LINAC98 Proceedings

LINAC98 Home

to LINAC98 HOME

Papers are organized according to session number. For example, session number **MO4037** represents: **MO** (Monday) **4** (sessions 1,2=invited; session 4=poster) **037** (order of presentation).

These papers are available in PDF format only. To view a paper, click on either the session number or the paper title. Papers should be viewed using Adobe Acrobat Reader 3.0 or 3.01, which can be downloaded from the Adobe site. Acrobat Reader 3.01 is available for the following platforms: Windows (32 bit), Windows (16 bit), Macintosh, IBM-AIX, SGI-IRIX, Sun Solaris, SunOS, HP-UX, Linux, Digital Unix, OS/2 Warp (Adobe Acrobat Reader 3.0 only).

Questions about these papers should be directed to: cee@aps.anl.gov

XIX International Linear Accelerator Conference

Fairmont Hotel, Chicago, Illinois, USA
August 23 - 28, 1998

Organized by Argonne National Laboratory in association with Fermi National Accelerator Laboratory

---

COMMITTEES:

International Organizing Committee

Program Committee

Local Organizing Committee

=> **Important Dates** <=

Questions?

Questions about the Conference should be directed to: linac98@aps.anl.gov

---

This page is maintained by: cee@aps.anl.gov

Disclaimer

Conference Chairman: Yanglai Cho, yc@aps.anl.gov

What's New?
Last Updated: September 22, 1998
What's new on this page

Abstracts
Abstracts received for LINAC98

Contributed Papers NEW
Final papers from the LINAC98 proceedings

Links to Chicago Area Sites of Interest:

Argonne National Laboratory
Home of the Advanced Photon Source

Chicago
Links for the Windy City

Fermi National Accelerator Laboratory **University of Chicago**

Other Accelerator-Related Links

LINAC98 International Organizing Committee

LINAC98 Home

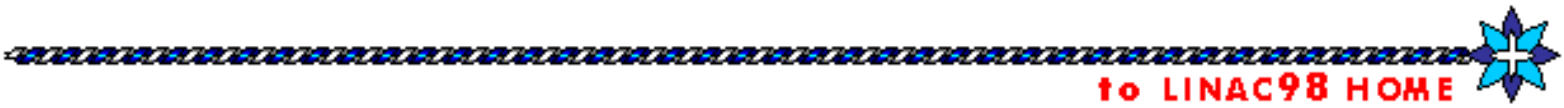

Conference Chairman: Yanglai Cho yc@aps.anl.gov

J. Alessi	BNL	Upton, NY USA	alessi1@bnl.gov
N. Angert	GSI	Darmstadt, Germany	N.Angert@gsi.de
B. Aune	CEA,DSM/DAPNIA	Saclay, France	aune@hep.saclay.cea.fr
Y. Cho	ANL-APS	Argonne, IL USA	yc@aps.anl.gov
G. Dutto	TRIUMF	Vancouver, BC, Canada	dutto@triumf.ca
L.W. Funk	SRS-APT	Savannah River, SC USA	warren.funk@srs.gov
R.L. Gluckstern	U. Maryland	College Park, MD USA	rlg@quark.umd.edu
H.D. Haseroth	CERN	Geneva, Switzerland	Helmut.Haseroth@cern.ch
H. Henke	TUB	Berlin, Germany	henke@tu-berlin.de
M. Inoue	ICR-Kyoto U	Kyoto, Japan	inoue@kyticr.kuicr.kyoto-u.ac.jp
H. Klein	IAP-Goethe U	Frankfurt, Germany	hklein@mikro1.physik.uni-frankfurt.de
A. Kolomiets	ITEP	Moscow, Russia	kolomiets@vitep5.itep.ru
L. Kravchuk	INR	Moscow, Russia	kravchuk@al20.inr.troitsk.ru
J. Le Duff	LAL	Orsay, France	leduff@lalcls.in2p3.fr
C.W. Leemann	TJNAF	Newport News, VA USA	leemannc@cebaf.gov
G.A. Loew	SLAC	Stanford, CA USA	galoew@slac.stanford.edu
G.E. McMichael	ANL-IPNS	Argonne, IL USA	mcmichael@anl.gov
W. Namkung	POSTECH	Pohang, Korea	namkung@vision.postech.ac.kr
R.C. Pardo	ANL ATLAS	Argonne, IL USA	pardo@anlphy.phy.anl.gov
C.W. Schmidt	FNAL	Batavia, IL USA	cschmidt@fnal.gov
S.O. Schriber	LANL	Los Alamos, NM USA	sschriber@lanl.gov
D.F. Sutter	US DOE	Washington, DC USA	hep-tech@oer.doe.gov
F. Tazzioli	INFN-LNF	Frascati, Italy	tazzioli@frascati.infn.it
D. Trines	DESY	Hamburg, Germany	trines@mail.desy.de
S.H. Wang	IHEP USMirror	Beijing, China	wangsh@sun.ihep.ac.cn
Y. Yamazaki	KEK	Tsukuba, Japan	yoshishi@kekvax.kek.jp
S. Yu	LBNL	Berkeley, CA USA	simon_yu@macmail2.lbl.gov

LINAC98 Program Committee LINAC98 Local Organizing Committee

Questions about the Conference should be directed to: linac98@aps.anl.gov
This page is maintained by cee@aps.anl.gov

LINAC98 Program Committee

LINAC98 Home

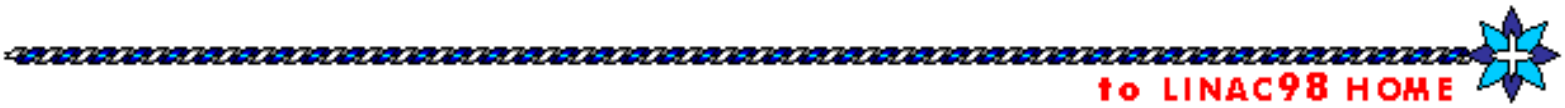

Program Committee Chairman: G. E. McMichael mcmichael@anl.gov

J. Alessi	BNL	Upton, NY USA	alessi1@bnl.gov
N. Angert	GSI	Darmstadt, Germany	N.Angert@gsi.de
V. Balakin	BINP	Novosibirsk, RU	balakin@vlepp.serpukov.su
J. Barnard	LLNL	Livermore, CA USA	barnard1@llnl.gov
M.H. Cho	POSTECH	Pohang, Korea	mhcho@vision.postech.ac.kr
Y. Cho	ANL-APS	Argonne, IL USA	yc@aps.anl.gov
G. Dutto	TRIUMF	Vancouver, BC Canada	dutto@triumf.ca
T. Garvey	LAL-Orsay	Orsay, France	garvey@lalcls.in2p3.fr
H.D. Haseroth	CERN	Geneva, Switzerland	Helmut.Haseroth@cern.ch
C. Hill	CERN	Geneva, Switzerland	Charles.Hill@cern.ch
N. Holtkamp	DESY	Hamburg, Germany	mpyhol@mail.desy.de
A. Kolomiets	ITEP	Moscow, Russia	kolomiets@vitep5.itep.ru
L. Kravchuk	INR	Moscow, Russia	kravchuk@al20.inr.troitsk.ru
G.E. McMichael	ANL-IPNS	Argonne, IL USA	mcmichael@anl.gov
R. Miller	SLAC	Stanford, CA USA	rhm@slac.stanford.edu
M. Mizumoto	JAERI	Tokai, Japan	mizumoto@linac.tokai.jaeri.go.jp
O. Napoly	CEA-Saclay	Gif/Yvette, France	napoly@hep.saclay.cea.fr
G. Neil	TJNAF	Newport News, VA USA	neil@cebaf.gov
R.C. Pardo	ANL ATLAS	Argonne, IL USA	pardo@anlphy.phy.anl.gov
M. Popovic	FNAL	Batavia, IL USA	popovic@fnal.gov
A. Schempp	IAPRFQ Goethe U	Frankfurt, Germany	A.Schempp@em.uni-frankfurt.de
S.O. Schriber	LANL	Los Alamos, NM USA	sschriber@lanl.gov
C.W. Schmidt	FNAL	Batavia, IL USA	cschmidt@fnal.gov
K.W. Shepard	ANL ATLAS	Argonne, IL USA	kwshepard@anl.gov
J. Staples	LBNL	Berkeley, CA USA	JWStaples@lbl.gov
D.F. Sutter	US DOE	Washington,DC USA	hep-tech@oer.doe.gov
F. Tazzioli	INFN-LNF	Frascati, Italy	tazzioli@frascati.infn.it

S.H. Wang	IHEP USMirror	Beijing, China	wangsh@sun.ihep.ac.cn
M. White	ANL-APS	Argonne, IL USA	mwhite@aps.anl.gov
Y. Yamazaki	KEK	Tsukuba, Japan	yoshishi@kekvax.kek.jp

LINAC98 International Organizing Committee LINAC98 Local Organizing Committee

---

Questions about the Conference should be directed to: linac98@aps.anl.gov
This page is maintained by cee@aps.anl.gov

LINAC98
Local Organizing Committee

LINAC98 Home

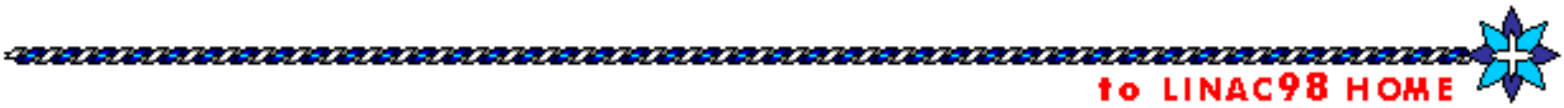

Joan Brunsvold	jbrunsvold@anl.gov
Lucinda Carroll	linac98companion@aps.anl.gov
Yanglai Cho	yc@aps.anl.gov
Joanne Day	jsd@aps.anl.gov
Jeff Dooling	jcdooling@anl.gov
Catherine Eyberger	cee@aps.anl.gov
Richard Fenner	fenner@aps.anl.gov
Barbara Grelick	linac98companion@aps.anl.gov
Elliott McCrory	mccrory@fnal.gov
William McDowell	wpm@aps.anl.gov
Gerry McMichael	mcmichael@anl.gov
Geraldine Nolen	linac98companion@aps.anl.gov
Jerry Nolen	nolen@anl.gov
Anne Owens	owens@aps.anl.gov
Richard Pardo	pardo@anlphy.phy.anl.gov
Charles Schmidt	cschmidt@fnal.gov
Ken Shepard	kwshepard@anl.gov
Carolyn Tobin	ctobin@anl.gov
Marion White	mwhite@aps.anl.gov
Marcia Wood	wood@aps.anl.gov

LINAC98 International Organizing Committee LINAC98 Program Committee

Questions about the Conference should be directed to: linac98@aps.anl.gov

This page is maintained by cee@aps.anl.gov

LINAC98 Important Dates to Remember

LINAC98 Home

to LINAC98 HOME

MARCH 15, 1998	**Deadline for Submitting Invited Abstracts** Abstract submission form and instructions are now online
APRIL 17, 1998	**Deadline for Submitting Contributed (Poster) Abstracts** Abstract submission form and instructions are now online
JULY 24, 1998	**Deadline for Early Registration** After July 24 the conference registration fee becomes $600.00
JULY 24, 1998	**Deadline for Guaranteed LINAC98 Hotel Rates** Reservations received after deadline are accepted on a space-available basis at regular rates
AUGUST 7, 1998	**Deadline for Cancelling Conference Registration** No refunds for conference-related fees will be made after this date

LINAC98 News and Information

LINAC98 Home

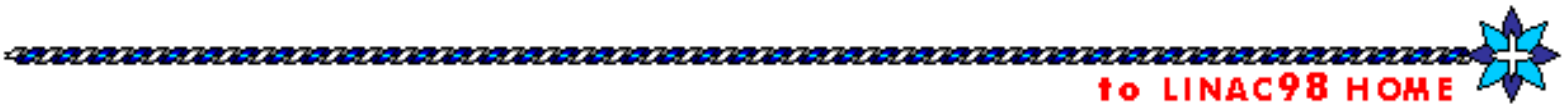

- **Tuesday 22 September 1998** Home page changed to remove registration and outdated conference info. Conference papers put online.
- **Friday 21 August 1998** Online Web forms removed for Expression of Interest, Registration, and Abstract submission.
- **Tuesday 4 August 1998** Location of exhibitor booths added.
- **Tuesday 21 July 1998** List of exhibitors was added.
- **Monday 8 June 1998** Abstracts were added.
- **Wednesday 3 June 1998** Exhibitor Information was added.
- **Tuesday 2 June 1998** Links to instructions on preparing and submitting manuscripts were added.
- **Friday 22 May 1998** Instructions on preparing manuscripts were mailed to authors. Web pages will follow shortly.
- **Wednesday 1 April 1998** Links to conference information, companion program, and registration pages were added to home page.
- **Friday 20 February 1998** Home page was revised, and new links were added:
  Preliminary Program, Expression of Interest form, Abstract Submission form, Abstract Instructions.
- **Thursday 18 December 1997** `Important Dates' added to home page.
- **Friday 5 December 1997** Home Page v.3 online.
- **Tuesday 16 September 1997** Second Draft. Public.
- **Monday 21 July 1997** The first draft version of the LINAC98 Home Page is available.

Questions about the Conference should be directed to: linac98@aps.anl.gov
This page is maintained by cee@aps.anl.gov

LINAC98 Abstracts

LINAC98 Home

to LINAC98 HOME

Invited Papers

Contributed Papers

Author Index

Questions about the Conference should be directed to: linac98@aps.anl.gov

This page is maintained by cee@aps.anl.gov

Information About Chicago

LINAC98 Home

to LINAC98 HOME

- Chicago Convention and Tourism Bureau
- The Chicago Transit Authority (CTA)
- City of Chicago government and services
- The Tezcat Chicago page
- Chicago Citylink
- Chicago Information System
- Chicago Psyber View
- Chicago Weather

This page is maintained by cee@aps.anl.gov

Other Accelerator-Related Links of Interest

LINAC98 Home

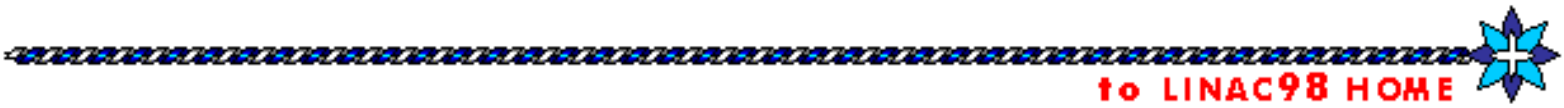

Linacs and Accelerator Facilities

- LANL - Accelerators and Accelerator Laboratories
- SLAC - Accelerator Labs around the World
- CERN - High Energy Physics Laboratories

Links to Upcoming or Recent Accelerator-Related Conferences

- PAC99 HomePage
- FEL98 HomePage
- EPAC98 HomePage
- APAC98 HomePage
- PAC97 HomePage

- LINAC96 Proceedings
- PAC EPAC APAC Joint Website - Conference Proceedings

- EPAC - Help for Electronic Publication
- APAC98 - Help for Electronic Publication, especially using MACs

---

Preprints

- Accelerator Physics Preprints
- LANL Preprint Server
- CERN Preprint Server
- RHIC Instrumentation Publications

Journals and Newsletters

- ICFA Beam Dynamics Newsletters and Beam Physics Page
- SLAC Beamline
- CERN Courier

Conferences

- Upcoming HEP Conferences

Other

- US Particle Accelerator School HomePage
- LANL - General Physics Links
- DOE Phone List
- LLNL List of Lists

Questions about the Conference should be directed to: linac98@aps.anl.gov

This page is maintained by cee@aps.anl.gov.

LINAC98 Papers - Monday

LINAC98 Home Tuesday papers Wednesday papers Thursday papers Friday papers Author Index

to LINAC98 HOME

INVITED TALKS
Session MO1: Monday, August 24, 1998

INVITED TALKS
Session MO2: Monday, August 24, 1998

ORAL POSTERS

Session MO3: Monday, August 24, 1998

POSTERS
Session MO4: Monday, August 24, 1998

LINAC98 Papers - Tuesday

LINAC98 Home Monday papers Wednesday papers Thursday papers Friday papers Author Index

INVITED TALKS
Session TU1: Tuesday, August 25, 1998

INVITED TALKS
Session TU2: Tuesday, August 25, 1998

ORAL POSTERS
Session TU3: Tuesday, August 25, 1998

POSTERS
Session TU4: Tuesday, August 25, 1998

LINAC98 Papers - Wednesday

LINAC98 Home Monday papers Tuesday papers Thursday papers Friday papers Author Index

INVITED TALKS
Session WE1: Wednesday, August 26, 1998

INVITED TALKS
Session WE2: Wednesday, August 26, 1998

LINAC98 Papers - Thursday

LINAC98 Home | Monday papers | Tuesday papers | Wednesday papers | Friday papers | Author Index

to LINAC98 HOME

INVITED TALKS
Session TH1: Thursday, August 27, 1998

INVITED TALKS
Session TH2: Thursday, August 27, 1998

ORAL POSTERS
Session TH3: Thursday, August 27, 1998

POSTERS
Session TH4: Thursday, August 27, 1998

LINAC98 Papers - Friday

LINAC98 Home | Monday papers | Tuesday papers | Wednesday papers | Thursday papers | Author Index

to LINAC98 HOME

INVITED TALKS
Session FR1: Friday, August 28, 1998

INVITED TALKS
Session FR2: Friday, August 28, 1998

LINAC98 Author Index for Papers

LINAC98 Home

to LINAC98 HOME

A

A B C D E F G H I J K L M N O P Q R S T U V W X Y Z

B

A B C D E F G H I J K L M N O P Q R S T U V W X Y Z Back to top

C

A B C D E F G H I J K L M N O P Q R S T U V W X Y Z Back to top

D

A B C D E F G H I J K L M N O P Q R S T U V W X Y Z Back to top

E

A B C D E F G H I J K L M N O P Q R S T U V W X Y Z Back to top

F

A B C D E F G H I J K L M N O P Q R S T U V W X Y Z Back to top

G

A B C D E F G H I J K L M N O P Q R S T U V W X Y Z Back to top

Gobin, R. , TH3006 , TH4059
Godot, J.C. , MO3002 , MO4017
Goldenberg, K. , MO4005
Golub, G. , WE2002
Gonzales, A. , WE1003
Gonzales, G. , TU4083 , WE1003
Gooch, C.M. , MO3012 , MO4097
Gorelov, D.V. , TU4106
Goto, A. , TU4085 , TH4008
Gough, R. , MO4090 , TU4054 , TU4084
Gräf, H.-D. , TU4007
Granatstein, V.L. , TU4100
Gray, E.R. , TU4012 , TU4107
Greer, J. , MO4056 , TU4084
Grelick, A.E. , TH4065
Gross, M. , MO4028
Grote, D.P. , MO4027 , TU2004
Guignard, G. , MO1004 , MO4043 , TU4040
Gutowski, W. , MO4070
Guy, F.W. , TU4103
Guzek, J. , TH3011 , TH4106

H

A B C D E F G H I J K L M N O P Q R S T U V W X Y Z Back to top

Haagenstad, H. , WE1003
Haber, I. , TU2004
Habib, S. , WE2002
Habs, D. , MO4028 , TH4006 , TH4021
Haffner, R.L. , TU4094
Hagel, J. , MO4043 , TU4040
Hahn, E. , TU4101
Halaxa, E. , MO4027
Hameister, J. , MO4068 , TH3007 , TH4066
Hamm, R.W. , TH3011 , TH4106
Hampel, T. , TU4007
Han, B.S. , TH4005
Han, J.M. , TH4005

I

A B C D E F G H I J K L M N O P Q R S T U V W X Y Z Back to top

J

A B C D E F G H I J K L M N O P Q R S T U V W X Y Z Back to top

K

A B C D E F G H I J K L M N O P Q R S T U V W X Y Z Back to top

L

A B C D E F G H I J K L M N O P Q R S T U V W X Y Z Back to top

M

A B C D E F G H I J K L M N O P Q R S T U V W X Y Z Back to top

N

A B C D E F G H I J K L M N O P Q R S T U V W X Y Z Back to top

O

A B C D E F G H I J K L M N O P Q R S T U V W X Y Z Back to top

P

A B C D E F G H I J K L M N O P Q R S T U V W X Y Z Back to top

Q

A B C D E F G H I J K L M N O P Q R S T U V W X Y Z Back to top

R

A B C D E F G H I J K L M N O P Q R S T U V W X Y Z Back to top

S

A B C D E F G H I J K L M N O P Q R S T U V W X Y Z Back to top

T

A B C D E F G H I J K L M N O P Q R S T U V W X Y Z Back to top

U

A B C D E F G H I J K L M N O P Q R S T U V W X Y Z Back to top

V

A B C D E F G H I J K L M N O P Q R S T U V W X Y Z Back to top

W

A B C D E F G H I J K L M N O P Q R S T U V W X Y Z Back to top

X

A B C D E F G H I J K L M N O P Q R S T U V W X Y Z Back to top

Y

A B C D E F G H I J K L M N O P Q R S T U V W X Y Z Back to top

Z

A B C D E F G H I J K L M N O P Q R S T U V W X Y Z Back to top

Last Update December 23, 1998 13:27:58

LOW-β SC LINACS: PAST, PRESENT AND FUTURE*

Lowell M. Bollinger
Argonne National Laboratory, Argonne, Illinois 60439 USA

Abstract

This paper is a general review of superconducting low-β technology and applications from its beginning in 1969 into the near-term future. The emphasis is on studies of accelerating resonators and on SC linacs that boost the energy of heavy-ion beams from tandem electrostatic accelerators used for nuclear-physics research. Other topics are positive-ion SC injectors to replace tandems and the need for accelerating structures with β outside of the present proven range, $0.008 < \beta < 0.2$.

1 EARLY HISTORY

The development and construction of the superconducting (SC) electron linac at Stanford stimulated others to investigate SC technology needed to accelerate low-β ions [1]. This effort started (1969) at Karlsruhe, Germany. Much of this work was devoted to Nb helix resonators and related technology. Accelerating fields of 2 to 3 MV/m were achieved for $\beta = 0.04$, suggesting that it was feasible to build a useful SC low-β linac. However, it was difficult to control the RF phase of a helix because of its mechanical instability.

In 1970, a small group at Cal Tech also started studies of the helix, but later found that other geometries provided greater accelerating fields and mechanical stability. These new units included the "split ring", two curved RF arms driving two drift tubes with opposite phases. Unlike the helix, for the split ring the RF and the field-formation elements are independent, thus allowing the RF arms to be mechanically stiff. All of the low-β structures at Cal Tech used lead plated on copper as the SC.

In 1971, a group at Argonne joined the study of SC low-β technology and, from the beginning, the goal was to build a SC linac to boost the energy of heavy ions from a tandem electrostatic accelerator. Again, this work started with the single-cell helix, and two such Nb structures ($\beta = 0.06$) with independent phase control accelerated an ion beam (proton) for the first time. This and other achievements led to a proposal to build a small SC low-β linac.

A fourth effort (1973) on a low-β structure was at Stanford, where a small group studied a Nb cavity with $\beta = 0.04$ and $f = 430$ MHz. For these parameters, the accelerating gap was very narrow (~ 1 cm), which required the accelerating field to be exceptional large for this unit to be competitive with other structures, which had active gaps ranging from ~ 5 to 15 cm.

*Work supported by the U.S. Department of Energy, Nuclear Physics Division, under Contract W-31-109-ENG-38.

2 FIRST SC ION LINAC

The demands on SC low-β studies at Argonne changed greatly in 1974 when the Atomic Energy Commission agreed to support construction of a small SC linac, i.e., we had to consider all aspects of the system: RF phase control, beam optics, cryogenics, etc. - not just the accelerating structures. Our initial plan was to use 5-cell helix resonators for a 13-MV linac to boost the energy of heavy ions from our 8.5-MV tandem. Fortunately, before our funding arrived in late 1975 we were able to replace the helix with the Cal Tech split ring, but with several changes: (1) Nb as the SC, (2) a smaller frequency (97 MHz) so as to increase the active length, and (3) an outer housing made of Nb explosively bonded to copper. Figure 1 compares our design to other structures that were available at the time.

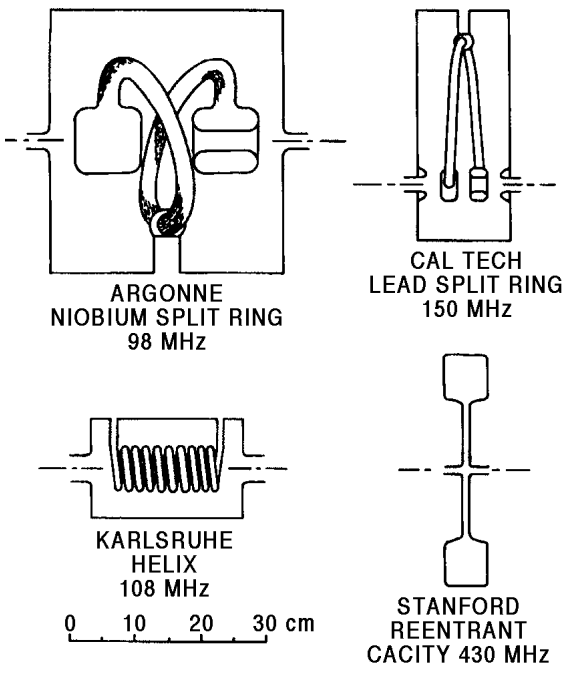

Figure 1: Heavy-ion accelerating structures in 1977.

The layout of the tandem-booster linac system [2] is shown in Fig. 2. Note the beam bunching system [3], 2 bunchers and a chopper, which converts ~ 65% of the DC beam of the tandem into narrow beam pulses (~ 200 ps). Initially the pulse rate of the beam was 97/2 = 48.5 MHz but, at the user's request, it was soon reduced to 97/8 = 12.125 MHz. Two classes of resonators are used in the booster: $\beta = 0.065$ and $\beta = 0.105$. The split rings are closely mounted in groups of 2 separated by SC beam-

focusing solenoids, the first accelerator of any kind in which SC was used for both acceleration and beam optics.

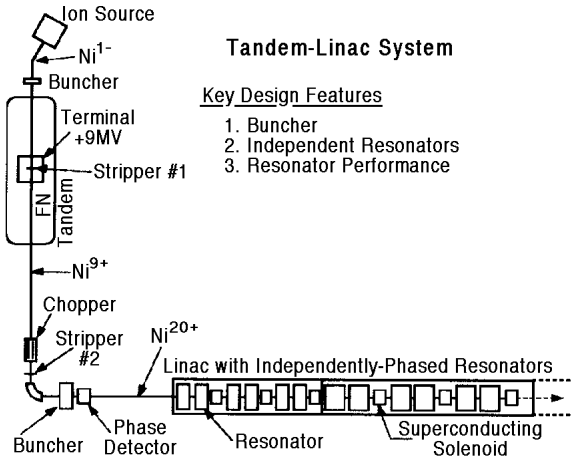

Figure 2: Main components of a tandem-linac system.

The phase control of each resonator is controlled by a VCX (voltage control reactance) but, in spite of the sturdy arms of our split rings, our initial VCR's provided only marginal control. After several major upgrades, the control problem was removed by a VCX that has a stored energy of 30 kW.

As soon as a small part of the booster was operable it was tested (June, 1978) and soon used for research (September, 1978). This step-by-step approach was continued for the next 3 years until the booster was completed. The goals of the project were more than met: an accelerating voltage of ~ 22 MV, excellent beam quality, short beam pulses, adequate acceptance of the tandem beam, easy change of beam energy, and future expandability.

In late 1983 funding was obtained to extend the booster linac and to add an adequate experimental area. The goal was to be able to accelerate ions with $A \leq 130$ to energies above the Coulomb barrier (~ 5.5 MeV/A). Since the original linac was operating well, we used the same technology for the addition. After completion in 1985, the entire linac provides ~ 38 MV; and the enlarged tandem-linac system [1,4] was named ATLAS.

3 EXISTING SC LOW-β LINACS

During the twenty-year period following the initial success of the tandem-linac system at Argonne, other laboratories undertook similar projects [5-15], listed in Table 1. Their primary goals were the same as discussed in Sec. 2, but often with significant differences in technology, as indicated in Table 1 and in [1,16]. For lack of space, only a few of these tandem-linac systems are mentioned below. Accelerating structures are treated in Sec. 4.

Table 1. Heavy-Ion Tandem-Linac Accelerators

Location	Accelerating Structure	f (Mhz)	β
Argonne--(In USE)	Split Ring (Nb)	97	.065 → .105
Stony Brook--(In USE)	SR + 1/4 Wave (Pb)	150	.06 → .10
Florida State--(In USE)	Split Ring (Nb)	97	.105
Saclay--(Terminated)	Helix (Nb)	135	.08
U. Washington--(In USE)	1/4 Wave (Pb)	150	.10 → .20
JAERI (Japan)--(In USE)	1/4 Wave (Nb)	130	.10
Kansas State--(In USE)	Split Ring (Nb)	97	.105
Legnaro (Italy)--(In USE)	1/4 Wave (Pb, Nb, Nb/Cu)	80, 160	.055 → .11 → .15
Sao Paulo--(?)	Split Ring (Nb)	97	.105
Bombay--(?)	1/4 Wave (Pb)	?	?
Delhi--(Under Construction)	1/4 Wave (Nb)	97	.08
Canberra--(In USE)	Split Ring (Pb)	150	.10

The second SC linac was built at Stony Brook [5] with split-ring Pb/Cu resonators provided by Cal Tech. The other parts of the linac were handled by a small group of faculty members and students at Stony Brook. I was especially impressed that students, after training, did work such as welding large pipes.

The linac at U. of Washington [8] was the first to use the quarter-wave resonator (QWR), a new class of structure developed at Stony Brook [17]. Two types of units are used: $\beta = 0.10$ and $\beta = 0.20$, both with Pb/Cu as the SC. These relatively large values of β indicate that the goal was to accelerate rather light ions, including protons, as needed by the research program.

The linac at JAERI (Japan) [9] was the first to use Nb for QWR. The oval-shaped outer shell of these units are explosively-bonded Nb to Cu. These units provide an average accelerating field > 5 MV/m, much greater than other SC low-β linacs in routine use.

The most ambitious of all SC low-β projects [11-13] is at Legnaro (Italy). It's injector is a 15-MV tandem, and the linac is designed to provide 48 MV, both substantially larger than any other tandem-linac system. The initial plan was to use QWR units with Pb/Cu as the SC, and some such units were installed, tested, and used. These initial structures are now being replaced by several kinds of RFQ units in which the SC is bulk Nb metal in some and Nb sputtered on Cu in others [11,12,13,18].

An interesting aspect of the teams that have designed and built the SC low-β linacs is that very few persons who played major roles had much experience in accelerator technology before entering the SC low-β game; indeed, I can think of only one American who did have earlier experience. On the other hand, most of the leading figures were physicists who had a thorough understanding of their goals.

4 ACCELERATING RESONATORS

The SC low-β resonators available in 1977 are shown in Fig. 1. Since then, many other structures have been studied, starting with the quarter-wave resonator (QWR) developed [17] at Stony Brook in 1983. The laboratories involved in these investigations are listed in Table 2, which includes (a) work before 1983, (b) other designs

that have been fully tested, and (c) work now in progress. Most of these units were designed for use in planned or existing linacs.

Table 2. Development of Accelerating Structures

Split Ring		**1974-1982**
Cal Tech -	Pb	
Argonne -	Nb	
Stony Brook -	Pb	
2-Gap Quarter Wave		**1982 →**
Stony Brook -	Pb	
Rehovot (Israel) -	Pb	
U. of Washington -	Pb	
Argonne -	Nb	
Bombay -	Pb	
JAERI (Japan) -	Nb	
Legnaro -	Pb, Nb, Sput. Nb, NsSn	
Canberra -	Sputtered Nb	
4-Gap Interdigital		**1985-1990**
Argonne -	Nb	
2-Gap Half-Wave		**1990 →**
Cal Tech + Argonne -	Nb	
Argonne + CEBAF -	Nb	
2-Gap QW with Nb Outer Jacket		**1992 →**
Legnaro -	Nb	
2-Gap QW with SS Outer Jacket		**1992 →**
Argonne + Delhi -	Nb	
RFQ		**1990-1993**
Stony Brook	Pb	

Figure 3 shows some of the resonators initiated in the 1980's; all but the half-wave unit are now in use. The units in Fig. 4 are more recent products for which an important objective is to reduce fabrication costs. Design changes and improvements in welding appear to have reduced costs by a factor of ~ 1.5.

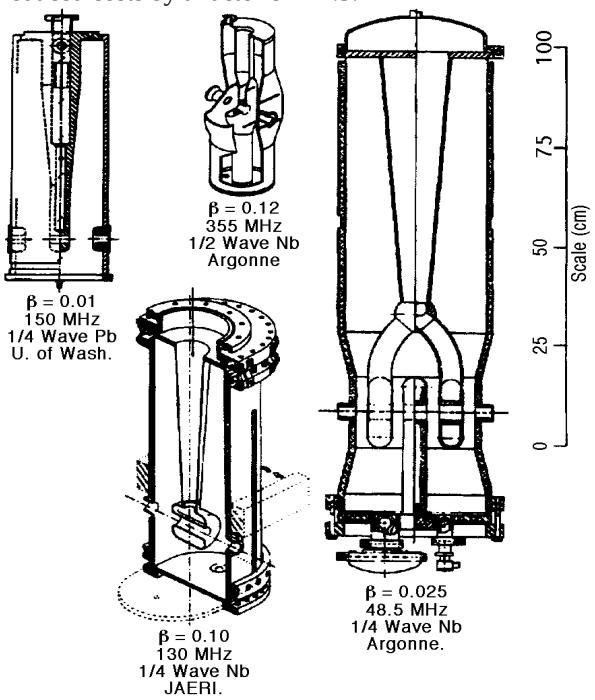

Figure 3: SC resonators from the 1980's.

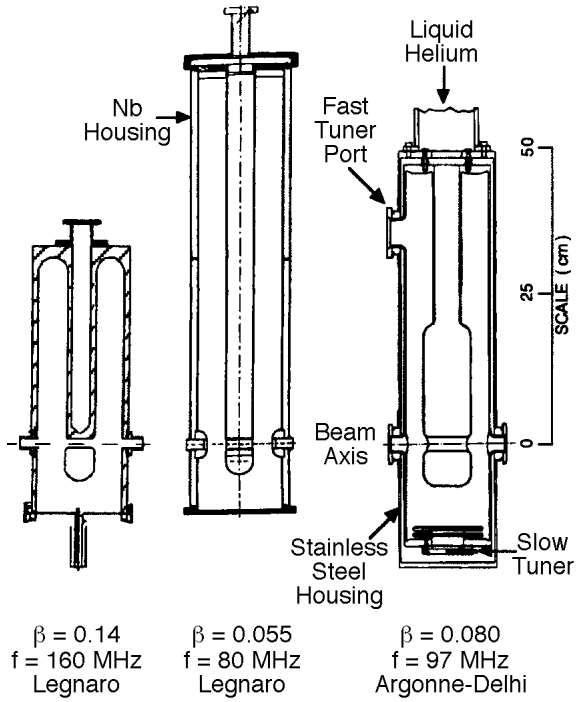

Figure 4: New resonators.

The long-term efforts at Legnaro and Canberra to use sputtered Nb on Cu as the SC surface are now being tested on the linac at Legnaro and the results are very encouraging [18,19]. It seems unlikely that sputter Nb will be superior to bulk metal, but it may reduce costs.

In SC low-β resonator design, many factors need to be considered: the SC material, RF frequency, optimum β, number of accelerating gaps, mechanical stability, the number of different resonator types needed, the ratio of accelerating field to maximum surface field, fabrication difficulties, and costs. Many of these factors interact with each other, making it impossible to determine a unique solution. For example, for resonators in routine use, the split ring in ATLAS has the greatest accelerating voltage because of its large size generated by its three gaps, low frequency, and high β. However, the higher-frequency 2-gap QWR in the JAERI linac has a greater accelerating field, is more stable mechanically, and is effective over a wider range of β. Which one is better?

5 POSITIVE ION INJECTOR

The linacs discussed above were energy boosters for tandems, an injector which requires a negative-ion source. By 1983 we at Argonne recognized that our tandem needed to be replaced because it could not produce useful beams for the upper half of the periodic table. After considering several possibilities, including a much larger tandem, we decided to build a positive-ion injector (PII) consisting of an ECR ion source on a voltage platform followed by a very-low-β SC linac [20,21].

Since ECR sources were well developed by the mid-1980's and the bunching concept used at our tandem could

be used at PII, the main challenge was the linac, which had to accelerate ions from $\beta = 0.008$ up to $\beta = 0.05$ without destroying the excellent quality of beams from the ECR. The front end of the linac seemed especially difficult because of the very low velocity and the rapid change in velocity of the beam.

One of the four interdigital resonators [22] used to span the required β range is shown in Fig. 3. The housing is Nb explosively bonded to Cu, and this housing is compressed around the beam line so as to form an oval-like shape. As in the booster linacs, SC solenoids are located after one or two resonators so as to minimize the beam size within resonators. The PII linac is easily tuned and, in practice, the whole ATLAS linac (including PII) is now usually tuned to the same recorded velocity profile for many ion species, and consequently tuning is exceptionally easy and rapid [23].

A different positive ion injector [24] is planned for the SC linac at Legnaro. The ion source is an ECR, of course, and its output is injected into an array of three Nb SC RFQ's followed by a QWR section. These RFQ 80 MHz units are designed to cover the β range 0.009 to 0.05. A full-scale stainless-steel model of an RFQ has been studied and a Nb unit is under construction. Based on the experience for other SC low-β resonators, phase control for a large SC RFQ may be difficult. In the early 1990's a SC low-β RFQ was built and tested at Stony Brook [25], but phase control was not attempted.

6 OPERATIONAL EXPERIENCE AT ATLAS

ATLAS is the largest and most intensively used SC low-β linac now in operation. The overall layout of the system is shown in Fig. 5. The primary injector is PII, where a second, more powerful ECR ion source has been added recently. The tandem is still used for very light ions and for radioactive species.

The first experiment with a small part of ATLAS was 20 years ago, Sept. 1978. Since then the system has been used steadily as the linac grew, and in recent years its beam has been used for research and occasionally development for more than 5,000 hr. annually [23]. Overall, since 1978 ATLAS has provided ~ 70,000 hr. of useful beam time.

Because of its positive ion injector, ATLAS provides beams for all parts of the periodic table. This wide range is used regularly; for example, 28 different isotopes ranging from hydrogen to uranium were used in FY1997. Altogether, there were 63 separate runs ranging from 8 hr. to 8 days.

7 NEEDS FOR NEW ACCELERATING STRUCTURES

Several future applications of SC linacs come to mind: (1) small linacs for purposes other than nuclear physics, (2) accelerating structures for intermediate-β ions, and (3) radioactive ion accelerators (RIB).

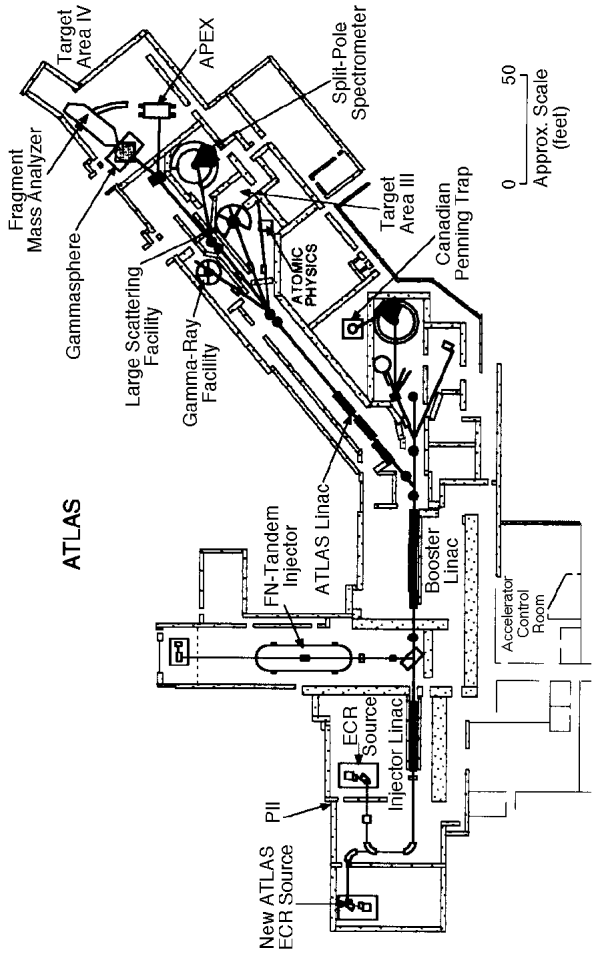

Figure 5: ATLAS in 1998.

Small linacs might be useful in materials science and industry. For example, most ion implantation is done with small electrostatic accelerators which provide limited depths of implantation and range of ion species. These limitations could be removed by a small SC low-β linac. However, it is not obvious that this approach is optimum, especially since CW operation may not be needed.

SC accelerating structures for intermediate-β ions may be attractive for a number of accelerators now being considered, of which I will mention two. One class is the high-current high-energy machines that have been studied at Los Alamos. They have tested 700 MHz SC cavities with $\beta \approx 0.48$, 0.64, and 0.82, and have concluded that for them, room-temperature structures are better for $\beta = 0.48$, and SC is optimum for the other two [25].

Another active proposal is a radioactive ion beam accelerator (RIB) at Argonne. The driver of this system is to be a 200-MV linac that can accelerate both protons and much heavier ions. CW operation is highly desirable, which makes SC technology very attractive. In an

Argonne-CEBAF collaboration [27], a SC 1/2-wave resonator with f = 350 MHz and $\beta = 0.4$ is being built for possible use in the RIB driver. An important feature of the 1/2-wave design (see Fig. 3) is that its ratio of accelerating field to surface field is substantially greater than for all other low-β resonators and, consequently, in an earlier test [28] on a $\beta = 0.10$ unit, the maximum accelerating field was 18 MV/m, ~ 50% greater than other low-β units as shown in Table 3 of [20]. However, additional experience is needed before the optimum structure can be chosen.

The third need for resonators is in the range below $\beta = 0.008$, the present limit set for SC by the first resonator in PII at Argonne. The requirements for the Argonne RIB are extreme: to accelerate a CW beam of radioactive ions with q/A = 1/120 through the range from $\beta = 0.001$ to $\beta = 0.008$ without seriously deteriorating the beam quality. The system planned [29] has two steps: a CW room-temperature 12.125 MHz RFQ on a 300 kV platform for the β range 0.001 to 0.0025, followed by a second RFQ on an independent voltage platform for the β range 0.0025 to 0.008. The first RFQ is undergoing tests now [29] and seems likely to be an excellent solution, and the second RFQ should be less demanding than the first because of the greater velocity of the beam. Note that the very low RF frequency is an essential design feature because of its low RF-power requirements. It appears, then, that if a very low RF frequency is acceptable and if the 12.125 MHz RFQ's function as well as expected, then SC structures are not competitive below $\beta \approx 0.008$.

As has been hinted by the topics mentioned in this section, there are still many questions to be answered about SC low-β linacs. Unlike most of the past, these questions are concerned with the two fringes of the low-β spectrum, and answers are needed for small but important parts of future accelerator systems. The subject is still interesting - but, for me, not as exciting as it was in the 1970's.

ACKNOWLEDGEMENTS

The author is indebted to K. W. Shepard, R. C. Pardo, and G. P. Zinkann for providing information for many parts of this paper.

REFERENCES

[1] L. M. Bollinger, "Superconducting Linear Accelerators for Heavy Ions", Ann. Rev. Nucl. Part. Sci. 36, 475-503 (1986). This published review gives a summary of work before 1986, including references to topics in Sec. 1 of the present review.

[2] J. Aron et al., Proc. 1979 Linear Accel. Conf., Montauk, NY, 511-34 (1979).

[3] F. J. Lynch et al., Nucl. Instr. Meth. 159, 245-263 (1979).

[4] J. Aron et al., Rev. Sci. Instrum. 57, 737-739 (1986).

[5] J. R. Delayen et al., IEEE Trans. Nucl. Sci. NS-26 (3), 3664-3666 (1979).

[6] J. D. Fox et al., Rev. Sci. Inst. 57, 763 (1986).

[7] B. Cauvin et al., Proc. 1989 Particle Accel. Conf. IEEE, 601 (1989).

[8] D. W. Storm et al., Nucl. Instr. Meth. A287, 247-252 (1990).

[9] S. Takeuchi et al., Nucl. Instr. Meth. A382, 153-160 (1996).

[10] T. J. Gray, Rev. Sci. Instr. 57, 783 (1986).

[11] G. Fortuna et al., Nucl. Instr. Meth. A308, 236 (1993).

[12] G. Fortuna et al., Proc. XVIII Intl. Linear Accel. Conf., Geneva, 905-909 (1996).

[13] A. Dainelli et al., Nucl. Instr. Meth. A382, 100-106 (1996).

[14] A. Roy, Proc. 8Th Workshop RF Superconductivity, Legnaro, 1997, to be published.

[15] A. E. Stuchbery and D. C. Weisser, Nucl. Instr. Meth., A382, 172-175 (1996).

[16] D. W. Storm, Nucl. .Instr. Meth. A328, 213-220 (1993); K. W. Shepard, Nucl. Instr. Meth. A382, 128-131 (1996).

[17] I. Ben-Zwi and J. M. Brennan, Nucl. Instr. Meth. 212, 73 (1983).

[18] V. Palmieri, in proceedings of this conference.

[19] A. M. Porcellato et al., to be published.

[20] L. M. Bollinger, Nucl. Instr. Meth. A328, 221-230 (1993).

[21] R. C. Pardo et al., 1992 Linear Accel. Conf. Proc., AECL-10728, 70-72 (1992).

[22] K. W. Shepard, Proc. 1986 Linear Accelerator Conf., Stanford, 269 (1986).

[23] G. Zinkann et al., Nucl. Instr. Meth. A382, 132-139 (1996).

[24] A. Lombari, Proc. Linac 96 Conference, CERN96-07, 125 (1996).

[25] A. Jain et al., Nucl. Instr. Meth. A328, 251 (1993).

[26] T. Wangler, personal communication (1998).

[27] K. W. Shepard et al., in proceedings of this conference.

[28] J. R. Delayen et al., Nucl. Instr. Meth. B56/57, 1025 (1991).

[29] K. W. Shepard, in proceedings of this conference.

STATUS OF THE TESLA DESIGN

D. Trines for the TESLA Collaboration [*]
Deutsches Elektronen-Synchrotron DESY, 22603 Hamburg, Germany

Abstract

The status of the layout of the linear collider project, TESLA, which employs superconducting accelerating structures, will be presented. Latest results from the R&D program on 1.3 GHz superconducting cavities, the accelerating gradients and quality factors which were achieved will be shown as well as the performance of the TESLA Test Facility linear accelerator.

1 INTRODUCTION

Since the first proposal for a superconducting linear $e^+ e^-$ collider by M. Tigner [1] in 1965, accelerator builders [2,3,4] have been fascinated by the potential of superconductivity for high energy linear $e^+ e^-$ colliders. The low resistive losses in the walls of superconducting cavities yield a high conversion efficiency from mains to beam power. As energy can be stored very efficiently in the cavities, a large number of bunches can be accelerated spaced far apart in a long RF pulse. This allows for a fast bunch to bunch orbit feedback which guarantees that bunches from the opposing beams hit head on at the IP despite ground motion effects.

The shunt impedance per unit length for superconducting cavities depends on RF frequency ω as

$$r_s \sim \frac{\omega}{A\omega^2 + R_{res}} \qquad (1)$$

favouring RF frequencies in the range of 0.5 to 3 GHz. A is a function of temperature and material and R_{res} is the residual surface resistance. Because low frequencies are preferred for s.c. cavities, this make them ideally suited to accelerate low emittance beams, as the emittance dilution by wakefields is small ($W_\perp \sim \omega^3$). In addition tolerances on the fabrication and alignment of cavities are very relaxed.

The luminosity of a linear collider is given by [5,6]

$$L \approx const. \frac{\sqrt{\delta_B}}{E_{CM}} \cdot \frac{\eta}{\sqrt{\varepsilon_{yN}}} \cdot P_{AC} \cdot H_D \qquad (2)$$

where δ_B is the relative energy loss caused by beamstrahlung, E_{CM} is the centre of mass energy of the $e^+ e^-$ collision, η is the conversion efficiency from mains power P_{AC} to beam power, ε_{yN} is the normalised vertical emittance at the IP and H_D is the disruption factor. Thus, the figure of merit [7] for the luminosity performance of a linear collider is given by $\eta/\sqrt{\varepsilon_{yN}}$. Therefore the combination of high conversion efficiency and small emittance dilution makes a superconducting linear collider the ideal choice with respect to the achievable luminosity.

2 A SHORT HISTORY OF TESLA

The major challenges to be mastered so that a superconducting linear collider becomes feasible were to increase the accelerating gradients from about 5 MV/m to 25 MV/m and to reduce the cost per length from existing systems by about a factor of four to obtain ~ 2000 $/MV. Encouraged by results from R&D work at CEBAF, CERN, Cornell, DESY, KEK, Saclay and Wuppertal [12,13,14], several institutions - the nucleus of the TESLA Collaboration formally established in 1994 - decided in 1991 to set up the necessary infrastructure at DESY [8] to process and test 40 industrially produced 9 cell 1.3 GHz solid Niobium cavities. The aim was to achieve gradients of 15 MV/m at a Q value of $3 \cdot 10^9$ in a first step and finally reach 25 MV/m at a Q value of $5 \cdot 10^9$ suitable for the linear collider. The infrastructure of the TESLA Test Facility TTF consists of cleanrooms, chemical treatment installations, a 1400° C purification furnace, a high pressure water rinsing system, a cryogenic plant to operate vertical and horizontal cavity test stands at 1.8 K and a 1.3 GHz RF source. A detailed description of the infrastructure, which was completed by the end of 1995, will be given in [9].

In addition the collaboration decided to build a 500 MeV linac as an integrated system test to demonstrate that a linear collider based on s.c. cavities can be constructed and operated with confidence.

Considerable attention has been given to the subject of cost reduction [10,11]. For example:

- The number of cells per accelerating structure was increased to 9 compared to the customary 4-5. This

[*] TESLA Collaboration: **Armenia:** Yerevan Physics Institute, **P.R. China:** IHEP Academia Sinica, Tsinghua Univ., **Finland:** Inst. of Physics Helsinki, **France:** CEA/DSM Saclay, IN2P3 Orsay, **Germany:** Max-Born-Inst. Berlin, DESY Hamburg and Zeuthen, GH Wuppertal, Univ. Hamburg, IAP Univ. Frankfurt, GKSS Geesthacht, FZ Karlsruhe, IfH TU Darmstadt, ITE TU Berlin, IKK TU Dresden, RWTH Aachen, Univ. Rostock, **Italy:** INFN Frascati, Legnaro, Milano, Univ. Roma II, **Poland:** Polish Acad. of Sciences, Univ. Warsaw, INP Krakow, Univ. of Mining & Metallurgy, Polish Atomic Energy Agency, Soltan Inst. for Nuclear Studies, **Russia:** JINR Dubna, IHEP Protvino, INP Novosibirsk, **USA:** Argonne National Lab., Cornell Univ., Fermilab, UCLA

reduces the number of RF input and HOM couplers, tuning systems and cryostat penetrations, it also simplifies the RF distribution system and increases the filling factor.

- Costly cryostat ends and warm to cold transitions were avoided by combining eight 9 cell cavities and optical elements, which were all chosen to be superconducting, into one long, simple cryostat. Also the complete helium distribution system has been incorporated into the cryostat using the cold low pressure gas return tube as support structure for cavities and optical elements.

From the work starting in 1990 [13] a concept for a 500 GeV cm energy superconducting linear collider emerged, operating at 1.3 GHz with a gradient of 25 MV/m at $Q=5\cdot10^{9}$ and a luminosity of some $5\cdot10^{33}$ cm^{-2} sec^{-1}. A conceptual design report (CDR) was published in May 1997 [15] giving a complete description of the machine including all subsystems. The report includes a joint study with ECFA on the particle physics and the detector layout.

Since 1990 interest has grown [16,17] in linac driven X-ray FEL radiation, based on the Self-Amplified Spontaneous Emission (SASE) principle [18,19]. As the requirements on the emittance of the beam for a short wave length FEL are very demanding, again a superconducting low RF frequency linac lends itself as the best choice for such an application. The CDR includes the layout of an X-ray FEL facility integrated into the linear collider as well as various scientific applications of the FEL radiation. A detailed report on the status of the X-ray facility will be given at this conference [20].

3 R&D RESULTS AND ACTIVITIES

Up to now 25 9-cell Niobium cavities have been tested at the TTF. The majority of the cavities exceeded the initial TTF design goal of 15 MV/m at $Q=3\cdot10^{9}$. Fig. 1 shows the measurements in the vertical test stand [26] of all cavities excluding only those with a well identified fabrication error. On average a gradient of 22 MV/m at $Q=10^{10}$ is obtained. In the most recent measurement in the horizontal test [25] a gradient of 33 MV/m at $Q=4\cdot10^{9}$ has been achieved.

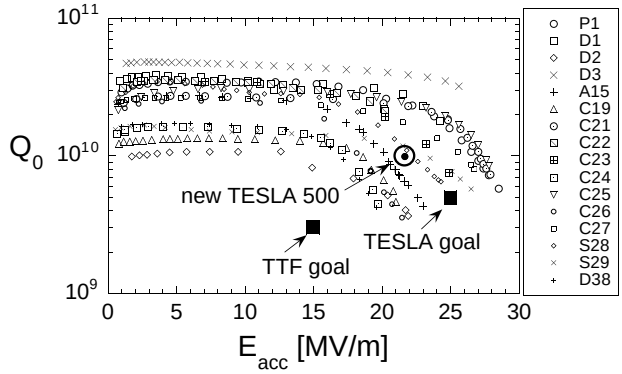

Figure 1: Quality factor Q versus acc. gradient for all 9-cell cavities without fabrication error (vertical test).

The performance limitations seen in six cavities were due to an improper welding procedure and could be eliminated in the subsequent cavity production. The remaining cavities not performing to expectations showed inclusions of Tantalum grains in the Niobium. Such defects will be avoided by scanning all Nb sheets for impurities with an eddy-current method. For a detailed information on cavity treatment procedures and results see [9,21].

All components for beam acceleration through the first cryomodule were installed in May 97. As the 14 MeV injector was already in operation at design values [22], stable beam acceleration in the first module could be established within a few days. Although the module contained 5 out of 8 cavities with fabrication errors, acceleration gradients of 16.7 MeV/m were obtained in a RF pulse of 100 μsec. For more details see [21,27].

The measurement of cryogenic properties of the module such as cryogenic loads, behaviour of cavity positions during thermal cycles and vibrations stayed well within the expected limits [23]. Detailed reports on the low level RF control, achieving a very impressive stability of phase and amplitude of the accelerating fields, will be given at this conference [24].

Several alternatives to the welding of dumb-bells for the production of 9-cell Niobium cavities - like hydroforming [28,32], spinning [29], or plasma spraying of copper on thin walled Nb cavities [30] - are being pursued within the collaboration. If successful, these methods may eventually lead to a further cost reduction in the cavity fabrication.

A very important new development was initiated by the proposal of a cavity "superstructure" [31]. In this scheme the spacing between adjacent cavities is reduced from 1.5 to 0.5 RF wavelengths and a group of 4 or more of these closely spaced cavities is supplied with RF power by only one input coupler. In this way the filling factor - the ratio of active to total length - increases from 66 % to 76 % or more, thus reducing the required gradient for 500 GeV cm operation from 25 to 21.7 MV/m for fixed linac length. The cost reductions due to the smaller number of RF input couplers and cryostat penetrations, and the simplification of the RF distribution system are obvious.

4 TESLA PARAMETERS

In the Conceptual Design Report the machine parameters were chosen such that luminosity and beamstrahlung energy loss were comparable to other linear collider designs [33]. The potential of the superconducting linac to accelerate a very small emittance beam with small emittance dilution was not exploited intentionally, keeping requirements on the alignment and stability of the linac and final focus components quite relaxed. Since the completion of the CDR, however, this strength of the TESLA concept has been investigated to some extent [34] leading to a new parameter set [35] suited for high luminosity operation at 500 GeV cm energy (see Table 1). The bene-

fits of the new "superstructure" concept have been incorporated into the design.

Table 1: Updated parameters at E_{cm}=500GeV in comparison with the original reference parameters.

	TESLA (ref.)	TESLA (new)
site length [km]	32.6	32.6
active length [km]	20	23
acc. Gradient [MV/m]	25	21.7
quality factor Q_0 [10^{10}]	0.5	1
t_{pulse} [μs]	800	950
# bunches n_b/pulse	1130	2820
bunch spacing Δt_b [ns]	708	337
rep. rate f_{rep} [Hz]	5	5
N_e/bunch [10^{10}]	3.6	2
ε_x / ε_y (@ IP) [10^{-6}m]	14 / 0.25	10 / 0.03
beta at IP $\beta_{x/y}^*$ [mm]	25 / 0.7	15 / 0.4
spot size σ_x^*/σ_y^* [nm]	845 / 19	553 / 5
bunch length σ_z [mm]	0.7	0.4
beamstrahlung δ_B [%]	2.5	2.8
Disruption D_y	17	33
P_{AC} (2 linacs) [MW]	95	95
efficiency $\eta_{AC\to b}$ [%]	17	23
luminosity [10^{34} $cm^{-2}s^{-1}$]	0.68	3

The reduction of the required gradient (25→21.7 MV/m) leads to an increase of the quality factor from $5\cdot10^9$ to 10^{10}. Both effects lower the required power for the cryogenics. This power savings has been invested in the beam power. The resulting lower loaded Q-value corresponds to a shorter filling time of the cavities, which in turn results in an increased conversion efficiency from mains to beam power (17→23 %).

Although the vertical emittance has gone down by almost an order of magnitude as compared to the CDR, tracking simulations [36] show that the emittance only grows by 23 % and 17 % due to single bunch and multi bunch effects respectively. However, most of the growth due to multibunch effects is not an incoherent spot size dilution but a systematic variation of the beam center along the bunch train at the IP. In combination with the larger disruption parameter - as compared to the CDR - these offsets may drive the opposing beams apart and critically reduce the luminosity. Fortunately, being mostly systematic, the offsets can be strongly reduced by the fast bunch to bunch orbit feedback. Further investigations of this topic will be needed, however.

As is to be expected the smaller spot sizes of the colliding beams put stronger requirements on the accuracy of the fast orbit feedback at the IP [37]. To keep the luminosity loss below 7 % the relative offset of the opposing beams at the IP has to be kept below 0.1 σ_y [38]. This requires a bpm resolution at the final focussing quadrupoles of 2 μm, which should be feasible.

As, for a given beam energy and beam power, the disruption parameter D_y is proportional to the product of luminosity and bunch length [35], the increase of D_y at a higher luminosity can be compensated by shortening the bunchlength. This handle has been applied only moderately up to now in the new design due to problems in the damping rings.

The TESLA damping rings are quite unconventional machines. At a beam energy of only 3.2 GeV they have a circumference of 17 km, of which 95 % are straight sections, located inside the TESLA tunnel (see Figure 2). Only two short return bends on either side with extra tunnels are needed ("dogbone"), thus saving substantially on civil engineering costs. However, the large circumference C and the low energy lead to an unfavourable enhancement factor of the incoherent space charge tune shift:

$$\Delta Q \sim \frac{C}{E^2}\cdot\frac{N_e}{\sigma_z\sqrt{\varepsilon_x\varepsilon_y}} \qquad (3)$$

Already for the CDR parameters the vertical tune shift amounted to -0.18. Further reductions of bunchlength and emittances therefore would lead to uncomfortably large tune shifts. The proposed cure for this problem [39] is to increase the beam size in the long straight sections by coupling the longitudinal or horizontal emittance to the vertical plane. First calculations [40] show that the space charge tune shift can be very effectively reduced in this way without trading in problems due to intra-beam scattering.

5 LAYOUT OF THE COLLIDER FACILITY

There has been consensus within the collaboration that the linear collider facility must be built at an existing high energy physics laboratory to make use of the existing infrastructure and staff. In the CDR two possible sites have been envisaged, one being DESY, the other Fermilab. Both sites allow for a future option to collide 500 GeV e^-/e^+ with high energy protons circulating in HERA or the Tevatron.

This option fixes the possible direction of the linear collider. At DESY the tunnel is foreseen with the main linac axis being tangential to the West straight section of HERA, extending about 32 km into the state of Schleswig-Holstein. The countryside is flat at about 10 m above sea level with maximum height variations of some 10 m. The tunnel axis is foreseen at 8 m below sea level, giving more than sufficient soil coverage for radiation protection. The soil, consisting mainly of sand, allows for easy tunneling by the hydroshield method, which was also used at HERA. The tunnel follows the earth's curvature

over most of its length, except for a section of about 5 km length to direct the tunnel axis tangentially to HERA.

A view into the planned tunnel (diameter 5.2 m) is shown in Fig. 2 at a section which contains the straight sections of the "dogbone" damping ring (upper left side) and several beam lines (right below the cyromodule) to the FEL facility. At the top of the tunnel there is a monorail for the transportation of equipment and personnel.

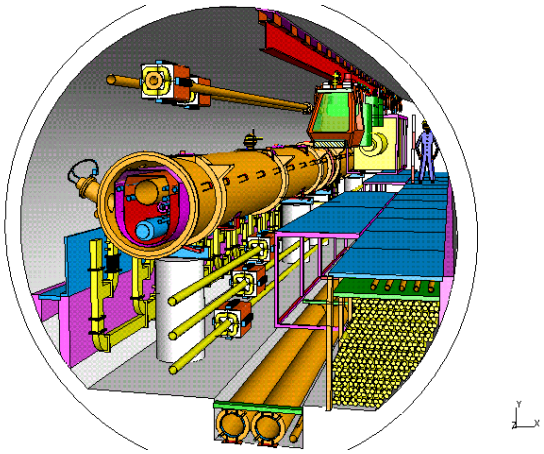

Figure 2: View into the TESLA Tunnel.

Klystrons and their pulse transformers are installed horizontally below the floor in the middle of the tunnel above the cooling water tubes. There is a total of about 625 10 MW klystrons including about 2.5 % spare. Each klystron feeds 32 9-cell cavities corresponding to a length of about 48 m. With a lifetime of 40,000 hours about 10 klystrons will have to be replaced in a one day interruption once per month.

The experience of the SLC [41] on the failure rate of modulators does not permit an installation into the tunnel, inaccessible during machine operation. Therefore in the present layout the modulators are housed in service halls above ground connected to the pulse transformers in the tunnel by long cables (Fig. 2, lower right). However, the design of modulators reliable enough to be installed into the tunnel is being investigated.

Service halls, spaced along the collider at a distance of about 5 km are needed for the cryogenic plants [42] in any case. The length of superconducting linac that can be cooled by a cryoplant is about 2.5 km. This distance is mainly determined by the pressure drop in the large return tube (300 mm diameter) for low pressure Helium gas at about 2 K. The pressure in tube determines the vapour pressure of the superfluid helium surrounding the cavities and thus the operating temperature of the cavities.

Each service hall houses two cryoplants each supplying a 2.5 km section of the linac. In case of a failure of one plant, the other one can supply two sectors operating the collider at a reduced repetition rate. The big cryogenic boxes are planned to be installed in the 14 m diameter shaft connecting the service hall with the tunnel (see Fig. 3).

Due to the large spacing between consecutive bunches, there is no crossing angle required at the IP and consequently no angle between the tunnel axis of the two linacs. The beams are deflected by electrostatic separators, having passed the interaction region and the large aperture, superconducting quadrupole doublet. A tunnel length of about 1.2 km between the IP and the ends of either superconducting linac is needed for the beam delivery system [15] containing beam collimation systems, beam diagnostics and orbit correction elements, and the final focus system, demagnifying the beam size and correcting chromatic effects. These tunnel sections also house the beam dumps and the positron source.

As the amount of positrons needed for a beam pulse exceeds the potential of conventional positron sources, the electron beam having passed the interaction region is used to produce the required number of positrons. In this scheme, proposed in the original VLEPP design [43], the spent electron beam is collimated and passed through a wiggler producing large quantities of γ-rays, which convert in a thin rotating target into $e^+ e^-$ pairs. The fraction of positrons which can be captured by the source optics, accelerated to 3 GeV and stored in the dogbone damping ring yields a sufficient number of particles for the operation of the linear collider. With the new design parameters the fraction of the spent electron beam usable for positron production actually increases from 86 % to 93 % due to the smaller beam emittance, thus substantially reducing the power load on the collimators [44]. Although a detailed technical layout of the positron source is still missing, first investigations indicate that the whole system can well be accommodated into the tunnel.

6 ENERGY UPGRADE POTENTIAL

With the new "superstructure" concept the gradient needed for 800 GeV cm energy is 34 MV/m. From the results on cavity R&D (section 3) the optimism, that average gradients well above 30 MV/m at Q values of $5 10^9$ can be reached within the near future, is well justified. The theoretical maximum gradient for our structures limited by the critical magnetic field is at about 55 MV/m.

All subsystems of the collider have been laid out for 800 GeV operation. The number of klystrons and modulators will be doubled. With the present layout of the cryogenics the repetition rate of the collider will have to be reduced from 5 to 3 Hz to maintain the level of available cooling capacity. By further reducing the normalised vertical emittance by a factor 3 to 10^{-8} m , a luminosity of $5 \cdot 10^{34}$ cm^{-2} sec^{-1} can be obtained [35], the beamstrahlung energy loss staying below 5 %. The mains power requirement will go up to 130 MW. An upgrade of the cryogenic cooling capacity will allow luminosities close to 10^{35} cm^{-2} sec^{-1} to be reached by running the collider at a repetition rate of 5 Hz.

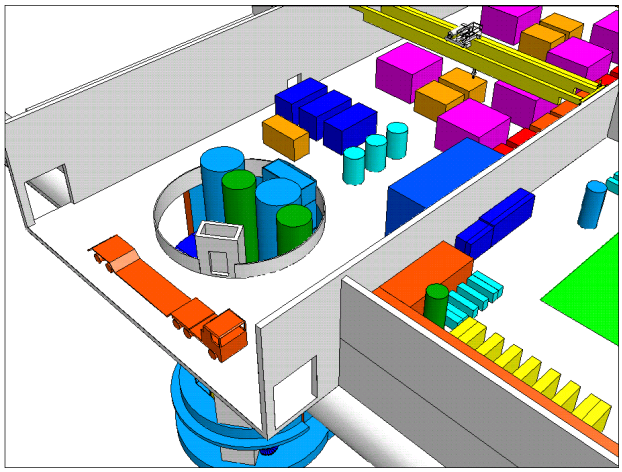

Figure 3: Service hall with shaft connection to the tunnel.

7 OUTLOOK

On the basis of the existing knowhow, orders to industry are being issued to evaluate the requirements of large scale industrial cavity production. Together with a detailed layout of all subsystems of the collider the information from the industrial studies will allow for a proposal containing technical design of the facility, and a reliable schedule and cost evaluation, to be submitted in two to three years from now. To obtain public acceptance the states, the communities, and the residents involved have been informed about the planning. An administrative procedure to eventually ensure the necessary legal conditions for the construction of the facility - if approved - is underway.

8 ACKNOWLEDGMENTS

I would like to express my respect to the many people in and outside the collaboration who have been working on the cavity R&D over the years. This work has been certainly cumbersome at times but finally lead to the beautiful cavity results, which we have today. Many people have contributed to the present status of the TESLA design, whom I cannot give proper credit to. But I would like to give special credit to the late G. Horlitz for designing the complete cryogenics system of TESLA.

9 REFERENCES

[1] M. Tigner, Nuovo Cimento, 37 (1965) 1228.
[2] U. Amaldi, Phys. Lett., B61 (1976) 313.
[3] J. Kirchgessner et al., HEACC, Geneva 1980.
[4] H. Gerke and K. Steffen, DESY PET-79/04 (1979).
[5] R. Palmer, New Developments in Particle Acceleration Techniques, Orsay 1987, CERN 87-11, ECFA 87/110.
[6] R. Brinkmann, DESY M-95-10 (1995).
[7] J.P. Delahaye, G. Guignard, T. Raubenheimer and I. Wilson, LC97, Zvenigorod, Russia, Vol. I, p. 428.
[8] TTF-Proposal, DESY-TESLA-93-01.
[9] H. Weise, Contribution to this conference.
[10] H. Padamsee, EPAC92, Berlin.
[11] D. Trines et al. HEACC92, Hamburg, Vol. II.
[12] 4th Workshop on RF Superconductivity, Tsukuba 1989, KEK Report 89-21, Ed. Y. Kojima.
[13] 1st International TESLA Workshop, Cornell 1990, CLNS 90-1029.
[14] 5th Workshop on RF Superconductivity, Hamburg 1991, DESY M-92-01.
[15] Conceptual Design of a 500 GeV e^+e^- Linear Collider with Integrated x-ray Laser Facility, Ed. R. Brinkmann, G. Materlik, J. Rossbach, A. Wagner, DESY 1997-048, ECFA 1997-182.
[16] L. Serafini, M. Ferrario, C. Pagani, A. Ghio, P. Michelato, A. Peretti, LNF-90/035 (R).
[17] C. Pellegrini, Workshop on Fourth Generation Light Sources, SSRL Report 92/02, p. 364.
[18] R. Bonifacio, C. Pellegrini, L. N. Narducci, Opt. Communi Vol. 50, No. 6 (1984).
[19] Ya. S. Derbenev, A. M. Kodratenko and E. L. Saldin NIM, A193, 415 (1982).
[20] J. Rossbach, Contribution to this conference.
[21] M. Pekeler, EPAC98, Stockholm.
[22] T. Garvey et al., PAC97, Vancouver.
[23] J. G. Weisend II et al., ICEC98, Bournemouth, UK.
[24] S. Simrock, Contribution to this conference.
[25] P. Clay et al., ICEC95, Columbus, Ohio.
[26] T. H. Nicol et al., IEEE Proceedings PAC93, Vol. 2.
[27] W.-D. Möller, Contribution to this conference.
[28] I. Gonin et al., TESLA 98-09
[29] V. Palmieri, Contribution to this conference.
[30] M. Fouaidy et al., EPAC98, Stockholm.
[31] J. Sekutowicz, M. Ferrario and C. Tang, EPAC98, Stockholm and TESLA 98-08.
[32] C. Z. Antoine et al., 8th Workshop on RF Superconductivity, Abano Terme 1997, DAPNIA/SEA-98-10.
[33] G. Loew (ed), Int. Linear Collider Technical Review Commmittee Report, SLAC-R-95-471.
[34] R. Brinkmann, TESLA 97-13.
[35] R. Brinkmann, EPAC98, Stockholm.
[36] A. Mosnier, unpublished contribution.
[37] I. Reyzl, PhD Thesis, TU Berlin, 1998, to be published.
[38] O. Napoly, D. Schulte, unpublished contribution.
[39] N. Walker, unpublished contribution.
[40] K. Balewski, unpublished contribution.
[41] A. R. Donaldson, J. R. Ashton, 20th Int. Power Mod. Symp., Myrtle Beach, South Carolina, 1992.
[42] S. Wolff et al., ICEC98, Bournemouth, UK.
[43] V. E. Balakin, A. A. Mikhailichenko, Preprint INP 79-85.
[44] R. Glantz, unpublished contribution.

RESEARCH AND DEVELOPMENT FOR AN X-BAND LINEAR COLLIDER*

C. Adolphsen
Stanford Linear Accelerator Center, Stanford University, Stanford CA 94309 USA

Abstract

At SLAC and KEK research is advancing toward a design for an electron-positron linear collider based on X-Band (11.4 GHz) rf accelerator technology. The nominal acceleration gradient in its main linacs will be about four times that in the Stanford Linear Collider (SLC). The design targets a 1.0 TeV center-of-mass energy but envisions initial operation at 0.5 TeV and allows for expansion to 1.5 TeV. A 10^{34} cm^{-2} s^{-1} luminosity level will be achieved by colliding multiple bunches per pulse with bunch emittances about two orders of magnitude smaller than those in the SLC. The key components needed to realize such a collider are under development at SLAC and KEK. In this paper we review recent progress in the development of the linac rf system and discuss future R&D.

1 INTRODUCTION

For the next generation electron-positron linear collider, one wants to generate at least one TeV center-of-mass collisions to complement the physics reach of the Large Hadron Collider (LHC) that is being constructed at CERN. At SLAC and KEK research has been focused on a collider design that uses X-Band (11.4 GHz) rf technology to achieve this goal [1,2]. The design has evolved largely from the experience gained from operation of the Stanford Linear Collider (SLC) where S-Band (2.9 GHz) rf technology is used to accelerate beams to about 50 GeV. Increasing the rf frequency allows for higher gradients (72 MeV/m versus 17 MeV/m in the SLC) which keeps the machine cost from becoming prohibitive at the higher energies.

To be efficient, multiple bunches (95) will be accelerated on each rf pulse (120 Hz repetition rate). There will be about 10^{10} particles per bunch and the bunch spacing will be 2.8 ns. These 0.6 A beams will reduce (load) the gradient in the 1.8 m long X-Band accelerator structures by 16%. Including energy overhead, the effective gradient in the structures will be 55 MeV/m. The structures will fill 86% of the lineal distance along the main linacs so 10.4 km long beam lines will be required to accelerate the electron and positron beams from their 10 GeV injection energies to 500 GeV. However, the collider will be operated initially with a 500 GeV center-of-mass energy where only the first half of each of the opposing linacs will contain rf components, and the beams will 'drift' through the remaining halves.

The main components of the linac rf system are the modulators that power the klystrons, the 75 MW klystrons that generate the rf, the distribution system that transports the rf to the accelerator structures, and the structures themselves. In the following sections, we review the designs, recent R&D and future development plans for these components.

2 MODULATORS

The modulators that are used in the SLC are conventional line-type with pulse-forming networks (PFN). These networks are composed of discrete inductors and capacitors that are slowly charged and then rapidly discharged (via a thyratron) through a step-up transformer to generate the high voltage pulse needed to drive an SLC klystron. A similar approach is being pursued at SLAC to produce the 490 kV, 260 A, 1.5 μs long pulses required for the X-Band klystrons that are being developed [3]. The current design has a single modulator powering two klystrons through a 14:1 transformer. A prototype version has been built using high-energy-density glass-type capacitors, and tested with a single S-Band klystron at a lower voltage (290 kV) to produce the same impedance as two X-Band klystrons. In this configuration, 89% of the stored energy is transferred from the modulator to the klystron, and 82% of the transferred energy is within the 1.5 μs long pulse flattop, between the pulse rise (350 ns) and fall (450 ns) periods. The charging power supply used in the test was not particularly efficient; however, if the goal of 90% is achieved, the overall energy transfer efficiency from AC to usable klystron beam power would be 66%.

To improve efficiency, KEK is working with a Blumlein modulator configuration [2]. Here a step-up transformer of half the turns-ratio as the conventional configuration sits between two PFNs of the appropriate impedance to double the primary voltage. In principle, this should yield a faster rise time due to the lower leakage inductance of the transformer [4]. However, tests thus far with klystron loads have yielded values comparable to the SLAC results. Both groups will continue to upgrade their test setups to improve

* Work Supported by DOE Contract DE-AC03-76F00515.

efficiency, reduce costs, and handle the full klystron pulse requirements.

One drawback of these modulator designs is their use of thyratrons which in general have relatively short lifetimes (10-20 khour) and require periodic tuning. As an alternative, a solid-state induction-type modulator is being developed at SLAC and LLNL that has the potential of better reliability and higher efficiency [5]. The basic idea is to sum many low voltage sources inductively to yield the desired klystron voltage. This has been realized by having each source drive a transformer made from a 4.5 inch ID, by 11.5 inch OD, by 2 inch thick Metglass core. The cores are stacked so the secondary windings, which sum the output voltages, can be threaded through their IDs. Each source is essentially a capacitor that is slowly charged and then partially (20%) discharged through a solid-state switch to generate the pulse.

Recent improvements in Isolated Gate Bipolar Transistor (IGBT) switches, which are used in electric trains for example, have made this induction scheme conceivable. They have relatively fast rise and fall times (< 100 ns between 10% and 90%) with turn-off occurring after a fixed delay of about 100 ns from the end of the gate pulse. Tests so far have been done with resistive loads: a single source has directly (no core) switched 1.5 kA at 2 kV, and an 18 kV pulse has been generated inductively through a six-core stack with single-turn primaries and a four-turn secondary.

Although the switching times are fast in these cases, the rise and fall times in actual operation will be somewhat longer due to the combination of the modulator leakage inductance and the klystron capacitance. Simulations have shown that a 1:1 turns-ratio is needed to produce fast enough rise and fall times (≈ 200 ns) to yield an overall efficiency of 75%. Part of this efficiency would come from including circuitry in each source that would recover much of the stored energy remaining in stray inductances and capacitances after the IGBTs shut off.

For the 1:1 turns-ratio design, one hundred 5 kV, 2 kA sources are summed to drive 8 klystrons. IGBTs capable of switching such power are expected to be available soon. Failure of any single source should be benign; the core will saturate and be nearly transparent to the pulse. Some overhead in voltage capability will be included to offset such a loss. Also, the sources will be independently timed to better shape the pulse, for example, to offset the natural droop. One potential problem in driving many klystrons is that an arc in one will be fed by the stored energy in the others (the circuit itself can be shut off in time to not be a problem). Adding inductors in the power feeds that fan out to the klystrons should reduce the discharge power to a manageable level. In the next year a more realistic prototype will be built to better evaluate this induction modulator scheme.

3 KLYSTRONS

During the past decade at SLAC and KEK, research has been directed at developing X-Band (11.4 GHz) klystrons in the 50 to 130 MW range [1,2,6,7,8]. Until the last few years these klystrons have used large solenoid magnets to focus the beam in its path from the gun through the bunching and output sections to the collector. However, the power used by these magnets, around 20 kW, is comparable to the average rf output power so it has a big impact on efficiency. This has prompted the development of a focusing scheme that uses permanent magnets so there is no associated power loss.

Before discussing this scheme however, we review results from the latest and perhaps last generation of solenoid-focused X-Band klystrons that SLAC and KEK will develop. They operate with a perveance (I [Amps] / $V^{3/2}$ [Volts]) of 1.2×10^{-6} and contain four-cell traveling wave output cavities. At SLAC, the XL4 klystrons are the culmination of its 50 MW klystron development program. Six of these tubes have been built, and they are used as X-Band rf sources for component testing and beam acceleration in the Next Linear Collider Test Accelerator (NLCTA). They reliably generate 1.5 μs long, 50 MW pulses with a 41% beam-to-rf efficiency. In a brief test, one klystron produced 75 MW, 1.2 μs long pulses at 48% efficiency. At KEK, the XB72K #9 tube, which was developed with BINP, has recently produced 72 MW with a 31% efficiency although the pulse length was limited to 200 ns by the modulator. KEK, in collaboration with Toshiba, has also recently completed assembly of a tube that is expected to produce 126 MW, 1.5 μs long pulses at 48% efficiency. It uses longer cavity cells with a lower Q_{ext} to be able to operate at higher currents for the same cavity surface fields. Testing of this tube has just started.

At SLAC, permanent magnet tubes are now being developed. In these designs, about 40 magnet rings with alternating polarities are interleaved with iron pole pieces to generate a periodic (i.e., sine-like) axial field along the ≈ 0.5 meter region between the gun anode and beam collector. The resulting focusing strength is proportional to the RMS of this axial field. About 2 kG can be achieved practically, which is smaller than the ≈ 5 kG field in the solenoid-focused tubes. This has led to a lower perveance (0.8×10^{-6}) design where the space charge defocusing is smaller. To handle the increased voltage drop along the output cavity, it was lengthened to five cells. The lower perveance has the advantage of increasing efficiency through improved bunching, but it makes the modulator harder to build due to the higher voltage hold-off (490 kV). The efficiency goal for these Periodic

Permanent Magnet (PPM) klystrons is at least 60% when generating 75 MW, 1.5 μs long pulses at 120 Hz.

Thus far, SLAC has built a 50 MW PPM klystron using samarium cobalt magnets. This tube has produced 2 μs long pulses with a 55% efficiency at the design power. A 75 MW PPM tube has also been built but has had operational problems that are thought to arise in part from using magnets that do not fully meet specifications. A switch to NbFeB magnets was made for machining and cost reasons, but they proved harder to manufacture within the desired magnetic tolerances. The present program is to improve the operation of this tube and concurrently to build a new version that is more suited for mass production. It should be completed by the end of 1999. At KEK, a 75 MW PPM tube that was designed and built by BINP was tested with limited success. Work there has recently focused on more accurate klystron modeling using the MAGIC code. These studies have resulted in a better understanding of existing tubes and will be used as the basis for designing the first PPM tube at KEK.

4 RF DISTRIBUTION

The function of the rf distribution system is to transport the klystron output power to the accelerator structures. This task is made more difficult by the fact that the klystrons optimally generate a lower power and longer pulse than that needed for the structures. In past linac designs and in the NLCTA, the solution was to use pulse compression, namely the SLED II system which is a delay line version of the SLAC Linac Energy Doubler (SLED) [1]. It consists of a 3 dB hybrid divider that routes the klystron output power equally to two delay lines made of circular waveguide. These lines are shorted at the far end and have irises at the near end that partially reflect the rf. During operation in the NLCTA, for example, the two 40 m long lines are resonantly filled during the first $5/6^{th}$ of the 1.5 μs long klystron pulse, and then effectively discharged through the remaining hybrid port by a 180º reversal of the klystron phase during the last $1/6^{th}$ of the pulse. This yields a shorter ($1/6^{th}$ as long), higher power pulse that is used to power two NLCTA accelerator structures. Although it works well, it is not particularly efficient; about 30% of the power goes to the structures during the filling of the delay lines, so the power gain is about four.

Although there are more efficient pulse compression methods, the scheme now being pursued sums the power from four pairs of klystrons, 'slices' it into four equal time intervals, and then distributes it up-beam to four sets of accelerator structures that are appropriately spaced so that the beam-to-rf arrival time is the same in each case. Hence no power is wasted although there are still resistive wall losses.

In the original version of this Delay Line Distribution System (DLDS), which was proposed by KEK, the power is summed with 3 dB hybrid combiners and distributed up-beam through individual circular waveguides to each set of structures [2,9]. The power routing is accomplished by varying the relative rf phases of the four sources. In the circular waveguides, the power is transported in the low-loss TE_{01} mode as is done in the SLED II delay lines. To reduce the length of waveguide, a multimode version of this system has been proposed at SLAC in which the power is distributed through a single circular waveguide, but in four different modes [10]. In this case the power from the four klystron pairs is sent to a 'launcher' that generates the modes based on the relative rf phases of the four inputs. During operation, the phases are varied to excite the four modes sequentially in equal time intervals. The circular waveguide modes are TE_{01}, TE_{12H}, TE_{12V} and TE_{21} where the H and V subscripts refer to horizontal and vertical polarizations. Three of modes travel up-beam and are extracted at appropriate locations to arrive 100 ns (the structure filling time) before the beam. Each 'extractor' couples out only one mode and passes the remaining modes. The fourth mode (TE_{21}) is extracted at the launcher. KEK is considering a similar scheme but with the power distributed in two circular waveguides where two modes (TE_{01}, TE_{12H}) are launched and extracted in each waveguide.

For the rf transport between the klystrons and launcher, and between the extractors and the structures, the TE_{01} circular waveguide mode is used. The extracted power in each case feeds three contiguous accelerator structures. To power a contiguous array of structure triplets, nine DLDSs (a nonet) are interleaved to form a 225 m long sector. The sector length is set by the 1.5 μs klystron pulse length and the relative beam-to-rf group velocity (about 2c). Twenty-two sectors are required to produce a 500 GeV beam.

An important requirement of this distribution system is its power handling capability. With eight 75 MW klystrons, 600 MW of rf power will be launched, extracted and 'taped-off' in thirds to feed 200 MW to each structure. Based on operational experience, the goal is to keep the surface fields in all transport components below about 40 MeV/m [11]. Recently, two planar-style 3 dB hybrids and several rectangular (TE_{10}) to circular (TE_{01}) mode converters were successfully tested to 420 MW with 150 ns long pulses. To test components at their design power level and beyond, the NLCTA is being upgraded to produce 800 MW, 240 ns long pulses.

Concepts for the launcher, extractors and bends are in hand and development programs have begun at SLAC and KEK. In addition to reducing the surface fields, the designs aim for a power reduction of < 1% in each component due to mismatches and resistive

wall losses. Overall, a klystron-to-structure transfer efficiency of about 85% is expected where only a small portion of the power loss occurs in the long circular waveguides. This assumes no mode conversion in these sections. A joint experiment is under way to verify that such conversion losses are small, especially from rotation of the polarized modes.

5 ACCELERATOR STRUCTURES

SLAC and KEK have enjoyed an active collaboration in X-Band accelerator structure development for more than five years. This has led to a common structure design that uses an electrical scheme developed at SLAC and assembly techniques pioneered at KEK. The electrical design addresses both the requirement of efficient beam acceleration and the need to suppress the long-range transverse wakefield generated when a beam travels off-axis through the structure. Unless the wakefield is reduced by about two orders of magnitude, the coupling of the bunches in a multibunch train will resonantly amplify any betatron motion of the train by a significant amount. This difficult goal has been met by using a combination of two methods.

The first to be developed was mode detuning whereby the frequencies of the lowest (and strongest) band of dipole modes are systematically varied along the 206 cell structure to produce a Gaussian distribution in the product of the mode density and the mode coupling strength to the beam [12]. With this detuning, the modes excited by an off-axis bunch add deconstructively, yielding an approximately Gaussian falloff in the net wakefield generated after each bunch. A sigma of 2.5% was chosen for the 206-mode frequency distribution to produce more than a hundred-fold wakefield suppression by 1.4 ns, the nominal bunch spacing in the early linear collider designs.

This detuning works well to suppress the wakefield for about the first 30 ns, after which its amplitude increases due to a partial recoherence of the mode excitations. This has led to the introduction of weak mode damping to offset this rise [13]. The damping is achieved through the addition of four single-moded waveguides (manifolds) that run parallel to the structure and couple to the cells through slots. For each dipole mode, the power flow to the manifolds occurs in that region of the structure where the cell-to-cell phase variation of the mode matches that of the manifold mode. When terminated into matched loads, the manifolds reduce the mode Q's from about 6000 to 1000, enough to keep the wakefield from significantly increasing again.

To date, three of these Damped Detuned Structures (DDS) have been constructed. The cells for the most recent version were manufactured at LLNL using diamond-point turning. The mating surfaces of the cells were machined flat to < 0.5 μm and smooth to < 50 nm. The cells were then assembled in Japan using a two-step diffusion bonding technique. In the first step, the cells were stacked on an inclined V-block and pressed by 600 kg of force for 48 hours in a 180 °C environment. This procedure partially bonded the surfaces which prevented cell-to-cell slippage when the stack was placed upright to be fully bonded. For this step, the stack was placed under 24 kg of force at 890 °C for 4 hours.

The straightness of the resulting structure varied with scale, increasing from a few μm cell-to-cell to a few hundred μm over its 1.8 m length. However, the long wavelength (> 0.5 m) offsets were reduced by counter bowing the soft copper structure. A straightness of +/- 20 μm was achieved, yielding an overall alignment that meets the requirements of the linear collider design. In this design, the long wavelength alignment of the structures will be set and maintained by the support system. The structures will be attached to girders in sets of three with a single rf feed per girder that is 'tapped-off' to each structure. Each girder will have remote adjustment capability and will be positioned to best center the beam in the three structures based on the information obtained from processing the dipole mode signals from the structure manifolds. Thus, only the internal alignment of the structures along the girders will have to be established with precision (about +/- 20 μm) and be kept stable. Studies of long-term stability have been done with mock structures on a prototype girder. They show that the desired level of alignment is maintainable in an operating-like environment.

In the most recent DDS prototype, the rf match through the output ports of the manifolds was improved and the dipole frequency profile was changed slightly to increase the wakefield suppression. To gauge the effect of these changes, the long-range wakefield of the structure was measured in the Accelerator Structure Setup (ASSET) facility in the SLAC Linac [14]. Here a positron beam was used to induce a wakefield in the structure and an electron beam was used to 'witness' it. The measurements show larger than expected values for the wakefield, particularly at short times (< 20 ns). This increase is thought to be the result of systematic errors in the cell dimensions. Errors of roughly the size required to explain these data were observed in a sample of cells measured for QC purposes prior to assembling the structure.

Centering tests were also done in ASSET in which the dipole signals were used as a guide to position the positron beam. Measurements of the resulting short-range wakefield (< 300 ps) indicated that the beam had been centered to < 20 μm in the structure which is roughly the requirement during linear collider operation. However, monopole-like components of the

transverse wakefield were also observed and need to be understood.

The next structure that will be built will have rounded shaped cavities instead of the cylindrical shape used so far. This increases the shunt impedance of the structure by 12% which yields a 6% increase in the rf-to-beam efficiency. This rounded-DDS or RDDS will have an average iris radius equal to 18% of the X-Band wavelength. This value was derived from a joint SLAC and KEK study to optimize the linac performance. The main design difficulty thus far has been in damping the modes in the few cells at the downstream end of the structure that cannot be coupled to the manifolds due to space limitations. Several solutions are being considered including adding individual absorbers in these cells. Otherwise, the electrical design is nearly complete; SLAC and KEK will jointly build and test an RDDS by the end of 1999.

The suppression of the long-range wakefield is not the only difficult structure performance requirement. The structures must also operate reliably at a high gradient, about 70 MeV/m. Three structures have been rf conditioned to this level, the most recent one up to 85 MeV/m after 440 hours of operation [15]. It is a 1.3 m long, diamond-turned structure built at KEK to study detuning. During its conditioning, the rf power was slowly increased until a breakdown occurred in which > 5 MW of power was reflected back toward the source. The rf was then shut off for 2-4 minutes to allow the structure to pump down, and then it was slowly ramped up again. This procedure was continually repeated under computer control during most of the conditioning period.

At the highest gradient, the dark current emitted from the downstream end of the structure was about 5 mA and the mean time between breakdowns was less than a minute. Reducing the power to yield a 70 MeV/m gradient reduced the dark current to about 0.5 mA and increased the periods between breakdowns to several hours. Even at the highest gradient, however, the loading due to the dark current should not have been significant.

Another dark current related concern is the excitation of transverse fields. To the extent that such fields are the result of excitations of the lowest band of dipole modes, an estimate of their size was made by measuring the dipole signals from a manifold of a DDS during rf conditioning to 70 MeV/m. No significant signals were observed (except during breakdown) which puts a limit on the transverse field amplitude that is within the tolerance required in the linear collider design. The latest DDS prototype will be conditioned in the near future as part of a more systematic program to understand high gradient limits in the structures.

6 SUMMARY

The four major components of an rf system for an X-Band linear collider - the modulators, klystrons, rf distribution system and accelerator structures - are being actively developed at SLAC and KEK. Once their designs are more mature, an integrated rf system with eight klystrons will be built that will serve as a model element of a full-scale linac.

7 REFERENCES

[1] "Zeroth-Order Design Report for the Next Linear Collider," SLAC Report 474 (1996).

[2] "JLC Design Study," KEK (April 1997).

[3] R. Koontz et al., "NLC Klystron Pulse Modulator R&D at SLAC," http://www.slac.stanford.edu/grp/kly/mkw/nlc.htm (June 1998).

[4] M. Akemoto et al., "Pulse Transformer R&D for NLC Klystron Pulse Modulator," SLAC-PUB-7583 (July 1997).

[5] Dick Cassel, talk presented at the Third Modulator-Klystron Workshop at SLAC (1998), see http://www.slac.stanford.edu/grp/kly/mkw/.

[6] G. Caryotakis, "Development of X-Band Klystron Technology at SLAC," SLAC-PUB-7548 (May 1997).

[7] D. Sprehn et al., "Periodic Permanent Magnet Development for Linear Collider X-Band Klystrons," these proceedings.

[8] Y. H. Chin, "Modeling and Design of Klystrons," these proceedings.

[9] H. Mizuno, "RF Pulse Compression for Linear Colliders," these proceedings.

[10] S. Tantawi et al., "A Four-Port Launcher for a Multi-Moded DLDS Power Distribution System," these proceedings.

[11] A. Vlieks et al., "High Power RF Component Testing for NLC," these proceedings.

[12] K. A. Thompson et al., "Design and Simulation of Accelerating Structures for Future Linear Colliders," *Particle Accelerators* **47**, 65-109 (1994) and SLAC-PUB-6032 (Nov. 1993).

[13] R. H. Miller et al., "A Damped Detuned Structure for the Next Linear Collider," SLAC-PUB-7288 (Sept. 1996).

[14] C. Adolphsen et al., "Wakefield and Beam Centering Measurements of a Damped and Detuned X-Band Accelerator Structure," to be presented at PAC99.

[15] R. Loewen et al., "SLAC High Gradient Testing of a KEK X-Band Accelerator Structure," to be presented at PAC99.

SCALING LAWS FOR NORMAL CONDUCTING e^+ e^- LINEAR COLLIDERS

J.-P. Delahaye, G. Guignard, I. Wilson/CERN, T. Raubenheimer /SLAC.

Abstract

Design studies of a future TeV e^+e^- Linear Collider (TLC) are presently being made by five major laboratories within the framework of a world-wide collaboration. A figure of merit is defined which enables an objective comparison of these different designs. This figure of merit is shown to depend only on a small number of parameters. General scaling laws for the main beam parameters and linac parameters are derived and prove to be very effective when used as guidelines to optimize the linear collider design. By adopting appropriate parameters for beam stability, the figure of merit becomes nearly independent of accelerating gradient and RF frequency of the accelerating structures. In spite of the strong dependence of the wakefields with frequency, the single bunch emittance preservation during acceleration along the linac is also shown to be independent of the RF frequency when using equivalent trajectory correction schemes. In this situation, beam acceleration using high-frequency structures becomes very favourable because it enables high accelerating fields to be obtained, which reduces the overall length and consequently the total cost of the linac.

1 INTRODUCTION

A lot of progress has been made in the last ten years on design and development studies towards high-luminosity TeV-range Linear Colliders (TLC). Various options for efficient beam acceleration have been explored and periodically compared within the framework of a world-wide collaboration [1]. Two basic technologies have been developed for beam acceleration: TESLA proposes to use 1.3 GHz super-conducting (SC) structures whereas SBLC, JLCc, JLCx, NLC,VLEPP and CLIC have chosen normal-conducting travelling-wave (NCTW) structures operating at the very different frequencies of 3, 5.6, 11.4, 14 and 30 GHz, respectively. General scaling laws have been derived [2] for multi-bunch TLCs which use NCTW structures, taking into account the basic physics processes which have been used to optimise the different designs. For completeness, the graphs also include data points for both TESLA and VLEPP in spite of their respective SC and single bunch operation. The motivation for the scaling study is two-fold. First, by comparing the parameters adopted by the various design studies which cover a decade in operating frequency, the study provides an insight into the way the different optimisations have been achieved. Secondly, it provides a logical strategy based on objective, physics-based arguments for designing or re-optimising any new or presently-proposed linear collider.

2 LUMINOSITY - FIGURE OF MERIT

The luminosity of an e^+/e^- linear collider is given by:

$$L = \frac{k_b N_b^2 f_{rep}}{4\pi\bar{\sigma}_x^*\bar{\sigma}_y^*} = \frac{N_b P_b}{4\pi e U_f \bar{\sigma}_x^*\bar{\sigma}_y^*} = \frac{H_D N_b \eta_{RF}^{AC}\eta_b^{RF} P_{AC}}{4\pi e U_f \sigma_x^*\sigma_y^*} \quad (1)$$

where P_{AC}, η^{AC}_{RF} and η^{RF}_{b} are the AC power, the AC-to-RF and RF-to-beam efficiencies, U_f, P_b, and N_b are the beam energy, beam power and number of particles per bunch, $\bar{\sigma}_x^*$ and $\bar{\sigma}_y^*$ are the r.m.s. beam sizes at the Interaction Point (I.P.) after being pinched by the beam-beam interaction, and H_D is the corresponding luminosity enhancement factor. Each particle is decelerated by the beam-beam interaction losing on average an energy δ_B and emitting n_γ γ-rays. At c.m. energies < 2 TeV the parameters are chosen such that δ_B does not exceed a few %, this is the so-called low beamstrahlung (LB) regime. At higher energies, to get adequate luminosity, the parameters are chosen in the high beamstrahlung (HB) regime [3]. In the HB regime, where $n_\gamma = 3.5\delta_B$, choosing $n_\gamma \approx 2$ ensures a reasonable compromise between the fraction of total luminosity contributed by particles with energies within 1-2 % of the maximum, and the number of $e^\pm$ pairs which appear as background in the detector. In both regimes therefore δ_B is an essential design parameter. The assumption of flat beams ($\sigma_x >> \sigma_y$) to enhance the luminosity and to decrease δ_B leads to the following expressions in the LB and HB regimes:

$$\delta_B \propto \frac{U_f}{\sigma_z}\frac{N_b^2}{\bar{\sigma}_x^{*2}} \quad \text{and} \quad \delta_B \cong \frac{n_\gamma}{3.5} \propto \frac{\sigma_z^{1/3}}{U_f^{1/3}}\frac{N_b^{2/3}}{\bar{\sigma}_x^{*2/3}} \quad (2)$$

Using (1), (2), and assuming in the LB regime a vertical beta function at the I.P. equal to the bunch length to minimise the "hourglass" effect, the luminosity scales as:

$$L \propto \frac{\delta_B^{1/2} H_{Dy}\eta_{RF}^{AC}\eta_b^{RF} P_{AC}}{U_f \varepsilon_{ny}^{*1/2}} \text{ and } L \propto \frac{\delta_B^{3/2} H_{Dy}\eta_{RF}^{AC}\eta_b^{RF} P_{AC}}{U_f^{1/2}\beta_y^{*1/2}\sigma_z^{1/2}\varepsilon_{ny}^{*1/2}} \quad (3)$$

In both cases, the luminosity only depends on a small number of parameters. For objective comparisons, a figure of merit M, is defined as L normalised to P_{AC}, δ_B, and U_f. Neglecting the variations of H_D (small for a flat beam) and of η^{AC}_{RF} (similar in all designs), M becomes:

$$M = L\frac{U_f}{\delta_B^{1/2}P_{AC}} \propto \frac{\eta_b^{RF}}{\varepsilon_{ny}^{*1/2}} \text{ and } M = L\frac{U_f^{1/2}}{\delta_B^{3/2}P_{AC}} \propto \frac{\eta_b^{RF}}{\sigma_z^{1/2}\varepsilon_{ny}^{*1/2}} \quad (4)$$

The TLC design optimisation consists of selecting beam parameters, and choosing a technology that is able to accelerate, at a reasonable cost, a high power beam with an optimum AC-power to beam-power conversion efficiency (Sections 3 and 4) while preserving a very small vertical normalised beam emittance (Section 5).

3 RF POWER TO BEAM EFFICIENCY

The RF-to-beam conversion efficiency is directly related to the choice of the RF frequency and the beam parameters. In order to obtain a high RF-to-beam transfer efficiency, all TLC designs (except VLEPP) have chosen to operate with a large number of bunches. In the extreme case of an infinite number of bunches, the formulation of the RF to beam efficiency becomes extremely simple [2] with a dependency on only two parameters: the field attenuation constant of the structures, τ, and the normalised beam current, J:

$$\eta_b^{RF} = \frac{2\tau g(\tau) J}{\left[1+\frac{J}{2}\left(1-\frac{e^{-2\tau}}{g(\tau)}\right)\right]^2} \qquad (5)$$

where $$J = \frac{R' q_b}{G_a \Delta_b} = \frac{R' I_b}{G_a} \qquad (6)$$

and R', I_b, q_b, Δ_b, G_u, G_a are respectively the shunt impedance per meter, the beam current, the charge per bunch, the interval between bunches, the unloaded and loaded accelerating gradient. For a given J, there is a value τ_{opt} which maximises the RF to beam efficiency:

$$\tau_{opt} = \frac{G_u \Delta_b}{R' q_b} = \frac{1}{J(1-\delta)} \qquad (7)$$

Using accelerating structures with an optimum field attenuation, τ_{opt}, following equation (7), and for the more usual range of beam parameters, $0.5 \le J \le 2$, where the beam loading parameter δ is limited to 50% (Fig. 1), the scaling of η^{RF}_b and τ_{opt} is approximated by:

$$\eta_b^{RF} \propto (J)^{1/2} = \left(\frac{R' q_b}{G_a \Delta_b}\right)^{1/2} \quad \text{and} \quad \tau_{opt} \propto J^{-9/10} \qquad (8)$$

Here, $\propto$ is the approximate proportionality implied by the straight line fit in Fig. 1 over the range of parameters considered. The figure of merit then becomes:

$$M \propto \frac{\eta_b^{RF}}{\varepsilon_{ny}^{*1/2}} \propto \left(\frac{J}{\varepsilon_{ny}^{*}}\right)^{1/2} = \left(\frac{R' q_b}{\varepsilon_{ny}^{*} G_a \Delta_b}\right)^{1/2} \qquad (9)$$

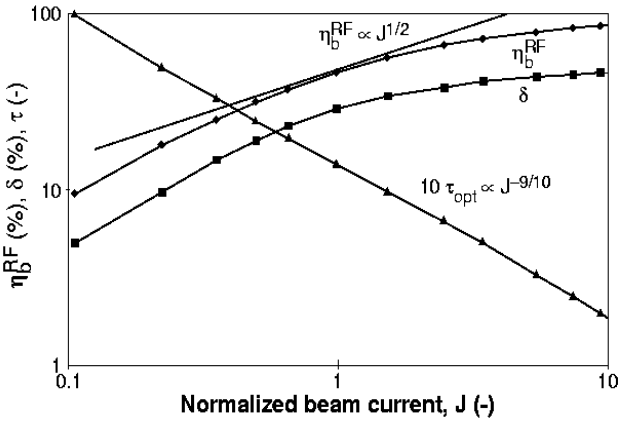

Figure 1: Optimum RF to beam efficiency, η^{RF}_b, field attenuation, τ, and beam loading parameter, δ.

4 THE NORMALIZED BEAM CURRENT

To optimise the design of a linear collider, the beam and linac parameters are therefore chosen to maximise the J parameter while preserving the initial vertical normalised beam emittance. All four parameters in the expression for J, (eq. 6) are directly related to the RF frequency, ω, of the accelerating structures. This is why the different TLC designs are mostly frequency driven.

- The well known scaling with frequency of R', when taking into account the iris to wave-length ratio, a/λ, is well verified in the TLC designs (Fig.2):

$$R' = r'Q \propto \omega^{1/2} (a/\lambda)^{-1} \qquad (10)$$

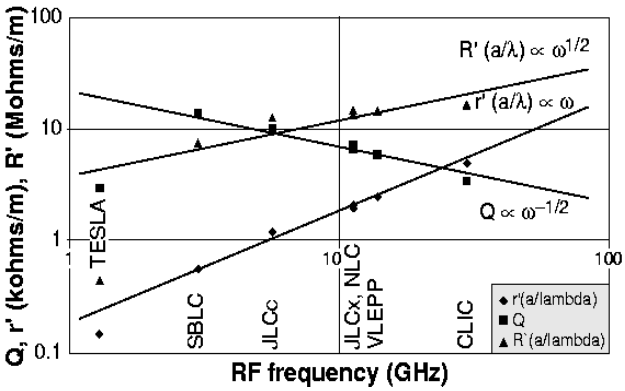

Figure 2: Accelerating structure parameters.

- The minimum distance between bunches is limited by the transverse wakefield level that can be obtained at the second and subsequent bunches by damping and/or detuning. For a given type of structure the number of RF periods needed for the same relative wakefield reduction is constant. This is reflected in Fig. 3 which shows that in spite of the different structure designs, the distance between bunches adopted in the various TLC designs scales with the RF wavelength:

$$\Delta_b \propto \omega^{-1} \qquad (11)$$

The J parameter then becomes:

$$J = \frac{R' q_b}{G_a \Delta_b} \propto \omega^{3/2} (a/\lambda)^{-1} G_a^{-1} N_b \qquad (12)$$

The charge per bunch is therefore made as high as possible to maximise J. Its maximum value is limited by beam stability considerations as developed in section 5.

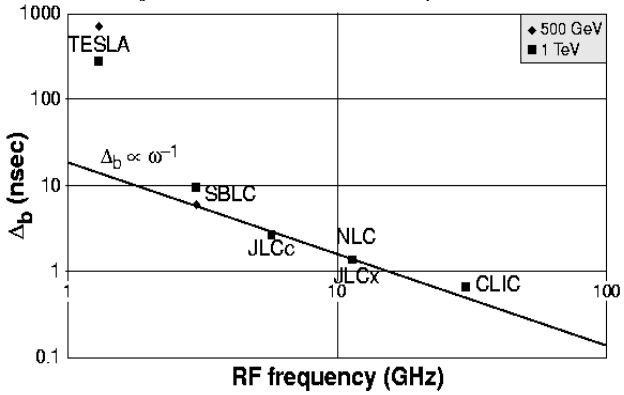

Figure 3: Time interval between bunches.

5 BEAM EMITTANCE PRESERVATION

Very small vertical normalised beam emittances of a few 10^{-8} rad-m are expected from state-of-the-art damping rings presently under development. During acceleration along the several-kilometer-long linacs however, the beams suffer a transverse blow-up $\Delta\varepsilon_n$, which is especially important in the vertical plane because of the particularly small initial emittance. One of the primary causes of emittance blow-up comes from the transverse wake-fields induced by the misalignment of the accelerating structures and by the beam trajectory deviations.

5.1 BNS damping

The single-bunch beam stability is greatly improved by so-called BNS damping [4] using a correlated energy spread which is introduced along the bunch such that:

$$\Delta p / p = \delta_{BNS} \propto N_b \langle W_T \rangle \frac{\langle \beta \rangle \langle L_{CELL} \rangle}{U} \qquad (13)$$

where $<\beta>$ is the mean betatron amplitude of the focusing optics along the linac, and W_T is the short range transverse wakefield averaged over the bunch with an r.m.s. length, σ_z, and scaling as:

$$\langle W_T \rangle \propto W_T' \sigma_z \propto \omega^4 (a/\lambda)^{-7/2} \sigma_z \qquad (14)$$

Under BNS damping conditions when taking into account equation (14), the vertical blow-up induced by the transverse wake-fields [5] shows a strong dependence (to the eighth power) on the frequency:

$$\left(\Delta\varepsilon_{ny}\right)_{RF} \propto N_b^2 \sigma_z^2 (a/\lambda)^{-7} \omega^8 G_a^{-1} \langle \beta_0 \rangle L_s \left\langle \Delta y_{RF}^2 \right\rangle \qquad (15)$$

but the other parameters in equation (15) also scale strongly with the frequency as shown hereafter.

5.2 Bunch length

The bunch length, σ_z, is made as small as possible in order to decrease the average transverse wakefield in the bunch according to equation (14). However, the minimum acceptable bunch length is determined by the need to compensate, towards the end of the linac, the energy spread associated with the longitudinal wake-fields, by positioning the bunch off the crest of the accelerating RF wave. Thus:

$$\frac{N_b W_L}{G_a} \propto \sigma_z \omega \sin(\Phi_{RF}) \Rightarrow \sigma_z \propto N_b G_a^{-1} (a/\lambda)^{-2} \omega \qquad (16)$$

where W_L is the short range longitudinal wakefield and Φ_{RF} is the off-crest RF phase which is limited to small values for the sake of beam acceleration efficiency.

5.3 Ratio of iris radius to RF wavelength

As shown in Fig. 4 for the different TLC designs, the ratio of iris radius to RF wavelength, a/λ, increases with increasing frequency in order to minimise the effect of the transverse wakefields (equation 14):

$$a/\lambda \propto \omega^{1/5} \qquad (17)$$

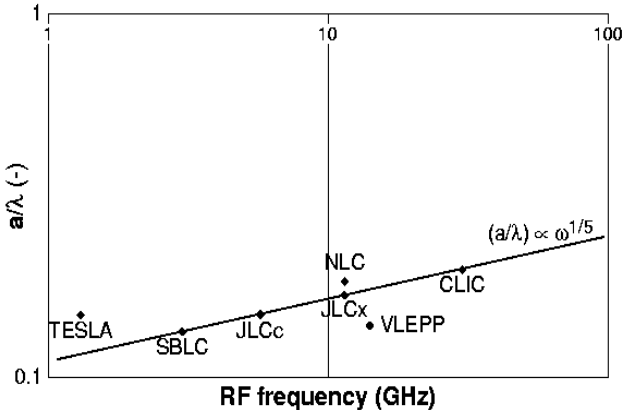

Figure 4: Iris to wavelength ratio.

5.4 Focusing optics of the linacs

In order to limit the BNS momentum spread needed for beam stability (eq. 13), the focusing strength along the linac is usually increased with the operating frequency as shown in Fig. 5. This is possible at higher frequencies because of the reduction in size of the linac components. Assuming the inner diameter, *D*, of the quadrupoles is scaled inversely with frequency in the same way as the inner radius of the iris, a, of the RF structures, then for the same magnetic field on the poles, *B*, the same phase advance per cell, β_0, and the same quadrupole filling factor, *F*, the FODO cell length, L_{cell}, scales as follows:

$$L_{cell} \propto \frac{D}{F L_{cell} B} \Rightarrow \langle \beta_o \rangle \propto L_{ocell} \propto (a/\lambda)^{1/2} \omega^{-1/2}$$

5.5 Pre-Alignment tolerances of the RF structures

Since the size of the accelerating structures becomes smaller with increasing frequency, the accuracy with which they can be made and pre-aligned is expected to approximately scale with the inverse of the frequency. As seen in Fig. 6, the variation of the pre-alignment tolerances of the RF structures in all TLC designs is well approximated by the following scaling law with frequency, which indeed is very close to expectation:

$$\langle \Delta y_{RF} \rangle \propto \omega^{-3/4} \qquad (19)$$

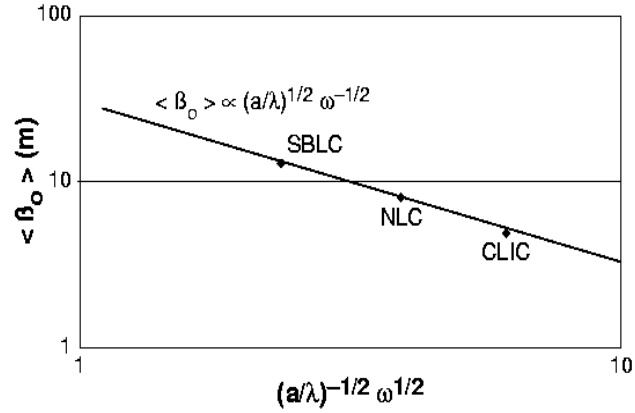

Figure 5: Focusing optics at injection into the linac.

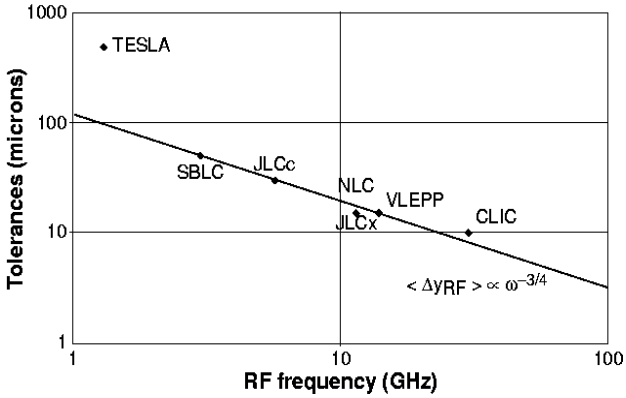

Figure 6: Pre-alignment tolerances of RF structures.

5.6 Accelerating section length

The length of the accelerating section, L_s, is adjusted to obtain an optimum field attenuation parameter, τ_{opt}, to maximise the RF-to-beam efficiency (equation 7)

$$L_S = \frac{2Qv_g\tau_{opt}}{\omega} = \frac{2Qv_g}{\omega J(1-\delta)} \qquad (20)$$

Neglecting the variation of the beam loading parameter δ, for small δ values, and introducing the scaling for J (eq. 6) as well as of the quality factor Q and the group velocity v_g, the optimum length of the accelerating sections, in the extreme case of an infinite number of bunches, becomes:

$$L_S \propto \omega^{-3}(a/\lambda)^4 G_a N_b^{-1} \qquad (21)$$

5.7 Charge per bunch

Finally, it is possible to derive the scaling of the maximum charge per bunch. This is the charge which produces a tolerable and frequency-independent beam blow-up during acceleration. It is deduced by substituting the relations for the scaling of all the different parameters (eq. 16, 17, 18, 19 and 21) in eq. 15.

$$\left(\Delta\varepsilon_{ny}\right)_{RF} \cong Const. \Rightarrow$$

$$N_b \propto \omega^{-5/3}(a/\lambda)^{13/6} G_a^{2/3} \propto \omega^{-6/5} G_a^{2/3} \qquad (22)$$

After substitution of eq. 22 for N_b in eq. 13, 16, and 21, σ_z, L_s, and δ_{BNS} become:

$$\sigma_z \propto \omega^{-2/3}(a/\lambda)^{1/6} G_a^{-1/3} \propto \omega^{-2/3} G_a^{-1/3} \qquad (23)$$

$$L_S = \frac{2Qv_g\tau_{opt}}{\omega} \propto \omega^{-4/3}(a/\lambda)^{11/6} G_a^{1/3} \propto \omega^{-1} G_a^{1/3} \qquad (24)$$

$$\delta_{BNS} \propto \omega^{2/3}(a/\lambda)^{-1/6} G_a^{1/3} \propto \omega^{2/3} G_a^{1/3} \qquad (25)$$

As shown in Figs 7, 8, 9 and 10, the charge per bunch, the bunch length, the length of the accelerating structure and the theoretical momentum spread for BNS damping adopted in the TLC designs compare favourably with the above scaling laws.

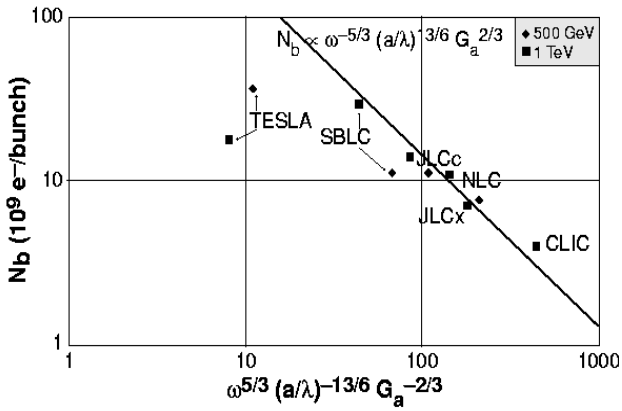

Figure 7: Charge per bunch.

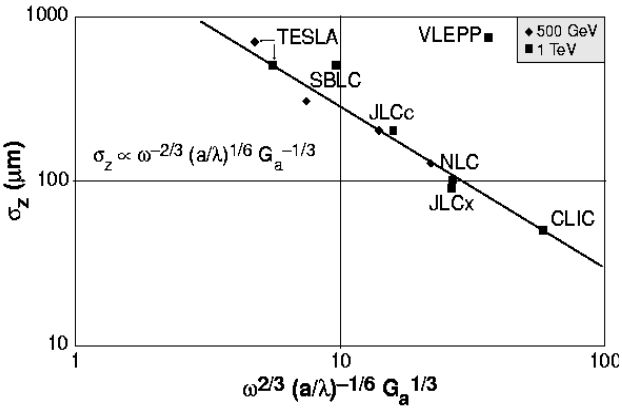

Figure 8: Bunch length.

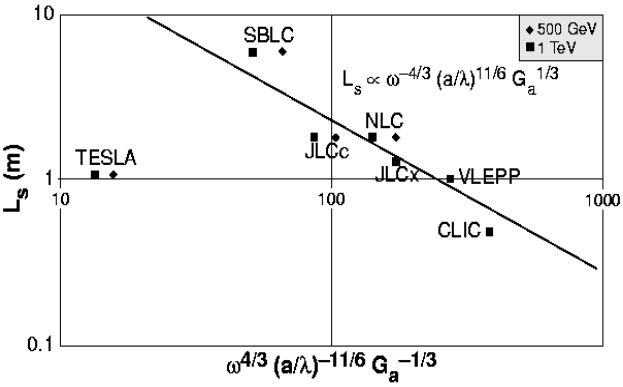

Figure 9: Length of the accelerating structures.

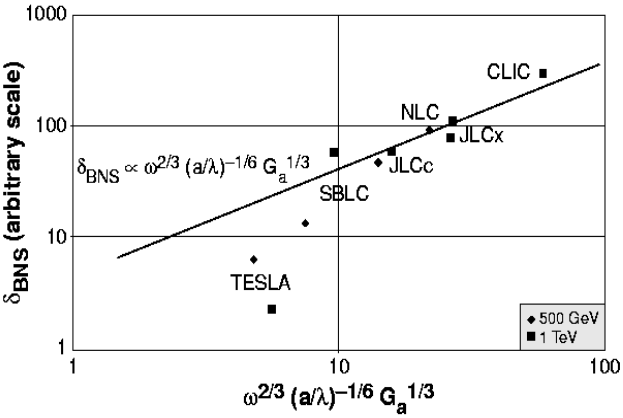

Figure 10: Momentum spread for BNS damping.

The strong dependence on frequency of the vertical blow-up induced by transverse wakefields is therefore cancelled by an appropriate choice of the other parameters and reduced to an acceptable level in all the TLC designs, independently of the RF frequency:

$$\varepsilon_{ny}^{*} \propto \varepsilon_{ny} = \varepsilon_{nyo} + \Delta\varepsilon_{ny} \quad \text{with} \quad \Delta\varepsilon_{ny} \cong Const. \qquad (26)$$

There is also a contribution [5] to $\Delta\varepsilon$ coming from the beam position monitor (BPM) misalignments. The same condition (26) on the emittance growth produces for Δy_{BPM} the generally expected dependence with ω^{-1} (Section 5.5),

$$\langle \Delta y_{BPM} \rangle \propto \omega^{-1/4} G_a^{1/6} \langle \Delta y_{RF} \rangle \propto \omega^{-1} G_a^{1/6} \qquad (27)$$

Finally, by introducing the frequency laws obtained up to this point, the normalised beam current and the RF-to-beam efficiency become roughly independent of the RF frequency and accelerating gradient,

$$\eta_b^{RF} \propto J^{1/2} \propto \omega^{-1/12} (a/\lambda)^{7/12} G_a^{-1/6} \propto \omega^{1/30} G_a^{-1/6} \qquad (28)$$

6 SENSITIVITY TO GROUND MOTION

The slow ground motion, modelled by the standard ATL law [6], causes all linac components to move with time. If uncorrected, the resulting trajectory variation will lead to emittance dilution [7]. The dominant effect comes from the quadrupoles with a contribution

$$\Delta\varepsilon_{nQUAD} \propto ATN_{cell}^3 \delta_{BNS}^2 \qquad (29)$$

where N_{cell} is the number of focusing cells in the linac, which is proportional to L_{cell} and G_a. Thus, using the above scaling laws, the time interval required between corrections to limit the emittance growth is

$$T_{QUAD} \propto \frac{G_a^{7/3} \varepsilon_{ny}}{A\omega^{5/2}} \left(\frac{\Delta\varepsilon_{ny}}{\varepsilon_{ny}} \right)_{ATL} \qquad (30)$$

The equivalent time interval related to cavity drift shows a similar dependence $\propto G_a^{1/3} \omega^{-5/3}$. Finally, the high frequency vibration of the focusing magnets induces a pulse-to-pulse trajectory variation which cannot be corrected with beam-based feedbacks. In local beam-size units, this induced beam jitter is [5]:

$$\frac{\langle \Delta y^2 \rangle}{\sigma_y^2} \approx \langle y_{QUAD}^2 \rangle \frac{4U_0 N_{CELL}}{\varepsilon_{ny} L_{oCELL}} \left(\frac{U_f}{U_o} \right)^{(1-\alpha)} \tan\left(\frac{\Psi}{2} \right) \qquad (31)$$

where y_{QUAD} is the focusing magnet movement. As a consequence, the vibration tolerance scales as:

$$\langle y_{QUAD}^2 \rangle \propto \frac{\langle \Delta y^2 \rangle}{\sigma_y^2} \frac{G_a}{\omega^{2/3}} \varepsilon_{ny} \qquad (32)$$

7 CONCLUSION

The figure of merit *M*, defined in Section 2, has been used to optimise the design of a future TeV e^+e^- Linear Collider. ***M is only dependent on two parameters: the AC-to-beam power transfer efficiency and the vertical beam emittance at the IP.*** Scaling laws have been derived for both the linac and beam parameters for an infinite number of bunches, stable beam operation and minimum energy spread at the linac end. Under these conditions, the main beam parameters are fully determined. Using them, and choosing an optimum field attenuation for the RF structures in order to obtain an optimum RF-to-beam efficiency, it is found that:

- ***The RF-to-beam efficiency is a weak function of the frequency and accelerating gradient*** (Eq.28)
- In spite of the large increase of the wake-field amplitude with frequency, ***the wakefield effect and the corresponding beam emittance blow-up are independent of the RF frequency*** (Eq. 26), ***for equivalent beam trajectory correction techniques.***
- ***In the low-beamstrahlung regime,*** generally adopted for intermediate-energy TLC designs (0.5 to 2 TeV), ***the luminosity slightly increases with RF frequency and slightly decreases with accelerating gradient***

$$L \propto \frac{\delta_B^{1/2} \eta_{RF}^{AC}}{U_f} \frac{\omega^{1/30} G_a^{-1/6}}{\varepsilon_{nyo}^{1/3} \left[1 + \Delta\varepsilon_{ny}/\varepsilon_{nyo} \right]^{1/2}} P_{AC}$$

- ***In the high-beamstrahlung regime,*** usually adopted for high-energy TLC designs (3 to 5 TeV), ***the luminosity increases with RF frequency but is independent of accelerating gradient***

$$L \propto \frac{\delta_B^{3/2}}{U_f^{1/2}} \frac{\eta_{RF}^{AC}}{\beta_y^{*1/2}} \frac{\omega^{1/3}}{\varepsilon_{nyo}^{1/2} \left[1 + \Delta\varepsilon_{ny}/\varepsilon_{nyo} \right]^{1/2}} P_{AC}$$

Finally, the use of high frequencies in accelerating structures for main linacs of future TeV e^+e^- Linear Colliders is particularly appropriate, since they allow operation with high accelerating gradients, which minimise the overall length and therefore the cost of the linacs. Provided that the beam and linac parameters are chosen to fulfil beam stability criteria and optimum RF-to-beam transfer efficiency, high frequency designs benefiting from high accelerating gradients result, when compared to lower frequency designs with lower gradient and similar beam quality, with the same or better RF efficiency and figure of merit.

8 REFERENCES

[1] Int. Linear Collider Technical Review Committee Report, ed. G. Loew, SLAC-R-95-471, 1995.

[2] J.P. Delahaye *and 3 co-authors,* CERN/PS/97-51, 1997 and CLIC Note 333.

[3] J.P.Delahaye *and 6 co-authors,* Proc. PAC97, Vancouver, Canada, and CERN/PS 97-23, 1997.

[4] V.E. Balakin, *and 3 co-authors,* Proc. 12th Int. Conf. On High Energy Accelerators, Fermilab, 1983.

[5] T.O. Raubenheimer, CLIC Note 347, 1997.

[6] B. Baklakhov, *and 5 co-authors,* INP 91-15; Tech. Ph.38, 984, 1993.

[7] A. Sery and O. Napoly, Phys. Rev. E 53, 5323 ,1996.

AN INDUCTION LINAC FOR THE SECOND PHASE OF DARHT

H. L. Rutkowski
Lawrence Berkeley National Laboratory
One Cyclotron Road, Berkeley, CA 94720, USA

Abstract

The Dual Axis Radiographic Hydrodynamics Test facility (DARHT) is under construction at Los Alamos National Laboratory. The facility will contain two electron accelerators arranged perpendicular to each other. The second accelerator is a long pulse induction linac using Metglas core technology and will provide a beam pulse at 20MeV with flat top current of 4KA. The focal spot should be less than 1.2mm in diameter. Generation of beam breakup (BBU) and corkscrew motion at the focal spot must be minimal. Very flat beam energy, excellent alignment of transport magnets, and low values for TM mode impedances in the accelerator cavities are needed. The accelerator will consist of a diode injector using a dispenser cathode, providing 3.2MeV energy together with a linac with 88 acceleration cells. Marx generators will provide pulsed power for both injector and linac. The pulse will be transported to a kicker (designed by Lawrence Livermore National Laboratory) which selects four 60ns pulses for transport to the final focus and the conversion target. The status of the design of the accelerator system will be presented along with results from prototype tests. Effect of operational requirements on the design of the accelerator will also be discussed.

1 INTRODUCTION

The accelerator for the second axis of the DARHT facility is a long pulse induction linear accelerator that provides an electron beam that will be used to produce a series of fast high energy X-ray pulses. The fast electron beam pulses, nominally 60 ns in duration, will be chopped out of a 2 μs single pulse and will be transported to a set of X-ray conversion targets. The X-rays will be used to image dense metal objects driven by high explosives. Initially four short pulses are required from the machine though the system could be upgraded to use the remaining part of the long pulse to provide additional views or more time resolution. Lawrence Livermore National Laboratory has the responsibility for the system from the point where the beam exits the accelerator up to the final focus on the X-ray conversion target or targets. The subject of this paper is the injector, accelerator and pulsed power systems that are being designed and built by Lawrence Berkeley National Laboratory.

* This work was supported by the U.S. Department of Energy under Contract No. DE-ACO3-76SF00098.

The injector is a dispenser cathode diode driven by a long pulse Marx generator at 3.2 MV peak flat voltage. The injector beam pulse enters a first cell block of 8 large bore induction cells that accelerate it to 4.6 MeV energy. The rest of the accelerator consists of 10 cell blocks of 8 cells each that accelerate the beam to the full 20 MeV energy. The exit current is 4kA maximum for 2μs. Between each cell block, an intercell provides a pumping point and a station for inserting diagnostics. The entire system is 175 ft. long, from the injector to accelerator exit. The induction cells use Metglas as the ferromagnetic material. The first cell block has a 14" diameter beam pipe while the bulk of the cells have a 10" beam pipe. This is to reduce generation of BBU in the front end. The system is presently in the design stage with prototyping work supporting the design. The injector design is fairly detailed and two options exist for the design of the accelerator cells. A concept of the accelerator sitting inside the building is shown in Fig. 1. The downstream transport and chopper are also shown. The pulsed power units are in an adjacent hall not shown.

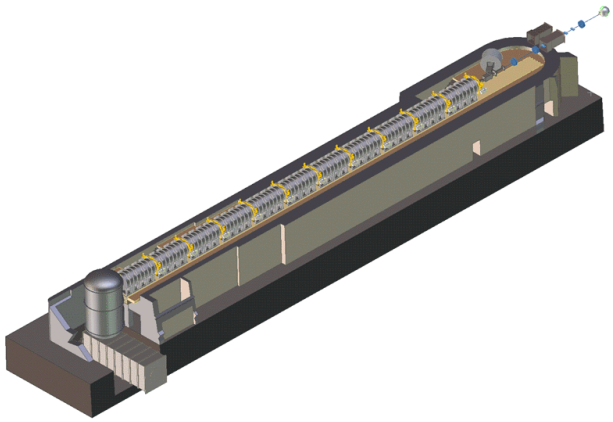

Fig. 1 Accelerator in Second Axis Building

2 INJECTOR

The injector is shown in Fig. 2 together with its first block of 8 cells. The first block of 8 cells is included here because the physics design of these cells is intimately connected with the injector design.

The injector itself is a simple diode designed for rapid acceleration of the electrons emitted by the cathode to 3.2 MeV in order to minimize emittance growth at the start. The emittance required at the final focus at the X-ray converter target is 1500 π mm-mrad normalized. This emittance limit is derived from the 1.2mm focal spot desired at the converter. This spot size is in turn required by the spatial resolution desired in the radiographs. The

required maximum flat current is 4 kA for 2.1 μs. However, the current must also be adjustable to allow for operation of the accelerator down to 1 kA to accommodate various commissioning and operational modes. There are a few options for achieving this such as changing cathodes and reducing voltage. The power supply for the diode is a Marx generator being designed by Pulse Sciences Inc. The Marx must provide matched voltage pulses of up to 3.5 MV to the combination diode and ballast resistor load with a flatness of ± 0.5%. The dielectric for the high voltage system is oil and it is being designed to survive a variety of failure modes. The maximum rep rate is 5 shots per minute. The insulator column itself is made of glued Mycalex sections with resistive grading and MOV's for damage protection. The injector is still being designed with fabrication to begin in October 1998.

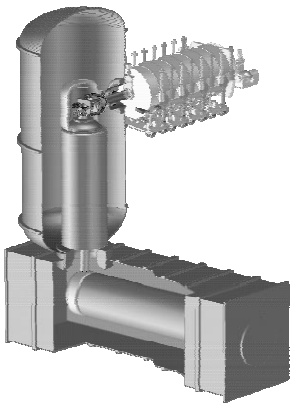

Fig. 2 Injector and First Cell Block

A more detailed drawing of the diode itself is shown in Fig. 3. The cathode is a type M dispenser cathode (8" diameter) which can deliver up to 20 A/cm^2 in a space charge limited mode. The operating temperature will be 1050°C with a uniformity of ±1% across the face. The cathode shroud is partially water cooled near the source and will be made of optically polished molybdenum, stainless steel, or coated stainless steel. Small scale tests on breakdown in vacuum are being carried out on these materials and molybdenum appears to be the best choice so far. However, full size shrouds using all three materials will be tested in the injector. The peak enhanced field stress on the cathode shroud is 162 kV/cm. The shroud material must not only be good to this level of enhanced stress but it must also survive in case of breakdown. Comparison with other machines and the test results so far indicate that the configuration can be made to work at this stress. The plate on which the cathode mounts is attached to a hexapod mounting system that is moved for alignment by six pressure activators. A bucking solenoid can be seen inside this mount in Fig. 3. This solenoid serves to cancel the field at the cathode caused by the focusing solenoids located inside the anode surface. The anode itself is stainless steel and the diode gap is 30cm. As can be seen in Fig. 2, the main current feed from the Marx makes a right angle bend. The vertical part of the feed is 1.5m behind the cathode face. This current feed geometry results in a dipole error field of 3-5 gauss in the diode gap. A quadrupole error field also exists. Correcting coils for these fields are being designed. The sextupole field which could increase emittance was shown to be negligible in calculation as were all higher order fields. A gate valve isolates the diode from the accelerator.

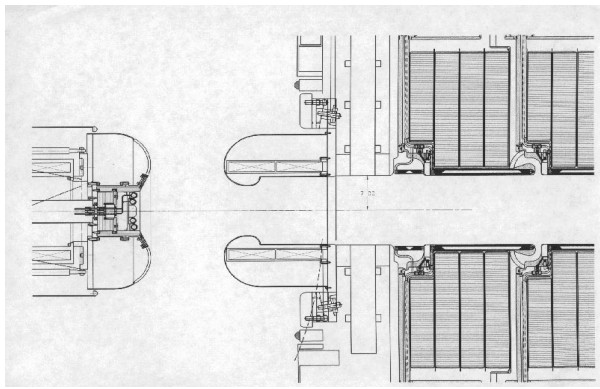

Fig. 3 Diode and First Cells

The rise time of the injector is required to be less than 400 ns and the design point is 200 ns. The fall time is planned to be 100 ns with use of a laser triggered crowbar. The off energy particles produced in the rise and fall must be dumped in a non-destructive way. Conical scapers will be placed in the first 8 cells to remove these electrons. The design of the accelerator cells will be discussed below in the next section.

The insulator column in the injector is designed with a combination of Mycalex insulator rings and high purity aluminum oxide rings. The rings will be glued (Hyso 9359.3) with metal grading rings. The overall height is almost 13 ft. with grading rings and joints. The Mycalex rings were obtained from LANL where they were spares for the column of a decommissioned Van de Graaff accelerator. These rings are 47.5" outside diameter with 3" wall thickness. They offer very large cost savings over building a ceramic brazed column of the same size or a column made of new Mycalex. Mycalex which is a mica-glass mixture seems to be mechanically tougher than ceramic and to have very good breakdown resistance. The clear space inside the insulator column is 38" diameter after the grading resistors (liquid), metal oxide varistors (MOV's) for damage protection, and shock guard rings are in place. Shock guard rings are incorporated to shield the insulator material from any shock waves generated by a breakdown in the oil dielectric. Mycalex is expected to be more survivable than alumina with respect to such shocks.

The original dielectric choice of high pressure SF_6 was discarded for oil because of the fear of insulator catastrophic failure after the column aged and was subject

to damage from electrical breakdown. The injector pulse generator is an 88 stage PFN Marx. It can be used to drive different beam currents by varying the resistance of the liquid grading and ballast resistors. The entire high voltage system is being designed to 3.5 MV for safety factor. A laser triggered spark gap is included in the design to reduce unwanted beam in the pulse tail and to aid in shorting the pulse for lower pulse energy applications. The pulse can be shortened in six steps by shorting out PFN stages in the Marx. The design will accommodate diode impedances from 714Ω to open circuit (875Ω nom). A high voltage dome is located at the end of the Marx and contains a hydraulically driven motor generator that provides 15KW power to the cathode dome, power supplies, and diagnostic/controls units to bring information out to the cathode dome. Voltage flatness will be ± 0.5%. The injector Marx and all the accelerator pulsers are required to hold charge for up to one minute to accommodate firing site needs with no more than one failure in 20 attempts. This is an experimental diagnostic requirement. In the experimental shot firing mode the accelerator system cannot fail more than one shot in 600 where failure is defined as detonating the explosive without obtaining beam.

In addition to the design activity there are several testing activities underway. Materials for the cathode shroud are being tested at small scale for field emission threshold, breakdown, and breakdown dependence on vacuum. So far, optically polished Mo has shown the best results with a field emission threshold of 300 kV/cm (200 kV total voltage). Breakdown thresholds above 400 kV/cm have been shown for both Mo and uncoated stainless steel. The breakdown threshold doesn't seem to depend significantly on vacuum between 10^{-8} and 10^{-5} Torr. A scaled version of the injector gun is being set up on the Relativistic Two-beam accelerator (RTA) at LBNL. The RTA machine operates at 1MV total gun voltage, 1.2 kA maximum current, and 0.3 μs pulse length. This test with a 3.5" diameter dispenser cathode will test the beam optics and breakdown at full field stress, current density and in a space charge dominated regime. This scaled gun will be used to test diagnostics and to benchmark the EGUN, IVORY SLICE, and GYMNOS codes that are being used for design to ensure that correct emittances are being calculated. A cathode test stand and a Long Pulse Development Facility are being assembled at LANL to allow testing of full size cathodes and to perform beam tests of accelerator cells respectively. Once the parts for the full injector are ready, the entire system will be assembled and tested as a unit at an industrial location near LBNL prior to being sent to LANL for final commissioning.

Use of a dispenser cathode in the diode dictates an excellent vacuum system and clean servicing environment. The system design calls for three 16" cyro pumps. The design baseline pressure in the tank in 2×10^{-8} t. There is sufficient pumping to reach this pressure in less than 1 hour after roughing.

3 ACCELERATOR

The accelerator must take the 3.2 MeV injector beam up to 20 MeV while not growing the emittance by more than 1000 π mm-mrad normalized. The other major requirement is that the beam at exit cannot have transverse motion of its centroid greater than ± 10% of the beam radius due to all sources. This means both corkscrew and BBU motion. Corkscrew motion of the beam centroid arises because of the misalignment of solenoids in the transport line and energy variations during the beam pulse. BBU arises if transverse magnetic (TM) modes are excited in the accelerating cavities. Since these modes have axial E fields that change direction across the beam axis they can extract beam energy and put it into mode energy. The transverse B field of the mode creates a transverse kick in the beam. In order to reduce corkscrew motion the pulsers for the cells must generate voltage pulses that are flat to ± 0.5%. After the solenoids have been aligned mechanically as well as possible the corrector coils in each cell can be used together with a "Tuning-V" algorithm [1] developed by LLNL to reduce corkscrew motion to a minimum. The voltage for each cell is nominally 193 kV for the small bore cells and 168 kV for each of the first 8 cells. The first block of 8 cells (injector cells) is designed with a 14" beam pipe while the rest of the machine (generic cells) is designed with a 10" beam pipe. This was done because use of a larger bore at low energy reduces the transverse mode impedance in an area particularly susceptible to BBU growth. In a pillbox cavity design the transverse mode impedance scales as [2] w/b^2 where w is the gap and b is the beam pipe radius. Another way to reduce BBU generation besides increasing the pipe size is to increase the solenoid field. However, one cannot arbitrarily increase the transport solenoid field at low energy because it causes emittance growth. The original cell design for the entire accelerator is shown in Fig. 4a
The original 10" cell was designed with a conical section Mycalex insulator. Originally the insulator was to be Rexolite because of the favorable experience LANL has had with this material. However tests at LBNL indicated that it does not survive breakdown from microsecond scale pulses well even though it works very well in the regime below 100ns. Therefore Mycalex was chosen because of its mechanical toughness, good breakdown behavior, and good vacuum properties. A Rexolite insulator will however be tested in the prototype cell. A disadvantage of Mycalex is its high dielectric constant (6.9) which increases the transverse mode impedance of the cavity compared to a Rexolite insulated version. Calculations with AMOS for a cavity without Metglas gave values of 450 Ω/m for the dominant mode. Measurements have been done on a full scale cavity without Metglas and with a cast epoxy insulator of the same dielectric constant as Mycalex. The result for a damped cavity was 330 Ω/m for the dominant mode (TM110). This measurement technique which uses loops to drive modes selectively and probes inserted into the

cavity on axis to displace field gives a measurement of Z/Q through interpretation of the frequency shift of a mode due to the probe [3]. This measurement becomes more unreliable as the mode is increasingly damped. Since one wants to damp these modes as much as possible other methods must be used to get definitive results with strong damping. This original cell design is a shielded gap with peak field stress of 100 kV/cm on the negative electrode and 40 kV/cm on the insulator surface.

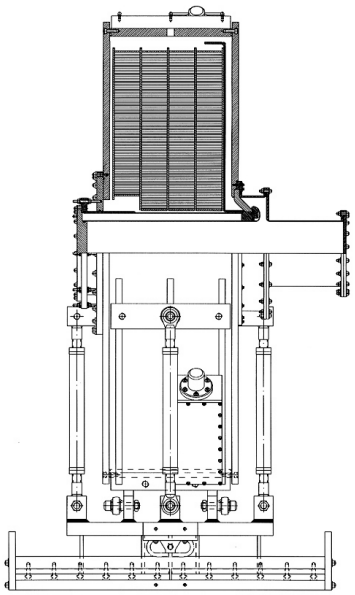

Fig. 4a Original Cell

The process of designing the special cells for the first block led to the design shown in Fig.4b. This design used a different insulator shape and created a space for diagnostics which were desired in the first cells because of the importance of beam motion at the beginning of the machine. Another reason for the change was to create a mode frequency shift between the two types of cells. This configuration will probably be used for the smaller bore cells as well because of the opportunity to place diagnostics anywhere and because of some mechanical design advantages. AMOS calculations give transverse mode impedances of 185 Ω/m at 170 MHz and 170 Ω/m at 450 MHz for this design with a Mycalex insulator and a 14" beam pipe. Applying the same configuration to the smaller bore cells gives 300 Ω/m at 200MHz and 310 Ω/m at 540 MHz. The mode frequencies are shifted between the first block and the rest of the machine which reduces BBU.

Corkscrew motion is combatted by generating flat voltage pulses in the pulsers which are E type Marx PFN's. The transport solenoid fields must also be well aligned to reduce corkscrew. LANL [4] experience in using the Stretched Wire Alignment Technique (SWAT) leads to the expectation of aligning the magnetic center of each solenoid to ± 0.1 mm and the tilt to ± 0.3 mrad. A precise calculation of the final corkscrew motion requires a final machine tune.

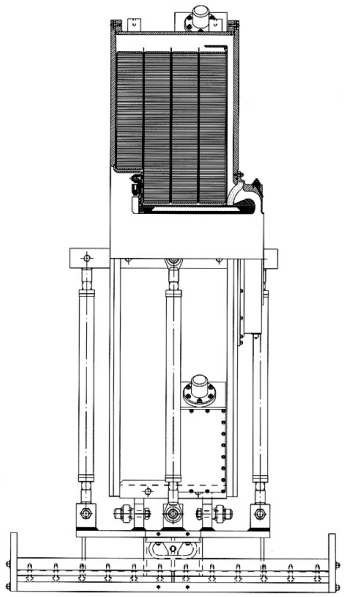

Fig. 4b Injector Cell

The transport solenoids in the generic cells are 12 layer fine wire solenoids 16" long impregnated with epoxy. The 8 injector cell solenoids are only 6 layers thick. The total power for running these solenoids plus the 5" long coils in the eleven intercells is 1.5 MW steady state if each solenoid is at maximum field (0.22T generic, 0.11T injector). The solenoids reside in cavities within the beam pipe and are DC, water cooled units. They float electrically from the machine. PC board type corrector coils are also placed between the solenoid and the pipe wall. An initial tune has been calculated for these solenoids and the beam envelope at exit is 1 cm diameter. Based on the use of the two pipe sizes in the machine, a BBU amplification relative to a straight pipe has been calculated. The values are 12.2 at 170 MHz, and 11.0 at 535 MHz. These numbers are based on a resonant seed at the exit of the injector at the relevant frequency. The amplification is the ratio between the displacement with cavity impedances present to displacement in the presence of continuous beam pipe with no cavities.

The intercells shown in Fig. 1 serve as pumping points with a turbo pump and a cryo pump at each intercell. Design vacuum in the accelerator is 10^{-6} t. The intercells also provide a place for intercepting diagnostics for beam profile and emittance measurement, B-dot loops for beam motion, and beam position monitors.

An important part of the pulsed power design is the Metglas core material. Allied Signal 2605 SC is the baseline design material because of its high ΔB of 2.8T with relatively low drive current. The magnetization current is relatively linear and the short pulse losses relatively low. 2605 SA1 has been tested at LBNL in the unannealed state and is just marginally acceptable. The

drive current is very non-linear and the ΔB is about 2.4T. Another candidate is Hitachi Finemet material if it can be obtained at an acceptable cost. The pulser used to drive both types of cells is an E-network Marx PFN. The pulser will feed to the cores at four points to eliminate production of quadrapole fields near the beam. The voltage pulse must be flat to ±.5%. The cell units will be mounted on rails. Removal of a cell requires removal of an intercell to create space for movement. The cells themselves will be capable of individual alignment using a differential screw system developed at the LBNL Advanced Light Source. Each cell weighs about 5 Tonnes. The differential screw system allows accurate movement of such massive structures to 0.001 inches manually. The cells will be vacuum sealed to each other with an inflatable bladder technique.

In addition to RF cavity tests mentioned above, two prototype cells are being constructed. The first uses the original cell design and will be used to measure damped transverse mode impedances and pulsed power tests of breakdown and core compensation. It has SA1 cores. This time Metglas will be in the cell and termination conditions at the outer radius will be realistic. The test cavity had a simple short at the outside. After the coupled loop-probe measurements are performed for comparison with the previous cavity measurements, breakdown tests with Rexolite, Mycalex, and cast epoxy will be performed and the core compensation will be optimized. Finally two wire [5] impedance measurements of the actual damped cell-cavity structure will be performed. The second prototype is a large bore unit that will have SC cores. It will be tested for pulsed power properties and then sent to LANL for beam spill tests. In 1999, 8 small bore cells will be put on the Long Pulse Development Facility at LANL to study beam effects in a full cell block before design of the generic cells is frozen for the large production phase.

ACKNOWLEDGEMENT

The author wishes to thank all the members of the LBNL-DARHT project team for their contributions especially D. Anderson, R. Briggs, E. Burgess, Y-J Chen, S. Eylon, W. Fawley, J. Fockler, E. Henestroza, T. Houck, T. Jackson, C. Peters, L. Reginato, M. Vella, and S. Yu.

REFERENCES

[1] Y-J Chen, Nuc. Inst. Meth. A398, p.139, 1997
[2] G. J. Caporaso, A.G. Cole, Proc. 1990 Linear Accelerator Conf., September 10-14, 1990, Albuquerque, p.281
[3] D. Birx, R. Briggs, T. Houck, L. Reginato, LBNL Eng. Note M7700, July 2, 1998.
[4] J. Melton, Private Communication
[5] L.S. Walling, D.E. McMurray, D.V. Neuffer, HA Thiessen, Nuc. Inst. Meth., A281, p. 433, 1989

HIGH-POWER PROTON LINAC FOR APT; STATUS OF DESIGN AND DEVELOPMENT

G. P. Lawrence
Los Alamos National Laboratory, Los Alamos, NM, 87545, USA

1 INTRODUCTION AND OVERVIEW

In one of two options being considered for a new source of tritium, the US Department of Energy (DOE) is planning an Accelerator Production of Tritium (APT) plant [1] that would be built at its Savannah River Site in South Carolina. The facility will employ a high power linear accelerator to produce neutrons by spallation reactions of protons in tungsten and lead contained in a target/blanket (T/B) assembly. The fast neutrons produced in the target are moderated in the light water that cools the blanket elements, and then captured by ^{3}He gas to produce tritium. The tritium is separated from the ^{3}He by permeation through a palladium membrane, with cryogenic distillation used for isotopic purification.

The APT design is based on a 1700-MeV proton linac operated at 100 mA CW. However, changing tritium requirements may reduce the energy to 1030 MeV, so the plant has been designed in a modular configuration to provide construction flexibility. Figure 1 shows the architecture of the modular plant. Heavy shading and lines indicate the 1030-MeV configuration; light shading and dashed lines show the portions added in a 1700-MeV system.

The project Conceptual Design Report [2] was issued in April, 1997, and formal design of the plant technical and conventional systems has now begun. A program of engineering development and demonstration (ED&D) has been underway since 1995 to support the plant design and subsequent construction.

2 ACCELERATOR DESIGN

The APT linac is designed as a two-stage machine [3], using both normal-conducting (NC) and superconducting (SC) accelerating-cavity technologies. Except for the first accelerating structure, a 350-MHz RFQ, the entire linac operates at a frequency of 700 MHz, with rf power supplied by 1-MW CW klystrons. After acceleration, a high-energy beam transport system (HEBT) consisting of magnetic focusing and bending elements conveys the beam to the T/B assembly. The architecture of the transport system depends on the machine energy, as indicated in Fig. 1. At the end of the HEBT, a raster beam expander transforms the beam into a rectangular, uniform large-area distribution, providing an acceptable power density in the target.

The linac design is driven strongly by the large amount of rf power required to accelerate the 100-mA CW beam. Efficient conversion is needed at each stage in the power train (from the ac grid to the beam) to minimize capital and operating costs. Other important design factors and considerations are the need to keep beam losses at a very low level, avoiding generation of beam halo, tight control of the high-power beam (in terms of the coupled beam/cavity/rf-drive interaction), current-independent operation and tuning, and high operational availability. Parameter selection and cost/performance modeling to achieve these objectives have been discussed previously [4]; key parameters are listed in Table 1.

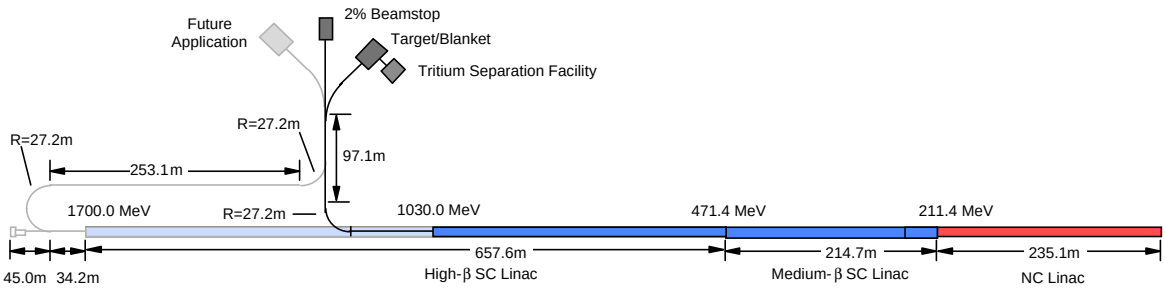

Fig.1 Modular design architecture for APT Plant.

2.1 Normal-Conducting Low-Energy Linac

The low-energy NC linac accelerates a 100-mA proton beam to 211.4 MeV in copper water-cooled structures. A 75-keV injector using a microwave-driven ion source produces a continuous 110-mA proton beam. From this input, a 350-MHz, 8-m-long RFQ (radio-frequency quadrupole) produces a CW 100-mA beam at 6.7 MeV. This RFQ is built in four resonantly-coupled segments, with rf drive provided by three 1.2-MW CW klystrons through 12 windows; it provides a current independent match into the next accelerating section.

Parameter	Normal-Conducting Linac			Superconducting Linac		
	RFQ	**CCDTL**	**CCL**	**β = 0.64-1**	**β = 0.64-2**	**β = 0.82**
Output energy (MeV)	6.7	96.6	211.4	242.0	471.4	1700 (1030)
Struct. gradient E_0T (MV/m)	1.38	2.04-1.68	1.68-1.82	4.3-4.5	4.3-5.0	5.25
Avg. gradient (MV/m)	1.38	0.77-1.12	1.12-1.22	1.21-1.54	1.21-1.54	2.05
Peak surface field (MV/m)				14.1-17.7	14.1-17.7	13.1-17.5
Quadrupole lattice period (m)		8-9 βλ	9 βλ	4.877	6.181	8.540
Section length (m)	8.0	112.8	110.4	29.3	185.4	657.6 (298.9)
Phase-adv./period (deg)	–	79-44	44-35	79-46	79-46	79-82
No. of quadrupoles	–	243	114	12	60	154 (70)
Quadrupole G•L prod. (T)		2.6-1.5	1.5-1.0	1.96 – 1.79	1.93 – 2.12	2.25 – 4.39
Synchronous phase (deg)	- 90 to -33	- 90 to -30	-30	- 30 to -35	- 30 to -42	-30
Shunt impedance (MΩ/m)	–	16-49	24-35			
Copper rf losses (MW)	1.26	5.0	6.8			
Power to beam (MW)	0.67	8.99	11.48	3.06	26.00	122.86 (55.86)
Power per klystron (MW)	0.77	0.80-0.84	0.81-0.84	512-560	765-840	798-840
Number of klystrons	3	17+6	24+5	6	30	154 (70)
Trans. emitt. (mm-mrad)*	0.16	0.17	0.17	0.16-0.19	0.16-0.19	0.19-0.17
Long. emitt. (MeV-deg)*	0.32	0.33	0.33	0.33-0.32	0.33-0.32	0.32-0.41
Aperture radius (mm)	2.3-3.4	10-17.4	17.4-31.9	65	65	80
Aperture/beamsize ratio	–	6.5-10	10-27	28-31	28-31	32-76

* Normalized rms values, 700 MHz. Quantities in parentheses are for a 1030-MeV output energy.

The RFQ is followed by π/2-mode coupled-cavity accelerating structures, each optimized for maximum rf-to-beam efficiency over a specific velocity range [5]. The first set of structures, which accelerates the beam to 96.6 MeV, is a 700-MHz CCDTL (coupled-cavity drift-tube linac) made up of 2-gap and 3-gap DTL cavities that are embedded in a FODO singlet focusing lattice. The latter begins with an 8-βλ period and transitions to a 9-βλ period at 10 MeV to provide additional space for quadrupoles and beam diagnostics. The quadrupoles are external to the cavity structures, separating the focusing and accelerating functions, and providing easy beam energy and is free from phase-space transitions after the RFQ. Beam dynamics analyses and simulations show these factors to be important in terms of minimizing core emittance growth [6] and the generation of beam halo [7]. As seen in Table 1, both transverse and longitudinal emittance growth are negligible. To obtain a current-independent match between the NC linac and the SC linac (which has weaker focusing), the quadrupole strength is reduced gradually as the transition energy is approached.

The CCDTL and CCL are sectioned into rf super-modules, which are each powered by 4 to 7 klystrons. Each klystron distributes power to the accelerating struct-

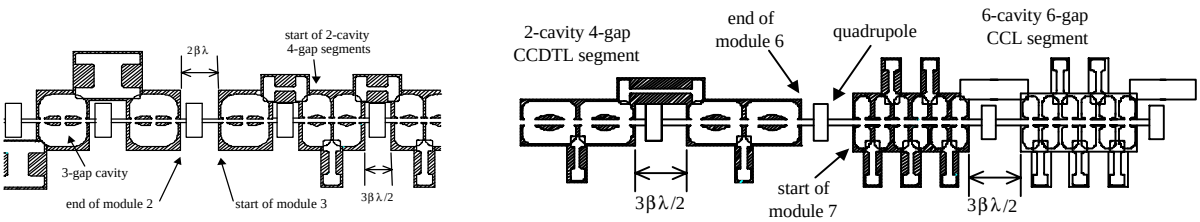

Fig. 2. CCDTL and CCL accelerating structure segments

alignment. Acceleration proceeds to 211.4 MeV in a 700-MHz side-coupled CCL that continues the 9-βλ focusing period. Fig. 2 displays representative segments of the CCDTL and CCL.

The NC linac has a short focusing period that elongates with beta, and the average accelerating gradient is ramped up gradually from 0.77 to 1.2 MV/m. The result is a linac that has strong focusing at low beam ure through four coaxial ceramic windows that are tested to 1-MW power levels [8]. The maximum rf power input to the cavities that is required from any of the klystrons is 0.84 MW, which allows for 10% control margin as well as rf transmission line losses. There are six supermodules in the CCDTL, with 28-57 segments per module. The CCL is divided into five supermodules, with 21-54 segments per module.

2.2 Superconducting High-Energy Linac

The SC high-energy linac consists of cryomodules containing two, three, or four 5-cell 700-MHz niobium SC accelerating cavities. Focusing is provided by NC quadrupoles in a doublet lattice located in the warm regions between cryomodules; these regions also contain the beam diagnostics. There are two kinds of SC cavity shapes, each type designed for efficient acceleration in a different velocity range. The cavity shape in the medium-beta section (211.4 MeV to 471.4 MeV) is optimized for $\beta = 0.64$, and in the high-beta section (471.4 MeV to 1700 MeV) for $\beta = 0.82$. The shapes are similar to the well-established elliptical designs for electron machines, but are compressed longitudinally in proportion to beta. Because the cavities are short and are driven independently, each section of the SC linac has a broad velocity bandwidth, which allows the gradient profile and output energy to be adjusted over a wide range. Because of the high beam current, the major design issue is not attainment of high cavity gradients, but high power rf coupler capability. Performance specifications of 140 kW and 210 kW have been chosen for the medium-β and high-β couplers respectively, values that are at the advancing edge of the demonstrated technology base. Each cavity is supplied by two antenna-type coaxial couplers mounted on opposite sides of the beam tube. Dual coaxial (warm) windows are planned, located so that they do not see the beam directly.

Figure 3 depicts the cryomodule, rf, and focusing-lattice architecture for the different sections of the SC linac. The high-β section contains 77 (35) of the four-cavity cryomodules shown in the right-hand sketch. Two 1-MW 700-MHz klystrons are used to power pairs of adjacent cavities. The nominal energy gain per cavity is 4.0 MeV. The medium-β SC linac is divided into two sections, both containing $\beta = 0.64$ cryomodules. The first section, starting at 211.4 MeV consists of six 2-cavity cromodules, and the second, starting at 242.0 MeV, consists of thirty 3-cavity cryomodules. Nominal energy gain per cavity is 2.6 MeV. The first section provides a transition between the short focusing period of the NC linac and the longer focusing period of the SC linac, and allows a current independent match to be obtained with minimal emittance growth.

The left-hand sketch in Fig. 3 shows the 3-cavity $\beta = 0.64$ cryomodules; the 2-cavity unit is not shown, but looks structurally like one-half of the high-β unit. Both are powered by a single 1-MW klystron. Earlier doublet-lattice medium-β linac designs with 2-cavity cryomodules attempted a configuration in which a klystron powered cavities in adjacent cryomodules. In beam simulations that included machine errors, it was found that this architecture gave rise to significant emittance growth because of the large cavity-to-cavity phase/energy errors that were introduced.

Table 1 lists key parameters of the SC linac. The selection of cavity gradients and numbers of cells per cavity were restricted by the need to keep peak surface fields below a safe level and by the power-coupler specifications. The rf power distribution is governed by the need to fully utilize the 840-kW power available from each 1-MW klystron. The design specification for the average cavity Q_0 is taken as 5×10^9. A 2.15 K operating temperature for the niobium cavities has been selected to minimize the static and rf heat loads to the LHe refrigerator and cryo-distribution system. Total cryoplant loads are estimated at 14.5 kW at 2.15K and 22.4 kW at 45K, for a 1700-MeV linac. These loads will be handled by three identical LHe refrigerators that are about 50% larger than those in service at CEBAF.

2.3 Beam Dynamics

The key beam dynamics [9] goal is to achieve very low losses (< 0.1 nA/m at 1700 MeV) in order to assure unrestricted hands on maintenance for the linac. This is provided by strong focusing at low energies and avoidance of phase-space mismatches, coupled with apertures that are much larger than the rms beam size, with the largest aper-tures at high energies where the activation threat is greatest. In the NC linac, the aperture increases in steps to 64 mm, while in the SC linac it jumps to 130 mm at 211.4 MeV, and then to 160 mm at 471.4 MeV. Figure 4 shows 100,000-particle beam simulations for both an error-free machine design, and for one with a set of randomly chosen imperfections, with magnitudes about a factor of two worse than typical errors expected in operation. The simulations compare the linac aperture dimension with both the rms beam size and the radius of the outermost particle in the distribution (the halo). At full energy, the aperture ratio (ratio of aperture to rms-beam-size) is close to 80, providing a very large clearance for the beam halo. At low energies,

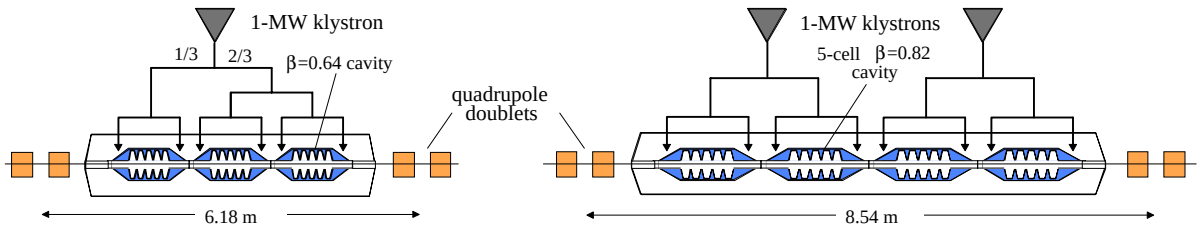

Fig. 3. Medium-β and high-β cryomodule and rf architecture in superconducting linac.

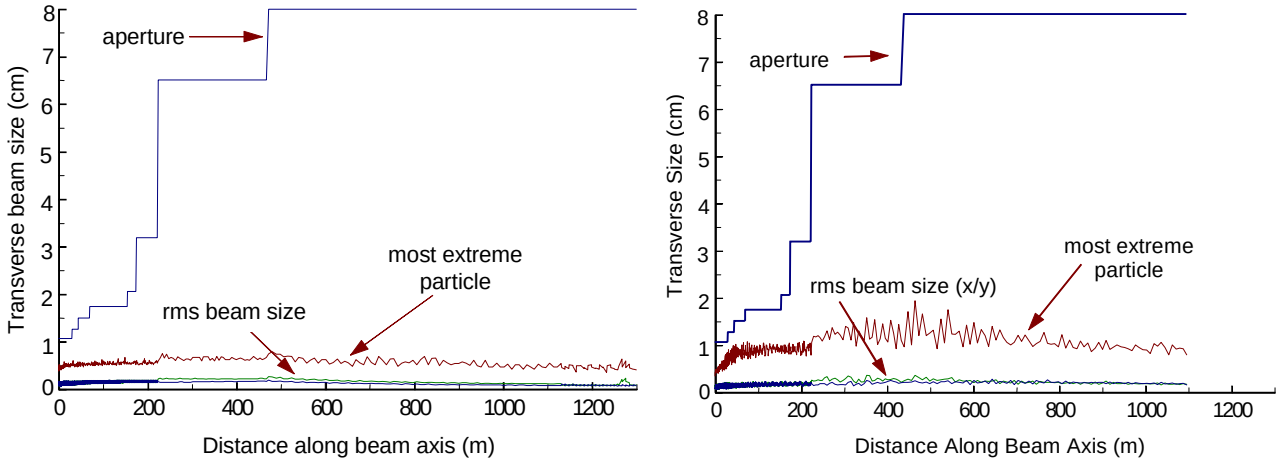

Fig. 4. Beam simulations for APT linac design showing rms beam size and radius of outermost particle, compared with aperture. Left: No machine errors. Right: Standard set of machine errors.

the clearance is less generous, and some small losses may occur.

2.4 Availability

Because the SC linac operates with short independently-driven accelerating cavities, the linac output energy may be adjusted over a wide range, providing considerable operational flexibility. Simulations confirm that, because of this feature, the SC linac is insensitive to a broad range of construction or operating errors and also can continue to function in a variety of off-normal conditions, such as having single klystrons, cavity pairs, and quadrupole pairs out of service. In order to meet the high annual availability goal for the accelerator (> 85%), redundancy schemes are used to provide excess rf drive in both the NC and SC linacs, but are implemented differently in each. The NC linac is divided into supermodules consisting of 100-150 coupled accelerating cells, with each unit supplied by n klystrons (typically 4 to 7), where only n-1 units are need-ed for operation. When an rf station fails, it is isolated by a waveguide switch and the accelerating structure drive iris is shorted. Power from the remaining klystrons is increased to compensate for the lost unit, and the supermodule continues to provide the full energy gain needed in that section. In the SC linac, redundancy is achieved by providing a modest level of reserve power in each rf station, above that needed to deliver the nominal output beam power, allowing increased energy gain in adjacent cryomodules to compensate for failed units. The power reserve is 5% in the high-β section and 9% in the medium-β section.

3 HIGH ENERGY BEAM TRANSPORT

A High Energy Beam Transport (HEBT) system [9] delivers the beam from the end of the linac to the (T/B). The HEBT focusing lattice continues the doublet-quadrupole optics in the high-β linac to a magnet switchyard. Here the beam is directed either to a tuning beamstop that can take up to 2% of the full-energy beam power, or into the beam line serving the T/B assembly. This beam line terminates in a raster beam expander, which converts the small-diameter Gaussian-like beam distribution into a large-area rectangular (19 cm wide x 190 cm high) uniform distribution at the target. The beam expander consists of two sets of four sweep magnets driven with triangular waveforms by IGBT modulators at frequencies close to 500 Hz. One set is for the horizontal-plane sweep, and the other for the vertical plane. Because the sweep frequencies are slightly different, the raster system paints the T/B uniformly once per 30 ms. A multiply-redundant modulator fault detector system protects the T/B from excess beam power density due to degradation or interruption of the sweep pattern. In the modular plant configuration, the T/B is located near the end of the 1030-MeV linac, following a 10-period drift and a 90-degree bend. If the linac is built to 1700 MeV, the beam returns to this target line through a transport system consisting of a 180-degree bend, a straight beam channel parallel to the linac, and a reverse 90-degree bend. Beam dynamics studies have shown that the insertion of these bends, which are first-order achromats, have essentially no effect on beam loss and on the beam performance on the target. They do, however, introduce some additional operational complexity.

4 ENGINEERING DEVELOPMENT AND DEMONSTRATION (ED&D)

The APT accelerator design is supported by a broad ED&D program that will demonstrate and prototype key components and systems. The program (Fig. 5) consists of 1) a Low-Energy Demonstration Accelerator (LEDA) that will prototype the APT linac front end up to 20 MeV, 2) development of high-β and medium-β SC-cavity and cryomodule prototypes, and several smaller programs. LEDA [10] will consist ultimately of a proton injector, a

6.7-MeV 350-MHz RFQ, and a 20-MeV CCDTL section. Its purpose is to confirm beam performance parameters, demonstrate integrated operation at full CW power, assess overall availability, and identify component failure modes. The major stages involve 1) construction and testing of a 75-keV, 110-mA proton injector; 2) addition of a 350-MHz RFQ to accelerate a 100-mA CW proton beam to 6.7 MeV; and 3) addition of a 700-MHz CCDTL to accelerate the beam to 20 MeV.

The LEDA injector has been built and successfully tested at APT performance specifications (110 mA H^+, <0.2 mm-mrad emittance). Construction and assembly of the RFQ is well advanced; the eight sections have been fabricated, and initial rf tuning of the whole structure is complete. The injector was recently successfully operated with a 1.25-MeV 267-MHz CW RFQ available from another program. Beam output current and transmission (100 mA, 85%) were as predicted, a strong validation of the codes used to design the APT RFQ.

A prototype of the highest-energy CCDTL segments (near 97 MeV) will be built and tested at full rf power to demonstrate RF coupling, manufacturability, and thermal performance of the section of the NC linac that is the most difficult to cool.

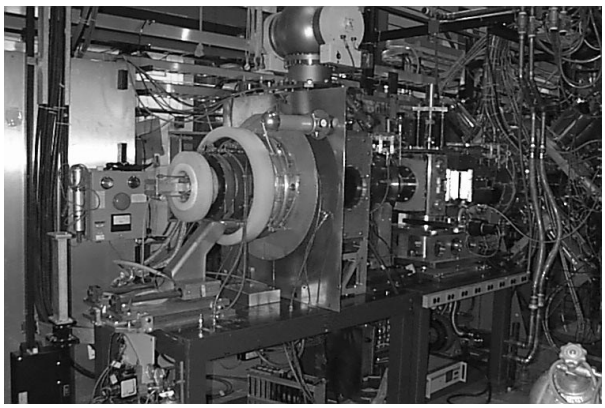

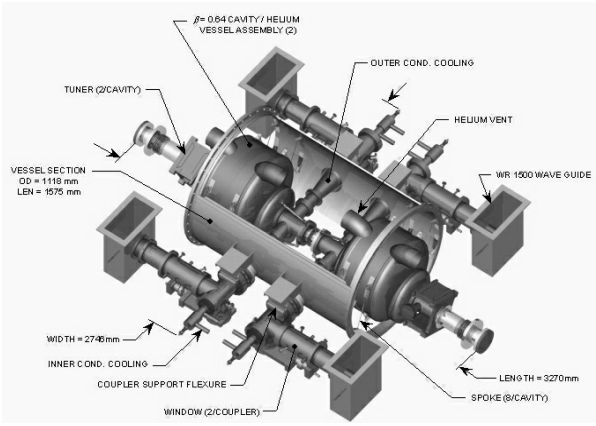

Fig. 5. ED&D program elements. Top: LEDA injector. Bottom: β = 0.64 2-cavity cryomodule.

The SCRF ED&D program [11] has as its basis the β = 1 cryomodules operating successfully in several electron accelerators. For the APT SC linac, it is necessary to develop cryomodule prototypes containing the lower-β cavity shapes needed for a proton accelerator. Development of these prototypes will confirm design parameters, component integration, and constructibility, and will support transfer of the technology to industry for manufacture of plant cyromodules. The elements of the SCRF program include: 1) fabrication and high-field testing of single-cell cavities; 2) evaluation of radiation damage to a prototype cavity; 3) fabrication and testing of high-power rf couplers; 4) fabrication and testing of multicell SC cavities; and 5) assembly and tests of complete prototype cryomodules. The first and second of these activities have already been successfully accomplished.

Other elements of the ED&D program include: 1) development of a prototype 1-MW 700-MHz High-Order-Mode Inductive-Output tube, which would offer improved efficiency and reliability (lower operating voltage) compared with a klystron, 2) construction and testing of a full scale raster beam expander prototype, 3) development and testing of high-power rf components (windows, waveguide valve, etc.), and 4) development of prototype diagnostics for measuring beam profiles at medium and high energies.

5 REFERENCES

[1] P.W. Lisowski, "The Accelerator Production of Tritium (APT) Project," Proc. 1997 Particle Accelerator Conf., Vancouver (May 1997).

[2] APT Conceptual Design Report, Los Alamos Report LA-UR-97-1329, April 15, 1997.

[3] G.P. Lawrence and T.P. Wangler, "Integrated Normal-Conducting/Superconducting High-Power Proton Linac for the APT Project," Proc. 1997 Particle Accelerator Conf., Vancouver (May 1997).

[4] G.P. Lawrence, et al., "Conventional and Superconduct-ing RF Linac Designs for the APT Project," Proc. 1996 Int. Linac Conf., Geneva, 710 (August 1996).

[5] J.H. Billen et al., "A Versatile High-Power Linac for Accelerator-Driven Transmutation Technologies, Proc. 1995 Particle Accelerator Conf., Dallas, IEEE No. 95CH35843, 1137 (1995).

[6] S. Nath, et al., "Beam Dynamics Design for the APT Integrated Linac," Proc. 1997 Particle Accelerator Conf., Vancouver (May 1997).

[7] T.P. Wangler, "New High Power Linacs and Beam Physics Issues," ibid.

[8] D. Rees, "Design of 250-MW CW RF System for APT," ibid.

[9] R.E. Shafer et al., "Overview of the APT High Energy Beam Transport and Beam Expanders," ibid.

[10] D. Schneider, "A Review of High Beam Current RFQ Accelerators and Funnels," Proc. 1998 European Particle Accelerator Conference, Stockholm (June, 1998).

[11] K.C.D. Chan et al., "Engineering Development of Super-conducting RF Linac for High-Power Applications," ibid.

HEAVY ION FUSION EXPERIMENTS AT LBNL AND LLNL*

Larry Ahle (presented for the groups at LBNL and LLNL)
Lawrence Livermore National Laboratory, Livermore, CA 94551 USA

Abstract

The long-range goal of the US Heavy Ion Fusion (HIF) program is to develop heavy ion accelerators capable of igniting inertial fusion targets to generate fusion energy for electrical power production. Accelerators for heavy ion fusion consist of several subsystems: ion sources, injectors, matching sections, combiners, induction acceleration sections with electric and magnetic focusing, beam compression and bending sections, and a final-focus system to focus the beams onto the target. We are currently assembling or performing experiments to address the physics of all these subsystems. This paper will discuss some of these experiments.

1 HEAVY ION FUSION DRIVER

In a heavy ion inertial power plant, particle beams are focused onto a target causing ignition. These targets consist of a hohlraum with a Beryllium (or other low Z ablator material) capsule inside. The capsule surrounds a frozen spherical shell of D-T, which is heated and compressed by X-rays created from the stopping of the ions in the holhraum. The accelerator will need to provide approximately 5-MJ of energy on a time scale of ~ 10-ns for ignition [1] and at a rate of ~5-Hz for a cost effective power plant [2]. Further, the range of the ion beams should be roughly 0.1-g/cm^2 which implies a total kinetic energy per beam particle of a few GeV.

The target specifications above are now based on sophisticated simulation validation and are generally demanding lower emittance beams than believed necessary a few years ago. There also appears to be a trade off between beam current and ion kinetic energy. Higher beam current implies a higher technical risk but the resulting lower energy may produce a cheaper power plant.

Current conceptual designs for a heavy ion fusion driver start with ~100 beam 2-MeV injector and ESQ matching section providing a initial pulse of 20-μs with approximately 1-A of current for each beam with radius of several centimeters. This is followed by an accelerator section. Whether the initial part of the accelerator is electrostatically focused, followed by beam merging, or magnetically focused is still being studied, but the end of the accelerator will be magnetic. The acceleration is accomplished through magnetic induction cores at the rate of 1-MV/m through most of the machine. The pulses on these induction cores are tilted to longitudinally compress the pulse from an initial length of ~30-m to ~10-m, which corresponds to a pulser duration of about 100-ns at the end of the accelerator. Following this is the drift compression, final focus, and target chamber section. The drift compression will do the final longitudinal compression to ~1-m in length. The final focus section will focus the beam to the target in the chamber reducing the radius of the beam to a few millimeters.

* Work supported by the US DOE under contract No. DE-AC03-76SF00098 (LBNL) and W-7405-ENG-48 (LLNL).

2 SOURCE AND INJECTOR

In developing sources and injectors for a driver, high current density is desired because it allows smaller and/or fewer beams and thus a cheaper injector. The current density is limited by voltage breakdown in the injector and transport limitations in the accelerator section and not by the emission limit of the source itself. Currently the design goal of an injector for a driver is many beam channels in one single vacuum chamber with a current density of 8-mA/cm^2 Cs equivalent.

2.1 Source Development

There are many possible types of ion sources for HIF, generally producing singly charged ions but higher charge states are also of interest in some driver designs. Surface ionization sources provide alkali metal ions, while a gas source is suitable for generating Hg, Xe, Ar and Ne ions, and a metal vapor vacuum arc source (MEVVA) would be more appropriate for ions such as Gd and Bi. Most HIF induction linac designs have used surface ionization sources because their performance already approaches the HIF requirements.

LBNL has been working with two types of surface ionization sources, contact ionizer and aluminosilicate. In a contact ionizer, alkali atoms are continuously fed to a heated surface, which ionizes the atoms. This type of source routinely produces low emittance and highly uniform beams. It also has the potential for a long lifetime source, but since alkali metal vapor deposits can deteriorate the high voltage property of accelerator components, it is important to minimize the cesium flow. In a recent experiment [3], the Cs^+ beam current from a 2-cm diameter contact ionizer was measured to be > 15-mA/cm^2 at 1145°C. In addition, the rate of the cesium neutral current evaporation was measured to be 1.7x10^{14}/cm^2/s or equivalently 0.14 mg/cm^2/hr. To test these sources in a real application, a Cs^+ contact ionizer will be installed in the scaled final focus experiment

described in section 4.2. This source will provide a factor of four increase in the current density and a more uniform beam.

For aluminosilicate sources, a layer of aluminosilicate doped with an alkali metal, is melted on a tungsten surface. This tungsten surface is then heated during operation. The neutral current for these sources should be lower than for the contact ionizer [4], but its lifetime for a driver before ion depletion is about one month [5]. Current densities of ≈15-mA/cm^2 of potassium, 7.9-mA/cm^2 Cs equivalent, have been achieved with a 2-cm aluminosilicate source [3]. For these sources to achieve uniform emission and high current density, a smooth layer must be melted on a large spherical area, which has proven to be a significant technical challenge. Recently, a different method to produce the aluminosilicate sources, in which a mixture of aluminosilicate and tungsten powder is sintered to form an emitter has been adopted [6].

2.2 2 MeV Injector

Based on ESQ beam transport considerations, a 2-MeV driver-scale injector should provide beams with a line charge density of approximately 0.25x10^{-6} C/m. A prototype injector, as shown in figure 1, was built for the Elise/ILSE project. It consists of a 17-cm diameter potassium aluminosilicate source as part of a 750-kV extraction diode which is in series with a 1250 kV ESQ accelerator. Both diode and ESQ are powered by a Marx Generator using a resistive divider. The column is completely enclosed in a steel tank (at 80 PSI compressed gas atmosphere) for compatibility with using SF_6.

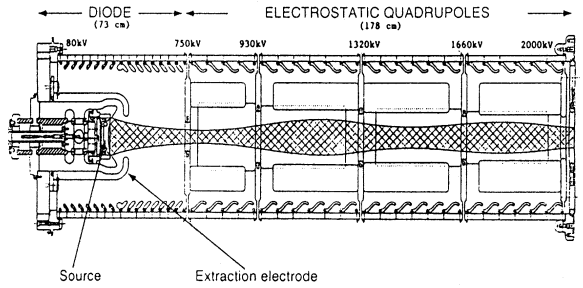

Figure 1: Schematic diagram of the 2-MeV injector.

Earlier tests have demonstrated beam current of up to 0.8 A of potassium ions (space-charge-limited) with a ε_{4rms} projectional emittance < 1.0 π-mm-mrad [7]. However, it was also discovered that the beam current density profile at the end of the injector has a hollow shape instead of the calculated uniform shape. In order to find out what causes the beam non-uniformity, a movable Faraday cup array was recently constructed to measure the beam profile at locations (along beam axis) inside the ESQ accelerator. Some preliminary data indicates the problem may occur at the extraction diode. At present, a new contact ionizer source of the same dimension is being prepared to replace the aluminosilicate source in order to determine if the phenomenon is related to non-uniform ion emission.

3 THE ACCELERATOR

3.1 Beam Merging

Transverse beam combining at the transition from electrostatic to magnetic quadrupole transport could lower the cost of a multiple beam induction linac driver. The cost of induction core material and HV breakdown dictate a small aperture in electrostatic quadrupoles, while magnetic quadrupole transport -- very effective at higher kinetic energy, favors larger apertures (and fewer beams). The challenge for beam merging is to limit resulting emittance growth (minimized by closely packing the merged beams in phase space [8]).

The 4-to-1 beam combining experiment [9] is designed to establish the ability to merge beams with considerable space charge, and measure the phase space evolution of the merged beams. The four initial Cs^+ beams are generated in 160 kV diodes and initially converge at a 6^o angle relative to the combiner center line. Four arrays of electrostatic quadrupoles (Q1-Q4) followed by the combined function dipole-quadrupole element ("wire cage", QD5) focus each beam and straighten its trajectory to be parallel to the downstream transport line. After the wire cage, the merged beam is transported and diagnosed at several locations along the merged beam transport line (Q6-Q67).

We reported earlier [10] measuring 88% transmission through the combiner. These data indicated that the beam edge to beam edge separation was <4 mm at the merge point, with the 1 mm tungsten rods (of the wire cage) in between. The measured phase space between Q7 and Q8 (one lattice period downstream of the cage) was in agreement with the 2D PIC simulations. The initial beams (4.5-mA) had a factor 1.65 more current than originally thought compatible with the transport of merged beams in the (previously existing) downstream transport lattice. As a consequence of the higher current there was not enough clearance between the merged beam and electrodes in the matching quadrupoles (Q6-Q11) to enable further transport without significant beam loss.

Recently, each initial beam current has been lowered to 2.7-mA by altering the Pierce electrodes. This has improved beam matching through the combined function element and the 10.4-mA merged beam through the first downstream lattice period has several millimeters more clearance to the quadrupole electrodes. Beam loss in the transport lattice following the merge should also be negligible, allowing a more quantitative interpretation of the merged beam distribution function.

Figure 2 shows the phase space measured in the vertical plane between Q7 and Q8. Though the beam distribution function has not equilibrated at this point, the rms emittance, $\varepsilon_n \approx 0.2$ π-mm-mR, has decreased by a factor

~0.5 compared to the previous measurements with the higher beam current reported in [10]. Transport measurements through Q67 are currently underway. These results will establish some limits on emittance growth through for this approach to beam merging.

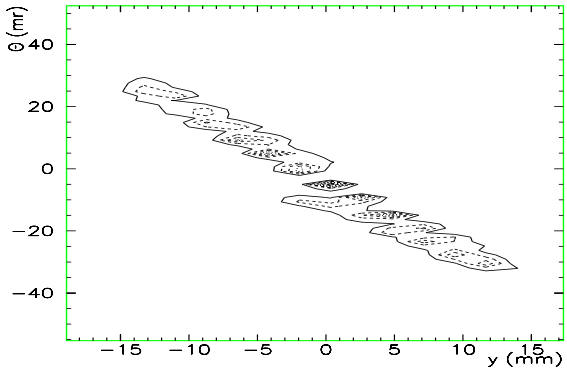

Figure 2: Contour plots from two-slit emittance scan of the merged beams between Q7 and Q8.

3.2 The Recirculator

Most designs of a driver are linear machines, but using a circular machine may provide significant cost savings. Such a machine, a circular ion induction accelerator for space charge dominated beams, or recirculator, have never been built before. Thus, a group at LLNL has been developing a small recirculator in order to validate the recirculator concept for an IFE power plant driver.

In designing this machine, all of the important dimensionless beam parameters, such as perveance, were kept the same as a full scale driver machine. Each half lattice period (HLP) of the recirculator consists of a permanent magnetic quadrupole for focusing, an electrostatic dipole for bending the beam, and an induction core, or modulator, for acceleration and longitudinal compression. The dipole plates are designed to provide a 9 degree bend to the beam while the modulators are designed to provide 500-eV of acceleration.

In the fall of 1997, the machine was extended from a 45 degree bend to a 90 degree bend section. Figure 3 shows the current layout of the machine. Initially, a 4-μs beam pulse is injected by a source diode with an energy of 80-keV through an aperture of diameter 1-cm which provides an initial beam current of 2-mA. Upon injection the beam enters an electrostatic matching section which is followed by a short magnetic transport section before the 90 degree bend section. Following the bend section is the End Tank which houses several diagnostics. As part of the upgrade, magnetic induction cores were added to 5 of the 10 HLP's as shown.

The first attempts at beam transport through the 90 degree section were done with no acceleration and DC voltages (+/- 6.575-kV) on the bending dipole plates. Full current transport was achieved with less than 1% loss as measured by Faraday Cups. The RMS normalized emittance for the 90% of full beam current was also measured at the source injector, 0.021 π-mm-mR, and after 90 degrees, 0.045π-mm-mR in x and 0.068 π-mm-mR in y. The growth seen is within the design specifications.

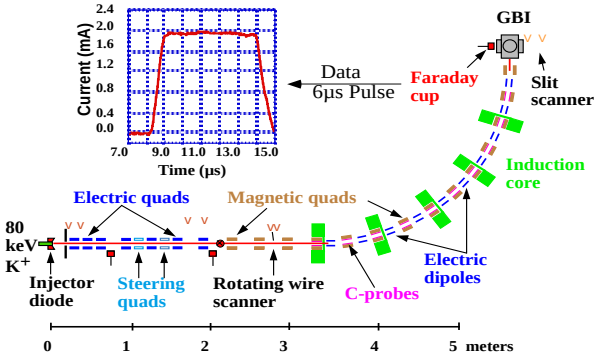

Figure 3: Current Recirculator Layout.

A network of C-probes (capacitively coupled beam position monitors) before and throughout the bend section has been enabled to measure the transverse beam position as a function of time. All four signals from each C-probe are amplified, digitized, and analyzed through the computer control system to obtain the charge centroid. Bench tests of the system using a conducting rod to simulate the beam have yielded a resolution of 70 μm. Figure 4 shows the x position measured by the C-probes for various dipole voltages.

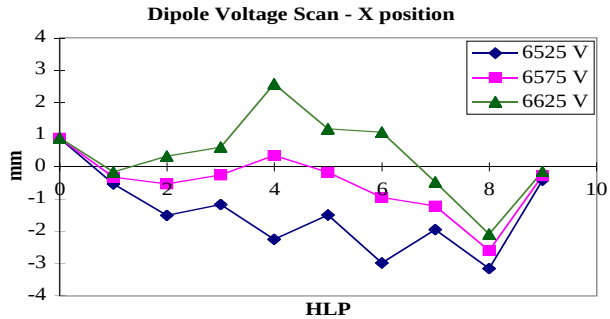

Figure 4: Time averaged X positions as measured by C-probes for various dipole voltages.

LLNL has developed a new device to measure the emittance, the Gated Beam Imager (GBI). The GBI is based on the pepperpot design in which the beam is incident on a hole with 100 μm diameter holes creating many beamlets. Each beamlet is allowed to drift to a micro channel plate(MCP) which is coated with a thin layer of stainless steel, ~150 nm, to stop the ions and produce secondary electrons. After passing through the MCP, the electrons are proximity focused on to a phosphor screen, and the light generated is focused and captured on a CCD camera. Recently, after the analysis of the GBI images was changed to more closely mimic the more traditional slit scan, the GBI was fully reconciled with the slit scanner.

Currently the initial implementation of the electronics necessary for acceleration and ramped dipole voltages, is underway. The first attempts at acceleration should occur shortly. For more information about the recirculator, please refer to the paper in these proceedings [11].

3.3 Induction Core Material

Currently one of the major cost items for a driver is the price of magnetic material for the induction cores. Recently, a survey of various commercially available material was done [12]. Two type of materials were tested, amorphous alloys and nanocrystalline alloys. The amorphous alloys cost less, have slightly higher flux swing (about a factor of 1.2), but have a significantly higher energy loss (about a factor of 5) than the nanocrystalline material. The important figure of merit for selection of material is the final cost of electricity. Obviously the nanocrystalline material will mean a lower operating cost, but a higher capital cost. System studies to determine which of these two materials produces a lower cost of electricity are underway.

4 FINAL FOCUS

There are several proposed schemes, depending on the intensities of the beams, for achieving the final spot size necessary to hit the target. At low intensities, vacuum ballistic focusing would suffice, but at high intensities a scheme involving charge neutralization or establishing a focusing current in a plasma must be invoked. Currently experiments are being performed investigating the ballistic focus scheme and one of the more exotic schemes, plasma channel transport [13].

4.1 Plasma Channel Transport

Plasma channel experiments, for heavy ion transport, are being conducted at LBNL to measure their time and space resolved plasma density evolution. These channel experiments are scaled versions that provide understanding of the channel's behavior under different regimes or parameter space, such as pressure, gas type, and discharge energy deposition, which directly relate to the transport efficiency. A working reactor ion transport design relies on proper selection of these parameters.

The plasma channel in these experiment are produced by a double voltage discharge technique initiated by the creation of a preferential discharge path produced by a KrF excimer laser. Plasma density space profiles have been obtained at several times during the first quarter cycle of channel current (peak current 29 kA). The measured pinch occurring (7 Torr N_2, 200 mTorr Benzene, 15 kV discharge) at t=2.2 microseconds is in agreement with previous experiments.

These measurements were made using a Michelson-type optical interferometer (1064 nm) with a time resolution of approximately 20 ns, determined by the probe laser pulse width. The on-axis plasma density time evolution (n_e = 1.3 x 10^{17} cm^{-3} at pinch time) provides input to the determination of a plasma conductivity model to be implemented in computer simulations.

Future experiments include the use of spectroscopy of the plasma's emitted radiation to measure the Zeeman and Stark broadening, as well as the Faraday rotation technique. These experiments will permit the mapping of the channel's magnetic field distribution and time evolution as well as the determination of its electron temperature.

4.2 Scaled Focusing Experiment

Vacuum ballistic focusing is one method to achieve the heavy ion beam spot size necessary for an inertial confinement fusion target. Proper scaling of particle energy, mass, beam current, beam emittance, and magnetic field replicates the dynamics of a full driver beam in a small laboratory beam. Thus, a one-tenth scale experiment, based on the HIBALL II design, is currently being assembled at LBNL. This scaled experiment uses a K^+ ion source to send a 120 keV beam through an aperture and electrostatic matching section. Approximately 80 μA of beam is then sent through a set of six magnetic quadrupoles that comprise the final focus. By expanding the beam and then focusing to a very small spot, the effects of aberrations and space charge on this method of final focus can be studied. Figure 5 shows the beam envelope for the final focus section.

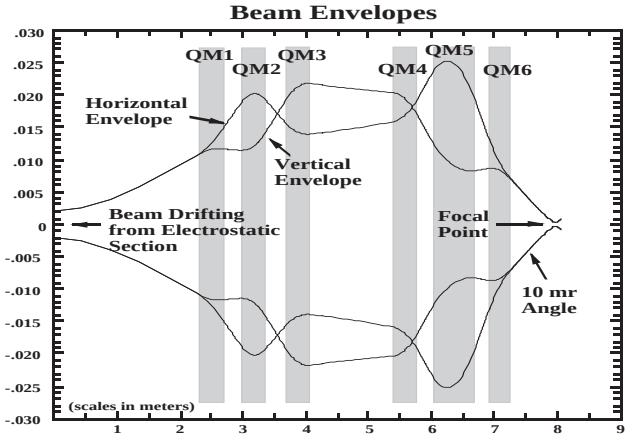

Figure 5: Plot of beam envelopes for magnetic focusing section.

Two-slit scanners measure beam properties after the electrostatic matching section, as well as after the third and sixth magnetic quadrupoles. Measurements of the beam have already been made through the first three magnets with encouraging results, and the second set of three magnets has just been installed, aligned, and pulsed. The beam spot size measurement will be made with a single slit probe that will translate along the beam axis as well as in the transverse directions so as to determine the precise nature of the beam waist.

Subsequently, a separate target injection experiment (section 4.3) may be coupled to the final focus in order to demonstrate the ability to hit a simulated heavy ion fusion target "on the fly". This will require a set of steering electrodes that have been designed to provide a real time correction to the beam to account for the shot-to-shot variation in target position. The emerging beam from the magnetic section will also be suitable for studying electron neutralization of space charge, and its effect on the focus.

4.3 Fusion Target Injecting and Tracking

An experiment is being conducted at LBNL to investigate and demonstrate the engineering feasibility of accurately injecting and tracking IFE targets into a vacuum chamber [14]. As indicated in figure 6, a gas gun is used to inject non-cryogenic, aluminum and delrin (plastic) target-sized projectiles. These projectiles are optically tracked at three locations using photodiodes to accurately provide real-time transverse and longitudinal target position prediction. This real-time information would then be used to trigger the ion beam and control small beam steering magnets to direct the beam on target.

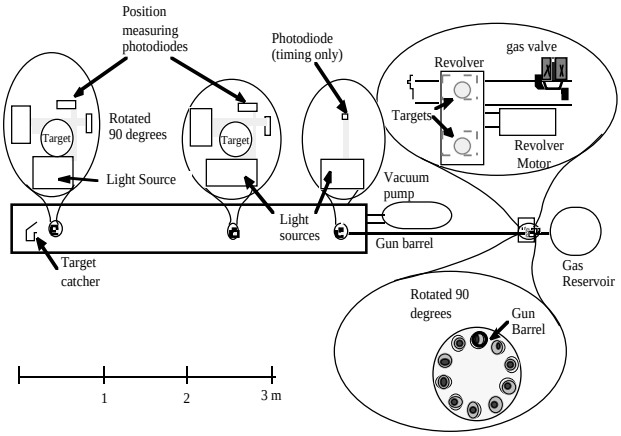

Figure 6: Schematic of Target Injector.

The position prediction is achieved by sending voltage data from one photodiode detector near the gun barrel and another 1 m downstream to a real-time target position prediction circuit. This circuit electronically latches the voltage as the center of the target passes the second detector, and compares this voltage with that when the target is not present. The voltage ratio and the time of passage between these detectors are used to predict the transverse position at which the target passes a third detector located 3 m from the gun barrel. The prediction is in the form of an output voltage that is proportional to the target's transverse position at detector 3; it is available microseconds after the target passes detector 2.

Although the standard deviation in projectile position in each transverse direction is about 2 mm, a standard deviation of 0.1 mm between predicted and measured positions in both transverse directions is achieved. Using an up-down counter, the arrival time of the target has been predicted such that the standard deviation in predicted target position along the direction of motion is 0.37 mm. These prediction capabilities are adequate for a heavy ion driver.

5 OUTLOOK

The road to a heavy ion IFE power plant is still a long one. Before a machine that achieves fusion with heavy ion beams can be realized, a scaled facility to test many, if not all of the accelerator issues in an integrated way must be built. We plan on being in a position to propose such a facility in a few years. To be in that position, the groups at LBNL and LLNL will continue conducting small experiments to explore issues in HIF.

6 ACKNOWLEDGMENTS

I would like to acknowledge the efforts of Joe Kwan, Peter Seidl, David Ponce, Ron Petzoldt, and Steve Maclaren of LBNL and Art Molvik of LLNL for providing the necessary input for this document.

7 REFERENCES

[1] M. Tabak et al., *Nuclear Fusion* **38** (4), 509 (1998).
[2] R. Moir, "Inertial Fusion Energy Power Plants Based on Laser or Ion Beams," Proc. of ICENES 98, Tel-Aviv, Israel, June 28 -July 2, 1998, to be published.
[3] J. W. Kwan et al., "High Current Density Ion Sources for Heavy Ion Fusion Accelerators," Proc. of Part. Accel. Conf., Vancouver, BC, May 1997.
[4] A. N. Pargellis and M. Seidl, *J. Appl. Phys.* **49**, 4933 (1978).
[5] S. Eylon et al., *Il Nuovo Cimento* **106A** (11), 1509 (1993).
[6] K. K. Chow et al., *Appl. Phys. Lett.* **10**, 256 (1967).
[7] S.S. Yu et al, *Fusion Engineering and Design* **32-33**, 309, (1996).
[8] C. M. Celata et al., Proc. of 1987 Part. Acc. Conf., Washington, D.C., **2** 1167 (1987).
[9] C. M. Celata et al., Proceedings of the 1995 Part. Acc. Conf., 3220 (1995). C. M. Celata et al., *Fusion Eng. and Design*, **32-33**, 219 (1996).
[10] P. A. Seidl et al., "Progress on the Scaled Beam Combing Experiment at LBNL," Proc. of Inter. Symp. on Heavy Ion Inertial Fusion, Heidelberg, Germany Sept. 24-27, 1997, to be published in *Nucl. Inst. and Meth. A.*.
[11] L. Ahle et al., "Recent Progress in the Development of a Circular ion Induction Accelerator for Space Charge Dominated Beams at LLNL," these proceedings.
[12] A. W. Molvik et al., "Induction Core Performance," these proceedings.
[13] A. Tauschwitz et al., *Fusion Eng. and Design*, **32-33**, 493-502 (1996).
[14] R. Petzoldt, LBNL Report 41360, (1998).

LINEAR ACCELERATORS FOR EXOTIC ION BEAMS

Pierre Bricault
TRIUMF
4004 Wesbrook Mall, Vancouver, BC, V6T 2A3, Canada

Abstract

One of the new frontiers in nuclear science is the use of exotic ion beams. In the past, nuclear reaction studies were restricted to the use of stable projectiles or a few long-lived isotopes. The possibility of producing intense exotic ion beams opens a wide variety of research opportunities in nuclear astrophysics, nuclear physics, material sciences, etc. This field has grown considerably in the past ten years owing to progress in the production techniques of isotopic separation on-line and in particular in the field of heavy-ion accelerators. One of the breakthroughs is the possibility to accelerate very low energy heavy-ions using a low frequency RFQ at the front end of a linear accelerator.

This paper will review exotic ion beam facilities, based on the ISOL method, using or proposing a linear accelerator as a post-accelerator.

1 INTRODUCTION

The opportunities offered by beams of exotic nuclei for research in the areas of nuclear physics, nucleosynthesis and nuclear astrophysics, and for critical tests of fundamental symmetries, are very exciting. The worldwide activity in the installation of different types of facilities for exotic nuclei reflects the strong scientific interest in the corresponding physics.

The choice of the post accelerator depends on the physics program, which defines the energy and mass range, duty factor and pulse characteristics of the desired ions. This paper reviews only exotic ion beam facilities using LINAC's as post-accelerators. One LINAC has already being built for exotic beam applications, this is the prototype of the JHF E-arena at INS-Tanashi, now, KEK-Tanashi. Two more LINAC's are under construction: one at ISOLDE-CERN and the other at ISAC-TRIUMF. Proposals for second generation exotic ion beams facilities based on the ISOL method which have selected a LINAC as post-accelerator are: JHF E-arena, Argonne National Laboratory, Oak Ridge National Laboratory, Munich and ISAC2 at TRIUMF. A proposed upgrade of the accelerator of the BRNBF in Beijing will also be mentioned.

2 EXISTING RIB LINAC FACILITIES

2.1 E-arena Prototype at Tanashi

A prototype radioactive ion beam facility has been built at KEK-Tanashi. The main components are: target/ion source, mass separator, RFQ and IH linear accelerators. The exotic species are produced using the ion beams extracted from the INS SF cyclotron. The exotic ions are then accelerated to energy ≤ 1 MeV/u through a split-coaxial RFQ (SCRFQ) and an interdigital-H type (IH) linacs. The project is regarded as a prototype of the more ambitious RIB facility for the E-arena in the proposed Japanese Hadron Facility (JHF). The main accomplishments were:

1) Test off- and on-line of target/ion-source systems, ECR, plasma and surface ion sources;
2) Off- and on-line beam tests of the ISOL system as well as the construction of the beam-transport system;
3) Construction and operation of a 25.5 MHz split-coaxial 4-rod RFQ;
4) Construction and operation of a 51 MHz IH linac composed of 4 tanks;
5) Construction and operation of the stripping and matching section between the RFQ and the IH LINACs.
6) Pilot experiments with exotic beams.

2.1.1 Split-Coaxial RFQ LINAC

The split-coaxial RFQ is designed to accelerate ions with charge-to-mass ratio (q/A) ≥ 1/30 from 2 to 172 keV/u. The split coaxial resonant cavity was invented by R. W. Müller[1] and development and investigation took place in several institutes: GSI[2], Frankfurt[3], and Argonne[4].

Various kinds of electrode structure have been proposed: modulated vanes, circular rods, drift tubes with fingers. At INS they selected modulated vanes. In order to achieve easy assembly of the vanes and a stable mechanical structure, a multi-electrode cavity is employed. Two opposite electrodes are fixed and electrically grounded at one end of the cavity. The other opposite electrodes are fixed and grounded at the other end of the cavity. That is, the electrodes are supported at only one point.

The module length, 0.7 m, was determined so that the drop of the vanes due to gravity may not exceed 35μm, with the cavity diameter not exceeding 1m. By introducing spacer rods, it was possible to align the vanes with accuracy better than ± 40 μm before installation into the unit-cavity tank.

The cavity, comprising 12 module cavities, is 0.9 m in diameter and 8.6 m long. The measured resonant resistance is 25.55 ± 0.44 kΩ. The measured unloaded Q-value is 5800. The nominal vane voltage is 109 kV for q/A ≥ 1/30 ions. This corresponds to an input power of 240 kW. The maximum duty factor is 30%.

2.1.2 Medium Energy Beam Transport (MEBT)

The MEBT system between the SC-RFQ and the IH LINAC comprises a charge stripper (Carbon foil of 10 $\mu g/cm^2$), a rebuncher and two quadrupole doublets. Since a frequency of 25.5 MHz is required for the rebuncher, a double-coaxial resonator with 6 gaps was developed to maintain the size of the cavity small and the power low.

2.1.3 Interdigital-H type LINAC

The Interdigital-H LINAC is composed of four tanks. It accelerates ions with charge-to-mass ratio ≥ 1/10 from 172 to 1053 keV/ nucleon. In order to obtain high shunt impedance, the accelerating mode is π-π, and no transverse focusing element is installed into the drift tubes. The operating frequency is twice the RFQ frequency. Each gap length between drift tubes is equal to one half of the first cell length. Both end structures of the cavity, *i.e.*, the magnetic flux inducer and the gaps between end-wall and ridges are determined experimentally so that the longitudinal field distribution becomes flat over the cavity. The synchronous phase is –25° to assure a stable longitudinal motion.

The tuning of the cavities is achieved using three kinds of tuners: a capacitive tuner (C-tuner), an inductive end-tuner (End L-tuner) and an inductive piston tuner (L-tuner). The C-tuner is a manually movable disk facing a ridge; The L-tuner is moved automatically to compensate for the frequency shift.

The first acceleration of an exotic ion beam has been carried out successfully on Mach 14th, 1997 at the INS prototype E-arena.

2.2 ISAC-TRIUMF

2.2.1 RFQ

A cw radio-frequency quadrupole provides the initial acceleration of the ion beam delivered by the ISOL. The total length of the vane-shaped rods is 7.60 m. Given that the radioactive ion beam intensity will be small, space charge can be neglected. A truncated Yamada-style recipe was used for the vane profiles. Due to a requirement from the experimenters for 86 ns time structure, beam bunching is achieved in an external, quasi-sawtooth pre-buncher. The shaper and gentle buncher portions of the RFQ are omitted, leading to substantial shortening. The pre-buncher is located in the LEBT section ~ 5 meters from the RFQ. A 4-rod split-ring RFQ structure has been chosen because of its relatively high specific shunt impedance, its mechanical stability, and the absence of voltage asymmetries in the end region[6]. It is a variation of the 4-rod RFQ built by Schempp[5]. The thermal and dynamic stability have been measured and are well within tolerance[7]. The final RFQ will be composed of 19 modules, but in order to test the beam dynamics and the injection of a bunched beam into the RFQ a 7-ring-RFQ section has being built installed in the 8 m long tank and tested first.

A $^{14}N^+$ beam test with the ISAC split-ring 4-rod RFQ has been successfully completed in June 1998. 7 of the 19 rings were installed for a final beam energy of 54 keV/u. The RFQ was operated in continuous wave (cw) mode. Operation at the nominal peak voltage of 74 kV was achieved in July 1998. This allowed the acceleration of $^{14}N_2$ (q/A = 1/28). The beam transmission was 80% at the nominal voltage in perfect agreement with PARMTEQ calculations. The energy spread of both bunched and unbunched ^{14}N and $^{14}N_2$ beams was measured and showed good agreement with PARMTEQ calculations.

2.2.2 Stripper and matching section

The charge-state selector is composed of a symmetric QQDDQQ section. A four-quadrupole system and a 35 MHz $\lambda/4$ rebuncher provide transverse and longitudinal match into the DTL. Provision is also made for installation of a rebuncher between the RFQ and the stripping foil to produce an upright ellipse for the longitudinal emittance at the stripping foil.

Several options for the 35 MHz $\lambda/4$ rebuncher were investigated. It is likely that a spiral $\lambda/4$ will be used.

2.2.3 Drift-Tube Linac

The drift tube linac is required to accelerate, in cw mode, ions with a charge to mass ratio ≥ 1/7 from 0.15 MeV/u to a final energy variable between 0.15 and 1.5 MeV/u. An IH structure[8] is chosen because of its very high shunt impedance. A *separated function* DTL concept has been adopted[9]. Five independently phased IH tanks operating at $\Phi_S = 0^o$ provide the main acceleration. Longitudinal focusing is provided by independently phased three-gap split-ring resonator structures positioned before the second, third and fourth IH tanks. When operating at full voltage the beam dynamics resembles that of a so-called 'Combined 0° Synchronous Particle Structure'[8]. To reduce the final energy, the last IH tanks may be turned off while voltage and phase of the last powered tank are varied. The split-ring resonators are all designed for β = 0.023 and are effective over the whole DTL velocity range. They also permit the beam to be kept well bunched over the entire energy range.

The first ISAC-IH-DTL tank has been built and is waiting for copper plating. Cooling channels are machined in bulk copper material to assure efficient cooling.

2.3 REX-ISOLDE

REX-ISOLDE is a first generation RIB project aimed at exploring the possibility of an efficient post acceleration of exotic ions based on LINAC after charge breeding with a trap-EBIS system.

The LINAC complex is composed of a 4-rod RFQ, an IH-structure and three seven-gap spiral resonators. To match the phase spread of the ion beam out of the RFQ to the longitudinal phase acceptance of the IH-structure a

three-gap split ring resonator is used. The maximum duty cycle is 10% with a maximum repetition rate of 50 Hz.

To reduce the cost of the LINAC a charge-to-mass ratio of 1/4.5 was chosen. Highly charged ions can be produced using an Electron Cyclotron Resonance Ion Source (ECRIS) or an Electron Beam Ion Source (EBIS). For a RIB facility it is essential to get high efficiency charge state breeding from 1+ to n+ ions and in a short time compared to the half-life of the nucleus considered.

2.3.1 REX-ISOLDE charge breeding scheme

In the REX-ISOLDE scheme a Penning trap is used for accumulation, cooling, and bunching[10]. The Penning trap is however limited in the number of particles which can be trapped. The maximum ion density for the REX-Penning trap is estimated for A = 140 at 10^6 ions/mm^3, which correspond to some 10^8 ions per accumulation cycle.

The Penning trap is located on a high voltage platform an the same potential as the singly charged ion source at the ISOLDE target. The transfer line consists of two electrostatic benders and two electrostatic quadrupole doublets. The confinement time required to reach a charge-to-mass ratio larger than 1/4.5 is less than 20 ms. The EBIS magnet has a magnetic field of 2 T with an homogeneity of about 2.5‰ along the confinement length of 0.8 m. The ions ejected from the EBIS are mass analyzed with a magnetic achromat composed of two 90° dipoles.

2.3.2 The 4-rod RFQ

The ions are accelerated from 5 to 300 keV/u by a 4-rod RFQ. This RFQ is similar to the one used for the High-Current -Injector at Heidelberg[11] and the GSI HLI-RFQ[5]. The results from these two RFQ show that about a quarter of the power is dissipated on the ground plate of the resonator. The new REX-RFQ will have additional cooling of the ground-plate, which must have a better electrical contact to the stems along the entire structure. Furthermore, for the cooling of the electrodes a new stem design has been made at Hiedelberg. The main characteristic of the new design is that channels for cooling water are now completely inside the stem.

Regarding the particle dynamics, they add to the present design a so-called “matching out section” at the high-energy end of the RFQ. The focusing strength is reduced stepwise at the last cells of the accelerator. This leads to decreased beam divergence at the exit of the RFQ and thus reduces the required field gradients of the following matching section between the RFQ and the IH LINAC.

2.3.3 REX-MEBT

The beam dynamics concept of the 0° synchronous phase of the IH structure requires a small longitudinal phase spread and a converging beam in both transverse directions at the entrance of the IH-LINAC. Thus, the matching section includes a rebuncher and two quadrupole triplets. The three-gap split-ring rebuncher operates at the RFQ’s frequency with a gap-voltage of 50 kV.

2.3.4 REX-IH LINAC

The IH-structure is a short version of the GSI HLI-IH-structure[12]. The energy gain required is about 0.9 MeV/u, which corresponds to 5 MV absolute voltage. The IH-structure uses the “Combined Zero Degree Structure” beam dynamics concept developed by Ratzinger[8]. A new approach of the REX-IH resonator is the possibility to vary the final energy between 1.1 and 1.2 MeV/u by adjusting the gap voltage distribution via two capacitive plungers and by adjusting the RF-power level in the resonator[13].

2.3.5 REX-7-Gap Resonators

The final energy of 2.2. MeV/u at the target is achieved by three 7-gap spiral resonators. These type of resonators were developed and built first at the Max Plank Institute in Heidelberg for the High-Current-Injector[14]. The resonators have a single resonance structure, which consists of a copper half shell and three arms attached to both ends of the shell. The resonators are optimized for synchronous particle velocities of 5.4%, 6.0% and 6.6%. The total resonator voltage is about 2 MV for a power consumption of 90 kW. The output of the IH structure is matched with a triplet lens to the first 7-gap resonator. Between the first and second 7-gap resonator there is a doublet for transverse focusing.

3 PROJECTS AND PLANNED UPGRADES

3.1 Japanese Hadron Facility E-arena

The E-arena is a second-generation exotic ion beam facility based on ISOL and post-accelerator scheme. It aims at new regions in nuclear physics and related fields of science by supplying high-quality intense RIB of energies from nearly zero to 6.5 MeV/u for ion mass up to 240.

The RIB facility will utilize 10 μA from the 3-GeV proton booster synchrotron for the production of unstable nuclei. A wide variety of intense exotic ion beams can be produced via spallation, multi-fragmentation and/or fission process of target nuclei. After selection the exotic ion beam can be accelerated through a heavy ion linac, consisting of a split-coaxial RFQ (SCRFQ), and two IH type linacs, IH1 and IH2. The maximum output energy at each stage being 0.17, 1.05 and 6.5 MeV/u, respectively, with a duty cycle of 30% for q/A equal to 1/30.

The proposed E-arena is a natural extension of the RIB facility at the Institute for Nuclear Study (INS) of Tokyo. The new merits of the E-arena are:

1) Primary accelerator: 3-GeV protons are known to produce exotic nuclei with large probability, while reaction residues produced with low-energy beams available from the K=68 cyclotron, are limited to nuclei close to the stability line.

2) The secondary beam energy: this would be increased, by adding a new IH linac, from 1 to 6.5 MeV/u. Nuclear reactions become therefore possible over the whole region of target nuclides.

3.2 ANL Exotic-Ion-Beams Facility

Argonne National Laboratory proposes a two-accelerator ISOL-type facility to provide intense exotic ion beams at energies required for nuclear structure research and for reactions of astrophysics interest[15]. The heart of the exotic-ion-beam accelerator is the present ATLAS superconducting LINAC[16] which can accelerate ions from protons through Uranium to an energy range from 6 to 15 MeV/u. The ATLAS accelerator complex can presently accelerate ions of $q/A \geq 1/6.6$. The new front end has to accelerate ions of low charge-to-mass ratio $\geq 1/132$ to the energy necessary for efficient stripping to higher charge state, while maintaining excellent beam quality to match the actual ATLAS beam characteristics.

The new front end accelerator can be divided into three distinct sections. A short RFQ1 operating at low frequency will be installed on a high voltage platform. After gas stripping the ions of $q/A \geq 1/70$ will be accelerated by a combination of a second RFQ and a 48 MHz superconducting LINAC. After a second stripper, which will increase the q/A to over 1/6.6, a 72 MHz superconducting LINAC module which match the velocity profile to the present ATLAS LINAC will be installed.

Work started on the room temperature cw RFQ at low frequency. Ions with $q/A \geq 1/132$ call for a 12 MHz frequency range. The selected Split-Coaxial RFQ-structure is a modified version of the MAXILAX built at GSI[1].

The status of the RFQ development is the following; a 2 m prototype section has been constructed and operated cw at the design voltage (100 kV). They are currently preparing a prebuncher and LEBT section for beam tests scheduled for end of August 1998[17].

3.3 ORNL Facility

ORNL operates the Hollifield Radioactive Ion Beam Facility based on the ORIC cyclotron and on the 25 MV tandem accelerator as a post-accelerator. A second-generation ISOL facility based on the utilization of the driver of the Spallation Neutron Source (SNS) is proposed [18]. A decision on the construction of the SNS is expected by late 1998. The scheme for the post-accelerator is not yet finalized; but a low frequency RFQ would be utilized to accelerate low charge-to-mass ratio exotic ions $\geq 1/140$ to an energy suitable for stripping. The second stage would used superconducting quarter-wave resonators similar to the ones developed at Argonne[16].

Three take-off points are foreseen at 1, 6 and 15 MeV/u, which will cover most of the nuclear physics studies.

3.4 ISAC2 at TRIUMF

The aim of ISAC-II is a final energy of 6.5 MeV/u for a mass range up to A = 150[21]. The energy increase can be achieved by adding cavities at the end of the present LINAC. However, the mass limitation comes from the stripping at 0.15 MeV/u. The optimum stripping energy for mass 150 is 400 keV/u. To take these ions from 0.15 to 0.4 MeV/u requires a new LINAC, very similar to the ISAC1 DTL. To reach 6.5 MeV/u from 0.4 MeV/u with $A/q = 7$ requires a total voltage gain of 42.7 MV. Independently phased superconducting cavities similar to the ones developed at ANL for ATLAS[16] or LNL for ALPI [22] will be used. The maximum energy of particles with $q/A > 1/3$ will be around 15 MeV/u.

A charge state breeder based on an ECRIS will be placed upstream of the 35 MHz RFQ to increase the charge to mass ratio to 1/30 or greater.

The plan is to build and install superconducting modules downstream of DTL1 as they become available. This would allow higher energy-experiments (~ 5 MeV/u) to start before the end of 2003.

3.5 LINAC for the Munich Fission Fragment Accelerator

A Linear accelerator is proposed for the new Munich high flux reactor, FRMII. This LINAC is based on a charge state breeding of singly charged ions coming from the ISOL system. The required charge-to-mass ratio from the CSB is $q/A>0,16$. The LINAC will operate with a duty cycle of 10% and the final energy will be between 3.7 and 5.9 MeV/u. The LINAC complex will be composed of an RFQ, three IH structures similar to the Lead LINAC at CERN and two 7-gap IH-resonators for the variation of the final energy[20].

3.6 Beijing LINAC

The Beijing Radioactive Nuclear Beam Facility (BRNBF) proposal consists of three accelerators, a compact cyclotron which would deliver 70 MeV proton for the production of radioactive nuclei, an existing Tandem (13 MV) and a superconducting LINAC which will boost the final energy. The superconducting LINAC will use Niobium-sputtered Copper quarter-wave-resonators, currently developed at Peking University[19].

4 DISCUSSION AND CONCLUDING REMARKS

With the new exotic ion beam facilities based on the ISOL method it will be possible to have access to new extreme neutron-to-proton ratios to identify new phenomena and improve our understanding of nuclei, their origin and their properties.

These opportunities are possible because of the development of efficient accelerating structures for very low velocity heavy-ions. All sorts of linear accelerating structures are used or proposed. Both room temperature

and superconducting Drift-Tube LINACs are envisaged, see Table 1.

The injection scheme can vary from very low to very high charge-to-mass ratio using Charge State Breeders (CSB). We can highlight four major schemes:

1) High-charge state breeding as used by REX-ISOLDE for experiments with neutron rich isotopes of Na, Mg, K and Ca. The charge-to-mass ratio required is 1/4,5.
2) Medium-charge state breeding as proposed for ISAC2 and E-arena for nuclear physics up to the Coulomb barrier (6.5 MeV/u). The charge-to-mass ratio required are 1/7 and 1/10, respectively. Such a charge-to-mass ratio remove the need for the medium energy stripper.
3) Low-charge state breeding as proposed for ISAC2 for nuclear physics with masses lower then 150 up to the Coulomb barrier (6.5 MeV/u). The charge-to-mass ratio required is 1/30. In that case a medium energy stripper is required.
4) Low-charge-state LINAC injector as proposed by ANL and ORNL for nuclear physics with masses up to 140. Low frequency RFQ and two strippers are used to reach Coulomb barrier energies.

From the available information on the intensity out of the CSB for a given charge state we can say that the fourth option will give a larger final exotic ion beam intensity on target. However, this may also be the most costly option.

Table 1: Summary of the LINAC for Exotic Beams

	q/A	Type	Type	Mass range	E range MeV/u
KEK-Tanashi	.≥ 1/30	SCRFQ (RT)	IH (RT)	6 ≤ A ≤ 30	0.172 to 1.05
REX-ISOLDE	≥ 1/4.5 CSB	4-rod RFQ (RT)	IH, 7-gap (RT)	6 ≤ A ≤ 60	0.3, 0.8 - 2.2
ISAC-I	≥ 1/30	Split-ring 4-rod RFQ (RT)	IH, 3-gap Split-ring (RT)	6 ≤ A ≤ 60	0.15 – 1.5
ISAC-II	≥ 1/30	Split-ring 4-rod RFQ (RT)	IH(RT), QWR (SC)	6 ≤ A ≤ 150	0.15 – 1.5 0.4 – 6.5
E-arena	≥ 1/30	SCRFQ (RT)	IH (RT)	6 ≤ A ≤ 238	0.17 – 6.5
ANL	≥ 140	SCRFQ (RT)	QWR, 3-gap Split-Ring(SC)	6 ≤ A ≤ 238	0.1 – 6.5
ORNL	≥ 140	SCRFQ (RT)	SC-QWR (SC)	6 ≤ A ≤ 238	0.1 – 6.5
BRNBF		Tandem	QWR (SC)	A ≤ 70	≤ 6.5
FRMII	≥ 1/6.5 CSB	IHRFQ (RT)	IH (RT)	A ≤ 100	≤ 6.5

5 ACKNOWLEDGEMENTS

The author would like to thank all the colleagues from other laboratories who provided information for the preparation of this talk, Dr. S. Araï, Dr. M. Tomizawa, Dr. O. Kester, Dr. J. Nolen, Dr. K. Sheppard, Dr. J. Garrett, Dr. J. Staples. And from TRIUMF we would like to thank, Dr. G. Dutto, Dr. R. Laxdal Dr. R. Poirier, and Dr. P. Schmor for helpful comments.

6 REFERENCES

[1] R. W. Müller et al, GSI-report 79-7, May 1979, R. W. Mueller, GSI Report GSI-90-25, ISSN 0171-4546 (1990).
[2] R. W. Müller et al, Proc. Of the 1984 Inter. LINAC Conf. Seeheim, Germany (1984) p. 77.
[3] H. Klein et al, GSI-Report 82-8, 1982.
[4] A. Moretti et al, Proc. Of the 1981 Inter. LINAC conf. Santa Fee, NM, USA, p. 197.
[5] A. Schempp, *et al.*, Nucl. Instrum. And Meth., **B 10/11**, (1985).
[6] P. Bricault et al, "Simulation of the TRIUMF Split-Ring 4-rod RFQ with MAFIA" Proc. of the 1995 Particle Accelerator Conf. Dallas, (1995) p. 1125.
[7] R. Poirier et al, "The RFQ prototype for the Radioactive Ion Beam Facility at TIUMF", Proc. Of the 1996 Int. LINAC Conf. CERN, Geneva, (1996). P. 405.
R. Poirier et al, "Construction criteria and Prototyping of the ISAC RFQ accelerator at TRIUMF", Proc. 1997 Particle Accelerator Conference.
[8] U. Ratzinger, "Interdigital IH structures, Proc. 1990 Linear Acc. Conf., Los Alamos, 525 (1990) and U. Ratzinger, PAC'91, San Francisco, 1991, p. 567.
[9] R. Laxdal and P. Bricault, "Design of the Drift Tube LINAC for the ISAC project at TRIUMF", Proc. Of the 1996 Int. LINAC Conf. CERN, Geneva, (1996).
[10] D. Habs, *et al.*, Nucl. Phys. A **616**, 29c (1997)., D. Habs, *et al.*, Nucl. Intrum. Methods B 139 (1998) p. 128.
[11] C. M. Klefffner, *et al.*, EPAC-1992, p.1340.,
[12] U. Ratzinger, N. Angert, J. Klabunde, GSI scientific report, 1987.
[13] D. Habs,*et al*, Nucl. Instrum. And Meth. B 139 (1998), p. 128.
[14] R. von Hahn, *et al.*, Nucl. Instrum. Methods, **A 328**, (1993) p. 270.
[15] Concept for an Advanced Exotic Beam Facility based on ATLAS, Working paper, Argonne Nat. Lab., 1995.
[16] K. W. Shepard *et al*, Proc. Of the 1990 Inter. Linear Accelerator Conference, p 510., L. M. Bollinger and K. W. Shepard, Proc. Of the 1984 Inter. Linear Accelerator Conference, p. 217.
[17] K. Shepar et al, "Low charge state CW RFQ", This conference.
[18] Jerry Garrett, private communication.
[19] Jiankui Hao *et al*, Proc. Of the First Asian Particle Accelerator Conference, March 1998, KEK, Tsukuba, Japan.
[20] O. Kester *et al*, "The LINAC for the Fission Fragment Accelerator", This conference.
[21] R. Baartman et al, "Long Range Plan Proposal to ISAC", this conference.
[22] G. Fortuna et al, Nucl. Instr. And Meth. A328 (1993) p. 236.

μ^+-μ^- COLLIDER: μ^+-μ^- GENERATION, CAPTURE AND COOLING

David Neuffer
Fermilab, P. O. Box 500, Batavia IL 60510

Abstract

A μ^+-μ^- collider requires a high-intensity proton source for π-production, a high-acceptance π-μ decay channel, a μ-cooling system, a rapid acceleration system, and a high-luminosity collider ring for the collision of short, intense μ^+-μ^- bunches. Critical problems exist in developing and compressing high-energy proton bunches for producing π's, in capturing π's and their decay μ's, and in cooling μ's into a compressed phase-space at which high luminosity collisions are possible. These problems and some possible solutions are discussed; the current μ^+-μ^- collider research program is described

1 INTRODUCTION

Considerable interest has developed in the possibility of a high-energy high-luminosity μ^+-μ^- collider [1,2,3,4], and a multi-laboratory collaboration has been formed to study this concept [4]. Initially the concept of a 4 TeV collider with a luminosity of $L = 10^{35}cm^{-2}s^{-1}$ was developed [1]. Recently the research has concentrated on developing a design concept for a lower-energy first μ^+-μ^- collider at ~100GeV, and in developing the new technologies needed for that and any μ^+-μ^- collider [5].

Particle physics has identified some clear physics goals for μ^+-μ^- collider technology. Recent LEP and SLC results imply that the Higgs mass is in the 100-170 GeV range. A small energy spread μ^+-μ^- Collider at that energy would be uniquely capable of precise Higgs studies [6]. Also, ν-oscillations have been recently reported. These could be checked by ν-beams that are produced through μ^+-μ^- collider methods of intense π production, μ collection and cooling, with the ν-beams produced by μ-decay in a storage ring [7,8].

The first μ^+-μ^- collider would be a low-energy machine (possibly at 50×50 to 70×70 GeV), designed both to test the basic concepts as well as to provide significant physics at the Higgs mass, and may be at somewhat lower intensity. This machine would be particularly valuable if it could deliver high luminosity at very small energy spreads, matched to the expected Higgs width of $\delta E \sim 1.5$ KeV. Later, higher-energy machines could probe energy frontiers beyond that accessible to existing technology.

Table 1 shows parameters of possible μ^+-μ^- colliders, including a ~100GeV Higgs factory, a 400 GeV and a 4 TeV machine, and Fig. 1 shows a layout view of a 100-GeVcollider facility. The collider requires a high-intensity proton source for π-production, a high-intensity π-production target with a high-acceptance π-μ decay channel, a μ-cooling system to cool the beams to collider requirements, a rapid acceleration system, and a high-luminosity collider ring for the collision of short, intense μ^+-μ^- bunches.

In Table 1, nearly identical proton source parameters are shown for each collider case. This is based on an assumption that a single new high-intensity source is developed and is used to drive different colliders. Also in developing parameters for different energy colliders, we have assumed that the cooling system can cool in 6-D normalized phase space to a fixed emittance, which can then be distributed betweeen transverse and longitudinal for differing collider requirements. (Lower-energy colliders require smaller longitudinal phase-space, and a Higgs Collider should have very small energy spread.) Greater variations in p-source and cooling scenarios are possible.

The critical property of muons in a collider is that the muons decay, with a lifetime of $\tau_\mu = 2.2\ (E_\mu/m_\mu)\ \mu s$. This is sufficient for multiturn acceleration and storage, but only a few hundred turns can be allotted to the μ^+-μ^- collection, cooling, and acceleration, which means that obtaining high luminosity requires frequent production of high-intensity μ-bunches and compressing and cooling the bunches to high densities.

Table 1: Parameter lists for μ^+-μ^- Colliders

Parameter	Higgs Factory (Small-LargeδE)	Top Source	4TeV
Collision Energy ($2E_\mu$)	100	400	4000 GeV
Energy per beam (E_μ)	50	200	2000 GeV
Luminosity ($L=f_0 n_s n_b N_\mu^2/4\pi\sigma^2$)	10^{31}-10^{32}	10^{33}	$10^{35}\,cm^{-2}s^{-1}$
Source Parameters (4 MW p-beam)			
Proton energy(E_p)	16	16	30 GeV
Protons/pulse(N_p)	$4\times2.5\times10^{13}$	$4\times2.5\times10^{13}$	$4\times3\times10^{13}$
Pulse rate(f_0)	15	15	15Hz
μ acceptance(μ/p)	0.2	0.2	.2
μ-survival (N_μ/N_{source})	0.4	0.4	.4
Collider Parameters			
Collider mean radius(R)	50	150	1200m
μ /bunch (N_{μ_c})	4×10^{12}	2×10^{12}	2.5×10^{12}
Number of bunches(n_B)	1	2	2
Storage turns($2n_o$)	1000	1500	1800
Norm. emittance(ε_N)	0.028-.01	10^{-2}	5×10^{-3}cm-rad
μ-beam emittance ($\varepsilon_t=\varepsilon_N/\gamma$)	$(5.6\text{-}2)\times10^{-5}$	5.3×10^{-6}	2.5×10^{-7} cm-rad
Interaction focus β_o	13-4	1	0.3 cm
IR Beam size $\sigma=(\varepsilon\beta_o)^{1/2}$	270-90	23	2.1 μm
δE/E at collisions	0.003-0.12	0.12	0.12%

In this paper we discuss the key technologies which are needed to develop these high intensity μ^+-μ^- beams, identify the critical difficulties, and describe the current

and planned research program on these topics. We also discuss the remaining unsolved problems and challenges.

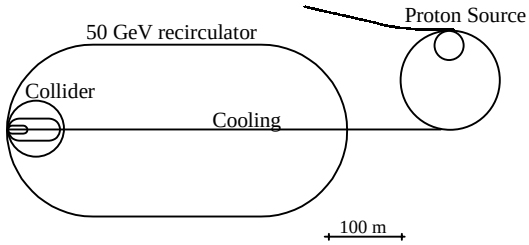

Figure 1. Overview of a 100 GeV μ^+-μ^- Collider facility showing p-source, μ-Cooling, recirculating-linac acceleration (RLA) and collider.

2 PROTON SOURCE

The collider requires an intense source of protons for $\pi \Rightarrow \mu$ production. Present studies indicate that a proton beam at energies of 16-30 GeV at a beam power of ~4 MW is optimal. This is an intensity comparable to that proposed for a KAON factory [9] or a spallation neutron source [10], but with the significant difference that the beam is extracted in short bunches to set up rf rotation (i. e., bunches of 2.5×10^{13}p of ~1 ns). Strategies to reach this intensity are being developed [5], and considerable variation is possible, as long as the high beam power in a bunch structure suitable for development of intense μ-bunches is obtained.

Table 2 shows parameters of a possible proton driver, which consists of a 1 GeV linac, a 3 GeV prebooster and a 16 GeV booster. The parameters are from a Fermilab-based plan for a multipurpose proton source upgrade (K-ν factory/μ-collider/Tevatron, etc.), which would replace the existing Fermilab booster [11]. A new booster tunnel would be required, and the linac would be either extended from its current location or moved.

The 1 GeV Linac is based on the Fermilab 400MeV linac, which consists of a 18 kV magnetron ion source which feeds a 0.75 MV Cockroft-Walton column, followed by a 100 MeV 201 MHz linac, and a 300 MeV 805 MHz side coupled linac. The upgrade requires a magnetron source which can provide 100 mA of beam in 250μs pulses (~1.2×10^{14} H^- ions). The additional 600 MeV structure is an extension of the 805 MHz linac, using 11½ additional modules (131.3m).

The H^- ions are multiturn injected through a foil stripper into the 3 GeV prebooster (500 turns), where they are captured in 6.64 MHz buckets and accelerated as 4 bunches of 2.5×10^{13} protons to 3 GeV in 33ms. The four bunches are then transferred into matched buckets in the 16 GeV booster for acceleration to full energy. At full energy, the bunches are compressed to minimal lengths (σ_z ~ 0.3m) and extracted to the π-production target. The 16 GeV ring circumference is matched to that of the existing Fermilab booster for compatibility with existing Fermilab accelerators.

A key limitation is transverse space charge and the design goal is to keep the space-charge tune-shift $\delta\nu = r_pN/(4\varepsilon_n\beta\gamma^2B)$ less than ~0.25-0.4 throughout the cycle, where r_p is the classical proton radius, N the number of protons, B the bunching factor(average/peak current), and ε_n is the normalized rms emittance. This is minimized by higher injection energies, and large emittances, and larger B. ε_n is increased to ~ 33 mm-mrad (rms) by painting the beam across the foil in multiturn injection. B is conservatively set at 0.25 at injection into the prebooster, which is initially filled with 4 bunches (large B). The beam bunches as it accelerates, and is transferred to the larger ring at 3 GeV, at $\delta\nu \cong 0.25$ (small B but larger γ), with minimal bunch lengths at the extraction bunch rotation.

The beam transports of both rings consist of rapid-cycling separated-function magnets. The peak dipole field is set at 1.3 T in both lattices, and the transition energy ($\gamma_t m_p c^2$) is set above extraction so that the beams are always below transition, which avoids instabilities due to "negative mass" and at transition crossing, and maintains a stable natural chromaticity. The high-γ_t is obtained by use of a "flexible-momentum-compaction" lattice, which gives a tuneable γ_t [12]. The large emittances imply large apertures (13cm for the 3 GeV ring and 10cm for the 16 GeV ring). To minimize eddy currents from rapid-cycling, a high-impedance beam pipe using Inconel or ceramic with conducting wires/strips is needed.

Griffin has developed an acceleration scenario with rf system designs for each ring [13]. The rf cavities are 1m long units with ceramic accelerating gaps and metal-alloy tape-wound cores, with outboard inductive tuners containing NiZn ferrite rings with bias current windings for tuning from 6.6 to 7.4 MHz during the acceleration. Power amplifiers for cavity excitation and transient beam loading compensation are coupled directly to the accelerating gaps. 10 such cavities can generate up to 200 kV in the prebooster, and 40 cavites can produce 1.5 MV in the booster. Bunches injected with ~100ns full-width in the prebooster are compressed to ~20ns after booster acceleration, and rotated to ~6ns (σ_{rms}• 1ns and $\delta E = \pm 200$ MeV) at booster extraction. An inductive insert to cancel space charge is helpful in the final compression. Simulations of this acceleration and bunching have been performed [14].

Some critical experiments testing elements of the proton source design have been performed. A set of inductive ferrite modules was placed in the LANL Proton Storage Ring. Longitudinal space charge effects were reduced without generating instability, and the results supported the use of inductive inserts to cancel space charge [15]. At the BNL AGS experiments in bunching the beam near transition were performed, at parameters similar to the post-acceleration bunching of the proton source. The rms bunch length of the 3 MHz, 8 GeV

bunches was reduced from 6.7 to 2.1 ns [16]. The results support the proposition that initially long proton bunches can be accelerated and compressed to ns lengths, as is required for the μ^+-μ^- collider.

3 π-PRODUCTION AND μ-COLLECTION

The purpose of the production target and subsequent transport is to produce the maximum number of muons which can be subsequently accepted and cooled into collider bunches. From recent studies, maximal capture is obtained by immersing the production target in a high-field solenoid, with sufficient aperture such that most π's are trapped (a 20T solenoid with 7.5cm radius is proposed). This is followed by a solenoid transport which accepts most of the low energy μ's (100-600 MeV/c) produced by π-decay. (see Fig. 2) An rf system within that decay transport reduces the energy spread by "rf rotation", in which the faster particles decelerate while slower ones accelerate. This transforms the short-bunch beam on target producing a large momentum spread in μ's to a longer μ-bunch with reduced δp/p.

Table 2: Parameters of 16 GeV Proton Source

Parameter	Linac	PreBooster	Booster
Final kinetic energy (E_p)	1	3	16 GeV
Pulse rate(f_0)	15	15	15Hz
Protons/pulse($n_B \times N_p$)	$40000 \times 3\ 10^9$	$4 \times 2.5\ 10^{13}$	$4 \times 2.5\ 10^{13}$
Length/circumference	+134	158	474 m
Emittance (95%, 6×rms)	6	200	240πmm-mrad
Dipole packing factor (1.3 T peak field)		0.39	0.575
Aperture		13	10 cm
Tunes(ν_x,ν_y)		3.9,2.4	9.4,4.9
Transition γ (γ_T)		7	25
rf Parameters			
rf frequency(f_{RF})	201→805	6.6-7.4	7.4-7.5MHz
rf harmonic	-	4	12
rf voltage /turn		0.2	1.2 MV
rf length		10	40 m

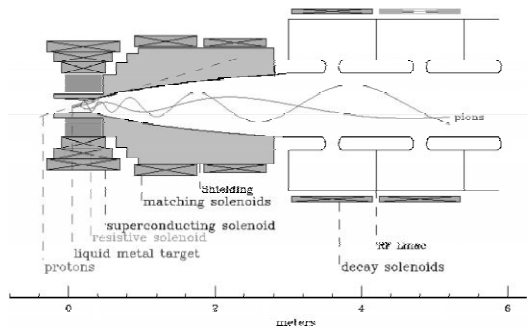

Figure 2. Capture solenoid and match to transport for π→μ decay + rf rotation (from ref. 5).

Extensive simulations on π-production as a function of proton energy, target material and geometry within a capture geometry have been performed, using Monte Carlo codes such as MARS [17] (and DPMJET [18] and ARC [19])and these codes have been verified by comparison with experiments, particularly the recent pion production experiment 910 at BNL [20]. They show that the target should be ~2-3 interaction lengths of a high-density, relatively high-Z material. Optimal proton energy was in the 10-30 GeV range. A target radius of ~1cm appears optimal, maximizing secondary production while minimizing absorption. Tilting the target by 100-150mrad was found to minimize absorption of low-energy π's, which follow helical trajectories through the magnetic region. π-yield is maximal for longitudinal momenta of the same order as the rms transverse momentum (~200 MeV/c). The magnetic field (20T, r=7.5cm) is designed to capture these momenta in helical orbits [21].

About 400 kW of energy is deposited in the target and handling that is a serious problem. Cooling with a thermal bath would lead to large π-absorption and thermal radiation is insufficient. Moving solid metal and flowing liquid jet targets are under consideration. Conducting liquid jets may be distorted by the magnetic fields; however, nonconducting jets are considered. A moving cable or "band-saw" target is possible.

Following the target, the magnetic field is adiabatically decreased and the beam size is increased, following Br^2 = constant to B=5-1.25T (r=15-30cm). The magnetically confined transport continues through a sufficient length for π-decay. This transport also contains a multiharmonic ~30-150MHz rf system embedded in a short-period solenoid transport. In studies rf rotation section solutions with lengths of 40-80m containing a total of 200-500 MV of rf cavities. In simulations ~0.35 μ's (of one sign)/proton are captured from 16-30 GeV protons within an acceptance window of a bunch length of ~6m and δE ~±100 MeV. This is roughly half the number of initially produced π's [1,22,23]. Energy selection in the μ-decay can be used to select a relatively high polarization in the μ-beams [24].

Significant problems exists in designing the rf + focusing system, since it requires combining large low-frequency, relatively high-gradient cavities with relatively high-field superconducting solenoids. Several design iterations have been considered; a recent one (see Fig. 2) uses low-field 1.25T magnets completely outside the cavities; a previous one uses 5T magnets placed in the cavity irises.

An experiment is proposed at the AGS on targetry related issues, which will test some of these systems [25]. It would include tests of liquid jet and other targets, placed within magnets, and then with beam, measuring π-production. An rf cavity with solenoid would be added to test rf rotation components.

4 μ-COOLING

After rf rotation the beam still has both a large momentum spread (δp/p ≅ 10%) and transverse phase space ($\varepsilon_T \cong 0.015$ m-rad). The μ^+-μ^- collider concept relies on ionization cooling to compress the beam phase-space volume to obtain high luminosity. In ionization cooling [2,3], the beam loses transverse and longitudinal

momentum while passing through a material medium, and regains only longitudinal momentum in acceleration cavities. Cooling by large factors requires successive stages of energy loss and reacceleration (20 to 50 stages) [1]. Since ionization cooling does not directly cool the beam longitudinally, these stages must include wedge absorbers at non-zero dispersion to exchange longitudinal and (cooled) transverse phase-space.

The differential equation for rms transverse cooling is:

$$\frac{d\varepsilon_T}{ds} = -\frac{1}{\beta^2 E}\frac{dE}{ds}\varepsilon_T + \frac{\beta_\perp E_s^2}{2\beta^3 m_\mu c^2 L_R E}$$

where the first term is the frictional cooling effect and the second is the multiple scattering heating term. Minimal heating requires that $\beta_\perp$, the betatron focusing amplitude at the absorber, be small, and that L_R, the absorber radiation length, be large (light elements; i.e. Li or Be or H). The energy loss mechanism also causes energy-loss straggling, which naturally sets rms $\delta p/p$ at the ~4% level, even with longitudinal cooling.

The beam dynamics problems in μ-cooling include the beam-material interactions intrinsic to the cooling process, the single-particle beam transport problems associated with obtaining strong foci at the absorbers, the chromatic effects of ~4% $\delta p/p$, dispersion and transverse matching at wedge absorbers, as well as longitudinal motion control with rf reacceleration, and the multiparticle constraints imposed by space-charge and wake-fields in the short intense bunches, where the beam intensifies as it is cooled.

Lattices for cooling have been developed and a favored design includes sequences of solenoid cells with rf cavities and LiH or H absorbers at low-β of the lattice [26]. Another desirable focusing situation is obtained by confining the cooling beam within a high-current Li rod which both focuses and cools the beam [27]. The transport must include arc segments with wedges for cooling longitudinally; obtaining large $\delta p/p$ acceptance configurations with cooling and transport stability is nontrivial.

An outline design scenario for μ-cooling has been developed, and critical sections of the cooling section have been simulated [28,29]. Figure 3 displays transverse phase space before and after a cooling section which cools transverse phase space by $10^4\times$. However an integrated design including the full complexity of the beam transports, reacceleration and bunching, and including nonlinear beam dynamics coupled with the ionization interactions, has not yet been fully developed. Initial cooling experiments verifying cooling efficiency must also be developed. Because effective μ-cooling has not yet been demonstrated and because of its importance in establishing the feasibility of a μ^+-μ^- collider, an extensive R&D program has been established.

Simulation efforts have been intensified, by developing the codes ICOOL [30] and DPGeant [31] and extending their capabilities to include a complete description of μ-material interactions and beam optics. These tools will be used to develop and optimize complete cooling systems.

An experimental collaboration called MUCOOL has been formed in order to establish and demonstrate the technologies needed for effective μ-cooling [32]. In MUCOOL, a muon beam line will be built which would include equipment for precision measurement of muon trajectories entering and leaving a cooling system test channel. Beam cooling sections will be inserted into the test channel, and measurement of muon beams entering and leaving the channel will determine the degree of cooling effectiveness. The cooling sections consist of arrays of absorbers within focusing systems with reacceleration rf. As an initial example a cooling system which includes H_2 cooling elements within strong (15T) solenoids and 800MHz rf cavities has been designed. Detailed designs of rf systems, solenoids and detector components have been developed, and construction of a prototype rf cavity with Be windows has begun [33]. MUCOOL will also include development of Li lenses for cooling, with construction and testing of a 1m long, 1cm radius, 10 T lens.

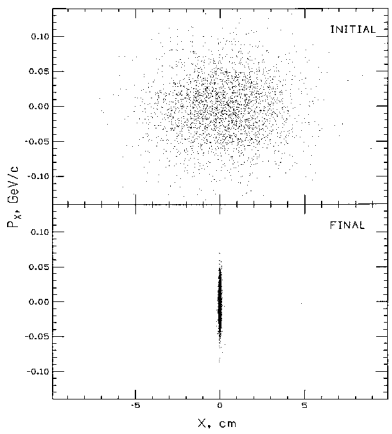

Figure 3. Transverse phase space (p_x-x) before and after a Li lens cooling channel which reduces ε_T from 0.01 to 0.00009 m-rad.

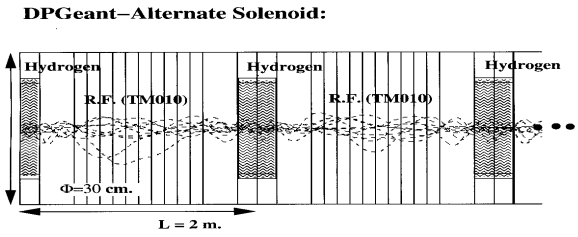

Figure 4. Schematic view of 2 cells of an alternate solenoid cooling system, with H_2 absorbers and 1.3m multicell Cu copper cavities with Be windows. Simulation tracks through the transport are shown.

5 μ-ACCELERATION AND COLLISIONS

Acceleration must be completed before μ-decay. This constraint can be written as the equation:

$$eV_{rf}' >> \frac{m_\mu c^2}{L_\mu} \cong 0.16 \text{ MeV/m},$$

where eV_{rf}' is the acceleration rate, and L_μ is the μ decay length (660m). Relatively fast acceleration is required, and two alternatives have been developed: recirculating linacs (RLAs) or very rapid-cycling synchrotrons (RCS). In both cases significant challenges exist in obtaining acceleration without phase-space dilution. Simulations show that longitudinal matching is relatively straightforward [34], and transverse matching is possible. However precise matching in rapid-cycling systems may be difficult, and beam decay within the transport and acceleration must be tolerated.

After acceleration to full energy, the μ^+-μ^- beams are inserted into a storage ring for multiturn collisions at full energy until μ-decay. The number of storage turns before decay is ~300B, where B is the mean ring bending field in T, or ~2000 turns at B=6.7 T. High luminosity requires that the beams be focussed to small spots and short bunches at the interaction points (IPs). It also implies high beam densities and that could allow multiparticle instabilities. The small focus at the IP with the geometric and chromatic acceptance requirements is a significant design challenge [35].

6 CURRENT R&D PROGRAM

Following initial studies presented at Snowmass, the high-energy physics advisory panel recommended expanded research including simulations and experiments to determine the feasibility of μ^+-μ^- colliders [36]. In response the μ^+-μ^- collaboration is expanding its efforts, including experiments on targetry/production at BNL and cooling at Fermilab. (discussed above) Much research and innovation is needed toward obtaining complete and optimal solutions to the difficult problems in developing a practical μ^+-μ^- collider.

We acknowledge the assistance of the many contributors to the μ^+-μ^- collider studies, based at BNL, Fermilab, LBL, and other universities and laboratories, including R. Palmer, S. Geer, A. Tollestrup, A. Sessler, J. Gallardo, D. Cline, K. MacDonald, R. Noble and many others.

REFERENCES

[1] $\mu^+\mu^-$ Collider - A Feasibility Study, BNL-52503, Fermi-Lab-Conf.-96-092, LBNL-38946 (1996), presented at the Snowmass 96 workshop (1997).

[2] A. N. Skrinsky and V.V. Parkhomchuk, Sov. J. Nucl. Physics 12, 3(1981), E. A. Perevedentsev and A. N. Skrinsky, Proc. 12th Int. Conf. on High Energy Accel., 485 (1983).

[3] D. Neuffer, Fermilab Note FN-319, July 1979, D. Neuffer, Particle Accelerators 14, 75 (1983), D. Neuffer, Proc. 12th Int. Conf. on High Energy Accelerators, 481 (1983), D. Neuffer, Nucl. Inst. and Meth. A350, 27 (1994)

[4] D. Neuffer and R. Palmer, Proc. 1994 EPAC, p. 52 (London, 1994).

[5] C. M. Ankenbrandt et al., "Status of Muon Collider Research", submitted to Phys. Rev. Special Topics (1998).

[6] V. Barger, M. Berger, J. Gunion, and T. Han, Nucl . Phys. B (Proc. Suppl.) 51A, 13 (1996)., Physics Reports 286, 1 (1997).

[7] D. Cline and D. Neuffer, AIP Conf. Proc. 68, 856 (1981).

[8] S. Geer et al., unpublished report, 1998.

[9] KAON Factory Study, Accelerator Design Report TRIUMF, Vancouver BC, Canada. (1990)

[10] 5 MW Pulsed Spallation Neutron Source, Preconceptual Design Study, BNL-60678, 1994.

[11] S. D. Holmes, ed.."A Development Plan for the Fermilab Proton Source", Fermilab-TM-2021 (1997).

[12] S. Y. Lee, K. Y. Ng, and D. Trbojevic, Phys. Rev. E48, 3040 (1993).

[13] J. Griffin, "rf System Considerations for Muon Collider Proton Driver Synchrotrons.", unpublished, April 1998.

[14] I. Kourbanis and Z. Qian, unpublished (1998).

[15] J. E. Griffin et al. "Passive Compensation of Space Charge in the LANL PSR", FN-661 (1998)

[16] C. Ankenbrandt et al.,"Bunching Near Transition in the AGS", Phys. Rev. Special Topics AB 1, 030101 (1998).

[17] N. V. Mokhov, The MARS Code System Users Guide, Fermilab FN-628 (1995).

[18] J. Ranft, DPMJET version II.3 and II.4, INFN-AE-97045 (1997).

[19] D. Kahana and Y. Torun, BNL-61983 (1995).

[20] Experiment 910 at BNL-AGS (1997).

[21] N. V. Mokhov and A. Van Ginneken, FNAL-Conf-98/041 (1998); N.V. Mokhov and S. I. Striganov, FNAL-Conf-98/053 (1998).

[22] W. Turner and H. Kirk, Proc. New Directions for HEP - Snowmass 96, 242 (1996).

[23] D. Neuffer and A. Van Ginneken, submitted to NIM A (1998).

[24] R. Palmer and J. Gallardo (unpublished) 1997.

[25] BNL targetry experiment proposal (1998)

[26] R. Palmer, (unpublished) 1997.

[27] G I. Silvestrov ,AIP Conf. Proc. 372, 168 (1996)

[28] R. C. Fernow et al., to appear in Proc. 8th workshop on Advanced Accel. Concepts, Baltimore, MD (1998)

[29] A. Van Ginneken, Nucl. Inst. and Meth. A362, 213 (1995); D. Neuffer and A. Van Ginneken, Nucl. Inst. and Meth. A 403,1 (1998); and paper 4W.31, Proc. PAC 1997.

[30] R. Fernow, ICOOL (unpublished) 1998.

[31] P. LeBrun and P. Spentzouris, DPGeant simulations (1998).

[32] S. Geer, spokesperson, et al. FNAL proposal P904(1998).

[33] A. Moretti et al., these 1998 Linac Conf. Proc. , Chicago (1998)

[34] D. Neuffer, Nucl. Inst and Meth, A384, 263 (1997).

[35] A. Garren et al., Nucl. Physics B, Proc. Suppl., 51A, 148(1996).

[36] F. Gilman, et al., HEPAP subpanel report on Planning the Future of US High-Energy Physics (1998).

BEPC INJECTOR UPGRADE

-For-
Electron Linac Division
Pei, Guoxi
Institute of High Energy Physics, Academia Sinica, Beijing 100039,China

Abstract

BEPC is a 2.2×2 GeV electron- positron collider with luminosity of $2\times10^{30}cm^{-2}s^{-1}$. Its injector is a 1.3GeV electron Linac. As a part of BEPC upgrades for higher luminosity, the Linac energy will be increased to 1.55 GeV of J/• physics energy region, and further to 1.75 GeV or higher. The main measures we took are: 1) to use 4 sets of high power RF sources, including newly designed 65MW klystrons and 150 MW modulators; 2) to rebuild local control system for more stable operation. After a few years effort with collaborating companies, main upgrades and relevant improvements (15 dB high power directional coupler, high power vacuum valve, RF pulse widening to increase the multiplication factor of SLED etc.) are completed. Now the machine can be operated stably at 1.55GeV.

Keywords: BEPC injector, high power RF source, Linac control system

1 INTRODUCTION

Full energy injection is necessary for any high luminosity storage rings, such as PEP-II• KEKB etc., because it can avoid beam loss during ramping or omit ramping process to shorten the injection time. For BES, the most important physics is J/• of 1.55GeV. So, to increase BEPC injector energy from 1.3GeV to 1.55GeV for J/• and further to 1.75GeV for other physics is significant.

BEPC injector [1], built in 1987, was a 1.3GeV• 200-meter electron Linac. HK-1 klystrons (35MW) were the RF power sources. The standard acceleration unit consists of four 3-meter constant gradient accelerator tubes, driven by one klystron with SLED. The energy gain can be expressed as W (MeV) = 20 M $\sqrt{P}$, where M is the multiplication factor of SLED, and P the klystron output power. It is clear that higher energy can be obtained by both increasing the klystron output power and enhancing multiplication factor. There are 12 such acceleration units downstream of BEPC positron production system. If we replace three of them with 65MW klystrons (operating at 45MW at the first stage), we can hope to get 200MeV energy gain. For the rest RF power supplies, we are going to make some modifications. Widening the pulse width from 3.2•s to 3.7•s by adjusting the modulator PFN, we can increase the multiplication factor of SLED from 1.4 to 1.5. Using higher ratio of 1:14 pulse transformer, we can arise the pulse voltage a little bit from 260KV to 270KV, so that the average output power of the klystrons can be increased from 19MW to 22MW. By all measures mentioned above, it is hopeful to increase the positron energy to 1.75GeV as shown in Table 1.

Table 1: Energy Upgrade

	Before upgrade	After Upgrade
RF Power Source	11×19MW	8×22MW 3×45MW
RF pulse width	3.2μS	3.7μS
EMF of SLED	1.4	1.5
Injector Energy	1.3GeV	1.75GeV

Besides energy upgrade, another important upgrade is to rebuild the local control system. The old one was manually operated, complex and inconvenient, especially in our case, both electrons and positrons use the same beam line. When we made mode change, say from e^- to e^+, a lot parameters should be changed. Computer can do it very easily.

In what follows, the author will present the technique issues underneath the energy upgrade and the local control system rebuild.

2 TECHNIQUE UPGRADE

2.1 65MW klystron

Table 2: 65MW Specifications and Test Results

Parameters	Design	1st Tube	2nd Tube	3rd Tube
Frequency (MHz)	2856	2856	2856	2856
Cathode	Dispenser	Dispenser	Dispenser	Dispenser
Heater Volt.(V)	22	20.5	23	21.6
Heater Curr.(A)	36	38	41	38
Pulse Volt.(KV)	350	330±5	342	350
Pulse Curr. (A)	415	406	401	444.1
Microperv. (•P)	2.0±0.1	1.91~2.13	2.0	2.145
PPS	50	12.5	12.5	12.5
Pin •W•	600		~600	~800
Pout •MW•	65	50.4	58.5*,66**	63*,76**
RF Width (•s)	3.5	3.0	3.3~3.35	2.5~3.0
Efficiency (%)	45	37.6	42.6*,48**	
Gain (dB)	51		~50	
Lifetime (Hrs)	•15000	3500	8000	Alive

*Measured by thermocoupler

**Measured by peak power meter

The new high power klystron[2] was designed in 1992, the prototype was SLAC 5045 tube. After many trials, we got the first tube in 1995, manufactured by 4404 company in Wuhan. The output power on the test stand was about 50MW, not bad for the first tube. In succession, we totally got three 65MW klystrons from the company. Their test

results and operation records at the gallery are listed in Table 2. From this table we can see, the output power is acceptable both on the test stand and at the gallery, but the lifetime is too short. Now we are trying to open the two failure tubes and analyse the problems with company people.

2.2 150MW modulator

Referring to high power modulator techniques of world class labs, such as SLAC, KEK, DESY, etc., and our own 80MW modulator experience, we designed the 150MW modulators [3] for 65MW klystrons. The specifications and pulse voltage output waveform are listed separately in Table 3 and Figure 1. We have made four 150MW modulators, two of them are now working at klystron gallery for a few years, very stable and low noise.

Table 3: Parameters of New and Old Modulators

	Old	New
Output Power	80MW	150MV
Output High Voltage	260KV	350KV
Repetition Rate	12.5Hz	25Hz
Anode Voltage of Thyratron	42KV	44KV
Anode Current of Thyratron	3240A	6500A
Pulse Transformer	1:12	1:15
Pulse Width	3.0•s	3.5•s
Rise Time	0.7•s	0.9•s
PFN Impedance	6.2•	3.3•
PFN Total Capacitance	0.34•f	0.9•f
Charging Current	3.7A	2.53A
Charging Time	5.5ms	2.6ms
Charging Inductance	10H	30H

2.3 Local control system

Linac control system[4] reconstruction includes following parts as illustrated in Fig.2.

a. *RF power source*

A new local control system based on the PLC was installed and the communication between the control room and modulators was accomplished. PLC was used to replace the original relay control logic circuits of the modulators. The control PC inspects the PLCs through the RS-232 port. The DC voltage, charging current, external failure signal and filament current are sent to the control room. DC voltage can be remotely controlled.

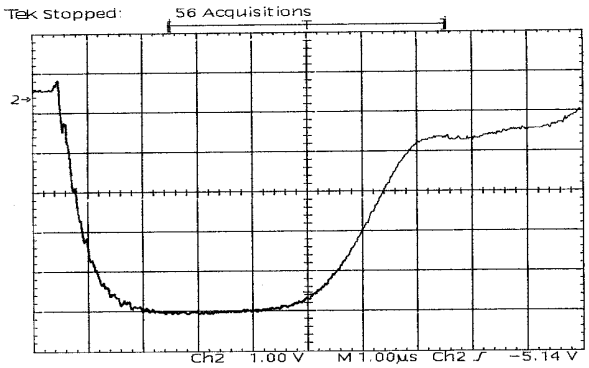

Figure 1: 150MW Modulator Output Waveforme

b. *Magnet power supplies*

There are 88 sets of DC power supplies used for quadrupoles, steering coils and focusing solenoids. Now the adjustment can simply be done by the PCs. Good data are saved on the hard disk for further analysis and reference.

c. *Vacuum*

A PC is used for inspecting the status of the Linac vacuum. All parameters can be shown on the screen with proper colours. When there is any trouble, a sound and red colour warning will appear.

d. Mode change and RF phase

As mentioned above, in our Linac e^- and e^+ beams use the same beam line. When changing modes, we need switch the stepping motor to arise or put down the target, and adjust the capture section RF phase and all the optical parameters downstream. In order to get the highest energy, the RF phases of the klystrons are controlled. All these are now accomplished by a PC.

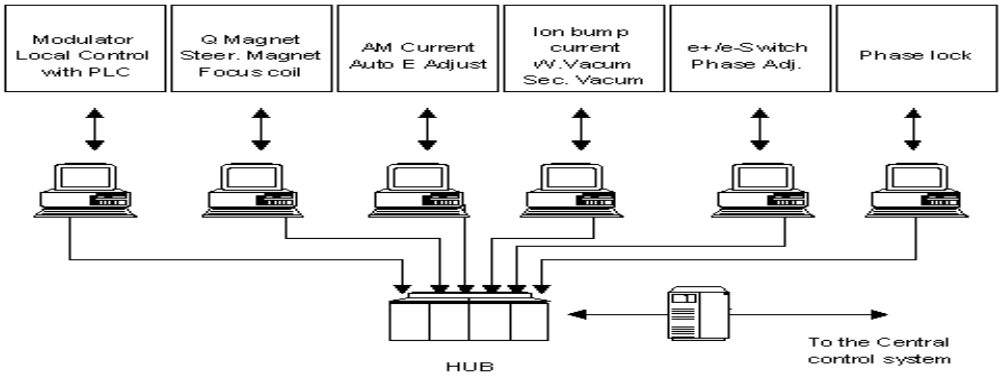

Figure 2: Linac Control System

2.4 High power vacuum valve[5]

Between klystron window and the downstream RF structure, there is an valve for vacuum separation. The one used for HK-1 klystron is SLAC old design, which is Indium sealed and only can bear 35MW power. For 65MW klystron, we must use new one. The new design is a two part U type waveguide. These two parts can be set apart a little bit to let seal plate with fluorine O ring insert into the gap to separate vacuum.

2.5 15dB high power coupler

In our system, the first klystron is driven by an RF amplifier. The following tubes are driven with part of the power from No.1 tube by directional coupler. In order to ensure enough driving power for 65MW klystrons, 15dB directional coupler was designed and used to replace the original 20dB one.

3 CONCLUSION

Except the lifetime of 65MW klystron need to be further studied, all other upgrades have reached the design targets. They are working smoothly on the machine, especially the modulators and local control system. Because only two 65MW klystrons were installed (including one SLAC 5045 tube) at the gallery, not four as planned ,the linac can only work at 1.55GeV.

4 REFERENCES

[1] Wang Jin, Han Qian, Ling Dachun. The status of BEPC 1.3GeV Linac, LINAC 94.

[2] Hong Bo, Dong Dong. Improvements of BEPC Linac klystrons, APAC 98.

[3] Chi Yunlong et al., BEPC Pulse modulator Upgrade, 98CATC (in Chinese)

[4] Gu Pengda et al., The status of BEPC Linac control system, ICALEPCS 97

[5] G. Li et al., Design and Test of WV1 High Power Waveguide Valve, Internal report (in Chinese)

DEMONSTRATION OF TWO-BEAM ACCELERATION IN CTF II

R. Bossart, H.H. Braun, G. Carron, M. Chanudet, F. Chautard, J.P. Delahaye, J.C. Godot, S. Hutchins, I. Kamber, C. Martinez, G. Suberlucq, P. Tenenbaum*, L. Thorndahl, M. Valentini, I. Wilson, W. Wuensch, CERN, 1211 Geneva 23, Switzerland

Abstract

The second phase of the Compact LInear Collider (CLIC) Test Facility (CTF II) at CERN has demonstrated the feasibility of two-beam acceleration at 30 GHz using a high-charge drive beam, running parallel to the main beam, as the RF power source. To date accelerating gradients of 59 MV/m at 30 GHz have been achieved. In CTF II, the two beams are generated by 3 GHz RF photo-injectors and are accelerated in 3 GHz linacs, before injection into the 30 GHz modules. The drive beam linac has to accelerate a 16 ns long train of 48 bunches, each with a nominal charge of 13.4 nC. To cope with the very substantial beam-loading special accelerating structures are used (running slightly off the bunch repetition frequency). A magnetic chicane compresses the bunches to less than 5 ps fwhm, this is needed for efficient 30 GHz power generation. The 30 GHz modules are fully-engineered representative sections of CLIC, they include a 30 GHz decelerator for the drive beam, a 30 GHz accelerator for the main beam, high resolution BPM's and a wire-based active alignment system. The performance achieved so far, as well as the operational experience with the first accelerator of this type, are reported.

1 INTRODUCTION

After successfully completing the first phase of CTF in 1995 [1], the construction of CTF II was launched in 1996 with the following goals:

1. To demonstrate the feasibility of the CLIC two-beam accelerator scheme [2] and its associated 30 GHz technology.
2. To build and test prototypes of the 30 GHz modules
3. To study the dynamics of a high-charge, multibunch drive beam.
4. To test the active alignment system in a realistic accelerator environment.
5. To test CLIC beam monitoring equipment.

The layout of CTF II with its two beam lines is shown in figure 1. The drive beam generates 30 GHz power, while the main beam probes the accelerating field in the 30 GHz accelerator. Both beams are generated by S-band RF-photo-injectors. The RF-photo-injectors have photo-cathodes illuminated by a common short pulse (8 ps fwhm) laser. The cathodes and the laser system are described in [3].

The main beam operates with a single bunch of 1 nC charge. A second bunch, with a variable delay relative to the first, can be added later to allow wakefield studies in the 30 GHz structures. Before being injected into the 30 GHz accelerator the main beam is accelerated to 46 MeV in an S-band travelling wave structure. This is necessary to obtain a small enough geometric emittance to fit into the small acceptance of the 30 GHz accelerating structures which have a beam aperture of only 4 mm diameter. Magnetic spectrometers before and after the 30 GHz accelerator are used to measure the beam energy. The details of the 30 GHz accelerator are described in [4].

The drive beam RF-photo-injector is a 3-cell design optimised for high charge acceleration [5]. The nominal charge is 640 nC in 48 bunches with a bunch spacing of 10 cm. The photo-injector accelerates these bunches to 6 MeV. The photo-injector is followed by two short travelling wave S-band structures optimised for high-charge acceleration [6]. These structures are also used

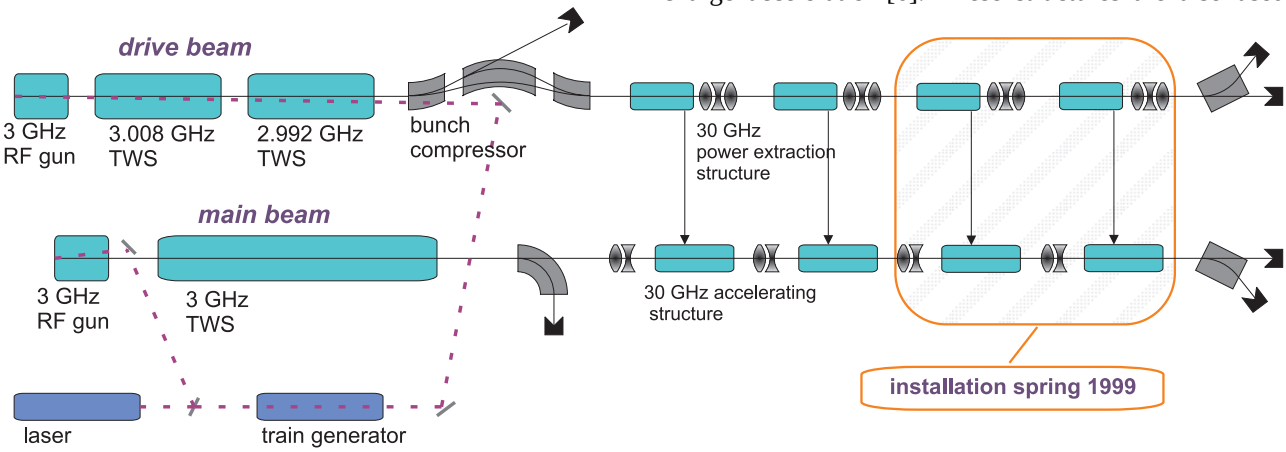

Figure 1: Layout of CTF II (TWS=travelling wave structure)

* Present address: Stanford Linear Accelerator Center, Stanford, California

for beam-loading compensation, as described in below. As a result of the counteracting longitudinal RF focusing and space-charge defocusing forces, the bunch length after acceleration is about 8 ps fwhm for the nominal charge. A magnetic chicane, together with proper phasing in the accelerating structures, compresses the bunches to ≤ 5 ps; this is needed for efficient 30 GHz power production. The first magnet of the chicane is also used as a spectrometer magnet. After bunch compression, the beam is injected into the 30 GHz decelerator [4] where a part of its energy is converted into 30 GHz power. A downstream spectrometer magnet measures the energy of the beam after power extraction.

2 DRIVE BEAM ACCELERATION AND BEAM LOADING COMPENSATION

The nominal drive beam train of 640 nC during 16 ns extracts 2.2 GW of power from the two 3 GHz accelerating sections. The related energy has to be provided by the energy stored in the accelerating structures. For this reason, the structures are operated at a high field (design 60 MV/m, achieved 36 MV/m) and their geometry is optimised for a low r'/Q (2.2 kΩ/m) to maximise the stored energy. Nevertheless the energy drop due to transient beam-loading would be 17.5 MeV at nominal charge. Since such an energy spread is neither acceptable for the bunch compression nor for the transverse matching into the 30 GHz decelerator, a two-frequency beam-loading compensation is used. The two accelerating structures operate 7.8 MHz below and above the drive-beam bunch repetition frequency of 2998.6 MHz. This introduces a change of RF phase from bunch to bunch which allows an approximate compensation of the beam-loading. Due to the curvature of the RF wave, a residual energy spread remains, leading to somewhat lower energies of the early and late bunches compared with bunches at the center of the train. This effect is visible in figure 2, which shows a longitudinal phase-space image of a 24 bunch train with a total charge of 120 nC. This is taken with a streak camera from a transition radiation screen in the first drive beam spectrometer. A plot of the calculated energy distribution is shown for comparison. For a 48 bunch train the total energy variation from bunch to bunch due to this effect is 7%. Without beam loading compensation it would be 30% for the nominal charge. By using two frequencies, the single bunch energy spread introduced in the 1st structure is compensated by the 2nd structure. However, using correct phasing and a slight reduction of the field amplitude in the 2nd structure, it is possible to introduce a correlated energy spread in the individual bunches which is approximately equal for all bunches. This is essential for bunch compression in the magnetic chicane. Adding a correlated energy spread to allow for bunch compression, the energy spread with beam loading compensation increases to 14%.

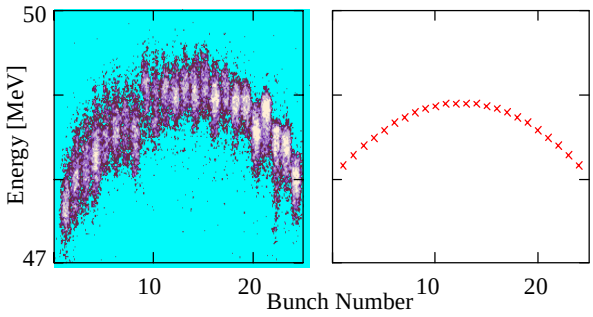

Figure 2: Longitudinal phase space with beam loading compensation. Left side: measured; right side: predicted.

3 TWO BEAM ACCELERATION AT 30 GHZ

In June and July of this year two-beam acceleration was tested by simultaneously passing the drive beam through the 30 GHz decelerator and the main beam through the 30 GHz accelerator. At present two power extraction structures are installed in the 30 GHz decelerator. Each power extraction structure is connected to one 30 GHz accelerating structure of the main beam. One of the power extraction structures is an older prototype (soon to be replaced) and gives about half the power of the other. The numbers quoted below for power and accelerating field refer to those measured with the newer structure. The following quantities were measured: drive beam charge before and after the decelerator, drive beam bunch length [7], main beam charge and bunch length, drive beam momentum before and after the decelerator, 30 GHz power (input, reflected and transmitted) for each of the two accelerating structures and main beam momentum. Table 1 summarises the performance achieved in comparison with the design goals. As already experienced in CTF I, no RF breakdowns were observed in either the 30 GHz waveguide networks or the structures. The 30 GHz power production is limited for the moment by the drive beam charge which can be transported through the decelerator.

		design	achieved
drive beam	maximum accelerated charge	640 nC	755 nC
	acc. charge giving max. 30 GHz power	640 nC	475 nC
	max. charge through decelerator	640 nC	374 nC
	number of bunches	48	48
	bunch length fwhm	5 ps	5 ps
30 GHz power at output of power extraction structure		71 MW	27 MW
30 GHz power pulse length		14 ns	14 ns
mean accelerating field in 30 GHz acc. structure		95 MV/m	59 MV/m

Table 1: Nominal and achieved performance.

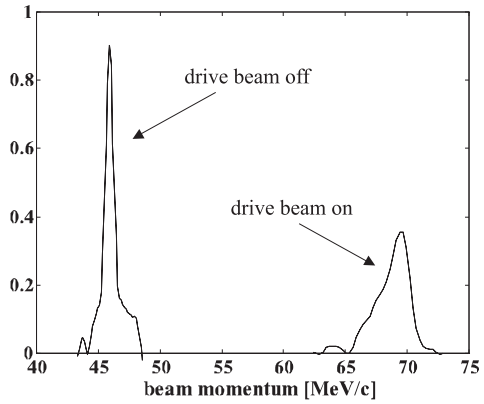

Figure 3: Momentum spectra of the main beam measured with drive beam on and off.

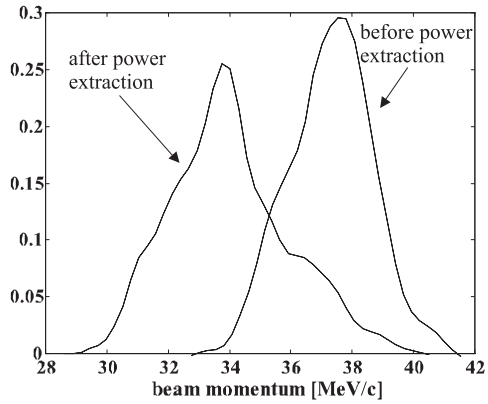

Figure 4: Drive beam momentum spectra measured before and after the 30 GHz power extraction structures.

Possible reasons for the still unsatisfactory transmission at high charges include the gradient in the drive beam accelerator which is still below the design value, transverse matching problems and various problems with the laser system.

Figure 3 shows energy spectra of the main beam measured downstream of the 30 GHz accelerator with and without 30 GHz acceleration. The larger energy spread of the accelerated beam is caused by laser energy jitters and by the bunch-length of the main beam, which is 6 ps fwhm corresponding to a phase extension of 65o at 30 GHz. Figure 4 shows the drive beam energy spectra before and after passage through the 30 GHz decelerator. These spectra were measured with a drive beam charge of 400 nC and a transmission of 85% in the decelerator. The measured power and acceleration are compatible with the values expected from theory. However, the precision of this comparison is presently limited by the beam losses in the decelerator.

4 SINGLE BUNCH EXPERIMENTS

The drive beam accelerator of CTF II can also be operated in single bunch mode. This mode of operation allows the study of the dynamics of single bunches with high charges. Recently a single bunch of 112 nC was produced and accelerated. Effects leading to emittance growth in the magnetic bunch compressor were studied experimentally [8]. The single bunch mode of operation is also used for beam monitor testing [9].

5 CONCLUSION AND OUTLOOK

The CTF II has demonstrated the principle of two-beam acceleration at 30 GHz. Although not all the design specifications have been met until now, the accelerating gradients achieved are already well above those in more conventional electron accelerators, and the charge and beam current obtained from the drive beam accelerator are unprecedented for RF-photo-injectors.

For the coming year it is planned to add two more power extraction and accelerating structures. A test with a special power extraction structure of considerably higher shunt impedance is foreseen, which will allow to generate even higher power than with the standard structures. This power will be used to explore the as yet unknown gradient limits of 30 GHz structures.

To improve the quality of the drive beam a new RF-photo-injector [10] and an idler cavity are under construction. The new gun will improve the drive beam quality while the idler cavity will reduce the residual energy spread of the beam loading compensation scheme.

REFERENCES

[1] H.H. Braun and 16 co-authors, “Results from the CLIC Test Facility,” EPAC, Sitges 1996

[2] J.P. Delahaye and 30 co-authors, “CLIC, a 0.5 to 5 TeV e^+/e^- Compact Linear Collider,” EPAC, Stockholm 1998

[3] E. Chevallay, J. Durand, S. Hutchins, G. Suberlucq, H. Trautner, “Photo-Cathodes for the CERN CLIC Test Facility,” this conference

[4] I. Wilson, W. Wuensch, W. Coosemans, C. Achard, “The CLIC 30 GHz Two-Beam Test Accelerator,” this conference

[5] R. Bossart, H.H. Braun, M. Dehler, J.-C. Godot, “A 3 GHz Photoelectron Gun for High Beam Intensity,” FEL Conf., New York 1995

[6] G. Bienvenu, J. Gao, “A Double High Current, High Gradient Electrons Accelerating Structure,” EPAC, Sitges 1996

[7] C. Martinez and H.H. Braun, , “Non-Intercepting Bunch Length Monitor for Picosecond Electron Bunches,” EPAC, Stockholm 1998

[8] H.H. Braun, F. Chautard, R. Corsini, T.O. Raubenheimer, P. Tenenbaum, “Emittance Growth during Bunch Compression in the CTF II,” submitted to Physical Review Letters

[9] T. Kamps and 9 co-authors, “Design and Tests of a new microwave beam position monitor for the Undulator of the TTF-FEL,” EPAC, Stockholm 1998

[10] R. Bossart, M. Dehler, “Design of a Gun for Heavy Beam Loading,” EPAC, Sitges 1996

RESULTS FROM HARDWARE R&D ON C-BAND RF-SYSTEM FOR e^+e^- LINEAR COLLIDER

T. Shintake, N. Akasaka and H. Matsumoto, KEK, 1-1 Oho, Tsukuba, 305 Japan
J.-S. Oh, PAL POSTECH, Pohang, Kyungbuk, 790-600, Republic of Korea
M. Yoshida, ICEPP, University of Tokyo, Tokyo, Japan
K. Watanabe, Tohoku University, Sendai, 982 Japan
Y. Ohkubo, H. Yonezawa, TOSHIBA Co., Tokyo, Japan
H. Baba, NIHON KOSHUHA Co., Ltd., 1119 Nakayama, Yokohama, 226 Japan

Abstract

Hardware R&D on the C-band (5712 MHz) RF-system for an electron/positron linear collider started in 1996 at KEK. During two years R&D, we have developed two 50-MW C-band klystrons (TOSHIBA E3746 #1, #2), the "Smart Modulator", the traveling-wave resonator (TWR) and the cold model of the rf-pulse compressor [1,2]. A C-band accelerating structure, which uses the choke-mode cavity, is under development. Its HOM-damping performance will be tested at ASSET beam-line in this year. Since the C-band system is designed to accelerate high-current beams at a high accelerating gradient of 36 MV/m, there are various applications in the future beside the linear collider. For example, we can build an injector for the SR-ring in a limited site-length. Additionally, since the C-band components are compact, it has a big potentiality to be widely used in various medical and industrial applications, such as an electron-beam radiotherapy machine, or a compact non-destructive X-ray imaging system.

1 INTRODUCTION

The e^+e^- linear collider is a large-scale project. In the main linac for two beams, we need more than 7000 accelerating structures, 3500 klystrons and their pulse modulators. Therefore, the hardware has to meet the followings:

(1) Highly reliable,
(2) Simple,
(3) Low construction cost,
(4) Reasonably power efficient and
(5) Operationally ease.

The above list provides a guideline and boundary conditions to our R&D works. Among the system parameters, the choice of the drive rf-frequency plays the most important role concerning to the system performance as well as the hardware details. We proposed the C-band frequency as the best choice to meet all of the demands listed above [1].

2 SYSTEM DESCRIPTION

Figure 1 shows a schematic diagram of one unit in the main linac rf-system. The deigned value of the accelerating gradient in ref. [1] was 32 MV/m. It is now 36 MV/m, which has been increased by a new idea concerning the RF pulse compressor (see later) and improved shunt impedance in the accelerating structure. The required number of unit for 500 GeV c.m. energy was reduced to 1800 units (it was 2040 units).

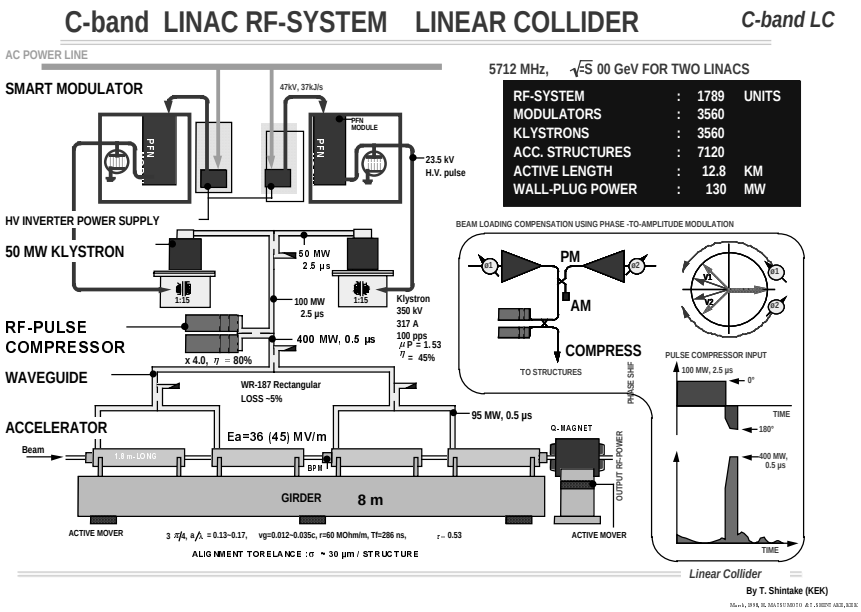

Fig. 1 One unit of the C-band RF system.

3 PROGRESS ON HARDWARE R&D

3.1 Waveguide Components

Since this is the first project to use the C-band frequency as the beam acceleration, no high-power waveguide component of vacuum-tight design was available in the market. We newly developed various waveguide components, including a ceramic window, at EIA-WR187 size (Fig.2). [3] We assembled a traveling-wave resonator (TWR), and tested it up to 90 MW of the accumulated power with 2.4 μsec pulse-width. No difficulty concerning to the high-power operation was found at this power level.

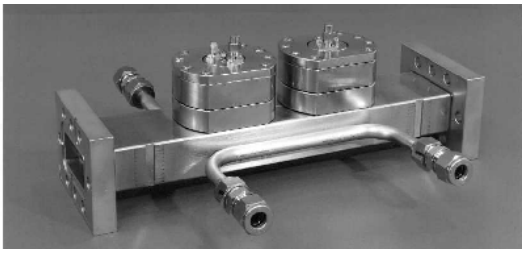

Fig.2 C-band waveguide component (Bethe holecoupler).

3.2 RF Pulse Compressor

The authors have proposed a new type RF pulse compressor in 1996 [4]. It can generate a flat output pulse from an energy-storage cavity of 1 meter long. It eliminated the long pipes required in SLED-II type compressor. To compensate ringing response associated with the multi-cell coupled cavity, the amplitude modulation is applied on the input RF power. In 1997, we demonstrated generation of a flat pulse using a cold model pulse-compressor cavity (Fig. 3, Fig. 4). The energy gain of 3.25 was obtained [5].

To improve the power gain, we started a study on a new idea: recovering rf-energy from the front part of the modulator pulse. A phase modulator is used to compensate a phase slip in the klystron. Since the pulse-compression cavity acts as the energy storage, the rf-energy in the front part is accumulated and contributes to the output energy.

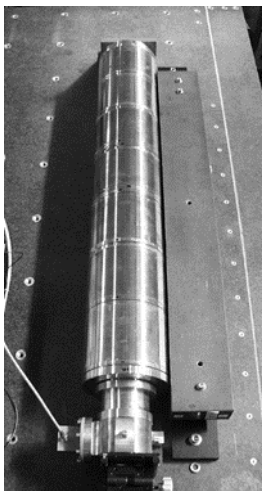

Fig. 3 Three-cell pulse compression cavity.

A tentative test showed enhancement of the power gain of 1.3 [6]. To apply this idea in the practical accelerators, we need to develop a RF feedback module (IQ-modulator and demodulator, a microprocessor and a solid-state RF amplifier of 500 W output level). This RF feedback module will be also useful in various accelerators to compensate the beam loading effects, such as in a beam buncher system or a rf-gun to generate a stable beam into FEL oscillators.

3.3 C-band Klystron R&D

In 1996 FY, we developed the first tube E3746 #1, which employed conventional design: the single-gap output structure and the solenoid focus. It generated 50 MW power into 1 μsec width at 20 pps repetition [7,8]. We continuously operated the klystron at C-band test-lab until the second tube being ready.

In 1997 FY, we developed the second tube E3746 #2. This is an upgrade version of the first klystron, in which the single-gap output structure was replaced with a newly developed 3-cell traveling-wave output structure shown in Fig. 5. The second tube generated 54 MW peak power in 2.5 μsec at 50 pps. The power efficiency was improved to 44%. Fig. 6 shows the output waveform from the second klystron. Details are reported at this conference [9].

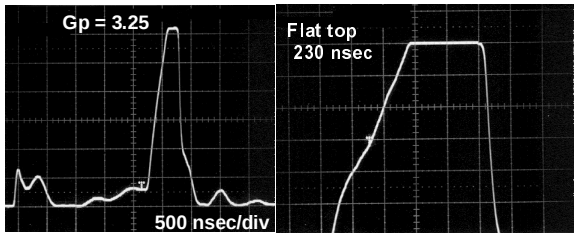

Fig. 4 Flat-top rf pulse compression using 1-m long 3-cell delay-line.

Recently we have developed an advanced calorimetric method for the absolute rf-power measurement. To eliminate uncertainty in flow-rate measurement of cooling water, we introduced an electric heater in the cooling water system. Since we can accurately determine the dissipation power on the heater by VI product, this method enables to determine the absolute power accurately.

3.4 Smart Modulator (Klystron Power Supply)

The C-band klystron uses a high-voltage pulse of –350 kV peak and 3.5 μsec width. The conventional PFN line-type pulse-modulator is suitable to generate this pulse, and no essential difficulties are expected. Therefore, R&D work was focused on reducing cost and improving reliability. In 1993, Prof. M. H. Cho and Prof. H.

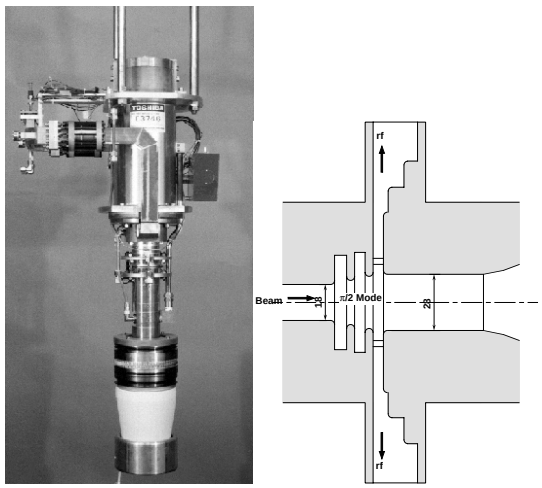

Fig. 5 The C-band klystron: TOSHIBA E3746 #2, and its traveling-wave output structure..

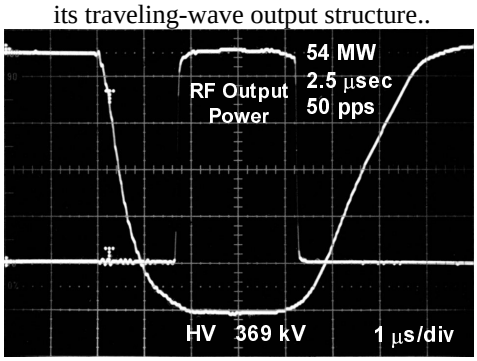

Fig. 6 RF output power of the second E3746 C-band klystron.

Matsumoto proposed a concept of “Smart Modulator”, which is an ideal modulator: simple, compact, reliable and low cost. As the first step, we developed a prototype of the smart modulator, which is

1. Direct HV charging from an inverter power supply.
2. No deQ-ing circuit.
3. Much smaller size than conventional modulators.
4. Uses existing reliable circuit components.

The developed smart-modulator is shown in Fig. 7. The main cabinet size is 1600x2000x1200 mm only, which is now running daily driving the 50 MW klystron [10,11,12].

Fig. 7. The smart-modulator (white box at upper-right), the C-band klystron (middle), and the C-band members.

3.5 Accelerating Structure

A C-band accelerating structure is under development at MITSUBISHI heavy industry [13]. It uses a special rf cavity called the choke-mode cavity, which strongly damps all higher-order-modes using microwave absorbers made by SiC [14]. The rf power for the beam acceleration is confined in the main cavity by means of a choke-filter. Figure 8 shows the structure under fabrication. It uses Matsumoto-coupler for symmetric field at input/output coupler. To align beams on its center, two RF-BPMs will be mounted at both ends, and one HOM pickup will be used at middile. The basic performance of the RF-BPM was tested at FFTB-beam line, and 25 nm of resolution was measured [15]. The RF-BPM in Fig. 8 is the upgraded version, which does not have the common-mode leakage. The HOM damping performance will be tested at ASSET beam line of SLAC in this year.

4 FUTURE R&D

The first stage of the R&D was successful. For the next step, in order to examine the system performance under a realistic situation, one-unit of the C-band system has to be installed and tested with beam in an existing machine, such as KEK-B injector. Daily operation will tell us what we should do next.

ACKNOWLEDGMENT

We thank Mr. Kazuharu Nishitani for his various contributions to build the experimental equipment. We thank Profs. H. Sugawara, G. A. Loew, W. Namkung and Prof. G. A. Voss, for their encouragement to our work. We also thank all contributors to this project.

REFERENCES

[1] T. Shintake *et al.*, “C-band Main Linac RF System for Linear Collider”, LINAC96, KEK preprint 96-122, Sep. 1996 A

[2] T. Shintake *et al.*, “C-band RF-system Development for e+e- Linear Collider”, APAC98, KEK preprint 98-30, April 1998 A

[3] H. Matsumoto *et al.*, "Development High Power Waveguide Components..", PAC97, KEK Preprint 97-50, June 1997

[4] T. Shintake *et al.*, "A New RF Pulse-Compressor using Multi-Cell Cavity", EPAC96, KEK Preprint 96-71, July 1996

[5] T. Shintake *et al*, "Development of C-band RF Pulse Compression..", PAC 97, KEK Preprint 97-48 June 1997 A.

[6] M. Yoshida *et a*, “Efficiency Enhancement of RF-pulse Compressor for C-band RF-System”, this conference.

[7] T. Shintake *et al.*, "Development of C-band 50 MW Pulse Klystron..", PAC97, KEK Preprint 97-47, June 1997 A

[8] H. Matsumoto *et al.*, “Operation of the C-band 50 MW Klystron..”, APAC98, KEK preprint 98-31, April 1998 A.

[9] Y. Ohkubo, “C-band 50 MW Klystron using Traveling-wave Output Structure”, this conference.

[10] J. S. Oh *et al.*, “Efficiency Issue in C-band Klystron-Modulator...”, PAC97, KEK Preprint 97-51, June 1997 A

[11] J. S. Oh *et al.*, “Efficiency Analysis of 111-MW C-Band Modulator…”, APAC98, KEK preprint 98-32, April 1998 A.

[12] H. Baba *et al.*, “Pulsed Modulator for C-band Klystron”, APAC98, KEK preprint 98-33, April 1998 A.

[13] H. Matsumoto *et al.*, “Fabrication of The C-band Choke Mode-type Damped Accelerating Structure”, this conference.

[14] N. Akasaka *et al.*, “Optimization of Wakefield Damping in C-band Accelerating Structure”, this conference

[15] T. Slaton *et al.* “Development of Nanometer Resolution C-band Radio Frequency Beam Position Monitors in the Final Focus Test Beam” , this conference

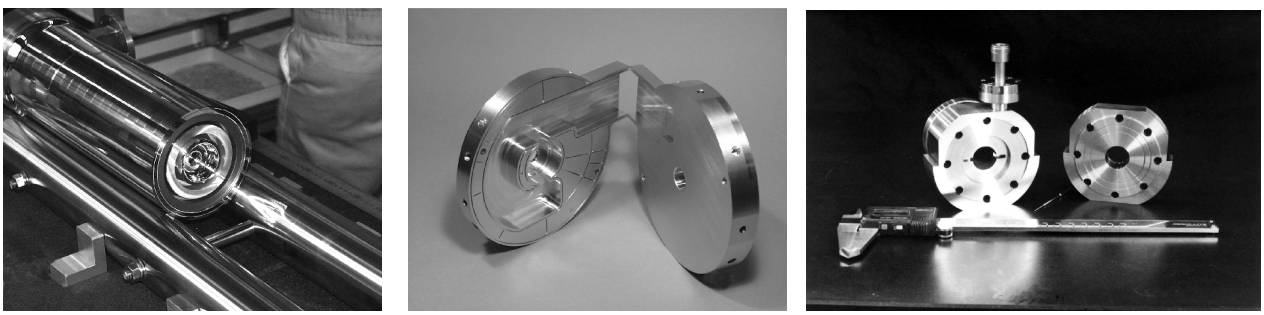

Fig. 8 C-band accelerating structure fabrication.
(left)choke-mode cell with SiC ring, (middle) Matsumoto-coupler and (right) common-mode free RF-BPM.

THE DRIVE BEAM DECELERATOR OF CLIC

A. Riche, D. Schulte, CERN, Geneva, Switzerland

Abstract

In the Compact Linear Collider (CLIC) a high-current, low-energy beam will be decelerated in a chain of power extraction structures to produce the RF-power necessary to accelerate a low-current, high-energy beam in the main linac. The transverse dynamics of the decelerated beam is discussed, based on results of the programs WAKE [1] and PLACET [2]. The very large energy spread and strong transverse wakefields as well as the high group velocity of these fields and the considerable length of the bunch train are important factors. Static and dynamic imperfections are considered including ground motion. The choice of parameters for the structures is investigated. A promising beam-based alignment technique is presented that makes use of a low emittance beam.

1 INTRODUCTION

CLIC [3] is based on a two-beam scheme. The RF power used to accelerate the main beam (at $30\,\mathrm{GHz}$) is produced by a second high-current low-energy beam (drive beam) running parallel to the main one [4], which is decelerated in power extraction structures, to produce the RF power.

Each drive beam decelerator is on average $767\,\mathrm{m}$ long and contains 550 power extraction structures. The train producing the power consists of 1824 bunches. Along the train the bunch charge increases over the first 320 bunches and then stays constant (at $17.6\,\mathrm{nC}$). This charge ramp is necessary to compensate the beam-loading in the main linac [5]. In the following simulations, the charge of the first bunch is assumed to be half of the charge of a bunch on the flat top. Within the ramp the bunch charge increases linearly with the bunch number.

Depending on the beam-loading compensation in the drive beam accelerator, the ramp may be different from the model used and the flat top may be followed by a tail of bunches with decreasing charge. However, first simulations indicate that the different ramps have little influence.

The bunches are separated by a distance of $2\,\mathrm{cm}$, have a length of $\sigma_z = 400\,\mu\mathrm{m}$ and have normalised transverse emittances of $\gamma\epsilon_x = \gamma\epsilon_y = 150\,\mu\mathrm{m}$. The initial energy is $E = 1.2\,\mathrm{GeV}$ and the initial energy spread is assumed to be $\sigma_E/E \approx 1\,\%$ RMS [6]. During deceleration the energy spread increases to about $90\,\%$ of the initial energy.

2 MODULE LAYOUT

To simplify the longitudinal matching of the drive beam decelerators and the main linac they both consist of modules of equal length. A main linac module contains up to four structures—one to four of which can be replaced by quadrupoles if necessary. A drive beam decelerator module consists of two structures, quadrupoles and beam position monitors (BPMs) forming a FODO-cell. Each drive beam structure has an active length of $0.8\,\mathrm{m}$ and feeds two main linac structures, its total power is $512\,\mathrm{MW}$.

In modules where main linac structures are replaced by quadrupoles, decelerator structures will be replaced by drifts or special types that feed one structure only.

3 STRUCTURE MODEL

Here, only on the so-called four-waveguide structure [7] is considered. The inner bore of the structures is cylindrically symmetric, except for the four longitudinal waveguides that are cut into the surface.

The longitudinal and transverse wakefields can each be described very well by a single mode. These modes have almost the same frequency—longitudinally it is $30\,\mathrm{GHz}$, transverly it is $24\,\mathrm{MHz}$ lower.

In contrast to most structures in accelerators, the group velocities of the longitudinal and transverse modes $\beta_{\parallel,\perp}$ are comparable to the speed of light—e.g. $\beta_\parallel \approx \beta_\perp \approx 0.44c$.

The maximum, minimum and mean energy of each bunch is shown in Fig. 1 at the end of the decelerator.

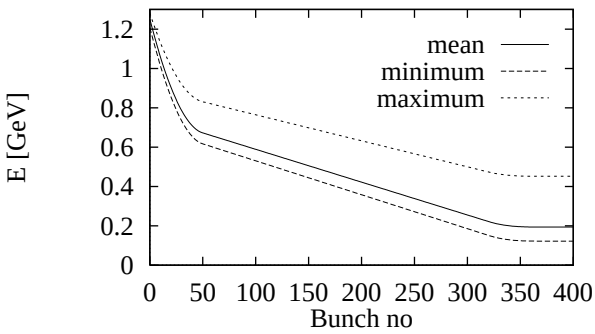

Figure 1: The final minimum, maximum and mean energy of each bunch as a function of the bunch number. Only the first 400 bunches are shown, on the flat top the values are constant.

4 LATTICE

The lattice consists of simple FODO-cells with a quadrupole spacing of half a girder length or $1.115\,\mathrm{m}$. Ignoring the additional drifts or special structures, each decelerator consists of 275 modules supporting 550 structures. For the same normalised emittance the maximum envelope in a periodic lattice is given by the particles with the lowest energy [8]. The lattice is scaled to have constant beta-functions for the lowest energy. The dependence of the final envelope on the final energy is shown in Fig. 2. A phase advance of $\Delta\Phi = 88°$ per cell was chosen. Larger phase advances reduce the sensitivity to transverse wakefields but increase the maximum transverse beam size. The three-sigma envelope of the beam is shown in Fig. 3. It shows the adiabatic undamping due to the decreasing energy.

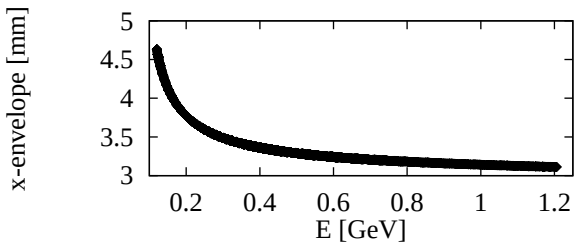

Figure 2: Final beam size versus final energy in the drive beam.

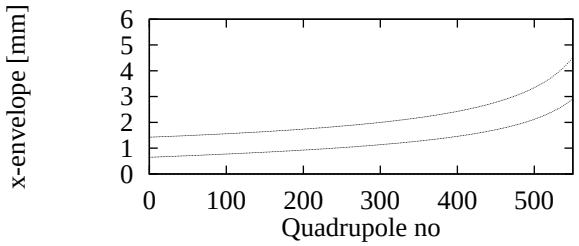

Figure 3: The envelope of a three-sigma beam along the decelerator in the focusing and defocusing quadrupoles.

5 STABILITY

In order to find the optimum iris radius a of the decelerating structures a scaling law for the longitudinal and transverse wakefields was derived using three different structures with $a = 10,\ 12$ and $20\,\mathrm{mm}$. The wakefields were found to scale as $\hat{W}_\perp \propto a^{-5}$ and $\hat{W}_L \propto a^{-3}$. The group velocity remains about constant.

Simulations were performed for different values of a and Q, ignoring the field non-uniformity. The layout of the decelerator was kept constant. In order to achieve the same power and initial-to-final energy ratio, the charge per bunch and initial energy were adjusted. Figure 4 shows the maximum amplitude reached by a three-sigma particle. The initial beam offset was $\Delta x = \sigma_x$. As can be seen, larger radii lead to a more stable beam. For very small values of Q, the envelope is larger at large radii, just because the emittance is larger due to the smaller energy.

The maximum charge per bunch is fixed by the drive beam injector to about $20\,\mathrm{nC}$. The parameters are thus chosen to be $a = 12\,\mathrm{mm}$ corresponding to $R/Q = 31\,\Omega/\mathrm{m}$. The necessary output power of $P = 512\,\mathrm{MW}$ can then be provided by $q \approx 17.6\,\mathrm{nC}$. The achievable Q is 50 [5].

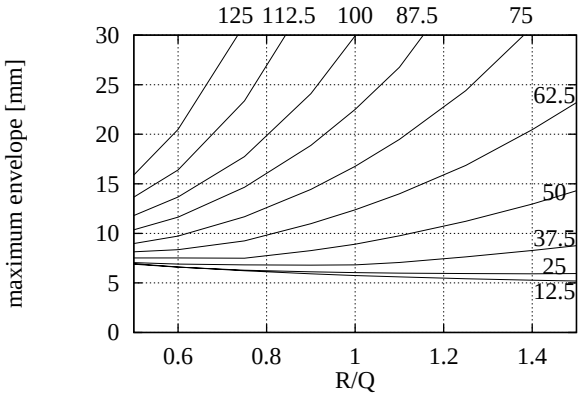

Figure 4: The maximum envelope of a three sigma beam with an initial offset of one sigma for different four-waveguide structures. The radius was varied to achieve different values of R/Q. The curves correspond to different Q-values.

6 NON-UNIFORMITY OF THE FIELD

The waveguides lead to a variation of the longitudinal field with the transverse offset r and ϕ. This in turn gives rise to a transverse kick

$$\Delta p_\perp(r,\phi) = \Delta p_{z,0} \sum_{k=1}^{\infty} 4k \frac{r^{4k-1}}{a^{4k}} \frac{\lambda}{2\pi} \sin(2\pi s/\lambda)$$
$$c_k[-\vec{e}_r \cos(4k\phi) + \vec{e}_\phi \sin(4k\phi)]$$

Here, $\phi = 0$ lies in a symmetry plane in the centre of a waveguide.

In the simulation only $k = 1$ and $k = 2$ are taken into account. The higher-order terms will cause a significant field only at large radii due to the $(r/a)^{4k}$ dependence.

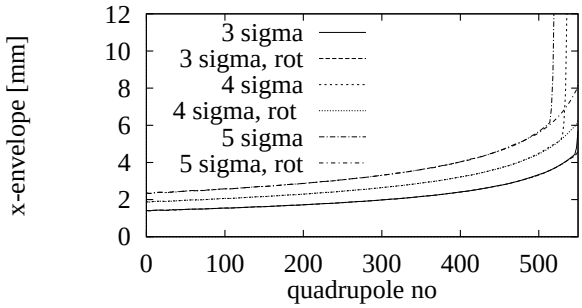

Figure 5: The envelope of an on-axis beam with and without rotating the structures at the focusing quadrupoles.

Figure 5 shows the envelopes for on-axis beams for particles with Courant-Snyder invariants $A_x^2 = c^2\epsilon_x$ and $A_y^2 = 0$. In this symmetry plane the forces are purely radial. The three-sigma particles barely pass. The situation improves significantly if every second structure is turned by 45° to get a cancellation of focusing and defocusing deflections. Here, the term with $k = 2$ may become important since it is not cancelled, but even the five-sigma particles turn out to be stable.

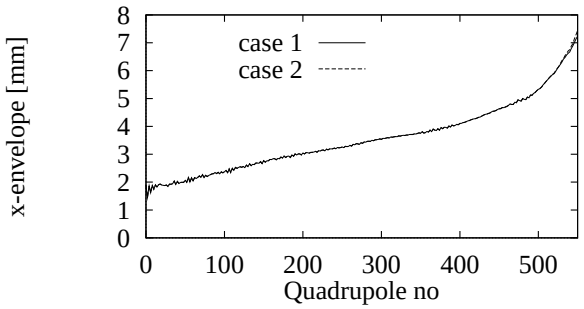

Figure 6: The envelope for a three sigma beam with an initial offset of $\delta_x = \sigma_x$ with (case 2) and without (case 1) taking into account the non-uniformity of the field.

To see the effect of the non-uniformity in the presence of beam jitter, the envelope for particles starting with $A_x^2 = 3^2\epsilon_x$ and $A_y^2 = 0$ for a beam with an initial offset $\delta_x = \sigma_x$ is calculated, with and without taking the non-uniformity into account. If the structures are rotated as described before, the difference is negligible, see Fig. 6. The same behaviour is expected for $A_x^2/\epsilon_x + A_y^2/\epsilon_y \leq 3^2$, but this needs more investigation.

7 ALIGNMENT AND STEERING

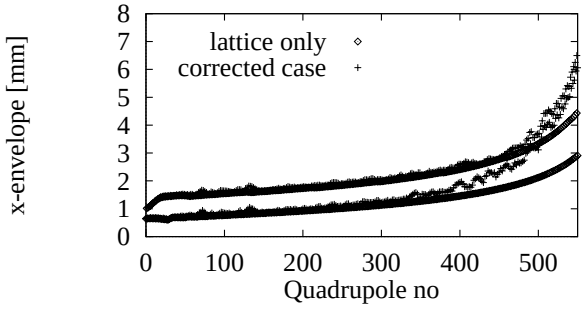

Figure 7: The envelope along the beamline after applying the ballistic correction.

Beam-based alignment is used to reduce the effect of the initial position errors of the beamline elements. One such method is the so-called "ballistic correction" [9], in which the beamline is divided into bins containing a number of quadrupoles and BPMs. The bins are aligned one after another in two steps that can be iterated if necessary. In the first step the quadrupoles in the bin are switched off. The beam is steered into the last BPM of the bin using a correction coil. The centres of the other BPMs are then shifted onto the beam trajectory—either using software or hardware. In the second step the quadrupoles are switched on and a few-to-few steering is performed. In this method, the beam has to be transported over some distance without focusing. This is not possible with the large emittance drive beam without major beam loss. Therefore it is necessary to use a low emittance beam such as, for example, the main beam after the damping ring. This beam has a bunch length of $\sigma_z = 300\,\mu\mathrm{m}$ and an energy of $E = 1.98\,\mathrm{GeV}$. Its emittance is less then $\gamma\epsilon_x \leq 2\,\mu\mathrm{m}$ in the horizontal plane. After aligning the BPMs, a simple one-to-one steering can be performed using the whole bunch train. The resulting envelope in a test case—not taking the non-uniformity into account—is shown in Fig. 7.

8 CONCLUSIONS

For a given type of power extraction structure it was found that increasing the aperture, and simultaneously decreasing the initial beam energy and increasing the bunch charge, improves the stability. Therefore the maximum beam current achievable by the injector has been chosen. The required output power then defines the structure aperture.

The non-uniformity of the longitudinal field effectively reduces the available aperture since particles at large radii are lost rapidly. Rotating every second structure improves the situation considerably, using a structure with a higher order of symmetry solves the problem. For example six-waveguide and eight-waveguide structures are under investigation.

With the present parameters a three-sigma beam is expected to pass the whole decelerator even if it has an uncorrected offset of one sigma at the beamline entry.

Further studies are necessary to understand the effect of the field non-uniformity on the correction scheme.

9 REFERENCES

[1] A. Riche, To be published.

[2] D. Schulte, to be published.

[3] J.-P. Delahaye and 30 co-authors, "CLIC a 0.5 to 5 TeV Compact Linear Collider." *EPAC 1998*.

[4] H.H. Braun and 14 co-authors, "The CLIC RF Power Source." to be published in CERN/PS 98-011 (LP).

[5] L. Thornadahl, private communication.

[6] D. Schulte, "The drive beam accelerator of CLIC." This conference.

[7] G. Carron, A. Millich, and L. Thorndahl, "Transfer structure for the CLIC study." To be published at ICAP 1998.

[8] A. Riche, "Maximum energy transfer efficiency in CLIC drive beam. *CLIC-Note 266*, 1994.

[9] D. Schulte, to be published.

OPTICS ELEMENTS FOR MODELING ELECTROSTATIC LENSES AND ACCELERATOR COMPONENTS IV. ELECTROSTATIC QUADRUPOLES AND SPACE CHARGE MODELING

George H. Gillespie
G. H. Gillespie Associates, Inc., P.O. Box 2961, Del Mar, CA 92014, U.S.A.

Abstract

Optical models for a variety of electrostatic elements have been developed for the computer code TRACE 3-D. TRACE 3-D is an envelope (matrix) code that includes a linear space charge model and is primarily used to model bunched beams in magnetic transport systems and radiofrequency (RF) accelerators. New matrix models have been developed that allow the code to be used for modeling beamlines and accelerators with electrostatic components. These new models include a number of options for simulating: (1) einzel lenses, (2) dc accelerator columns, (3) electrostatic deflectors (prisms), and (4) electrostatic quadrupoles. A prescription for setting up the initial beam appropriate to modeling 2-D (continuous) beams has also been developed. The models for (4) are described in this paper and examples of their use are illustrated. The relationship between the 3-D (bunched beam) and 2-D (dc beam) space charge modeling is discussed and comparisons of numerical results to other calculations are presented.

1 INTRODUCTION

The TRACE 3-D program [1] is one of the standard codes used in the design of standing wave radiofrequency linacs and transport lines for high-current bunched beams. Considerable work has been done on extending the program to model a new array of accelerator problems, including wakefields [2], traveling wave structures [3], and electrostatic lenses [4]. This paper describes recent work at further extending the capabilities of TRACE 3-D.

2 ELECTROSTATIC QUADRUPOLES

Two electrostatic (ES) quadrupoles models have been developed for use in TRACE 3-D. One is a hard-edge model where the magnitude of the quadrupole field is constant over the quadrupole length and zero elsewhere. The second models fringe fields as linear functions that act over specified fringe field entrance and exit distances.

2.1 Hard-Edge ES Quadrupole

The first order optics for a particle moving in the field of an ES quad are the same as those for the motion in a magnetic quad using an equivalent field gradient B':

$$B' = 2V_o/(a^2\beta c) \quad , \qquad (1)$$

where V_o is the electrode voltage of the ES quadrupole, a is the radial aperture of the ES quadrupole, and βc is the velocity of the particle. The hard-edge ES quad model [2] in TRACE 3-D simply calls the hard-edge magnetic quadrupole subroutine using a gradient given by (1).

2.2 ES Quadrupole with Fringe Field

Electrostatic quadrupoles with fringe fields are often modeled in terms of a potential function of the form:

$$\phi(x,y,z) = + V(z)\,(x^2 - y^2)/a^2 \quad , \qquad (2)$$

where V(*z*) is a smooth function used to model the longitudinal variation of the quadrupole strength. The electric field is given by the gradient of ϕ: $\boldsymbol{E} = -\nabla\phi$. However, this electric field does not, in general, satisfy Maxwell's equation $\nabla\bullet\boldsymbol{E} = 0$. For the special case in which $V(z)$ is a piece-wise linear (or constant) function of *z*, then $\nabla\bullet\boldsymbol{E} = 0$ almost everywhere. The fringe field ES quadrupole uses a function $V(z)$ which rises linearly from zero to a maximum value V_o over an entrance length d_1, remains constant at V_o for a distance given by the effective electrode length *l*, and then decreases linearly to zero over an exit length d_2.

2.3 R-Matrix Elements and Example

A first-order 6×6 transfer matrix (R-matrix) is used to describe particle optics in the paraxial approximation. The elements of the R-matrix are computed directly from the electric fields using standard methods [4,5]. For the fringe field ES quadrupole, the region over which the fields act is divided into small steps of length Δz and four R-matrices are computed for each step: a drift matrix [1] of length Δz /2, a lens matrix which computes the quadrupole impulse, another drift matrix of length Δz /2, and a space-charge impulse matrix to model the linear space-charge forces (described in Section 3).

The non-trivial elements of the quadrupole lens R-matrix at location *z* are:

$$R_{21} = - R_{43} = - 2q\Delta z\, V(z)/(a^2\beta^2\gamma mc^2) \quad . \qquad (3)$$

Table 1 summarizes test TRACE 3-D calculations carried out for the hard-edge and fringe-field models with short fringe lengths, which are compared to magnetic quadrupole results. The fringe-field ES quad calculations required a maximum step size of $\Delta z = 0.1$ mm to obtain the results shown, whereas accurate results were obtained for the magnetic and hard-edge ES quads with $\Delta z = 2.0$ mm. Using the relation (1), the agreement is good between all cases.

Table 1. Comparison of quad fitting (matching) results (Example B of reference [1] without RF elements) for hard-edge ES quads, fringe-field ES quads (small d_1 and d_2), magnetic quads, and expected ES values from Eq. (1).

Quad Model	MMF (10^{-6})	Quad 1 (V_o or B')	Quad 2 (V_o or B')	Quad 3 (V_o or B')	Quad 4 (V_o or B')
Magnetic	2	- 20.2647 T/m	22.4726 T/m	- 19.6900 T/m	18.3534 T/m
Equation (1)	-	- 14.0189 kV/cm	15.5463 kV/cm	- 13.6213 kV/cm	12.6967 kV/cm
Hard-Edge ES	17	- 14.0189 kV/cm	15.5464 kV/cm	- 13.6214 kV/cm	12.6967 kV/cm
Fringe-Field ES	55	- 14.031 kV/cm	15.559 kV/cm	- 13.629 kV/cm	12.706 kV/cm

3 2-D SPACE CHARGE MODELING

Space charge is treated in TRACE 3-D as a linear force using the equivalent uniform beam model. The electric field components inside a uniformly charged 3-D ellipsoid, with semiaxes given by r_x, r_y and r_z, are [1]:

$$E_x(x,y,z) = (\kappa/\gamma^2)\,[(1\text{-}f(p))/(r_x(r_x+r_y)r_z)]x \quad , \quad (4)$$

$$E_y(x,y,z) = (\kappa/\gamma^2)\,[(1\text{-}f(p))/(r_y(r_x+r_y)r_z)]y \quad , \quad (5)$$

and

$$E_z(x,y,z) = \kappa\,[f(p)/(r_x r_y r_z)]z \quad , \quad (6)$$

where $\kappa=3\lambda I_b/(4\pi\varepsilon_o c)$, γ is the relativistic energy factor of the beam, and f(p) is the 3-D ellipsoidal form factor. I_b is average beam current, where each bunch passes a given point once per RF cycle (wavelength is λ). The form factor depends on $p=\gamma r_z/(r_x r_y)^{1/2}$: for p>1, f(p) is:

$$f(p) = [p\,ln\,[p+(p^2+1)^{1/2}]/(p^2+1)^{3/2}] - 1/(p^2+1)^{1/2} \quad . \quad (7)$$

Equations (4)-(6) for the bunched beam electric fields can simulate dc beam fields by taking appropriate limits.

3.1 Space Charge for Continuous Beams

For r_z much larger than r_x and r_y, the 3-D ellipsoidal beam bunch becomes elongated and the shape near the center approaches that of a 2-D beam with an elliptical cross section whose semiaxes are given by r_x and r_y. The electric fields in this case are obtained in the limit where p becomes very large. In the limit of large p, the 3-D ellipsoidal form factor becomes:

$$f(p) = [ln(2p) - 1] / p^2 \quad , \text{ for } p>>1. \quad (8)$$

The electric field becomes:

$$E_x(x,y,z) = (\kappa'/\gamma^2)\,[1/(r_x(r_x+r_y))]x \quad , \quad (9)$$

$$E_y(x,y,z) = (\kappa'/\gamma^2)\,[1/(r_y(r_x+r_y))]y \quad , \quad (10)$$

$$E_z(x,y,z) = (\kappa'/\gamma^2)\,[[ln(\gamma r_z/(r_x r_y)^{1/2}) - 1]/(r_z^2)]z \quad , \quad (11)$$

where $\kappa'=(\kappa/r_z)$. The field components (9) and (10) are of the same form [8] as those for a continuous uniformly charged, 2-D elliptical cross section beam, with semiaxes r_x and r_y, when the parameter $\kappa'=I_{dc}/(\pi\varepsilon_o\beta c)$. I_{dc} is the current for the continuous (dc) beam. Consequently, the transverse electric fields computed by TRACE 3-D are the same as those for a dc beam if the bunched beam current is related to the continuous beam current by:

$$I_b = (4/3)(r_z/\beta\lambda)\,I_{dc} \quad . \quad (12)$$

The longitudinal electric field (11) varies very slowly (logarithmically) with the transverse beam dimensions, and becomes small for large r_z. The bunch length r_z will not change due to the longitudinal space charge force if the total beamline length L over which the envelope equations are integrated is small compared to the initial r_z. Therefore, two conditions on the initial bunch length need to be satisfied so that the bunched beam space charge fields reduce to those for a continuous beam:

$$r_z >> (r_x r_y)^{1/2}/\gamma \quad \text{and} \quad r_z > L \quad . \quad (13)$$

Both conditions are achieved in the normal situation where the transverse dimensions are small compared to the beamline length, and one selects an initial value for the bunch length greater than L. The longitudinal emittance and Twiss parameters are:

$$\varepsilon_z = r_z(\Delta p/p) \quad \pi\text{-meter-radian} \quad , \quad (14)$$

$$\alpha_z = 0 \quad , \quad (15)$$

and

$$\beta_z = r_z/(\Delta p/p) \quad \text{meter/radian} \quad , \quad (16)$$

where r_z is in meters and $\Delta p/p$ is the momentum spread.

Using the formulas (12) and (14)-(16), the TRACE 3-D space charge fields reduce to those for a 2-D continuous beam when the conditions (13) are satisfied.

3.2 Comparisons to Semi-Analytic Calculation

The accuracy of the 2-D simulation has been verified using TRACE 3-D by comparing the space charge radial expansion of cylindrical beams with results for the semi-analytic solutions. Table 2 summarizes one comparison.

The space charge expansion of a zero emittance, cylindrical beam can be expressed in terms of Dawson's integral. For a beam with radius r_o and no divergence at z=0, the downstream r and z are related by [7]:

$$(z/r_o) = (2/K)^{1/2}\,(r/r_o)\,D[ln((r/r_o)^{1/2}] \quad , \quad (17)$$

where $D[\xi]$ is the value of Dawson's integral at ξ, and is available in tabulated form [9]. $K=2(I_{dc}/I_o)\,\beta^{-3}\gamma^{-3}$ is the generalized beam perveance and I_o is the Alfven current.

Table 2. Comparison of the simulated beam radius, for the space-charge expansion of 10 keV, 2 Ampere, dc (2-D uniform) e-beam, with the semi-analytic radius. The beam's initial phase space parameters are given in the text.

Length z (mm)	Drift Number	Drift Length	$\ln(r/r_o)^{1/2}$	Radius (mm) Semi-Analytic	Radius (mm) TRACE 3-D	Deviation (%)
1.6368	2	1.6368	0.02	10.00400	10.00400	0.00000
3.2750	3	1.6382	0.04	10.01601	10.01603	0.00020
8.2104	4	4.9354	0.10	10.10050	10.10057	0.00069
16.5869	5	8.3765	0.20	10.40811	10.40850	0.00375
119.6891	6	103.1022	1.00	27.18282	27.19945	0.06118
332.4853	7	212.7963	1.50	94.87736	94.94152	0.06763
548.5548	8	216.0694	1.70	179.93310	180.04664	0.06310
724.5571	9	176.0023	1.80	255.33722	255.49130	0.06034
976.9775	10	252.4205	1.90	369.66053	369.87306	0.05749

The Alfven current $I_o=4\pi\varepsilon_o[mc^3/q]=0.03335641 \times[mc^2(MeV)/q(e^-)]$ amps. The values $\xi=ln((r/r_o)^{1/2}$ shown in Table 2 were selected so that tabulated entries for D [ξ] could be used to determine the corresponding values of z/r_o. The perveance used (K=0.02986778) corresponds to a 2 amp, 10 keV beam with particle mass 0.511 MeV. A beamline of drift elements was constructed [10], whose lengths correspond to the intervals between the values of z/r_o. For a beam radius r_o = 10 mm, the resulting drift lengths and accumulated length z are given in Table 2.

The initial transverse phase space used values of $\varepsilon_x=\varepsilon_y=0.04$ π-mm-mrad, $\beta_x=\beta_y=2500$ mm/mrad and $\alpha_x=\alpha_y=0$. For the longitudinal parameters (14)-(16), initial values of $\Delta p/p = 5\times10^{-4}$ and r_z=100 meters were used. Simulations using I_b=0 confirmed that no beam expansion occurred due to finite transverse emittances.

The TRACE 3-D results shown in Table 2 used a radiofrequency of 2.998 MHz (λ just under 100 meters). Then, from Eq. (12), I_b=13.676 amps. The TRACE 3-D radii computed for this current agree with those from the semi-analytic calculation to better than 7 parts in 10,000. Other simulations to confirm the Eq. (12) scaling, and to explore limitations imposed by (13), were also performed with different λ, r_z, I_b, and with equal perveance beams.

4 SUMMARY

Optical elements for electrostatic quadrupoles have been developed for use in the TRACE 3-D code. A prescription for using TRACE 3-D to accurately simulate dc space charge effects has also been developed. Together with einzel lens [4], acceleration column [5], and deflector prism [6] models, TRACE 3-D has been expanded to model a spectrum of electrostatic systems.

ACKNOWLEDGEMENTS

The hard-edge ES quadrupole model was implemented by W. Lysenko [2] under CRADA number LA95C10203 between the Los Alamos National Laboratory and G. H. Gillespie Associates, Inc. The fringe-field ES quad model was developed using *PowerTrace*™ [10].

REFERENCES

[1] K. Crandall and D. Rusthoi, "TRACE 3-D Documentation," third edition, Los Alamos National Laboratory Report LA-UR-97-886 (1997) 106 pages.

[2] W. P. Lysenko, D. P. Rusthoi, K. C. D. Chan, G. H. Gillespie and B. W. Hill, "Wakefields in the TRACE 3-D Code," Proc. XVIII International Linear Accelerator Conf. (Geneva), Vol. 2, 845-847 (1996).

[3] M. C. Lampel, "A Self-Consistent Beam Loaded Traveling Wave Accelerator Model for Use in TRACE 3-D," to be published in the Proc. 1997 Particle Accelerator Conf. (Vancouver), 3 pages.

[4] G. H. Gillespie and T. A. Brown, "Optics Elements for Modeling Electrostatic Lenses and Accelerator Components I. Einzel Lenses," to be published in the Proc. 1997 Particle Accelerator Conf., 3 pages.

[5] G. H. Gillespie and T. A. Brown, "Optics Elements for Modeling Electrostatic Lenses and Accelerator Components II. Acceleration Columns," to be published in Nuclear Instruments and Methods in Physics Research B (1998) 4 pages.

[6] G. H. Gillespie, "Optics Elements for Modeling Electrostatic Lenses and Accelerator Components III. Deflector Prisms," in preparation.

[7] M. Reiser, *Theory and Design of Charged Particle Beams*, J. Wiley & Sons, New York (1994), p. 199.

[8] D. C. Carey, *The Optics of Charged Particle Beams*, Harwood Academic Publishers (1987), p. 284.

[9] M. Abramowitz and I. A. Stegun, *Handbook of Mathematical Functions with Formulas, Graphs and Mathematical Tables*, Ninth Printing, Dover Publications, New York (1972), p. 319, Table 7.5.

[10] *PowerTrace*™ is available from AccelSoft Inc., www.ghga.com/accelsoft.

RECENT DEVELOPMENTS IN THE ACCELERATOR DESIGN CODE PARMILA*

H. Takeda and J. H. Billen
Los Alamos National Laboratory, Los Alamos, New Mexico 87545 USA

Abstract

The PARMILA code, which originated in the 1960s for designing drift-tube linacs (DTLs), now designs and simulates the performance of many types of rf linear accelerator. The structure types include the DTL, coupled-cavity drift-tube linac (CCDTL) [1], conventional coupled-cavity linac (CCL), and several types of superconducting linac. This new code can handle multiple types of linac structures in a single run. This code features a more logically organized input sequence for the different linac structures and their properties. A PARMILA run can include sequences of beam-transport elements. In this paper, we describe the new user interface, highlighting the implementation of multiple rf structures. Also, we discuss the algorithm used for designing superconducting linac structures.

1 LINAC STRUCTURES

In designing a linac system, one first determines the types of linac (DTL, CCDTL, CCL, etc.). If a linac uses different rf structures, for example, one part of the linac requires a different number of cavities between focusing magnets then another, then we assign a new linac structure for that portion of linac. Starting from the low-energy end of the linac toward higher energy, up to 30 structures are allowed in an input file. The PARMILA code also calculates the beam-dynamics performance of the designed linac.

Each line of the PARMILA input file starts with a keyword, which in this paper we write in lower case letters in double quotes. At the beginning of the input file, we specify the global parameters on the "linac" line. Included parameters are: starting beam energy, bunch frequency, beam current, the beam particle mass and charge state. We specify whether the simulated particle distribution is read from a file created by another code (e.g. PARMTEQ [2] or a previous PARMILA run) with a "readdist" line, or if the distribution should be created anew by PARMILA according to data on the "input" line. After the global parameters for the whole linac are specified, each rf structure type starts with a "structure" line.

Figure 1 shows schematically the sections of a PARMILA input file. At junction between structures, the program keeps track of the ending state of beam characteristics in the linac. For typical room-temperature linacs, the inter-structure spacing is corrected so that the particle enters next structure with a correct phase. While the code designs the linac, it automatically creates a file of TRACE 3-D [3] elements which can be used for beam matching or optical element adjustment. For a multiple structure run, the sequence of rf structures follow the same order in the accelerator. Each structure is terminated as specified by a cell number on the "structure" line. Also, the particle distribution snapshots are stored in a file for later viewing with the DTLPROC postprocessor.

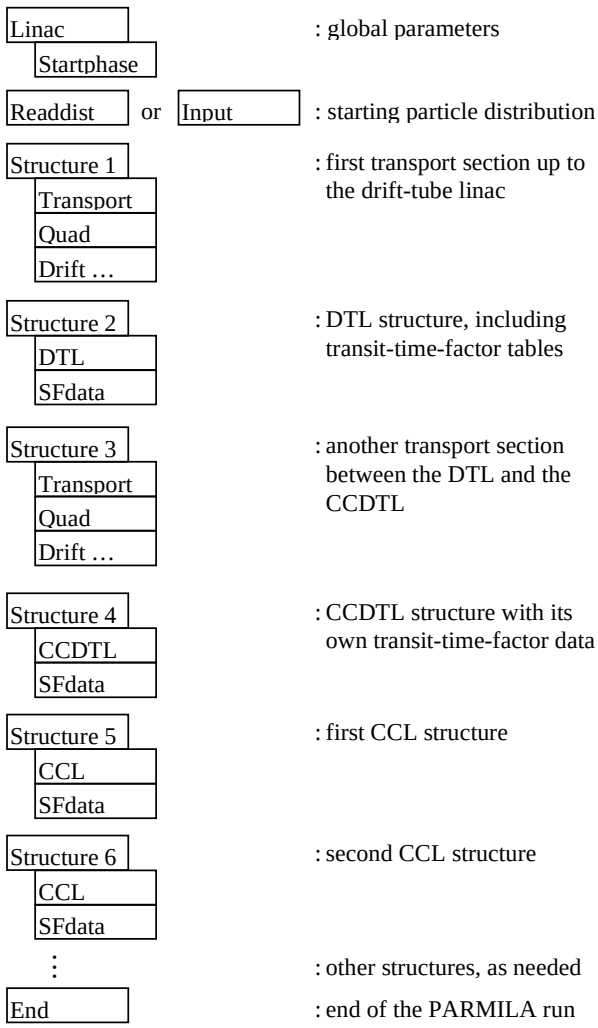

Figure 1. Schematic of a typical PARMILA input file.

*This work sponsored by the Division of Materials Sciences, US department of Energy, under contract number DE-AC05-96OR22464 with Lockheed Martin Energy Research Corporation for Oak Ridge National Laboratory.

2 INDIVIDUAL STRUCTURES

The keyword "structure" identifies and delimits the current linac structure. It includes the structure identification number, particle-dynamics termination cell number, frequency of the linac and the frequency used for the transit-time factors calculated by SUPERFISH [4]. All the phase coordinates of the initial particle distribution can be displaced by a specified amount if the rf module is driven by a separate power supply. Normally, one designs each linac structure one or more segments beyond the point where the beam-dynamics simulation ends. (Segments refer to contiguous sections of rf cavities, usually separated by focusing magnets.) This approach allows the code to calculate the distance between structures correctly. This can be specified by a design end energy parameter. For a CCDTL or CCL, one can design linac segments either with individual cell lengths proportional to particle velocity βc or with each segment made of cavities of identical length. In the latter case, the cell lengths are designed for a particle having the velocity $\beta_g c$, where the subscript g stands for geometrical.

One may specify several rf structure types such as "ccdtl", "ccl", "sc1", and "sc2". These keywords define parameters of a coupled-cavity drift-tube linac (CCDTL), a conventional coupled-cavity linac (CCL), or two particular types of superconducting cavity layout. For each of these structure types, PARMILA requires one or more tables of transit-time-factor data headed by one of the keywords "sfdata," "sfdatae," or "sfdataq." The three tables correspond to different boundary conditions imposed upon the fields in the bore tube at the edge of the cavity. The "scheff" keyword (for space-charge effects) specifies the initial space charge mesh size in each rf structure section. Once the particle dynamics starts (after a "begin" line), PARMILA adjusts the mesh size automatically to fit the extent of the particle distribution. An "output" keyword directs the code to store particle distribution snapshots at specified cell positions. The multiple structure run stops after encountering an "end" keyword.

3 TRANSPORT STRUCTURE

The "transport" structure type contains only beam optical elements. The code does not design an rf cavity layout for this sections an input file. A file can contain several "transport" sections, for example to match the beam's phase-space properties between accelerator sections. The user specifies transport elements such as "drift" and "quad" elements. After a "begin" keyword the code does the beam dynamics simulation through the specified optical elements. To assist designing the linac, PARMILA includes the transport elements in the TRACE 3-D input file that it automatically creates for the entire linac. A PARMILA run can consists only of a transport structure to simulate the beam dynamics. For a "transport" structure, the user can specify the starting design phase , if necessary.

4 CCDTL AND CCL STRUCTURE

The "ccdtl", or "ccl" line defines an rf structure of the same name. Both lines include data that specify the design termination energy, starting design phase angle, starting cavity field E_0, number of drift tubes per cavity (for the CCDTL), number cavities per segment, segment spacing, default quadrupole-lens parameters and other transverse focusing lattice settings. Other input lines ("extquad," "change") appearing after the "ccl" line or "ccdtl" line can be used to modify these default settings for specific rf cavities or magnets. There is considerable flexibility in the methods for defining the focusing magnet layout. For example, singlet or doublet quadrupoles can be placed a fixed distance from the end of each cavity segment, or each magnet location can be set individually. Also, their positions can be gradually moved within successive magnet spaces according to the beam velocity. The cavity field and amplitude can be set globally or automatically ramped using the "setramp," "e0ramp," and "phaseramp" lines. If one wants to maintain a constant real estate E_0T (accelerating field averaged over a transverse focusing period) across the segments, the "etfixed" line will compute the required acceleration.

After quadrupole and rf cavity definitions in the input file are the transit-time-factor tables. These tables list as a function of beam velocity βc several integrals computed by the SUPERFISH postprocessor SFO for a number of representative cavities. The "sfdata" table corresponds to symmetric cells, the "sfdatae" table is for cells at the edge of an internal cavity facing another cavity operated in the π mode, and the "sfdataq" table is for cell at the end of a segment where the electric field penetrates into the bore tube. The presence of these tables completes the linac design.

Once the linac is designed, one can modify the operating phase, amplitude, or quadrupole settings for a dynamics calculation. The "linout" line writes details of the designed linac to the output file. The "start" and "stop" lines tell the program the cell numbers on which to start and stop the beam-dynamics simulation. The "output" line specifies cell numbers for storing beam snapshots for later display by the DTLPROC postprocessor. If one simulates a well-matched 0-mA beam and saves the pseudo-particle coordinates at the center of each quadrupole magnet of a FODO lattice or a doublet lattice, the postprocessor DTLPROC can use the data to calculate the phase advance per focusing period along the linac.

5 SUPERCONDUCTING STRUCTURES

The "sc1" line defines a particular type of superconducting linac structure, which is characterized by

a missing segment at regular intervals. The "sc1" line includes number of cells per segment, missing segment interval, the energy gain per segment, the design end energy, design phase, segment separation and default quadrupole settings. The "sc2" line defines a superconducting linac structure, which is characterized by groups of cavity segments with quadrupole magnets between groups. The "sc2" line includes the energy gain per segment, segment spacing, number of segments between quadrupoles, and the lattice type: either a "singlet" lattice or "doublet" lattice. Like the room-temperature structures, the quadrupole settings for both superconducting layouts can be customized by "extquad" lines. The transit-time-factor tables used in the superconducting cavities are calculated by the SUPERFISH code for a number of beam particle velocities βc for the cavities with an identical cell length $\beta_g c/2$.

6 SUPERCONDUCTING LINAC DESIGN ALGORITHM

There are important differences between conventional room-temperature linacs and superconducting (SC) proton linacs now being proposed for some projects. In a SC linac of the type being designed for the Accelerator Production of Tritium project, multiple segments driven by the same power supply deliver equal power to the beam. Thus, each equally powered segment gives the same energy gain. Also, the segment spacing is fixed for large portions of the linac. Many cavity segments have identical lengths so that only a few different cavity shapes are manufactured for the entire linac. Unlike the conventional CCL, most cell lengths in the SC linac will differ considerably from $\beta\lambda/2$ (the distance traveled by a particle of velocity βc in one rf period). Instead of the usual phase difference of 180 degrees from cell to cell seen in a CCL, the phase changes may be tens of degrees larger or smaller than 180 degrees. By using active phase shifters, the rf power for each SC cavity segment can be driven independently. Within a segment, which consists of a series of coupled cells operated in the π mode, the relative rf phase between cells is fixed. Because of the usual large bore diameter in SC cavities, the fields in the end cavities extend out into the bore tube. This field penetration results in an effective shift of the electrical center from its geometrical center. The shift can be as large as ~2 cm for a 700-MHz cavity. These phase shifts are all included in the PARMILA code.

Because the lengths and positions of the of the SC linac cavities are predetermined, the design of the linac in PARMILA means finding the correct rf phase and the rf power at which to operate each segment. Because of the large phase slip from cell to cell, we trace a test particle through each segment recording the center-of-gap phases and energy gains of the particle. The code then requires two conditions simultaneously: 1) the energy gain must equal the design energy gain for the segment, and 2) the average phase must equal the design phase. This iterative process is performed by a two-dimensional optimization routine in PARMILA. After calculating the amplitude of rf electric field applied on one segment, and the entry and the exit phases of that segment, the code can compute the rf drive phase for the next cavity segment based upon the distance between segments and the difference between the exit phase of the upstream segment and the entry phase of the downstream segment.

7 SUMMARY

Format of PARMILA code input file was upgraded. The code can design and perform beam dynamics simulation of multiple linac structures in a single run including DTL, CCDTL, CCL, and superconducting linacs. Each linac structure is logically separated in the input file and the state of the beam at the end of each structure is transferred automatically to next structure type in the beam-dynamics simulation. Currently, a comprehensive PARMILA code documentation is in preparation.

8 REFERENCES

[1] J. H. Billen et al., "A New Rf Structure for Intermediate Velocity Particles," Proceedings of the 1994 Linear Accelerator Conference (August 21-26, 1994 Tsukuba, Japan).

[2] K. R. Crandall et al., RFQ Design Codes, Los Alamos National Laboratory report LA-UR-96-1836 (Revised May 20, 1998).

[3] K. R. Crandall and D. P. Rusthoi, TRACE 3-D Documentation, Los Alamos National Laboratory report LA-UR-97-886.

[4] J. H. Billen and L.M. Young, "POISSON SUPERFISH," Los Alamos National Laboratory report LA-UR-96-1834 (Revised April 22, 1997).

COMPARISON OF BEAM SIMULATIONS WITH MEASUREMENTS FOR A 1.25-MeV, CW RFQ†

H. Vernon Smith, Jr., Gerald O. Bolme, Joseph D. Sherman, Ralph R. Stevens, Jr.,
Lloyd M. Young, and Thomas J. Zaugg
Los Alamos National Laboratory, Los Alamos, NM 87545

Abstract

The Low-Energy Demonstration Accelerator (LEDA) injector is tested using the Chalk River Injector Test Stand (CRITS) radio-frequency quadrupole (RFQ) as a diagnostic instrument. Fifty-keV, dc proton beams are injected into the 1.25-MeV, CW RFQ and transported to a beamstop. Computer-simulation-code predictions of the expected beam performance are compared with the measured beam currents and beam profiles. Good agreement is obtained between the measurements and the simulations at the 75-mA design RFQ output current.

1 INTRODUCTION

To test the LEDA injector [1] under operating conditions, the ion-source extraction system is altered from a tetrode at 75 keV to a triode at 50 keV [2]. The rest of the 2.54-m-long LEDA injector is about the same as it will be when the initial tests of the LEDA RFQ [3] are made. We match the LEDA microwave-driven source H^+ beam (50 keV, 70-100 mA, >90% H^+ fraction) to the CRITS RFQ [4] using the two-solenoid, gas-neutralized low-energy beam transport (LEBT) [5] described in Ref. [6]. Two steering-magnet pairs provide the desired beam position and angle at the RFQ match point. Beam neutralization of 95-99% occurs in the LEBT residual hydrogen gas [7]. The RFQ accelerates the beam to 1.25 MeV and a simple HEBT transports that beam to the beamstop. The RFQ transmission and spatial profiles are measured as a function of injected current and LEBT solenoid excitations [2]. The expected beam performance is calculated using the computer codes TRACE [8] and SCHAR [9] to model the LEBT [10], PARMTEQM [11] to model the CRITS RFQ, and PARMELA [12] to model the HEBT.

2 INPUT PARAMETERS

The input H^+ beam parameters are determined from measurements on the prototype LEDA injector (Fig. 3 of Ref. 1) using a procedure described in [10]. A beam with 90-mA total current, proton fraction >90% (H^+ current >81 mA), rms normalized emittance ε_N = 0.146 π mm mrad, and α = -0.546 and β = 8.254 mm/mrad at 10% threshold is measured at the emittance-measuring unit (EMU).

Using TRACE [8] to drift the beam back along that 2.1-m long LEBT, from the EMU to the ion source, gives a predicted 6.98-mm-diam H^+ beam size, close to that of the 6.8-mm-diam ion source emitter, for an unneutralized current I_{eff} = 1.825 mA, α = 0.411, β = 0.215 mm/mrad, and ε_N = 0.146 π mm mrad (Table 1). Using these TRACE parameters as SCHAR* [9] input, and scaling them using $\alpha_{new} = \alpha_{old}[\varepsilon_{old}/\varepsilon_{new}]$ and $\beta_{new} = \beta_{old}[\varepsilon_{old}/\varepsilon_{new}]$, gives the measured ε_N to within 0.1% after two iterations. The resulting SCHAR-predicted input beam (Table 1) has ε_N = 0.134 π mm mrad. When SCHAR transports the beam parameters in Table 1 through the 2.1-m LEBT, the approximate phase-space shape at the 10% contour (Fig. 1) and beam profile at the video diagnostic (Fig. 2) result. Although the beam-profile data in Fig. 2 were obtained three days earlier than the phase-space data in Fig. 1, the source parameters were nearly identical for both data sets.

Table 1. TRACE and SCHAR input H^+ beam parameters.

TRACE (I_{eff} = 1.825 mA)	SCHAR (I_{eff} = 1.825 mA)
E = 50 keV	$v_o = 3.095 \times 10^6$ m/s
α = 0.411	r_{12} = -0.4131
β = 0.215 mm/mrad	$x_{max} = 4.271 \times 10^{-3}$ m
ε_N = 0.146 π mm mrad	$v_{x\,max} = 6.117 \times 10^4$ m/s

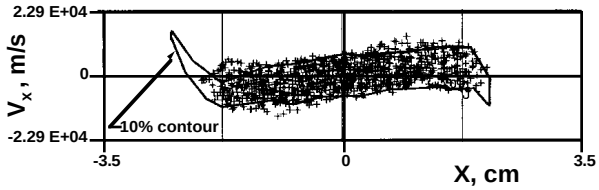

Fig. 1. The SCHAR-calculated phase space (crosses) at the EMU for the LEDA prototype LEBT. The solid line is the 10% phase-space contour measured with the EMU.

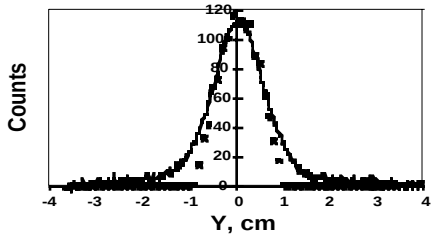

Fig 2. Hydrogen beam profile 42.9 cm from the source measured with a video camera (line) and predicted by SCHAR (squares).

3 LEDA LEBT SCHAR SIMULATIONS

The LEBT (Fig. 3) is simulated with the non-linear space-charge computer code SCHAR. These simulations use a 4-volume distribution and the line mode with 999

† Work supported by the US DOE, Defense Programs.
* $v_o = [2E/m_pc^2]^{1/2}c$, $r_{12} = -\alpha/[1+\alpha^2]^{1/2}$, $x_{max} = [\beta\varepsilon(6rms)]^{1/2}$, $v_{x\,max} = [\gamma\varepsilon(6rms)]^{1/2}v_o$

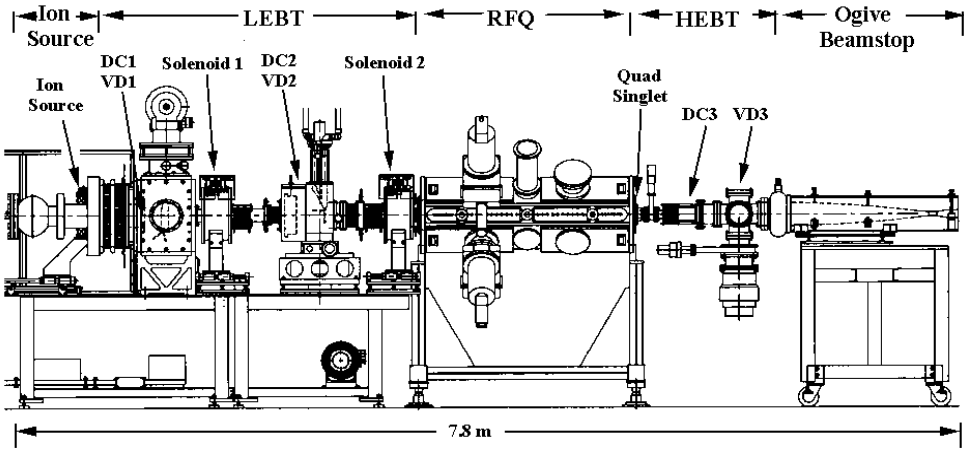

Fig. 3. The CRITS RFQ experiment beamline. The LEDA injector, ion source plus LEBT, is at the left. The CRITS RFQ is in the center, and the LEDA prototype ogive beamstop is at the right. The locations of the two LEBT solenoids (Solenoid #1 and Solenoid #2), RFQ exit quadrupole singlet, three Bergoz dc current transformers (DC1, DC2, and DC3), and three videocamera diagnostics (VD1, VD2, and VD3) are indicated.

lines. The LEBT dimensions are extractor to solenoid 1, 89.8 cm; solenoid 1 to solenoid 2, 138.4 cm; and solenoid 2 to RFQ match point, 25.6 cm. A beam neutralization of 98.0% (I_{eff} = 1.825 mA) is used. SCHAR predicts no proton beam loss in the LEBT. Using SCHAR input files, PARMTEQM predicts that the best match to the RFQ (Fig. 4) is obtained for $B_{sol\ 1}$ = 2100 G and $B_{sol\ 2}$ = 3675 G, giving ε_N = 0.169 π mm mrad at the RFQ match point. The actual $B_{sol\ 1}$ setting for the measurements, 1940-2010 G, is close to the SCHAR prediction whereas the actual $B_{sol\ 2}$ setting, ~4000 G, is 10% higher than the SCHAR prediction. The $B_{sol\ 2}$ setting is underestimated because of the absence in the SCHAR model of the un-neutralized section of beam transport just in front of the RFQ. Most of the SCHAR-calculated emittance growth (26.2%) is due to spherical aberrations in solenoid #1 (6.0%) and solenoid #2 (15.1%). The non-linear, space-charge-induced emittance growth is low (3.4%).

To obtain the 75-mA design RFQ output current requires operating the proton source at ~1200 W microwave power, 50% higher than used to obtain the SCHAR input parameters given in Table 1 (~800 W). The result is a larger-diameter beam at VD1 (Fig. 5) than in the case of the prototype LEBT measurements. At the ~1200 W power level the measured beam profile at VD2 (152.6 cm from the source) is also larger than SCHAR predicts.

4 CRITS RFQ PARMTEQM SIMULATIONS

The SCHAR output file is used to generate a 5,000 particle input beam for the PARMTEQM computer code to calculate the RFQ transmission and output ε_N. The proton fraction can be as high as 95% [13], but plasma effects caused by beam interactions with the beam-pipe walls [2] reduce the observed DC2 current by ~5%. These effects offset each other, so we use the measured DC2 current for the PARMTEQM input current. The result (Case 2, Table 2) is transmission = 75.1% and output ε_N = 0.207 π mm mrad (Fig. 6) for 97.5 mA input beam current and known RFQ intervane voltage (70.4, 72.6, 74.4, and 68.5 kV for Cases 1-4, respectively [14]). The predicted CRITS RFQ output current for other measured input beam currents [2] and RFQ vane voltages are given in Table 2. The SCHAR input parameters in Table 1 for a 90-mA beam (measured just in front of the EMU) are used for all of the simulations summarized in Table 2. Although RFQ output currents of up to 100 mA were measured [2], we limit our analysis to just those cases that have a complete set of beam currents and profiles.

5 HEBT PARMELA SIMULATIONS

The PARMELA [12] model of the HEBT uses the CRITS RFQ PARMTEQM output files for input. PARMELA,

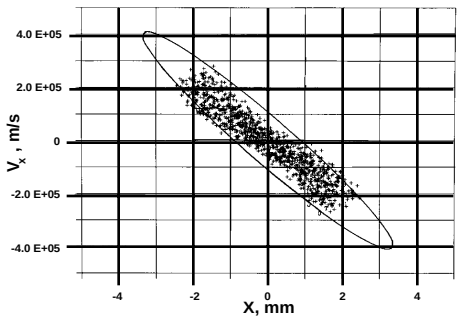

Fig. 4. SCHAR-calculated phase space (crosses) at the RFQ match point and the RFQ acceptance (curve) at 90-mA and 0.20-π mm mrad.

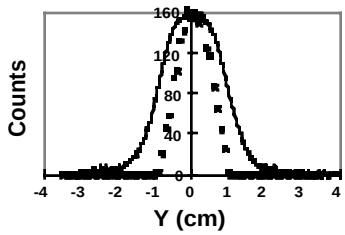

Fig. 5. Measured Hydrogen beam profile at VD1 (42.9 cm from the source) for case #2 in Table 2 compared with the SCHAR prediction calculated using the parameters in Table 1. Note the increase in the measured beam size over that in Fig. 2 as discussed in the text.

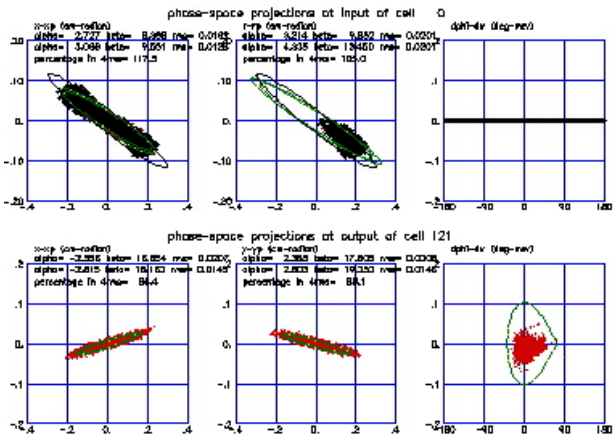

Fig. 6. PARMTEQM-calculated RFQ input (top) and output (bottom) phase space for Case 2 (Table 2).

set up to transport H^+ ions, predicts the beam transmission from the RFQ to the dc toroid (DC3 in Fig. 3), 57.5 cm downstream from the RFQ vanes, and also the x and y beam profiles at video diagnostic #3 (VD3 in Fig. 3), 87.7 cm downstream from the RFQ, for the known fields in the quadrupole singlet, located 7.8 cm downstream from the RFQ vanes. Table 2 lists the PARMELA predictions (note that the predicted beam loss between the RFQ and DC3 is small) along with the measured DC3 currents. Figure 7 shows the predicted x and y beam profiles at VD3 for Case #2.

Table 2. Results of the LEBT, RFQ, and HEBT simulations with SCHAR, PARMTEQM, and PARMELA, respectively. The measured LEBT beam currents at DC1 and DC2, the assumed PARMTEQM RFQ input current, the PARMTEQM-predicted RFQ output current, and the PARMELA-calculated and the measured HEBT current at DC3 are given in columns 2-7, respectively.

Case No.	Meas. LEBT current (DC1) mA	Meas. LEBT current (DC2) mA	PARMTEQM RFQ in current mA	PARMTEQM RFQ out current mA	PARMELA HEBT current mA	Meas. HEBT current (DC3) mA
1	123	94	94.4	70.33	69.95	74
2	124	98	97.5	73.18	73.16	76
3	123	96	96.0	75.11	74.96	75
4	138	102	102.1	71.98	71.61	90

6 DISCUSSION

There is good overall agreement between the measured beam currents and those predicted by the simulations for the 3 cases that have measured HEBT currents near the 75-mA CRITS RFQ design output current. These 3 cases are for the RFQ exit quadrupole singlet defocussing in x (Case 1), focusing in x (Case 2), and off (Case 3). The best agreement between the predicted current and the measured current is Case 3, but the best agreement between the predicted profiles and measured profiles is Case 2. The simulation of the 90-mA exit beam from the RFQ gives much lower beam transmission (DC2/DC3 = 70%) than the measured value (88%). It is likely that the beam input parameters in Table 1 are not as accurate a representation of the ~140 mA output beams (DC1) as they are for the ~120 mA beams. The measured and code-calculated RFQ transmissions are larger than those in [4] because of the steering and focussing flexibility of the LEDA LEBT (Fig. 3), features missing in the no-steering-magnet, single-solenoid LEBT employed in [4].

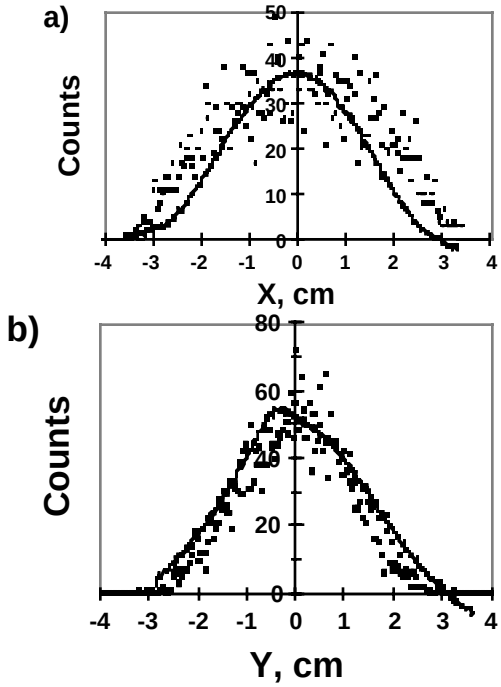

Fig. 7. PARMELA-predicted x (a) and y (b) beam profiles (squares) and the measured x and y beam profiles (lines) at VD3 for Case #2.

REFERENCES

[1] J. Sherman *et al.*, Rev. Sci. Instrum. **69** (1998) 1003-1008.
[2] J. Sherman *et al.*, "Development and Test Results of the Low Energy Demonstration Accelerator (LEDA) Proton Injector on a 1.25-MeV CW Radio Frequency Quadrupole," this conf.
[3] D. Schrage *et al.*, "CW RFQ Fabrication and Engineering," ibid.
[4] G. M. Arbique *et al.*, Proc. 1992 LINAC Conf. (AECL-10728, November, 1992) 55-57.
[5] R. R. Stevens, Jr., "High-Current Negative-Ion Beam Transport," AIP Conf. Proc. No. 287 (1994) 646-655.
[6] L. D. Hansborough *et al.*, "Mechanical Engineering for the LEDA Low-Energy Beam Transport System," to be published.
[7] R. Ferdinand, *et al.*, "Space-Charge Neutralization Measurement of a 75-keV, 130-mA Hydrogen-Ion Beam," Proc. PAC97 (Vancouver, 12-16 May 1997), paper 6W010 (in press).
[8] K. R. Crandall "TRACE: An Interactive Beam-Transport Program," Los Alamos Scientific Laboratory report LA-5332 (October, 1973).
[9] R. J. Hayden and M. J. Jakobson, "The Space-Charge Computer Program SCHAR," IEEE Trans. Nucl. Sci. **NS-30** (1983) 2540.
[10] H. V. Smith, Jr. *et al.*, "Simulations of the LEDA LEBT H^+ Beam," Proc. PAC97 (Vancouver, 12-16 May 1997), paper 6W022 (in press).
[11] K. R. Crandall *et al.*, "RFQ Design Codes," Los Alamos National Laboratory report LA-UR-96-1836 (revised February 12, 1997).
[12] L. M. Young, "PARMELA," Los Alamos National Laboratory report LA-UR-96-1835 (revised May 11, 1998).
[13] J. H. Kamperschroer *et al.*, "Doppler-shift Proton Fraction Measurement on a CW Proton Injector," this conf.
[14] G. O. Bolme *et al.*, "Proton Beam Studies With a 1.25 MeV, CW Radio Frequency Quadrupole LINAC," ibid.

STUDY OF COMPENSATION PROCESS OF ION BEAMS **

A. Jakob*, H. Klein, A. Lakatos, J. Pozimski, L. Wicke

Institut für Angewandte Physik, University of Frankfurt, 60054 Frankfurt, Germany

Abstract

For investigation of space charge compensation process due to residual gas ionization and the experimentally study of the rise of compensation, a Low Energy Beam Transport (LEBT) system consisting of an ion source, two solenoids, a decompensation electrode to generate a pulsed decompensated ion beam and a diagnostic section was set up. The potentials at the beam axis and the beam edge were ascertained from time resolved measurements by a residual gas ion energy analyzer. A numerical simulation of self-consistent equilibrium states of the beam plasma has been developed to determine plasma parameters which are difficult to measure directly. The temporal development of the kinetic and potential energy of the compensation electrons has been analyzed by using the numerically gained results of the simulation. To investigate the compensation process the distribution and the losses of the compensation electrons were studied as a function of time. The acquired data show that the theoretical estimated rise time of space charge compensation neglecting electron losses is shorter than the build up time determined experimentally. To describe the process of space charge compensation an interpretation of the achieved results is given.

1 INTRODUCTION

Space charge forces within ion beams lead to a notable divergence of the beam ions and to a disadvantageously emittance growth. To enhance the maximum transportable current and reduce the increasing emittance during the transport of the ion beams in a Low Energy Beam Transport (LEBT) line, it is essential to reduce the space charge forces. Therefore space charge compensation of positive beam ions by electrons [1], which are produced by residual gas ionization, enhance the maximum transportable ion current.

Measurements by use of a residual gas ion energy analyser based on the detection of residual gas ions produced by the interaction between beam ions and residual gas atoms. The produced residual gas ions are radial expelled by the beam potential. Therefore the kinetic energy of the residual gas ions corresponds to the beam potential at the point of production under the assumption of negligible start energy. Hence the residual gas ions energy distribution contains all necessary information about the radial distribution of the beam potential and thus about the degree of compensation [2]. For investigation of the space charge compensation process a time resolved residual gas energy analyser with a channeltron was used [3].

Calculated beam potential by self-consistent numerical simulations [4] were compared with the potentials yielded from the measured spectra. The combination of simulation and measurement allows the determination of all relevant beam plasma parameters [5].

2 MEASUREMENT AND CALCULATION

Time resolved measurements of ions repelled radially by the beam potential passing an energy analyser [6] with an inserted channeltron were done to investigate the rise time of compensation of a periodically decompensated 10kV, 3mA DC He^+ ion beam [7].

The simulation of the self-consistent equilibrium states of the beam requires the temperature and the relative density of the compensation electrons at the beam axis as varying free parameters and radial distribution of the beam ions as input data. A CCD-camera was used to investigate the radial distribution of the beam ions by observing the light emitted by the intersection of the beam ions with the residual gas atoms (photon emission). In fig. 1 a CCD-camera profile measurement I(x) of an 3.9 mA He^+ ion beam is shown, the corresponding density profile $\rho(r)$ can be calculated via Abel inversion.

Significant advantages of this profile measurements in comparison to measurements by a flying wire beam profile monitor [5] are the high time resolution and that the CCD-camera is an undisturbing diagnostic instrument. Therefore there is no disturbance of the equilibrium state of the compensated ion beam due to the production of secondary electrons. In addition to the residual gas ion energy analyser the CCD-camera was used to estimate the rise time of compensation in the present experimental set up.

** Work supp. by BMFT under contract No. 06 OF 841

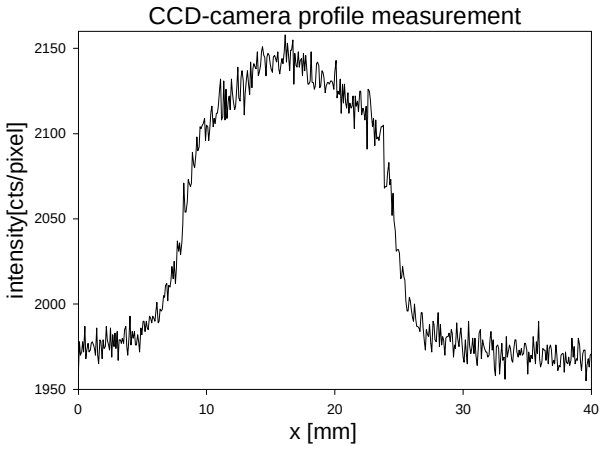

Fig. 1: Beam profile measurements by a CCD-camera. The exposure time was 2.5 s.

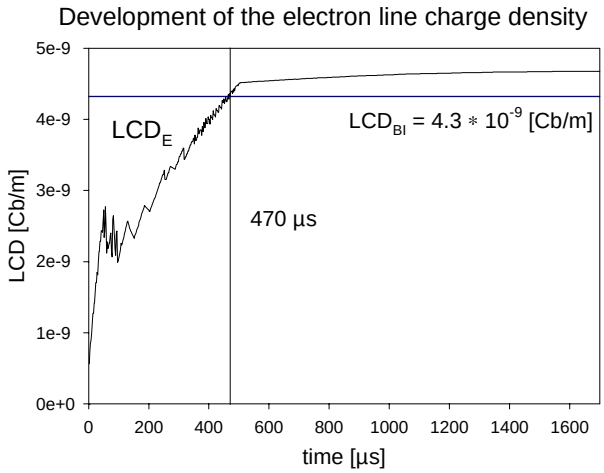

Fig. 2: Line charge density of compensation electrons and beam ions.

The minimum rise time of compensation τ can be estimated by a simple expression [5, 8], which is valid for idealized conditions (cylinder symmetry, electron losses neglected). Although the rise time of compensation determined by CCD-camera measurements are in good agreement with the calculated minimum rise time of compensation the evaluation of the residual gas ion energy analyser measurements shows that the compensation process is not finished at the minimum rise time mentioned above.

The following figures illustrate results gained from measurements for a residual gas pressure of $5*10^{-5}$ hPa, accordingly the calculated minimum rise time of compensation is 220 µs.

The determination of the plasma parameters, like the temperature of the compensation electrons (CE), the line charge density of the CE, the kinetic and potential energy of the CE by comparison of the simulation with the measured data reacts sensitive to fluctuation of the measured record. Therefore the measured data are fitted mathematically to smooth fluctuations of the measured data. The smoothed curves in the following figures show the appraisal of mathematically fitted measured data.

Fig.2 shows the development of the electron line charge density during the compensation process. The rise time of compensation is determined by the intersection point of the increasing electron (LCD_E) and the beam ion line charge density (LCD_{BI}) and is given by 470 µs.

The rise time of compensation estimated by the residual gas ion energy measurements exceeds the minimum rise time compensation τ by a factor of two due to electron losses, which is not taken into account in the above mentioned theoretical estimation.

Fig. 3 shows the evolution of the **e**lectron **c**harge **d**ensity (CD_E) during the compensation. The straight line indicates the CD_E on the beam axis, the dashed line is the CD_E at the beam edge. Fig. 3 clarify that the compensation process continues over the estimated minimum rise time of compensation τ of 220 µs. The minimum rise time indicates the time, which is needed to produce enough electrons (without consideration of electron losses) to compensate the space charge of the beam ions. With decreasing space charge forces during the compensation the electron losses increases continuously until an equilibrium state of electron losses and electron production is reached. The increasing electron losses yields to a prolongation of the compensation process up to 470 µs. Furthermore fig.3 and fig. 4 illustrate that redistribution processes are finished not until 1000 µs.

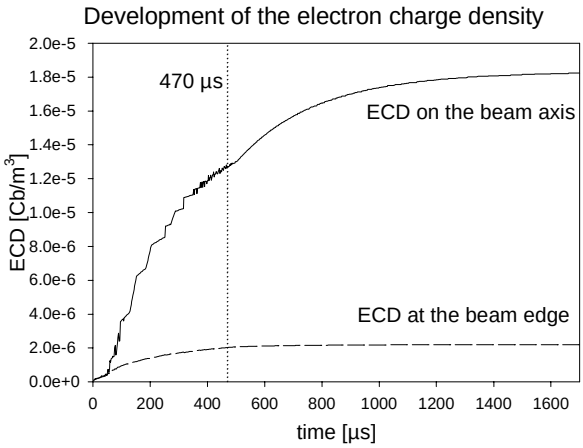

Fig. 3. Development of the electron charge density.

Fig. 4 shows the development of the kinetic (dotted line), potential (straight line) and total (dashed line) energy line density of the CE. The kinetic energy decreases continuously due to the dominant effect of decreasing temperature. The electron temperature decreases due to cooling processes by losses of „hot“ electrons. The maximum of the kinetic energy curve at 320 µs, represented in an antecedent presentation [5], which has not cleared till then, is an effect of the above mentioned fluctuations of the measured data. A new execution of the represented appraisal with smoothed measured records do not show this maximum.

From 80 µs on the potential energy exceeds the kinetic energy, hence the compensation electrons are trapped in the beam potential, this shows that the used theory and simulation is valid. Up to the maximum at 220 µs the potential energy increases, due to accumulation of produced compensation electrons in the beam potential, then electron losses and the decrease of the beam potential causes the progression of the energy. All three curves saturate after 1200 µs, then all redistribution-, production- and loss-processes reach an equilibrium state. The total curves shows clearly, that the energy still decreases, although the compensation process is complete. This effect is attributed to the above mentioned cooling process and redistribution within the ion beam, without a further accumulation of compensation electrons.

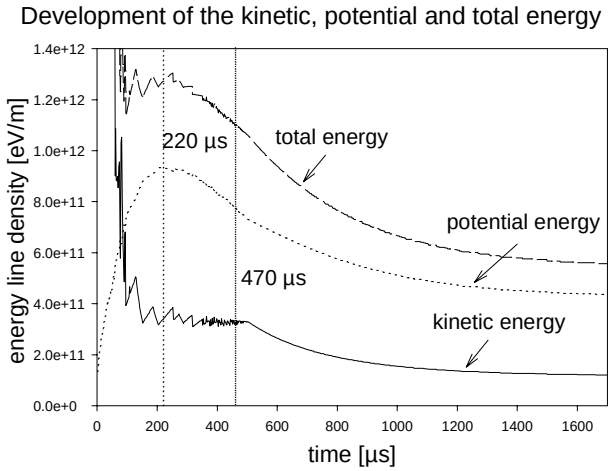

Fig. 4: Comparison of the development of kinetic, potential and total energy line density of the CE. The kinetic energy has a maximum at 220 µs. After 470 µs the compensation process is completed, after 1200 µs the development of the kinetic, potential and total energy line density saturates.

3 SUMMARY

The compensation processes of a periodically decompensated 10 keV DC He^+ ion beam has been investigated by usage of a time resolved ion energy spectrometer with installed channeltron. By application of an appraisal procedure of time resolved measurements using self-consistent calculations the rise time of compensation can be determined. A derivation by a factor of two was found between the experimentally detected rise time of compensation and the minimum rise time calculated for idealized conditions. The rise time of compensation was experimentally determined and has a value of 470 µs.

In the future work the time resolved residual gas ions measurements will perform on a pulsed ion beam, instead of a pulsed decompensated ion beam. For this investigation the gas discharge of the ion source will be pulsed directly.

REFERENCES

[1] A.F.T. Holmes, “Theoretical and experimental study of space charge in intense ion beams”, Phys. Rev. A. 19, 1979, pp.389

[2] J. Pozimski et.al., “Determinarion of Electron Temperature in Partial Space Charge Compensated High Perveance Ion Beams”, Proc. International Symposium on Heavy Ion Inertial Fusion, Il Nuovo Cimento 106A N.11, Frascati, Italy, May 1993, pp.1713[2]

[3] K. Reidelbach et al., “Development of a Time-Resolving Ion Energy Spectrometer for Investigation of Space Charge Compensated Pulsed Ion Beams”, ANNUAL REPORT 1993, GSI-94-10 REPORT, June 1994, pp.36

[4] J. Pozimski et.al., “Numerical calculations of charge density distributions in space charge compensated ion beams”, ANNUAL REPORT 1992, GSI-93-17 REPORT, Darmstadt, GER., May 1993, pp.38-40

[5] A. Jakob et.al., “Investigation of the Rise of Compensation of High Perveance Ion Beams Using a Time Resolving Ion Energy Spectrometer”, Proc. Sixth European Accelerator Conference, EPAC’98, Stockholm, 22-26 June 1998

[6] P. Bryce, r. Dalglich, J.C. Kelly, “The 127° Electrostatic Analysor: Performance as a Spectrometer”, Can. J. Phys. 51, CAN., 1971, pp.574

[7] K. Reidelbach, et al., ANNUAL REPORT 1994, GSI-95-06 REPORT, Darmstadt, GER., May 1995, pp.31

[8] P.K. Janev, W.D.Langer, K.Evans Jr., De Post Jr., “Elementary processes in hydrogen-helium-plasmas”, *Springer, Berlin, Heidelberg*, GER. ,1987

DESIGN, ANALYSIS AND TESTING OF A HIGH THERMAL CONDUCTIVITY WAVEGUIDE WINDOW FOR USE IN A FREE ELECTRON LASER *

T. Schultheiss, V. Christina, M. Cole, J. Rathke, Q. Shu**,
Northrop Grumman Corp, Bethpage, NY.

T. Elliott, V. Nguyen, L. Phillips, J. Preble, Jefferson Lab, Newport News, Va.

Abstract

Design, Analysis, and testing of a waveguide window with a goal of propagating greater than 100 kW average power operating at 1500 Mhz has been performed. This is made possible by the favorable material properties of Beryllia (BeO). Brazing the window to a soft copper frame and then brazing the frame to a KOVAR flange provides the vacuum seal. RF analysis combined with thermal/structural analysis shows the benefits of the material. The KOVAR flange with a CTE, coefficient of thermal expansion, that matches that of BeO enables a strong braze joint. RF testing to 35 kW has been successful, and higher powers will be tested in the near future. The basics of this design can be expanded to applications with lower frequencies and higher average power.

1 INTRODUCTION

The Free Electron Laser Facility being developed at Jefferson Lab requires much higher RF power throughput than is needed for their main facility. Much of the accelerator technology for the free electron laser is taken from the main facility which uses a two window design. The window design for the FEL consists of a room temperature warm window and a 2K cold window like the main facility. The warm window design from the main facility does not work at the power levels required for the FEL, therefore, Jefferson Lab initiated the development of a warm window using the cold window design as a baseline. In a corroborating effort, Northrop Grumman began developing a backup warm window design to enable greater than 100 kW average power operating at 1500 Mhz. The design was developed as a direct replacement in the FEL warm window location.

2 MECHANICAL DESIGN

The design evolved with the primary consideration to develop a backup warm window that would fit in the TJNAF envelope. Preliminary comparisons between alumina and beryllia windows showed that for standard grade material the high thermal conductivity of beryllia, shown in Table 1, resulted in low thermal gradients, and therefore low thermal stress within the window.

Table 1: Comparison of Thermal Conductivity's at 25C

Material	W/mK
Copper	380
Beryllia	300
SiC	270
AlN	240
Al	230
Mo	140
Alumina	20

To match the thermal expansion of beryllia, KOVAR was chosen as the flange material, minimizing thermal stresses in the beryllia during the braze cycle. A thin OFHC copper frame, .010 inches thick, between the beryllia window and the relatively stiff flange was added for strain relief. High thermal conductivity of the copper is also a benefit. Figure 1, shows a solid model of the window, the copper frame and the KOVAR flange. The KOVAR flange included a copper plating for high electrical conductivity.

The preferred BeO window geometry was an 'off the shelf' flat piece of Thermalox 995, .100 inches thick, from Brush Wellman. The thickness was chosen to keep the stress due to pressure low while using a stock size of standard grade material, ensuring repeatable material properties. Presently there is no multipacting coating on the window.

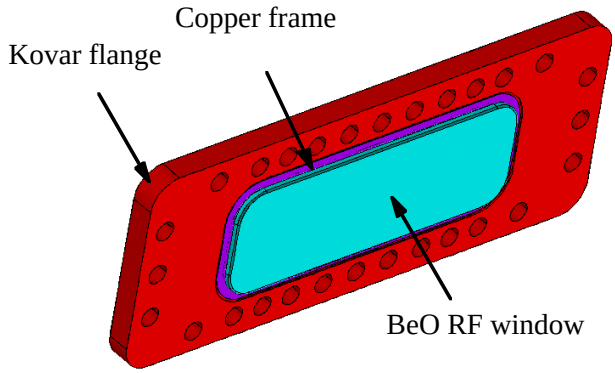

Figure 1: BeO RF Window, Flange and Frame

* Work supported by CRADA between NGC and Thomas Jefferson National Accelerator Facility SURA 95-S003 CRADA
** Q. Shu now at AMAC, LLC, Newport News Va.

3 BRAZE PROCESS

A two step braze process was used, first the copper frame was brazed to the BeO window then the copper frame was brazed to the KOVAR flange. The following steps were used to attach the frame to the BeO window:

- Molymanganese metallization 1/4" wide around the surface to be brazed. Silk screen technique was used then fired at 1450 C.
- Nickel plate metallized area then sinter at 1000 C
- Nicoro ribbon is used with a (apprx. 15 lb.) weight on fixture brazed at 1050 C
- A nioro wire (20 mil O.D.) braze around the outer edge between the BeO and copper and fired at 970 C
- Helium leak check 1x 10-8 std cc/sec
- Light blasting was done with aluminum oxide particles

The second step of the process was to braze the copper frame to the KOVAR flange.

- Incusil-10 wire in a vacuum braze oven and fired to 750 C
- Mask the copper plated KOVAR and apply a light blasting with aluminum oxide particles to clean beryllia surface

4 RF DESIGN

RF analysis was used to determine the S parameters for the structure and to optimize the structure within the requirements set by the envelope and mechanical design. Table 2 compares the electrical properties of BeO with other standard grade candidate materials.

Table 2: Comparison of Electrical Properties

Material	Dielectric Const (1MHz)	Loss Tangent
Beryllia (Thermalox 995)	6.7	.0003
AlN	9.0-10.0	
Alumina	9.0	.0003

To optimize the structure with a .100 inch thick BeO window, metal "wings" forming an iris were added to the flange. These wings were added to both sides of the window as shown in figure 2. Results for wings on just one side were not acceptable. The following MAFIA RF analysis results were obtained for a wing width of .750", and a wing thickness of .100".

Table 3: S Parameter Results

S11 amplitude	S11 phase	S21 amplitude	S21 phase
.0066	87.30	.99956	-2.740

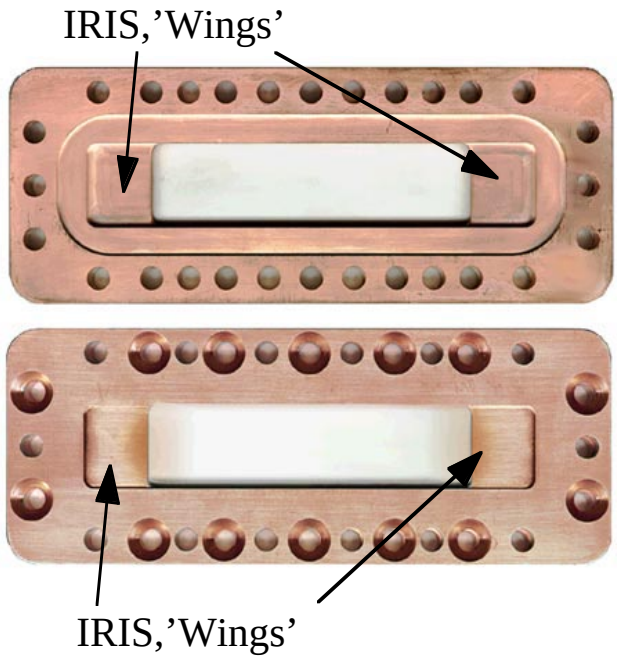

Figure 2: RF window and Iris('wings') and flange

After this configuration was selected, the power deposited into the ceramic and the fields in the waveguide were calculated. Contours of the heat deposited in the window are shown in figure 3 after scaling to a loss tangent of .0003 and 100 kW of through power.

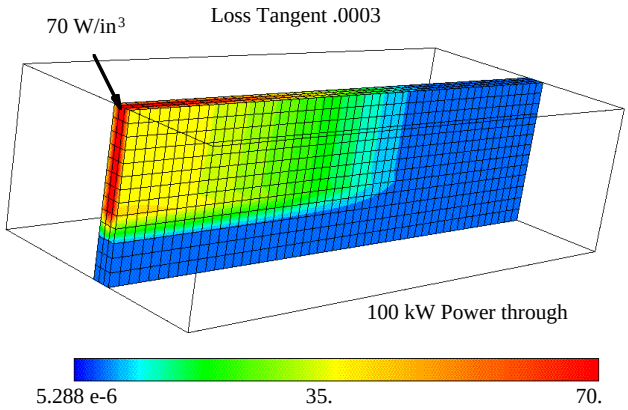

Figure 3: Heat loss contours determined by MAFIA

5 THERMAL ANALYSIS

The power loss distribution calculated in MAFIA was then mapped into an ANSYS finite element model. This model was used to determine thermal gradients and stresses in the window. Figure 4 shows the resulting temperature contours in the window, the frame, and the flange. On the edge of the flange a boundary temperature of 20C was set. The results show very small gradients in the window and a temperature rise of 29C between the window and the flange edge. These small thermal gradients result in small stress in the window.

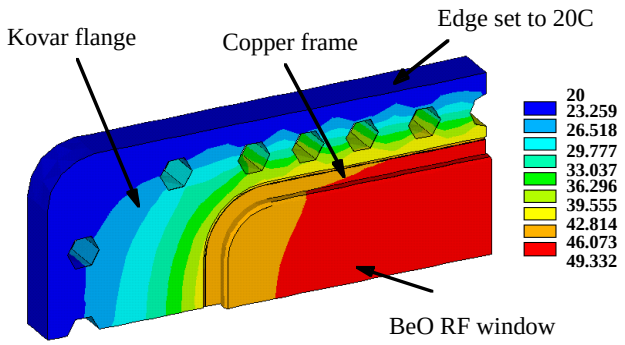

Figure 4: Temperature contours from ANSYS

6 RF TESTS

Thomas Jefferson National Accelerator Facility (TJNAF) provided the facility and manpower to test the window. Figure 5 shows the layout of the high power test. The space between the PN001 JLAB window and the BeO test window was evacuated by a 160 l/s Vac-Ion pump while the waveguide between the BeO window and the load was at atmospheric pressure. The window flanges were water cooled. The baseline pressure prior to testing was 1.4x10-9 torr. Temperatures at different locations of the waveguide and window flanges were monitored by thermocouples. Temperature of the BeO ceramic was measured by an infrared thermometer through a viewing port on the waveguide elbow. The waveguide between the two windows was equipped with a pick-up probe to monitor the electron current. A vacuum interlock and an arc detector interlock were used to prevent a catastrophic destruction of the ceramic. During the test, the incident and reflected powers, the vacuum pressure, the electron current, the temperature of the BeO ceramic and the temperatures of the window flanges were continuously monitored and recorded.

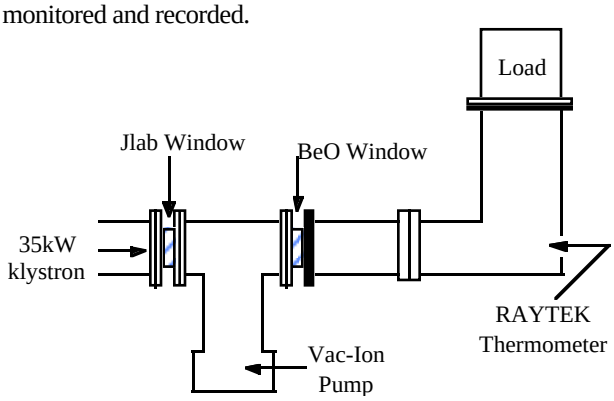

Figure 5: RF window test set up

Prior to applying high CW power, the windows were first submitted to high pulsed power (pulse length .01 ms - .1 ms, with a repetition rate of 100 Hz). Table 3 shows the temperature rise of the BeO ceramic as the power is increased. The temperature of the ceramic at zero power was 28C. The vacuum pressure increased to 9.4x10-8 torr at 35 kW and no electron current was detected.

Table 4: Temperature Rise In BeO Ceramic

Power (kW)	BeO Temp C	T(BeO)-27.7 ΔT C
0	27.7	0
5.04	35	7.3
10.1	40.8	13.1
15.1	45.7	18
20.2	51.2	23.5
25.2	58.2	30.5
35	70.9	43.2

The temperature rise between the coolant and the BeO window was much higher than expected from analysis. This could be from high losses in the braze material and/or poor thermal contact between the coolant line and the flange. This will be looked at more closely as additional tests are run.

7 CONCLUSIONS

Analysis shows that for the expected power lost in the window the goal of 100 kW of through power at 1500 Mhz is achievable. The high thermal conductivity of BeO results in low thermal gradients within the ceramic. Further tests are planned for 50 kW of through power. Modifications to the design which would include coolant nearer the ceramic would ensure lower ceramic temperatures. BeO as an RF window material shows promise based on the analysis and tests to date.

8 REFERENCES

[1] E. Chojnacki, et al., "Design Of A High Average-Power Waveguide Window"; Proceedings of the Particle Accelerator Conference, 1997, Vancouver, Canada.

[2] M. Neubauer, et al., "High-Power RF Window and Coupler Development for the PEP-II B Factory"; Presented at 16th IEEE PAC 95 Conference and International Conference on High Energy Accelerators, Dallas, Texas, May 1-5, 1995.

[3] D. Proch, et al., "Measurement of Multipacting Currents of Metal Surfaces in RF Fields"; Proceedings at the 16th IEEE PAC 95 Conference and International Conference on High Energy Accelerators, Dallas, Texas, May 1-5, 1995; pp 1776-1778.

[4] Conversations with Brush Wellman.

THE DIPOLE WAKEFIELD FOR A ROUNDED DAMPED DETUNED LINEAR ACCELERATOR WITH OPTIMISED CELL-TO-MANIFOLD COUPLING

R.M. Jones[†], N.M. Kroll[†‡], R.H. Miller[†], T. Higo[¥], K. Ko[†],
Z. Li[†], R.D. Ruth[†], V. Srinivas[†], and J. W. Wang[†]
[†]Stanford Linear Accelerator Center, M/S 26, P.O Box 4349, Stanford, CA 94309
[‡]University of California, San Diego, La Jolla, CA 92093-0319.
[¥]KEK, National Laboratory for High Energy Physics, 1-1 Oho, Tsukuba-shi, Ibaraki-ken 305, Japan

Abstract

A redesign of the basic cell configuration of the Damped Detuned Structure has been briefly reported in [1] where the cells are referred to as ellipsoidal cavities, and accelerator structures incorporating them are designated DDS 5 and DDS 6. This new structure type has been renamed RDDS 1, and the first of this series, RDDS 1, is presently under design and fabrication. The carefully sculpted cell profile (fabricated on computer controlled lathes at KEK incorporating diamond point machining) provides a 20% increase in shunt impedance which, when combined with other parameters, allows for a dramatic reduction in the RF power required for the NLC (Next Linear Collider). The detuning profile, damping manifold taper, and the cell to manifold coupling contant profile have all been carefully optimised so as to permit decoupling the cells at the ends of the structure from the manifolds while still adequately minimising the transverse wake. The decoupling is required in order to fit adequately matched terminations into the structure. The single structure analysis has been supplemented with studies of wake degradation arising from systematic fabrication errors and wake improvement obtained by combining manifold damping with structure interleaving.

1 INTRODUCTION

In the design of the NLC (Next Linear Collider) the heart of the system will consist of 4,752 X-band accelerator structures, each indiviual structure being 1.8025m in length. Any misalignment in the structure, or transverse motion of the structure over time, or beam misalignment from the electrical center of the structure will give rise to a transverse wakefield which will result in the beam being kicked off axis and can lead to a beam break up instability (as originally observed on the Stanford Linear Collider). In order to mitigate these effects, which may seriously degrade the beam emmitance, and hence reduce the luminosity of the beam, the transverse wakefield must be carefully controlled and damped. The method described herein, incorporates both detuning by gently tapering the iris parameters such that they follow an Erf function distribution and, damping the long range wake field, by coupling the wakefield out of the structure to a set of four manifolds which are located along the circumference of the accelerator structure.

In order to obtain the maximum efficiency of interaction, the shunt impedance is required to be maximised. The shunt impedance, R_{sh} is defined in terms of the potential across the structure V and, the power dissipated within the structure, P_d

$$R_{sh} = |V|^2 / P_d$$

In our current design, we maximise the $R_{sh}/Q = |V|^2/(2\omega U_E)$, where ω is the angular resonance frequency and U_E is the energy stored within the electric fields, so that we obtain a value that is 10% larger than that obtained over a set of pillbox cavities and, we enhance the Q value by 10%, both achieved by carefully shaping the contours of the irises and cavities. This together with a larger klystron pulse length, led to our initial design for RDDS with elliptical features having a 30% more efficient source-to-beam, or "wall plug", efficiency. In this design the average a/λ was approximately 0.171 (a being the radius of a particular iris). However, short range wakefield considerations has led to the iris being widened considerably in order to reduce the wake and, this leads to a 6% degradation in the overall efficiency. In this design the average a/λ is approximately 0.18. Furthermore, our initial design incorporated elliptically shaped cavities and irises. However, driven by mechanical engineering considerations, all shapes have been made circular. This reduces the efficiency by 1% or so, and at the same time it facilitates more rapid verification between the specified design and the fabricated cell.

Here we calculate the wakefield for the accelerator with a 30% improvement in efficiency the elliptical RDDS and, the RDDS with circular cells and cavities, which has an efficiency enhancement of approximately 20%.

2 WAKEFIELDS FOR CIRCULAR AND ELLIPTICAL RDDS

The wakefield in each 206 cell structure cannot be computed accurately, with a finite difference or finite element code as at present the memory and time requirements required to run the code are prohibitive and thus, we utilise a circuit model [3] and spectral function

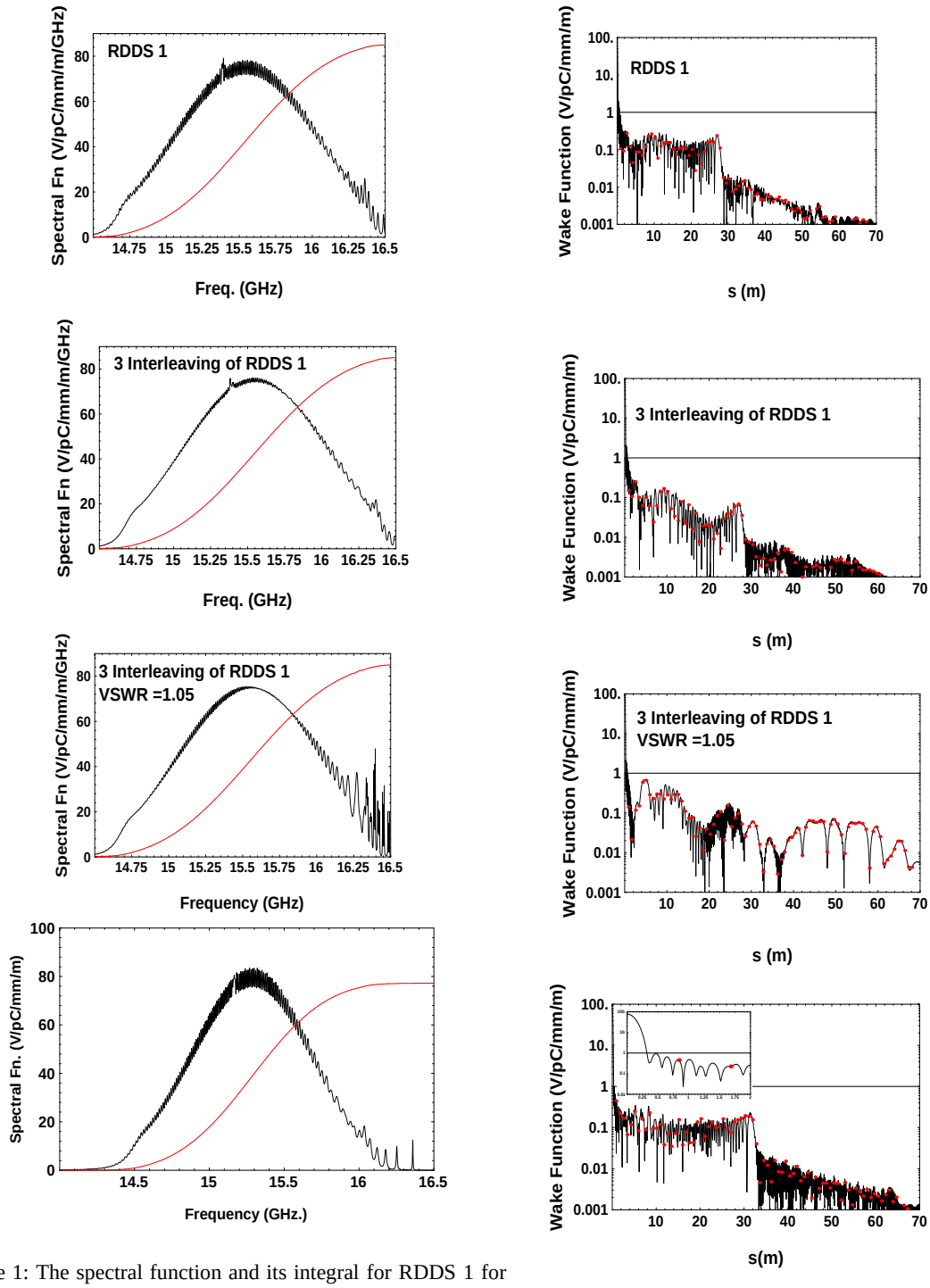

Figure 1: The spectral function and its integral for RDDS 1 for an initial design. The uppermost is the spectral function for a structure with perfectly matched HOM (Higher Order Mode) couplers and all cells coupled. The second is for series of three interleaved structures in which the synchronous frequency of each structure differs form its neighbor by 3.8 MHz. The third curve is for the case of three interleaved structures with six cells decoupled and a HOM load with a VSWR of 1.05. The fourth is for the most up-to-date design, RDDS1 with circular contours.

Figure 2: The wake function and its integral for RDDS 1. All wakes are the counterparts of the spectral functions given in fig. 1. The dots are located at the bunch locations. One V/pC/mm/m is indicated as beam emmitance considerations dictate that the transverse wake function, at the bunch locations, may not be larger than this value. The lowetmost curve is for RDDS1 with cicular features to the irises and cavities. The load has is assumed to have a VSWR = 1.

method [2] expressly developed for this purpose. The model we use assigns 9 parameters to each cell and this allows the dipole band of the brillioun diagram to be accurately described. The structure geometrical parameters have been designed to vary slowly in an adiabatic manner and thus we interpolate between, 5 cells to obtain the behavior of all 206 cells. The model we use incorporates many features present in the real structure as fabricated, viz., the non-perfect terminations of the manifolds in the higher mode loads and, the details of the coupling of the cells to the manifold (the modal composition of the accelerator is mainly TE at the low energy end and, it becomes progressively more TM towards the higher end of the structure). The spectrum function for a single elliptical structure is calculated and the coupling of the manifold to the structure is carefully optimised. The result of a final optimisation for the design with an $a/\lambda = 0.171$ is shown in Fig.1 for perfectly matched HOM couplers (higher order mode) and the wakefield corresponding to this spectral function is shown in Fig. 2. By interleaving the structures with structures whose central frequency is slightly shifted from their neighbours the wakefield is forced to decohere successively more so than a single structure. In Fig. 1 the spectral function is shown for three structures whose central dipole synchronous cell frequencies differ by 3.8 MHz from their neighbours, both with matched terminations to higher mode couplers and with terminations with a VSWR of 1.05 and with six cells decoupled either end of the accelerator structure.

The magnitude of the oscillations imposed on the spectral function is seen to be significantly reduced, particularly in the upper end of the spectral function. And, the wakefield is seen to be 3 times smaller in the region 0 to 30 m or so. Furthermore, the system is considerably stablised with respect to oscillations in the spectral function, on decoupling the last few cells. The last lowermost curve in Fig. 1 corresponds to the present RDDS with circularly shaped irises and cells. The spectral function corresponding to this latest design, is shown lowermost in Fig. 1. In this design, all ellipses have an eccentricity of 1 and the VSWR =1 of all loads in this preliminary realisation.

3 EFFECT OF SYSTEMATIC ERRORS ON THE WAKEFIELD

In the fabrication of the RDDS cells systematic, or repeatable errors, in the machining of the cells us likely to occur and in this section we consider the effect of such errors on the transverse wakefield. We consider a specific case, viz, a sinusoidal perturbation of amplitude 2MHz in the synchronous frequencies, in the central region of the structure (cells 75 through 125). The spectral function, illustrated in Fig. 5 is seen to be significantly modulated in the central region.

However, this significant modulation has little effect on the long-range wake function (Fig. 6). Although, for the first few bunches the wake field is slightly enhanced, it is a very small effect. We also consider random errors and, for a Gaussian spread in the synchronous frequencies with a σ of 10^{-4} (corresponding to approximately 1.5 MHz) the wakefield is largely unaffected.

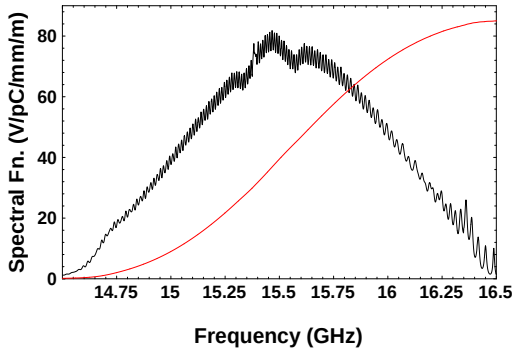

Figure 3: Spectral function for RDDS1 with all cells coupled and a perfectly matched HOM coupler. A systematic error in the fabrication is assumed to occur leading to a sinusoidal perturbation in the cell dimensions and the synchronous frequencies. The synchronous frequency perturbation has amplitude of 2 MHz.

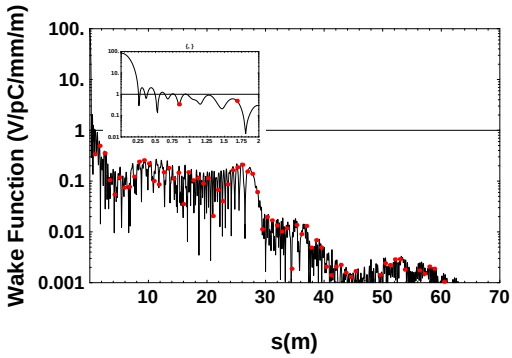

Figure 4: Wake function including the effects of a systematic fabrication error which results in a sinusiodal deviation in the synchronous frequency in the middle of the frequency band of the structure. Shown inset is the short-range wake in the range 0 to 2m.

4 ACKNOWLEDGMENTS

This work is supported by Department of Energy grant number DE-FG03-93ER40759‡ and DE-AC03-76SF00515†.

5 REFERENCES

[1] R.M. Jones., N.M. Kroll, R.H. Miller, R. Ruth and J.W. Wang, Advanced Damped Detuned Structure Development at SLAC, Proc. Particle Accelerator Conference, Vancouver, Canada, 1997. http://www.cern.ch/accelconf

[2] R.M. Jones., N.M. Kroll and R.H. Miller, A Spectral Function Method Applied To The Calculation Of The SLAC Damped Detuned Structure. Proc. Intl. Linac Conf. Geneva Switzerland, 1996 (SLAC-PUB 7287).

BASIC RESEARCH ON HORIZONTAL ASSEMBLY METHOD OF SC CAVITIES WITH HIGH Q AND HIGH GRADIENT

K.Saito, P.Kneisel*, E.Kako, T.Shishido, S.Noguchi, M.Ono, and Y.Yamazaki,

High Energy Accelerator Research Organization (KEK)
1-1, Oho, Tsukuba-shi, Ibaraki-ken, 305-0801 Japan
*: Thomas Jefferson National Accelerator Facility
12000 Jefferson Avenue, Newport News, Virginia 23606 USA

Abstract

The fabrication technology of the high gradient superconducting(sc) cavities has been made much progress in the last 10 years. As a next issue, one has to develop a horizontal assembly method of sc cavities which makes no performance degradation in order to exhibit the excellence in the accelerator. Among many candidates of the cause with the degradation, here, the influence of breaking cavity vacuum after the vertical test and indium contamination effect are investigated.

1 INTRODUCTION

By the R&D of high gradient sc niobium cavities done at KEK so far, its technology level has come to the high gradient of 30 - 40 MV/m. Our next R&D target is to realize the excellence in the horizontal cryomodule. Performance of the sc cavity is very sensitive to the surface contamination, so generally speaking it is hard to reproduce the performance of the vertical test in a real accelerator. Really in the TRISTAN sc project, we observed a degradation in both Q value and the maximum accelerating gradient (Eacc,max) by the horizontal assembly. If the same degradation happens in the future advanced sc applications, the effect is very serious because the machines will be operated at 2K. The study of assembly method of cryomodule is an essential R&D issue.

2 HORIZONTAL ASSEMBLY

2.1 Horizontal assembly

In the TRISTAN sc project, after the vertical test of individual cavities, the cavity vacuum was broken introducing pure(6-N) and particle free (> 0.01 μm) nitrogen gas into the cavity for one night, then end flanges at the beam tubes were opened in the class 100 clean room and the remained scraps of indium used for the vacuum sealing on the flanges were carefully cleaned up. Two cavities were paired at the end flange of the beam tube with indium seal again. Blanket extension tubes were joined to each cavity at the other beam tube. After that, blanket flanges on the HOM ports were taken off and cleaned up indium scraps on the ports, then put on HOM couplers on them. The paired cavities were installed in the helium vessel of the horizontal cryostat outside of the clean room, then input couplers were put on the each port under a clean environment which was produced by a portable small clean booth. While this work, nitrogen gas was flowed the pair to prevent particle contamination from the outside. Then all the parts were assembled on the cryostat.

2.2 Degradation of cavity performance

After the horizontal assembly, the cavity pair was evacuated and cold tested. The unloaded Q value (Qo) was scattered after the horizontal tests and degraded in average as: 2.7×10^9 (vertical)→1.7×10^9 (horizontal).
This means that a surface resistance of 60 nΩ was added. $E_{acc,max}$ was also decreased as:
10 MV/m (vertical)→7 MV/m (horizontal).
However, the cavity performance in the accelerator did not change from the horizontal test.

2.3 Possible causes for the degradation

The degradation happens in the future application of sc cavities like a sc proton linac or TESLA, the influence is very serious. For instance, JAERI is considering a sc proton linac (600 MHz) for an intensive neutron source for the neutron science and nuclear waste transmutation. For this machine, electric power efficiency in the operation is an important issue, therefore 2 K operation will be applied. In this case the typical surface resistance of the cavities is about 10 nΩ. Adding 60 nΩ by the horizontal assembly, Qo value takes a figure down so that there is no meaning of the 2 K operation. The field degradation is also very serious for the machine. It is to be operated at Ep = 16 MV/m (surface peak field). The field limitation of 7 MV/m corresponds to 14 MV/m in Ep. There is no way for the operation.

One has to take a cure to prevent the degradation if he use the same assembly procedure. The possible causes of the degradation will be followings: 1) influence of breaking cavity vacuum, in other words particle contamination, or oxidation of niobium surface while the horizontal assembly, 2) indium contamination, 3) absorption gas, 4) contamination problem from RF accessories like input coupler or HOM couplers, 5) field emission, 6) multipacting so on. In this paper we investigate qualitatively used L-band single cell cavities with higher sensitivity on the issues 1) and 2) among these candidates.

3 INFLUENCE OF BREAKING CAVITY VACUUM

3.1 Effect of introducing N_2 gas

A concerning of breaking cavity vacuum is the particle contamination from the vacuum system or in the used N_2 gas. As a result the residual surface resistance (Rres) might increase or field emission happens. The faster N2 gas flow may bring the more particles into the cavity. In this experiment, flow rate of nitrogen gas was changed from 1.5 cc/min. to 900 cc/min. We used the vacuum

evacuation system presented in figure 1. The flow rate is adjusted by the valve(V2). Particles bigger than 0.01 μm size in the gas are eliminated by the final filter. By the particle counter measurement, manipulating of the final valve V2 produces particles, so it has to be handled carefully. The vacuum pressure of the sealed cavity is worse than 2-3 x 10^{-5} torr after the cold test (while cold testing the cavity vacuum is also sealed.). Prior to open the cavity valve V6, the space between V1 and V6 is evacuated to less than 1.5 x 10^{-5} torr, then V6 is opened. By opening V4 very carefully, it is checked whether the cavity was fully filled with N_2 gas. Vacuum evacuation

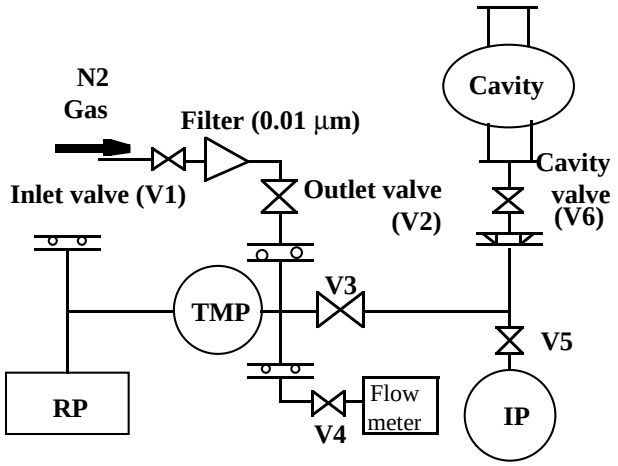

Figure 1: The used vacuum system for N_2 gas leak.

was started as soon as it was filled. Typical results of breaking cavity vacuum are shown in figure 2 on residual surface resistance and in figure 3 on field gradients. The summary is presented in Table 1. The concerned increase of Rres is not observed in the measurement error up to the flow rate of 900 cc/min. A clear field emission was observed from 20 MV/m at the flow rate 5 cc/min. but the other cases were not significant. That might be a mistake in manipulating the valves. Eacc,max decreases a little : 8 - 18%. This influence are too small to explain the degradation in the TRISTAN horizontal assembly.

Table 1: Summary of influence of breaking cavity vacuum with N_2 gas.

Flow rate of N2 [cc/min.]	Rres [nΩ] before / after (difference)	Eacc,max [MV/m] before / after (difference)	F.E at Eacc < 25 MV/m before / after
1.5	14.0 / 11.3 (-2.7)	31.3 / 31.8 (+2%)	No / No
5.0	7.7 / 4.8 (-2.9)	36.3 / 29.7 (-18%)	No / Yes from Eacc = 20
21.5	7.7 / 7.2 (-0.5)	40.3 / 34.2 (-15%)	No / No
120	12.1 / 14.4 (+2.3)	30.9 /28.4 (-8%)	No / No
900	5.4 / 7.4 (+2.0)	31.8 / 32.4 (+2%)	No / No

3.2 Influence of air exposure

Even nitrogen gas was flowed into the cavity while the horizontal assembly, there is a chance for the cavity inner surface to be exposed to the air. In this case, oxidation of niobium surface is concerned. A cavity once exposed to nitrogen gas in the experiment of *3.1* was exposed to the air by the same method as *3.1* for one day to one week

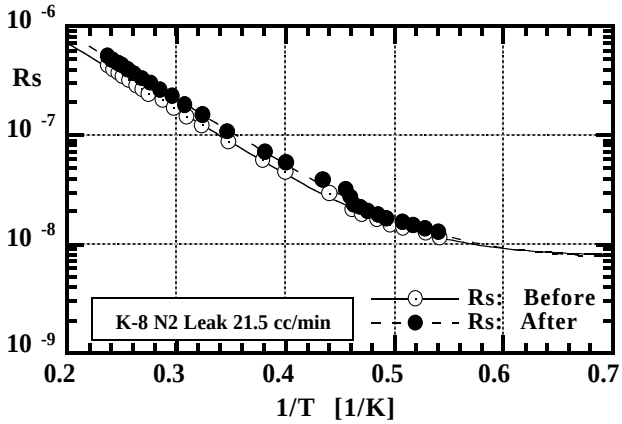

Figure 2: Effect on Rres with N_2 leak.

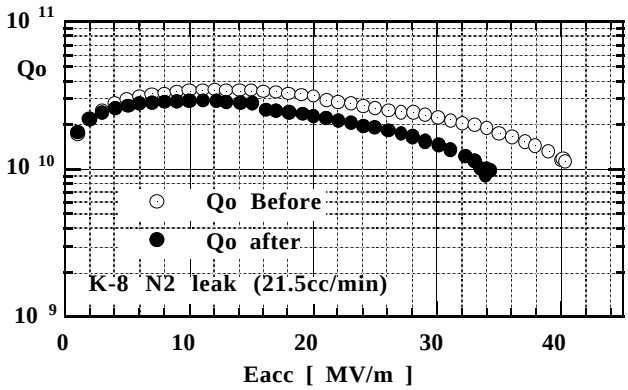

Figure 3: Effect on the Eacc with N2 leak.

Table 2: Summary of the effect of air exposure.

Exposed time	Rres [nΩ]	Eacc,max [MV/m]	F.E. onset field [MV/m]
0	7.4	32.4	29
< 45 min.	8.3	34.2	29
1 day	12.5	32.2	23
3 days	12.3	28.9	23
7 days	16.2	28.0	22

without disassembly. The results are summarized in Table 2. Only introducing the air into the cavity has no influence on Rres and Eacc,max but the exposure for one week produces the additional Rres of 8 nΩ and reduces the gradient by 9 % due to field emission. The onset point of field emission becomes lower with increased air exposure time. The exposure time of one day is enough for the horizontal assembly procedure. The resultant Rres of 5.1 nΩ and Eacc,max reduction of 0 % are too small to explain the degradation in the horizontal assembly. Especially the additional Rres is out of sight in the measurement error at 4.2 K because BCS surface resistance (100 nΩ at 500 MHz) is dominate in this

temperature, however, this additional Rres is very serious in the 2 K operation. It reduces the Qo value to about one half. Some cure might be need for this degradation with the 2 K operation.

4 INFLUENCE OF INDIUM CONTAMINATION

KEK has used indium wires or ribbons for the vacuum sealing of sc cavities. It has a high reliability but has a contamination problem by its scraps in disassembly. An experiment to see qualitatively the influence was carried out at CEBAF using a 1.5 GHz single cell cavity. In this experiment a flat indium fragment was attached intentionally on the cavity inner surface at the place 25 mm inside from the iris. The size was changed by four kinds : 35, 1.5, 0.5 mm^2 and no indium. After every measurement, the cavity was disassembled, soaked with nitric acid to eliminate the indium, then taken BCP(1:1:1) with a 30 μm material removal. The indium fragment was attached in the class 100 clean room after the surface treatment. The results are presented in figure 4 with the Eacc vs. Qo, in figure 5 on Rres and in figure 6 on the Eacc,max. Indium produces a big influence on both Rres and $E_{acc,max}$. The additional Rres and reduction of the $E_{acc,max}$ with the indium size (S; mm^2) are estimated from this experiment as follows:

Δ Rres (1.5GHz) =1.12 $\mu\Omega/mm^2$ · · ·(1),

$\Delta E_{acc,max} = 1 - \exp(-S/1.75)$ · · ·(2).

The thermal valance between a heating at the indium

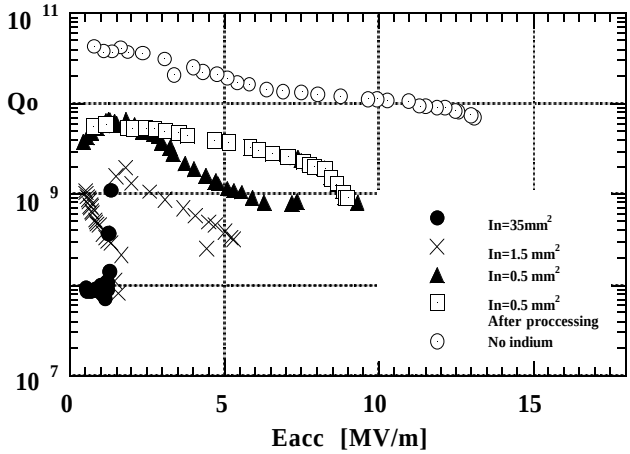

Figure 4: Indium size effect on Qo and Eacc,max.

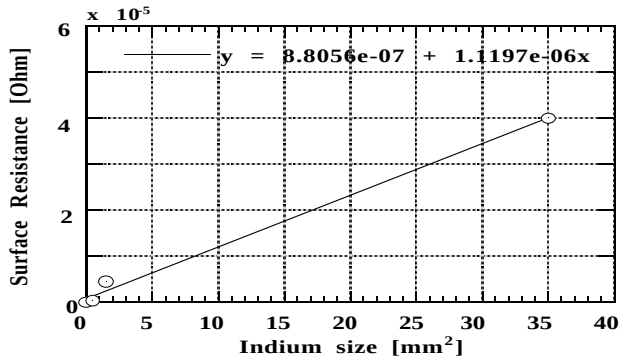

Figure 5: Increased surface resistance with indium size.

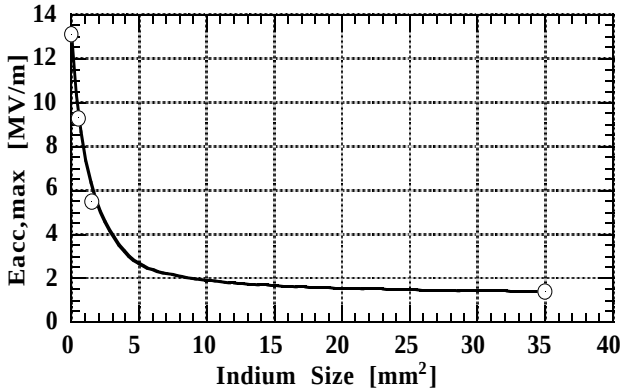

Figure 6: Limitation of field gradient with indium size.

fragment and the thermal conductivity of niobium determines the $E_{acc,max}$. Therefore the $E_{acc,max}$ does not depend on the frequency of the microwave. On the other hand, the sensitivity of the additional Rres of the eq. (1) depends on the rf frequency. For instance, from the definition and the scaling of rf frequency Qo value of 0.5 GHz cavity is presented by the Qo of 1.5 GHz cavity for the same Eacc as following:

$Qo(0.5GHz) = \omega_{1.5}U_{1.5}/(Pc_{1.5} + 1/9 \cdot P_{loss}(indium))$.

Here, U is a stored energy in the cavity, ω the angular velocity of microwave, Pc the intrinsic wall loss of the cavity, and Ploss(indium) the heating power at the indium. The 0.5 GHz cavity has the larger surface 9 times than the 1.5 GHz cavity, so the indium effect becomes small relatively to 1/9. Addition to it, the TRISTAN sc cavity is a 5 cell structure. The indium effect of eq. (1) should be changed for the TRISTAN sc cavities as follows:

$$\Delta \text{ Rres}(0.5\text{GHz}) = 1.12/(9\text{x}5)\ \mu\Omega/mm^2, \\ = 25\ n\Omega/mm^2 \qquad (3).$$

Suppose the reduction of 30% in Eacc,max by the TRISTAN horizontal assembly comes from the indium contamination, the size is about 0.6 mm^2 from eq. (2). Even if such an indium or scraps entered the cavity during cleaning the cavity flanges in the assembly work, it is not strange. The indium adds an additional Rres of 15 nΩ from eq. (3) and finally brings to field emission as presumed from figure 4 (▲ and ❒). A possible explanation of the performance degradation in the TRISTAN horizontal assembly is the indium contamination and the resultant field emission.

5 SUMMARY

Among possible causes of the cavity performance degradation in the TRISTAN horizontal assembly, the influence of breaking cavity vacuum and the effect of indium contamination are investigated. The former is not guilty with the 4.2 K operation but some cure is needed for the 2 K operation. The later has a serious effect on both Qo and field gradient. The degradation can be explained the indium contamination with the size about 0.6 mm^2, however, the other possibility should be investigated like contamination from cavity accessories or multipacting. The research program is now under going at KEK.

SIMULATION OF HIGH-AVERAGE POWER WINDOWS FOR ACCELERATOR PRODUCTION OF TRITIUM*

L. D. Daily, C. C. Shang, C. M. Gooch, D. J. Mayhall, S. D. Nelson
Lawrence Livermore National Laboratory, Livermore, California 94551 USA
K. A. Cummings
Los Alamos National Laboratory, Los Alamos , New Mexico 87545 USA
J. Salem
NASA Lewis Research Center, Cleveland, Ohio 44135 USA

Abstract

Development of a robust, high-average-power (210 kW, CW) microwave transmission line system for the Accelerator Production of Tritium (APT) facility is a stringent engineering and operational requirement. One key component in this RF transmission system is the vacuum barrier window. The requirement of high-power handling capability coupled to the desirability of good mean time to failure characteristics can be treated substantially with a set of microwave, thermal-structural, and Weibull analysis codes. In this paper, we examine realistic 3-D engineering models of the ceramic windows. We model the detailed cooling circuit and make use of accurate heat deposition models for the RF. This input and simulation detail is used to analyze the thermal-structural induced stresses in baseline coaxial window configurations. We also use a Weibull-distribution failure prediction code (CARES), using experimentally obtained ceramic material failure data and structural analysis calculations, to infer probability of failure.

1 INTRODUCTION

The Accelerator Production of Tritium (APT) project is a Department of Energy (DOE) sponsored investigation into the feasibility of using linear accelerator technology (as opposed to traditional reactors) to produce tritium. A major technical issue is the design of vacuum barrier ceramic windows inside the RF transmission system. Specifications call for material transparent to microwaves at as much as 700 MHz and 500 kW, CW (actual operation will be at half that power). Compromise of the system results in vacuum breach and costly down time for the accelerator.

The objective of this analysis is to develop a simulation that will model the thermal and structural effects of transmission inefficiencies coupled to an atmospheric load to determine if, and more appropriately, when the ceramics will fail.

Since ceramics have much higher deviations in strength and wear properties than conventional structural materials, the output of the continuum, thermomechanical, Finite Element Analysis (FEA) will be coupled to a Weibull statistics code. Weibull analysis is performed with CARES (Ceramic Analysis and Reliability Evaluation of Structures) [1], a finite element probabalistic software developed by NASA. Probability of Failure (POF) is inferred from calculated Weibull parameters using data from four point bending tests on AL300 (97.6% alumina ceramic).

2 PHYSICAL DESCRIPTION

Two RF waveguide geometries are presented in this paper: (1) a generic, single window, design that has been used in experiments, and (2) one of the competing designs for the power coupler on the APT linac (courtesy of CPI Communications & Power Industries).

Electric fields from microwave transmission produce heat loads from imperfections in the electrical properties of copper and alumina. For the test geometry, there is active cooling from air flowing through the inner conductor and out across the window surface. The walls of the inner conductors, outer conductors, and t-bars are plated with copper (for electrical properties) and are otherwise aluminum and stainless steel. For the CPI geometry, the active cooling circuit is a more aggressive, water cool, in the inner conductor coupled with airflow between the ceramics. The conductors are copper and copper-plated stainless steel. The windows are kept in place by a brazed joint.

3 FINITE ELEMENT MODEL

The single window Finite Element (FE) model is built using 8-node bricks and 4-node shell elements and the CPI model is built as a 2-D axisymmetric simulation with 4-node quads. Using a 2-D axisymmetric simulation for the CPI geometry (as opposed to the 3-D implemented in the single window test case) is assumed from the observation that very little problem insight is gained from the addition

* The work was performed under the auspices of the U.S. Department of Energy by LLNL under contract W-7405-ENG-48.

of 3-D effects. There is geometric axisymmetry of the problem (in the region that we are interested) and our main concern is the stress state of the windows, not the entire system.

The heat deposition as a result of the electric field calculation along the walls of the inner and outer conductor and the ceramic is conservatively approximated to be axisymmetric with the maximum azimuthal values represented. The values of the electric field are calculated using a 3-D direct Maxwell equation solver. The values for power deposition are determined from the calculated electric field averaged over a RF cycle for the perfectly matched case.

Convective cooling is accounted for by computing heat transfer coefficients from correlations for fluid flow [2]. Enclosure radiation is accounted for in the vacuum cavities (in the 2-D axisymmetric case) using gray diffuse view factors. Natural convection and radiation exchange with the surroundings are accounted for on all outside surfaces.

The simulation is performed in two steps: (1) solution of the thermal profile from the given power load (using TOPAZ [3]) and (2) solution of stress contours throughout the window from the sum of thermal stress and mechanical stress from the vacuum pull (using NIKE [4]). These combine to give the thermal stress result.

4 RESULTS

There are three significant results presented here and each allow insight into to the fundamental physics of the problem.

4.1 Single Window Geometry

An experiment was performed at Argonne National Laboratory (ANL) [5] (using an EEV/WESGO AL300 ceramic) and is used for comparison with the test FE model. This experiment provides the temperature at the outer radius of the window and a temperature profile across the vacuum surface courtesy of an infrared camera. These experiments were done in the range of 1000 kW, CW at 350 MHz. The test FE model has been run and benchmarked to these experiments. This model helps us understand the significance of the cooling circuit in the stress distribution of the window. Running 1000 kW at 350MHz, the effects of too aggressive an inner conductor cooling without adequate attention to the air cooling across the window could be disastrous. It is discovered from varying the heat transfer coefficients (effectively changing the flow rates of air and water in the system) the stress is significantly effected. The results are seen in Figure 1.

It can be seen that as the heat transfer coefficient value on the inner conductor is decreased, the maximum principal stress in the window actually decreases. This is an important result - that less cooling results in less stress.

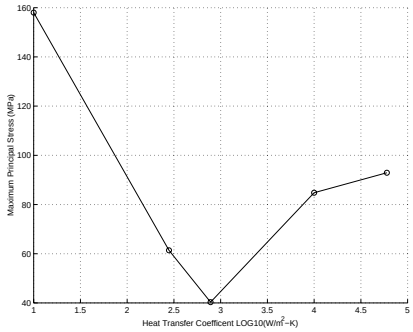

Figure 1: Maximum principal stress at various flow rates inside the inner conductor (window cooling held constant).

Conventional heat transfer rule-of-thumb would suggest the opposite, that less cooling will result in higher thermal stress. Further analysis shows that the magnitude of the face cooling is just as important. Figure 2 shows the variation of stress when the flow rates across the window are varied.

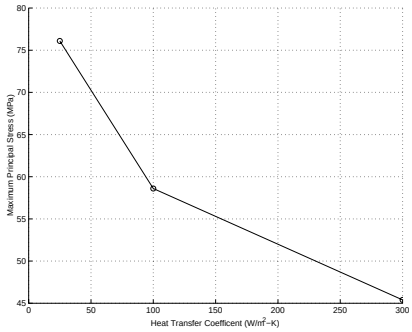

Figure 2: Maximum principal stress at various flow rates across the ceramic windows (inner conductor cooling held constant).

This geometry provided the first look of the effects of RF shields on the resultant heat load on the ceramic. These shields are place in the transmission line before and after the ceramics to prevent significant loading on the brazed joint. In preventing this build-up, the shield creates high electric fields at the same radial location in the ceramic (off the conductor walls). The resultant temperature peak, at a distance out from the inner conductor, results in high thermal loading in that position. This has been a significant influence in the temperature gradient driven thermal stress, because the peak temperature occurs away from the inner conductor wall, rather than directly at the wall, as theory would say. Couple that to the fact that the inner conductor is cooled to low temperatures, creates a strong temperature gradient right at the inner radius.

4.2 Dual Window Geometry

The CPI geometry includes a feature on the inner conductor that mitigates the aforementioned cooling issue (especially when using high flow rate water-cooling). The design features a thin-walled sheet of Oxygen Free

Electronic Copper (OFE-Cu) that the ceramic is directly brazed to. This plate is supported only at the ends, allowing the ceramic to expand, unconstrained, under a thermal load. The resultant stresses decrease by a factor of three over the ridged body assumption. Table 1 shows a comparison of the ridged and flexible support models with inner conductor and window cooling set at 60,000 W/m^2-K and 50 W/m^2-K respectively.

Table 1: Resultant principal stresses.

Maximum Principal Stress (MPa)	Ridged support	Flexible support
(σ_{mean}~250 MPa)	92.9	28.7

The implementation of flexible boundaries, although quite clever, leaves many questions lingering about the integrity of the brazed joint. Stresses in the copper plate are approaching the yield strength of the material and could create some fatigue problems in the long run.

4.3 CARES Predictions

CARES is a probabilistic, public domain software program that was developed at NASA Lewis Research Center. CARES calculates the POF for brittle ceramic materials from Weibull parameters and fatigue parameters for sub-critical crack growth. These parameters are calculated by CARES from test sample data.

Using data for WESGO AL300 ceramic [6], the probability of failure is calculated for extreme stress. Figure 3 shows the POF (as calculated by CARES) is only significant above 189 and below 273 MPa. Since our problem is the 30 MPa range (see Table 1), preliminary results suggest that the probability of failure will be quite low.

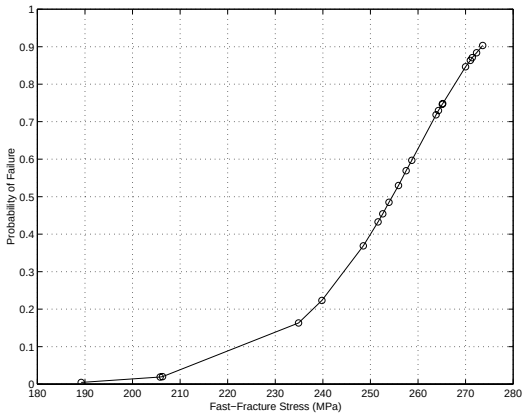

Figure 3: Probability of Failure in AL300 as a function of Stress State.

5 CONCLUSION / WORK IN PROGRESS

The analysis thus far has given much insight into the physics of the problem, significant design features, and their contribution to failure. From the aforementioned analysis we are able to infer trends in stress state when the cooling flow rates are changed. Thus, we are able to recommend optimum values to mitigate premature breakage due to thermally induced stresses. We also discovered that implementation of flexible boundaries for the ceramic vacuum barrier windows proved an excellent means of preventing thermal stress buildup.

Future analysis will be focused on continuing refinement of the current simulations to assure accuracy, as new experimental data becomes available in the coming months. More effort will be put on the interpretation of CARES results for fast-fracture as well as the failure time as a result of sub-critical crack growth (static fatigue). Other emphasis will be placed on the EEV design for the APT power coupler that was not treated here. A major feature of the EEV design is the use of an expanding outer conductor, rather than a shield, to protect the brazed joints. Preliminary results also suggest that the EEV design may not be plagued by the same cooling concerns because of the smooth distribution of power absorption in the ceramic (from the absence of shields) and the more than adequate use of air cooling across the window faces.

More future analysis will examine the structural response to the perfect mismatched case in the transmission (when the RF wave effectively encounters a short and is reflected back down the line) for both the CPI and EEV designs.

6 ACKNOWLEDGEMENTS

Completion of this analysis would not have possible without the contributions of colleagues at LLNL and LANL. The authors acknowledge stimulating discussions with Dr. A. Shapiro and Dr. C. Landram at LLNL, and Dr. B. Rusnak at LANL.

7 REFERENCES

[1] Baker, E., L. Janosik, J. Gyekenyesi, N. Nemeth, and L. Powers, "CARES Users and Programmers Guide-Preliminary Draft," 3/10/97.

[2] DeWitt, D. and F. Incropera, "Fundamentals of Heat and Mass Transfer," 4th ed., John Wiley & Sons: New York (1996).

[3] Shapiro, Arthur B., "TOPAZ3D: A three-dimensional finite element heat transfer code," LLNL UCID-20484, Livermore, CA (1985).

[4] Maker, Bradley N., "NIKE3D: A non-linear, implicit, three dimensional finite element code for solid and structural mechanics," LLNL UCRL-MA-105268 rev. 1, Livermore, CA (1995).

[5] Cummings, K., "EEV RF Window experiments," LANL Memo L-5:97-028, 3/20/97.

[6] Cummings, K., "Theoretical Predictions and Experimental Assessments of the Performance of Alumina RF Windows", Ph.D. Dissertation, UC Davis, June 1998.

LINAC LUE - 200 TEST FACILITIES

S. Dolya, W. Furman, K. Goldenberg, A. Kaminsky, A. Krasnykh[*] ,
E. Laziev[**] , V. Shvets, A. Sumbaev, V. Zamrij
Joint Institute for Nuclear Research (JINR), Dubna, Russia;

N. Dikansky, P. Logachev, V. Skarbo
Budker Institute of Nuclear Physics (BINP), Novosibirsk, Russia;

E. Begloyan, E. Gazazian, Yu. Nazarian, V. Nikogossian, G. Oksuzian
Yerevan Physics Institute (YerPhI), Yerevan, Armenia;

V. Senyukov
Moscow Engineering Physics Institute (MEPhI), Moscow, Russia

Abstract

The Intense REsonant Neutron Source (IREN) [1] with 200 MeV driver electron linac LUE-200 is being created at JINR by JINR, BINP and MEPhI. The average power of the electron beam will be 10 kW. For optional decision of a lot of problem we are planning to use a few test-installations (test-facilities). One of them is the Full Scale Test Facility (FSTF) [2] and the second one - the Electron Gun Test Facility (EGTF) at JINR. The JINR's operable installation (LUE-40 + IBR-30) [3], along its direct aim, also being used as the IREN's test-facility. The Electron Linacs of the Yerevan Physics Institute being planned to use as the IREN's test-facilities too. The description of the specified test-facilities is presented.

1 INTRODUCTION

The Intense Resonant Neutron Source (IREN) was designed and is being created at JINR by JINR, BINP and MEPhI. The IREN includes three main parts: the 200 MeV Electron Linac LUE-200 (beam average power will be 10 kW), tungsten target and plutonium booster-multiplicator [1]. On account of the IREN installation must be placed instead of the presently operating neutron source (IBR-30 and its driver - 40 MeV Electron Linac), the designed value of the accelerating gradient of the LUE-200 is chosen relatively high (35 MV/m) for providing the necessary energy and power of electron beam.

So far as the IREN must be instead of the operable facility (IBR-30 + LUE-40) it is reasonable to test, using test facilities, the most part of the IREN's equipment, and first of all the LUE-200 equipment, before its installation. For this purpose is expected to create some of those facilities at JINR and use existing facilities in BINP and YerPhI as well. The description of those facilities is given below. The program of works to be carried out at those facilities is also presented. Note that the possibility to provide the necessary accelerating gradient as well as the determination of the dark current are the principal problems for us.

2 FULL SCALE TESTING OF THE ACCELERATING SECTIONS

For full scale testing of the LUE-200 accelerating sections we are planing to use the special facility (FSTF) (see Fig. 1) at JINR (under construction [2]), as well as the BINP's available test-facilities. Since the BINP is the designer and producer of both - the accelerating sections and the SLED cavities - it is expected that the sections and cavities will be tested at the suitable BINP test-facilities in cooperation with the JINR representatives and get certificate of quality originally. At the FSTF the M-350 modulator for the 5045 klystron [4] was already installed, and klystron is being installed now. The M-350 modulator was created using of the M-250 modulator of the OLIVIN klystron station. This station was developed and created for the YerPhI linac and supplied to the JINR according to the agreement between JINR and Armenian government. All jobs on putting the modulator in operation are completed. The thermostat, cooling, monitoring and emergency systems are under construction. The vacuum system's equipment produced by the Vacuum Praha is ready for installation, and some of it is already installed.

The main problems to study at this facility are the obtaining of the expected accelerating gradient and measuring of the dark current. Along the accelerating section the scintillation detectors will be placed for measuring X-radiation induced in the section body by the dark current. Energy spectrum of the dark current and accordingly accelerating gradient will be measured in the usual way by magnet spectrometer. Moreover the RF-

[*] Also SLAC
[**] Also YerPhI

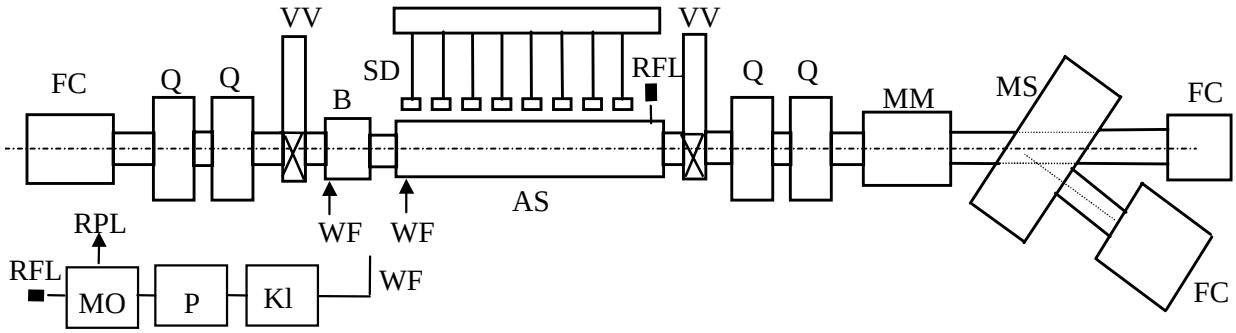

Fig. 1. Schematic layout of the full scale LUE-200 IREN test facility.
AS - accelerating section, B - buncher, Q - quadrupole lenses, FC - Faraday cup, Kl - klystron, MO - master oscillator, P - preamplifier, MS - magnetic spectrometer, RFL - RF-load, VV - vacuum valve, SD - scintillation detector, WF - waveguide feeder, MM - measuring module, RPL - reference phase line.

power multiplier system, the waveguide elements, the LUE-200 control, monitoring and protection systems are expected to test at the FSTF. Note the another no less important role of this facility. It is expected that all the LUE-200 elements will be tested and get the certificate of quality on it before installation in the standard place.

3 ELECTRON GUN (EG) TESTING AND SETTING-UP FACILITY.

In Fig. 2 the EG test - facility layout is presented. The LUE-200 electron gun is under construction at JINR now. It was designed on the basis of the prototype created earlier at BINP for the F-factory. EG products the electron beam having the parameters: 200 KeV energy; 5 A pulse current at 0.25 μsec pulse duration. At the present time most of the EG parts are produced and its assembly being carried out. In addition to the electron gun the facility includes the following equipment:

- 100 cm length beam transport channel equipped with two focusing solenoid lenses and beam position correctors (transverse magnetic field coils);
- beam current monitor;
- beam position monitor;
- beam profile monitor;
- beam emittance monitor;
- magnet analyzer;
- auxiliary technological equipment.

The research program involves: cathode emission characteristics measurement, beam energy (total energy and energy spectrum) and space-angular (profile, emittance) electron beam characteristics measurement

4 TEST RESEARCH OF THE LUE-200 ELEMENTS AND RF SYSTEM DEVICES

The LUE-200 RF-system is based on two 5045 klystrons produced by SLAC. The RF-system includes the master oscillator, reference phase line, preamplifier, SLED system, and two waveguide feeds. The each waveguide feed provides incident and reflected power monitoring, RF-pulse envelope monitoring, phase monitoring (of the buncher and the accelerating sections RF channels relative to the reference phase), control and protection (on RF breakdown and VSWR in the waveguide feeds or the sections). The LUE-200 RF

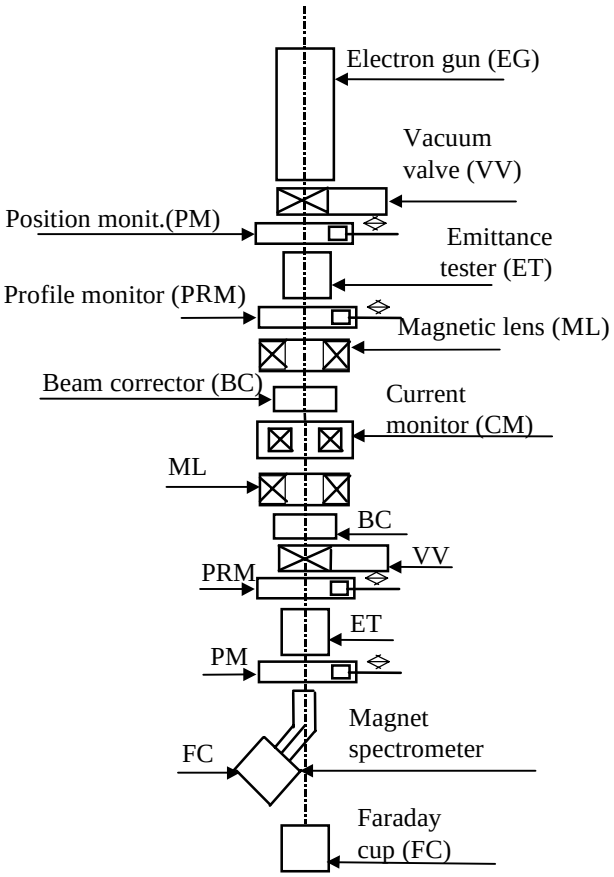

Fig. 2. Schematic layout of the EG test facility

system also includes high-power matched RF loads placed at the outputs of the sections. The RF system elements (except the SLED's cavities and the loads) were designed at MEPhI and produced by the ISTOK specialized manufacture. Some monitoring and RF-system control devices were designed at YerPhI and are being tested at the test facilities in Yerevan. When the testing will be finished that devices will be placed in own positions at the FSTF and at the LUE-200. Fig. 3 shows the layout of the IREN RF test-facility at YerPhI.

5 IREN MONITORING DEVICES

Within the project realization a number of basic principles on the IREN monitoring are being tested at the operable installation (LUE-40 + IBR-30) which is used as the IREN's test-facility. We try to build a stabile and reliable control system using free software base: FreeBSD and Linux operating system, free implementation of SQL server, HTTP server, etc. The use of the software which source codes are open gives us some advantage in comparison with commercial (and closed) software.

Such a monitoring system of the (LUE-40 + IBR-30) was created and put in experimental operation during the 1997-98. A set of pulse and continuous parameters are measured and stored with a real repetition rate 100 Hz. All the functions of the control systems (measuring, database storing, public access providing) are distributed between different UNIX workstations. Main attention is paid to provide a stability of the control system at emergency situations, such as AC power shutdown, network cable tearing, etc.

We also try to develop a software to provide an effective communication between personnel and users of the existing facility. All the information interesting for the users are available from the WWW, and WWW to SQL interface is used to access the databases.

6 CONCLUSION

The IREN project aimed to create the new JINR's base installation for fundamental research is being realized in the rigorous of the total crisis, caused by economic, political and social cataclysms of the recent years all over the territory of the Former Soviet Union. In spite of all the difficulties the IREN team does not lose hope to complete the project in the foreseeable future.

Work supported by .JINR Facilities Development Plan under contract .#0993. and partially by ISTC under contract A 087 at YerPhI.

7 REFERENCES

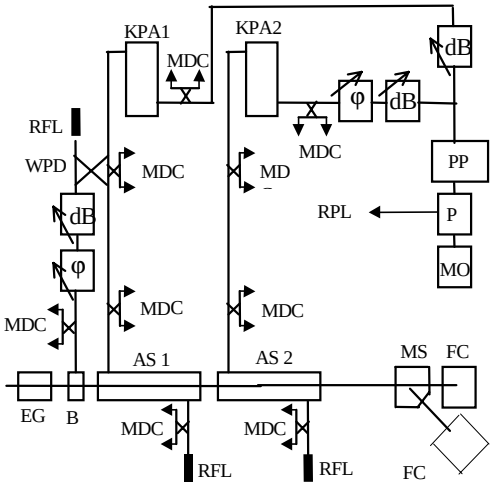

Fig. 3. The IREN test facility at YerPhI.

MO - master oscillator, P - continuous signal preamplifier, PP - pulse signal preamplifier, MDC - coupler, RPL - reference phase line, WPD - waveguide power divider, EG - electron gun, B - buncher, RFL - RF load, AS - accelerating section, KPA - klystron pulse amplifier, MS - magnetic spectrometer, FC - Faraday cup.

[1] A.Kaminsky et al., "Lue200 - Driver Linac For Intense Resonant Neutron Spectrometer (IREN)", Proceedings of LINAC96 Conference, CERN, August 26-30, 1996, 508-510 (1996).

[2] V. Antropov, et al., "IREN Test Facility At JINR", Proceedings. of LINAC96 Conference, CERN, August 26-30, 1996, 505-507 (1996).

[3] I. M. Frank. Particles and Nucleus, Vol. 1, Part 2, 805-860. Dubna, 1972.

[4] A. A. Kaminsky et al, "The M350 Modulator for JINR Intense Resonant Neutron Source (IREN)" Proceedings of the XV International Workshop on Charged Particle Linear Accelerators, Kharkov, September 16-21, 1997; Publeshed in "Voprosy Atomnoi Nauki i Tehniki", Issue 2,3(29,30), 131-134, Kharkov, 1997.

CONSTRUCTION OF THE 8-GEV e^- / 3.5-GeV e^+ INJECTOR LINAC FOR KEKB

A. Enomoto, KEK e-/e+ Injector Linac Group*, and Linac Commissioning Group**
KEK, 1-1 Oho, Tsukuba-shi, Ibaraki-ken, 305-0801, Japan

Abstract

The KEK/PF 2.5-GeV linac has been upgraded since 1994 by upgrading the existing linac as well as extending it towards the upstream site. It has been almost completed and commissioned during May and June, 1998. This paper summarizes the construction status and the beam performance of the new injector.

1 INTRODUCTION

KEKB includes an 8-GeV electron (e^-) ring and a 3.5-GeV positron (e^+) ring, which has been under construction since the TRISTAN accelerator was removed. KEKB aims at a luminosity of 1 x 10^{34} $cm^{-2}s^{-1}$ with collisions between 1.1-A electrons and 2.6-A positrons.

One of the requirements of the injector linac is to deliver full-energy beams for both rings. The other is to increase the positron beam intensity to 0.64 nC (4 x 10^9 particles) /bunch with a repetition rate of 50 Hz. This positron intensity is ten-times as much as what the old linac produced, and when the beam could be injected without any beam loss, it takes 13.5 minutes to accumulate from 0 to a maximum charge of 26 μC, since the KEKB ring has a circumstance of about 3 km.

In order to achieve these requirements, the linac has been reconstructed and expanded [1]-[3]. For the energy upgrade, the number of accelerator modules was increased from 40 to 57, as well as the acceleration gain of each module from 70 to 160 MeV. The old positron generator was moved to a higher energy point of about 3.7 GeV from 0.25 GeV in order to increase the positron intensity.

2 CONSTRUCTION

The KEKB injector has been constructed since FY 1994 as a five-year program. Reconstruction of the old linac was finished by the end of FY1996; the linac expansion was constructed during FY1997 and the combination with the old linac was completed by the end of FY1997 (March, 1998).

2.1 Energy Upgrade of the accelerator module

In order to increase acceleration gradient, the rf source of the old accelerator modules has been upgraded from the downstream to the upstream using summer and winter shutdown terms. For increasing the rf peak power, the klystron modulator power was increased by twice, the 30-MW klystrons replaced by 50-MW klystrons, and rf pulse compressors (SLED: SLAC energy doubler) used. Including newly fabricated ones, 58 upgraded accelerator modules were so far constructed and the number of the remaining modules to be installed is only one.

	summer	winter	annual
-FY1994			5
FY1995		7	7
FY1996	12	15	27
FY1997	12	6	17
FY1998	1		1
		total	58

Among 58 accelerator modules, the SLEDs are not used in the most upstream module (pre-injector) and the accelerator module just after the positron radiator, in order to avoid any troubles due to electric breakdown.

2.2 High-power klystrons and modulators

The newly developed 50-MW klystrons are compact, size-compatible with the old 30-MW klystrons. They have been satisfactorily fabricated and installed according to the schedule described above.

Forty-seven klystron modulators were improved to double the pulse energy and 11 modulators were newly produced. The high-voltages applied to the klystrons were tuned so that the pulse width is 3.7 μs with ripples less than 0.3%. The high voltage control and the interlock monitor are made using programmable logic controllers.

During the linac commissioning in May and June 1998, the klystrons were operated at 25 pps and the output power was 38.6 MW in average of 55 modules with SLEDs; and corresponding calculated no-load accelerator gain was 164 MeV /module.

---

*1: K. Nakahara (head), I. Abe, S. Anami, A. Enomoto, S. Fukuda, K. Furukawa, H. Hanaki, H. Honma, H. Iijima, M. Ikeda, K. Kakihara, N. Kamikubota, T. Kamitani, H. Katagiri, H. Kobayashi, T. Matsumoto, S. Michizono, K. Nakamura, K. Nakao, Y. Ogawa, S. Ohsawa, T. Oogoe, T. Shidara, A. Shirakawa, T. Suwada, T. Urano, S. Yamaguchi
*2: N. Akasaka, A. Enomoto, J. Flanagan, H. Fukuma, Y. Funakoshi, K. Furukawa, N. Iida, T. Kamitani, M. Kikuchi, H. Koiso, K. Nakajima, T.T. Nakamura, Y. Ogawa, S. Ohsawa, K. Oide, K. Satoh, M. Suetake, T. Suwada

All the accelerator modules had been conditioned up to about ten-percent higher peak power, and the trip rate was low during the beam commissioning, ex., 0.31 times/klystron.hour during June 7 to 13. Since the operation started, two klystrons has been replaced owing to trouble in the output window and the gun cathode, respectively; and 4 more klystrons are to be removed during this summer shutdown in order to tune the focusing field again.

2.2 Low-power rf systems

The low-power rf systems have been extensively changed for the KEKB injector [4]. In order to synchronize the linac beam with the ring rf buckets within a requested precision of +-30 ps, the common factors between the linac and the ring rf frequencies were searched under the condition that the linac frequency was fixed and considering the ring rf bandwidth. The highest common factor was consequently chosen to be 10.38545 MHz, which is the 275 (11 x 5 x 5) -th subharmonic of the linac rf as well as the 49 (7 x 7) -th subharmonic of the ring rf (508.8872 MHz). This means the linac beam and the ring rf bucket are synchronized at 10.38545 MHz.

The subharmonic bunchers (SHBs), which produce single bunch beams from the gun beam pulses with a width of about 2ns, are to be operated at the fifth (571.2 MHz) and the 25-th subharmonic (114.24 MHz). For the former rf, a 10-kW solid-state amplifier was newly fabricated, however, for the latter, an old amplifier using vacuum tubes was still utilized with slight improvement.

The frequency of a master oscillator was chosen to be the fifth subharmonic (571.2 MHz). Using an optical fiber cable, the linac fundamental rf (2856 MHz) is transferred from a main-booster to sub-booster stations located at the upstream of every 8 accelerator modules.

For the SLED system, the sub-booster rf drive systems were improved so as to inverse phase at the latter part of the rf. The switching time is changeable. During the rf conditioning, it was set around 200 ns in order to avoid the rf breakdown.

Sub-booster klystrons were replaced by newly developed 60 kW klystrons in order to drive 8 klystrons instead of 4 klystrons in the old linac case. These klystrons are water-cooled. During the commissioning, the correlation between the rf phase shift and the cooling-water temperature was studied and measured 1 deg /0.1 deg.C. The temperature stability for the rf systems has been improved to be around 0.2 deg. by changing cooling-tour fan switching to continuous control of a 2-way valve.

2.3 SLEDs

So far 55 SLEDs has been operated. These SLEDs are of two-hole coupling type and are modified in order to facilitate handling in the existing linac: the tuner with smooth adjustments with the necessary resolution (2 kHz in resonant frequency); the drive mechanism of the detuner needle using solenoid. The radiation from the SLEDs is sufficiently low and the shielding is not necessary, though there are several SLEDs with relatively higher radiation. The tuners and the detuners are also well working.

2.4 Accelerator sections

About seventy 2-m sections, which are $2\pi/3$-mode traveling-wave structures, were fabricated using electro-plating method. One of them was tested up to 36 MV/m (21 MV/m is operational), where any limitation was not found. By the linac commissioning, all of the new sections were conditioned without any problem up to more than the operational gradient.

An accelerator section used just after the positron radiator is one meter long; the input coupler has two symmetric coupling holes in order to reduce electric field around the coupler and the input waveguides. This section is operated in the solenoidal magnetic field of 0.5 T and fed by an rf of about 30 MW, 1 μs without a SLED, producing an acceleration gradient of 17 MV/m. Rf conditioning for the accelerator sections used in the magnetic field was carefully performed. Consequently the klystron trip due to electric breakdown was hardly experienced during the commissioning for the positron beam in June. This was a drastic change from the four-meter sections which had been used in the old positron source.

2.5 Pre-injector

The KEKB injector requires the pre-injector to produce single bunches with a bunch length of about 10 ps (FWHM) and a charge of more than 10 nC. The gun is able to emit pulsed beams with a pulse width of about 2 ns (FW) and a peak current of about 10 A. In order to compress the gun beam to the single bunch beam, a 114.24-MHz SHB and a 571.2-MHz SHB were installed before the 2856-MHz bunchers. The gun beam energy was increased up to 200 kV (100 kV in the old electron linac) for suppressing space charge effect on the basis of a computer simulation. The pre-injector showed a good beam performance in the commissioning.

2.6 Positron production

The main improvement for the positron source was to replace 4-m accelerator section by shorter sections. In the KEKB injector, two 1-m sections and two 2-m sections were installed and rf pulses with shorter width are to be fed. This improvement was very effective for stable operation of the positron beam. The electron-to-positron conversion rate normalized by the incident electron energy was about 3.3%/GeV at the end of the linac.

2.7 Beam Instrumentation and control

One of the great progress of the KEKB injector from the old injector is to have developed a beam instrumentation system based on beam position monitors (BPMs)

which were installed at every location of quadrupole magnets [5]. The BPMs were widely utilized to tune linac beam in such cases as orbit correction and dispersion correction of the linac beam transport system.

The BPMs comprises stripline-type beam position monitors and associated signal analyzing systems. For solving man-power problem to develop a data acquisition system, 17 digital sampling oscilloscopes, which are of 5 GHz, 2 ch, and communicated with a VME computer, were distributed every half of the linac sector (typically 38.4 m). The signals are combined by combiners so that each peak is not overlapped and their peaks are measured using the oscilloscope functions and analyzed by VME. The position signals for one beam pulse are measured by a beam-trigger signal distributed to the monitor station. The position information from all BPMs is renewed every 1.4 second at present.

The other important monitor is a streak-camera system to observe the bunch structure of the linac beam [6]. The streak-camera system was also used in the old linac. However, it was not so easy to handle, because it consisted of separate devices, such as an optical system, a trigger and its delay system, a synchronization circuit between the trigger and the rf to reduce trigger jitters, as well as a streak camera proper. Further, air-Cherenkov light emitted by a beam was used as a light source into a streak camera; therefore, it has for a long time been used only for experiments.

Newly developed streak-camera systems are more simply arranged, computer controlled, and they utilize optical transition light (OTR) emitted from a metal mirror which can be easily inserted to the beamline. Thus four streak-cameras were installed after the pre-injector, after the linac arc, after the positron radiator, and the linac end. So far they were frequently used at the pre-injector as a real time bunch tuner.

2.8 Linac Alignment

All the buncher system are operated in the Helmholtz coil of about 0.1 T. In this low energy region, the alignment of the equipment was carefully checked; by changing the gun beam energy, the position change on beam screens was investigated. However the alignment has been still checked in this summer shutdown, because it was essential to use steering coils before the buncher during the commissioning.

The linac alignment has not been sufficient at present. One of the reason is the girder slide rollers were superannuated. They have been replaced during this summer shutdown. And the linac alignment will be selectively improved upstream of the positron radiator in order to increase the primary electron beam intensity.

3 BEAM PERFORMANCE

The linac commissioning was carried out as scheduled in May and June and the results near to the design were obtained as follows:

electron			positron	
	dsgn	achvd	dsgn	achvd
energy (GeV)	8	>8	3.5	>4
charge (nC/bunch)	1.2	1.5	0.64	0.6
energy width (% FW)	0.5	----	0.5	0.8
emittance (1σ, mm)	1.1	----	1.6	2.3

A remarkable feature of the linac commissioning was use of the beam instrumentation system and SAD (strategic accelerator design) computers in various stages of the beam tuning. Especially it was indispensable to tune high-current electron beams for positron production while suppressing emittance growth.

4 SUMMARY

(1) A linac upgrade was almost completed. A total energy of more than 8 GeV and average module gain of more than 160 MeV (20 MeV/m) were obtained.

(2) A positron beam near to the design quality has been achieved.

(3) To achieve a complete performance in the KEKB commissioning, the remaining issues, such as the linac alignment check, replacement of the old devices, and preparation for the 50-Hz operation, is to be still continued during this summer.

REFERENCES

1) J. Tanaka, et al., "Operation of the KEK 2.5 GeV Electron Linac", Proc of the 1984 Linear Accelerator Conference, Darmstadt, Germany, May 7-11, 1984.
2) I. Sato, et al. edited, “Design Report of PF Injector Linac Upgrade for KEKB” (in Japanese), KEK Report 95-18.
3) A. Enomoto, “Upgrade to the 8-GeV Electron Linac for KEKB” , Proc. of LINAC96, Geneva, Switzerland, 26-30 August, 1996, pp.633-637.
4) H. Hanaki,et al., "Low-Power RF Systems for the KEKB Injector Linac", Proc. of APAC98, Tsukuba, Japan, 23-27 March, 1998, to be published.
5) T. Suwada, N. Kamikubota, K.Furukawa: "NEW DATA ACQUISITION SYSTEM OF A BEAM-POSITION MONITOR AND A WALL-CURRENT MONITOR FOR THE KEKB INJECTOR LINAC", Proc. of APAC98, Tsukuba, Japan, 23-27 March, 1998, to be published.
6) Y. Ogawa, et al.: "NEW STREAK-CAMERA SYSTEM FOR THE KEKB LINAC", Proc. of APAC98, Tsukuba, Japan, 23-27 March, 1998, to be published.

SINGLE BUNCHED BEAM TESTING FOR SPRING-8 LINAC

T. Kobayashi, T. Hori, H. Yoshikawa, H. Sakaki, T. Asaka, K. Yanagida, A. Mizuno, S. Suzuki, T. Taniuchi, H. Abe and H. Yokomizo
Japan Synchrotron Radiation Research Institute, SPring-8, Kamigouri, Ako, Hyogo 687-1298

Abstract

A new grid pulser for a short pulse was installed in the electron gun system. The emission pulse length can be changed from 250ps to 1ns with the peak current of 1.6A. The single bunch operation in the storage ring was successfully achieved with the purity of 10^{-6} order.

1 INTRODUCTION

The SPring-8 is a third generation synchrotron radiation X-ray facility with a 1GeV linac, 8GeV booster synchrotron and 8GeV storage ring. We succeeded in the acceleration to 1GeV by the linac in August 1996, and in acceleration to 8GeV by the booster synchrotron in December 1996. In March 1997, the storage ring was accumulated the 20mA beam current with long life time. In May 1998, the storage ring was stored the electron beam with maximum current of 100mA.

SPring-8 linac with maximum energy of 1GeV is consisted of 13 high power klystrons(E3712,80MW) and 26 acceleration tubes[1,2]. The preinjector of the linac is composed of 200kV thermionic gun[3], two single-cavity prebunchers, a standing wave buncher and a high-gradient acceleration tube. The emission current from the linac has been produced various kinds of the pulse length from 10ns to 1μs and an energy of 60MeV, which are requested by the operation modes of the storage ring. We have been planned the 1ns emission of the linac for the efficient injection to the storage ring. Since this autumn, 1GeV storage ring(so called New SUBARU) which is under construction in SPring8 site will be also injected the 1ns emission from the linac. However, the 1ns emission have not been supplied in the 8GeV storage ring. Recently, the single bunched beam operation of the storage ring was achieved by using the new grid pulser(three fixed outputs 250ps,500ps,1ns).

2 PERFORMANCE OF GRID PULSER FOR SINGLE BUNCH EMISSION

The grid pulser system is shown in Fig.1. This system has three grid pulsers; a single-mode grid pulser(less than 1ns), a short-mode grid pulser (10-40ns) and long-mode grid pulser(1μs). The single-mode pulser has three outputs with the fixed pulse length of 250ps, 500ps and 1ns through the front panel N-type connectors, and the rise time of each pulse is about 200ps. These grid pulser are installed on the gun high-voltage deck. In order to achieve rapid exchange of the grid pulsers, the grid pulser system is connected with a coaxial rotary switch controlled remotely from the control room. The emission test was carried out with the 1ns pulse length of the single-mode grid pulser.

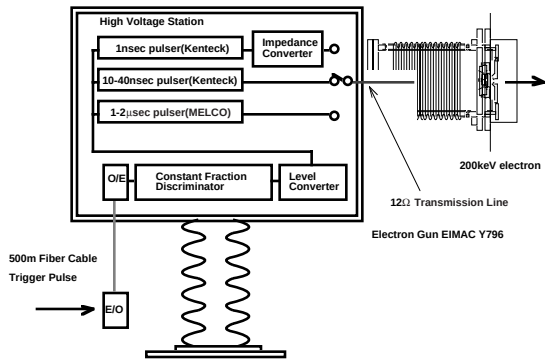

Figure 1: Schematic drawing of the grid pulser system.

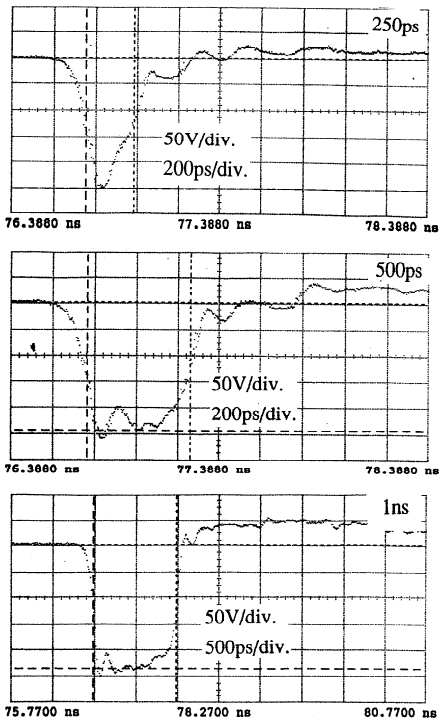

Figure 2: Waveform of three fixed outputs of single-mode grid pulser(250ps,500ps,1ns)

The external grid pulser trigger was transmitted through a single-mode optical fiber, which has low dependence on the room temperature, developed by Sumitomo electric industries. This fiber has a thermal coefficient for a delay of less than 0.4ppm. We use circuits made by ORTEL Co. as electrical-to-optical(E/O) and optical-to-electrical(O/E) converters, with a jitter of less than 2ps(rms) and a maximum frequency of 10GHz. The external trigger of grid pulser is synchronized both 508MHz(synchrotron, storage ring) and 60Hz(line frequency).

The waveform of the three fixed outputs of the single-mode grid pulser is shown in Fig.2. The peak-to-peak time jitter of three fixed output(250ps,500ps and 1ns) is 26ps, 28ps and 25ps, respectively. The relationship between pulser control voltage and pulser output voltage is shown in Fig.3. The output voltage of grid pulser is changed from 120V to 300V at the port of 1ns output.

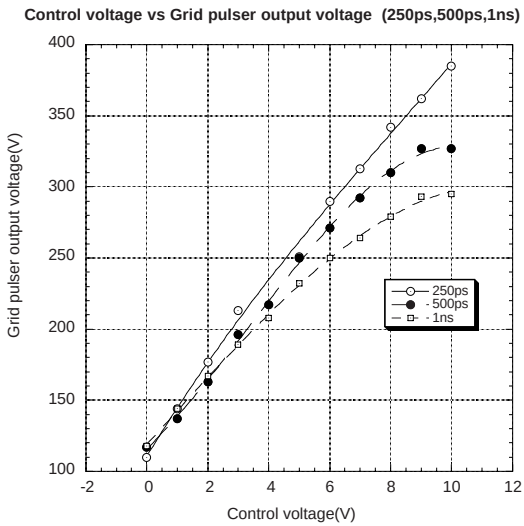

Figure 3: Control voltage vs grid pulser output voltage

3 EMISSION & ACCELERATION TESTING

The waveform of the emission current from Y796 electron gun is measured by the SCM(wall current monitor) as shown in Fig. 4[4,5]. The maximum emission current is 1.6A with pulse length of 1ns.

Fig.5 shows the relationship between emission current and the output voltage of the single-mode grid pulser. The 1ns emission current shows the good linearity. We measured the characteristics of the 1ns beam which was accelerated up to the maximum energy of 1GeV. The beam position and shape were adjusted by checking screen monitors and the beam current was measured by wall current monitors. After fine adjustment of the beam transport, the transmission efficiency of the bunching section of linac was about 60%, and the transmission efficiency of the whole linac from the bunching section to an 1GeV beam dump was 95%. Using the chicane after the last acceleration tube, the energy spread and the beam energy was measured. The energy spread of beam was observed by the profile of screen monitor at the chicane center point(dispersion function 1m). The x-direction distribution of screen monitor at the chicane center point was 7mm. Consequently, energy spread of beam was within 0.7%.

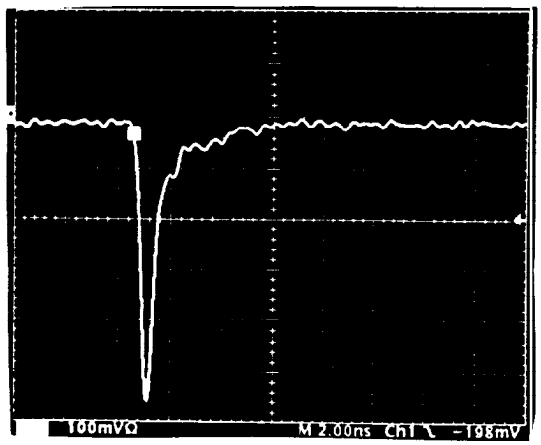

286mA/div. , 2ns/div.

Figure 4: Waveform of 1ns emission

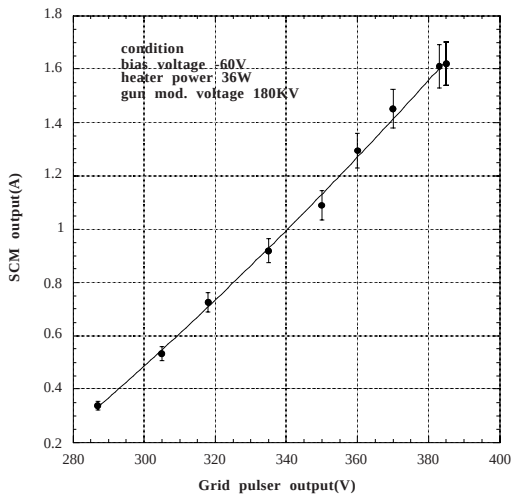

Figure 5: Relationship between grid pulser output and emission current

4 SINGLE BUNCH OPERATION OF STORAGE RING

We tried single bunched beam operation which accumulated the 1ns beam from the linac at the 21 buckets of the storage ring. Because Y796 cathode assembly was used for last 3 years, the grid was coated with Ba so that the grid emission has been increased. The current of the grid emission of 10^{-4} compared with the peak current of 1ns electron beam. By kicking the satellite

beam by the RF-KO of the synchrotron, the pure single bunched beam was obtained. The purity of the single bunched beam was observed by the technique of the optical measurement as shown in Fig.6. The purity of the single bunched beam was achieved to be the order of 10^{-6}.

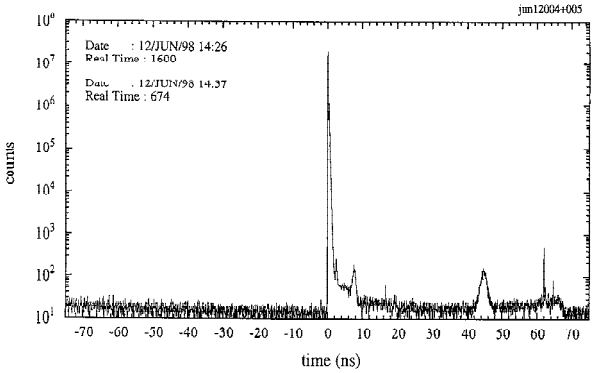

Figure 6: Measurement of single bunched beam of storage ring

5 CONCLUSIONS

We succeeded for accelerating the 1ns electron beam and accumulating the single bunched beam at the 8GeV storage ring. The grid emission was observed to be order of 10^{-4} compared with the electron beam. The purity of the single bunched beam of the storage ring was obtained to be order of 10^{-6} by means of eliminating the satellite beam by RF-KO of synchrotron.

6 ACKNOWLEDGEMENTS

The authors would like to acknowledge K.Nakajima, S. Nagasawa, H.Akimoto, SPring8 engineering service(SES) for their continuous support.

7 REFERENCES

[1] H. Yokomizo et al.,"Construction of SPring-8 Injector System",Proceedings of 10th Symp. Acc. Scie. and Tech.,14-16(1995)

[2] S. Suzuki et al.,"Initial data of Linac Preinjector for SPring-8",Proceedings of 93 PAC, Washington D.C., May 1993.

[3] H. Yoshikawa et al., "Bunching System of the Linac for SPring-8",Proceedings of 8th Symp. Acc. Scie. and Tech., November 1991,304-305(1991)

[4] K. Yanagida et al.,"Performance of Beam Diagnostics for SPring-8 Linac",Proceedings of 9th Symp. Acc. Scie. and Tech.,1993

[5] T. Kobayashi et al.,"Beam Monitors for SPring-8 Injector Accelerators",Proceedings of 14th Internatioal Conference,Application of Accelerators in Research and Industry",761-763(1997)

PERFORMANCE OF AN *AccSys Technology* PL-7 LINAC AS AN INJECTOR FOR THE IUCF COOLER INJECTOR SYNCHROTRON

D.L. Friesel and W. Hunt, Indiana University Cyclotron Facility, Bloomington, IN, 47408

Abstract

An AccSys Technology Model PL-7 Linac is used to pre-accelerate H^- ions to 7 MeV for strip injection into a new 2.4 T-m injector synchrotron now being commissioned at IUCF. The Cooler Injector Synchrotron (CIS) is designed to inject over 10^{10} polarized protons or deuterons per pulse at 5 Hz into an existing electron cooled synchrotron-storage ring (Cooler) for nuclear research [1]. The linac, a 3 MeV RFQ coupled directly to a 4 MeV Drift Tube Linac, is designed to transmit over 1 mA of 7 MeV H^- ions to the CIS injection beam line with 85% transmission, 1 π mm mrad normalized emittance and 1% energy spread. Two 350 kW, 425 MHz rf amplifiers power the linac which accelerates variable pulse width H^- ions at duty factors up to 0.2%. We discuss the beam performance of this unique linac after a year of service as a synchrotron injector, and compare measured beam properties with calculations made during design and fabrication.

1 INTRODUCTION

Negative ion strip injection into the CIS booster synchrotron is required by the relatively low intensities ($\leq$ 5 mA) of polarized proton and deuteron beam ion sources. Strip injection and accumulation calculations for H^- ions on thin Carbon foils (2 – 8 μgm/cm^2) predict that a minimum energy of 5 MeV is required to achieve the intensity goals desired for Cooler injection, with higher energies yielding higher intensity gains [2]. This led to the selection of an AccSys Technology Model PL-7 Linac as the H^- pre-accelerator for CIS. The PL-7 linac design consists of a modified AccSys Technology 3 MeV RFQ directly coupled to a 4 MeV, 22 cell drift tube linac. Beam matching from the RFQ into the DTL is done internally at the RFQ exit and the DTL entrance. Indiana University and AccSys technology entered into an "Industrial Partnership" agreement whereby AccSys designed and built the accelerating structures and power amplifiers. IUCF supplied the source, LEBT, RFQ vacuum vessel, commercial hardware and some manpower support. Fabrication of the IUCF 7 MeV H^- linac, the prototype of the present AccSys Model PL-7 design (serial No. 001), began at AccSys in June, 1995 and was completed by December, 1996.

Construction of a booster synchrotron (CIS) to replace the IUCF cyclotrons as an injector for the Cooler [1] began in late 1994. Beam commissioning of the H^- linac pre-accelerator and the ring strip injection system began in January 1997 with a 25 keV unpolarized H^- beam and resulted in the injection, accumulation and capture of both 3 and 7 MeV protons in CIS. Construction of an intense pulsed H^- polarized ion source (CIPIOS) [3] also began in January 1997. Beam acceleration studies beginning in Nov. 1997 resulted in the acceleration of 10^{10} protons to 240 MeV by May 1998. Beam extraction and Cooler injection development will begin during the last quarter of 1998 and CIPIOS will deliver polarized H^- beam to CIS and the Cooler in the first quarter of 1999. The CIS lattice design [4], beam performance goals [5,6], and initial H^- beam strip injection and acceleration commissioning results were previously reported [7,8,9].

2 LINAC DESCRIPTION

Design specifications for the IUCF Model PL-7 Linac are listed in Table I, and were determined from modified versions of the linac design codes PARMTEQ and PARMILA. Beam measurements made during the last year, described below, are compared with these predictions. A layout of the PL-7 RFQ/DTL pre-accelerator is shown in Fig. 1, and details of the 4 vane RFQ and 22 cell DTL accelerating structures and 350 kW amplifier systems are provided in Ref.[7]. The RFQ

TABLE I
PL-7 Linac Performance Specifications and Parameters

RFQ/DTL Operating Frequency		425 MHz
Input Energy (H^-)		25.0 keV
Output Energy (H^-)		7.0 MeV
Duty Factor		$\leq$ 0.2 %
Repetition Rate (variable)		0.1 – 10 Hz
Pulse Width (Variable)		35 – 350 μs
Maximum RFQ and DTL RF Power		0.35 MW
Normalized RFQ Acceptance (90%)		$\leq$1.0 π μm
Normalized DTL Output Emittance (90%)		1.0 π μm
Output Energy Spread		$\pm$75 keV
Guaranteed Beam Transmission		$\geq$80 %
A) RFQ Parameters:		
Overall Length:		228.4 cm
-Matching:	1.0 cm	
-Shaper:	22.3 cm	
-Bunching:	17.1 cm	
-Acceleration:	190.1 cm	
Ave. Bore Radius:		0.248 cm
Vane Voltage:		71 kV
Cavity Q:		7547
Peak Operating Power:		295 kW
B) DTL Parameters:		
Overall Length:		153.7 cm
No. Cells:		22
Quad Length (SmCo Perm Magnets):		2.54 cm
Cavity Q:		30,000
Peak Operating Power:		285 kW

for these measurements is designed for q/A=1 particles (H^+, H^-). To accelerate deuteron beams, this structure can be replaced in the RFQ with a separate q/A = ½ structure through a removable lid on the RFQ vacuum vessel.

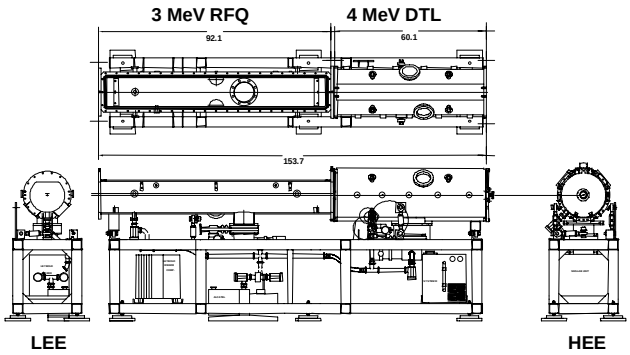

Figure 1. AccSys Technology Model PL-7 7 MeV Linac

3 LINAC PERFORMANCE

For all measurements reported here, a ≤ 1.0 mA peak, 25 keV unpolarized H^- beam from a duoplasmatron source is focused at the entrance of an AccSys Technology model PL-7 Linac. Beam is matched to the Linac (RFQ) acceptance requirements (symmetric 1.3 mm beam radius and 125 mrad convergence half angle, normalized emittance of 1.0 π μm) via a Low Energy Beam Transport (LEBT) system consisting of three Einsel lenses, an x/y steering magnet and an electron beam sweep magnet. Diagnostics including a multi-wire harp, an emittance scanner and a beam stop were designed into the LEBT. Measurements of the 25 keV H^- beam properties at the RFQ entrance are $\varepsilon \leq 0.6\ \pi$ μm, $\alpha = 0.62$ and $\beta = 0.012$, well within the AccSys specifications. The small source emittance is not necessarily an advantage for the PL-7 linac, which was designed for an acceptance of 1.0 π μm. The new polarized source, however, will have a beam emittance more closely matched to the PL-7 emittance requirements.

The 425 MHz three stage power amplifiers for the linac must provide the required RFQ and DTL cavity fields with amplitude and phase stabilities of ± 0.5% and ± 0.2° respectively to achieve the 7 MeV H^- beam properties listed in Table I. Significant improvements to the frequency, phase and amplitude loops were required at IUCF to meet these specifications, which are critical to the injection performance goals for CIS. The frequency and phase loops operate to specification. Until recently, however, the cavity amplitudes were run open loop to achieve the RFQ and DTL required threshold fields because the amplifiers, based on the EIMAC YU-176 triode tube, had insufficient power to maintain stability with these loops closed. The amplifiers must typically run above 295 kW.

The performance of the linac was characterized by measuring the properties of the 7 MeV H^- beam using several diagnostic systems in the 9m transfer beam line between the linac and the CIS ring. The RFQ cavity field threshold (V_o) was determined to be 4.35 V on a diode attached to a small pickup loop by measuring the transmission of beam through the linac with the DTL turned off as a function of cavity field. Typically, beam transmission through the linac is 80%, although transmissions as high as 90% have been observed. Beam time-of-flight pickups in the 7 MeV transfer beam line are used to monitor the energy and energy stability of the beam from the linac. The orbit period of the strip injected proton beam in the CIS ring is also used to independently verify the energy of the H^- beam extracted from the DTL. At the measured DTL threshold diode voltage of 3.57 V, the rf capture frequency of an optimally stored proton beam in CIS is 2.09730 MHz (h=1), corresponding to a circulating proton beam energy of 6.990 MeV. The 7 MeV H^- beam emittance was measured to be between 0.6 and 1.0 π μm.

The FWHM energy spread of the H^- beam was measured to be ± 85 keV via elastic scattering from a 2.5 mg/cm^2 Au foil with planar Si surface barrier stopping detectors at 30° scattering angles. This slightly larger than the predicted value of ±75 kV by AccSys was caused by our inability to close the DTL amplifier cavity field amplitude loop. This is illustrated in Fig. 2. The upper trace is an oscilloscope display of the TOF energy measurement of a single 200 μsec long, 7 MeV H^- beam pulse from the linac. The two initial peaks in this trace are instrumental "turn-on" noise, while the energy fall off (≈200 keV) during the last 40 μsec is real and mimics the DTL cavity field amplitude fall-off with pulse length. The vertical scale for this trace is 100 keV/div. The lower trace is the intensity of strip injected proton beam in the CIS ring (0.2 mA/div), which exhibits a similar decrease with pulse length that is not evident on the H^- beam stop prior to injection. When amplifier upgrades allowed the amplitude loops to be closed, the TOF energy fluctuations were reduced to 25 keV, which reduced intensity fluctuations for strip injected beams.

These data illustrate the importance of stable linac cavity fields on the injection efficiency of protons into the CIS ring. The TOF energy monitor is continuously displayed during routine CIS operations to diagnose and correct linac (DTL) stability problems. Even with the DTL amplitude loop open, injection stability is quite acceptable for long running periods when the Linac is properly tuned and has reached thermal equilibrium after startup. With the loop closed, accumulated

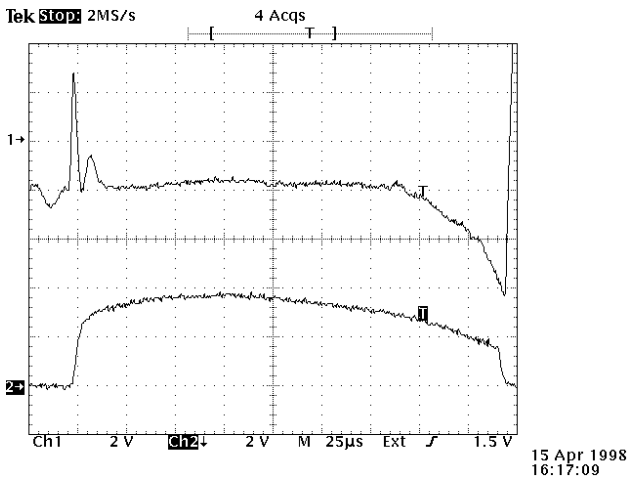

Figure 2. Scope displays of the 7 MeV H^- beam TOF energy (upper) and first turn proton beam intensity in CIS (lower).

and stored beam intensity typically varies by less than a few percent from cycle to cycle.

The focussing properties of the 7 MeV H^- beam exiting the linac were determined to be very close to the predictions provided by AccSys, which were used to design the transfer beam line optics that match the linac beam to the synchrotron acceptance. The beam line focussing elements and measured beam envelope are within 5 % of the values predicted using the optics code TRACE 3D, and beam transmission from the linac to the stripper foil in the ring is better than 85%.

4 BEAM INJECTION & RF CAPTURE

The linac delivers a 300μsec H^- beam pulse on a 4.5 $\mu g/cm^2$ stripper foil in the CIS at up to 5 Hz repetition rates for the injection and accumulation of 7 MeV protons. Two bumpers displace the ring equilibrium orbit onto the foil for strip injection and proton accumulation. Typically, an equilibrium accumulation of 8×10^{10} protons occurs in 200 μsec, after which the bumpers are turned off and adiabatic turn-on of a 1st harmonic rf cavity is started. Only about 2×10^{10} protons are rf captured and stored 2 msec latter because of the short 1/e beam lifetime (< 0.5 sec) in the 0.2 μTorr average ring vacuum. The captured beam bunch factor is 2.5 for an rf cavity voltage of 250 volts.

A schematic diagram of the RFQ, DTL and bumper fields, the linac H^- beam pulse and the injected proton beam accumulation relative timing required for optimal strip injection is shown in Fig. 3. We were surprised to find that the DTL cavity field must be at threshold before the 25 keV H^- beam from the source is injected into the linac or the DTL cavity field clamps to zero. This phenomenon was not observed when testing the linac at AccSys with protons. It is likely that stripped electrons produced in the RFQ cause multipactoring in the DTL which prevent its' rise to full field. This inconvenience was resolved by pulsing the source extraction HV in time with the RFQ cavity field, delayed by

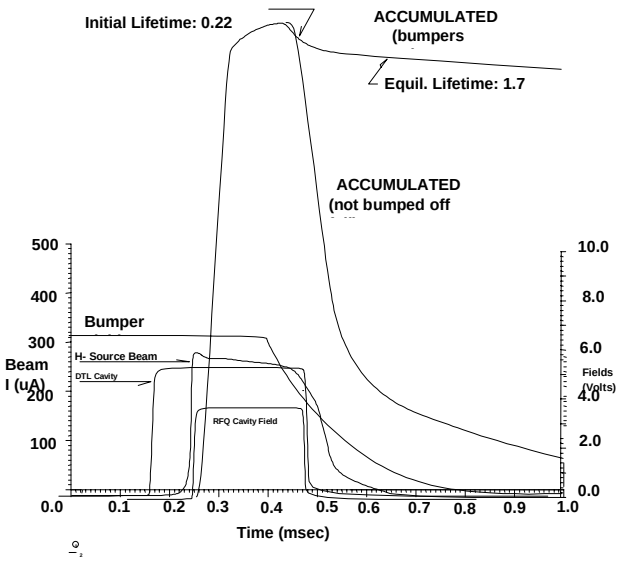

Figure 3. PL-7, bumper, and beam timing diagram.

as little as 30 μsec after the DTL cavity reaches full field. The RFQ pulse width must reside within the bounds of the DTL field anyway to insure that only 7 MeV H^- ions enter the transfer beam line, since 3 MeV H^- ions transmit through the Linac with equal efficiency as 7 MeV ions when the DTL cavity field is turned off.

5 CONCLUSIONS

The PL-7 linac has been used for over 1400 hours during the last year to inject 7 MeV protons into the new IUCF Cooler Injector Synchrotron. While some development of the RF amplifiers was required to achieve the guaranteed beam properties reported here, this linac has proven to be a reliable and stable source of 7 MeV H^- ions for strip injection into CIS. When delivered, the PL-7 linac was yet another new accelerator type introduced into the IUCF inventory. With continuous support from AccSys Technology, we have undertaken the effort to upgrade the amplifiers at IUCF ourselves to facilitate our understanding and maintainability of this system. The accelerating structures have proven to be rugged and reliable while the beam properties from this accelerator are reproducable to the point where no tuning of the transfer beam line and little tuning of the ring injection parameters are required to routinely achieve optimum strip injection performance. Turn-on during startup is usually quick (30 minutes), and once tuned up, the linac performs reliably for long periods of time, becoming invisible during other ring development activities such as beam acceleration and extraction studies. We are confident that these accelerator properties will be maintained as the CIS ring moves from developmental to operational status.

6 ACKNOWLEDGEMENTS

The work reported here was made possible by the skill and dedication of the technical and profession staff of IUCF, who were involved in all phases of this construction and commissioning effort. Clearly, this report could not have been made without the expertise and generous support of the professionals at AccSys Technology, Inc.

7 REFERENCES

[1] R.E. Pollock, IEEE 89CH2699-0, 17 (1989).
[2] K. Hedblom *et al.*, IEEE95CH35843, 336 (1995).
[3] V. Derenchuk *et al.*, PAC97, Vancouver, BC, to be published.
[4] D. Li *et al.*, IEEE 95CH35843, 357 (1995).
[5] D.L. Friesel *et al.*, IEEE 95CH35843, 336 (1995).
[6] D.L. Friesel & S.Y. Lee, EPAC'96 Spain, 548 (1996).
[7] D.L. Friesel *et al.*, PAC97, Vancouver, BC, to be published.
[8] D.L. Friesel & R. Hamm, PAC97, Vancouver, BC, to be published.
[9] D.L. Friesel & G.P. Berg, EPAC98, Stockholm, SE, to be published.

A 100 MeV SUPERCONDUCTING PROTON LINAC: BEAM DYNAMICS ISSUES

M. Comunian, A. Facco, A. Pisent
INFN Laboratori Nazionali di Legnaro, Legnaro, Padova 35020 ITALY

Abstract

Proton linacs with beam intensities between 10 and 120 mA in CW are under study in various laboratories, for applications that go from fundamental physics to energy production and nuclear waste transmutation. The majority of the projects consider, for energy above 100 MeV, the use of a superconducting linac, which is particularly convenient for "moderate" currents (10-50 mA). For the low energy part the situation is unclear, and the advantages of a superconducting structure have not been generally recognized yet. In this paper we consider a possible architecture for a 100 MeV linac based on independently phased resonators, and we give a first analysis of the beam dynamics issues, and the resulting cavity specifications. The flexibility of such a linac, for the use with different charge over mass ratios and beam currents, will be underlined.

1 INTRODUCTION

The interest for a superconducting proton linac covering the traditional DTL energy range has recently grown, in connection with various high intensity linac studies. We considered in this paper an Independently phased Superconducting Cavity Linac (ISCL) similar to those used for low energy heavy ions in many nuclear physics laboratories like ours, but at much higher beam intensity, and in a wider beta range. Development of cavities for this kind of applications has been done mainly at ANL[1], and other studies can be found in literature[2]. The high power coupler design and the beam losses control are specific problems related to the high beam power.

We show here a preliminary analysis at 352 MHz. Our attention is centered on beam dynamics issues: we determined a preliminary set of parameters that could help in cavity development. The classical chain of LANL programs (PARMTEQM, PARMILA…) was adapted to this specific problem so to have results based on well proven codes (especially for what space charge and initial distributions are concerned). We checked various approaches, like single and double gap cavities, 176 MHz and 352 MHz [3].

The most promising design for 30 mA beam current is based on the so-called “reentrant cavities”, that are modified pillbox, cylindrically symmetric and therefore theoretically dipole free.

2 THE ISCL

The linac was designed taking the main beam parameters used for TRASCO, the INFN-ENEA feasibility study for a waste transmutation Accelerator Driven System (ADS). In Tab. I we list the main specifications and the beam characteristics from the 352 MHz 5 MeV RFQ, with some emittance dilution in the matching line[4]. In the last two rows we specify the two main constraints of the independently phased resonators: the surface field and the beam loading per cavity. In particular the second constraint is specific of high current machines: in our case we want to feed each cavity with a single solid state amplifier and the limitation to 15 kW seems consistent with the present technology.

Table I: Main specifications of the linac.

Particle species		p	
Input energy		5	MeV
Output energy		100	MeV
Beam Current		30	mA
Duty cycle		100%	
Input RMS Emittance	Trans (norm)	0.4	mmmrad
	Long.	0.2	MeVdeg
Frequency		352	MHz
Maximum beam loading/cavity		15	kW
Maximum surface field		25	MV/m

3 THE REENTRANT CAVITIES

Various kind of superconducting resonators were developed or proposed for this β-range. Among them an attractive choice is a modified version of the reentrant cavities developed at Stanford [5]; in this early work the feasibility of low-β, single-gap niobium structures with good RF performance and no serious multipacting problems was demonstrated [6]. At the frequency of 352 MHz and in the presence of a relatively large bore, these cavities present many advantages: the axially symmetric shape avoids dipole field components; the single gap guarantees the widest velocity acceptance and the possibility of covering the full interval from 5 to 100 MeV with only one type of resonator; the simple geometry, which requires very few electron beam welds, allows for a low construction cost in the view of mass production. The maximum field achievable in superconducting cavities is usually limited by the onset of field emission; single gap structures, then, could

appear less attractive than multigap, high shunt impedance ones. However the relatively low energy gain per cavity which is required in our linac design and the low surface electric field ratio E_p/E_a of reentrant cavities make them perfectly adequate to the aim. The ISCL resonator characteristics, calculated by means of the program SUPERFISH, are listed in Tab. II. In fig.1 the shape of the new resonators and the design of the Stanford cavity are shown.

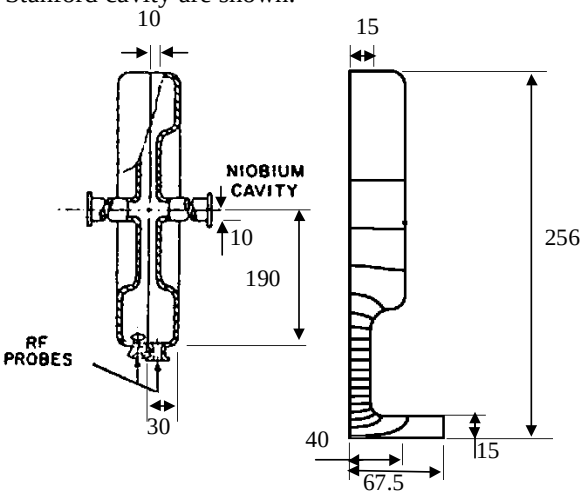

Figure 1: Reentrant cavity: the Stanford cavity (430 MHz [6]) and the proposed ISCL geometry (352 MHz).

Table II: Main cavity parameters (SUPERFISH).

Effective length	80	mm
Effective gap	53	mm
E_p/E_a	3.01	
H_p/E_a	32	Gauss/(MV/m)
$\Gamma=R_s\times Q$	82	Ω
R'_{sh}/Q	18	kΩ/m

4 BEAM DYNAMICS

We have chosen a FODO focusing structure with period $6\beta\lambda$. As the period becomes longer, a larger number of cavities can be installed between the quadrupoles. This design gives the advantage of an almost constant quadrupole gradient and beam envelope in the whole energy range. The zero current transverse phase advance per period is about 55 deg and the initial depressed one 45 deg. Moreover the adiabatic increase of the period makes the beam matching easier at the two extremes, with the RFQ and with the main linac.

The quadrupole parameters can be reached both by normal conducting and superconducting quads. Nevertheless, due to the lack of space, it is necessary to use superconducting quadrupoles installed inside the same cavity cryostat. A cost-effective design of such magnets is an open point.

The preliminary power consumption figures in Table III are rather conservative.

Table III: ISCL Parameters (30 mA).

Total length		65	m
Synchronous phase		-30	deg
Average acceleration		1-1.8	MeV/m
Number of cavities		253	
Cavity bore radius		1.5	cm
Quadrupole gradient		30	T/m
Quad aperture/length		2/5	cm
Output	Trans. (nor)	0.6	mmmrad
RMS Emittance	Long.	0.2	MeVdeg
Current limit (losses<10^{-4})		>50	mA
RF dissipation (R_s=100nΩ)*		890	W(@4.5)
Beam loading		2.85	MW
RF sys. pwr. cons. (η_{RF}=50%)		5.7	MW
Static cryo. losses (10 W/m)		650	W
Cryo. sys. cons. (η_{cryo}=1/500)		0.8	MW
Quadrupoles and ancillaries		0.5	MW
Mains power		7	MW
Pwr conversion efficiency		41%	

Table IV: ISCL Structure.

Energy [MeV]	Cavities/period	# of Periods	# of Cavities
5 ÷ 12.5	1	23	23
12.5 ÷ 28	2	30	60
28 ÷ 30	3	4	12
30 ÷ 55	3	18	54
55 ÷ 100	4	26	104
	Total	101	253

The linac has been simulated with PARMILA (standard PC version), using 10000 macro particles and about 700 elements (concatenated runs). Each cavity is represented by an accelerating gap. The structure of the linac, following the scheme of Tab. IV, is generated by an EXCEL workbook that writes the input files for PARMILA and reads the results preparing automatically several plots.

In Fig. 2 (upper part) the most significant parameters are plotted as a function of length. The transit time factor is in the range 50-98%. The voltage per cavity is chosen as to maintain a constant energy gain per linac length in the two linac parts; from the W plot the first (about 1 MeV/m) and the second (about 1.8 MeV/m) part of the linac can be distinguished. The plots of the surface field and of the energy gain per cavity show that the constraints are fulfilled.

In Fig. 2 (lower part) we plot the RMS envelopes, less then 1/7 of the aperture, and the emittances. Due to the non adiabatic change of the period structure some residual mismatch cannot be avoided. The emittance increase is acceptable, and can be partly seen heuristically as an exchange of energy (equipartitioning) between the longitudinal and the transverse degree of

* The BCS resistance is 58 nΩ.

freedom. The transverse degree of freedom is colder because the ISCL period is 6 times the RFQ period.

We have simulated currents up to 50 mA , and we did not see losses (10000 macro particles). Smaller losses must be investigated by other means.

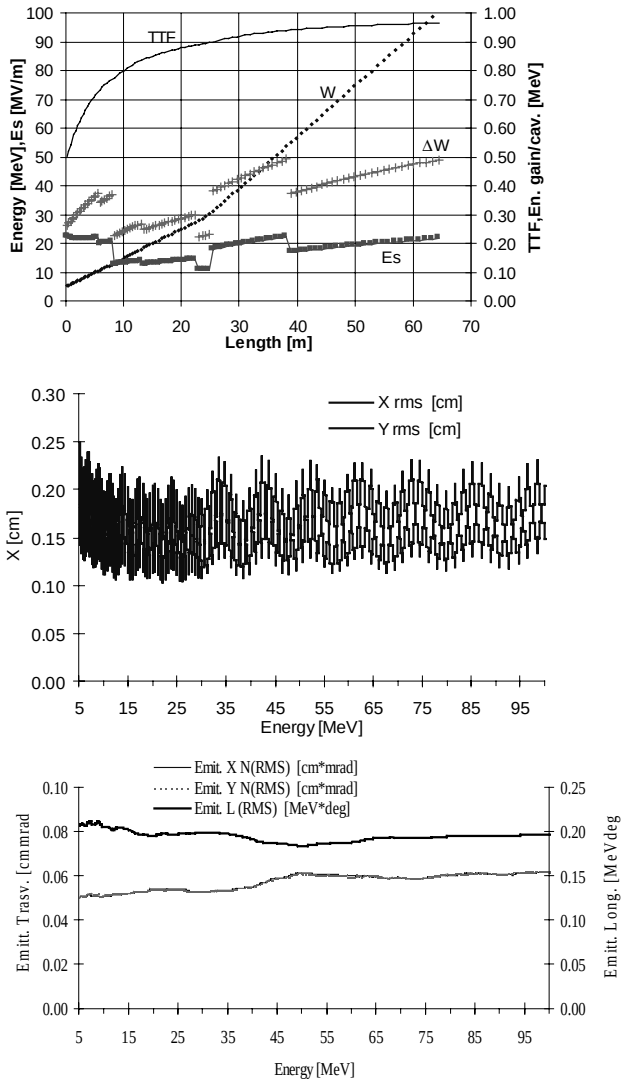

Fig. 2: Linac parameters as a function of position, RMS envelopes and Beam Emittance as function of energy.

5 DIFFERENT MODES OF OPERATION

The ISCL, in addition to a lower power consumption, has, with respect to a traditional DTL, the advantage of a considerable flexibility. It allows (see Tab. IV):

1. The compensation of the lack of performance of some cavities with the adjacent ones;
2. The use of the linac, with reasonable efficiency, at lower intensity keeping the CW characteristic of the beam;
3. If the linac is used as stand alone at low current (~1 mA) the field can be increased so to get almost 140 MeV of final energy (Exotic Beam production);
4. A moderate current of particles with q/A= ½ can be accelerated up to a final energy of 70 MeV/u.

Table IV: ISCL Operation modes (CW).

Particles	p	p	d	
Peak Current	30	1	<1	mA
Final energy	100	140	70	MeV/u
Beam Power	3	0.14	<0.15	MW
Mains Power	7	2	2	MW
Efficiency	41	7	7	%

6 CONCLUSION

We have designed a 352 MHz superconducting linac, able to accelerate a 30 mA CW beam up to 100 MeV, to be injected in the superconducting linac of a waist transmutation driver, but also able to accelerate, with good efficiency, 1 mA up to 140 MeV CW, as required for exotic beams production. Single gap axially symmetrical cavities (with a single design in the whole energy range) have been used. Many points of this design work are preliminary, but can be used as a base for cavity R&D.

7 ACKNOWLEDGMENTS

This work was developed within the TRASCO-A project. We thank G. Fortuna, A. Lombardi, A. Porcellato, G. Bisoffi, and G. Bassato for many illuminating discussions.

8 REFERENCES

[1] J.R. Delayen, W.L. Kennedy and C.T. Rohe, Proceedings of the 1992 Linac conference, Ottawa, AECL-10728 (1992) 695.

[2] Y. Tanabe, T.Ota, Y. Wachi, C.Yamazaki, S.Kawatsu and A.Miyahara, Proceedings EPAC 96 conference, Sitges (1996), Institute of Physics Publishing Bristol and Philadelphia, (1996) p. 569.

[3] A. Pisent, M. Comunian "Beam dynamics issues of a 100 MeV superconducting proton linac." The eight workshop on RF superconductivity Abano Terme (Padova) Italy,1997.

[4] A. Pisent, M. Comunian, G. Fortuna, A. Lombardi, M.F. Moisio "The DTL approach for a 100 MeV CW linac" LNL internal note LNL-INFN(REP) 111/96 (1996).

[5] P.H. Ceperly, I. Ben-Zvi, H.F. Glavish and S.S. Hanna, " Superconducting re-entrant cavities for heavy ion linacs", IEEE Trans. Nucl. Sci. NS-22, N.3, June 1975, p. 1153-1156.

[6] P.H. Ceperly, J.S. Sokolowski, I. Ben-Zvi, H.F. Glavish and S.S. Hanna, "Beam test of a superconducting niobium cavity for a heavy ion accelerator", Nuclear Instruments and Methods 136 (1976) 421-42.

STATUS OF THE SUPERCONDUCTING HEAVY-ION TANDEM-BOOSTER LINAC AT JAERI

S. Takeuchi and M. Matsuda

Japan Atomic Energy Research Institute, Tokai Research Establishment
Tokai, Naka, Ibaraki 319-1195 Japan

Abstract

An independently phased superconducting linac has been used over four years as the heavy ion booster for the JAERI Tandem accelerator at Tokai since its completion in 1994. This report describes the status of the resonator performances, especially the relief of Q degradation of hydrogen-polluted resonators by applying a sequential fast precooling method and other possible methods. A big air leak which happened to cold resonators is also reported.

1 INTRODUCTION

The superconducting heavy ion booster for the JAERI Tandem accelerator at Tokai is an indepependently phased linac composed of 46 superconducting quarter wave resonators, which are made of solid niobium and niobium-clad copper, and all of which optimum velocities are 0.1c[1]. There has been no resonator troubles resulting in cryomodule opening since the completion in 1994. Heavy ions of Ni, Ge, Se, Zr, I, Au and etc from the 20UR folded type pelletron tandem accelerator were boosted at accelerating fields of 3 - 5 MV/m per resonator and transported to the targets for experiments of nuclear or solid-state physics.

We have a problem called *Q-disease* that the resonators in the first four linac cryomodules suffer from hydrogen Q-degradation, which is due to significant hydrogen absorption during the electro-chemical surface treatment and precipitation of hydrides on the resonator surfaces during slow pre-cooling by the cryogenic system. A sequential precooling method was applied to the resonators to increase cooling rates across the temperatures from 130K to 90K in order to suppress the Q-degradation.

Recently, a big air leak happened in the linac due to a beam hit. This paper mainly reports the results of the fast precooling and the air leak accident. Our efforts to extract hydrogen from the niobium walls are also reported.

2 RESONATOR PERFORMANCES

2.1 Recovery of Q by Fast Precooling

We found that a severe Q-degradation happened to a resonator after it was cooled taking a long time between 130K and 90K[2]. The cooling rate of 10 -12 K/h by the cryogenic system is too slow and should be increased to 20 -40 K/h in order to moderate the Q-degradation. Fortunately, the cold helium gas was designed to flow into the cryomodules in parallel. The helium flow could be concentrated to a few cryomodules while the resonators in them were cooled down across the precipitation zone of 130K to 90K, and sequentially switched to others.

The first four linac cryo-modules which contain the resonators ill of Q-disease belong to seven cryo-modules cooled by a cryogenic system. We tried two modes of a three-modules-by-three-modules sequence and a two-modules-by-two-modules sequence. The cooling rates obtained by the two modes were 17 -27 K/h and 21-48 K/h, respectively. The reason that the rates were spread wide is that the four resonators are cooled in series in a cryo-module.

The low-field Q values of the 20 resonators measured after the two precooling modes as well as the normal precooling mode are shown in Fig. 1. Resonators of no.1 to no.16 are the ones in the first four cryomodules. The Q values were recovered to 65 - 80 % of the off-line test results by the two-modules-by-two-modules mode, except the two severely sick resonators no. 2 and 4. Those two resonators may need a treatment of hydrogen outgassing to recover satisfactorily.

Figure 2 shows the accelerating field gradients of the first 20 resonators measured at rf input of 4 watts after normal precooling in 1995 and after the two-modules-by-

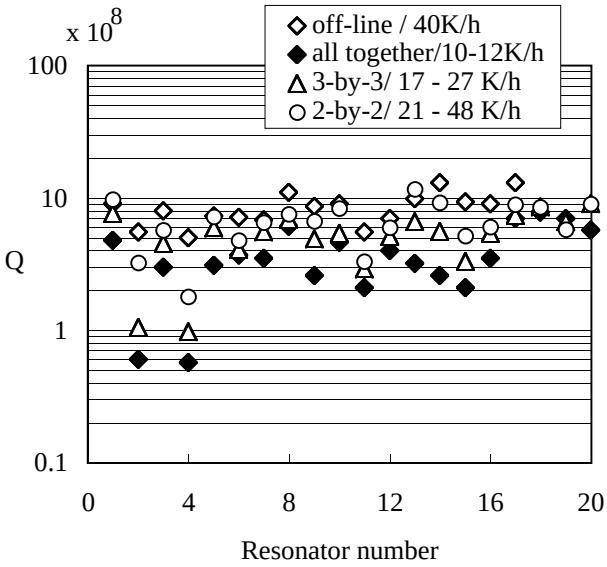

Fig.1 Low field Q of the first 20 resonators measured after four different precooling rates across the range of 130K to 90K; in the off-line tests, after the normal all-together precooling mode and after three-by-three and two-by-two sequential precooling modes.

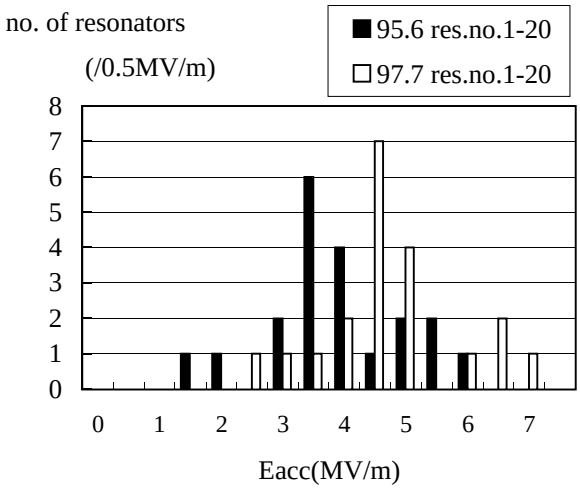

Fig.2 Histograms of the field gradients at rf input of 4 watts of the first 20 resonators measured in June, 1995 after normal all-together precooling mode and July, 1997 after three-by-three module sequential mode.

two-modules mode sequential precooling in 1997, as a histogram. The mean of the field gradients was recovered from 4.1 to 5.0 MV/m associated with the Q recovery.

The other 20 linac resonators which belong to the other cryogenic system have Q values between 0.6 and 1.2×10^9 so that the sequential precooling was not applied to them. In Fig.3, the accelerating field gradients of all the 40 linac resonators at 4 watts were shown as a histogram, which were measured at the same time together with the first 20 resonators. The overall mean value was 5.4 MV/m so that the originally designed value of 5 MV/m was attained.

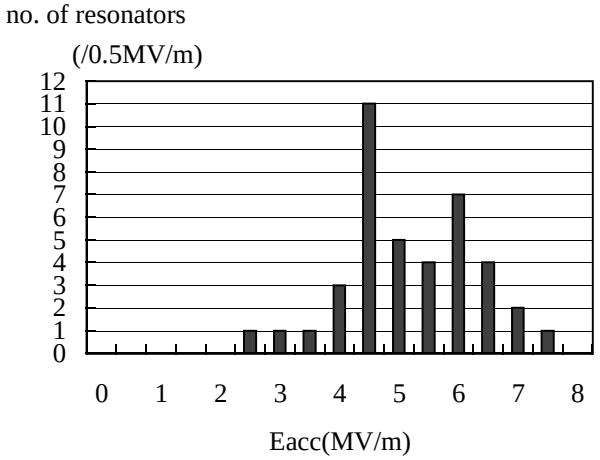

Fig. 3 Histogram of the field gradients of all the 40 resonators in the linac measured at rf input of 4 watts in July 1997.

2.4 Resonator Performances after Air Leak

A big air leak happened to the bellows between the first two cryo-modules on Sunday, May 31, 1998. The resonators were cold. The leak continued for about 12 hours untill the resonators were warmed across 80K. The pressure in the two cryostats were in the range of 10^{-1} Pa. The liquid level and helium pressure in the dewars were fortunately stable. The increase of the heat flow into the cryogenic system was about 23 watts, which was smaller than the refrigeration capacity per cryo-module of 28 watts. The resonators were once warmed up to the room temperature. The bellows had pin holes which seemed to be made by a sharp beam of 180MeV $^{32}S^{11+}$ of about 1 eμA. The leak rate measured later was 17 ml/s. Only from this rate, a lot of gas, as much as 1 kg, is supposed to be deposited on the cold surfaces of the resonators, the dewars and etc. From an additional fact that a big increase of leak rate have occured during the warming-up process, the deposition might be an order of 0.1 kg.

The accelerating field gradients of the resonators in the first two cryomodules are shown in Fig.4, in comparision with the data obtained before the leak(The sequential precooling was not applied to that machin time period, because of no demands for very high energies). The degradation of the resonator performances was not appreciably heavy, fortunately. They did not need heavy rf processing after the cool-down, either. It seemed that the niobium resonator surfaces were well protected from the gas deposition by the outer cans which have only two small beam holes of 25 mm in diameter.

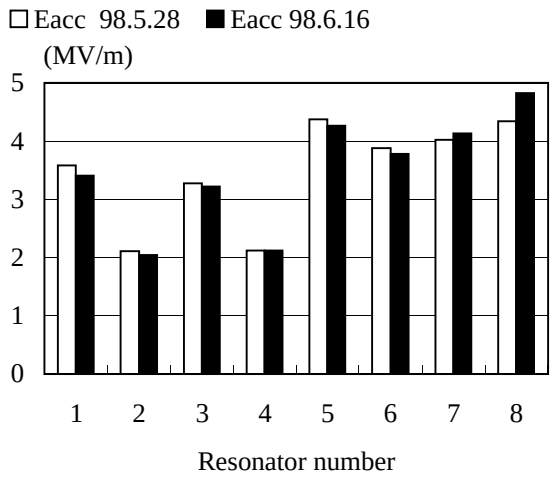

Fig. 4 Field gradients at rf input of 4 watts measured before and after an air leak trouble for the resonators on which air was deposited.

3 HYDROGEN OUTGASSING

It is idal to extract hydroden from the niobium walls by warming them up or by other methods if possible in order to cure the Q-disease. The quarter wave resonators are composed of a center conductor made of only niobium and an outer conductor made of niobium and copper and both conductors are welded together. It is, at least, possible to partially heat up only the center conductor.

3.1 Partial Heat Treatment

A spare resonators which was also ill of Q-disease was used to test the partial heating of the center conductor. A heater of 1.5 kW was set inside the center conductor, of which space is evacutated to 10^{-3}Pa. The top of the resonator was cooled by water. Lower 1/2 - 2/3 part of the center conductor was warmed up to about 600°C and hydrogen of an order of $1x10^{-3}$ mol was outgassed, which corresponded to a decrease of hydrogen content of 1 - 2 wppm in the niobium. The low field Q value measured after a slow precooling at a rate of about 12K/h was increased from 1×10^8 to 3.3×10^8 and the accelerating field gradient at 4 watt rf input from 2.7 MV/m to 4.0 MV/m. It looks worth applying this heat treatment to heavily hydrogen-polluted resonators such as the ones no.2 and 4.

3.2 Plan of ECR Plasma Surface Treatment

A method of hydrogen extraction without heating is wanted for the resonators made of bi-metals. Any of our attempts resulted in vain. Our next attempt is a plasma surface treatment utilizing electron cyclotron resonance at a micro-wave frequency. Gaseous elememts such as hydrogen, carbon and oxigen can be sputtered chemically from the surface[3]. We expect this method as a dry method of surface treatment for the superconducting niobium structures; that is, as a final surface treatment of rf superconducting cavities in place of heat treatment or high pressure water rinsing, or as a non-chemical surface re-processing method in case of heavy pollution.

A conceptional plan is illustrated in Fig.5. The ECR condition will be a frequency of 2.45GHz and a magnetic field of 0.09T. A resonator is co-axially placed in a solenoid. Investigations will be made with hydrogen, helium, oxigen or nitrogen gas.

4 OTHERS

4.1 Resonator control

Every resonator is controlled in a strongly coupled self-excited loop with phase lock and amplitude feed back functions. Six control modules made by Applied Superconductivity Inc. are used, each of which can control eight resonators. The rf power amplifiers were recently tuned up from 100 watts to 150 watts and moved close to the cryomodules in order to improve the stability at high field gradients. The resonator control is working well on the whole.

4.2 Cryogenic System

The cryogenic system is divided into two identical systems with refrigeration power of 250 watts. They have been working well except valve control troubles. The proportional valves are pneumatically driven and sometimes did not open as demanded. So that, an operator must make sure when time comes in a precooling period.

4.3 Beam Transport

The beam transmission was 40 - 100 % from the expectation in the past. After mis-alignment of 0 - 2 mm was found and fixed, the transmission was improved to about 80 - 100 %. An improvement was also given to the nine quadrupole doublet lenses placed between the cryomodules. They have now alternative focusing(F)-defocusing(D) planes as FD-DF-FD-DF- - -. The first four of them and the last four of them are simultaneously controlled, respectively, and the center one is turned off because there should be a beam waist point near the position. It made beam handling easier.

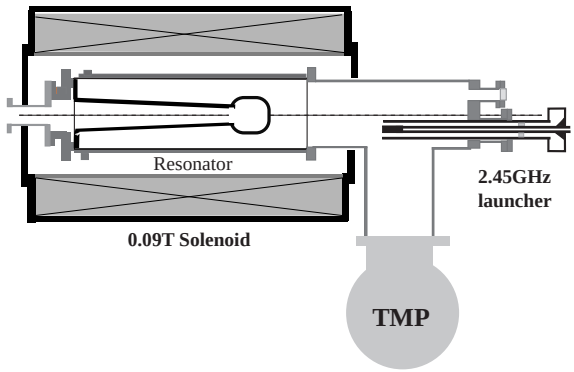

FIG. 5 Set-up plan of ECR plasma surface treatment for superconducting quarter wave resonators

5 CONCLUSIONS

The superconducting quarter wave resonators in the JAERI tandem superconducting booster have a mean field gradient of 5.4 MV/m, which is higher than the designed acceptance value of 5 MV/m, at the rf input of 4 watts, after carrying out the sequential fast precooling for the first 20 resonators. Resonator performances were found to be stable against a big air leak. Effective methods of hydrogen extraction from niobium are being investigated.

REFERENCES

1) S. Takeuchi,M. Shibata, T. Ishii, H. Ikezoe and T. Yoshida, Proc. of the 1994 International Linac Conference, Tsukuba Japan(1994)pp758-761
2) T. Ishii, M. Shibata and S. Takeuchi, Nucl. Instr. and Methods A328(1993)pp231-235
3) S. Kato, N. Noda, H. Oyama, K. Akashi, T. Senju. K. Kaneko, O. Motojima, Y. Sakamoto and A. Iiyoshi, J. Nucl. Mater. 162-164(1989)pp763-768

MEBT DESIGN FOR THE JHF 200-MeV PROTON LINAC

T. Kato and S. Fu*
KEK, High Energy Accelerator Research Organization
1-1 Oho, Tsukuba-shi, Ibaraki-ken, 305-0801, Japan

Abstract

The medium-energy beam-transport line of 2.7 m long for the JHF 200-MeV proton linac was designed. It consists of eight quadrupole magnets, two bunchers and two RF choppers, and has two purposes: matching the beam from the RFQ with the acceptance of the DTL; chopping the beam to produce a gap of 222 nsec between pulses of 278 nsec for the injection into the following rapid-cycling ring. The JHF proton linac is an intense beam accelerator with an average current of 0.2 mA in the first stage and of 0.8 mA for the future upgrade. Therefore, the key point in the MEBT design was focused on the control of the beam emittance growth in the beam line and the beam loss during transient times of the chopper. An RF deflector is utilized for the chopper owing to its characteristics of high deflecting field and compactness. The beam edge separation between the chopped and the unchopped beams reaches to 6 mm with a deflecting field of 1.6 MV/m. The field distribution (both E and B) of the RF deflector from MAFIA calculation is directly read into the modified TRACE3-D for the beam line design. The beam losses during RF transient times of the chopper, analyzed by both LEBT and PARMILA codes, are less than 0.08% at the exit of the 50-MeV DTL.

1 INTRODUCTION

In the JHF linac the beam intensity is high in terms of both the pulse current and average current[1]. Therefore, beam-loss control is a very essential requirement in the accelerator design. Beam-quality degradation mainly occurs in the low-energy sections. It has been realized that beam matching is of great significance for minimizing the emittance growth and avoiding beam-halo formation, which has been recognized as one of the major causes for beam losses[2].

The 500 μsec-long macropulses from the ion source need to be chopped into sub-pulses for injection into the following 3-GeV ring. After chopping, the macropulse consists of 278 nsec long pulses and 222 nsec long gaps in between the pulses. The chopped pulses should have a clean cut at the head and tail to avoid beam losses during injection into the ring. During the rise and fall times of the chopping field, however, there are some unstable particles, which are partially deflected; they may be accelerated to high energy and lost or get into the ring. Therefore, a fast-chopper design is being pursued in order to decrease the number of unstable particles.

The medium-energy beam-transport line (MEBT) between the RFQ and DTL has been designed to accomplish the two tasks: beam matching and chopping. It consists of quadrupoles, bunchers and RF deflectors. To conserve the beam quality, the line should not be too long and the beam needs to be well focused without large-amplitude oscillation. The line must also leave sufficient space for the beam diagnostics. The RF power requirement for the RF deflectors should be within the capability of the up-to-date solid RF power supply.

In this report, the design details are delineated. At first, the MEBT design is proposed in the second section. Section three describes the RF cavity of the deflector. The fourth section presents analysis of unstable particle. Finally conclusions are drawn out.

2 DESIGN OF THE MEBT

In order to describe the beam-deflection behavior, TRACE3-D[3] has been modified so as to include a new element: RF deflector. The field distribution in the cavity is calculated from MAFIA[4] and directly read into TRACE3-D. In this way, the fringe E&H fields beside the deflecting electrode can be taken into account.

The output beam from the RFQ is assumed to have the parameters listed in Table 1. Type A stands for the 30 mA case and Type B for the 60 mA case for upgrading in the future. The MEBT design is proposed with a total length about 2.7 m (Fig. 1). In the beam-profile plot at the bottom of the figure, the beam centroid offset in the x-direction by the RF deflectors is depicted by the dark curve. The beam dump will be positioned at the element 18 for the chopped beam. The design procedure has two steps. At first, the beam line up-stream of the element 18 is designed aimed at the largest separation between the unchopped and chopped beams at the element 18. Then, the unchopped beam is further transferred so as to match with the acceptance of the DTL.

Table 1. Input beam parameters at the MEBT entrance.

Parameters	Type A	Type B
I (mA)	30	60
$\varepsilon^{x,y}_{RMS}$ (πmm-mrad)	0.187	0.375
ε^{z}_{RMS}(πMeV-Degree)	0.133	0.266

* On leave from China Institute of Atomic Energy

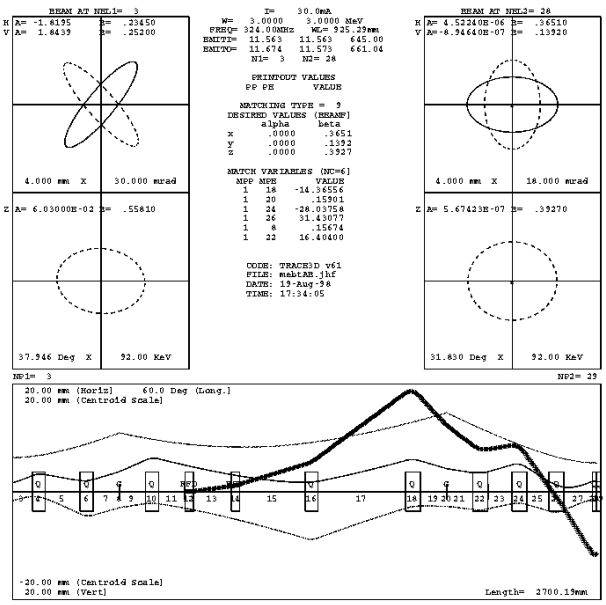

Fig. 1, TRACE3-D output of the MEBT for Type A. The up-left gives the input beam phase spaces and the up-right gives the matched beam with DTL. The bottom shows the beam profiles in the z, x and y directions respectively. The dark curve traces the beam centroid offset by the two RFDs. The element numbers are denoted under the beam axis.

The edge separation between the chopped and unchopped beam is 6 mm at the dump, when both of the RF deflectors have a deflecting field of 1.6 MV/m. This large separation is contributed from not only the two RF deflectors, but also the fourth quadrupole-element 16. The deflection is initiated by the two RF deflectors at an angle of 6 mrad for each, and is then amplified more than two times by the quadrupole. Downstream of the quadrupole, the deflection angle becomes 30 mrad. Owing to this reason, the RF deflectors do not require much RF power for an adequate deflection.

The first three Q magnets also contribute to the realization of the large separation. They should be adjusted for a small beam profile in the deflecting direction at the fourth Q magnet. Since the deflected beam centroid is more distant from the quadrupole's axis than is the undeflected beam envelope at the Q magnet it gives a larger defocusing to the deflected beam, but less defocusing to the undeflected beam. The first three quadrupoles should also keep the beam envelope in this section not too large in the y-direction in order to avoid any large emittance growth in this direction. In the RFD section, the beam size in the x-direction must be smaller than the gap between the deflecting electrodes so as to avoid beam losses on the electrodes.

In case that the beam emittance from the RFQ is larger than the assumed value for Type A, a relatively larger initial emittance between Type A and Type B for 30 mA beam was input into the designed beam line. The result shows that the same beam line is still applicable. Of course, the edge separation becomes smaller (about 3.6 mm for the input rms emittance of 0.25 π mm-mrad). But it is still sufficiently large for chopping the beam.

The beam emittance growth for the undeflected beam has been studied by means of PARMILA[5] simulation with 10,000 particles. Figure 2 shows the RMS emittance variation versus the element of the beam line. The beam has an RMS emittance growth of 7.7%, 9.5% and 4.8% in the x, y, z directions respectively.

The same beam line can also be used for input beam Type B. Only a very slight adjustment in the gradient of the Q magnets and the bunchers is necessary for large deflection and matching. For Type B, a higher deflecting field of 2 MV/m is needed to generate a 5-mm beam edge separation, due to the fact that the beam envelope is larger than that in Type A. The PARMILA run shows that the RMS emittance increases by 10%, 6%, 8% in the x, y, z directions, respectively.

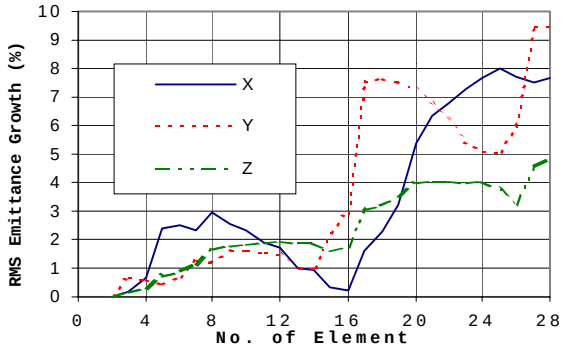

Fig.2. RMS emittance growth vs. the beam line elements for Type A.

3 RF CHOPPER DESIGN

A 324-MHz RF deflector cavity was designed and a cold model was tested[6]. The design philosophy is a low power demand from an RF power source and a fast rise time during pulse transient time. To hit the first target, the cavity geometry was optimized for maximum Z/Q_0 with MAFIA code under the limitation of the beam size; here Z is the transverse shunt impedance and Q_0 the unloaded Q value. To reach a fast rise/fall time, the cavity is heavily loaded by two coupling loops as input/output ports. Simulation with HFSS code shows the cavity can reach a very low loaded Q of 10 by means of two large loops with the size of 75×218 mm in the maximum-flux plane. To generate the deflecting field of 1.6 MV/m in the electrode gap, an input power of 22.2 kW is demanded from an RF power source, according to HFSS simulation. If the loaded Q becomes 15, the demanded power decreases to 14.8 kW. An additional power is needed to account for the deflection of the beam bunch with a half phase-length about 25° (see Fig.1). Therefore 1.2 times of power are required.

An aluminum cold model cavity was manufactured for demonstration of the low loaded Q. The results show a good agreement with the simulation: the measured Q_L=9.7.

4 ANALYSIS ON UNSTABLE PARTICLES

It is very crucial for the chopper to have as few unstable particles as possible during the RF rise and fall times. It is noted that the beam will not become totally unstable particles during the transient times because the scraper at the element 18 in Fig. 1 can stop some part of the particles in a beam when the RFD field is not at its full amplitude. To investigate the unstable particles during the transient times, PARMILA simulations with 5000 particles in uniform initial phase space were conducted. A particle scraper with an aperture of 20 mm in the x-direction is positioned at the element 18. As the RFD field increases toward its full value of 1.6 MV/m, the unstopped particle ratio in a bunch declines, as the curve shows in Fig. 3.

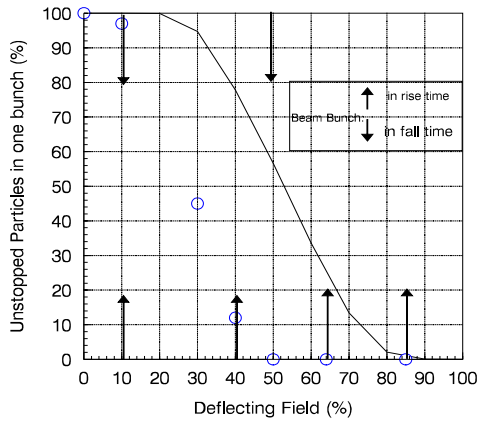

Fig.3 Unstopped particles ratio in one bunch vs. the deflecting field variation. The arrows indicate the bunch distribution during the RF rise and fall times. The curve indicates the ratios at the entrance of DTL and the circles those at the exit of DTL.

In order to obtain a quick rise and fall time, an improved method was proposed. The initial amplitude of the incident RF field to the cavity is 1.4 times the required full field. Some time after saturation, it is adjusted to one time the required full value. A rapid phase shift of 180^0 is added at the time just two or three periods before the power is turned off. These methods speed up the rise and fall times in terms of the required full field. Even though it needs an rf power two times higher, the solid RF power source is still within the commercially available range. Then, there are four micro-bunches during the rise time when the required full-field value is reached. Also only two bunches appear during fall time. These bunches meet the field amplitude, as denoted by the arrows in Fig.3.

When the field is more than 80% of the full value, the particles in a micro-bunch are almost totally stopped by the scraper. On the other hand, when the field is less than 30%, the unstopped portion of the particles can be injected into the acceptance of the DTL, according to TRACE3-D simulation. Thus only during the field-variation time from 30% to 80% of the full value, the beam will become unstable. However, not all the particles in the beam become unstable, because some of them can still be stopped by the scraper, as illustrated in follows.

During the rise time, two bunches at field of 10% and 85% amplitude do not become unstable beams. The other two bunches at 40% and 65% field amplitude partially contribute to the unstable particles. During the fall time one bunch is subjected to a field of 50%. Thus, for this bunch, only 58% of the particles become unstable. Totally, during transient times, the particles in 1.6 bunches become unstable at the exit of the MEBT.

A further investigation concerning the behavior of the transmitted unstable particles in the following 50-MeV DTL is conducted by means of the LEBT and PARMILA codes. Three scrapers are mounted in between the three DTL tanks with a slit full width of 6 mm. At the exit of the DTL, the ratio of the transmitted unstable particles is further reduced to less than 0.08% by the scrapers, as denoted by the circles in Figure 3. Also the scrapers do not block the unchopped beam.

5 CONCLUSIONS

The MEBT for the JHF linac is designed for matching and chopping the beam. The beam line is compact with a length of 2.7 m, owing to application of RF deflector. With the help of a quadrupole the chopper has a high deflection efficiency. The unstable particle ratio in the RF transient times can be reduced to less than 0.08% at the exit of the 50-MeV DTL.

ACKNOWLEDGMENTS

The authors are very grateful to Y. Yamazaki and F. Naito for their great support to this work and fruitful discussions.

REFERENCES

[1] T. Kato, “Design of the JHF 200-MeV Proton Linear Accelerator,” KEK Report 96-17, Feb.1997.
[2] Yamazaki, “Design Issues for High-Intensity, High-Energy Proton Accelerators,” Proc. of 1996 Inter. Linac Conf., 26-30,Aug. 1996, Geneva, Switzerland.
[3] K.R.Crandall,D.P.Rusthoi,TRACE3-Documentation, LA-UR-97-886, May,1997.
[4] T.Weiland, Part. Accl. , Vol.17 (1995)227.
[5] LANL accelerator code group, PARMILA Documentation, May,1995.
[6] S. Fu, et al., “ 324MHz RF Deflector Design and Test,” in these Proceedings.

FIRST BEAM STUDY FOR THE 432-MHZ DTL

F. Naito, K. Yoshino, T. Kato, Z. Igarashi, M. Kawamura, E. Takasaki,
Y. Morozumi, C. Kubota, T. Kubo, M. Ono, S. Anami and Y. Yamazaki
KEK, High Energy Accelerator Research Organization
1-1 Oho, Tsukuba-shi, 305-0801 JAPAN

Abstract

The first beam extraction from the 432-MHz DTL has been carried out in the test stand of KEK. Both MEBT and HEBT were assembled in the beam line for the beam test. The DTL has accelerated the 3-MeV H^- ion ejected from the RFQ up to 5.47 MeV. The measured ratio of the beam transmission is 91 %.

1 INTRODUCTION

The low-energy part of the 1-GeV linac for the Japanese Hadron Project (JHP [1]) has been constructed in order to establish the construction techniques and study the beam properties. (The scheme of the JHP is different from that of the Japanese Hadron Facility (JHF [2]) which was proposed recently as the modified version of the JHP.)

The test linac system consists of the H^- ion source, the radio frequency quadrupole (RFQ) linac and the short Alvaretz-type drift-tube linac (DTL). The beam-transport lines connect them. The high-power test of the DTL was completed in summer of 1994. The preparation for the beam study of the DTL was started since 1997, because the beam study of the RFQ had been completed.

2 SETUP FOR THE BEAM STUDY

The components of our linac system are as follows: 1) the H^- ion source; 2) the low-energy beam-transport line (LEBT); 3) the radio frequency quadrupole (RFQ) linac; 4) the medium-energy beam-transport line (MEBT); 5) the Alvaretz-type drift-tube linac (DTL); 6) the high-energy beam-transport line (HEBT). The layout of the linac system from the RFQ to the HEBT is shown in figure 1.

2.1 Ion source, HEBT and RFQ

The volume-productive ion source [3] supplies the H^- beam of the maximum 16-mA peak current. The extraction voltage of the ion source is 50 kV. The LEBT is composed of two solenoid magnets. The RFQ has the four-vane type structure. It accelerates the H^- ions from 50 KeV to 3 MeV. The resonant frequency of the RFQ is 432 MHz. The accelerating field of the RFQ is stabilized by the pi-mode-stabilizing loop. [4]

2.2 MEBT

The MEBT [5] consists of eight quadrupole electromagnets (Q-magnets [6]), a buncher and two steering magnets. All components of the MEBT are aligned on the same table. Thus, the alignment of the MEBT has been done by tuning the position of the table.

The buncher is a single-cell reentrant cavity. The gap length is 8.99 mm. The resonant frequency and measured Q_0 value of the buncher are 432 MHz and 21700, respectively. The maximum rf-power of 10 kW is supplied by the solid state power amplifier through the WX39D coaxial waveguide. The buncher is set in the middle of the MEBT. Two small steering magnets are installed between the QD1 and QF2.

2.3 DTL

The DTL has 18 drift tubes (DTs). The total length of the DTL is about 1.2 m. A permanent quadrupole magnet (PQM) is installed in each DT. The average field gradient of the PQM is 211 ± 1.3 T/m, which is about 20 % stronger than the design field (175 T/m). [7] The observed Q_0 value is 43500. It is about 90 % of the calculated value. The Q_0 value is sufficiently high. The measured

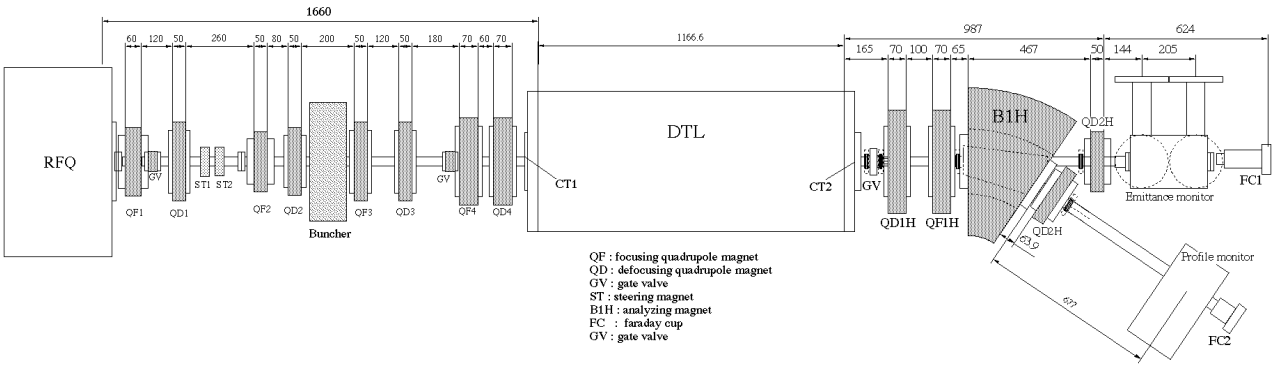

Fig.1 Setup of the DTL beam experiment

shunt impedance (Z) is 82 MΩ/m. It suggests a peak power of 128 kW for the 3-MV/m accelerating field. Thus rf-power of about 150 kW is required for the acceleration of 10-mA beam. The maximum electric field on the drift tube corresponds to 75% of Kilpatrick's limit. [8]

The accelerating field is stabilized by the eight post couplers. The field distribution stabilized by post couplers is sufficiently uniform (± 0.3%) and stable.

The current transformers (CT1, CT2) for the beam current measurement are installed in each end plate of the DTL.

2.4 HEBT

The HEBT consists of four Q-magnets, a bending magnet [9], a profile monitor, a transverse emittance monitor and two faraday cups. (We did not use the QD2H magnet between the bending magnet and the profile monitor.) The bending angle of the bending magnet is 34 degrees. The momentum distribution is measured by using a set of the bending magnet and the profile monitor. The effective area size of the profile monitor is 16 mm x 16 mm. The beam distribution is read by tungsten wires (0.1 mm in diameter) of 1-mm pitch.

The faraday cups (FC1, FC2) measure the total beam current. The FC1 works as the beam dump and the FC2 measures the beam current of the selected momentum.

3 MEASUREMENT

Because this study is the first beam acceleration by the DTL, the average beam current is reduced in order to minimize the beam loss. Then, the pulse length of the beam is reduced to 50 μsec, which corresponds to the rf-pulse length of the RFQ. The repetition rate is 10 Hz. Thus, the duty factor of the beam is 0.05 %. (The designed duty factor is 3 %.) The rf-pulse length of the DTL and the buncher are 200 and 140 μsec, respectively. The peak current of the beam, comes from the ion source, is about 13mA during the study. The coupling constant of the input coupler to the DTL tank has been increased from 1.0 to 1.25 (over coupling) against the beam loading by rotating the coupling loop before the beam experiment.

The DTL, MEBT and the HEBT were aligned in the RFQ beam axis by using a laser alignment system.

3.1 Tuning of the Parameters

The main parameters to be tuned are as follows: 1) The field strength of the Q-magnets of the MEBT; 2) The level and the phase of rf-field in the buncher; 3) The level and the phase of rf-field in the DTL; 4) The strength of the steering magnets. These parameters were tuned in order to maximize the beam transmission in the DTL and minimize the momentum spread of the beam ejected from the DTL.

The buncher requires the rf-power of 5.6 kW. The rf-power in the RFQ was adjusted to about 480 kW, which is an adequate power level for the standard operation of the RFQ. The rf-power level of the DTL is adjusted to 170 kW by parameter survey. Figure 2 shows the rf-field patterns for the DTL and the buncher

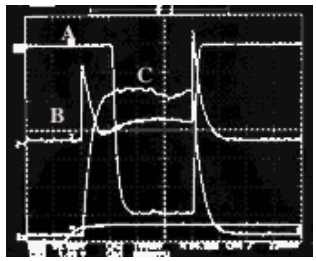

Fig. 2 Tank rf-field.
A: RF-field in the Buncher
B: Reflection from the DTL
C: RF-field in the DTL
(Abscissa: 50 μsec/div)

3.2 Beam Transmission

Figure 3 shows the output signals from CT1 and CT2. The upper line ("A" line) shows the beam current at the entrance of the DTL and the lower ("B" line) the output beam current from DTL. One vertical division corresponds to the current of 2 mA. It shows that the input and the output beam currents are 10.7±0.13 and 9.7±0.13 mA, respectively. Thus, the transmission of the DTL is 91 ± 2 % in this stage. Because the beam current from the ion source is 13±0.9mA and the transmission of the RFQ is 82.5%, the estimated beam current from the RFQ is 10.7±0.7 mA, which consists with the input beam current in the DTL. The reason for the missing beam of about 9 % is still unknown. We will check the followings in order to find its origin; 1) Transverse mismatching at the DTL entrance due to a 21-% excess in the strength of the PQM; 2) Alignment of the total accelerating system, especially, the Q-magnets of the MEBT; 3) a fraction of particles other than H^- ions.

3.3 Beam Energy

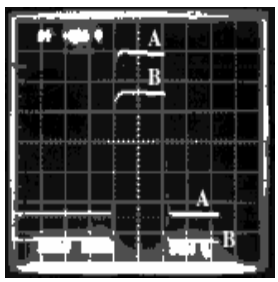

Fig. 3 Current monitor signal.
A: Incident beam into the DTL
B: Output beam from the DTL

Abscissa: 20 μsec/div
Ordinate: 2 mA/div

The beam momentum is measured on the profile monitor by changing the excitation current of the bending magnet in the HEBT. The beam momentum has been calibrated by using the beam from the RFQ without the acceleration in the DTL since the beam energy from the RFQ was already measured. The results (figure 4) include three kinds of data taken by changing the excitation current of the bending magnet. The abscissa is the energy of the beam. The Gaussian distribution curve has been fitted to the data in order to estimate the center value and the width of the kinetic-energy distribution. The averaged center value and the full width at half maximum of the

fitted curves are 5.47 and 0.21 MeV, respectively. The width of the distribution will be checked by the simulation.

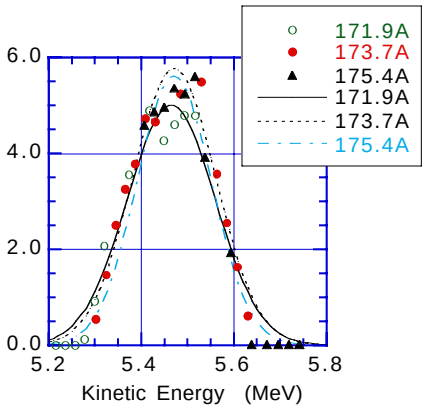

Fig. 4 Energy distribution of the beam from the DTL. Markers indicate the measured data. Gaussian curves are fitted to the data. The figures (171.9, 173.7 and 175.4) are the excitation current of the bending magnet used for the data taking.

3.3 Phase Dependence of the Beam Transmission

Figure 5 shows the variation of the beam transmission measured by changing the rf-phase of the DTL relative to that of the RFQ. The beam is measured by the FC2 after the bending magnet, which is adjusted by changing the excitation in order to collect the beam in the faraday cup FC2. The ordinate values are normalized at the maximum point. The width of the flat top of the plot is about 30 degrees. It is reasonable value, because the longitudinal bunch length of the beam from the RFQ is about 50 degrees and the acceptable longitudinal phase of the DTL is about 90 degrees.

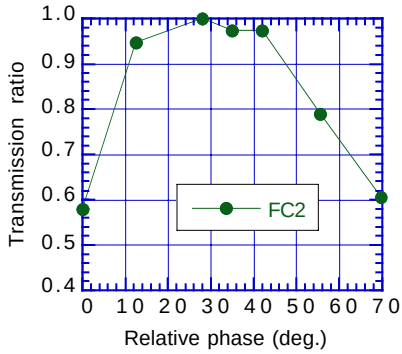

Fig. 5 Relative phase dependence of the beam transmission.

4 CONCLUSION

The first experiment of the beam acceleration by the 432-MHz DTL has been successfully performed in the test stand of KEK. The DTL accelerates the 3-MeV H^- ion ejected from the RFQ up to 5.47 MeV. Both MEBT and HEBT, assembled for the beam test, worked well. After the survey of the Q-magnet strength and the rf-pulse parameter for the tanks, the transmission of 91 ± 2 % has been obtained. The measurement of the beam emittance will be done soon.

5 ACKNOWLEDGEMENTS

We would like to thank Prof. M. Kihara for his continuous support. We also acknowledge Dr. A. Ueno and Dr. S. Fujimura for their useful suggestions for the operation of the RFQ and the ion source.

6 REFERENCES

[1] Y. Yamzaki and M. Kihara, Proc. of the 1990 Linear Accelerator Conf., Albuquerque, USA, LA-12004-C, 543 (1990)

[2] JHF Project Office, KEK-Report 97-16, JHF-97-10, KEK, Japan

[3] S. Fujimura and A. Ueno, Proc. of the 1996 Linear Accelerator Conf., Geneva, Switzerland, CERN 96-07, 343 (1996)

[4] A. Ueno, et al, Proc. of the 1996 Linear Accelerator Conf., Geneva, Switzerland, CERN 96-07, 293 (1996)

[5] T. Kato, Proc. of the 1994 Linear Accelerator Conf., Tsukuba, Japan, 59 (1994)

[6] K. Yoshino, et al, Proc. of the 1994 Linear Accelerator meeting in Japan (in Japanese), Tokai, Japan, JAERI-Conf 94-003, 202 (1994)

[7] F. Naito, et al, Proc. of the 1994 Linear Accelerator Conf., Tsukuba, Japan, 134 (1994)

[8] F. Naito, et al, Proc. of the 1994 Linear Accelerator Conf., Tsukuba, Japan, 137 (1994)

[9] K. Yoshino, et al, Proc. of the 1995 Linear Accelerator meeting in Japan (in Japanese), Osaka, Japan, Free Electron Laser Research Institute, 314 (1995)

RECENT DEVELOPMENTS AT THE NIRS-HIMAC INJECTOR

Y.Sato, T.Honma, T.Murakami, A.Kitagawa, K.Tashiro, M.Muramatsu, S.Yamada and Y.Hirao
National Institute of Radiological Sciences (NIRS), 4-9-1 Anagawa, 263 Inage-Chiba Japan

T.Fujimoto, H.Sakamoto, M.Yamamoto and T.Okada
Accelerator Engineering Corporation (AEC), Chiba, Japan

Abstract

At NIRS-HIMAC, 473 patients have already been treated using carbon beams by August, 1998. Therapy is scheduled in the daytime, while basic research is carried out during the nights and on weekends. Various ion species from Proton to Xenon have been used for basic research. Much effort was made to develop a time-sharing-acceleration system to well utilize the capability of three ion sources (PIG, 10GHz-ECR, 18GHz-ECR). Such recent developments in the injector are described in this paper. Several applications of linac beams with an energy of 6MeV/n are also briefly presented.

1 INTRODUCTION

Since 1994, HIMAC has been routinely used for both clinical trials of cancer therapy and basic research. Details concerning the HIMAC facility and its design philosophy have already been reported at linac and accelerator conferences [1, 2].

Taking account of an increase in both the number of patients and requests for basic experiments, it is necessary to effectively increase the available beam time and the kinds of ion species. During this year 16 themes in medicine, 64 in biology, and 47 in physics are actually being carried out in basic research. To answer these various requirements, a time-sharing-acceleration (TSA) scheme has been developed in the injector [3]. By using this scheme, three kinds of ion species can be simultaneously delivered from the injector to two synchrotron rings and a medium-energy (6MeV/n) experimental cave.

In order to expand the usable ion species, improvements in the ion sources have also been made. In order to precisely and actually measure the ion-stopping position in a human body, the application of positron emitter nuclei with a PET camera is in progress. A secondary-beam course was installed, and a preliminary test has been made for the production of ^{11}C by bombarding a thick beryllium target with high-energy ^{12}C beams through the reaction process of projectile fragmentation. The production rate of ^{11}C was around 0.2% and its purity 97%. A considerable increase in the primary beam is necessary to obtain sufficient intensity in the secondary beams for medical application; particularly developments in the ion sources are expected. Related improvements in the RF system of the injector are also necessary to stably accelerate heavy ions with an *e/m* of around 1/7, which corresponds to the maximum design value.

The above-mentioned developments in the injector are mainly discussed from the viewpoint of reliability; also, the status of some experiments in basic research using 6MeV/n beams (from the injector) are briefly reported.

2 TIME-SHARING ACCELERATION

2.1 Magnet

As previously mentioned, the purpose of this TSA-scheme is to simultaneously supply different ion species from three ion sources to three courses: two synchrotron rings and the medium-energy experimental course. Figure 1 shows a schematic drawing of the HIMAC injector. All of the DC magnets in the existing injector were replaced by pulsed magnets by the end of March, 1998. For designing these pulsed magnets, a response time of 100ms is necessary for the normal TSA operation, in which the injector is operated with a repetition rate of 3Hz at maximum and a typical pulse width of 1ms. Practical improvements and modifications concerning the beam diagnostic devices are under progress for routine TSA operation.

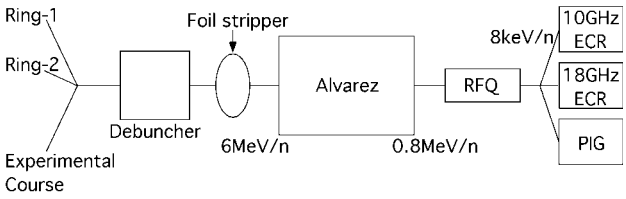

Fig.1 Schematic drawing of the HIMAC injector. Under TSA operation, one injector works as if it were three.

2.2 RF

An important point is to stably operate the RF system of RFQ and Alvarez cavities (100MHz) under different power levels, each of which corresponds to a different ion species (*e/m*). It is generally impossible to quickly control the tuning of cavities with mechanical tuners. In our case the highest power level is chosen; then, the tuning is optimized to this fixed condition. Although the cavities

are not precisely tuned for the other two power levels, the RF operation is now satisfactorily stable for *e/m*-values between 1/2~1/6. Careful tests are now under way in terms of the stability for the case of very wide *e/m*-values, such as 1~1/7.

Another RF problem was occasional sparks in the final amplifier for Alvarez at a high power level. This phenomenon seems to mainly originate in the reflected power from the loop coupler of the Alvarez tank when sparking occurs, and to be enhanced at the amplifier output-cavity. It was thus difficult to stably accelerate heavy ions with an *e/m* of around 1/7. Concerning this problem, an idea has been tested, which is to slightly detune the amplifier output-circuit seen by the feedline, in order to make its impedance smaller at 100MHz and to suppress the amplitude of standing waves (SW). Along this line, a cold test was carried out by adjusting the position of a short panel in the output cavity while observing the SW-signal through the directional coupler, as shown in Fig.2. All of the results, including a high-power test, show that a frequency shift by 0.32MHz from 100.93 to 101.25MHz allows the amplitude of sparks to be reduced down to 30% with no reduction in the RF-power transmission. RF-down times due to sparks has thus become rare; it is possible to stably accelerate heavy ions, such as Xe^{20+}, though small sparks may still occur in the tank.

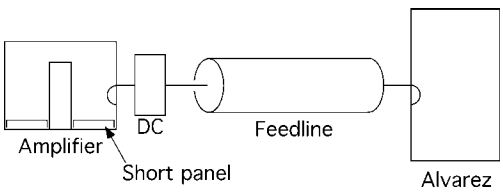

Fig.2 Schematic drawing between the final amplifier and Alvarez. A network analyzer is connected to a directional coupler (DC) to analyze the spectra of standing waves.

3 ION SOURCES

In the HIMAC injector, three ion sources have been operated in the pulse mode: PIG, 10GHz-ECR, 18GHz-ECR. All sources are normally operated at around 1Hz, according to the trigger pulses from synchrotrons; meanwhile the pulse width depends on the sources and elements. The detailed design of these sources has already been presented [4-6]. The present performance for typically-used ion species is listed in Table I. Each intensity is measured in front of the RFQ. In addition to Table I, several hundred eμA of N^{3+} and O^{3+} can also be easily supplied from three sources, though they are not usually used. Although the transmission efficiency between the source and RFQ is quite good for 10GHz-ECR (~70%), it has not yet been well optimized both for PIG and 18GHz-ECR, depending on the elements.

TABLE I. Typical peak intensities at the RFQ, in which the normalized acceptance is 0.6π mm·mrad. The transmission efficiency through the RFQ is about 93% for the below-listed intensity region.

PIG		10GHz-ECR		18GHz-ECR	
Elements	eμA	Elements	eμA	Elements	eμA
He^{1+}	550	H_2^+	360	Ar^{9+}	280
C^{2+}	650[#1]	C^{4+}	250	Fe^{9+}	35[#2]
Ne^{4+}	500	Ne^{4+}	350	Kr^{15+}	60
Si^{5+}	200[#1]	Ar^{8+}	200	Xe^{20+}	50[#3]
Ar^{7+}	300				

#1: by sputtering the graphite with (N_2+Ne) for C^{2+}, and the silicon single crystal with Kr for Si^{5+}.
#2: $Fe(C_5H_5)_2$ powder is used with O_2 for Fe^{9+}.
#3: abundance of ^{132}Xe is 27% and ^{84}Kr 57%.

3.1 PIG

In the typical production of Si^{5+} by PIG, the arc power is 6kW in peak (5A, 1200V), and the arc pulse width is 1.5ms; the duty factor is 0.15%. An extracted intensity of 400eμA has been routinely obtained by sputtering the silicon single crystal with Kr (~0.15cc/min). The stably-usable lifetime will be on the order of one week, depending on the arc power and elements; the recent results for Si^{5+} showed that it is 70hr with no adjustment. The electron bombardment power (~500W) to the upper cathode is stabilized in such a way that the error signal is fed back to the filament current, which is effective for stable operation in such a low-duty pulse mode. Figure 3(a) shows a pulsed beam-waveform of Ar^{8+}.

3.2 10GHz-ECR

Usually, carbon beams for radiotherapy are supplied from 10GHz-ECR with CH_4 (0.07cc/min); this source is basically maintenance free as long as gas materials are used. For the production of C^{4+}, the microwave power is about 500W with a pulse width of 8ms. An extracted intensity of around 350eμA has so far been routinely obtained owing to optimization for the position of the extraction electrode. A few hundred eμA of $^{13}C^{4+}$ and $^{36}Ar^{8+}$ are also produced for the nuclear physics experiments. Figure 3(b) shows a pulsed beam-waveform of C^{4+}.

3.3 18GHz-ECR

The production of heavy-metal ions has just started by using a newly-installed 18GHz-ECR with high extraction voltage (~60kV). For producing Fe^{9+}, $Fe(C_5H_5)_2$ powder has been preliminarily used with gas-mixing of O_2 (0.02cc/min). The lifetime is mainly subject to the amount of powder (0.15g at most), and the test results suggest that it is on the order of 70~80hr. Under the after-glow mode, a 45eμA of Fe^{9+} has been obtained from the source; the

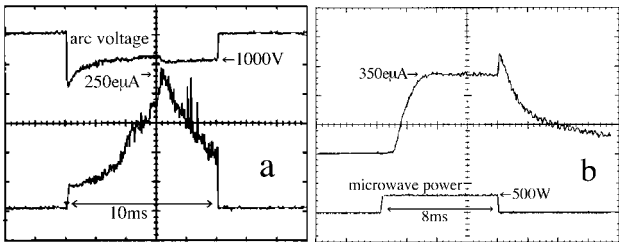

Fig.3 Pulsed beam-waveforms for PIG (a) and 10GHz-ECR (b). In such a low-duty pulsed PIG, the output of Ar^{8+} (highly-charged ions) is high during the early 6-7ms [4]. For the production of C^{4+} in the 10GHz-ECR, a smooth and rapid rising, and a clear afterglow-peak seem to be essential as an indication of stable operation.

microwave power is 1.2kW with a pulse width of 6ms. After its acceleration up to 6MeV/n, about 6eμA of Fe^{24+} or 10eμA of Fe^{23+} can be obtained by stripping through the thin carbon foil (100μg/cm^2). In the latter case, the usable intensity from the synchrotron is on the order of $1x10^8$pps. The pulse width of the afterglow peak is about 1ms, which is sufficiently long compared to the injection time (~160μs) of a synchrotron ring. The sextupole magnet was optimized in order to expand an ECR zone (size of plasma), which resulted in an improvement of the yield by a factor 2-3 for gaseous ions; hence, 750eμA of Ar^{8+} and 400eμA of Ar^{9+} can be obtained from the source. Careful cleaning and sufficient aging of the gas-feeding quartz tube are essential to well maintain the source operation.

According to the requests from basic research groups, Mg^{5+}, Ca^{7+}, Ti^{7+} will be produced by PIG, and S^{5+}, Cl^{5+}, Ni^{9+} by 18GHz-ECR. B^{3+} and F^{4+} will also be tested by one of three sources.

4 BASIC RESEARCH

Several groups in atomic- and bio-physics have conducted experiments using 6MeV/n heavy-ion beams from the NIRS-HIMAC injector linac [7].

The projectile charge (z) dependence on the electron-emission rate from Al-foil (300μg/cm^2) has been measured using fully-stripped ions (He~Ar). The forward enhancement and its strong dependence on z were observed; the ratio between the forward and backward was 1.67 for z=18. This would be due to much forward δ-electrons pulled by the strong Coulomb field of the projectile in the outgoing projectile direction.

Through collisions with fully-stripped ions, the total ionization cross sections have been determined for both atoms and molecules with a good accuracy by using a parallel-plate electrode. Another group made a similar experiment using a secondary-ion mass spectrometer (magnet type).

Pulse-radiolysis experiments were carried out using He^{2+} in order to measure the time-dependent yields of water-decomposition products by the scavenger method. The product yields were found to be smaller than those determined by electron beams.

The energy loss of Ar^{18+} in a Z-pinch helium plasma has been observed using a TOF method. The standard Stark-broadening diagnostics gives an electron density ranging from 4 to $5x10^{17}$/cm^3 for a helium plasma. The observed energy loss exceeds the value for cold helium gas, and agrees with the Bethe theory modified for the plasma.

The micro-structure of plasmid DNA (pBR322) irradiated with C^{6+} was analyzed using time-resolved fluorescence spectroscopy. The molecular behaviors of ethydium bromide (EB) intercalated between the base-pairs of DNA showed that the distance between the base pairs was expanded by 50% with the irradiation. The anticipated deformation in the double strand of the DNA has thus been proposed.

In order to strongly promote biophysical experiments, the dosimetory of C^{6+} beams has been conducted behind a thin Harvar (metal) foil with a thickness of 2.2μm and a diameter of 20mm. The results showed that the range of the beams was 14.2cm in air, and the long-time durability of this foil against the atmospheric pressure was satisfactory. A secondary-electron emission-type profile monitor (SEEM) has also been developed for irradiating biological materials, such as cells.

The authors would like to thank their colleagues at the Div. of accelerator physics and engineering of NIRS headed by Dr. F.Soga for many friendly discussions concerning injector linacs as well as their application to basic research.

REFERENCES

[1] S.Yamada, et al. "Present Status of the HIMAC Injector", Proc. 1994 Int. Linac Conf. p768(1994).

[2] S.Yamada, et al. "Commisioning and Performance of the HIMAC Medical Accelerator", Proc. 1995 PAC, Dallas, (1995).

[3] M.Murakami, et al. "Status of the HIMAC Injector", Proc. 1996 Int. Linac Conf. Geneva, (1996).

[4] Y.Sato, et al. "Heavy-Ion Sources for Radiation Therapy", *J. of Appl. Phys.* **76**, 3947(1994).

[5] A.Kitagawa, et al. "Development of the NIRS-ECR ion source for the HIMAC medical accelerator", *Rev. Sci. Instrum.* **65**, 1087(1994).

[6] A.Kitagawa, et al. "Development of 18GHz NIRS electron cyclotron resonance ion source with high-voltage extraction configuration", *Rev. Sci. Instrum.* **69**, 674(1998).

[7] HIMAC Report-020, (NIRS-M-15).

PARAMETER STUDY FOR A HIGH CURRENT HEAVY ION LINAC*

G. Parisi, A. Sauer, H. Deitinghoff, H. Klein
IAP - Frankfurt University, Robert-Mayer-Str. 2-4, 60054 Frankfurt am Main, Germany

Abstract

In present scenarios of a heavy ion inertial fusion facility, a combination of linacs and storage rings has been proposed as a driver. After some funnelling steps, the main linac has to accelerate and focus an intense heavy ion beam (e.g. Bi^+, 400 mA) to a final energy of 10 GeV.

Using well known analytical formulae an attempt has been made to find a range of beam and structure parameters (e.g. frequency, shunt impedance, beam current, emittances, focusing scheme), in which the requirements on a DTL can be fulfilled. Beam dynamics aspects have been checked by numerical simulations.

1 INTRODUCTION

Since about 20 years, studies have been performed on inertial confinement fusion for potential application in energy production. Laser facilities, light and heavy ion accelerators and storage rings have been investigated as drivers; one study for a heavy ion driven fusion power system (HIBALL) was completed in the 1980's already [1]. Main progress has been achieved during the last years in the understanding of pellet dynamics after ignition, i.e. in the physics of extremely hot and dense matter, leading to new conditions for pellet ignition which impose also new requirements on the layout of the driver accelerator facilities. Progress and changes can nicely be seen in the proceedings of the Symposia on Heavy Ion Inertial Fusion, held every two years at different places, e.g. [2,3,4].

2 THE HIDIF STUDY

A combination of linacs and storage rings has been proposed by a European study group as an rf approach of a driver for a Heavy Ion Driven Ignition Facility (HIDIF) [5]. The scheme is shown in Fig. 1.

For pellet ignition, a beam energy of 3 MJ must be brought to the pellet within 5 ns, focused to spot sizes of about 1.7 mm radius. The ion species is Bi^+, the final ion energy was fixed to 10 GeV. These requirements determine mainly the driver layout and the beam parameters like beam current, beam emittance and pulse duration.

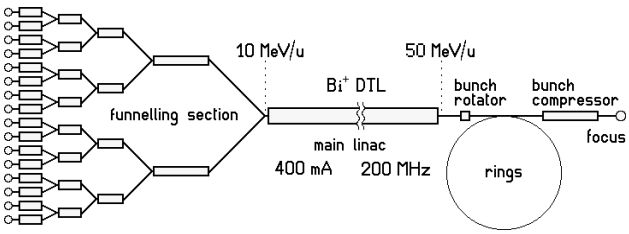

Figure 1: Scheme of the heavy ion driven ignition facility.

Since the capability of high current acceleration in a rf linac is limited, an array of rings and bunch compressors will be needed for the necessary current multiplication and pulse compression for the final focus. By tracking back the parameters needed at the final focus, limits on output conditions at the linac end are pre-given: beam current of 400 mA in a total transverse emittance of $4\,\pi$ mm mrad, and longitudinal maximum momentum spread of $\pm 2\times10^{-4}$ for 99% of the particles after bunch rotation for tolerable losses at ring injection. Following the scheme of funnelling [6] (already proposed for HIBALL) and taking some measured values for ion source currents and emittances, there are only few degrees of freedom for the choice of parameters in the layout of the main linac.

3 LAYOUT OF THE MAIN LINAC

Existing ion sources are not able to produce a current of 400 mA Bi^+: for a seven hole extraction, values up to 70 mA have been recently reported; with a lower extraction voltage, a 21 mA beam has been achieved within an emittance of $0.065\,\pi$ mm mrad (80% rms, norm.) [7]. Moreover, RFQs cannot accept such a high current; then beams from several sources must be extracted, accelerated and merged in a funnel tree as indicated in Fig. 1. In each funnel step the frequency of the linac and the current are doubled: assuming 3 funnel steps and including some losses at beam formation, an ion source current of 60 mA is required; for 4 funnel steps it is lowered to 30 mA.

The first accelerator will be an RFQ, which is able to capture, focus and bunch the beam even at high space charge forces. Its frequency is chosen with respect to the input ion velocity: an appropriate choice is 12.5 MHz, since one has about 1.2–1.5 keV/u Bi^+ with a dc post-acceleration of 250–300 kV after extraction; 60 mA are still accepted but already close to the RFQ current limit.

In the RFQ the dc current is formed to bunches of about $\pm 30^\circ$ phase width. Due to the high space charge forces in the beam, the initial bunch length will nearly stay constant, i.e. before the frequency can be doubled in the next step the ion energy should be increased by a factor of four to avoid dilution in the longitudinal phase space. With these assumptions one ends up, after 3 funnel steps, with 100 MHz for the main linac and an injection energy of about 3 MeV/u; or, after 4 funnel steps,

* Work supported by BMBF under contract 06OF841I.

with 200 MHz and about 12 MeV/u. The standard formulae of Mittag [8] show that in both cases the longitudinal acceptance is large enough to capture a beam with an rms emittance of 0.2 π°MeV/u without filamentation in the following acceleration to a final energy of 50 MeV/u.

Taking into account a 100 MHz DTL structure, the shunt impedance, which is a measure of the efficiency, drops already to the end of the linac. To improve the efficiency, a frequency jump in the main linac would be necessary, leading to a higher peak current and empty rf buckets. For a 200 MHz Alvarez type structure the effective shunt impedance changes only slightly in the whole velocity range; the technology is well proven in different laboratories. Therefore a preliminary layout for a 200 MHz DTL from 10 to 50 MeV/u has been made; the main parameters are summarized in Table 1.

The effective accelerating field E_oT is 2.8 MV/m; the average shunt impedance is 26 MΩ/m. For a total voltage gain of 8.4 GV, the length of the linac sums up to 3.4 km.

Table 1: Linac and beam parameters.

Mass number	209 (Bi+)	
Frequency	200.0	MHz
Current	400	mA
Number of cells	9775	
Total length (10-50 MeV)	3383	m
Min. aperture radius	1.6	cm
Max. pole tip field	1.15	Tesla
Electric field amplitude E_oT	2.80-2.88	MV/m
Total energy gain	40.0	MeV/u
Peak beam power, 60% chopping	690	kW/m
Peak dissipated power	320	kW/m
Average shunt impedance	26	MΩ/m
Transv. rms norm. emittance	0.176-0.183	π mm mrad
Long. rms norm. emittance	1.66-1.83	π ns keV/u

4 BEAM DYNAMICS ASPECTS

When generating the linac geometry, a drift tube aperture of about 1.6 cm radius came up; with a maximum pole tip field of 1 Tesla the transverse focusing turned out to be too weak for the FD or FFDD quadrupole configuration normally used. Going to a FFFFFDDDDD scheme, as proposed in [9], resulted in a maximum pole tip field of 1.16 T and a transverse phase advance of 35°–55° per period. Schemes from 3F3D to 7F7D seem to be possible too; no optimization has been done for these. In Fig. 2 the focusing scheme is plotted, showing a low flutter factor.

The normalized transverse emittance for proper ring injection of 1.3 π mm mrad is rather small. Assuming a safety factor of 10 between full and rms emittance, to reduce the risk of particle losses and structure activation, the required value of 0.13 π mm mrad has to be compared to the value of 0.06 π mm mrad measured directly at the ion source. This allows only a factor of 2 for the unavoidable emittance growth along the whole linac complex.

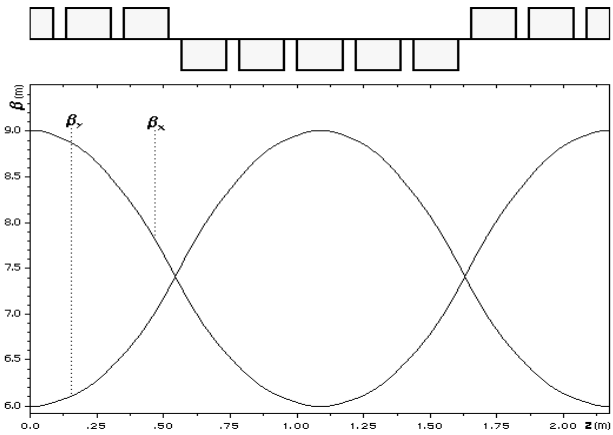

Figure 2: Chosen focusing scheme: plot of β_x and β_y.

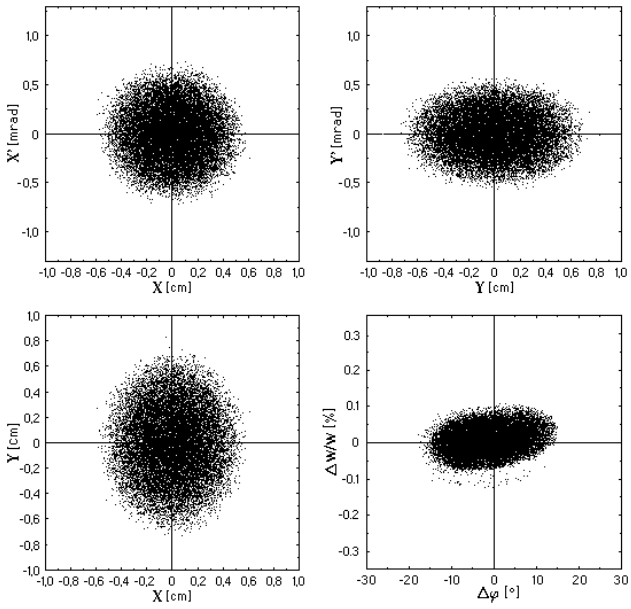

Figure 3: Output distribution at the linac end for 20,000 particles; 6D waterbag input, phase and amplitude errors.

Therefore particle dynamics calculations have been done with a 6D waterbag distribution including rf field amplitude and phase errors with an rms input emittance of 0.176 π mm mrad, allowing for some more emittance growth in the front part. It could be demonstrated that the requirements for ring injection can be fulfilled [10,11].

As an example, in Fig. 3 the output emittances at the linac end are plotted for the nominal design, including rf phase and amplitude errors. There is only a slight increase of beam size in the real transverse space. The energy spread in the longitudinal phase space is smaller than $\pm 4\times10^{-4}$ after debunching.

5 LINAC OPTION FOR TELESCOPING

An additional complication for the layout of the linac is the need to accelerate ions of different masses to the same momentum, to allow for "telescoping" of the different bunches in the final transport line. Telescoping is a

non-Liouvillean method: bunches with different ion species but same momentum are started with an appropriate delay time in a single beam line. The delay time and the velocity difference have to be chosen in such a way that the bunches fully overlap in real and momentum space at the end of the final transport, i.e. when hitting the pellet [12].

In the present scheme a mass difference of ±10% is required, which would correspond to the ions ^{187}Re, ^{209}Bi, ^{232}Th [5]. In Fig. 4 kinetic energy versus momentum is plotted for different masses for the velocity range of the main linac. At the design output energy for Bi (50 MeV/u) the momentum is 64 GeV/c; to get the same momentum, the kinetic energy for Re and Th must be 61 and 40 MeV/u.

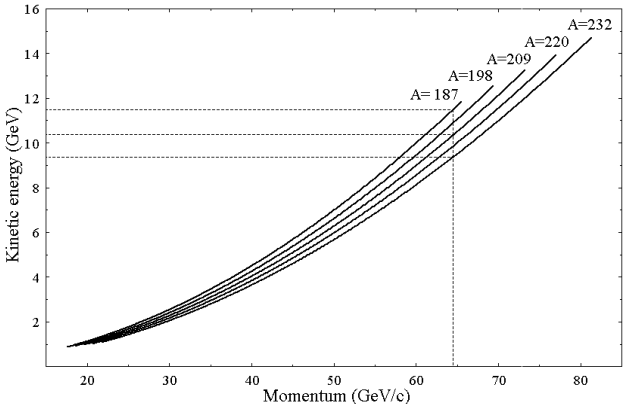

Figure 4: Energy vs. momentum for different masses.

But a DTL has a fixed velocity profile, accelerating all ions from the same specific input energy to the same specific output energy when the voltage is scaled accordingly to the mass ratios. Different velocity profiles can be obtained only if the frequency can be adjusted to the change in ion velocity, to fulfill the condition for synchronous acceleration. A large frequency variation of ±10% for an Alvarez type structure seems not to be realistic. Therefore the following concept has been investigated:

- the linac length has to be increased to accelerate the lightest ion to the higher required energy;
- the design mass has to be transported through the additional part only, keeping the beam bunched;
- the heaviest ion (which reaches the lower required energy already before the linac end) has to be transported through the rest of the main linac and the additional part.

For a mass 10% lighter than the design mass (ion energy difference of 20%) the linac becomes 20% longer; Th must be accelerated with a higher electric field E_oT of 3.1 MV/m and then transported without loss of beam quality through 1.6 km.

Preliminary beam dynamics calculations indicate that the beam can be transported through several DTL cells, when single resonators are installed in between the tanks, acting as rebuncher [11]. The time for switching all parameters between two pulses with different ion species is 0.075 ms. Any reduction in the required mass differences would simplify also the linac architecture and operation.

Table 2: Change of linac parameters for telescoping.

Mass numbers	187 (Re), 209 (Bi), 232 (Th)	
Number of new cells	1540	
Additional length	760	m
Electric field amplitude E_oT	2.4-3.1	MV/m
Momentum at output	64.3	GeV/c

5 CONCLUSIONS

From the point of view of particle dynamics, a conventional Alvarez type DTL can serve as main linac in the present HIDIF scheme. Some critical points exist: the alignment of drift tubes and quadrupoles in a 3 km long linac, the acceleration of ions with different masses to the same momentum at the linac end, the required peak power of about 1.1 MW/m. A higher beam current, as discussed for energy production, or a higher acceleration rate would increase this value. Beam dynamics calculations including errors and tolerances gave good results for the design ion Bi^+ and the linac layout of Table 1. The telescoping option must still be reconsidered.

6 ACKNOWLEDGEMENTS

The authors would like to acknowledge the good spirit of collaboration present in the HIDIF study group and the constant readiness for always open-minded discussion.

7 REFERENCES

[1] R. Badger et al., “HIBALL - A Conceptual Heavy Ion Beam Driven Fusion Reactor Study”, KFK 3203, Karlsruhe and UWFDM-450 (1981).
[2] Proceedings of the Symposium on Accelerator Aspects of Heavy Ion Fusion, March 29 - April 2, 1981, GSI-82-8, Darmstadt.
[3] Proceedings of International Symposium on Heavy Ion Inertial Fusion, Frascati, Italy, May 25-28, 1993 and *Il Nuovo Cimento*, Vol. 106, Nr. 11 (1993).
[4] Proceedings of International Symposium on Heavy Ion Inertial Fusion, Princeton, USA, September 6-9, 1995; *Fusion Engineering and Design*, 32-33 (1996).
[5] I. Hofmann, “HIDIF - An approach to high rep-rate inertial fusion”, Proc. of 12th International Symposium on Heavy Ion Inertial Fusion, Heidelberg, September 24-27, 1997, *Nucl. Inst. & Meth.-A*, in print.
[6] K. Bongardt and D. Sanitz, “Funnelling of Heavy Ion Beams”, in [1].
[7] M. Weber, K. Volk et al., “Development of a Bi^+ source for a heavy ion driven ignition facility”, in [5].
[8] K. Mittag, “On parameter optimization for a linear accelerator”, KfK-255, Karlsruhe (1978).
[9] D.G. Koshkarev, I.L. Korenev, L.A. Yudin, “Conceptual design of linac for power HIF driver”, Proc. of LINAC96, CERN, August 1-5, Geneva (1996).
[10] G. Parisi, H. Deitinghoff, K. Bongardt, M. Pabst, “Error effects and parameter analysis for a HIDIF DTL”, Proc. of EPAC98, June 22-26, 1998, Stockholm, in print.
[11] G. Parisi, Ph.D. Thesis, Institut für Angewandte Physik, Universität Frankfurt am Main, in preparation.
[12] U. Oeftiger et al., “Longitudinal particle dynamics in a heavy ion driven ignition facility”, in [5].

LUMINOSITY MONITOR OPTIONS FOR TESLA

Olivier Napoly † and Daniel Schulte ‡
† CEA, DSM/DAPNIA/SEA, CE-Saclay, F-91191 Gif-sur-Yvette Cedex, France
‡ CERN, PS/LP, CH-1211 Genève 23, Suisse

Abstract

The feasibility of a luminosity monitor based on a radiative Bhabha, beamstrahlung photons or e^+e^- detectors, is investigated in the context of the TESLA [1] linear collider.

1 INTRODUCTION

During the normal operation of a linear collider, while the beam are in collisions, the detuning of the final focus optics must be controlled in such a way that the luminosity stays maximum. The required on-line tuning procedure should be the least invasive in order to lose the least luminosity up-time. The beam-beam deflection scan method in use at the SLC [2] allows one to measure the convoluted spot sizes of both beams with a limited impact on the machine operation. For TESLA [1] however, the large vertical disruption of the colliding beams (cf. Table 1), characterised by the disruption parameter $D_y = 33$, precludes the measurement of the vertical spot size by this method. However,

Table 1: TESLA parameters at the IP for $\sqrt{s} = 500$ GeV

Beam sizes	σ_x^*, σ_y^* [nm]	558 , 5
Emittances	$\gamma\epsilon_x^*, \gamma\epsilon_y^*$ [μm]	10 , 0.03
Bunch length	σ_z [mm]	0.4
Bunch population	N_e [10^{10}]	2.0
Number of bunch	n_b	2820
Bunch spacing	Δt_b [ns]	337
Luminosity	$\mathcal{L}$ [$10^{33}\,\mathrm{cm}^{-2}\mathrm{s}^{-1}$]	32
Beamstrahlung	δ_B [%]	2.5

the combination of beam-beam horizontal deflection scans ($D_x = 0.3$) and luminosity monitoring is a valid procedure to correct both horizontal and vertical aberrations. Luminosity monitoring, recently re-investigated at the SLC [3], offers the advantage that the beam aberrations can be measured in the vicinity of the optimum head-on collision parameters and that a relative measurement of the luminosity is sufficient for its optimization.

We study three options to provide such a measurement based on detecting either the bremsstrahlung leptons, the beamstrahlung photons or the e^+e^- pairs. We use the beam-beam program GUINEA_PIG [5] to generate these processes and track the trajectory of the low energy leptons, from pair creation or bremsstrahlung, through the coherent e.m. field of the opposite bunch. The bremsstrahlung cross-section is corrected for the finite beam size effect [4]. It can be artificially multiplied by a factor n_b which allows one, with a single beam-beam simulation, to track the bremsstrahlung particles and integrate the bremsstrahlung signal originating from n_b bunch-crossings assuming that the bunch parameters are fixed and their fluctuations can be neglected. This is a valid assumption since the bunch population is about 6 orders of magnitude larger than the bremsstrahlung one.

The e^+ and e^- bunches are replaced by 320 000 macroparticles with 6-D Gaussian distributions set by the beam parameters given in Table 1. The luminosity for the optimum parameters is about $3.2 \times 10^{34}\,\mathrm{cm}^{-2}\mathrm{s}^{-1}$ including a factor about 2.0 from the pinch effect. The statistical relative error on the luminosity is about $7.5 \cdot 10^{-5}$ from numerical origin. This is small enough to be able to identify, from the simulations, rate fluctuations of the order of 10^{-3} as physical fluctuations.

2 BREMSSTRAHLUNG MONITOR

Bhabha monitors are a well proven instruments for luminosity measurement at e^+e^- and e^-p colliders [6]. The radiative Bhabha process $e^+e^- \to e^+e^-\gamma$, also called bremsstrahlung has a much higher event rate at small angles than the elastic Bhabha process $e^+e^- \to e^+e^-$, and is more suitable for on-line monitoring. This rate can be measured by detecting the low-energy lepton emitted away from the intense beamstrahlung cone around the beam axis. Since they are strongly deflected by the opposite beam, the rate of the outgoing low energy bremsstrahlung leptons deflected at angles usable for a luminosity detector is enhanced. This more than counterbalances the finite beam size correction [4] of roughly 1/2 to the total bremsstrahlung rate. Because of its sensitivity to the beam-beam effect, the bremsstrahlung signal *within a fixed kinematical acceptance* is no longer an absolute measurement of the luminosity but it can still be used for measuring luminosity variations induced by beam parameter changes at the interaction point (IP) such that the horizontal beam sizes which control the beam-beam effect, are unchanged. This includes the most important vertical aberrations.

For this study the luminosity monitor, assumed to be a hollow disk around the beam axis with 24 mm inner radius. As shown in Fig.(1) its location, 8.5 m from the IP, is optimised for detecting about 40 GeV particles. The number of hits is about 550 with about 20 TeV deposited per side and per bunch crossing. Integrating over 10 bunch cross-

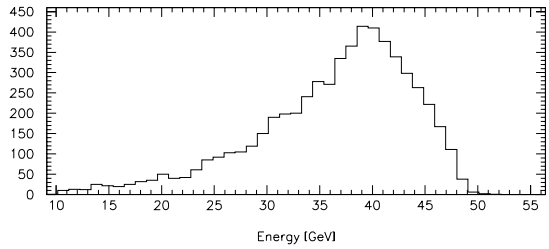

Figure 1: Bremsstrahlung energy distribution on luminosity monitor

ings and both sides leads to over 10,000 hits, enough to reduce the statistical error to the 1% level. The most important vertical beam parameters to be tuned are the beam matrix "rotations" which affect the vertical beam size, namely the vertical waist shift w_y, the vertical dispersion η_y and the yx'-coupling c_y. The definition of these aberrations and the beam matrices associated to them are given in [7]. Fig.(2) displays the results of luminosity optimisations obtained by varying the waist-shift w_y of the electron beam matrix, keeping the positron beam constant. The central configuration is such that

$$w_y^{(0)} = 0.9\,\beta_y^*, \quad \eta_y = c_y = 0 \tag{1}$$

for both beams. It is also the optimal configuration since, due to the pinch effect, the luminosity is maximized when both vertical waists are shifted by $0.9\,\beta_y^*$ in front of the IP. The gain in luminosity is about 16% with respect to the configuration where the waists are centered on the IP. In this figure, the calculated luminosity (right) is compared to the number of hits (left) from bremsstrahlung particles on the luminosity monitors, adding both sides. The scan involves 11 points and therefore a total of 110 bunch-crossings. The "optimum" luminosity as determined by the parabolic fit through the bremstrahlung rate, is less than 10^{-3} relatively smaller than the maximum of the calculated luminosity. This optimum can be determined equally well from the number of hits (counter) or from the energy deposited (calorimeter), and similar resolutions are obtained for the dispersion and coupling scans [7] as well.

In practice, each scan could be implemented with fast quadrupole pairs in the chromatic correction section (CCS) [8]. A vertical waist-scan like in Fig.(2) for instance, would be performed by symmetrically exciting the quadrupoles in the vertical CCS over 110 bunch crossings and measuring the luminosity for 110 monotonically increasing values of

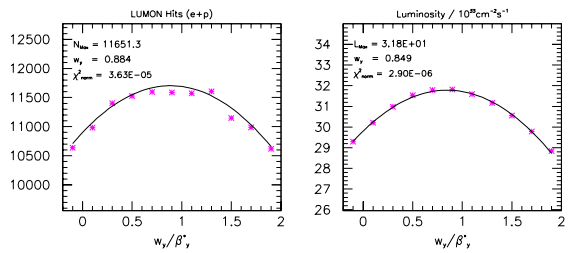

Figure 2: Scan of the vertical waist. Parabolic fits are drawn through the data points

the waist-shift w_y at the IP. In this way, a single TESLA bunch train with 2820 bunches would allow one to measure the vertical waist-shift, the vertical dispersion and the coupling of both beams, provided the implementation of the necessary excitations of the fast quadrupoles is manageable within one pulse.

3 BEAMSTRAHLUNG MONITOR

The beamstrahlung photons, with a ratio $N_\gamma/N_e \simeq 1.65$ for TESLA, provide a very strong signal which is directly related to the beam energy loss but less directly to the luminosity. In fact, this signal goes through a maximum when the two beams are vertically offset and deflect each other strongly. In order to decouple this effect from the luminosity optimization, we select the photons emitted in the $\pm 25 \times 5\mu\text{rad}^2$ forward cones whose intensities decrease with the beam offset. Fig.(3) shows the dependance of these intensities in the e^- (left) and the e^+ (right) directions on the e^--beam vertical waist (up) and dispersion (low). Unlike the bremsstrahlung, the beamstrahlung signal is not e^-/e^+ symmetric and signs which beam matrix is changing. As can be seen by comparing Fig.(3) to Fig.(2), the e^--beamstrahlung is not effective for the e^--waist tuning. Vertical dispersion, and $x'y$ the coupling as well, can however be tuned with a resolution better than 10^{-3} in terms of relative luminosity. In these scans, the 1% error in the intensity is due to the purely numerical limitation in the number of macro-photons, about 11,000, representing the physical photons contained in the forward cones.

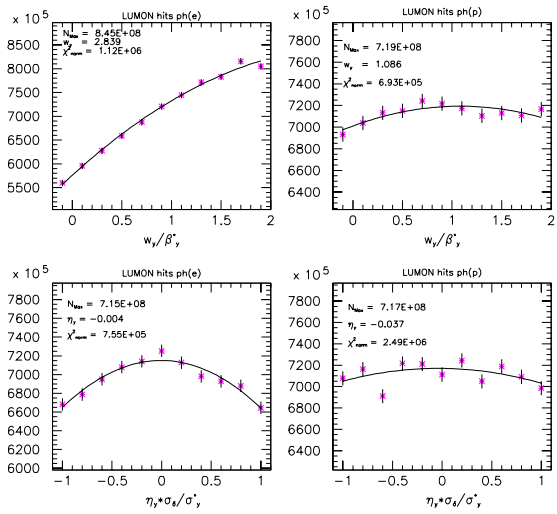

Figure 3: Beamstrahlung photon intensity per bunch-crossing vs. vertical waist (up) and dispersion (low)

4 $E^+ - E^-$ PAIR CALORIMETER

Inside the main mask a combined inner mask and luminosity monitor will be installed. This inner mask will be hit by a large number of pairs deflected by the beams. At small

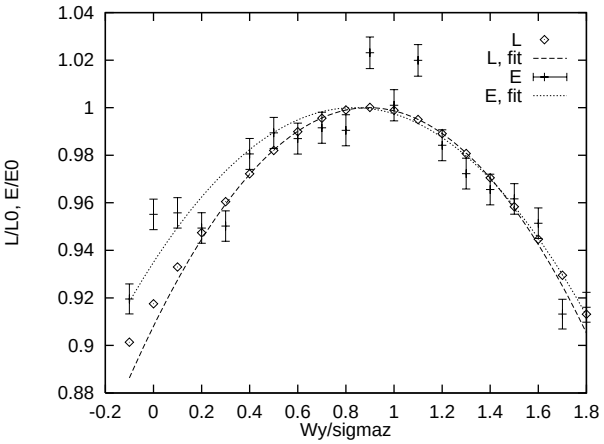

Figure 4: Scan of the vertical waist shift: energy deposited in the calorimeter and luminosity normalised to the maximal values.

radii it is covered with a low-Z material (graphite) to prevent the backscattering of low energy particles. At larger radii, where the background due to the deflected pairs is small, it will be used to measure the Bhabha events with larger angles. The rate of these events will be a few per second, much higher than those measured in the main detector for the reconstruction of the luminosity spectrum but too low for fast monitoring.

The total energy deposited by the pairs in this mask can be measured calorimetrically, but details have to be worked out. This energy is about $12000\,\mathrm{GeV}$ per bunch crossing and per side. This values varies from simulation to simulation due to physical and numerical effects. Running 25 cases with the same initial distribution (read from a file) but different seeds for the random number generators showed an RMS-spread of $1.2\,\%$ and $1.4\,\%$ for the two sides. This is in reasonable agreement with the expectation from the counting rate alone ($\approx\ 1.0\,\%$ from about 9200 hits). In practice one can expect significant contributions to the error from energy leaking out at the inner aperture of calorimeter and from jitter of the beam.

The scan was performed moving the waist of one beam, while the one of the other was about in the right position. For each point only a single bunch crossing was measured. The optimal position of the waist was determined by maximising the sum of the two signals, leading to $w_y = 0.83\,\beta_y^*$ (note that $\beta_y^* = \sigma_z$). The luminosity thus obtained is lower by a fraction of $4 \cdot 10^{-4}$ than the optimal value, which is reached for $w_y = 0.89\sigma_z$. The scan was repeated decreasing the positron bunch charge to $1.5 \cdot 10^{10}$ particles, increasing its horizontal emittance by $50\,\%$ and increasing its vertical emittance by $50\,\%$. In all three cases the luminosity for the found optimal waist position were smaller than the optimal by a fraction of about 10^{-3}.

In contrast to the bremsstrahlung process where the production of particles depends strongly on the luminosity and only weakly on the other beam parameters, the number and energy of pairs produced depends also on the number and energy of the photons produced by beamstrahlung. The deflection is however very different in the two cases. The beam particles which have emitted bremsstrahlung are still relatively high in energy and are focused by the oncoming beam. Most of the particles from pair production that hit the calorimeter are low in energy and are defocused by the same charge oncoming beam. Combining the two methods one could thus hope for reducing possible ambiguities.

5 CONCLUSION

We believe that a luminosity monitor will be a necessary instrument for the fast tuning of the collision parameters of TESLA. In this study we have shown that a radiative Bhabha counter or calorimeter can monitor the luminosity to a 1% resolution by integrating the bremsstrahlung signal over about 10 TESLA bunch-crossings, that is about 3.3 μs. The powerful beamstrahlung signal in a very narrow forward cone can also be used for tuning dispersion and coupling. A promising complementary option is a calorimeter in the masking system around the IP to measure the energy deposited by the pair-created e^+e^- particles. The 1% level can then be reached with one bunch-crossing.

With either monitor, scanning the usual vertical linear aberrations with about 10 points should permit to determine the optimal luminosity to better than 0.1% relative resolution. Implementing such scans within a single TESLA bunch train should be possible: it would reduce considerably the influence of beam jitter on the luminosity measurement errors.

6 REFERENCES

[1] "Conceptual Design of a 500 GeV e^+e^- Linear Collider with Integrated X-ray Laser Facility", R. Brinkmann, G. Materlick, J. Rossbach and A. Wagner Editors, DESY 1997-049 and ECFA 1997-182 (1997).

[2] P. Emma, L.J. Hendrickson, P. Raimondi and F. Zimmermann "Limitations of Interaction-Point Spot-Size Tuning at the SLC" SLAC-Pub-7509 (1997).

[3] P. Raimondi et al, "Recent Luminosity Improvements at the SLC" 6th EPAC (EPAC-98), Stockholm June 1998

[4] G.L. Kotkin, V.G. Serbo and A. Schiller "Process with Large Impact Parameters at Colliding Beams" Int. J. Mod. Phys. A, 4707 (1992).

[5] D. Schulte, "Study of Electromagnetic and Hadronic Background in the Interaction Region of TESLA", Ph.D. thesis, University of Hamburg 1996, and DESY report TESLA 97-08, April 1997

[6] V.N. Baier, V.S. Fadin, V.A. Khoze and E.A. Kuraev "Physics Reports 78, 3 (1981) 293-393.

[7] O. Napoly and D. Schulte, "Luminosity Monitor Studies for TESLA", Saclay Preprint CEA/DAPNIA/SEA-97-14 and TESLA Note 97-17, 1997

[8] Following suggestions by N.J. Walker and R. Brinkmann.

THE CLIC 30 GHz TWO-BEAM TEST ACCELERATOR

I. Wilson, W. Wuensch, W. Coosemans, C. Achard
CERN, Genève 23,1211 Switzerland

Abstract

As part of the experimental effort to demonstrate the feasibility of the CLIC scheme, a 3 m long representative section of the CLIC accelerator has been constructed, installed in the CLIC Test Facility (CTF) and successfully commissioned with beam. Prototype 30 GHz components developed during the course of the CLIC study including accelerating structures, power generating transfer structures, and high power RF loads, have been successfully integrated with the micron-precision active alignment system, the vacuum system, the water cooling system, and the high power RF distribution system to produce a very compact two-beam test accelerator. This paper describes the layout and gives details of the important subsystems.

1 INTRODUCTION

A 3 m long 30 GHz two-beam test accelerator has been constructed and is presently operating with beam in the new CLIC test facility (CTF2). The test accelerator layout follows that currently foreseen for CLIC but has a higher density of quadrupoles - and consequently a lower RF filling factor - due to lower beam energies. The test accelerator is equipped with a prototype active alignment system in order to gain operating experience in a real accelerator environment. The bunched electron beams needed for the drive and main linacs are supplied by two separate 3 GHz linacs.

Since both CLIC and the test accelerator are composed of repeated two-beam 'modules', the construction of two fully equipped modules has enabled many of the technical difficulties of the full length linacs to be solved. All necessary subsystems including water cooling and vacuum have been included. The layout of a test accelerator module is shown in figure 1. Two such modules have been installed and a further two will be installed in 1999.

Prototypes of components developed in the course of the CLIC study have been used wherever possible. These include: accelerating sections, high power RF loads, main linac beam position monitors, main linac quadrupoles, support girders and the active alignment system. The power extracting structures are similar to those of CLIC but have a stronger coupling to the beam to compensate for the lower drive beam charge. Other components including waveguides, phase shifters, vacuum and beam line components were specially developed for the accelerator.

The test accelerator is shown in figure 2. Commissioning with beam started in the autumn of 1997. A maximum accelerating gradient of 50 MV/m [2] has so far been achieved and is currently limited by available drive beam charge.

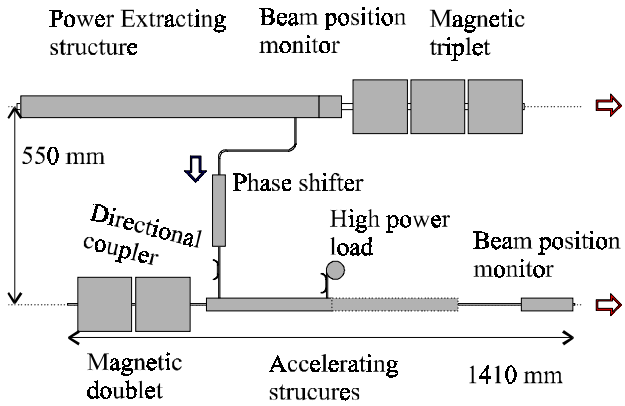

Figure 1: Schematic layout of one module of the main (lower) and drive (upper) linacs.

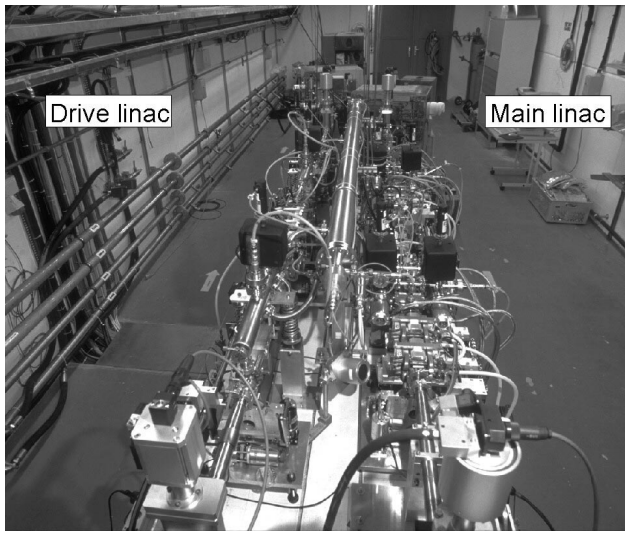

Figure 2: Downstream view of the test accelerator installed in the CTF.

2 RF SYSTEM

Each two-beam accelerator module has one power extracting structure, shown in figure 3, which feeds two accelerating sections. An extracting structure has four output waveguides - opposing pairs are combined to feed the two accelerating sections. For the moment all four output waveguides are combined to produce a higher

accelerating gradient for a given drive beam charge (but less total energy gain). RF power is combined in 'Y' junctions that are split in the magnetic field plane. The output of each accelerating section is connected to a high-power stainless-steel load which is vacuum pumped. The area around the accelerating section in the first module is shown in figure 4.

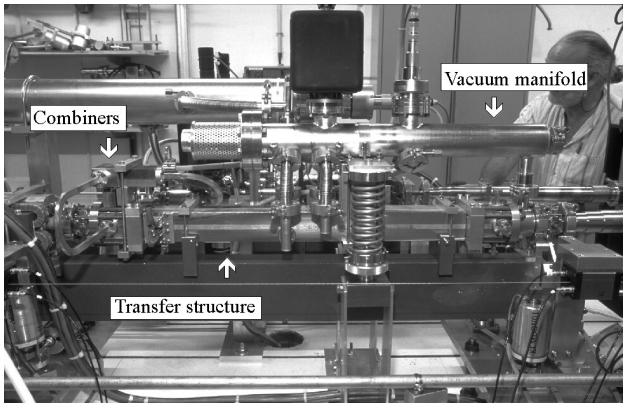

Figure 3: Installation around a power extracting structure.

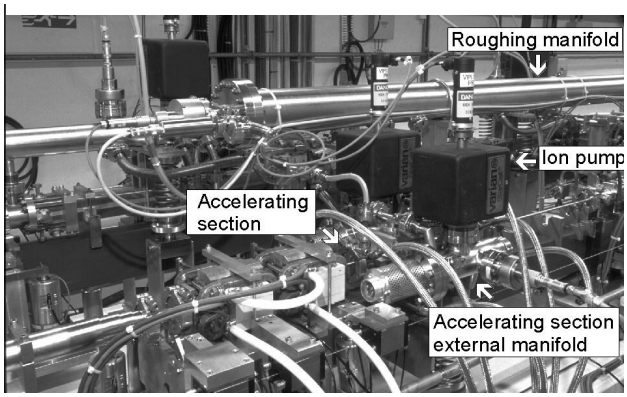

Figure 4: Installation around an accelerating section. The view of the section is obstructed by the vacuum manifolds.

The upstream ends of the power extracting structure waveguides are terminated with vacuum compatible loads containing ceramic absorbing elements. In order to maintain free movement of the support girders, all RF connections between components on the girders and those on the concrete support block contain lengths of flexible waveguide. These are made from copper plated commercially-available hydro-formed waveguide tube. The flexible waveguides also provide vibration isolation. The waveguide between the power extracting and accelerating structures contains a phase shifter.

Vacuum-tight high-power RF connections were made using a flange design with a flat face-to-face contact and a Helicoflex seal. There are no windows anywhere in the high power RF line. Low power signals are extracted from the high power system via vacuum-to-air 56 dB directional couplers before and after each accelerating section, providing calibrated incident, reflected and transmitted power signals. 1 mm diameter ceramic disks brazed into the coupling holes separate vacuum from air in these couplers. 12 m long WR-28 waveguide runs connect the outputs to the signal processing electronics in the klystron gallery.

3 BEAM POSITION MONITORS

A prototype 30 GHz resonant cavity BPM [4] with an integrated phase and charge reference cavity is installed in each main linac module. Common mode rejection is made in vacuum-compatible magic Ts. Position signals pass from vacuum to air-filled waveguide via alumina windows mounted on the difference ports of the magic Ts. Signal processing electronics is mounted in the klystron gallery.

A four-button BPM is mounted in each drive linac module. Each button electrode is connected directly to a coaxial vacuum-to-air feed-through. 20 to 30 cm lengths of standard flexible coaxial cable connect the BPM on the support girder to fixed semi-rigid coax fixed onto the concrete block.

4 ALIGNMENT SYSTEM

The entire accelerator is mounted on a concrete block that is grouted to the floor - a precaution that would only be meaningful in a proper stable linear collider tunnel. The block also contains niches where radiation sensitive alignment control electronics are mounted. All other components of the alignment system have been designed to be radiation hard

The test accelerator is actively aligned and held to within a few microns using a stretched wire system [3]. All beam line components other than quadrupoles are mounted on 1.41 m long (length of one module) silicon carbide support girders. The components are directly supported by ± 1.5 μm precision V blocks. Continuity of the beam axis from girder to girder to a similar precision is provided by a system of link rods that connect the ends of the successive girders. The link rods create articulation points at the beam axis intersections. The articulation points, and thus the linacs, are aligned by moving the ends of the girders with 0.1 μm step linear actuators, which are shown in figure 4.

Actuator movements are calculated from readings of the 0.1 μradian resolution tilt meters and the 0.1 μm resolution capacitive sensors of the stretched wire system. The vertical positions of the ends of the wires are measured by a hydrostatic leveling system.

Quadrupole doublets and triplets are mounted on independent platforms with their own wire sensors, tilt meters and actuators. The quadrupoles are referenced to the same stretched wire as the support girders.

The system operates in a closed feedback loop holding the linacs within an alignment window of ± 2 microns.

The end-station of the stretched wire system is shown in figure 5.

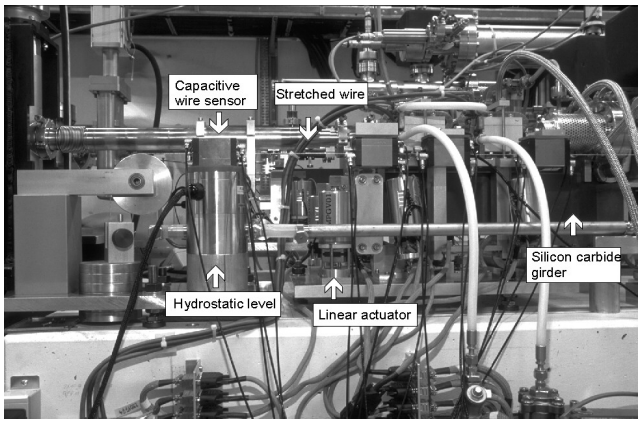

Figure 5: End station of the stretched wire system.

5 BEAM LINE COMPONENTS

The internal diameters of the main and drive linacs are 4 and 22 mm respectively. The main and drive linac beam pipes have been designed to present low transverse impedances. The drive linac beam pipe must also carry high image currents without arcing or heating locally. Maintaining these design objectives has been most difficult for the inter-girder articulations, which must also be flexible and vacuum tight. In the current design, the articulation points have a 1-2 mm beam pipe gap with a 50 mm diameter bellows placed around the gap region to contain the vacuum.

Connections between fixed drive-linac beam-line components are made using a flange design derived from the vacuum RF flange. The requirements for the RF flange, a small impedance mismatch and a high current capability, are identical to those of the drive-linac beam-line flange.

The prototype main and drive linac quadrupoles have internal apertures of 10 and 30 mm respectively. The resulting ± 2 mm clearances between the quadrupoles and the beam pipes allows the beams to be steered using quadrupole offsets. The field gradient in the main linac quadrupoles is 100 T/m.

6 VACUUM SYSTEM

The primary design challenges for the vacuum system are to provide adequate pumping to the very low conductance main linac beam pipe and to allow unconstrained movement of the alignment system. The design level of 10^{-8} torr has been achieved.

This vacuum level in the main linac is obtained by pumping each accelerating section cell with four 1 mm diameter radial holes. It is sufficient to pump only accelerating sections since in CLIC they make up most of the main linac length. Each accelerating section is pumped by a pair of local manifolds each of which contains a getter and an ion pump. The manifolds (weighing some 20 kg) are mounted on spring supports and follow girder movements with little applied force. Power extracting structures are pumped by a single local manifold also with a getter and an ion pump.

All of the local manifolds are connected via flexible tubing to a central roughing manifold, which appears prominently in all photographs of the test accelerator such as figure 1. After an appropriate vacuum has been reached the roughing manifold is isolated from the manifolds by valves. The accelerator can be isolated from the rest of the CTF with valves at the ends of each linac.

7 WATER COOLING SYSTEM

With average RF and beam power levels in the test accelerator a small fraction of those anticipated in CLIC, the water cooling requirement is less demanding. Nonetheless, the water connections must still remain sufficiently flexible when pressurized not to constrain the alignment system. Hydro-formed thin walled stainless steel tubing has been used to connect to the accelerating sections but the solution is unsatisfactory because the tubing is a vibration source. Latex tubing was later chosen for the quadrupoles and appears to function very well.

8 CONCLUSIONS

The successful installation and operation of the test accelerator represents an important step in the demonstration of the feasibility of the CLIC scheme. Difficulties of layout and assembly resulting from the high density of components of the 30 GHz accelerator have been overcome. The active alignment system has been successfully integrated with all the other subsystems, maintains alignment within a ± 5 micron window and operates reliably in a high radiation environment without any evidence of deterioration. A precise agreement between drive beam, generated power and main beam energy gain indicates that the RF system is functioning correctly.

9 REFERENCES

[1] J. P. Delahaye et.al., "CLIC, a 0.5 to 5 TeV e± Compact Linear Collider", Proceedings of EPAC98, Stockholm (1998).

[2] R. Bossard et. al. "Demonstration of Two-Beam Acceleration in CTFII", These proceedings.

[3] W. Coosemans, J.M. Bouche, R. Pittin, "Active alignment for CLIC modules in CTF2", Proceedings of IWAA, Argone (October, 1997).

[4] J. P. H. Sladen, I. Wilson, W. Wuensch, "CLIC Beam Position Monitor Tests", Proceedings of EPAC96, Sitges (1996).

BEAM LOADING COMPENSATION USING PHASE TO AMPLITUDE MODULATION METHOD IN ATF

S. Kashiwagi, The Graduate University for Advanced Studies, Ibaraki, Japan
H. Hayano, K. Kubo, T. Naito, K. Oide, T. Shintake, S. Takeda,
N. Terunuma and J. Urakawa, KEK, Ibaraki, Japan
T. Korhonen, Paul Scherrer Institut, CH-5232 Villigen PSI, Switzerland
S. Nakamura, Yokohama National University, Kanagawa, Japan

Abstract

For future linear colliders, one of the essential techniques to get a sufficient luminosity is to accelerate multi-bunch beam of small bunch spacing. Beam loading voltage in an accelerating structure generates a large energy spread along the bunch train. This energy spread is critical for the lattice design and, if not properly compensated, induces emittance growth and in turn lowers the luminosity. A method to compensate for beam loading effects in a multi-bunch beam is under development at Accelerator Test Facility (ATF) in KEK [1]. We will report the beam tests for early injection and a phase to amplitude modulation method using multi-bunch beam of 2.8 ns bunch spacing. This energy compensation method compresses energy spread of multi-bunch beam by changing the input rf waveform properly into accelerating structures.

1 INTRODUCTION

A scheme of multiple bunches (87 bunches) being accelerated on each rf pulse is adopted in the Japan Linear Collider (JLC) design [2]. This scheme improves the energy transfer efficiency from wall plug power to the beam and luminosity of the machine. However, it results in turn significant beam loading. In JLC, an energy spread which is generated by the beam loading has to be reduced to a few tenth of a percent.

There are several possible methods to compensate the multi-bunch energy spread with keeping bunch spacing constant, such as ΔF method [3], ΔT method and so on. The ΔF method is to use one or more accelerator structures running at the frequency slightly higher and lower than the fundamental frequency and roughly in 90 degree out of phase from the acceleration. The ΔT method is to inject a beam before an rf pulse has filled in an accelerating structure. Power efficiency of ΔF method is higher than ΔT method, however this method is only adaptive in case that the energy of beam drops approximately linearly as a result of beam loading.

On the other hand, the transverse emittance dilution due to a random misalignment A_{rms} of quadrupole magnets with respect to the beam is estimated approximately to be

$$\frac{\Delta\epsilon}{\epsilon} \approx \frac{A_{rms}^2}{2\gamma_0\epsilon_0} \sum_i \gamma_i \beta_i k_i^2 (\frac{\Delta E}{E})_i^2 \qquad (1)$$

where $\gamma_0\epsilon_0$ is initial normalized emittance and γ_i, β_i, k_i and $(\Delta E/E)_i$ are Lorentz energy factor, beta function, focusing strength of quadrupole magnet and energy spread at the i-th quadrupole in the linac, respectively [4]. Since the emittance growth is connected to the energy spread at each quadrupole according to Eq. 1, energy spread correction should be done locally at each quadrupole. The ΔT method which compensates an energy spread in every accelerating structure is the local compensation, while ΔF method compensates it through several quadrupoles in average. In the low energy part in the linear colliders, the local correction method will be an important method where $\Delta E/E$ is not enough small.

2 PHASE TO AMPLITUDE MODULATION METHOD ($\Delta\phi - A$)

The most simple compensation of the beam loading in ΔT method can be done by injecting the beam before the rf pulse has filled the accelerating structure. If we use this simple early injection method, the beam current at which the energy compensation acts effectively is limited to some range, and acceleration efficiency will be poor. We apply

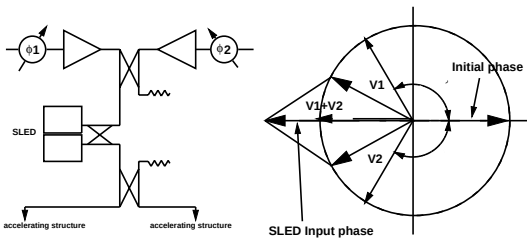

Figure 1: $\Delta\phi - A$ beam loading compensation

thus the amplitude modulation on the input rf pulse for the pulse compression. Therefore in case of using the SLED-I system [5], we can obtain the desirable slope of unloaded voltage by changing input rf waveform for SLED cavities. As discussed in Ref. [6], it is not a good idea to directly modulate the amplitude of the driving rf power to klystron. For a stable operation, a klystron usually needs to be used in the saturation condition. Thus, modulating the drive rf phase of klystron would be a better method. To modulate the amplitude of rf pulse for the SLED-I cavities at constant phase, two klystrons are needed. They run in saturation, keeping the input rf level constant. Then, we control their phases and combine the rf power from two klystrons by using a 3 dB hybrid combiner. Figure 1 shows a scheme in which the rf phases of two klystrons are rotated into opposite directions relative to each other. The sum of two

phase modulated rf makes amplitude modulated rf with constant phase, which is fed into the SLED cavities. The phase modulation of the two klystrons effectively realizes amplitude modulation using this method ($\Delta\phi - A$ method).

If bunch population of each bunch is not uniform, thus the energy spread of beam does not drop linearly with time. Even in the case of it, phase modulation to amplitude modulation ($\Delta\phi - A$) method can properly compensate by changing the speed of phase rotation.

3 BEAM TEST OF $\Delta\phi - A$ ENERGY COMPENSATION

To verify that the $\Delta\phi - A$ beam loading compensation scheme works as predicted, we performed preliminary beam test in the ATF injector linac of the damping ring. The ATF s-band linac consists of 80 MeV pre-injector, 8 regular accelerating units, two units of energy compensating structure for ΔF energy compensation. Each regular unit contains SLED-I pulse compression system and the compressed rf power is fed into the two accelerating structures. For this experiment, the first and second regular sections were used and a chicane to measure the multi-bunch energy distribution was constructed downstream from this two regular units. ATF linac accelerates a multi-bunch beam that consists of 20 bunches with 2.8 ns spacing.

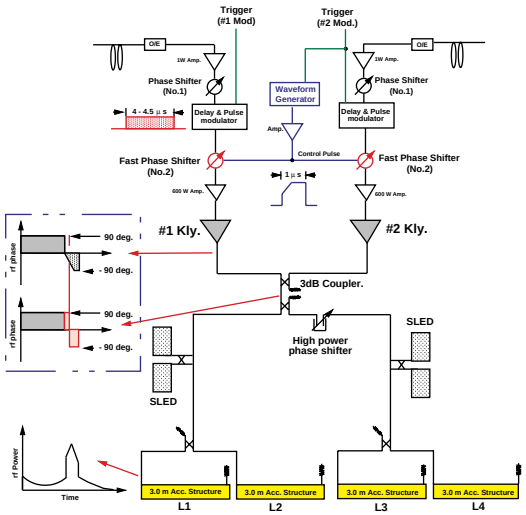

Figure 2: Experimental setup for $\Delta\phi - A$ beam loading compensation

3.1 *Experimental setup*

We preliminary tested $\Delta\phi - A$ method using two-klystron combination, Figure 2 shows the rf system of this experiment. It consists of two 85 MW klystron (TOSHIBA 3712), two dual-iris s-band SLED cavities, 3 dB hybrid combiner, high power wave guides, rf loads and an high power mechanical phase shifter. In this rf set up, rf power from the two klystrons were combined using 3 dB hybrid combiner, after that combined power was divided again to avoid a break-down at SLED cavities. High power mechanical phase shifter was used to adjust the relative phase between two rf units (L1,2 and L3,4 structures). Rf power is measured by using -70 dB Bethe-Hole coupler at several points which are each klystron out, the combined point, input of the SLED cavity and the entrance and exit of the accelerating structure. In the low level rf circuit, the 2856 MHz phase shifters (No.1) tune the rf phase of the input CW rf to the beam. By using Delay and Pulse Modulator, it is modulated into a short pulse with 4.5 μs width and the rf timing to klystron voltage is adjusted. The fast phase shifters (No.2) using varactor diode are used to rotate the drive rf phase. A control pulse with 1.0 μs width for the fast phase shifters is generated by an arbitrary waveform generator, and changes the rotating speed of drive phase. In this beam test, rotating speed of rf phase was changed at constant rate.

3.2 *Measurement system of the beam energy*

Figure 3 shows the layout of the beam line to measure the energy variation along the bunch train. For energy

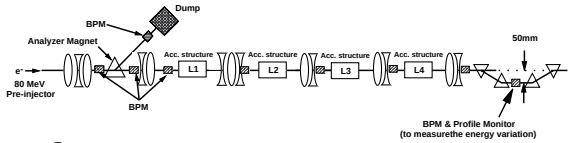

Figure 3: Beam line layout for energy compensation experiment

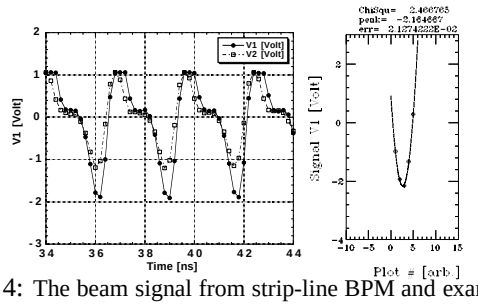

Figure 4: The beam signal from strip-line BPM and example of fitting to sample data

measurement, the horizontal chicane was installed down stream from the four regular accelerating structures which were filled amplitude modulated rf power. This chicane contains a strip-line-type beam position monitor (BPM) which is mounted at the center of the chicane to measure the beam energy. At this BPM, the horizontal dispersion function η_x is 50 mm. The multi-bunch beam signal from the BPM was measured by using a digital oscilloscope of real-time 5.0 GHz sample and a personal computer. A pulse height of each bunch signal was determined by a parabolic curve fitting to the sampled data. In this measurement, the position resolution was about 130 μm which was derived from three BPMs correlation and this position resolution corresponds to 0.26 % energy resolution. The position resolution was mainly limited by a systematic error of the fitting, so it may be improved using other functions for the fit. On the other hand, the only horizontal orbit of all bunches in the same pulse was measured using 7 BPMs in the linac, this measurement was free from the pulse-to-pulse energy jitter.

3.3 Preliminary result of beam test

In this experiment, the multi-bunch of 19 bunches/pulse accelerated with intensity of 0.82×10^{10} electrons/bunch at pre-injector exit. At the 80 MeV pre-injector, the energy of multi-bunch beam was compensated using the simple ΔT compensation technique (only early injection) to make the energy flat as an input of $\Delta\phi - A$ compensation section.

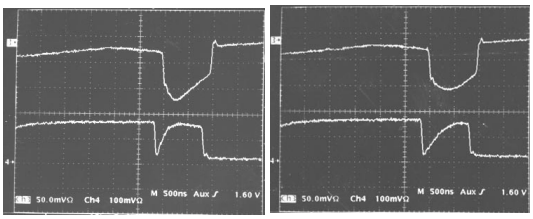

Figure 5: Rf waveform at the structure input (up) and the combined point (down) in different phase rotating speed. (right:90 deg./400 ns, left:90 deg./800 ns)

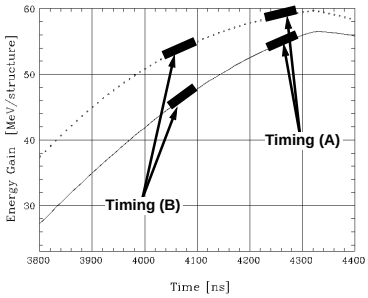

Figure 6: Calculation result of unloaded energy gain. Phase rotating speed are 90 deg./400 ns (dashed) and 90 deg./800 ns (solid)

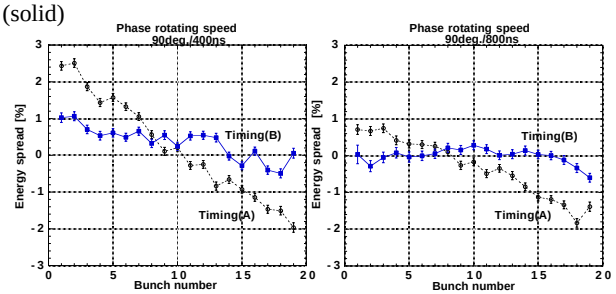

Figure 7: Measured multi-bunch energy spread with different phase rotating speed

We observed the difference of compensating voltage along the multi-bunch beam by changing the phase rotating speed and the relative timing of rf pulse to the beam in the two klystrons. Figure 5 shows rf waveforms at the input of accelerator and the combined point in the two cases of different rotating speed of drive rf phase. The calculation result of unloaded energy gain slope for the previous two different phase speed is shown in Figure 6. In this calculation, klystron output power is assumed to 20 MW which is the same value with the real beam test setup and the parameters of SLED cavities and structure are also the same. The two slopes of the unloaded energy gain curve are different by phase speed before first filling time of the structure. In the slow rotation case in which the phase speed is 90 deg./800 ns, the compensating voltage is larger than another case (see in Figure 6). Figure 7 shows energy distribution of multi-bunch beam in the two different rotating speed of drive phase and the two different beam injection timing to rf pulse which are shown as timing (A) and (B) in Figure 6. Assuming that the beam loss at $\Delta\phi - A$ compensation region was 10 % at the entrance of the first structure, the calculated beam loading voltage was about 2.7 MV/structure. Then the calculated energy spread with 90 deg./400 ns rotating speed are about 4.0 % at timing (A) and 1.8 % at timing (B), while in the another case with 90 deg./800 ns rotating speed they are about 2.8 % and 0.5 % at the each timing. From the Figure 7, the measured energy spread were 4.5 % (with timing A) and 1.5 % (with timing B) for 90 deg./400 ns, 2.6 % (with timing A) and 0.5 % (with timing B) for 90 deg./800 ns speed. The calculated values and the measured energy spread were consistent, so the amplitude modulation of the input rf acted to the multi-bunch beam so as to compensate the beam loading. However, the measured energy distribution inside the multi-bunch beam had a fluctuation from monotonous change. This fluctuation correlated to the intensity of each bunch. If we can measure the intensity variation along the bunch train and monitor the rf power correctly, the energy spread of multi-bunch beam will be minimized by setting the rotating speed of rf phase and injection timing as calculated. Its experiment is planed in this fall.

4 SUMMARY

The beam test of $\Delta\phi - A$ energy compensation was performed by using two klystron combination. Phase modulation of two klystrons was used to obtain an amplitude modulated input for the SLED. The modulation of accelerating waveform could be realized by modulating the amplitude of the SLED input. Energy gain of each bunch along a bunch train was changed by changing a rotating speed of an input rf phase, as a result the beam loading was compensated as expected.

5 ACKNOWLEDGMENTS

The authors would like to acknowledge the continuous encouragement of Professors M. Kihara, K. Takata, Y. Yamazaki. This experiment could not be performed without the help of Mr. D. Aizawa and E-CUBE corporation. We wish to thank these people for their help. The authors also appreciate to Drs. K. Egawa and M. Masuzawa of accelerator laboratory in KEK for the reason that they have readily lent us the dipole magnets.

6 REFERENCES

[1] F. Hinode et al, 'ATF Design and Study Report', KEK Internal95-4 (1995)

[2] JLC Design Study Group, 'JLC Design Study Report', KEK Report 97-1 A (1997)

[3] S. Kashiwagi et al., "Preliminary Test of $\pm\Delta F$ Energy Compensation System", Proceedings of the 18th Int. Linac Conf., Geneva, p.848 (1996)

[4] K. Kubo, Private communication

[5] P. B. Wilson SLAC-TN-73-15 (1973)

[6] T. Shintake, "C-band Linac RF-system for e^+e^- Linear Collider", Proceedings of RF96, April, 1996, Kanagawa, Japan, p37–46

RK-TBA STUDIES IN KA-BAND

S.M. Lidia, S.S. Yu
E.O. Lawrence Berkeley National Laboratory, Berkeley, California 94720, USA

J. Gardelle, T. Lefevre, J.L. Rullier
CEA/Centre d'Etudes Scientifiques et Techniques d'Aquitaine, BP 2, 33114 Le Barp, France

G.A. Westenskow
Lawrence Livermore National Laboratory, Livermore, California 94551, USA

J.T. Donohue
Centre d'Etudes Nucleaires de Bordeaux-Gradignan, BP 120, 33175 Gradignan, France

Abstract

It is well established that operating frequencies in the 30-GHz range and higher are required to obtain the high accelerating gradients needed by linear collider systems that wish to probe center-of-mass energies significantly higher than 1 TeV. As an rf power source for high-energy linear colliders, relativistic klystron two-beam accelerators (RK-TBAs) have been shown theoretically to scale favorably to frequencies higher than X-band. To complement our studies of RK-TBA systems at 11.424 GHz, we are undertaking experimental tests of components at both 35 and 30 GHz. These studies will be conducted at the CEA/CESTA facility using the LELIA and PIVAIR electron linear induction accelerators (LIAs), respectively, and will concentrate on the interaction of the intense, modulated electron beams with rf cavity structures, compact induction modules, and permanent magnet quadrupole transport lattices. Details of the rf cavity design and the proposed experiments are discussed.

1 INTRODUCTION

To explore center-of-mass energies in the multi-TeV range with electron-positron linear colliders will require accelerating gradients of several hundred MeV per meter. Scaling of conventional, copper-based structure technology shows that this can be considered at operating frequencies around 30 GHz (Ka band) [1]. Among the myriad ways of producing pulsed, high-power microwaves to drive accelerating structures, RK-TBA technology has been shown theoretically to be one of the most efficient [2]. As a testbed for RK-TBA physics and engineering studies, the 11.4-GHz prototype RTA is currently being commissioned [3]. To complement these studies, we will conduct tests of rf output structures and bunched beam transport at 30-35 GHz. This work is conducted through a collaboration of LBNL personnel with groups at CEA/CESTA and CERN. This paper discusses these upcoming experiments, with emphasis on rf cavity design and measurements of longitudinal bunching.

2 TESTS ON LELIA

Since 1995, the induction linac LELIA at the CEA/CESTA facility has been used to produce a 2-MeV, 800-A, 60-ns beam modulated at 35 GHz by a free-electron laser. This work has been conducted with support of CERN to study the generation of a suitable drive beam to power CLIC Transfer Structures (CTS). Of equal interest is the possibility of using the modulated beam to drive inductively detuned rf structures in an RK-TBA. In this case, the rf properties of the cavities determine the longitudinal beam dynamics. Hence, measurements of longitudinal phase space bunching are important to make. Diagnostics techniques developed at CESTA have, for the first time, enabled us to directly view the electron bunching, and to capture the image with a streak camera [4,5].

2.1 Inductively Detuned SW RF Cavities

The first set of experiments will study the interaction of the modulated beam with standing wave rf cavities. Three different cavities are to be constructed and studied sequentially, one idler and two single-output cavities. We have modeled these structures with the Superfish, URMEL-T, and GdfidL codes [6]. The characteristics of the cavities are listed in Table 1.

	Idler	Low Q	High Q
f [GHz]	34-36	35	35
Q	363	6	45
R/Q [Ω]	45	45	45
P_{out} [MW]	-	0.7	5.0
E_{peak} [MV/m]	400	7	50

Table 1. Parameters of rf cavities.

The idler cavity has been designed to accept variable-radius 'tuning rings' in the inner pillbox region. These rings adjust the inner radius of the cavity to permit tuning the fundamental mode frequency over the range 34-36 GHz. The frequency of the cavity can be adjusted so that the longitudinal impedance seen by he beam is resonant, or detuned (capacitively/inductively). The idler cavity assembly is shown in Figure 2.

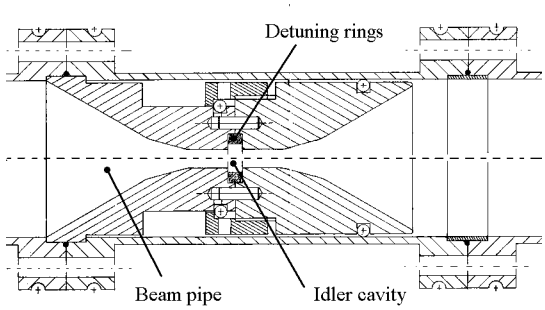

Figure 2. Idler cavity assembly.

The tuning rings will be manufactured by wrapping a layer of stainless steel (304SS) around a narrow spool that exhibits a slight taper. Individual rings will then be cut from this spool. This permits an accurate measure of the ring's inner radius, as well as differences in the radii between different rings.

The output cavities are designed with only a single output port. This port is attached to a connecting waveguide which is expanded to mate with standard WR-28 guide. Figure 3 shows a quarter of the geometry.

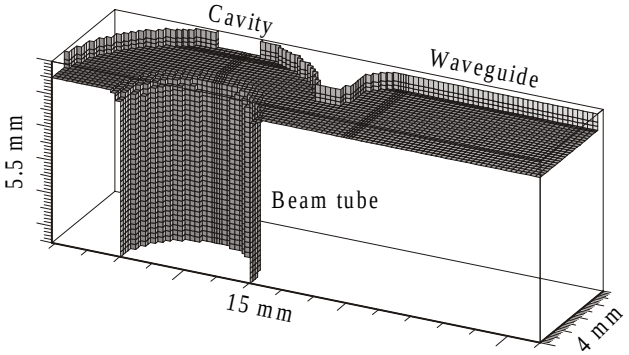

Figure 3. Output cavity quarter-geometry. The beam travels vertically through the beam tube.

This single output port can introduce an unwanted transverse impulse to the beam as it traverses the structure. The pillbox region of the cavity has been designed slightly off-center from the beamline axis to compensate for this. As a result, the linear variation of the longitudinal electric field has been strongly suppressed. A small quadratic variation is still present. However, any quadrupole interaction is slight. A cross-section of the longitudinal electric field distribution in the cavity midplane normal to the beam axis is shown in Figure 4.

The expected performance of these cavities is listed in Table 1. As can be seen, only a modest amount of output power is expected from these structures. These first experiments will concentrate mostly on beam dynamics issues: generation and transport of an intense, modulated beam through a narrow aperture cavity; and observation of the interaction of the cavity upon the beam. Later experiments may involve more sophisticated cavity designs, intended to produce rf output levels sufficiently high to drive accelerating structures.

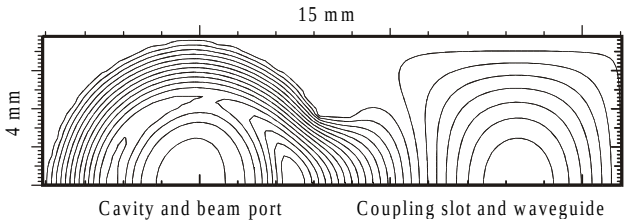

Figure 4. Cross-section of output cavity showing symmetrization of the modal longitudinal electric field.

2.2 Longitudinal Beam Dynamics Studies

Optical measurements will be performed to study the time-dependent beam-cavity interaction. Bunches will be extracted, and their longitudinal bunching characteristics measured. This allows us to make a comparison between our simulation codes and experiment. The primary measurement will be of the bunching parameter of the beam before and after it exits the cavity region. This will be compared with measurements of bunching when the beam is freely propagating. Simulation results of the evolution of the bunching parameter along the beamline following the FEL are shown in Figure 5. The cavity is located 28.5 cm from the end of the FEL. Measurements will also be made of the relative phase of the output rf power with respect to the FEL output.

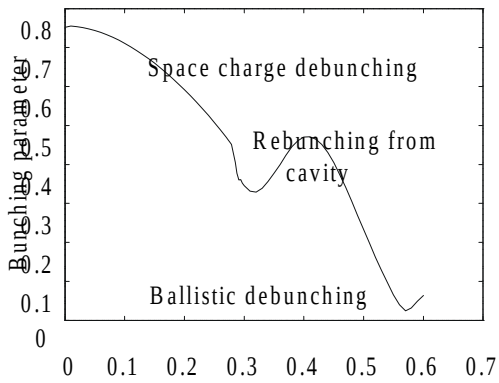

Figure 5. Evolution of the bunching parameter from the end of the FEL through the cavity.

2.3 Observation Of Bunching Characteristics

An optical diagnostic based on Cerenkov emission will be used to measure the bunching characteristics. The beam is stopped by a movable, fused-silica target. A gated CCD camera and a fast streak camera (2-ps resolution) will be used to collect and analyze a small part of the visible Cerenkov light. Figure 6 shows an example of the streak camera output, clearly displaying the bunching.

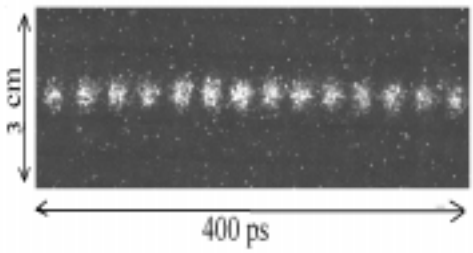

Figure. 6. Streak images of 35GHz bunches.

3 TESTS ON PIVAIR

The PIVAIR induction linac generates a nominal 7.2-MeV, 3-kA, 60-ns beam. These values make it very attractive as an injector for a 30-GHz RK-TBA system to power a multi-TeV linear collider. A preliminary point design for a multi-TeV-scale linear collider system using an RK-TBA driver and operating at 30 GHz has already been presented [7]. The RK-TBA drive beam architecture is shown in Figure 7.

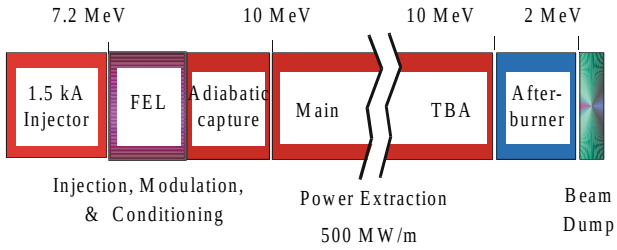

Figure 7. 30-GHz RKTBA architecture.

The front end of the drive beam injector for the Main TBA is composed of an electron gun and accelerator ('Injector'), a free electron laser ('FEL') to provide the modulation, and an 'Adiabatic capture' section to provide for bunch compression, additional acceleration, and other pulse conditioning. This latter effect may include shaping of the front-end current profile to provide a ramped current pulse. Power extraction and reacceleration then occurs in the Main TBA section.

A current proposal [8] seeks to use PIVAIR for TBA-related studies. An FEL to provide 30GHz modulation is to be constructed, followed by a beamline to support TBA studies. PIVAIR operated as a test stand thus will provide a valuable resource in the effort to examine beam dynamics and to test designs of beamline components for a high frequency RK-TBA. Of particular concern are the rf output structures and induction modules in the Main TBA section. Prototypes may be designed and then tested on the PIVAIR beamline, once a modulated beam is present.

4 CONCLUSIONS

Current experiments are studying the beam-cavity interaction in RK-TBAs at frequencies around 30GHz, ostensibly extending the utility of RK-TBA power sources to higher frequencies and to higher peak output power levels. These studies will enable us to more accurately predict and model beam dynamics in a large scale driver for a multi-TeV electron-positron linear collider.

5 ACKNOWLEDGMENTS

We wish to thank our collaborators in the CLIC group at CERN, and Colin Johnson and Walter Wuensch in particular, for their work in constructing the output cavities. SML also wishes to thank Warner Bruns for the time spent on extra development of the code GdfidL, which was used considerably in the cavity design. Work in the U.S. was performed under the auspices of the U.S. Department of Energy by LBNL under contract AC03-76SF00098, and by LLNL under contract W-7405-ENG-48.

6 REFERENCES

[1] J.P. Delahaye, et. al., "A 3 to 5 TeV Linear Collider at 30 GHz", Proceedings of VII International Workshop on Linear Colliders, Zvenigorod, Russia, Sept. 29-Oct. 3, 1997.

[2] T.L. Houck, et. al., "Scaling the TBNLC collider design to higher frequencies", Proceedings of LINAC96, CERN, August 1-5, 1996, 396-398 (1996).

[3] G.A. Westenskow, et. al., "RTA Gun Performance", these proceedings.

[4] J. Gardelle, et. al., *Phys. Rev. Lett.* **76**, 4532 (1996).

[5] J. Gardelle, et. al., *Phys. Rev. Lett.* **79**, 3905 (1997).

[6] K. Halbach and R. Holsinger, *Part. Acc.* **7**, 213 (1976); T. Weiland, *Nucl. Inst. Meth. Phys.* **A216**, 329 (1983);W. Bruns, *IEEE Trans. Magn.*, **32**, n. 3, (1996).

[7] S. Yu, "30-GHz, 200-MV/m Relativistic Klystron Two-Beam Accelerator", Proceedings of VII International Workshop on Linear Colliders, Zvenigorod, Russia, Sept. 29-Oct. 3, 1997.

[8] J. Gardelle, et. al., "Proposal to use PIVAIR as a 30-GHz High-Power Generator", these proceedings.

HIGH CHARGE SHORT ELECTRON BUNCHES FOR WAKEFIELD ACCELERATOR STRUCTURES DEVELOPMENT*

M.E. Conde, W. Gai, R. Konecny, J.G. Power, P. Schoessow
Argonne National Laboratory, Argonne, Illinois 60439 USA

Abstract

The Argonne Wakefield Accelerator group develops accelerating structures based on dielectric loaded waveguides. We use high charge short electron bunches to excite wakefields in dielectric loaded structures, and a second (low charge) beam to probe the wakefields left behind by the drive beam. We report measurements of beam parameters and also initial results of the dielectric loaded accelerating structures. We have studied acceleration of the probe beam in these structures and we have also made measurements on the RF pulses that are generated by the drive beam. Single drive bunches, as well as multiple bunches separated by an integer number of RF periods have been used to generate the accelerating wakefields.

1 INTRODUCTION

In order to study and demonstrate the wakefield acceleration scheme and also the two beam acceleration concept, we have designed and constructed a facility called Argonne Wakefield Accelerator (AWA). The AWA consists of three major components: (i) a photocathode based RF electron gun capable of producing up to 100 nC (drive gun) followed by two standing wave linac sections for post acceleration, (ii) a second photocathode based RF electron gun capable of generating low charge short electron bunches synchronized with the drive bunches (witness gun), and (iii) an experimental section for wakefield measurements, in which the witness beam is accelerated by wakefields generated by the drive beam. We have obtained electron bunches of 10 - 100 nC with FWHM of 10 - 40 ps, which have been used for initial wakefield experiments in both dielectric loaded structures [1] and plasmas [2]. These unprecedented high-charge short-electron bunches, allied with the uniqueness of having two photocathode RF guns with adjustable delay between their beams, make AWA an ideal facility for the study of electron beam driven wakefield acceleration.

2 AWA ELECTRON GUNS AND LINAC STRUCTURES

Figure 1 shows a schematic of the AWA layout. The half-cell drive gun was designed to have a high accelerating field (92 MV/m at the photocathode surface) to allow the extraction of high charge electron bunches, and to produce a 2 MeV beam with the limited RF power available at the design time (1.5 MW at 1.3 GHz) [3]. The high intensity of the accelerating field in the gun permits the generation and acceleration of short electron bunches, without having to rely on magnetic pulse compression. Magnesium was chosen to be the photocathode material for its ruggedness and quantum efficiency (5×10^{-4}). The 2 MeV bunches generated by the drive gun subsequently

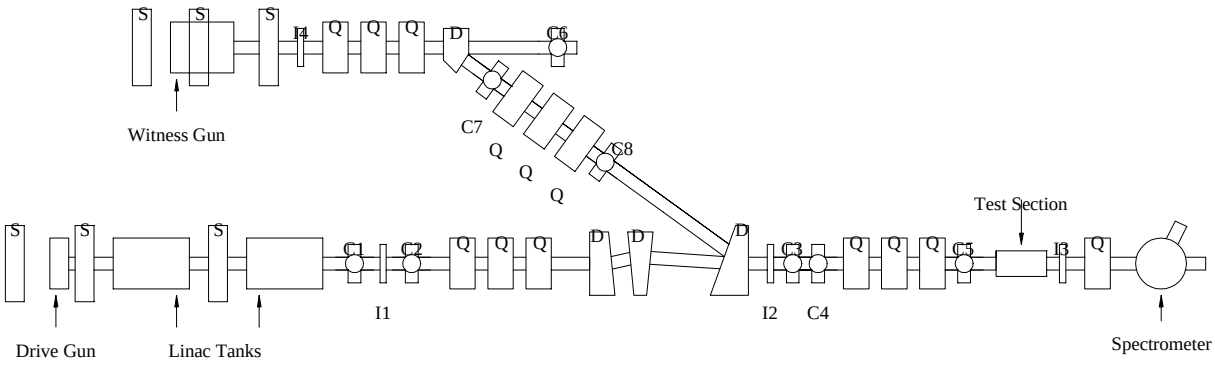

Figure 1: Schematic of the AWA experimental setup: S, Q, and D indicate solenoids, quadrupoles, and dipoles, respectively; the four integrating current transformers are labeled I1 through I4; the eight diagnostic ports are labeled C1 through C8.

*Work supported by the Department of Energy, Division of High Energy Physics, under contract W-31-109-ENG-38.

pass through two standing-wave, $\pi/2$ mode linac tanks (shunt impedance of 21.5 MΩ/m), increasing the beam energy to about 14 MeV. The linac structures have large irises (10.16 cm diameter) to minimize the generation of wakefields by the propagation of the high charge drive bunches [4]. The beam is then focused by quadrupoles and bent by three dipoles to allow for the injection of both the drive beam and the witness beam into the wakefield experimental section. The witness gun [5] is a 6-cell standing-wave $\pi/2$ mode structure that generates 4 MeV bunches of 300 pC. Its photocathode material is copper. The witness beam goes through combining optics and then through the wakefield device (plasma or dielectric structure) trailing the drive beam, thereby probing the wakefields excited by the drive bunches. Energy changes of the witness beam are measured by a spectrometer magnet located downstream of the wakefield experimental section.

The two RF guns and the two linac structures are powered by a single klystron (Thomson TH2022D; 24 MW, 4 μs pulses), via necessary power splitters and phase shifters. The laser system is comprised of a dye oscillator (496 nm) pumped by a tripled YAG, which is then followed by a dye amplifier, a doubling crystal and finally an excimer amplifier. This laser is capable of producing up to 8 mJ with 6 ps FWHM at 248 nm. The laser beam is then split and a small fraction of it (~ 15%) sent to the witness gun. There is an adjustable delay between the drive gun and the witness gun laser beams. This allows us to vary the delay between the drive and the witness electron bunches (obviously the RF phases have to be adjusted accordingly, in order to maintain the same launching phase).

3 DIAGNOSTICS AND BEAM CHARACTERIZATION

There are four integrating current transformers (Bergoz ICT - 082-070-20:1) installed on the beamlines to measure bunch charge at various locations as indicated in Fig. 1. Bunch length measurements [6] are performed using radiation emitted by the electron beam as it passes through a Cerenkov radiator. The Cerenkov light is sent to a Hamamatsu M1952/C1587 streak camera for pulse length measurements. Insertable quartz or aerogel plates are used as Cerenkov radiators. The aerogels require a more elaborate holder than the quartz plates, but offer several advantages. The aerogels need to be in a vacuum-tight holder which is inserted in the beam path. The electron beam enters our holder through a thin aluminum window (0.15 mm). It then traverses the aerogel (under atmospheric pressure) and emits Cerenkov radiation, which leaves the aerogel holder through a quartz window. Our aerogels have an index of refraction of 1.009, therefore the Cerenkov light is emitted at an angle of 7.4° with respect to the direction of propagation of the 14 MeV electrons. The light is then reflected by a mirror and leaves the vacuum chamber through a diagnostic view port.

Figure 2 shows measurements of pulse length as a function of bunch charge. In these plots the charge was measured by the integrating current transformer I1 (see Fig. 1), and the bunch length was measured using the aerogel radiator and the streak camera. In Fig. 2a we show a detailed charge scan in the range 15 - 35 nC and the corresponding FWHM of the pulses; many pulses were measured in this range and then binned in groups of 51. The plot shows the average value of charge and bunch length for seven bins, indicating that in this charge range the pulse length is almost constant, fluctuating between 15 and 20 ps. The plot in Fig. 2b shows a charge scan over a much wider range, but each point in this graph is the average of only three pulses. We have plotted the FWHM of the bunch lengths and also the 95% RMS values (this was calculated taking into account only the section of the pulse profile with intensity within 95% of the peak value, with the purpose of discarding the effect of the small background noise at the wings of the distribution). The ratio between the 95% RMS and the FWHM values shows that the pulses are not gaussian. The large fluctuation in the FWHM of the pulses also shows that the detailed shape of the temporal profile varies considerably from pulse to pulse. In all of these bunch length measurements the changes in bunch charge are accomplished by varying the laser pulse energy (either by purposely attenuating the laser beam, or due to

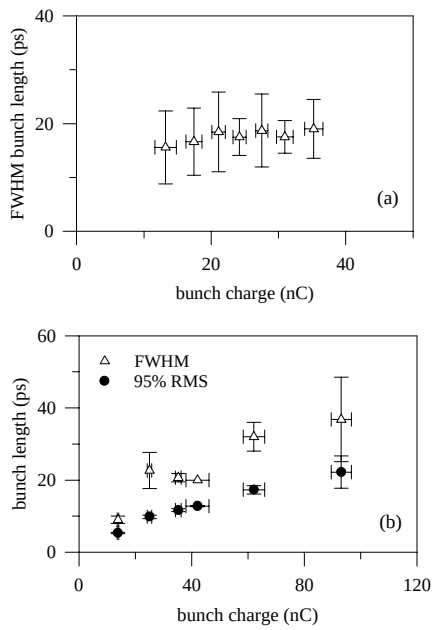

Figure 2: Measurements of electron bunch length as a function of bunch charge: (a) detailed pulse length measurement in the 15 - 35 nC range; (b) measurement over a wider range of charges, each point represents the average of three pulses.

the natural fluctuations in the laser power); when the change in the emitted bunch charge is large, it becomes necessary to readjust the solenoids and RF phases to compensate for the changes in the space charge forces.

4 WAKEFIELD MEASUREMENTS

We can map out the wakefields in a dielectric loaded structure by varying the delay between the drive bunch and the probe (witness) bunch. By measuring the change in energy of the witness beam, we obtain a direct measurement of the wake potential. This detailed mapping of the wakefields [1] was performed in a structure consisting of a hollow borosilicate glass cylinder ($\varepsilon \sim 4$) with inner radius of 5.0 mm and outer radius of 7.7 mm. Figure 3 shows the wake potential as measured from the energy change of the centroid of the witness beam as a function of the delay between the two bunches. The largest energy shift of the centroid is about 2.5 MeV/m (for drive bunches of 11 nC). Because the 2.5 mm FWHM length of the witness beam is a significant fraction of the wavelength of the wakefield (in this specific case the wakefield has an RF frequency of 15 GHz), the actual gradient is larger than the gradient measured from the witness beam centroid change in energy. By comparing the data with numerical simulations convolved with a Gaussian witness bunch shape, a true gradient of 3.6 MeV/m is inferred. Additional optimization of the laser injection phase and beamline magnet settings resulted in a gradient of approximately 6 MeV/m with a 20 nC drive beam intensity.

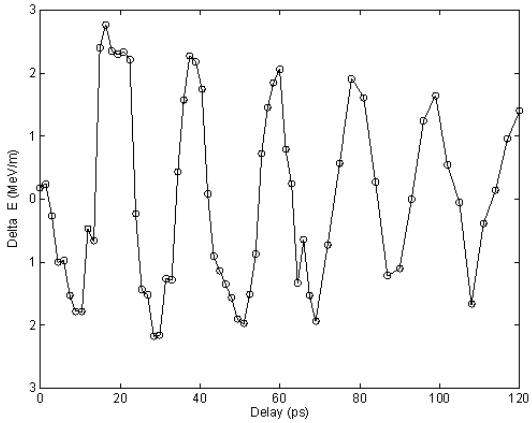

Figure 3: Wake potential measurement for a 15 GHz dielectric structure. Each data point is the change in the bend view centroid of the witness beam at the spectrometer 60° port.

5 DIELECTRIC WAKEFIELD TRANSFORMER

There are advantages in building a dielectric wakefield accelerator with two separate dielectric structures, in a transformer configuration. The drive beam generates an RF pulse as it passes through one of the structures. This RF pulse is coupled to the second dielectric structure (via a waveguide) where the witness beam is accelerated. The second tube has the same fundamental frequency but lower group velocity and transverse dimensions, thus providing an accelerating field step-up by compressing the RF pulse. Multiple drive bunches can be used, spaced by an integral multiple of the RF period, to provide a long accelerating pulse. Another advantage of having two separate dielectric structures is that the drive structure can be designed with sufficiently low transverse impedance to avoid beam breakup problems.

We have recently been designing and building dielectric wakefield transformers [7] operating at 7.8 GHz and also at 15.6 GHz. We have also succeeded in generating multiple drive bunches, by optically splitting and appropriately delaying the laser pulse to the drive gun. Figure 4 shows the envelope of the RF macropulse generated by a bunch train consisting of 4 bunches separated by 3.077 μs.

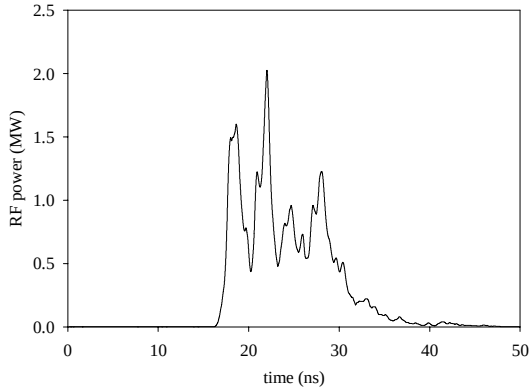

Figure 4: RF macropulse envelope for train of four drive bunches in a 7.8 GHz structure.

6 REFERENCES

[1] P. Schoessow et al., *J. Appl. Phys.* **84**, 663 (1998).

[2] N. Barov et al., *Phys. Rev. Lett.* **80**, 81 (1998).

[3] W. Gai et al., Proceedings of PAC89, Chicago, IL, 612 (1989).

[4] E. Chojnacki et al., Proceedings of PAC93, Washington, D.C., 815 (1993).

[5] J.G. Power et al., *Rev. Sci. Instrum.* **69**, 1295 (1998).

[6] M.E. Conde et al., submitted to *Phys. Rev. Special Topics - Accelerators and Beams.*

[7] M.E. Conde et al., submitted to Proceedings of Advanced Accelerator Concepts, Baltimore, MD, (1998).

LASER SYSTEM FOR A SUBPICOSECOND ELECTRON LINAC*

R. A. Crowell, C. D. Jonah, A. D. Trifunac, and J. Qian
Chemistry Division
Argonne National Laboratory,
Argonne, Illinois 60439 USA

Abstract

At the Argonne Chemistry Division efforts are underway to develop a sub-picosecond electron beam pulse radiolysis facility for chemical studies. The target output of the accelerator is to generate electron pulses that can be adjusted from 3nC in .6ps to 100nC in 45ps. In conjunction with development of the accelerator a state-of-the-art ultrafast laser system is under construction that will drive the linac's photocathode *and* provide probe pulses that are tunable from the UV to IR spectral regions.

1 INTRODUCTION

From the start time-resolved investigations of fast chemical processes have been part of radiation chemical studies. Recent advances in accelerator technology are making it possible to generate subpicosecond electron pulses. Additionally, solid state laser development is making it more routine to generate subpicosecond optical pulses. A merging of these two technologies will provide an invaluable tool for probing ultrafast radiation induced processes. In this contribution the development of a state-of-the-art laser system that will be capable of both driving the photocathode of a subpicosecond linac and simultaneously and provide a widely tunable (UV to mid-IR) stroboscopic detection capability will be described

2 FEMTOSECOND LASER SYSTEM

2.1 Femtosecond Laser System

In order to generate subpicosecond electron pulses a state-of-the-art laser systems must be developed to drive the photocathode. The accelerator under consideration at Argonne National Laboratory requires the laser operate within very strict specifications[1]. The following key problems must be addressed:

- Development of an intense (>3mJ) 5ps UV laser pulse that is needed to drive the photocathode.
- A .1ps probe pulse must be derived from the same laser and be independently tunable from the UV to the IR.
- The UV pump and the probe laser pulses must be synchronized to the RF of the accelerator to within .5ps
- Development of novel, sensitive and specific detection techniques to make the fullest use of the potential information.

For the photocathode the laser must provide high energy UV (~260nm) pulses that can be varied in energy from .1mJ to 3mJ. The low UV pulse energy corresponds to operation of the accelerator in the low charge short pulse mode (i.e., 3nC, .6ps), while the high UV pulse energy corresponds to operation in the long pulse high charge mode (i.e., 45ps, 100nC) mode. In addition to variable UV pulse energy the UV pulsewidth must be made variable from 5ps to 60ps. Some of the laser pulsewidth and energy requirements are summarized in Table 1.

To make use of the full capabilities of the experimental system, the laser must also produce pulses with less than 0.1 ps duration with enough energy (~1mJ) to pump a series of widely tunable optical parametric amplifiers that will provide probing wavelengths from the UV to IR spectral regions. The laser is to operate from single shot to 60 Hz with a pulse-to-pulse jitter less than .5ps with respect to a 1.3 GHz master clock. *Minimization of the jitter is the is the most crucial and difficult aspect of the laser design.*

Table 1: Laser Energy and Pulsewidth Specifications

Linac Pulsewidth	Charge	Laser Pulsewidth	Laser Pulse Energy
.6ps	3nC	5ps	.1mJ
3.0ps	10nC	15ps	.3mJ
8.0ps	50nC	45ps	1.5mJ
45ps	100nC	60ps	3mJ

2.2 Generation of Intense UV Laser Pulses

A block diagram of the laser amplification scheme is shown on the following page. Briefly, a diode-pumped frequency-doubled Nd:YVO laser will be used to pump a femtosecond Ti:Sapphire (Ti:S) laser that will produce a

* Work performed under the auspices of the Office of Basic Energy Sciences, Division of Chemical Science, US-DOE under contract number W-31-109-ENG-38.

81.25MHz pulsetrain of 3nJ 50fs pulses centered at 800nm. The 50fs pulses will be passed through a grating pulse stretcher which will increase the pulsewidth to 500ps. This will reduce the peak power of the laser pulses enough to prevent optical damage in the following two stages of amplification (chirped pulse amplification). After the stretcher a polarizer-Pockels cell-polarizer combination will be used to select pulses out of the 81.25MHz pulse train at 60Hz (linac repetition rate).

The first preamplifier stage (AMP1) is a multipass (8 pass) Ti:S amplifier that will produce ~5mJ pulses at 800nm[2]. AMP1 is pumped with 50mJ pulses from a high power Nd:YAG laser (HP Nd:YAG). The output of AMP1 will be used to seed a power amplifier (AMP2) that will boost the energy up to >100mJ. AMP2 is also a multipass amplifier (4 pass) and will be pumped by 450mJ from a HP Nd:YAG laser.

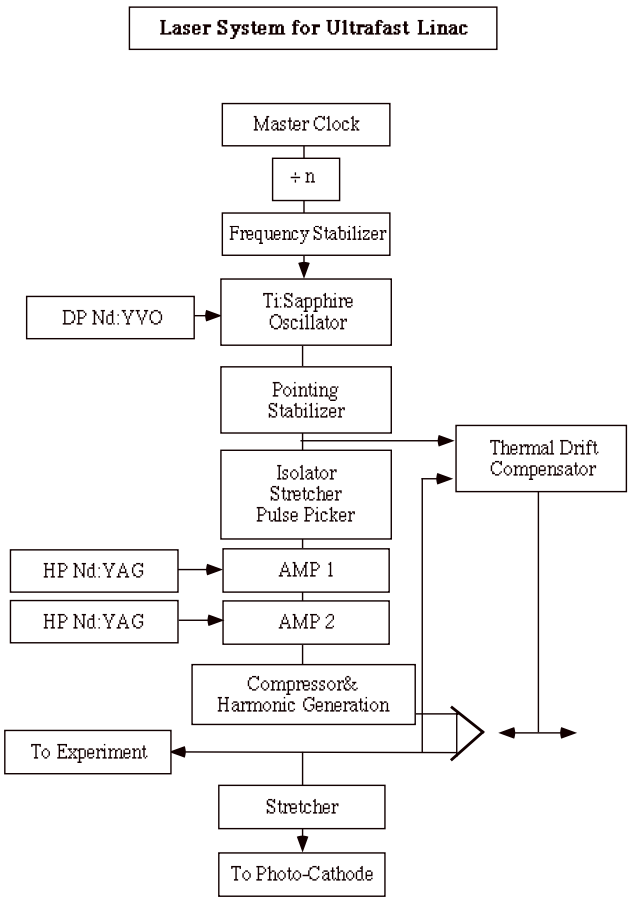

Fig. 1. Block diagram of the amplified femtosecond laser system. See text for details.

The amplifier output will be compressed in a standard grating pulse compressor to <.1ps and passed through a series of specially designed nonlinear crystals to generate the third harmonic at 260nm. The UV pulse energy is expected to exceed the required maximum of 3mJ. Dichroic mirrors will be used after the harmonic conversion step to divert the residual fundamental towards the optical parametric amplifiers while directing the third harmonic towards the linac cathode. Before illumination of the photocathode the UV will be temporally stretched by passing it through several centimeters of suprasil. The pathlength of the suprasil will be determined by the amount of UV pulse stretching that is required for the desired electron pulse charge and pulsewidth (see Table 1).

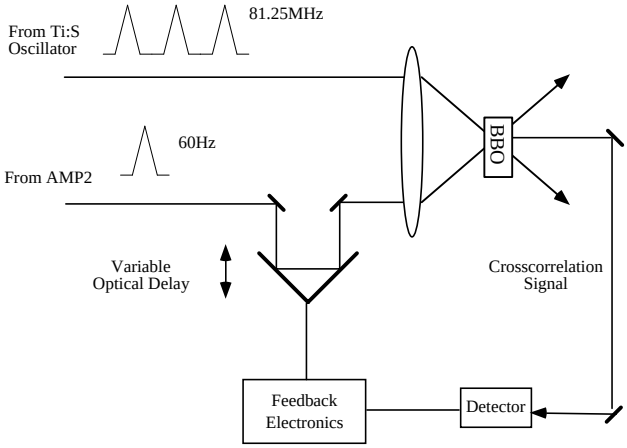

Fig. 2. Thermal drift compensation of the Ti:S amplifiers using the crosscorrelation technique. BBO (beta barium borate) is a nonlinear frequency mixing crystal. See text for details.

2.3 Minimization of Jitter

To generate .6ps electron pulses from a photocathode driven linac it is necessary to synchronize the phase of the RF that drives the photocathode and the UV laser pulses to within .5ps[1] of each other. The master clock for the RF will operate at a frequency of 1.3GHz. Expected sources for loss of synchronization will come from a variety of sources. Most importantly will be, drifting in the output frequency of the Ti:S oscillator, slow thermal drifting in the optical components, mechanical vibrations, and air currents.

The 16th subharmonic (81.25MHz) of the master clock will be used as a reference frequency for the Ti:S oscillator. Using commercially available electronics (Spectra Physics, Mountain View, CA) it is possible to reduce the jitter/synchronization out of the Ti:S oscillator to better than .1ps rms.

During the amplification process the synchronization will degrade due to the slow thermal drifting of the optical components and vibrations that result from mechanical and audio interference. To reduce effect of the slow thermal expansion and contraction of the optical components the pathlength that the laser pulse travels through the amplifier must be minimized. This dictated the choice to use a multipass amplifier design rather that a more efficient regenerative amplifier for AMP1. A multipass amplifier should reduce the path length by ~20m relative to a regenerative amplifier.

Compensation for slow thermal drifts will be actively achieved by passing the pulse out of the amplifiers through a stepper motor/piezo driven optical delay that will compensate for thermal drifts on a shot-to-shot basis (see Figure 2). The error signal for driving the optical delay will be derived from the crosscorrelation between the Ti:S oscillator and the output of AMP2 in a BBO crystal. This technique has been previously used to maintain subpicosecond synchronization between a Ti:S amplifier and an infrared optical parameteric amplifier[3]. Specially designed optical tables and evacuated beam tubes will minimize the sensitivity of the system to mechanical vibrations.

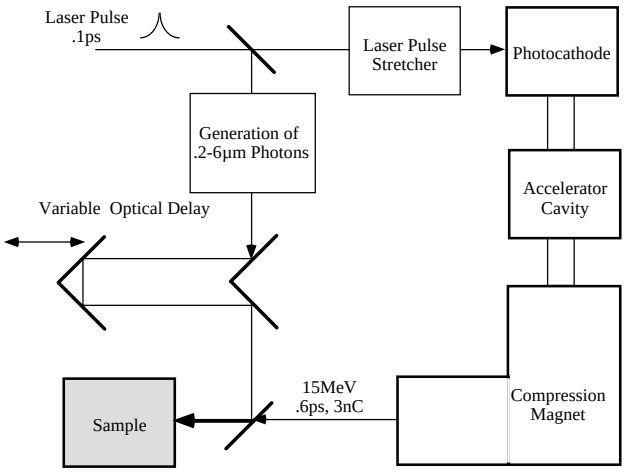

Fig. 3. Block diagram depicting a typical electron linac pump/laser probe experiment.

3 CONSEQUENCES OF LASER SYNCHRONIZATION

A significant advantage of this system is that the laser that "drives" the photocathode is inherently synchronized with the electron pulse, with very little jitter in the synchronization. This fact translates into considerable improvements in sensitivity and capabilities for detection schemes. Figure 3 shows a the setup for a typical pump/probe experiment in which the subpicosecond electron linac acts as pump source to initiate a radiological event that is subsequently probed by a laser pulse.

Detection schemes can now be based on laser produced interrogating light pulses as opposed to linac produced light pulses (Cerenkov radiation) that are presently used. Thus, the intensity and wavelength range will be available to develop new detection schemes for examination of transient species that are impossible to study at this time.

A new type of detection that will become available is transient infrared spectroscopy, which can be used to determine the role of excess thermal energy and vibrational energy transfer in radiation chemistry. In addition to providing a window through which to view the role of vibrational dynamics, the structural selectivity of infrared spectroscopy can be used to follow the progression of and identification of transient species. To this extent we have recently developed a unique optical parametric amplifier based on potassium niobate that is tunable throughout the chemically important 2.5-5.5 micron spectral region.

Other new types of detection under development include time resolved coherent spectroscopy (e.g., CARS, transient grating spectroscopy, photon echo spectroscopy), and time-resolved resonance Raman spectroscopy. Such techniques will provide new information on energy levels, lifetimes of transient species, collisional processes, coupling strengths, and diffusion processes.

4 SUMMARY

A femtosecond laser system for driving a subpicosecond photocathode electron linac has been described. The main design criteria center around the necessity to achieve .5ps synchronization between the high energy UV pulses and the phase of the RF that drives the photocathode. As a consequence of the synchronization between the linac and the laser a wide variety of sensitive detection schemes now become available for probing radiation induced chemical events on fast timescales.

5 ACKNOWLEDGEMENTS

We gratefully acknowledge the input from Drs. Illya Shkrob, D. M. Bartels, and D. Werst in the preparation of this manuscript.

6 REFERENCES

[1] "Argonne National Laboratory CHM Linac Upgrade Study Final Report," Northrop Grumman, Princeton, NJ, March 30, 1998.

[2] P.Georges, F. Estable, F. Salin, "A High-Efficiency Multipass Ti:Sapphire Amplifier for a Continuous Wave Single Mode Laser," *Optics Lett.*, **16**, 144 (1991).

[3] R. A. Crowell, G. R. Holtom, and X. S. Xie, "A High Repitition Rate Femtosecond Optical Parametric Oscillator-Amplifier System Near 3 Microns," *J. Amer. Optic. Soc. B*, **12**, 1723 (1995).

FEASIBILITY STUDY OF A 2 GEV SUPERCONDUCTING H⁻ LINAC AS INJECTOR FOR THE CERN PS

R. Garoby, H. Haseroth, C.E. Hill, A.M. Lombardi, P.N. Ostroumov*, J.M. Tessier**, M. Vretenar
PS Division, CERN, CH 1211 Geneva 23, Switzerland
(*: on leave of absence from INR, Moscow, Russia **: SL Division)

Abstract

This preliminary feasibility study is based on the availability of the CERN LEP2 superconducting RF system after LEP de-commissioning. The option that is explored is to use this system as part of a high energy H⁻ linac injecting at 2 GeV into the CERN PS, with the aim of reliably providing at its output twice the presently foreseen transverse beam brightness at the ultimate intensity envisaged for LHC. This requires the linac to be pulsed at the PS repetition rate of 0.8 Hz with a mean beam current of 10 mA which is sufficient for filling the PS in 240 μs (i.e. about 100 turns) with the ultimate intensity foreseen for injection for the LHC.

The linac is composed of two RFQs with a chopping section, a room temperature DTL, a superconducting section with reduced beta cavities up to 1 GeV, and a section of LEP2 cavities up to 2 GeV. This study deals, in particular, with the problems inherent in H⁻ acceleration up to high energy and in the pulsed operation of SC cavities. Means for compensating microphonic vibrations in the SC cavities are considered, with the aim of reducing the final overall energy spread to the tight requirements for injection into a synchrotron. Other possible applications of such a machine are also briefly reviewed, that make use of its potential for working at a higher duty cycle than required for LHC alone.

1 INTRODUCTION

Most of the RF equipment of the CERN LEP-2 will be available after the year 2000. Among the possible re-uses of this valuable hardware [1-4] the realisation of a 2 GeV Linac injector for the PS is an attractive option with many benefits with respect to the present scheme for LHC injection [5].

As a result of the smaller emittance of the Linac beam and of the higher injection energy into the PS (at present 1.4 GeV), the LHC would profit from an increased brightness of the proton beam delivered by the PS injector complex. The peak beam intensity in the PS could be improved as well by filling the entire aperture. Beam losses would be reduced by the efficient charge exchange injection in the transverse planes, and by the chopped beam in the longitudinal phase plane. The injectors of the PS could be modernised and re-built with standardised equipment, with advantages in terms of reliability and maintenance.

Other potential applications of this facility at a higher duty cycle justify the use of SC cavities. They include: 1) neutron production with a spallation target, using the PS as an accumulator ring; 2) feeding a second generation ISOL facility for the production of radioactive ion beams; and 3) any physics application requiring intense secondary beams.

A small study group has concentrated on the main accelerator technology topics and on the most promising scenario. A first report indicating the feasibility of such a facility is being prepared [6].

2 PARAMETERS AND LAYOUT

The Superconducting Proton Linac, SPL, (Figure 1) is made of an H⁻ source, two RFQs with a chopper in between, a Drift Tube Linac up to 100 MeV and a superconducting section up to 2 GeV. The main design parameters are given in Tables 1 and 2.

Table 1: Linac Beam Parameters

Number of Particles / PS Pulse	1.5	10^{13}
Mean Linac Current during Pulse	10	mA
Pulse Length	250	μs
Repetition Rate	0.83	Hz
Filling Factor of Linac Buckets	½	
N. of Linac Bunches per PS Bucket	11	
SPL Micropulse (11 bunches)	59.6	ns
Chopping Factor	46	%
Mean Bunch Current (in an RF period, for a full bucket)	37	mA
Source Current	20	mA
Beam Duty Cycle (for PS filling)	0.021	%
Maximum Design Duty Cycle	5	%
Maximum Average Current	500	μA
Transverse Emittance, source exit, rms	0.2	μm
Transverse Emittance, PS input, rms	0.6	μm
Longitudinal Emittance (5 rms)	3	°MeV

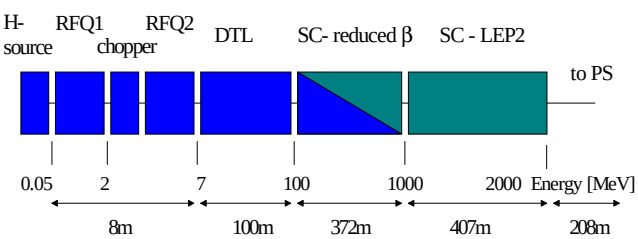

Figure 1: Schematic layout of the Linac.

Table 2: Linac structure parameters.

	W_{out} [MeV]	Freq. [MHz]	#of cav.	Power [MW]	# of klyst	Length [m]
RFQ1	2	176.1	1	0.45	-	2.3
RFQ2	7	352.2	1	0.5	1	4
DTL	100	352.2	29	5.8	6	99
SC - red. β	1027	352.2	152	13	19	372
SC - LEP2	2000	352.2	136	14.2	17	407
Line	2000	352.2	1	-	-	208
Total					43	1094

The facility is designed to provide 1.4 10^{13} particles at the exit of the PS, corresponding to the LHC beam-beam limit ("ultimate beam"). For a mean linac current of 10 mA, this number of particles can be obtained by injecting 110 turns into the PS, with a linac pulse length of ~250 μs. For the PS repetition period of 1.2 sec, the resulting linac beam duty cycle is only 0.021%. The injection energy into the PS, 2 GeV, has been chosen to use most of the existing LEP equipment, to improve transverse beam stability in the PS and to profit from the high accelerating efficiency of the LEP cavities at high energies.

The LEP RF frequency of 352.2 MHz is also used for most of the room temperature section. A significant number of klystrons with their power distribution systems can therefore be recovered, and a standard RF system can be used throughout the linac.

Due to the low duty cycle, the SC cavities need to be pulsed to minimise heat dissipation and wall plug power. The linac is foreseen for a beam duty cycle of 5%: up to this value the cryogenic system is dimensioned mainly to handle static losses and RF pulsing has no impact on the cryoplant. The main additional investment for this duty cycle comes from the shielding needed to cope with the higher activation due to losses in the linac.

The relative particle loss at 2 GeV and 5% duty must be smaller than 10^{-6}/m to allow hands-on maintenance; this is not a strong design constraint as a large fraction of the halo particles are transported through the large aperture of the SC cavities (>20 cm) and can be properly removed before PS injection.

An important design constraint is the high beam brightness needed by the LHC: this requires an emittance of 0.2 μm from the source because a factor 3 blow-up between the source and the PS has been conservatively assumed to account for space-charge, mismatch, and misalignment effects.

3 ROOM TEMPERATURE SECTION

The room temperature section is composed of a front-end (source, RFQs, chopper) injecting into a Drift Tube Linac (DTL). The 20 mA beam coming from the source is accelerated to 2 MeV by a 176.1 MHz RFQ. The beam is then chopped and injected, filling every other bucket, into an RFQ at double frequency (352.2 MHz), which brings the beam energy to 7 MeV. Matching to and from the chopper is performed by dedicated sections integrated in the first and second RFQ respectively.

A distance of 1.6 m is provided between the RFQs to house a wide-band electrostatic chopper of the BNL design [7] and some diagnostics. The chopper voltage required is 1.7 kV, and, to avoid partially filled buckets in the Linac, a 4.2 ns rise time is required: should it be too challenging, a chopper/antichopper line will be chosen.

The DTL has been divided in two sections. The first one (7-20 MeV) consists of one standard Alvarez tank, with FODO focusing. The second, up to 100 MeV, is of the separated-focusing DTL type, made of 28 8-cell tanks separated by 3 βλ drifts containing a quadrupole triplet. This structure offers higher shunt impedance and simpler mechanical construction than a standard DTL. Triplet focusing is preferred because of the resulting round beam inside the tank, which minimises the emittance growth due to RF defocusing. The transmission of the room temperature part is 99% (without taking into account stripping losses after the source) and the transverse emittance increase is 10%.

4 SUPERCONDUCTING SECTION

The superconducting part of the Linac consists of four different sections, with cavities optimised for beta 0.48, 0.6, 0.8 and 1. LEP-2 standard cavities (β=1) and cryostats are used between 1 and 2 GeV, while 5-cell cavities optimised for β=0.8 would be built and installed in the existing LEP-2 cryostats to cover the energy range between 450 MeV and 1 GeV [3]. Two additional sections of 4-cell cavities optimised for β=0.48 and β=0.625, arranged in shorter cryostats, cover the energy range between 100 MeV and 200 MeV, and between 200 and 450 MeV respectively. A development program is underway at CERN for the production of reduced-β (β=0.5 to 0.8) cavities with the niobium on copper technique [8]. In case the sputtering is not be feasible, the lowest beta cavities would be made of bulk niobium and the DTL energy increased up to 150 MeV. The layout of the superconducting part is given in Table 3.

Table 3: Layout of the superconducting section.

Sec.	Cryo stats	klyst rons	Cavi ties	cells / cav.	output energy [MeV]	length [m]	RF power [MW]
1	8	4	32	4	191	58	1.3
2	14	7	56	4	452	126	3.7
3	16	8	64	5	1027	188	8.0
4	34	17	136	4	2041	407	14.2
tot.	72	36	288			779	27.2

This layout makes use of 34 LEP2 4-cavity modules with their cryostats, i.e. 53% of the 68 installed in LEP. Including the cryostats used for the β=0.8 cavities, only 50 cryostats would be re-used, leaving some margin for reaching a higher linac energy if needed.

Due to the pulsed mode of operation, static cryogenic losses will dominate. Assuming a static loss of 180 W per 4-cavity module as in LEP [9], the 72 cryostats of the SPL would have an overall static loss of 13 kW, i.e. slightly more than the cooling capacity of a LEP-type cryoplant (12 kW).

The mean field used in this design is 6 MV/m although operation at a higher gradient should be possible in pulsed mode. The focusing for the superconducting section is provided by a doublet (two 400-mm long quadrupoles spaced by 100 mm) placed outside each cryostat. It has so far been optimised for zero current. For 40 mA the emittance increase is 45%, coming from the long focusing period at low (<1 GeV) energy and from mismatches between the different sections. A new layout for the low energy part and a more accurate matching should reduce the emittance blow-up.

5 ENERGY STABILITY

Mechanical vibrations in the SC cavities change their resonant frequency, leading to oscillations of the bunch in the longitudinal phase plane and finally to a pulse-to-pulse jitter in the mean bunch output energy. The effect of the vibrations can be greatly reduced by a self-excited loop and an RF feedback of the cavity voltage. For the SPL, a feedback scheme and calculation tools originally developed for the TESLA project [10] have been adapted for a proton beam. Since the correction is applied at the klystron input, the beam motion cannot be compensated completely when the klystron feeds several cavities as is the case in the SPL (8 cavities per klystron). In the simulations, the gains of the regulation loops are set to 100 and 500 respectively for the amplitude and for the phase. 20 % extra power is required for the amplitude loop and 20% for the phase loop.

The effect of the Lorentz detuning at 6 MV/m field is very small: the cavity phase can be cancelled by the feedback loops when the beam is injected, and the corresponding peak-to-peak energy error at 2 GeV is only 0.006 MeV.

The effect of mechanical vibrations has been studied assuming a pessimistic maximum cavity-to-cavity variation in resonant frequency of ± 40 Hz. The motions of the beam centre and the energy and phase errors at linac exit have been calculated for 500 uniform random distributions of frequency errors. The scatter in the position of the beam centre in the longitudinal plane at 2 GeV is shown in Figure 2.

Inside the single pulses, energy and phase are very stable (the period of the mechanical vibrations is much longer than the pulse length), while from pulse to pulse the rms energy variation is 0.3% (6 MeV). The energy jitter can be reduced to ± 3 MeV (total), by an energy-correcting cavity placed 200 m downstream, resulting in a good match to the PS bucket.

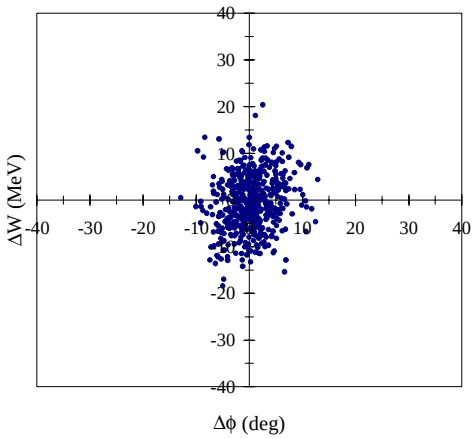

Figure 2: Relative position of the bunch centre in the longitudinal plane at 2 GeV for 500 random error distributions.

6 REFERENCES

[1] R. Corsini, A. Hoffmann, “Considerations on an FEL based on LEP superconducting cavities”, CERN/PS 96-04.

[2] C.Rubbia, J.A.Rubio, “A tentative program towards a full scale energy amplifier”, CERN/LHC 96-11.

[3] D. Boussard, E. Chiaveri, G. Geschonke, J. Tuckmantel, “Preliminary Parameters of a Proton Linac using the LEP 2 RF System when Decommissioned”, SL-RF Technical Note 96-4.

[4] C. Pagani, G. Bellomo, P. Pierini, “A high Current Linac with 352 MHz SC Cavities”, Proceedings of the 1996 Linac Conference, Geneva, p. 107.

[5] R. Garoby, M. Vretenar, “Proposal for a 2 GeV Linac Injector for the CERN PS”, PS/RF/Note 96-27.

[6] G. Bollen, D. Boussard, R. Cappi, R. Garoby, H. Haseroth, C.E. Hill, P. Knaus, A. Lombardi, M. Martini, P.N. Ostroumov, J.M. Tessier, M. Vretenar, “Report of the Study Group on the Superconducting Proton Linac as a PS Injector”, CERN/PS, in preparation.

[7] J.M. Brennan, L. Ahrens, J. Alessi, J. Brodowski, J. Kats, “A Fast Chopper for Programmed Population of the Longitudinal Phase Space of the AGS Booster”, Proc. of the 1988 EPAC, Rome, p. 1003.

[8] C.Benvenuti, D.Boussard, S.Calatroni, E.Chiaveri, J. Tückmantel, “Production and Test of 352 MHz Niobium Sputtered Reduced-Beta Cavities”, CERN-SL 97-63 RF.

[9] G.Geschonke, “Superconducting Structures for High Intensity Linac Applications”, Proceedings of the 1996 Linac Conference, Geneva, p. 910.

[10] J.M. Tessier, “Field Stabilisation in Superconducting Cavities in Pulsed Mode”, Ph.D. Thesis, Paris XI, Orsay 1996.

RECENT PROGRESS IN THE DEVELOPMENT OF A CIRCULAR ION INDUCTION ACCELERATOR FOR SPACE CHARGE DOMINATED BEAMS AT LLNL*

L. Ahle, T. C. Sangster, D. Autrey, J. Barnard, G. Craig, A. Friedman, D. P. Grote,
E. Halaxa, R. L. Hanks, M. Hernandez, H. C. Kirbie, B. G. Logan, S. M. Lund,
G. Mant, A. W. Molvik, W. M. Sharp
Lawrence Livermore National Laboratory, Livermore, CA 94551 USA
D. Berners**, S. Eylon, D. L. Judd, L. Reginato
Lawrence Berkeley National Laboratory, Berkeley, CA 94720 USA
A. Debeling, W. Fritz
Bechtel Nevada Corporation, Las Vegas, NV 89193 USA

Abstract

The Heavy Ion Fusion Group at Lawrence Livermore National Laboratory has for several years been developing the world's first circular ion induction accelerator. This machine has recently been extended to 90 degrees, or 10 half-lattice periods(HLP) with full beam transport. In addition, induction cores have been installed on five of the HLP's, each with an independent arbitrary waveform pulser. An arbitrary waveform pulser for the bending electrostatic dipoles has also been enabled. Together, they have allowed the first attempts at coordinated bending and acceleration of the beam. The results of these first attempts will be reported on in the paper by examining the output of various diagnostic devices, such as the capacitive Beam Probes(C-probes), slit scanners, and the Gated Beam Imager(GBI).

1 INTRODUCTION

Currently, heavy ion beams are being pursued as a candidate for a driver of an Inertial Fusion(IFE) power plant. In such a power plant, ion beams would provide the input energy necessary to ignite small D-T capsules [1]. The accelerator for such a driver would need to accelerate space charge dominated ion beams to a total kinetic energy of a few GeV while providing pulse compression and be able to operate at a rate of ~5-Hz [2,3]. Usually the conceptual design of such a machine is linear, but an alternative concept, which may provide significant cost savings [4], is a circular machine, or recirculator. However, a space charge dominated, ion induction, circular machine has never been built before. Thus, the HIF Group at LLNL has been developing a small recirculator in order to investigate the validity of such a concept.

* This work has been performed under the auspices of the US DOE by LLNL under contract W-7505-ENG-48.
** Present Address: Stanford University, Palo Alto, CA 94305, USA

2 THE RECIRCULATOR

In order to validate the recirculator for an IFE power plant driver, coordinating bending and acceleration of the beam while maintaining transverse and longitudinal control beam brightness must be demonstrated [5]. Table 1 lists some important characteristics of the recirculator. In designing this machine, all of the important dimensionless beam parameters, such as perveance, were kept the same as a full scale driver machine. Each half lattice period(HLP) of the recirculator consists of a permanent magnetic quadrupole for focusing, an electrostatic dipole for bending the beam, and an induction core, or modulator, for acceleration and longitudinal compression. The dipole plates are designed to provide a 9 degree bend to the beam while the modulators are designed to provide 500-eV of acceleration.

Table 1: Recirculator Specifications

Circumference	14.4m	
Beam Species	K^+	
# of laps	15	
Max. Beam Radius	1.5 cm	
Beam Statistic	Lap 1	Lap 15
Beam Energy	80 keV	320 keV
Pulse Duration	4 μs	1 μs
Beam Current	2 mA	8 mA
Undepressed Phase Advance	78°	45°
Depressed Phase Advance	16°	12°

In the fall of 1997, the machine was extended from a 45 degree bend [6] to a 90 degree bend section. Figure 1 shows the current layout of the machine. Initially, a 4-μs beam pulse is injected by a source diode with an energy of 80-keV through a 1-cm diameter aperture which provides an initial beam current of 2-mA. Upon injection the beam enters an electrostatic matching section used to convert the uniformly expanding beam to an AG focused

beam. A short magnetic transport section follows which then leads to the 90 degree bend section. Following the bend section is the End Tank which houses several diagnostics (a Faraday cup, parallel slit scanner, and a gated beam imager) to measure beam quality. Also as part of the upgrade, magnetic induction cores were added to 5 of the 10 HLP's as shown.

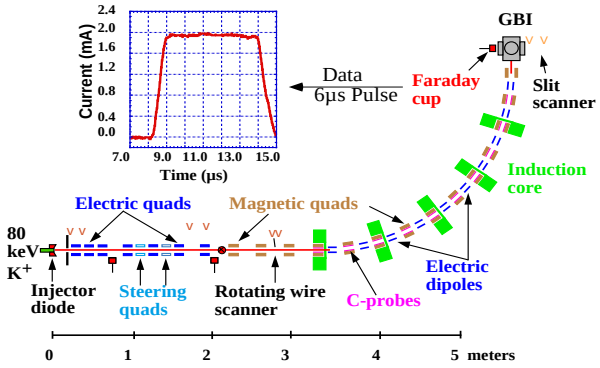

Figure 1: Current Recirculator Layout and Faraday cup data at 90 degrees.

The first attempts at beam transport through the 90 degree section were done with no acceleration and DC voltages (+/- 6.575-kV) on the bending dipole plates. Full current transport was achieved with less than 1% loss as measured by Faraday Cups. The RMS normalized emittance,

$$\varepsilon_{rms}^2 = 4\gamma\beta\left(\langle x^2\rangle\langle x'^2\rangle - \langle xx'\rangle^2\right)$$

for 90% of full beam current was also measured after 90 degrees. In the bend plane (x), the measured value is 0.045π-mm-mR while the out-of-plane (y) emittance is 0.068π-mm-mR. This compares to 0.021π-mm-mR measured directly after the source aperture. The growth seen is within the design specifications.

3 CAPACITIVE BEAM PROBES

In order to monitor the beam as it travels through the accelerator, a capacitive beam probe (C-probe), which measures the transverse beam position as a function of time, was also installed in each HLP as part of the upgrade. The C-probe [7] is a ceramic cylindrical shell whose inside is coated by copper. The copper coating is divided into four equal areas by divisions parallel to the cylinder axis. The C-probe is placed inside the beam pipe and as the beam passes through it, a charge is induced on each pad. The induced charge is a function of the charge centroid and the total current of the beam. Each signal is amplified and digitized through the computer control system and analyzed to obtain the charge centroid. Bench tests of the system, using a conducting rod to simulate the beam, have yielded a resolution of 70 μm [6].

Figures 2 and 3 show the x position and y position as a function of HLP number. HLP 0 corresponds to a C-probe in the straight section while HLP n refers to the C-probe immediately after the nth dipole plate. The different curves represent different applied voltages on the dipole plates. From the y position plot, the shot to shot repeatability of the measurement is clearly seen, while the x position shot demonstrates the sensitivity of the system to small perturbations. From tests characterizing the digitizing electronics, a systematic error of ~700-μm is estimated for each point. That systematic error should decrease upon adding some refinements to the algorithm that calculates the position.

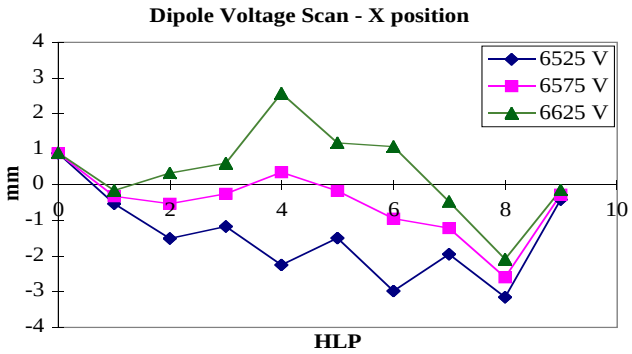

Figure 2: X positions as measured by C-probes for various dipole voltages.

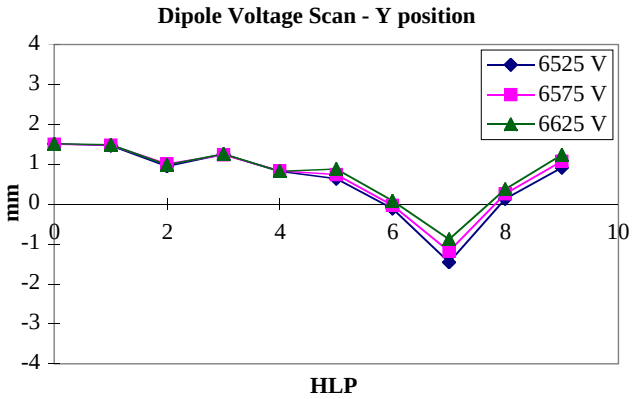

Figure 3: Y positions as measured by C-probes for various dipole voltages.

4 GATED BEAM IMAGER

In addition to beam position, the emittance growth of the beam as it travels through the bend section is of critical importance. In a full scale driver, the final beam pulse must be compressed to ~10 ns and a final spot size of a few mm. If the emittance is growth is too large, this final focus on the target will not be possible. Traditionally, a parallel slit scan has been used to measure the emittance of space charge dominated beams, but LLNL has developed a new device to measure the emittance, the Gated Beam Imager [8].

The GBI uses a pepperpot design in which the beam is incident on a hole with 100 μm diameter holes creating many beamlets. Each beamlet is emittance dominated and is allowed to drift to a micro channel plate(MCP). The MCP is coated with a thin layer of stainless steel, ~150

nm, which stops the ions and produces several few eV electrons per ion. After passing through the MCP, the electrons are proximity focused on to a phosphor screen. The light generated is focused and captured by a CCD camera that sits outside of vacuum. The image can then be analyzed to determine the emittance in both transverse directions. The MCP also allows time gating of the GBI to measure emittance as a function of time.

As of fall of 1997, the functionality of the GBI had been achieved, but there was still some slight discrepancy in direct comparisons between slit scanner data and GBI data [6]. After the analysis of the GBI images was changed to more closely mimic the slit scan, agreement between the two devices was achieved. At 90 degrees, the slit scan measurement yielded ε_x=0.045 and ε_y=0.068 π-mm-mR while the GBI yielded ε_x=0.043 and ε_y=0.065 π-mm-mR. Both of these comparison are well within the estimated 15% systematic error associated with each measurement.

5 ACCELERATION

In order for the acceleration of the beam to be controlled throughout the bend section, the voltage on the dipole plates need to be ramped up. For the full ring, the dipoles need to ramped from approximately 7-kV to 28-kV in ~240-μs. To meet this challenge, LBNL has developed a prototype dipole pulser [9]. This pulser delivers only the positive polarity, but the design can be used with only slight modifications to build a pulser for the negative polarity. Bench tests of the pulser system indicate that it delivers the necessary voltage ramp.

Currently, we are in the process of enabling the pulser on the 90 degree bend section. When connected the pulser provide voltages for the positive plates in HLP 6-10. The rest of the plates are operated with DC voltages. The initial test of the system has shown that is does not yet have the desired shot to shot repeatability at the low voltage level necessary on the initial lap. Figure 4 shows C-probe data from three successive pulses taken within a minute of each other. This clearly shows the variance from pulse to pulse. From the DC voltage data presented in figure 2, the pulse to pulse variance is less than 2%. Currently, we are exploring ways to modify the feedback loop of the pulser to obtain the necessary repeatability.

Presently the electronics for the modulator are just going through their initial implementation on the bend section. While the bench tests are very encouraging, there is no data to show at this time.

6 CONCLUSION

Lawrence Livermore National Laboratory is currently developing the world's first circular ion induction accelerator, the recirculator. This machine has been extended to 90 degrees with full current transport. The emittance growth in this bend section is well within the design requirements. The C-probe system has been enabled and has allowed for accurate beam position monitoring throughout the bend section and, the GBI has been fully reconciled with the more standard slit scanner. Initial test for the pulser to do the necessary ramping of the dipole voltage during acceleration have been performed. Currently we are performing the initial test of the electronics for the modulators. In the next month, we expect to make the first attempts at coordinating bending and acceleration.

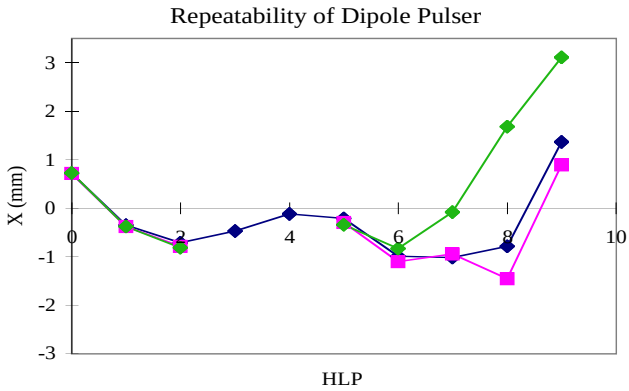

Figure 4: C-probe X positions for three consecutive pulses with dipole plates in HLP 6 through 10 connected to pulser.

7 REFERENCES

[1] R. O. Bangerter, *Nuovo Cimento* **106A** (11), 1445-1456 (1993).

[2] M. Tabak et al., *Nuclear Fusion* **38** (4), 509 (1998).

[3] R. Moir, "Inertial Fusion Energy Power Plants Based on Laser or Ion Beams," Proc. of ICENES 98, Tel-Aviv, Israel, June 28 -July 2, 1998, to be published.

[4] W. R. Meier et al., "An Integrated Systems Model for Heavy Ion Drivers," Proc. of Inter. Symp. on Heavy Ion Inertial Fusion, Heidelberg, Germany, Sept. 24-27, 1997, to be published in *Nucl. Inst. and Meth. A.*

[5] A. Friedman et al., *Fusion Engineering and Design* **32-33**, 235-246 (1996).

[6] T. C. Sangster et al., "Status of Experiments Leading to a Small Recirculator," Proc. of Inter. Symp. on Heavy Ion Inertial Fusion, Heidelberg, Germany, Sept. 24-27, 1997, to be published in *Nucl. Inst. and Meth. A.*

[7] F. J. Deadrick et al., "Development of Beam Position Monitors for Heavy Ion Recirculators," Proc. of Particle Accelerator Conference, Dallas, TX, May 1995, 2557 (1995).

[8] L. Ahle and H. S. Hopkins, "Gated Beam Imager for Heavy Ion Beams", Proc. of Beam Instrumentation Workshop, SLAC, May 4-7, 1998, to be published.

[9] D. P. Berners and L. L. Reginato, "Arbitrary Waveform Generator for Electrostatic Dipoles ina Heavy Ion Recirculator," Proc. of Particle Accelerator Conference, Vancouver, B.C., Canada, May 12-16, 1997, (1997).

THE LINAC OF THE MUNICH ACCELERATOR FOR FISSION FRAGMENTS (MAFF)

O. Kester, D. Habs, R. Rao, T. Sieber, H. Bongers, A. Kolbe, M. Gross, P. Thirolf, J. Ott
LMU München, Garching, Germany
U. Köster, TU München, Garching, Germany
A. Schempp, J.W. Goethe-Universität, Frankfurt, Germany
U. Ratzinger, GSI, Darmstadt, Germany

Abstract

A linear accelerator for the new Munich high flux reactor FRM-II is under design [1,2]. This LINAC will be able to deliver intense beams of very neutron rich fission fragments from a target ion source located inside a through going reactor tube for the production of very heavy elements [3]. In order to obtain an efficient acceleration in the LINAC, charge breeding of the 1+ ion beam from the reactor to a q/A > 0.16 is required. The LINAC will work with 10% duty cycle with a final energy between 3.7 and 5.9 MeV/u. The LINAC of the Munich Accelerator for Fission Fragments (MAFF) will consist of an Radio Frequency Quadrupole (RFQ) accelerator, three interdigital H-type (IH) structures similar to the lead LINAC at CERN and two seven-gap IH-resonators for the adjustment of the final energy of the ions. In the present paper the concept, particle dynamics calculations and first cavity design calculations with MAFIA will be presented.

1 INTRODUCTION

Advanced radioactive nuclear beam facilities have a strong scientific case which is centered in three areas of basic science, namely Nuclear physics, Nuclear Astrophysics and the limits of the Standard Model. This physics and the application of neutron-rich fission fragment beams were discussed in [4]. With the ISOL (Isotope Separation On-line) technique intense high quality beams of radioactive ions can be supplied using very different reactions for the production: i) high energy protons, ii) fast neutrons and iii) thermal neutrons. The high neutron flux of a reactor and the high cross section of U^{235} for thermal fission (580b) allows to produce beam intensities comparable to those of stable beams which are used at GSI for the production of superheavy elements (SHE). The MAFF-Project at the new high flux reactor FRM-II at Garching will be the only facility world wide which uses this concept. A first realization of this concept was studied in the PIAFE project [5], which was stopped at 1. July 1998 for political reasons.

Compared to other radioactive beam accelerators under construction the MAFF project expects beam intensities (10^{11}/s) of fission fragments which are typically larger by a factor of 1000. Very intense neutron-rich ion beams accelerated to energies at the Coulomb barrier are of special interest for the production of very heavy elements. Fig.1 shows the calculated lifetimes for the elements Z=104 to Z=114 in dependence on the number of neutrons in the nuclei. The calculations are compared to measurements, which fit very well to the theoretical values.

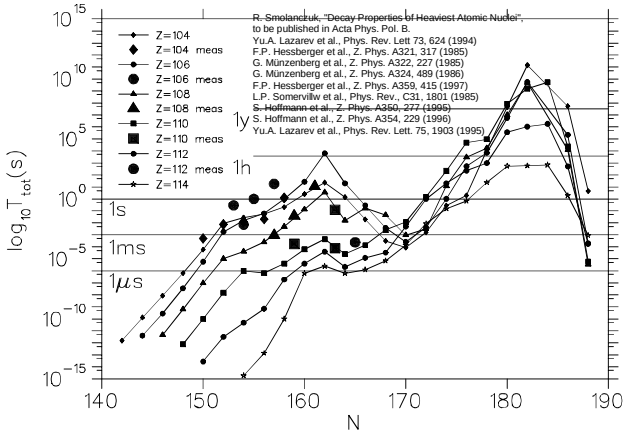

Figure 1: Calculated half-lifetimes for the elements Z=104 -114 in comparison to measurements [6].

In fig.1 is shown with very neutron rich isotopes as projectiles and implanted in a target very heavy elements with higher neutron numbers (165-180) can be produced, which lifetimes are extended to minutes and hours compared to the fusion products produced at GSI. The peak at lower neutron numbers (N=162) is derived from effects of magic shell closure.

2 ACCELERATION CONCEPT AND BEAM DYNAMICS

To achieve adequate final energies close to the Coulomb barrier several acceleration schemes have been proposed [2,7]. For MAFF the singly charged ions out of the reactor source will be injected into a high charge state ion source, presumably an electron cyclotron resonance ion source (ECRIS) and charge bred to an A/q < 6.3. The LINAC of MAFF is sketched in fig.2. The key parameters of the LINAC are shown in Table1.

2.1 The resonant structures

The LINAC consists on an RFQ which accelerates the ions from 2.5 keV/u to 300 keV/u which requires a rod

voltage of 59 kV for the present design which is similar to the REX-ISOLDE RFQ. First examination have been carried out [8] to use a quadrupole structure which is driven by an IH-resonator. Such an RFQ will be used for the high current injector at GSI. The booster LINAC consists of three IH-cavities where a jump in frequency is done at the second tank to reduce the length of the accelerator [2].

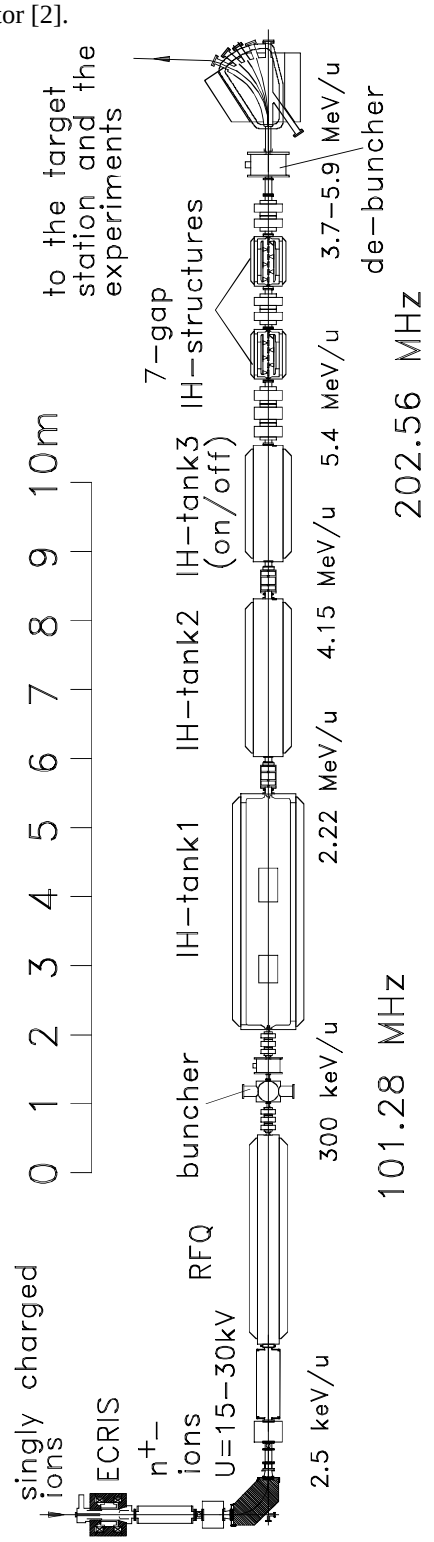

Figure 2: Lay-out of the MAFF LINAC.

Table 1: Key parameters of the MAFF LINAC

resonance frequency	101.28 / 202.56 MHz
injection energy	2.5 keV/u
final energy	3.7 - 5.9 MeV/u
A/q	< 6.3
max. duty cycle	10%
required energy spread at the target	<0.2 %
beam intensities	$4*10^{11}$ ions/s (^{91}Kr)
mass range (A)	75 -150
elements (Z)	Ni - Eu (28 - 63)

2.2 Variation of the final energy

The variation of the final energy over the large range of 2.2 MeV/u is done by using two 7-gap resonators and the tank 3 of the booster LINAC. So deceleration and acceleration is done at two different injection energies with the same 7-gap accelerators at 4.15 and 5.4 MeV/u. The 7-gap resonators of the MAFF-LINAC are IH-cavities in order to reach higher resonator voltages (2.1 MV) in comparison to the cavities used for REX-ISOLDE [9]. The 0°-synchronous particle structure is used in the beam dynamics, which means that the mean particle of the bunch will reach the center gap at 0° phase of the RF. The voltage of tank3 of the booster LINAC must be twice the effective voltage of the 7-gap resonators. In order to achieve the required low energy spread de-buncher is required after the second 7-gap cavity.

2.3 Beam dynamics

Beam dynamics calculations have been carried out to prove the possibility of the energy adjustment with only two 7-gap resonators.

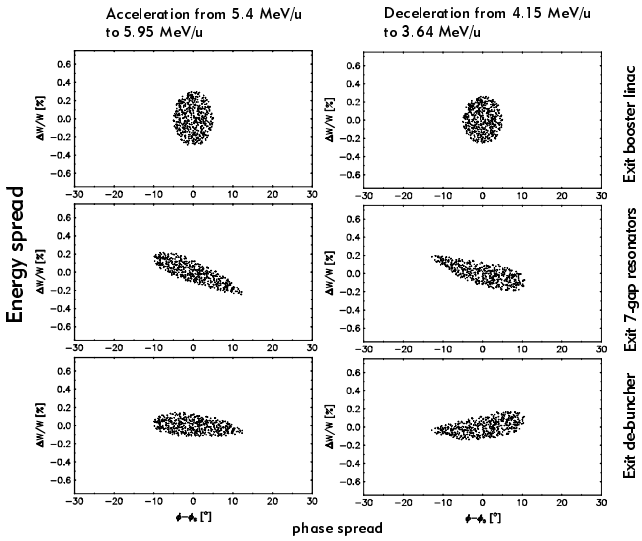

Figure 3: Development of the longitudinal phase space for the minimum and maximum energy of the MAFF LINAC

Fig. 3 shows calculations of the development of the longitudinal phase space of the beam from the exit of tank3 of the booster to the exit of the de-buncher. Table 2 summarizes the energies which can be achieved by deceleration and acceleration with both 7-gap cavities.

For the transverse emittances, the typical emittance of an ECRIS of about 0.6 π mm mrad (normalized) has been assumed. For the longitudinal phase space at the exit of the booster a phase spread of $\pm 5^{\circ}$ and an energy spread of +0.2% have been taken into account. From fig. 3 it can be seen that even in the worst case of maximum deceleration at lower starting energy the low energy spread at the exit can be provided.

Table 2: Achievable energies using the two 7-gap IH-resonators for deceleration and post acceleration.

E_{inj} [MeV/u]	E_{min} [MeV/u]	E_{max} [MeV/u]
4.15	3.64	4.77
5.4	4.78	5.94

3 CAVITY DESIGN AND MAFIA CALCULATIONS

The structures which will be examined first are the IH-RFQ and the 7-gap-IH-resonators. In order to get some cavity characteristics both resonator types have been examined by MAFIA calculations.

3.1 The IH-RFQ

The investigation of an IH-type RFQ at frequencies around 100 MHz is motivated by a higher shunt impedance compared to a 4-rod RFQ and that a direct rod cooling is not required due to a higher number of stems and herewith lower electrode currents. Fig.4 shows the 3m MAFIA model of the IH-RFQ. The parameters determined with MAFIA [8] are an R_p-value of 288 kΩm, a quality factor of 11657 at a frequency of 93.5 MHz, concerning a stem distance of 8 cm.

Figure 4: MAFIA model of the 3m IH-RFQ for the MAFF LINAC.

3.2 The 7-gap IH-resonator

The central issue of the MAFF-LINAC are the 7-gap IH-cavities. For the beam dynamics calculations a total resonator voltage of 2.1 MV have been assumed. For an incoupled power of 80 kW a shunt impedance of 110 MΩ/m is required to fulfill these requirements. Fig.5 shows the MAFIA model of one half of the 7-gap-IH-cavity. The cell length is 74 mm, the drift tube length 50 mm. The half shell radius is about 135 mm. The calculated quality factor is 15000, the shunt impedance about 300 MΩ/m. The calculated resonance frequency of the cavity was 225 MHz. Model measurements will done soon to prove the MAFIA calculations of the IH-RFQ and of the 7-gap cavity. Assuming the calculated values, the maximum resonator voltage of 2.1 MV can reached with low rf-power of about 50 kW.

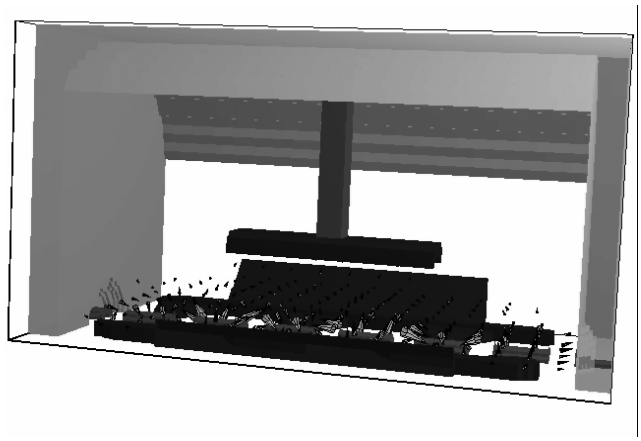

Figure 5: MAFIA model of one half of the 0.55m IH-7-gap resonator for the MAFF LINAC. Shown is the electric field of the TE_{111} mode.

REFERENCES

[1] D. Habs et al., „The Munich Fission Fragment Accelerator“, *Nucl. Phys.* **A616** 39c (1997).

[2] O. Kester et al., „Fission Fragment Accelerators for the Grenoble and Munich High Flux Reactors,“ *Nucl. Instrum. and Meth.* **B139**, 28-36 (1998).

[3] P. Thirolf et al., „Concept for a High Resolution Online Mass Separator of the Munich Fission Fragment Accelerator“, *Nucl. Instrum and Meth.* **B 126**, 242-245 (1997).

[4] Proc. of the International Workshop on Research with Fission Fragments, Benedikbeuern, Germany, ed. by T. von Egidy, D. Habs, F.J. Hartmann, K.E.G. Löbner and H. Nifenecker, World Scientific, 1997.

[5] PIAFE Collaboration, Technical report of the project covering the period 1993-1996, ISN report ISN97-52.

[6] R. Smolanczuk, „Decay Properties of Heaviest Atomic Auclei“, subm. to *Acta Phys. Pol.* B., 1998.

[7] O. Kester and J. L. Belmont, „Charge Breeding and Post Acceleration“, PIAFE project report, ed. U. Köster and J.A. Pinston, March 1998.

[8] T. Sieber et al., „RFQ-Accelerators for Radioactive Ion Beams“, proc. EPAC98, Stockholm, June 1998.

[9] H. Podlech et al., „The 7-Gap Resonator-Accelerator for the REX-ISOLDE-Experiment at CERN“, *Nucl. Instrum. and Meth.* **B139**, 447-450 (1998).

FIELD DESCRIPTION IN AN RFQ AND ITS EFFECT ON BEAM DYNAMICS

R. Ferdinand, R. Duperrier, J-M. Lagniel, P. Mattei
S. Nath*
CEA-Saclay/DSM/DAPNIA/SEA, Bat 706, 91191 GIF-sur-Yvette, FRANCE
* On sabbatical from LANL, Los Alamos, NM, USA.

Abstract

In a Radio Frequency Quadrupole (RFQ) linac, the electric field distribution is generated by four poles arranged symmetrically around a central z-axis. It's a customary practice to use a formulation based on cylindrical harmonics. That leads to inaccurate description of the fields near the boundary walls. Here, we present an analysis of errors based on an alternate numerical method to map the field correctly in the entire space between the vanes. This is especially important for high currents when the beam tends to fill nearly all available cavity-space [1]. The difference in the field-description and its effect on beam dynamics in a typical RFQ end cell will be presented. Two ways for calculating harmonic coefficients, the harmonic analysis and the fit to the cell geometry, are described.

1 INTRODUCTION

Radio Frequency Quadrupole (RFQ) linacs are widely used in the accelerator community. They have the remarkable capability of simultaneously bunching low-energy ion beams and accelerating them up to the MeV range. Several types of vane-tip geometries have been considered, and it is important to know the electric fields produced by these various geometries. In R.F.Q. linacs, the impedance in the beam zone is such that the electrodes can be considered as isopotential surfaces, and the vector potential can be ignored. Solving the Laplace equation in cylindrical coordinates, the electric potential seems to be able to be represented by the expansion:

$$U(r,\theta,z) = \frac{V}{2}\left(\sum_{p} A_{0(2p+1)} r^{2(2p+1)} \cos[2(2p+1)\theta] + \sum_{m,n} A_{nm} I_{2n}(mkr)\cos(2n\theta)\cos(mkz)\right)$$

The first eight terms give satisfactory accuracy [2]. Different methods are found in literature for calculating the coefficients of the expansion. The most common ones are the projection on the base [3] and the fit to the cell geometry [4,5]. This paper is a discussion on the accuracy that can be achieved with these two different methods.

2 CALCULATION OF THE ELECTRIC POTENTIAL IN A RFQ CELL BY TOSCA

We have first simulated the electric potential in a RFQ cell with the code TOSCA[1] (Figure 1).

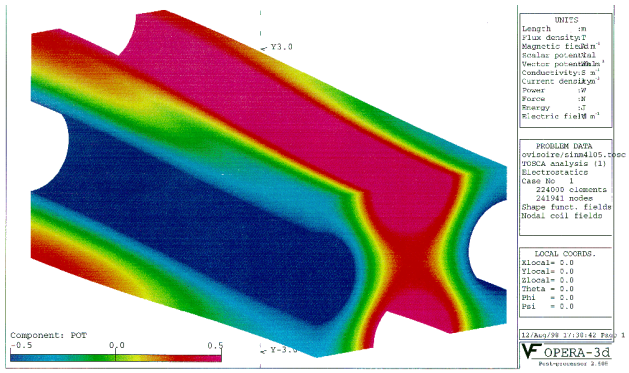

Figure 1: Electric potential in a RFQ cell.

This simulation will be the reference for validation and calculation in following stages. A typical RFQ end cell is chosen. The characteristics of the cell are:

- ρ = 0.89 (transverse radius of curvature)
- L_c = 11 (cell length)
- m = 2 (modulation factor)
- Sinusoidal profile in longitudinal direction

All distances are in R_0 units. The mesh of this simulation has been optimized for calculation of the peak surface electric field [6].

3 CALCULATION OF THE COEFFICIENTS BY PROJECTION ON THE BASE

To use the properties of harmonic analysis, we need to consider a limited space in which the boundaries satisfy the homogeneous conditions [7]. In cylindrical co-ordinates, the volume is a cylinder. The maximum value for the radius of this cylinder is "a", the minimum

[1] Vector Fields code for electromagnetic design

aperture radius. The coefficients can then be determined by the projection of the solution calculated by TOSCA on the lateral surface of this cylinder:

$$A_{0m} = \frac{16}{\pi V a^{2m} L_c} \int_0^{\frac{\pi}{2}} \int_0^{L_c} U(a,\theta,z).\cos(2m\theta).d\theta.dz$$

$$A_{n0} = \frac{8}{\pi V I_0(nka) L_c} \int_0^{\frac{\pi}{2}} \int_0^{L_c} U(a,\theta,z).\cos(nkz).d\theta.dz$$

$$A_{nm} = \frac{16}{\pi V I_{2m}(nka) L_c} \int_0^{\frac{\pi}{2}} \int_0^{L_c} U(a,\theta,z).\cos(2m\theta).\cos(nkz).d\theta.dz$$

Due to symmetry, only one quarter of a RFQ structure is necessary for the calculations. The results for the eight first order terms are shown in Table 1.

Table 1

A_{01}	A_{03}	A_{10}	A_{12}
0.9267	0.0012	0.6006	307.6125
A_{21}	A_{23}	A_{30}	A_{32}
-0.8337	-30753.6794	-0.0109	-7.0949

The difference between the real potential and the values obtained from the expansion derived coefficients is shown in Figure 2.

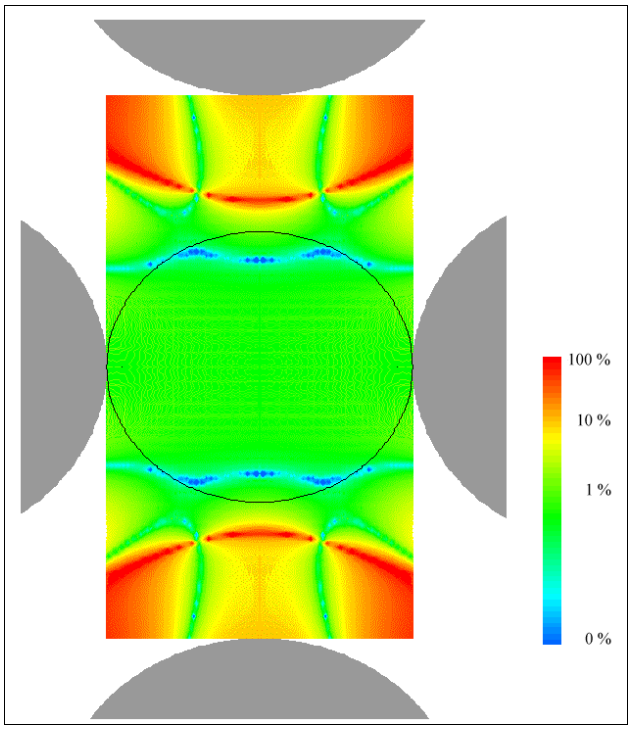

Figure 2: Difference between the real potential and the eight term potential. The accuracy is poor outside the cylinder used for calculations (black circle). A logarithmic scale is used.

It is apparent that the solution can't be extrapolated outside the volume used for integration. However, the accuracy is quite satisfactory with in the cylinder as is shown in Figure 3.

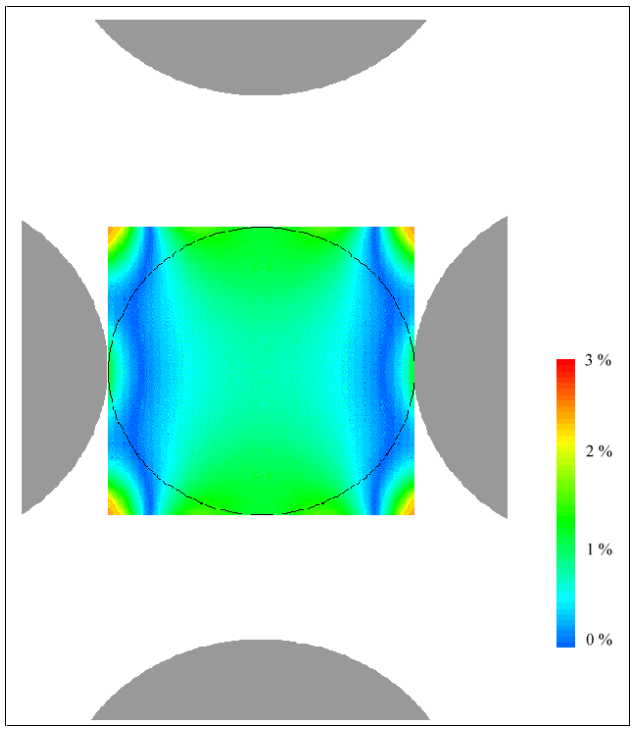

Figure 3: Same as in Figure 2 with a close-up view around the beam axis. A linear scale is used.

4 CALCULATION OF THE COEFFICIENTS BY FIT TO THE CELL GEOMETRY

The coefficients are calculated by the least-squares fit [8] using the isopotential surfaces defined by the conductors. This method is faster than the previous one for calculation of the expansion's coefficients. Table 2 contains the results of the fit obtained using the code MATHEMATICA[2].

Table 2

A_{01}	A_{03}	A_{10}	A_{12}
0.9587	0.0211	0.6064	3489.55
A_{21}	A_{23}	A_{30}	A_{32}
-0.5960	3493.32	-0.0093	-4.1060

The difference between the real potential and that obtained form the expansion using fit is shown in Figure 4.

[2] Environment for technical and mathematical computing.

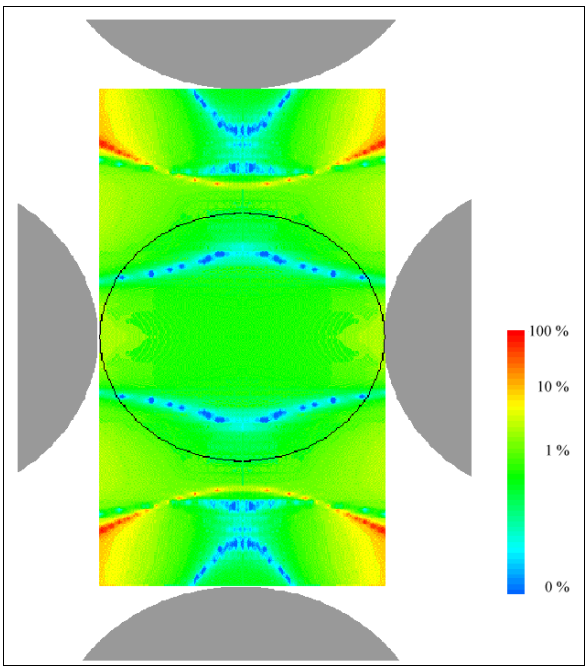

Figure 4: Difference between the real potential and the eight term potential with fit coefficients. A logarithmic scale is used.

The accuracy is better outside the cylinder used for projections (black circle). However, the deviation is about a few percent everywhere, which exceeds the tolerance for linacs (≈1% of maximum error).

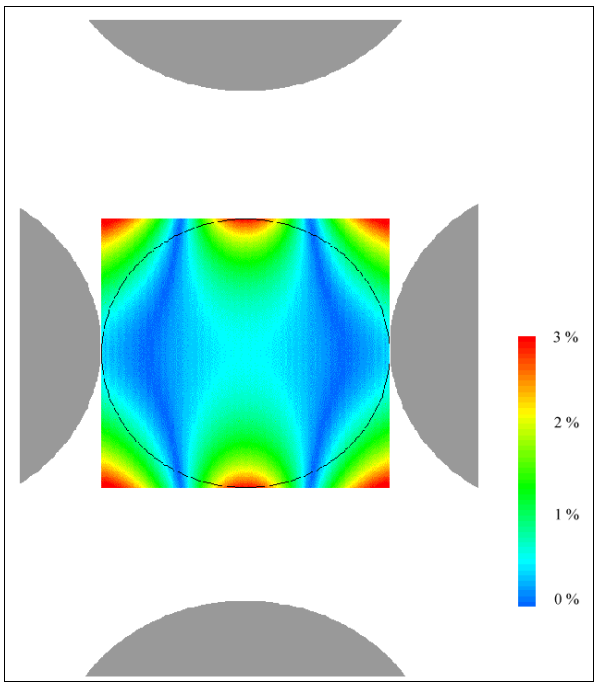

Figure 5: The same as in Figure 3 with a close-up view around the beam axis. A linear scale is used.

5 CONSEQUENCE ON BEAM DYNAMICS

In order to assess the influence of the difference induced by these two methods, beam dynamics simulation were done with particles that lay outside the cylinder of reference. 1035 particles of 1 MeV are uniformly distributed in a square with coordinates ($x = 0$, a; $y = a$, $m \times a$; $z = 0$) without any energy spread and zero transverse speed component for the injection. The transport is realized without any space charge and image effects. The intervane voltage is equal to 97 kV. The transmissions for three cases are summarized in Table 3.

Table 3

Real Fields	Projection	Fit
16.04 %	40.97 %	49.37 %

6 CONCLUSION

The projection on a cylindrical harmonic base gives the best accuracy of field around the beam axis. The fit to cell geometry by least-squares method doesn't give accuracy better than a few percent. However, regardless of the method used, cylindrical harmonics don't allow simulation with some accuracy in all region of the beam [2]. An alternative is to simulate the fields numerically. This is time consuming and needs a lot of memory to store the mesh for several cells. A good compromise would be to use 8 terms obtained by projection around the z-axis and a numerical mapping for the halo. A reduced mesh size is necessary in such case.

7 REFERENCES

[1] B. BONDAREV, A. DURKIN and S.V. VINOGRADOV, «Multilevel Codes RFQ.3L For RFQ Designing»,. Proc. IFMIF Accelerator Team PARIS Meeting, CDE Workshop May 26-30,(1997).

[2] R. DUPERRIER, «Le potentiel électrique dans la zone utile d'un RFQ»,. CEA/DSM/SEA/9844, (1998).

[3] K.R. CRANDALL, «Effects of vane-tip geometry on the electric fields in Radio-Frequency Quadrupole linacs», LANL report LA-9695-MS, (1983).

[4] A. LETCHFORD and A. SCHEMPP, «A comparison of 4-rod and 4-vane RFQ fields», EPAC Stockholm (1998).

[5] A. M. TODD and M. F. REUSCH, «RFQ beam dynamics model development», Linear Acc. Conf.., 326-328 (1990).

[6] R. DUPERRIER, «Calcul du champ électrique maximum dans une cellule RFQ»,.CEA/DSM/SEA/9843, (1998).

[7] E. DURAND, «Electrostatique, Tome II, Problèmes généraux, Conducteurs», Masson & C^{ie} (1964).

[8] W.E. MILNE, «Numerical calculus, approximations interpolation, finite differences, numerical integration, and curve fitting», Princeton University Press (1949).

WAKE FIELD EFFECTS IN APT LINAC*

Sergey S. Kurennoy
LANSCE-1, Los Alamos National Laboratory, Los Alamos, NM 87545, USA

Abstract

The 1.7-GeV 100-mA CW proton linac is now under design for the Accelerator Production of Tritium (APT) Project [1]. The high current leads to stringent restrictions on allowable beam losses (< 1 nA/m), that requires analyzing carefully all possible loss sources. While wake-field effects are usually considered negligible in proton linacs, we study these effects for the APT to exclude potential problems at such a high current. Loss factors and resonance frequency spectra of various discontinuities of the vacuum chamber are investigated, both analytically and using 2-D and 3-D simulation codes with a single bunch as well as with many bunches. Here we concentrate on two features specific to the APT linac: loss factors for the design $\beta < 1$ and CW beam structure.

1 INTRODUCTION

A wake-field analysis for a high-intensity accelerator includes wake computations, followed by calculations of loss factors and heating due to various elements of the vacuum chamber. The wake fields are typically computed with time-domain codes like ABCI [2] or MAFIA [3]. However, these codes are only applicable for ultrarelativistic bunches with $\beta = v/c = 1$. Two specific features of proton (or H^-) high-intensity linacs are essential for the wake-field analysis: first, β is significantly less than 1 for the most part of the machine, and second, the beam is either CW (in APT) or consists of macropulses containing many regularly spaced bunches (spallation neutron sources). Usual $\beta = 1$ estimates, while useful, can be quite different from those for the design β values, e.g., [4]. In particular, the resonance impedances and corresponding loss factors can strongly depend on β. Frequency-domain calculations can provide an answer for a given $\beta < 1$, but they require information on individual modes, and are typically limited to just a few lowest ones. In Sect. 2, we consider β-dependence of the loss factors for lowest modes in the APT 5-cell superconducting (SC) cavities.

Due to the CW beam structure, the beam frequency spectrum is concentrated only near the multiples of the bunch repetition frequency f_b. While the spectrum envelope is still defined by the bunch shape, it rolls off at frequencies many times higher than f_b, due to a very short bunch length. Therefore, an important question is whether any higher-order mode (HOM) has its frequency close to a multiple of f_b. The presence of such modes, especially at relatively low frequencies, can lead to undesired coherent effects. One can use time-domain computations with multiple bunches to answer this question. The idea is to apply a time-domain code with a few identical bunches at $\beta = 1$, but to set the bunch spacing s to $s = c/f_b$ for having the correct bunch repetition frequency. Since the resonance frequencies are essentially independent of β, so is a conclusion from such simulations. In Sect. 3 we compute the wakes in the APT 5-cell SC cavities varying the number of bunches in the bunch train, and look for coherent wake-field effects.

* Work supported by the US Department of Energy

2 LOSS FACTORS VERSUS β

For a Gaussian bunch of rms length $2l$, the loss factor k_s for the s-th cavity mode having the frequency ω_s depends on β as (see [4] for more details)

$$\frac{k_s(\beta,l)}{k_s(1,l)} = \exp\left[-\left(\frac{\omega_s l}{c\beta\gamma}\right)^2\right]\frac{|I_s(\beta,\omega_s)|^2}{|I_s(1,\omega_s)|^2}\,. \qquad (1)$$

Here $I_s(\beta,\omega) = \int_L dz\exp(-i\omega z/\beta c)E_{sz}(0,z)$ is the overlap integral, $\gamma = 1/\sqrt{1-\beta^2}$, and $E_{sz}(0,z)$ is the mode longitudinal electric field on the chamber axis.

For 5-cell APT SC cavities the lowest resonances are split into 5 modes which differ by phase advance per cell $\Delta\Phi$, and their frequencies are a few percent apart [5], see Table 1. MAFIA-computed on-axis fields of these modes [5] are used to calculate numerically overlap integrals in Eq. (1) and to find the loss factors for a given β. The results for the lowest monopole modes are presented in Table 1. We are mostly concerned about only these two resonance bands, since the higher modes are above the cutoff and can propagate out of the cavity depositing most of their energy in the beam pipes. Our results for the design values of β are in agreement with those obtained in [5]. Remarkably, the total loss factors for a given resonance band in Table 1 are lower for the design β than at $\beta = 1$, which is not always the case, see [4] for detail. The only exception here is the TM_{020} band for the $\beta = 0.82$ cavity, but it includes some propagating modes, and its contribution is very small.

Time-domain simulations with ABCI [2] give us the loss factor of a bunch at $\beta = 1$. The loss factor spectrum for the $\beta = 0.64$ cavity, integrated up to a given frequency, has two sharp steps, 0.5 V/pC near 700 MHz, and about 0.1 V/pC near 1400 MHz. They correspond to the two bands of the trapped monopole modes in the cavity, cf. Table 1. The totals for the TM_{010} and TM_{020} bands for $\beta = 1$ in Table 1 agree very well with the time-domain results.

The β-dependence of the loss factor for two TM_{010} modes — 0-mode and fundamental, π-mode — is shown in Fig. 1. Obviously, the shunt impedance (and the loss factor) dependence on β is strongly influenced by the mode field pattern.

Table 1: Loss Factors (in V/pC) in APT 5-cell Cavities

$\Delta\Phi$	f, MHz	$k(\beta)$	$k(1)$	$k(\beta)/k(1)$
$\beta = 0.64$, TM_{010}-band				
0	681.6	$7.2\,10^{-6}$	$3.7\,10^{-4}$	0.020
$2\pi/5$	686.5	$4.8\,10^{-5}$	$2.9\,10^{-2}$	0.0016
$3\pi/5$	692.6	$1.1\,10^{-4}$	0.218	0.0005
$4\pi/5$	697.6	$1.2\,10^{-3}$	0.250	0.0049
π	699.5	0.184	$9.2\,10^{-3}$	19.92
Total		0.185	0.507	0.365
$\beta = 0.64$, TM_{020}-band				
0	1396.8	$6.5\,10^{-4}$	$5.4\,10^{-4}$	1.187
$2\pi/5$	1410.7	$1.2\,10^{-6}$	$9.0\,10^{-4}$	0.0014
$3\pi/5$	1432.7	$1.8\,10^{-5}$	0.0173	0.0011
$4\pi/5$	1458.8	$8.0\,10^{-7}$	0.0578	$1.4\,10^{-5}$
π	1481.0	$3.5\,10^{-7}$	0.0095	$3.7\,10^{-5}$
Total		$6.7\,10^{-4}$	0.086	$7.8\,10^{-3}$
$\beta = 0.82$, TM_{010}-band				
0	674.2	$0.3\,10^{-6}$	$6.9\,10^{-4}$	$4.5\,10^{-4}$
$2\pi/5$	681.2	$7.3\,10^{-5}$	$1.6\,10^{-5}$	4.64
$3\pi/5$	689.9	$1.8\,10^{-6}$	0.034	$5.1\,10^{-5}$
$4\pi/5$	697.2	$1.3\,10^{-3}$	0.220	$5.9\,10^{-3}$
π	699.9	0.285	0.240	1.188
Total		0.286	0.494	0.579
$\beta = 0.82$, TM_{020}-band				
0	1357.7	$4.2\,10^{-5}$	$0.8\,10^{-6}$	52.4
$2\pi/5$	1367.7	$1.4\,10^{-4}$	$8.0\,10^{-5}$	1.71
$3\pi/5$	1384.5	$1.6\,10^{-6}$	$1.4\,10^{-4}$	0.011
$4\pi/5^{*}$	1409.6	$8.0\,10^{-7}$	$1.3\,10^{-3}$	$5.6\,10^{-3}$
π^{**}	1436.9	$1.6\,10^{-2}$	$2.2\,10^{-3}$	7.5
Total		$1.6\,10^{-2}$	$3.7\,10^{-3}$	4.32

*Mode near the cutoff.

**Propagating mode, above the cutoff.

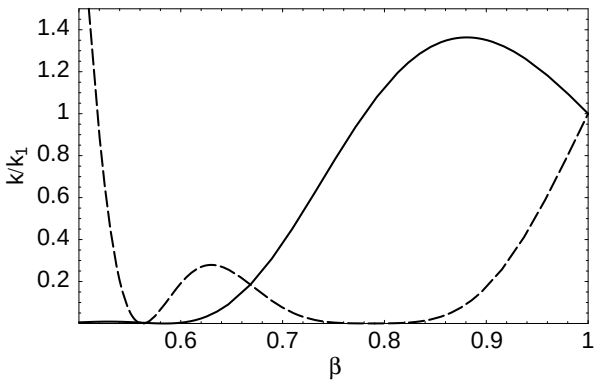

Figure 1: Loss factor ratio (1) versus β for 0-mode (dashed) and π-mode in the 5-cell APT $\beta = 0.82$ cavity.

3 MULTIPLE-BUNCH EFFECTS

Wake potentials of a train of a few identical Gaussian bunches passing through 5-cell APT SC cavities have been computed with the code ABCI [2]. Cavity parameters are given in [6], the bunch rms length was chosen to be 4.5 mm in the β=0.82 section of the linac, and 3.5 mm for β=0.64. While these bunches have β=1, their separation is set to s=0.85657 m, which gives the proper bunch repetition frequency f_b=350 MHz.

We study the loss factors for the 5-cell APT SC cavities as a function of the number of bunches N_b in the bunch train. The loss factor per bunch is expected to tend to a constant for incoherent wakes, but it should increase linearly when wakes are coherent. The coherent effects would occur if higher-mode resonances are close to multiples of f_b. The results for the transverse loss factor k_{tr} per bunch are shown in Fig. 2, both for β=0.64 and β=0.82 cavities. As one can see, k_{tr} reaches its asymptotic already for N_b between 5 and 10 in the case of β=0.82. This asymptotic value is, in fact, lower than k_{tr} for a single bunch. For β=0.64, however, we observe an almost linear growth up to N_b about 20, and only after that the transverse loss factor per bunch saturates. Therefore, in the β=0.64 cavity higher-order dipole resonances are closer to multiples of f_b than those for β=0.82. For comparison, the longitudinal loss factor per bunch for both cavities increases linearly as N_b increases. This is, of course, due to the fundamental accelerating mode of the cavity at 700 MHz. The maximal values of the transverse wake potentials also saturate as N_b increases, unlike the longitudinal ones, see [7].

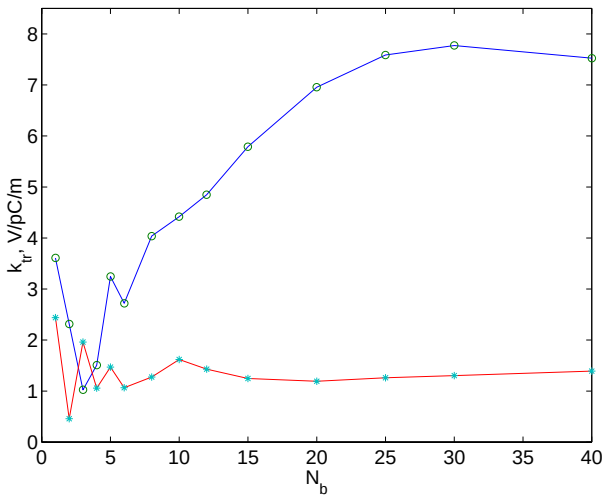

Figure 2: Transverse loss factor per bunch for 5-cell APT SC cavities versus the number of bunches: circles for $\beta = 0.64$, stars for $\beta = 0.82$.

As the number of bunches in the train increases, its frequency spectrum is getting more and more concentrated near the multiples of the bunch repetition frequency. Stronger peaks in the wake power spectrum for a relatively long bunch train indicate the frequency regions where the cavity resonances are close to multiples of f_b=350 MHz. To identify such frequency ranges we plot in Fig. 3 the power spectra of the wake potentials produced by a 30-bunch train in the cavities. The wake potentials have been calculated for 30 m after the leading bunch; they include about 60,000 points, and their Fourier transforms have been performed with $N = 2^{16} = 64K$. One can see a regular

structure of peaks at multiples of f_b, as well as a peak near 950 MHz, which corresponds to the band of the TM110 dipole mode [5]. Comparison of the wake power spectra for different N_b shows that the magnitude of this last peak decreases quickly as one goes to longer and longer bunch trains, since there is a smaller and smaller excitation at this frequency. Comparing relative peak heights in the frequency spectra shows where higher-order modes are close to multiples of the bunch frequency. Obviously, it is the strong peak near 1750 MHz — the multiple of the bunch frequency — that produces a coherent increase of the dipole loss factor in the APT SC β=0.64 5-cell cavity. Fortunately, its resonance frequency is close to the cutoff frequency of the pipe, which means this resonance can be effectively damped by HOM power couplers. Nevertheless, a more detailed analysis of this frequency range with frequency-domain codes is required to identify the corresponding eigenmode(s), and take its (their) properties into account in designing HOM couplers.

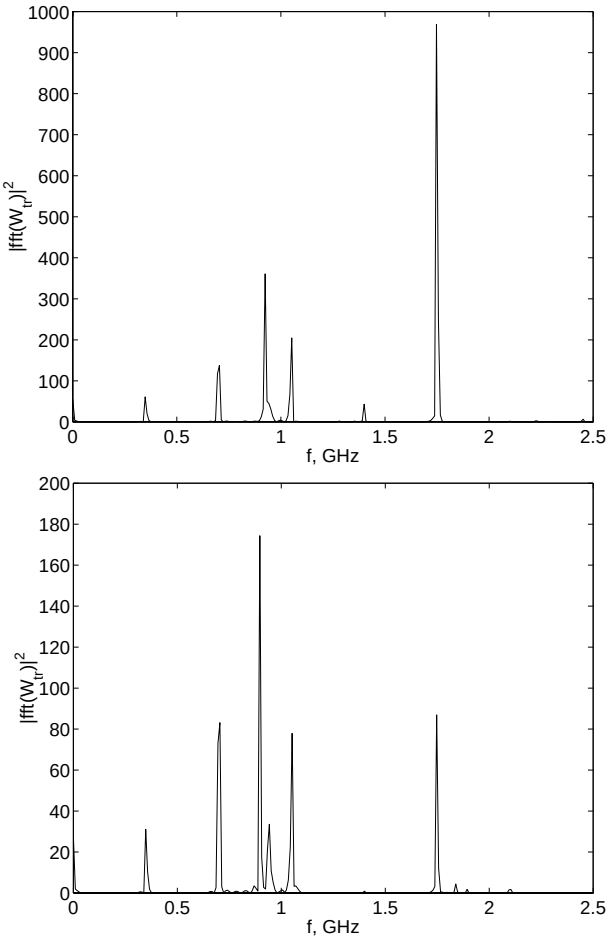

Figure 3: Power spectra of the transverse wake potentials for 30 bunches in the APT 5-cell cavities: $\beta = 0.64$ (top) and $\beta = 0.82$ (bottom).

Clearly, the potentially dangerous regions for the 5-cell β=0.64 APT SC cavities with respect to the dipole modes are around 1750 MHz and 1050 MHz, and for 5-cell β=0.82 cavities they are around 1750, 700, and 1050 MHz (but all those contributions are relatively weak). Also, some additional attention is probably required to the transverse modes near 950 MHz for β=0.64 and in the range 900–950 MHz for the β=0.82 cavities. While these frequencies are not close to a multiple of f_b, the corresponding dipole resonances are strong enough that their effects are observed even for rather long bunch trains.

A similar analysis has been performed for the longitudinal wakes, see [7] for detail. The power spectra of the monopole wakes are dominated by the fundamental mode at 700 MHz, but in a log plot one can see higher-mode peaks. There is one near 2100 MHz for β=0.64 cavities (since 2100 MHz is above the beam-pipe cutoff, one should expect a trapped monopole mode near this frequency), and two, near 1750 and 1050 MHz, for the β=0.82 case.

4 CONCLUSIONS

A simple approach to study HOM effects in cavities for CW or long-pulse non-ultrarelativistic ($\beta < 1$) beams is developed. Time-domain simulations with standard codes are applied to the bunch trains moving with β=1, but having a correct bunch repetition frequency f_b. As the number of bunches N_b increases, the details of the beam frequency spectrum, dependent both on β and N_b, become unessential since the cavity is excited mostly at multiples of f_b. This allows us to find potentially dangerous frequency ranges where HOM frequencies are close to multiples of f_b.

A further analysis with frequency-domain codes should be used to identify the modes in these frequency ranges. Computed fields of these HOMs are used then to calculate their loss factors for the design value of β and to take their properties into account in designing HOM couplers, if required.

Our main conclusion for the APT linac is that the only noticeable wake-field effect is the HOM heating of the 5-cell SC cavities. It has, however, an acceptable level and, in addition, will be taken care of by HOM couplers.

Useful discussions with R.L. Gluckstern, F.L. Krawczyk and T.P. Wangler are gratefully acknowledged.

5 REFERENCES

[1] G.P. Lawrence and T.P. Wangler, in Proceed. PAC97, Vancouver, BC (1997); also in LA-UR-97-2582, Los Alamos, 1997.

[2] Y.H. Chin, Report LBL-35258, Berkeley, 1994.

[3] T. Weiland et al., Proc. 1986 Lin. Acc. Conf., SLAC Report 303, p.282; *MAFIA Release 4.00* (CST, Darmstadt, 1997).

[4] S.S. Kurennoy, Report LA-CP-98-55, Los Alamos, 1998; in Proceed. EPAC98, Stockholm, Sweden (1998), p. 1294.

[5] F.L. Krawczyk, in Proceed. PAC97, Vancouver, BC (1997); also LA-UR-97-1710, Los Alamos, 1997.

[6] F.L. Krawczyk, et al., in Proceed. PAC97, Vancouver, BC (1997); also LA-UR-97-1700, Los Alamos, 1997.

[7] S.S. Kurennoy, Report LA-CP-98-151, Los Alamos, 1998; in Proceed. EPAC98, Stockholm, Sweden (1998), p. 1291.

DESIGN STUDIES OF THE DARHT PHASE II INJECTOR WITH THE GYMNOS PIC CODE*

W.M. Fawley, E. Henestroza
Lawrence Berkeley National Laboratory, Berkeley, CA 94720 USA
Y.-J. Chen, D.W. Hewett
Lawrence Livermore National Laboratory, Livermore, CA 94550 USA

Abstract

We have used the GYMNOS 2D (r-z) electro-/magnetostatic PIC simulation code to help design a high current, high brightness, 3.2-MV injector for the DARHT Phase II accelerator. GYMNOS is particularly noteworthy for its use of piece-wise linear approximations to curved boundaries within a regular orthogonal mesh, which aids in modeling complex surfaces. We present a number of comparisons between GYMNOS and EGUN results, both in terms of "coarse" parameters such as emitted current and beam envelope dynamics, and "fine" details such as the transverse phase space distribution.

1 INTRODUCTION

The DARHT Phase II accelerator is a 20-MV, 4-kA, induction linac to be built at LANL with a nominal pulse length of $2-\mu$s. This pulse will subsequently get chopped into four short duration ($\Delta\tau \sim 60$ ns) pulses which will then be focused onto a metallic converter for radiographic imaging purposes; a more detailed summary is available in Ref. [1]. Among the various challenging physics aspects of the injector and accelerator design is the need to produce a very low transverse emittance over the full temporal pulse width. At present, our goals for ε_n(edge) are $\leq 500\pi$ mm-mrad for the injector and $\leq 1200\pi$ mm-mrad at the x-ray converter approximately 20-m downstream of the accelerator. Success in this area for the injector requires, among other things, a very "quiet" and highly uniform emission surface, very careful design of the electrode geometry to minimize nonlinear electrostatic fields and to prevent unwanted electrical breakdown, and appropriate longitudinal shaping of the solenoidal magnetic field in the A-K gap and beyond to prevent radial oscillations of the beam from converting space charge energy into transverse emittance.

This paper presents the current status of LBNL/LLNL PIC simulations of the DARHT II injector with the time-dependent, azimuthally symmetric GYMNOS code[2] and compares its results with those obtained with the EGUN ray-tracing code[3]. GYMNOS is a fully relativistic, 2-1/2 D, electro- and magnetostatic code which uses an iterative ADI approach to solve the necessary elliptic field equations. Both electric and magnetic collective fields are determined, including the diamagnetic A_θ induced by beam rotation in external solenoidal focusing fields. GYMNOS employs the "Embedded Curved Boundary" (ECB) method[4] for representing curved boundaries via a piecewise linear approximation on a uniformly-spaced Cartesian mesh. The ECB method is far more detailed than simple staircase approximations to curved surfaces while remaining more computationally efficient than most adaptive mesh techniques.

We first discuss the overall injector geometry and compare the the steady-state GYMNOS and EGUN beam envelope results. We then examine details of the emission near the cathode/Pierce shroud boundary where apparent limitations of the simulation grid resolution and/or present ECB formulation results in difficulties when modeling extremely low emittance beams.

2 INJECTOR GEOMETRY AND FULL VOLTAGE CURRENT FLOW

In order to minimize the possibility of electrical breakdown in the 30-cm A-K gap, the present injector design uses a relatively large (10-cm radius), heated dispenser cathode surrounded by a Pierce shroud extending radially outwards to 40 cm. "Velvet" cathodes, while more robust in terms of insensitivity to vacuum contamination, are believed to produce too transversely warm and possibly insufficiently uniform emission to satisfy the high brightness requirements. The anode surface facing the cathode has a radius of curvature of 8 cm and 16 cm for r less than and greater than 20 cm, respectively. At a 3.2 MV potential drop, the peak electric field is approximately 162 kV/cm on the shroud and 189 kV/cm on the anode. The anode entrance opening radius asymptotes to 12.5 cm. Within the anode is a solenoid magnet, typically run at a current sufficient to produce a peak field of about 500 G to keep the beam well-confined radially as it drifts from the anode into the first accelerator cell magnets. Equidistant behind the cathode is an identical bucking solenoid to zero out any B_z field at the emission surface.

Given this configuration, the EGUN code predicts a steady-state beam current of 4.1 kA for a nominal injector voltage of 3.2 MV. The beam envelope radius smoothly shrinks down to approximately 7 cm as it passes into the anode opening and remains at that radius until it enters the first accelerator cell another 40 cm downstream. In these runs the beam rays were emitted at the 5 kV potential con-

* Work supported by U.S. DOE under Contracts No. DE-AC03-76SF00098 (LBNL) and W-7405-ENG-48 (LLNL).

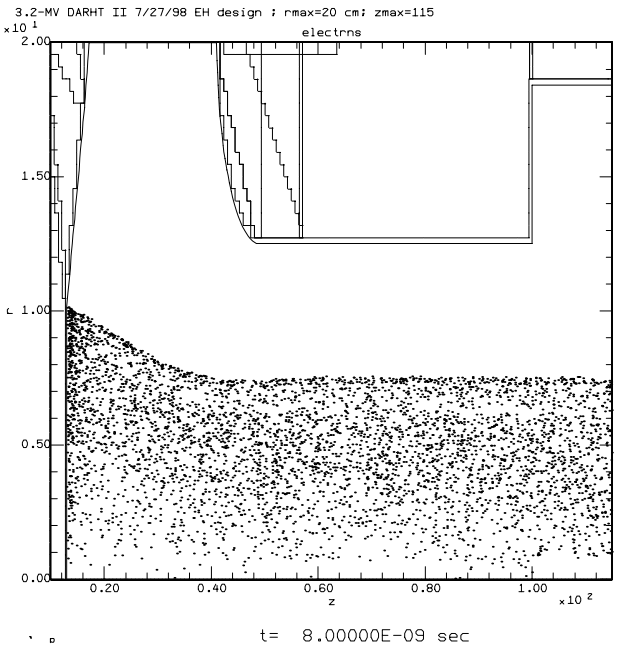

Figure 1: $r - z$ particle scatter plot from a GYMNOS simulation of the DARHT II injector

tour, approximately 4 mm downstream of the cathode surface, and very fine ($\Delta r = \Delta z = 1$ mm) gridding was used. More information on the design and EGUN results are available in Ref. [5].

GYMNOS runs with the same injector parameters show similar but not identical results. Since GYMNOS is a "normal" time-dependent PIC code, it is necessary to gradually ramp up the electrode voltages to minimize "shock" excitation of beam and electric field oscillations. We found that a 2-ns voltage risetime gave a smooth increase of emitted beam current and minimal radial bounces and/or particle reflection from virtual cathodes. The beam envelope evolution with z is quite similar to that predicted by EGUN. Figure 1 displays an r-z scatter plot of a GYMNOS simulation at $t = 8$ ns. Of the actual 100,000+ macroparticles in the simulation volume at this time, only ~10% are shown. For the simulation volume of 120 cm in z and 20 m in r, we used 126 and 45 grid points in z and r, respectively, leading to $\Delta r = 0.45$ cm and $\Delta z = 0.7$ cm.

Despite the good agreement in the beam envelope dynamics, there is a surprising disagreement in the magnitude of the emitted current with GYMNOS results being consistently $\sim 10 - 15\%$ higher. Some numerical tests have shown that while this discrepancy is insensitive to the grid cell size, there is an apparent sensitivity of I_{emit} to details of the macroparticle "birth" algorithm for space-charge limited flow. In each timestep GYMNOS places newly born particles within a "sheath" approximately one longitudinal grid cell wide downsteam of the emitting surface. As the sheath width is decreased by up to a factor of four, the total emitted current can change by some tens of percent. Since other tests at non-relativistic energies and previous GYMNOS modeling of ion injectors[2] showed

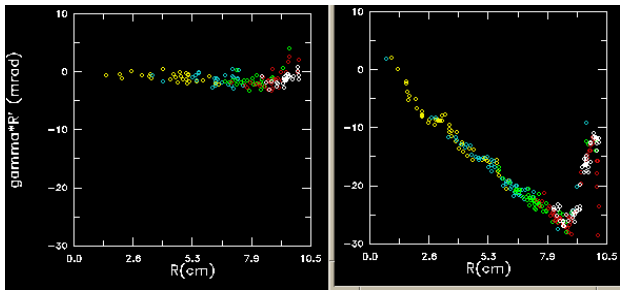

Figure 2: $r - \gamma r'$ snapshots at $z = 13.05$ and $z = 13.65$ cm for the same simulation shown in Fig. 1; the cathode surface is at $z = 13.0$ cm. Each plot includes particles within 0.05 cm of the nominal z position. The ordinate ranges from -30 to 10 mrad, the abscissa from 0 to 10.5 cm.

good agreement between Child's Law and the emitted current, we suspect that the emission algorithm need improvements for accurate resolution of the current sheath density and velocity profile for the relativistic injector energies relevant to DARHT.

3 PHASE SPACE EVOLUTION AND MODELING DIFFICULTIES NEAR THE CATHODE/SHROUD BOUNDARY

Given the high brightness wanted from the DARHT II injector, a great deal of effort has been spent on optimizing the gap geometry and solenoidal focusing profile downstream. At present, EGUN predicts that the normalized emittance jumps to approximately 1000 pi mm-mrad some 50 cm downstream of the cathode, stays this high for about one additional meter, and then (according further single-slice transport by the SLICE code[6]) oscillates and damps down to an exit emittance of ~500 pi mm-mrad at the exit of the first 8-cell block 5-m downstream of the cathode. These numerical values correspond to the "edge" emittance, defined as $4 \times \varepsilon_{RMS}$.

GYMNOS runs, which have been limited by CPU constraints to ~1 m of transport beyond the cathode, have shown consistently higher transverse emittance values, generally by a factor of 2-3X. After some development of post-processing tools to permit detailed investigations of particle dump "snapshots" (we cannot stress too highly how useful tools like these are in examining the fine details available in multi-dimensional PIC codes), we discovered that transverse phase space anomalies began appearing immediately downstream of the cathode surface. Specifically, a "hook" in $r - \gamma r'$ develops for $r \geq 9.0$ cm such that the smoothly increasing radial convergence for lesser values of r suddenly drops by a factor of two. An example of this behavior is shown in the $r - \gamma r'$ phase plots of Fig. 2, 0.5 and 6.5 mm downstream of the cathode. The equivalent normalized transverse emittance increase is close to 1000 pi mm-mrad within 1 cm downstream of the cathode, many times greater than found in the EGUN simulations.

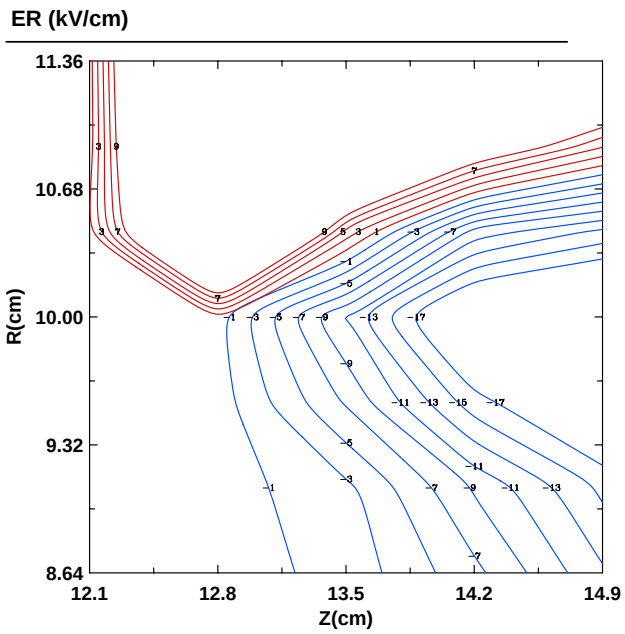

Figure 3: Contours of E_r near the outer radial boundary of the cathode. Between $r = 8.6$ and $r = 10.0$ cm the magnitude of this defocusing field nearly triples, leading to strongly nonlinear behavior in the electron beam's transverse phase space. Most of the nonlinearity occurs within $1 - 2\,\Delta r$ of the beam edge.

The origin of the hook drives from a strong increase in the defocusing E_r at radii just inside the cathode-Pierce shroud boundary. Inspection of the $r - z$ contours of the electrostatic potential show an enhanced "bowing" inward (toward smaller z) for $r \geq 9.5$ cm, one radial grid cell below the cathode/shroud boundary at 10.0 cm. At present, we believe the underlying cause for the bowing in Φ and nonlinear E_r dependence is a numerical artifact arising from a unwanted interaction of the 5-7 mm grid resolution, the sharp edge of the emitted beam, and the "kink" in the zero potential surface at the cathode-shroud boundary as modeled by the ECB formulation. We hope to find an appropriate solution that will not require decreasing the grid resolution to the 1-mm size of the equivalent EGUN calculations. Otherwise, the required number of grid points and macroparticles might jump by greater than an order of magnitude.

4 CONCLUSIONS

The underlying rationale for our use of GYMNOS in simulating the DARHT II injector behavior was to provide an independent check of both the EGUN results and overall physics design. Despite the problems discussed in the previous paragraphs, we note that GYMNOS does confirm that the injector design will produce ≈ 4 kA of emitted current together with a well-behaved envelope as the beam passes through the anode. While the GYMNOS results cannot confirm the high brightness EGUN runs, even with the present numerical limitations they indicate that the design is no worse than a factor of ~ 2 from the desired result.

5 REFERENCES

[1] H. Rutkowski, "An Induction Linac for the Second Phase of DARHT", Paper MO2001, these proceedings.

[2] D. W. Hewett and Y.-J. Chen, "PIC Space-Charge Emission with Finite Δt and Δz", *Proc. 1993 Comp. Accel. Physics*, **AIP Conf. Proc. 297**, 532-539 (1994).

[3] W.B. Herrmannsfeldt, "Electron Ray Tracing Programs for Gun Design and Beam Transport", *Linear Accelerator and Beam Optics Codes*, **AIP Conf. Proc. 177**, Ed. Charles R. Eminhizer, (Amer. Inst. Physics, New York, 1988), p. 45.

[4] D. W. Hewett, "The Embedded Curved Boundary Method for Orthogonal Simulation Meshes", *J. Comp. Physics*, **138**, 585-616 (1997).

[5] E. Henestroza, "Physics Design of the DARHT Electron Beam Injector", Paper TH40456, these proceedings.

[6] B. E. Carlstein, "Emittance Growth Due to Radial Density Variations of an Emittance-dominated Electron Beam in a Channel with Continuous Acceleration and Focusing", *Physics of Plasmas*, **5**, 1148-1161 (1998).

EMITTANCE GROWTH FROM BEND/STRAIGHT TRANSITIONS FOR BEAMS APPROACHING THERMAL EQUILIBRIUM*

John J. Barnard and Bojan Losic
Lawrence Livermore National Laboratory, L-645, Livermore, CA 94550

Abstract

In certain applications such as heavy ion fusion, intense beams with large space charge tune depressions will be transferred from linear transport sections into bent transport sections. In some designs, such as recirculating induction accelerators, transport through bends will occur over thousands of betatron periods and in some driver designs the final transport through a bend will occur over tens of betatron periods. Over such distances, non-linear space charge forces are expected to produce particle phase space distributions which are close to thermal equilibrium, especially with respect to lower order moments. Here we calculate the properties of thermal equilibrium beams in bends assuming uniform focusing, as a function of two dimensionless parameters We also outline the calculation of the change in emittance for a beam that is initially in thermal equilibrium in a straight transport section, and that finally reaches thermal equilibrium in a bent system, using an energy conservation constraint to connect the two states.

1 INTRODUCTION

The conditions for equilibria of beams in a bent system were determined in ref. [1], under the assumption of uniform focusing and bending, with dispersion included through linear order in the equations of motion. The equilibria were determined by requiring that the derivatives of the second order moments with respect to path length vanish. A further assumption of this calculation was that space charge was distributed uniformly in an elliptical cross section, although as pointed out in refs. [2,3], distributions that are functions only of $x^2/\langle x^2\rangle + y^2/\langle y^2\rangle$ are also exact solutions to the moment equations of ref. [1], where x is the coordinate in the bend plane, y is the out-of-plane coordinate, and $\langle\ \rangle$ indicates average over the distribution.

Recently, in refs. [4,5] equilibrium distributions have been calculated that are fully self-consistent solutions to the coupled Vlassov and Poisson equations. Distribution functions which are functions only of the single particle transverse hamiltonian $h_\perp$ are solutions of the Vlasov equation, since $h_\perp$ is a constant of the motion. In refs. [4,5], the properties of a generalized KV distribution, (i.e. a delta-function of $h_\perp$) were investigated in detail. Although, the KV beam in bends is interesting because of its analytic tractability, beams which have equilibrated (e.g.due to space charge non-linearities), are likely to be better characterized by thermal equilibrium distributions. Although longitudinal/transverse coupling can be strong [6], it is of general interest to examine beams with distinct temperatures in the two directions.

The purpose of this paper, is to examine thermal equilibrium beams in bends with longitudinal temperatures which are not necessarily equal to the transverse temperatures (and hence the final temperature equilibration has not necessarily been reached.)

2 THEORETICAL MODEL

Equilibrium distribution functions f which satisfy the Vlassov/Poisson equations, for a system with constant focusing and bending radius have been found previously having the following form (refs. [4,5]):

$$f = f(h_\perp)\exp[-(\delta/\delta_0)^2] \tag{1}$$

where $2h_\perp = p_x^2 + p_y^2 + k_{\beta 0}^2(x^2+y^2) + 2g\phi - 2x\delta/\rho$. Here $f \equiv \mathrm{d}N/\mathrm{d}x\mathrm{d}y\mathrm{d}p_x\mathrm{d}p_y\mathrm{d}\delta$, is the number of particles per element of phase space, with the in-bend plane (horizontal) coordinate x, and vertical coordinate y, dimensionless momenta $p_{x,y}$ normalized to the design momentum in in the longitudinal direction $P_0 \equiv \gamma_0 m v_0$. The quantity $\delta = (P_s - P_0)/P_0$, is the fractional deviation of a particle with longitudinal momentum P_s from the longitudinal design momentum, and m is the particle rest mass. The quantity $k_{\beta 0}$ is the zero current spatial betatron frequency in the postulated uniform focusing channel, and ρ is the radius of curvature in the uniform bending field. The quantity ϕ is the electrostatic potential, and $g \equiv q/\gamma_0^3 m v_0^2$.

In this paper, we focus on the distribution of the form:

$$f(x,y,p_x,p_y,\delta) = f_0\exp(-h_\perp/T_\perp)\exp(-\delta^2/\delta_0^2) \tag{2}$$

Here, $T_\perp \equiv k_b\mathcal{T}_\perp/\gamma_0^2 m v_0^2$ where $\mathcal{T}_\perp$ is the comoving beam transverse temperature, k_b is Boltzmann's constant. The density $n(x,y)$ is given by:

$$n(x,y) = \int_{-\infty}^{\infty}\int_{-\infty}^{\infty}\int_{-\infty}^{\infty} f(x,y,p_x,p_y,\delta)dp_x dp_y d\delta \tag{3}$$

$$= n(0,0)\exp\frac{-1}{T_\perp}\left(\frac{k_{\beta 0}^2}{2}([1-\eta]x^2+y^2) + g\Delta\phi(x,y)\right). \tag{4}$$

Here $\eta \equiv \delta_0^2/2k_{\beta 0}^2\rho^2 T_\perp$, and represents the effects of dispersion in a bend on off-momentum particles, and $\Delta\phi \equiv \phi(x,y) - \phi(0,0)$. We find solutions to the non-linear poisson's equation $\nabla^2\phi = -qn(x,y,\phi(x,y))/\epsilon_0$ for which the beam pipe (radius r_p) is sufficiently far from the beam edge such that image forces can be ignored.

* Work performed under the auspices of the U.S. D.O.E. by LLNL under contract W-7405-ENG-48.

3 DIMENSIONLESS FORM OF MODEL

Without dispersion ($\eta = 0$) the beam density profiles in this problem recover azimuthal symmetry. In that case, the density profiles can be characterized by a single parameter (see e.g. [8]) which we define here as $\alpha_0 \equiv n(0,0)/n_{cold}$. Here $n(0,0)$ is the central density and n_{cold} is given by: $n_{cold} \equiv 2\gamma^3 m v_0^2 \epsilon_0 k_{\beta 0}^2/q^2$. The quantity n_{cold} is the density of a beam with focusing constant $k_{\beta 0}$, but at zero T_p and zero η.

When dispersion is added, the second dimensionless parameter η appears and all solutions may be characterized by the two dimensionless parameters α_0 and η. We define $X \equiv k_{\beta 0} x/T_\perp^{1/2}$, $Y \equiv k_{\beta 0} y/T_\perp^{1/2}$, $\Phi \equiv g\phi/T_\perp$, and $\Delta\Phi \equiv \Phi(X,Y) - \Phi(0,0)$. We may then cast Poisson's equation into the dimensionless form:

$$\frac{\partial^2 \Phi}{\partial^2 X^2} + \frac{\partial^2 \Phi}{\partial^2 X^2} = -2\alpha_0 \exp -\Psi. \qquad (5)$$

Here, $\Psi \equiv (1-\eta)X^2/2 + Y^2/2 + \Delta\Phi$. The boundary condition is $\Phi = 0$ at $X^2 + Y^2 = R_p^2$, where $R_p \equiv k_{\beta 0} r_p/T_\perp^{1/2}$ is the dimensionless pipe radius. Note that we have neglected the curvature terms in Poisson's equation, which is appropriate when $r_p << \rho$. Note also that R_p adds a third dimensionless parameter to the problem, but results presented here will be in a regime where R_p is large enough so that the beam parameters are nearly independent of R_p. We solve this equation numerically, using standard SOR techniques.

Once a solution is obtained, it is useful to calculate dimensionless moments of the density distribution:
$I_1(\alpha_0,\eta) \equiv \int\int dX dY \exp -\Psi$;
$I_{X^2}(\alpha_0,\eta) \equiv \int\int dX dY\, X^2 \exp -\Psi$;
$I_{Y^2}(\alpha_0,\eta) \equiv \int\int dX dY\, Y^2 \exp -\Psi$;
and $I_\Phi(\alpha_0,\eta,R_p) \equiv \int\int dX dY\, \Phi \exp -\Psi$. Here,the integration occurs over the interior of the beam pipe, $X^2 + Y^2 < R_p^2$, and the explicit dependence on α_0 and η is displayed. From these quantities, averages can be obtained: $\langle X^2\rangle \equiv I_{X^2}/I_1$, $\langle Y^2\rangle \equiv I_{Y^2}/I_1$, and $\langle\Phi\rangle \equiv I_\Phi/I_1$.

Using these integrals and averages, which depend only on α_0 η, (and in the case of I_Φ, R_p), we may calculate physical parameters of the beam. For example, the current $I = qv_0 n_{cold}\alpha_0 T_\perp I_1/k_{\beta 0}^2$, the perveance $K \equiv qI/2\pi\epsilon_0\gamma_0^3 m v_0^3 = \alpha_0 T_\perp I_1/\pi$, x-emittance $\epsilon_x = 4(\langle x^2\rangle\langle p_x^2\rangle - \langle x p_x\rangle^2)^{1/2} = 4T_\perp(I_{X^2}/I_1)^{1/2}$, and space charge parameter $S = 4K\langle x^2\rangle/\epsilon_x^2 = K/4T_\perp = \alpha_0 I_1/4\pi$. The rms tune depression $\sigma_x/\sigma_0 = (1/\langle X^2\rangle + \eta)^{1/2}$, and $\sigma_y/\sigma_0 = 1/\langle Y^2\rangle^{1/2}$.

4 RESULTS

Figure 1 displays a surface plot of the normalized beam density with a relatively large dispersion, and moderate tune depression. The beam has an apparent elliptical shape with a flattop similar to the thermal equilibrium beams in straight transport sections (cf. [8]).

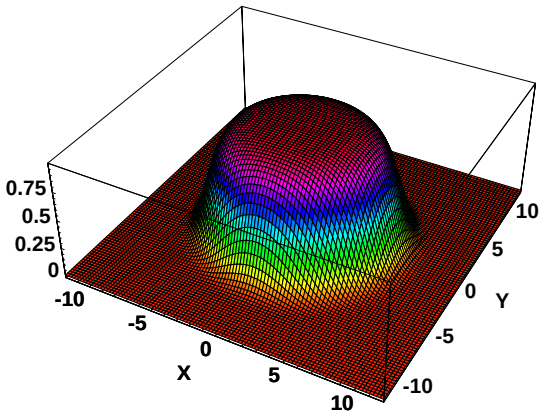

Figure 1. Scaled density $n(X,Y)/n_{cold}$ vs. X and Y for the parameters $\alpha_0 = 0.974$, and $\eta = 0.05$.

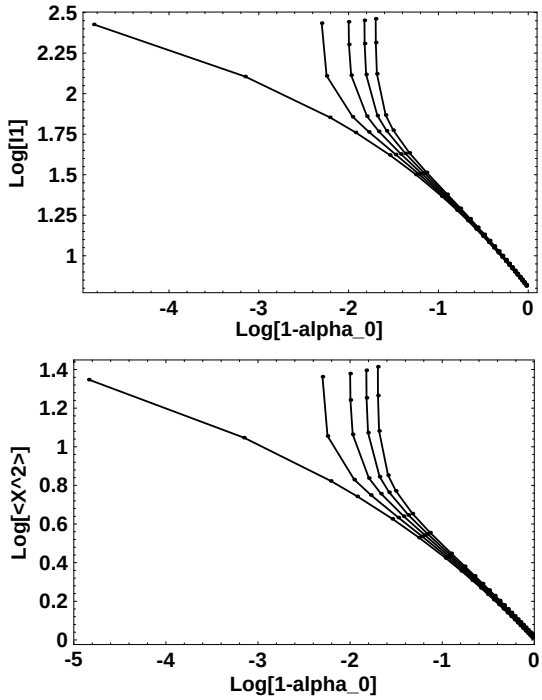

Figure 2. $\log(I_1)$ vs. $\log(1-\alpha_0)$ (upper) and $\log\langle X^2\rangle$ vs. $\log(1-\alpha_0)$ (lower) for five different values of η (starting from the left-most curve and proceeding to the right, $\eta =$ 0.00, 0.01, 0.02, 0.03, and 0.04).

The curves asymptote to $\alpha_0 = 1 - \eta/2$ for large space charge depressions (derivable from the envelope equations below with zero emittance), and I_1 tends to $2\pi/\sqrt{1-\eta}$, while $\langle X^2\rangle$ tends to $1/(1-\eta)$ in the limit of zero space charge.

5 EQUILIBRIUM EQUATIONS

In ref. [1], moment equations including dispersion were derived, and in ref. [9], the effects of images on a uniform density elliptical beam in a circular pipe were derived. The envelope equations with these two effects included (in addition to the usual external focusing, space charge and emittance terms are):

$$\frac{\mathrm{d}^2 a}{\mathrm{d}s^2} = -k_{\beta 0}^2 a + \frac{\epsilon_x^2}{a^3} + \frac{4}{\rho}\langle x\delta\rangle + \frac{2K}{a+b} + K\frac{(a^2-b^2)a}{4r_p^4} \qquad (6)$$

$$\frac{\mathrm{d}^2 b}{\mathrm{d}s^2} = -k_{\beta 0}^2 b + \frac{\epsilon_y^2}{b^3} + \frac{2K}{a+b} - K\frac{(a^2-b^2)b}{4r_p^4} \qquad (7)$$

Here $a \equiv 2\sqrt{\langle x^2\rangle}$ and $b \equiv 2\sqrt{\langle y^2\rangle}$. Setting $\mathrm{d}^2 a/\mathrm{d}s^2 = \mathrm{d}^2 b/\mathrm{d}s^2 = 0$, and transforming to the dimensionless variables, we find the equilibrium moments satisfy:

$$0 = -(1-\eta)\sqrt{\langle X^2\rangle} + \frac{1}{\sqrt{\langle X^2\rangle}} + \frac{\alpha_0 I_1}{2\pi\left(\sqrt{\langle X^2\rangle}+\sqrt{\langle Y^2\rangle}\right)} + \frac{\alpha_0 I_1\left(\langle X^2\rangle - \langle Y^2\rangle\right)}{\pi R_p^4}$$

$$0 = -\sqrt{\langle Y^2\rangle} + \frac{1}{\sqrt{\langle Y^2\rangle}} + \frac{\alpha_0 I_1}{2\pi\left(\sqrt{\langle X^2\rangle}+\sqrt{\langle Y^2\rangle}\right)} - \frac{\alpha_0 I_1\left(\langle X^2\rangle - \langle Y^2\rangle\right)}{\pi R_p^4}$$

It has been found that in all cases examined, that given I_1, and solving for $\langle X^2\rangle$ and $\langle Y^2\rangle$, these equilibrium equations accurately predict the moments derived from the SOR code, and the final term accurately gives an indication of the importance of image charge effects on the solution.

6 EMITTANCE GROWTH FROM BEND/STRAIGHT TRANSITIONS

As discussed in [1], if a beam abruptly enters a bend from a straight transport section, off momentum particles will tend to oscillate in x about centers which are displaced from the design orbit of the machine. This causes an envelope mismatch, and if the non-linear space charge forces are sufficiently strong to allow phase mixing and energy equi-partition between the x and y directions, then a new equilibrium will result. In ref. [1], the moment equations yield an exact energy invariant, when $k_{\beta 0}$ is independent of s, under the assumption that density is constant on nested ellipses ($n(x,y) = n(x^2/\langle x^2\rangle + y^2/\langle y^2\rangle)$). More generally, a dimensionless average transverse energy may be written:

$$H_\perp = \frac{1}{2}\left((1-2\eta)\langle X^2\rangle + \langle Y^2\rangle + \langle \Phi\rangle + 2\right) \qquad (8)$$

Because of the choice of normalization, it is the quantity $H_\perp T_\perp$ which is conserved. Note that the factor of 1/2 multiplying $\langle\Phi\rangle$ is necessary to correctly calculate the self-assembly energy from space charge. To calculate the the change in beam parameters from a straight/bend transition, we first calculate the current I and the transverse energy $H_\perp T_\perp$ of the beam in the straight section. Because we tabulate $H_\perp(\alpha_0, \eta, R_p)$ for fixed R_p we must account for the change in R_p as $T_\perp$ changes even though r_p remains fixed. But $H_\perp(\alpha_{0f}, \eta_f, R_{pf}) = H_\perp(\alpha_{0f}, \eta_f, R_{pi}) + (K/2T_{\perp f})\times(\ln R_{pf} - \ln R_{pi})$, where subscripts i, f indicate initial, final. For $k_{\beta 0}$ and r_p held constant, we find $T_{\perp i}[H_\perp(\alpha_{0i}, \eta = 0, R_{pi}) + (K/4T_{\perp i})\ln K/T_{\perp i}] = T_{\perp f}[H_\perp(\alpha_{0f}, \eta_f, R_{pi}) + (K/4T_{\perp f})\ln K/T_{\perp f}]$. For a finite value of η, we iterate $T_\perp$ and α_0, until the current and this relation for $H_\perp$ is satisfied. This allows calculation of all final beam parameters and using $\langle\delta^2\rangle = (1+\eta\langle X^2\rangle)\delta_0^2/2$, we may a posteriori, determine the initial value of δ_0. The change in emittance calculated using this algorithm agrees within numerical accuracy to the calculation done using the moment equations in ref. [1] and compared with simulations in ref. [7].

7 CONCLUSIONS

We have solved the self-consistent Vlasov Poisson system for beams in bends with thermal distributions, and with temperatures not necessarily equal in the longitudinal and transverse directions. We have characterized these beams by two dimensionless parameters α_0 and η and have graphed two of the quantities which characterize the solutions. We find that such beams have profiles which are constant on nested ellipses, to within numerical errors when the beam pipe is sufficiently large. This validates moment and envelope equations in refs. [1] and [3] for this class of beams. Emittance growth from bend/straight transitions, using energy and current conservation constraints was found to be the same as that calculated in ref. [1] again to within numerical uncertainties.

ACKNOWLEDGMENTS

The authors wish to thank Alex Friedman and Steven Lund for many useful discussions on the properties of beams in thermal equilibrium and on numerical techniques.

REFERENCES

[1] J.J. Barnard, H.D.Shay, S.S. Yu, A. Friedman, and D.P. Grote, "Emittance Growth in Heavy-Ion Recirculators,"1992 Lin. Acc. Conf. Proc.,1992 Aug. 24-28, Ottawa, Canada, C.R. Hoffman, ed. (1992), AECL 10728 p. 229. Also J.J. Barnard et al, in Proc. of the Workshop on Space Charge Effects in Hadron Rings, May 4-7, 1998, Shelter Island NY, (AIP, NY) in press.

[2] F. J. Sacherer, "RMS Envelope Equations with Space Charge," IEEE Transactions on Nuclear Science **NS-18**, 1105, (1971).

[3] Marco Venturini and Martin Reiser, "RMS Envelope Equations in the Presence of Space Charge and Dispersion," Phys. Rev. Letters **81** 96-99 (1998).

[4] Marco Venturini and Martin Reiser, "KV Beam in a Dispersive Channel," Proceedings of the 1997 Particle Accelerator Conference.

[5] M. Venturini and M. Reiser, "Self-consistent beam distributions with space charge and dispersion in a circular ring lattice," Phys. Rev. E, **57** 4725, (1998).

[6] I. Haber et al "Characteristics of an Electrostatic Instability Driven by Transverse- Longitudinal Temperature Anisotropy", Nucl. Instr. and Meth. A, in press (1998).

[7] S.M. Lund et al, "Numerical Simulation of Intense-Beam Experiments at LLNL and LBNL," Nucl. Inst. Meth. A (in press).

[8] M. Reiser, "Theory and Design of Charged Particle Beams," (Wiley & Sons, New York, 1994).

[9] E. P. Lee, E. Close, L. Smith, "Space Charge Effects in a Bending Magnet System," Proc. 1987, IEEE Particle Accelerator Conference, p. 1126 (1987).

COUPLING SLOTS MEASUREMENTS AGAINST SIMULATION FOR TRISPAL ACCELERATING CAVITIES

Pascal Balleyguier, CEA/DPTA, 91680 Bruyères-le-Châtel, France

Abstract

At the LINAC96 conference, we presented a new coupling scheme for the Trispal CCL accelerating cavities: the "4-petal" slots [1]. It resulted from a MAFIA optimization in which we tried to maximize the shunt impedance. Since that time, we designed and built a mock-up for an accurate measurement of the Q-drop. Indeed, we achieved a good accuracy and reliability in Q-drop measurements, but the value was rather disappointing: -22.5% (+/-0.5), instead of 5% as predicted. As a consequence, the "4-petal" coupling scheme was abandoned, and we learned that local power losses computed by cavity simulation codes can be widely underestimated. Further simulation showed that improving the mesh resolution could give better results though we felt that only a more subtle meshing method (like triangular cells or partially filled cells) could lead to realistic values.

1 INTRODUCTION

The TRISPAL linac [2] will deliver a 40 mA CW beam of 600 MeV protons. Above 100 MeV, it will be made of 352-MHz π-mode coupled cavities. Their coupling slots had been optimized with MAFIA in a way to minimize the shunt impedance drop that they induce [1]. Starting from a "2-bean" configuration of slots inspired by LEP cavities [3], the optimization resulted in a new "4-petal" scheme, for which MAFIA predicted a -6 % Q-drop (about half that of the "2-bean" slots), with the same coupling coefficient. Moreover, this Q-drop was found to be approximately canceled by an improvement of R/Q, resulting in a quasi-negligible loss in shunt impedance.

These characteristics were weakly dependent on the resolution, and variations versus various geometrical parameters were rather coherent. For verification, the optimized geometry was also computed by other codes: Soprano [4] and Antigone [5]. Roughly, all the codes agreed about coupling factor and R/Q improvement. The Q-drop values were rather close too, except for the one computed with Antigone-H (-17 %) which seemed very pessimistic.

To settle the point of the Q-drop, a 1/3 scale aluminum alloy cold model has been build (fig. 1). The central part, which contains the coupling slots, can be removed for single-cell measurements. A major issue is to get a reliable Q value in spite of successive assembling and dismantling. The electrical seal is made of a 0.8-mm solder wire squeezed to 0.4 mm with a mechanical limitation that makes the contact quality independent of the tightening strength.

Coupling antennas were made of N connectors screwed outside each end plate (fig. 2) and did not need to be dismantled at changes of configuration (single or double-cell). The central stem of the connector was extended somewhat toward the cavity to make an on-axis electrical antenna, but the coupling remained low enough (<-25 dB) to neglect the external Q.

Fig. 1. The 2-cell cold model

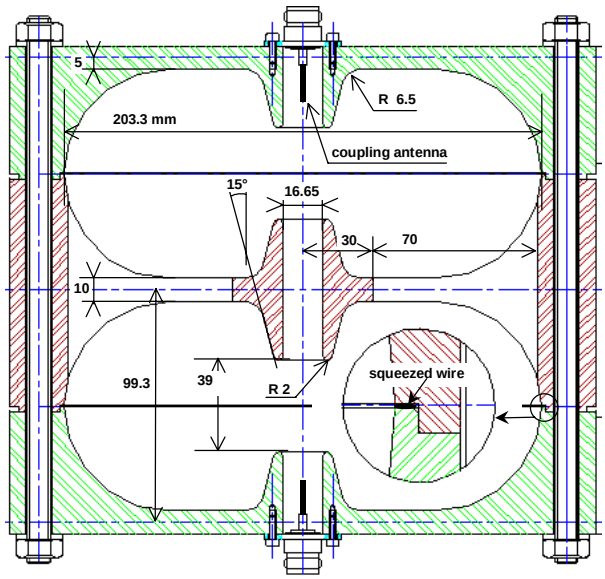

Fig. 2. Longitudinal section (transverse view on fig.4)

2 MEASUREMENTS VS. SIMULATIONS

In the MAFIA computation of the cold model, no symmetry is assumed in the center of the cell. So it represents a true double cell cavity, rather than infinitely long structure. We computed the coupling coefficient γ and the slot frequency drift α with the following

formulas:

$$\gamma = 2\frac{f_0 - f_\pi}{f} \quad , \quad \alpha = 2\frac{f_1 - f_0}{f},$$

in which f is the goal frequency (3×352 MHz). Indices π, 0 and 1 indicate the pi-mode, 0-mode and single cell cavity mode (i.e., a cell without any coupling slots), respectively. The factor two is to extrapolate the data to the case of an infinitely long structure with coupling slots on both sides of the cell as computed in [1]. The mesh used was exactly the same for the three modes, but in the case of a single-cell cavity, slots were filled with metal instead of vacuum. We used about 60000 points for a quarter of a cell, resulting in a 2.5 mm resolution in the vicinity of the slots.

Table 1 shows a +8 MHz systematic frequency error in simulation versus the cold-model that probably results from gap length and nose shape changes due to discretization. But this bias is constant, and should not alter relative differences. Indeed, α and γ computed values are close to the measured ones: the agreement is pretty good, from the coupling-factor and slot-frequency-drift points of view.

Table 1. Frequency and quality factor (4-petal).

	MAFIA	cold model
pi-mode (MHz)	1073.912	1064.415
zero-mode (MHz)	1081.556	1072.412
single-cell (MHz)	1088.948	1080.841
coupling γ (%)	1.45 (1.40*)	1.51
fq. drift α (%)	1.40 (1.42*)	1.60
Q pi-mode	11924	11340
Q zero-mode	12922	12938
Q single-cell	12236	12880
δQ_π (%)	-5.0 (-5.9*) (-16.9**)	-22.5
δQ_0 (%)	+11.5 (+11.3*) (+4.7**)	+0.9

(*MAFIA and **Antigone-H simulations in [1])

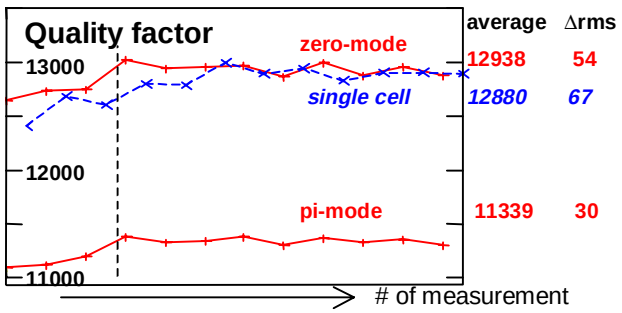

Fig. 3. Statistical variation of the measured Q.

The resistivity of the alloy (Al: 96%, Cu: 4%) was 51 nΩ.m, and the measured single-cell cavity Q was 12880, slightly above the computed value (12236). But, because of surface imperfection and seal losses, we should expect the measured Q to be 10% to 15% lower. We conclude that the MAFIA Q-value is probably underestimated, an effect that had already been established [1]. Anyway, as this bias is rather small and should be identical for the three modes computed here, the relative differences should not be significantly altered.

To estimate the quality factor reliability, we made a series of measurements alternating both configurations (single or double-cell) and changing the seal each time. The gradual Q improvement in the left-hand part of the curves (fig. 3) shows the improvement of the operator's skillfulness during the first measurements. Disregarding the first three points in each curve, the statistical variation on the measured Q is about 0.4 % r.m.s.. The accuracy on the mean value is then 0.15 %, leading to a 0.5 % absolute accuracy on δQ (see definition below).

Table 1 also gives measured quality factors against predicted ones. Here, relative variations versus single-cell mode (δQ) have been doubled by squaring the ratios to represent the case of an infinitely long structure with coupling slots at both sides of each cell:

$$\delta Q_\pi = \left(\frac{Q_\pi}{Q_1}\right)^2 - 1 \qquad \delta Q_0 = \left(\frac{Q_0}{Q_1}\right)^2 - 1.$$

We can see that MAFIA prediction of δQ_π is widely underestimated: -5 % instead of -22.5 %. Furthermore, we measured a very small δQ_0: +0.9 %, instead of +11.5 % as predicted. Other codes used in [1] gave results close to MAFIA ones, except for Antigone-H. This code predicts δQ values closer to measurements but still not very satisfactory.

3 BACK TO "2-BEAN" SLOTS

Previous measurements showed that the 4-petal slots did not yield the performance we expected from them. So, we built a new central-part for the cold model, with two classical bean-shaped slots. A single measurement (i.e., no statistics) in each configuration was performed this time. According to measured results (fig.4), the 2-bean slots are definitely preferable to 4-petal ones.

Unfortunately, we did not have time and material to make R/Q measurements with the bead-pull technique. Anyway, even if MAFIA predictions were right (the pi-mode R/Q variation versus single-cell is +5.2 % for 4-petal, and -0.2 % for 2-bean), the net result in shunt impedance would still be in favor of conventional slots.

For 2-bean slots, the simulated frequency is also 8MHz higher than measured, and a rather good agreement is obtained for relative frequency differences (table 2). The slot frequency drift α is pretty well predicted. The actual coupling factor is a little bit smaller than computed (1.27 % instead of 1.51 %). Perhaps the actual 5 mm radius due to the machining method, instead of right angles (at the slot corners), explains a part of this discrepancy. For linac designing, such a discrepancy is non-negligible and the slot width should be slightly increased in order to reach the desired 1.4 % coupling factor.

About Q-variations, this time the agreement between measurement and simulation is not bad. Apparently,

losses are inaccurate in the case of composite coupling (like 4-petal), and not in case of pure magnetic coupling (like 2-bean), but we have no explanation. This is a possible track for further investigations.

Table 2. The 2-bean coupling.

	cold model	MAFIA
pi-mode (MHz)	1069.976	1076.629
zero-mode (MHz)	1076.702	1084.604
single-cell (MHz)	1080.922	1088.554
coupling γ (%)	1.27	1.51
fq. drift α (%)	0.80	0.75
Q pi-mode	12083	13269
Q zero-mode	12959	14118
Q single-cell	12825	13928
δQ_π (%)	-9.2	-11.3
δQ_0 (%)	+2.8	+2.1

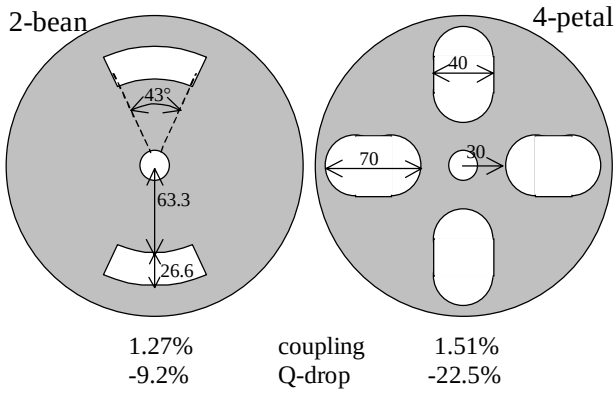

Fig.4. "2-bean" vs. "4-petal" slots (actual performances).

4 CONCLUSIONS

About the cold model: we managed to get a reliable quality factor in a cold model cavity, despite successive assembling and dismantling. Thus, we can estimate the percentage Q-drop induced by the coupling slots in an infinitely long structure, with an accuracy of ± 0.5. This accurate experimental data can be a benchmark for future codes.

About simulation: cavity code accuracy has been widely discussed until today (see, for example [6]). But most of the time, only the frequency or the on-axis field has been taken care of. The present study gives accurate experimental data involving the quality factor. We conclude that, at the present time, 3D codes tested here are not suitable for minimizing cavity losses.

In a closed vacuum-filled cavity, the quality factor is the ratio between two integrals: a volume integral (field energy) and a surface integral (losses). The first integral should be good, because if there were a bias in the whole volume, the resonant frequencies could not be predicted accurately. Thus, we probably should suspect the surface losses to be inaccurate. For a given field in the center of the cell, losses should be identical between a single-cell cavity and a multi-cell one, as long as walls are identical. Thus, only small areas in which surface currents are deviated by coupling slots (i.e., nearby the slot edges) should yield different losses. The discrepancy between computed and measured Q-drop is rather important though only small areas of the cavity walls may cause this difference. So, we suspect the local power dissipation to be very inaccurately computed in some cases, particularly in areas where the fields are strongly non-uniform.

Further analyses have been carried out at CST to explain the discrepancy between MAFIA results and measured ones. It appeared that the computed Q-drop would depend on the resolution, and be a little closer to experimental values with a much larger number of points. Anyway, no clear convergence was found, and the conclusion was that one should not try to get this kind of information from MAFIA at the present time. The future "Partially Filled Cells" algorithm, should lead to more accurate Q-drop values.

About Trispal: the 4-petal coupling slots must be abandoned. As we have no reliable way to optimize the slots, we will use the more classic 2-bean ones, which have proved to be not so bad.

Right now, we should take a great care when designing cooling circuits. If possible hot spots are suspected, a more important margin should be used. This remark is also valid for the Trispal RFQ design.

ACKNOWLEDGMENTS

The author thanks F.Appolaire who designed the cold-model, M.Fabry (from AMAFA) for having it built, and P. Hahne (from CST) for investigations with Mafia. The author is grateful to R.Wood (from LANL) for careful reading of the manuscript.

REFERENCES

[1] P. Balleyguier, "Coupling slots without shunt impedance drop", Linac Conference, Geneva, 1996, p. 414.

[2] M. Prome, "Conceptual studies of a high proton linac", Linac Conference, Tsukuba, 1994, p.146.

[3] I. Wilson and H. Henke, "The LEP main ring accelerating structure", CERN report 89-09, 1989.

[4] D. Walsh et al., "Resonant cavity design using the finite element method", EPAC, Sitges, 1996.

[5] G. Le Meur and F. Touze, "Priam/Antigone: a 2D/3D package for accelerating design", EPAC, London, 1994.

[6] T. Weiland,"High precision eigenmode computation", Particle Accelerators, Vol. 56, 1996, pp. 61.

EXTERNAL Q STUDIES FOR APT SC-CAVITY COUPLERS

Pascal Balleyguier, CEA/DPTA, 91680 Bruyères-le-Châtel, France

Abstract

Coupling coefficients for the APT superconducting cavity couplers have been predicted using an improvement of the method previously developed for the French Trispal project [1]. We here present the method and a proof of the formula used to compute the external Q. Measurements on a single-cell copper cold model exhibited a very good agreement against simulation. Then, we established that the original coupler design lead to an insufficient coupling in β=0.64 cavities. Different solutions were proposed to fix this problem, like combining impedance discontinuities in the line and an off-centered disc end tip. Finally, it was decided to increase the beam tube diameter though it has some influence on the cavity end-cell performance.

1 INTRODUCTION

The superconducting accelerating cavity prototype for the Accelerator Production of Tritium project and its associated power coupler have been intensively studied in Los Alamos [2]. Among the main characteristics is the external quality factor of the cavity. This parameter determines the coupling between the cavity and the RF line that feeds it.

Some methods to compute the external Q already exist. In 1990, Kroll and Yu [3] proposed one based on a fit on a branch of Slater's diagram. Unfortunately, this method is limited to low Qext values (less than a few hundreds) and is not suitable for our purpose. The author of the present paper recently proposed a new method [4]. It has been improved since, and the resulting method in fact is equivalent in its principle to another one described in 1993 by Hartung and Haebel [5]. But our method differs both in the proof and in the practical way to operate. Moreover, we derive from it a procedure to compute fields and local power losses under operation in a cavity and its power coupler.

2 METHOD

Let us consider a lossless cavity initially containing some RF energy W at its resonant frequency ω. If this cavity is weakly coupled to an infinite line, this line drives out a certain RF power P and the energy stored in the cavity gradually decreases. The external Q then is:

$$Q_{ext} = \omega W / P .$$

Only a single mode is assumed to travel along the line. The power transported by the travelling wave along the line may be computed either from the electric or the magnetic field amplitude:

$$P = \frac{1}{2\eta} \iint_{\text{line x sect}} |E|^2 \, ds = \frac{\eta}{2} \iint_{\text{line x sect}} |H|^2 \, ds ,$$

assuming that η is the mode impedance. The stored energy in the cavity (assumed to be under vacuum) is:

$$W = \frac{1}{2} \iiint_{cavity} \varepsilon_0 |E|^2 \, dv = \frac{1}{2} \iiint_{cavity} \mu_0 |H|^2 \, dv .$$

We assume the line mode is a TEM, and that the dielectric is vacuum: $\eta^2=\mu_0/\varepsilon_0$. Then, the external Q can be expressed as:

$$Q_{ext} = \frac{\omega \iiint_{cavity} |F|^2 \, dv}{c \iint_{\text{line x sect}} |F|^2 \, ds} , \qquad (1)$$

F being either the electric (*E*) or magnetic (*H*) field. (If the line is not under vacuum and/or the mode is not a TEM one, a coefficient taking the line mode impedance into account has to be introduced in equation (1)).

Unfortunately, computing the Qext with the formula (1) would require the use of a dissipative code. Though such codes now exist, they are more difficult to use and much slower than non-dissipative ones.

Inverting the sign of time gives a second solution of Maxwell's equations that represents the same cavity slowly gaining energy from an incoming wave travelling in the line. According to the superposition theorem, we can add these two solutions (fig. 1).

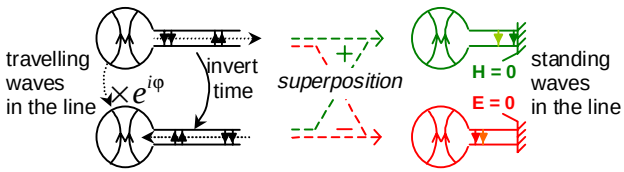

Fig. 1. Transforming a travelling-wave problem into a standing-wave one.

Inside the line, the two added travelling waves drive the same RF power P in either direction, and they interfere into a standing wave. Let us choose the reference plane at an electric field antinode: the standing wave field amplitude is there twice the one of the travelling waves. Inside the cavity, the two added fields have an arbitrary phase difference φ, so the amplitude of the resulting field is $|1+e^{i\varphi}|$ times the one of the original field. Using the same formal expression as in equation (1), we can define the quantity Q_1 as:

$$Q_1 = \frac{\omega \iiint_{cavity} |E_1|^2 \, dv}{c \iint_{\text{ref. .plane}} |E_1|^2 \, ds} = \frac{|1+e^{i\varphi}|^2}{4} Q_{ext} ,$$

where the suffix *1* indicates the resulting field after addition. This field is a pure standing wave in both the cavity and the line. The line can be terminated at the

reference plane with the appropriate boundary condition (perfect magnetic wall) without changing the fields, making this problem computable by MAFIA or any other cavity code.

Now let us use the superposition theorem again, but by subtracting the two solutions instead of adding them (the resulting fields will be noted with the suffix *2*). At the same reference plane, we now have a magnetic antinode which field amplitude is twice the one of the travelling wave. Inside the cavity, the resulting field is now $|1\text{-}e^{i\varphi}|$ times the original field. We define Q_2 as:

$$Q_2 = \frac{\omega \iiint_{cavity} |H_2|^2 dv}{c \iint_{ref.\,plane} |H_2|^2 ds} = \frac{|1 - e^{i\varphi}|^2}{4} Q_{ext}.$$

This problem can also be computed by MAFIA with the other boundary condition (perfect electric wall) at the reference plane. As for any value of φ, $|1+e^{i\varphi}|^2 + |1\text{-}e^{i\varphi}|^2 = 4$, we have then: $Q_{ext} = Q_1 + Q_2$.

So, two MAFIA runs (with the same mesh) are sufficient to predict the external Q. The reference plane position has no influence on the external Q and can be chosen anywhere in the line. Indeed, tests showed that the computed Qext was within a 0.5% variation when computed in double precision with different line lengths.

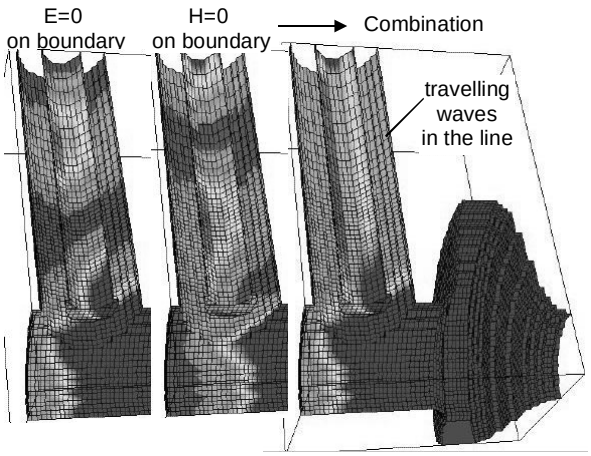

Fig. 2. Losses in the coupler under normal operations

Reciprocally, the travelling wave can be reconstituted from the two standing wave solutions in order to compute the fields in normal operation. For this purpose, one just has to combine the two standing waves solutions in quadrature phase. Before combining, one has to make sure that the electromagnetic energy at an arbitrary line cross section of the line is the same for the two waves.

This operation also permits to compute the losses in the coupler under normal (i.e. travelling waves) operation. As the solutions combine are in quadrature phase, the resulting losses is just the sum of the losses of the two solutions after normalizing them with respect to the energy density at the line end plane. As an example, the local losses in the final coupler (sect. 3) have been computed. As expected, we obtained a pure travelling wave with uniform losses along the line (fig. 2).

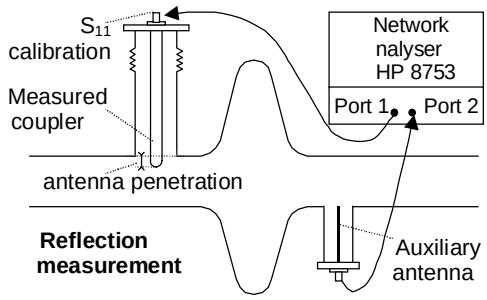

Fig. 3. Qext measurement in the 1-cell copper mock-up.

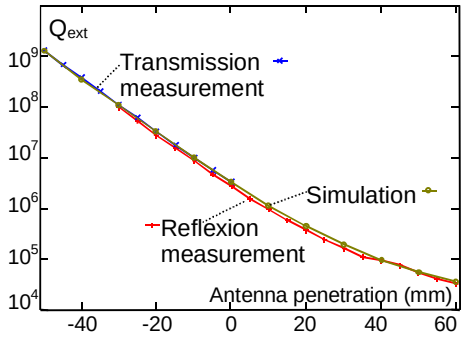

Fig. 4. Computed and measured Qext in the mock-up.

To prove the validity of this method, we tested it on a β=0.64 single-cell copper mock-up of APT cavities (fig.3). The coupling could be changed by moving the electrical antenna more or less into the beam tube. The Q_{ext} has been computed and measured (by reflection and/or transmission) for various penetrations of the coupler antenna. The result (fig. 4) shows an excellent agreement between simulation and measurements. The discrepancy of measurements versus simulation is <20 % for reflection and <7 % for transmission.

3 THE β=0.64 APT CAVITY

To cancel the reflected wave on the β=0.64 APT cavity, the external Q must equal the internal Q which is:

$$Q_{\text{int}} = \frac{\omega W}{P_{beam}} = \frac{\beta \lambda/2 \, E}{2 \, r/Q \, I \cos\varphi},$$

where *W* is the stored energy, P_{beam} the power gained, E=4.8 MV/m is the accelerating gradient, r/Q (single-cell circuit-definition)=17.1Ω, I=100mA is the beam current, φ=30° is the phase angle between the proton bunch and the RF voltage. The goal value is then: $Qext=0.22\times10^6$.
The cavity [6] has been simulated with the originally designed power coupler (fig.5). The computed Qext (assuming two couplers per 5-cell cavity) was: 1.5×10^6, which is off by a factor 6.7. With such a design, the antenna would have had to be pushed 26 mm into the beam pipe in order to reach the goal: this is not acceptable in a real accelerator.

At first, we tried to increase the coupling, without modifying the cavity design, but only the coupler itself (fig. 6). Replacing the hemisphere antenna end tip with a disc was found to be efficient if the disc axis was shifted toward the accelerating cells. A further improvement was

obtained by introducing an impedance step in the coaxial line. Such a discontinuity generates a reflected wave that partially cancels the one at the antenna end, if the distance between the reflections planes is chosen suitably. It appeared that two such steps would be necessary: an impedance increase about λ/2 from the end tip, and an impedance diminution λ/4 further. These steps would also make the transition between the coupler dimensions and the feeding coaxial line, thus avoiding the use of a taper.

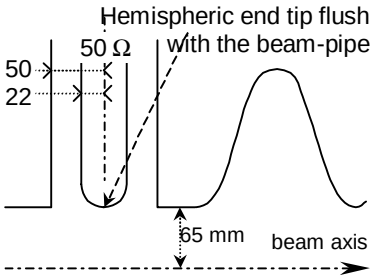

Qext=1.5×10^6 (–8.3 dB from goal)

Fig. 5. Original coupler design

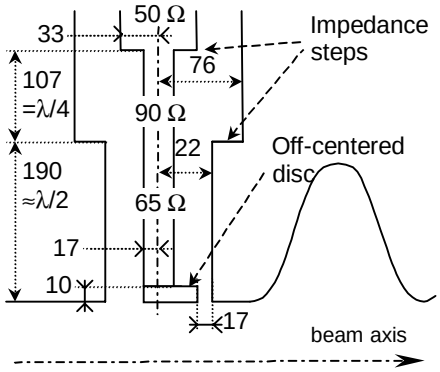

Qext=0.22×10^6: goal achieved

Fig. 6. Solution without cavity modification

However, the above solution only barely gave the necessary Qext and would have let no margin in case of unexpected behavior. For this reason, we preferred another one that consisted in expanding the end-cell beam-pipe radius from 65 to 80 mm. This change was rather soft because 80 mm is already the beam pipe radius of the β=0.82 cavities. Computations showed that such a beam-tube expansion would almost give the required Qext. In order to further improve the coupling, a 10-mm thick symmetrical disc was added at the antenna end tip (fig. 7). The Qext obtained (0.20×10^6) is even a little lower than required.

Such a modification in the cavity geometry has of course some influence on the cavity performance. First of all, the end cell profile has been adjusted to keep a 700 MHz resonance frequency. As well, the transit time factor is poorer with the enlarged pipe, and the geometric impedance (r/Q) drops by 19 %. But, as this happens only in the end-cell, the global cavity impedance is only 4 % lower, which is acceptable.

For a final adjustment, couplers will be tuned by adjusting the penetration into the beam pipe. The Qext has been computed versus antenna penetration, and the slope is 0.38 dB/mm around nominal position. So, a ±5-mm possible antenna adjustment will permit to vary the Qext within a factor 2.4.

The influence of a possible antenna tilt was simulated by a parallel displacement of the antenna in the z-axis direction. In fact, this effect is very small: 0.12 dB/mm. A ±1-mm misalignment can be compensated by a ±0.3-mm penetration of the antenna.

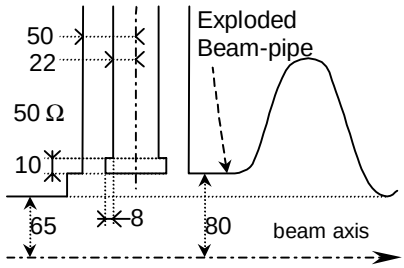

Qext=0.20×10^6: +0.6 dB more than goal

Fig.7. Final geometry

4 CONCLUSION

The Qext can be easily and efficiently computed by lossless cavity codes in frequency domain. The losses in the coupler associated with the travelling wave can also be derived from the same simulation.

The desired Qext in APT β=0.64 cavities has been obtained by expanding the beam-pipe. If necessary, an asymmetrical end tip and appropriate impedance steps could further improve the coupling.

The author thanks Brian Rusnak and all the coupler group for including me in their team during my stay in Los Alamos. I want to thank specially Frank Krawczyk for all his help, and Henri Safa for his suggestions about the possible ways to improve the coupling.

REFERENCES

[1] M. Prome, "Conceptual Studies for a High Power Proton Linac", LINAC-94, Tsukuba, p 146.

[2] F. Krawczyk et al., "The Power Coupler Design for the APT Superconducting Accelerator", LA-UR-97-3190, 8th Workshop on Superconducting RF, Abano Terme, Italy,1997.

[3] N.Kroll and D.Yu, “Computer determination of the external Q and frequency of wave guide loaded cavities”, Particle Accelerators, Vol 34, p 231, 1990.

[4] P.Balleyguier “A straightforward method for cavity external Q computation”, Particle Accelerators, Vol 57, p 113, 1997.

[5] W.Hartung and E.Haebel, “Search of trapped modes in the single-cell cavity prototype for CESR-B”, 1993 Particle Accelerator Conf., Washington DC, p 898.

[6] F. Krawczyk, et al, "Superconducting Cavities for the APT Accelerator", LA-UR-97-1700 and Proceedings of the 1997 PAC Conference in Vancouver, Canada.

2.5D CAVITY CODE WITH HIGH ACCURACY

Y. Iwashita
Accelerator Laboratory, Nuclear Science Research Facility
Institute for Chemical Research, Kyoto University
Gokanosho, Uji, Kyoto 611-0011, JAPAN Gokanosho, Uji, Kyoto 611-0011, JAPAN

Abstract

PISCES II calculates Eigensolutions of any axi-symmetric cavity with 2.5D Finite Element Method and can handle periodic boundary conditions. Dipole and higher multipole solutions are obtained by hybrid finite elements. The accuracy of the frequency in a solution obtained from PISCES II is improved by use of higher order elements. In order to reduce the computation time, the Eigenvalue solver is improved.

1 INTRODUCTION

An RF cavity code with high accuracy is necessary for design with high precision. There are still some needs of an axisymmetric cavity because of its simplicity.

PISCES II can calculate all Eigensolutions in a cavity with axisymmetric boundaries including multipole modes[1,2]. Periodic boundary conditions can also be handled in this code.

2 FORMULATION AND FINITE ELEMENT MODEL

Because either $\vec{E}$ or $\vec{H}$ can be used as the field variable, only the electric field will be shown here. The differential equations to be solved are [3,4,5],

$$\nabla\times\nabla\times\vec{E}+k^2\vec{E}=\vec{0},\quad \nabla\cdot\vec{E}=\vec{0}\qquad (in\quad \Omega), \tag{1}$$

where $k^2=\omega^2\varepsilon\mu$. In vacuum space $k^2=\omega^2/c^2$, where c is the speed of light. Boundary conditions are

$$\vec{E}\cdot\vec{n}=0 \qquad \text{on magnetic boundaries } (\Gamma m) \tag{2}$$
$$\vec{E}\times\vec{n}=\vec{0} \quad \text{on electric boundaries } (\Gamma e) \text{ and} \tag{3}$$
$$\vec{E}_{right}=e^{i\varphi}\vec{E}_{left} \quad \text{on periodic ones } (\Gamma p), \tag{4}$$

where $\vec{n}$ denotes the outward normal on the boundary, and φ is the phase advance in the problem .

Because only the problems on axisymmetric domains are considered, we can assume $\sin m\theta$ and $\cos m\theta$ dependencies for E_r, E_z and E_θ components, and then the problem can be reduced to two-dimensional problem:

$$\vec{E} = (E_\theta \sin m\theta, E_r \cos m\theta, E_z \cos m\theta). \tag{5}$$

Then (E_θ, E_r, E_z) are functions of r and z only. The field variables are (rE_θ, E_r, E_z) for $m\geq 1$ and (E_θ, H_θ) for $m=0$.

Using Finite Element Method, Eqs. (1-3) can be reduced to a matrix form of a general Eigenvalue equation:

$$\boldsymbol{M}\cdot\vec{x}=k^2\boldsymbol{K}\cdot\vec{x}, \tag{6}$$

where $\boldsymbol{M}$ and $\boldsymbol{K}$ are large sparse symmetric matrices, and $\vec{x}$ is an Eigenvector[6]. Because of the hybrid elements, any spurious mode has zero-Eigenvalue and is well separated from the real modes. Usually several Eigensolutions starting from the smallest one but zero are of interest. Unfortunately, this Eigenvalue problem has many zero-Eigenvalue solutions, which correspond to the spurious modes, and thus special care should be taken. For axisymmetric solutions, such as TM0xx or TE0xx, the problem can be expressed by field variable of E_θ or H_θ, which has no zero Eigensolution.

3 PERIODIC BOUNDARY

The periodic boundary condition is implemented using Floquet's theorem[7]. Although $\vec{x}$ has to be a complex vector for this analysis, the final Eigenvalue problem to be solved can be rewritten as real and symmetric by splitting the component into real and imaginary part. Because of this technique, the Eigenvalue solver for the usual boundary conditions is used.

4 GENERAL EIGENVALUE SOLVER

Because Eq. (5) is a general Eigenvalue problem for large sparse symmetric matrix with many zero Eigenvalue solutions, special care had to be taken. The solver is based on the subspace method[8] and uses zero and upper filtering technique[9].

The zero filtering technique requires a rough estimate of the lowest Eigenfrequency(FLO), which can be obtained by the physical dimension of the problem. If FLO is not given by a user and solution with the second order element or multiple solutions are required, PISCES II evaluates FLO from a single mode solution with lowest order element starting with the "guess" value from the physical dimension.

Using similar technique, upper filter is also applied for acceleration of the convergence. If the upper frequency (FUP) are not given by a user, PISCES II uses the highest Eigenvalue in the subspace after it settled. In this case the FUP value is adjusted adaptively.

Because the method is based on the iterative method, initial vectors should be given at the beginning. For the problem with the lowest order element, the initial vectors are given by random numbers. Before starting with the second order element, the solution vectors are obtained from the lowest order element and "prolonged" to the

second order solutions by linear interpolation. Because fairly good initial solutions are obtained by this way and FUP is also available from the beginning, the solution time is reduced up to half comparing with direct start with the random vectors.

5 INPUTS TO PISCES II

A mesh data example for a sphere as shown in Fig. 1 is listed in Fig. 2. All the internal units are in SI. The first line contains a title with less than 80 characters. The second line is problem constants, where only the unit scale for cm is specified in the list. The options are explained later. The third line has three numbers, which are the number of nodes, the number of elements and the number of boundary points plus one for closure of the line. Node coordinates are specified being enclosed by brackets. Followings are the element data, which specifies the three coordinates of the vertices by the sequential numbers of the coordinate sets. The fourth positions are reserved. Then the boundary points are specified in the same way as above. Each boundary condition for a segment between n and n+1 boundary points is specified by a character constant. The encoding of the boundary conditions are listed in Table 1. The last group is the curvature data which specifies the radii of the segments in the same sequence as the boundary conditions. Zero in radius should read as straight line. Each group is read by free format read statement. The mid-line points will be generated in the code if the second order elements are needed. For a periodic boundary problem, the radial coordinates of both the left and right side nodes should coincide.

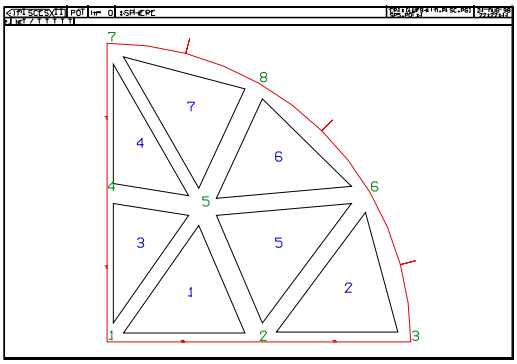

Fig. 1 Mesh example for a sphere.

```
:SPHERE
 &PROBLEM   UNIT=0.01 &END
      8      7      8
(0,0)  (5,0)  (10,0)  (0,5)  (3.1,4.5)  (8.66025,5)  (0,10)
(5,8.66025)
1,2,5,,2,3,6,,4,1,5,,4,5,7,,5,2,6,,5,6,8,,7,5,8,,
   1,   2,   3,   6,   8,   7,   4,   1,
'A' 'A' 'E' 'E' 'E' 'E' 'E' 'A'
0 0 10 10 10 0 0  0
```

Fig. 2 Mesh data for a sphere with radius of 10 cm.

Table 1: The encoding of the boundary conditions

Code	Boundary condition
'A'	on axis (r=0)
'E"	on electric boundary (metal surface)
'M'	on magnetic boundary (symmetry plane)
'P'	left side boundary for periodic boundary
'Q'	right side boundary for periodic boundary

MESHNET program[10] can convert a TAPE35 data that is generated by LATTICE[11] to an input file for PISCES II. Because the curvature information is not included in TAPE35 data, the curvature data has to be added by hand or by NETREF (NET REFine) program.

Table 2 explains the major problem constants and their default values. Table 3 shows the encoding of the element type. For example, LMTYP=22, the second order nodal elements are used for axisymmetric modes (m=0) while the mixed linear edge/nodal element are used for multipole modes (m>0). For the default setting of LTYP=1, both TE0xx and TM0xx are obtained simultaneously at m=0 so that any mode is not missed in the solution. Although such Eigenvalue problem can be separated into two independent problems, it is solved altogether.

Table 2: The problem constants

name	Default	description
OPTNF	T	The problem constants will be read again
EM	1.0	m in Eq. (5)
MSTEP	1	increment of m
MNUM	1	iterations
PHASE	0.0	phase advance
PHSTEP	0.0	increment of phase
NUMPH	1	iterations
BCLR	''	override boundary condition at left/right sides(2chars)
UNIT	1.	unit scale
CVF	T	enable curved boundary
FIELD	'E'	field variable E or H
LMTYP	1	element mode
NMODE	5	modes to be solved
FUP	0.0	highest frequency
FLO	0.0	lowest frequency
EPS	1E-5	accuracy
ITMX	200	iterations for subspace
MGF	T	enable two step solve
MCG	2	method of CGM
INFILE	''	file for initial value
OTFILE	''	output file

Table 3: The element mode encoding

LMTYP	0	1	2	10	11	12	20	21	22
LTYP (EM=0)	0	1	2	3	1	2	4	1	2
LTYP (EM>0)	I	0	0	0	3	3	3	4	4

LTYP=0 E/H with mixed constant edge/nodal element
LTYP=1 E&H with linear nodal element
LTYP=2 E/H with 2nd order nodal
LTYP=3 E/H with mixed linear edge/nodal element 12 params
LTYP=4 E/H with mixed linear edge/nodal element 14 params

6 EXAMPLE

Figs. 5 and 6 show the relative frequency errors and CPU time as functions of the number of unknowns for the hemisphere problem shown in Fig.1 (r=10cm). The CPU time depends on only the number of unknowns, although the number of nonzero elements in the matrices are about twice. The second order solutions give better accuracy with doubled memory requirement.

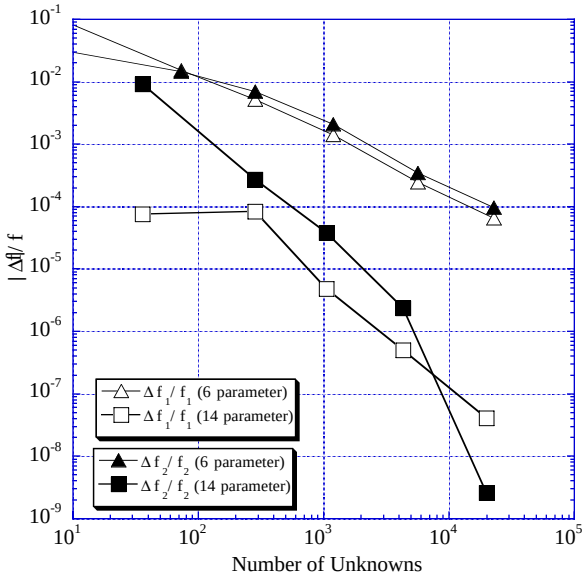

Fig. 5 Relative frequency errors of the second and the third lowest modes in a spherical cavity as a function of the number of unknowns.

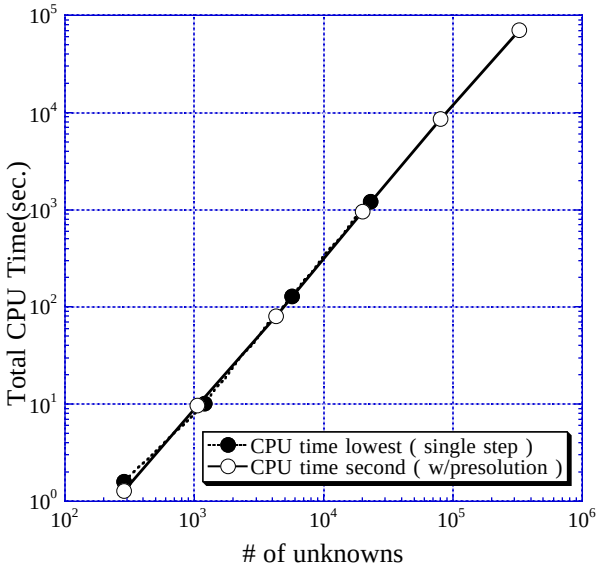

Fig. 6 CPU times as functions of the number of unknowns.

7 CONCLUDING REMARKS

After the improvement of initial vectors and parameters, the dipole problem with 324388 unknowns—23572 nodes, 46519 elements, 624 boundary points, 93662 point (including mid-line points generated internally)—takes about 20 hours for seven Eigensolutions. If FLO and FUP are given, the CPU time is reduced to about 70%. The most time consuming portion is the linear matrix solver. PCGM (Preconditioned Conjugate Gradient Method) with SOR as a preconditioner is currently used for the linear matrix solver. More efficient preconditioner will reduce the CPU time.

8 REFERENCES

[1] E. M. Nelson, "A finite element field solver for dipole modes", 1992 Linear Accelerator Conference Proceedings, Ottawa, Ontario, Canada, AECL-10728, Vol2, pp.814-816, August 1992

[2] M. Koshiba, S. Maruyama and K. Hirayama, "A vector finite element method with the high-order mixed-interpolation-type triangular elements for optical waveguiding problems", Journal of Lightwave Technology, Vol.12, No.3, March 1994, pp.495-502.

[3] K. H. Huebner and E. A. Thornton, "The finite element method for engineers", (J.Weiley, New York); and A.R.Mitchell and R.Wait, "The Finite Element Method in Partial Differential Equations" (J.Weiley, New York, 1977)

[4] M. Hara, T. Wada, T.Fukasawa, and F. Kukuchi, "A three dimensional analysis of RF electro-magnetic fields by finite element method", IEEE Trans., MAG-19 No. 6 Nov. 1983

[5] F. Kikuchi et al., "A finite element method for 3-D analysis of cavity resonators", Distributed Parameter Systems: Modeling and Simulation, Elsevier Science Publishers B. V. (North-Holland) ©IMACS,1989

[6] Y. Iwashita, "Accuracy of Eigenvalue with Hybrid Elements on Axisymmetric Domains", Proc. of the 11th Conference on the Computation of Electromagnetic Fields, Rio de Janeiro, Brazil, 165-166 (1997)

[7] R. L. Gluckstern and E. N. Opp, "Calculation of dispersion curves in periodic structures", IEEE Trans. MAG-21 No. 6 Nov. 1985 pp. 2344-2346

[8] K.J. Bathe, "Solution Methods for Large Generalized Eigenvalue Problem in Structural Engineering", Doctoral thesis, University of California, Berkeley, 1971

[9] Y. Iwashita, "General Eigenvalue Solver with Zero and Upper Filters for Large Sparse Symmetric Matrix", Proc. of the Eighth Biennial IEEE Conference on Electromagnetic Field Computation CEFC'98, June-3,1998, Tucson, Arizona, p.253

[10] Y. Iwashita, "PISCES II:2.5D RF Cavity Code", Computational Accelerator Physics, Williamsburg, VA, AIP conference proceedings No. 361 Sept. 1996, pp.119-124

[11] "User's Guide for the POISSON/SUPERFISH Group of Codes", LA-UR-87-115, Los Alamos National Lab.

COMPUTING EIGENMODES IN HIGHLY LOSSY ACCELERATING STRUCTURES

S. Setzer*, T. Weiland
Darmstadt University of Technology, Fachbereich 18,
Fachgebiet Theorie Elektromagnetischer Felder, Schlossgartenstrasse 8, 64289 Darmstadt, Germany

Abstract

The numerical calculation of eigenvalues in structures containing high loss dielectric and permeable materials is of importance in the field of accelerators as well as in many other high frequency applications. While satisfying algorithms exist for loss free and small-loss problems, the numerical problem of highly lossy material insertion is still a big challenge. We examine the Jacobi-Davidson method that proves to be a rather suitable method for calculating a set of eigenvalues even in the case of highly absorbing materials. Furthermore, unlike the commonly used sub-space methods, this algorithm is not limited to calculate extreme eigenvalues only. It is also capable of finding the eigenfrequencies located around any user specified frequency. Another practical advantage of this method is the absence of parameters such as the upper limit for an eigenvalue spectrum.

1 INTRODUCTION

Many problems in the field of electroctromagnetic design require the determination of a set of eigenvalues and corresponding eigenvectors. In the absence of lossy dielectric and permeable material or even for small loss problems, existing algorithms are functioning satisfyingly. In the presence of highly lossy material new methods like the Jacobi-Davidson technique as shown in [1] must be used. This algorithm has been implemented in the eigenvalue module of the electromagnetic CAD software MAFIA which is based on the FI-Technique. Besides the basic theory we present results for typical accelerator components such as the preliminary model of a high order mode damped accelerating cavity built at Fermilab.

2 BASIC CONCEPTS

2.1 The FIT-Method

The formulations of the Finite Integration Technique (FIT) according to Weiland [2] provides a general spatial discretization scheme usable for different electromagnetic applications of arbitrary geometry. The so called Maxwell Grid Equations and the material relations are given in the following notation:

$$C\hat{e} = -\dot{\hat{\tilde{b}}} \quad (1)$$

$$\tilde{C}\hat{h} = \hat{\tilde{j}} + \dot{\hat{\tilde{d}}} \quad (2)$$

$$S\hat{\tilde{d}} = q \quad (3)$$

$$\tilde{S}\hat{\tilde{b}} = 0 \quad (4)$$

$$\hat{\tilde{d}} = \hat{\tilde{D}}_\varepsilon \hat{e} \quad (5)$$

$$\hat{\tilde{b}} = \hat{D}_\mu \hat{h}. \quad (6)$$

The geometry is discretized on a dual orthogonal grid system with the vectors of the electrical grid voltage $\hat{e}$ and the magnetic flux $\hat{\tilde{b}}$ located on the normal Grid G while the vectors of the electrical flux $\hat{\tilde{d}}$ and the magnetic grid voltage $\hat{h}$ are based on the dual Grid $\tilde{G}$. The analytical curl operator results in the curl matrices (C,$\tilde{C}$) and the divergence operator in the source matrices (S,$\tilde{S}$).
The presence of lossy dielectric and permeable materials can be included by introducing complex diagonal material matrices $\underline{\hat{\tilde{D}}}_\varepsilon$ and $\underline{\hat{D}}_\mu$. The eigenvalue equation can be obtained by combining equations 1 and 2 in the frequency domain with the now complex grid voltages $\underline{\hat{e}}, \underline{\hat{h}}$:

$$C\underline{\hat{e}} = -i\omega \underline{\hat{D}}_\mu \underline{\hat{h}} \quad ; \quad \tilde{C}\underline{\hat{h}} = i\omega \underline{\hat{\tilde{D}}}_\varepsilon \underline{\hat{e}}$$

$$\Rightarrow \underline{\hat{\tilde{D}}}_\varepsilon^{-1} \tilde{C} \underline{\hat{D}}_\mu^{-1} C\underline{\hat{e}} = \omega^2 \underline{\hat{e}} \quad (7)$$

2.2 The Jacobi-Davidson Method

The Jacobi-Davidson method as described in [3] is applicable to the standard as well as to the generalized eigenvalue problem with a complex system matrix. Here, we will only concentrate on the standard eigenvalue problem as it arises when using the FIT as presented above.
The idea of Jacobi-Davidson techniques is to generate a search subspace on which the projected eigenvalue problem of a now much smaller dimension is solved. This is the "Davidson" part and leads to an approximation for the eigenvalue and eigenvector of the unprojected problem. In the Jaccobi part of the algorithm, a correction equation is solved defining an orthogonal correction for the current eigenvector approximation. This correction is also used to expand the orthogonal search subspace.
Although no estimations of extreme eigenvalues are needed, there is a practical problem with the Jacobi-Davidson algorithm, namely the convergence towards a

* Work supported by DFG (GK-GRK 410/1)

specific eigenvalue. Usually one is interested in calculating a set of eigenvalues located around a user specified target which is more effectively done by using a modified method, the JDQR algorithm, as described in [4]. Here the Jacobi-Davidson method is used to generate a partial Schur-form for the standard eigenvalue problem. A explicit deflation technique is introduced which leads to a modified correction equation. After identifying the first eigenvalue, the speed of convergence towards the succeeding ones is increased by reusing already generated subspace information.

3 NUMERICAL RESULTS

The JDQR-algorithm, a modified version of the Jacob-Davidson method, has been implemented for rz-problems in the eigenvalue module of the electromagnetic CAD software MAFIA. As an example the preliminary design of a high order mode damped cavity developed at Fermilab [5] has been chosen. The damping of the unwanted higher modes excited by the beam itself is achieved by inserting rings of lossy dielectric and permeable material with $\underline{\varepsilon} = 5 - 5i$ and $\underline{\mu} = 100 - 3i$. The geometry of the cavity is shown in figure 1.

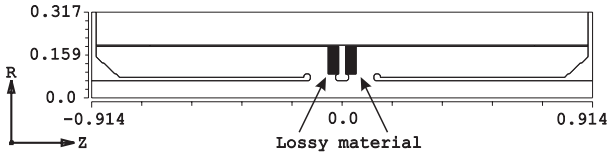

Figure 1: High order mode damped accelerating cavity

The first ten eigenmodes and the corresponding quality factors have been calculated , the results are summarized in table 1. To ensure that the lowest ten modes are identified, the user given eigenvalue target has been set to zero.

The speed of convergence for each eigenmode is depicted in figure 2. Usually, the identification of the first eigenfrequency takes more iteration then for the higher modes. This is due to the fact that subspace information generated for the first eigenvalue can be used to speed up the convergence of the following ones.

$Mode$	f_{re}/MHz	f_{im}/MHz	Q
1	54.608	0.657	41.56
2	63.723	15.888	2.01
3	64.833	16.357	1.98
4	87.578	1.902	23.02
5	98.203	36.505	1.35
6	98.278	36.606	1.34
7	137.547	53.701	1.28
8	137.630	53.829	1.28
9	171.255	52.872	1.62
10	171.340	53.066	1.61

Table 1: First ten Eigenmodes of a high order mode damped cavity

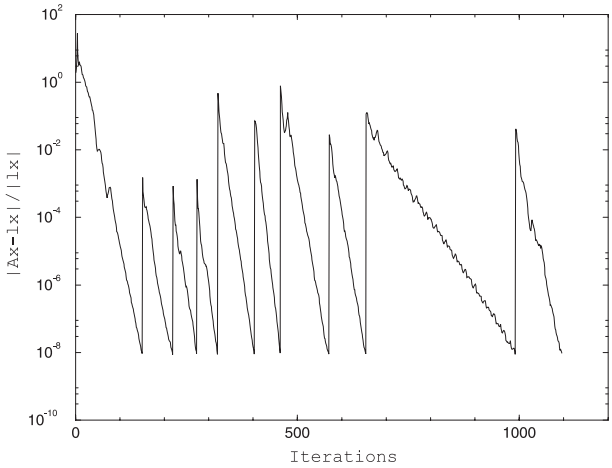

Figure 2: Relative error of eigenvalues vs. number of iterations

4 CONCLUSION

The Jacobi-Davidson method has proved to be a successful approach to the identification of resonating modes in structures containing highly absorbing materials. The algorithm is also capable of finding the eigenfrequencies located around an user given frequency which is useful for the examination of special frequency ranges. Another practical advantage of this method is the absence of parameters such as the upper limit for an eigenvalue spectrum.

5 REFERENCES

[1] S. J. Cooke, B. Levush,"Eigenmodes of Microwave Cavities containing High-Loss Dielectric Materials",Proceedings of the Particle Accelerator Conference PAC 97, Vancouver, to be published

[2] T. Weiland, "A Discretization Method for the Solution of Maxwells Equations for Six-Component Fields", Electronics and Communication (AEÜ), Vol. 31, pp. 116-120, 1977

[3] G. L. G. Sleijpen , H. A. van der Vorst, "A Jacobi-Davidson iteration method for linear eigenvalue problems",SIAM J. Matrix Anal. Appl., 17(2), pp. 401-425,1996

[4] D. R. Fokkema, G. L. G. Sleijpen, H. A. van der Forst,"Jacobi-Davidson style QR and QZ algorithm for the partial reduction of matrix pencils", Preprint 941, Department of Mathematics, University Utrecht, Janur 1996, to appear in SIAM J. Sc. Comput.

[5] W. Chou, private communication

SIMULATION RESULTS WITH AN ALTERNATE 3D SPACE CHARGE ROUTINE, PICNIC

N. Pichoff, J.M. Lagniel, S. Nath*
CEA-Saclay/DSM/DAPNIA/SEA,
* On sabbatical from LANL, Los Alamos, NM, USA.

Abstract

One of the major problems in the beam dynamics calculation dealing with high current linacs is the treatment of space charge effects. The widely used SCHEFF routine - originated and developed at Los Alamos, is often critiqued as being simplistic because of its inherent assumption of transverse symmetry. Here we report preliminary work on an alternate fully 3D space-charge routine for a bunched beam. It is a particle-in-cell approach based on numerical-calculation of the interaction between cubes (PICNIC). The principle underlying the method and the comparative results of simulation with SCHEFF and PICNIC are reported.

1 INTRODUCTION

Increase in the interest for high-current accelerators with very low loss-rate demands a high degree of confidence to the space-charge simulation tools. PARMILA is one of the more well known and widely used tools in the design of such accelerators [1]. Its space-charge routine, SCHEFF, is fast, but is not a fully 3D code. It assumes cylindrical symmetry around the longitudinal axis. We have written a new 3D space-charge routine, PICNIC, based on the same principle as SCHEFF, but making no assumption on the bunch shape. We made simulations with PARMILA, both with SCHEFF and PICNIC. Studies were done for the front section of the APT linac [2] (98 mA RFQ-output beam with energy form 6.7 MeV to 100 MeV) as well as in continuously linear focusing 3D channel (50 m, $k_{x0}=k_{y0}=k_{z0}=1\ m^{-1}$, with 10 space charge calculations per meter).

2 LIMITATION OF SCHEFF

In the SCHEFF routine the space is mapped with a 2D (r, z) mesh, r and z being respectively the radial and the longitudinal position in the beam. The number of particle in each elementary volume (a ring such that $r \in [r,r+\delta r]$ and $z \in [z,z+\delta z]$) is calculated, and the field induced by each ring, considered as uniformly charged, is computed at the mesh node. The field at each particle position is interpolated from that of the neighbouring nodes. Thus, SCHEFF is very well suited for transverse round-beam, but becomes increasingly inaccurate as when the transverse aspect ratio $\alpha = Y/X$, **X** and **Y** being respectively the x and y beam rms-sizes, differs significantly from 1, or when the beam has no cylindrical symmetry (e.g. in the RFQ output beam due to image charge forces).

In PICNIC, the space is mapped with a 3D (x, y, z) mesh. The number of particles in each elementary volume (cube) with $x \in [x,x+\delta x]$, $y \in [y,y+\delta y]$ and $z \in [z,z+\delta z]$ is calculated, and the field induced by each cube (considered as uniformly charged) is computed at the mesh node. The field at each particle position is then interpolated from those of the neighbouring nodes. No beam symmetry is assumed.

In figure 1 we represent the results of emittance-growth calculation of a non cylindrical ($X=Z=Y/\alpha$) beam (100mA, 6.7 MeV) in a continuously focusing channel ($k_{x0} = 1\ m^{-1}$). For both SCHEFF and PICNIC. The initial beam distribution is of type 8 in PARMILA (uniform); 9,000 particles are used. It clearly shows the problems with SCHEFF calculations for larger values of α. Simulations have also been done under the same conditions but with a transversally round beam ($X=Y=Z/\alpha$). In those cases PICNIC and SCHEFF give nearly the same results, i.e. those of fig.1.b.

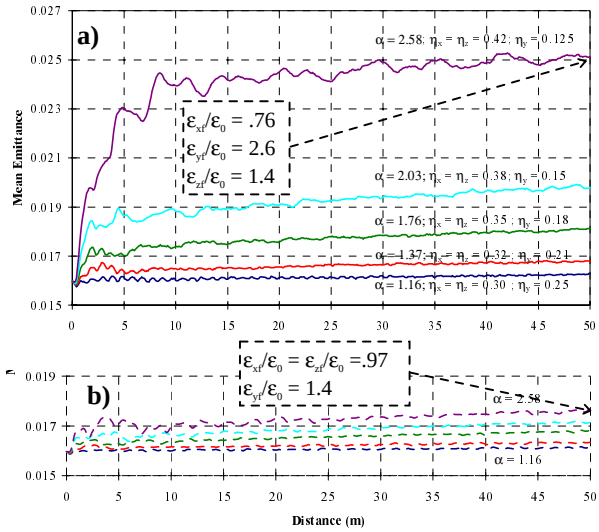

Figure 1: Emittance growth of non cylindrical beam in a continuously focusing channel. a) SCHEFF results, b) PICNIC results. We have Z = X.

The emittance growth observed at the beginning with PICNIC comes from the initial beam relaxation towards a space-charge equilibrium; the nonzero slope of the curves

is due to a poor statistics for this severely depressed-tune beam (see **§ 3.b**).

3 PICNIC PROPERTIES

a) Choice of the number of cells

With PICNIC, as with SCHEFF, one must choose number of cells ($\mathbf{N_c}$ is the half cell number) in each direction. The PICNIC mesh extends to ±3.5·X, ±3.5·Y and ±3.5·Z. Electric field at positions outside the mesh is calculated as that of a gaussian beam with the same rms-sizes. For example, a value of N_c=7 means step-size=.5X.

Figure 2 shows the transverse emittance growth versus N_c for 2 different particle number $\mathbf{N_p}$ (10K and 100K) for the APT linac at 100 MeV. It exhibits the existence of an optimised mesh number dependent on the number of particles used in the simulation.

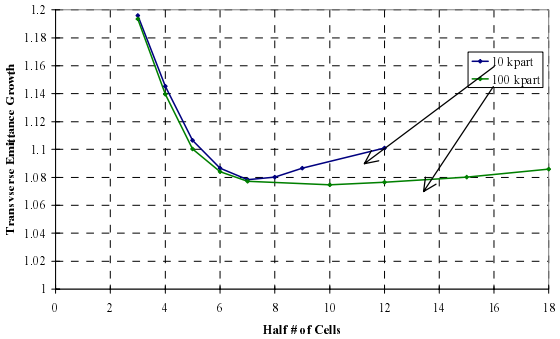

Figure 2: Emittance growth dependence on the number of cells and the number of particles.

When N_c is small, we have a lack of resolution inducing an emittance growth. When N_c large, the number of particles per cell is small inducing statistical noise and emittance growth, this is less sensitive with a higher number of particles. There is a optimum value for N_c, depending on N_p, which gives the best results. Choosing N_c=8 seems to be a good choice; it will induced an error lower than 1 %, whatever the particle number. However, results presented in **§4** in a continuous channel favour larger Nc.

b) Sensitivity to the statistics

When the beam is highly tune depressed, and the transverse and longitudinal temperatures are not the same (non-equipartionned), the rate of emittance growth per meter dε/dz in the direction with lower temperature depends on the number of particles. However, theoretically once at equilibrium (after some betatron periods), the beam should not undergo any emittance growth. This dependence on statistics is nearly the same with SCHEFF and PICNIC, it has been illustrated in fig. 3.

This results from an spurious exchange of energy between the "hotter" transverse direction to the "colder" longitudinal direction. This phenomenon has been demonstrated in [3]. A space-charge routine should therefore be validated in the context of "spurious collision" in order to avoid erroneous conclusion in term of equipartitioning. In all cases, however, it is better to work with large N_p. Even in such case, a very small emittance growth is observed. This is explained in **§4.c**.

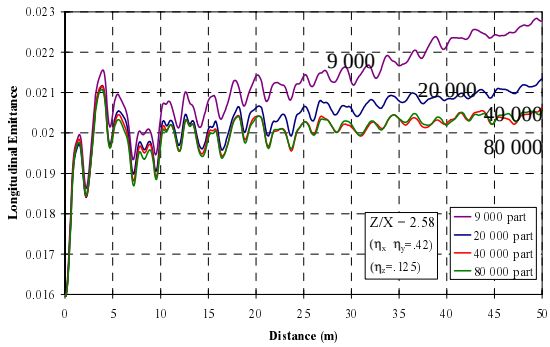

Figure 3 : Longitudinal Emittance growth of a highly tune-depressed beam, for different number of particles (PICNIC results) with X = Y = Z/2.58.

c) Computation time

Computation time for PICNIC and SCHEFF has been explored in terms of particles and cell numbers. They are represented in fig.4.

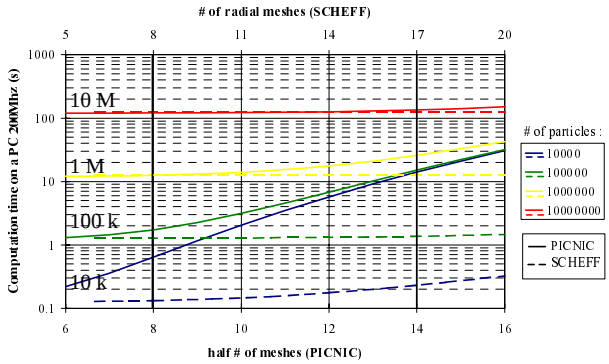

Figure 4: Space-charge computation time with a PC (fortran 77) for SCHEFF and PICNIC.

In a PIC code, one part of the computation-time depends linearly on N_p. It represents the time used to count the particles in the mesh cells (~10%), and to compute the field at each particle position (~90 %). This linear dependence can be seen when N_c tends to 0.

The other part of the computation-time depends on the method used to calculate the field at the mesh nodes. It depends only on N_c. For SCHEFF it is nearly proportional to N_c^4 and for PICNIC to N_c^6 ! New developments in PICNIC, not reported here, should reduce this part by a factor 5 to 10.

PICNIC computation-time is very reasonable with Nc=8. It is nearly the same as that of SCHEFF (with Nc=20) with more than 100,000 particles. Use of fully 3D

routines thus seems to be feasible even with a small computer (PC) !

4 LIMITATIONS

a) Highly tune-depressed beam emittance growth

The transport of a highly tune-depressed beam (η down to 0.1) has been studied in a continuous focusing channel with phase advance per meter without space-charge $k_0 = 1m^{-1}$. The initial beam is a uniform sphere (type 8), filled with 9,000 particles.

Simulations with PICNIC (fig. 5) and SCHEFF have shown a linear emittance growth, important for $\eta < 0.3$.

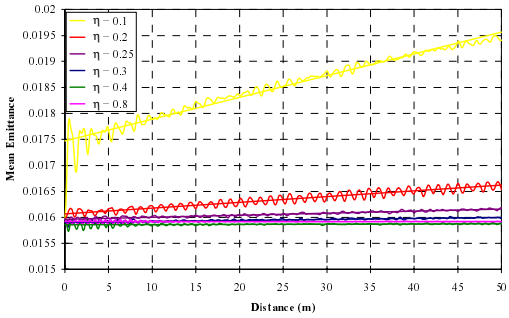

Figure 5 : Emittance growth observed with PICNIC for different tune depressions.

The growth rate (fig. 6) increases with the severity of tune-depression, and varies with the number of mesh: a large N_c seems to be better for η=0.2 (optimum for N_c=14).

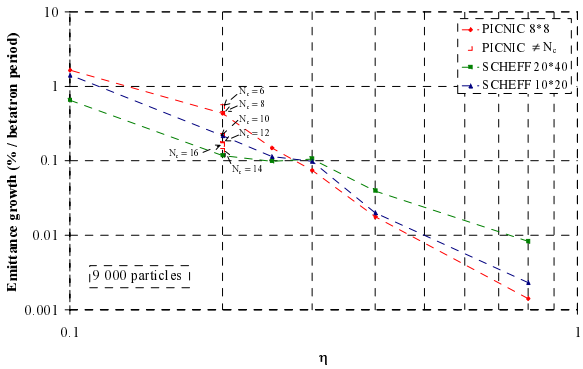

Figure 6 : Emittance growth rate in % per betatron period with depressed tune. Both PICNIC and SCHEFF results are shown

The origin of this observed emittance growth is under study. The growth-slope however quickly decreases when the beam density distribution is smoothed out. For example, the slope decreases by a factor ~3.5 when each cell is assigned the mean value of the neighbouring 27 ($=3^3$) cells with N_p=9,000 and N_c=8. It is independent on the initial beam distribution (as type 22 (~Water-Bag)) and the number of particles (up to 80,000).

b) Field calculation accuracy with small N_c

Figure 7 shows the space-charge field applied on the particles of a spherical Gaussian beam. Calculations were done with PICNIC and SCHEFF for 2 different N_c values and results are compared with the theoretical curve. With a too small value of N_c, the field is calculated as if the beam was less dense at the centre. This effect seems to be a common feature for all PIC routines; the same has been observed with the routine 3DPIC [4]. However, this seems to have a negligible effect on the emittance growth, but might change the space-charge equilibrium of the beam somewhat.

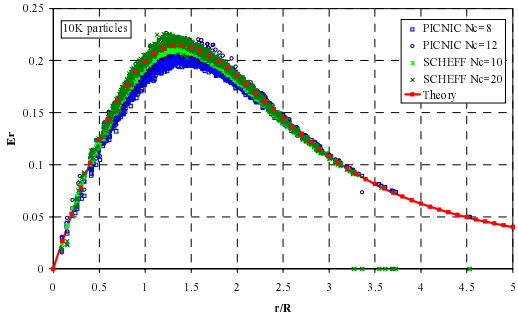

Figure 7 : Computed space-charge field on particles of a spherical Gaussian beam, compared with analytic prediction.

5 CONCLUSION

3D space-charge calculations appears to be realistic on a personal computer and PICNIC is a good candidate for this. It benchmarks very well with SCHEFF for test cases. It should be emphasised tha each space-charge routine needs to be carefully studied before application for appropriate parameters (i.e. N_c, N_p, number of space charge calculation per betatron period ...).

Some of the parameters could be used to quantify and compare the applicability of the routines, e.g. the coupling between directions (**§3.b**), the emittance growth per betatron period (**§4.a**), the computation speed (**§3.c**)... All these parameters depend on N_p and N_c (or parameters such as the screen distance in a PPI routine).

6 REFERENCES

[1] G.P. Boiscourt, «Linear Accelerator and Beam Optics Codes», Proc. of AIP Conf., 177 (1988).

[2] J. D. Schneider, «APT Accelerator Technologie», Proc. of LINAC96 (1996).

[3] J. Struckmeier, «Concept of entropy in the realm of charged particle beams», *Phys. Rev. E* **54** (1), 830-837 (1996).

[4] R. D. Ryne and S. Habib, «Beam dynamics calculations and particle tracking using massively parallel processors», *Part. Acc.*, **Vol. 55**, 365-374 (1996).

MUSTAFA-A TOOL FOR NUMERICAL SIMULATIONS OF THE BEAM BEHAVIOR IN A LINAC

G. Guignard, J. Hagel, CERN, Geneva, Switzerland

Abstract

MUSTAFA stands for **MU**ltibunch **S**imulation and **T**racking **A**lgorithm for **F**uture linear **A**ccelerators and provides an environment for tracking a multibunch beam accelerated in the linac of a collider. It is made of three parts: i) an interactive utility MBUNCH which allows to run the simulations, edit the input data, systematically vary some parameters, launch statistics on misalignment realisations and select the outputs, ii) the tracking program itself MBTR that includes magnetic focusing, acceleration, wakefields, misalignments and trajectory correction, and iii) a graphics facility called MOVIE that provides an animated representation of the transverse motion within each bunch of a train, either in the geometric space or in the phase space. While MBTR is written in FORTRAN, the other two codes are written in QUICKBASIC (MS V4.5). They run on PC Pentium computers in a stand-alone mode, independent of any network. Hence MUSTAFA is easily transportable and offers a unique graphics facility. It has been extensively used for multibunch simulations in the Compact Linear Collider scheme (CLIC) as well as for demonstrations of the beam behaviour in different stability or beam break-up conditions.

1 INTRODUCTION

The transverse oscillations of many bunches under the influence of longitudinal and transverse wake fields are of fundamental importance for beam stability in linear colliders. Since these oscillations are governed by many coupled forced-oscillator equations, their behaviour is generally complex and not yet completely understood. Simulation codes therefore are important to analyse the question of the bunched beam stability for various sets of linac parameters. MUSTAFA provides a user-friendly environment for such a tracking and result analysis. Only a short description of the three parts of MUSTAFA is given below and the potential user is recommended to look at the published MUSTAFA description and users' guide [1] for more details.

2 TRACKING CODE MBTR

The central piece of the MUSTAFA codes which have been written for beam tracking and multibunch simulations in a linac is the FORTRAN program named MBTR. This program is based on the MBTRACK codes [2], issued themselves from the single bunch tracking application MTRACK [3]. MBTR is a result of an evolution that followed the needs related to the CLIC studies and emphasizes portability as well as graphical visualization.

Since the beam of a linear collider is highly relativistic, the space charge forces can be neglected and the longitudinal positions along the bunches are fixed (no mixing). This has two impacts on the beam model. The absence of radial forces makes the use of a 3D-model with macro-particles unnecessary and each bunch can simply be longitudinally divided into elements with constant relative positions. The main parts of the numerical model are described below:

– The beam is a train of equidistant bunches. Each bunch is divided in turn into equidistant slices of width δ_z, small w.r.to the r.m.s. bunch length σ_z. Each slice is defined by the transverse positions of its center of gravity and its r.m.s. transverse dimensions deduced from the emittances. The charge per bunch is distributed in all slices according to a (truncated) gaussian distribution.

– Magnetic focusing is achieved by quadrupoles arranged in a FODO lattice that also includes drifts, accelerating structures, beam position monitors (BPM) and microwave quadrupoles (RFQ). There are two versions of the MBTR code which only differ by the way the focusing is scaled along the linac with the energy of the bunches. The first version called MBTRSCAL corresponds to a continous and adiabatic scaling (small steps not requiring any matching) while the second called MBTRSECT gives a more realistic lattice implementation, that approximates to the continuous scaling solution but is based on linac sectors with constant FODO geometry, joined by matching insertions.

– The RF system is characterized by a few parameters, such as the RF frequency of the fundamental accelerating mode ω_{RF} in s^{-1}, the RF wave length λ_{RF} in m and the maximum amplitude of the loaded acceleration gradient G_a in MV/m. The relative position of the bunch train with respect to the RF wave is defined by the phase ϕ_{RF} of the reference slice of the first bunch which is equal to zero at the peak of the wave. The phase ϕ_{RF} can be different in each sector and adjusted for optimum BNS damping. The relative phases of all the slices of the bunches are then calculated from this reference value and from the z-position of each slice resulting from the beam definition.

– Short-range wakefield Green's functions are computed with the code MAFIA [4] and defined as usual via the loss factors k_n and frequencies $\omega_n/(2\pi)$ of a large number of synchronous modes. The short-range, delta-function wake potentials are then given by the subsequent summation over these structure normal modes [5].

– Long-range wakefield Green's function is obtained either from an analytical approximation or MAFIA output data, that directly provides the field in the time domain, i.e. as a function of the distance behind a point-charge. Different models can be used. They all assume that beam loading in a train of bunches is compensated, but they differ by the

drop-off of the transverse wakefield behind bunch 1. Fig. 1 shows the Green's function of three particular models, two analytical ones based on piece-wise exponential decays and one numerical (termed here CG-DS) associated with individual damping of each cell and frequency detuning via linearly tapered iris dimensions. At the level of bunch 2, the wakefield is equal to 1 or 1.5 % of its maximum.

– The transport through the linac of the coordinates and geometrical emittances defined by the Σ matrix is done for every slice of each bunch, using the transfer matrices of the linac components. Hence, the slice emittance that includes the contribution of its off-set with respect to the average position of the train can be computed at any point s. Adding these contributions weighted by the slice population, gives the geometric emittance of a bunch or the whole train, depending on the selection. Calculating the (square root of the) determinant of Σ and multiplying by the Lorentz factor γ give the normalized bunch and beam emittances which are then used for further analysis.

– Trajectory correction is implemented in the presence of random misalignments of quadrupoles, accelerating structures and beam position monitors . It is based on a standard 'one-by-one' correction in which the beam is centred in a BPM by moving the preceding upstream quadrupole, taking into account the actual wakefields. A minimisation over several BPMs is also possible and errors in the measurements or in the displacements of the quadrupoles can be introduced.

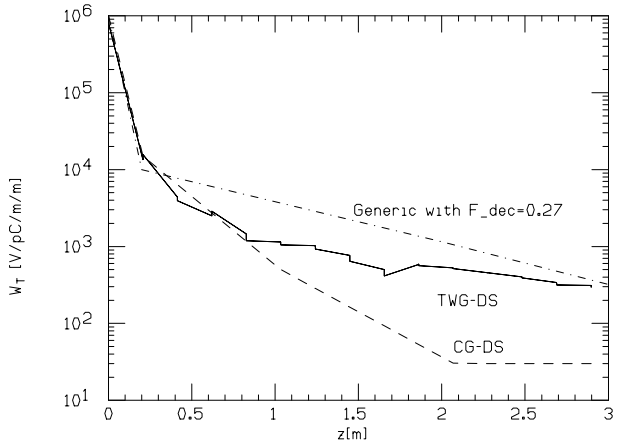

Figure 1: Long-range transverse wakefields in various CLIC structure models.

3 MBUNCH UTILITY

The MBUNCH program has been written to provide an effective and easy tool for working with the multibunch tracking code MBTR. It is fully menu driven and therefore self explanatory to a large extent, however, the basic parts are shortly described in this section.

MBUNCH handles the input and output of MBTR in an interactive way and allows to run the simulation code with specified input parameters. In addition, it postprocesses the output data providing both an online visualization of the results obtained and a statistical evaluation originating from many simulation runs. It also provides a link to the animated graphics facility which makes it possible to visualize a train of many bunches through the given linac. Finally MBUNCH gives the possibility to run either MBTRSCAL, the scaled lattice version of MBTR, or MBTRSECT, the sector lattice version of the simulation code (Section 2).

Like the simulation code MBTR, MBUNCH runs on IBM compatible PCs. It has been written using the language Microsoft Quickbasic V 4.5 [6] and is available in its executable form under the name MBUNCH.EXE. To run it efficiently together with MBTR and MOVIE, it is strongly recommended to use a PC with at least 16 Mbytes of internal RAM, a clock frequency of not less than 100 MHz, the available space on hard disk not being less than 30 Mbyte and a Pentium type processor. Although MBUNCH has been written under MSDOS (version 3.3 at least), WINDOWS 95 is well suited to run the code starting either in an MSDOS window or directly from Windows 95 Explorer.

The main menu of this program appears as:

```
****************************************
*  MUSTAFA -MULTIBUNCH SIMULATION      *
*      AND TRACKING ALGORITHM          *
*                                      *
*      G. GUIGNARD , J. HAGEL          *
*                                      *
*   (Version 1.0 , January 1998)       *
****************************************

Edit the input CLIC(SCAL)SECT.INP.... <===
Run the simulation ..................
Look at the output summary ..........
Look at the emittance graphs ........
Vary an Input parameter .............
Run the movie .......................
Save Results on Subdirectories ......
More ................................
End .................................

Pick an option via the cursor UP/DOWN keys
and  execute the command with the ENTER key.
```

The first command enables the user to interactively change the input file via the KEDIT editor and displays a copy. The second command runs the requested simulation and produces the following files: i) a summary of the results with the echo of the input data that can be displayed via command 3, ii) four files containing the orbits and emittances as functions of position s for the first, an intermediate, and the last bunch as well as the whole train (graphs previewed with command 4, see example in Fig. 2. Command 5 varies any single input parameter within specified limits and steps, providing four files [as under ii)] with the vertical emittance versus this parameter, that can be displayed. The next command initiates the 'movie' (animated graphics) described below and the last one stores all the generated files in a sub-directory for later use. Commands 4 to 6 open (mostly self-explanatory) sub-menus.

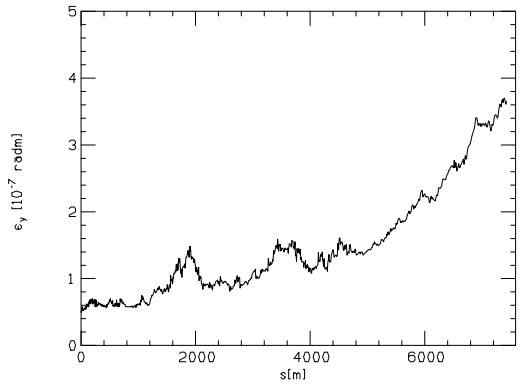

Figure 2: Vertical emittance growth averaged over a train of 10 bunches, along the 1 TeV linac, in the presence of a weak instability due to long-range wakefields

4 MOVIE FACILITY

The idea of the MOVIE code is to have a tool for direct visualization of transverse bunch oscillations as the train passes through all the parts of the linac. This helps to understand the instability mechanisms as well as the attempts to correct them. The MOVIE code shows the vertical oscillations (the most important for the flat beams of linear colliders) of all the slices of all bunches along the bunch coordinate z in the form of an animated graphics (real time corresponding to s). It uses an input file containing all the coordinates of all slices of all bunches along the entire linac (at every quadrupole position). This input file (CK.OUT) has to be created by the simulation code MBTR before MOVIE is run. Up to five bunches can be seen at any one time on the screen and it is possible during one run to scroll along the train using the right and left arrow keys. MOVIE van visualize bunches of up to 50 slices. The program MOVIE, as well as MBUNCH has been written using Microsoft Quick Basic (V. 4.5) [6] and can be run on any PC after importing and starting the executable file MOVIE.EXE. It can be run independently or via the MBUNCH utility which provides a comfortable way to launch it. The sub-menu for the 'movie' appears as:

```
   MOVIE SHOWING THE MOTION OF THE
        BUNCHES IN THE LINAC

Use the File CK.OUT created by the
stand alone program ................. <===
Use a different File ................
Run the Movie .......................
Preview the Frozen Pictures .........
Return to main menu .................
```

The proposed commands run the MOVIE facility from the last CK.OUT file created by MBTR simulations or from previously stored MOVIE-files with different names but the same extension. Command 3 initializes the animated graphics routine itself, requiring the full screen, using colors and displaying the bunch slice positions at successive quadrupoles at a nominal speed of 10 frames/s, giving the feeling of oscillating bunches with time when they travel down the linac (the related s-values appear on the screen).

The movie can be run with or without the subtraction of betatron motion, in the geometric- or phase-space, and offers on-line options to change the animation speed, stop on an image and save it in a file for later viewing with a graphics package. Figs 3 and 4 show examples of such frozen pictures in the geometric- and phase-space respectively, generated for a CLIC main beam. In the animated graphics, rapid succession of pictures of Fig.3-type gives the sensation of the oscillatory motion of the bunch tails. Colors are used to represent the particle gaussian distribution in a bunch (e.g. 'red' for the dense core and 'blue' for the tails).

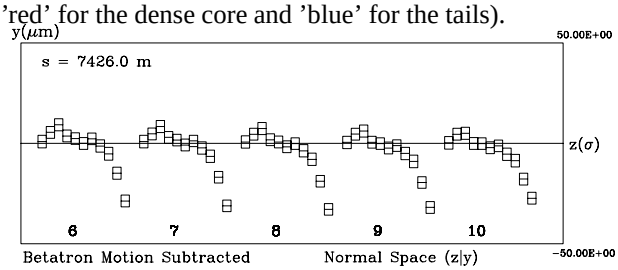

Figure 3: Vertical off-sets of the last five bunches at the linac end, for the same weak instability as in Fig. 2.

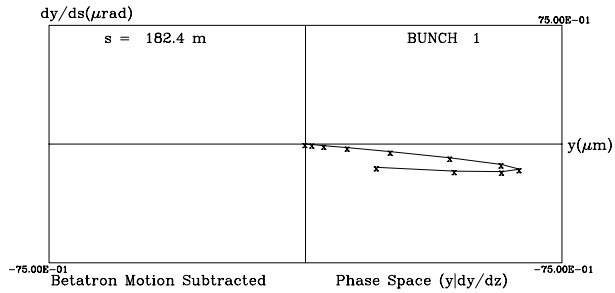

Figure 4: Vertical coordinate off-sets of bunch 1, in the phase space, at the linac beginning and with BNS damping.

5 CONCLUSION

The MUSTAFA programme 'trilogy' has proved to be user-friendly and very useful for both the design of the CLIC linear collider and the definition of the required parameters or tolerances. It also provides a practical graphic illustration of the possible single-bunch or multi-bunch instabilities. Its modularity makes additions easy and its portability has showed to be extremely convenient when movie-examples are projected during seminars or conferences. The code is available on request to any potential user.

6 REFERENCES

[1] G.Guignard and J.Hagel, CERN-SL-98-002(AP), 1998.

[2] G.Guignard and J.Hagel, CERN-SL-96-60 (AP), 1996.

[3] G.Guignard, CERN-SL-91-19(AP),1991, and XVth Int. Conf. on H.E. Part. Acc. Conf., Hamburg, 1992.

[4] MAFIA collaboration, CST GmbH, Darmstadt, Germany.

[5] A.Millich, CERN-SL-91-27(CO), 1991.

[6] J.R.Ottensmann, Quickbasic Quick Reference, Que Corporation, Carme, Indiana, 1988.

SIMULATION OF HALO FORMATION IN BREATHING ROUND BEAMS IN A PERIODIC FOCUSING CHANNEL*

Zhibin Huang, Yinbao Chen
China Institute of Atomic Energy, Beijing 102413

Abstract

Halo formation in high-intensity axisymmetric beams in a periodic focusing channel is analyzed using particle-in-cell simulations. In order to explore self-consistently the fundamental properties of breathing round beams propagating in a periodic focusing channel, the initial phase-space distribution of a beam injected into a linac is adopted to be a sufficiently realistic distribution such as Gaussian, waterbag and parabolic. Numerical results such as halo intensity and emittance growth are obtained by means of multiparticle simulations.

1 INTRODUCTION

Recent interest in using high-current ion linacs for production of tritium, the transmutation of nuclear waste, etc. has enhanced activitities for halo study. It is necessary to understand mechanisms of intense-beam losses, especially, beam instabilities and halo formation, because machines must operate with a very low beam losses to avoid serious radioaction.

K-V distribution of particles in transverse phase space is used to adopt to predict the behavior of real beam in most theoretical studies [1,2]. Because K-V beam density is uniform, then space-charge forces are linear. Particle-core model has contributed to an understanding of the underlying causes of halo formation from mismatched beams [3-6]. In order to obtain more meaningful simulation results nonlinear particle-density distributions are adopted in a uniform channel [7-11], the codes calculating space charge have been replaced by those with more simple and accurate representation of practical distributions [12,13]. Moreover, it is important to understand the mechanism of halo formation in a periodic focusing channel, since the periodicity of the external field can cause a strong resonant instability [14,15]. The chaotic behavior caused by structure-driven resonance has recently been studied and connected with halo formation [16-19]. We had investigated the mechanism which enables some particles to escape from deep inside core in a uniform channel [11]. In present paper, we discuss the properities of halo formation in breathing round beams in a periodic focusing channel.

We first describe the simulation method in section 2, then apply the code to the phase-space distributions and obtain some simulation results in section 3.

2 SIMULATION METHOD

The Hamiltonian of the transverse motion is given by

$$H_\perp(r,r_\perp;z)=r_\perp^2/2+\kappa_z(z)r^2/2+q\phi(r,z)/\left(m\gamma^3\beta^2c^2\right), \qquad (1)$$

where m, q, βc denote, respectively, the ion mass, charge and longitudinal velocity, $\kappa_z(z)$, whose profile is shown in Fig.1, is the periodic function representing the variation of the focusing strength, and z is the distance measured along the beam line. $\gamma=\left(1-\beta^2\right)^{-1/2}$, $r=\left(x^2+y^2\right)^{1/2}$ is the distance from the z-axis in the transverse plane, and $r_\perp=\left(x'^2+y'^2\right)^{1/2}$ is the dimensionless transverse velocity with $x'=\dot{x}/\beta c$, $y'=\dot{y}/\beta c$, $\phi(r,z)$ is the space charge potential, which must meet with the Poisson eqution:

$$\nabla^2\phi(r,z)=-\frac{q}{\varepsilon_0}\iint f\left(r,r_\perp;z\right)d\bar{r}_\perp\,, \qquad (2)$$

where $f(r,r_\perp;z)=f(x,y,x',y';z)$ is the distribution function in the transverse nonrelativistic four-dimensional phase space.

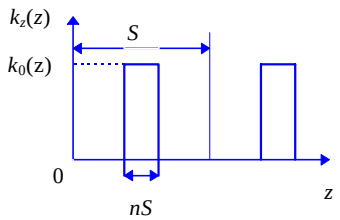

Figure 1: The profile of solenoidal periodic focusing field

All distributions that are function of the transverse Hamiltonian $H_\perp$ are stationary for a uniform focusing channel because $H_\perp$ is a constant of motion in this case. However, in the case of periodic focusing channels $H_\perp$ is no longer constant, and the only stationary state for which an analytic representation could be found is the K-V distribution. For a more general investigation one must rely on numerical simulations by means of adopting nonstationary distributions. Here nonstationary distribution functions used in computer simulation studies are defined as functions of the radius in four-dimensional trace space and not as functions of the Hamiltonian $H_\perp$. For a detailed discussion of nonstationary distributions see [20].

In order to compare different distributions on the same basis, we consider rms-equivalent beams which have the same perveance, rms radius, and rms emittance. To obtain the rms radius, we introduce the envelope eqution:

$$\frac{d^2a}{ds^2}+\kappa(s)a-\frac{\Lambda}{a}-\frac{1}{a^3}=0\ , \qquad (3)$$

where a, Λ and $\kappa(s)$ are dimensionless variables: $s=z/S$, $\Lambda=KS/\varepsilon$, K is the generalized perveance, ε the emittance and S is the periodic length of a single focusing cell, and $\kappa(s)=\kappa_z(z)S^2$. The matched normalized radius $a_0(s)$ can readily be derived from Eq.(3) when Λ and $\kappa(s)$ are determined. The vacuum phase advance over one axial period of such a focusing field is approximately given by $\sigma_0=\left[\int_0^1\kappa(s)ds\right]^{1/2}=\left[nk_0(z)\right]^{1/2}$. Then we notice that $a_0(0)$ corresponds to the minimum radius of a matched beam because the original coordinate is located at the center of a drift.

We determine the mismatched initial phase-space distribution $a_i=\mu a_0$, $a'_i=a'_0/\mu$, where a_0, a'_0 correspond to the matched one, and mismatch parameter $\mu\le 1$. The radial space-charge field of an axisymmetric beam can be calculated from Gauss law by counting the number of particles in cells of a finite radial grid which extends up to 5 times the beam matched radius. We monitor the total energy through the transport channel, and keep the total energy constant. Here we employ 10^4 particles and 100 radial meshes over the length $a_0=a_0(0)$.

3 NUMERICAL SIMULATION RESULTS

We take into account the transport channel with enough length so that the beam reaches saturated states before arriving at the exit. Here the filling factor n seen in Fig.1 is 40 percent of the length of a single cell.

If an input beam is perfectly matched to a transport system, there is no reason to expect the growth of a halo unless the distribution is intrinsically unstable against perturbation or there is structure-driven resonances. However, it is impossible to provide a perfect beam, actually, there is an inevitable initial mismatch which generates a halo.

We perform multiparticle simulations, to consider a beam as realistic as possible, several different types of initial phase-space distributions such as Gaussian, parabolic and waterbag distributions are adopted.

3.1 Emittance growth of various nonstationary distributions

To consider a beam as realistic as possible, several various initial phase-space distributions such as Gaussian (GA), parabolic (PA) and waterbag (WB) distributions are adopted to estimate emittance growth. Figure 2 shows emittance growth defined as the ratio of the final rms-emittance to the initial rms-emittance vs the cell number of the transport channel for tune depression η=0.4, which is defined by $\eta=\sigma/\sigma_0$, where σ is the space-charge phase advance over one axial period of such a focusing field and σ_0=75°, and different mismatch parameter (a) μ=0.7, (b) μ=0.8. From Fig.2 we can find that the more realistic the distribution is, the smaller the ripple of emittance growth changes through the transport channel.

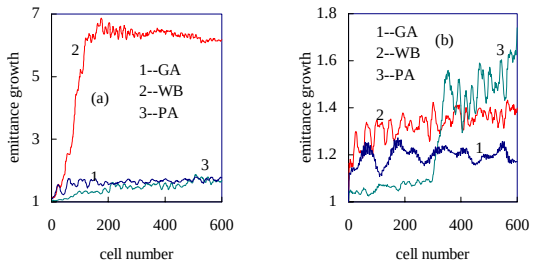

Figure 2: Emittance growth of various distributions vs cell number for (a) μ=0.7, (b) μ=0.8.

3.2 The structure-driven resonance

The periodicity of the external field can cause a strong resonant instability. Since the unstable particles can easily escape from the core getting a large betatron amplitude, it is necessary to investigate halo formation mechanism in the structure-driven instability. The instability growth rate increases with increasing σ_0, and at sufficiently high values of σ_0 there is an intensity threshold beyond which the beam is unstable for all values of $\sigma\to 0$ [20], that is to say, the second-order even mode occurs from the Vlasov equation perturbation analysis. For σ_0>90° and sufficiently large Λ, the envelope oscillations become chaotic for some mismatched beams [17].

Figure 3(a) shows emittance growth of rms-matched beams with Gaussian distribution, the phase advance without space charge is fixed at 105^0. We find emittance growth rises rapidly from η=0.23 to η=0.25, there is the region where the second-order even mode exists. The beam is trapped by the second-order resonance in the phase-space configuration shown in Fig.3(b).

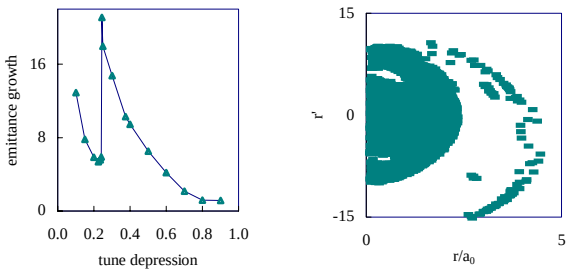

Figure 3: (a) Emittance growth of rms-matched Gaussian beams vs η and (b) phase-space distribution of rms-Gaussian beam at cell number=600 and η=0.245.

3.3 Halo intensity and the maximal radial extent

We firstly consider mismatched beams with Gaussian distribution, the phase advance without space charge is 65°,75°, 85°, respectively. The number of particles which go into the halo seen in Fig.4, gets rather small as mismatch parameter μ tends to 1.0. Here we define halo intensity *h* as the number of particles outside the boundary $r_b=1.75a_0$ divided by all of particles we employ.

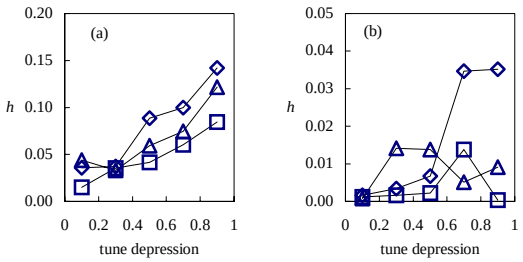

Figure 4: Halo intensity vs η for mismatch parameter (a) μ=0.6, (b) μ=0.8, with different σ_0: ◊-85°, Δ-75°, -65°.

In addition, let us look at Fig.5 where the maximal radial extent r_{max} has been displayed. It is obvious that the maximal radial extent is almost independent of σ_0, but the maximal radial extent is larger as mismatch parameter is lower than 1.0.

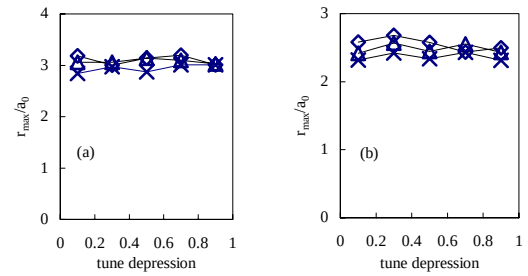

Figure 5: Ratio of the maximal radial extent to radius of matched beam vs η for mismatch parameter (a) μ=0.6, (b) μ=0.8, with different σ_0: ◊-85°, Δ-75°, ×-65°.

4 CONCLUSIONS

It has been confirmed that the periodicity of the channel induces resonant instibility in some region. There is no prominent emittance growth in the region when σ_0<90°, however, the strong instibility, especially the second-order resonance, occurs when σ_0>90°, and emittance growth is very large. Therefore, we do our best to set σ_0 at a value below 90° in a linear transport design. We can also set σ_0 above 90°, but we need to select the region where there is no resonance.

Simulation results show halo intensity and maximal radial extent are more increased as the magnitude of initial mismatch increases, and they is not dependent of the tune depression when σ_0<90°.

ACKNOWLEDGEMENTS

The authors thank professor Robert L. Gluckstern for helpful discussions and guidance. The authors also want to thank Dr. M. Ikegami for useful communications.

REFERENCES

[1] I. M. Kapchinskij and V. V. Vladimirskij, in Proceedings of the International Conference on High Energy Accelerators. CERN, Geneva, 1959.

[2] Robert L. Gluckstern, W-H Cheng, S. S. Kurennoy et al., Phys. Rev. E, 1996, 54(6):6788

[3] Robert L. Gluckstern Phys. Rev. Lett., 1994, 73(9):1247

[4] J. S. O'Connell, T. P. Wangler, R. S. Mill et al., Proc. 1993 Particle Accelerator Conf., Washington D C, 1993, p.3657

[5] J. M. Lagniel, Nucl. Instrum. Methods Phys. Res., 1994, A345(3):405

[6] T. P. Wangler, R. W. Garnett, E. R. Gray et al., Proc. of the 1996 International Lianc Conference, p.372

[7] Robert A. Jameson, Proc. 1993 Particle Accelerator Conf., Washington D C, 1993, p.3926

[8] J. M. Lagniel, Proc. of the 1994 International Linac Conference, p.529

[9] H. Okamoto and M. Ikegami, Phys. Rev. E, 1997, 55(4):4694

[10] Robert L. Gluckstern and S. S. Kurennoy, Proc. 1997 Particle Accelerator Conf.

[11] Huang Zhibin and Chen Yinbao, High Energy Physics and Nuclear Physics, in published.

[12] P. Lapostolle, A. M. Lombardi, E. Tanke et al., Proc. of the 1994 International Linac Conference, p.552

[13] P. Lapostolle, A. M. Lombardi, S. Nath et al., Proc. of the 1996 International Linac Conference, p.375

[14] I. Hofmann, L. J. Laslett, L. Smith and I. Haber, Particle Accelerators, 1983, 13:145

[15] J. Struckmeier and M. Reiser, Particle Accelerators, 1984, 14:227

[16] C. Chen and R. C. Davidson, Phys. Rev. Lett., 1994, 49:5679

[17] C. Chen and R. C. Davidson, Phys. Rev. Lett., 1994, 72(14):2195

[18] Q. Qian and R. C. Davidson, Phys. Rev. Lett. E, 1996, 53:5349

[19] M. Ikegami and H. Okamoto, Jpn. J. Appl. Phys., 1997, Vol. 36:7028

[20] M. Reiser, *Theory and Design of Charged Particle Beams*. John Wiley & Sons, Inc, 1994

*The work is supported by the National Natural Science Foundation of China and the Science Foundation of Chinese Nuclear Industry.

BEAM DYNAMICS IN A HIGH CURRENT SC PROTON LINAC FOR NUCLEAR WASTE TRANSMUTATION

G. Bellomo, P. Pierini,
INFN Milano - LASA, Via Fratelli Cervi, 201, I-20090 Segrate (MI), Italy

Abstract

INFN is studying a 100 MeV to 1.6 GeV high current (25 mA) proton linac for waste transmutation and energy production. The beam dynamics in the superconducting linac have been studied with multiparticle tracking codes. The results of this activity will be presented here, with a description of a simulation code that we are developing for space charge dominated beam dynamics.

1 THE LINAC DESIGN

INFN has started a two year program (TRASCO) for the design study and for R&D on components of a high power superconducting proton Linac for nuclear waste trasmutation. The status of the program is reported in a separate contribution at this Conference [1].

The 352 MHz superconducting linac, operating at 25 mA in the energy range 100-1600 MeV, uses five cell elliptical cavities designed for synchronous β of 0.5, 0.65, 0.85. The rationale of this choice, based on the efficiency of the cavities, has already been presented in Ref. [2].

The peak energy gain in the cavities, at the nominal synchronous phase ϕ_s=-30 deg, is 4, 6.5 and 10 MeV, respectively. The cryostats accommodate 2, 3 and 4 cavities in the three sections.

The transverse focusing is provided by a periodic array of quadrupole doublets, and the cavity cryostats are placed in the drift between the doublets. The lengths of the focusing periods are 8.0, 11.2 and 15.3 m.

The lattice parameters have been chosen so that the zero current phase advances in the first period of each section are close to 90 degrees and the tune depression is around 0.7.

The quadrupoles in each section have an almost constant gradient, so that the transverse phase advance is smoothly decreasing at approximately the same rate of the longitudinal phase advance.

The matching between sections is controlled with the gradient of the doublet at the interface and the tuning of the synchronous phases of the cavities close to the interface.

The rms beam sizes along the linac are shown in Figure 1. The input rms emittances are 0.4 π mm mrad and 0.2 π deg MeV.

Since the beam pipe radius is 100 mm the ratio between the aperture and the rms beam size is larger than 25 and reaches the value of 40 at the end of the linac.

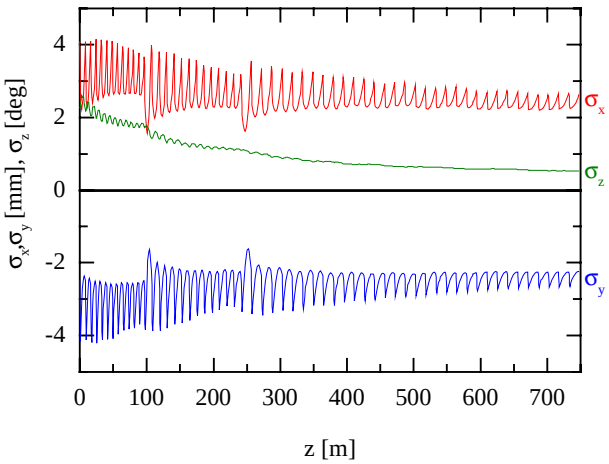

Figure 1: Rms beam sizes along the linac. On the positive ordinates: horizontal and longitudinal, On the negative ordinates: vertical.

2 MULTIPARTICLE SIMULATIONS

2.1 Initial results

Initial multiparticle tracking has been performed with a preliminary version of a code we are developing, using a limited number of particles (up to 5000) and space charge calculations via a direct point-to-point scheme. The results, reported at EPAC 98 [3], are summarized here.

For the rms emittances assumed in these simulations, 0.2 π mm mrad and 0.2 π deg MeV, an increase of 70% of the transverse rms emittances and a decrease of 40% longitudinal emittance was observed. The growth occurred mostly in the first linac section (100-200 MeV). Using as a guideline the equipartitioning criteria two alternatives were found to limit the emittance growth:

- a decrease of the period length of each section (this can be reached with 1, 2, 2 cavities per cryomodule in the sections, but results in a linac lengthening);
- an increase by a factor two of the transverse rms emittances. The beam sizes increase approximately by 50%, but the ratio aperture to rms is still larger than 20.

The latter solution, presented in Figure 1, has been chosen to be explored in more detail with the enhanced capabilities of the code, using up to 10^5 particles, and will be reported in the following subsection.

The first solution will be examined in the future, in connection with the foreseen increase of the current up to 50, or even 100 mA [1].

2.2 The multigrid code

A multiparticle beam dynamics code has been developed for the SC linac simulations. The particles are advanced through direct integration of the equations of motion along a beamline composed of quadrupoles, drift spaces and RF cavities.

The on-axis longitudinal field of the cavities is either assumed as an analytical expression for an ideal cavity or provided as an input. An iterative method to set the RF field phases of each cavity to the synchronous values, defined at the cavity center, has been implemented.

Space charge kicks are applied every few integration timesteps. A 3D space charge routine based on a fast multigrid[4] Poisson solver and a Cloud in Cell (CIC) charge assignment algorithm have been implemented in the code. The charge distribution is evaluated in the reference particle rest frame, using a CIC density smoothing algorithm. The Poisson equation for the electric potential is then solved on a square mesh (typically consisting of 33x33x33 points, extending at least to 6 rms) using a fast multigrid solver. The electric field in the rest frame is then computed from the potential, transformed to the laboratory frame and the corresponding kick, interpolated from the grid values, is applied to each particle of the beam.

Multigrid methods are surely among the fastest iterative methods for the solution of elliptic problems[4]. The model problem is represented on a series of coarser grids, obtained, for example, doubling the mesh size. Appropriate operators allow to "transport" the information (i.e. the source term, the residuals or an estimate of the solution) down one coarser grid level ("coarsening") or up one finer grid level ("prolongation"). The approximate solutions at each grid level are then used to form a better solution of the problem on the finest. The approximate solutions at each grid level are obtained with a few cycles (2-4) of an ordinary relaxation method (here the Gauss-Seidel algorithm).

The multigrid scheme makes use of the smoothing properties of relaxation schemes: the high frequencies (relative to the grid in use) of the error decay very rapidly. This, together with the use of a hierarchy of coarser and coarser grids, allows a very effective improvement in the convergence with respect of a standard relaxation scheme on a single grid, which has to face a poor performance with the smooth components of the error. V-cycle multigrid schemes converge (to 10^{-6} in norm) in 4 to 6 iterations, independently from the grid size.

A further acceleration in the convergence to the required accuracy for the space charge fields in a beam dynamics code is the use of the potential map evaluated in the previous space charge step, in order to have a better initial guess for the unknown potential.

The multigrid Poisson solver has been employed for beam dynamics simulations with up to 10^5 particles for the 750 m TRASCO linac, as reported in the following.

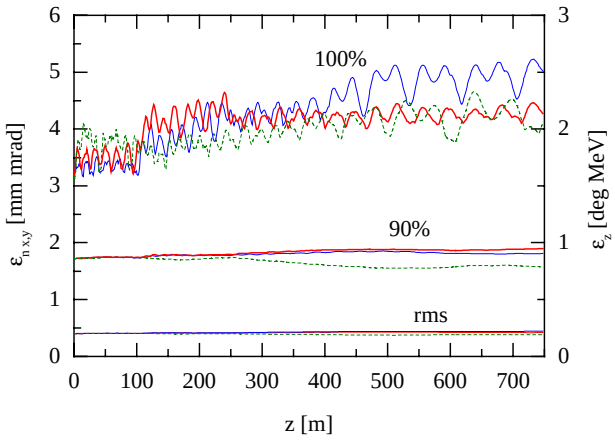

Figure 2: The rms, 90% and total (100%) normalized emittances along the linac. Solid curves (left axis): transverse emittances; dashed curve (right axis): longitudinal emittance. 10^5 particles in the simulation.

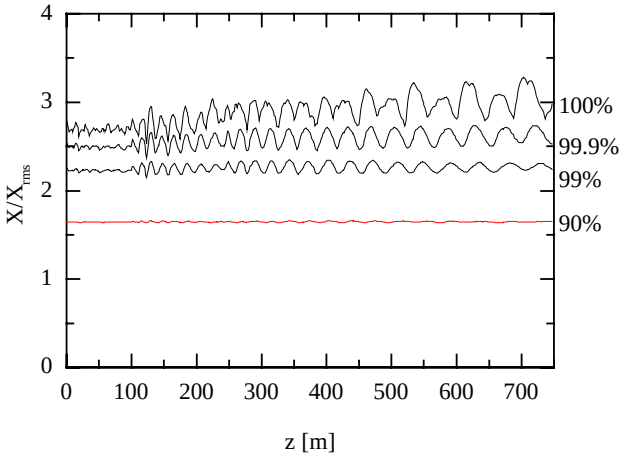

Figure 3: Ratio of the horizontal beam size to the rms value along the linac, for different beam fractions (10^5 particles in the simulation).

2.3 Matched beam case

The simulations with the multigrid code, using 10000 particles, have confirmed the results obtained with the point to point space charge routine. Simulations with 10^5 particles were then performed to explore in more details the tails of the beam distribution.

The simulations discussed here have been performed using a 6D waterbag distribution for the particle loading with a quiet random number generator [5]. However, more particle loading options still need to be implemented in the code, in particular the stationary distributions described in Ref. [6].

The input rms beam Twiss parameters and the matching conditions for the section transitions have been calculated with a linear space charge code [7].

The evolution of the rms, 90% and total emittances along the linac is plotted in Figure 2. The rms emittance growth is less than 10%.

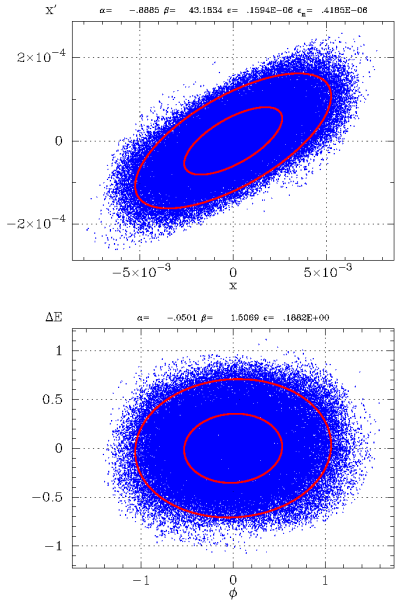

Figure 4: Transverse (upper) and longitudinal (lower) phase space projections at the end of the linac (1.6 GeV). Also plotted are the rms and the 90% beam ellipses. The simulation has been performed with 10^5 particles. Units are m, rad and deg, MeV.

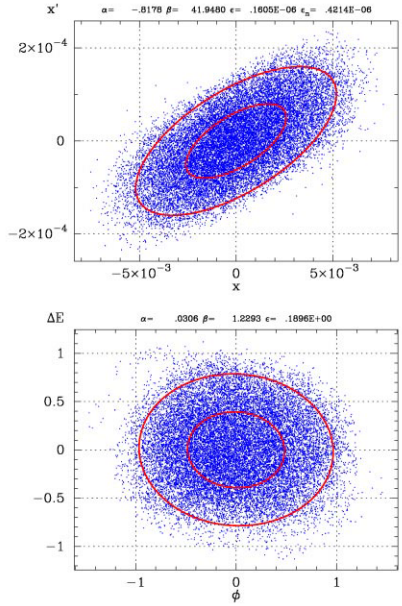

Figure 5: Transverse (upper) and longitudinal (lower) phase space projections at the end of the linac for an initial mismatched beam (10% in x,y and z). The simulation has been performed with 20000 particles. Units are m, rad and deg, MeV.

The increase of the total emittance is moderate (less than 50%), so that the ratio total/rms grows approximately from 8 to 12. The discontinuity at the interface between section 1 an section 2 (approximately at z=100 m) can be seen from Fig. 2.

The regular behavior of the beam is more apparent in Fig. 3, where we plot the ratio X/Xrms corresponding to various beam fractions. The 100% beam size is remarkably constant in the first linac section (up to z=100 m), indicating, in our opinion, a good matching of the beam distribution in the linac. In the second and third linac sections the betatron oscillation of the beam tails (99% and beyond) can be clearly seen, indicating a mismatch of the tails of the distribution. Similar plots can be shown for the vertical and longitudinal distributions.

A close examination of the phase space projections at the end of the beamline, see Fig. 4, show the formation of beam tails, in both the transverse and longitudinal planes. The deformation of the phase space is also evident looking at the beam fraction outside the 90% ellipses.

2.4 Initial beam mismatch

Simulations with a 10% mismatched initial beam (in a single plane and in all planes) have been performed with 20000 particles. No appreciable variations of the rms beam emittances have been observed. The total beam emittances increase by 20% with respect to the matched beam case, in agreement with similar calculations [8].

The phase space projections for a mismatch of +10% in the three planes are shown in Fig. 5; signs of filamentation in the longitudinal plane are barely visible.

3 CONCLUSIONS

The beam dynamics multiparticle simulations of the linac, using up to 10^5 particles, have shown a modest 10% increase of the rms emittances and a good behavior of the total beam sizes and distribution along the linac.

Initial calculations with mismatched input beams (10%, in one plane or in all planes) have shown a remarkable stability in the rms emittances, with no significant sign of halo development.

A revision of the linac design will be undertaken in the future to increase the current up to 50 mA and to explore the constraints imposed by the 100 mA operation.

4 REFERENCES

[1] C. Pagani, D. Barni, G. Bellomo, R. Parodi, P. Pierini, paper TH4108 at this Conference.

[2] C. Pagani, G. Bellomo, P. Pierini, G. Travish, D. Barni, A. Bosotti, R. Parodi, in Proceedings of the 1997 Part. Acc. Conf., Vancouver, Canada.

[3] G. Bellomo, P. Pierini, in Proceedings of the 1998 European Part. Acc. Conference, Stockholm, Sweden.

[4] W.L. Briggs, "A Multigrid Tutorial", SIAM, Philadelphia, Pennsylvania 1987.

[5] J.M. Hammersley, D.C. Handscomb, "Montecarlo methods", (Methuen, London 1964).

[6] A.V. Fedotov, R.L. Gluckstern, S.S. Kurennoy, R.D. Ryne, in Proceedings of the 1998 European Part. Acc. Conference, Stockholm, Sweden.

[7] TRACE3-D, LANL Report LA-UR-90-4146 (1987).

[8] M. Pabst et al, in Proceedings of the 1998 European Part. Acc. Conference, Stockholm, Sweden.

SIMULATIONS OF THE NONLINEAR TRANSVERSE RF FIELD EFFECTS ON THE BEAM DYNAMICS IN LOW ENERGY X-BAND SW LINACS*

Sun Xiang and Lin Yuzheng
Department of Engineering Physics, Tsinghua University, Beijing 100084, PRChina

Abstract

The detailed beam dynamics simulations in a low energy X-band SW linacs are presented. The codes *CAV* and *TRACK* are developed. They are used to investigate beam dynamics in a model structure including the nonlinear transverse RF fields. Examples are given of the study of transverse effects in different cavity shapes and in different synchronous states. The results are compared and found to agree well with those from analyses.

1 INTRODUCTION

In ref.[1], we discuss the RF fielde nonlinear effects on the emittance dominated beam in low energy linacs analyticly. In low ernergy linacs, the initial phase region of captured particles is very large and usually in the decelerating region. From the simply theory, the nonlinear transverse effects on the beam is associate with the relative radial positon of particles, the nonlinear components of RF fields and the synchronous state between particles and RF fields. The RF nonlinear transvers effects on the beam and the emittance growth mainly occurs in the first cavity, especially over the decelearting phase region. These effects weaken quickly and vanish in the quasi-synchrous section and synchrous. In the symmetric π mode cavities, the nonlinear components of RF fields are least. But the nonlinear effects on the beam in an assymetric first cavity can be less than the beam with the same initial phase in a symmetric one.

A few formulas for longitudinal and transverse dynamics have been derived including bunching, accelerating and higher space harmonics. The results of the theory should be compared with the ones of simulation to test and verify this theory.

We mainly concentrate on the first cavity in simulation.

2 MODEL

A model linac structure is considered to compare the analysis of this structure by the methods in ref.[1] with the numerical simulation by *CAV* and *TRACK*. In order to amplify the effects of the nonlinear RF fields, a larger beam radius and RF power are chosen. This model structure opperates in *9300MHz* and consists of *8* cavities (shown in Fig. 1). The microwave power inputed in the structure is *1.1MW* and the initial *rms* normalized tranceverse emittance of the electon gun is *12.02mm.mrad*. The initial phase region of captured particles is from -150^0 to -30^0.

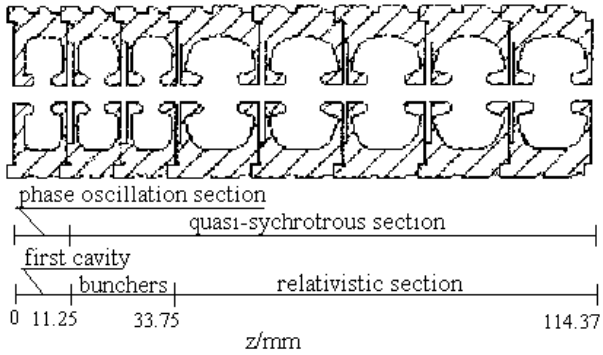

Fig. 1 Schematics of the model structure

3 DESCRIPTION OF THE SIMULATION CODES

The RF fields in the linacs are calculated by CAV. TRACK is coded by multi-particle tracking and calculates the beam dynamics including the nonlinear RF fields. It uses the time as independent variable and calculates the effects of Coulomb interactions among the electrons by variable-radius-disc model[2]. The electrons are emitted randomly with a profile that can be arbitrary distribution in radius. Both forward and backward particles are tracked. We introduce *power distribution factors* to TRACK to changing the RF field distribution conveniently.

4 EMITTANCE GROWTH

4.1 Emittance Growth Occurs in the First Cavity Mainly

The rms normalized emittances at the entrance of the model, at the exit of the first cavity, at the exit of the bunchers and the exit of the model are calculated separately. From simulation results (shown in Fig. 2), we can see the emittance growth due to RF nonlinear fields occurs in the first cavity mainly. The drop of emittance at the exit of the model whose initial phase is -150^0 results

*Work supported by the National Science Foundation of China

from the particles loss on the wall. So we concentrate on the first cavity when investigating the emittance growth.

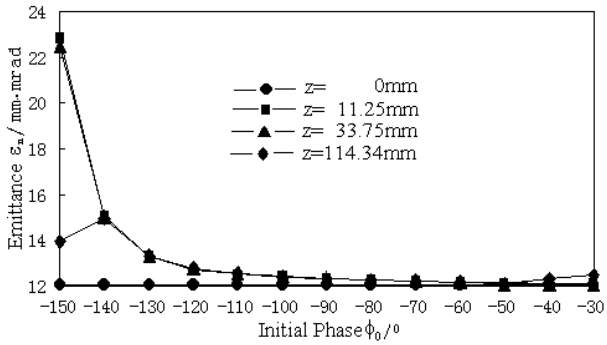

Fig. 2 Comparison of ε_n at different cross section

4.2 The Influence of the Cavity Shape

The nonlinear transverse effects on the beam is associate with the nonlinear components of RF fields which are deceded by the cavity shape. The RF fields in the assymetric cavity lift slowly along the axis and the decelearting for the particles in the asymmetric cavity is smaller than the particles with the same initial phase in the symmetric cavity (shown in Fig. 3). The emittance growth in the asymmetric cavity is smaller because the synchronous state of particles in the asymmetric cavity is better than in the symmetric cavity, even though the nonlinear components of RF fields in the asymmetric cavity is larger than in the symmetric cavity.

ε_{n1}*=22.81mm.mrad* at the exit of the symmetry first cavity as compared to ε_{n1}*=12.51mm.mrad* at the exit of in the assymytry first cavity at the initial phase ϕ_0*= -150*^{0}.

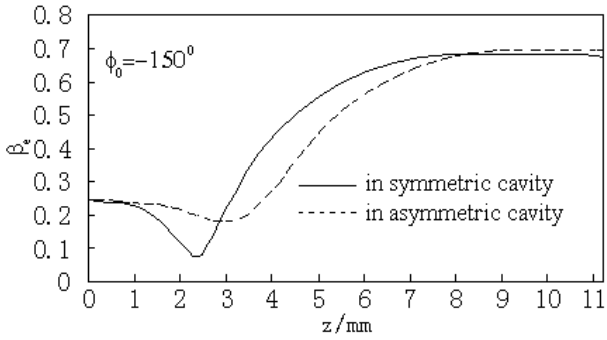

Fig. 3 Schematics of β_e in the different shape first cavity

4.3 The Influence of the Synchronous State

The synchronous state is associated with the initial phase, injecting voltage and RF field amplitude. The following ε_{n1} is the rms normalized emittance at the exit of the first cavity.

If the initial phase is near the sychrotrous phase (*0*^{0}), the sychrotrous state is better (shown in Fig. 4). ε_{n1}*=22.82mm.mrad* at the initial phase ϕ_0*=-150*^{0} as compared to ε_{n1}*=12.72mm.mrad* at the initial phase ϕ_0*=-120*^{0} in V_{inj} *=16.0kV* and P_0 *=1.1MW*.

If V_{inj} is higher, the sychrotrous state is better (shown in Fig. 5). ε_{n1}*=22.82mm.mrad* in V_{inj} *=16.0kV* as compared to ε_{n1}*=26.80mm.mrad* in V_{inj} *=14.5kV* at the initial phase ϕ_0*=-150*^{0} and P_0 *=1.1MW*.

If P_0 is higher, a_n is higher and the decelerating is larger, then the sychronous state is worse (shown in Fig. 6). ε_{n1}*=22.81mm.mrad* in P_0 *=1.1MW* as compared to ε_{n1}*=13.72mm.mrad* in P_0*=0.9MW* at the initial phase ϕ_0*= -150*^{0} and V_{inj} *=16.0kV*.

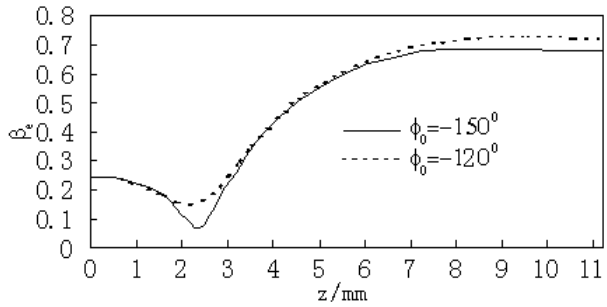

Fig. 4 Schematics of β_e in the first cavity for different ϕ_0

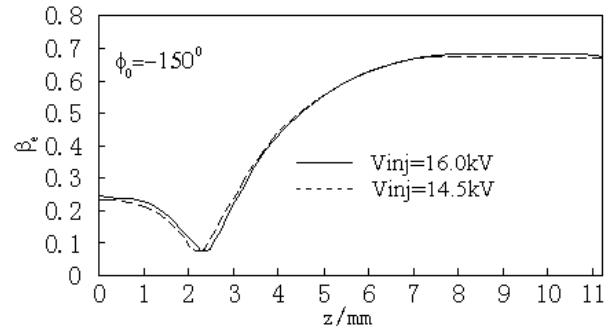

Fig. 5 Schematics of β_e in the first cavity for different V_{ini}

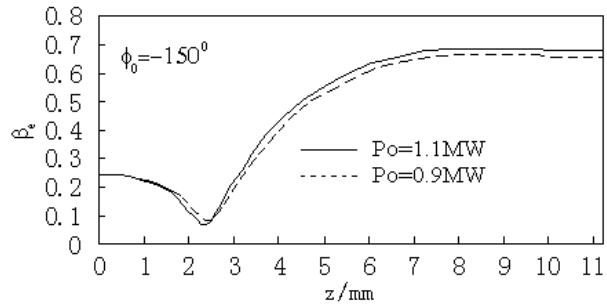

Fig. 6 Schematics of β_e in the first cavity for different P_0

5 COMPARISON BETWEEN ANALYSIS AND SIMULATION

The relativistic factor at the exit of the first cavity,

$$\gamma_1 = \gamma_0 + \frac{e}{m_0 c^2}\frac{\bar{\beta}_{e0}}{k}\left[\sum_{n=1}^{\infty} a_n \frac{Sin\left(\frac{n\bar{\beta}_{e0}}{\beta_{p1}}\phi_0\right) - \frac{n\bar{\beta}_{e0}}{\beta_{p1}} Sin(\phi_0)}{1-\left(\frac{n\bar{\beta}_{e0}}{\beta_{p1}}\right)^2}\right]$$

$$+\frac{e}{m_0c^2}\frac{\bar{\beta}_{e1}}{k}\sum_{n=1}^{\infty}a_n\left[\frac{-Cos\left(\frac{\bar{\beta}_{e0}}{\bar{\beta}_{e1}}\phi_0\right)Sin\left(\frac{n\bar{\beta}_{e0}}{\beta_{p1}}\phi_0\right)}{1-\left(\frac{n\bar{\beta}_{e1}}{\beta_{p1}}\right)^2}\right.$$

$$\left.+\frac{n\bar{\beta}_{e1}}{\beta_{p1}}\frac{(-1)^n Sin\left(\frac{\beta_{p1}}{\bar{\beta}_{e1}}\pi\right)+Sin\left(\frac{\bar{\beta}_{e0}}{\bar{\beta}_{e1}}\phi_0\right)Cos\left(\frac{n\bar{\beta}_{e0}}{\beta_{p1}}\phi_0\right)}{1-\left(\frac{n\bar{\beta}_{e1}}{\beta_{p1}}\right)^2}\right] \quad (1)$$

Corresponding, the phase at the exit of the first cavity

$$\phi_1 == \frac{k}{\bar{\beta}_{e1}}(D_1 - D_0) \quad (2)$$

where $D_0 = -\frac{\bar{\beta}_{e0}}{k}\phi_0$ defined in ref.[1].

After one cavity under the nonlinear RF fields,

$$\Delta\varepsilon_{xn} = 4\pi\left(\frac{1}{\beta_{p1}\lambda}\right)^3 |N(\phi_0)|\sqrt{\langle r^4x^2\rangle\langle x^2\rangle - \langle r^2x^2\rangle^2} \quad (3)$$

If the distribution of electrons is uniform distribution at the plane which is perpendicular to the axis,

$$\Delta\varepsilon_{xn} = 4\pi\left(\frac{R}{\beta_{p1}\lambda}\right)^3 |N(\phi_0)|\times 0.06R \quad (4)$$

where R is the envelope radius of beam.

For the first cavity,

$$N(\phi_0) = \frac{D_1 e}{m_0c^2}\frac{\pi^2}{2}\left(\frac{1}{\beta_{p1}} - M_0^2\right)\sum_{n=2}^{\infty}\frac{n(n^2-1)}{1-(nM_0)^2}[Cos(nM_0\phi_0) - Cos(\phi_0)]$$

$$-\frac{D_1 e}{m_0c^2}\frac{\pi^2}{2}\sum_{n=2}^{\infty}\frac{(n^2-1)a_n}{1-(nM_1)^2}\left\{M_1\left(\frac{n^2}{\beta_{p1}}-1\right)Sin\left(\frac{M_0}{M_1}\phi_0\right)Sin(nM_0\phi_0)\right.$$

$$\left.+n\left(\frac{1}{\beta_{p1}}-M_1^2\right)\left[-(-1)^n Cos\left(\frac{\pi}{M_1}\right)+Cos\left(\frac{M_0}{M_1}\phi_0\right)Cos(nM_0\phi_0)\right]\right\} \quad (5)$$

where $M_0 = \frac{\bar{\beta}_{e0}}{\beta_{p1}}$, $M_1 = \frac{\bar{\beta}_{e1}}{\beta_{p1}}$.

RF acceleration and RF effects on longitudinal phase space distribution γ_1 and ϕ_1 of analysis is in rough agreement with γ_1 and ϕ_1 of simulation (shown in Fig. 7 and 8). So is the RF field effects on transverse phase space distribution ε_{n1} (shown in Fig. 9).

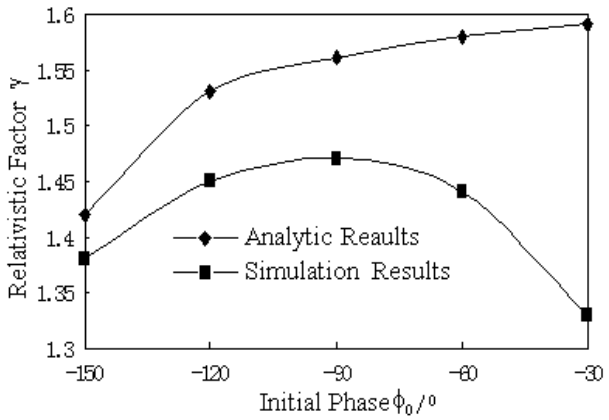

Fig. 7 Comparison of γ at the exit of the first cavity

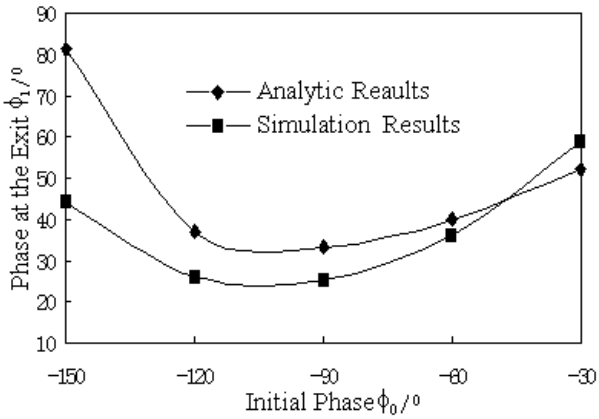

Fig. 8 Comparison of ϕ at the exit of the first cavity

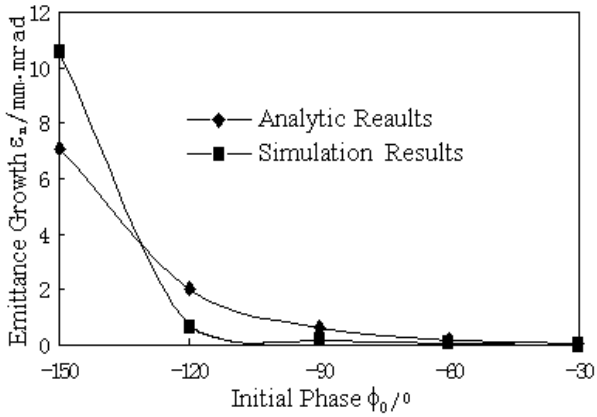

Fig. 9 Comparison of ε_n at the exit of the first cavity

6 CONCLUSIONS

A simulation to investigate the beam dynamics in the presence of nonlinear RF fields in a low energy SW X-band linac structure has been performed. The results have been compared and found to agree well with those from analyses. These programs *CAV* and *TRACK* should be useful in designing the low energy, high beam quality and high shunt resistance SW linacs opperating in higher frequencies.

A *6 MeV* X-band SW linac structure has been designed including the nonlinear RF fields and is presently under construction.

REFERENCE

[1] Sun Xiang and Lin Yuzheng. The Nonlinear Transverse RF Field Effect on the Beam Dynamics. These proceedings.

[2] Yao Chongguo. Electron Linear Acclerators. China Science Press. (1986)

A NOVEL STRUCTURE OF MULTI-PURPOSE RF GUN

E. Tanabe, A. Nakayama*, F. Oda*, M. Yokoyama*
AET Associates, Inc., 20370 Town Center Lane, Ste. 252, Cupertino, CA 95014
USA
*Kawasaki Heavy Industries Ltd., 118 Futatsuzuka, Noda, Chiba, 278 JAPAN

Abstract

RF guns have recently been very commonly used in high-energy research accelerators, as well as in various applications of accelerators such as FEL, because it offers significant advantages over the conventional techniques, which use electron guns and bunchers. In this paper, the novel structure of the RF gun, utilizing the π/2 mode, standing wave, on-axis coupled structure (OCS), is described. The new structure offers much higher group velocity and lower emittance over the structure that is commonly used. As a result, the new structure has a more stable operation for higher beam current without sacrificing beam emittance. Moreover, the structure offers unique characteristics in reduction of back bombardment for the application of thermionic cathodes in RF guns. The cavity structure and beam parameters were optimized by using EMSYS (2D) and MAFIA (3D). An overview of design detail and prototype structure, which can be used with either thermionic cathodes or photocathodes, will be presented.

1 INTRODUCTION

Since RF guns offer various advantages over the high voltage DC guns, many of today's electron injectors for physics accelerators and accelerators for FEL utilize this concept in order to obtain a higher brightness beam within a smaller space [1]. Although laser driven cathodes have been used in conjunction with RF gun, the complexity, the lifetime of cathode material, and cost have been the obstacles. Meanwhile, the RF Gun with the thermionic cathode offers a compact and low cost injector, but it suffers by pulse shortening due to electron "back-bombardment".

Here, we propose a new RF-Gun utilizes the π/2 mode, on axis coupled standing wave structure (OCS), that can offer highly stable, high current beam with lower emittance. The new structure can be used with both the photo cathode and thermionic cathode.

2 DESIGN CRITERIA AND CONCEPT

There are several very important criteria for designing RF guns, including:

2.1 The first accelerating cavity and the cathode for initial acceleration should be made electrically and mechanically as axis-symmetric as possible.

2.2 The accelerating field within the first cavity contains the least transverse components on an off-axis where the beam initially gains longitudinal momentum.

2.3 The amplitude and phase of accelerating field within the accelerating cavities should be stable with beam loading, frequency shift, and thermal instabilities.

2.4 Accelerating gradient must be as high as possible, but less than the RF breakdown and field emission threshold.

In order to satisfy these criteria, we have designed an S-Band RF Gun as shown in Fig. 1. The standing wave π/2 mode was chosen as the accelerating mode to satisfy criterion 2.3 [2]. The on-axis coupling structure (OCS) was used in order to satisfy criteria 2.1 and 2.2.

The selection of this mode and structure offers several other advantages, such as a) ease of machining the structure; b) ease of tuning; and c) flexibility of choosing the ratio of accelerating field in the first cell and the third cell.

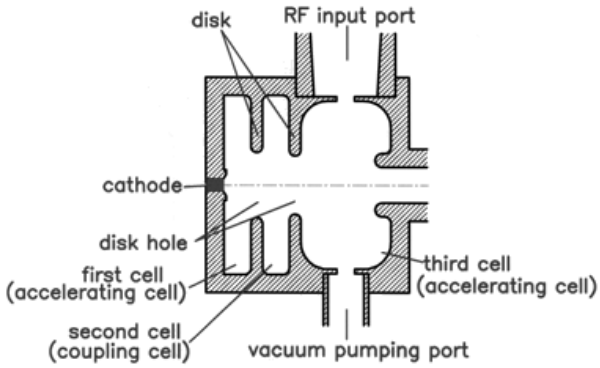

Fig. 1. Cross sectional view of OCS type RF gun

The RF input power will be fed to the third cell where a vacuum pump out-port is placed at the opposite side of the RF input-port in order to minimize the non-axis symmetry within the cavity as shown in Fig 1. A demountable cathode structure is designed by using a tungsten wire spring in the form of a toroid for RF contact. It employs an impregnated tungsten dispenser cathode for operation at around 1000°C.

Fig. 2 shows an equivalent circuit for three cavity couple resonator models with the nearest neighbor coupling (k_{12} and k_{23}) and the second nearest neighbor coupling (k_{13}). Assuming Q is very high, one can obtain the relation of the couplings and the amplitude ratio of the first and third cavity as:

$$\frac{k_{12}}{k_{23}} = \frac{|X_3|}{|X_1|} = \alpha$$

for $\pi/2$ mode operation. This indicates that one can choose any α by changing the radii of the coupling disk holes.

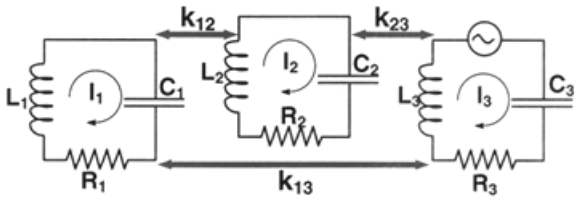

Fig. 2. Coupled resonator model for OCS type RF gun

3 NUMERICAL SIMULATION AND DESIGN OPTIMIZATION

The electromagnetic field profiles were computed using SUPERFISH and EMSYS. The beam dynamics were calculated by the 2D particle-in-cell (PIC) code EMSYS and 3D PIC Code (MAFIA).

Fig. 3 shows the relation of computed coupling coefficients, k_{12} and k_{23}, vs. disk hole radius in millimeters.

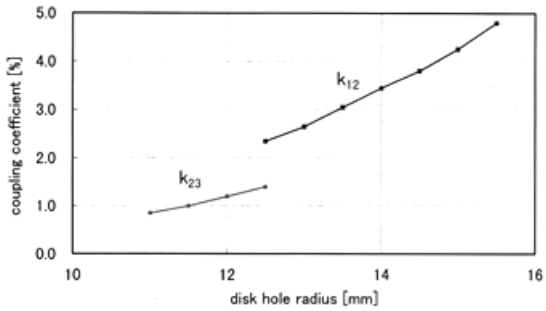

Fig. 3. Disk hole radii vs. coupling coefficients

Fig. 4 shows the dependence of output beam emittance and back bombardment power on coupling ratio α, assuming cathode diameter of 6mm and current density 16A/cm^2. In order to optimize the output beam energy spectrum, the length of the first cell and the second cell are varied along with α. A larger α offers lower back bombardment power, but aggravates the emittance of the beam, since the accelerating field on the cathode surface will be reduced. The optimum α will be around 2.5 and the normalized emittance is 12πmm·mrad. The average back bombardment power is about 1.1W, assuming the pulse width of 5μsec and a repetition rate of 10pps [3].

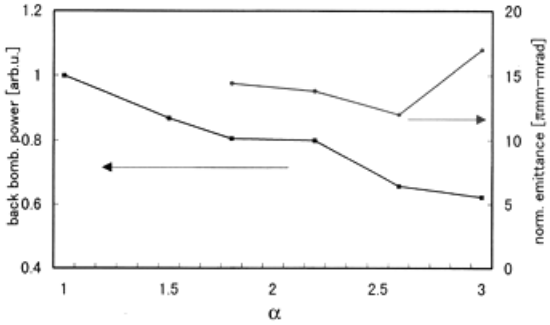

Fig. 4. Field balance (a) vs. beam emittance and back bombarding power

Fig. 5 shows the computed energy spectra of back bombarding beam for α=2.6 and for α=1.0. This figure clearly shows that the lower accelerating field within the shorter first cavity will generate much less electron back bombarding energy as 0.2MeV, compared to the back bombarding energy of higher accelerating field within the longer first cavity as 0.6MeV.

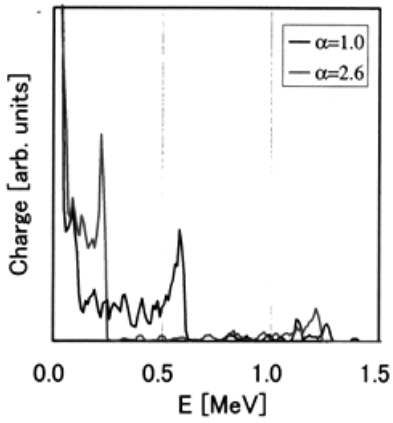

Fig. 5. Energy spectra of back bombarding beam

Fig 6 shows the radial distribution of back bombardment power density for α=2.6. The back bombardment power density is much higher in the center of the cathode due to the back bombarded higher energy electrons being focused by the radial RF field. This indicates that the back bombardment effect and pulse shortening will be completely eliminated by introduction of a hollow beam cathode with a Faraday cup of 2mm hole in the center of the cathode and a Faraday cup placed behind. Fig. 7 and Fig. 8 show an energy spectrum of output beam and energy spread as a function of time, respectively. The FWHM of the energy spectrum is about 25KeV and the charge contained during 10psec is about 0.17nC.

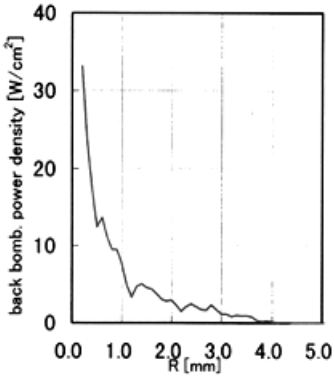

Fig. 6. Radial distribution of back bombarding power density

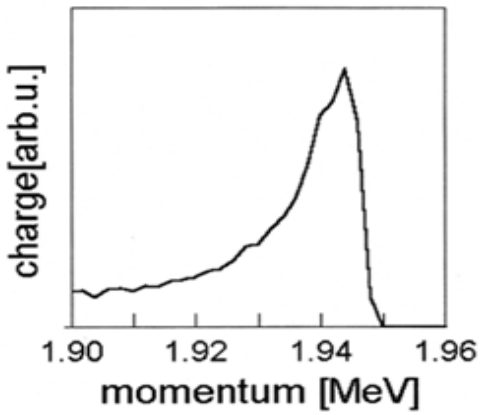

Fig. 7. Energy spectrum of output beam

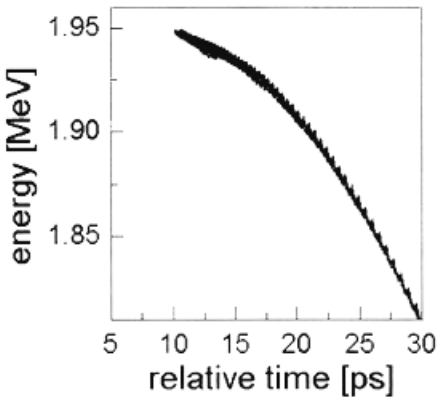

Fig. 8. Time dependence of energy of output beam

Table I summarized the optimized design parameters of the S-Band OCS RF gun. A prototype RF gun is under construction. The beam test will be expected to begin in early 1999.

Fig. 9 shows a comparison of experimental result of an axial field distribution and EMSYS computation.

Table I

Frequency:		2856MHz
Band Width:		103MHz
Peak Beam Energy:		1.9MeV
Peak RF Power:		5.0MW
β (Input Coupling):		3
Coupling Coefficients	k_{12}:	1.4%
	k_{23}:	3.6%
Peak Beam Current:		17A
Normalized RMS Emittance:		11πmm·mrad
Energy Spread (FWHM):		25KeV

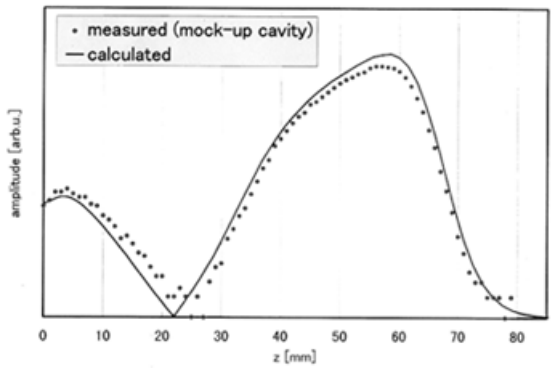

Fig. 9. Measured and calculated longitudinal field profile

4 CONCLUSION

The new on-axis coupled standing wave RF gun structure is presented. This structure offers numerous advantages over the RF guns, which are commonly used. It can be used with either the photocathode or thermionic cathode. Two prototype RF guns are under construction along with a hollow beam thermionic cathode with a beam dumper placed in the center of the cathode.

REFERENCE

[1] J.E. Clendenin, "RF Photo Injector," Linear Accelerator Conference Proceedings, 1996.

[2] E.A. Knapp, et al., "Standing Wave High Energy Linear Accelerator Structure," *Rev. Sci. Instr.* **39**, 979 (1968).

[3] E. Tanabe, et al., "A 2-MeV Microwave Thermionic Gun," Linear Accelerator Conference Proceedings, 106 (1989).

THE HIGH VOLTAGE SYSTEM FOR THE HIGH INTENSITY CERN PROTON SOURCE

C.E. Hill, M. O'Neil
PS Division, CERN, 1211 Geneva 23, Switzerland

Abstract

For the RFQ injector mounted on the CERN 50 MeV proton linac, the source needs to provide about 300 mA of 100 keV beam in pulses of 20 to 150 μs at 1 Hz. Although the high voltage supply is fairly conventional, a number of measures had to be taken to ensure not only the reliability of the source electronics, but also other equipments installed in the near vicinity. In view of the high current demanded from the source, a new and very simple form of beam load compensation was developed to stabilise the preinjector voltage to values acceptable to the RFQ.

1 BACKGROUND

The original 750 kV preinjector for the CERN Proton Linac (Linac2) used a Cockroft-Walton (C-W) high voltage supply with dynamic beam load voltage stabilisation [1]. In 1993, this injector was replaced by a Radio Frequency Quadrupole (RFQ) system whose injection energy was 90 kV. This voltage was chosen to be close to that of standard commercial high voltage power supplies whilst still allowing a small margin for injector column conditioning.

The ion source is a standard CERN Duoplasmatron with the steel body adapted to the length of the injector column. This two-section column uses two porcelain rings 300 mm diameter by 60 mm thick which were recovered from parts of the original CERN Linac1 preinjector [2]. The porcelains are glued with Araldite to the end flanges and an intermediate disk which is fitted internally with a stress relief electrode. Corona plates which also carry bleeder resistors complete the assembly.

Source supplies and controls were installed inside the Faraday cage in open racks supported on polyethelyene insulators,. This assembly gave a very compact system at a location where space was at a premium, whilst also allowing easy access for maintenance. The minimum clearance between racks and the cage is about 330 mm.

Following problems with backstreaming oil vapours from turbopumps on the RFQ test stand, virtually oil-free magnetic bearing turbopump systems were adopted to pump the high hydrogen load.

2 HIGH VOLTAGE SYSTEM

For the operational injector a modified standard commercial high voltage supply was chosen. The supply was specified for 120 kV, 1.2 mA with a current limiting mode and modified for interlock and control purposes. High voltage was led into the Faraday cage via a length of RG218 cable.

Figure 1 shows the layout of the high voltage system which can probably be described as fairly conventional. During off-line tests of the RFQ, a 100 nF capacitor was used as an energy reservoir to maintain the voltage during the beam pulse. As this did not give rise to problems, it was adopted for its simplicity for the operational machine. A single point earth very similar to that used on the test stand was also installed. It soon became obvious that the selected earth point had been badly chosen as HT flashovers often resulted in trips of the vacuum pump electronics (and other power supplies).

A new star point was found which resulted in a complete elimination of the problems with the vacuum pump controllers although there are still occasional problems with power supplies latching up.

Flashovers are detected and cause the HT reference to be automatically reduced to a low value. A programmed ramping of the reference then takes place bringing the voltage back to normal after about one minute. During this time the source is inhibited until the HT has reached about 95% of the nominal. Depending on the weather the typical flashover rate varies from zero to about five per week. An additional interlock is provided to protect the system from the consequences of bursts of flashovers.

The control interface between ground and the source racks in this system has always been via fibre optic interfaces. Originally, it was based on a Camac serial loop. Now, in order to economise rack space, to reduce maintenance costs and to prepare for the obsolescence of certain Camac modules, an industrial based CAN bus controller interfaced to the ground level VME is in use [3]. Present experience has shown this to be rather resistant to the consequences of HT flashovers.

3 BEAM LOADING COMPENSATION

The original C-W set had stringent requirements for voltage stability. Fortunately, the RFQ is much more tolerant in its requirements for injection energy stability. With the chosen power supply, passive energy storage with a 100nF capacitor could maintain the voltage for the 120 μs beam to within 0.5%. However, with the desire to reduce the stored energy of the system, a simple active compensation scheme was developed.

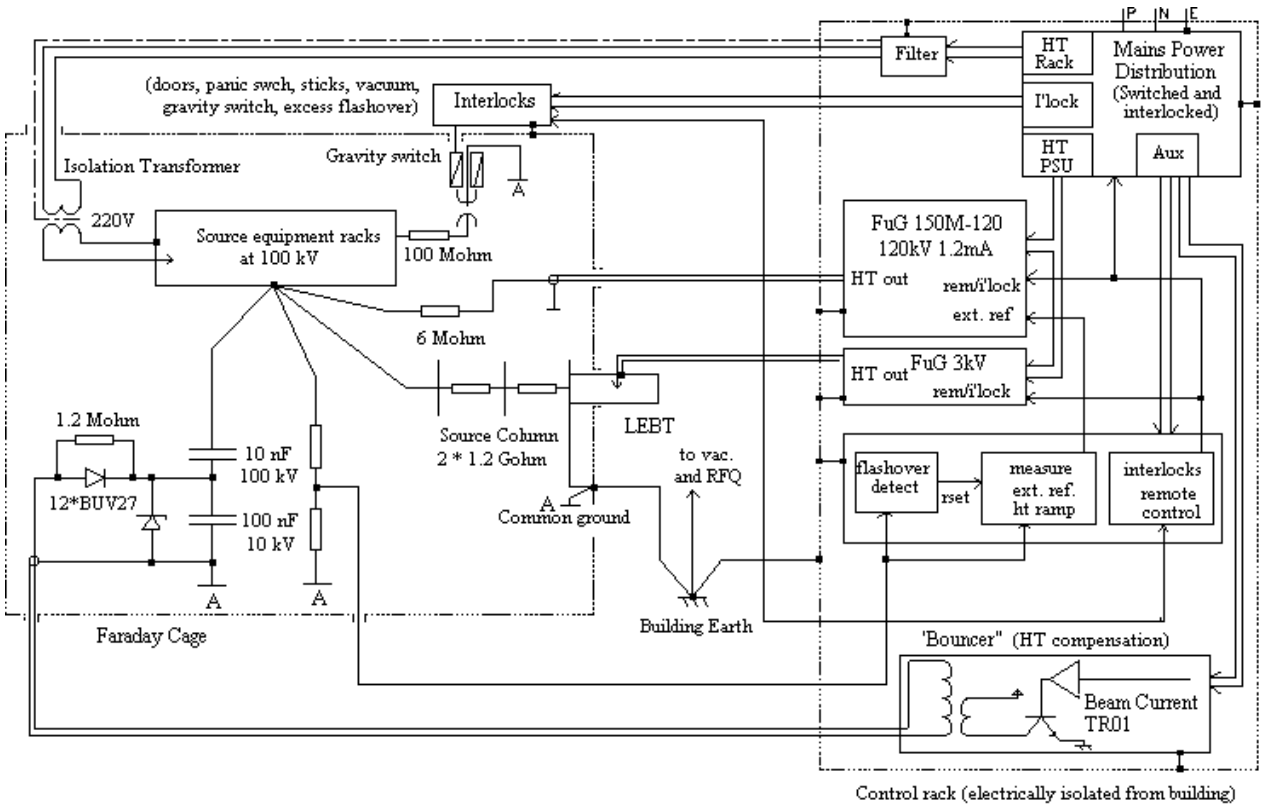

Figure 1: Schematic layout of the High Voltage system

If capacitor (C2) in Fig.2 is charged at constant current, the voltage at its high terminal increases linearly. It is then only necessary to arrange that the increase in voltage compensates the fall due to beam loading on the system capacitance. For a beam of constant intensity and length, a square pulse synchronous with the beam would be suitable to charge the capacitor. Unfortunately, at CERN pulse to pulse modulation of the beam length is used to provide only the number of protons that are actually demanded by the user. This results in the proton pulse length varying from 20 to 150 μs.

A beam transformer downstream of the source provides a quasi square wave signal which reflects both the intensity and length of the beam pulse. This signal is amplified in a transistorised power amplifier which drives a 100:1 pulse transformer. The output pulse of the transformer charges capacitor C2. Typically, the primary current is of the order of 300 A. Figure 3 shows the HT with and without beam load compensation for a source current pulse of 300 mA (trace 2), with a useable length of 92 μs. Figure 4 shows laboratory measurements on the system for a simulated beam of 300 mA and the linear rise of the voltage at C2 can be clearly seen for a constant charging current (traces 3 and 2).

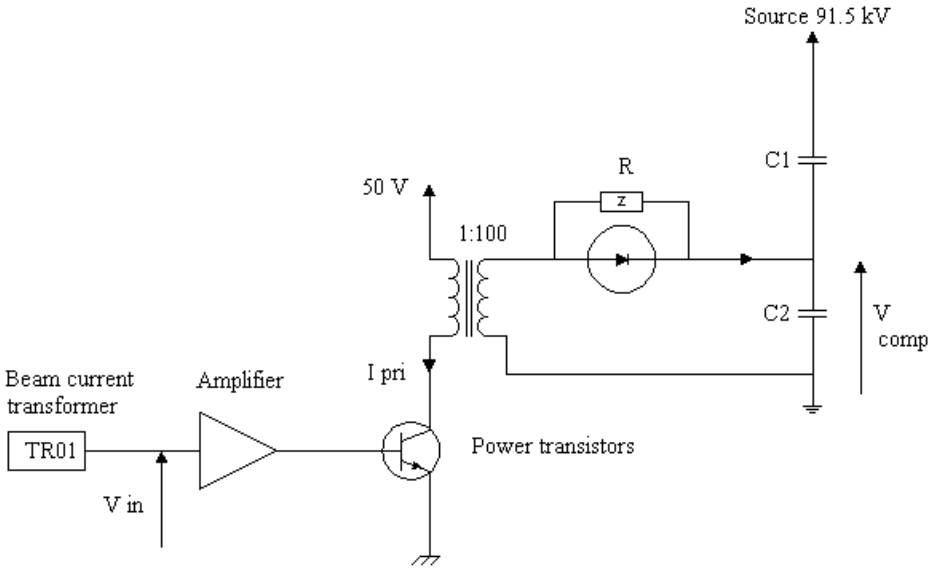

Figure 2: Block diagram of compensation scheme

The transistorised power amplifier consists of 240 BUV27 transistors in parallel made up into eight removable modules and is placed between the pulse transformer and

ground, the high side of the transformer being connected to the supply rail. A RG213 cable 6 m. long connects the secondary to the capacitive divider. After the passage of the beam, C2 is discharged through the resistor R in preparation for the next cycle. In the laboratory the compensation has run at up to 5 Hz but could probably run at a higher frequency.

Fine tuning of the compensation is achieved by trimming the gain of the preamplifier and the high voltage can be maintained to better than 0.1% during the passage of the beam (trace 1 Fig 3). Apart from amplification of the beam current signal no other treatment of this signal has proved necessary.

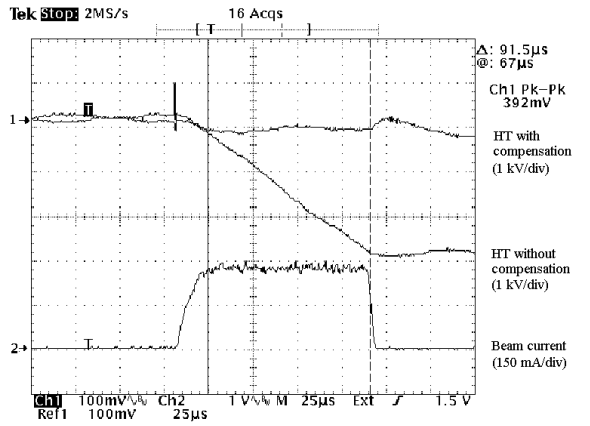

Figure 3: Comparison of high voltage stability with and without beam loading compensation.

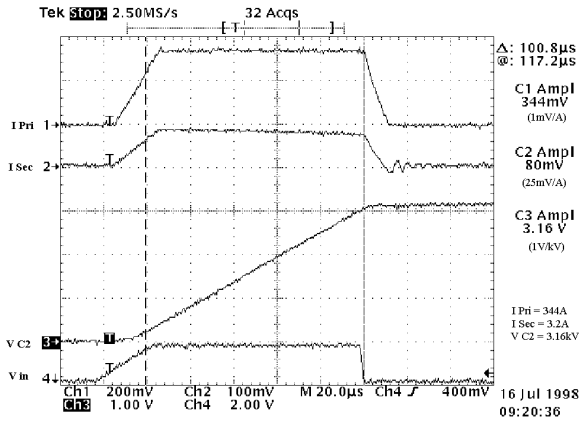

Figure 4: Voltage and current waveforms at key points in Fig.2 under simulated operation at 1 Hz.

4 RELIABILITY

Reliability of the injector is of prime importance, especially with the increasingly longer operational periods now becoming common at CERN. In 1998, the longest continuous period will be of 29 weeks. For the systems described here, the commercial power supplies have shown themselves to be particularly reliable and it has proved to be of great advantage to use a current limiting HT power supply. After a particularly severe flashover which caused some damage to the accelerating electrodes in the HT column, current limiting enabled the problem to be diagnosed quickly without repeated tripping of the high voltage.

Surprisingly, the transistorised drive amplifier for the beam loading compensation has not suffered any failure in its six years of operation. However, the main problems experienced to date concern the pulse transformers. Although specified for the required service in consultation with, and manufactured by, industry, they have suffered internal insulation failures. Investigations showed that the insulation was inadequate and badly designed. To overcome this problem, the transformers are being rewound "in house".

The high voltage system and the beam loading compensation now meet the requirements of simplicity and reliability. In the near future, as new modules pass flashover immunity tests, it is intended to replace the residual Camac and NIM based cards to Eurochassis standards thus eliminating obsolete, ageing and expensive equipment.

5 REFERENCES

[1] H. Haseroth, M. Hone, J. L. Vallet, "The Compensation for Beam Loading on the Preinjector of the New CERN 50 MeV Linac", Proc. 1979 Linear Accelerator Conference, Montauk, BNL 51134, 444, 1979

[2] E. Regenstreif, "The CERN Proton Synchrotron (2nd Part)", CERN 60-26. 1960

[3] G. Gräwer, W. Heinze, "Using a Fiber Optic CAN Bus for the Proton Source Control of the CERN PS Linac", CERN/PS/97-76, 1997, Presented at Int. Conference Accelerator and Large Experimental Physics Control Systems (Icalepcs'97), November 3-7, 1997, IHEP, Bejing, China

FIRST EXPERIENCE OF WORKS WITH COMPACT INJECTORS FOR TRIALS AND DRILLS OF RF LINAC STRUCTURES

V.V.Kushin, N.A.Nesterov, S.V.Plotnikov, D.N.Seleznev, A.S.Suvorov, A.B.Zarubin, V.P.Zubovsky
Institute of Theoretical and Experimental Physics (ITEP), Moscow, Russia
E.P.Bogolyubov, V.T.Bobylev, Y.K.Presnyakov, V.A.Samarin
All-Russia Research Institute of Automatics (ARRIA), Moscow, Russia

Abstract

The problem of gas loading on vacuum conditions in RF linac structures from traditional ion injectors based on duoplasmatron type source is well known. At the stage of starting high power linac trials and drills it often requires significant increase of pumping capacity to maintain the working vacuum level in resonators. The problem is mostly vital at development of multiple aperture linac structures. To simplify the problem new compact test injectors based on spark ion sources are discussed.

1 INTRODUCTION

Recently there has been a great deal of interest in studying of possible methods of remote non-destructive object composition testing by means of nuclear detection of targets irradiated by accelerated beams of light ions.

The approach known as pulsed fast neutron analysis (PFNA) is based on measuring of gamma ray spectra from remote target after its irradiation with extremely short neutron pulses produced by RF linac [1]. The obtained time and energy gamma spectra are used for material interrogation. The information is stored by means of time-of-flight analysis between the accelerator pulse and the arrival of γ-rays to *NaI* detectors located far enough from an examining object [2]. On the other hand, pretty low angular divergence of accelerated beam is required to transport it to remote target with minimal losses. The method of simultaneous acceleration of many short pulse ion beams in the same RF accelerator structure is expected to be the most promising for this purpose. Two approaches of multiple beam injection are under consideration. The first approach is based on the ion injector with multiple individual channels. The other way is based on generation of wide common ion beam with low angular divergence within ion source placed in the nearest close to multiple aperture RF structure with beam multiple channel collimating before the structure.

A compact injector of deuterium ions based on spark ion source is one of possible decision for the second approach. On the other hand, such kind of injectors may be used as test equipment for any RF structures trials and drills due to its feature to avoid the problem of gas loading on accelerator cavity.

2 MULTIPLE BEAM SYSTEMS

2.1 General comparison of single and multiple channel accelerator systems

It is well known requirements of simultaneous high intensity and small divergence of charged beams are in contradiction because of space charge loading, and only multiple beam accelerator systems are principally able to resolve the problem [3]. Let us compare properties of single and multiple channel systems with strong focusing.

If every the channel with aperture radius of a which is among multiple $(M\cdot N)$ beam system is able to accelerate maximum beam current of i_{Mm} then total current of the system is

$$I_M=(M\cdot N)\, i_{Mm},$$

And for traditional single channel linac with aperture radius of R and the same channel characteristics, maximum beam current is I_1 and it is easy to see that

$$I_M / I_1 = (a/R)^2 (M\cdot N). \qquad (1)$$

At analogous comparison of angular divergence α at the output of single and multiple beam linac systems their relationship may be estimate as

$$\alpha_1 / \alpha_M = R / a.$$

So taking into account (1) we have

$$\alpha_M = \alpha_1 [I_M / (M\cdot N \cdot I_1)]^{0,5}.$$

It is easy to see that at the same value of total current beam angular divergence at the output of multiple channel system is by factor of $(M\cdot N)^{0,5}$ times less than it is in a single channel system. It means that at given value of beam current its output angular divergence may be decreased by increasing of number of channels.

2.2 Multiple aperture RF accelerator system with space lattice focusing

Design features of multiple channel accelerator systems with alternating phase focusing (APF) as well as with some multiple channel RFQ modification [4] considered below are promised to be adequate decision for simultaneous acceleration of some hundred beams.

Let us consider the multiple beams RFQ system by using a new focusing element called "space lattice" (SL-focusing) [5]. The main idea is based on the following feature of RF accelerating fields. At the edges of drift tubes particles are exposed to transversal focusing or defocusing pushes from RF field. In particular, in drift tube linac a particle is pushed by defocusing RF field at the input and by focusing field at the output edges of drift tubes while it is roughly free from RF field action within both drift tubes and accelerating gaps. We considered a possibility of substantial amplification of focusing action from RF field by increasing a number of indicated boundary edges. It may be possible if some additional electrodes are placed within every accelerating gap.

By making *M* horizontal grooves from one flat side of the thin electrode plate to the middle of its thickness as well as *N* vertical grooves from the other side of this electrode again to its middle we get metal space lattice with *(M· N)* rectangular aperture holes with relatively thin walls in between (see fig.1).

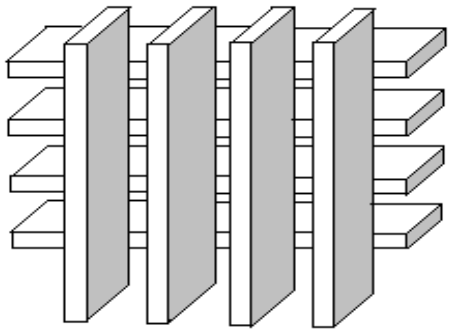

Fig.1.The fragment of Space Lattice electrode.

If several thin SLs are arranged along the common axis one after another at the equal distances between them within accelerating gaps of the multiple channel linac we have a system which can accelerate some hundred beams simultaneously. In case of circular apertures in thin electrodes focusing and defocusing forces at both edges of thin electrodes are almost mutually compensated while in SL every particle is pushed in vertical direction at the input and in horizontal direction at the output edges even at very thin electrode depth. If we arrange *n* SLs within an accelerating gap particles will be *n* times pushed by focusing strength in the vertical plane and *n* times pushed by defocusing strength in the horizontal plane. When SLs are arranged within every gap particles will be suffered some focusing action in one of transversal direction and defocusing action in other transversal direction. By turning SLs by an angle of 90^0 in every the following gap it is possible to create a sequence of sign-alternating strengths analogous to field strengths at space-homogeneous RFQ focusing. In fig.2 some possible realization of SL focusing electrodes with 324 aperture holes as well as their use in multiple channel accelerator structure is presented.

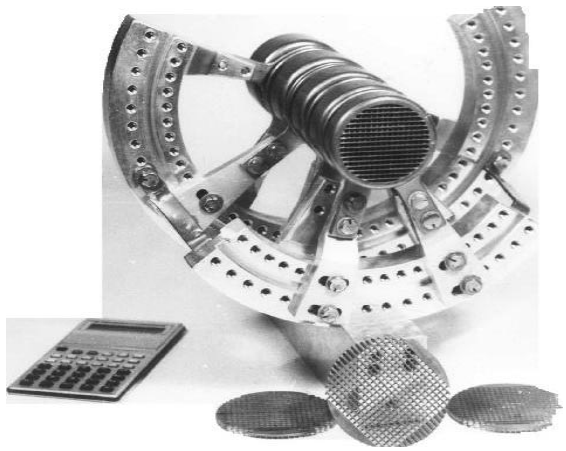

Fig.2. Space lattice electrodes and their possible arrangement in RF structure

3 SHORT PULSE TEST INJECTOR

The injector is designed for generation of very short pulses of ion beam as well as its preliminary acceleration in the range from 50 keV up to 150 keV [6]. The important feature of the injector is its small sizes due to possibility of placement both ion source and high voltage accelerator block within the same metal-ceramic package of *680 mm* long and *130 mm* in diameter. Such a configuration may produce protons, deuterons or heavy ions formed with pulses of nanosecond or microsecond ranges and followed with repetition rate up to some tens or hundred pps. On the other hand, such injector may be fixed at input flange of multiple channel RF accelerator structure at once due to the property of discharge initiation with no initial gas concentration (gas is stored in source electrodes as hydride of metal).

Vacuum accelerating tube of TNT-147 designed earlier in ARRIA for neutron generators is used as the main part of the injector. Ion generation is based on the property of desorption of deuterium occluded in metal cathode at spark charge, and its ionization in arc of spark discharge. Ion pulses are generated by formation of accelerating voltage of nanosecond range at microsecond pulse current of ion source. Ions are extracted from plasma bunches at electric field supplied between plasma gun anode and extracting electrode. Plasma gun is switching on at the moment of capacity discharge or inductive energy storage on the anode-cathode gap of the gun.

A spark-type ion source is based on the feature of some metals, such as *Ti, Zr, or Sc,* heated in the condition of hydrogen or its isotopes, to form hydride of metal as result of exothermic reaction. The process leads to saturation of a metal cathode with hydrogen. The saturated metal cathode in the form of washer is placed within the body of the ion source (fig.3).

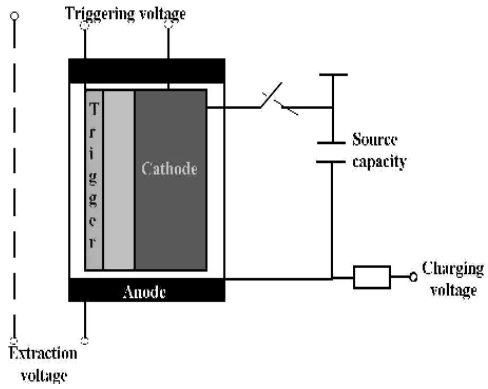

Fig.3. Short pulse spark ion source

The trigger electrode placed near the cathode supplies initial electrons to heat the cathode for gases desorption in the source volume. The electric arc is formed between cathode and anode electrodes. It is drifting to an open edge of plasma gun where ions of hydrogen are extracted and accelerated by high voltage potential. Pulse source is used as a source of trigger voltage. Pulse duration of extracted ion beam is in strict accordance with the duration of pulses of extraction which is able to be varied in rather wide time range from some nanoseconds to several tens of microseconds. The problem of electrical insulation is simplified in short pulse mode of source work. The unit of pulse formation is based on the scheme with electric capacity energy storage and pulse transformer. High voltage pulses are generated at the transformer's secondary and supplied to the gap between trigger electrode and anode.

The acceleration block of the injector includes spark ion source and trigger pulse former which contains high voltage transformer, accumulator capacitors and high voltage throttle. The elements of the acceleration unit are mounted within the same frame of metal ceramic tube. One of butt-ends of the tube is covered hermetically with the lid supplied with high voltage connectors, the other one serves to join injector with RF accelerator structure. The output flange of the accelerator structure is connected with the injector body by bellows for adjusting purpose.

Independent tests were carried out with proton and deuteron short pulse injectors. The cathode of the proton source was saturated with hydrogen. Pulse ion beam with output energy varied from *60 keV* to *120 keV* at pulse duration of about *1 μs* and repetition rate up to *30 pps* was formed.

We investigated regimes of pulse output current depending on ark trigger voltage at different values of anode voltage at pulse repetition rates of *1, 10,* and *30 pps.* The beam collimator with a single aperture diameter of *10 mm* was placed *100 mm* behind the injector with output aperture diameter of *60 mm*. At the distance of *80 mm* behind the collimator beam current has been measured by the system of 13 current pickups of *5 mm* in diameter every. The pickups were placed symmetric by the beam axis in three transversal layers - the central pickup and two peripheral layers of 6 pickups every. The distances from the beam axis to peripheral pickup layers are *16 mm* and *28 mm*.

The central part of the transversal beam distribution of *20 mm* in diameter contains about *60%* of total beam current while the tendency of both beam current and core diameter rising at injection voltage increase was also noted. The instability of pulse amplitude at this stage was observed rather high and sometimes exceeded *± 100%*.

The short pulse proton injector based on spark ion source was used for first trials of experimental deuteron APF linac structure with output energy of *4 MeV* at half level of RF gradients in accelerator gaps (*85 kV/cm)*. At that stage the main purpose was to calibrate all the technological units including RF level required for supply, level of optimal injection energy, etc. The *1 m* long *148.5 MHz* RF accelerator structure based on *H*-resonator with drift tubes was jointed to the injector output edge due to the injector feature of working at pretty high vacuum. The collimator with a single axis aperture hole of *10 mm* was arranged at the flange of vacuum tank *50 mm* before the first drift tube of the RF accelerator channel.

The tests of the structure have confirmed abilities of the injector to be prepared quickly for the working with high vacuum RF accelerator structure with injection current level of some tens *mA* and its easy of handling. On the other hand, the tests have pointed to the necessity of improving some injector parameters and its stability firstly.

4 REFERENCES

[1] D. R. Brown, T. Gozani. Cargo inspection system based on pulsed fast neutron analysis. - Nucl. Inst. & Meth. In Phys. Res., B 99, (1995), p.753-756.

[2] I. V. Chuvilo et al. "Accelerator-based approach experiments for remote identification of fissionable and other materials". - Nucl. Inst & Meth. In Phys. Res., B 139 (1998), p.298-300.

[3] T. P. Wangler "Summary for Working Group on Multiple Beams and Funneling", Proc. of High-Curr., High-Bright., High-Duty Fact. Ion Injectors Workshop, 173-177 (1986).

[4] E. V. Gromov, V. V. Kushin, S. V. Plotnikov, "Multiple Channel Structure For Ion Linac", Inventor's Certificate of USSR No. 256492 (1986).

[5] S. V. Plotnikov "Operating variables of RF focusing in linac structures", Thesis, 2 (1986) (in Russian)

[6] V. V. Kushin, N. A. Nesterov, S. V. Plotnikov et al. "Some features of short pulse test injector for linac", VANT, Ser.: Yaderno-fizicheskie issledovaniya, **2,3** (29,30), 146-148 (1997) (in Russian).

THE CATHODE TEST STAND FOR THE DARHT SECOND-AXIS*

C. Fortgang, C. Hudson**, D. Macy**, M. Monroe, K. Moy**, D. Prono
Los Alamos National Laboratory, Los Alamos, New Mexico 87545 USA
** Bechtel Nevada, Santa Barbara, California 93111 USA

Abstract

The injector for the DARHT second-axis will use an 8" thermionic dispenser cathode. Because the cathode is relatively large and requires a large amount of heat (5 kW) there are certain engineering issues that need to be addressed, before the DARHT injector reaches the final design stage. The Cathode Test Stand (CTS) will be used to address those concerns. The CTS is a new facility, presently under construction. The CTS will consist of a high-voltage pulse modulator, a high-vacuum diode test-chamber, and a short beam-transport section with diagnostics. This paper discusses the status of the project.

1 INTRODUCTION

The DARHT second-axis (DARHT-2) requires a 3.2 MV, 4 kA, 2 μsec injector [1]. The injector will use an 8" diameter thermionic dispenser cathode. Because such a cathode has requirements exceeding existing cathode assemblies, we are building a facility for measuring its most important engineering features. The cathode will be tested in situ as part of an operational electron-gun which has most of the design features envisioned for the DARHT-2 injector. The cathode requires 5 kW of heater power. We will measure: temperature uniformity over the cathode surface, differential thermal expansion between the cathode and focusing electrodes, and outgassing and vacuum properties. We will also test field-emission from the focusing electrodes up to an electric-field strength of 160 kV/cm. We will extract a 500 kV, 500 A beam using a PFN and a step-up transformer to generate a 1-μsec pulse. After a modest compression of the beam and a short transport section, we will measure the beam profile to assess electron-current emission-uniformity, paying particular attention to beam halo in preparation for further studies of emittance growth due to non-linear focusing forces.

2 GUN DESIGN

The electron-gun design for the CTS is very similar to that being designed for DARHT-2 by Lawrence Berkeley National Lab [2]. It is not identical because the electrical characteristics of the CTS (500 kV, 500 A) are more modest than DARHT-2 (3.2 MV, 4 kA). However, compared to the DARHT-2 design the CTS gun uses the same 8" thermionic cathode, has focusing electrodes with the same shape and is also a high perveance design (1.4 μP). The gun is designed using the computer code EGUN. The gun geometry and the electron-beam trajectory are shown in figure 1.

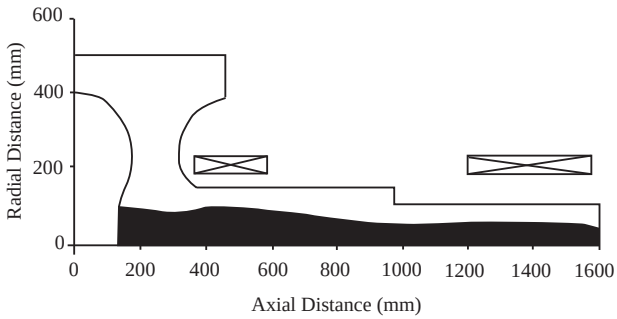

Figure 1: Electron gun design and beam envelope. Note axes are not scaled equally.

The injector uses two focusing solenoids to extract and transport the beam. Both solenoids are located down stream of the anode and have a peak magnetic field on axis of about 200 Gauss. The primary purpose of the magnetic optics is to transport the beam with a small amount of beam compression and negligible emittance growth. Under these circumstances a beam profile measurement at the end of the beam transport section can be used to determine electron-emission uniformity at the cathode.

The gun uses a M-type dispenser cathode, i.e., BaO impregnated into a tungsten matrix with a few thousand Angstrom Os/Ru coating sputtered on the surface to enhance emission and life. The cathode is heated with two counterwound filaments supplying about 5 kW of heater power. The focus electrode follows the standard Pierce diode design (67 degrees) and extends out to a large (stainless steel or molybdenum) radius shroud to minimize electric field stress.

3 EXPERIMENTAL SETUP

The configuration of the gun inside its vacuum chamber is shown in figure 2. After initial thermo-mechanical experiments, that don't require beam extraction, a beam transport line will be attached to the diode vacuum chamber. The cathode is supported by a 22" long ceramic insulator stack. Stainless steel rings are used to grade the

* Work supported by the US Department of Energy.

electrical stress along the stack. On the oil side, torlon rods under tension are used to maintain the insulator stack under compression and help support the cantilevered cathode assembly which weighs about 400 pounds. Radial and upstream heat shields surround the cathode structure to prevent heat loss and to maintain temperature uniformity. Water cooling is provided to the cathode support structure and shroud.

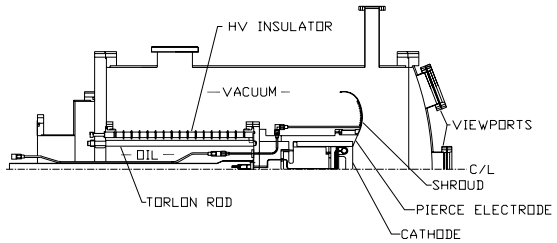

Figure 2: An assembly drawing of the gun and vacuum test chamber.

The vacuum chamber for the gun has 1 cryopump (4000 liters/sec) and 2 turbo pumps (500 liters/sec each). Because the cathode can be easily poisoned by contaminants (e.g. water, hydrocarbons) only metal seals are used and all components are to be baked for 10^{-9} Torr vacuum operation. There are several viewports on the vacuum chamber to be used for instrumentation. Ports are also available to insert quartz heating elements for in situ baking.

4 HIGH VOLTAGE MODULATOR

The HV modulator consists of a solid-state switching power supply, two 7-section PFNs wired in parallel, and a HV step-up (13:1) transformer. The modulator is presently being commissioned using a 1 kΩ dummy load. Each PFN has a characteristic impedance of about 11 Ω. An example of the modulator output and a simulation of the output are shown in figure 3.

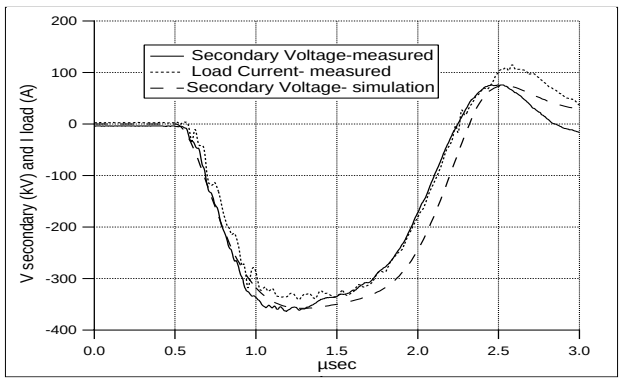

Figure 3: Modulator output waveforms compared with a circuit model simulation.

The modulator output voltage shown in figure 3 has unacceptable droop. We are in the process of replacing the PFN inductors with variable inductors. This will give us the ability to vary the waveform pulse shape and make it more constant. The modulator is capable of running at 10 Hz but we envision running the gun between 0.1 Hz and 1.0 Hz.

5 PLANNED EXPERIMENTS

The experiments to be performed on the CTS can be grouped into two categories, those without beam and those with beam. Experiments without beam will consist of measuring thermal, mechanical, and vacuum properties of the gun. Because of the high heat load (5 kW) some differential thermal expansion of components is expected. In particular, we will measure relative movement between the cathode, Pierce electrode, and shroud. EGUN simulations indicate that relative displacements of ~1mm have adverse effects on the beam quality. Pyrometers will be used to measure thermal uniformity on the cathode surface. The cathode is heated to 1100 degrees centigrade and a temperature uniformity of ±5 degrees is desired to maintain electron emission uniformity to a few percent over the 324 cm^2 cathode surface area. If we find that the temperature uniformity is greater than desired the 2 cathode filaments will be reconfigured to run off independent power supplies to gain more control of the heat deposition profile.

Another important experiment for the CTS regards field emission from the shroud. Field emission can cause breakdown and contamination of the cathode. The peak electric field at the shroud surface for the DARHT-2 injector is 160 kV/cm. The peak electric field during beam extraction for the CTS gun is only 39 kV/cm. Therefore to test for field emission from the shroud we plan to use a small grounded electrode placed close to the shroud to locally enhance the electric field. The experiment will be performed using a HV pulser with little energy storage. In this way we will achieve a high-electric field with negligible current emission from the cathode. This experiment will be performed with a hot cathode providing the same vacuum environment (dominated by the barium outgassing from the cathode) that is present when the gun is being pulsed normally.

After the first phase of experiments are complete a short beam line (~ 1m) will be installed to transport the beam to a beam profile diagnostic (see figure 1). Simulations show that with two solenoids (20 cm and 40 cm long) the beam can be transported with negligible emittance growth. By measuring current density at the end of the transport section with a beam profile diagnostic we will assess beam current-emission uniformity at the cathode surface.

6 SUMMARY

The CTS is a new facility under construction. It will be used to investigate critical engineering issues for the DARHT-2 electron gun. The modulator is built and operating. The gun is in the final design stage and fabrication of some parts has begun.

7 REFERENCES

[1] H. Rutkowski, An Induction Linac for the Second Phase of DARHT, presented at this conference.

[2] E. Henestroza, et al., Physics Design of the DARHT Electron Beam Injector , presented at this conference.

THE SNS FRONT END ACCELERATOR SYSTEMS*

John Staples, Daniel Cheng, Martin Fong, James Greer, Matthew Hoff,
Roderich Keller, Kurt Kennedy, Matthaeus Leitner, Robert MacGill,
Daryl Oshatz, Alessandro Ratti, Justin Remais, Steve Virostek
Lawrence Berkeley National Laboratory, Berkeley California, USA 94720

Abstract

The Spallation Neutron Source front end comprises a 35-70 mA volume H^- source, a multi-element electrostatic LEBT including chopping and steering, a 402.5 MHz RFQ with low output emittance and a 2.5 MeV MEBT also including chopping. The beam duty factor is 6%, with possible extension to 12%. This system, along with an LANL-supplied 1 GeV linac and a BNL-supplied storage ring, provides an average beam power of 1-2 MW to an ORNL and ANL-supplied neutron target and beam instruments facility. The current status of the front end design is described, along with results of several R&D projects leading to the final design.

1 INTRODUCTION

Over the last year the SNS design has undergone two DOE reviews and the project is expected to receive authorization for construction start. This paper reports on physics and engineering progress since the last report[1]. Hardware models have been built to test various subsystems, and some technical systems are now moving into prototype engineering design stages.

2 ION SOURCE

The design of the SNS prototype H^- ion source will be based on experiences gained with the SNS R&D ion source number 1, which is currently mounted on an ion source test stand at LBNL. A schematic of such an rf-driven (2 MHz) multicusp H^- ion source is shown in figure 1. A detailed design of this ion source has already been described elsewhere[2] .

Last year the ion source development was mainly concentrated on the extraction system[3]. Because of the high electron fraction in the beam extracted from a volume H^- ion source, an efficient electron removal scheme is essential for the 6% duty factor operation of the SNS H^- extraction system. We have chosen a novel design which deflects most electrons back to the ion source by a strong (1300 Gauss) magnetic field across the extraction hole as described in reference[4]. Only a small electron leakage current, which diffuses through the strong magnetic field, has to be dumped at a downstream electrode. To

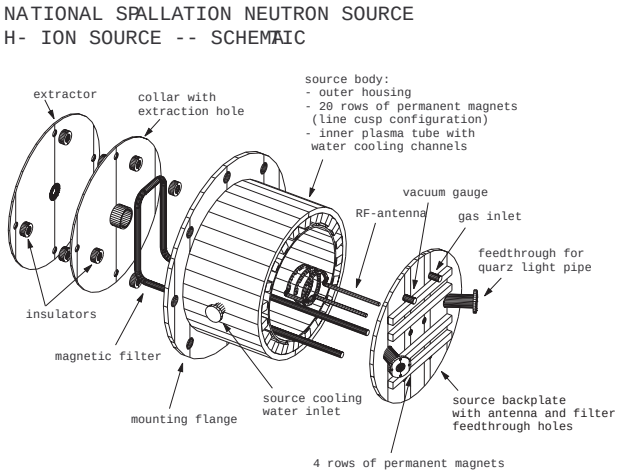

Figure 1: Ion Source Cross Section

further reduce this unavoidable power load, we have added an intermediate electrode between the plasma outlet and the extractor electrode as shown in figure 2. All electrons leaking out of the magnetic deflector will be caught on this intermediate electrode, which has only a 3kV potential difference to the ion source potential.

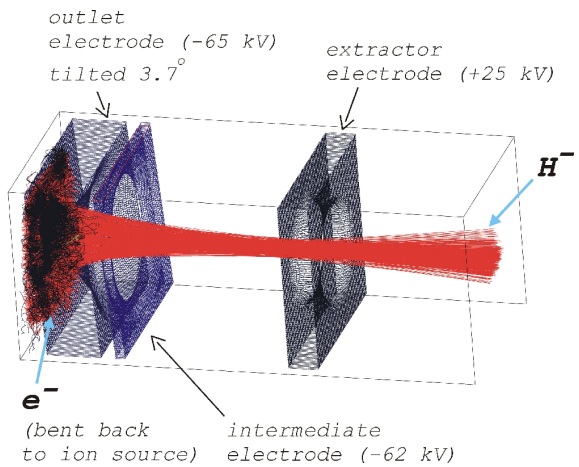

Figure 2: Ion Source Trajectories

The design of the magnetic field distribution across the extraction hole has been optimized with the 3D-ion-optics code KOBRA in combination with the 3D-magnet code TOSCA[5]. To compensate for the H^- ion beam deflection the outlet electrode must be tilted (see figure 2). It has been found that no transverse shift of the electrode is nec-

* This research is sponsored by the Lockheed Martin Energy Research Corporation under the U.S. Department of Energy, Contract No. DE-AC05-96OR22464, through the Lawrence Berkeley National Laboratory under Contract No. DE-AC03-76SF00098.

essary to inject a straight H^- ion beam into the LEBT. This feature eases the mechanical design and alignment of the SNS LEBT considerably.

3 LEBT

The Low Energy Beam Transport system has undergone some modification, described below. The all-electrostatic transport system provides a 65 keV beam to the RFQ entrance with a normalized emittance of less than 0.15π mm-mrad, with twiss parameters α = 1.6 and β = 6.5 cm.

Figure 3 shows a cross section of the LEBT electrode arrangement. The beam enters from the plasma generator off to the left, and is delivered to the RFQ through the tank endwall on the right.

The electrode geometry includes two pseudo-einzel lenses, allowing both α and β twiss parameters at the RFQ to be varied independently over a large range, and the last electrode, split into quadrants, allows beam angular steering by biasing the four segments, and beam chopping, by applying a $\pm$3 kV bipolar waveform to each segment, deflecting the beam in a stepped rotary pattern onto a four-segment beam stop. The length of the last focusing electrode has been extended to enhance the steering and chopping sensitivity. The electrically isolated four-segment beam stop, integrated into the RFQ endwall, will provide diagnostic signals of beam intensity and steering during the 35% of the time the beam is deflected away from the RFQ entrance by the LEBT chopper.

Tests on a prototype LEBT at LBNL show that the 3 kV bipolar chopper power supply rise/falltime is less than 40 nsec, and that the beam extinction time is 25-30 nsec.

The entire LEBT assembly is movable with respect to the RFQ for beam centering.

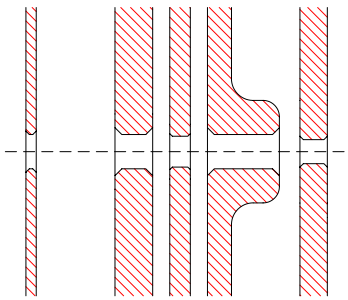

Figure 3: LEBT Cross Section

4 RFQ

The 3.7 meter-long RFQ accelerates 60 mA of H^- beam at greater than 95% transmission from 65 keV to 2.5 MeV. The r.f. duty factor is initially 6%, but the RFQ is capable of operating at 12% for a possible future upgrade of the facility to extend the average beam power to 4 MW. The RFQ comprises a single 402.5 MHz cavity, with pi-mode stabilizing loops[6] maintaining the quadrupole field symmetry in the presence of assembly errors. The one technical recommendation from the first DOE review committee was to increase the maximum current the RFQ could accommodate. This was done by increasing the peak field at the vanetips from 1.75 to 1.85 kilpatrick.

A r.f. cold model has been constructed and operated. It is full size in cross section and one-quarter length of the actual RFQ, with six pairs of pi-mode stabilizers, spaced 15.5 cm apart, as shown in figure 4. Perturbing one of the four quadrant frequencies by 1.53 MHz with plunger-type tuners causes a change in the quadrupole field balance by 2.7% worst case, with field levels in the remaining quadrants varying less. This substantial field stability will provide good field balance with normal mechanical assembly errors.

The pi-mode stabilizers move the quadrupole operating frequency down by 11 MHz and the two degenerate dipole modes up by 36 MHz from the non-stabilized cavity frequencies, with a resulting quadrupole-dipole separation of 35 MHz. No longitudinal stabilization is provided. The RFQ is five free-space wavelengths long, comparable to the JHF RFQ[6], which has no longitudinal stabilization and a measured field longitudinal field flatness of $\pm$1%.

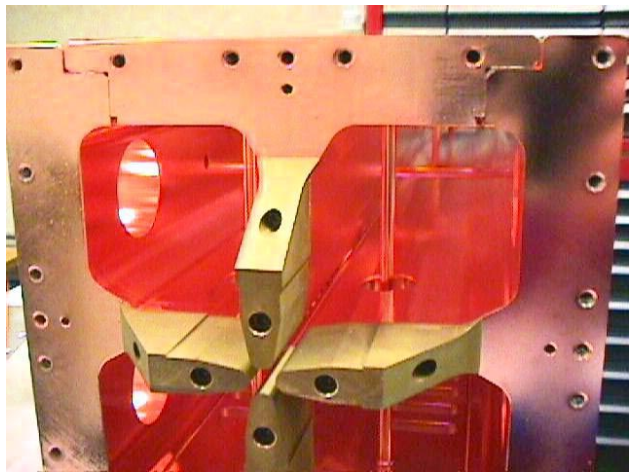

Figure 4: Cold Model End Detail, with Stabilizer

The RFQ mechanical design incorporates four separate vane quadrants which are brazed together to create the final cavity configuration. This design eliminates the need for demountable rf joints in regions of high rf wall currents. The vanes and cavity walls are made from OFE copper and they are backed by a brazed-on one inch thick piece of Glidcop AL-15©. Cooling water channels will be milled into the OFE prior to brazing on the Glidcop. Four of the 93 cm long completed modules will be joined using bolted joints with vacuum and rf seals. This method is acceptable since the longitudinal rf currents across the interfaces will be much lower than the azimuthal currents in each module. Rather than a flanged connection, the joint design will incorporate axial bolts inserted into recesses in the Glidcop

layer. Benefits of this type of joint include higher strength, more reliable seal loading and a lower profile. Canted coil springs will be used in the area between adjoining vane tips to ensure good electrical contact.

Vacuum ports will consist of an array of slots small enough to attenuate any rf leakage. The ports will be incorporated identically in all four quadrants to ensure rf symmetry. Nearby tuners will be used to compensate the locally depressed cutoff frequency near the pumping ports, leveling out local variations in the vane tip voltage distribution. The RFQ vacuum level will be maintained in the 10^{-7} Torr range.

The RFQ mechanical design and prototype RFQ models are covered further in two other papers at this conference[7] [8].

5 MEBT

The MEBT transports the 2.5 MeV H^- beam from the RFQ to the DTL, and accommodates a fast traveling-wave clean-up chopper, supplied by LANL[9]. Three rebuncher cavities and 18 quadrupoles transport the beam over the 3.6 meter length. Nonlinear space charge emittance blowup is reduced to less than 20% by the large number of closely-spaced quadrupoles, which adiabatically taper the transverse betatron period length up at the entrance, focus the beam for the traveling-wave chopper, and then adiabatically refocus the beam into the DTL.

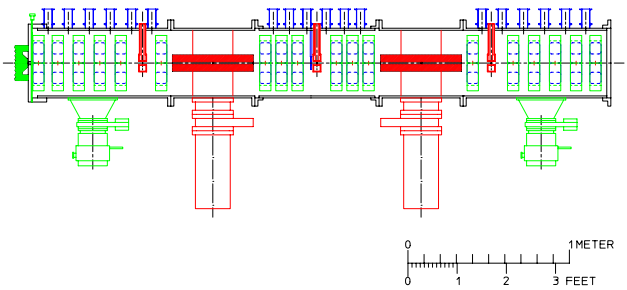

Figure 5: MEBT in Common Vacuum Chamber

The original MEBT physical configuration consisting of individual diagnostic boxes between the quadrupoles has been supplanted by a design where all components are contained inside a common vacuum chamber as shown in figure 5. Spool pieces between the beam line elements are used to maintain a low wall impedance, damping the excitation of wake fields in the vacuum chamber. The previous concept, which used a combination of EM and permanent magnet quadrupoles, has been replaced by a design incorporating only EM quadrupoles. The MEBT's high quadrupole filling factor necessitates minimizing the physical length of the magnets in order to maximize the inter-quad gaps for diagnostic devices. The associated fringe fields allow the length of an EM quadrupole to be up to one aperture radius shorter than an equivalent PM quad. To provide steering, six of the quadrupoles will be equipped with additional trim windings to create magnetic dipole fields of up to 0.03 T. All coils will be wound with solid conductor and the cores will be water-cooled.

The quadrupoles will be locally aligned to each other in groups of six on three separate strong-back structures. Mechanisms for mounting and aligning the individual strong-backs within the vacuum chamber will be provided. A distributed pumping system will be used to achieve a pressure of less than 5×10^{-8} Torr at the DTL entrance. The MEBT vacuum will be isolated from the RFQ and DTL by a pair of thin gate valves.

MEBT diagnostics will include two-slit emittance devices, Faraday cups, beam position monitors and a beam calorimeter. Additionally, toroidal beam transformers, capacitive phase probes and profile monitors will be used during routine operation of the neutron source since they are non-intercepting diagnostics.

6 ACKNOWLEDGEMENTS

The authors wish to thank Rick Gough, Craig Fong and Ron Yourd for their leadership. In addition the authors thank Jim Ayers, Don Williams, and the many other support persons who participated in this work.

7 REFERENCES

[1] John W. Staples, "The NSNS Front End Accelerator System", PAC97, May 1997, Vancouver.

[2] M.A. Leitner, R.A. Gough, K.N. Leung, M.L. Rickard, P.K. Scott, A.B. Wengrow, M.D. Williams, D.C. Wutte, Rev.Sci.Instrum. 69, 962 (1998).

[3] M.A. Leitner, D.C. Wutte, K.N. Leung, 2D Simulation and Optimization of the Volume H^- Ion Source Extraction System for the Spallation Neutron Source Accelerator, to be published in Nucl.Instrum. Methods A

[4] M.A. Leitner, D.C. Wutte, K.N. Leung, Rev.Sci.Instrum. 69, 965 (1998).

[5] M.A. Leitner, K.N. Leung, Optimization of the Volume H^- Ion Source Extraction System for the Spallation Neutron Source Accelerator Utilizing 3D Magnet and Ion Optics Codes, to be published in Nucl.Instrum. Methods A

[6] A. Ueno et al,. "Beam Test of the Pre-Injector and the 3-MeV H^- RFQ with a New Field Stabilizer PISL", Linac 96, August 1996, Geneva.

[7] A. Ratti et al,. "Conceptual Design of the SNS RFQ", Paper MO4090, Linac 98, August 1998, Chicago.

[8] A. Ratti et al,. "Prototype Models for the SNS RFQ", Paper MO4084, ibid.

[9] S. Kurennoy, J. Power, "Development of a Fast Traveling Wave Beam Chopper for the SNS Project", Paper TH4023, ibid.

FERROELECTRIC CERAMICS: A NOVEL EFFICIENT AND ROBUST PHOTOCATHODE

I. Boscolo, R. Parafioriti, A. Scurati
University and INFN, Via Celoria 16, 20133 Milano, Italy
M. Castellano, L. Catani, M. Ferrario, F. Tazzioli
INFN-LNF, Via E. Fermi, 00044 Frascati - Roma, Italy
A. Doria, G.P. Gallerano, L. Giannessi, E. Giovenale
ENEA-CRE, Via E. Fermi, 00044 Frascati - Roma, Italy

Abstract

Ferroelectric ceramics of the PLZT type, i.e. lead zirconate titanate lanthanum doped, in form of thin disks have been tested as photocathodes. The disc of material, with the back surface only metallized and held in place by a metallic ring, was set in front of a solid anode. The applied accelerating field reached 20 kV/cm and the light pulse was 25 ps long, 532 nm wavelength and its energy arrived up to 6 mJ on an area of about 10 mm^2. The vacuum was very poor. The maximum output charge was 1 nC, but it was clearly limited by space charge. A theoretical explanation of the results is only hinted because the material surface structure is very complicated and various emission mechanism concur.

1 INTRODUCTION

The photoemission from ferroelectric material has become interesting after the experiments at CERN [1, 2]. The reasonably good emissivity at wavelength varying from green to UV, coupled to robustness makes this ferroelectric lead zirconate titanate lanthanum doped (referred as PLZT) ceramic a real subject of research for an efficient and robust photo-cathode for induction linac [3], next generation of accelerators [4], FEL, ultrashort x-ray sources.

The problem of the physical interpretation of the photoemission from these materials appeared soon very difficult. In reference [5] a new physical model has been proposed in order to account for the different experimental observations.

An experimental program has been set with the aim to investigate further the physics of the emission. The green light has been chosen because it seemed more suitable for that investigation.

The sketch of the experimental setup is shown in fig. 1.

The experiment has been carried out with PLZT having composition 8/65/35 and 4/95/5, where the numbers refer to lanthanum (in relation to lead), zirconium and titanium relative atom percentage and with lead titanate, PTO_3, sample. The ceramics 8/65/35 and PT are in ferroelectric phase at room temperature, while the 4/95/5 is in antiferroelectric phase, but it undergoes a transition from antiferro to ferroelectric phase under the action of an enough high electric field [6]. These materials have a high density of defects [7], whose activation energy is about 1 eV. The samples were not prepoled. The cathodes are disks of 16 mm diameter and 1 mm thickness, coated by a uniform metallic film at the back surface and by an external ring only at the front surface, see fig. 1 b).

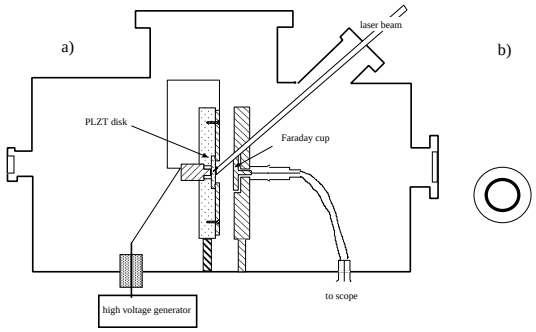

Figure 1: a) Sketch of the experimental apparatus used in the photoemission experiments; b) sketch of the cathode with the ring electrode at the front surface. The passively mode locked Nd-YAG laser provides some mJ of light at λ = 532 nm for a pulse length of 25 ps.

2 EXPERIMENTAL RESULTS

2.1 Experiments on PLZT 8/65/35 with bare front surface.

The results of the emission from a PLZT 8/65/35, fig. 1 b), are given in figures 2 and 3. The emission reached such a level that the saturation effect becomes evident. From the shape of the emitted charge versus the incident laser power, we can see that: there is a threshold and the yield in logarithmic scale increases linearly with an angular coefficient nearby 4. Extrapolating with an accelerating field high enough to avoid saturation effects, the emitted charge at 6 mJ of laser light would be 2 nC. The value of quantum efficiency results around 10^{-6}.

2.2 Experiments on PLZT 4/95/5.

We have investigated the emission from antiferroelectric PLZT 4/95/5 samples. The results are summarized in figures 4, 5 and 6.

The charge emitted increased from some picocoulombs to a couple of hundreds of picocoulombs when the applied field passed from 3.5 kV to 7 kV (equivalent to 20 kV/cm).

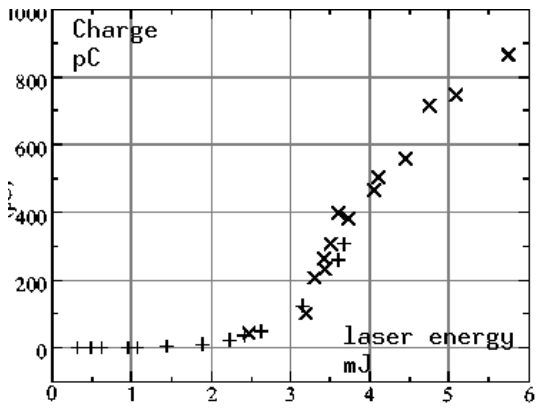

Figure 2: Emitted charge versus laser energy for a PLZT 8/65/35 without the front grid. Notice the clear bending of the curve due to the space charge effect.

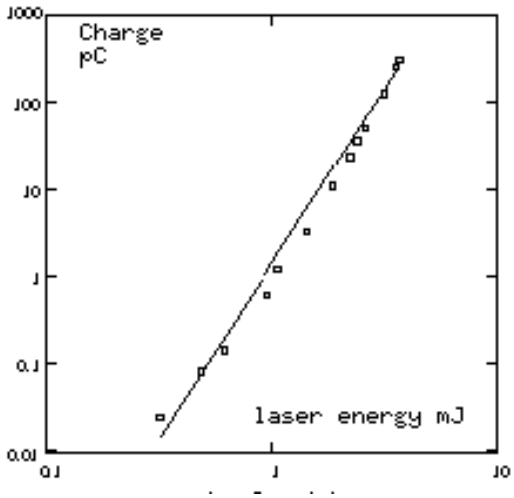

Figure 3: Emitted charge versus laser energy for a PLZT 8/65/35 without the front grid in log-log frame. The continuous line is a fit with $Q\alpha I^4$ scaling law.

In addition the log-log plot of emitted charge as function of laser power changed the slope from about 2 to the higher value around 3.

2.3 Experiments on PT.

This lead titanate material is a hard ferroelectric, good absorber of radiation in optical range. It emitted at much lower level as shown in fig. 7. We remark that the emission from this sample follows the two-photon absorption law [8], as the case of 4/95/5 sample at relatively low electric field in the diode gap.

We have, finally, tested the emission with two light pulses separated by 2 ns. The two emissions are substantially stable. The system seems able to provide pulse trains with nanosecond time separation.

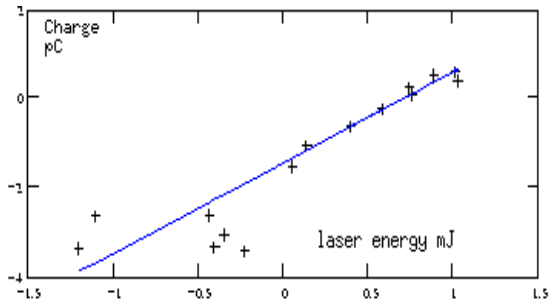

Figure 4: Emitted charge versus laser energy in logarithmic scale for a PLZT 4/95/5 sample when the applied voltage through the gap was 3.5 kV. The continuous line fits with $Q\alpha I^2$ scaling law.

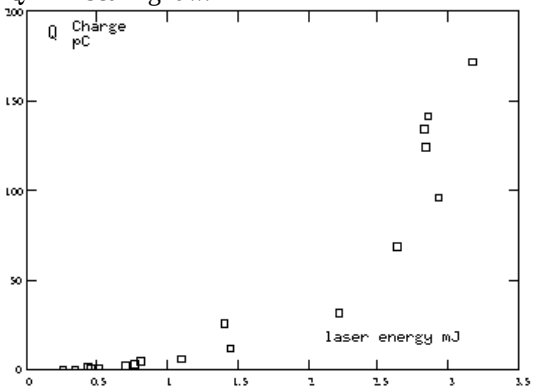

Figure 5: Emission versus laser energy for a PLZT 4/95/5 sample when the applied voltage was 7 kV.

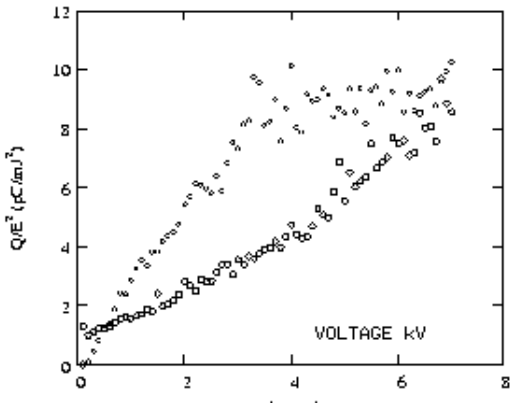

Figure 6: Emitted charge versus laser energy: the lower points are obtained at 7 kV of applied voltage, while the points of the upper curve are obtained in succession but after having reduced the voltage to 3.5 kV. The hysteretic behavior was not observed keeping constant the voltage.

3 DISCUSSION

The two main characteristics of the strong emission are: the almost negligible emission up to a laser intensity of about 1 GW/cm^2 (i.e. 2 mJ) and the high non-linearity starting from that point. In addition to this, the other notable fact is the change of the operational regime for the PLZT 4/95/5

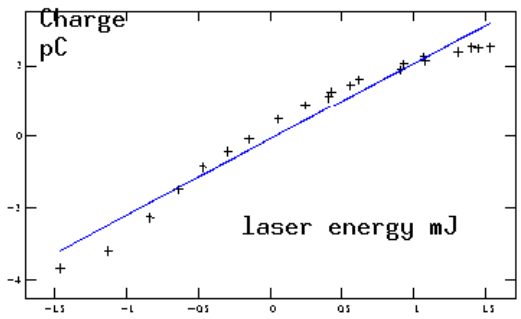

Figure 7: Charge versus laser energy in log-log scale for PT. The continuous line fits with $Q \alpha I^2$ scaling law.

sample when it is immersed in a relatively high electric field. The PT sample has stably two-photon emission.

The generalized Fowler-Dubrige theory [8] cannot explain these results. An average potential barrier higher than 4 eV is estimated in these materials for the electrons of the defect traps. The electron affinity E_a is not well defined because the surface state is un-defined: is like a patchwork of pieces with different physical characteristics, which range from insulating to metallic [9, 10, 11]. That value of the potential barrier is a fairly crude approximation.

Furthermore, our disk is immersed in the electric field applied through the diode gap, hence a counter field is created by the induced polarization. When the crystal is polarized, there is a band bending at the surfaces with a potential well for electrons at the positive side of the polarization, while there is a barrier at the opposite side [12].

The emission at 2.3 eV and its non-linearity with a power equal or greater than 4 would envision the anomalous heating regime [13], cooperating with the Auger effect [5].

More generally, we should have the concurrence of different contributions: one and two-photon emission, thermally assisted and Auger emission.

The increase of the emission of 4/95/5 sample as a function of the applied field, together with the hysteretic behavior of fig. 6 tells that the polarization is very important: when the polarization builds up in the sample, the emission steps up, then the sample remains polarized when the electric field is reduced because of the hysteresis loop. The experiment with PT material says that the polarization by itself is not sufficient for obtaining strong emission, but a strong doping, that is a large number of defects, must be also present.

Assuming that the electron pulse length is strictly correlated to the light pulse length, that is $\approx 25ps$, since the illuminated area is about 10 mm^2, the current density would be higher than 1 kA/cm^2. The laser power is well below the damage threshold.

4 CONCLUSIONS

A new very efficient configuration for ferroelectric photocathodes has been investigated. We got 1nC level of emission only because the charge was limited by space charge effect. Since the damage threshold of a ceramic is relatively high, a large amount of extracted charge can be foreseen.

The emission has shown to be very sensitive to the sample polarization. This fact allows to foresee a large enhancement of the quantum efficiency just increasing the polarization. This polarization increasing occurs naturally with the high electric field that are customary applied in electron guns.

The characteristics of these cathodes, are: a)strong robustness, they work in any kind of vacuum showing a long life; b) they do not require any particular processing; c)they can be operated with green light. In the near future the extracted electron beam will be characterized in terms of time structure. If the electron pulse duration is strictly related to the laser pulse duration, these cathodes promise to deliver current densities larger than 1 KA/cm^2 and to be valid competitors of both metallic and alkali cathodes.

5 ACKNOWLEDGEMENTS

We want to thank H. Riege for the part of apparatus he supplied us and for the encouragement to start this research; we must also recognize the technical support given by R. Sorchetti.

6 REFERENCES

[1] K. Geissler, H. Gundel, H. Riege, J. Handerek, Appl. Phys. Lett. 56, 895, 1990.

[2] K. Geissler, A. Meineke, H., Riege, S. DE Silvestri, N. Nisoli, O. Svelto, I. Boscolo, J. Handerek, Nucl. Instrum. Meth. Phys. Res.A 372, 567-571,1996.

[3] T. Srinivasan-Rao, J. Fisher, T. Tsang, J. Appl. Phys. 69, 3291, 1991.

[4] C. Pagani, P. Michelato, L. Serafini, Nucl. Instr. Meth. Phys Res. A 340, 17, 1994 and other papers in that volume.

[5] G. Benedek, I. Boscolo, Appl. Phys. Lett. 72, 522, 1998.

[6] M. E. Lines and A.M. Glass, *Principles and Applications of Ferroelectric and Related Materials*, Clarendon Press, Oxford, 1977.

[7] H. Gundel, J. Handerek, H. Riege, E.J.N. Wilson and K. Zioutas, Ferroelectrics 109,137,1990.

[8] J.H. Bechtel, W.L. Smith, N. Bloembergen, Phys. Rev. B. 15, 4557, 1977.

[9] K. Szot, M. Pawelczyk, J. Herion, Ch. Freiburg, J. Albers, R. Waser, J. Hullinger, J. Kwapulinski, J. Dec, Appl. Phys. A 62,335,1996.

[10] K. Szot, W. Speier, S. Cramm, J. Herion, Ch. Freiburg, R. Waser, M. Pawelczyk, W. Eberhardt, J. Chem. Solids, 57,1765,1996.

[11] K. Szot, W. Speier, J. Herion, Ch. Freiburg, Appl. Phys. A 64,55,1997.

[12] G. Benedek, I. Boscolo, J. Handerek, H. Riege, J. Appl. Phys, 81,1396,1997.

[13] J. P. Girardeau-Montaut, C. Girardeau-Montaut, Phys. Rev. 51, 13560, 1995.

FIELDS INDUCED BY CHOPPED BEAMS IN THE TANK CAVITY

E. Takasaki, Z. Igarashi, F. Naito, K. Nanmo and T. Takenaka
High Energy Accelerator Research Organization, KEK
1-1 Oho, Tsukuba-shi, Ibaraki-ken, 305-0801, JAPAN

Abstract

In order to accelerate high-intensity beams at the 12-GeV proton synchrotron complex at KEK, the 40-MeV proton linac has been successfully operated as an injector. The 40-MeV proton linac consists of two tanks. Recently, an acceleration of chopped beams has been tried to obtain good transmission from the Booster to the 12-GeV main ring. We thus measured the fields induced by chopped beams in the second tank, where the accelerating field is stabilized by post-couplers. The effects of the induced field on the longitudinal motions have also been observed. In this report, the measured results are described.

1 INTRODUCTION

The KEK 40-MeV Proton Linac has worked very well to supply beams to the 500-MeV Booster Synchrotron since the upgrade from the accelerating energy of 20-MeV to 40-MeV. Recently, an increase in the beam intensity of the 12-GeV Proton Synchrotron is required for experiments about neutrino oscillation. It is thus very important to accelerate beams with good quality and high intensity. Therefore, at first, we arranged a beam-monitor system and then improved the control system, the RF-source for a prebuncher and the RF-source for a debuncher system [1]. The effects of the tuning procedure of the linac on the transversal motions have been studied [2]. Otherwise, a beam-chopping system [3] has been developed and the acceleration of chopped beams has been attempted in order to control the bunch shape in the Booster.

At KEK, a 200-MeV proton linac for the Japanese Hadron Facility (JHF) has been designed [4]. The main features of the linac are a high peak current, a high average current, a high duty factor and a high performance for beam-loss problems. Therefore, an RF-source with high specifications must be fabricated, where we must guarantee that the accelerating field is stabilized within about ±1% in amplitude and within about ±1° in phase. In this linac, also, the acceleration of chopped beams with a micro structure and a long-pulse high intensity is required to paint the linac beams onto the longitudinal phase space in the next accelerator.

We think that in the near future chopped beams with a high peak current can be accelerated in a proton linac. We thus measured the fields induced by chopped beams and those effects on the longitudinal motions. In this report we describe the results measured with chopped beams produced by a beam-chopping system.

2 INDUCED FIELDS

Nominal beams accelerated by the proton linac have only the frequency components of (driving frequency) × n and a small fraction due to the phase spread. However, chopped beams have many frequency components, like (driving frequency) × n ± (chopping frequency) × m and the fraction. Figure 1 shows the frequency components of chopped beams accelerated in the first tank at KEK.

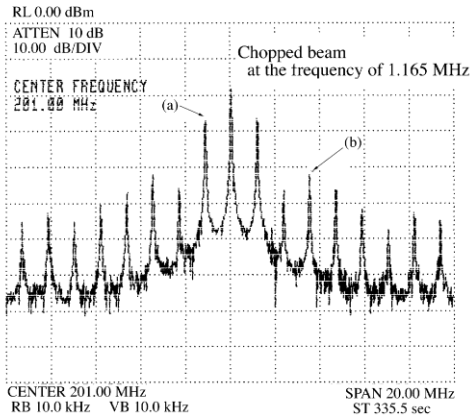

Fig. 1 Frequency components of chopped beams. Chopped beams were produced by using a beam-chopping system developed at KEK. An average beam intensity was about 8 mA. The post-1 and TM012-modes were excited by the frequency components of (a) and (b), respectively.

Furthermore, the proton linac comprises many tanks, each of which also has many resonance modes, like the TM and TE modes, and which must accelerate long-pulse high intensity beams with good quality. Therefore, when such beams pass through a tank and the beam-frequency component is near to a resonance mode in the tank, the mode would be strongly excited by the beams.

In general, such a field would be given by [5]

$$E_{bl}=\alpha_l I_l\{\exp(-j\Omega_l t)-\exp(-\omega_l t/2Q_l)\} \times \exp\{j(\omega_l t+\phi_b)\}\cos(\pi z/L). \quad (1)$$

where α_l = coefficient which is dependent upon parameters regarding to the l-mode,

I_l = beam-frequency component of beam bunches,

ω_l = l-mode frequency,

Ω_l = (TM010 mode frequency) - (l-mode frequency),

Q_l = total Q for the l-mode,

ϕ_b = accelerating phase angle,

L = tank length = 12.84 m.

Thus, the total field in the tank is given by the following superposition,

$$E = E_0 \exp(j\omega t) + \Sigma E_{bl}$$
$$= E_0 \exp(j\omega t)\{X + jY\}. \quad (2)$$

Therefore, the phase shift relative to the driving field is Y/X and wiggles with a frequency of ω-ω_l, which would correspond to the chopping frequency. We can then estimate a phase shift of about 4°, where the ratio of the induced field to the driving field is assumed to be about -40 dB. A variation of the phase shift due to the induced field is larger than a phase stability of about ±1° required for stable operation of the JHF proton linac. At the KEK proton linac, the driving frequency is 201.07 MHz and the chopping frequency is about 2.2 MHz, which is near to a post-2 mode in the second tank.

3 MEASUREMENTS

3.1 Fields Induced by Chopped Beams at KEK

The second tank has 17 rf-loop monitors for checking the field distribution of the accelerating modes. Thus, the TM01n-like mode has only been observed by using those loop monitors. At first, we measured fields induced by chopped beams in the second tank as variations of the chopping frequencies. Figure 2 shows the relation between the chopping frequency and the induced field. The measured frequencies of all the modes are consistent with the frequencies given in Reference [6]. All of the modes were determined by measuring the field distributions along the second tank. The strength of the induced field depends upon the frequency components of the beam bunches injected to the second tank and the operational phase between the first tank and the second one. We measured the ratios between the strength of the induced field and the frequency components, as shown in Figure 3. The measured results show that the higher post-modes would be not strongly excited by the beam-frequency component.

3.2 Effects of the induced field on the longitudinal motion

Though an average intensity of the chopped beams was about 8 mA, the ratio of the field strength of the post-1 mode to the main field strength (201.07 MHz) was about -43 dB, as can be seen in Fig. 2. This ratio is comparable to the ratio of the field induced by the nominal beam with an intensity of about 130 mA [5]. We thus think that the post-1 mode excitation might affect the longitudinal motion of the beams. Therefore, we measured an acceptable phase area to the second tank at beam positions (1) and (2) and on conditions whether the mode has been excited or not, as shown in Figures 4a and b.

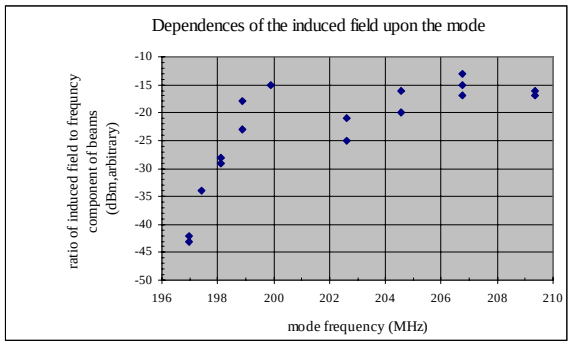

Fig. 3 Ratios of the induced field to the frequency component of bunched beams injected into the second tank. Higher modes of the post-type modes are weakly excited. However, the TM01n modes are almost equally excited.

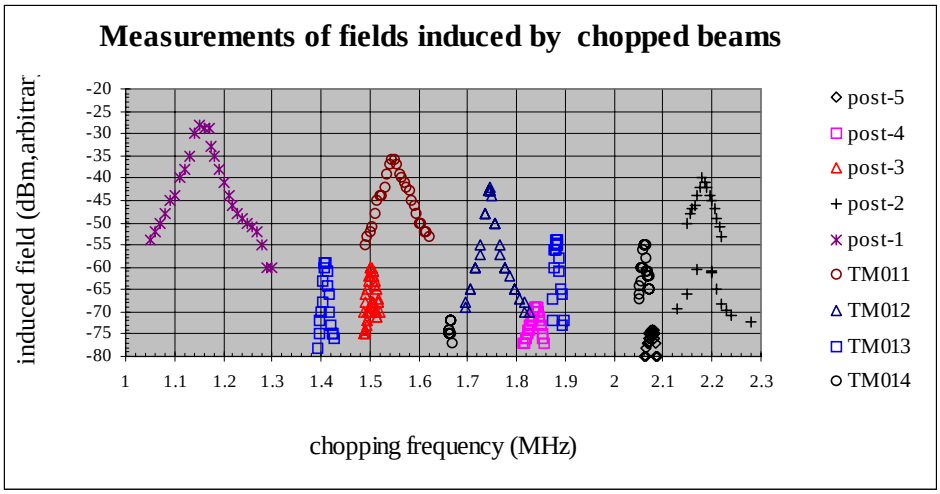

Fig. 2 Relation between the chopping frequency and the induced field. We measured the field distributions using 17 rf-monitors installed along the second tank, and then determined all modes of the measured fields. In our case, the post-2 mode is excited because the rf-frequency in Booster is about 2.2 MHz.

The measured results are shown in Figures 5, 6 and 7. Fig. 5 shows that the field levels of the post-1 mode are dependent on the operational phase between two tanks. We could observe some differences in those dependence between the post-1, post-2 and TM-modes.

Fig. 6 shows the energies accelerated in the second tank under conditions of different excitation levels of the post-1 mode. We thus conclude that the average energy would be independent of the induced field levels.

We can see variations of the acceptable phase areas in Fig. 7, which were measured at different beam positions and under different conditions of excitation levels of the post-1 mode. We can now conclude that the field induced by chopped beams in the tank might disturb the longitudinal motion of beams, and then narrow the acceptable phase area. Hence, it would be very important to study the relations between the resonance mode of the tank cavity and the chopping frequency. Next time, we will study the induced fields, like the TE-modes and their effects.

REFERENCES

[1] Z. Igarashi et al., 1992 Linear Accelerator Conf. Proc., Ottawa, 109-111 and 112-114 (1992).
Z. Igarashi et al., " Introduction of the Solid State RF Source at KEK 40-MeV Proton Linac", to be published in the Proc. of the 11th Symp. on Accelerator Science and Technology, Harima, (1997).
Z. Igarashi et al., " A New RF System for the Debuncher at the KEK 40-MeV Proton Linac", submitted to this Proceedings.

[2] E. Takasaki et al., " Effects of Controlling the 40-MeV Proton Linac on Transversal Motions", to be published in the Proc. of the 11th Symp. on Accelerator Science and Technology, Harima, (1997).

[3] K. Shinto et al., Rev. Sci. Instrum. 67(3), p. 1048, March (1996).

[4] JHF Project Office, KEK Report 97-16.

[5] T. Kato and E. Takasaki : IEEE Trans. Nucl. Sci. Vol. NS-28 NO.3 (1981) p.3507.

[6] T. Kato, KEK Report 86-5.

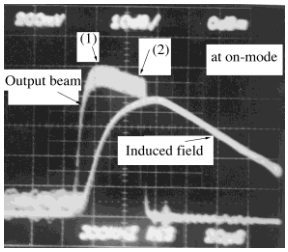

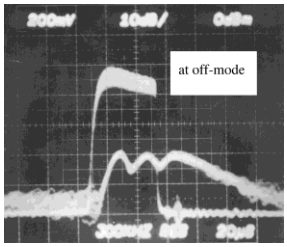

Fig. 4-a; “on-mode” Fig. 4-b; “off-mode”

In Fig. 4, the conditions are given for when we observed the effects of the induced field on the longitudinal motions. Both 91) and (2) are the beam positions measured on a long beam pulse. We selected these positions while considering that the strength of the induced field would increase exponentially.

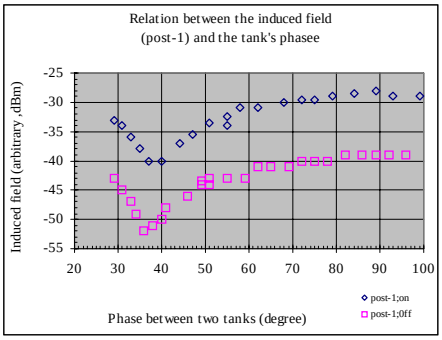

Fig. 5. Relation between the field level of the post-1 mode and the operational phase between two tanks.

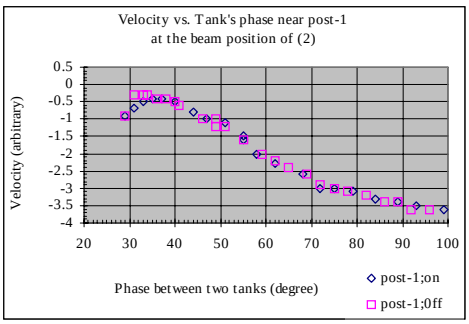

Fig. 6 Relation between the velocities and the operational phase.

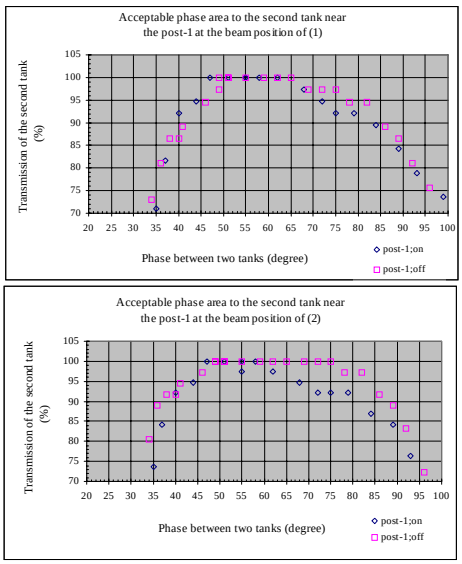

Fig. 7. Acceptable phase area on the second tank. The results measured at the beam position of (2) show that the variation in the acceptable phase area strongly depends on whether the post-1 mode is excited or not.

DESIGN AND DEVELOPMENT OF THE LEDA SLOW WIRE SCANNER PROFILE MEASUREMENT*

J. F. O'Hara, ALLIEDSIGNAL FM&T**; J. F. Power, LANL;
J. Ledford, LANL, J. D. Gilpatrick, LANL; J. Sage, General Atomics, M. Stettler, LANL

Abstract

The Low Energy Demonstration Accelerator (LEDA) [1, 2] is being developed at Los Alamos National Laboratory as part of the Accelerator Production of Tritium (APT) project. One of the diagnostics being developed to commission LEDA [3] is a slow wire scanner beam profile measurement. Initial profile measurements will be made at 6.7 MeV beam energy and 100 mA beam current. The wire scanner is an interceptive device that will move two silicon carbide coated graphite mono-filament fibers (wires) through the beam, in order to obtain the profile. Some of the design considerations discussed are; Mechanical design, wire temperature analysis, secondary electron detection, signal processing, and system control.

1 SCANNER MECHANICAL DESIGN

Fig. 1 shows the LEDA Slow Wire Scanner. The wire scanner will be mounted at 45° angle to the beam line in the diagnostic pump port of the LEDA High Energy Beam Transport (HEBT) [4]. The sensing wires are 100 μm silicon carbide fibers mounted on an aluminum fork. This material was selected based on the successful use of silicon carbide at LANSCE (Los Alamos Neutron Science Center) [5]. In order to prevent the x and y scanning wires from being in the beam at the same time the wires are mounted in a "V" design. Two biasing wires surround each signal wire. The biasing wires are also silicon carbide and will have a high voltage on them. The biasing wires prevent the secondary electrons from back streaming on to the signal detection wires and also will optimize the Secondary Electron Coefficient (SEC) of the wires. This configuration called for approximately 370 mm of travel to get both signal fibers fully through the beam scanning area. To clear the fork back out of the scanning area requires an additional 90 mm of travel.

1.1 Drive System

A fractional horsepower stepper motor moves the scanner through the beam. Coupled to the stepper motor is a modified Huntington Labs linear motion feed through. The stepper motor drives a ball screw that converts rotary to linear motion.

*Work supported by the US Dept. of Energy.
**Operated for the US Dept of Energy under Contract No. DE-ACO4-76-DP00613.

There are two separate position feedback systems, a rotary potentiometer and a linear optical encoder. Preliminary system testing shows the rotary potentiometer has an uncertainty of 0.17 mm and the linear optical encoder has an uncertainty of 0.013 mm.

1.2 Vacuum Considerations

The drive system lies outside the vacuum boundary of the beam line. A flexible welded bellows seals the actuator to atmosphere. The actuator mounts to the beam line with the use of metal sealed flange connections. Inside the vacuum chamber the actuator bolts to the fork that is in turn connected to a recirculating ball linear bearing. The linear bearing moves on a precision guide rail. The linear bearing guide rail system stabilizes the wire configuration during data acquisition.

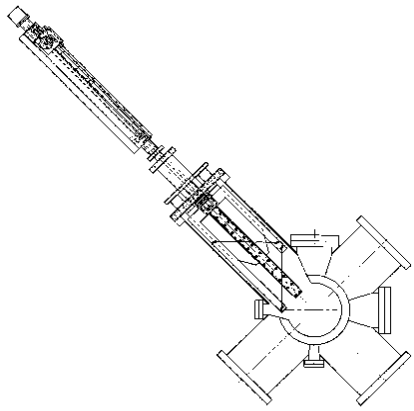

Figure 1. LEDA Slow Wire Scanner

2 WIRE TEMPERATURE ANALYSIS

The sensing wires will intercept the beam as they move through it. The protons that move through the wire will interact with the electrons in the wire material atoms. The electron will sense an attractive force due to the oppositely charged proton. This force can cause the electron to move to a higher lying shell (excitation) or if it is large enough it can actually remove the electron (ionization) [6]. The energy lost to the wire material comes at the expense of the proton, and this energy will cause a temperature increase in the wire material. The problem with this measurement technique is that if the energy deposited in the wire becomes too great it can cause the destruction of the wire. In order to predict the operating parameters that the wire is capable of surviving it was necessary to do a thermal analysis of the sensing wires.

2.1 Governing Equations

The analysis began by performing an energy balance on a control volume around the wire [7] and arriving at the following governing equation:

$$0 + \rho \frac{dE}{dx} I_{peak} V - \varepsilon\sigma\left(T^4 - T_{surr}{}^4\right)A_s = \rho V c_p \frac{dT}{dt}$$

Where,

ρ - wire material density (gm/cm^3).
dE/dx - stopping power (MeV-cm^2/g).
I_{peak} - peak current of the beam (μA/cm^2).
V - the volume of the wire under consideration (cm^3).
ε - emissivity of the wire material.
σ - Stephan-Boltzman coefficient (W/(cm^2-K^4)).
T - temperature of the wire (K).
T_{surr} - temperature of the surroundings (K).
A_s - surface area of the wire (cm^2).
c_p - specific heat capacity of the wire material (J/(g-K).
dT/dt - time rate of change of temperature (K/s).

The first term represents the energy entering the control volume that, in this case, is zero. The second term represents the energy generated inside the control volume, which is due to the stopping power [8] of the wire material and to the beam current. The third term represents the energy out, or the radiant cooling of the wire. The term on the right hand side represents the energy stored inside the control volume.

2.2 Numerical Analysis

A numerical integration technique is used to determine the time rate of change of temperature (dT/dt). Early on in the development of the scanner it became clear that no material would be able to withstand the intense CW beam conditions. It was therefore necessary to determine what pulsed mode operating parameters the wire material could tolerate. Fig. 2 shows a typical plot of the temperature rise in a 100 μm silicon carbide wire at a 500 μs beam macro pulse length and a 1 Hz beam repetition rate.

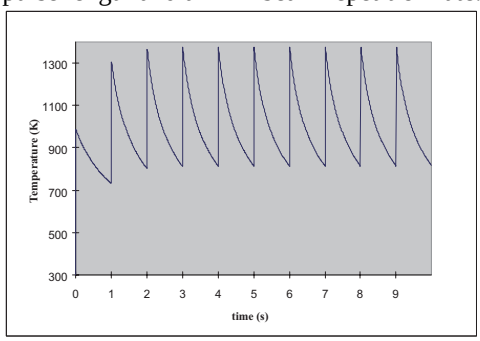

Figure 2. Temperature rise in SiC Wire

A series of analyses were done at various pulse lengths and repetition rates in order to determine the safe operating conditions of the wire. Fig. 3 shows the safe wire operating conditions based on a 500 ms beam pulse length at different repetition rates. The primary requirement was to keep the wire temperature below 1400 K, based on manufacture supplied data (Textron Systems, Wilmington, MA).

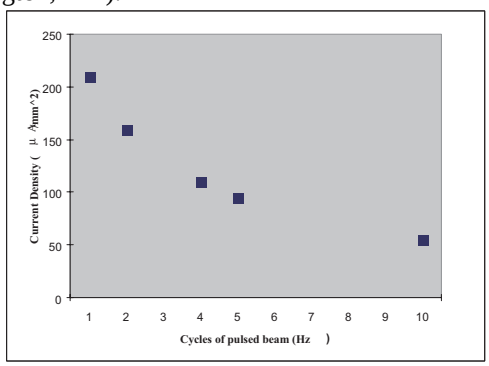

Figure 3. Scanner operating parameters for 500 μs beam pulse length.

2.3 Finite Element Analysis

A finite element analysis (FEA) was also done on the wire. Included in the FEA was the effect of the thermal conductivity of the material. Fig. 4 shows the results of an FEA model of a SiC fiber exposed to a 500 μs beam pulse and the conduction effects as the heat is being transferred along the wire axis.

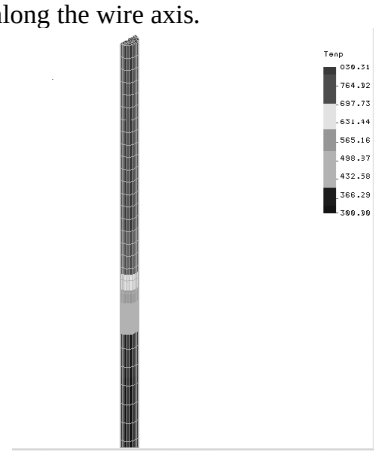

Figure 4. FEA model showing conduction effects

3 SECONDARY ELECTRON DETECTION

The signal for this measurement is taken directly from the sensing wires. The signal will be the sum of the protons stopped in the wire and the secondary electrons leaving the wire surface.

3.1 Secondary Electron Yield

Protons passing through the wire surfaces generate secondary electrons, both as they enter and as they exit. Using Sternglass's theory [9] the amount of secondary electrons generated can be stated as follows:

$$Y = \frac{Pd}{\varepsilon}\frac{dE}{dx}.$$

Where,

Y = electron yield.
P = probability that electron will escape (0.5).
d = average depth from which the electron escapes (nm).

e = average kinetic energy lost by an ion per ionization in material (MeV).
dE/dx = stopping power (MeV-cm^2/g).
The anticipated secondary electron yield for the LEDA wires is: Y= 0.012, which corresponds to a 16 mA signal at the distribution peak with 100 mA beam current.

3.2 Signal Processing

The current or charge measurement electronics will be packaged in VXI format. An onboard Digital Signal Processor (DSP) will enhance measurement and data analysis features. An on-line calibration and verification system will also be included.

3.3 Secondary Electron Coefficient, Ψ, Calculation

One of the features being incorporated into the scanner control system will be the ability to do an on-line calculation of the SEC, Ψ. This is done by measuring a beam profile, normalizing the average beam current present during each point in the scan, as measured by the ac Beam Current Monitor system. The average SEC is calculated as the measured wire current divided by the theoretical current intercepted by the wire, assuming a Gaussian distribution.

4 SYSTEM CONTROL

The wire scanner will be controlled by the Experimental & Physics Industrial Control System (EPICS) [10, 11]. Motion control sequences are written in State Notation Language, the EPICS implementation of a finite state machine. There will be three main screens.

4.1 Calibration Screen

This screen will be used to perform the on-line system verification. The operator will have the capability to check the condition of the sensing wires and verify the voltage on the biasing wires. The operator will also be able to verify the scanner position accuracy by running the scanner, acquiring position information and comparing this information against past performance.

4.2 Status and Scan Execution Screen

This screen will provide the operator information about the scanner and other accelerator functions. There will be links to the Run Permit system, information on beam pulse width, beam repetition rate, and the measured beam current. The operator will select from five types of scans.

Fast scan: This scan is intended to provide a quick, coarse resolution profile.

Slow scan: This scan is intended to provide a high resolution profile.

Find peak scan: This scan is a combination of the fast and slow scans.

Go to position and stay: The scanner will move to the operator-defined position and remain there.

User-defined scan: The operator has the ability to define the scan range (for both x and y axes) as well as the desired bin size (distance between data points).

4.3 Data Analysis Screen

This screen is where the profiles will be displayed. There will be two plots, one for each axis profile. Interactive Data Language (IDL) will be used for data reduction. IDL is a commercial software package used for analysis and display of scientific data. The operator will have the ability to display calculated moments of the raw data and the parameters determined from a Gaussian fit.

5 SUMMARY

Wire Scanner system testing and development are continuing. The scanner is scheduled for use this fall during The LEDA commissioning process.

6 ACKNOWLEDGEMENTS

The LEDA Slow Wire Scanner design was based heavily on scanners currently in use at LANSCE. The LANSCE-2 group was responsible for the design of these scanners. We gratefully acknowledge their generosity and assistance.

7 REFERENCES

[1] J. D. Schneider, "APT Accelerator Technology," Proceedings of XVIII Int. LINAC Conf., (Geneva, 26-30 Aug. 1996), pp. 22-26.

[2] H. Vernon Smith, Jr. and J. D. Schneider, "Status Update on the Low-Energy Demonstration Accelerator (LEDA)," this conf.

[3] J. D. Gilpatrick *et al*, "LEDA and APT Beam Diagnostics Instrumentation," Proc. 1997 Particle Accelerator Conf., (Vancouver, 12-16 May. 1997), Paper 8P058.

[4] W. Lysenko and M. Schulze, "High Energy Beam Transport Beamline for LEDA," this conf.

[5] M. Plum and M. Borden, "Intense Beam Profile Workshop", Santa Fe, NM. Nov 6-7, 1997.

[6] G. F. Knoll, *Radiation Detection and Measurement*, 2nd ed, NY: John Wiley and Sons, 1989.

[7] F. P. Incropera and D. P. DeWitt, *Fundamentals of Heat and Mass Transfer*, 2nd ed, NY: John Wiley and Sons, 1985.

[8] W. H. Barkas and M. J. Berger, "Tables of Energy Losses and Ranges of Heavy Charged Particles", NASA SP-3013, 1964.

[9] E. J. Sternglass, Phys. Rev. 108 (1957) 1.

[10] L. R. Dalesio *et al*., "Nucl. Instrum. Meth. In Phys. Research A352 (1994) 179-184.

[11] M. Moore and R. Dalesio, "A Development and Integration Analysis of Commercial and In-House Control Subsystems," this conf.

IMPROVEMENTS ON THE ACCURACY OF BEAM BUGS

Yu (Judy) J. Chen and T.J. Fessenden
Lawrence Livermore National Laboratory, Livermore, CA 94550

Abstract

At LLNL resistive wall monitors are used to measure the current and position of intense electron beams in electron induction linacs and beam transport lines. These, known locally as "beam bugs", have been used throughout linear induction accelerators as essential diagnostics of beam current and location. Recently, the development of a fast beam kicker has required improvement in the accuracy of measuring the position of beams. By picking off signals at more than the usual four positions around the monitor, beam position measurement error can be greatly reduced. A second significant source of error is the mechanical variation of the resistor around the bug. In addition, in-situ bugs used on ETA-II show a droop in signal due to a fast redistribution time constant of the signals. This paper presents the analysis and experimental test of the beam bugs used for beam current and position measurements in and after the fast kicker. It concludes with an outline of present and future changes that can be made to improve the accuracy of these beam bugs.

1 DESCRIPTION

Perhaps the most important diagnostic developed for electron induction accelerators is the device that monitors the beam current and position in the accelerator and associated beam transport lines. This type of monitor [1] was first developed for use on the LBL ERA accelerator about 1970. It was rapidly adapted [2] for use on the Astron Accelerator [3] and has been used on all LLNL induction accelerators since. These instruments, commonly called "beam bugs", are capable of measuring kiloampere beam currents and beam position with rise times of less than 0.2 ns and relative position resolutions less than 100 μm. Signals are generated by placing a resistor in series with the inner wall of the beam transport lines and detecting the currents induced in the wall by the passage of the beam. The resistors are made of 0.2 mil nichrome foil (5.4 μm) that is spot welded across an insulated break in the beam tube wall to form a band that encircles the inside of the beam pipe. The diameter of the band equals the inner diameter of the beam pipe so that the beam sees no abrupt steps or extraneous capacitance during its passage through the bug. A small overlap is formed as the band wraps around the inside diameter of the pipe.

Figure 1 shows the design [4] of the beam bug used with the ATA accelerator [5]. The ETA-II bugs are only slightly different. The resistance of the resistor foil was approximately 20m• with a resulting sensitivity of the instrument of 1 kA/V. Also shown are measurements of the response of the bug to a 10 amp fast rising current

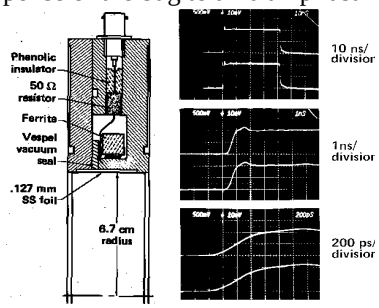

Fig. 1. Drawing of an ATA beam bug. ETA-II bugs use 5.4 μm nichrome foil and have no 50 Ohm resistor in series with the outputs. Also shown is the response of the bug (lower trace) to a 10 Amp pulse (upper trace) along the bug axis from a mercury pulser.

flowing around the resistor. Because of the very low foil resistance, the *L/R* time for the current to decay is very much longer than the beam pulse. Eight pickoffs around the circumference of the bug are used to develop the current and position signals. Two of the pickups encircle the ferrite in a direction opposite to that of the other six thus producing a negative signal. The current signal is formed by adding four positive signals from cardinal points around the bug. The *x* and *y* position signals are formed adding positive and negative signals from opposite sides of the bug. Additional information on beam bugs and other diagnostics for high current linacs can be found in [6] and [7].

2 ANALYSIS

Consider a beam moving within a conducting pipe as sketched in Fig 2. It is possible to show (by the method of images for example) that a current *I* flowing within a pipe of radius *a* at a distance *r* off axis causes a surface current to flow on the inner pipe wall.

Consider interrupting the beam pipe with a resistive band or ring placed at the inner circumference of the pipe with total resistance R. The surface current passing through the resistor that initially or for a short time develops a voltage around the pipe *V(•)* given by [7].

$$V(\theta) = IR\frac{\rho^2 - 1}{1 + \rho^2 - 2\rho\cos\theta}. \qquad (1)$$

where • = *r/a* is the normalized beam displacement. The angle • is defined by Fig. 2b. For most of the ETA-II accelerator and transport the beam current signal comes from adding the voltages of the four sum ports, S1 to S4. It is fed through a resistive summing circuit in which care

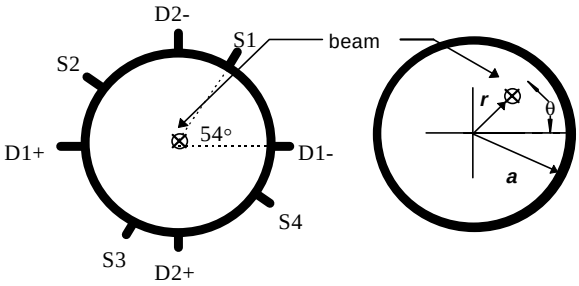

(a) (b)

Fig. 2. (a) ETA-II's beam bug port configuration and (b) Sketch of a beam off-axis in a conducting pipe

is taken to avoid reflections in the cabling. Therefore,

$$V_I = [V(54^o) + V(144^o) + V(234^o) + V(324^o)] \quad (2)$$

Similarly, the position signals are obtained with

$$\begin{aligned} V_x &= V(0) - V(180^\circ) \\ V_y &= V(90^\circ) - V(270^\circ) \end{aligned} \quad (3)$$

Combining (1)-(3) and taking the limit of small beam displacement (• << 1), we obtain

$$V_I = 4IR \quad (4)$$

and

$$V_x = 4IR\rho\cos\theta \quad (5)$$

or

$$\frac{x}{a} = \rho_x = \frac{V_x}{V_I}; \qquad \frac{y}{a} = \rho_y = \frac{V_y}{V_I} \quad (6)$$

3 IMPROVED CURRENT AND POSITION FUNCTIONS

The determination of beam current and position can be improved by using all eight pickoffs to determine beam current and position which already exists on ETA-II's beam bugs (see Fig. 2a). Define the beam x and y-position relations as:

$$\begin{aligned} V_x &= V(0) - V(180) + [V(54) - V(234)]\cos(54) \\ &\quad - [V(144) - V(324)]\sin(54) \\ V_y &= V(90) - V(270) + [V(54) - V(234)]\sin(54) + \\ &\quad [V(144) - V(324)]\cos(54) \end{aligned} \quad (7)$$

and the relation for the beam current is given by

$$\begin{aligned} V_I &= V(0) + V(54) + V(90) + V(144) + \\ &\quad V(180) + V(234) + V(270) + V(324) \end{aligned} \quad (8)$$

The relationships for *x* and *y* are the same as (6).

Let us consider in detail the error in the position signal resulting from the assumption of small beam displacement •. Fig. 3 shows plots of the error in measured beam position by the bug as a function of the normalized beam displacement • for the case of two and six pickoffs as defined above. These curves were obtained from Eq. (3) and (7). Each pair of curves show the values to be expected for the case of the beam displacement angle toward a pickoff point and for the case of the beam displacement angle half-way between two pickoff points. For an arbitrary displacement these curves bound the measurements to be expected. At a normalized displacement of •• = 1/2, the position error ranges from -37% to 48% for the case of two pickoffs and -7% to 3% for six pickoffs, a drastic improvement.

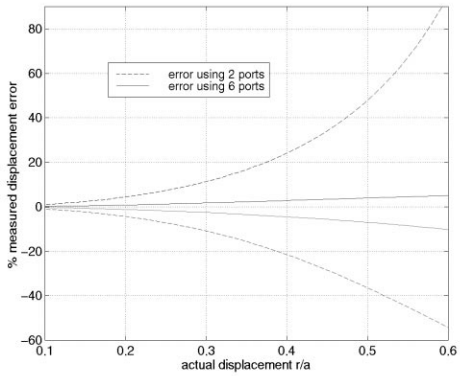

Fig. 3. Plots of the measured error as a function of the normalized beam displacement from axis for two and six pickoffs as defined above. For arbitrary angle, the point will be bounded by the two curves.

4 MECHANICAL ERRORS

Beam bugs are tested and calibrated using a mercury pulser and a test fixture. The fixture consists of two coaxial cylinders; the larger has an inside diameter equal to that of a beam bug that is attached in its center. The second simulates the beam and threads the assembly. It is smaller in diameter by a ratio of 2.3 to achieve a 50 Ohm impedance. The two cylinders are attached with tapers to a coax line that is driven by a mercury pulser. The pulser generates current pulses with a rise time of 0.2 ns that are typically 200 ns long. The oscillograms presented in Fig. 1 were obtained from such a fixture.

Measurements of the eight output signals from the beam bug show random amplitude variations of approximately ± 2%. For the ETA-II bugs this implies an uncertainty in beam position of ±1.4 mm. These errors result from variations in the resistance of the foil around the circumference of the bug. These variations arise principally from two causes. Measurements revealed that the thickness of the 5.4 μm foils randomly vary by about 2%, and variations in the spot welds that attach the foil also contribute to the error. This latter effect is evident in Fig. 4. The foil on Beam Bug 26 was re-welded with extreme care. This reduced the variation between pickoffs by about a factor of two.

5 SIGNAL DROOP

The beam bugs are fabricated of metal and essentially shorted by the housing as shown in Fig. 1. The inductor provides time isolation for the monopole current signal for times long compared with the beam pulse. This time is determined by the *L/R* time constant developed by the ferrite inductor and foil resistor. For ETA-II parameters this time is typically hundreds of microseconds. Thus the

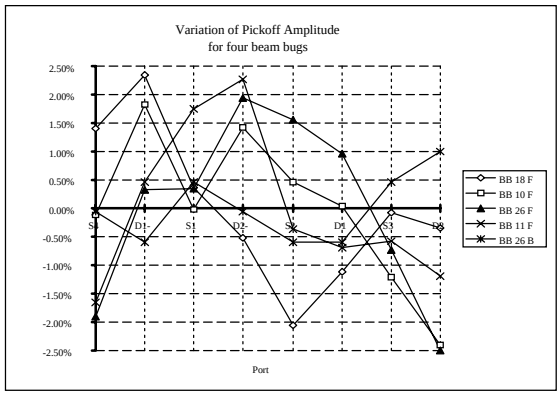

Fig. 4. Variations between electrical signals at the eight ports of four ETA-II beam bugs. The foil on Beam Bug 26 was re-attached with extreme care.

current signal will droop by less than 0.1% in the time of the 70 ns ETA-II pulse. The position signal is generated by an off-axis beam which produces a dipole excitation of the bug. The dipole component of the excitation does not link the ferrite inductor. As a consequence the droop of the position signal is much faster.

The center cylinder of the calibration fixture can be moved with respect to the outer cylinder so as to simulate an off-axis beam. Fig. 5 shows bug signals developed at opposite sides of a one centimeter offset of this center cylinder. Adding these signals together produces a signal that is proportional to the offset of the center conductor. For the parameters shown here the decay time constant is approximately 200 ns. Thus, in the 70 ns of the ETA-II pulse, the position signal droops by approximately 30%. For centering the beam this droop is of little consequence. However, for determining the position of an off-axis beam this droop must be compensated by either processing the position signal or partially integrating the signal.

The present droop compensation scheme on ETA-II is to correct it in software, thus preserving signal strength. A simple yet accurate approach is to calculate the amount of droop by finding the value the signal immediately reset to (and it is usually non-zero) and add a ramp to the signal with that amplitude. In addition, RC circuits have been built to boost the RC time constant. The advantage of using hardware compensation is speed of data processing but signal strength is compromised. These circuits have not been used yet.

6 CONCLUSION

A wealth of extremely detailed characterization on two generations of beam bugs (ATA and ETA-II) has pointed to a number of improvements that can be made on the accuracy of these diagnostics. It has been known that increasing the number of pickoff points increases off-axis accuracy. However, one must be careful about implementing this idea. The increased number of pickoffs also increases the inherent error in port to port variations as shown in Fig. 4. To combat this source of error, one should document port amplitude variation for each port on each beam bug. This can be stored in a look-up table and compensated in software. This necessitates individual measurement of each pickoff and summing and differencing is processed in software, not hardware as has been traditionally done. This also increases on-axis precision as long as bit noise is not a major source of error (if one goes to 16-bit data acquisition).

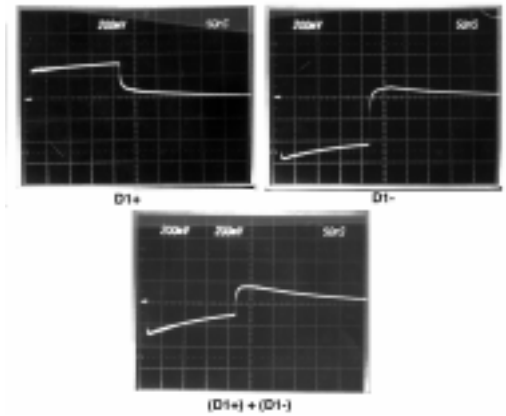

Fig 5. Oscillograms showing bug signals generated from a 1 cm offset of the center conductor of the test fixture.

The dipole *L/R* droop on ETA-II beam bugs has been corrected in software. In addition, a real-time display of processed I, X, and Y values has been implemented. In the long term, beam bugs around the fast kicker (which require a high level of precision) will have it's pickoffs individually routed to the control room.

7 ACKNOWLEDGMENTS

We are grateful to C. Holms and J. C. Clark for their assistance. This work was performed under the auspices of the U.S. Department of Energy by the Lawrence Livermore National Laboratory under Contract No. W-7405-Eng-48.

8 REFERENCES

[1] Avery, R. et al., UCRL-20166, LBL, (1971).
[2] Fessenden, T. et al., Rev. Sci. Instru., **43** , 1789, (1972).
[3] C. Christofolis et al., Rev. Sci. Instru., **35**, 886, (1964).
[4] K. Struve, "The ATA Beam Bug," internal communication, LLNL.
[5] Reginato, IEEE Trans. Nucl. Sci., **NS-30**, 2970, (1983).
[6] K Struve, Meas. Elect. Qty. in Pulse Power Sys.-II, NBS, Gaithersburg, MD (1986).
[7] Fessenden, T, Conference Proceedings No. 252: Beam Instrumentation Workshop, p. 225, AIP (1992).
[8] Chambers, F. et. al., Proc. of the 1991 PAC, SF, 3085, (1971).

A COAXIAL CABLE BEAM LOSS MONITOR ION CHAMBER SYSTEM FOR HIGH POWER MULTI-BUNCH BEAMS*

M. C. Ross and D. McCormick
Stanford Linear Accelerator Center, Stanford University, Stanford, CA 94309

Abstract

Gas filled coaxial cable beam loss monitors are a proven diagnostic in short pulse linacs and transport lines. At the SLAC linear collider (SLC), where the bunch length (σ_z) is ~ 1 mm, monitor cables with lengths ranging from 100 m to 3 km are used to locate beam losses of 5 x10^8 particles (1.5% of the nominal intensity) with a resolution of +/- 1 m. The monitor is effective because of the simplicity of its installation and signal interpretation. Future linear colliders (LC) will use beams made up of trains of many closely spaced bunches and will therefore require more careful signal processing in order to locate losses. Typical collider operation will involve the use of pilot pulses, made up of only one bunch, to test subsystem performance prior to full power operation. A simple signal processor will be able to locate losses by comparing the evolution of the loss monitor signal as the number of bunches is increased. The monitor must have 10 times greater sensitivity than the SLC monitors in order to provide a prediction of the expected beam loss at full power using only the signal from the pilot pulse. This paper describes the proposed linear collider loss monitor system.

1 INTRODUCTION

Future LC differ from the SLC in that they will use multi-bunch, very high power beams. The machine protection system (MPS) role is therefore more critical than in older, lower power machines [1] and the consequences of its failure are more severe.

The MPS for LC consists of two primary sensors: a device controller monitor and an errant beam detector (EBD). The purpose of the device controller monitor is to query the state of all appropriate devices before allowing the system to produce beam pulses. The monitor can be as simple as an analog comparison of magnet currents and will be queried and tested before each pulse. The EBD is typically comprised of loss monitors, such as gas filled ion chambers, current monitor toroid comparators and solid state radiation detectors as well as simpler devices such as thermal sensors. In an ideal system, the device controllers would be adequate to ensure that the machine is not in danger of damage from simple failures.

Some failures, such as instabilities in upstream systems, will not be identified by the device controllers. In this case, it may not be possible to recover stable operation without a diagnostic process that includes the generation of a sequence of beam pulses that may then be analyzed in order to determine the underlying cause of the fault. An essential aspect of the EBD system operation is to allow the generation of the diagnostic pulses and eventually to allow the recovery of full power operation.

2 MACHINE PROTECTION SYSTEM

The linear collider MPS will control both the termination of operation in the case of a device controller signal or an EBD signal and the restoration of full power operation. The system must at the same time protect the accelerator structure from possible single pulse induced failure (SPIF), i.e. failure that results from a single errant pulse without any warning. SPIF is a concern in future LC because the charge density, and therefore the power density, is high enough to cause substantial material damage.

Restoration of full power operation proceeds in 5 stages as outlined in table 2; 1) generation of a low repetition rate benign, low intensity, high emittance single bunch pulse which cannot cause SPIF, 2) generation of the same pulse at high repetition rate, 3) at full repetition rate, increase the single bunch intensity, 4) reduce the emittance to the nominal value, and finally, 5) raise the number of bunches (n_b) to the nominal.

The purpose of the coaxial cable loss monitor (CCLM) system is to aid in predicting what the beam loss profiles will be in order to allow the steps listed above to proceed. We will focus only on the last step, increasing n_b, since it involves the highest power beams. Collider systems are designed such that the difference between the trajectory and phase space volume of a single bunch and the projected volume of the entire train is small. However, following a system failure or an interruption, this cannot be guaranteed, so the response of the loss monitor must be checked and evaluated as full power operation is restored.

Typical Next Linear Collider (NLC) parameters are listed in table 1. Table 2 shows a typical full power recovery sequence from a 'benign' pilot beam at low repetition rate to full power operation.

* Work supported by the Department of Energy, contract DE-AC03-76SF00515

Table 1: NLC beam parameters [2]

Bunch intensity (I_b)	1 x 10^{10} e+/e-
Number of bunches (n_b)	90
Bunch spacing (τ_b)	2.8 ns (total Δz=77m)
$\gamma\varepsilon_x$(horizontal invariant emittance)	100 x 10^{-8} m-rad
$\gamma\varepsilon_y$	10 x 10^{-8} m-rad
Energy	500 GeV
Repetition rate	120 Hz
Typ. linac beam size (σ_x)	10 μm
σ_y	1 μm

Table 2: Five step full power operation start sequence for NLC. Note that beam power increases by 10^5. The multi-step sequence is required in order to use the benign pilot beam as a diagnostic and smoothly make the transition to full power operation.

Step	Parameters n_b, I_b, typ. $\sigma_{x,y}$	Charge density (C/m^2)	Average beam power
Pilot beam	1, 1 x 10^9, 30μm(1Hz)	.04	80
Full rate	120 Hz	.04	10KW
Nominal I	1, 1 x 10^{10}, 30μm	.3	100KW
Nominal ε and I	1, 1 x 10^{10}, 3μm	23	100 KW
Nominal	90, 1 x 10^{10}, 3μm	2100	8MW

The rate at which the sequence proceeds depends on the characteristic stabilization times of systems used to control the beam parameters such as the emittance controller and beam energy loading compensation. Typically, the transition between steps may require 10 or more machine pulses or sub-steps so that, for example, n_b might follow a 1,5,10,20,40,60,80,90 progression.

Table 3: Loss monitor sensitivity requirements and test results using SLC beam (see figure 3).

Trip threshold energy(V_{thres})	2 J (corresponds to 240W at full rate)
Required sensitivity	250 mV/J (5mV/(V_{thres}/n_b))
Nominal SLC system sensitivity [3]	60 mV/J
Fast gas –Ar CF_4	150 mV/J – test result
Ar CF_4, larger cable, HV gradient doubled	450 mV/J – test result

The threshold used in the MPS is determined using an estimate of the average power that can cause damage in a given mechanical subsystem (typically a few hundred watts). Operation with CCLM signals greater than the threshold voltage is not permitted. Since the nominal pulse rate is 120 Hz, the threshold against which each pulse will be compared is about 2 J (V_{thres}). An electronic sensitivity of 5mV/(V_{thres}/n_b) is required so that an estimate the losses at full n_b is possible. Table 3 summarizes the threshold and CCLM sensitivity requirements.

3 LOSS MONITOR SYSTEM

Gas-filled coaxial cable loss monitors have been used at SLC and other accelerators for the last few decades [3, 4, 5]. They offer excellent position resolution (1m) and good sensitivity for short bunches. As the gas in the cable is ionized, a signal propagates in both directions along the cable. In the direction opposite that of the beam, the signal carries position dependent loss information. For multi-bunch trains, the signal from losses of a small portion of each bunch in the entire train at a single location and that from a few bunches at more than one location can be similar. One way to resolve the ambiguity is by monitoring the evolution of the signal during the n_b progression. Figure 1 shows the expected waveform from a single point loss and illustrates how the signal evolves through the power up sequence.

The complete MPS will also rely on discrete loss monitor EBDs. These devices indicate the local energy deposition less ambiguously but do not have the comprehensive geometric coverage of a CCLM.

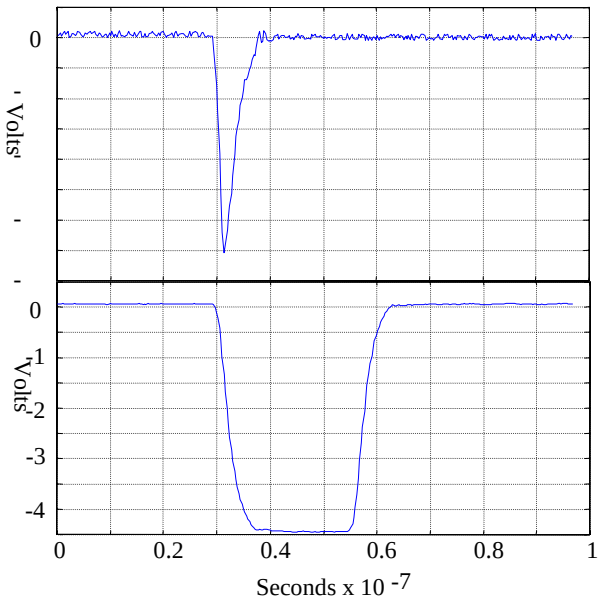

Figure 1: Simulation showing the expected CCLM performance as n_b is increased from 1 (top half of figure) to 90 (bottom half). The top half of the figure was recorded during SLC operation and illustrates a beam loss of 0.2J.

The loss monitor MPS signal processing schematic is illustrated in figure 2. Because the bunch train is long compared to the rise and fall time of signals in the cable, a simple V_{thres} comparator does not provide an accurate estimate of the local power deposition and an integrator with a time constant of $n_b\tau_b$ must be used.

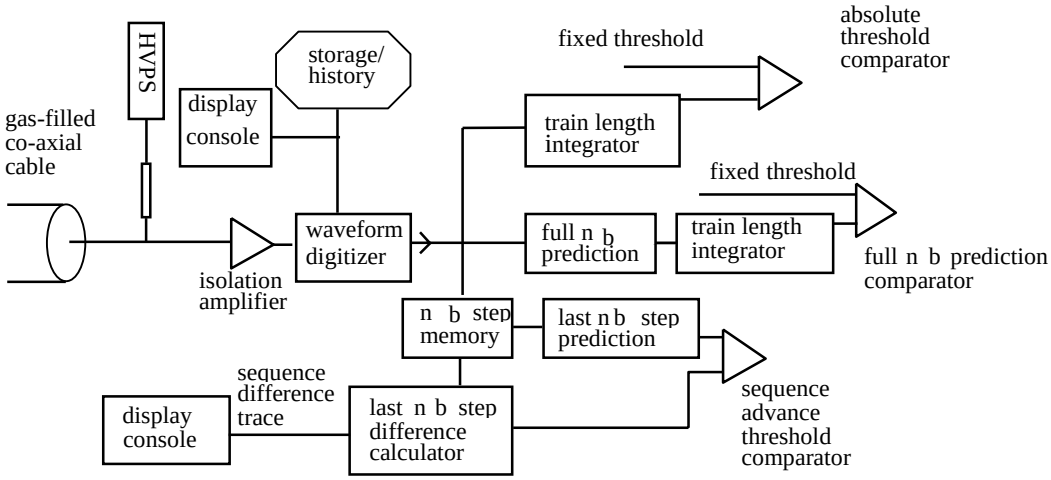

Figure 2: Signal processing schematic for CCLM MPS. The loss monitor signal emerges from the cable at the left side of the figure, is separated from the DC HV, and is amplified and digitized on each 120/s pulse. The signal is then processed and checked using the 3 comparators shown at right. If any threshold is exceeded, the sequence is terminated and a diagnostic process begins.

The electronics will use three comparators: 1) a local power threshold (V_{thres}), 2) anticipated V_{thres} for full n_b, and 3) a comparison of the observed vs. expected difference between the latest steps in the n_b sequence. It will analyze the signal evolution and abort the sequence, if necessary, before actually producing the pulse that exceeds the threshold.

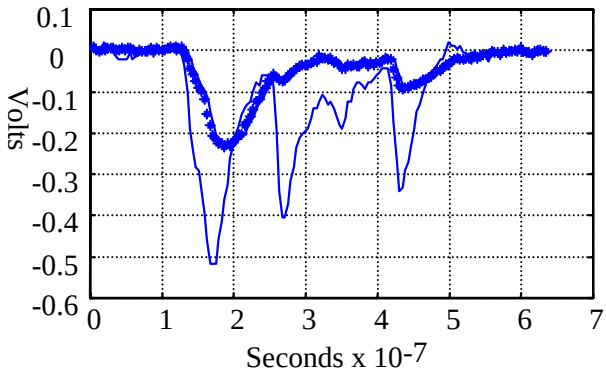

Figure 3: Loss monitor signals, (recorded during 1.2 GeV SLC beam operation), showing the difference between the Ar/CO_2 (95/5%) gas mixture (*) and the Ar/CF_4 (90/10%) gas mixture (-)[6]. The figure shows CCLM signals from a beam loss of about 4 x 10^9 particles distributed over three locations (0.8J total). The CCLM was mounted 0.3 m from the beamline.

Figure 3 illustrates results of tests aimed at increasing the sensitivity of the CCLM. As indicated in Table 3, the cable gas volume and the high voltage gradient were increased and a 2 x higher drift velocity gas was used. The combination of the three improvements provided adequate sensitivity.

4 CONCLUSION

The purpose of the pilot project is to develop a system for use of CCLM and determine its role in the LC MPS. While the CCLM does not replace discrete loss monitors, it has several advantages and will be used at future LC.

5 REFERENCES

[1] M.C. Ross, “Machine Protection Schemes for the SLC”, Proceedings of IEEE Particle Accelerator Conf. 1991, San Francisco, CA, May 6-9, 1991, Particle Accel.Conf: IEEE 1991:1502-1504.

[2] T. Raubenheimer et al., “Zeroth-Order Design Report for the Next Linear Collider”, SLAC-Report-474, 1996.

[3] D. McCormick et al., “Long Ion Chamber Systems for the SLC”, Proceedings of IEEE Particle Accelerator Conf., Chicago, Ill., Mar 20-23, 1989. IEEE Part.Accel.1989.

[4] W. K. H. Panofsky, “The Use of a Long Coaxial Ion Chamber Along the Accelerator,” SLAC TN-73-57 (1963).

[5] M. Fishman and D. Reagan, “The SLAC Long Ion Chamber for Machine Protection,” IEEE Transactions on Nuclear Science (June 1967). IEEE Trans. Nucl. Sci. 14:1096-1098, (1967) (issue No.3).

[6] D. McCormick, “Fast Ion Chambers for SLC” Proceedings of the 1991 Particle Accelerator Conference, San Francisco CA, May 6-9 1991. IEEE 1991, PAC, vol. 2 1240-1242.

TIME RESOLVED, 2-D HARD X-RAY IMAGING OF RELATIVISTIC ELECTRON-BEAM TARGET INTERACTIONS ON ETA-II*

C. E. Crist, SNL; S. Sampayan, LLNL; M. Krogh, AlliedSignal FM&T; G. Westenskow, G. Caporaso, T. Houck, J. Weir, D. Trimble, LLNL,

Abstract

Advanced radiographic applications require a constant source size less than 1 mm. To study the time history of a relativistic electron beam as it interacts with a bremsstrahlung converter, one of the diagnostics we use is a multi-frame time-resolved hard x-ray camera. We are performing experiments on the ETA-II accelerator at Lawrence Livermore National Laboratory to investigate details of the electron beam/converter interactions. The camera we are using contains 6 time-resolved images, each image is a 5 ns frame. By starting each successive frame 10 ns after the previous frame, we create a 6-frame movie from the hard x-rays produced from the interaction of the 50-ns electron beam pulse.

1 INTRODUCTION

Of the variety of diagnostic tools available to an experimenter, an image or picture representing salient features under investigation is a significant tool. At ETA-II, one of the diagnostics that provides reliable data is a 6-frame x-ray camera. This instrument, created at Sandia National Laboratories in 1985 by Dr. William A. Stygar, provides six time-resolved images and one time-integrated image of the hard x-rays produced by relativistic electron beam as it interacts with a bremsstrahlung converter.

2 THE CAMERA

To operate in a high, x-ray noise environment, the camera, (fig 1) consists of a 26-inch diameter, 32-inch long, lead filled housing with an opening of 12 ½-inches (fig 2).

Figure 1

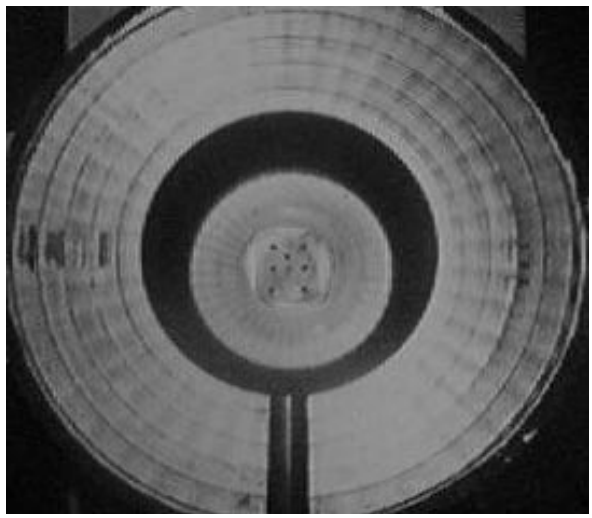

Figure 2

The reasons for the extensive lead shield is to minimize the signal from sever scattered x-ray noise. Inside the camera housing are the camera's six micro-channel plate (MCP) intensifier tubes and film holders. (fig 3)

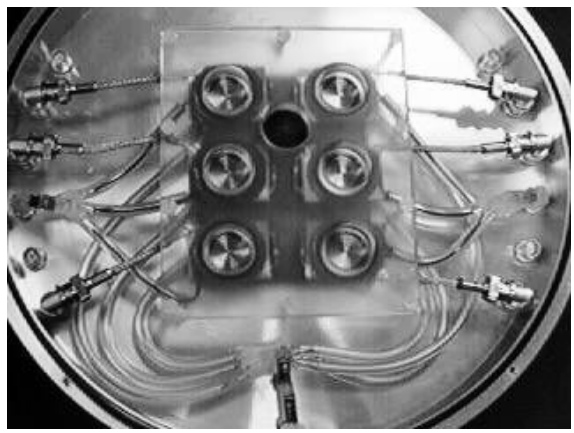

Figure 3

This housing provides a minimum of nine inches of lead shielding in front, seven inches of shielding on the sides and three inches of shielding aft, between the x-ray source and micro-channel plate MCP tubes. For imaging the x-ray spot, we are using tapered tungsten pinholes that are ~ 6 inches long with a final aperture of

.015 inch diameter. This provides us with an image resolution of ~ .3 mm with an on axis signal x-ray to scattered x-ray of over 1×10^{6} and off axis of over 1×10^{3} (fig 4).

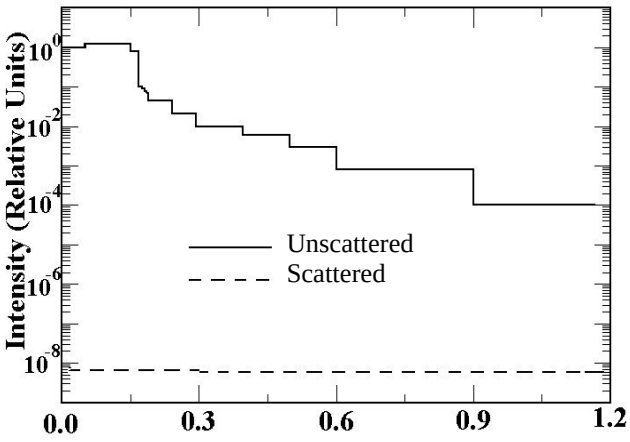

Figure 4

3 DRIVE ELECTRONICS

To control the timing of the individual MCP tubes in the camera, we use high-speed avalanche pulsers assembled at LLNL by Stephen Fulkerson [1]. The pulsers provide the 1-kV signal across the MCPs that in turns controls the precise gain or gating of the camera. For the experiments on ETA-II, the pulsers provide a signal for 5-ns, with each successive pulse arriving 10-ns later. This creates a 6-frame movie with an integration time or frame time of 5-ns with an inter-frame time of 5-ns (fig 5).

Figure 5

For monitoring the individual MCP sequencing, a sample from each pulser is summed via a resistive network. This signal is then combined to a signal from a beam current monitor which is located ~2.5 m upstream of the bremsstrahlung converter. All signals are then combined via the summing function of a Tektronix 7104 oscilloscope and recorded on film. The film is later scanned via the flatbed scanner and archived for later processing (fig 6).

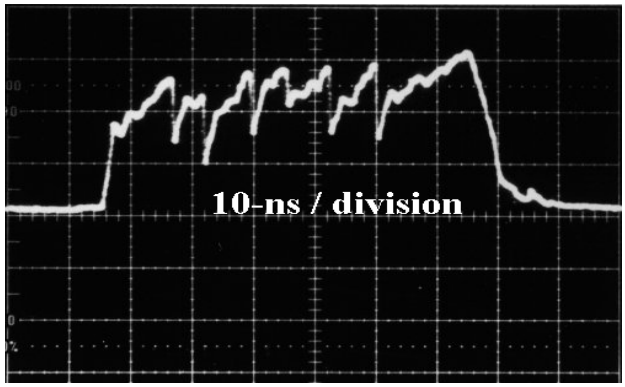

Figure 6

4 DATA RECORDING

Recently, we are using Polaroid Type 52 and Type 57 file for our data recording. While this is not the optimum recording medium, this camera/film combination provides a relatively convenient recording format. After developing the film, we utilize a standard flatbed scanner with an optical resolution of 1200 dots per inch (dpi). The film is scanned as an eight-bit gray scale image at 1200 dpi. The result 22-Mb image is then stored in a Joint Photo. Expert Group (JPEG) format image file. The files are then available for image processing and data reduction

5 RESULTS

For the applications at ETA-II, we are presently measuring beam profiles with feature sizes from ~ .5-mm to 2.0-mm. This combination of optics, shielding, film, and digitalization, provides us with a reasonable representation of the x-ray spot behavior as a function of time. As a result of utilizing this diagnostic we have performed several critical experiments in support of DARHT and AHF programs [2,3]. An example of the raw data provided by this system, clearly demonstrates some of the unique advantages of this instrument (fig 7 & fig 8).

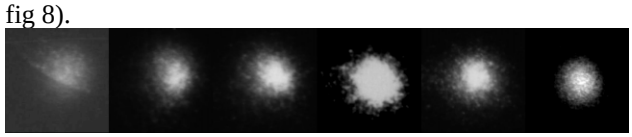

Example of stable beam
Figure 7

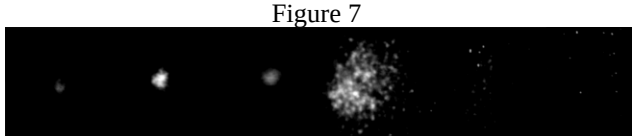

Beam blowup stimulated by laser induced plasma
Figure 8

6 FUTURE PLANS

Future activities include installing an array of video type cameras with a resolution in excess of 30 lp/mm. The cameras, CID Technologies Corporation's model TN 2250, create an image using a 512 element by 512 element Charge Injection Device (CID) sensor. The individual square pixels are 15-μm by 15-μm on a side. The input of the CID arrays are coupled to the output of the micro-channel plate intensifiers by means of fiber-optic tapers. This provides a convenient means of matching the 18-mm diameter MCP to the camera's ~0.3-inch x 0.3-inch CID array. With video frame-grabbers, from Imaging Technologies, containing eight-bit flash A/D converters, direct digitization and computer storage of the images is possible. This configuration should allow us to acquire, store, and pre-analyze the spatial and temporal history of the beam at a rate consistent with the accelerator operation.

7 ACKNOWLEDGEMENTS

*Work performed jointly for the U.S. DOE by Sandia National Laboratories, managed by Lockheed Martin Corp., under contract DE-AC04-94AL85000, Lawrence Livermore National Laboratory under contract W-7405-ENG-48 and by AlliedSignal FM&T under contract DE-ACO4-76-DP00613.

The authors would like to thank Dr. William A. Stygar from Sandia National Laboratories, Roger Van Maren, Stephen Petz from Lawrence Livermore National Laboratory, and the rest of the ETA-II team for their help and assistance. Without their help many of these experiments and results would not have been possible.

8 REFERENCES

[1] E. Stephen Fulkerson et al., "Driving Pockel Cells Using Avalanche Transistor Pulsers," Proceedings of 11th IEEE International Pulsed Power Conference, June 29-July 2, 1997, Baltimore, Maryland

[2] G. A. Westenskow et. al., "Experimental Investigation of Beam Optics Issues at the Bremsstrahlung Converters for Radiographic Applications," Proceedings of LINAC98, August 23-27, 1998

[3] G. J. Caporaso et al, "Analytic Model of Ion Emission from the Focus of an Intense Relativistic Electron Beam on a Target," Proceedings of LINAC98, August 23-27, 1998

ABSOLUTE BEAM POSITION MONITORING USING HOM-DAMPER SIGNALS *

C. Peschke, G. Schreiber, P. Hülsmann, H. Klein
Institut für Angewandte Physik, Universität Frankfurt/Main, Germany

Abstract

To preserve the required beam quality in an e^+/e^--collider it is necessary to have a very precise beam position control at each accelerating cavity. An elegant method to avoid additional length and beam disturbance is the usage of signals from existing HOM-dampers. The magnitude of the displacement is derived from the amplitude of a dipole mode whereas the sign follows from the phase comparison of a dipole and a monopole HOM. To check the performance of the system, a measurement setup has been built with an antenna which can be moved with micrometer resolution to simulate the beam. Furthermore we have developed a signal processing to determine the absolute beam displacement. Measurements on the HOM-damper cell can be done in the frequency domain using a network analyser. Final measurements with the nonlinear time dependent signal processing circuit has to be done with very short electric pulses simulating electron bunches. Thus, we have designed a sub nanosecond pulse generator using a clipping line and the step recovery effect of a diode. The measurement can be done with a resolution of about 10 micrometers. Measurements and numerical calculations concerning the monitor design and the pulse generator are presented.

1 INTRODUCTION

To explain the principle of operation, we take a look to the modes of a single pillbox resonator. On the one hand, the monopole modes have a nearly constant longitudinal electrical field near the axis. Therefore their excitation by a bunch of charged particles does not depend on the displacement. The amplitude after a passing of a bunch is proportional to the charge of the bunch, the starting phase is independent of the displacement. On the other hand, the dipole modes have no longitudinal electrical field on the axis. Off-axis the field rises with the first Bessel function. Near the axis, the amplitude after a passing of a bunch is proportional to the magnitude of displacement and the charge, the starting phase ($0^\circ/180^\circ$) depends on the sign of the displacement.

So we can use the complex amplitude of a dipole mode to measure the absolute beam position in one azimuthal direction. A higher monopole mode serves as a phase reference to detect sign of bunch displacement. The accelerating mode is not useful for this purpose since amplitude is dominated by the klystrons.

One possibility for the choice of a suitable monopole mode is the TM_{011} pillbox mode. Due to the fact of different frequencies of the TM_{011} and TM_{110} mode phase comparison of both modes is very difficult. This method was described in a preceding paper [1].

To simplify the method it is desirable to have the same frequency for both modes. This would simplify the synchronisation with the bunch and reduces the number of intermediate frequency stages which leads to a considerable reduction of costs. Thus one needs an additional monopole-like mode with the frequency of the TM_{110} dipole mode. This is ensured by the presence of reflections in waveguide corners of the HOM-damping system attached (see for example the SBLC [2] HOM-damping system).

One suitable mode was found by a MAFIA-simulation (eigenmode solver) of the coupler cell closed by electrical boundaries within the iris and waveguide flanges. The mode on the left hand side of Figure 1 is the desired monopole mode with electrical field on axis. On the right hand side one sees the dipole pillbox mode geometry changed by the damping system attached. Due to the strong damping effect on both modes, the resonance curves are widely overlapped. Thus one can choose a frequency near both resonances. To proof the existence of the monopole mode and their coupling to the beam a MAFIA time domain simulations have been done.

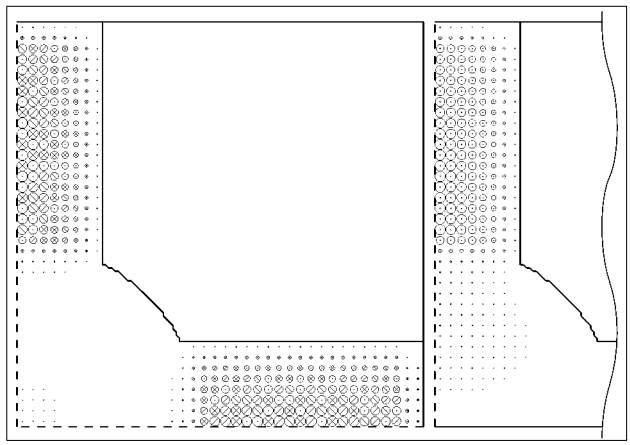

Figure 1: MAFIA[3]-simulation of the coupler cell: monopole-like waveguide mode at 4.1682 GHz and dipole mode at 4.1115 GHz.

* Work supported by DESY/Hamburg and BMBF under contract 06OF841

2 FREQUENCY DOMAIN MEASUREMENTS

For the measurements the beam was simulated by a movable antenna nearby the axis. Therefore a positioning system has been build with a mechanical resolution of 1.23 micrometers. As long as all components of the signal processing electronics are linear and time invariant, the measurements can be done in frequency domain. During the measurements the RF-source was connected to the movable antenna. The signals of the modes were detected by two pick-up antennas mounted in the waveguides of the damping system. The separation of monopole and dipole signals were done by a 180˚ ring hybrid which delivers the sum and the difference of the signals. Figure 2 shows mag-

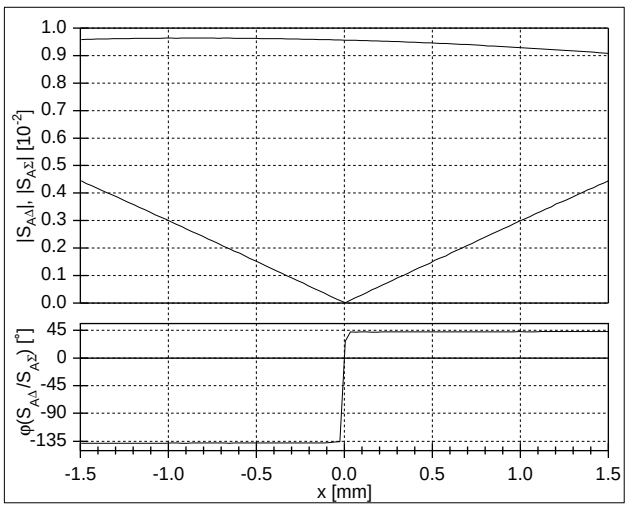

Figure 2: Transmission from antenna to Σ- and Δ-Port at 4.198 GHz in dependence of the displacement.

nitude and phase of the transmission from the movable antenna (A-Port) to the Σ- (monopole signal) and the Δ-Port (dipole signal) of the hybrid depending on the position of the input antenna. As expected, the dipole signal rises linearly with the magnitude of displacement and the phase between monopole and dipole signal jumps by 180˚ at zero displacement. Furthermore the result shows a much stronger coupling to the monopole than the dipole mode. Even at positions far off axis (1.5 mm) the monopole transmission is two times the dipole transmission. Thus it is clearly shown that the 180˚ ring hybrid is necessary.

Figure 3 shows the ratio of dipole to monopole transmission in magnitude and phase with the maximum resolution of the positioning system. This measurement was performed at optimum frequency of 4.197 GHz. We found a phase jump within 1.23 micrometers on axis. Apart from the optimum frequency the minimum is flatter and is further away from zero. Due to the fact of mechanical tolerances of the damping system, the electrical axes of the monopole and the dipole modes are different (Figure 2). Thus the electrical field of the monopole mode is not constant near the axis of the dipole mode. Together with the

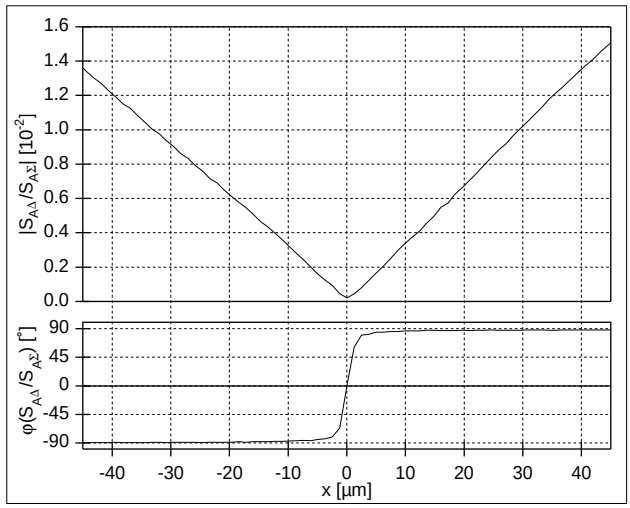

Figure 3: Transmission ratio at 4.197 GHz in dependence of the displacement.

limited isolation of the hybrid the signal is not symmetric, which causes a relative inaccuracy of 6 % of the beam displacement.

Further measurements with the nonlinear time dependent signal processing circuit have to be done with very short electric pulses simulating electron bunches.

3 BEAM SIMULATIONS BY SHORT PULSES

The requirements to produce a short pulse are small transition time and small pulsewidth. A 10 MHz oscillator pulse is shaped by a clipping line and the transition time is shortened by a step recovery diode. The pulse generator is realized on a single microstrip line printed circuit board completely. The schematic configuration is shown in Figure 4.

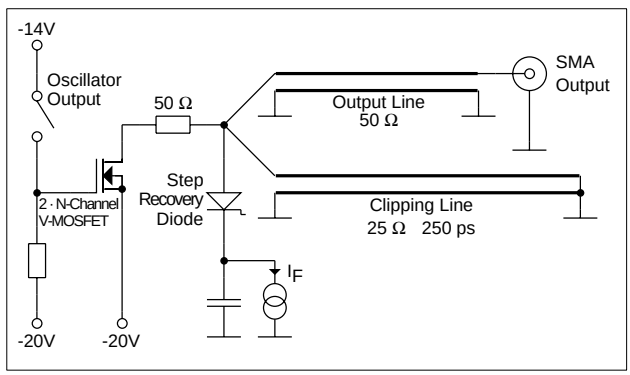

Figure 4: Schematic of a fast pulse generator (simplified).

The step recovery diode can be described as fast switch reducing the fall time of the oscillator pulse. A forward bias I_F stores charge and the negative oscillator pulse, powered by two V-MOSFETs, causes a reverse bias I_R which depletes this charge, and when fully depleted the step recovery diode ceases to conduct current. The action of turning

off takes place within 100ps or less depending on forward and reverse bias and the specific carrier life time of the diode.

The clipping line changes the falling edge into a pulse, and pulse length is given by two times the delay of the clipping line which has to be longer than two times the rise time of negative edge. Otherwise the resulting pulse height decreases. To avoid multiple reflections the entrance of the clipping line, seen from the short end, should be matched. But due to presence of the diode capacity and parasitic inductances of the MOSFETs perfect matching is impossible. The effect of multiple reflections on the resulting pulse can be seen in Figure 5, after the desired negative pulse,

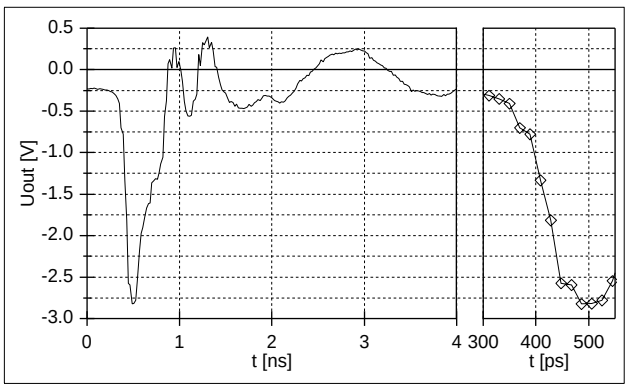

Figure 5: Measured output signal of the pulse generator in Figure 4.

which ends around 800 ps, the signal is oscillating around zero.

One possibility to get rid of the undesired multiple reflections caused by the mismatch of the clipping line is to connect the diode directly to the common drain of the MOSFETs. The disadvantages are now the parasitic inductances and capacities of the MOSFETs which influence the pulse stronger than before. On the other hand due to the inductances the pulse height is increased. Additionally length and impedance of the clipping line were optimized to achieve a more proper pulse. This is ensured by destructive interferences eliminating the parasitic oscillations. Furthermore leading parasitic oscillations can be minimized using a second line with an open end. All these precautions were verified numerically with the program SPICE [4] and are not yet realized experimentally. The configuration is shown in Figure 6 and the results are presented in Figure 7.

4 CONCLUSION

The resolution of the HOM-damper beam position monitor is limited by strongly excited monopole modes. It has been shown that a resolution of 10 µm seems possible. The relative inaccuracy caused by the axes offset of the monopole mode, which is in the order of 6 %, can be decreased by the construction of a new HOM-damping system which can be machined more precisely. Furthermore an inaccuracy due

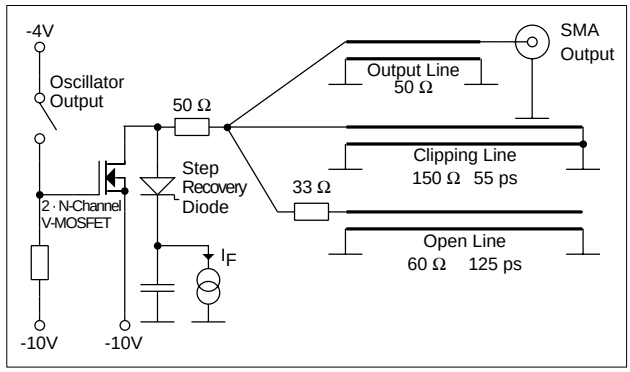

Figure 6: Schematic of a optimized pulse generator (simplified).

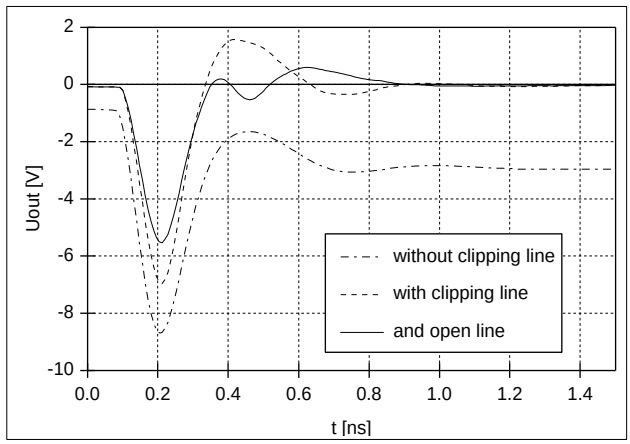

Figure 7: Calculated output signals of the pulse generator in Figure 6.

to the evanescent accelerating mode in the HOM-damping waveguides is expected. But this influence depends strongly on the signal processing electronics and has not yet been proven. For measurements with the pulse generator the new proposed setup (Figure 6) will be built and tested.

This concept of a beam position monitor can be applied to any high energy cavity type linac with symmetric HOM-damping system. Due to the synchronisation with a higher monopole mode, external synchronisation to the timing system of the linac is not necessary. Thus beam position monitoring is also possible in non accelerating cavities.

5 REFERENCES

[1] Peter Hülsmann, H. Klein, W.F.O. Müller, C. Peschke: "Beam Position Monitoring for SBLC Using HOM-Coupler Signals"; proceedings of the 5th European Particle Accelerator Conference (EPAC 96); Sitges (Spain), 1996

[2] R. Brinkmann et al.: "Conceptual Design of a 500 GeV e^+e^--Linear Collider with Integrated X-Ray Laser Facility", DESY 97-048, Hamburg (Germany), 1997

[3] T. Weiland et al.: "Solutions of Maxwell's Equations using the Finite Integration Algorithm"; Version 3.2; Darmstadt 1993

[4] "Simulation Program with Integrated Circuit Emphasis"; Version 3f4; Department of Electrical Engineering and Computer Science, University of California, Berklay, California 1993

DESIGN OF THE RF PHASE REFERENCE SYSTEM AND TIMING CONTROL FOR THE TESLA LINEAR COLLIDER

A. Gamp, M. Liepe, T. Plawski, K. Rehlich, S.N. Simrock, DESY
Notkestr. 85, D-22603 Hamburg, Germany

Abstract

The frequency distribution system for the TESLA linear collider must deliver a highly phase stable rf signal to the 616 rf stations over a length of 33 km. At the operating frequency of 1300 MHz a short term and long term stability of the order of 1 degree with respect to the accelerated beam is required. Our solution involves three coherent oscillators, a 9 MHz low loss coaxial cable distribution, 1.3 GHz fiber optics, and continuous calibrations based on beam phase measurements. This system is transparent to beam operation and will continually monitor and correct slow phase drifts.

1 INTRODUCTION

The overall layout of the TESLA linac [1] is sketched in Figure 1. The main elements are two linacs with a length of 2×12 km, the damping rings which make use of the linac tunnel, the source for electrons (laser driven rf photocathode gun), the source for the positrons which is based on the concept of high-energy photon conversion into e^+e^-, and a 3 km region for the beam delivery system in between the two linacs. The photon are generated by the spent high-energy electron beam passing a wiggler. The acceleration system in each linac consists of 9856 superconducting cavities which are powered by 308 klystrons (32 cavities per 10 MW klystron)

The various rf system that must be phase synchronized with picosecond stability over the full accelerator length are:

- the 616 rf systems operating at 1300 MHz in the two superconducting linacs.
- The 433 MHz rf systems for the damping rings
- the 1300 MHz rf system providing power to the photocathode rf gun of the electron source and the associated laser for illumination of the photocathode.

The timing system must guarantee that the bunches which are spaced by 337 ns (3 MHz repetition rate) arrive at the same time at the interaction region.

2 RF DISTRIBUTION STABILITY REQUIREMENTS

The phase stability requirements for the accelerating field in the linac cavities are dictated by the low beam energy spread requirement of $\sigma_E/E < 7\times10^{-4}$ and the timing requirements for the bunch arrival at the interaction point. Assuming that a third of the energy spread contribution originates from phase fluctuations of the accelerating field a correlated phase error of only σ_ϕ =0.4° at 1300 MHz corresponding to a timing error of 0.8 picoseconds can be tolerated.

The phase stability of the 433 MHz rf systems of the damping rings determines that arrival time of the bunches at the interaction point. The interaction position error should not exceed one bunchlength (1 mm) resulting in the same timing stability requirements as dictated by the low energy spread.

In addition to the rf phase reference system a timing system with event coding capability is required to allow for real time synchronization of the various rf and other subsystems. The electron and positron bunches must be accelerated in selected rf buckets (every 438^{th} bucket, this number is given by the ratio of bunch spacing and the period of one rf cycle) to guarantee that the collision takes place in the center of the detector. A misplacement by 1 bucket would result in a collision position error of 23 cm (λ=c/f=23 cm). Therefore the timing system for the rf gun must guarantee a trigger signal stability of better than 770 ps. The timing system clock will also be synchronized to the master oscillator and can therefore provide phase stable timing for the digital feedback and rf system monitors.

3 DESIGN CHOICES AND ISSUES

The four basic choices for a phase stable reference system are:

- coaxial distribution system
- fiber optic distribution system
- coherent oscillators
- beam pickup

All systems with the exception of the beam pickup require a beam based calibration scheme since calibrations by measurement of the electrical length of the subsystems is not sufficiently accurate. It is desirable to use a fast coarse calibration scheme for initial start-up of the accelerator and a slow and precise calibrations scheme which is active during accelerator operation and which is transparent to the beam experiments.

The rf distribution system for the TESLA linear collider has been designed as a combination of all of the above options to utilize the advantages of each of the systems thereby maximizing performance and providing some level of redundancy.

The design employs a coaxial distribution system in the linacs. It provides a phase stable 9 MHz signal to all of the 616 rf stations in the linacs and the 433 MHz systems in the damping rings. The signals are locally multiplied by 144 or 36 respectively. Coherent oscillators operating at 9 MHz are located at the beginning of each linac close to the 433 MHz rf systems (also close to rf gun for electrons and auxiliary positron source) and in the experimental hall

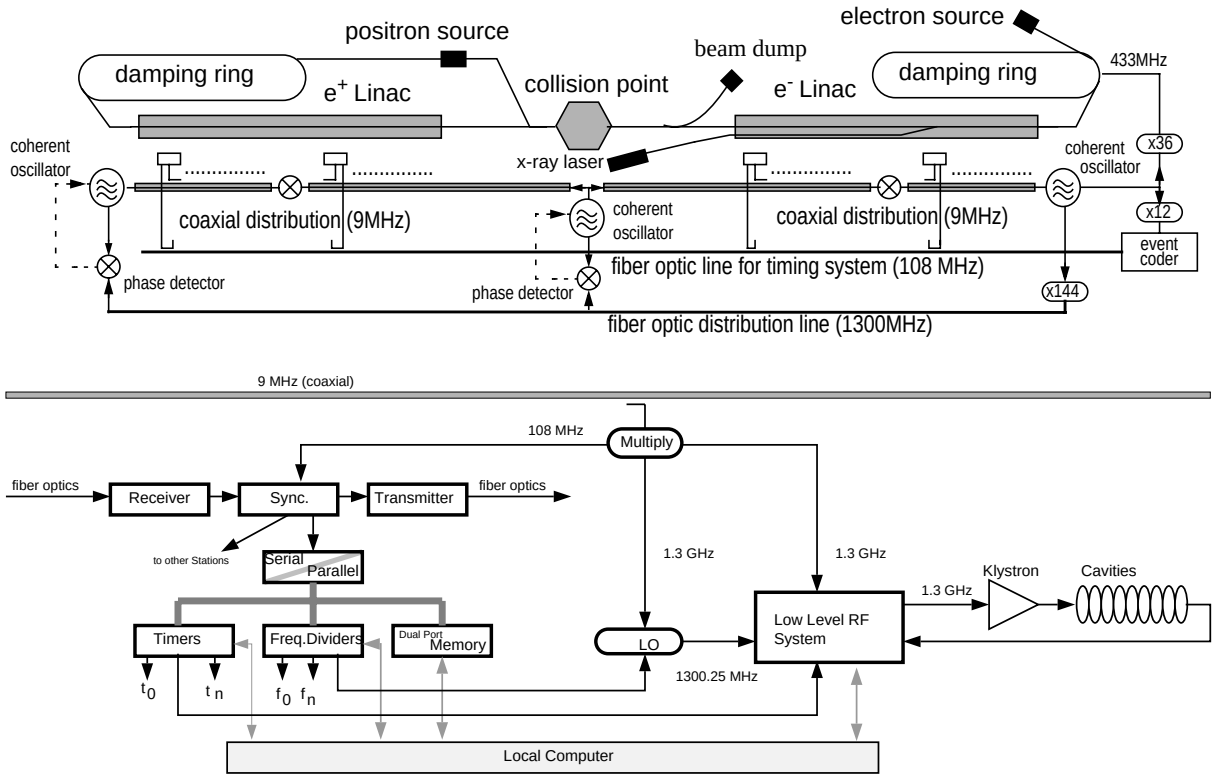

Figure 1 : Overall layout of the TESLA Linac. The phase reference system and timing control distribution are shown.

between the linacs. The three oscillators are synchronized by a optical fiber system. Each of the oscillators provides the reference signal for half of the linac closest to it. All systems are measured against each other and calibrated with reference to the beam utilizing the beam induced transients.

3.1 Coaxial Distribution System

The distribution of rf signals by coaxial cables or waveguides appears to be the most obvious solution since the rf signal can be transported directly to its destination. For the distribution to many rf stations directional couplers are recommended for good isolation between the tap points. This scheme allows for relatively high power levels of up to a few hundred watts at the input of the distribution line and can provide several milliwatts to several watts of rf power to each station. The main parameters that need to be considered for a coaxial distribution system are:

- frequency to be distributed
- distance between signal source and destination
- numbers of destinations to which the signal must be supplied
- power level of signal required at destinations
- power level available at signal source
- attenuation of coaxial cable
- power handling capability of the cable and the directional couplers
- thermal stability (phase stability of cable)
- number of amplifier needed within the distribution system
- sensitivity to microphonics

In the case of TESLA it is advisable to distribute a lower frequency and to convert the frequency locally to the operating frequency by use of multipliers. This method reduces the rf losses in the distribution system significantly. The lower frequency limit is given by the efficiency, noise characteristics, and phase stability of the local frequency multipliers.

For the TESLA accelerator the operating frequency is 1300 MHz but the coaxial frequency distribution along the linac is operated at 9.0278 (= 1300/144) MHz. The signal sources - H^--masers controlled low noise oscillator operating at 9 MHz and boosted by 200 W amplifiers - are located at the beginning of each linac and in the experimental hall between the linacs. For the coaxial distribution system a 1 5/8" (type LDF-50A1-5/8-inch Heliax) cable has been chosen because of its low insertion loss of 0.2 dB/100 m, the excellent phase stability (10 ppm/deg. C) and power handling (42 kW) capability. With a group velocity of 0.88c this results in a phase sensitivity of 177 deg./°C/10 km. The actual sensitivity may deviate from this number since the cable cannot expand freely due to its own mass.

The directional couplers (type HDC1460 from HD Communications) exhibit an insertion loss of 0.15 dB /

coupler. The distribution scheme for the linac is shown in Figure 1. Input power for each of the 7 km long sections is 200 W. The number of couplers has been reduced to 50 with a spacing of 120 m. A three way power splitters feeds a subnet consisting of LDF 1/2" cable to the two adjacent stations. The 9 MHz signals are then locally multiplied by 144 in the linacs and 36 at the damping ring rf systems.

3.2 Fiber Optic Distribution

Over the past years, fiber optic distribution links have replaced coaxial cable distribution for phase reference systems [2]. Optical fibers are the preferred medium for distribution because of their low attenuation, immunity to EMI/RFI, and temperature stability.

The thermal coefficient of delay for a typical optical fiber is of the order of 7 ppm/°C and therefore comparable to that of phase stabilized coaxial cables. A LCD coated optical fiber from Sumitomo [3] which has been specifically designed for high thermal stability provides a stability of better than 0.4 ppm/°C at an operating temperature close to 0°C. At a more realistic operating temperature of 30°C the coefficient increases to 1 ppm/°C. The group velocity in this fiber is 0.66c resulting in a phase sensitivity of 23.6 deg./°C/10 km.

The phase noise characteristics of a fiber optic distribution system suffers from the low signal levels retrieved at the individual receivers. The minimum phase noise level at 1300 MHz is expected to be around -100 dBc (> 10 kHz) [2] corresponding to an rms phase error of 0.57 deg. or 1.2 ps timing jitter which is marginal for our application.

3.3 Coherent Oscillators

The timing stability requirements between two remote locations such as the rf stations for the damping rings which are separated by a distance of 32 km could be fullfilled with two absolutely coherent oscillators. Present technology utilizing a H^- Maser allows for a frequency stability of $2x10^{-13}$/s corresponding to a phase stability of about 0.1 deg./s (or 0.2 ps/s) thereby exceeding the requirements for intrapulse and pulse-to-pulse stability. Even oven stabilized crystal oscillators can achieve a stability of the order of 2×10^{-12}/s which might be sufficient.

The coherent oscillators will be synchronized with the fiber optic distribution system with a time constant of 10 - 100 s to ensure long term stability.

3.4 Beam Based Phase Calibration

The ultimate reference for the rf systems in the linacs, the damping rings, and the timing of the bunches at the collission point will be the beam itself. It is therefore foreseen to synchronize all rf systems with respect to the beam. To achieve a measurement accuracy of better than 0.5 deg. or 1 ps, the transient beam loading based algorithm must average over several hundred measurements resulting in a measurement time of up to 100 seconds. Therefore the beam based phase correction can take place at a time scale of 100-1000 s.

4 TIMING CONTROL

The timing system provides various triggers and fixed frequency signals as well as machine parameters in a dual-port memory. A central timing signal source is synchronized with the master oscillator. This signal source generates encoded telegrams and sends them via a fiber optic distribution system to all devices along the linac and the damping rings. Repeaters every 120 meter receive the signals, resynchronize them with the 9 MHz, distribute the data to the local equipment and retransmit the signals to the next stations. The received serial telegrams have to be encoded and converted into parallel data streams. This data stream contains events and data words from the master station. Since the telegrams are synchronized with the main oscillator fixed frequencies with low phase errors can be derived from the telegrams also. The data stream is used to filter events in a timer unit and data words in the dual port memory. Programmable timers are triggered by these events to generate the start pulses for the klystrons or digital signal processors for instance. A timer unit provides several independent output channels. Some machine parameters that change from macro pulse to macro pulse need to be delivered in time to run all digital feedback loops in parallel. The data words from the telegrams are stored in a dual port memory. This information is readable from the local connected computers or signal processors.

5 CONCLUSION

The design of a rf phase reference and timing system for the TESLA linear collider is a challenging task due to the tight timing stability requirements of about 1 picosecond over a distance of more than 30 km. It should be possible to meet these requirements if a combination of coaxial distribution, optical fiber distribution, coherent oscillators and beam based calibration is used. It is planned evaluate the performance of such a scheme at the TESLA Test Facility.

REFERENCES

[1] R. Brinkmann, Linear Collider Projects at DESY, EPAC98, Stockholm, Sweden, June 22-26, 1998, in print.

[2] M. Calhoun, *Fiber Optic Reference Distribution to Remote Beam Waveguide Antennas*, JPL Report 95-0037, Reston, VA, December 5, 1994

[3] Kakuta, Tanaka, *LCD Coated Optical Fiber with Zero Thermal Coefficient of Transmission Delay Time*, Sumitomo Electric Industries Ldt., Yokohama, 244, Japan.

[4] A.N. Luiten, A.G. Mann, E.N. Ivanov, D.G. Blair, *Latest Results of the UWA Cryogenic Sapphire Oscillator*, Proc. 49th Annual Frequency Control Symposium. San Francisco, CA, 1995, pp 433-437.

FREQUENCY SOURCE FOR THE ISAC RFQ

K. Fong, S. Fang and M. Laverty
TRIUMF, 4004 Wesbrook Mall, Vancouver, B.C., Canada

Abstract

The ISAC RFQ cavity nominally operates at a frequency of 35 MHz. It can operate in either self-excited or driven mode. In the self-excited mode, the RFQ cavity itself is one of the frequency-determining elements. In the driven mode, the frequency is slaved to an external stabilized, digitally synthesized frequency source. In order to achieve glitchless transitions between the two modes, the RFQ frequency source is buffered by a phase-locked loop. When operating in the driven mode, RF switches in the loop configure the loop to lock to the external direct digital synthesizer. Reconfiguration of the RF switches in the self-excited mode turns the phase-locked loop into an oscillator whose frequency is determined by the phase shift of the RFQ cavity. The overdamping characteristic of the phase-locked loop prevents sudden transitions in either frequency or phase during switching between operating modes.

1 INTRODUCTION

The ISAC RFQ accelerator is a high Q, 4-rod RFQ with a peak potential between the electrodes of 74 kV. When operating under the fixed frequency mode, a stabilized direct digital synthesizer, whose frequency can be controlled remotely, drives the RFQ. During the powering and warming up phase, before the RFQ cavity reaches its operating temperature, the preferable mode is the self-excited mode, where the rf frequency is slaved to the resonance frequency of the RFQ cavity. The rf control system must be able to switch between these two modes under full power. Since the DDS frequency and the self-excited frequency are often different in frequency as well as in phase, this switching must be performed in such a way that will result in a gradual phase transition to prevent overloading the final RF power amplifier. A rf switch is used to provide the frequency switching, while a phase-lock loop is used to buffer the resultant switching transition. The phase-lock loop is designed with a large overdamp factor to enable the RFQ rf system to switch from one mode to another without generating large phase excursion.

2 DIRECT DIGITAL SYNTHESIZER

For operation of the RFQ in the driven mode, a frequency source whose output frequency ranges from 35.654517MHz to 35.851119MHz is needed. A digital direct synthesizer (DDS) is used to provide a very stable source with fine resolution, and is able to change frequency without generating phase jumps. As shown in Figure 1, a DDS is used as the core of this frequency source.

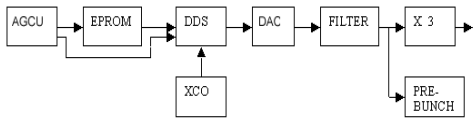

Figure 1: Block diagram of DDS

The phase data, which is stored in the EPROM shown in Figure 1, and the clock frequency are directly related to the output frequency by the equation (1).

$$f_o = \frac{f_c x(-\,phase)}{2^{32}} \qquad (1)$$

where f_c is clock frequency generated by an 80 MHz crystal oscillator (XCO), *-phase* is the phase data. The DDS input phase resolution is 32 bit, but the phase bus between the DDS and the EPROM is only 8 bit. Therefore, it is necessary to transfer the phase data four times from the EPROM to the DDS to obtain a new frequency. This control logic is performed by the Address Generator Control Unit(AGCU).

The DDS output frequency is the third sub-harmonics of the RFQ frequency (i.e. 11.884839MHz to 11.950373MHz). The DAC is used to convert the frequency digital data to analog voltages. A 3-pole Butterworth bandpass filter removes any spurious frequency components and splits the signal into two paths: one is used as the frequency source for a buncher placed upstream the RFQ and another requires tripling the frequency in order to obtain the desired frequency for the RFQ. The design frequency resolution is 6Hz and its stability is better than 1ppm.

3 PHASE-LOCK LOOP

The RFQ can be operated either under the driven mode, in which the DDS is used as the master frequency source, or in the self-excited mode, in which the signal from the RFQ cavity is used to determine the excitation frequency. An internally terminated high-isolation rf switch is used to select between the two frequency references. A phase-lock loop (PLL), with its versatility in frequency control, acquisition times, and step response, is used as a buffer

after this mode selection switch. A low phase drift limiting amplifier with 30-dB dynamic range is placed between the switch and the PLL to eliminate the amplitude dependency of the circuitry. The performance requirements of this RFQ PLL are different from that of an ordinary frequency synthesizer. In particular, it is designed to have a slow step response in order to satisfy the following two requirements.

1. The ability to switch from self-excited to driven operations under full power without phase jumps.
2. The ability of the entire system to recover from sparking in a rf cavity.

A spark can collapse the rf field in the cavity. Sometimes within several microseconds the RFQ voltage may recover after the spark has dissipated. The inclusion of the PLL circuitry is designed to be highly overdamped such that its VCO frequency does not react to the disturbance during this time interval. The power amplifier keeps energizing the cavity with rf power at the last resonance frequency allowing the cavity field to recover. The transfer function of the PLL is given by

$$\frac{\theta_o}{\theta_i} = \frac{G}{1+GH} \tag{2}$$

with

$$G = \frac{K_v K_p F}{s} \tag{3}$$

and

$$H = 1.$$

In equation (2), θ_i is the phase at the input of the PLL, and θ_o is the phase at the output of the PLL. In equation (3), K_V is the VCO sensitivity, K_p is the phase-detector gain constant, and F is the transfer function of the filter. Together they determine the response characteristics of the PLL. A unity gain bandwidth in the order of kHz and a phase margin of more than 45^o provides enough damping for spark recovery. Using a type 2, second-order PLL, zero frequency error at dc is guaranteed. The schematic of the PLL filter is shown in Figure 2.

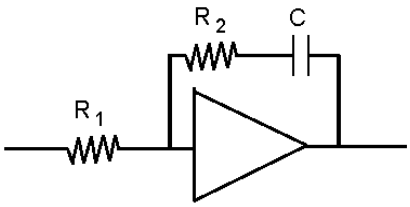

Figure 2: Schematic of PLL integrator/filter

In equation (3), the filter transfer function, F, is given by

$$F = -\frac{1+sT_2}{sT_1} \tag{4}$$

where $T_1 = R_1 C$ and $T_2 = R_2 C$. Figure 3 shows the output spectrum of the PLL. The x-axis shows the frequency at 5 kHz/div. The y-axis shows the power at 10 dB/div. This spectrum displays typical noise distribution of PLL output. The background noise is -70 dBc, while the oscillator noise with a bandwidth of 20 kHz is –55 dBc.

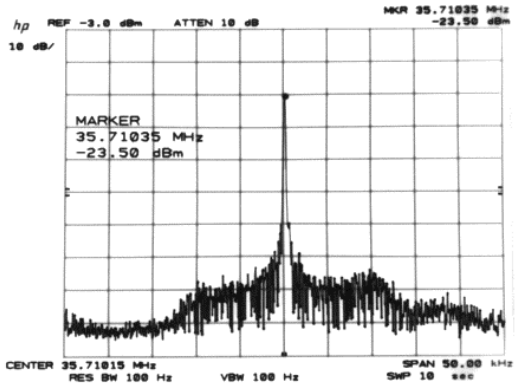

Figure 3: Output spectrum of PLL

4 SELF-EXCITED OSCILLATION

In the self-excited mode, the RFQ cavity determines the rf frequency. This is achieved by feeding the signal voltage at the RFQ cavity back into the input of the PLL. Thus θ_i is given by

$$\theta_i = \theta_o + \Delta\theta_m + \Delta\theta_l + \theta_c \tag{5}$$

where $\Delta\theta_m$ is the phase shift from the VCO to the output of the vector modulator. $\Delta\theta_m$ is the sum of the phase delay due to the VCO to the modulator and the phase shift of the vector modulator. $\Delta\theta_l$ is the phase shift due to the transport lag of the feedback loop. θ_c is the phase shift caused by the RFQ cavity. When the excitation frequency ω is close to the resonance frequency ω_o of the cavity,

$$\theta_c = -\frac{2(\omega - \omega_o)}{\omega_o} Q \tag{6}$$

Q is the quality factor of the cavity. These phase shifts must be adjusted to satisfy several constraints. In order to reduce crosstalks between channels in I/Q feedback loops, it is necessary to set the phase shift from the vector modulator to the vector demodulator to be integer multiples of 360^o (i.e. $\Delta\theta_l + \theta_c \cong 0.$). For proper operation of the self-excited mode, the phase shift from the output of the VCO to its input should also be integer multiples of 360^o. As a result, $\Delta\theta_m + \Delta\theta_l = 0$. This also implies that for the Q channel, the regulation is disabled and the open loop drive is set to zero. The overall phase relationship is illustrated in Figure 4.

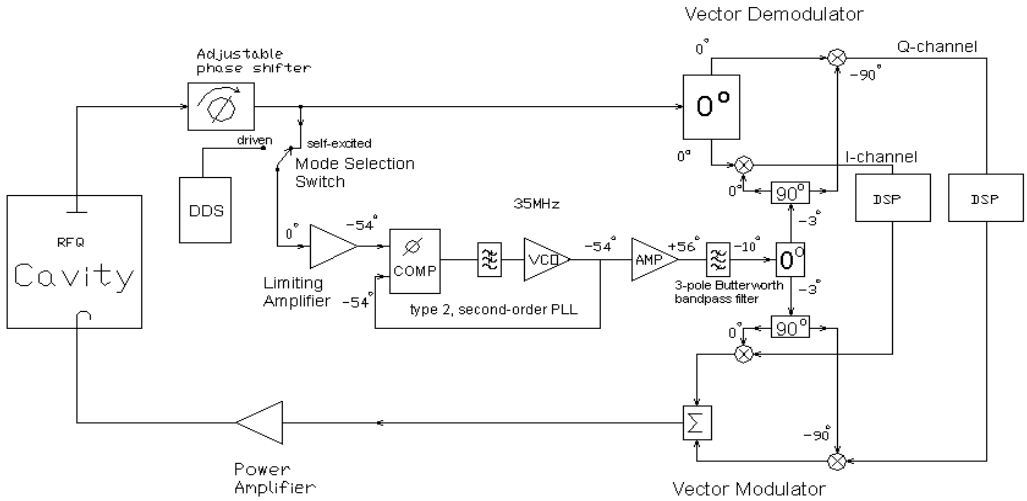

Figure 4: Phase relationship for proper operation of self-excited oscillation

When the above conditions are satisfied, the PLL will oscillate at

$$\omega = \frac{1+sT_2}{1+s\left(\frac{T_1\omega_o}{2K_pK_vQ}+T_2\right)}\omega_o \qquad (7)$$

The PLL in the ISAC RFQ has the following parameter values:

$$T_1 = 330\mu s$$
$$T_2 = 50\mu s$$
$$K_p = 0.16V/rad$$
$$K_v = 500\times10^3\ rad/s/V$$
$$\omega_o = 35.75\times10^6\cdot 2\pi\ rad/s$$

With these parameter values, Equation 7 then reduces to

$$\omega = \frac{1+\frac{s}{3\times10^3}}{1+\frac{s}{9\times10^3}}\omega_o \qquad (8)$$

where ω_o, the resonance frequency of the cavity, is the only varying factor. Since the variation in ω_o is due to thermal expansion, it varies slowly and thus,

$$\omega \cong \omega_o$$

Thus, the PLL tracks the resonance frequency of the RFQ cavity.

All the above mentioned circuitries (i.e. the PLL, the mode selection switch, the limiting amplifier, the vector modulator and the vector demodulator) are placed into a single C-size VXI module. In operation, the low pass filter at the PLL output is adjusted to give the desired phase shift as shown in Figure 4. Final phase adjustment is carried out using the variable phase shifter after the cavity. During self-excited mode operation, the Q-channel is disabled and the phase shifter is adjusted for minimum VSWR.

5 SUMMARY

The mixing of digital and analog technology in the frequency source for the RFQ allows for both performance and flexibility. A direct digital synthesizer is able to generate a highly stable and programmable frequency source. An overdamped phase-lock loop allows the rf power amplifier to switch from a self-excited mode to a driven mode without sudden phase jumps. To date, the system has been running in close-loop operation with the ISAC RFQ cavity. Stable operation has been achieved with both self-excited and driven modes. Switching between the two modes has been demonstrated at different power levels including full power without tripping the rf power amplifier. Spark recoveries at both modes are also observed to be similar. The rf system is able to recover from short duration sparks. In the driven mode, the digital direct synthesizer (DDS) as a frequency source is capable of reaching high stability, high resolution and is proving to be easily controlled.

REFERENCE

[1] M. Laverty, K. Fong, and S. Fang, "A DSP-based Control System for the ISAC Pre-Buncher," International Conference on Accelerator and Large Experiment Physics Control System, Beijing, Nov. 1997

A DEVELOPMENT AND INTEGRATION ANALYSIS OF COMMERCIAL AND IN-HOUSE CONTROL SUBSYSTEMS

D. M. Moore (WSRC), L. R. Dalesio (LANL)
Los Alamos National Laboratory, Los Alamos, New Mexico 87545 USA

Abstract

The acquisition and integration of commercial automation and control subsystems in physics research is becoming more common. It is presumed these systems present lower risk and less cost. This paper studies four subsystems used in the Accelerator Production of Tritium (APT) Low Energy Demonstration Accelerator (LEDA) at the Los Alamos National Laboratory (LANL). The radio frequency quadrupole (RFQ) resonance-control cooling subsystem (RCCS), the high-power RF subystem and the RFQ vacuum subsystem were outsourced; the low-level RF (LLRF) subsystem was developed in-house. Based on our experience a careful evaluation of the costs and risks in acquisition, implementation, integration, and maintenance associated with these approaches is given.

1 INTRODUCTION

There were several reasons the control systems for major subsystems were outsourced for the LEDA project. A major reason was that delivery of the subsystem control system along with the subsystem allowed complete testing at the supplier's location before shipment. From our experience with several subsystems, we will analyze aspects of these implementations and provide strategies for successful acquisition of future subsystems.

2 SUBSYSTEM OVERVIEWS

Provided below is a summary of each subsystem included in this study. Brief descriptions of the computer system hardware, software, and external interfaces are presented. These subsystems have been, or are being, integrated into the integrated control system for LEDA, which is based on the Experimental and Physics Industrial Control System (EPICS). [1]

2.1 RFQ Resonance-Control Cooling Subsystem

The RCCS is a water cooling system used to maintain the RFQ's temperature, thereby controlling the resonant frequency of the accelerating cavity. Provided by Allied Signal, the RCCS includes an EPICS input/output controller (IOC) connected to devices like flow meters, thermocouples, valves, variable-speed pumps, etc.

2.2 High-Power RF Subsystem

The high-power RF subsystem control system is comprised of two PLCs used to control each klystron. An Allen-Bradley PLC-5/40 interfaces to the klystron control electronics (called the "transmitter"), and an Allen-Bradley SLC 5/03 interfaces to the high-voltage dc power supply. The transmitter provides magnet power, ac filament power, and crowbar triggering for the klystron, and the power supply provides the cathode voltage for the 1.2 MW continuous wave klystron amplifiers. Both PLCs were provided and programmed by the vendors as part of the purchase specifications for the equipment – Continental Electronics Corp. supplied the transmitter, and Maxwell Technologies supplied the power supply.

2.3 RFQ Vacuum Subsystem

The RFQ vacuum subsystem is used to achieve high vacuum. This subsystem was contracted to Lawrence Livermore National Laboratory (LLNL), and consists of five cryo pumps, two scroll pumps, and one turbo pump. Control is implemented using a Modicon PLC for equipment interlocks, Granville Philips ion-gauge controllers, and a Labview system for operator display and automatic shutdown.

2.4 LLRF Subsystem

The low-level RF subsystem is comprised of 5 VXI boards used to control the cavity field and resonance and to provide high-power RF protection and RF reference frequency generation and distribution. The clock distribution module provides the master timing signals to the other modules. The field control module provides feedback/feedforward I/Q control based on beam and field I/Q inputs. The amplifier control module compensates for individual klystron phase differences to 10 kHz. The resonance control module controls cavity resonance and allows for frequency agility during cavity warm-up. The high-power RF module protects the klystrons, windows, loads, and the accelerator from excessive reflected power.

The VXI boards were developed and programmed by the LANL RF group, and the external interface is via the slot zero controller mounted in the VXI chassis.

3 EVALUATION OF COST AND RISKS

All four subsystems described above are, or will be, integrated into the LEDA instrumentation and control system. This integrated system is implemented in EPICS, a control system tailored for accelerator and research applications. Whether the subsystems were outsourced or developed in-house had a definitive impact on the cost

and risks involved in acquisition, implementation, integration, and maintenance. Each of these areas is discussed below.

3.1 Acquisition

The acquisition cost for outsourced subsystems is difficult to quantify, particularly when the control systems portion is not identified as a separate, billable expense. However, a general estimate on the materials and effort involved is possible.

In the case of the RCCS, it was developed using hardware specified by the LANL Accelerator Controls and Automation group, which has primary responsibility for the integrated LEDA control system. When compared to a typical EPICS system design as developed by the Controls group, the only extra component added by the supplier is the learning curve required to become productive with the EPICS toolkit. This has been estimated at 3 man-months effort for this supplier.

In the case of the high-power RF subsystem, the materials include the two PLCs and their associated input/output modules, sensors, and cabling. Approximate costs of these are on the order of $25K. The effort includes the PLC programming, installation and testing by the vendor's control system engineer, as well any support provided by LEDA personnel involved in factory and site acceptance testing. This has been estimated at 12 man-months for the system.

In the case of the RFQ vacuum subsystem, it was developed using Labview due to LLNL's familiarity with that software, and the steep learning curve for EPICS. Interlocks were programmed into the PLC's ladder logic, and the automatic shutdown sequence was implemented in Labview. This Labview system is being replaced with an EPICS implementation for LEDA. The effort to support requirements definition and equipment testing has been estimated at 9 man-months.

In the case of the LLRF subsystem, the acquisition cost and risks are nonexistent. They are instead reflected in the implementation section.

3.2 Implementation

The RCCS took approximately 10 man-months to implement. Collecting requirements took 4 months, developing device drivers took 5 months, and testing took 1 month. Had the subsystem been implemented in-house by the LANL Controls group, it is estimated that 4 man-months could have been eliminated. However, this would have impacted the schedules of other subsystems due to resource limitations. Also, problems were encountered during device driver development and integration with the RCCS that required additional implementation time.

Since the high-power RF subsystem used two different models of PLCs, implementing the EPICS interface proved somewhat difficult. The PLC-5 communicates to other PLCs via Allen-Bradley's DataHighway Plus or DF1 protocols, while the SLC communicates via DH-485 or DF1. Since DF1 is the common protocol, an EPICS device driver was written to allow communication between a PC IOC and the PLCs. Coding and testing of this driver took approximately 4 man-months, and development of a fault logger similar to the vendor's implementation took approximately 2 man-months. There will be three klystrons connected to the LEDA RFQ. A commercial, off-the-shelf (COTS) hardware board was ordered for each klystron's PC IOC, at a cost of $750 each, to communicate with the transmitter PLC via DataHighway Plus. Communication with the power supply PLC is via the PC's serial port. Interfaces to the integrated control system were allowed for, but integration details were not initially designed. Had the LANL Controls group implemented the klystron controls, a large portion of the PLCs ladder logic would have instead been implemented in the EPICS IOC to reduce maintenance costs.

The RFQ vacuum subsystem was implemented in 4 man-months, which was spent developing the Labview display, automatic pumpdown sequence, and Modicon PLC program. Device drivers for the GPIB communications protocol were already supported in EPICS, but the Modicon PLC interface driver had to be created.

In the case of the LLRF subsystem, control system materials include only the slot zero controller and associated software licenses. Costs of these are on the order of $10K. The effort includes the software installation and configuration, ethernet wiring, and device driver development for each VXI module. This is estimated at about 11 man-months.

3.3 Integration

The RCCS was easily integrated into the LEDA control system, since it was designed as an EPICS application. Integration costs included implementing the database, sequences, and displays, and is estimated at 9 man-months.

For the high-power RF subsystem, EPICS database and operator screen development took 12 man-months for the first klystron. A considerable amount of time was spent analyzing the data available in the two PLCs and determining how best to duplicate this information for the other klystrons to be added to the network. Subsequent klystrons will be added rather easily due to the repetitive nature of the design, and this is estimated to take 0.5 man-months per additional klystron.

The RFQ vacuum subsystem was integrated into the LEDA control system by porting the Labview application to EPICS, and took 2 man-months. This includes reviewing the requirements, using the ladder logic and Labview programs as a foundation. Integrating a GPIB

device took 2 days, and overall system testing by LLNL and LANL is expected to require another man-month.

Integrating the LLRF subsystem is ongoing. EPICS device drivers are being written for each VXI module as they are delivered, and engineering databases and screens are being developed for testing and commissioning purposes. This effort was included in the implementation section. Further integration with the high-power RF subsystem databases and screens will take another 3 man-months, after obtaining all operational requirements.

3.4 Maintenance

Maintenance costs for these subsystems are affected by formality of the vendor relationships and the familiarity the LANL Controls group has with the overall system design. For instance, maintenance of the RFQ vacuum subsystem is not expected to take any extra time, since the ladder logic is the only component remaining from the original system design, and familiarization with that software was required to implement the porting into EPICS. Also, the LANL Controls group will now have maintenance responsibility for that software. However, high-power RF subsystem maintenance is complicated by the fact that all ladder logic changes will remain the responsibility of the vendors. This is likely to result in longer response times for software revisions, which could impact LEDA operations since some control algorithms and sequences are implemented in the PLC and not in the EPICS IOCs. Maintenance concerns are minimized for the RCCS and the LLRF subsystem since these are strictly EPICS implementations, and are only limited by the resources available to the LANL Controls group to perform these tasks.

4 SUMMARY

The effort involved in implementing a control system with subsystems developed by both outside suppliers and in-house personnel is affected by many factors. Included in these are the overall complexity of the subsystem, the amount of software to be developed while integrating new modules, and the amount of communication between subsystem developers and the integrated controls group. Table 1 lists efforts in man-months for the acquisition, implementation, and integration of the four subsystems discussed above.

Phase	RCCS	HPRF	RFQ Vacuum	LLRF
Acquisition	3	12	9	0
Implementation	10	6	4	11
Integration	9	13	3	3

Table 1. Effort (man-months) for Each Subsystem

5 CONCLUSIONS AND RECOMMENDATIONS

Although the LEDA control system is not yet fully operational, the following conclusions can be drawn from the experience gained to date in this effort:

- The amount of involvement in subsystem design and implementation by the LANL Controls group is inversely proportional to the effort to integrate each subsystem in the LEDA control system.
- Surprisingly the largest amount of time spent developing and integrating these subsystems into the LEDA control system has been in collecting requirements.
- When there are repeating elements in the control system, as is the case with the klystron PLCs, time spent replicating added elements is greatly reduced by carefully evaluating and planning the initial design.

The following recommendations can be made to improve future developments, both in outsourcing and in developing in-house:

- Ensure the personnel responsible for the integrated control system are involved in establishing subsystem requirements.
- Ensure the personnel responsible for the integrated control system are involved in periodic reviews of subsystem implementation.
- Reduce the role of PLCs in the design to that of equipment protection interlocking, and implement all sequencing and control algorithms in the EPICS IOCs. This will reduce complexity of the PLC design, and improve the flexibility of the integrated control system.
- When outsourcing, include in the purchase requisitions a minimum response time to software and hardware change requests, and add a minimum time period where there are no fees for these changes.
- When developing custom hardware in-house, the schedule must include time to integrate and test these components into the overall control system.

6 ACKNOWLEDGEMENTS

We gratefully acknowledge the support of the United States Department of Energy.

7 REFERENCES

[1] M. E. Thuot et.al., "The Success and The Future of EPICS," Proceedings of XVIII International Linac Conference, Geneva, Switzerland, August 26-30, 1996.

PERFORMANCE OF THE KLYSTRON MODULATORS AT THE S-BAND TEST FACILITY AT DESY

S. Choroba, J. Hameister, M. Kuhn
Deutsches Elektronen-Synchrotron, DESY, 22603 Hamburg, Germany

Abstract

The klystrons at the S-band test facility at DESY require high voltage pulses of 550kV at a flat top pulse duration of 3μs, at a current of 700A and a repetition frequency of 50Hz. Two HV pulse modulators with a nominal power of 375MW were built. The design and results of the commissioning of the first system were described in [1]. The second system came into operation and was operated at an output power up to 475MW (610kV, 780A). In addition it was modified to investigate capacitor charging power supplies, which might be used in a linear collider tunnel. This type of power supply promises a better efficiency than the conventional resonant charging method and also saves space in the linear collider tunnel. This paper describes the operation experience with the HV modulators at the test facility especially with the second system. It reports the modifications, which were required to operate the modulator with the new type of HV power supply and presents results of the operation.

1 INTRODUCTION

The S-band test facility at DESY is a 400MeV electron linac, which serves for the development and evaluation of components which might be used for an S-band linear collider. Two pulse klystrons operating at 2.998GHz with a nominal output power of 150MW are installed at the test facility. The pulse duration is 3μs and the repetition rate 50Hz. In order to generate the microwave power of 150MW a klystron cathode voltage up to 550kV and a current up to 700A are required. The high voltage pulses of 3μs flat top pulse duration are produced by line type modulators. Although the resonance charging method, used in both modulators, is a well established and reliable technique to charge the capacitors of pulse forming networks, a new type of capacitor charging power supply, which is now available from different manufacturers, was installed at the second modulator. It can be used alternately with the existing resonance charging system. Constant current capacitor charging power supplies have a high efficiency and a compact size. Both are properties, which are especially desirable for modulators, which need to be installed in a linear collider tunnel, but of course are also of interest for other linear accelerators. The first modulator is in operation since three years and the second since one year. In the following we present a short overview of the modulator system and report on our operation experience so far. After that we describe the modifications required to install the new charging power supply and present results of the measurements performed on the system.

2 LINE TYPE MODULATOR LAYOUT

Table 1 shows the parameters of the modulator and figure 1 shows the basic circuit diagram.

Table 1: Modulator parameters

Pulse Voltage	550 kV
Pulse Current	700 A
Flat Top Pulse Duration	3 μs
Repetition Rate	50 Hz
Equivalent Square Wave Duration	4.8 μs
Rise Time 10 - 90 %	700 ns
PFN	four lines parallel, each line ten sections
PFN Impedance	1.34 Ω
Total Capacitance	1.8 μF
Capacitor Capacitance	45 nF
Coil Inductance	1.3 μH
Charging Voltage	50 kV max.
Peak Current (primary side)	16 kA
Pulse Transformer Ratio	1 : 23

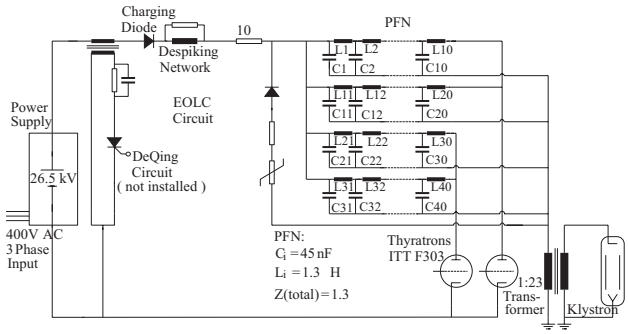

Figure 1: Basic circuit diagram

The pulse forming network is formed by four parallel lines of ten sections. They are discharged by two thyratrons, ITT F303, via the pulse transformer into the klystron. There is a slight positive mismatch between the pulse forming network and the klystron. The capacitors of the lines are charged by a resonant charging system consisting of a DC power supply (26.5kV, 5A), a charging choke of 16H and a charging diode capable to withstand

80kV. The PFN can be charged up to 50kV by a sinus half wave current of 17ms duration. This allows to operate the modulator at a repetition rate up to 50Hz. The DeQing system shown in the figure 1 was not installed, because the DC power supply has good regulation properties, which already allow a pulse to pulse variation smaller than 0.5%. Figure 2 shows typical waveforms at more than 500kV.

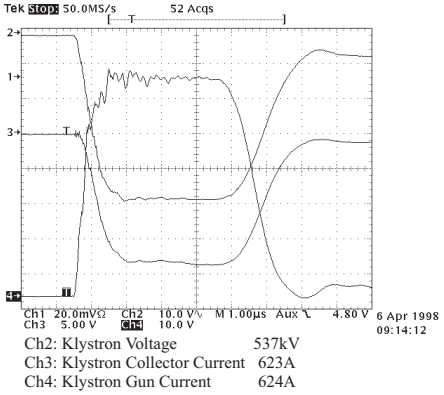

Figure 2: Typical waveforms

More detailed information can be found in [1].

3 OPERATION EXPERIENCE

At the beginning of operation electromagnetic noise generated by the modulators was a major concern. It entered the interlock system or other components and could lead to interruptions of the modulator operation. In the worst case it could even muddle up the thyratron driver trigger logic and damage components in the driver, especially the drivers thyristor switches. Since the source of noise could not be eliminated, we installed RC filters in the drivers and also in other components, which were affected by the noise. This solved our problem and allowed to operate without interruptions.

It is necessary to control the thyratrons reservoir voltage carefully. Otherwise the situation can occur, that instead of firing both thyratrons simultaneously, the thyratrons fire at different times or in the worst case one thyratron fails to fire. This does not harm the klystron, but leads to large thyratron grid spikes and can damage the thyristor switches in the driver circuits.

Besides these we had no major problems.

The klystron output power of 150MW could be reached with a cathode voltage of 550kV. With a PFN charging voltage of 50kV even 610kV could be achieved at the klystron. At this voltage an output power of 213MW could be extracted from the klystron. Since the klystron was developed for an RF power of 150MW at 3µs pulse duration and a repetition rate of 50Hz, we reduced the RF and HV pulse duration to 1µs and the repetition rate to 12.5Hz. The reduction in pulse width was accomplished by removing five capacitors per PFN line. At a flat top pulse duration of 1µs a maximum voltage of 610kV at 780A, which corresponds to a power of 475MW, was achieved and could be handled without problems. Longer pulses might be even possible but have the risk of damaging the klystron or the modulator. Since we need the klystron to operate the test facility linac, we refrained from running at longer pulse width at this power level.

4 MODIFICATION

The second modulator was modified in order to investigate the properties of a constant current capacitor charging power supply. This type of power supply might be able to replace the resonant charging method. It charges a pulse forming line with a constant current to the desired voltage without the use of a charging choke. Maxwell (San Diego, USA) offers power supply modules up to a voltage of 50kV and a power rating of 10kJ/s. Modules can be connected in parallel to build one power supply with more output power. In a first stage we installed three modules, which are sufficient to operate the modulator at maximum peak power, but at a reduced repetition rate of 12.5Hz instead of 50Hz. In a later stage the new power supply could be upgraded to full average power by installing up to twelve modules in parallel. In the meantime the existing resonance charging system must be used, if operation at 50Hz repetition rate is required. Therefore all modifications of the existing modulator needed to be done in a way, which allows to switch easily between the two charging methods.

A freewheeling diode and two series resistors must be installed between the pulse forming network and the constant current charging power supply output. This is necessary, because the charging power supply must be protected from negative voltage at its output. In this case a current could flow through the power supply rectifier diodes, which might exceed their capabilities. Negative voltage at the power supply output arise during fault conditions like klystron arcing or PFN breakdown and even also during normal operation conditions. The EOLC diode is not sufficient to protect the power supply, because it does not connect the power supply output and ground. We therefore installed a another diode at the thyratron side of the PFN. Figure 3 shows the diagram of the modified circuit.

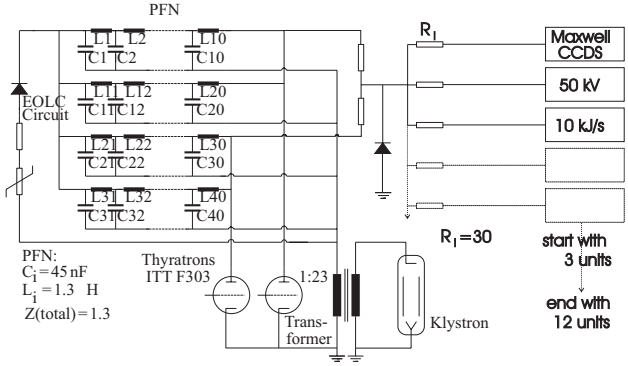

Figure 3: Diagram of the modified circuit

The protecting diode is made of 25 high voltage diodes in series (4kV each), each with a varistor in parallel. Two 30Ω series charging resistors serve for the decoupling of the two thyratrons. This allows switching of both thyratrons at the same time. Each of the power supply modules has a separate output cable, which is terminated by a another series resistors. We did not combine the output of modules directly after the output and did not use just one cable and resistor instead of many, because this would have made it more difficult to install or remove modules for test purposes. For a set up, which does not require this flexibility, a connection with just one cable could of course be made. The protecting diode and the resistors were installed in the PFN cabinet.

The compact size of this new type of power supply makes it attractive if space availability is an important aspect, e.g. in the case of a linear collider tunnel. The size of each of the modules in use is 220mm high, 508mm long and 19 inch wide. All modules, which would be sufficient for a modulator operation at full average power, would fit in two 19 inch racks. This reduces the space required by the existing DC power supply and the charging unit by about a factor of ten.

Another motivation to test the new type of power supply results from the efficiency demands of a linear collider. The existing resonance charging method has an efficiency of 88% for the charging path from the mains to the PFN, partly caused by the DC power supply efficiency and partly caused by ohmic and eddy current losses due to the charging choke. We measured the efficiency of the power supply at various output voltage settings. At the maximum voltage of 50kV it reaches 93%. Even if one includes the losses in the series charging resistors, the efficiency for the charging path from the mains to the PFN is still 91.5%.

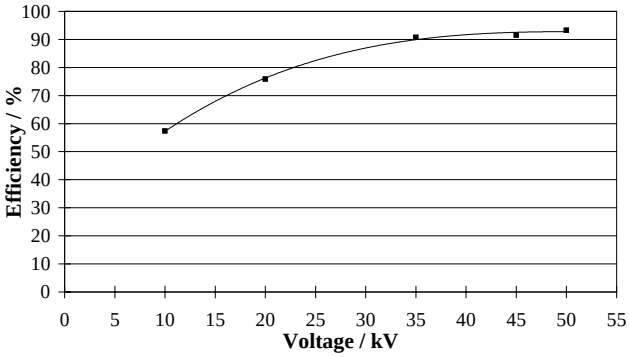

Figure 4: Charging power supply efficiency versus PFN voltage

The pulse to pulse variation was measured in the same way as for the resonance charging method by superposing 1500 klystron voltage pulses. The variation did not change significantly. and is still smaller than 0.5%.

An important aspect for a linear collider is the impact of the modulator power supplies on the line. Therefore we measured the voltage and the current of each of the input phases and calculated the input power of each phase. Figure 5 shows the linear ramp of the PFN voltage and the power extracted from the three phases of the mains. It is basically a picture one would expect from a three phase double way rectifier, which has do provide a linear increasing output power. This process is repeated with the modulators repetition rate. The power consumption from the mains is not constant and in case of a large number of modulators would probably disturb the mains. Further development to limit this effect is required.

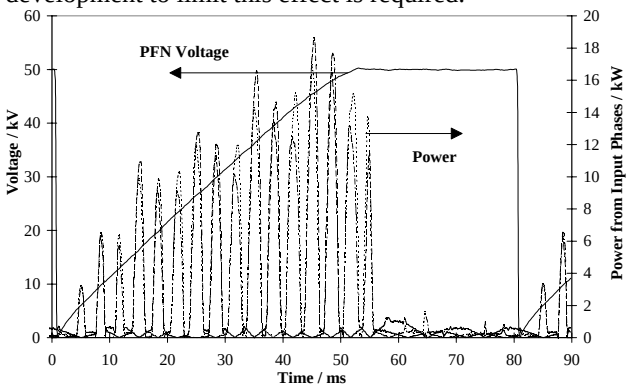

Figure 5: Charging voltage and power extracted from the three phases of the mains during one charging cycle

More detailed information about the modification of the second modulator can be found in [2].

5 CONCLUSION

The high voltage pulse modulators at the S-band test facility are in operation at nominal conditions of 550kV at 3μs pulse duration and a repetition rate of 50Hz. The second system can be even operated at a higher power level up to 475MW (610kV, 780A) at 1μs pulse duration and 12.5Hz repetition rate. The operation of the modulators is reliable, but the thyratron reservoir voltage setting needs careful control and adjustment. A new type of charging power supply was installed at the second system. It has a high efficiency and is of compact size, which makes it attractive for linear collider applications. Its reaction to the mains was investigated, but further work is necessary to limit disturbing effects to the mains.

6 REFERENCES

[1] S. Choroba, M. Bieler, J. Hameister, Y. Chi, A 375MW Modulator for a 150MW Klystron at the S-Band Linear Collider Test Facility at DESY, Proceedings of the XVIII International Linear Accelerator Conference, Linac96, Geneva, Switzerland, 26 -30 August, 1996, P 785-787

[2] S. Choroba, J. Hameister, M. Kuhn, "Operation of a HV Pulse Modulator at the S-Band Test Facility at DESY with a Constant Current Capacitor Charging Power Supply", to be published in the Proceedings of the 1998 Third Modulator-Klystron Workshop, SLAC, Stanford, June 29 - July 2, 1998

ADVANCED BUCK CONVERTER POWER SUPPLY "ABCPS" FOR APT *

R. Street, T. Overett, E. Bowles
General Atomics, San Diego, California 92186-5608 USA

Abstract

To meet the Nation's needs for Tritium one proposal is to use a high-power proton Linac, The Accelerator for the Production of Tritium or APT project **. The 1700 million electron volt (MeV) proton beam accelerator will be powered by radio frequency (RF) klystrons. A direct current (DC) power supply is required for each of the approximately two hundred and fifty 1-megawatt (MW) continuous wave klystrons in the RF power system. The requirements are that the power supply meet output performance specifications, provide fault protection for the klystron, have high efficiency, high reliability, good maintainability, and be readily manufacturable. As the power supplies are one of the largest cost elements in the accelerator, a technology review was made to determine the most economical approach to satisfy the requirements. A switch-mode power supply employing a buck-regulator was identified as being potentially the lowest cost approach. As the switch represents a certain development risk, a small-scale prototype has been constructed for evaluation, and has resulted in the decision to fabricate a full-scale prototype power supply. The prototype design and performance test information will be made available to potential suppliers. A description of the concept follows.

1 INTRODUCTION

The proposed APT plant will use proven accelerator based technology. The 1700 MeV proton accelerator will utilize three standard 350 megahertz (MHz) klystron RF sources to drive the RF Quadrupole. There will be two hundred and forty one 700 MHz klystron RF sources to power the normal temperature low-energy linac and the super-conducting radio frequency cavities in the high energy linac to create the high-energy proton beam.

2 APT RF POWER SYSTEM

The APT plant requires one high voltage power supply (HVPS) for each of the 244-klystron RF power sources. Three HVPS provide 2 MW DC to 1.2 MW (RF) klystrons and the rest supply 1.6 MW DC to 1 MW (RF) klystrons. Two-MW DC power supplies rated for 95 Kilovolts (kV) @ 21 Amperes (A) DC are planned throughout for commonality.

*Work supported by DOE under contract DE-AC04-96al89607.

** George P. Lawrence's invited talk at this conference.

In addition to meeting specification requirements in section 4, the HVPS must also provide fault protection for the klystron, have high efficiency, high reliability, good maintainability, and be readily manufacturable. As the HVPS are one of the largest cost elements in the accelerator, a technology review was made to determine the most economical approach to satisfy the requirements. The results of that review indicated a switch-mode power supply employing a buck-regulator was potentially the lowest cost approach to satisfy all plant requirements.

The buck-regulator topology is potentially the most economical because the high voltage rectifier bridge and the high voltage step-up rectifier transformer are removed from the power supply. All other topologies, including the resonant power supply utilize expensive magnetic components, which increase their costs and complicate their manufacturability.

To accomplish this, the 230-kV high voltage, utility distribution transformers would become the rectifier transformers. The transformer secondary voltage is rectified to provide twelve pulse DC power to the system. This also simplifies and reduces the cost of the utility distribution system for APT because the usual branch circuits and components used to step-down the utility voltage to a workable medium voltage are not required.

The utility source 230-kV, 677 megavolt-ampere (MVA) line feeds four substations. Each of four substations (Fig. 1) will contain two, 60 MVA isolation transformers for a total substation capacity of 120 MVA. This allows each substation to feed twenty five percent of the HVPSs. For redundancy, two high voltage rectifier bridges would be connected to the secondary of each distribution transformer. There would be a total of eight rectifier-transformers and sixteen rectifier bridges. Interphase transformers tie the rectifier outputs from the phase-shifted transformers to make twelve pulse ripple. The transformer secondary is eighty-two kV rms. It is then rectified to 115 kV DC. Each rectifier bridge will be sized to support twice the usual number of HVPSs, in case one rectifier is out of service. Each of the four DC transmission grids would feed a minimum of sixty-one power supplies. Only three HVPSs will actually operate at 21 A. The remaining HVPSs will operate at 17 A. Fig. 1 shows a typical distribution substation pair of rectifier transformers including the DC rectifiers dedicated to the RF power system.

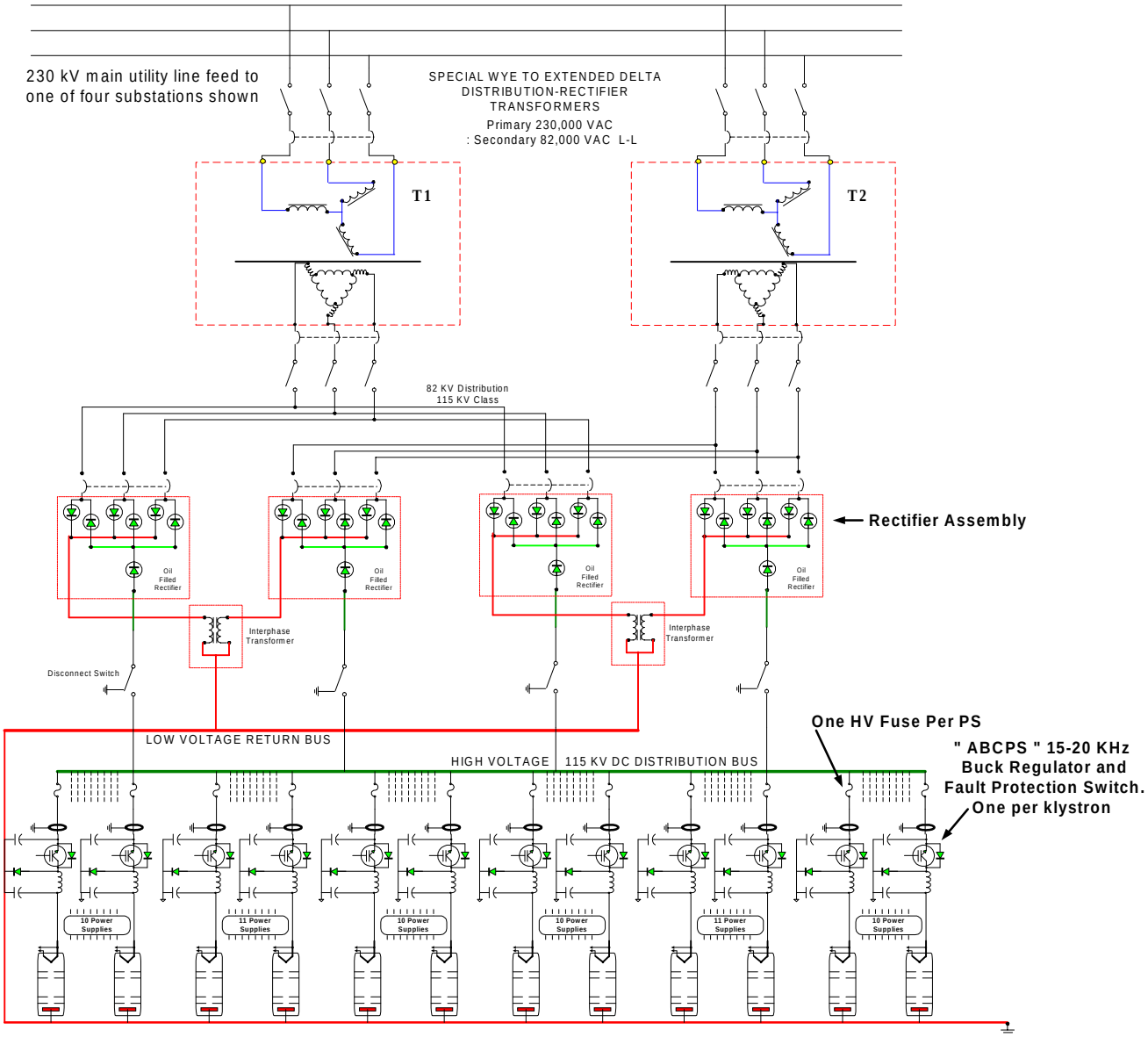

Figure 1: "ABCPS" DC Distribution System for APT

3 ABCPS

The Advance Buck Converter Power Supply, (ABCPS) is connected directly to the DC distribution bus. The topology of this converter is a DC to DC buck chopper which regulates the applied voltage to one klystron. A circuit schematic of a single ABCPS is shown in Fig. 2. The raw HVDC input is switched at approximately 20 kilohertz by a HV IGBT switch and charges the output capacitor through a switching inductor. A freewheeling diode transfers the inductor energy into the output capacitor during the IGBT switch off time. The circuit operates in the discontinuous current mode.

Additional output filter sections reduce output ripple voltage and also provide instantaneous fault energy limiting to the klystron. During operation, when the klystron may arc internally, the IGBT switch will interrupt the high voltage power supply output current in one microsecond or less. To prevent damage to the klystron, less than 40 joules will be deposited during an internal plasma arc. Individual primary high voltage fast acting fuses will be used for back-up power supply and klystron load protection.

The high voltage IGBT switch assembly is designed for ease of maintenance. The IGBTs, heat sinks, and gate drive circuits are mounted on plug-in circuit cards. Fiber optic signal isolation is utilized throughout the HVPS. The entire switch assembly can be bench manufactured and does not require special manufacturing or heavy assembly equipment. In addition no large magnetic cores

are needed. All the HVPS inductors are single layer wound air-core coils. The majority of the HVPS components are standard off the shelf types. This manufacturing approach reduces cost and procurement lead-time.

The most critical circuitry in this ABCPS is the high voltage solid-state switch. This switch is a string of paired IGBTs connected in series to hold off the 115-kV DC input. References [1] through [6]. The IGBTs are paired to provide redundancy. Uniform voltage sharing across each device is critical under all operating conditions. Each IGBT will have an independent gate control circuit. Once the fault is detected, the IGBT switch can operate in less than one microsecond to protect the klystron and provide fast voltage regulation and control.

4 HVPS OUTPUT CHARACTERISTICS

Output DC voltage: Continuously variable- 4 to - 95 kV
Output DC polarity: Negative with respect to ground
Output voltage set-point accuracy: +/- 400V
Output voltage rate of increase: 10 kV / second max.
Output current rate of increase: 200A / second max.
Regulation range: 10 – 95 kV
Regulation requirements (line & load): +/- 400 V max.
Ripple @ any 60 Hz harmonic: 800 V pk to pk max.
Total ripple (all causes): 1100 V peak to peak max.
Voltage stability: +/- 0.4% max.
Output DC current: 0 - 21 A
Load fault protection: 40 Joules max.

REFERENCES

[1] V.Chitta, S. Hong, and David A. Torrey, “Series Connection of IGBTs with Active Voltage Balancing”, IEEE 1997

[2] P.R. Palmer and A.N.Githiari, “The Series Connection of IGBTs with Active Voltage Sharing”, IEEE PESC 1997, pp.637-644

[3] C.Gester, P. Hofer, N Karrer, “Gate-control Strategy for Snubberless Operation of Series Connected IGBTs”, PESC 1996, pp.1739-1742.

[4] P.R. Palmer and A.N. Githiari, “The Series Connection of IGBTs with Optimized Voltage Sharing in the Switching Transient” Proceedings of IEEE PESC 1995, Vol. 1, pp.44-49.

[5] C.Gester, “Fast High Power/High Voltage Switch Using Series Connected IGBTs with Active Gate-Controlled Voltage Balancing”, APEC 1994, pp.469-472.

[6] M.Tsuneoka, M. Takeuchi, and I. Takahashi, “The Design of RF Power Supply using DC-DC Converter”, IEEE 1989, pp.1206-1209.

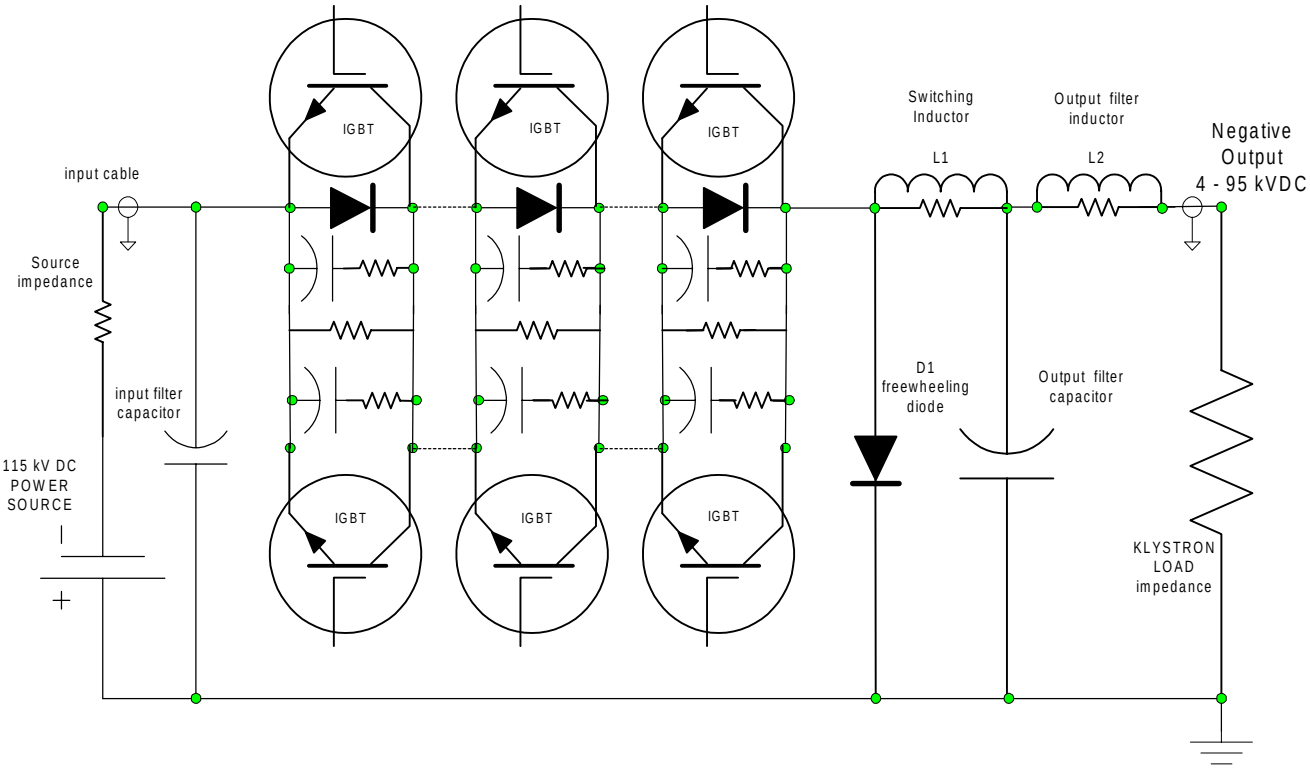

Figure 2: ABCPS Schematic

STATUS OF THE 36 MHZ RF-SYSTEM FOR THE HIGH-CURRENT-INJECTOR AT GSI

W. Vinzenz, W. Gutowski, G. Hutter, GSI, Planckstr. 1, D-64291 Darmstadt, Germany
B. Rossa, Thomcast AG, Bahnhofstr. 10, CH-5300 Turgi, Switzerland

Abstract

Within the beam intensity upgrade program at GSI some significant changes of the rf equipment will take place. The replacement of the four Wideröe tanks means at the same time the elimination of the 27 MHz operating frequency at GSI. To supply the new 36 MHz structures, rf amplifiers with a peak power of about 2 MW are needed. These stages will be designed and built up in house. 200 kW amplifier stages were specified, ordered and delivered. They act as driver stages for the 2 MW final stages and as final stages for feeding smaller cavities, respectively. The frequency change, as well as the future operation with beam load implies the replacement of more than 60 % of the present UNILAC low level distribution and control.

1 INTRODUCTION

In 1999 the 1.4 MeV/u prestripper section will be replaced by the High Current Injector HSI with an accepted mass over charge ratio for heavy ions up to 65 and with beam currents up to 0.25 A/q (mA) [1]. A 36 MHz RFQ and two IH drift tube tanks will replace the four tank Wideröe section. Each of the three new cavities will be fed by 2 MW final amplifier stages designed at GSI (see fig.1). The duty factor is up to 2% at maximum rf level, the specified rf power fraction into the beam is ranging up to 40%. Though the RFQ will need only up to 500 kW input power it was decided to have three identical amplifier chains. Beam dynamical aspects, as well as the dimensions of the cavities caused the choice of the new frequency 36 MHz. Because of the future UNILAC time share operation with two 1.4 MeV/u – Injectors and with up to three ion sources running in parallel, it was necessary to change the master frequency from 27 MHz to 108 MHz, the Poststripper LINAC frequency. The new 36 MHz system includes the following structures : RFQ, Superlense, IH 1, IH 2, a rebuncher at the 1.4 MeV/u gas stripper section and a debuncher at the 11.4 MeV/u transfer line to the synchrotron SIS. The operating modes of the 36 MHz Injector LINAC are :

a) up to 20 Hz repetition rate with 1 ms flat top at maximum power and full beamload;
b) up to 50 Hz repetition rate with 6 ms flat top at 40% of maximum power without appreciable beamload;
c) replacement of single pulses out of the pulse train in case b) with short high current pulses like in case a) resulting in a mixed mode operation.

Additionally, a small rebuncher structure focusing to the input of the Alvarez 1 tank will be driven by an existing 200 kW amplifier [2], which has been modified from 27 to 36 MHz.

2 AMPLIFIERS 200 KW

The required driving power for the 2 MW stages, as mentioned before, is calculated to be up to 200 kW. Further two 36 MHz final stages in the power range from 120 kW to 150 kW are needed to supply the Superlense and a debuncher cavity in the injection line to the synchrotron SIS (see fig.1). Therefore it was decided to procure five identical stages. Within a call for tenders rf amplifiers including all these features have been specified. Details about the design philosophy can be found in Ref.[3].
The major design part as well as the construction was performed by Thomcast AG (Turgi, Switzerland) after the order was placed (see Fig. 3). These stages use a class A/B solid state amplifier with a maximum peak output power of about 2 kW as driver . For the layout of the following tube stages the current use of the Siemens tetrode RS1084CJ at GSI and the working mode of the 2 MW final stages have been taken into account. The 200 kW stage works in a grounded cathode circuit in a class A/B mode (quiescent current at 2 Amp). To reduce power dissipation between the rf pulses the operating point will be switched to class C during the intervals. The anode circuit is a capacitively shortened $\lambda/4$ resonator in strip line design, tuneable by a vacuum capacitor at the tube side. The input (grid) circuit is a tuneable Π-network loaded with a capacitivly coupled 50 Ω.
The stages are designed as an 'all including' system. It means that all electronic components are installed inside the rack system, including the power supplies for plate, grids and heater of the 200 kW stage. In three amplifiers the grid supplies for the 2 MW final stages are included. In addition the amplitude and phase control units, the analogue value measuring and tube protection units, the free programmable control (SPS), the computer interface and also the automatic tank tuning system are housed in these cabinets. The timing information for rf pulse width, pulse space and sampling time, transmitted via a GSI two-wire-bus, is decoded in a special timing interface. The identification of a high current pulse is also done within this system [4].
With regard to the pulsed beam operation of the UNILAC (max. 16 virtual accelerators and low duty factor in the

high current mode) the analogue measurement unit had to be sampled. This allows to gate the measured values with the according beam pulse. For acceptable beam operation at unstable beam intensities, the frequency response of the amplitude and phase control loops had to be improved. For that reason a redesign of the existing control units of the Alvarez rf-transmitters was performed. Now the bandwidth of the amplitude control is set to f_{cutoff} = 500 kHz while the accuracy is up to ± 0.1%. The phase control unit attains a bandwidth of 1 MHz and an accuracy of ± 0.1 degree.

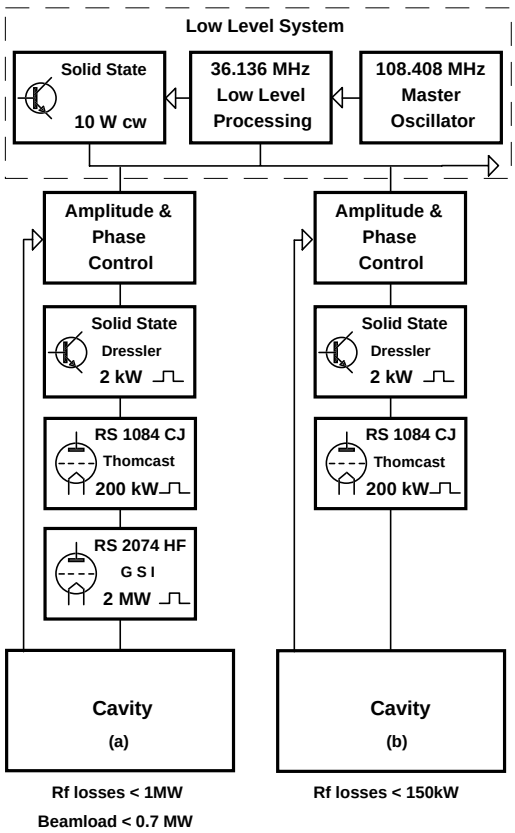

Fig. 1: Amplifier Chains of the New High Current Injector: (a) RFQ, IH1-DTL and IH2-DTL, (b) Superlense and Buncher

The delivery of the five stages to GSI started in December 97 and had been finished in July 98. Individual acceptance tests, including laboratory measurements, as well as electrical parameter tests (rf test with dummy load) and measurements of unwanted radiation leaks have been accomplished at the manufacturer. The observance of the very tight EN (European Harmonised) standards for electromagnetic compatibility and the IEC/VDE directives required an extension of the development time. Nevertheless this part of the project is terminated successfully with a delay of only three months. For tests of the RFQ tank and one 200 kW rf stage on resonant load, two of ten RFQ modules have been assembled to built a test cavity. They were powered by pulses of 90 - 100 kW peak at 1 ms / 20 Hz rep. rate and also by 20 kW at 6 ms / 50 Hz rep. rate. The results of the above mentioned RFQ tests showing excellent performance of the transmitter at 150 % of the nominal power level for the RFQ modules. Starting this test operation a parasitic oscillation at 190 MHz was observed at the plate circuit by switching the operating point to class A/B mode**.** This spurious mode could be eliminated by placing a frequency dependent attenuation circuit inside the anode circuit. An earlier detected oscillation at 280 MHz had already been eliminated at the manufacturer. At tests with the 2nd to the 5th stage at Thomcast AG by a pulsed grid voltage (-350 volts to 0 volts) with a resulting plate current up to 20 ampere, no parasitic effects could be seen. Tests were done with 50 Ω load, open and shortened amplifier output.

3 LOW LEVEL RF SYSTEM

The planned UNILAC upgrading requires also extended modifications within the low level rf equipment, including the master oscillator system and the low level rf distribution. The present system is driven by an oscillator frequency at 27 MHz. The frequency for the Poststripper section (108 MHz) is generated by quadruplicating the master oscillator frequency. This system will be replaced by a new 108 MHz master oscillator and a phase locked loop (PLL) synchronised slave oscillator at 36 MHz. Both low level systems are separately amplitude and phase controlled and can be supplied by different phase set values from the operating software. Thereby both 1.4 MeV/u UNILAC injector LINACs can be shifted in pulsed mode against the 11.4 MeV/u Poststripper LINAC. This feature is very important because the injectors can be operated in time share operation with different ions [5]. All input and output levels are normalised to +24 dBm (250 mW). Components like detectors, phase shifters, filters, oscillators, frequency dividers and amplifiers are designed and made in-house. Figure 2 shows the block diagram of the low level set-up and the rf-distribution.

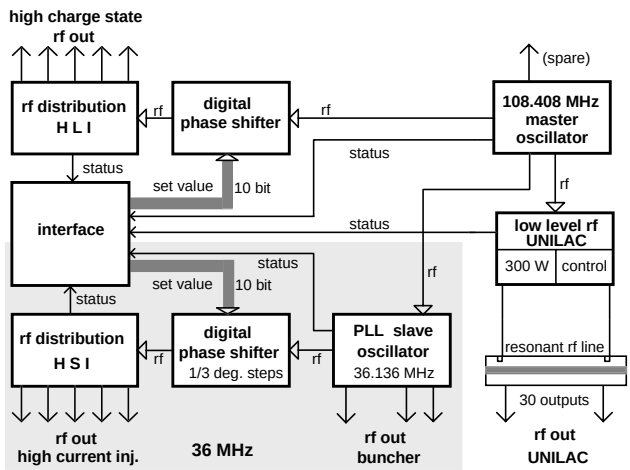

Fig. 2: Upgraded Low Level System

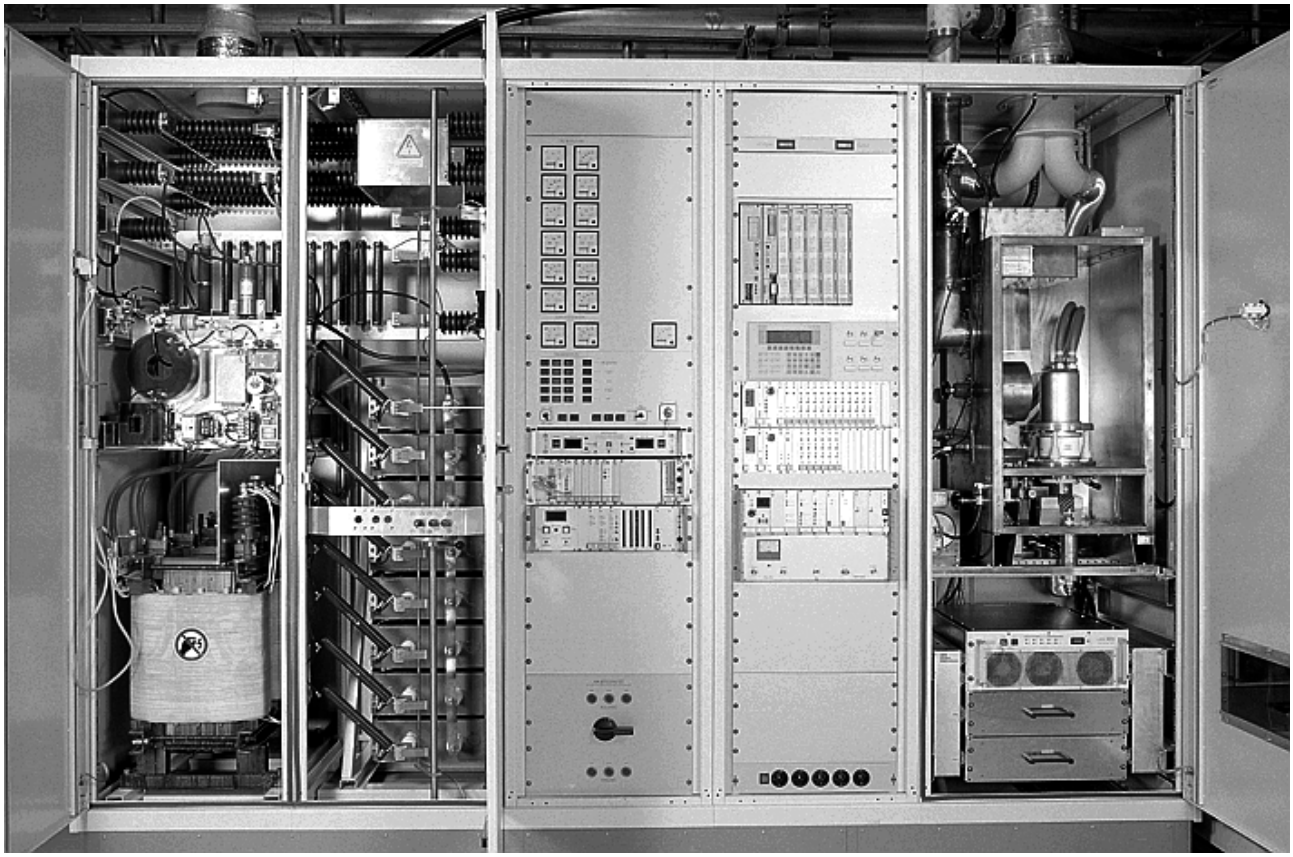

Fig. 3 : Front View of the 200 kW / 36 MHz Amplifier (by Thomcast AG) : the plate supply (two cabinets left); the local operation panel with computer interface and plunger control (3rd cabinet); Program controlled computer [Simatic] with the measuring device and amplitude & phase controls (4th cabinet); opened anode & grid circuit of the 200 kW stage with the 2 kW solid state amplifier (by Dressler) and the tube grid supplies below (right cabinet)

4 AMPLIFIERS 2 MW

The Siemens tube RS 2074 HF of the 2 MW final stages is the same tube as used at the final stages of the Poststripper LINAC (Alvarez 1 to 4). All the necessary calculations (partly performed with the Supercompact$^{\rightarrow}$ code) have been done for a 50 Ω load at the output of the amplifier. They were confirmed by cold measurements with a 1:1 model of the anode circuit using a dummy tube. The input circuit showed a good tunability. For a power range of 1:10 the load of different cathode currents at different power levels was simulated by variable resistors for this measurement. At present a prototype is under construction. The amplifier will be tested with rf on a dummy load early in autumn 1998. The construction of the three transmitters for the new injector should start by the end of this year. Commissioning of the RFQ and IH-Linacs with beam is scheduled for April to July 1999. A detailed report of the amplifier layout and the first results will be given elsewhere.

REFERENCES

[1] U. Ratzinger; "The New GSI Prestripper LINAC for High Current Heavy Ion Beams" Proc. of the 1996 LINAC Conf., Geneva, 288.

[2] G. Hutter et al; "New Power Amplifiers for 200 kW at 27 MHz" Proc. of the 1992 EPAC Conf., Berlin, 1203.

[3] D. Böhne; "Beam Intensity Upgrade of the GSI Accelerator Facility" GSI-95-05 report.

[4] W. Vinzenz; "The Computer Interface for the RF Amplifiers of the new HLI" GSI annual report 1992, GSI 93-1, 433.

[5] N. Angert et al; "Two-Ion Time Share Operation of the UNILAC" Proc. of the 1994 LINAC Conf., Tsukuba, 707.

KLYSTRON RF STABILIZATION USING FEEDFORWARD CIRCUIT

H. Hayano, M. Akemoto, T. Naito, S. Takeda, KEK, Tsukuba, Ibaraki, Japan
D. Aizawa, M. Higuchi, T. Sakamoto, Tohoku-Gakuin University, Tagajo, Miyagi, Japan

Abstract

Klystron rf stability in the linac of ATF, Accelerator Test Facility at KEK, is important to make beam injection into the damping ring stable. The current pulse-to-pulse fluctuation of the output rf is 0.4% peak-to-peak in the amplitude and 1.5degree in the phase. The linac beam energy is correlated with rf amplitude fluctuation directly. In order to make more stable beam injection, storage and extraction in the damping ring, pulse-to-pulse jitter of injected beam energy should be reduced to half of it. By the analysis of rf fluctuation, the amplitude and the phase jitter are correlated with a charging voltage of the modulator. The charged voltage of the modulator is also correlated with the slope of charging rise cycle. The peak of the charging waveform slope which is a few ms in advance of a deQ trigger control gives a possibility of a feedforward to stabilize the charged voltage. We developed a new deQ circuit with a feedforward function which reduces a charged voltage fluctuation into about a half of it. The rf fluctuation of the klystron and the feedforward circuit test are described.

1 INTRODUCTION

ATF[1] is a test-stand of key components to realize a linear collider such as multi-bunch beam generation, high gradient acceleration, low emittance beam generation and its instrumentation development. ATF consists of 1.54GeV S-band Linac[2], damping ring[3] and extraction beam line[4]. The main purpose of the damping ring is to develop an extremely low emittance beam($1x10^{-11}$ m for vertical). After the commissioning on end of January 1997, single bunch operation and development were performed continuously. The emittance performance was confirmed as $1.3x10^{-9}$ m for horizontal $3.6x10^{-11}$ m for vertical with 1.29GeV energy and maximum $1x10^{10}$ electrons of single bunch storage. It is comparable with the design value within a few factor difference. One of the problem to be solved in ATF operation is extracted beam intensity fluctuation of pulse-to-pulse. The required specification for the intensity fluctuation in the linear collider is less than 1%, however, ATF beam is fluctuating more than 10%. This is coming from the injection efficiency fluctuation which is caused by the energy jitter and the wide energy spread expanded into whole damping ring acceptance of 1% full width. The energy spread will be reduced to half of it by the bunching section upgrade in this summer. The energy jitter of pulse-to-pulse has been studied by measuring correlation with various possible sources. The results of the correlation measurements showed that the most strong source was rf amplitude jitter of the klystron output. It is directly connected with driving pulse voltage jitter supplied by a klystron modulator. In order to reduce the energy jitter pulse-to-pulse, a stabilization of the klystron modulator output is essential. This paper describes a new deQ circuit with feedforward compensation to stabilize the output pulse amplitude of the existing modulator for the pulse klystron.

2 ATF KLYSTRON MODULATOR PERFORMANCE

In the ATF linac, 9 klystrons are in operation with 25Hz repetition. The first klystron which is used for the bunching section is operated with 70MW 1μs rf pulse output. The rest of them which are used for 8 regular accelerating unit are operated around 56MW 4.5μs rf pulse output with rf pulse compression. The average accelerating gradient is 25.6MV/m which gives 1.3GeV beam energy at the end of linac. There are two type of klystron modulators; one is a conventional resonant charging type from AC 200V. The other is a common DC power supply type with resonant charging. In both case, a deQ circuit stabilize the charged voltage less than 0.2% peak-to-peak. The charged voltage of the PFN capacitor is around 43kV in the operation. The following pulse trans makes about 340kV 7.5μs HV pulse which is applied to the klystron. The operational parameter of the modulator and klystron are summarized in Table.1. Also, the simplified diagram of the modulator is shown in Fig. 1.

Klystron	Toshiba E3712
frequency	2856MHz
output rf power	56MW, 4.5μs
cathode voltage	340kV, 7.5μs
Modulator	
PFN & pulse trans	12stage, 2 para., 3.0Ω, 1:16
PFN charged voltage	43kV with deQ
repetition	25Hz
pulse flatness	<1%p.p.
pulse amplitude jitter	<0.2%p.p.

Table.1 operation parameter of ATF klystron modulator

Since the AC line stability is not good by a conflict with the other accelerator operation and other power supply operation, there is a few % voltage fluctuation in the input AC line. By using a deQ circuit for PFN

charging and an AC line synchronized thyratron trigger, the PFN charged voltage is well regulated less than 0.2% peak-to-peak which is the design value of the modulator. In this condition, the correlation measurement between PFN charged voltage and the klystron output rf has been done using digital oscilloscope with offset function and vertical axis expansion. The results of this correlation are shown in Fig. 2. The amplitude and the phase of klystron output rf are well correlated with the PFN charged voltage.

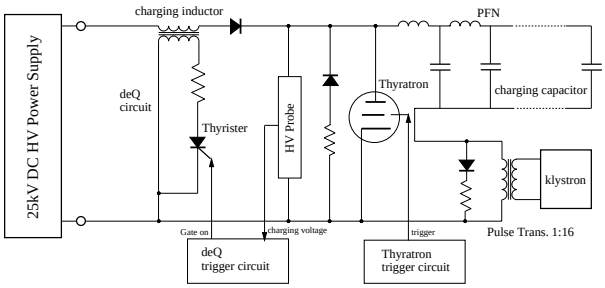

Figure 1: The simplified diagram of the modulator

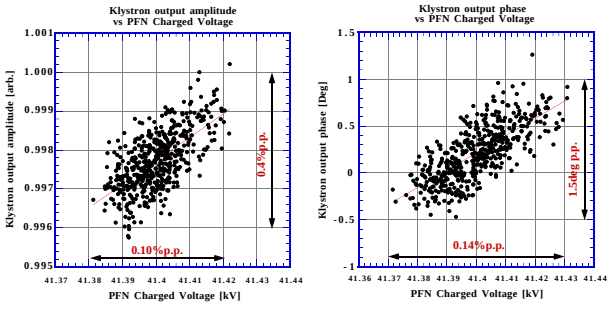

Figure 2: correlation plot between an amplitude and a phase of klystron output rf and PFN charged voltage

3 FEEDFORWARD FUNCTION FOR DEQING STABILIZATION

The deQ circuit of the ATF modulator consists of charging inductor which is a part of resonant charging circuit, its secondary winding circuit including a thyrister and a resister, PFN voltage monitor and thyrister trigger circuit, as shown in Fig. 1. The thyrister trigger circuit outputs 20V trigger pulse to make it on-state when the PFN voltage reached the set reference voltage. The charging current into the PFN capacitor is cut by this close action of the inductor secondary circuit. In this way, the charged voltage is stabilized.

Since there is a small time delay from the deQ trigger timing to charged voltage equilibrium, a small change of charging voltage slope at the reference voltage will make small overshoot or undershoot for the equilibrium. In this case, a change of the charging voltage slope is correspond to an amplitude fluctuation of the AC line which is slow compared to 25Hz. The correlation plot between a charging voltage slope and charged voltage equilibrium shows a good correlation relation as shown in Fig.3. The charging slope is detected by differentiating the charging voltage electrically.

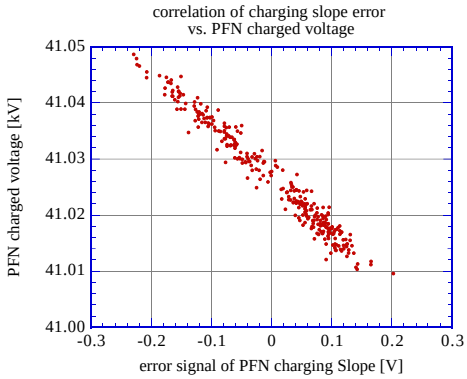

Figure 3: correlation plot between a charging voltage slope and charged voltage equilibrium

The maximum of the charging voltage slope is about 5ms in advance to the deQ trigger timing in case of the ATF modulator. Therefore, there is a possibility of feedforward from the slope information to the timing of deQ trigger in order to compensate overshoot and undershoot charging. A 5ms time duration is enough long for determination of the feedforward amount by a digital calculation or an analog circuit.

4 FEEDFORWARD TEST CIRCUIT

Using this slope detection, a feedforward test circuit was designed and built by the analog circuitry. The conversion function from the slope change to the delay of the deQ trigger was assumed to a linear for the circuitry simplicity. The charging slope detection circuit, the slope error signal generation, the amplifier for feedforward gain adjustment and deQ trigger delay circuit were added to the existing deQ circuit. The block diagram of the circuitry is shown in Fig. 4. The slope detection is done by a sample/hold at the peak signal of the differentiated charging waveform. A comparator outputs an error signal voltage from the reference which is coming from the deQ

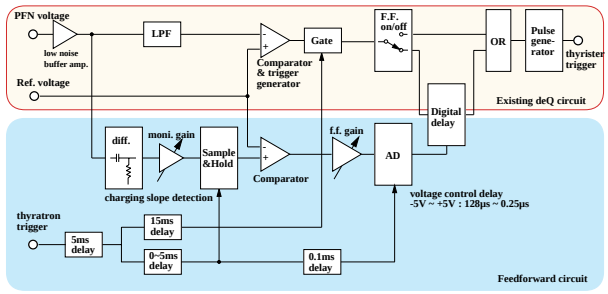

Figure 4: The block diagram of the feedforward circuitry

reference voltage. The error signal level is adjusted by the following amplifier and converted into a digital signal. The digital error data is converted to a time delay which is used for a deQ trigger delay. The amount of the delay is 0.25 to 128μs for +5 to -5V error voltage. By adding this delay circuit, the deQ trigger has an offset delay of about

60μs for the nominal control compared to the case of without feedforward.

5 RESULTS OF FEEDFORWARD TEST

The test of the feedforward circuit has been done using one of the ATF modulator which is the first modulator used for the bunching section. The charged voltage was 41kV which generated 328kV of the klystron cathode voltage and 49MW 1μs rf pulse. The measurement of the charged voltage and the klystron output rf has been done using the digital oscilloscope(Tektronics TDS684B) with offset function and vertical axis expansion into its maximum. The bit resolution is about 2 order small compared with the measured fluctuation width. In order to remove high frequency noise coming from a thermal noise and a thyratron noise, 20 sequential sampling points were averaged. The acquisition bandwidth of 20MHz was used only for the charged voltage measurement.

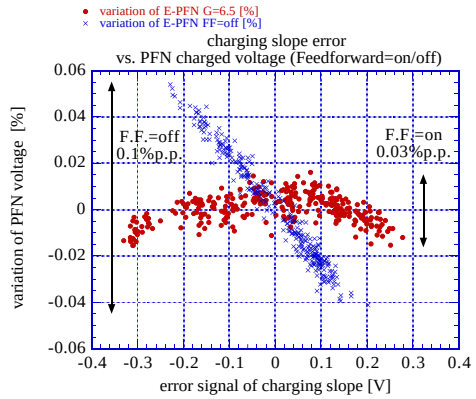

Figure 5: correlation between a charging voltage slope and charged voltage equilibrium with feedforward on/off

After the adjustment of the feedforward gain, the PFN charged voltage fluctuation was measured together with the error signal of the charging slope. The read-out time from the oscilloscope into PC was around 3 seconds for one correlation. The total number of the data points is 300 for each plot which is correspond to about 15 minutes duration. The plot shown in Fig.5 includes the correlation of the PFN charged voltage with feedforward and without feedforward. It shows the fluctuation is reduced from 0.1% to 0.03% peak-to-peak by the feedforward. As for the output rf stability shown in Fig. 6, the effect on the output rf is about factor 2 reduction, that is, from 0.3% to 0.13% peak-to-peak in amplitude and from 0.8degree to 0.5degree peak-to-peak in phase. A residual fluctuation in phase still remains. It seems that it may come from a noise conflict for the phase measurement and from the phase noise of the drive input rf of the klystron.

6 CONCLUSION

In order to reduce the energy jitter pulse-to-pulse, the stabilization of klystron modulator output has been tested by using new deQ circuit with feedforward compensation. The achieved performance on the PFN charged voltage stability was 0.03% peak-to-peak which was about factor 3 reduction from the existing deQ circuit. The rf stability of the klystron outputs were 0.13% peak-to-peak in amplitude and 0.5degree peak-to-peak in phase which were about factor 2 reduction. This method will provide easy modification of an existing deQ circuit and more than factor 2 reduction for an rf amplitude fluctuation.

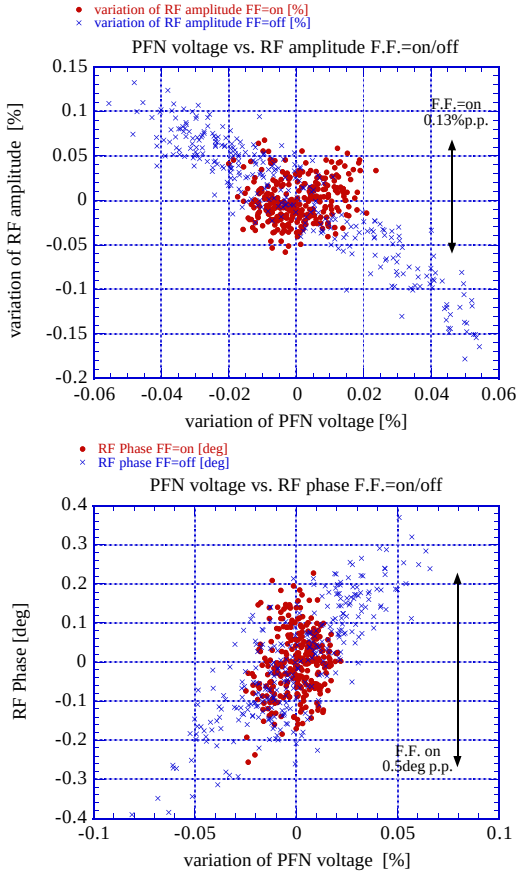

Figure 6: correlation between a charging voltage slope and klystron output rf with feedforward on/off

7 ACKNOWLEDGMENT

The authors would like to acknowledge Prof. H. Sugawara, director of KEK organization, for the support under the program of cooperation & development research. We also thank to all the member of the ATF group for their cooperation and useful discussion.

REFERENCES

[1] F. Hinode et. al., “ATF Design and Study Report” KEK Internal 95-4, (June 1995).

[2] H. Hayano, “ATF Linac Commissioning” Proc. of 18th Int. Linac Conf., Geneva (August 1996)

[3] K. Kubo, “Beam development in ATF Damping Ring,” Proc. of 6th European Particle Accel. Conf., Stockholm (June 1998)

[4] S. Kashiwagi et. al., “Diagnosis of the low emittance beam in ATF DR Extraction Line,” Proc. of 6th European Particle Accel. Conf., Stockholm (June 1998)

IMPROVEMENT IN THE UPGRADED MODULATOR OF THE KEKB INJECTOR LINAC

H. Honma, T. Shidara, S. Anami and K. Nakahara
High Energy Accelerator Research Organization
1-1 Oho, Tsukuba-shi, Ibaraki-ken, 305-0801, Japan

Abstract

An upgrade of the klystron modulator for the KEKB injector linac was completed before March, 1997. In this linac, SLED (SLAC Energy doubler) along with an upgraded klystron (which has an rf output power of 46 or 50 MW) is utilized to accelerate electron and positron beams up to 8 and 3.5 GeV, respectively. It is desirable to increase the pulse flat top of the modulator output pulse voltage for SLED operation. An improvement of the output waveshape had been carried out and a flat-top width of about 4μs was finally obtained. In addition, the time jitter of the modulator output pulse voltage was reduced to about 8ns by modifying the driver circuit for a thyratron.

1 INTRODUCTION

The upgraded modulators in the KEKB injector linac are capable of producing pulses with a 110 MW peak power and a 5.6μs pulse duration (calculated as one without a pulse transformer) for the upgraded klystron. SLED along with this klystron is utilized in order to obtain an energy gain of 160 MeV per one acceleration unit. At the initial stage of SLED operation, it became clear that there were some problems concerning the waveshape and the time jitter of the modulator output pulse voltage.

In order to obtain the aimed energy gain, it became important for the flat-top width of the klystron rf output to be increased as much as possible. A basic concept of the modulator upgrade was doubling the total capacitance of the PFN (pulse-forming network). The size of the PFN housing was therefore enlarged and the inductance of the wiring in the PFN output circuit was increased. The upgraded klystron causes the distributed capacitance of the pulse transformer to be increased, since its step-up ratio must have been increased compared to that in the old modulator [1]. These two factors deteriorated the pulse flat-top width of the output pulse voltage, i.e. the klystron rf output.

A reduction in the time jitter of the output pulse voltage is also important in order to obtain a stable beam energy. Since the time jitter of the modulator output pulse voltage is strongly dependent on a thyratron operation, improvements to the driver circuit for the thyratron were intensively performed. This paper describes the improvements mentioned above.

2 IMPROVEMENTS TO THE OUTPUT CIRCUIT

2.1 Improvement to the Waveshape of the Output Pulse Voltage

By considering the total number of acceleration units and available output power of the upgraded klystron, a SLED energy multiplication factor of 2.0 was selected as the design value. Taking into account the characteristics of the SLED cavity, a flat-top width of 4μs was reqired for the klystron rf output pulse [2].

Figure 1 shows the calculated output voltage waveshapes in the old (a) and upgraded (b) modulators using the circuit-simulation code “ISSPICE”. It can be seen from these figures that the increase in the flat-top width is less than that of the pulse duration due to the slower rise-and fall-time than those in the old modulator. It is therefore necessary to reduce the inductance of the wiring in the PFN output circuit.

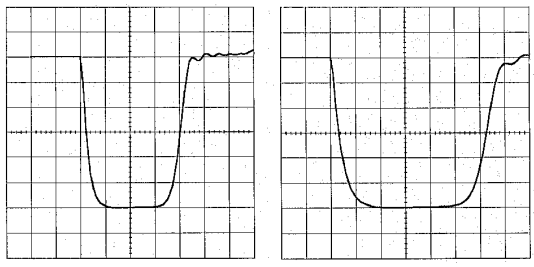

(a) old (b) upgraded
horizontal scale: 1μs /div
Fig. 1 Output voltage waveshapes (calculated).

Figure 2 shows the arrangement and the wiring of the output circuit in the upgraded modulator. A copper pipe was being used as the wiring (a) between the thyratron anode and the high-voltage side of the PFN. The length of this wiring became longer than that in the old modulator and its inductance was increased. As for the wiring (b) between the thyratron cathode and the feeder, a copper plate perpendicular to low voltage side of the PFN was being used.

We carried out the following improvements to the output circuit in order to increase the flat-top width of the output voltage pulse (see fig.2):

(1) Another copper pipe was added to the wiring (a) in such a way that the two pipes are separated from each other as much as possible,

(2) The wiring (b) was made parallel to the low-voltage side of the PFN in order to reduce the area of the loop surrounded by the wiring,
(3) The capacitance of the added PFN capacitors was increased from 0.0146μF to 0.0155μF .

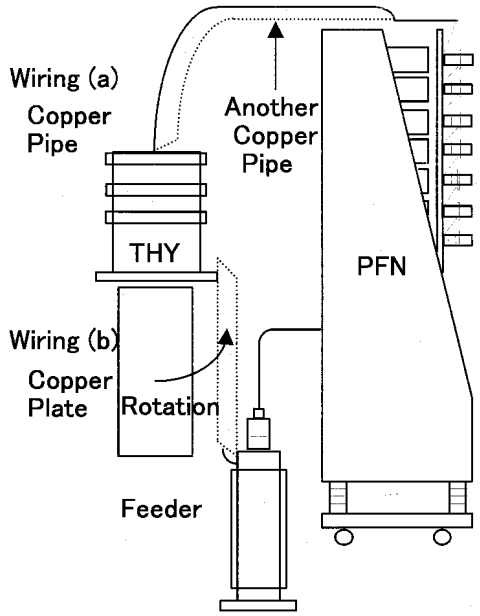

Fig. 2 Wiring of the output circuit.

Figure 3 shows the output-voltage waveshape of the modulator with the improved output circuit. It can be seen from this figure that the pulse duration is increased and the rise-time is being improved compared to fig.1(b). Figure 4 (a) shows an expanded trace of the flat-top of the waveshape. It can be seen that the flat-top width within 0.4% of peak pulse voltage is 3.8μs. Taking into account a recovery time of the oscilloscope, it is possible to say that the flat-top width of about 4μs was obtained. Figure 4 (b) shows an similar trace of the waveshape in the modulator without improvement to the wiring. It can be seen from this figure that the flat-top width increase of 0.4μs was obtained by carrying out the improvement to the wiring. An rf output pulse with the aimed flat-top width was obtained using this improved modulator.

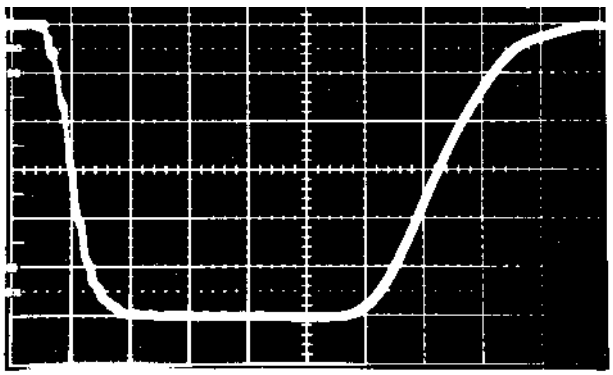

Fig. 3 Output voltage waveshape by the improved output circuit.
(horizontal scale: 1μs /div, peak voltage: 286kV).

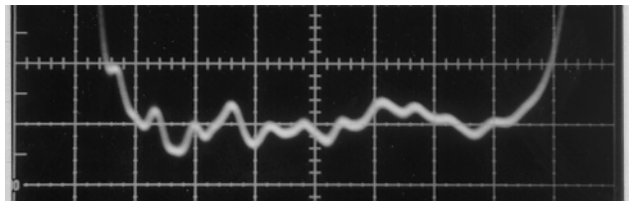

Fig. 4 (a) Expanded trace of the flat-top of an output-voltage waveshape (after improved). (horizontal scale: 0.5μs/div, vertical scale: 0.4% of peak pulse voltage/div).

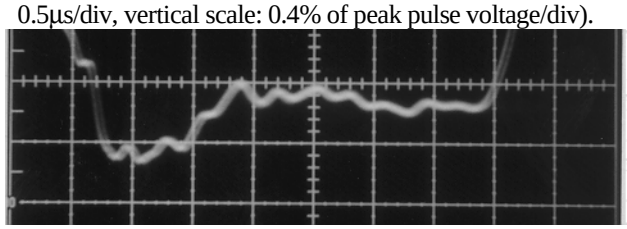

Fig. 4 (b) Expanded trace of the flat-top of an output voltage waveshape(before improved). (horizontal scale: 0.5μs /div, vertical scale: 0.4% of peak pulse voltage/div).

2.2 Improvement to the Thyratron Grid Driver

There are the following four factors which control the time jitter of the output pulse voltage: (1) the thyratron resorvoir voltage, (2) the output impedance of the thyratron grid driver, (3) the rise time of the pulse output voltage in the driver and (4) the input impedance of the thyratron input circuit. Figure 5 shows both the output circuit of the thyratron grid driver and the input circuit of the thyratron. The output impedance is derived from the impedance of the PFN and the step up ratio of the pulse transformer. In the old modulator, the output impedance of the thyratron driver was 100 Ω was equal to the value of the input impedance in the thyratron input circuit.

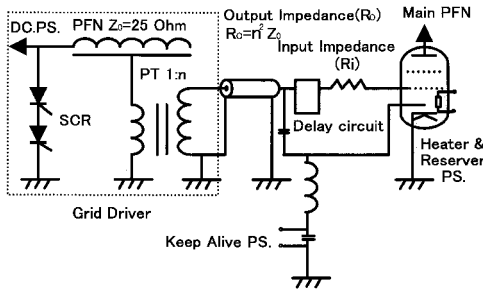

Fig. 5 Circuit between the driver and the thyratron.

Figure 6 shows the dependence of the time jitter in the output pulse voltage on the thyratron resorvoir voltage (jitter-resorvoir relation) measured under repetition rates of 25 and 50 pps in the old modulator. In this figure, it was impossible to measure the time jitter outside of both edges in each curve due to an unstable operation of the thyratron. It can be seen from this figure that the time jitter at each repetition rate and the difference between the values at two repetition rates increases when the resorvoir voltage decreases. This means that the thyratron driver of the old modulator has not fed sufficient power to the thyratron grid. It is also necessary to decrease the time jitter further for SLED operation .

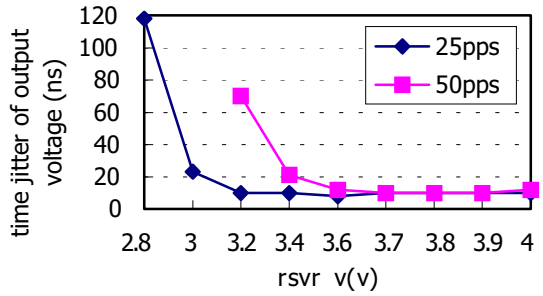

Fig.6 Jitter-resorvoir relations by an old driver.

In order to modify the old driver into one capable of feeding sufficient power to the thyratron grid, the jitter-resorvoir relation was investigated by changing the output impedance (Ro) of the thyratron driver and the input impedance (Ri) of the thyratron input circuit under repetition rate of 50 pps. Figure 7 shows the result of this investigation. The result obtained by changing the input impedance from 100 Ω to 22 Ω while maintaining the output impedance of the driver is almost same as that of the old driver. It is also known that the smaller is the output impedance, the smaller does the time jitter become. Though an output impedance of 28 Ω gives the smallest time jitter, such a modification costs too much, since it needs another PFN. Therefore, we adopted a driver with an output impedance of 56 Ω. Figure 8 shows the results of the jitter-resorvoir relations of this driver under both 25 and 50 pps operation. Since two jitter-resorvoir relations nearly coincide with each other, this driver feeds sufficient power to the thyratron grid.

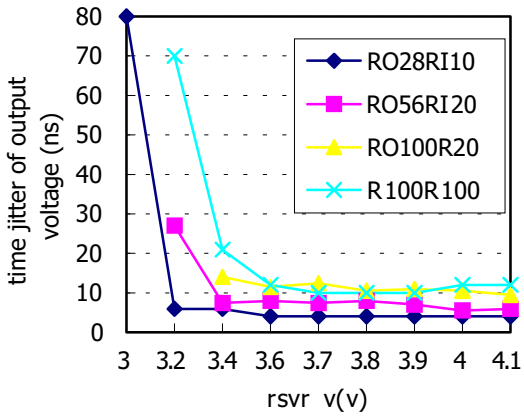

Fig. 7 Jitter-resorvoir relations investigated by changing the impedances (Ro, Ri).

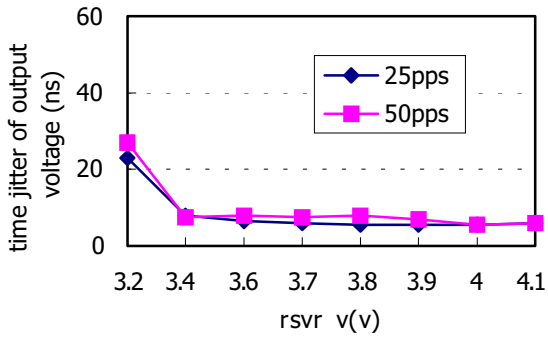

Fig. 8 Jitter-resorvoir relations by a new driver.

REFERENCES

[1] S. Fukuda et al., "Development of the B-Factory Linac 50-MW Pulse Klystron", Proceedings of Linac94, Tsukuba, Japan, August 21-26, 1994, 427-429(1994).

[2] H. Hanaki et al., "Use of SLEDS for high-gradient acceleration" , Proceedings of Linac94, Tsukuba, Japan, August 21-26, 1994, 430-432(1994).

NEW HIGH POWER 200 MHZ RF SYSTEM FOR THE LANSCE DRIFT TUBE LINAC*

J. Lyles, C. Friedrichs, and M. Lynch, Los Alamos National Laboratory,
Los Alamos, New Mexico 87544 USA

Abstract

The Los Alamos Neutron Science Center (LANSCE) linac provides an 800 MeV direct H^+ proton beam, and injects H^- to the upgraded proton storage ring for charge accumulation for the Short Pulse Spallation Source. Accelerating these interlaced beams requires high average power from the 201.25 MHz drift tube linac (DTL) RF system. Three power amplifiers have operated at up to three Megawatts with 12% duty factor. The total number of electron power tubes in the RF amplifiers and their modulators has been reduced from fifty-two to twenty-four. The plant continues to utilize the original design of a tetrode driving a super power triode. Further increases in the linac duty factor are limited, in part, by the maximum dissipation ratings of the triodes. A description of the system modifications proposed to overcome these limitations includes new power amplifiers using low-level RF modulation for tank field control. The first high power Diacrode® is being delivered and a new amplifier cavity is being designed. With only nine power tubes, the new system will deliver both peak power and high duty factor, with lower mains power and cooling requirements. The remaining components needed for the new RF system will be discussed.

1 PRESENT HIGH POWER RF SYSTEM

The Los Alamos Neutron Science Center (LANSCE) linac provides high power proton beams for neutron science, Tritium target development for APT, nuclear physics, material science, isotope production, and weapons research. The number of simultaneous beam users places heavy demands on the RF powerplant, especially the 201.25 MHz final power amplifiers (FPA) driving four Alvarez DTL tanks for 0.75 to 100 MeV. Designed nearly 30 years ago, these amplifiers have operated at up to 3 Megawatts with duty factors of 12%. The large number of power tubes in the PA plate modulators, the age of the cooling and control subsystems, tube manufacturing problems, and operation near maximum PA tube ratings have all affected the system reliability.

For the past six years we have designed and installed system upgrades that have reduced the number of power tubes in the system from fifty-two to twenty-four [1,2]. A block diagram of the present RF system is shown in Figure 1. The maximum duty factor is rated at 12% where the plate dissipation of the final amplifier tube, a Burle Industries 7835 triode, is approximately 250 kW. The peak power from the final cavity amplifier for the largest DTL tank (tank 2) is slightly over 3 MW for some tunes. The triode FPA is unstable if operated with plate voltage but no RF drive. Consequently, the FPA is driven with constant RF drive from the IPA, using a Burle Industries 4616 tetrode. The plate voltage is simultaneously pulsed on and varied by the amplitude controller in order to adjust the saturated output and provide tank field control. This high voltage modulation technique requires four additional power tubes. The modulator has an internal voltage drop of about 10 kV when fully on, so the high voltage capacitor bank must be maintained above the level needed by the FPA by at least this amount. This causes an additional power dissipation of nearly 250 kW each, in three of the four plate modulators. The forth RF system drives DTL tank 1, which requires less than 500 kW of peak RF, relatively low power compared to the other units. In this report, this unit is not shown in the diagrams for simplicity.

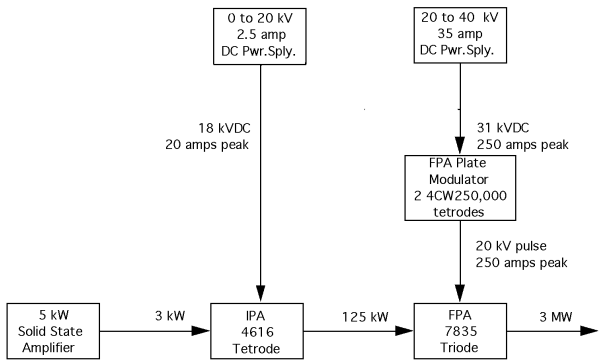

Figure 1. Present configuration - high power RF modules

The FPA triode has an output ceramic seal length of 7.62 cm. This requires that it be operated within a pressure vessel operating with 2.4 bar dry air at Los Alamos (2120 meters above sea level) to maintain voltage standoff. Because of the high average power, the pressurized air must be circulated through the cavity and cooled. The high-pressure turbine and pressurized heat exchanger require annual maintenance, and have contributed to system down time. Replacement of the FPA tube takes approximately 16 hours due to the enormous pressure vessel that must be removed first.

Higher beam current for new linac applications such as the proposed Long-Pulse Spallation Source [3] cannot be

* Work supported by the US Department of Energy

delivered simultaneously with other beams at high duty factor. Table 1 shows the RF power requirements for the present 18 mA and proposed 21 mA peak current needs. The RF pulse parameters are for up to 1350 microseconds width at 120 pulses per second repetition rate, resulting in up to 16.2% duty factor for the RF amplifiers. These requirements are within the fundamental capabilities of the 805 MHz RF System for the coupled-cavity linac that accelerates from 100 to 800 MeV; only the 201 MHz system needs this substantial upgrade.

Table 1. RF power requirements for DTL

RF Operating Levels						
Module	Energy	Tank Pwr.	21 mA Beam Pwr	8% margin	Peak Req'd	Ave. Req'd
	MeV	MW	MW	MW	MW	kW
1	4.64	0.37	0.10	0.04	0.51	82
2	35.94	2.57	0.75	0.27	3.59	582
3	31.39	2.10	0.66	0.22	2.98	483
4	27.28	2.23	0.57	0.22	3.03	491

2 POWER AMPLIFIER REPLACEMENT

We plan to install a new cavity amplifier, which will operate as a linear amplifier and eliminate the need for modulation of the high voltage. Output power control will be accomplished by varying the low-level RF drive to the preamplifier stage. This eliminates four more tubes in each system, leaving only two RF amplifier tubes per module (three in module 2), or nine for the entire DTL RF powerplant. In addition, the voltage overhead of the plate modulator will disappear, as the tube will operate with DC plate voltage and be pulsed into conduction with the control grid bias.

2.1 RF Power Tube Selection

Until very recently, there has been no reasonable alternative to the 7835 for the LANSCE 200 MHz DTL. Thomson Tubes Electroniques embarked on a program to develop a tube capable of delivering 3 MW peak, 600 kW average RF power, at 200 MHz. The tube was proposed for fusion heating as early as 1991 [4]. Employing double-ended RF geometry (as in the 7835 triode) can extend the frequency-power limits of gridded tubes. The TH628 Diacrode® is a double-ended tetrode, derived from the single-ended TH526 tetrode. The tube uses pyrolytic graphite grids, a thoriated-tungsten mesh cathode, and a multiphase-cooled anode rated to dissipate 1.8 MW. Pyrolytic graphite grids allow elevated grid operating temperatures without seconday electron emission. This allows for higher screen power dissipation, and higher output power without adverse effects. The first cathode-driven TH628 Diacrode® has recently passed acceptance tests at the factory, and is being delivered to LANSCE. No other modern tetrode has delivered this level of high power 200 MHz performance. Table 2 lists significant results from the tests.

Table 2. Thomson TH628 Test Results – June, 1998

Peak Power Output	3 MW peak
Average Power Output	600 kW
RF pulse duty cycle	20 %
DC-to-RF Efficiency	>60%
DC plate voltage	26 kV
Screen (G_2) Voltage	1.6 kV
Filament Power	18 VDC, 910 A.
RF Power Gain	>14 dB
Zero Drive Stability	No emissions 0 to 1 GHz
Coolant Flow	360 l/min deionized water

The planned configuration for DTL modules 3 and 4 is shown in figure 2. Two combined amplifiers may be required only for module 2, and this scheme is shown in figure 3. The upgraded system will employ circulators between the FPA and DTL. Air pressurization is not planned for these amplifier cavities, as the ceramic seal is longer on the TH628. Tube replacement time will be decreased from about 16 hours to 2 hours.

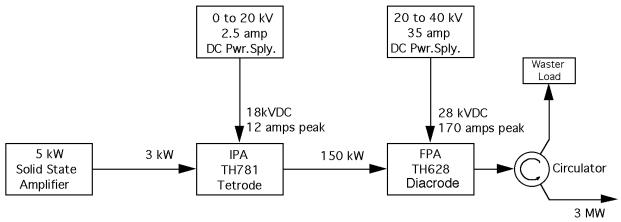

Figure 2. New configuration for RF modules 3 and 4

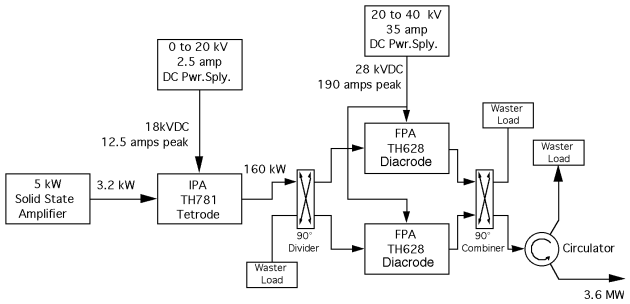

Figure 3. New configuration for RF module 2

2.2 Intermediate Power Amplifier

The existing 4616 tetrode intermediate power amplifier is capable of 150 kW peak power at our present duty factor. The statistical lifetime of these tubes has varied with variations in manufacturing, including component changes such as different filament alloys and sources of mica. As a grid-driven tetrode, the 4616 is capable of very high gain. Along with this high gain is a system sensitivity to variations in the screen emission and VHF resonances or back-cavity modes from the internal mica screen bypass capacitor assembly. We have a choice of continuing to utilize the existing amplifiers, or converting to a cavity amplifier using a Thomson TH781 tetrode, which has pyrolytic graphite grids, a thoriated-tungsten mesh cathode, and a multiphase-cooled anode rated to dissipate 250 kW. A nearly identical tetrode (TH681) is in

successful operation driving the CERN PS 40 MHz bunching cavity [5].

2.3 Power Supplies

The existing plate HV power supply/capacitor banks are adequate for the conversion, after the plate modulators are removed. The HV power supplies for DTL modules 2 through 4 are rated for 40 kV maximum, at 35 Amperes DC. With the existing capacitor banks, they were designed to drive the FPAs at 120 Hz, with 1200 uS pulses. The DC voltage will be reduced from the present charging level. The module 1 power supply will also be reused.

The 7835 triode requires 6900 Amperes of DC filament current. The original filament power supplies are very large. Removal of the present power supply will provide much floor space for the upgrade. The TH628 requires less than 1000 Amperes, supplied from a small power supply without water-cooled cables.

2.4 RF Output Components

The new FPA will be isolated from reflected power from the DTL by using a coaxial Y-junction circulator. Advanced Ferrite Technology has proposed a 35.5 cm coaxial device, which has less than 0.16 dB of insertion loss and 25 dB of isolation. This is especially important for the combined amplifiers for module 2, driving the high Q DTL. A water-cooled dummy load will be connected to the third port.

The power splitter and combiner for module 2 will be 3 dB hybrids, available from several manufacturers. Examples of the successful use of power combiners of this size are found at the MIT/Lincoln Labs ALTAIR radar in which two super-power triodes are combined at 160 MHz. At the CERN SPS, sixteen 35 kW tetrodes are successively combined at 200 MHz for 500 kW, and four 125 kW CW tetrodes are combined for 500 kW of total power [6]. A water-cooled dummy load (waster) will be required on the combiner, rated at one quarter of the overall power.

The full output power is to be transmitted to the DTL through the existing 35.5 cm diameter coaxial line. This line is theoretically capable of 40 MW peak and over 600 kW of average power at 200 MHz when pressurized with dry nitrogen, according to the manufacturer. The Brookhaven National Laboratory AGS Linac has used 30.5 cm line for up to 6 MW peak at low duty factor [7].

The present RF window seals the DTL vacuum while passing through the coaxial center conductor to connect to the drive loop. It is made of crosslinked polystyrene, or Rexolite®. Presently these windows are replaced about every 2 years of service, or when the following damage is noticed during inspection: Excess radiation darkening, evidence of streamer tracks, mechanical deformation, or evidence of sputtered metallization on the vacuum side. Further work is anticipated to improve the voltage standoff and lifetime of the windows for the higher peak and average powers proposed for LANSCE.

2.5 Cooling Plant

The cooling requirements will not add additional load to the plant, as the modulator heat load will be removed, and the waster loads on the circulators and combiner are only dissipating transient loads during tuning and unbalances. The water flow though each new FPA tube is 36% less than the present tubes, due to the more efficient multiphase cooling regime in the tubes.

3 CONCLUSION

The proposed upgrade to the LANSCE DTL RF powerplant is based on changing the FPA to a new type of tetrode, which has demonstrated excellent performance during testing. The other system changes will require RF, electrical, mechanical and thermal engineering, but nothing appears to be significantly challenging to prevent long term success. This project will be a significant improvement to the LANSCE linac RF system.

ACKNOWLEDGEMENTS

The authors wish to thank the LANSCE-5 RF team for their assistance in keeping the RF plant operating with high reliability and in their suggestions and assistance in all of the upgrades.

REFERENCES

[1] W. Harris, J. Lyles, M. Parsons, “Modulation Improvements in the 201.25 MHz RF Generators at LAMPF,” 20th International Power Modulator Symposium, Myrtle Beach, SC, June 1992.

[2] C. Friedrichs, J. Lyles, “LANSCE 201.25 MHz DTL RF Power Status,” Proceedings of Linac Conference, Geneva, Switzerland, August 1996.

[3] G. Bolme, J. Lyles, A. Regan, “LANSCE Linac RF Performance for a Long Pulse Spallation Source,” Proceedings of Linac Conference, Geneva, Switzerland, August 1996.

[4] G. Clerc, J. Ichac, M. Tardy, “ICRH Thomson Tetrodes: From Long Pulses to CW,” 14th IEEE/NPS Symposium on Fusion Engineering, San Diego, 1991, pp. 488-491.

[5] Personal communication with D. Grier, CERN, Geneva, Switzerland, November 1996.

[6] H. Kindermann, W. Herdich, W. Sinclair, “The RF Power Plant of the SPS,” IEEE Transactions on Nuclear Science, Vol. NS-30, No. 4, August 1983, pp. 3414-3416.

[7] J. Keane, R. McKenzie-Wilson, “High Power RF Transmission Line for the 200 MeV Linac at AGS,” Proceedings of the 1970 Proton Linear Accelerator Conference, Batavia, Illinois, October 1970, pp. 601-619.

ACCELERATOR PRODUCTION OF TRITIUM 700 MHz AND 350 MHZ KLYSTRON TEST RESULTS

D. Rees, M. Lynch, P. Tallerico
Los Alamos National Laboratory, Los Alamos, New Mexico 87545 USA

Abstract

The Accelerator Production of Tritium project (APT) utilizes a 1700 MeV, 100 mA proton Linac. The radio frequency (RF) power is provided by 244 continuous wave (CW) klystron amplifiers at 350 MHz and 700 MHz. All but three of the klystrons operate at a frequency of 700 MHz. The 350 MHz klystrons have a nominal output power of 1.2 MW at a DC-to-RF conversion efficiency of 65 %. They are modulating-anode klystrons and operate at a beam voltage and current of 95 kV and 20 A. The design is based on the CERN klystron. The 700 MHz klystron is a new development for APT. Three 700 MHz klystrons are currently under development. Two vendors are each developing our baseline klystron that has a nominal output power of 1.0 MW at a DC-to-RF conversion efficiency of 65%. A 700 MHz klystron is also under development that promises to provide an efficiency in excess of 70%. The 700 MHz klystrons operate at a maximum beam voltage of 95 kV and a maximum beam current of 17 A. The test results of these klystrons will be presented and the design features will be discussed.

1 KLYSTRON REQUIREMENTS

The design requirements for the 350 MHz and 700 MHz klystrons are included below in table 1.

The 350 MHz klystron was supplied by English Electric Valve (EEV). Two vendors developed the 700 MHz klystrons, EEV [1] and Communication and Power Industries (CPI). The design parameters for these two tubes are different but still within the requirements. EEV chose a lower perveance design with respect to CPI.

In addition to the standard 700 MHz klystron design, EEV also pursued an advanced klystron design utilizing a second, second harmonic cavity just prior to the output cavity. This klystron had to meet the requirements in Table 1 and the development was directed towards increasing the efficiency to 70%.

The 350 MHz klystrons have all been tested and installed on the Low Energy Demonstration Accelerator (LEDA) [2], and have satisfied all design requirements. The standard EEV 700 MHz klystron has been tested, demonstrated all requirements, and is being installed on LEDA. The high-efficiency EEV klystron has been tested and demonstrated compliance with the baseline design requirements. In addition, the efficiency was increased from the required 65% to 68%. Higher efficiencies were achieved but found to be inconsistent with the 1.2:1 VSWR requirement at any phase. However, at the nominal 68% efficiency into a matched load, the klystron achieves efficiencies in excess of 72% at some phases of a 1.2:1 mismatch.

Table 1. Klystron Requirements

Frequency	350 MHz	700 MHz
Output Power	1.2 MW	1.0 MW
Test Power	1.3 MW	1.1 MW
Gain	40 dB Min.	40 dB Min.
Beam Voltage	95 kV Max.	95 kV Max.
Beam Current	20 A Max.	20 A Max.
Efficiency	65 % Min.	65 % Min.
Bandwidth 1 dB	+/- .35 MHz	+/- .7 MHz
Collector Dissipation	Full Beam Power	Full Beam Power
VSWR Tolerance	1.2:1 Max. Any Phase	1.2:1 Max. Any Phase
Mod-Anode	Yes	Yes

The CPI 700 MHz Klystron has demonstrated that the klystron physics design satisfies our performance and operating requirements; however, the entire klystron package has not yet satisfied all electrical and mechanical requirements and is still in process.

2 KLYSTRON TEST RESULTS

2.1 350 MHz Klystron

The 350 MHz klystron is shown in Fig. 1. The klystron is a six cavity klystron with a second harmonic cavity. As is seen in the picture, the klystron has a horizontal orientation. Although there is some supplemental lead shielding around the collector, the klystron is operated in a lead garage, and the supplemental shielding allows for a lead thickness of 0.125" to be suitable for suppressing x-ray radiation. The klystron output window is a coaxial window. The coaxial section containing the window can be seen in the picture protruding from the top of the tube. A t-bar is used to transition from the coaxial line to waveguide. The klystron requires three cooling circuits. Up to 400 gpm is provided to the collector, and two body circuits require up to 10 gpm. The RF window on the klystron is air cooled. A small oil tank is included with the klystron for high voltage insulation and is visible in the photos.

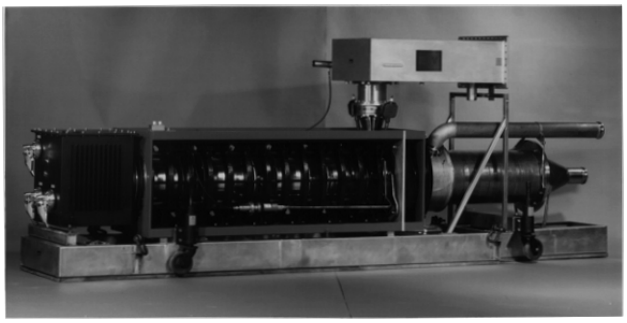

Figure 1: EEV 350 MHz Klystron.

Table 2 contains the recorded operating parameters and characteristics of one of the 350 MHz klystrons. In addition to this data the tube undergoes a 24 hour run with only 2 tube-caused trips allowed at 110 % of rated power and also must demonstrate the full 1847 kW of beam power into the collector for one hour.

Table 2. EEV 350 MHz Recorded Klystron Data

Heater Voltage	22.8 V
Heater Current	22.8 A
Main Focus Current	6.4 A
Main Focus Voltage	227 V
Output focus Current	8.2 A
Output focus Voltage	123 V
Beam Voltage	94.1 kV
Beam Current	19.63 A
Mod Anode Voltage	51.8 kV
Mod Anode Current	0.4 mA
Drive Power	93 W
Output Power	1210 kW
Efficiency	65.5 %
Body Power	3.5 kW
Output Cavity Power	3.3 kW

2.2 700 MHz Klystron

The CPI version of the 700 MHz klystron is illustrated in Fig. 2. At the level of detail allowed by the picture the differences between this klystron and the EEV klystrons is not easily distinguishable, so in the interest of space conservation only the CPI photo is included. The EEV klystrons do have a slightly longer output coax prior to the T-bar transition to insure mode purity in the window ceramic.

The physical description of the 700 MHz tube is identical to the description provided above for the 350 MHz klystron and is not repeated. The 700 MHz klystrons also is subject to the 24 hour test at 110% of rated power.

The recorded test data from the CPI 700 MHz klystron, the standard EEV 700 MHz klystron, and the high efficiency EEV 700 MHz klystron are included in tables 3 and 4. Table 4 includes results for both the EEV standard klystron and the high efficiency klystron.

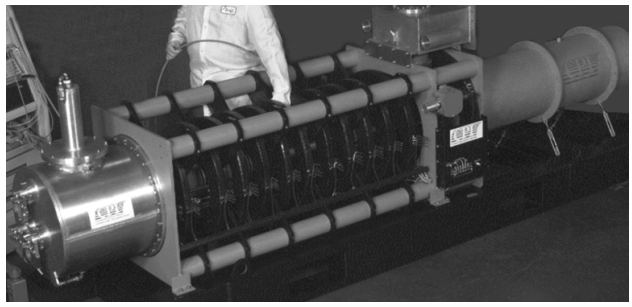

Figure 2: CPI 700 MHz Klystron

Table 3. CPI 700 MHz Klystron Recorded Data

Heater Voltage	21.2 V
Heater Current	19 A
Main Focus Current	17 A
Main Focus Voltage	< 120 V
Output focus Current	22A
Output focus Voltage	< 120 V
Beam Voltage	92 kV
Beam Current	16.6 A
Mod Anode Voltage	78 kV
Mod Anode Current	1.4 mA
Drive Power	12.3 W
Output Power	1000 kW
Efficiency	65.5 %
Body Power	3.7 kW
Output Cavity Power	8.6 kW

Table 5 illustrates the efficiency of the EEV high-efficiency klystron as it drives a mismatch of nominally 1.2:1 at variable phase. The table shows that for some phases of the mismatch very high efficiencies were achieved. However, by noting the mod-anode current and body power for the high-efficiency phases of the mismatch, it can be concluded that some of the electrons are being stopped and turned around and are not only hitting the tube body but also traveling back down the beam pipe and impacting on the mod anode, increasing the mod anode current. These returned electron can lead to sideband oscillations [3,4]. During early testing an efficiency approaching 70 % was achieved into a matched load but was unstable at some phases of a 1.2:1 VSWR. The guide wavelength in WR1500 waveguide is 52 cm so each 4 cm change in position of the mismatch in Table 5 represents a phase change of 28 degrees.

Figs. 3 and 4 illustrate the power transfer curve of the CPI 700 MHz klystron and the klystron's measured frequency response. These plots are useful to the designers of the feedback circuitry to control the accelerating-cavity amplitude and phase by modulation of the klystron drive signal.

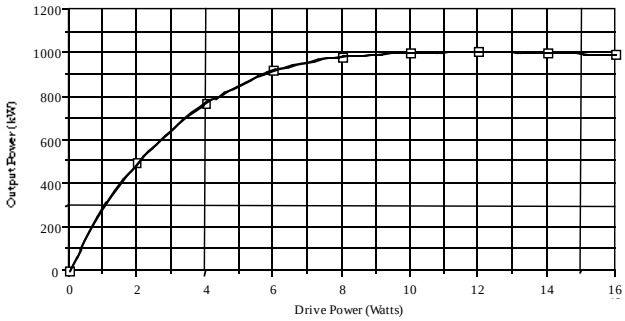

Figure 3: CPI klystron power transfer curve.

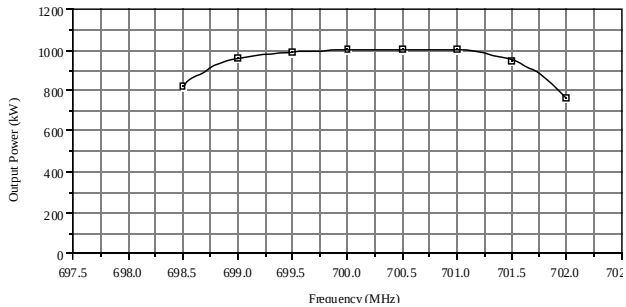

Figure 4: CPI klystron frequency response.

3 CONCLUSIONS

Successful klystron developments have been completed for the APT project. The test data show the klystrons meet or exceed all requirements. Commencing in October we will begin to gather long term reliability data on these klystrons with the LEDA accelerator.

4 REFERENCES

[1] D. Bowler et al., "Design of a High Efficiency 1 MW CE Klystron at 700 MHz For Low Energy Demonstrator Accelerator," EPAC 98.

[2] D. Rees et al., "Operation and Test Results of the 350-MHz LEDA RF System," This conf.

[3] M. Yoshida et al., "Instabilities due to multipactoring, modulation and anode emission found for TRISTAN high power CW klystrons," 6th Symposium on Accelerator Science and Technology, Tokyo 1987.

[4] H. Frischolz, "The LEP Main Ring High Power RF System," PAC 89.

Table 4. EEV 700 MHz Standard Klystron Recorded Data

	Standard Effic.	High Effic.
Heater Voltage	22.8 V	22.8 V
Heater Current	23.8 A	24.3 A
Main Focus Current	12.8 A	12.3 A
Main Focus Voltage	141 V	163 V
Output focus Current	12.8 A	12.8 A
Output focus Voltage	91 V	106 V
Beam Voltage	95.1 kV	95.1 kV
Beam Current	16.28 A	15.57 A
Mod Anode Voltage	51.52 kV	46.67 kV
Mod Anode Current	0.15 mA	0.3 mA
Drive Power	75 W	96 W
Output Power	1013 kW	1007 kW
Efficiency	65.4 %	68 %
Body Power	4.0 kW	3.9 kW
Output Cavity Power	6.2 kW	6.9 kW

Table 5. EEV High-Efficiency Klystron Data as a Function of VSWR

POS (cm)	Ima (mA)	Effic. (%)	Body 1 Power (kW)	Output Cavity Power (kW)
0	.2	61.1	4.2	6.0
4	.3	60.6	3.8	5.8
8	.4	65.2	4.4	7.0
12	1.0	70.8	5.6	6.6
16	.9	74.2	5.8	8.7
20	.3	72.8	4.4	6.6
24	.2	65.7	4.1	5.9

ELECTROMAGNETIC COLD-TEST CHARACTERIZATION OF THE QUAD-DRIVEN STRIPLINE KICKER

Scott D. Nelson and James E. Dunlap
Lawrence Livermore National Laboratory, Livermore, California 94550 USA

Abstract

The first kicker concept design [1] for beam deflection was constructed to allow stripline plates to be driven; thus directing, or *kicking*, the electron beam into two subsequent beam lines. This quad-driven stripline kicker is an eight port electromagnetic network and consists of two actively driven plates and two terminated plates. Electromagnetic measurements performed on the bi-kicker [2] and quad-kicker were designed to determine: (1) the quality of the fabrication of the kicker, including component alignments; (2) quantification of the input feed transition regions from the input coax to the driven kicker plates; (3) identification of properties of the kicker itself without involving the effects of the electron beam; (4) coupling between a line current source and the plates of the kicker; and (5) the effects on the driven current to simulate an electron beam through the body of the kicker. Included in this are the angular variations inside the kicker to examine modal distributions. The goal of the simulated beam was to allow curved path and changing radius studies to be performed electromagnetically. The cold test results produced were then incorporated into beam models [3].

1 INTRODUCTION

The original kicker design was conceived to allow for the diversion of the electron beam dynamically during a long pulse; thus acting like a beam splitter. Experiments performed on the kicker [4] detail the operating parameters of the system. This paper outlines the electromagnetic cold-test measurements performed on the kicker as part of the analysis and concepts for the kicker pulser requirements.

Figure 1. The quad-kicker in the Experimental Test Accelerator (ETA-II) beamline as part of the verification experiments [4]. Note the four ports on each end of the quad-kicker. These ports connect directly to the deflection plates. Two of the white pulser cables are visible in the foreground.

Due to beamline usage and the motivations for the cold-test measurements, the kicker was tested in the LLNL Electromagnetics Laboratory using a variety of vector network analyzers (to sweep the frequency band) and time domain impulse generators and scopes.

Figure 2. The quad-kicker was tested using frequency- and time-domain scopes to cover the band for the swept frequency tests and instantaneous impulse tests.

2 KICKER PORT TESTING

Each of the eight input ports of the kicker were tested over a frequency band from 45 MHz to 500 MHz. Two ports connected to the input and output of each of the four plates through a tapered transition region through a coaxial connector. The pin on the plate connected directly to the center pin of the coax. The results of the measurements (shown in Figure 3) indicate a broadband match with the exception of resonances caused by the feed regions. The comparison in Figure 4 illustrates the feed region effects based on experience learned from the bi-kicker and quad-kicker development activities.

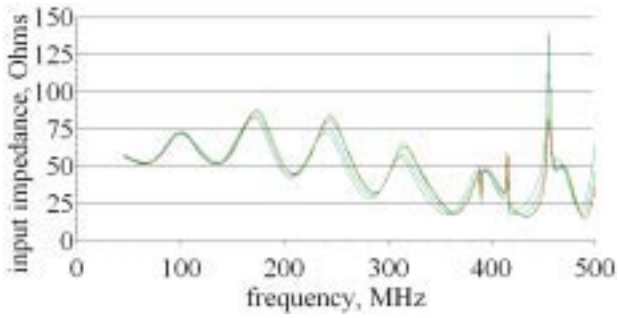

Figure 3. The input impedance of each of the ports is shown vs. frequency (margin of error is +/- 0.3 ohms). The spikes at 388.75, 414.0, 460 MHz are higher order mode resonances and correspond to Q's of 310 (quadrupole mode), 61 (dipole mode), and 29 (dipole mode) respectively.

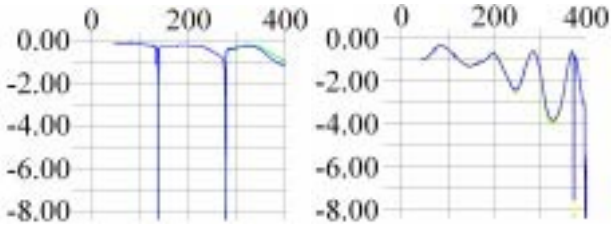

Figure 4. The input reflection coefficient (in dB) vs. frequency (in MHz) of the bi-kicker was much more uniform due to the more gradual transition region after the coaxial feeds. The quad-kicker had a more abrupt transition after the coax and has a larger input reflection coefficient. The spikes in the bi-kicker response curve are due to the grounded plate resonances and were eliminated in the quad-kicker.

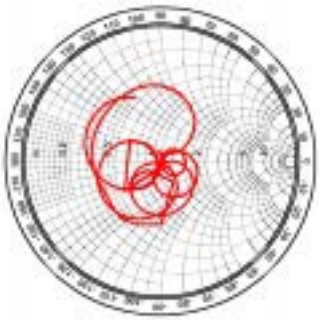

Figure 5. The complex input impedance of the kicker is shown for one of the ports (the variance between the ports is +/- 7 ohms due to fabrication differences). The three straight lines in the curve represent under sampling.

3 CROSS COUPLING TERMS

The cross-plate coupling terms of the kicker corresponded to the coupling between adjacent and opposite ends of the various plates to each other. These coupling terms represent energy that couples from the kicker pulser driven plate to those plates that are terminated, thus inducing fields onto plates that are not directly driven. These cross coupling terms are appreciable (8% and 20%) even at the lower frequencies.

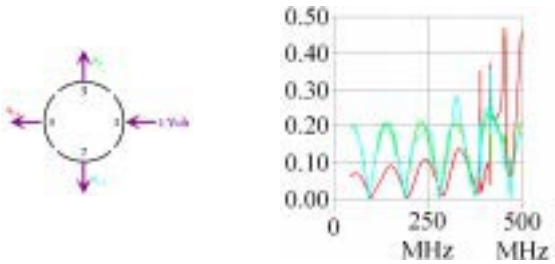

Figure 6. The magnitude of the coupling between adjacent plates vs. frequency shows significant cross coupling at multiples of 80 MHz. The adjacent plate coupling is 20% and the cross plate coupling is 8%.

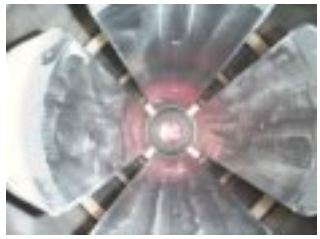

Figure 7. The quad-kicker plates are identical and each is connected to a 50-ohm coaxial port. For the experiments [4] using the existing kicker pulsers, two of the plates were driven and the other two plates were terminated in matched loads. Each plate is 78 ^{o} wide (12.87 cm radius) and is supported by rexolite.

4 FORWARD COUPLING TERMS

The kicker pulsers drive one end of the plates and the other end is mated to reduce reflections on the plate structure. The loss along the plates is less than 1 dB and the transfer function from one end of the plate to the other is shown in Figure 8.

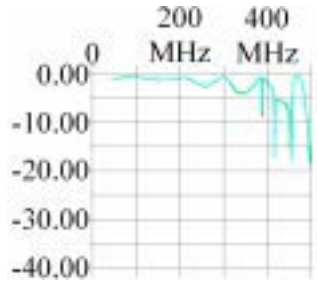

Figure 8. The transfer function (in **dB**) vs. frequency from one end of the plates to the other end. In the low frequency part of the spectrum, the curves for the various plates overlap to within 0.025 dB.

5 KICKER RESPONSE

For identification of the transient properties of the kicker and the association between a simulated beam and the kicker ports, a ramp pulse (0.95V per 300ns) was used to excite the wire-current. The resulting waveform that was induced on the downstream output port is shown in Figure 9.

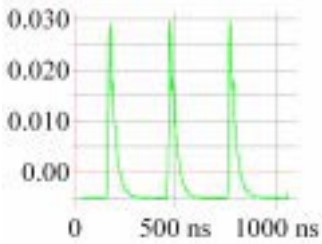

Figure 9. The effect of the 300 ns ramp pulse coupling from the wire-current to one of the kicker plates being monitored at a downstream port. Notice that after about 70 ns, the coupling stabilizes to -0.005 Volts (corresponds to -0.53%). The spikes occur at the transition of each 300 ns excitation ramp waveform.

When the central wire representing an electron beam was excited through the main body of the kicker, the ''pump-up'' time of the kicker was observed as an equivalent time constant of 70 ns. This corresponds to the cavity fill time between the simulated beam pulse and the ports.

6 AZIMUTHAL VARIATIONS

During the course of the measurements, the azimuthal variation caused by the offset-rotations of the current-wire was measured and compared against the theoretical solution for an offset wire in an ideal kicker. A comparison between this theoretical solution (dashed line) for an electrostatic coupling case and that for the experimental cases at the peak coupling points of 68.4, 139.2, and 209.4 MHz is shown in the above plot. The angular frequency spectrum of the above plots was taken to determine the relationships between the various modes (**D**ipole, **Q**uadrupole, and **S**extupole) in the kicker and those modal ratios are shown in the table below and are

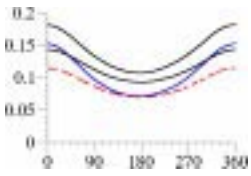

	static	**68.4**	**139.2**	**209.4**	**eq (1)**
$\mathbf{V_Q/V_D}$	0.136	0.134	0.140	0.169	0.174
$\mathbf{V_S/V_D}$	0.0252	0.0315	0.0327	0.0351	0.0203

in a similar range to that determined by integrating the simple analytic representation [5] along the plate boundaries shown in Equation 1,

$$\frac{V_S}{V_D} = \frac{4q\frac{a^3}{b^4}\int_{-\phi}^{\phi}\cos 3\theta d\theta}{4q\frac{a}{b^2}\int_{-\phi}^{\phi}\cos\theta d\theta} = \frac{1}{3}\frac{a^2}{b^2}\frac{\sin 3\phi}{\sin\phi} \qquad \frac{V_Q}{V_D} = \frac{1}{2}\frac{a}{b}\frac{\sin 2\phi}{\sin\phi}, \quad (1)$$

where ϕ is the plate half-angle (39^o) but 45^o was used to be consistent with the theory since Eq(1) assumes no gaps, b is the plate radius (12.87 cm), and a is the radius to the wire position (3.175 cm). Differences can be attributed to gap effects between plates, end effects near the feeds, and simplifications of the analytic representation.

The equivalent circuit model for the kicker is composed of a series of transmission line sections and cross-coupling terms representing the plate-to-plate effects.

7 CONCLUSIONS

Although the frequency range of interest for kicker applications is in the low hundreds of megahertz range and is based on the bandwidth of the kicker pulser, there were initial concerns about beam induced effects. For this frequency range: the cross coupling between adjacent ports is less than 14 dB; the input impedance for each port is between 50 and 90 ohms; transmission along the plates experiences less than 1 dB of loss; and cavity measurements show a cavity pump-up time, and a dI/dt coupling between the current-wire and the cavity.

The input reflection coefficient for some higher frequencies can approach 30%; but these frequencies are expected to be outside of the normal operating range of the kicker. However, in making the modifications from the bi-kicker design to the quad-kicker design, the frequency band where these effects make a pronounced difference was lowered and is closer to the operating band. Thus, subsequent changes in the kicker design would need to be leery of this limit. It should be emphasized however that the elimination of the shorted plates from the bi-kicker design substantially improved the operation of the quad-kicker [4].

8 ACKNOWLEDGMENTS

Thanks go to Brian Poole for numerous conversations about kicker development and to Judy Chen and John Weir for their experimental activities. This work was performed under the auspices of the U.S. Department of Energy by the Lawrence Livermore National Laboratory under contract No. W-7405-Eng-48.

9 REFERENCES

[1] G.J. Caporaso, Y.J. Chen, B.R. Poole, ''Transmission Line Analysis of Beam Deflection in a BPM Stripline Kicker,'' 1997 Particle Accelerator Conference, Vancouver, B. C. Canada, May 12-16, 1997, LLNL UCRL-JC-126073.

[2] S. D. Nelson, ''Electromagnetic (Cold Test) Characterization of the bi-Driven Kicker,'' Lawrence Livermore National Laboratory, UCRL-ID-129997, January 1998, http://www-dsed.llnl.gov/documents/em/sdnkick98/

[3] B.R. Poole, G.J. Caporaso, Y. J. Chen, ''Analysis and Modeling of a Stripline Beam Kicker and Septum,'' LLNL, 1998 Linear Induction Accelerator Conference (Linac98), Chicago, Ill. USA, August 24-28, 1998.

[4] Y.J. Chen, G.J. Caporaso, J. Weir, ''Experimental Results of the Active Deflection of a Beam from a Kicker System,'' LLNL, 1998 Linear Induction Accelerator Conference (Linac98), Chicago, Ill. USA, August 24-28, 1998.

[5] A. W. Chao, ''Physics of Collective Beam instabilities in High Energy Physics,'' John Wiley & Sons, Inc., pg 6, 1993, ISBN 0-471-55184-8.

SOLID-STATE SWITCH MODULATOR DECK FOR THE MIT-BATES S BAND TRANSMITTER

C. Wolcott, R. Campbell, A. Hawkins, W. North (Consultant), L. Solheim, R. Trepsas, Defa Wang, A. Zolfaghari, MIT-Bates, M. Gaudreau, M. Mulvaney, Diversified Technologies, Inc.

Abstract

This paper describes how to modernize and simplify the design of a pulse amplitude modulator for klystron power amplifiers. The existing modulator design uses two parallel-connected Litton Injectron ™ Beam Switch Tubes (BSTs) in series with the cathode of an RF amplifier klystron. A vacuum-tube based modulator sends high-voltage pulses to the modulating anodes of the BSTs to produce a current pulse through the klystron. In recent years, the vacuum-tube circuitry that drives the BSTs and klystron has become difficult and expensive to maintain. The new design replaces this circuitry with a single switch, comprising multiple series-connected, high-voltage, high-current Insulated-Gate-Bipolar Transistors (IGBTs). Figure 1 illustrates the basic design of the solid-state modulator deck.

The prototype of this system along with its control and feedback circuitry has been built at the Bates Linear Accelerator Center and has been successfully tested in one of the Bates accelerator RF transmitters. The new cathode switching design will not only replace obsolete and failing technology but will also significantly improve the reliability and performance of the accelerator and the RF transmitters.

1 INTRODUCTION

The MIT-Bates linear electron accelerator uses the output of six S-Band RF transmitters to produce the high-level electric fields that accelerate the beam. Each of these transmitters contains two klystron power amplifiers. The modulator in use today uses two parallel-connected Litton Injectron™ Beam Switch Tubes (BSTs) in series with the cathode of each klystron. A vacuum-tube based modulator sends high-voltage pulses to the modulating anodes of the BSTs to produce a current pulse through the klystron. In recent years, the vacuum-tube circuitry used in the present system to drive the BSTs and the klystron has proven difficult and expensive to maintain. As part of the MIT-Bates upgrade project, a new design has been created to replace this old and obsolete technology.

2 SOLID-STATE SWITCH

At the heart of the new modulator design is the 17.5 kV 100 Amp Solid-State Switch (SSS). In the spring of 1997, MIT Bates Linear Accelerator Center awarded a contract for a prototype 20 kV, 100-Ampere solid state switch to Diversified Technologies Inc. of Bedford MA. This switch utilized the core elements of their commercial unit, the HVPM 20-150.

The switch itself consists of 8 Insulated Gate Bipolar Transistor (IGBT) modules, connected in series, and a high-frequency inverter power source for the gate drive circuitry, designed to be compatible with immersion in insulating oil. Each switch module contains four series-connected IGBTs (actually two dual-IGBT assemblies), and their associated control, over-voltage protection and diagnostic circuitry. Each IGBT is rated at 1200 V and 100 A continuous. The overall switch comprises 32 IGBTs in series, with a total voltage rating of 38 kV, shunted by over-voltage clamping which begins to conduct at a voltage of 22 kV, utilizing DTI's patented design. The eight switch modules and the associated switch power supply were each mounted on aluminum heat sinks, approximately 7" x 15". These nine component modules were integrated into an insulating framework, and installed in the solid-state switch deck.

3 SOLID STATE DECK

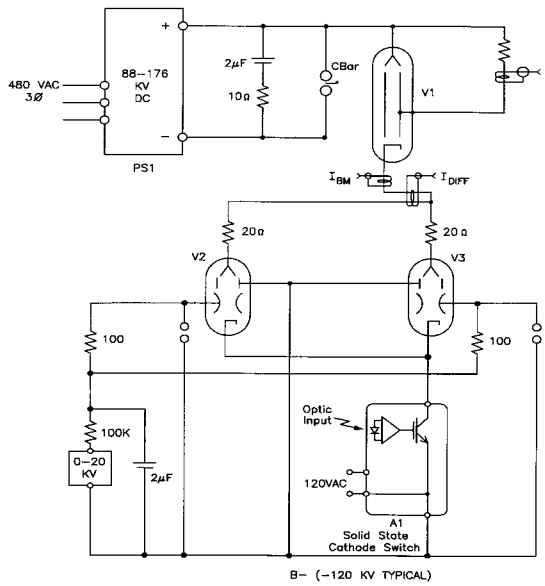

Figure 1: Basic Diagram of the Solid-State Deck

The purpose of the modulator is to send pulses of regulated current, up to 100 Amps, through the klystron power amplifier. When timed correctly, the klystron input RF power is amplified and injected into the beam line to accelerate the beam. The current pulses must have very quick rise and fall times (less than 1 μs) and must be very stable during the flattop portion of the pulse. The present design accomplishes this by sending pulses of high-voltage (up to 15kV) to the mod-anode of the BSTs. The new

design accomplishes the same thing with a constant precision DC high voltage (.001% ripple, .001% regulation) applied to the mod-anodes and by the use of the SSS in series with the cathodes of the BSTs (see Fig. 1). With the switch in the "open" condition, and with the mod-anode power supply at a nominal level, high voltage (up to 170kV) is applied across the klystron, BSTs, and the SSS connected in series. The only current flowing through the klystron in these conditions is the SSS leakage current (less than 1mA). In this situation, the cathodes of the BSTs assume the voltage, relative to the mod-anode, necessary to regulate this small current. Depending on the individual BST, this voltage could even be a small amount more positive than the mod-anode. The solid-state cathode switch is closed in response to fiber-optically-coupled pulses of light. When the switch closes, the current through the klystron rises (in less than 1 μs) to the level set by the mod-anode power supply. The switch stays closed for a time that is set by the trigger control circuitry (from 1-50 μs) and then opens again. When the switch opens, the current falls back to the leakage level in less than 1 μs. This process can take place at various pulse current levels (up to 100 Amps), various widths (up to 50 μs) and at various pulse repetition rates (up to 600 Hz.). The klystron current can be increased or decreased by increasing or decreasing the mod-anode power supply output voltage.

The peripheral equipment on the solid-state deck includes the mod-anode power supply, the dual filament power supply, and the dual solenoid supply. These power supplies are all necessary to run the BSTs.

The mod-anode power supply is a positive-output 300-Watt high-voltage power supply that is adjustable to 20 kV. This power supply, manufactured by Bertan Associates, is an extremely precise supply. The ripple and regulation specifications are both 0.001%. This amount of precision is necessary to regulate the klystron current without any noticeable pulse to pulse, phase, or amplitude jitter (the phase-pushing factor of the klystron is approximately 10 degrees per 1 percent beam voltage change, or per 1.5 percent current change). Shunting the output of the power supply is a 100,000Ω resistor and a 30 kV, 2μF capacitor that together form a low-pass filter to further attenuate any ripple on the mod-anode voltage.

The dual-filament power supply provides AC power to the filaments of each BST. Each BST filament requires 10 Amps at 12 volts to ensure that the tubes are never temperature limited. The dual-filament supply consists of two transformers. The first transformer is a SOLA AC regulator. This device takes the AC power that is floating at high voltage and converts it to a regulated 120 VAC. The second transformer is a 500 VA multi-tapped, step-down, isolation transformer. This transformer provides isolation for up to 30kV, which is necessary because when the SSS opens, the cathodes of the BSTs float at a voltage near the mod-anode power supply output. The secondary of the isolation transformer is tapped at 10.5, 11, 12 (nominal), 13, 14, 16, and 18 VAC. The taps below the 12V nominal tap are provided to run the filaments cooler in order to prolong the tube's lifetime. The taps above 12V are provided for when the tube begins to deteriorate and the filaments have to be run hotter to produce the desired klystron current. The filaments are connected to the supply in parallel and can be switched to a different tap by the use of a rotary switch.

The dual solenoid power supply provides regulated DC current (8 Amps nominal) to the solenoids of each BST.

4 PROTECTION

Along with the basic building blocks that make up the solid-state switch deck, there are many devices that are integral to the reliability, susceptibility, and durability of the design. First, all AC power circuits are protected with correctly rated circuit breakers and varistors to provide short circuit and transient protection. The SOLA AC regulator of the filament power supply also provides transient and inrush current protection. The mod-anode power supply is protected from arcs that conceivably could occur from the BST collectors to a mod-anode of one of the BSTs. The first line of defense is a 17kV arc-gap connected between the mod-anode of each BST and the negative high-voltage rail. These gaps ensure that the mod-anode power supply will never be destroyed by such a destructive occurrence. However, these arc-gaps take a small amount of time before they fire. They also work more reliably when the voltage across them ramps up slowly. The 2μF capacitor across the output of the mod-anode power supply provides the means to slow down the voltage transient and allows the arc-gaps to work more effectively. The capacitor is rated for 30kV and 5,000 Amps of transient current for this purpose. The arc-gaps also provide protection to the mod-anode of the BSTs, the filament power supply, and the SSS. If the mod-anode power supply output rises too high, all these circuits could be over-voltaged if not for the arc-gaps.

Another arc protection strategy uses the shield of the BSTs themselves. The inner geometry of the BST is such that the collector of the BST is most likely to arc to the shield electrode. On the solid-state switch deck, the shield is tied directly to B-, the reference of the deck. In this way, nearly every arc will go straight to the reference. The cathodes of the BSTs and the SSS are also protected from arcs by two components. A wire wrapped tube is connected between the cathodes of the BSTs and the SSS. In the event of an arc to the cathode, which would damage the SSS, this small inductance will limit the current and hold a portion of the voltage during the arc. The second stage of this arc protection is a very large metal-oxide varistor (MOV) across the entire SSS, which provides a great deal of transient protection. The third stage is the protection circuitry in the SSS itself. With all these safeguard strategies, the BSTs, the peripheral supplies, and the SSS are all protected.

5 INSTRUMENTATION

Signals from the SSS, the mod-anode power supply, the solenoid power supply, and the filament power supply are all transmitted from the deck, which is floating at high voltage, to the ground level instrumentation via fiber optic links.

The SSS sends a fiber optic signal from each IGBT module that indicates whether or not the IGBT module is open or closed. The mod-anode power supply sends back a 20kHz to 100kHz frequency signal that indicates the level of the power supply output. This signal is converted to a voltage and fed to a digital meter that displays the mod-anode power supply output in kilovolts. The solenoid power supply sends back a 0Hz to 100kHz frequency signal that indicates the current through the solenoids. This signal is converted to a voltage and fed to another digital meter that displays the solenoid current in Amps. The AC current to each BST filament runs through a small transformer. Across the secondary of the transformer is a resistor that is sized so that the output voltage of the transformer, when rectified, is 9 VDC when 10 Amps AC is flowing through the filament. This voltage is converted to a frequency that is sent to ground via a fiber optic cable. This frequency is converted back to a voltage and the current through each filament, in Amps, is displayed on a digital meter. In this way, all the necessary information from the solid-state deck is conveyed to ground level and displayed in the correct units.

6 CONTROL

The SSS is turned on and off by a gate signal that is converted to a fiber optic pulse. This pulse is transmitted to the SSS via a fiber optic cable and the switch is closed as long as there is light at the end of the cable. The width and frequency of the gating signal determines the width and frequency of the current pulses through the klystron. Pulse current transformers are used to monitor the collector, cathode, and body current of the klystron. The collector and cathode current can be viewed with an oscilloscope. In the event of a klystron arc, the body current transformer will produce a pulse and the SSS will be latched open. There is also a ground current pulse transformer that monitors all currents through ground. This transformer will also produce a pulse during a klystron arc but this pulse will fire the crowbar of the transmitter, thereby de-energizing the main high-voltage power supply and the energy-storing capacitor banks. It is undesirable to fire the crowbar in the event of a klystron arc. Therefore, any signal from the ground current transformer is integrated so that it does not reach its crowbar trigger level for 10μs. In this way a klystron arc may be extinguished without firing the crowbar, but any other fault through the ground path will fire the crowbar after 10μs.

There is also a pulse current transformer that monitors the amount of current difference between the two BSTs. If this current becomes too large, as in a BST arc, the crowbar is fired. With any of these crowbar events, the switch is latched in the open position. A 0-5 VDC voltage that is converted to a 20kHz to 100 kHz fiber optic signal controls the mod-anode power supply. This control signal must be as stable as the power supply in order to keep the ripple and stability percentages low.

7 PROTOTYPE PERFORMANCE

During the week of December 1, 1997 the prototype solid-state-switch-deck was installed into the oil tank of one of the Bates transmitters after having been extensively tested in air. On December 3, the deck was turned on and began to pulse. That day the transmitter was processed to a klystron current of 60 Amps with a pulse width of 20μs at 60 Hz. The system ran for 3 hours and experienced 3 major crowbars as part of processing and remained undamaged. The next day the system was processed to 80 Amps with a width of 22μs and with a pulse repetition rate of 600 Hz. The system ran at this level for 24 hours with no major failures. Figure 2 shows an oscilloscope picture of the klystron pulse current at 74 Amps at a pulse repetition rate of 600 Hz. Trace #1 is the trigger input to the control circuitry and trace #2 is the signal from the klystron collector current transformer, which has an output ratio of 0.1 volts per Amp.

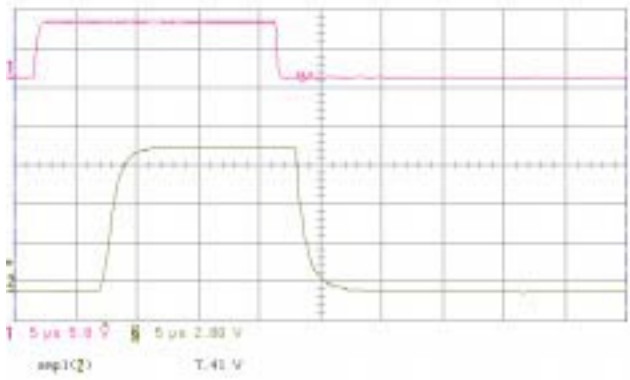

Figure 2: Klystron Current Pulse

This very successful test proved the functionality of the solid-state switch deck. The full-power 24 hour heat run did not reveal any weaknesses and there were no reliability problems associated with this test.

8 CONCLUSION

The new solid-state deck at the Bates Linear Accelerator is a vast improvement over the old modulator designs of the past. The new design uses less power, is much smaller, uses fewer components, is much more reliable, and is easier to control. The system has been thoroughly tested in the air and in the transmitters at Bates and has been proven to work successfully. This new modulator design will greatly increase not only the efficiency of the accelerator overall, but will improve the performance as well.

DESIGN CONSIDERATIONS FOR VERY HIGH POWER RF WINDOWS AT X-BAND*

W. R. Fowkes, R. S. Callin, E. N. Jongewaard
D. W. Sprehn, S. G. Tantawi, A. E. Vlieks
Stanford Linear Accelerator Center, Stanford, California 94309 USA

Abstract

RF window designs of the Pillbox type were capable of transmitting peak rf power up to about 10 MW. The power levels now being produced by advanced high frequency power sources is beyond the level that can safely be transmitted through a single rf window of conventional design. New approaches are required to keep the rf electric fields at a manageable level in the vicinity of the rf window.

This paper describes some of the recent rf window designs at SLAC and elsewhere and some of the test results. Windows that operate in larger waveguide in higher order modes such as TE_{01} and in a mix of modes such as TE_{11}, TM_{11} and TE_{12} are described. RF chokes and corona shields, circular polarization and forced electric field reduction are also discussed.

1 INTRODUCTION

The high power window presently used on all of the SLAC X-band klystrons has been reported on previously [1]. It is usually referred to as a TE_{01} reduced field traveling wave window. A pair of symmetrically located inductive irises are used to set up a standing wave in the region between the irises and the 47 mm diameter ceramic window surface. This results in "forcing" a lower impedance at the window surface that exactly matches the characteristic impedance inside the ceramic thereby causing a pure traveling wave condition inside the ceramic. This design has been tested successfully to over 100 MW in a traveling wave resonator (TWR) and has been serving as a single output window on the 50 MW XL-4 series klystrons. This design however, is considered marginal at this power level.

The new 75 MW periodic permanent magnet (PPM) focussed klystron presently uses a pair the windows described above, each passing 37.5 MW. Four TE_{10}/TE_{01} mode transducers are presently required—an expensive luxury due to the cost of the mode transducers.

2 LARGE DIAMETER TE_{01} TW WINDOW

2.1 Larger Single Window

A single window alternative has been sought that will safely handle the full 75 MW. The 47 mm TW window described above is considered to be very reliable up to a peak power level of about 40 MW where the peak rf electric field at the window is 3.4 MV/meter. Using this electric field level as a design criterion for a single 75 MW window, an increase in diameter to 65 mm would be required. This assumes of course that TE_{01} mode purity is maintained and the reduced field TW scheme is used. A problem that must be addressed in all all overmoded diameter circular windows windows is mode conversion. TE_{11} windows are susceptable to conversion to TM_{11}, TE_{12} and TM_{12} in the transitions (tapered or stepped) going from single moded to overmoded diameters. TE_{01} windows are not as vulnerable to mode conversion with increases in diameter providing the mode converter has launched TE_{01} with good purity. Gradual tapers maintain TE_{01} mode purity but are not usually very compact. Stepped transitions to larger diameters are normally susceptible to conversion to higher order TE_{0n} modes unless special attention is given to the step design.

2.2 TE01 TW Window with Compact Optimized Step

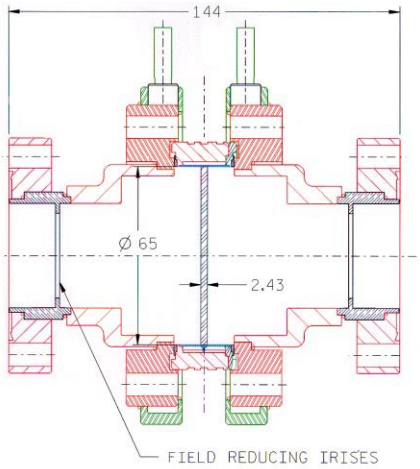

Fig. 1. Compact overmoded 65 mm diameter TE01 window. Field reduction is accomplish by a combination of the 2-stage steps and irises. The double step is optimized to cancel TE_{02} that is created at each indivdual step.

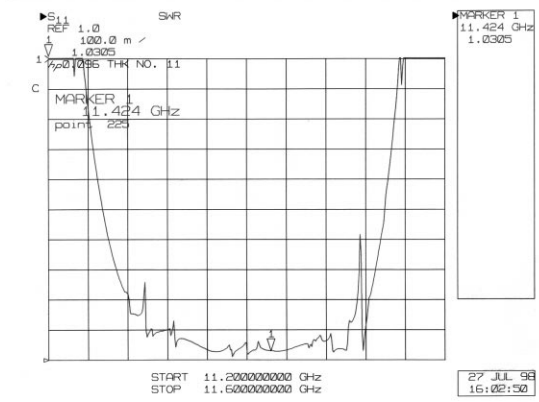

Fig. 2. Cold test results of window in Fig. 1 measured on HP 8510C NWA using old style "Flower-Petal" mode transducers which have narrower bandwidth than the window.

* Work supported by Department of Energy contract DE-AC03-76SF00515

This paper describes a compact 65 mm diameter TE_{01} TW window that is virtually free of higher order modes. The maximum electric field at the surface of this window at 75 MW is about the same as exists at for the previously described window at 40 MW; 3.4 MV/meter. The TE_{01} mode is created in 38 mm diameter circular waveguide using the recently designed compact wrap-around mode transducer [2] shown in Fig 4.

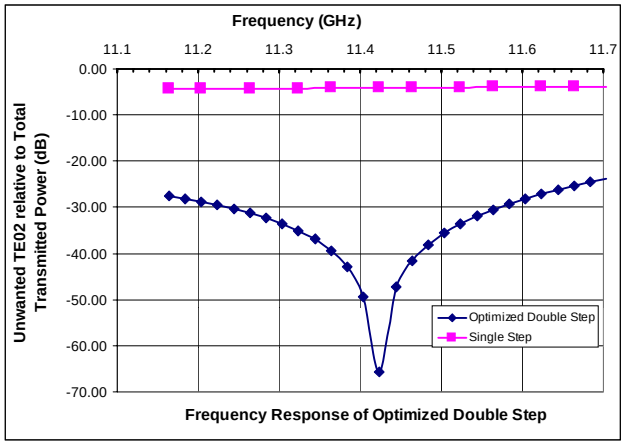

Fig. 3. Comparision of an optimized double step with a single step going from 38 mm to 65 mm with a launched TE_{01} mode.

The input and output ports for this window design are 38 mm diameter. The transition from 38 mm to 65 mm is a two-stage step designed using MLEGO© which sets up the cancellation of the TE_{02} mode excited at each step stage [3]. If one were to use a single sudden step in diameter from 38 mm to 65 mm, the resulting mode conversion is the following: S_{21} of 0.78 for TE_{01} and 0.62 for TE_{02} with only TE_{01} exciting the smaller diameter port. By going to a two-step design, the length and diameter of the intermediate step is optimized to null out the natural conversion to TE_{02}. The optimum intermediate diameter is 58.14 mm with a length of 19.48 mm. The residual S_{21} for TE_{02} drops to 0.00051. The effectivness of this optimized step is shown in the graph in Fig. 3. It is compared with a single abrupt step as a function of frequency. The unwanted conversion from TE_{01} to TE_{02} is mimized for the operating frequency of ll.424 GHz.

All this is accomplished at the expense of a residual TE_{01} mismatch S_{11} of 0.167 in the 38 mm port. This residual mismatch, however, can be used along some help from an additional iris to set up the standing wave that is necessary to force the electric field down at the surface of the ceramic. The result is a pure traveling wave inside the ceramic.

It can be shown that the optimum VSWR needed to produce the TW condition within the ceramic is

$$\sigma_{opt} = \frac{\lambda_g}{\lambda_g'}$$

and the total normalized iris susceptance that would give σ_{opt} is given by

$$\left|\frac{B}{Y_0}\right| = \frac{\lambda_g - \lambda_g'}{\sqrt{\lambda_g \lambda_g'}} = 1.3476$$

where λ_g and λ_g' are the guide wavelengths in the large diameter outside and inside the ceramic window respectively [1]. The double-step reflection of 0.167 corresponds to a normalized susceptance of 0.3388. The difference is made up with symmetrical inductive irises each having a normalized susceptance of

$$\left|\frac{B}{Y_0}\right| = 1.3476 - 0.3388 = 1.0088$$

located properly so that the stored energy between the iris and the 2-stage step is minimum. It is important that the irises be located in the smaller (38.1 mm) port since an inductive iris will convert to TE02 in the larger (65 mm) port.

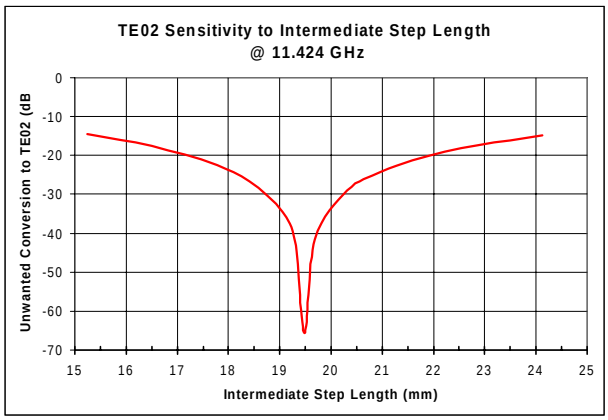

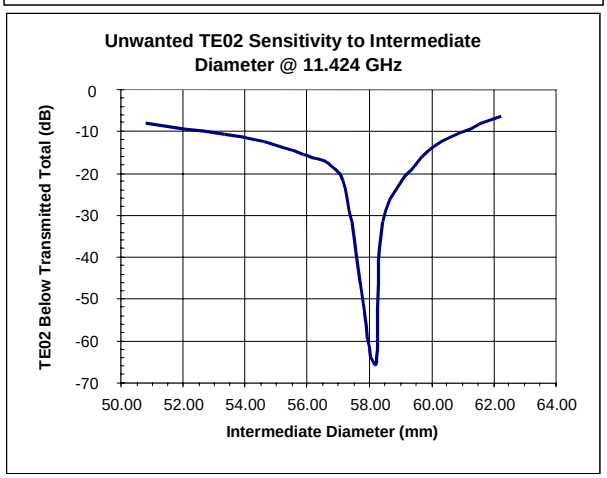

Fig. 3a and 3b. The Double step from 38.1 mm to 65 mm has been optimized to cancel out any TE_{02} conversion occurring at each step at the operating frequency of 11.424 GHz. This was accomplished using the mode matching code MLEGO. The variable parameters are the length and diameter of the intermediate step. The above graphs show the theoretical sensitivity of the conversion to unwanted TE_{02} to each of these parameters while the other is kept at the optimum value.

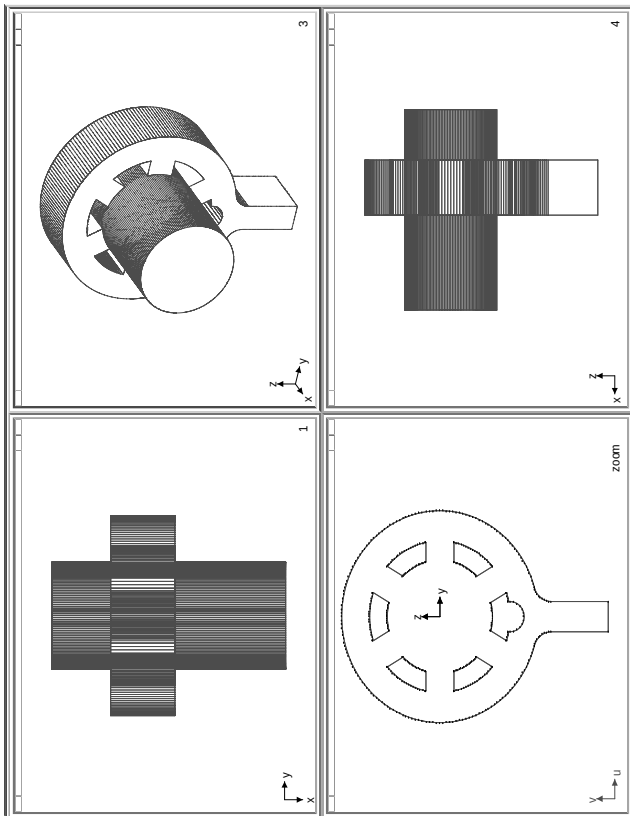

Fig. 4. HFSS output showing the geometry of the new compact Wrap-around TE_{10}/TE_{01} mode transducer that is used to excite the TE_{01} mode in 38 mm circular waveguide.

3 OTHER WINDOWS

3.1 Revisiting TE11 with Chokes

TE_{01} is preferred for technical reasons. The braze fillet is in a zero electric field region. The high cost of the TE_{10}/TE_{01} mode transducers however, diminishes the attractiveness of the TE_{01} design. TE_{11} window designs are not being abandoned entirely for some applications. A window has been designed that uses RF chokes to block RF from the region where the ceramic is brazed into its sleeve. A pair of symmetically placed inductive irises set up the reduced field TW condition similar the the TE_{01} version described earlier. The irises are necessarily thick with a full radius to reduce the local surface electric field as much as possible. A cold test version of this design was built and tested at SLAC. The diameter of the circular waveguide approaching the choke region is 27 mm while the cylinder housing the ceramic is 47 mm. This diameter is larger than necessary and was used because ceramic window blanks were available from the TE_{01} design.

This design has two main drawbacks. The surface electric field on the inside of the irises is high and there is also a strong axial component of RF electric field between the choke lobe tips and the ceramic surface, a fact that was overlooked in the beginning until it was modeled on a later version of HFSS that was capable of resolving total electric field into axial and radial components. A high power version of this design has not been built for these reasons. There was an effort to modify this design to a larger diameter but we were unable to solve the problem of mode conversion from TE_{11} to TM_{11} and TE_{12} in the larger diameter portion of the window.

3.2 Other Overmoded Windows

There have been some recent designs where the conversion of TE_{11} to combinations of TM_{11}, TE_{12}, TM_{12} were exploited successfully by Sergi Kazakov in a collaboration between BINP and KEK [4]. These designs have window diameters of either 53mm or 64 mm. These use the reduced field TW concept and in some cases the total electric field at the braze fillet has been reduced substantially and the axial component of electric field from TM_{11} is also greatly reduced.

4 REFERENCES

[1] W. R. Fowkes, R. S. Callin, S. G. Tantawi, and E. L. Wright, "Reduced Field TE01 X-Band Traveling Wave Window", Proceedings of 1995 Particle Accelerator Conference, Dallas, May 1995 pp 1587-9.

[2] S. G. Tantawi, "The Wrap-around Converter: A compact TE_{10}/TE_{01} Mode Transducer" (to be published).

[3] MLEGO© A mode matching code, Copyright S. G. Tantawi.

[4] S. Y. Kazakov, Presented at 2nd International Study Group Workshop on Next Linear Collider, ISG2, Tsukuba, Japan, July 1998.

STRATEGIES FOR WAVEGUIDE COUPLING FOR SRF CAVITIES*

Lawrence R. Doolittle
Thomas Jefferson National Accelerator Facility, Newport News, Virginia 23606 USA

Abstract

Despite widespread use of coaxial couplers in SRF cavities, a single, simple waveguide coupling can be used both to transmit generator power to a cavity, and to remove a large class of Higher Order Modes (HOMs, produced by the beam). There are balances and tradeoffs to be made, such as the coupling strength of the various frequencies, the transverse component of the coupler fields on the beam axis, and the magnitude of the surface fields and currents. This paper describes those design constraints, categories of solutions, and examples from the CEBAF Energy Upgrade studies.

1 USE OF COUPLERS

Fundamental power couplers form an important part of the design of any RF accelerating cavity, and have a history of difficult development in superconducting $\beta \approx 1$ designs[1]. Although waveguide couplers are relatively uncommon in this arena, they offer some intriguing advantages, including simplicity and the ability to operate while flexing mechanically.

The intended operation of a coupler is clear—it has to convert the TM_{01} mode of the circular beampipe (and possibly higher order modes as well) to the TE_{10} rectangular waveguide mode, eventually connected through a window and cold-warm transition to the power source.

Much of the following discussion depends on the propagation of various modes down the circular beampipe. Table 1 shows the calculation of attenuation

$$A = 20/\ln 10 \cdot \sqrt{(p/a)^2 - (2\pi f/c)^2}$$

for the cavities (designed at Cornell) used at Jefferson Lab, which have tube radius $a = 3.5$ cm. Most $\beta = 1$ cavities have similar behavior in this regard, although there will certainly be small differences due to the HOM band structure and the relative size of the beampipe. Note that the TM_{110} cavity mode couples to both the TM_{11} ($p = 3.832$) and TE_{11} ($p = 1.841$) waveguide modes, but the former decays more rapidly and is unimportant for pipes longer than 2 cm.

It is possible to ignore HOM properties of the coupler, and assert that separate HOM filter/absorbers will be used (this is the approach of Jefferson Lab's baseline design for its energy upgrade). That places stringent requirements on the HOM damping system. In particular it leaves intact a relatively tight ratio between the fundamental (which must not be absorbed) and the lowest frequency HOM (which must be absorbed). The Cornell/Jefferson Lab cell shapes set a ratio of 1.72 to 1.50 GHz for this requirement. The community's history of HOM absorbers (often designed to these tight frequency selectivity requirements) has been less than trouble-free. One might hope that moving the required absorption band edge from 1.7 GHz to 2.7 GHz could make for a simpler, more reliable filter.

Table 1: Mode attenuations in beampipe

mode	freq. (GHz)	p	attenuation (dB/cm)
TM_{010}	1.497	2.405	5.31
TE_{111}	1.72–1.97	1.841	2.83–3.33
TM_{110}	2.08–2.12	1.841	2.44–2.77

Note that the $Q_{\rm ext}$ required for HOM modes can be 100 times lower than the design point for $Q_{\rm ext}$ of the fundamental: Storage rings typically need $Q_{\rm ext}$ less than 10^4 for HOMs and 10^5–10^6 for the fundamental, and linacs typically need $Q_{\rm ext}$ less than 10^5 for HOMs and 10^6–10^7 for the fundamental.

2 A $\lambda/2$ STUB DESIGN

Cornell designed and tested a waveguide coupler for use in a storage ring. The basic design used a stub slightly shorter than $\lambda/2$, as shown in Figure 1[2, 3, 4]. The second stub is used for HOM purposes: the HOM coupler in that design was incapable of damping modes below 1.9 GHz, and there are cavity TE_{111} modes in the 1.7 to 1.9 GHz range that needed damping. The second stub enhanced coupling to these modes.

This coupler length has some interesting advantages: the fundamental can be rejected by a factor of $\sin(2\pi x/\lambda) \ll 1$. This condition does not hold for non-π TM_{010} modes and HOMs, since λ is appreciably different at other frequencies (1.7 vs. 1.5 GHz in the latter case). The resulting strong coupling to the former mode set is of great interest in a storage ring application, where the stub-on-stub design was demonstrated to give a factor of two reduction in $Q_{\rm ext}$ for the $4\pi/5$ TM_{010} mode[3].

Figure 2 shows the electric fields of this coupler in the direction of the beam axis, as computed by HFSS[7]. Examination of these shows the large resonance (14× amplitude) set up between the beamline and the end of the stub. The curve labelled "Real" is the component of a traveling wave

* Work supported by the U.S. DOE Contract # DE-AC05-84ER40150

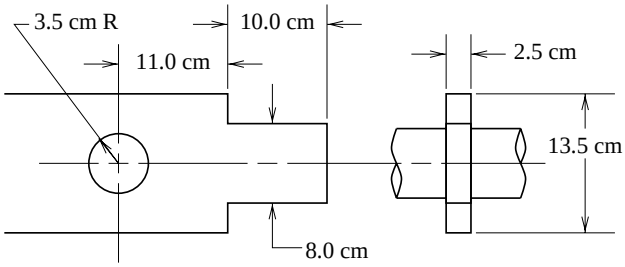

Figure 1: Schematic (interior dimensions) of $\lambda/2$ stub-on-stub FPC used by the Cornell/JLab cavity system.

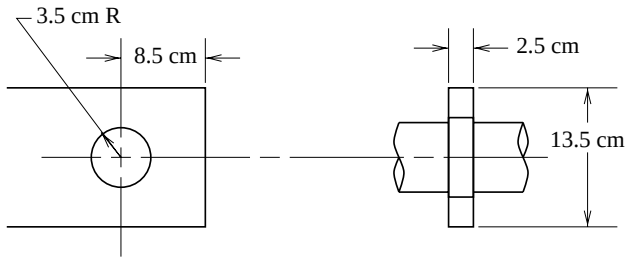

Figure 3: Schematic (interior dimensions) of $\lambda/4$ stub FPC proposed for the CEBAF energy upgrade cryomodule.

that is in phase with the evanescent fields in the beampipe. It is also the standing wave pattern when the cavity is filled, as would occur in steady state on resonance. The curve labelled "Imag" is the component of a traveling wave that is in quadrature with the evanescent fields in the beampipe. It is also the standing wave pattern when the cavity is empty, as would occur off resonance.

This design also provides a mechanism to tune $Q_{\rm ext}$ by mechanical deformation of the stub. A bow in the wide face of the waveguide will change λ, which in turn makes a large change in $\sin(2\pi x/\lambda)$ and therefore $Q_{\rm ext}$. For large changes in $Q_{\rm ext}$, this might make sense. The complexity of producing a reliable cold mechanism makes this unattractive for performing small adjustments, where an external three-stub tuner can perform adequately.

When the cavity shape was incorporated in Jefferson Lab's design for its Nuclear Physics accelerator, CEBAF, the $Q_{\rm ext}$ tunability was used to shift from the (storage ring) design point of 3×10^5 to the (recirculating linac) design point of 6×10^6. This factor of 20 reduction of $\sin(2\pi x/\lambda)$ made for touchy bench adjustments and increased concerns about how stresses in assembly and cooldown could affect $Q_{\rm ext}$. In retrospect, it might have been better to obtain some or all of the gross increase in $Q_{\rm ext}$ by increasing the length of beampipe between the coupler and end cell iris.

The coupler fields are quite asymmetric in the $\lambda/2$ stub design. The resulting beam kick was cancelled (to first order) in the CEBAF accelerator by arranging the feeds in a $++--\,--++$ pattern for the 8-cavity cryomodule. Further study of coupler kicks[5] has in some cases placed extra restrictions on the setup of cavity gradients[6]. The use of the stub to reject the fundamental mode also leads to high fields in the coupler, and the stub must be well cooled to keep it superconducting.

3 A $\lambda/4$ STUB DESIGN

The same waveguide–beamline topology can result in a near-zero coupler kick, if the stub is $\lambda/4$ long, as shown in Figure 3. Figure 4 shows E_z along the length of the coupler axis, again computed by HFSS.

For a given intensity of fundamental evanescent fields in the beampipe at the coupler location, this coupler design has a factor of 10 lower peak field in the coupler region. It passes a factor of 10 more wave intensity to its waveguide port than the $\lambda/2$ stub design. To keep $Q_{\rm ext}$ the same, therefore, one could either put more beampipe between the cavity and the coupler, or add a matching iris on the rectangular waveguide section.

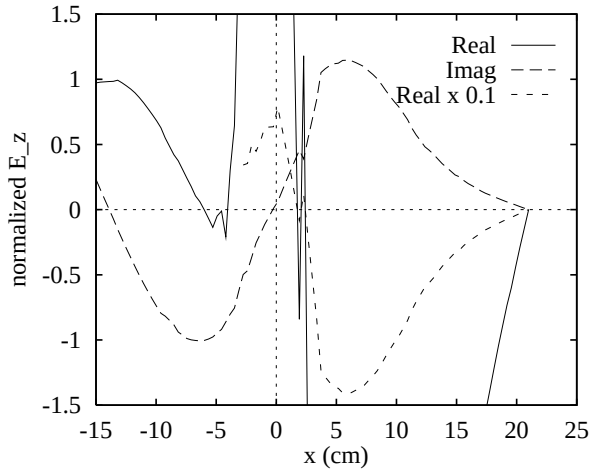

Figure 2: Electric fields in the centerline of $\lambda/2$ stub-on-stub FPC used by the Cornell/JLab cavity system.

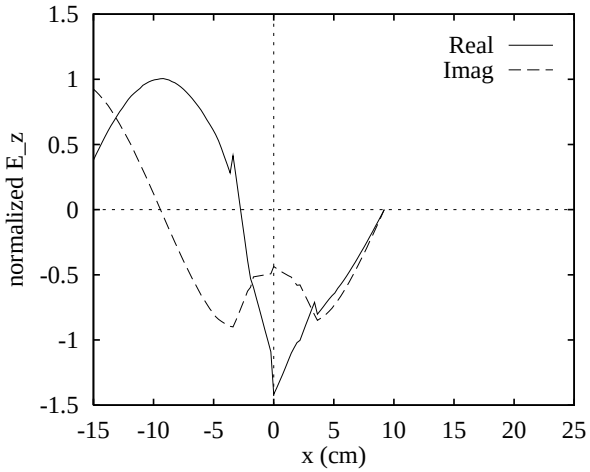

Figure 4: Electric fields in the centerline of $\lambda/4$ stub FPC proposed for the CEBAF energy upgrade cryomodule.

While the use of a matching iris may sound silly, a superconducting filter constructed out of H-plane steps in waveguide width can form an effective *narrowband* iris. An example design sets up a VSWR of 10 at 1.5 GHz, but less than 1.2 at 1.72 GHz and above[8]. It takes only 56 cm of waveguide length, zero beamline space, and does not induce asymmetric coupler fields.

4 POLARIZATION OF RF COUPLING

Normally the two polarizations of dipole (and higher rotational order) modes have slightly different frequencies, due to broken cylindrical symmetry by manufacturing defects and couplers. In the worst case, a single HOM coupler in the presence of otherwise degenerate polarizations will break the degeneracy in such a manner as to couple only one of the two polarizations. Conversely, a single coupler can function effectively if the nodal planes are pinned at a 45° angle from the coupler plane.

The lowest frequency mode (which is the hardest to separate from the fundamental in conventional HOM filters) is normally the TE_{111} dipole mode, so any attempt to extract this mode from the fundamental power coupler (waveguide or not) has to deal with polarization. The HOM coupler in the Cornell/Jefferson Lab cavity-coupler system is designed to polarize the TE_{111} mode in the ideal direction. Most measurements of mode Q's verify the success of this plan. This effect was not checked during manufacturing, however, and in two cases (in Jefferson Lab's Free Electron Laser) one of those modes shows very high Q_{ext}[9].

Some studies have shown [10] that polarized cells can be used to damp both polarizations with a single coupler. To date, no beam testing or production manufacturing of such cells has been attempted, so the cost and performance impact can not be fully characterized. The polarizing effects of the $\lambda/4$ stub waveguide coupler discussed here are rather small, so there is hope that an intentional disturbance (such as an elliptical section of beampipe near the coupler) could swamp both residual manufacturing and inherent coupler polarization, without the complexity of polarized cells.

5 RF WINDOWS

The design of windows is tightly bound to that of the coupler itself. In the original Cornell/JLab design, a cold window (originally Kapton$^{\mathrm{TM}}$, later ceramic) was used, primarily to keep the cells under clean vacuum during cryomodule assembly. That window had to meet a set of extreme design goals:

- Low VSWR over a wide frequency range (because of the HOM damping needs)
- Tolerance of high radiation flux (it's only 8 cm from the beamline)
- Low RF losses at the fundamental (since dissipation is taken by the 2 K helium circuit)
- Particulate free during assembly and operation (to avoid damaging cavity performance)

Meeting all of these needs simultaneously turned out to be a larger challenge than anticipated. Among other problems, many of the windows installed at CEBAF have developed pinholes during the years of operation[11].

The baseline design of the cryomodules for CEBAF's energy upgrade uses a single ceramic window at room temperature, away from line-of-sight of the cavities. The coupler system, window included, is not used for HOM damping, so the window can be implemented with a narrowband design (allowing a thicker ceramic with better puncture resistance). It still forms part of the beam vacuum envelope, and must be manufactured and assembled free of particulates.

6 CONCLUSIONS

The ultimate simplicity of a waveguide coupler makes it a worthy competitor to a conventional coaxial coupler. The Cornell/Jefferson Lab experience has led to clearer understanding of how to use waveguide couplers to meet design goals. A coupler based on this work is now in the prototyping phase at Jefferson Lab.

7 REFERENCES

[1] M. Champion, "RF Input Couplers and Windows: Performances, Limitations, and Recent Developments," Proceedings of the Seventh Workshop on RF-Superconductivity, B. Bonin, editor, Gif sur Yvette, France, 195 (1995).

[2] J. Kirchgessner, "Preliminary Studies on LCY Fundamental Power Coupler," Cornell University, Laboratory of Nuclear Studies report SRF-820902-EXA (1982).

[3] J. Kirchgessner, "Measurements on LCY Coupler," Cornell University, Laboratory of Nuclear Studies report SRF-830103-EXA (1983).

[4] J. Amato, "Summary of HOM Measurements to Date," Cornell University, Laboratory of Nuclear Studies report SRF-831002-EXA (1983).

[5] C. G. Yao, "Effects of Field Asymmetry in the Coupler," Jefferson Laboratory Tech Note CEBAF-TN-89-183 (1989).

[6] Jefferson Lab FEL Team, private communication.

[7] Ansoft HFSS, by Ansoft Corporation, http://www.ansoft.com, commercially licensed software.

[8] L. R. Doolittle, "Analysis and Design of Waveguide Filters Based on H-Plane Steps," Jefferson Laboratory Tech Note JLab-TN-98-034, http://recycle.jlab.org/∼ldoolitt/hstep/.

[9] Lia Merminga, I. E. Campisi, "Higher-Order-Modes and Beam Breakup Simulations in the Jefferson Lab FEL Recirculating Linac," these proceedings.

[10] "Azimuthal Shaping of Cylindrical Accelerating Cavities for Improved Higher Order Mode Extraction," J. C. Amato, et al., IEEE Trans. Nucl. Sci. NS-32, 3593 (1985).

[11] L. Phillips et al., "Some Operational Characteristics of CEBAF RF Windows at 2 K," Proc. of the Particle Accelerator Conference, 1993, 1007.

SYSTEMATIC DESIGN OF AN S-BAND PILLBOX-TYPE RF WINDOW

A. Jöstingmeier, M. Dohlus and N. Holtkamp, DESY, D-22607 Hamburg, Germany

Abstract

The scattering matrix technique and the MAFIA computer code are employed for the systematic design of an 75 MW S-band pillbox-type window. It is shown that with the standard pillbox-type design the window cannot be matched using ceramic disks with a thickness in the range from 4 mm to 8 mm. Nevertheless such disks are mechanically more robust and easier to manufacture than the usual 3 mm disks. Therefore a new design of the pillbox-type window with an additional inductive iris is presented so that ceramic disks of arbitrary thickness may be used. Furthermore it is demonstrated how the bandwidth of the window can be optimized by fine tuning the thickness of the ceramic disk. The final design of the pillbox-type window with smoothed edges is validated by the application of the MAFIA time domain module.

1 INTRODUCTION

The S-band linear collider at DESY requires approximately 2600 klystrons operating at an output power of 150 MW, a pulse duration of $3\,\mu$s and a repetition rate of 50 Hz. Until 1995 two klystrons have already been built and successfully tested [1]. The klystron has two output waveguides which are split and recombined so that each of the four rf windows has to withstand a peak transmission-power of about 37.5 MW. The production costs of the klystrons can significantly be reduced if each tube contains only two rf windows. In this paper we will report on the systematic design of such a window.

Fig. 1 presents the schematic drawing of a pillbox-type rf window. The practical use of rf-windows in the high-power regime is still a challenging task although strong efforts have been made during the past to improve their reliability [2]. The mechanismen which is responsible for an rf window failure has not yet been understood in detail. Nevertheless it seems to be clear that multipactor electron bombardment of the ceramic disk [3] is mainly responsible for a breakdown.

Computer simulations have demonstrated that the component of the electric field normal to the disk is mainly responsible for this phenomenon. Hence a long pillbox-type rf window has been suggested in [2] which has a length of more than 150 mm instead of 30 mm for the standard window. The axial electric field is effectively suppressed by this new geometry because only the TE_{11} mode is propagating in the empty circular waveguide sections of the pillbox cavity.

The higher order modes which are excited at the transition from the rectangular to the circular waveguide do not interact with the ceramic disk in a long window. Thus we can apply the scattering matrix technique taking only one propagating mode into account. From this analysis we get analytic expressions which are very useful for the window design. Only the scattering matrix corresponding to the waveguide transition will be calculated numerically using MAFIA [4]. Hence the scattering matrix technique leads to a numerically efficient formulation so that a large variety of parameter sets can be studied.

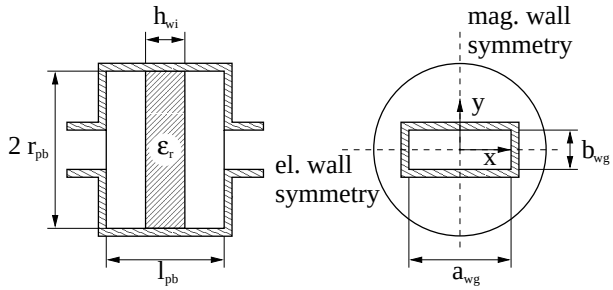

Figure 1: Schematic drawing of the pillbox-type rf window.

Pillbox-type rf windows usually contain ceramic disks with a thickness of about 3 mm. Especially if high purity alumina is to be used it is desirable to increase the thickness of this disks from the mechanical point of view. The analytic design formulas show that such windows cannot be matched if the thickness of the disk is in the range from 4 mm to 8 mm because the input reflection of the transition from the rectangular to the circular waveguide is too small. Therefore a new type of rf window is presented which contains additional inductive irises in order to increase the reflectivity of the waveguide transition.

Both features of the new window, which are an increased thickness of the ceramic disk and a long pillbox cavity, lead to a significant reduction of the bandwidth. Especially if the SLED-option [5] is taken into account the VSWR must be less than 1.1 over a band of about 90 MHz centered at 3 GHz. It is shown how a maximum bandwidth is obtained by properly adjusting the thickness of the ceramic disk.

In order to prevent the structure from arcing we have to round off the sharp edges at the waveguide transition which are characterized by $y =$ constant. Although the inductive irises do not give rise to a singularity of the electric field they are also assumed to be rounded off in the final design which is validated by the time domain module of the MAFIA code.

2 WINDOW DESIGN

Let us assume that the dimensions of the rectangular waveguide and the permittivity of the ceramic disk are

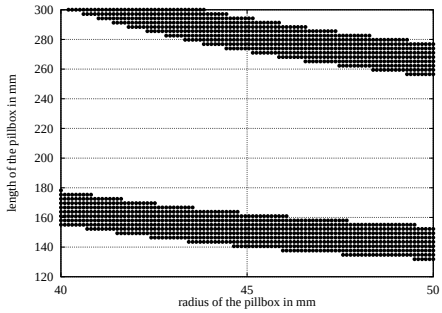

Figure 2: Distribution of possible solutions in the r_{pb} - l_{pb} plane. Parameter: $h_{wi} = 5$ mm.

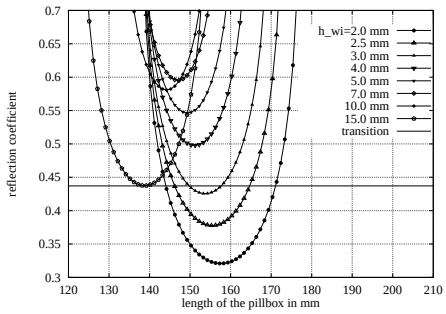

Figure 3: Required reflection coefficient of the waveguide transition as a function of l_{pb} and h_{wi}. Parameter: $r_{pb} = 46$ mm.

$a_{wg} = 72.14$ mm, $b_{wg} = 34.04$ mm and $\varepsilon_r = 10$.

From the application of the scattering matrix technique it turns out that the rf window can only be matched if the window parameters obey certain relations. Fig. 2 shows all possible solutions for which the window can be matched in the r_{pb} - l_{pb} plane assuming $h_{wi} = 5$ mm. In the considered parameter range two sets of solutions are found which are separated just by one wavelength of the TE_{11} mode in the empty circular waveguide.

For the variation of the radius of the pillbox cavity some transitions from the rectangular to the circular waveguide have been analyzed using MAFIA. Actually the radius of the pillbox cavity has been varied in steps of 2 mm. The scattering parameters at intermediate points are then found by the application of an interpolation scheme.

Fig. 3 presents the required input reflection of the waveguide transition as a function of the length of the pillbox cavity for a cavity radius of 46 mm whereas the thickness of the ceramic disk serves as a parameter. The input reflection of the waveguide transition is also given as a straight line.

Starting from $h_{wi} = 2$ mm, the required input reflection of the waveguide transition increases. For $h_{wi} = 2$ mm, 2.5 mm and 3 mm, Fig. 2 predicts two solutions for each thickness corresponding to different lengths of the pillbox cavity. But for thicker disks, the parabolas do not intersect with the straight line so that no solution exists. Only if we consider very thick disks, $h_{wi} > 10$ mm, the required input reflection decreases again. Consequently, the window can only be matched for disks in the range from 4 mm to

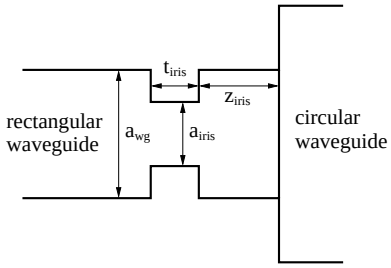

Figure 4: Schematic drawing of the waveguide transition with an inductive iris.

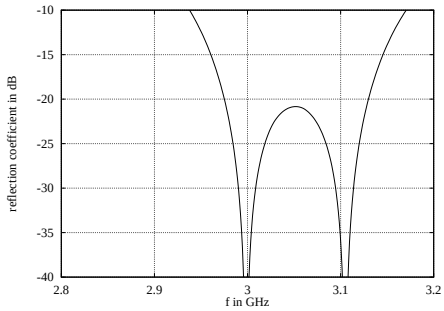

Figure 5: Reflection coefficient of the window as a function of frequency. Parameter: $r_{pb} = 46$ mm, $l_{pb} = 144.9$ mm, $h_{wi} = 5$ mm, $z_{iris} = 40$ mm and $a_{iris} = 57$ mm.

8 mm if we choose a waveguide transition with a higher input reflection.

In order to increase this quantity we introduce an inductive iris in front of the waveguide transition according to Fig. 4. t_{iris} is assumed to be 5 mm. For a given iris one gets a maximum increase of the reflectivity for $z_{iris} = 40$ mm. For the adjustment of a specific value of the input reflection, which is necessary for the proper design of a window, the width of the iris a_{iris} is used.

We have now all the data together which we need for a systematic design of the window. Let us start assuming the following parameters: $r_{pb} = 46$ mm, $h_{wi} = 5$ mm and $z_{iris} = 40$ mm. According to Fig. 3, the input reflection of the waveguide transition has to be greater than 0.55 in this case. We choose an input reflection of 0.57 which corresponds to an iris width of about 57 mm in order to show that really two solutions exist if the input reflection is larger than 0.55. Applying the scattering matrix technique, we actually find two matched windows for $l_{pb} = 144.9$ mm and $l_{pb} = 154.5$ mm. Fig. 5 shows the input reflection of the window for $l_{pb} = 144.9$ mm.

Both solutions have a bandwidth corresponding to a VSWR $= 1.1$ of approximately 30 MHz which is much too small. The bandwidth can significantly be enhanced if we make use of both solutions simultaneously. For that the two frequencies at which the window is matched have to be centered around the design frequency, see Fig. 6. This is achieved by properly choosing the length of the pillbox cavity.

The reflection coefficient at the design frequency which is related to the bandwidth of the window can then be adjusted by the thickness of the ceramic disk which is illus-

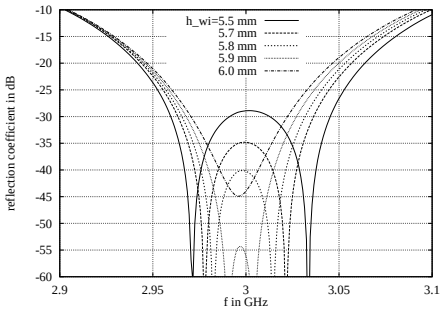

Figure 6: Reflection coefficient of the window as a function of frequency and the thickness of the ceramic disk. Parameters: $r_{pb} = 46\,\text{mm}$, $l_{pb} = 148.9\,\text{mm}$, $z_{iris} = 40\,\text{mm}$ and $a_{iris} = 57\,\text{mm}$.

#	h_{wi} in mm	Δf in MHz	
		VSWR $= 1.05$	VSWR $= 1.1$
1	5.5	–	94
2	5.7	67	83
3	5.8	60	77
4	5.9	52	72
5	6.0	44	66

Table 1: Bandwidth as a function of the thickness of the ceramic disk.

trated in Fig. 6. From Fig. 3 it is clear that the solutions move closer together if the thickness of the ceramic disk is increased. This leads to a smaller reflection coefficient at the design frequency but also to a reduction of the bandwidth. Thus one has to find a trade-off between these two quantities. In Table 1, the bandwidth of the window is given for several values of h_{wi}. E.g., the VSWR is still less than 1.1 over a frequency range of $94\,\text{MHz}$ for $h_{wi} = 5.5\,\text{mm}$. However in this case one has to cope with a reflection coefficient of $-28.9\,\text{dB}$ at the design frequency.

For the final design of the window we use a waveguide transition with rounded edges according to Fig. 7. Detailed investigations using the MAFIA electrostatic module yield that a rounding radius of $10\,\text{mm}$ leads to a field enhancement of about 30% which seems to acceptable. Furthermore it is preferred to use semicircular irises with a radius of $9\,\text{mm}$ instead of those which sharp edges which is also illustrated in Fig. 7.

Fig. 8 presents the input reflection of the final window design as a result of the scattering matrix technique and the MAFIA time domain module. The agreement between both methods is quite well. Optimizing the bandwidth yields a useful frequency range of about $80\,\text{MHz}$ and a reflection coefficient at the center frequency which is less than $-33\,\text{dB}$.

3 CONCLUSIONS

The scattering matrix technique and the MAFIA computer code have been applied in order to design a modified S-band high-power pillbox-type window. It has been shown that for a ceramic disk with a thickness in the range from $4\,\text{mm}$ to $8\,\text{mm}$ the input reflection of the rectangular-circular waveguide transition has to be increased so that

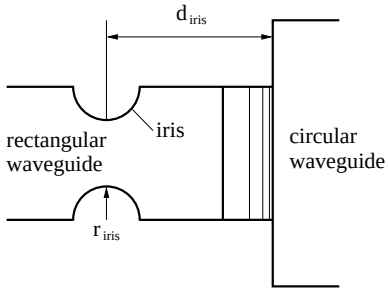

Figure 7: Schematic drawing of the waveguide transition with rounded edges.

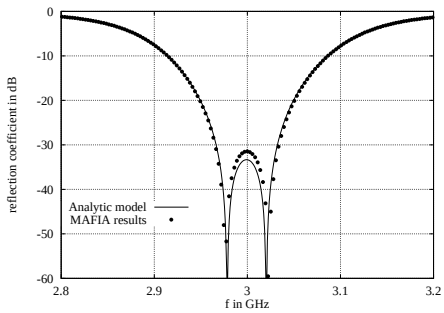

Figure 8: Reflection coefficient as a function of frequency with $r_{pb} = 46\,\text{mm}$, $h_{pb} = 150.4\,\text{mm}$, $h_{wi} = 6.1\,\text{mm}$, $d_{iris} = 40\,\text{mm}$, $r_{iris} = 9\,\text{mm}$.

the overall window is matched at the design frequency. It has been demonstrated by MAFIA computations that the required input reflection of the waveguide transition can be obtained by an inductive iris one quarter wavelength in front of the rectangular-circular waveguide transition. Moreover it has been shown that the thickness of the ceramic disk has to be properly chosen for an optimum bandwidth of the window. A final design of the window with rounded off edges has been proposed; and the performance of this structure has been checked applying the time domain module of the MAFIA computer code.

4 REFERENCES

[1] D. Sprehn, "Final report on the development of a 150-MW S-band klystron", to be published in *Proceedings of Pulsed RF Sources for Linear Colliders*, 1996.

[2] A. Miura and H. Matsumoto, "Development of an S-band high-power pillbox-type rf window", *Proc. of Int. Conf. for High Energy Accelerators*, 1992.

[3] W. J. Gallagher, "The multipactor effect", *IEEE Trans. on Nucl. Sci.* , vol. NS-26, pp. 4280–4282, 1979.

[4] T. Weiland, "On the numerical solution of Maxwell's equations and applications in the field of accelerator physics", *Particle Accelerators*, vol. 15, pp. 245–292, 1984.

[5] P.B. Wilson, "SLED: A method for doubling SLAC's energy", *Technical Note SLAC-TN-73-15*, Stanford Linear Accelerator Center, Stanford University, Stanford, California, 1973.

DESIGN OF A HOM BROADBAND ABSORBER FOR TESLA

M. Dohlus, A. Jöstingmeier, N. Holtkamp and H. Hartwig, DESY, D-22607 Hamburg, Germany

Abstract

For the TESLA FEL operation very short intense bunches of electrons have to be accelerated. These bunches excite a broad spectrum of HOM (Higher Order Modes) up to frequencies of some THz. Two HOM couplers per cavity are foreseen in the present design proposal in order to extract some of the low frequency HOM from the superconducting accelerating structure. In this contribution an additional HOM broadband absorber is suggested which is to be installed between two cryogenic modules at a temperature of $70\,\mathrm{K}$. Its task is to prevent that the really high frequency HOM are absorbed in the accelerator structure at the $2\,\mathrm{K}$ level. The absorption characteristics and the short range wake of four structures which make use of SiC as absorbing material are investigated using the MAFIA computer code. The proposed structures are easier to manufacture and better suited for the operation under vacuum conditions than the recently suggested waveguide array absorber.

1 INTRODUCTION

It is planned to operate TESLA in the FEL mode with very short bunches ($\sigma = 25\,\mu\mathrm{m}$) [1] which excite wakefields with spectral components up to some THz. If we do not extract these fields from the accelerating structure by a special absorber we expect a considerable reduction of the quality factor of the superconducting cavities because the photon energy gets larger than the binding energy of the Cooper pairs for frequencies larger than $700\,\mathrm{GHz}$.

This phenomenon would consequently lead to an excessive energy deposition in the $2\,\mathrm{K}$ cooling circuit which has to be prevented for the following reason: The time averaged power deposition due to the wakefields is about $25\,\mathrm{W}$ per module [1]; and a typical refrigerator requires about $800\,\mathrm{W}$ of wall plug power per Watt dissipated at $2\,\mathrm{K}$ [2]. Thus we would have to supply $20\,\mathrm{kW}$ of cooling power per module which is not tolerable.

A HOM absorber which is sketched in Fig. 1 has already been proposed in [2]. This absorber consists of an array of outward directed rectangular waveguides surrounding the beampipe. The extraction of the high frequency wakefields from the beampipe by such an array has been investigated in detail in [3]. The outward propagating waveguide fields are attenuated by the ohmic losses of the stainless steel waveguides which are considerably high for frequencies above the cutoff frequency of the fundamental waveguide mode which is $100\,\mathrm{GHz}$. Note that low frequency spectral components cannot penetrate much into the absorber.

A cutoff frequency of $100\,\mathrm{GHz}$ corresponds to a width of the waveguides of $1.5\,\mathrm{mm}$. The waveguide height is only

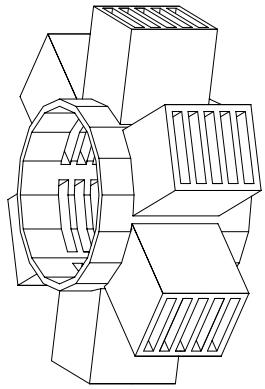

Figure 1: Schematic drawing of the waveguide array absorber.

$0.3\,\mathrm{mm}$ in order to have a high attenuation of the waveguide modes. Furthermore it is obvious that the waveguide walls should be as thin as possible for a good efficiency of the absorber. A wall thickness of $0.1\,\mathrm{mm}$ has been proposed which seems to be the lower limit from the mechanical point of view. The TESLA beampipe has a radius of $35\,\mathrm{mm}$; and approximately $100\,\mathrm{mm}$ of space are available for the absorber in the axial direction. Therefore the actual absorber consists of an array of about 140×250 waveguides in the azimuthal and the axial direction, respectively.

The manufacturing of such a structure is very difficult even if etching techniques are applied [2]. Moreover the problem of cleaning the waveguide array before it is installed in the TESLA vacuum system has yet not been solved. Thus four new absorber structures are proposed which do not have these disadvantages. The MAFIA computer code [4] is used in order to study their absorption characteristics as well as their contribution to the short range wake.

2 PROPOSED ABSORBERS

The absorbers which are investigated in this contribution are shown in Figs. 2-5. In each of these configurations the actual absorbing structure is accomodated in a shielding which is similar to a single cell of the TESLA accelerating structure. For the simulations we have assumed $r_{iris} = 30\,\mathrm{mm}$, $r_{cell} = 100\,\mathrm{mm}$ and $l_{cell} = 100\,\mathrm{mm}$.

We have chosen SiC as absorbing material because it is suitable to be used in a vacuum system; and it has a large loss-tangent which is about 0.3. This number has been confirmed by measurements at room temperature up to a frequency of $20\,\mathrm{GHz}$. For our simulations we assume that it is still valid in the THz region and that it does not change significantly if the absorber temperature is $70\,\mathrm{K}$.

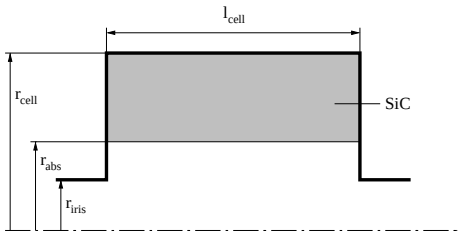

Figure 2: Solid SiC absorber.

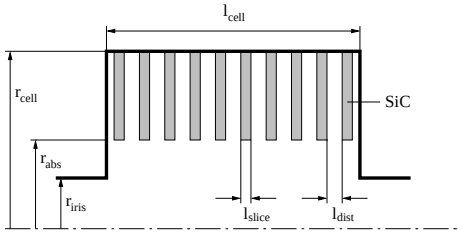

Figure 3: Laminated SiC absorber.

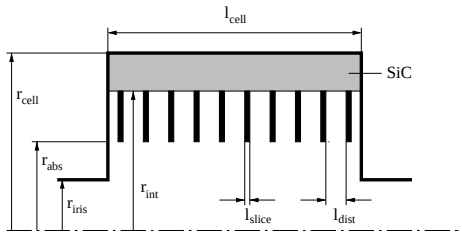

Figure 4: Combined absorber.

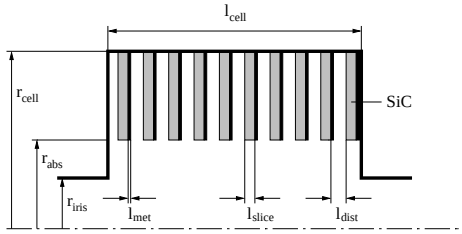

Figure 5: Metallized laminated SiC absorber.

For each proposed HOM absorber we are going to consider two versions. In the original version we have $r_{abs} = r_{iris}$. This seems to be favourable for a good coupling between the absorber and the HOM. On the other hand, the absorber itself also contributes to the beam impedance. This contribution can be decreased if we hide the absorbing structure behind the iris of the shielding cell. A bunch does not see the actual absorbing structure if the relation $r_{abs} - r_{iris} \geq \sqrt{5 l_{cell} \sigma}$ is fulfilled. In this case the short range wake of the HOM absorber is equal to that of a single accelerating cell. Bearing in mind that a module contains 72 such cells, the additionally introduced beam impedance due to the HOM absorber seems to be tolerable.

Note that in the above relation $r_{abs} - r_{iris}$ is proportional to $\sqrt{\sigma}$ which means that the absorbing structure may be arranged close to the beampipe for short bunches. Nevertheless it must also be possible to operate TESLA with $1\,$mm long bunches for which the condition for $r_{abs} - r_{iris}$ cannot be satisfied if we are interested in a good coupling between the HOM and the absorber. Thus we have to find a trade-off between the efficiency of the absorber and its contribution to the beam impedance. For our simulations we choose $r_{abs} - r_{iris} = 5\,$mm.

The first proposed absorber is a solid SiC tube accomodated in the shielding cell. This configuration is shown in Fig. 2. Since the permittivity of SiC is large ($\varepsilon_r \approx 30$) we expect considerable reflections at the SiC-vacuum interface. Therefore the second structure which is presented in Fig. 3 consists of a stack of 50 SiC washers with $l_{slice} = l_{dist} = 1\,$mm in order to reduce the effective permittivity of the absorbing structure.

The idea of the combined and the metallized laminated absorber which are shown in Figs. 4 and 5 is basically different than that of the first two structures in which all spectral components of the HOM are damped by the absorbing material in the shielding cavity. The combined and the metallized laminated absorber additionally contain a stack of stainless steel parallel-plate waveguides which attenuate the really high frequency HOM by ohmic wall losses similar to the previously discussed waveguide array absorber. In these structures SiC is used to suppress the long range wake. For this purpose it is sufficient that it has good damping properties up to a frequency of some $10\,$GHz. Hence the required bandwidth of the absorbing material is much less for these structures than that for the solid and the laminated absorber.

The difference between the combined and the metallized laminated absorber is that in the latter one the low frequency fields are continuously damped by the absorbing material while they are propagating outwards whereas they are absorbed at the ends of the waveguides in the combined absorber. The parameters of both structures read: $l_{slice} = l_{dist} = 1\,$mm and $r_{int} = 80\,$mm. Note that the actual thickness of the metallization l_{met} which is very thin can be neglected for the field analysis. In the MAFIA simulations we have assumed that l_{met} is equal to the thickness of one mesh layer.

3 SIMULATION RESULTS

The absorption characteristics of the proposed absorbers are given in Fig. 6. Here it is assumed that $r_{iris} = r_{abs}$.

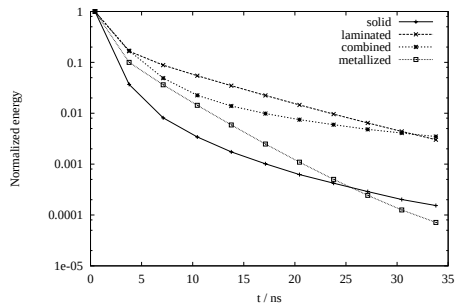

Figure 6: Absorption characteristics of the investigated structures.

The curves represent the total energy normalized to its value at the time $t = 0$. At this time the exciting bunch

has just left the absorber cell. The transient behaviour is then computed for the next 33 ns. An ultra-relativistic particle just travels 10 m during this time interval.

Two classes of absorbers can be well-distinguished with respect to their absorption efficiency. In the solid and the metallized laminated absorber the energy drops to about 10^{-4} of its initial value after 33 ns. On the other hand, the absorption of the laminated and the combined absorber is approximately two orders of magnitude less.

The transient absorption behaviour of the combined and the metallized laminated absorber and the corresponding hidden structures are compared in Fig. 7. It is expected that

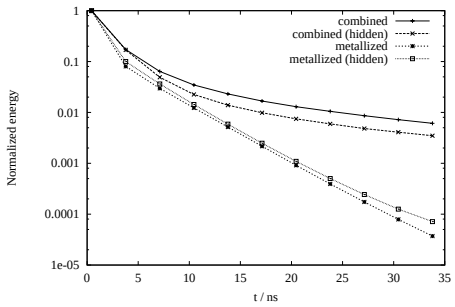

Figure 7: Comparison between the original and the hidden structure.

the hidden structures are less efficient than the corresponding absorbers with $r_{iris} = r_{abs}$. It is found that this is in fact true for the metallized laminated absorber. Nevertheless the efficiency of the hidden version of this absorber is only slightly less than that of the original structure. For the combined absorber it even turns out that the absorption can be improved a little bit if we hide the absorbing structure.

In order to illustrate the different absorption mechanisms of the metallized laminated and the solid absorber the relation between the total energy and that which is stored in the beampipe is shown in Fig. 8. Both energies are approx-

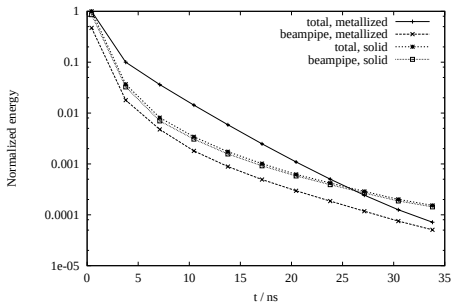

Figure 8: Total energy and energy which is stored in the beampipe.

imately the same for the solid absorber. This means that the electromagnetic field cannot penetrate significantly into the absorbing material because it is absorbed in the immediate vicinity of the dielectric-vacuum interface.

On the other hand the total energy is much larger than the beampipe energy in the metallized laminated absorber because the electromagnetic field propagates a considerably large distance into the parallel-plate waveguides before it is finally absorbed.

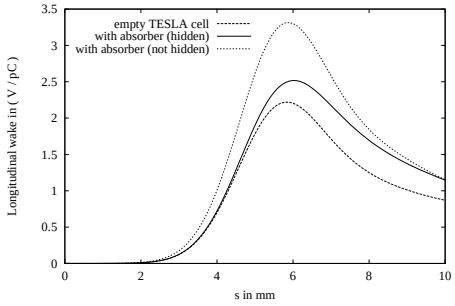

Figure 9: Short range wake of various structures for $\sigma = 1$ mm.

Fig. 9 shows the longitudinal short range wake of the empty TESLA cell, the laminated absorber with $r_{iris} = r_{abs}$ and the hidden version of this structure. The wake of the empty cell, which has a maximum value of 2.2 V/pC, is smaller than that of the two other structures as it is expected. The wake function corresponding to the non-hidden absorber is about 50% higher than this value. On the other hand, the short range wake is only 15% increased for the hidden version of the absorber which is acceptable.

4 CONCLUSIONS

Four types of HOM absorbers for TESLA which are easier to manufacture and more appropriate to be used in a vacuum system than the previously suggested waveguide array absorber have been investigated in this contribution. It has turned out that two of the absorbers, namely, the solid and the metallized laminated absorber have good absorption properties; and that the efficiency of the absorbers is not significantly decreased if we hide the absorbing structure behind the iris of the shielding. The short range wake of such a hidden structure is equal to that of a single TESLA accelerating cell for short bunches; and it is still tolerable for an intermediate bunch length. The solid absorber is less complicated concerning manufacturing and installation than the metallized laminated one. Nevertheless the simulation results for the solid absorber are based on the assumption that SiC has the same favourable attentuation properties in the THz region at a temperature of 70 K as in the frequency range up to 20 GHz at room temperature.

5 REFERENCES

[1] R. Brinkmann et al. (ed.), Conceptual design of a 500 GeV e^+e^- linear collider with integrated X-ray laser facility, DESY 1997-048, 1997.

[2] M. Dohlus, N. Holtkamp, A. Jöstingmeier, H. Hartwig and D. Trines, "Design of a HOM broadband absorber for TESLA", Meeting note: 31 Linear collider project meeting at DESY, 1998.

[3] A. Jöstingmeier, M. Dohlus, N. Holtkamp and M. Shahabadi, "Application of the mode matching technique for the computation of the beam parameters of an infinite periodic structure", will be published as TESLA report, 1998.

[4] The MAFIA collaboration, User's Guide MAFIA Version 3.2, CST GmbH, Lauteschlägerstr. 38, D64289 Darmstadt.

BIPERIODIC DISK-AND-WASHER CAVITY FOR ELECTRON ACCELERATION

H. Ao, Y. Iwashita, T. Shirai, A. Noda and M. Inoue,
Accelerator Laboratory, NSRF, ICR, Kyoto Univ.,
T. Kawakita and M. Matsuoka, Mitsubishi Heavy Industries, Ltd.

Abstract

Fabrication of the disk-and-washer(DAW) cavity is in the stage of high power model fabrication. In order to determine the final dimensions, we measured the frequencies of OFC models which were fabricated with the same fabrication process as the final cavity. This paper describes these measurement results.

1 INTRODUCTION

The biperiodic DAW [1] cavity has been investigated for these years. Basic dimensions of the DAW cavity have been studied by computer simulations and measurements on aluminum models (cold model). Eight units of such cold model were fabricated. The RF characteristics and the dependence of frequency on the number of units have been measured by these models. Before making a final high power structure, another test cavities made of OFC(OFC model) and high accuracy aluminum models(G2 model) were fabricated. The G2 model and the OFC model cavities were machined at the same shop. The OFC models were used for studying a fabrication process and final properties of cavities. The G2 models which had the same dimensions of OFC model on the drawing were used for optimization of the final dimensions. The G2 model is different from the OFC model in only two points: (i) the material is aluminum, (ii) each part is fixed by screws without brazing. Table 1 shows the frequency measurement results of these models.

	cold model	G2 model	OFC model
fa [MHz]	2857.4	2863.0	2859.6
fc [MHz]	2872.2	2873.0	2876.3

Table 1: Frequency of cold model, G2 model and OFC model. In the DAW structure, two modes should be tuned to an operating frequency(2857[MHz]). One is an accelerating mode(fa) and the other is a coupling mode(fc). In the accelerating mode, strong electric field is generated between the acceleration gap.

This results shows the slight difference in frequency among these models. The actual dimensions of each model measured by a coordinate measuring machine showed that there was no significant difference in the measurable region. The cause of frequency difference have been investigated, and it seemed to arise from the washer part [2]. The detail, however, has not been made clear yet. We discuss about this problem in a later session.

Assuming the reproducibility of fabrication process of washer part, we decided to tune the frequency to an operation one by correcting the dimensions of cavity. The frequency was measured for several sets of dimensions to accumulate correction data. All these measurement were performed on the G2-model for accuracy of dimensions.

2 MEASUREMENT RESULTS

2.1 Parameters of dimensions

Figure 1 shows the schematic view of the biperiodic L-support DAW. Frequencies were measured varying the washer radius (Rw), the inner radius of disk with supports (Rds) and the inner radius of disk without supports (Rdn).

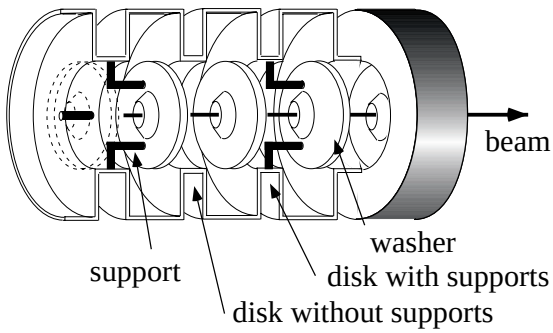

Figure 1: Disk-and-Washer structure

2.2 Accelerating mode

Coefficient of washer radius (Rw) The frequencies were measured with three washer sizes: Rw=44.0(original), 44.05, 44.5. (See Figure 2)

The frequency dependence of the number of units in Rw=44.0 or 44.05 is different from that of Rw=44.5. This is because an end plate has its intrinsic frequency tuned to 2857[MHz] (operating frequency), and thus the effect from both the end plates falls off with increase of the number of units. The intrinsic frequency of Rw=44.0 or 44.05 cavity is higher than 2857 [MHz], while that of Rw=44.5 is lower than 2857[MHz]. The coefficient for the frequency correction was calculated from the extrapolated frequencies at 24 units: the number of units in the high power model. Figure 3 shows the plots of the extrapolated value. Because the

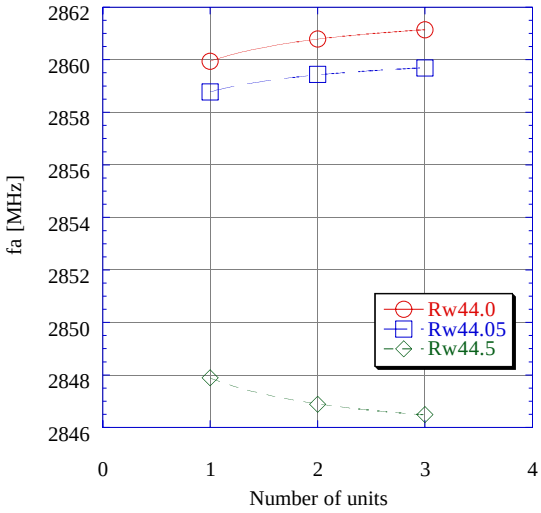

Figure 2: Frequencies as functions of the number of units at three Rw values

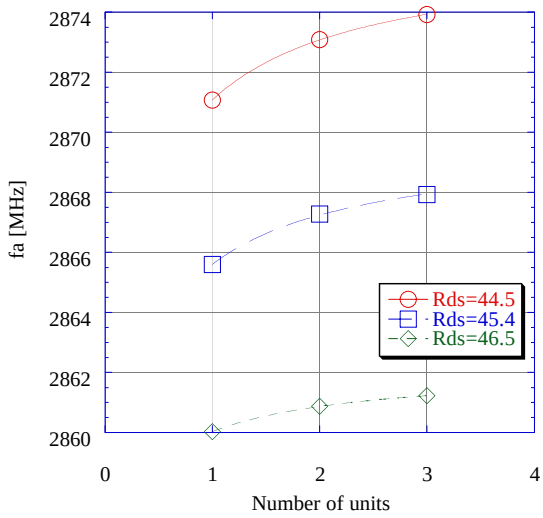

Figure 4: Frequencies as functions of the number of units at three Rds values

three frequencies (Rw=44.0,44.05,44.5) are lined up along a line, the linearity can be assumed. The correction coefficient for Rw was calculated as -32.8 [MHz/mm] from these results.

Coefficient of disk radius (Rds) Figure 4 shows the measured frequencies as functions of the number of units, in a similar way as Rw. The extrapolated frequency at 24 units was calculated for each Rds size. Thus the coefficient of Rds was obtained as -6.9 [MHz/mm]. There was a good linearity in these three points.

Coefficient of disk radius (Rdn) *N* units setup are required for *N* Rds disks and *N*-1 Rdn disks. Because there were only three G2-model cavity units, only two points data could be measured, while three data points at least are required for a curve fitting. Hence, we used the result from one unit setup, which had no Rdn disk, as the one data point. Thus the extrapolated frequency at 24 units was estimated and the correction coefficient for Rdn was obtained as -8.7 [MHz/mm].

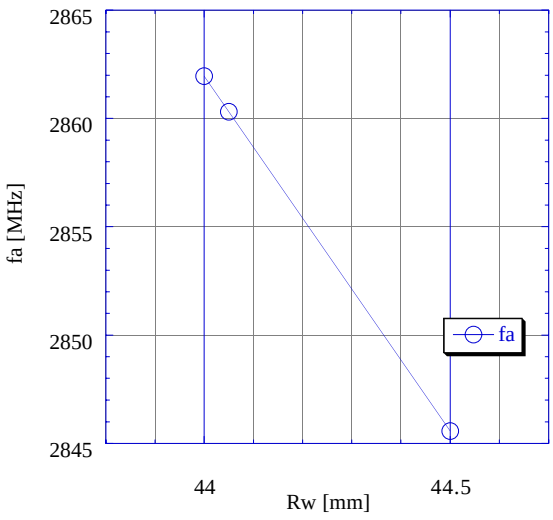

Figure 3: Correction coefficient for washer radius Rw

2.3 *Coupling mode*

Coefficient of washer radius (Rw) Figure 5 shows the measured frequencies for each washer radius. The dependence of the number of units in the coupling mode is larger than that of the accelerating mode. It should be noted that the scale of vertical axis is larger than that of accelerating mode in previous subsection. The extrapolated frequency was estimated by similar way in the accelerating mode and the correction coefficient was calculated as -32.8 [MHz/mm].

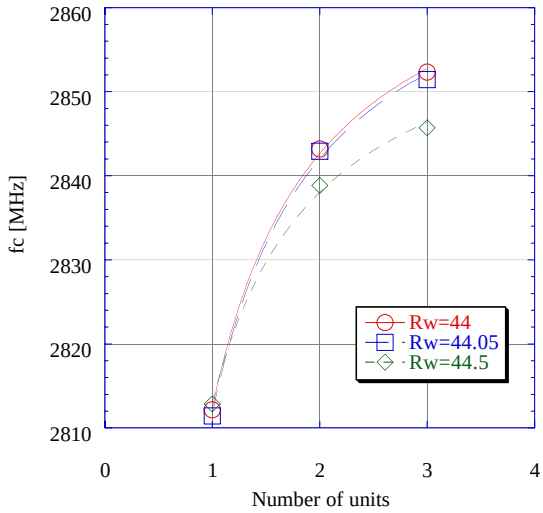

Figure 5: Frequencies as functions of the number of units at three Rw values (coupling mode)

Coefficient of disk radius (Rds) With similar way, the coefficient was obtained. Figure 6 shows the measurement results. The calculated coefficient was 9.8 [MHz/mm].

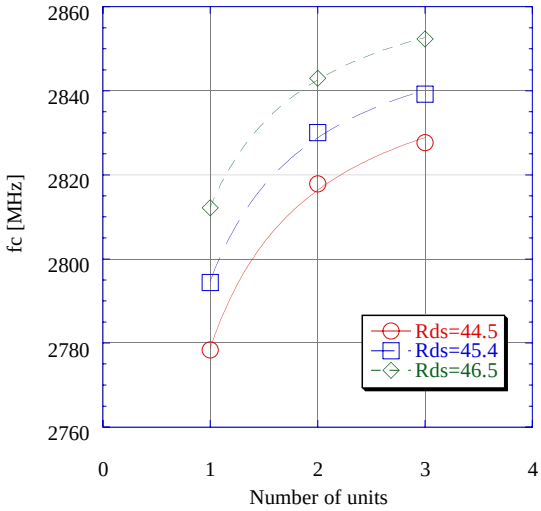

Figure 6: Frequencies as functions of the number of units at three Rds values

Coefficient for disk radius (Rdn) Figure 7 shows the measurement results, and the coefficient was calculated as 14.2 [MHz/mm].

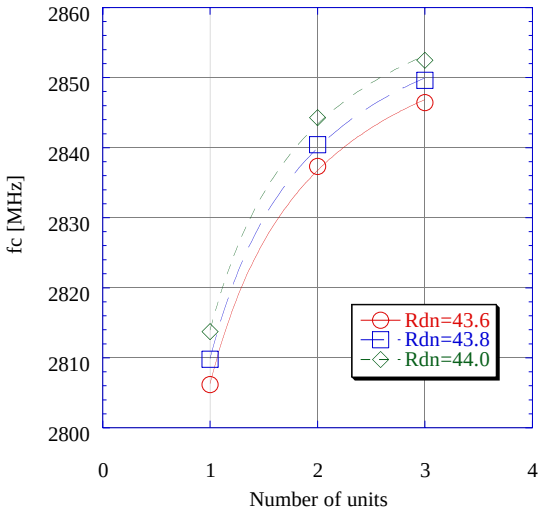

Figure 7: Frequencies as functions of the number of units at three Rdn values

3 DISCUSSION AND CONCLUSION

3.1 Correction coefficient

Because the frequency depends on the number of cavity units, an extrapolated frequency at 24 units was used to evaluate the correction value. Table 2 shows the summary about the coefficients obtained from these measurements.

	df/dRdn	df/dRds	df/dRw
fa [MHz/mm]	-8.7	-6.9	-32.8
fc [MHz/mm]	14.2	9.8	-19.4

Table 2: Summary of correction coefficient

As the coefficients of accelerating mode, df/dRdn=-9.2 [MHz/mm], df/dRds=-7.3 [MHz/mm] and df/dRw=-28.4 [MHz/mm] were calculated by SUPERFISH. These values are compatible with the measurement results. For the coupling mode, it is difficult to estimate the coefficient by SUPERFISH because the support effect was too large.

3.2 Frequency difference among three models

The frequency difference seems to arise from the washer part. Because washer has a curved surface (nose), it is difficult to measure all dimensions precisely. We tried to measure the more fine shape of nose part by a contracer (contour measuring device). An output from our device, however, is only a line drawing. The obtained data are analyzed to estimate the frequency difference. The shape of nose part is very sensitive to the accelerating frequency. It is important fabrication technology to fall in with the tolerance of frequency keeping the reproducibility of RF properties with available machining technique.

The curved surface is considered most critical point in the fabrication of the DAW. It is important fabrication technology to control the frequency with keeping the reproducibility of RF properties.

4 REFERENCES

[1] Y. Iwashita, "Disk-and-washer structure with biperiodic support", Nucl. Instrm. and Meth. in Phys. Res. A 348(1994)15-33

[2] H. Ao, et al., "Fabrication of disk-and-washer cavity", Proc. of the First Asian Particle Accelerator Conference, Tsukuba, Japan, in printing.

THE ESTIMATIONS FOR MECHANICAL VIBRATIONS OF STEMS-LIKE ELEMENTS IN RF CAVITIES

A.S. Levchenko, V.V. Paramonov, R.S. Ter-Antonyan
Institute for Nuclear Research, 117312, Moscow, Russia

Abstract

In such elements of accelerating cavities as stems, posts, spirals, split rings low frequency (several tens Hz) mechanical oscillations may excite. Analytical expressions for resonant frequencies are presented. If the channel for cooling liquid is placed inside the element, depending on flow parameters the source of noises may exists from turbulence. Estimation for flow parameters and possible spectrum of noises are given.

1 INTRODUCTION

A lot of rf cavities have in the design thin and long stem-like elements. It may be stems for drift tubes support in DTL structure (Fig. 1), post couplers for stabilisation of the accelerating field distribution (Fig. 1), straight (Fig. 2) or circular (Fig. 3) central conductors in double gap bunching cavities. In such thin elements small low-frequency mechanical oscillations may excite. This mechanical oscillations will lead to small changes in the resonant frequency of the cavity and amplitude modulation of accelerating voltage. If the external source of noises exists, it simplifies the excitation of oscillations. One possible source of excitation are the noises due to turbulent flow of the cooling liquid. In this paper the qualitative estimations for own frequencies of mechanical oscillations are presented and parameters of the liquid flow are considered.

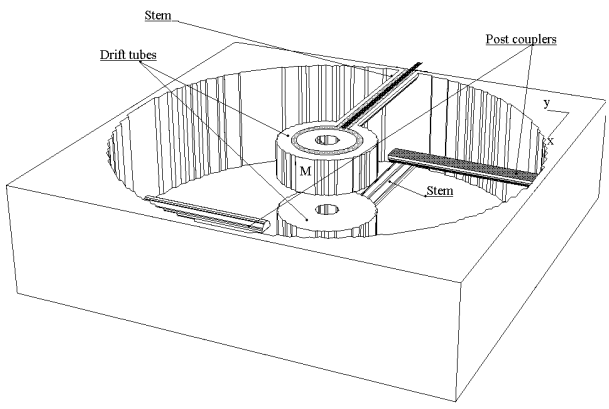

Figure 1: A sketch of DTL structure

2 MECHANICAL OSCILLATIONS

Let consider the stem with the mass m rigidly fixed at one end. At the another end of the stem the drift tube with the mass M are fixed. Two cases should be considered.

2.1 The heavy drift tube

If the mass of the drift tube $M \gg m$, we can neglect the mass of the stem m and consider oscillations of the heavy solid body at the weightless elastic stem. Supposing y is the displacement in the direction perpendicular to the stem axis one get [1] equation for small transverse oscillations:

$$I_c E \frac{d^2y}{d^2x} + M(l-x)(\frac{d^2y}{d^2t})_{x=l} = 0, \qquad (1)$$

where x is the current coordinate along the stem axis. I_c is the moment of inertia of cross section:

$$I_c = \int_S y^2 dS, \qquad (2)$$

E is the Young modulus of the material of the stem, l is the length of the stem. We suppose the mass M is concentrated in a point at the end of the stem. The eigenfrequency of this oscillations f_h:

$$f_h \approx \frac{1}{2\pi}\sqrt{\frac{3I_c E}{Ml^3}}, \qquad (3)$$

It should be pointed out here strong dependence of f_h from the length of the stem.

To simplify manufacturing procedure, DTL cavities are usually at constant radius and the radius of drift tubes is constant also. So, the stems have the same length, but the mass of drift tubes (together with the length of tubes) changes. For typical 200 MHz DTL, for example for $0.04 \leq \beta \leq 0.4$ with copper hollow stems (outer radius of the stem $R_2 = 20$ mm, the inner one $R_1 = 15$ mm, the length $l = 400$ mm, $I_c = \pi/4(R_2^4 - r_1^4)$) and drift with the mass M from 3.5 kg to 30 kg one will get estimation for $f_h \sim (58 \div 18)$ Hz.

2.2 The stem without drift tube

Another case to be considered is the case $M \ll m$ and we can assume $M = 0$. This case describes oscillations of post couplers (Fig. 1) and may be good approximation for oscillations in central conductors of bunching cavities (Fig. 2, Fig. 3). Considering small transverse oscillations [1]:

$$I_c E \frac{d^4y}{d^4x} + S\rho\frac{d^2y}{d^2t} = 0, \qquad (4)$$

and eigenfrequencies f_{ln} are:

$$f_{ln} \approx \frac{a_n^2}{2\pi l^2}\sqrt{\frac{I_c E}{\rho S}}, \qquad (5)$$

where ρ is the density if the stem material, S is the square of the stem cross section, a_n are the roots of the characteristic equation:

$$cos(a_n)ch(a_n) = -1, \qquad a_1 = 1.876, a_2 = 4.675.... \quad (6)$$

For the hollow copper post coupler with outer radius $R_2 = 40$ mm, the inner one $R_1 = 30$ mm, the length $l = 400$ mm one will estimate $f_{l1} \approx 140$Hz.

For circular central conductor of bunching cavity estimation (5) may be applied, if $R \gg R_2$, with transformation $l = \pi R$ (Fig.3).

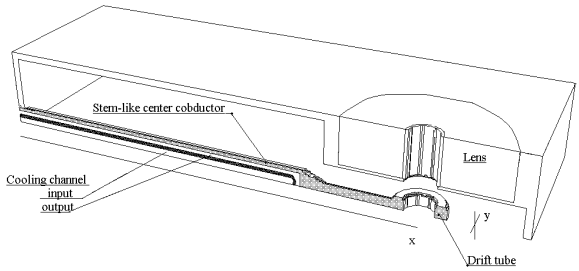

Figure 2: The double-gap bunching cavity with the straight central conductor

2.3 Oscillations of rotation

Let consider oscillations of rotation with respect the axis of the stem. Also two cases should be distinguished in comparison of inertia moments of the drift tube I_t and the stem I_s with respect to the stem axis. If $I_t \gg I_s$, the frequency for oscillations of rotation f_{th} is [1], [2]:

$$f_{th} \approx \frac{1}{2\pi}\sqrt{\frac{C}{lI_t}}, \qquad (7)$$

where C is the rotational rigidity, which strongly depends on the shape of cross section of the stem and for the coaxial tube is [1]:

$$C = \frac{\pi E(R_2^4 - R_1^4)}{4(1+\sigma)}, \qquad (8)$$

where σ is the Poisson coefficient. For cylindrical drift tube with radius R_t and the length l_t the inertia momentum I_t needed is [2]:

$$I_t = \frac{M(3R_t^2 + l_t^2)}{12}, \qquad (9)$$

and for the case considered in (2.1) ($l_t = 46 \div 380$ mm, $R_t = 75$ mm) $f_{th} \sim (300 \div 30)$ Hz.

If $I_t \ll I_s$ we can neglect I_t (the case of the post coupler) and the frequency for oscillations of rotation f_{tl} may be estimated as [1], [2]:

$$f_{tl} \approx \frac{1}{2\pi}\sqrt{\frac{C}{lI_s}} = \frac{1}{2\pi}\sqrt{\frac{\pi E(R_2^2 + R_1^2)}{2Ml(1+\sigma)}}. \qquad (10)$$

For the case considered in (2.2) $f_{tl} \approx 450$Hz.

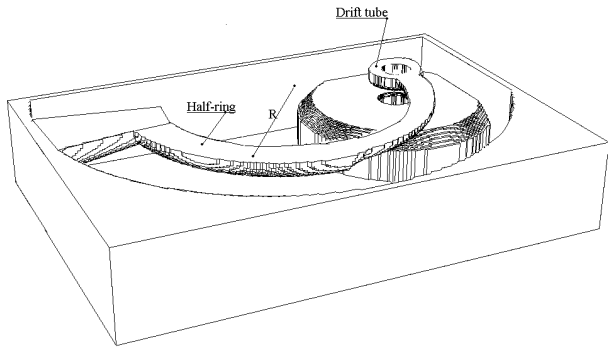

Figure 3: The double-gap bunching cavity with the ring central conductor

3 PARAMETERS OF LIQUID FLOW

It is known well that the character of the liquid flow in the channel is defined by the Reynolds number Re:

$$Re = \frac{Vd}{\eta}, \qquad (11)$$

where V ia the average velocity, d is the characteristic dimension of the channel and η is the kinematic viscosity of the liquid (for water $\eta \approx 10^{-6} m^2/sec$). If $Re \geq Re_{cr}$, the flow in the channel is turbulent. For cylindrical channel $Re_{cr} \approx 1800$, for coaxial one $Re_{cr} \approx 1000$ [3].

The main parameter in the cooling of accelerating cavities is usually the expenditure Q of the cooling liquid, because stabilised temperature of the cavity is needed. So, the average velocity of the flow may be estimated as $V \approx Q/S_c$, where S_c is the square of cross section of the channel. In most practical cases flow is the channel is turbulent , due to limited S and Q given. Another reason is because the heat exchange coefficient for turbulent flow is higher than for laminar one. (It is important to avoid case with $Re \gg Re_{cr}$, because for $Re \geq 6000$ in circular pipe the flow becomes unstable [3]. Due to this reason V is usually not higher than 5m/sec.)

In the turbulent flow the unstability with the frequency $f_{fl} \approx V/d$ can exists in the stream [3]. Estimating f_{fl}:

$$f_{fl} \approx \frac{V}{d} = \frac{\eta Re}{d^2}, \qquad (12)$$

for most practical cases $f_{fl} \geq (100 \div 200)$ Hz.

It means, that for correctly designed cooling channel the possibility of excitation for mechanical oscillation is low enough and this effect is not the main reason.

4 SUMMARY

Analytical estimations for resonant frequencies for different types of oscillations in stem-like elements are presented. It is shown that for typical dimensions of accelerating cavities the frequency range of oscillations may be from several tens Hz to hundreds Hz. This results are useful in the cavity design to take care from possible sources of noises from equipping hardware (cooling, pumping and so on).

5 ACKNOWLEDGMENTS

The authors thank Dr. Yu.V. Bilinsky for the discussions,

6 REFERENCES

[1] L D. Landau, E.M. Lifshiz, Theoretical physics. v. 7, Theory of elasticity, Nauka, Moscow, 1987 (in Russian)

[2] L D. Landau, E.M. Lifshiz, Theoretical physics. v. 1, Mechanics, Nauka, Moscow, 1973 (in Russian)

[3] L D. Landau, E.M. Lifshiz, Theoretical physics. v. 6, Hydrodynamics, Nauka, Moscow, 1988 (in Russian)

FABRICATION OF THE C-BAND (5712 MHz) CHOKE-MODE TYPE DAMPED ACCELERATOR STRUCTURE

H. Matsumoto, T. Shintake and N. Akasaka
KEK High Energy Accelerator Research Organization, 1-1 Oho, Tsukuba, Ibaraki, 305, Japan

Abstract

The first high power model of the C-band (5712 MHz) accelerating structure for the e+e- Linear Collider project is under construction. This is a full spec version: equipped with the Choke-Mode cavity for the higher-order mode damping, the double feed coupler for the symmetric power feed at input/output, and RF-BPM for the beam-based alignment at both ends.

Fabrication of the total 91-cells and their frequency tuning were completed. The cells were assembled in one structure by the electroplating of copper.

The integrated phase shift were measured, it was within ±5 degree at operation condition. It was confirm that a Higher-Order-Mode (HOM, TM_{110}) is successfully damped by a choke-mode cavity with an SiC type rf absorber [1].

1 INTRODUCTION

In the e^+e^- linear collider for 300-500 GeV C.M. energy region, one of the most important R&D issue for the accelerating structure is how to control the beam induced wakefield effects to achieve the nano-meter size beam at collision point.

From the beginning of the linear collider project, many ideas were proposed for damping the wakefield. However, most of those were not realistic; structure was very complicated, thus it was not suitable for mass production at a reasonable cost. In 1992, T. Shintake of KEK proposed a very simple HOM-free structure, so called Shintake-type "Choke-Mode" damped structure. [2] It is a kind of an open cavity. The beam induced power (HOM power) is strongly damped by the electromagnetic radiation through a radial line into open space, while the rf power necessary for the beam acceleration is trapped inside the cavity by a choke filter.

Its concept was confirmed by the experimental test performed at ATF-KEK in 1994, where the bunched electron beam was successfully accelerated in a prototype with S-band microwave power.

Figure 1 and 2 show the C-band model. The accelerating cavity, the annular slot for the choke and a room for the HOM absorber are machined on a copper disk on a turning lathe. The vacuum seal and mechanical structure is maintained by simply stacking them and plating copper layer from outside. The SiC ceramic ring is the HOM absorber, which is mounted in the disk with a metal spring insert (MC Multilum-contact). Since all parts are axial-symmetric, which can be machined on tuning lathe, the choke-mode type cavity has a big advantage on manufacturing than the other ideas proposed before.

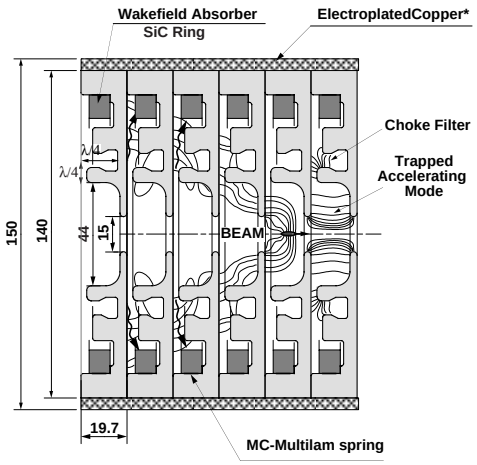

Figure 1: A cut of view of the C-band (5712 MHz) Choke-Mode structure.

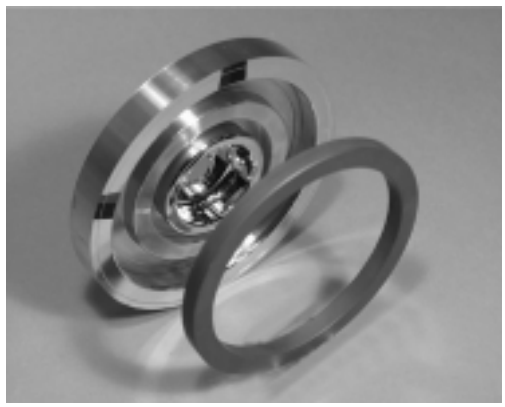

Figure 2: C-band structure with SiC rf absorber.

The Choke-Mode concept has solved the multi-bunch problem. However, there is still another type of wakefield field problem. The short-range transverse wakefield causes the bunch shape deformation, resulting in loosing luminosity. This wakefield is a strong function of the iris aperture, its is proportional to $a^{-3.5}$, thus it becomes very strong at higher frequency bands. Considering the technical difficulties related to the tight tolerance, we did not use higher frequency, but chose the C-band (5712MHz) as the best frequency. The straightness tolerance is ±50 μm (maximum bow) for 1.8 m long structure. At the higher frequency bands, straightness becomes close to ±10 μm or less for 1.8 m-long structure.

In 1996, hardware R&D on the C-band rf system was started at KEK. The first high power 1.8 m-long Choke-

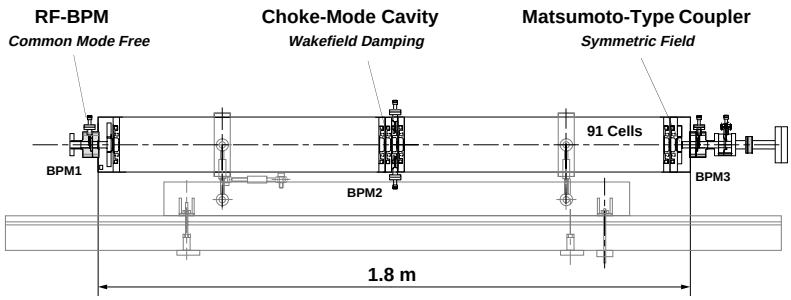

Figure 3: 1.8 m long high power C-band choke-mode structure.

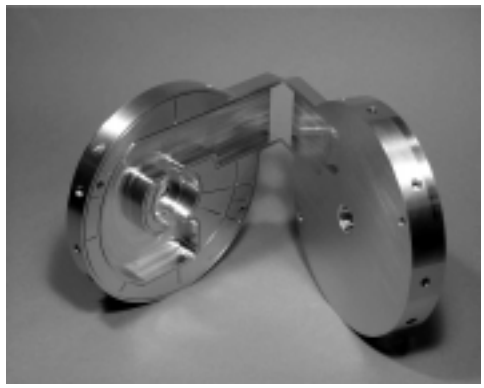

Figure 4: Machined copper parts of field symmetric double feed coupler. They will be brazed together and mounted at both ends of the structure by the electron-beam welding.

mode structure is under fabricating at MITSUBISHI HEAVY INDUSTRIES Ltd. The structure to be tested at ASSET in SLAC in December this year.

This paper describes details on fabrication of the cell and tuning on the acceleration mode. Optimization on the HOM damping performance is described in a separate paper [1].

2 CHOKE-MODE STRUCTURE

The first high-power model of the C-band choke-mode structure is composed of the regular section (89 choke-mode cells), input/output couplers attached at each end, two common-mode-free RF Beam-Position-Monitor (RF-BPM) as shown in Fig.3. A wake-field monitor is prepared in the center cell, by which we can observe the beam induced HOM spectrum, and determine the beam position. To avoid unwanted transverse kick due to asymmetric field, the double-feed coupler using J-shaped waveguide is used in the input/output couplers as shown in figure 4.

2.1 Main Parameters of the structure

The main parameter of the accelerating structure designed for 500 GeV C.M. energy linear collider is listed in Table 1. To increase the shunt impedance, we changed the disk-thickness from 4 mm of initial design to 3 mm. It improved the shunt-impedance by 13%.

3 MANUFACTURING AND ASSEMBLING

3.1 Machining of the cavity

The choke-cell, and the coupler cavity are made of the high purity Oxygen Free High Conductivity (OFHC, >99.99%) copper. The final machining uses a very high-precision tuning lathe with a diamond cutting-tool of rounded shape (R0.5). The dimensional accuracy of the accelerator cavity was kept within 2 μm, except for the rounded part of the beam hole, where it is 5 μm, which provides the frequency valuation of within ±100 kHz.

The surface roughness was kept to 30 nm at cavity inner surfaces and within 500 nm around the beam hole [3]. Since the stored energy in the choke slot is much smaller than that in the acceleration cavity, the dimensional tolerance is much looser than that in the cavity cell, it is around ±30 μm. The electric field gradient is also lower in the choke slot, thus the surface roughness of 3-6 μm is enough. Therefore, machining of choke can be made on ca standard turning lathe, and it does not increase the fabrication cost

Table 1: Main parameters of the accelerating structure

Frequency	5712	MHz
Phase shift per cell	$3\pi/4$	
Field distribution	C. G.	
Number of cells	91	cell
Active length	180	cm
Iris aperture (2a) : up-stream	1.74	cm
: down-stream	1.254	cm
Cavity diameter : up-stream	4.53	cm
: down-stream	4.33	cm
Disk thickness: t	0.3	cm
Quality factor: Q	10.7-10.3	$\times 10^3$
Group velocity : up-stream	0.035	c
: down-stream	0.012	c
Average shunt impedance: rs	53-67.3	MΩ/m
Attenuation parameter	0.53	
Filling time: T_f	286	nsec

3.2 Assembling the SiC RF Load

In order to mount the rf load on the cavity, we decided to uses a thin metal spring, which was inserted between the SiC- ring and the outer-groove as shown in figure 6. The reason why the brazing was not used is to eliminate the high temperature bonding process, which causes dimensional changes in the structure, resulting in a big error on straightness, which can exceeds the 50 μm limit.

The cooling of SiC-ring is not a big issue in this case, since the estimated wakefield power per cavity is as low as 2 W only. The leakage power of the accelerating field is also quite low, because the choke has enough isolation gain as high as -90 dB.

When a HV-discharge is happen in a choke, the acceleration field will flow into the SiC. However, it also causes the detuning of the cell frequency and the traveling

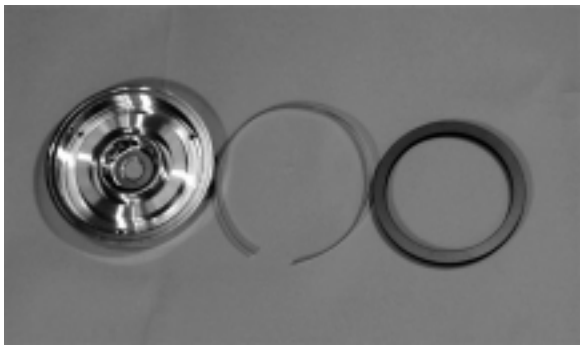

Figure 5: An SiC rf absorber components. Left: choke-mode cavity. Center: metal spring belt. Right: SiC rf absorber ring. An SiC rf-absorber ring is inserted smoothly into the outer groove by using a simple jig with pressure around 30 kgf.

rf power is reflected back to upstream. Only the stored energy in one cell will be dissipated on the SiC, which is only 0.2 J or less.

4 RF MEASUREMENT

After the precision machining, each cavity was stacked, and resonance frequency was measured. Since the relation between $\pi/2$ and $3\pi/4$ modes are known in advance, the $\pi/2$ mode frequency (cell resonance) was used for this check. The deviation from the target frequency of each cell was adjusted by slightly machining the inner dimension (2b) of the disk.

4.1 Choke Slot

The center frequency of the choke filter was measured with a special rf jig. The acceleration cavity part is electrically shorted by a metal disk, then a rf-signal is fed from the center terminal. The transmitted power through the choke is monitored by two pick-up antennas. Figure 6 shows the typical frequency response. The deviation of the center frequency from the target of all the cavities were within the specified values of ±1 MHz.

Figure 6: Frequency response of choke cavity.

4.2 Accelerating cavity

The cell resonance frequency was measured by a special jig, which detunes the neighboring cells and resonates at $\pi/2$ mode. Figure 7 show the frequency deviations from the operating point of 5712 MHz in vacuum. As can be seen in figure, all the data obtained within the specified frequency of ±200 kHz.

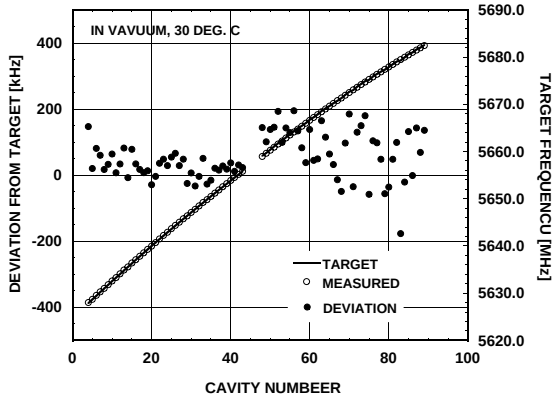

Figure 7: Frequency deviations from the target of each acceleration cavity.

5 ELECTROPLATING

To meet the straightness tolerance, we decided to uses the "Electroplating Method" (not to be confused with the prior electro-forming method), which plates a thick copper layer of 5 mm on the outer surface of stacked cavities. During this process, temperature of the structure raises, but only around 40 °C, which does not cause the dimensional changes in copper material and keeps the structure straightness [4].

6 SUMMARY

The deviation frequency from the target of the choke and accelerating cavity were obtained within each target value of ±1 MHz and ±200 kHz. An integrated phase error is around ±5° for 87 cavities.

It was confirmed that the conventional hardware technique, which has been used in fabrication of S-band accelerating structures, is enough to develop the C-band structure.

The fabrication will be completed in this fall, and its HOM performance will be tested with ASSET beam line at SLAC end of this year.

REFERENCE

[1] N. Akasaka et al., "Optimization on Wakefield Damping in A-band Accelerating Structure", Proceedings of LINAC98, Chicago, USA, August 23-28, 1998

[2] T. Shintake, "The Choke Mode Cavity", Jpn. J. Appl Phys. Vol. 31, pp. L1567-L1570, Part2, No. 11A 199.

[3] H. Matsumoto et al., "An Electroplating Fabrication Method for Electron Accelerator Structure", Proceedings of LINAC98, Chicago, USA, August 23-28, 1998..

[4] K. Kubo et al., "Alignment Issues for C-band Linear Collider", Proceedings of the EPAC96, June 10-14, 1996, Sitges, Barcelona, Spain

AN ELECTROPLATING FABRICATION METHOD FOR ELECTRON ACCELERATOR STRUCTURES

H. Matsumoto and T. Shintake
KEK High Energy Accelerator Research Organization, 1-1 Oho, Tsukuba, Ibaraki, 305, Japan
Y. Iino and Z. Kabeya
Mitsubishi Heavy Industries, Ltd., 10 Oye, Minato-ku, Nagoya, 455, Japan

Abstract

An electroplating fabrication method has been used since 1962 for S-band frequency electron accelerating structures in Japan. The electrical contact between disk and cylinder, and the vacuum integrity are maintained by an electroplated copper layer 5 mm thick, without any metal brazing. The typical integrated phase error after plating was kept below ±2° without any frequency tuning. The mechanical straightness was within ±100 μm over the 2 m length of the S-band accelerating structure.

Since this method does not require any high-temperature processes, such as the metal brazing commonly used for accelerator fabrication, the copper material does not crystallize and maintains a higher tensile strength. That makes this method very attractive for fabrication of the high-performance structures which will be required in various future projects, and especially for e+e- linear colliders.

1 INTRODUCTION

A special requirement for a large scale e^+e^- linear collider for 300-500 GeV C.M. energy reasion is to be able to accelerate a low emittance beam while achieving a nano-meter size beam at the collision point in order to provide the required high luminosity. One R&D issue for the accelerating structure is how to control beam induced wakefield effects. The multi-bunch instability problem has been mostly solved by the Choke-Mode concept and the detuned-structure. However, single bunch instability due to short-range wake-field is still a problem. Trade-offs are involves since lower rf frequencies minimize these instabilities, while higher frequency bands provide higher shunt-impedance which is also preferable. From consideration of the required straightness tolerance, we chose a compromise at the C-band frequency (5712MHz), where the straightness tolerance becomes ±50 μm (maximum bow) for a 1.8 m-long structure. At the higher X-band frequency, straightness becomes on the order of ±10 μm for the 1.8 m-long SLAC Detuned-Damped-Strucure [2,3]. It is clear that no laboratory or industry group currently has any experience with fabricating so many structures at this extraordinary level of accuracy.

Mitsubishi Heavy Industries Ltd. (MHI) and Professor J. Tanaka of KEK developed an electroplating fabrication method (not to be confused with the prior electro-forming method) for electron accelerator structures [4,5]. Their motivation was to improve the accuracy in the phase-shift per cavity, while ensuring mass productability. They introduced a high-precision machining lathe, and succeeded in fabricating accelerating structures, which did not require frequency tuning of any method after the copper plating.

In 1978, 160 accelerating structures were made this method and installed in the 2.5 GeV PF-injector at KEK. Recently, 68 more structures were added for an energy upgrade to 8 GeV for the KEK-B project [6,7].

Figure 1 shows the temperature dependence of the tensile strength, and also the dimensional elongation of high purity Oxygen-Free-High-Conductivity (OFHC, 99.996%) copper.

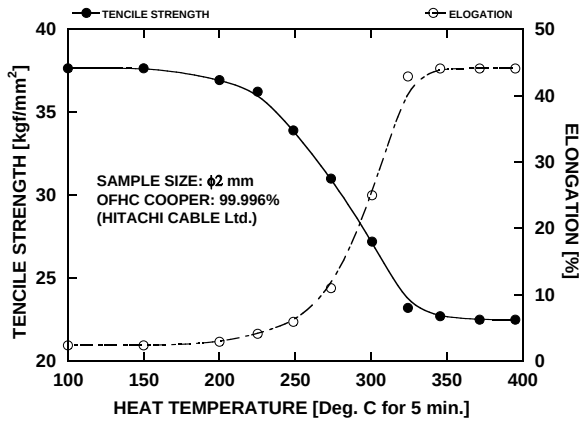

Figure 1: Mechanical properties of OFHC copper as a function of temperature. Each sample was heated up to a target temperature, and held there for 5 minutes.

As can be easily seen in the figure, at temperatures over 200 °C the tensile strength drops sharply and elongation becomes pronounced.

It is very clear that conventional brazing methods, which require temperatures of around 700-900 °C, present difficult problems with respect to mechanical performance. On the other hand, when using electroplating to join the cavities, the maximum temperature raise is only about 40 °C. From this fact, we believe that the electroplating method is a very attractive candidate for the preferred fabrication method for high-performance accelerators requiring tight mechanical tolerance and frequency control.

In this paper, we will describe the elector-plating fabrication method, and its related techniques.

2 MANUFACTURING

The regular section of the accelerating structure is composed of disks and cylinders. They are stacked alternately in series and held in place as a single structure by the electroplated outer copper layer as shown in figure 2. The disks and cylinders are made of high purity OFHC copper, and machined by a high-precision turning lathe. The electroplated copper layer is 5 mm, which provides good enough electrical contact as well as vacuum tightness without further metal bonding, such as the high-temperature brazing process.

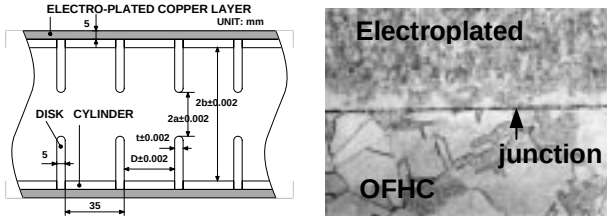

Figure 2: Figure 2: Left: cut away view of the structure. The thickness of the electroplated copper layer is 5 mm. Right: an expanded view of the electroplated layer (top), and OFHC copper (bottom). A horizontal dark black line shows boundary of electroplated copper and OFHC.

2.1 Disk and Cylinder Manufacture

The disk, cylinder, and the coupler cavity are made of the high purity OFHC (>99.99%) copper. Figure 3 shows a photograph of the machining of the disks for KEKB 8 GeV linac. The final machining uses a very high-precision tuning lathe with a diamond cutting tool of round shape (R0.5).

The dimensional accuracy was kept within 2 μm, except for the rounded part of the beam hole, where it is 5 μm. The surface roughness was kept to 30 nm at disk flat surfaces and within 500 nm around the beam hole. The inner surface of the cylinders have 30 nm of roughness. Figure 4 shows the typical surface roughness at the disk surface measured by an optical interferometer using a 600-nm wavelength monochromatic light source.

2.2 Assembly Accuracy Check

The dimensional tolerances for the disk and cylinder are ±2 μm as shown in figure 2, which corresponds 80 kHz in frequency error, and 0.34 degree of the phase error at vg of 0.01c at the S-band frequency. This result made it possible to eliminate the final phase adjustment such as the dimpling procedure which is needed after brazing the structure. The target resonant frequency of each cavity was intentionally lowered by 200 kHz from the operating frequency to allow for the mechanical compression effect associated with the electroplating process. The electroplated copper tends to shrink, and produces a small change in the resulting mechanical dimensions, mainly in that the cylinder diameter becomes smaller.

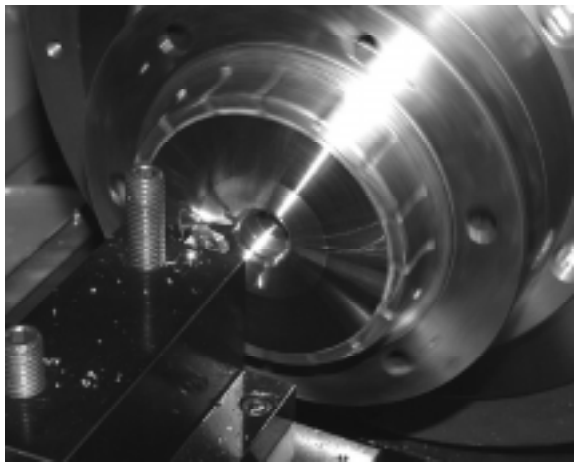

Figure 3: Figure 3: The final machining of a disk with a diamond tool.

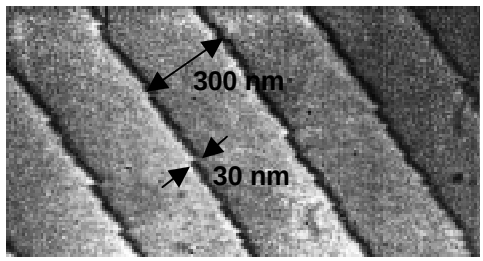

Figure 4: This photograph, taken by an optical interferometric method, shows the typical surface roughness of a copper disk machined on a precision turning lathe. The distance between dark lines is 300 nm (half-wavelength). Any deviation of the dark line from straightness shows the surface roughness. The peak to peak surface roughness is about 30 nm in this case.

2.3 High Speed Electroplating

After frequency checks of all the cavities for an acceleration structure, they are stacked together horizontally (56 cavities for 2 m length) on a precision support-bed. A steel mandrel is inserted through the staked cavities and tightened to a tension of 2500 kgf to which will be held during the electroplating. The mandrel has a bar-shape and is made of high-tensile-strength steel to maintain the tension throughout the electroplating procedure.

The oxide layer on the outside of the structure is removed by mechanical brushing, and then it is rinsed in pure water to remove any foreign matter such as dust which may be stuck on the surface. The structure is then immersed in the electroplating process fluid in a vertical bath.

A high-speed electroplating method is chosen [8,9]. In order to plate the copper at high current densities of 10 A/dm^2 or more, additives are included to the copper-sulfate. It takes 70 hours to deposit a layer 5 mm in thickness. The processing fluid mainly consists of copper-sulfite, sulfuric-acid (H_2SO_4, >95%), hydrochloric-acid (HCl, >35%) and ion-exchanged-water. During the plating the plating fluid temperature was controlled at 30 °C ± 1 °C. Also, close purity control of the plating fluid

is very important to prevent defects in the copper crystal structure such as the so called star and wrinkle defects.

The possibility of fluid leakage through a gap between disk and cylinder is very low. A key point in this is the surface smoothness. It is around 30 nm after the precision machining and the dimensional accuracy is also 2 μm. When the disk and cylinders are compressed with an appropriate contact pressure, the resulting vacuum tightness reaches the order of 10^{-4} Torr.

After the electroplating, the surface of the plated copper is machined to back to a 5 mm thickness. The hardness of the plated copper layer is really high, and is comparable to iron. This is due to the compaction force of ionized copper. During the plating the temperature rises, but only to 40 °C.

2.4 Assembling the Completed Accelerating Structure

After assembling, an accelerating section has a coupler attached at each end by electron beam welding (EBW) while pressure is applied by the mandrel. The position for the weld is designed to avoid excessive stress concentration and to obtain a good electrical contact. The structure is cooled with a water-jacket type pipe, which has both ends TIG welded to the couplers.

3 RF MEASUREMENT RESULTS

The structure is assembled from highly accurate disks and cylinders; it is easily checked for the specified resonance frequencies, thus in principle we see that it is possible to mass produce a high precision accelerating structure. However, the proof is in the final check to measure the phase shift of the all the cavities by Nodal-Shift method. Figure 5 shows the typical measured Nodal-Shift data before and after the electroplating process. The three solid lines in figure 5 are the specified phase-shifts (0°, 120° and 240°), the measured phase shifts of the cavities for $2\pi/3$ mode at the operating frequency are marked with open circles. As can be seen from figure 5, the integrated phase errors are within ±2° for the 2 m-long structure (two couplers and 54 regular cavities). After the electroplating process, the integrated phase errors slightly increase, but still only to 0.86 degree in rms. From this we conclude that the electroplating effects can be controlled quite precisely.

4 CONCLUSIONS

We conclude that the electroplating method is a attractive candidate for fabrication of the next generation advanced accelerators. As for the related technology, we have also shown that the simple frequency measuring of the assembly check can be use to obtain the same accuracy of the Nodal-Shift method. Finally, the straightness of the structure can be improved to within less than 30 μm of the target value.

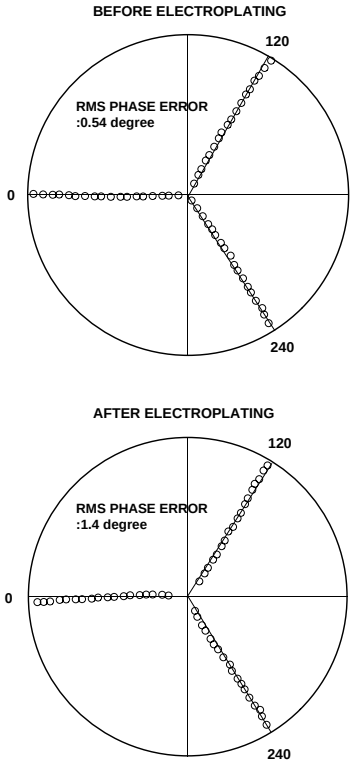

Figure 5: Typical phase characteristics of an electroplated S-band 2 m-long structure as measured by the Nodal-Shift method.

REFERENCE

[1] T. Shintake et al., “Result from Hardware R&D on C-band RF-System for e^+e^- Linear Collider”, Proceedings of LINAC98, Chicago, USA, August 23-28, 1998.

[2] T. Shintake, "The Choke Mode Cavity", Jpn. J. Appl Phys. Vol. 31, pp. L1567-L1570, Part2, No. 11A 199.

[3] K. Kubo et al., "Alignment Issues for C-band Linear Collider", Proceedings of the EPAC96, June 10-14, 1996, Sitges, Barcelona, Spain.

[4] J. Tanaka et al., "On Electroforming of Disk-Loaded of Linear Accelerator", Applied Physics in Japan 31, 1962, 146.

[5] N. Yamaguchi, "Mitsubishi Linear Accelerator tube Manufactured by Electro-forming method with copper spacer", Internal report of Mitsubishi Heavy Industries Ltd.

[6] A. Entomb, "Upgrade to the 8-GeV Electron Linac for KEKB", Proceedings of LINAC96, August 26-39, 1996, Geneva, Switzerland.

[7] S. Yamaguchi et al., "Design if Input and Output Coupler for Linear Accelerator Structures", Proceedings of LINAC96, August 26-39, 1996, Geneva, Switzerland.

[8] K. Takahashi, Internal report (in Japanese) of Mitsubishi Heavy Industries Ltd.

[9] S. Yoshida, Internal report (in Japanese) of Mitsubishi Heavy Industries Ltd.

STATUS OF ENGINEERING DEVELOPMENT OF CCDTL FOR ACCELERATOR PRODUCTION OF TRITIUM*

R. L. Wood, J. H. Billen, W. T. Hunter, P. O. Leslie, R. J. Roybal, F. E. Sigler
Los Alamos National Laboratory, Los Alamos, New Mexico 87545 USA

Abstract

The Coupled-Cavity Drift Tube Linac (CCDTL) is a relatively new RF accelerator structure which plays a major role in the APT Low-Energy Linac (LEL) design. Engineering development is pushing ahead on several fronts, including thermal management, fabrication procedures, cavity and coupling slot tuning, high-power prototype fabrication and testing, supports and alignment, vacuum, and provisions for beam diagnostics. Fabrication of the CCDTL Low-Beta Hot Model is nearly complete, and high-power RF tests will commence soon. In 1999, we will begin the fabrication of 11 meters of CCDTL to be added to the Low-Energy Demonstration Accelerator. In 2001, it will take the 100 mA beam from 6.7 MeV to 10.05 MeV, producing the world's most powerful proton beam. We are also starting the design of a CCDTL 96 MeV Hot Model to demonstrate cooling of an intermediate-beta version of the structure. The 14 cm-long, 9 cm diameter 96 MeV drift tube dissipates roughly 5 kW. This all leads to the final mechanical design of the 113 m long CCDTL for the APT plant linac.

1 INTRODUCTION

The CCDTL concept was invented in 1994 [1] to answer the stringent demands of the waste-transmutation and tritium production accelerator applications. Although several low-power aluminum "Cold Models" have been built and tested, no CCDTL has yet been operated at high power or with particle beam. Before taking that step, there are many "trivial" engineering details which must be worked out. This would be a significant effort, even if the first application were low power. Some unique fabrication and tuning methods must be developed, while vacuum pumping, cooling, resonance frequency control, and RF interfacing must be adapted from similar systems used on common Coupled Cavity Linacs (CCLs).

This paper presents the status of this engineering effort, without giving much background about how we got here, or why. The following discussion covers topics, results, and plans in four areas: mechanical prototype tests, RF cold models, the CCDTL Low-Beta Hot Model (LBHM), and the APT Low-Energy Demonstration Accelerator (LEDA), phase 3A (6.7-8 MeV) and 3B (8-10 MeV)[2].

* Work supported by the US Dept. of Energy, Defense Programs.

2 ARCHITECTURE

The APT LEL has evolved significantly since the presentation of the Conceptual Design, mostly in response to practical engineering considerations.[3][4] There are still three distinct types of CCDTL (single 2-gap, single 3-gap, and double 2-gap segments) to carry the 100 mA proton beam from 6.7 to ~100 MeV, but the transition points have been moved to eliminate mixing of types within a RF module. This mixing caused a variety of mechanical issues in earlier versions of the design, but there is not enough space to discuss them here.

Marked changes in the focusing period were made to provide needed empty space for magnets and beam diagnostics in the 10-to-50 MeV range. This in turn prompted a change from 6-cell to 7-cell CCL segments in the >100 MeV portion of the LEL [4].

This lattice change indirectly causes a "tolerance stack-up" problem in the CCDTL which is remedied by changing to 3-cell bridge couplers to join the brazed sections (see below). This solution does not work in the 10-to-21 MeV portion, where the 3-gap CCDTL type is used.

3 RF STRUCTURE MATERIALS AND FABRICATION METHODS

Several of the CCDTL's new mechanical features have been under development for the last three years. Most have to do with either fabricating or cooling drift tubes. We have previously reported on the design and predicted performance of coolant passages within the drift tubes[5]. Recently, we have performed experimental measurements which suggest that these passages are actually much more effective than originally thought[6]. We will be repeating these measurements on drift-tube prototypes from a different part of the LEL to further prove the cooling scheme before actual RF structures are built.

Material properties and brazing continue to be areas of concern, primarily with vacuum and RF attachments to OFE copper structures. Originally, we had chosen to use alumina-dispersion strengthened (Glidcop™) copper for all components which are exposed to RF and require strength, such as drift-tube stems and accelerating cavity flanges. Until recently, large equatorial flanges were planned to join the 1-to-1.6-m-long brazed sections into long RF modules. The aforementioned tolerance stack-up problem made it easy to choose to eliminate the flanges

from the design, but, as previously mentioned, we have not found a practical alternative for the 10-to-21 MeV portion of the LEL. For now, at least, there are about 15 of these flanged joints still in the plan.

Our first attempts at brazing OFE drift tubes and Glidcop™ stems into OFE cavities were very good, but recent attempts have had some problems. The 50-50 Au-Cu braze alloy has produced all leak-tight joints, but they do not look like the kind of clean cosmetic joints we want inside a high-power RF cavity. Although copper plating is expected to help, this added step may tip the scales back toward plated stainless steel.

There have also been several improvements made in our machining and braze fixturing which should insure good parts in our future fabrications.

The vehicle for much of this development is the LBHM, a 1-m-long piece of CCDTL corresponding to 7.6-8.8 MeV in the original LEDA design. At the time of this conference, all of the pre-tuning fabrication and brazing are complete, and cavity and slot tuning activity is about half complete. Following tuning, the assembly will go through its final assembly braze, be installed on its test stand, and tested at up to 135% of its intended RF fields.

4 RF STRUCTURE TUNING

Although 2-D and 3-D modeling can give us a very good understanding of the CCDTL cavities, we find that simple, relatively inexpensive aluminum "cold models" are the only sure way to determine complex 3-D properties like coupling coefficients and frequency dependency on coupling. Several cold models have been built to simulate various cavities in the 6.7-10 MeV range and we have developed many refinements in our testing and tuning methods[7].

These methods are being put to the test in the tuning of the LBHM, now underway. Despite our earlier cold modeling, we have encountered several new problems. Specifically, although the coupling slot predictions are very close, the accelerating cavity frequency predictions are off by more than 5MHz in some cases (<1%). Since the LBHM will not be used with beam, we have aggressive ways to deal with this, but this will not be acceptable on LEDA. Apparently, extrapolations from too few cold models is not a good idea, and 2MHz tuning range might not be enough, even with better data.

Our approach for LEDA phase 3A is to build more cold models, matching the 6.7 and 8 MeV endpoints, in hopes that interpolation over a short range of β will yield cavities which are closer to the target frequency. The 6.7 MeV Cold Model has already been built and is being very thoroughly tested. An extensive 8 MeV Cold Model has been designed, but we are waiting to see what new data will come from the 8 MeV LBHM and the 6.7 MeV cold model before starting fabrication. We hope to complete all work on these new cold models by December 1998.

5 ELECTROMAGNETIC QUADRUPOLES (EMQ)

The spatial constraints placed on the LEL EMQs are very stringent, requiring an innovative approach to their design. A 2-fold symmetric geometry has been developed, several prototype versions have been built and tested, and a "final" LEDA version is in the final design stage.

Because of the large number of magnets, and the overall congestion of all areas around the beam line, alignment of the magnets after installation could be a problem. For this, and to minimize personnel radiation exposure, we will be pre-aligning all of the magnets off-line, to a common standard, on semi-kinematic mounts. The calibration and pre-alignment standard has been designed, and is being assembled by General Atomics.

6 SUPPORTS AND ALIGNMENT

All alignment-critical components are mounted on hardened rails within the linac tunnel. The ultimate alignment of these components depends on the stable "straightness" of these rails. The rails are mounted atop rigid steel chassis, ranging from 2 to 4 meters in length, which are placed end-to-end for the entire length of the LEL. An afocal optical system is used to straighten the rails to within 25 μm. Internal optics and loading hardware provide means to sense and correct the mid-point deflection of each chassis, which will return the rails to within 10 μm of its original shape for almost any conceivable loading condition[8].

A detailed design and prototype are the next step. LEDA hardware is due by December 1999.

7 RESONANT FREQUENCY CONTROL/ COOLING AND VACUUM SYSTEMS

Again, the LBHM has been the vehicle for development. A cooling and resonant frequency control system has been fully implemented in miniature, by Allied Signal, for use on the 30-40 kW LBHM. The test of this system is one of the key objectives of the LBHM.

A brute-force approach has been taken for the vacuum system for the LBHM, but a conceptual design for the LEDA CCDTL vacuum system is under development at

LLNL. For maximum cost/performance and reliability, each 2 to 4 m chassis will have a dedicated large diameter manifold with 2 to 4 large ion pumps and one turbo pump attached. Detailed design of the LEDA Phase 3a hardware will commence soon, followed by fabrication, ready for installation in January 2000.

8 CCDTL LOW-BETA HOT MODEL EXPERIMENT

The LBHM will be the first high-power test of the CCDTL concept, and the driving force for fabrication and tuning method development. Various aspects of this effort are covered in the previous sections. The main objectives include the refinement of cooling and resonance control system designs, and to measure the system's ability to cope with errors in local coolant flow rates. We expect to install the completed LBHM in Oct 98, and to complete high power experiments by January 99. This data will be immediately applied to the design of the LEDA and plant accelerators.

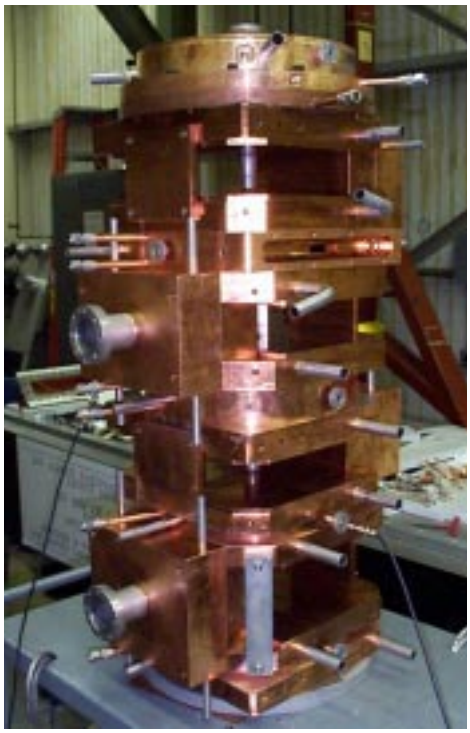

9 LEDA PHASE 3A CCDTL DESIGN

While we await the completion of the cold modeling effort, we have proceeded with the mechanical design of the 5 meters (24 accelerating segments with 20 "sideways" coupling cavities in four brazed sections, plus the three 3-cell bridge couplers) of LEDA Phase 3a CCDTL. Unigraphics™ Parametric Solid Modeling™ is used heavily, allowing us to "complete" most of the drawings without the final dimensions. Once the missing values are finalized, software will read the physics dimensions from spreadsheets, and the models and drawings will be automatically updated. Again, we are hoping for completion of the cold models by Dec. 98, the cavity tables by Jan. 99, and completion of the LEDA Phase 3A drawing package by Feb. 99, fabrication to commence immediately afterward.

10 96 MEV HOT MODEL

Most of the work described above is aimed at the low-energy end of the CCDTL, since that will be built and operated first. But the worst case thermal problems are at the other end of the CCDTL. We are planning to build and test a 1.4m-long high-power prototype of the final two CCDTL segments (@ 96 MeV) to address this part of the parameter space. Fabrication is expected to begin by mid-1999, with tests to begin by early-2000.

The drift tubes in the 96 MeV cavity are roughly the size of a beverage can and dissipate ~5 kW of RF power. This drift-tube will require a very dense coolant passage network. Prototypes are being fabricated now, and cooling experiments conducted as before.

11 CONCLUSION

Despite less than overwhelming funding to date, significant progress has been made toward the systematic completion of the APT LEL design. Key design topics have been, or soon will be, explored, leading to the completion of the LEDA Phase 3a CCDTL over the next two years. Subsequent steps are planned to cover any and all remaining topics.

12 REFERENCES

[1] J. H. Billen et al., "A New RF Structure for Intermediate-Velocity Particles," Proc. 1994 Int. Linac Conf., Tsukuba, p341 (1994).

[2] H. V. Smith Jr. et al., "Status Update on the Low-Energy Demonstration Accelerator", this conf.

[3] J. H. Billen et al., " A Versatile, High-power Proton Linac for Accelerator-Driven Transmutation Technologies". Proc. 1995 Particle Accelerator Conf., Dallas, p1137.

[4] L. M. Young et al., "Beam Dynamics Design of the 211 MeV APT Normal Conducting LINAC", this conf.

[5] R. L. Wood et al., "Thermal/Structural Design and Fabrication Development Of High Power CCDTL And CCL Structures", Proc. LINAC96, Geneva.

[6] P. O. Leslie et al., "Heat Transfer Coefficient in Serpentine Coolant Passage for CCDTL", this conf.

[7] M. Cole et al., "Test Results for a Cold Model of a 2-gap to 3-gap Transition Section for LEDA," this conf.

[8] R. L. Wood, "Conceptual Design for Support Chassis for LEDA CCDTL", Los Alamos National Laboratory internal memorandum LANSCE-1:TNM-98-040 (Feb.5, 1998).

TUNING THE LEDA RFQ 6.7 MEV ACCELERATOR*

Lloyd M. Young and L. Rybarcyk
Los Alamos National Laboratory, MS H817, Los Alamos, NM 87545, USA

Abstract

This paper presents the results of tuning the 8 meter long Radio Frequency Quadrupole (RFQ) [1] built for the Low Energy Demonstration Accelerator (LEDA)[2]. This 350-MHz RFQ is split into four 2-meter-long-RFQ's. Then they are joined with resonant coupling to form an 8-meter-long RFQ[3]. This improves both the longitudinal stability and the transverse stability of this long RFQ. The frequencies of the modes near the RFQ mode are measured. We show the effect on the RF fields of an error in the temperature of each one of the 2-meter-long RFQ's. Water-cooled copper slugs distributed along the outer walls tune the RFQ. The program RFQTUNE [4] is used to determine the length of the slug tuners. The tuners are machined to length when the final tuning is complete.

1 INTRODUCTION

The final tuning of the LEDA RFQ has been completed. All the tuners have been machined to length and installed. The RF drive ports are plugged with temporary inserts that are flush with the interior wall of the RFQ. Figure 1 shows the measured fields versus position along the RFQ. The RF magnetic fields near the outer wall are measured using the bead-perturbation technique. The vane gap voltage is inferred from the measured magnetic fields by comparison to SUPERFISH calculations of the RFQ cross section every 10 cm along the RFQ. In Figure 1 the measured fields are the lines with bumps. The smooth line through the measured quadrupole fields is the design field. The measured quadrupole field agrees so well with the design field that in this figure it is difficult to distinguish between the two lines except for the fact the design field has no bumps. These bumps in the fields are caused by the tuners. In Figure 1, the crosses (+) indicate locations between tuners where the measured field is valid. These bumps in the measured magnetic fields do not appear in the electric fields on axis. The large dips in the measured quadrupole fields are caused by the bead passing through holes in the coupling plates. The coupling plates join the four 2-meter-long RFQ's.

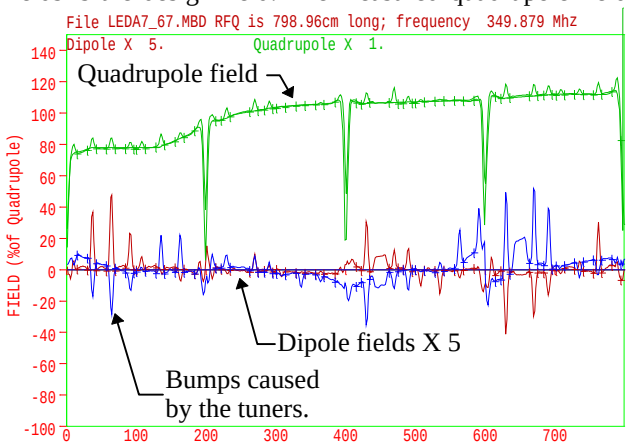

Figure 1. RFQ fields measured with the bead perturbation technique. The measured fields are within 1% of the design values. The dipole fields are multiplied by a factor of 5.

2 TUNING STEPS

The first step in the tuning of the LEDA RFQ occurred before the final brazing. Each 1-meter-long segment was checked for correct frequency and fields. The undercuts on one end of each segment have a large effect on the field tilt. Figure 2 shows the fields in section A1. The quadrupole fields are very nearly equal to the design fields, which means that the vane undercuts on the low-energy end are correct. The dipole fields of about 20% are correctable with the tuners. This measurement was performed with the tuners flush. The frequency is adjusted by machining the braze surfaces on the major vanes and moving the minor vanes in or out. Typically, the frequency of each 1-m segment was correct when the vane gaps were adjusted to the design dimensions.

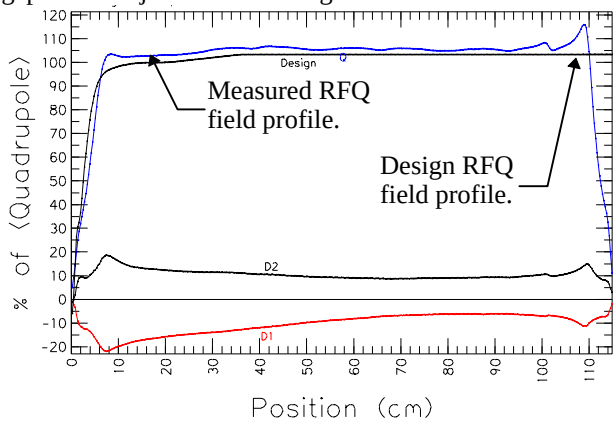

Figure 2. Perturbation measurement of the fields in section A1 before brazing. The measurement was performed with a short RFQ piece attached on the high energy end. This short piece has a vane undercut designed to properly terminate the RFQ with flat fields.

The next step in tuning occurred after the final section brazes. This step established the length of the dipole stabilizer rods. These rods, four of which are mounted on each of the end walls and on both sides of each coupling plate, adjust the frequency of the dipole modes. The

*Work supported by the US Department of Energy.

length of the rods are adjusted to approximately equalize the frequency difference between the quadrupole mode frequency and the nearest dipole mode above and below the quadrupole mode. Figure 3 shows the quadrupole modes in the frequency region near the operating mode that is free of dipole modes. This tuning scheme minimizes the dipole component in the quadrupole mode caused by asymmetric perturbations. The water cooled stabilizer rods are 1.27 cm in diameter and 15 cm long.

Step three in tuning adjusted the gap between the vane-tip ends at the segment joints. These gaps provide capacitive coupling between adjacent pairs of the four 2-meter-long RFQ's. The size of these gaps determines the capacitance between the vane-tip ends and thus the frequency of the coupling mode. The goal is to have the coupling mode frequency equal to the operating mode, which closes the stop band at the zero-phase-shift point in the dispersion curve shown in Figure 3. The fact that the dispersion curve is smooth through the operating mode shows that the frequency of the coupling mode is nearly equal to the RFQ operating mode. The operating mode has zero phase shift between the segments so the structure acts like one long RFQ. The resonant coupling provides longitudinal stability that is nearly as good as in a 2-meter-long RFQ.[5]

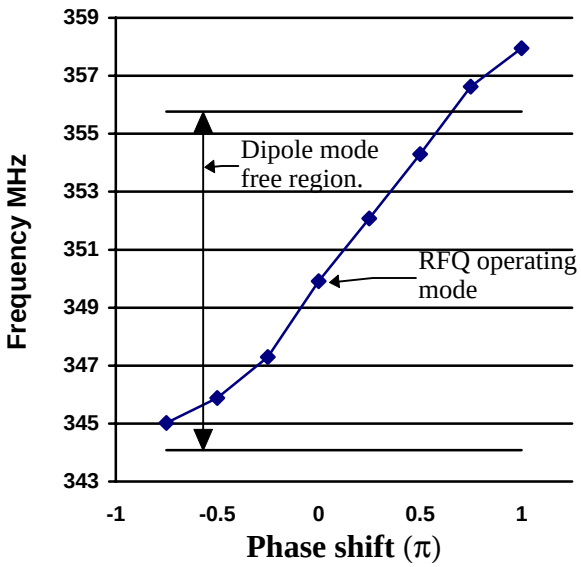

Figure 3. Quadrupole dispersion curve showing the RFQ operating mode and the frequency gap between the nearest dipole modes and the operating mode.

Step four in the tuning adjusted the RF field to the design values. This was done by moving the 128 movable tuners in accordance to the code RFQTUNE. A number of iterations were performed to adjust the field to within 1% of the design value. Figure 1 shows that the dipole component is less than 1% in over 90% of the RFQ. The D(2-4) dipole component is about 2% from 400 cm to 450 cm. When this tuning was completed the movable tuners were replace with water-cooled tuners machined to the final penetration of the movable tuners. Because the machined tuners raised the frequency slightly with respect to the movable tuners, this step was done in three stages. First 50% were replaced, then 25%, and finally the last 25%. After each stage the RFQ tuning was checked and the remaining tuners adjusted as necessary.

Step five in the tuning was to adjust the waveguide coupling irises. This RFQ is driven with three 1.2-MW klystrons. The RF power from each klystron is split 4 ways to reduce the power on the waveguide vacuum windows. The total coupling beta without beam with all three klystrons operating was chosen to be 2. The RFQ will be over coupled when all three klystrons are operating, but this RFQ is also expected to operate with only 2 of the 3 klystrons. With 2 klystrons operating, the total coupling beta without beam will be 1.33 and the RFQ will be under coupled with full beam current. A coupling beta of 1.58 would give the best match at full beam current.

A coupling beta of 2 with all twelve waveguides coupled to the RFQ requires each waveguide to be coupled with a beta of 0.167. To achieve this coupling a tapered ridge-loaded waveguide section reduces the size of the half-height WR2300 waveguide to 17.78 X 2.54 cm at the RFQ. The RF fields in this tapered section increase to the point where an iris only 9.144 cm long and 0.1575 cm wide is sufficient to achieve this coupling. The 12 RF waveguide ports were plugged with a copper piece flush with the interior walls during tuning. After the iris size was determined, the penetration of the tapered-waveguide test section was adjusted for minimum effect on the RF fields and frequency. This adjustment allows the final tuning to be completed with all the water-cooled tuners machined to length and installed before the waveguides are installed. Because the manufacturing of the tapered waveguides is taking longer than originally expected, we have completed the final tuning even though the fields may change a small amount after the waveguides are installed.

3 TUNING ERRORS

The RFQ cooling system controls the resonate frequency of the RFQ. The frequency is controlled by adjusting the temperature of the cooling water in the outer walls of the RFQ and maintaining 50° F water in the cooling passages near the vane tips. A +1° F change in temperature of the outer wall cooling water raises the resonant frequency of the RFQ by 17 kHz for constant temperature of the tip cooling water. Whereas if both the tip cooling and the wall cooling water raises by 1° F, the frequency of the RFQ will drop by 3.27 kHz. This dual temperature cooling system is required to keep the RFQ tuned to 350 MHz when dissipating 1.2 MW of RF power. The RFQ is tuned to 350 MHz at 70° F with low RF power. When it is operating, the average temperature will be ~84° F.

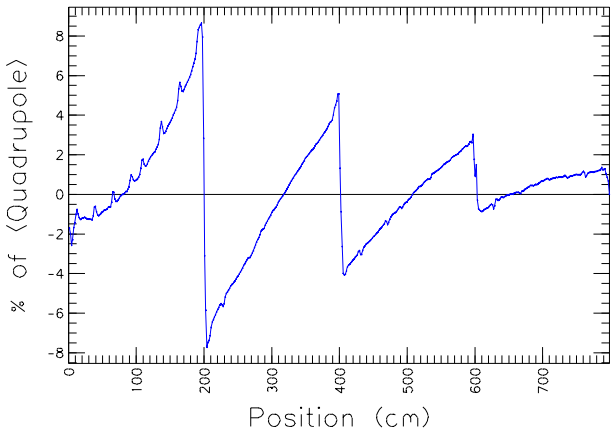

Figure 4. Change in quadrupole fields when segment "A" (0-200 cm) is tuned high in frequency by ~400 kHz. This corresponds to a cooling water temperature error of +23° F.

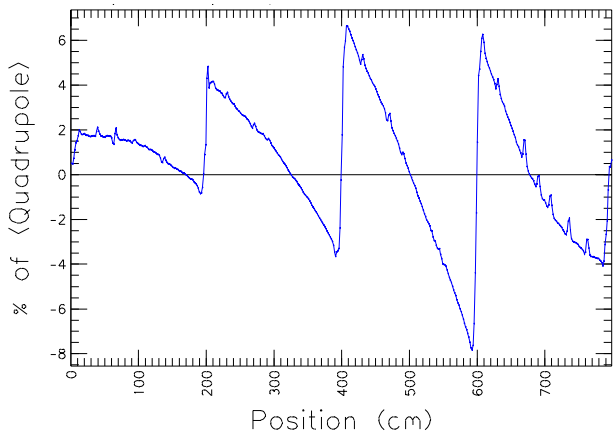

Figure 5. Change in quadrupole fields when segment "D" (600-800 cm) is tuned high in frequency by ~400 kHz. This corresponds to a cooling water temperature error of +23° F.

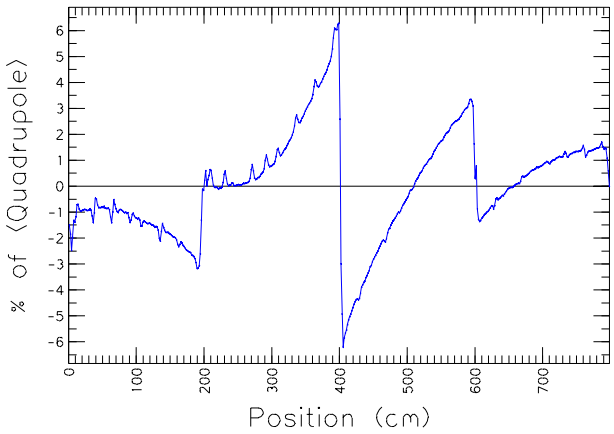

Figure 6. Change in quadrupole fields when segment "B" (200-400 cm) is tuned high in frequency by ~400 kHz. This corresponds to a cooling water temperature error of +23° F.

The cooling system has a separate cooling loop for each 2-meter section of the RFQ because each section dissipates a different amount of RF power. The cooling to the outer walls in each section have a cooling loop which mixes some of the cooling water heated by that section with the water from the outer cooling loop. This mixing ratio is adjusted manually with a remote control valve. An outer cooling loop mixes the water returning from all 4 inner loops with the 50° F supply water to control the resonate frequency of the RFQ. This outer loop is controlled by a PID feedback circuit.

The adjustment of the 4 manually controlled mixing valves will be performed by inspection of the field errors in the RFQ. RF pickup loops placed in 64 of the 128 tuners will measure the RF field distribution. Inspection of the errors in the field distribution will allow adjustment of the mixing valves. Figures 4, 5, and 6 show the changes in the quadrupole field for a temperature error in the outer wall cooling water in sections A, D, and B. The changes in the quadrupole field for section C looks like the mirror image of B. This type of perturbation does not effect the dipole component in the operating quadrupole mode.

Thus a cooling water temperature error of +23° F results in a maximum field error of only 8%. Therefore, it should be easy to set the manually controlled mixing valves to minimize the field errors by setting the mixing valves to obtain the predicted temperatures. The predicted temperatures of the 4 loops are 71, 65, 63, and 61° F respectively.

ACKNOWLEDGMENTS

Many people have been involved in the design and manufacturing of this RFQ. They include: D. Schrage, P. Roybal, A. Naranjo, D. Baca, W. Clark, F. Martinez, H. Haagenstad, J. Mitchell, D. Montoya, A. Rendon, F. Krawczyk, T. Davis, D. Casillas,A. Gonzales, G. Gonzales, S. Hidalgo, E. Kettering, G. Leeches, B. Ormond, R. Reinert, O. Smith, and J. Tafoya.

REFERENCES

[1] D. Schrage et al., "CW RFQ Fabrication And Engineering," these proceedings.

[2] H. V. Smith, "Status Update for the Low-Energy Demonstration Accelerator (LEDA)," these proceedings.

[3] L. Young, "Simulations of the LEDA RFQ 6.7 MeV Accelerator," *Proceedings of the 1997 Particle Accelerator Conference.*

[4] L. Young, "Tuning and Stabilization of RFQ's" *Proceedings of the 1990 Linear Accelerator Conference,* September 10-14,1990 Albuquerque, NM.

[5] L. M. Young, "An 8-meter-long Coupled Cavity RFQ Linac" *Proceedings of LINAC94,* Tsukuba, 1994

TEMPERATURE DISTRIBUTION CALCULATIONS ON BERYLLIUM WINDOWS IN RF CAVITIES FOR A MUON COLLIDER*

Derun Li, J. Corlett, W. Turner, LBNL, One Cyclotron Road, Berkeley, CA 94720, USA

Abstract

We report the temperature distribution calculations on beryllium windows in RF cavities for a muon collider. The cavity resembles a closed pill-box cavity with the conventional beam iris aperture covered by thin beryllium (Be) foils to enhance the electric fields on the beam axis. The design resonant frequency for the cavity is 805 MHz. To reduce the RF power losses, the cavity may be operated at liquid nitrogen (LN) temperature. The heating caused by RF power dissipations on the Be windows is a concern for either at the room or at the LN temperature operations. Based on the MAFIA simulations, considering the heat conduction inside the Be windows only, a pill-box and an approximated *linear* model are used to calculate the temperature distributions analytically on a flat and a tapered window, respectively. Preliminary calculations suggest that no special cooling designs be needed for 0.127 mm thickness of Be windows while the cavities operate at 30 MV/m of electric fields on beam axis with 30 μs pulse length and 10 Hz repetition rate.

1 INTRODUCTION

Significant efforts have been devoted to exploring the feasibility of designing and constructing a high luminosity muon collider. Among many technical challenges, experimental demonstration of ionization cooling for high intensity μ^+ and μ^- beams is one of the most critical paths towards the building of a muon collider. Initial simulation studies have indicated that the six-dimension phase space volume of muon beams can be cooled by as much as a factor of 10^5 or 10^6 through an ionization cooling channel [1]. The cooling channel under study is composed of 20 to 30 sections, while each section consists of liquid hydrogen absorber and RF acceleration cavities surrounded by alternating super-conducting solenoids. The muon beam loses its momentum (energy) both transversely and longitudinally while passing the absorber. Nevertheless the longitudinal momentum loss is compensated by coherent acceleration fields in the RF cavities and therefore a net transverse momentum loss is left $\Rightarrow$ **transverse cooling**! A highest possible acceleration gradient RF structure is a must for restoring the longitudinal momentum loss in the limited lifetime of the muon beam. Among few proposed RF structures [2], an interleaved $\pi/2$ standing wave (SW) structure, shown in Figure 1, is favored. The accelerating cavity cell resembles a regular closed cylindrical pill-box cavity, but with the beam iris aperture covered by thin Be foils. The structure produces an on-beam-axis field equal to the maximum surface field (e.g. $E_{\rm acc}/E_{\rm surface} = 1$) while for conventional RF structures with beam iris $E_{\rm acc}/E_{\rm surface} \approx 0.5$. Moreover the muon beams traverse these foils with negligible energy losses. MAFIA simulations indicate the cavity has an effective shunt impedance of 37 MΩ/m at $\beta = 0.87$ [2]. To further reduce RF power loss (or the costs for RF sources) the cavity may be operated at LN temperature. Potential benefits operating at LN temperature will depend on both the electrical and thermal properties of the Be windows. However, these properties at low temperature are not very well known. The thermal property in particular has strong influence on the mechanical and engineering designs for the windows and cavities. Experimental exploration on these issues is currently in progress at BNL. Nevertheless based on the limited data [4], we have estimated the temperature raise the Be windows so that proper temperature control or special cooling designs are employed if necessary. Two models, a pill-box and an approximated *linear* have been used to calculate the temperature distributions. Analytical formulae and numerical results are presented and compared. The linear model is also used for the calculation of tapered windows.

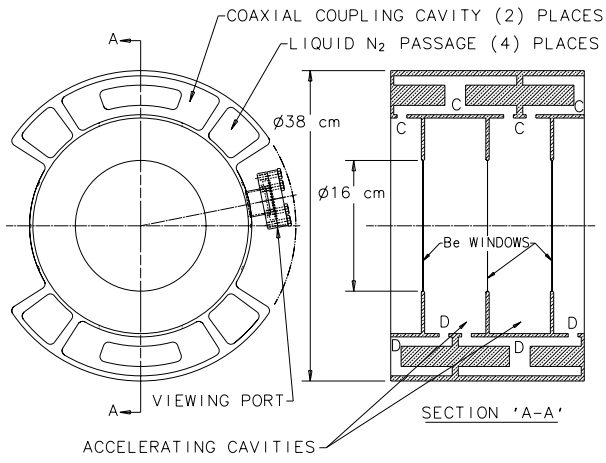

Figure 1: An interleaved $\pi/2$ SW RF structure proposed for a muon cooling experiment at FNAL. Two cavity chains are interleaved with a $\pi/2$ phase shift. Each chain operates at its own $\pi/2$ mode separately. Each cavity cell has a resonance frequency of 805 MHz. Conventional beam irises are covered by thin Be foils with radii of 8 cm. RF coupling between the cells is conducted through open slots on adjacent walls. The accelerating resembles a closed pill-box cavity and the coupling cell is a loaded coaxial type cavity.

* This Research Work is supported by the Director, Office of Energy Research, Office of High Energy and Nuclear Physics, High Energy Physics Division, of the U.S. Department of Energy, under Contract No. DE-AC03-76SF00098

2 RF POWER LOSSES

The electro-magnetic field continuously loses its energy to the cavity wall. In order to maintain the field, the energy loss has to be provided by rf sources. The total RF energy (power) flowing from the field into the wall can be computed by

$$P = \frac{R_s}{2} \oint_S H_t \cdot H_t^* ds, \quad (1)$$

where P is average power loss over one RF period; $R_s = \sqrt{\frac{\mu_0 \omega}{2\sigma}}$ is surface resistance of the wall; H_t is tangential component of magnetic field on the surface; S is the area of the cavity wall being studied. Equation (1) holds only if the conductor thickness and radii of curvature are much greater than δ, the skin depth. This is the case for most of the accelerator applications. H_t usually has to be obtained from numerical simulation codes such as MAFIA and SUPERFISH etc.. In some special cases (simple geometry), analytical solutions are available or can be used as good approximations. The $\pi/2$ interleaved SW structure, for example, the field in the accelerating cell can be well approximated by pill-box solutions. Using the analytical solutions and a *linear* approximation model solution in particular greatly simplify the calculation for temperature distributions. Considering the cylindrical symmetry of the accelerating cells, it is convenient to define a power loss and a density functions, $P(r)$ and $\rho(r)$ by re-writing Equation (1),

$$P(r) = \int_0^r \rho(r')(2\pi r')dr', \quad \rho(r) = \frac{R_s}{2} H_t \cdot H_t^*, \quad (2)$$

where we have assumed that only TM_{010} is the mode of our interest and $P(r)$ and $\rho(r)$ depend on r only. [1]

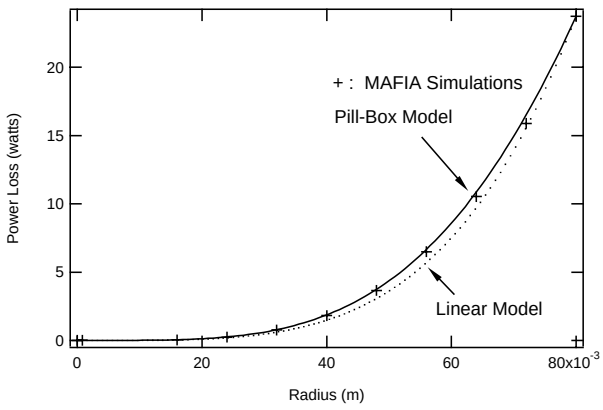

Figure 2: Power loss distribution on a flat Be window (conductivity of copper was used for this calculation, it should be easy to scale to the Be case once the data is available) calculated from the MAFIA simulations (+ sign), analytical formulae for the pill-box cavity (solid line) and the *linear* approximation (dotted line). The resonance frequency of the cavity is 805 MHz.

[1] The coupling slots in the cavities may introduce asymmetric field components, but these components are usually small and have negligible effects on on the power loss distribution.

2.1 The Pill-Box Model

For the TM_{010} mode in a pill-box cavity, its electro-magnetic fields can be expressed as,

$$E_z = E_0 J_0(kr), \quad H_\phi = H_t = \sqrt{\frac{\epsilon_0}{\mu_0}} E_0 J_1(kr). \quad (3)$$

The power loss and density functions are then given by,

$$\begin{aligned} P_{\mathrm{pb}}(r) &= \tfrac{\pi}{2}\eta R_s \left(\tfrac{\epsilon_0}{\mu_0}\right) E_0^2 \left\{ r^2 \left[J_0^2(kr) + J_1^2(kr)\right] \right. \\ &\quad \left. -\tfrac{2r}{k} J_0(kr) J_1(kr) \right\} \\ \rho_{\mathrm{pb}}(r) &= \tfrac{R_s}{2}\eta \left(\tfrac{\epsilon_0}{\mu_0}\right) E_0^2 J_1^2(kr) \end{aligned} \quad (4)$$

where $k = (\omega/c) = (u_{01}/a)$, with u_{01} as the first root of zero order Bessel function and a the outer radius of the accelerating cell; η is the duty factor of the RF source.

2.2 Linear Approximation Model

As indicated in Equation (3), $H_t \propto J_1(kr) \approx \frac{k}{2} r$ when $r << a$. We are interested only in the power loss on the Be windows with 8 cm of radii ($0 < r < R = 8$ cm and $R/a < 0.6$), we therefore may assume H_t to be linearly dependent on r, e.g. $H_t = \sqrt{\alpha} r$ and name it as the linear model. The power loss density in this case is given by,

$$\rho_{\mathrm{ln}}(r) = \alpha r^2, \quad (5)$$

which is **quadratically** proportional to r. The linear model diverges more from the pill-box solutions while r is approaching to R. To compensate this deviation, we calculate α by requiring,

$$P_{\mathrm{ln}}(r) = P_{\mathrm{Be}} \left(\frac{r}{R}\right)^4, \quad \alpha = \frac{2P_{\mathrm{Be}}}{\pi R^4}. \quad (6)$$

Where P_{Be} is the total average RF power loss on the Be window (one side). P_{Be} may come from the MAFIA simulations, analytical formulae from the pill-box model or even experimental measurement. For either cases we assume,

$$P_{\mathrm{pb}}(R) = P_{\mathrm{ln}}(R) = P_{\mathrm{Be}}. \quad (7)$$

With this assumption the power loss function by the linear model agrees well (within 6 %) with both the pill-box model and the MAFIA simulations. Nevertheless the linear model is much simpler mathematically, and therefore makes it possible for calculating the temperature distribution analytically tapered windows. As a comparison, Figure 2 shows the power loss calculations versus r on a flat Be window by different models. For all the calculations, we have assumed $E_0 = 30$ MV/m; $\sigma = 5.8 \times 10^7$ /(Ωm) (copper); $d = 0.127$ mm; $\kappa = 200$ W/mk and $\eta = 3 \times 10^{-4}$ (10 Hz repetition rate and 30 μs pulse length).

3 TEMPERATURE DISTRIBUTIONS

The RF power loss on Be windows is dissipated in the form of heat. The heat may be transfered by conduction, convection and radiation. However, the dominant form of the

transformation in metals is conduction. For the temperature distribution calculations we consider the heat conduction within Be windows only.

3.1 Heat Equation

It is well known that the conduction of heat obeys [3],

$$\frac{dQ}{dt} = -\kappa A \frac{dT}{dr} \text{ [watts]}, \tag{8}$$

where Q is the heat flow across area A, κ is a constant and known as the coefficient of thermal conductivity for the material of interest, and $\frac{dT}{dr}$ is the temperature gradient at r. Considering the cylindrical symmetry, and neglecting ionization energy loss of muons by passing through the windows, we assume the temperature distribution $T(\vec{r})$ depends on r only, e.g. $T(\vec{r}) = T(r)$. Equation (8) then can be re-written as,

$$\frac{dT}{dr} = -\frac{1}{\kappa d}\left[\frac{1}{r}\int_0^r \rho(r')r'dr'\right], \tag{9}$$

where d is the thickness of the Be window, for tapered windows d is dependent on r.

3.2 The Pill-box Solution

Substituting the power loss density function in Eq. (4) into Eq. (9), for a flat window we obtain,

$$T_{\rm pb}(r) = T_{\rm pb}(0) - \frac{R_s}{4}\eta\left(\frac{\epsilon_0}{\mu_0}\right)\frac{E_0^2}{\kappa d}\left\{r^2\left[J_0^2(kr)+J_1^2(kr)\right] - \frac{r}{k}J_0(kr)J_1(kr) + \frac{1}{k^2}\left[J_0^2(kr)-1\right]\right\}. \tag{10}$$

Where $T_{\rm pb}(0)$ is the temperature at the center of the window. Note the hottest spot is always at the center of the window (see Figure 3). We have assumed the cooling will keep the out-most edge $(r = R)$ at a constant temperature $T(R)$. The heat at the center takes the longest path to reach the cooling point even though there is no direct heating source in the center.

3.3 The Linear Model Solutions

Similarly by substituting the linear model solution in Eq. (5) into Eq. (9), we attain the temperature distribution for a flat window,

$$T_{\rm ln}(r) = T_{\rm ln}(0) - \frac{P_{\rm Be}}{8\pi\kappa d}\left(\frac{r}{R}\right)^4 \tag{11}$$

with $T_{\rm ln}(0) = T(R) + P_{\rm Be}/(8\pi\kappa d)$.

Based on the linear model solution, temperature distribution on a tapered Be window (see Figure 3) can also be calculated. We give the analytical formula below and with some numerical calculations shown in Figure 3.

$$T_{\rm ln}^{\rm tp}(r) = \begin{cases} T_{\rm ln}^{\rm tp}(0) - \frac{P_{\rm Be}}{8\pi\kappa d}\left(\frac{r}{R}\right)^4 & \text{if } r < r_0 \\ T_{\rm ln}^{\rm tp}(0) - \frac{P_{\rm Be}}{2\pi\kappa dR^4}\left\{\frac{r_0^4}{4} + \Phi(r)\right\} & \text{if } r > r_0 \end{cases} \tag{12}$$

$$\Phi(r) = \xi^3\left(1-\frac{r_0}{\xi}\right)^2(r-r_0) + 2\xi^2\left(1-\frac{r_0}{\xi}\right)(r^2-r_0^2) + \frac{\xi}{3}\left(r^3-r_0^3\right) - \xi^4\left(1-\frac{r_0}{\xi}\right)^3\ln\left[\frac{\xi+r}{\xi+r_0}\right], \tag{13}$$

where $\xi = \frac{R-r_0}{d^*-d}d$. For the tapered window simulations in Figure 3, in addition to the same parameters used in Figure 2 we have taken $d^* = 2d$ and $r_0 = 0.04$ m.

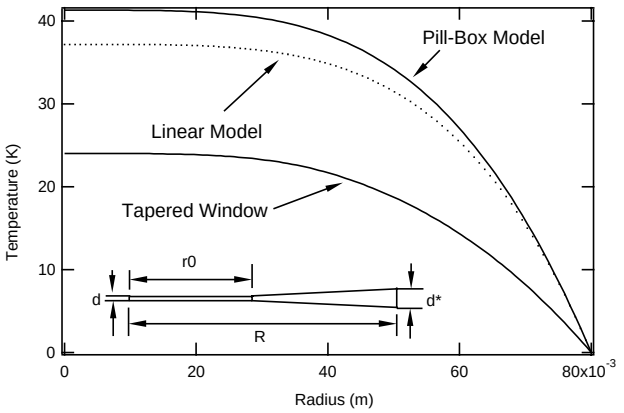

Figure 3: Temperature distribution on a flat Be window with thickness of 0.127 mm and on a tapered window with $d^* = 0.254$ mm. Note the temperature difference of $T(0) - T(R)$ is plotted here. $T(R) \approx 77$ K and $T(R) \approx 300$ K for the LN and room temperature, respectively. The temperature raise of the tapered window is about 15 K lower than the flat one.

4 CONCLUSION

Analytical formulae have been given for the temperature calculations. Numerical results presented here are for copper windows. It can be easily scaled to Be windows accordingly by $T_{\rm Be}(r) = \sqrt{\frac{\sigma_{\rm Cu}}{\sigma_{\rm Be}}}T_{\rm Cu}(r)$ once the Be data becomes available. Note both $\sigma_{\rm Be}$ and $k_{\rm Be}$ may vary with the temperature, but we did not take this into account in our models. However within small temperature range the models still give good approximations. Preliminary results show that the tapered window is better for the heat conduction and even a 0.127 mm thick flat window does not need special cooling designs and yet gives acceptable results from the viewpoint of beam dynamics for the muon cooling.

5 REFERENCES

[1] R. Palmer, *Muon Collider: Introduction and Status*, The Muon Collider Collaboration Report (1998)

[2] Derun Li, et al, *RF structure options for the muon collider*; A. Moretti, *An $\pi/2$ Interleaved SW Structure*; Y. Zhao, *A $2\pi/3$ Interleaved SW Structure*, Muon Collider RF Workshop at LBNL (1998); W. Turner, et al, *RF system concepts for a muon cooling experiment*, EPAC'98

[3] F. Tyler, *Heat and Thermodynamics*, Edward Arnold (Publishers) Ltd. (1964)

[4] Richard P. Reed and Alan F. Clark, *Materials At Low Temperatures*, American Society For Materials

CONCEPTUAL DESIGN OF THE SNS RFQ *

A. Ratti, C. Fong, M. Fong, R. MacGill, R. Gough, J. Staples, M. Hoff,
R. Keller, S. Virostek, R. Yourd
Lawrence Berkeley National Laboratory, Berkeley, CA, USA

Abstract

The conceptual design of the RFQ included in the front end injector of the Spallation Neutron Source is described. The RFQ operates at 402.5 MHz, with a maximum H^- input current of 70 mA and 6% duty factor. It is 3.72 m long and made out of four equally long modules. A brazed copper structure has been chosen due to the high power, high duty factor operation. The 800 kW peak r.f. power is coupled into the structure via eight ports, two per section. A set of tuners is provided for final frequency adjustment and local field perturbation correction. Quadrupole mode stabilization is obtained with a set of π-mode stabilizing loops. The conceptual design, assembly processes and status report are presented. This paper reports and updates the status of the design since it was last described [1].

1 INTRODUCTION

Lawrence Berkeley National Laboratory has been given the responsibility within the SNS collaboration of designing, building, installing and commissioning the Front End. This 2.5 MeV injector comprises the ion source, an electrostatic beam transport into the RFQ accelerator and the beam transport line that will deliver and match the beam into the linac. The radio frequency quadrupole (RFQ) accelerator is responsible for the bunching and acceleration of the beam from the energy of 65 keV after the source to the 2.5 MeV injection energy into the linac. A summary of the status of the SNS Front End is presented in another paper at this conference [2]. Intensive modeling has been done to support the RFQ conceptual design. The modeling results are in a separate paper [3].

2 PHYSICS DESIGN

The main parameters of the RFQ are summarized in Table 1. The RFQ accelerates the 65 keV H^- beam to 2.5 MeV in a 3.72 meter long cavity resonant at 402.5 MHz. The choice of operating frequency is dictated by the required peak output current, the desire of a compact structure and the need to inject into the higher energy sections of the linac (805 MHz) with an integer frequency ratio. This frequency also allows for the possibility of beam funneling in the first part of the linac.

Structure Type	4 vane
Total Length	3.723 m
RF Frequency	402.5 MHz
Input Energy	65 keV
Output Energy	2.5 MeV
Peak output Current	56 mA
Design Transmission	> 90 %
Rms Beam Size	0.7 mm
Norm. H rms Emittance	0.156 π mm mrad
Norm. V rms Emittance	0.156 π mm mrad
Vane-to-vane Voltage	83 kV
Peak Field	1.85 kilpatrick
Total Peak RF Power	800 kW
Beam loading	17 % @ 56 mA
RF Duty Factor	6.2%
Rep. Rate	60 Hz
Vacuum	$< 1\ 10^{-6}$ Torr

Table 1- Main RFQ Design Parameters

The RFQ is made of 449 cells, which are apportioned as 8 in the radial matcher, 48 in the shaper, 328 in the buncher ending at an energy of 780 keV, and 65 in the final accelerator section. The parameter selection is conventional, with the exception that the buncher section is slightly longer than usual to allow the longitudinal output emittance to remain below 95 keV-degree at 60 mA output and 75 keV-degree at 30 mA output, rather than increasing due to excessive bunching at lower current.

Eight-term RFQ beam dynamics simulations have been used in optimizing the buncher and acceleration section parameters, giving a normalized rms input acceptance of 0.2 π mm-mrad. In such simulations, the beam transmission is better than 95% at 60 mA of current, increasing to better than 99% at 30 mA.

The peak vane-to-vane voltage is 83 kV for a peak surface field of 1.85 kilpatrick, with a flat field distribution along the length of the RFQ to minimize longitudinal currents at the joints between the four modules that comprise the accelerator.

* This research is sponsored by the Lockheed Martin Energy Research Corporation under the U.S. Department of Energy, Contract No. DE-AC05-96OR22464, through the Lawrence Berkeley National Laboratory under Contract No. DE-AC03-6SF00098

The vane tip is machined with a constant transverse cross section of .351 cm, the same as r_0, the mean vane tip displacement from the axis.

3 RF CAVITY DESIGN

The 3.723 m long RFQ is built in four modules, each 93 cm long. The vanes and vacuum shell are made of OFE copper, with each quadrant brazed to a Glidcop (C) backbone to provide bolting strength for exterior components. The modules are joined with a copper-to-copper r.f. compression joint, backed up by a canted spring ring to provide a backup rf seal and a Viton O-ring vacuum joint. All this within the OFE part of the cavity. Figure 1 shows a conceptual view of one module.

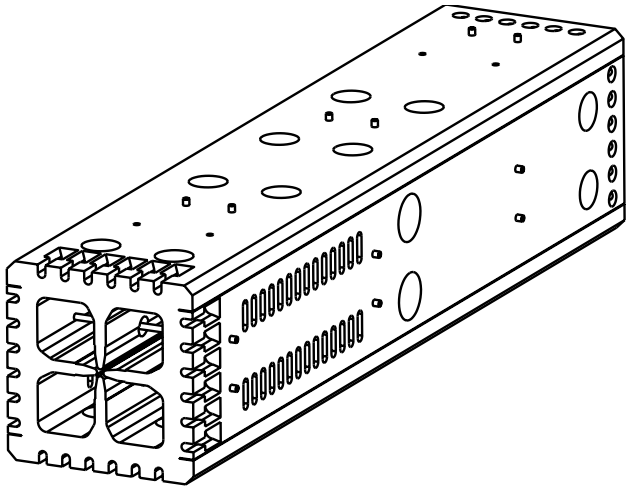

Figure 1 - Schematic view of one RFQ module

The quadrupole-dipole mode separation for the fundamental mode is 35 MHz, provided by π-mode stabilizer loop pairs [4] separated by 15.5 cm, for a total of 24 stabilizer pairs. The quadrupole mode frequency is decreased by 11 MHz and the dipole mode frequencies are increased by 36 MHz by the stabilizers. Perturbation tests show that changing the frequency of one RFQ quadrant by 1.53 MHz changes the azimuthal field symmetry by less than 2.7 percent. The RFQ is 5 free-space wavelengths long, and while no longitudinal stabilization is provided, the beam loading (for 60 mA) accounts for less-than 17% of the total power. Eight r.f. drive ports equally distributed in the four modules are expected to maintain the longitudinal field distribution within limits better than +/- 1%.

The average wall power density for 6% duty factor is 1.7 watts/cm^2, assuming the real losses to be about 67% of the ones in pure copper; computer simulations show that small areas near the vane end cutbacks approach 10 watts/cm^2. Each π-mode stabilizer rod will dissipate less than 10 watts.

The RFQ will be equipped with 80 tuners, 5 per module per quadrant, with a range of 2 MHz. Most, if not all, the tuners will be fixed, with the RFQ frequency fine control provided by a two-temperature water cooling system. In this scheme, the RFQ body is held fixed above ambient and the vane cooling channel temperature is kept at a lower and adjustable value.

4 MECHANICAL CONSTRUCTION

The RFQ mechanical design incorporates four separate vane quadrants containing the precision machined vane and cavity profiles. The quadrants are wire-brazed together to create the final cavity configuration. This design eliminates the need for demountable r.f. joints in the regions of high azimuthal r.f. wall currents. The vane and cavity wall surfaces are machined from solid blocks of oxygen-free copper (OFE). Since the copper is fully annealed during the brazing process, a 1" thick slab of GlidCop AL-15 is wire-brazed onto the rear surface of each copper quadrant to provide additional strength. This joint is obtained by brazing the copper cladding of the Glidcop to the OFE inner part. Provision has been made that no vacuum joint will cross the OFE-Glidcop braze. Figure 2 shows the final assembly of the four quadrants, as well as the external GlidCop layer.

The four completed modules are joined by means of a bolted connection. Rather than incorporating flanges at the ends of the RFQ modules, the joint design is preloaded by axial bolts recessed into the GlidCop outer layer, as shown in Fig. 1. Benefits of this type of joint include higher strength, reliable seal loading and a low profile. A slightly raised surface at the module ends around the perimeter of the cavity is used to provide a copper-to-copper r.f. compression joint. A canted spring ring seal provides back up to the r.f joint and protects an outer Viton O-ring vacuum. Canted springs are also used to ensure good electrical contact between adjoining vane tips. The r.f. and vacuum seals are all contained within the OFE portion of the cavity.

To conduct cooling water along the structure, the RFQ design uses milled channels in the back side of the OFE quadrants which are covered by the brazed-on GlidCop layer. This configuration allows internal manifolding and increased flexibility in the routing of the cooling passages. The integrity of the RFQ vacuum is maintained since no passages penetrate the ends of the modules.

This design has been studied with regards to cooling and stresses. Preliminary 2D finite element analyses have shown the RFQ operating temperature to be uniform within 3° C and thermal stresses to be 1200 psi or less.

Although the RFQ operating parameters call for a 6.2% duty factor, all thermal analyses are performed for operation at 10% to allow for possible future upgrades to a longer pulse length.

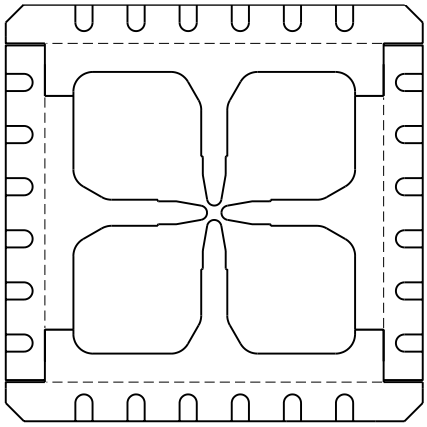

Fig. 2 – Four Quadrant RFQ cavity assembly

Vacuum ports are arranged in arrays of slots designed to attenuate the r.f. transmission into the vacuum system. The ports are incorporated identically in all four quadrants to ensure r.f. symmetry. In addition, nearby tuners are used to compensate the locally depressed cutoff frequency near the pumping ports, leveling out local variations in the vane tip voltage distribution. The RFQ vacuum level is maintained in the low 10^{-7} Torr range. All penetrations into the RFQ vacuum have been designed such that the GlidCop-to-OFE braze joint is not exposed to vacuum.

5 RF POWER SYSTEM

The peak power calculated is approximately 800 kW, including beam loading, when an additional 50% of power is allowed as the difference between the theoretical model of the RFQ and the real device built. This power is delivered by a single klystron, capable of 1.25 MW, that feeds the coupling ports via a circulator and a commercial eight-way power splitter. This splitter provides better than 40 dB of port-to-port isolation; at present no external longitudinal stabilization is planned.

The power is coupled in the cavity with a set of two coupling loops per module, with a total of eight ports. Each port will therefore carry a peak rf power of 100 kW, at a 6.2 % duty factor.

6 STATUS

A separate paper in this conference describes in detail the ongoing modeling efforts to support the conceptual design of the RFQ [3]. Benefiting from the results of such modeling, the detailed design of the first test module has begun. In the next months, a full cross-sectional size 93 cm long module will be built; it is designed with full capabilities, including vacuum, rf power, tuning and cooling. This module is intended to be identical to any of the four modules of which the RFQ will be built, apart from the specific vane modulations. The RFQ design and manufacturing procedures, as well as the operation under full r.f. power, will be tested with this device. A 1 MW klystron has been made available from the LANL collaborators and has been recently delivered to LBNL; its installation at LBNL is underway.

Upon successful completion of the first module's test, a full size prototype will be built incorporating the necessary changes that might be needed. This prototype RFQ will also be tested with beam.

7 ACNOWLEDGMENTS

The authors would like to acknowledge the generous help received from many colleagues. In particular, we would like to acknowledge the tremendous support provided by Dale Schrage and the design team for the LEDA RFQ project, by the LANL SNS collaborators Paul Tallerico and Bill Reass and by many LBNL colleagues, including R. Rimmer, K. Kennedy, J. Ayers, J. Greer and J. Remais.

8 REFERENCES

[1] M. Hoff, et al., "NSNS RFQ Mechanical Design", PAC97, Vancouver, BC, Canada

[2] J. Staples, et al, "The SNS Front End Accelerator Systems", Paper MO4056, LINAC98, August 1998, Chicago, IL USA

[3] A. Ratti, et al, "Prototype Models for the SNS RFQ", Paper TU4048, LINAC98, August 1998, Chicago, IL USA

[4] A. Ueno, et al, "Beam Test of the Pre-Injector and the 3-MeV H^- RFQ with a New Field Stabilizer PISL", LINAC96, August 1996, Geneva, CH

TEST RESULTS FOR A COLD MODEL OF A CCDTL TWO GAP TO THREE GAP TRANSITION REGION*

M. D. Cole, H. Bluem, Advanced Energy Systems, Northrop Grumman Corp. Bethpage New York 11714 USA,
J. H. Billen, P. O. Leslie, Los Alamos National Lab, Los Alamos New Mexico 87544 USA

Abstract

As part of the APT [1] project we have tested several cold models of a Coupled Cavity Drift-Tube LINAC (CCDTL) [2,3] 2 to 3 gap transition region. This is the region where cavities change from having 2 gaps and 1 drift tube per cavity to having 3 gaps and 2 drift tubes per cavity. We have established that frequency effects of coupling slots can be accurately predicted allowing calculation of the cavity frequencies within the allowed tuning range. The base cavity frequency is very accurately predicted by SUPERFISH and correction for stems and tuners is well established, the major uncertainty prior to these tests was predicting the frequency effect of the coupling slots. These tests have also shown that the cell-to-cell coupling for a given slot geometry can be predicted accurately enough to allow a minimum of slot tuning range to be left in the structure. A large desired field tilt between the two coupled accelerating cavities can be set up by varying the cell-to-cell couplings between the accelerating cells and the coupling cells. Further, the tilt can be predicted accurately enough to allow a minimum of slot tuning range to be left in the structure.

1 INTRODUCTION

We have tested and tuned 3 cold models (CMs) of a CCDTL 2-to-3 gap transition region. These three cold models differed only in detail dimensions, the first cold model was not extensively tested. The transition is the region in a CCDTL where the CCDTL cavities change from having 2 gaps and 1 drift tube (DT) per cavity to having 3 gaps and 2 DTs per cavity. The CMs are of structures from an early version of the APT LEDA [4], designed for a transition 8.09 MeV. A drawing of one of the CMs is shown in figure 1. In this design the transition occurred between Acc24 (accelerating cavity 24) and Acc25 (accelerating cavity 25). The CMs include ½ of a 2-gap cavity (Acc24), a complete coupling cavity (CC24-25), and ½ of a 3-gap cavity (Acc25). The current version of LEDA has the transition at 10.16 MeV between Acc49 and 50.

There were three principle issues to be addressed by these tests.

1) Could the required E_0 field tilt between the 2-gap and 3-gap cavities be established. Nominally the E_0TL for the two cavities should be equal, ignoring any additional field ramp? Since the 3-gap cavity is approximately 3/2 longer than the 2-gap cavity, the E_0 for the 3-gap cavity needs to be approximately 2/3 that of the 2-gap cavity. We needed to know if the tilt could be predicted accurately enough to minimize the required slot tuning range. The tilt is set by the difference in coupling between the respective cells and the common coupling cell.

2) Could the coupling produced by a given slot size be calculated accurately enough to allow a minimum of extra material to be left in the slot region, allowing the maximum use of available space in cramped areas? We are calculating the coupling produced by a given slot along the line described by J. Gao [1]. In addition if the coupling can be predicted accurately then the slots can be cut close to (or right on) the final dimension,

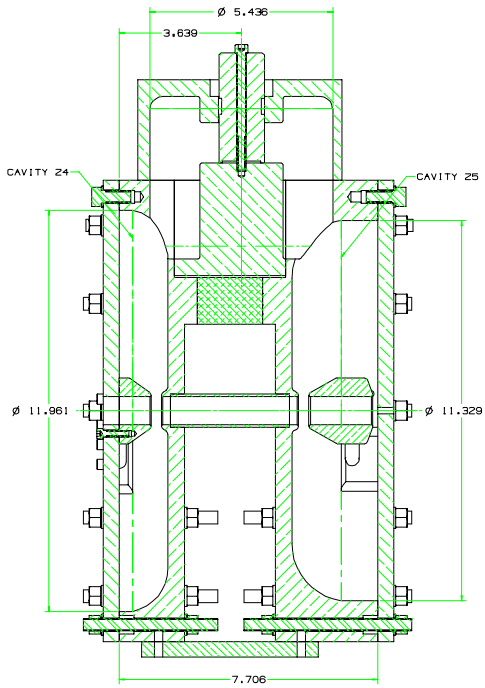

Figure 1: Drawing of transition region cold model.

* Funding provided by U.S. Department of Energy.

minimizing the coupling slot tuning required.

3) Could the frequency of the accelerating and coupling cavities be predicted accurately enough so that the cavities would be within the allotted tunable range? The base cavity frequency is very accurately predicted by SUPERFISH and corrections for stems and tuners are well established. The major uncertainty was predicting the frequency effect of the coupling slots.

2 FIELD TILT AND COUPLING MEASUREMENTS

The second cold model to be fabricated was slightly off frequency but was tunable and usable for field and coupling measurements. Table 1 shows the frequencies of Acc24, Acc25, and CC24-25 measured with the other cells shorted (with rods shorting the cavity gap along the cavity axis) as the cavities were tuned to 702 MHz with two rounds of tuning cuts.

Table 1: Measured individual cavity frequencies for the second cold model with all other cavities shorted.

Meas	1	2	3
Acc24 Fmeas	702.013	702.040	701.996
Acc25 Fmeas	705.253	702.639	702.589
CC24-25 Fmeas	707.645	702.310	701.982

During each tune step the mode frequencies were measured. These mode frequencies are used in the modal analysis program DISPER [2] to calculate the accelerating cavity frequency, the coupling cavity frequency, and the coupling for an infinite string of coupled cavities assuming that all of the coupling cavities, all of the accelerating cavities, and all of the couplings are the same. The "average" coupling, calculated by DISPER, is the best available for evaluating the cold model and is used throughout these tests. Table 2 shows the measured mode frequencies and the Acc and CC cavity frequencies and coupling calculated by DISPER. The final k_{avg} value calculated by DISPER is 4.63%, 93.72% of the target average coupling of 4.94%.

Table 2: Measured Mode frequencies, and DISPER calculated cavity frequencies and couplings.

Meas	1	2	3
0 Mode	689.900	686.764	686.602
$\pi/2$ Mode	703.300	702.369	702.337
π Mode	723.300	719.340	719.150
Disper Acc F_{avg}	703.300	702.369	702.337
Disper CC F_{avg}	708.748	702.603	702.285
Disper K_{avg}	4.66%	4.63%	4.63%

There is no way to measure the individual couplings from the coupling cavity to each of the accelerating cells, however, the field tilt that results from the different coupling values can be measured directly. The actual couplings need not be measured. The field profile was measured by performing a bead-perturbation measurement after the cavities were tuned. Figure 2 shows the plotted beadpull data. The plot shows (from left to right) the field in the gap in Acc24, the field in the first full gap in Acc25, and the field second (half) gap in Acc25. The measured field in the second (half) gap in Acc25 is not used in the analysis since the terminating wall and bore hole distort the field. A numerical integration of the fields in the Acc24 and Acc25 gaps was performed to generate a value for E_oL for each gap. The E_o value for a full Acc24 and a full Acc25 cavity was then calculated. For Acc24 the measured E_oL was simply doubled then divided by the actual full cavity length. For Acc 25 the cavity field profile from SUPERFISH was used to calculate the E_oL in the middle gap from the measured E_oL in the first gap, the result was added to twice the first gap E_oL and the sum divided by the actual full cavity length. The "measured" values for the single gap E_oL and the cavity E_o along with the SUPERFISH values are shown below for Acc24 and Acc25 in Table 3. Table 4 shows the "measured" field ratios, the target values, and the ratio of the measured to target values.

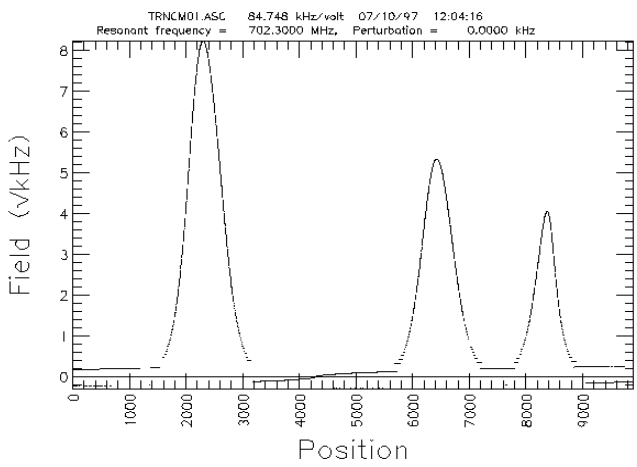

Figure 2: Results of beadpull on the cold model after frequency tuning.

Table 3: Relative single gap EoL and full cavity Eo.

	Acc24	Acc25
Measured single gap EoL	0.716757	0.445895
SUPERFISH single gap EoL	106.297	73.6647
Measured full cavity Eo	0.17124	0.094548
SUPERFISH full cavity Eo	2.5395	1.562

Table 4: Measured field ratios, and target ratios.

	Measured	Target	Meas/Target
EoL Ratio	62.21%	69.30%	89.77%
Eo Ratio	55.21%	61.51%	89.77%

The coupling can be increased by the small amount required during the assembly tuning phase, there is adequate space for the slots to be enlarged by the required amount. The E_o tilt of Acc25/Acc24 was 55.21%, 89.77% of the target 61.51%. Reducing the tilt can be done during the assembly tuning phase while the average coupling is increased.

The results of coupling and field tilt measurements with a third cold model were also quite good. The final k_{avg} value of 4.72% calculated by DISPER is 94.21% of the target average coupling of 5.01%. The E_o tilt of Acc25/Acc24 for this cold model was 58.00%, 94.30% of the target 61.51%.

3 FREQUENCY MEASURMENTS

Since we had good results with coupling and field tilt using the second cold model, the primary goal for the third cold model was to evaluate our frequency predictions.

All of the accelerating cells were designed with the intention having a small tuning range. This would be accomplished by nominally leaving a small amount of a fixed tuning ridge in place after the cell was tuned to 700 MHz. The cells would be fabricated with an additional amount of this ridge in place, hence the nominal fabrication frequency target of greater than 701 MHz. In theory, with all of the ring removed the frequency of the cells should be 699 MHz. For this model, the extra tuning ridge left in place was fixed at about 2.5mm for Acc24 and Acc25. The effect of this step on Acc24 and Acc25 is shown below for both the SUPERFISH predicted tune rate in Table 5 and the measured average tune rate in Table 6 (For these measurements, the cavity frequencies were not corrected for T, relative humidity, barometric pressure, or referred to vacuum).

Table 5: Tuning Step effects for Acc24 and Acc25.

	Acc24	Acc 25
SF Frequency with no step	699	699
Tune Step Height (in)	0.099	0.099
SF Tune Rate (MHz/in)	-22.0499	-36.0754
dF from step	2.18294	3.571464
Expected Fab Freq	701.1829	702.5715
Actual Fab Freq	700.541	702.766
Error	-0.64194	0.194536

Table 6: Tuning Step effects for Acc24 and Acc25.

	Acc24	Acc25
SF Frequency with no step	699	699
Tune Step Height (in)	.099	.099
Meas Tune Rate (MHz/in)	-16.7299	-34.3182
dF from step	1.656259	3.3975
Expected Fab Freq	700.6563	702.3975
Actual Fab Freq	700.541	702.766
Error	-0.11526	0.3685

The agreement between the expected and actual fabrication frequencies is within the tuning range provided by the tuning ridge. For Acc25 the agreement between the SUPERFISH tune rate and the measured tune rate is also good. It is not clear why it is not as good for Acc24.

4 CONCLUSION

We are quite satisfied with the results obtained with the transition region cold models. We have established that frequency effects of the slots in this region can be predicted allowing calculation of the cavity frequencies within the allowed tuning range. We have shown that the coupling can be predicted accurately enough to allow a minimum of slot tuning range to be left in the structure. Finally, we established that the required E_o tilt can be set up and that it can be predicted accurately enough to allow a minimum of slot tuning range to be left in the structure.

5 REFERENCES

[1] G. Lawrence, "High Power Proton Linac for APT; Status of Design and Development", these proceedings.

[2] J. H. Billen, et al, “A New RF Structure for Intermediate-Velocity Particles”, Proc. 1994 Int. Linac Conf., Tsukuba, Japan, p341 (1994).

[3] R. Wood, et al, "Status of the Engineering Development of CCDTL for the Accelerator Production of Tritium", these proceedings.

[4] H. V. Smith, "Status Update for the Low-Energy Demonstration Accelerator (LEDA)", these proceedings.

[5] J. Gao, “Analytical formula for the coupling coefficient β of a cavity-waveguide coupling system”, Nucl. Instr. And Meth., A309 (1991) p. 5.

[6] DISPER coupled cavity modal analysis program maintained and distributed by the Los Alamos Accelerator Code Group

EFFECTS OF ALTERNATING CELL MISALIGNMENTS ON THE DDS

R.M. Jones†, N.M. Kroll†‡, R.H. Miller† and T. Higo[¥]
†Stanford Linear Accelerator Center, M/S 26, P.O Box 4349, Stanford, CA 94309
‡University of California, San Diego, La Jolla, CA 92093-0319
[¥]KEK, National Laboratory for High Energy Physics, 1-1 Oho, Tsukuba-shi, Ibaraki-ken 305, Japan

Abstract

We study some effects of cell misalignments in accelerator structures in which each cell is displaced the same amount and direction but with sign which alternates from cell to cell. In particular we study the manifold radiation in a damped detuned structure (DDS1) and wakefield effects in a uniform constant impedance structure. A synchronous wave aliasing phenomenon is observed. In previous treatments the effect of cell misalignment has been modeled by replacing it by beam displacement. Here we compare finite difference simulation of cell misalignment with the beam displacement model. We conclude with discussions about the relevance of our results for general misalignment profiles.

1 INTRODUCTION

In a damped detuned accelerator structure the dipole modes are detuned such that their synchronous frequencies vary with error function profile along the length of the structure, so that the frequency distribution function is Gaussian. In addition four damping manifolds, connected to each cell, extend along the length of the structure. The detuning leads to a rapid initial fall off of the transverse wakefield and the damping prevents the recoherance reappearance which would otherwise occur [1]. The utility of the manifold radiation as a source of information about beam position within the structure and about structure misalignment is discussed in [2] and [3]. The spectral distribution of manifold radiation, computed by means of the equivalent circuit theory, was found to be in good agreement with observations [2, Fig. 1]. Furthermore it was shown, by computing the effect of beam displacements localized to a few cells within the structure, that there was a strong correlation between the localization position and the frequencies emitted into the manifold [2, Fig. 2] allowing manifold radiation frequency to be mapped onto cell position. Reference [3] reports measurements of beam position which minimizes manifold radiation as a function of frequency. By assuming that this minimum position is centered with respect to the cells which provide the frequency being observed and applying the mapping function defined above, one obtains a measure of cell position as a function of cell number and good agreement with mechanical misalignment measurements.

Implicit in the above is the assumption that localized cell displacements can be taken into account by replacing them with localized beam displacements in the equivalent circuit theory. In reference [4], which discusses the computation of wake functions associated with actual beam misalignments as well as with structure misalignments, the same assumption is made. Also the computational and experimental evidence does not really support the above simple picture for sharp discontinuities (such as actually occurred in DDS1).

The remainder of this paper is devoted to a partial study of the effect of a special misalignment. We assume the cells to be displaced alternately upward and downward by equal amounts as one proceeds along the structure. Because this is the opposite of a smooth misalignment it has some bearing on the issues raised above. It is also simple enough to allow a direct test of the equivalence of localized beam displacement and cell displacement. Such a structure can be analysed by treating each cell pair as a single cell and carrying out an analysis completely analogous to the standard DDS theory. While we have carried out only a small part of such a program, a number of interesting phenomena have emerged. The concluding section includes some discusions on the applicability of what we have learned to the more general misalignment problem.

2 RELATIVE DISPLACEMENT OF 2 IDENTICAL STRUCTURES

The study of both the detuned structure without damping and the DDS begins with the study of individual cells as part of a uniform structure. Proceeding analogously here we consider a cell pair as a unit in a structure of period 2p, where p is the period of the structure when the cell to cell displacement 2d vanishes. Mode patterns and frequencies as a function of phase advance over the 2p period were obtained from the finite difference program GdfidL [5] for a typical cell, similar to cell 103 of a detuned structure. The mesh for these calculations is shown in Fig. 1. Considerable care in mesh construction is required to preserve the symmetry of the problem, obtain sufficient accuracy, and avoid the introduction of mesh artifacts as d is varied. The Brillouin (dispersion) diagram for the accelerating mode and first two dipole modes is shown in Fig. 2.

As is conventional the diagram is folded so that the phase advance range is limited to 0 to 180 degrees. Also

shown on Fig. 2 is the (folded) light line. Computations were performed for d = 0, 0.1825, and 0.365 mm. For comparison we note that the diameter of the iris aperture is 9.5926 mm.

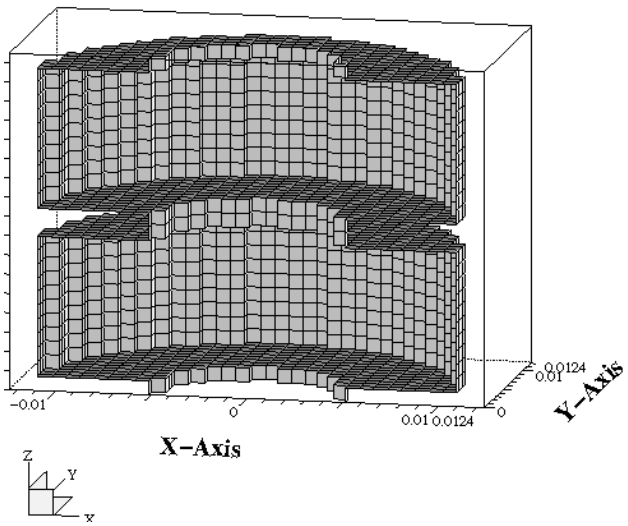

Figure 1: GdfidL mesh used for double period structure, viewed from the y symmetry plane. A coarse mesh is used to illustrate the geometrical features.

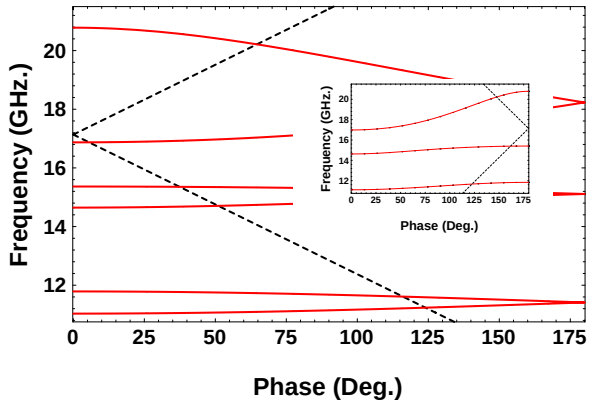

Figure 2: Brillioun diagram for double period structure with 0mm displacement of structure.

We first discuss Fig. 2 for the case d = 0. In that case the structure is periodic over the distance p (as well as 2p), and the conventional Brillouin diagram, folded with respect to p rather than 2p, is shown in the Fig. 2 inset. One sees that the single mode curves of the conventional form become doubled by folding back the 90 to 180 degree sections, leading to the paired curves of the 2p representation connected at 180 degrees. One also sees that the three synchronous frequency points (light line intersections) of the conventional representation become supplemented by three more which we refer to as alias synchronous frequencies. The longitudinal voltages for velocity of light particles vanish identically at these frequencies.

We next discuss what happens when one cell of the pair is offset to the left a distance d and the other offset to the right by d. As far as the Brillouin diagram is concerned there are small frequency shifts, varying as d^2, at each phase advance. The shifts of the six synchronous frequencies in KHz for d = 10 micrometers were inferred from the simulations to be -7.58, -13.2, 15.3, 27.5, 17.8, and -6.95 respectively, starting from the lowest frequency to the highest. Numbering them one to six, the odd numbers correspond to the alias cases. The fact that the coincidence of the curve pairs remains at 180 degrees is evidence that the mesh variation as d is varied is under control. The curves separate if the cells differ from one another.

The interaction of a v = c beam with a mode of the structure is controlled by the longitudinal voltage integral:

$$V_P(x,y) = \int_0^P E_z(x,y,z)\exp(j\omega z/c) \qquad dz$$

where P is the structure period (p or 2p in our case), and E_z and ω refer to the mode under study. We base our comparison of beam displacement with cell displacement on the behaviour of V_p and V_{2p}.

We consider the beam displacement model first. The beam displacement approximation is based upon the d = 0 structure, a structure with period p. At a synchronous point we have besides the expression given above:

$$V_p(x,y) = \int_p^{2p} E_z(x,y,z)\exp(j\omega z/c) \qquad dz$$

while for the alias synchronous modes this relation is

$$V_p(x,y) = -\int_p^{2p} E_z(x,y,z)\exp(j\omega z/c) \qquad dz$$

Thus at a synchronous point the beam displacement model yields $V_{2p}(x,y) = V_p(x-d) + V_p(x+d)$, while at an alias synchronous point it yields $V_{2p}(x,y) = V_p(x-d,y) - V_p(x+d,y)$. We recall that at a synchronous point of a periodic structure, V_p is a solution of the 2D laplace equation at all points within a region A defined by the area common to the beam apertures. Since the d = 0 structure is also rotationally symmetric about the beam axis, within A V_p is constant for the monopole case and a constant times x or y for the two dipole mode polarizations. Hence for all synchronous cases of the modes we study here, $V_{2p} = 2\ V_p$. Away from a synchronous point V_p no longer has this simple behaviour. However the departure from it is found to be very small, and the symmetry properties under reflection are preserved. It follows that

$$V_{2p} = -2d(d/dx)V_p$$

to an excellent approximation. This means that the alias synchronous modes have their x reflection behaviour reversed in parity. The monopole becomes an x dipole, the x dipoles become monopoles, and the y dipoles become quadrupoles. Note that to the extent that V_p

satisfies pure 2D laplacian behaviour the x dipoles behave like a pure monopole and the V_{2p} vanish for the monopole and y dipoles. Hence the alias dipole and quadrupole effects are very weak.

We have compared these results with the behaviour of GdfidL simulations at y = 0 and values of x over the interval [-4,4] mm. To compare different cases we require that all have the same stored energy over the [0,2p] interval. Also since the GdfidL simulations have an arbitrary overall phase, we compare absolute values of V_{2p}.

Comparisons were made at d = 0.365 and 0.1825 mm. First a few general observations. Since all modes are synchronous with respect to the 2p period, all of the V_{2p} satisfy the 2D laplace equation. The rotational invariance about the beam axis is, however, broken, and hence the simple x dependence of pure multipoles may be altered. On the other hand, one can show that the behaviour under x reflection should be preserved. Hence we expect the alias monopole to be principally dipole, and the alias x dipoles to be principally monopole, an expectation born out by the simulations.

We discuss the even numbered modes first. For the monopole case, there is no detectable difference between the displaced beam model and the simulation at 0.1825 and no detectable variation from pure monopole behaviour. For the first dipole there is a 0.1% deviation for d = 0.1825 and 0.25% for d = 0.365 and no evidence for departure from pure dipole behaviour. For the second dipole the discrepancy was 10% at d = 0.1825 and 30% at d = 0.365 and there was slight evidence for a deviation from pure dipole behaviour. We note that the voltage integral is abnormally small for this mode and therefore seems to be more sensitive to field changes associated with the displacement. The discrepancy does appear to be decreasing with d and may well become very small at d values likely occur in practice. These results provide no evidence against the use of the displaced beam approximation for calculating the transverse wakefunction as was done in [4].

For the odd numbered modes, which correspond to the aliased synchronous modes, the comparison is much poorer. The departure from pure multipole behavior is substantial but not significant at beam displacements which are likely to occur in practice. The result of most practical interest is the deflecting mode 1, which occurs at a frequency within the accelerating mode band and would thus be unaffected by manifold damping. The magnitude is 8 times as large as that given by the beam displacement model and appears to be proportional to d. The kick factor associated with it then varies as d^2, and assuming this to be the case is a factor 10^3 smaller than a typical first band dipole mode for d = 36 μm. For mode 3 the dominant monopole component is over estimated 15% for d = 0.1825 and 20% at 0.365 by the beam displacement model. The figures for mode 5 are 65 and 75% respectively. Being non deflecting and subject to manifold damping these modes are of little practical wakefield interest.

3 MANIFOLD RADIATION PHENOMENA

An equivalent circuit computation of the manifold radiation spectrum from DDS1 for beam displacements alternated from cell by equal amounts yielded a striking shift in the spectrum which we interpreted as implying that each cell was excited at its aliased synchronous frequency rather that its actual synchronous frequency. In the future we plan to investigate the extent to which this effect is localised. The other striking result was the the fact that the radiation was predominantly upstream rather than downstream, an effect which was consistent with the explanation of directional asymmetry given in [1].

4 CONCLUDING COMMENTS

While the evidence is limited to the special situations that we have studied, we attempt here to draw some tentative general conclusions. First, frequency shifts due to misalignments are unimportant compared to those likely to arise from dimensional errors in the cells. Second, for the computation of transverse wakes due to dipole modes the displaced beam approximation is reliable. These misalignment may also cause a longitudinal wake from the dipole modes, but it is small and of little practical importance. Third, we have no evidence that misalignment produces any significant effect on the accelerating mode band. The transverse wakes from aliasing are very small, and we have no evidence of transverse wakes produced directly by the RF drive.

5 ACKNOWLEDGMENTS

This work is supported by Department of Energy grant number DE-FG03-93ER40759‡ and DE-AC03-76SF00515†. We are pleased to acknowledge the timely advice and support of Dr. W. Bruns, the author of GdfidL.

6 REFERENCES

[1] N.M. Kroll, The SLAC Damped Detuned Structure, Concept and Design, SLAC-PUB-7541, PAC97 Proceedings*. [2] R.M. Jones, et al, Analysis and Application of Microwave Radiation from the Damping Manifolds of the SLAC Damped Detuned Structure (DDS), SLAC-PUB-7589, PAC97*

[3] M. Seidel, Studies of Beam Induced Dipole-Mode Signals in Accelerating Structures at the SLC, PAC97 Proceedings.*

[4] R.M.Jones et al, Spectral Function Calculation of Angle Wakes, Wake Moments, and Misalignment Wakes of the SLAC Damped Detuned Structure (DDS), SLAC-PUB-7538* [5] W. Bruns, A Finite Difference Program with Reduced Memory and CPU Usage, PAC97 Proceedings.*

* http://www.cern.ch/accelconf/

APPLICATION OF A MAPPING FUNCTION TECHNIQUE TO THE DESIGN OF DAMPED DETUNED STRUCTURES AND TO THE RAPID CALCULATION OF THEIR WAKEFIELDS

R.M. Jones†, N.M. Kroll†‡ and R.H. Miller†
†Stanford Linear Accelerator Center, M/S 26, P.O Box 4349, Stanford, CA 94309
‡University of California, San Diego, La Jolla, CA 92093-0319.

Abstract

In order to reduce the dipole wake encountered by the first few bunches accelerated in a multi-bunch NLC scenario the DDS (damped detuned structure) was re-designed such that a much improved Gaussian fall-off occurs in the initial wake-function. From the 9 parameterised model of DDS1 we use a mapping function to allow DDS 3 & 4 to be modeled and hence avoid additional and prohibitively time consuming MAFIA runs. The equivalent circuit parameters and geometrical parameters are treated as functions of the synchronous frequency and are readily mapped onto the new synchronous frequencies. The new geometrical parameters form a family where each is associated with the iris diameter.

1 INTRODUCTION

The first ever manifold DDS was designed such that the geometrical parameters (iris radius and cavity radius) of the cells were inverse functions of error functions, Erf. Further, the mode density function (the reciprocal of the derivative of the uncoupled frequencies with respect to mode number: dn/df) was prescribed to be Gaussian. However, the short range dipole wake function, is given by twice the inverse transform of the dipole kick-factor (K) weighted density function and under a Gaussian prescription of dn/df, 2Kdn/df is markedly asymmetric. The consequence of the asymmetry is a poor definition of the minima in the short range wake function. DDS 3 & 4 have been re-designed under a Gaussian 2Kdn/df prescription with a bandwidth of 4.71 units of sigma (with sigma 2.125% of the central frequency of the Gaussian) and this leads to a significantly improved short-range wake function.

The inverse Fourier transform of the spectral function [1] allows the global wake-function to be evaluated. However, in order obtain the new spectral function, all nine parameters of the structure must be obtained for 206 cells. This is a substantial computational task in running the MAFIA code required for the spectral function and in the careful fitting procedure required for all the new functions. However, the method used herein obviates this excessive computational work and requires that we fit all the 9 circuit model parameters together with the beam kick-factor to ten functions which all depend on the synchronous frequency only. The new set of new synchronous frequencies, dictated in our case by the requirement that 2Kdn/df be Gaussian, allows the 206 x 10 new characteristic parameters to be calculated. Similarly the 5 parameters, which define the geometry of the structure (the iris radius a, cavity radius b, iris thickness t, the radial distance of the edge of the manifold from the center of of a cell, H and the height of the manifold L) are also functionally dependent on the synchronous frequency of the beam and, under a new set of frequencies, 5 x 206 new dimensions are calculated for the DDS. Thus, in order to obtain the wake function and new geometrical parameters for fabrication all that is necessary is to obtain 15 functions.

However, under this new mapping one might express some concern as to whether the properties of the fundamental (i.e. accelerating) mode have been adversely affected and so with this in mind we conducted an intensive investigation as to the deviation of the cell dimensions, parameterised by the cavity diameter 2b, from their values designed in DDS 2 (all dimensions form an invariant family parameterised by the cavity diameter b). This is detailed in section 4 and successive sections.

2 THE MAPPING FUNCTION

In our design of DDS 2 we chose eleven representative sections to obtain frequency-phase pairs from detailed MAFIA simulations and hence obtain ten model parameters (nine circuit parameters plus the cell kick-factors) for each of the eleven sections. Parameters for all sections are subsequently obtained by error function fits and interpolation. A similar procedure may be followed to determine the five geometric parameters (i.e., cell and manifold dimensions) for all the sections from those for the original eleven. This is a substantial task for each structure design. However, as we now have all fifteen parameters as a function of synchronous frequency, we can take advantage of this functional dependence to explore new design distributions and to obtain the set of section dimensions which would be needed to realize them.

Based on our fit parameters we prescribe a smooth uncoupled spectral function, $S_0(f_s)\lambda$ and impose the condition that: $2K(f_s)dn/df = S_0(f_s)\lambda$, where K is the uncoupled kick factor, f_s the synchronous frequency and, λ is a scale factor to be determined. The upper and lower

truncation bounds on the synchronous frequencies are imposed, f_{s1} and f_{sN} and the normalisation condition is obtained:

$$\lambda = N / \int_{f_{s1}}^{f_{sN}} (\tfrac{1}{2} S_0 / K) df_s \qquad (2.1)$$

Then the new synchronous frequencies are determined according to:

$$\int_{f_{sn}}^{f_{sn+1}} \frac{1}{2K} \lambda S_0 df_s = 1 \qquad (2.2)$$

This enables all the cell synchronous frequencies to be determined and hence the new ten parameters are determined.

This procedure is implemented in the following section to calculate the spectral function and associated wake function for DDS 3.

3 CALCULATION OF THE WAKE FUNCTION

In the revised design for DDS 3 we chose a truncated Gaussian distribution for the uncoupled $2Kdn/df_{syn}$ distribution, with a bandwidth of 4.71 units of sigma, (a bandwidth of 10.159% of the central frequency and sigma is 2.125% of the central frequency) and this provides a basis for the determination of the 206 synchronous frequencies. The kick factor weighted density function for DDS 3 and DDS 1 are shown in Fig 1.

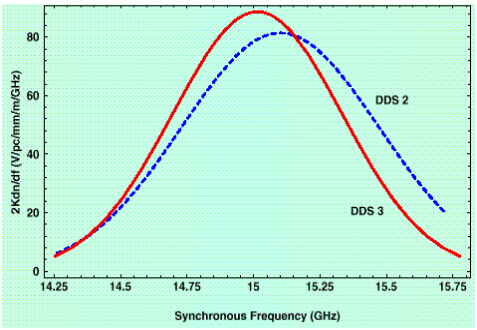

Figure 1: Twice the kick factor weighted density function for DDS 2 (shown dashed) and the corresponding function for the re-designed DDS3 and 4

It is evident that DDS 2 is markedly asymmetric and this adversely affects the sharpness and depth of the minima for the short range wake

In order to calculate the wake function we first are required to calculate the spectral function associated with the 9 mapped parameters. This spectral function calculated for DDS 3, and shown in Fig 2, maintains the Gaussian characteristics imposed upon it from the synchronous frequency distribution but modulated with oscillations of large amplitude (resulting in a large part from reflections occurring in the higher order mode couplers in the manifold).

Also, the spectral function exhibits the underlying damped mode structure as mentioned previously for DDS 2 [1] and is shifted with respect to the 2Kdn/df curves, as given in Fig. 1. The difference between the respective curves in Fig. 1 and Fig. 2 becomes more pronounced for higher frequencies and this is a consequence of the synchronous frequencies becoming more highly perturbed as one progresses down towards the higher energy end of the structure where the coupling to the manifold has been designed to be largest. These coupled synchronous frequencies will be discussed in a future publication [2]

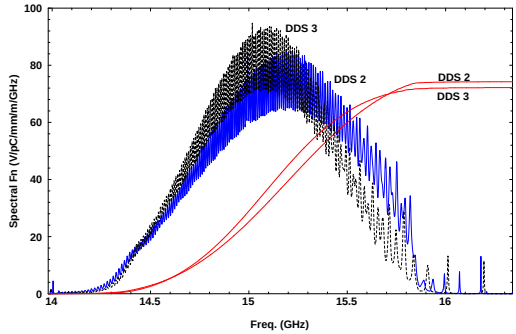

Figure 2: Spectral function for DDS 2 and DDS 3

It is important to note that the sharp, rather precipitous, fall-off in the spectral function in DDS 2 at approximately 15.8 GHz has detrimental affects on the short range wake function. In DDS 3 the spectral function falls off smoothly and gradually and this has beneficial effects on the range wake function in that it enables a faster fall-off to occur. Indeed for a perfectly smooth termination, which we refer to as our idealised case [1], it is possible to achieve more than an order of magnitude weaker wake function at the 90 bunch point.

It is interesting to note that the maxima of DDS 3 is a little larger than that of its counterpart DDS 2. However, the area under the curve (bounded by the upper & lower synchronous frequencies for each structure) corresponding to DDS 3 is slightly smaller than DDS 2. This reduction in the area of the curves is indicative of a reduced wake function at the origin (since the wake function is given by the inverse transform of the spectral function) and this is in itself a consequence of the larger iris dimension in DDS 3.

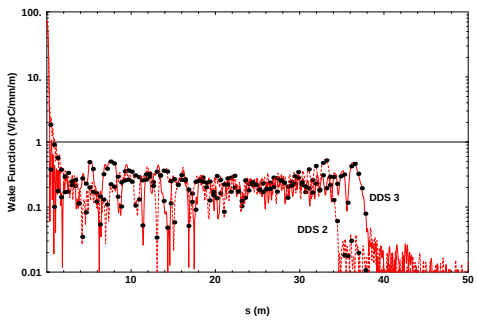

Figure 3: Long range wake function for DDS 2 (shown dashed) and DDS 3. The points are at the location of each of the bunches, of which there are ninety.

4 GEOMETRICAL PARAMETERS

Each of the five geometrical parameters are fitted with an interpolation function, the independent variable in each case being the synchronous frequency. Thence, armed with these new synchronous frequencies the new 206 x 5 parameters are readily obtained. Both a new and mapped cell parameter is shown in Fig. 4 and a manifold parameter in Fig. 5. The end points of DDS 2 and DDS 3 are identical by design so that no extrapolation is required in the determination of the DDS 3 parameters. Thus, in determining all parameters only third order interpolation between cell points has been employed, with a view to minimising any error in the generation of the new points.

It is evident from the curves that in the downstream end (or low energy end) of the structure the parameters are very close to that of the DDS 2 design whereas in the upstream end both the iris and the cavity diameter are increased significantly. This is a consequence of the asymmetry in the original design in which the kick factor weighted distribution reached too low a level in the upstream location of the structure and this has been corrected for in DDS 3. The thickness of the irises however, is reduced with respect to DDS 2, but this reduction is sufficiently small that the structure still maintains its mechanical integrity.

The manifold is tapered as one goes down the structure to enhance the coupling. This increased coupling is necessary because the modal composition of TE/TM is reduced as one moves towards the upstream end of the structure and to achieve a Q value in the neighborhood of a 1000 or so, increased coupling is required. There is a reverse in the taper towards the end cells in the upstream end and this is instituted in order to lower the cut-off frequency of the HOM (higher order mode) coupler and hence improve the match of the mitered bend of the HOMs at the lower frequency end of the band.

It is necessary to have well-matched HOM loads because the wake function is very sensitive to the power reflected back into the accelerator [1]. However, under the mapping the middle cell has effectively shifted forward by 11 cells and hence the upward taper (which occurs in cells 182 to 202 for DDS 2) maps the up-taper into a region where there are no manifold cells. Thus, in DDS 3 we change the mapped taper in this region by increasing the gradient of the taper and withdrawing its to cell 202. This will adversely affect the wake function but we are confident that its deleterious effect will minimal.

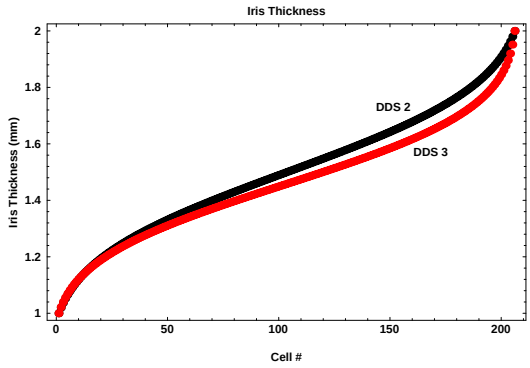

Figure 4: Cell geometrical parameters: iris thickness, t.

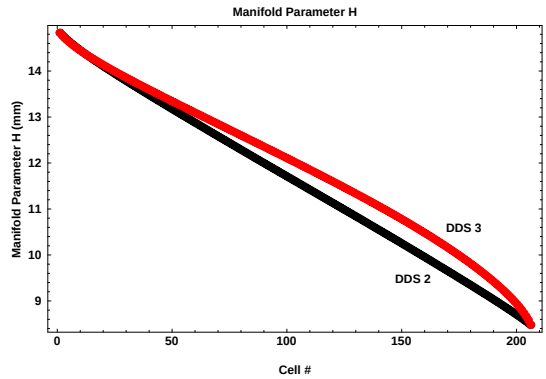

Figure 5: Manifold geometrical parameters: radial distance of the edge of the manifold the from center of a cell.

5 CONCLUSIONS

We have developed a method to rapidly design new DDSs based upon a mapping procedure. This method enables both the wake function and the new geometry of the structure to be evaluated. Indeed, we have applied this method to calculate the short range wake function for DDS 3 and we find that, on average, the wake function is reduced by a factor of 5 or more. The new geometrical parameters form an invariant family which are functionally dependent on the cavity iris diameter, 2 and the deviation of the new family of parameters from the old provides an indication as to the accelerating mode's phase advance of the new structure.

6 ACKNOWLEDGMENTS

This work is supported by Department of Energy grant number DE-FG03-93ER40759[‡] and DE-AC03-76SF00515[†].

7 REFERENCES

[1] R.M. Jones, et al. A Spectral Function Method Applied to the Calculation of the SLAC Damped Detuned Structure. Proc. Intl. Linac Conf. Geneva Switzerland, 1996 (and SLAC-PUB 7287)

[2] N.M. Kroll, The SLAC Damped Detuned Structure, Concept and Design, SLAC-PUB7589, PAC97

OPTIMUM OPERATING TEMPERATURE OF SUPERCONDUCTING CAVITIES

H. Safa
Los Alamos National Laboratory, Los Alamos, 87545, NM, USA
& C.E.A. Saclay, 91191 Gif/Yvette Cedex, France

Abstract

Superconducting radiofrequency (SCRF) cavities require cryogenic temperature to operate in the superconducting state where the RF power losses are extremely low. But this power has to be removed at very low temperatures using a refrigerator. While reducing the operating temperature results in lower losses for the cavities, it may severely impacts the cryogenic plant, drastically reducing its efficiency. On the other hand, the exponential dependence of the BCS surface resistance with temperature will ask for much higher refrigeration power at higher temperatures. Therefore, an optimum working temperature results, depending on frequency, accelerating field and cavity performance. This temperature should be determined by cost, performance, and risk minimization.

1 INTRODUCTION

While it is obvious that for frequencies over 1 Ghz, SCRF niobium cavities must operate in superfluid helium [1], the use of an intermediate frequency as 700 MHz for future proton linear accelerators requires a more thorough evaluation. For the sake of convenience, the APT (Accelerator Production of Tritium) high energy part [2] will be taken as an example. While reducing the operating temperature results in lower losses for the cavities, it severely impacts the cryogenic plant, reducing its efficiency (for example, going down from 2.0 K to 1.8 K will have a tremendous impact on the cryoplant's cold compressors, while achieving very little reduction of the cavity losses). On the other hand, a high operating temperature would require a very high-power refrigeration, due to the strong dependence of the BCS surface resistance with temperature (for example, operating at 4.5 K would require seven times more refrigeration power than for 2 K operation). Therefore, an optimal working temperature should exist in between these two limits.

2 COSTS ESTIMATION

2.1 Operation Cost

To properly optimize the operating temperature, all the items that may vary with this parameter should be taken into account. First, the two main items are the cryogenic plant and the electric power required to maintain the cryogenic temperature. The choice of the operating temperature will directly affect the total cryogenic power R required, which, in turn, will size the cryogenic plant. The AC electric power of the cryogenic plant can then be deduced using an overall efficiency η :

$$P_{AC} = \frac{R}{\eta} \qquad (1)$$

This will be the most important cost item in operation. The change in other operation costs of the cryoplant components (manpower, maintenance, etc.) will be assumed to be of second order when compared to AC power, and will be neglected here. Assuming a running time of 80% and an average price of (0.05 \$/kW$_e$h), the operating cost will amount to:

$$C_{op} = 0.35 \times P_{AC} \quad (\$/\text{year}) \qquad (2)$$

The total operating cost is obtained by multiplying C_{op} by the total lifetime of the accelerator.

2.2 Capital Cost

The change in capital cost C_{cap} with respect to operating temperature is assumed to be mostly due to the cryogenic plant. Green et al. [3] from Berkeley have estimated the capital costs of helium refrigerators and liquefiers based on a collection of existing systems, ranging from a few watts to 30 kW. They devised a simple formula[a] relating the cost C (in \$) to the refrigeration power R (in W)

$$C_{cap} = 12000 \left(\frac{\eta_{4.5K}}{\eta} R\right)^{0.7} \qquad (3)$$

$\eta_{4.5K}$ is the overall efficiency at 4.5 K.

These evaluations were mostly done for 4.5 K refrigerators of relatively small sizes. To take into account the additional needs for cold compressors while going to lower temperatures, a slightly modified formula will be used. The capital cost for one cryogenic system producing a refrigeration power R at temperature T will be taken as[b] :

$$C_{cap} = 3000 \left(3 + \frac{4.5}{T}\right) \left(\frac{\eta_{4.5K}}{\eta} R\right)^{0.7} \qquad (4)$$

If the accelerator requires an unusually large amount of refrigeration power, it will be assumed that the cryogenic plant is made of N identical cryogenic systems, each producing (1/N) of the total power.

$$C_{captotal}(R) = N \times C_{cap}(R/N) \qquad (5)$$

For APT, N = 3 will be taken. Although increasing the capital cost, this approach enables flexibility, enhances

[a] The factor has been adjusted to give the cryogenic power R in Watts.

[b] The temperature dependence should be theoretically already taken in account in the efficiency factor η. However, it will be assumed that the need for helium cold compressors will turn into additional costs higher than the efficiency ratios, taken here to increase linearly with (1/T). Whereas a lot of data points are available at 4.5 K, only a few are at 2 K (the most significant of these being CEBAF CHL).

availability, and relies on existing systems without requiring major technological developments.

2.3 Efficiency

The thermodynamic efficiency of the refrigerator system is roughly proportional to the ideal Carnot efficiency:

$$\eta_{Carnot} = \frac{T}{(T_a - T)} \qquad (6)$$

where T_a is the room temperature (generally taken as 310 K). Some systems can achieve up to 40% of Carnot efficiency. The efficiency goes up with size [3] and with temperature. If $\eta_r = \eta/\eta_{Carnot}$ is the ratio of the actual efficiency to the Carnot efficiency, the following approximate[c] formula will be used:

$$\eta_r = 0.035\ \mathrm{Ln}(R)\ \tanh(T/3) \qquad (7)$$

(In the case of a liquefaction mode, this efficiency is lower and has to be multiplied by a factor 75%±10%).
The overall efficiency will be:

$$\eta = \eta_r \cdot \eta_{Carnot} \qquad (8)$$

3 CRYOGENIC POWER REQUIREMENTS

The cryogenic power required is obtained by estimating the cryomodule heat loads which are the sum of the cavity losses plus a fixed heat flux amount (due to static losses, power couplers, transfer line losses, etc.). The latter losses (at the operating temperature T) are estimated for the time being to be around (10 W) per cavity in all cryomodules with an uncertainty of (± 5 W). Additional heat loads removed at the intercept temperature, assumed here to be 20 K, have to be added. Although these amount to roughly (80 W/cavity), they will play a minor role in the overall optimization and can be reasonably assumed to remain constant.

4 CAVITY LOSSES

Cavity losses will be the main item driving the optimization. The dissipated power in the cavity is :

$$P_d = \frac{V^2}{2R} = \frac{E_{acc}^2 l^2 R_s}{2(R/Q)\ G} \qquad (9)$$

where (R/Q) and G are both geometrical factors. E_{acc} is the accelerating field and l is the cavity accelerating length. Table I gives these numbers for the APT cavities. The surface resistance R_s can be calculated using the theoretical BCS value R_{BCS} (which increases exponentially with temperature) and adding a fixed residual resistance R_0 due to the residual static magnetic field, Q-disease, and surface impurities [4].

$$R_s = R_{BCS}(T) + R_0 \qquad (10)$$

[c] Ideally, this ratio should be almost constant. The variation with power is fitted from the curve given in [3]. The variation with temperature is extrapolated to other temperatures using a linear variation at low temperatures. The formula (7) used here is conservative.

The residual value is strongly dependent on the environment, as well as on the quality of the cavity niobium, fabrication, and preparation. An average value of (20 nΩ) will be taken with a uncertainty of ± (15 nΩ).

Table I - APT 5-cell Cavity Parameters

	E acc (MeV/m)	l (m)	(R/Q) (Ω)	G (Ω)
β = 0.64	4,8	0,685	85,7	151
β = 0.82	5,5	0,878	134,0	208

5 TOTAL HEAT LOADS

Considering the above uncertainties, three different cases are labeled as "average," "best," and "worst." The "average" case will be most likely observed in the actual accelerator, if all the steps and procedures are properly followed. The "worst" case will give the maximum heat load that will drive the total refrigeration capacity, whereas the "best" case would be the minimum that could possibly be achieved. Table II summarizes the heat loads in each case, from which the required power for sizing the refrigerator and calculating the operating cost can be deduced.

Table II - Residual Resistance and Non-cavity Losses in the Three Cases Considered. (All powers are in Watts)

	AVERAGE	BEST	WORST
Residual resistance R_0(nΩ)	20	5	35
Cryomodule losses /cavity	10	5	15
Total Losses (excluding cavities)	4100	2050	6150

6 RESULTS

Cost results will be given for the three heat loads cases: worst, average, and best. Most of the conclusions will be given using data from the average case.

6.1 Capital Cost

First, the "worst" case will be used to size the needed refrigeration power R (including a 50% margin). That will determine the total capital cost C_{cap}, using equation (5). This cost, together with the refrigeration power R, is shown in Figure 1 for temperatures ranging between 1.8 K and 3.0 K.

Based exclusively on capital cost, the temperature giving the lowest cryogenic plant cost is 2.70 K. But that minimum is very broad (any temperature between 2.10 K and 3.40 K would be within 15% of that minimum cost, while the formula used should not be trusted to that accuracy). An operation at 2.0 K would result in adding 22% (13.2 M$) over the lower cost.

6.2 Operating Cost

As expected, the operating cost, shown in figure 2, strongly varies with the cavity losses. There is a significant cost difference between the "best" and the "worst" case (it more than doubles at 2.0 K). This reflects

the importance of trying to increase the cavity quality factor Q. While the cost may widely change with cavity performance, there is no drastic variation of the optimum temperature. It increases from (2.00 K) in the best case to (2.50 K) in the worst, the average being (2.30 K). Again, this minimum is very broad and operating between (1.90 K) and (2.70 K) will only give less than 10% additional cost over the optimum.

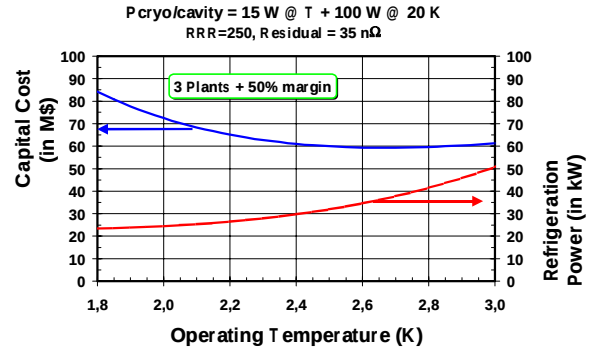

Figure 1 - Refrigeration power and capital cost as a function of the operating temperature.

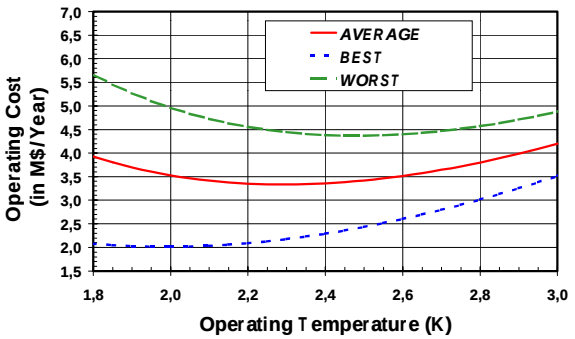

Figure 2 - Operating cost per year for the three cases considered.

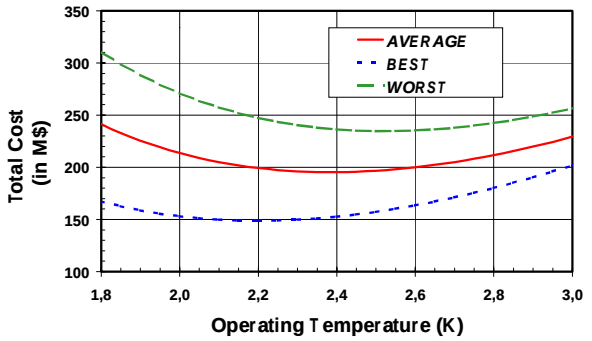

Figure 3 - Total cost for 40 years of operation.

7 TOTAL COST

The total cost is deduced by adding the capital to the operating cost integrated over the accelerator lifetime :

$$C_{Total} = C_{cap} + 40 \times C_{op} \qquad (11)$$

This total cost is plotted in Figure 3 as a function of temperature for the three cases. As expected, because the operation part amounts to 75% of the total cost, it will be driving the optimum temperature. The figures of the total cost (fig. 3) are very similar in shape to those shown in the preceding figure. The overall optimum temperature slightly shifts to higher values due to the lower capital cost. It moves from 2.20 K for the best case to 2.50 K for the worst, with a middle value of 2.40 K.

8 THE QUENCH FIELD

The above discussion implicitly assumes the cavities will reach the desired accelerating fields without any problem (no field emission, no quenches). But heat removal in a superfluid bath (He II at $T < T_\lambda = 2.17$ K) is much more effective than a normal liquid bath where nucleate boiling can occur that will limit the cavity performance at lower fields [5]. Boiling helium can also induce additional pressure vibrations that add to the microphonics induced in the SCRF cavities. This may result in a demand for additional RF input power which have to be carefully accounted for, as each additional 1% on the RF power is equivalent to adding 20% on the total cryogenic AC power. The expected quench field values in the normal fluid regime are around 50 mT as compared to more than 80 mT in superfluid helium. Therefore, superfluid operation can offer a much more comfortable margin in that respect. Moreover, the higher the helium temperature, the more heating one will have to extract from the RF surface, and the lower the quench field will be. This quench field issue is a very serious drawback that must be thoroughly addressed if operation above the λ point is decided.

9 CONCLUSION

The total cryoplant cost (including capital and operation) has been evaluated as a function of SCRF cavities temperature at a frequency of 700 MHz. The optimum operating temperature is found to be (2.4 ± 0.2) K. This optimum is broad and any operation between (2.0 K) and (2.8 K) would lead to less than a 10% excess cost. But operation in normal helium is risky, as performance may not even be achieved while gaining less than 3.5% on the total cost. Therefore, it is recommended that the operating temperature would be chosen in the superfluid helium regime (below 2.17 K).

REFERENCES

[1] "Cryogenic Optimization for Cavity Systems", C.H. Rode & D. Proch, 4th Workshop on RF Superconductivity, 751, Tsukuba, Japan, Aug. 1989

[2] "A feasibility study of the APT Superconducting Linac," K.C.D. Chan, LA-UR-95-4045, April 1996.

[3] "Estimating the Cost of Superconducting Magnets and the Refrigerators Needed to Keep them Cold," M.A. Green et al., Advances in Cryogenic Engineering, Vol. 37, Feb. 1992.

[4] "High Gradients in SCRF Cavities," H. Safa, 8th Workshop on RF Superconductivity, Padova, Italy, October 1997.

[5] "An analytical approach for calculating the quench field in superconducting cavities", H. Safa, Proc. of the 7th Workshop on RF Superconductivity, Gif-sur-Yvette, France (1995), p.413.

AN ACCELERATOR-ASSISTED NUCLEAR FUEL ASSEMBLY FOR A FUTURE PROJECT AT KURRI

Y. Kawase and S. Shiroya
Research Reactor Institute, Kyoto University, Kumatori. Sennan, Osaka 590-0494 Japan
M. Inoue
Institute for Chemical Research, Kyoto University, Uji, Kyoto, 611-0011 Japan

Abstract

A nuclear fuel assembly assisted by a linear accelerator has been proposed as a future neutron source of the Research Reactor Institute, Kyoto University (KURRI). The injector linac provides 300 MeV, 0.3mA protons to produce neutrons by a spallation reaction. Final goal of this project is to multiply neutrons by a subcritical nuclear fuel assembly. This system is expected to bring new opportunities as a second generation neutron source at KURRI and also to play an important role in the basic studies of the future hybrid reactor.

1 INTRODUCTION

The Kyoto University Reactor(KUR) has been providing low energy steady neutrons since 1964 for various research fields such as reactor physics, nuclear physics, nuclear chemistry, biology and medicine. Strong requirements for high energy and pulsed neutrons have been arising up recently according to the advancement in each field. To meet the requirements, a "new neutron source" has been discussed in the working group of the future plan committee of KURRI. A combination of a proton accelerator and a nuclear fuel assembly is proposed as one of possible candidates.

2 INJECTOR LINAC

The primary particles to produce neutrons efficiently are high energy proton and deuteron which can be accelerated advantageously by a linear accelerator(LINAC) at high beam intensity[1]. In order to obtain intense neutrons, it is desirable that the reactor technology is effectively applied to produce neutrons in combination with a moderate size linac.

The project " Neutron Factory" is proposed. It is composed of a hybrid system of particle accelerators and a subcritical assembly. The outline of the system is shown in Fig. 1.

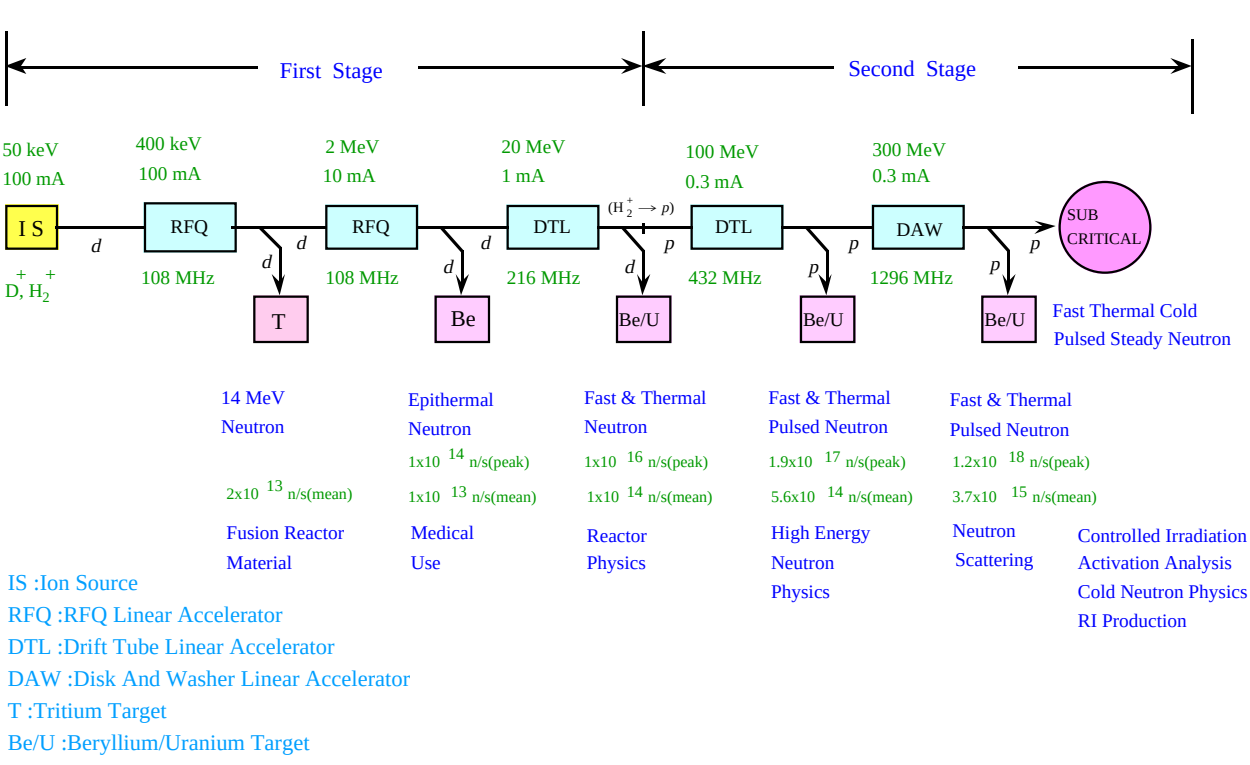

Figure 1: Block diagram of Neutron Factory

The brief report on this system has been given in Ref[2]. Deuterons or hydrogen molecules of 100 mA beam intensity extracted from a high current ion source are accelerated to 400 keV by the first RFQ . The beam energy is raised up to 2 MeV by the second RFQ at the 10% duty pulse operation. The drift tube linac(DTL) at 1% duty is employed to get the beam energy of 20 MeV . For the higher energy than 20 MeV, the proton acceleration is economical. Therefore, the 20 MeV H_2^+ beam which can be accelerated by the deuteron linac is stripped before the second stage DTL. Finally, we expect to obtain a proton beam of 300 MeV and 0.3 mA by a Disk and Washer (DAW) linear accelerator.

In each stage of the particle energy, every variety of neutrons become available as follows.

1) *14 MeV neutrons*

Among the neutron producing reactions, the (D,T) reaction has the largest cross section. It reaches 5 barns at 105 keV deuteron bombarding energy. By using 400 keV deuterons from the first RFQ, intense 14 MeV neutrons can be generated and used for the study on fusion reactor materials. Difficult problems arising from a large amount of tritium targets should be solved. For fusion reactor material irradiations, the ^{9}Be(d,n) reaction is also useful to produce neutrons with energy around 14 MeV by higher energy deuterons as proposed in the IFMIF project at JAERI.

2) *Epithermal neutrons*

The second RFQ generates about 3 MeV neutrons by the deuteron bombardment on the Be target. They can be moderated down to epithermal neutrons which are efficiently used for the BNCT. The fundamental study on the BNCT presently performed with thermal neutrons at KUR can be upgraded by utilizing high quality epithermal neutrons. To produce epithermal neutrons very efficiently, the p(^{7}Li,n) reaction by the 2.5 MeV proton is used at MIT[4]. Therefore, the 2.5 MeV proton beam by a small accelerator may be more favorable for medical use.

3) *High energy pulsed neutrons*

The 20 MeV deuterons obtained by the DTL linac can produce about 10 MeV pulsed neutrons by the ^{9}Be(d,n) stripping reaction. The DTL is operated at 1% duty and high energy neutron experiments such as the T.O.F. spectroscopy in reactor physics become possible.

4) *Intense pulsed neutrons*

The final energy and beam intensity of the primary particles are planned to be 300 MeV and 0.3 mA, respectively, which allow the mass production of high energy neutrons by a spallation reaction. We can expect the neutron intensity of 1.2×10^{18} n/s at peak and 3.7×10^{15} n/s in mean, which enables neutron scattering experiments such as the structure analysis of condensed matters.

5) *Neutrons for material irradiation*

The final goal of the Neutron Factory project is to inject spallation neutrons into a subcritical assembly to multiply them safely and efficiently. Details of the target system are studied preliminary for a simple case[3]. Intense neutrons can make great evolution in research fields such as precisely controlled irradiation of materials and the cold neutron physics which require much more neutrons than presently available at KUR.

An example of design parameters for proposed linacs is summarized in table 1. A conservative design is proposed by a working group as shown in table 1 in which higher energy section uses RF of 216 MHz and 432 MHz. The Disk-And-Washer(DAW) type is considered as an alternative design.

The deuteron beam with energies lower than 20MeV enters the Kyoto University Critical Assembly(KUCA) to be used for test experiments on the subcritical neutron target. At the 300 MeV terminal, a new target system of a subcritical nuclear fuel assembly is constructed to obtain intense neutrons for material irradiation and neutron scattering experiments.

Table 1 The example of design parameters for linacs.

	RFQ1	RFQ2	DTL1	DTL2	DTL3*
Particle	H_2^+,D^+	H_2^+,D^+	H_2^+,D^+	H^+	H^+
Energy(MeV)	0.4	2	20	100	300
Mean current(mA)	100	10	1	0.3	0.3
Duty(%)	CW	10	1	1	1
Frequency(MHz)	108	108	216	216	432
Cell number	90	67	78	138	329
Length(m)	1.182	3.065	10.316	62.73	134.81
RF power(MW)	0.3	0.8	3	12	48

*) Disk-And-Washer(DAW) type is considered as an alternative design.

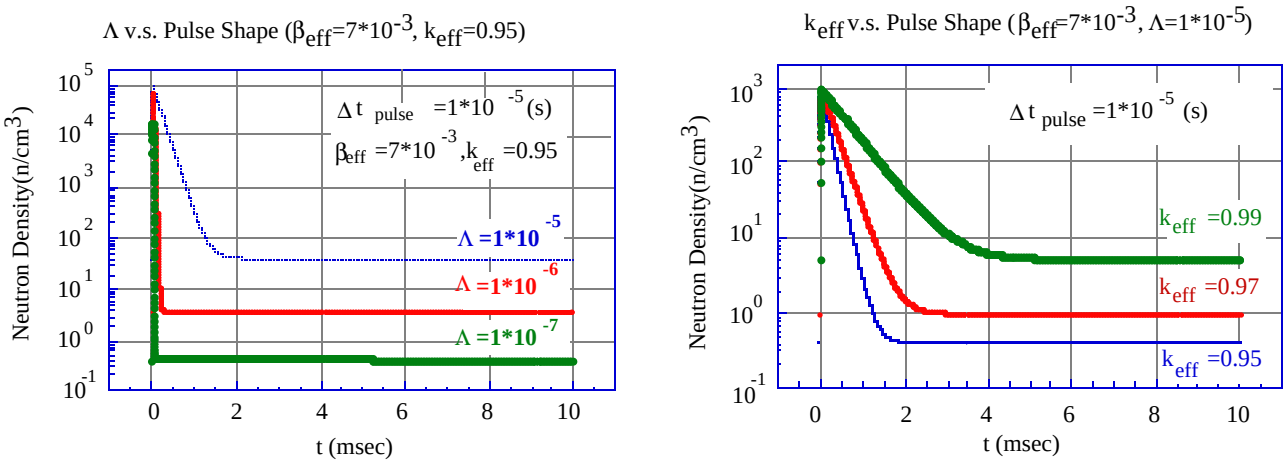

Figure 2: Dependence of the neutron pulse shape on k_{eff} and L at the equilibrium state.

3 NEUTRON PULSE SHAPE IN HYBRID REACTOR

Neutronics design calculations were carried out to obtain information on a hybrid system[3]. We report here some results of preliminary studies on the neutron pulse shape in the "hybrid" reactor calculated by the one-point reactor kinetics with an external source. It is well known that the neutron pulse shape strongly depends on values of k_{eff}, the effective delayed neutron fraction β_{eff} and the neutron generation time Λ.

Figure 2 shows the dependence of the neutron pulse shape on k_{eff} and Λ at an equilibrium state, when 100 neutron pulses with a density of 10^{10} cm^{-3} s^{-1} and a width of 10^{-5} s are introduced into the system per second. From this figure, it was found that the signal-to-noise (S/N) ratio of the neutron pulse, which is defined as a ratio between the peak and the background levels, becomes larger with reduced values of Λ and k_{eff}, whereas the peak level is maintained approximately at the same level. The decay of a neutron pulse becomes faster with reduced values of Λ and k_{eff}. The effect of β_{eff} on the decay of a neutron pulse was also investigated and was found to be remarkable when k_{eff} approaches to unity. For the neutronics design of the "hybrid" system, one should be careful that Λ and β_{eff} depends on k_{eff} on the basis of the reactor physics theory.

More detailed studies are required for the design of planned subcritical assembly. This can be performed in the first stage of the “Neutron Factory “ project by using the pulsed neutrons generated by the 20MeV linac.

4 SUMMARY

In order to offer opportunities to utilize high energy pulsed neutrons as well as low energy steady neutrons, the KURRI has started toward the realization of a multipurpose neutron source assisted by particle accelerators. The nuclear hybrid system itself is very interesting and worthwhile because it involves many technical subjects in both accelerator technology and nuclear engineering. We hope that this proposal will be discussed and polished up by those who are interested in neutrons, accelerators and nuclear systems.

REFERENCES

[1] "Neutron Sources for Basic Physics and Applications". An OECD/NEA Report, edited by S. Cierjacks, Pergamon Press, 1983.

[2] Y. Kawase, M. Inoue et al., Proceedings of the 11th Symposium on Accelerator Science and Technology, Harima, Hyogo, Japan,1997, p.133.

[3] S. Shiroya and H. Unesaki, Proceedings of the 9th International Conference on Emerging Nuclear EnergySystems ICENES'98, Tel-Aviv, Israel, 1998, Vol.1, pp.289-296

[4] J. C. Yanch, et al., Advances in Neutron Capture Therapy, edited by A. H. Soloway et al., Plenum Press, New York, 1993, p.95.

DESIGN OF 1 GEV, 30 mA PROTON LINAC WITH SUPERCONDUCTING CAVITIES

A.P.Durkin, V.M.Belugin, B.I.Bondarev, A.P.Fedotov, Yu.D.Ivanov, B.P.Murin, I.V.Shumakov, N.I.Uksusov

Moscow Radiotechnical Institute of RAS
MRTI RAS, 113519, Russia, Moscow, Warshavskoe shosse, 132

At the moment there are not problems of fundamental nature in CW proton linac construction with energy of 1 GeV and current of 30 mA. That is why the main problems have economic and technical aspects [1,2]: high economic efficiency (total electric efficiency >50 %), its reliability and radiation purity, linac design have to permit modernization with changing of beam performances demanded, linac design has to apply perspective methods and materials tested in actual practice.

The most expedient way of obtaining of such proton beams is acceleration in linear accelerator with superconducting (SC) accelerating resonators .

The scheme of CW proton and negative ion of hydrogen linear accelerator (LAP) with energy of 1 GeV and current up to 30 mA with superconducting accelerating resonators (SCR) in the main part is shown in Fig.1.

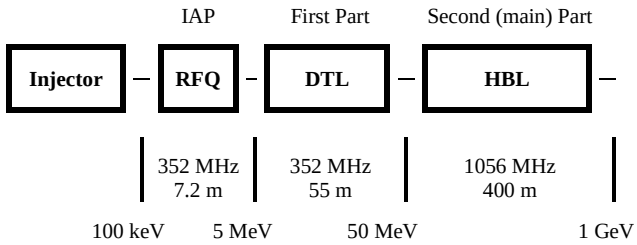

Fig.1.
1 GeV, 30 mA CW linac scheme.

The following main statements are used in its design.

1. Reliability: low voltage injector; low beam losses; CW mode; decreased number of RF channels.

2. Economic efficiency: superconducting cavities in the main part of linac; short length because of high accelerating rate.

3. Radiation purity: beam losses are not more than 10^{-4} [3] because of acceptance reserve of accelerating-focusing channels.

4. Linac consists of three parts. Initial part - RFQ structure, accelerating field frequency f_1 = 352 MHz. First part - three DTL resonators, frequency f_1 = 352 MHz. Main part - accelerating structure consists of 248 nine-cell axially symmetric cavities with elliptical shaped cells excited at the frequency f_2 = 1056 MHz.

Odd frequencies ratio $f_2/f_1 = 3$ allows if necessary to simultaneous acceleration of protons and negative hydrogen ions.

The main parameters of linac are presented in the Table 1. The parameters will not change for the case of acceleration of hydrogen negative ion beam.

The RF system and automatic control system are proposed as classic linac. For decrease of number of RF channels the possibility of excitation of several (6-2) SCR in main part by one RF amplifier is considered. Klystrons are used as RF amplifiers (1.3 MW klystrons - in initial and first parts, 400 kW klystrons - in main part).

In order to provide superconductivity in the SCR, its surfaces by layer are cooled to 2K by liquid helium. The total thermal power removed by helium is 5 kW.

Module of the main part of the linac with two SC cavities and PM quadruple lens is shown in the Fig.2.

Codes of LIDOS.Advisor package [4-7] were used for beam dynamic calculation Main problem is to prevent particle losses in high-energy accelerator part. Two main dangerous effects leaded to increase transverse beam size would be set: influence of phase motion on transverse one and random errors (within the limits of tolerances) in tuning and installations of channel elements. First effect is peculiar features of superconductng channel. In ordinary “warm” channel influence of phase motion on transverse one is weak effect, but in this case this influence is rather high because of high amplitude of accelerating field. This effect is most conspicuous in high-energy accelerator part with low (50-100 MeV) particle energy

High Beta Linac (HBL) part of LIDOS.Advisor package makes it possible to determined channel main parameters, demanded tolerances for elements installation, to reveal influence of various factors on beam parameters in the channel and at accelerator output. Initial and final particle energy, distribution of accelerating field amplitude and equilibrium phase along the accelerator, emittance, current are specified as initial information. Mean-squared errors of position of focusing lens ends, focusing fields, rotation of lens median axes, amplitude and phase of accelerating fields are used as additional initial data. Based on these data, channel random realization are calculated and statistic characteristics of beam parameters are derived. Simulations on the base of LIDOS.Advisor.HBL show that mismatching factor of transverse beam sections increases to the boundaries of

Table 1

Parameter	Initial Part	First Part	Second Part
Type of accelerator, resonator	RFQ	DTL	9-cell resonators
Injection energy, MeV	0.1	5	50
Output energy, MeV	5	50	1000
Frequency of accelerating field, MHz	352	352	1056
Number of resonators	1	3	248
Period of focusing, m	$\beta\lambda$	$2\beta\lambda$	$14\beta\lambda$
Acceptance, specified,π cm·mrad	0.27	2.0	2.0
Effective emittance, specified, π cm·mrad	0.1-0.15	0.15-0.3	0.3-0.4
Equilibrium phase, degree	-(40÷35)	-30	-30
Phase width, degree	360÷36	36÷20	60÷20
Pulse spread at output, %	0.32	0.1	0.04
Resonator length, m	7.2	18.5-17.6	0.4-1.12
Diameter of resonator, cm	20.2	55.0	29-26
Aperture diameter, mm	5	20	30
Accelerator length, m	7.2	55	400
Power for beam, MW	0.15	1.35	28.5

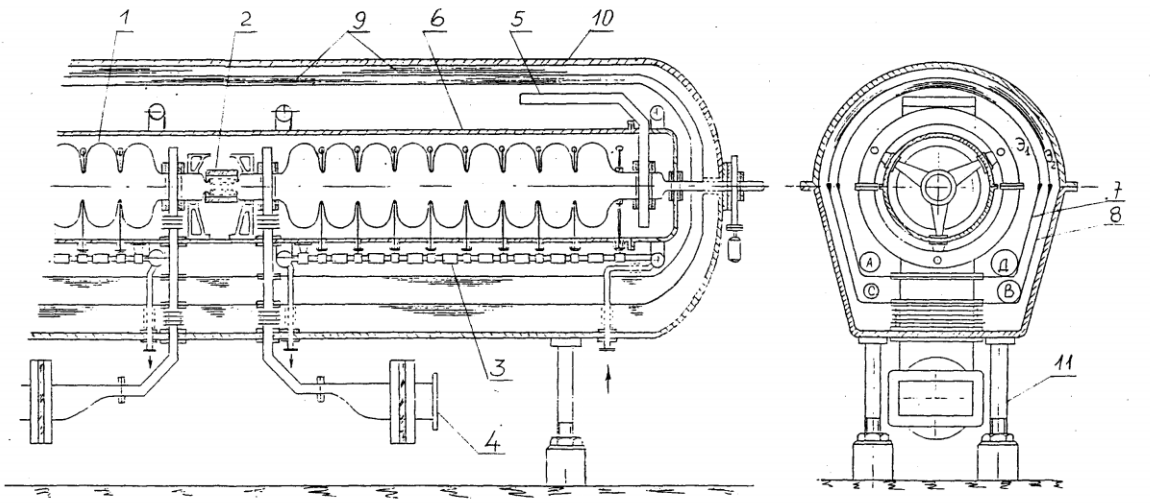

Fig.2.
Module of the main part of the linac with two SC cavities and PM quadruple lens.
1 – accelerating cavity; 2 – permanent magnet (PM) quadruple lens; 3 – nickel bar with cavity frequency fine-tuning elements; 4 – RF input; 5 – loading for high mode suppression; 6 – helium vessel; 7 – heat screen; 8 – radiation screen; 9 - superisolation; 10 - cryostat case; 11 – supports with adjusting devices; A, B, C, D – helium flow system

longitudinal oscillation separatrix up to the 1.8 – 2 in the considered case. If beam phase width at the channel beginning is 50^0, than maximal mismatching is 1.5. Beam phase characteristics at the accelerator output for the channel without disturbances and superposed beam phase portraits obtained with 50 channel random realization are shown in the Figs.3,4.

Phase width of initial beam is 50^0. Initial data were as follows: error of cavity field amplitude – 1%, error of cavity phase – 1^0, transverse displacement of quadruple lens ends – 50 mkm, error of magnetic field gradient in the lenses – 1%, rotation of lens median axes – $0{,}5^0$. Statistic characteristics of beam parameters obtained in 50 random realization are shown in the Fig.5.

Results analysis shows that because of influence of longitudinal phase oscillations and under the influence of random errors transverse beam size with high confidence coefficient will not exceed 5.5 mm. In this case the size of matched equilibrium section in the channel without errors is 3 mm.

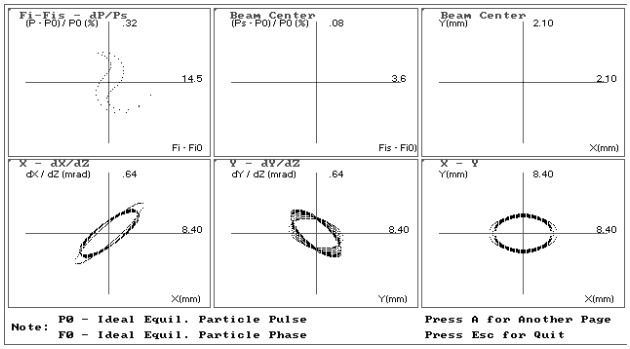

Fig.3.

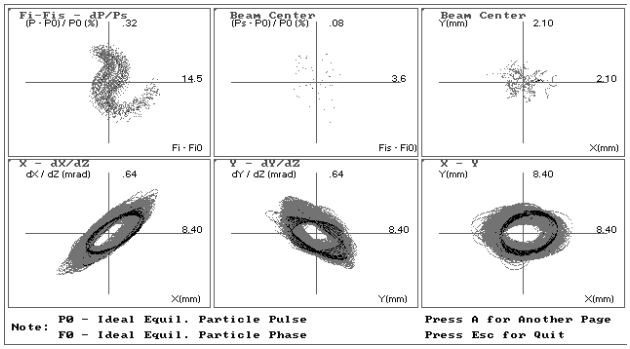

Fig.4.

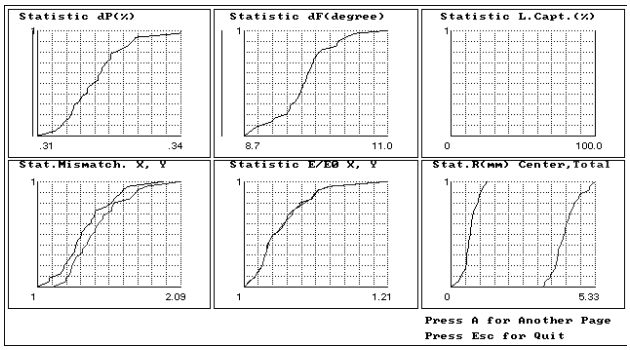

Fig.5.

Fulfilled investigations verify efficiency and reliability of described scheme as well as its practical feasibility.

REFERENCES

1. O.V.Shvedov, B.P.Murin, B.P.Kochurov, Yu.N.Shubin, V.I.Volk, P.V.Bogdanov. Weapon plutonium in accelerator driven power system. In "Joint United States/Russian Plutonium Disposition Study", pp.A1-A60, September 1996.

2. B.P.Murin et al. “Superconducting devices use in high-current linear accelerators for energy purposes” Proceedings of the Second International Conference on “Accelerator-Driven Transmutation Technologies and Applications”, June 3-7 1996, Kalmar, Sweden, Uppsala University, pp.1047-1053.

3. A.P.Fedotov, B.P.Murin. Towards a radiation-free linac of meson or neutron generator type. Proceedings of the Proton Linear Accelerator Conference, Chalk River Nuclear Laboratory, Canada, 1976, p.377.

4. B.I.Bondarev, A.P.Durkin, et al. LIDOS - Unconventional Helper for Linac Beam Designing,. Computational Accelerator Physics Conference, AIP Conference Proceedings 297, Los Alamos, NM 1993, pp.377-384.

5. B.I.Bondarev, A.P.Durkin, B.P.Murin, G.T.Nikolaishvili. LIDOS: Multilevel Codes For Ion Linac Designing. Proceedings of International Workshop "Beam Dynamics&Optimization", pp.35-44. (July 4-8, 1994, St.-Petersburg, Russia).

6. B.I.Bondarev, A.P.Durkin, G.H.Gillespie. Beamline Parameter Optimization In The Framework Of The Lidos.Advisor. Proceedings of Second International Workshop Beam Dynamics&Optimization, pp.61-64. (July 4-8, 1995, St. Petersburg, Russia).

7. "SUPERLINAC.Advisor, Image-based Codes for Ion Beam Optimization and Simulation", MRTI-ISTC Project No 147, Scientific Report, Moscow 1996.

BREMSSTRAHLUNG PAIR-PRODUCTION OF POSITRONS WITH LOW NEUTRON BACKGROUND*

E. Lessner, M. White
Argonne National Laboratory, Argonne, Illinois 60439 USA

Abstract

Minimization of component activation is highly desirable at accelerator-based positron sources. Electrons in the 8- to 14-MeV energy range impinging on a target produce photons energetic enough to create electron-positron pairs; however, few of the photons are energetic enough to produce photoneutrons. Slow positron production by low-energy electrons impinging on a multilayer tungsten target with and without electromagnetic extraction between the layers was studied by simulation. The neutron background from 14-MeV electrons is expected to be significantly lower than that encountered with higher-energy electron beams. Numerical results are presented and some ideas for a low-activation slow-positron source are discussed.

1 INTRODUCTION

Slow positrons are widely used in materials science and solid state physics research. Positron annihilation techniques are used to characterize vacancy-type defects in metals and alloys. Very low energy positrons are ideal probes for surface crystallography due to their shallow penetration and weak scattering with the atomic ion core.

The use of the Advanced Photon Source (APS) linac beam as a source of slow positrons has been investigated for incident electron beam energies between 200 and 400 MeV [1], [2]. Accelerator studies indicate that the electron linac is capable of producing about 13kW of incident beam power [3]. Simulation studies to optimize the target indicate that for those incident-electron energies, a high slow-positron yield can be obtained.

Activation of components in the area near the target is a potentially serious problem at positron sources. Component activation can be reduced if the input beam energy is low enough such that the cross section for photoneutron production is still quite low, yet high enough to create electron-positron pairs. In this paper, we study the production of slow positrons using electrons with energies between 8 and 14 MeV.

Monte Carlo simulation results of low-energy electrons impinging on a multilayer tungsten target are described. Positron production rates with and without electromagnetic extraction between target layers are compared. Some ideas for a low-background positron source are discussed.

* Work supported by U. S. Department of Energy, Office of Basic Energy Sciences under Contract No. W-31-109-ENG-38

2 CHOICE OF ELECTRON BEAM ENERGY

Several factors influence the choice of the incident electron beam energy for a slow-positron source with minimal neutrons. One factor is the efficiency with which the incident beam creates positrons, the other is the neutron yield. For high productivity, most of the incident electron beam should penetrate the target. The number of backscattered electrons increases exponentially with decreasing electron energy, as can be seen in Fig. 1. As shown in the figure, there is essentially no backscattering for energies above

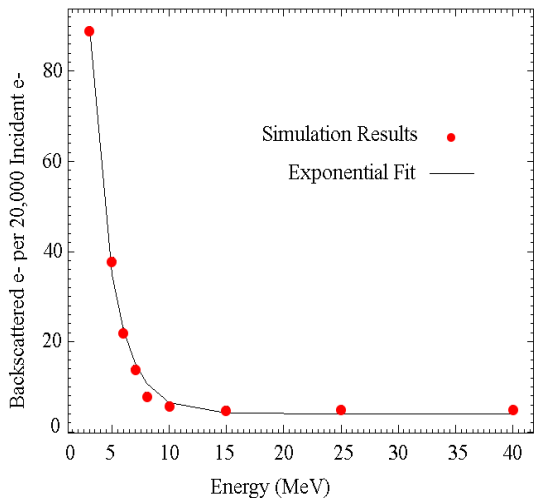

Figure 1: Number of backscattered electrons versus incident beam energy with a superimposed exponential fit.

8 MeV. At 3 MeV, about 0.5% of the incoming particles are backscattered, thus reducing overall efficiency. In our simulations, we chose an energy range between 8 and 14 MeV for the primary electron beam.

The neutron yield per incident electron in a high-Z target is low for energies below 14 MeV. The photoneutron cross-section for tungsten is about 400 mb for 14-MeV photons and becomes negligible for photons of 6-MeV energy and lower [4]. For one radiation-length-thick targets, measurements indicate that there are 2.5×10^{-4} neutrons per 14-MeV electron [5]. Shown in Fig. 2 is the photon energy distribution from 20000 14-MeV electrons impinging on a 1.2-mm tungsten target. An energy cutoff of 1.0 MeV

has been applied to the distribution prior to histogramming. Photons below 1.0 MeV are incapable of e^+e^- pair production. The distribution peaks at 1.5 MeV and has a standard deviation of 2.4 MeV. Less than 9×10^{-2} photons per electron have energies greater than 6 MeV.

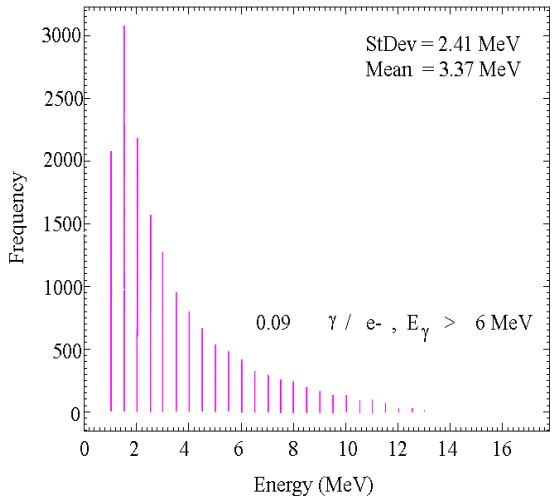

Figure 2: Photon energy distribution from 14-MeV electrons on a 1.2-mm tungsten target.

3 SIMULATION RESULTS

Our simulations were performed with the program EGS4 [6], together with a C-language user-interface code, "shower" [7]. We studied the positron-production efficiencies of single-block and multilayer targets at several energies. Optimized multilayer targets are able to produce more positrons than single-block targets for a fixed incoming beam energy. For multilayer targets, we examined the production rates with and without electromagnetic extraction between target layers.

The forward positron production as a function of single-block tungsten target thickness is shown in Fig. 3 for 8-MeV and 14-MeV electrons. For the higher-energy beam, the production peaks around target thicknesses of 2.5 mm. The production from the 8-MeV beam roughly follows a similar curve. The variations seen in the figure are within the statistical fluctuations of the Monte Carlo process. The number of positrons increases by a factor of 4.5 for a 1.75 increase in beam energy. For target thicknesses greater then 2.5 mm, many positrons are lost in the material decreasing the yield.

Figure 4 shows the forward positron production for a three-layer tungsten target of 1.2-, 0.6-, and 0.6-mm-long segments, respectively. The incident electron beam energy is 14 MeV.

In the figure, circles indicate the number of positrons produced when no electromagnetic field is applied between layers, and squares indicate the production when electromagnetic extraction is applied. In the latter simulations, the total output lepton distribution from each segment was removed and only the photon distribution was used as input to the simulation of the following segment. This possibly leads to an underestimation of the positron count after the second and third layers. In practice, energetic electrons would not be removed by the applied field, though the total beam divergence would be increased, and they could contribute to the positron creation through bremsstrahlung. As shown in the figure, photons produce 68% of the total positron count in the second segment, and 89% in the third segment.

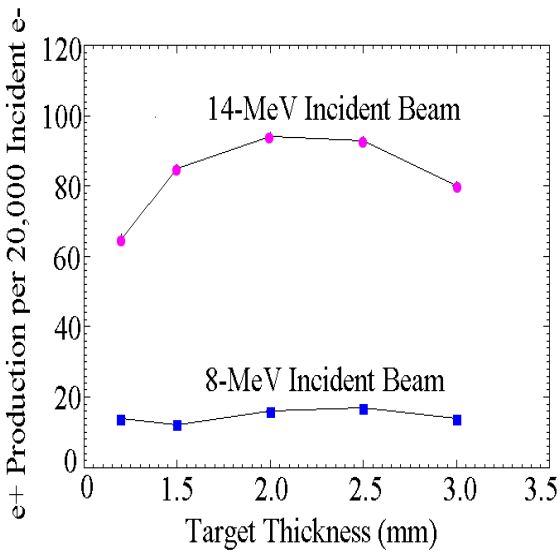

Figure 3: Positron production as a function of target thickness for two electron energies.

We used our high-energy simulation results as a guide to optimize the multilayer target for a 14-MeV incident beam. Specifically, we analyzed the positron production as a function of target thickness and the output electron and photon mean energy variations to determine the optimal segment thicknesses of a multilayer target. At 400 MeV, the best target configuration is a 10.5-mm-long, five-layer target. The 10.5-mm length is determined by the optimized single-block target length.

The highest production differentials between layers occur when there is a 25% variation in thickness from the first to the second layer and none or a small variation in thickness between the last two layers. The output electron mean-energy change from layer to layer is also a factor. Yield is best when the energy decreases by about 50% in the first two layers, and by 30% to 10% in the last layers. These observations, together with the single-block target results at low energies, led to a three-layer target with segment thicknesses of 1.2, 0.9 and 0.9 mm, respectively, as a candidate for an optimized low-energy target. Further simulations showed that the positron production is in-

creased by 26% when the last-segment is 0.6-mm long. For the optimized 1.2-/0.9-/0.6-mm target, the total number of positrons whose energies are $\leq$ 6 MeV is 1.3e$\times 10^{-2}$ per incoming 14-MeV electron.

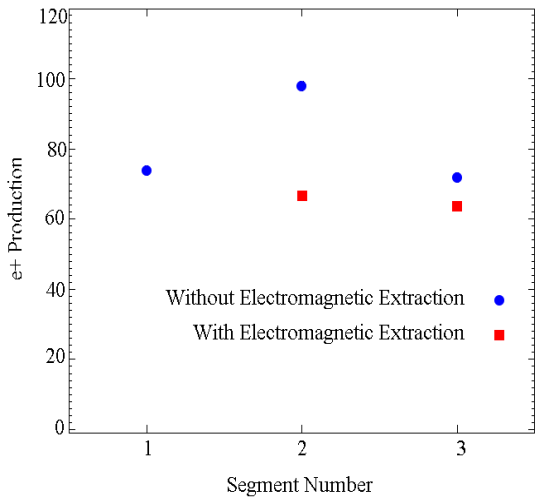

Figure 4: Comparison of the number of positrons produced by 14-MeV electrons on a three-layer target, with and without electromagnetic extraction between layers.

4 OPTIONS FOR A LOW-ENERGY POSITRON SOURCE AT APS

The linac's DC thermionic electron gun has been supplemented by a thermionic rf gun [8], and additional thermionic and low-emittance photocathode rf guns will soon be installed. These guns will be able to handle the task of storage ring injection, thus allowing the DC thermionic gun to be used for other purposes.

The DC gun is currently being re-packaged for greater space efficiency. The gun, together with its buncher and accelerating structure, could be located in the linac tunnel under the rf photocathode gun girder. Assuming good beam optics, at least 13 kW of beam power could still be obtained at 150 MeV. If used to produce a low-energy, high-power beam, the gun and its associated rf structures could operate semi-independently of the APS. The bunchers and accelerating structure could receive rf power from the output load of one of the linac accelerating structures. We estimate that the linac could produce a few kW of beam power in low-energy mode. Available beam power in such a low-energy machine could be significantly increased by changing from pulsed to CW operation, and using superconducting rf structures.

5 CONCLUSIONS

A slow-positron source with reasonable slow-positron yield and with a relatively low neutron background could be constructed. For an incident 14-MeV electron beam, we estimate that a flux of 10×10^{7} positrons per second can be achieved, assuming a conservative moderation efficiency of 10×10^{-3}.

Plans are now underway to measure the positron and slow positron yields at another local facility with beam characteristics similar to what we have considered in this paper. Use of low-energy electrons to drive a slow positron source has the advantage that it could be a semi-independent setup. Various configurations for such a source have been investigated. Some options allow operation of the slow positron source in parallel with other APS operations, while operation of other configurations is more constrained.

An additional advantage of the low-energy driver is that extraction and guide voltages for the unmoderated positrons can be lower, since they are produced at lower energies. The disadvantages are lower positron production rates per incident electron. The beam power and thus the positron production rate can be improved by increasing the electron current. At high power and low energy, target ablation will likely be a problem. Detailed thermal analysis must be carried out, and careful monitoring of the target and support structures must be envisioned.

6 ACKNOWLEDGMENTS

The authors appreciate J. Galayda's continuing support and enthusiasm. We would also like to thank P. Schoessow for useful discussions, D. Haid for graphics assistance, and C. Eyberger for editorial input.

7 REFERENCES

[1] M. M. White, E. S. Lessner, "The Advanced Photon Source (APS) Linear Accelerator as a Source of Slow Positrons," Applied Surface Science 116, 87-90 (1997).

[2] M. White and E. Lessner, "Slow Positron Target Concepts for the Advanced Photon Source (APS) Linear Accelerator," Proceedings of the 11th International Conference on Positron Annihilation, Material Sciences Forum Volumes 255-257, 778-780 (1997).

[3] M. White and E. S. Lessner, "High-power Beam Studies at the APS Linac," APS-LS Note, to be published.

[4] S. S. Dietrich and B. L. Berman, "Atlas of Photoneutron Cross Sections Obtained with Monoenergetic Photons," UCRL-94820 Preprint.

[5] W. C. Barber and W. D. George, "Neutron Yields from Targets Bombarded by Electrons," Phys. Rev. 116 (6) (1959).

[6] R. Nelson, H. Hirayama, D. W. Rogers, "The EGS4 Code System," SLAC-265 (1985).

[7] L. Emery, private communication.

[8] J. Lewellen, A. Lumpkin, S. V. Milton, A. Nassiri, S. J. Pasky, and M. White "Operation of the APS RF Gun," these proceedings.

THE KEK-PF SLOW-POSITRON FACILITY AT A NEW SITE

T. Shidara, T. Kurihara, A. Shirakawa, A. Enomoto, H. Kobayashi, K. Nakahara
KEK, 1-1 Oho, Tsukuba-shi, Ibaraki-ken, 305-0801, Japan

Abstract

The KEK-PF slow-positron facility was relocated to the 1.5-GeV point of the upgraded electron/positron injector linac relevant to the KEKB project. A dedicated linac for slow-positron use is also installed utilizing the remnants of the injector linac reformation. We expect a slow-positron intensity of more than 100 million positrons/sec with a maximum primary beam power of 1 kW for their application in various fields of solid-state physics.

1 INTRODUCTION

The KEK slow-positron facility, aiming at the use of slow-positron beams (ranging from eV to keV) in various fields of solid-state physics, was constructed. A slow-positron flux of $1x10^8$ positrons/sec was successfully achieved [1, 2] utilizing our 2.5-GeV electron linac [3, 4] with a 2.0-GeV, 2-kW primary electron beam power.

Although we had opened this facility to slow-positron users [5, 6], we had to relocate our facility relevant to the upgrade plan of the KEK 2.5-GeV linac. There are two major goals of the upgrade [7, 8]: 1) to increase the energy of electrons and positrons to 8 and 3.5 GeV, respectively, and 2) to increase the bunch intensities of positrons by roughly one order. In accordance with this upgrade plan, we must relocate our KEK-PF slow-positron facility to the 1.5-GeV point of the upgraded linac (the KEKB J-linac).

2 LAYOUT OF THE RELOCATED KEK-PF SLOW-POSITRON FACILITY

There are two primary-electron-beam sources for our slow positron facility; the 1.5-GeV beam of the KEKB linac and the test linac. The nominal beam power of the 1.5-GeV beam is 0.75 kW (an energy of 1.5 GeV, charge of 10 nC/pulse, a pulse length of 10 ps and a pulse repetition rate of 50 pulse/s). A dedicated linac for slow positron use only (the test linac) was installed utilizing the remnants of the J-linac upgrade plan. An average beam power of 1 kW can be expected from the test linac. A slow-positron intensity of more than 10^8 positrons/sec is easily expected in both cases.

Figure 1 shows the relocated KEK-PF slow-positron facility, which locates at the 1.5-GeV point of the KEKB J-linac. It comprises beam lines for the primary electron beams, a target-moderator assembly, a slow-positron beam-transport line and relevant assemblies.

The primary electron beam is injected into the target. The extracted slow-positron beam is directed by a 30-m long beam-transport line with an axial magnetic field of 100 G to an experimental area. Twelve sets of steering coils were installed along the slow-positron beam-transport line in order to adjust the slow-positron beam trajectory. A high-voltage station capable of applying 60 kV was installed in order to vary the energy of the positron beam. A device controller, combining a personal computer and a programmable sequence controller through optical fiber, has been adopted to control the monitors and power supplies at a high-voltage potential. Penning-trap electrodes are also installed at this station in order to make a dc beam from a pulsed beam.

At an experimental area, a slow-positron beam switch system, which comprises a pair of beam deflecting coils and two pairs of Helmholtz coils with magnetic-field directions crossing each other, was installed. This system enables us to direct slow-positron beams to several experimental stations one by one without breaking the vacuum.

As for experimental equipment, a transmission-type positron microscope, a positronium time-of-flight (TOF) apparatus, and a 2D-ACAR (two-dimensional angular correlation of annihilation radiation) equipment are now being prepared.

3 PRESENT STATUS

All components of the KEK-PF slow-positron facility were relocated. The accelerating structures and necessary magnets of the test linac have already been installed in the linac tunnel.

The commissioning of the slow positron beam was started from this April. We have already achieved a slow-positron intensity of more than 10^7 positrons/sec utilizing the 1.5-GeV J-linac beam as its primary beam source. Utilizing this positron beam, the 2D-ACAR equipment was checked and adjusted.

4 FUTURE PLAN

If we reinforce its primary beam source by adding other two accelerating units to the present test linac, we will be able to achieve a beam power of 6 kW from the upgraded test linac. This enables us to produce more than 10^9 positrons/sec in our slow-positron facility.

5 SUMMARY

The KEK slow-positron facility was relocated to the 1.5-GeV point of the KEKB J-linac relevant to the KEKB project. A dedicated linac for slow-positron use is also installed utilizing the remnants of the KEKB J-linac

upgrade plan. We have already achieved a slow-positron intensity of more than 10^7 positrons/sec utilizing the 1.5-GeV J-linac beam as its primary beam source and we expect more than 10^8 positrons/sec with a maximum primary beam power of 1 kW.

ACKNOWLEDGMENTS

The authors are greatly indebted to the Director General, Prof. H. Sugawara as well as to the staff of the KEK administration department for their encouragement and continuous support of this slow-positron project. They should also express their gratitude to prof. Y. Kimura, the director of the Institute of Materials Structure Science and to Prof. M. Kihara, the director of the Accelerator Laboratory, KEK, for their support. The staff of the KEK electron/positron linac is also gratefully acknowledged for machine operation and support.

REFERENCES

[1] A. Asami, A. Enomoto, H. Kobayashi, T. Kurihara, K. Nakahara and T. Shidara, "A Slow-Positron Source Project using the Photon Factory Electron Linac", Materials Science Forum, 105-110, 1833 (1992).

[2] T. Shidara, A. Enomoto, T. Kamitani, H. Kobayashi, T. Kurihara, A. Shirakawa, H. Hirayama, I. Kanazawa, A. Asami and K. Nakahara, "The KEK Slow-Positron Source", Materials Science Forum, 175-178, 205 (1995).

[3] J. Tanaka, "Construction of the Photon Factory 2.5 GeV Injector Electron Linac", Nucl. Instr. Meth., 177, 101 (1980).

[4] I. Sato, "Accelerator Structure and Beam Transport System for the KEK Photon Factory Injector", Nucl. Instr. Meth., 177, 91 (1980).

[5] Y. Morinaka, Y. Nagashima, Y. Nagai, T. Hyodo, T. Kurihara, T. Shidara and K. Nakahara, "Time-of-Flight Spectroscopy of Positronium Emission from SiO_2 Surface", Materials Science Forum, 255-257, 689 (1997).

[6] eds. T. Shidara and K. Nakahara, "Construction Report of the PF Slow-Positron Source (II)", KEK Report, 97-12, (1997).

[7] "KEKB B-Factory Design Report", KEK Report, 95-7, (1995).

[8] eds. I. Sato, S. Anami, A. Enomoto, S. Fukuda, H. Kobayashi and K. Nakahara, "Design Report on PF Injector Upgrade for KEKB", KEK Report, 95-18, (1996).

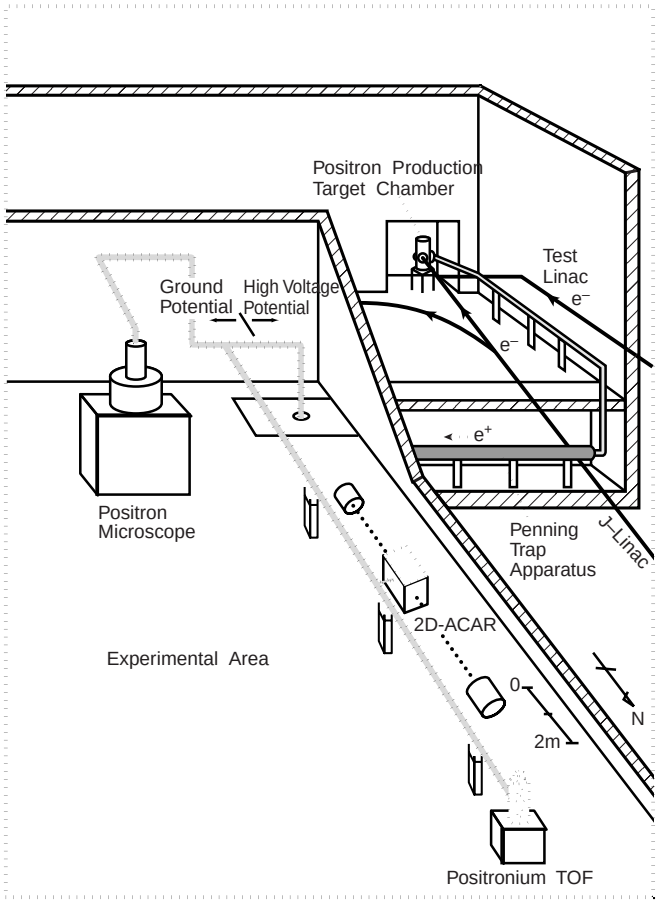

Figure 1. Bird's-eye view of the KEK-PF slow-positron facility.
It comprises beam lines for the primary electron beams, a target-moderator assembly, a slow-positron beam-transport line and relevant assemblies.

FARADAY CUP MEASUREMENTS OF THE PLASMA PLUME PRODUCED AT AN X-RAY CONVERTER*

T. Houck, M. Garcia, and S. Sampayan
Lawrence Livermore National Laboratory, Livermore, California 94550 USA

Abstract

The next generation of radiographic machines based on induction accelerators is expected to generate multiple, small diameter x-ray spots of high intensity. Experiments to study the interaction of the electron beam with the x-ray converter are being performed at the Lawrence Livermore National Laboratory (LLNL) using the 6-MeV, 2-kA Experimental Test Accelerator (ETA) electron beam. The physics issues of greatest concern can be separated into two categories. The multiple pulse issue involves the interaction of subsequent beam pulses with the expanding plasma plume generated by earlier pulses striking the x-ray converter. The plume expands at several millimeters per microsecond and defines the minimum transverse spacing of the pulses. The single pulse issue is more subtle and involves the extraction of light ions by the head of the beam pulse. These light ions might propagate at velocities of several millimeters per nanosecond through the body of the incoming pulse resulting in a moving focus prior to the converter. In this paper we describe Faraday cup measurements performed to quantify the plasma plume expansion and velocities of light ions.

1 INTRODUCTION

Radiographic machines based on induction accelerators produce an intense x-ray spot by focusing a short pulse of high current electrons onto a high Z material. Nominal parameters for the electron beam could be 50-100 ns pulse width, several kiloamperes, and 10-20 MeV. Producing a small and stable (constant diameter and position) x-ray spot is essential for radiographic imagining. The electron beam quality has been considered the limitation on the quality of the x-ray spot. For example, the emittance of the beam determines the smallest focus spot, and energy variation combined with transport focusing misalignments produces beam motion. Continuing advancements in induction accelerator technology has improved beam quality to a level where the interaction of the beam with the converter may be the limitation for the next generation of radiographic machines. Two areas of concern are the emission of light ions [1] that can "backstream" through the beam due to space charge potential, and interference between the beam and the plasma generated by previous pulses during multiple pulse operation.

*The work was performed under the auspices of the U.S. Department of Energy by LLNL under contract W-7405-ENG-48.

An on-going experimental program at LLNL is studying the interaction of an electron beam with the x-ray converter [2]. The goal is to quantify the effects of the plasma plume generated at the interaction on the initial and subsequent beam pulses, and to develop an appropriate x-ray converter configuration. Below we report on measurements from faraday cups incorporated into the experimental setup to characterize the plasma plume and determine the existence of backstreaming light ions.

2 EXPERIMENTAL LAYOUT

The faraday cups were comprised of two, electrically isolated, concentric cylinders as illustrated in Fig. 1. The inner cylinder could be biased up to 1.2 kV with respect to the grounded outer cylinder. Two geometries were used. The forward cup (refer to Fig. 2) had an OD of 5 cm and an aperture of 1.9 cm while the back cup had an OD of 1.3 cm and an aperture of 0.4 cm. The low ratio of aperture to cup length was to minimize the escape of secondary electrons generated by the impact of the positive ions with the inner cylinder. The forward cup was located about 25 cm from the beam/target intersection at an angle of 30° from the beam axis. The back cup was located about 5 cm from the intersection point and 75° from the beam axis. As shown in Fig. 2, the cups were situated at the entrance and exit, respectively, of a solenoid operating with an on-axis peak field of approximately 3 kG.

The inner cup discharged to ground through the 50 Ω input of an oscilloscope, permitting the rate of charge interception (current) to be measured. The sensitivity of the cups to ion density, assuming single ionization, is:

$$n_{\min} = \frac{I_{\min}}{Aev} \text{ , where} \qquad (1)$$

$n_{\min}$ is the minimum density, I_{min} is the minimum detectable current, A is the aperture area, and v is the ion velocity. For the forward and back cups, and for a nominal v of 5 mm/μs, $n_{\min}$ is $2\text{x}10^{8}$ cm^{-3} (I_{min} was 40 μA) and $5\text{x}10^{10}$ cm^{-3} (I_{min} was 480 μA), respectively.

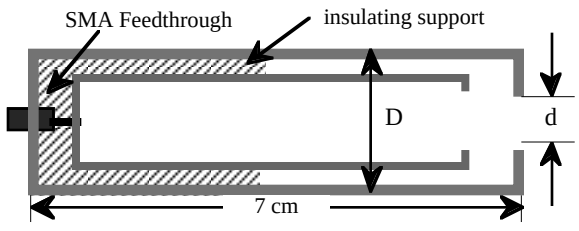

Figure 1: Schematic of the Faraday cup.

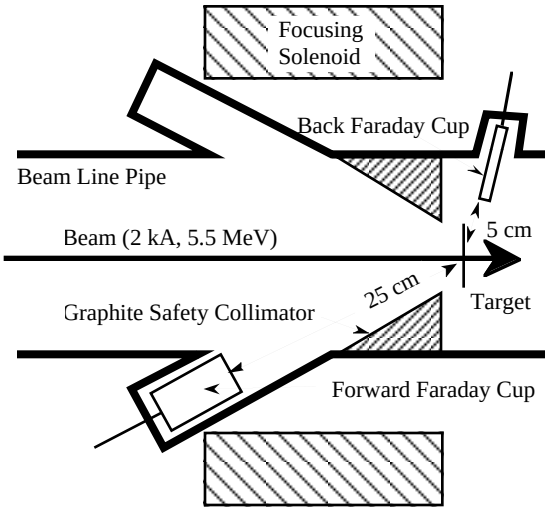

Figure 2. Schematic showing relative positions of the faraday cups with respect to the beam line and target.

The x-ray converter was comprised of a rotating wheel that held several "targets" to permit multiple shots before the x-ray converter had to be replaced. The majority of data was taken for tantalum targets of three thicknesses; 1 mm, 0.25 mm, and 0.1 mm. In addition, 1 mm thick stainless steel and 0.25 mm tungsten targets were used.

3 MEASUREMENTS

The faraday cup measurement consisted of the current (voltage) measured at the input (50 Ω termination) of an oscilloscope. See Fig. 3 and 4. Information that could be estimated from the measurements, with qualifications, included velocity, density, and beam radius. A third faraday cup was located approximately 50 cm upstream of the converter and recessed to avoid exposure to the plasma plume. This cup was directed at the beam line and served as a background reference for the other cups.

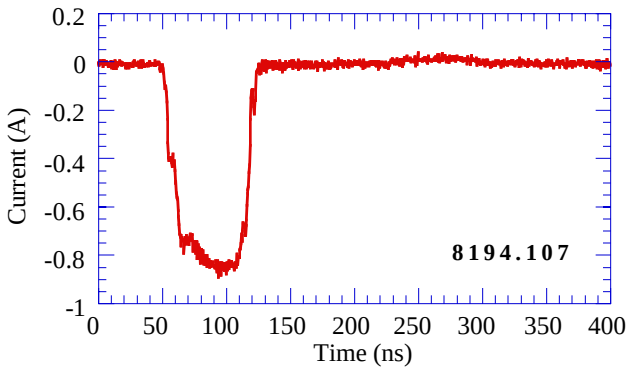

Figure 3. Typical output from the forward faraday cup.

3 .1 Prompt Signals (< 1 μs)

A large signal was generated by the faraday cups during beam passage. A typical signal from the back cup is shown in Fig. 3 and displays the same pulse shape as the beam current monitors installed on the beam line. The small positive signal between 250-300 ns was caused by cable reflections. The forward cup produced a similar signal, but a factor of 10 to 20 smaller in amplitude.

Estimates for the energy and density of extracted ions from the target are > 250 keV and 10^{12} cm^{-3} near the x-ray converter [3,4]. For protons, this equates to a velocity of 7 mm/ns and currents of 20-100 mA at the faraday cups. However, the signals would arrive within 50 ns of electron beam passage. Numerous comparisons were made of signals at the cups with and without the x-ray converter installed to discern such a signal with no success.

3 .2 Plume Velocity

Typical signals from the back and forward cups are displayed in Fig. 4. The back cup tended to have a single peak although the signal to noise ratio could have masked some features. The forward cup signal normally exhibited two peaks with the amplitude of the first peak varying from about 10% to over 130% of that of the second peak.

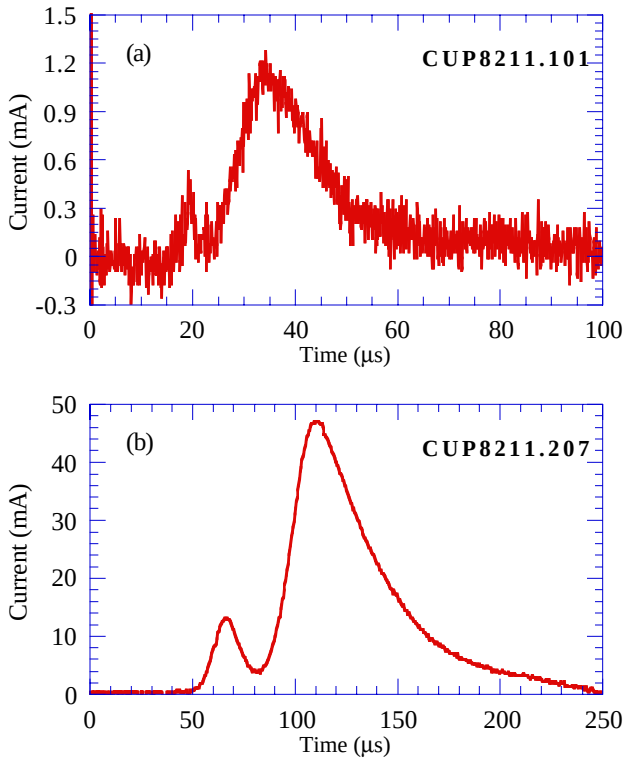

Figure 4. Typical output signals from the (a) back and (b) forward faraday cups. Beam interaction with the converter (1 mm thick Ta) occurred at time 0.

An estimate of the velocity can be made by assuming that the plasma was ejected promptly at beam time and quickly reached terminal velocity. With these assumptions the velocity would be simply the distance to the respective cup divided by arrival time at the cup after beam passage. The velocity can be related to spot size assuming a self-similar, isentropic expansion of a spherical gas cloud:

$$v = 1.64\sqrt{\frac{2E}{m}} = 2.32\sqrt{\frac{dE/dz}{\pi r^2 \rho}}, \text{ where} \qquad (2)$$

E is the energy deposited into a mass m by the beam, dE/dz is the rate of energy deposition along the axis, r is the radius of the beam spot, and ρ is the mass density. While approximate, eq. (2) indicates that the velocity should vary inversely with spot size and be insensitive to target thickness. In Fig. 5, the velocity of the leading edge of the plasma plume at the forward cup (25 cm/ time of arrival) is plotted as a function of x-ray spot size for two thicknesses of Ta targets. The x-ray spot sizes shown for the 1 mm targets were measured using the roll bar technique [5] while for the 0.25 mm targets a higher resolution pin hole camera [6] was used. Eq (2) was in general agreement with measured velocities and spot sizes.

The plume velocity measured at the forward cup consistently was faster than measured at the back cup. For the distances that the cups are located from the target, the plasma plume could be expected to be expanding approximately spherically. Thus, the velocity should not be strongly dependent on the angular locations of the cups with respect to the beam. A second explanation suggested by Fig. 6, a plot of the velocity ratio between the cups as a function of target thickness, is that the beam diameter expands during transit producing a larger spot size on the back surface. Ratios are shown for the leading edge and for the peak signal.

3 .3 Plasma Density

Equation (1) can be used to crudely estimate the plasma density. Current in the Faraday cups is the combined effect of the collection of ions and electrons, and of the ejection of electrons in reaction to ion impact. Heavy ions like Ta with kinetic energy of several eV are quite likely to eject electrons on striking metal surfaces. Escape of secondary electrons increases the current signal and collection of plasma electrons lowers the current signal. Attempts to bias the inner cylinder did not produce significant changes to the cup signal. Probably of more importance is the orientation of the cup with the magnetic field lines of the focusing solenoid. The forward cup was positioned such that the magnetic field would tend to preclude the flow of electrons into or out of the cup. However, the orientation of the back cup would enhance flow. The heavy ions would not be significantly affected. The relative long length of the back cup to its aperture should minimize the escape of secondaries, with the net result of a low estimate of the density at the back cup.

Table 1: Estimated density (10^{10} cm^{-3}) at faraday cup.

Ta thickness	1 mm	0.25 mm	0.1 mm
Forward Cup	30	5	1
Back Cup	50	100	30

4 SUMMARY

No evidence was found for fast, backstreaming, light ions. However, the plasma plume was found to expand at 3-4 mm/μs (peak density) with a leading edge velocity of 7-8 mm/μs in agreement with theoretical models.

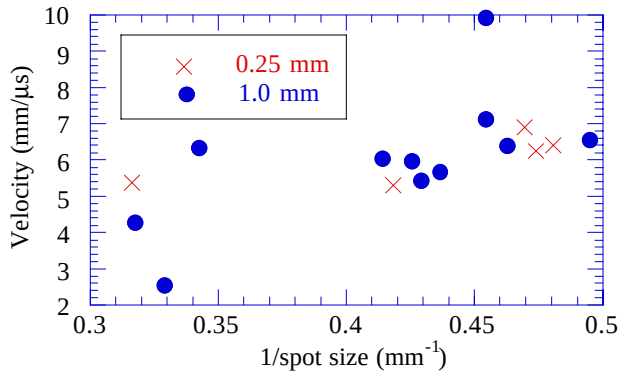

Figure 5. Velocity of the leading edge of the plume for Ta targets of two thicknesses as a function of spot size.

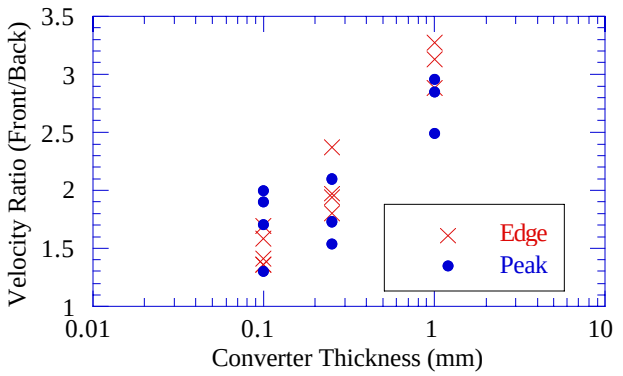

Figure 6. Ratio of the plume velocity at the forward and back faraday cups as a function of target thickness.

5 ACKNOWLEDGMENTS

We thank Phil Pincosy, Y-J Chen, Darwin Ho, and George Caporaso for their helpful explanations of the physics of the interaction. Cliff Holmes constructed the faraday cups. John Weir and the ETA crew provided the accelerator and experimental support.

6 REFERENCES

[1] G. Caporaso, "Analytic Model of Ion Emission From the Focus of an Intense Relativistic Electron Beam on a Target," this conference TH4027.

[2] S. Sampayan, "Experimental Investigation of Beam Optics Issues at the Bremsstrahlung Converters for Radiographic Applications," this conference MO4103.

[3] J. McCarrick, "Trapping Backstreaming Ions from an X-ray converter using an Inductive Cell," this conference TH4028.

[4] Y-J Chen, "Controling Backstreaming Ions from X-ray Converter Targets with Time Varying Final Focusing Solenoidal Lens and Beam Energy Variation," this conference TU3006

[5] R. Richardson, "Roll Bar X-ray Spot Size Measurement Technique," this conference TH4063

[6] C. Crist, "Time Resolved, 2-D Hard X-ray Imaging of Relativistic Electron-Beam Target Interactions on ETA-II," this conference MO4062

EXPERIMENTAL INVESTIGATION OF BEAM OPTICS ISSUES AT THE BREMSSTRAHLUNG CONVERTERS FOR RADIOGRAPHIC APPLICATIONS*

S.Sampayan, G. Caporaso, Y-J Chen, C. Crist†, M. Garcia, T. Houck,
M. Krogh††, R. Richardson, J. Weir, and G. Westenskow
Lawrence Livermore National Laboratory, Livermore, California 94550 USA

Abstract

As part of the Dual Axis Radiographic Hydrodynamic Test Facility II (DARHT II) and Advanced Hydrotest Facility (AHF) programs, we have began investigation of the possible adverse effects of (1) backstreaming ion emission from the Bremsstrahlung converter target and (2) the interaction of the resultant plasma with the electron beam during subsequent pulses. These effects would primarily manifest themselves in the static focusing system as a rapidly varying x-ray spot. To study these effects, we are conducting beam-target interaction experiments on the ETA-II accelerator (a 6.0 MeV, 2.5 kA, 70 ns FWHM pulsed, electron accelerator). From these experiments and the multiple diagnostics we have implemented, we are able to determine spot dynamics and characterize the resultant plasma for various configurations. Our data to date shows the first effect to be minimal. We report on the details of our experiments and our preliminary experiments to study the second effect.

1 INTRODUCTION

We are presently working on Linear Induction Accelerator (LIA) based radiography projects under the US Department of Energy (DOE). These projects, known as the Dual Axis Radiographic Hydrodynamic Test Facility II (DARHT II) and the Advanced Hydrotest Facility (AHF), are an element of the DOE's strategy of science based stockpile stewardship (SBSS). This program focuses on assuring the safety and reliability of the nuclear weapon stockpile without underground testing. The DARHT II is presently being built at Los Alamos National Laboratory and it is planned that AHF will be built at the Nevada Test Site. Both are national facilities optimized to address weapons issues with minimal environmental impact. The DARHT II machine is a multi-pulse, single-axis flash radiography machine. The AHF machine is a multi-pulse, multi-axis flash radiography machine designed for full 3D imaging. These machines are being designed to be capable of taking a sequence of closely spaced radiographic images so as to produce a time sequenced image of the test object.

On AHF, the process of producing these radiographic images consists of generating a 10-15 shot burst of electron beam pulses at a 1 MHz repetition rate. Each electron beam pulse is approximately 20 MeV energy, 6 kA current, and 200 ns long. These pulses are further chopped into a series of 50 ns sub-pulses and are redirected through a series of magnets to converter targets at each axis. The 20 MeV electron beam impacting the converter target generates an intense x-ray cone which produces a radiographic image on a fast detector array.

The converter target consists of an 0.5-1 mm thick tantalum or tungsten foil. The electron beam is focused to <1 mm and allowed to impinge on this target to create the x-ray pulse. Two effects are of concern. As the electron beam interacts with the target surface, a plasma quickly develops. As the beam electrons creates a strong space charge field in front of the target, ions can be extracted and accelerated in a direction opposite to the electron beam prorogation. These ions partially neutralize the beam space charge and defocusing of the beam results.

The second effect results from the direct interaction of electron beam with the target plasma on subsequent electron pulses. Such an interaction, depending on the interaction length and plasma density, may have an adverse effect on the beam propagation and the resultant spot on the converter target.

Our on-going experimental program at LLNL is to study the interaction of the electron beam with the x-ray converter target. In these experiments, we focus on the dynamics of the spot behavior using optical transition radiation (OTR), measuring x-ray spot blur across an edge (so called "roll-bar" technique), and a gated, multiframe, imaging pinhole camera. Further, we are characterizing the properties of the plume by using Faraday cups, interferometers, and a gated spectrometer. We report on our progress thus far.

2 EXPERIMENTAL

The overall layout of the experiment is shown in Fig. 1. Imaging instruments consist of gated, image intensified cameras for observation of Optical Transition Radiation (OTR) from the target surface. Ion diagnostics consist of multiple Faraday cups to observe plasma velocities and to obtain estimates of the plasma density. In addition, to resolve the spatial extent of the plasma as a function of time, an interferometer cavity imaged onto a fast gated or streak camera was implemented. An 0.5 m gated spectrometer allows observation of target optical

emissions for species identification and inference of plasma temperature.

As the principal objective of our experiment is to observe the dynamic behavior of the x-ray spot, we have implemented one method of direct observation of the beam spot and two methods to observe the x-ray spot. The first method of observation of the x-ray spot is with a so called "roll-bar" technique. This technique infers spot size from the blur across a hard edge. The second method is by the use of a time resolved x-ray pinhole camera. This latter device consists of tungsten pin-holes imaged onto an x-ray photocathode and amplified with a gated micro-channel plate (Fig. 2). The camera we are using creates 6 sequentially gated images so as to produce a 6 frame movie of the hard x-rays produced from the target interaction during the 70 ns (FWHM) beam pulse. Calculations show optimum sensitivity of the camera to be from 1-2 MeV with a 20% decrease at 5 MeV.

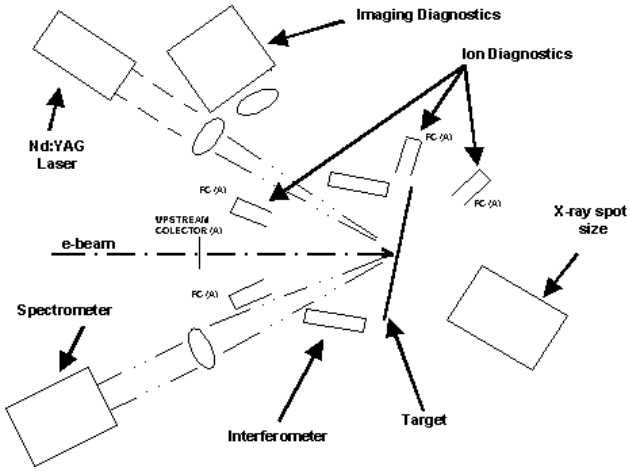

Figure 1. Target experiment layout

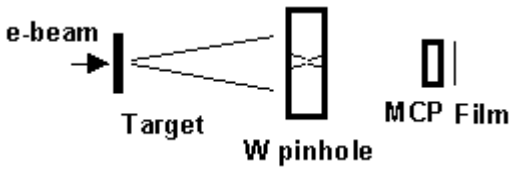

Figure 2. X-ray pinhole camera.

To simulate the effect of a high repetition rate multipulse, we have implemented an 0.8 J Nd:YAG laser focused on the target. The laser beam can be positioned and timed so as to produce a plasma of sufficient density so as to simulate target debris as would encountered in a mutipulse electron beam system.

3 RESULTS AND DISCUSSION

Results from the Faraday cup measurements indicate a plasma velocity dependence on spot size, beam parameters, and target thickness [1]. No evidence was found for fast, backstreaming, light ions. The plasma plume was found to expand at 3-4 mm/μs (peak density) with a leading edge velocity of 7-8 mm/μs in agreement with theoretical models.

Target emissions as measured with the spectrometer showed evolution of a prompt line spectra evolving to a black-body like spectra with a peak at about 600 nm when integrated over 8 μs after beam time.

Observations of OTR did not show strong promise as a radius diagnostic when used in conjunction with converter materials of interest (Ta and W). Calculations show that energy deposited into the target at these fluences elevates the material temperature in excess of 1 eV within 4 ns. As a result, prompt thermal radiation with a decay exceeding 1 ms results and observation of a time varying spot becomes difficult. The radiation is so intense and spectrum sufficiently broad that even with the inclusion of high quality short wavelength pass filters in the optical chain, extraction of the OTR signal was not possible.

Roll bar measurements were also performed. As scatter and depth of field issues can reduce the system resolution, a significant effort was necessary to optimize the trade-off between scintillator thickness (used in conjunction with a gated or streak camera for imaging) and pixel noise. Never-the-less, system resolution was limited from 0.75-1.5 mm. Correlation was also attempted with the OTR images under identical accelerator tuning conditions. Generally, we observed reasonable correlation (order 50%) between these measurement techniques. Additional reporting of this data is contained in a separate paper [2].

Figure 3 shows a representative sample of image data from the x-ray pinhole camera [3]. In this particular data, the orientation of the target was changed from 15° off normal (top) to normal incidence (bottom).

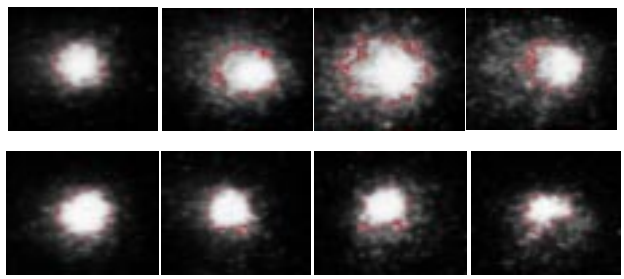

Figure 3. Time resolved x-ray spot comparison between 15° off normal (top) and normal incidence (bottom).

The top images were taken with the target at 15° off normal show expansion and filamentation of the beam. Gate time of each image is approximately 6 ns and spacing between images is 7-10 ns.

This effect can be explained by the asymmetric foil focusing forces which occur at the target as result of the angled target. The lower images, taken with the beam at

normal incidence with all other remaining conditions identical, show an almost constant spot diameter. An intensity profile through the center of other similar images taken at a 1 mm spot diameter (FWHM) and 1.4 kA are shown in Figure 4. Again, these data show an almost constant spot radius with a variation of approximately 25%. Shown with these data, is the expected expansion of the spot resulting from backstreaming H^+ ions. From this comparison, we have concluded that backstreaming ion defocusing is not a strong effect with these beam parameters.

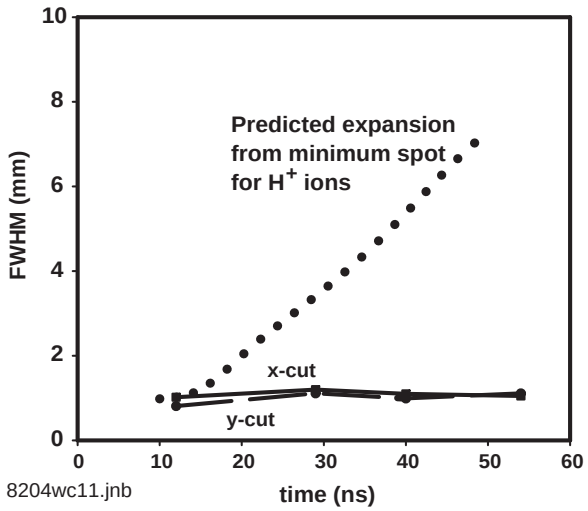

Figure 4. Time resolved images of x-ray spot (6 ns gate time, 10 ns intervals).

Figure 5. Spot expansion resulting from a laser induced plasma.

Initial data from the interaction of the electron beam with a laser induced plasma is shown in Figure 5. The beam maintains a 1 mm (FWHM) core and the 2σ threshold expands from 1.5 mm to 12 mm (last frame). With this particular data set, the laser was fired at approximately 100 ns before beam time and co-located with the electron beam position on target. Faraday cups indicate an expansion velocity of approximately 5 cm/μs and density at the Faraday cup (spaced 24 cm from the target) of 2 x 10^{10} cm^{-3}. Combing these data indicates an interaction length of 0.5 cm and an inferred density within that region of 5 x 10^{18} cm^{-3}. Initial analysis of the data shows this behavior is dominated by a backstreaming ion affect.

To minimize the interaction of the plasma with the beam, we are considering dynamic targets in our baseline development program. Such a technique will provide fresh target material pulse-to-pulse and also add a transverse component to the plasma so as to inhibit a direct beam-plasma interaction.

The dynamic target delivery scheme required study of several relatively mature technologies: high velocity fly wheels, shape charge jets, and both the burning propellant and compressed gas driven versions of high performance guns, i.e., light gas guns..

The fly wheel offers a significant advantage over all of the other methods because it does not need to be synchronized with other hardware in the system or the test object. Velocities are limited to 5 mm/μs, however. Shape charged jets offer the advantage of a very short cycle time for the total operation of injection of the target material. They also can reach the required velocities but work is required to create the necessary target crossection. Gas guns have the capability for deliver of materials with the velocity required to meet the replenishment need of the radiography systems. Velocities of 8 mm/μs, consistent with the target requirements, are not uncommon from these guns and some research guns are proposing speeds of nearly a factor of 2 faster Calculations have been performed with a basic two-stage system and indicate that a total system jitter for the gun will be 1.5 μs for a gun operated in the 5 mm/μs range.

4 SUMMARY

We have described our ongoing experiments to determine the effects for a multipulse Bremsstrahlung converter target used for radiography. An ion backstreaming and plasma interaction effect have been defined as the two of the most predominant mechanisms which could degrade the focal spot on the target. The first effect was studied, no obvious effects were found. Study of the second effect was initiated and appeared to be dominated by an ion effect. Alternative target systems are being studied to minimize this second effect.

5 REFERENCES

[1] T. Houck, et.al., "Faraday Cup Measurements of the Plasma Plume Produced at an X-ray Converter", these proceedings.

[2] R. A. Richardson, et.al., "Roll Bar X-ray Pot Measurement Technique", these proceedings.

[3] C. E. Crist, et.al., "Time Resolved, 2-D X-ray Imaging of Relativistic Electron-Beam Interactions on ETA-II", these proceedings.

* The work was performed under the auspices of the U.S. Department of Energy by LLNL under contract W-7405-ENG-48.

† Sandia National Laboratory

†† Allied Signal

RF POWER DISTRIBUTION AND PHASING AT SSRL INJECTOR LINAC

Sanghyun Park
Stanford Linear Accelerator Center, P.O. Box 4349, Stanford, California 94309, USA

Abstract

At the Stanford Synchrotron Radiation Laboratory injector linac, each of three linac sections was powered by an XK-5 klystron for 5 years starting from 1990. The RF power from the second klystron was then branched out to drive the thermionic RF gun. Due to dwindling performance of XK-5's, two of them were replaced by one SLAC type 5045, which powered the RF gun and the first two linac sections. In the summer of 1997, the linac system was further modified to have one 5045 power all three sections and gun. During this process a 5dB waveguide directional coupler was developed, and RF phasing was done by cold tests and by beam-based tuning of the waveguide network at full power. The remaining two XK-5's are currently being utilized at the Gun Test Facility located in the injector linac vault to drive a photocathode gun followed by a linac.

1 INTRODUCTION

The SSRL Booster synchrotron[1] accelerates a bunch of 10^9 electrons from 100 MeV to 2.3 GeV at the rate of 10 bunches per second, which is limited by the White circuit, before it is injected to the SPEAR storage ring. When the stored beam current reaches 100 mA, the beam energy is ramped to 3 GeV for user run.

In order to maximize the injection rate in terms of mA/min, it is very important to maintain a shot-to-shot reproducibility and a long term stability of the linac beam energy, which is proportional to the square root of the RF power. To this end, all the DC voltages applied to the klystron (focusing magnet and core bias) and modulator (PFN and thyratron reservoir) are regulated through switching or linear power supplies. Constant voltage transformers stabilize the AC power to the klystron cathode and thyratron heater.

The beam voltage and the input RF power is selected in such a way that $\delta P_O/\delta P_I = 0$ when the beam voltage stays constant (output power saturation). In general, higher klystron beam voltage requires less RF input power for the RF output power to saturate. Therefore, one sets the beam voltage first and adjusts input RF power level by a PIN diode-based attenuator until the klystron output is saturated. If the power is not right for the desired linac beam energy, the klystron beam voltage is changed and the process is repeated.

Another factor that affects the beam energy is the temperature at the gun and linac. For them to stay tuned at the operating frequency of 2.856 GHz, there are two systems that supply temperature controlled water (TCW); one for the gun and the other for linac that operates in different temperature range from the gun. The temperature regulation is better than 0.1^{O}F in both systems. Considering the thermal expansion coefficient of copper at $1.7\text{x}10^{-5}$ / ^{O}C, the resonance frequency of both structures remains unchanged within 3 kHz.

2 RF POWER DISTRIBUTION

When 4 linac sections are powered by one klystron, which is the case with the SLAC main linac, the RF power from the klystron is divided evenly twice by three of 3-dB hybrids so that each section is driven by equal level of RF power. When the number of linac sections to be driven is three, the power needs to be divided by 1:2 ratio, then the main line is evenly divided by a 3-dB hybrid. This is how the SSRL injector linac is powered by a single klystron.

The power branching ratio of a 3-dB hybrid is 1:1, and deviation from the design value is usually very small. Any other coupling between 3 and, say, 15 dB requires multi-hole narrow wall coupler. While it is possible to achieve precision coupling in calculations, errors from the process of machining make it very hard to predict what the actual coupling would be.

Therefore, the sequence of building a high power waveguide directional coupler is to choose a design of smaller coupling. For example, if a 5-dB coupler is to be made, choose a 7-dB coupler, duplicate the coupling strip of some 10 pairs of holes. Then clamp the two waveguide pieces together, with the strip inserted in between. Take data on coupling and phase delay at the main line and coupled port. In order to increase the coupling, the width and/or the length of all the holes are to be made larger. One repeats the process of mechanical modification of the coupling holes and cold tests until the coupling is within the tolerance. The final stage is to braze all the components together. As it turns out, the

brazing process does not alter the RF characteristics of a directional coupler very much.

The heart of a multi-hole directional coupler is the coupling strip. A sketch of it is shown below. The most important dimensions are A (6.016 in.= λ_g), B (=λ_g/4), and C (= 0.600 in.).

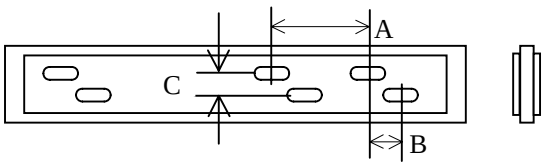

Figure 1: A coupling strip for a multi-hole narrow wall waveguide directional coupler. Only three pairs are shown for clarity. The endview is shown at the right.

This copper strip has overall dimension of 1.686 in. width, 21.632 in. long, and 0.375 in. thick. The mesa on either side is 0.086 in. above the middle part, and is to be mated with the waveguide. The holes are 0.3 in. wide rectangles, ending with a semi-circle at the ends. Each has overall length of about 1.5 inches. Typically, there are 10 pairs. If this number is reduced, directivity is also lowered. With the dimensions A, B, and C remaining the same, the hole size determines the coupling coefficient.

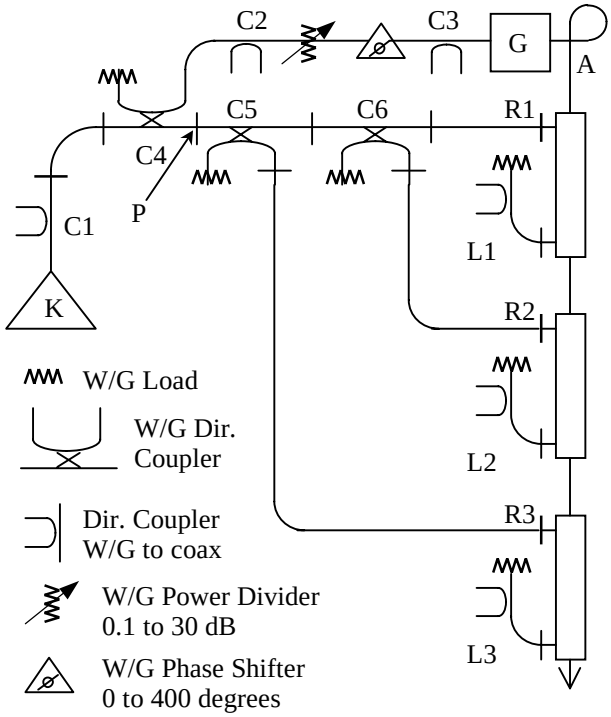

Figure 2 : The system layout of the S-band RF power distribution at the SSRL injector linac including the RF gun (G). The klystron (K) is a SLAC type 5045. The directional couplers C1 and C3 are for the power level monitoring, and C2 at 37 dB coupling is to drive another klystron, such as XK-5, for the Gun Test Facility. [2]

In the Fig.2, C4 has 8.5 dB coupling. The coupled out power is reduced by the power divider and drives the RF gun (G) at about 2 MW. The thermionic electrons bunches at about 2 MeV are compressed from about 100 ps to about 1 ps or shorter by the alpha magnet (A). At this point, there are about 3000 bunches. In order to minimize the beam loading to the linac, all but 4~5 bunches are diverted to the beam dump by the chopper (not shown). C6 in Fig.2 is a 3-dB hybrid.

The C5 measured coupling was 5.21 dB at 2.856 GHz. For the best efficiency, this should have been 4.77 dB, or exactly 1:2 branching ratio. Assuming that L1~L3 are all perfectly phased, and ignoring any parasitic losses, the energy gain by the linac is given by

$$\Delta E = 10.7\left(\sqrt{rP} + \sqrt{2P(1-r)}\right)$$

where ΔE is in MeV, r is the branching ratio at C5, and P is the RF power in MW at the C5 input. At 5.21 dB, r is $10^{-0.521}$ = 0.301 and ΔE = 117.1 MeV at 40 MW. At the same power, if r is 1/3 (4.77 dB), energy gain is 117.2 MeV. As one can notice from this example the energy dependence on the C5 coupling coefficient is very weak. If r<1/3, more power is available at the first two sections. If it is more, then the third section adds more to the total gain while the first two add less. Therefore the coupling requirement is then 4.8±0.5 dB.

3 RF PHASING BEWTEEN LINACS

As has been shown in the previous section, the linac energy is insensitive to how the power is divided up to drive each linac section. When it comes to the phasing, one has to be extra careful to maximize the energy at a given RF power. Here the gun is out of the picture for two reasons: one is that at about 2 MeV, the initial energy out of the gun is only a small perturbation to the total energy of the beam, which is steered into the booster synchrotron. The other is that the gun RF power is adjusted in amplitude and phase by the power divider and the waveguide phase shifter, as shown in Fig. 2.

The three linac sections are aligned to a straight line passing through the electrical centers of each. They are separated from each other by $34\lambda_0$ longitudinally, which is 140.510 inches. Then the requirement for maximum acceleration is that the RF phase must be the same at all three RF input ports. Therefore the phase lengths from the C5 input (P in Fig.2) to the L1~L3 input have to be adjusted to make them the same.

In a straight section, male (female) Skarpaas flange adds 0.641 (0.559) in. to the tip-to-tip copper waveguide length, including one half the thickness of copper gasket. In waveguide directional couplers, 3-dB hybrids, H-mitres, H- bends, and E-bends, the path length is very different from geometric length. Therefore the phase

length of each individual component must be measured with a vector network analyzer in the air, to arrive at the side arm length of a U tube at the final leg of the waveguide network. Of course the vacuum inside gives rise to mechanical deformation of the waveguide that leads to a change in path length, but it is small enough to ignore in the first order.

Once all the parts are fabricated and assembled, the entire network of waveguide from C5 to male flanges for RF input to each linac sections was moved by one inch away from linac. Then modulator flanges[3] were inserted, and entire network starting from the point *P* to linac sections L1~L3 was pumped down to about 1 torr. This flange is about 0.5 inch thick. One side is Skarpaas male and the other female for vacuum seal. It has germanium diode at the center of broad side. When it is reverse biased at –20V at 1 kHz it causes total reflection.

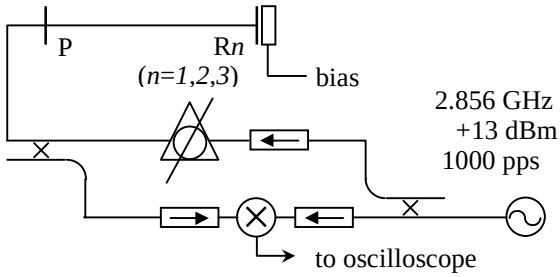

Figure 3 : Circuit diagram for phase measurement of the reflected wave, for P to R*n* path lengths.

By adjusting the phase shifter, the mixer output can be made zero. If the phase shifter setting is $\phi 1$ for n=1, the difference in phase readings shows the phasing error of each branch. The error correction is done by squeezing the waveguide wall. The guided wavelength of RF is

$$\lambda_g = \lambda_0 / \sqrt{1-(\lambda_0/2a)^2}$$

where a =2.840 in. is the inside dimension of broad wall. By squeezing the narrow wall to make a smaller, the guided wavelength λ_g is made longer. If broad wall is squeezed, it forces the narrow wall to bulge out resulting in a shorter λ_g. This procedure is performed using a C-clamp while monitoring the null on oscilloscope. The accuracy of this method is better than $\pm 4^o$ of RF phase.

At the conclusion of the process above, it was found that one modulator flange was inadvertently reversed in direction. After the commissioning, additional efforts were made to correct the error caused by the mistake. Hardware was assembled around the waveguide inside the linac vault, to have it squeezed by hydraulic jacks operated from the outside, while the system is up to full power. The assembly consists of two pairs of steel bars (one inch square, 12 inches long, and tapered 3 inches both ends), aluminum holder, two hydraulic jacks, two dialed indicator gauges, and a TV camera to read the gauges. For better reliability and safety, a phase bridge was made to monitor incremental phase as shown below.

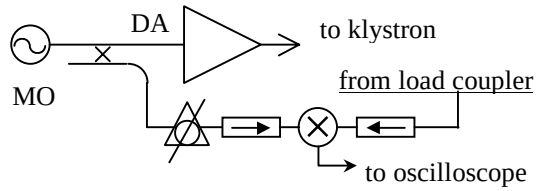

Figure 4: Linac incremental phase monitor. The master oscillator (MO) has +14 dBm cw output. The drive amplifier (DA) has 7μs pulse length at 10 Hz.

The manual phase shifter was set to produce a null reading. Then setting was changed by 2.856^o, to be nulled by squeezing the waveguide remotely. At every step of phase correction, the linac beam energy was measured by a bending magnet. The ΔE plot against $\delta\phi$ was close to a sine curve. At the end, the energy gain from the phase correction was peaked at 2.5 MeV.

4 CONCLUSION

The linac system has been modified to have one klystron drive the RF gun and all three linac sections for improved stability and reliability. A 5-dB coupler was produced for the purpose. Now it became possible to design and fabricate precision high power directional coupler of any coupling coefficient through interpolation of existing designs and analyzer measurements prior to assembly. RF phasing between klystron and linac sections was accomplished locally at low power (20 mW), and remotely at full power (40 MW), to achieve highest possible linac beam energy for a given klystron output power.

5 ACKNOWLEDGEMENT

This work was supported by US DoE through SLAC AIP project. Technical supports from SSRL Vacuum, MSG, and EDM groups are gratefully acknowledged. Contribution from J. Weaver has been indispensable. The author regrets to announce that he passed away on 2 July 1998 after more than two years of illness.

6 REFERENCES

[1] H. Wiedemann, *et al*., Proc. 1991 Part. Accel. Conf. (San Francisco), p. 2688
[2] S. Park and J. Weaver, Proc. 1996 Linac Conf. (Geneva), p. 528
[3] J. Weaver and R. Alvarez, IEEE Trans. **MTT-14** (1966), p. 624

INDUCTION CORE PERFORMANCE*

A. W. Molvik, W. R. Meier
Lawrence Livermore National Laboratory, Livermore, California 94550 USA
A. Faltens, L. Reginato
Lawrence Berkeley National Laboratory, Berkeley, California 94720 USA
C. Smith
Nonvolatile Electronics, Inc., 115 Lafayette Ave. Chatham, New Jersey 07928 USA

Abstract

Large masses of magnetic core material are required for many of the induction accelerator-based projects currently under study; the quantities required exceed 10^7 kg for a linear heavy-ion fusion driver, so core performance and cost are critical issues. We have evaluated cores of amorphous alloys from AlliedSignal and MRTI (Moscow Radio Technical Institute) and nanocrystalline alloys from Hitachi and Vacuumschmelze. The cores were of moderate size, between 1 and 11 kg. We characterized the materials in terms of the flux swing ΔB from $-B_{remanent}$ to $+B_{saturation}$, and the energy loss versus dB/dt. We found sources for each material that could coat, wind, and then anneal the cores. This required the development of thin coatings that withstand 350-550° C anneal temperatures. The result is core performance near the ultimate small sample performance of each material, with higher ΔB and lower losses than the earlier approaches of using as-cast material or rewinding after anneal, in both cases usually cowinding with thin mylar (~4μm thick). We are beginning system code studies of tradeoffs between ΔB and losses.

1 INTRODUCTION

In a previous paper[1] we showed that tape wound magnetic induction cores, processed by annealing after winding, produced superior performance to cores wound of as-cast material and not annealed, or to cores wound with previously annealed material. Annealing after winding is advantageous both to gain the full flux swing, and to wind while the material is still ductile. With annealing after winding, we achieved performance near the ultimate small sample performance[2]. The major technical challenge in annealing cores after winding is providing an interlaminar insulation[3], that reduces eddy current losses at high magnetization rates. The insulation must withstand annealing temperatures the order of 360° C without applying mechanical stress to the amorphous metal ribbon, and must meet other requirements related to cost, lifetime and packing fraction which have been described in greater detail [1]. Two insulation techniques were used, mica paper in ribbon form of 18 μm thick, and inorganic coatings of <1 μm thick.

In this paper, we extend the previous work with measurements on cores manufactured from alloys produced by four manufacturers: the amorphous alloys 2605SC and 2605SA1 from AlliedSignal (USA), 9KCP, 30KCP, 2HCP, and 7421 from Amet (Russia); and the nanocrystalline alloys FT-1H from Hitachi (Japan), and VitroVac 800 from Vacuumschmelze (Germany). The 2605SC was insulated with mica paper, wound and annealed by LLNL (USA) [1]. The other materials were coated, wound, and then annealed: FT-1H by Hitachi (Japan), the four Amet alloys by MRTI - Moscow Radiotechnical Institute (Russia), 2605SA1 and VitroVac 800 by National-Arnold Magnetics (USA).

2 RESULTS

Our experimental methods for measuring core parameters have been discussed previously [1]. Briefly, we discharge a 1 μfd capacitor bank through a thyratron switch into 1 to 32 primary turns wrapped around the minor cross section of the toroidal cores. The core has been reset to $-B_{remanent}$. We measure the current through the primary and the voltage across a 1-turn secondary. The flux swing ΔB and the losses u(J/m^3) are referenced to the area and volume of alloy, determined by weight, not the geometrical area and volume of the core, i.e., we correct for the packing factor. The digital oscilloscope calibration was checked by the manufacturer to be within specifications (errors<1% of full scale), the voltage probe attenuation was adjusted to be within 1% over the range of time bases used (10-100 ns resolution), and the current transformer/terminator were also checked to be within 1%.

We summarize our findings in Table 1. We list each alloy by the manufacturers designation, and each core with an abbreviation of its manufacturers labeling. Each row represents a different core, except for 2605SA1, where data from one core is analyzed at 4 different flux swings, to allow direct comparison of the losses at the same flux swings as other alloys can achieve. We note that the loss increases more rapidly than the square of the flux swing (see scaling in Eq. 1 below) so that one can tradeoff increased core capital costs for reduced pulser capital and operating costs.

* Work supported by the U.S. Department of Energy under contract No. W-7405-ENG-48 (LLNL) and DE-AC03-76SF00098 (LBNL).

Table 1: Core flux swing and loss for various alloys, all annealed after winding.

Alloy	Core No.	ΔB_{max}(T) (1 μs dur.)	ΔB_u(T)	C_1	C_2	u(J/m3) (1 μs dur.)	ID(m)
2605SC	C-12	2.46	2.30	171	583	651	0.125
2605SC	C-13	2.30	2.20	130	612	609	0.125
2605SC	C-14	2.39	2.30	144	591	633	0.125
2605SA1	NA-97	2.84	2.70	144	1341	1720	0.125
"	"	"	2.50	136	1158	1294	0.125
"	"	"	2.30	129	1068	1023	0.125
"	"	"	2.00	123	993	734	0.125
FT-1H	982-1	2.03	1.95	41.5	355	248	0.06
FT-1H	982-2	1.97	1.90	25.0	367	231	0.06
FT-1H	982-3	2.06	2.00	27.5	354	249	0.06
FT-1H	982-4	1.99	1.90	28.0	354	226	0.06
VitroVac800	NA-1	2.28	2.15	18.4	304	241	0.102
VitroVac800	NA-2	2.21	2.10	39.7	240	203	0.102
VitroVac800	NA-3	2.14	2.10	27.6	284	224	0.102
9KCP	06-01	2.40	1.85	84.6	773	486	0.327
9KCP	06-02		2.25	78.2	934	827	0.327
9KCP	08-01	2.79	1.75	-30.3	807	374	0.336
30KCP	00-01	2.69	2.60	221	848	1147	0.115
30KCP	01-01	2.53	2.45	139	1027	1123	0.110
30KCP	05-01	2.30	2.25	65.5	1032	895	0.326
2HCP	03-01	2.49	2.3	137	530	575	0.110
2HCP	03-02	2.59	2.30	263	440	614	0.110
2HCP	07-01	2.26	2.15	77.3	756	626	0.327
7421	04-01	2.07	1.90	128	843	584	0.110

The usable flux swing ΔB_u is slightly smaller than $\Delta B_{max} = B_{saturation} - (-B_{remanent})$. It is obtained by applying four criteria to a sampling of the 20-70 data records of primary current and secondary voltage for each core, each record at a different level of pulser charge or number of primary turns. The four criteria are:

(1) The primary voltage is dropping;
(2) The current is beginning to rapidly increase above its average level;
(3) The loss per unit flux change approximately doubles; and
(4) The core impedance drops to 0.1-0.25 of peak value.

While these criteria are only semi-quantitative, the uncertainty in the flux swing is usually within 0.1 T. A more precise, engineering, determination of the usable flux swing depends on the design of the pulser and the requirements on the precision of the core voltage output. The values listed in Table 1 are a reasonable match to the assumptions of the systems code[4] with which we are evaluating accelerator architectures and components. This code assigns portions of the flux swing to the rise and fall of the pulse voltage, before and after the beam passes, while the central portion of the pulse must accurately match the desired pulse form in order to properly accelerate and shape the beam. The sag in the voltage can then be assigned to the fall time. For comparison, ΔB_{max} and the loss u(J/m3) for a 1 μs pulse duration are also listed. We note that ΔB_{max} in Table 1 is generally less than published small sample values; this may indicate that further development is needed in core manufacturing technologies.

The losses are fit with the 2-term loss criterion of Faltens' [1],

$$u\left(\frac{J}{m^3}\right) = C_1\left(\frac{\Delta B}{2.5T}\right)\left(\frac{t}{25\mu m}\right) + C_2\left(\frac{\Delta B}{2.5T}\right)^2\left(\frac{1\mu s}{\tau}\right)\left(\frac{t}{25\mu m}\right)^{1-2}$$

where τ(μs) is the pulse duration, and t(μm) is the thickness of the ribbon with an exponent of 1 or 2 (an exponent of 1 is used in here). We set t = 25 μm to compare cores made with alloys of unknown thickness. The ultimate capabilities of the different materials would be more fairly compared if the tape thicknesses were used in Eq. 1. C_1 (which represents dc hysteresis losses) and C_2 (which represents the fast-pulsed losses due to eddy currents and domain wall motion) are determined by a least-squares fit to the data.

The data and fit are shown in Figs. 1-3 for 2605SC, 2605SA1, and VitroVac 800 respectively. The fit is seen to be best for the VitroVac 800, but lies above the data

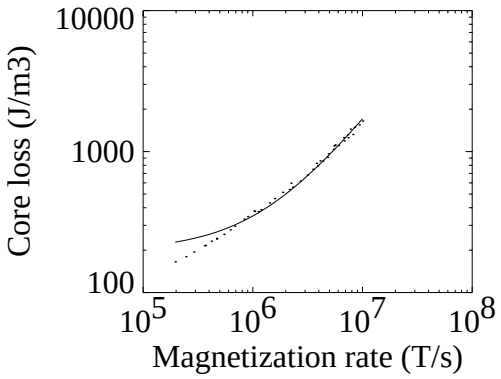

Fig. 1. 2605SC C-14 data shown by dots, fit by line, $\Delta B = 2.3$ T.

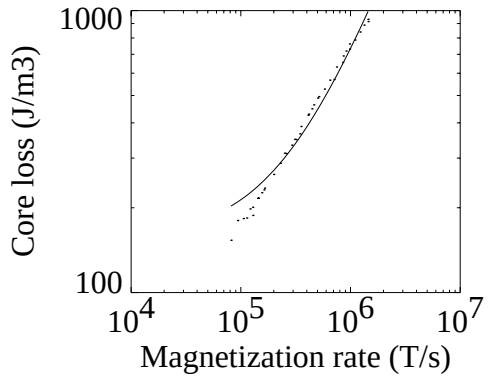

Fig. 2. 2605SA1 NA-97 data, $\Delta B = 2.7$ T.

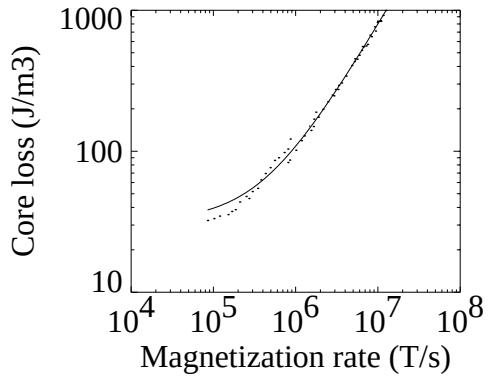

Fig. 3. VitroVac 800 NA-2 data, $\Delta B = 2.1$ T.

for low magnetization rates in each example. In some cases, the fit is very poor, e.g. core 08-01 where C_1 is negative. We are looking at alternative models with which to better characterize the data.

The consistency of amorphous metal cores has been an area of concern, see for example, Ref. [5] where the standard deviation in loss per volume ranged from 14-29% for 3 sizes of 38 cores of 2605SC. While we don't have sufficient cores of any one alloy to obtain reliable standard deviations, we compute 3% with 2605SC and we find three other alloys that also have <10% standard deviations of loss: FT-1H, VitroVac800, and 2HCP. The first two are nanocrystalline alloys. The MRTI cores (the bottom 10 rows) come in three geometries: The inside diameter of the cores is listed in the last column of Table 1. Cores with diameters near 0.1 m have masses between 1.6 and 2.3 kg. Cores with diameters near 0.3 m have masses between 5.4 and 6.1 kg. All of the MRTI cores use 0.020 m wide ribbon, except for 08-01 that uses material slit to 0.009 m wide and weighs 2.5 kg. We see that cores with a similar geometry are grouped more closely than those of different geometry.

The capital cost of cores is minimized with 2605SA1, which is manufactured in large quantities for use in 60 Hz transformers. Its cost varies from $20/kg in small quantities to an estimated <$4/kg in lots larger than 10^5 kg. It also has the largest flux swing, which minimizes the amount of core material needed. However it has the highest loss per pulse, at the same flux swing its losses are about 1.5-2 x that of 2605SC, and at maximum flux swing they are near 3x that of 2605SC. And compared with nanocrystalline, the losses are 3-7x higher.

The operating costs of an accelerator are minimized with the nanocrystalline alloys: the losses are down a factor of 7 compared with 2605SA1 at maximum flux swing. However, more material is needed, by at least the ratio of the flux swings (2.7/(1.9-2.15) = 1.25-1.4), and by more if a large build-up is needed. The material is also more expensive: most of the components are similar to those in the amorphous alloys 2605SC and 2605SA1, the major difference is the addition of 3% niobium. The niobium will increase the ultimate cost of the materials in large quantities by ~$1/kg of alloy. The additional capital costs will be partially offset by the reduced cost of pulsers. These and other tradeoffs are being investigated with a systems code [4].

3 REFERENCES

[1] A. W. Molvik et al, "Magnetic Core Studies at LBNL and LLNL," To be published in Nuclear Inst. and Methods in Physics Research, A.

[2] Carl H. Smith, "Applications of amorphous materials at very-high magnetization rates," J. Appl. Phys. 67 (9), 5556-5561 (1990).

[3] Carl H. Smith et al, "Insulations for Metallic Glasses in Pulse Power Systems," IEEE Transactions on Electron Devices 38 (4), 750-757 (1991).

[4] W. R. Meier, et al, "Systems Modeling for Heavy Ion Drivers – An Induction Linac Example," Proceedings of 17th IEEE/NPSS Symposium Fusion Engineering, IEEE 598-602 (1998).

[5] S. Lidia et al, "RK-TBA Studies at the RTA Test Facility," in Advanced Accelerator Concepts, edited by S. Chattopadhyay, J. McCullough, and P. Dahl, AIP Press, New York, 842-851 (1997).

HIGH RESOLUTION BPM FOR FUTURE COLLIDERS

C. Magne, M. Juillard, M. Lalot, A. Mosnier, B. Phung, DAPNIA/SEA, CEA-Saclay, France
Y. Lussignol, DAPNIA/SIG, CEA-Saclay, France
R. Bossart, CERN, Geneva, Switzerland

Abstract

A beam position monitor using a coaxial reentrant RF cavity has been designed and tested. Main advantages are the small size, the high precision, excellent linearity, and the broadband operation. The measured resolution is 10 microns on the low current beam of the TTF linac. The expected resolution is 700 nm for the high current beam of TTF.

1 INTRODUCTION

High resolution beam position monitors (BPM) will be needed for the future linear colliders. Large band-widths will also be important to operate fast feedback systems. We have designed and tested on TTF (Tesla Test Facility) a broadband BPM which can also be operated at liquid helium temperature.

The TTF superconducting linac at DESY is now in operation with a low charge injector delivering bunches at 216 MHz. In the next step an RF gun will provide high charge (8 nC) bunches at the frequency of 1 MHz. The BPM is suited to both operating modes. In the first case the tests have shown a resolution of 8 μm. In the second case a resolution of 0.7 μm is expected.

2 PRINCIPLE OF THE BROADBAND BPM WITH A REENTRANT CAVITY

A reentrant cavity (fig.1) has a small size and the broad band is well adapted to the measurement of high charge short-bunched beams, such as they will be in future colliders [1]. The beam coupling impedance is advantageously weak. The measurement frequency is chosen well below the monopole (TEM) and dipole (TE011) modes of the cavity, and below the cut off frequency f_c of the dipole TE_{11} mode of the cavity considered as a coaxial transmission line (table 1). The beam excites an "evanescent" TE011 mode [2], in proportion of its displacement off axis, damped towards the bottom of the reentrant cavity. The energy is concentrated in the gap where the antennae are located. The higher order modes are damped much more strongly so their contribution is negligible and the linearity of the measurement is ensured.

If U_1, U_2, U_3, and U_4 are the voltages induced on each antenna, U_m the voltage induced by the monopolar mode on each antenna, I the beam current, x and y the beam displacements from the axis, then the transfer impedance is defined by:

$$Z_t = \frac{U_m}{I}$$

and the dipolar constant L is defined by:

$$x = L\frac{U_1 - U_3}{U_1 + U_3} \qquad y = L\frac{U_2 - U_4}{U_2 + U_4}.$$

Zt and L are calculated analytically in [2] and the BPM sensitivity is

$$S = 2\frac{Z_t}{L}.$$

3 FABRICATION OF THE CAVITY

The BPM precision at room and cryogenic temperatures (cooling without deformation) relies on the axial symmetry obtained by machining the cavity with a lathe. The beam pipe radius is 78 mm and the gap of the reentrant cavity is 8 mm. A demountable cavity was fabricated (figure 1) and severe tolerances were applied on the radii and the perpendicularity of the assembling surface (2/100). The concentricity of the cavity walls actually measured on the cavity is better than 20 μm.

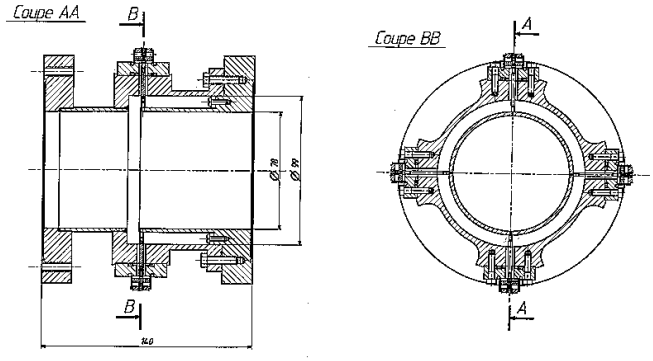

Figure 1: BPM cavity

The feedthrough have a standing wave ratio below 1.02 at 650 MHz. They ensure vacuum tightness between the linac 10^{-11} vacuum and the 2 K helium bath. To achieve broadband operation the cavity is strongly overcoupled by fixing the antenna tips to the inner diameter of the cavity. The external Q factor is about 4.

4 RF MEASUREMENTS OF THE CAVITY ALONE

The transmissions between two opposite antennae have been measured with a network analyser for two positions of the antennae: pulled out or fully pushed. The first

position (resonant mode) is used to spot the precise resonance frequencies and the second one (broadband mode) to visualize the bandwidth really used in the operation mode (figure 2 and table 1).

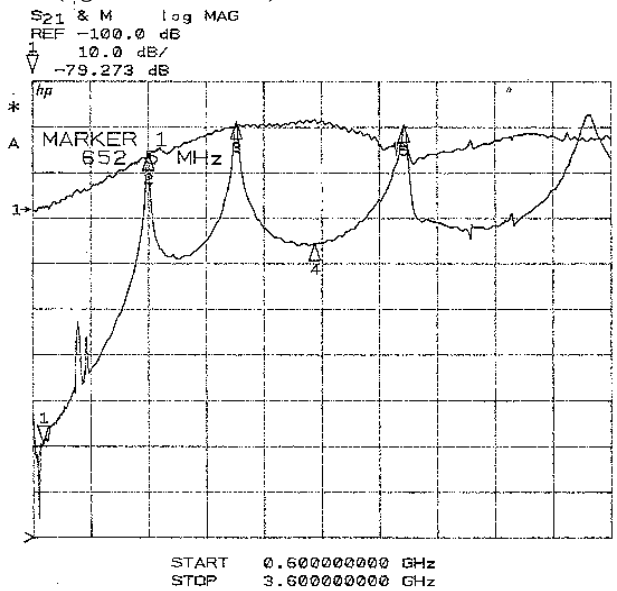

Fig. 2: Cavity transmission, broadband(1) and resonant(2)

5 SIGNAL PROCESSING

A 180° hybrid junction is connected to each pair of opposite antennae, yielding directly the sum and difference RF voltages proportional to the beam current and position. These RF signals are then filtered, amplified, and demodulated with a superheterodyne reception. To achieve a good balance between the 4 ports the hybrid coupler is placed in a box as close as possible to the cavity. And a "perpendicular balance" is done: A reference signal is input through the horizontal antennae while attenuators and phase shifters are adjusted to cancel the vertical power output.

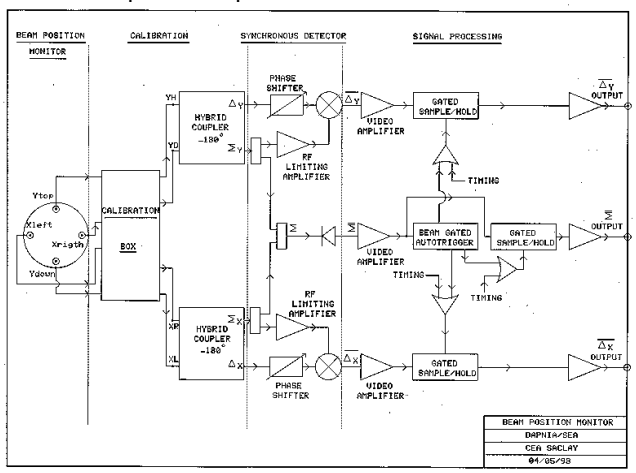

figure 3: BPM electronics

The acquisition board yields analog output for noise measurements and digitized 14 bit output for the control system. The software used is EPICS.

6 CALIBRATION ON A TEST BENCH

A test bench has been assembled to calibrate the BPM without beam, at room temperature. The beam is simulated by a moveable rod. The cw RF power equivalent to the beam current is injected through transition cones as shown on figure 11. The cones have a reflection coefficient of 0.25.

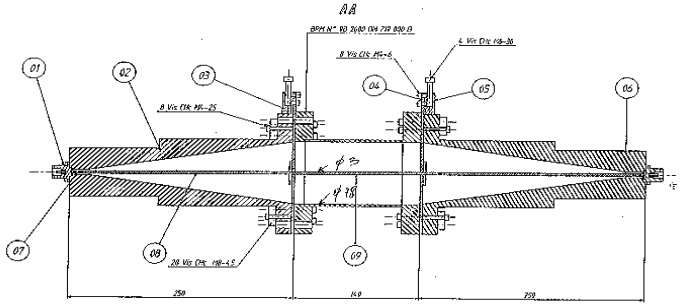

figure 4: Test bench for the BPM cavity and electronics

The characteristics measured with a network analyser are compared with the theoretical values in table 1. The linearity is shown in fig. 5. The noise measured is 20 mV for a 4 V/mm signal, so the resolution is 5 µm.

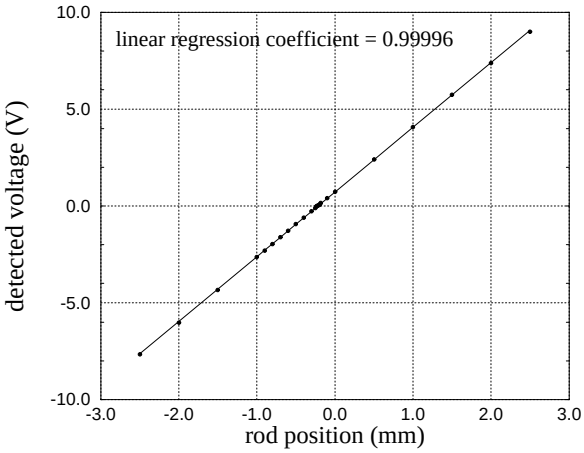

Fig.5: BPM test on bench

The precision after calibration is given in table 2. Micrometric shifters should be used to evaluate the relative precision better.

Table 1 (measurement frequency = 0.650 GHz)

	calculated	measured
fc (GHz)	1.0	
f TEM (GHz)	1.24	1.20
f TE011 (GHz)	1.7	1.658
Z_t (Ω)	6.2	8
L (mm)	37.5	
S (mV/mm/mA)	0.331	0.26

Table 2

absolute precision	0.2mm
relative precision	<50µm

7 MEASUREMENTS WITH THE TTF BEAM

One BPM has been tested inside the capture cavity cryostat at 2 K and the other at room temperature.

a) Absolute precision Δ: The BPM error Δ_{bpm} and the alignment error Δ_{align} give:

$\Delta = \Delta_{bpm} + \Delta_{align} = 0.2$ mm + 0.1 mm = 0.3 mm.

b) Beam current measurement: The beam current is measured between 0.1 mA and 8 mA. By adding a high gain preamplifier the dark current emitted by the cavity (as low as 100 nA) can also be measured.

c) Resolution: The measured noise is 40 mV when the RF amplifier is 54dB and the video amplifier has a gain of 100. With the 5 V/mm BPM calibration for a beam current of 8 mA this leads to a resolution of 8µm.

e) Linearity: The x and y beam displacements were measured with an 8 mA, 35 µs, 10 Hz beam while horizontal and vertical steerers were varied. The steerers are 1.513 m upstream. Their linearity is such that $\delta x/I_{steerer}$ = 2.188mm/A with a precision of .002 mm/A over the range -4V, +4V. (The DC power supplies are stabilised to 10^{-3}).

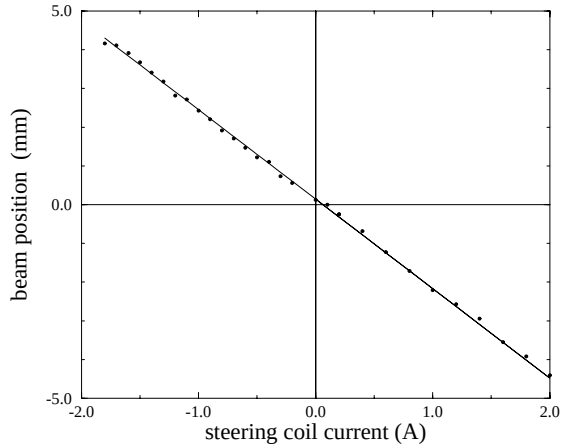

Figure 6: Measurement of the TTF beam position

The linearity in y is observed with a regression coefficient of R = 0.9996 (fig. 6). In that example a fluctuation of the beam position is seen with a standard deviation of 150 µm, about 5% of the beam size.

8 EXPECTED RESOLUTION IN THE CASE OF INJECTOR 2

The short bunch signal is filtered at the output of the hybrid coupler. Bessel filters of order 7 have been chosen as they have the less distorted time-domain response and shortest rise time. The 4 MHz bandwidth Bessel filter entirely determines the time response of the electronic chain. The 10 ps bunch can be considered as a Dirac impulse and the input current is: $I_{in}[A]=8x10^{-9}x\delta(t)$. Calculating the output current from the transfer function of the filter we find an envelope amplitude of $8x10^{6}xI_{in}$ with a time response width fitting inside the 1 µs bunch separation. A comparison with the current of the injector #1 shows that a factor 12 is gained on the sensitivity. As the noise level will be unchanged (since the same electronics are kept except for a modified acquisition card) the resolution will be: 8 µm / 12 = 700 nm.

9 CONCLUSION

a) Results of the tests (low bunch charge)

The axial symmetry of the RF cavity allowed a high fabrication precision (2/100) and the absolute precision of the BPM was measured on a test bench (0.2 mm).

On the Tesla Test Facility the BPM was tested at 2 K and at 300 K; the beam position is measured in the ranges 0 to 1 mm, and 1 mm to 10 mm; the beam current and the dark current can be measured. The pass-band is 4 MHz due to the RF filter chosen. The acquisition time is 1 µs. The resolution (at low bunch charge) is 8 µm.

b) Plans for injector 2 (high bunch charge: 8 nC)

By modifying slightly the acquisition card (changing the sample-and-hold amplifier) the BPM is presently being adapted to the high charge 1 MHz bunches of the injector #2. The resolution will be 700 nm if nothing else is changed (same RF amplifier, same RF filter).

c) New technical developments

Changing the RF amplifier to a low noise amplifier and broadening the pass-band of the RF filter from 4 MHz to 20 MHz will increase the resolution in the case of high bunch charge beams. A resolution of 100 nm should be obtained at 8 nC bunch charge.

d) New applications

It is possible to use the BPM without the present electronics (4 MHz band-width) and benefit from the real bandwidth of the BPM cavity and hybrid coupler (about 200 MHz) if a degraded resolution (about 100 µm) is accepted. This is presently tested to measure the HOM impedances of the TTF 9-cell superconducting cavities. Resonances due to the HOM are excited by an offset of the beam position and a modulation of the beam current at frequencies from 5 MHz to 100 MHz. The growth of the resonances inside the 35 µs bunch train is observed with an oscilloscope and a spectrum analyser.

An other application is to build a new acquisition board with flash components. In that case the BPM would have a 25ns measurement time and could be inserted in a fast position feedback loop.

10 REFERENCES

[1] R. Bossart, “High precision beam position monitor using a re-entrant coaxial cavity” Proceedings of LINAC94, KeK, (1994).

[2] R. Bossart, “Microwave beam position monitor using a re-entrant coaxial cavity,” CERN report PS 91-59 (1992).

HEAT TRANSFER COEFFICIENT IN SERPENTINE COOLANT PASSAGE FOR CCDTL*

P. Leslie, R. Wood, F. Sigler, A. Shapiro, A. Rendon
Los Alamos National Laboratory, Los Alamos, NM 87545, USA

Abstract

A series of heat transfer experiments were conducted to refine the cooling passage design in the drift tubes of a coupled cavity drift tube linac (CCDTL) [1]. The experimental data were then compared to numerical models to derive relationships between heat transfer rates, Reynold's number, and Prandtl number, over a range of flow rates. Data reduction consisted of axisymmetric finite element modeling where the heat transfer coefficients were modified to match the experimental data. Unfortunately, the derived relationship is valid only for this specific geometry of the test drift tube. Fortunately, the heat transfer rates were much better (approximately 2.5 times) than expected.

1 INTRODUCTION

The objective of this experiment was to use experimental results combined with numerical simulation to measure heat transfer rates in drift tube coolant passages for the cavities in the Accelerator Production of Tritium (APT) [2], Low Energy Demonstration Accelerator (LEDA) [3] CCDTL Hot Model. The hot model is a full scale, copper brazed structure that will be exposed to full RF fields, but will not have beam through it. A goal of the experiment is to refine the design of the cooling passages and coolant systems for the LEDA CCDTL. The results of this experiment were used to give a better estimate of the heat transfer rates within the drift tube coolant passages and are just a first look at the drift tube thermal problem. Since the experiment is not error-free, the Nusselt equation coefficients determined are probably not an exact representation of all the physics of the problem, but a match with this empirical data using the specific geometry of the test item.

In the CCDTL, the drift tube is located within an RF cavity and provides a region of no electric field which shields the beam when the electric field would decelerate the beam (for an in-depth description, see [4]). A great deal of RF power is dissipated on the outer surface of the APT drift tubes. A method was developed to form an elaborate network of cooling passages within the body of each drift tube [5]. The coolant passages within the drift tubes are rectangular, short, and curved, a situation which is not well covered in the literature.

In the literature [6], the heat transfer coefficient in long, straight, circular passages is given as

$$\bar{h}_c = \frac{k_{water}}{D_{Tube}} * 0.023 * Re^{0.8} * Pr^{0.4} \qquad (1)$$

where k_{water} is the thermal conductivity of water, Re is the Reynold's number, Pr is the Prandtl number. Since these drift tube passages are not round, the convention is to use the equivalent hydraulic diameter for a rectangular cross section which is given by

$$D_h = \frac{4A}{P} \qquad (2)$$

where A is the flow area and P is the wetted perimeter. It is much more difficult to account for the passages being short and curved. The complex three dimensional geometry of the drift tube coolant passages make it difficult to determine an effective heat transfer coefficient directly from published data. It was necessary to use a finite element, thermal/structural model to extract an approximate value for the heat transfer coefficient. From that data, an approximate relationship between the Nusselt number, the Reynold's number, and the Prandtl number for this geometry was derived.

2 SETUP

The test setup consisted of a water chiller, approximately 5 gallon reservoir, a flow meter with range of 0 to 2 gpm, water filter, 17 heater cartridges, rheostat, 100X amplifier, a modified drift tube slug placed on a styrofoam base with styrofoam "popcorn" completely over it, tubing to connect these components together, two thermocouples to measure drift tube temperatures, another thermocouple to measure coolant inlet temperature, a two pass thermopile to measure the coolant temperature rise through the drift tube, and a data acquisition system to record the data. Figure 1 shows a schematic of the setup. For data reduction purposes, the flow rate was determined from the heater power and the temperature rise within the coolant from inlet to outlet. Much depends on this measurement, so a two pass thermopile was used to increase the sensitivity of the measurement and lessen the effect of noise in the data.

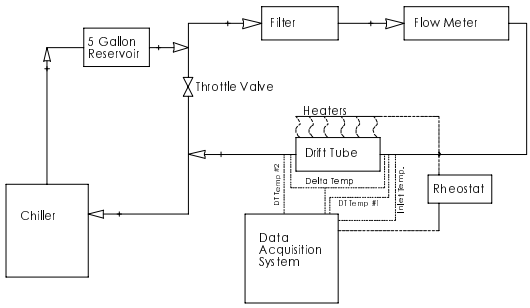

Figure 1. Schematic of the experiment.

* Work supported by the US Department of Energy, Defense Programs

The drift tube slug used in the heat transfer experiments was a three passage drift tube that is identical to those from which CCDTL hot model drift tubes were made. Figure 2 shows the cross sectional drawing showing the 3 concentric cylinders and the 3 coolant passages. The center, longitudinal holes were drilled in 1 inch each side (not shown in Figure 2) with a type T thermocouple inserted into each. These thermocouples were labeled Body Temp 1 and Body Temp 2. Because the water temperature increases with each successive passage, the area of the drift tube that dissipates the most power and/or most affects the cavity frequency needs to be cooled first. So the placement of the drift tube coolant passages is not arbitrary and the experimental drift tube passages closely resembled an actual drift tube.

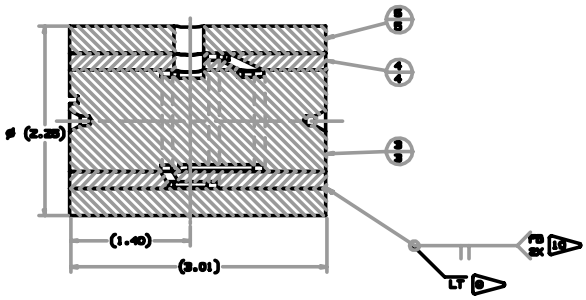

Figure 2. Drift Tube Slug Showing Cross Sections of Cooling Passages.

The heater cartridges were placed in longitudinal slots cut into the drift tube slug with thermal conducting grease, copper shim stock wrapped around, and hose clamps to keep them in place. Figure 3 shows the assembly in the styrofoam box with associated hardware prior to filling the box with styrofoam "popcorn" and topping it with a foam pad. The inlet thermocouple and the thermopile were installed into the hardware at the ends of the copper tubes protruding from the drift tube shown in Figure 3.

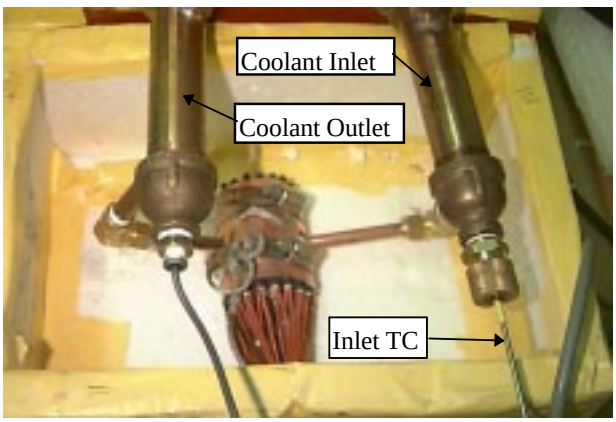

Figure 3. Drift Tube in Styrofoam box.

The reservoir was used to increase the thermal mass of the system so each time step was more closely steady state. The rheostat was used to control the power to the heaters. The data acquisition system consisted of a computer running Labview software, two Keithley 2002 Multimeters, three type T thermocouples with electronic "ice point" and one type T thermopile, and the data was recorded into text files for easy transfer to other data manipulation software. A thermistor was used to monitor the outlet temperature, but it was not recorded.

3 THERMOCOUPLE CALIBRATION

The process began by identifying the offset inherent in the system. This was done by setting the thermostat on the chiller to its lowest point of 42° F. Once the system reached this temperature, the flow rate was throttled way down (~0.30 to 0.35 gpm) to minimize heating due to pressure loss across the drift tube, the thermostat on the chiller was raised to approximately 110° F, and the data acquisition system began recording the data. The heaters and rheostat were turned off and unplugged from the wall. It took the system 2 to 2 ½ hours to reach approximately 75° F and much longer if the desired system temperature was near 100° F. When the system reached ~75° F, the data recording was stopped, the flow rate was turned up, and the temperature on the chiller was set down to its lowest point.

4 TEST PROCEDURE

Each measurement was assumed to be steady state due to the high thermal conductivity of copper and the 5 gallon reservoir added to increase the thermal mass of the system. The chiller system's compressor cycled too much to hold the temperature constant so it was used only as a pump and as a means to cool the entire system to an initial <45° F condition. Quasi-steady state data was then taken as the drift tube heaters gradually drove the system temperature upward.

When the system temperature was 42° F, the heaters and rheostat were turned on, near 1000 watts, and the desired flow rate was set. Once the system reached quasi-steady state, the chiller thermostat was set to 100° F and the data was then recorded as the system temperature gradually climbed to >100° F. The process took 1½ to 2 hours, depending on the flow rate. Figure 4 shows a plot of the data collected at one specific flow rate.

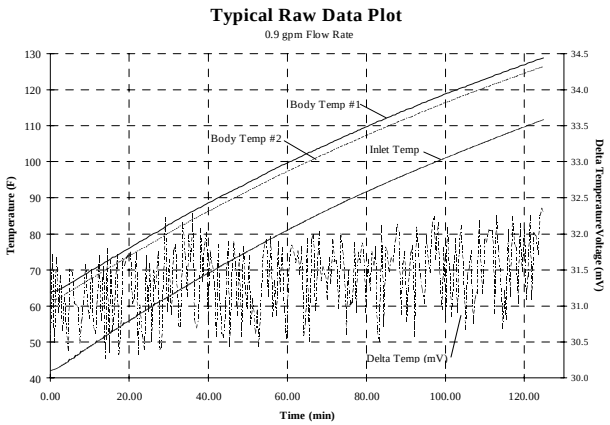

Figure 4. Data Collected During Experiment.

The thermocouple data was smooth with very little noise; however, the thermopile data (Delta temperature)

had a 3% noise range throughout due to the sensitivity of the measurement. This is believed to be stray electrical noise, not variations in the flow rate. Once the inlet temperature reached approximately 100° F, the data collection was stopped, the heaters and rheostat were turned off, and the chiller thermostat was turned down to its lowest setting. It took approximately 1 hour to return to the 42° F starting point. The procedure was then repeated using a different flow rate.

5 ANALYSIS

The analysis was performed in two sections. The first was to analyze the data collected to determine the delta temperature between the outlet and inlet. The thermocouple calibration was "backed out" and the resulting measurements converted to temperatures. As can be seen in Figure 4, there was a significant range of data for the voltage measurement which translates over to the temperature measurement. To smooth out this data, a weighted time average was taken from the surrounding data points. The weighted average equation is

$$\overline{X}_N = \frac{X_{N-2} + 3X_{N-1} + 5X_N + 3X_{N+1} + X_{N+2}}{13} \qquad (3)$$

where X_{N-x} was a data point x steps before or after the N^{th} data point. All quantities (temperatures and heater power) were averaged this way. This smoothed data was then entered into a spreadsheet [7] that calculated the average heat transfer coefficients and temperatures for each passage on the drift tube.

The second part of the analysis used numerical simulation, specifically COSMOS/M finite element analysis (FEA) software [8]. An axisymmetric model was generated within COSMOS where the boundary conditions were taken from the spreadsheet [7] which calculated the average heat transfer coefficients, average coolant temperatures, and the heat flux from the heaters. The model was then thermally analyzed to determine the nodal temperatures in the model. The comparison between the measured data and the numerical data was made by averaging the two measured body temperatures and comparing them to the average nodal temperatures that correspond to those thermocouple's location. One iteration required modifying the heat transfer coefficient, applying the calculated boundary conditions to the FEA model, running the thermal analysis, averaging the temperatures at the nodes corresponding to the thermocouple's location, and comparing it to the averaged measured body temperature and repeating until the two averages were within ±0.03° F (even though the accuracy of the measurement was much worse). These iterations were performed at 4 to 5 temperatures within the measured temperature range for each flow rate.

6 RESULTS

Four flow rates were analyzed in this experiment: 0.9, 0.7, 0.5, 0.3 gallons per minute (gpm) which corresponded to approximately 15, 12, 9, and 6 feet per second (fps) (4.57, 3.66, 2.74, and 1.83 m/s) flow velocity in the coolant channels, respectively. The Reynold's numbers corresponding to these flow rates are 15,549; 11,159; 8,275; and 5,291, respectively. The data can be fairly well described by the following equation.

$$Nu = .0862 * Re^{.75} * Pr^{.42} \qquad (5)$$

Figure 5 compares the data to this equation graphically.

The design flow velocity within the passages of the drift tube is a critical factor due to erosion of the copper passages at higher flow velocities. A rule of thumb is to keep flow velocities within copper coolant channels below 15 fps (4.57 m/s) to minimize this erosion. Therefore, there was no need to test a flow rate higher than 0.9 gpm.

Note that, for this geometry, the heat transfer rates are ~2.5 times greater than predicted by Eqn (1) (long, straight, circular passages). For the design on the APT/LEDA CCDTL Low Beta Hot Model drift tubes, a value of 1.5 times better was used to offset any experimental errors that may have influenced the data and to stay on the conservative side of the design. Thorough tests of the Low Beta Hot Model will be done to verify and refine these results.

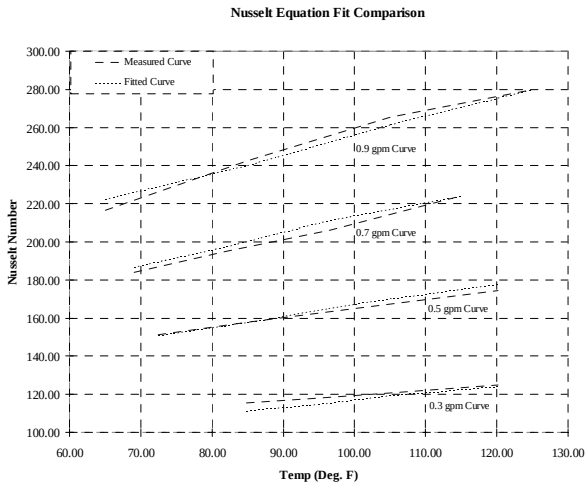

Figure 5. Data fit comparison.

7 REFERENCES

[1] Billen, J. et al, "A New RF Structure for Intermediate-Velocity Particles", Proceedings for LINAC94, Tsukuba, 1994.

[2] Lawrence, G., "High Power Proton Linac for APT; Status of Design and Development", this conference.

[3] Smith, H., "Status Update for the Low-Energy Demonstration Accelerator (LEDA)", this conf.

[4] Wangler, T., "RF Linear Accelerators", John Wiley & Sons, Inc., 1998.

[5] Wood, R. et al, "Thermal/Structural Design and Fabrication Development of High Power CCDTL and CCL Structures", Proceedings for LINAC96, Geneva.

[6] Incropera, F. P.; DeWitt D. P. "Fundamentals of Heat and Mass Transfer", John Wiley & Sons, Inc., 1985

[7] Wood, R. Los Alamos National Laboratory, Personal Communication.

[8] Structural Research and Analysis Corp. (SRAC) 12121 Wilshire Blvd., Los Angeles, CA 90025.

DOUBLE DYNAMIC FOCUSING FOR LINEAR COLLIDERS

J. Irwin†, SLAC, 2575 Sand Hill Road, Menlo Park, CA, USA

Abstract

Dynamic focusing refers to the use of secondary beams to form final-focus lenses for the primary high energy beams of linear colliders. In double dynamic focusing an initial lens-lens beam collision focuses the lens beams for their collision with the primary beam. This paper describes the techniques for the formation of a uniform lens shape from an initial Gaussian shape, the necesary main- and lens-beam parameters and their scaling, and requirements for a 1 TeV c.m. application. Advantages of this scheme include the complete elimination of the conventional final focus and collimation systems, elimination of beamline elements within the detector, and the promise of looser main-beam linac alignment, energy spread and ground motion tolerances.

1 INTRODUCTION

1.1 Motivation

Our original motivation was a search for a viable final focus system for linear colliders above 1.5 TeV cm. Now our motivation is the complete elimination of the final focus and collimation systems and reduction of backgrounds and cost in all future colliders, including the next linear collider (NLC) [1].

1.2 A simple large momentum-bandpass focusing system

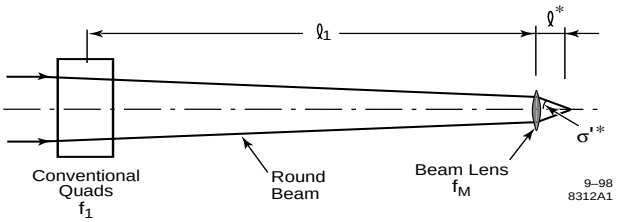

Figure 1. A schematic of a simple final focus system. A very strong lens is placed 1 cm from the IP. The total length is about 4 m.

We will use a secondary beam to create a small strong lens about 1 cm from the IP [2, 3]. Figure 1 shows the full system, with final conventional quads outside the detector at a distance $l_1 \geq 4m$. If the focal length, f_1, of the convential quads is chosen equal to l_1, and the focal length of the beam lens, f_M, is chosen so that a ray originating at the convential quad is focused to the IP, then the final spot size demagnification is $\rho = l^* / l_1$, and

$$\sigma^{*2}(\bar{\delta}) = [\rho^2 + (\lambda^2 - 2\rho)\bar{\delta}^2 + \bar{\delta}^4]\,\sigma_1^2$$

where $\lambda = l_1 / \beta_1$ is the demagnification to the beam lens. If $\lambda < \sqrt{2\rho}$, a condition easily satisfied, the second order term in $\bar{\delta} \equiv \delta / (1+\delta)$ is actually negative. Under these circumstances the bandpass of the system is given by $\bar{\delta}^2 < \rho$, which for a typical demagnification of 1/400 gives $\bar{\delta} < 1/20$, implying a huge momentum bandpass.

1.3 Double dynamic focusing

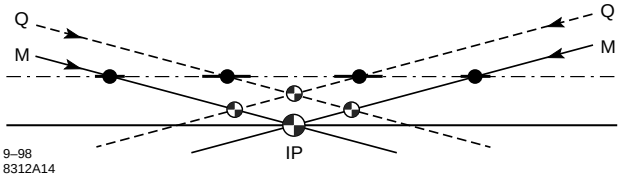

Figure 2. An overview showing the trajectories of the lens beams and main beams. There are three collisions: lens-lens, 2 lens-main and the final main-main. This figure also shows the "crabbing" of the beams and the fact that all beams lie on a common line as they traverse the IP.

Figure 2 shows an overview of the incoming lens and main beams. Because room-temperature colliders must have multi-bunch beams, a non-zero crossing angle is required. Crab cavities are used to twist the bunch so that they pass through each other as if head-on, and by control of their relative phases, they place the bunches along a common transversely-moving line.

The two lens beams must necessarily collide before their interaction with the main beam. This collision can be put to advantage for either aligning the lens bunches or to completely focus the lens beam. It is the latter case which we refer to as double dynamic focusing.

2 LINEAR COLLIDER IP PARAMETERS

With dynamic focusing, arguments for the flat beam geometry are all but eliminated. Round beams are favored because they require lower main-beam bunch charge (facilitating a lower lens-beam energy) and have a larger IP vertical size and β-function. Presumably, for main- linac efficiency, main-beam current is held constant. A lower short-range wakefield is advantageous, but long-range wakes could be worse. Damping ring rf design is changed dramatically. At 1 TeV cm with $n_\gamma = 1$, round IP parameters are $N = 0.7\ 10^9$, $\sigma = 12\,nm$ and $\sigma_z = 60\,\mu m$.

†Work supported by the Department of Energy, contract DE-AC03-76SF00515.

3 DYNAMIC FOCUSING PARAMETERS

3.1 Lens beam charge per bunch

For a charge $\bar{N}_Q$ in a uniform disk of radius R_Q the focal length is given by $\frac{1}{l^*} = \frac{2\bar{N}_Q r_e}{\gamma_M R_Q^2}$. This condition yields $\bar{N}_Q = N_{Q_0}\frac{R_Q^2}{2\sigma_M^2}$ where $N_{Q_0} = \frac{(\gamma\varepsilon)_M}{r_e}\xi$, and $\xi = \frac{l^*}{\beta^*}$ is the inverse demagnification from the beam lens to the IP. Since the fraction of the main beam not incident on the uniform disk is given by $\Delta N / N = \exp[-R_Q^2 / 2\sigma_M^2]$, the exponent will lie between 3 and 4.

3.2 Uniform lens distributions

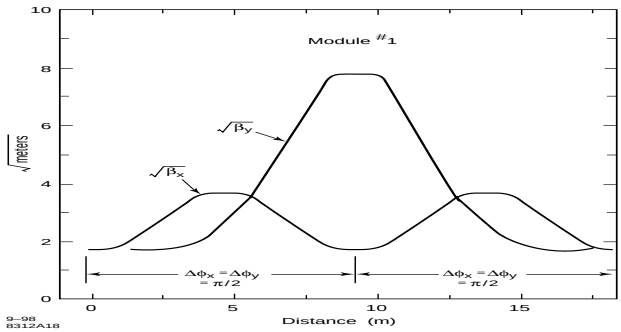

Figure 3. A module for inserting an octupole in a beamline.

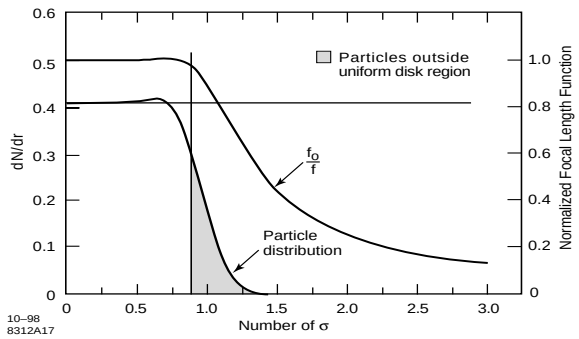

Figure 4. An example of a particle distribution and its focal length function achieved with a 3-octupole system. 85% of the distribution is accurately focused.

A Gaussian distribution can be made almost uniform by using 3 octupoles in 3 similar modules (see Fig. 3), each rotated by 60 degrees from the previous module. An example of a distribution achieved in this way is shown in Fig. 4. The lens-lens collision can further reduce the population in the tails for the main-lens collision.

3.3 Pinch effect

Figure 5 shows the lens beam colliding with the main beam. Each beam focuses the other and the ratio of the focal lengths is the beam-power ratio: $f_M / f_Q = (\gamma N)_M / (\gamma N)_Q$. The focusing of the lens beam will cause a change in its focal length for the latter part of the main beam. This is improved by arranging that the lens beams diverge when they meet the main beams. See Fig. 6. Ignoring effects of disruption, the luminosity loss due to the change in focal length is about $\frac{\Delta L}{L} \approx \frac{1}{120}\left(\frac{l^*}{f_Q}\frac{\sigma_z}{\beta^*}\right)^2$.

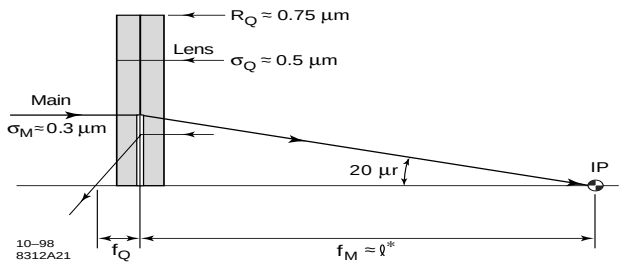

Figure 5. The lens beam, moving to the left, is pinched by the main beam moving to the right.

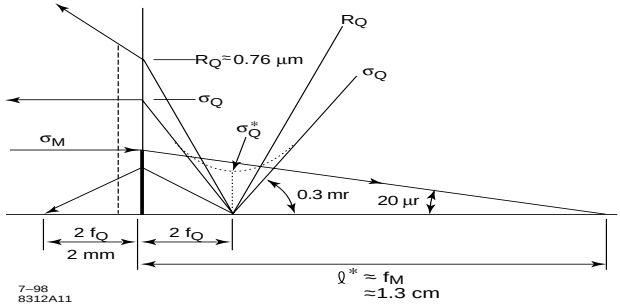

Figure 6. A lens beam which is diverging when it meets the main beam will reduce the pinch effect.

3.4 Parameter summary

Figure 7 summarizes the relationships of the parameters in this problem. $c_p = \sqrt{120(\Delta L / L)_p}$ comes from the pinch-loss equation and n_{l^*}, the number of l^* chosen for the focal length of the lens-lens collision, equals 1 for double dynamic focusing and 2 for self alignment. A possible parameter choice for 1 TeV cm [ξ=30, $\gamma_M / \gamma_Q = 100$, D=0.9, and H=3] lies very close to the zero 2nd order chromaticity condition.

These parameter relationships scale well to higher energies, and dynamic focusing appears viable up to 10 TeV cm. At 1 TeV cm it may be possible to put the lens

beam in a storage ring. At higher energies a modified scheme including a linac will be necessary. See Fig. 8.

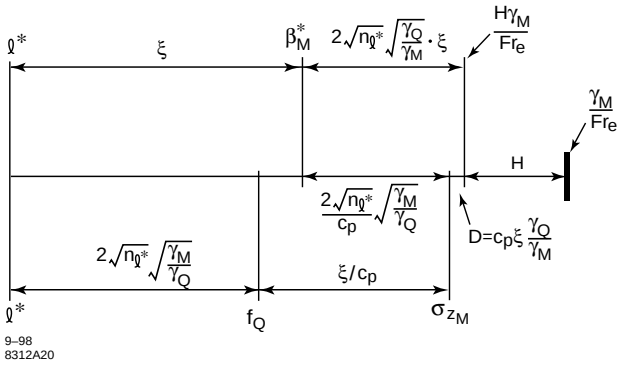

Figure 7. A log-scale diagram showing the relationship of the parameters in a "double" dynamic focusing system. See text.

4 OPTICAL BENCH CONDITIONS

4.1 Jitter

In addition to a uniform lens profile, it is crucial to have small beam jitter because the lens position determines the focal point for the main beam. With the demagnifications assumed, the inter-bunch lens-beam jitter would have to be 1% for the self-aligning case and 0.1% for double dynamic focusing. 1% is the ZDR specification for the NLC damping ring, and appears achievable. 0.1% probably requires a feed-forward loop after extraction from the lens-beam damping ring. Such a scheme is indicated in fig. 8. The main obstacle is the short inter-bunch spacing, presumably at S-band or less. An accurate fast BPM is under study. Lens train alignment can be achieved by using precursor bunches in the lens train.

4.2 The crab cavity

Crab cavity phase tolerance are an order of magnitude tighter with round beam parameters: the relative phases should drift no further than 0.01 degrees X-band. Systems for evaluating the feasibility of this tolerance are being developed.

5 SUMMARY

The prospect of total elimination of the final focus and collimation systems offered by dynamic focusing is very attractive. Additionally backgrounds in the IP region can be dramatically reduced, removing the tension between luminosity and backgrounds present in the SLC operation. Lens-beam energy should be minimnized to reduce cost. The minimum will depend on the lens quality that can be achieved, but appears to be less than 1% of the main beam energy.

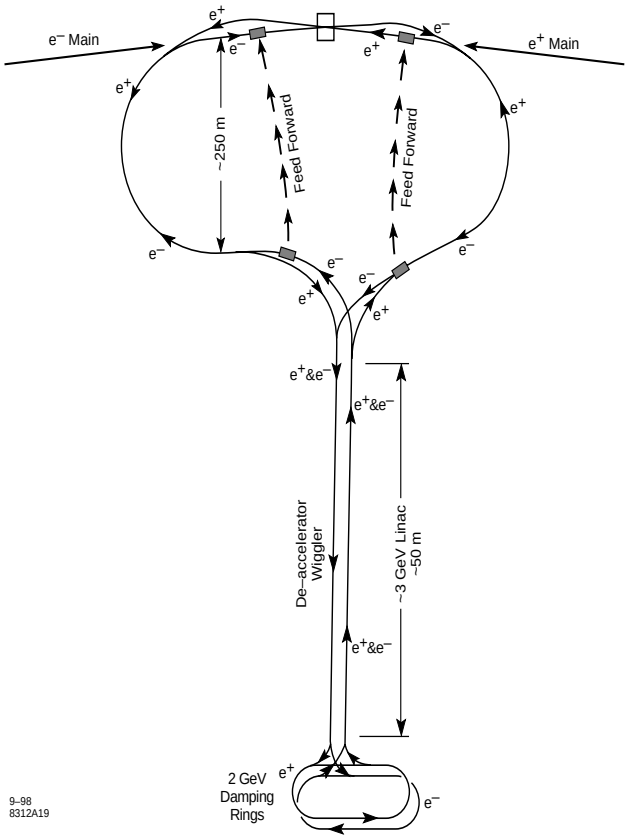

Figure 8. A possible geometry for the lens-beam system. The lens beam is stored in a 2 GeV damping ring between collisions, accelerated to the required collision energy, then decelerated and re-injected into the damping ring. A feed-forward scheme removes bunch to bunch jitter.

6 ACKNOWLEDGMENTS

I would like to thank the Institute of Theoretical Physics, Santa Barbara, for hosting a session on accelerator physics, where this work began. I thank Y. Cai, P. Chen, A. Dragt, K. Oide, V. Telnov, K. Thompson, T. Raubenheimer, and F. Zimmermann for encouragement and helpful conversations.

REFERENCES

[1] Zeroth-order design report for the Next Linear Collider, SLAC-Report 474 (1996)

[2] The idea of using particle bunches to focus is attributed to D. Leith and first described by R. Palmer: 'Super disruption and its use in linear colliders', SLAC-PUB-3688 (1985)

[3] J. Irwin, Final focus and beam alignment in TeV electron-postron colliders using particle bunches as lenses, AIP Conf. Proc. 156, 531 (1986)

[4] N. Tsoupas, R. Lankshear, C.L.Snead, Jr., and H.A. Enge, Uniform beam distribution using octupoles, Proceedings IEEE Particle Accelerator Conference (PAC95), San Francisco, CA, p1695 (1995)

2 MeV LIA INJECTOR DESIGN

L. Zhang, N. Cheng, G. Dai, H. Wang, L. Chengjun, J. Deng, B. Ding
Institute of Fluid Physics, CAEP P.O.Box 523-56, Chengdu, China, 610003

Abstract

This paper describes a design for 2 Mev LIA Injector. The injector is composed by eight accelerating cells in which for four accelerating cells form an anode and others make a cathode. A foilless diode or a diode with a tungsten mesh anode is used in the injector, and the voltage for the diode is 2 Mev. The electron beam current is more than 3kA in the end of injector. The pulse power system, beam transport system. Auto-control system and auxiliary system also are discussed.

1 INTRODUCTION

The purpose for the injector is to produce a high-brightness, low energy spread electron beams [1,2]. The injector is consisted of 8 accelerating cells, foilless diode, solenoid magnet and pulse power system. The length of the injector is 6 m. In order to satisfy the requirement of resistant match, the cathode bar and anode bar are formed as cylinder stairup-like. Internal diameter of anode accelerating cell is bigger than that of cathode for accommodating focusing solenoid. The cathode is cold cathode field-emission and the cathode material is velvet. We use solenoid producing a focusing magnet to transport electron beams.

2 DESIGN OF THE INJECTOR

It is necessary to improve beams brightness, lower beam energy spread and control transversal movement of beams. We make following design.

2.1 The design of diode

To design a diode, first of all, we must optimize the shape of diode by using foilless anode or tungsten mesh anode so that the field in the cathode is uniform. This is beneficial to increase the brightness of electron beams. The optimizing choice is carried out by using numeral simulation and experiment. The experimental result shows that a plane diode can produce a high-quality electron beam which brightness is higher than 1.5×10^{8}A/(m·rad)^{2}

2.2 The system design for pulse power

To realize the wide flat top in the diode, the pulse power source need good synchronism [3]. Then the influence of resistant variance should be controlled. in the process of electron emission, the plasma moves toward anode and the emission current gradually increased, the resistance of diode decrease. In this way, the diode voltage induces. The way to induce this kind of influence of to choose the proper resistance of accelerating cavity and proper diode shape. While design pulse power system, we use a Max generator and Blumlein line to produce a 250 kv 110 ns pulse. The Max generator charge four Blumlein lines and each line provide pulse power to two accelerating cells. We use spark gap switch to control the synchronism.

2.3 The system design for beam transport

Eight solenoids are used to build up a beam transport magnet, two solenoids for introducing electron beam out the diode, one solenoids for producing a compensate magnet field at cathode, four solenoids in the accelerating cavity for transporting electron beams and others for adjusting output beams.

2.4 Auto-control system and auxiliary system

We use personal computer and Bitbus net to build up our auto-control system. A personal computer is used as central control computer and several industrial control computers are used as station. A data analyze system for analyzing experiment result is also accomplished. The auxiliary system includes vacuum (4×10^{-4} Pa), pure water (5 MΩcm), gas (N_2, SF_6) and oil.

3 CONCLUSION

The injector should arrival following criterion:

$$energy \geq 2Mev$$
$$beam \geq 3KA$$
$$pulsewidth \geq 60ns$$
$$energyspread \leq 1.5\%$$
$$emission \leq 0.28\ cm \bullet rad$$
$$brightness \geq 1.5\times10^{8}\ A/(m \bullet rad)^{2}$$

The 2 Mev LIA injector was resemble in 1997 and the first experimental result show that our design is reasonable.

REFERENCES

[1] Mascurea J. De, et al, A Progress of the AIRIX Induction Accelerator 1993.
[2] B.N Ding, Performance of 10 Mev LIA. Proceeding of 10 Mev LIA 1994.
[3] Jaitly N.C et al, Design and Testing of a Multi-output 300 kv Prototype Induction Cell Pulse Power Supply for DARHT.

ADVANCED CONCEPTS FOR HIGH-GRADIENT ACCELERATION*

D. H. Whittum
SLAC, Stanford University, Stanford, California 94309 USA

Abstract

The promise of high-gradient accelerator research is a future for physics beyond the 5-TeV energy scale. Looking beyond what can be engineered today, we examine basic research directions for colliders of the future, from mm-waves to lasers, and from solid-state to plasmas, with attention to material damage, beam-dynamics, a workable collision scheme, and energetics.

1 INTRODUCTION

The technology of colliders could be scaled to energies well beyond the frontier of high energy physics today, but for limits to physical size. To reach beyond the next-generation machines requires not scaling nor engineering, but basic research in beam physics. The need for "advanced accelerator research" is not new; the subject extends back decades, to the beginnings of high-energy physics, the invention of the klystron by the Varian brothers, the resonant-cavity accelerator by Hansen, and strong-focusing by Christofilos. However it is only in the last decade that it has become recognized as the critical path for experimental particle physics in our lifetime. Here we consider one view of the latest chapters in the story of high-gradient accelerators for colliders.

In Sec. 2, we review the relevance of high-gradient to a collider. We then review the state of research in high-gradient acceleration mechanisms. Solid-state accelerators are covered in Sec. 3, and plasma-accelerators in Sec. 4. Conclusions are offered in Sec. 5.

2 COMPACT COLLIDER

Efforts to conceive of a compact collider meet with numerous difficulties. For example, if one were to extrapolate the "conventional" picture of a collider [1] to 5-TeV center-of-mass energy, a luminosity of 10^{35} $cm^{-2}s^{-1}$, and an accelerating gradient of 1 GeV/m, one would hear objections at every turn. At conventional frequencies, one would need a multi-GW power source that doesn't exist. Even if one had such a source, it would ablate the accelerator structure surface in a single pulse, due to Ohmic heating. At high frequencies, the peak power requirement would be lower, but Ohmic heating would still be untenable, due to copper fatigue from thermal cycling. In addition, high-frequency structures are difficult to fabricate. Even if one could fabricate 10^5 of them, and align them, their wakefields would destroy the beams. Even if the beams survived the linac, then to focus them one would need a 20 km optical system. With such a big machine, why bother with high gradient? In collision the beams would pinch each other producing mostly backgrounds, so why bother at all?

These problems can be taken either as discouragement, or motivation. Actually it appears that most of them are simply symptoms of a naive collider concept. A different concept for a collider has been described by Zimmermann [2], as seen in Fig. 1, with parameters as in Table 1. To avoid beam disruption, neutralized beams or $\gamma\gamma$ collisions are employed. To form a compact final focus, chromatic correction is abandoned. Instead, it is assumed that each main linac is followed by two much shorter accelerators operated at harmonics of the fundamental. To improve luminosity for a given site-power, one combines single bunches from the linac. This requires a half-chicane, and synchrotron radiation there requires that bends be gentle, extending over 1.3 km. Control of single-bunch beam dynamics in the linac is consistent with permanent magnet quadrupoles.

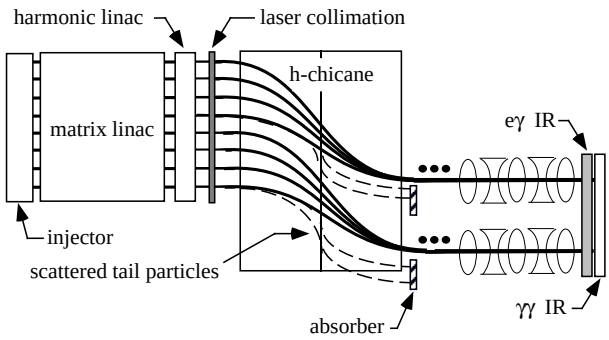

Figure 1: A new concept for a compact collider, as described by Zimmermann [2].

Even if one accepts that such concepts could be reduced to practice, one significant problem remains: how to make a high-gradient linac? This linac should be frugal with stored energy per unit length, and should be consistent with multi-beam collisions, either through beam-combining as seen in Fig. 1, multiplexed collisions, or a continuous focus in the interaction region. For example, if one could collide each of 50 bunches, the luminosity corresponding to Table 1 would approach 10^{35} $cm^{-2}s^{-1}$. In the meantime, work of [2] suggests that the collider problems-of-principle soon may be reduced to just

* Work supported by DE-AC03-76F00515.

one: the accelerator. Let us consider then recent work on advanced accelerator concepts.

Table 1: Example Parameters for a Compact Collider.

parameter	W-Band example
center of mass energy	5 TeV
gradient	1 GeV/m
collision spot-size	1.8 nm
normalized emittance	10^{-7} m-rad
charge per linac bunch	60 pC
frequency	91.392 GHz
repetition frequency	120 Hz
main linac length	2.5 km
harmonic linac length	0.1 km

3 SOLID-STATE STRUCTURES

At high-gradient, solid-state structures are prone to breakdown [3] and cyclic stress arising from pulsed Ohmic heating [4]. Associated with breakdown are the phenomena of field-emission and trapping. A discussion of the phenomenology can be found in [5]. To summarize, breakdown is inhibited on short time-scales. Trapping occurs for gradient-wavelength product $G\lambda$>1.6 MeV. All such considerations favor short-wavelength for high-gradient. For G>1 GeV/m, frequencies of 10^2 GHz and higher are indicated. However, it is difficult to conceive of a resonantly-excited structure that can survive the Ohmic heating associated with such gradients. Thus pulsed-heating is the first motivation for research into new structure concepts.

There are four research directions one might pursue to lower cyclic stress limits: disposable (plasma) accelerators, advanced materials, composite structures, and active circuits. Plasma accelerators are discussed in the next section. Advanced materials include dispersion-strengthened conducting alloys [6], and dielectrics. Dielectric accelerators include wakefield-driven [7], and resonantly-driven [8] structures. Lin has analyzed a composite structure employing a diamond layer to reduce pulsed heating [9]. Diamond is attractive due to its high thermal conductivity, high dielectric strength, and low loss tangent [10,11]. Active circuits have been studied for some years, for applications external to the accelerator [12]; incorporation into the structure is a relatively new area [13]. One new concept for an active accelerator is seen in Fig. 2, employing a high-Q resonant cavity coupled by switches to loaded transmission lines, forming a matrix of accelerating cells. [14]. For the active element, silicon is inadequate at high-fields, and thus plasma and diamond are of interest. Use of diamond as the photoconductor requires 220-nm photons; carrier lifetime is adequate depending on the purity.

While the ultimate gradient attainable in a solid-state accelerator is unknown today, it appears that application of strengthened copper alloys, diamond layers, and active circuits may permit more than an order of magnitude improvement in stress-limited gradient.

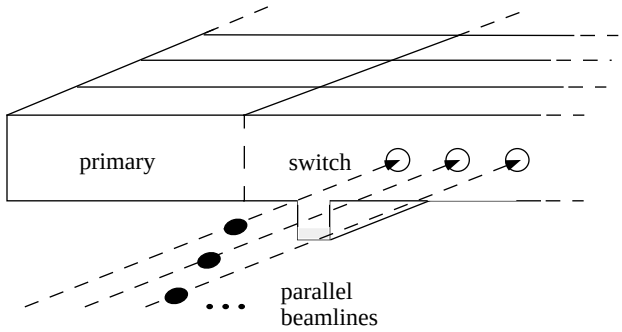

Figure 2: A new concept for an accelerator, employing an active circuit and parallel beamlines.

Structure fabrication and bench-measurement are critical to structure development. At W-Band (75-110 GHz) such work is being pursued by Kang, *et al.*, [15] via deep X-ray lithography, and D.T. Palmer via electrodischarge machining [16]. The primary challenge for fabrication at present is bonding. Brazing appears difficult due to the detuning effect of fillets; diffusion bonding is discussed in [16]. Meanwhile, good tune and quality factor have yet to be demonstrated in a multi-cell W-Band structure. In the meantime, other fabrication techniques merit attention, particularly where they may be extensible to the THz range [17].

A short-wavelength structure also requires a power source. To-date power levels adequate for 1-GeV/m fields have been demonstrated up to 140 GHz [18], and there in a mode consistent with the two-beam accelerator (TBA) concept. For TBA-driven colliders one is interested to assess drive beam stability at beam currents consistent with the stored energy requirement for the linac, typically 10^1 J/m. Tube concepts at 10^2 GHz meanwhile are making rapid progress at the 10^{-1} MW level [19,20], and a 10^1 MW design study is complete [21].

For structure dimensions in the 10^{-5} m range, lasers are adequate to produce GeV/m gradients, limited by structure damage [22]. However, it is important to keep in mind that for first-order accelerators [R/Q] is a crucial figure of merit for the energetics of the machine. Theoretical maximum in idealized cylindrical or rectangular geometries is 221 Ω, and this diminishes rapidly as the volume of the accelerating cell or the beam-port is enlarged. Higher-mode losses must be accounted for, particularly for small beam-ports [23].

For all short-wavelength solid-state structures, machine issues are in an early state. A glimpse of what is to come can be seen in the work on SLC collimator damage [24]. For structure protection, laser and resonant spoliation and collimation are being pursued [2]. Associated beamline instrumentation will require: manipulation of THz frequencies and beyond for bunch-length and beam-timing

information; beam position monitor resolution below the 10^{-7} m level for orbit analysis; single-pulse emittance measurement [25] for tune-up; use of the structure as a self-registered beam-position monitor [26] for control of emittance.

Given the benefits of harmonic-acceleration for energy-spread compensation [2], a linac proposed to operate at frequency f, should be accompanied by concepts for frequencies extending up to 10^2 f. Thus one is inevitably interested in structure development across the spectrum. Note that harmonic structures need not meet the same stringent requirements as the main linac structures, so that [R/Q], efficiency and gradient can be lower.

Structure research for the injector is equally critical. While the parameters of Table 1 are consistent with expected scalings for rf photocathode guns, the scaled field approaches 1 GV/m. Thus the problems of high-gradient appear in the injector as well. Possible alternatives include a pulsed photocathode-gun [27]. An injector providing a low-emittance, high-polarization electron beam remains a critical problem.

4 PLASMA STRUCTURES

The first plasma wakefield experiments employed a uniform plasma, demonstrating the principles of operation with injected beam; plasma wakefields were observed to exhibit a high Q, of order 10^2, in the linear regime (small $G\lambda$) [28]. In the intervening years, the plasma beat-wave accelerator has produced 2 GeV/m, and the laser wakefield accelerator, 100 GeV/m [29]. In a uniform plasma, however, the laser-driven concepts are limited by the diffraction of the drive pulse; thus observed beam spectra extend up to only 10^2 MeV.

To extend the interaction length numerous groups are presently pursuing experimental studies of laser-driven wakefield acceleration in a hollow plasma channel as seen in Fig. 3. Such a channel can serve as an optical fiber, permitting acceleration over many Rayleigh lengths [30]. With these efforts, and continued work on beam-driven wakefields [31], it is quite likely that a 1 GeV beam spectrum will be produced from a plasma accelerator, within the next year.

As the plasma accelerator concepts develop into a new generation of experiments, oriented on 1-GeV spectra and staging, it is timely to compare them quantiatively to the conventional multi-cell accelerator. Schroeder, *et al*., have recently analyzed the plasma channel in such a fashion [32], providing the first rigorous characterization as an accelerator. Let us summarize this work briefly.

In a uniform channel, there are two free parameters, the plasma frequency ω_p and the channel radius, b, measured in units of the plasma skin-depth $B=\omega_p b/c$. The accelerating mode of a plasma channel may be characterized by an [R/Q] (per plasma period) a function only of B, and a resonant frequency scaling with ω_p and a function of B. Moreover, Schroeder has discovered that for this monopole excitation, and for each higher azimuthal harmonic, the channel supports *only one* synchronous mode. This is possible since the channel is axially uniform, eliminating diffractive losses, and the plasma susceptibility is negative, suppressing Cherenkov losses.

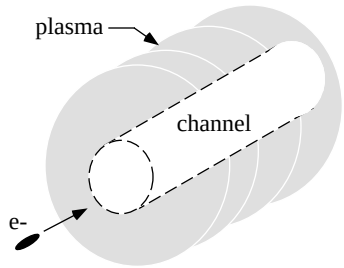

Figure 3: A hollow channel in a plasma can function as an accelerating structure.

The "single-mode" character of the channel implies lower parasitic losses than in a scaled conducting structure, and permits *shorter* bunches and *higher* single-bunch charge than in a scaled collider design. Analysis of the dipole mode shows that for multi-bunch operation, channels can be stagger-tuned to inhibit beam break-up. However, multi-bunch operation requires good Q for the accelerating mode and this requires a sharp-edged channel [33]. The high Q of the uniform plasma has not yet been demonstrated experimentally in the channel geometry, and vigorous efforts are underway to produce and diagnose tailored plasma channels [30].

The promise of this work is an accelerator concept superior in principle to the conventional circuit, immune to damage, and operating with an existing power source. The first challenge for such a disposable accelerator is accurate structure fabrication and diagnosis "on-the-fly", at the machine repetition frequency. To operate a series of such structures in concert, phasing and alignment must be provided for. Finally, incorporation into a multi-beam collision scheme should be addressed.

5 CONCLUSIONS

While the naive extrapolation of the conventional collider concept is fraught with problems, more sophisticated collision schemes are conceivable. In the last two years, we have seen new results emerge across the spectrum that appear capable of solving the problems of the compact collider, and its high-gradient linac. Work summarized here was not arrived at by scaling known technology, nor by contemplating only what can be engineered. Advanced accelerator research today is simply basic physics research, carrying us into the state- of-the-art in laser science, micro-fabrication, instrumentation and mm-wave and infrared technology --- and to the frontiers of plasma, beam, and high-energy physics. The results of

recent years suggest that the next-generation colliders will not be the last.

6 ACKNOWLEDGEMENTS

Collaboration with Carl Schroeder, Sami Tantawi, Jonathan Wurtele, and Frank Zimmermann was essential. Conversations with Wim Leemans were most helpful. I thank Angie Seymour for her support.

7 REFERENCES

[1] R. B. Palmer, *Ann. Rev. Nucl. Part. Sci.* **40** 529-592 (1990).

[2] F. Zimmermann, "New Final Focus Concepts at 5 TeV and Beyond", *Advanced Accelerator Concepts*, W. Lawson, ed., (to be published), SLAC-PUB-7883.

[3] J.W. Wang and G.A. Loew, "Field-emission and RF breakdown in high-gradient room-temperature linac structures", *Proc. Joint School RF Engineering for Accelerators* (IOP, to be published), SLAC-PUB-7684.

[4] D. Pritzkau, *et al.*, "Experimental study of pulsed-heating of electromagnetic cavities", *Proc. 1997 Particle Accelerator Conference*, (IEEE, New York, to be published).

[5] D. Whittum, "Ultimate gradient in solid-state accelerators", *Advanced Accelerator Concepts*, W. Lawson, ed., (to be published), SLAC-PUB-7910.

[6] A.V. Nadkarni, "Dispersion strengthened copper properties and applications", in *High Conductivity Copper and Aluminium Alloys*, E. Ling and P.W. Taubenblat, eds. (AIME, Los Angeles, 1984) pp. 77-101.

[7] W. Gai, *et al.*, *Phys. Rev. Lett.* **61** (1988) pp. 98-100.

[8] J. Rosenzweig, A. Murokh, and C. Pellegrini, *Phys. Rev. Lett.* **74** (1995) pp. 2467-2470.

[9] X. Lin, "Diamond coating in accelerating structure", *Advanced Accelerator Concepts*, W. Lawson, ed., (to be published).

[10] L.S. Pan and D.R. Kania, eds., *Diamond: Electronic Properties and Applications* (Kluwer, Boston, 1995).

[11] M. Thumm, *International Journal of Infrared and Millimeter Waves* **19** (1998) pp. 3-14.

[12] S.G. Tantawi, "Active high power RF pulse compression using optically switched resonant delay lines", *Advanced Accelerator Concepts*, AIP Conf. Proc. **398** (AIP, New York, 1997) pp. 813-821; M.I. Petelin, A.L. Vikharev and J.L. Hirshifield, "Pulse compressor based on electrically switched Bragg reflectors", *ibid.*, pp. 822-831.

[13] C. Bamber, *et al.*, *Nucl. Instrum. Meth.* **A 327** (1993) pp. 227-252.

[14] D.H. Whittum and S.G. Tantawi, "Switched matrix accelerator" (submitted to Rev. Sci. Instrum.), SLAC-PUB-7848.

[15] Y.W. Kang, *et al.*, *Rev. Sci. Instrum.* **66** (1995) pp. 1-5 and "DXRL Fabrication and Measurement of Millimeter-Wave Accelerating Structures" (these proceedings).

[16] D.T. Palmer, "W-Band structure research at SLAC", *Advanced Accelerator Concepts*, W. Lawson, ed., (to be published).

[17] T.L. Willeke and A.D. Feinerman, *J. Vac. Sci. Tech.* **B 14** (1996) pp. 2524-2530.

[18] S.L. Allen, *et al.*, "Generation of high-power 140 GHz microwaves with an FEL for the MTX experiment", *Proc. 1993 Part. Acc. Conf.* (IEEE, New York, 1993) pp. 1551-1553.

[19] M. Blank, *et al.*, "Experimental investigation of a W-Band gyroklystron amplifier", *Proc. 1997 Part. Acc. Conf.* (IEEE, New York, to be published).

[20] G. Caryotakis, *Phys. Plasmas* **5** (1998) pp. 1590-1598.

[21] M.R. Arjona and W. Lawson, "Design of a 7-MW, 95-GHz, three-cavity gyroklystron" (submitted to *IEEE Trans. Plasma Sci.*).

[22] T. Plettner, *et al.*, *Advanced Accelerator Concepts*, W. Lawson, ed., (to be published).

[23] F. Zimmermann, *et al.*, "Wakefields in a mm-wave linac", *ibid.*

[24] F.-J. Decker, *et al.*, "Design and wakefield performance of the new SLC collimators", *Proc. XVIII International Linac Conference* (CERN, Geneva, 1996) pp. 137-139, SLAC-PUB-7261.

[25] J.-S. Kim, *et al.*, "Pulse-to-pulse emittance measurement system", FARTECH Inc., 3146 Bunch Ave., San Diego, CA 92122 (unpublished).

[26] M. Seidel, *et al.*, *Nucl. Instrum. Meth.* **A 404** (1998) pp. 231-236.

[27] T. Srinivasan-Rao, *et al.*, "Optimization of gun parameters for a pulsed power electron gun", *Advanced Accelerator Concepts*, W. Lawson, ed., (to be published).

[28] J.B. Rosenzweig, *et al.*, *Phys. Fluids* **B 2** (1990) 1376.

[29] W. Leemans, "Summary of the Plasma Acceleration Working-Group", *Advanced Accelerator Concepts*, W. Lawson, ed., (to be published).

[30] T.C. Chiou, *et al.*, *Phys. Plasmas* **2** (1995) 310.

[31] R. Assmann, *et al.*, "Proposal for a 1-GeV Plasma Wakefield Acceleration Experiment at SLAC", SLAC E-157

[32] C.B. Schroeder, J.S. Wurtele, and D.H. Whittum, "Multimode analysis of the plasma channel accelerator" (submitted to *Phys. Rev. Lett.).*

[33] B.A. Shadwick and J.S. Wurtele, "Numerical studies of wake excitation in plasma channels", *Proc. 6th European Part. Accelerator Conf.* (to be published).

HIGH INTENSITY INJECTOR LINACS FOR SPALLATION SOURCES

K. Bongardt, M. Pabst, FZJ, Jülich, Germany
A. Letchford, RAL, Didcot, U.K.

Abstract

A review is given of the layout and the design problems for recently proposed spallation neutron sources with up to 5 MW average beam power. The accelerator part consists of an H^- - injector linac followed by compressor rings. Different to the design of high intensity proton linacs are the low energy front end and the restrictions at high energy for loss free ring injection. The linac energy spread has to be reduced by a bunch rotator requiring an unfilamented beam in longitudinal phase space. Uncollected ring injection losses should be kept below 10^{-4}. Due to intensity limitations of the H^- ion source a funneling line is needed at the front end. For loss free ring injection the linac pulse has to be chopped after the first RFQ. Special emphasis is given to either transverse or longitudinal halo production due to mismatch of a high intensity bunched beam. Concerning particle loss in the linac itself the loss rate has to be smaller than 10^{-7}/m for unconstrained hands on maintenance. Design criteria are discussed for 10% pulsed RF systems. Comments are given about the use of pulsed superconducting cavities above 200 MeV beam energy.

1 PROPOSALS FOR HIGH POWER SPALLATION SOURCES

Recent proposals for spallation neutron source facilities require up to 5 MW average beam power. The accelerator part consists of a high intensity pulsed H^- linac followed either by a compressor ring or a rapid cycling synchrotron. The high intensity compressor rings are summarized in ref. [1,2]. Detailed proposals exist for the following projects :

1.1 Japanese Hadron Facility (JHF)

The JHF aims at an interdisciplinary facility based on a high intensity proton accelerator [3]. It is planned to replace the existing KEK 12 GeV booster synchrotron by a high intensity 3 GeV booster. A 3 GeV, 200 μA proton beam , upgradeable to 800 μA, can be sent either to a spallation source target or a muon production target or nuclear physics area. By adding a 50 GeV proton synchrotron an average current of 10 μA can be given to a Kaon area or a neutrino experimental hall.

The H^- - injector linac has to accelerate a 30 mA peak current beam up to 200 MeV in a first step. The repetition rate is 25 Hz and the pulse length 400 μ sec, leading to 200 μA average current [4]. This results in a 3 GeV, 0.6 MW spallation neutron source. The final goal is to accelerate 60 mA peak current up to 400 MeV, leading to 800 μA average beam current at 50 Hz rep. rate. This would lead to a 3 GeV, 2.4 MW spallation source facility.

Quite recently the Japanese government decided to provide an additional fund to supplement the KEK 1998 budget. With this additional fund the JHF project team is preparing to construct a high intensity linac up to 60 MeV.

1.2 Neutron Science Project (NSP) at JAERI, Japan

The Japan Atomic Energy Research Institute (JAERI) is proposing the Neutron Science Project NSP. The objective of the NSP is to explore technologies for nuclear waste transmutation and basic research science in combination with a high intensity proton storage ring [5]. The 1.5 GeV linear accelerator is required to operate with H^+ and H^- particles in a pulsed or CW mode. 5 MW average H^- power is envisaged for a spallation neutron source facility, whereas 8 MW CW H^+ beam can be provided for nuclear waste transmutation experiments.

Above 100 MeV a 5 cell superconducting (SC) cavity at 600 MHz is foreseen with 16 MV/m peak surface field. Single SC cavities at β=0.5 have reached peak surface fields of 44 MV/m at 2.1 K already [6].

1.3 Spallation Neutron Source (SNS) Project

Oak Ridge National Laboratory is coordinating for the Department of Energy in the US the SNS project [7]. As a first step a 1 MW beam power facility with one target is envisaged with a final energy of 1 GeV. The whole facility is upgradeable up to 4 MW beam power and a second target station.

Design parameters of the first step are for the H^- injector linac pulse current of 30 mA for 1 msec long pulses. The 4 MW upgrade will be achieved by doubling the ion source current and installing a funnel line at 20 MeV. The high energy part of the linac is a conventional room temperature 805 MHz coupled cavity linac (CCL).

The project will be built by a consortium of 5 DOE laboratories. Lawrence Berkeley National Laboratory (LBNL) is responsible for the SNS linac front end [9], Los Alamos National Laboratory (LANL) is designing the linac [8]. The transport line between linac and compressor rings and the compressor ring layout itself is the responsibility of Brookhaven National Laboratory (BNL).

1.4 European Spallation Source (ESS)

The 5 MW beam power short pulse ESS facility [10] consists of a 6% duty cycle H^- linac with 1.334 GeV final en-

ergy. The pulse compression to less than 1μ sec is achieved by two compressor rings in a shared tunnel. Various R+D work is going on, especially for building an ESS test stand with ion source, chopper and RFQ at Rutherford Appleton Laboratory (RAL) U.K. and continuing beam loss studies [11].

2 BASE LINE LAYOUT OF HIGH INTENSITY INJECTOR LINACS

The dominating design feature of a high intensity injector linac is to bring particle losses down to about 1 W/m and to guarantee less than 10^{-4} uncollected ring injection losses. All accelerator sections have to be designed to be far away from the space charge limit.

As an example, the layout for the 5 MW H^- injector linac of ESS is shown in Fig. 1. Both RFQs operate at 175 MHz followed by a conventional 350 MHz drift tube linac (DTL) up to 70 MeV. The high β CCL operates at 700 MHz. Different from a proton linac is a bunched beam chopping line at 2 MeV between two 175 MHz RFQ structures and a bunch rotation cavity at the linac end. For achieving loss free ring injection, the linac pulse has to be chopped at the ring revolution frequency and the energy spread has to be reduced by the bunch rotator.

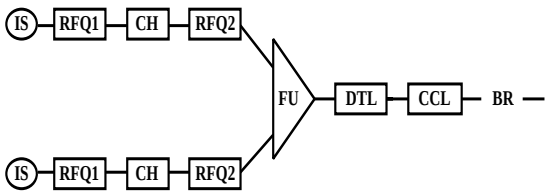

Figure 1: ESS linac layout: IS: I ion source, CH: chopper, FU: funneling, BR: bunch rotator

2.1 Low Energy Front End

Ion source requirements of more than 100 mA, 10% duty cycle H^- currents cannot be met with existing ion sources. R and D prototype programs are going on for all the above mentioned spallation source projects. For ceasiated RF-driven H^- volume sources a current of 70 mA at 7% duty cycle will be reached soon [9,12].

The beam transport between the H^- ion source and the first RFQ can be space charge compensated or uncompensated [9]. Integrated ion source RFQ test stands are set up for both possibilities.

Cooling problems for a 10% duty cycle RFQ are not so severe as for a CW H^+ RFQ, but more demanding than in RFQ structures built up to now. Field stability at 10% duty cycle can be achieved by 'π-mode stabilization loops' (PISL) for 4 vane structures [13]. Less than 1% unwanted field contamination has been experimentally verified. The 4-rod RFQ offers some advantage over the 4-vane design in terms of RF properties and ease of manufacture. The limited cooling capacity of a conventional 4-rod RFQ can be overcome [14], allowing up to 10% duty cycle. New RFQ-codes are available, taking into account rod or vane shaped electrodes, 8 term potential function, dipole components and complete 3d space charge subroutines [15].

A bunched beam transfer line at about 2 MeV is a good solution for a clean chopped beam with sharp edges and small longitudinal emittance increase. Chopping efficiencies of about 60% are required for loss free ring injection. Fast traveling wave choppers with 3 nsec rise time are under development [16]. Layouts of a chopping line with regular betatron oscillations as equal as possible in both planes results in quite small rms emittance growth [2].

The use of a funneling scheme implies a second bunched beam transfer line, but relaxes the constraints on the chopping line and on the ion source considerably. The peak current per ion source is halved and the first RFQ can operate at lower frequency. In a funneling section with conventional elements the two beams are merged together by an arrangement of septum magnets and an array of RF deflection elements. Care has to be taken to match the dispersion and its angle to zero even under space charge conditions [2]. By implementing a Two-Beam Funnel RFQ [17] lower energies for the funneling section seem to be possible.

2.2 Halo Production due to Mismatch in Bunched Beams

The major problem of the design in high current proton linacs is the loss of particles at higher energies. Particle loss leads to activation of accelerator components and reduces the flexibility of hands on maintenance. As a rule of thumb, hands on maintenance is possible if the loss is less than 1 W/m. In a linac losses occur radially due to the formation of a beam halo. The beam halo consists of a 'small' number of particles which oscillate around the beam core. In addition filamentation of the particle distribution in the longitudinal phase space can cause activation problems when injected into compressor rings. The design goal is less than 10^{-4} uncollected lost particles at ring injection.

In recent years substantial progress has been achieved by identifying the parametric resonance condition as a major source of halo production of DC and bunched beams. For realistic particle distributions with nonlinear space charge forces particles even inside the core have a tune spread. Parametric resonances can occur between single particle tunes and the frequency of the oscillating mismatched beam core [18].

Due to the two transverse and one longitudinal bunch dimensions 3 eigenmodes exist for a bunched beam. The frequencies of these modes can be approximately expressed by the full and zero current transverse and longitudinal tunes only. There exists a pure transverse quadrupolar mode and high and low modes which couple the transverse and longitudinal directions. The high mode represents a 'breathing' of the ellipsoidal bunch. For the low mode the bunch breathes in transverse direction but the oscillation in

the longitudinal direction is of opposite phase. For exciting the high or low mode only, the longitudinal mismatch is normally different in amplitude than the transverse ones [18,19].

For a mismatched bunched beam a 1/2 parametric resonance between a single particle tune and the frequency of an eigenmode is always excited radially by the quadrupolar mode. The high or low mode can excite a parametric resonance in the transverse and/or the longitudinal direction.

Fig. 2 and Fig. 3 show Monte Carlo simulations with 20000 particles which interact in full 3d for a 70 MeV bunched beam transfer line. A 6d waterbag distribution is used as input. The transverse and longitudinal tune depressions are 0.7 and 0.8 respectively. The transverse temperature is 1/3 of the longitudinal temperature. Shown is the 99.9% total to rms emittance ratio in the x-direction. In Fig. 2 the matched case is compared to a 20% quadrupolar mode excitation. A substantial increase of the 99.9% emittance is visible due to the 1/2 parametric resonance excitation. In Fig. 3 the same emittance ratio as in Fig. 2 is shown but comparing the matched case with a 20% radially and 30% longitudinally excited high mode. Here, no single particle tune is as large as half the high mode frequency and, as predicted, no resonance effect can be seen [18,19].

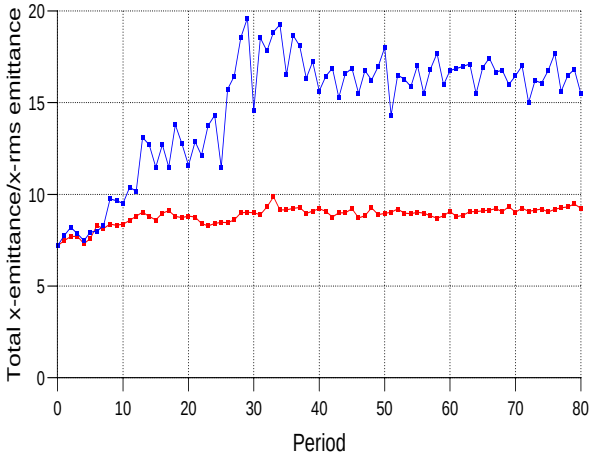

Figure 2: 99.9% total to rms emittance ratio for a matched (bottom) and a quadrupolar mode excited case (top)

During the startup period of high intensity linacs more than 20% initial mismatch is expected especially in the longitudinal plane. For a spallation source linac with its additional restriction on loss free ring injection a design is required where the transverse and longitudinal halo production is insensitive to all kinds of mismatch. Linac designs with both transverse and longitudinal tune depressions above 0.8 and transverse to longitudinal temperature ratios between 1/3 and 2 fulfill these conditions if no high mode envelope instability is excited [18]. The 214 mA ESS CCL has design parameters which meet these conditions for most of it's length and transverse and longitudinal halo formation is acceptable for a 20% initial mismatch. Space charge dominated designs with tune depressions below 0.4 [20] or large temperature anisotropy [21] can lead to chaotic single particle motion [22] and enormous halo production due to mismatch which is absolutely unwanted for high intensity injector linacs.

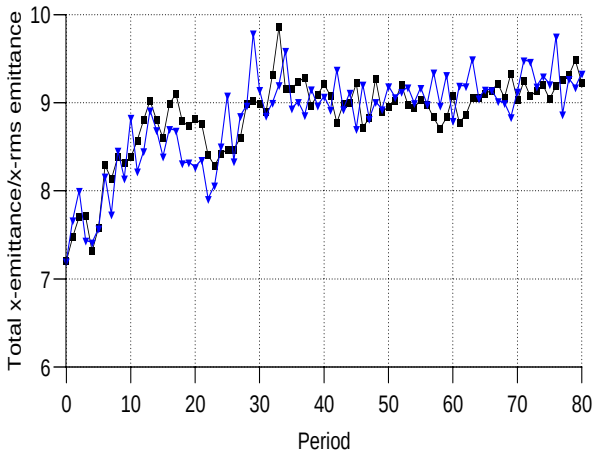

Figure 3: 99.9% total to rms emittance ratio for a matched (squares) and a high mode excited case (triangles). Please note the enlarged scale

2.3 High β Transfer Line

The transfer line from the H^- linac to the compressor rings differs in some respects from the H^+ transferline between a high intensity H^+ linac and a high power target station either for tritium production or waste transmutation. In both lines the linac beam is not kept bunched. Space charge forces are small but still effective, especially in the longitudinal plane [23] resulting in an increase of the energy spread.

For loss free ring injection into a circular machine the energy spread of the linac bunches has to be reduced by placing a bunch rotator at some distance behind the linac. After bunch rotation there should be less than 10^{-4} particles outside an energy spread of $\pm$ 2 MeV as a typical figure. For the ESS bunch rotation system there are less than 10^{-4} particles outside $\pm$ 0.8 MeV for the matched case, but more than 10^{-4} outside $\pm$ 1 MeV for the mismatched case. Longitudinal space charge effects are still visible after the bunch rotation system.

Uncorrelated RF amplitude and phase errors of $\pm$ 1% and $\pm$ 1^o respectively can cause an oscillation of the beam center by as much as 1 MeV [24]. As the energy spread collimation has to be guaranteed for all bunch currents including much larger RF tolerances during the start up procedure achromatic bending systems have to be installed in the high β transfer line. The influence of a conducting pipe has to be considered as the bunch length is equal or larger than the pipe radius. [23]

3 PULSED RF SYSTEM

The high β section from about 100 MeV onwards is the most expensive part of the whole linac for both the capital cost and the operating cost. Typically operating frequencies are between 600 and 800 MHz. Cost optimization of the accelerating gradient leads to about 2.8 MV/m for 10% duty cycle pulsed operation. Including focusing quadrupoles and diagnostic elements this value corresponds to an average real estate energy gain of 2 MeV/m for a room temperature linac design.

The layout of the RF system is a trade off between capital cost and overall RF efficiency. Conventional 2.5 MW peak power klystrons at 805 MHz, 8% duty cycle, with a modulating anode and a floating deck modulator are proposed for the SNS [25]. Such a RF system is expected to be very robust, can almost be built today and does not need circulators for protecting the klystron. The klystron efficiency is 60% at 100 kV beam voltage.

Prototyping is necessary for a 2.5 MW peak power, 7% duty cycle cathode modulated klystron with a transformer coupled bouncer type modulator. More than 65% RF efficiency is expected for 120 kV beam voltage at 1.4 msec pulse duration. No circulator is required. The modulator cost can be substantially decreased by connecting 2 klystrons to one modulator. The modulator efficiency is about 85%, the pulse flatness better than $\pm$ 0.5% [26]. A test stand with commercially available IGBT switches (EUPEC FF 800) mounted on individually water cooled boards has been set up in order to study temperature rise and life time problems at 50 Hz repetition rate for ESS.

Low voltage 2 MW peak power HOM-IOT (higher order mode inductive output tube) without a modulator are expected to be an attractive solution in the near future due to their smaller size and lower production costs compared to high power klystrons. Prototyping is needed therefore. A 1MW CW, 700 MHz HOM-IOT is under development for the Los Alamos APT project [27] requiring only 40 kV beam voltage for an anticipated RF efficiency $>$ 70% [28]. For a 700 MHz HOM-IOT with 2 MW peak power pulsed at 7% duty cycle, only 65 kV beam voltage is required and an efficiency of $>$ 70% is expected [29].

Attention has to be given to the RF control system. For H^- injector linacs uncorrelated amplitude and phase errors have to be limited typically to $\pm$ 1% and 1^o respectively in order to prevent intolerable oscillation of the beam centre at the linac end. The strict amplitude and phase tolerances counteract in some respects the use of high peak power multi beam klystrons (MBK) as power splitting is mandatory here. Circulators are necessary for protecting the MBK. Doubling the number of cells per tank is not recommended as the field flatness is proportional the square of the cell number.

4 SUPERCONDUCTING HIGH β LINAC

Superconducting cells are a very interesting option for the high β linac. Superconducting cavities are now being routinely used in many accelerators. Experience gained during building these machines strongly suggests that RF superconductivity is approaching mature technology, even if it is still far from its limit. In order to accelerate a high intensity proton beam from 100 MeV to about 1.3 GeV, various technical and physical difficulties have to be overcome, which do not exist in the acceleration of low intensity relativistic electron beams.

For the 100mA CW APT proton linac a 5 cell 700 MHz superconducting cavity at 2 K is proposed from 217 MeV on [27]. Focusing is provided by conventional quadrupole doublets located in the warm region between cryomodules. Only 2 different cavity length are foreseen with an on axis accelerating gradient of about 5 MV/m. The real estate energy gain in the SC linac is 1.5 MeV/m. Each 5 cell SC cavity is equipped with 2 power input couplers, limited to 210 kW each. The 5 cell cavities are arranged in cryomodules fed by 1 MW DC klystrons. About $\pm$ 3% amplitude and $\pm$ 5% phase errors in each cavity are tolerable caused by the power splitting procedure.

The layout of a SC high β linac for 10% pulsed H^- injector differs in some respects from the layouts for a CW proton linac. Normal conducting, 700 MHz, 10% pulsed coupled cavity linacs for energies from 100 MeV on have an real estate energy gain of 2 MeV/m. For msec long pulses the achievable accelerating gradient in a SC cavity is almost the CW value limited by the peak surface field especially at β values below 0.5, corresponding to 150 MeV proton energy. Peak surface field values of 25 MV/m for a 2 K 5 cell cavity around 600 MHz are expected to be reached quite soon. The corresponding accelerating gradients inside the SC cavity are 6 MV/m at 200 MeV and 10 MV/m from 900 MeV on leading to a real estate energy gain of 3 MeV/m. 5 different geometries are needed for such a SC linac. 240 kW and 600 kW peak power is needed for a 5 cell cavity at 200 MeV and 900 MeV respectively. Substantial R+D is needed for developing input couplers at about 600 MHz, capable of handling 1 MW peak reflected power during the 100 μsec long filling time, corresponding to 4 MW peak forward power. Circulators are mandatory for klystron protection.

The input coupler power limitation can in principle be overcome by having 2 couplers per cavity. As pointed out before power splitting is a problem for a high intensity H^- linac due to the $\pm$ 1% and $\pm$ 1^o amplitude and phase error limits in each cavity. Another difficulty for the RF control system is the field stabilization at the beam arrival time, complicated due to microphonic noise varying from cavity to cavity and pulse to pulse. The startup cavity frequency can oscillate by $\pm$ 30 Hz, intolerable with $\pm$ 1^o phase error. Unlike electron linacs phase errors in different cavities connected to one klystron do not add up to a common energy fluctuation [30]. Large but predictable RF errors due to Lorentz force detuning may be compensated by stiffening the cavities and applying digital feedback and feedforward from lookup tables [31].

Below 200 MeV or β = 0.6 elliptical shaped SC struc-

tures suffer from mechanical instability problems [5]. The real estate energy gain is lower compared to a 10% pulsed room temperature linac due to the uneconomic use of space in a low β cryomodule. Also the RF control problems are more severe here due to the reduced cavity bandwidth.

Different groups have R+D plans to study β=0.5 cavity structures [5], new fabrication techniques [32] and pulsed RF control problems including power splitting [33].

For a 10% pulsed H^- injector linac limiting the peak surface gradient to 25 MV/m in the SC cavity for an energy range from 200 MeV to 1.5 GeV, the SC linac has 2/3 of the length of a competitive room temperature one. The capital costs are expected to be equal or even slightly higher for the SC option. A 5 MW average beam power spallation neutron source needs about 75 MVA AC power where about 12 MVA can be saved with such a superconducting linac

5 REFERENCES

[1] I. S. K. Gardner, " A Review of Spallation Neutron Source Accelerators", Proc. EPAC '98, Stockholm, Sweden

[2] C. R. Prior, "Progress Report on the European Spallation Source", Proc. of the Workshop on Space Charge Physics in High Intensity Hadron Rings, Shelter Island, New York, May '98

[3] JHF Accelerator Design Study, KEK Report 97-16, March '98

[4] T. Kato, "Design of the 200 MeV Proton Linac for the Japanese Hadron Facility", these proceedings

[5] M .Mizumoto, "A High Intensity Proton Linac Development for the JAERI Neutron Science Project", these proceedings

[6] J. Kusano at al., "Development of Superconducting Cell Cavity for a Proton Linac in the Neutron Science Project", Proc. APAC '98, March 23-26, 1998, Tsukuba, Japan

[7] National Spallation Neutron Source Conceptual Design Report, Vol. 1 and 2, NSNS CDR-2 V1,2m May '97

[8] A. Jason, "A Linac for the Spallation Neutron Source", these proceedings

[9] J. Staples, "The SNS Front End Accelerator System", these proceedings

[10] "The European Spallation Source Study", vol. 1 - 3, March '97

[11] I. S. K. Gardner et al., "Status of the European Spallation Source Design Study", Proc. PAC97, Vancouver, Canada, '97

[12] K. Volk, "The Frankfurt H^- Source for the European Spallation Source ESS", these proceedings

[13] A. Ueno et al., Proc. Linac '96, Geneva, p157

[14] G. R. Murdoch, H. Vormann, "Thermal Design of an RFQ Cell for the Radio Frequency Quadrupole Under Construction for ISIS", Proc. EPAC '98,Stockholm, Sweden

[15] A. Letchford, A. Schempp, "A Comparison of 4-rod and 4-vane RFQ Fields", Proc. EPAC '98, Stockholm, Sweden

[16] S. Kurrennoy, "Development of a Fast Travelling Wave Beam Chopper for the SNS Project", these proceedings

[17] A. Firjahn-Andersch et al., "First Results of the Two-Beam Funneling Experiment", these proceedings

[18] M. Pabst et al., "Progress on Intense Proton Beam Dynamics and Halo Formation", Proc. EPAC '98, Stockholm, Sweden

[19] M. Pabst, K.Bongardt, A. Letchford, "Halo Formation by Mismatch for High Intensity Bunched Beams", these proceedings

[20] Y. Chen et al., "Halo Formation in Intense Linacs", these proceedings

[21] S. Lund et al., "Temperature Anisotropy Instabilities in Space Charge Dominated Beams", these proceedings

[22] J. M. Lagniel, Nucl. Instr. Meth. A, vol. 345, 1994, p405

[23] K. Bongardt et al., Proc. EPAC '96, Sitges, Spain, p1224.

[24] M. Pabst, K. Bongardt, Proc. PAC '95, Dallas, p3197.

[25] P. Tallerico, "The RF Power System for the SNS Linac", these proceedings.

[26] W. Bothe, "Dual Mode Pulse Generation for the ESS", ESS report 96-40-L, April '96

[27] G. Lawrence, "High-Power Proton Linac for APT: Status of Design and Development", these proceedings

[28] M. Lynch et al, "RF System Developments for CW and/or Long Pulse Proton Linacs", these proceedings

[29] H. Bohlen, CPI Inc, Palo Alto, California, USA, Private Communication

[30] S. Simrock, "Requirements for RF Control of the Vector Sum for Superconducting Proton Linacs", these proceedings

[31] S. Simrock, "Time Delay Compensation for the Digital RF Control at the TESLA Test Facility", these proceedings

[32] J. M. Lagniel, "High Intensity Linac Studies in France", these proceedings

[33] W. Bräutigam, Forschungszentrum Jülich, Germany, Private Communication

HIGH BRIGHTNESS ELECTRON SOURCES

J.B. Rosenzweig
UCLA Dept. of Physics and Astronomy, Los Angeles, CA 90095

Abstract

The production of unprecedentedly high brightness electron beams is a critical aspect of many applications, from free-electron lasers to advanced accelerators. The preferred method for obtaining these beams is the radio-frequency photoinjector. The physics and technology aspects of this device are reviewed here, along prospects for future progress in high-brightness beam development.

1 APPLICATIONS

Several applications of high brightness electron beams are driving the worldwide development of electron sources. These include free-electron sources of coherent radiation, such as self-amplified spontaneous emission free-electron lasers [1] (SASE FEL) and Compton scattering sources [2]. In the FEL, the beam is the lasing medium, and must thus be very dense to provide high gain. A measure of this is the brightness, which is the ratio of the current (linear density) to the square normalized rms emittance

$$B \equiv \frac{2I}{\varepsilon_n^2}. \qquad (1)$$

The brightness is a measure of the practical focusibility of a beam. Other applications include very high peak current, short pulse, and moderately low emittance beams which are needed to drive wake-field accelerators [3], and linear collider sources of polarized electrons [4]. For the FEL and wake-field accelerator, a high-brightness, pico-second electron beam is a critical technology. The need for these sources in linear colliders is not as clear, as positron sources are additionally needed, and the necessary emittances may not be achieved without damping rings.

The demanded parameters for typical future applications are given in Table 1. The pulse lengths needed are given in the absence of pulse compression, which may be necessary for all applications. The parameters for the TESLA linear collider may be approachable by electron sources using slightly exotic, asymmetric rf structures [5]; for other designs, damping rings will be required.

Table 1: Electron source parameters for applications. Emittance and pulse duration are rms quantities.

Application	I (A)	ε_n (mm-mrad)	σ_t (psec)
SASE FEL	200	<2	<3
Wake driver	>1000	<100	<2
TESLA-LC (polarized)	800	1 (y), 20 (x)	<3

2 RF PHOTOINJECTORS

The state-of-the-art in high brightness electron sources is achieved with the rf photoinjector. This type of device, an example of which is shown in Figure 1 (the Neptune photoinjector at UCLA [6]), uses a photocathode source embedded in a high gradient rf gun. The laser pulse which excites photoemission in the gun is very short, at the level of picoseconds or below. For promptly emitting photocathodes this implies that one can create the psec electron pulses of the sort given in Table 1 in this device.

The gun is followed by a transverse focusing element (usually a solenoid), which aids in beam size and emittance control. It additionally must be post-accelerated to bring the beam to a usable energy, and to mitigate space-charge effects. This acceleration is accomplished in a booster linac, which may be physically separated, or integrated into the same rf structure as the gun.

As the effects of space-charge and wake-fields during the acceleration process often conspire to lengthen the pulse. Because of this, it is often necessary to include in the rf photoinjector system a magnetic chicane [7] for pulse compression. The chicane can give additional capabilities and design flexibility in advanced electron sources.

The analysis, design, and operation of rf photoinjector sources entail a working understanding of many diverse areas of beam physics, and accelerator and laser technology. We begin by discussing the physics of these beams, which is dominated by space-charge and violent acceleration effects.

3 PHOTOINJECTOR BEAM PHYSICS

3.1 Longitudinal dynamics

The longitudinal dynamics in an rf photoinjector are characterized by violent acceleration. This is due to two effects: the need to mitigate detrimental space-charge effects, and the requirement that the beam be captured in the rf wave within the initial cell of the standing wave rf cavity. This can be quantified by defining a unitless parameter which must exceed approximately unity [8]

$$\alpha \equiv \frac{eE_0}{2k_{RF}m_e c^2} = \frac{\gamma'}{k_{RF}} > 1 \qquad (2)$$

This parameter allows a classifcation of injector types: high gradient injectors have $\alpha \cong 1.5 - 2.5$, whereas the lowest gradient injectors operate with $\alpha \cong 1$. The typical range of peak on-axis accelerating field encountered for a common rf wavelength, $\lambda_{RF} \equiv 2\pi/k_{RF}$ = 10.5 cm, is eE_0 = 60 – 150 MeV/m. These high gradients allow good

control of the beam dynamics, but only within limits, as the space-charge field at the cathode due to the surface charge density there can easily be near the applied rf field. Thus we have the requirement

$$E_0 >> 4\pi e\Sigma_b = 2eN_b/\sigma_r^2 \ . \qquad (3)$$

This inequality guarantees only that the beam fields are perturbative. If in addition we wish to ensure that the beam not lengthen appreciably during acceleration, then we require a short acceleration length $\gamma'^{-1} = (k_{RF}\alpha)^{-1}$,

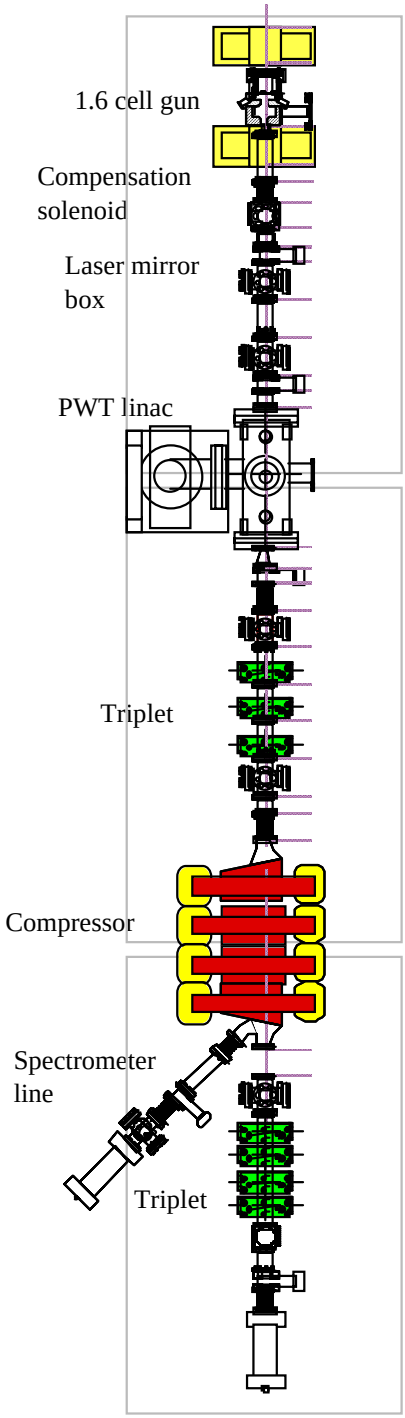

Figure 1. The Neptune photoinjector at UCLA.

$$c\sigma_t \geq \gamma'^{-1} \ . \qquad (4)$$

When inequalities 3 and 4 are satisfied, the beam pulse length may be preserved, and even compressed by rf focusing effects during capture in the initial cell.

Longitudinal bunch compression in photoinjectors is now a commonly employed, yet not completely understood, tool. Magnetic chicanes have been employed in a number of photoinjector facilities; space-charge limits on compressibility, and the effects of non-inertial space-charge and radiation fields on emittance growth [9] are the subjects of present and future experiments.

3.2 Transverse dynamics

Violent acceleration carries with it large transverse forces, which for an accelerator cavity terminate on a conducting (cathode) plane, gives a net first order kick to an off-axis accelerating particle. Further, this kick is rf phase dependent, and thus for a finite pulse length beam, an effective "rf" emittance is [8]

$$\varepsilon_{RF} \propto \gamma k_{RF}^2 \sigma_r^2 \sigma_z^2 \propto \alpha k_{RF}^3 \sigma_r^2 \sigma_z^2 \ . \qquad (5)$$

The first order rf kick can be thought of as originating at the end of the structure. All other irises in the rf structure have a balance in first order inward/outward kicks, but have a second order alternating gradient focusing (of strength $\propto \gamma'^2$) [10]. The combined effect of the rf focusing can be included in envelope and matrix treatments of the beam dynamics. The analytical model has been recently verified experimentally [11].

Photoinjector beams are generally space-charge dominated. The rms envelope equation, including acceleration and space charge, can be written as

$$\sigma'' + \left(\frac{\gamma'}{\gamma}\right)\sigma' + \left[k_\beta^2 + \frac{\eta}{8}\left(\frac{\gamma'}{\gamma}\right)^2\right]\sigma = \frac{I}{2I_0\gamma^3\sigma} + \frac{\varepsilon_n^2}{\gamma^2\sigma^3} \ . \qquad (6)$$

The emittance term is negligible for these beams (cold plasma, or quasi-laminar flow limit), with ratio of defocusing terms

$$\rho = \frac{I\sigma^2}{2I_0\gamma\varepsilon_n^2} >> 1 \ . \qquad (7)$$

For high-brightness beams this situation persists until the beam is very energetic (>100 MeV), or at tight focus.

As the enclosed current in bunched beams depends on longitudinal position, or "slice", within the bunch, the differential defocusing of the slices can produce a sheared total projected phase space. This leads to emittance growth, or, in systems with proper external focusing, emittance oscillations.

A useful heuristic model for understanding the process of emittance oscillations is shown in Figure 2. In this case, we suppose that a beam is injected with size smaller than the equilibrium sizes of the slices. As the equilibria in amplitude are dependent on the current at a given slice, the subsequent oscillations are larger for smaller currents, but the (plasma) frequency of oscillation is the same

($\omega_p = k_\beta c$). Thus the beam edges, which define angles in phase space, line up, regardless of slice, twice per oscillation, at the beam minimum and maximum. At these points, the projected emittance is also a minimum. The process of emittance compensation is essentially the arresting of these oscillations after an integer number of beam plasma periods. The plasma oscillations are adiabatically terminated, of course, by acceleration, which diminishes the strength of the space-charge.

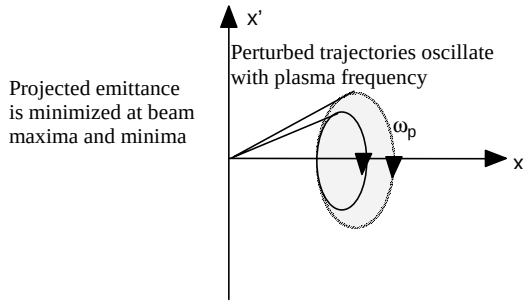

Figure 2. Emittance oscillations caused by slices about rotating in phase space about different equilibria.

The recently developed analytical theory of emittance compensation is based on Eq. 6, and examines a new type of equilibrium laminar flow (analogous to Brillioun flow) the invariant envelope [12]

$$\sigma_{\text{inv}} = \frac{2}{\gamma'}\sqrt{\frac{I}{3I_0\gamma}} \tag{8}$$

The invariant envelope has the property that the phase space angle $\sigma'_{\text{inv}}/\sigma_{\text{inv}} = \gamma'/2\gamma$ is independent of current. This guarantees that once all slices are aligned in phase space, they remain so. Slices not aligned to the invariant envelope oscillate in a Liouvillian space about the invariant envelope, giving rise to emittance oscillations. It should also be noted that the beam becomes smaller as it accelerates, driving the residual emittance down as $\gamma^{-1/2}$.

The model for the compensation of time-dependent space-charge forces is well understood analytically, through simulation, and experiment. New theoretical work concerning the role of nonlinear forces in optimized beam transport, is now underway.

3.3 Scaling of Designs

One recent advance in the understanding of photoinjector beam physics is the development of charge (Q) and wavelength (λ) scaling laws [14]. Charge scaling allows change of design charge while keeping dynamics of compensation identical, thus permitting a high Q, low brightness design (*e.g.* TTF) to a low Q, high brightness design (*e.g.* TTF-FEL). Wavelength scaling allows the taking of a design from one rf wavelength, and move it to a different value of λ. This permits expertise to be shared among different laboraratories, and the performance of seemingly disparate devices to be compared. It also is a tool which can, as we will see below, point to promising new directions in source development.

In charge scaling, we do not change external forces (or wave-numbers), and must therefore preserve plasma wave-number. This in turn implies that we preserve bunch density and aspect ratio, or $\sigma_i \propto Q^{1/3}$. Deviations from strict Q-scaling arise from space charge at cathode, and rf effects, as the beam size changes relative to rf wavelength. Following this scaling, it can be shown that the emittance arises from two components: space-charge, which contributes $\varepsilon_x^{sc} \propto \sigma_x^2 \propto Q^{2/3}$, and rf/chromatic focusing effects, which contribute $\varepsilon_x^{rf} \approx \sigma_z{}^2\sigma_x^2 \propto Q^{4/3}$. PARMELA simulations of a family of Q-scaled cases in an S-band emittance compensated injector gives the results shown in Fig. 3.

The fit for the data shown is

$$\varepsilon_x \cong \sqrt{\tfrac{4}{5}Q^{4/3} + \tfrac{1}{2}Q^{8/3}} \tag{9}$$

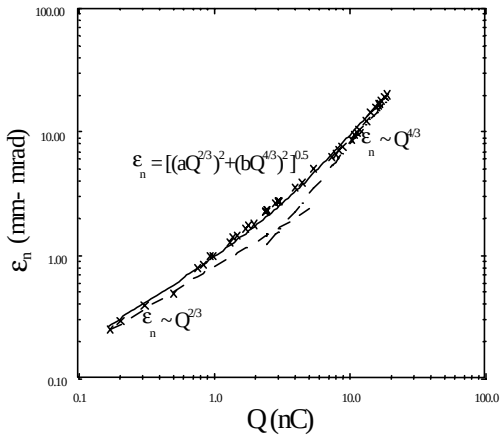

Figure 3. Emittance for family of Q-scaled cases in an S-band emittance compensated injector.

For wavelength scaling, we must preserve longitudinal dynamics, which requires α = constant, or $E_0 \propto \lambda^{-1}$. To additionally preserve the energy spread and beam aspect ratio, we have that all beam dimensions scale as $\sigma_i \propto \lambda$. Further, making the betatron frequency scale properly requires that the solenoid field $B_0 \propto \lambda^{-1}$, and the scaling of the beam-plasma frequency requires $Q \propto \lambda$.

There are no inherent deviations from λ-scaling laws, and use of these laws can be shown to yield an emittance scaling of $\varepsilon_x \propto \lambda$. Note also, that brightness scales as $B \propto \lambda^{-2}$; the advantage of short λ operation is apparent.

Nevertheless, several aspects of scaling to short λ merit discussion. Technologically, the laser laser pulse length and jitter are as well as emittance measurements are more difficult at short λ. The scaling of external forces requires large rf fields, which may be "natural" - high-gradient implies short λ because of breakdown limits, power considerations, etc. The scaling of the focusing fields is less natural, however, as the current density in the solenoid scales as $J_{sol} \propto \lambda^{-2}$. In addition, many applications require a certain charge per bunch. With large charge, short wavelength implies rf dominated operation. The optimum emittance and brightness occur

at a certain wavelength in the transition between the space-charge and rf-dominated regimes — for Q=1 nC, the optimum deduced from Eq. 9 is approximately 9 GHz.

4 TECHNOLOGY

Many of the performance limitations in photoinjectors are technological, not fundamentally physical. We now review the status of rf photoinjector technologies.

4.1 RF cavities

Rf cavities for photocathode gun use have gone through considerable development in the last decade. The most successful designs have been the low-α, integrated photoinjectors typified by the LANL devices, and the high-α short (1.5-6 cell) guns pioneered at BNL.

The high-α S-band gun has been improved recently by making the photocathode cell of length 0.625 times a π-mode standing wave cell. This improves the ratio of peak on-axis to wall fields, and provides stronger rf focusing near the cathode, enhancing the emittance comp-ensation process. The coupling to the waveguide is perf-ormed only in the full cell, using symmetrized slots or a coaxial coupler, with on-axis coupling to the 0.5-cell.

The integrated photoinjector, in which a large number of cells are coupled together, cannot be easily coupled on axis in the π-mode while maintaining good mode separation. The solution employed at LANL entails coupling through on-axis vestigial cells in a π/2-mode configuration. A new S-band design being pursued by a UCLA/DULY Research collaboration uses a plane wave transformer (PWT) structure. This structure has excellent coupling through a coaxial region outside of the accelerat-ing mode-supporting disks. The emittance compensation optics in this device were the first to be derived from analytical theory [12]. It is interesting to note, however, that the optics in the PWT could have been deduced by scaling of the L-band optics of the AFEL injector at LANL — they are nearly identical when scaled. Scaling of the PWT design to X-band is in fact discussed below.

4.2 Lasers

Several years ago, the necessary drive laser pulses (picoseconds, total energy from tens of μJ to tens of mJ) were very difficult to achieve [14]. The amplification process often used flash-lamp pumping and chirped-pulse amplification, both of which tend to introduce unwanted fluctuations in pulse energy. This problem has been mitigated by use of diode-pumping technology. Advanced development in photocathode drive lasers now concentrates on production of long pulse trains [15], and on obtaining an illumination which is relatively uniform in time and transverse position, to make the space-charge forces as linear as possible. This goal may now be in reach through use high-bandwidth, short pulse lasers (*e.g.* Ti:Sapphire) combined with Fourier-plane filtering, as well as soft aperturing and relay imaging of the pulse.

4.3 Photocathodes

The search for a robust, high quantum efficiency (QE) cathode is now localized on two types of materials. Metals such as magnesium have been found to be prompt, with fsec response, but with QE no better than 10^{-3} (with uv illumination) and significant dark current. In addition, metal cathodes are surprisingly sensitive to vacuum conditions, and typically must be "laser cleaned" to produce anything approaching uniform emission.

A more promising candidate for high-brightness cathode development is Cs_2Te. This material is relatively immune to vacuum problems, can be revived after contamination, has QE as large as 15%, and a low inherent emittance. On the other hand, it still requires uv illumination to photo-emit, and is undoubtedly slower in emission delay than a metal photocathode.

Linear collider electron sources demand polarization. The development of a polarized photocathode in an rf gun, which entails addressing vacuum, field, and charge limitation problems, is only now beginning. Testing of GaAs cathodes in a high gradient rf gun has been reported at the CLIC Test Facility [16].

5 PRESENT PERFORMANCE

The state-of-the-art in beam parameters obtained from rf photoinjectors has advanced rapidly in the last few years.

- The charge measured from these devices has been as high as 100 nC [16,17]. Pulse trains with as much as mC have been reported.
- The pulse length, which is typically space-charge limited, has been measured at the level of a picosecond, for relatively low charge. For higher charge, the highest current reported is a few kA [16]. Picosecond pulses can be measured by streak cameras (which also provide imaging information) or rf sweeping techniques. At this pulse length, and below, it is now popular to use coherent transition radiation interferometry, which can resolve times as small as 0.2 psec.
- The normalized rms emittance has been measured in a variety of laboratories [18] to be at the level of 2 mm-mrad/nC. This is expected to be reduced by a factor of two with the advent of shaped laser pulses. The measurement of the emittance in space-charge dominated beams has presented a challenge in its own right, with the standard quadrupole scan method being prone to space-charge induced problems in interpretation. Nevertheless, at BNL these problems have been overcome, and a time-resolved emittance measurement, which verified the slice-model of emittance compensation reported [19]. Alternatively, a slit-based measurement system can be employed which mitigates space charge and allows single shot reconstruction of the beam's phase space.

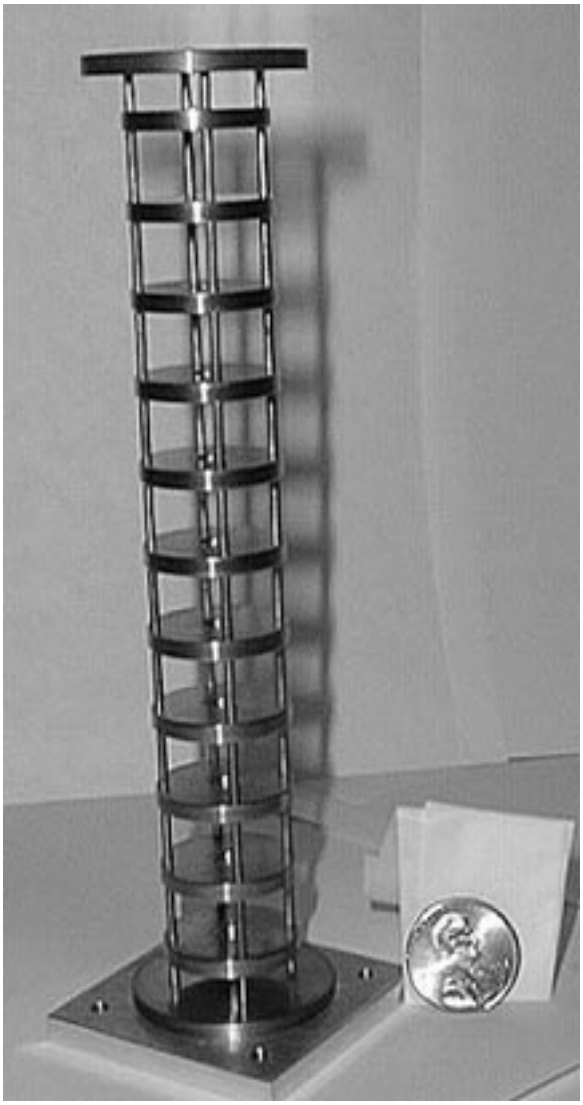

Figure 4. Interior of 11.4 GHz PWT cold test structure.

6 FUTURE DIRECTIONS

The choice between integrated and split photoinjectors is not simple, as there are advantages and unattractive features to both. The split photoinjector is flexible; one can choose booster linac gradient/phase, and gun-linac drift length for compensation can be optimized. One can naturally include a compressor. One actually must choose a high gradient in the gun, or the drift section will produce pulse lengthening and larger residual transverse emittance — the TTF gun is run at relatively α. As the defocusing kick at the gun exit is proportional to the beam size, the compensation solenoid must be stronger, and is difficult to build at short λ. Also because of the exit kick, the beam size oscillation is larger, and this produces larger residual emittances.

For an integrated injector, the gradient in the structure is lower, and the scaling to short λ is easier. At lower gradient however, the space-charge pulse lengthening near the cathode is larger than that in a high-gradient gun, but because of continuously applied longitudinal focusing in the structure, the bunch does not appreciably lengthen after the initial cell. The needed solenoid field lower is also lower, again allowing easier scaling to short λ. As the beam exits the structure small (near the invariant envelope) the rf kick at the structure exit is not large, and the rf-derived emittance can be greatly mitigated.

It can thus be seen that the high gradient gun generally produces shorter pulse lengths, but the integrated injector gives better emittance performance at a given λ. But if one chooses a short λ, then the achievable pulse length becomes smaller. Because of this, we have proposed, and are now seriously developing a scaled X-band version of the PWT injector at UCLA, in collaboration with DULY Research and LLNL. Simulations of an 11.4 GHz injector indicate [5] that this device can produce 120 μm rms bunch lengths at 1 nC, with ε_n = 0.8 mm-mrad, for a brightness, $\varepsilon_n = 3 \times 10^{15}$ cm^{-2}, which is a factor of 30 times greater than the present state of the art. In this development we are concentrating on the issues of structure cooling and solenoid design, which both become quite challenging in X-band. A cold-test model of an 11.4 GHz structure's interior is shown in Fig. 4. Development of the injector will probably take place at 8.6 GHz, however, due to availability of rf power, and solenoid design issues. It should also be noted that this is near the optimum value of λ predicted to minimize the emittance at 1 nC.

7 REFERENCES

[1] M.Hogan, et.al, Phys. Rev. Lett. **80**, 289 (1998)
[2] R. W. Schoenlein, et al., Science **274**, 236 (1996).
[3] W. Gai, et al., Phys. Rev. Lett. **61**, 2765 (1988).
[4] H. Tang, et al, 1997 Part. Accel. Conf. 2849 (1998).
[5] J. Rosenzweig, et al., Proc. 1997 Part. Accel. Conf. 1965 (1998).
[6] J. Rosenzweig, et al., NIM A **410**, 437 (1998).
[7] J.B. Rosenzweig, N. Barov and E. Colby, IEEE Trans. Plasma Sci**. 24**, 409 (1996).
[8] K.J. Kim, NIM A **275,** 201 (1989).
[9] B.E. Carlsten and T.O. Raubenheimer, *Phys. Rev. E* **51**, 1453 (1995).
[10] J. Rosenzweig and L. Serafini, *Phys. Rev. E* **49**, 1499 (1994).
[11] S. Reiche, et al., Phys, Rev. E **56**, 3572 (1997).
[12] Luca Serafini and James Rosenzweig, Phys. Rev. E **55**, 7565 (1997).
[13] J. Rosenzweig, and E. Colby, Proc. 1995 Advanced Accelerator Concepts Workshop 337 (AIP, 1996).
[14] See Proc. Lasers for RF guns, Brookhaven National Laboratory Report, 1994.
[15] TESLA Test Facility Design Report, D.A. Edwards, Ed. TESLA Rep. 95-01 (Hamburg, 1995).
[16] E. Chevallay, et al., these proceeedings.
[17] M.E. Conde, et al, Phys. Rev. ST-Accel. Beams **1**, 041302 (1998)
[18] D.T. Palmer, et al., Proc. 1997 Part. Accel. Conf. 2687 (1998).
[19] X. Qiu, *et al, Phys. Rev. Lett.* **78**, 3723 (1996).

A HIGH INTENSITY PROTON LINAC DEVELOPMENT FOR THE JAERI NEUTRON SCIENCE PROJECT

M. Mizumoto, J. Kusano, K. Hasegawa, N. Ouchi, H. Oguri, M. Kinsho, E. Chishiro, T. Tomisawa, Y. Touchi, M. Ikegami,Y. Honda, K. Mukugi, H. Ino, F. Noda, N. Akaoka, H. Kaneko
JAERI, Tokai-mura, Naka-gun, Ibaraki-ken 319-1195, Japan

Abstract

JAERI has been proposing the Neutron Science Project (NSP) which will be composed of a high intensity proton accelerator and various research facilities. The accelerator with an energy of 1.5GeV and a beam power of 8MW is required to operate both with pulse mode for basic research fields and CW mode for nuclear waste transmutation studies. A superconducting (SC) linac is a main option for the high energy portion from 100MeV to 1.5GeV. A beam test with an ion source and an RFQ has been performed with a current of 80mA and a duty factor of 10 % at the energy of 2MeV. A hot test model of DTL has been fabricated and tested with a duty factor of 20%. A test stand for SC linac cavity with equipment of cryogenics, vacuum, RF and cavity processing and cleaning system has been prepared to test the fabrication process and physics issues. The vertical test of a β=0.5 (145MeV) single cell SC cavity has been made resulting in a maximum electric field strength of 44MV/m at 2K.

1 INTRODUCTION

JAERI has been proposing the Neutron Science Project which aims at exploring the fields of basic science and nuclear technology using a high intensity proton accelerator[1]. The design studies are being carried out for a high intensity pulsed and cw spallation neutron sources for basic research fields of material science and biology and for accelerator-driven transmutation technology of long-lived radioactive nuclides from nuclear power generation The major facilities to be constructed under the project are, 1) a superconducting proton linac with a proton energy of 1.5GeV and a maximum beam power of 8MW, 2) a spallation neutron target station with input beam power of 5MW for neutron scattering, and 3) a research facility complex for accelerator-driven transmutation experiment, neutron physics, material irradiation, isotopes production, RI beam experiment for study of exotic nuclei. A conceptual layout for the NSP LINAC is given in Fig.1.

JAERI had originally planned to build a pulsed linac with an energy of 1.5GeV and a peak current of 100mA with 10% duty factor. The design study has been made to confirm technical feasibility to accelerate high peak current with high duty operation from the beam dynamics point of view. In this accelerator development, the R&D work has been performed on high brightness ion source, radio frequency quadrupole linac (RFQ), drift tube linac (DTL) and RF source, as well as the conceptual design of the whole accelerator components.

JAERI has altered the original plan by proposing an option of superconducting (SC) linac to meet requirements for a variety of basic research fields mentioned above and an ultimate goal for waste transmutation[2]. This SC linac will be operated in pulse as a first stage for the spallation neutron source and upgraded in CW for engineering test as a second stage. These two operational modes, pulse and CW operation, will be realized with time sharing manner, not simultaneously, and is the most challenging technical issues for the accelerator development.

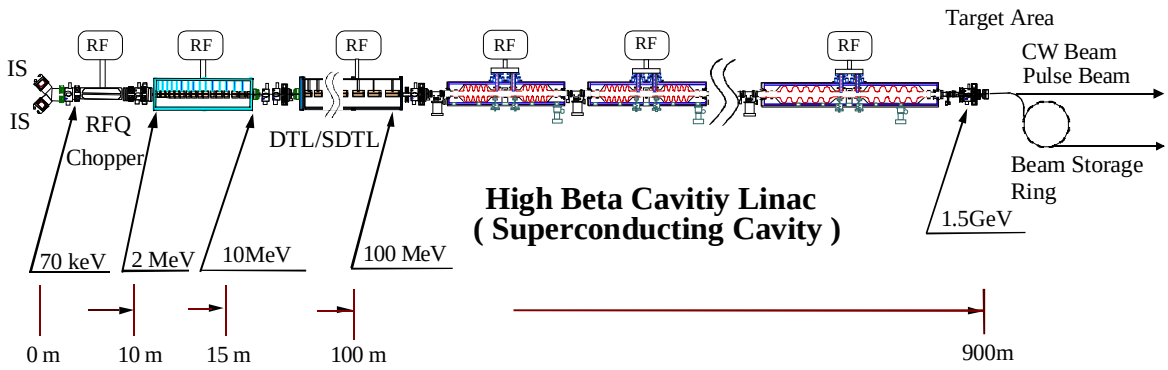

I S : High Brightness H Ion Source
RFQ : Radio Frequency Quadrupole Linac
DTL : Alvarez Type Drift Tube Linac
RF : Radio Frequency Power Source

Fig. 1 A conceptual layout of the JAERI NSP-LINAC

The SC linacs have several favorable characteristics as follows; the large bore radius results in low beam loss, the length of the linac can be reduced, and high duty and CW operation can be made for engineering purposes. The possibility to inexpensive operation cost may be also expected in comparison with normal conducting (NC) option.

Several R&D items have been studied for high intensity accelerator development; 1) the beam dynamic calculation including the high β linac. 2) the development of the negative ion source and the fabrication of high power test models for CW-RFQ and CW-DTL. 3) the SC cavity development, 4) the high intensity proton storage ring and 5) high power RF source development. A specification of the JAERI NSP LINAC is given in Table 1.

Table 1 A specification of JAERI NSP LINAC

Particles	Negative and positive ion
Energy:	1.5GeV
Beam current:	
1st stage;	Pulse average 1mA, peak 16.7mA (duration 2ms, repetition rate 50Hz)
2nd stage	CW<5.33mA Pulsed average<5.33mA, peak 30mA
Low energy:	RFQ &DTL/SDTL Normal-
High energy:	Conducting linac: 200MHz
Chopping:	Superconducting linac: 600MHz 60% (intermediate pulse width of 400ns)

2 2MeV RFQ BEAM TEST AND DTL HIGH POWER TEST

The R&D work for the low energy portion has been carried out as a first step in the development with a positive hydrogen ion source and a pulsed RFQ. This R&D-RFQ is a four-vane type and designed to accelerate 100mA (peak) of protons to 2MeV with a duty factor of 10%. The low power tuning, the high power conditioning and the beam tests were carried out[3]. The layout of the 2MeV RFQ and the R&D results are shown in Fig.2. The proton beam from the 100keV ion source was focused by the two solenoids to match the RFQ acceptance. The maximum RFQ output current, which was currently achieved, was 80mA at the ion source extraction current of 155mA with 10% duty factor. The transmission in the low energy beam transport (LEBT) from the ion source to the RFQ was about 65% with the proton fraction of about 80% in the ion source beam. The maximum transmission rate through the RFQ was obtained to be 90% at the most optimum ion source condition. The rms emittance values from the ion source and RFQ are minimum to be 0.15 πmm.mrad and about 0.62 – 0.76 πmm.mrad at the beam current of 170mA, respectively. These emittance values are not satisfactory and the further improvement is needed.

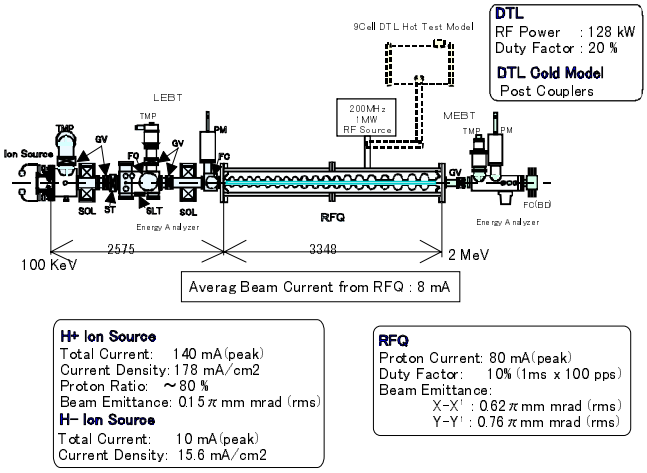

Fig.2 The R & D Results of Low Energy Accelerator Parts

An R&D-DTL hot test model with 9 cells for mock-up of the first part of the DTL has been fabricated to study the RF characteristics and the cooling capabilities. The 20% duty operation was achieved with a RF power of 128kW. The further test of CW operation with this hot model is being prepared. The 1/3 scaled DTL cold model installed with post couplers and 60 DT cells, which corresponds to the energy region of 2-10MeV, was also fabricated. The effects with post coupler such as field distribution, the detuning sensitivity and mode spacing were tested. The parameters of post coupler configurations (total numbers and positioning) has been obtained for stabilization of the accelerating fields[4].

3 LOW ENERGY PART BE LOW 100MeV FOR THE NSP LINAC

3.1 New Design for the Low Energy Part

In order to realize the short pulse for basic research with the proton storage ring and the final CW operation, new R&D's are carried out including negative ion source and CW-RFQ/CW-DTL in addition to the SC linac development. At the high energy part of DTL, the SDTL (separated type of DTL) proposed by Kato[5], KEK, has been studied. The SDTL, which has higher shunt impedance and simpler mechanical structure than DTL, is an attractive option for CW operation in the energy region of 50 - 100MeV where the SC linac can not be applicable.

3.2 Ion Source

A negative ion beam is required for basic research to inject the beam into the storage ring which produce 1 μs pulse. The beam extractor of the existing positive ion

source used for previous beam experiment was modified to produce negative ion beams from source ion plasma by providing the transverse magnetic field. The characteristics of the negative ion beam have been examined with the maximum observed beam current of 21mA at an arc discharge power of 35kW[6].

A new negative ion source has been fabricated to accumulate experimental data to fulfil the requirement to the NSP linac. A schematic drawing of the ion source is shown in Fig. 3. A plasma chamber is installed outside the insulator to change easily the configuration of the cusp magnet fields. The vacuum pumping system is also improved. The preliminary data have been obtained to be 11mA beam extraction without Cesium from the test experiment.

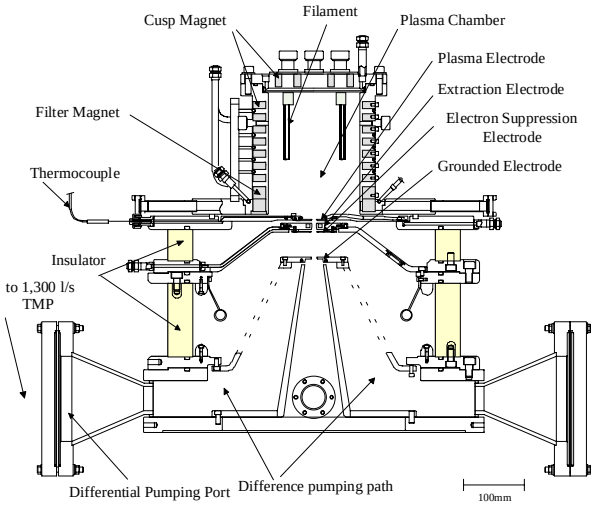

Fig.3 A schematic drawing of new negative ion source

3.3 RFQ for Pulse and CW operation

The low energy part should be capable for the CW mode operation as well as the pulse mode, because the SC linac has been operated with CW. The scheme to prepare two independent RFQs together with ion sources for pulse and CW operation is considered to meet these two different operational conditions[7]. The pulse mode RFQ is optimized at a beam current of 30mA. The maximum peak electric field of 1.65Ek is chosen. The CW mode RFQ is optimized below a current of 10mA with lower electric filed of 1.5Ek. Figure 4 shows design parameters vs length for the pulse mode and the CW mode RFQs. The beam simulation is performed with the PARMTEQ and PARMTEQM codes. The similar performance for transmission rate and transverse and longitudinal emittances were obtained with the calculations. Because the most important problem for the R&D-RFQ was found to be the RF contact between vane and tank, the RFQ will be made as integrated type by brazing between vane and tank. The high power model 50cm long was fabricated and tested with a power of 60kW and a duty factor of 20%.

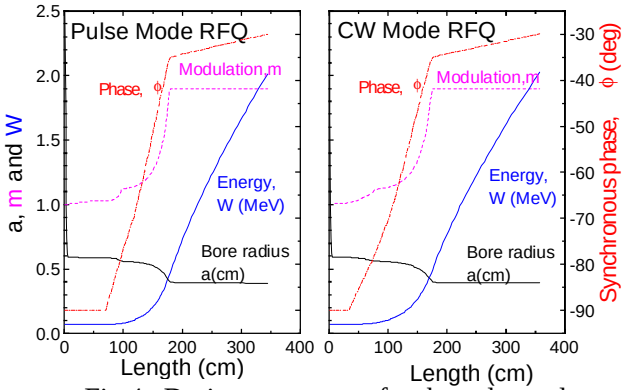

Fig.4 Design parameters for the pulse and the CW RFQs

3.4 CW-DTL/SDTL

The parameters for the CW-DTL are also re-evaluated to match the CW operation for the SC linac design concept. The SDTL concept has been also adopted to improve the performance for CW operation. Relatively low accelerator gradient of 1.5MeV/m is taken in order to reduce the RF power consumption and the RF heating. The expected maximum magnetic field gradient for the focusing magnet is about 50T/m using the hollow conductor type Q-magnet. The end point energy for the SDTL is 100MeV which is determined from the beam dynamics and mechanical consideration of the high β structure.

The beam dynamics study is conducted to obtain the optimized parameters for each accelerator structure. An equipartitioned design approach is taken for the DTL/SDTL to maintain the good beam quality and to prevent emittance growth causing beam losses. Figure 5 shows a concept of the CW-DTL and SDTL[4].

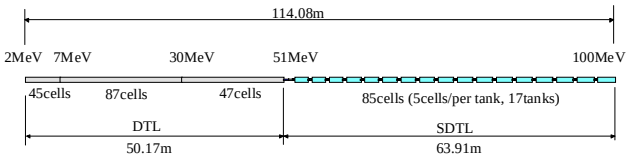

Fig. 5 A concept of DTL and SDTL

4 HIGH ENERGY ACCELERATOR PART

4.1 The layout of the superconducting linac

In the SC linac part, the proton velocities β gradually change from 0.43 to 0.92 corresponding to the energies

for 100MeV and 1.5GeV. Accordingly, the length of the cavity is also changed. Main concern is the strength of the cavity under the vacuum load for the low β (β<0.7) region. The mechanical structure calculations with the ABAQUS code have been made to determine the cavity shape parameters as well as electromagnetic ones with the SUPERFISH code.

are shown in Fig.7. The equipartitioning factor of about 0.9, which is defined by $\gamma_0(\varepsilon_{nx}/\varepsilon_{nz})(z_m/a)$ where z_m and a are radius and longitudinal half length of ellipsoidal bunch, respectively, shows the design parameters nearly equipartitioned. There is only 1% increase of the transverse and the longitudinal rms emittances.

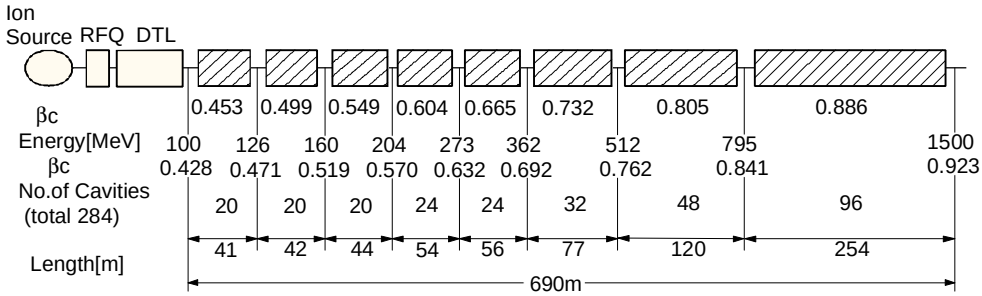

Fig. 6 Basic parameters for superconducting(SC) linac.

In order to determine the layout of the SC accelerating structure, the case of the SC linac, which is composed of 8 different β sections has been studied[8]. The cavities in each β section will be made with identical 5 cells and designed at the specific beam energy but also can be operated at slightly different beam energy with lower efficiency. The maximum peak surface field is set to be 16MV/m. Two cavities are laid in one doublet focusing period. The conceptual layout and basi parameters of the superconducting linac are shown in Fig. 6. The structure of the cryomodule, input/HOM couplers and tuning devices etc. are being designed based on the KEK-TRISTAN (high energy e+, e- colliding machine) experiences. Using these parameters, calculations for the beam dynamics have been made with the modified PARMILA code. The equipartitioned design approach is also taken for the SC linac. The design and beam simulation results of the SC sections such as wave numbers, the beam sizes and the equipartitioned factors

4.2 Fabrication and test of a superconducting cavity

The test stand for a superconducting cavity development with the cryostat 80cm dia. x 350cm long and a clean room has been constructed[9]. Two sets of single SC test cavities have been fabricated for β =0.5 which corresponds to the proton energy of 145MeV. Fabrication process such as cold rolling and press of pure Niobium metallic sheet, electron beam welding, surface treatment (barrel polishing, electro-polishing and high pressure water rinsing, etc.) has been performed based on the KEK experiences for 500MHz TRISTAN cavity. Vertical tests have been conducted to examine the RF and mechanical properties. Figure 8 shows the results of performance test for two prototype cavities. The measurements were made several times for each cavity. The maximum surface peak field strength of 24MV/m at 4.2K and 44MV/m at 2.1K have been successfully

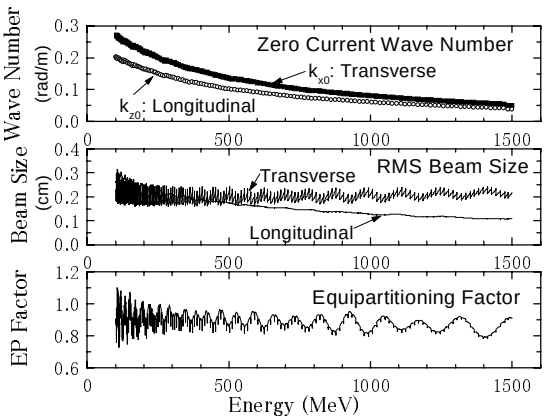

Fig.7 Design and beam simulation results of the superconducting linac section

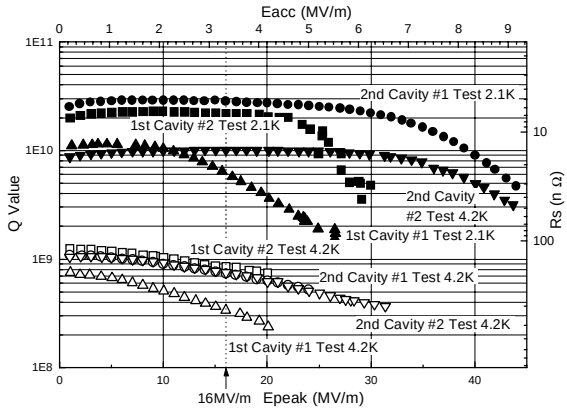

Fig.8 Results of the performance tests for two prototype cavities; Q valuses as a fuction of the surface peak electric field (Epeak)

obtained for 2nd cavity. The Q values of 2.8×10^{10} at 2K and 7.3×10^{8} at 4.2K were obtained at E_{peak}=16MV/m[10]. This result was reconfirmed at the recent 2nd experiment although the Q values this time was lower to be 1×10^{10} at 2K because some deterioration of the surface condition occurs during the intermediate period. Those test results have satisfied the specification for the conceptual layout of the superconducting linac.

5 RF SOURCES

The RF sources are main components to determine the availability and reliability, and most costly parts for the accelerator system. Two frequency choices, 200MHz and 600MHz, have been selected in the conceptual study for low energy and high energy part, respectively, where total peak RF powers of about 300kW for RFQ, 9MW for DTL/SDTL and 25MW for SC linac are required for pulse operation. Due to the different two mode operations and gradual upgrade path, optimization for RF configuration is one of the most important technical issues. An RF system based on the Grid tube (Tetrode) Klystron and IOT has been carried out[11]. As an example, Figure 9 shows RF power requirements for 8 different β sections for each operating condition in the SC linac.

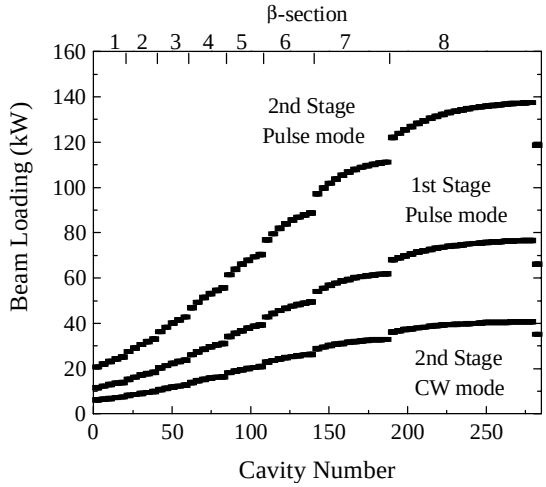

Fig.9 Beam loading for each cavity

6 SUMMARY

The R&D work for the prototype linac structures has been performed. The good performances of the components such as ion source, 2MeV-RFQ, RF-source have been achieved. The test stand for the SC cavities was constructed. The vertical SC cavity test has been successfully conducted resulting in the satisfactory maximum surface electric field strength for the SC proton accelerator. The design work on the RFQ and DTL/SDTL as well as SC cavities for the CW operation is performed.

7 ACKNOWLEDGEMENT

The authors would like to thank Drs. S. Noguchi, K. Saito H. Inoue and E. Kako of KEK for discussion and help on the SC cavity development. They also thank Drs. T. Kato and Y. Yamazaki of KEK, and Dr. R.A. Jameson of LANL about the beam dynamics calculations and accelerator system optimization.

8 REFERENCES

[1] M. Mizumoto et al., "Development of Proton Linear Accelerator and Transmutation System", Proc. of GLOBAL'93, September 12-17, 1993 Seattle, p357-362

[2] M. Mizumoto et al., "A High Intensity Proton Linac Development for Neutron Science Research Program" XVIII International Linac Conference, LINAC96, Geneva, Switzerland 26-30 August 1996, p662-664

[3] K. Hasegawa et al., "The Development of a High Intensity RFQ at JAERI", J. Nucl. Sci. Technol., Vol.34, No.7, (1997) p622-627

[4] H. Ino et al., "A Conceptual Design of the DTL-SDTL for the JAERI High Intensity Proton Accelerator", JAERI-Tech 98-028, 1998

[5] T. Kato, "Proposal of a Separated-type Proton Drift Tube Linac for a Medium-Energy Structure", KEK Report 92-10 (1992)

[6] H. Oguri et al., "The Development of a Negative Ion Source for a High Intensity Linac", Proc of EPAC98, June 22-26, 1998, Stockholm

[7] K. Hasegawa et al., "Beam Dynamics Study of High Intensity Linac for the Neutron Science Project at JAERI", Proc. of APAC98, March 23-27, 1998, Tsukuba

[8] Y. Honda et al., "A Conceptual Design Study of Superconducting Proton Linear Accelerator for Neutron Science Project", ibid

[9] J. Kusano et al., "Development of Superconducting Single Cell Cavity for a Proton Linac in the Neutron Science Project at JAERI", Proc. of EPAC98, June 22-26, 1998, Stockholm

[10] N. Ouchi et al., "R&D Activities for Superconducting Proton Linac at JAERI", Proc. of APAC98, March 23-27, 1998, Tsukuba

[11] E. Chishiro et al., "An RF Power System for the NSP High Intensity Proton Accelerator", ibid.

THE TESLA FREE ELECTRON LASER – CONCEPT AND STATUS

J . Rossbach, for the TESLA FEL Collaboration
Deutsches Elektronen-Synchrotron, DESY, 22603 Hamburg, Germany

Abstract

The aim of the TESLA Free Electron Laser (FEL) is to develop and realize an Angstrom wavelength, high gain FEL in parallel with the TESLA superconducting e+/e- linear collider. As a first step, an FEL for the VUV wavelength regime is now under construction at DESY, making use of the TESLA Test Facility (TTF).

The VUV FEL at the TTF comes in two phases, which are both approved. The paper describes the over-all layout of each phase and the status of components.

1 FREE ELECTRON LASERS FOR SHORT WAVELENGTH

Over the past 30 years, synchrotron radiation has turned into a most powerful research tool that has been applied in many fields of science ranging from physics, chemistry and biology to material sciences, geophysics, and medical diagnostics. This rapid progress was driven by the development of new, increasingly brilliant sources based on electron storage rings. Due to the recent progress in accelerator technology the possibility has been opened up to complement storage ring based sources by ultra-brilliant Free-Electron Lasers operating in the soft X-ray regime.

In a Free Electron Laser (FEL), an electron beam radiates photons at much higher power and better coherence than it does due to spontaneous synchrotron radiation. The key point is that electrons moving in a transverse magnetic field of alternating polarity (undulator) may amplify an existing electromagnetic radiation field (see e.g. [1]). For properly chosen phase and wavelength (see eq. 1) the scalar product of the electron's velocity vector and the electric field vector does not vanish on average, resulting in an average energy transfer between the electron beam and the radiation field. As a consequence of this interaction, depending on the relative phase, some electrons get accelerated and others decelerated. This results in a longitudinal density modulation of the electron beam at the optical wavelength during the passage through the undulator. With the onset of this "micro-bunching", coherent emission at the resonant wavelength sets in which results in an exponential growth of the power in the radiation field (high gain mode), characterized by the gain length L_{gain} :

$$I(z) = I_0 \cdot \exp(z / L_{gain})$$

Similar to synchrotron radiation sources, there is no fundamental limit in the choice of the photon wavelength.

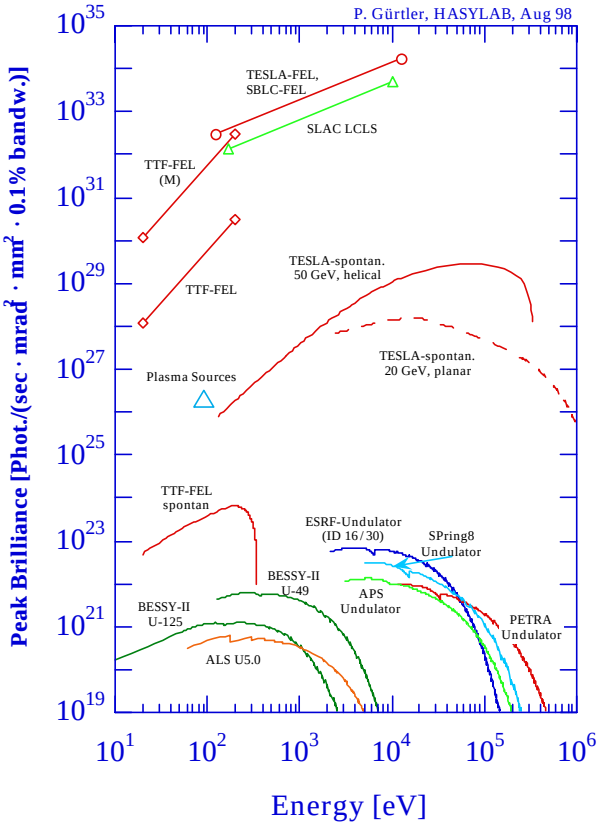

Fig. 1. Spectral peak brilliance of short-wavelength FELs compared with third generation radiation sources and plasma lasers. For comparison, the spontaneous spectrum of an X-ray FEL undulator at 20 GeV is also shown.

The photon wavelength λ_{ph} of the first harmonic is related to the period length of a planar undulator λ_u by

$$\lambda_{ph} = \frac{\lambda_u}{2\gamma^2}\left(1 + \frac{K^2}{2}\right) \quad , \qquad (1)$$

where $\gamma = E/mc^2$ is the relativistic factor of the electrons and $K = eB_u\lambda_u/2\pi mc$ the 'undulator parameter', e being the elementary charge, m the electron rest mass, c the speed of light, and B_u the peak field in the undulator. It is seen that very short photon wavelength can be achieved if only the electron energy (i.e. γ) is chosen sufficiently high.

For most FELs presently in operation, the electron beam quality and the undulator length result in a gain of only a few percent per undulator passage, so that an optical cavity resonator and a synchronized multi-bunch electron beam have to be used. For the TESLA FEL however, we aim at very short wavelength, for which normal-incidence mirrors of high reflectivity are not

available. Thus we have to provide an electron beam quality (emittance, peak current, energy spread) good enough and an undulator long enough to reach the power saturation level within a single passage. At the saturation length $L_{sat} \approx 4\pi L_{gain}$, the electrons run out of resonance due to their energy loss.

Since the desired wavelength is very short, there is no conventional laser to provide the "initially existing radiation field". Instead, one may consider the spontaneous undulator radiation from the first part of the undulator as an input signal to the downstream part of it. FELs based on this principle of Self-Amplified-Spontaneous-Emission (=SASE) [2,3] are presently considered the most attractive candidates to deliver extremely brilliant, coherent light with wavelength in the Angstrom regime[4-6]. Compared to state-of-the-art synchrotron radiation sources, one expects full transverse coherence, larger average brilliance, and, in particular, up to eight or more orders of magnitude larger peak brilliance (see Fig. 1) at a pulse lengths of about 200 fs FWHM. An important step has been done recently in demonstrating a SASE FEL gain larger than 10^5 at 12 μm wavelength [7].

2 SASE FEL RADIATION

Theoretical description of SASE distinguishes three steps of the process: The start-up-from-noise (or lethargy) regime, the steady-state regime and the saturation regime. The steady-state regime, where a well-defined external electromagnetic input wave is linearly amplified resulting in exponential growth, is accessible for analytical and numerical treatment since many years. The start-up from noise process, however, is much more difficult to analyze, since it is determined by statistical properties and by mutual interaction of more than 10^9 radiating particles. Fully 3-dimensional simulations became available only recently. One of these codes uses Cartesian coordinates and performs direct solution of the paraxial equations for the radiation field and is thus capable of dealing with arbitrary undulator field errors [22]. The other one [23] uses a Greens-function approach for calculation of the radiation field, is much faster and includes far-field mode analysis of the radiation. Results of these codes are in perfect agreement with a SASE proof-of-principle experiment performed recently in Los Alamos at 12 μm wavelength [7, 23]. Finally it is noted, that fluctuation properties of SASE FEL radiation have been analyzed both in the linear and in the saturation regime [24]. Experimental results obtained for the linear regime are again in agreement with theory and simulation, while experimental results on saturation are not yet available.

3 THE TESLA FEL CONCEPT

TESLA aims at a 500 GeV e+/e- collider with integrated X-ray laser Facility [6]. The TESLA linac is indeed exceptionally well suited for a short-wavelength Free Electron Laser: Excellent beam quality is maintained during acceleration and a large variety of pulse train patterns can be provided to users.

The problem with SASE FELs is that, in going to shorter and shorter wavelengths, several technical problems arise such as:

- Some 100m long undulators
- Small (normalized) emittance around 1 π mrad mm for a 1 nC bunch charge
- Bunch compression down to 25 μm bunch length

The ambitious goal of an 1 Å FEL is approached in three steps. Table 1 summarizes main parameters of both electron and photon beams for all these steps.

1. **TTF FEL Phase 1** (approved) [8]: A SASE FEL experiment at wavelength down to 42 nm using the 390 MeV TESLA Test Facility (TTF) linac at DESY[9], see Fig. 2. Besides proving the principle, technical components will be tested: the rf photoinjector, bunch compressors, a 14m long undulator, diagnostics for both electron and photon beams. First operation is scheduled for 1999.

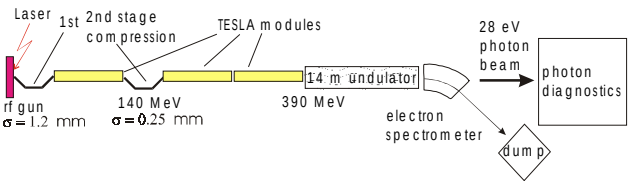

Fig. 2: Schematic layout of phase 1 of the SASE FEL project based on the TESLA Test Facility at DESY.

2. **TTF FEL Phase 2** (approved) [10,11]: By adding 5 more TESLA modules [12], the linac will be upgraded to (at least) 1 GeV, bringing the wave-length down to 6 nm, see Fig. 3. The undulator will be 27m long and the rms bunch length will be reduced to 50 μm by a further compressor stage. Open to users by the year 2003, this facility will give the opportunity to develop experimenting techniques with extraordinary photon beam characteristics like high peak power, short pulse length and fluctuating, spiky substructure typical for SASE FEL photon pulses [13].
3. **TESLA** linear collider with Integrated X-ray Laser (in its technical design phase) [5,6]. For large field gradients, even a superconducting linac has to operate in a pulsed mode. Thus there is room for adding further rf pulses between those driving the high-energy physics beam. By adding a specialized injector providing the electron beam properties needed for the FEL, one can utilize a linear collider installation for driving an X-ray FEL without mutual interference. The plan is to eject the electron bunch train for the FEL at the required beam energy (e.g. at 50 GeV) in the TESLA tunnel, and then transport it to the TESLA interaction region, where a big enough area could accommodate both the high energy physics experimental halls and the X-ray laboratory. A schematic of a switchyard distributing the bunch train over different radiation facilities is shown in Fig. 4.

Concerning the necessary electron beam parameters, all the critical issues are being addressed during phases 1 and 2 (see also Table 1): An rf photoinjector with small emittance and many thousand bunches within each rf pulse [14], bunch length compression by magnetic chicanes including control of coherent radiation effects [15], acceleration without beam degradation [16], and long undulators combined with a periodic FODO lattice [17,18]. In the remainder of this paper we briefly address some key issues of these components.

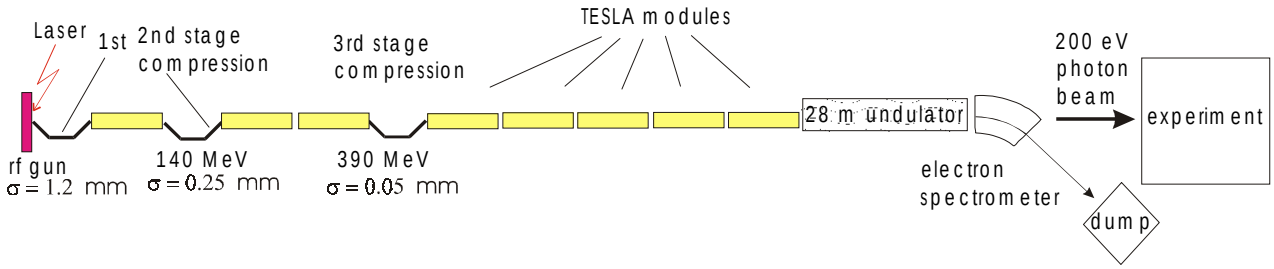

Fig. 3. Schematic layout of phase 2 of the SASE FEL project based on the TESLA Test Facility at DESY. The linac consists of 8 TESLA modules, each 12.2m long. The over-all length of phase 2 is some 300 meters.

Parameter	**Units**	**TTF FEL Phase 1**	**TTF FEL Phase 2**	**TESLA X-ray FEL***
beam energy	GeV	0.300	1.000	25.0
λ_{ph} (radiation wavelength)	nm	71	6.4 (193 eV)	0.1
λ_u(undulator period)	mm	27.3	27.3	50
Effective undulator length	m	13.5	27	87
rms beam size	μm	70	50	18
ε^n (normalized emittance) in the undulator	π mrad mm	2.0	2.0	1.0
peak electron current	A	500	2490	5000
No. of electrons per bunch		6.24E+9	6.24E+9	6.24E+9
No. of photons per bunch		1.7E+14	4E+13	7E+12
rms energy spread σ_γ/γ	10^{-3}	1.7	1.00	0.04 at entrance
rms bunch length σ_S	μm	250.	50.	25
L_g (power gain length)	m	0.6	1.00	4.1
P_{sat} (saturated peak power)	GW	0.3	2.6	65
Average brilliance [photons/s/mm^2/mr/0.1%]		up to 2E+21	up to 6E+22	8E+25
bunch train length	μsec	800	800	1052
Number of bunches per train		Up to 7200	up to 7200	Up to 11315
Repetition rate	Hz	10	10	5

Table 1: Main parameters of the TESLA Test Facility FEL (TTF FEL), phases 1 and 2 [10] and of the TESLA X-ray FEL[6]. The insertion devices are planar hybrid undulators. These values should be used as a guideline only since experimental experience has still to be gained in this wavelength regime.
*) For the TESLA X-ray FEL there will be a beam switchyard serving a number of FELs operating at different wavelengths down to 1 Angstrom, and using different beam energies. The parameters given are typical for the 1 Angstrom case.

4 THE PHOTOINJECTOR

The electron source consists of a 1½ cell , 1.3 GHz normal conducting resonator and a photocathode located at the mid-plane of the first (1/2) cell, where the accelerating field is maximum (approx. 45 MV/m). The klystron must provide 4.5 MW power at up to 800 μs pulse length for the long bunch train that can be accelerated in the s.c. linac,. Thus, since the gun cavity is normal conducting, thermal load is a critical issue. The mechanical design provides direct water cooling of the irises and avoids any brazing between water channels and vacuum. For achieving minimum emittance in all 3 dimensions, the design criteria are

- High accelerating gradient to reduce transverse space charge effects.
- Coaxial rf input coupling to reduce rf asymmetries in the cavity.
- Optimum position of the solenoid focussing field to achieve, in the subsequent drift space, “space charge compensation” [19].
- Short laser pulses.

5 THE BUNCH COMPRESSOR

In phase 1, two stages of longitudinal bunch compression are foreseen to reach the high peak current (500A) that is needed to achieve high FEL gain. This compression is done at beam energies high enough so that space charge forces are tolerable. The key compression step is at 140 MeV from 1 mm to 0.25 mm rms bunch length and consists of a 4 dipole magnet chicane. While magnet chicane compression, using path length differences of particles with different momenta, is the only possible way for ultra-relativistic particles, this method unavoidably involves radiation effects when electrons pass the dipole magnets. It has been shown [17,20] that space charge forces and coherent radiation need to be treated simultaneously in order to describe properly beam dynamics. Radiation effects are the dominant contribution to emittance growth in our chicane, see Fig. 5.

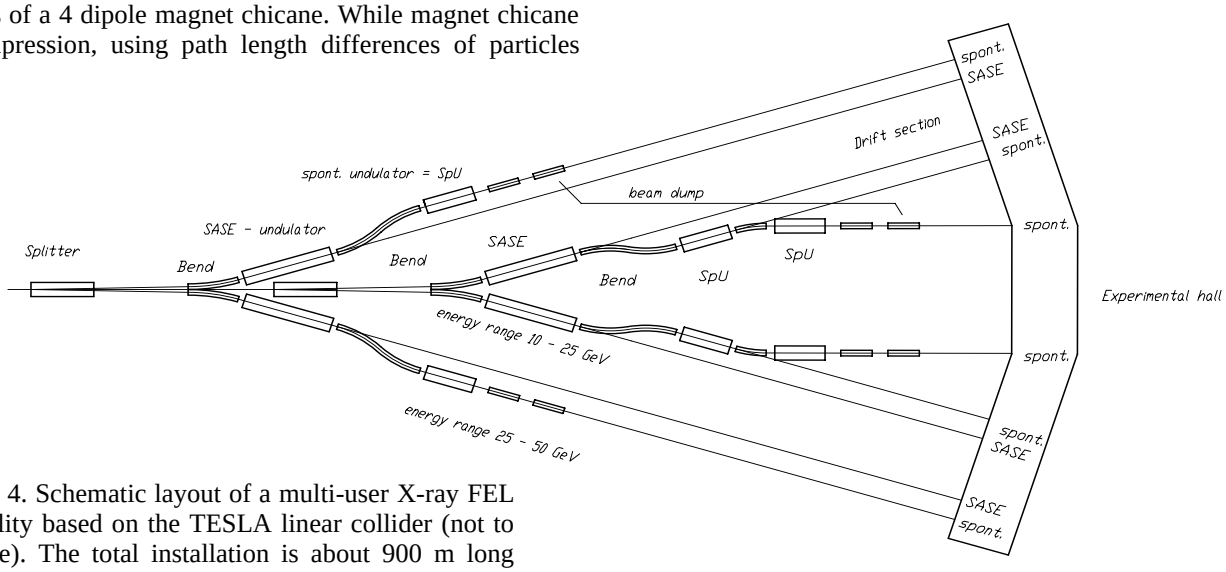

Fig. 4. Schematic layout of a multi-user X-ray FEL facility based on the TESLA linear collider (not to scale). The total installation is about 900 m long and 200 m wide and would be located on the same site as the linear collider interaction region.

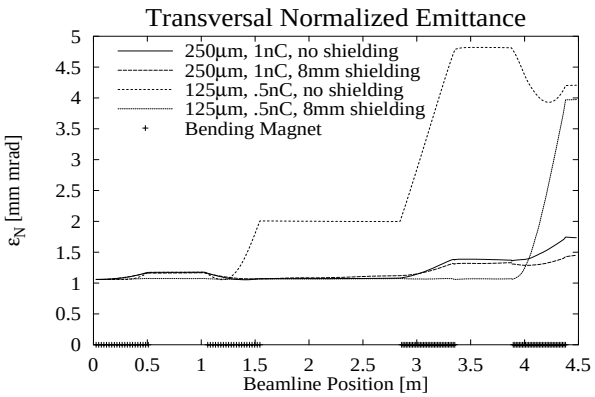

Fig. 5: Evolution of the uncorrelated emittance at the longitudinal center of the electron bunch passing bunch compressor 2. Coherent radiation and space charge are taken into account in this simulation [17]. Two different parameter set are considered, corresponding both to 500 A peak current in the bunch. It is seen that the 125 μm case is more heavily affected.

Significant suppression of coherent radiation by the metallic vacuum chamber is expected at a vacuum chamber height below 8 mm. For experimental verification of this theoretical prediction, the chamber height of bunch compressor 2 will be varied during phase 1 operation. Another issue of test operation will be the stability of rf phase vs. laser phase, since this determines stability of the bunch length, particularly in view of compressor 3. Phase stability below 1 ps has been demonstrated for both the laser and the klystron, which should be sufficient to reach 50 μm rms bunch length in phase 2.

Although compression takes place at high beam energies, space charge turns out to be critical for the whole TTF FEL beam line, from the gun to the undulator, and needs to be taken into account even in the linear optics calculation.

6 BEAM DYNAMICS IN THE ACCELERATOR

Besides space charge and coherent radiation, also wakefields may degrade beam quality. In spite of the low rf frequency of TESLA, longitudinal wake fields are still a concern due to the extremely small bunch length (or to be more precise, due to the large time derivative of the bunch current). It has been shown in [16] that the wake potential of a short bunch is considerably modified while the bunch is passing a longer and longer accelerator structure. For the TTF, the asymptotic case of an infinitely long, periodic structure is reached well before the end of the linac. The bunch still generates extremely high frequency components >680 GHz for which Niobium is known to loose superconductivity. Absorption of these frequency components in the Niobium walls does not seem to be a problem regarding superconductivity, nevertheless, but it may increase the dynamical cryogenic load on the 2K Helium level [21]. Experimental studies on this issue is a subject of TTF FEL, as well as the optimum technical realization of higher order mode absorbers

and additional wake fields due to surface roughness of the vacuum pipe.

7 LONG UNDULATORS

The main technological challenge of the FEL undulator is that the electron beam trajectory must be straight within a tolerance of 10 μm over several meters. This is particularly difficult to achieve since strong quadrupole focussing is superimposed to the undulator field in order to realize the small β function of about 1 m which is optimum for maximum FEL gain. The undulator for TTF FEL phases 1 and 2 is made in permanent magnet, hybrid technology with modules 4.5 m long each [17], see Fig. 6. Since it is impossible to guarantee this straightness from undulator field measurement alone, a beam based alignment strategy has been worked out using a large number of high-resolution beam position monitors [18].

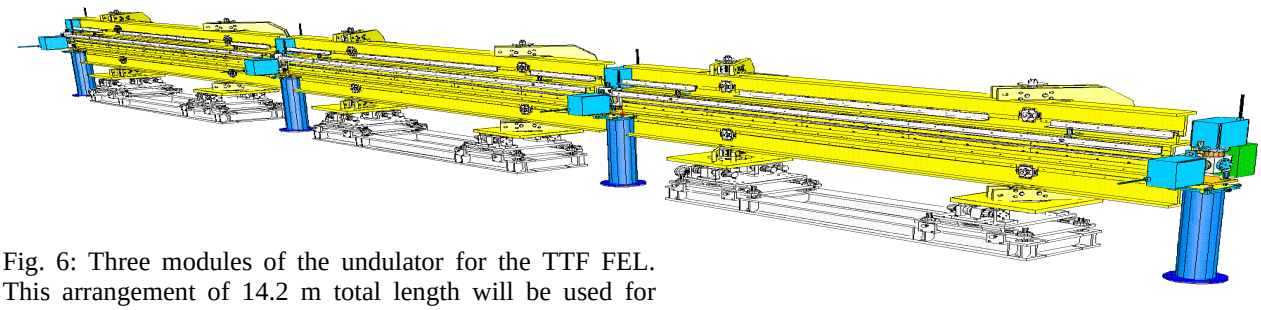

Fig. 6: Three modules of the undulator for the TTF FEL. This arrangement of 14.2 m total length will be used for phase 1. 10 correction coils and 10 beam position monitors per module are squeezed into the 12 mm magnet gap.

8 REFERENCES

[1] J.M. Madey 1971 *J. Appl. Phys.* **42** 1906

[2] A.M. Kondratenko, E.L. Saldin 1980 *Part. Accelerators* **10**, 207

[3] R. Bonifacio, C. Pellegrini, L.M. Narducci 1984 *Opt. Commun.* **50** 373

[4] H. Winick, et al. 1993 *Proc. PAC Washington* and SLAC-PUB-6185

[5] R. Brinkmann et al. 1997 *Nucl. Instr. and Meth. in Phys. Res.* **A 393** 86-92

[6] R. Brinkmann, G. Materlik, J. Rossbach, A. Wagner (eds.) 1997 DESY 1997-048 and ECFA 1997-182

[7] D.C. Nguyen, et al. 1998, Proc. 1998 FEL Conf., to be published in *Nucl. Instr. and Meth. A*

[8] W. Brefeld, et al. 1997 *Nucl. Instr. and Meth. in Phys. Res.* **A 393** 119-124

[9] D. Trines, Status of the TESLA Design, this conference

[10] T. Åberg, et al. 1995, A VUV FEL at the TESLA Test Facility at DESY, Conceptual Design Report, DESY Print TESLA-FEL 95-03

[11] J. Rossbach 1996 *Nucl. Instr. Meth. in Phys. Res.* **A 375** 269

[12] H. Weise, High Gradient Superconducting RF Structures, this conference

[13] Proceedings of workshops on these issues are available at DESY-Hasylab

[14] S. Schreiber et al., The RF-gun based Injector for the TESLA Test Facility Linac, Proc. 1998 EPAC

[15] M. Dohlus, A. Kabel, T. Limberg, Uncorrelated emittance growth in the TTF-FEL Bunch Compression Sections due to Coherent Synchrotron Radiation and Space Charge Effects, Proc. 1998 EPAC

[16] A.N. Novokhatski, A. Mosnier 1996 DAPNIA/SEA-96-08

[17] J. Pflüger et al., *Proc 1996 FEL Conf. Rome* II-107 and *Nucl. Instr. Meth. in Phys. Res.* **A 393** 380

[18] P. Castro: Orbit Correction by Dispersion Minimization in an Undulator with Superimposed FODO Lattice, , Proc. 1998 EPAC, Stockholm

[19] B. Carlsten 1989 *Nucl. Instr. Meth.* **A 285** 313

[20] E.L. Saldin, E.A. Schneidmiller, M.V. Yurkov, 1997 *Nucl. Instr. Meth.* **A 398** 373

[21] P. Schmüser, private communication

[22] S. Reiche, Proc. 1998 FEL Conf., to be published in *Nucl. Instr. and Meth. A*

[23] E.L. Saldin, E.A. Schneidmiller, M.V. Yurkov,, Proc. 1998 FEL Conf., to be published in *Nucl. Instr. and Meth. A*

[24] E.L. Saldin, E.A. Schneidmiller, M.V. Yurkov,, Proc. 1997 FEL Conf., to be published in *Nucl. Instr. and Meth. A*

THE LINAC COHERENT LIGHT SOURCE AT SLAC*

P. Emma
Stanford Linear Accelerator Center, Stanford, California 94309, USA

Abstract

A design study [1] has been completed at SLAC for a linac-based Free Electron Laser (FEL) known as the Linac Coherent Light Source (LCLS), which aims at the production of high peak power coherent x-rays with a wavelength of 1.5 Å. A 1-nC electron beam produces coherent radiation through self-amplified spontaneous emission (SASE) in a long undulator with a projected peak output power of ~10 GW. The design utilizes the last kilometer of the SLAC linac, not used by the PEP-II project, to compress and accelerate a single electron bunch, generated by a photocathode rf gun, to a peak current of ~3.4 kA at 15 GeV. We describe here the acceleration, compression and preservation of this high brightness electron beam through the S-band linac and related transport lines, and outline some of the required beamline modifications. Specific challenges such as emittance growth generated by coherent synchrotron radiation, compensation of the correlated electron energy spread after compression, and overall pulse-to-pulse machine stability issues drive the parameter choices and system designs outlined here.

1 INTRODUCTION

The LCLS is based on the principle of Self-Amplified-Spontaneous-Emission (SASE) where high power, transversely coherent, radiation is generated in a single pass of a high peak current electron beam through a long undulator eliminating the need for optical cavities, which are difficult to build in the x-ray spectral region.

The requirements on the electron beam are, however, quite demanding and, until recently, difficult to achieve. The LCLS will utilize the experience and technical advances gained at the Stanford Linear Collider (SLC) [2] and the Final Focus Test Beam (FFTB) [3] and make use of recent progress in the production of intense electron beams with radio-frequency photocathode guns [4].

With the advent of the PEP-II asymmetric B-factory, which employs only the first 2/3 of the 3-km SLAC linac, the final kilometer will be available to accelerate and compress an electron beam up to 17 GeV. With these developments, as well as ongoing studies for the next linear collider (NLC) [5], SLAC is in an ideal position to construct a linac based x-ray FEL. This was first proposed in 1992 [6]. This new '4th generation' source will produce coherent radiation many orders of magnitude greater in peak power and brightness than present 3rd generation sources, opening new research potentials in chemistry, physics, biology and other applied sciences. The main parameters, at the undulator, are outlined in Table 1.

Table 1: LCLS parameters at 15 and 1.5 Å operation.

Parameter	unit	15 Å	1.5 Å
Electron beam energy	GeV	4.54	14.35
Repetition rate	Hz	120	120
Normalized emittance†	μm	2.0	1.5
Peak beam current	kA	3.4	3.4
Coherent energy spread†	%	<0.2	<0.1
Incoherent energy spread†	%	<0.06	<0.02
Bunch length†	μm	20	20
Beam size†	μm	37	31
Field gain length	m	3.7	11.7
Undulator period	mm	30	30
FEL parameter	10^{-4}	12.9	4.7
Peak brightness	10^{32} ‡	1.2	12
Average brightness	10^{22} ‡	0.42	4.2
Peak saturation power	GW	11	9
Peak spontaneous power	GW	8.1	81

† RMS, ‡ photons/sec/mm^2/mrad^2/0.1%-BW

Table 1 shows parameters at the low and high energy ends of the operational range, with radiation wavelengths of 15 and 1.5 Å, respectively. The 100-m, permanent magnet, planar undulator will be located in the existing FFTB tunnel, directly following the linac. The accelerator is divided into several sections to provide two-stage bunch compression. A schematic layout of the accelerator is shown in Fig. 1 which includes the RF-gun (at the 2-km point in the linac), four linac sections (Linac-0…3), two dog-leg transport lines (DL1,2) two bunch compressors (BC1,2) and the undulator. System parameters and electron beam quantities are indicated at various points.

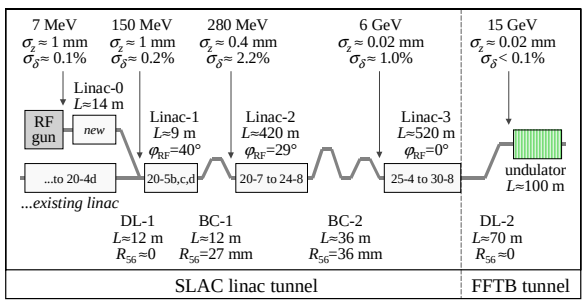

Fig. 1: LCLS accelerator and compressor schematic.

The first linac (Linac-0) is a new section installed adjacent to the existing linac which accelerates the 1 mm

* Work supported by the Department of Energy, contract DE-AC03-76SF00515

long bunch to 150 MeV and also compensates the space charge induced transverse emittance growth. The first bend section (DL1) injects the beam into the main linac and provides emittance and energy spread diagnostics. Linac-1 (L1) accelerates the 1 mm bunch 'off-crest' to 280 MeV and generates an energy correlation along the bunch such that the first chicane bunch compressor (BC1) shortens the bunch to 0.38 mm. L2 then accelerates the bunch to 6 GeV and also generates an energy correlation so the double chicane system (BC2) compresses the bunch to its design value of 20 μm. Finally, L3 nominally accelerates the beam to 15 GeV (a range of 4-17 GeV is available) and also cancels the remaining correlated energy spread with its geometric wakefield. The high-energy dog leg (DL2) is designed for energy and energy spread analysis, transverse emittance measurements, final beam transport, and variable matching into the undulator.

All of the linac sections, except L0, are existing and require only minor modifications. Both L2 and L3 (~950 meters of linac) require primarily quadrupole power supply modifications, while L1 (9 meters) requires the insertion of a few quadrupole magnets. The bunch compressors and DL1 will be composed of some new and some existing magnet designs and replace a total of 15 3-meter rf structures (4 klystrons) for an energy loss of ~2% of the nominal 50 GeV SLAC linac. DL2 and the post-undulator electron beam dump will use the existing FFTB tunnel as well as its magnets.

The peak current required for 1.5-Å SASE saturation in the 100-m undulator is dependent on the final emittance as shown in Fig. 2. Plotted is the 'slice' emittance, defined as the transverse phase space area over of a small slice (~0.5 μm) of the 20 μm bunch length. Conversely, the whole-bunch emittance, 'projected' emittance, may be significantly larger, with little impact on saturation. The LCLS design budgets a 50% slice emittance increase over the entire accelerator. Considering most dilution mechanisms affect the projected emittance, rather than the slice, this is a relatively conservative budget.

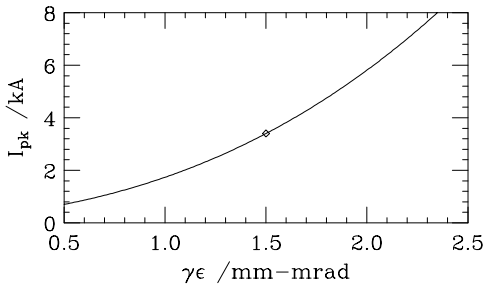

Fig. 2: Peak current required for 1.5 Å SASE saturation in the 100-m undulator vs. rms normalized 'slice' emittance.

2 LONGITUDINAL DYNAMICS

To achieve the high peak current in the undulator, the bunch must be compressed in a series of magnetic chicanes. These will be arranged and located along the linac such that non-linearities in the compression and acceleration process (wakefields, rf curvature, and 2nd order momentum compaction) are mutually canceled. With a careful arrangement the compression process is more linear which reduces the minimum bunch length achievable. An optimum choice of parameters cancels the final correlated energy spread, minimizes transverse emittance growth effects and desensitizes the system to phase and charge variations.

2.1 Bunch Compression

The bunch is compressed by accelerating at an off-crest rf phase, thereby introducing a correlated energy spread along the bunch. This is followed by a bending section, a magnetic chicane, with linear path length dependence on particle energy. The peak current generated by the rf photocathode gun is ~100 Amps. Generating the 3.4 kA necessary for 1.5-Å SASE saturation at $\gamma\varepsilon = 1.5$ μm requires a compression factor of ~35. For a single stage compressor using an rf phase of φ_0, the relative change in final bunch length, $\Delta\sigma_f/\sigma_f$, produced by a change in initial beam phase, $\Delta\varphi$, (timing jitter at the gun) is given by [7]

$$\frac{\Delta\sigma_f}{\sigma_f} \approx -\left(\frac{\sigma_i}{\sigma_f} \mp 1\right)\Delta\varphi \cot\varphi_0 \ , \qquad (1)$$

with 'under-compression' ($<\pi/2$ phase space rotation) expressed by the minus sign and 'over-compression' the plus sign. For $\varphi_0 = 20°$ and a compression factor of $\sigma_i/\sigma_f = 35$, initial phase jitter of just $\Delta\varphi = 0.1°$ S-band (0.1 psec) results in final bunch length (undulator peak current) jitter of $\Delta\sigma_f/\sigma_f \approx 16\%$.

Clearly, a single stage compressor is too sensitive. Furthermore, the final bunch length of a single stage compressor is limited by non-linearities, such as rf curvature, which make single-stage compression from 1 mm to 20 μm very difficult. A two-stage compression system, however, brings about cancellations which can reduce this phase jitter sensitivity by an order of magnitude. This also allows the first compressor to be located early in the accelerator so that the next linac section accelerates a shorter bunch. The reduced transverse wakefield of the shorter bunch provides looser quadrupole and rf-structure alignment tolerances. Conversely, a single compression stage needs to be placed at a high enough energy so that space charge forces are not significant for a 20 μm bunch. This extends the length over which the long bunch is accelerated tightening alignment tolerances. For these reasons, a two-stage compressor is used.

The compressors are simple 4-dipole chicanes with no quadrupoles. These offer ease of adjustment and the dispersion function is closed to all orders in energy.

The first compressor (BC1) is at 280 MeV and shortens the bunch from 1 mm to 385 μm rms at a correlated energy spread of 2.2% rms. The second compressor (BC2) is a double chicane designed to reduce and

compensate the transverse emittance growth generated by coherent synchrotron radiation (CSR) [8] (explained below). BC2 is at 6 GeV and compresses the bunch from 385 μm to ~20 μm rms at a correlated energy spread of 1.0% rms. Bunch length diagnostics, using e.g. CSR [9], are included after each bend section. Table 2 summarizes the chicanes.

Table 2: Bunch compressor chicane parameters.

Parameter	unit	BC1	BC2	
			chic-1	chic-2
Beam energy	GeV	0.28	6	6
Total length	m	2.8	13.2	13.2
Momentum compac.	mm	27	31	4.5
Dipole length	m	0.2	1.5	1.5
Bend angle/dipole	deg	7.1	3.4	1.3
Drift between bends	m	0.75	3.35	3.35
Max. dispersion	m	0.12	0.29	0.11

Fig. 3 shows a simulation of longitudinal phase space before and after each compressor. The non-linear correlation after BC1 (Fig. 3b) is primarily due to the long bunch on the S-band rf curvature in L1. It is later compensated by the geometric wakefield of L2 resulting in the nearly linear correlation of Fig. 3c. Finally, after BC2, the large correlated energy spread (Fig. 3d) is cancelled by acceleration and the strong geometric wakefield of the L3 linac (see Fig. 4, lower right).

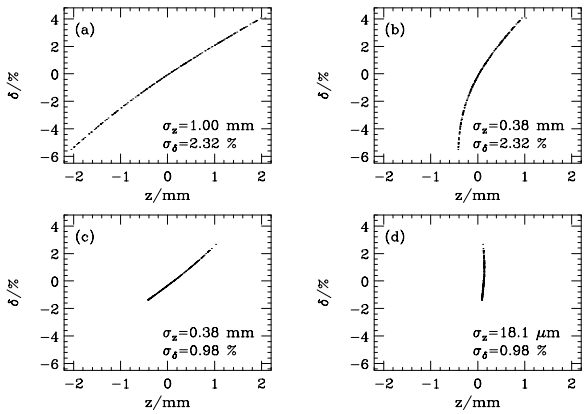

Fig. 3: Longitudinal phase space on fixed scales at (a) BC1-start, (b) BC1-end, (c) BC2-start and (d) BC2-end (bunch head at left).

The core of the beam (85%) is shown, prior to the undulator, in Fig. 4. The final energy spread is 0.035% rms with a very acceptable incoherent component (over a 0.5 μm slice) of 0.006%. Large energy tails (~1%) which encompass 15% of the bunch charge are not shown. The simulations [10] include geometric wakefields, the sinusoidal character of the rf accelerating field, the 1st and 2nd order momentum compaction of the chicanes, and the incoherent energy spread generated by synchrotron radiation in BC2 and DL2. The resistive wall wakefields of L3/DL2 and CSR effects of BC2/DL2 are not included in the figures, and are expected to contribute <0.05% rms to the coherent energy spread, some of which is correctable through small adjustments in the rf phasing.

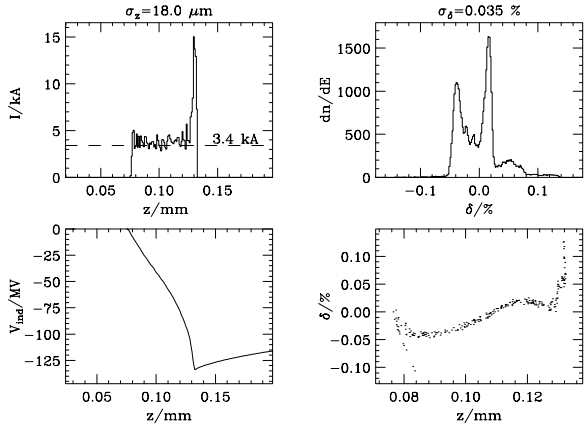

Fig. 4: Longitudinal phase space (low-right), axial (up-left) and energy (up-right) distributions and L3 bunch induced voltage (low-left) at undulator input (15 GeV).

The chosen chicane locations, the intermediate bunch length, and the rf phases form a system with significantly looser tolerances on pulse-to-pulse gun jitter. Gun timing jitter of 0.8 psec rms or initial bunch population jitter of 3% rms will each produce a 10% rms peak current jitter. Although challenging, they are achievable.

2.2 Coherent Synchrotron Radiation

When a microbunch follows a curved path, as in a chicane, the bunch radiates at wavelengths which may be large compared to the bunch length. This coherent radiation produces an energy-spread-generating wakefield along the bunch which can induce significant transverse emittance growth; a potential problem for many future microbunch accelerators.

In the LCLS, this is controlled by using a double chicane [11] for the 2nd bunch compressor. Chicane-1 of the double system is designed to partially compress the bunch, keeping the emittance growth due to incoherent synchrotron radiation less than 2%. A second chicane is then added with reduced bend angles and separating optics (four quadrupoles forming a **–I** transfer matrix) to complete the compression and approximately cancel the net CSR emittance increase. Fig. 5 shows a schematic.

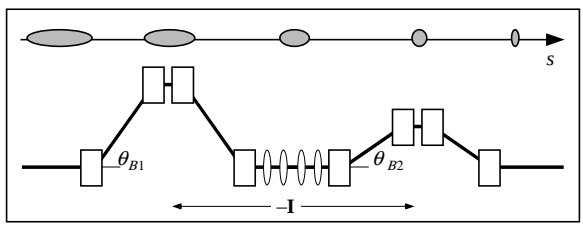

Fig. 5: Schematic of the double chicane compressor.

The cancellation can be understood by imagining an electron which loses energy in the *n*th dipole (n = 1...4) of chicane-1. In this steady-state model, the CSR-wakefield

increases with compression, but its shape along the bunch, is preserved through the chicane. The electron will then receive an extra horizontal kick, with respect to an on-energy electron, in the *n*th bend. This same electron, with its unchanged relative axial position, will lose even more energy in the *n*th bend of chicane-2 (because of the shorter bunch there), but due to the **–I** transfer matrix between paired bends and the weaker bends of chicane-2, the net horizontal kick is zero. This assumes the electron does not shift axially with respect to the remainder of the bunch as would occur in the case of over-compression or a highly non-linear phase space transformation. The double chicane also significantly weakens the CSR effect by using strong bends when the bunch is long (chicane-1) and weak bends where the bunch is short (chicane-2).

Calculations of the CSR-induced emittance dilution have been made using both a simple steady-state model and also the DESY *WAKE* code [12] which includes CSR field transients and bend-to-bend coupling effects. These calculations predict an emittance growth after BC2 of 0.3% and 3-5%, respectively. Fig. 6 shows the dispersion, bunch length, and the CSR induced energy spread and emittance growth through the BC2 double chicane for the steady-state model. CSR effects in DL2 are similarly controlled with a ~1% emittance growth expected.

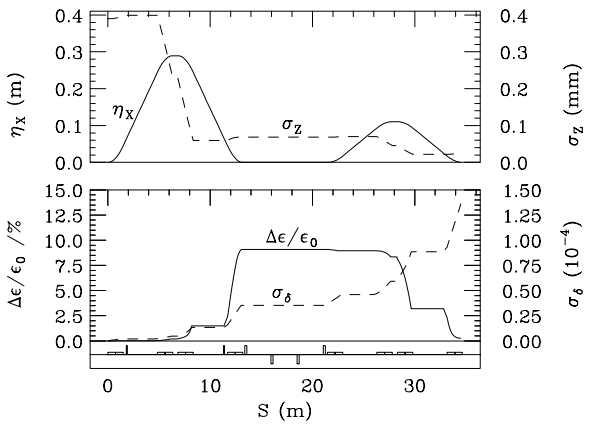

Fig. 6: The dispersion (η_x), bunch length (σ_z), and the CSR rms energy spread (σ_δ) and emittance growth ($\Delta\varepsilon/\varepsilon_0$), generated in BC2 calculated with the steady-state model.

3 TRANSVERSE DYNAMICS

The four separate S-band linac sections each have different beam parameters which motivate different lattice parameter choices. The lattices are designed to minimize 'projected' emittance dilution due to wakefields and dispersion which are generated through component misalignments. For example, a large beam energy spread and short bunch length require weak focusing.

3.1 RF Gun and Booster Linac

The high brightness electron beam is initially generated in a 1.6-cell S-band rf photocathode gun driven by a 500 μJ UV laser system with temporal pulse shaping capability and <1 psec stability. The injector is required to produce a single electron bunch of 1-nC and 100 A peak current at a repetition rate of 120 Hz with normalized rms emittances of 1 μm. The gun design includes a solenoidal field, located near the copper cathode, which initiates a compensation of the space charge induced transverse emittance growth. The L0 booster linac completes the compensation and provides acceleration to 150 MeV. L0 is a new beamline constructed parallel to the existing linac and is displaced 1 meter horizontally. It includes four 3-meter rf-structures and no quadrupole magnets. Following L0 is an adjustable optical matching section and an emittance diagnostic section. The first dog leg, DL1, provides energy diagnostics and bends the beam onto the main linac axis (L1). The existing 3-meter rf-structure there is removed to provide space for injection.

3.2 Linac-1

L1 initiates the compression process by accelerating off crest, thereby generating the necessary energy-*z* correlation so the first chicane, BC1, will compress the bunch. L1 is composed of three existing 3-meter rf-structures. Because of the large rf phase angle and the long bunch, the rms energy spread in L1 rapidly increases from 0.2 to 2.2%. Therefore, both dispersion and transverse wakefields are potential emittance dilution mechanisms. Space charge forces here are insignificant.

The quadrupole spacing and strength requirements were determined by simulating several different lattice schemes using the computer code *LIAR* [13]. This computer program calculates the transverse emittance dilution induced along a linac by wakefields and dispersion via random quadrupole, BPM (beam position monitor), and rf-structure misalignments. It also provides various steering algorithms and empirical emittance correction techniques. With 300 μm rms quadrupole, BPM, and rf-structure transverse misalignments and one quadrupole added after each 3-meter structure, the optimum phase advance per cell is found to be near 75°. The expected emittance dilution over L1 is then ~5%.

3.3 Linac-2

The energy spread is large (1-2%) over the entire 430-meter length of L2, and the bunch is only partially compressed making L2 the most problematic linac section for emittance preservation. The lattice choice for L2 was made, as for L1, using *LIAR*, including misalignments, and varying the phase advance per cell and quadrupole spacing. By increasing the density of quadrupoles, the expected emittance dilution can be reduced, but the gains do not clearly justify the additional costs. Therefore, the existing quadrupoles are used in their present locations with an optimum phase advance of ~70°/cell. Fig. 7 shows the dilution versus phase advance per cell after 'one-to-one' steering for the existing quadrupole spacing. Note, only the 'projected' emittance is affected here.

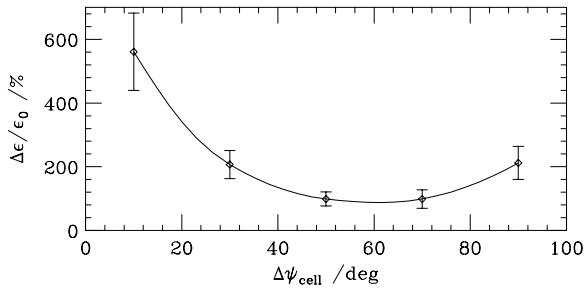

Fig. 7: Emittance after L2 vs. phase advance/cell. Quad, BPM and structure misalignments of 150,150 and 300 μm rms, respectively, and steering are applied (10 seeds).

Even though the L2 uncorrected emittance growth can easily reach 100%, localized trajectory oscillations ('bumps'), as used in the SLC and FFTB, can be applied to restore the emittance. Simulations of trajectory-based emittance corrections are performed using *LIAR*. 'Bumps' of ~300 meters in length, with 100-300 μm peak amplitude, are used to empirically minimize the measured emittance in both planes. Beam position and angle, per plane, are varied near the beginning of L2 to optimize emittances at the end. As at the SLC, oscillations are terminated with an orbit controlling feedback system. A high resolution 4-wire-scanner emittance diagnostic section is planned for the end of L2. Fig. 8 shows emittance bump correction simulations. Using 100 misalignment seeds, an average projected emittance growth of ~100% is corrected to <10% in both planes. At the FFTB, with the SLAC linac, this technique has been used to preserve an initial vertical emittance of 1.5 μm to ~50% dilution [7] while accelerating a 1-nC, 0.5-mm *long* bunch over a linac three times the length of the LCLS.

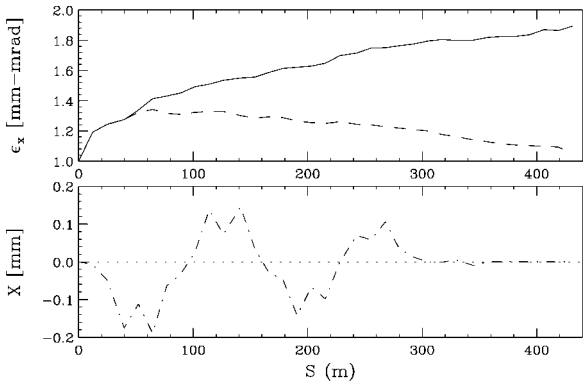

Fig. 8: Emittance along L2 before (top-solid) and after (top-dash) bumps applied. Curves are an average over 100 seeds. The bottom plot shows a typical oscillation.

3.4 Linac-3

The short bunch of L3 effectively eliminates transverse wakefields, and the rms energy spread shrinks from 1% to <0.1% due to acceleration and the strong longitudinal wakefield of the short bunch. In this case the dominant emittance dilution mechanism is due to dispersion generated by quadrupole and BPM misalignments. The dispersion can be minimized by a weak focusing lattice. *LIAR* simulations were run for L3 using the existing linac quadrupoles and varying the phase advance per cell. In this case an optimum was found at ~30°/cell with an expected emittance dilution of <10%. A 4-wire-scanner diagnostic section presently exists at the end of L3. Finally, DL2 will include high resolution energy, energy spread and emittance diagnostics prior to the undulator.

4 SUMMARY

The LCLS offers a unique opportunity for the creation of a coherent x-ray beam with unprecedented gains in peak power and brightness using, for the most part, existing components, techniques and facilities at SLAC. Although the design is based on a consistent and feasible set of parameters, some components, such as the RF-gun, undulator construction and CSR compensation, require further research and development to guarantee performance. The present proposal includes a 3 year R&D phase with pre-fabrication engineering beginning in FY2001, construction in 2002 and major systems commissioning starting in 2005.

5 REFERENCES

[1] LCLS Design Study Report, SLAC-R-521, (1998).
[2] SLC Design Report, SLAC-PUB, (1984).
[3] FFTB Design Report, SLAC-REP-376, 1990.
[4] R.L. Sheffield, "Photocathode rf guns", *Physics of Particle Acc.*, *AIP* Vol. 184, pp. 1500-1531, (1992).
[5] Zeroth-order Design Report for the Next Linear Collider, SLAC-REP-474, May 1996.
[6] C. Pellegrini, *Workshop on Fourth Generation Light Sources*, SSRL Report 92/02, pp. 364-375, 1992.
[7] T. Raubenheimer, Nuclear Instruments and Methods in Physics Research A, 358 (1995), 40-43.
[8] See for example, Ya. S. Derbenev et al, "Microbunch Radiative Tail-Head Interaction", *DESY*, Sep. 1995.
[9] D.X. Wang, "Electron Beam Instrumentation Techniques Using Coherent Radiation", *PAC*, Vancouver, B.C., 1997.
[10] Simulations performed with the computer code *LiTrack*, written by K.L.F. Bane (SLAC).
[11] P. Emma, R. Brinkmann, "Emittance Dilution Through Coherent Energy Spread Generation in Bending Systems", *PAC*, Vancouver, B.C., 1997.
[12] M. Dohlus, T. Limberg, "Emittance Growth due to Wake Fields on Curved Bunch Trajectories", *XVIII International Free Electron Laser Conference* (Rome, 1996); DESY print *TESLA-FEL 96-13*.
[13] R. Assmann et al., "*LIAR* - A New Program for the Modeling and Simulation of Linear Accelerators with High Gradients and Small Emittances", *18th Linac Conference*, Geneva, Switzerland, August, 1996.

MODELING AND DESIGN OF KLYSTRON

Y. H. Chin
KEK, 1-1 Oho, Tsukuba-shi, Ibaraki-ken, 305, Japan

Abstract

We have developed a new method for a realistic and more accurate simulation of klystron using the MAGIC code. MAGIC is the 2.5-D or 3-D, fully electromagnetic and relativistic particle-in-cell code for self-consistent simulation of plasma. It solves the Maxwell equations in time domain at particle presence for a given geometrical structure. It uses no model or approximation for the beam-cavity interaction, and thus keeps all physical processes intact. With MAGIC, a comprehensive, full-scale simulation of klystron from cathode to collector can be carried out, unlike other codes that are specialized for simulation of only parts of klystron. It has been applied to the solenoid-focused KEK XB72K No.8 and No.9 klystrons, the SLAC XL-4 klystron, and the BINP PPM klystron. Simulation results for all of them show good agreements with measurements. We have also developed a systematic design method for high efficiency and low gradient traveling-wave (TW) output structure. All these inventions were crystallized in the design of a new solenoid-focused XB72K No.10. Its predicted performance is 126 MW output power (efficiency 48.5%) with peak surface field of about 77 MV/m, low enough to sustain a 1.5 μs long pulse. It is now in manufacturing and testing is scheduled to start from November 1998.

1 JLC KLYSTRON PROGRAM

The 1-TeV JLC (Japan e^+e^- Linear Collider) project[1] requires about 3200 (/linac) klystrons operating at 75 MW output power with 1.5 μs pulse length. The main parameters of solenoid-focused klystron are tabulated in the second column of Table 1. The 120 MW-class X-band klystron program at KEK[2], originally designed for 80 MW peak power at 800 ns pulse length, has already produced 9 klystrons with solenoidal focusing system. To reduce the maximum surface field in the output cavity, the traveling-wave (TW) multi-cell structure has been adopted since the XB72K No.6. Four TW klystrons have been built and tested. All of them share the same gun (1.2 microperveance and the beam area convergence of 110:1) and the buncher (one input, two gain and one bunching cavities). Only the output structures have been redesigned each time at BINP. XB72K No.8 (5 cell TW) attained a power of 55 MW at 500 ns, but the efficiency is only 22%. XB72K No. 9 (4 cell TW) produced 72 MW at 520 kV for a short pulse of 200 ns so far. The efficiency is increased to 31% and no sign of RF instability has been observed. The limitation in the pulse length attributes a poor conditioning of the klystron. The latest tube, XB72K No.10, was designed at KEK, and is being build in Toshiba.

Apart from the solenoid-focused XB72K series, KEK has also started a PPM (periodic permanent magnet) klystron development program. The design parameters are shown in the last column of Table 1. Its goal is to produce a 75MW PPM klystron with an efficiency of 60 % at 1.5 μs or longer pulse. The first PPM klystron was designed and build by BINP in the collaboration with KEK. It has a gun with beam area convergence of 400:1 for the microperveance of 0.93. The PPM focusing system with 18 poles (9 periods) produces the constant peak magnetic field of 3.8 kG. The field in the output structure is still periodic, but tapered down to 2.4 kG. There are two solenoid coils located at the beam entrance for a smooth transport of a beam to the PPM section. It achieved 77 MW at 100 ns, but there is a clear sign of RF instability at higher frequencies. The DC current monitor in the collector shows about 30 % loss of particle when RF is on. The second PPM klystron, XB PPM No.1, is being designed at KEK.

Table 1: Specifications of X-band solenoid-focused and PPM-focused klystrons for JLC.

	XB72K	PPM
Operating frequency (GHz)	11.424	11.424
RF pulse length (μs)	≥ 1.5	≥ 1.5
Peak output power (MW)	75	75
Repetition rate (pps)	120	120
RF efficiency (%)	47	60
Band-width (MHz)	100	120
Beam voltage (kV)	550	480
Perveance ($x10^{-6}$)	1.2	0.8
Maximum focusing field (kG)	6.5	
Gain (dB)	53-56	53-56

2 MAGIC CODE

After a series of disappointing performance of XB72K series, several lessons had been learned. First, KEK should have its own team to specialize the klystron design and overhaul the design process. Second, a new klystron simulation code was needed for a more realistic design of klystron, particularly, that of a TW output structure. The one-dimensional disk model code, DISKLY, had been used by BINP for design of the TW structure from XB72K No.5 till No.9. This code uses an equivalent circuit model (port approximation) to simulate a TW structure and tends to predict the efficiency much larger (nearly twice larger) than the experimental results. For the design of a new klystron, XB72K No.10, we have developed a method to use the MAGIC code[3] to simulate and design a klystron. MAGIC is the 2.5-D or 3-D, fully electromagnetic and relativistic particle-in-cell code for self-consistent

simulation of plasma. It solves the Maxwell equations directly at particle presence by the finite difference method in time like ABCI [4] or MAFIA. It requires only the geometrical structure of the cavity and assumes no model (neither port approximation nor equivalent circuit) for the beam-cavity interaction. The static magnetic field can be applied to a structure. Advantages of MAGIC are its accuracy and versatility. Even an electron gun can be simulated with results in good agreements with measurements. Simulation results can be imported/exported from one section of klystron to another, allowing a consistent simulation of the entire klystron without loss of physics. Only disadvantage is that it is time consuming.

3 FUNCTIONAL COMPARISON OF AVAILABLE CODES

Table 2 shows the functional comparison of computer codes available for klystron simulations. MAGIC is the only code that can simulate all parts of klystron from gun to collector. ARSENAL[5] is closest to MAGIC in functional performance, but cannot handle a TW multi-cell structure. CONDOR[6] can simulate a TW structure, but requires a beam input from a gun that needs to be simulated by other code such as EGUN[7]. In the migration of beam and fields from one code to another, two programs must be well matched to avoid any incomplete transfer of information and resulting unphysical phenomena.

Table 2: Functional comparison of available codes.

	Dimen-sion	Gun	Bun-cher	Single -cell output cavity	Multi -cell output cavity
MAGIC	2.5, 3	O	O	O	O
EGUN	2.5	O	×	×	×
CONDOR	2.5	×	O	O	O
FCI [8]	2.5	×	O	O	×
ARSENAL	2.5	O	O	O	×
JPNDISK	1	×	O	O	×
DISKLY	1	×	O	O	×

4 SIMULATION METHOD USING MAGIC

We divide a klsytron into three sections:

- Electron gun
- Buncher section (an input, gain and bunching cavities + drift space)
- TW output structure

The simulation techniques are described in detail in Ref. [9]. Here, we briefly summarize them.

3.1 Electron Gun

The gun simulation is done by specifying an emission area (cathode) and an applied voltage along a line between a wehnelt and an anode. The number of emitted particles can be specified per unit cell volume and unit time-step. The applied magnetic fields (both B_z and B_r) must be specified over the structure, not just on beam axis. They can be calculated using codes such as POISSON (for solenoid field) and PANDIRA[10] (for PPM). These programs requires the exact configuration of coils, yokes, or permanent magnets and their properties as input.

Figure 1 shows the comparison of beam profile simulated by EGUN and MAGIC for the XB72K-series gun. They look nearly identical. The simulated perveance for three different guns and the measured values are tabulated in Table 3. MAGIC simulations are in excellent agreement with the measurements, while the EGUN tends to produce a 5-10 % larger value than the measurements. This behavior was also reported in simulation of SLAC 50 MW PPM klystron by EGUN [11].

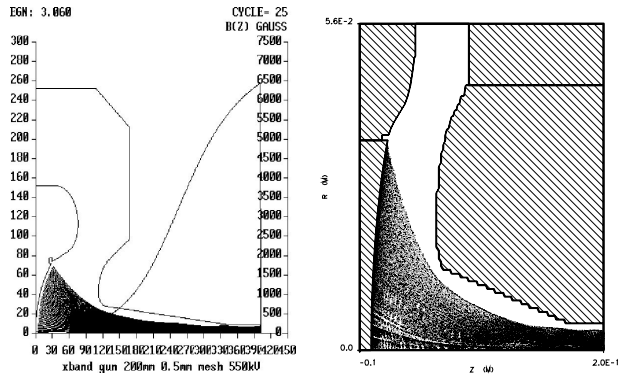

(a) EGUN (b) MAGIC

Figure 1: Beam profile from the XB72K gun simulated by (a) EGUN and (b) MAGIC.

Table 3: Comparison of the simulated perveances and the measured values.

		Micro perveance		
Klystron	Frequency (MHz)	MAGIC	EGUN	Measured
XB 72K (KEK)	11,424	2.03	1.89	2.05
PV3030 (KEK)	2,856	1.19	1.10	1.2
5045 (SLAC)	2,856	1.99	1.78	2.0

3.2 Buncher Section

The input cavity needs a different treatment from other cavities, because the RF power is given externally, rather than being induced by a beam. Since a beam stays almost

as DC while passing the input cavity, the beam induced voltage is negligible. Therefore, we just need to specify the applied RF voltage along an electric filed line between the cavity gap. The field distribution of the fundamental mode should be computed by MAGIC priory and used as input. Other cavities need to be tuned to correct fundamental frequencies by adjusting the cavity aperture on mesh. The beam-induced voltage in cavities are monitored to measure the necessary RF cycles for saturation. In most of cases, about 200-300 RF cycles are enough. To speed up the saturation, a DC beam current from gun is increased smoothly and slowly from zero to the full value at the first 10-20 RF cycles.

Figures 2 (a) and (b) show spatial distributions of beam in the input+gain cavity section and in the bunching cavity section of the XB72K No.10 buncher, respectively. The strong bunching of beam (RF current/DC current ≈ 1.7) is created toward the end of the buncher section.

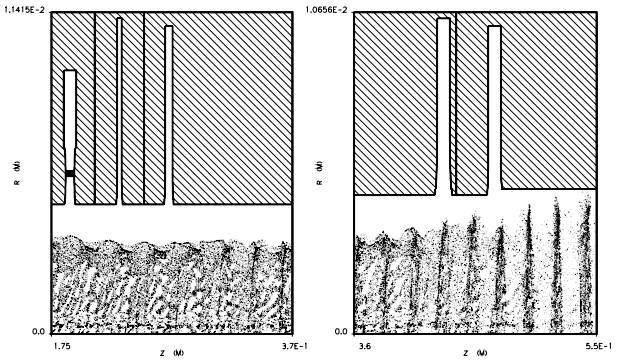

(a) (b)

Figure 2: Spatial distribution of beam (a) in the input+gain cavity section and (b) in the bunching cavity section of the XB72K No.10 buncher.

3.3 Traveling-Wave (TW) Output Structure

Simulation of TW output structure is quite straightforward as any other cavity. In order to simulate effects of a non-axis-symmetrical output coupler by the 2.5-D version of MAGIC, we model it by a ring-shaped conductor which has the same complex S_{11}-matrix element (i.e., the reflection coefficient for amplitude and phase). This is illustrated in Fig. 3. There are three free parameters to fit the frequency dependent S_{11}-matrix element: the conductance, and the inner and the outer radii of the conductor. For details of the output coupler modeling, refer to Ref.[9]. As shown later, simulation results for many klystrons seem to verify the validity of this approximation.

Before inventing the above conductor approximation, we have considered a use of an axis-symmetrical radial transmission line to model a 3-D coupler. However, this method cuts the output structure into two disconnected parts, and thus an artificial DC voltage is induced by the DC component of beam at the output cell to which the output couplers are attached. This artificial DC voltage causes a non-negligible effect to the particle dynamics, and results in error. Figure 4 shows the simulation results for the output structure of XB72K No.10.

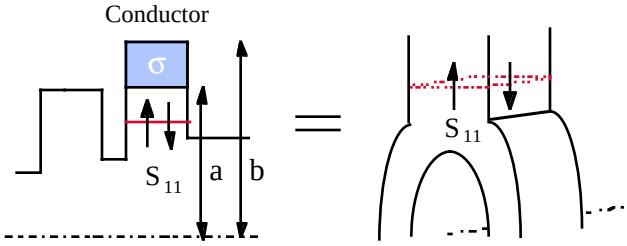

Figure 3: Illustration for 2.5-D modeling of 3-D output coupler using a conductor.

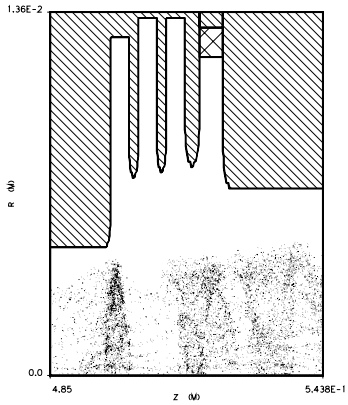

Figure 4: Simulation of XB72K No. 10 in the output structure.

5 SIMULATION RESULTS AND MEASUREMENTS

Figure 5 shows the simulation results of MAGIC and the experimental data for the saturated output power vs. beam voltage for XB72K No.8 klystron. Excellent agreements can be seen. The closed triangles in Fig. 5 are DISKLY simulations. It reveals the accuracy limitation of the 1-D disk model code.

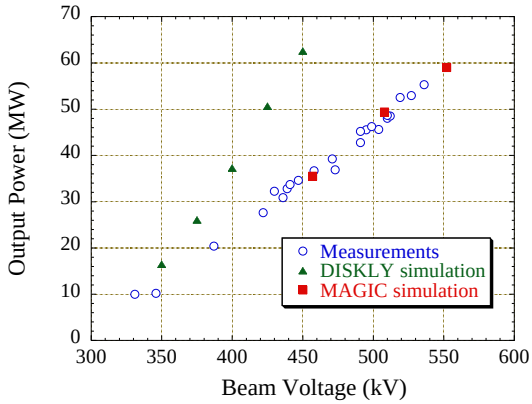

Figure 5: Simulation results of MAGIC and DISKLY and the measurement data for XB72K No.8 klystron.

Let us move to the simulation of SLAC XL-4 klystron. XL-4 klystron produced50 MW at 400 kV with

1.5 μs pulses at 120 pps. It attained 75MW at 450 kV, but the pulse length could go up only to 1.2 μs before the RF breakdown in the output cavity. The simulation results for the output power are compared with the measurements in Fig. 6. MAGIC simulations reproduce the measurement data quite well. The CONDOR prediction at 450 kV, denoted by the closed triangle, was at 10% too high. Figure 7 shows the output power vs. the input power for XL-4. It is clear that the simulation reproduces the measured gain curve well.

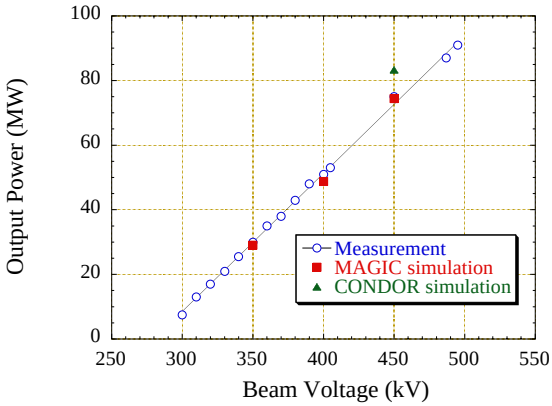

Figure 6: Simulation results of MAGIC and CONDOR and the measurement data for the SLAC XL-4 klystron.

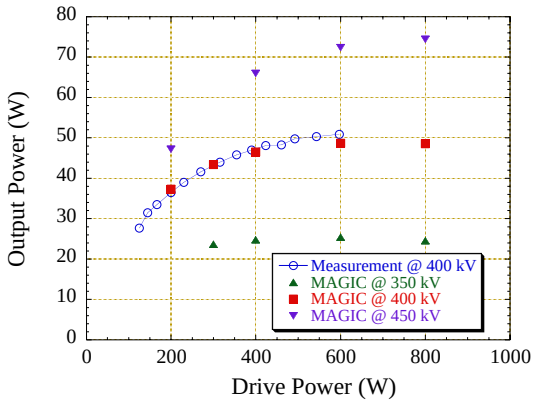

Figure 7: Simulations and measurement data of the output power vs. the input power for the SLAC XL-4 klystron.

Our simulation method can also make an accurate prediction of performance for a PPM klystron. Figure 8 shows the simulation results and the measured values of output power for the BINP PPM klystron. The evolution of DC and RF beam current as a function of distance from the gun is plotted in Fig. 9. The sudden drop of the DC current is due to the particle interception at the final cell of the output cavity. The interception is caused by lack of focusing for particles that drop to the stop-band voltage after losing energy to the traveling-wave. This simulation result explains the experimental observation of significant particle loss described in Section 1.

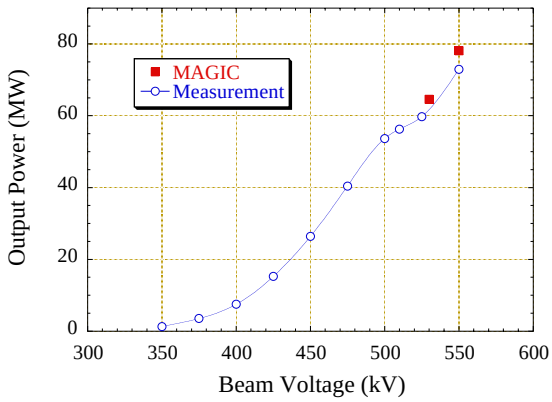

Figure 8: Simulation results for the BINP PPM klystron.

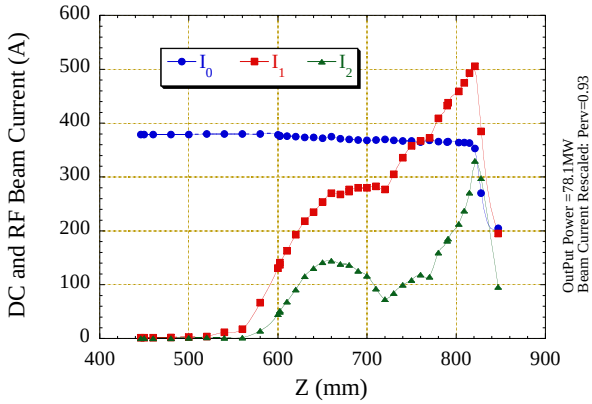

Figure 9: Evolution of the DC and RF beam current in the BINP PPM klystron.

3 XB72K NO.10 DESIGN

XB72K No.10 is the last solenoid-focused klystron in the XB72K series. Main changes from the previous XB72K klystrons are the buncher section and the TW output structure. The operational experience with the previous klystrons proved that the gun portion of XB72K has sufficient performance (1.2 microperveance at 2μs pulse length) and no interception of particles has been observed. The old buncher has two gain cavities and only one bunching cavity. It has a poor RF power generation capability: the RF current /DC current is only 1.2 at the entrance of the output structure. In XB72K No.10, one more bunching cavity was added and the drift space was lengthened to 16cm. The stagger tuning of gain cavities was also adopted to increase the band-width to the current specification of 100 MHz.

The most challenging part of XB72K No. 10 design is a high efficiency and low gradient TW output structure. MAGIC is quite useful for getting an accurate estimate of klystron performance, but the design of an effective TW structure is another matter. A systematic design method was needed to avoid getting lost in the freedom of too many parameters.

For this end, we have developed a simple-minded theory of a constant group/phase velocity TW structure. The idea

is to let the power flow with a constant group velocity throughout the structure, while evolving due to merge of the extracted power from a beam. The Q-value at the output port is matched to this group velocity so that the power exits at the same speed as it flows in the structure. This smooth flow of power prevents congestion at local spots and thus the electromagnetic energy density is more equally distributed in the structure

It is also better to keep the phase velocity constant (approximately equal to the average beam velocity) from the first to the last cell, rather than being matched with the declining beam velocity. When the perfect synchronization of traveling-wave and the beam is tried, the beam loses energy too quickly to the wave, and its velocity becomes too slow to be matched with the wave after a few cells (XB72K No. 10 has four cells). The beam then moves to the acceleration phase of the wave and starts to get energy back. The energy extraction efficiency of each cell does not have to be too good. Only the total efficiency of all cells matters. It is more important to keep the beam in the deceleration phase of the wave all the time. In our method, the traveling-wave travels behind the beam at first, and catches it up with in the middle of the structure. It then moves ahead of the beam, but exits from the output port before the beam slips into the acceleration phase of the wave.

We also demand that each cell is operated in $2/3\pi$ mode at 11.424 GHz. The cell length is also constant except the last cell (slightly longer to reduce the field gradient). As the result, the cells become almost identical. We then tapered up the iris aperture slightly to equalize the field gradient among the cells. In this method, once the group and the phase velocities are chosen, the geometry of the structure are almost uniquely determined. The structure of output port can be adjusted to control the reflection of power to maximize the output power.

The predicted output power vs. the beam voltage is plotted in Fig. 10:

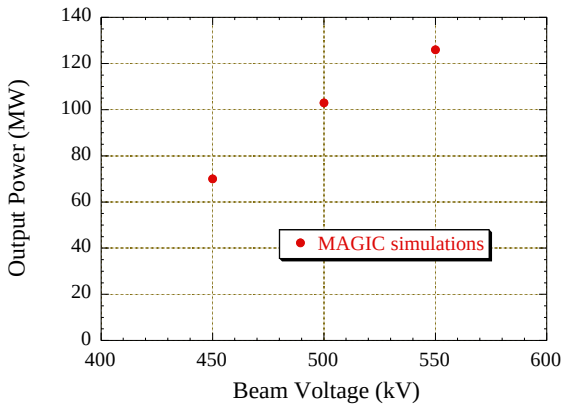

Figure 10: Predictedoutput power vs. beam voltage for the XB72K No.10.

The predicted performance is summarized in Table 4. Figure 11 shows comparison between XB72K No.10 and SLAC XL-4 for the saturated power vs. the maximum field gradient in the output structure. Both have similar efficiencies of about 48%, but the maximum gradient of XB72K No.10 is about 20% lower than that of XL-4, though the power is 67% larger. In XB72K No.10, the fairly constant gradient is achievedin the output structure. This comparison indicates that the XB72K TW output structure can attain 120 MW power at a longer pulse than XL-4 at 75 MW without cavity breakdown. At 75MW, XB72K can tolerate an even longer pulse. It is now in manufacturing and testing will begin in November 1998.

Table 4: Predicted performance of XB72K No. 10.

Peak output power	126 MW
Beam voltage	550 kV
Efficiency	48.5%
Maximum field gradient in TW	77 MV/m
Pulse length	1.5 μs or longer
Band-width	100 MHz
Gain	53 dB

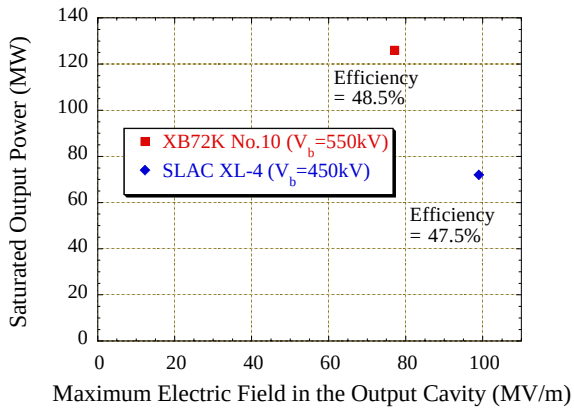

Figure 11: Saturated power versus the maximum field gradient in the output structure for XB72K No.10 and SLAC XL-4.

REFERENCES

[1] JLC Design Study, KEK, April 1997.

[2] Y. H. Chin, et. al., in Proc. of EPAC98, 1998.

[3] MAGIC User's Manual, Mission Research Corporation, MRC/WDC-R-409, 1997.

[4] Y. H. Chin, "User's Guide for ABCI Version 8.8", LBL-35258 and CERN SL/94-02 (AP (1994)..

[5] A. N. Sandalov, et. al., in Prof. of RF96, KEK Proc. 97-1, pp.185-194, 1997.

[6] B. Aimonetti, et. al., "CONDOR User's Guide", Livermore Computing Systems Document, 1988.

[7] W. B. Herrmannsfeldt, SLAC-PUB-6498 (1994).

[8] T. Shintake, Nucl. Instr. Methods A363, p.83, 1995.

[9] S. Michizono, S. Matsmoto, and H. Tsutsui in this proceedings.

[10] J. H. Billen and L. M. Young, "POISSON SUPERFISH", LA-UR-96-1834 (1997).

[11] D. Sprehn et.al, in Proc. of RF96, KEK Proc. 97-1. pp.81-90, 1997.

THEORY OF AN ELECTROSTATIC INSTABILITY DRIVEN BY TRANSVERSE-LONGITUDINAL TEMPERATURE ANISOTROPY IN SPACE CHARGE DOMINATED BEAMS *

S.M. Lund[a], D.A. Callahan[a], A. Friedman[a], D.P. Grote[a], I. Haber[b], and T.F. Wang[c]
[a] Lawrence Livermore National Laboratory, Livermore, CA 94550 USA
[b] Naval Research Laboratory, Washington, DC 20375, USA
[c] Los Alamos National Laboratory, Los Alamos, NM 87545, USA

Abstract

An unstable electrostatic mode has been observed in particle-in-cell simulations that, for unbunched ion beams with sufficient intensity and thermal anisotropy, transfers thermal energy from the transverse ($\perp$) to the longitudinal ($\|$) directions[1-4]. This instability can be important and appears to be insensitive to the details of the initial distribution as well as the nature of the applied focusing. The unstable mode is characterized by an axial wavelength comparable to the beam radius and growth rates comparable to the frequency of $\perp$ particle betatron oscillations. We present a theory of this instability based on the work of Wang and Smith[5]. This theory employs a continuous focusing model in the limit of strong thermal anisotropy with a warm, $\perp$ KV distribution and a cold, $\|$ distribution. The predicted mode structure is found to compare favorably with simulations carried out over a range of space-charge strength.

1 INTRODUCTION

In a continuous focusing (CF) channel, a thermal equilibrium (TE) beam distribution represents a stable, maximum entropy state that an arbitrary initial distribution will relax to under the influence of collisions[6]. Although collective processes and phase mixing can enhance the rate of relaxation, the beam lifetime in the machine is often insufficient to allow significant relaxation. Moreover, in real accelerators, the focusing is usually periodic, and in this situation there is no known TE distribution. Nevertheless, distributions that more closely resemble a CF TE distribution are expected to have less free energy to drive instabilities. This renders thermodynamic concepts like beam temperature useful for non TE distributions.

Although temperature is, strictly speaking, a thermodynamic quantity, one can define local kinetic temperatures (energy units) by $T_i/2 = \langle (p_i - \langle p_i \rangle)^2 \rangle / 2m = m v_{th,i}^2/2$, where m is the particle mass, p_i is the $i = x, y, z$ particle momentum, $v_{th,i}$ is the ith local thermal velocity component, and $\langle \cdots \rangle$ denotes an average over the momentum space degrees of freedom in the particle distribution. Here and henceforth, we have adopted a nonrelativistic model for simplicity in presentation. Differences in these kinetic temperatures (or equivalently momentum spreads) provide a measure of deviations from an isotropic TE, and such differences can provide free energy for so-called "equipartitioning" instabilities that drive the beam closer to TE[7].

$\perp$-$\|$ temperature anisotropies tend to naturally develop in accelerators[6,8]. For example, consider an ion diode with particle energy $\mathcal{E}_b$ (~ 50 keV typical) and source temperature T (~ 0.1 eV typical). In the absence of $\perp$-$\|$ coupling, one would expect the final axial (z-direction) temperature to be strongly cooled with $T_z = T^2/2\mathcal{E}_b$. On the other hand, one would expect little accelerative change in $\perp$ temperatures with $T_x = T_y \sim T$, consistent with any $\perp$ beam compression, $\perp$ instabilities, etc. These effects suggest a strongly anisotropic beam emerging from the diode. Further $\perp$-$\|$ anisotropy can develop in the transport following the diode. Neglecting $\perp$-$\|$ coupling, $T_z \tau \simeq const$, where τ is the beam pulse duration, and T_z will evolve consistently with any $\|$ beam expansion or compression during acceleration. Some change in T_z can also be caused by the thermalization of $\|$ space-charge waves launched by acceleration errors. On the other hand, nonlinear forces associated with focusing aberrations and nonuniform space charge (from instabilities, various beam manipulations, etc.), can lead to increased $\perp$ normalized beam emittance ($\propto r_b \sqrt{T_x}$, where r_b is the beam radius) while only producing small changes in T_z.

In high intensity applications such as Heavy-Ion Fusion (HIF), the need for a small focal spot radius r_s leads to interrelated constraints on the beam $\perp$ emittance, space-charge strength, and $\|$ momentum spread, as well as machine misalignments and abberations in the final focus optic[9]. For a final magnetic optic, dispersion results in a limit of allowable $\|$ momentum spread that can be estimated as $\Delta p/p < r_s/8\theta d$. Here $p = \langle p_z \rangle$ and $\Delta p = \sqrt{2\langle (p_z - p)^2 \rangle}$ are the axial momentum and momentum spread, d is the distance from the final optic to the focal spot, and θ is the beam convergence angle to the spot. This typically results in spread limits of less than $\Delta p/p \sim 1\%$. If the $\perp$ and $\|$ beam temperatures must remain similar, this will introduce an additional constraint that must be considered. Moreover, if any bends are present, dispersion can result in further momentum spread limits that $\perp$-$\|$ equilibration can influence[8].

In most accelerators, particle collision times are generally much longer than the beam lifetime in the machine. Hence collision induced equipartitioning is usually negligible. On the other hand, rapid kinetic instabilities can result in significant equipartitioning. Thus it is prudent to understand any such instabilities so they can be properly

* This research was performed under the auspices of the US DOE by LLNL, NRL, and LANL under contracts W-7405-ENG-48, DE-AI02-93ER40799, and DE-AI02-94ER54232.

accounted for in machine design.

In this paper, we present simulation (Sec. 2) and theory (Sec. 3) on an intense-beam collective mode that produces a rapid transfer of thermal energy from the $\perp$ to the $\parallel$ degrees of freedom for sufficient $\perp$-$\parallel$ thermal anisotropy. The beam is unbunched, and nonlinear space-charge forces associated with the unstable electrostatic mode produce this energy exchange rather than $\perp$-$\parallel$ coupling induced by the shape of the beam ends. For simplicity, all analysis is carried out for an axisymmetric ($\partial/\partial\theta = 0$) beam propagating without acceleration in a continuous focusing channel with a linear radial focusing force. This focusing arrangement can represent the average effects of a lattice of alternating gradient electric or magnetic quadrupoles, or a periodic solenoidal magnetic field for a beam with zero total canonical angular momentum[10].

2 PIC SIMULATIONS

Particle-in-cell (PIC) simulations were carried out with the electrostatic WARP code[2,8]. An axisymmetric (rz) package of the WARP code suite that neglects self-magnetic field effects was employed with periodic boundary conditions axially, and a grounded, perfectly conducting cylindrical beam pipe transversely. Simulations employed 100 k to 1 M particles, and typical grid dimensions consisted of 32 radial and 256 axial zones. When T_z was sufficiently cold, Gaussian smoothing was employed in the axial direction to suppress a $\parallel$ numerical grid instability. The initial $\perp$ distribution of beam particles had zero canonical angular momentum and was either KV [uniform density and a parabolically decreasing temperature profile in the radial coordinate $r = \sqrt{x^2 + y^2}$, see Ref. 6 and Sec. 3] or semi-Gaussian (SG) [uniform density and a uniform temperature Gaussian in $\perp$ momentum space]. The initial $\parallel$ distribution had uniform density and Gaussian momentum spread. The instability is seeded from noise associated with the finite particle statistics.

Typical runs employed: K^+ ion at $\mathcal{E}_b = \langle p_z \rangle^2/2m = 10$ MeV axial kinetic energy, equilibrium beam radius $r_b = 2.5$ cm, beam current $I = 5$ A, and conducting pipe radius $r_p \geq 2r_b = 5$ cm. The spatial average $\perp$ beam temperature $\hat{T}_x = \hat{T}_y = (2\pi \int_0^{r_b} dr\ r T_x\ )/\pi r_b^2$ was then consistently set as follows (in an rms equivalent beam sense[6] for an initial SG distribution). Denote the angular frequency of $\perp$ particle oscillations in the equilibrium fields in the absence (i.e., $I = 0$) and presence (specified I) of space charge by ν_0 and ν, respectively. Using the equilibrium envelope equation, these so-called "betatron" frequencies can be expressed as[10]

$$\begin{aligned} \nu_0^2 &= 4\hat{T}_x/mr_b^2 + \hat{\omega}_p^2/2, \\ \nu^2 &= \nu_0^2 - \hat{\omega}_p^2/2 = 4\hat{T}_x/mr_b^2, \end{aligned} \qquad (1)$$

where $\hat{\omega}_p$ is the beam plasma frequency. Then $\hat{T}_x$ was set to achieve a specified tune depression ν/ν_0 satisfying $0 \leq \nu/\nu_0 \leq 1$, where $\nu/\nu_0 \to 1$ and $\nu/\nu_0 \to 0$ correspond to the warm- and cold-beam limits, respectively. With $\hat{T}_x$ fixed, ν_0 (i.e., the external focusing) was then set consistently with Eq. (1). For $\nu/\nu_0 \sim 0.1$ to 0.4, these parameters are representative of those in the low energy end of linear induction accelerators for Heavy Ion Fusion[9]. The $\parallel$ temperature T_z was set as a fraction of $\hat{T}_x$. Axial grid lengths were chosen sufficiently short for the $\parallel$ variations of the unstable mode to be well resolved, but sufficiently long where 5 or more wavelengths of variation were simulated to reduce the influence of the periodic boundary conditions. This resulted in grid lengths of 10 to 25 cm. Timesteps for the particle advance were chosen such that $dt < 0.01/\nu_0$.

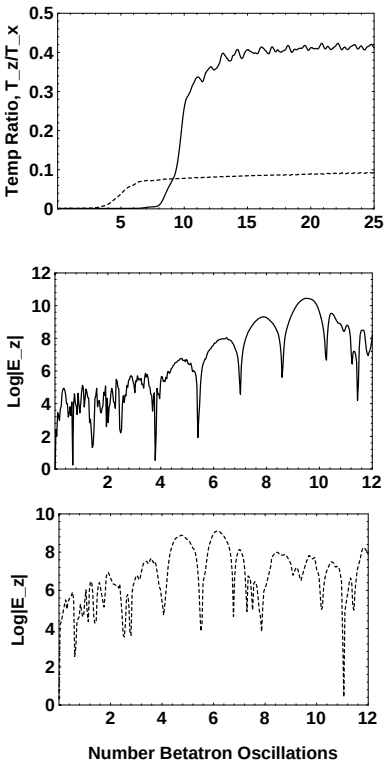

Figure 1: Temperature anisotropy $T_z/\hat{T}_x$ (top, SG and KV) and the log of the absolute value of the axial electric field $\ln|E_z|$ (middle for KV, and bottom for SG) verses the number of undepressed betatron oscillations $\nu_0 t/2\pi$.

Results of simulations illustrating properties of a space-charge mode that transfers thermal energy from the $\perp$ to the $\parallel$ directions are presented in Figs. 1 and 2. The simulations are for initial $\nu/\nu_0 = 0.45$, $T_z = 0.01\hat{T}_x$, a 13.4 cm axial beam length, and $r_p = 2r_b$. Results are shown for both initial KV (solid curves) and SG (dashed curves) $\perp$ distributions. In Fig. 1, the anisotropy ratio $T_z/\hat{T}_x$ is plotted as a function of the number of undepressed betatron oscillations of an equilibrium particle, $\nu_0 t/2\pi$, where t is the time. Evidently, in the initial quiescent period the growth in $T_z/\hat{T}_x$ starts from the noise, followed by a period of exponential growth, and then saturation with $T_z/\hat{T}_x \sim 0.4[0.1]$ (results given for initial KV with SG values in "[]" brackets). This instability leads to increased T_z and decreased $\hat{T}_x$ as energy is exchanged. Phase space plots of the mode have been presented elsewhere[3,4]. Also in Fig. 1, the log of the abso-

lute value of the axial electric field, $\ln|E_z|$, is plotted (arbitrary units) for a fixed location moving with the equilibrium beam as a function of $\nu_0 t/2\pi$. Little variation in structure is observed with the choice of location, suggesting an absolute instability. These plots suggest that a single unstable mode is dominating the evolution with an oscillation period and e-fold time of approximately 3.2[2.8] and 0.82[1.1] undepressed betatron oscillations, respectively. The radial and axial structure of the perturbed electrostatic potential $\delta\phi$ describing this mode was extracted with a discrete Fourier transform diagnostic. The dominant axial wavelength λ of $\delta\phi$ was well expressed with $\lambda/r_b = 1.3[1.1]$ and the radial mode structure of this harmonic component is shown in Fig. 2 for $\nu_0 t/2\pi = 9.2[3.9]$. Note that $\delta\phi$ is peaked at the center with one radial node within the beam ($r < r_b = 2.5$cm) and has small amplitude outside the beam ($r_b < r \leq r_p = 5$cm).

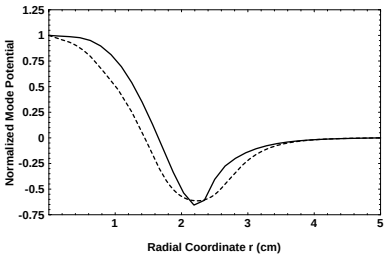

Figure 2: Normalized electrostatic potential of the unstable mode $\delta\phi/\delta\phi(r=0)$ verses radial coordinate r.

The simulations indicate that the essential features of this instability are similar for both initial KV and SG $\perp$ distributions. However, since the SG is not a real equilibrium, the lack of detailed radial force balance influences the initial evolution of the mode, complicating the interpretation of the onset of instability (note the shift in Fig. 1). Moreover, details of the saturation are different for the KV and SG $\perp$ distributions, with wave breaking in the KV distribution leading to a trapped particle phase-space that may represent an intermediate state on a longer timescale evolution. The KV and SG initializations also have differing numerical collision properties, further complicating interpretations. Preliminary data is presented in Table 1 on the space-charge threshold (ν/ν_0 less than indicated values leads to instability) and the saturation level (in $T_z/\hat{T}_x$) of the instability. Data is tabulated for both initial KV and SG $\perp$ distributions for several values of initial temperature anisotropy ($T_z/\hat{T}_x$). Note that the threshold is a strong function of the initial anisotropy and depends weakly on the type of initial distribution. Saturation occurs when T_z is a fraction of $\hat{T}_x$, with the value depending on the initial anisotropy, space-charge strength, and distribution type. Growth rates of the unstable mode are larger for strong initial anisotropy and space-charge strength. Smaller growth rates can render simulations difficult due to the noise associated with the finite particle statistics.

Finally, previous studies[1,4] suggest that the instability only transfers $\perp$ thermal energy to the $\parallel$ direction and not vice-versa when $T_z > \hat{T}_x$. Full 3D simulations have also been carried out with both alternating gradient and CF channels and the results are similar those presented here.

Table 1: Instability threshold and saturation properties.

Initial	Threshold ν/ν_0	
T_z/T_x	KV	SG
0.001	0.69	0.74
0.01	0.76	0.80
0.1	0.48	?

Initial	Saturated T_z/T_x for Initial KV and $\nu/\nu_0 =$				
T_z/T_x	0.4	0.5	0.6	0.7	0.8
0.001	0.55	0.18	0.04	—	—
0.01	0.59	0.31	0.07	0.09	—
0.1	0.42	—	—	—	—

Initial	Saturated T_z/T_x for Initial SG and $\nu/\nu_0 =$				
T_z/T_x	0.4	0.5	0.6	0.7	0.8
0.001	0.10	0.14	0.19	0.08	—
0.01	0.12	0.10	0.16	0.14	0.11

3 THEORY

Neglecting particle correlations and collisions, the beams simulated in Sec. 2 are described in terms of a single-particle distribution function f that is a function of the coordinate $\mathbf{x}$, momentum $\mathbf{p}$, and time t, and evolves according to the Vlasov equation

$$\left\{\frac{\partial}{\partial t} + \frac{\partial H}{\partial \mathbf{p}}\cdot\frac{\partial}{\partial \mathbf{x}} - \frac{\partial H}{\partial \mathbf{x}}\cdot\frac{\partial}{\partial \mathbf{p}}\right\} f(\mathbf{x},\mathbf{p},t) = 0. \qquad (2)$$

Here, $H = \mathbf{p}^2/2m + m\nu_0^2 r^2/2 + q\phi$ is the Hamiltonian, q is the particle charge, and ϕ satisfies the Poisson equation $\nabla^2\phi = 4\pi q\int d^3p\, f$ subject to the boundary condition $\phi(r = r_p) = const.$ To perform a conventional equilibrium/stability analysis, we expand

$$\begin{aligned} \phi &= \phi^0(r) + \delta\phi(r,\omega,k_z)e^{-i(\omega t - k_z z)}, \\ f &= f^0(\mathbf{x},\mathbf{p}) + \delta f(r,\mathbf{p},\omega,k_z)e^{-i(\omega t - k_z z)}, \end{aligned} \qquad (3)$$

where equilibrium quantities (superscript zero) correspond to $\partial/\partial t = 0$ solutions to Eq. (2) with $\delta\phi = 0 = \delta f$ and $\delta\phi$ and δf are normal mode perturbations with angular frequency ω and wavenumber $k_z = 2\pi/\lambda$. We assume a $\perp$ KV and $\parallel$ Gaussian f^0 defined by[6,10]

$$f^0 = \frac{\hat{n}}{2\pi m}\delta\left(H_\perp^0 - 2\hat{T}_x\right)\frac{\exp\left[-\frac{(p_z - m v_b)^2}{2mT_z}\right]}{(2\pi m T_z)^{1/2}}. \qquad (4)$$

Here, $v_b = \langle p_z\rangle/m$ is the axial beam velocity, $\delta(x)$ is the Dirac delta-function, and $H_\perp^0 = \mathbf{p}_\perp^2/2m + m\nu_0^2 r^2/2 + q\phi^0$ with $\mathbf{p}_\perp = p_x\hat{\mathbf{x}} + p_y\hat{\mathbf{y}}$. The form of f^0 is consistent with undepressed and depressed $\perp$ particle oscillations with frequencies ν_0 and ν given by Eq. (1) with $\hat{\omega}_p^2 = 4\pi q^2\hat{n}/m$ and beam edge radius r_b. For $0 \leq r < r_b$, Eq. (4) also corresponds to uniform density, $\int d^3p\, f^0 = \hat{n} = const$, and a parabolic $\perp$ temperature profile, $\int d^3p\, (\mathbf{p}_\perp^2/2m) f^0 = 2\hat{n}\hat{T}_x(1 - r^2/r_b^2)$.

The linear eigenvalue equation for the perturbed potential $\delta\phi$ can be derived by linearizing the Vlasov equation (2) and inverting the resulting equation for δf with the method of characteristics and inserting the result in Poisson's equation. After some algebraic manipulation, this results in

$$\left\{\frac{1}{r}\frac{\partial}{\partial r}r\frac{\partial}{\partial r}-k_z^2\right\}\delta\phi=\frac{\hat{\omega}_p^2 r_b}{4\hat{T}_x/m}\delta(r-r_b)\;[\delta\phi+\kappa_1]\big|_{p_\perp=0} + \hat{\omega}_p^2\Theta(r_b-r)\left[\frac{m^2}{p_\perp}\frac{\partial}{\partial p_\perp}\kappa_1+ik_z^2\kappa_2\right]\Bigg|_{p_\perp^2/2m=T_x}, \quad (5)$$

where $\Theta(x)$ is the Heaviside step-function, and κ_1 and κ_2 are equilibrium orbit integrals defined by

$$\kappa_1 = i\int\frac{d\psi}{2\pi}\int_{-\infty}^{0}d\tau\;\left(\Omega-i\frac{k_z^2T_z}{m}\tau\right) \times \delta\phi[\tilde{r}(\tau)]\exp\left[-\frac{k_z^2T_z}{2m}\tau^2-i\Omega\tau\right], \quad (6)$$

$$\kappa_2 = i\int\frac{d\psi}{2\pi}\int_{-\infty}^{0}d\tau\;\tau\delta\phi[\tilde{r}(\tau)]\;\exp\left[-\frac{k_z^2T_z}{2m}\tau^2-i\Omega\tau\right].$$

Here, $T_x\equiv 2\hat{T}_x(1-r^2/r_b^2)$, $\Omega\equiv\omega-k_zv_b$, and the equilibrium characteristics are defined by $\tilde{r}^2(\tau)\equiv r^2\cos^2(\nu\tau)+(rp_\perp/m\nu)\cos(\;\;)\sin(2\nu\tau)+(p_\perp/m\nu)^2\sin^2(\nu\tau)$.

Equation (5) is a difficult integro-differential equation that must be solved for Ω and $\delta\phi$ simultaneously. Wang and Smith[5] derived the dispersion relation corresponding to Eq. (5) in the limit of infinite thermal anisotropy ($T_z/\hat{T}_x\to 0$ by coupling together earlier transverse solutions ($T_z=0$ and $k_z=0$) by Gluckstern[11] for $k_z\neq 0$. In this procedure $\delta\phi$ is expanded within the beam ($0\le r\le r_b$) as

$$\delta\phi(r)=\delta\phi(r=r_b)+\sum_{n=1}^{\infty}A_n\delta\phi_n(r), \quad (7)$$

where $\delta\phi_n(r)=(1/2)[P_{n-1}(1-2r^2/r_b^2)+P_n(1-2r^2/r_b^2)]$ is an nth order $\perp$ Gluckstern eigenfunction, $P_n(x)$ is a nth order Legendre Polynomial, and $\delta\phi(r=r_b)$ is the potential at the beam edge (generally nonzero). The expansion coefficients A_n generally depend on k_z and Ω and satisfy recursion relations, which together with an interface ($r=r_b$) jump condition on $\delta\phi$, yields a dispersion relation expressible in terms of an infinite determinant.

Approximate numerical solutions to this dispersion relation can be found by truncating the series [$n<n_{max}$ in Eq. (7)] to obtain a finite determinant dispersion relation[5]. Solutions for $\Omega/\nu_0=(\omega-k_zr_b)/\nu_0$ are parameterized by ν/ν_0, k_zr_b, and r_b/r_p. The number of distinct mode branches found is $n_{max}(n_{max}+2)$ or $(n_{max}+1)^2$ for n_{max} even or odd. The branches are characterized according to their limiting properties. For $k_zr_b\to 0$, $n_{max}(n_{max}+1)$ branches corresponding to nth order $\perp$ Gluckstern modes[11] are found (labeled T_n) with $\delta\phi\propto\delta\phi_n$ for $r\le r_b$ and $\delta\phi=0$ for $r\ge r_b$. Properties of this $\perp$ limit dispersion relation have been described elsewhere[10,11]. For long wavelength perturbations with $k_zr_b\ll 1$ and $\hat{T}_x\to 0$ ($\nu\to 0$), a single branch (labeled L_1) corresponding to an "ordinary" cold-beam $\parallel$ mode is found. This limiting form mode has $\delta\phi\propto I_0(k_zr)$ for $r\le r_b$ with $I_0(x)$ a 0th order modified Bessel Function and $\Omega^2=(\hat{\omega}_p^2/2)(k_zr_b)^2\ln(r_p/r_b)$. Other branches (labeled L_n with $n=2,4,\cdots,n_{max}-1$ or n_{max}) are found to reduce for long wavelengths ($k_zr_b\ll 1$) and weak space-charge ($\nu\to\nu_0$) to a little known class of $\perp$ coupled $\parallel$ modes. These modes have $\delta\phi\propto\delta\phi_n$ within the beam and

$$\Omega^2=\frac{\hat{\omega}_p^2}{8n(n+1)}(k_zr_b)^2\int_0^{2\pi}\frac{dx}{2\pi}\;P_n(\cos x).$$

In general, a large n_{max} truncation will result a high-order polynomial dispersion relation with many branches; some of which describe low-order modes and others, high-order modes. One takes n_{max} sufficiently large to accurately represent modes of interest, but small enough to reduce the number of branches and facilitate mode identification. Instabilities arise in parameter regimes where two or more branches of Ω "collide" and coalesce. Unfortunately, many of these instabilities, particularly higher-order ones, are associated with unphysical features of the KV model[10]. Nevertheless, we believe that a low-order confluent branch where the T_2 and L_2 branches coalesce describes the instabilities observed in Sec. 2. This low-order T_2-L_2 confluent branch may also represent a non-pathological KV instability that persists for more realistic (non-singular) equilibrium distribution functions.

Comparisons between the confluent T_2-L_2 mode branch and simulations are presented in Figs. 3 and 4. All simulations were seeded from noise and it is assumed that a single unstable mode dominates the evolution. In the theory, an $n_{max}=4$ truncation was employed. In Fig. 3, the radial eigenfunction $\delta\phi$ of the T_2-L_2 mode (k_z selected for maximum growth rate) is compared with simulation and $\perp$ ($k_z\to 0$) theory for $\nu/\nu_0=0.45$ and $r_p/r_b=2$. Note that the T_2-L_2 has similar structure to the $\perp$ T_2 mode, but has finite amplitude at the beam edge ($r=r_b$) and is unstable, in contrast to the $\perp$ mode. Also in contrast to the $\perp$ T_2 mode, where $\delta\phi_2$ is independent of ω, the radial structure of $\delta\phi$ varies with Ω and k_z for the T_2-L_2 mode. In Fig. 4 the normalized axial wavenumber, oscillation frequency, and growth rate of the T_2-L_2 mode is compared to the simulation results over the range of space-charge strength $0.3\le\nu/\nu_0\le 0.5$. The theory curves were generated employing the wavenumber k_zr_b with maximum $\mathrm{Im}\,\Omega/\nu_0$ growth rate at specified ν/ν_0. The spreads about the simulation points indicate measurement uncertainties. For $\nu/\nu_0\ge 0.4$ the theory agrees reasonably well with the simulations outside of a slightly lower simulated growth rate that is likely due to the finite axial temperature employed in the simulations (initial $T_z<0.01\hat{T}_x$). For $\nu/\nu_0<0.4$, low-order KV instabilities of the T_2, T_3, and T_4 $\perp$ Gluckstern modes[10] may produce the systematic deviations observed from the results predicted by the T_2-L_2

branch. Extension into this strong space-charge regime will likely require systematic mode seeding to avoid exciting such unphysical $\perp$ KV instabilities. Approximate expressions for the mode density, temperature, and flow velocity perturbations have been derived from a fluid theory[10] (using the kinetic theory dispersion relation) for use in future mode seeding studies.

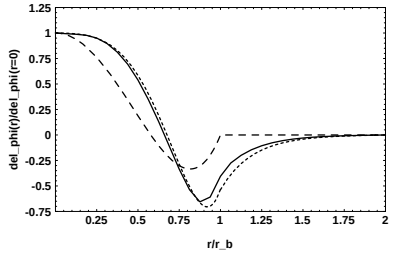

Figure 3: Eigenfunction comparisons for simulation (solid), 3D T_2-L_2 confluent mode theory (dotted), and $\perp$ T_2 mode theory (dashed).

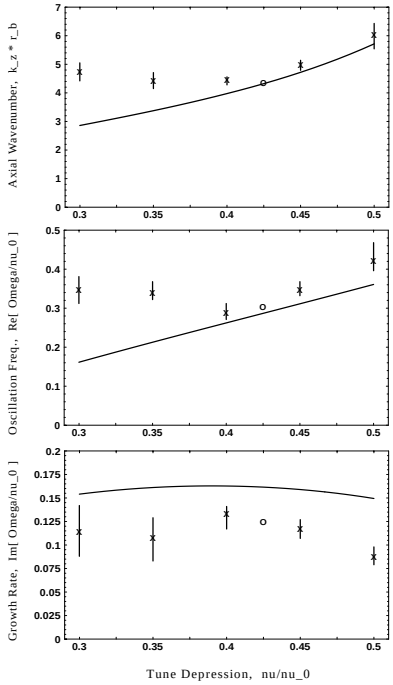

Figure 4: Normalized mode axial wavenumber ($k_z r_b$), oscillation frequency ($\mathrm{Re}\,\Omega/\nu_0$), and growth rate ($\mathrm{Im}\,\Omega/\nu_0$) verses tune depression (ν/ν_0) from theory and simulation.

4 CONCLUSIONS

Simulation and theory have been presented characterizing an electrostatic instability that can transfer thermal energy from the $\perp$ to the $\parallel$ directions for an intense, unbunched beam with sufficient thermal anisotropy ($T_z/\hat{T}_x < 1$). General features of this instability are insensitive to the specific form of the applied focusing and initial distribution, and therefore, a $\perp$ KV model was used to explore the idealized mode structure. The instability has short axial wavelength ($\lambda \sim r_b$) with growth rates and oscillation frequencies comparable to the depressed betatron frequency ($\mathrm{Re}\,\Omega \sim \mathrm{Im}\,\Omega \sim \nu$). The unstable mode has an anisotropy (initial value of $T_z/\hat{T}_x$) dependent threshold in space-charge strength (ν/ν_0) and saturates when the $\parallel$ temperature (T_z) is a fraction of the $\perp$ temperature ($\hat{T}_x$). Since $\parallel$ accelerative cooling and $\perp$ emittance increases can contribute to the anisotropy that drives the instability, the mode needs to be better understood to access impact on machine design. The energy exchange associated with the instability leads to decreased $\perp$ emittance with increased $\parallel$ momentum spread. Whether this effect is beneficial or harmful will depend on the details of a particular application. Possible consequences of the instability can be estimated by assuming that T_z remains saturated during transport at a set fraction of $\hat{T}_x$ if significant $\perp$-$\parallel$ anisotropy would have developed in the absence of the unstable mode. Equipartitioned design concepts have also been applied to bunched beams in rf linacs[12], where the $\perp$ and $\parallel$ focusing can be adjusted to maintain equilibration. Proper modeling this instability also has implications for simulations, since it requires the resolution of short axial wavelengths in simulations of long, "unbunched" beams.

ACKNOWLEDGMENTS

The authors wish to acknowledge useful conversations with J.J. Barnard, R.C. Davidson, and E.P. Lee.

5 REFERENCES

[1] A. Friedman, D.A. Callahan, D.P. Grote, A.B. Langdon, and I. Haber, "Studies of Equilibration Processes in Heavy-Ion Fusion Beams," Bull. Am. Phys. Soc. **35**(9), 2121 (1990).

[2] D.A. Callahan, "Simulations of Longitudinal Beam Dynamics of Space-Charge Dominated Beams for Heavy Ion Fusion," Ph.D. Thesis, University of California, Davis, 1994.

[3] I. Haber, D.A. Callahan, A. Friedman, D.P. Grote, and A.B. Langdon, J. Fusion Eng. Design **32**, 159 (1996).

[4] I. Haber, D.A. Callahan, A. Friedman, D.P. Grote, S.M. Lund, and T.-F. Wang, "Characteristics of an Electrostatic Instability Driven by Transverse-Longitudinal Temperature Anisotropy," Nuc. Inst. Meth., in press (1998).

[5] T.F. Wang and L. Smith, Part. Accel. **12**, 247 (1996).

[6] M. Reiser, *Theory and Design of Charged Particle Beams* (John Wiley, New York, 1994), and references therein.

[7] I. Hofmann, Phys. Rev. E **57**, 4713 (1998).

[8] S.M. Lund, J.J. Barnard, G.D. Craig, A. Friedman, D.P. Grote, H.S. Hopkins, T.C. Sangster, W.M. Sharp, S. Eylon, T.J. Fessenden, E. Henestroza, S. Yu, and I. Haber, "Numerical Simulation of Intense-Beam Experiments at LLNL and LBNL," Nuc. Inst. Meth., in press (1998).

[9] E.P. Lee, in *Heavy Ion Inertial Fusion*, M. Reiser, T. Godlove, and R. Bangerter, Eds. (American Institute of Physics, New York, NY, 1986; AIP Conference Proceedings **152**), p. 461.

[10] S.M. Lund and R.C. Davidson, "Warm-Fluid Description of Intense Beam Equilibrium and Electrostatic Stability Properties," Phys. Plasmas, in press (1998).

[11] R.L. Gluckstern, in *Proceedings of the 1970 Proton Linear Accelerator Conference*, Batavia, IL, edited by M.R. Tracy (National Accelerator Laboratory, Batavia, IL, 1971), p. 811.

[12] M. Reiser and N. Brown, Phys. Rev. Lett. **74**, 1111 (1995).

DECELERATING AND ACCELERATING RFQS

A.M. Lombardi
PS Division, CERN, 1211 Geneva 23, Switzerland

Abstract

This paper presents an overview of RFQ working principles, highlights the relevant parameters and summarises the different design approaches for the high, medium and low intensity cases. Attention is then focussed on the beam dynamics design in decelerating RFQs and, in particular, on how to cope with the intrinsic problems of deceleration (e.g. physical emittance increase and reduction of the longitudinal stable area). Fields of application for decelerating RFQs and their advantages with respect to conventional decelerating techniques will also be highlighted. The beam dynamics of the RFQD, the post decelerator for the CERN Antiproton Decelerator (AD) ring, will be presented in detail. This RFQ is intended to decelerate the 5.3 MeV antiproton beam coming from the AD down to an energy of virtually zero. Several decelerating schemes have been studied to fit the experimenters' need for a high quality beam with the final energy varying in the range 0 to 100 keV. Various potential solutions will be presented and discussed, with particular attention given to the intended approach.

1 INTRODUCTION

The idea of a Radio Frequency Quadrupole Accelerator (RFQ) was born in 1970 in Russia [1,2]. Its highlights are: an alternating-gradient velocity-independent focusing and a remarkable efficiency in bunching and accelerating a continuous low energy ion beam while preserving the transverse beam quality. The efficiency of an RFQ for injection into a Drift Tube Linac can reach values as high as 90% - making it extremely attractive when compared to the 50% attainable with standard quadrupoles-and-bunchers transfer lines. It has become the key machine for attaining high-current low-emittance beams. Nowadays there are more than 100 RFQ accelerators in operation, mainly as H+,H- and heavy ion injectors but also in medical facilities, material research and material production facilities. Recently the physicist community manifested an interest [3] in using an RFQ to post-decelerate a beam coming from a ring to energies of some ten keV. This could potentially broaden the range of application of such a machine, as the theoretical deceleration efficiency is one to two orders of magnitude higher than the more widespread degrader foil technique.

2 (ACCELERATING) RFQS

The RFQ is a linear accelerator that focuses, bunches, and accelerates a continuous beam of charged particles: all three functions are performed by the electrical radio-frequency (RF) field. The RFQ consists of a cylindrical cavity resonating in the TE21 mode with four electrodes placed along the direction of propagation of the beam, which present a longitudinal modulation. The four-fold symmetry provides an alternating focussing channel, and the longitudinal modulation produces a field in the direction of propagation, which bunches and accelerates the beam. A sketch of an RFQ is reported in Fig. 1, with characteristic parameters indicated. The ratio between the focusing and the acceleration, the bunching and accelerating rates and the synchronicity between the longitudinal field and the beam are determined by the geometry of the electrodes, i.e. the aperture, the modulation and the distance between peaks and troughs on the electrode surface. Once the electrodes are machined, the RFQ is a “one-button” machine, as only the power going into the cavity can be varied. This feature, while making the RFQ easy to operate, necessitates a rigorous design phase and has given rise to the development of powerful computer codes to simulate the beam dynamics [4].

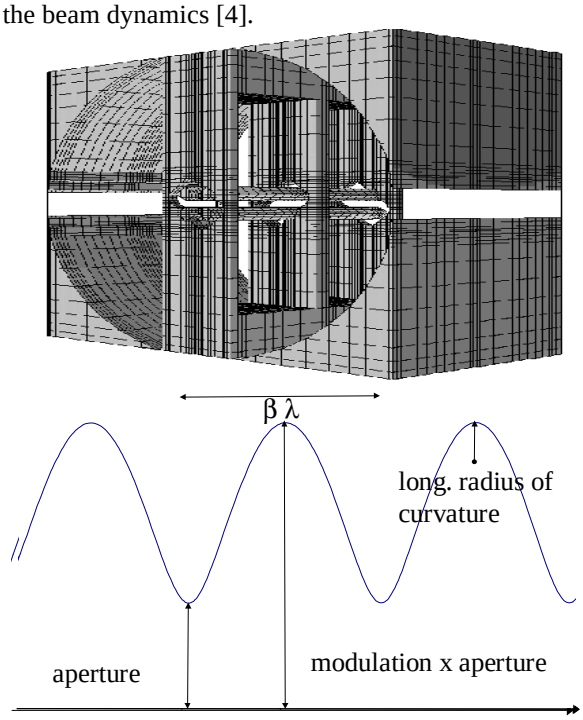

Figure 1: Sketch of an RFQ structure (top) and electrode microstructure (bottom).

2.1 Basic parameters and initial choices

For sake of completeness a list of the RFQ basic parameters [5,6,7] used throughout this paper is reported in the following.

- The focussing parameter:

$$B = \left(\frac{q}{m_0 f^2} \right) \left(\frac{V}{a^2} \right) \left(\frac{I_o(ka) + I_o(mka)}{m^2 I_o(ka) + I_o(mka)} \right)$$

linked to the phase advance per focussing period:

$$\sigma = \sqrt{\frac{B^2}{8\pi^2} - \frac{\pi q E_0 T \sin(\varphi)\lambda}{m_o c^2 \beta \gamma^3} - \frac{3 Z_0 q I \lambda^3 (1 - f(p))}{8\pi m_o c^2 \gamma^3 r^2 b}}$$

- The accelerating efficiency:

$$A = \frac{m^2 - 1}{m^2 I_o(ka) + I_o(mka)}$$

linked to the effective accelerating field:

$$E_0 T = AV\left(\frac{2}{\beta \cdot \lambda}\right)\frac{\pi}{4}$$

- The longitudinal radius of curvature

$$\rho_l = -\frac{A \cdot k \cdot r_o^2 \cdot I_1(mka) - 2 \cdot m \cdot a}{A k^2 r_o^2 I_o(mka)}$$

which determines the maximum dimension of the cutting tool.

In the above: *a*=bore radius, *b*=the average beam length, β,γ=relativistic parameters, *c*=speed of light, *f*= rf frequency, *I*=beam current, *I0,1*=zero,first order Bessel function, *k*=wave number, λ=wavelength, *m*=electrode modulation, *m0*=rest mass, *f(p)*= geometrical factor, *p*=ratio of the transverse beam dimensions, *q*=charge, *r*= average transverse beam dimension, *r0*=average bore, *V*=vane voltage, *Z0*=free-space impedance (376.73 Ohm).

There are several factors that influence the choice of the basic parameters of an RFQ and each RFQ is a "special" case.

The beam-dynamics quality factors are mainly the beam output quality (transverse and longitudinal emittance, intensity), the current limit and the sensitivity to input condition, mechanical alignment and to the RF field quality (flatness, frequency stability,..). Several other "external" factor can influence the RFQ design as e.g. budget, availability of RF power and frequency of the downstream accelerator. Additionally, the structure length is always an issue, not only because of cost but also because of machining and alignment concerns.

Frequency is a fundamental design consideration as it strongly influences the focussing power and the length of the RFQ. Due to the strong frequency dependence of the focussing parameter frequencies lower than 200 MHz are more indicated for ions or very-high-current proton beams while higher frequency (300-400MHz) are more suitable for protons.

The maximum field on the vane-tip (and the maximum voltage between the electrodes) influences the acceleration rate (and consequently the length of the RFQ) and the probability of breakdown. The Kilpatrick field [8] gives a guideline: values up to 2 Kilpatrick are commonly used for low-duty-cycle machines but require a careful surface cleaning and RF conditioning.

The minimum and maximum modulation, which define the minimum and maximum acceleration rate, are determined by machining limitation. For standard machining ρ*l* should be bigger than some 5 mm.

The phase advance per focussing period is a measure of the transverse stability [5] and it should be set at a value between 20 and 40 degrees.

2.2 Design recipes

Designing an RFQ co-ordinates three aspects: the mechanic design, the RF design and electrode profile design. The field pattern in the beam region is given by the electrode micro-structure; the beam dynamics depend mainly on the electrode design, which is the only aspect this paper deals with.

An RFQ is conceptually divided into four sections [9]: the Radial Matching Section (R.M.S.), the shaper, the gentle buncher, and the accelerator. In the R.M.S. (4-6 cells) the focussing parameter is tapered up to its final value in order to adapt the beam to a time-dependent focussing system. In the shaper the longitudinal field is slowly increased in order to form the beam longitudinal structure. The shaper determines the final value of the longitudinal emittance: a smooth shaping (over several cells, up to 20-40) guarantees a small output longitudinal emittance. In the gentle buncher the synchronous phase is adiabatically changed towards a stable accelerating phase, the beam is bunched and its energy gradually increased. The end of the gentle buncher, where the modulation is maximum and the aperture minimum, defines the transverse acceptance. Finally, in the accelerator the phase, aperture, and modulation are kept constant while the beam is brought to the final energy. An exit matching section can then be added to adapt the beam to the downstream user needs. The laws of change of the defining parameters (aperture, modulation and phase) determine the transition between the different sections in the RFQ. The smoother the transition the better the output beam quality but also the longer the RFQ.

A fundamental issue when choosing an RFQ design "recipe" arises from space charge effects. These are difficult to address in the design phase as they strongly couple the longitudinal and the transverse dynamics. As a consequence it is not possible to separate bunching and acceleration because the space-charge force increase, due to bunching, must be compensated by acceleration. This imposes an extremely smooth transition both between the

"shaping" and the "bunching" as well as between the "bunching" and the "acceleration". The result is that for the same beam energy increase the high-intensity RFQs turn out to be longer than the corresponding low-intensity one and that an emittance increase is unavoidable (due to bunching in the presence of space charge). During the design phase a careful trade-off between RFQ length and emittance increase has to be chosen. For low-intensity RFQs it is possible to have a fast pre-bunching section, and a boosting section (before acceleration) where the synchronous phase and modulation are varied very rapidly. Typical designs for a high and for a low intensity RFQ are shown in Fig. 2. Both these RFQs are currently operating at CERN and their nominal performances have been attained [10,11].

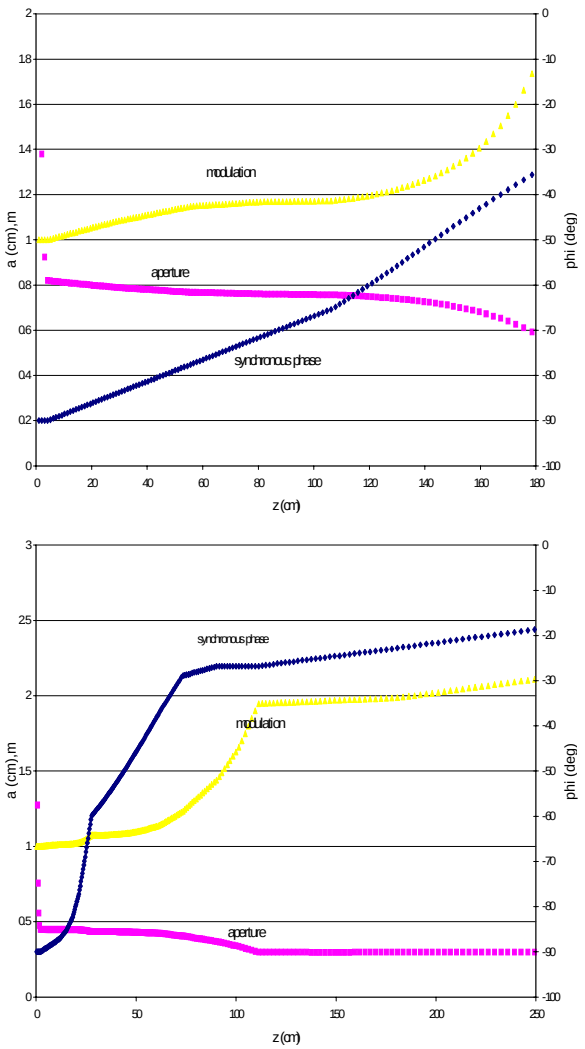

Figure 2: Evolution of modulation, aperture and synchronous phase along the axis for (top) CERN RFQ2 (200 mA protons, 90-750 keV, 200 MHz) and (bottom) for CERN LEAD ION RFQ (100 μA lead ions, 2.5-250 keV/u, 100 MHz)

3 DECELERATING RFQS

The concept of a decelerating RFQ is fundamentally different than that of a "reversed" accelerator. The main difference lies in the fact that the process of shaping and bunching the incoming beam can not just simply be done in reverse. This is not only for the inconvenience of generating an unreasonably long structure but also because of the fact that the longitudinal critical point (minimum bucket stable area) is located at the last cell of the machine. Therefore a completely different longitudinal approach needs to be applied to a decelerator RFQ.

3.1 Longitudinal dynamics and the need for a matcher

The stable motion in the longitudinal phase space in any linear accelerator can be described as an oscillation around the synchronous phase and energy along a characteristic pattern. Stable patterns lie within a separatrix [7]. In the case of an RFQ the maximum energy excursion of a particle moving along the separatrix can be expressed as:

$$\Delta W = \sqrt{2 \cdot W_s \cdot V \cdot A \cdot (\varphi_s \cdot \cos(\varphi_s) - \sin(\varphi_s))}$$

and the phase excursion (φ) follows

$$tg(\varphi_s) = \frac{\sin(\varphi) - \varphi}{1 - \cos(\varphi)}$$

where *W*s is the synchronous energy, and the rest has the same meaning as in Section 2.1

Due to the energy dependence, the stable area shrinks during the deceleration process and the separatrix of the last decelerating cell defines the acceptance of the machine. Hence the first design criterion for an RFQ decelerator is to maximise the expression above at the last cell by 1) choosing the highest vane voltage that the sparking limit allows and 2) keeping the accelerating factor (A) as high as machining limits allow. The phase should be kept as close as possible to -180°. This first criterion determines the vane voltage and the aperture and modulation of the last cell. The design of the RFQ starts then from the high-energy end: the modulation of the first cell is set to a high value (between 2 and 3) and the aperture to a value that gives the desired transverse phase advance per focussing period. From here the RFQ is generated cell-by-cell with the following procedure: with a fixed minimum acceptable longitudinal radius of curvature (ρ*l*), the maximum allowable modulation is chosen. The aperture is tentatively set to keep the focussing constant, although it can be changed to allow for a higher accelerating efficiency. With this method a rough design for the RFQ is generated. This is then

refined by tuning the parameters of each individual cell to optimise locally: 1) the transverse phase advance per focussing period; 2) the maximum field on the vane-tip, and; 3) the smoothing of abrupt changes in aperture and/or modulation.

Once the design of the decelerating part is complete, the next step is to determine the longitudinal matched condition: the separatrix at the last cell is traced backwards to the input of the RFQ. This assumes that the points of the boundary rotate counter-clockwise around the synchronous phase and synchronous energy with a cell-by-cell angular velocity given by the longitudinal phase advance. The backtracked stable area defines the "decelerating acceptance": only the particles falling in this area are successfully decelerated. It should be stressed that the decelerating acceptance is only a small fraction of the separatrix at the high-energy end and is not necessarily upright. The RFQ decelerator system therefore needs a front-end longitudinal matching section. This task can be accomplished by an adiabatic buncher system (for example a special shaping section of an RFQ) or by a discrete buncher system (conventional RF cavity). In general it is more convenient to use a discrete bunching system - the long RFQ cell length that goes with the high energy and the number of such cells typically required for smooth shaping would result in an unreasonably long machine.

The efficiency of an RFQ decelerator is determined by its front-end longitudinal matching system. The longitudinal output-beam quality depends instead on the decelerating rate at the lower energies: the faster the deceleration rate the better. This can be explained by the fact that the beam, towards the lower energies, gets closer and closer to the separatrix line and moves along an unstable path with the characteristic shape of a golf club (reversed in this case, see Fig. 3).

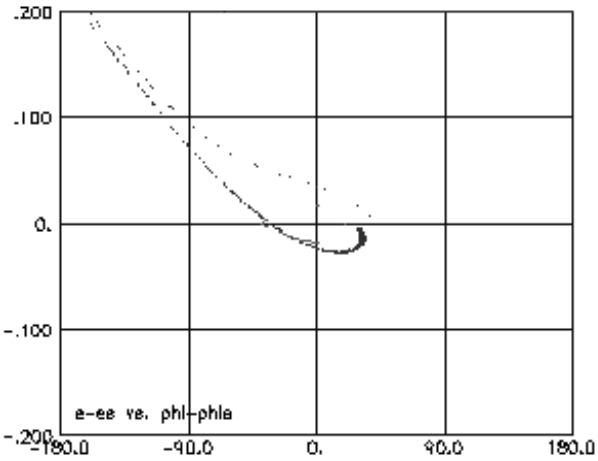

Figure 3: Characteristic path followed by particles at the boundary of the decelerating acceptance (stable particles have been removed from the plot for sake of clarity). PARMULT [4] simulation result.

3.2 Transverse dynamics

The transverse dynamics in a decelerator RFQ poses fewer problems than the longitudinal one as the process can be reversed. A standard R.M.S. can be employed at the beginning. The physical emittance increases during deceleration, and the focussing period is shortened proportionally to the beam velocity. The phase advance per focussing period (σt) is tentatively kept constant so that the beam envelope is constant along the decelerator. Conversely the divergence of the decelerated beam increases. In the critical points where σt can not be kept constant due to the more stringent longitudinal constraint, some extra cells are inserted to provide a smooth transition. This fix has been proved sufficient, in absence of space charge, for avoiding emittance increase due to mismatch.

Due to the strong beam divergence at low energy an exit matcher, to make the beam round as it exits the RFQ, facilitates the transport from the RFQ.

The RFQ is an effective focussing channel also for particles outside the longitudinal acceptance, which exit from the machine un-decelerated.

4 THE RFQD

The ASACUSA collaboration [3] is planning to use the antiproton beam coming from the CERN AD ring [12] for gas target and trap experiments. The 5.3 MeV beam coming from the ring should be post-decelerated with as-wide-as-possible energy variability around 50keV. The acceptable output energy spread is ±5 keV and the beam dimensions, a few mm.

4.1 Proposed decelerating schemes

The energy deceleration from 5.3 MeV to 50 keV is quite large: the longitudinal decelerating acceptance is 10 times smaller than the separatrix at the high energy. The possible frequencies (availability and expertise at CERN) are 200 or 100 MHz: 100 MHz makes the designing easier but would also result in an extremely long machine.

Optimisation following the criteria of Section 3 has led to the conclusion that, for a frequency of 200 MHz, the minimum energy attainable with acceptable beam quality is 50 keV. The decelerator length is about 4 meters; the equivalent structure at 100 MHz would be double this length, making it unattractive. A RF cavity performs the front-end longitudinal matching.

Some extra device must provide the energy variability, as the RFQ itself does not have this capability. Several set-ups have been considered [13], amongst which the most representative are:

- A 200 MHz RFQ decelerator to 80 keV followed by a double gap RF cavity. Energy variability: 30-130keV. The design of the double gap buncher is

quite challenging due to the poor efficiency for a 200 MHz cavity at low energies.

- Use two frequencies: a high-energy section (till 400 keV) at 200 MHz, a low-energy section at 100 MHz. Energy variability: 10-140,300-500 keV. This is the best-performing solution but requires a longer drift length between the pre-buncher and the RFQ.
- The RFQ tank would be divided in two sections independently powered and phased, the second one with flat electrodes. The first part of the RFQ would decelerate the antiproton down to 100 keV, the potential drop between the wall of the second cavity and the electrodes would provide energy variability in the range 80-120 keV.
- An RFQ decelerator to 60 keV, whose inner structure, mounted on a ceramic insulator, can be raised to a DC voltage of ± 60 keV. This solution gives energy variability in the range 10-110 keV with excellent beam quality for all the output energies.

The beam quality and the cost are comparable for all the solutions; the variation in the energy range, however, is quite different. The last solution was eventually chosen based on its simplicity and the advantage of bringing the beam to an energy of virtually zero. It will be described in more detail in the next section.

4.2 The chosen solution

Particles coming from the ring at 5.3 MeV and with an energy spread of 0.2% and an overall physical emittance of 10π mm mrad are bunched by a coaxial TEM resonator loaded with double gap with an effective voltage of 47 keV. The drift (6.15 m) to the RFQ contains magnetic elements to match the beam to the RFQ transverse acceptance. The voltage and the length of the drift are optimised to maximise the number of particles in the RFQ decelerating acceptance. The RFQ, a four-rod structure, is 3.44 m long and it decelerates the beam to 63 keV. The structure holding the electrodes can be raised to a potential (± 60 keV) to further accelerate/decelerate the beam as it exits the RFQ. A corrector cavity, identical to the one at the beginning of the line, placed at the RFQ entrance, counteracts the unwanted electrostatic effect at the input. This cavity can also correct for small variations in the input beam energy.

The normalised transverse emittance is constant along the RFQ, and 46% of the incoming particles are decelerated within ± 5 keV of the nominal energy. The RFQ defining parameters are given in Fig. 4.

5 ACKNOWLEDGEMENTS

I would like to acknowledge the constant guidance and support of the RFQ-section leader W. Pirkl, and the invaluable contributions of B. Couturier and F. Grandclaude.

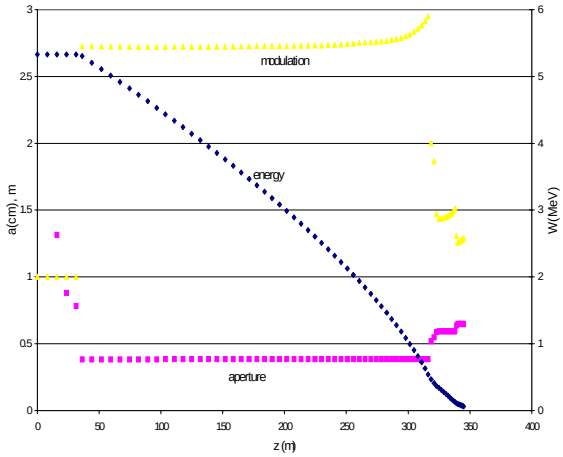

Figure 4: Modulation, aperture and synchronous energy along the decelerator RFQ

6 REFERENCES

[1] I. M. Kapchinskii and V. A. Teplvakov, Prib.Tekh. Eksp. No. 2, 19 (1970).

[2] I. M. Kapchinskii and V. A. Teplvakov, Prib.Tekh. Eksp. No. 4, 17 (1970).

[3] T. Azuma et al., "Atomic Spectroscopy And Collisions Using Slow Antiprotons," ASACUSA Collaboration, CERN/SPSC 97-19, CERN/SPSC P-307 (1997).

[4] K.R.Crandall, J.H.Billen, R.S.Mills, D.L.Schrage, R.H.Stokes, G.H.Neuschaefer, T.P.Wangler and L.M.Young,"RFQ design codes",LA-UR-96-1836.

[5] T.P.Wangler, "Space charge limits in linear accelerator", LA-8388 (Los Alamos).

[6] R.H.Stokes and T.P.Wangler, "Radio Frequency Quadrupole and their applications",*Annual Rev. of Nuclear and Particle Science* , 1989.

[7] M.Weiss, " Radio Frequency Quadrupole", CERN-PS/87-51, CAS Aarhus,(1986).

[8] W.D. Kilpatrick, "Criterion for Vacuum Sparking Designed to Include both rf and dc," *Rev. Scient. Instr.* **28** (10), 824-826 (1957).

[9] K.R. Crandall, R.H.Stokes and T.P.Wangler, " RF Quadrupole Beam dynamics Design study", Proceedings of LINAC79, Montauk, Sept. 10-14, 1979, 205-216 (1979).

[10] C.E. Hill, A.M. Lombardi, W. Pirkl, E. Tanke, M. Vretenar, "Performance of the CERN Linac2 with a High Intensity Proton RFQ" Proc. 1994 Linear Accelerator Conference, Tsukuba, 175-177, 1994.

[11] G. Bezzon et al. "Construction and commissioning of the RFQ for the CERN Lead-Ion Facility", Proc. 1994 Linear Accelerator Conference, Tsukuba, 722-724, 1994.

[12] S. Baird et al., "The Antiproton Decelerator: AD" CERN/PS 97-36 (HP), 1997

[13] W.Pirkl editor, "Feasibility Study Of A Decelerating Radio Frequency Quadrupole System For The Antiproton Decelerator AD", CERN/PS/HP Note 97-36 (1997).

A LOW-CHARGE-STATE CW RFQ

K. W. Shepard, M. Kedzie, and R. A. Kaye
Argonne National Laboratory, Argonne, Illinois 60439 USA

Abstract

A two-meter long, 12 MHz RFQ has operated cw at an intervane voltage above 100 kV, the voltage required to accelerate singly-charged ions of mass 132. The prototype unit is the first of three that will be required to provide for efficient injection of exotic beams into the existing ATLAS heavy-ion linac, while maintaining the high beam quality characteristic of ATLAS beams. The room-temperature, normal conducting RFQ utilizes indium gasketed joints, originally developed for the superconducting resonators of ATLAS, to maintain good vacuum, thermal, and rf properties while permitting a highly modular design. Another unusual feature of the design was the use of aluminum for the main structure, which was electroplated with 100 microns of silver to minimize rf losses in critical areas. Preparations are currently underway for beam tests to be performed later this year.

1 INTRODUCTION

The superconducting heavy-ion accelerator ATLAS can provide ion beams of any mass, including uranium, with state-of-the-art beam quality, particularly with respect to longitudinal emittance [1]. A related characteristic of ATLAS is very large transverse acceptance. Because of these characteristics, ATLAS is highly suitable for the task of accelerating radioactive ion beams [2,3]. ATLAS is presently injected by an electron cyclotron resonant (ECR) ion source capable of producing high charge-state ions, for example uranium 26+ [1]. For hard-to-produce exotic species, however, we require the use of more efficient ion sources, which produce singly-charged ions. For such charge states obtaining sufficient transverse focussing to maintain good beam quality becomes problematic, particularly for the heavier ions. Adapting ATLAS to radioactive beams requires development of a low-charge-state injector capable of maintaining the good features of ATLAS. The design of the entire injector system has been discussed elsewhere [2,3]. This paper discusses the design and development of the entrance section [4].

For heavy ions of charge state 1+ and energies of a few hundred keV, an electric quadrupole provides the strongest possible transverse focusing, and thus the greatest possible transverse acceptance. This consideration dictates the choice of an RFQ structure for the entrance section. The primary technical challenge arises from the requirement of maintaining substantially smaller longitudinal emittance than is typical for an RFQ.

Table 1: RFQ Design Parameters

Parameter	Value
Frequency	12.125 MHz
Structure	Split-coaxial
Voltage (vane-vane)	100 kV
Peak Electric Field	12.8 MV/m
Minimum Aperture	8 mm radius
Modulation Factor	1.5
Benchmark Beam	$^{132}Sn^{1+}$
Entrance Energy	378 keV
Exit Energy	1508 keV
Number of cells	44
Length	222 cm
Synchronous phase	-30 degrees

2 DESIGN FEATURES AND PARAMETERS

The RFQ design parameters are shown in Table 1. These parameters provide for our initial development goal of producing high-quality beams of singly-charged ions as heavy as mass 132. Ions of less mass can then be accommodated by turning down the RFQ operating voltage.

The split-coaxial geometry was chosen since it has already been shown to be suitable for very low frequencies [5], and to maximize the aperture of the device, we want the RFQ to operate at as low a frequency as practicable. In this way we both maximize the transverse acceptance and also minimize longitudinal emittance growth.

The primary reason we chose to inject the RFQ with a pre-bunched beam was to maintain a smaller longitudinal emittance than results from bunching within the RFQ

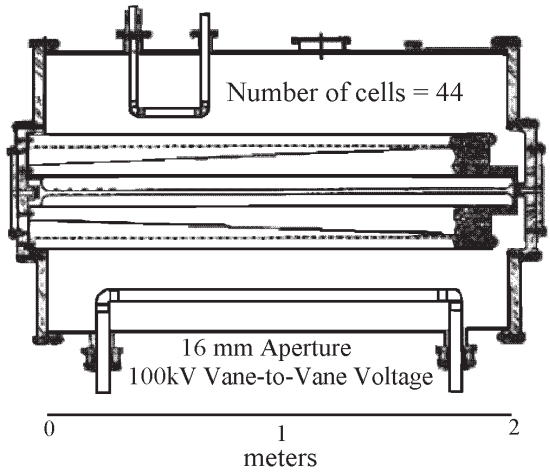

Figure 1: Section of 12 MHz split-coaxial RFQ

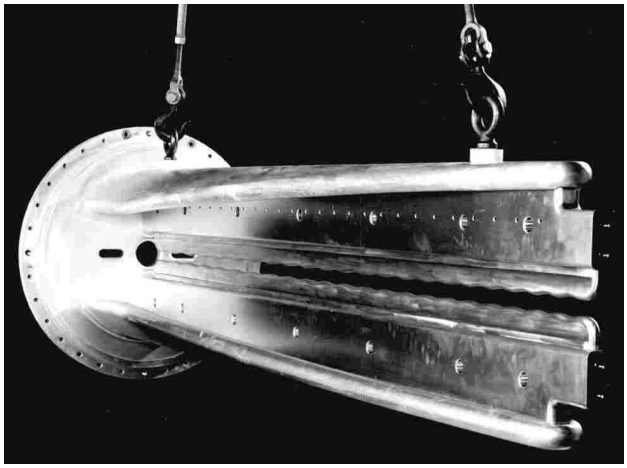

Figure 2: Two-meter long vertical vane pair.

structure [6]. There are several additional benefits from pre-bunching. By separating out the bunching function, the entire length of the RFQ can be used for acceleration, providing more voltage gain. A less obvious benefit results from the fact that the split-coaxial structure is characterized by a voltage offset at entrance and exit of half the vane-vane voltage. With a pre-bunched beam, we are able to make use of the voltage offset by attaching a drift tube to the high-voltage vane pair at both the entrance and the exit of the RFQ. The two drift tubes provide appreciable accelerating field, and increase the voltage gain through the structure by more than 20%.

3 MECHANICAL CONSTRUCTION

Figure 1 shows a section of the cavity. The structure is fabricated as several elements which are demountably joined using an indium-gasket seal described in more detail below. All elements are of 6061 aluminum, except for the RFQ vane tips which are formed of copper. Assembling the cavity from several elements greatly simplifies the machining and forming of the structure. Mechanical tolerances are effectively relaxed, since the structure can be assembled and examined, then disassembled and critical surfaces re-machined to correct mechanical misalignments or errors in rf tuning or field distribution.

A major sub-assembly, the vertical vane pair, is shown in Figure 2. The two-meter long vanes are cantilevered from the end flange which mounts at one end of the cylindrical outer housing. The low density of aluminum permits massive, monolithic structural elements providing good thermal and mechanical stability, while keeping mechanical resonant modes at high frequency. This helps minimize the effects of ambient vibration on the rf eigenfrequency.

Using a demountable joint to attach the vane tips provides several advantages. It is relatively inexpensive to completely replace the vane tips, and by so doing modify virtually any RFQ beam parameter. Also, we can then use copper in the high electric field region of the cavity, where the use of aluminum would possibly increase sparking and reduce the maximum attainable voltage.

Aluminum is appreciably inferior to copper or silver as an rf conductor. To reduce rf losses, those areas of the RFQ supporting high rf currents were electroplated with a 100 micron thick layer of silver.

3.1 Demountable Indium Gasket Joint

The demountable joint used was developed more than two decades ago: several thousand such seals have been used in the superconducting cavities and cryogenic plumbing of the ATLAS accelerator. The design has been found to provide a highly reliable seal with good vacuum and thermal properties. The rf losses in metal to metal joints formed in this way are known to be small from direct measurement in superconducting cavities.

A section of a typical gasketed joint is shown in Figure 3. The gasket is 1.6 mm diameter, high-purity indium wire. One surface of the joint is planar. The opposing surface is grooved to hold the indium wire, the groove having a cross-sectional area typically 65% of the wire cross-section. A key feature of the seal design is that the region to either side of the indium groove is relieved. The relief provides that when the mating surfaces are clamped together, excess indium is extruded into the relief volume. In this way, the compressed area is well-defined and limited in size. The loading on the seal is uniform, and the flow of indium when the seal is made up proceeds rapidly, with a short relaxation time.

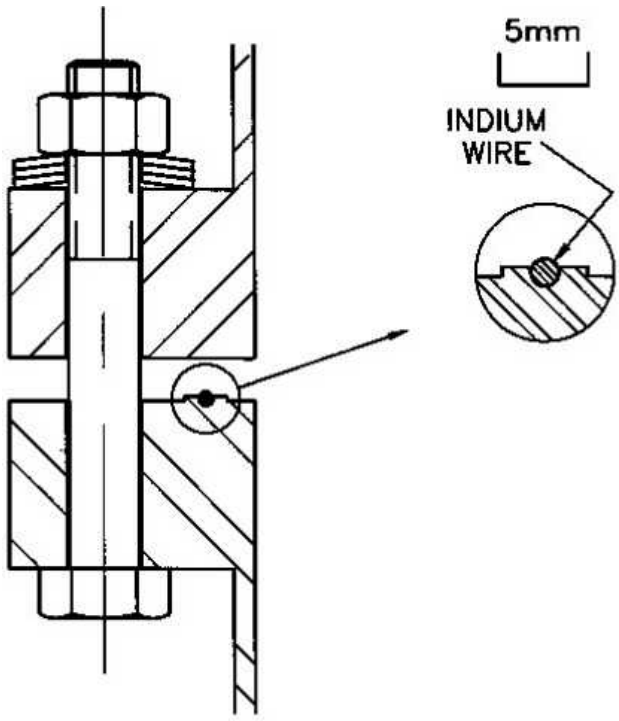

Figure 3: Details of the indium gasket seal used to make a joint with good RF, thermal, and vacuum characteristics.

4 EXPERIMENTAL RESULTS AND DISCUSSION

Optical measurements following initial assembly indicate that the errors in transverse position of the vane tips are everywhere less than 0.8 mm and the rms error is 0.5 mm. Note that the mean aperture is 20 mm, as is the vane thickness. The observed level of error is expected to be tolerable both for tuning and for the beam interaction. The definitive test, however, will be the planned measurements with beam.

When assembled, the rf eigenfrequency was found to be 11.6 MHz. The loop-coupled tuner can bring the frequency up to 11.9 MHz, still slightly below the design value of 12.125 MHz. For initial testing, and even testing with beam, this discrepancy is of no consequence. For eventual use with the ATLAS linac, a slight change in the vane tips will be required to tune to the design frequency.

The measured intrinsic Q of the RFQ resonant cavity is 8863, a result that indicates the rf losses to be appreciably less than were expected from earlier tests of a (nominally) half-scale model [4]. This result implies that the rf loss properties of the silver plating are excellent, as is discussed further below. To operate at a vane to vane voltage of 100 kV, the RFQ requires 16.6 kW of rf input.

Because of the high Q, the 3 dB bandwidth is slightly more than 1 kHz. In designing the RFQ, there was some concern that the effects of ambient acoustic noise might induce troublesome fluctuations in the rf eigenfrequency. Measured microphonic frequency jitter was less than 100 Hz peak to peak, a small fraction of the intrinsic bandwidth and too small to present any operational problems.

Water cooling to the cavity was configured in nine separate loops to enable calorimetric measurement of the detailed distribution of rf power. The distribution, shown in Table 2, was determined by measuring the flow rate and temperature rise (typically 2 C) in each loop separately. The summed total of calorimetric power agrees quite well with the measured rf input power of 17.4 kW. Of particular interest is the fact that one vane exhibits 40% higher rf loss than the other three. This result indicates the critical nature of the plating process in obtaining good rf performance.

Table 2: Calorimetrically measured RF heating

RFQ Element	Calorimetric Power
Top Vane	2.75 kW
Right Vane	2.72 kW
Bottom Vane	2.86 kW
Left Vane	3.90 kW
Entrance End Flange	1.40 kW
Exit End Flange	1.61 kW
Housing	2.19 kW
Drive Loop	0.07 kW
Tuner Loop	0.87 kW
TOTAL	18.37 kW

The cavity vacuum is maintained by two 500 l/sec turbopumps. With no baking, the vacuum in the cavity reached $6.4 \cdot 10^{-7}$ torr in 72 hours. On initial application of rf power, sparking was first encountered at a vane-vane voltage of approximately 60 kV and the input power was limited by outgassing. The cavity quickly conditioned up in voltage. After a few hours of conditioning the vacuum outgassing diminished and the RFQ could be operated above 100 kV. During initial tests, the RFQ was operated continuously for some 90 minutes with the vane voltage between 100 and 108 kV and vacuum in the low 10^{-6} torr range. Thermal stability of the RFQ during these tests was excellent.

In the design phase, the performance of the RFQ was projected using the Kilpatrick model. Figure 4 shows the frequency and gap dependent voltage limit (parallel-plate) as originally put forward by Kilpatrick [7]. It should be noted that the often quoted value for the Kilpatrick limit is the asymptotic limit for large gaps from the model shown in Figure 4. For most RFQ implementations, the frequency is sufficiently high that typical vane spacing is in the asymptotic region, where the gap dependence of the voltage limit can be ignored. As we have shown both in the earlier in the half-scale model pulsed rf tests [4] and also in the present 12 MHz cw result, the gap dependence is important in establishing the voltage limits for very low frequency RFQ's.

5 CONCLUSIONS AND FUTURE PLANS

The basic design concepts, i.e., indium rf joints, silver-plated aluminum rf surfaces, demountable copper tips, etc. have proven feasible as evidenced by the voltages achieved in initial tests of the low-charge-state RFQ.

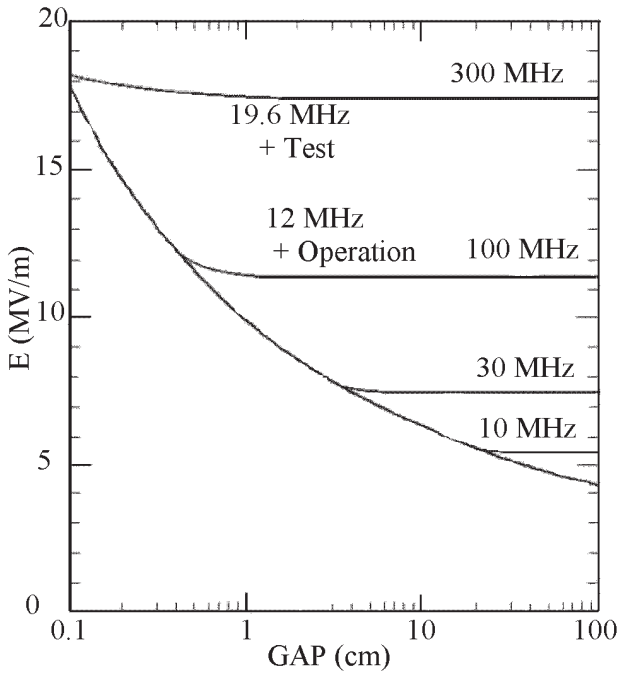

Figure 4: Sparking electric field limits in the Kilpatrick model, including electrode gap dependence.

The vane voltages achieved are sufficient to permit high-quality beams as heavy as uranium to be injected into ATLAS. Although our initial design was for Sn^{132} beam with a transverse acceptance of 0.25 π·mm-mrad, numerical simulation indicates that acceleration of uranium with a transverse acceptance of 0.16 π·mm-mrad while maintaining longitudinal emittance of a few keV-nsec is possible with the voltages achieved.

A remaining development task is demonstration of the expected transverse acceptance and longitudinal beam quality by beam tests. Preparation for such tests are currently underway.

6 ACKNOWLEDGEMENTS

The authors gratefully acknowledge the help of John Vincent in design of the 25 kW drive amplifier. Many helpful discussions of RFQ design were held with Rolf Muller, John Staples, and Alvin Schempp.

We are indebted to Pete Smith of Norbet Plating, Chicago for electroplating the silver films that exhibited such excellent properties. Also, Ed Bonnema and others at Meyer Tool and Manufacturing were most helpful in fabrication of the prototype.

This work was supported by the U. S. Department of Energy, Nuclear Physics Division, under contract number W-31-109-ENG-38.

7 REFERENCES

[1] R. C. Pardo, et al., in the Proc. 1992 Linear Accelerator Conference, August 24-28, Ottawa, Ontario, AECL-10728, p70 (1992).

[2] J. A. Nolen, in the Proc. 1995 IEEE Particle Accelerator Conference, May 1-5, Dallas, Texas, 95CH35843, p354 (1996)

[3] K. W. Shepard and J. W. Kim, in the Proc. 1995 IEEE Particle Accelerator Conference, May 1-5, Dallas, Texas, 95CH35843, p1128 (1996).

[4] K. W. Shepard and W. C. Sellyey, in the Proceedings of the 1996 Linear Accelerator Conference, 26-30 August, Geneva, Switzerland, p68 (1996).

[5] R. W. Muller, GSI Report GSI-90-25-ISSN 0171-4546, (1990).

[6] F. J. Lynch, R. N. Lewis, L. M. Bollinger, W. Henning, and O. D. Despe, Nucl. Instr. and Meth. **159**, p245 (1979).

[7] W. D. Kilpatrick, Rev. Sci. Instr. **28**, p824 (1957).

DESIGN OF THE 200-MEV PROTON LINAC FOR THE JAPAN HADRON FACILITY

T. Kato and Y. Yamazaki
KEK, High Energy Accelerator Research Organization
1-1 Oho, Tsukuba-shi, Ibaraki-ken, 305-0801, Japan

Abstract

A 200-MeV proton linear accelerator for the JHF has been designed [1][2]. A peak current of 30 mA with a 500 μsec pulse duration will be accelerated at a repetition rate of 25 Hz. The designed average current will be 200 μA at the beginning, and nearly 1 mA in the future. The linac consists of a 3-MeV radio-frequency quadrupole linac (RFQ), a 50-MeV drift tube linac (DTL) and a 200-MeV separated-type drift tube linac (SDTL) [3]. A frequency of 324 MHz has been chosen for all of the rf structures. A future upgrade plan of up to 400 MeV is also being considered, in which annular-coupled structures (ACS) of 972 MHz are to be used over an energy range of above 150 or 200 MeV. The balanced beam quality in both the transverse and longitudinal motions is one of the main features of the design. It can be achieved both by using an equipartitioning focusing scheme and by adopting an SDTL structure for the medium-energy range.

1 REQUIREMENTS

The required main parameters for the JHF proton linac are listed in Table 1. The construction plan of the linac consists of two stages. An output energy of 200 MeV and a peak current of 30 mA with a pulse length of 500 μsec at a repetition rate of 25 Hz are required in the first stage of construction. The required momentum spread of the output beam is ±0.1%. In order to reduce any beam losses after injection into the ring and to achieve high-intensity operation in the ring, a fast beam chopper in the low-energy region is required. It is crucial for the fast chopping system that the fraction of particles during the rising and falling times of the chopping pulse is very small.

Tabel 1: Required main parameters of the linac

1-1 Oho, Tsukuba-shi, Ibaraki-ken, 305-0801, Japan	Initial stage	Final stage	
Particles	H^-	H^-	
Output energy	200	400	MeV
Peak current	30	60	mA
Beam width	500	500	μsec
Repetition rate	25	50	Hz
Average current	200	800	μA
Length	< 150	~ 220	m
Momentum spread	±0.1	±0.1	%

2 DESIGN OF THE LINAC

2.1 Design features

The design is summarized in Table 2. The features of the design are as follows: (1) a frequency of 324 MHz has been chosen for all of the rf structures up to 200 MeV, resulting in no longitudinal transition; (2) an SDTL has been chosen in the energy range from 50 to 200 MeV, resulting in a higher effective shunt impedance and a separation of the transverse transition at 50 MeV from the longitudinal one at 200 MeV; (3) a 3-MeV RFQ has been chosen, resulting in the adoption of quadrupole magnets for the following DTL with sufficient focusing forces; (4) a transition energy of 150 or 200 MeV from the SDTL to the ACS has been selected in the upgrade plan; (5) the equipartitioning focusing method is applied; and (6) klystrons are used for all of the accelerating structures.

2.2 Ion source and RFQ

A promising experimental result (a peak injection current of 13.2 mA with a 90% emittance of 0.55 πmm-mrad was accelerated in the RFQ with a transmission efficiency of 83%) was achieved in the preinjector system

Table 2: Parameters of the JHF 200-MeV proton linac (DTL and SDTL).

	DTL	SDTL	
Frequency	324	324	MHz
Injection energy	3.0	50.3	MeV
Output energy	50.3	200.2	MeV
Length (structure only)	26.7	65.6	m
Length (including drift space)	27.1	91.1	m
Number of tank	3	31	
Number of klystron	3	14	
Rf driving power	3.3	16.6	MW
Total rf power (30 mA)	4.7	21.1	MW
Total length		119.1	m
Total power (30 mA)		25.8	MW
Peak current		30	mA
Beam width		500	μsec
Repetition rate		25	Hz
Average current		200	μA
chopping ratio		~0.56	

Table 3: Parameters of the DTL.

Tank number	1	2	3	
Output energy	19.7	36.7	50.3	MeV
Length	9.9	9.4	7.3	m
Number of cell	76	43	27	
Rf driving power	1.06	1.17	1.06	MW
Total rf power (30 mA)	1.56	1.68	1.47	MW
Accelerating field	2.5	2.7	2.9	MV/m
Stable phase	-30	-26	-26	degree
Bore diameter	13	22	26	mm

(a volume production negative-hydrogen ion source and a 432-MHz RFQ) at KEK [4]. Therefore, a peak current of more than 30 mA from the ion source will be realized if some increases in the transverse emittance are allowed. A four-vane type 324-MHz RFQ has been designed [5]. It accelerates ions from 50 keV to 3 MeV. The detailed design is under development.

2.3 DTL

A 324-MHz DTL accelerates beams from 3 to 50 MeV. It consists of three post-stabilized tanks [6]. An accelerating field of 2.5 MV/m is determined from the viewpoints of satisfying the equipartitioning condition and being sufficiently low for avoiding any discharge problem. All drift tubes contain quadrupole magnets. Model magnets of the hollow-conductor type with a magnetic-field gradient of 117 T/m were designed and successfully fabricated [7]. The parameters of the DTL are listed in Table 3.

2.4 SDTL

A 324-MHz SDTL is adopted for medium-energy acceleration from 50 to 200 MeV. Each tank consists of five unit cells. Since the focusing magnets (doublet) are placed between two adjacent SDTL tanks, the shunt impedance can be freely optimized without any geometrical restriction from the quadrupole magnets, which are placed in the drift tubes in the conventional DTL system. There are many other advantages in the SDTL system: the number of required focusing magnets has been reduced, fabrication of drift tubes has become easier, stabilizing devices are not necessary, and the required alignment accuracy of the drift tubes and each tank has been reduced. The parameters of the SDTL are listed in Table 4.

2.5 ACS

An extensive beam-dynamics calculation regarding an upgrade of the output energy up to 400 MeV by using the CCL-type structure was performed [1]. It was concluded that an accelerator complex of DTL, SDTL and the ACS is a good choice from the viewpoints of both the output

Table 4: Parameters of the SDTL.

Length of unit tank	1.48 - 2.61	m
Number of tank	31	
Number of cell	155	
Rf driving power	0.34 - 0.71	MW
Total rf power (30 mA)	0.46 - 0.86	MW
Accelerating field	3.75	MV/m
Stable phase	-26	degree
Bore diameter	30	mm

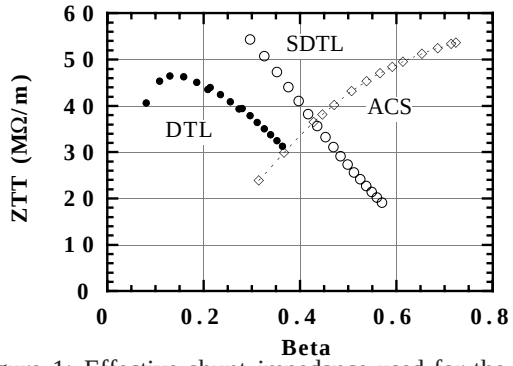

Figure 1: Effective shunt impedance used for the JHF proton linac.

beam quality and the accelerating efficiency. Also, it was pointed out that the ACS has more balanced characteristics concerning both the shunt impedance and the field symmetry [8]. A frequency of 972 MHz, three-times as high as the fundamental frequency, and a transition energy of above 150 or 200 MeV were selected. The fundamental RF issues concerning the ACS have already been solved, and a number of high-power RF tests using the 1296-MHz prototype cavities were successfully performed [9]. Therefore, a future extension using a 972-MHz ACS will be possible with some modification efforts.

The effective shunt impedance for the three kinds of rf structures mentioned above is plotted in Fig. 1.

3 BEAM DYNAMICS

A beam simulation was performed using the code LINSAC [10]: the code includes an accurate field distribution in an accelerating gap, and takes into account any space-charge effects by the particle-particle method. It includes all space harmonics into the calculation. Both the emittance growth and halo formation during acceleration were carefully studied, since they are one of the main issues in designing the high-intensity JHF proton linac.

3.1 DTL and SDTL

Both the transverse and longitudinal focusing parameters were determined based on equipartitioning theory combined with coupled envelope equations for the bunched beam [11][12][13]. The equipartitioning condition is approximately satisfied during acceleration in the design. Figure 2 shows both the transverse and longitudinal phase

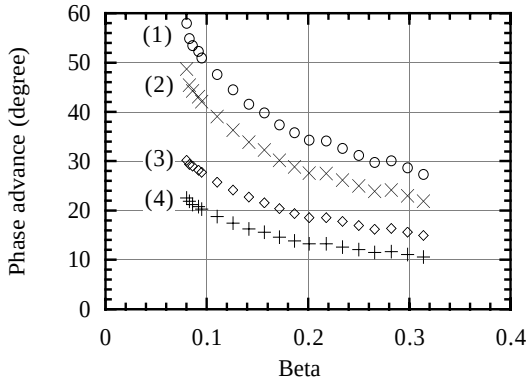

Figure 2: Phase advance in both the transverse ((1) 0 mA and (2) 30 mA) and longitudinal ((3) 0 mA and (4) 30 mA) phase spaces along the DTL vs. beta (v/c).

advances in the DTL. Two sets of normalized rms emittances at the entrance of the DTL were used in the simulation through the DTL and the SDTL (Type A: 0.187 πmm-mrad and 0.133 πMeV-deg and Type B: 0.375 πmm-mrad and 0.266 πMeV-deg). Compared with the transverse-focusing design with a constant phase advance of 60 degrees, the calculated results with the equipartitioning focusing design show better beam qualities totally, especially in both the emittance growth and halo formation in longitudinal phase space [2]. For the type-A beam, the ratios of the emittance growth between two focusing methods (the equipartitioning focusing and the constant phase advance one) are 1.22 and 0.62 in the transverse and longitudinal rms emittances, respectively. It has been found that the ratio of halo-like particles is about on the order of 10^{-3} ~10^{-4} in a simulation with 48000 particles. The ratios of halo formation between these two focusing methods are nearly equal in the transverse motion and 0.52 in the longitudinal motion. Here, halo-like particles in the transverse motion are defined by those outside 6.5 times as far as the standard deviation of the radial distribution of the output beam, while halo-like particles in the longitudinal motion are defined by those outside 12.5 times as far as the longitudinal output rms emittance.

3.2 MEBT

A beam-transport line, 2.7 m long between the RFQ and the DTL (MEBT), has three purposes: achieving both transverse and longitudinal beam-matching, chopping the beam for reducing beam losses after injection into the ring and measuring the beam properties before injection into the DTL [14][15]. It consists of eight quadrupole magnets, two bunchers and two rf-chopping cavities (referred to as RFD) [16]. Detailed simulation results show that high performance in the chopping operation can be achieved by using the RFD: the number of unstable particles at the DTL exit (50 MeV) during the transient times is less than 0.08% of the total injection particles [14][15].

Table 5: Parameters of the RF power source.

Repetition rate	50	Hz
Pulse width	620	μsec
Number of klystrons	19	
Peak output power	2.0	MW

4 RF POWER SOURCE

A high-power rf system has been designed on the basis of accumulated knowledge and experience during the construction and operation of the JHP test stand [17]. The main parameters are listed in Table 5.

ACKNOWLEDGMENTS

The authors wish to express their gratitude to M. Kihara regarding his encouragement. They wish to express their gratitude to R. A. Jameson, K. Bongardt, S. Ohnuma, M. Mizumoto, L. V. Kravchuk, P. N. Ostroumov, V. V. Paramanov and V. A. Moiseev regarding valuable comments and discussions.

REFERENCES

[1] T. Kato, 'Design of the JHP 200-MeV Proton Linear Accelerator,' KEK report 96-17 (1997).
[2] T. Kato et al., 'JHF Accelerator Design Study Report, Section 4, 200-MeV Linac,' KEK report 97-16 (1998).
[3] T. Kato, 'Proposal of a Separated-type Proton Drift Tube Linac for a Medium-Energy Structure,' KEK Report 92-10 (1992).
[4] A. Ueno et al., 'Beam Test of the Pre-Injector and the 3-MeV H RFQ with a New Field Stabilization PISL,' Proc. 1996 International Linac Conf., p.293 (1996).
[5] A. Ueno, 'JHF Accelerator Design Study Report, Section 4.4, Preinjector,' KEK report 97-16 (1998).
[6] F. Naito et al., 'Rf Characteristics of a High-Power Model of the 432 MHz DTL,' Proc. 1994 International Linac Conf., p.137 (1992).
[7] K. Yoshino et al., 'JHF Accelerator Design Study Report, Section 4.5, Accelerating structure,' KEK report 97-16 (1998).
[8] Y. Yamazaki, 'Recent Technological Development of Accelerating Structures,' Proc. 1992 Linear Accel. Conf., p.580 (1992).
[9] T. Kageyama et al., 'Development of Annular Coupled Structure,' Proc. 1994 International Linac Conf., p. 248 (1994).
[10] T. Kato, 'Beam Simulation Code Using Accurate Gap Field Distributions in a Drift Tube Linac,' Proc. 1994 International Linac Conf., p.523 (1994).
[11] R. A. Jameson, 'Beam-Intensity Limitations in Linear Accelerators,' IEEE Trans. Nucl. Sci. NS-28, 2408 (1981).
[12] R. A. Jameson, 'On Scaling & Optimization of High-intensity Low-beam-loss RF Linacs for Neutron Source Drivers', AIP Conference Proceedings 279 (1993) 969.
[13] M. Reiser, 'Theory and Design of Charged Particle Beams,' Section 5, John Willy & Sons, 1994.
[14] S. Fu and T. Kato, 'JHF Accelerator Design Study Report, Section 4.3.4, The medium energy beam-transport line,' KEK report 97-16 (1998).
[15] T. Kato and S. Fu, 'MEBT Design for the JHF 200-MeV Proton Linac,' submitted to this conference.
[16] S. Fu et al., '324-MHz RF Deflector Design and Test,' submitted to this conference.
[17] S. Anami et al., 'JHF Accelerator Design Study Report, Section 4.6, RF source,' KEK report 97-16 (1998).

A LINAC FOR THE SPALLATION NEUTRON SOURCE*

Andrew J. Jason with the SNS Linac Team
Los Alamos National Laboratory, Los Alamos, NM 87545 USA

Abstract

The Spallation Neutron Source Project (SNS), to be constructed at Oak Ridge National Laboratory, accelerates H^- ions to an energy of 1.0 GeV with an average current of 1-mA for injection into an accumulator ring that produces the short intense burst of protons needed for the spallation-neutron source. The linac will be the most intense source of H^- ions and as such requires advanced design techniques to meet project technical goals. In particular, low beam loss is stressed for the chopped beam placing strong requirements on the beam dynamics and linac construction. Additionally, the linac is to be upgraded to the 2- and 4-MW beam-power levels with no increase in duty factor. We give an overview of the linac design parameters and design choices made.

1 OVERVIEW

The SNS project is described in depth elsewhere [1,2]. Los Alamos is responsible for the design and construction of a linac suitable to meet project specifications. H^- beam enters the linac at an energy of 2.5 MeV with a peak current of 27.7 mA and a normalized rms emittance of 0.23 π-cm-mrad. The linac input beam is produced by a "front-end" assembly that sequentially consists of an ion source, RFQ, and transport line that contains a chopper. The chopper provides a gap in the beam as required by the accumulator ring extraction scheme. Lawrence Berkeley Laboratory is responsible for the front end [2] except for the chopper system that is to be constructed by Los Alamos. The linac output energy is 1.0 GeV with little emittance growth or current loss and will maintain the nominal time structure of the input beam. Beam then enters a transport line and is conveyed to an accumulator ring, to be constructed by Brookhaven National Laboratory [3]. It is also a Los Alamos task to construct and power a bunch rotator in the transport line. The ring, at constant energy, accumulates the nominal 1-ms-long linac macropulses to an intense proton pulse of 590-ns duration for impingement on the spallation target. The average beam power on the target is 1.0 MW with a pulse rate of 60 Hz. The beam-power is upgradeable to up to 4 MW by increasing the peak linac current.

* Work supported by the U.S. Department of Energy, Office of Energy Research, Office of Basic Energy Sciences.

2 BASIS OF DESIGN

Requirements on the linac included cost effectiveness, high operational availability, low beam loss, upgradability, high beam quality, and insensitivity to chopping. We believe that the present design meets these criteria. A block diagram of the linac is shown in Figure 1.

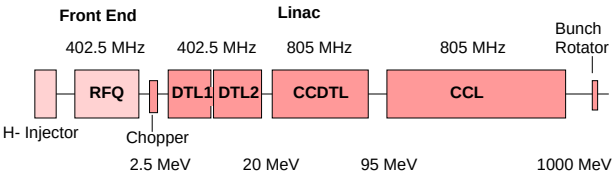

Figure 1. Block diagram of SNS linac

The linac consists of a drift-tube linac (DTL) up to 20 MeV, a coupled-cavity drift-tube linac (CCDTL) to nominally 95 MeV and a coupled-cavity linac (CCL) to the full energy. The DTL and the CCL are well known structures, appropriate to their energy ranges. The CCDTL, though a recent invention, has received cold-model testing and is considered a good intermediate structure between the DTL and CCL in terms of beam-dynamics matching and shunt impedance. This structure has other advantages and is believed to be the optimum choice in the given energy range.

In order to minimize cost, a tradeoff study was conducted early in the project that varied the linac gradient. On the basis of this study an average gradient (E_0T) of 2.7 MV/m was chosen. Later and more accurate costing showed this to be near the optimum value. The length arrived at was 493 m giving a real-estate energy gradient of 2.02 MeV/m. Although higher than many previous proton linacs, the peak field is everywhere less than 1.5 Kilpatrick, a safe value. Because of the high gradient, a relatively large amount rf power (slightly less than 100-MW peak delivered to the linac) is needed.

The linac rf frequency was similarly chosen; assessment of this and other design choices showed that frequencies near 800 MHz have best performance and lower cost. The exact frequency of 805 MHz was chosen because of our familiarity with the LANSCE linac and subsequent ease of technology transfer as well as an assessment of klystron cost and availability. The 402.5-MHz value for the structure frequency below

20 MeV was chosen to allow funneling in future upgrades.

Low beam loss and high availability are closely related. The linac structure must suffer only low levels of activation so that maintenance and upgrade can be done quickly. A spacious aperture and adequate steering are important in this regard and are part of the design. Furthermore, our calculations show that with good matching, halo formation will contribute negligibly to beam loss. However, it is expected that the predominant beam loss will occur by stripping of the negative hydrogen ions through collision with background gas. Calibration of the LANSCE-linac activation and loss-transport calculations are convincing that, at 1 GeV, a loss of 1 nA/m will cause activation of greater than 10 mrem/hr an hour after shutdown at a distance of 1 ft. To achieve this low-loss level at the 4 MW upgrade, a vacuum of $5x10^{-8}$ torr is required and, with proper design, is achievable.

A room-temperature structure was chosen over a superconducting structure largely to minimize technical and schedule risk. An assessment showed that if an R&D program were successful in addressing the issues of transient control and power coupling, the capital cost and schedule would be little affected and that the operating costs would be decreased by nearly 4 M$ per year. Nonetheless, if such an R&D program were to run into difficulties, the program schedule and cost would be strongly affected.

3 CHOPPING

A 35%-duty-factor chopping at 1.189 MHz (just slightly off the ring revolution frequency) is applied to the beam before entering the linac by a traveling-wave deflector. This decreases the average macropulse current to 18.8 mA for the 1-MW case. The chopper rise time should be under 2.5 ns to prevent partially chopped pulses from entering the linac and possibly creating additional loss downstream. R&D work [4] is in progress to define a deflecting structure and modulator that can provide the required 18-mrad deflection in a 0.5-m deflecting structure with such a challenging rise time. FET drivers with the required rise time are not commercially available; development work with a semiconductor manufacturer is scheduled. A device with 5-ns rise time is judged to be immediately feasible and construction of a prototype is underway. This decreased rise time may be adequate for the 1-MW scenario.

The chopper plays a secondary role in providing time-width modulation of the beam in order to maintain constant peak current during the 20-μs ramp up planned at the macropulse start.

Transient analysis has been done to evaluate the effect of chopping on the linac-cavity fields. Negligible excitation of high-order modes was found. The main effect predicted is a 3% field variation in the 4-MW case throughout the linac at the chopping frequency. The major effect is a broadening of the energy and phase width, small compared to the unperturbed parameters. The effect is inversely proportional to the accelerating field, thus further justifying the high linac gradient.

4 STRUCTURES

The 402.5-MHz DTL is 8.7-m long and uses a FOFODODO lattice with period 8 βλ (at 805 MHz). This was chosen over a FODO lattice to allow feasibility of permanent-magnet quads in the drift tubes. To achieve good field stabilization, the DTL is broken into two tanks at the 10-MeV point. The structure tune is maintained by regulating water temperature.

The 68.8-m long CCDTL uses a 12-βλ FODO lattice. Each of the 101 segments (structure between quads) contains two cells of length 3βλ/2, each with one drift tube. The space for quadrupole magnets, containing a coupling cavity is 6βλ/2, allowing sufficient room for quadrupole magnets and diagnostics but requiring a low acceleration gradient of 1.08 MeV/m. An adequate prototype quadrupole magnet has been made.

The CCL comprises the remaining 85% of the structure length and uses a 12-βλ FODO lattice. Up to 166 MeV the structure has eight cells per segment with 2-βλ quad spaces. The large intersegment spacing provides adequate space for quads and diagnostics. At higher energies, where βλ has increased sufficiently, a 10 cell segment is used with 1-βλ quad spaces.

The segments are joined by coupling cells to form isolated rf modules. Bridge couplers are not used; the modules are driven by from 1 to 3 klystrons in a symmetrical feed-point arrangement that minimizes field droop in a module. Partitioning of the modules has been chosen to facilitate upgrades. The choice of an even number of half βλ cells in the segments permits all segment couplers to remain on one side of the structure for simplified mounting, fabrication, and vacuum pumping. Structure tune is maintained by regulating the cooling water temperature for each module against cavity frequency offset.

5 BEAM DYNAMICS

The linac beam dynamics along with the physics design is discussed elsewhere [5]. We here note a few salient features. Variants of the code PARMILA were used to define and find a matched beam for each structure. The structures are joined and smooth matching done across structure transitions with appropriate phase and field ramping. There are no explicit matching sections; matching is done between structures by the quads and structure design. As well as matched beam studies, error studies and end-to-end

simulations have been done using 10,000-particle sets starting from the RFQ output. We plan to increase the size of this particle set by using massively parallel processing.

The aperture size is maintained at 10 times the beam rms size to promote low beam loss; predicted halo growth will not intercept the aperture even with alignment errors and can be readily scraped in the transport line to the ring. A plot of aperture versus energy is shown in Figure 2.

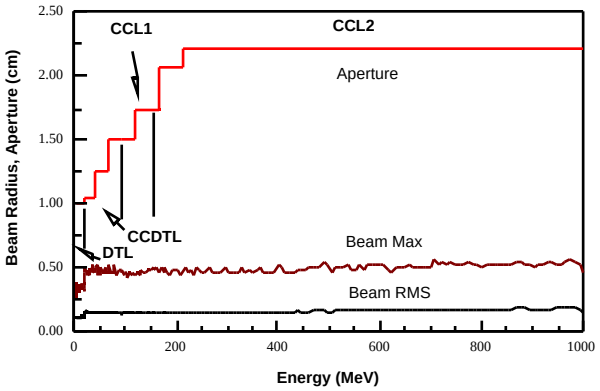

Figure 2. Aperture and beam size in the linac

6 RF SYSTEM

The rf system [6] will deliver approximately 99 MW peak power at 7.02% duty factor to the structure for an average power of 6.74 MW. The ac wall-plug power has been specified at 22 MW. Two 1.25-MW peak-power klystrons drive the DTL and a third klystron will be provided for the RFQ. The remainder of the structure uses 56 anode-modulated 805-MHz 2.5-MW klystrons in the baseline design. Allowing for control margin and system losses, 2-MW are available to the structures. Klystron size was determined from optimization of cost, technical feasibility, and relation to linac-structure. The anode modulation was judged to be the most technically feasible method of pulse switching. However, recent developments indicate that an IGBT switching system is likely feasible and will be substantially more cost effective; R&D work is planned for this approach. A two klystron modulator, developed in previous projects, is planned, also for economic reasons. The klystron modulators are located above and lateral to the linac tunnel in a gallery that contains the water systems, vacuum pump controls, low-level rf controls and beam-diagnostics electronics. The rf system will control the cavity fields to within ±1% and ±1° through a stable reference system and using sophisticated feedback techniques, including fast adaptive feed forward.

7 UPGRADES

The requirement that the SNS is to be readily upgradeable to beam powers up to 4 MW in a staged approach strongly affects the 1-MW design. An upgrade to 2-MW, with doubling of the ion-source current, could be accomplished by redefinition of the linac rf modules and the addition of rf power (14 klystrons). Upgrade to 4 MW requires beam funneling at 20 MeV because of likely ion-source limitations and the inability of the RFQ to accelerate the 108-mA current at 805 MHz. A second linac reconfiguration is then required along with addition of 14 more klystrons. The linac reconfiguration could be done without structure replacement by redefining the number of segments (half focusing periods) of the rf modules and terminating the module ends with special λ/10-cavity sections. Thus a module end could be defined by removing a CCDTL or CCL coupling cavity and terminating the two cells previously joined by the coupling cavity. Correspondingly a module could be extended by removing adjacent terminating cells and joining the terminating segments with a full coupling cell. Drive points and waveguide runs would have to be built into the design at initial construction. However, substantial effort would be required to effect the reconfiguration as well as in the initial design. A simpler scheme has recently been discussed that would use two klystrons for each of 26 rf modules and eliminate any structure reconfiguration in a direct upgrade from 1 to 4 MW. Here a third klystron would be added to the center of each module. and provision would be made for the appropriate (small) change in rf matching during the initial design.

8 REFERENCES

[1] B. R. Appleton, "The National Spallation Neutron Source," PAC 97 proceedings, Vancouver (to be published).

[8] "Conceptual Design Review of the National Spallation Neutron Source," ORNL, June, 1997. Available on the web at http://www.ornl.gov/~nsns/CDRDocuments/CDR.html.

[2] J. Staples, et al., The SNS Front End Accelerator Systems," PAC 97 proceedings, Vancouver (to be published).

[3] W.T. Weng et al., Accumulator Ring Design for the NSNS Project," PAC 97 proceedings, Vancouver (to be published).

[4] S. S. Kurennoy et al., "Development of a Fast Traveling-Wave Beam Chopper for the National Spallation Neutron Source," PAC 97 proceedings, Vancouver (to be published).

[5] H. Takeda, J. H. Billen, and S. Nath, "Physics Design of the National Spallation Neutron Source Linac," PAC 97 proceedings, Vancouver (to be published).

[6] P. Tallerico et al., "The Rf System for the National Spallation Neutron Source Linac," PAC 97 proceedings, Vancouver - to be published.

FIRST RESULTS OF THE TWO–BEAM FUNNELING EXPERIMENT*

A. Firjahn–Andersch, H. Liebermann, A. Schempp, J. Thibus,
H. Vormann, E. Winschuh, H. Zimmermann
Institut für Angewandte Physik, Johann Wolfgang Goethe–Universität,
Robert–Mayer–Straße 2–4, D–60054 Frankfurt am Main, Germany

Abstract

High intensity accelerator concepts for **H**eavy **I**on **I**nertial **F**usion (HIIF) injectors require small emittance, high current and high energy beams. The improvement of brightness in such a driver linac is done by several funneling stages at low energies, in which two identically bunched ion beams are combined into a single beam with twice the frequency, current and brightness. For the **H**eavy–**I**on **D**riven **I**gnition **F**acility (HIDIF) we have proposed the use of a two–beam accelerator structure which provides two beams within one cavity, and a single r.f. deflector structure which bends the two beams to one common axis. The progress of the experiment and first beam–test results will be presented.

1 INTRODUCTION

By the use of the two–beam RFQ the two beams are brought very close together while they are still radially and longitudinally focused. Additional discrete elements like quadrupole–doublets and –triplets, debunchers and bending magnets, as they have been proposed in first funneling studies [1, 2, 3], are not necessary. A short r.f. funneling deflector will be placed around the beam crossing position behind the RFQ. The layout of the proposed HIDIF–injector with two–beam RFQs in front of the first and second funneling sections is shown in Figure 1. The HIDIF linac starts with 16 times 3 ion sources for three different ion species to allow so–called "telescoping" at the final focus [4]. With four funneling stages the frequency has been increased from 12.5 MHz to 200 MHz accordingly.

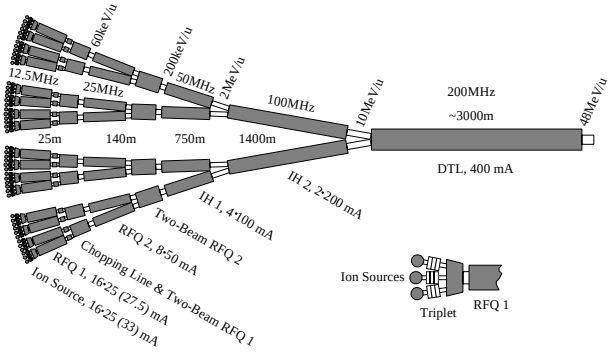

Figure 1: Layout of the 12.5. . .200 MHz HIDIF linac system for 400 mA of Bi^+.

* Work supported by the BMBF

For studies of the new two–beam RFQ structure and the r.f. deflector, the first two–beam funneling experiments will be carried out with He^+–ions at low energies to facilitate ion source operation and beam diagnostics. Two small multicusp ion sources and electrostatic lenses, built by LBNL (Lawrence Berkeley National Laboratory) [5, 6], are used. The ion sources and injection systems are attached directly on the front of the RFQ with an angle of 76 mrad, the angle of the beam axes of the two–beam RFQ. Figure 2 shows the experimental set–up of the two–beam funneling experiment. In Table 1 the main parameters of the experiment with He^+ and the design parameters of a first HIDIF funneling stage for Bi^+ are shown.

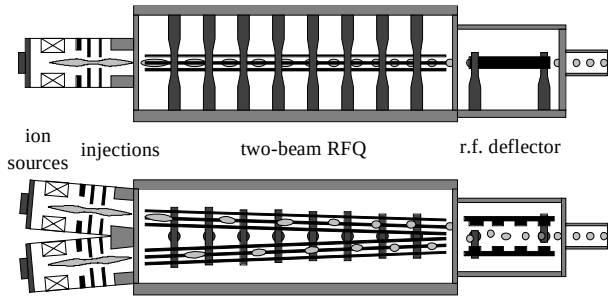

Figure 2: Experimental set–up of the two–beam funneling experiment.

Table 1: Main parameters of the experiment with He^+ and the design parameters of a first HIDIF funneling stage for Bi^+.

Two–beam RFQ	He^+	Bi^+
f_0 (MHz)	54.5	12.5
Voltage (kV)	10.5	180
R_p value (kΩ m)	80	250
Q_0 value	1800	5000
T_{in} (keV)	4	209
T_{out} (MeV)	0.16	12.54
Angle between beam axes (mrad)	76	76
Beam separation at output (mm)	40	40
Multigap funneling deflector		
f_0 (MHz)	54.5	12.5
Voltage (kV)	6	450
Length ($\frac{\beta\lambda}{2}$)	9	2

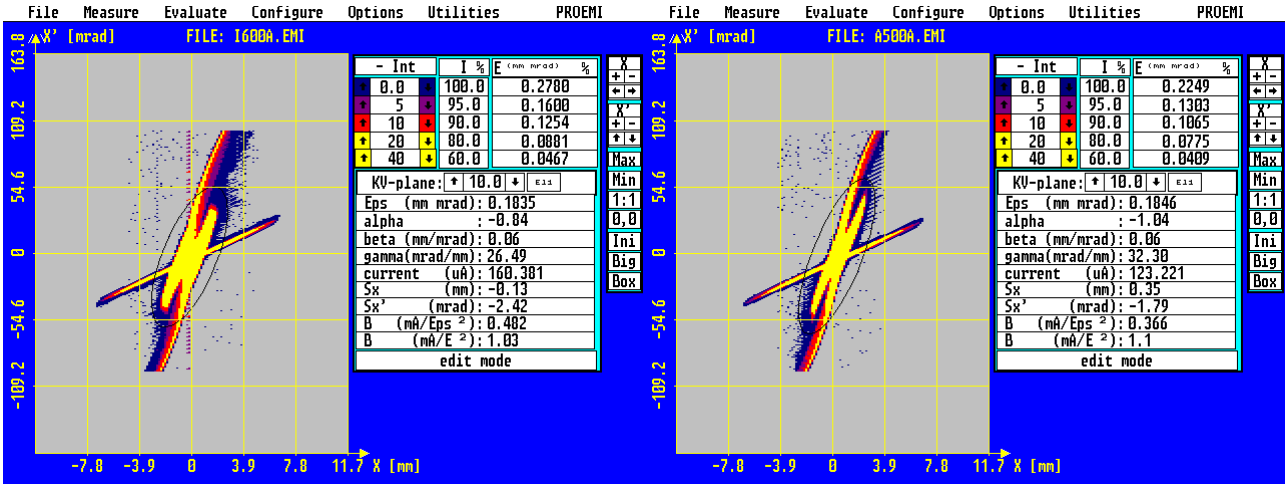

Figure 3: Comparison between the emittances of the extracted beams of the two ion sources at 0.8 mA. The ellipses correspond to the 90% normalized KV–emittances which are ϵ_{KV} =0.1835 π mm mrad for the first source and ϵ_{KV} =0.1846 π mm mrad for the second source.

2 ION SOURCES AND INJECTION SYSTEMS

To optimize the synchronous operation, both ion sources and injection systems have been tested on an emittance measurement device. Figure 3 shows the measured emittances of the extracted ion beams of the two ion sources at 0.8 mA, which scales to a beam current of 40 mA of Bi^+. The minimum difference of the two normalized 90% KV–emittances was 0.5%. The values are dependent on the included divergent neutral beam.

3 THE TWO–BEAM RFQ

The two–beam RFQ consists of two sets of quadrupole electrodes, where the beams are bunched and accelerated with a phase shift of 180° between each bunch, driven by one resonant structure. With the use of identical RFQ electrode designs for both beam lines, the electrodes of one beam line are installed with a longitudinal shift of 2.55 cm (i.e. $\frac{\beta\lambda}{2}$) to achieve the 180° phase shift between the beam bunches of each beam line. In Figure 4 a photograph of the two–beam RFQ, with the first section of the electrodes mounted, is shown.

The RFQ electrodes are divided into two sections with different functions. While the first section, 140 cm long, bunches and accelerates the ions to the final energy of 160 keV, the second 60 cm long section consists of a drift and a matching section. So an x, y focus is at the funneling deflector position, while the axial focus will be behind the deflector for a matching into the next accelerator stage [7].

In Figure 5 the measured energy spectra behind the RFQ are shown. The final beam–energy of 166 keV is reached at an electrode voltage of 10 kV. Up to 4 kV electrode voltage the He^+ beam is only transported.

At the beam crossing position behind the two–beam RFQ emittance measurements have been done. In Figure 6

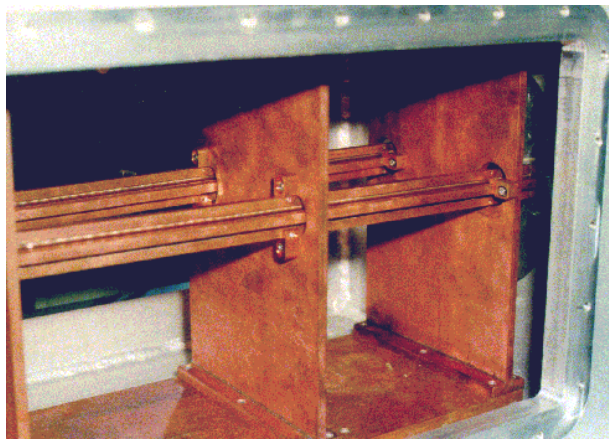

Figure 4: Photograph of the two–beam RFQ with the first section of the electrodes mounted.

the 2D– and 3D–view of the two emittances at an electrode voltage of 11.5 kV is shown. The difference between the two emittances is mainly dependent on the parameters of the injection systems.

4 THE FUNNELING DEFLECTOR STRUCTURE

The electrode geometry of the multigap deflector consists of several deflector plates divided by sections with larger aperture with equal length. In this geometry, the particles will see the deflecting field in one direction several times but the deflection in the opposite direction is always less. The length of the sections have to be proportional to the particle velocity and to the inverse frequency of the deflector system. For beam funneling, the frequency of the deflector has to be the same as the accelerator frequency, so that the bunches from different beam axes will see opposite

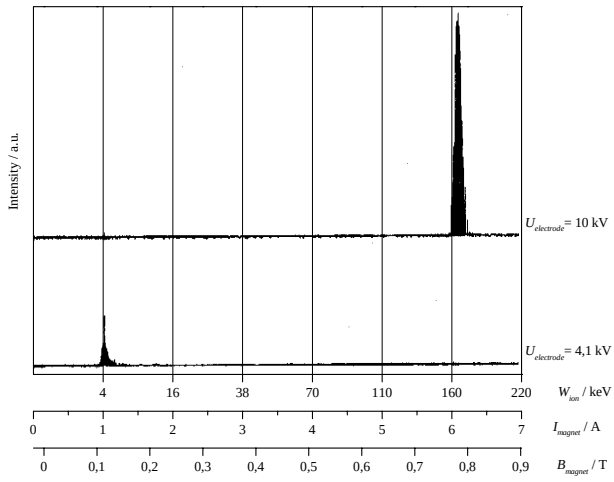

Figure 5: Energy spectra behind the RFQ. With the design voltage of 10 kV the final beam–energy of 166 keV is reached.

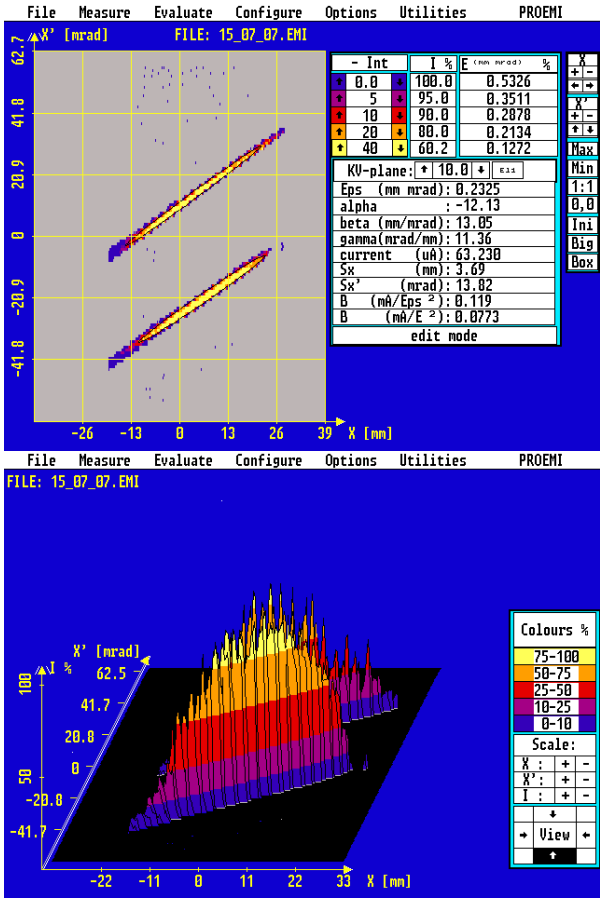

Figure 6: 2D– and 3D–view of the measured emittances behind the RFQ at the place of beam crossing. The ellipses correspond to the 90% normalized KV–emittances which is about ϵ_{KV} =0.25 π mm mrad for each beam.

field directions because of the phase shift of 180° between each bunch. Figure 7 shows a schematic drawing of the 9–gap funneling deflector which will be used.

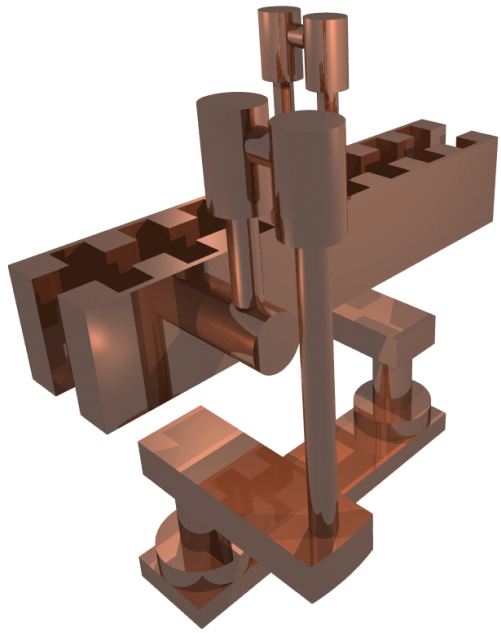

Figure 7: View of the multi–gap funneling deflector.

5 CONCLUSION

The beam tests results of the injection systems and the two–beam RFQ have shown that the chosen set–up can deliver two nearly identical ion beams for the planned funneling experiment. Next step will be the installation of the r.f. funneling deflector behind the two–beam RFQ.

The experiment with He^+ is a scaled version for funneling of Bi^+ at 60 $\frac{\text{keV}}{\text{u}}$ as it is required in the first funneling section of HIDIF, but can also be scaled to higher energies for e.g. the second section at 200 $\frac{\text{keV}}{\text{u}}$ or other funneling applications like spallation source.

6 REFERENCES

[1] K. Bongardt and D. Sanitz, Funneling of Heavy Ion Beams, Primary Report, Kernforschungszentrum Karlsruhe, 11 04 02P14C (September 1982).

[2] J.F. Stovall, F.W. Guy, R.H. Stokes and T.P. Wangler, Beam Funneling Studies at Los Alamos, Nucl. Instr. and Meth. A278 (1989) p. 143.

[3] K.F. Johnson, O.R. Sander, G.O. Bolmer, J.D. Gilpatrick, F.W. Guy, J.H. Marquardt, K. Saadatmand, D. Dandoval and V. Yuan, A Beam Funnel Demonstration: Experiment and Simulation, Particle Accelerators, Vols. 37–38 (1992) p. 261.

[4] M. Basco, M. Churazov, D. Koshkarev, Fusion Engineering and Design 32–33 (1996) p. 73.

[5] K.N. Leung, Multicusp Ion Sources, Rev. Sci. Instrum. 65(4) (1994) p. 1165.

[6] R. Keller in: The Physics and Technology of Ion Sources, Edited by I. G. Brown, Wiley–Interscience Publication, New York.

[7] A. Schempp, Design of Compact RFQs, Proc. Linear Accelerator Conference 1996, p. 53.

PRESENT PERFORMANCE OF THE CERN PROTON LINAC

C.E. Hill, A.M. Lombardi, E. Tanke, M. Vretenar
PS Division, CERN, 1211 Geneva 23, Switzerland

Abstract

The original 1973 design specification of the CERN 50 MeV Proton Linac was for a 150 mA beam but this intensity was rarely used. Preliminary tests for the high brightness beam required for LHC indicated that 170 mA could be produced for short pulses (30 μs). Since then further optimisation has enabled the 170 mA to be delivered reliably, within the nominal emittances and dispersion, in long pulses (120 μs) to the user, the PS Booster (PSB), about 80 m downstream of the linac. The improvements will be described along with the steps envisaged to attain a goal of more than 180 mA.

1 INTRODUCTION

Linac2 has now been the primary source of protons for the CERN accelerator complex for the last 20 years [1]. In spite of its age, the machine performance has been steadily improved over the past few years in anticipation of the demands that will be made on it in the LHC era. Table 1 indicates the evolution of the beam intensity delivered to the PS Booster (PSB) over recent years. Figure 1 shows the layout of the linac and PSB injection lines.

In the early years, there was no particular demand for high intensities from the linac as, usually, more than sufficient protons could be supplied to the users, and high intensity beams were only produced as an academic exercise or to supply special test beams. It was generally felt that 150 mA out of tank 3 of the linac was a limit defined by the RF power available. However, the anticipated requirements of LHC started investigations into the possibilities of accelerating higher currents. By limiting the beam pulse length to around 30 μs, it proved possible to accelerate around 170 mA. However, existing high intensity users required a beam pulse length of the order of 120 μs. The measures taken to attain the present performance for a long beam will now be described.

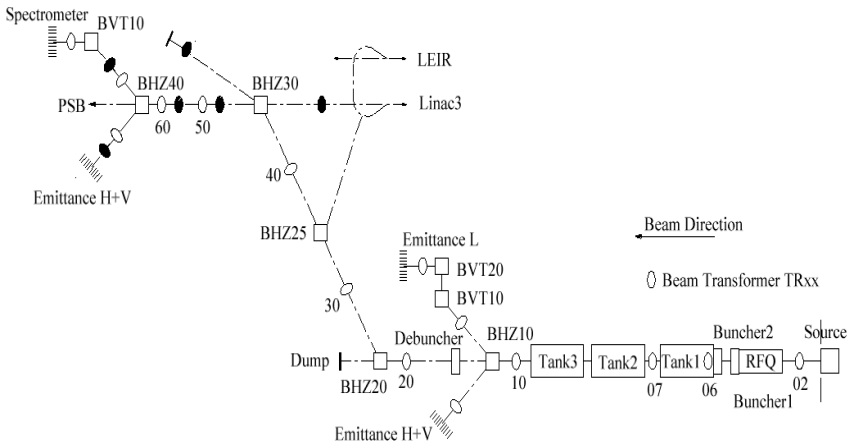

Figure 1: Schematic layout of Linac2 and its transfer lines.

Table 1. Evolution of operational beam intensity at transformer TR60 in Linac2 since 1992.

Date	Event	mA
up to1992	C-W injector operation	140
1993	RFQ2 installed	135
1994	Typical operation	135
1995	Realignment RFQ+LEBT	142
1996/I	Annual startup	140
1996/II	New high energy optic	145
1997/I	Annual startup	145
1997/II	New setting RFQ	160
1977/III	Source + LEBT adjustment	170
1998/I	Annual startup (reduced)	158
1998/II	Stable operation	173

2 INSTALLATION OF RFQ2

The high beam brightness required by the LHC requires some modifications to its injectors, and in particular an increase in the linac peak current. The consequent reduction in the number of turns needed in PSB injection leads to a smaller emittance at the end of the process. A major step towards a higher linac current was the replacement in 1993 of the old 750 kV Cockroft-Walton and Low Energy Beam Transport (LEBT) by a new 90 kV platform, a 750 keV RFQ (RFQ2) with compact (<1m long) beam transport lines between source and RFQ, and RFQ and linac [2]. After two months of installation work and one month of setting-up, the linac was able to provide 135 mA for the normal operation and 165 mA for high intensity studies.

3 RFQ2 ALIGNMENT

Whilst the RFQ was still on the test stand, it was found that the beam at its output was mis-steered. After installation on Linac2, the high-energy end of the RFQ had to be positioned off axis to get a good transmission through the linac. On

the stand, the beam emittance measured directly behind the source showed that the beam was off axis in position and angle. Although the source anode hole had been centred to better than 0.1 mm, it was not perpendicular to the beam axis. This same error was also found on Linac2 and corrected [3].

The line between the source and the RFQ contains two solenoids. Due to coupling, a beam passing through a solenoid off axis in, say, the horizontal plane can cause errors in beam position and angle in both transverse planes at the output. Originally, the solenoids had been aligned on their mechanical, not on their magnetic axes. Moving the solenoids whilst checking the beam centre (position and angle in both transverse planes) enabled the beam to be brought onto axis into the RFQ. As a result the overall performance of the RFQ improved with a reduction of RF breakdowns, which were often induced by ions hitting the electrodes, and the RFQ could be realigned mechanically to the theoretical axis.

4 RFQ2 CONDITIONING

The RFQ was designed to accelerate a space charge dominated beam of 200 mA. For this reason the design vane voltage had to be relatively high (178 kV) [4] which corresponds to surface electric fields of more than 2 times Kilpatrick on a large fraction of the electrodes and locally as high as 2.5. Conditioning on the test bench was only partially successful; only about 95% of the nominal voltage was attained before heavy sparking started. Once installed at the linac, the RFQ was operated at 92% of the design voltage to avoid excessive breakdowns that would have perturbed the whole CERN proton acceleration chain. This resulted in a 10% reduction in beam transmission.

It turned out that a defective drag pump in the RFQ vacuum system used to pump the large amount of hydrogen coming from the source, was backstreaming oil vapours into the cavity. The hydrocarbon deposit on the vane surface enhanced field emission (dark current) that finally resulted in RF breakdown.

Steady operation at high field level in the following years slowly eliminated the hydrocarbon from the electrodes. Figure 2 shows Fowler-Nordheim, ($ln(I/V^{2.5})$ vs. $1/V$), plots of dark current, derived from the excess power going to the electrons [5], as function of vane voltage at different moments of the RFQ2 history. The derived field enhancement factor β is a figure of merit for electrode roughness and cleanliness. Between 1993 and 1997 the dark current in the RFQ (operating at 92% of the nominal level) went down from about 70 mA to virtually zero. A comparison of the beta-factors deduced from Figure 2 shows that the cavity after delivery from the workshop (1990) was already somewhat polluted (β=220), while at the installation at the linac (1993) pollution was extremely high (β=920), It went down drastically (β=67 in 1997) after removing the source of pollution and slow RF conditioning. The present value is reasonable for the standard of surface finish used in the RFQ.

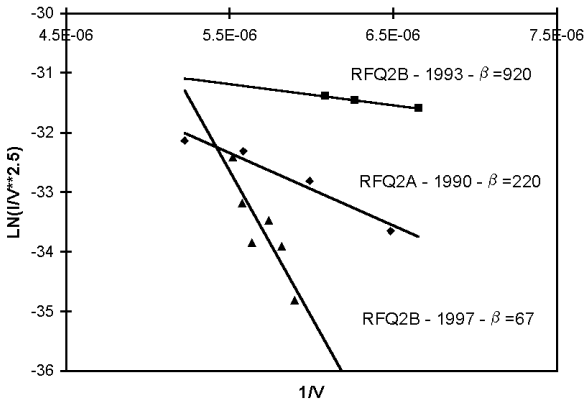

Figure 2: Fowler-Nordheim plots for the RFQs.

Following the discovery of the reduced β, the RFQ was reconditioned from 92% up to 100% of the nominal level during normal operation. The level was increased in small steps, taking care to limit the breakdowns so as not to perturb the users. As a result, the current delivered by the linac went up from 145 to 160 mA.

5 RF IMPROVEMENTS

The RF power needed for the design current of 150mA (cavity plus beam loading) is about 2.1 MW for each of the 5 final amplifiers, well within the capabilities (2.5MW) of the amplifiers [6]. For LHC, allowing for 5% beam losses, the 180 mA at the PSB correspond to 190 mA in the linac. For this, the final amplifiers will have to provide about 2.5 MW. With a 10% margin for phase and amplitude control, tuning precision and amplifier balancing, at least 2.7 MW per final amplifier will be needed

Some upgrades were gradually applied to the RF chains to increase their output power. The final amplifier tubes (TH170R) are rated for 2.5 MW power at a duty cycle greater than that used at Linac2, but they can deliver more power provided that enough drive power is available. Initially an additional amplifier stage was added in the Tank 1 chain which experiences the heaviest beam loading. Then modern 4.5 kW solid state amplifiers were installed in all the chains to replace aging tube units which generally had a lower power output. These more reliable transistor amplifiers have also contributed to a decrease in the linac fault rate.

Great attention was also given to the correct adjustment of the feedback loops which have not only to compensate for an increased beam loading but also have to stabilize amplifiers which are often working in the non-linear region close to saturation.

6 HIGH ENERGY OPTICS

The 80 metre 50 MeV proton beam line from the linac to the PSB is composed of 20 quadrupoles, 2 bending magnets, 8 steering magnets, and a debuncher cavity and is also equipped with eight position pick-ups and two emittance measurement lines. The optics of the line has been studied and optimised for the high current.

The space charge force varies considerably along this line as the beam comes out of the linac with a very marked longitudinal microstructure that is gradually lost. The beam is strongly space charge dominated at the beginning of the line and becomes emittance dominated after about 50 metres. The focusing of the line has been set-up in such a way so as to provide a "quasi" FODO system with constant phase advance per focusing period: this arrangement turned out to be the most convenient for optimising transmission and beam qualities, and minimising the sensitivity to steering. This last parameter is particularly critical, as the stray field of the PS machine penetrates the transfer line and sensitivity to steering has been considerably reduced with this configuration. Figure 3 shows the measured beam centre displacement before and after the change.

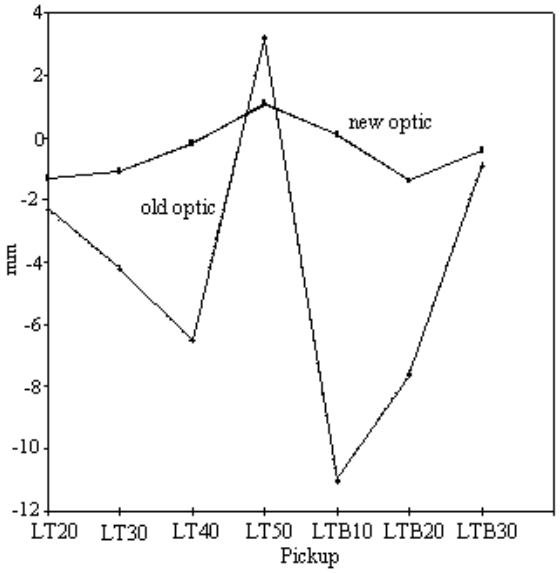

Figure 3: Measured beam centre displacement for 0.25 mrad variation in steering after the linac.

7 SOURCE OPTIMISATION

Normally, the total beam out of the duoplasmatron source is around 275 mA with a hydrogen consumption of about 7 std.ml/min. This results in a N_2 equivalent pressure of approximately $3.5*10^{-5}$ mbar in the preinjector housing falling to the high 10^{-7}s in the RFQ. With this relatively high pressure in the LEBT, neutralisation is very high. Thus, the effective focusing of the solenoids is highly dependent on the gas flow from the source. Gains in intensity of around 10% were obtained by iterative re-optimisation of source parameters and solenoid focusing strengths. Naturally, as source parameters and the injector vacuum quality change with time, this optimisation process must be repeated at regular intervals.

8 LINAC OPTIMISATION

In parallel to these major changes to the linac, a major long term effort was initiated to reduce the losses in the machine and transfer lines. A consequence of the new optics, and its inherent stability against perturbations, was that it became much simpler to control losses in the high energy transport line. Equally it is also easier to optimise both transverse and longitudinal parameters in the linac itself. Computer programmes are being developed to try to optimise the linac on-line using hill climbing techniques to find the optimum combinations of these parameters.

9 THE FUTURE

During one short study period in 1997, a peak current of 176 mA in 120 μs was passed to the PSB. This demonstrated that there is still potential for further improvements in intensity. The goal is to try to pass the 180 mA barrier in the near future. However, it is also known that there are serious bottlenecks at the beginning of the linac that will require ingenuity to overcome . It is also appreciated that this higher performance will place new demands on the linac with attendant consequences on reliability.

10 REFERENCES

[1] E. Boltezar, H. Haseroth, W. Pirkl, T. Sherwood, U. Tallgren, P. Tetu, D. Warner, M. Weiss. "The New CERN 50MeV Linac", Proc. 1979 Linear Accelerator Conference, Montauk, BNL 51134, 66, 1979

[2] C.E. Hill, A.M. Lombardi, W. Pirkl, E. Tanke, M. Vretenar, "Performance of the CERN Linac2 with a High Intensity Proton RFQ", Proc. 1994 Linear Accelerator Conference, Tsukuba, 175, 1994

[3] E. Tanke, "Realignment of the Linac2 LEBT During the 1994/1995 Machine Shutdown", PS/HI-Note 95-10 (MD)

[4] J.L. Vallet, M. Vretenar, M. Weiss, "Field Adjustment and Beam Analysis of the High-Intensity CERN RFQ", Proc. EPAC 90, Nice, Editions Frontieres, 1234, 1990

[5] M. Vretenar, "Field Emission Measurements on RFQ2 and Recalibration of the Vane Voltage", PS/RF/Note 97-11 (MD).

[6] J. Cuperus, F. James, W. Pirkl, "The RF System of the CERN New Linac", Proc. 1979 Linear Accelerator Conference, Montauk, BNL 51134, 344, 1979

ACHIEVING 800 KW CW BEAM POWER AND CONTINUING ENERGY IMPROVEMENTS IN CEBAF*

C. E. Reece
Thomas Jefferson National Accelerator Facility, Newport News, Virginia 23606 USA

Abstract

During the past year, CEBAF at Jefferson Lab has demonstrated its full capacity of sustained 800 kW beam power. All systems performed as intended. The energy stability at the design parameters of 4.0 GeV, 200 μA CW beam was measured to be better than 3×10^{-5} rms. During the fall of 1997, physics experiments were conducted using 4.4 GeV beam. Having demonstrated the benefits of *in situ* helium/rf processing of SRF cavities for increasing the energy reach of CEBAF, we began a program of processing all installed cryomodules. This processing has proven effective against the principal gradient limitation of the SRF cavities in CEBAF: discharges at the cold rf waveguide window, induced by electron field emission in the cavities. Such effects limit approximately half of the cavities. Regular operation at 5.0 GeV is just beginning, and preparations are underway to support 5.5 GeV in early 1999.

1 CEBAF DESIGN

CEBAF was designed and constructed as a 4.0 GeV, 200 μA CW recirculating electron linac. [1] The acceleration system employs 330 superconducting radiofrequency (SRF) cavities operating at 1497 MHz and 2.0 K. Each cavity is individually regulated and powered by a 5 kW klystron. Beam may be recirculated through the split linac up to five passes before delivery to the three experimental halls.

2 OPERATING EXPERIENCE

The accelerator has been supporting physics experiments since October 1995. Routine multi-hall operation has proceeded for the past two years. Tolerable CW beam currents are typically either limited to very low currents (100 pA–100 nA) by event discrimination constraints—for example, in the Hall B Large Acceptance Spectrometer—or to ~130 μA by heating of cryogenic targets in Halls A and C.

The first physics run above 4 GeV took place during November 1997. One experiment took 4.4 GeV beam while another received four-pass 3.5 GeV beam.

*Work supported by the U.S. Department of Energy, contract DE-AC05-84ER40150.

The SRF cavities in CEBAF as well as the rest of the acceleration system have been quite stable and reliable. By August 1998, over 4,000,000 cavity-beam hours had been accumulated.

3 FULL POWER TEST

On September 16, 1997, a test was performed on the CEBAF accelerator to demonstrate its full design capability of 200 μA CW beam at 4.0 GeV. This beam was delivered to the Hall C dump with minimal difficulties and with stability characteristics consistent with normal operations. Since no physics target was available that could handle 200 μA, the test was performed without a target in place. Rastered beam went directly to the dump. One clear indicator of the robustness of the integrated accelerator system was the ability to place 200 μA on the injector Faraday cup, retract that cup, and immediately transport lossless, full-power beam to the Hall C dump and maintain this current for at least tens of minutes with all orbit locks off. The duration of the full test was 10 h.

As illustrated in Figure 1, the test demonstrated the economy of exploiting SRF technology. A typical cavity operating at 6.5 MV/m fully matches the input 3.8 kW rf to the beam.

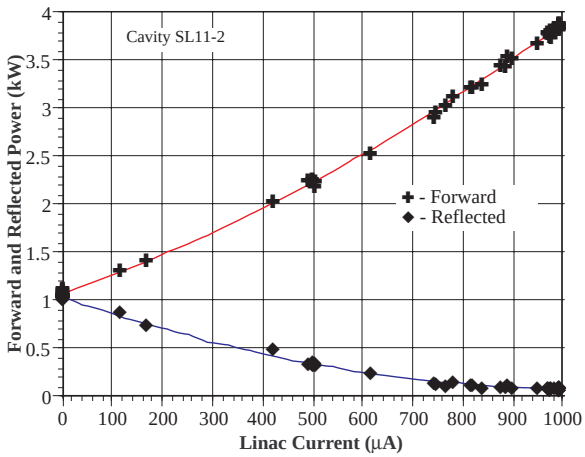

Figure 1. Matched rf load at full current.

During delivery of 200 μA to Hall C, measurements were made of the stability of beam position and energy. The dominant features observed were at 60 Hz. Beam motion in high dispersion and zero dispersion regions was comparable with comparable beta functions, so it's unlikely to be due to energy variation which, based on

a set of BPM measurements, had a fractional peak-to-peak amplitude of 4×10^{-5}.

There was no problem with input waveguide vacuum pressures as the input rf power increased and shifted to full travelling-wave conditions. An increase in the 2 K heat load was observed, increasing quadratically with total linac current, with an additional 200 W from the maximum 1 mA circulating current. The source of this heat has yet to be fully explored.

The beam dump cooling systems had no problem handling the 800 kW of beam power. The high-power beam dumps were designed to accept well over 1 MW. The test also challenged the beam current monitoring system used as part of the safety interlock system. We were able to approach the administrative limits with absolute beam accounting to better than 1%.

4 ENERGY IMPROVEMENTS

4.1 Limitations

The CEBAF cavities, though performing substantially better than initial specifications, are primarily limited in performance by internal electron field emission. Periodic arcs at the cold ceramic rf window are strongly correlated with field emission in the associated cavity.[2] Over a third of the 330 SRF cavities are now limited in usable gradient by this arcing phenomenon. Post-production tests have demonstrated that this arcing may be eliminated by moving the ceramic window away from the beamline and adding a dogleg in the cold waveguide section. All future rework will implement at least this change.

The other effects of field emission are x-ray production and spoilage of the cavity Q. Because it is more easily measured, we use the radiation as an indicator of decreasing Q and presently tolerate 2 R/h outside the cryostat from each cavity.

4.2 Helium Processing

The most economical route for incremental extension of the CEBAF energy reach has been through *in situ* conditioning of the SRF cavities, seeking to reduce the internal field emission and thus also the periodic arcing. Helium/rf processing, first attempted on an installed CEBAF cryomodule in September of 1996, has proven to be an effective method of improving cavity performance.[3]

Because of CEBAF's very full run schedule, we have continued to upgrade the processing methods in order to minimize any impact on run time. Beginning in 1998, the normal rf control system was used during processing rather than one of three stand-alone systems. A local ~70 MHz VCO was substituted for the fixed-frequency 70 MHz IF line. Including this VCO in a phase-locked loop then enabled dealing with the low-level multipacting barrier, as previously described.[4]

Also, to maximize the yield from helium processing, it is now preceded by a thermal cycle up to 40 K in order to desorb and remove any accumulated He and H. This is followed by several hours of detuned pulsed rf conditioning of the input cold waveguide region.

The actual processing is accomplished with 10^{-4} torr He on the beamline while driving the cavity at its highest sustainable field level for ~1 h. A subsequent thermal cycle to 40 K is used to remove the He. Following this procedure there have been no difficulties immediately resuming normal operation. The markers for effective processing are reduced arcing and reduced generation of x-rays by field-emitted electrons.

This upgraded processing scheme was commissioned on two cryomodules in February 1998. Using staggered crews, 16 additional cryomodules were processed during seven days allocated in July. The number of cryomodules processed was limited only by the capacity of the cryogenic system to handle the thermal cycles.

In addition to direct processing gains, other cavity gradient limitations are revisited during the processing work, and in many cases additional voltage has been found through reducing margin based on accumulated operating experience.

4.3 Results

To date, we have applied helium-rf processing at 2 K to 224 cavities in 29 of the 41 installed CEBAF cryomodules. Figure 2 shows the shift of limits after processing.

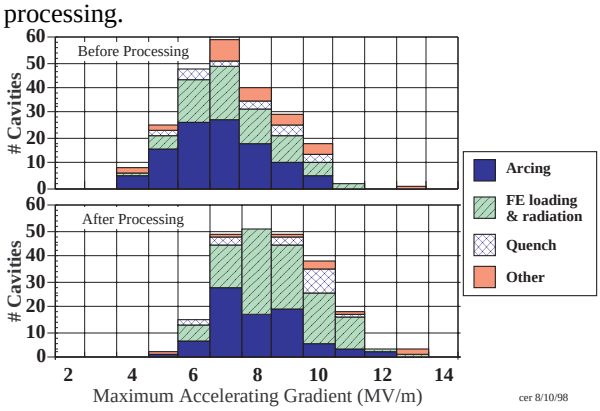

Figure 2. Change of limitations with processing.

Helium processing and requalification of cavities have increased the available installed CEBAF voltage by 155 MV, corresponding to an added 775 MeV for five-pass beam. At this rate we project an additional 55 MV gain from processing the balance of the machine, which would be adequate for extending the energy reach of CEBAF above 6 GeV. Figure 3 presents the present voltage capacities of the 41 CEBAF cryomodules.

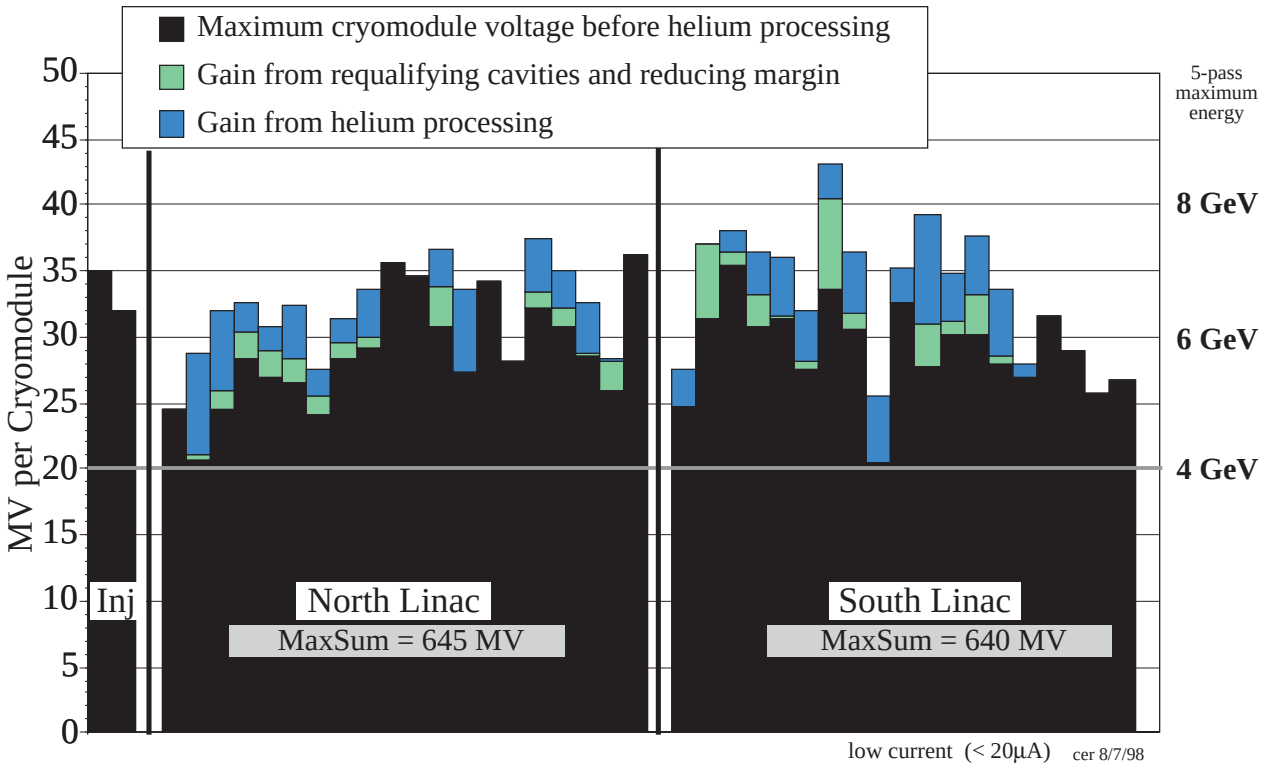

Figure 3. Maximum SRF Cavity Voltage per Cryomodule in CEBAF.

The distribution of present cavity performance limits is discussed in another contribution to this conference.[5]

5 UPGRADE PLANS

Beyond the virtually complete improvement to 5.5 GeV, upgrades to several arc dipole power supplies are being implemented in order to handle 6 GeV beam. Realization of this energy is planned for 1999.

Plans are presently being developed for a possible upgrade of CEBAF to 12 GeV. The most economical route includes the construction of new 80 MV cryomodules to populate the ten slots left empty by the early design switch for CEBAF from a four- to five-pass machine. Such new cryomodules will have improved filling factor by incorporating seven-cell rather than five-cell cavities, and take advantage of the process improvements in SRF technology of the last decade.[6]

6 ACKNOWLEDGEMENTS

J. Bisognano, J-C. Denard, L. Doolittle, V. Lebedev, B. Dunham, M. Spata, M. Tiefenback, and M. Wiseman all made important contributions to the success of the full-power demonstration test. A large number of Jefferson Lab staff have participated in the helium processing improvement work. Particular credit goes to G. Myneni, V. Nguyen, E. Strong, D. Dotson, T. Powers, G. Marble, G. Lahti, and C. Hovater for their creative efforts. All of this work has been solidly supported by the Operations and AES groups.

7 REFERENCES

[1] H. Grunder, "CEBAF Commissioning and Future Plans," PAC 95 Proceedings, 1–3 (1995).

[2] V. Nguyen-Tong *et al.*, "Electronic Activity at CEBAF Cold RF Window Induced by Cavity Operation," EPAC 94 Proceedings, 2200–2202 (1994).

[3] C. E. Reece *et al.*, "Improvement of the Operational Performance of SRF Cavities via in situ Helium Processing and Waveguide Vacuum Processing," PAC 97 Proceedings, in press.

[4] C. E. Reece, "Operating Experience with Superconducting Cavities at Jefferson Lab," contribution to The Eighth Workshop on RF Superconductivity, Abano Terme, Italy, 6–10 October 1997. (To appear in *Particle Accelerators*.)

[5] J. R. Delayen *et al.*, "Analysis of Performance Limitations for Superconducting Cavities," these proceedings.

[6] J. R. Delayen "Development of an Upgrade of the CEBAF Acceleration System," these proceedings.

CONTROLLING BACKSTREAMING IONS FROM X-RAY CONVERTER TARGETS WITH TIME VARYING FINAL FOCUSING SOLENOIDAL LENS AND BEAM ENERGY VARIATION

Yu-Jiuan Chen, George J. Caporaso, Arthur C. Paul
Lawrence Livermore National Laboratory, Livermore, California 94550 USA

Abstract

Backstreaming ions emitted from an x-ray converter hit by a tightly focused intense electron beam can form an ion focusing channel and over-focus the electron beam. As the ions move upstream in time, the net focusing strength increases. The final beam spot size on the target would then change in time and typically be larger than intended. We have developed a model to estimate the backstreaming ions' neutralization factor in a potential sheath near the target surface and away from the sheath. Performance of high resolution x-ray radiography facilities requires high current electron beams to be focused to a millimeter spot size on an x-ray converter through out the entire current pulse. We have studied the possibility of maintaining a constant final spot size for the entire pulse by using either a time varying final focusing solenoid field or beam energy variation to compensate the time varying ion focusing effects.

1 INTRODUCTION

Performance of high resolution x-ray radiography facilities requires several kiloamperes of electron beams to be focused to a millimeter spot size on an x-ray converter target through out the entire current pulse. D. Welch claimed that it would be difficult to maintain the tight focus of electron beams on a converter during the entire pulse length because of the existence of backstreaming ions[1]. He stated that a high density electron beam can heat the target surface up to 400°C and lead to rapid desorption of surface contaminants within a few nanoseconds. These desorbed gases form a plasma layer on the converter surface. Meanwhile, the charge redistribution on the target after the electron beam hits the surface creates a large potential drop and an ion diode on the target surface. The space charge field of the electron beam would pull ions out of the plasma layer into the beam. These ions trapped by the electron beam move upstream, form an ion focusing channel and over-focus the electron beam. As the ions move upstream in time, the net focusing strength increases. The final beam spot size on the target would then change in time and typically be larger than intended. The potential backstreaming ions are protons and oxygen from the water vapor on the target surface, carbon and tantalum or tungsten from the target itself. The lighter ions have a greater potential to destroy electron beam's final focus since they would travel upstream at a higher speed and form a longer ion channel. The ions from the target material itself are usually too heavy to have a large effect on the beam spot size during the beam pulse time. On the other hand, the backstreaming protons would have the worst effects on the electron beam's final focusing if these backstreaming protons do exist. Single-pulse experiments at various radiography facilities and laboratories [2-4] (except at CESTA's PIVAIR linac [5]) have not yet been able to provide a strong evidence of existence of backstreaming protons. However, The simulated double-pulse experiments on ETA-II indicated a different backstreaming ion emission mechanism [4]. The space charge field of the electron beam would pull ions out of a pre-existing target plasma generated by the preceeding pulse. The ETA-II results also indicated that the backstreaming ion emission follow a the Child-Langmuir law. In this paper, we study the possibility of maintaining a constant final spot size for an entire current pulse by using either a time varying final focusing solenoidal field or beam energy variation to compensate the time varying ion focusing effects. We have found that the required time varying rates for both the solenoidal field and the energy variation are too large to be feasible.

2 MODEL

To model the backstreaming ion effects consistently with the beam and target geometry, we should study this problem with particle simulations. Typically, the electron beam size at a converter target is about 1 mm, and the beampipe wall radius is about several centimeters. The backstreaming ion channel can vary from a few millimeters at the beginning of an electron beam pulse to a meter at the tail of a pulse. The simulation volume has to be large enough to include the pipe wall and the entire ion channel in order to model the space charge potential and the backstreaming ion focusing effect properly. At the same time, the simulation mesh size has be small enough to model the backstreaming ion emission in a millimeter size A-K gap. These requirements make examining time varying focusing field and energy with particle simulations very time consuming. Therefore, we study the feasibility of controlling the electron beam's spot size with a time varying final focusing solenoidal field or beam energy variation by solving the envelope equation given as

$$R'' + \frac{k_{co}^2}{4\gamma^2\beta^2} R - \frac{2I}{\gamma\beta^3 I_o R}\left\{1 - f_i(z) - f_T(z) - \beta^2\right\} - \frac{E^2}{R^3} = 0 \quad (1)$$

where R and E are the beam's edge radius and edge emittance, f_i is the backstreaming ions' charge neutralization factor, and f_T is the foil focusing effect provided by the x-ray converter. In our model, all backstreaming ions are trapped within the electron beam.

Both the electron density and the ion density are constant in radial positions within the beam radius.

2.1 Beam Potential near a Target

Let the x-ray converter target locates at $z = z_T$. At a location far away from the converter surface ($z_T - z >> a$), the radial scale length of the beam is much less the longitudinal scale length, where a is the beam radius at the z location. Let the wall potential be zero. The space charge suppressed potential inside the beam at this location is well known and given by

$$\phi(r, z_T - z >> a) = \phi_o + \frac{I}{\beta c a^2} r^2 \quad , \tag{2}$$

where

$$\phi_o = -\frac{I}{\beta c}\left(1 + 2\ln\frac{b}{a}\right) \quad , \tag{3}$$

and b is the wall radius. Let's assume that the beam potential is separable in r and z such that

$$\Phi(r, z) \approx \phi(r, z_T - z >> a)\psi(z) \quad . \tag{4}$$

Substituting Eqs. (2) and (4) into Poison equation, we find that the beam potential is given in the form

$$\phi(r, z) \approx \phi(r, z_T - z >> a)(1 - e^{-(z_T - z)/\lambda}) \quad , \tag{5}$$

where

$$\lambda = \frac{a}{2}\sqrt{1 + 2\ln\frac{b}{a}} \tag{6}$$

is the scale length of the potential sheath at the target. Note that the sheath thickness is always about several times of the beam radius regardless of the wall radius since λ varies from $0.5a$ to $1.49a$ as the b/a value varies from 1 to 50. The radial, electrostatic space-charge field is given by

$$E_r(r, z) = -\frac{2I}{\beta c r}(1 - e^{-(z_T - z)/\lambda}) \quad . \tag{7}$$

Comparing Eq. (1) with Eq. (7), it is obvious that the focusing effect provided by the x-ray converter is given by

$$f_T(z) = e^{-(z_T - z)/\lambda} \quad . \tag{8}$$

By integrate Eq. (8) over z, we find that the target's effective focusing length is λ, and the effective foil focusing factor is 1. For the case that the wall radius is 5 cm and the beam radius is 0.5 mm, the effective foil focusing length is 0.8 mm. For simplicity, we ignore the target's focusing effects.

2.2 Backstreaming Ions

According to Eq. (5), the potential drop over the distance $d = 3\lambda$ from the target is 95% of ϕ_o. An ion diode is formed across this potential drop. To estimate the amount of an ion current could be extracted from this diode, we assume that the ion emission is space charge limited. We further assume the extracted ion current follows the planar Child-Langmuir law,

$$J_i = \frac{1}{9\pi}\sqrt{\frac{2q}{M}}\frac{|\phi_o|^{3/2}}{d^2} \quad , \tag{9}$$

where q and M is ion's charge and mass, respectively. After leaving the A-K gap, i.e., $z < z_T - d$, ions move backstream with a velocity $v_i = \sqrt{2q|\phi_o|/M}$. From Eq. (3), it is obvious that the length of the ion channel would depend on beam current, spot size, wall radius and ion species. We find that the backstreaming ions' charge neutralization factor outside the A-K gap is given by

$$f_i \approx \frac{4}{9}\left(\frac{\lambda}{d}\right)^2 \approx 5\% \tag{10}$$

as $z > z_T - v_i t$. A 5% charge neutralization factor has been observed in the PIC simulations for the backstreaming protons [6]. Note that the backstreaming ions' charge neutralization factor within an ion channel is independent of beam parameters, wall radius and ion types. A re-entry (beer-can) target configuration would help to reduce the spot size blow-up rate by reducing the beam space-charge potential, hence the length of the ion channel. However, the ion charge neutralization factor remain the same. Caporaso has shown that the backstreaming ions' charge neutralization factor is 6.4% in a beer-can model that both the electron beam and the ion beam fill a beampipe [7].

The ions' neutralization factor varies along the z location within the A-K gap region and approaches infinity. The neutralization factor averaged over the gap is

$$f_i \approx \frac{4}{3}\left(\frac{\lambda}{d}\right)^2 \approx 14.8\% \quad . \tag{11}$$

For the case that the wall radius is 5 cm and the beam radius is 0.5 mm, the A-K gap distance d is only 2.4 mm. For a 6 kA beam, backstreaming protons would travel 1.9 cm, that is much longer than the A-K gap distance, within 1 ns. For simplicity, we assume the ion neutralization factor constant (5%) for the entire ion channel.

3 TIME VARYING SOLENOID FIELD

A potential way to compensate for the increasing backstreaming ions' focusing strength is to reduce the final focal lens strength in time. For the Advanced Hydrotest Facility's (AHF) [8] 6 kA, 20 MeV beams with 1200π mm-mr normalized edge emittance, we use a solenoid focusing field of 6350G to focus beams at a waist with a radius of 0.5 mm. Figure 1(a) shows that we need at lease to reduce the focusing field at the rate of 30 G/ns to compensate the backstreaming protons' focusing effects. We have found that varying the focusing lens' strength is not effective once the protons have traveled upstream and passed the final lens (t > 35 ns). Figure 1(b) indicates that at least 14 G/ns is needed to maintain the spot size for backstreaming carbon. For both cases, the required reduction rate in the final lens' strength would be hard to achieve due to the pulse power limitation.

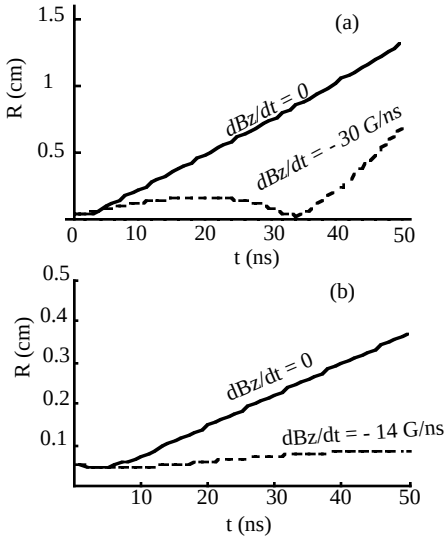

Fig.1 The time varying beam radius on a target with backstreaming (a) protons and (b) carbons and a constant (solid) and time reducing (dashed) focusing field.

4 TIME VARYING BEAM ENERGY

We now examine the feasibility of maintaining the beam spot size on a target by varying the beam energy. For simplicity, we assume that the beam energy increases linearly within a pulse, and there is no envelope variation in the pulse. For the same AHF beam, Fig. 3(a) and (b) show the compensation results for the focusing effects of backstreaming protons and carbons, respectively. Even with 150 kV/ns of energy variation rate, we can only maintain the beam spot size to a small value for about 35 ns for the backstreaming proton case (see Fig. 2(a)). For the backstreaming carbons, by varying beam energy at the rate of 40 kV/ns, we can successfully maintain the beam spot size constant (see Fig. 2(b)). For a 50 ns long, 20 MeV beam, this would require a 10% energy variation through a pulse. It would be difficult to transport a beam with such a large energy variation to the final focus region without any envelope variation.

5 CONCLUSIONS

We have developed a model to estimate the neutralization factor of backstreaming ions emitted from an x-ray converter hit by a tightly focused intense electron beam. We have found that the neutralization factor is always 5% regardless of the ion mass and charge, the electron current, beam radius and the wall radius. We have also studied two schemes, reducing the final focus lens' strength in time and increasing beam energy in time, to compensate for the increase in focusing produced by these ions. We have found that neither methods are effective in maintaining a small beam spot size if the backstreaming ions are protons. In the case of backstreaming carbons, both methods can maintain a small beam spot size. However, the required solenoid field variation rate and the energy variation rate are quite large.

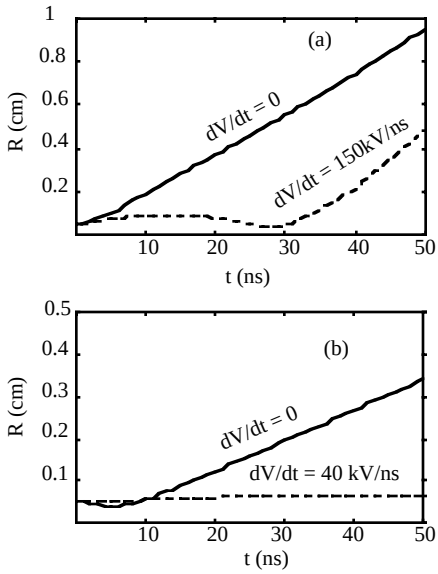

Fig. 2 The time varying beam radius on a target with backstreaming (a) protons and (b) carbons for a constant (solid) and for a time varying beam energy (dashed).

ACKNOWLEDGMENTS

We would like to thank J. McCarrick for numerous discussions. The work was performed under the auspices of the U.S. Department of Energy by LLNL under contract W-7405-ENG-48.

REFERENCES

[1] Dale Welch, Target Workshop, Albuquerque, NM. Feb. 6, 1997

[2] P. Rambo, et. al., "EM-PIC Simulations of e-Beam Interaction with Field Emitted Ions from Bremsstrahlung Target," this conference.

[3] D. Prono, Target Workshop, Livermore, CA, May 21, 1998; T. Hughes, Target Workshop, Livermore, CA, May 21, 1998.

[4] S. Sampayan, et. al., "Experimental Investigation of Beam Optics Issues at the Bremsstrahlung Converters for Radiographic Applications," this conference.

[5] C. Vermare, et. al., "Experimental Results of Electron Beam Neutralization Induced by a Limited Space-Charge Emission," this conference.

[6] J. McCarrick, et. al., "Trapping Backstreaming Ions from an X-ray Converter using an Inductive Cell," this conference.

[7] G. J. Caporaso, Y.-J. Chen, "Analytic Model of Ion Emission from the Focus of an Intense Relativistic Electron Beam on a Target," this conference.

[8] G. J. Caporaso, Proceeding of 1997 Particle Accelerator Conference, Vancouver, Canada, May 1997.

ELECTRON GUN SIMULATION USING MAGIC

S. Michizono, H.Tsutsui, S. Matsumoto, Y. H. Chin and S. Fukuda
High Energy Accelerator Research Organization (KEK), Tsukuba, Ibaraki 305-0801 Japan

Abstract

The electron gun plays an important role concerning klystron performance, especially for X-band klystrons with a small drift-tube diameter. This paper describes a new method for an electron-gun simulation by using MAGIC. MAGIC solves the Maxwell equations in the presence of charged particles on a time-domain. The results simulated by MAGIC are compared with those by EGUN and measured values. It reveals that the perveance is almost the same as the measured values, and that the current-density distribution and beam angle are almost the same as those of EGUN. Although it takes half days to simulate the gun, the simulation has the potential that a single code can enable one to simulate the whole structure of a klystron.

1 INTRODUCTION

It is important to design the electron gun precisely when we design klystrons. In a future linear collider, such as Japan Linear Collider (JLC) and SLAC NLC, high-power klystrons at the X-band (11.424 GHz) will be used. In these klystrons, the beam (>350A) should be compressed to around a radius of 3 mm and the area-convergence ratio of the beam should be more than 100.

In order to simulate a whole structure of a klystron precisely by a single code, we started to use a 2.5D particle-in-cell (PIC) program, called "MAGIC"[1], which is used in plasma-physics problems. In MAGIC, neither a port approximation nor an equivalent-circuit model is used, and only the geometry of the structure is necessary to be input. By using a general program ("MAGIC"), one can modify and develop a simulation system by oneself, even if a new idea for klystrons occurs.

In the klystron, the gun and all rf components are electromagnetically divided from each other, and the simulation is executed at three parts (gun, buncher and output) [2-4]. We report on the results of some klystron-guns (S- and X-band) simulated by MAGIC.

2 BOUNDARY PREPARATION

2.1 Spatial geometry of "large" and "small" area

In MAGIC, arbitrary rectangular grids are used and the spatial grid is the primary determinant of accuracy. It is especially necessary to define fine grids in a spherical cathode and the small aperture of the drift tube radius. Since the electrons emitted due to the electric-field strength on every grid of the cathode, a careful configuration of the cathode surface is important to avoid edge emission. In order to construct the boundary condition easily, we made a program similar to the boundary-definition-program POLYGON [5] used for EGUN [6]. Figure 1 shows a schematic of the electron-gun boundary. The grid dimensions, such as Δr and Δz, must be defined in the program. Since the grids should be located on the drift tube wall, the number of grids existing in the r-direction of the drift tube is necessary as an input. There are restrictions in the number of grids (r- and z-directions and total numbers), and the grid sizes depend on the geometry size.

It is possible to simulate a "small area" (divided by "GAP" line in Figure 1) after the simulation of a "large area" (total area of Figure 1). In a small-area simulation, the electric-field (Ez) distribution on "GAP" obtained by a "large-area" simulation is used for the voltage input. Although a "small-area" simulation is possible only when the "GAP" can be treated as a Neumann boundary, this is convenient to reduce the number of cells or to make a precise simulation.

By using this boundary program, it becomes easy to compare the data obtained by EGUN.

2.2 Time step of "rough" and "fine" simulation

The data of particles and electromagnetic fields are repeatedly imported at the next buncher and output region, and the time step should be a divisor of the period of the operation frequency. When we simulate the entire structure of a klystron, it is selected as 0.24315 ps ("fine" simulation) in an X-band klystron (XB-72k [7]), which corresponds to 1/360 of the period (1 degree). The default time step with 0.5 mm grids is about 0.8 ps, which reduces the simulation time ("rough" simulation). This is convenient when we simulate only the electron-gun

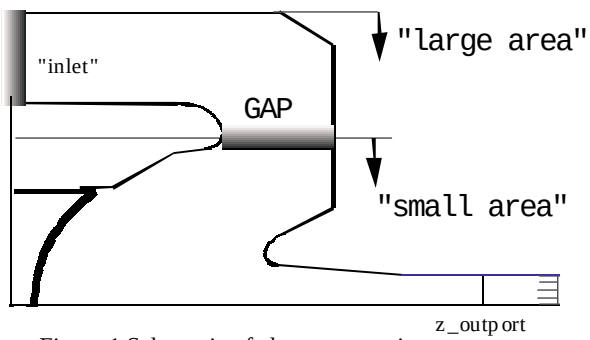

Figure 1 Schematic of electron gun giometry.

region. Both “rough” and “fine” simulations gave the same results in the gun region.

2.3 Magnetic fields

The magnetic fields used for electron-beam convergence can be introduced from the output of the LANL POISSON/PANDIRA codes [8].

2.4 Cathode voltage

In MAGIC, the voltage is applied at “inlet” in Figure 1 is a “large-area” simulation and at “GAP” in Figure 1 in a “small-area” simulation.

Since MAGIC is a time-domain code, the applied voltage should gradually be increased so as to avoid any numerical oscillations: we set 0.8 ns for the rise time.

3 PERFORMANCE OF MAGIC

3.1 Execution procedure

The execution of a MAGIC simulation is done as follows:

(1) “Large-area” simulation with a “rough” time step

If the “GAP” (in Figure 1) can be treated as a Neumann boundary, then

(2) Input the electric-field distribution on “GAP”

(3) Make a “small-area” simulation with a “fine” time step

After the simulation, the particle and field data can be exported to the next buncher and the output region of the klystron.

3.2 Output data

Since MAGIC is a general code for plasma problems, we can specify the output of the simulations. (1) A phase plot (particle trajectory) is obtained by MAGIC. Figure 2 shows the trajectories of XB-72k with an applied voltage

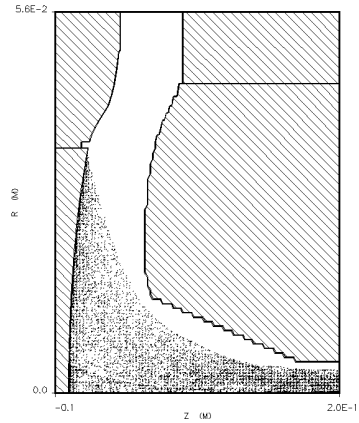

Figure 2 Particle trajectories of XB-72k with “small-area” and “fine” time step. The applied voltage and beam current are 550 kV and 490 A respectively.

of 550 kV. Due to a careful grid configuration, edge emission is not observed. (2) The transition of the beam current and voltage between a wehnelt and an anode are monitored in order to evaluate the machine time necessary to be stable. A simulation of the XB-72K with 0.5 mm grids requires 15 ns (about 60,000 time steps with “fine” simulation) to be stable.

By using exported particle data, (3) the current density distribution and (4) beam angle (v_R/v_z) are also obtained.

We can compare results (1), (3) and (4) with those of EGUN. Figure 3 shows the current-density profile of XB-72K by MAGIC together with that obtained by EGUN. The results obtained by MAGIC agree well with that by EGUN. Figure 4 shows the radial distribution of the beam angle obtaiend by MAGIC and by EGUN. Since the position of the beam waist was different between EGUN and MAGIC, probably caused by a difference in the total beam current (450 A in EGUN and 490 A in MAGIC), the beam angle by MAGIC is about half that obtained by EGUN.

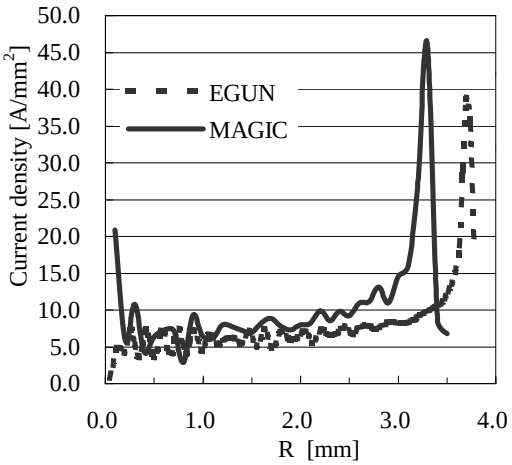

Figure 3 Current-density distribution of the electron gun (XB-72k) at 175 mm in the Z-direction.

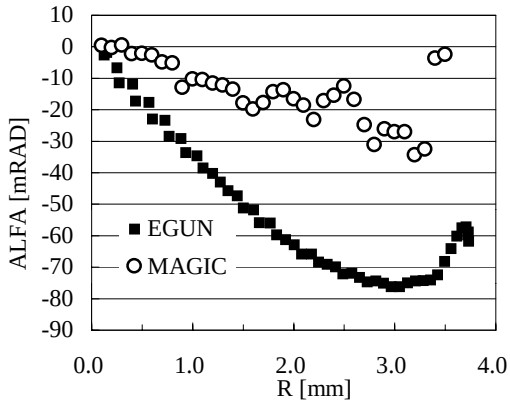

Figure 4 Electron-beam angle (vr/vz) of the electron gun (XB-72k) at 175 mm in the Z-direction. About half the value of MAGIC is due to the difference in the beam oscillation position (see Figure 5).

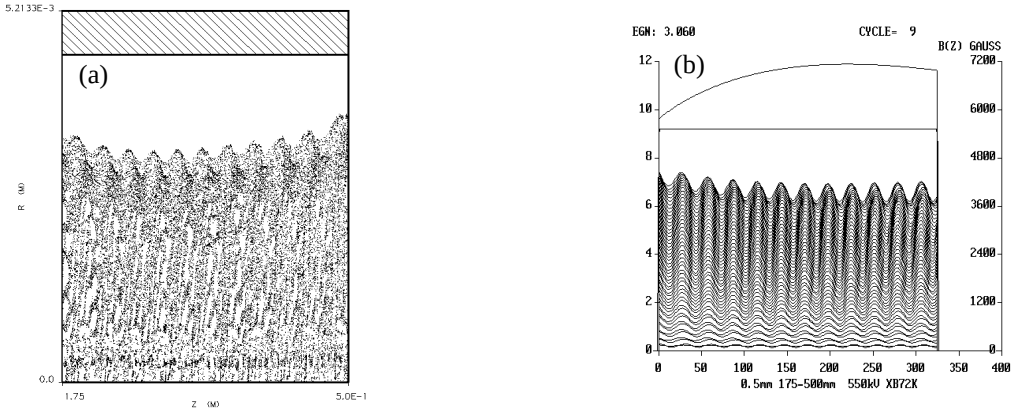

Figure 5 Beam trajectories obtained by MAGIC (a) and EGUN (b) from z=175 mm to 500 mm of XB-72k. The oscillation is almost the same, but the phase is different, probably due to a difference in the total current.

3.3 Diode simulation

By importing particle data from electron-gun region, we can simulate the drift-tube region. Figure 5 shows the particle trajectories of the diode together with that by EGUN. The trajectories obtained by MAGIC are almost the same as those obtained by EGUN.

3.4 Performance and machine time

The performance and machine time are summarized in Table.1. Simulations by MAGIC are carried out not only for an X-band klystron, but also for the S-band klystrons used in the KEK(PV3030A2)[9] and SLAC(5045)[10,11]. The perveances are almost the same as the measured values and 5-10% larger than those obtained by EGUN.

The machine time depends on the grid size and time step; it takes about 15 hours to simulate "15 ns" with a "small-area" and "fine" time step by PentiumPro-200MHz PC. Now, the pentiumII-300MHz PC is used, which reduces the simulation time by half.

Table 1 Performance of a MAGIC simulation.

Klystron	PV3030A2	5045	XB-72K
Frequency	2,856 MHz	2,856 MHz	11,424 MHz
Voltage	300 kV	315 kV	550 kV
Experimental			
μperveance	2.05	2.0	1.2
EGUN			
Grid size	0.5 mm	0.5 mm	0.5 mm
μperveance	1.89	1.78	1.10
machine-time*	2 min.	2 min.	6 min.
MAGIC			
Grid size	0.5 mm	0.5 mm	0.5 mm
Time step	0.9726 ps	0.9726 ps	0.24315 ps
μperveance	2.03	1.99	1.19
machine-time*	5 hours	5 hours	15 hours

*The time simulated by PentiumPro200MHz PC.

4 SUMMARY

An electron-gun simulation was successfully carried out by MAGIC. A boundary-formation program was developed which makes it convenient for comparisons with EGUN. (1) The particle trajectories, (2) transitions of the voltage and beam current, (3) current-density distribution, and (4) beam angle were obtained; the results agree well with those obtained by EGUN. The obtained perveances were almost the same as the measured values for the S- and X-band klystrons. Although it takes more than a half day to simulate with a fine time-step used for a whole-structure calculation, the machine time can be reduced by using a faster PC. Since the whole-structure simulation reveals good agreements with the measured values, this simulation method is useful for the final stage of klystron design.

5 REFERENCES

[1] Mission Research Corporation, Virginia, USA.
[2] Y.H.Chin, "Computational Modeling of Klystrons", this conference.
[3] S.Matsumoto et al., "Simulation study of the bunching section of X-band klystrons", this conference.
[4] H.Tsutsui et al., "X-band klystron output cavity simulation", this conference.
[5] R. Becker, "Easy boundary definition for EGUN", Nucl. Inst. Meth. B42,162-164 (1989).
[6] W.B.Herrmannsfeldt, "Developments in electron gun simulation", SLAC-PUB-6498 (1994).
[7] J.Odagiri et al., "FCI simulation on 100 MW class klystron at X-band", Proceedings of the 17th International Linac Conference, Tsukuba, Japan, 469-471(1994).
[8] J.H.Billen and L.M.Young, "POISSON SUPERFISH", LA-UR-96-1834(1997).
[9] S.Fukuda et al., "Design and evaluation of a compact 50-MW rf source of the PF linac for KEKB project", Nucl. Instr. Meth. A363,83-89 (1995).
[10] T.G.Lee et al., "A fifty megawatt klystron for the stanford linear collider", SLAC-PUB-3214 (1983).
[11] M.A.Allen et al., "Performance of the SLAC linear collider klystrons", SLAC-PUB-4262 (1987).

DOPPLER-SHIFT PROTON FRACTION MEASUREMENT ON A CW PROTON INJECTOR

J. H. Kamperschroer (General Atomics, San Diego, CA),
J. D. Sherman, T. J. Zaugg (LANL, Los Alamos, NM),
A. H. Arvin, A. S. Bolt, and M. C. Richards (WSRC, Aiken, SC)

Abstract

A spectrometer/Optical Multi-channel Analyzer has been used to measure the proton fraction of the cw proton injector developed for the Accelerator Production of Tritium (APT)[1] and the Low Energy Demonstration Accelerator (LEDA) at Los Alamos. This technique, pioneered by the Lawrence Berkeley National Laboratory (LBNL), was subsequently adopted by the international fusion community as the standard for determining the extracted ion fractions of neutral beam injectors. Proton fractions up to 95 ± 3% have been measured on the LEDA injector. These values are in good agreement with results obtained by magnetically sweeping the ion beam, collimated by a slit, across a Faraday cup. Since the velocity distribution of each beam species is measured, it also can be used to determine beam divergence. While divergence has not yet been ascertained due to the wide slit widths in use, non-Gaussian distributions have been observed during operation above the design-matched perveance. An additional feature is that the presence of extracted water ions can be observed. During ion source conditioning at 75 kV, an extracted water fraction >30% was briefly observed.

1 INTRODUCTION

A diagnostic developed by the magnetic fusion energy community has been successfully utilized on the LEDA injector test facility[2] at Los Alamos. The technique was developed in the late 1970s at LBNL[3] as a means of determining the composition of neutral beams used to heat magnetic fusion plasmas. Extracted H^+, H_2^+, and H_3^+ interact with background gas to produce fast, excited hydrogen atoms with energies of E, E/2, and E/3, where E is the ion source extraction potential. By observing the beam at an angle relative to the direction of propagation, the Doppler-shift separates the light from the three species. The wavelength of the Doppler-shifted light is $\lambda = \lambda_0 (1 - \beta \cos \theta)$, where λ_0 is the unshifted wavelength, β = v/c, and θ is the angle between the viewing line of sight and the beam's direction of propagation. Beam composition is determined from the quantity of light associated with each Doppler-shifted line. Cross sections for Balmer-α (Hα) production from H^+, H_2^+, and H_3^+ incident on hydrogen gas have been measured[4], permitting a quantitative measure of the beam composition. In addition to the Doppler shift due to the differing β's, the light from each species is broadened due to cos θ. For small beam divergence, and neglecting broadening due to the instrument, the line shape is a direct measure of the velocity distribution. In principle, a quantitative measure of the divergence can be made[5]. Collisions of extracted water ions with the background gas produce excited hydrogen atoms with energy E/18, where E is the extraction potential. Water contamination becomes apparent at a level of <1%

Experiments carried out at Los Alamos have been a successful proof-of-principle test on a proton injector, even though photon fluences from the injector are orders of magnitude below that of large fusion ion sources. The photon production rate is proportional to the beam current, the background gas density, and the Hα production cross sections. While the current densities of fusion and APT ion sources are similar, fusion ion sources have much larger extraction areas. Fusion ion source currents are of order 100 A versus 100 mA for the LEDA/APT injector. Another significant difference is the background gas density. In neutral beam injectors, the goal is to convert the extracted ions into neutrals by collisions with background gas. For a proton injector, it is important to avoid proton loss via charge exchange to H^0. Near the ion source, the background gas density is ~10 times lower than in a fusion neutral beam injector. The net result is that the Hα production rate in a proton injector is ~10^4 times less than in a fusion neutral beam injector.

Several factors favor the proton injector. The APT ion source is cw compared to pulse-lengths of a few seconds for fusion ion sources; long integrations are therefore possible. Another advantage is that the neutralization and dissociation of the extracted ion beam, that takes place in the neutral beam injector before the beam reaches the observation point, occurs to a much smaller degree in a proton injector. The problem created by changing the state of the beam is that the Hα production cross sections are different for the daughters than for their parents. Therefore, the composition of the beam at the observation point must be known to deduce the composition at the extraction plane. Due to the low gas pressure between the ion source and observation point in a proton injector, a beam composed of H^+, H_2^+, and H_3^+ can be assumed.

Initial data collection occurred at 50 kV, during experiments supporting a 1.25 MeV cw radio-frequency quadrupole (RFQ)[6]. The RFQ for LEDA and APT has been designed to accept a 75 keV proton beam. A small amount of data was obtained after the ion source was regapped for operation at 75 keV.

2 DESCRIPTION OF THE HARDWARE

A complete Doppler-shift spectroscopy system[7] was borrowed from the Princeton Plasma Physics Laboratory (PPPL). It consists of a 135-mm Canon lens to focus collimated light onto a 600-μm glass fiber; an Instruments S.A. 640-mm Czerny-Turner spectrometer; a Princeton Applied Research Corp. vidicon detector; a detector controller; and a computer control console.

The beam was observed 34 cm downstream from the extractor as it exits the cone that follows the accelerator. The 7-cm exit diameter of the cone equals the 7-cm diameter of the light collection cylinder. At this location the 4-rms beam diameter is 2.2 cm. Since light is collected from the entire horizontal extent of the beam, all of x phase space is observed.

Each pixel in the 500x500 square detector is 25 μm. When integrating light from a 43-cm tall PPPL neutral beam injector, the slits of the spectrometer were set at 3 μm. In the present case, they were opened to 50 μm, providing additional light. Opening the slits beyond the 50-μm size of the pixels caused broadening of the lines and merging of the two molecular lines. 50 μm is a compromise between signal and resolution.

3 DATA AND ANALYSIS

Figure 1 is a spectrum obtained at 50 kV with 120 mA of ions measured at the first DC current toroid. (All quoted beam currents were measured with this toroid.) The viewing angle, θ, was 60°, the entrance slit of the spectrometer was 50 μm, and light was integrated for 16 s. Since the beam came towards the line of sight, the Doppler shift was in the blue direction. Left to right, the first three lines are the Doppler-shifted lines from incident H^+, H_2^+, and H_3^+. The rightmost, and tallest, line is unshifted Hα (656.3 nm).

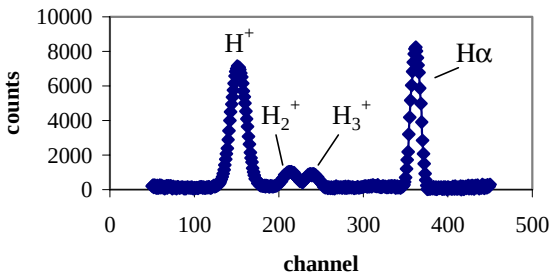

Figure 1. Spectrum at 50 kV and 120 mA with 50 mm slits.

Light falls on a portion of the height of the detector corresponding to the diameter of the fiber. Each channel was defined to be one pixel wide by 60 pixels tall (sufficient to include all pixels illuminated by the fiber). The wavelength corresponding to a particular channel can be determined by assigning 656.2 nm to channel 362 and using a dispersion of 0.016 nm/channel. The ordinate represents the number of counts detected in each channel.

Proton fractions were obtained by fitting the three Doppler-shifted lines to Gaussians. Error bars of ±3% for the proton fraction, 17% for H_2^+, and ±20% for H_3^+ are based on uncertainties of ±10% in calculating the line areas, ~±5% in cross sections[4], and assuming that the gas line density between the ion source and observation point could be as high as 1.5×10^{14} cm^{-2}.

4 RESULTS

Proton fractions have been measured for scans of the ion source microwave power and gas throughput. In both cases, the spectrometer and detector were operated in the as in figure 1. Figure 2 shows the results of scanning the 2.45 GHz microwave power to the source over the range of 500 to 1500 W while the beam energy and gas throughput were fixed at 50 keV and 2.22 standard cubic centimeters per minute (sccm). Beam current varied from 36 mA to 140 mA. Due to the wide range over which the beam current changed, the currents to the two electron cyclotron resonance (ECR) solenoids needed to be varied to maintain stable operation.

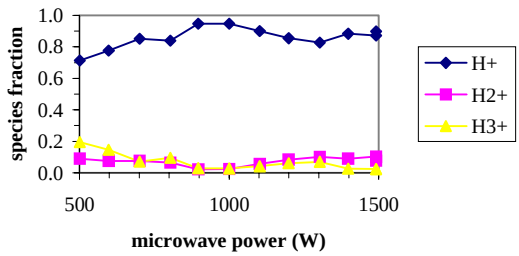

Figure 2. Beam composition as a function of microwave power.

Proton fractions of 0.95 ± 0.03 were found at 900 and 1000 W. These values agree with measurements made using an emittance measuring unit modified with a deflection magnet preceding the Faraday cup[2].

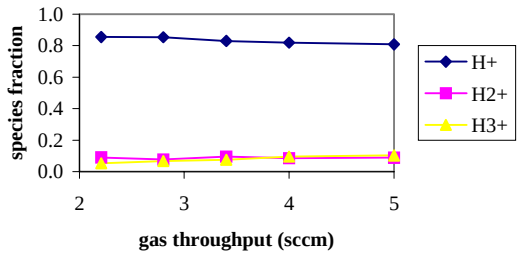

Figure 3. Beam composition as a function of gas throughput.

Figure 3 is the result of a scan where the gas throughput was varied from 2.2 to 5 sccm, at a constant

microwave power of 1000 W. As the throughput increased from 2.2 to 5 sccm, beam current decreased from 92 mA to 71 mA. As above, the currents to the two ECR solenoids were adjusted to maintain stable source operation.

It is important to note that the proton fraction corresponding to the 2.2-sccm data point in figure 3 (85%) does not agree with the 1000 W data point in figure 2 (95%). Source microwave power and throughput were the same in these two cases, but the proton fractions differ by 10%. Inspection of the raw data supports the measured difference. ECR solenoid settings were slightly different. This observation, together with the variations in figure 2, indicates that the proton fraction is sensitive to minor variations in ion source setpoints.

Figure 4 is a spectrum from 50 kV, 132 mA source operation. The source is operating above its design-matched perveance (110 mA at 50 kV). An important difference between the way this spectrum was acquired and all of those discussed so far is that the slit width was reduced to 20 μm.

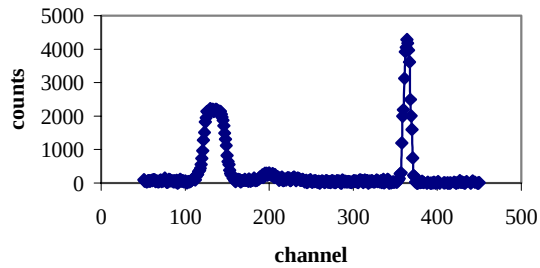

Figure 4. Spectrum taken at 132 mA with 20 μm slit width showing a non-gaussian proton peak.

Note the non-Gaussian shape of the proton line. Such a distribution is indicative of poor beam optics. In this case, it can be attributed to overdense beam extraction. Other data taken with 20-μm slits show a return to Gaussian shape as the current was reduced to 110 mA. The data taken with 50-μm slits is more Gaussian because the natural line width is convolved with a wider instrument function.

Data were also taken during several hours of ion source operation at 75 keV. Immediately prior to when this data was taken, the ion source was exposed to air for accelerator maintenance. The spectrometer slit width was back to 50 μm.

An interesting spectrum was noted and is shown in figure 5. Situated at channel 300 is a line due to hydrogen atoms extracted as water ions. The presence of significant water in the beam is attributed to the fact that the ion source was just beginning to be conditioned and that water became absorbed on the source walls during its exposure to air.

Cross sections for the production of Hα from water incident on hydrogen have not been measured. To estimate the water fraction, the required cross sections were estimated from cross sections for the production of Hα for hydrogen atoms incident on water[8].

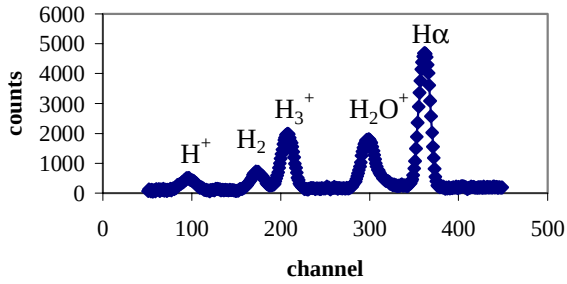

Figure 5. Spectrum at 75 kV, just after the ion source was open to air.

The proton fraction is estimated to be in the range of 30 to 40% while water is 40 to 25%, respectively. There is a large uncertainty in the beam fractions in this case due to the facts that protons are no longer the dominant line and that estimates of the water cross sections differ by a factor of two.

After approximately 10 minutes of cw operation, the water level in the beam decreased by over an order of magnitude. However, the proton fraction was still poor due to the low source power. Residual gas analysis of the injector vacuum always indicates the presence of water contamination for several days after exposure to air. Water in the ion source cleans up at a more rapid rate due to its active removal by the plasma and the beam.

ACKNOWLEDGMENTS

This work has been supported by the US Department of Energy contract DE-AC04-96AL89607. We would also like to thank the neutral beam operations group at the Princeton Plasma Physics Laboratory for the loan of the Optical Multi-channel Analysis system.

REFERENCES

[1] G. Lawrence, "High-Power Proton Linac for APT; Status of Design and Development", these proceedings.
[2] J. Sherman et al., Rev. Sci. Instrum. **69**, 1003 (1998).
[3] C. F. Burrell, W. S. Cooper, R. R. Smith, and W. F. Steele, Rev. Sci. Instrum. **51**, 1451 (1980).
[4] I. D. Williams, J. Geddes, and H. B. Gilbody, J. Phys. B **15**, 1377 (1982).
[5] G. Bracco, C. Breton, C. de Michelis, M. Mattioli, and J. Ramette, J. Opt. Soc. Am. **71**, 1318 (1981).
[6] B. G. Chidley, F. P. Adams, G. E. McMichael, T. T. Ngoc, and T. S. Bhatia, in *Proceedings of the 1990 Linear Accelerator Conference.*
[7] J. H. Kamperschroer et al., Rev. Sci. Instrum. **58**, 1362 (1987).
[8] F. B. Yousif, J. Geddes, and H. B. Gilbody, J. Phys. B. **19**, 217 (1986).

DESIGN, CONSTRUCTION AND OPERATIONAL RESULTS OF THE IGBT CONTROLLED SOLID STATE MODULATOR HIGH VOLTAGE POWER SUPPLY USED IN THE HIGH POWER RF SYSTEMS OF THE LOW ENERGY DEMONSTRATION ACCELERATOR OF THE ACCELERATOR PRODUCTION OF TRITIUM (APT) PROJECT

J. T. Bradley III, D. Rees, R. S. Przeklasa, Los Alamos National Laboratory, Los Alamos, NM;
M. C. Scott, Continental Electronics Corporation, Dallas TX

Abstract

The 1700 MeV, 100 mA Accelerator Production of Tritium (APT) Proton Linac will require 244 1 MW, continuous wave RF systems. 1 MW continuous wave klystrons are used as the RF source and each klystron requires 95 kV, 17 A of beam voltage and current. The cost of the DC power supplies is the single largest percentage of the total RF system cost. Power supply reliability is crucial to overall RF system availability and AC to DC conversion efficiency affects the operating cost. The Low Energy Demonstration Accelerator (LEDA) being constructed at Los Alamos National Laboratory (LANL) will serve as the prototype and test bed for APT. The design of the RF systems used in LEDA is driven by the need to field test high efficiency systems with extremely high reliability before APT is built. We present a detailed description and test results of one type of advanced high voltage power supply system using Insulated Gate Bipolar Transistors (IGBTs) that has been used with the LEDA High Power RF systems. We also present some of the distinctive features offered by this power supply topology, including crowbarless tube protection and modular construction which allows graceful degradation of power supply operation.

1 POWER SUPPLY REQUIREMENTS

The High Voltage Power Supplies are required to convert standard AC distribution voltages to regulated HV DC power. The efficiency of this power supply was required to be greater than that of proven power supply technologies. The large number of power supplies required by APT implies that each power supply must be extremely reliable. Protection of the personnel who will service the power supply systems in the APT plant is of primary importance. Protection of the klystron from damage during a klystron arc is secondary to safety but still a crucial requirement. The humidity and temperature of the environment around the APT plant at Savanna River Site impose additional requirements on the power supply.

1.1 Performance

While over 100 of the klystrons in the APT plant will require a maximum of 17 A of current at 95 kV, the three klystrons which drive the RFQ of the accelerator will require up to 21 A at 95 kV. In contrast, the RFQ klystrons will make up approximately half of the klystrons in the LEDA RF systems. The function and reliability of all candidate power supply designs must first be proven out in the LEDA accelerator before they can be considered for the APT plant. In order for candidate power supply designs to gain significant testing time on LEDA, all candidate power supply designs must be capable of providing currents of up to 21 A at 95 kV.

The output voltage regulation was required to be within ±400 V around the setpoint and the ripple was required to be ≤1100 Vpp while the input line voltage varied ±5% and the input voltage phase unbalance was ≤3.8%.

The input voltage of this power supply design was required to be 4160 V three phase service. The power supplies were required to have a power factor ≥0.98 for all output voltage levels between -60 kV and full power and all current levels between 10 and 21 amps. The harmonic distortion of the current drawn from the input lines was required to meet IEEE Std 519-1992 specifications.

When operating at -95 kV and currents between 17 and 21 amps, the efficiency was required to be ≥97%. When operating between -80 kV and -95 kV and currents between 12 and 21 amps, the efficiency was required to be ≥96%. When operating at or between -60 kV and -80 kV and currents between 10 and 21 amps, the efficiency was required to be ≥95%. The requirements on efficiency are summarized in Figure 1.

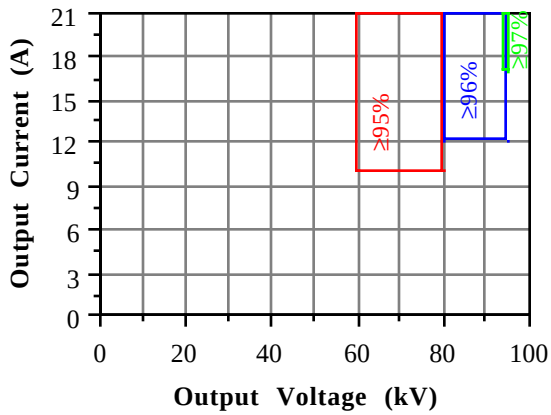

Figure 1: The efficiency requirements were specified over a range of currents and voltages.

1.3 Reliability and Maintenance

The goal for power supply Mean Time Between Failure (MTBF) was 25,000 hours. This goal was driven by the combination of the MTBF for all other components in each RF system and the large number of high power RF systems that will be required in the APT plant.

Serviceability was given consideration from the beginning the power supply design. The goal for the Mean Time To Repair (MTTR) of the supply was one hour or less to minimize the cost of maintaining the APT accelerator.

1.4 Safety and Klystron Protection

The Kirk® Key locks on the power supplies were required to integrate with the existing Kirk® Key lock system used in the existing LEDA High Power RF systems.

The power supplies were also required to meet all existing safety requirements at LANL including the requirement that debugging the low level power supply control circuits could be done without exposure to voltages in excess of 24 V.

The power supply was required to NOT use a crowbar but still limit the energy deposited in a klystron arc to less than 40 Joules and have a backup means of shutting off the power in the event that the principal system failed.

1.5 Environment

The environmental requirements were specified such that they covered both the expected environmental conditions at the Savanna River Site and the environmental conditions at LANL. The power supply was required to function over an ambient temperature range of 10°C to 32°C (50° F to 90° F) which was determined by the indoor location of the power supply. The power supply was required to function over a humidity range of up to 85% non-condensing which was chosen based on the environment at Savanna River Site. Finally, the power supply was required to function at an altitude of up to 2438 m (8000 feet) to allow it to be tested at LANL.

2 POWER SUPPLY DESCRIPTION

The design of the IGBT controlled Solid State Modulator High Voltage Power supply is based on the design of Solid State Modulators sold by Continental Electronics. Over 100 of these modulators are now in use and offer impressive AC to DC conversion efficiency.

2.1 Electrical Design.

The power supplies utilize 96 separate rectifying modules stacked in series. Each module is fed from an isolated secondary winding on one of four transformers as shown in Figure 1. The primary windings of each transformer are extended by different amounts to produce 24 pulse rectification at the power supply output.

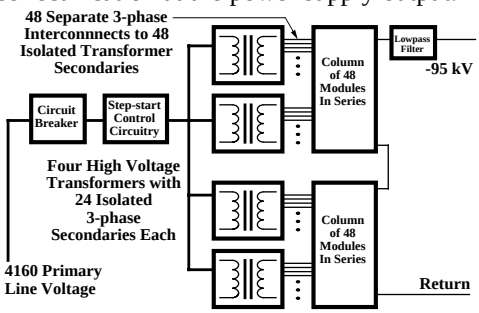

Figure 1: Two transformers serve each power column.

Each module uses an IGBT for current control as shown in Figure 2, eliminating the need for a crowbar. Each module also contains independent control circuitry to monitor the module output and inhibit the SCRs in the six pulse bridge in the event that an IGBT fails closed. Failed modules are bypassed by the control system to provide graceful degradation of operation. If more than five modules have failed, then the maximum voltage the supply can produce under the condition of 5% input voltage droop is reduced by roughly 1 kV per failed module after the first five.

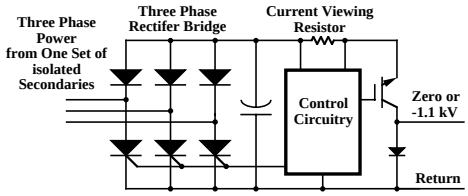

Figure 2: Each module contains independent control circuitry to disable the module in the event of module control failure.

2.2 Physical Structure.

The whole power supply is located behind a 6.1 by 5.5 m fence. Each module is contained on a removable circuit card. The circuit cards are arranged in the two power columns in four rows of twelve. This arrangement allows cooling air from fans at the bottom of the columns to be blown across each module. The columns support corona rings on each row to hide sharp edges on the modules from high electric fields and to grade the electric field as the potential increases toward the top of each column.

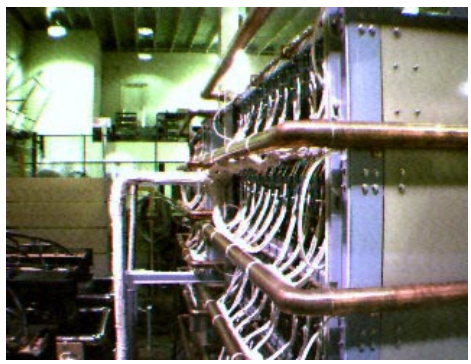

Figure 3: Each module is connected to a unique isolated 3-phase secondary on one of the four transformers.

The backplanes of the power columns contain connections to the 24 isolated 3-phase secondaries on each of the four transformers as shown in Figure 3. The backplanes also contain the shorting mechanisms that insure that all modules are shorted out before the fence is opened when the power supply is to be serviced.

2.3 Mean Time Between Failure and Mean Time To Repair

The MTBF was calculated after the design was finalized. The power supply was designed such that up to five modules could fail before the supply's ability to produce 95 kV under the conditions of a 5% input voltage droop was impaired. A block diagram of the method used to calculate the MTBF is shown in Figure 4.

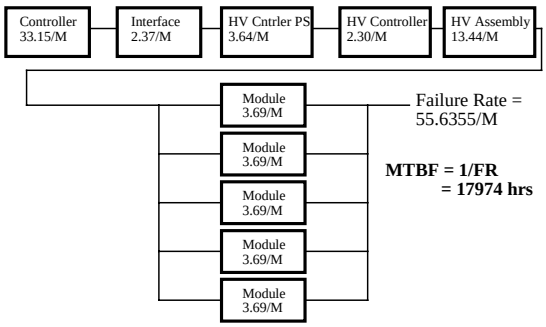

Figure 4: The total MTBF for the supply was calculated from published MTBF data for each component in the power supply.

The power supply was designed with serviceability in mind. A 44 minute MTTR was achieved in part by designing the power columns such that it possible to remove and replace any modules in the power columns without the use of tools once the Kirk® Key locked fence has been opened and the columns have been grounded.

3 ACCEPTANCE TEST RESULTS

Acceptance testing of the power supply is done in two parts. Almost all required functions of the power supply (including output power quality, safety systems and klystron protection systems) are tested at the vendor's facility before the power supply is shipped. The testing of power supply efficiency and a full power heat run is done at LANL due to the availability of a 95 kV, 2 MW resistive load at the LEDA facility.

Three of these power supplies are on order from Continental Electronics. The first has passed its factory acceptance tests and is being shipped to LANL.

3.1 Factory Acceptance Test Results

All methods of triggering the Fast Shut Down Mode (FSDM or the equivalent of a "crowbar") were tested successfully. The power supply shut down quickly enough to prevent a 0.614 meter long 35 gauge copper wire (40 Joules) from melting placed across the high voltage output. This test was performed 192 times at full voltage over a period of 48 hours. Calculations made of the energy deposited in the wire indicate that the energy that will deposited into a klystron arc will be less than 10 Joules when the power supply is operating at full voltage and current.

The power supply was tested into a 640 Ω load at 21 A for 48 consecutive hours. During this test a heat wave combined with an air conditioning failure at the vendor's facility caused the ambient temperature and humidity rise above the maximum specified levels. Despite the extreme temperature, the full current test was passed without failure. Figure 5 shows the core temperature of the first transformer during this run. The time required to reach a relatively constant core temperature was approximately ten hours, significantly less than the length of the 48 hour test..

The harmonic content of the input current during the 21 A output current tests showed magnitudes that were all below 20 dB down from the 60 Hz fundamental. While all of these values are significantly below the maximum allowed values of IEEE Std 519-1992, these measurements will be taken again at LANL where the test can be repeated with loads in the MW level. The utility connections at LANL are also expected to provide a more realistic source impedance to the supply.

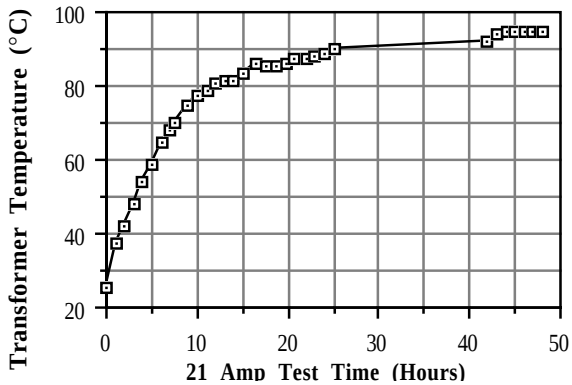

Figure 5: Transformer core temperature while running at 21 Amps in an ambient temperature of greater than 38° C.

3.2 Final Acceptance Tests

The final acceptance tests will be performed at LANL where a 2 MW, 95 kV resistive load is available. The power supply is being shipped to LANL for installation. Final acceptance tests will take place in September, 1998.

4 CONCLUSIONS

The first IGBT Controlled SSM High Voltage Power Supply has successfully passed the factory acceptance tests. This power supply is being shipped to LANL for final acceptance tests. Final acceptance tests will include measurement of efficiency at output power levels in the MW range and more detailed measurements of the input current harmonic content.

THE COLD MODEL OF THE CDS STRUCTURE

V.V. Paramonov, L.V. Kravchuk, V.A. Puntus
Institute for Nuclear Research, 117312, Moscow, Russia

Abstract

The Cut Disk Structure (CDS) was proposed as the compensated accelerating structure for high energy linacs. Cold rf model was manufactured to examine CDS parameters, partially for S-band electron linacs. In agreement with design parameters, coupling coefficient near 22% was obtained together with high shunt impedance. Results of experiments are presented.

1 INTRODUCTION

The Cut Disk Structure (Fig. 1) was proposed [1] as the result of investigations for coupling coefficient k_c increasing in compensated accelerating structures. Results of numerical simulations [1], [2] have shown attractive features of the structure - high k_c value together with high effective shunt impedance Z_e. Nine cell $\beta = 1$ cold model with operating frequency $f_0 = 2450$ MHz was produced to proof CDS design parameters for high β region.
This paper describes CDS design parameters, rf model, tuning procedure and results of experiments.

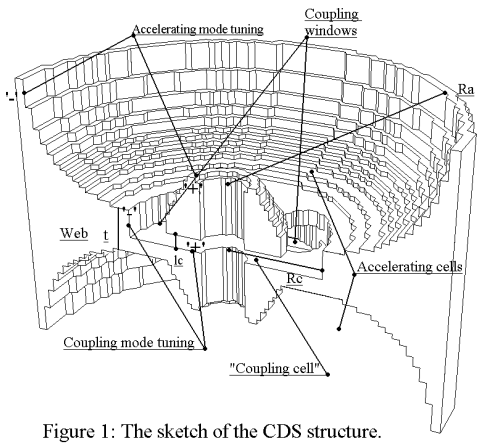

Figure 1: The sketch of the CDS structure.

2 THE CDS PARTICULARITIES

Instead of CDS is very similar outwardly (Fig. 1) to On-axis Coupled Structure with coupling slots, it realise another idea. In CDS accelerating mode is distributed in accelerating cell of usual Ω-shape with distributed electric and magnetic fields. For coupling mode electric field is concentrated in the short space between half tubes (in "coupling cell", Fig. 1), but main part of magnetic field is distributed in the volume of accelerating cell. It results in strong overlapping for magnetic fields of coupling and accelerating modes and high k_c [2],[3] value. In CDS coupling windows serve as real 'window' trough which main part of magnetic field for coupling mode penetrates in the volume of accelerating cells and some conclusions, based on extensive experience with coupling slots, are not correct for CDS. For example, k_c is practically not sensitive to the thickness of window. For $\beta = 1$, $f_0 = 2450$ MHz increasing of the window thickness from 3.5 mm to 6 mm (and total increasing of the web between accelerating cells from 10 mm to 15 mm) k_c reduces only from 22% to 19%. The frequency shift for accelerating mode due to coupling windows is also smaller than for slot coupled structures.
May be several (2,3,4...) coupling windows at one side of the cell. The dependencies k_c on total windows opening are shown in (Fig. 2a) together with plots for calculated Z_e (Fig. 2b). At (Fig. 2b) Z_0 is the effective shunt impedance of solid accelerating cell without any windows. For small k_c values $Z_e > Z_0$ [2] and for every β there exists such k_c^0 value when calculated $Z_e = Z_0$. Due to increasing of the volume for accelerating cell with β increasing, k_c^0 decreases from $\approx 30\%$ at $\beta = 0.4$ to $\approx 22\%$ at $\beta = 1$.

3 CDS MODEL

3.1 Design parameters

As in all Coupled Cells (CCL) structures with Ω-shaped accelerating cells, Z_e value for CDS decreases with increasing of the web thickness t between accelerating cells. As an example, at (Fig. 3a) 2D calculated plots of Z_e are shown for "electron" CCL option (aperture diameter 10 mm, nose cone radius 2.0 mm). At (Fig. 3b) plots for normalised (to Z_{emax} at zero web thickness) are shown. (For "proton" CCL option Z_e reduction at low β with t increasing is

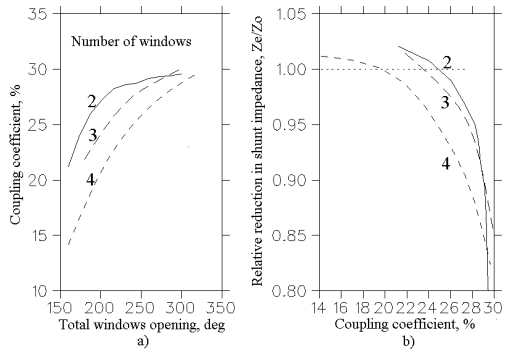

Figure 2: Parameters of the CDS structure

not so drastic.) In the CDS design we allow Z_e reduction due to increased web thickness hoping this reduction be compensated with CDS particularities (Fig. 2) and resulting Z_e value will be not less than for another CCL structures, which loose Z_e with k_c increasing. The shape of accelerating cells was 2D optimised for accelerating gradient $E_0T = 10.0$ MV/m to have $Z_{e2D} = 89.7$ MOhm/m, $Q_{2D} = 17900$. The web thickness $t = 10$ mm.

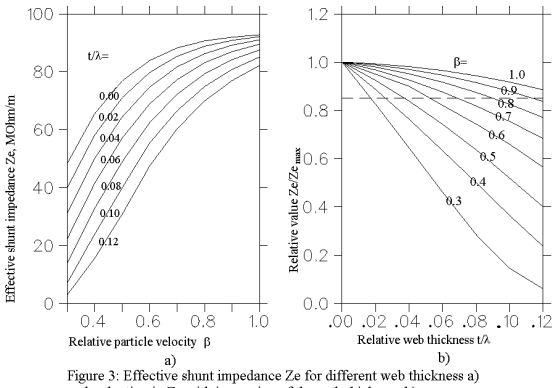

Figure 3: Effective shunt impedance Ze for different web thickness a) and reduction in Ze with increasing of the web thickness b).

3.2 The model description

The cold CDS model was manufactured from aluminum alloy to simplify the manufacturing procedure. The units of the model have been manufactured in INR with using reliable, but usual (not numerically controlled) equipment. Enough soft tolerances (not stronger than $\pm 50\mu$) were accepted for essential dimensions of the structure - dimensions of "coupling cell", coupling windows and accelerating cell. The radius of accelerating cell R_a and the length of "coupling cell" l_c (see Fig. 1) were reduced with respect to design values to have ≈ 50 MHz reserve for rf tuning.

The model contains nine periods of the structure. The termination of the model is with two plates in the middle of end accelerating cells. In each period of the structure there are two caps. Joint between caps (the place of rf contact) are in middle-planes of accelerating and "coupling cells". To reduce quadruple perturbation of accelerating field by coupling windows, at opposite sides of accelerating cell windows are placed face-to-face. Because rf properties of material are not known well, to have information about quality factor Q, special reference cylindrical cavity was manufactured from the same material, at the same equipment, with the same requirements, with the same length $\beta\lambda/2$, with the same number of rf joints.

The usual equipment was used to provide rf and bead-pool measurements. As the bead-pool the aluminium sphere 3 mm in diameter was used.

3.3 Tuning procedure

As usual, tuning of compensated accelerating structure should have three procedures:
- tuning of the accelerating mode frequency f_a to f_0 one;
- tuning of the coupling mode frequency f_c to confine with f_a (closing of the stop-band);
- tuning of the accelerating field distribution (if needed).

During the mode frequencies tuning there were no tuning of individual cells. Both for accelerating mode tuning and coupling one the change in dimensions was the same for all cell in the section. But after each step of the frequencies tuning the frequencies of accelerating mode and coupling one were determined by measuring frequencies of two 0 type and one π type modes in the assembly from two caps terminated with end plates. It was just for purpose of investigation.

The accelerating mode frequency tuning in CDS do not differs from the same procedure in another CCL and may be performed by R_a increasing (decreasing of f_a) or drift tube shortening (increasing of f_a) (Fig. 1). Starting f_a value was 2598 MHz and f_a tuning has been performed in three steps. Two steps (draft) were done by increasing of R_a value to achieve $f_a = 2451$ MHz. Because this kind of f_a tuning is soft enough ($df_a/dR_a \approx 45$ MHz/mm), there were no problems. Last step of f_a tuning was done after f_c tuning by providing narrow circular ditch at the spherical surface of accelerating cavity.

Due to big k_c value, direct determination of the coupling mode frequency both for each cell and for total section, which is reasonable in usual CCL structures, provides big error $\Delta f_c \approx f_c k_c^2/2$. The coupling mode frequency f_c tuning is based on our experience in the tuning of Disk and Washer accelerating structure. In all compensated sturcures the stop-band width $\delta f = f_a - f_c$ may be determined [4] as:

$$\delta f = \frac{\Delta F_m - \Delta F_n}{m^2 - n^2}, \Delta F_m = f_m^+ + f_m^- - 2f_0, \qquad (1)$$

where f_m^+ is the mode frequency of $\frac{(N-m)\pi}{N}$ type at the top branch of dispersion curve (Fig. 4), and f_m^- - at the bottom one.

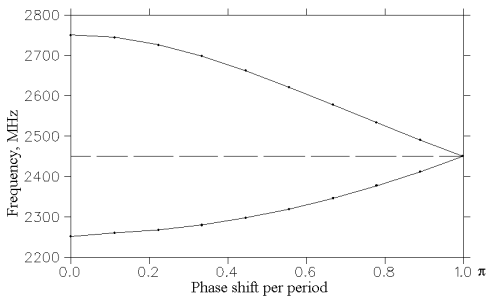

Figure 4: Dispersion curves for operating passband (experiment).

The coupling mode frequency tuning in CDS may be performed by R_c increasing (decreasing of $f_c, df_c/dR_c \sim$ 30MHz/mm) or by increasing the gap between half drift tubes l_c (increasing of $f_c, df_c/dl_c \approx 285$ MHz/mm) (Fig. 1). Starting f_c value was 2413 MHz and f_c tuning has been performed in two steps. The first step (draft) to achieve $f_c = 2447$ MHz was done by increasing of l_c value at total area of "coupling cell". Because this kind of f_c tuning is not soft, the second step has been performed by providing washer-type ditch in the space between half drift tubes. For coupling mode in CDS the tuning procedure should be under special attention.

In this study no efforts have been performed to tune accelerating field distribution, because coupling windows in this model should be identical. The mutual orientation of caps, to fix mutual orientation of windows, has been controlled with maximum deviation not more 0.25^o.

4 RESULTS OF EXPERIMENTS

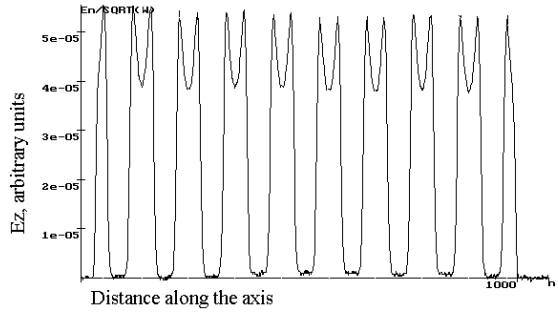

Figure 5: Electric field distribution along the axis of the model

After the model tuning, operating frequency $f_0 = 2450.1$ MHz, the stop-band width $\delta f = 400$ kHz (relative value $\delta f/f_0 = 1.9 * 10^{-4}$) were obtained. The relative values for standard deviation for frequencies of accelerating cells σ_{fa}/f_0 and "coupling cells" σ_{fc}/f_0 are $1.63 * 10^{-4}$ and $1.42 * 10^{-3}$ respectively. This σ_{fc} value is due to only soft tolerances for "coupling cell" dimensions. The measured dispersion curve is shown at Fig. 4 and calculated with this curve the coupling coefficient value $k_c = 22\%$ confirmed the designed one. In spite of one can look through the structure (there is overlapping of windows), the CDS has practically "ideal" shape of the dispersion curve. The fitting with the standard five parameters lumped circuit model shows neighbour coupling coefficients k_1 and k_2 being practically zero. Nearest high order modes of TE_{11n}-like type are placed at frequencies ≈ 3670 MHz with the passband width ≈ 160 MHz. The experimental results for spectral parameters of the CDS model confirm fine the design values.

The electric field distribution as the result of bead-pool measurements is shown at Fig.5. and exhibits the standard deviation value $\sigma_E = 1.05\%$. The main part in σ_E contribute deviations of k_c, because contribution due to deviations in frequencies of cells σ_{ef} is estimated as $\sigma_{ef} \approx 0.12\%$ for k_c, σ_{fa}, σ_{fc} and δ_f given. The measured value of the quality factor for aluminium model $Q_{eCDS} = 7880$, and for cylindrical reference cavity $Q_{eref} = 9850$. Taking into account additional rf losses in two end walls (42% from rf losses in one CDS period) and assuming 2D calculated Q factor for the solid copper reference cavity $Q_{cref} = 19400$, we are expecting Q for solid regular copper CDS structure as $Q_{CDS} \approx 16240$. The calculated from bead-pool measurements R/Q value is $(R/Q)_e = (3.6 \pm 0.07)$ kOm/m, in good agreement with calculated by using 3D MAFIA $(R/Q)_c = 3.625$ kOm/m. Together with transit time factor $T = 0.861$ for solid regular copper CDS we obtain $Z_e \approx 85.5$ MOm/m, 95% from 2D calculated one. This value do not takes into account the surface imperfectness and possible rf contacts, but is not less in comparison with another CCL structures (with low coupling) and confirm that CDS practically do not lose in shunt impedance due to strong coupling.

5 CONCLUSION

The results of experiments with 9-period $\beta = 1$ cold model of the CDS structure confirm parameters as high coupling ($k_c \approx 22\%$) and high effective shunt impedance. Another attractive CDS features are in simple design, manufacturing and tuning procedures, small transverse dimensions.

As the results of experiments, recommendation for CDS design and manufacturing procedure improvements are developed. The treatment of "coupling cells" and windows regions should be careful.

With the combinations of these parameters, CDS looks as very attractive structure for electron and high energy proton linacs. The study of the structure continues for medium β in investigation of the structure cooling, possibility of multipactoring, accelerating field "quality".

6 ACKNOWLEDGMENTS

The authors thank their colleagues from INR Accelerator Department for their help, support and creative discussions during different periods of this study, the model production and rf measurements.

7 REFERENCES

[1] V.V. Paramonov, The methods of the coupling coefficient increasing ..., Proc. of the 15 Workshop on Charged Part. Accel., Protvino, v.1 p. 161, 1996 (in Russian)

[2] V.V. Paramonov, The Cut Disk Accelerating Structure ..., Proc. of the 1997 PAC, Vancouver, (to be published).

[3] I.V. Gonin, V.V. Paramonov, Proc. of 10-th Part. Accel. Conf., Dubna, v.l, p. 182, 1985, (in Russian)

[4] I.V. Gonin et al, Some Methods of the Stop-band Width Evaluation ..., IEEE Trans. , NS-32, n.5, p. 2818, 1985

324-MHz RF DEFLECTOR DESIGN AND TEST

S. Fu*, T. Kato, F. Naito and K. Yoshino
KEK, High Energy Accelerator Research Organization
1-1 Oho, Tsukuba-shi, Ibaraki-ken, 305-0801, Japan

Abstract

In the design of JHF linac, the beam needs to be chopped for the injection into the following rapid-cycling ring. The chopper has been decided to locate in the 3-MeV medium-energy transport line between the RFQ and the DTL. A 324-MHz RF deflector (RFD) is adopted as a fast beam-chopper for its various merits, such as compactness and high deflecting field, which benefit for an efficient deflection of the beam within a short beam line. In the application of an RF deflector for an intense-beam linac, the beam loss in the transient time is a major concerned issue. The shunt impedance should be as large as possible to make the cavity to be powered by a commercially available solid RF source. An RFD cavity is designed by the HFSS code to have a very low loaded-Q value of about 10 by means of two large coupling loops, and meanwhile to keep the higher order modes sufficiently far away from the deflecting mode. An aluminum cold- model cavity was made for a test. In this paper, the design, simulation and the test results are described in detail.

1 INTRODUCTION

The JHF 200-MeV linac provides a H^- beam of 30 mA–60 mA peak current for injection into the following 3-GeV rapid-cycling ring[1]. A beam chopper must be used in the linac in order to produce a pulsed beam with a pulse length of 278 nsec and a pulse separation of 222 nsec. This chopper is located in the 3-MeV medium-energy beam-transport line (MEBT) between the 324-MHz RFQ and DTL[2]. As a high-current linac, beam-quality preservation and beam-loss control are of superior importance in the design. The MEBT should be short so as to avoid emittance growth, since the beam energy is low. An RF deflector (RFD)[3] was chosen as the chopper cavity owing to its compactness and high deflecting field. A fast rise/fall time is a fundamental requirement for the RFD to minimize the beam losses due to partial deflection to the beam during the transient time. This can be achieved in an RF cavity with a very low loaded Q value. On the other hand, a high transverse shunt impedance is pursued in the design in order to keep the RF power demand from a solid RF source within a reasonable range.

In this paper, a design study of the RF deflector cavity is presented. We first give the cavity simulations by MAFIA[4] and HFSS[5] codes in order to show the detailed design investigation in the geometry needed to meet the requirements mentioned above. Then the measurements of a cold model cavity are presented and shown to have a good agreement with the code simulation and a satisfactory result for our purpose.

2 CAVITY DESIGN STUDY

The RF deflector cavity is operated in a TE_{11}-like mode with two electrodes, as shown in Fig.1. A transverse electric field oscillating at 324 MHz between the two electrodes deflects the beam bunches away from the beam axis to a beam dump downstream during the beam-cutoff time of 222 nsec.

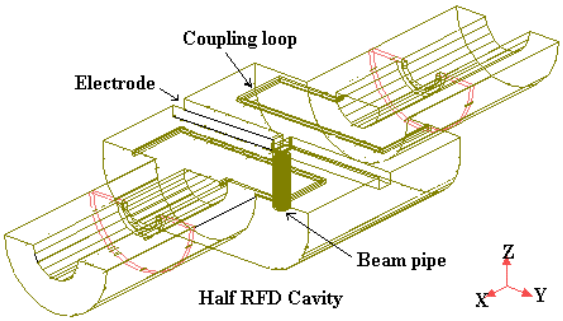

Fig.1 RF deflector cavity with large coupling loops.

One of the design target of the cavity is a high value of Z/Q_0, while keeping in mind the beam dynamics limitation. Here, Z is the transverse shunt impedance and Q_0 the unloaded Q value. In order to achieve a very short rise/fall time, the cavity will be heavily loaded by two coupling ports. In this case, the power demand from a solid RF source for operating the cavity becomes very high. To minimize the power demand P, a large value of Z/Q_0 should be pursued according to the approximate relation

$$P \cong \frac{V^2}{\omega_0 \tau (Z / Q_0)} \quad , \qquad (1)$$

where V is the deflecting voltage, ω_0 the oscillation frequency and τ the rise time.

2.1 Geometry of the electrode region

The ratio Z/Q_0 is determined by the equivalent capacitance C according to the relation

$$Z/Q_0 = \frac{1}{\omega_0 C} \quad . \qquad (2)$$

* On leave from China Institute of Atomic Energy

The C for the mode is mainly dependent on the geometry of the electrode gap region. Therefore, the parameter choice around this region must be carefully made.

The fringe fields of the electrode along the beam axis should be taken into account in the beam dynamics to calculate the effective deflection. To avoid an inverse deflecting effect of the high fringe field, the length of the electrode along the beam axis should not be equal to, but less than $\beta\lambda/2$, with β being the relative speed of a particle (v/c) and λ the free-space RF wavelength. To determine the length, MAFIA runs were conducted and the electromagnetic field distribution from MAFIA was used in a modified TRACE3-D[6] for beam-deflection tracking. The result showed that the length of the electrode should be slightly less than $\beta\lambda/2$. In this way, Z/Q_0 is larger (due to smaller C) and the high fringe field beside the electrodes can work in phase with the field in the central part of the electrodes, while keeping the effective deflecting length long. It was concluded that the electrode length along the beam axis should be 29 mm. Furthermore, the fringe field between the electrodes and the cavity wall needs to be sheltered so as to minimize its inverse effect. A beam-deflection simulation of a cavity without beam pipes showed that the net deflection is less than half that in a cavity with beam pipes. Therefore, two beam pipes are added beside the electrodes with 5.5 mm gaps between the pipes and the electrodes.

Of course, the two electrodes should be as close as possible to generate high deflecting field between them. This gap is, however, limited by the full beam size. The beam envelope from TRACE3-D suggests that the gap should be around 10 mm in order to guarantee no particle losses on the electrodes.

Also, the size of the electrode in non-deflection direction should be small in order to obtain a large Z/Q_0 value. Again, the beam envelope sets the minimum limit. The necessary size is 20 mm according to TRACE3-D simulation on beam size and the MAFIA result concerning the field distribution.

2.2 Cavity shape optimization

After the electrode size has been decided, the other dimensions of the cavity is then further optimized for the value of Z/Q_0 to be as high as possible. Since two RFD cavities will be cascaded in the beam line, the cavity should not be too long along the beam axis, due to a lack of focusing to the beam in this space, which may result in a beam emittance increase. Taking all of these factors into account, MAFIA runs suggested a cavity of 324 MHz with Z/Q_0= 437 Ω. It can be estimated from Eq.(1) that the demanded power from an RF source is reasonably about 27 kW (more accurately, HFSS gives the power of 22 kW in the next subsection) to generate a necessary deflecting field of 1.6 MV/m if a rise time of 10 nsec is assumed. Such a fast rise time indicates that the loaded Q of the cavity should be decreased down to about 10.

2.3 Cavity design with a very low loaded Q

The use of two large input/output loops is an easy option to realize a low loaded Q. A loop-coupled cavity was redesigned using the HFSS code on the basis of the previous design by MAFIA, provided that the electrode region maintains the same geometry. A modification to the cavity shape is necessary because of the introduction of large loops into the cavity, which shift the cavity resonant frequency due to the additional inductive reactance.

Two large loops with the same size are inserted into the cavity. The loops are connected to a coaxial transmission line of 50 Ω. To reach such a low loaded Q value, the size of the loop is 75×218 mm in the surface with the maximum flux. An HFSS simulation gives the S parameters, S_{21} and S_{11}, versus the frequency, as shown in Fig.2. From the figure, it can be found that the resulting Q_L is about 10, assuming it is given by the whole frequency width, Δf (31 MHz), at 70% maximum value.

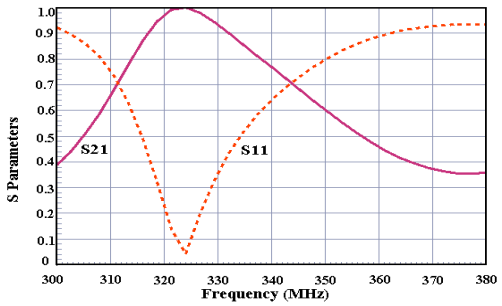

Fig.2 S-parameters from the HFSS for the cavity with Q_L=10.

The two loops of the same size are placed asymmetrically with respect to the middle plane. This induces a spectrum asymmetric with respect to the central frequency: the high-frequency side is wider than the other side, as depicted in Fig.2. It thus helps to reach a larger Δf. On the other hand, it also makes the fundamental mode to be close to and mix with the higher mode. To avoid such a problem, the loop should not be too deeply inserted into the cavity. It must keep a sufficient distance between the loop and the electrode in order to insure that the electric field between them remains extremely low. We thus increase the other dimension of the loop to a very large value (i.e. 218 mm) so as to guarantee a sufficient coupling as well as a wide mode separation.

HFSS simulations also showed the dependence of the large coupling on the diameter of the coaxial transmission line. A large coaxial line of WX-152D was adopted for the input/output of the cavity, resulting in a

loaded Q of 10. However, the loaded Q became 17 if a coaxial line of WX-77D was used.

The variation of the deflecting field (Ey) in three directions calculated with HFSS is plotted in Fig.3. The original point corresponds to the center of the cavity. The beam radii in x and y directions are both less than 5 mm according to the TRACE3-D result. It can be observed from the figure that the field has no obvious variation within the beam-size region, and hence that the beam can be deflected by a field having the same magnitude. HFSS gives Ey=1.6 MV/m in the deflecting gap when the input power is 22 kW.

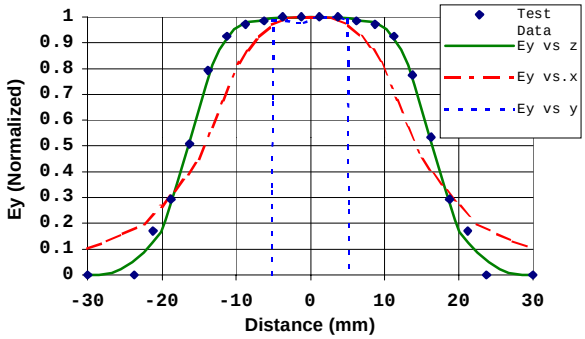

Fig. 3 Ey field distribution in three directions (test data is in the z-direction).

3 COLD MODEL TEST

An aluminum cold-model cavity was manufactured according to the design by HFSS. A series of measurements were conducted to check the applicability of the design.

A direct measurement of the rise time was performed by means of a digitizing oscilloscope with the result shown in Fig.4. It indicates that the rise time (Delta T) is 18.3 nsec, which includes about a 9 nsec contribution from the pulsed RF signal source. The effect of the transient time on the beam dynamics is discussed in Ref. [2], in which an improved method is proposed for the cavity, and the unstable particles are estimated.

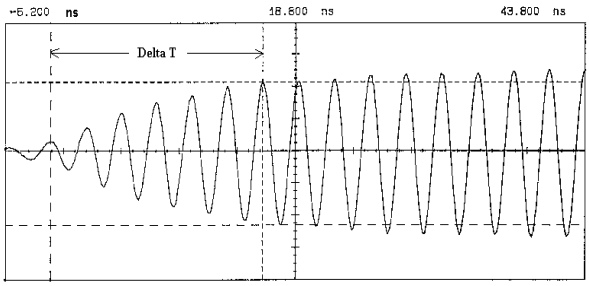

Fig.4 Measured rise time (Delta T) of the RFD cavity.

Network Analyzer depicted the scattering parameter S_{21} versus frequency in Fig.5. It gave a loaded Q of 9.7 and a resonance frequency of 324 MHz. The results are well concordant with the HFSS simulation. Some small coupling loops were prepared for a test of the dependence of the loaded Q on the size of the loops. For example, when the loops size became 65×218 mm, the loaded Q increased to 23. With two very small coupling loops, the loaded Q equaled 1463 and S_{21} was –2.18 dB. The unloaded Q was deduced to be 6580.

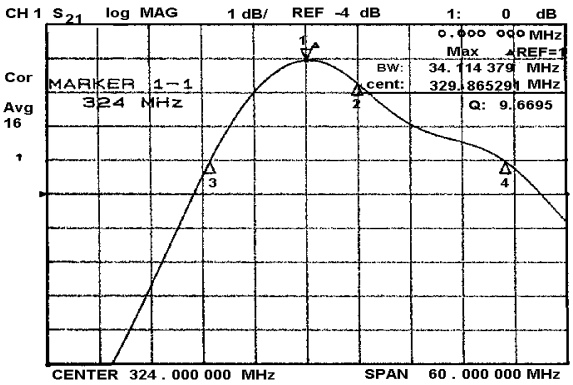

Fig.5 Spectrum of S_{21} showing the Q_L=9.7.

The field pattern in the deflecting gap was measured with a pulling bead of 5 mm in diameter. In Fig.3 the measured deflecting field (Ey) along the beam axis (z direction) is dotted. It shows a good agreement with the calculation result from HFSS.

Since the cavity is heavily loaded with a very wide spectrum, it is possible to operate it without a tuning device. To verify the temperature dependence of the resonance frequency, the cavity was heated. It was found that the cavity has a frequency shift of 60 KHz when the temperature rises up to 10°C.

CONCLUSIONS

A 324-MHz RF deflection cavity used for JHF linac was designed and a cold model was tested with satisfactory results. The measurement gives a loaded Q of about 10, which is necessary for a fast rise/fall time. The test results are in good agreement with the design calculations with MAFIA and HFSS. To meet the deflection requirement, the cavity with a loaded Q of 10 requires an input power of 22 kW according to HFSS.

ACKNOWLEDGMENTS

The authors are very grateful to Y. Yamazaki and X. Wang for their great support and many helps.

REFERENCES

[1] JHF Project Office, JHF Accelerator Design Study Report, KEK Report 97-16, March,1998.
[2] T. Kato, S. Fu, “MEBT Design for the JHF 200-MeV Proton Linac,” in these Proceedings.
[3] T. Kato, “New Design of an RF Beam Chopper,” Proc. of 7th Symp. On Acc. Sci.& Tech. (1989) 288.
[4] T.Weiland, Part. Accl. , Vol.17 (1995)227.
[5] HFSS Ver. A.04.01, Ansoft Corp, HP Co..
[6] K.R.Crandall, D.P.Rusthoi, TRACE3-D Documentation, LA-UR-97-886, May,1997.

DESIGN OF AN OGIVE-SHAPED BEAMSTOP

T. H. Van Hagan, D.W. Doll
General Atomics, La Jolla, California

J.D. Schneider, F.R. Spinos
Los Alamos National Laboratory, New Mexico

Abstract

This paper addresses the evolution, design, and development of a novel approach for stopping cw (continuous-wave), non-rastered proton beams. Capturing the beam *in vacuo* within a long, axisymmetric surface of revolution has the advantages of spreading the deposited energy over a large area while minimizing prompt neutron backstreaming and reducing shield size and mass. Evolving from a cylinder/cone concept, the ogive shape avoids abrupt changes in geometry that produce sharp thermal transitions, allowing the beam energy to be deposited gracefully along its surface. Thermal management at modest temperature levels is provided with a simple, one-pass countercurrent forced-convection water passage outside the ogive. Hydrophone boiling sensors provide overtemperature protection. The concept has been demonstrated under beam conditions in the CRITS (Chalk River Injector Test Stand) facility at Los Alamos.

1 INTRODUCTION

The Accelerator Production of Tritium (APT) program [1] requires several commissioning beamstops [2]. This paper discusses the first of these, which will be used to commission the Radio Frequency Quadripole (RFQ) and the first Coupled-Cavity Drift Tube Linac (CCDTL sections in the Low Energy Demonstration Accelerator (LEDA) presently being built at LANL (Los Alamos National Laboratory) [3]. The first LEDA beamstop must accommodate a 0.1 A proton beam in cw operation at energy levels of up to 6.7 MeV. Early studies showed that conventional beamstop approaches (e.g., plate-type with beam rastering to distribute the heat) would result in a large, costly, immobile installation with significant radiation back-streaming issues—attributes which would severely complicate the job of developing and maintaining the Linac. These issues are addressable with an approach that minimizes the projected area (footprint) presented by the beamstop normal to the beam.

Eliminating rastering reduces this footprint to that of the beam spot size, but requires management of sharply higher energy fluxes imposed by the Gaussian beam. The circular spot shape of the beam suggests a conical impact surface for the beamstop, a concept which has been successfully used on other Linac applications.

Even smaller orthogonal footprints result when the conical geometry is combined with an upstream cylindrical scraper section that exploits the divergent qualities of the beam to spread the heat distribution. The conical end section then would capture the central portion of the beam while the wings of the Gaussian distribution are deposited in the cylindrical section. The cone/cylinder beamstop proportions are governed by the practical combination of radius and length that captures the beam within a minimum radius without spillage. This typically results in a long, thin structure, with a re-entrant configuration that inherently minimizes both the back-streaming potential and the radial shield thickness requirement. The circular cross-section also minimizes edge effects which could produce hot spots. However, the abrupt cone/cylinder intersection creates a sharp thermal gradient that needs to be smoothed out. The graceful, continuous inflection obtained by replacing the cone/cylinder with an ogive shape is a logical solution to this problem.

The ogive shape addressed here is generated by revolving a circular arc about a centerline to produce a surface of revolution, as shown in Figure 1. The ogive

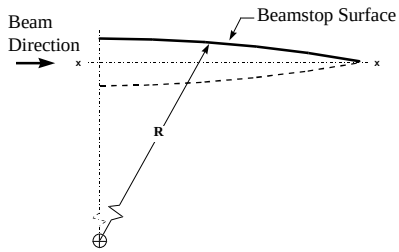

Figure 1: Ogive Shape

contour adjusts the angle of incidence as needed to accommodate the variable power density of the diverging beam: the greatest angles occur where the power density is lowest, and vice versa, resulting in a smooth, relatively mild heat flux profile on the beamstop surface.

2 DESIGN CONSIDERATIONS

Table 1 summarizes the LEDA beamstop design, which is based on the ogive concept.

Table 1: LEDA Beamstop Design

BEAM CHARACTERISTICS	
Energy x Current	6.7 MeV x 0.1 A, Gaussian
Operation	1 Hz to cw (~ 6 mos. At cw)
PHYSICAL FEATURES	
Overall Dimensions	~ 109-in Height x 133-in Length
Beam Centerline Height	72-in
Target Geometry	Axisymmetric; Tangent Ogive
Target Dimensions	6-in ID x 92-in L x 0.1-in Thick
Target Material	Electroformed Nickel
Coolant	Water outside (vacuum inside)
Coolant Flow Arrangement	1-Pass Forced Convection, Counterflow to Beam Direction
Neutron Shield	Water
Neutron Shield Tank Material	Aluminum
Gamma Shield	1-in Lead Wall on Upstream Face
THERMAL MANAGEMENT	
Heat Removal	670 kW
Peak Heat Flux	212 W/cm^2 incident to surface
Peak Wall Temperatures	275 F water; 430 F beam
Water Conditions	305 gpm, 60 F/75psig in; 35 psid

The ogive beamstop is integrated into a simple, replaceable water-cooled cartridge that connects directly to the upstream beam pipe. In the arrangement shown in Figure 2, a flow shroud around the ogive creates an annular passage for once-through, forced-convection water cooling.

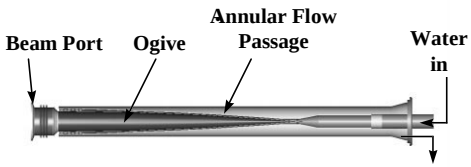

Figure 2: Ogive Beamstop Cartridge

The shielding advantages of the ogive approach are evident in Figure 3, which presents a cutaway view of

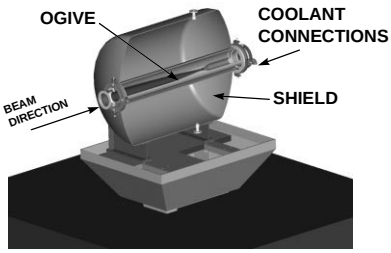

Figure 3: Integrated Beamstop Arrangement

the integrated beamstop assembly. The deposition of the beam energy deep within the small-diameter ogive makes it possible to have a near-4-pi, minimum-size neutron shield. The gamma shield wall is not shown.

2.1 Thermal Management

The thermal design is based on the quasi-Gaussian beam characteristics predicted for the LEDA linac, including the location and severity of hot spots produced by beam focus and steering errors. Figure 4 shows the mild axial heat flux and waterside temperature profiles predicted for the 6.7 MeV LEDA ogive at the nominal operating condition. The beam direction is from left to right.

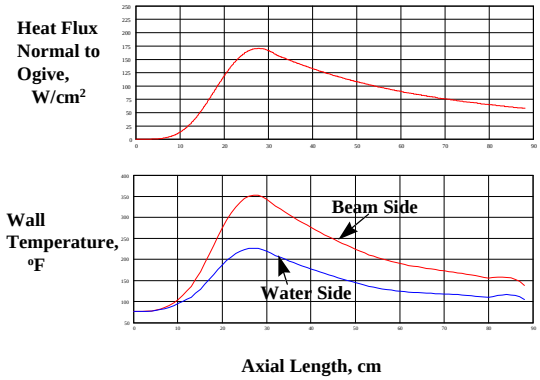

Figure 4: The heat flux normal to the ogive surface is about 1/30th of that normal to the beam cross-section, resulting in modest temperatures.

The thermal design is based on cooling with high-velocity water flow under sufficient static pressure to suppress boiling. Since the flow passage near the tip of the ogive is a venturi, care must be taken to ensure that the static pressure in this region will remain above the boiling limit.

2.2 Structural Design

The ogive structural analysis considered buckling, flow-induced vibration, thermal stress due to heat flux, thermal bowing due to misaligned beam, and the potential for thermal/flow feedback instability. Figure 5 is an example of the analytical sophistication needed to confirm structural adequacy.

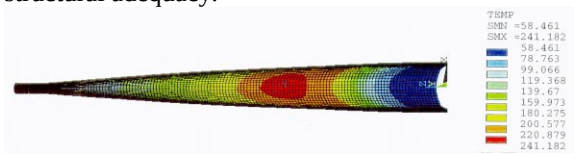

Figure 5 : Temperature Distribution of Ogive Coolant for One Case of Beam Misalignment

3 DEVELOPMENT

Although the LEDA beamstop has not yet gone into service, valuable experience has already been obtained on the fabricability and performance of the ogive concept.

3.1 CRITS BeamstopTesting

By happy coincidence, an adjunct proton Linac program at LANL urgently needed a new beamstop just as the LEDA design was being finalized, affording the opportunity to test out the ogive concept under actual cw, beam-on conditions similar to those of LEDA, but at reduced power levels. The water-cooled copper 6.5-in ID x 42-in long ogive, shown in Figure 6, was designed to accommodate a 1.25 MeV proton beam at 75 mA. With a proton energy well below the

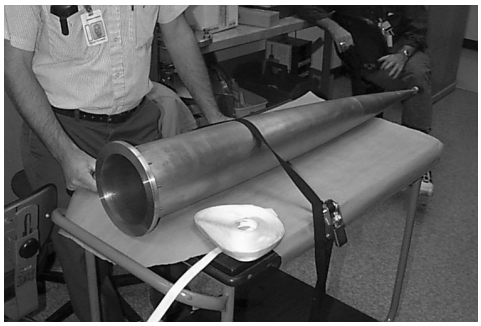

Figure 6: CRITS Ogive

2.2 MeV neutron activation threshold for copper, neutron shielding was not required. The ogive easily met design performance, permitting the CRITS linac to reach the highest cw 1.25 MeV beam power ever demonstrated [4]. During this testing, calorimetry performed on the ogive cooling water circuit helped verify the beam power measurements. The excess cooling capacity in the beamstop design defeated attempts to confirm the functionality of the hydrophone boiling sensors installed on the ogive flow shroud.

3.2 *LEDA Beamstop Fabrication*

Unlike its CRITS predecessor, which was spun from a copper cylinder, the nickel ogive for LEDA was produced by electroforming. This plating method produced a robust, one-piece, seamless, near-net shape ogive section to which a machined nose was added, using an electroformed cold-weld process. Figure 7 shows the completed LEDA ogive beamstop before it was inserted into its cartridge (see Figure 2).

Figure 7: Electroformed Ogive for LEDA

The 6.7 MeV LEDA beamstop has been installed at LANL and is now undergoing precommissioning checkouts. Testing should begin later this year.

4 CONCLUSIONS

The CRITS and LEDA experience gained to date have validated the ogive approach, which is now being applied to the design of the beamstops needed to commission the low to intermediate energy sections of the APT.

5 ACKNOWLEDGMENTS

This joint GA/LANL project was sponsored by the Department of Energy under Contract No. DE-AC04-96AL8907. Key members of the GA/LANL team included Ken Redler, Paul Wegner, Chuck Charman, Hank Brodnick, Ralph Senior, Herb Newman, Denise Pelowitz, Ross Meyer, Jr, and Dave Hodgkins. The support of Joe Sherman and the CRITS project team is particularly appreciated.

6 REFERENCES

[1] G. P. Lawrence, “High-Power Proton Linac for APT; Status of Design & Development,” LINAC 98 Invited Paper MU1004.
[2] D. W. Doll et al, “Low to High Energy Beamstops for APT,” LINAC 98 Poster TU4090.
[3] H.V.Smith et al, “Status Update on the Low-Energy Demonstration Accelerator,” LINAC98 Poster TU4014.
[4] J.D.Sherman et al, “A DC Proton Injector for Use in High-Current cw Linacs,” Proceedings of the European Particle Accelerator Conference, 22-26 June 1998, Stockholm, Sweden.

UPGRADING OF LINEAR INDUCTION ACCELERATOR X-RAY FACILITY (LIAXF)

J.J.Deng, B.N.Ding, J.S.Shi, Y. He, J.Li, Q.Li, G.G.Cao, L. Wen, G.S.Dai
LAPA, Institute of Fluid Physics, CAEP

Abstract

Linear Induction Accelerator X-ray Facility(LIAXF) is a pulsed X-ray machine at Institute of Fluid Physics which produced X-ray by impacting an electron beam on target with beam parameters of 10MeV, 2kA with 90ns pulse width(FWHM). The machine was upgraded to LIAXFU by increasing energy and current and reducing its spot size in 1996 in order to increase the capability of penetration. Description of the LIAXF and upgrades to LIAXF are presented. Simulation on the redesigned drift and focusing section is also given. Experimental results of 12MeV, 2.6kA with 90ns pulse width, about 4mm spot size have been obtained.

1. INTRODUCTION

Linear Induction Accelerators are powered by causing a large, pulsed, time-varying current to once circle a ferrite annulus. This results in a large, time-varying, azimuthal magnetic field to be imbedded in the ferrite annulus. A particle beam threading the center of the annulus acts as the secondary of this 1:1 pulsed transformer and is accelerated by the induced electromotive force. Stacking many such transformers in series and having the particle beam be the secondary common to all modules enables high beam energy to be obtained.

Induction Linac has many application in the fields such as free electron laser[1], high power microwave, flash X-ray radiography[2], heavy ion fusion[3], and so on due to its distinct advantage of high peak power, capacity of producing high current, high energy beams with pulse durations ranging from tens of nanoseconds to microseconds. LIAXF is a linear induction accelerator designed to produce X-ray by impacting the electron beams onto a tantalum target with the nominal beam parameters of 10MeV, 2kA with 90ns pulse width, which was developed by scientists at Institute of Fluid Physics, CAEP, in the early 1990s'. LIAXF was assembled with a four-induction-cell injector and 28 accelerator cells. The first 12 induction modules were used as driver for SG-1 free electron laser[4].To improve the capability of the LIAXF, the upgrades to the LIAXF centered on improving beam quality and increasing beam energy and current.

2. DESCRIPTION OF THE LIAXF

2.1 Injector

The injector is composed of four induction cells and a field emission diode, each cell of the injector is applied to 250kV, for a 90ns(FWHM) high voltage pulse. The voltage contribution of the four cells is summed along the hollow stainless steel stem to drive the diode. The surface of the cathode is covered by the velvet cloth, the anode aperture is closed off with fine tungsten mesh. The emitting current is collimated and matched into the accelerating section by axial magnetic field.

2.2 Accelerating Section

There are total 28 accelerating cells that are arranged in four-cell blocks in the LIAXF. Each accelerating cell contributes about 320keV energy to the beam. The electron beam from the injector is guided by a near-continuous array of solenoids that are positioned both internal and external to the accelerating cell. The current view resistor(CVR) between the four-cell blocks give the beam current and position information for machine tuning. The capacitor probe at each cell measures the accelerating voltage of each cell.

2.3 The Ferrite Toroids Used in LIAXF

The characteristics of the ferrite are very important to the accelerating cells. In order to obtain a non-distorted high voltage pulse, Large saturated and residual fluxes are expected. The ferrite toroids used in the LIAXF were developed by ourselves. It worked very well. The characteristics of the ferrite toroids are as follows:

B_S:	3.9kG
B_r:	3.0kG
μ:	350
ρ:	10(6)Ohm-cm

Dimensions:

OD:	508mm
ID:	230mm
Ht:	25mm

2.3 Beam Drift and Focusing Section

The beam drift and focusing section of the LIAXF is composed of five solenoids and three thin magnetic

lenses, and a tantalum target. The total length of this section is about 4.5m.

2.4 The Pulsed Power System

The pulsed power system can be divided into charging system and triggering subsystem. There are five Marx Generators in charging subsystem. Each charges six or seven Blumlein pulse forming lines through inductors.

There are three stages of triggering switches. One first stage switch triggers five second stage switches that then trigger 32 Blumlein switch in turn. Therefore the output voltage of each Blumlein was synchronized with the beam and applied to the induction cell to accelerate the electron beam.

3. UPGRADES TO LIAXF

The first task was to add four induction cells to the end of LIAXF, then increase the working voltage of each accelerating module from original 320kV to 350kV. The total beam energy can be more than 12MeV.

The next tasks in improving LIAXF beam quality were to realign the mechanical axis of the whole machine for reducing the corkscrew motion and improve the synchronization of the accelerating voltage with the beam for reducing the beam energy sweep.

The injected beam current into accelerating section was also increased to about 3kA.

The drift and focusing section was redesigned to achieve smaller spot size. The length of this section was shortened to about 2cm. Only two solenoids and two thin magnetic lenses were employed. Simulation showed that 4mm spot size can be achieved.

4. CONCLUSION

With the completion of these upgrades, LIAXFU produced the electron beam with parameters of 12MeV, 2.6kA with 90ns pulse width. The spot size was reduced from 6mm of LIAXF to about 4mm. LIAXFU has stronger capability of penetration and smaller spot size.

REFERENCES

[1] W.E.Nexen, et al., “The ETA-II Induction Linac as a High-Average-Power FEL Drive," Nuclear Instruments and methods, NIM-A296(1990).

[2] Kulke B., et al., “Initial Performance Parameters on FXR," Proceedings of the 15th IEEE Power Modulator symposium, Baltimore, MD, 1982.

[3] Friedman A., et al., “Progress toward a prototype recirculating induction accelerator for heavy-ion fusion," Proceedings of the 1995 16th Particle Accelerator Conference, Vol. 2, Dallas, TX, USA, P828-830.

[4] Ding B.N., Deng J.J., et al., “Free electron laser amplifier experiment based on 3.5MeV LIA," Proceedings of 1995 Particle Accelerator Conference, Dallas, TX, USA, 1995.

INSTALLATION OF THE AIRIX INDUCTION ACCELERATOR

E. Merle, R. Boivinet, M. Mouillet, O. Pierret
CEA / B3-M / PEM 51490 Pontfaverger-Moronvilliers - France

Ph. Anthouard, J. Bardy, C. Bonnafond, A. Devin, P. Eyl, C. Vermare
CEA / CESTA BP n°2 33114 Le Barp - France

Abstract

The AIRIX flash X-Ray Radiographic facility will consist of a 3.5kA/4.0MeV/60ns injector and 64 induction cells powered by 32 H.V. generators (250 kV per cell). The induction cells studies made on the PIVAIR accelerator [1], which is the prototype of AIRIX, have allowed to design specific vacuum technology cells (ferrite are under vacuum). In this paper, we will present the technical features of the injector, and particularly the time-resolved energy measurement, the pepper-pot emittance measurement and the results of the three gradient method experiment which has been made by optical transition radiation and Cerenkov radiation observation. In a second part, we will present the design of the induction cells and their HV performances. We will see also the different tests and characterizations we make on each cell, and how we install the accelerator. Finally, we will expose the intermediate experiment we plan to do with the electron beam, after the first 16 cells, that are just installed. Those experiments will be a comparison between PIVAIR and AIRIX accelerators. They will allow to characterize the electron beam, and to optimize beam transport and beam centering procedures, before continuing the installation.

1 INTRODUCTION

The AIRIX induction accelerator has been designed to generate an intense bremsstrahlung X-ray pulse of 500 rads @ 1m using a 3.5kA/20MeV/60ns electron beam. It is made up by an injector that delivers a 3.5kA/4MeV/60ns electron beam, and 64 induction cells powered by 32 H.V. generators (250 kV per cell).

The PIVAIR prototype at CESTA, that is a validation step of AIRIX up to 8MeV, has allowed to test two different technologies for induction cells [1] and to improve beam transport and centering procedures [2].

The AIRIX installation at PEM has begun in 1997 with the reception of the injector. The accelerator part (H.V. generators and induction cells) is now under construction and partly installed.

We present in the first section the experimental results obtained with the injector. In the following paragraphs we expose the different tests made on the H.V. generators and induction cells before their installation. We will see, in particular, the magnetic alignment constraints for the cells. Finally, we expose the beam characterization experiments we plan to do at the end of this year in order to validate industrial production.

2 INJECTOR

The AIRIX injector is a reproduction of the PIVAIR one, and has been made by PSI corporation [3]. The association of a 4 MV pulsed generator and a vacuum diode create a 4MeV,3.5kA,60ns electron beam. The time-resolved energy spectrometer that we use [4], has shown that the energy spread is very low: $\Delta E/E = 1\%$ over 60ns (figure 1).

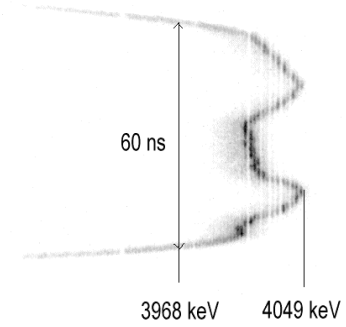

Figure 1: energy spectrum of the AIRIX injector

The next table gathers the results of the acceptance test of the AIRIX and PIVAIR injectors. The essential difference is the cathode configuration.

Table 1: injectors acceptance test results

Injector	**PIVAIR**	**AIRIX**
Diode voltage (spectrometry)	4029keV± 4 keV	4027keV± 4 keV
Voltage flatness	< ± 1% over 60ns	< ± 1% over 60ns
Voltage reproducibility	1%	1%
jitter	< 1 ns	< 1 ns
Cathode diam.	76 mm	89 mm
Velvet recess	2.8 mm	6.1 mm
Beam current	3.5 kA	3.5 kA
Normalized RMS emittance	1650 Π.mm.mrad	1900 Π.mm.mrad

We have been obliged to increase the cathode diameter and the velvet recess in order to hold the 3.5kA current value and to have the smaller emittance value as possible. The beam normalized RMS emittance has been measured

with the Pepper-pot method [5]. Nevertheless, the differences we observe (table 2) in the measurement of this parameter, for similar cathode configuration between the two injectors aren't yet explained.

Table 2: RMS emittance comparison between AIRIX and PIVAIR with: cathode diameter=76mm, recess=2.8mm

	ε rms (π mm mrad)
PIVAIR	1600 ± 100
AIRIX	2100 ± 100

The determination of the initial parameters of the beam, (Ro=beam diameter, R'o=beam envelope slope at the origin) is made with the three gradient method [5]. Images of the beam are made by an intensified and gated camera, observing Cerenkov radiation (CR) or Optical Transition Radiation (OTR) created when the beam passes through a 5µm thin aluminized mylar foil. The analysis of the beam profile, with a 5ns gate placed at different temporal position of the pulse, has shown important differences. More precisely, at the end of the pulse, we observe an abnormal and centered peak (figures 2-5).

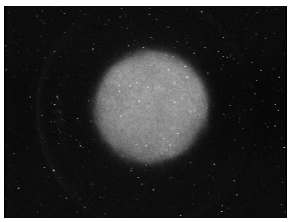

2

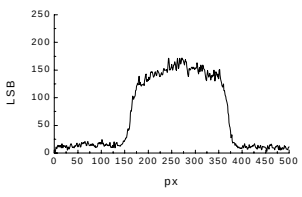

3

Figure 2: image of the beam observed with a gate of 5ns placed in the firts 10 ns of the flat-top of the pulse

Figure 3: the associated and centered beam profile

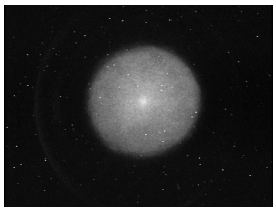

4

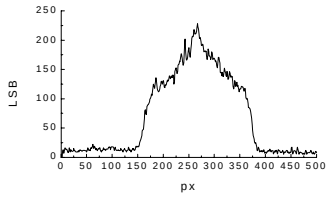

5

Figure 4: image of the beam observed with a gate of 5ns in the last 10 ns of the flat-top of the pulse

Figure 5: the associated and centered beam profile

Those images have been made when we used the 89mm diameter and 5.7mm recess cathode. We have obtained equivalent results with the 76mm diameter cathode and a recess of 4, 5 and 6mm by observing in the same way OTR or CR. We have experimentally demonstrated that the importance of the phenomenon is coupled to the value of the recess. When we use the 76mm diameter cathode, and a recess of 2.8 or 3.2 mm, the beam profiles are quiet different to those obtained with big recess, and the peak seems to be less important but the emittance is higher. In that configuration, the beam profiles are very similar to those obtained on the PIVAIR injector with the same apparatus.

However, the peak apparition is perhaps produced by combined effects between cathode emission and the optical diagnostic that visualizes the beam. Future experiments for optical diagnostic studies will check if there is a diagnostic effect or no.

We are now continuing tests on the injector to find the best configuration of the cathode (lower emittance, stable beam profile during the pulse) before determining the initial parameters of the beam.

3 H.V. GENERATOR

The AIRIX high voltage pulsed generator have been designed to drive two induction cells with a 250 kV, 75 ns pulse (flat top deviation less than ± 1%).

Some improvements have been necessary in order to reach specifications and reliability:

- the spark gap geometry has been corrected and a polarization added;
- thyratron command unit: initially built by EEV, a new one designed by EUROPULSE has been successfully tested.
- minor modifications on magnetic switch reset circuit and H.V. delay line.

Table 3: H.V. pulsed generators characteristics

	PIVAIR gen.	**AIRIX gen.**
Blumlein operating range	100 to 270 kV	100 to 270 kV
Main switch polarization	none	V/3
SF6 nominal pressure	3 bars	1 bar
Thyratron command unit	EEV (gas switch)	EUROPULSE (solid state switch)
jitter peak-peak jitter rms (1 σ)	18. 9 ns 3 ns	12 ns 2,6 ns

4 INDUCTION CELLS

Each induction cell comprises:

- 13 ferrite cores (270 mm I.D., 500 mm O.D., 24 mm thick) housed in a non magnetic stainless steel body
- a guiding solenoid magnet
- two printed circuit dipoles coils for beam centering
- two quadrupoles to correct possible transverse beam dissymmetry.

The 19 mm width accelerating gap has been shaped in order to give good high voltage behavior and minimize the beam coupling with the gap cavity to reduce BBU instability.

Compare to PIVAIR cells, the ferrite section has been increased by 9% in order to delay ferrite saturation and to optimize the timing of the acceleration.

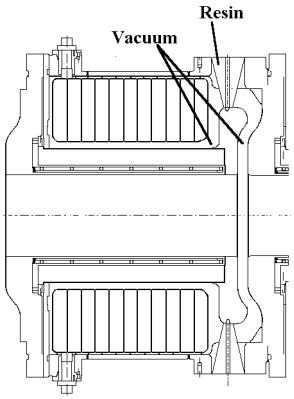

Figure 6: AIRIX induction cell

The H.V. test performed on the 16 first cells loaded with resistors confirmed the flux gain.

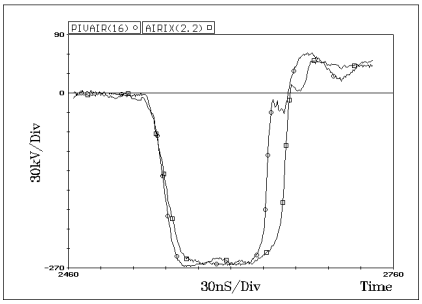

Figure 7: PIVAIR and AIRIX cells H.V. response on resistive loads

The next table shows the cell changes from PIVAIR to AIRIX design.

Table 4 : induction cells characteristics

	PIVAIR cell	**AIRIX cell**
ferrite length	12 x 25 mm	13 x 24 mm
available flux	24.4 mV.s	26 mV.s
gap spacing	19 mm	19 mm
flat top duration at 250 kV	65 ns	75 ns
Quadrupole coil	none	2

This should lead to a better behavior after beam loading, according to PSPICE calculations

5 CELLS ASSEMBLY

After vacuum and high voltage tests, the cells are aligned and assembled 4 by 4 [8]. We consider after this step only the block of four cells with his alignment references.

To minimize chromatic effects, the specific criteria impose that all the cell magnetic axes have to be enclosed in a 250 µm diameter cylinder with an angle spread lower than 500 µrad around the reference beam axis. In order to install only cells which have consistent magnetic axes with the criteria, we characterize magnetic defaults with the pulsed wire field technique.

6 ‘‘AIRIX 16 CELLS’’ EXPERIMENT

To make a comparison with PIVAIR, and to improve industrial realization, we are preparing different experiments with the electron beam accelerated by 16 cells. In a first step, we will characterize the acceleration with the time-resolved spectrometer. This diagnostic will confirm also the good machine timing [6].

We will measure the emittance with the Pepper-pot method. We will improve also the beam transport calculation code ENV [7] with CR beam imaging, and the beam centering procedure with the use of new Beam Position Monitors.

We plan to make experiments during 6 weeks at the end of this year to well characterize the electron beam and then validate the AIRIX technological choices.

7 CONCLUSION

Today 19 H.V. voltage generator have been assembled and tested at PEM. Three blocks of 4 cells have already been installed.

The accelerator will be completely assembled in march 99. After the final alignment of the machine with HLS and WPS technology [8], we will test the entire accelerator. The complete machine is planed to be operational for the radiographic experiments at the beginning of 2000.

REFERENCES

[1] E. Merle et al., ‘‘AIRIX prototype technological results at CESTA’’, Proceedings of PAC 97.

[2] Ph. Eyharts et al., ‘‘Beam transport and characterization on AIRIX prototype at CESTA’’, Proceedings of PAC’97.

[3] Pulse Sciences Inc., 600 Mc Cornick street, San Leandro, CA 94577, USA.

[4] D. Villate et al., ‘‘AIRIX alignment and high current beam diagnostics’’, Proceedings of PAC 95.

[5] C. Bonnafond et al., ‘‘Optical and time-resolved diagnostics for the AIRIX high current electron beam’’, Proceedings of DIPAC 97.

[6] Ph. Anthouard et al. ‘‘AIRIX and PIVAIR accelerator status’’, Proceedings of Power Modulator Conference 98.

[7] J. Bardy, ENV ‘‘Envelop electron beam transport code’’, Private communication.

[8] C. Bonnafond et al., ‘‘Status of AIRIX alignment and high intensity electron beam diagnostics’’, Proceedings of EPAC 96.

EXPERIMENTAL RESULTS OF ELECTRON BEAM NEUTRALIZATION INDUCED BY A LIMITED SPACE-CHARGE EMISSION

C. Vermare, J. Labrouche, D. Villate, P. Le Taillandier
Commisariat à l'Energie Atomique, Centre d'Etudes Scientifiques et Techniques d'Aquitaine
Bp n°2, 33 114 Le barp - FRANCE

Abstract

At the exit of the flash X-ray photography accelerator AIRIX, an intense relativistic electron beam (4 kA, 16-20 MeV, 80 ns) impinges on a high-Z target. The quality of the radiograph obtained is directly tied to the properties of the electron beam (RMS size and position, energy and current).

In a study on the LELIA linac (1 to 2 MeV, 1 kA) to study optical diagnostics, a very strong time-dependent focusing effect near the target was observed. The size of the spot emitting Cerenkov light was found to vary with time during the beam pulse. This observation was confirmed on the last Optical Transition Radiation (OTR) studies with the PIVAIR linac (7.2 MeV, 4 kA, 80 ns).

After analysis of this experimental results, an explanation of the effect in terms of the emission of positive ions by the target, and their subsequent tendency to move upstream has been simulated using a PIC code. The results support the concept of backstreaming ions adding an additional time-dependent focusing force that acts on the electron beam.

1 THE EXPERIMENTS

After a short description of the experimental set-up, we present the observed phenomena. An hypothesis is proposed to explain this observation.

1.1 Description of the accelerators and the optical diagnostics

Two different induction linear accelerators have been used. The first, LELIA, delivers a 1 kA electron beam with an energy up to 2.2 MeV. Initially developed to perform microwave FEL experiments [1-2] it has also been used as a test bed for the AIRIX induction accelerator [3], in particular for beam transport studies and diagnostics development.

The second, PIVAIR, is the prototype of AIRIX. It operates at 3.5 kA with an energy from 3.5 MeV up to 7.3 MeV.

At low energy, as in the case of LELIA, the optical observation is based on the emission of Cerenkov light which occurs when the beam hits a transparent target. The analysis of a part of this light, collected by optical cameras, allows us to measure the e-beam transverse dimensions [4]. Above 3 MeV, as in the case of PIVAIR, our optical diagnostic is based on the OTR [5] process.

Figure 1 presents the two different configurations we have adopted.

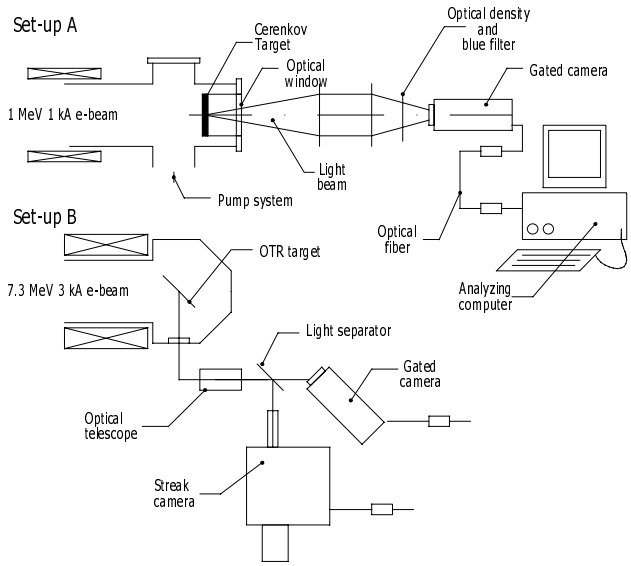

Figure 1: Schematic drawings of the two different set-up.

1.2 Results of the observation

During a "Cerenkov" measurement which used a 1 mm-thick fused silica foil (set-up A), we have observed a dependence of the beam radius as a function of time. Neither the beam current nor the beam energy exhibit a time variation fast enough to explain this behavior. An empirical solution has been found to reduce this effect by coating the target with aluminum to increase its conductivity. An example of the results obtained is given in Figure 2.

2 THE IONIC EMISSION HYPOTHESIS

2.1 General description

It is well-known that [6-7] the energy deposited in a target by an electron beam can produce free positive ions. In our case, their dynamic behavior is very interesting. The strong axial electric field generated near the target can accelerate and propagate upstream this ionic current to the primary beam. This mechanism is different from the one described in the references mentioned above. A neutralization of the strong electron beam current can appear and explain its focusing to small radii.

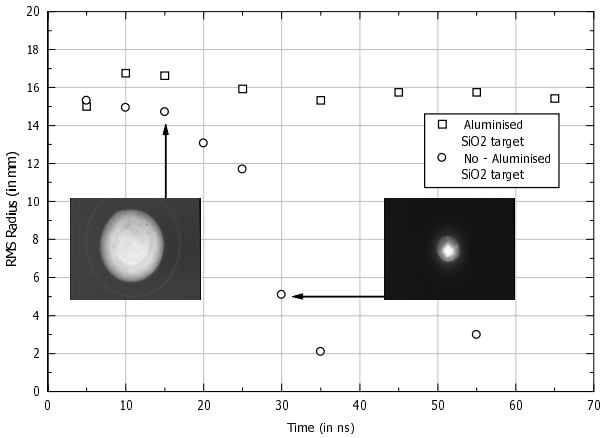

Figure 2: Behavior of the beam radius as a function of time. Two Cerenkov images of the beam at different times show its convergence.

2.2 Analytical approach

A simple model can be used to take into account the effects of the ions in the calculation of e-beam transport. We have computed the stationary longitudinal electric field generated by the e-beam itself [8]. By neglecting its transverse variations we have shown that close to the target, the electric field variations with z can be linearized. Then, the motion of the ions in this field can be calculated and the corresponding space charge-limited current is given by the following equation:

$$I_{ion} = \left(\frac{e}{M\varepsilon_0}\right)^{\frac{1}{2}} \left(\frac{I_e}{\pi c}\right)^{\frac{3}{2}} \qquad (1)$$

where M is the ion mass, e the elementary charge, I_e the e-beam current and c the light velocity. The ion energy becomes constant after a distance at which the electric field vanishes and is given by:

$$E_{ci} = \left(\frac{3e}{\pi^3 \varepsilon_0 c}\right) I_e \qquad (2)$$

If the e-beam current is 1 kA we find a proton current of 4 A and a maximum energy of 40 keV. These 2 values can be used to introduce a neutralization factor in the space charge term of the envelope equation in order to determine the influence of the ionic emission on the radius of the electron beam. The results of this calculation have shown a substantial focusing effect over in the pulse duration.

2.3 "PIC" simulations

We have developed a "Particle In Cell" code to simulate the experiment. It uses a 2D "Maxwell-Vlasov" algorithm in a cylindrical space. The electron beam initial conditions are determined thanks to the transport code ELECTRA [9]. Different species of ions are generated at the target position, the electromagnetic field and the particle dynamics are computed in order to obtain the effects of the ions on the electron beam radius.

3 COMPARISON BETWEEN NUMERICAL AND EXPERIMENTAL RESULTS

3.1 The parameters of the simulation

The main parameters are the mass and the charge of each kind of ion, their production rates and their initial energies. We have compared the experimental results by considering only protons. Their production rate is chosen to obtain the limited space charge ion current and they are emitted with a kinetic energy close to zero (10 eV).

3.2 Variations with the beam density

In the case of the experiment performed with the LELIA linac, we have varied the magnetic fields of the guiding coils in order to obtain, at a fixed total current, different values of the initial e-beam size, i.e. different beam densities. The current density has a strong influence on the evolution of the beam radius as a function of time. As shown in Figure 3, the higher the beam density the earlier the focalisation appears.

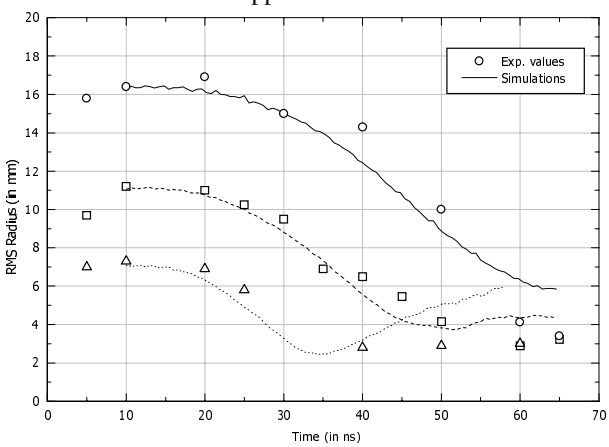

Figure 3: Numerical and experimental behavior of the beam radius versus time for three different initial beam densities.

4 OBSERVATIONS ON PIVAIR

The existence of this phenomenon, which has been observed with LELIA at CESTA as well as at LANL with ITS [10], has to be understood in order to evaluate its effects on the final focus of the AIRIX accelerator. Consequently, we have installed the experiment at the PIVAIR facility (Set-up B, figure 1).

4.1 OTR Time resolved measurement

The behavior of the e-beam size has been measured with an OTR diagnostic. The optical system was developed to obtain both the transverse dimensions of the

beam with a 5 ns gated camera and a time resolved 1D image with a streak camera. In this way, we are able to know the position of the slit of the streak camera in the transverse beam spot. Two images from the streak camera are displayed in Figure 4. They have been obtained for two distinct initial electron beam radii. As in the case of LELIA, we observe a variation of the radius during the beam pulse. It appears earlier for the small radius which corresponds to a higher beam density. The images from the gated camera exhibit the same behavior. Furthermore, these images reveal an unexpected bump in the beam transverse profile.

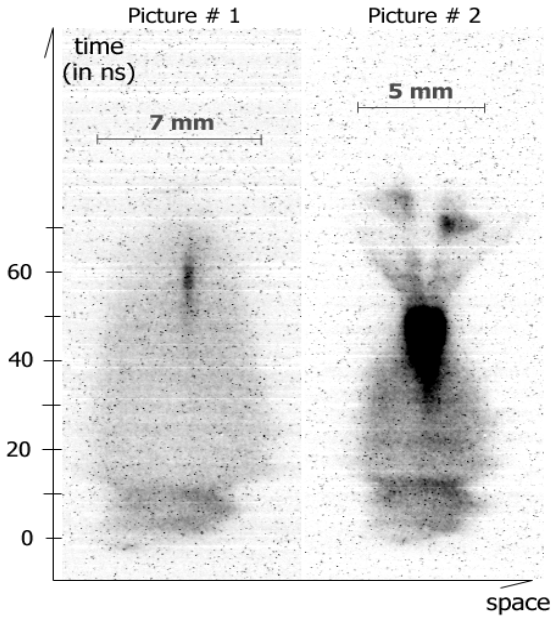

Figure 4: Examples of time resolved OTR images for 2 different beam radius at the target position.

4.1 Time behavior of the radial beam profile

The radial profile of the beam as a function of time has been studied and compared with the results of the PIC code. In Figure 5, we present the charge density of the electron beam at different times, both for LELIA and PIVAIR, the experiment shows a bump on the axis which blows up as the time increases. The numerical results reproduce this effect as indicated in the figure 5 for the LELIA case. We think this behavior, associated with the decrease in beam radius versus time, is the signature of the ionic focusing effect. It is present in the PIVAIR experiment though the beam parameters are very different. Consequently, the ionic focusing could be of prime importance in a higher energy accelerator like AIRIX.

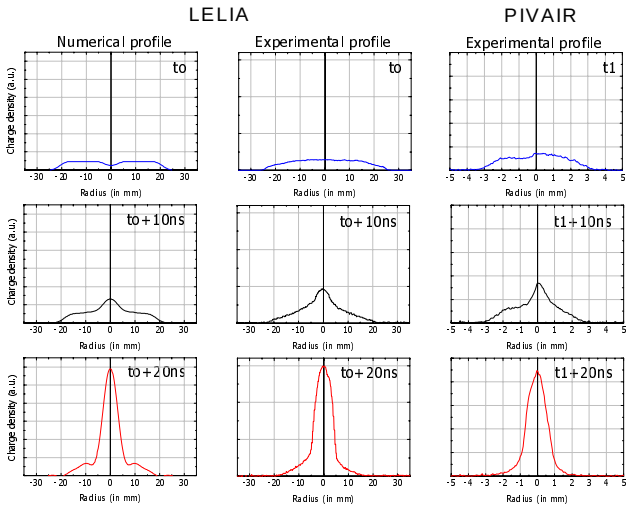

Figure 5: The structure of the e-beam radial profile versus time. The signature of the "ionic effect" appears with the two different accelerators.

5 ACKNOWLEDGEMENTS

The authors wish to acknowledge the valuable support and participation of the PIVAIR team.

We thank the CESTA/FEL team for their encouragement and support.

REFERENCES

[1] J. de Mascureau et al., "An induction linac developed for FEL application", Nuclear Instruments and Methods in Physics Research" A318 (1992), 460-4640.

[2] J. Gardelle, J. Labrouche, G. Marchese, J. L. Rullier, and D. Villate, "Analysis of the bunching produced by a free electron laser", Phys. Plasmas 3 (11) November 1996.

[3] E. Merle, "Installation of the AIRIX Induction Accelerator", Session 4 Posters, LINAC98.

[4] E. Merle, "Diagnostics optiques de faisceaux d'électrons de 1 à 17 MeV", Thèse spécialité: physique, Université de Bordeaux I, 1994.

[5] L. Wartski, Thèse de docteur es-science, Université d'Orsay, 1976.

[6] T. E. Madey, "Electron- and Photon-Stimulated Desorption: Probes of Structure and Bonding at Surfaces" Science vol. 234, p316, (October 96).

[7] T. W. L. Sanford, J. A. Halbleib, J. W. Poukey, A. L. Pregenzer, R.C. Pate, C. E. Heath, R. Mock, G. A. Mastin and D. C. Ghiglia, "Measurement of the electron energy deposition necessary to form an anode plasma in Ta, Ti, and C for coaxial bremsstralung diodes" J. Appl. Phys. **66**, 10 (1989).

[8] This work will be submitted for publication.

[9] P. Le Taillandier, C. E. A. Internal report

[10] D. C. Moir, D. Prono, Private Communication.

PICOSECOND AND SUB-PICOSECOND, HIGH CHARGE ELECTRON LINACS*

A. M. M. Todd, H. P. Bluem, C. C. Paulson, M. F. Reusch and I. S. Lehrman[a]

Northrop Grumman Advanced Systems & Technology,
9 Jeffrey Lane, Princeton Junction, New Jersey 08550, USA

Abstract

We have built and are presently designing, photocathode-based accelerator systems for radiation chemistry applications. One of these accelerators is in operation at Brookhaven National Laboratory. All feature a photocathode electron gun and produce a short, intense electron pulse with a variable repetition rate. The designs range from 1 nC to 100 nC per pulse, with bunch lengths of 0.6 psec at lower charge levels to less than 50 psec at higher charge. A compact design which can deliver 10 nC of charge in less than 5 psec and a larger machine designed to deliver up to 100 nC of charge in less than 50 psec, are described. Data on the operating system is also presented.

1 INTRODUCTION

Linear accelerators based upon photocathode RF electron guns are ideally suited for a number of scientific applications. The unique properties of these systems include the ability to produce a single, intense pulse of electrons at a variable repetition rate whose timing can be precisely controlled. These electrons can be used directly, through a thin window, or to generate an intense burst of gamma rays.

For the past few years, we have been designing photocathode-based linacs for scientific research [1]. In particular, we have delivered one accelerator beamline to Brookhaven National Laboratory (BNL) for pulse radiolysis chemistry research, and have designed two others for similar applications. The installed accelerator has been operating successfully for almost two years, producing in excess of 10 nC per pulse. The design and performance of this accelerator follows. Thereafter, the other two designs with their differing performance and packaging, are described.

2 BNL SYSTEM PERFORMANCE

The machine presently in operation at Brookhaven includes two beamlines. The first is a beamline deflected 90 degrees from the straight path, and the other is a beamline along the straight path. Two further deflected path beamlines can be installed. The electrons are delivered to one beamline or the other through energization of the bend magnets.

The bent path fulfills several important functions. Firstly, when properly designed, it provides a certain amount of longitudinal bunch compression which leads to higher peak current and better time resolution. The bent path can also be used for energy analysis of the electrons, if desired, and provides excellent suppression of the dark current due to energy selectivity.

The electron source is a 3.5 cell S-band photocathode RF gun which can produce electron energies up to 9 MeV. The electrons are produced in a single microbunch through illumination of the photocathode with a picosecond laser pulse synchronized to the RF that drives the gun cavities. A variable laser pulse width can be used to tailor the electron bunches to suit the needs of the experiment. The system runs at a repetition rate of 10 Hz, but this is not a fundamental limit. Quadrupole, dipole steering, and dipole bending magnets transport the electron pulse to the desired target.

The system has achieved the design goals that correspond to the present photocathode drive laser performance. The deflected beamline was designed to produce 10 nC bunches with a pulse width of less than 5 psec on target. The straight beamline was specified to deliver greater than 20 nC with pulse lengths of less than 30 psec. The transverse spot size on both targets can be varied over a wide range. To date, up to 12 nC have been delivered to both target stations with laser energies of 180 μJ per pulse. The dark current on the deflected path is measured to be less than 0.1 nC summed over the entire 4 μsec RF pulse.

3 NEW DESIGNS

Two new but related designs, with very different performance parameters, have recently been developed. The first is a very compact machine with only two target stations. The second machine is much larger and presently envisages five target stations.

The compact design is very similar to the BNL machine. An S-band 3.5 cell gun produces the 9 MeV electron pulses. These pulses can be delivered to one of two target stations via either a straight path or a bent

* Funding for this work was provided by the Office of Basic Energy Sciences, United States Department of Energy, under Brookhaven National Laboratory Contract # 703171 and Argonne National Laboratory Contract # 972582401, and by the Northrop Grumman Corporation.

[a] Present address: General Instrument Corporation, 101 Tournament Drive, Horsham, PA 19044, USA.

path. The pulses contain over 10 nC in a FWHM length of less than 10 psec on the straight path, and less than 5 psec on the bent path. The entire beamline, from the gun to the target stations, fits onto an optical table with dimensions of 2 meters by 3 meters.

The final design is a significant departure from the two previously described systems. It was driven by two separate goals, namely, very high charge and very short bunch lengths.

Achieving much higher charge necessitated a switch to an L-band accelerator. Operation of the gun in L-band allows a longer laser pulse and a larger laser spot size before beam quality starts degrading significantly. The longer pulse and larger spot allow more charge to be extracted before charge shielding becomes a major issue. They also allow more laser energy to be incident upon the cathode without exceeding the maximum permissible intensity.

To make it possible to attain the shorter bunches, the design includes a four cell booster accelerator after the 2.5 cell photocathode electron gun. The booster's RF phase is used to adjust the electrons longitudinal phase space in order to achieve optimal compression in the subsequent magnetic pulse compressor. In addition, the gun has been designed to provide a nearly linear relationship in longitudinal phase space. Through careful matching of the gun and booster, compression ratios of around 15 between the output of the gun and the end of the beamline have been achieved.

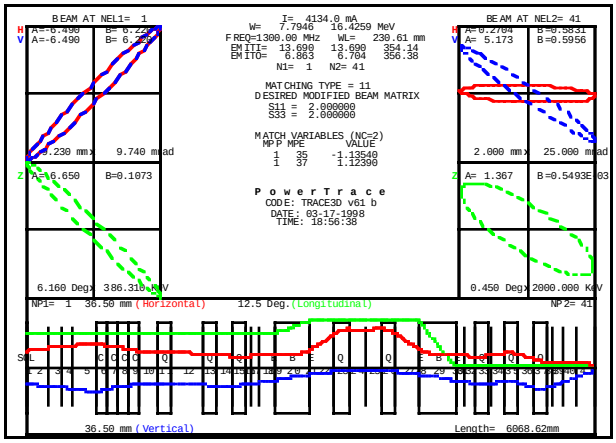

Figure 1. L-Band system beamline envelopes at 3.2 nC.

Figure 1 is a TRACE-3D [2] illustration of the beamline envelopes, showing the bunch compression. Nonlinear analysis of the beam on target using the TOPKARK [3] code yields, after aperturing, the transverse and longitudinal phase space plots of Figure 2.

The booster accelerator also assists in achieving the high charge operation. This is because, given a fixed amount of available RF power, the shorter gun can be operated at a higher gradient than would be possible with a longer gun. The gun and booster produce electron pulses up to an energy of 15 MeV while allowing the gun to be operated at maximum gradients. A higher gradient in the gun both raises the threshold for charge shielding considerations and raises the effective quantum efficiency of the cathode through the Schottky effect.

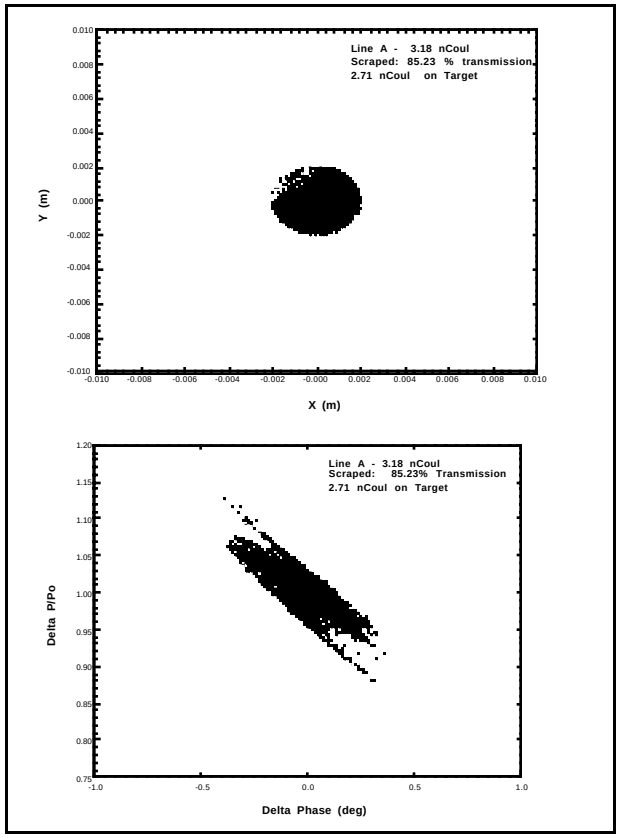

Figure 2. Transverse (upper) and longitudinal (lower) phase space plots for a 2 mm apertured, 2.7 nC, 0.67 psec FWHM bunch.

The beamline has multiple target stations, as shown in Figure 3, and the layout was designed to fit into an existing facility.

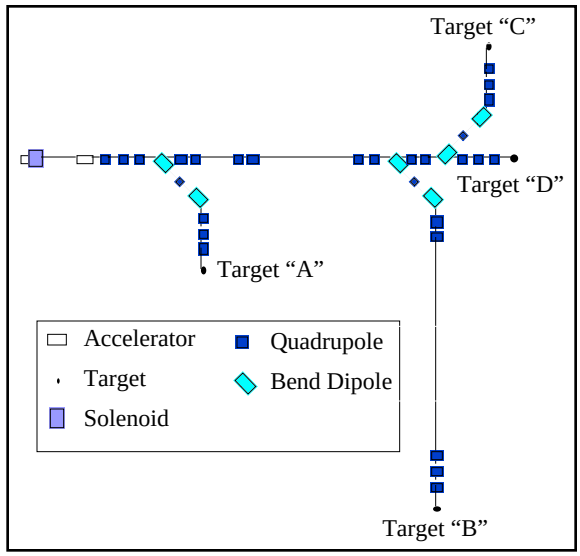

Figure 3. Four target L-band beamline layout.

The closest target to the accelerator, "A", is optimized for short pulse operation. Also, it is intended that the electron pulse at this target be synchronized with a sample of the photocathode drive laser to provide precise timing for pump-probe type experiments. At this target station, a pulse length of 0.67 psec FWHM has been achieved with 2.7 nC on target after aperturing a 3.2 nC beam and focusing the electrons to a transverse spot size of 2 mm radius. Lesser charge can be delivered in even shorter pulse lengths, while a 10 nC bunch can be compressed to less than 2 psec FWHM. At this target, we have achieved, in our non-linear simulations, peak currents in excess of 5 kA and peak densities in excess of 30 kA/cm^2.

The other two target stations on bent paths cannot match the performance of target "A" due to their distance away from the accelerator, smaller space for the achromat, and the necessity to have long sections of drift space. They were designed primarily to transport the high charge pulses.

The gun can produce up to 100 nC depending upon the available laser energy. After acceleration in the booster, this current can be delivered to either the first target station or any of the other targets. At target "A", the transport efficiency for the high charges approaches 100% and the pulse length can be compressed to less than 20 psec FWHM for 90 nC. The other two targets on bent paths have transport efficiencies of 81% and 89% with pulse lengths of around 25 psec FWHM. For comparison, the straight path target "D" has close to 100% transport with a pulse length of a little over 50 psec. A summary of the on-target performance at each of the four target stations is shown in Table 1.

4 SUMMARY

Northrop Grumman has built or designed three state-of-the-art electron accelerators. Although all three designs were driven by chemistry research applications, accelerators of this type have a much broader range of applications. These accelerators, based upon photocathode RF guns, can deliver very intense, very short (sub-picosecond) pulses of electrons or longer (20-30 psec), very high single bunch charge. The accelerator presently in use has met or exceeded all expectations.

ACKNOWLEDGMENTS

The assistance and collaboration of Dr. James Wishart at Brookhaven National Laboratory, Professor Jacqueline Belloni at the Université de Paris-Sud and Dr. Charles Jonah at Argonne National Laboratory, together with their various colleagues is gratefully acknowledged.

REFERENCES

[1] e.g. I. S Lehrman, et al., "Design and Operation of the Compact Infrared Free Electron Laser (CIRFEL)," Electron-Beam Sources and Charged-Particle Optics, Proceedings of the SPIE, Eric Munro and Henry Freund, Eds., 2522 (1995) 451.

[2] K. R. Crandall and D. P. Rusthoi, "TRACE-3D Documentation, Third Edition," Los Alamos National Laboratory Report LA-UR-97-886 (May 1997).

[3] D. L. Bruhwiler and M. F. Reusch, "High-Order Optics with Space Charge: The TOPKARK Code," Computational Accelerator Physics, AIP Conf. Proc. **297** (1993) 524.

ID #	Target	Energy (MeV)	Charge (nC)	X FWHM (mm)	Y FWHM (mm)	T FWHM (psec)
5	A	16.11	3.2	2.6	2.6	0.87
6	***A***	***16.11***	***2.7***	***2.0***	***2.0***	***0.67***
7	A	16.08	10.2	3.8	2.0	1.90
8	***A***	***16.83***	***87.2***	***4.7***	***5.4***	***19.6***
9	B	16.54	3.0	5.7	0.7	3.61
10	B	17.87	10.0	13.3	4.2	5.04
11	B	16.42	72.9	7.4	3.5	27.73
13	C	16.07	3.2	3.6	5.9	1.92
14	C	17.26	10.2	4.1	1.7	3.72
15	***C***	***16.48***	***80.1***	***5.3***	***5.3***	***25.81***
16	D	16.03	3.2	1.2	1.5	16.29
17	D	16.49	10.2	2.7	5.0	13.31
18	D	16.45	89.1	4.8	3.8	51.53

Table 1. Summary of on-target performance simulations

DEVELOPMENT OF AN UPGRADE OF THE CEBAF ACCELERATION SYSTEM*

J. R. Delayen
Thomas Jefferson National Accelerator Facility, Newport News, Virginia 23606 USA

Abstract

Long-term plans for CEBAF at Jefferson Lab call for achieving 12 GeV in the middle of the next decade and 24 GeV after 2010. Such energies can be achieved within the existing footprint by fully populating the accelerator with cryomodules capable of providing 3 to 4 times as much voltage as the design value of the existing ones within the same length. In particular, this requires the development of superconducting cavities capable of operating at gradients above 12 MV/m and Q close to 10^{10}.

1 CEBAF DESIGN AND STATUS

CEBAF was designed and constructed to accelerate an electron beam to 4 GeV by recirculating five times through two 1497 MHz superconducting linacs, each providing 400 MeV per pass at the accelerating gradient of 5 MV/m. The two anti-parallel linacs are connected by 180 degree isochronous, achromatic recirculating arcs. The design maximum current is 200 μA cw, corresponding to a beam loading current of 1 mA [1].

The superconducting RF (SRF) system consists of 20 cryomodules in each of the two linacs and 2 ¼ cryomodules in the injector. Each cryomodule contains 8 accelerating cavities for a total of 338 cavities. The cavities, which are 50 cm long, were designed to operate at a gradient of 5 MV/m, which corresponds to an energy gain of 20 MV for each cryomodule. Each cavity is individually powered by a 5 kW klystron and controlled by a low-level rf control system to stabilize the phase and amplitude of the rf field. Having each cavity individually controlled allows for precise and careful optimization of the system and results in excellent phase and amplitude stability of the accelerating fields in the cavities.

The central helium refrigerator provides 2 K helium to the cavities with availability above 98%. The system, capable of providing 4800 W of refrigeration, presently operates with a constant heat load of 3100 W, of which 1500 W is the actual rf heat load.

From the beginning the performance of the acceleration system exceeded the design goal [2]. Early in 1996 a one-pass energy of 1 GeV was achieved, and in the spring of 1997 a 90 μA beam was accelerated to 1.16 GeV in a single pass (equivalent to a 5.6 GeV, 18 μA 5-pass beam). The average accelerating field in the active cavities was 7.8 MV/m, more than 50% above their design field. In the fall of 1997, the full capacity of CEBAF was demonstrated with the delivery of a 4 GeV, 200 μA beam [3]. Some of the arc dipole power supplies are being upgraded in order to deliver high-energy multipass beams, and physics experiments at 5.6 GeV are being scheduled for the first half of 1999.

The initial performance of the CEBAF cavities corresponded to a 5-pass energy of about 5 GeV. The performance was predominantly limited by electron field emission that can manifest itself in additional cryogenic losses, x-ray production, and periodic arcs at the cold window which is located close to the beam line [4].

In order to reduce field emission and increase the operational energy of CEBAF, a program to perform *in situ* helium processing of the cavities was initiated in the fall of 1996. To date 224 cavities in 29 of the 40 installed cryomodules have been processed [3]. This has increased the installed voltage by 155 MV, which corresponds to an added energy of 775 MeV for a 5-pass beam. The *in situ* processing program will be completed in February 1999 and it is expected that the additional gain will allow operation close to 6 GeV.

2 UPGRADE OPTIONS FOR THE ACCELERATION SYSTEM

CEBAF's long-term institutional plan calls for an energy upgrade to 12 GeV in the middle of the next decade, and to 24 GeV after 2010. The short-term goal is to have developed, installed in the accelerator, and demonstrated by 2002 prototypes of the key components of such an upgrade.

While the details of the upgrade path are still being developed, a top-level parameter list has been generated which guides the selection between the various options:

- The highest energy beam of 12 GeV needs to be delivered to only one experimental hall.
- CW operation must be preserved.
- The maximum circulating beam current will be 400 μA (corresponding to an 80 μA beam for a 5-pass design).
- The maximum installed refrigeration capacity will be 8.5 kW at 2 K.
- Cost and impact on accelerator operation during the upgrade must be kept to a minimum.
- Since the purpose of the 12 GeV electron beam is to generate an 8 GeV photon beam, the requirements on

*Supported by US DOE Contract No. DE-AC05-84ER40150

the electron beam quality can be relaxed from the existing requirements.

- Since the ultimate goal is an upgrade to 24 GeV, an upgrade path to 12 GeV that could be extended to higher energy would be preferable.

The original upgrade plan for CEBAF called for a maximum energy of about 9 GeV. The most attractive option to achieve this goal called for a systematic "reworking" of the cryomodules. This consisted of removing the cryomodules from the accelerator one at a time, reprocessing the superconducting cavities, and replacing or modifying some of the limiting components (for example relocating the cold windows and shielding them from field-emitted electrons). While this option seemed attractive to 9 GeV, it could not be easily extended beyond, either because it could not provide enough energy or because the cryogenic consumption would be excessive.

The most attractive option that has emerged from the studies that have been conducted during the last year consists of:

- addition of a fourth experimental Hall D at the end of the North Linac (turning CEBAF into a 5-pass machine for Halls A, B, and C, and a 5 1/2-pass machine for Hall D),
- development of high-voltage, high-Q cryomodules that would be installed in the 5 empty slots in each of the linacs,
- replacement of a limited number of existing cryomodules by the new ones (typically 3 in each of the linacs and 2 in the injector),
- upgrade of the refrigeration capability to 8.5 kW,
- addition of a 10th arc and upgrade of the existing ones.

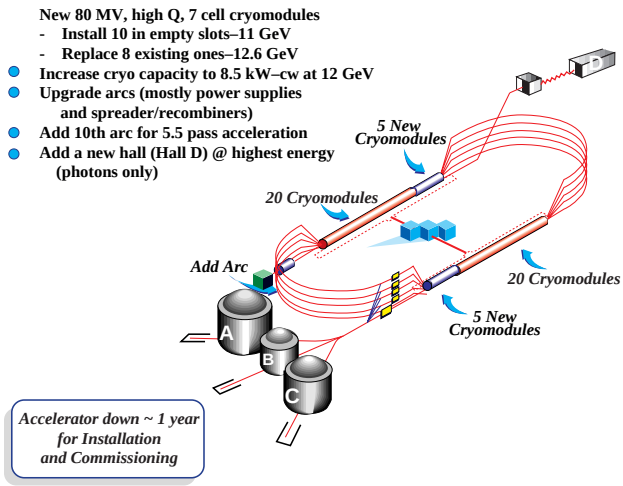

3 DESIGN OF THE UPGRADE CRYOMODULE

The Upgrade Cryomodule is clearly the key component of the upgrade of the acceleration system. Its design is also somewhat insensitive to the details of the upgrade option that is ultimately chosen, once the top-level parameters have been defined, and it can be viewed as a building block that can be applied to a large number of upgrade options. For these reasons, most of the development efforts in support of the upgrade are directed toward the development and demonstration of prototype Upgrade Cryomodules.

3.1 Cavities

In order to increase the voltage that is provided by a cryomodule within a given length, one can either increase the gradient at which the cavities are operating, or increase the effective accelerating length, or both. While it may be argued that maximizing the accelerating length is the approach that presents the least technological risk, for cw accelerators such as CEBAF, maximizing the length instead of the gradient has the added advantage of lower dynamic load on the refrigeration system.

For this reason, it was decided early that the Upgrade Cryomodule would still include 8 cavities, but that these would be 7-cell cavities (70 cm) instead of the present 5-cell (50 cm). The option described in Section 2 calls for these cavities to provide a minimum voltage of 8.75 MV with a maximum power dissipation of 17.5 W, *i.e.* their Q must be at least 6.5×10^9 at 12.5 MV/m. Thus the greatest challenge is not so much in achieving a high gradient but in maintaining a high Q at high gradient. Given the constraint imposed by the available refrigeration, cw operation at 15 MV/m would be practical only if the Q at that field were at least 10^{10}.

While the CEBAF cavity cell design could have been improved, the potential benefits did not seem important enough at that time, and the first 7-cell cavity prototype was built using the existing cell design. The first prototype met the requirement of a Q of 6.5×10^9 at 12.5 MV/m. A redesign of the cells is still an option, although a low priority one.

3.2 Cryostat Concept and Cavity String Assembly

The existing CEBAF cryomodule is constructed from 4 cyounits, each containing a sealed cavity pair. These cyounits are then joined with bridging sections. In order to increase the number of cells from 5 to 7 while maintaining the same cryomodule length, this approach had to be abandoned. The Upgrade Cryomodule will include a continuous 8-cavity string assembly without isolation valves between the cavities. The present design calls for a 30 cm separation between cavities into which must fit the fundamental power coupler, the higher mode extraction system, the pick-up probe, connecting flanges and bellows, and connections to the helium tank and mechanical tuners.

Several cryostat concepts were explored:

- Cylindrical cryostat with radial penetrations for the power couplers,

- Cylindrical cryostat with axial (through the end plates) penetrations,
- Bathtub-type cryostat where all the innards are suspended from a top plate.

While all designs had advantages and disadvantages, a cost/benefit analysis did not reveal an obviously preferred option. The overriding consideration was the limited amount of time and resources expected to be available, and the radial design was chosen as it was deemed the one that would require the least amount of development given the on-site experience with the radial design.

3.3 Fundamental Power Coupler

Both coaxial and waveguide couplers were explored. The waveguide concept was retained because of its simplicity and flexibility at 1500 MHz. Unlike the present design, though, we have decided to completely separate the functions of fundamental power coupling and higher mode extraction. This produces a coupler design that, unlike the existing CEBAF design, is free of transverse kick imparted to the beam and allows a cryostat design where all the power couplers are on the same side [5].

3.4 Higher Order Modes Damping

The requirements for high order modes (HOM) damping for the 12 GeV Upgrade have been substantially relaxed from the original CEBAF design. Not only is the energy increased from 4 to 12 GeV but the maximum circulating current is being reduced from 1000 to 400 μA. Additionally, the experience acquired during CEBAF operation has led to a reduction of the "safety factor" for the stability threshold current. As a result an upper limit of 10^6 was adopted for the Q_{ext} of the HOMs.

The design of the HOM couplers is a departure from the existing design: we do not rely on any HOM being extracted from the fundamental power coupler, the 2 HOM couplers will be of a coaxial type as opposed to a waveguide type, the HOM couplers will be located outside the helium tank and the HOM power can be deposited at a temperature other than 2 K.

3.5 Frequency Tuning

The frequency tuners perform several functions: bring the cavities on resonance after installation, detune the cavities that are not operating, and track the changes in frequency due to Lorentz detuning, pressure and temperature fluctuations. For the Upgrade Cryomodule, the bandwidth will be small (~75 Hz), the Lorentz detuning large (~500 Hz), and we want to track the frequency accurately (~2 Hz) in order to minimize the rf power requirements. For this reason the baseline design incorporates two different tuning schemes: a coarse mechanical tuner with 400 kHz range and 100 Hz resolution that will be used infrequently, and a fine tuner, probably piezoelectric, with 1 kHz range and 1 Hz resolution that will provide the fine, frequent tracking.

3.6 Processes and Procedures

While the gradients required are modest compared to those for proposed linear colliders, a high Q is of primary importance. Furthermore, since rf power will be a hard constraint, "good" cavities cannot operate at higher gradient in order to compensate for "weaker" ones. For these reasons our main goal is to achieve consistent performance as opposed to the less frequent exceptional one. We have engaged in a complete review of all the processes and procedures involved in the fabrication and assembly of cavities and cryomodules. Modifications to the processing and assembly facilities, such as implementation of final chemistry and rinsing in the cleanroom, are under way.

3.7 Microphonics, RF Control, and RF Power

In order to contain the cost of the upgrade we have adopted as a goal only a modest increase of the rf power per cavity from 5.5 to 6 kW. This puts stringent requirements on microphonics and the control system. At 12.5 MV/m and 400 μA circulating current, the maximum allowable amount of detuning (including static and microphonics) is 25 Hz. The optimum Q_{ext} is $2x10^7$, and the Lorentz detuning is much larger than the loaded bandwidth; for this reason a new low-level rf control system will be required. The baseline concept is an agile digital system capable of implementing a self-excited loop on I/Q feedback.

4 ACKNOWLEDGEMENTS

This paper summarizes the work of the Upgrade Cryomodule Development Team: I. Campisi, L. Doolittle, E. Feldl, J. Hogan, P. Kneisel, J. Mammosser, G. Myneni, V. Nguyen, L. Phillips, J. Preble, C. Reece, W. Schneider, D. X. Wang, M. Wiseman.

5 REFERENCES

[1] H. Grunder, “CEBAF Commissioning and Future Plans,” Proceedings of the 1995 Particle Accelerator Conference, 1-3 (1995).

[2] C. Reece et al., “Performance Experience with the CEBAF SRF Cavities,” Proceeding of the 1995 Particle Accelerator Conference, 1512 (1995).

[3] C. Reece, “Achieving 800 kW CW Beam Power and Continuing Energy Improvements at CEBAF,” these Proceedings.

[4] J. R. Delayen, L. R. Doolittle and C. E. Reece, “Analysis of Performance Limitations for Superconducting Cavities,” these Proceedings.

[5] L. R. Doolittle, “Strategies for Waveguide Coupling for SRF Cavities,” these Proceedings.

LATEST DEVELOPMENTS FROM THE S-DALINAC AND ITS FREE-ELECTRON-LASER*

M. Brunken, S. Döbert, R. Eichhorn, H. Genz, H.-D. Gräf, T. Hampel, S. Kostial, U. Laier, H. Loos, A.Richter, B. Schweizer, A. Stascheck, O. Titze and T. Wesp
Institut für Kernphysik, TU Darmstadt, Schlossgartenstrasse 9, D-64289 Darmstadt, Germany

Abstract

The FEL at the superconducting electron accelerator S-DALINAC has been operated at wavelengths between 6.6 and 7.8 µm corresponding to electron beam energies between 31.5 and 29.6 MeV respectively. In house developments like active stabilization of the optical cavity's length based on a laser interferometer and a fast 10 channel online-spectrometer for the near infrared laser radiation were incorporated and used for investigation of the properties of the FEL itself. In addition a simple focusing system produced power densities of 10^8 W/cm^2 and enabled us to perform first ablation experiments from different tissues. To optimize the complicated bunching process, the low energy part of the S-DALINAC was carefully studied by tracking calculations in order to achieve bunch length < 3 ps corresponding to peak currents > 1.5 A, necessary to operate the FEL reliably in the saturated regime. For operation at higher energies using two recirculations of the electron beam, longitudinal tracking simulations show that off crest acceleration together with nonisochronous recirculation introduce longitudinal stability resulting in significant improvement in energy spread.

1 S-DALINAC

The S-DALINAC operating since 1991 is a recirculating electron linac using superconducting (sc) accelerating cavities allowing for a continuous wave (cw) electron beam [1]. The machine provides beam to serve a variety of nuclear and radiation physics experiments and is since 1996 also used as a driver of a Free-Electron-Laser in the mid infrared wavelength region. A layout of the accelerator and the FEL is shown in Fig.1.

The electron beam is generated by a thermionic cathode, on a high voltage terminal providing a 250 kV electrostatic preacceleration. The beam gets its time structure in a chopper/prebuncher section at room temperature (see Sec. 3.) and is then accelerated up to 10 MeV in the sc injector linac consisting of a 2-cell (β=0.85) and a 5-cell (β=1) capture cavity and two 20-cell (β=1) accelerating cavities. Each of them is made of bulk niobium and operates at 2 K in a liquid helium bath at a resonant frequency of 3 GHz. Behind the injector the beam can be used in a low energy experimental area or bent 180° by a magnetic arc to be injected into the 40 MeV main linac consisting of eight 20-cell cavities. For nuclear physics experiments with electron energies up to 130 MeV the beam can be recirculated twice passing through dedicated beam transport systems.

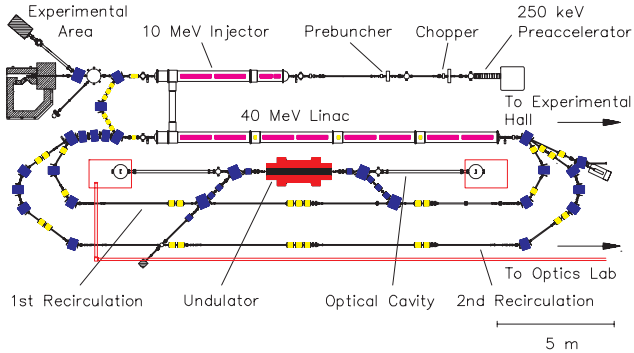

Figure 1. Layout of the S-DALINAC and its Free-Electron-Laser

The FEL is driven by transporting the beam from the first recirculation into the undulator through a magnetic bypass system. The infrared radiation generated and amplified in the 80 periods hybrid undulator is accumulated in a 15 m long optical cavity formed by two dielectric mirrors. For experiments part of the stimulated radiation is coupled through the downstream mirror and guided through an evacuated transfer to an optical laboratory.

Since its commissioning the S-DALINAC delivered some 16000 hours of beam time for experiments covering a wide range of beam parameters. Energies ranging from 2.5 MeV up to 120 MeV and currents from a few nA to 50 µA could be realized in a 3 GHz mode. The FEL is driven in a 10 MHz cw mode using a subharmonic injection scheme leading to peak currents of about 2 A at energies between 30 and 38 MeV.

2 FREE-ELECTRON-LASER

The FEL at Darmstadt benefits from the superconducting drive linac enabling time structures of the laser ranging from 100 µs long macro pulses to 10 MHz cw operation. The FEL has been operated so far at wavelength between 6.6 and 7.8 µm corresponding to electron energies between 31.5 and 29.6 MeV respectively. The wavelength could be tuned continuously in this range determined by the bandwidth of the dielectric

* Supported by BMBF under contract number 06 DA 820 and by DFG under contract number Ri 242/12-1 and through the Graduiertenkolleg "Physik und Technik von Beschleunigern"

mirrors by changing either the magnetic gap of the undulator or the electron energy. During the commissioning [4] of the FEL using an electron beam with an energy of 30.4 MeV and a measured bunch length of 3 ps corresponding to a peak current > 1.5 A, we were able to extract an average cw laser power of 3 W at a wavelength of 7.4 µm through a mirror with 99 % reflectivity. The net gain of the arrangement was measured to 3-5 %.

The laser output power turned out to be very sensitive to length variations of the optical cavity in the micrometer range. These perturbations are caused by vibrations on the optical tables due to cryogenic pumps and the heavy machinery of the helium liquifier as well as long time drifts caused by air pressure and room temperature changes. Therefore it was essential to develop an active feedback system to stabilize the length of the optical cavity. A commercial michelson interferometer (HP 5527A Laser Position Transducer) measures the length variations and generates a drive signal for the piezo transducers holding the mirrors. The control parameters can be software adjusted. The remaining length variation due to vibrations was measured to be a gaussian distribution with 232 nm FWHM, as shown in Fig.2., while the long time drifts were eliminated completely. Without feedback the position error is about 500 nm FWHM with drifts of 20 µm within 24 hours preventing stable laser operation.

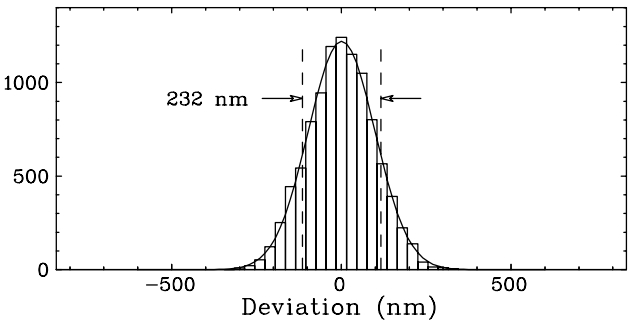

Figure 2. Length variation of the optical cavity with interferometric feedback active.

In order to control and optimize the laser performance an online- spectrometer was developed with a typical Czerny Turner setup for the spectral splitting and a ten element pyroelectric strip detector. The detector output is monitored online on a LED display or connected to ADC's for further analysis. The resolution of this device is 20 nm per element. Drifts and changes in the electron beam steering through the undulator leading mostly to longer wavelengths could be easily corrected with this device. The laser beam stabilized and monitored in such an way could be used for first ablation experiments on different tissues performed in cooperation with J. F. Bille and his group from the university of Heidelberg. The laser beam was focused by a single CaF_2 lens with a focal length of 350 mm to a spot size of 160 µm providing a power density of some 10^8 W/cm^2. The resulting ablation depths were measured with a scanning electron microscope and the ablation mechanism was described by an analytical model. It turned out that the ablation was due to thermal interaction. The measured ablation depths could be explained by a model assuming the tissue as water, being heated and vaporized by the radiation pulses. Ablation sufficient for medical purposes demands at least a 10^3 times higher power density in order to avoid too much thermal damage for nearby tissue. We are sure to reach this goal by means of more sophisticated focusing optics and by optimizing the optical transfer system. The use of regenerative amplifiers for the laser beam is also envisaged to reach even higher power densities in the future.

3 TRACKING CALCULATIONS OF THE INJECTOR LINAC

The quality of the laser output depends on the parameters of the electron beam entering the undulator, especially the longitudinal properties energy spread and bunch length are critical for the shape of the spectrum and the output power. These properties are almost fixed after the injector, therefore the beam dynamics in the low energy part of the accelerator was studied intensively by tracking calculations. For driving the FEL the thermionic cathode is pulsed with a repetition rate of 10 MHz. Pulses with a duration of 1 ns are extracted from the gun at 250 keV. The subharmonic chopper/prebuncher section working at the 5th subharmonic cuts out 370 ps corresponding to a charge of 6 pC and compresses these bunches to a length of 5 ps at the entrance of the capture cavity. For FEL operation we so far used only the 5-cell capture cavity followed by two 20-cell standard accelerating cavities.

The tracking simulations of this part of the machine are performed using the code GPT [5] including space charge forces and electromagnetic fields of the rf-resonators calculated by MAFIA [6]. The simulations are performed to find an optimized parameter set for the injector as well as to compare empirically found parameter sets and measured beam properties with the simulation results. The gauging relation between the tracking code parameters and the machine parameters like rf-phases and amplitudes were determined from separate calibration measurements. The nice agreement between measured beam properties from a previous FEL beam time and the simulation results confirmed this calibration method. Searching for an optimized setting with respect to bunch length and energy spread revealed an enormous sensitivity concerning the choice of rf-phases and amplitudes for the first two accelerating cavities due to non relativistic behavior in this section. In contrast to the common feeling (accelerate as fast as possible) the simulations suggested to reduce the field amplitude of the first 20-cell cavity. Since the longitudinal phase space is found to be correlated at the exit of the injector we can benefit from magnetic

bunching in the 180° bending arc towards the main linac. According to the tracking results a bunch length of 2 ps (FWHM) with sufficient energy spread of ± 33 keV (rms) at an energy of 8 MeV can be achieved at the entrance of the main linac as shown in Fig.3. below.

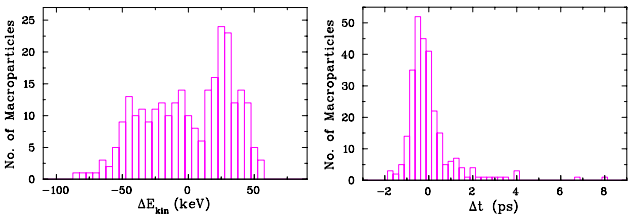

Figure 3. Distributions of particle energy and arrival time at the main linac for an optimized injector setting.

For the next beam time it is envisaged to verify this calculated parameter set hopefully leading to an increased small signal gain and higher peak power of the laser because of the shorter electron bunch. The simulations also showed that even at a quite modest bunch charge of 6 pC space charge effects influence the beam dynamics in our injector.

4 NONISOCHRONOUS RECIRCULATION

The principle of phase focusing is well known and used in circular machines like synchrotrons and microtrons. Recirculating linacs with only a few separate recirculations however, like the S-DALINAC, are usually operated with an isochronous beam transport system and on crest acceleration. The energy spread is then determined by the bunch length and the stability of the rf field in the accelerating cavities. But as pointed out by [7] the choice of an off crest synchronous phase together with a nonisochronous beam transport system offers a welcome longitudinal stability, thus reducing the effects of amplitude and phase jitter in the linac.

We simulated the situation at the S-DALINAC with two recirculations and 3 passes through the linac by simple tracking of the longitudinal phase space. We assumed a relativistic electron beam coming out of the injector uniformly distributed in longitudinal phase space with an energy spread of ± 0.1 % and a bunch length of 2° with respect to the rf-period. The eight cavities of the main linac are assumed to have an uncorrelated field amplitude jitter of 10^{-3} and a phase jitter of ± 1°. The longitudinal phase space distribution was calculated at the exit of the linac after 3 passes as a function of the synchronous phase ϕ_s and the longitudinal dispersion of the recirculating beam transport system. The simulations showed that at a working point of ϕ_s = -9.7° and r_{56} = 5.3° / % we can gain a factor of four in energy spread compared to isochronous recirculation. The remaining energy spread is mainly caused by the injected beam, while the contribution of amplitude and phase jitter in the linac becomes almost negligible. In Fig.4. the tracking calculations are summarized in a two parameter plot of the resulting energy spread. These concepts, highly relevant for improving the beam quality for nuclear physics experiments, could be verified already qualitatively and will be measured quantitatively soon.

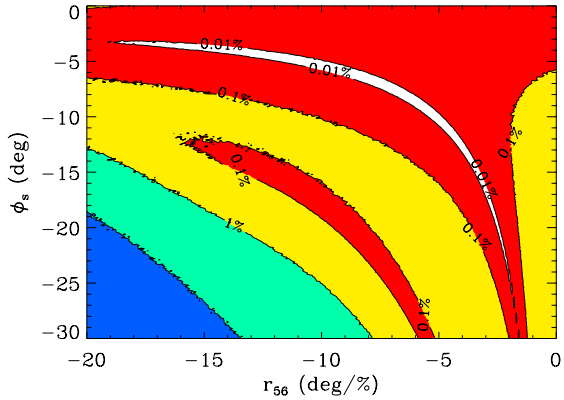

Figure 4 Energy spread after three linac passes as function of the synchronous phase ϕ_s and the r_{56}-matrix element of the recirculating beam transport system.

5 CONCLUSION

The successful operation of the FEL at the S-DALINAC has opened a wide new field of research possibilities. Therefore from now on besides the nuclear and radiation physics activities, both, user oriented experiments with the infrared light from the laser as well as investigations of basic FEL properties will be carried out. Improvement of the accelerator itself is focused on a better understanding and an optimization of its low energy part. To assure that the influence of space charge effects is taken into account correctly, we have already started to investigate the pulsed emission in the gun and electrostatic preacceleration using the time dependent Particle in Cell module of the MAFIA code.

6 REFERENCES

[1] A. Richter, Proc. Fifth EPAC, eds. S. Meyers et al., IOP Publishing, Bristol (1996)110.

[2] S. Döbert et al. , Proc. Eighth Workshop on rf superconductivity, to be published.

[3] H.-D. Gräf et al. , Proc. Eighth Workshop on rf superconductivity, to be published.

[4] M. Brunken et al. , Proc. 20th Int. FEL98 Conference, 1998, to be published.

[5] S. B. van der Geer, M. J. de Loos, Proc. Sixth EPAC, Stockholm (1998) , to be published.

[6] Th. Weiland, Int. Jour. Num. Modeling 9, (1996)295

[7] H. Herminghaus, Nucl. Instr. Meth. A314 (1992)209.

1-GeV LINAC UPGRADE STUDY AT FERMILAB*

M. Popović, A. Moretti, R. Noble and C.W. Schmidt
Fermilab, Batavia, Illinois, USA

Abstract

A linac injector for a new proton source complex at Fermilab is assumed to have a kinetic energy of 1 GeV. This linac would be sized to accelerate 100 mA of H^- beam in a 200 microsecond pulse at a 15 Hz repetition rate. This would be adequate to produce $\sim 10^{14}$ protons per pulse allowing for future improvements of the new proton source complex. An alternate proposal is to add 600 MeV of side coupled cavity linac at 805 MHz to the existing 400 MeV Linac. This addition may either be in a new location or use the present Booster tunnel. A discussion of these possibilities will be given.

1 INTRODUCTION

This study investigates a possible upgrade of the Fermilab Linac to meet hypothetical muon collider needs, increased antiproton production and higher neutrino fluxes. Muon collider is the most demanding and anticipates 1.25×10^{14} protons per pulse at 15-Hz rate and an energy of 1 GeV. Presently, the Linac can deliver 45-50 mA peak current at 15 Hz with a pulse length of 35 to 57 μs for high energy physics or cancer therapy respectively[1]. With a small effort it is likely that pulses of 60 mA and 90 μs can be achieved at 400 MeV[2]. This represents a beam of 3.4×10^{13} protons per pulse at 15 Hz. Producing 20000 μs - mA, 1.25×10^{14} protons per pulse, is significantly more difficult and would require modifications at every stage of acceleration. For 1 GeV as a final energy, an additional accelerating structure is needed. Two options have been considered. Moving the operating Linac to a new location and extending the present side-coupled accelerating structure to 1 GeV. The other is to leave the operating Linac where it is, extend the side- coupled structure through part of the Booster tunnel and use existing tunnels to transfer the 1-GeV beam to a new booster[3].

2 1-GEV EXTENSION

To have a 1 GeV linac at Fermilab site which will satisfy the muon collider needs, there are three possible options, (Figure 1);

- Build a completely new Linac based on designs adopted for spallation neutron sources,
- Build a new Linac tunnel near the Main Injector which will house the whole linac and a new Booster. Move the existing linac into the new tunnel, make necessary modifications needed for higher beam peak current and longer pulse length, and add-additional accelerating structures to reach 1 GeV as the final kinetic energy.
- Leave the existing linac at its present location, make necessary modifications needed for higher beam peak current and longer pulse length, and use the existing Booster tunnel and galleries to house accelerating structure for acceleration from 400 MeV to 1 GeV.

The first option is the least controversial but may be the most expensive. The second option assumes increasing the linac energy in a conventional way, simply adding new structure to the existing Linac in the new tunnel to achieve 1 GeV. The additional 600 MeV structure is assumed to be an extension of the recent Linac Upgrade using the same side coupled cavity modules. A preliminary design requires 11 modules for acceleration and a "half" module for controlling the energy spread of the exiting linac beam. The total physical length of the structure is 131.3 meters. The design is based on the following assumptions:

- Values for transit time, Emax/Eo and ZTT are extrapolated from the fits calculated with SUPERFISH for the values of β from 0.46 to 0.72.
- Maximum allowed electric field is 1.55 Kilpatrick which for 804.96 MHz is equal to 40.3MV/m.
- Maximum power for a four section module should be less than 9 MW. This power limit includes power to the copper and power needed to accelerate 75 mA of beam.

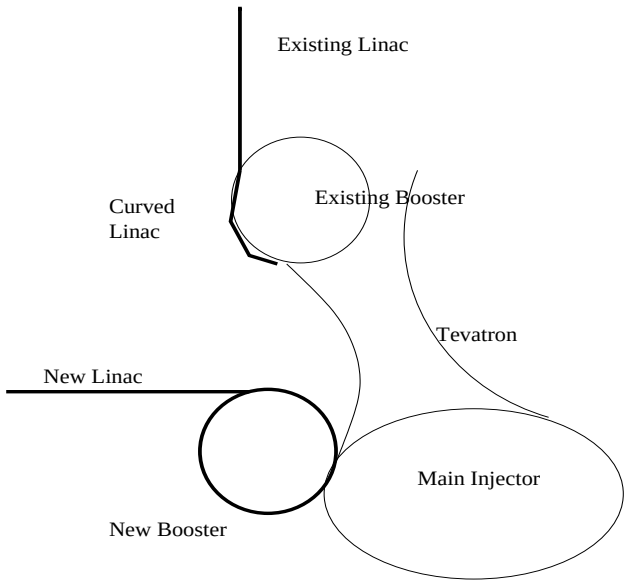

Figure 1: Location(s) of extended Linac and new Booster

* Operated by the Universities Research Association under contract with the U. S. Department of Energy

- ZTT used in the calculations is 85% of the value extrapolated from SUPEFISH calculations.
- Each module is made of four sections. The sections are made of 16 cavities of equal β. The value of β is equal to the beam's β at the mid point of the section. The sections are connected with bridge couplers and spaced for $3/2\lambda\beta$.
- Acceleration phase is -32 degrees.
- A FODO lattice is assumed using quads between each section with a phase advance of 90 degrees.

The third option, a 1-GeV linac extension in the present Booster tunnel, could prove to be economically and operationally viable. The H- beam from the 400 MeV Linac would be transported with the present 400 MeV transfer line to the Booster tunnel. To preserve the bunched beam we will use a buncher cavity at the entrance to the chute and/or retune the phase of the last module of the 400 MeV Linac. Recent experiments show that bunch length can be preserved for injection into the side coupled cavity. In this experiment linac pulses with pulse lengths less than a full Booster turn were injected in the Booster. The wall current monitor which is 334.3 meters from the injection point to the Booster was used to observe changes in the bunch length as a function of the debuncher phase and/or phase of the last accelerating module. The debuncher is located in the transfer line 33.2 meters from the exit of the Linac. The total length of 400 MeV transfer line is 62.2 meters, and by design it is dispersion free in both planes. Figure 2, shows the signal from the wall current monitor. The upper trace is a

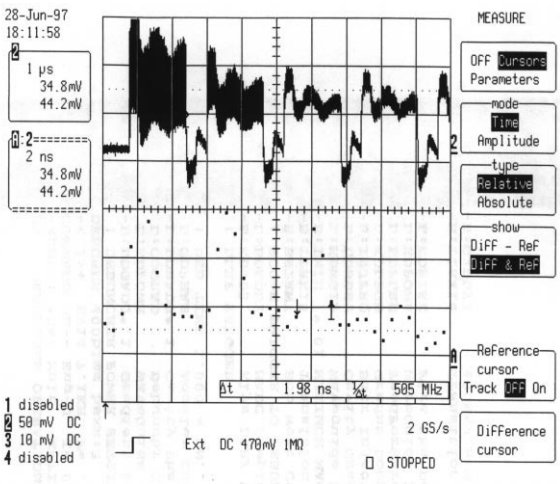

Figure 2: Bunch lenght at injection in the Booster

record of a little more than four Booster turns. The width of the trace is a measure of the strength of the 200-MHz signal. The lower trace is an expansion of the last three 200-MHz bunches seen by a detector on the first turn, after injection. The full width measured at this point is 1.98ns and this is at a location which is 396.6 meters away from the exit of the linac. On the second turn (474 meters away) the full width of the same bunch was measured to be 3.52ns. In the Booster tunnel the new linac will start 30 meters from the exit of the 400 MeV linac and will have two horizontal bends. The first bend is after three modules at a beam energy of 557 MeV. The bend consists of one FODO cell with two 11 degrees bend magnets. The next bend is at 703 MeV with the same type of bending magnets. The magnets are two meters long with a field of $\sim 3kG$. The H^- stripping probability is less than 4×10^{-12} at 557 MeV and less then 5×10^{-8} at 704 MeV. Each bend will introduce horizontal dispersion. TRACE3D calculations show an "increase" in horizontal emittance. Figure 3 shows the output

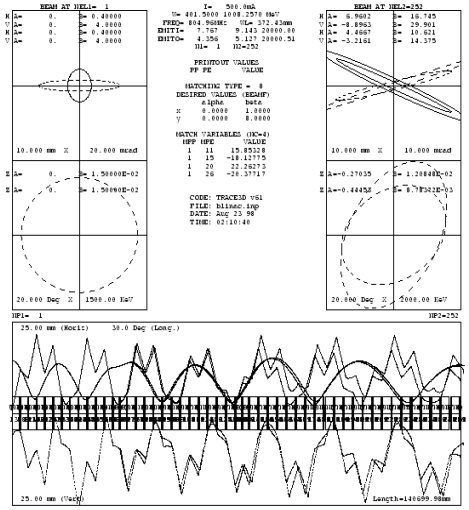

Figure 3: 1GeV Linac with bends

of TRACE3D where the beam was traced for two different cases. Input to the calculations is the linac as describe above, 13 accelerating modules and four bending magnets. The first trace simulates a "no bend" situation. In these calculations the bending angles were set to be 0.1 degree and the radius of curvature was adjusted to have the length of the "magnet" 2 meters. The second trace is for the case of four 11 degree bends. The output emittance printed by TRACE3D in this case is about two times bigger than for the "no bend" situation. In these calculations there was no attempt to adjust dispersion trough the linac after the first bend. The three quadrupoles around each bend can be tuned to minimum dispersion. The phase advance to the second bend can be arranged to supress if not cancel the dispersion.

3 PRESENT LINAC

To achieve 1.25×10^{14} protons per pulse will require considerable upgrading of the operating Fermilab Linac at the source, preaccelerator, low-energy linac and the high- energy linac. The maximum current the Linac is likely to achieve is 80-100 mA. This is limited by many constraints, most strongly by the ion source, RF power of the low-energy linac and the lattice design of the high-energy linac. Extending the pulse length is the other option, given that the

repetition rate is fixed at 15 Hz. The lower limit of 80 mA beam current sets the pulse length at 250 μs. These parameters set the conditions to which the present Linac must be capable.

3.1 Ion Source

The magnetron H^- ion source currently in use delivers a current of 65-75 mA with a pulse length of 90 μs[4]. Of this $\sim 5\%$ is lost in transport and 70% is captured in Tank 1 for a linac current of ∼45 mA through the Linac. To achieve the desired current of 80 mA an H^- ion source of ∼120 mA is necessary. BNL achieves 90 mA from a slightly modified magnetron source at an extraction voltage of 35 kV with a pulse length of 500 μs at 7.5 Hz[5]. The Fermilab source extracts at 18 kV. It is expected that a higher extraction voltage could give the desired current. A RF-driven H^- volume source may be another possibility having long lifetime. Such a source is undergoing R&D for other accelerator projects to produce 60 mA, 6% duty factor and a normalized emittance of 0.2 π mm- mr[6].

3.2 Preaccelerator and low energy transport

Two 750-kV Cockcroft-Walton generators are used as injectors to the Linac. Since neither has a bouncer, a voltage drop of ∼7 kV occurs for present beam pulses. At higher currents and pulse lengths a bouncer or other correction will be required. If the Linac were to be moved, one could consider a new tank 1 from 2 or 2.5 to 10.25 MeV, the energy of tank 2, and a set of RFQ's replacing the preaccelerators. This could also significantly improve the emittance[7].

3.3 Low-energy linac

The Fermilab Linac was designed for 75 mA and four turns of beam to the Booster (12 μs plus RF stabilizing time)[8]. At 90 mA the 5-MW RF power tubes will limit the beam current. However they can handle longer pulse lengths as shown by other U.S. accelerator facilities in table 1.

Table 1: US Proton Linacs

Beam	**BNL**	**FNAL**	**LAMPF**
Peak Current(mA)	37	48	18
Pulse Length(μsec)	500	57	900
Repetition rate(Hz)	7.5	15	120

Thus pulse lengths of 250 μs are possible with only a modest modification of the RF systems. To achieve longer pulses the quadrupole system for the drift tube linac will need modification. The pulsed power supplies will need to incorporate a second harmonic to give a relatively flat 250 μs pulse.

3.4 High-energy linac

The upgraded high-energy linac had a design goal[9] for the side-coupled accelerating cavities of 50 mA. The bridge couplers connecting the cavities were cut for a power level corresponding to 35 mA of beam, the traditional beam current when the upgrade was built. The cavities and couplers have handled up to 50 mA of beam. Whether they can handle 80-90 mA is questionable, and this is probably an upper limit. It may require rebuilding the bridge couplers. For 90 mA the 12 MW klystrons would need to be increased to 14.5 MW. The modulators, cooling systems, pulse transformers, oil tanks and low level rf systems would need to be redesigned for the higher power and pulse length.

3.5 Shielding and Losses

At the 1.0×10^{14} protons per pulse and 15Hz, the enclosure shielding, extrapolated from our present running, appears adequate except for a few areas that can be corrected. The radiation at the exterior high energy berm may exceed the permissible limit for an open unmarked area but could be corrected with a fence and signs or by adding soil. The door at the 400 MeV labyrinth into the Linac tunnel and the 400 MeV cable penetrations may exceed their allowed limits. This may require closing off the labyrinth and sealing the cable penetrations. The worst possible loss is the case of a spark in the last accelerating module if the extended structure for 1 GeV is located in the Booster tunnel. In this case about 2 μs of the beam located between the end of the 400 MeV Linac and the end of the 1 GeV linac will be lost in the Booster tunnel. This is less than the present losses in the Booster during normal operations. The beam in the 400 MeV part of the Linac will be dumped in the present Linac dump.

4 REFERENCES

[1] L.J. Allen, M. Popovic and C.W. Schmidt. "Operation and Inprovements of the Fermilab 400 MeV Linac". Proccedings of the 1996 Linear Accelerator Conference, September 1996, CERN, p329.

[2] M. Popovic, "Present Near Future and Future Performance of Fermilab Linac", Fermilab-Pub-96/046

[3] S.D. Holmes(editor). "Development Plan for the Fermilab Proton Source", TM- 2021, August 1997, Fermilab.

[4] C.W. Schmidt. "Review of Negative Hydrogen Ion Sources", Proccedings of the 1990 Linear Accelerator Conference, September 1990, Albuquerque, NM, USA, p259.

[5] J.G Alessi et al.. "Upgrade of the Brookheaven 200 MeV Linac", Proccedings of the 1996 Linear Accelerator Conference, September 1996, CERN, p329.

[6] L. Schroeder et al., editors. "Proceedings og the Ion Source Issues Relevant to a Spallation Neutron Source". LBL, October 24-26, 1994, LBL-36347 CONF-9410233 UC-404.

[7] C. Schmidt et al.," Redesign of the Low Energy Section of the Fermilab Linac to Improve Beam Brightness". Proccedings of the 1988 Linear Accelerator Conference, October 1988, Newport News, Virginia, USA, p188.

[8] Design Report, Nacional Accelerator Laboratory, July 1968.

[9] Fermilab Linac Upgrade Conceptual Design, Revision 4A, November 1989.

DEVELOPMENT OF A COMMISSIONING PLAN FOR THE APT LINAC

L. W. Funk[+], K. R. Crandall*, J. D. Gilpatrick**, E. R. Gray**, A. H. Regan**,
A. Rohlev**, L. J. Rybarcyk**, and T. P. Wangler**

[+]Westinghouse Savannah River Company, Aiken, SC 29808
*TECHSOURCE, Santa Fe, NM 87594-1057
**Los Alamos National Laboratory, Los Alamos, NM 87545

Abstract

The Accelerator Production of Tritium (APT) facility [1,2] is based on a linac which incorporates both normal-conducting and superconducting RF technology and accelerates a 100-mA cw proton beam to an energy of 1030 MeV or higher, depending on the desired production rate. Commissioning plans to achieve full power operation with minimum beam-induced activation of components have been evolving [3]. This paper presents the main issues and the basic approaches that are now being discussed.

1 COMMISSIONING OBJECTIVES

By commissioning of the accelerator, we refer to the process whereby the components are brought into operation with beam for the first time as a functioning integrated accelerator system. Commissioning need not await the complete installation and alignment of all the accelerator components, but may be done in stages. Two main activities make up the commissioning process. First is the initial setting of parameters, which includes the focusing and steering fields, and cavity-field amplitudes and phases, to values determined by the physics and engineering design. Second are the measurements to characterize the functioning of the integrated system, especially the beam and the RF system. These data will be compared with the predictions of simulation code. Discrepancies that are outside of error tolerances must be understood and, if appropriate, used to update the codes. The commissioning process is the time to detect and resolve any unanticipated performance problems that might arise. Also needed for evaluation of the overall performance are tests of different operating modes. For APT this includes operation with some superconducting cavities turned off, simulating fault conditions, where the rest of the linac is reset to continue beam operation.

2 SPECIAL CONSIDERATIONS FOR COMMISSIONING APT

The experience gained from operating and restarting the LANSCE proton linac, a pulsed machine with multiple beam operation that includes a 6%-duty-factor, 1-mA average current, and 800-MeV final energy, will be our reference point. LANSCE experience has shown that minimizing beam loss during normal operation is important, because beam loss produces radioactivity that restricts hands-on maintenance, and can cause equipment damage. Beam loss could be a concern during commissioning because the parameters are adjusted over a wide range and at times can deviate substantially from the design values. Many steps, including alignment, polarity setting, and calibration of focusing quadrupoles and steering dipoles, alignment and calibration of beam-diagnostic components, and relative phasing of multiple power feeds should be carried out prior to the start of beam tests. Also, commissioning operations that require beam should be done using pulsed beam with as small a beam duty factor and as small a peak current as is practicable, consistent with the capabilities of the beam diagnostics and the ion source. Beam-pulse lengths should be long compared with the transients in the low-energy beam transport and the RF system. We anticipate using cw RF power and pulsed beams with approximately 200-μs pulse length and a repetition rate from 1 to 10 Hz. Depending on the beam current, an RF-system settling time of 30 to 100-μs is expected before steady state is reached. The choice of peak current depends on the procedure. We expect a peak current of about 1 mA to be adequate for measuring the transverse beam-centroid alignment and setting the transverse beam steering. The 1-mA peak current, for which the space-charge forces are small, is suitable for phase scans used to set the phases and amplitudes of the cavity fields. After the 1-mA procedures are completed, the peak current will be increased to 100 mA to evaluate beam and system performance at full space charge and with full beam loading. To limit the beam losses during the commissioning, LANSCE experience suggests that the commissioning procedures should be as simple as possible, and should be done one section at a time, where each section to be commissioned consists of one of more accelerating modules.

After all the parameters have been set, beam measurements will be made to characterize the output beam from that section, using a commissioning beam-diagnostic package placed at the output. After the diagnostic package, a beam stop is installed, which prevents the commissioning beam from inducing radioactivity downstream of the section being commissioned. The beam stops must have sufficient cooling capability to absorb the beam power at 100-mA peak current with materials chosen to minimize long-lifetime activation. After the commissioning of a given section is completed, the diagnostic package and the commissioning beam stop are removed, making room for installation of the next section.

Although dividing the linac into sections helps to locate and fix problems, to keep the commissioning time within reasonable bounds, it is desirable to commission the linac in no more separate sections than is necessary, consistent

with the requirement that simple operational procedures be used. For practicality and simplicity, LANSCE experience suggests that all the commissioning steps, including the cavity phase scans, during which the beam energy varies over a large fractional range, be carried out with fixed quadrupole gradients. This requirement leads to a preliminary estimate of perhaps six commissioning-section final energies: 6.7, 10, 21, 54, 211 MeV, and 1030 MeV. A systematic study to determine the optimum number of sections and their final energies is now in progress.

3 SETTING THE PARAMETERS

Setting the parameters affecting the transverse beam dynamics, primarily quadrupole gradients and beam-steering fields should be straightforward except for outright mistakes or possible component failures. Quadrupole gradients can be set accurately to values determined from the physics design by using magnetic-field calibrations. Beam-profile measurements made near the major focusing-lattice transitions can be used to make adjustments in the quadrupole gradients if needed to improve the beam quality. As the beam energy increases, the apertures increase and good transmission can be expected over a wide range of the amplitudes and phases of the accelerating cavities.

The main task for the parameter-setting part of the commissioning process is expected to be setting the amplitudes and phases of the cavity fields. Beam measurements are required for this because direct RF field-measurement methods are not accurate enough. Cavity-field parameters can be set using a phase-scan method, in which the phase of each accelerating cavity relative to the input beam is varied, and for each phase, corresponding output beam parameters are measured. The beam measurements for commissioning can be made using both an interceptive method, such as the absorber/collector technique at low energies that measures the accelerated beam intensity above an energy threshold set by the thickness of a copper absorber, or a non-interceptive method based on beam-image-current probes in which signals are induced by the string of beam bunches. Advantages of the absorber/collector method for setting phase and amplitude at low energies are simplicity, and the ability to measure directly the phase width of the bunch from the shape of the curve of accelerated-beam intensity versus input phase.

The beam-probe method allows a measurement of beam arrival time or phase using a single probe, or beam-energy using a pair of probes separated by a drift distance. The non-interceptive beam-probe method allows more accurate measurements over the full range of beam energies and at full peak current. In the normal-conducting linac, plots of either the output-beam energy from a pair of probes or the output-beam phase from a single output probe, versus cavity phase are made as a function of the cavity amplitude. By comparing these curves with corresponding curves predicted by the simulation code, the RF parameters that produce the design values of the cavity amplitude and phase can be determined. The method based on a plot of output-beam phase versus cavity phase gives greatest accuracy when the longitudinal phase advance between the beginning of the cavity and the output probe is near an odd-integer multiple of 90°. The method involves plotting the curves for two amplitudes, one for the amplitude corresponding to 90° phase advance, and one for the design amplitude, which is known from simulation relative to the former amplitude. The two curves intersect at a known phase near the design phase. This method has the advantage that intertank spaces will generally be available allowing us to install an output probe near a location within the accelerating module corresponding to an odd-integer multiple of 90° phase advance. The other method based on a plot of output energy versus cavity phase is most accurate when the longitudinal phase advance is an integer multiple of 180°, a property that is not generally satisfied if the probes are installed in the drift space after the module.

A phase-scan procedure is also planned for the cavities in the high-energy superconducting linac. In this case the RF modules consist of either two or three independent superconducting cavities, driven by one klystron, and the longitudinal phase advance is small compared with 90°. Each cavity has an RF pickup probe that samples the field in the cavity, and whose amplitude can be calibrated in the laboratory using measurements of power and quality factor Q to an accuracy of about ±5%. After the cavities are installed in their cryostats in the tunnel, and before beam is injected into the linac, the cavity resonant frequencies are set by calculation to compensate for beam loading, the cavity fields are set to approximate values based on the laboratory calibrations, and relative phases of the cavities within the same module are set using low-power RF measurements and by adjusting mechanical phase shifters. This one-time setting of the mechanical phase shifters is determined by the design values of the cavity phases relative to the beam and the nominal value of the beam velocity at that location.

After presetting these parameters, we use the beam to determine the required RF drive phase that gives optimum phasing of the whole RF module relative to the beam, using a phase-scan measurement. In this case we obtain from the measurements a curve of output energy from a pair of beam probes versus RF drive phase. The curve is a skewed sinusoid, and using the phase locations of the peak and valley from the measured curve, we can set the RF drive phase to the design value. A complete analysis of tolerances has yet to be completed, but if uncertainties are limited to those from the beam diagnostics, the phase can be set to within a degree of the design value.

Because of the accuracy of the beam-energy measurement, the klystron amplitudes can be adjusted at each stage to minimize cumulative energy errors as we proceed down the linac. The beam energy from the pair of beam probes is obtained from the relation $\phi(\mathrm{deg})=360L/\beta\lambda$ and solving for β, where ϕ is the measured phase difference of the signals induced by the beam in the probes, L is the spacing of the two probes, β is the beam velocity relative to the speed of light, and λ is the wavelength at the bunch frequency of 350 MHz. For example, at 1 GeV (β = 0.875), L = 8.54 m (using the

spacing of two detectors separated by a lattice period), and λ = 0.857 m, we find that ϕ = 4102° or 142° (mod 360°). We are more interested in the energy uncertainty ΔW from the measurement. This can be calculated from

$$\Delta W = mc^2\gamma^3\beta^3\left(\frac{\lambda}{L}\right)\left(\frac{\Delta\phi(\text{deg})}{360}\right).$$

If we use mc^2=938.3MeV, L=8.54m, γ=2.066, β=0.8750, λ=0.857m, and $\Delta\phi$ =±3.1° (a conservative estimate of the "accuracy" from the beam diagnostics) we obtain a corresponding uncertainty in the beam-energy of ±4.8 MeV, which is only ±0.48%, sufficient to prevent a significant accumulation of an energy error.

4 CHARACTERIZATION OF THE ACCELERATOR SYSTEM

Experience from commissioning accelerators over the years has shown that as new parameter regimes are explored, new and unanticipated effects can appear. Especially because of the need to control beam loss to maintain high availability, carrying out a comprehensive set of measurements of the beam properties after setting the parameters of each stage is an important requirement. Such data taken at the end of each newly commissioned section will be compared with the predictions of the numerical simulation code. Discrepancies can be used to identify problems, which may include either component errors or physics effects that may not be included in the beam-dynamics model. Measurements made at the low-velocity end of the linac, where space-charge is important, are particularly important because discrepancies between measurements and simulation can provide an early warning of possible problems that could lead to beam loss at the high-energy end of the machine.

Measurements should be chosen so that, by comparison with the simulation code, we can answer three main questions. First, do we observe the expected low-peak-current beam characteristics, where space-charge effects are negligible? Second, do we observe the expected rms properties of the beam at the full peak current? These rms properties depend on the space-charge force, and should be compared with the numerical simulation code. Finally, do we understand the observed beam distribution including the beam halo, its density profile and its extent?

Using a commissioning beam-diagnostic package placed at the output of the section being commissioned, we plan to measure the beam current, beam loss, transverse beam profile, transverse rms emittance, transverse beam halo, final beam energy centroid, and bunch length at the output of each commissioning section [4]. Beam-loss measurements depend on the beam-halo characteristics, which depend on beam mismatches in either the longitudinal or transverse phase space [5]. Multiple transverse profile measurements using permanently installed beam-profile monitors will be compared directly with the simulations, and will also be used to determine the rms emittance during both commissioning and nominal operation. Because of its interceptive nature, a separate phase-space measurement using a conventional slit and collector device will provide beam-emittance measurements during low peak current operations. Comparison of the emittance measurements from the two methods will provide a calibration of the multiple profile measurements, which will be used to characterize beam operation after the commissioning process. Also, transverse beam-halo measurements will be obtained in which we acquire the transverse projected profiles of the beam from 3 to 5 rms-widths at multiple locations. Finally, for the longitudinal dynamics, we depend primarily on beam-centroid phase and energy measurements, and bunch length or phase spread measurements [4].

Prior to implementing supermodule RF systems in the normal conducting linac, klystron phase calibration measurements must be performed. These measurements are made to ensure that the RF phase of the klystrons have a unique and fixed relation to one another. In addition, the low-level RF (LLRF) control system has built in some on-line system-characterization capabilities [6]. These enable the operator to inject a signal of known frequency characteristics and measure the system response. After the RF parameters are set, measurements will be made to characterize the RF system performance under full beam-loaded conditions. These measurements will include the reflected power, and the errors signals associated with phases and amplitudes of the cavity fields, which are controlled by the LLRF system.

5 ACKNOWLEDGMENTS

We acknowledge support by the U.S. Department of Energy. We thank Jim Stovall for sharing with us his studies for setting the cavity parameters in the low energy linac, and Andrew Browman for helpful discussions.

6 REFERENCES

[1] Lawrence, G. L. "High-Power Proton Linac for APT: Status of Design and Development", these proceedings.

[2] Lisowski, P. W., "Accelerator Production of Tritium Plant Design and Supporting Engineering Development and Demonstration Work", Proceedings of the American Nuclear Society Topical Meeting on Nuclear Applications of Accelerator Technology, Albuquerque, NM, November 16-20, 1997.

[3] Chan, K. C. D. et al., "Commissioning Plan for a High-Current Proton Linac", Proceedings of the Particle Accelerator Conference, Vancouver, BC, May 1997.

[4] Gilpatrick, D. et al, "LEDA and APT Beam Diagnostics Instrumentation", Proceeding of the Particle Accelerator Conference , Vancouver, BC, May, 1997.

[5] Wangler T. P., Gray, E. R., Krawczyk F. L., Kurennoy S. S. , Lawrence, G. P., and Ryne, R. D., "Basis for Low Beam Loss in the High-Current APT Linac", these proceedings,

[6] Regan, A. H., et al, "LEDA LLRF Control System Characterization", these proceedings.

STATUS UPDATE ON THE LOW-ENERGY DEMONSTRATION ACCELERATOR (LEDA)*

H. Vernon Smith, Jr. and J. David Schneider, APT Technical Project Office,
Los Alamos National Laboratory, Los Alamos, New Mexico, 87545

Abstract

As part of the linac design for the accelerator production of tritium (APT) project, we are assembling the first approximately 10-MeV portion of this cw, 100-mA proton accelerator. The primary objective of this low-energy demonstration accelerator (LEDA) is to verify the design codes, gain fabrication knowledge, understand beam operation, and improve prediction of costs and operational availability for the full 1000- to 1700-MeV APT accelerator. This paper provides an updated report on this past year's progress that includes extensive beam tests of the LEDA injector using the Chalk River Injector Test Stand (CRITS) radio-frequency quadrupole (RFQ) accelerator. The CRITS RFQ produces a cw, 100-mA, 1.25-MeV RFQ output beam. We also report on fabrication, assembly, tuning, and installation of the 6.7-MeV LEDA RFQ; installation and testing of the 350-MHz RF system; fabrication of the high-energy beam transport (HEBT); installation (as well as prototype testing) of the LEDA ogive beam stop; and upgrades to the facility. First tests with the 6.7-MeV, 100-mA, cw beam from the RFQ are scheduled for late fall, 1998. References are given to many detailed papers on LEDA at this conference.

1 INTRODUCTION

This overview paper summarizes activities completed and initiated on LEDA since the publication of ref. [1]. LEDA is designed as a prototype [2] of the first 10- to 20-MeV portion of the APT linac [3] that will be built at Savannah River. LEDA's beamline components now include a 75-keV proton injector, a 6.7-MeV RFQ, a HEBT, and a beamstop (Fig. 1). Initially, a 10 MeV CCDTL (coupled-cavity drift-tube linac, a hybrid between a standard DTL and a CCL structure) will be added after the RFQ tests are complete.

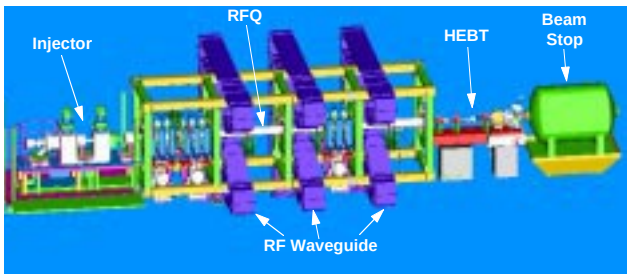

Fig. 1. Conceptual layout of the LEDA accelerator, showing the injector, RFQ (behind waveguides), HEBT, and beamstop.

* Work supported by the US Dept of Energy, Defense Programs.

Even though the output energy is low (10 MeV), the average beam power (1.0 MW) of LEDA will rank it with the LANSCE accelerator as the two highest power proton linacs in the world. Clearly, radiation shielding and power handling are important design issues. We summarize the LEDA status as of early August, 1998.

2 SUBSYSTEM DESCRIPTION

Injector:

The injector must match a dc proton beam of at least 110 mA at 75 keV into the RFQ. A 2.45-GHz microwave proton source, a single-gap extractor, and dual magnetic solenoids provide this beam. The ion source requires only 500-800 W to create a suitable plasma from which a beam having >90% proton fraction and >30% gas efficiency is extracted [4]. The single-gap, spherically convergent extractor provides a beam with emittance <0.2 π mm-mrad (normalized).

The low-energy beam transport (LEBT) uses two solenoids and two steering coils to ensure a proper match into the RFQ. A well-cooled variable-iris device is used to control injected current [5], and a microwave power modulator is used to provide beam pulsing [6] for commissioning and beam-tuning activities. Multiple extended beam runs with this injector have shown it capable of the required current, emittance, and stability. Measured erosion rates show a predicted maintenance-free lifetime exceeding 400 hours. The LEBT physics design [7, 8] is in good agreement with the mechanical design [9] and detailed measurements [10]. The LEDA injector is now installed in the beam tunnel (Fig. 2).

Fig. 2. LEDA injector installed in the beam tunnel.

The LEDA injector was used to inject a 50 keV proton beam into the CRITS RFQ. Beam operation with this 1.25-MeV cw RFQ is summarized in several papers at this conference [11, 12, 13]. Beam currents up to 100 mA

were accelerated by the CRITS RFQ [12]. A modification of the source-plasma 2.45-GHz microwave power feed lowers the rms noise on the output proton beam to < ±1% [14]. Also, an on-line method for measuring the proton fraction of the hydrogen beam confirms the previously-measured ~90% H^+ fractions [15].

RFQ:

LEDA's RFQ [16-18] is unique in terms of its long physical length (8 meters), high output energy (6.7 MeV), large beam power (670 kW), and cooling requirements (1.2 MW). It is constructed as an all-brazed, 100% copper (OFE) structure, assembled from eight separate 1-meter-long sections [17]. When in operation, its only active resonance control is by modulation of the input water temperature.

Of the eight separate sections, three are used for 350-MHz RF power feed [19] via four 250-kW coupling irises (12 total) and three sections provide vacuum pumping. Each section includes 16 static slug tuners, used only for tailoring the initial field distribution. Fabrication of the LEDA RFQ [20], the vacuum system [21, 22] and the resonance-control cooling system [23] is complete; this equipment is installed in the LEDA beam tunnel (Fig. 3); and the RFQ RF-field tuning procedure is complete [24].

Fig. 3. LEDA RFQ installed in the beam tunnel.

CCDTL:

This new 700-MHz structure [25] captures features of a DTL and a CCL, using either one or two simple drift tubes inside each π-mode cavity. Test results [26] for a CCDTL "cold model" confirms the 2-gap to 3-gap transition section for the LEDA CCDTL. A CCDTL 'hot model' has been fabricated to test structure cooling and response [27]. The LEDA CCDTL will be installed after the LEDA RFQ has been commissioned and tested.

RF Power Systems:

Three 1.2-MW, 350-MHz, cw RF-power systems are installed to power the RFQ [28-30]. The first of three 700-MHz, 1.0-MW systems that will be used to test the CCDTL have also been installed [29]. A 95-kV IGBT (insulated-gate, bi-polar) power supply that will drive the 700-MHz klystrons is being developed [31]. Each of sixteen 350-MHz RF vacuum windows have been tested at power levels >950 kW [32]. During operation, twelve of these windows will be run at power levels up to 250 kW each. The high-power RF system is ready for RF conditioning of the LEDA RFQ.

Low-Level RF Systems:

The LLRF controls system will perform a number of functions including: set and maintain the proper phase and amplitude of all accelerating cavities [33], distribute reference signals along the beam line, monitor cavity resonance condition, and provide many field signals from cavity pickup loops.

Controls:

LEDA is using a distributed control system based on EPICS [34, 35]. Many LEDA sub-systems have localized control with dedicated PLCs (programmable logic controllers), but all operational status and control commands can be accessed through the EPICS operator interfaces. An EPICS station and all peripherals have been controlling the LEDA injector for more than three years. An automated control routine provides prompt, hands-off, full-beam recovery from injector high-voltage sparkdowns. The safety and protection systems are monitored using EPICS - in the case of the fast-protect system the beam is shut down within 10-20 μsec of an interrupt and the first fault is recorded by EPICS.

HEBT and Beam Stop:

The HEBT safely transports and matches the RFQ output beam to the high-power beamstop. The HEBT (described in [36]) contains beam diagnostics that allow confirmatory measurement of the beam parameters.

For tests at 6.7 MeV, the beam will impinge on a nickel ogive beamstop [37] that is mounted inside an aluminum vessel that contains borated water (Fig. 4) to provide excellent shielding against prompt neutrons. Preliminary calculations indicate this ogive beamstop apparatus will be suitable for use at 8- and 10-MeV operation with the CCDTL sections.

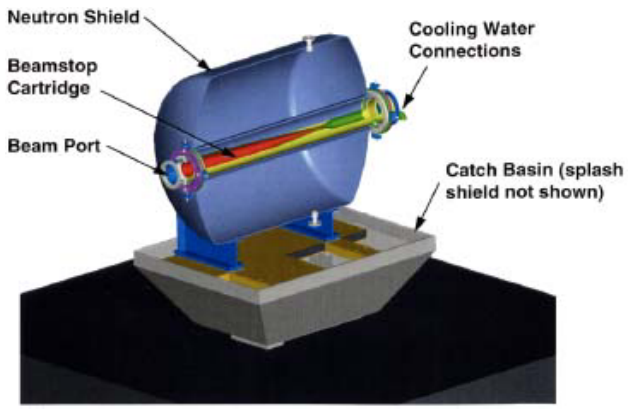

Fig. 4. LEDA ogive beamstop.

Beam Diagnostics:

The LEDA (mostly non-interceptive) diagnostics [38] measure and characterize the beam position [39] and the beam profile [40]: they also measure the beam current to obtain the RFQ transmission. This information will be used to operate the LEDA accelerator and to confirm the accelerator component designs.

Facility Modifications:

LEDA is installed in, and will be operated in, a pre-existing building that has a 140-m-long buried beam tunnel. The upgrades required to provide >10 MW of ac power and cooling water are nearly complete.

Safety Systems and Analysis:

A safety analysis document (SAD) has been prepared, reviewed, and approved. The LEDA accelerator readiness assessment is scheduled for this September. Operational run-permit is incorporated into the EPICS control system, with scores of interlocks to ensure that components and systems operate only when the risk of equipment damage is very low. A hard-wired fast-protect system ensures the near-immediate (10- to 20-μs) turnoff of the beam in event of beam spill as detected by fast ionization chambers. Totally separate from both these equipment safety systems, a personnel access control system (PACS) ensures that all personnel are excluded from the beam tunnel whenever beam or high rf power might be present. This PACS is very similar to the recently upgraded system in use at LANSCE.

3 SUMMARY

The LEDA project is on schedule to progressively assemble and test major components of a high-power, cw accelerator, first at 6.7 MeV, then 8 MeV, and then at 10 MeV. The possibility of testing the APT plant CCDTL at up to 20 MeV remains.

4 REFERENCES

[1] J. D. Schneider and K. C. D. Chan, "Progress Update on the Low-Energy Demonstration Accelerator (LEDA)," Proc. 1997 Particle Accelerator Conf. (Vancouver, 12-16 May 1997), Paper 5W024 (in press).

[2] J. D. Schneider, "APT Accelerator Technology," Proc. XVIII Int. Linac Conf. (Geneva, 26-30 Aug. 1996), pp. 22 -26.

[3] G. Lawrence and T. Wangler, "Integrated Normal-conducting/Super-conducting High Power Proton Linac for APT," Proc. 1997 Particle Accelerator Conf. (Vancouver, 12-16 May 1997), Paper 5W020 (in press).

[4] J. D. Sherman *et al.*, Rev. Sci. Instrum. **69** (1998) 1003-1008.

[5] L. Hansborough *et al*., "Mechanical Design for the LEDA Low-Energy Beam Transport System," to be published.

[6] T. Zaugg *et al*., "Operation of a Microwave Proton Source in Pulsed Mode," this conf.

[7] H. V. Smith *et al*, "Simulations of the LEDA LEBT H^+ Beam," Proc. 1997 Particle Accelerator Conf. (Vancouver, 12-16 May 1997), Paper 6W022 (in press).

[8] L. M. Young, "Simulations of the LEDA LEBT with H^+, H_2^+, and e^- particles," Proc. 1997 Particle Accelerator Conf. (Vancouver, 12-16 May 1997), Paper 6W023 (in press).

[9] L. Hansborough *et al*., "Mechanical Engineering for the LEDA Injector," Proc. 1997 Particle Accelerator Conf. (Vancouver, 12-16 May 1997), Paper 6W020 (in press).

[10] R. Ferdinand, *et al*., "Space-Charge Neutralization Measurement of a 75-keV, 130-mA Hydrogen-Ion Beam," Proc. 1997 Particle Accelerator Conf. (Vancouver, 12-16 May 1997), Paper 6W010 (in press).

[11] G. O. Bolme *et al.*, "Proton Beam Studies with a 1.25 MeV, CW Radio Frequency Quadrupole LINAC," this conf.

[12] J. Sherman *et al*., "Development and Test Results of the Low Energy Demonstration Accelerator (LEDA) Proton Injector on a 1.25 MeV CW Radio-Frequency Quadrupole," this conf.

[13] H. V. Smith *et al*., "Comparison of Beam Simulations With Measurements for a 1.25-MeV CW RFQ," this conf.

[14] P. Balleyguier *et al*., "Suppression of the 1-MHz Beam Current Modulation in the LEDA/CRITS Proton Source," this conf.

[15] J. Kamperschroer *et al*., "Doppler-Shift Proton Fraction Measurement on a CW Proton Injector," this conf.

[16] L. M. Young, "An 8-m-Long Coupled Cavity RFQ Linac," Proc. 1994 Int. LINAC Conf. (Aug., 1994, Tsukuba, Japan), 178.

[17] D. Schrage *et al*, "A 6.7-MeV CW RFQ Linac," Proc. 1997 Particle Accelerator Conf. (Vancouver, 12-16 May 1997), Paper 2W025 (in press).

[18] L. M. Young, "Simulations of the LEDA RFQ 6.7-MeV Accelerator," Proc. 1997 Particle Accelerator Conf. (Vancouver, 12-16 May 1997), Paper 6W024 (in press).

[19] R. Valdiviez *et al.*, "The Mechanical Design and Fabrication of a Ridge-Loaded Waveguide for an RFQ," this conf.

[20] D. Schrage *et al*., "CW RFQ Fabrication and Engineering," this conf.

[21] S. Shen *et al*, "APT/LEDA RFQ Vacuum Pumping System," Proc. 1997 Particle Accelerator Conf. (Vancouver, 12-16 May 1997), Paper 4P017 (in press).

[22] K. Kishiyama *et al.*, "Testing of Vacuum Pumps for the APT/LEDA RFQ," this conf.

[23] R. Floersch and G. Domer, "Resonance Control Cooling System for the APT/LEDA RFQ," this conf.

[24] L. Young and L. J. Rybarcyk, "Tuning the LEDA RFQ 6.7-MeV Accelerator," this conf.

[25] R. L. Wood *et al.*, "Thermal/Structural Design and Fabrication Development of High-Power CCDTL and CCL Structures," Proc. XVIII Int. Linac Conf. (Geneva, 26-30 Aug. 1996) pp. 752-4.

[26] M. Cole *et al.*, "Test Results for a Cold Model of a CCDTL Two-gap to Three-gap Transition to be used in the Accelerator Region," this conf.

[27] R. L. Wood *et al.*, "Status of Engineering Development of the CCDTL for Accelerator Production of Tritium," this conf.

[28] D. Rees *et al*., "Design, Operation, and Test Results of the 350-MHz LEDA RF System," this conf.

[29] D. Rees *et al.*, "Accelerator Production of Tritium 700-MHz and 350-MHz Klystron Test Results," this conf.

[30] W. T. Roybal *et al.*, "LEDA RF Distribution System Design and Component Test Results," this conf.

[31] J. Bradley *et al.*, "Design, Construction, and Operational Results of the IGBT Controlled Solid State Modulator High Voltage Power Supply used in the High Power RF Systems of the Low Energy Demonstration Accelerator of the Accelerator Production of Tritium (APT) Project," this conf.

[32] K. Cummings *et al.*, "Results and Lessons Learned from Conditioning 1-MW, 350-MHz Coaxial Vacuum Windows," this conf.

[33] A. Regan, *et al.*, "LEDA LLRF Control System Characterization," this conf.

[34] L. R. Dalesio *et al.*, Nucl. Instrum. Meth. In Phys. Research **A352** (1994) 179-184.

[35] M. Moore and R. Dalesio, "A Development and Integration Analysis of Commercial and In-House Control Subsystems," this conf.

[36] W. Lysenko, J. D. Gilpatrick, and M. Schulze, "High-Energy Beam Transport Beamline for LEDA," this conf.

[37] T. VanHagan *et al.*, "Design of an Ogive-Shaped Beamstop," this conf.

[38] J. D. Gilpatrick *et al.*, "LEDA and APT Beam Diagnostics Instrumentation," Proc. 1997 Particle Accelerator Conf. (Vancouver, 12-16 May 1997), Paper 8P058 (in press).

[39] J. D. Gilpatrick *et al*., "LEDA & APT Beam Position Measurement System: Design and Initial Test Results ," this conf.

[40] J. F. O'Hara *et al*., "Design and Development of the LEDA Slow Wire Scanner Profile Measurement," this conf.

BEAM DYNAMICS DESIGN OF THE 211 MEV APT NORMAL CONDUCTING LINAC *

L. M. Young, J. H. Billen, H. Takeda, R. L. Wood
Los Alamos National Laboratory, MS H817, Los Alamos, NM 87545, USA

Abstract

This paper describes the normal conducting linac design that is part of the Accelerator for Production of Tritium (APT) project [1]. The new version of PARMILA [2] designed this linac. This linac accepts the beam from the 6.7-MeV radio-frequency quadrupole (RFQ) [3,4] without a separate matching section. At about 10 MeV, it has a smooth transition in the length of period from 8βλ to 9βλ in quadrupole focusing lattice. This adjustment of the period was needed to provide sufficient space for the quadrupole focusing magnets and beam diagnostic equipment. The linac consists of the coupled-cavity drift-tube linac (CCDTL) [5] up to 97 MeV and coupled-cavity linac (CCL) above 97 MeV.

1 INTRODUCTION

The first 211 MeV of the APT linac consists of the 700-MHz CCDTL and CCL. The CCDTL accepts the beam from the 350-MHz, 6.7-MeV RFQ without a separate matching section. The CCDTL accelerates the 100-mA beam to 97 MeV. The CCL accelerates the beam to 211 MeV. The CCDTL uses a transverse focusing period of 8βλ from 6.7 MeV to about 9.5 MeV. At this point the transverse focusing period is smoothly increased to 9βλ to make more room for the quadrupole focusing magnets. The 8βλ section of the CCDTL uses one accelerating cavity with 1 drift tube between each quadrupole magnet leaving plenty of space for the quadrupole. After the transition to 9βλ the CCDTL has one accelerating cavity with 2 drift tubes between each quadrupole. The rest of the CCDTL and CCL accelerator use the 9βλ focusing period. Figure 1 shows the particle coordinates versus cell number from a PARMILA simulation though the 211-MeV linac and the first 6 “Cryomodules” of the Superconducting linac. A “Cryomodule” is a cryostat with two or more accelerating cavities. Each accelerating gap and each quadrupole increments the cell number in this figure.

2 RFQ TO CCDTL MATCHING

We used no separate matching section to match the beam from the RFQ to the CCDTL. By adjusting the length of the fringe-field cell at the output of the RFQ, we matched the beam into the CCDTL quadrupole focusing channel. In addition, we adjusted the transverse focusing strength per cm of the RFQ to equal that of the CCDTL so that the match would be current independent. The longitudinal matching was a little more difficult because the longitudinal focusing goes to zero at the end of the final accelerating cell in the RFQ. Also, the beam drifts to the first cavity of the CCDTL before it sees any longitudinal focusing. Another complication is that the RFQ operates at 350 MHz and the CCDTL at 700 MHz. This problem was solved by setting the synchronous phase of the first accelerating cavity at -90° and increasing the RF fields in this cavity by a factor of 1.65. The second accelerating cavity was operated at -30° synchronous

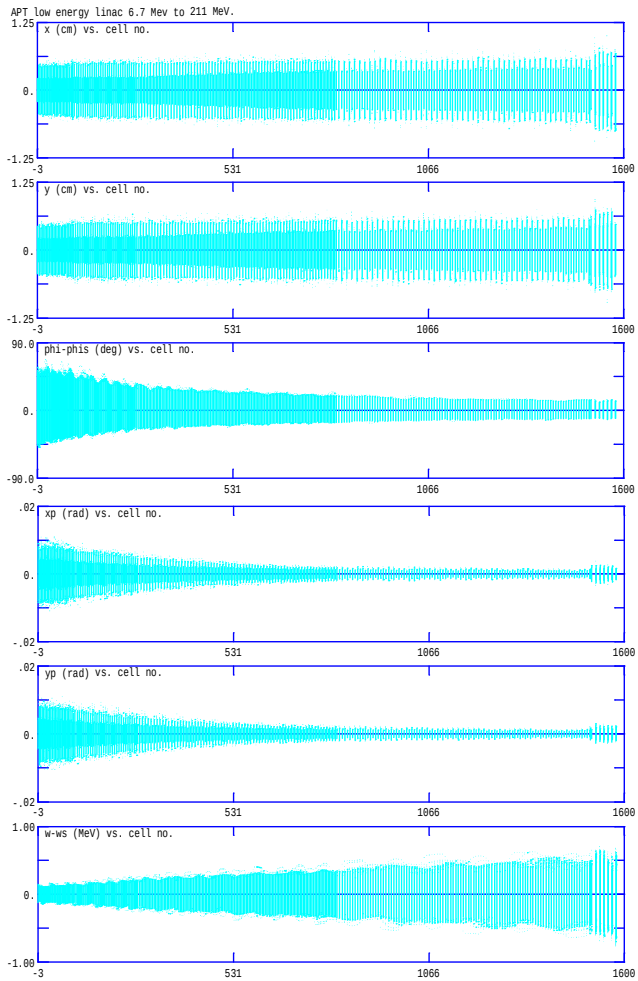

Figure 1. Beam size versus cell number of the 211-MeV APT Linac. Plotted versus cell number respectively from the top down are particle coordinates x, y, phi, xp, yp, and energy. The phase “phi” and the energy are plotted with respect to the phase and energy of the synchronous particle. Divergence coordinates are xp=dx/dz and yp=dy/dz. This data comes from a PARMILA simulation with 95405 particles.

*Work supported by the US Department of Energy.

phase and normal RF fields. The third and subsequent accelerating cavities operate at -60° synchronous phase to provide a large enough longitudinal acceptance to capture the beam bunches from the 350-MHz RFQ. We chose the RF amplitude at the beginning of the CCDTL to provide nearly the same longitudinal focusing strength per cm as provided by the RFQ near its exit. Figure 2 shows the longitudinal and transverse zero-current phase advance divided by the transverse-focusing-period length plotted versus energy from 1 MeV (in the RFQ) to 245 MeV (in the first part of the superconducting accelerator). The small discontinuities in the focusing strength in this figure at 6.7 MeV, show the match in the focusing between the RFQ and the CCDTL.

3 CCDTL

The RF amplitude slowly increasees and the synchronous phase approaches -30° as the energy increases. At 10 MeV, after the transition to the 9βλ focusing period, the real-estate accelerating field is too high for the 1-drift-tube CCDTL. The term real-estate refers to an average over a transverse focusing period. The CCDTL uses 2 drift tubes in each cavity from 10 MeV to 21.6 MeV. At 21.6 MeV the synchronous phase has progressed to -40° and the accelerating field to 1.863 MeV/m. The accelerating structure only occupies 5/9^{ths} of the real estate. Therefore the real-estate accelerating field is 1.035 MeV/m.

The CCDTL uses 2 cavities with 1 drift tube in each between each quadrupole magnet from 21.6 MeV to 96.7 MeV. The synchronous phase reaches its final value of -30° at 92 MeV. At that point the effective real-estate accelerating field, E_0T, is 1.12 MeV/m. We made the changes in the accelerating field and synchronous phase to keep the ratio of the longitudinal and transverse phase advance per cm nearly constant below 25 MeV. Below 25 MeV the transverse phase advance was keep constant at ~78° per period.

The effect of changing the period from 8βλ to 9βλ can be seen between 9.5 and 10 MeV in Figure 2. At energies above 25 MeV, we slowly decreased the quadrupole focusing strength as the energy increased. We reduced the quadrupole focusing strength at higher energies for two reasons. First, by keeping the ratio of the longitudinal focusing strength to the transverse focusing strength constant the bunch shape remained nearly constant. Also, as shown in Figure 3, the longitudinal tune depression did not fall to extremely low values as it would have without reducing the transverse focusing strength. Second, we had to reduce the transverse focusing strength at the end of the normal conducting linac to equal that available at the beginning of the superconducting linac.

4 CCL

The linac uses the CCL structure from 96.7 MeV to 211 MeV. The first segment in each module uses 6 accelerating cavities while the rest of the segments have 7 accelerating cavities. The accelerating structure occupies 7/9^{ths} of the real estate in this part of the linac. The first segment uses only 6 cavities to make room for a beam-line vacuum-isolation valve. The field in the first segment is increased to give the same energy gain as the 7 cavity segments. At the end of the normal conducting linac the real estate accelerating field is 1.427 MeV/m at 211 MeV. Figure 4 shows the transverse and longitudinal emittance in the normal conducting linac and the first part of the superconducting linac.

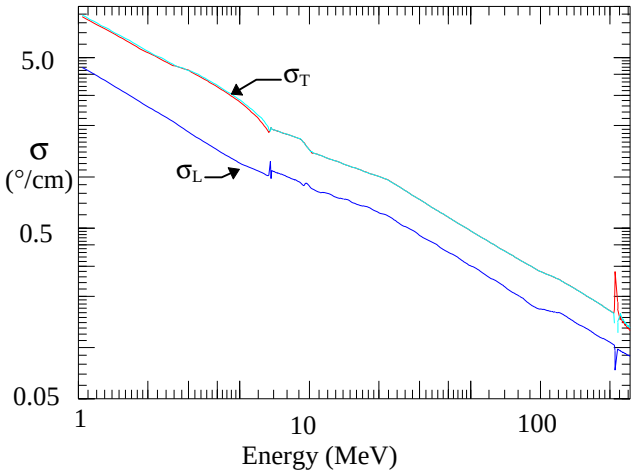

Figure 2. A log-log plot of the longitudinal (σ_L) and transverse (σ_T) zero-current phase advance divided by the transverse-focusing-period length. The transition from the quad-singlet focusing in the normal conducting linac to the quad-doublet focusing in the superconducting linac causes the spikes at 211 MeV.

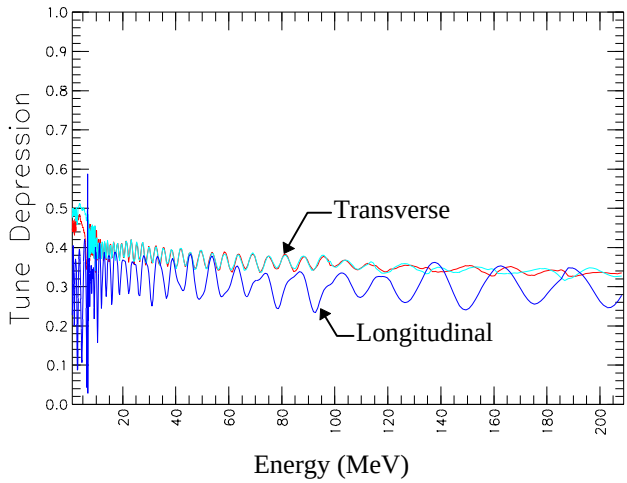

Figure 3. The longitudinal and transverse tune depression from 1.0 MeV to 211 MeV in the APT linac plotted versus energy. The tune depression is the ratio of the phase advance with 100 mA to the phase advance with "zero" current.

5 CURRENT INDEPENDENT MATCH

A current independent match means the beam match between two parts of the linac does not depend on the beam current. The APT linac must operate with a 100-mA

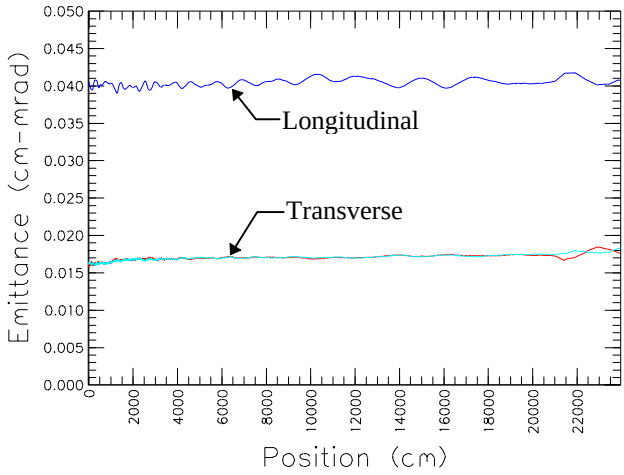

Figure 4. The transverse and longitudinal emittance versus position in the 6.7-MeV-to-211-MeV linac and the first 6 "Cryomodules" of the superconducting linac. The superconducting linac starts at ~21000 cm in this figure.

CW beam. We must keep the beam loss to a very small level even during commissioning. During commissioning we will use beam pulses of about 200 μsec duration and with low peak current at first. Under these conditions we can allow a larger fraction of the beam to be lost. Later in the commissioning process the pulsed beam will have a peak current of 100 mA and only a small fraction can be lost. During commissioning with a pulsed beam we will optimize the quadrupole magnet strengths and the RF amplitudes and phases for extremely small beam loss. We must not change these settings for the CW beam. Therefore, we need a current independent match so that we can operate the accelerator at any current up to 100 mA without readjusting the quadrupole focusing magnets or the RF settings. The current independent match between the RFQ and CCDTL has been checked by running PARMTEQ simulations of the RFQ with input beams with currents of 0, 40, 57, 103, and 110 mA. These output beam distributions from the PARMTEQ simulations were then used as the input beam distributions for PARMILA simulations of the beam through the CCDTL and CCL without changing any parameters. The PARMILA code uses the beam current contained in the input distribution file. The match in all cases was satisfactory.

We used the following philosophy throughout the design of the linac to ensure current independent matching between different parts of the linac. We kept the ratio of the longitudinal to the transverse focusing strength nearly constant and without steps in either the longitudinal or transverse focusing strengths. This philosophy results in a linac design with a beam that is nearly equipartitioned [6,7]. With a nearly equipartitioned beam there may be less beam in the halo for a well matched beam such as that shown in Figure 1. Reference [8] shows that a halo can develop even with a well matched beam if it is not equipartitioned. With a poorly matched beam, a halo will develop whether or not the beam is equipartitioned.

6 CONCLUSIONS

The PARMILA design of the normal conducting linac for APT is complete. The simulations show essentially no emittance growth in this linac. The match between the RFQ and the CCDTL is current independent. The match between the various sections of the CCDTL and the CCL is extremely good because there is no change in the transverse focusing period and the variation in the real-estate accelerating field is smooth.

The beam can be matched to the superconducting linac. Although we have not checked this match with a complete set of simulations (only with 0 and 100 mA) we expect the match to the superconducting linac to be current independent, because we kept the focusing strength per cm continuous across this transition.

REFERENCES

[1] G. Lawrence, "High Power Proton Linac for APT; Status of Design and Development," these proceedings.

[2] H. Takeda, J. H. Billen, "Recent Developments in the Accelerator Design Code PARMILA" these proceedings.

[3] L. M. Young, "Tuning of the LEDA RFQ 6.7 MeV Accelerator," these proceedings.

[4] L. M. Young, "Simulations of the LEDA RFQ 6.7 MeV Accelerator," Proceedings of the 1997 Particle Accelerator Conference.

[5] J. H. Billen et al., "A New RF Structure For Intermediate-Velocity Particles" *Proceedings of the 1994 Linear Accelerator Conference*, August 21-26, 1994 Tsukuba, Japan.

[6] R. A. Jameson, "On Scaling & Optimization of High Intensity, Low-Beam-Loss RF Linacs for Neutron Source Drivers", AIP Conf. Proc. 279, ISBN 1-56396-191-1, DOE Conf-9206193 (1992) 969-998, Proceedings Third Workshop on Advanced Accelerator Concepts, 14-20 June 1992, Port Jefferson, Long Island, NY, (LA-UR-92-2474, Los Alamos National Laboratory).

[7] M Reiser, "Theory and Design of Charged Particle Beams," John Wiley & Sons, Inc., p. 573 (1994).

[8] L. M. Young, "Equipartitioning in A High current proton Linac", Proceedings of the 1997 Particle Accelerator Conference.

FERMILAB LINAC 1997-98 OPERATIONS, STUDIES AND IMPROVEMENTS

L. J. Allen, C. W. Schmidt and M. Popovic
Fermi National Accelerator Laboratory*
Batavia, Illinois

Abstract

The Fermilab Linac operated as an injector for the Tevatron Fixed Target Program, booster studies and as a neutron source for cancer treatment during 1997 and 1998. Operational reliability was 98% of the scheduled operating time. Beam currents were generally in the 45 to 48 mA range with a high of 52 mA during studies. After completion of the Fixed Target Program, the Linac embarked on a series of studies. The studies were intended to verify visual survey data indicating a misalignment of the low energy linac, correct the misalignment, and install and use new wires for determining emittance. Operations data and studies results will be presented.

1 OVERVIEW

The Fermilab Linac operates at 400 MeV for linac studies and injection into the 8-GeV Booster for further studies and high energy physics (HEP). It also operates at 66 MeV as a neutron source for treating cancer in the Neutron Therapy Facility (NTF). There are two ion sources, feeding DC accelerating columns powered by Cockcroft-Walton generators at 745 kV. The Linac RF pulse repetition rate is 15 Hz, useable RF pulse length is 120 μsec and the maximum source beam pulse length is ~80μsec. The operating beam pulse length is dependent upon on its ultimate use and determined by choppers in the 750-keV line. Pulse lengths for HEP beam are determined by the Booster requirements, typically 15-25 μsec. NTF uses the unused 15-Hz pulses with a 57-μsec length. Linac studies use typically a 20 μsec pulse generally at 3 Hz.

2 FIXED TARGET RUN

In 1996 and 1997 Fermilab operated a Fixed Target Run providing 800-GeV beams to experimenters in the external beam-lines and 8 GeV antiproton beams to experimenters in the Accumulator Ring. The Linac provided 12 pulse bursts of beam for HEP and single pulses at 2.5 second repetition rates for antiproton production along with NTF. In September 1997 the Fixed Target program ended and the Linac embarked on a one year program of maintenance and studies with the Booster. Aside from the usual preventive maintenance a drift tube was replaced in tank two, a resurvey was done and scanning profile wires were added at the 400-MeV output of the Linac. Studies included the sampling of drift tube quadrupole placement to investigate a suggested vertical misalignment between tank 5 and the high-energy linac.

* This work supported by the U.S. Department of Energy through the Universities Research Association under contract DE-AC35-89ER40486.

Beam intensity, during the Fixed Target Run, averaged 45 to 48 mA as shown in Figure 1. Problems with the 2400 l/sec ion pumps used to maintain column vacuum on the preaccelerators, forced the use less efficient roughing turbo pumps. The resulting increase in pressure reduced the intensity slightly until they could be rebuilt. After the run was over and beam level safety permits were readjusted the Linac achieved 52 mA.

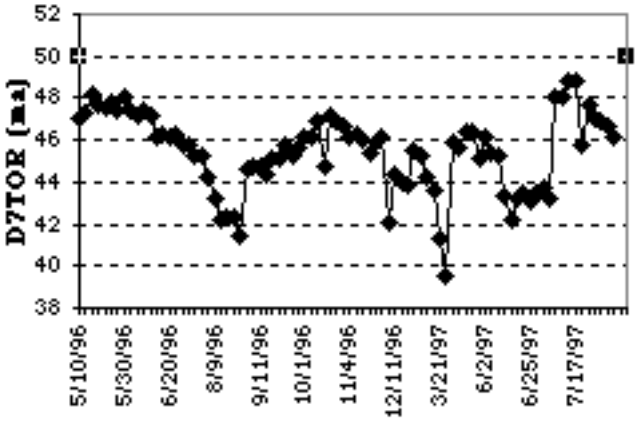

Figure 1. Linac intensity during fixed target run.

There are 35 loss monitors in the high-energy linac. They are of the Tevatron type [1] with Main Ring style amplifiers. They are not calibrated, but used as tuning aids and for comparison with previous data. The maximum value of the relative computer signal is 100 equivalent to 10V from the amplifier. By saving and averaging these values the tuning quality and level of losses in the Linac can be monitored. Reviewing this average since the high-energy linac was installed, Table 1, shows that the losses have decreased especially in the RF accelerating structures. Typical beam loss through the Linac from tank 2, after the beam has been captured, to the 400-MeV output is ~1% or less. Of the 65-70 mA of the preaccelerator beam 70% or more is captured in tank 1.

Table 1. Relative beam loss levels for each period for the total Linac structures and along the RF accelerating cavities.

Time	Whole Linac	RF Cav. Only
March, 1994	3.06	2.18
Beginning of run	2.82	1.43
End of run	2.61	0.95

Linac operated for 98% of the 10442 scheduled operating hours. As has historically been the case the vast majority of downtimes are very short. There were 1166 downtime entries, of which 80% are less than six

minutes and while 4% are one hour or longer they account for 66% of the 212 hours of downtime. Downtime by major system is shown in Fig. 2. The three major causes of downtime during the run were; the failure and replacement of klystron 3, replacing the power amplifier for low energy RF station 4 with an unconditioned spare and multiple failures of the SCR switches in klystron charging supplies and PFN's.

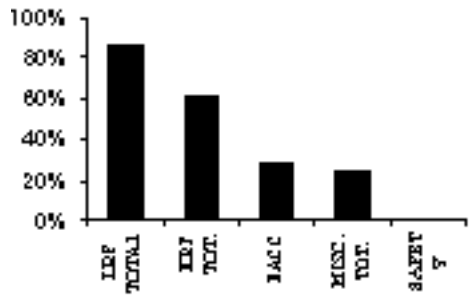

Figure 2. Linac downtime for fixed target run by major system

Klystron 3 was the first failure of a klystron and caused 7.8% of linac downtime. Being the first klystron to fail in use from aging, it had ~35,000 hours of operating time, the problem was at first unclear. Diagnosing the klystron emission failure, assembling the people and replacing the klystron assembly required a total of 16.5 hours over two days.

The power amplifier for RF station 4 was the last in an series of 7835 failures during a time when the test stand was unavailable for conditioning spares due to moving the test stand and an error by the manufacturer for a new dummy load. Total downtime for this failure was 7.4% of the linac downtime.

There have been repetitive problems with SCR switches and other components in the charging supplies and PFN's for the klystrons. This has caused 10.3% of the linac downtime. Solutions have been implemented and the failure rate has decreased dramatically.

3 STUDIES

In an effort to confirm survey data which showed a vertical misalignment between tank 5, the last tank of the low-energy linac, and the beginning of the high-energy linac, studies were done of the beam centering for each of the drift tube quadrupoles. This procedure was first used about ten years ago and now repeated where the current of each drift tube quadrupole pair (in the Fermilab Linac the DT quads are connected in FD pairs except for the two at the beginning and end of each tank) is individually changed by 10% up and/or down. The resulting beam motion at a downstream position detector (BPM or wire scanner) gives an indication of the beam centering at the changed DT quadrupole. If the beam center coincides with the magnetic center of the quadrupole, no motion of the beam center at the detector is observed. However, if the beam is off center relative to the quadrupole, when the current is changed a kick is given to the beam. This kick would then start an oscillation which continues down the Linac to be observed at an appropriate position detector. Usually two detectors, ~90^{O} apart in phase and at the farthest downstream position of the Linac are used so all DT quad positions could be observed relative to the same detectors. This is analogous to observing beam motion due to quadrupole misalignment in a transport line.

This procedure was used on the Linac in the late 1980's and predicted a large quadrupole misalignment in tank 2 by showing a cusp in the data. The drift tube was subsequently found to be off center by 1 mm. After correction the cusp was gone and the downstream beam oscillations reduced. It also indicated tank misalignments by showing increased errors from one tank to the next. Figure 3 shows a typical set of measurements for the old Fermilab Linac before tanks 6 through 9 were removed and replaced by the side-coupled cavities. The low errors in tanks 7, 8 and 9 are a result of steering magnets at the entrance and exit of tank 6 (~90% separated in phase) to remove beam errors and have the beam leave the Linac on axis of the 200-MeV beam line.

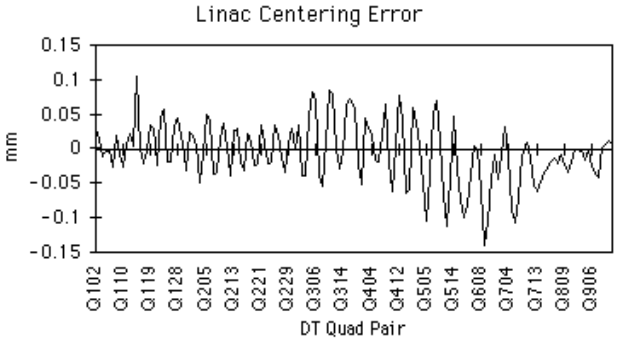

Figure 3. Detected beam motion for a 10% decrease in each Linac DT quad pair.

Recently similar measurements were made for the current Linac, figure 4, and consentrating on tank 5, figure 5. The mismatch in tank 5 is a result of beam leaving the tank off axis and at an angle for lowest losses in the high-energy linac. The steering magnets at the beginning of the high-energy linac were on hard to correct the angle. Moving the downstream end of tank 5 down 0.75 mm as indicated by the survey and beam, reduced the mismatch, allowed steering changes to reduce the errors in tank 5 (see figure 6), decreased the steering at the beginning of the high-energy linac, and reduced the losses significantly throughout the high-energy linac.

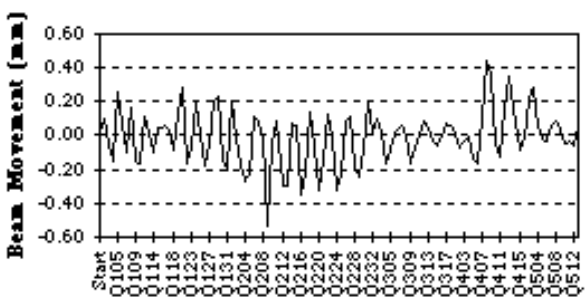

Figure 4. Recent detected beam motion for a 10% decrease in each Linac DT quad pair.

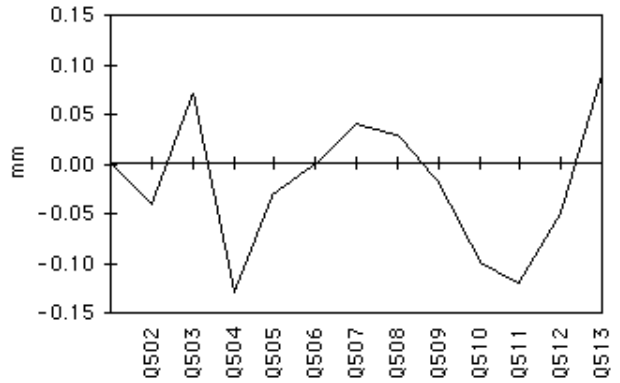

Figure 5. Error measurements before tank 5 change.

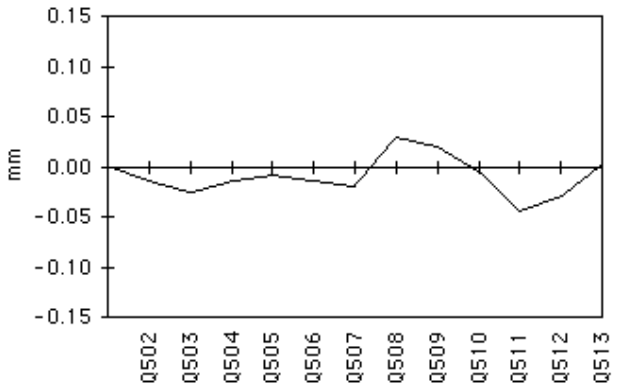

Figure 6. Repeat of figure 5 after lowering the downstream end of tank 5.

The condition of tank 5, indeed the complete Linac, depends on the tuning of earlier components. Tank 5 does not remain this good at all times, never-the-less the losses in the high-energy linac have remained very low. Table 2 shows current loss averages. Some loss monitors were moved to places where they are more sensitive to beam loss.

Table 2. Losses after moving tank 5.

Time	Whole Linac	RF Cav. Only
After studies	2.17	1.20

4 IMPROVEMENTS

During the recent shutdown, three wire scanners were installed in a drift space just beyond the 400-MeV output on the Linac. These wires will give better monitoring of the beam size, position and emittance leaving the Linac.

REFERENCES

[1] M. Johnson, "Loss Monitors". AIP Conference Proceedings 212 Accelerator Instrumentation, 1989, pg. 156.

MOSCOW MESON FACTORY LINAC - OPERATION AND IMPROVEMENTS*

L.V. Kravchuk, Y.V. Bylinsky, S.K. Esin, P.N. Ostroumov, V.L. Serov
Institute for Nuclear Research RAS, 117312, Moscow

1 INTRODUCTION

Moscow Meson Factory Linac (MMFL) [1] has provided in 1997-1998, 4400 beam hours for physics, isotope production and machine development. The lack of adequate funding for machine operation (electricity etc.) has put severe limitation on the beam production time. Beam energy was limited by 305 MeV and in some production shifts even by 209 MeV. A significant part of the beam time has been devoted to isotope production for medical use at an energy of 160 MeV. The maximum average proton current during regular operation is 65 μA with a pulse duration of 85 μs and repetition rate of 50 Hz. In 1998 a proton beam has been delivered for the first time to the Pulsed Neutron Source. A number of improvements have been implemented, with a strong impact on the operation efficiency. One of the most important measures is the creation of a new control network (based on PCs) for the beam diagnostics data acquisition. The injection beam transport channel and RF power supply system are presently undergoing reconstruction. The aim of this reconstruction is to increase the beam pulse up to 140 μs and repetition rate up to 100 Hz which will result to the growth of average beam current to 200 μA.

2 LINAC OPERATION

The total scheduled time of the linac operation includes the beam delivery to users, the tuning of the linac and unexpected down time. On average for the last two years the beam delivery time to users was ~60%. About 30% of the time was spent for tuning and accelerator experiments and developments, the rest was down time. Essential development has been done on the linac RF system with the main aim of increasing the reliability and linac operation efficiency, as well as to prepare the RF system for operation at 100 Hz and a 140 μs beam pulse. Obtaining of 100 Hz repetition rate is simpler task than providing of the beam pulse length more than 100 μs, because of operation at 100 Hz is the design specification of all linac equipment. The design beam pulse duration of the linac is 100 μs. Therefore the modulators and preamplifiers have been revised. The automatic temperature control system of the accelerating cavities has been tuned in order to provide 100 Hz repetition rate of rf amplifiers.

Although the linac control system is based on old computer equipment, it is adequate for the linac operation. This system is mainly used for the support of RF and other technical equipment. Major profit from the control system has been obtained by development of software in order to support the RF system operation. In many cases the restoration of the RF system immediately after the malfunction has increased operational time. This is an important issue for the system with large electrical power consumption which is the case of the MMF linac. However the original control system has very restricted ability for the data processing and presentation. The existing beam monitors already produce large amount of information which is not fully available from the original control system. In addition, many beam diagnostic devices have been developed and installed on the linac, including:

- A new type of detector allowing the measurement of the transverse density distribution was installed in the 750 keV transport line.
- A new Bunch Length and Velocity Detector (BLVD) is installed in the 160 MeV transition line.
- Several beam profile harps.
- Non-interceptive beam position monitors.

Therefore the new control system was developed based on PCs which are connected to the local area network. The analogue and digital hardware is housed in CAMAC crates (up to 4 crates per sector). The system is based on MOON-Lab (Multi-tasking Object-Oriented Network Lab System) - a software run-time system and an application programming technology developed at INR [2].

The new control system serves different types of beam diagnostic monitors: beam current transformers, wire scanners, profile harps, BLVD, beam loss monitors, a monitor for the measurement of transverse beam density and neutron detectors. Fig. 1, 2 and 3, represent examples of graphical information obtained by new control system.

The beam delivery system to the isotope production area includes 27° bending magnet and ~12 m long transport channel [3]. The control of beam losses in the vicinity of the bending magnet is a problem of great importance due to high level of the average beam

* Work supported partly by the RFFI, grant 97-02-17475.

current. Discrepancy between the beam energy and the magnet current as well as the violation of the correcting element parameters can lead to instantaneous melting of the vacuum pipe during an extremely short time. To prevent such accidents, a number of protections measures have been undertaken.

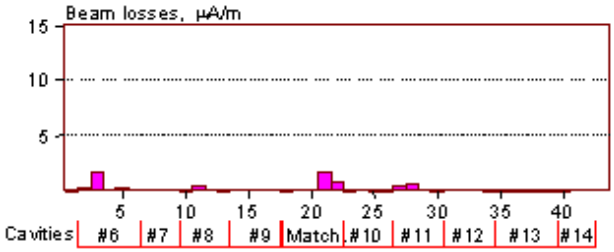

Figure 1: Scintillating beam loss counters (#1-40) along the 3rd sector of the MMFL. (Tanks #6-14)

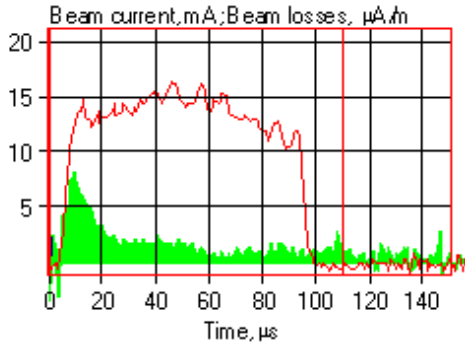

Figure 2: Beam current and particle losses along the macropulse. 3rd sector. Beam loss monitor # 21

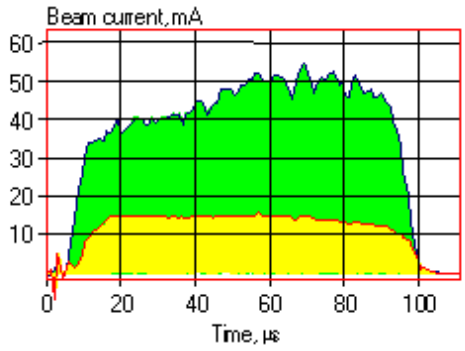

Figure 3: Capture coefficient control. Comparison of current transformer signals: at the input of the Tanks # 1 and at the output of the Tanks # 8.

The bending magnet in the 750 keV injection line is switched off and the 750 keV beam is deflected by a chopper, as well as the injector trigger being shifted with respect to the RF pulse if one of the following cases occurs: 1) Difference of the pulse charge in a given cycle registered with current transformers upstream and downstream of the bending magnet is in excess of the tolerance limit; 2) Beam loss monitor signal is in excess of the tolerance; 3) Phase and amplitude parameters of any RF system is out of tolerance; 4) Beam profile on the isotope production target moves too close to the edge of the target. Fig. 4 shows 2 signals from current transformers. The difference between the signals is well inside the tolerance. For initial accelerator tuning at the repetition rate of 1 Hz the protection is not used. At a repetition rate of 2 Hz and higher, the loss threshold may be reduced from 10% to 1%. As a result of careful tuning the total beam loss in the course of an isotope production shift does not exceed 0.5% and is usually kept near 0.1%.

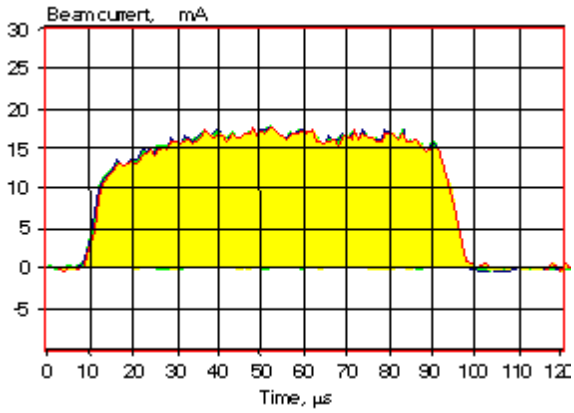

Figure 4: Two overlapped beam pulses: upstream of the bending magnet (almost invisible) and downstream of the bending magnet.

The MMFL contains two transition regions at 100 MeV and 160 MeV. It is important to verify the longitudinal bunch length in these regions. The bunch length measurement (BSM) system is well established at INR, and the most recently modified device, the Bunch Length and Velocity Detector (BLVD) has been installed in the 160 MeV area. The high resolution of the detectors, which is 14 ps, allows monitoring of the quality of the Linac beam during operation. The devices use a 100 μm wire which allows the measurements to be performed at up to 50 Hz repetition rate. After many years experience with the BSM and BLVD systems, we are able to detect the source of any deviation of the longitudinal profiles form the nominal state. Fig. 5 shows the bunch shape evolution along the macropulse at the energy of 160 MeV.

3 INJECTION CHANNEL UPGRADE

The essential reconstruction of the injection channel is under way. Fig. 6 a) shows the existing layout of the channel (equipment of 1st and 2nd parts of channel is not shown for simplicity). The channel is designed to inject 750 keV H^+ and H^- beam simultaneously into the Alvarez tank. However, the electrical strength of the 750 kV pulsed transformer is not sufficient for operation at 100 Hz repetition rate, hence the linac operates at 50 Hz

with half the average beam current of the maximum possible.

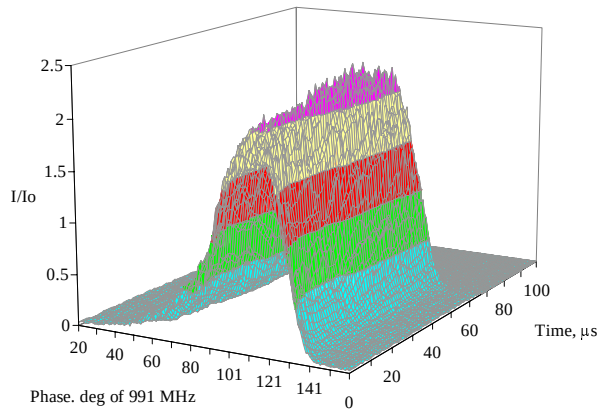

Figure 5: Bunch shape evolution along the macropulse at 160 MeV.

A decision was taken to insert the RFQ booster section into the 3rd part of the injection channel (Fig. 6 b)). The RFQ has been designed to accelerate hydrogen ions from 400 keV to 750 keV. The high voltage equipment of the injector works with good reliability up to the level of 400 kV. Moreover, the pulse length can be increased up to 140 μs without pulsed transformer saturation. It will allow the average beam current to beam increased up to 200 μA. The limited space does not permit to the realisation of adiabatic capture in the RFQ. To provide the longitudinal capture efficiency up to 80% at the peak current of 70 mA, the 400 keV prebuncher is placed upstream of the RFQ. A 750 keV buncher and four quadrupoles provide 3D beam matching between the RFQ and DTL tank. Fig. 7 shows the RFQ booster section which is now under high power test.

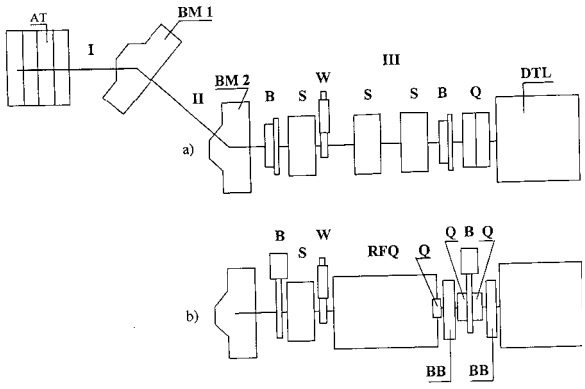

Figure 6: Injection channel layout.

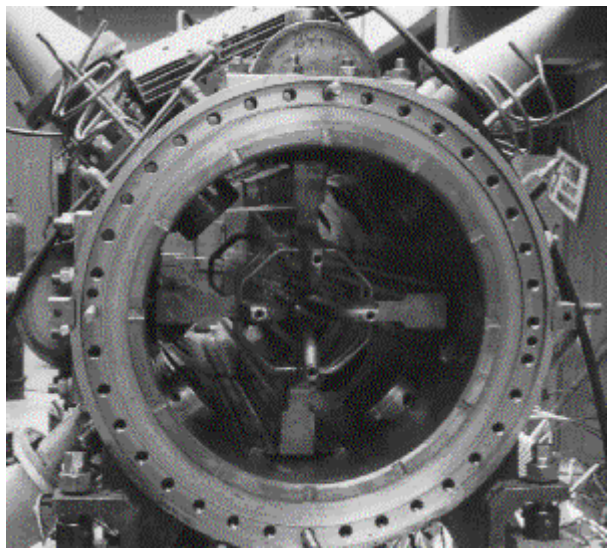

Figure 7: RFQ booster section.

High power modulators in the RF power supply permit to introduce moderate modification which will guarantee operation with longer rf pulses in order to accelerate 140 μs beam pulse.

Thus we hope increase the average beam current by up to a factor three over that presently attained.

4 ACKNOWLEDGEMENTS

In conclusion authors express their deep gratitude to the whole staff of the MMFL, who made the machine operational in recent times, which are not easy for scientific activity.

5 REFERENCES

[1] S. K. Esin, L. V. Kravchuk et. al. Commissioning / Operation of the Moscow Meson Factory Linac. Proc. of the 1994 Linac Conf. August 21-26, Tsukuba, Japan, pp.31-35.

[2] S. A. Kryukov. New Programming Technologies for Beam Diagnostics. Proc. of the Epac-96. Sitges, Vol3, pp. 1781-1783 (1996).

[3] S. K. Esin et al. Isotope Production for Medical and Technical Use at Moscow Meson Factory Linac. Proc. of 1996 Linac Conf. Geneva, 1996, v.1, p. 213.

[4] A. V. Feschenko and P.N. Ostroumov. Bunch Shape Measuring Technique and Its Application for an Ion Linac Tuning. Proc. of 1986 Linac Conf. Stanford, June 2-6, pp. 323-327.

STATUS OF A NEW SWITCHYARD DESIGN FOR LANSCE*

R. W. Garnett, C. Rose, F. Shelley, and J. D. Zumbro**,
LANSCE Division, Los Alamos National Laboratory, Los Alamos, NM 87545, USA

Abstract

Funding was recently received to study modifications of a section of the LANSCE beam switchyard. At present, the switchyard is used to deliver a proton beam to experimental Area A and an H^--ion beam down Line D. The total H^- repetition rate is 120 Hz. 100 Hz is transported to the Weapons Neutron Research (WNR) area. The remaining 20 Hz is injected into the Proton Storage Ring (PSR). In order to provide H^- beam to other experimental areas without interfering with the PSR operations, a new design of the switchyard is in progress. We are presently investigating a solution that would use pulsed kicker magnets to deflect a fraction of the WNR H^- beam down a separate existing beam-line at the demand of the experimenters.

1 INTRODUCTION

The Los Alamos Neutron Scattering Center (LANSCE) accelerator complex consists of an 800-MeV linear accelerator, a proton storage ring (PSR), and a number of experimental areas. Two beams are presently accelerated simultaneously on alternating cycles of the rf. The linear accelerator consists of two 0.75-MeV Cockroft-Walton injectors, one supplying protons and the other supplying H^- ions. A separate low-energy beam transport line exists for each beam species. A 0.75-MeV to 100-MeV drift-tube linac operating at 201.25 MHz, a 100-MeV transition region, and a 100 to 800-MeV side-coupled linac operating at 805 MHz is used to accelerate the two beams. Typically, peak beam currents as high as 18 mA are transmitted for variable duty factors to give a maximum average beam current of 1 mA for the H^+ beam and up to 100 μA for H^-.

A beam switchyard is used to direct beams from the linac to various experimental areas and for injection into the PSR. The 800-MeV proton beam is presently sent to an experimental area (Area A) via a separate beam-line where it presently interacts with a series of different targets for the Accelerator Production of Tritium program and for isotope production. Up to 3 μA of the 800-MeV H^- beam is sent to the Weapons Neutron Research Facility (WNR) where it strikes a target producing an intense white-neutron source. Since variable proton pulse widths are available, time-of-flight experiments for neutron energies ranging from a few MeV to 800 MeV are possible.

The PSR functions as a high-current accumulator or pulse compressor to provide intense pulses of 800-MeV protons to the Manual Lujan Jr. Neutron Scattering Center (Lujan) spallation neutron-production target. This target was upgraded for higher-average-current operation this year. The PSR operates at a repetition rate of 20 Hz. An entire linac macro-pulse is accumulated each turn around the ring with up to 2800 turns accumulated prior to single-turn extraction.

We recently received internal funding to study technical options that would greatly enhance our existing capabilities. We are presently performing simulation and conceptual design studies to determine the most cost-effective reconfiguration of a section of the beam switchyard. A diagram of the unmodified switchyard is shown in Fig. 1. The desired solution should allow simultaneous, uninterrupted beam delivery to Line D (PSR injection) and delivery of a "tailored" H^- beam-pulse to either Line B or Line C on the demand of the experimenters. The beam-pulse delivered on-demand will be diverted from the 100 Hz beam normally delivered to WNR.

Simultaneous beam delivery to Line B/C and Line D is not possible at present. A few hours are required to accomplish the required changes to allow the H^- beam to be directed from Line D to Line B/C. Delivery of beam to all users of this beam is interrupted during this transition period.

Immediate beneficiaries of this study will include the proton radiography program, neutron resonance spectroscopy studies, Lujan neutron scattering users, and WNR users at LANSCE. Other programs that may also benefit may include an ultra cold neutron facility and the future Dynamic Experimentation Laboratory. Implementation of a proposed solution will be contingent upon receiving additional project funding.

2 TECHNICAL REQUIREMENTS

Beam delivery for the present Line B/C users requires delivery of 800-MeV protons with ~2-3x10^8 protons per 5 ns (201.25 MHz) micro-pulse. The present ion-source and linac are capable of delivering this beam to the switchyard. The number and sequence of micro-pulses delivered, per macro-pulse, is determined by the accelerator master-timer and controls software. Modifications to this software will be required to fully

*Work supported by the U. S. Department of Energy Contract W-7405-ENG-36.
**Physics Division, Los Alamos National Laboratory.

implement any proposed solution and satisfy programmatic requirements.

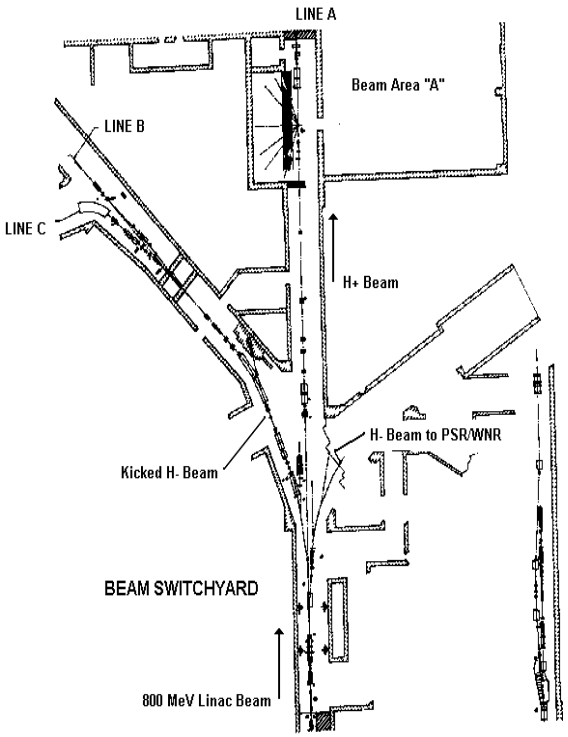

Figure 1 – LANSCE Beam Switchyard

Any proposed kicker solution must be capable of continuously delivering full-beam macro-pulses, for tuning, at a repetition rate of 1-20 Hz to Line B/C. The magnet response time requirement is 8 ms. This is the time between beam macro-pulses (120 Hz). Additionally, the capability to deliver a single macro-pulse on demand must be possible. Preserving the capability to operate in all the other existing facility modes is also a requirement. In particular, operation should not interfere with the 20 Hz H^- beam delivery for injection into the PSR. A desired feature, although not absolutely necessary, is that the solution be achromatic.

3 A TWO-KICKER SOLUTION

A schematic diagram of the unmodified H^- beam-line where the split between Line B/C and Line D occurs is shown in Fig. 2. The diagram is not to scale, but shows the general features of this area of the beam switchyard that we are proposing to modify.

3.1 TRANSPORT Results

We have modeled a two-kicker solution using TRANSPORT [1]. This solution requires the removal of the disabled kickers, the dipole bender, and the beam vacuum box just before the beam-line split (See Fig.2). These components would be replaced with two d.c. dipole magnets and two pulsed dipole kicker magnets. A new vacuum beam box design would also be required to match the new configuration to the existing beam-lines. Figure 3 shows a conceptual layout for this solution. The figure is not drawn to scale and only illustrates the relative positioning of the beam-line components.

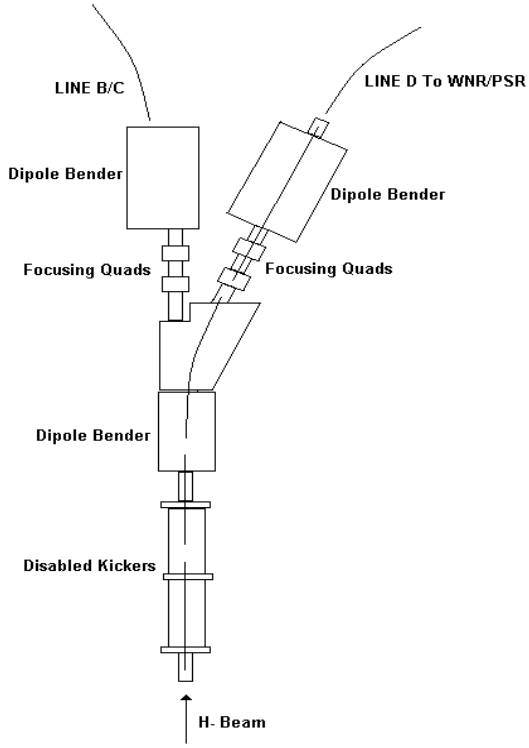

Figure 2 – Schematic of the Line B/C and Line D split in the LANSCE beam switchyard.

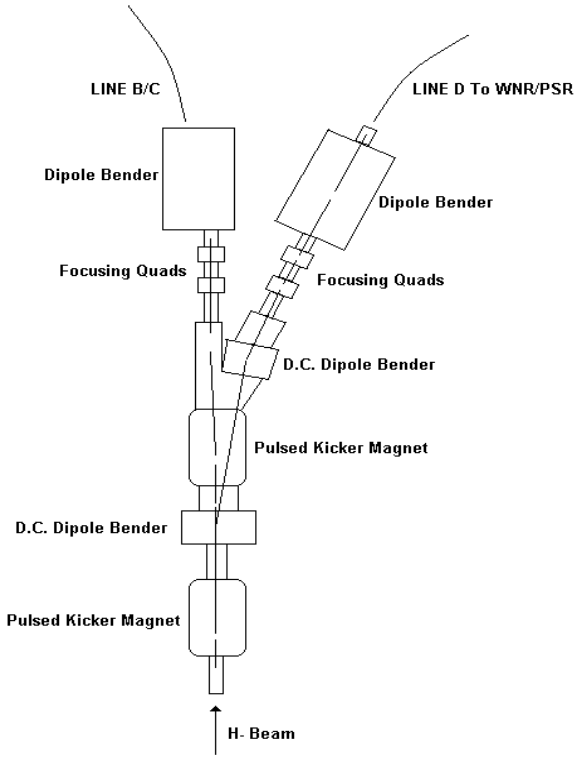

Figure 3 – Schematic of the proposed two-kicker solution

The two smaller d.c. dipole magnets will provide the same total bend angle of the single larger dipole magnet for the normal operation mode where beam is delivered down Line D. When the two kickers are fired, the beam is deflected in each kicker an amount equal to the bend of the first d.c. dipole, thus canceling out its effect. Beam is then delivered down Line B/C when the kickers are on.

The solution shown is also achromatic. This should help to preserve the relatively small linac energy spread. Table 1 gives the bend angle, field, and effective length requirements for the new magnets based on the simulation results.

Table 1 – New magnet parameters for the two-kicker solution.

Magnet	**Effective Length (m)**	**Field (KG)**	**Bend Angle (deg)**
Pulsed Kicker	1.016	1.26	1.5
DC Dipole	0.724	3.53	3.0
Pulsed Kicker	1.016	1.26	1.5
Dipole	0.656	3.53	2.7192

3.2 Kicker Magnet and Pulsed-Power System

The magnet requirements, as determined by the simulations, for this solution will allow use of a pulsed magnet and power-supply similar in design to that of the pulsed ring injection kicker magnet (RIKI) for the PSR at LANSCE [2].

The RIKI magnet is typically operated at 20 Hz. It can, however, also be operated in d.c. mode. This magnet is a laminated H-magnet with 20-turns/coil using hollow water-cooled conductor.

The pulsed-power system will provide a controlled current pulse to each kicker magnet. The RIKI pulsed-power system is capable of producing a current pulse with an amplitude that can be set in a range from 180 to 220 A with a flat-top width of up to 1.4 ms. Repetition rates ranging from 1 to 40 Hz have been tested with pulse regulation better than ± 0.5 %.

This system operates by resonantly discharging a capacitor of known voltage into a kicker magnet of known inductance through the following cycle. Initially, the current in the magnet builds resonantly. After the current has peaked, the circuit goes into "Freewheel" mode producing a settable flat-top of up to 1.4 ms width. Finally, the circuit goes into recovery mode where most of the stored energy in the magnet is recovered by returning it to the pulse capacitors. Implementing the firing of both kickers simultaneously and the potential problems that may be caused by timing errors have not yet been investigated.

3.3 Hardware Controls Requirements

We have estimated the approximate number and types of data channels that will be required for a flexible implementation scheme able to accommodate the final versions of the kicker power supplies. Our estimation is based on our past implementation of the RIKI magnet power-supply controls into the LANSCE control system. The RIKI power supply has control functions that use 9 binary input channels to indicate status and 5 binary command channels to provide on/off controls and reset functions. Two analog read-back channels are required to indicate voltage and current. One analog command channel is used to set the output current level. The modular design of the control system hardware provides the adaptability and flexibility required to implement the actual power supply controls.

One possible controls-hardware configuration is as follows. A VME crate using a Motorola processor module connected to the control system's Ethernet network can provide the foundation for the system and create an Experimental Physics and Industrial Control System (EPICS) input/output controller [3]. The use of the EPICS system allows existing operator interfaces to be used with a minimum of modifications, thereby reducing the cost of the system. The addition of VME Industry Pack carriers and Industry Packs, to provide the necessary signal conditioning, will complete the system. Industry Packs are small cards that perform specific I/O functions and are mounted on carrier boards for the bus system they are housed in. The interface between the Industry Pack and the carrier board is defined in the standard, ANSI/VITA 4-1995. Selection of Industry Packs similar to those already used in the control system can reduce the cost of software development. Local control for the power supply must be provided on each unit. This implementation has the advantage of providing isolation of the power supply control from the rest of the control system along with a modular design to increase maintainability and reduce system downtime.

4 SUMMARY

A solution for modification of the LANSCE switchyard has been described. In future studies, other solutions will be sought and compared to the two-kicker solution presented here.

REFERENCES

[1] K. L. Brown and S. Howry, "TRANSPORT, computer Program for Designing Charged Particle Beam Transport Systems," SLAC Report No. 91, July 1970.

[2] C. R. Rose and D. H. Shadel, "Proton Storage-Ring Injection-Kicker Pulsed-Power System," Accelerator Operations and Technology Technical Note AOT-1: 95-162, Los Alamos National Laboratory, June 26, 1995.

[3] Dalesio, L. R., Kraimer, M.R., Kozubal, A. J., "EPICS Architecture," in Proceedings of International Conference on Accelerator and Large Experimental Physics Control Systems, C. O. Pac, S. Kurokowa and T. Katoh, Eds. (ICALEPCS, KEK, Tsukuba, Japan, 1991), pp. 278-282.

UNDERSTANDING ACCELERATOR RELIABILITY

Christopher M. Piaszczyk
Advanced Science & Technology Center
Northrop Grumman Corporation
Bethpage, NY

Abstract

The event data collected during operation of the LANSCE accelerator facility are being analyzed as part of an effort to understand accelerator reliability in support of current design activities for future large scale accelerator systems. In this paper, the sequence of failures and repairs of the system is represented as a composition of alternating stochastic failures and repairs processes and the process parameters are estimated. The derived estimates can also be used for practical maintenance planning.

1 PREAMBLE

Previous work [1] has identified the current state of the art as lacking in the area of reliability database information for components typically used in rf accelerator systems, such as rf stations, rf drives, rf transport, cooling, vacuum systems, magnets, and magnet power supplies. This led to intensive data collection efforts [2]. The data has already been used to derive initial estimates of failure and repair rates for typical individual accelerator components [3].

The present paper examines the data set of failure events for Cycle #71 for the complete LANSCE 800 MeV DTL/SCL accelerator facility. Instead of deriving failure and repair rates for individual components, we estimate here the parameters of the failures and repairs processes for the complete system [4].

2 ESTIMATING THE FAILURES/REPAIRS PROCESS

An accelerator is an example of a repairable system [5]. Reliability of a non-repairable system is determined by reliabilities of its individual components and the typical problem of interest for this kind of system is that of the first failure. For a repairable system, the analysis must also include the interactions between the system and the repair policies, maintenance procedures, spare parts policies, etc.

2.1 The Failures Process

We tend to think of a complex, repairable system such as an accelerator facility as a set of sockets, each carrying its corresponding part. The cycle of operation and repair of the component in each socket is described as a superposition of two alternating Poisson processes: one consisting of times between failures and the other consisting of down times. Each one is generally a nonhomogenous Poisson process (NHPP), with the number of failure events per unit time, typically called the rate of occurrence of failures (ROCOF), and the rate of "occurrence" of repairs (ROCOR), functions of time. The two processes are usually uncorrelated.

Thus, the analysis of data collected for a repairable system seeks to determine the type of the stochastic process represented by the data, rather than estimates of component population statistics. Of particular interest is the existence of any trends. If ROCOF is increasing, it is an indication of the system's deterioration and a potential basis for a significant action, such as a major improvement program (or abandonment: for example, by sending an old car to the junk yard). Decreasing ROCOF, on the other hand, is an indication of reliability growth.

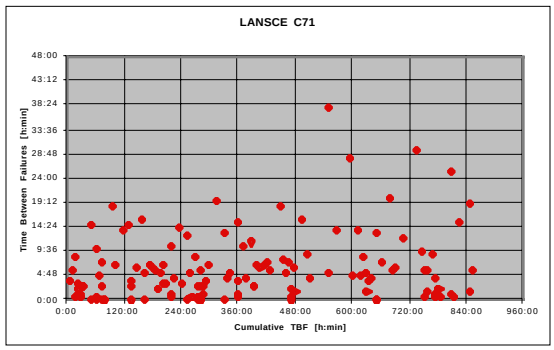

Figure 1. Times Between Failures

Application of this analysis procedure is illustrated here with the LANSCE Cycle 71 data. This data set was selected because it provides an example where the failures process is truly nonstationary. Over long periods of time stretching over many cycles, the observed tendencies are more balanced.

Raw data comes in the form of a sequence of times of occurrence of the failure events. One can extract from this data the sequence of times between failures shown in Figure 1.

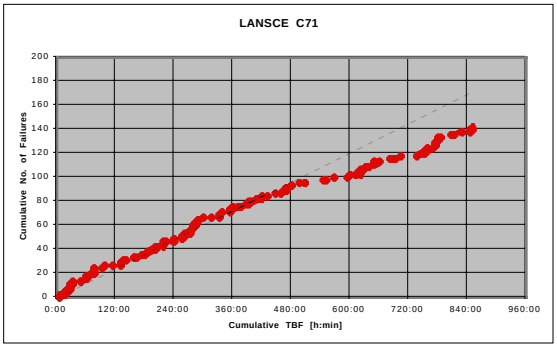

Figure 2. Cumulative Number of Failures

Figure 2 shows the cumulative number of failures as a function of cumulative operating time (sum of the times between failures). Comparison with the straight line fit indicates that the rate of occurrence of failures drops with time (after about 480 hours of operation).

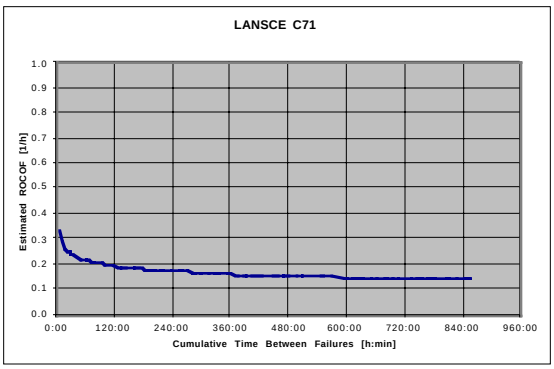

Figure 3. Estimated ROCOF

The Rate of Occurrence of Failures (ROCOF) is the limit of a series of discrete functions obtained by dividing the number of failures counted over a fixed delta interval when the length of the interval tends to zero.

Searching for ROCOF as a limit of the sequence of such discrete approximations is not practical. Direct statistical estimate of the parameters of the ROCOF assumed in the power form:

$$\lambda(t) = \alpha\beta t^{\beta}$$

results in $\alpha = 0.5036$, and $\beta = 0.8339$, which is shown in Figure 3.

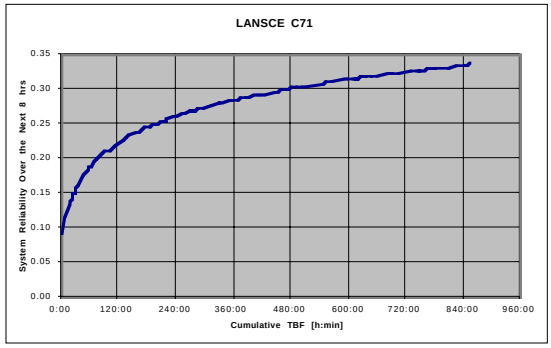

Figure 4. Expected Reliability over the Next 8 Hours

Once an estimate of ROCOF is obtained, we can use it to predict the system behavior, such as the expected number of failures in the next 8 hours or the expected system reliability in the next 8 hours for any desired instant of time shown in Figure 4 (since ROCOF is a function of time, both are functions of time as well).

Assuming a power relationship for MTBF(t) one can estimate the constants from the sample (resulting fit is shown in Figure 5):

$$MTBF(t) = 0.1056\, t^{0.2457}$$

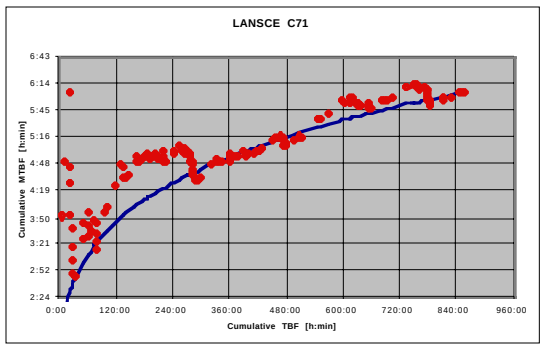

Figure 5. Estimating MTBF (t)

2.2 The Repairs Process

Figure 6 shows the cumulative number of repairs as a function of the cumulative down time (sum of the down times).

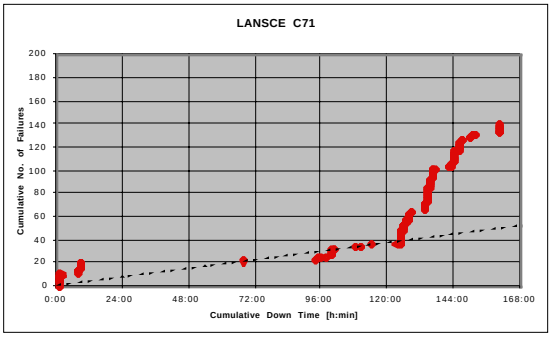

Figure 6. Cumulative Down Times

The down times are random just like the times between failures. However, in LANSCE Cycle 71, the down times history is dominated by a long 59 hour down time in the beginning of the cycle caused by the Magnet Power controller.

The ROCOR can still be assumed in the form of a power law. This time, this function is growing, indicating that the durations of the individual down times have a diminishing trend:

$$\mu(t) = 0.24114\ t^{1.3063}$$

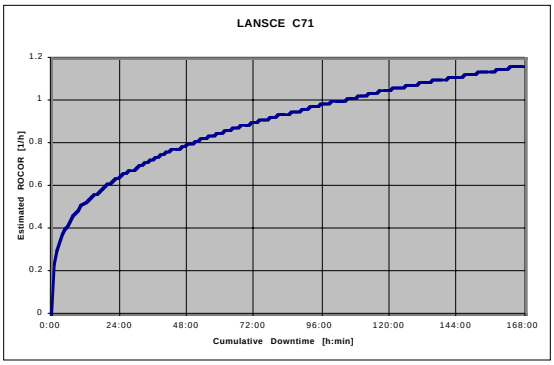

Figure 7. Estimated ROCOR - Rate of Occurrence of Repairs

A diminishing system MDT(t) can be fitted to the last part of the data (past 96 hours):

$$MDT(t) = 5.7302\ t^{-2.5186}$$

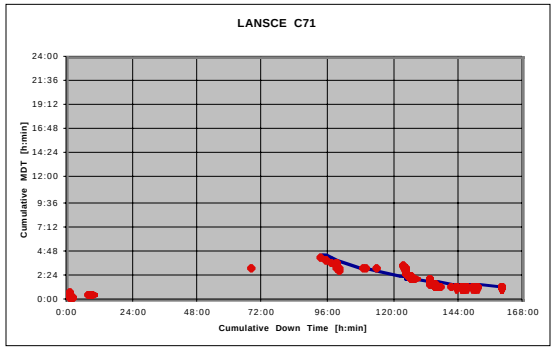

Figure 8. Estimated MDT(t)

3 CONCLUSIONS

The capability to predict the behavior of a repairable system is important for many reasons. Maintenance scheduling, advance spare parts procurement, and early detection of trends are essential in management and operation of the facility and planning for reliability improvement. The type of analysis presented in this paper may be used to gain such a capability from records of operational data.

REFERENCES

[1] C. M. Piaszczyk, “Reliability Analysis of the IFMIF”, AccApp ‘98, 2nd Topical Meeting on Nuclear Applications of Accelerator Technology, September 20-23, 1998, Gatlinburg, TN

[2] C. M. Piaszczyk, “Reliability Survey of Accelerator Facilities”, Maintenance and Reliability Conference, May 12-14, 1998, Knoxville, TN

[3] M. Eriksson and C.M. Piaszczyk, “Reliability Assessment of the LANSCE Accelerator System”, AccApp ‘98, 2nd Topical Meeting on Nuclear Applications of Accelerator Technology, September 20-23, 1998, Gatlinburg, TN

[4] P. Tobias and D.C. Trindade, “Applied Reliability”, Van Nostrand Reinhold, 1995

[5] H. Asher and H. Feingold, “Repairable Systems Reliability”, Marcel Dekker, Inc. 1984

STATUS OF 200 MeV ELECTRON LINAC AND ITS APPLICATION

Y.J.Pei, Y.F.Wang, S.Dong, X.F.Luo, G.R.Huang
G.C.Wang, W.Wang, Y.X.Li
National Synchrotron Radiation Laboratory
University of Science & Technology of China
Hefei, Anhui 230029

Abstract

200 MeV Electron LINAC is an injector of HLS. The LINAC has been running well for ten years since 1987. A typical operation parameters are energy of 200 MeV, Current of 50 mA and energy spread of 0.8%. Some improvements are described in this paper, such as developing an energy stabilized system, developing a two mode combined pulser for the electron gun to meet single-bunch and multi-bunch mode running in the storage ring. Some applications are briefly described here also.

Keywords LINAC Synchrotron Radiation Gun Single bunch Isotope production

1 INTRODUCTION

200 MeV Electron LINAC is an injector of HLS(Hefei Synchrotron Radiation Light Source) [1], which layout is shown in Fig.1. The LINAC has been running well for ten years since 1987. A typical operation parameters energy of 200 MeV, Current of 50 mA and energy spread of 0.8%. Since 1991 some improvements were done, such as developing an energy stabilized system, adding a post-transport line in order to guide the beam into a nuclear physics experimental hall, developing a two mode combined pulser for the electron gun to meet single-bunch and multi-bunch mode running in the storage ring. The LINAC is also an electron beam source for some application users, such as detector crystal calibration, isotopes products using photonuclear reaction, and so on.

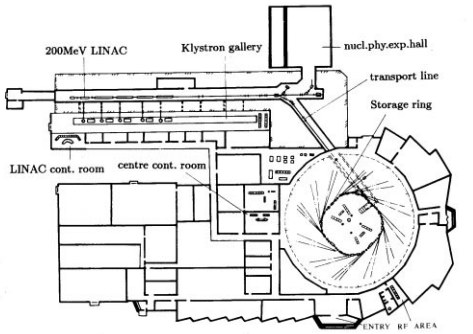

Figure 1. Plan of HLS

2 IMPROVEMENTS

2.1 Energy Stabilities

The 200 MeV LINAC has been run for 50,000 hours since 1987. The LINAC is running for both injecting the electron beam into HLS storage ring and providing the beam for producing some short lifetime isotopes, irradiation biology effects etc. The typical operation parameters are summarized in table 1.

Table 1. Operation Parameters of LINAC

Energy(MeV)	200.5
Current (mA)	70
Frequency (MHz)	2856.04
cavities' temperature ($^{\circ}$C)	42
output power of Klystron (MW)	
1# Klystron	9.7
2# Klystron	16.2
3# Klystron	15.7
4# Klystron	16.8
5# Klystron	9.3
beam pulse length(μs)	0.2~1.0
Energy spread (FWHM)	0.8%
Vacuum (mbar) (without beam)	$<1\times10^{-8}$
(with beam)	$<1\times10^{-7}$

In the beginning of the LINAC, its energy was not so stable that sometime it was difficult to inject the beam into the storage ring. After machine study, we adopted some measures. The energy stability has been improved. The main improvement was established an automatic energy stabilization system(AESS). Fig.2 showed a layout

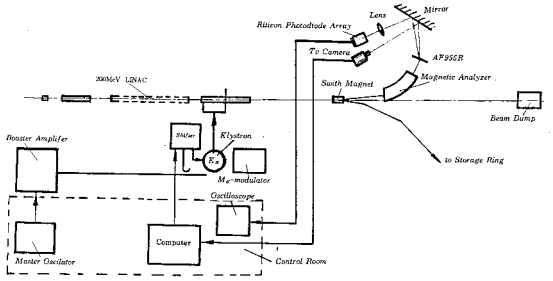

Figure 2. Layout of the automatic energy stabilizer

of the AESS. The energy stabilizing system was successful in stabilizing the energy. Typical running results are as following. When the AESS was not on, the central energy change rate $\Delta E_0/E_0$ was more than 0.8%. When the AESS was on, the $\Delta E_0/E_0$ was reduced down 0.4%. Now the LINAC has been running stably [2].

2.2 Combination pulser

The electron gun has been running for providing a pulse of μs beam for injection since 1989, so that there are multi-bunch running in the storage ring. Some users hope the ring running on a single bunch mode. This means that the beam pulse length from the LINAC must short than 4ns and the jitter time of the timing system is less than 0.5 ns. In order to meet the requirement, we need to improve the timing system, trigger system, beam diagnostic system and develop a ns pulser, and so on.

In order to produce a short pulse beam with width less than 3 ns, a grid pulser was developed and tested. The electronic circuit diagram is shown in Fig. 3. A key element of the circuit is employed a high frequency transistor 3DA87C with avalanche characteristics. The pulser can produce a short pulse of 2.5 ns (FWHM) and its amplitude is 120 volts. The waveform of the pulse is shown in Fig.4.

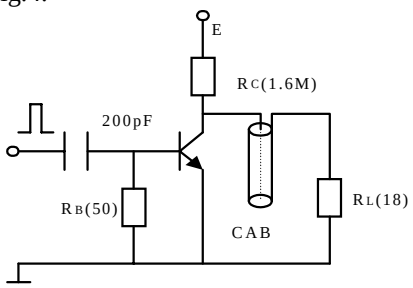

Figure 3. Circuit diagram of the ns pulser

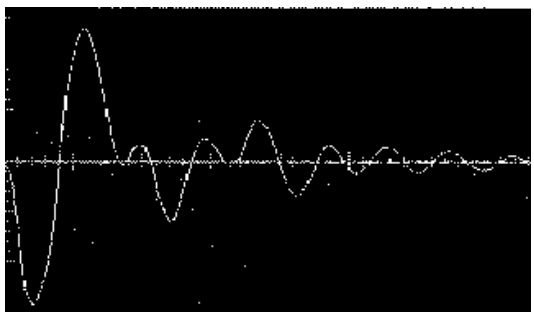

Figure 4. Waveform of the ns pulse

To transmit a trigger signal from the ground potential to a high potential, an optical fiber is most suited. The trigger signal transmission system consists of an electric-optical signal conversion circuit (E/O), and an optical- to -electric signal conversion (O/E). Time jitter including timing system, trigger system and pulser is less than 0.5 ns which is better enough for us.

Both grid pulser for long and short beam are assembled together in a circuit board, and employed a power splitter/combiners to transmit their signal respectively and isolate them each other. The trigger signals for the long and short beam are from a center control room and LINAC control room respectively.

Both long pulse and short pulse have been got and measured by means of Toroid monitors and wall current monitors which are installed in the LINAC and the transport line. The beam waveform are shown in Fig. 5(a),(b).

(a)

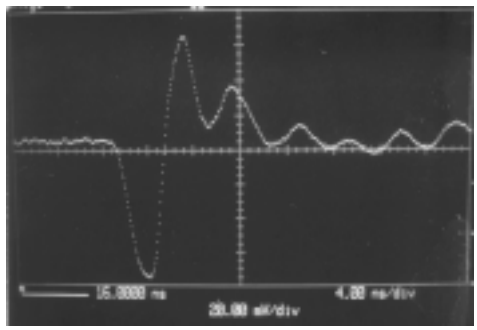

(b)

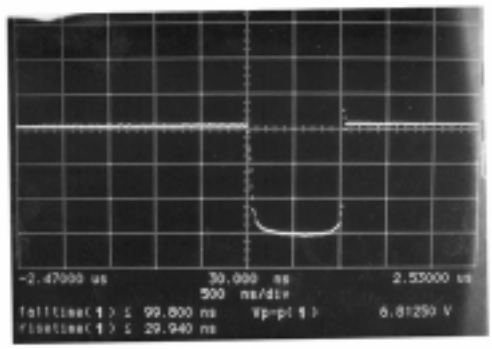

Figure 5. Waveform of output voltage of the combination pulser (a) ns waveform, (b) μs waveform

A single bunch mode running in the HLS storage ring has been successful using the combination pulser and a new timing system with jitter time less 100 ps (3σ) [3]. A waveform of the single bunch in the storage ring is shown in Fig. 6.

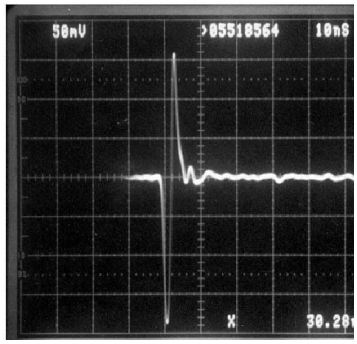

Figure 6. Waveform of a single bunch in the ring

3 APPLICATIONS

In the beginning the 200 MeV LINAC was designed for two purposes, one was as an injector of the HLS storage ring, another was to provide an electron beam of 200 MeV or less so that the machine can meet requirements from different scientific fields. Meanwhile the budget was shortage, a transport line for guiding the electron beam into a nuclear experimental hall and necessary experimental equipment were not constructed yet. last year a post-transport line for guiding the beam into the hall was added and an electron beam line was also established. The beam line will be used for studying the properties of single piece of P_bWO_4, such as light yield, decay time of the light and uniformity of the light output etc..

In order to utilize the electron beam from the LINAC fully, we established an equipment for photonuclear reaction at the end of the LINAC. As everyone knows, radioactive isotopes with short lifetime have been widely applied in medicine as tags or traces to study complex bodily processes and to diagnose some illness. Sequentially some new technologies , such as PET (positron emission tomography), SPECT (single photon emission computed tomograpgy), have developed. All of these have promoted a requirement of short-lived isotopes.

How do we get the radioactive short- lived isotopes? Neutron-capture reactions have long been used to induce them. By contrast, photon-induced nuclear reaction have been relatively neglected. But photonuclear reaction have great potential because they can results in medically important biological elements, such as carbon, nitrogen, oxygen and fluorine etc.

Since 1994, some researches on producing short-lived isotopes have been done in our LINAC. Some short lifetime isotopes, such as ^{18}F, ^{15}C, ^{11}C, ^{123}I, were got using the following photonuclear reaction ,

$$^{19}F(\gamma,n)\rightarrow{}^{18}F$$

$$^{16}O(\gamma,n)\rightarrow{}^{15}O$$

$$^{12}C(\gamma,n)\rightarrow{}^{11}C$$

$$^{124}X_e(\gamma,n)\rightarrow{}^{123}X_e\xrightarrow{\beta^+}{}^{123}I$$

Fig.7 showed a typical Gamma spectrum of the products of photonuclear reaction of natural Xenon which was irradiated by bremsstrahlung beam of 200 MeV, half hour generated via Tungsten convertor of 6 mm thick.

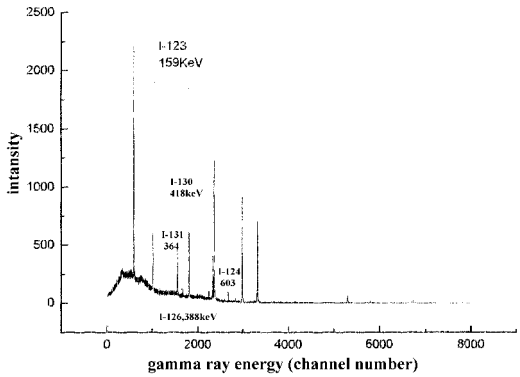

Figure 7. Gamma spectrum of products of photonuclear reaction of Xenon

REFERENCE

[1] Y.J. Pei, D.F. Wang, D.H. He, Proc. of the 3rd International Conference on Synchrotron Radiation Instrumentation, Review of Scientific Instruments, Vol. 60, No. 7, 1701 (1989)

[2] Y.J. Pei, M. Bai, G.R. Huang, Proc. of the 1994 International Linac Conference, p.196 (1994)

[3] Y.J. Pei, G.C. Wang, P.J. Zhang, et al., Proc. of 2nd National Symposium on Particle Accelerator Technology, p.107 (1998)

STATUS OF PLS 2-GEV ELECTRON LINAC PERFORMANCE

M.H. Cho, K.R. Kim, J.S. Oh, S.H. Park, S.S. Park, I.S. Ko, and W. Namkung
Pohang Accelerator Laboratory, POSTECH
Pohang, 790-784 Republic of Korea

Abstract

The 2 GeV electron linac at the Pohang accelerator laboratory (PAL) has been operated continuously as a full energy injector for the Pohang Light Source (PLS) since its completion on Dec. 7, 1994. There has been continuous effort to make the linac system more stable and reliable, such as the modifications of the klystron modulators, temperature stabilization of the main rf drive line, installation of one more klystron-modulator station with the addition of two sets of acceleration sections. The average high voltage operation time of the klystrons (E-3712, Toshiba) installed at the very beginning, 8 tubes are survived out of total 11 tubes, has been reached near 32,000 hours as of May 1998. Current overall system availability is well over 90%. In this paper, we report the major linac system upgrade for the nominal 2.5 GeV operation as well as the system performance and relevant machine statistics such as lifetime of klystrons and thyratrons, and overall system's availability, and others.

1 INTRODUCTION

PLS linac[1] has been injecting 2-GeV electron beams to PLS (Pohang Light Source) storage ring since September 1994. The linac klystron modulator system (K&M system[2]) has started its normal operation at the end of 1993, and the total accumulated high voltage run time of the oldest unit has reached beyond 37,000 hours. At the end of 1997 we have installed one more additional K&M module (total 12 modules with 44 accelerating structures), for the higher beam energy margin. The K&M system is normally operating in 70 to 80% of the rated peak power level to avoid the multipactoring phenomena occurring occasionally in random fashion in the waveguide networks and accelerating structures. The sum of all the high voltage run time of the K&M system is approximately 360,000 hours as of June 1998.

In this paper we have reviewed overall system performance statistics of the high power K&M system of the PLS linac for the period of September 1994 to June 1998. During this 4.5-year period the machine has been in operational mode for total 27,072 hours (counted only the scheduled run time).

2 K&M SYSTEM OVERVIEW

Key features of the K&M system design include 3-phase SCR controlled DCHV power supply, resonant charging of the PFN, resistive De-Q'ing, end-of-line clipping with thyrite disks, pulse transformer with 1:17 step-up turn ratio, and high power thyratron tube switching. The major operational parameters of the K&M system (PLS-200MW modulator) are listed in Table-1. The shot-to-shot beam voltage stability is controlled by the (1) the feedback of the DC high voltage to SCR primary input voltage control and (2) the resistive De-Q'ing. SCR DC feedback provides less than 0.5% fluctuation and additional De-Q'ing stabilizes the beam voltage better than 0.1% level. The details of the system design and performance characteristics are described elsewhere [2].

Table 1: K&M operation parameter summary.

Peak beam power	200MW*max.* (400kV @500A)
Beam vol. pulse width	ESW 7.5μs, 4.4μs flat-top
Pulse rep. rate	120pps *max.* (currently 30pps)
PFN impedance	2.64Ω (5% positive mismatch)
Voltage stabilization	SCR, DC feedback & 5% De-Q'ing
Pulse transformer	1:17(turn ratio), L_L:1.3μH, C_D:69nF
Thyratron switch	heating factor: 46.8x10^9VApps, 8.5kA peak anode current
Klystron tube	drive power:~300W, efficiency.:40%, gain:~53dB, peak power:80/65 MW (currently running at 50 to 65MW)

For the fault free stable operation of the system the thyratron tube is one of the most important active components which require continuous maintenance and adjustment. The thyratron tubes which meet the PLS-200MW K&M system specifications are listed in Table-2 together with their specifications, i.e. ITT/F-303, EEV/CX-1836A, and Litton/L-4888. We have all 3 types of tubes installed in our system, and the performance evaluations are underway. This effort is initiated to improve the system from the frequent occurring fault caused by the irregular recovery action of the thyratrons, which strongly depends upon the reservoir control.

There are three types of system's interlocks, namely dynamic, static, and personal protection interlocks. All the static fault activation is initiated by the relay logic circuit, and dynamic faults which require fast action response are activated using the electronic comparator circuit. When the system operation is interrupted by the static fault it can be recovered either by the automatic remote control computer or by the manual reset switch.

Table 2: Comparison of the thyratron tubes

ITEM	ITT F-303	Litton L-4888	EEV CX-1836A
Heater (Vac/A) *max*	6.6 / 80	6.7 / 90	6.6 / 90
Reservoir (Vac/A) *max*	6.0 / 20	5.5 / 40	6.6 / 7
Peak anode (kV/kA) *for*	50 / 15	50 / 10	50 / 10
Peak anode vol.(kV) *inv*	50	*n/c*	50
Avg. anode cur.(A) *max*	8	8	10
Min DC anode vol.(kV)	2	10	5
Heating factor ($x10^9$) *max*	300	400	*n/c*
dI/dt (kA/μs) *max*	50	16	10
Anode delay (μs) *max*	0.3	0.4	0.35
Trigger jitter (ns) *max*	2	10	10

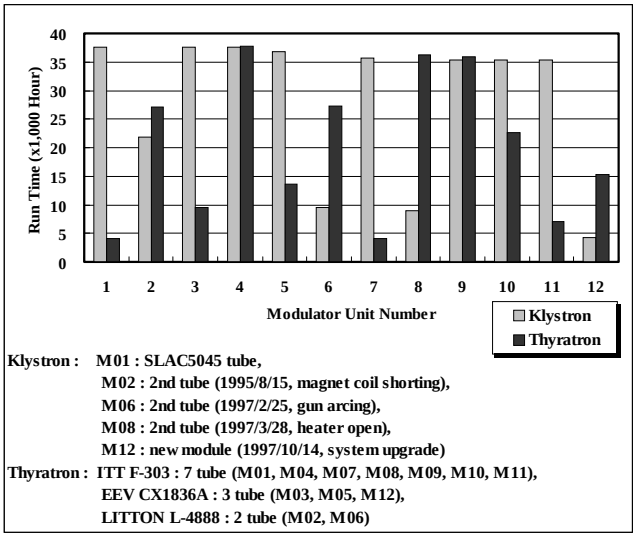

Figure 1: Run time statistics of all klystron and thyratron tubes (as of June 15, 1998).

3 SYSTEM AVAILABILITY STATISTICS

Since the completion of the PLS 2-GeV linac in December 1993 all the K&M systems have been operating continuously except scheduled short term and long term maintenance shut down. Fig-1 shows the accumulated run times of klystron and thyratron tubes as of June 15, 1998. As one can see in the figure rather shorter bars indicate that corresponding tubes have been replaced at least once or more. In fact we have replaced total 3 klystrons and 14 thyratrons during the total ~360,000-hr of operation time (run time sum of all 12 K&M modules). Table-3 & 4 show the calculated statistics of mean time to failure (MTTF) for the klystrons and thyratrons, respectively.

Machine availability analysis has been performed based on the data using the techniques described in detail in reference[4]. The results are summarized in Table-5. The MTBF (mean time between failure) is calculated by dividing the sum of the accumulated modulator run time with the total fault count (*MTBF = N*TO/FC*). The MTTR (mean time to repair) is equal to the total down time divided by total fault counts, *MTTR = TD/FC*.

During the early phase of the operation, from the late 1993 to early 1995, relatively low machine availability (*A = 1-MTTR*FC/TO*) has been obtained. This is due to the maintenance crew training as well as system debugging exercise. Most of time for the repair was spent for the extensive system diagnostics. The major changes that we implemented at the beginning of 1996 were the computer controlled automatic static fault reset and the modification of the circuit breaker (CB) trip interlock. They greatly contributed to the improved availability reaching over 90% as shown in the Table-5. Fig-2 shows the MTTF (mean time to failure) and the MTTR statistics of key component replacement works for the K&M system. For instance, the klystron replacement takes about 16 hours, and the thyratron tube replacement takes around 8 hours. Time estimation counted from the time of the fault to the time of complete recovery of the system.

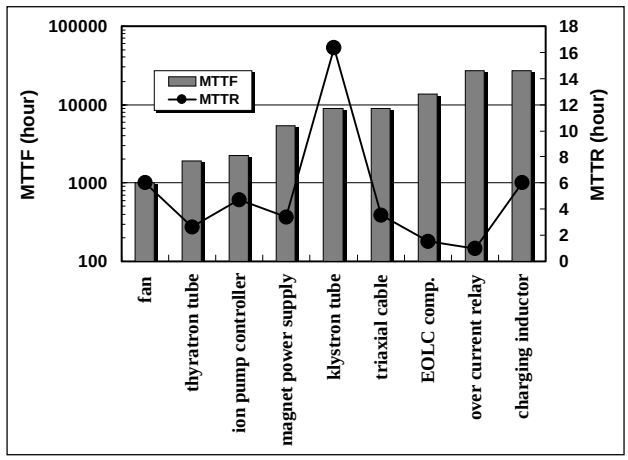

Figure 2: MTTF & MTTR for component replacement (data collection period: 94.9~98.6).

4 COMMENTS ON SYSTEM FAULTS

It has been observed that the most frequent system fault is the circuit breaker (CB) trip. This is mainly due to the problems in thyratron recovery characteristics which depend on the elaborate reservoir ranging (hydrogen gas pressure control in the tube). Thyratron tubes of F-303 and L-4888 require ranging adjustment (see Table-2), and according to our experience they are very sensitive to the effects which may cause internal gas pressure change. Once out of normal operating point self-fire, firing miss, or slow recovery (causes shorting of the PFN charging power supply) can occur. The CX-1836A thyratron tubes require not so delicate ranging according to the manufacturer's specifications.

Other occasional troubles were corona discharges that are found to occur when there are bad contacts in high voltage components. It has been found also that even a small corona discharge disturbs the ground potential, which are configured to have a single point ground

connection inside the modulator, causing noise interference in digital displays as well as SCR phase controls.

5 SUMMARY

It has been approximately 5 years since the PLS 2-GeV linac has started its normal operation. We have analyzed the klystron modulator system's performance record for the period, which is the major source of the beam injection failure. It is observed that the average lifetime expectancy of the klystron is over 25,000-hr, and it is getting longer. Lifetime of the thyratron tube also appears to be reasonable except the occurrence of the infant failure, however the major improvement is necessary for the reservoir control which is the main source of the system trouble. The machine availability statistics of the K&M system for the beam operation mode is calculated to be over 90%. It appears to us that there are still lots of rooms for the improvement of the availability more than 95% with the smart design of the protection circuits and control schemes.

6 ACKNOWLEDGEMENTS

Authors gratefully acknowledge the sincere efforts performed by PAL linac division members to keep the PAL linac system at an excellent condition. This work was supported partly by POSCO and MOST, Korea.

7 REFERENCES

[1] W. Namkung *et. al*, "PLS 2-GeV Linac," Proc. of 17th Int'l Linac Conf., Tsukuba, Japan, Aug. 21-26, pp.14-16 (1994)

[2] M.H. Cho *et. al*, "High Power Microwave System for PLS-2GeV Linac," Proc. of 17th Int'l Linac Conf., Tsukuba, Japan, Aug. 21-26, pp.418-420 (1994),

[3] I.S. Ko *et. al*, "Control of PLS 2-GeV Linac," Proc. of 17th Int'l Linac Conf., Tsukuba, Japan, Aug. 21-26, pp.825-827 (1994)

[4] A.R. Donaldson and J.R. Ashton, "SLAC Modulator Operation and Reliability in the SLAC Era," IEEE Conf. Proc. 20th Power Modulator Symposium, pp.152-156 (1992)

Table 3: Klystron MTTF of the PLS linac.

Period	Per Period			Cumulative					
	Failed		MTTF (hrs)	Total no. of tubes	Failed		Living		MTTF (hrs)
	no. of tubes	Mean age (hrs)			no. of tubes	Mean age (hrs)	no. of tubes	Mean age (hrs)	
1994	0			11	0		11	9,990	
1995	1	18,833	89,671	12	1	18,833	11	16,430	199,558
1996	0			12	1	18,833	11	24,244	285,517
1997	2	27,031	24,960	15	3	24,298	12	21,879	111,812
1998	0			15	3	24,298	12	25,818	127,569
Jyear	Nfp	Tfp	T(MTTFp)	Nt	Nfc	Tfc	Nlc	Tlc	T(MTTFc)

Table 4: Thyratron MTTF of the PLS linac.

Period	Per Period			Cumulative					
	Failed		MTTF (hrs)	Total no. of tubes	Failed		Living		MTTF (hrs)
	no. of tubes	Mean age (hrs)			no. of tubes	Mean age (hrs)	no. of tubes	Mean age (hrs)	
1994	4	5,070	25,885	15	4	5,070	11	7,569	25,885
1995	3	8,828	26,416	18	7	6,680	11	12,366	26,112
1996	3	16,837	26,973	21	10	9,727	11	15,130	26,371
1997	4	23,820	20,712	26	14	13,754	12	12,833	24,754
1998	0			26	14	13,754	12	18,203	29,356
Jyear	Nfp	Tfp	T(MTTFp)	Nt	Nfc	Tfc	Nlc	Tlc	T(MTTFc)

*Note; T(MTTFp) = {(Nfc*Tfc+Nlc*Tlc) of jyear – (Nfc*Tfc+Nlc*Tlc) of j-1year}/Nfp
T(MTTFc) = {(Nfc*Tfc+Nlc*Tlc) of jyear}/Nfc

Table 5: K&M system availability of the PLS linac.

Operation period	1994	1995	1996	1997	1998	Total
Total no. of modulators	11	11	11	11	12	11.2
Operation time (hr)	2,298	7,152	6,432	7,128	3,432	27,072
Total failure counts	103	175	131	130	147	686
Total down time (hr)	563	1,076	413	529	232	2,813
Modulator MTTF (hr)	313	450	540	603	280	442
System MTTF (hr)	28	41	49	55	23	39
MTTR (hr/failure)	5	6	3	4	2	4
Availability (%)	81	85	94	93	93	90

THE DRIVE BEAM ACCELERATOR OF CLIC

D. Schulte, CERN, Geneva, Switzerland

Abstract

The drive beam of the Compact Linear Collider (CLIC) requires a current of several amperes. The time structure of this beam is discussed. First simulation results on longitudinal single bunch effects are presented and achievable bunch lengths and sensitivity to jitter of the gradient, initial energy and charge are analysed. The transverse stability of the beam is discussed based on the present structure model. Requirements on the damping and detuning of the cavities are given in detail. A beam-based alignment technique is presented and the stability with respect to jitter and ground motion is investigated.

1 INTRODUCTION

CLIC [1] is based on a two-beam scheme. The RF power used to accelerate the main beam (at $30\,\mathrm{GHz}$) is produced by a second beam (the drive beam) running parallel to the main one [2] through so-called "power extraction structures". This beam has a high current but low energy and is decelerated thus producing the RF power.

The drive beam is accelerated to a final energy of $1.2\,\mathrm{GeV}$ in a fully-loaded low-frequency linac ($937\,\mathrm{MHz}$), consisting of 99 $3.1\,\mathrm{m}$ long structures with a loaded gradient of $3.8\,\mathrm{MV/m}$. The beam is then separated into trains of bunches. In so-called "combiner rings", 16 of these trains are merged to form a single one. The length of the final train is the same as that of one of the inital ones, but the distance between bunches is reduced by a factor 16. These short pulses are then sent to the decelerator sectors.

The total length of the charge pulse to be accelerated is equal to twice the main linac length. Assuming a fill factor of $80\,\%$, the main linac will be $13.75\,\mathrm{km}$ long, and the pulse length will therefore be $92\,\mu\mathrm{s}$.

2 TIME STRUCTURE

At the combiner rings, the beam must consist of short trains of bunches, separated by gaps that are larger than the rise time of a kicker. In the drive beam accelerator these gaps would however lead to a significant variation in multi-bunch beam-loading, so it would be difficult to keep the bunch-to-bunch energy variation small, see Fig. 1a. On the other hand, the tolerance on the final energy is tight.

A solution to this problem is not to fill every bucket, but instead only every second one, increasing the train length by a factor of two. Each train is split into two half-trains,

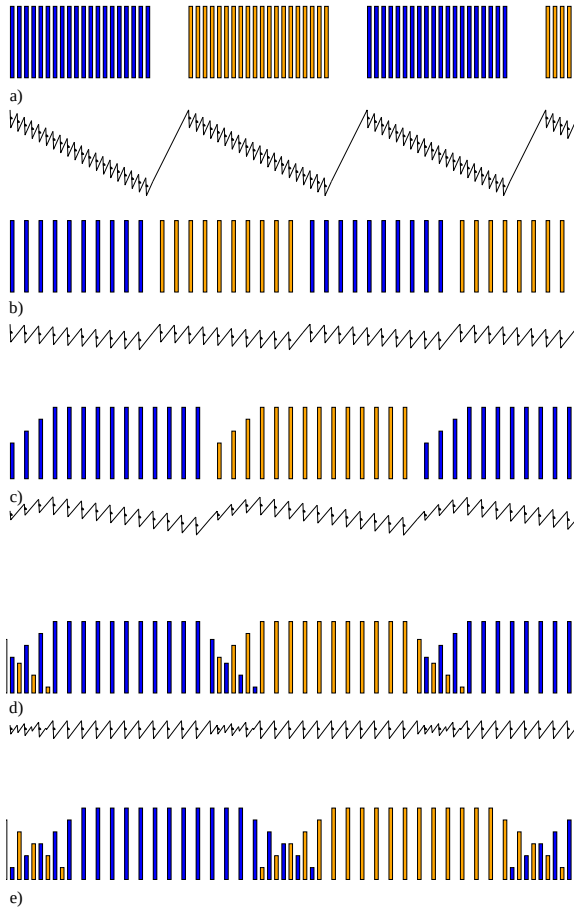

Figure 1: The charge distribution along the pulse—in case a) different trains are shown in different tones, in the other cases different half-trains are shown different tones. The number of bunches on the flat top is constant but different from the real value. The curves indicate the variation of the energy gain. Depending on the injector, a distribution in the range of d) to e) will be chosen.

the bunches of the first half are put into even buckets, and the bunches of the second half into odd ones, see Fig. 1b. In this case the beam-loading is not constant only where one switches from odd to even, or even to odd buckets. The first half of each train is sent into a delay line, using an RF-deflector at the end of the linac, running at half the linac frequency. The second half is deflected to the other side and passes with no delay. The delay line is adjusted to interleave the two halves of the train to form one, with

every bucket filled. This train has the length of an initial half train and is followed by a gap of the same length.

While this solves the problem in the case of constant charge per bucket, the beam-loading compensation in the main linac requires that each half-train starts with a charge ramp. The charge is thus increasing over the first few bunches. This would also create a significant variation in beam-loading (Fig. 1c). This is solved by adding a tail of bunches to the previous half-train which overlaps the ramp (Fig. 1d). This is feasible since different buckets are used for consecutive half-trains. The charge in the tail can be adjusted to make the beam-loading constant.

If the injector is only able to vary the charge per bunch slowly along the train, a longer ramp and a longer tail would be required, see Fig. 1e. In the following simulations, it is assumed that the charge rises linearly from zero to full intensity over the 20 bunches in the ramp and decreases, also linearly, in a tail of the same length.

The flat top of each train contains 47 bunches each with a charge of $q \approx 17.6\,\mathrm{nC}$ [2]. The total pulse ($92\,\mu\mathrm{s}$) is thus sufficient to feed 20 drive beam decelerator sectors.

3 COMPRESSION

The initial bunch length is assumed to be about $\sigma_z = 4\,\mathrm{mm}$ at an energy $E_i = 50\,\mathrm{MeV}$ with an energy spread of $0.75\,\%$ (L.Rinolfi [3]). While this spread is partly correlated with the longitudinal position, in the following it is assumed to be completely incoherent—to be pessimistic.

A simple calculation of the achievable compression was performed using a linear approximation. Since the exact longitudinal wakefield was not available, the values derived for an S-band structure [4] were used. The longitudinal wakefield amplitude $\hat{W}_L$ scales as $\hat{W}_L \propto f^2$ with the acceleration frequency f. The ratio of aperture a to wavelength λ is also different, here the scaling $\hat{W}_L \propto (\lambda/a)^2$ was used as an approximation.

In order to avoid large energy losses due to coherent synchrotron radiation in the combiner rings and in the bends into the decelerator, the bunch length in these sections has to be at least $\sigma_z = 2\,\mathrm{mm}$ (R. Corsini [3]). The final compression is therefore done afterwards. For the compression two different approaches are possible. One can either compress the bunch to a length of $\sigma_z = 2\,\mathrm{mm}$ inside the linac (preferably at low energy) and do the final compression after the bends. Or one can compress the bunch inside the linac in several stages as much as possible. Then it has to be uncompressed at the end of the linac to $\sigma_z = 2\,\mathrm{mm}$. Finally it has to be compressed again after the bends.

An example of the first approach uses an RF-phase for the beam of $\Phi_{RF} = -12^\circ$. The first compression is done at $E \approx 100\,\mathrm{MeV}$, achieving the required $\sigma_z = 2\,\mathrm{mm}$. The final compression step at the decelerator entrance yields $\sigma_z = 290\,\mu\mathrm{m}$ and an RMS energy spread of $\sigma_E = 18\,\mathrm{MeV}$ (case 1). Without wakefields (case 2) one would reach $\sigma_z = 340\,\mu\mathrm{m}$ and a final energy spread of $\sigma_E = 8.5\,\mathrm{MeV}$—this shows the relative independence of the result on the wakefield model.

Using the second approach, the bunch is compressed as much as possible at three positions along the linac, then uncompressed to $2\,\mathrm{mm}$, and recompressed after the bends (case 3). The bunch length achievable with this method is $\sigma_z \approx 170\,\mu\mathrm{m}$. This is significantly shorter than in for case 1 and the final energy spread of $\sigma_E = 13.4\,\mathrm{MeV}$ is also smaller. If the RF-phase is set to $\Phi_{RF} = 0^\circ$ after the first two compression steps (case 4) one can still achieve $\sigma_z \approx 200\,\mu\mathrm{m}$ with an energy spread of $\sigma_E \approx 11.4\,\mathrm{MeV}$. Figure 2 shows the phase space distribution after the final compression for this case.

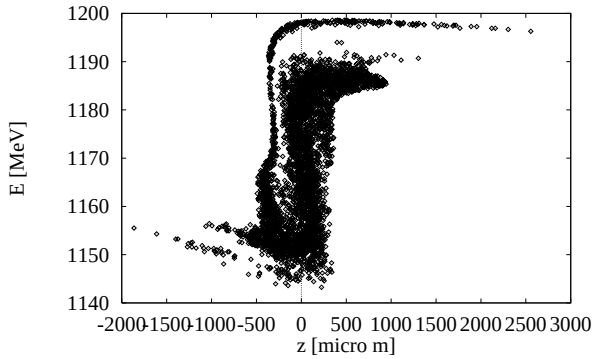

Figure 2: The phase space distribution of the particles after the last compression step in case 4. The particles represent different charges.

Table 1: Deviations from nominal values that result in a longitudinal shift of the bunches of about $10\,\mu\mathrm{m}$.

case		1	2	3	4
$\Delta G/G_0$	$[10^{-4}]$	0.45	0.4	0.5	0.4
$\Delta E_i/E_{i,0}$	$[10^{-4}]$	0.8	16	0.9	0.8
$\Delta\Phi_{\mathrm{RF}}$	$[0.1^\circ]$	0.12	0.1	0.12	0.12
$\Delta q/q_0$	$[10^{-2}]$	0.2	—	0.25	0.2

Energy variations of the bunches are transformed into longitudinal position errors by the bunch compression. These energy variations can be caused by variations of the initial beam energy E_i, the acceleration gradient G, the RF-phase and the bunch charge. Table 1 shows the size of these variations that lead to a longitudinal shift of $10\,\mu\mathrm{m}$. The differences in gradient and RF-phase are assumed to be constant along the accelerator, not random errors.

4 LATTICE

The lattice of the drive beam accelerator consists of simple FODO-cells with a constant quadrupole spacing of $3.9\,\mathrm{m}$. The phase advance per cell is about 116°. One $3.1\,\mathrm{m}$ long accelerating structure, consisting of 29 cells, and a beam position monitor (BPM) are placed between two quadrupoles. The iris radii of the cells of the structure vary from 42.2 to $54.4\,\mathrm{mm}$. The initial beam energy after the injector is $50\,\mathrm{MeV}$.

5 STABILITY

To evaluate the beam stability, simulations with PLACET [5] were performed for the first 2000 bunches assuming initial transverse emittances of $\epsilon_x = \epsilon_y = 100\,\mu\mathrm{m}$. Each of the 29 cells of a structure is simulated using its two most important transverse modes. Three cells were calculated with ABCI (L. Thorndahl [3]) at a frequency $f = 3\,\mathrm{GHz}$ and frequencies and loss factors of the modes were derived by interpolation. A short model structure using a single cell size has been built (L. Thorndahl [3]).

Due to the length of the pulse the structures have to be damped to avoid beam breakup. The measured upper bound of the damping Q of the transverse mode is $Q \leq 100$. The limit was due to the experimental setup, calculations for perfect loads predict $Q \approx 11$ (M. Luong [3]).

In the simulations each bunch is cut longitudinally into 21 slices. Using an undetuned structure with $Q = 100$ leads to an amplification of an initial beam jitter by a factor 15 for some of these slices. A reduction to $Q = 20$ reduces this to a factor of less than 2.

Detuning the structures by varying the iris radii from 42.2 to $54.4\,\mathrm{mm}$ reduces the amplification factor to less than 2 for a damping of $Q = 100$. Figure 3 shows the final positions of the slices after the linac. Within the region of constant charge, the bunch to bunch variations are relatively small, while in the transient parts where the trains overlap they are significantly larger. From train to train the variations are also small. Using the detuned structures, even a damping of $Q = 500$ does not increase the amplification factor significantly.

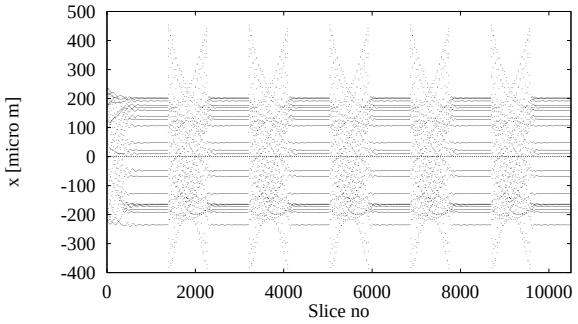

Figure 3: The final slice position for detuned structures with $Q = 100$. Each bunch is cut longitudinally into 21 slices, the first 500 bunches are plotted. The horizontal lines visible, are formed by equivalent slices of successive bunches. The slices of each bunch are filling the space between the minimum and maximum position.

An uncorrelated jitter of the quadrupoles of $\sigma_{quad} = 1\,\mu\mathrm{m}$ leads to a small movement of the beam of less than 0.06σ for any slice at the accelerator exit. The simple ATL-law is used to estimate the sensitivity to ground motion. In this model, the relative transverse offset Δy of two points, separated by a distance L, is given after a time T by $(\Delta y)^2 = ATL$. The value of the constant A is site dependent and can have a value of less than $A = 0.5 \cdot 10^{-6}\,(\mu\mathrm{m})^2/(\mathrm{sm})$[6]. For a test case, the maximum offset after $T = 10^5\,\mathrm{s}$ of any slice was 0.02σ and the average was 0.01σ without any feedback or steering. The linac is thus insensitive to ground motion.

The fast beam-ion instability [7] can also increase the beam emittance. A charged beam can ionise the rest gas in an accelerator. An electron beam will deflect the electrons that are set free in this process towards the outside. The positive ions however are accelerated towards the beam centre. In an unbunched beam they would oscillate. If in a bunched beam the ion oscillation frequency is smaller than the bunch frequency, the ions will be trapped. For the drive beam accelerator this condition is fulfilled. At the moment, simulations of this effect are not available for the drive beam, and analytic formulae [7] give no clear indication of importance of the problem.

6 ALIGNMENT AND STEERING

The initial position errors for quadrupoles are assumed to be $\sigma_{quad} = 500\,\mu\mathrm{m}$ and for beam position monitors and structures $\sigma_{BPM} = \sigma_{struct} = 100\,\mu\mathrm{m}$.

Already with a simple one-to-one steering the total emittance growth along the linac was found to be $3.5\,\%$ in a test case. The maximum position deviation of a slice from the beam centre at the linac exit was about 0.2σ.

7 CONCLUSION

The drive beam accelerator seems to be very stable if detuned and damped accelerating structures are used. Initial beam jitter is amplified by less than a factor 2 for any particle. The alignment tolerances are rather relaxed even when only simple steering is used for correction. The fast beam-ion instability remains to be investigated in detail.

8 REFERENCES

[1] J.-P. Delahaye and 30 co-authors, "CLIC a 0.5 to 5 TeV Compact Linear Collider.", EPAC 1998.

[2] H.H. Braun and 14 co-authors, "A new method of RF power generation for two-beam linear colliders.", EPAC 1998.

[3] H.H. Braun and 14 authors, "The CLIC RF power source", to be published in CERN/PS 98-011 (LP).

[4] K. Bane, M. Timm, and T. Weiland, "The short range wake fields in the SBLC linac.", *DESY-M-97-02*.

[5] D. Schulte, to be published.

[6] R. Assmann, C. Salsberg, and C. Montag, "Beam stability measurements with a stretched wire system in the FFTB.", Linac 1996.

[7] F. Zimmermann and 8 co-authors, "Experiments on the fast beam-ion instability at the ALS.", *SLAC-PUB-7617*.

HIGH CURRENT TRANSPORT AND ACCELERATION AT THE UPGRADED UNILAC

W. Barth, J. Glatz, J. Klabunde
GSI, Planckstraße 1, 64291 Darmstadt, Germany

Abstract

The UNILAC will be upgraded as a high current injector for SIS. This paper focuses on beam dynamics studies in the newly designed stripper section, the poststripper Alvarez accelerator and the transport line to SIS considering space charge effects along the UNILAC. Simulation results for the matching to the Alvarez linac, emittance growth effects in the poststripper linac and the beam transfer line to the SIS including the modified foilstripper and charge separation system will be discussed. The beam brilliance loss due to foil straggling and space charge forces will be calculated. Beam experiments at the present UNILAC under comparable space charge conditions are reported.

1 INTRODUCTION

Within the GSI high-intensity program, the present prestripper linac will be replaced by an RFQ and two IH-tanks [1] designed for the acceleration of high current, low charge state beams. The beam behavior influenced by space charge forces is simulated for different input phase space distributions through the complete system to the SIS. Emittance growth occurs in all sections of the UNILAC. A reduction of emittance growth could be expected by the newly designed gasstripper section at $1.4\,\mathrm{MeV/u}$. Beam dynamics calculations within the poststripper and the transfer line will be presented.

2 HIGH CURRENT BEAM MEASUREMENTS

At the present UNILAC, beam experiments with neon ions were carried out under comparable space charge conditions as expected for the upgraded UNILAC, particularly in the stripper region. The SIS could be operated at the space charge limit with Ne^{10+} beam. Measurements in the gasstripper section at $1.4\,\mathrm{MeV/u}$ are shown in Fig. 1. The Ne^{1+} beam accelerated by the Wideröe linac passes the gasstripper and is transported through the charge state analyzing system by four 30° bending magnets. The most abundant Ne^{7+} is selected for further acceleration, the stripping efficiency is about 40%. The emittance growth rates are shown at different current levels. For intensities up to $10\,\mathrm{emA}$ total current behind the $9\,\mathrm{mm}$ stripper aperture, the emittance growth is in good agreement with computer simulations, neighbouring charge states are taken into account. Simulations have indicated that the emittance growth can be reduced by increasing the diameter of the stripper tube from 9 to $16\,\mathrm{mm}$. Experimental and simulation results supported the new design of the stripper section described in the following paragraph.

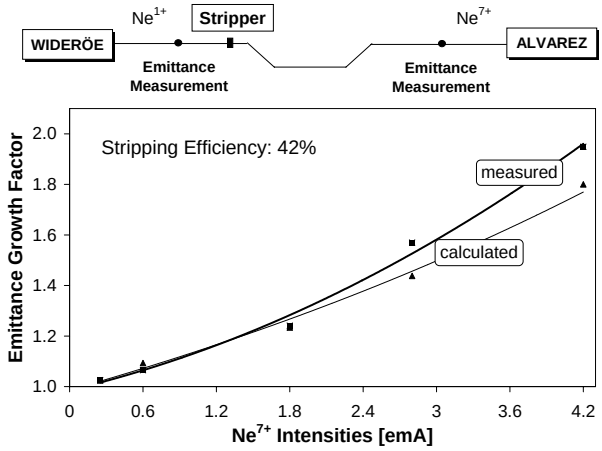

Figure 1: Measured and calculated emittance growth factors at different neon current levels.

3 THE NEW GASSTRIPPER SECTION

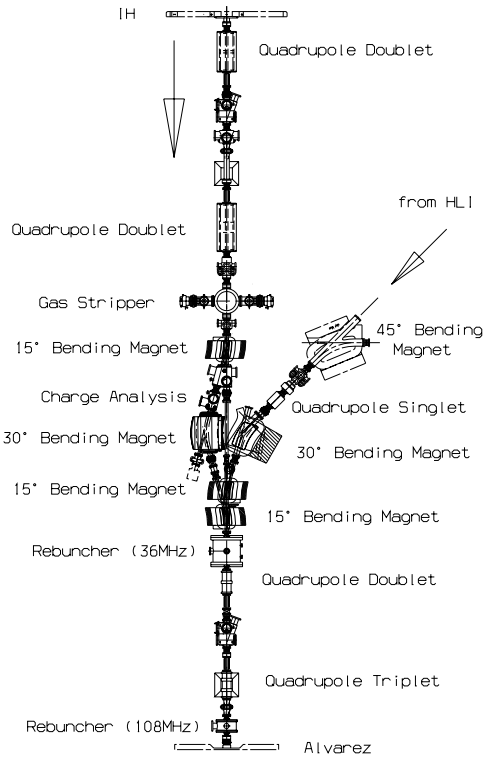

Figure 2: Layout of the new stripper section.

The design of the new transport line between the prestripper and the Alvarez linac is faced with different requirements: lowest emittance growth under considerable

space charge forces, charge state separation, achromatic transport after the bending magnets, transverse and longitudinal matching to the poststripper. The new design has to cope with the ion time-share operation on a $50\,\mathrm{Hz}$ pulse-to-pulse basis. The layout of the gasstripper section is shown in Fig. 2. The beam from the IH section is matched to the stripper tube by two magnetic doublets. After stripping the beam goes immediately into the first 15° bending magnet. The analyzing slit is directly before the second dipole (30°). The last dipole bends the beam back to the UNILAC axis. In the following transport line the longitudinal matching (with two rebunchers) and the transversal matching (with a quadrupole doublet and a triplet) to the poststripper accelerator is accomplished without any particle loss. The beam from the second injector (HLI) is delivered to the poststripper by a 180° bending section. All magnetic lenses, dipoles of the stripper section and the kicker magnet of the HLI transport line allow the pulsed operation.

4 CALCULATED EMITTANCE GROWTH FROM THE PRESTRIPPER TO THE SIS

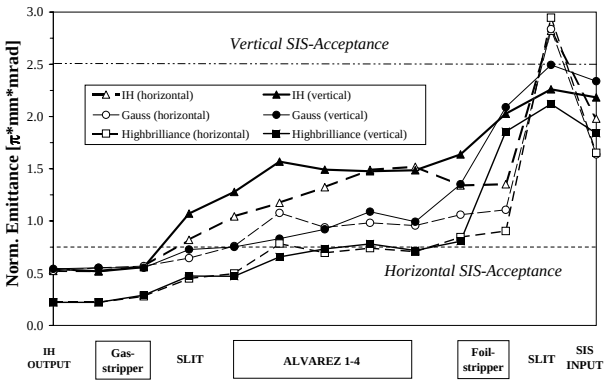

Figure 3: Variation of the horizontal and vertical 90% emittances from the UNILAC stripper section to the SIS input for different input beams. The transmission in all cases is approx. 95%.

For the simulations three input distributions are selected: the 'IH distribution' will be expected behind the new prestripper linac [2]. This particle distribution was calculated from an initial Gaussian distribution at the prestripper entrance with a current of $16.5\,\mathrm{emA}$ U^{4+}. In order to exclude effects of the distorted IH distribution, simulation begin with an ideal Gaussian distribution with the same 90% values of emittance at the IH exit. The limit of the system is evaluated by a high brilliant transversal Gaussian distribution as expected from the RFQ. In all three cases the beam was transformed through the stripper section, the poststripper accelerator and the transfer line with the same settings of the quadrupole gradients and rebuncher fields. In Fig. 3 and Fig. 4 the development of the horizontal and longitudinal 90% emittance. The calculated beam transmission in all cases is approx. 95%. In addition the space charge parameter SPC (relatively) is exposed in Fig. 5: $SPC \sim ParticleCurrent \cdot ChargeState^2 \cdot \beta^{-1} \cdot Bunchvolume^{-1}$.

In the following the beam behavior in the several UNILAC sections is discussed.

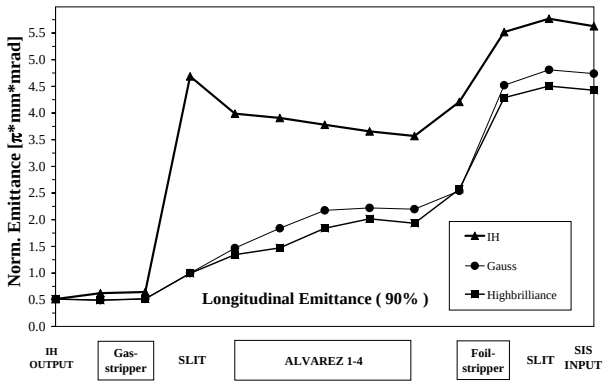

Figure 4: The longitudinal 90% emittances complementary to Fig. 3.

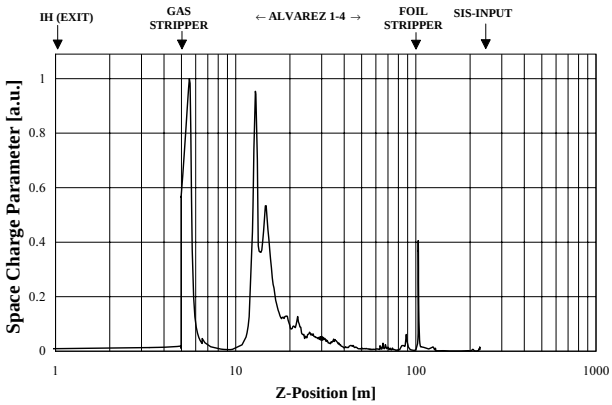

Figure 5: The Space Charge Parameter (SPC) along the stripper section, the Alvarez and the transfer line.

4.1 Gasstripper section

In the matching section to the gasstripper no significant emittance growth occurs, the jump of the charge state after stripping increases the SPC dramatically. Amplified by the reduction of the bunch volume, the emittance in all three planes accumulates until the slit of the charge state analysis, where the particle current abruptly decreases. To match the beam to the Alvarez a very small bunch length is indispensable. For the Gaussian distribution the transversal emittance growth factor at the Alvarez input is only 1.37, compared to 2.18 for the IH distribution, which occurs due to the longitudinal phase space aberrations in interaction

with the strong space charge forces after the stripping process. The emittance growth factor is optimized by iteration of the transversal beam divergence at the gasstripper. The transversal emittance of the high brilliant beam increases by a factor of 2.2, but the absolute emittance growth is comparable with the Gaussian case.

4.2 Poststripper Accelerator

Particularly in the first Alvarez section emittance growth is high, thereafter the effect is moderate because the acceleration gain becomes higher. The stripper section is optimized for low horizontal emittance growth at the expense of vertical beam quality. Because of that equipartitioning takes place for the IH distribution in the poststripper accelerator caused by strong space charge forces. If the same transverse distribution combined with a matched Gaussian one in the longitudinal phae space (IH modified) is used, the transversal emittance growth is reduced from 30% to 15%. To minimize emittance growth for beams with higher brilliance (Gauß, High Brilliance) the zero current phase advance in the periodic structure has to be increased from 45° to 54°. This can be achieved by 11% higher quadrupole field strengths.

4.3 Transfer Line to the SIS

In the transfer line the transverse matching to the foilstripper is not critical. With a narrow upright beam spot on the stripperfoil the emittance growth in the horizontal plane is minimized, while an increase of the vertical emittance is tolerated in view of the acceptance of the synchrotron (see Table 1: IH distribution with and without stripping) [3, 4]. Comparing the Gaussian and the high brilliant distribution with the IH one, an conspicuous increase of the vertical emittance caused by stripping effects has to be considered.

Table 1: Emittance growth (90 %) in the transfer line

		Foil (in)	Foil (out)	Charge Sep.	TK (out)
IH	horizontal	0.88	0.89	1.86	1.30
(with stripping)	vertical	1.10	1.36	1.52	1.47
IH	horizontal	0.91	0.91	1.16	1.31
(without stripping)	vertical	1.11	1.11	1.11	1.07
Gauß	horizontal	1.11	1.16	2.97	1.71
(with stripping)	vertical	1.36	2.11	2.51	2.36
High Brilliance	horizontal	1.20	1.28	4.18	2.34
(with stripping)	vertical	1.12	2.59	2.96	2.57

Fig. 6 displays the emittance growth factor due to particle scattering as a function of the distribution fraction at the same vertical beam size. The IH distribution has a very intense core (peaked distribution), the emittance growth is much lower for the outer area of the distribution. An inverted characteristic for the emittance growth as a function of intensity results from a transverse homogeneous KV distribution.

Increasing the charge state from $28+$ to $73+$ entails in a SPC boost which is only 40% of the effect in the gasstripper section.

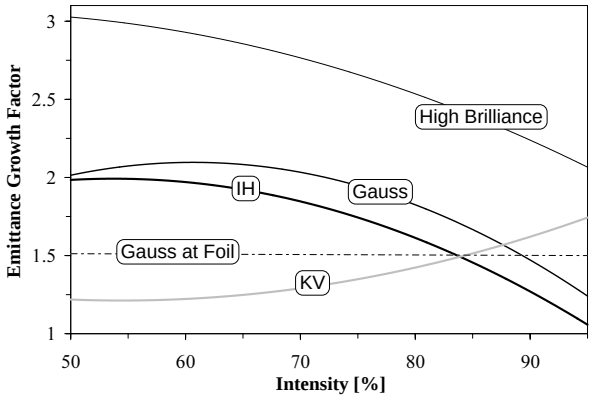

Figure 6: Emittance growth factor due to particle scattering at the foilstripper for several phase space distributions.

5 SUMMARY

The calculated deformation in the phase space distribution coming from the prestripper accelerator results in high emittance growth. The new stripper section may work very well for a Gaussian distribution. If a high brilliant beam is preserved the zero current phase advance in the poststripper has to be increased to minimize emittance growth. Beside the gasstripper section the first Alvarez tank is the most critical part due to space charge effects. The transport through the transfer line does not lead to considerable horizontal emittance growth. The vertical scattering effect in the foilstripper is much higher because of the upright beam spot and depends strongly on the phase space distribution. The final transverse emittance exceeds the acceptance of the SIS in all three cases. Nevertheless, the SIS can be filled up to the required 2×10^{10} particles per pulse U^{73+}.

6 REFERENCES

[1] U. Ratzinger,"The New GSI Prestripper Linac for High Current Heavy Ion Beams", Proc. of LINAC96, p. 288, Geneva, 1996

[2] W. Barth, J. Glatz, J. Klabunde, U. Ratzinger, "Space Charge Dominated Beam Transport in the 1.4 MeV/u-UNILAC Stripper Section", Proc. of LINAC96, p. 131, Geneva, 1996

[3] W. Barth, L. Dahl, J. Glatz, J. Klabunde, U. Ratzinger, A. Schempp, "High Current Beam Dynamics for the Upgraded UNILAC", Proc. of 1997 PAC, in press, Vancouver, 1997

[4] J. Glatz, B. Langenbeck, "A High Duty Foil Stripper System in the Injection Line to the Heavy Ion Synchrotron SIS at GSI", Proc. of EPAC96, p. 2406, Sitges, 1996

ANALYSIS AND MODELING OF A STRIPLINE BEAM KICKER AND SEPTUM

B. R. Poole, G. J. Caporaso, Y. J. (Judy) Chen, L. –F. Wang
Lawrence Livermore National Laboratory, Livermore, California 94550 USA

Abstract

A fast stripline beam kicker and septum are used to dynamically switch a high current electron beam between two beamlines. The transport of the beam through these structures is determined by the quality of the applied electromagnetic fields as well as temporal effects due to the wakefields produced by the beam. In addition, nonlinear forces in the structure will lead to emittance growth. The effect of these issues is investigated analytically and by using particle transport codes. Due to the distributed nature of the beam-induced effects, multiple macro-particles (slices) are used in the particle transport code, where each slice consists of an ensemble of particles with an initial distribution in phase space. Changes in the multipole moments of an individual slice establish electromagnetic wakes in the structure and are allowed to interact with subsequent beam macro-particles to determine the variation of the steering, focusing, and emittance growth during the beam pulse.

1 INTRODUCTION

The stripline kicker is designed to spatially separate a high current electron beam for transport into two separate beamlines. However, to provide a significant angular kick to the beam, a magnetic dipole septum is required. This system is shown schematically in Figure 1.

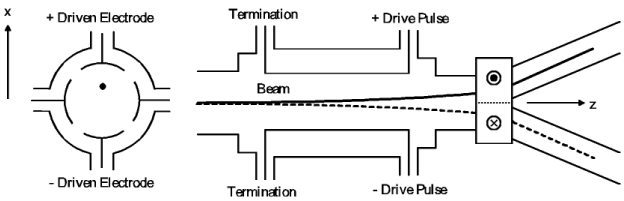

Figure 1 Kicker and septum configuration for dynamic beam steering in one plane

The operation of the system is as follows: A high voltage pulse is applied to the downstream ports of the kicker and the beam is spatially separated (kicked) by a combination of the transverse electric and magnetic dipole forces associated with the TEM waves propagating on the strip transmission lines. The beam is then directed into a septum magnet with opposite polarity dipole fields on either side of the plane separating the two downstream beam lines. All the upstream ports and the two downstream ports in the non-kick plane are terminated in a matched load impedance for the dipole transmission mode on the structure. It should be noted that steering in both planes can be accomplished by also driving the other pair of plates.

2 KICKER TEM FIELDS AND BEAM DEFLECTION

To steer the beam in *x*, opposite polarity high voltage pulses are applied to the downstream ports in the *y=0* plane. The potential within the kicker plates ($r<b$) is given by

$$V = \frac{4V_p}{\pi}\sum_{m=odd}\left(\frac{1}{m}\right)\sin\left(\frac{m\phi_0}{2}\right)\cos(m\phi)\left(\frac{r}{b}\right)^m \quad (1)$$

where b is the interior radius of the kicker plates, and ϕ_0 is the angle subtended by the kicker plates. The voltage applied to the plate is V_p giving a total steering voltage of $2V_p$. The solution is determined by solving for the potential in the region $r<b$, and using the boundary condition that the potential at $r=b$ is given by the appropriate applied plate voltages and that the potential in the gaps between the plates is zero. The TEM fields can be easily derived from this scalar potential. The *m=1* term in Equation (1) represents a transverse dipole force which provides the beam steering while the higher order terms will contribute to emittance growth in the beam. The beam deflection due to the combined electric and magnetic dipole forces is given by

$$\Delta x = \frac{\pi b V_p}{I_c Z_k \sin(\phi_0/2)} \quad (2)$$

where the critical current, I_c is defined by

$$I_c = \frac{\pi}{16}\frac{\gamma\beta^2 I_0}{\sin^2\left(\frac{\phi_0}{2}\right)}\frac{Z_0}{Z_k}\left(\frac{b}{L}\right)^2 \quad (3)$$

and I_0 = 17 kA, Z_0 = 377 Ω, L is the length of the kicker, b is the inner radius of the kicker plates, Z_k is the kicker impedance, and γ is the usual relativistic factor.

3 DIPOLE WAKE IMPEDANCE AND BEAM INDUCED STEERING

In our application, the beam current is sufficiently large as to induce substantial voltages and currents on the strip transmission lines. These voltages and currents are introduced on the transmission lines as the beam traverses the upstream and downstream gaps as well as from changes in the dipole return current as the beam is deflected. A detailed model has been previously described [1],[2]. The *m=1* transverse dipole wake impedance for this structure [3] is given by

$$Z_{\perp}(\omega)=\frac{8cZ_k}{\pi^2 b^2}\sin^2\left(\frac{\phi_0}{2}\right)\left(\frac{1}{\omega}\right)\left[\sin^2\left(\frac{\omega L}{c}\right)+j\sin\left(\frac{\omega L}{c}\right)\cos\left(\frac{\omega L}{c}\right)\right]. \tag{4}$$

The imaginary part of the dipole impedance, $Z_{\perp 0}=\mathrm{Im}[Z_{\perp}(\omega=0)]$ is a measure of the asymptotic beam deflection due to the beam-induced fields. It has been shown that the asymptotic beam deflection for an initially offset beam with current I_B injected into the kicker has the form [1]

$$x_{\infty}=x_0\cosh\left(\sqrt{\frac{2I_B}{I_c}}\right) \tag{5}$$

where x_0 is the injection offset of the beam. It is easily shown for sufficiently small beam currents that

$$x_{\infty}\approx x_0\left[1+\left(\frac{2\pi L}{\gamma\beta^2 I_0 Z_0}\right)I_B Z_{\perp 0}\right]. \tag{6}$$

To examine the relevant physics issues, a kicker has been designed and installed on the Experimental Test Accelerator (ETA-II). The ETA-II kicker has the following set of parameters: b=12.87 cm, ϕ_0=78°, Z_k=50 Ω, L=164 cm and I_c=3.9 kA. The outer enclosure has a radius of 19 cm. To verify the validity of the transmission line model the structure was modeled using a 3-D time domain electromagnetic code to determine the dipole impedance spectrum. Figure 2 shows a comparison of the dipole impedance as calculated from Equation (4) with numerical results from a 3-D time domain electromagnetic code for the ETA-II kicker. As can be seen there is a good agreement between the transmission line model and the 3-D code results. The differences can be attributed to end cavity effects associated with the feeds to the external ports and effects due to higher order modes in the structure.

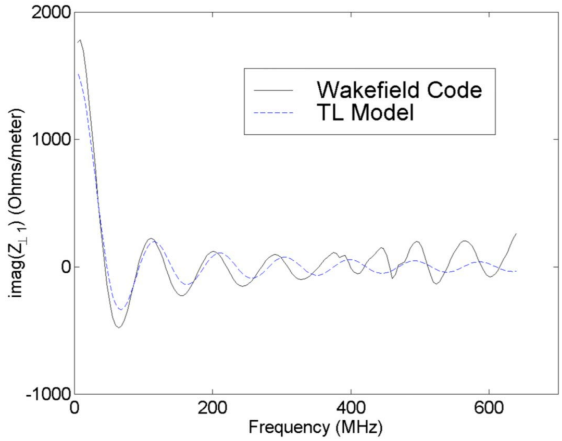

Figure 2 Dipole wake impedance

The effect of the wake impedance on the deflection of the beam can be quite dramatic. For example, for a 6 MeV, 2 kA beam initially offset by 2 cm going into the kicker, the tail of the emerging beam will be offset by 3.1 cm at the exit of the structure. These effects have been observed experimentally [4] and are consistent with theory.

4 NONLINEAR FORCES AND EMITTANCE GROWTH

From Equation (1) it is seen that for a dipole excitation of the kicker, all higher order odd multipoles will be excited in the structure. Although the higher order multipoles reduce in strength as $(r/b)^m$ it is possible under certain conditions that the beam will experience these fields, especially the *m=3* sextupole component. For example, with ETA-II parameters the space charge fields due to the beam may require that the beam entering the kicker have a large radius to enable the downstream beam to be at or near a waist when entering the dipole septum. This is important in order to minimize any emittance growth due to the nonlinear fields associated with the septum magnet. In order to estimate the effect of the higher order multipoles due to the kicker on the beam emittance, a simple particle transport code was developed. The code includes the external fields in the kicker region as defined by Equation (1) and is being expanded to include the beam-induced effects and space-charge effects self-consistently. Presently, the particles respond only to the external fields. However, we can estimate the emittance growth in the structure by using the external fields only. As an example, using the ETA-II kicker previously described, a 6 MeV beam is injected into the kicker with an unnormalized edge emittance of 13 cm-mrad and a convergence angle of .03 rad. The injected beam radius is 4 cm, which allows the beam to experience the higher order multipoles. Figure 3 shows a configuration space image of the emerging beam from the kicker showing a centroid location of 2.7 cm consistent

with Equation (2). The triangular image has been observed experimentally [4].

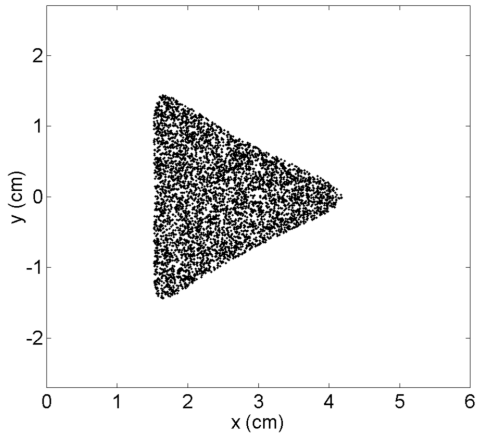

Figure 3 Configuration space image of beam emerging from kicker experiencing a large sextupole field

Despite the strong deformation of the beam image the emittance growth is predicted to be about 53% for this beam. However, transport calculations have also shown that it is possible to transport a smaller radius high current beam ~2 kA through the kicker giving an estimated emittance growth on the order of 2%.

5 MAGNETIC DIPOLE SEPTUM

The septum magnet provides an additional angular kick to the beam as it emerges from the kicker. The kick is in opposite directions on either side of *x=0*. The septum is shown schematically in Figure 4.

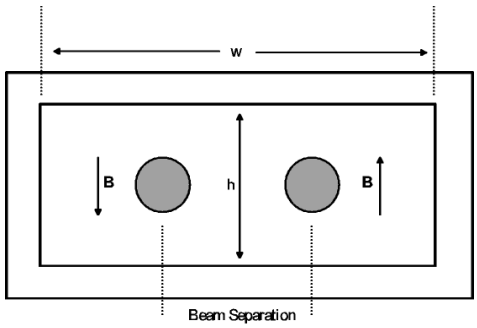

Figure 4 Magnetic dipole septum magnet

The dipole magnetic field required to produce a beam exit angle of ~15° is determined from

$$B\ell = \frac{mc}{e}\sqrt{\left(\frac{E_b}{mc^2}\right)^2 + 2\left(\frac{E_b}{mc^2}\right)} \times \left[\sin(\theta_i + \Delta\theta) - \sin(\theta_i)\right] \quad (7)$$

where ℓ is the axial length of the magnet, θ_i is the incident beam angle, $\theta_i + \Delta\theta$ is the desired exit beam angle, and E_b is the beam energy. A preliminary design for a dipole septum magnet to be used with the ETA-II kicker is being developed. The parameters for the design are an axial length of 20 cm, and a magnetic field of about 276 Gauss for a beam energy of 6.3 MeV. The dimensions of the aperture are about h=6 cm high and w=31 cm wide. Careful optimization of the design is required to minimize possible emittance growth in the transition region where the field changes sign. Currently, magnetic modules are being developed for particle transport codes to estimate the emittance growth through the septum magnet. With careful design including shims preliminary estimates show an emittance growth on the order of 4% through the septum magnet.

6 CONCLUSIONS

Self-consistent models are being developed for modeling the transport of high current space-charge dominated beams through fast beam kickers and dipole septum magnets. The effect of beam-induced forces due to the wakefields of the beam are included in the analysis. In addition, emittance growth due to nonlinear forces associated with higher order multipoles in both the kicker and septum have been estimated. Preliminary estimates of beam-induced steering are consistent with the experimental program [4]. The effect of space-charge, image forces, and fringe fields in the structures have yet to be included.

7 ACKNOWLEDGEMENTS

This work was performed under the auspices of the U. S. Department of Energy by the Lawrence Livermore National Laboratory under contract No. W-7405-Eng-48.

8 REFERENCES

[1] G. J. Caporaso, Y. J. Chen, B. R. Poole, "Transmission Line Analysis of Beam Deflection in a BPM Stripline Kicker," 1997 Particle Accelerator Conference, Vancouver, B. C. Canada, May 12-16, 1997, LLNL UCRL-JC-126073.

[2] B. R. Poole, G. J. Caporaso, W. C. Ng, "Wake Properties of a Stripline Beam Kicker," 1997 Particle Accelerator Conference, Vancouver, B. C. Canada, May 12-16, 1997, LLNL UCRL-JC-126075.

[3] K. –Y. Ng, "Impedances of Stripline Beam-Position Monitors," *Particle Accelerators* **23**, 93-102 (1988).

[4] Y. J. Chen, G. J. Caporaso, J. Weir, "Experimental Results on the Active Deflection of a Beam from a Kicker System," XIX International Linac Conference (Linac98), Chicago, Ill. USA, August 23-28, 1998.

HIGHER-ORDER-MODES AND BEAM BREAKUP SIMULATIONS IN THE JEFFERSON LAB FEL RECIRCULATING LINAC*

L. Merminga, I.E. Campisi
Thomas Jefferson National Accelerator Facility, Newport News, Virginia 23606, USA

Abstract

Measurements were performed of the frequencies and external Q's of the first two Higher-Order Mode (HOM) dipole passbands in the eight superconducting cavities of the cryomodule used in the recirculating linac of the driver accelerator of JLab's IRFEL. Anomalous high-Q resonances were found, which could lead to beam instabilities at currents close to the operating current of the machine. These results led to more detailed simulations of its beam breakup (BBU) behavior. The analysis indicates that a few modes are responsible for the relatively low value of 27 mA of the threshold current. A simple modification of the superconducting cavities could lead to an increase of the threshold current by an order of magnitude.

1 INTRODUCTION

The Jefferson Lab Free Electron Laser is presently being commissioned at current levels of about 1 mA [1]. The driver accelerator is based on a recirculation design, which incorporates energy recovery as an important feature. The accelerating-decelerating linac consists of a slightly modified CEBAF 2 K cryomodule, containing eight 5-cell superconducting cavities operating in the TM_{010} π mode at 1497 MHz.

The Higher Order Modes (HOM) are extracted by two mutually orthogonal waveguides, with a frequency cutoff of 1900 MHz, terminated in loads thermally anchored at 50 K. Modes at frequencies below 1.9 GHz can only be extracted via the fundamental power couple (FPC). Four out of five dipole modes of the TE_{111} passband fall into this category, and their external Q's can be lowered only if some component of their fields is aligned with the FPC. In the case of strong polarization, orthogonal modes could exhibit large values of Q_{ext}.

Due to the energy recovery feature of this accelerator and the relatively low number of superconducting cavities involved in the process, even a few poorly damped modes can have a devastating effect on the beam, especially at the low energy end in either one of the passes through the cavities.

In this paper we describe the results of the measurements of frequencies and Q_{ext} values of the first two HOM dipole bands (TE_{111} and TM_{110}).

* Work supported by the US Department of Energy, contract DE-AC05-84ER40150

From these measurements, rough estimates of the upper and lower limits of the BBU threshold current were derived, which bracketed the operating current of 5 mA. This result forced us to more carefully re-evaluate the instability threshold by using the simulation code TDBBU [2] and the actual measured values, as described below.

2 MEASUREMENTS OF HOM'S

The TE_{111} and TM_{110} passbands' frequencies and Q's were systematically measured for all the superconducting cavities in the FEL linac [3]. Several modes exhibited high Q's (see table 1), with the highest Q's associated with the vertical polarization of the TE_{111} π/5 mode.

Figure 1 shows the correlation of Q's for all the modes observed. All modes except the TE_{111} π/5 (large circles) show a direct correlation, pointing to no preferred polarization alignment. The TE_{111} π/5 does not follow this correlation, indicating that the extraction efficiency is subject to strong polarization. Since this particular mode has most of the energy stored in the center cell, the strong polarization is possibly associated with overall mechanical bending of the cavity in the vertical plane, thus preventing that polarization to couple to the FPC.

Although the TE_{111} π/5 mode has been observed to have the highest Q_{ext}, it is actually the 4π/5 mode which contributes more to possible beam instabilities because of its substantially higher transverse impedance (Table 1).

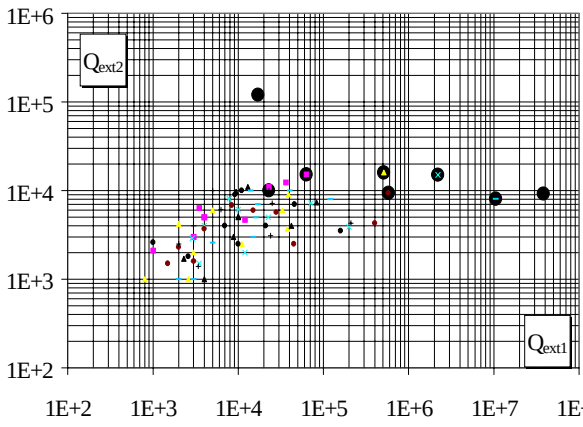

Figure 1 Distribution of external Q's for the first two dipole passbands in the eight FEL superconducting cavities. • represents the TE_{111} π/5 modes.

Table 1. Previously reported by Amato [4] (denoted by subscript A) and presently measured (subscript M) parameters for the most relevant modes for the FEL. The Q_M's in this Table are the highest measured in the whole cryomodule.

TE_{111}	$(Z"T^2/Q)_A$	$(Z"T^2/Q)Q_A$	Q_M	$(Z"T^2/Q)Q_M$
$\pi/5$ -x	2.0 E2	6.2 E6	1.2 E5	2.4 E7
$\pi/5$-y	2.0 E2	6.2 E6	3.8 E7	7.6 E9
$4\pi/5$-x	7.0 E4	1.1 E9	1.2 E4	8.6 E8
$4\pi/5$-y	7.0 E4	1.1 E9	4.0 E5	2.8 E10

Six out of eight cavities show that the vertically polarized TE_{111} $4\pi/5$ mode has a Q high enough to generate a shunt impedance of 1-3 10^{10}, two orders of magnitude larger than what originally measured by Amato [4]. The frequency of this mode falls right below the cutoff of the HOM extraction waveguides. A more effective extraction of this dangerous mode could be attained if a slight modification of future cavities could be made to allow propagation of this mode.

The simulations described below were performed both for the real system and for a modified system with realistically decreased Q_{ext} of the six cavities TE_{111} $4\pi/5$ modes.

3 SIMULATIONS

3.1 Method

Simulations of beam breakup were performed using the code TDBBU [2]. In it, every bunch is characterized by a phase space vector which gets updated according to the fundamental equations of dynamics described in Reference [5], as deflecting modes in each cavity impart kicks in the horizontal and vertical directions.

In the FEL simulations, a 10 MeV beam is injected into the linac, interacts with the HOM fields of each cavity, gets transported around the recirculation path and enters the linac again, 180° out of phase for energy recovery. As the decelerated beam traverses the RF cavities, it interacts with the HOM fields of the cavities again, and, as the beam energy becomes smaller, the transverse deflections imparted to the beam have a stronger effect. Therefore, we expect the threshold current to be lower in the case of recirculation with energy recovery than in the absence of energy recovery.

The beam is injected into the linac with energy equal to 10 MeV with a bunch repetition frequency of 37.4 MHz, the 40th sub-harmonic of the RF frequency. Each cavity is described by a 0.25m drift delivering an energy gain of 2 MV, followed by the "HOM-kick" section for the particular cavity and this is followed by another 0.25m drift delivering 2 MV energy gain, for a total of 8 MV/m acceleration gradient per cavity.

The "HOM kick" section includes all five TE_{111} and five TM_{110} horizontal and vertical modes. Each mode is characterized by its Q value, frequency, and transverse shunt impedance, as given in Ref. [4] scaled by the frequency of the mode.

The total path length of the recirculation is 501.5 RF wavelengths [5] and the transport matrix elements are calculated using DIMAD.

3.2 Results

The threshold current for a system containing the real cavity parameters and optics for the FEL was determined via several runs and found to be about 27 mA.

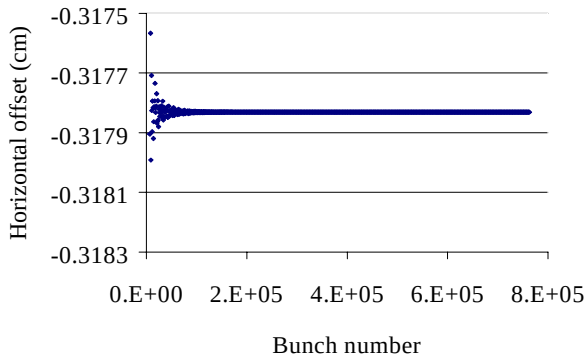

Figure 2 Horizontal bunch offset as a function of bunch number at 25 mA. The beam damps rapidly to a stable condition in the horizontal plane.

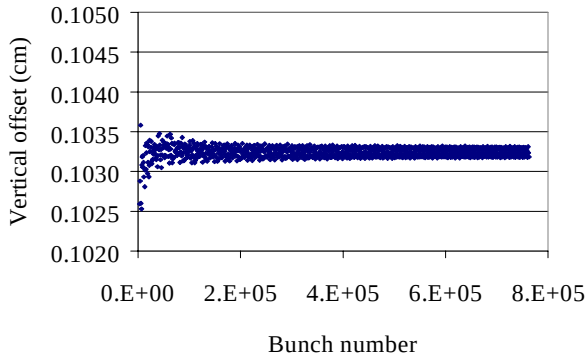

Figure 3 Vertical bunch offset at 25 mA. In the vertical plane the damping occurs more slowly than in the horizontal plane.

Figure 2 shows the convergence behavior at 25 mA for the horizontal plane and Figure 3 shows the convergence in the vertical plane at the same current. A clear divergence in the vertical place is observed at 28 mA (Figure 4).

In the horizontal plane, on the contrary, no instability is observed at these current values, since the relevant modes are polarized in such a way that those aligned with the horizontal axis are well damped by the fundamental power coupler.

Several other simulations with currents well above threshold were performed to determine the growth rate of the instability and to extract the functional dependence of growth rate on current. Figure 5 shows a typical run performed for currents well above threshold. In Figure 6 the growth rate is plotted as a function of current. From it, it is possible to get a relatively good agreement with the actual estimate of the threshold by direct simulation, by making only two simulation runs above threshold and extrapolating the threshold via the plot in Figure 6. The value thus obtained is approximately 35 mA, about 25% higher than what obtained by direct simulation.

The analysis of the mode impedance for the real cavities shows clearly that the TE_{111} $4\pi/5$ mode is in most cavities the one responsible for a major part of the current limitations. This mode often falls only a few MHz below the threshold for propagation in the HOM waveguide and it would be damped more effectively if the cutoff frequency of the HOM waveguide could be lowered by only one percent or so.

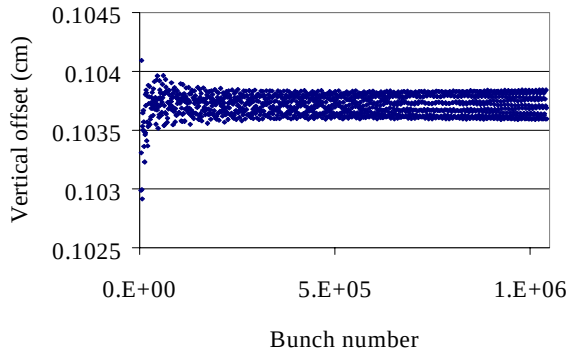

Figure 4 Vertical bunch offset at 28 mA. The beam becomes unstable at this threshold current.

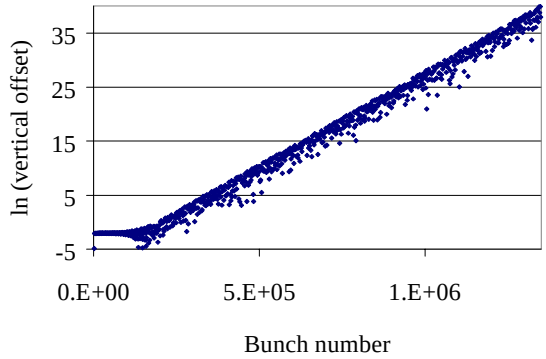

Figure 5 Logarithmic representation of the bunch offset for a current well above threshold, 200 mA in this case.

Such mechanical modification of the coupler might be possible with minimal effort [6]. Based on that assumption, we have recalculated the threshold current for the case in which the Q's of the TE_{111} $4\pi/5$ modes are lowered by a factor of 10 if above 10^5. This was done for cavities 1-6 in the cryomodule. The cavities with Q's already below 10^5 (7 and 8) were left untouched.

It is possible that the Q's of these modes is limited to about 5×10^5 because at these frequencies, slightly below the HOM waveguide cutoff, there is enough leakage of the evanescent mode in the waveguide to effect some damping. The $\pi/5$ mode, being at lower frequencies, exhibit considerably higher Q's, even two orders of magnitude larger.

The results of the simulations, performed in exactly the same manner as for the real measured Q's, indicate that the threshold current is now increased to 207 mA.

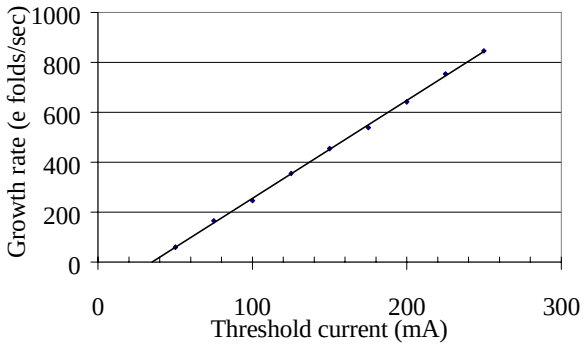

Figure 6 Growth rate of the bunch offset as a function of current. This plot can be used to estimate the threshold current as the abscissa intercept.

4 CONCLUSIONS

Detailed measurements of the Q's and frequencies of the first two dipole Higher Order Modes in the FEL linac indicated that the vertical polarization of some modes in several cavities are only marginally damped.

TDBBU simulations of the Beam Breakup threshold performed with the actual configuration yield a value of threshold current of 27 mA, only a factor of 5 higher than the design operating current.

Analysis of the mode shunt impedance indicates that with a slight modification of the cavities, a few dangerous modes could be more adequately damped. With such modification, the TDBBU estimate of the threshold current would be increased above 200 mA.

5 REFERENCES

[1] C. Bohn et al., "Performance of the Accelerator Driver of Jefferson Laboratory's Free-Electron Laser," Proceedings of the 20th International FEL98 Conference, August 16-21, 1998 Williamsburg, VA
[2] TDBBU was written by G. A. Krafft at JLab
[3] I. E. Campisi and L. Merminga, "Higher-Order-Mode Spectra in the FEL cavities", JLAB TN 98-011, 1998
[4] J. Amato, "Summary of HOM Measurements to date", Cornell LNS Tech Note SRF-831002, 1983
[5] D. Douglas, Private communication, 1998
[6] J. Preble, Private communication, 1998

TESLA INJECTOR SIMULATIONS WITH MAFIA*

P. Schütt, T. Weiland
Darmstadt University of Technology, Fachbereich 18,
FG Theorie Elektromagnetischer Felder, Schloßgartenstraße 8, 64289 Darmstadt, Germany

Abstract

The TESLA Test Facility (TTF) is a test bed for the superconducting option of a linear e+/e- collider in the TeV regime. The injector delivers a 20 MeV beam with 1 nC charge per bunch of 1 mm length. It consists of an RF-gun, a superconducting 9-cell Capture Cavity and a chicane bunch compressor. The MAFIA modules TS2 and TS3, the particle in cell programs in 2D and 3D, as well as the module L, a tracking program, have been used to study the particle dynamics in the TTF, e.g. the emittance growth due to space charge effects in the bunch compressors. Dedicated interfaces for the three different simulation tools allow to study components separately and to hand over beam data from one accelerator section to another or one simulation tool to another, respectively.

1 INTRODUCTION

A typical linear accelerator consists of a diversity of components, which are usually developed with different design tools. When the beam dynamics in an accelerator is studied, the low energy part near the particle source usually requires the use of a simulation program that includes the calculation of space charge forces. On the other hand, the tracking of ultrarelativistic particles can be done much faster with a different class of simulation codes.

Problems may arise when parameters of the beam must be communicated between the different programs. Often, definitions e.g. for the units of the emittance differ. More over, beam models may be different: e.g. macroparticles in one code versus gaussian bunches in the next.

Within the electromagnetic CAD package MAFIA[1], three solvers are offered which allow the simulation of the full electrodynamics in the low energy part of the accelerator as well as the fast tracking in the high energy part. Interfaces are being developed to ease the handover of parameters from one code to the next.

In the low energy region, a handover of beam parameter from one accelerator element to the next is challenging even in the case where both are handled in the same code. This is due to the fields which accompagny the beam and must be interpolated from one calculation grid to the other without inducing numerical noise.

The status of this project is described in this paper.

* work supported by DFG (Deutsche Forschungsgemeinschaft)

2 SIMULATION TOOLS

2.1 MAFIA-TS2 and -TS3

TS2 and TS3 are the names of the Particle in Cell (PIC) modules in MAFIA. They have been used successfully for the computer aided design of klystrons and other RF sources[2]. The PIC programs solve Maxwell's equations in the time domain with a FDTD algorithm and in parallel, selfconsistently, integrate the equations of motion of the charged particles. These particles, in turn, are the source of the electromagnetic fields.

TS2 is the axisymmetric, two dimensional version, TS3 works with three dimensional cartesian coordinates. Both are fully relativistic and due to their basic physics algorithm a priori include all interaction of the charged particles and electromagnetic fields. Therefore, space charge, self magnetic fields, wake fields etc. are all included. Furthermore, both codes can use precalculated static and resonant fields, which are provided by other solvers in the MAFIA package.

2.2 MAFIA-L

L is a specialized module for the tracking of relativistic particles in an accelerator. It has been used to study single bunch and multibunch instabilities[3]. Featuring a modular description or the accelerator, including alignment errors, as well as optimization strategies, it is a tool for the overall design of a linear accelerator. The statistical description of the beam allows an uncorrelated energy spread and a phase jitter.

L calculates the longitudinal as well as the transversal dynamics of the beam. It includes realistic external fields. The transversal space charge forces may be calculated in a fast approximation, wake fields can be included by a quasi Green's function algorithm, where the Greens functions are provided by MAFIA-T2.

2.3 Interfaces

Several interfaces have been developed to facilitate the data exchange from one accelerator section to the next.

If both sections are calculated by L, the data exchange is trivial: beam data can just be reused.

In the case of the PIC codes, it is necessary to store not only beam data but also the field data for one period in a steady state. Furthermore, to avoid noise in the downstream component, the beam current must be artificially raised to

its nominal value over several RF periods. The algorithms for interfaces from TS2 to TS2 or TS3 have been published earlier[2].

Especially for the use in accelerator design, an interface from TS2 to L has been developed. This requires the translation between two different beam models: in TS2, the beam is described by a number of macro particles, characterized by their position and momentum at a fixed time. In L, the bunch at a fixed position in the accelerator is described by a number of time slices. These slices are characterized by their first and second order statistical moments of transversal position and momentums as well as their energy and their longitudinal position in time.

The interface has been built into TS2. During the calculation, all particles are registered when they cross the monitor plane, which is located at the beginning of the structure to be simulated in L. The slice parameters for L can then be calculated via statistics formulae. In order to keep as much information as possible, no further smoothing of the data is used.

It will rarely be necessary to hand data from L to TSx. But it can be useful to calculate single elements without the calculation of all upstream components in TSx. In order to facilitate the input of starting parameters, we plan to enable the input of Twiss parameters into TSx and to develop an interface from L to TSx.

3 NUMERICAL RESULTS

3.1 *Injector Layout*

Figure 1 shows schematically the layout of the TESLA FEL injector. A Laser RF gun delivers a beam with about 5 MeV. In a first superconducting TESLA structure, the capture cavity, it is accelerated to 15 - 20 MeV, then longitudinally compressed in a chicane and delivered to the first complete TESLA module.

The beam dynamics in the gun and possibly in the capture cavity must be simulated in TS2, because of the strong collective forces. Either at the end of the gun, or at the end of the capture cavity, L may take over.

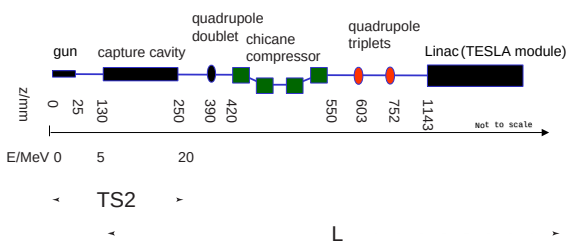

Figure 1: Schematic Layout of the Injector. The application regions of the MAFIA modules TS2 and L are indicated.

3.2 *The Gun*

Simulation results for the TESLA TTF gun have been published elsewhere [4]. For a correct treatment of the collective forces, a very fine resolution of the calculation grid is required: typically $\Delta z = 20\mu m$. The results have been compared to PARMELA calculations: when wake fields are artificially suppressed in MAFIA-TS2, both codes give the same results.

3.3 *The Capture Cavity*

The capture cavity has also been simulated with TS2 (see figure 2, next page). Since the spatial bunch dimensions are bigger here than in the gun, the resolution may be somewhat coarser: we used $\Delta z = 100\mu m$ and $\Delta r = 120\mu m$.

In order to reduce the numerical noise in the calculation, data were not taken from previous calculations, but initialized at the entrance of the cavity. The bunch length was $\sigma_z = 800\mu m$, the radius $\sigma_r = 600\mu m$. In the test case, we used an injection phase of $\Delta\varphi = -10°$. The start energy was 5.3 MeV with an uncorrelated energy spread of 13.3 keV. The maximum field amplitude in the cavity was 15 MeV/m.

3.4 *Handing Data over to L*

Close to the end of the capture cavity, an interface to L was placed in the TS2 simulation.

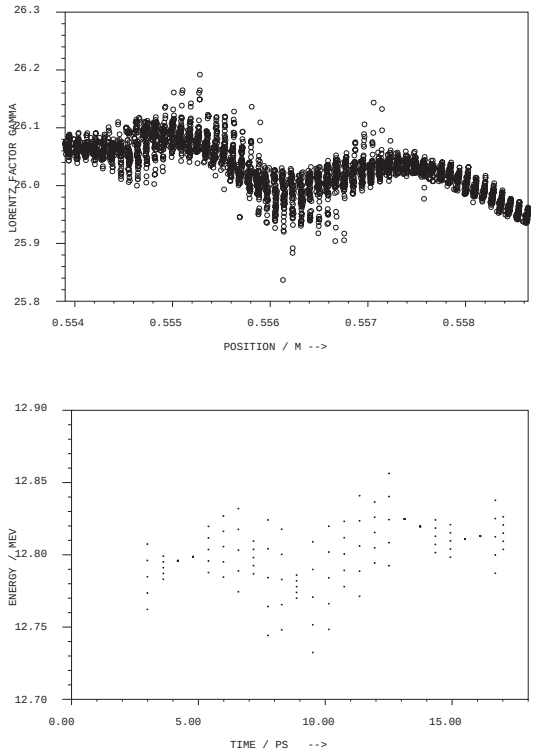

Figure 3: Energy distribution in the bunch at the end of the TS2 simulation (top) and at the start of L (bottom).

Figure 3 shows the energy distribution in the bunch as represented in TS2 and in L. In the TS2 graphic, the bunch moves from left to right, so the head of the bunch is on the right. In L, the energy is plotted as a function of time, therefore the head of the bunch is on the left. Slices in L

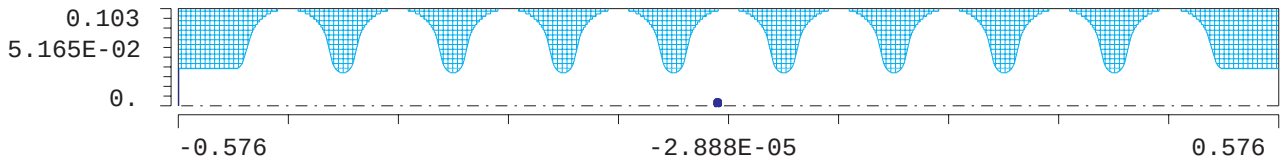

Figure 2: Capture Cavity as simulated in TS2. The structure is rotationally symmetric, the bottom line is the axis of rotation. The spot near the center shows the tiny dimensions of the electron bunch that moves along the axis from left to right.

carry different charges. The number of slices was chosen very high. Statistics is better for fewer slices at the cost of details in the distribution.

4 CONCLUSION

MAFIA provides tools to simulate the low energy part of a linear accelerator as well as a fast calculation of ultra relativistic particles with some approximations. Interfaces allow to use the result of one calculation as starting conditions for the next one.

5 ACKNOWLEDGEMENT

The authors wish to thank Stefan Setzer for his calculation of the capture cavity.

6 REFERENCES

[1] The MAFIA collaboration, *User's Guide MAFIA Version 4.00*, CST GmbH, Lauteschlägerstr. 8, D-64289 Darmstadt, Germany

[2] U.Becker, M.Dohlus, T.Weiland, *Three Dimensional Klystron Simulation*, Particle Accelerators, 1995, Vol. 51, pp. 135-154

[3] M.Drevlak, *On the Preservation of Single- and Multi-Bunch Emittance in Linear Accelerators*, Thesis, DESY 95-225, Nov. 1995

[4] M.Zhang, P.Schütt, *TESLA FEL Gun Simulations with PARMELA and MAFIA*, Proc. of the 1996 Computational Accelerator Physics Conference, Williamsburg, Virginia, September 1996

HALO FORMATION IN 3-D BUNCHES WITH DIFFERENT PHASE SPACE DISTRIBUTIONS *

A.V. Fedotov, R.L. Gluckstern
Physics Department, University of Maryland, College Park, MD 20742
S.S. Kurennoy, R.D. Ryne
LANSCE Division, Los Alamos National Lab, Los Alamos, NM 87545

Abstract

We recently constructed, analytically and numerically, a new class of self-consistent 6-D phase space stationary distributions [1], which allowed us to study the halo development mechanism without being obscured by the effect of beam redistribution. In this paper we consider non-stationary distributions and study how the halo characteristics compare with those obtained using the stationary distribution. In contrast to bunches with a large aspect ratio we find that the effect of coupling between the r and z planes is especially important as the bunch shape becomes more spherical.

1 INTRODUCTION

A realistic treatment of halo formation must take into account 3-D beam bunches and 6-D phase space distributions. Barnard and Lund [2] performed numerical studies with a 3-D beam bunch using the particle-core model, drawing attention to the existence and importance of a longitudinal halo for a spheroidal bunch. However, all studies based on the particle-core model do not address the question of whether halo formation is influenced by the density redistribution which follows for a non-stationary beam, even if it is rms matched (See for example [3]). In fact, halo formation in 2-D due to the redistribution process in rms matched beams was shown, for example, by Okamoto [4] and Jameson [5]. We therefore continued our effort to study the halo development mechanism in 3-D beam bunches in the absence of the redistribution process [1]. Such an approach allowed us to study the fundamental mechanism of halo formation associated with the beam mismatch. To accomplish this we constructed a new class of stationary 6-D phase space distributions for a spheroidal beam bunch [1]. We then explored the formation of longitudinal and transverse halos in 3-D bunches in great detail [1].

Now that we have established the parameters which lead to halo formation in 3-D beam bunches for the 6-D self-consistent phase space distribution, we explore distributions which are not self-consistent, to determine the extent to which the relatively rapid redistribution in the 6-D phase space contributes to the formation of halos. This is the focus of the present paper.

* Work supported by the U.S. Department of Energy

2 NUMERICAL SIMULATIONS

In this paper we compare particle simulations performed for the 6-D stationary distribution given in [1] with the non-stationary 6-D Gaussian distribution, and the non-stationary 6-D uniform distribution. We also consider an axisymmetric beam bunch by putting $a = b$ with a, c being the minor and major semiaxes of our spheroidal bunch, respectively. Both the Gaussian and uniform distributions are constructed in the rms matched sense.

2.1 Stability of the Matched Distribution

Both numerical studies of the unstable modes and multi-particle simulations for the 2-D breathing KV beam with zero mismatch confirmed that the beam is unstable for tune depressions below $\eta = 0.4$ [6]. However, no halo was observed in the corresponding 2-D simulations. Similar studies for other 2-D rms matched distributions which are not stationary solutions of the Vlasov equation showed the existence of a halo for severe tune depression and zero mismatch [4]. The existence of a halo for such rms matched distributions was attributed to the unavoidable plasma oscillations generated by the initial density-redistribution process which is clearly shown in [4].

In our recent 3-D simulations [1] with the stationary distribution no such redistribution occurred. However, for the Gaussian distribution one can see the strong redistribution process which occurs very quickly in both the transverse and longitudinal planes. In contrast to the 2-D simulations [4] this redistribution process happens for both modest and severe space charge. In Fig. 1 we plot the maximum x and z among the million particles in our run for severe ($\eta_z = 0.27, \eta_x = 0.38$) and modest ($\eta_z = 0.65, \eta_x = 0.75$) tune depressions, respectively. Figure 2 shows the phase space $z - p_z$ diagram for $\eta_z = 0.27, \eta_x = 0.38$ without and with a low-density cut [1] which enables us to observe the halo structure clearly. Similarly, one can see the redistribution process for the uniform distribution. One again finds halo formation for both modest and severe space charge [7]. Thus, we have found that an rms matched 3-D beam can produce transverse and/or longitudinal halos (of relatively small extent) for a wide range of space charge intensity even when it is initially perfectly matched. Of course, from a practical point of view such halos are not important because the halo extent is very small for the mismatch factor $\mu = 1.0$. The important consequence is that the redis-

tribution process by itself (zero initial rms mismatch) does not lead to significant emittance growth.

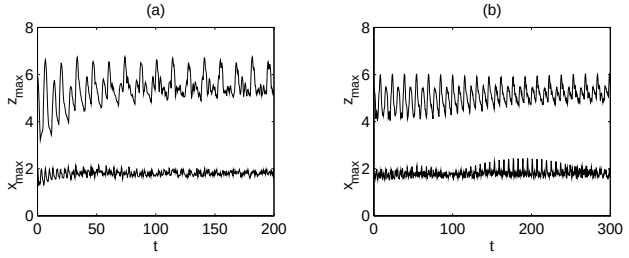

Figure 1: Maximum x and z as a function of time for initially matched beam $\mu_x = \mu_y = \mu_z = 1.0$ with 6-D Gaussian distribution ($c/a = 3$) a) $\eta_x = 0.38$, $\eta_z = 0.27$ b) $\eta_x = 0.75$, $\eta_z = 0.65$.

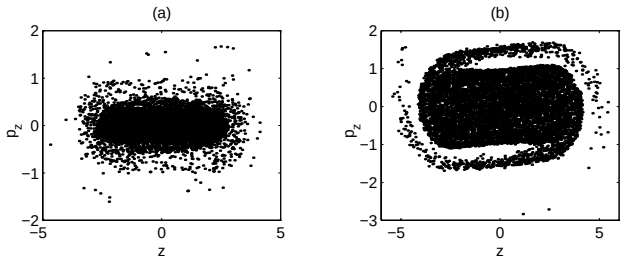

Figure 2: Longitudinal phase space diagram at $t = 50$ of initially matched beam $\mu_x = \mu_y = \mu_z = 1.0$ with 6-D Gaussian distribution ($c/a = 3$, $\eta_x = 0.38$, $\eta_z = 0.27$) a) without low-density cut (with 32,768 particles plotted) b) with low-density cut (with 20,000 particles plotted).

2.2 Initially Mismatched Beam

Numerical 3-D simulations with the initially mismatched non-stationary distributions described above confirm all the characteristics of halos observed for the stationary distribution [1]. The main difference is that for a non-stationary distribution the halo extent is larger (especially for the Gaussian) than the halo extent of the stationary distribution with the same initial mismatch parameters. As an example, in Fig. 3 we show the maximum x, z, emittance growth, $z - p_z$ diagram without the low-density cut and $r - p_r$ diagram (with angular momentum $|L_z| < 0.1$ to make the "peanut" diagram relatively clear) with initial $\mu_x = \mu_y = \mu_z = 1.5$ for the uniform distributions. The 6-D stationary distribution constructed in [1] gives a picture of halo development almost identical to the uniform non-stationary distribution except for a slight difference in the halo extent.

A systematic study for bunches of different shape (c/a) and mismatch factor μ (with simultaneous mismatch in all planes) was presented recently [1]. Below we present some examples of the mismatch in the transverse plane only. To compare our results with those available for a transverse

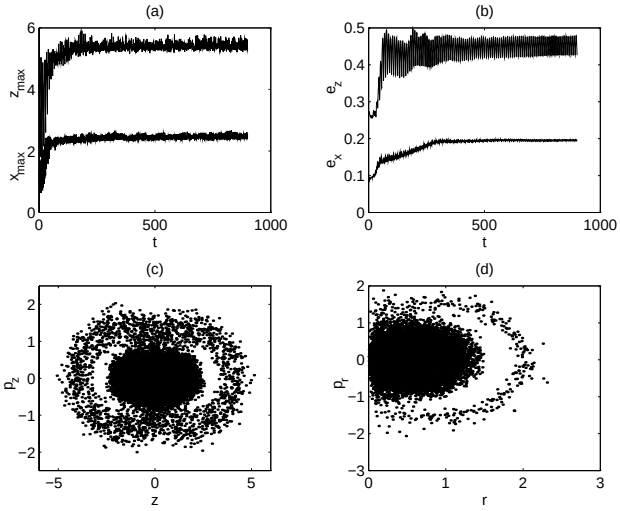

Figure 3: 6-D uniform distribution $\mu_x = \mu_y = \mu_z = 1.5$ ($c/a = 3$, $\eta_x = 0.53$, $\eta_z = 0.39$) a) maximum x and z b) emittance growth c) $z - p_z$ diagram at $t = 900$ (with 32,768 particles plotted) d) $r - p_r$ diagram at $t = 900$ for particles with the angular momentum $|L_z| < 0.1$ (with 25,000 particles plotted).

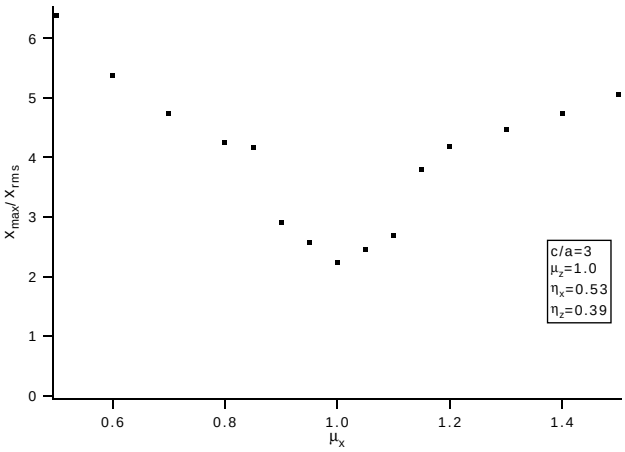

Figure 4: Extent of the transverse halo for the 6-D stationary distribution with zero longitudinal mismatch $\mu_z = 1.0$ ($c/a = 3$, $\eta_x = 0.53$, $\eta_z = 0.39$).

halo [8] we show in Fig. 4 the dependence of the transverse halo extent on the mismatch for fixed space charge, with tune depressions $\eta_z = 0.39$, $\eta_x = 0.53$. The main difference is the behavior near $\mu = 1.0$ which clearly shows the existence of threshold for halo formation in beams with stationary distributions. Similar behavior exists for the longitudinal halo [7] (the extent of the longitudinal halo is smaller than that of the transverse halo).

However, the existence of a threshold for halo formation observed in 2-D simulations and then confirmed by our 3-D particle simulations turns out to be a feature only observed for self-consistent stationary distributions. For example, Fig. 5 for the 6-D uniform non-stationary distribution has

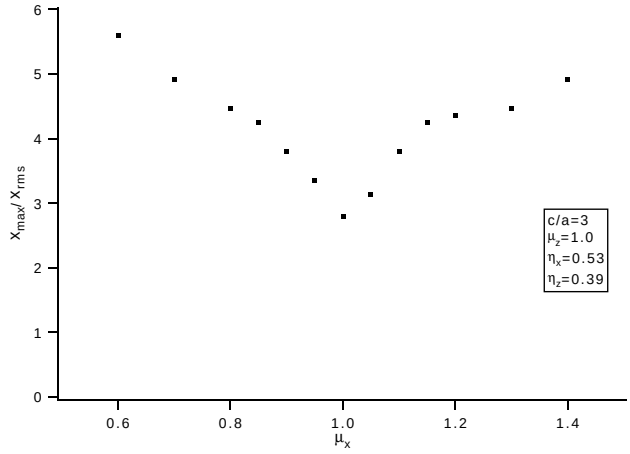

Figure 5: Extent of the transverse halo for the 6-D uniform distribution with zero longitudinal mismatch $\mu_z = 1.0$ ($c/a = 3$, $\eta_x = 0.53$, $\eta_z = 0.39$).

no obvious threshold behavior. In fact, we showed above that, in a non-stationary beam, a halo can form even for a zero initial mismatch. Therefore, in a "real" beam which goes through a redistribution and relaxation process one should not expect a threshold for halo formation due to a mismatch.

2.3 Coupling Effects

In performing 3-D simulations we encounter halo formation in a beam bunch, where we clearly see coupling between the longitudinal and transverse motion. It was already noted [1] that due to the coupling between r and z, a transverse or longitudinal halo is observed even for a very small mismatch (less than 10%) as long as there is a significant mismatch in the other plane. Further numerical investigation of this question showed that the effect of coupling becomes extremely important for nearly spherical bunches ($c/a \leq 2$) which is typical of the parameter range of interest for the APT design [9]. For example, for the short bunch with $c/a = 2$, with only a longitudinal initial mismatch ($\mu_z = 1.5$, $\mu_x = \mu_y = 1.0$), one finds particles at large amplitude in both the longitudinal and transverse directions, as can be seen in Fig. 6 for the 6-D stationary distribution. Of course, the intensity of particles in the transverse halo is much smaller than it is when there is in addition a transverse initial mismatch. (In our example in Fig. 6, we have 0.05 percent of the particles in the transverse halo with zero transverse mismatch compared with several percent in the longitudinal halo.) A similar effect due to coupling was seen for the non-stationary distributions.

3 SUMMARY

Recently we constructed, analytically and numerically, a new class of 6-D phase space stationary distributions for an azimuthally symmetric beam bunch which allowed us

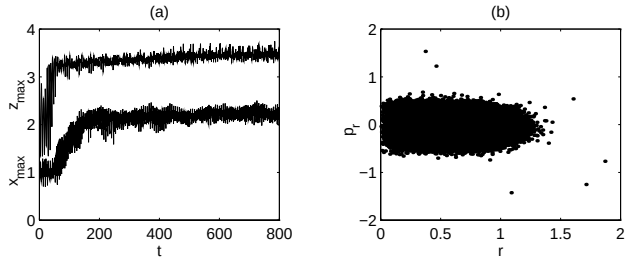

Figure 6: Coupling effect for the 6-D stationary distribution with zero transverse mismatch $\mu_x = \mu_y = 1.0$, $\mu_z = 1.5$ ($c/a = 2$, $\eta_x = 0.55$, $\eta_z = 0.45$) a) maximum x and z b) $r - p_r$ diagram at $t = 800$ for particles with the angular momentum $|L_z| < 0.1$ (with 25,000 particles plotted).

to study the halo development mechanism in 3-D beam bunches where no phase space redistribution occurs. After we established the parameters which lead to halo formation in 3-D beam bunches for the self-consistent 6-D phase space stationary distribution [1], in this paper we explored rms matched distributions which are *not* self-consistent, to determine the extent to which the relatively rapid redistribution of the 6-D phase space contributes to the formation of halos. We also found that the effect of coupling between the r and z planes is very important in the halo development mechanism and can lead to serious consequencies, especially for a very short beam bunch.

4 ACKNOWLEDGMENT

We thank Tom Wangler for helpful conversations. In addition RLG and AVF wish to thank Andy Jason and the LANSCE1 group for its hospitality during part of these studies.

5 REFERENCES

[1] R.L. Gluckstern, A.V. Fedotov, S.S. Kurennoy and R.D. Ryne, Univ. of Maryland Physics Dept. Preprint 98-107, scheduled for publication in Phys. Rev. E (October 1998).

[2] J.J. Barnard and S.M. Lund (I), and S.M. Lund and J.J. Barnard (II), in Proceedings of the 1997 Particle Accelerator Conference, Vancouver, Canada (unpublished).

[3] M. Reiser, Theory and Design of Charged Particle Beams, Wiley, New York (1994).

[4] H. Okamoto and M. Ikegami, Phys. Rev. E **55**, 4694 (1997).

[5] R.A. Jameson, Los Alamos Report No. LA-UR-93-1209 (unpublished).

[6] R.L. Gluckstern, W-H. Cheng, S.S. Kurennoy and H. Ye, Phys Rev. E **54**, 6788 (1996).

[7] A.V. Fedotov, R.L. Gluckstern, S.S. Kurennoy and R.D. Ryne, Univ. of Maryland Physics Dept. Preprint 98-108 (1998).

[8] T. Wangler et al., in Proceedings of the 1997 Particle Accelerator Conference, Vancouver, Canada (unpublished).

[9] APT Conceptual Design Report, Los Alamos Report No. LA-UR-97-1329, 1997.

STUDY OF THE TRANSVERSE BEAM MOTION IN THE DARHT PHASE II ACCELERATOR*

Y.-J. Chen and T.L. Houck
Lawrence Livermore National Laboratory, Livermore, California 94550 USA
W. M. Fawley
Lawrence Berkeley National Laboratory, Berkeley, California 94720 USA

Abstract

The accelerator for the second-axis of the Dual Axis Radiographic Hydrodynamic Test (DARHT) facility will accelerate a 4-kA, 3-MeV, 2-μs long electron current pulse to 20 MeV. The energy variation of the beam within the flat-top portion of the current pulse is ± 0.5%. The performance of the DARHT Phase II radiographic machine requires the transverse beam motion to be much less than the beam spot size which is about 1.5 mm diameter on the x-ray converter. In general, the leading causes of the transverse beam motion in an accelerator are the beam breakup instability (BBU) and the corkscrew motion. We have modeled the transverse beam motion in the DARHT Phase II accelerator with various magnetic tunes and accelerator cell configurations by using the BREAKUP code. The predicted sensitivity of corkscrew motion and BBU growth to different tuning algorithms will be presented.

1 INTRODUCTION

Transport simulations of the beam from the exit of the injector to the accelerator exit have been performed for the second axis of the Dual Axis Radiographic Hydrodynamic Test (DARHT) facility [1]. The motivation for performing these simulations was to establish engineering tolerances and design criteria to ensure that the DARHT-II facility meets performance goals. These goals are to produce four 60-ns long pulses, each with a time-integrated x-ray dose of 1000 R at one meter, with a 1 - 2 mm time-integrated x-ray spot. Transverse motion of the beam is a principle limitation in achieving the desired accelerator performance. Leading causes of the transverse beam motion typically are the beam breakup instability driven by injector noise and misalignments, and the corkscrew motion [2] caused by misalignments and chromatic aberration of optical elements. In this paper, we show that both corkscrew motion and misalignment driven beam breakup instability can be controlled effectively by using the corkscrew tuning V algorithm [3].We have also examined growth of beam breakup instabilities in these cells for various accelerator configurations.

*The work was performed under the auspices of the U.S. Department of Energy by LLNL under contract W-7405-ENG-48 , and by LBNL under contract AC03-76SF00098.

2 CONFIGURATION AND DESIGN PARAMETERS FOR DARHT II

The accelerator is arranged in eleven 8-cell blocks with pumping ports located between cell blocks. About one hundred solenoids are used to transport the beam. Three different cell configurations were used in the transport simulations. Two configurations are for a beam line aperture of 25.4 cm and differ only in the insulator/gap design of the cells. The final configuration has a larger, 35.6 cm, aperture for the first 8-cell block followed by ten 8-cell blocks with a 25.4 cm aperture.

To achieve the performance criteria of x-ray dose and spot size, the normalized Lapostolle emittance (95% of beam current) at the x-ray converter has to be no greater than 1500 π-mm-mr, and the transverse beam motion should be no greater than 10% of beam radius. The designed beam parameters are:
1) current of 4 kA in a 2 μs pulse with 200 ns rise time,
2) energy at the injector exit of 3 MeV ± 0.5% increasing to 20 MeV ± 0.5% at the accelerator exit, and
3) emittance (4 x Lapostolle emittance) at the injector exit of 500 π-mm-mr increasing to less than 1000 π-mm-mr at the accelerator exit.

3 BBU INSTABILITY AND TRANSVERSE IMPEDANCE

The beam breakup instability arises from the beam interacting with the accelerating cells' dipole TM modes. The transverse impedance is a measurement of the strength of the interaction. As the beam axis is offset from the cavity axis, these modes extract energy from the leading part of the beam and deflect the trailing part of the beam transversely. This instability typically sets the upper limit for a transportable beam current and the lower limit for the focusing field.

3 .1 Equations Governing BBU

The BBU instability is a convective instability. For the misalignment driven beam breakup instability, the maximum number of e-fold in the beam breakup instability growth is given by

$$\alpha = \frac{c}{l}\frac{I}{I_o} Z_\perp \int_0^L \frac{dz'}{\gamma k_c(z')} \ , \qquad (1)$$

and the peak growth will occur in the pulse after a time

$$\tau = 2\alpha Q/\omega_o \quad , \qquad (2)$$

where I is the beam current, I_o = 17 kA, $Z_\perp$ is the transverse cell impedance for the BBU mode frequency ω_o. The gap separation is l, and the accelerator length is L. For an electron beam pulse with a long rise time, the beam breakup instability driven by misalignment starts to grow at the head of the pulse and may not propagate into the flat-top portion of the pulse before the beam leaves the accelerator. Therefore, the beam breakup instability driven by misalignment is generally not a threat to a DARHT-II pulse with long rise time. In contrast, the beam breakup instability driven by injector noise would appear throughout the pulse length. BBU growing from injector noise a significant concern for the DARHT-II beam transverse motion.

3 .2 Transverse Impedance

Three DARHT-II accelerator cell configurations have been designed [4]. The configurations differ primarily in the geometry of the insulator and aperture size. However, only the impedance and frequency of the primary resonant modes are required for the purpose of the simulations. Table 1 lists the pertinent cell characteristics for BBU calculations. Note that $Z = c\, Z_\perp/\omega_o$. "Initial" and "current" refer to the insulator/gap designs under consideration.

Table 1: Impedances of different cell configurations

Design	Freq. (MHz)	Z/Q (Ω)	Q
Initial (25.4 cm ID)	262	34.9	2.0
	580	1.1	7.2
	672	3.9	6.9
Current (25.4 cm ID)	200	37.6	1.9
	535	7.3	3.8
Current (35.6 cm ID)	171	25.4	2.0
	443	4.3	4.2

4 CORKSCREW MECHANISM AND TUNING STRATEGY

Corkscrew motion is a differential oscillation of the beam centroid between the leading and trailing portions of a beam pulse driven by chromatic aberration of the focusing elements and misalignment of the machine. The DARHT-II accelerator's alignment requirement is to meet the alignment specification of the first axis of DARHT accelerator's: random 3-σ magnetic tilt to be 1.95 mrad and random 3-σ magnet offset to be 0.45 mm. There are about one hundred of solenoids with steering/correction coils along the DARHT-II accelerator.

The magnetic tune was chosen to focus the electron beam from an 8 cm radius at the exit of the injector to a 6 mm radius as rapidly as possible without adversely affecting the current distribution. The 6 mm radius is then maintained through the remember of the accelerator. The rapid increase in magnetic field slows the BBU growth as seen in equation (1).

The DARHT-I alignment specifications is expected to produce a corkscrew amplitude of several millimeters by the end of the accelerator without corrective measures. The "tuning-V" steering algorithm has demonstrated an order of magnitude reduction in corkscrew on the ETA-II accelerator. In the simulations described below, only one steering coil per 8-cell block was used to implement the steering algorithm.

5 SIMULATION RESULTS

The BREAKUP code was used to model the beam centroid's transverse motion in the DARHT-II accelerator. Both motion due to the BBU instability and corkscrew motion was included. Three different configurations were simulated. The gain factor, a figure of merit for BBU growth, is defined as BBU amplitude divided by the injector noise amplitude. The goal is to have a gain factor ≤ 20, or 3 e-folds based on an injector noise amplitude of 100 microns. The goal for the amplitude of the transverse motion, including corkscrew and BBU, is 0.6 mm.

Examples of the simulation results for misalignment errors are shown in Figures 1 and 2. The beam pulse was simulated for 350 ns including a 200 ns rise time. An energy variation of ±5% was imposed on the 150 ns of flat-top to model the effect of corkscrew on the longer 2-μs pulse. Two observations can be made from the results. First is that the BBU motion, the fast oscillation at the start of the pulse, extends only a short distance into the pulse and is insignificant compared to the corkscrew amplitude. Second, the V-tuning steering correction reduced the corkscrew amplitude by over an order of magnitude. The effects of injector noise and misalignment are shown in Fig. 3. The BBU motion extends throughout the pulse as expected while the corkscrew amplitude is relatively unchanged from the no noise case.

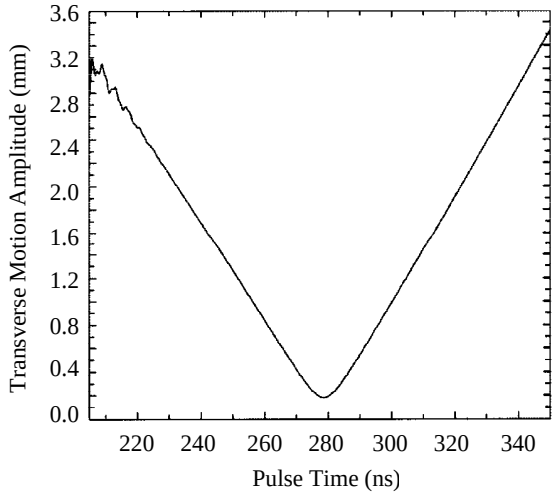

Figure 1. Simulated transverse beam centroid motion driven by misalignments with no steering correction.

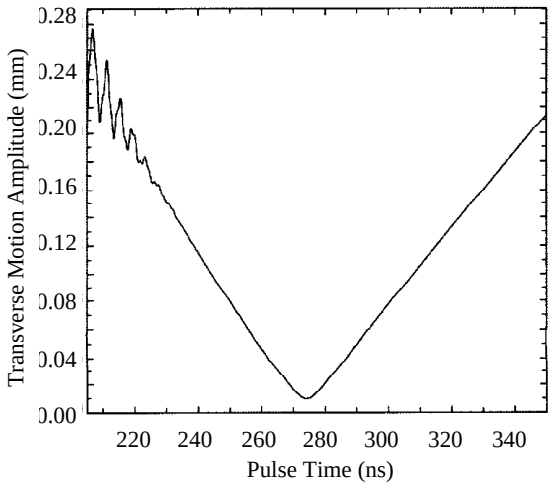

Figure 2. Simulated transverse beam centroid motion driven by misalignments with steering corrections. Note the change in vertical scaling from Fig. 1.

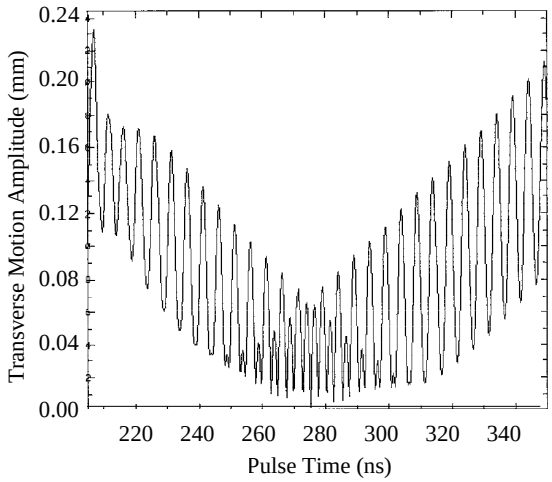

Figure 3. Simulated transverse beam centroid motion driven by misalignments and injector noise. V-tuning steering corrections used.

Results of the different configurations are summarized below. For all cases, the simulations included both misalignment and injector noise. The gain factor at the end of the first 8-cell block is listed in the results to emphasize the effect of the low focusing fields at the start of the accelerator. The first configuration modeled consisted of eleven 8-cell blocks with an aperture of 25.4 cm and used the "initial" cell impedance parameters. Results are shown in Table 2.

Table 2. BBU growth for "initial" accelerator cell design

Mode Frequency (MHz)	Gain Factor at exit of 1st block	Gain Factor at accelerator exit
262	2.9	132.7
672	2.1	115

Corkscrew amplitude at accelerator exit is 0.24 mm.

The second configuration modeled consisted of eleven 8-cell blocks with an aperture of 25.4 cm and used the "current" cell impedance parameters. Results are shown in Table 3.

Table 3. BBU growth for "current" accelerator cell design

Mode Frequency (MHz)	Gain Factor at exit of 1st block	Gain Factor at accelerator exit
200	3.1	34.3
535	3.1	34.3

Corkscrew amplitude at accelerator exit is 0.24 mm.

The third configuration modeled consisted of a 35.6 cm aperture 8-cell block followed by ten 8-cell blocks with apertures of 25.4. All cells used the "current" cell impedance parameters. Results are shown in Table 4.

Table 4. BBU with larger aperture first 8-cell block

Mode Frequency (MHz)	Gain Factor at exit of 1st block	Gain Factor at accelerator exit
170	1.9	12.2
200	1.5	10.7

Corkscrew amplitude at accelerator exit is 0.16 mm.

6 SUMMARY

Corkscrew motion can be kept well within design goals for the expected accelerator misalignments by applying the V-tuning algorithm. The BBU instability growth required the lower impedance characteristics associated with the larger aperture cells to stay below the desired gain factor. A possible factor not considered in the BBU growth is loss of the low energy head of the beam. This would lead to a faster rise time as the pulse travels down the accelerator. The gain factor will remain the same, so the issue is the magnitude of the shock excitation due to the short rise time and misalignments. If this excitation is no more than the injector noise, the BBU growth should remain within design goals.

7 ACKNOWLEDGMENTS

R. Briggs, G. Caporaso, D. Prono, and S. Yu provide valuable advice and guidance.

8 REFERENCES

[1] H. Rutkowski, "An Induction Linac for the Second Phase of DARHT", this conference MO2001.
[2] Y.-J. Chen, Nucl. Instr. and Meth. A 292 (1990) 455.
[3] Y.-J. Chen, Nucl. Instr. and Meth. A 398 (1997) 139.
[4] T. L. Houck, et. al., "Physics Design of the DARHT 2nd Axis Accelerator Cell," this conference TH4040.

EM-PIC SIMULATIONS OF e-BEAM INTERACTION WITH FIELD EMITTED IONS FROM BREMSSTRAHLUNG TARGETS*

P. W. Rambo and S. Brandon
Lawrence Livermore National Laboratory, Livermore CA 94550

Abstract

We investigate electron beam defocusing caused by field emitted ions from the bremsstrahlung target of a radiography machine using fully electromagnetic particle-in-cell simulations. This possibly deleterious effect is relevant to both current radiography machines (FXR) and machines being built (DARHT-2) or planned (AHF). A simple theory of the acceleration of ions desorbed from the heated target, and subsequent beam defocusing due to partial charge neutralization is in reasonable agreement with the more detailed simulations. For parameters corresponding to FXR (I_b=2.3 kA, ε_b=16 MeV), simulations assuming space-charge-limited emission of protons predict prompt beam defocusing. Time integrated spot-size measurement, however, is dominated by early-time small spot brightness, and so is not a sensitive diagnostic. Comparisons are made to available FXR data. We also investigate use of a recessed target geometry to mitigate field emitted ion acceleration; only modest improvements are predicted.

1 INTRODUCTION

Current radiography machines such as FXR, as well as future machines such as DARHT-2 and the proposed Advanced Hydrodynamic Facility (AHF), make use of an intense electron beam striking a high-Z target to generate high-energy bremsstrahlung radiation. It is necessary that the electron beam be focused to a small spot for good radiographic definition. In FXR and DARHT-2, and the proposed AHF machine, the beam is created in a linear induction accelerator (LIA), and is focused in a low applied-field drift region. Dale Welch [1] at MRC first identified a potential problem due to ion field emission for DARHT–2, arguing that target heating from the beam would quickly provide a source of ions which can be accelerated by the beam space-charge, and back stream toward the beam source. The excess charge neutralization then causes the beam to pinch, and subsequently defocus.We describe results from electromagnetic PIC simulations for FXR parameters, which predict prompt defocusing for space-charge-limited proton emission. Comparison to available experimental data suggests that the emission onset is substantially delayed in time or reduced from the space-charge-limit, if not absent entirely.

2 SPACE CHARGE LIMITED EMISSION AND BEAM DEFOCUSING

Welch has argued that once the target surface is heated beyond 400 °C, impurities are readily desorbed and ionized. These impurities, including both protons and carbon ions, are then free to be accelerated by the beam space charge potential. Nominally, FXR operates at a total current of I_b≈2.3 kA focused to a spot size of r_b≈0.1 cm; thus the current density is approximately J_b≈70 kA/cm^2 and particle flux J_b/e=5×10^{23} /cm^2·s. At the beam energy ε_b =16 MeV, ionization energy loss in Ta is $d\varepsilon/dx$≈20 MeV/cm at solid density, and the average energy increase per atom is approximately 0.2 eV/ns. Thus the target is very quickly heated, and any surface contaminants are expected to be available for ionization and subsequent acceleration.

A simple theory serves to estimate the properties of these emitted ions and their interaction with the electron beam; units are Gaussian, except where results in more convenient units are specifically indicated. Approximate the beam as a cylinder of radius r_b with uniform density n_b, both corresponding to the target focus. The beam is traveling at nearly the speed of light, c, with relativistic factor γ_b. The potential difference between the center of the beam and its edge, as well as the (radial) electric field are easily calculated; the axial field at the target will be approximately the same,

$$\Phi_b \approx \pi e n_b r_b^2 \approx I_b / c\,; \quad E_z \approx E_r = 2\Phi_b / r_b\,. \qquad (1)$$

For FXR parameters, this predicts an electric field at the target surface of order E_z≈1.4 MeV/cm. The current of emitted ions (mass $M_i=A_i m_p$ and charge $q_i=Z_i e$, with m_p the proton mass) may be estimated using the well known result for Child-Langmuir space-charge-limited current. Using the beam potential just estimated and a distance equal to the beam radius,

$$J_i \approx \frac{\left(2q_i / M_i\right)^{1/2} \Phi_b^{3/2}}{9\pi r_b^2}\,; \quad I_i \equiv \pi r_b^2 J_i\,, \qquad (2)$$

which predicts an emitted ion current I_i/I_b ≈0.2% for FXR. The ions are quickly accelerated to an energy of the order of the beam potential, and hence velocity $v_i=(2q_i\Phi_b/M_i)^{1/2}$. The ion density is then estimated from $n_i=J_i/v_i q_i$, showing the surprising result that the charge neutralization fraction f is a constant: f≈1/9. The contribution to the radial field from this ion charge is equal to the field generated by the beam decreased by the factor f, $E_+=fE_r$. In a time τ, the ions will move a length $L\approx\tau v_i$ and beam electrons will be radially accelerated as they traverse this distance to the target, t≈L/c. Equating the radial deflection to the beam radius gives an estimate for the time τ required to defocus the beam,

$$\delta r \approx \frac{1}{2}\frac{eE_+}{\gamma_b m_e}t^2 \approx \frac{1}{2}\frac{e}{\gamma_b m_e}\left(f\frac{2\Phi_b}{r_b}\right)\left(\frac{\tau v_i}{c}\right)^2 \equiv r_b\,, \qquad (3)$$

$$\tau \approx 5ns\frac{r_b(mm)}{I_b(kA)}\sqrt{\frac{\gamma_b A_i}{Z_i}}\,.$$

* This work was performed under the auspices of the U. S. Department of Energy by Lawrence Livermore National Laboratory under contract No. W-7405-Eng-48

For FXR parameters, this theory predicts a time to defocus of $\tau \approx 10$ ns for proton emission, well within the pulse time of 60 ns. Of course this theory is quite simplified; we next turn to self consistent simulations.

3 EM-PIC SIMULATIONS

Direct particle-in-cell (PIC) simulation of intense beams has a long and successful history, both at LLNL and elsewhere. We have simulated ion emission and subsequent beam defocusing with both CONDOR, a well-tested design code developed over many years within A-division, and a new code, CODA, that allows non-rectangular zones. Both codes are fully relativistic, 2-1/2 dimensional (2-spatial dimensions in axisymmetric *Z-R* geometry, 3-velocity dimensions) electromagnetic (EM) PIC codes. The simulation geometry is a cylinder of radius 4 cm and length 25 cm with conducting boundaries. The beam is injected at the left hand boundary with an initial radius of 2.0 cm, and with uniform current density. The beam is injected with finite emittance so as to be focused at the target; no externally applied fields are present. The injected beam current is linearly ramped up in 10 ns, constant for 40 ns, then linearly ramped down again in 10 ns. The right hand end-plate forms the absorbing target, from which ions are emitted. No modeling of the target heating or surface physics is included; the space-charge-limited emission is simply turned on at a preselected time, over a specified radial region. Simulations presented here were all performed with CODA utilizing a converging mesh that allows much better resolution at the target surface, $\Delta r = 200$ μm and $\Delta z = 600$ μm.

The time history of the RMS beam radius at the target is shown in Fig. 1 from a typical simulation. The injected beam is characteristic of FXR, with $I_b = 2.3$ kA, $\varepsilon_b = 16$ MeV ($\gamma_b \approx 32$) and initially focused to a root-mean squared (RMS) radius $r_b = 0.06$ cm. Proton emission is turned on at t=15 ns, in the region $0 < r < 0.06$ cm. The initial pinch and subsequent defocus occur very quickly in

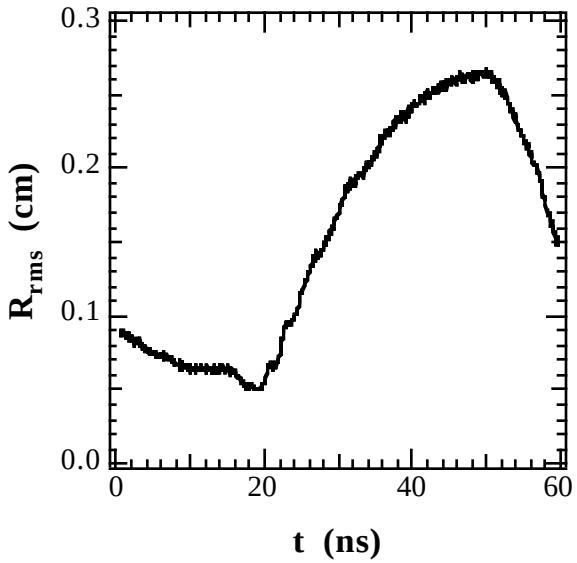

Fig. 1 Time dependent beam radius at target from a simulation of FXR with proton emission turned on at t=15ns.

agreement with our previous estimate. As the beam defocuses, emission decreases (from a peak of $I_i \approx 8$ A) because of the reduced electric field at the emission area. Many aspects of the simple theory previously developed are observed in these simulations, namely the magnitude of the axial electric field at the target surface, the time for pinching to occur, and the small ratio of emitted ion current to beam current (<1%). The scaling of the time to defocus, Eq. (3), with ion mass and beam current has also been confirmed by additional simulations. An important observation is that the total number of field emitted ions, N_i, is quite small: for this simulation $N_i = 5.7 \times 10^{11}$ at t=30 ns. This corresponds to a fraction of approximately 10^{-4} from a monolayer of equal area, suggesting that surface cleaning would be a very difficult proposition.

4 COMPARISON WITH FXR DATA

We now consider available data from FXR. Two principle measurements are used to assess spot quality at FXR; both are time-integrated radiographic measurements. The first uses an opaque "roll bar" to cast a shadow from the bremsstrahlung spot; the width of the edge of this shadow reflects the finite spot size. Careful unfolding of the data shows a central peak with FWHM spot size of 1.1mm, surrounded by a low density "halo" with relative brightness of a few percent of the central peak [2]. In the second measurement, forward bremsstrahlung dose is measured both with and without an 800 μm diameter collimator. The collimated dose is observed to be approximately 1/3 of the forward dose in the absence of the collimator; this is observed to be the case both for beam currents of 2.3 kA and 3.3 kA [3].

Although the experimentally observed small spot seems at odds with the defocusing seen in the simulations, e.g. Fig. 1, this is not necessarily so. Because the beam density at the target is inversely proportional to the square of the spot size, $n_b \propto I/r^2$, the bremsstrahlung emission from the defocused beam is very dim and a time integrated measurement can be dominated by the early-time small spot brightness. In Figure 2, we show the time integrated beam density at the target (normalized) as a function of radius from the simulation illustrated in Fig. 1. As can be seen, the contribution from the defocused beam is a low density halo. The level of the halo relative to the central peak is determined by the relative duration of the focused and unfocused periods of the time history. This is illustrated in Fig. 2, which also shows results from simulations with the ion emission turned on at 10 and 30 ns. The level of the halo is also affected by the defocused radius; allowing ion emission from a larger area increases the defocused beam spot, decreasing the relative beam density in the halo.

We next consider the collimated dose measurements. The angular spectrum of bremsstrahlung photons created by 16 MeV electrons striking a 1mm thick Ta target was calculated using a Monte Carlo code [4]; this angular spectrum is then used to determine the contribution to the forward dose from each simulation electron as it strikes the target. Figure 3 shows the time dependent forward

dose (normalized) for the simulation shown in Fig. 1. Because the electrons strike the target with larger angles

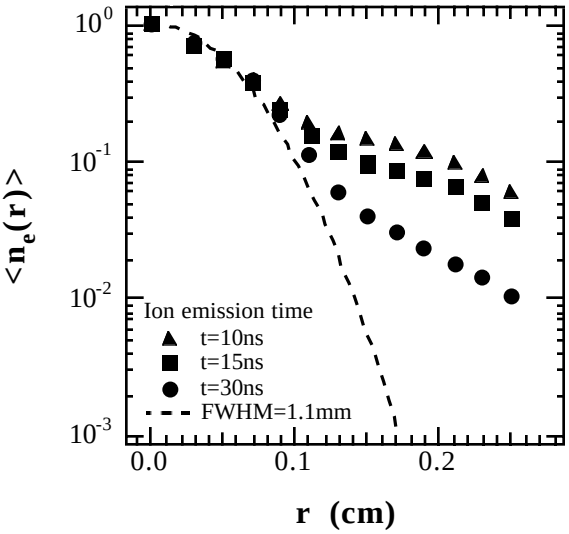

Fig. 2 Time averaged beam density at target from FXR simulations including proton emission; three different emission onset times are shown.

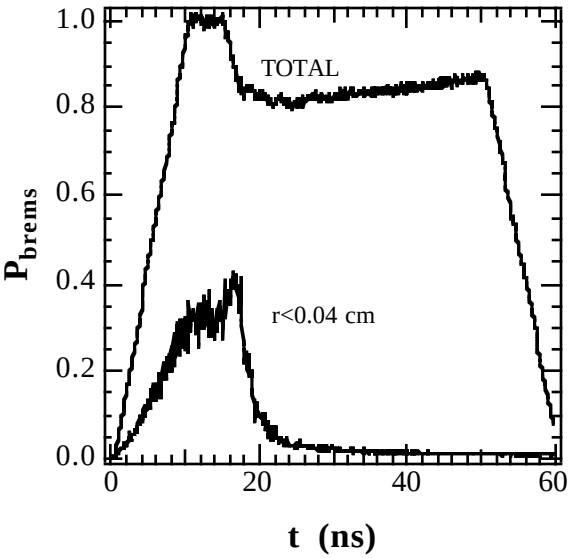

Fig. 3 Time dependent forward dose from FXR simulation including proton emission for t>15 ns.

after pinching, the total forward dose decreases approximately 20%. More importantly, however, the forward dose from electrons striking the target with r<400 μm is abruptly cut-off as the spot size increases. For this case the time integrated forward dose from electrons entering the target with r<400 μm is 0.14 of the total calculated forward dose. Again, this fraction varies with the onset time for ion emission; for onset times of 10 ns and 30 ns (see Fig. 2) the forward dose fractions are 0.10 and 0.23 respectively. With the beam current increased to I_b=3.3 kA, similar results are obtained except that the forward dose fraction is further decreased: for proton emission onset times of 15 ns and 30 ns the forward dose fractions are 0.11 and 0.20 respectively. The forward dose fraction for these simulations in the absence of ion emission is 0.30. Decreasing the focused beam radius to r_{RMS}= 0.05 cm (by decreasing the injection emittance) increases the unperturbed fractional transmission to 0.40; for this focus and I_b=3.3 kA, proton emission turned on at t=30 ns decreases the time integrated fractional forward dose to 0.26. Further decrease of the focused beam radius would be in disagreement with the spot size measurements.

Simulations were also performed with singly ionized carbon emission for comparison. Turning on C^+ emission at t=15ns for the I_b=3.3 kA case gives a forward dose fraction of 0.20 due to the slower defocusing, still significantly less than observed; delaying the C^+ emission until t=30 ns results in a forward dose fraction of 0.28.

5 DISCUSSION

We have seen from simulations with parameters relevant to FXR, that beam defocusing occurs quickly after the onset of proton emission. Time integrated spot size measurements are not a sensitive measure of defocusing, however, because the defocused beam only contributes a dim halo compared to the central peak from the small spot emission. But the level of the halo, observed to be a few percent relative to the central peak in FXR measurements, does rule out prompt proton emission, t<15 ns. The collimated dose is a more stringent test. Proton emission beginning at time earlier than t≈30 ns is inconsistent with the observation that one third of the forward dose is transmitted through an 800 μm collimator. Bounds on the emission of singly ionized carbon are only slightly less restrictive.

The simplest explanation is that ion emission is not occurring on FXR, or at currents reduced far below the space charge limit (approximately a factor of 30 decrease is necessary). This does not preclude a disastrous effect on machines with higher current densities, however, since there may still be a threshold for ion formation. Because of this, methods to minimize this effect are being pursued. In particular, we have simulated the effect of recessing the target so as to reduce the emitted ion current. Although the time for defocusing is increased, and the defocused beam spot size decreased, this still does not appear to be satisfactory. Used in conjunction with other means for isolating the emitted ions, however, might be acceptable. We look forward to experimental results from ETA-II (to be reported at this conference), including time resolved measurements that may give a more definitive answer concerning these effects.

ACKNOWLEDGMENTS

The authors wish to acknowledge numerous useful discussions with Y.-J. Chen, G. Caporaso, N. Back, R. Scarpetti, M. Aufderheide, D. Ho, and P. Bergstrom.

REFERENCES

[1] D. R. Welch, "Effects of electron-ion streaming due to beam-target interactions," presented at the DARHT-2 Review (January 16, 1997).
[2] N. Back, internal memorandum (March 24, 1997).
[3] R. Scarpetti, private communication (May 14, 1998).
[4] P. Bergstrom, private communication (October 3, 1997).

TRANSVERSE WAKEFIELD EFFECT MEASUREMENT VIA MODEL-INDEPENDENT ANALYSIS *

John Irwin, Chun-xi Wang, Karl Bane, Yiton Yan, Michiko Minty, Franz J. Decker, Gennady Stupakov
Stanford Linear Accelerator Center, Stanford University, Stanford, CA 94309 USA

Abstract

Transverse wakefield effects due to structure misalignments can be an important source of emittance degradation in a linear collider. Though important, it is difficult to measure local wakefield effects and identify the sources. Recently, we have developed a novel method for analyzing the beam dynamics in an accelerator based on BPM readings, that is independent of any machine models. This method relies on, instead, statistically analyzing an ensemble of readings from a large number of BPMs and for a large number of pulses. In addition, pulse-by-pulse information of beam (and machine) parameters are used. By taking advantage of the spatial correlation and temporal structure of all these signals, such analysis allows observation of beam dynamics at a level well below the single BPM resolution as well as studies of subtle beam dynamics effects. Using this method, which is quick and non-invasive, we are able to measure the transverse wakefield effects due to structure misalignments in the SLC linac.

1 INTRODUCTION

A beam, when passing by a misaligned accelerator structure, will excite transverse wakefields that kick different parts of the beam by different amounts and therefore blow up the beam emmittance. Such a wakefield effect can be a major source of luminosity degradation in a linear collider. However, it is very difficult to measure transverse wakefield effects due to the weakness of the signals and the difficulty of separating such effects from other sources of perturbations. Using the current dependency of the wakefield, one can separate the wakefield effects from other effects. One idea is to measure beam orbits at different currents and then calculate the difference. Unfortunately, such measurements hardly succeed. One reason is the limited resolution in orbit measurements. More importantly, when beam current is changed, many other beam parameters (as well as the orbit) will be changed also. To avoid problems coming with current change, bunch length change has been used but with limited success. To illustrate this problem, Table 1 shows the correlations of current (bunch length) change with other beam parameters that we are able to monitor in the linac of Stanford Linear Collider (SLC). It was computed with 5000 electron pulses collected under normal running conditions. Clearly such correlations have to be taken into account in order to measure the wakefield effects correctly.

* Work supported by the Department of Energy under Contract No. DE-AC03-76SF00515

Table 1: Correlation coefficients of beam current and bunch length with other beam parameters

	current ΔI	bunch length σ_z
horizontal position x	-0.17	-0.52
horizontal angle x'	-0.03	-0.15
vertical position y	-0.08	0.01
vertical angle y'	0.10	0.20
long. beam phase	-0.48	-0.20
beam energy	-0.37	-0.18
bunch length	0.05	1
beam current	1	-0.05

Recently, a novel approach to analyze beam dynamics has been developed which we call "Model Independent Analysis (MIA)". It is a statistical analysis of BPM data and does not rely on any particular machine model. There are two major parts in MIA. One is noise reduction and degree-of-freedom analysis via singular value decomposition of a BPM-reading matrix. The other is a physical base decomposition of the BPM-reading matrix based on the time structure of beam (and machine) parameters. The combination of these two methods allows one to go below the resolution limit set by individual BPMs and to observe the beam dynamics at a much finer level. Physical base decomposition is particularly useful for understanding various beam dynamics issues, because it takes all known signal correlations into accounts. In the next section we describe MIA. Then, in the following section we apply MIA to obtain information about the structure misalignments in the SLC linac and their transverse wakefield effects.

2 MODEL INDEPENDENT ANALYSIS [1]

The transverse beam position of a pulse depends on various physical variables such as the initial conditions of the pulse, the settings of magnets, and the RF conditions. We can Taylor expand the beam position b over all variables as

$$b = b(\bar{x}_1, \bar{x}'_1, \bar{\delta}, \bar{\sigma}_z, \cdots) + \sum_{v \in \{x_1, x'_1, \cdots\}} \left.\frac{\partial b}{\partial v}\right|_{v=\bar{v}} \Delta v + \frac{1}{2} \sum_{v_1, v_2 \in \{x_1, x'_1, \cdots\}} \left.\frac{\partial^2 b}{\partial v_2 \partial v_1}\right|_{\substack{v_1=\bar{v}_1 \\ v_2=\bar{v}_2}} \Delta v_1 \Delta v_2 + \cdots \quad (1)$$

where x_1, x'_1, δ, σ_z are respectively initial beam position, angle, relative energy, and bunch length, given as examples of possible physical variables; the over bar indicates the expansion points; $\Delta v = v - \bar{v}$ and so on. The zero order term may have complicated dependency on the variables

and is sensitive to the unknown BPM offset errors. To get rid of it, we subtract the average over a large ensemble of pulses and study the difference

$$b - \langle b\rangle = \sum_v \left.\frac{\partial b}{\partial v}\right|_{v=\bar v} (\Delta v - \langle \Delta v\rangle) + \frac{1}{2}\sum_{v_1,v_2} \left.\frac{\partial^2 b}{\partial v_2 \partial v_1}\right|_{\substack{v_1=\bar v_1\\ v_2=\bar v_2}} (\Delta v_1 \Delta v_2 - \langle \Delta v_1 \Delta v_2\rangle) \quad (2)$$

where $\langle\ \rangle$ indicates the average over an ensemble of pulses. Although we have found that some second derivatives (which characterize, e.g. the chromatic dependency of the betatron motion) may be significant at times, the third and higher order terms are generally negligible and will be dropped. We treat the first and second order terms on the same footing and rewrite Eq.(2) in a concise form:

$$b - \langle b\rangle = \sum_{\{q\}} q\, f_q \quad (3)$$

where the variable $q = \frac{\Delta v - \langle \Delta v\rangle}{\mathrm{std}(\Delta v)}$ or $\frac{\Delta v_1 \Delta v_2 - \langle \Delta v_1 \Delta v_2\rangle}{\mathrm{std}(\Delta v_1 \Delta v_2)}$ and f_q is the corresponding derivative $\left.\frac{\partial b}{\partial v}\right|_{\bar v} \cdot \mathrm{std}(\Delta v)$ or $\frac{1}{2}\left.\frac{\partial^2 b}{\partial v_2 \partial v_1}\right|_{\bar v_1,\bar v_2} \cdot \mathrm{std}(\Delta v_1 \Delta v_2)$. The physical variables are normalized by their standard deviations over the ensemble of pulses, so that all the q's are dimensionless and reflect the relative changes, while all the f's have the same dimension as the BPM readings.

For an ensemble of P pulses monitored with M BPMs, according to Eq.(3), the BPM-reading matrix B, consisting of $b - \langle b\rangle$, can be factorized as

$$B = QF^T + N \quad (4)$$

where $Q_{P\times d} = [\vec q_1, \cdots, \vec q_d]$, $F_{M\times d} = [\vec f_1, \cdots, \vec f_d]$, and $N_{P\times M}$ contains the noise associated with each BPM reading. The column vector $\vec q_i$ contains the P values of the i-th physical variable and $\vec f_i$ contains the M components of the corresponding physical pattern. The q's are referred to as temporal patterns or time structures of the pulses, while the f's as spatial patterns or physical vectors. Note that the BPM-reading matrix B is the central object of MIA analysis. Eq.(4) is called the physical base decomposition.

We assume all the physical vectors are linearly independent, i.e. F has full column rank given by d. They form a complete basis for the row space of the BPM-reading matrix (i.e. range of B^T). Unlike P and M which can be chosen at will, dimension d is determined by the dynamics. One of the MIA achievements is to determine d. Generally, d is a small number and, we choose P and M so that $d \ll M \ll P$ to obtain statistical benefits. Typical numbers that we use are $d \sim 10$, $M \sim 10^2$, and $P \sim 10^3$. For convenience, we normalize B, Q, and N by $\sqrt{P}$, so that the important (variance-)covariance matrices of BPM readings and temporal patterns (q's) can be formed simply as $C_B = B^TB$ and $C_Q = Q^TQ$.

According to Eq.(3), a beam orbit is a linear combination of a limited number of "basic" orbits given by the f_qs. In other words, the BPM reading pattern generated by each pulse is a superposition of certain basic patterns. This fact allows us to apply linear algebra concepts and matrix analysis techniques to the BPM data analysis. The statistical meaning of C_B and C_Q provides the connection between matrix analysis and statistical analysis.

Though SVD analysis of the BPM-reading matrix B (statistically, it is the principle components analysis of BPM readings) is a major aspect of MIA, it will not be described here due to space limitation. However this analysis is not crucial in the discussion of the wakefield effect measurements. What we will use is physical base decomposition of B using various kinds of pulse-by-pulse beam and machine parameters as tags –signals form a subset of the matrix Q. Mathematically, we know Q (or a subset of it) and B of Eq.(4), and need to solve for F. If we know all the physical variables with sufficient accuracy, the corresponding physical basis can be computed as

$$F^T = (Q^TQ)^{-1}Q^TB = C_Q^{-1}Q^TB \quad (5)$$

and the errors due to noise are generally proportional to $\frac{1}{\sqrt{P}}$. The first expression reflects the least-squares fitting aspect of the solution, while the second expression emphasizes the importance of taking care of correlations among the observed variables.

The accuracy of Eq.(5) does not rely on the number of BPMs used. It simply fits each BPM reading to various temporal patterns individually and ignores any correlations among BPM readings. In fact, the BPM noise can be reduced statistically by taking into account the correlations among BPM readings. Therefore, if we cut the noise first and then apply Eq.(5), the noise level can potentially be reduced by a factor of $\frac{1}{\sqrt{M}}$, and we have

$$F^T = C_Q^{-1}Q^TU\,\underline{S}V^T + O(\frac{1}{\sqrt{P\,M}}) \quad (6)$$

where USV^T is the SVD of B, and $\underline{S}$ indicates the zeroing of small singular values that are due to noise. This statistical error limit may be hard to achieve however due to problems such as machine instability and incomplete information in Q.

Usually we know only a subset of Q, say Q_s of $Q = [Q_s, Q_r]$. We can still calculate F_s according to Eq.(5) with Q_s, The error due to the missing part is

$$(F_s - F_s^{exact})^T = (Q_s^TQ_s)^{-1}Q_s^TQ_rF_r^T \quad (7)$$

Therefore, if the known subset Q_s are uncorrelated with (orthogonal to) the remaining unknown temporal patterns, i.e. $Q_s^TQ_r = 0$, then we would obtain the same results as if we had measured all Q. Otherwise, the unknown part of the physical basis (i.e. F_r) will be mixed into the measured parts. This is the major limitation of this method.

3 TRANSVERSE WAKEFIELD EFFECT MEASUREMENT

Because of the detrimental effects of transverse wakefield due to structure misalignments, various methods [2, 3] have been used for the detection and correction of such wakefield effects. In the following, we present some preliminary results where MIA is used to measure the transverse wakefield effects. At the SLC, in addition to the beam transverse position, we can monitor beam current, bunch length, incoming beam (longitudinal) phase, and relative beam energy on a pulse-by-pulse basis. Other signals such as klystron phases along the linac have not been used in the present analysis. As is shown in Table 1, there are significant correlations among these signals, especially for the wakefield sensitive variables. MIA takes all known correlations into account, and therefore should provide a better measurement of the wakefield effects. To investigate this, we generated a 5 corrector, 1.2mm, local bump in the linac of SLC and measured its wakefield effect via MIA. We used readings from the beginning to about the 1/3 point of the linac (LI02–LI13), and collected 3 sets of 5000 pulses under the conditions: before the bump was applied (a), after it was applied (b), and after the bump was removed (c). Each set of data took a few minutes to collect.

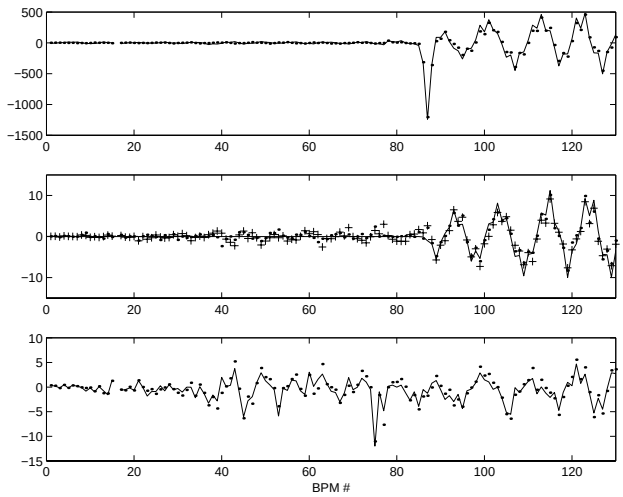

Figure 1: wakefield effect measurements in vertical plane

We applied MIA on all sets of data and then compared the vectors corresponding to the current jitter, and the results in y are shown in Figure 1 (all ordinate units are in μm). The top frame shows the differences of the averaged beam orbits. The solid line shows the difference between conditions b and a, while the dots are between conditions b and c. The corrector bump is clearly visible (it is not closed). The middle frame shows the difference of current vectors–the vectors correponding to current jitter. The dots are the differences between b and a, while the crosses are between b and c. The solid curve shows the calculated wakefield effect due to the bump. We see that the agreements are fairly good, especially when considering the fact that the BPM resolution is about 10 μm, which is as large as the signals. Furthermore, no external beam perturbation was used, and the signal is a rather weak 1.3% natural current jitter. As far as we know, such accurate transverse wakefield effect measurements in a linac are unprecedented. Note that the errors are on the order of a few microns, which is much larger than the statistical limit. Therefore, it is still possible to further improve both measurement and analysis. Frames 1 and 2 demonstrate that the current vectors obtained via Eq.(5) are correct. The bottom frame shows the current vectors of conditions a and c, which are the wakefield effects due to misalignments (and corrector offsets, etc.) in the normal running machine. An immediate application of such current vectors is the detection of structure misalignments and confirmation of wakefield calculations.

We performed a similar analysis in x also. We found that, one set of results agrees with the calculation while another has much larger deviations. The discrepancy in the horizontal cases may be due to some unknown jitter sources that are correlated with the current. We repeated these experiments several weeks later and obtained similar results in both the vertical and horizontal planes.

Our measurement results are still preliminary because limited machine time prevented us from thorough investigation. Nonetheless, they are very encouraging and promising. Since such measurements need not perturb the beam, they are basically non-invasive to normal machine operation and in principle can be done parasitically and quickly after the method matures. On the other hand, intentionally introduced larger current variation will improve the sensitivity to the misalignments. This method can potentially become a powerful tool for finding structure misalignments.

4 ACKNOWLEDGMENTS

We would like to thank M. Ross and N. Phinney as well as the SLC operation crew for their support. Special thanks is due to L. Hendrickson for her updating the SLC solo control program (SCP) to support our data acquisition. We would also like to acknowledge A. Chao, M. Lee, P. Raimondi, S. Smith, F. Zimmermann, and P. Tenenbaum for helpful discussions.

5 REFERENCES

[1] A comprehensive documentation of MIA will soon be published under the title “Model independent analysis of beam dynamics in accelerators”

[2] T.O. Raubenheimer, K. Kubo, “A technique for measuring and correcting emittance dilutions due to accelerator structure misalignments,” NIM A370, p. 303-311

[3] F.-J. Decker, et al., “Super-ASSET: a technique for measuring and correcting accelerator structure misalignments at the SLC,” Proceedings of PAC97

MULTIPLE COUPLING AND BEAM LOADING OF A RF CAVITY

H. Safa
Los Alamos National Laboratory, Los Alamos, 87545, NM, USA
& C.E.A. Saclay, 91191 Gif/Yvette Cedex, France

Abstract
Future high power accelerators are aiming at increasing the power transferred to the beam through radiofrequency (RF) cavities. Consequently, multiple main coupler drives may be required to withstand the high RF power needed per cavity. An analysis including multiple couplers and beam loading is described here, featuring the interaction between all couplers, the beam and the cavity. In this description, the beam is shown to act as if it were merely an additional drive for the cavity. Special focus is given to the case of superconducting cavities in a continuous (CW) operation mode. Some important conclusions derived from this analysis are briefly discussed as, for example, power coupler fault conditions or a way to handle the commissioning of an accelerator in a CW mode.

1 INTRODUCTION

The superconducting radiofrequency APT (Accelerator Production of Tritium) cavities will be driven simultaneously by two power couplers. Consequently, an analysis involving multiple couplers will be needed to understand the behavior of the interaction between the beam, the cavity and all the couplers, extending the beam loading introduction given in reference [**1**].

2 CAVITY, BEAM AND COUPLERS

Standard notations will be used to define the cavity parameters. If W is the stored energy, P_c the dissipated power and ω_0 the resonance pulsation ($\omega_0 = 2\pi F_0$), then the shunt impedance R and the quality factor Q_0 are defined by $P_c = |V_c|^2 / 2R$ and $Q_0 = \omega_0 \tau_0 = \omega_0 W / P_c$, $\tau_0 = Q_0/\omega_0$ is the filling time of the cavity. A superconducting cavity will have a very high R ($10^{12}\ \Omega$) compared to a normal copper cavity ($5.10^6\ \Omega$). This reduction of losses by more than 10^5 will increase the cavity filling time and the available beam power by the same amount. The cavity voltage V_c is arbitrarily defined through the effective length *l* of the cavity and the effective accelerating field E_{acc} :

$$V_c = E_{acc}\, l \qquad (1)$$

The cavity impedance is

$$Z_0 = \frac{R}{1 + jQ_0\left(\frac{\omega}{\omega_0} - \frac{\omega_0}{\omega}\right)} \cong \frac{R}{1 + jQ_0\frac{2\Delta\omega}{\omega_0}} \qquad (2)$$

If the injected time of a particle passing through the cavity is shifted by $\delta t = \phi/\omega$ as compared to the maximum energy gain, then the accelerating voltage will be

$$V_{acc} = V_c \cos\phi \qquad (3)$$

It can be shown that the induced voltage of a crossing particle with charge q on each mode of the cavity will simply reduce to $V_{ind} = -q\,(R/Q)\,\omega_0$ and the corresponding energy deposited $W = (R/Q)\omega_0 q^2/2$ will decay after the particle had passed with the time constant τ_0. Therefore, in a steady state regime, a current beam I_b will induce a total voltage $V_0 = -R\, I_b$. The induced voltage is always decelerating the particles. The beam can then be merely seen as a drive line having a fixed current source I_b with an equivalent voltage V_0 and will therefore be labeled drive 0 from now on. Let us now consider many RF lines (labeled 1,2,k) with characteristic impedances Z_{ck} coupled to the cavity through a coupling factor β_k. The external Q of each line k is defined as $Q_k = Q_0/\beta_k$ and the loaded quality factor Q_l results from $Q_l^{-1} = (\sum Q_k^{-1})$. Introducing the alpha coefficients $\alpha_k = Q_l/Q_k = \alpha_0\beta_k$, these will always be between 0 and 1[a], and obey the closure relation $\sum_k \alpha_k = 1$. The cavity detuning angle ψ is, by definition, $\tan\psi = -Q_l\,(2\Delta\omega/\omega_0)$. Each drive k will see the cavity impedance Z_0 in parallel with all the other drive impedances transformed to the cavity (R/β_m) through its own coupling coefficient β_k (Fig. 1). Consequently, drive k will see the overall impedance :

$$Z = \left(\frac{\beta_k Z_{ck}}{R}\right)\frac{1}{\frac{1}{Z_0} + \sum_{m\neq 0,k}\frac{\beta_m}{R}} = \frac{\alpha_k Z_{ck}}{(1-\alpha_k) - j\tan\psi} \qquad (4)$$

Therefore, the reflection coefficient ρ_k of drive k will be :

$$\rho_k = 2\alpha_k \cos\psi\, e^{j\psi} - 1 \qquad (5)$$

In order to get the different RF powers traveling on each line, we will use the incident and reflected voltages normalized to their relative coupling coefficient, that is $\left(V_{ik}/\sqrt{\beta_k}\right)$ and $\left(V_{rk}/\sqrt{\beta_k}\right)$. Each normalized drive should exhibit the same voltage $\frac{\left(V_{ik} + V_{rk}\right)}{\sqrt{\alpha_k}} = \text{constant}$. The cavity voltage is $V_c = V_{i\,0} + V_{r\,0}$, equal to the sum of all the induced voltages from each drive :

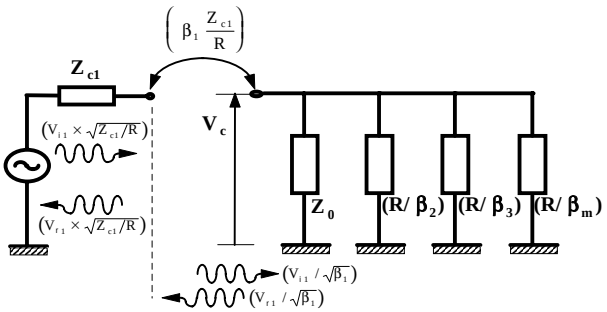

Figure 1. Impedance transform as seen from drive 1.

[a] This is an advantage over the use of the β (those can be infinite) as it significantly reduces computation errors.

$$\frac{V_c}{\sqrt{\alpha_0}} = \sum_m (1+\rho_m)\frac{V_{im}}{\sqrt{\alpha_m}} = \frac{(V_{ik}+V_{rk})}{\sqrt{\alpha_k}} \quad (6)$$

The above basic equations (6) will give all the return voltages including the cavity one. Once the incident powers (with their phases) and the coupling coefficients α_k are set, all the reflected powers in each line, the beam power and the cavity accelerating field may be deduced.

3 EXAMPLE OF TWO COUPLERS

Let us look more deeply at the case where two couplers are driving a single cavity. If the injected powers are P_1 and P_2 with phases θ_1 and θ_2, then, the corresponding normalized incident voltages are :

$$\begin{cases} V_{i1} = \sqrt{2RP_1}\, e^{j\theta_1} \\ V_{i2} = \sqrt{2RP_2}\, e^{j\theta_2} \end{cases} \quad (7)$$

And the reflected voltages derived from equations (6) :

$$\begin{cases} \frac{|V_c|e^{j\phi}}{\sqrt{\alpha_0}} = 2\alpha_0\cos\psi e^{j\psi}\frac{|V_{i0}|e^{j\theta_0}}{\sqrt{\alpha_0}} + 2\alpha_1\cos\psi e^{j\psi}\frac{|V_{i1}|e^{j\theta_1}}{\sqrt{\alpha_1}} + 2\alpha_2\cos\psi e^{j\psi}\frac{|V_{i2}|e^{j\theta_2}}{\sqrt{\alpha_2}} \\ \frac{V_{r1}}{\sqrt{\alpha_1}} = 2\alpha_0\cos\psi e^{j\psi}\frac{|V_{i0}|e^{j\theta_0}}{\sqrt{\alpha_0}} + \left(2\alpha_1\cos\psi e^{j\psi}-1\right)\frac{|V_{i1}|e^{j\theta_1}}{\sqrt{\alpha_1}} + 2\alpha_2\cos\psi e^{j\psi}\frac{|V_{i2}|e^{j\theta_2}}{\sqrt{\alpha_2}} \\ \frac{V_{r2}}{\sqrt{\alpha_2}} = 2\alpha_0\cos\psi e^{j\psi}\frac{|V_{i0}|e^{j\theta_0}}{\sqrt{\alpha_0}} + 2\alpha_1\cos\psi e^{j\psi}\frac{|V_{i1}|e^{j\theta_1}}{\sqrt{\alpha_1}} + \left(2\alpha_2\cos\psi e^{j\psi}-1\right)\frac{|V_{i2}|e^{j\theta_2}}{\sqrt{\alpha_2}} \end{cases} \quad (8)$$

The cavity voltage phase is, like in equation (3), noted ϕ, the reference phase taken opposite to the beam induced voltage, $V_{i0} = -R\, I_b$ with $\theta_0 = \pi$. The cavity power is $P_c = |V_c|^2/2R$, the beam power $P_b = \mathrm{Re}(V_c I_b^*) = |V_c| I_b \cos\phi$, and $\sum_k (P_{ik} - P_{rk}) = \sum_{k\neq 0}(P_{ik} - P_{rk}) - (P_c + P_b) = 0$ show that power is conserved. The reflected voltages are :

$$V_{rk} = \sqrt{\beta_k}\, V_c - V_{ik} \quad (9)$$

To minimize the generator power, all V_{rk} should be set to zero. That imposes to have for any line k :

$$\begin{cases} \theta_k = \phi \\ V_{ik} = \sqrt{\beta_k}\, V_c \end{cases} \quad (10)$$

And the external Q of each line have to be chosen so that

$$Q_k = \frac{P_c}{P_{ik}} Q_0 = \frac{|V_c|^2}{2(R/Q)P_{ik}} \quad (11)$$

A specific relation follows between the detuning angle ψ of the cavity and the beam phase ϕ :

$$\tan\psi = -(1-2\alpha_0)\tan\phi \quad (12)$$

In particular, if ($\alpha_0 = 1/2$), corresponding to the case of a matched single coupler ($Q_1 = Q_0$), then $\psi = 0$ for any phase ϕ. Whereas if ($\alpha_0 \ll 1$), general case for running a superconducting cavity with beam ($Q_0 \gg Q_1$), then $\psi \approx -\phi$. The cavity will have to be detuned by an angle equal to the opposite of the beam phase. For the APT cavities, where the beam phase is (- 30 degrees), this corresponds to a frequency shift of 947 Hz off resonance.

4 SENSITIVITIES

In order to match the beam, external couplings have to be adjusted using (11), powers and phases using (10), and detuning frequency using (12). Correlatively, the cavity voltage V_c and the phase beam ϕ will be the desired ones. Table I gives the sensitivity of each parameter.

Parameter	Nominal Values	Drive Phase	Drive Power	External Q	Beam Current
Variation	-	$\theta_i = \theta_{i\,nom} + - 10°$	$P_i = P_{i\,nom}(1+ -10\%)$	$Q_i = Q_{i\,nom}(1+ -10\%)$	$I_b = I_{b\,nom}(1+ -10\%)$
P_1 Reflected (W)	0	1500	119	472	2097
P_2 Reflected (W)	0	4872	393	0	2097
Beam Power (kW)	420	414	420 + - 20	420	416
Phase Angle Φ (°)	-30	-30 + - 7,7	-30 - + 1,15	-30 + - 0,02	-30 + - 5,1
Energy Gain (MeV)	4,20	4,14	4,20 + - 0,20	4,20	4,20 - + 0,42

Table I - Sensitivities of reflected powers, beam power, phase angle and energy gain on various parameters.

One can notice the importance of the drive phases. If the maximum allowable reflected power is for example 1‰ (200 W), they should be set equal to the phase angle ϕ to better than 2 degrees. Whereas the drive power, the external Q or the beam current may vary by as much as 6.3% for the same amount of reflection. Note the negligible effect of an external Q variation on ϕ. As a matter of fact, one can even get by without any adjustable coupling. Coupling can be pre-adjusted for each cavity, taking in account the variation of (R/Q) along the linac. Fixed coupling has the advantage of simplicity, reliability, and can avoid unwanted failures. On the other hand, adjustable coupling may reduce the total AC power consumption of the accelerator when operated at reduced current (at half current of 50 mA, a fixed coupling would require 12%[b] more RF power than an adjustable coupler).

5 FAULT SCENARIOS

5.1 Beam Failure

If the beam trips, then the couplers will have to withstand almost full reflection. The accelerating energy gain will exactly double in the cavity. The energy increase will rise with the time constant $\tau = \alpha_0\tau_0$ (46 μs for the 0.82 cavity). The amplitude control loop of the cavity should correct and bring back the voltage to its nominal value. This RF control feedback has generally a bandwidth exceeding 10 kHz and should easily compensate for the field variation. Therefore, the couplers will see the full 210 kW reflection only for about tens of microseconds, while hundred of microseconds after beam failure, the RF drive should be set back to 105 kW per coupler (again with full reflection). By that time, the RF drive can be shut down. Consequently, beam failure has no severe impact, provided RF control ensure that the cavity field would not exceed a given level.

5.2 Cavity Failure

The cavity may fail in many ways. It may experience a sudden change in its resonance frequency (due to mechanical stress or pressure), it may leak, it may exhibit field emission and finally it may quench. In the case of a quench, we are back to the above discussion during beam trip and that should be handled by a quench interlock. A

[b] This reduces to 9% for the whole accelerator taking in account the warm section, the cryoplant load and klystron efficiency.

shift in the resonance frequency would mainly impact the phase and should be corrected by the phase loop. If field emission occurs (inducing excessive Q losses and/or high X-ray levels), then the impact should be minimal. No effect will be seen on the couplers. The Q losses will induce higher cryogenic losses and the X-ray level can be monitored. In either case, the cavity field can be reduced accordingly to an acceptable level without having to react promptly by shutting down the RF or the beam (Here, one may allow a slow reaction time). Finally, in the case of a leak, a vacuum interlock should be set.

5.3 RF Power Failure

The RF system failure may concern power supply, klystron, circulator, divider or waveguide. In any case, the klystron is turned off. Cavity voltage will then be exactly opposite to the one without beam, the beam inducing exactly as much power as what it has been designed to receive. The required action is to detune the cavity far enough from resonance, reducing the beam induced voltage. A detuning frequency of 10 bandwidths (34 kHz) will reduce the beam power loss to less than 0.65% (1.37 kW).

5.4 Coupler Failure

The coupler might fail either because of a window problem (ceramic cracking, multipacting, breakdown, ...) or because of the coaxial part itself (breakdown, leaks, cooling, high dissipation, multipacting, ...). A coupler failure might lead to a serious failure (case of a leak, for example) where the beam and RF should be shut down and the cavity isolated.

6 ACCELERATOR COMMISSIONING

During commissioning, one might use either a pulsed beam and increase the duty cycle, or start at a very low CW current slowly increasing to reach its nominal value. Let us examine this latter case. In order to get the same accelerating energy and the same phase angle ϕ in the cavity, equations (8) give

$$\left|V_c\right|e^{-j\psi} = -2\alpha_0 \cos\psi R I_b e^{-j\phi} + 2\sqrt{\alpha_0\alpha_1}\cos\psi\left|V_{i1}\right| + 2\sqrt{\alpha_0\alpha_2}\cos\psi\left|V_{i2}\right| \quad (13)$$

If one recalls that the nominal value of cavity voltage for the nominal beam current I_{bnom} is

$$V_c = 2\alpha_0 \cos\phi\,(RI_{bnom}) \quad (14)$$

then, taking the imaginary part of (13) leads to the relation $\tan\psi = -(I_b/I_{bnom})\tan\phi$ which is equivalent to :

$$\left(\frac{\Delta F}{F}\right) = \frac{\tan\phi}{2Q_l}\left(\frac{I_b}{I_{bnom}}\right) \quad (15)$$

Therefore, the cavity frequency shift should be kept proportional to the current beam.

Taking the real part of (13) and using (14) with the nominal input voltages given by (10), one gets

$$2\left(\alpha_1\left|\frac{V_{i1}}{V_{i1nom}}\right| + \alpha_2\left|\frac{V_{i2}}{V_{i2nom}}\right|\right) = \left(1+\frac{I_b}{I_{bnom}}\right) \quad (16)$$

which, considering that the two ratios are identical, gives the input powers on each coupler

$$\left(\frac{P_{ik}}{P_{iknom}}\right) = \frac{1}{4(1-\alpha_0)^2}\left(1+\frac{I_b}{I_{bnom}}\right)^2 \quad (17)$$

In the case of the superconducting cavities, α_0 is very small and can be neglected. The input power required to achieve the same accelerating field at zero current beam is one fourth of the full power at nominal beam. Of course, almost all this power is then fully reflected. If the cavity frequency is changed according to (15) (linearly with beam current) and the input power according to (17) (quadratic with current), everything should remain stable while increasing the beam current. This should provide an easy way for commissioning the accelerator.

7 TRANSIENT ANALYSIS

In a transient mode, the use of the Laplace transform will make all the above relations, established for a steady state regime, straightforwardly extended. The Laplace transform of the cavity impedance is $Z_0 = R\dfrac{p}{p^2+\frac{p}{\tau_0}+\omega_0^2}$

which gives, once transformed through each drive k :

$$Z = \alpha_k Z_{ck}\frac{p/\tau}{p^2+(1-\alpha_k)\frac{p}{\tau}+\omega_0^2} \quad (18)$$

with the time constant $\tau = \alpha_0\tau_0$.

The reflection coefficient is like in equation (5)

$$(\rho_k+1) = \frac{2\alpha_k(p/\tau)}{p^2+\frac{p}{\tau}+\omega_0^2} \quad (19)$$

The basic equations (6) are still valid in the Laplace transform. In particular, using (6) and (19), one may write the cavity voltage as

$$V_c(p) = \frac{(p/\tau)}{\left(p^2+\frac{p}{\tau}+\omega_0^2\right)}\left(\sum_k 2\sqrt{\alpha_0\alpha_k}V_{ik}\right) \quad (20)$$

This function has two poles, solution of $\left(p^2+\frac{p}{\tau}+\omega_0^2\right)=0$, which are $p_\pm = -\frac{1}{2\tau} \pm j\omega_0\sqrt{\left(1-\frac{1}{4Q_l^2}\right)} \approx -\frac{1}{2\tau} \pm j\omega_0$. The cavity voltage as a function of time is then deduced by inverting the Laplace transform $V_c(t) = \int e^{pt}V_c(p)\,dp$:

$$V_c(t) = \left(Ap_+e^{p_+t} + Bp_-e^{p_-t}\right) + \left(\sum_k 2\sqrt{\alpha_0\alpha_k}V_{ik}\right)\cos\psi\, e^{j\psi}e^{j\omega t} \quad (21)$$

The first bracket is the transient one, with the time constant (2τ). The second term is the stationary solution. Finally, using the simplification $Q_l \gg 1$, the solution is :

$$V_c(t) = V_c(0)e^{-\frac{t}{2\tau}}e^{j\omega_0 t} + \left(\sum_k 2\sqrt{\alpha_0\alpha_k}V_{ik}\right)\cos\psi\, e^{j\psi}(e^{j\omega t} - e^{-\frac{t}{2\tau}}e^{j\omega_0 t}) \quad (22)$$

References

[1] P. B. Wilson, "High Energy Electron Linacs: Applications to Storage Ring RF Systems and Linear Colliders", SLAC-PUB-2884, February 1982.

ANALYTICAL TREATMENT OF SINGLE BUNCH STABILITY IN A LINAC

G. Guignard, J. Hagel, CERN, Geneva, Switzerland

Abstract

Single bunch stability is analysed by solving the equation of motion of the particles travelling in a linac, for a Gaussian distribution of charge, a linear variation of the transverse wakefield along the bunch, a smooth focusing and negligible acceleration. The treatment is based on a non-standard perturbation expansion that has been specifically developed for this study and preserves at each order the intrinsic detuning likely to stabilise the resonant beam break-up. It provides a closed expression for the tune shift along the bunch resulting from BNS damping and autophasing, methods proposed in the past to control the emittance, and a first-order solution for the transverse off-sets within the bunch. The analytic result obtained makes it possible to study the behaviour of the solution and compute the emittance dilution in specific cases. The present theory is a useful complement to the numerical simulations done with the MUSTAFA code in the Compact Linear Collider scheme (CLIC). It also gives an interesting as well as comprehensive view of the physics involved in the single-bunch motion and the damping of the instability.

1 EQUATION OF MOTION

Since in most linear colliders a flat beam design (low vertical to horizontal beam size ratio) is used, emittance blow up due to transverse wakefields is most critical in the vertical plane. Disregarding acceleration, using a weak focusing model for the betatron motion and assuming a linearly varying wakefield within a single bunch the equation of motion reads as (refs [1, 2])

$$\frac{\partial^2 x(s,z)}{\partial s^2} + q^2[1+\Delta k(z)]x(s,z) = \frac{CW_0}{\gamma_0 l_B}\int_0^z \rho(z^*)(z-z^*)x(s,z^*)dz^* \qquad (1)$$

The two independent variables s and z describe the position of the bunch inside the linac, and the position inside the bunch, respectively. The quantity $q = 1/\bar{\beta}_y$ is the weak focusing tune, $\Delta k(z)$ a z-dependent additional focusing force (arising from a correlated energy spread and/or RF quadrupoles) and $\rho(z)$ the line charge density distribution. The constant C is defined by $C = 4\pi\epsilon_0 r_e N$ where N is the number of particles inside the bunch and r_e is the classical electron radius. W_0 is the value of the transverse wake at the tail of a truncated bunch in units of $V/(Asm^2)$. For $\rho(z)$ a truncated Gaussian distribution ($\pm 2\sigma_z$) has been used. In order to facilitate the analysis, the Gaussian has been replaced by its 4-th order Chebyshev approximation within $\pm 2\sigma_z$ which results into an error of not more than 4%. After normalisation the thus approximate expression for ρ becomes

$$\rho(z) = \frac{75}{46 l_B}\left[1 - \frac{41}{100}\left(\frac{4z}{l_B}-2\right)^2 + \frac{1}{20}\left(\frac{4z}{l_B}-2\right)^4\right] \qquad (2)$$

where $l_B = 4\sigma_z$.

We choose to deal with the effect of an initial offset α_0 as well as an initial slope along z. Although we do not consider here randomly misaligned quadrupoles and accelerating cavities, it has to be noted that these off-set and slope represent well the misalignment of a single component of the linac. The initial conditions are then

$$x(0,z) = \alpha_0 + \alpha_1 z \qquad (3)$$

$$\frac{dx}{ds}(0,z) = 0 \qquad (4)$$

2 SEPARATION OF VARIABLES AND AUTOPHASING

Equation (1) is a linear, partial, homogeneous integro-differential equation of second order. This type of equation can often be solved analytically by separating the two independent variables, i.e. s and z. Rewriting $x(s,z)$ as $x = X(s) + y(s,z)$ and performing some algebra leads to the following new equations for X and y

$$\frac{d^2X}{ds^2} + q^2 X = 0 \qquad (5)$$

$$\frac{\partial^2 y}{\partial s^2} + q^2[1+\Delta k(z)]y = X(s)\left[-q^2\Delta k(z) + \frac{CW_0}{\gamma_0 l_B}\int_0^z \rho(z^*)(z-z^*)dz^*\right] + \frac{CW_0}{\gamma_0 l_B}\int_0^z \rho(z^*)(z-z^*)y(s,z^*)dz^* \qquad (6)$$

The coherent motion (5) is given by the unperturbed betatron equation and its solution according to the initial conditions given above is

$$X(s) = \alpha_0 \cos qs = \alpha_0 \cos\frac{s}{\bar{\beta}_y} \qquad (7)$$

Considering the case of no z dependent focusing across the bunch ($\Delta k(z) = 0$), we face a resonant situation due to the fact that the frequency q of the unperturbed betatron motion appears on the right hand side and generates a secular solution in s. This is related to the well-known head to tail instability of a single bunch traveling through a structure with wakefields. In order to suppress the resonance excitation term, it is necessary to introduce a tune spread along

the bunch [3] cancelling the coefficient of $X(s)$ in Eq. (6).

$$\Delta k(z)_{AUTO} = \frac{CW_0}{\gamma_0 l_B q^2}\int_0^z \rho(z^*)(z-z^*)dz^* \quad (8)$$

In this paper we do not specify the mechanism creating the detuning (RF quadrupoles or correlated energy spread). However, in order to also study the bunch dynamics in the case of no correction or only partial correction through a z-dependent focusing, the actual detuning is defined as

$$\Delta k(z) = \lambda \Delta k(z)_{AUTO} = \lambda \frac{CW_0}{\gamma_0 l_B q^2}\int_0^z \rho(z^*)(z-z^*)dz^* \quad (9)$$

where $\lambda = 0$ means no correction while $\lambda = 1$ corresponds to the **autophasing condition** (8) (resonance suppressed). Inserting our definition (9) into Eq. (6) gives

$$\frac{\partial^2 y}{\partial s^2} + q^2\left[1 + \frac{\lambda CW_0}{\gamma_0 l_B q^2}\int_0^z \rho(z^*)(z-z^*)dz^*\right] y = (\lambda-1)\frac{CW_0}{\gamma_0 l_B} X(s)\int_0^z \rho(z^*)(z-z^*)dz^* + \frac{CW_0}{\gamma_0 l_B}\int_0^z \rho(z^*)(z-z^*)y(s,z^*)dz^* \quad (10)$$

3 PERTURBATIVE SOLUTION

Introducing the normalised bunch coordinate $\zeta = z/l_B$ and further separating y such as $y(s,\zeta) = \alpha_1 l_B \zeta \cos qs + v(s,\zeta)$ results in

$$\frac{\partial^2 v}{\partial s^2} + \bar{q}^2(\zeta) v = \frac{CW_0}{\gamma_0 l_B}\cos qs \times \left[[\alpha_0(1-\lambda) - \alpha_1 l_B \zeta \lambda]\int_0^\zeta l_B^2 \rho(l_B\zeta)(\zeta-\zeta^*)d\zeta^* + \alpha_1 \int_0^\zeta l_B^3 \zeta^* \rho(l_B\zeta)(\zeta-\zeta^*)d\zeta^*\right] + \frac{CW_0\epsilon}{\gamma_0 l_B}\int_0^\zeta l_B^2 \rho(l_B\zeta^*)(\zeta-\zeta^*)v(s,\zeta^*)d\zeta^* \quad (11)$$

where

$$\bar{q}^2(\zeta) = q^2\left[1 + \lambda E \frac{CW_0}{\gamma_0 l_B q^2}\int_0^\zeta l_B^2 \rho(l_B\zeta^*)(\zeta-\zeta^*)d\zeta^*\right] \quad (12)$$

In order to avoid secular terms and preserve the detuning of the oscillatory motion we use a specific **partial perturbation expansion** of the solution $v(s,\zeta)$. It consists of separating the perturbation of the (analytically) solvable part of the equation of motion (11), marked with E in (12), from the integral driving-term on the right hand side of (11) marked with ϵ. Both ϵ and E indicate that the associated terms contain products of the wakefield W_0 with the oscillation amplitude due to the wakefields $v(s,\zeta)$ and are perturbations w.r.t. the rest of the equation. The expansion is only done w.r.t. ϵ and not w.r.t. E describing the z-dependent tune shift. Then the perturbation series reads as $v = v^{(0)}(s,\zeta;E) + \epsilon v^{(1)}(s,\zeta,E) + \cdots$ and no resonant terms arise at any order. At the end of the computation, both ϵ and E are set to unity. A detailed description and justification of the partial expansion method introduced for this study is given in [2]. Setting $\epsilon = 0$ in eq. (11) leads to a linear, inhomogeneous differential equation of second order and its solution is

$$v^{(0)} = \left[\alpha_0\frac{\lambda-1}{\lambda} + \left(\frac{3\zeta}{7\lambda} - \zeta\right)\alpha_1 l_B\right][\cos qs - \cos(\bar{q}(\zeta)s)] \quad (13)$$

with

$$\bar{q}(\zeta) = q\left[1 + \frac{\lambda CW_0}{\gamma_0 q^2}\times \left(\frac{16}{23}\zeta^6 - \frac{48}{23}\zeta^5 + \frac{79}{46}\zeta^4 + \frac{1}{23}\zeta^3 + \frac{3}{23}\zeta^2\right)\right]^{\frac{1}{2}} \quad (14)$$

The equation for the first order perturbation contribution $v^{(1)}$ becomes

$$\frac{\partial^2 v^{(1)}}{\partial s^2} + \bar{q}^2(\zeta)v^{(1)} = \frac{CW_0 l_B}{\gamma_0}\int_0^\zeta \rho(l_B\zeta)(\zeta-\zeta^*)v^{(0)}(\zeta^*,s)d\zeta^* \quad (15)$$

The detailed solution of this equation is given in Ref. [2].

As a first example, Fig. 1 shows a typical solution (to order zero of the perturbation) of the form $y = \alpha_1\zeta l_B \cos qs + v^0(s,\zeta)$ at a distance of 520 m downstream of the linac. The increasing frequency of the incoherent bunch oscillations from the head ($\zeta = 0$) to the tail ($\zeta = 1$) of the bunch becomes clearly visible.

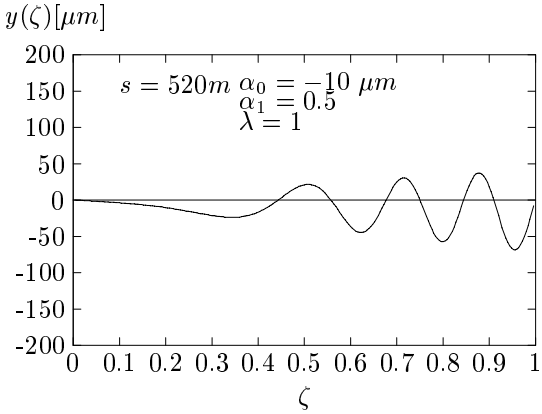

Figure 1: Autophasing solution in CLIC

Next we show in Fig. 2 the solution (including the first order term $v^{(1)}$ of the perturbation) for $\lambda = 0$, i.e. in the absence of detuning along the bunch. While the full line represents the analytical solution, the points indicate the results obtained with the tracking code MUSTAFA [4].

By comparison with the detuned example of Fig. 1, the amplitude of the oscillation increases significantly because of the resonant effect. However, some residual detuning remains visible due to the influence at large amplitudes of the last integral term in Eq. (11).

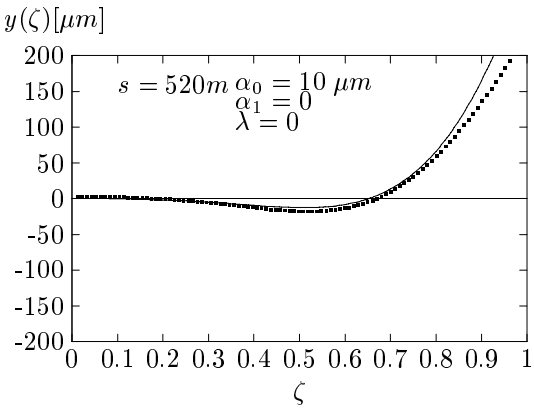

Figure 2: Resonant solution in CLIC at $s = 520$ m

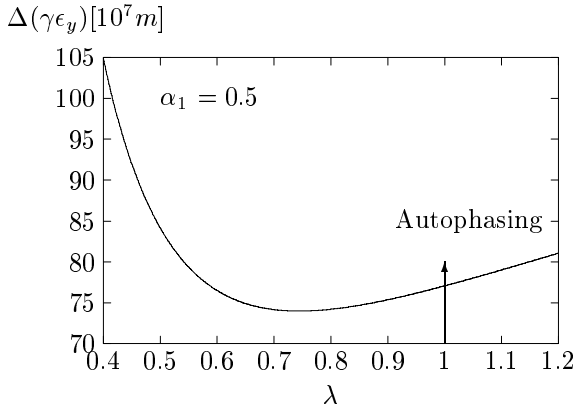

Figure 3: Asymptotic emittance growth as function of λ

4 EMITTANCE DILUTION

Since a low emittance beam is needed at the interaction point to provide high luminosity collisions, it is interesting to study the emittance dilution due to wakefields in the accelerating structures of the collider. If we consider the emittance increase due to transverse wakes in a single bunch, the total normalised emittance at the end of the main linac is given by

$$\gamma\epsilon_{tot} = \gamma\epsilon_{inj} + \Delta(\gamma\epsilon_y) \tag{16}$$

where

$$\Delta(\gamma\epsilon_y) = l_B\gamma_0 \int_0^1 \rho(\zeta) \left[qy^2(s,\zeta) + \frac{1}{q}\left(\frac{\partial y}{\partial s}(s,\zeta)\right)^2 \right] d\zeta \tag{17}$$

and $y = \alpha_1 l_B \zeta \cos qs + v(s,\zeta)$. Instead of v we use $v^{(0)}(s,\zeta)$ as given in Eq. (13) since it is believed to give the strongest contribution. Although y has then a relatively simple form, the integral in (17) becomes non elementary, leading to complicated expressions of trigonometric and Fresnel functions. However, it can be demonstrated that the emittance in the case of an initial offset tends to an asymptotic value as s goes to infinity. It is straightforward to compute this limit by only considering slowly oscillating terms in ζ as s increases and averaging the fast oscillating terms before performing the quadrature. As above, all the details are described in Ref. [2]. The result for the asymptotic emittance becomes

$$\lim_{s\to\infty}(\gamma_0\epsilon_y) = \gamma_0\epsilon_{inj} + \frac{a_{-2}}{\lambda^2} + \frac{a_{-1}}{\lambda} + a_0 + a_1\lambda + a_2\lambda^2 \tag{18}$$

where the parameters a_{-2} to a_2 are polynomial expressions of the transverse wakefield W_0 with coefficients that are rational functions of α_0 , α_1 , q and l_B. They are all listed in Ref. [2]. The form of the expression (18) makes it obvious that ϵ_y must have a certain minimum as a function of λ, since the first and second terms decrease with λ while the last two increase. Evidently $\lambda = 0$ leads to an infinite asymptotic emittance due to the resonance effect.

Fig. 3 gives an illustration of this effect for the case of $\alpha_0 = -10\ \mu m$, $\alpha_1 = 0.5$ and $0.4 < \lambda < 1.2$.

The same figure 3 clearly shows for $\alpha_1 = 0.5$ that **the autophasing condition is not leading in general to the minimum single bunch emittance**. Instead, the minimum is shifted to a lower value of λ where two effects are best balanced: namely an increase of the decoherence of the bunch with λ that leads to an emittance growth and a rise of the distance from the resonance with λ that induces an emittance reduction. The actual (flat) minimum of the emittance in this example appears at a value of λ near 75% of the one corresponding to the autophasing condition.

5 CONCLUSIONS

The equation of the transverse single-bunch motion has been analytically solved for initial off-set and slope along the bunch, similar to those generated by the misalignment of a single linac element. Weak focusing is used and the acceleration within a linac sector is not included. The transverse wakefield along the bunch is taken as linear and the charge density approximated by Chebyshev polynomials. The transverse displacement $x(s)$ is split into a coherent term $X(s)$ and a part $y(s,z)$ that depends on the position z in the bunch. A particular partial perturbation treatment worked out by the authors is then applied in order to keep the detuning property through all orders and prevent the creation of artificial resonances. In this way, zero and first order solutions for x as well as the asymptotic emittance dilution for $s \to \infty$ have been derived as functions of the fraction λ of the wakefield that is damped. They all agree with the results of the code MUSTAFA and confirm the existence of a given λ where the single-bunch emittance blow-up is minimum. This minimum is proven not to correspond generally with autophasing.

6 REFERENCES

[1] See for instance A.W.Chao, B.Richter, C.Y.Yao, *Nucl. Instr. Meth,*, **178**, 1 (1980), and H.Henke, W.Schnell, report CERN-LEP-RF 86-18 (1986).

[2] G.Guignard, J.Hagel, report CERN-SL-98-015 AP (1998).

[3] V.Balakin, *Proc. 1988 Workshop on Lin. Coll*, SLAC-report-355, 55 (1988).

[4] G.Guignard, J.Hagel, MUSTAFA users' guide CERN-SL-98-002 AP (1998) and *this conference*.

APPLICATION OF THE MODE MATCHING TECHNIQUE TO THE ANALYSIS OF WAVEGUIDE ARRAYS

A. Jöstingmeier, M. Dohlus and N. Holtkamp, DESY, D-22607 Hamburg, Germany

Abstract

In this contribution the mode matching technique is applied to compute the absorption characteristics of a two-dimensional array of rectangular waveguides. This analysis is motivated by a proposal of a broadband absorber for TESLA. Outside the waveguide array the so-called Rayleigh expansion is used which represents the electromagnetic field in terms of space harmonics whereas the complete modal spectrum of eigenmodes is taken into account inside the waveguides. In the case of normal incidence the validity of the presented method is confirmed by MAFIA computations. The absorption characteristics for various angles of incidence are calculated for a broad frequency range. The accuracy of the results is checked by a study of convergence. It is shown that the Rayleigh expansion has to be modified if the waveguide array is excited by an ultra-relativistic beam instead of an incoming plane wave. Numerical results for the beam parameters are presented for an array of parallel-plate waveguides and compared with those obtained by other methods.

1 INTRODUCTION

A HOM (higher order modes) absorber for TESLA has been proposed in [1] which consists of an array of rectangular waveguides surrounding the beampipe (Fig. 1). This absorber is used to extract the HOM in the THz region from the superconducting accelerating structure and to attenuate the extracted fields by the ohmic wall losses of the rectangular waveguides.

For the sake of simplicity we consider instead of the circular waveguide array a two-dimensional infinite planar grating (Fig. 2). The absorption characteristics of this model are expected to be very close to those of the original absorber because the free-space wavelength is much shorter than the curvature of the structure in the relevant frequency range.

Such a grating can be analyzed by the application of the mode matching technique. Above the grating the electromagnetic field is expanded in terms of an infinite series of spatial harmonics, which is known as the Rayleigh expansion; and inside the waveguides the field is represented by the complete spectrum of TE and TM waveguide modes. Matching the waveguide aperture tangential electromagnetic field, yields an infinite algebraic system of equations the unknown of which are the field expansion coefficients [2].

The ratio describing how much of the power of the incoming wave is coupled into the waveguides is denoted as the grating efficiency. It is used to estimate the power absorption properties of the structure. This quantity is calculated for a grating with typical absorber dimensions over a broad frequency range and for various angles of incidence.

If we use a grating as HOM absorber we have to keep in mind that such a structure itself also contributes to the beam impedance. The second part of this paper is therefore dedicated to the computation of the beam parameters of infinite periodic structures.

The mode matching technique is employed to calculate the electromagnetic field which is excited by an ultra-relativistic bunch of particles in the presence of an infinite array of parallel-plate waveguides (Fig. 3). Subsequently the beam parameters are calculated by making use of the results of the field analysis. In [3] it has been demonstrated that the results of this planar model can also be used for a circular configuration if certain scaling laws are taken into account.

The Rayleigh expansion for the field representation above the grating is known to be complete which means that it can be used to represent any kind of pseudo-periodic field. Nevertheless it has to be modified for an ultra-relativistic beam since the phase advance of the exciting

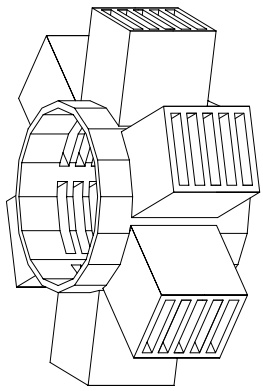

Figure 1: Sketch of the waveguide array absorber.

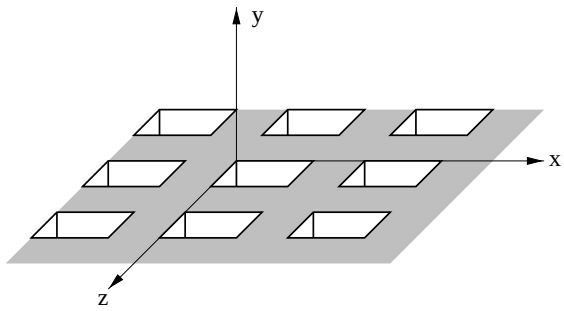

Figure 2: Two-dimensional planar grating.

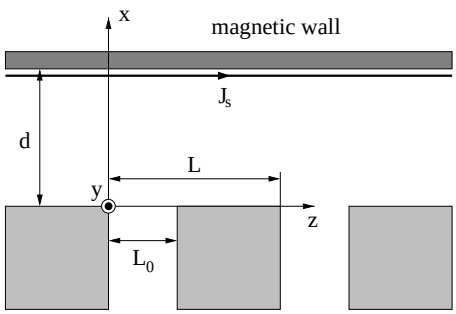

Figure 3: Infinite array of parallel-plate waveguides which is excited by an ultra-relativistic current backed by a magnetic wall.

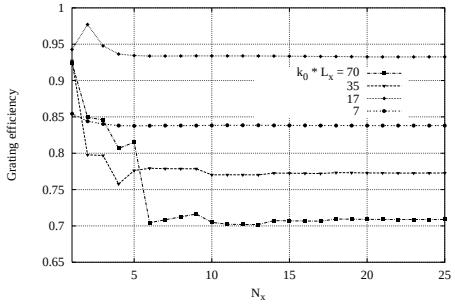

Figure 4: Grating efficiency as a function of the number of field expansion terms for various frequencies.

current is in this case equal to the vacuum wavenumber. Consequently the zeroth order spatial harmonic satisfies the Laplace equation instead of the usual wave equation. Thus we have to use a constant and a linearly increasing function in the x-direction as expansion terms for the y-component of the magnetic field instead of the zeroth order spatial harmonic of the standard Rayleigh expansion.

2 ABSORPTION CHARACTERISTICS OF A RECTANGULAR WAVEGUIDE ARRAY

The mode matching technique leads to an infinite system of equations for the unknown field expansion coefficients which has to be truncated if the method is implemented on a computer. Therefore it is essential to study the convergence of the results with respect to the number of field expansion functions.

Fig. 4 shows the grating efficiency as a function of the maximum order of the spatial harmonics in the x-direction for a grating with typical dimensions of the proposed absorber. The normalized wavenumbers $k_0 L_x = 70$, 35, 17 and 7 correspond to frequencies of approximately 2000, 1000, 500 and 200 GHz, respectively. For a frequency of 200 GHz accurate results are already obtained for $N_x = 5$ whereas $N_x = 20$ is required for a frequency of 2000 GHz. Thus $N_x = 20$ is used for all further calculations which means that approximately a (1500×1500) linear system of equations has to be solved. Assuming this parameter, a typical frequency scan with 1000 points requires about 2 d of cpu-time on a modern workstation.

If the electric field vector of the incoming wave goes along the x- or the z-direction the grating analysis reduces

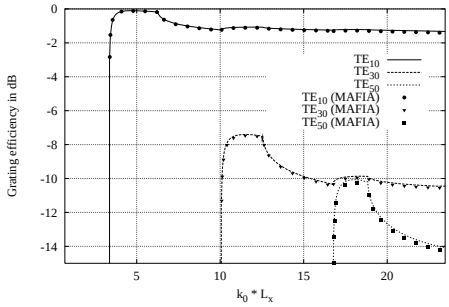

Figure 5: Comparison between the MAFIA computer code and the presented mode matching technique.

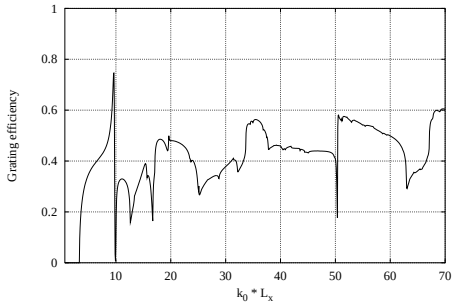

Figure 6: Absorption characteristics for a nearly grazing incident field.

to a waveguide discontinuity problem which can also be solved using the MAFIA computer code [4]. Fig. 5 shows the excitation of the TE_{10}, the TE_{30} and the TE_{50} rectangular waveguide modes as a result of both methods. It is found that in the investigated frequency range from 100 GHz to about 700 GHz the results agree very well.

In the case of normal incidence the grating efficiency is greater than 0.6 (except for frequencies which are very close to the cutoff frequency of the fundamental mode of the rectangular waveguide) which means that more than 60% of the power of the incoming wave is extracted by the grating. Nevertheless the grating efficiency decreases for obliquely incident fields. But even if the angle between the direction of propagation of the incoming wave and the grating interface is only $15°$ the average grating efficiency is still about 40% (Fig. 6).

3 BEAM PARAMETERS OF AN INFINITE PERIODIC STRUCTURE

Fig. 7 shows the real part of the beam impedance for a planar grating as a function of frequency. The maximum normalized wavenumber which is $k_0 L = 200$ corresponds to a frequency of about 10 THz for a period length of the grating of 1 mm. The beam impedance is calculated at 32768 frequency points and 200 spatial harmonics are taken into account.

The beam impedance is a smooth function of $k_0 L$ in the frequency range from dc to $k_0 L = \pi$. On the other hand it starts to oscillate rapidly at for higher frequencies where the first higher order spatial harmonic turns from evanescent to propagating with respect to the x-direction. This leads to resonances between the magnetic wall and

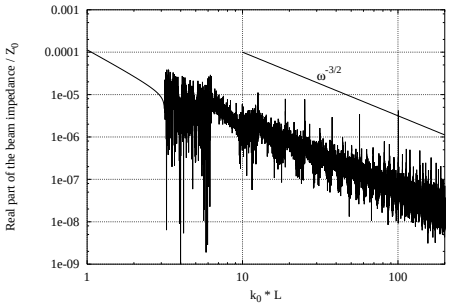

Figure 7: Real part of the beam impedance for a planar grating as a function of frequency. Parameters: $L = 4/15\,\text{mm}$, $L_0 = 0.5L$ and $d = 35\,\text{mm}$.

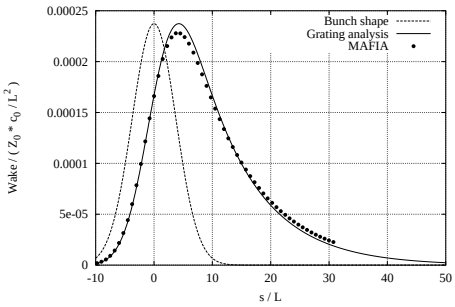

Figure 8: Comparison of the wakefields between the presented mode matching analysis and the MAFIA computer code. Parameters: $L = 4/15\,\text{mm}$, $L_0 = 0.5L$, $a = 5\,\text{mm}$ and $\sigma = 1\,\text{mm}$.

the grating interface with a high spectral density because $d = 35\,\text{mm} \gg L = 4/15$ mm.

In Fig. 7 a logarithmic scale is used for both axis. Thus a curve which is proportional to $\omega^{-3/2}$ corresponds to a straight line with a slope of $-3/2$ which is also given in this Fig. From the two curves it can be concluded that the averaged beam impedance also drops as $\omega^{-3/2}$ which has already been shown in [5].

In Fig. 8 the wakefields corresponding to the presented mode matching analysis and the MAFIA computer code [4] are compared. For the MAFIA calculations a corrugated circular beampipe with a length of 200 periods is assumed. The wakefield corresponding to the mode matching technique is obtained by scaling the result from the equivalent planar model. The agreement of the two wakefields is quite good which confirms the validity of the presented method.

The dependence of the wakefield on the bunch length is illustrated in Fig. 9. The results which are presented in this Fig. are valid for a circular configuration with a radius a. The curves converge to an asymptotic wakefield corresponding to an infinitely small bunch length. For the given parameters the wakefield gets very close to the asymptotic curve ($\sigma/L = 0.1$) for a bunch length in the order of one grating period. Such an asymptotic wakefield has also been used in [6] where it is approximated by a special fit.

4 CONCLUSIONS

The mode matching technique has been applied for the analysis of a two-dimensional array of rectangular waveguides which serves as a model for a HOM absorber. A

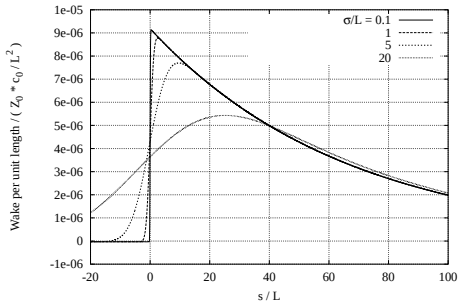

Figure 9: Dependence of the wakefield on the bunch length. Parameters: $L_0 = 0.5L$, $a = 262.5L$.

detailed study of convergence has been carried out in order to demonstrate the accuracy of the presented method. Furthermore the validity of the results has been checked by comparing the excitation of the rectangular waveguide modes with corresponding numbers from MAFIA computations for the special case of normal incidence. The analysis of a grating with typical absorber dimensions has shown that the average grating efficiency is quite high. Although this quantity decreases as we approach the case of grazing incidence the overall absorption properties of such a grating seem to be acceptable. In the second part of this contribution the mode matching technique has been applied to compute the electromagnetic field excited by a bunch of ultra-relativisitic particles traversing a planar grating. It has been shown that the standard Rayleigh expansion which is usually used to represent the field above the grating has to be modified in this case. The beam parameters have been calculated for various structures; and the validity of the presented method has been checked.

5 REFERENCES

[1] A. Jöstingmeier, M. Dohlus, N. Holtkamp and M. Shahabadi, "Computation of the absorption characteristics of a two-dimensional rectangular waveguide array using the mode matching technique", will be published as TESLA report, 1998.

[2] A. Wexler, "Solution of waveguide discontinuities by modal analysis", *IEEE Trans. Microwave Theory Tech.*, vol. MTT-15, pp. 508–517, 1967.

[3] A. Jöstingmeier, M. Dohlus, N. Holtkamp and M. Shahabadi, "Application of the mode matching technique for the computation of the beam parameters of an infinite periodic structure", will be published as TESLA report, 1998.

[4] T. Weiland, "On the numerical solution of Maxwell's equations and applications in the field of accelerator physics", *Particle Accelerators*, vol. 15, pp. 245–292, 1984.

[5] S. A. Heifets and S. A. Keifets, "High-frequency limit of the longitudinal impedance of an array of cavities," *Phys. Rev. D*, vol. 39, pp. 961–970, 1989.

[6] R. Brinkmann *et al.* (ed.), *Conceptual design of a 500 GeV e^+e^- linear collider with integrated X-ray laser facility*, DESY 1997-048, 1997.

SIMULATION STUDY OF THE BUNCHING SECTION OF X-BAND KLYSTRONS

S.Matsumoto, S.Michizono, H.Tsutsui, Y.H. Chin and S.Fukuda
High Energy Accelerator Research Organization (KEK), Tsukuba, Ibaraki, 305-0801 Japan

Abstract

A precise simulation of a klystron is useful not only to understand its operation but for the design work. For this purpose, MAGIC code, which is a 2.5 dimensional PIC code for self-consistent simulation of plasma physics problems, is used to simulate the entire klystron performance including the production of the beam at the gun, the modulated beam motion and the beam-cavity interaction at the output cavity as well as the gain cavities. In this article, the simulation of the buncher section of KEK XB72K, a relativistic X-band klystron, is described.

1 INTRODUCTION

An X-band klystron is a possible RF power source in future linear colliders. The design performance of such a klystron is high. In R&D of such a klystron, a precise simulation of the performance is preferred. For this purpose, we recently adopted MAGIC code at KEK. MAGIC is a 2.5 dimensional fully electromagnetic and relativistic Particle-in-Cell (PIC) code for self-consistent simulation of plasma physics problems[1]. The primary inputs of MAGIC simulation are the electromagnetic boundary condition on the perimeter (simulation boundary) and the initial condition of beam.

In a klystron simulation, the geometry of the klystron determines the physical boundary (conductor perimeter), while in the gun region, for example, an external DC field should be given properly along a line between the cathode and the anode. This kind of lines is also a part of the perimeter. As for the initial condition of beam, MAGIC can simulate the thermal emission from the cathode surface. The focusing solenoidal field is included as an external field in the simulation. We calculate this field by POISSON code[2].

In our simulation study, the whole klystron structure breaks into three simulation sections. This separation is technically unavoidable since the whole length (from the gun to the output cavity) of our klystron is too long for a single simulation. In a MAGIC simulation, 1024 is the maximum number of the grids (cells) in z direction (the direction of beam axis). If the grid size in z is 0.2 mm (this is the case of our simulation), about 20 cm is the maximum length.

The stream of beam particles and electromagnetic fields from the upstream simulation section can be transferred to the downstream by MAGIC IMPORT/EXPORT command. Once EXPORT command is invoked, MAGIC records the fields and particles on the "export line" for a specified duration of time. The data is launched by IMPORT command on the "import line" in the downstream simulation section which should be matched to the export line. This technique works if there is no backward wave and particles and a klystron is the case. The separation into these simulation sections is done at the middle of the long drift tubes.

The first section is the gun section where the DC beam from the gun is simulated[3]. The beam energy is specified here by the cathode voltage. The next region is the buncher section which includes the input cavity, the gain cavities and the penultimate cavity. The RF voltage supplied at the input gap modulates the beam. The last section simulates the output cavity. The actual output cavity has two ports to conduct the power. The ports are represented by an equivalent axisymmetric load in the simulation[4]. The output power is estimated as the consumed power in this load.

In the present paper, the simulation of the buncher section of XB72K, an X-band klystron developed at KEK [5], is described. This section is divided into 2 subsections, since the whole section is still long for a single simulation. The first half covers the input and gain cavities while the last half includes the penultimate cavity.

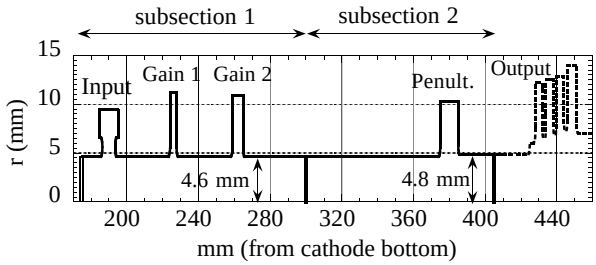

Figure 1: The structure of the buncher section of XB72K. The import line from the gun section is located at 170 mm and the export line is at 410 mm. There is another line at 300 mm, which divides the section into two. These lines are indicated by the double lines in the figure. The TW output structure of XB72K#9 is also shown in the figure.

2 SIMULATION METHOD

2.1 Input cavity

MAGIC can simulate straightforwardly the gain cavities or the penultimate cavity. However, the simulation of the input cavity is not straightforward since it has a port (not axisymmetric) through which the power comes in (or out). In our simulation, the input cavity is removed and its electrical effect is represented by an external field on the gap line, a new boundary which is defined as the (shortest) straight line between the nose cones of the cavity. The external field, $E_z(z,t)$, is calculated primarily as the electric field of the trapped mode of the input cavity with the operation frequency. It is

$$E_z(z,t) = \frac{V_g}{d}\,\bar{e}(z)\sin\omega t,$$

where V_g is the gap voltage, d is the gap length (7 mm in our case) and $\bar{e}(z)$ is a function shown in Fig. 2. In the simulation (with beam), $E_z(z,t)$ is applied on the gap line as an external field. Fig. 3 shows the electric field generated by $E_z(z,t)$. The gap voltage V_g is related to the input power P as

$$V_g^2 = \rho P.$$

We adopt ρ such that $V_g = 2.0\,\mathrm{kV}$ when $100\,\mathrm{W}$ input power. The dependence of ρ on the beam energy or beam current is small thus we neglect it.

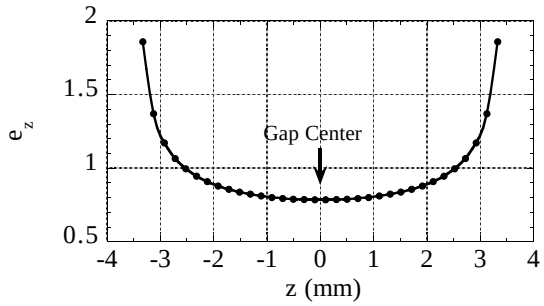

Figure 2: The function $\bar{e}(z)$ of XB72K input cavity.

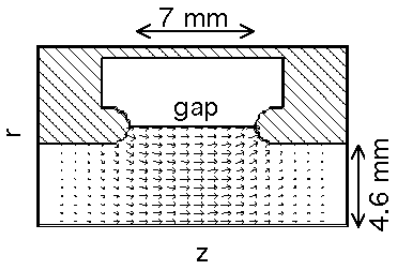

Figure 3: A snapshot of the electric field. The external field is given on the gap. The arrows indicate the direction and strength of the electric field at this moment.

2.2 Gain and Penultimate cavities

The resonant frequency of the gain and penultimate cavities is shifted from the operation frequency (11.424 GHz) as tabulated below. The resonant frequency can be measured by EIGENMODE command. All the cavities were tuned within at most 0.5 MHz by a tiny change of the cavity radius.

Table 1: Frequency Shift of cavities

Cavity	*df* (MHz)	Cavity	*df* (MHz)
1 (input)	0	3 (Gain)	+26
2 (Gain)	+12	4 (Penult.)	+376

2.3 Other issues

We use uniform spatial grids. The grid size in z is 0.2 mm overall while that in r is $4.6\,\mathrm{mm}/15 \sim 0.3$ mm in the drift tube and a little small grid is used in the cavity space. We set the time step manually to be $1/360$ cycle (for the entire simulation sections). This step is smaller than the default step set by MAGIC automatically from the given grid size.

The external field on the boundary should be started from zero value and slowly raised to its desired value. Otherwise we often see the numerical oscillation occurs. The similar treatment should be done when we import particles. SCALE is a MAGIC command for this trick.

We are interested in the beam and fields in their stationary state. Realization of such a state requires a finite duration of time in the simulation. For example, in Fig. 4, the evolution of the gap voltage at the 2nd gain cavity is shown. The voltage becomes constant after about 20 nsec, which is 230 RF cycles. Although the relaxation time should depend on the current carried by the beam or the beam energy as well as the frequency shift of the cavity, the duration of 300 cycles is enough for the first subsection while 200 cycles is enough for the second subsection.

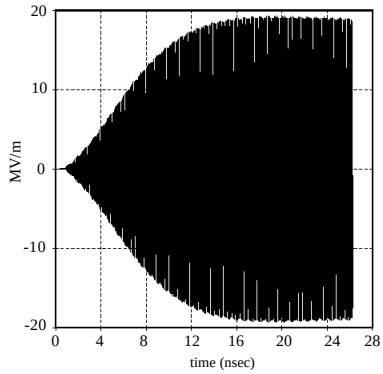

Figure 4: The averaged electric field strength (in unit of MV/m) on the gap line of the 2nd gain cavity. It saturates after about 20 nsec. Beam energy is 525 kV and input power is 300 W.

3 SIMULATION RESULTS

3.1 Modulation and its enhancement

Let us see how the bunching process is seen in the MAGIC simulation. As an example, we show the case of XB72K#9 with the beam energy being 525 kV and input power being 300 W. Fig. 5 is a snapshot of the beam energy in the first subsection as a function of z. We clearly see the enhancement of the energy modulation occurred at the gain cavities. The modulation in energy (velocity) is turned to be the density modulation downstream and this is actually seen in the next subsection. See Fig. 6. The cavity in the figure is the penultimate cavity which enhances the bunching process. The bunching process can be more clearly seen in the current growth along the z direction, which is calculable from

MAGIC output. See in Fig. 7. The enhancement of bunching by the cavity can be seen as a kink of the growth curves.

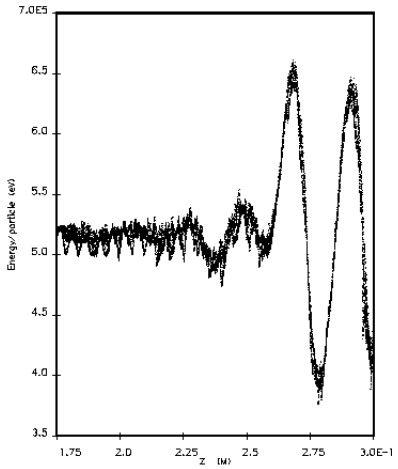

Figure 5: The snapshot of the beam energy along the longitudinal direction z.

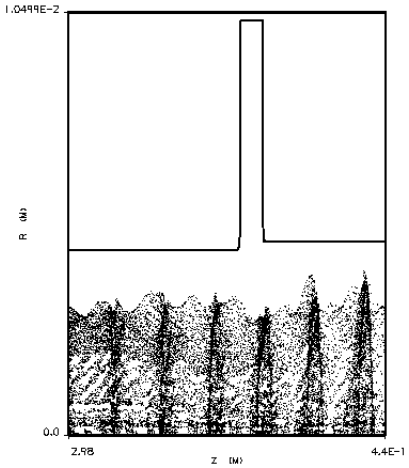

Figure 6: The snapshot of the particle distribution in subsection 2.

The output power can be estimated in the next simulation section by using the exported data from the buncher section. The simulation of the #9 TW output structure predicts 80.5 MW in this particular case. Since DC current is 458 A (the perveance is 1.2×10^{-6}), therefore MAGIC simulation for XB72K #9 predicts the efficiency of 33% at 525 kV. A discussion on the MAGIC predictions and experimental results is found in Ref. [6]. The MAGIC predictions agree well to the observations so far [7].

3.2 Required CPU time

Required CPU time is 10.5 hours for first subsection (duration 300 cycles) and 7.5 hours for the second subsection (200 cycles) in pentiumII-300 MHz PC. The number of the

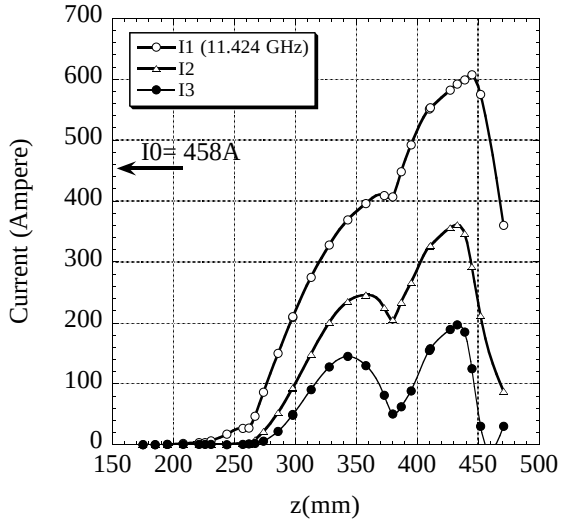

Figure 7: The RF current growth in XB72K #9. Beam voltage is 525 kV, 300 W input. The fundamental ($I1$) as well as the second ($I2$) and third ($I3$) harmonics are shown. The ratio of $I1$ to $I0$ (DC component) reaches about 1.3 in the output cavity but decays rapidly.

macro-particles emerge from the import line of the first subsection is about 3800 per a single cycles (360 time steps). This number is not changed throughout the whole simulation sections (unless the particles hit the wall). CPU time depends largely on the number of the macro particles appeared in the simulation region. The grid size, the time step and the number of macro particles that we used so far are rather conservative.

4 SUMMARY

The basic techniques for simulating a klystron by 2.5D MAGIC code are established. Although the code primarily solves the problem, we still need a trick like the port approximation for the input cavity, as shown above. Eligibility of the trick is checked by the experiment or by the other code. So far the MAGIC model is a good simulator of a klystron.

5 REFERENCES

[1] Mission Research Corporation, Virginia, USA.

[2] J.H.Billen and L.M.Young "POISSON SUPERFISH", LA-UR-96-1834,(1997).

[3] S.Michizono, et al., "Electron Gun Simulation using MAGIC", these proceedings.

[4] H.Tsutsui, et al., "X-band klystron output cavity simulation", these proceedings.

[5] J.Odagiri, et al., "FCI Simulation on 100MW Class Klystron" in Proc. 1994 Int. Linac Conf., Tsukuba, Japan.

[6] Y.H. Chin, et al., "Computational Modeling of Klystrons", these proceedings.

[7] Y.H. Chin et al., "The 120 MW X-band Klystron Development at KEK", in Proc. of EPAC 98.

HIGH ENERGY BEAM TRANSPORT BEAMLINE FOR LEDA*

W. P. Lysenko, J. D. Gilpatrick
Los Alamos National Laboratory, Los Alamos, NM 87544 USA
M. E. Schulze
General Atomics, Los Alamos, NM 87545

Abstract

Here we describe the High Energy Beam Transport (HEBT) for the Low Energy Demonstration Accelerator (LEDA), which is part of the Accelerator Production of Tritium (APT) project. We used the TRACE 3-D linear design code[1] for the first-order design and performed r-z and 3-D particle-in-cell (PIC) simulations to study the beam distribution and halo. TRACE 3-D predicts rms beam properties well. The PIC simulations are important for determining the presence of beam halo, which is present for some tunes. We propose halo experiments to help validate our simulation codes for modeling nonlinear space charge.

1 REQUIREMENTS

The HEBT, which matches the 6.7 MeV 100 mA CW beam from the RFQ into the water-cooled nickel beamstop must meet the following requirements:

- **Match beam to beamstop**. The rms size of the beam at a point 45 inches past the entrance of the beamstop must be 44 mm in both transverse directions.
- **Provide space for equipment.** Diagnostics and other equipment take up a certain amount of length.
- **Have rms beam sizes $<$ 1/5 of aperture radius.** Inside the HEBT, we require the rms beam sizes to be less than than one-fifth of the bore radius.
- **Be insensitive to beam or quadrupole errors.** The rms beam sizes and phase-space centroids must be within the safe operating range of the beamstop.
- **Minimize beam halo generation.** Under normal operation, we do not want any beam to be scraped off in the beamline. To meet his requirement, we must ensure that no beam halo is introduced.

2 BEAM PHYSICS

We can increase the focusing strength of the lattice by decreasing the distance between quadrupoles. With sufficient external focusing, the relative strength of the space-charge force is decreased to harmless levels. The 100 mA beam current forces us to use four quadrupoles. If there were less space charge, only two or three quadrupoles would have been sufficient to match the RFQ beam to the beamstop.

* Work supported by the US DOE, Defense Programs.

When the beam reaches the last quadrupole, the bunch length is 4.5 times its original value and space charge is no longer important. In the drift to the beamstop the beam is in the zero-emittance regime ($\epsilon_x << x_{max} x'_{max}$). We can approximate the beam by a point source located near the final quadrupole. Emittance growth does not significantly affect the beam size. The linear TRACE 3-D code is a good predictor of beam size even though it cannot model emittance growth produced by space-charge nonlinearities.

The beam from the RFQ has a fairly uniform core and no long tails in the x and y distributions. The HEBT should preserves these qualities and not introduce any beam halo. To compute these effects, we need particle simulations, which can take into account details in the phase-space distribution and nonlinear space-charge forces.

3 DESIGN PROCEDURE

We used TRACE 3-D to design the beamline. We fixed the quadrupole positions, providing space for beamline instrumentation and diagnostics. The input beam used rms values from RFQ simulations. We specified the beam at the match point, 45 inches past the start of the beamstop, and let the TRACE 3-D optimizer determine the magnet gradients. Our results depended on the specified values of α_x and α_y at the match point. (These determine the cross-over points, which must be near the final quadrupole.) We searched for tunes having rms beam sizes everywhere less than one-fifth the bore radius.

When we ran particle simulations (see below), we found some tunes developed halos. That is, the distributions in x or y developed long, Gaussian-like tails. This happened in two situations. First, we got halos whenever the quadrupoles were too far apart. We also got halos whenever the beam size in x or y was very small at some point in the upstream part of the HEBT. Because of this effect, we accepted only tunes with fairly constant beam sizes.

4 TRACE 3-D DESIGN

Figure 1 shows the TRACE 3-D output for our standard tune. The graph shows the initial and final phase-space ellipses at the top and the transverse profiles at the bottom. The beam is traced from the RFQ end wall to the 45-inch match point, i.e., 45 inches past the start of the nickel beamstop. The scale for the x and y profiles (4.5 mm total) is appropriate for the beam in the region of the quadrupoles. The

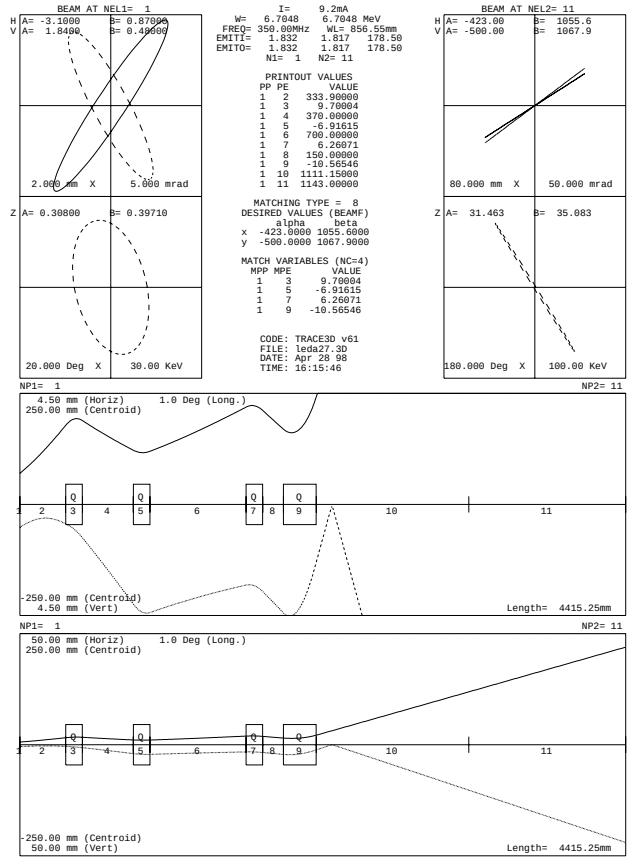

Figure 1: TRACE 3-D output for the standard tune. The beam is traced from the RFQ end wall to the 45-inch match point. The transverse profile plot is repeated at the bottom with a larger scale to show the beam in the beamstop.

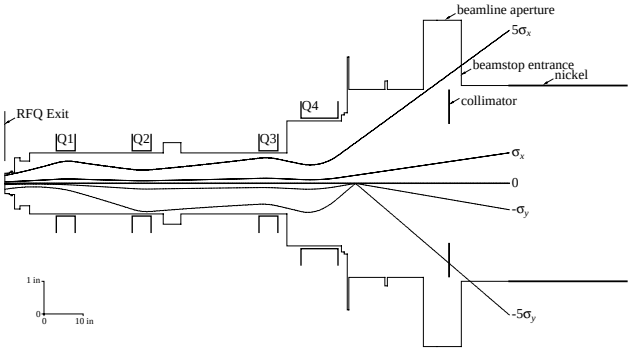

Figure 2: The 1-σ (rms) and 5-σ beam profiles compared to the minimum aperture in the HEBT beamline.

lower part of Fig. 1 shows the profile with a scale of 50 mm total to show the expansion of the beam in the beamstop. In our TRACE 3-D simulations, we use rms emittances and thus the plots show the rms beam sizes. The current we use (9.19 mA) is the actual current (103 mA) divided by $5/\sqrt{5}$. Figure 2 shows the rms and 5$\times$rms profiles together with the minimum beam apertures in the HEBT.

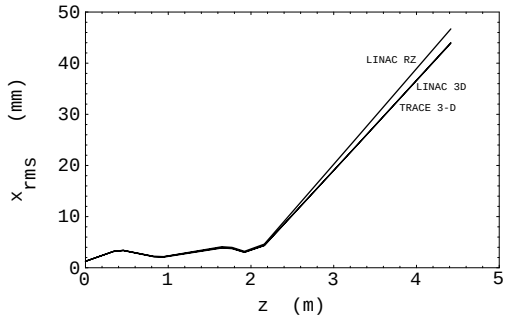

Figure 3: Rms value of x as a function of z for the r-z and 3-D PIC simulation using the LINAC code and the TRACE 3-D code. The two 3-D codes produced similar results.

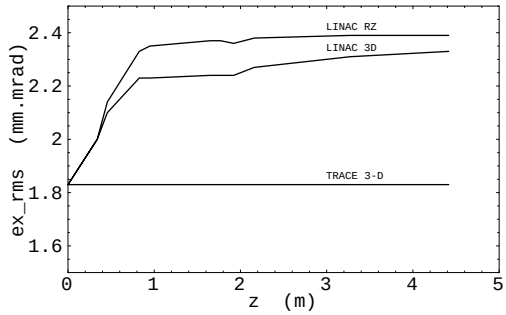

Figure 4: Rms value of x emittance as function of z.

5 SENSITIVITY STUDY

We studied the sensitivity of the beam at the beamstop to errors in the quadrupoles (strengths and offsets) and to various errors in the input beam. We found no errors that could not be handled by our diagnostics and control system. The beam spot at the beamdump depends on the beam current. While lower-current beams have a smaller spot size, the current density (current per unit area) is smaller than for the normal, full-current beam. There is no need to retune for different currents.

6 PIC SIMULATIONS

We verified our TRACE 3-D designs with particle-in-cell (PIC) simulations. We ran r-z and fully 3-D PIC simulations. Figure 3 shows $x_{\rm rms}$ as a function of z for our standard tune as predicted by TRACE 3-D and the r-z and 3-D versions of the PIC code LINAC[2]. The two 3-D codes agree very well but the r-z code produces slightly different results. As Fig. 4 shows, there is about a 30% emittance growth. This did not affect the TRACE 3-D result for the beam size because the emittance is so small. The conclusion is that 3-D effects are important but nonlinearities are not in predicting rms beam size. Our TRACE 3-D designs produce the correct rms beam at the match point.

PIC simulations are essential in determining if our tunes generate halos. Figure 5 shows the TRACE 3-D output for

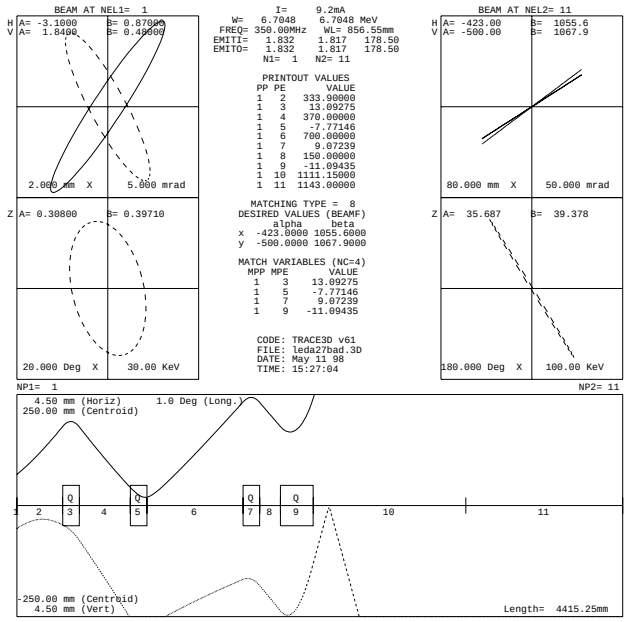

Figure 5: TRACE 3-D output for a bad tune, which has a halo in the x-direction. Halo-generating tunes have a small waist in the upstream part of the beamline.

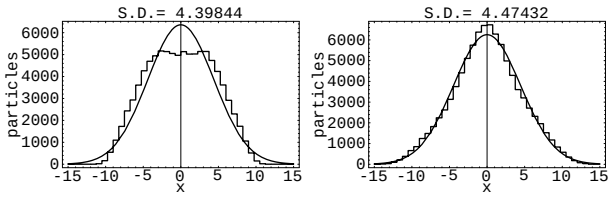

Figure 6: Beam profiles in the x-direction at the match point for the standard tune (left) and the bad tune (right).

another tune that produces the same beam at the 45-inch match point. Only the quadrupole settings are different. The input and final beams and all lengths are the same as before. We see that the beam has a small waist in x early in the HEBT. We find this characteristic is always associated with the existence of a halo. Figure 6 shows the x distribution in a 3-D PIC simulation at the 45-inch match point for both the standard and bad tunes. Also shown are Gaussians having the same rms values as the actual distributions. The halo is generated in the first part of the second quadrupole, just before the waist. Figure 7 shows the phase-space scatter plots in the x direction at the beginning and the center of Q2. We see that the distribution becomes very nonelliptical because of the nonlinear space-charge forces.

7 HALO EXPERIMENTS

Table 1 shows properties of the x profile at the wire scanner for both the standard tune and the bad tune. Also shown are a uniform (rectangular) and Gaussian distribution having the same sigma ($<x^2>^{1/2}$) value. A good way to characterize whether or not we have a halo is to determine the

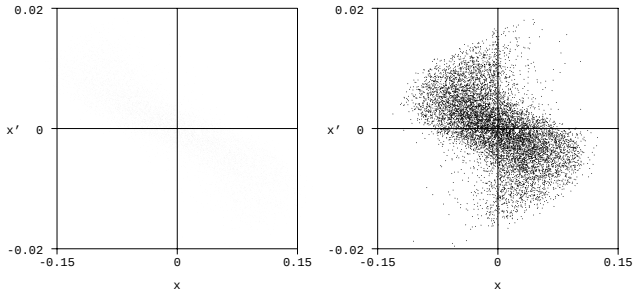

Figure 7: The x-x' phase-space scatter plots for bad tune at start of Q2 (left) and center of Q2 (right).

Table 1: Properties of x distributions at wire-scanner.

Beam	$<x^2>^{1/2}$ (mm)	$x_{\max}$ (mm)	$<x^4>/<x^2>^2$
Uniform	16	28	1.8
Gaussian	16	∞	3.0
Standard	16	41	2.2
Bad	16	56	2.9

kurtosis of the x or y distribution. The kurtosis is simply the fourth moment of the distribution, normalized by the square of the second moment to obtain a dimensionless quantity. The fourth moment depends on the whole beam distribution. It should be easy to measure even if the wire scanner does not have a large dynamic range (the amount of beam for the bad tune that is past the maximum $|x|$ value of the standard tune is only 0.35%).

8 CONCLUSION

Our HEBT design meets all readily quantifiable requirements. Our 3-D PIC simulations verify that the TRACE 3-D design code can accurately predict rms beam properties. Nonlinear space-charge effects are important, however. We have found that having adequate focusing (no less than four quadrupoles) and a good tune are essential to avoid halo formation, which could result in undesirable particle losses before the beamstop.

The codes clearly indicate when halo formation occurs. We therefore propose that we do some halo experiments at LEDA. We can obtain the required information from the wire-scanner data. If we verify the simulations' predictions about the differences between the good and bad tunes, we will have greatly increased confidence in the ability of our codes to correctly model nonlinear space-charge effects.

9 REFERENCES

[1] D.P. Rusthoi, W.P. Lysenko, and K.R. Crandall, "Further improvements in TRACE 3-D," Proceedings of the 1997 Particle Accelerator Conference.

[2] K. Crandall and R. Ryne, private communication, 1998.

BEAM DYNAMICS SIMULATION OF THE SPALLATION NEUTRON SOURCE LINEAR ACCELERATOR*

H. Takeda, J. H. Billen, T. S. Bhatia
Los Alamos National Laboratory, Los Alamos, New Mexico 87545 USA

Abstract

The accelerating structure for Spallation Neutron Source (SNS) consists of a radio-frequency-quadrupole-linac (RFQ), a drift-tube-linac (DTL), a coupled-cavity-drift-tube-linac (CCDTL) [1], and a coupled-cavity-linac (CCL). The linac is operated at room temperature. We discuss the detailed design of linac which accelerates an H^- pulsed beam coming out from RFQ at 2.5 MeV to 1000 MeV. We show a detailed transition from 402.5 MHz DTL with a 4 βλ structure to a CCDTL operated at 805 MHz with a 12 βλ structure. After a discussion of overall feature of the linac, we present an end-to-end particle simulation using the new version of the PARMILA code [2] for a beam starting from the RFQ entrance through the rest of the linac. At 1000 MeV, the beam is transported to a storage ring. The storage ring requires a large (±500-keV) energy spread. This is accomplished by operating the rf-phase in the last section of the linac so the particles are at the unstable fixed point of the separatrix. We present zero-current phase advance, beam size, and beam emittance along the entire linac.

1 LINAC STRUCTURES

We consider the DTL, CCDTL and two types of CCL part of linac structure. At the linac structure change between structures, we apply discontinuous accelerating electric fields between structures to maintain a continuous real-estate phase advance per unit length. The design phase was made continuous at the structure junctions to avoid the abrupt longitudinal separatrix change. The DTL with focusing lattice FOFODO structure accelerates the 2.5-MeV H^- beam from the RFQ to 20 MeV. Between the RFQ and the DTL, we have a symmetric beam chopper section which consists of a number of quadrupoles and three buncher cavities.

The CCDTL then takes the beam from the DTL and accelerates it to 94 MeV. To match the beam from the DTL to the CCDTL, we use the first two cavities (4 cells) of the CCDTL operating at –90° and adjust the first four quadrupole magnet strengths. Each cavity in the CCDTL contains a drift tube. A focusing (or defocusing) quadrupole magnet follows every two CCDTL cavities. In the DTL the transverse lattice is of type FOFODODO with a 4 βλ period at 402.5 MHz. Starting in the CCDTL the transverse lattice changes to FODO with a 12 βλ period at 805 MHz. The term FODO (pronounced "foe-doe") refers to singlet quadrupole magnets arranged in an alternating gradient focusing system. The letter O was originally a numeral zero, and indicates a drift space between a focusing magnet F and a defocusing magnet D.

Above about 95 MeV the efficiency of a conventional CCL exceeds that of the CCDTL. The 805-MHz CCL continues the 12 βλ periodic transverse lattice of the CCDTL. The first part of CCL consists of 8-cavity segments separated by singlet quadrupole magnets and accelerates the beam to 165 MeV. Above 165 MeV, the CCL consists of 10-cavity segments and completes the acceleration to 1000 MeV. The 8-cavity segments are used at lower energy to provide more space for the quadrupole magnets and diagnostic elements. This entire CCL maintains the FODO lattice structure with a transverse period of 12 βλ [3]. Table 1 shows the linac characteristics. Figure 1 shows the cavity field along the linac. The field is discontinuous, but the "real-estate" longitudinal focusing force which is proportional to E_0T averaged over a transverse focusing period is continuous, where E_0 is the average axial electric field and T is the transit-time factor. Figure 2 shows the design phase along the linac. Figure 3 shows the zero-current phase advance per transverse focusing period through the CCDTL and CCL.

Table 1. Linac characteristics

Linac Type	Energy (MeV)	Length (m)
DTL	2.50 to 20.275	8.712
CCDTL	20.275 to 94.428	68.78
CCL1	94.428 to 164.65	46.24
CCL2	164.65 to 1000.	369.94

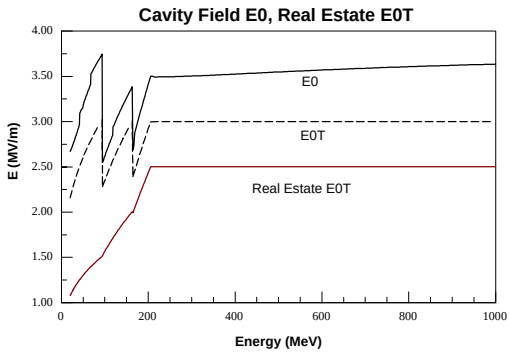

Figure 1. The cavity field E_0 E_0T real estate E_0T from CCDTL to CCL2.

*This work sponsored by the Division of Materials Sciences, US department of Energy, under contract number DE-AC05-96OR22464 with Lockheed Martin Energy Research Corporation for Oak Ridge National Laboratory.

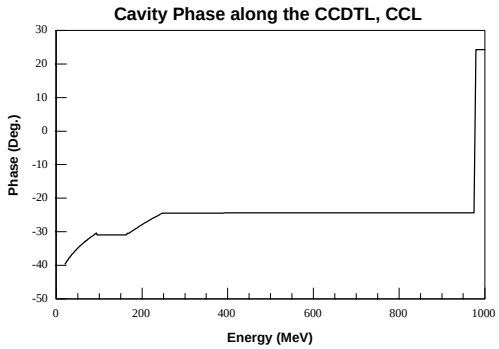

Figure 2. The design phase starting in the CCDTL. The phase change near the end of the CCL from –24 to +24 degrees increases the energy spread as required for ring injection.

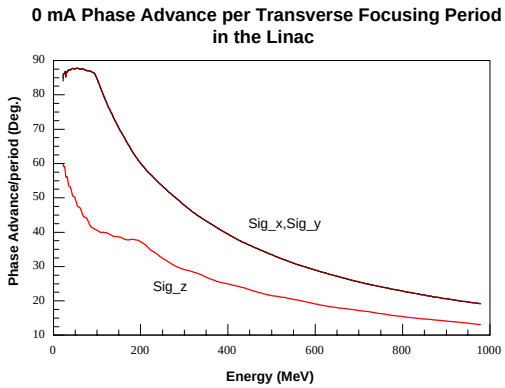

Figure 3. Zero-current phase advance per 12 βλ in the CCDTL and CCL.

2 DTL TO CCDTL TRANSITION

To achieve a smooth beam match between the DTL and the CCDTL, we require that the transverse and longitudinal real-estate phase advances are continuous across the matching section. The longitudinal matching section consists of the first two CCDTL cavities with a total of 4 accelerating gaps operating at –90°. The transverse matching section consists of four quadrupole magnets after the first segment of the CCDTL. The zero-current transverse phase advance at the end of the DTL is 57.35° with a transverse period 4 βλ at 402.5 MHz. The equivalent phase advance at the entry to the CCDTL, which operates at 805 MHz is 86.025° (= 57.35*12/(4*2)). The longitudinal phase advance is 40° over the transverse period 4 βλ. This translates to 60° at the CCDTL entry. Table 2 shows the matching section linac parameters. Figure 4 shows the transverse and longitudinal beam profiles at the matching section performed with the TRACE 3-D code [4].

Table. 2. Matching section parameters at the CCDTL.

Beam Element	Parameters
Drift	13.27 cm
Q between DTL and CCDTL	–2.692 T
Drift	7.0 cm
Q1	+2.161T
Q2	–2.278T
Q3	+2.261T
Q4	–2.199T
First 2 Cavities	1.9529 MV/m, –90°

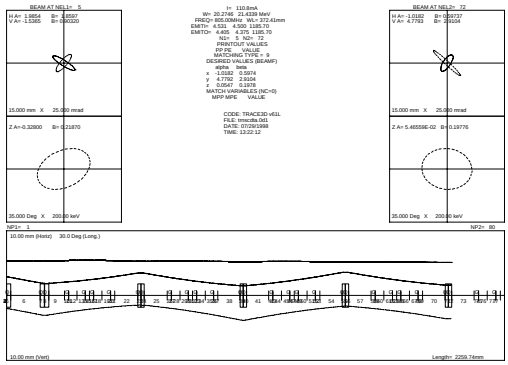

Figure 4. Beam profiles in the first few lattice periods of the CCDTL. This part of the structure is used to match the beam from the DTL.

3 PARMILA SIMULATION FROM DTL TO CCL

Starting at the entry to the DTL with the RFQ exit beam distribution we performed a PARMILA 10,000-particle simulation. The normalized rms emittance was 0.01845 π cm-mr in the transverse phase plane, and 0.1056 π deg-MeV in the longitudinal plane. The beam microbunch current was 55.4 mA. Figure 5 shows the rms beam radius, the maximum radius, and the linac aperture along the linac. It shows that we have sufficient beam clearance along the linac. Figure 6 shows the normalized rms emittances through the linac. The artificial discontinuity in longitudinal emittance at 20 MeV is caused by the doubling of the rf frequency.

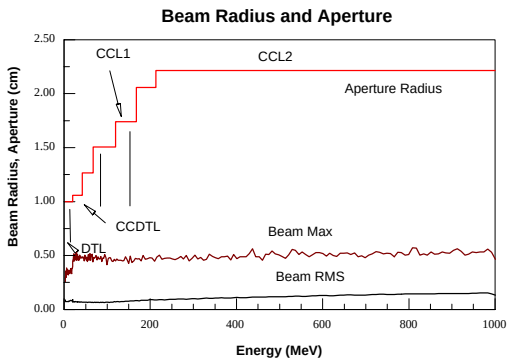

Figure 5. Linac aperture and beam size along the linac.

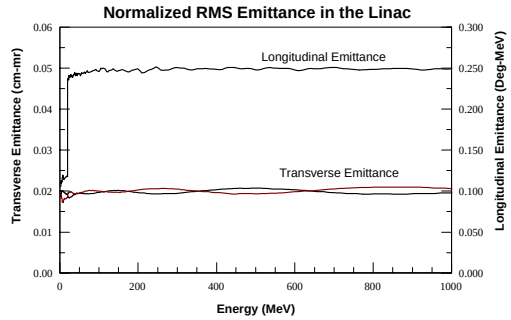

Figure 6. The normalized rms emittances are constant along the linac.

The beam profiles x, y, phase ϕ and energy W through the entire linac from DTL to CCL are plotted in Figure 7. By shifting the rf phase to operate at +24 degrees for the last five 10-cavity segments of the structure, the energy width increases from ±163 keV to ±667 keV.

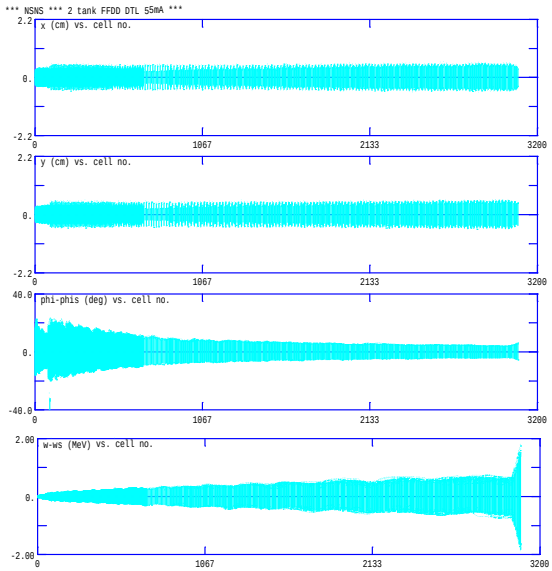

Figure 7. The beam profiles x, y, phase ϕ, and energy W along the linac from DTL. Shifting the rf phase to +24° expands the beam energy width.

4 END-TO-END PARMILA SIMULATION FROM RFQ TO CCL

A 30-mA beam with normalized transverse rms emittance 0.2 π mm-mrad was generated with 4-d waterbag distribution for the RFQ input. The RFQ accelerates the beam to 2.5 MeV. Then a medium-energy beam transport section (MEBT), which houses the chopper and consists of 18 quadrupole magnets and 3 buncher cavities, guides the beam to the DTL. At the entry to the MEBT, the normalized rms beam emittances are 0.206 π mm-mrad transversely and 0.1π MeV-deg longitudinally. Figure 8 shows the x and y beam profiles at the interface between the MEBT and the DTL.

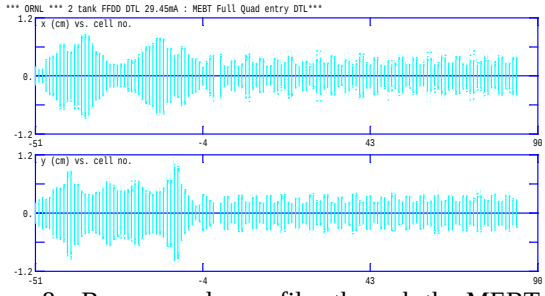

Figure 8. Beam x and y profiles through the MEBT and DTL for a 29.4-mA beam.

Figure 9 shows the x, y, phase, and energy profile of the end-to-end simulation showing from the MEBT through the CCL. The beam starts at the RFQ.

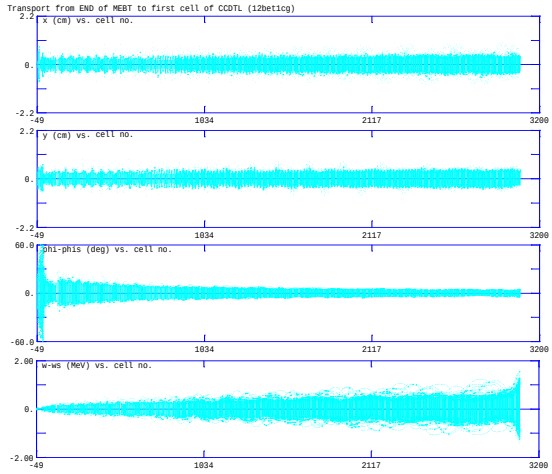

Figure 9. End-to-end simulation for a 29.4-mA beam. The profiles are the same as in Figure 7. The plot shows the profiles starting at the MEBT, but the simulation started at the RFQ entrance.

5 SUMMARY

The PARMILA simulation from the DTL to the end of CCL shows that the beam could be accelerated to 1000 MeV without loss by the sequence of linacs DTL, CCDTL, and CCL.

6 REFERENCES

1 J. H. Billen et al., “A New Rf Structure for Intermediate Velocity Particles,” Proceedings of the 1994 Linear Accelerator Conference (August 21-26, 1994 Tsukuba, Japan).

2 H. Takeda and J. H. Billen, “Recent Developments in the Accelerator Design Code PARMILA,” this conference.

3 T. S. Bhatia et al., “SNS Linac: Revised Configuration” Los Alamos National Laboratory Report LA-UR-98-3595.

4 K. R. Crandall and D. P. Rusthoi, Trace 3-D Documentation, Los Alamos National Laboratory Report LA-UR-97-886.

CW RFQ DESIGNING USING THE LIDOS.RFQ CODES

Boris Bondarev, Alexander Durkin, Stanislav Vinogradov
Moscow Radiotechnical Institute,
132, Warshavskoe Shosse, Moscow, Russia, 113519

Jean-Michel Lagniel, Robin Ferdinand,
CEA-Saclay, DSM/DAPNIA/SEA, France

New criteria arise when high-current CW linacs are considered. The main requirements for such linacs are beam acceleration with very low beam losses and reduced intervane voltage. In such cases the traditional algorithms can lead to undesired versions of the RFQ.

New concepts for parameter choices based on optimization methods and scientific visualization of space charge-dominated beam are incorporated in the new multilevel codes RFQ.3L [1]**.**

This new RFQ code package gives users the possibility to proceed successfully from input data up to accelerating-focusing channel design and space-charge-dominated (SCD) beam simulation. There are two main features: a maximum of scientific visualization for each calculation step and the possibility to cut off undesired linac versions long before the time-consuming calculations start. The package contains codes with three levels of mathematical model complexity.

The first-level codes make only a preliminary choice of the main parameter arrays on the basis of a simplified physical model. These codes are richly supplied with visual information, which helps to quickly find the best linac version.

The second-level codes are used for channel data calculations with the real shape of the RFQ vanes. Information from the first level codes is used as input data.

The third-level codes are based on information from the first and second level codes and on complex PIC-models that are needed for a correct beam simulation in the chosen channel version.

In the case of the IPHI high-current CW RFQ, radiation purity (minimum of lost particles) and reduced intervane voltage are considered as the main optimization criteria**.**

RFQ.3L codes have been used to find the region of RFQ parameter space most likely to satisfy the design requirements. The process is fast because the beam simulation is used only for the final RFQ version. RFQ.3L gives an user intellectual advises and helps him to come to the best RFQ version by the shortest way.

The first level stage the channel, data must be chosen in a way that beam transmission can be as large as possible. The periods of vane modulation are calculated at the second stage taking into account the "ideal" vane shape (2 terms potential) and nonlinear space charge forces. The functions $U(n)$, $m(n)$, $\varphi_s(n)$ and $R(n)$ obtained at the first stage are used as input data. The third level codes LIDOS.PIC are used for beam simulation. Beam is represented as a set of macro-particles and Poisson equation is solved at every step with boundaries in the form of "ideal" vane shape. The amount of macro-particles is 50 000. A saved cartoon is used for the presentation of the beam transport. Phase portraits all along the RFQ are showed on cartoon's pictures, as well as plots of several beam parameters (transmission factor, rms emittance, mean longitudinal and transverse kinetic energies…). Information on lost particles, their input distribution, total lost power and maximal lost power per unit length are also obtained. Distribution of lost particles as functions of length along the RFQ, number of RFQ periods and particle energy are presented.

When the RFQ structure is chosen (first level) and primarily checked (third level), the 3D calculation of the real external electrical fields (i.e. fields from the electrodes, without the beam Coulomb field) is performed for the real form of the electrodes. On this stage the second-level codes are used. These codes calculate the distribution of the field potential for each cell in an electrostatic approach. The calculations are the solution of the Laplace equation with the relaxation method. As the field is supposed to be quadruple-symmetrical, the potential distribution is calculated only for one quarter of the whole region. As the parameters of neighbor cells (modulation, mean radius, length) are very close to each other and the fields differences in them occur to be less than the calculations accuracy, then base cells are used for the definition of the fields in the whole channel. The field in a cell is calculated as a function of two parameters: m - the electrodes modulation- and the ratio $s = R_0/L$, where L is the cell length. Cells are chosen based on those parameters and the fields $E(m_n,s_n)$, $E(m_n,s_{n+1})$, $E(m_{n+1},s_{n+1})$ are then calculated. Thereafter, the field in cells with intermediate values of m and s is calculated with a linear interpolation between the three base fields. Total number of base points is 39. The new length of the cells are calculated taking into account the efficiency of acceleration in real fields using the dependencies of $\varphi_s(n)$ and $m(n)$ defined previously.

On the last stage, the calculations of the particles dynamics is performed taking into account Coulomb forces and real shapes of the electrodes. The code

LIDOS.PIC is used for this task where the calculated real fields are used instead of the ideal fields. On this stage study of different tolerance influence (channel axis displacement, different sorts of voltage deviations) on beam dynamics are also performed.

The above code tools were used for RFQ designing in favor of IPHI Project (CEA, France) [2]. The following parameters were preset as well as some restrictions and requirements:

Accelerating Particles	protons
Input Energy	0.095 MeV
Output Energy	5 MeV
Beam Current	100 mA
Total Beam Emittance	0.15π cm·mrad
Operating Frequency	352 MHz
Peak Surface Field	< 29.5-30 MV/m
Kilpatrick Factor	< 1.6
Length	about 8 m
Beam Transmission	> 90%
Power of Lost Particles	< 1–1.5 KW

Minimum of Lost Particles with energy more than 3 MeV

A strategy was elaborated for creating a RFQ version who satisfies the conditions set above. A lot of versions were examined to create the needed channel. Following is the essence of this strategy: If the calculations show that particles capture in the accelerating regime is sufficiently high (~ 95%) then one can conclude that the regularities for the equilibrium phase φ_s variation and for the acceleration rate *UT* are defined finally. To prevent transverse particles losses in the last part of the channel (particles with high energy), it is necessary to increase the focusing strength when they achieve the first minimum of phase oscillations (first focus) and to increase the aperture of the following channel part. Besides, it is necessary to satisfy the upper limit of the field $E_r=U/R_0$. The aperture increase must be accompanied with the proportional voltage increase. The increasing of the focusing strength diminishes the size of the beam halo in the region of first focus. Simultaneously, the aperture decrease at this location leads in halo losses in a channel region where particle energy slightly differs from the input value. According to calculations and investigations there is a range where the raise of the transverse beam size due to the decreasing focusing strength is compensated by the aperture increasing. Thus we can avoid losses of high-energy particles in the last channel part. To keep the product $U \cdot T$ constant, we must also change the vane modulation.

The best RFQ version with constant U and R_0 was first calculated (U = 91.6 kV, R_0 = 4 mm). This version gave good transverse and longitudinal captures but leads in losses of high energy particles. In order to minimize power of lost particles the plots $U(n)$ and $R_0(n)$ were chosen and correction of $m(n)$ was made. In optimal case the mean bore was decreased from 4 to 3.6 mm and then increased up to 5 mm. Intervane voltage must be increased up to 25% from input to output. Vane modulation at the RFQ output does not exceeded 1.5. It means that bore radius is increasing not only at the cost of $R_0(n)$ increasing, but also at the cost of $m(n)$ decreasing. The chosen parameters are showed on Figs. 1-2 as functions of the period number. In Tables 1 and 2 RFQ parameters are given.

Table 1. Main RFQ Parameters

Operating Frequency	352 MHz
Length (w/o output part)	7.906 m
Electrical Length	9.28 (λ=0.85 m)
Number of Periods	267 (534 cells)
Bore Radius, mm	4 → 3.43 → 3.95
Vane Modulation	1→ 1.53
ρ/R_0	0.85
Vane Voltage, kV	91.6→ 82.4→ 114.4
Kilpatrick Factor	1.62 – 1.64

Table 2: Parameters of RFQ Parts

	W, MeV	φ_s, deg	Cell Nos	L, m
Matching Section and Shaper	0.104	-83	180	1.098
Gentle Buncher	0.72	-40	190	1.7
Acceleration	5	-35	164	5.108
Total	5		534	7.906

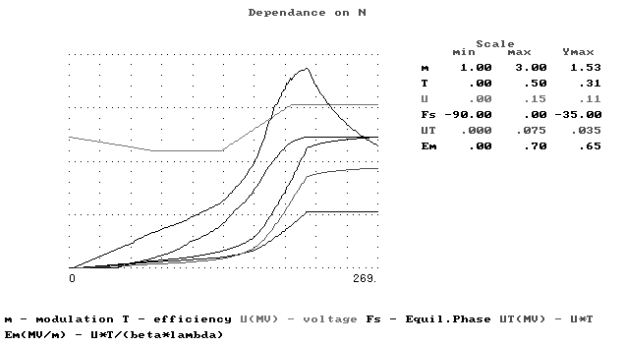

Fig.1.

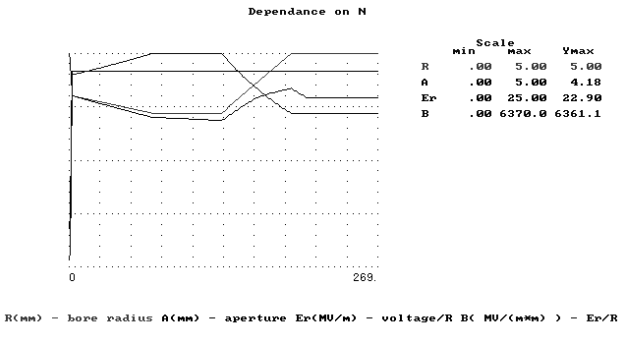

Fig.2.

The arrays of the calculated fields in the input section and in regular channel are got united. The united array is used for beam dynamics calculations We have not understood that sentence.

The results for different RFQ versions are presented below in Tables 3-5. We indicate the beam normalized emittance, *E*, the overall beam transmission, *Trans*., the accelerated particle, *Acc*., as well as the integrated power of lost particles, *P*. All results are presented for a beam current of 100 mA. The initial particles distribution is a uniform filling in the 4-dimensional ellipsoids in phase space X,X',Y,Y' with uniform distribution along the longitudinal coordinate *Z* and without longitudinal velocities spread. Version 0 is with constants *U* and R_0. Versions 1a and 1b correspond to RFQ structure with ideal RF fields (no multipoles, with images effect), 1c – with real RF fields. The next versions are presented for real RF fields and beam emittance of 0.15π cm·mrad.

Table 3

Version	• *(π·cm·mrad)*	*Trans* (%)	*Acc* (%)	*P* (kW)
0	0.1π	97.7	97.0	1.55
1a	0.1π	98.1	96.8	0.59
1b	0.15π	97.6	96.2	0.80
1c	0.15π	95.9	92.8	0.92

As it is seen from the Table 3 new version 1b with ideal fields leads practically to the same results as version 0, even for greater emittance (0.15π versus 0.1π). The comparison of versions 1b and 1c shows that in real field the overall current transmission suffer a diminution of 1.7% and a capture diminution of 3.5%. For the investigation of the influence of real fields, non-linearity in matching section on overall current transmission there was performed the calculation of the particles dynamics for the intermediate version when the real regular part was combined with ideal matching section. The difference occurs to be practically zero. One may conclude that the non-linearity of the regular channel field diminishes both the overall current transmission (95.9 versus 97.6) and the number of accelerated particles (96.8 versus 98.6). Note that the definition of the input beam parameters matching with real nonlinear channel represents itself a separate problem. When the mean square emittance $\langle xx' \rangle$ calculated in z points only slightly oscillates through z, then we have a good beam matched.

Among all calculated effects, a great interest was expressed to study the influence of a channel axis displacements on output beam parameters as well as influence of a tilt of intervane voltage. In Table 4 resume this analysis.

Version 2a – the channel axis is uniformly shifted of 0.1 mm in x and y.

Version 2b – the channel is divided in 4 sections, the ends of sections are shifted of ± 0.1 mm in *x* and *y*, and the axis represents broken line without tears.

Version 2c – the channel is divided in 4 sections, the beginning of each section is shifted on –0.1 mm in *x* and *y*, the end of each section is shifted on +0.1 mm, the channel axis has tears at sections ends.

Table 4

Version	*axis*	*Trans* (%)	*Acc* (%)	*P*
1c	ideal	95.9	92.8	0.92
2a	straight	95.5	92.6	1.05
2b	broken	95.5	92.5	1.06
2•	disrupt	93.6	90.6	2.18

As it is seen from the table, the most dangerous are the independent shifts of sections ends (no continuity of the channel).

The influence of RF fields tilts in RFQ sections on beam motion was a goal of the next series of beam simulation. There are results for the following versions:

3a - RF fields are decreased at the beginning of each of four sections by 5%, and increased at the ends by 5%; 3b – reversed for 3a, +5% then –5%; 3c - RFQ linac was considered as unique section. At the beginning of the linac, RF fields are increased by 5%, at the ends - decrease by 5%; 3d - RFQ linac was considered as unique section. At the beginning of linac RF fields are decreased by 5%, at the ends - increased by 5%. All RF variations are linear.

Table 5

Version	*Section Nos*	*RF Field*	*Trans (%)*	*Acc (%)*	*P*
1c	1	Nominal	95.9	92.8	0.92
3a	4	Increasing	93.2	90.5	2.58
3b	4	Decreasing	95.3	92.0	1.54
3c	1	Increasing	94.9	91.3	1.32
3d	1	Decreasing	96.4	93.9	0.73

As is easy to see, the RF field tilts from smaller values at the beginning of sections to larger ones at its ends decrease beam transmission in a greater extent that the opposite case. Nevertheless, the last case (version 3b) leads to a beam halo growth on longitudinal phase plane.

The third level code formally called LIDOS.PIC also implement error studies (vane voltage, misalignment and tears…). It can be used to help the designer to set the manufacturing precision and to get the expected transmission for multi errors.

REFERENCES

1. B.I.Bondarev, A.P.Durkin, S.V.Vinogradov "Multilevel Codes RFQ.3L for RFQ Designing", CAP-96, Williamsburg, Virginia, USA.

2. R.Ferdinand et al. "Optimization of RFQ Design", EPAC-98.

MULTI-FIDUCIAL TECHNIQUES FOR TRACKING LARGE PHASE SPACE DISTRIBUTIONS IN NON-LINEAR FIELDS

S.M. Lidia*
E.O. Lawrence Berkeley National Laboratory, Berkeley, CA 94720 USA

Abstract

One of the challenges in tracking intense beams through linacs is to account for the differences in non-linear forces experienced by portions of the beam separated by large regions of phase space. In many situations, the high-order maps generated by a single fiducial trajectory fail to capture or describe the dynamics of distant particles within the beam. I describe here a technique which overcomes this difficulty by piecing together lower-order maps induced by multiple fiducial orbits. This atlas of maps can more accurately track the evolution of a beam spread over a large phase space region. I discuss applications of this technique to simulating beam dynamics in two-beam accelerators.

1 INTRODUCTION

Particle dynamics in relativistic klystrons pose several thorny problems for simulations. Possibly the most important element of the dynamics in a relativistic klystron two-beam accelerator (RK-TBA) [1] occurs in the longitudinal phase space. The beam is modulated at high frequencies (11 - 40 GHz), and each bunch carries a charge of 10's-100's of nC. Space charge effects will produce debunching forces (a capacitive impedance) which is counteracted by (inductively) detuning the rf output structures. A bunch will undergo numerous synchrotron oscillations during transport through the full-scale device. Also, the bunches are not short compared to the rf wavelength; they typically subtend 60°-120° of rf phase. Hence, they sample very non-linear fields in the rf output structures.

From this description we can identify the main problems present in a device simulation. The beams are sufficiently intense that space charge forces present more than a small perturbation. The beamline elements are necessarily spaced close together, and this requires treatment of overlapping, non-linear fringe fields. Transverse focusing is strong so that a complete betatron oscillation occurs between rf output cavities (~1 m). Transverse emittance, while low, is still sufficiently large that particles at the beam edge sample significant non-linearities present in the beamline elements. The instantaneous energy spread is large (~10%) to handle the low-frequency BBU, and to produce the bunching by rf rotation. The particle simulation, of necessity, must track many, many particles to provide adequate sampling of both the beam phase space and the fields experienced.

One of the main disadvantages of tracking by mapping can be seen immediately. The resultant map is fundamentally a power series expansion about the initial and final coordinates of the fiducial orbit. When the extent of the beam distribution in phase space is no longer 'small' in some sense, then the map generated about the given fiducial orbit loses accuracy when applied to the outlying particles. There are various solutions that may be applied to this problem. The pre-calculated fiducial may not faithfully represent the orbit of the beam centroid, but another fiducial may be found which does. The order of non-linearity carried by the calculation may be too low to adequately describe the given external field structure. Increasing the order of the calculation may be sufficient. However, these 'fixes' make for a good solution only when the beam occupies a small enough region of phase space such that a single fiducial orbit and the map it induces captures the essential dynamics.

In many applications of intense, modulated beams, however, this is not the case. These beams are most often present in single pass, linear beamlines, with constantly changing parameters. The beams may also have a relatively long pulse length with respect to any time-dependent rf fields they encounter. To sufficiently capture that interaction via a single map would require a degree of non-linearity far too high, and involve the computation of too many map coefficients, that the intrinsic efficiency of the method would be quickly lost. This problem is only compounded when self-field effects are included.

2 CONSTRUCTION OF A MULTI-FIDUCIAL MAP

The construction and evaluation of the multi-fiducial map upon the particle coordinates is straightforward. Algorithmically, it may be described by a sequence of simple steps. In any calculation, the beamline under consideration is initially divided into a set of mapping intervals. Beam particles are propagated by mapping successively through each interval. We define a 'center' fiducial as a single orbit that continuously threads through all the mapping intervals. This single fiducial is important to maintain as it provides a single reference frame, and hence a reference 'clock' and 'meter stick', for

* The author may be contacted via email at SMLidia@lbl.gov.

the problem. Each mapping interval is defined by referring to the coordinates of this center fiducial.

For each interval, the beam phase space is partitioned and a set of nominal values of coordinates are selected, one set for each region. These nominal coordinate sets provide the initial values for 'sub-fiducials' and their associated maps to be constructed. The particles in each region are then propagated according to these local maps. The number and method of partitioning is highly dependent upon the physics to be modeled. Partitioning should represent a balance between the order of non-linearity carried by the calculation, the degree of non-linearity present in the external fields and sampled by the beam, and the non-homogeneity of the beam density profile when self-fields are a concern. For example, in a magnetostatic transport region, only a single fiducial and map may need to be calculated. Whereas, in a region with time-dependent rf fields where the wavelength and period of the external fields is comparable to the bunch length and transit time of the beam, then perhaps 10 or more fiducials may be required. When self-field effects are included, the number of partitions may depend upon the non-uniformity of the beam density profile.

3 LONGITUDINAL BEAM DYNAMICS IN AN RF CAVITY

As an example to illustrate the method, I consider the problem of tracking a bunched beam through an rf cavity. Here, I follow only a single bunch, where the modulation carried by the beam is comparable to the rf period of the cavity, as in the case of an RK-TBA. Also, I will only consider the longitudinal phase space. The center fiducial is placed at the center of the beam distribution, with the sub-fiducials at locations that span the interval in arrival time (t) of the bunch at a given beamline position (z). The initial bunch distribution and fiducial positions is shown in Figure 1.

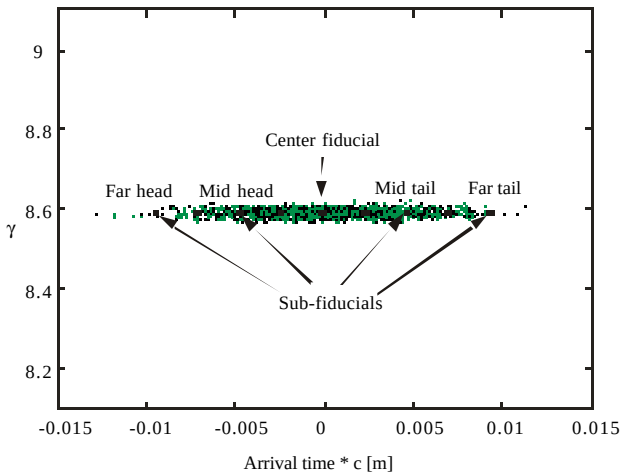

Figure 1. Initial fiducial coordinates and beam distribution in longitudinal phase space.

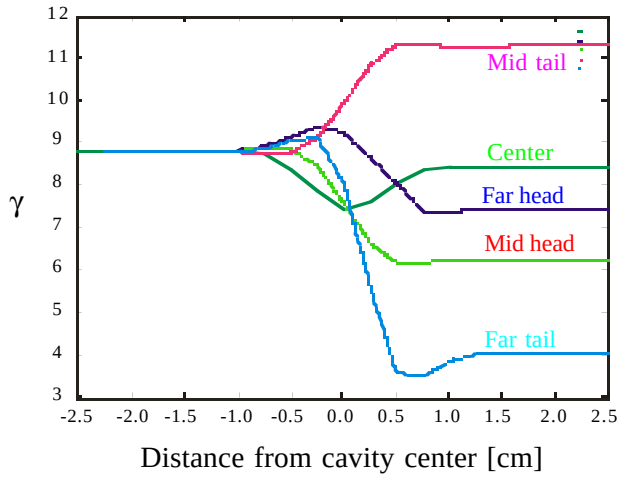

Figure 2. Fiducial trajectories in an rf cavity

3.1 Fiducial Particle Trajectories

The fiducial trajectories are calculated using the exact single-particle equations of motion. During transit through the rf cavity field, different fiducials will experience different forces due to arrival time differences. The final coordinates of the various fiducials will generally differ in a non-linear way. The fiducial trajectories in this case are shown in Figure 2.

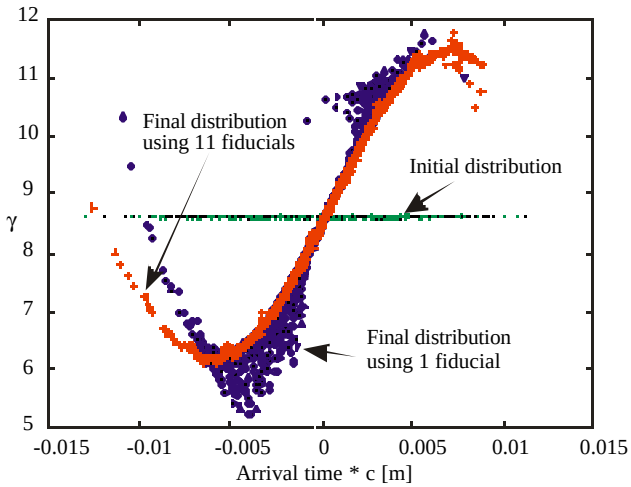

Figure 3. Final longitudinal beam distribution under a 3rd order map with multiple fiducials

3.2 Comparison of Single Vs. Multiple Fiducial Calculation

The maps induced by the fiducial orbits can, in principle, be calculated to arbitrary order. The accuracy of the mapping for outlying particles is determined by this order parameter. In Figure 3 is shown the results of the mapping through the rf cavity for two cases. The first case uses a 4th order Hamiltonian, with a single fiducial (identical to the center fiducial in Figures 1 and 2). The second case uses a 3rd Hamiltonian, but with 11 fiducials. In the first case, the combined effect of sampling only low-order field variations and tracking outlying particles

leads to inaccuracies. The final distribution suffers additional local energy spread growth, and does not exhibit the appropriate curvature, as seen in the head of the bunch. The second case avoids these problems by sampling the fields at the location of the outlying particles. The effects of errors in the field evaluation and in large coordinate deviations between particles and their associated fiducials are kept small.

4 INCLUSION OF SELF-FIELD EFFECTS

4.1 Split Operator Algorithm

Two separate mappings are applied to the particle phase space coordinates using split-operator techniques [2]. These techniques are based on splitting the Hamiltonian into pieces that can be solved exactly (or through some desired order of accuracy), and then combining the separate maps to produce an approximate map for the full Hamiltonian. Split operator symplectic integration algorithms, including the well known 'leap-frog' algorithm of plasma physics simulations [3], are widely used in the treatment of Hamiltonian systems.

The total Hamiltonian is represented in the form

$$H_{tot} = H_{kin} + H_{ext} + H_{self} , \qquad (1)$$

where H_{kin} is the kinetic portion describing single-particle motion in the absence of all fields, H_{ext} is the contribution from external fields, and H_{self} is the contribution from self-fields. The maps from the first two contributions are calculated together, while the map resulting from self-forces is calculated separately. A combined map is then produced to advance particles over an interval τ. Accurate through second order in this step, the combined map is expressed as

$$M_{tot}(\tau) = M_{kin+ext}(\tau/2)\, M_{self}(\tau)\, M_{kin+ext}(\tau/2). \qquad (2)$$

The self-fields are determined by numerical solution of Poisson's equation on a 3-D Cartesian grid in the beam's rest frame. Standard techniques are used to solve for the fields at the grid nodes. For accurate representation of the 3-D fields from a bunched beam, we may use grid sizes up to 64x64x512 nodes, as well as 10^4-10^5 macroparticles.

4.2 Changing Representations

Since we are solving the Maxwell equations at a given instant in time, the particle distribution be represented at a given moment. However, for the single particle maps, we represent the particles at a given beamline location (z), with a spread in arrival time (t). To faithfully calculate the self-forces, then, we must change the distribution from a 'constant-z' to a 'constant-t' representation.

The multi-fiducial approach again provides some utility. A visual aid to the process of changing representations is provided by the 'world-line' diagram of the fiducials, Figure 4. The fiducial trajectories (z vs. t) are shown as world-lines. The constant-z beam distribution is shown as black line segments. The first step is to calculate the motion of the sub-fiducials about the center fiducial, and the associated non-linear maps. This brings all the fiducials to the same time, but at different beamline positions (green lines and arrows). The particles attached to a given sub-fiducial are still spread in time (red line segments). The last step is to apply a linear transformation to all the particles associated with a given fiducial, to bring them to the nominal time (blue line segments). The beam distribution now exhibits a spread in beamline position consistent with observation at a given moment in time.

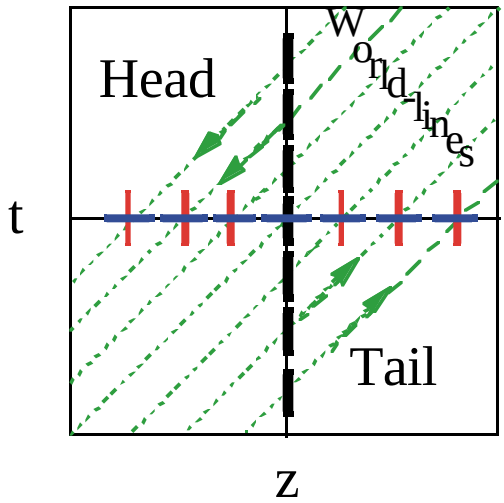

Figure 4. Changing beam distribution representation from constant-z to constant-t.

5 CONCLUSIONS

I have presented a new method for improving the accuracy of tracking algorithms, by using low-order integrators and multiple fiducials. Extensions to self-field calculations have also been made.

6 ACKNOWLEDGMENTS

I would like to thank Simon Yu and Glen Westenskow for their continued support of this work. This work was performed under the auspices of the U.S. Department of Energy under contract AC03-76SF00098.

7 REFERENCES

[1] A.M. Sessler and S.S. Yu, *Phys. Rev. Lett*. **54**, 889 (1987); G.A. Westenskow and T.L. Houck, *IEEE Trans. Plasma Sci.* **22**, 750 (1994).

[2] E. Forest and R.D. Ruth, *Physica D* **43**, 105 (1990); H. Yoshida, *Phys. Lett. A* **150**, 262 (1990); E. Forest, et. al., *Phys. Lett. A* **158**, 99 (1991).

[3] C.K. Birdsall and A.B. Langdon, *Plasma Physics Via Computer Simulation*, Adam Hilger, Bristol,1991.

PRODUCTION OF NEGATIVE HYDROGEN AND DEUTERIUM IONS IN MICROWAVE-DRIVEN ION SOURCES*

David Spence, Keith R. Lykke **
Argonne National Laboratory, Argonne, Illinois 60439 USA

Abstract

We report progress we have made in the production of negative hydrogen and deuterium atomic ions in magnetically-confined microwave-driven (2.45 GHz) ion sources. The influence of source surface material, microwave power, source gas pressure and magnetic field configuration on the resulting ion current is discussed. Results strongly suggest that, at least in our source, vibrationally excited molecular hydrogen, the precursor to atomic negative ion production, is produced via a surface mechanism suggested by Hall et al. [1] rather than via a gas phase reaction as is generally believed to be the case in most ion sources.

1 INTRODUCTION

In order to accumulate (store) or accelerate large currents of protons (H^+) in circular machines, it is necessary, from phase-space considerations, that the ions be injected into the circular storage/acceleration ring in the form of negative ions, H^-, with the H^- being stripped of its electrons to form H^+ at the point of injection. Linac accelerator performance can also be significantly improved through simultaneous acceleration of positive and negative ion beams. Suitable positive ion sources are available now, but negative ion source development has lagged somewhat.

All advanced high current H^- sources currently available, including surface sources and RF driven (2MHz) volume sources require the addition of cesium in order to achieve high H^- current. This is undesirable for several reasons, not the least being the technical problems associated with introduction of cesium into the source in a controllable manner over a long period of time. Moreover, all high current RF H^- and D^- sources developed to date consume tens of kilowatts of power and can only produce beams of a few mA per square centimeter of extraction aperture when operating cw (i.e., 100% duty factor).

Our novel approach to high current cw H^- and D^- formation involves modification of an extremely simple low power consumption (100's of watts vs. 10,000's for other type) microwave-driven source.

*Work supported by US DOE via Laboratory Directed Research and Development Funds.

Previous attempts elsewhere [3] at negative ion extraction from this type of source have been singularly unsuccessful. Our approach involves application of pioneering studies by Hall et al. [1] which demonstrated the effectiveness of freshly evaporated tantalum surfaces in producing copious quantities of vibrationally excited molecular hydrogen (a required precursor to H^- formation). The observations of Hall et al. appear to never have been deliberately, or successfully, applied to the production of high-current cw H^- or D^- beams.

2 APPARATUS AND SOURCE DIAGNOSTICS

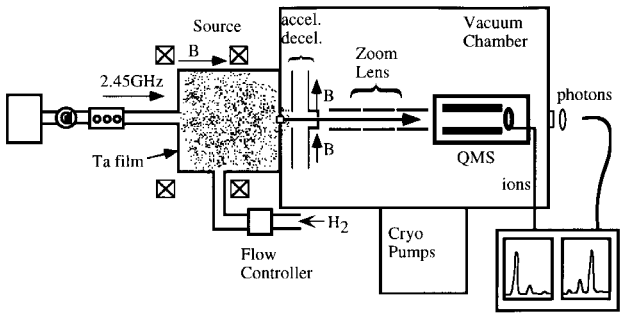

Figure 1: Schematic of apparatus.

The major components of our apparatus shown in Fig. 1 include a magnetically-confined microwave-driven (ECR) source purchased from Atomic Energy of Canada, Ltd. which is powered by a 2.45 GHz microwave generator (2 kW). The microwave generator is coupled to the source via a circulator and a four-stub autotuner. The ion source is attached to a large high-vacuum oil-free diagnostic chamber with a base pressure of $1x10^{-8}$ Torr.

Ion beams extracted at few hundred volts from the 5 mm source aperture by an accel-decel arrangement are primarily collected on the decel electrode that is in the configuration of a faraday cup. A 0.5 mm aperture in the decel electrode allows a small portion of the beam to be transported to a quadrupole mass spectrometer (QMS) via an electrostatic zoom lens for quantitative beam composition measurement. Light from the ion source is monitored by an optical monochromator by a clear line-of-sight through the QMS (sapphire window). The monochromator continuously monitors the atomic hydrogen Balmer α radiation (656 nm) to give a measure

of the atom concentration in the source under varying conditions.

3 H^-, D^- PRODUCTION MECHANISMS AND RESULTS

The mechanism for production of H^- is via the dissociative attachment of slow (<2 eV) electrons to vibrationally excited molecular hydrogen [H_2(v)], i.e.,

$$e_{slow} + H_2(v) \rightarrow H^- + H \quad (1)$$

The initial production of H_2(v), the precurser of H^-, is generally accepted to be by excitation of ground state hydrogen H_2 in the gas phase by fast electrons, i.e.,

$$H_2 + e_{fast} \rightarrow H_2(v) + e_{fast} \quad (2)$$

It is the initial production of H_2(v) that is the limiting step in the production of H^-.

Our novel cw H^- source takes advantage of observations (in experiments not directly related to ion sources) that copious quantities of H_2(v) are produced by recombinative desorption of two hydrogen atoms on a tantulum surface (M) (the Eley-Rideal reaction mechanism) i.e.,

$$H(g) + H(ads)M \rightarrow H_2(v)(free) \quad (3)$$

where H(g) is an atom in the gas phase and H (ads) is an atom adsorbed on a tantalum surface.

In order to produce H_2(v) via equation (3) we have sputtered a thin layer of Ta on the inner surface of our ion source. Our earlier experiments [3] used a bulk Ta liner to the source, which, though effective in producing H^- ions led to strong effects. Namely, Ta like other transition metals strongly absorbs hydrogen, which would periodically escape the metal in large pressure bursts. Use of a thin Ta film avoids this unwanted effect. Also, in order to prevent destruction of H^- by fast electrons in the source the solenoids are centered over the microwave window rather than over the center of the source. This results in the magnetic field diverging at the extraction aperture and diverting hot electrons. Failure to do this initially resulted in no H^- ions being extracted.

Electrons necessarily extracted along with the negative ions were removed from the beam prior to mass analysis by a weak (~30 Gauss) transverse magnetic field in the region of the accel-decel electrodes. About 100 mA of extracted electrons were collected on these electrodes.

Simple arguments show that if production of H_2(v) occurs via equation (2) (as previously generally believed), then production of H^- (D^-) is proportional to $[e]^2$, where [e] is the electron density in the plasma, whereas if it is via equation (3) then H^- (D^-) production is proportional to $[e]^3$. If one assumes that [e] is proportional to microwave power (as we can demonstrate for H^+ production), then the H^- current will be proportional to $(power)^3$. This is indeed what we observed, shown in Fig. 2 below, thus confirming a novel mechanism for production of H^- and D^-.

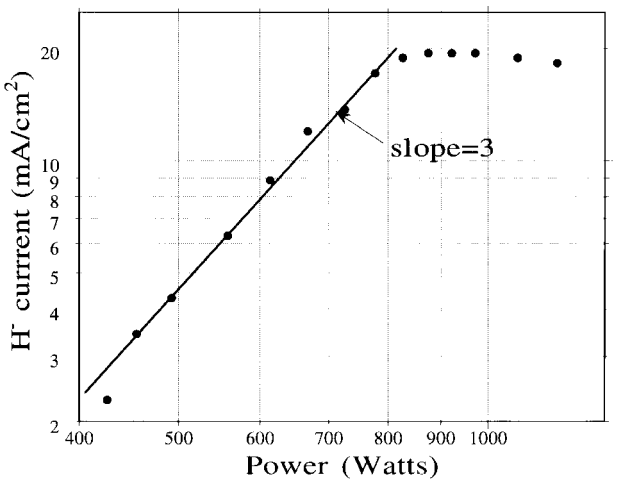

Figure 2: Log-log plot of H^- (D-) current extracted from microwave driven (ECR) source vs. microwave power to source. Plot indicates current is proportional to cube of power and strongly supports the surface production of H_2(v) hypothesis.

Based on the ratio of total H^+ extracted to H^+ sampled by the mass spectrometer in other experiments, we estimate that a total H^- current of 4-5 mA being extracted from the 5 mm diameter source aperture.

A comparison of the performance of our H^-, D^- ECR source compared with the arc-driven CWDD source at ANL, the previous D^- cw current record holder, is shown in the table below.

	Current	Beam Aperture	Current Density	Power Consumption
Present cw source H^-, D^-	4-5 mA	5 mm	20 mA/cm^2	700 W
CWDD source D^-	22 mA	23 mm	4 mA/cm^2	50,000 W

Because of H_2/D_2 isotope effects, the production rate for D- is generally much lower than H^-, often by a factor greater than ten. This results from H_2(v) production via equation (2) leading to low vibrationally excited levels from which the isotope effect is pronounced, whereas H_2(v) via equation (3) is expected to lead to populations of high vibrationally excited levels from which the isotope effect can disappear. This is what we observe in our experiments. Figure (2) shows H^- and D^- mass spectra obtained under identical experimental conditions where the cw ion currents are represented by the areas of the peaks and are essentially the same for H^- and D^- and indicating little or no isotope effect.

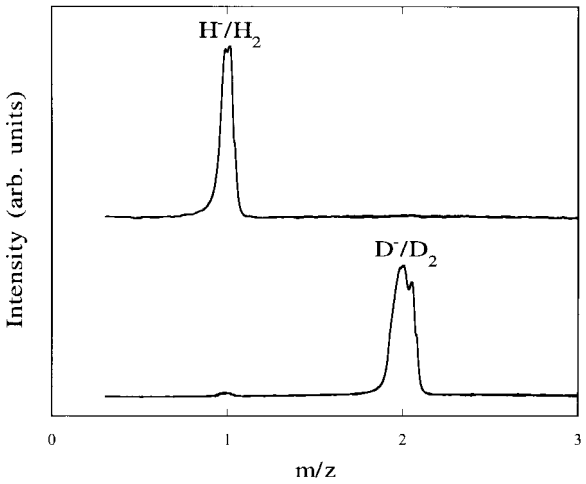

Figure 3: Mass spectra of H^-/H_2 and D^-/D_2 extracted from modified microwave driven (ECR) ion source. Spectra obtained under identical source conditions (power, density, etc.) shows no isotope effect for H^- D^- production. A first for any type of source.

4 ACKNOWLEDGEMENTS

We thank C. Batson for continued technical expertise in this project.

**Present Address: National Institute of Standards and Technology, Washington, D.C.

5 REFERENCES

[1] R. I. Hall, I. Cadez, M. Landau, F. Pichou, and C. Schermann, "Vibrational Excitation of Hydrogen via Recombinative Desorption of Atomic Hydrogen Gas on a Metal Surface," Phys. Rev. Lett. **60**, 337 (1988).

[2] J. S. C. Wills, Chalk River Laboratory, private communication.

[3] D. Spence, K. R. Lykke, and G. E. McMichael, "Plasma Modified Production of High-Current, High-purity cw H^+, D^+ and H^- Beams from Microwave-driven Sources." Proc. 1996 Int. LINAC Conf. Geneva, Switzerland, 26-30, Aug. 1996.

BEAM SIMULATIONS FOR THE H-INJECTOR UPGRADE AT LANSCE

Ralph R. Stevens, Jr., William Ingalls, Oscar Sander, Ben Prichard,
and Joseph Sherman
Los Alamos National Laboratory, Los Alamos, New Mexico 87545

Abstract

An upgrade program is being carried out at Los Alamos to increase the peak beam current from the present H^- injector to provide 200 μA average current for the proton storage ring at LANSCE. In order to meet this objective, the injector must provide at least 30% more current than presently available. More optimal operation, however, requires a factor of two higher peak current in order to reduce circulating losses in the ring. At these higher currents, a lower beam emittance is needed to limit beam losses in the linac. Beam simulations have been carried out to model the operation, of the present injector and to determine what changes will be required to operate with these higher beam currents. A collaboration with the Lawrence Berkeley National Laboratory (LBNL) is now in progress to modify our present converter ion source to produce 40-mA peak of H^- beam current with reduced beam emittance. Beam simulations show that a new 80-kV accelerating column will be needed to accelerate and transport these higher current beams with acceptable beam size and divergence. Experimental results for the initial phase of this program are presented together with a comparison to these beam simulations.

1 INTRODUCTION

The upgraded H^- injector must produce high-duty factor, low-emittance H^- beams with good reliability and availability in order to meet the operational requirements at the Los Alamos Neutron Science Center (LANSCE). The present surface converter ion source provides the reliability and availability needed [1]. Previous work at LBNL with a similar barium converter source [2,3] has demonstrated that a factor of two increase in converter efficiency can be obtained for this type of ion source by filtering the primary plasma. Experiments carried out with a cesiated molybdenum converter [4] have demonstrated that the required 40 mA of beam current can be produced.

The design of a new accelerating column was carried out by first benchmarking the ray-tracing code PBGUNS against the operation of the present accelerating column. Then this code was used to determine what changes were needed to design a column capable of accelerating higher beam currents with the required exit beam parameters.

2 LANL ION SOURCE

The configuration of the present LANL converter ion source together with the 80-kV accelerating column is shown in Fig. 1.

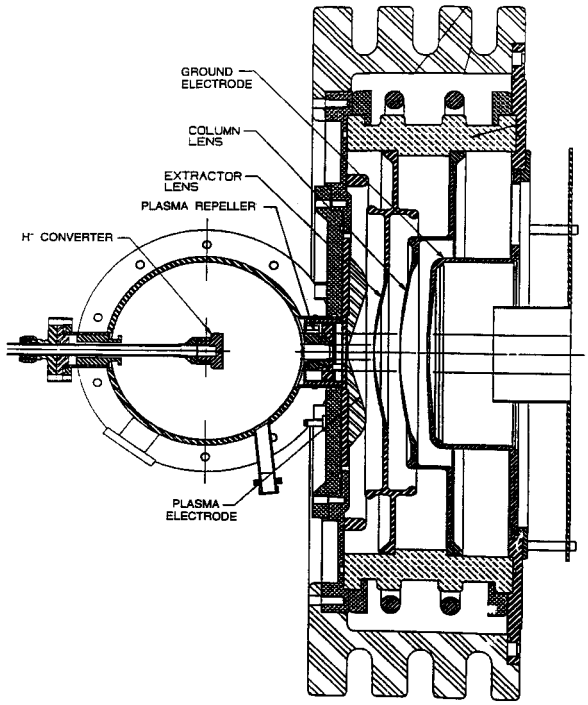

Figure 1: Layout of the LANL converter ion source with the present accelerating column.

The H^- ions are sputtered from the surface of a cesiated molybdenum converter electrode and are subsequently accelerated to several hundred electron volts by the cathode sheath formed at the converter surface by the applied bias voltage. These ions are self-focused by the spherical surface of the converter and form a converging beam that exits the source at the plasma electrode. The ion beam is collimated both by the 1.0-cm diam. plasma electrode aperture and by the plasma repeller assembly within the source itself. The emittance of the beam extracted from the ion source is determined by the geometrical admittance. For low converter voltages, the beam fills the phase space available and the beam emittance is equal to the ion source admittance. The extraction electrode is located 2.5 cm from the plasma electrode and has a 2.2-cm diam. aperture. The extraction voltage required for our present 16-mA production beam is only 12 kV. This is

a consequence of the high energy (250 eV) of the converter beam and of the relatively low plasma density at the plasma electrode. The difference between the extraction voltage and the total column voltage is applied across two high-voltage gaps in the column with the intermediate voltage being variable. For the present operation, this voltage difference is split equally between these two high-voltage gaps.

3 BEAM SIMULATIONS

The ray-tracing code PBGUNS Version 3.20 [5] has been used to model the production of the H- beam in the ion source and the subsequent acceleration in the 80-kV accelerating column. This code computes beam trajectories starting at the converter surface and propagates the beam through the ion source plasma and then subsequently accelerates the beam through the 80-kV accelerating column into the low-energy beam transport (LEBT) line. Emittance plots can be produced at four positions along the beam line, and the evolution of the beam phase space can be followed through the system as the ion source and accelerating column parameters are varied.

4 TEST STAND PROGRAM

To carry out the development of a new ion source, the LANSCE ion source test stand (ISTS) was rebuilt to have the same configuration as the injector in the accelerator. Thus, it now provides a means for testing ion source improvements and modifications in an off-line environment [6]. A spare converter ion source was mounted on the ISTS, and beam tests were carried out which demonstrated that the operation of the ion source on the test stand was the same as that on the injector.

Although the PBGUNS code had been benchmarked against experiments for positive ion sources, there has not yet been a similar validation for the negative ion sputter sources that we are using [7]. We decided, therefore, to carry out an experimental program to compare the simulation predictions to the emittance data taken with our present ion source. A series of emittance scans were taken at the first emittance station (EM-1) in which the ion source parameters were held constant and the extraction voltage was varied from 8 kV to 15 kV. A typical emittance scan for the 12-kV case is shown in Fig 2.

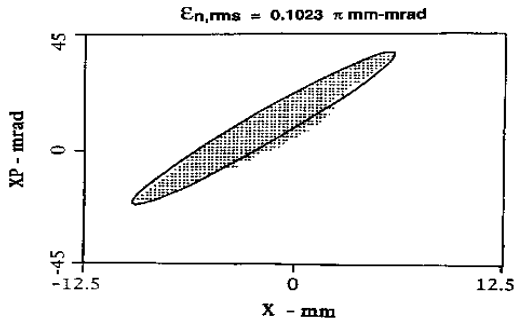

Figure 2: Horizontal emittance scan of a 16-mA H^- beam at the column exit with 12-kV extraction voltage.

Simulations were then run for all the extraction voltages with the ion source parameters fixed at the production values. The calculated phase-space distribution for the 12-kV extraction voltage case is shown in Fig. 3.

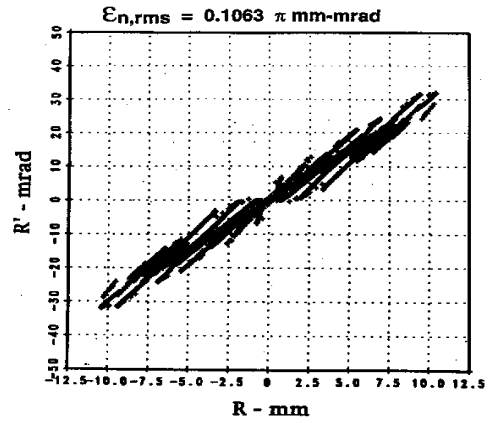

Figure 3: Calculated emittance distribution of a16-mA H^- beam at the column exit for 12-kV extraction voltage.

The experimental data observed at EM-1 and the corresponding PBGUNS simulations are compared in Table I.

Both the ray-tracing code and the emittance analysis code

Table 1: Comparison of Emittance Data and PBGUNS Simulations

kV Extraction Voltage	π mm-mrad Normalized rms Emittance		Mismatch Factor	cm Beam Size		mrad Beam Divergence	
	EM-1	PBGUNS		EM-1	PBGUNS	EM-1	PBGUNS
8.0	0.0984	0.1096	1.53	0.880	0.879	29.19	18.41
9.0	0.1096	0.1065	1.53	0.893	0.924	31.34	21.88
10.0	0.1003	0.1071	1.30	0.853	0.948	30.68	24.85
11.0	0.1032	0.1040	1.23	0.848	0.941	31.86	25.79
12.0	0.1023	0.1063	1.20	0.803	0.939	31.08	27.44
13.0	0.1018	0.1044	1.26	0.763	0.913	30.78	27.21
14.0	0.0100	0.1036	1.27	0.714	0.891	29.97	27.44
15.0	0.0972	0.1028	1.32	0.672	0.856	29.86	27.57

carry out a second moments analysis to determine the rms emittance of the beam. We see that for the rms emittance the experimental data and beam simulations agree to within a few percent. We note that for the converter source being modeled, the beam size and divergence values given by PBGUNS on the emittance plots are closely approximated by the 2rms values calculated by this code, i.e., by the beam parameters of a 4rms beam. We have, therefore, chosen to compare the beam parameters for the experimental beams with the 4rms beam parameters calculated by PBGUNS. We see that the beam sizes for the observed EM-1 beams are typically 10% smaller than the calculated 2rms beam size and that the observed beam divergences at EM-1 are approximately 15% larger than the 2rms divergence values. Thus, while the beam code calculates the phase space area correctly, there are still systematic differences between the measured and simulated beam size and divergence which probably arise from errors in the location of beam transport elements or errors in the assumed space-charge neutralization model. Work is in progress to resolve these discrepancies.

5 HIGH-VOLTAGE COLUMN SIMULATIONS

Having established that the LANSCE H^- injector beam can be modeled with the PBGUNS code, we carried out simulations for the higher beam currents. We first determined the performance of the present injector systems as we increased the extracted beam current. We increased the extraction voltage to keep the beam perveance constant in the extraction gap as the extracted current was increased. Thus, as the beam current was increased from 16 mA to 40 mA, the extraction voltage was varied from 12 kV to 22 kV. The variation of beam emittance and beam sizes at several locations in the beam line are shown in Fig. 4.

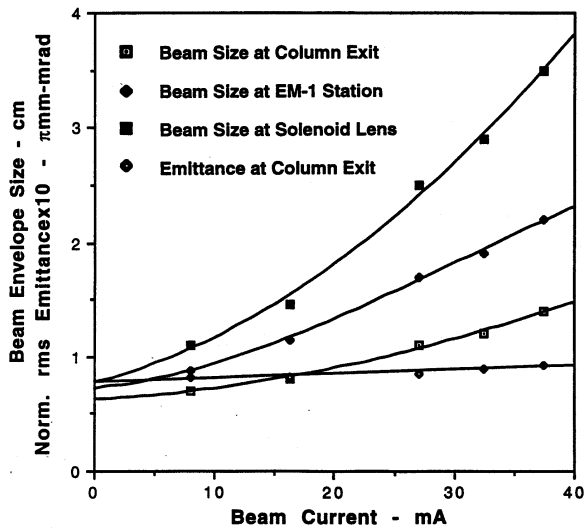

Figure 4: Beam emittance at the column exit and beam sizes in the LEBT as a function of extracted current.

We see that the emittance of the beam at the column exit remains essentially constant over this range of currents for the perveance matching employed in the extractor gap. The beam size in the beam line increases continuously with increasing current and exceeds the aberration limit in the solenoid lens (half the bore aperture) for 27 mA and fills the bore aperture for currents approaching 40 mA. Thus, the present injector can be used for beam currents up to 27 mA without emittance degradation, but a new accelerating column with stronger focusing will be required for beam currents at the 40 mA level.

Several accelerating column designs have been studied using this simulation code. The beam profiles for a high gradient tetrode column with a decel ion trap and for the present accelerating column are presented in Fig. 5. The beam envelope sizes in the LEBT for the tetrode design with 40 mA are essentially the same as those with the present column for 16-mA beams.

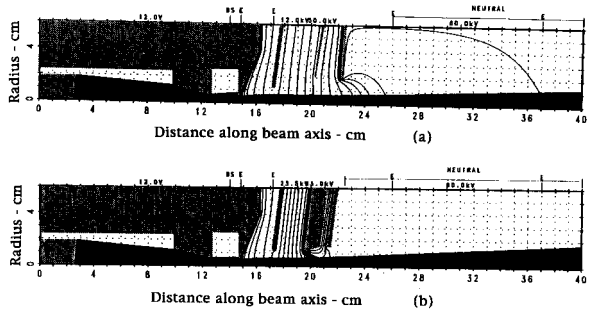

Figure 5: Trajectories and equipotentials for the 16-mA production beam with the present accelerating column (a) and for a 40-mA beam with a high gradient tetrode column (b).

REFERENCES

[1] R. L. York and Ralph R. Stevens, Jr., "Third International Symposium on Production and Neutralization of Negative Ions and Beams," Brookhaven National Laboratory, 1983, p 410.

[2] C.F.A. van Os, K.N. Leung, and W.B. Kunkel, *Appl. Physics Letters*, **57** (9), August, 1990, p 27.

[3] C.F.A. Van Os, K.N. Leung, and W.B. Kunkel, J. Appl. Physics, **69** (6), March 15, 1991, p 3485.

[4] M. Williams et al., "Ion Source Development for LANSCE Upgrade," Proc. of 1998 LINAC Conf., to be published in these proceedings.

[5] Jack E. Boers, Proc.of 1995 Particle Accelerator Conference, May 1995, p 2312.

[6] W. Ingalls et al "Enhanced H^- Ion Source Testing Capabilities at LANSCE," Proc. of 1998 LINAC Conf., to be published in these proceedings.

[7] Jack E. Boers, private communication.

ION SOURCE DEVELOPMENT FOR LANSCE UPGRADE

M. Williams, R. Gough, R. Keller, K. Leung, D. Meyer[i] and A. Wengrow
E. O. Lawrence Berkeley National Laboratory, Berkeley, CA 94720

O. Sander, W. Ingalls, B. Prichard, and R. Stevens
Los Alamos National Laboratory, Los Alamos, NM, 87545

Abstract

Design and testing of the prototype ion source for the Los Alamos Neutron Science Center (LANSCE) Facility is described.

1 INTRODUCTION

The next generation spallation neutron sources, such as the upgrade of the Los Alamos Neutron Science Center (LANSCE) Facility will require high intensity negative hydrogen (H^-) beams. Lawrence Berkeley National Laboratory has been contracted by Los Alamos National Laboratory to develop an H^- ion generator that can meet the upgrade LANSCE neutron source requirement. Specifically, the output current of the new H^- ion source has to increase from 16 to 40 mA. In addition, source emittance, reliability, and availability will need to be improved. All of which must be achieved while operating under the facility's prescribed 12% duty factor (1 ms pulse at 120 Hz).

In order to meet the LANSCE source requirement, the Ion Beam Technology (IBT) Program at LBNL chose the surface-conversion multicusp ion source as the base candidate. The present LANSCE H^- source is also a surface-conversion source [1]. However, the H^- output current doesn't improve much beyond 20 mA with higher discharge power. Previous experimental study at LBNL demonstrated that if the surface converter source is operated with a magnetic filter, the H^- output current generated by a barium converter can increase without saturation with increased discharge power [2]. Based on this study, a prototype ion source has been developed to utilize the multicusp magnet arrangement as a filter. Cesium is used to enhance the H^- yield.

2 ION SOURCE CONFIGURATION

LBNL has been developing multicusp surface conversion ion sources for many years [3,4]. The typical multicusp H^- surface conversion source is primarily composed of a plasma chamber and a negatively-biased converter electrode as illustrated in Figure 1.

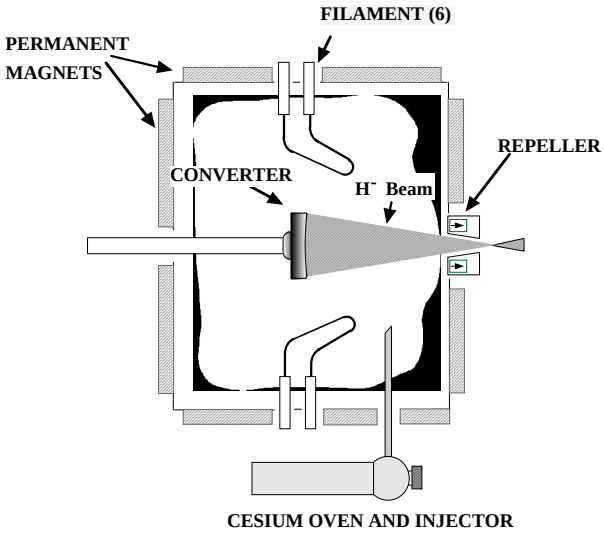

Figure 1: Schematic of the surface conversion ion source.

The positive ions present in the hydrogen plasma (H^+, H_2^+, H_3^+) are accelerated towards the converter surface. H^- ions can then be formed either by a backscattering process or by a sputtering process when the ions impinge on the converter surface. The converter is coated with a low work-function metal such as cesium to enhance negative ion conversion.

The current LANSCE ion source has a cylindrical body and the negative ions are extracted radially. The two filament cathodes are located on the cylinder end flanges. The LBNL prototype, Figure 2, is also of cylindrical design, however the negative ions are extracted along the source axis. This allows six filaments to be placed within the magnetic field generated by the cusp magnets on the wall (Figure 3).

The magnets provide a filter field which reduces the number of energetic electrons in the main plasma volume. This reduces the negative ion stripping due to energetic electrons. A converter of twice the area of the current converter is also used. The radius of curvature is increased to maintain the same projection angle. The axial position of the converter was optimized for maximum H^- output.

[i] Permanent address: Kernfysisch Versneller Instituut, The Netherlands.

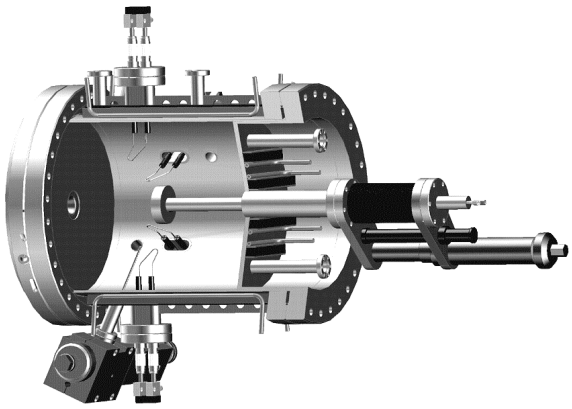

Figure 2: A 3-D rendering of the prototype ion source.

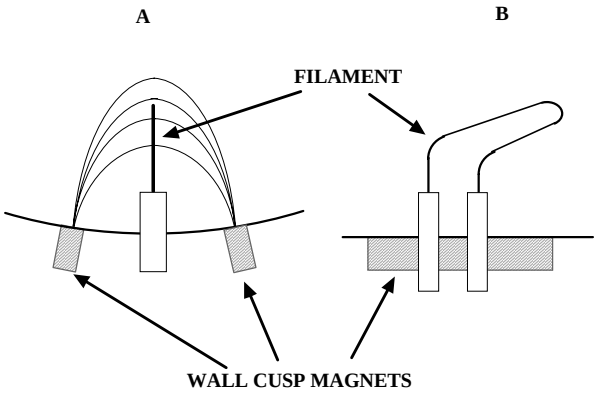

Figure 3: Location of the filament within the wall cusp magnet field. A. View along longitudinal axis. B. Viewed side on.

The prototype source utilizes a repeller electrode similar to the one in the current LANSCE ion source [1] This electrode is typically biased a few volts positive with respect to the anode to repel electrons. It also incorporates a dipole cusp arrangement in the extraction region which deflects the energetic electrons produced by secondary emission from the converter surface.

Figure 2 shows a 3-D rendering of the prototype ion source. The vacuum manipulator is used to optimize the converter position. In order to reduce cesium consumption, the ion source is designed for the walls to run at approximately 100° C, so as to avoid condensation of cesium in cool areas.

3 EXPERIMENTAL RESULTS

The prototype ion source has been operated at the design specifications. Figure 4 is a plot of H^- output as a function of arc power. The arc voltage was 80 volts, the source pressure was 1.2 mTorr and the converter voltage was 330 volts. It can be seen that the highest H^- current measured exceeded the required 40 mA. The duty factor was 12 %, 1 msec pulses at 120 Hz. Figures 5 and 6 show the H^- beam pulses at 12 % duty factor. These results were obtained without the normal LANSCE accelerator system.

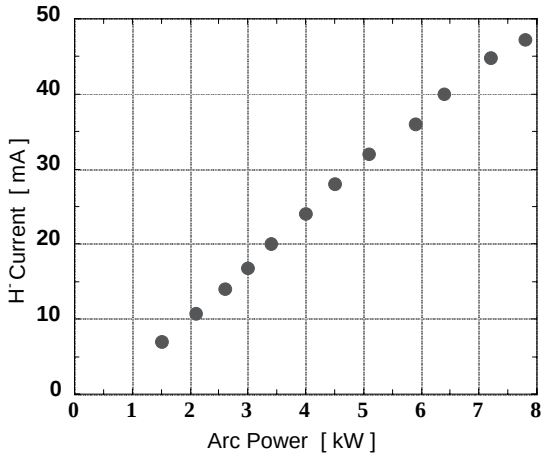

Figure 4: Plot of H^- current as a function of arc power

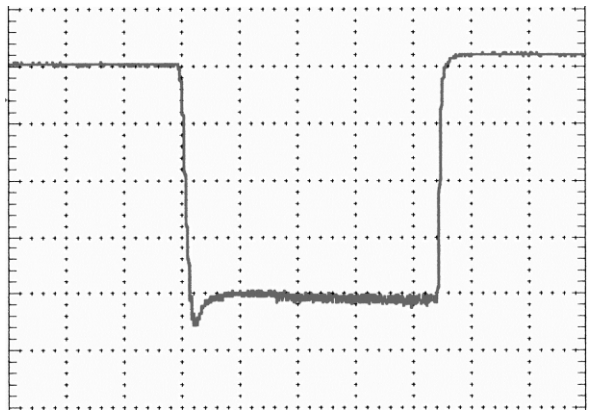

Figure 5: An oscilloscope display of the 40 mA H- pulse. The vertical scale is 10 mA/div. The time scale is 250 µsec/div.

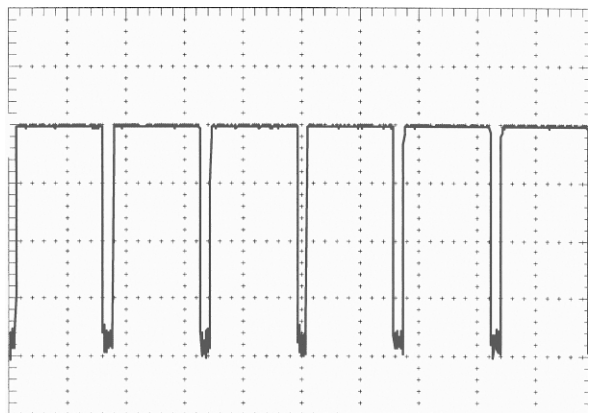

Figure 6: An oscilloscope display of the H- pulse at 12% duty factor. The vertical scale is 10 mA/div. The time scale is 5 msec/div.

4 CONCLUSIONS AND FUTURE PLANS

It has been demonstrated that the prototype ion source for the LANSCE upgrade can produce the required 40 mA of H^- at a 12 % duty factor. When operating with diligence the day to day operations show well reproducible results. The most significant problem with this source is getting a compromise between wall temperature and cesium injection. A low wall temperature requires constant cesium injection. If the wall is too hot, the cesium vapor pressure gets too high and the plasma is dominated by cesium ions and the H^- output tapers off requiring higher arc power to attain the 40 mA output. However, the present source is not constructed to allow for simple control of wall temperature; this issue will be addressed in the next design.

An earlier version of the proposed source design fabricated from existing components was tested at LBNL and is now being tested on the LANSCE Test Stand. The results obtained at both laboratories are similar. LANSCE is planning to make emittance measurements with the prototype source to compare with the present LANSCE operation source.

At this time a new production source is under design that will include features indicated by testing of the prototype ion source. One of the main concerns is the ability to adjust the wall temperature. The design is near completion and fabrication is expected to take about two months. Testing is expected to begin in early November.

5 ACKNOWLEDGMENTS

We would like to thank C. A. Matuk, R. Low S. B. Wilde, P. J. Rosado, T. A. Mc Veigh, M. L. Rickard and L. W. Mills for their technical assistance. This work was supported by Los Alamos National Laboratory and the U.S. Department of Energy under Contract No. AC03-76SF00098.

REFERENCES

[1] R. R. Stevens Jr., R.L. York, R. Kendarian, Proceedings of the 1984 Linear Accelerator Conference.

[2] C.F.A. van Os, K. N. Leung, and W. B. Kunkel Appl. Phys. Lett. **57** (9), 27 Aug. 1990.

[3] K. W. Ehlers and K. N. Leung, Rev. Sci. Instrum. **51**, 721 (1980).

[4] K. W. Ehlers and K. N. Leung, Rev. Sci. Instrum. **53**(6), 803 (1982).

HIGH POWER TEST RESULTS OF THE FIRST SRRC/ANL HIGH CURRENT L-BAND RF GUN

C.H. Ho, S.Y. Ho, G.Y. Hsiung, J.Y. Hwang, T.T. Yang,
Synchrotron Radiation Research Center, No.1 R&D Road VI, Hsinchu 30077, Taiwan
M. Conde, W. Gai, R. Konecny, J. Power, P. Schoessow
Argonne National Laboratory, 9700 S. Cass Avenue, Argonne, Illinois 60439, USA

Abstract

A joint program is underway between the SRRC (Synchrotron Radiation Research Center, Taiwan) and ANL (Argonne National Laboratory, USA) for developing a high current L-band photocathode rf guns. We have constructed an L-Band (1.3 Ghz), single cell rf photocathode gun and conducted low power tests at SRRC. High power rf conditioning of the cavity has been completed at ANL. In this paper we report on the construction and high power test results. So far we have been able to achieve > 120 MV/m axial electric field with minimal dark current. This gun will be used to replace the AWA (Argonne Wakefield Accelerator)[1] high current gun.

1 INTRODUCTION

The generation of high gradients (> 100 MV/m) in wakefield structures requires a short pulse, high intensity electron drive beam. The goal of the AWA is to demonstrate high gradients and sustained acceleration of charged particle beams using wakefield methods. The main technological challenge of the AWA program is the development of a photoinjector capable of fulfilling these requirements. The laser photocathode source was designed to deliver 100 nC bunches at 2 MeV to the drive linac. The photocathode gun is a single cell standing wave cavity with designed peak field of 90 MV/m on the cathode[2]. However, due to surface contamination and damage during the initial rf conditioning of the original gun, the peak electric field on axis is only limited to 55 ~ 65 MV/m rather than the designed field 92 MV/m due to the severe dark current beam loading[3].

A collaboration between SRRC and ANL has been established to construct a new L-band single cell photocathode rf gun and associated test stand. The goals of this collaborative research effort are to characterize the beam produced by this gun, and to study high field breakdown phenomena, dark current, and quantum efficiencies of various photocathode materials.

2 FABRICATION AND COLD TESTING

The gun cavity structure is shown in Figure 1. The cooling channel is built inside the cavity body instead of just attaching it to the outer surface. The cavity is also equipped with a tuner and a field strength monitor.

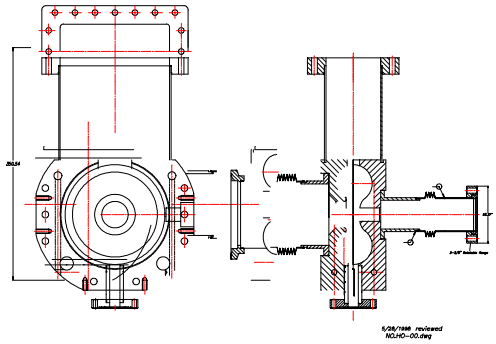

Figure 1: Assembly drawing of the gun cavity

The cavity was CNC machined several times to reach the correct resonant frequency and critical coupling. The cavity surface (mounted on a rotating stand) was then polished using 3M Imperial Lapping Films (60, 40, 30, 15, 12, 9, 5, 3, and 1 micron) and then Buehler Micropolish II Alumina Suspensions (1, 0.3 and 0.05 micron).

The cavity components were brazed together in a vacuum furnace in several stages to allow the joining of various components. After brazing and applying Vac Seal to eminent possible small leaks around the joints between the WR-650 waveguide and the cavity, it was vacuum tested using a Helium leak detector (Balzers HLT 160) and found to be Helium leak tight to better than 10^{-10} standard c.c./sec. However, it was found that the resonant frequency had been shifted down by 2.5 MHz and the

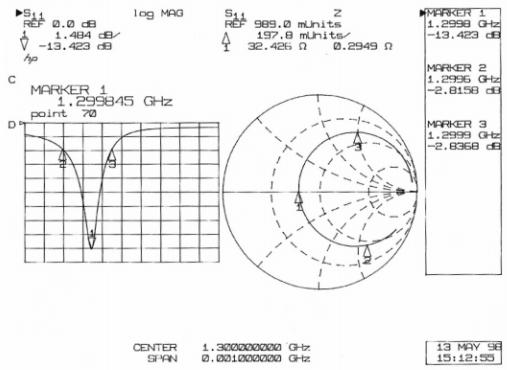

Figure 2: Reflection coefficient of gun cavity measured using HP8510C network analyzer.

coupling coefficient shifted from 1 (critical coupling) to around 1.5 (over coupled). The frequency shift is corrected back to 1.3 GHz using the tuner. Figure 2 is the measured plot in atmosphere and room temperature from the HP 8510C network analyzer after the cavity was installed and tuned at ANL. The measured unloaded quality factor is around 13000, while the URMEL prediction for the unloaded quality factor is around 15000.

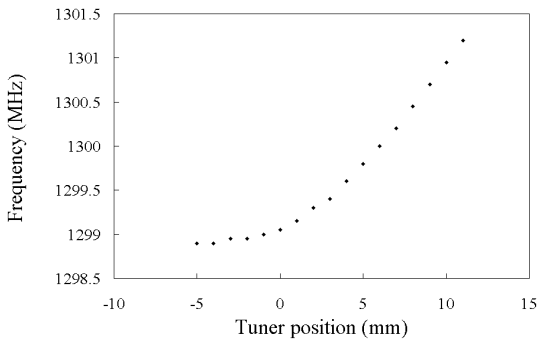

Figure 3: Measured resonant frequency dependence of tuner position.

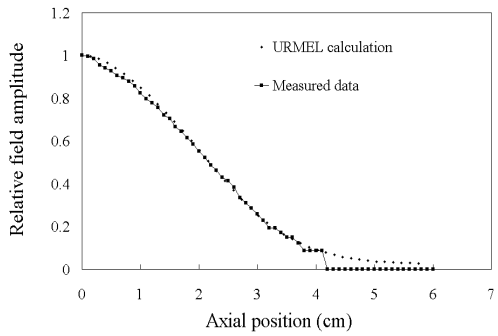

Figure 4: Longitudinal E-field profile on axis.

Figure 3 shows the measured frequency response to the tuner position (the tuning sensitivity is appear to be 1.8 MHz/cm in the linear region of the curve). Since the frequency is very sensitive to the cathode slug position, we use the tuner to fine tune the frequency. The cathode is held flush with the cavity inner surface to avoid arcing due to the discontinuity.

A ceramic bead of 2 mm diameter was used to perform the bead pull measurement. Figure 4 shows the longitudinal E-field profile along the central axis of the cavity from the bead pull measurement results and the URMEL prediction.

Bucking and focussing solenoids were also designed, constructed and measured at SRRC. The measured magnetic field profile is in close agreement with the POISSON calculation.

3 EXPERIMENTAL SETUP

The layout of the L-band rf gun test stand is shown in Figure 5. The whole system was first assembled and vacuum tested at SRRC and then shipped and installed at ANL in May, 1998. Two Molecular Drag pumps (16 CFM) and two oil free magnetic suspension Turbo Molecular Pumps (400 l/s) were used for roughing and baking. Two sputtering ion pumps (60 l/s) and one Non-Evaporable Getter (NEG) pump (500 l/s) were used to reach a base pressure of around 1.6 nTorr and maintain the pressure at around 13 nTorr during conditioning of the cavity.

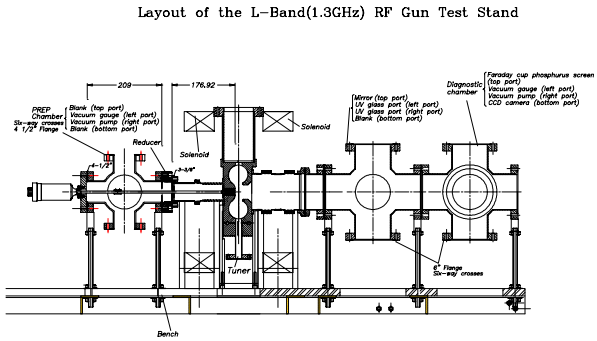

Figure 5: Layout of the L-band rf gun test stand.

4 HIGH POWER TEST RESULTS

RF conditioning of the gun proceeded smoothly. During the conditioning, the vacuum was kept under 50 nTorr and the occurrences of breakdown were kept to minimum. The forward, reflected rf power and dark current were also monitored continuously. Figure 6 shows the forward power to the gun with peak power of 2 MW. Figure 7 gives the reflected rf power and it shows almost no detuning of the gun due to the dark current.

In fact, because this gun was over coupled after brazing, the loading from the dark current will move it toward critical coupling to some extent. Since the field monitor was not instrumented yet for this test, one can only estimate the surface field using the rf reflection coefficient and the dark current. For 2 MW forward power with no reflection, we have estimated the surface field at the cathode center to be 100 MV/m[2]. This is somewhat larger than the designed value of 92 MV/m at 1.5 MW. At 100 MV/m, dark current is about 13 nC per rf pulse, in comparison with the original AWA gun which is 40 -60 nC at ~ 60 MV/m.

Further rf conditioning has been done to further reduce the dark current and increase the axial electric field to 120 MV/m. With a few additional days of conditioning, we have increased the rf forward power to 3 MW, still with no dark current induced rf reflection, with the equivalent photocathode field of 117 MV/m. The peak electrical field on the nose cone is 152 MV/m. Measured dark current is 25 nC /pulse. This is a 40% above the designed field and should be able to provide improved performance over the original AWA gun. Figure 8 shows the dark current transported out of the gun versus the forward rf power (surface field). It clearly shows the exponential dependence of the surface field. Below 70 MV/m, no significant dark current was observed. However, it goes up quickly as the surface field increases.

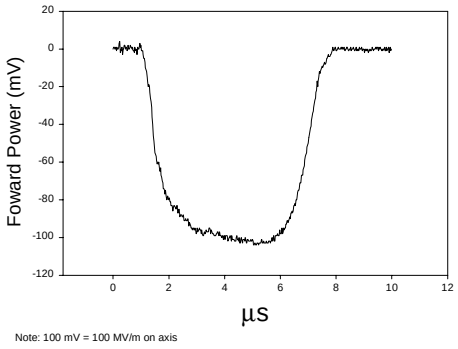

Figure 6: Measured forward rf power to the gun. This is a scope trace that measures envelope of rf pulse with calibrated diode detector. The peak voltage corresponds to 2 MW peak rf power.

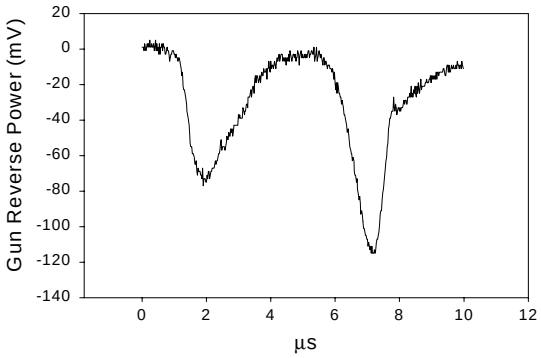

Figure 7: Reflected rf power from the gun. It shows that after the gun was filled, no reflection was observed.

5 SUMMARY

The first L-band rf gun cavity resulting from the joint collaboration between SRRC and ANL has been constructed, installed and conditioned. The high power test results are very encouraging. Input rf power was applied to rf cavity and increased from 100 kW level to 2 MW level within two days. Further conditioning increased the accelerating gradient in excess of 120 MV/m at the photocathode. The dark current measurement results show little effect of beam loading at this power level. We will replace the current AWA drive gun with this new gun, which should enable us to obtain shorter electron beams, and thus improve the gradients obtained in wakefield acceleration experiments.

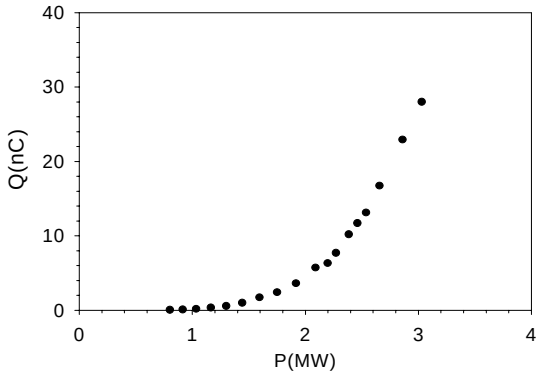

Figure 8: Measured dark current at the down stream against the surface field (forward rf power). It shows the exponential dependence and the maximum dark current observed was 30 nC at 120 MV/m (3 MW).

6 ACKNOWLEDGMENTS

We would like to thank Mr. T.T. Wu from ITRI for operating the vacuum brazing furnace. We would also like to thank Mr. M.H. Huang and Mr. C.H. Chang of SRRC for helping the construction of the solenoid, and Mr. F.Y. Lin and Dr. C.S. Hwang of SRRC for helping the measurement of the solenoid field profile. We would also like to thank the kind help from Mr. V. Svirtun, Mr. R. Nielson, and Dr. J. Noonan of ANL-APS, and Mr. R. Taylor of ANL-HEP during installation of the gun. This work is supported in part by the National Science Council (Taiwan) under contract No. NSC 87-2613-M-213-012, as well as by the Department of Energy (USA), Division of High Energy Physics, Contract No. W-31-109-ENG-38.

7 REFERENCES

[1] W. Gai et. al., in AIP Conf. Proc. 398 for the 7th Workshop on Advanced Accelerator Concepts Oct. 12-18, 1996, Lake Tahoe, California, p.116.
[2] C.H. Ho, PhD Thesis, UCLA, 1992.
[3] M. Conde et. al., to be appeared in Physical Review Special Topics- Accelerators and Beams, 1998.

EXTRACTION AND LOW ENERGY TRANSPORT OF NEGATIVE IONS*

A. Lakatos, J. Pozimski, A. Jakob, H. Klein,
Institut für Angewandte Physik, Universität Frankfurt, 60054 Frankfurt, Germany

Abstract

High perveance negative ion beams with low emittance are essential for several next generation particle accelerators (i. g. spallation sources like ESS [1] and SNS [2]). The extraction and transport of these beams have intrinsic difficulties different from positive ion beams. Limitation of beam current and emittance growth have to be avoided. To fulfill the requirements of those projects a detailed knowledge of the physics of beam formation the interaction of the H^- with the residual gas and transport is substantial. A compact cesium free H^- volume source delivering a low energy high perveance beam (6.5 keV, 2.3 mA, perveance K= 0.0034) has been built to study the fundamental physics of beam transport and will be integrated into the existing LEBT section in the near future. First measurements of the interaction between the ion beam and the residual gas will be presented together with the experimental set up and preliminary results.

1 INTRODUCTION

The production and transport of high current negative ion beams is a key issue for future high current accelerators. For ESS, as an example, an H^- beam with 70 mA at 55 keV (K=0.0035) and ε_n = 0.1 πmmmrad is required using non Liouvillian stacking schemes for the accumulation rings. An ion source has been developed in Frankfurt, which is now able to deliver an H^- current even higher than necessary [3]. To reduce particle losses at high beam energy (above the coulomb barrier) and to maximise the available current the beam has to be treated carefully between the plasmaelectrode and the first RFQ. External and internal fields can induce emittance growth, space charge forces and interactions of the beam with the residual gas can limit the transportable current.

Different extraction and ion beam transporting schemes are under discussion [4,5], each have various positive and negative aspects. To improve the H^- to e^- ratio magnetic filterfields (i. g. dipoles) are used. In our case these filterfields are in conjunction with dipole fields for electron dumping. The quality of beam extraction simulations suffers from these additional magnetic fields in the low energy part of the extractor. The destruction of the rotational symmetry together with the space charge forces causes emittance growth and particle losses within the extraction system. High residual gas pressure near the extractor together with the high cross section for stripping will influence the transmission as well as space charge compensation.

LEBT of high perveance ion beams suffers from high space charge forces. Generally two systems are used:

electrostatic or magnetic lenses. The use of electrostatic lens systems has to deal with the full space charge and therefore has limited current transport capabilities. They suffer from high space charge forces causing in conjunction with field aberrations serious emittance growth. Magnetic lens systems can use space charge compensation to reduce the necessary focusing force and the radius of the beam in the lenses. Hence the emittance growth due to lens aberrations and self fields is reduced. In Frankfurt an experiment is under construction to investigate the influence of various parameters on beam formation and transport under space charge compensated and decompensated conditions. On behalf a H^- source has already been built. After the essential operation conditions for the source are studied the source will be incorporated into the existing **L**ow **E**nergy **B**eam **T**ransport (LEBT) line.

The details of the beamline layout are shown in Fig. 1.

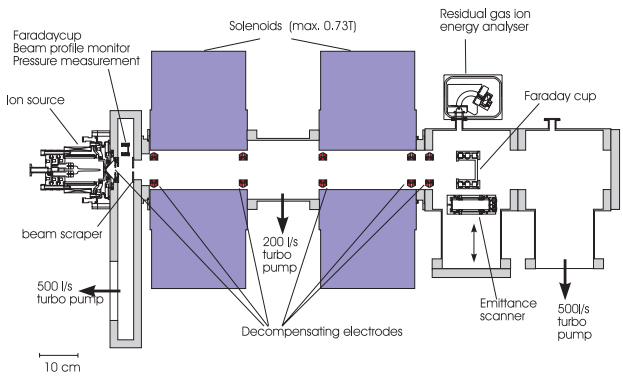

Figure 1: Schematic drawing of the experimental set up of the Frankfurt LEBT line.

An existing double solenoid (max. field 0.73 T) LEBT capable with the ESS scenario will be used for our investigations of high-current beam transport of negative ions. Therefore different beam diagnostic elements have been installed. Emittance measurement device and residual gas ion energy spectrometer and Faradaycups are available along the beampath. The degree of

* Work supported by BMBF under contract No. 06 OF 841

compensation can be regulated by decompensating ring electrodes as well as by varying the residual gas pressure in the LEBT. The measured beam properties, e. g. transverse emittance, degree of space charge compensation support the design of the future LEBT for negative ions.

2 ION SOURCE

An schematic drawing of the ion source for our experiment is shown in Fig. 2.

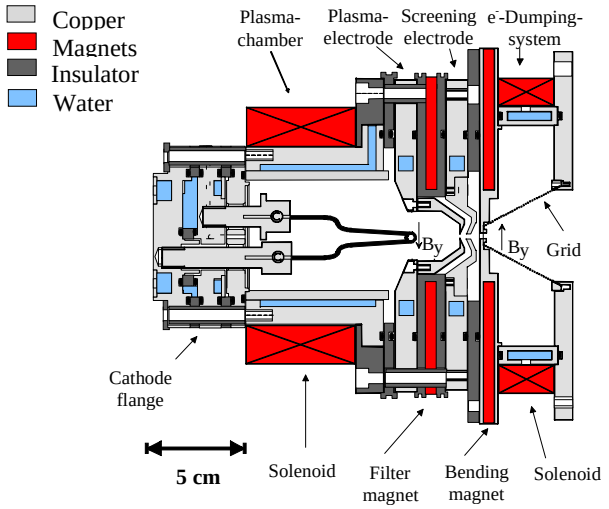

Figure 2: schematic drawing of the ion source.

The ion source [6], is of the volume type using a gas discharge driven by a hot cathode to atomize the H_2 molecules. The electrons are radially enclosed by a solenoidal field. A magnetic dipole filter field (electrical exited) near the extraction area is used to separate slow and fast electrons and therefore enhance the H^- production [7]. To inhibit influence on the diagnostic devices the source will be operated cesium free. This will limit the plasma density and therefore the ion current. The design value for the current density delivered by the plasma was chosen to be 20 mA/cm^2 a commonly reached value for cesium free H^- sources [8]. The H^- to e ratio has to be above 0.02 due to current restrictions by the high voltage power supply.

For the ion beam formation a single aperture accel - decel system is used. Various numerical simulations of the beam extraction using the IGUN [9] code have been performed for different extraction geometries. The goal was to build a compact triode extraction system insensitive to plasma density variations delivering a high perveance ion beam with minimised emittance.

The simulations have been performed for different ion current densities (0-50 mA/cm^2), different extraction voltages (4,5 and 6 kV) and aspect ratios between 0.2 and 1.2. The simulations showed that the boundary conditions are fulfilled for an aspect ratio of S = 0.375 and an extraction of 3 mm diameter. For the matched case a beam emittance of $\varepsilon_{n,RMS}$ = 0.001 πmmmrad (4kV) is calculated. For a current density of app. 25 mA/cm^2 delivered by the plasma generator a 4 keV H^- beam with 1.77 mA beam current is delivered. This will correspond to a beam perveance of K=0.0045 which is app. 30 % higher than proposed for the ESS project [6].

3 EXPERIMENTAL SET UP

To study the fundamental behavior of the ion source for different parameters of the plasma generator a test bench was installed. The details of the test bench layout are shown in Fig. 3.

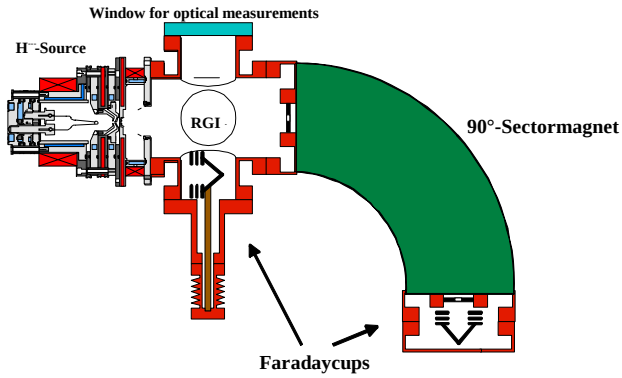

Figure 3: : Schematic drawing of the experimental set up of the test bench for the H^--source.

Multiple beam diagnostic elements like a magnetic spectrometer, a residual gas ion (RGI) energy spectrometer and Faradaycups have been installed. A window gives the opportunity to analyse the radial density profile of the extracted beam by using the incident light emitted by collisions of the beam ions with the residual gas atoms. Additionally the residual gas pressure can be varied in the test bench.

4 MEASUREMENTS

After the design parameters of our H^--source have been reached, the mass spectra of the emerging particle beams have been investigated by the use of the 90° sectormagnet, to prove that H^- has been measured in the Faraday cup.

Fig. 4 shows two spectra measured using a H^--beam of appr. 2 mA at a beam energy of 6.5 kV. The gas pressure inside the ion source has been 0.133 hPa and $5*10^{-6}$ hPa in the diagnostics chamber (mostly H_2 due to the gasflow from the source). The lower curve (for the negative charged particles) show peaks according to the extracted electrons and H^--ions (due to the electron dumping the spectrum does not indicate the extracted H^-/e^- ratio).

By changing the polarity of the magnetic dipole field we observed also positive ions. The mass of the ions have been calculated under assumption of an ion energy of 6.5kV as well.

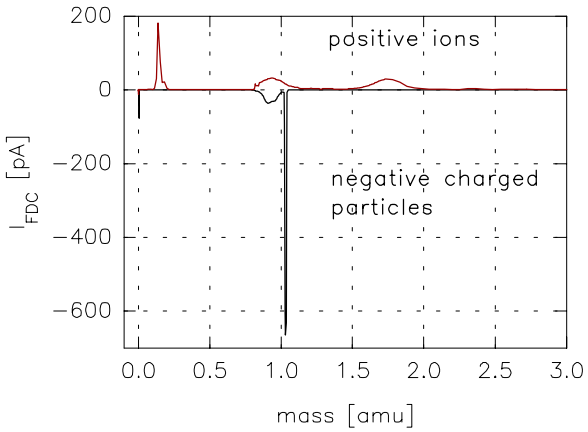

Figure 4: mass spectra of an extracted beam.

The ion energy of the positive ions which possibly are produced by interaction of H^- and electrons with residual gas atoms in the extraction area (at highest gas pressure) cannot be determined without additional investigations due to the fact that neither the ion mass (possible candidates are H^+, H_2^+, H_3^+, N^+, N_2^+, H_20^+) nor the energy is known. To exclude most of the possibilities two additional experiments already have been performed.

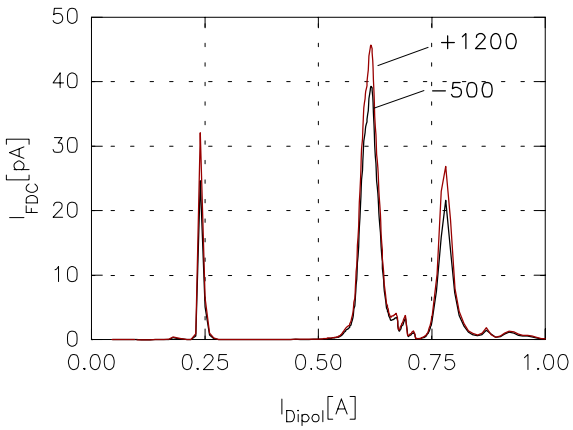

Figure 5: mass spectrum with decelerate potential of 1.2 kV and reference spectrum.

Fig. 5 shows the results of an experiment were the polarity of the secondary electron suppression electrode in front of the Faradaycup of the sector magnet has been changed from negative to positive (compared to ground potential). The electrode was biased up to +1200V (limited by constructional reasons). It is supposed that all positive ions with a kinetic energy below 1200 eV will be suppressed and therefore not detected. As shown in Fig. 4 the detected current is higher (due to the secondary electrons) than for the reference spectra and therefore it is likely that most of the positive ions have energies above 1200 eV. This indicates that their origin is not from inelastic collisions of H^- and e^- with heavy atoms (like N_2,H_20). Fig. 6 shows spectra measured at different extraction voltages (4.5-6.5 kV). We expected a change of the energy of the positive ions.

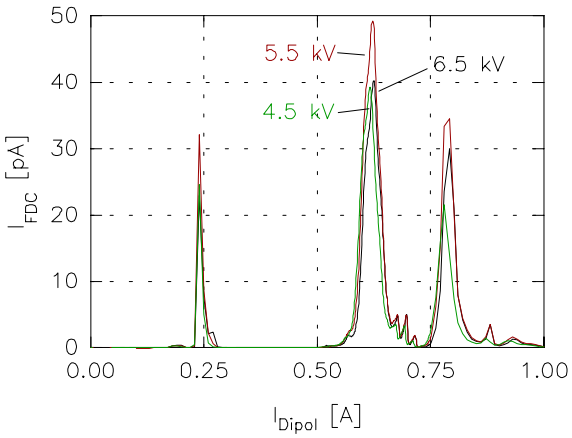

Figure 6: spectra gained for different extraction voltages.

if their energy is determined by the momentum exchange at interaction, but only minor changes of the measured positive spectra can be observed**.** Therefore an additional process determining the energy of the positive ions have to be assumed. Further work to understand these results in more detail are planed.

5 OUTLOOK

After the source tests on the separate test bench the source will be incorporated into the existing LEBT. The experiments will start with a DC beam to study the influence of the external parameters (filter fields, solenoids, residual gas pressure, voltage on decompensation electrodes, source noise) on emittance and transmission. For a next step the set up is already prepared for pulsed mode operation.

REFERENCES

[1] H. Klein et. al., "The ESS Technical Study", ESS-96-53-M, November 1996
[2] B.R. Appleton, J.B. Ball and J.R. Alonso , “The National Spallation Neutron Source”, EPAC’96, Sitges, June 1996. p. 575
[3] K. Volk, A. Maaser, H. Klein,“ The Frankfurt H- source for the E.S.S.“, LINAC’98
[4] J. W. Staples et al. , “All Electrostatic Split LEBT Test Results”, LINAC’96, Geneva, August 1996. p. 157
[5] J. Pozimski, P.Groß, R. Dölling, K. Reidelbach and H.Klein, "LEBT-Design Studies for ESS" , Proc. of ESS-PM4, October 1995, Weinfelden, PSI-Proc. 95-02
[6] A. Lakatos, J. Pozimski, A. Jakob, K. Klein, Proc. of EPAC 98, June 22-26, 1998, Stockholm, in print
[7] Ehlers, K. N. Leung et. al., "Increasing the efficiency of a multicusp ion source", Rev. Sci. Instr. 53(2), 1982, p. 1429
[8] Ehlers, K. N. Leung et. al., "Effect of a magnetic filter on hydrogen ion species in a multicusp ion source", Rev. Sci. Instr. 52(2), 1981, p. 1452
[9] R. Becker, W. B.Herrmansfeldt, Proc. of the 4th International Conference on Ion Source, Bensheim, Germany (1991)

STABLE AMPERE LEVEL EMISSION OF ENERGETIC ELECTRONS BY ELECTRICALLY EXCITED FERROELECTRIC CERAMICS

I. Boscolo, A. Scurati
University of Milano and INFN, Dipartimento di Fisica via Celoria 16, 20133 Milano, Italy

Abstract

Stable emission of energetic electrons from ferroelectric ceramic of PLZT type, i.e. lead zirconate titanate lanthanum doped, in form of thin disks have been obtained with a proper design of the front electrode. The current is about 1 A square centimeter and the energy is a couple of keV. High density, more than 50 A square centimeter, is obtained in the plasma assisted configuration. The electron expulsion from the surface is due to the spontaneous polarization switching induced by a high voltage pulse applied to proper metallic electrodes deposited as thin film on the two surfaces of the disk. In passing from the usual front electrode having the structure of an interconnected grating, to an electrode being a pattern of disconnected patches contained within a ring, the electron emission passes from erratic with samples and decaying with the number of shots to stable in both cases. This change in the behavior is explained by the fact that the sandwich of the continuous electrode and the grating constrains the domain switching and the relevant charge carriers motion within the part of material covered by metal, whilst a quasi-free surface allows the domain switching all over the whole area with the consequent flux of electrons in and out of the sample surface. In the plasma assisted emission, the front electrode must be the normal grating because the plasma in this electrode configuration is homogeneous.

1 INTRODUCTION

Electrons emitted from a ferroelectric cathode [1] come from ground to the crystal surface and then they are acted upon by the spontaneous polarization. This vector can be set in either direction with respect to the front (emitting) surface, depending on the sign of the voltage pulse applied at the rear electrode. With positive excitation (negative voltage), surface domains switch with the positive side pointing towards the front surface and then relax back. Therefore, in the first stage they attract screening electrons, then they push them out. With negative excitation, the negative side of the spontaneous polarization sweeps out the electrons loosely bound at the surface defects.

The process of excitation and relaxation must be of non-equilibrium type in order to have strong emission, so that the surface electron diffusion in the evolution towards an equilibrium state occurs through the material-vacuum interface [2]. Hence, the ceramics suitable for electron emission are the so-called ferroelectric relaxors [3] and antiferroelectric material with fast transition under the action of an electric field. The material used in the emission experiments was lead lanthanum zirconate titanate, called PLZT, with components proportion 4/95/5 and 8/65/35, where the numbers refer respectively to lanthanum, zirconium and titanium atom percentage. PLZT 4/95/5 material is in antiferroelectric (AFE) phase at the working room temperature, and it makes the transition to FE phase under the action of an electric field higher than 15 kV/cm, while PLZT 8/65/35 is in FE phase [4]. The emission observed [4, 5] with ceramic disks having the usual grating interconnected by a metallic ring, see fig.1, as front electrode had stable behavior neither with the number of shots in a single sample, nor in the level of emission (many times the emission was zero) for samples equal in composition, preparation and electroding. Instead, the emission obtained with an ensamble of

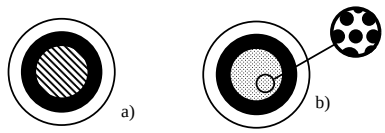

Figure 1: Sketch of the two electroding types of the front surface: the stripes are 200 μm with an interdistance of the same width.

metal islands surrounded by a metal ring was quite stable.

The application of an electric field higher than 10 kV/cm through the samples, induces not only the spontaneous polarization switching within the crystal, but also the plasma formation on the cathode surface [4]. Both processes generate electrons, but the former process generates a group of electrons that are energetic, whilst the latter generates only non-energetic electrons.

We call the emission due to the switching of the spontaneous polarization, ferroelectric emission (FE).

2 DISCUSSION OF THE RESULTS WITH THE GRATING AS ELECTRODE

The set-up is described in ref [5]. A virgin emitting sample typically starts to emit FE electrons, then the emission slows down and finally stops after about one hundred shots. This cycle repeats after the rejuvenation of the sample. PLZT 4/95/5 samples show always switching peaks, because of the antiferro-ferroelectric transition, while non-emitting PLZT 8/65/35 samples show no sign of switching current after a certain number of shots. We have ob-

served that the ferroelectric emission is recovered, at least partially, after the reversion of the electrical pulse and after a long rest of the sample, one-two days.

The fact that switching and emission currents go to die in pair, lead to think that there is a mechanism which progressively blocks the domain switching of the uncovered stripes and/or confines the electric field under the metal stripes. This blocking mechanism could be due whether to a domain screening process, or to the formation of macrodomains so the spontaneous polarization does not relaxes back, as it occurs in normal ferroelectrics. The fact that many times there is no emission even if a well pronunced switching current is present (as is the case with PLZT 4/95/5) leads to say that either the switching occurs only inside the zones covered by metal, that is it does not propagate laterally, or the surface becomes passivated for screening and surface mutation due impurities, gas desorption, electron reduction, etc., or finally, the switching mechanism is not enough fast to prevent an evolution of the crystal configuration after the excitation through a complete internal migration of the charge carriers after multishots operation. The possibility of the confinement of the electric field under the metal area is supported by the growth of oxygen-deficient dendrite tips under the metal [6] which cause the increasing of the local field and the decreasing of the switching time.

3 RESULTS WITH A PATTERN OF METALLIC ISLANDS AS ELECTRODE

Different pattern of metallic islands have been tested: a) a pattern obtained by deposition of a uniform 100 Ågold film (this deposition auto-arranges itself in separate patches), b) a very thin silver paste film, which auto-arranges as a patchwork; c) a uniform filling of the surface holes (we remember that the material is porous) by a carbon paste and d) an Au evaporation with a mask of 50 μm diameter islands with an interdistance of 50 μm. A sketch of the pattern is shown in fig. 1.

The samples without the metal islands (with the external metal ring only) did not work.

We have observed that the samples emit always with the new type of electrode, but the nearer the interdistance between the islands the more stable the emission resulted. The results obtained by holes filling are reported.

No accelerating voltage has been set through the diode gap by purpose, because we wanted to catch at the anode Faraday cup only the energetic ferroelectric electrons. An accelerating voltage would have mixed the relatively few FE electrons within the huge amount of electrons extracted from the plasma sheet.

a) Negative pulse at the rear electrode

The signals of the emitted current reported in figs. 2,3 show a good stability. With PLZT 4/95/5 there are two current peaks, while there is only one for PLZT 8/65/35 and in this second case the signal amplitude is 2-3 times higher and longer than the first. These characteristics were

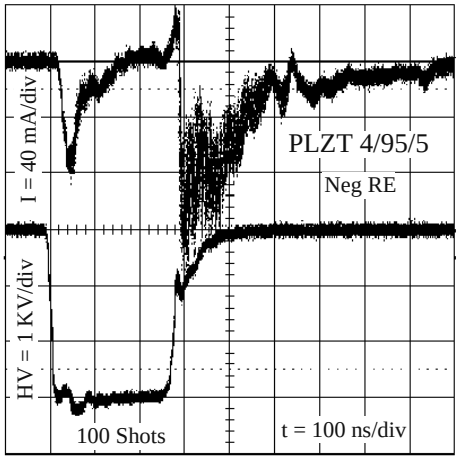

Figure 2: The superposition of 100 current signals, upper trace, and voltage signals, lower trace, is reported. The voltage pulse is applied to the rear electrode (RE), and the sample was a PLZT 4/95/5, as written in the frame, of 0.7 mm thickness.

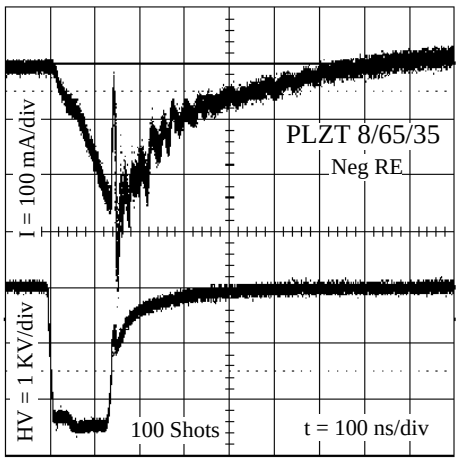

Figure 3: Ibidem as previous figure, but here the sample was a PLZT 8/65/35 of 1 mm thickness.

observed also with the grating, but here the second pulse in 4/95/5 material is substantially stable in time. For all the comparisons the reader is referred to the signals published in references [4, 5, 7]. The almost linear increasing of the 8/65/35 signal is explained by the continuous spontaneous polarization switching all along the excitation pulse. We notice that the very narrow pulses superimposed on the signals resemble the well known Barkausen pulses.

The first pulse is due to the building up of the spontaneous polarization oriented towards the rear electrode [5], while the second peak is due to the relaxation of the spontaneous polarization. The relaxation process of the spontaneous polarization is longer than its building up because in this latter case it is driven by the fast voltage pulse, and in the former case the ferroelectric state is metastable.

b) Positive pulse at the rear electrode

The signals of the emission are shown in fig.4 and 5.

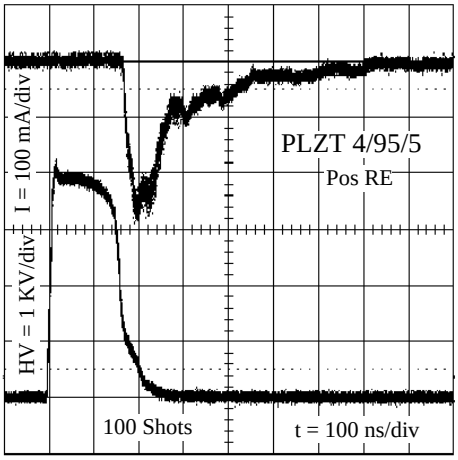

Figure 4: As in fig. 2 but with positive pulse to the rear electrode of a PLZT 4/95/5 sample.

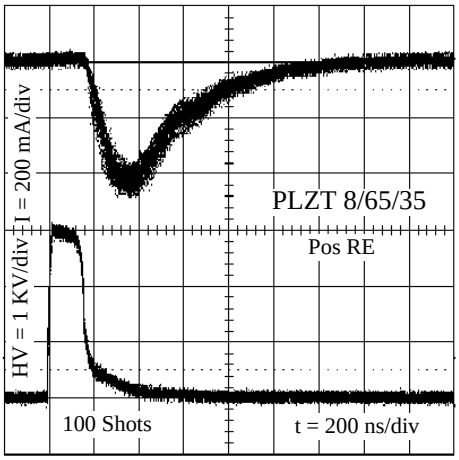

Figure 5: As fig.4 but for PLZT 8/65/35.

In this case the emission occurs at the relaxation of the spontaneous polarization P_s.

For the samples electroded with 100 Åfilm, the emission stopped after a certain number of shots because of the sweeping out of the metal islands.

4 DISCUSSION

The observations on samples with the grating lead to claim that a fast aging process is present for the application of a sequence of unipolar pulses. The neat separation of the cathode material in two parts, one under the metal stripes and the other one outside should induce a process of switching limitation within the covered zones and passivation of the uncovered surface.

The plasma which forms on the surface, owing to the high voltage of the excitation pulse, pushes further towards the surface passivation.

The screening and passivation processes do not occur for samples having disconnected metal patches as electrode. The disconnected electrode avoids the possible segregation of the electric field and so of the polarization switching under the covered zones. Our phenomenological view of operation is that the front of the voltage pulse propagates as a wave to the front surface, so inducing the co-propagation of polarization switching. As a consequence the surface switches into a substantial conduction state: in fact, the dP/dt current signal results in this configuration as high as with a completely electroded surface, further, in ref. [8] it was measured a high mobility of the charge carriers within the stressed region.

When the voltage excitation pulse is over, the surface goes to equilibrium by diffusion of the charge carriers through the surface towards the external ring or through the bulk. The paths of the electrons through the surface are not fixed because the surface state of a ferroelectric ceramic is dynamical and the surface is like a patchwork of peaces, whose properties [9] range from metallic to insulating.

We notice that in the grating case the plasma starts along all the rims of the stripes and covers the 200 μm in few hundreds of nanoseconds, in the other case that time is much longer because the plasma starts from the rim of the outside metal ring (it is connected to the pulser) and has to cover some millimeters of surface space.

It must be recognized that we are not able to give a clear phenomenological model explaining both the substantial unreliable operation with the first electroding and the reliable operation with this second electroding.

5 CONCLUSIONS

A stable copious emission of energetic ferroelectric electrons from a ferroelectric ceramic disk, under the application of a fast high voltage pulse, has been obtained when the electrode of the emitting surface was made as a uniform pattern of un-connected metal patches contained within a metallic ring.

6 REFERENCES

[1] H. Gundel, J. Handerek, H. Riege, E.J.N. Wilson and K. Zioutas, Ferroelectrics 100,1,1989.

[2] H. Glaefeke, *Topics in Applied Physics*, vol 37, 225-273, ed. P. Brorintich, New York, 1979.

[3] D. Viehland, S. J. Jang, L. Eric Cross, J. Appl. Phys. 68, 2916, 1990

[4] G. Benedek, I. Boscolo, J. Handerek, H. Riege J. Appl. Physics, 81/1396/ 1997

[5] G. Benedek, I. Boscolo, J. Handerek, A. Moscatelli, A. Scurati, J. Appl. Phys, 83,2776,1998.

[6] J. F. Scott, C. A. Araujo, B. M. Melnick, L. D. McMillan, R. Zuleeg, J. Appl. Phys. 70,382,1991.

[7] G. Benedek et al. NIM Phys. Res.A, 393,469-473, 1997.

[8] W. Mock, Jr. and W. H. Holt J. Appl. Phys. 50, 2740, 1979.

[9] K. Szot, W. Speier and W. Eberhardt, Appl. Phys. Lett. 60 (10), 1190-1192, 1992.

TIME-RESOLVED IMAGING FOR THE APS LINAC BEAMS*

A. H. Lumpkin, W. J. Berg, B. X. Yang, M. White
Advanced Photon Source
Accelerator Systems Division
Argonne National Laboratory
Argonne, IL 60439 USA

Abstract

The particle-beam imaging diagnostics for the Advanced Photon Source (APS) injector linac have been enhanced by the installation of optical transition radiation (OTR) screens and the use of Ce-doped YAG crystals as beam profile monitors. Both converters have improved spatial resolution and time responses compared to the standard Chromox (Al_2O_3:Cr) screens used elsewhere in the linac. These enhancements allow us to address the smaller beam sizes (< 100 μm) and the critical micropulse bunch length of higher brightness gun sources. For the linac macropulse of 30-ns duration composed of 86 micropulses at S-band frequency intervals, only the OTR mechanism is prompt enough to separate individual micropulses and to allow streak camera measurements of the micropulse averaged bunch length. Tests have been performed at 400 to 625 MeV using the gated DC thermionic gun source. Beam sizes less than σ_x=30 μm have been observed with a micropulse bunch length of σ_t= 2-3 ps using OTR. First results on the lower-emittance rf thermionic gun are briefly discussed.

1 INTRODUCTION

The imaging of particle beams on linacs via intercepting screens and video cameras is a well-established practice. However, the time-resolving of individual micropulses in an rf linac macropulse and the measuring of micropulse bunch length requires a radiation conversion mechanism that is prompt compared to the time scale of interest [1]. In the case of the Advanced Photon Source (APS) injector linac, the addition of a lower emittance gun and the critical need for high peak currents in the developing self-amplified spontaneous emission (SASE) free-electron laser (FEL) application have motivated our enhancement of these diagnostics [2]. Optical transition radiation (OTR) screens and Ce-doped YAG crystals have been installed in selected places in the beamline. Both converters have improved spatial resolution and time responses compared to the standard Chromox (Al_2O_3:Cr) screens used elsewhere in the linac. Of the three converters only the OTR screens provide the response required to separate the S-band micropulses and to allow streak camera measurements of the micropulse averaged bunch length and longitudinal profile. At low currents the YAG:Ce provides good spatial resolution like OTR, but we report an apparent "size-blurring" effect for the YAG:Ce converter as current is increased that may limit its usefulness. Many tests have been performed at 400 to 625 MeV using the gated DC thermionic gun source to commission the diagnostics, and the first results with the rf thermionic gun were obtained in the summer of 1998.

*Work supported by U.S. Department of Energy, Office of Basic Energy Sciences, under Contract No. W-31-109-ENG-38.

2 EXPERIMENTAL BACKGROUND

The APS facility's injector system uses a 250-MeV S-band electron linac and an in-line 450-MeV S-band positron linac. The primary electron gun is a conventional gated DC thermionic gun. For one alternate configuration an rf thermionic gun, designed to generate low-emittance beams (< 5 π mm mrad) and configured with an α magnet, injects beam just after the first linac accelerating section [3,4]. Then both in-line linacs can be phased to produce 100- to 650-MeV electron beams when the positron converter target is retracted.

The rf gun's predicted, normalized emittance at higher peak current is lower than that expected of the DC gun, and correspondingly smaller beam spot sizes (< 100 μm) should result. In an early test we used a Ti OTR foil to cover half of a standard intercepting screen based on Chromox of 0.25 mm thickness (rotated 45° to the beam). The 45° angle also directed the OTR light out the same 90° port as the Chromox radiation. Previous experiences on the Los Alamos linac-driven FEL with a low-emittance photoelectric injector (PEI) showed the OTR screens could be used for profiling small beams [5]. This assembly allowed us to steer the e-beam from one converter to the other to compare observed beam spot sizes for spatial resolution tests and assess response time. Because the Chromox decay was so slow, we used a Spiricon video digitizer that could digitize and save images to disk at a 15-Hz rate. This proved more than adequate to track the Chromox decay time.

In addition, we subsequently installed a Ce-doped YAG single crystal of 0.5 mm thickness (obtained from Startec) normal to the beam direction with a polished metal mirror at 45° to the beam just behind it. A separate actuator was used to insert the OTR screen (Molybdenum mirror from Melles Griot) so that its surface was at 45° to the beam.

The light was transported out of the linac tunnel to an optics table via two 150-mm-diameter achromat lenses. The Chromox, OTR, or YAG:Ce light could be viewed by a Vicon charge-coupled device (CCD) camera; a charge-injection device (CID) camera; a Stanford Computer Optics Quik-05 gated, intensified camera; and/or a Hamamatsu C5680 dual-sweep streak camera. The synchroscan unit was phase-locked to 119.0 MHz, the 24th subharmonic of the 2856-MHz linac frequency. A low jitter countdown circuit has been built using Motorola ECLIN PS logic to generate the 24th subharmonic with sub-ps jitter [6].

3 EXPERIMENTAL RESULTS

3.1 Radiation Converter Comparison

As mentioned in the previous section, comparisons were made for Chromox versus OTR and YAG:Ce crystals versus OTR in the past year. In the first series, the beam was initially steered into the high efficiency Chromox. The electron beam optics were then adjusted to give the "best focus" on the OTR screen. The size was recorded, and then the beam was steered back to the Chromox. For beam sizes in the 150-μm regime as measured by OTR, we observed a larger size in the Chromox. We then estimated the Chromox-limiting resolution by subtracting the OTR image size from the total observed Chromox image size in quadrature. This resulted in a limiting value of σ_{res} ~ 200 μm as reported previously [7].

The response time of the Chromox was determined by triggering a single macropulse from the DC gun at 1 Hz and recording the succession of video images on the Spiricon hard disk. The digital images were then analyzed and intensities plotted as a function of elapsed time from the trigger. The 30-ns-long macropulse was like a delta-function in time compared to the Chromox decay time. In Fig. 1 this decay of image intensity is shown, and the 1/e value was determined as 300 ms. Using the OTR screen, only one frame had an image since OTR is indeed prompt versus video rates. The Chromox decay time is even long compared to macropulse separations of 30 ms at the 30-Hz rate.

In the YAG:Ce and OTR comparison, the tests were performed in a similar manner. Over the course of brief tests at 100-mA average beam current (about 3 nC in a macropulse), we repeatedly observed a larger beam size with YAG:Ce than with OTR. In the June 12, 1998 experiments we first established our beam size comparisons at low currents of 30 and 60 mA. We used an elongated vertical focus (aspect ratio H/V of 1/10) because this seemed to result in the smallest sizes we could make: 70 μm (FWHM) or 30 μm (σ). This value is close to the calculated resolution of the transport line. The neutral density filter difference of 2.0 was used at this reference point, and the camera position in Z was adjusted to compensate for

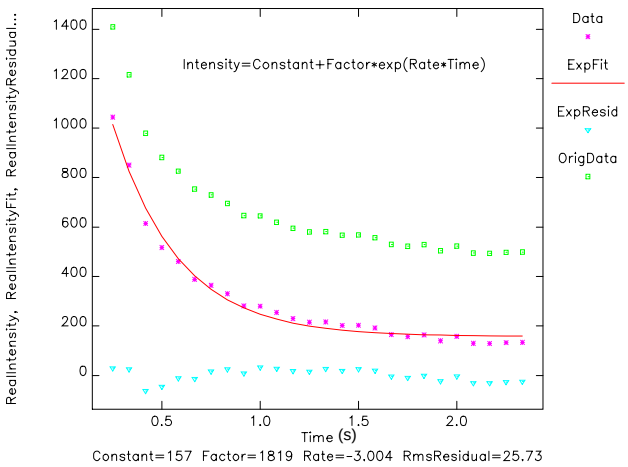

Figure 1: "X" Data with background subtracted are fitted to an exponential. The 1/e time is about 300 ms.

the YAG surface and OTR mirror surface location difference. These low-current data basically normalize and validate the screen comparison in terms of calibration factors, source strength compensation, camera saturation, and bremsstrahlung effects in the YAG:Ce. As shown in Fig. 2, at 100 mA and higher the YAG:Ce images are observed to be increasingly larger with current than the OTR images. There is a slight increase in the OTR image with current. The threshold for this "size-blurring" effect for this particular crystal/mirror and these conditions is 1.1 to 1.6 pC/μm^2 using the FWHM size. If the one-sigma beam sizes are estimated using a Gaussian shape assumption, the threshold is $(2.35)^2$ times smaller or 0.2 to 0.3 pC/μm^2.

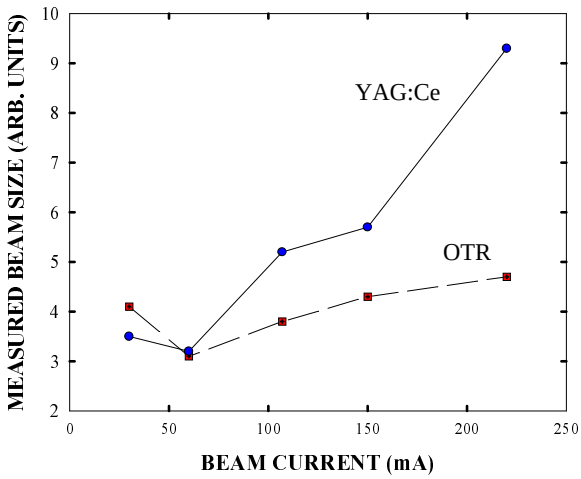

Figure 2: Comparison of observed beam image sizes using OTR (dashed line) and the YAG:Ce converter screens. Noticeable YAG:Ce (solid line) image size growth is observed beginning at ≤ 100mA and with spot size of about 40×400 μm^2 ($\sigma_x \times \sigma_y$).

Simplistically speaking, there may be a saturation-like phenomenon in the peak-intensity regime that results in the half-maximum intensity points growing relative to the peak. How the very large number of Ce-related impurity levels could be exhausted is unclear. Alternatively, mechanisms involving radiation trapping or photoionization may be involved [8]. The very small beam spots from a PEI that involve several hundred pC could easily approach this threshold observed in these 625-MeV tests. These charges and beam energies are higher than used in the single micropulse experiments previously [9]. Further tests and a search for alternative explanations are planned.

The reported response time for this YAG:Ce is 80 ns (FWHM) [9] so it averages the micropulses in a 30-ns macropulse. A measure of this was shown by comparing the micropulse bunch length seen with OTR to the YAG:Ce result. The OTR result was 4 ps (FWHM) while the YAG:Ce decay filled the 150-ps field of view and completely obscured the micropulse structure and a fortiori, the bunch length. The OTR result is very similar to that obtained previously by an rf phasing technique [10].

Table 1 summarizes these comparisons of the radiation converter spatial resolution, temporal response, and conversion efficiency. The limiting resolution number for APS-installed screens of Chromox and YAG:Ce are given and the OTR number estimated. The OTR response time is only an estimate, but this surface phenomena should be in the regime of the skin depth for visible light in a metal [11].

Table 1: Comparison of the Chromox, YAG:Ce, and OTR Converter Screens for Particle Beam Imaging at 600 MeV at APS

Screen	Spatial Resolution σ (μm)	Temporal Response	Intensity Arb. Units
Chromox (0.25 mm)	200	300 ms	1
YAG (0.5 mm)	<30 low current <100 200 mA	80 ns	1
OTR	<10	~ 10 fs	$\sim 2 \times 10^{-3}$

3.2 RF-Gun Accelerated Beam

On August 12, 1998 our first images of the rf-gun beam at 400 MeV were obtained at this station at the end of the linac. Both OTR and YAG:Ce images were obtained with the YAG:Ce size again being larger than the OTR size for ~160-mA average current and an approximate 130×130 μm^2 spot size. A preliminary synchroscan streak image gave a σ_t = 3 to 6 ps result even though no optimization of the rf gun had yet been done.

4 SUMMARY

In summary, the time scales for time-resolved imaging on the APS linac have been significantly enhanced. The targeted beam spot sizes of 100 μm (σ) can be addressed by YAG:Ce at low current (areal charge density) and OTR at higher currents. Micropulse bunch lengths at the ps-regime can also be addressed now. Optimization of the accelerated rf gun beam will be facilitated by these enhanced techniques.

5 REFERENCES

[1] Alex H. Lumpkin, “Advanced Time-Resolved Imaging Techniques for Electron-Beam Characterization,” 1990 Accelerator Inst. Workshop, AIP #229, 151-179 (1991).

[2] Stephen V. Milton et al., “Status of the APS Low-Energy Undulator Test Line,” Nucl. Inst. and Meth. A407, 210-214 (1998).

[3] M. Borland, “An Improved Thermionic Microwave Gun and Emittance Preserving Transport Line,” Proc. of the 1993 Particle Accelerator Conference, Washington, DC, May 17-20, 1993, 3015-3017 (1993).

[4] J. Lewellen et al., “Operation of the APS RF Gun,” Proc. of the LINAC’98, Chicago, Illinois, August 24-29, 1998 (to be published).

[5] A. H. Lumpkin et al., Nucl. Inst. and Meth. A296, 769-775 (1990).

[6] R. Laird and F. Lenkszus, Argonne National Laboratory, private communication, April 1997.

[7] A. H. Lumpkin, W. Berg, B. Yang, and M. White, “Preliminary Tests of the Optical Diagnostics for the APS LEUTL Particle Beam,” Proc. of the FEL’97, Beijing China, August 18-22, 1997 (to be published).

[8] M. Shinn, Thomas Jefferson National Accelerator Laboratory, private communication, August 1998.

[9] W. S. Graves, R. D. Johnson, and P. G. O’Shea, “A High Resolution Electron Beam Profile Monitor,” Proc. of the 1997 Particle Accelerator Conference, Vancouver, B.C., May 12-16, 1997 (to be published).

[10] N. Sereno et al., “Bunch Length Measurements at the Advanced Photon Source (APS) Linear Accelerator,” Proc. of the 1995 Particle Accelerator Conference, Vol. 2, 1070-1072 (1996).

[11] D. Rule, Naval Surface Warfare Center, private communication, June 1996.

LEDA & APT BEAM POSITION MEASUREMENT SYSTEM: DESIGN AND INITIAL TESTS*

J. D. Gilpatrick, J. F. Power, R. B. Shurter, M. Stettler
Los Alamos National Laboratory, Los Alamos, NM, 87545, USA
J. F. O'Hara
AlliedSignal Inc., Albuquerque, NM, 87196, USA
D. Martinez
General Atomics, San Diego, CA, 92186, USA

Abstract

Beam position measurements are being designed and fabricated for the Low Energy Demonstration Accelerator (LEDA), a 20-MeV, 100-mA-cw proton-accelerator, presently under construction at Los Alamos [1]. Similar position measurements will provide position information for a steering scheme within the Accelerator Production of Tritium (APT) linac magnetic lattice. The steering scheme, which centers the beam in the magnetic lattice, uses two position measurements and two translatable quadrupole magnets every 5.5-FODO-lattice periods. What makes these beam position measurements unique is how they will attain, maintain and verify the required accuracy. The position measurement systems consist of micro-stripline beam position monitors (BPMs) and RF coaxial cables, log-ratio processors, on-line error correction sub-systems, and a control system interface including associated algorithms and computer software. This paper discusses the mapping of the BPM probe response, the algorithm used to calculate low beam-velocity response, and the expected log-ratio processor performance.

1 INTRODUCTION

1.1 Beam Position Measurement Purpose

During the commissioning and operation of the LEDA radio frequency quadrupole (RFQ), beam position measurements serve two purposes. They provide sufficient beam position information for centering the 6.7-MeV beam both in the high energy beam transport (HEBT) magnetic lattice and on the high power beamstop, and they verify that the quadrupole magnetic field settings are properly set.

For APT, position measurements provide sufficient information for centering the beam in the magnetic lattice throughout the linac and HEBT. By placing BPM pairs within quadrupole magnet bores separated by ~90 degrees of phase advance, both beam position and trajectory angle are acquired. For example, early in the coupled cavity drift tube linac (CCDTL), where the phase advance per FODO lattice period is 78 degrees, two BPMs are installed in two focusing quadrupole magnets separated by a defocusing quadrupole magnet.

1.2 APT Steering Schemes

The CCDTL BPM placement scheme repeats every 5.5-lattice periods, allowing operators to correct for various static random errors. This scheme was simulated using budgeted beam-position-measurement errors similar to those shown in Table 1 and multiple quadrupole magnet misalignments, field amplitude errors, and other errors. For a 25-mm radius BPM, the total budgeted position-measurement precision and accuracy is 0.06- and 0.21-mm, respectively. Typical accuracy errors include BPM alignment errors and precision errors include RF cable isolation and BPM vibration.

Table 1: Beam-position measurement-error budget table using a 25-mm radius BPM.

Measurement Components	Precision (mm)	Accuracy (mm)
BPM	0.01	0.12
RF Cable Plant	0.0003	0.02
On-line Calibrator	0.03	0.16
Log-Ratio Processor	0.04	0.04
TOTAL	0.05	0.21

APT beam steering is accomplished by translating a quadrupole magnets pair for each BPM pair with the last steerer residing in the same focusing quadrupole magnet as the first BPM [2]. The additional half FODO lattice in the steerer/BPM-pair placement period allows a single axis of the beam's central trajectory to be corrected every 11-lattice periods.

2 MEASUREMENT SYSTEM

2.1 System Description and BPM Design

The position measurement system consists of four components; the BPM and its associated set of RF cables, an electronics processor, on-line error correction circuitry,

* Work supported by the US Department of Energy

and an Experimental & Physics Industrial Control System (EPICS) interface [3,4,5].

The BPMs are a four-electrode micro-stripline design with electrode characteristic impedances of 50-Ω. Each BPM has a physical feature that provides alignment verification with respect to the facility alignment references and ultimately with respect to the linac magnetic lattice. These alignment features also serve as a method to mate the BPM to its mapping fixture so that it's mapped electrical characteristics are directly related to the measured beam position. For the pictured LEDA HEBT BPM shown in Fig. 1, four optical-alignment-monument mounts are welded on the downstream vacuum flange. Those APT BPMs that are mounted within quadrupole magnets have additional constraints. For these BPMs, construction processes and materials are used to minimize the BPM's permeability and to ensure that the quadrupole magnetic fields are undistorted.

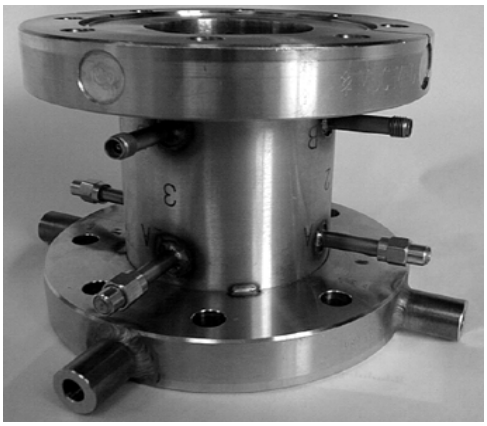

Figure 1: This LEDA 5-cm-aperture micro-stripline BPM has a 45 degree subtended angle and a 5-cm-length electrode.

2.2 Log-Ratio Electronics Processor

The electronics processor uses a log-ratio technique for analyzing the beam's position by demodulating and converting each BPM-electrode 350-MHz-signal current into a logarithmic signal voltage [6]. Each logarithmic lower-bandwidth analog voltage is digitized. The opposite-electrode converted signals are then subtracted from each other to produce a stream of digital words that represent the detected log-ratio beam position.

Previously, demodulating logarithmic amplifiers were only available with limited input bandwidths. These limited bandwidth amplifiers forced the addition of a RF down converter to translate the BPM-electrode's fundamental RF signal to a frequency within these earlier amplifier's operational range. However, low-cost very-broad-bandwidth logarithmic amplifiers are now available and allow the exclusion of down converter circuitry in log-ratio processor designs. For example, the Analog Devices, Inc. AD8307 logarithmic amplifier has a 500-MHz bandwidth over a 92-dB dynamic range and can operate at frequencies near 900-MHz with a reduced dynamic range.

As with previous versions, the logarithmic function is created by a series of amplifier stages that successively detect the RF signals and approximate the logarithm function in a piecewise linear fashion. Due to the detection technique, this type of logarithmic amplifier systematically deviates from the ideal logarithmic function. Fig. 2 shows how these deviations will effect the operation of the log-ratio processor. These data were acquired from a single AD8307 amplifier detecting a 350-MHz RF signal. The output signal mean and rms noise were acquired for each 1-dBm step of input signal power. The mean data were fitted to a logarithmic function and the residuals were plotted to show function-deviation information versus input beam current, where input beam current is derived from input signal power. Note that the logarithmic function deviation is approximately ±0.7-mm for a 50-mm aperture BPM over four decades of beam current. This deviation represents a worst case condition. In previous log-ratio processors, these amplifiers exhibited very similar logarithmic-function systematic errors. When used in pairs, the log-ratio detection method has a lower sysetmatic error behavior [5].

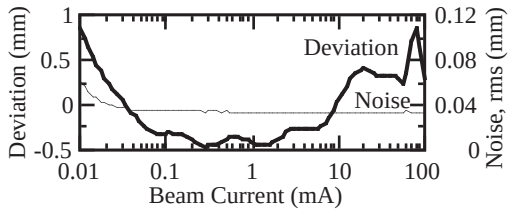

Figure 2: The above data show expected 350-MHz log-ratio position-detector performance using an AD8307 integrated circuit.

Fig. 2 also displays the rms noise characteristics of the AD8307 amplifiers. Because these logarithmic amplifiers contain many stages of detection and amplification, their noise figures are typically much larger than other beam position processing techniques. However, the AD8307 noise characteristics are sufficiently low to easily meet the APT and LEDA position measurement precision requirements. Note that these amplifiers are expected to provide beam position measurement precision of 0.04 mm within a 50-mm aperture BPM.

2.3 Error Correction and EPICS Interface

A unique feature of this particular measurement system is how the system's accuracy is maintained. During normal BPM operation, an RF relay connects a properly matched terminator to the downstream port of each BPM electrode. Additionally, this relay may also be switched to inject a 350-MHz signal from a stable and well-characterized 4-way RF splitter into each BPM electrode for measurement-system error correction. This error correction method will allow accelerator operators and commissioners, from within the accelerator control room, to verify and correct most measurement system errors. Early implementations of the log-ratio processor have

shown that systematic errors may be corrected to within a factor of X2 of the precision error using signal injection techniques [4,5].

Another unique feature is the method used to interface the log-ratio circuitry to EPICS. The current design calls for both the log-ratio processor and on-line correction module to be implemented as register-based VXI modules, and located in the same VXI crate. This module organization allows direct control and rapid automatic operation of both modules from the same control computer, typically referred to as an input/output controller (IOC). Both modules will implement full digital control and data acquisition via the VXI bus.

3 BPM CHARACTERIZATION

3.1 Mapping Characterization Process and Data

A mapping fixture was developed for LEDA and APT to accurately characterize the BPM beam-position response [7]. As a thin wire with an injected 350-MHz signal is accurately moved across a BPM aperture, the RF fields from the injected signal induce RF currents on the BPM electrodes. RF signal data from individual electrodes are acquired and the power ratios between opposing electrodes are calculated for each wire location. The resultant data maps are then fitted in a least squares sense to a 3rd-order 2-dimensional equation [8].

Fig. 3 shows a typical map of the 50-mm aperture BPM planned for use in the LEDA HEBT with its fitted 3rd-order surface fit. Typical mapped offsets and sensitivity terms are 0.07 mm and 1.36 mm/dB, respectively. The typical sensitivity terms are within a few percent of the theoretical values of 1.39 dB/mm based on a analytic circular-BPM model [6,9].

3.2 Low Beam-Velocity Correction

Because the relative beam velocities are low for the LEDA and APT CCDTL and coupled cavity linac (CCL) beams, the bunched beam fields deform such that the BPM offset, sensitivity, and 3rd-order terms will be slightly different from those acquired by the mapping fixture. A technique has been developed to correct these terms for low velocity beams and has been verified with beam experiments [9]. The technique consists of the following steps:

1. With β=1, adjust the electrode subtended angle and radius in the analytic model so that a new model-based map agrees with mapping fixture data.
2. Decrease β in the analytic model to agree with the expected beam velocity.
3. Produce new analytically-derived map.
4. Perform forward and inverse least-squares fits.
5. Change manufactured offsets in the initial mapped data by using the new low-β BPM sensitivity.

This procedure has been performed on 50-mm aperture LEDA BPMs and has shown sensitivities will increase to 1.76 dB/mm.

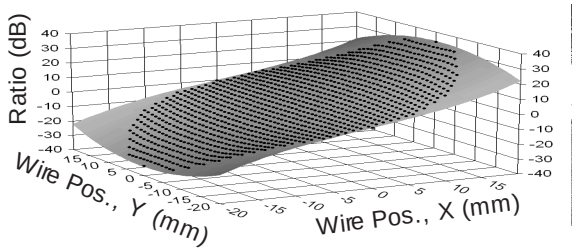

Figure 3: Position-sensitivity map of a BPM showing an opposing-electrode signal ratio for each wire location.

4 SUMMARY

This paper has discussed current LEDA and APT beam position measurement developments. These developments include the APT and LEDA beam steering scheme, changes to the log-ratio processor, the BPM characterization processes, and corrections to the BPM sensitivity due to low beam-energy effects.

5 REFERENCES

[1] J. D. Gilpatrick, et al., "LEDA and APT Beam Diagnostics Instrumentation," PAC '97, Vancouver, BC, Canada, June, 1997.

[2] K. Crandall, private communication, TechSource Inc., Santa Fe, NM.

[3] C. R. Rose, et al., "The LEDA Beam Position Measurement System," PAC '97, Vancouver, BC, Canada, June, 1997.

[4] C. R. Rose, et al., "Description and Operation of the LEDA Beam Position /Intensity Measurement Module," PAC '97, Vancouver, BC, Canada, June, 1997.

[5] C. R. Rose, et al., "Test Results of the LEDA Beam-Position/Intensity Measurement Module," BIW '98, Stanford, CA, May 4-7, 1998.

[6] J. D. Gilpatrick, "Comparison of Beam-Position-Transfer Functions using Circular Beam-Position Monitors," PAC '97, Vancouver, BC, Canada, June, 1997.

[7] R. B. Shurter, et al., "An Automated BPM Characterization System for LEDA," BIW '98, Stanford, CA, May 4-7, 1998.

[8] J. D. Gilpatrick and T. Hardek, "Known Problems and Solutions for the RI Beam Position Measurement Systems," AOT-1 Technical Note No. 95-98, May 10, 1995.

[9] J. D. Gilpatrick, et al., "Experience with the Ground Test Accelerator Beam-Measurement Instrumentation," AIP Conf. Proc. 319, Santa Fe, NM, pp 154-169, May, 1993.

LASER DIAGNOSTIC FOR HIGH CURRENT H⁻ BEAMS*

Robert E. Shafer
Los Alamos National Laboratory, Los Alamos, NM 87545

1 INTRODUCTION

Laser systems have been in use at the Los Alamos LAMPF 800-MeV proton linac and on various low energy H^- beamlines since about 1980 to do research or diagnostics on the accelerated H^- beam. The basis for these systems is that the threshold for photodetaching an electron is about 0.75 eV, and the photodetachment cross section rises to about 4 x 10^{-17} cm^2 for photons of about 1.5 eV (800 nm).

A Q-switched laser, when triggered, fully discharges in a few ns. Thus a small Q-switched laser with, say 50 mJ pulse energy and 10 ns pulse length, has the instantaneous power of 5 MW. Furthermore, a 50 mJ pulse at 1064 nm wavelength contains over 2 x 10^{17} photons. Because of the large photodetachment cross section, a significant fraction of the beam can be neutralized during the laser pulse. The Q-switched laser beam can either be focused to select a thin slice of the transverse beam profile, or defocused to nearly uniformly illuminate the entire beam.

Because neither the laser photon nor the recoiling photodetached electron transfer significant momentum to the H^0 atom, the neutralized beam maintains nearly the original phase-space parameters of the H^- beam from which it was extracted.. Furthermore, because the neutralized beam will not be deflected by either electric or magnetic fields, the H^- beam parameters can be deduced from measurements on the drifting neutral beam, even after it is separated from the H^- beam by magnetic fields. Measurements on the neutral beam are neither disruptive to the primary beam, nor destructive to the beam diagnostic.

2 THEORY

2.1 Photodetachment Cross Section

A plot of the photodetachment (stripping) cross section vs. photon energy, in the rest frame of the H^- atom, is shown in Fig. 1 [1-3].

The threshold is at about 0.75 eV and the peak cross section, 4 x 10^{-17} cm^2, is at about 1.5 eV. Because the binding energy of the remaining 1s electron in the neutral hydrogen atom is 13.6 eV, it will not be stripped by the laser.

*Work supported by the U.S. Dept. of Energy.

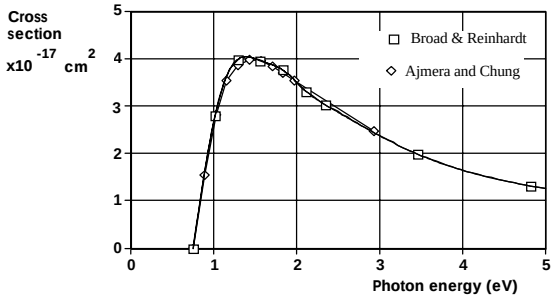

Figure 1. Photodetachment cross section of H^- vs. photon energy in the H^- rest frame.

2.2 Lorentz Transformation

Because H^- beams can be accelerated to energies of 1 GeV or more, there is a very sizable relativistic shift of the laser photon energy to higher energies in the H^- rest frame, often referred to as a "Lorentz boost". The photon energy E_{CM} in the H rest frame is related to the laser photon energy E_L by the equation

$$E_{CM} = \gamma E_L (1 - \beta \cos\theta_L)$$

where β and γ are the Lorentz parameters of the H^- beam, and θ_L is the laboratory angle of the laser beam relative to the H^- beam.

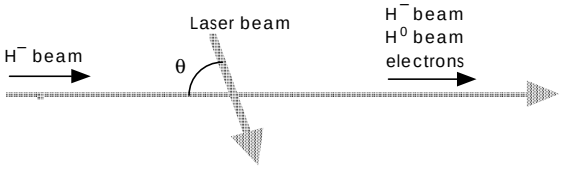

Figure 2. Geometry for laser photodetachment

2.3 Photodetachment Yield

For a Gaussian-profile laser beam with N_L photons intercepting a Gaussian-profile H^- beam of current I_b at an angle θ_L, the yield Y_1 (number of neutral hydrogen atoms produced per laser-H^- beam crossing) is given approximately by

$$Y_1 = \frac{I_b N_L}{e\beta c}\frac{1-\beta\cos\theta_L}{\sin\theta_L}\frac{\sigma_N(E_{cm})}{2\pi\sigma\ \sigma_L}\int_{-\infty}^{\infty}\exp\left(\frac{-x^2}{2\sigma_b^2}\right)\exp\left(\frac{-x^2}{2\sigma_L^2}\right)dx$$

$$= \frac{I_b N_L}{\sqrt{2\pi}\, e\beta c}\frac{1-\beta\cos\theta_L^b}{\sin\theta_L}\frac{\sigma_N(E_{cm})}{\left(\sigma_b^2+\sigma_L^2\right)^{1/2}}$$

where σ_b and σ_L are the transverse rms sizes of the H^- and laser beams normal to the plane of incidence, and $\sigma_N(E_{cm})$ is the photodetachment cross section at photon energy E_{cm} in the H^- rest frame.

The yield of photodetached H atoms for a 50 mJ 1064 nm Nd:YAG laser pulse on a 50 mA, 1-GeV H^- beam, using θ_L = 85º, E_{cm} = 2.22 eV (Lorentz-boosted photon energy in rest frame of H^-), βc = 0.875 x 3 x 10^{10} cm/s (beam velocity) N_L = 2.68 x 10^{17} (photons per laser pulse), $\sigma_b = \sigma_L$ = 0.2 cm (rms width of laser and H^- beams), σ_N (E) = 3 x 10^{-17} cm^2 (photodetachment cross section at energy E_{cm}), is Y_1 = 1.25 x 10^8 H^0 atoms per laser pulse (single crossing). For a 10 ns laser pulse, this is an instantaneous H^0 'current" of 2 mA (4% of H^- current).

This technique can also be used for low-energy (< 10 MeV) H^- beams, because the detachment cross section (Fig. 1) is 3.5 x 10^{-17} cm^2 at 1.17 eV (1064 nm). Because the yield is inversely proportional to β, the H^0 yield is larger for low energy beams. In the above example, if the beam energy is lowered to 2.5 MeV, the yield increases to 1.6 x 10^9 atoms (51% of H^- current).

2.4 Yield Enhancement

A variety of mirror configurations for reflecting the laser beam through the H^- beam many times are possible. The simplest configuration is two parallel front-surface mirrors. Another configuration is an internally-reflecting cylindrical mirror with its axis aligned along the beam. To take advantage of the temporal resolution of a very short Q-switched laser pulse, which is useful in maximizing signal to noise, the effective photon lifetime in the mirror should not exceed a few ns. An effective lifetime of 10 ns corresponds to a photon path length of about 300 cm, equivalent to about 30 reflections inside a 10-cm diameter mirror assembly. Thus the optimum mirror assembly needs to reflect the laser beam through the H^- beam only about 30 times, an easily achievable number even with modest mirror reflectivities.

2.5 Backgrounds

There are two sources of background uniquely associated with H^- beams. They are magnetic stripping and residual gas stripping. If not controlled, these stripping mechanisms can contaminate the signal obtained by laser stripping. For high current, high energy H^- beams, these loss mechanisms can also contribute to a significant amount of activation. A beam loss of a watt per meter at 1 GeV can lead to activation levels in the range of 10's of mrad/hr.

A relativistic H^- beam can be stripped by the Lorentz-transformed magnetic field of a typical beamline magnet. The theory of electric and magnetic field stripping of H^- beams is discussed by Sherk [4] and by Jason [5]. As an example, the stripping loss rate of a 1-GeV H^- beam in magnetic fields of 0.3 T, 0.35 T, and 0.4 T is 0.12, 7.4, and 164 ppm per meter respectively.

A relativistic H^- beam can also be stripped by inelastic collisions with residual gas atoms. The cross sections for this process have been evaluated by Gillespie [6]. As an example, the cross sections for stripping a 1-GeV H^- beam in hydrogen and nitrogen gas are about 1.2 and 8.9 x 10^{-19} cm^2/atom, and scale approximately as $1/\beta^2$. For a 1 x 10^{-7} torr (273 K) vacuum, these cross sections represent stripping losses of about 0.08 and 0.6 ppm per meter respectively.

3 EXPERIMENTAL APPLICATIONS

3.1 Commercially Available Q-Switched Lasers.

Inexpensive shoe-box sized Q-switched Nd:YAG lasers can produce 10-ns long, 50 mJ, 1064-nm pulses (or harmonics) at 60 Hz. These units are totally enclosed, and can be installed directly on a beamline. The 1064-nm line is nearly ideal for general diagnostics on H^- beams, because of its proximity to the peak in the photodetachment cross section. The 10-ns pulse width is adequate for many applications where good temporal response is required, and this can be improved if necessary by using external polarizers and pockels cells.

Solid state laser diodes, with outputs of several watts, may be useful as a device for extracting very small average currents from a H^- beam, but they are probably not suitable as a beam diagnostic. This is because the solid state laser cannot achieve the very high peak power available in a Q-switched laser, required to discriminate against the backgrounds.

3.2 Experimental Layouts and Measurements

A generic layout for a laser diagnostic is shown in Figure 3. In Fig. 3, the Q-switched laser beam intercepts the H^- beam at an angle θ_L. A mirror assembly produces multiple passes of the laser beam. A dipole magnet separates the neutral beam from the H^- beam. If a dipole magnet, such as in a bend, is not possible, then a weak dipole field will deflect the detached electrons, which can be detected. After the neutral beam emerges from the dipole magnet, it may be foil-stripped to produce a proton beam. A variety of beam diagnostics for characterizing the resultant proton beam are possible. Because the proton beam is low power, the diagnostic may totally intercept the protons.

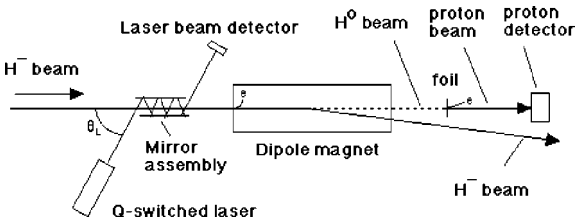

Figure 3. A generic arrangement for laser beam diagnostics.

A laser beam for transverse beam diagnostics can either be a thin "laser wire", neutralizing only a thin slice of the incident H^- beam, or intercept the entire beam [7-9]. The width of the laser wire can be of the order of 0.2 to 0.4 mm. If used in a high dispersion region, it may be

possible to measure the H^- energy spread. For measuring the proton yield, possible proton diagnostics include phototube-scintillator assemblies, Faraday cups, secondary-emission monitors, etc. Because the photodetachment yield is higher at low energies, lasers may be a good substitute for intercepting wire scanners, which are particularly hard to use in low energy, high dE/dx H^- beams.

A very specific application in the proposed Spallation Neutron Source project is to measure the beam current in a 1.18 MHz, 280-ns-wide, beam chopper gap, which must be less than about 1 x 10^{-5} of the 28 mA H^- beam (about 0.3 μA). The laser system with mirrors can extract a neutral current of about 0.10 μA from this gap for 10 ns, equivalent to about 6200 particles. This can be measured using either charge or scintillator pulse detection techniques to determine the cleanliness of the gap. The very high dynamic range and charge sensitivity required for the beam-in-gap measurement is also useful for exploring the halo region of the primary beam. This is a difficult measurement to make with normal beam profile diagnostics.

When measurement of the photodetached H^0 atom or proton is difficult, measurement of the photodetached electron is possible. The electron has about $1/1840^{th}$ of the proton rigidity, and is easily deflected into detectors by weak magnetic fields. This technique has been used in photodetachment experiments. The photodetached electron is easily deflected by space charge forces in high current H^- beams, however, so the electron signal cannot be analyzed for obtaining accurate H^- beam emittance information.

Resonances in the photodetachment total cross section near the n=2 threshold (10.953 eV) have been used to measure H^- beam momentum and momentum spread [10]. In this experiment, a 50 mJ Q-switched Nd:YAG laser operating at 266 and 355 nm was used. Both the Feshbach resonance (10.926 eV, width 30 μeV) and the shape resonance (10.975 eV, width 25 meV) can be used for this measurement, although the widths and strengths of these resonances are not ideal.

4 CONCLUSION

Laser photodetachment can be used on high current, high energy H^- beams to carry out a wide variety of beam diagnostic measurements parasitically during normal operation, without having to operate the facility at either reduced current or duty cycle. Suitable Q-switched laser systems are small, inexpensive, and can be mounted on or near the beamline. Most of the proposed laser-based diagnostics techniques have already been demonstrated.

5 REFERENCES

[1] J. T. Broad and W. P. Reinhardt, "One and Two-Electron Photoejection from H^- Atoms", Phys. Rev. A14, page 2159-72 (1976). See Table IV.

[2] M. P. Ajmera and K. T. Chung, "Photodetachment of Negative Hydrogen Ions", Phys. Rev. A12, pages 475-79 (1975).

[3] M. Daskhan and A. S. Ghosh, "Photodetachment Cross Section of the Negative Hydrogen Ion", Phys. Rev. A28, pages 2767-69 (1983)..

[4] L. Scherk, "An Improved Value for the Electron Affinity of the Negative Hydrogen Ion", Can. J. Phys. Vol. 57, 558 (1979).

[5] A. J. Jason, D. W. Hudgings, and O. B. VanDyck, "Neutralization of H– Beams by Magnetic Stripping", IEEE Trans. Nucl. Sci., Vol. NS-28, pages 2704-6 (1981).

[6] G. H. Gillespie, "Electron-Loss Cross Sections for High Energy H^- Collisions with Low and High Z atoms", Phys. Rev. A15, pages 563-573 (1977), and A16, pages 943-950 (1977).

[7] D. R. Swenson, E. P. MacKerrow, and H. C. Bryant, "Non-Invasive Diagnostics for H– Ion Beams using Photodetachment by Focused Laser Beams"; Proc. 1993 Beam Instrumentation Workshop (Santa Fe), pages 343-52, A.I.P. Conf. Proceedings # 319 (1994).

[8] R. C. Connolly et al., "A Transverse Phase Space Measurement Technique for High Brightness H– beams", Nucl. Inst. and Meth. Vol. A312, pages 415-419 (1992).

[9] D. P. Sandoval, "Non-Interceptive Transverse Emittance Measurement Diagnostic for an 800-MeV H– Transport Beam", 1994 Beam Instrumentation Workshop (Vancouver). A. I. P. Conference Proceedings 333

[10] E. P. MacKerrow et al., "Laser Diagnostics For H– Beam Momentum And Momentum Spread," Reference 8, pages 226-35 (1994).

HORIZONTAL EMITTANCE MEASUREMENT IN ATF EXTRACTION LINE

T. Okugi, T. Hirose, Tokyo Metro. Univ., Tokyo, Japan,
H. Hayano, K. Kubo, N. Terunuma, J. Urakawa, KEK, Ibaraki, Japan
S. Kashiwagi, The Graduate University for Advanced Studies, Ibaraki, Japan

Abstract

The beam operation of the damping ring of the KEK accelerator test facility (ATF) has been started since January 1997 for the development of the technologies to achieve a low emittance beam, which is required in future linear colliders. The ATF consists of a injector linac, the damping ring and a beam extraction line for a beam diagnosis. An operation of the extraction line has been started since November 1997. However, the beam position at the extraction line was not stable for the reason why extraction kickers did not work stable and the longitudinal beam oscillation is still remained in the damping ring at extraction timing and so on. Therefore, we established the method to correct measured beam size and evaluated the horizontal emittance. In this paper, we report the performance of jitter subtraction method for the horizontal beam size. The amount of the evaluated horizontal emittance was 1.37 ± 0.03nm.

1 INTRODUCTION

It was reported that a small beam emittance was measured by synchrotron radiation at several synchrotron radiation storage rings. In ESRF, extremely small horizontal and vertical emittances, 3.5nm and 0.04nm, were evaluated with X-ray pinhole camera[1]. It is difficult to measure the horizontal emittance with small systematic error by utilizing the synchrotron radiation in the ATF damping ring, because a fraction of horizontal beam size due to horizontal dispersion and energy spread was comparable or greater than that from horizontal emittance. However, ATF has a beam extraction line, which contains a beam diagnosis section of the extracted beam. Operation of the ATF extraction line has been started since November 1997.

2 ATF EXTRACTION LINE

In the ATF extraction line, there is a beam diagnostic section, which is designed to be horizontal dispersion free and the quadrupole magnets are designed to form FODO cells.

There are an integrating current transformer (ICT) and 14 single path strip-line type beam position monitors (BPMs) at the extraction line. And four wire scanners are located to measure a beam size and to evaluate a beam emittance[2]. Wires of each wire scanner are mounted to wire mounts. And the wire mounts are rotated by $45°$ to horizontal plane as shown in Figure 1. The wire positions are read out by measuring the wire mount positions with digital position gauges. And scattered γ-rays by wire scanners are detected by an air Čerenkov detector with photomultiplier (PMT). All of these beam monitors at the ATF extraction line are read out in the single beam passage simultaneously. Thereby, we can examine a correlation between all monitors in the ATF extraction line.

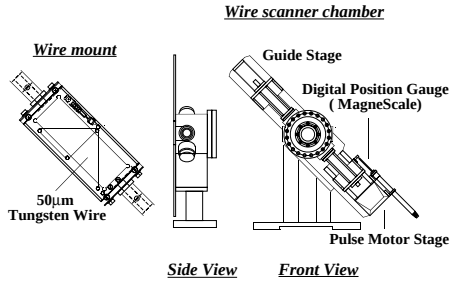

Figure 1: Schematic figure of wire scanner used in ATF.

3 DISPERSION CORRECTION

The magnet setting, especially steering magnets, is often changed for various beam studies, because ATF damping ring is a test accelerator. It changes dispersion in the damping ring and as consequence in the extraction line. Residual horizontal dispersion at the beam diagnostic section produces an additional beam size and a longitudinal beam oscillation make additional horizontal position jitter as proportional to the dispersion. Thereby, we must make dispersion correction every time at the beginning of beam diagnosis on the extraction line. The dispersion function at the extraction line is evaluated by measuring orbit difference with different rf frequency in the damping ring (rf ramp method). At a beam injection timing, the damping ring rf must be synchronized with a linac rf. However, the damping ring rf frequency can be changed between a beam injection and the next beam injection in order to measure the dispersion function.

Dispersion correction was carried out as following procedures. At first, beam positions were measured by BPMs for five rf frequency offsets, +2kHz, +1kHz, 0kHz, -1kHz and -2kHz. Slopes $\Delta x_{\mathrm{ramp}}/\Delta f_{\mathrm{RF}}$ were evaluated with linear fitting using MINUIT[3] software package and horizontal dispersions were evaluated as

$$\frac{\eta_x}{\alpha_{\mathrm{M}}} = -f_{\mathrm{RF}} \frac{\Delta x_{\mathrm{ramp}}}{\Delta f_{\mathrm{RF}}} \tag{1}$$

for each BPM locations in the extraction line. Horizontal dispersions at locations of wire scanners were evaluated using a fitting with two parameters of η_x, η_x' at the entrance of extraction line on restricted condition of design momentum compaction factor α_{M}. Linear optics model for the extraction line was used for the fitting. Finally, a calculation of magnet settings to suppress horizontal dispersion at beam

diagnostic section were carried out based on the dispersion measurement. Consequently, strength of some quadrupole magnets were changed to suppress horizontal dispersion.

4 JITTER SUBTRACTION

Horizontal beam position of the extracted beam was not stable for the reason why one of extraction kickers[4] discharged, which was located at the extraction line. An amount of horizontal beam position fluctuation was 50-200μm at the beam diagnostic section and the beam fluctuation affected to horizontal beam size measurement, because a typical horizontal beam size of 30-100μm at the beam diagnostic section was comparable to the beam fluctuation. We applied a position jitter subtraction to a beam size measurement.

Horizontal beam offset at arbitrary position x_3 is calculated from offsets at other two locations x_1, x_2 as follows

$$x_3 = \frac{R_{12}(s_3,s_1)}{R_{12}(s_2,s_1)}x_2 - \frac{R_{12}(s_3,s_2)}{R_{12}(s_2,s_1)}x_1 \qquad (2)$$

at the dispersion free section. Where $R_{12}(s_j,s_i)$ is a transfer matrix component from s_i to s_j. As more than two horizontal positions are possible to be measured by BPMs, we can estimate a horizontal beam offset at arbitrary position. An expected position resolutions for the position estimation depends upon a BPM readout resolution as follows

$$\begin{aligned}\sigma_{x_3} &= \sqrt{\left(\frac{R_{12}(s_3,s_1)}{R_{12}(s_2,s_1)}\right)^2 + \left(\frac{R_{12}(s_3,s_2)}{R_{12}(s_2,s_1)}\right)^2}\,\sigma_{x,\mathrm{BPM}} \\ &= f(s_1,s_2,s_3)\,\sigma_{x,\mathrm{BPM}} \end{aligned} \qquad (3)$$

with $\sigma_{x,\mathrm{BPM}}$ the BPM readout resolution. As any set of BPM readout positions can be applied to x_1, x_2 in Eq. (2), the set of BPMs should be chosen to make the resolution factor $f(s_1,s_2,s_3)$ minimize for each noticeable locations s_3.

We applied the position estimation method to beam size measurement using wire scanners. The set of BPMs used for position estimation and corresponding resolution factor $f(s_1,s_2,s_3)$ are listed in Table 1. As mentioned above, horizontal beam positions at the wire scanners were fluctuated pulse by pulse. However, we can expect a beam position with respect to wires by using the position estimation of Eq. (2). And the beam position with respect to a wire can be expressed as

$$x_{\mathrm{WS}} = \frac{x_{\mathrm{DG}}}{\sqrt{2}} - \left(\frac{R_{12}(s_{\mathrm{WS}},s_1)}{R_{12}(s_2,s_1)}x_2 - \frac{R_{12}(s_{\mathrm{WS}},s_2)}{R_{12}(s_2,s_1)}x_1\right) \qquad (4)$$

with s_{WS} the wire scanner location, x_{WS} the beam position with respect to the wire and x_{DG} the digital position gauge readout on the wire scanner, which was divided by $\sqrt{2}$ to convert the horizontal position by its 45° tilt. A typical readout of PMT signals for wire scanner MW1X is shown in Figure 2(a) as a function of wire positions. It was found that PMT signals were scattered over wide range. On the other hand, Figure 2(b) shows PMT signals as a function of the x_{WS} in Eq. (4) and horizontal position jitter was well corrected.

Wire Scanner Name	BPM1	BPM2	$f(s_1,s_2,s_3)$
MW1X	ML11X	ML10X	0.758
MW2X	ML12X	ML10X	0.432
MW3X	ML12X	ML9X	0.868
MW4X	ML10X	ML11X	0.370

Table 1: The list of resolution factor for each monitors located at beam diagnostic section. BPM1, BPM2 are the set of BPMs for the minimum resolution factor.

5 EMITTANCE EVALUATION

Two different methods are used for horizontal emittance evaluation. One is a waist scan method, and the other is a four wire method. The waist scan method is the method to evaluate a beam emittance by measuring a beam size with single wire scanner while changing strength of a quadrupole magnet located upstream of the wire scanner. The beam size square changes as quadratic as shown in Figure 3. We evaluated a horizontal emittance by the waist scan method with MW1X, MW2X and MW3X. Waist scan method with MW4X was not carried out, because a horizontal beam size at MW4X was insensitive to a strength change of quadrupole magnets located upstream of the monitor. The results are listed in Table 2.

The four wire method is the method to evaluate a beam emittance by measuring beam sizes with four wire scanners. In this method, Twiss parameters α_x, β_x and horizontal emittance are evaluated from a fitting for the beam sizes at the four wire scanner locations, knowing the optics information between them. The result of the fitting are shown in Figure 3(d). The ellipse shows the evaluated beam distribution in phase space (x,x') at the entrance of the extraction line. And four lines show the measured beam size boundaries converted to the same phase space. Result is also listed in Table 2. All evaluated horizontal emittances with both of waist scan and four wire methods agreed within 2σ and the averaged horizontal emittance was obtained as

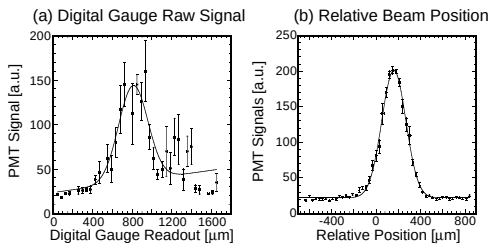

Figure 2: Result of a position jitter subtraction to magniscale readout position of wire scanner. (a) PMT signals as a function of wire readout position, (b) PMT signals as a function of evaluated relative beam position to wire.

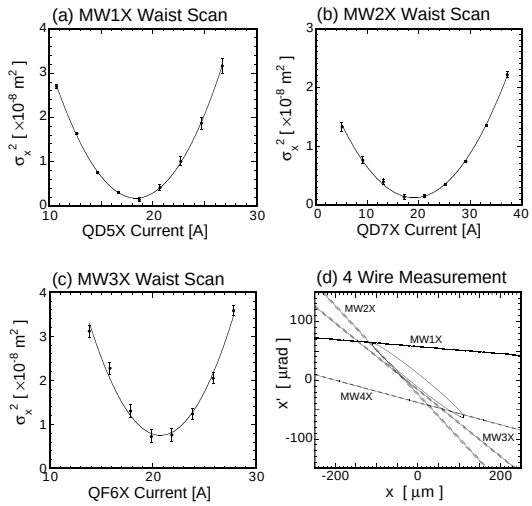

Figure 3: Beam size measurement result. (a),(b),(c) are results of waist scan method for each monitors, and (d) shows a result of four wire method.

1.37 ± 0.03nm.

The fitted Twiss parameters were compared for a verification of consistency of the horizontal emittance evaluations. Factor $B_{\rm mag}$ is defined as

$$B_{\rm mag} = \frac{1}{2}\left[\frac{\beta_2}{\beta_1} + \frac{\beta_1}{\beta_2} + \beta_1\beta_2\left(\frac{\alpha_1}{\beta_1} - \frac{\alpha_2}{\beta_2}\right)^2\right] \quad (5)$$

for two different set of Twiss parameters α, β. The evaluated $B_{\rm mag}$'s are also shown in Table 2. In the calculation of $B_{\rm mag}$, each measurement was used as one set of Twiss parameter and an averaged Twiss parameter of the other three measurement weighted by their errors was used as the other. It was found that all $B_{\rm mag}$ were close to unity. Thereby, evaluated horizontal emittance had the consistency each other.

6 CONSIDERATION

The evaluated horizontal emittance was a little bit larger than design natural emittance of 1.12nm. A momentum spread was evaluated by measuring a beam size with screen monitor at about 1.7m of huge horizontal dispersion region of the extraction line and the evaluated momentum spread was increased with increasing a bunch current as shown in

Method	Emittance [nm]	$B_{\rm mag}$
MW1X Waist Scan	1.47 ± 0.06	1.05 ± 0.09
MW2X Waist Scan	1.27 ± 0.06	1.00 ± 0.03
MW3X Waist Scan	1.38 ± 0.05	1.07 ± 0.11
Four Wire	1.29 ± 0.11	1.07 ± 0.34
Average	1.37 ± 0.03	α_x:3.83 β_x:6.77

Table 2: The results of horizontal emittance. "Average" is an averaged data weighted by their errors.

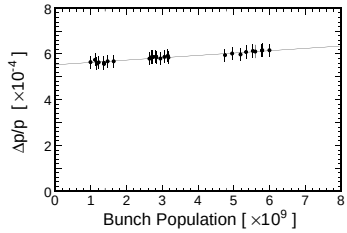

Figure 4: Result of momentum spread measurement. There was clearly intensity dependence.

Figure 4. A horizontal emittance is expected to increase with the momentum spread as

$$\epsilon_x = \frac{J_\epsilon}{J_x}\left\langle \frac{1}{\beta_x}\left[\eta_x^2 + (\beta_x\eta_x' + \alpha_x\eta_x)^2\right]\right\rangle_{\rm arc}\left(\frac{\sigma_p}{p}\right)^2, \quad (6)$$

where J_x and J_ϵ are the damping partition number for horizontal and longitudinal direction and the angular bracket means average over the arc section. As momentum spread was enhanced by about 8-12% at the bunch population of 3-5$\times 10^9$ in Figure 4, the horizontal emittance should be 1.31-1.41nm for the beam intensity. This horizontal emittance agreed with the evaluated horizontal emittance of 1.37 ± 0.03nm.

7 SUMMARY

The horizontal emittance was evaluated by the horizontal beam size measurement at the ATF extraction line with position jitter subtraction method. The horizontal emittance was 1.37 ± 0.03nm and this was a little bit larger than the design natural emittance. However, this difference can be explained by intensity dependence of the emittance. Measured horizontal emittance well agreed with the designed one.

8 ACKNOWLEDGEMENT

We would like to express our thanks to Professors H. Sugawara, Y. Kimura, M. Kihara and K. Takata for their encouragement of this work. And we wish to thank to Drs. S. Kamada, T. Naito, K. Oide, S. Takeda and N. Toge of KEK and M. Takano of Toho Univ. and D. McCormick, M. Minty, M. Ross, M. Woodly and F. Zimmermann of SLAC for various useful discussions. We also thank to the ATF operation group for their support to the beam experiment.

9 REFERENCES

[1] P. Elleaume et al., Jour. of Synchr. Rad. **2** (1995) 209.

[2] S. Kashiwagi et al., "DIAGNOSIS OF THE LOW EMITTANCE BEAM IN ATF DR EXTRACTION LINE", Proc. of the 6th EPAC, Stockholm (1998).

[3] MINUIT Reference Manual, edited by F. James, CERN Program Library Long Writeup D506.

[4] H. Nakayama, KEK Proceedings 92-6 (1992) 326.

REQUIREMENTS FOR THE RF CONTROL OF THE VECTOR SUM FOR SUPERCONDUCTING PROTON LINACS

M. Hüning, S.N. Simrock, DESY, Notkestr. 85, D-22603 Hamburg, Germany
T. Schilcher, PSI, CH-5232 Villigen, Switzerland

Abstract

Superconducting accelerator technology has demonstrated its superior performance in large scale machines such as CEBA at TJNAF and is increasingly used for new accelerator designs. Until now this technology has found its main application in electron accelerators. However nowadays proton accelerator designs for the European Spallation Source (ESS) and the Accelerator Driven Transmutation Technology (ADTT) also study the feasibility of superconducting linacs. In contrast to the highly relativistic electron beams the proton beam exhibits an increased susceptibility to voltage fluctuations in the acceleration system induced by microphonics and dynamic Lorentz force detuning. Although low beam loss is an important criterion for linac design, studies of the longitudinal dynamics appear to be a good indicator for beam stability in presence of fluctuations of the accelerating field. Control of the vector sum of multiple cavities driven by one klystron is desirable for cost reasons but does not allow for control of individual cavity fields. In this paper we study the performance of such a system.

1 INTRODUCTION

The technology of proton accelerators has progressed considerably in the past three decades [1]. Several high intensity proton accelerators with high peak or average beam currents of the order of 100 mA are presently under study for applications such as: spallation neutron sources, kaon factory, nuclear transmutation technology, energy amplifier, and muon collider drivers. The implementation of superconducting acceleration systems [2,3] appears to be attractive since it could lead to substantial cost savings in machine operation especially if multiple cavities are driven by one common high power klystron.

An important design criterion for a high intensity proton linac is beam loss control since the beam loss should not exceed 1 nA/m to allow for hands-on maintenance after a long operation period. Particle loss is caused by a small number of particles outside the dense beam core, called the beam halo. The origin and formation and dynamics of the halo have been studied intensively and significant progress has been made in recent years. In superconducting linacs where multiple cavities are driven by a single klystron beam loss may be enhanced by microphonics which are a result of mechanical vibration modulating the resonance frequency of the high Q cavities. In this paper we develop a simple model to determine the impact of fluctuations of the accelerating field on beam energy. For simplicity only the longitudinal dynamics of the bunch centroid are analyzed. Bunches with excessive energy deviations are considered as potential candidates for beam loss. An important result of this model is an upper limit for the microphonics noise levels permitted for accelerator operation.

2 BEAM DYNAMICS MODEL

The energy gain of the bunch centroid when passing a single cavity can be described as

$$\Delta V = V_o \cdot T \cdot \cos(\phi_S),$$

where V_o is the cavity voltage, T is the transit time factor, and ϕ_S the phase angle between beam current and accelerating field. The transit time factor is a function of the bunch velocity $\beta = v/c$ and the phase angle depends also on β according to $\Delta\phi = (2\pi f L)/(c\beta)$, where f is the operating frequency of the rf cavities, and L the drift space between the center of two adjacent cavities. Thereby the dynamics inside the cavities have been approximated by a cavity with length zero and the surrounding drift space.

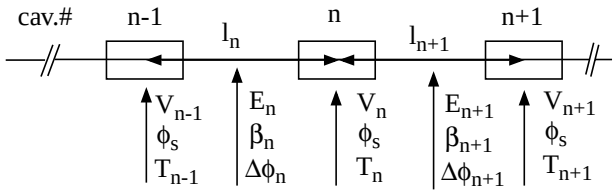

Figure 1: Definition of parameters used for the beam dynamics model.

Changes in transit time factor due to finite cavity length are however considered. For a given linac configuration one can calculate the deviations of beam energy, bunch velocity, and phase of the accelerating field with respect to a reference particle.

$$E_{n+1} = E_n + V_n \cdot \cos(\Delta\phi_n + \phi_s) \cdot T_n(\beta_n)$$

$$\beta_{n+1} = \sqrt{1 - \frac{m_p^2 c^4}{(E_{n+1})^2}}$$

$$\Delta\phi_{n+1} = \Delta\phi_n + \frac{2\pi f l_n}{c} \cdot \left(\frac{1}{\beta_n} - \frac{1}{\beta_{ref}}\right)$$

In the model the transit time factor of a m-cell cavity is derived from the transit time factor $T_1(\beta)$ of a single cell cavity as:

$$T(\beta) = T_1(\beta) 2 \cdot \frac{\cos\left(\frac{m-1}{2}(x-\alpha)\right) - \cos\left(\frac{m+1}{2}(x-\alpha)\right)}{m \cdot (1-\cos(x-\alpha))}$$

with

$$T_1 = \frac{\sin(x/2)}{(x/2)} \text{ for } E(z) = \text{const.}, \; x = \frac{2\pi L_n}{\beta\lambda}, \; \alpha = \frac{k}{m}\pi$$

k=1...m depending on selected passband mode. Here k/m=1 i.e. $\alpha = \pi$ for a standing wave structure. L_n is the length of the cavity.

3 LINAC PARAMETERS

To determine the impact of fluctuations of the accelerating field on the longitudinal dynamics of the bunch centroid the parameters of two recently proposed linac designs have been selected (see Table 1).

4 SIMULATION RESULTS

Based on the beam dynamics model and the sample linac parameters the quantities of interest have been determined for several cases:

1. stochastic cavity amplitude and phase errors along the linac with uniform distribution. The simulation has been performed with various sets of errors for injector and linac.
2. stochastic cavity amplitude and phase errors along linac but the vector-sum of an ensemble of 2 or 4 cavities perfectly regulated.

Table 1: Sample Linac Parameters

	LINAC 1	LINAC 2
Frequency [MHz]	700	700
Linac Energy [MeV]	1700	1300
Number of cavities	102 & 308	166
Number of cells / cavity	5 & 5	5
Injection energy [MeV]	211 & 470	70
Beta of cavity	0.64 & 0.82	0.37 .. 0.91
Cav. centroid spacing [m]	2.0 & 2.1	0.5 .. 1.36
Synchronouse phase [deg]	-35 & -30	-20
Energy gain/cav. [MV]	2.5 & 4.0	3.9 .. 9.8
Cavity gradient [MV/m]	5.2 & 5.9	10

The deviation of the final linac energy from the reference energy can be used to determine the potential for beam loss. The simulations show that small field fluctuations result in a moderate increase in energy spread while larger errors - depending on the distribution along the linac - may result in basically zero energy gain in the linac due to phase slippage. Particles which do not experience a net energy gain in the linac are likely to be lost due to the lack of rf focusing. Some of the results of the simulations for the different case studies are shown in Table 2. The probability of beam loss is equivalent to linac energy gain less than 90%.

Table 2: Linac Energy Spread (Bunch-to-Bunch) and Particle Loss

Injector Error[1]		Linac cavity error[1]		probability of energy gain < 90% [10^{-5}] [2]						σ_E/E [10^{-4}]					
$\Delta\phi$[°]	ΔE [%]	$\Delta\phi$[°]	ΔV [%]	no control[3]		vector-sum (2)[4]		vector-sum (4)[4]		no control[3]		vector-sum (2)[4]		vector-sum (4)[4]	
		Linac type:		1	2	1	2	1	2	1	2	1	2	1	2
1	1	1	1	12	-	-	-	-	-	18	11	18	8.7	18	9.1
1	1	3	3	24	-	-	-	-	-	22	25	18	9.4	19	12
1	1	5	5	270	13	-	-	-	-	27	42	18	11	19	16
1	1	7	7	1580	30	-	-	-	-	33	57	18	12	20	21
1	1	10	10	9500	610	-	-	10	7.8	40	72	19	15	21	31
0	0	1	5	- 5	- 5	- 5	- 5	- 5	- 5	15	29	1.8	6.2	4.0	11
0	0	5	5	- 5	- 5	- 5	- 5	- 5	- 5	20	39	2.3	7.8	5.2	15
0	0	1	10	300	120	- 5	- 5	- 5	- 5	28	54	3.4	10	7.6	20
0.5	5	1	5	- 5	- 5	- 5	- 5	- 5	- 5	19	30	10	10	11	14
0.5	5	5	10	1600	1400	- 5	- 5	- 5	- 5	33	61	10	14	14	24
0	0	0.1	1	- 5	- 5	- 5	- 5	- 5	- 5	3.2	7	0.7	4	1.7	4.5
0.5	5	0.1	1	- 5	- 5	- 5	- 5	- 5	- 5	10	10	9.7	8.9	9.7	9.0
1	5	0.1	1	- 5	- 5	- 5	- 5	- 5	- 5	19	12	18	11	18	11
1	5	1	5	80	- 5	- 5	- 5	- 5	- 5	23	31	18	12	19	15
5	5	0.1	0.1	80000	60000	80000	60000	80000	60000	27	41	25	41	26	41

[1]All errors assume a uniform distribution; [2]total number of runs is 100000 [3]no rf feedack applied; [4]vector-sum of 2 repectively 4 cavities is perfectly regulated; [5] number of runs only 12000;

The number of random error sets for most simulations has been 100000 which means there is still a chance of the order of 10^{-5} that a bunch might get lost. The table shows that for a reasonable phase and amplitude injection error of 1 deg. and 1% respectively the linac can tolerate phase and amplitude perturbation levels of severals degrees and percent. A summary of the results is shown in Figure 2.

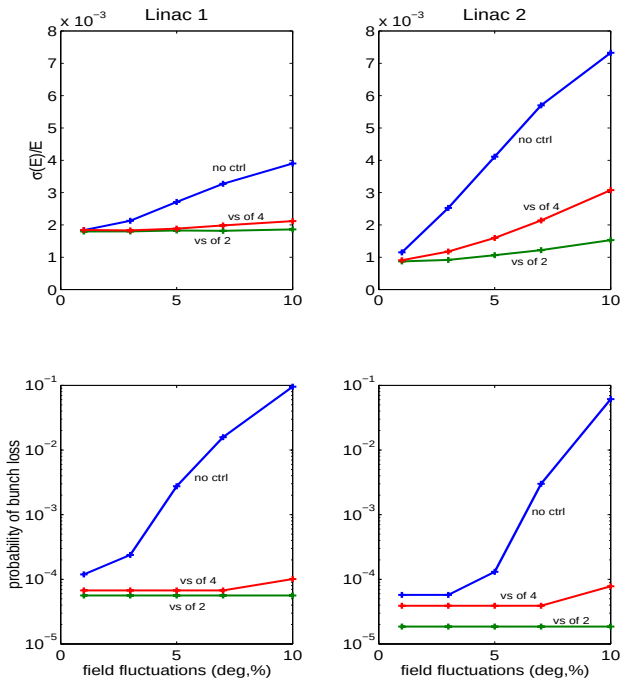

Figure 2: Energy spread and bunch loss as function of amplitude and phase errors in the linacs.

5 CONSIDERATIONS FOR THE CONTROL OF THE VECTOR SUM

The rf control for the vector sum of multiple cavities can be improved significantly if the energy gain and the beam arrival time or beam phase at the entrance of the following ensemble of multiple cavities can be controlled. This can be accomplished by control of the vector sum amplitude and phase which provide linear independent control of the beam energy gain and beam phase in the vicinity of the synchronous phase.

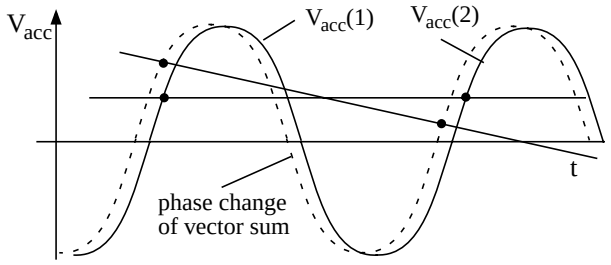

Figure 3: Principle of beam energy and beam phase control

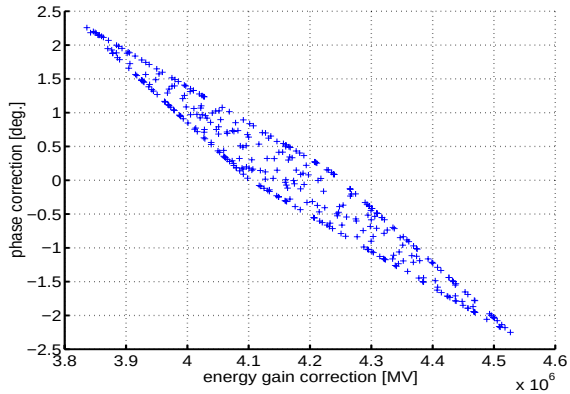

Figure 4: Energy gain and beam phase correction range at the low energy end of Linac 1. The vector sum of 2 cavities is controlled and varied by ±3 deg. in phase and ±10% in amplitude.

The principle of beam energy and beam phase control is shown in Figure 3. A change in cavity phase or amplitude will result in the arrival time at the following cavity. With proper choice of vector sum amplitude and phase the energy and beam phase at the following cavity can be controlled within the boundaries shown in Figure 4. The control range is larger at the low energy end of the linac.

6 CONCLUSION

The control of microphonics and Lorentz force detuning in superconducting cavities for proton accelerators has been a major concern. This is especially true if only vector sum of several cavities which are driven by one common klystron is controlled. The simple model presented for the analysis of the accelerating mode driven longitudinal dynamics of the bunch centroid has shown that surprisingly large levels of microphonics are acceptable even in the case of vector sum control of 4 cavities.

REFERENCES

[1] M. Pabst and K. Bongardt, *Halo simulation in a realistic proton linac design*, PAC97, Vancouver, B.C., Canada, May 12-16, 1997, in print.

[2] G.P.Lawrence and T.P. Wangler, *Integrated Normal-conducting/Superconducting High-Power Proton Linac for the APT Project*, PAC97, Vancouver, B.C., Canada, May 12-16, 1997, in print.

[3] B. Aminov, A. Gamp, E. Haebel, H. Heinrichs, H. Piel, J. Pouryamout, Th. Schilcher, D.L. Schrage, G.Schulz, S. Simrock, C.H. Rode and R. Röth, *Conceptual Design of the Superconducting High Energy Linear H⁻-Accelerator for the Future European Spallation Source (ESS)*, ESS 96-60-L, 1996.

TIME DELAY COMPENSATION FOR THE DIGITAL RF CONTROL AT THE TESLA TEST FACILITY

H. Imsieke, A. Kholodnyi, S.N. Simrock, DESY
Notkestr. 85, D-22603 Hamburg, Germany

Abstract

Time delays or dead times between inputs and outputs are an inherent characteristic of digital feedback systems. The time delay limits the maximum allowable gain required for system stability. Modern control theory provides a scheme called Smith predictor which has the potential to improve control performance significantly. The method is based on model internal control which works well if the dynamics of the plant are slow compared to the time delay. In this paper we analyze the performance improvement that can be achieved in the TTF rf control system where the time delay is dominated by computational delay. In this system the time delay of 4 microseconds and sampling period of 1 microsecond are short compared to the cavity time constant of 700 microseconds. Attention is paid to both theoretical and practical aspects.

1 INTRODUCTION

The cavities in the TESLA Test Facility are operated in pulsed mode at gradients of up to 25 MV/m with each klystron driving multiple cavities. Significant Lorentz force detuning and control of the vector-sum are the main issues for the low level rf controls. A digital feedback system has been developed [1] to provide flexibility in the control algorithms, precise calibration of the vector-sum, and extensive diagnostics and exception handling. The main features are a sampling rate of 1 MHz for the individual cavity signals, digital in-phase and quadrature detection, calculation of the vector-sum which includes gradient calibration and the correction of phase offsets, and feedback algorithm.

The presently implemented version of the feedback employs a proportional controller and has demonstrated excellent performance [2] especially in combination with the adaptive feed forward [3]. Due to the large time delay of 4 microseconds in the feedback loop the loop becomes unstable at gains exceeding 40 dB. The need for a high gain to maximize error suppression results in a small range of usable gains. Therefore a compensation of the loop delay appears to be attractive since it could improve the robustness and possibly increase the performance of the feedback loops.

2 TIME DELAY

The time delay in the feedback loop is given by:

- 500 ns conversion time of the 14 bit, 2 MHz ADC
- 200 ns writing to the comm-port of the TMS320C40
- 1000 ns multiplication with rotation matrix for individual field calibration and calculation of the vector-sum
- 200 ns writing to next comm-port of C40
- 1000 ns for the feedback algorithm (subtract setpoint, multiply with gain table, and add feedforward)
- 200 ns to write to the DAC
- 200 ns delay in the klystron
- 800 ns cable delay

The sum of the delays is about 4 µs. The implementation of the Smith-Predictor and Kalman filter might add up to 2 µs to the total delay. Time delay increases the phase shift between input and output signals and thus limits the maximum allowable gain. The system becomes unstable if the loop gain exceeds unity gain while the phase exhibits 180 deg. The phase shift due to delay is proportional to the frequency and is 180 deg. at 125 kHz for a delay of 4 µs. The phase margin of the rf system with a loop gain of 40 dB, and the cavity pole (first order) at 200 Hz is approximately 60 degrees at the unity gain frequency of 20 kHz.

3 SMITH PREDICTOR STRUCTURE

In 1957 O.J. Smith presented a control scheme to predict the reaction of a plant P to the output of a controller C thereby providing the potential of improving the control loops with delay (Figure 1).

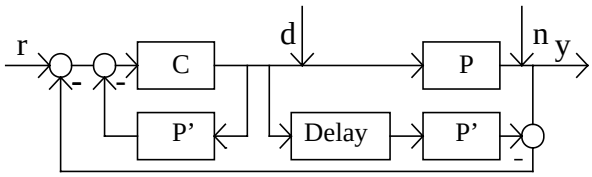

Figure 1: Smith Predictor structure

The total delay time in the feedback loop can be ascribed to the plant. P' is the model of the plant without delay time, r is the setpoint, y the output, d disturbances in and before the cavity and n measurement noise. With exact model matching and no disturbances or noise, the controller would only get signals from the model and the delay would be removed from the control loop as shown in Figure 2. The outer feedback loop in Figure 1 accounts for uncertainties of the model and disturbances.

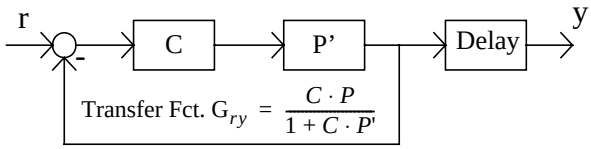

Figure 2: Desired Feedback with SP.

4 IMPLEMENTATION

The response of a single cavity to the beam current and the generator current can be described by two coupled first order differential equations for the envelope of the cavity voltage:

$$\begin{bmatrix} \dot{V}_{Re} \\ \dot{V}_{Im} \end{bmatrix} = \begin{bmatrix} -\omega_{1/2} & -\Delta\omega(t) \\ \Delta\omega(t) & -\omega_{1/2} \end{bmatrix} \begin{bmatrix} V_{Re} \\ V_{Im} \end{bmatrix} + \begin{bmatrix} R \cdot \omega_{1/2} & 0 \\ 0 & R \cdot \omega_{1/2} \end{bmatrix} \begin{bmatrix} I_{Re} \\ I_{Im} \end{bmatrix}$$

where V is the complex cavity voltage, I the complex current (generator + beam), $\omega_{1/2}$ (=π*operating frequency of 1.3 GHz/loaded quality factor ~$3*10^6$) the half width of resonance, $\Delta\omega$ the cavity detuning, and R the cavity shunt impedance.

A macropulse consists of cavity filling (500 μs), flat top with beam injection (800 μs), and field decay. The goal of the control system is to maintain a constant accelerating voltage during the flat top. The cavity is predetuned to minimize the power required to control the dynamic detuning which is a result of the Lorentz force. The cavity detuning should be zero in the middle of flat top. The cavity model used in the predictor should reflect the dynamics of the time varying Lorentz force detuning but has been omitted for simplicity. The field error resulting from such a simplification is comparable to the error caused by 1% quality factor or shunt impedance difference between model and plant (worst case: around 0.01%). The error caused by detuning is slowly changing and repetitive and can therefore be compensated by adaptive feedforward.

With a peak detuning of one bandwidth (realistic for 25 MV/m gradient) a step input on the real part of generator current would cause an error in the imaginary part of 7×10^{-4} after 1us. This crosstalk corresponds to a loop phase error of 0.04 deg. and can therefore be neglected.

The cavity is thus represented by a decoupled discrete State Space model with complex input and output vectors. The model parameters are calculated from the cavity bandwidth, which itself is calculated from the voltage decay time constant, and the cavity shunt impedance

$$V_{t+1} = (1 - (\omega_{1/2} \cdot T)) \cdot V_t + R \cdot \omega_{1/2} \cdot T \cdot I_t$$

where V and I stand for either real or imaginary component at time t. T is the sampling time of 1μs.

The model for multiple cavities can be obtained by superposition and can be approximated by that of a single cavity if the spread of the loaded quality factor is not too high. The spread should not exceed 25% to keep the model error below 3%. An improved model could consist of two cavities with different bandwidths. The model parameters are determined off-line.

The delay time can be adjusted in 1 μs steps by storing the control signal in memory and even in finer steps of 0.02 μs by selecting the time at which the 50 MHz DSP writes the data to the DAC. The delay is measured with a test program and then the program with correct DAC output time is written into the DSP. With model delay errors up to 0.1 μs, there's a decrease in maximum allowable gain off about 1% for every 0.01 μs mismatch.

5 PERFORMANCE

The performance of the rf system can be measured in terms of achieved field stability or disturbance rejection, the quality of setpoint tracking (important for fast varying setpoints as needed for FEL operation), and feedback loop stability which should be tolerant (or robust) with respect to parameter variations.

5.1 Stability

The maximum gain for stable operation is limited to 1400 (exactly two times the optimum gain, because overcorrection by more than 100% means instability) due to the 1 μs delay in the internal feedback loop.

While the bode plot without model uncertainties is easily interpreted due to the separation of the delay time, its meaning for the SP with parameter uncertainties is not easily understood. However since a numerical model analysis and the pole-zero map (obtained with a rational approximation of the closed loop SP transfer function) give similar results near the ideal case, stability margins were obtained with these methods. They show that realistic model mismatch of a few percent reduces the critical gain to ~1200.

If the klystron is operated close to saturation, its nonlinearity limits the maximum gain, so that it could be necessary to replace the actuator signal with the measured incident wave to the cavity. This scheme would also include time varying phase errors in the klystron and the vectormodulator. The measured klystron output would provide the correct control signal, thereby increasing stability and reducing sensitivity to klystron power fluctuations.

5.2 Setpoint Tracking

Figure 3 shows the response of the SP to a change of the setpoint. Operation with optimum gain will cause the cavity field to reach the desired setpoint in 1 μs time assuming availability of sufficient power from the klystron. If a beam current induces a voltage ΔV in steady state, the cavity field will change ΔV/700 in 1 μs. The optimal gain for reference tracking is therefore around 700 which is well below critical gain.

5.3 Disturbance Rejection

The ability to suppress disturbances is not improved significantly by the smith predictor, as shown in Figure 4. The slow response to a beam induced perturabtion is due to the presence of the cavity poles in the transfer function from the disturbance to the output,

$$G_{dy} = P \cdot (1 - G_{ry}).$$

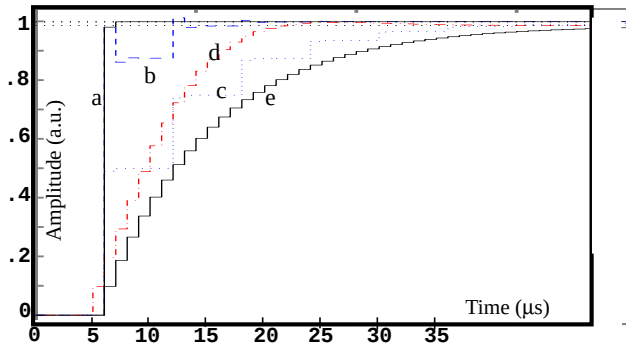

Figure 3: Step response of the transfer Function G_{ry} for a) optimal SP b) SP with 20% lower cavity quality factor c) SP with 50% gain decrease due to klystron nonlinearity d) normal feedback with gain of 70 e) SP with gain of 70.

The first term in the bracket is independent of the feedback gain. This means that the time constant of the error correction is not a function of the gain. It is however possible to modify the model and the controller so that the pole cancels with a zero of the transfer function [4] or to add the difference between cavity and model to the input of the model in order to adapt it to the disturbed cavity (a scheme called observer). Pole cancellation reduces the maximum allowable gain, is sensitive to parameter uncertainties, and slower than the latter method.

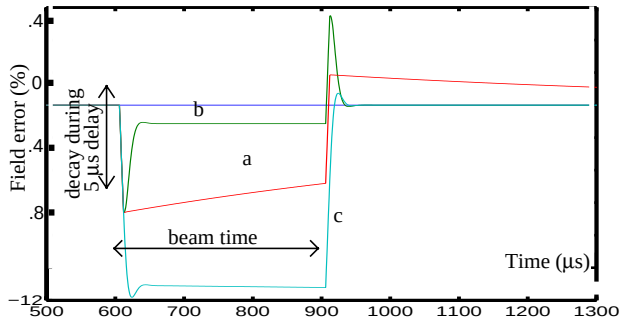

Figure 4: Reaction of the cavity field to a beam induced transient, a) optimal SP b) SP with Observer c) normal feedback.

Even with faster disturbance correction, the beam still causes a drop in the cavity field of 1/700 ~ 0.14 % per µs delay time in the feedback loop after injection. This can only be prevented by the use of feedforward. For the klystron noise, a faster disturbance rejection would have no influence. Errors caused by detuning would be reduced approximately by 50% on flat top with a gain of 700, but much better with an additional observer. The observer is useful against stochastical detuning by microphonics which cannot be suppressed by feedforward.

A controller with an integrator does not perform significantly better, and decreases stability margins due to phase advance.

6 FEEDFORWARD SCHEMES

Because the digital control system can measure the beam current in real time it can compensate it with a delay of about 1-2 µs. This scheme can reduce the beam induced transients considerably.

Another approach is the calculation of a feed forward table which is added to the control signal sent to the plant. This accounts for the absence of the beam in the model and microphonics influences. The feed forward table is repeatedly calculated from the difference between model and plant, with the error decreasing each step. In this way it also adapts itself to slowly changing system parameters. In contrast to this adaptive feed forward, a feed forward table needed to trace the setpoint optimally in the ideal case is calculated with model parameters and proportional gain and is added to both model and plant. This has to be updated only when these parameters are changed. Without Smith Predictor, there would be only one (adaptive) feed forward for all repetitive errors.

7 CONCLUSION

The main advantage of the Smith Predictor is faster setpoint tracking. With the existing feed forward, this workload is removed from the feedback with the exception of stochastic errors. These errors act almost exclusively in or before the plant, so the SP offers only little improvement. A major drawback is the amplification of measurement noise with higher gains, which has to be suppressed significantly. For this purpose a Kalman filter, which estimates the state of the plant in presence of klystron and measurement noise, is currently under development. The measurement is also disturbed by an offset in the rf mixer output which varies over the macropulse. This has to be cancelled out too to allow better performance than present feedback.

The klystron nonlinearity restricts the SP performance. The power margin could be too little for the desired high gains, and with equal gain, a standard feedback controller would outperform the SP. To assure stability the nonlinearity has to be known for the model calculations.

REFERENCES

[1] S.N. Simrock, I. Altmann, K. Rehlich, T. Schilcher, *Design of the Digital RF Control System for the TESLA Test Facility*, EPAC 96, Sitges (Barcelona), Spain, June 10-14, 1996, p. 349

[2] A. Gamp et al., *Experience with the Control of the Vector Sum in the TESLA Test Facility*, EPAC98, Stockholm, Sweden, June 22-26, in print

[3] M. Liepe, S.N. Simrock, *Adaptive Feed Forward for Digital RF Control System for the TESLA Test Facility*, Stockholm, Sweden, June 22-26, in print

[4] William S.Levine editor, *The Control Handbook*, CRC Press 1996, p. 231

RF CONTROL STUDIES FOR MODERATE BEAMLINE COUPLING BETWEEN SRF CAVITIES*

Lawrence R. Doolittle and D. X. Wang
Thomas Jefferson National Accelerator Facility, Newport News, Virginia 23606 USA

Abstract

When an SRF accelerator is designed, there is motivation to move the cavities close together on the beamline. Assuming the beamline apertures are not shrunk as well, this compaction (which will increase the overall accelerating gradient and/or lower the dynamic cryogenic heat load) increases the inter-cavity coupling. Within certain limits, the control system can compensate for this coupling by retuning each of the cavities. This paper describes constraints on the RF system, tuners, couplers, and control systems that are required to provide stable operation of cavities in the presence of inter-cavity coupling that exceeds the loaded bandwidth of an individual cavity.

1 INTRODUCTION

Many cost optimizations have discussed the tradeoff between accelerator capital and operating costs, acceleration gradient, cryogenic capacity, and RF Power. One contributing term in those equations is η, the ratio of the active accelerating cavity length to the overall accelerator length, sometimes called the "filling factor" or "packing fraction." While the effect of packing fraction on a new machine is debatable (since the relative cost of cavity meters and other meters can be hard to identify), when upgrading an existing machine with fixed total length, η has a clear effect, particularly on the cryogenic load. A cavity cell and the manufacturing technology will set the familiar cavity parameters ω, Q_0, and the shunt impedance per unit length (r/Q). For a given acceleration voltage V and active accelerator cavity length ηL, the cryogenic power dissipation is

$$\mathrm{Power} = \frac{V^2}{\eta L Q_0 (r/Q)}.$$

Thus, η is the only parameter under the designers' control that can change the relationship between voltage gain and dynamic cryogenic load.

Historic values of η are in the 0.3 to 0.6 range. The existing CEBAF accelerator linac has $\eta = 0.42$, and the baseline design of our Energy Upgrade studies calls for raising η to 0.58, by increasing the number of cells per cavity from 5 to 7[1].

Between cavities is a beam pipe of length b, whose radius a is normally set by beam impedance or beam aperture needs. The coupling $d\omega$ between two cavities is given by $\Delta\omega \cdot \exp(-kb)$, where $k^2 = k_0^2 - (2.405/a)^2$, and the proportionality constant $\Delta\omega$ represents the coupling between the resonant fields in the end cell and the evanescent TM_{01} fields in the beam pipe.

Increasing η will normally involve decreasing b, at which point the coupling $d\omega$ has the potential to rise enormously. Accelerators to date have kept $d\omega$ much smaller than the cavity bandwidth, to avoid potential problems that could arise from stronger coupling. The rest of this paper will discuss those problems in detail, and how they could be worked around.

2 DEFINING EQUATIONS

In the most general form, ignoring wall losses in the cavity ($\beta \gg 1$), in the rotated coordinate (phasor) sense where the instantaneous gradient $E(t)$ in a cavity is given by $\mathrm{Re}\{Ee^{j\omega_0 t}\}$,

$$\frac{dE}{dt} = -(\omega_f - j\omega_d)\cdot E - jd\omega_- \cdot E_- - jd\omega_+ \cdot E_+$$

$$+2\omega_f \sqrt{R_c}\cdot K - \omega_f R_c \cdot I_b$$

For cavities at the end of a string, this formula involves phantom cavities, which should be treated as if they had zero gradient.

Table 1: notation

ω_f	bandwidth, $\omega_0/2Q_L$
ω_d	frequency offset from ω_0
E_-	gradient of upstream cavity
E_+	gradient of downstream cavity
$d\omega_-$	coupling to upstream cavity
$d\omega_+$	coupling to downstream cavity
K	specific drive amplitude
R_c	coupling impedance per length, $Q_L(r/Q)$
I_b	beam current

Typical self-consistent units of K and R_c are $\sqrt{\mathrm{Watts/m}}$ and Ω/m. The quantities E, K, and I_b are complex numbers; the rest of the parameters are real. The definitions of E, K, R_c, and I make physical and numerical sense on a macroscopic scale. Over a length l, a beam of current I gains El energy using KK^*l power, when the matching condition $E = IR_c$ holds.

The per-cavity ω_0 component of the beam current depends on the string beam current I_{bs} according to $I_b =$

* Work supported by the U.S. DOE Contract # DE-AC05-84ER40150

$I_{bs}e^{j\phi}$, where ϕ is the phase-of-flight along the beamline to cavity of interest.

If we restrict ourselves to the steady-state where $dE/dt = 0$, and additionally set $E_- = v_- E e^{-j\theta_-}$, $E_+ = v_+ E e^{j\theta_+}$, and $I_b = i_b E e^{j\phi}$,

$$\frac{K}{E} = \frac{1}{2}\sqrt{R_c} i_b e^{j\phi} + \frac{1}{2\sqrt{R_c}\omega_f}\left(jd\omega_- v_- e^{-j\theta_-} + \right.$$

$$\left. \omega_f - j\omega_d + jd\omega_+ v_+ e^{j\theta_+}\right)$$

When the right hand side is separated into its real and imaginary components, the quantity ω_d (controlled by the tuners) only appears in the imaginary part. Moving the tuners to minimize the power therefore results in the zeroing of that imaginary part, which happens when

$$\frac{\omega_d}{\omega_f} = i_b R_c \sin\phi + v_- \frac{d\omega_-}{\omega_f}\cos\theta_- + v_+ \frac{d\omega_+}{\omega_f}\cos\theta_+$$

Indeed, the tuner operation is equally sensitive to tuning with no inter-cavity coupling, when all cavity voltages are held fixed. The remaining real part gives the power at optimum cavity tune,

$$\text{Power} = \frac{1}{4}R_c E^2 \left(i_b \cos\phi + \right.$$

$$\left. \frac{1}{\omega_f R_c}(v_- d\omega_- \sin\theta_- + \omega_f - v_+ d\omega_+ \sin\theta_+)\right)^2$$

If $\sin\theta_- \neq 0$ and $\sin\theta_+ \neq 0$, only small amounts of coupling can be tolerated without requiring excessive Klystron power. The bad cases are one end of the string (which end depends on the sign of $\sin\theta$), and any case where $v_- d\omega_- \sin\theta_-$ does not exactly cancel $v_+ d\omega_+ \sin\theta_+$. Ordinarily one wants the ability to adjust each cavity gradient independently based on its performance capabilities. This independence can be recovered by setting $\sin\theta_+ = \sin\theta_- = 0$, at which point the coupling terms all but disappear from the Power equation.

3 DISCUSSION

The coupling between the cavities can provide an opportunity to measure the relative phases of the cavities. Without this measurement, the cavities' phase relative to the beam must be individually measured. Of course, with strong coupling, the relative phases must be set properly or the limited klystron power will not allow operation at full gradient. Figure 1 shows this phenomenon—curves show the input drive required as a function of phase for 10 Hz and 1 kHz coupling, under no-beam conditions. The flat reference line shows the power needed for 400 μA beam current. Other parameter values assumed for this example are $\omega_f = 235\text{s}^{-1}$, $R_c = 1.34 \times 10^{10}\Omega/\text{m}$, $E = 12\text{MV/m}$, $l = 0.7\text{m}$, and $v_- = v_+ = 1$.

One would certainly hope to operate a cavity string by attaching single-cavity control systems to each individual

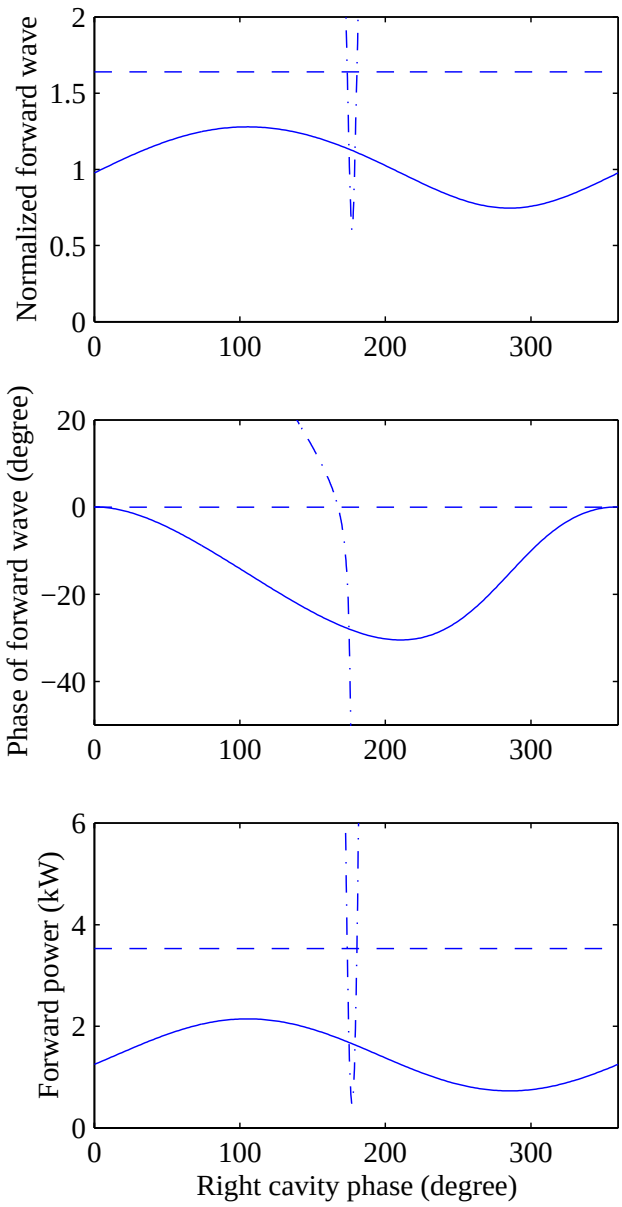

Figure 1: Drive required *vs.* neighboring cavity phase for 10 Hz coupling (solid) and 1 kHz coupling (dash-dot). A reference line (dashed) is given for the power required with beam.

cavity, so that $2\omega_f\sqrt{R_c}K = A(s)\cdot(E_s - E)$, where $A(s)$ is the (diagonal matrix) gain and E_s represents the setpoints. The undesirable alternative is some hopelessly complex centralized control that understands the $n \times n$ inverse of the coupling matrix. The equation of motion of the simpler system is

$$M \cdot E = A(s)E_s$$

where if we make the simplifying assumption that all cavities and coupling terms are identical, $M_{i,i} = s + \omega_f + j\omega_d + A(s) = p$ and $M_{i,i+1} = M_{i+1,i} = jd\omega$. The stability criteria are based on the zeros of $\det(M)$; to first order

in $d\omega$,

$$\det(M) = p^{n-2}(p_i^2 + (n-1)d\omega^2),$$

where n is the number of cavities in the string. One can clearly see that there are $n-2$ unperturbed stability criteria based on zeros of $s + \omega_f + j\omega_d + A(s)$. There are also two more cases involving global string modes, based on zeros of $s + \omega_f + j\omega_d + A(s) \pm j\sqrt{n-1}d\omega$.

Strong inter-cavity coupling makes a string more difficult to turn on. One sensible approach is to turn them all on slowly and proportionally, so that v_- and v_+ are constant. The tuners can center the system for minimum RF power under low gradient conditions, when there is plenty of available RF power. The only phenomenon the tuners have to compensate for during the ramp to full gradient is the ponderomotive frequency shift with gradient.

If a cavity trips, it's probably best to immediately turn RF off to the whole string and let it coast to a stop. Even if the adjacent cavities' RF systems could maintain their fields (a job made easier since the beam is probably turned off by the first cavity trip), some of their power would flow to the tripped cavity, which is not desirable.

Longitudinal alignment sensitivity can be significant. Historical assembly patterns at CEBAF, where that axis of alignment was not relevant, showed fluctuations of 6 mm. Between thermal contraction, manufacturing and assembly errors, and coarse tuning, 2-4 mm is a reasonable target for our 0.5 to 0.7 m long, λ=20 cm, cavities. Still, that implies uncontrolled phase differences between cavities of ϕ=0.1 radians. This error can be accommodated in two ways: If $\sin\theta = 0$, power does not flow between cavities. RF characteristics without beam are ideal, but individual cavities are miscrested with respect to the beam. The total crest for the module can still be zeroed, but the overall voltage gain has slipped some. If $\sin\phi = 0$, individual cavities are crested properly, but large amounts of RF power move from cavity to cavity. For a given (measured) set of cavity gradient and Klystron power capabilities, inter-cavity and external coupling bandwidths, and longitudinal cavity positions, numerical optimization can construct a set of phases that optimizes the total voltage delivered to the beam.

As discussed above, the sensitivity of a coupled cavity string to tuner motion is unchanged from the uncoupled case. That is, the curvature of the Power *vs.* tuner position relationship is not affected by the coupling. On the other hand, the position of that curve's minimum becomes sensitive to the voltage ratio between adjacent cavities (v_- and v_+). This sensitivity is one more reason to demand a tuner subsystem capable of short response times and no backlash. If a coarse tuner/fine tuner pair is used, the required range of the fine tuner is the sum of all effects that must be corrected. To the traditional list of pressure and ponderomotive compensation, inter-cavity coupling adds another term: the estimated maximum value of $v_- d\omega_- \cos\theta_- + v_+ d\omega_+ \cos\theta_+$. A reasonable choice for the maximum voltage ratio is in the 2 to 3 range, when cavities are more mismatched than that one would probably turn off the weak cavity.

When a cavity is turned off, it must also be detuned. Normally this is done to keep the cavity fields low in the presence of exitation from the beam. In a coupled-cavity system, excitation will also come from neighboring cavities. The neighbors of a detuned cavity must have their tuning corrected to reflect the changed pattern of voltage setpoints.

4 CONCLUSIONS

With the right phase relationship between cavities, coupling equal to or greater than the bandwidth of the cavity appears technically feasible. Tuning individual cavities can cancel all the reactive elements of the system. For any particular gradient pattern, proper tuning will result in drive requirements unchanged from the no-coupling case. The dynamic stability of the string is perturbed, and some reduction in feedback performance should be expected. The control system needs to be agile enough to measure the coupling and implement turn-on scenarios that involve coordination between the cavities.

5 REFERENCES

[1] J. R. Delayen, "Development of an Upgrade of the CEBAF Acceleration System," these proceedings.

THE RF SYSTEM FOR THE CEBAF POLARIZED PHOTOINJECTOR*

Mark Crofford, Curt Hovater, George Lahti, Chip Piller and Matt Poelker
Thomas Jefferson National Accelerator Facility
12000 Jefferson Ave., Newport News, VA 23606

Abstract

Jefferson Lab's CEBAF electron accelerator has recently begun delivering spin-polarized electrons for nuclear experiments. Spin-polarized electrons are emitted from a GaAs photocathode that is illuminated with pulsed laser light from a diode laser synchronized to the 3rd subharmonic (499 MHz) of the accelerating cavity frequency (1497 MHz). Up to three experimental halls (A, B and C) are served by the photoinjector each with their own beam requirements. To accomplish this, three independent diode lasers are synchronized and combined to illuminate the GaAs photocathode emitting a 1497 MHz pulse train of electrons. In addition an RF bunching cavity approximately 2 m down stream from the photocathode is used to compensate for space charge effects at the higher beam currents. The RF system that controls these elements is a modified VME based system. Custom RF VME modules control phase and amplitude for each laser diode and the bunching cavity. Power requirements were satisfied with commercial RF amplifiers, 5 W for the diode lasers and 10 W for the bunching cavity. Simple software algorithms using the EPICS control system correct phase and amplitude drifts. The RF system is compact, simple and allows for easy hardware or software modifications.

1 INTRODUCTION

The 5.5 GeV CEBAF accelerator at Thomas Jefferson National Accelerator Facility (Jefferson Lab) is arranged in a five pass racetrack configuration, with two superconducting radio-frequency (SRF) linacs joined by independent magnetic 180° transport arcs. The continuous electron beam is composed of three interlaced variable intensity beams that can be independently directed from any of the five passes to any of the three experimental halls. This allows three simultaneous experiments at the same or different energies and currents. Electrons are emitted through a polarized photocathode [1]. All of the experimental halls (A, B and C) are fully operational.

Recently a new laser system for the polarized source has begun operation that allows each of the experimental halls to independently choose current and operational duty factor [2]. Three diode lasers are biased with an RF frequency of 499 MHz. The light from the lasers is then optically combined to form a 1497 MHz pulse train. The light then illuminates a GaAs photocathode, producing polarized electrons. Precise phase control between the lasers is essential for proper acceleration. The 499 MHz laser pulses must be 120° apart to construct the 1497 MHz signal. Amplitude control is also important since each laser's pulse length is determined both by the dc bias and the RF bias. The laser's pulse length determines the electron bunchlength leaving the photocathode. The RF system also includes a bunching cavity to help reduce space charge effects over the wide current range (100's pA to 180 μA) demanded by the users.

Previously a CEBAF RF control module had controlled the laser for the photocathode (single laser) [3]. This system is based around a CAMAC interface and is designed to control a superconducting accelerating cavity. While this control system has been excellent for superconducting accelerating cavities, it has only been marginal for controlling RF systems like laser diodes and normal conducting cavities. Therefore it was decided to design a system that better met the needs of the laser diodes and was compatible with the EPICS/VME interface.

2 LASER RF SYSTEM

The laser RF controls are a VME based system using the EPICS control system [4]. Drifts associated with these RF systems are mostly thermal; thus we chose a rather slow (10 Hz) feedback system. A dedicated EPICS IOC (Motorola MV 167) is used to control the phase and amplitude of the three laser diodes and the bunching cavity. The update rate of the EPICS control system met our need. Should faster update rates be necessary, speeds up to 1 kHz are possible by putting the software into VxWorks directly on the IOC. Choosing the VME bus allowed us to use economical and readily available VME cards. In addition the EPICS collaboration already had the drivers available for the ADC/DAC (VMIVME 4514A) and I/O (VMIVME 2532A) cards and only slight modifications were necessary. The VME crate is a custom crate with a modified P2 backplane to handle the control signals. RF signals are hard wired to the back of the crate. Blindmate™ connectors allow for easy VME module removal.

* Work supported by the Department of Energy, contract DE-AC05-84ER40150.

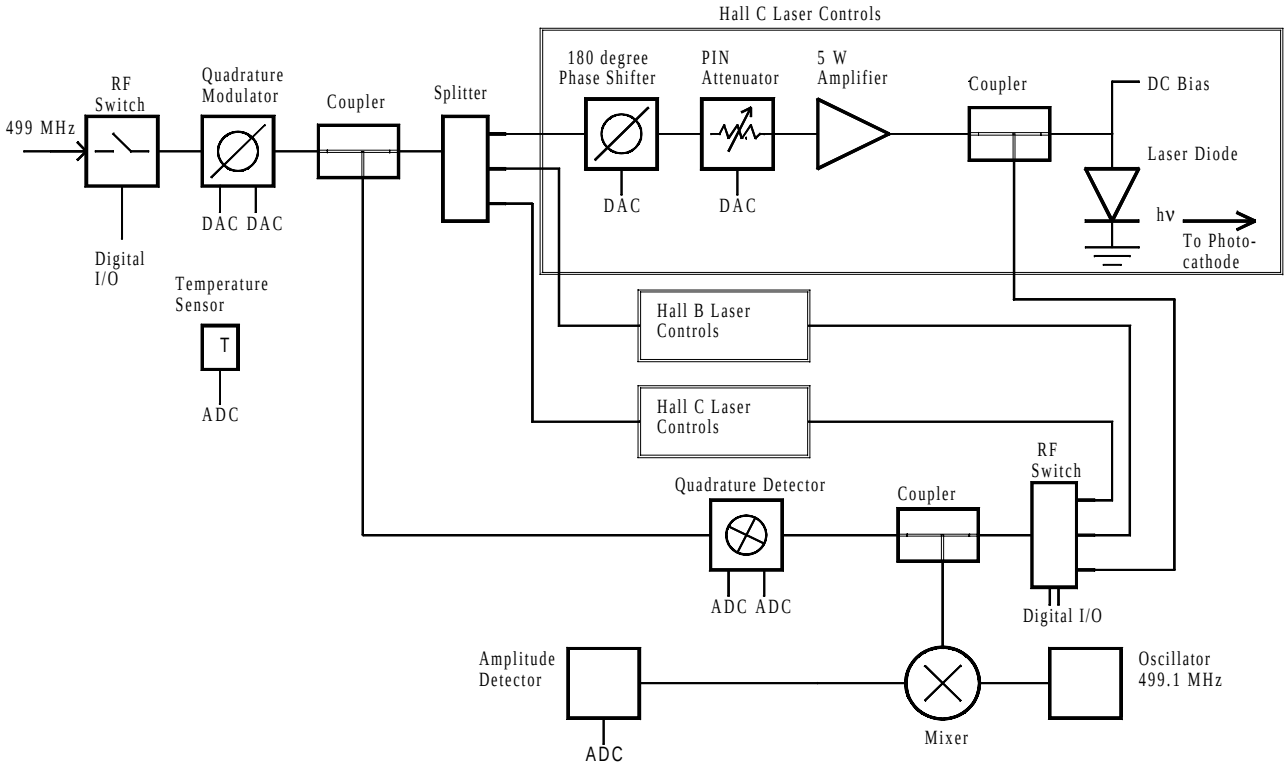

Figure 1 Block diagram of the laser diode RF system.

Figure 1 shows a block diagram of the RF system. The specifications for phase and amplitude control are 1^o and 1% respectively. Considering the relaxed control specifications it was decided to do the entire signal processing at the operating frequency of 499 MHz. This also allowed the system to use one of the pre-existing 499 MHz chopping cavities as a reference; the cavity is located less than 3 m away. The controls are divided into three VME modules: Reference Drive, Phase Shifter Module, and Detector Module. The reference module consists of a 360^o (I/Q) phase shifter for global phase adjustments and a 3-way splitter to supply the RF to the individual laser diodes. In addition it provides a coupled signal to the detector module. The phase shifter module consists of three 180^o varactor capacitor phase shifters (Synergy Microwave) used to align the phase between the three laser diodes. The phase between the lasers is coarsely (+/- 5^o) set using hard-line. The varactor phase shifters were chosen over I/Q phase shifters for cost reasons and since it was not necessary to have 360^o of phase shift capability. The phase shifters are controlled by 12 bit DACs. 5 W solid state amplifiers (Microwave Power Equipment) are used to RF bias the laser diodes. Inside each amplifier a voltage controlled PIN attenuator is used to control the RF bias on the laser diode. Approximately 1 W of RF power is needed for the laser diode RF bias. The detector module detects drifts due to cable or components (most notably the amplifiers). An RF signal is coupled back from each laser diode to the detector module. To economize on RF parts the three RF signals are muxed through an RF switch into a 360^o phase detector (quadrature detector) and amplitude detector. The EPICS control software continuously switches among the three RF signals. The error signals are then fed through the VME back plane to the ADC. The amplitude detector is an Analog Devices RMS to DC converter operating at an IF of 100 kHz. This was chosen over a typical Shottky diode because it is less susceptible to temperature drifts.

Key to the design process was minimization of thermal drifts. All RF electronics is next to the laser diodes in the tunnel (previously the RF electronics had been located up in the klystron gallery, 10 m above the tunnel). Temperature sensors on the VME cards are continuously monitored for any abnormalities. All the RF components on the VME cards and components were thoroughly characterized in an environmental chamber. It was intended to use the temperature sensors to provide a mechanism to remove thermal drifts using the component characterizations. This was deemed unnecessary after measurements in the CEBAF tunnel showed that temperatures vary less than 2^o C over long periods of time (weeks).

The feedback for the system presently only includes the cables to the laser diodes. Drifts across the laser diodes and optics are assumed to be minimal (< 0.5^o). If tighter tolerances are needed in the future, a laser diode detector can be incorporated in the optical path and the signal fed back into the controls.

3 BUNCHER RF SYSTEM

The buncher cavity is a pillbox design with reentrant nosecones that is operated in the TM_{010} mode at 1497 MHz. The cavity is constructed from stainless steel with copper plating on the RF surfaces, a process with which we have had good success at Jefferson Lab [5]. Three equally spaced ports located around the circumference of the pillbox cylinder are used to interact with the magnetic field of the TM_{010} mode. Manual adjustment of the resonant frequency is achieved via a micrometer controlled plunger mechanism, which is attached to the first port. RF power is delivered to the cavity via a critically coupled inductive coaxial loop probe located at the second port. A small undercoupled loop probe mounted on the third port samples the field for feedback and control. The cavity loaded Q is approximately 2500 and the R/Q is 125.

The cavity is designed to operated between 1 kV/m and 35 kV/m. Since power requirements are small, less than 5 Watts, heating from conductive losses is not a concern and so no internal cooling is necessary. Temperature stabilization is realized through the use of an external water jacket and insulating blanket. The RF phase and amplitude regulation requirement for the cavity control system is 1^{o} and 1%. As with the laser diodes the feedback takes place through EPICS. Phase control is provided by an I/Q phase shifter (IF Engineering) operating at 1497 MHz and, similarly, phase detection is performed using an I/Q phase detector. Amplitude control is accomplished using a pin attenuator (Anaren) and diode detector in a similar fashion as with the diode laser controls. The reference frequency (1497 MHz) is provided from a pre-existing bunching cavity located further downstream. A single VME card controls the buncher cavity and it is housed along side the other cards for the diode laser controls.

4 SOFTWARE

The software is a low-level application built on the EPICS control system. The interface to the VME hardware is via specifically written EPICS device support that communicates with the commercially available boards. This is mostly a straightforward EPICS database application, using standard records. It uses 12 Capfast database schematics with about 270 records, 26 ".c" subroutine files, and 2 ".st" sequencers. Most of the database records scan at 1 Hz, with the feedback loops running at 10 Hz.

The feedback loops are implemented in software, using the standard feedback control model (i.e. compare the measured hardware value to the user requested value, and vary the hardware set point to drive this comparison toward zero). Each of the three seed lasers and the buncher has independent feedback loops, a phase loop and gradient loop for each. Temperature regulation can be handled by these loops using a 1 Hz scan rate. However, for the buncher beam loading effect, a 10 Hz rate was needed. If a higher rate is desired, then part of the EPICS database will need to be converted into ".c" code to be run as a VxWorks task.

The software incorporates alarms and addresses trouble shooting. The feedback loop parameters can be altered for diagnostics (e.g. variable scan rates, free running or manual trigger modes, and hardware simulation). The user's interface to the alarms and troubleshooting begins with a basic set of good-bad indicators. The top indicator is for the combined status of both subsystems (three laser and buncher). If it shows good, then there is no need to look further. The rest of the basic indicators show more specific status. If an indicator shows bad (warning or fault), then the user can bring up various screens that show the specific problems (e.g. analog value out of range, loss of communication). The built-in troubleshooting screens provide condensed information of what needs to be done and by whom and in what order, and gives reference to the full troubleshooting guide document.

5 SUMMARY

The system has been operational since March of 1998 and has had no major problems. During commissioning of the system, a bug in the phase feedback algorithm caused the systems to run off crest, but this was quickly discovered and fixed. The decision to go with the VME platform over existing CEBAF RF controls has made the system much easier to upgrade and maintain, especially considering the compatibility with the EPICS control system.

REFERENCES

1. B. M. Dunham, “Investigations of the Physical Properties of Photoemission Electron Sources for Accelerator Applications”, Ph.D. Dissertation (physics), 1993, University of Illinois.
2. M. Poelker, et al., to be published in Nuclear Instrumentation and Methods.
3. S. Simrock, “RF Control System for CEBAF,” 1991 IEEE Particle Accelerator Conference, Conference Record.
4. L. R. Dalesio, et al., “The Experimental Physics and Industrial Control System Architecture: Past, Present and Future”, International Conference on Accelerator and Large Experimental Physics Control Systems, Oct. 1993.
5. C. Hovater et al., “The CEBAF RF Separator System”, 1996 Linear Accelerator Conference, Conference Proceedings, August 1996.

WAVEGUIDE HARMONIC DAMPER FOR KLYSTRON AMPLIFIER*

Yoon Kang, Ali Nassiri
Argonne National Laboratory, Argonne, Illinois 60439 USA

Abstract

A waveguide harmonic damper was designed for removing the harmonic frequency power from the klystron amplifiers of the APS linac. Straight coaxial probe antennas are used in a rectangular waveguide to form a damper. A linear array of the probe antennas is used on a narrow wall of the rectangular waveguide for damping klystron harmonics while decoupling the fundamental frequency in dominent TE_{01} mode. The klystron harmonics can exist in the waveguide as waveguide higher-order modes above cutoff. Computer simulations are made to investigate the waveguide harmonic damping characteristics of the damper.

1 INTRODUCTION

In the APS linac klystron amplifiers, the connectors for the high-voltage connection to the ion pump were burned by the klystron harmonics power. The metallic tube connected to the ion pump passes the higher frequency harmonics power, and the metal screen used to decouple the harmonics was not very effective. Even though more effective rf shielding may be possible, it was not desirable for quality vacuum pumping. The tube to the pump has a cutoff frequency higher than the fundamental klystron frequency, but the harmonic spectrum power, shown in Figure 1, is not attenuated sufficiently. In the APS, five klystrons are used. Each klystron normally delivers 5-microsecond 35-MW peak power pulses to the accelerating structures. The average power of harmonic spectrum in the waveguide is estimated as several tens of watts. In order to eliminate the heating due to the harmonic power, a damping circuit is needed in the waveguide. The harmonic frequency power in the output cavity of the klystron amplifier may couple to the waveguide in the form of waveguide higher-order modes as well as the dominant mode. The klystron harmonic frequency power caused some problem in the APS storage ring, so the harmonics were damped by multiple probe antennas mounted on the narrow wall of the waveguide. A damper design of similar function is needed in the 2.856-GHz linac system. For this reason, the waveguide harmonic damper designs were studied using computer simulation.

* Work supported by U.S. Department of Energy, Office of Basic Sciences under Contract No. W-31-109-ENG-38.

2 HARMONIC DAMPER

In the waveguide transmission line, during normal operations, the fundamental frequency propagates as a travelling wave to the load cavity structure that works as a matched load. However, since the accelerating cavity structure is a narrowband load, the harmonic frequency spectrum may form standing wave resonances in the waveguide between the klystron output cavity and the cavity structure.

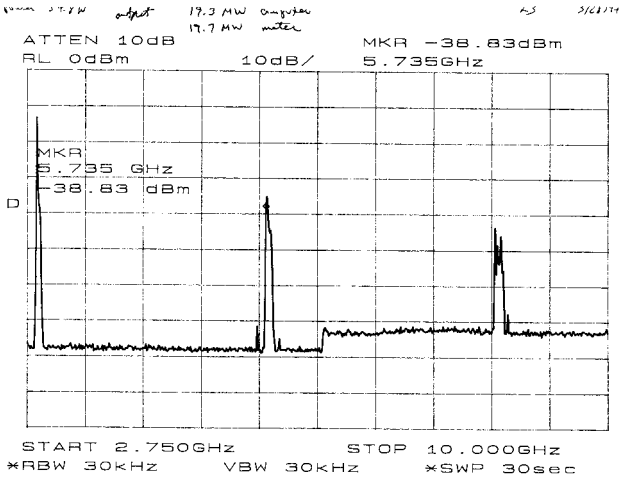

Figure 1. Harmonic spectrum of 2.856-GHz klystron amplifier output.

Figure 2 shows the waveguide harmonic damper design employing coaxial probe antennas. A linear array of five probe antennas is used on a narrow wall of the rectangular waveguide for damping klystron harmonics while decoupling the dominent TE_{01} mode. The rf power for the accelerating structure from the klystron is transmitted in the dominant TE_{01} mode. The harmonic frequencies from the klystron amplifier not only exist in the TE_{01} mode but also in higher-order waveguide modes. Higher order TE_{mn} and TM_{mn} modes couple to the antennas if m=odd and do not couple to the antennas if m=even. The index n must be nonzero for both TE and TM modes.

For the fundamental frequency, the antennas may reflect some power without delivering power to the matched load of the coaxial probes. The input matching of the damper section is important for power transmission of the fundamental frequency. Ideally, the probe antennas do not disturb the TE_{01} mode at the fundamental frequency. However, actual antennas can cause some

mismatch for the frequency. Therefore, it is important to find the optimum antenna spacing for minimum reflection at the input.

The waveguide with uniformly spaced antennas is considered a periodic loaded transmission-line structure with a matched load at the output. From [1] it can be shown that minimum reflection occurs if the spacing between antennas is a quarter wavelength. In Figure 2 the antennas are spaced by a quarter wavelength so that the combined reflection from all antennas is minimized at the input. However, since mutual coupling between the antennas and the higher-order mode excitation exist due to finite antenna dimensions, it may be necessary to check the optimum spacing of the antennas for minimum reflection at the input.

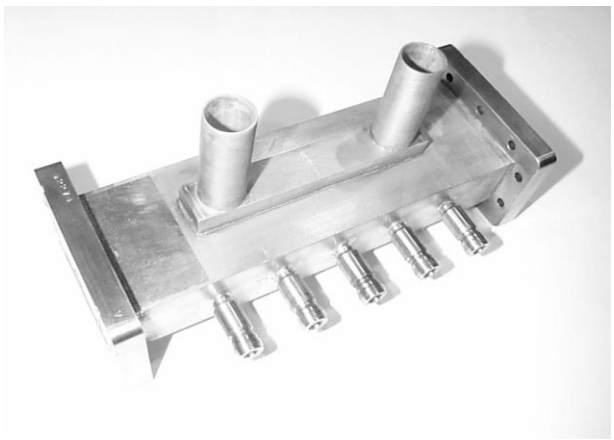

Figure 2. Waveguide harmonic damper with coaxial probe antennas.

3 SIMULATION

The damper structure has been simulated using the High Frequency Structure Simulator (HFSS) code [2]. In the simulations, eight modes were used to predict the input matching and harmonic damping with the structure. The simulations showed that the antennas convert the fundamental TE_{01} mode to some higher-order modes, and these modes do not couple to the antenna terminations if a mode is below cutoff. Since a uniform rectangular waveguide works as a high-pass filter for each mode, the harmonic frequencies, nf_o (n=2,3,4,5,…), can couple to antennas as higher-order waveguide modes.

The distance between the antennas is no longer a quarter wavelength at the higher harmonic frequencies that exist as higher-order waveguide modes. Note that the higher-order modes have pass-bands only above the cutoff frequencies of corresponding higher-order modes. Figure 3 shows the structure used in the simulation.

Figures 4 and 5 show the calculated generalized scattering parameters, $S_{1\_n,1\_n}$ and $S_{2\_n,1\_n}$, respectively, for the first four modes. Figure 6 shows the propagation loss of the four modes in the waveguide damper. Only four modes are shown in the plots for convenience. The fundamental frequency propagates in the dominant TE_{01} mode and the S_{11} is lower at the frequencies around 3GHz. These results of simulations show the properties of reflection, mode excitation and conversion, and damping characteristics of the waveguide modes due to the probe antennas. Probe antennas used in the calculation were 1.2” long and 0.121” in diameter.

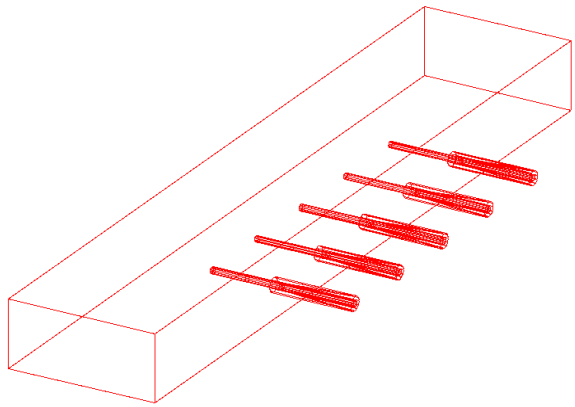

Figure 3. Damper structure with coaxial probe antennas.

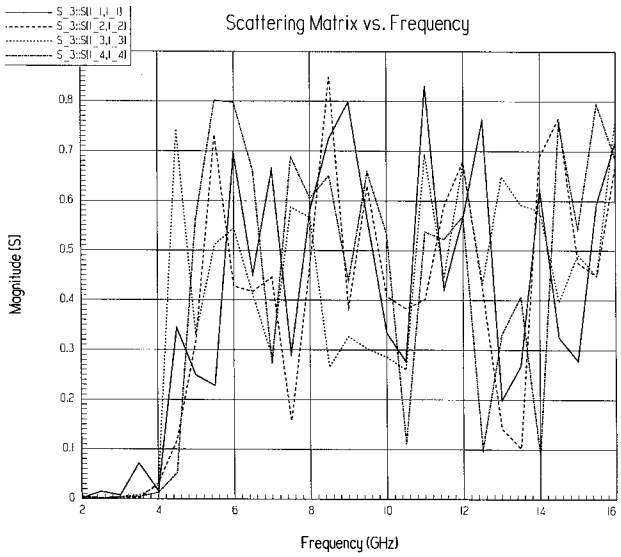

Figure 4. Calculated input reflection of the waveguide modes of the damper.

Since the simulation did not include the klystron amplifier and the accelerating structure as the load, the calculated damping characteristics did not directly describe the actual damping performance. The spacing between the antennas was varied to see the optimum antenna separation. The length of the antennas was also varied. The propagation loss characteristics shown in Figure 6 for the first four modes show that the waveguide higher-order modes can be damped effectively.

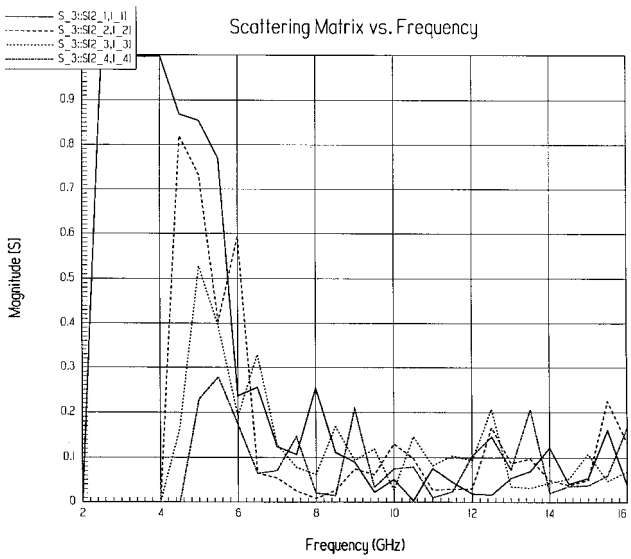

Figure 5. Transfer characteristics of waveguide modes through the harmonic damper.

The input matching and the insertion loss are good only at around 2.5-4GHz for the fundamental mode. Note that the generalized S-parameters are shown in the figures, so that the propagation loss in Figure 6 includes the waveguide cutoff loss for each mode.

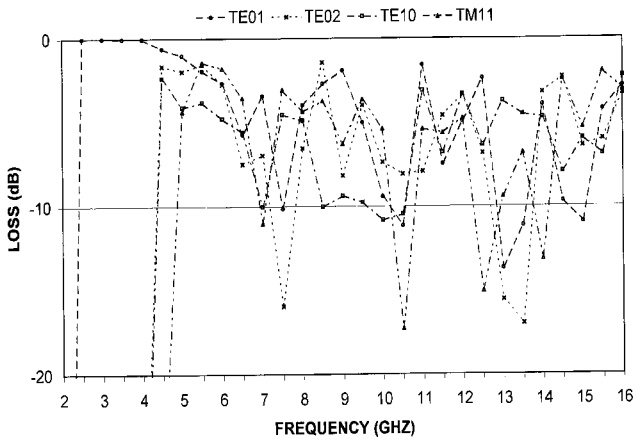

Figure 6. Propagation loss of first four waveguide modes in the waveguide harmonic damper.

4 FABRICATION AND MEASUREMENT

A prototype waveguide damper with coaxial probes has been fabricated and a low-power measurement was made. Five Ceramaseal CDP-20001 coaxial feedthroughs have been used as the probe antennas in the WR-284 waveguide. The antenna feedthroughs are welded to the copper waveguide. The fabricated damper was shown in Figure 2. The coaxial section of the antenna has a 50Ω characteristic impedance and a 50Ω coaxial termination is used in each antenna. Measurement of scattering parameters of the damper at 2.856GHz with a network analyzer confirmed good impedance matching with low insertion loss. At the fundamental frequency, the input return loss and the insertion loss were <–23dB and <0.02 dB, respectively.

The damper was to be inserted in the waveguide between the klystron and the accelerating structure. At the time the prototype was tested, the APS linac system was delivering beam to the users and, unfortunately, the damper could not be used with the actual accelerating structures. Preliminary testing of the damper between a klystron amplifier and a matched load has been planned. Since the accelerating cavity structure is a narrowband load to the klystron, measurement with a broadband resistive load may not show the characteristics of the damper. Testing with an actual accelerating structure is needed and will be performed in the near future.

5 CONCLUSION

The klystron harmonic waveguide damper employing five coaxial antennas in the narrow wall of a rectangular waveguide was simulated, fabricated, and low-power tested for the S-band linac application. The design is applicable to any system using a high-power transmitter with high harmonics content in the spectrum. The damping obtained in the design is considered adequate to protect the high-voltage connectors of the ion pumps. The design may also be useful for damping the cavity higher-order modes coupled to the waveguide.

6 REFERENCES

[1] R. E. Collin, “Field Theory of Guided Waves,” Second Edition, IEEE Press, New York, 1991.

[2] HP 85180A, High-Frequency Structure Simulator, Hewlett Packard.

DEVELOPMENT OF A 114.24MHz SUB-HARMONIC BUNCHER FOR THE KEKB INJECTOR LINAC

S. Yamaguchi, S. Ohsawa, M. Ikeda, A. Enomoto and Y. Igarashi*
High Energy Accelerator Research Organization (KEK), Oho, Tsukuba, Ibaraki 305-0801 JAPAN
* Mitsubishi Heavy Industries, Ltd., Nagoya Aerospace Systems,
Oye, Minato, Nagoya, Aichi 455-8515 JAPAN

Abstract

A 114.24-MHz sub-harmonic buncher cavity was newly developed to improve the single-bunch purity of the KEKB injector linac. The cavity was designed so as to have a high shunt impedance and a low maximum surface field at the acceleration gap. To reduce the probability of rf breakdown, the inner wall of the cavity was electrolytic-polished and a vacuum pump-out was put at the end wall of the cavity. Copper was selected as the structural material (it was copper-plated stainless steel for the old cavity) in order to improve the water-cooling capability and to reduce the resonant frequency shift by the gap-distance change when the input power increases. A cold test showed a shunt impedance of 1.2 MOhm, which is twice as large as that for the old cavity. The design, fabrication and results of low- and high-power tests and a beam-acceleration test are described.

1 INTRODUCTION

The upgraded KEKB injector linac (8.0-GeV e^- / 3.5-GeV e^+) is now at the stage of initial commissioning [1, 2]. The pre-injector of this linac has to provide single-bunch beams of 10nC in 10ps to produce intense positron beams. To satisfy this requirement, in this pre-injector, two sub-harmonic bunchers (SHB), i.e., SHB1 (114.24MHz) and SHB2 (571.2MHz) were introduced [3,4]. However, the bunch purity had not been sufficiently good; the percentage of the main-bunch current to the total current was only 80%. For this reason, we have developed a new SHB1 cavity having a large shunt impedance. Another problem of the old SHB1 cavity is low stability of the resonant frequency because of the gap-distance shift, due to poor cooling performance. Redesigns of the structural material and cooling-pipe configuration have been made.

2 DESIGN

According to the PARMELA simulation, it is possible to reduce the amount of the satellite bunch to less than 1% if the shunt impedance of the SHB cavity is increased by 1.7 times[4]. The dimensions of the new cavity was determined for this goal on the condition that the cavity can be install in the existing focusing coils (ϕ200mm).

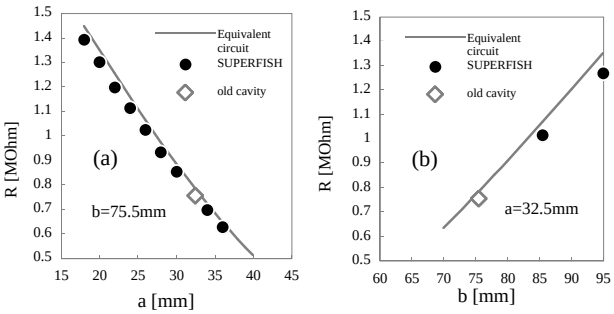

Figure 1: Dependence of shunt impedance on cavity dimensions; (a) inner radius, *a* ; (b) outer radius, *b*.

Figure 1 shows the dependence of the shunt impedance (*R*) on the inner radius (*a*) and the outer radius (*b*) of the cavity calculated by SUPERFISH and an equivalent-circuit model (quarter-wavelength-long short-circuited antiresonant transmission line). This figure shows that the required shunt impedance can be obtained when the values of *a* and *b* are selected as 30mm and 90 mm, respectively; these values were 32.5mm and 75.5 mm, respectively, for the old cavity.

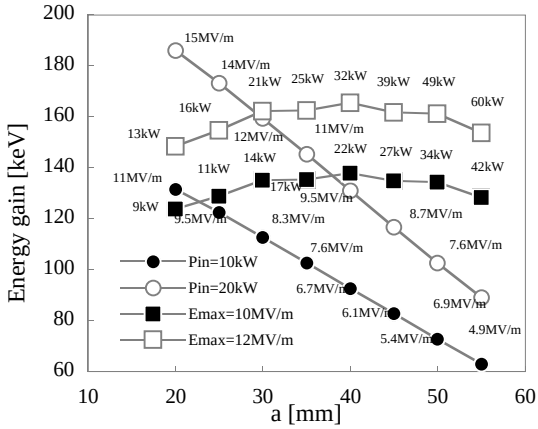

Figure 2: Relation between the energy gain and the inner radius (*a*). The numbers beside each mark show the maximum electric field for P_{in} = constant or the required source power for E_{max} = constant.

Figure 2 shows the relation between the energy gain of SHB1 and the inner radius (*a*). When the input power is constant, the smaller is *a*, the larger is the energy gain. However, when the maximum surface field is constant,

the energy gain is maximum at a = 40mm. Finally we set the value of a at 30mm because the power source available at present is limited to 10kW and beam handling would be difficult if the value of a is too small.

The distance of the acceleration gap was determined as being 40 mm (it was 18mm for the old cavity) because the longer is the gap distance, the lower is the maximum surface field. Though the shunt impedance also decreases for a wider gap distance, it is only a few percent (see Figure 3).

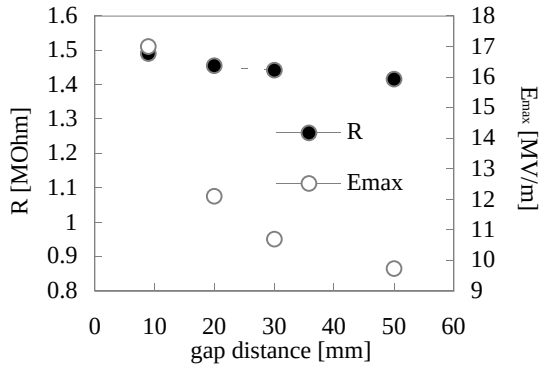

Figure 3: Shunt impedance, maximum electric field *vs* gap distance.

As the structural material, copper-plated stainless steel has been used for the old cavity. Also, only the outer conductor has been water-cooled. Consequently, the cooling performance is not good, which causes a change in the resonant frequency when the input power is changed. In the new cavity, copper (oxygen free copper) is selected as the structural material, and the inner conductor and both end plates are water-cooled.

The calculated value of the shunt impedance for the final dimensions (see Figure 4) is 1.28MΩ, which is 1.7-times that for the old cavity (0.77MΩ).

As an rf input coupler, a loop antenna of coaxial waveguide (20D) has been selected instead of that of coaxial line, which is used in the old cavity, because it has a high possibility of rf breakdown. A copper rod (ϕ24mm) is used as the tuner. According to a MAFIA calculation, a frequency change of 200kHz can be obtained by a stroke of 40mm. The tuner is remote-controlled using an ultrasonic motor

An ion pump (10l/s) is put at the end plate (see Figure 4) to improve the vacuum level of the cavity. All inner parts of the cavity were electrolytic-polished (20μm).

3 LOW POWER TEST

The resonant frequency was tuned by adjusting the length of the short nose (d_L). The sensitivity of the dimensions on the resonant frequency is given in Table 1.

Table 1: Sensitivity of the dimensions on the resonant frequency. Units of kHz/mm.

	$\partial f/\partial L_R$	$\partial f/\partial L_L$	$\partial f/\partial d_R$	$\partial f/\partial d_R$
SUPERFISH	174.18	0	210.73	36.95
Measurement	-	-	200.0	36.3

The results of a low-power test are given in Table 2. The ratio of the measured Q_0 to the calculated Q_0 (Q_0^m/Q_0^c) has increased from 0.75 for the old cavity to 0.93. This may be due to an improvement in the electrical contact because end-plates were connected using bolts and nuts in the old cavity but are connected by electron-beam welding in the new cavity.

Table 2: Results of low-power tests.

SUPERFISH	measurement				
Q_0	Q_0	Q_c	Q_L	β	Q_0^m/Q_0^c
7523	6989	6741	3433	1.04	0.93

The shunt impedance was obtained from R/Q values measured by Slater's bead perturbation method [5]. Figure 5 shows the electric-field distribution on the beam axis near to the acceleration gap.

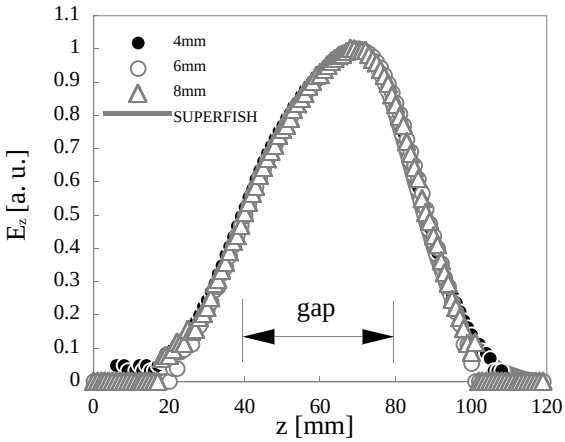

Figure 5: Distribution of the axial electric field measured by the bead-perturbation method.

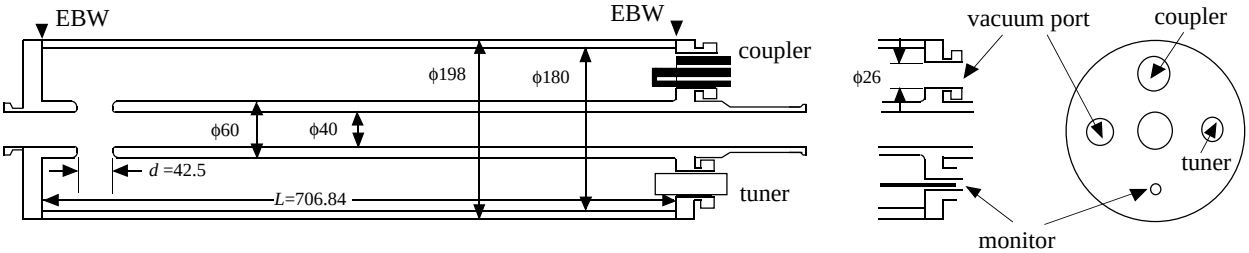

Figure 4: Cross-sectional view of the new Sub-harmonic buncher cavity.

Aluminum spheres of diameter 4, 6, and 8mm were used as perturbaters. When these values are extrapolated to the limit of zero volume, the value of shunt impedance of 1.15MOhm was obtained (see Figure 6).

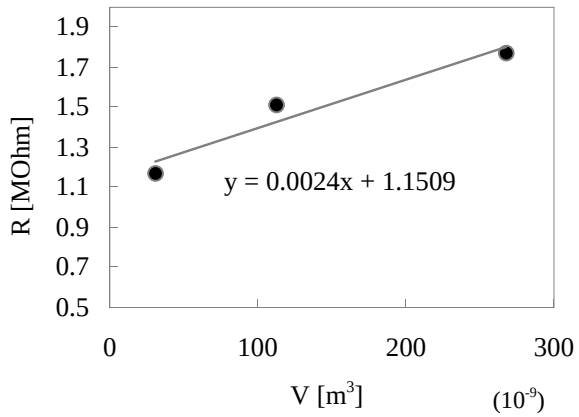

Figure 6: Relation between volume of bead and shunt impedance.

4 HIGH POWER TEST

Electric discharges by multipactoring have been observed during the initial stage of rf conditioning; it took ten days to reach an input power of 10kW without focusing coils and two days after the addition of coils. During rf conditioning, no change in the resonant frequency was observed. The pulse shapes for an input power of 10kW are shown in Figure 7. The time constant calculated from this pulse shape is about 10μs. The theoretical value is 9.6μs (= $2Q_L/\omega$).

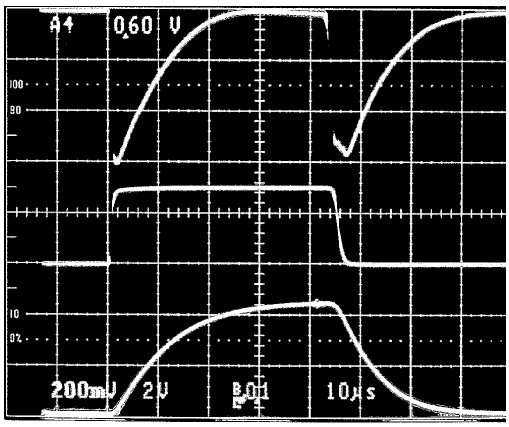

Figure 7: Photograph of rf pulses. Top trace, Reflection; Middle trace, Input; Bottom trace, Transmission. Input power, 10kW; 10μs per division.

5 BEAM ACCELERATION TEST

After installation of the SHB cavity on the beam line, a beam-acceleration test was performed. The beam charge was 12nC at the gun output. Figure 8 shows the bunch shape observed by a streak camera [6]. The bunch purity was improved from 80% to almost 100%.

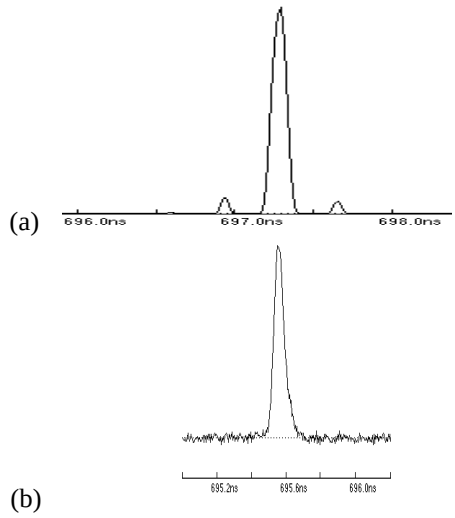

Figure 8: Shape of 12nC single bunch. (a) old SHB; (b) new SHB.

6 SUMMARY

In order to improve the bunch purity of the KEKB injector linac, a new 114.24MHz SHB cavity was designed, fabricated and tested. As a result, the shunt impedance was increased twice as large as that for the old cavity (70% came from the geometry and 20% from an increase of Q_0(measured)/Q_0(theoretical), and a bunch purity of almost 100% was obtained for a 12nC single-bunch beam. Good stability of the resonant frequency was obtained by improving the cooling performance.

7 ACKNOWLEDGEMENTS

The authors wish to thank H. Hayano for his valuable comments on the design of the SHB cavity. They acknowledge Y. Morozumi for his help in fabricating the input coupler.

8 REFERENCES

[1] A. Enomoto et al., “Construction of the 8-Gev e- / 3.5-GeV e+ Injector Linac for KEKB,” these Proceedings.

[2] Y. Ogawa, “Commissioning of the KEKB linac,” these Proceedings.

[3] J-Y Choi et al., “Bunching system of the KEKB Linac," Proceedings of LINAC96, CERN, August 26-30, 1996, 340-342 (1996).

[4] S. Ohsawa et al., “Pre-injector of the KEKB 8-GeV Linac," these Proceedings.

[5] J. C. Slater, “Microwave Electronics," D.Van Nostrand Company, Princeton, 1950.

[6] Y. Ogawa et al., “New Streak-Camera System for the KEKB Linac," Proceedings of APAC 98, KEK, March 23-27, 1998, to be published.

DESIGN, OPERATION, AND TEST RESULTS OF 350 MHZ LEDA RF SYSTEM

D. Rees, J. Bradley III, K. Cummings, A. Regan, T. Rohlev, W. Roybal, Y.M. Wang
Los Alamos National Laboratory, Los Alamos, New Mexico USA

Abstract

The Low Energy Demonstration Accelerator (LEDA) being constructed at Los Alamos National Laboratory will serve as the prototype for the low energy section of Acceleration Production of Tritium (APT) accelerator. The APT accelerator requires over 244 RF systems each with a continuous wave output power of 1 MW. The reliability and availability of these RF systems is critical to the successful operation of APT plant and prototypes of these systems are being developed and demonstrated on LEDA. The first completed LEDA RF systems are three, 1.2 MW, 350 MHz, continuous wave, klystrons driving a radio frequency quadrapole (RFQ). This paper present the design and test results for these RF systems including the klystrons, cathode power supply, circulators, RF vacuum windows, and RF components. The three RF systems driving the RFQ use the accelerating structure as a power combiner and this places some unique requirements on the RF systems. These requirements and corresponding operational implications will be discussed.

1 LEDA RF SYSTEM DESIGN

The LEDA RF system provides RF power to an RFQ which accelerates a proton beam to a final energy of 6.7 MeV. To accomplish this acceleration the RFQ requires structure and beam power of 1900 kW. The power to the RFQ is provided by three 1.2 MW klystron amplifiers with the structure serving as the power combiner.

The LEDA RF systems utilize modulating-anode klystrons with individual power supplies to maximize operating flexibility and efficiency. Each klystron has an individual power supply, and the modulating anode voltage is derived from the cathode voltage using a regulator tube. The high-efficiency klystrons are protected from reflected power by circulators. The power from a klystron is divided into four equal parts using 3 dB hybrids to reduce the power passed through the accelerating structure vacuum windows. For the RFQ waveguide runs, the power from the three klystrons is carried in three full height WR2300 through a waveguide switch to hybrid splitters. The hybrid splitters divide the power into twelve waveguide feeds that transition to half-height WR2300 and deliver the power to the RFQ through coaxial vacuum windows.

Because the LEDA systems are, in part, meant to serve as prototypes for the APT plant, the approach to achieving high availability is also being prototyped on LEDA. Only two of the three RF systems connected to the RFQ are required for operation of the RFQ. The RFQ serves as the power combiner. Should any component of any one of the RFQ RF systems fail, a waveguide switch is used to isolate the failed system from the RFQ. The waveguide switch also reflects a short circuit at the appropriate phase to the RFQ irises associated with the failed system allowing the RFQ to continue to operate with the two remaining systems.

This approach results in some additional requirements on the RF system. With the RFQ serving as the power combiner, it is necessary to balance the output power and phase of the two or three RF systems connected to the RFQ or unwanted reflected power will result. To accomplish this, local phase control loops are implemented around each klystron and the group of klystrons is treated as if it were a single RF source by the low level control system, which modulates the amplitude and phase of the klystron drive to control the RFQ field amplitude and phase. Also, an RF arc in a window or circulator requires that all RFQ RF systems be disabled, not just the system associated with the arc, to prevent the other RFQ systems from continuing to drive the arc through the RFQ. This logic also holds true for a crowbar or interlock trip in any one of the RF systems. The other RFQ RF systems must be disabled to prevent the disabled system from being driven through the cavity by the remaining RF systems.

The low-level RF control (LLRF) system performs various functions. Foremost is feedback control of the accelerating fields within the cavity in order to maintain field stability within ±1% amplitude and 1° phase. Other functions of the LLRF control system are implementation of the local phase control loops of each klystron and RFQ resonance condition monitoring. The resonance of the RFQ is controlled by varying cooling water temperature. Because the RFQ will rapidly cool when RF is shut down, drive frequency agility in the main feedback control subsystem is incorporated to quickly restore the cavity to resonance with RF heating.

2 RF COMPONENT DESCRIPTIONS

2.1 Klystrons

The LEDA RFQ RF systems utilize 1.2 MW CW klystrons at 350 MHz. The klystron is based on the CERN klystron with one major design modification. The LEDA 350 MHz klystrons are designed to dissipate the

full beam power (1.85 MW) in the klystron collector in the steady state. This design requirement is driven by the size of the APT plant and the impact that turning off all klystrons would have on the local power grid.

The design requirements and measured performance for the 350 MHz klystron are summarized in Table 1. The 350 MHz klystrons have demonstrated all design requirements in the acceptance tests and have approximately 300 hours of operation in test stands at Los Alamos. A picture of the klystron is shown below in Figure 1.

Table 1: Klystron Requirements

Requirement	Specified	Measured
Voltage (Max)	95 kV	94 kV
Current (Max)	21 A	19.6 A
Output Power (Min)	1.2 MW	1.2 MW
Efficiency (Min)	65 %	65 %
Gain (Min)	40 dB	41 dB
Operating VSWR (Max)	1.2:1	1.2:1
1 dB Bandwidth	.7 MHz	>.7 MHz

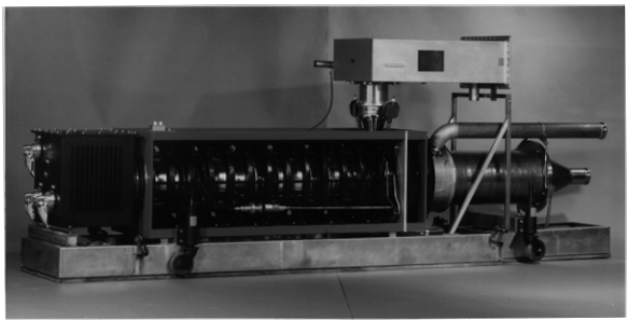

Figure 1: Picture of EEV 350 MHz klystron.

2.2 Power Supplies

LEDA is prototyping two power supply topologies that are under consideration for the APT plant: a Silicon Controlled Rectifier (SCR) center point controlled power supply and a solid state modulator power supply using Insulated Gate Bipolar Transistors (IGBTs). Both topologies provide a klystron beam voltage of up to 95 kV and a maximum beam current of 21 A and protect the klystron from excessive energy deposition in the event of a tube arc.

The SCR power supplies utilize two SCR bridges with filter inductors at the center tapped transformer primaries to produce 12 pulse rectification as shown in Fig 2. In the event of a klystron arc, the crowbar circuit protects the klystron from the filter capacitor stored energy. These power supplies must have an efficiency of ≥95%, a power factor of ≥0.93 at full power and the harmonic distortion at the input must meet IEEE Std 519-1992 requirements. Three of these power supplies have been delivered by Maxwell Labs and have met all performance requirements.

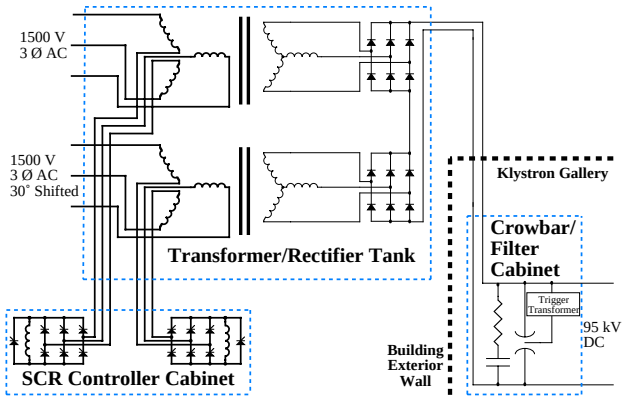

Figure 2: SCR bridges are in the center of the primaries.

The IGBT power supplies utilize 96 separate rectifying modules stacked in series. Each module is fed from an isolated secondary winding on one of four transformers. The primary windings of each transformer are phased for 24 pulse rectification at the series output. Each module uses an IGBT for current control, eliminating the need for a crowbar. Failed modules are bypassed by the control system to provide graceful degradation of operation. These power supplies must have an efficiency of ≥97%, a power factor of ≥0.98 and meet IEEE Std 519-1992 requirements. Three of these power supplies are on order from Continental Electronics and the prototype power supply has passed all acceptance tests. A picture one of the power columns containing half (48) of the 96 rectifying modules is included below in Fig. 3.

2.3 RF Vacuum Windows

The window design we have selected is a coaxial geometry. The 350 MHz window is illustrated in Figure 4. The air side is a half-height WR2300 waveguide. A T-bar is used to transition to a coaxial line. A high-purity alumina coaxial window separates the air and vacuum side of the window assembly. Another T-bar is used to transition back to half-height WR2300 which is then connected to ridge loaded waveguide to drive the iris coupled RFQ. Each RFQ window has been tested under vacuum in a back-to-back configuration to 1.0 MW of CW RF power for a minimum of four hours. In the RFQ the windows are utilized at a maximum nominal power of 300 kW. Prior to the 1.0 MW acceptance test, the windows must be conditioned to this power level. The conditioning time for each of the RFQ windows and spares is indicated in Figure 5. The average time was 18.5 hours.

2.4 Cavity Field Control

The cavity field control system controls the in-phase and quadrature (I/Q) errors of the cavity field. It consists of three VXIbus modules. The Clock Distribution Module receives a phase-stable 10 MHz reference and produces coherent frequencies needed for field signal

downconversion and I/Q sampling. The Field Control Module (FCM) houses all of the digital and analog electronics, which perform the high-precision I/Q detection and control. The Amplifier Control Module serves as an interface between the control system and the multiple klystrons driving the cavity. It takes the control signal from the FCM, splits it, and then individually modifies each output leg to compensate for the aberrations of each particular klystron. The closed-loop bandwidth of the field control system is approximately 200 kHz. A block diagram of the entire LLRF system is shown in Figure 6.

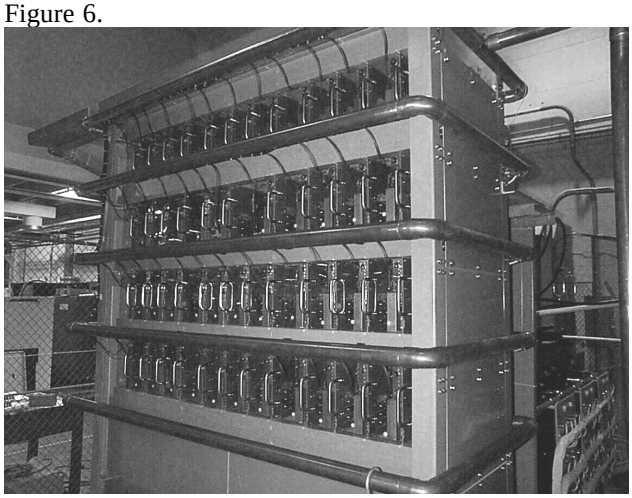

Figure 3: Power Column For IGBT Power Supply

2.5 Resonance Control

The resonance condition of the RFQ will be determined by monitoring a sample of its forward, reflected, and transmitted signals. The signals will be run through a simple algorithm in a digital signal processor on board the Resonance Control VXIbus Module to calculate the RFQ's resonant frequency. Should the resonance frequency differ from the fundamental, an error signal will be sent to the RFQ's water-cooling system indicative of the need to increase or decrease the cooling water temperature. This module also implements the frequency agile function, based on direct digital synthesis mentioned earlier. This frequency agility will be utilized only when the cavity is far from nominal resonance, not during normal operation.

2.6 RF Protection

A flexible RF Protection function has also been built into the LLRF VXIbus Control system. The RF Protect Module monitors the HPRF transmission system and turns off the drive to the klystrons should a fault occur anywhere within the system. The RF Protect function protects against arcs in the waveguide, klystron, or RFQ; high reflected power at the RFQ ports, loads on the circulator, and waveguide splitters; crowbars; and bad VSWR at the klystron output.

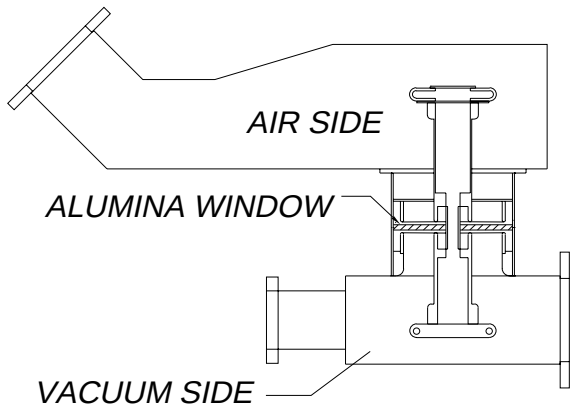

Figure 4: RFQ coaxial window.

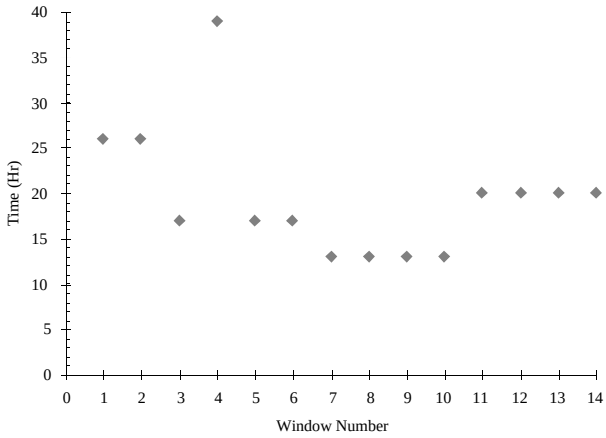

Figure 5: RFQ vacuum window conditioning time.

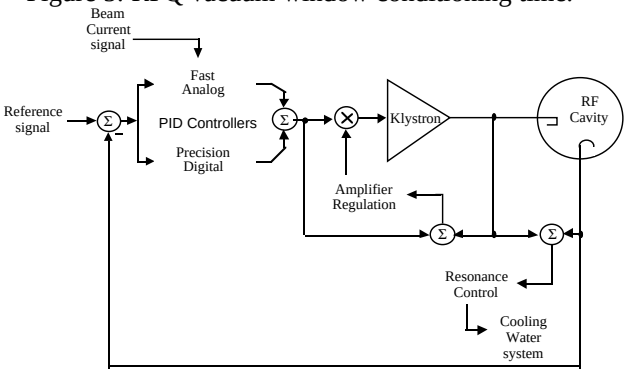

Figure 6: LLRF control system.

3 CONCLUSIONS

The RF systems for the LEDA accelerator have been installed at Los Alamos and are ready to provide RF power to the RFQ in early October. These systems have been designed as prototype equipment for the APT plant and will be used to demonstrate not only the reliability of RF equipment, but also the redundancy concepts for the APT plant that will allow for very high RF system availability. The individual RF system have demonstrated that each system meets the design requirements. The integrated testing with the RFQ in October is the next step in the validation of the APT RF system design.

THE RF POWER SYSTEM FOR THE SNS LINAC*

Paul J. Tallerico and William A. Reass
Los Alamos National Laboratory, Los Alamos, NM 87545 USA

Abstract

The initial goal of the SNS project is to produce a 1 MW average beam of protons with short pulse lengths onto a neutron-producing target. The objective of the SNS RF system is to generate 117 MW peak of pulsed 805 MHz microwave power with an accelerated beam pulse length of 1.04 ms at a 60 Hz repetition rate. The power system must be upgradeable in peak power to deliver 2 MW average power to the neutron target. The RF system also requires about 3 MW peak of RF power at 402.5 MHz, but that system is not discussed here. The design challenge is to produce an RF system at minimum cost, that is very reliable and economical to operate. The combination of long pulses and high repetition rates make conventional solutions, such as the pulse transformer and transmission line method, very expensive. The klystron, with a modulating anode, and 2.5 MW of peak output power is the baseline RF amplifier, an 56 are required in the baseline design. We discuss four power system configurations that are the candidates for the design. The baseline design is a floating-deck modulating anode system. A second power system being investigated is the fast-pulsed power supply, that can be turned on and off with a rise time of under 0.1 ms. This could eliminate the need for a modulator, and drastically reduce the energy storage requirements. A third idea is to use a pulse transformer with a series IGBT switch and a bouncer circuit on the primary side, as was done for the TESLA modulator. A fourth method is to use a series IGBT switch at high voltage, and not use a pulse transformer. We discuss the advantages and problems of these four types of power systems, but we emphasize the first two.

1 THE FLOATING DECK MODULATOR SYSTEM

The floating-deck modulator is an old technology that is well suited to pulse lengths above 0.5 ms, and pulse rates below 1 kHz. The RF duty factor, is 6.84%, since some scores of μs must be added for cavity fill time, and control loop settling time. The pulsed power duty factor is 7.5%, since the 0.1 ms rise and fall time must be added to the RF pulse length. Each 805 MHz klystron can deliver 2.5 MW of peak power into its load, and each klystron requires 120 kV and 40 A, peak. The average power into each klystron is thus 328.3 kW. We add 20% to allow for losses in the modulator, and capacitor bank slump, and arrive at 394 kW per klystron. In this floating-deck system, each power supply drives eight klystrons, so each power supply is rated at 130 kV and 3.25 MW. The current pulses are drawn from a capacitor bank. For 5 kV maximum voltage droop during the pulse, the capacitor bank must be at least 90 μF, and the bank energy is 760 kJ. A fast acting crowbar switch is used to protect the klystrons from this energy when they arc, since as little as 20 J in an arc may damage a klystron. Figure 1 illustrates the major parts of this power system.

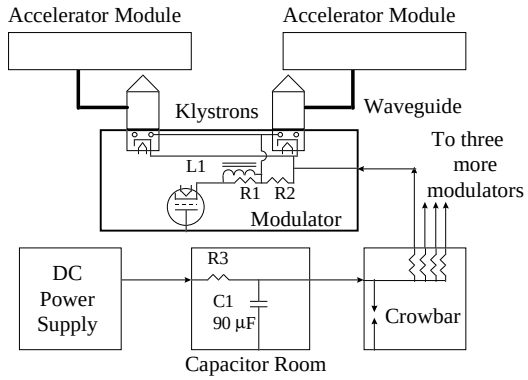

Fig 1. Block diagram of the floating deck modulator system.

With the single switch tube, rise times of 80 μs and fall times of 120 μs are typical with 100 kΩ as the sum of R1 and R2 in Fig. 1 in series with the switch tube. The efficiency of this modulator is high, since only 1.2 A flows through the modulator resistors, compared to the 75.8 A in the two klystrons. The power losses are 51.7 kW in the resistors (at 6 Ω per resistor) in the capacitor room, 43.2 kW in the modulator resistors, and only 0.6 kW in the 800 pF stray capacity in the modulators. The total energy efficiency is then 93.5% in the pulsed power part of the circuit, including the rise-time losses.

Many variations of the circuit are possible to reduce the capacitor bank droop, and Fig. 1 shows a passive compensation method. Active compensation methods are more effective, but require a higher parts count, so they usually have a reliability penalty. At voltages below 100 kV the floating-deck modulator and its klystron can be very reliable, and a Mean Time Between Failure (MTBF) of 25,000 hours for the combination of the klystron and the modulator is our estimate for those at LANSCE. However, there is dc voltage stress on the electron gun, and the MTBF decreases rapidly with voltage. The

* Work supported by the U.S. Department of Energy.

reduction in MTBF may be as high as a factor of 2 for 120 kV operation, so we look for alternative modulators. Another serious problem with this circuit is that the energy storage in the capacitor bank must be 10 times the energy in the klystron pulse to limit the droop to 5% in the klystron's voltage, and even more energy must be stored to reduce the droop below 5%. This energy must also be stored at high voltage, above 125 kV in the SNS case, and we have to deal with difficult corona control and serious safety issues.

2 THE FAST CONVERTER MODULATOR

It is possible to make dc-to-dc converters that raise a voltage to a much higher value, and many consumer products do this. A newer concept is to design a dc-to-pulsed power supply that takes power at a moderate dc voltage, and produces the 1 ms, 120 kV pulses at a 60 Hz repetition rate for the klystron. The concept is shown as a block diagram in Figure 2. The dc-to-dc converter is a multiphase chopper, operating between 10 and 20 kHz, making the high-voltage transformer very compact compared to that required for 60 Hz operation. Most of the problems with this type of circuit have been solved in the past few years by the gradual perfection of the insulated gate bipolar transistor (IGBT), that are massed produced for high-power applications, especially in motor control. The IGBT may be considered a combination of a voltage driven MOSFET coupled to a bipolar transistor. The energy left in the leakage inductance of the transformer after each pulse must be dissipated in snubber circuits, and we expect an efficiency of somewhat above 80% with this circuit.

However, it looks feasible to build such a converter that can deliver almost 10 MW pulses for 1 ms to a pair of klystrons. The dc power is provided by an inexpensive, unregulated, full wave rectifier that operates directly from a 3-phase, 4160 V source. More details on this circuit are available in [1]. Energy must be stored for the pulses, so there is a 10 kV capacitor bank on the output of the power supply.

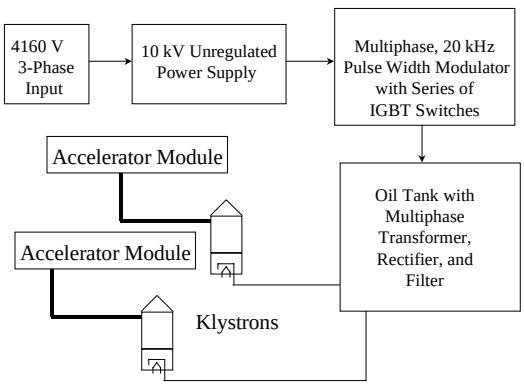

Fig. 2. Block diagram of the fast converter modulator.

Preliminary calculations are quite encouraging, and indicate that significantly less energy must be stored for this circuit than for the floating-deck modulator. Rise and fall times of 50 μs have also been calculated with a fairly detailed computer model. Another difficult component in this design is a multiphase, very tightly coupled, transformer. Measurements on a scale model of the transformer have shown that it should be possible to achieve both the high turns ratio and very low leakage inductance that we require.

3 THE BOUNCER-COMPENSATED PULSE TRANSFORMER MODULATOR

Perhaps the first method of utilizing modern semiconductor switches to drive a long-pulse, multi-megawatt klystron was the bouncer-compensated pulse transformer circuit that was developed by Pfeffer et al. [2] at Fermi National Laboratory. A simplified second version of this circuit, using IBGT's as the main switch elements, is shown in Fig. 3 below. Here the main capacitors, (C1 in Fig. 3) store only slightly more than the energy required for each klystron pulse. Normally, the voltage droop during a 1 ms pulse would be intolerable with a simple pulse discharge circuit, but the LC circuit (the bouncer) in the return leg of the pulse transformer is charged by each pulse, and the bouncer starts to oscillate before each main pulse. By appropriate design, the bouncer voltage can add to the discharging capacitor voltage to produce an output pulse that only has a few percent variation over the pulse. Earlier versions of this circuit were developed using GTO switches [3].

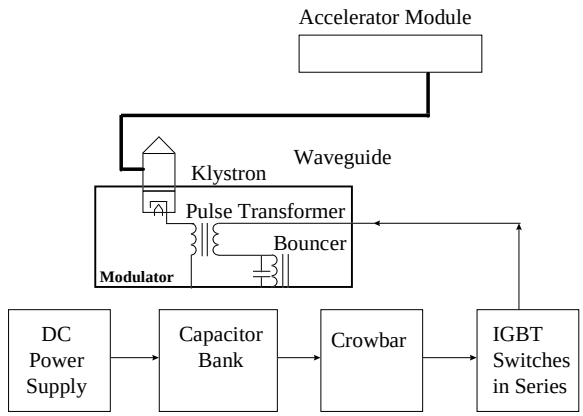

Fig. 3. Block diagram of the pulse-transformer, bouncer corrected modulator.

4 THE SERIES SWITCH MODULATOR

Rather than drive a step-up transformer, in some cases it is more economical to directly switch the high voltage between the power supply and the klystron load. Older versions of this circuit were used at the Bates linac, and in

the some Free-Electron Lasers, using electron tube technology. Solid-state versions are also possible, using IGBT switches, for example. The engineering issues are rather significant with this solution, since the switches must operate at high voltages, so isolation becomes a problem. A simplified block diagram of the series switch modulator is shown in Fig. 4. In this system, two separate switches is series, as well as many series IGBT's in each switch, are sometimes required: one chain pulses the klystron, and another provides regulation. This system has the disadvantage of storing the pulse energy at high voltage, so there are corona and safety issues associated with this energy storage.

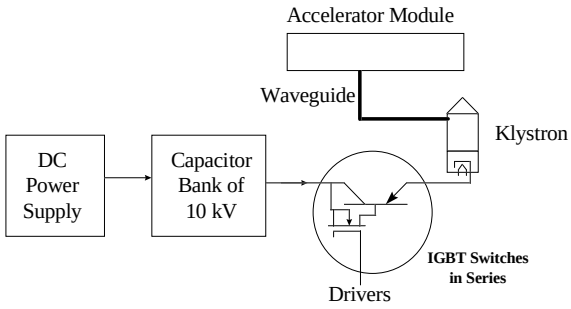

Fig 4. Block diagram of the series high voltage modulator.

5 SUMMARY AND CONCLUSIONS

Cathode pulsing is the best method for high-power, long pulse systems. The baseline RF system for the SNS is moving towards the converter-modulator option. Since all the cathode-pulsed systems do not require modulation anodes in the klystrons, the klystrons should be more reliable, and their cost should be reduced by at least a few percent. Another advantage of the converter modulator and the other new systems discussed here is that most of the electronics is out of the oil tank in these circuits, so maintenance is easier, and the environmental impact is more benign with the smaller oil tanks.

The semiconductor implementations of the power system can save capital costs by reducing the amount of energy that must be stored for the pulsed system, and some expensive or troublesome components, such as the crowbar and high-voltage capacitors, can often be eliminated.

ACKNOWLEDGMENTS

The assistance and encouragement of the SNS project management, both at Oak Ridge and at Los Alamos, has been essential in performing this work. The assistance of J. Daniel Doss of Los Alamos in performing the circuit analyses is also gratefully acknowledged.

REFERENCES

[1] W.A. Reass, P.J. Tallerico, "An Alternative Approach for an Advanced Power Conditioning Modulator for the Oak Ridge SNS Linac RF System," Los Alamos SNS Tech Note, to be published, (1998).

[2] H. Pfeffer, et al., "A Second Long Pulse Modulator for TESLA Using IGBT's," Fifth European Particle Accelerator Conference, June 10-14, 1996, 1285-1287, (1996).

[3] H. Pfeffer, et al., "A Long Pulse Modulator for Reduced Size and Cost," Proceedings of the 1994 Modulator Conference, June 27-30, 1994, 48-52, (1994).

HIGH POWER RF COMPONENT TESTING FOR THE NLC*

A.E. Vlieks, W.R. Fowkes, R.J. Loewen, S.G. Tantawi
Stanford Linear Accelerator Center, Stanford University, Stanford, CA 94309, USA

Abstract

In the Next Linear Collider (NLC), the high power rf components must be capable of handling peak rf power levels in excess of 600 MW. In the current view of the NLC, even the rectangular waveguide components must transmit at least 300 MW rf power. At this power level, peak rf fields can greatly exceed 100 MV/m. We present recent results of high power tests performed at the Accelerator Structure Test Area (ASTA) at SLAC. These tests are designed to investigate the rf breakdown limits of several new components potentially useful for the NLC. In particular, we tested a new TE_{01}–TE_{10} circular to rectangular 'wrap-around' mode converter, a modified (internal fin) Magic Tee hybrid, and an upgraded 'flower petal' mode converter.

1 INTRODUCTION

In SLAC's version of the NLC, sources, such as klystrons, transport rf power to accelerator structures primarily in circular overmoded waveguide. Various rf components—such as mode converters, 90° bends, and 3-dB hybrids (each consisting in part of single-moded rectangular waveguide)—route rf power from one circular guide to another.

In order to verify that these components can handle the required power levels of up to 300 MW, we conducted a series of tests to establish breakdown limits and to investigate mechanisms of breakdown. We present the results of experiments, which led to the identification of components capable of operating reliably at rf power levels in excess of 300 MW. In earlier tests [1], two key components of SLED-II—a $TE_{01}^{(circ.)}$–$TE_{10}^{(rect.)}$ flower petal mode converter and the Magic Tee hybrid—failed at a power level of 220–250 MW [2]. These components were modified and subsequently retested along with the newly designed wrap-around mode converter.

2 EXPERIMENT

2.1 General Layout

The general setup is shown in Figure 1. The experimental setup consists of an rf source, a SLED-II pulse compressor, and a high power load assembly. Two 50 MW klystrons operating at 11.424 GHz supply the rf power. The pulse width of each klystron is 1.05 μs running at a repetition rate of 60 Hz. Each klystron is driven by its own TWT driver which in turn is driven by a common signal generator. The power from these klystrons combine through a Magic Tee 3-dB hybrid and feed the input to the SLED-II system. The combiner was previously conditioned to full klystron power by being connected to the load assembly.

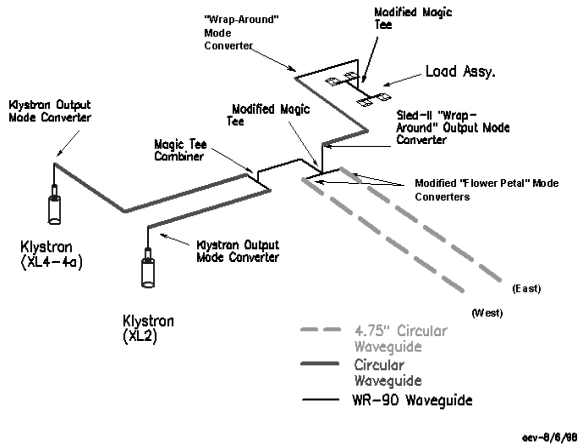

Figure 1. Schematic of the initial experimental setup.

The SLED-II pulse compression system operates with a compression ratio of 7 and a peak power gain of ≈4. Hence, this configuration can potentially yield up to 400 MW of peak power with a flat top of 150 ns. The primary components under test are the 3-dB hybrid, the two delay line mode converters, and the output mode converters.

The load assembly consists of four choked, stainless steel 'dry' loads [3] arranged in parallel. (A Magic Tee first splits the incoming power and then two additional Magic Tees divide each of the split power levels again.) In earlier tests, an individual load of this type was successfully tested to ≥100 MW at a pulse width of 150 ns.

2.2 Preparation

During all phases of the experiment, the vacuum system is baked out to approximately 150°C for at least 24 hours (plus a ramp-up/cool-down of 24 hours each). At the end of this cycle, the vacuum in the system is $\leq 1\times10^{-9}$ Torr. In addition, any new components added to the system during the course of the experiment are first high temperature baked to 400°C before installation in order to remove residual hydrogen and other contaminants.

* Work supported by Department of Energy contract DE-AC03-76SF00515

2.3 Initial Experiment

In the first phase of the experiment, two modified flower petal mode converters were installed in the SLED-II delay lines. As described in [1], these components are modified from an earlier design to alleviate the rf erosion at the bifurcation in the rectangular waveguide section. The 3-dB hybrid is a modified Magic Tee configured with the H-arm as input and the E-arm as output. The modification consists of replacing the matching post in the throat of the Tee by a broad fin with fully rounded corners and rounding the edges at the E-arm throat. (This was motivated from witnessing significant erosion of the post during previous testing). A newly designed wrap-around mode converter was placed at the output of SLED-II.[4]

Results of the initial phase of the experiment show that all components work well up to ≈240 MW. Above this power level, there were significant rf breakdown events at the SLED-II Magic Tee as well as enhanced, steady state X-ray emission. One of the two delay line mode converters—labeled the 'West' mode converter—also exhibited enhanced X-ray emission albeit far less than the Magic Tee. The wrap-around mode converter was essentially breakdown-free and radiation levels at this mode converter were about the same level as the nearby rectangular WR90 waveguide.

Figure 2 shows typical radiation levels measured at the waveguide surface of the Magic Tee by an X-ray survey meter. One curve shows a typical dose rate when the system is well conditioned. The other curve shows the effects of conditioning. Initially, at low power levels, the dose rate is anomalously high. Then, after an rf breakdown event occurs and testing is resumed, the radiation levels reduce to the typical values. These typical values did not improve or deteriorate with time.

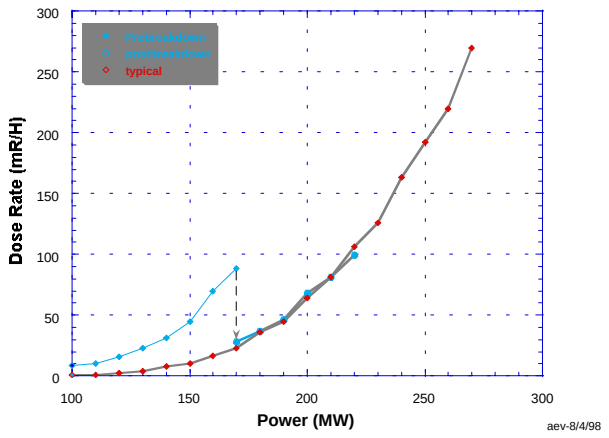

Figure 2. Radiation Intensity at the SLED-II Magic Tee.

An interesting result from radiation measurements is that the Magic Tee at the entrance of the load had much lower radiation levels than the SLED-II Magic Tee even though the peak power levels are approximately the same. It appears that the standing wave set up between the delay line iris and the SLED-II Magic Tee enhances the peak fields. Simulation verifies that the increased fields from this standing wave pattern can greatly enhance the peak fields in critical regions of the Magic Tee. It also became clear that reversing the input and output ports of this Magic Tee would significantly reduce these peak fields.

2.4 Phase Two

At the conclusion of the initial experiment, the SLED-II and load entrance Magic Tees were removed and cold tested. Their RF properties were found to be unchanged from their pre-test values although some erosion was observed in the SLED-II Magic Tee along the fin. The West delay line mode converter was also checked and found unchanged. It was decided that the positions of the two Magic Tees would be exchanged and that the new SLED-II Magic Tee would be installed with the roles of the input and output ports interchanged, i.e. now the E-arm is input and the H-arm is output. It was also decided to coat the problematic West flower petal mode converter with Titanium Nitride to try to reduce the X-ray radiation by decreasing the electron secondary emission yield.

The interchange of input and output ports of the SLED-II Magic Tee had a marked improvement on system performance. The steady state radiation level at the Magic Tee was reduced by a factor of 18. Unfortunately, the radiation levels at the West delay line mode converter remained the same with no effect due to the TiN coating. As the peak power levels approached 270 MW, it became clear that the limiting component was this mode converter. Figure 3 compares the radiation levels from the East and West mode converters and Magic Tee. It is remarkable that the radiation levels of the East mode converter are 150 times smaller than the West even though the system is apparently symmetric.

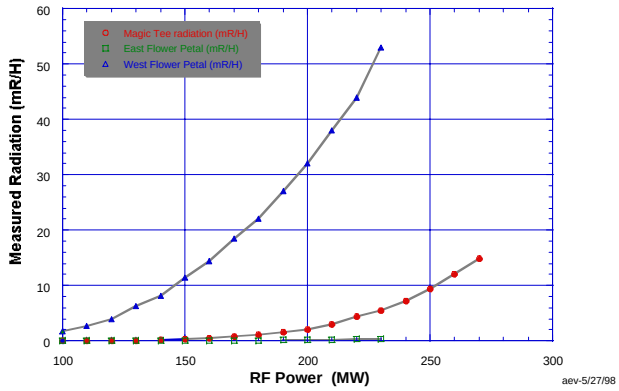

Figure 3. SLED-II Radiation levels.

To further pinpoint the location of this radiation, measurements were made through a 0.64-cm aperture of a lead-shielded survey meter in 1-cm intervals along the centerline of the mode converter (see Figure 4). The results, as shown in Figure 5, indicate that the radiation is

emanating at or behind the coupling irises (or 'flower petals').

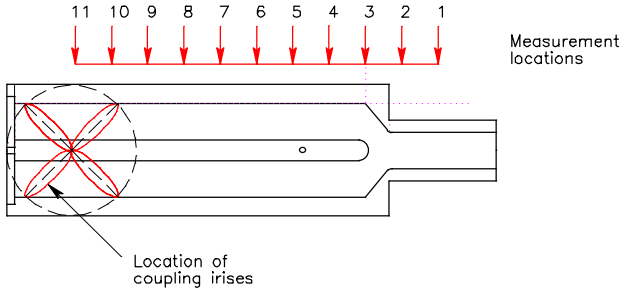

Figure 4. Location of measurement points along the rectangular portion of the mode converter. Additional measurement points are located out of the paper along the circular portion of the converter.

To estimate the energy of these X-rays, aluminum and copper absorbers of various thicknesses were used to measure the X-ray attenuation coefficient at a power level of 200 MW. Since the slope of the attenuation is quite linear (on a semi-log plot) with absorber thickness, we may assume that the walls of the mode converter selectively removed the low energy portion of the X-ray spectrum leaving only X-rays with the highest energies. Under these assumptions, we find the peak X-ray energy to be near 150 KV as shown in Table 1. For electrons accelerated from rest across the petal gap, this corresponds to a peak gradient of 510 KV/cm. This value is in excellent agreement with earlier computer simulations of 523 KV/cm at 200MW [6].

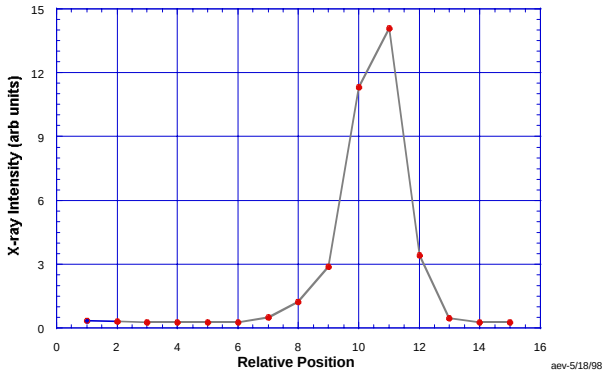

Figure 5. X-ray radiation intensity at the West flower petal mode converter at 130 MW power.

2.5 Phase Three

At the conclusion of the second phase of this experiment, both delay line mode converters were replaced with wrap-around mode converters and testing resumed.

This time we were able to drive the SLED-II system to a power level of 320 MW with no evidence that a power limit had been reached. The X-ray intensity at the Magic Tee was similar to previous measurements, and the wrap-around mode converters showed no evidence of excessive radiation (i.e. no greater than WR90 waveguide).

Table 1. Comparison of measured attenuation coefficient with tabulated values near 150 KV.

Absorber	**Measured attenuation (cm^2/g)**	**Tabulated attenuation[5]**
Copper	0.136	0.134@ 150KV
Aluminum	0.191	0.203@ 150KV 0.148@ 200KV

3 SUMMARY AND CONCLUSION

A series of experiments were performed to determine the peak power performance of various rf components. The mode converters of the modified flower petal type are adequate up to peak power levels of approximately 225 MW. Wrap-around mode converters perform well at least up to 320 MW and in all likelihood much higher. The modified Magic Tee 3-dB hybrid transmits 320 MW without difficulty but when used in applications where standing waves can enhance peak fields (such as SLED-II), the details of the installation becomes important.

At the moment, the exact reason for the heightened X-ray emission in the West mode converter is unclear. However, the measured energy of the X-rays corresponds to the expected peak field levels based on simulation.

4 REFERENCES

[1] A.E.Vlieks, W.R. Fowkes, R.J. Loewen, and S.G. Tantawi, "Upgrade of the SLAC SLED-II Pulse Compression System Based On Recent High Power Tests", PAC 97, Vancouver, Canada, May 1997.

[2] S.G. Tantawi, A.E.Vlieks, K. Fant, T. Lavine, R.J. Loewen, C. Pearson, R. Pope, J. Rifkin, and R.D. Ruth, "The Next Linear Collider Test Accelerator's RF Pulse Compression and Transmission Systems", Advance Accel. Concepts (1997), p805.

[3] Sami G. Tantawi and A. E. Vlieks, "Compact X-band High Power Load Using Magnetic Stainless Steel", PAC 95, Dallas Texas, May 1995, and SLAC-PUB-95-6826.

[4] S. Tantawi, "The Wrap-around Mode converter: A Compact TE_{10}-TE_{01} Mode Transducer", To be published.

[5] NSRDS-NBS 29 (1969)

[6] S. Tantawi, K. Ko, and N. Kroll, "Numerical Design and Analysis of a Compact TE_{10} to TE_{01} Mode Transducer". CAP93 Pleasanton, CA Feb. 1993, and SLAC-PUB 6085 (April, 1993)

LINEAR INDUCTIVE VOLTAGE ADDERS (IVA) FOR ADVANCED HYDRODYNAMIC RADIOGRAPHY*

M. G. Mazarakis, J. D. Boyes, D. L. Johnson, J. S. Lash, J. E. Maenchen,
P. R. Menge, C. L. Olson, S. E. Rosenthal, D. C. Rovang
Sandia National Laboratories, Albuquerque, NM 87185 USA

B. V. Oliver, D. R. Welch
Mission Research Corporation, Albuquerque, NM 87106

V. L. Bailey and I. D. Smith
Pulse Sciences Incorporated, San Leandro, CA 94577

Abstract

The electron beam which drifts through the multiple cavities of conventional induction linacs (LIA) is replaced in an IVA by a cylindrical metal conductor which extends along the entire length of the device and effectuates the addition of the accelerator cavity voltages. In our approach to radiography, the linear inductive voltage adder drives a magnetically immersed electron diode with a millimeter diameter cathode electrode and a planar anode/bremmstrahlung converter. Both anode and cathode electrodes are immersed in a strong (15-50 T) solenoidal magnetic field. The electron beam cross section is approximately of the same size as the cathode needle and generates a similar size, very intense x-ray beam when it strikes the anode converter. An IVA driven diode can produce electron beams of equal size and energy as a LIA but with much higher currents (40-50 kA versus 4-5 kA), simpler hardware and thus lower cost. We present here first experimental validations of our technology utilizing HERMES III and SABRE IVA accelerators. The electron beam voltage and current were respectively of the order of 10 MV and 40 kA. X-ray doses of up to 1 kR @ 1 m and spot sizes as small as 1.7 mm (at 200 R doses) were measured.

1 INTRODUCTION

Up to the cessation of the nuclear tests, radiography of an imploding primary (with surrogate material) was utilized to supplement the information gathered from these tests. However, this is now the only means available to probe and characterize such a device.

To radiograph very thick objects, a high-energy, high-flux, and very small spot x-ray source is required. The small spot (~ 1 mm in diameter) will provide the necessary spatial resolution while the high-energy photon flux is required to penetrate the thick object and produce a clear image of its interior. To generate those penetrating x-rays an electron accelerator is being used. The electron beam strikes a tantalum x-ray converter plate. The forward x-ray beam illuminates the surrogate primary and produces a photograph on a package of films or imaging detectors located on axis downstream from the radiographed object, similar to medical or industrial radiography.

Presently, two types of accelerators are being utilized for x-ray radiography: first, linear RF (PHERMEX) or induction accelerator (FXR); and second, single gap pulsed power devices using a high-voltage Blumlein pulse forming line (AWE). The first can produce high-energy, small-diameter (2-3 mm) electron beams relatively easily, but the current is limited to 1-2 kA yielding low photon fluences. The Blumlein pulsed power devices can produce much higher beam currents (50-100 kA), but the beam spot diameter is relatively large (~ 6 mm) and the beam energy is limited to 8-10 MV.

Our linear inductive voltage adder accelerator (IVA) coupled to a magnetically immersed foilless diode can successfully bridge the gap between the two devices. It can produce small spots (~ 1 mm), high voltages (15-20 MV), and high currents (40-50 kA) at a fraction of their cost.

In the next sections, we present first experimental validations of our technology utilizing available Sandia National Laboratories IVA accelerators.

2 SABRE EXPERIMENTS

For these experiments, SABRE was modified to increase the output voltage and proportionally reduce the current, delivering the same energy. It was, therefore, operated at 9-12 MV and 100-120 kA. The design of the MITL voltage adder and the foilless diode (Fig. 1) were validated with a large number of particle-in-cell simulations.

* Sandia is a multiprogram laboratory operated by Sandia Corporation, a Lockheed Martin Company, for the United States Department of Energy under Contract DE-ACO4-94AL85000.

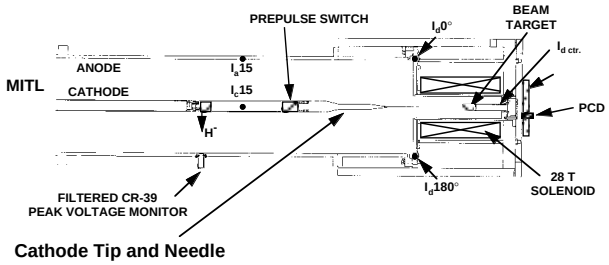

Figure 1 Schematic diagram of diode design utilized in both SABRE and HERMES-III experiments.

The intense electron beam produced by the SABRE foilless diode quickly produces an ion-emitting anode plasma. The ions are accelerated toward the cathode. The electrostatic attraction between the two beams is considerable and an ion-hose two-stream instability is excited. If left uncontrolled, this instability can cause large deflections and heating of the beam which would substantially increase the beam spot size. A strong axial magnetic field (B_z) controls this behavior. The beam offset (ε) grows until it reaches the gyrodius value. A simple model matches the simulations:

$$\varepsilon = \left(2\gamma \;\; \mathrm{I}/17 \;\; kA\right)^{1/2} \times \left(0.17 \;\; Tesla/B_z\right) \;\; cm$$

$$r_b\left(FWHM\right) = 0.83\sqrt{\varepsilon^2 + r_k^2} \;\; ,$$

where I is the beam current and r_b and r_k are respectively the beam and cathode needle radius. According to this model and IPROP simulations, a 30-T magnetic field should control the ion-hose instability and produce a 0.75-mm radius beam. The experimental results (Fig. 2) are in very good agreement with theory and simulations [1].

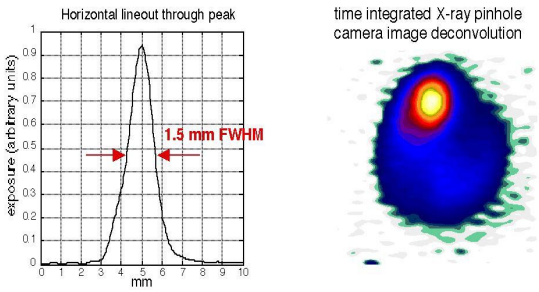

Figure 2. Time integrated x-ray image of the beam for B_z = 29 T, SABRE results. Beam size agrees with theory and simulations.

3 HERMES-III EXPERIMENTS

HERMES III is larger than SABRE, having twenty 1-MV inductively insulated cavities. It routinely produces 18-20 MV, 700-kA electron beam in normal operation, but in the present experiments, we operate it at lower voltage (12 MV), reduced current (150 kA), and longer pulse (~ 70 ns FWHM).

The outer cylinder of the extension MITL has conical sections to reduce the radius down to SABRE size. Thus, the same magnetically immersed diode (Fig. 1) assemblies are utilized with HERMES III. In addition, a smaller, 50-Tesla, cryogenic diode was designed and constructed (Fig. 3) for these experiments.

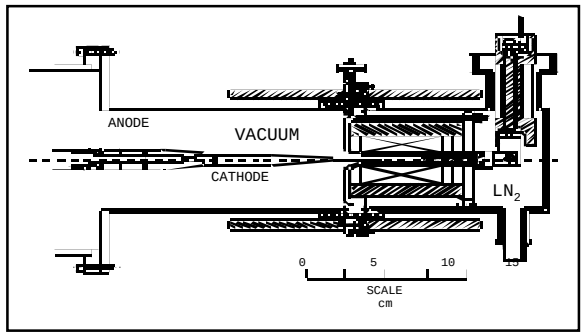

Figure 3. The 50-Tesla cryogenic diode design utilized only with HERMES-III.

During SABRE experimentation we observed a severe decrease in the diode impedance near the peak of the voltage pulse. It was attributed to a 100-kV prepulse arriving 200 ns before the main pulse. A flashover prepulse suppression switch solved the problem. The impedance remained constant during the entire duration of the voltage pulse (30-ns FWHM). In HERMES III, we installed two flashover switches in series and we made sure that no appreciable prepulse was making it into the diode. In addition, special care was taken to improve the diode vacuum to 1-3 10^{-7} torr levels. Despite all this the diode impedance still exhibited a collapse at about 10-30 ns into the voltage pulse (Fig. 4). The onset of this abnormal impedance decrease was delayed by opening the AK gap (Fig 5). While the diode impedance remained normal (~ 300 Ω) the beam spot size was small and in good agreement with numerical simulations (Fig. 6). As soon as the impedance started plummeting, the beam spot size increased and the x-ray intensity decreased. All the above are characteristic of diode shorting.

Figure 4 shows typical behavior of the diode current. At the beginning it is consistent with a monopolar flow of electrons from the cathode to the anode. About 20 ns into the pulse the expected bipolar flow sets up with a 30% increase of the total current. Finally ~ 33 ns later the current breaks away from the voltage trace and keeps increasing to 150-180 kA until the end of the voltage pulse. Analytical calculations and numerical simulation [2,3] explain the late time current behavior as due to counterstreaming heavy ions emitted from the cylindrical anode walls and the converter target. Very high-intensity heavy-ion (carbon, nitrogen, oxygen, etc.) beams, while in transit toward the cathode, suffer many electron stripping ion-ion collisions and increase their charge. When this increased ion charge density reaches the cathode, it bootstraps currents into an abnormal impedance collapse. Forty-five degree slant targets and larger anode cylindrical

walls appear to delay impedance collapse for the same AK gap (Fig. 5).

A number of impedance collapse mitigation methods have been extensively studied [4] and will be implemented in future experiments. Among them, an increase in magnetic insulation will prevent ions from the diode cylindrical walls reaching the axis. The ions emitted from the target can be reduced by utilizing a small 1-mm diameter target. Finally, the counterstreaming ions following the magnetic field lines can be prevented from striking the needle if a less-immersed cathode tip is utilized. A new 60-T diode is being designed that will offer those capabilities which, we believe, will enable us to achieve the advanced hydrodynamic radiography goals of 0.6-mm (FWHM) x-ray spot, 1-kRad dose @ 1 meter from a 12-14 MeV electron beam.

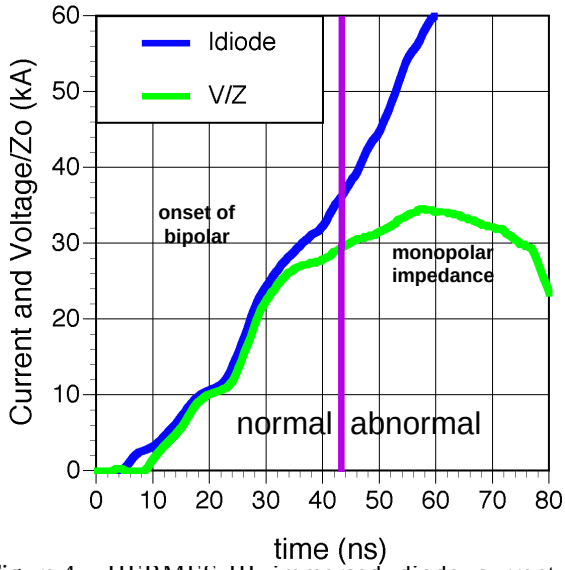

Figure 4. HERMES-III immersed diode current and voltage time behavior for a 22-cm AK gap.

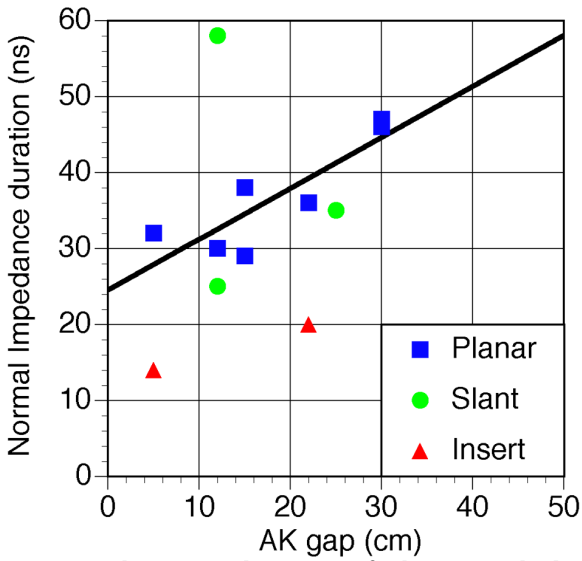

Figure 5. The time duration of the normal diode operation increases with the AK gap spacing and orientation of the converter front surface.

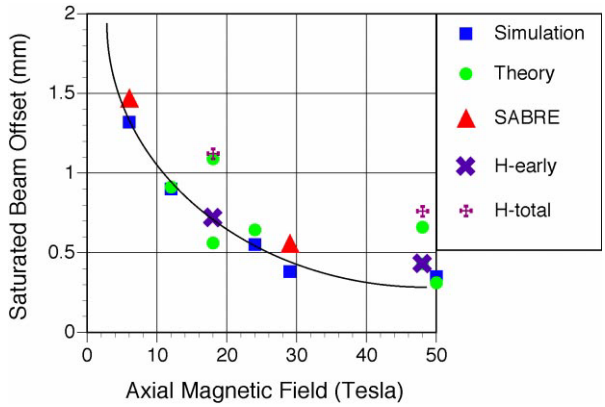

Figure 6. Measured beam offsets (ε) in SABRE and HERMES III are in very good agreement with theory and numerical simulation.

4 SUMMARY

SABRE and HERMES III experiments demonstrated that IVA/immersed diode technology can produce millimeter size x-ray sources capable of penetrating very dense objects. The observed ion hose instabilities can be controlled to acceptable levels with 50-60-T confining magnetic fields. The abnormal diode impedance behavior is well understood and mitigating diode designs are under construction for future IVA experiments. SABRE and HERMES-III results (normal diode operation) are in full agreement with theory and numerical simulations.

5 REFERENCES

[1] M. G. Mazarakis, et al., *Appl. Phys. Lett.* **70**, 832, 1997.

[2] C. L. Olson, et al., "Physical Picture of Immersed Diode Experiments on HERMES-III and SABRE," *Proc. IEEE 25th Int. Conf. On Plasma Science*, Raleigh, NC, p. 211 (1998).

[3] B. V. Oliver, et al., "2-D Electron Dynamics in a Magnetically Immersed Foilless Diode," *Proc. IEEE 25th Int. Conf. On Plasma Science*, Raleigh, NC, p. 256 (1998).

[4] D. R. Welch, "Impedance Reduction Mechanisms in a Magnetically Immersed Electron Diode," *Proc. IEEE 25th Int. Conf. On Plasma Science*, Raleigh, NC, p. 256 (1998).

HIGH PERFORMANCE PULSE MODULATOR FOR 80MW S-BAND KLYSTRON IN SPring-8 LINAC

T.Hori, H.Yoshikawa, T.Kobayashi, T.Asaka, H.Sakaki, S.Nagasawa, and H.Yokomizo
Japan Synchrotron Radiation Research Institute
SPring-8,Mihara, Mikazuki-cho, Sayo-gun, Hyogo, 679-5198, Japan

Abstract

An 190MW compact pulse modulator is constructed to test spare 80MW S-band klystrons(E3712 TOSHIBA) and 2 different type thyratrons(F351 TRITON, CX1937A EEV), as well as to provide R&D tool for the development of high performance modulator. Typical specifications of the modulator are 190MW peak power, 390kV peak beam voltage, 60pps pulse repetition rate, 2.2μS flat-top pulse width with less than $\pm$ 0.15% of beam voltage. Compared with conventional modulator, new technologies were used in the several points such as a 40MHz inverter power supply, a command charging, a remotely controlled tunable slug of PFN coil to improve the stability of the output voltage, to prevent a thyratron prefire and to achieve an easy adjustment of pulse flatness.

1 INTRODUCTION

The S-band injector linac of SPring-8 is 140m long, and maximum electron energy is 1.15GeV. The main high power RF components of linac are composed of 13 units of E3712 S-band klystron tube and conventional pulse modulator. Table 1 shows the specifications of E3712 klystron.The conventional pulse modulator for 80MW klystron have been operated for 11,000hr in the past two years. It is a line type pulser because of its well-established technology and reliability. In order to make a pulse modulator more efficient, the high performance modulator was designed since last years,aiming at easy maintenance, compact size, low cost, high stability. A test modulator was constructed using three inverter type HV power supplies in paralled for the charging power supply. This paper presents the circuit design, specifications and the performance data.

2 MODULATOR SPECIFICATION

Table 2 shows the main specifications of test modulator. As the 80MW klystron tube requires about 400 kV on its cathode voltage and the thyratron anode voltage should be less than 50kV, a pulse transformer with turn ratio of 1:17 was selected.Therefore, the modulator generates pulses with the peak voltage of more than 23.5kV and the peak current of more than 8160A. In order to accelerate an electron beam with the pulse width of 1μsec, the flat-top of klystron beam voltage is required to be more than 2μsec. The long-term regulation and the pulse flatness of the klystron beam voltage is decided to be less than $\pm$ 0.15% to prevent RF phase modulation and microwave power fluctuation.

Table 1: Specifications of E3712 S-band Klystron

	typical	max.	
Peak RF output power		80	MW
Beam voltage	396		kV
Beam current	480		A
Efficiency	44		%
Gain	55		dB
Microperviance	1.96		
Pulse width (beam)		6.2	µS
Pulse width (RF)		5.0	µS
Drive power	300	500	W
Pulse repetition rate		60	pps
Frequency	2856		MHz

Table 2: Main specifications of the test modulator

Peak output power	190 MW
Average output power	78 kW
PFN charging voltage	50 kV
PFN impedance	2.85 Ω
Peak swiching current	8772 A
Pulse width (ESW)	5.5 µS
Pulse width (flat top)	> 2µS
Pulse flatness	±0.15%
Pulse risetime	<1.5µS
Pulse falltime	< 3.0 µS
Pulse repetition rate	60 pps
Pulse transformer turn ratio	1 : 17

3 MODULATOR CIRCUITS

Fig.1 shows simplified circuit diagram of the test modulator. The features of this modulator are :

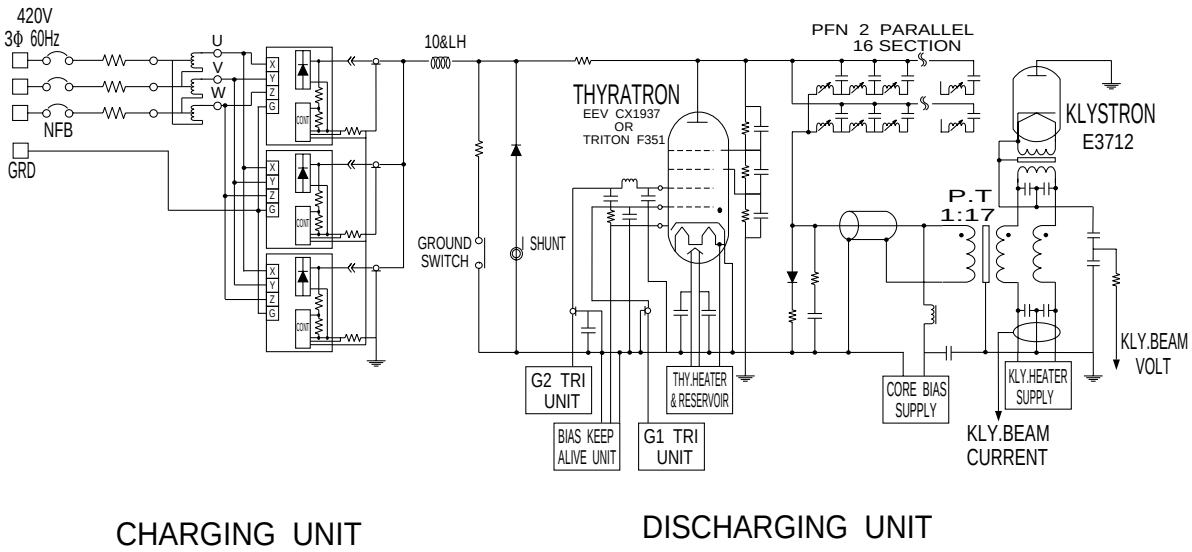

Figure 1: The simplified circuit diagram of the test modulator

Table 3: Specifications of major parts in the test modulator

Inverter power supply	Model 303S A.L.E SYSTEMS, INC. Output voltage 50kV current 1.5A Charge rate average 30kJ/s peak 37.5kJ/s Voltage regulation < 0.1% Efficiency 90%
Thyratron shunt	diode 45 (2.5kV,7.7A) in series R 8 (15Ω,500W) in series,parallel
Tail clipper	diode 10 (5kV,4.5A) in series R 4 (10Ω,500W) in series,parallel
Serge dispiker	C 0.0325μF, 55kV DC R 6 (25Ω,500W) in series,parallel
PFN	2 parallel, 16section C total 32 (0.0325μF, 55kV) L total 32 (0.28μH, max.)
Thyratron	CX1937A EEV (75kV, 15,000A) F351 TRITON (55kV, 10,000A)
Triaxial cable	model# TRIAXIAL Isolation Design
Pulse transformer	1 : 17 ratio SI - 8164 Stangenes Industries, Inc.

1. Direct constant current charging by three inverter power supplies.
2. Without De-Qing circuit.
3. Command charging.
4. Improvement of maintenance due to reduction of several high voltage components,for example IVR,charging choke,hold-off diodes,etc.

In addition to these points , we designed as follows :

1. Remote control for tunable slug of PFN coils.
2. Counter circuit to detect thyratron misfire.

The modulator cabinet size (involved power supplies rack) is 2700(W) × 2300(H) × 1500(D), this is 57% of the current cabinet volume of the SPring-8 modulator. Table 3 shows the specifications of major parts in test modulator.The inverter power supplies are state of the art switch mode power supply,designed primarily for use in pulsed power applications such as laser system and capacitor charging.The voltage reversal which is cause by mismatching a PFN characteristics impedance and klystron tube impedance forces a large surge current to flow through the output rectifiers in the inverter power supply. Therefore,the protection circuit with series terminating resistors and freewheeling diodes was carefully designed.

4 ACHIEVED PERFORMANCE

A preliminary test of new modulator was started in April and initial data have been obtained. Fig.2 shows the one cycle of charging voltage profile of PFN capacitors, as set a PFN voltage of 20∼35kV at 5kV step. The time added charge time to dwell time is fixed 15ms, and the charge time was varied linearly along with PFN charging voltage. In the case of change a pulse repetition rate, only the dead time is changed. Fig.3 shows the typical waveform of klystron beam voltage and its flat-top(Beam voltage and current are 396kV,480A). In this case, the test modulator was operated at repetition rate of 30pps and a PFN charging voltage of 51.1kV. After carefully adjusting tunable slug of PFN coils, the flat-top pulse width of klystron beam voltage was achieved the 2.2μs with $\pm$0.15% which is designed values. The long-term(30hr)operational characteristics of klystron beam voltage was investigated in condition at repetition rate of 30pps, a PFN charging voltage of 40kV, two inverter power supplies. As a result, test modulator has achieved the

output voltage fluctuation of less than $\pm 0.15\%$.

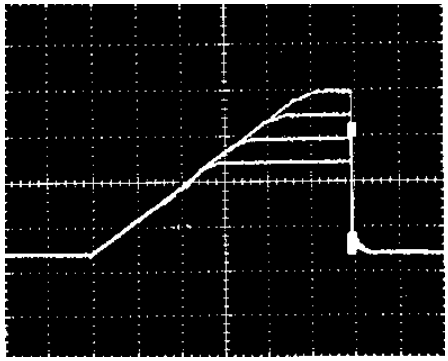

Vertical :10kV/div
Horizontal :2.5mS/div

Figure 2: Charging Voltage Waveform of PFN

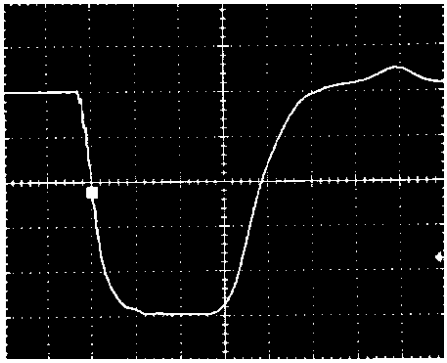

Vertical :80kV/div
Horizontal :2μS/div

Figure 3: Klystron Beam voltage waveform

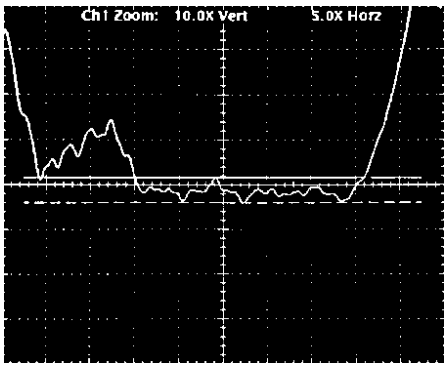

Vertical :2kV/div
Horizontal :400nS/div

Figure 4: Flat-top of klystron beam voltage

5 DISCUSSION

We have fabricated a test modulator and tested its performance. This modulator have not yet satisfied with full operation, which is to be used three inverter power supplies, a repetition rate of 60pps and a PFN voltage of 50kV. Speculated causes of the problem are as follows,

1. The deficiency of cooling water capacity supplied for inverter power supply

   The high voltage parts of inverter power supply is mounted in Freon liquid, and the cooling method which is condensed evaporated Freon by cooling water was adopted. In case of repetition rate of 60pps and a PFN voltage of 50kV, inverter power supply was stopped by internal temperature interlock after 40 minutes operation.Our cooling water system is able to supply at a rate of 8ℓ/min. and 32$\sim$34°C water through three inverter power supplies. Even thought these values are within the upper limit of required cooling water specifications, the cooling water deficiency may be a main reason to stop long-term operation.

2. The power factor of inverter power supply

   It is described that the power factor of inverter power supply is 0.9 in instruction manual. But in present, the power factor was measured to be about 0.67 in case of repetition rate of 40pps and a PFN charging voltage of 50kV. It is necessary to improve the power factor of inverter power supply by way of reconsidering both the choke coil inductance in smoothing circuits and the charging time of PFN.

6 CONCLUSION

High performance modulator for 80MW klystron was designed and fabricated,good performance which the flat-top width of klystron beam voltage with $\pm 0.15\%$ flatness was 2.2μs and voltage regulation was less than $\pm 0.15\%$ for long-term operation has achieved. To operate continuously the test modulator for full operation, the deficiency of cooling water capacity and the power factor of inverter power supply should be improved.

7 ACKNOWLEDGMENTS

The authors would like to express their thanks to Messrs. H.Misawa, K.Nishio and H.Kouzu of TOSHIBA Co. for the fabrication and adjustment of the test modulator and to operators of SPring-8 service corporation for the useful support.

8 REFERENCES

[1] H.Yonezawa et al.,"Development of a 100MW S-band Pulse Klystron",Particle Accelerators,1990,Vol.30,pp.219-224.

[2] J.S.Oh et al.,"Efficiency Issue in C-band Klystron-Modulator System for Linear Collider",PAC97,KEK Preprint 97-51,June 1997A.

[3] T.Shintake et al.,"C-band Klystron & RF-System Development", The 11th Symposium on Accelerator Science and Technology,October 21-23 1997,pp.335-337.

THE BRIDGE COUPLING CAVITIES IN THE SEPARATED DRIFT TUBE LINAC STRUCTURE

V.V. Paramonov, L.V. Kravchuk, A.S. Levchenko
Institute for Nuclear Research, 117312, Moscow, Russia
T. Kato, F. Naito, Y. Yamazaki,
KEK, National Laboratory for High Energy Physics, Oho 1-1, Tsukuba-shi, Ibaraki-ken, 305, Japan

Abstract

The Separated Drift Tube Linac (SDTL) structure was proposed for medium energy range of proton linacs. The accelerating cavity consists of several SDTL units with focusing lenses between sections. To drive several SDTL sections from single RF source, application of both RF power dividers and coupling bridge cavities seems feasible. Through bridge couplers, the field distribution, in both amplitude and phase, is automatically stabilised among connected sections in the lowest order. Additional rf power dissipation of an order of several percents is inevitable in the bridge coupler because of its standing-wave operation. In this paper particularities and limitations for coupling bridges in the SDTL tanks are considered. Well known cylindrical bridge cavities (CBC) may be used. To maintain features of the SDTL structure as the easy-to-do low-cost one, Rectangular Directly Coupled Bridges (RDCB) look more preferable. Developed and realised in Moscow Meson Facility linac, RDCB operates in TE_{10N} mode and originally has no mode mixing problem. To simplify manufacturing procedure, RDCB design is based on parts of standard waveguide. The philosophy of SDTL-RDCB tank and results of preliminary consideration are presented.

1 INTRODUCTION

Attractive features of the bridge coupled system are well known and have been proved experimentally for Coupled Cells accelerating Structures (CCS) at high frequencies ≈ 1000 MHz in several laboratories. The bridge coupling cavities can also be applied for SDTL structure [1], taking into account SDTL particularities. The consideration of bridge coupler in SDTL structure has been performed [2] as one option possible for 200 MeV linac accelerating structure. Two concepts of coupling bridges are possible. Both CBC and RDCB have been considered. Below we summarise results of consideration [2] and results of further investigations for SDTL-RDCB tank.

2 CONCEPTS OF COUPLING

2.1 Coupling with intermediate coupling cell

Application of CBC for high frequency (700 MHz) SDTL was considered in [3]. Following the well known concept [4], a CBC is attached to the SDTL section through intermediate coupling cell (Fig.1a). In the chain of coupled cells, which describes total tank, bridge cavity is equivalent to modified accelerating cell which is displaced from beam axis. In order to reduce the rf losses in the bridge cavity one should provide asymmetrical coupling in intermediate cell $k_2 > k_1$. If total tank has M SDTL sections, $M-1$ bridges

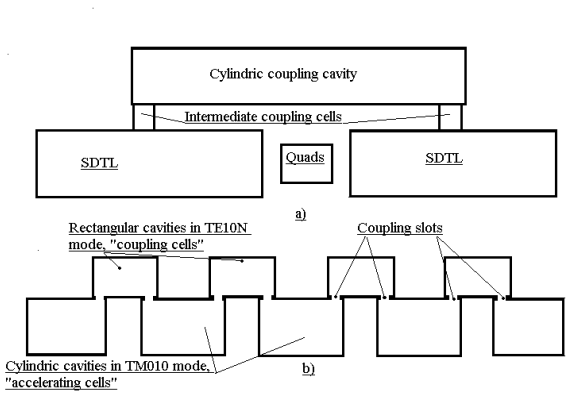

Figure 1: A sketch of the tanks coupled by CBC (a) and RDCB (b).

and $2(M-1)$ coupling cells, there will be $4M-3$ modes in the TM_{010}-like passband. Central operating mode is the $\pi/2$ mode, position of nearest modes mainly depends on k_1 value, the bandwidth of the passband - on k_2 value. Additional rf losses for such option were estimated as 3.3% for $k_2/k1 = 4$, k_2=1.8% [2]. As the result of comparison of different CBC types, the multy-cell bridge cavity [5] looks as a preferable CBC solution.

2.2 Direct coupling

Another concept of coupling bridge cavities is possible [6]. To illustrate the philosophy of RDCB, let consider bi-periodic chain of coupled cavities (Fig.1a) . First type of cavities are cylindrical ones, exited in TM_{010} mode. The second type of cavities are rectangular ones, exited in TE_{10n} mode. To simplify manufacturing procedure for rectangular cavity, let chose transversal dimensions equal to dimensions of standard waveguide recommended at operating frequency. With such choice we automatically solve mode-mixing problem for RDCB, because dimensions of waveguide are defined for single mode operation of TE_{10} wave. Both types of cavities are coupled trough coupling slots, forming the chain of coupled cavities, in which cylindrical cavities are equivalent to accelerating cells, and rectangular cavities - for coupling ones. The coupling slots are placed to couple H_ϕ component in cylindrical cavity

with H_x in rectangular one. Let define the mode in the rectangular cavity, for example TE_{10N}, and choose the length of the cavity to have the frequency of this mode equal to operating frequency of accelerating cells. We get usual chain of coupled cavities which is well known from CCS description [4]. If one match frequencies of accelerating mode (operating mode of the tank, really it is the frequency of SDTL sections taking into account effect of coupling slots) and coupling mode (the frequency of rectangular cavity also taking into account effect of coupling slots), one will have accelerating system, consisting from two types of cells, with continuous dispersion curve. If we have M SDTL sections in the tank and $(M-1)$ bridges, operating passband will have $2M-1$ modes. Central, operating mode is $\pi/2$ mode, with strong field in accelerating (SDTL) sections and weak field in coupling cells (RDCB) and with all properties of stabilisation. One should take into account that for odd N mode TE_{10N} has H_x component of different signs at the ends of the bridge. This case at operating $\pi/2$ mode phase shift between SDTL sections is 2π. For even N coupling coefficients k_c at the ends of RDCB has the same sign and phase shift between SDTL sections is π. The evident question to be answered - how can we match such directly coupled bridges with the driving waveguide, if there are no field in the bridge cavity at operating mode? This statement is only the result of our analysis based on single-mode approximation to describe RDCB. In the study of multy-mode approximation for RDCB description, one will find weak, but nonzero field in bridges at operating mode, sufficient to match with driving waveguide. For odd N the field in RDCB at operating $\pi/2$ mode can be represented as the sum over TE_{10n} modes with even n, for even N - with odd n. RDCB were proposed for high energy accelerating structures, tested at high rf power level with the Disk and Washer and Annular Coupled structures [7] and long time successfully operate in the main part of the Moscow Meson Facility linac.

3 PARTICULARITIES

If coupling bridges are attached to the ends of SDTL sections, they will couple both operating TM_{010} modes and all high order TM_{01m} modes, including nearest TM_{011} ones. With increasing of k_c bandwidths rise both for TM_{010} passband and for TM_{011} one too. If passbands will overlap, one will have mode mixing problem, leading to serious problems with the field distribution at the operating mode and reduction of the stability. There will be slope in the field distribution at operating frequency, related with TM_{011} mode influence which is especially dangerous in the transient. The frequency difference ΔF between TM_{011} and TM_{010} modes can be estimated as:

$$\Delta F \approx \frac{f_0}{8N_p^2\beta^2} \qquad (1)$$

where N_p is the number of periods in the SDTL section, β is relative velocity of particles. For particular case 5 period SDTL sections with operating frequency f_0 =324 MHz [2] TM_{011} mode is far enough for β =0.3, ΔF =17 MHz, and closer, ΔF =3.8 MHz, for β =0.55. To reduce TM_{011} mode passband influence, one should restrict the value of coupling coefficient k to keep the bandwidth of the TM_{010} passband several times less than ΔF. The coupling with TM_{011} (and all odd TM_{01n} modes too) mode can be avoided by the coupling of the bridge coupler in the middle of the SDTL cavity [3]. This [2] case CBC should have the length $7\beta\lambda$ and for f_0 =324 MHz it is equal to 1940-3560 mm, $0.3 \geq \beta \leq 0.55$. Practically we have to place in parallel additional line of cylindrical cavities, comparable in dimensions with SDTL sections. It leads to increasing of the costs for accelerating system manufacturing.

If 4, 6 or 8 sections are coupled with bridges, coupling at the ends of SDTL sections is possible, because coupling with TM_{011} mode at one end compensates such coupling at another end. If two SDTL sections are coupled with bridge couplers, coupling in the middle of the section looks reasonable.

Coupling slots decrease the frequency and we have local detuning of order $2 \div 4$ MHz in one SDTL period. This detuning is big enough and should be compensated by increasing of the gap length to avoid deterioration of the field distribution inside SDTL section.

4 THE EXAMPLE OF SDTL-RDCB TANK

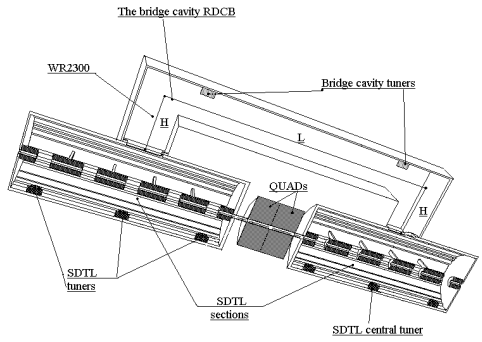

Figure 2: The sketch of SDTL-RDCB tank

Let consider two SDTL sections coupled in the middle with RDCB (Fig.2). The inter-section length is $2\beta\lambda$ [2] and RDCB should provide 0 phase shift between sections, so TE_{10N} mode with odd N should be chosen. It means, that RDCB length along 'middle line' $L+2H$ (see Fig.2) should be close to $N\Lambda/2 \approx L+2H$, where Λ is wavelength of the TE_{10} wave in the waveguide. In addition to [2], below we consider RDCB produced from standard waveguide WR2300 (Λ =151.53 cm at f_0 =324.0 MHz). To combine requirements of distance between cou-

pling slots $L = 7\beta\lambda$ and the total length of the bridge coupler $L+2H \approx N\Lambda/2$, RDCB should be formed in Π-shape (Fig.2). For the beginning of the SDTL accelerating structure β=0.314 TE_{105} RDCB mode is suitable. With the increasing of β along the structure H decreases to maintain total length $L+2H$ and when H becomes insufficient from technological requirements, TE_{105} RDCB mode have to be changed to TE_{107} one. RDCB is equipped with two plug tuners (Fig.2). With simultaneous moving of RDCB tuners we can change own frequency of RDCB, tuning position of nearest modes practically without changing of operating frequency of total cavity. With opposite moving of RDCB tuners one changes level of rf field between SDTL sections. It is very useful also to have several tuners in SDTL section. Two tuners near ends are intended to control operating frequency and field distribution inside SDTL section. It may be shown, that standard deviation of the electric field distribution σ_e in SDTL section (without post couplers) is related with standard deviation of frequencies of SDTL cells σ_f as:

$$\sigma_e \approx \sigma_f \sqrt{\frac{4}{N_p} \sum \frac{f_m^4}{(f_0^2 - f_m^2)^2}} \qquad (2)$$

where f_m are the frequencies of high TM_{01m} modes and TM011 one provides the biggest contribution into σ_e. Two tuners near ends of the SDTL section allow to compensate TM_{011} mode contribution and release tolerances for SDTL manufacturing in 3 times. Moreover, SDTL tuners in the first and last cells are useful to compensate detuning of cells due to absence of a half of stems. Central SDTL tuner is intended to compensate detuning of the middle cell due to coupling slot. If this compensation is done, the central tuner is not necessary. Numerical simulation of rf parameters has been performed for the SDTL-RDCB tank cavity for β =0.314 by using 3D code MAFIA with total number of mesh points near $1.5 * 10^6$. RDCB tuners are suggested 15 cm in diameter and 4 cm in length. SDTL tuners are supposed 10 cm in diameter and 4 cm in length. At first, reference values for SDTL section (without RDCB) have been obtained for operating frequency. RDCB tunes by adjusting H parameter (see Fig.2). The coupling slot 24 cm x 27 cm reduces the frequency of middle SDTL cell at 2.61 MHz and this reduction was compensated by increasing of the gap length at 2.4 mm. After RDCB tuning for TM_{010} mode passband were obtained - operating frequency f_0 =323.999 MHz, another TM_{010}-like modes with frequencies f_- =322.286 MHz and f_+ =325.627 MHz. The k_c value for this case is $k = \frac{f_+ - f_-}{f_0} = 1\%$. For this SDTL-RDCB options numerical calculations show no additional rf losses with respect to reference values for SDTL sections (reduction in shunt impedance Z_e is 0.16%). There are two reasons for additional rf losses - rf losses in the RDCB cavity and redistribution of rf currents at the SDTL walls due to coupling slot influence. The own quality factor Q of RDCB cavity is high ($\approx$ 48000) and comparable with Q-factor of SDTL sections ($Q \approx$ 53000). By choosing high Q RDCB cavity we decrease additional rf losses in the bridge. The dimensions of coupling slot were optimized to reduce rf currents redistribution in SDTL walls. Results of SDTL-RDCB with usual coupling slots also show [2]. tolerable decrease in Ze ≈0.5 ÷ 7% for coupling k_c ≈0.4 ÷ 3%. No significant distortions in the field distribution at operating mode in SDTL sections have been found (σ_e ≈0.1%). With increasing of the at 1 cm length of one RDCB tuner and decreasing for another the ratio of average electric field between SDTL sections changes at 1.67%, operating frequency changes at 1.5 kHz. With the removing of one SDTL end tuner (it corresponds detuning of the end SDTL cell at 650 kHz) operating frequency of the tank changes at 70 kHz (in fine agreement with averaging of frequency errors) and the change in average field level between SDTL section is 0.05%. Inside detuned SDTL section field slope 2.9% exists in good agreement with estimation (2).

5 SUMMARY

The multi-cell CBC may be used for coupling of the SDTL sections. For the operating frequency 324 MHz bridge cavity diameter is ≈ 650 mm, diameter of coupling cell is ≈ 420 mm. To avoid mode mixing in SDTL cavities, coupling coefficient should be small, leading to the reduction in the passband width and closing of the nearest modes.
RDCB may be a good option for the coupling of SDTL sections. In comparison with CBC with intermediate coupling cells RDCB have:
- better mode separation with smaller rf losses,
- smaller transverse dimensions,
- flexible tuning of rf field between SDTL sections,
- simpler manufacturing and tuning procedure.

6 ACKNOWLEDGMENTS

The authors thank Dr. P.N. Ostroumov, Dr. V.G. Andreev and Prof. S.K. Esin for valuable discussion.

7 REFERENCES

[1] T. Kato, Proposal of a Separated Type Proton Drift Tube Linac... , KEK Report, 92-10, (1992).

[2] JHF Accelerator Design Study Report, KEK Report 97-16, JHF-97-10, Sec. 4.5.8 Bridge Coupler.

[3] R. Garnett et al. Design and Simulation of a Bridge-Coupled DTL..., Proc. of the Linac92 Conference, v.2, p.824.

[4] E.A. Knapp et al, Standing wave high energy accelerating structures, Rev. of Sci. Instr. v. 39, p. 979, (1968)

[5] Y. Morozumi et al, Multy-Cavity Bridge Coupler, Proc. of the Linac90 conference, p.153.

[6] V.G. Andreev et al, Bridge Device for Cavities of a Proton Linac..., RTI, Moscow, N20, p47, 1974 (in Russian).

[7] V.G. Andreev et al, Results of the high power test, RTI, Moscow, N25, p123, 1976 (in Russian).

OPTIMIZATION ON WAKEFIELD DAMPING IN C-BAND ACCELERATING STRUCTURE

N. Akasaka, T. Shintake and H. Matsumoto
KEK, High Energy Accelerator Research Organization, 1-1 Oho, Tsukuba, Ibaraki, 3050801 Japan

Abstract

Multi-bunch acceleration in the future e^+e^- Linear Collider projects requires sufficient suppression of transverse wakefield for high luminosity. The C-band accelerating structure consists of the choke-mode cavity to damp the wakefield. In order to achieve the maximum damping, optimization of wakefield absorber was necessary. After the optimization, the transverse wakefield is sufficiently damped below the desirable level.

1 INTRODUCTION

In the future e^+e^- linear colliders, multi-bunch operation is necessary for high luminosity. In multi-bunch operation, long-range transverse wakefield, which is generated by the leading bunches passing the accelerating structure with an finite offset, deflects the orbit of the following bunches. In order to prevent the degradation of the luminosity due to the orbit deflection, the wakefield must be sufficiently damped after the bunch spacing with practical alignment tolerance.

Long-range ringing of the wakefield can be shortened by broadening its spectrum. There are two promising techniques to increase the spectrum width of the wakefield in an accelerating structure: detuning and damping. In the former scheme, the distribution of the higher order mode (HOM) frequency in one or more accelerating structures is deliberately arranged to realize fast smear out of the wake field. In the latter scheme, on the other hand, the HOM's are damped and the HOM spectrum becomes broad even for one cell.

In the C-band linear collider project [1,2], choke-mode cavity [3] is adopted for the accelerator structure in the main linac. Figure 1 shows the C-band accelerating structure. The whole accelerating structure is constructed by stacking axially-symmetric cells. The wakefield generated by a bunch goes out of the cell through the radial line, whereas the accelerating field is confined by the choke. The wakefield is absorbed by the SiC ring at the outside of the choke. The choke-mode cavity is sometimes referred to as "heavily damped structure" because of its high damping performance.

The C-band accelerating structure is now under fabrication [4] to be tested at ASSET in SLAC, where the long-range transverse wakefield will be measured using a driving bunch and a witness bunch passing through the accelerating structure with an offset.

In this paper, its design procedure relating to wakefield damping is presented. First, the optimization of the wakefield absorber for a single cell is described in section 2. Next, the transverse wakefield averaged over the accelerating structure is calculated in section 3.

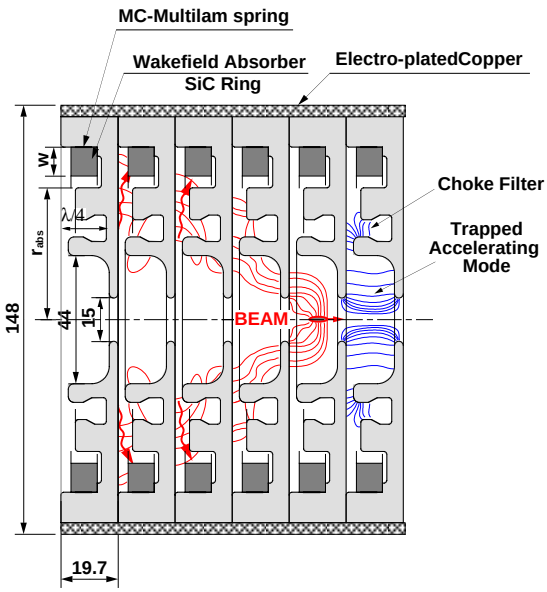

Figure 1: C-band choke-mode structure.

2 OPTIMIZATION PROCEDURE OF SINGLE-CELL DAMPING

The frequency of HOM's is not constant along the accelerating structure since it is a semi-constant gradient structure. The result of the optimization is different depending on the dimensions of the cell.

2.1 Reflection of the Wakefield by the Choke

A part of the wakefield is reflected at the choke even

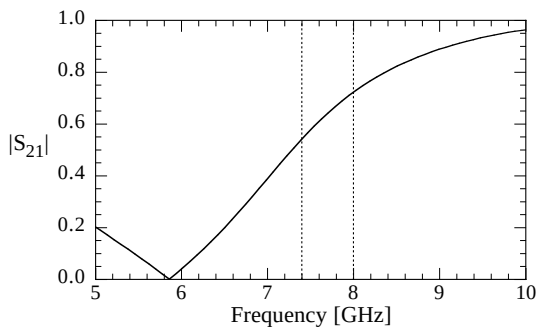

Figure 2: Dipole transmission of the choke.

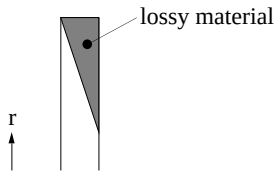

Figure 3: Dummy absorber for calculating optimum reflection coefficient.

though the radial line of the choke-mode structure effectively extracts the wakefield. This can be a serious problem when the main frequency component of the wakefield is near the dipole stop frequency of the choke. In our case, the main contribution to the transverse wakefield comes from TM110, whose peak frequency ranges from 7.4 to 8 MHz depending on the iris aperture 2*a*.

Figure 2 is the transmission coefficient of the choke for the lowest dipole mode calculated with MAFIA 2D time-domain solver (T2). The peak frequency of TM110 is in the region between the two dashed lines, which indicates that only 1/3~1/2 of the energy of TM110 wakefield is transmitted to the absorber. Because of this effect, simple matched (no reflection) absorber at the outer end of the radial line does not provide sufficient damping. This problem was solved by deliberately introducing reflection to the absorber.

2.2 Optimum Reflection from the Absorber

Before designing a realistic absorber, a simple wedge-shaped lossy material, which is shown in Fig. 3, was used in the calculation of the optimum reflection coefficient. The amplitude and phase of the reflection coefficient can be changed by the imaginary part of the permittivity and the radial position of the lossy material, respectively. Then the transverse wakefield and impedance were calculated by MAFIA T2. The optimum reflection coefficient was determined where the peak height of TM110 becomes the lowest. Typical amplitude of the optimum reflection coefficient is 0.55.

Table 1: Parameters of the C-band accelerating structure. The form $n1$ - $n2$ indicates $n1$ at upstream and $n2$ at downstream.

Frequency	5712	GHz
Phase Shift per cell	$3\pi/4$	
Field distribution	semi C.G.	
Number of cells	91	
Iris aperture ($2a$)	17.4 - 12.54	mm
Cavity diameter ($2b$)	45.3 - 43.3	mm
Disk thickness (t)	3	mm
Group velocity	0.035 - 0.012	c
Quality factor	10.7 - 10.3	10^3
Shunt impedance	53.0 - 67.3	MΩ/m

2.3 Determining the Absorber Dimensions

As shown in Fig. 1, the wakefield absorber is an ring of SiC ceramics with a rectangular cross-section. This simple shape was adopted for three reasons: (i) it is easy to fabricate, (ii) the reflection coefficient at the TM110 frequency can be easily changed by changing its width w, and (iii) the reflection coefficient above the TM110 frequency is relatively low. The width of the SiC ring is determined to realize the amplitude of the optimum reflection coefficient at the frequency of TM110. Although the reflection coefficient is optimized only at the frequency of TM110, absorbing all the field energy is sufficient for smaller peaks at higher frequency as can be seen in the next section.

The calculated transverse wakefield is shown in Fig. 4 for the most upstream cell ($2a$ = 17.4) and the most downstream cell ($2a$ = 12.54). In the figure, the thin lines are the wakefield with a matched absorber and the thick lines are with the optimized absorber. With an optimized absorber, the damping time is 2 or 3 times shorter than with a matched absorber. The damping time of the upstream cell is longer than that of the downstream cell since the frequency of TM110 is lower at the upstream cell.

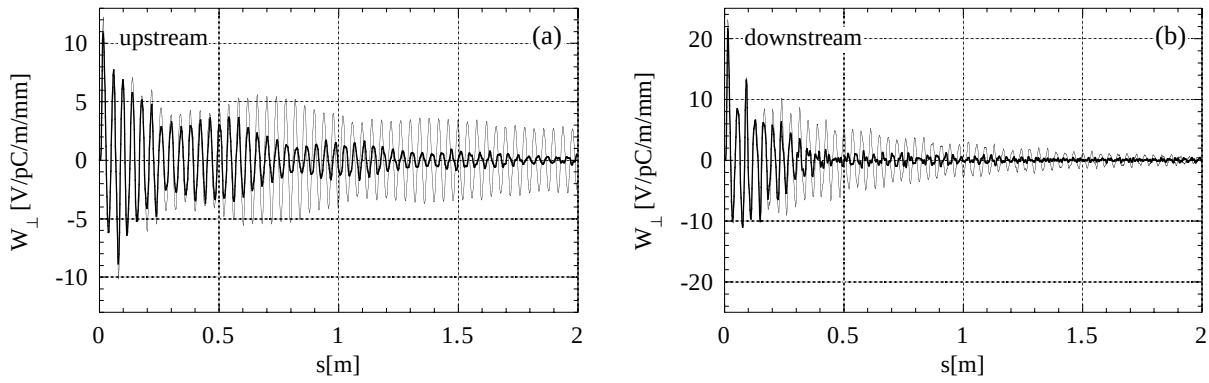

Figure 4: Dipole wakefield calculated by MAFIA T2 for (a) the most upstream cell ($2a$ = 17.40) and (b) the most downstream cell ($2a$ = 12.54). The thin lines are the wakefield with the matched (no reflection) absorber and the thick lines are with the optimized absorber.

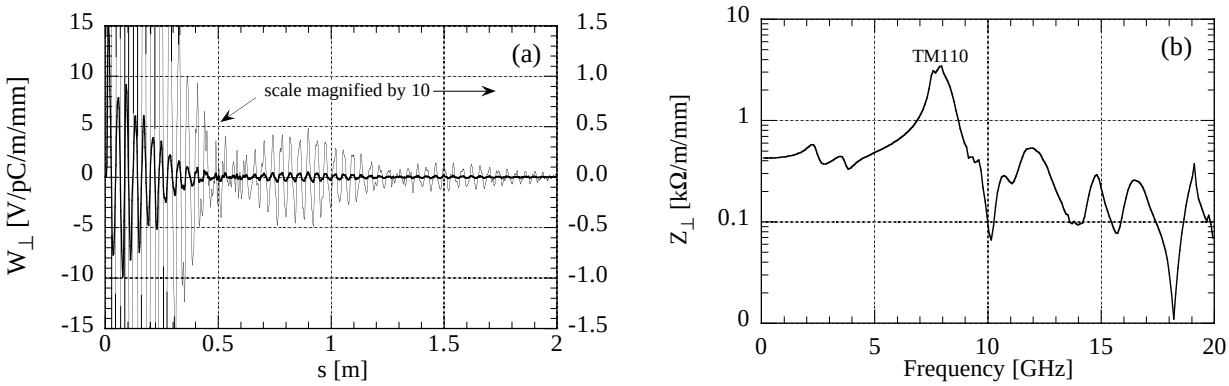

Figure 5: (a) The dipole wakefield averaged over the whole accelerating structure. (b) The impedance calculated from the wakefield.

3 DAMPING OF THE WHOLE STRUCTURE

The parameters of the C-band accelerating structure is summarized in Table 1. The iris aperture 2*a* changes linearly with the cell number from 17.4 to 12.54 and the cell diameter 2*b* also changes to keep the frequency of the fundamental mode constant. This variation of the cell structure introduces detuning of HOM's and additional spectrum broadening. All the choke dimensions including its radial position are the same for the whole structure.

3.1 Absorber Dimensions

For simplicity of the absorber design, the whole structure is divided into four regions of equal length. In each region, the absorber dimensions are determined by the optimization procedure descried above at the center cell.

Table 2: Optimized absorber dimensions. w and r_{abs} are defined in Fig. 1.

cell No.	2 - 22	23 - 45	46 - 68	69-90
w	10.0	10.0	10.0	10.0
r_{abs}	46.5	46.5	45.5	44.5

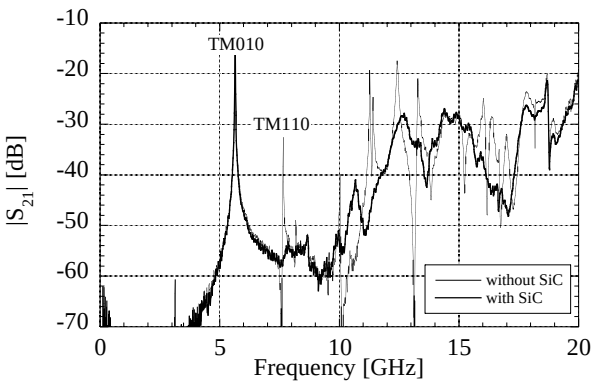

Figure 6: Measured transmission spectrum of the 44th cell.

The result of the optimization is listed in Table 2. The width of the SiC ring is decided to be constant along the accelerating structure since the optimized amplitude of the reflection coefficient was almost the same for the four regions.

3.2 Total Wakefield

The wakefield of the whole accelerating structure is obtained approximately by averaging the wakefield calculated at equally spaced 12 points. Figure 5 shows the averaged transverse wakefield and impedance. The peak of TM110 is still the highest one even after the optimization.

In the case of C-band main linac, the bunch separation is 2.8 nsec (0.84 m). The upper limit on the transverse wakefield corresponding to 30 μm alignment tolerance is 0.7 V/pC/m/mm at s = 0.84 m. From Fig. 5(a), the averaged wakefield is below this upper limit.

4 LOW-LEVEL MEASUREMENT

The transmission of a single cell was measured with two antenna-type probes on both sides of the cell. The distance of the probes from the center axis of the cell is 5 mm and their azimuth is the same. An example of measured spectrum with and without SiC absorber is plotted in Fig. 6. With SiC, sharp peaks are all damped. Further wake measurement for the whole accelerating structure will be done at ASSET.

REFERENCES

[1] T. Shintake et al., "C-band RF-system Development for e^+e^- Linear Collider," APAC98, KEK, March 23-27, 1998.

[2] http://c-band.kek.jp/.

[3] T. Shintake, "The Choke Mode Cavity", *Jpn. J. Appl. Phys.* **31**, L1567-L1570 (1992).

[4] H. Matsumoto et al., "A Fabrication of the C-band (5712 MHz) Choke-Mode Type Damped Accelerator Structure," in this conference.

DESIGN CONSIDERATIONS FOR MULTIPLE-BEAM RFQ STRUCTURES

V. Kapin, M. Inoue, Y. Iwashita and A. Noda
Accelerator Lab., Inst. Chem. Res., Kyoto University
Gokanosho, Uji, Kyoto 611, Japan

Abstract

There are applications, which require MeV-range multiple-beams consisting of a large number of identical highly packed beamlets. The multiple-beam RFQ (MB-RFQ) arranged as a matrix array of longitudinal rod-electrodes is appropriate candidate. A configuration of MB-RFQ resonator should ensure identical quadrupole fields in every accelerating channel. The MB-RFQ resonators based on TEM transmission lines are studied. The resonators are designed by a periodical multiplication of a 4-rod unit cell in transverse direction. To understand fields of resonator the normal mode technique is applied. The resonator field is expanded into normal modes having simple field patterns. In general case of resonator with an arbitrary number of rods and normal modes, analysis becomes difficult. To simplify problem, only normal modes composed from four normal modes of a 4-rod unit cell are selected. Similar to normal modes of a 4-rod unit cell (coaxial, quadrupole and two dipole modes), selected normal modes of multi-rod resonator have clear field patterns. Novel configurations of MB-RFQ resonators based on these normal modes are generated. The RF properties of resonators are verified with computer simulations done with MAFIA code.

1 INTRODUCTION

Several multiple-beam RFQ (MB-RFQ) structures has been proposed to accelerate a number of identical beamlets [1]. These structures consist of matrix array of longitudinal electrodes. The problem is to define a configuration of resonator, which ensures identical accelerating fields in every accelerating channel and preserves high packing of beamlets.

In this paper, MB-RFQ structures are treated as the TEM transmission line resonator. The normal mode technique is applied to decompose a complicated field resonator into fields of normal modes.

2 MB-RFQ AS THE TEM RESONATOR

Let us consider MB-RFQ resonator with N quadrupole electrodes as a resonator based on the N-conductor shielded TEM transmission lines (NCSTL). The propagation of TEM waves is described by the system of the telegraph equations. To facilitate solution of the telegraph equation the normal mode technique is usually applied. The resonator field is expanded into normal modes having simple field patterns. In the transmission line with N-conductors there are N normal TEM modes.

This technique has been applied to study 4-rod RFQ using the four-conductor shielded transmission line (4CSTL) [2]. In the case of N>4, the analytical definition of normal modes becomes difficult. To facilitate the study, let us restrict a number of considered normal modes in the NCSTL. A 4-rod configuration with known normal modes is considered as a unit cell. Normal modes of the NCSTL are composed by a periodical multiplication of a 4-rod unit cell in transverse direction.

The normal modes in the 4CSTL can be observed in the resonator shown in Fig.1. All four electrodes are grounded at the same longitudinal position, z=0 and have open ends at the another end of resonator, z=l.

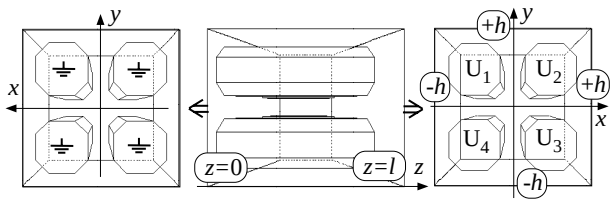

Figure 1: 4-rod RFQ allowing an observation of normal modes.

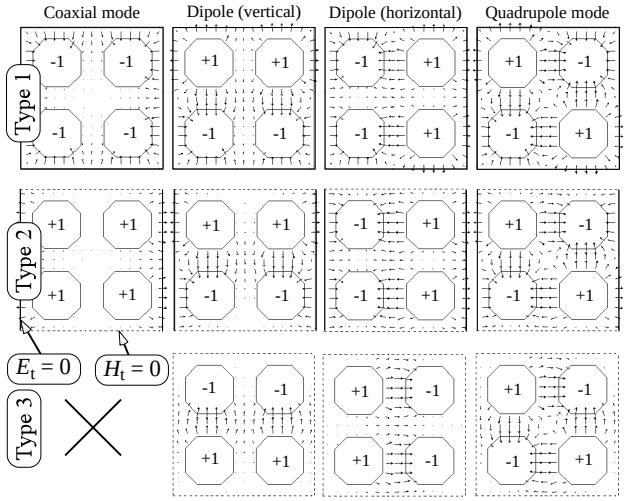

Figure 2: The E-line patterns of normal modes in the 4CSTL for three types of boundary conditions on shield.

Figure 2 shows the E-line patterns of TEM normal modes in the 4CSTL calculated with MAFIA code. Three different combinations of two boundary conditions (perfect conductor, E_t=0 or infinitely permeable, H_t=0)

on the shield are presented. The first and second type has four normal modes (coaxial, quadrupole and two dipole). The third type with H_t =0 on all four sides of the shield has only three modes, because it corresponds to opened transmission line.

The normal modes in the NCSTL can be observed by the similar way. The MB resonator with 4x4-matrix array of electrodes is shown in Fig.3. All electrodes are grounded at the same longitudinal position, z=0 and have open ends at the another end of resonator, z=l.

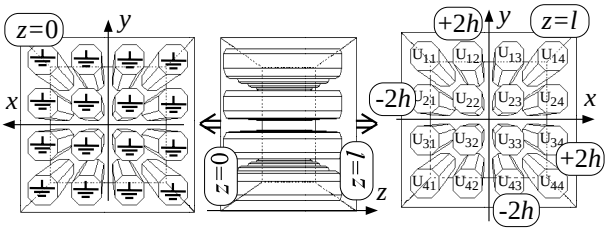

Figure 3: MB-RFQ resonator with a 4x4-matrix array of electrodes allowing an observation of normal modes.

Figure 4 shows the E-line patterns of normal TEM modes calculated by MAFIA code. Three types of boundary conditions on the shield are presented. The values of conductor potentials are shown on the conductor cross-sections.

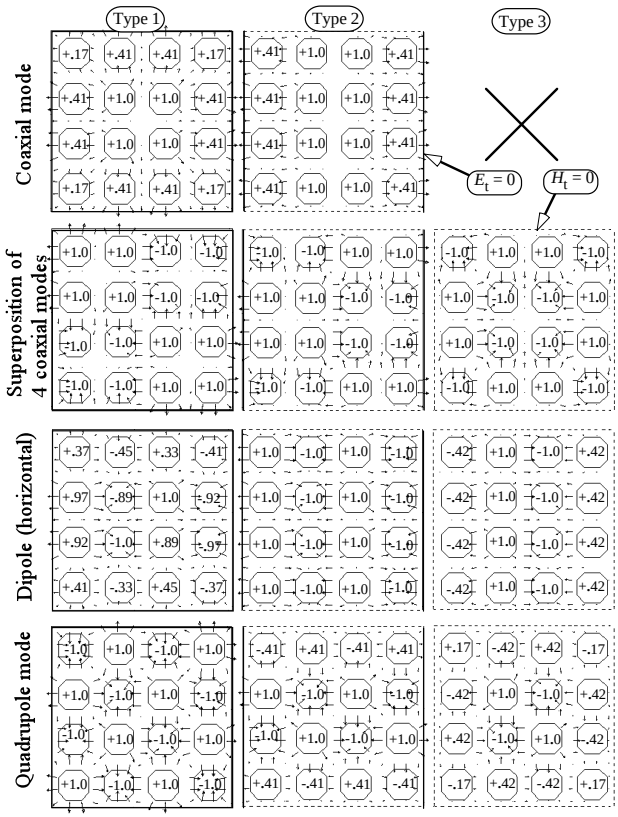

Figure 4: The E-line patterns of normal modes in the MB-RFQ resonator for three types of boundary conditions on the shield.

The quadrupole mode of the type 1 has correct-balanced quadrupole potentials for all channels. The field of the quadrupole mode increases sinusoidally along z-direction. This MB-resonator can be used as an initial matching section.

Figure 5 shows the MB resonator designed using an extension of 4-rod RFQ in the transverse direction. All electrodes are divided into two groups in a chess order. The electrodes of two groups are grounded in opposite manner.

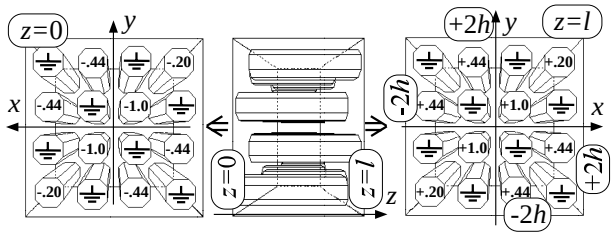

Figure 5: MB-RFQ resonator composing by an extension of 4-rod RFQ.

The field in this MB-resonator can be interpreted in terms of normal mode technique. The field of the original 4-rod resonator is described by combination of quadrupole and coaxial mode, which has been presented in [2]. In contrast to 4-rod resonator, the coaxial mode of MB-RFQ (see Fig.4, Coaxial mode of type 1) has unequal potentials of electrodes. Therefore, the combination of quarupole and coaxial modes in the MB resonator does not provide a correct excitation of the electrodes. The voltages on the electrodes surrounding RFQ-channels deviate from quadrupole symmetry.

Figure 6 shows the MB resonator designed using a periodical multiplication of 4-rod unit cell in the transverse direction. The field of the 4-rod unit cell of the resonator is described by combination of the quadrupole mode and the normal mode shown in the second row of the first column of Fig.4. The voltages on electrodes provide a balanced excitation and every second RFQ-channel can be used for an acceleration of beamlets.

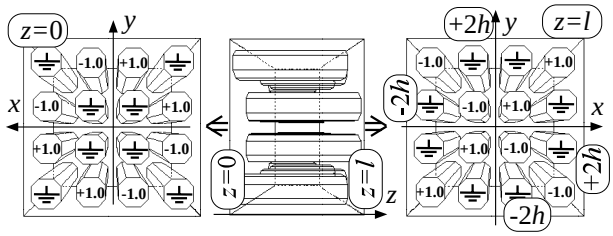

Figure 6: MB-RFQ resonator composing by a periodical multiplication of 4-rod unit cell.

Recently, a new MB-RFQ structure has been proposed [1,3]. To preserve high packing of beamlets this structure allows discrete connections of adjacent RFQ electrodes. The beam dynamics in RFQ-channels is modified. Beams perform "slalom" motions, utilizing

transverse oscillations. The Figure 7 shows the MB-resonator.

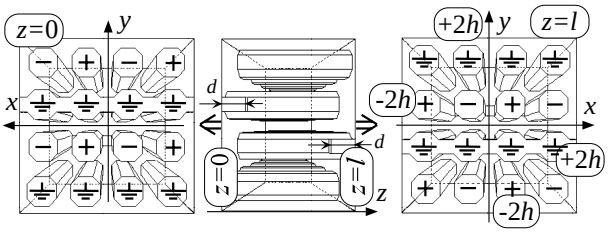

Figure 7: MB-RFQ resonator with 4x4-matrix array of electrodes.

The field of the MB-resonator with a "slalom" beam is superposition of quadrupole mode and dipole mode, which are summed at a $\lambda/4$ phase shift between each other. Figure 8 shows voltage distributions for this combination of quadrupole and dipole modes in the case of 4-rod unit cell. The result of summation is given on the right side of the Fig. 8.

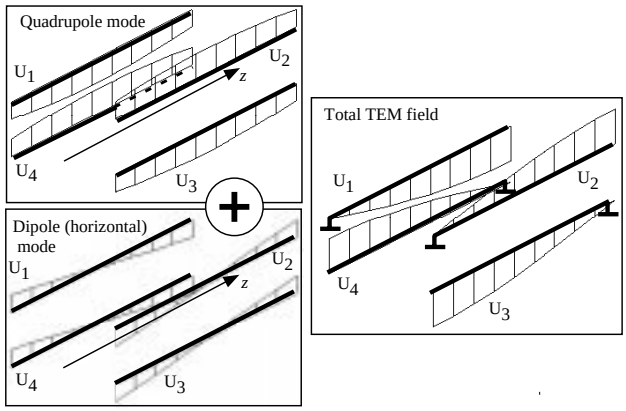

Figure 8: The superposition of quadrupole and dipole modes shifted by $\lambda/4$ to each other.

For the case of MB-RFQ, this combination is extended to the superposition of quadrupole mode of type 1 and dipole mode of type 2 (see Fig.4). For a real configuration of MB-RFQ resonator, the boundary conditions on all tank walls must correspond to a perfect conductor. The dipole mode of type 2 is replaced by the dipole mode of type 1 (see Fig. 2). In contrast to the dipole mode of type 2, potentials of electrodes surrounding RFQ-channels for the dipole mode of type 1 deviate from a correct dipole field (see Fig.4). As the result, a total field in the MB-resonator is distorted.

A difference between dipole modes of type 1 and type 2 is appeared as different boundary conditions on the shield for the upper and lower rows of 4-rod unit cells. Free frequencies of the outer cells deviate from their values for cells in the middle rows of MB-resonator. The free frequencies of the outer cells should be tuned. The free frequency of a 4-rod unit cell depends on an electrical length of conductors. For the MB-resonator shown in Fig.7, the length of conductors in the middle rows is less than the length in the outer cells on the value, d.

Fig. 9 shows the distributions of the quadrupole and dipole voltages in separate channels calculated with MAFIA code. The quadrupole voltage V_{ij} in the ij-channel is calculated from the voltages of electrodes surrounding the channel by the relation

$$V_{i,j} = (U_{i,j} - U_{i,j+1} + U_{i+1,j+1} - U_{i+1,j})/2$$

The voltages of horizontal and vertical dipole modes, Dh_{ij} and Dv_{ij} are defined by the following formulas:

$$Dh_{i,j} = (U_{i,j} - U_{i,j+1} - U_{i+1,j+1} + U_{i+1,j})/2$$

$$Dv_{i,j} = (U_{i,j} + U_{i,j+1} - U_{i+1,j+1} - U_{i+1,j})/2$$

For the case of d=0, the values of quadupole voltage, V_{ij} are different for the middle and outer channels. The phase shift between quadrupole and dipole voltages deviates from $\lambda/4$ for outer channels. For the optimal value of d=1.8cm, curves of quadrupole voltages became very similar and the required phase shift of $\lambda/4$ is restored.

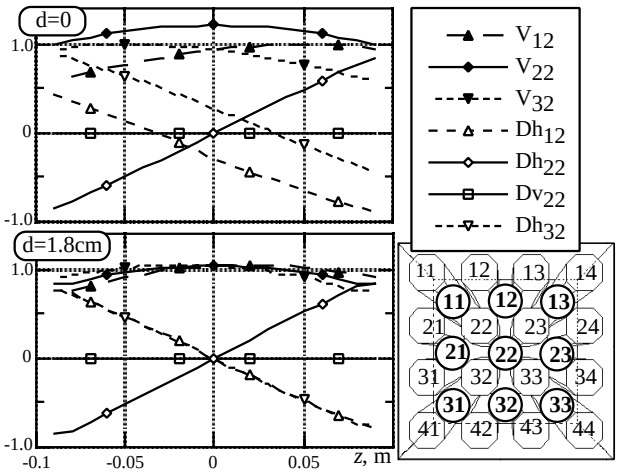

Figure 9: The distributions of the quadrupole and dipole voltages in separate channels calculated with MAFIA code.

3 ACKNOWLEDGEMENTS

This study has been conducted under the Postdoctoral Fellowship Program for Foreign Researchers of Japanese Science Promotion Society and supported in part by the Grant-in-Aid for JSPS Fellows from the Ministry of Education, Science, Sports and Culture of Japan.

4 REFERENCES

[1] V.Kapin, A.Noda, Y.Iwashita and M. Inoue, Proc. XVIII Linear Accelerator Conference, CERN 96-07, 1996, pp. 722-724 and references therein.

[2] V.Kapin, M.Inoue, Y.Iwashita and A.Noda, ICR Annual report, Kyoto Univ., Vol.4, 1997, pp. 56-57 and references therein.

[3] V.Kapin, M.Inoue and A.Noda, to be published in Proc. EPAC'98.

PROTON BEAM STUDIES WITH A 1.25 MeV, CW RADIO FREQUENCY QUADRUPOLE LINAC*

G.O. Bolme, T.W. Hardek, L.D. Hansborough, D.J. Hodgkins, D.R. Keffeler, J.D. Sherman, H.V. Smith, R.R. Stevens, L.M. Young, T.J. Zaugg (LANL, Los Alamos, NM), P.P. Balleyguier (CEA-Bruyeres le Chatel, France), A.H. Arvin, A.S. Bolt, M.C. Richards (SRS, Aiken, SC), and J.H. Kamperschroer (GA, San Diego, CA)

Abstract

A high-current, cw linear accelerator has been proposed as a spallation neutron source driver for tritium production. Key features of this accelerator are high current (100 mA), low emittance-growth beam propagation, cw operation, high efficiency, and minimal maintenance downtime. A 268 MHz, cw radio frequency quadrupole (RFQ) LINAC section and klystrode based rf system were obtained from the Chalk River Laboratories [1] and were previously installed at LANL [2] to support systems development and advanced studies in support of cw, proton accelerators. A variation of the **L**ow **E**nergy **D**emonstration **A**ccelerator (LEDA) proton injector, modified to operate at 50 keV, was mated to the RFQ and was operated to support advance developments for the **A**ccelerator **P**roduction of **T**ritium (APT) program. High current, proton beam studies were completed which focused on the details of injector-RFQ integration, development of beam diagnostics, development of operations procedures, and personnel and equipment safety systems integration. This development led to acceleration of up to 100 mA proton beam.

1 INTRODUCTION

The **C**halk **R**iver **I**njector **T**est **S**tand (CRITS) was the LANL designation given to a proton accelerator designed, built, and tested at the **C**halk **R**iver **L**aboratories (CRL) in Canada. The CRITS accelerator apparatus includes a 1.25 MeV RFQ accelerator section and a prototype klystrode-based rf system for powering the RFQ. An earlier independent study at LANL, utilizing the RFQ, focussed on the high-power operation of the rf structure [2].

The LEDA program has the objective of developing a high-current, cw injector and the initial rf accelerating structures for APT. The LEDA injector is comprised of the proton ion source and a **L**ow **E**nergy **B**eam **T**ransport (LEBT) section to the RFQ. A 75 kV, cw proton ion source was developed for LEDA and has produced a proton beam with measured current and emittance meeting program requirements. A state-of-the-art LEBT was designed and built to match the ion source beam to the LEDA RFQ [3].

*Work supported by the US Department of Energy.

The functionality of an injector is best confirmed by injecting its beam into an RFQ. In preparation for installing the injector as a component of LEDA, the availability of the CRITS RFQ provided the opportunity for an initial shakedown of the injector. The modification of the ion source to 50 kV and adaptation of the LEBT exit section to the CRITS RFQ made the LEDA injector/CRITS RFQ configuration a realistic testbed for injector development. Furthermore, this configuration also supported RFQ experiments to evaluate the system modeling codes and to learn the details of cw RFQ operations. Figure 1 shows the full beamline used in this project.

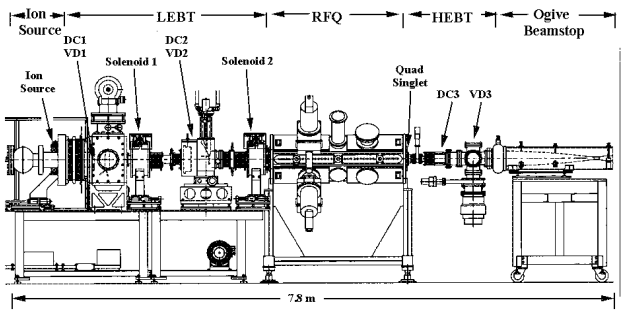

Figure 1. The LEDA Injector/CRITS RFQ experiment beamline.

In order to meet the project objectives, the RFQ specific studies focussed on verifying the RFQ field configuration, successfully operating the RFQ at high fields, verifying the accelerating fields in the RFQ, and accelerating proton beam from the modified LEDA injector.

2 RFQ FIELD DISTRIBUTIONS

Although the Q and resonant frequency of the RFQ were close to the expected values following shipment of the RFQ from CRL, the verification of the modeling codes mandated that the field distribution in the structure be confirmed. The insertion of a probe through the vacuum pumping holes in each of the quadrants gave a perturbation measurement of the cavity fields from which the dipole field contributions to the quadrupole field were calculated. The uncorrected dipole fields across quadrants 1 and 3 (dipole 1) were measured up to 14% of the quadrupole field and up to 8% across quadrants 2 and 4 (dipole 2). The dipole field distribution along the RFQ

length indicated that the vane coupling rings near the ends held the distribution close to the desired quadrupole configuration, thus, dipole field reduction at the center should achieve an acceptable field pattern in the RFQ. Adjustment of movable tuners in quadrants 2 and 4 and modification of the fixed tuner in quadrant 3 corrected the field distribution to less than 4% dipole contribution. This was considered acceptable for the beam studies. Figure 2 displays the corrected and uncorrected dipole contributions for dipole 1, the larger of the two dipole field distributions.

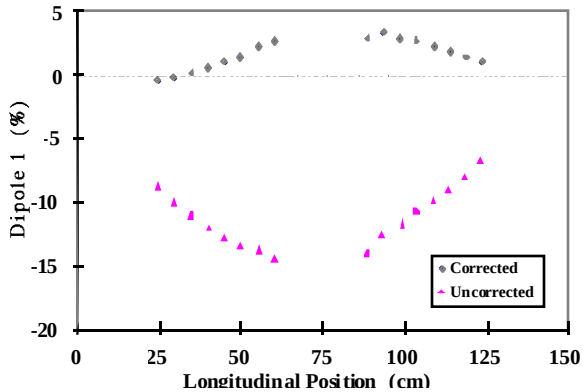

Figure 2. Dipole 1 contribution to the quadrupole field distribution.

A subsequent intervane gap measurement verified that the vanes had shifted away from their initial 1 mil tolerance and these gap differences were in agreement with the uncorrected dipole distributions.

3 HIGH-POWER FIELD LEVEL VERIFICATION

The calibration of the field sampling loops were completed using a Hewlett Packard 8753 Network Analyzer, and the rf signals from these loops at high power were monitored using power meters and oscilloscope measurements of the raw rf signals and diode rectified signals. The RFQ was conditioned to high power based on the SUPERFISH prediction of the design power level. High-power measurements of the actual field level were made using the x-ray endpoint method [4], a technique pioneered by accelerator scientists at CRL. Measurements made throughout the duration of the proton beam studies verified that the peak intervane gap voltage tracked the measured power levels according to the expected square root dependency. Figure 3 displays the gap voltage data and the curve used to project the peak intervane gap voltage as a function of measured power.

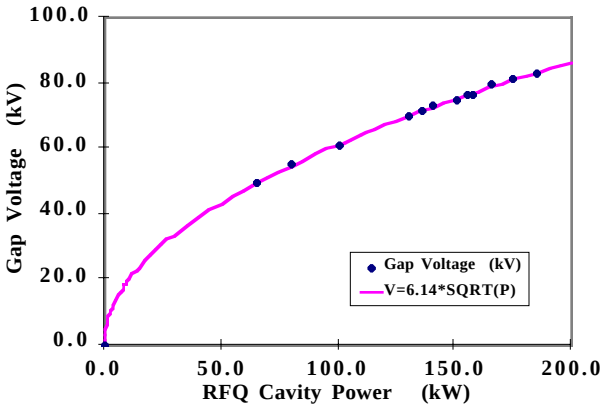

Figure 3. Peak intervane gap voltage versus RFQ cavity power.

4 SPARK RATE ANALYSIS

During the CRITS RFQ operation, the spark rate has been systematically measured and stored. Every second, the total number of sparks was read on a counter. Every minute, the raw number of sparks was stored as well as the number of seconds with at least one spark. In fact, this last information was found to be more relevant, since avalanches of sparks do not bias it. The rf power levels (forward, reflected and in cavity) were also recorded, as well as the residual vacuum pressure (Figure 4). We established that the spark rate has some influences on vacuum, but there is no evidence of any reciprocal effect.

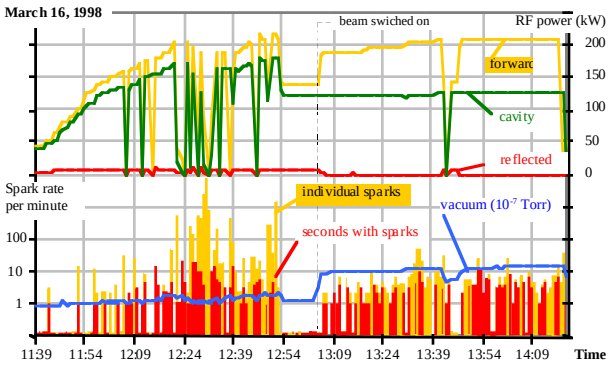

Figure 4. Example of archived rf power operations.

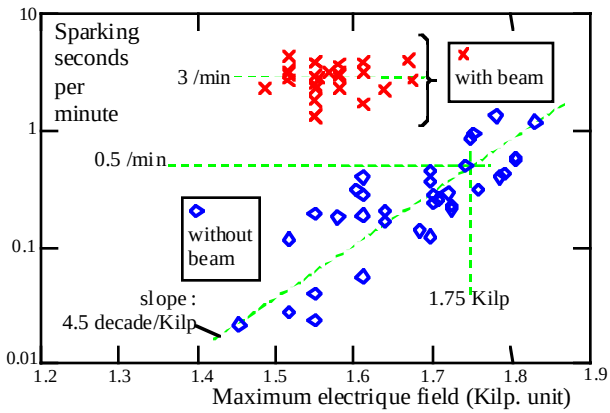

Figure 5. Average spark rates during long runs.

Within the stored data, a set of long runs (between 22 and 163 minutes long) of continuous operation have been extracted: 34 runs without beam and 24 with beam. For each run, the average rate of sparking seconds was computed. As some runs yielded no sparks at all, one spark has been added arbitrarily to each data point in order

to be able to plot the zero-spark points on a log scale (figure 5). This induces a slight bias to the data, but takes into account the fact that rates are more accurate if acquired over a long run.

Without beam, the rate is typically 0.5 per min at the design field (1.75 Kilpatrick, 77.4 kV intervane voltage, 159 kW measured in the RFQ), i.e. the average time between two bunches of sparks is two minutes. The slope shows that a 0.22 Kilpatrick decrement in the electric field lowers the sparking tendency by an order of magnitude.

During beam operations, the RFQ was run about 10% below the design field because of a peak rf power limitation. The rate jumped to 3.0 per minute, depending neither on the beam current (20 to 80 mA) nor on the field (1.5 to 1.7 Kilpatrick tested). This is about 6 times more than without beam at 1.75 Kilpatrick.

With rates such as the ones measured here, one could not hope to build an RFQ that would be free of sparks over several months of continuous operation. For LEDA proton beam operations, it will probably be necessary to deal with a spark rate which requires that the LINAC restart automatically after a short power interruption.

5 PROTON BEAM MEASUREMENTS

The proton beam studies with the RFQ proceeded cautiously by increasing current only as the injector match to the RFQ could be confirmed by the beam transmission. The desired field level for the RFQ was set from the x-ray endpoint measurement, but a measurement of beam transmission as a function of the RFQ cavity power was also used to confirm the expected behavior. As expected, a knee in the transmission curve was observed below the design field level.

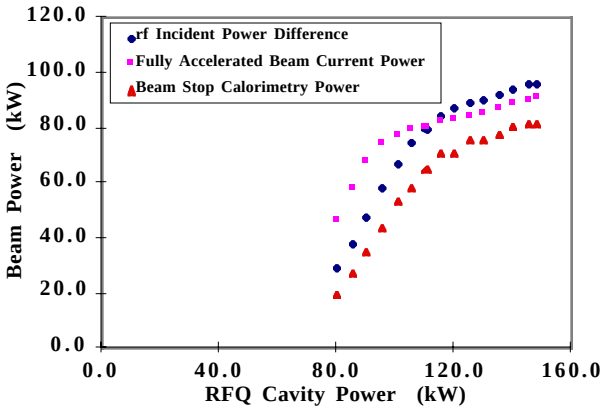

Figure 6. Beam power measurements from rf incident power difference, beam stop calorimetry, and predicted power assuming fully accelerated transmitted beam versus RFQ cavity power.

As a separate check for accelerated beam, the incident power difference and beam stop calorimetry were compared to the expected beam power under the assumption that the entire proton beam was accelerated. This assumption is known to be false but allows us to compare the beam transmission data with the two beam power measurements using the same units. These data are shown in Figure 6. The rf incident power difference and calorimetry measurements of the beam as a function of RFQ cavity power show a discrepancy in absolute calibrations, but the knee in the curve for both measurements agree. The lower RFQ cavity power correlated with the knee for beam transmission compared with the other power measurements indicates that beam is transmitted even though it is not accelerated.

6 SUMMARY

The CRITS RFQ proved to be the best test device for checking out all components of the injector. By optimizing the current through the RFQ, all injector systems demonstrated that they could operate across the required parameter space. The procedures developed in preparing the RFQ for beam and in accomplishing beam studies should expedite successful operations with the LEDA RFQ. The successful transmission of beam currents with good agreement to the simulations [5] also provides confidence in the codes as we proceed into future projects.

7 ACKNOWLEDGMENTS

We would like to thank and express our appreciation to the personnel at Chalk River Laboratories who designed, fabricated, assembled, and commissioned this accelerator section under the RFQ1 program. They provided an RFQ which met its design goals and proved to be robust enough to operate reliably through a long sequence of structure studies. Furthermore, their brilliant and innovative work provided not only the basis for the x-ray endpoint measurement which has proven so valuable at LANL, but also the underlying technical knowledge for cw, proton accelerator development which has been the cornerstone of the upcoming LEDA project.

REFERENCES

[1] J.Y. Sheikh, *et al.*, "Operation of a High-Power CW Klystrode with the RFQ1 Facility", Proc. 1993 Particle Accel. Conf., IEEE 93CH3279-7, p. 1175.

[2] G.O. Bolme, *et al.*, "High-Power RF Operations Studies with the CRITS RFQ", Proc. 1995 Particle Accel. Conf., IEEE 95CH35843, p. 923.

[3] J. Sherman, *et al.*, Rev. Sci. Instrum. **69** (1998) 1003-1008.

[4] G.O. Bolme, *et al.*, "Measurement of RF Accelerator Cavity Field Levels at High Power from X-ray Emissions" in Proceedings of the 1990 Linear Accelerator Conference, LA-12004-C,219 (1990).

[5] H.V. Smith, *et al.*, "Comparison of Beam Simulations with Measurements for a 1.25-MeV, CW RFQ", these Conference Proceedings.

THE MECHANICAL DESIGN AND FABRICATION OF A RIDGE-LOADED WAVEGUIDE FOR AN RFQ*

R. Valdiviez, P. Roybal, B. Clark, F. Martinez, D. Casillas, G. Gonzales, J. Tafoya
Los Alamos National Laboratory, Los Alamos, NM, 87545

Abstract

The APT/LEDA Radio Frequency Quadrupole (RFQ) accelerator has an RF power input of 2 MW and an H^+ beam output current of 100 mA at 6.7 MeV CW. The RFQ utilizes twelve nearly identical ridge-loaded vacuum waveguides to couple the RF power to the RFQ accelerating cavity. The mechanical design and fabrication of the ridge-loaded waveguides are the topics of this paper.

1 RFQ AND RF POWER SUPPLY DESCRIPTION

The RFQ linac [1] is made of eight different sections that are joined together with a flange type design. Each section is approximately one meter in length and weighs approximately 680 pounds. RF power is supplied at three different sections of the RFQ. RF feed sections have four rectangular shaped ports each that are sized to accept the nose piece of the ridge-loaded waveguide. The nose piece of the waveguide actually becomes part of the cavity wall, with the face being part of the cavity surface.

The RF power is supplied to the RFQ by three separate klystrons, each rated for 1 MW operation at 350 MHz. The output of each klystron is divided four ways to create twelve waveguide runs of nominally 167 kW each. An RF window [2] is used to separate the air and vacuum waveguide runs on each waveguide arm.

2 BASIC RF CHARACTERISTICS DESIGN OF THE RIDGE-LOADED WAVEGUIDE

The tapered ridge-loaded waveguide operates in the dominant TE10 mode, the same mode as in the half-height WR2300 waveguide used for the airside RF waveguide. The ridge in the waveguide begins at a location in the waveguide approximately twenty-four inches from the RFQ inner wall and increases in height toward the RFQ, while both the height and width of the waveguide are reduced. The RF fields have intensified sufficiently at the end of the ridged waveguide to couple the RF power into the RFQ cavity with an iris slit small enough to not perturb the tuning of the RFQ. The cutoff frequency of any cross section through the tapered ridge-loaded waveguide is equal to the cutoff frequency of the WR2300 waveguide.

3 THERMAL/STRESS ANALYSIS OF THE RIDGE LOADED WAVEGUIDE

3.1 First Ridged Waveguide Section

The waveguide arm connecting the RFQ to the RF window is actually made up of three vacuum waveguide sections. The first two sections are the ridge-loaded sections. The third section is a straight section of waveguide that includes a vacuum pumping port for pumping the waveguide arm [3].

A section view of the ridged waveguide is shown in Figure 1. The total weight of the waveguide is 97 pounds.

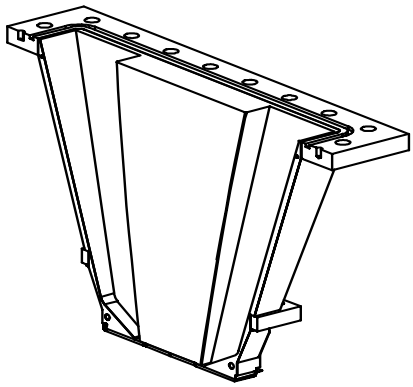

Figure 1. First Ridged Waveguide Longitudinal Section View

The first waveguide section inserts into the RFQ, and has a plate with an iris slit machined through it brazed to the bottom, rectangular face. The iris plate becomes the cavity inner wall surface. The slit aligns longitudinally with the gap between the ridges, and exposes the gap to the cavity. The Rf coupling takes place via the slit. This configuration places a considerable heat load on the waveguide. Integral coolant channels within the waveguide body are used to provide the necessary temperature control of the waveguide. Water from the

* Work supported by the US Department of Energy, Defense Programs

Resonance Control Cooling System (RCCS) [4] is used in the waveguide coolant channels. Since the waveguide becomes part of the resonating cavity wall it must be thermally controlled along with the rest of the cavity walls.

Two parallel coolant channels run down through the ridge, make six turns in a region immediately behind the iris plate, and flow up and out of the waveguide. The bulk coolant velocity is 15 ft/s in the iris region, and 12.8 ft/s in the supply and return channels in the ridge bodies. This cooling configuration allows for the power loss heat load, that ranges from 13.0 watts/cm^2 to 0.3 watts/cm^2 to be accommodated. The high thermal conductivity of the copper material allows for using only two discrete coolant channels to cover a rather wide surface area without creating substantial temperature gradients.

The thermal/stress Finite Element Analysis (FEA) model of the waveguide was created and analyzed using the program COSMOS/M, version 1.75A [5]. The waveguide geometry was obtained from the solid modeling software Unigraphics, version 11.1.3 [6] by using an IGES translation file.

To model the waveguide the thermal profile throughout the body was first predicted. The peak temperature predicted was 106 °F for normal conditions, with an inlet coolant temperature of 66 °F. This peak temperature occurs in the iris region where the peak heat load is located. This thermal profile is then used as one of the boundary conditions in a displacement and stress model. The largest displacement is predicted to be 0.0022 inch at the top of the waveguide. The peak von Mises stress is predicted to be 6540 lb$_f$/in^2 and occurs in the iris region. The iris region is locked between the lower mounting flange of the waveguide and the RF seal that the nose piece of the waveguide presses against. The RF seal acts as a very stiff spring that has some pliability, yet still offers significant resistance to the thermal growth of the nose portion of the waveguide.

Due to the value of the predicted peak von Mises stress in the waveguide the high strength copper material Glidcop AL-15 [7] was chosen as the construction material for the waveguide.

3.2 Second Ridged Waveguide Section

Figure 2 is a section view of the second ridged waveguide that connects directly to the first section. The second ridged waveguide is the section where the ridge begins, and weighs 186 pounds. One end of the waveguide matches the half-height WR2300 waveguide dimensions. The bottom-end dimensions of this waveguide match to the first waveguide to within a few thousandths of an inch.

The waveguide has four separate coolant-flow channels. The channels are located in the corner regions of the ridge. The bulk coolant velocity in each channel is 6 ft/s. The coolant water from the first section is split and sent into the second section. The power-loss heat load on the second section ranges from 0.21 watts/cm^2 to 0.05 watts/cm^2.

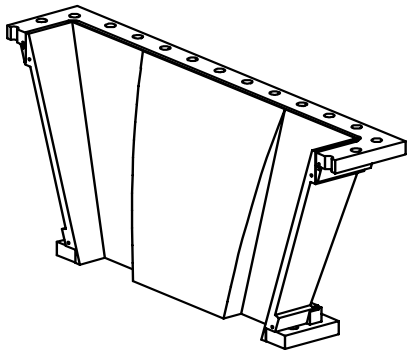

Figure 2. Second Ridged Waveguide Longitudinal Section View

The thermal/stress Finite Element Analysis (FEA) model of the second waveguide was created and analyzed using the program COSMOS/M, version 1.75A. The waveguide geometry was obtained from the solid-modeling software Unigraphics, version 11.1.3 by using an IGES translation file.

The FEA model was first used to predict the thermal profile of the second waveguide. The peak temperature was predicted to be 81 °F at a location in the lower part of the waveguide sidewall, for an inlet coolant temperature of 72 °F. This location is one of the furthest from a coolant channel in the section. The predicted thermal profile was used as a boundary condition for the displacement and stress model. The largest displacement was predicted to be 0.0013 inch at the top of the waveguide. The peak von Mises stress is predicted to be 3680 lb$_f$/in^2 located in a lower corner region of the waveguide.

The predicted von Mises stresses are not too high for the second section. For this reason OFE C10100 copper was chosen as the material of construction.

4 MECHANICAL DESIGN OF THE RIDGE-LOADED WAVEGUIDE

The mechanical design used the results of the thermal and stress analyses to determine a final design that would meet both strength and space-envelope constraints. Initial

concepts for each of the waveguide designs had been created using the solid modeling software Unigraphics, version 11.1.3.

The thermal and stress analyses of both waveguide sections predicted some areas where the initial design required some modification. The size of the coolant channel in the iris waveguide, in the region immediately behind the iris piece was changed in order to obtain the thermal/hydraulic conditions needed to achieve the desired thermal profile in this part of the waveguide body. The body of the second waveguide section was predicted as needing reinforced sections in the flange areas in order to reduce the combined stress levels.

5 FABRICATION METHODS EMPLOYED

The ridged-waveguide sections are machined copper assemblies with the individual parts joined together by brazing . The internal ridge and pocket configuration of both sections along with the tapering in two planes over the length of the section requires skillful machining. The geometry of, and the mechanical loads placed on the braze joints requires equally skillful preparation and brazing.

5.1 Machining

Each waveguide section is machined in two halves that are eventually joined together. By using this approach the internal ridge and pockets can be machined in an open-face configuration. The dimensional tolerance of the internal features was +/- 0.005 inch or less. Five three-axis machines and one five-axis machine were used to produce the waveguide bodies.

Due to the fact that the internal surfaces and features see high RF power, the surface finishes and feature sizes (such as corner radii) took on more importance than they normally would as in a non-RF power component. Sample pieces were machined out of aluminum for both waveguide sections to check for surface finish and feature sizes obtainable, and to check the machine programming. After undergoing a few iterations with samples the actual copper machining was begun.

5.2 Brazing

Gold-copper alloys are used to braze the various pieces of the waveguides together. Brazing the OFE C10100 presented no major problems due to long experience in brazing this copper material. Brazing OFE C10100 to Glidcop AL-15 presented some problems with joint sealing and joint strength. Brazing Glidcop AL-15 to Glidcop AL-15 presented increased sealing and strength problems.

In order to overcome the problem of Glidcop joint seal and strength integrity several vacuum and tensile specimens were fabricated and put through variations of the basic brazing procedure being used. In summary, the first sample investigations provided some improvement steps, but nothing that achieved consistent seal and strength integrity. Throughout this testing process other users of Glidcop were consulted about the problem. The Stanford Linear Accelerator Complex (SLAC) advised that their best success in brazing Glidcop came from first plating the surfaces to be brazed with a 0.0008 inch thick copper strike in a cyanide-copper plating process. This method of preparing the braze surface was employed on several sample pieces with very good, consistent results in sealing and strength. The preparation method was added to the fabrication sequence of the waveguide sections, and has worked well on the parts brazed to date.

6 RESULTING WAVEGUIDE HARDWARE

At the time of preparing this paper the ridged waveguide sections were still being fabricated, so no high RF power operation has been conducted yet with this ridged waveguide design. Since the desired RF design has been able to be manufactured with no major changes the waveguides are expected to perform as required.

7 REFERENCES

[1] D. Schrage et al, “CW RFQ Fabrication and Engineering,” these proceedings.

[2] K. Cummings et al, “Results and Lessons Learned From Conditioning 1 MW CW 350 MHz Coaxial Vacuum Windows,” these proceedings.

[3] S. Shen et al, “APT/LEDA RFQ RF Window Vacuum Pumping System-Conceptual Design Report,” LLNL Report APT/RFW-091797-001.

[4] R. Floersch, “Resonance Control Cooling System for the APT/LEDA RFQ,” these proceedings.

[5] Structural Research and Analysis Corp., “COSMOS/M User Manual,” version 1.75A, March, 1996.

[6] EDS Corporation, “Unigraphics User Manual,” version 11.1.3, 1996.

[7] OMG Americas Corp., “Glidcop Dispersion Strengthened Copper, Glidcop AL-15 (C15715),” Technical Data Sheet, August, 1989.

PROTOTYPE MODELS FOR THE SNS RFQ*

A. Ratti, J. Ayers, R. Gough, J. Greer, M. Hoff, R. Keller, R. MacGill,
J. Remais, J. Staples, R. Yourd
Lawrence Berkeley National Laboratory, Berkeley, CA, USA

Abstract

Prototype models that simulate components of the RFQ which is part of the Spallation Neutron Source front end injector [1] are described. The RFQ operates at 402.5 MHz, a maximum current of 70 mA H^- and 6% duty factor. The first model, made of copper plated aluminum is a full size version of one of the four sections of the RFQ and is used to perform low level r.f. measurements of frequency, r.f. tuning, field structure and power coupling port studies. It serves to benchmark the 3D computer simulation studies and to test assembly and field measurement procedures. The second model is a quarter-wave coaxial resonator is used to perform full-power tests of high current seals and joints. This model is also used to test the prototype of the RFQ tuners. The design and construction of both models are presented, as well as test results.

1 INTRODUCTION

The detailed design of the RFQ [2] requires intensive computer simulations to define the cavity shape as well as the optimal configuration of many of the components like the π-mode stabilizers (PISL) [3], tuners and power ports. While some of the work can be done with a 2D code like Superfish, whose accuracy is quite satisfactory, the lack of radial symmetry mandates the use of 3D codes like MAFIA, which are not accurate enough to determine final dimensions. A test model has been built to perform low level measurements to validate and refine the computer simulations results. A quarter wave cavity has also been built to study tuners and seals under vacuum and rf power.

2 COMPUTER MODELING

The main cavity body geometry for the SNS RFQ has been developed with Superfish. With the adoption of the PISL stabilizer scheme, the structure has also been analyzed for mode separation and stabilization. The insertion of the stabilizer bars has the twofold effect of lowering the resonance frequency of the quadrupole mode and of raising the frequency of the degenerate dipole mode. A family of MAFIA simulations, summarized in Fig. 1, shows the effect of the stabilizer rods on both the quadrupole and the dipole modes as a function of the rods' spacing.

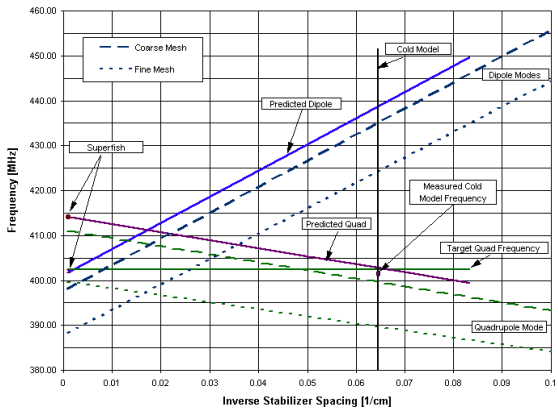

Figure 1 – Computer analyses of the quadrupole and dipole modes as a function of stabilizer spacing.

As a result of these analyses, the spacing between each set of stabilizers has been chosen to be 15.5 cm, from a horizontal pair to a vertical one (and vice-versa). This resulted in a predicted quadrupole mode shift of –11 MHz and of the dipole modes of +36 MHz. These effects were factored in the main frequency calculations performed with Superfish to determine the reference shape of the cavity. The measurements on the cold model proved the validity of this method.

3 COLD MODEL

A full size, 93 cm long RFQ cold model has been built, representing one quarter of the actual length of the full RFQ. This model is intended to validate the computer studies performed and to help defining the geometry to a better degree of accuracy than is achievable with MAFIA.

The model is made of aluminum, with a hard (acid) copper plating to guarantee a stable and strong surface to make good rf contacts between adjacent quarter sections. A picture of the cold model is shown in Fig. 2. This model has all vacuum penetrations, power coupling ports and tuner ports, but it is not built to operate under vacuum or with substantial rf power. Piston tuners are also provided,

* This research is sponsored by the Lockheed Martin Energy Research Corporation under the U.S. Department of Energy, Contract No. DE-AC05-96OR22464, through the Lawrence Berkeley National Laboratory under Contract No. DE-AC03-6SF00098

as well as adjustable end flanges to properly define the tuning of the vane ends. A set of six π-mode stabilizers, three in the horizontal and three in the vertical plane, is installed to validate the mode separation analysis.

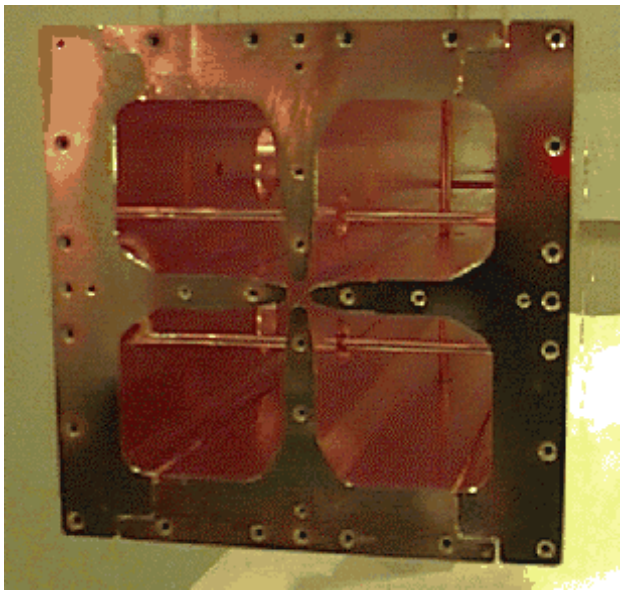

Figure 2 - The Cold Model Cavity

A computer based motion control and data acquisition system has been used to perform field perturbation measurements with the well known bead-pull method. The setup has been modified from the existing structure that was used at LBNL to map the higher order mode structure of PEP-II cavities [4]. In order to be able to observe both the H and the E fields, a set of four alumina spheres were run along the vane tips, whereas a set of four aluminum beads were run along the wall of each quadrant. To accomplish this, four motors were employed, with each motor servicing one quadrant and controlling one dielectric and one metallic bead.

The data acquisition system, based on the IGOR commercial software package running on a Macintosh platform, controls the motors via the RS232 bus. The program determines the bead positions and ensures that only one bead is inside the cavity at any given time. An HP8510 network analyzer is used to perform the S21 measurement that is used to observe the effects of the beads on the cavity. The instrument is software controlled via the GPIB bus which allows also for the transfer of the acquired data to the computer. Data analysis is later performed using separate software.

4 COLD MODEL TEST RESULTS

The perturbation measurements allowed the validation of the chosen cavity geometry. The waveguide cut-off frequency was found at 402.18 MHz, close to the required 402.5 MHz frequency. The tuners will bring the cavity to the operating frequency. This means that the cavity cross-sectional dimensions do not need to be changed, given the chosen stabilizer bars spacing. Figure 1 shows the measured quadrupole mode in comparison with the results from computer simulations.

Quadrant perturbation tests were performed using the available 12 tuners with the goal of judging the quality of the π-mode stabilization. The perturbation of one quadrant by 1.53 MHz changes the azimuthal field symmetry by less than 2.7 %. This satisfactory result finalized the current stabilization scheme.

Another important result obtained from the cold model perturbation measurements is the tuning of the end plates. The vane to end plate capacitance is balanced against the inductance of the vane undercut at a resonant frequency of 402.5 MHz that matches the cut-off frequency of the wave guide. With the help of detachable vane ends of various length it has been possible to find the optimum vane termination geometry.

The overall performance of the tuners was also verified. By moving all twelve tuners to their fully inserted and fully extracted position, a total tuning range in excess of 2 MHz was measured.

5 HOT MODEL

The hot model is designed to test rf sealing configurations on fully annealed OFE copper as well as tuner designs. To accomplish these tasks a quarterwave geometry was chosen for its simplicity and ease of fabrication. The cavity is designed to reach peak surface currents of the same density as the ones reached in the RFQ walls. This implies that the cavity operate under vacuum and be capable of taking a 6% duty factor rf high power pulse.

The cavity is powered by a tetrode-based 15 kW peak power amplifier, the components of which were provided by LANL. Using the energy stored in a capacitor bank, the system will run at a 1 ms long pulse with 60 Hz repetition rate, thus matching the operating conditions of the SNS RFQ.

The less than 1 kW average power is removed from the cavity by a spit-tube flooding the inner conductor of the resonator. The power coupling loop is also cooled in its outside wall.

The rf sealing geometry is designed to allow for testing of several types of seals. In particular, a copper-to-copper configuration was compared to sealing techniques based upon indium or tin. The hot model cavity is shown in Fig. 3.

Figure 3 - The Hot Model Cavity

The rf tuner is designed to help optimizing the piston. Clearance gap, moving rf contacts and vacuum sealing techniques will be tested under power.

6 HOT MODEL TEST RESULTS

The hot model measurement program is still underway. So far, the low level measurements have been completed.

The cavity quality factor Q has been calculated by measuring the reflection coefficient as seen on the optimally matched power coupling loop. These measurements showed no improvement in the rf performance of the cavity by adopting an indium or a tin seal. The observed values are listed in Table 1.

Configuration	Quality Factor Q
Calculated (Sfish)	4600
Cu-cu	4160
In	4140
Tin	4125

Table 1 – Rf seal measurements results.

The good performance of the copper-to-copper seal led to the decision to adopt it as the baseline in the first RFQ test module currently under design. This avoids the problems associated with using a metal seal on the fully annealed OFE surfaces and allows for the use of a rubber elastometer as the main vacuum seal.

The cavity is going to be powered soon to develop the tuner design. This phase will also allow to validate the adopted rf seal.

7 STATUS

The final dimensions of the RFQ cavity, including the vane undercuts and end plate positions have been determined and finalized aided by the measurements performed on the cold model. The bead-pull setup is now available for use to characterize the fields and assembly accuracy during the cavity manufacturing, assembly and brazing processes.

The baseline rf and vacuum sealing design has been established and will be tested in the hot model power tests that are soon to begin. These tests will also allow the conceptual development of the rf tuners.

8 ACKNOWLEDGMENTS

The authors would like to acknowledge the support received from the Beam Electrodynamics Group at LBNL, who made available the bead-pull test laboratory and provided the hardware used in the measurements. John Corlett, Bob Rimmer and John Byrd also contributed with their extensive experience in the field of cavity design and measurements.

9 REFERENCES

[1] J. Staples, et al, “The SNS Front End Accelerator Systems”, Paper MO4056, LINAC98, August 1998, Chicago, IL USA

[2] A. Ratti, et al, ”Conceptual Design of the SNS RFQ”, Paper MO4090, LINAC98, August 1998, Chicago, IL USA

[3] A. Ueno, et al, “Beam Test of the Pre-Injector and the 3-MeV H- RFQ with a New Field Stabilizer PISL”, LINAC96, August 1996, Geneva, CH

[4] D. A. Goldberg and R. A. Rimmer, “Automated Bead Positioning System for Measuring Impedances of RF Cavity Modes”, Proc. US PAC, Washington DC, May 17-20th 1993.

DESIGN OF A CHARGE-STATE MULTIPLIER SYSTEM FOR THE RIKEN RI-BEAM FACTORY

O. Kamigaito, A. Bandyopadhyay, M. Kase, Y. Miyazawa, T. Chiba,
M. Hemmi, S. Kohara, E. Ikezawa, A. Goto, and Y. Yano,
The Institute of Physical and Chemical Research (RIKEN),
Wako-shi, Saitama, 351-0198 Japan

Abstract

In the RIKEN RI-beam factory project, a Charge-State Multiplier system (CSM) is planned to be placed between the existing heavy ion linac (RILAC) and the ring cyclotron (RRC). It consists of an accelerator, a charge stripper and a decelerator. The accelerator section increases the stripping energy further and the decelerator section brings the beam energy down to the initial value. By use of this system, the charge-to-mass ratio (q/A) of the heavy-ion beams will be increased so that the ring cyclotrons can accept the beams without changing the injection radius of the RRC. For the accelerator and decelerator sections, drift tube linacs of variable-frequency type will be used, whose rf-frequency is varied from 36 to 76 MHz. The total accelerating voltage required for the accelerator section is about 26 MV and that for the decelerator section is about 13 MV. Initial design of the low energy part of the CSM, based on a quarter wavelength resonator with a movable shorting plate, is described in this paper.

1 INTRODUCTION

In the on-going RI-beam Factory project[1], a cascade of a K930-MeV ring cyclotron (IRC) and a K2500-MeV superconducting ring cyclotron (SRC) will be constructed as an energy booster of the existing K-540 ring cyclotron (RRC). The final energy will be increased up to 400 MeV/u for light ions such as Oxygen and 150 MeV/u for Uranium with this new cyclotron system. As the injector for the accelerator complex, the existing heavy-ion linac (RILAC) will be used, whose pre-injector has been recently upgraded[2]. The intended beam intensity is 1 pμA for light ions and 100 pnA for heavy ions.

For very heavy ions, a charge-stripping process is necessary before the RRC so that the cyclotrons can accept the beams by reducing the magnetic rigidity. There is, however, a significant problem that the beam energy from the RILAC is too low to provide the required charge state with the existing charge-stripper between the RILAC and the RRC.

We illustrate this problem in Fig. 1 by taking the case of Uranium acceleration as an example. If the beam is accelerated to 150 MeV/u with the SRC, the corresponding rf-frequency and the output energy of the RILAC are 27.2 MHz and 1.48 MeV/u, respectively. To be accepted in the IRC and the SRC, the charge state must be at least 58^+. The most probable charge state at this energy is, however, 42^+ and the production rate of 58^+ is almost zero[3].

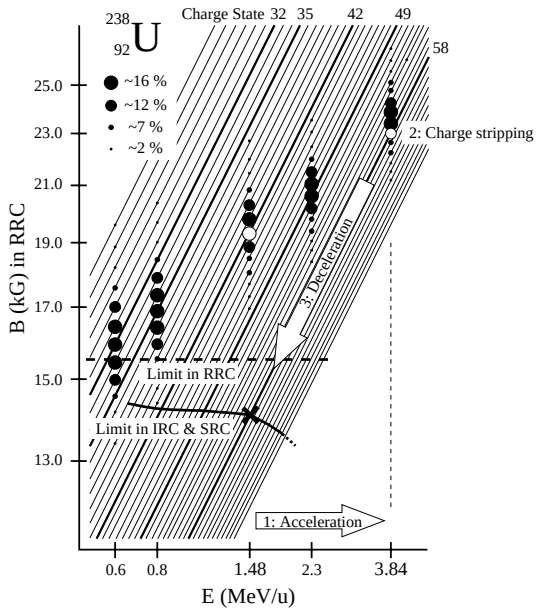

Figure 1: Principle of the CSM. The size of the dots corresponds to the production rate of Uranium ions with respective charge state at the stripping energy, E, when using a carbon foil for the stripper. The ordinate represents the necessary bending power in the RRC. The bending limit in the IRC and SRC is also indicated.

The proposed method[1] to solve this problem is also described in Fig. 1. The output beam from the RILAC is accelerated further up to 3.84 MeV/u. After charge-stripping at this energy, where the production rate of 58^+ is sufficiently high, the obtained ions are decelerated to the initial energy. It should be noticed that the injection radius of the RRC need not be changed because the input speed remains the same. This is the principle of the Charge-State Multiplier (CSM) system.

The CSM consists of an accelerator, a charge-stripper, and a decelerator as described above. Several designs have been proposed for the drift tube linacs used in the

accelerator and the decelerator sections[4,5]. In the recent design[5], four accelerating tanks and two decelerating tanks are proposed, where 16 or 18 gaps are included in each tank. The resonator is based on the Interdigital H-mode (IH) structure with a movable shorting plate, whose rf-frequency is twice the fundamental frequency. In order to put the whole CSM in a present experimental room, the maximum gap voltage is chosen to be 430 kV. However, the power consumption per tank is estimated to exceed 100 kW and the calculated current density reaches 90 A/cm on the sliding contact around the corner of the ridge of the IH structure. This design has another problem that the tank becomes too long to make the structure rigid especially in the high energy part.

2 CSM DESIGN

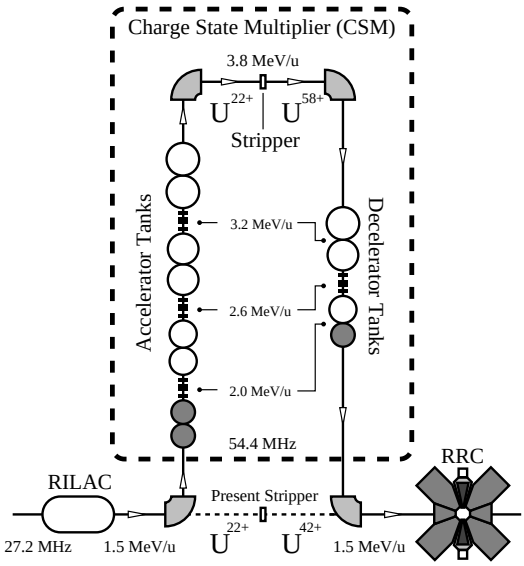

Figure 2: Schematic layout of the CSM. The energies at the fundamental frequency of 27.2 MHz are also indicated.

Figure 2 shows the schematic layout of the present configuration of the CSM. We plan to put eight tanks in the accelerator and four tanks in the decelerator. The tanks are independently operated at the doubled frequency of the fundamental one, which means that the required frequency for the CSM ranges from 36 MHz to 76 MHz. The synchronous phase of the accelerator tanks has been chosen to be -25° while that of the decelerator tanks has been 25°, in order to maintain the longitudinal focusing in the tanks. Each tank has eight gaps in it. The maximum gap voltage is chosen to be about 500 kV. The power consumption per tank will be made less than 100 kW by adopting this configuration.

The last tank of the decelerator covers the same energy-range as the first two tanks of the accelerator. In the same way, there are a pair of accelerator tanks and a decelerator tank which work in the same energy-range. Quadrupole

Table 1: Main Parameters of the Low Energy Part of the CSM

Tank	Acc.1	Acc.2	Dec.
Frequency (MHz)	36-76	36-76	36-76
Mass to charge (m/q)	26-6	26-6	12-2.7
Input energy* (MeV/u)	1.48	1.74	2.01
Output energy* (MeV/u)	1.74	2.01	1.48
Inner length (m)	1.3	1.3	1.3
Number of gaps	8	8	8
Bore radius (cm)	1.75	1.75	1.75
Synchronous phase (ϕs)	-25°	-25°	+25°
Max. gap voltage (kV)	450	450	450
Max. power loss (kW)	50	52	50
Z_{eff} (MΩ/m)*	148	154	146
Max. current (A/cm)**	58	61	58

* : At 54.4 MHz.
**: Maximum current density on the sliding contacts.

triplets are placed between every two tanks. The total length of the accelerator and that of the decelerator will be about 16 meters and 8 meters, respectively.

Construction of the low energy part, indicated by the hatched circles in Fig. 2, has started and the mechanical design of the resonators is under progress. The main parameters are listed in Table 1. The output energy of the accelerator section of this part is 2 MeV/u at the fundamental frequency of 27.2 MHz.

The resonator of the low energy part is based on a quarter-wavelength resonator of circular cylinder, as shown in Fig. 3. All the three resonators have the same dimensions except for the drift tubes and their stems. The resonant frequency is changed by a movable shorting plate. The rf-power is fed through a capacitive feeder. A capacitive tuner is used for the fine tuning of the frequency.

The rf-characteristic of the resonators has been studied with the MAFIA code[6]. The size of the coaxial part as well as the shape of the stems for the first and final drift

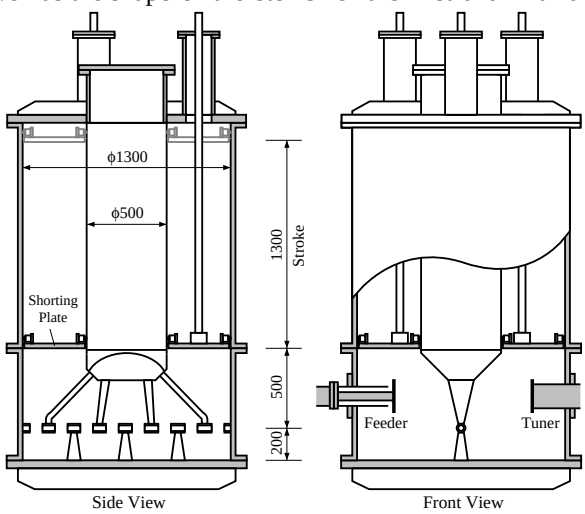

Figure 3: Schematic drawing of the resonator.

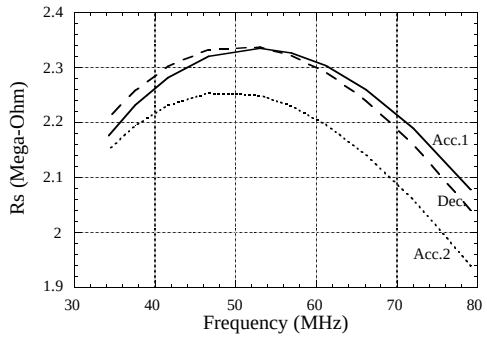

Fig. 4: Shunt impedances of the tanks of the low energy part. The solid, dotted and dashed curves represent the impedance of the first, second and the last tank of the CSM, respectively.

tubes are optimized so that the current density on the sliding contact could be as small as possible.

The calculation predicts that a stroke of 1300 mm of the movable shorting plate covers the required frequency-range from 36 to 76 MHz in the three tanks. The current density on the sliding contacts is estimated to be 60 A/cm at the maximum gap voltage of 450 kV.

Figure 4 shows the calculated shunt impedances. The shunt impedance R_s is defined in this paper by $V^2/(2P)$, where P is the rf-power consumption and V is the peak value of the gap voltage. From this result, the maximum power loss is calculated to be about 50 kW per tank. The calculated Q-values are about 30000 and they are almost constant in the frequency range.

The actual shunt impedances of the resonators will be less than the calculated ones mainly due to the sliding contacts used around the stem. Therefore, we are planning to construct the amplifiers whose maximum power is 100 kW in the required frequency-range.

Cooling is one of the most important problems in these resonators. According to the calculation, the power loss in the stem for the end drift tube is 9 kW at the maximum gap voltage. The arrangement of the cooling channels is under design based on the heat analysis.

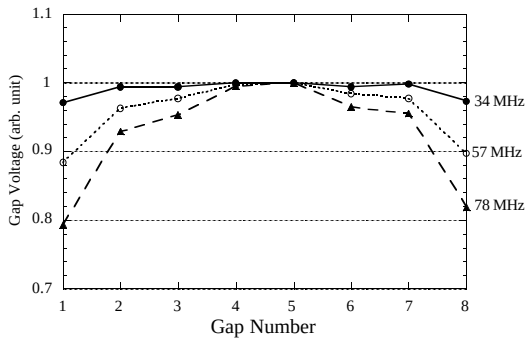

Fig. 5: Calculated gap voltage of the second tank of the CSM.

The voltage distribution is not flat along the accelerating cells in these resonators, particularly in the high frequency region. A calculated example is shown in Fig. 5 for the second tank. As shown in the figure, the gap voltage at the end cells is about 80 % of that of the inner cells at the highest frequency. The effect of this voltage distribution on the beam transmission has been estimated with a first-order calculation. According to that, the transmission will be good enough when the average gap voltage is larger than the designed voltage.

3 SUMMARY AND OUTLOOK

A design for the CSM has been proposed consisting of eight accelerator tanks and four decelerator tanks, independently operated in the frequency range from 36 MHz to 76 MHz. Three tanks of the low energy part of the CSM are under design based on a quarter-wavelength structure of circular cylinder with a movable shorting plate.

The construction of the low energy part will be completed in 1999. The three tanks will be installed and tested in the beam line between the RILAC and the RRC in the same year. The rest of the CSM tanks will be designed and constructed based on the test of the low energy part.

In parallel with the resonator design, study on the charge-stripper should be done, which can withstand the intended high intensity beams.

4 ACKNOWLEGDEMENT

The authors are grateful to Dr. M. Tomizawa at KEK for informative discussions and valuable comments on beam dynamics as well as on IH structures.

5 REFERENCES

[1] Y. Yano et al., “RIKEN RI-Beam Factory Project,” Proceedings of PAC97, TRIUMF, May 12-16, 1997, in press.

[2] O. Kamigaito et al., “Recent Developments of the Folded-Coaxial RFQ for the RILAC,” in this proceedings.

[3] K. Shima et al., *Atomic Data & Nuclear Data Tables.* **51**, 173 (1995).

[4] M. Tomizawa, RIKEN Accel. Prog. Rep. **29**, p.228 (1995).

[5] A. Bandyopadhyay et al., RIKEN Accel. Prog. Rep. **31**, p.203 (1997).

[6] The MAFIA collaboration, User's Guide MAFIA Version 3.2, CST GmbH, Lauterschlaegerstrasse 38, D-64289 Darmstadt, Germany.

THE PRESENT STATUS OF DEVELOPMENT ON SUPERCONDUCTING CAVITIES AT SHI

Y. Matsubara, M. Hirose, T. Hori, H. Saito*, F. Yukawa**
H. Inoue***, M. Ono***, E. Kako***, S. Noguchi***, K. Saito***, T. Shishido***

Research and Development Center, Sumitomo Heavy Industries, Ltd. (SHI)
2-1-1, Yato-Cho, Tanashi-City, Tokyo 188-8585 Japan
*Quantum Equipment Business Center, Sumitomo Heavy Industries, Ltd. (SHI)
5-2, Soubiraki-Cho, Niihama-City, Ehime-Ken, 792-8588 Japan
**Sumiju Technical Center Co., Ltd. (STC).
1-2, Kuryoutsutsumi, Hiratsuka-City, Kanagawa-Ken, 254-0801 Japan
***High Energy Accelerator Research Organization (KEK)
1-1, Oho, Tukuba-City, Ibaraki-Ken, 305-0801 Japan

Abstract

We have started development on superconducting cavities with KEK from 1997. First, we checked out the effect of removal thickness with electropolishing (EP) . In the results, We could obtain the maximum accelerating field of 32MV/m by a repeatedly small removal thickness (30μm) up to 150 μm material removal. Next, when fabricating the second, we directly removed as much the thickness as the optimized depth by the first cavity using heavy chemicalpolishing (CP) and final light EP in sequence. We are now in the stage of fabricating the third one, 3-cell cavity. In this paper, we report on these results and activities at Sumitomo Heavy Industries, Ltd.

1 INTRODUCTION

Last year, We set up three purposes as follows. First; fabricating a single-cell L-band niobium cavity to study surface treatment, and testing it to learn many operating systems in this fields. Second; fabricating multi-cell cavities by our own technics. Third; design and fabrication of a cryo-module.

On the first step, we have acquired two important data, namely, superiority of EP [1] and hydrogen Q-disease [2]. For the former, it showed the good relationship between an amount of removed thickness and accelerating gradient(Eacc), which could be obtained with only EP as surface treatment. Finally, the cavity obtained 32MV/m of gradient. For the latter, we checked out hydrogen Q-disease with our first fabricated cavity SHI-3. This cavity surface was removed 130μm in depth with CP. Annealing was not practiced for this cavity. After the first vertical test, the cavity was kept at 100K for two hours. Before and after this process (holding 100K) , the performance almost unchanged.

On the second step, we needed to check out the proper welding condition on niobium by our electron beam welding (EBW) machine, because of the different conditions from KEK's. Then, we applied our own conditions to single-cell and 3-cell cavities .

The all fabricated cavities are named individually as shown in Table 1. SHI-1 which was fabricated at KEK was applied to study the relationship between the removed thickness by EP and maximum gradient of the cavity. SHI-2 was only used to optimize EBW condition. For SHI-3 without annealing and mechanical treatment, it was used to investigate hydrogen Q_disease. SHI-4 is a 3-cell cavity and under fabrication at SHI factory.

Table 1: List of fabricated cavities.

Name	# of cell	Factory	Remarks
SHI-1	1	KEK	Investigate effect of EP :max. E_{acc}=32MV/m
SHI-2	1	SHI	Researching only EBW condition .
SHI-3	1	SHI	Investigate anneal effect :max. E_{acc}=7.3MV/m
SHI-4	3	SHI	Not measured

2 SURFACE TREATMENT ON SHI-1

The purpose of SHI-1 cavity was to study the dependence between the cavity performance and the removed thickness with EP. A similar relationship was already studied by P. Kneisel et al. using CP [3]. First, a light chemical polishing (20μm) was carried out on this cavity to remove the contaminated surface layer, and then annealing at 760° was done to prevent the hydrogen Q-disease. After that , the performance of this cavity was measured with adding a light EP(30μm) and high-pressure water rinsing (HPR) repeatedly. The experiments were continued until 210μm removed thickness. These experimental data are shown in Figures

1~3. All tests were executed using the KEK's vertical measuring system.

X-ray was detected at the 1st, 3rd and 4th measurements in Figure 1. X-ray was observed over the higher gradients than 16MV/m at 3rd and 4th. This radiation should be due to field emission by the reason that the relative X-ray intensity is enhanced in accordance with increasing field gradient.

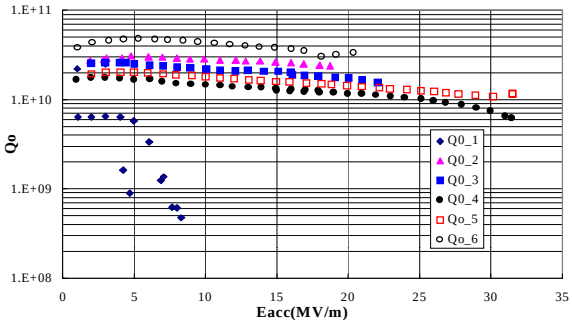

Figure 1: Q_o vs. E_{acc} at SHI-1 cavity.

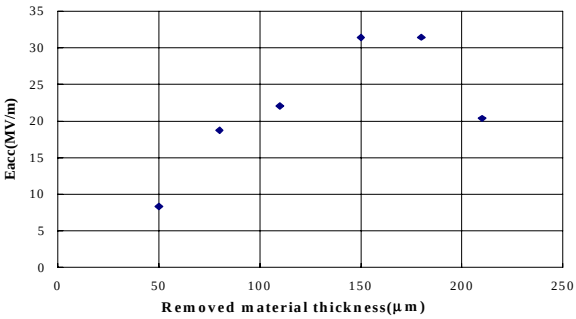

Figure 2: E_{acc} vs. removed thickness on SHI-1 cavity.

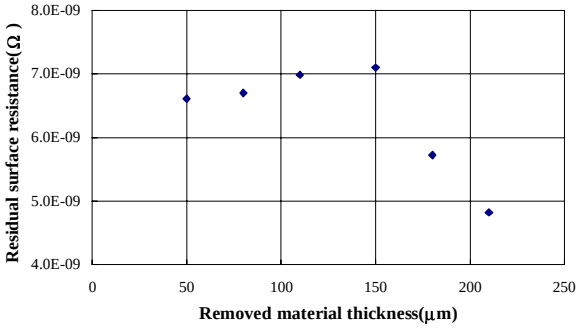

Figure 3: Residual resistance vs. removed thickness on SHI-1 cavity.

This cavity had a large pit (diameter: ~600μm) and many tiny pits (diameter: ~50 μm) on the initial stage. The tiny pits have gradually vanished with adding EP. The field gradient increased with adding 30μm EP until 150μm as shown Figure 2. At the 5th measurement (the removed thickness was in total 180μm), the performance just kept the same value as the case of 150μm removing and X-ray was not observed. After the 5th measurement, we inspected the inner surface of SHI-1 cavity and confirmed that the tiny pits have almost vanished except the large one.

Although we did not measure the temperature mapping, it is considered that the maximum performance at 6th measurements was limited by the pit. The magnetic field strength on the inner wall at 32MV/m is shown in Figure 4. At the 6th measurement (the removed thickness was in total 210μm), Eacc decreased to 20.5MV/m and X-ray was not observed. By the inspection after 6th measurement, we found the existence of many tiny pits similar to the initial stage. It might be due to EP processes.

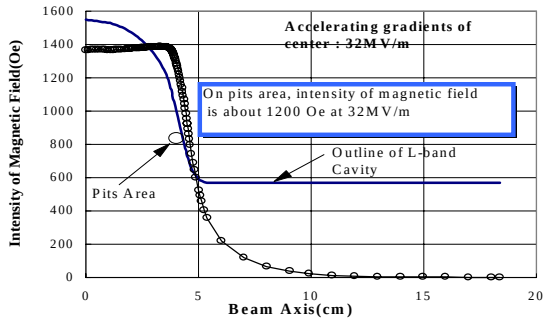

Figure 4: Distribution of magnetic field on the wall at 32MV/m on the axis.

3 SHI-3 CAVITY

3.1 Fabrication And Surface Treatment

We started fabricating a L-band single-cell cavity by our own factory while measuring SHI-1 cavity. First, we optimized an appropriate EBW condition with Nb flat sheets (thickness: 2.5mm) by our EBW machine(Table 2), and next, with beampipes (inner diameter: ϕ76mm, thickness: 2.5mm, length: 40mm). Then, we assembled SHI-2 cavity with two half-cells and two beampipes. SHI-2 got a small hole on the one iris EBW seam, because of the high electron beam currents. After modifying the EBW condition, we finished the assembling of SHI-3.

Table 2: Current condition of EBW

SECTION	VOLTAGE(kV)	CURRENT(mA)
Iris	150	14
Equator	150	16
Machine: JE-114 : Osaka henatsuki , Ltd. : Beam power-15KW (150KV- 100mA)		

Although the EBW is not perfectly optimized, our current condition is shown in Table 2. From the results of SHI-1, we decided the optimum removed thickness as 150-180μm to obtain over 30MV/m of high gradients. The subjects of SHI-3 were testing the high gradients and making sure of a hydrogen Q-disease without

annealing. The treatments on SHI-3 are shown in Table 3.

Table 3: Surface treatments on SHI-3 cavity.

No	Treatment	Method	Remarks
1	Pre_polishing	CP	130 μm
2	Final polishing	EP	30 μm
3	Cleaning 1	HWMR*	80°C / 90min.
4	Cleaning 2	HPR	8.3 MPa / 90min.

* : Hot Water with Megasonic Rinsing

3.2 Measurement Results of SHI-3

The measurements were carried out twice on the cavity. First cooling was to check out SHI-3 cavity performance after our treatment. After that, SHI-3 was kept constant temperature at 100K for two hours to make sure of a hydrogen Q-disease. From the second measurement, Q-degradation did not observed as shown Figure 5. A hydrogen Q-disease might not happen by removing sufficient amount with CP before light EP. We showed have to study the process of making Nb sheets and aging effect on the material properties.

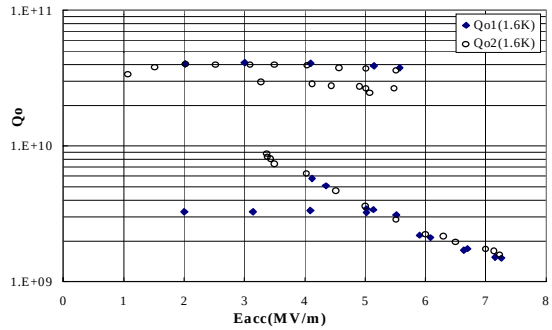

Figure 5: Q_o vs. E_{acc} at SHI-3 cavity.

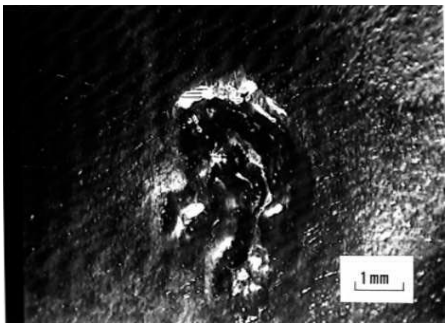

Figure 6: Equator defect found on SHI-3.

The Qo vs. Eacc curve in Figure 5, we can observe that Qo was switched to the lower level after the first quench at 5.7MV/m. The maximum Eacc was limited at 7.4MV/m. On the reverse process when decreasing Eacc from 7.4MV/m, Q jump did not appear at 5.7MV/m and kept the lower values. I suppose that this phenomenon is related to two defect. Through the inspection after measurement, we discovered a big defect on nearly the equator portion as shown in Figure 6. At the time of assembling, no such defect had been found.

4 FABRICATION OF A 3 CELL CAVITY

The manufacturing of a 3 cell cavity (SHI-4) has just been finished. Whole view is in Figure 7. This will be cold testing soon.

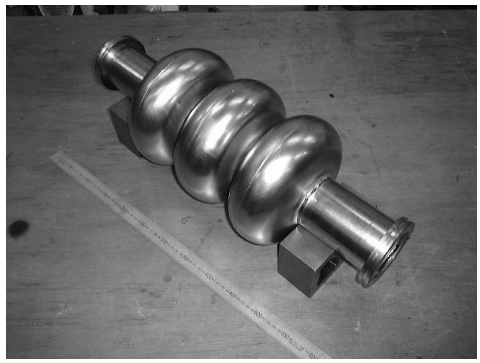

Figure 7: Overall view of 3 cell-cavity.

5 SUMMARY

We obtained the dependence of accelerating gradient upon an amount of removed thickness using EP. The optimum removal by EP to get high gradient is in over 150μm. In case of using a large amount of CP, annealing process for hydrogen degassing does not always need to avoid hydrogen Q-disease.

ACKNOWLEDGMENTS

The authors would like to thank Mr. N. Yasumitsu, Y. Kumata and K. Sawada at SHI, Mr. T. Minakuchi and Y. Tateishi at STC, and Mr. Shiratake at Nomura Techno Research Co. Ltd. for helpful discussions and their supports.

REFERENCES

[1] K. Saito et al. “Superiority of Electropolishing over Chemical Polishing on High Gradients” Proc. 8th Workshop on RF Superconductivity, 1997.

[2] K. Saito and P. Kneisel “Q_o-degradation Due to Hydrogen in High Pure Niobium Cavities” Proc. 18th Linear Accelerator Meeting in Japan, 1993.

[3] E. Mahner, P. Kneisel, N. Pupeter, G. Muller “Effect of Chemical Polishing on the Electron Field Emission of Niobium Samples and cavities” Proc. 7th Workshop on RF Superconductivity, 1995.

RF TESTS ON THE INITIAL 2.8m SECTION OF THE 8m LONG ISAC RFQ AT TRIUMF

R. L. Poirier, P. Bricault, G. Dutto, K. Fong, R. Laxdal, A. K. Mitra, B. Uzat
TRIUMF, Vancouver, B. C., CANADA

Abstract

The ISAC RFQ is an 8 meter long, 4-rod split-ring structure operating at 35 MHz in cw mode. The rods are vane-shaped and are supported by 19 rings spaced 40 cm apart. The rings are unique in that the rf surfaces have been structrurely de-coupled from the mechanical support structure to improve dynamic stability. An initial 2.8m section of the accelerator (7 of 19 rings) was installed and aligned in the 8m, square cross-section, vacuum tank to allow rf and beam tests to be carried out. The stringent, +/- 0.08 mm, quadrature positioning tolerance of the four rod electrodes was practically achieved and a relative field variation along the 2.8 meter of the RFQ was measured to within +/- 1%, using the standard bead pull method, signal level measurements gave a frequency of 35.7 MHz, a Q of 8700 and a resonant shunt impedance of 292 k Ω.m. Compared to the initial 3 ring prototype, this represents a 21% increase in Q and a 30 % increase in shunt impedance. The seven ring section has been successfully tested with beam at full power.

1 INTRODUCTION

The accelerating system of the ISAC radioactive ion beams facility consists of an RFQ and a post - stripper DTL. Ion beams with A/q $\leq$ 30 from the on line mass separator will be accelerated from 2 keV/u, to 150 keV/u through the RFQ and then to an energy up to 1.5 MeV/u through the DTL structure. The low charge-to-mass ratios of the ions dictate a low operating frequency to achieve adequate transverse focusing, and cw operation is required to preserve beam intensity. The reference design [1] for the RFQ is a four rod split ring structure operating at 35 MHz. The RFQ accelerator section is 8 meters long and is designed in 40 cm long modules with a peak potential between the electrodes of 74 kV. Full power tests on a single module [2] and on a three module assembly[3] enabled us to complete the basic electrical and mechanical design for the RFQ accelerator. The theodilite intersection method[4] was used to align two platen bases in the tank to allow 7 of the 19 rings to be installed in the first section of the 8m long vacuum tank. The alignment of the ring assemblies on the platens was accomplished by the same method. Because of the manufacturing procedures and alignment philosophy adopted [4], when the electrodes were installed on their mounting surfaces they were aligned by default with no shimming required. Figure 1 shows the vacuum tank installed on the concrete mounting pad in the accelerator building with seven rings assembled. The coupling loop, which was tested in the prototype test facility for 100 hours at 40 kW, was installed and used to feed the rf signal for calibrating the monitoring probes. The inside groove on the tank flange is for an rf spring contact.

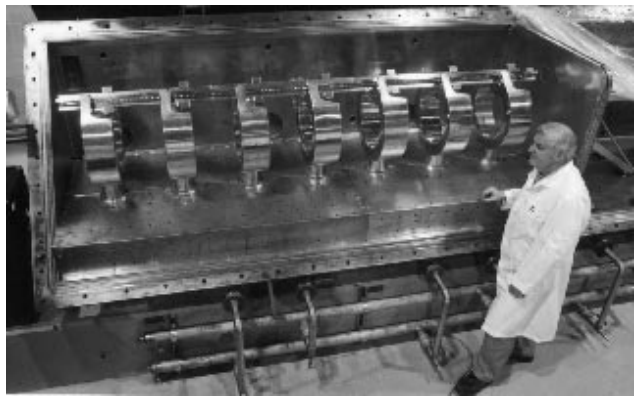

Figure 1. Seven rings assembled, installed and aligned in the bottom section of the vacuum tank

2 SIGNAL LEVEL TESTS

2.1 Frequency, Q and Shunt Impedance Measurements

The frequency and Q are measured with a network analyzer and the shunt impedance is derived from two independent R/Q measurements; ΔC method and input admittance method [5]. The input admittance of a parallel resonant circuit when plotted against frequency, produces a V-curve in the vicinity of the resonance. R/Q can be obtained from the slope of such a curve and is given by the equation,

$$R/Q = (2/f_o)*df/dy \quad (1)$$

where f_o = resonant frequency, dy = change in input admittance and df = corresponding change in frequency.
It can also be shown that R/Q is related to the change in frequency with change in capacitance and is given by the equation

$$R/Q = (1/pi*f_o)* df/dc \quad (2)$$

Results are compared to MAFIA calculations in table 1.

Table 1. Comparison of measured values to calculated MAFIA values.

Parameter	MAFIA	Measured
Frequency (MHz)	34.7	35.7
Q	15175	8700
R_{shunt} (k-ohms)	174.9	104.4
R_{shunt} (k-ohms-m)	489.9	292.3
R/Q	11.53	12.0
Capacity (pfd/m)	142	132.6

Because of the size of the mesh used in the MAFIA calculations one would expect the calculated MAFIA frequency to be lower than the measured frequency.

2.2 Bead-pull measurements

The first set of bead pull measurements were made with a set of test electrodes made of aluminum with a radius of r_o and no modulation. Because the electrodes have no shoulder to rest the dielectric bead on when measuring the lower gap, the sagging of the bead was overcome by fabricating a bead carriage from Teflon that traveled down the centre bore of the RFQ and was captured by the tips of the four electrodes. Five bead pull runs were made for each set of measurements; carriage only and four separate runs with the dielectric bead in each of the four quadrants. The carriage only run was used as the average perturbation reference and the other four runs corrected accordingly.

Both the average peak field variation and the quadrupole field asymmetry were deduced from the measurements and are shown in figure 2. The results are within the target of +/- 1% field strength variation.

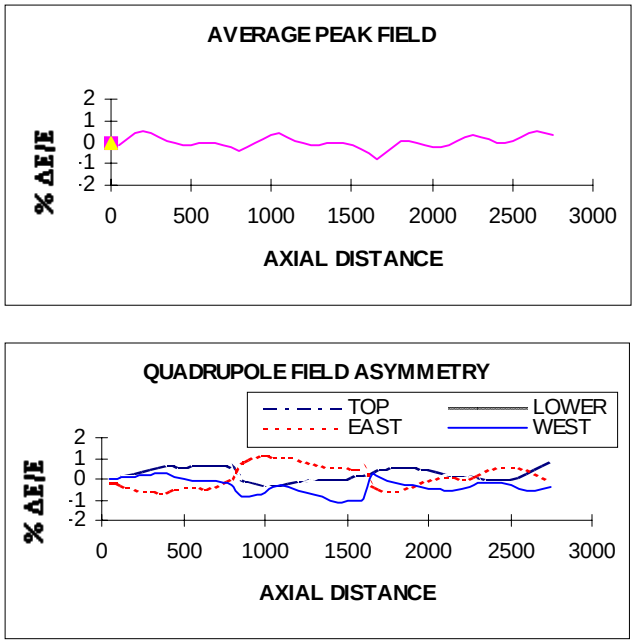

Figure 2. Average peak field and quadrupole field asymmetry for the non-modulated electrodes.

A similar set of results is shown in figure 3 for the copper electrodes with modulation. Because of the modulation, the teflon carriage for these bead pull measurements was guided by the straight edges of the electrodes. There is only one small area where the variation is slightly beyond the target of +/- 1%.

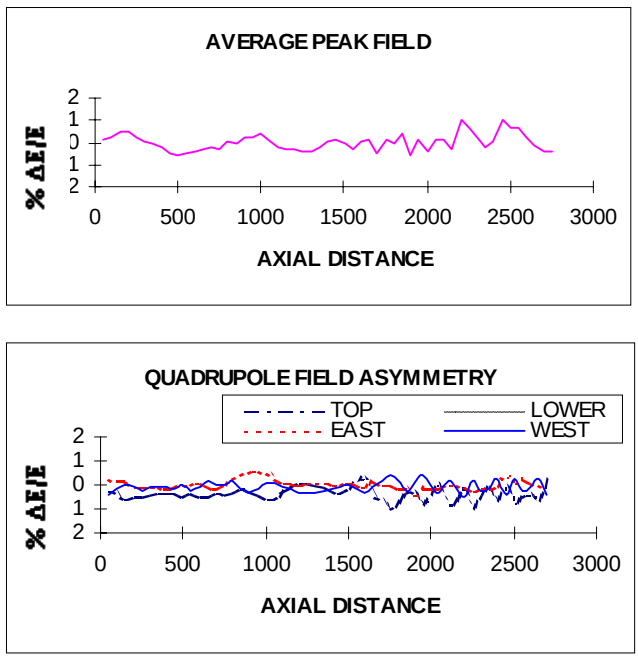

Figure3. Average peak field and quadrupole field asymmetry for the modulated electrodes.

3 FULL POWER TESTS

In preparation for full power tests the RFQ tank was baked out for three days at 60° C by uniformly mounting eighty-four 500W heaters on the tank walls, covered with a glass fibre blanket to contain the heat. At the same time 60 degree water was circulated through the structure cooling system. A base pressure of 1.4 *10-7 torr was achieved, which increased to 4.0*10-7 torr with full RF power applied. Although the bake-out temperature created a longitudinal growth of ~ 2.0 mm in the tank, the elasticity of the mounting system coped with this and the growth returned very close to zero at operating temperature. The RFQ tank went through several bake out cycles as we encountered a few water leaks. Initial tests were carried out at half voltage (36 kV) in order to do beam tests with N14 [6]. Following beam tests, 76 kV (2kV above design value) was achieved on the electrodes within four hours at the anticipated power level of 30 kW. The x-ray level during this time was 0.5 microseverts at 0.5m from the tank wall. We were able to maintain this condition for two hours before our first major amplifier overload occurred. Subsequently, we were never able to achieve the above voltage for the same power. A voltage versus power curve in figure 4 shows the power

requirement for three different days of operation, although it did remain at the lower power level for the beam tests with N28 [7]. The RFQ operated continuously for 15 hours at nominal voltage plus various runs for 5 and 10 hours before being interrupted by an amplifier trip. Automatic recovery from a high standing wave ratio is being incorporated in the RF controls to cut the RF drive rather than trip the amplifier.

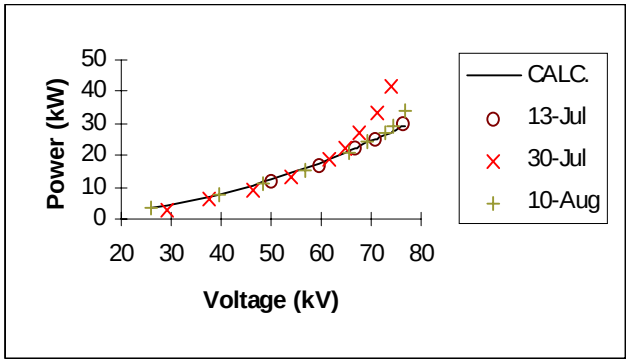

Figure 4. Voltage versus Power for the RFQ

When the lid was removed there was evidence of strong multipacting in the 7 cm gap between the RF shroud and the tank lid front wall as shown in figure 5. This could be the explanation for the additional power requirement at higher voltages. We plan to short out this gap to prevent multipacting in that region.

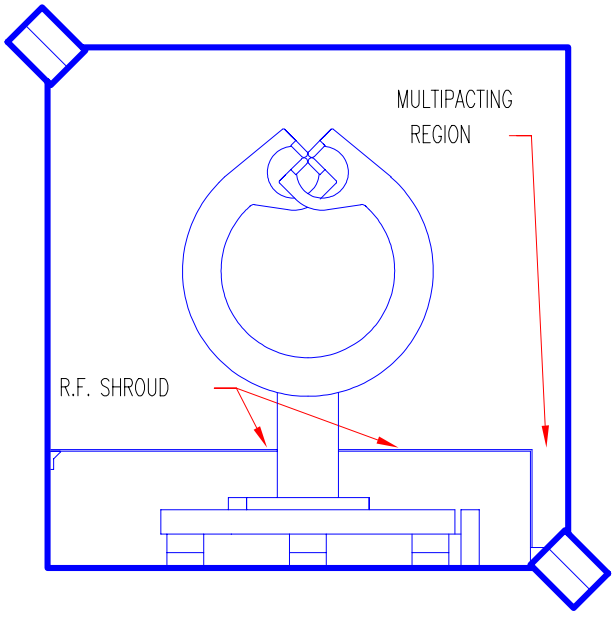

Figure 5. Cross-section schematic of RFQ tank and rings

4 CONCLUSION

Except for the increased power requirement, the RF behaved very well and agreed with the calculated predictions. The successful beam tests [7] in giving full agreement between expected and measured beam behavior (beam capture ~ 80%), indicate that the mechanical design, fabrication and alignment philosophy adopted was very successful. The remaining 12 rings will be installed in Spring 99 and commissioning of the RFQ in its final configuration by the end of 99.

5 ACKNOWLEDGMENT

We are especially grateful to Roland Roper (machine shop) who took on the responsibility of the fabrication and manufacturing details of rings, jigs and fixtures.
A special thanks to Bhalwinder Waraich for the mechanical assembly and installation of the rings, and to Peter Harmer for the organization and integration of the RFQ with all the ancillary systems.

6 REFERENCES

[1] P.G. Bricault and H. R. Schneider, "Simulation of the TRIUMF Split Ring 4-Rod RFQ with MAFIA", Proc. 1995 Particle Accelerator Conf. and Int. Conf. on High-Energy Accelerators, p1125 (1995)
[2] R.L. Poirier, P.J. Bricault, K. Jensen and A. K. Mitra, "The RFQ Prototype for the Radioactive Ion Beams Facility at TRIUMF", Proc. XVIII LINAC Conference, CERN, p405 (1996)
[3] R.L. Poirier, P. Bricault, G. Dutto, K. Fong, K. Jensen, R. Laxdal, A.K. Mitra, G. Stanford, "Construction Criteria and Prototyping for the ISAC RFQ Accelerator at TRIUMF", Proc. 1997 Particle Accelerator Conference.
[4] G. Stanford, D. Pearce, R. L. Poirier, "Mechanical Design, Construction and Alignment of the ISAC RFQ Accelerator at TRIUMF", These Proceedings.
[5] P. Bourquin, W. Pirkl and H.-H. Umstatter, "RF and Construction Issues in the RFQ for the CERN Laser Ion Source", Proc. XVIII LINAC Conference, CERN, p381(1996)
[6] R. Laxdal, et al, "Testing the ISAC LEBT and 35 MHz RFQ in an Intermediate Configuration", EPAC98.
[7] R. Laxdal, et al, "First Beam Tests with the ISAC RFQ" This conference.

DEVELOPMENT OF A RASTER ELECTRONICS SYSTEM FOR EXPANDING THE APT PROTON BEAM *

S. Chapelle, E. L. Hubbard, T. L. Smith
General Atomics, San Diego, California 92121 USA
M. E. Schulze, R. E. Shafer
General Atomics, Los Alamos, New Mexico 87544 USA

Abstract

A 1700 MeV, 100 mA proton linear accelerator is being designed for Accelerator Production of Tritium (APT). A beam expansion system is required to uniformly irradiate a 19 x 190 cm tritium production target. This paper describes a beam expansion system consisting of eight ferrite dipole magnets to raster the beam in the x- and y-planes and also describes the salient features of the design of the electronics that are unique to the expander. Eight Insulated Gate Bipolar Transistor (IGBT)-based modulators drive the raster magnets with triangular current waveforms that are synchronized using phase-locked loops (PLLs) and voltage controlled crystal oscillators (VCXOs). Fault detection circuitry shuts down the beam before the target can be damaged by a failure of the raster system. Test data are presented for the prototype system.

1 BACKGROUND

In the proposed raster-type beam expander, there will be four horizontal and four vertical raster magnets. They will be modulated so that the target is "painted" by the 1 x 2 cm proton beam in a pattern somewhat like the ones shown in Fig. 1. The pattern is achieved by modulating the vertical- and horizontal-axis magnets with triangular current waveforms at slightly different frequencies in the 500 to 600 Hz range [1]. The entire target is then irradiated in a period of approximately 20 ms.

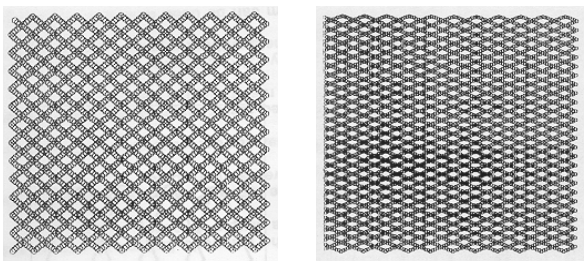

Figure 1: Sample patterns that are available by changing the ratio of the x- and y-plane rastering frequencies.

* Work supported by the DOE under contract DE-AC04-96AL89607.

An obvious requirement of using a rastered approach to beam expansion is that the beam must not be allowed to dwell on one spot of the target for very long (on the order of 0.5 ms) or else damage to the target could result. The prevention of common mode and single point failures has been a major design driver. The eight magnet systems are purposely designed to operate synchronously and independently, so that a failure of one system will not affect the operation of any other system, and therefore the beam will always be moved across the target (see Section 2.2). Fig. 2 shows the raster magnets as they fit into the high energy beam transport (HEBT) portion of the APT Linac.

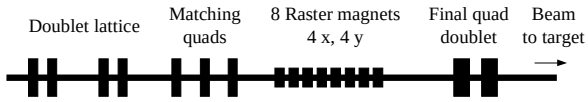

Figure 2: Raster magnets in HEBT

2 SYSTEM DESCRIPTION

The block diagram of the Raster Magnet System is shown in Fig. 3. The logical blocks of the system are the 1) Master Clock, 2) PLL/IGBT Gate Driver, 3) IGBT Modulator, 4) Raster Magnet and 5) Fault Detection Circuitry.

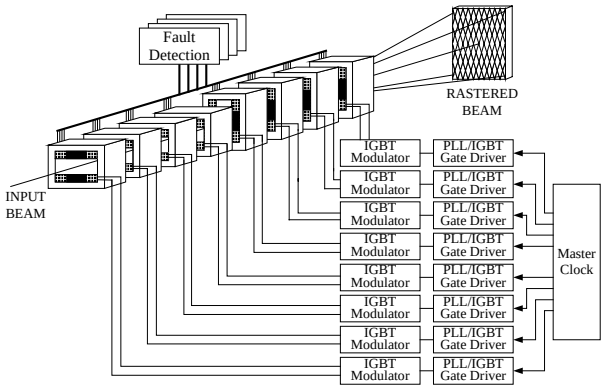

Figure 3: Raster system concept

2.1 Master Clock

The Master Clock produces two different frequencies, one for the four x-plane magnets and a second for the four y-plane magnets. The choice of frequencies is carefully made to avoid beat patterns. Important design issues of

the Master Clock are related to accurately splitting out a 1.024-MHz crystal-controlled master oscillator to two different "divide by N" circuits to drive the horizontal and vertical planes with a minimum amount of skew between the channels. The Master Clock includes on-card fault check circuitry that monitors the clocks to notify the user of a fault. The clock fault outputs are sent to four independent divisions in the Beam Enable circuitry to turn off the Linac beam before a raster system failure causes damage to the target.

2.2 PLL/IGBT Gate Driver

Each magnet gets its timing signal from the Master Clock described above. Each of the magnets has a PLL/IGBT Gate Driver that will, using a phase-locked loop, synchronize itself to the Master Clock, or else if the Master Clock fails, is able to produce its own clock so that the beam continues to be rastered onto the target. This design approach is used to preclude a common mode failure that might cause damage to the target blanket.

For this application a sequential type of phase detector, rather than an analog multiplier type, is used in each PLL to generate error signals for the VCXOs in each IGBT gate driver. The sequential phase detector results in modulator-to modulator phase errors less than about 50 ns at the rastering frequencies. The phase detector then outputs the error signal to a VCXO that varies the frequency accordingly. If the Master Clock signal fails, the VCXOs of each modulator will maintain a clock signal, although the modulators will no longer be synchronized. However, the drift is slow, allowing ample time for the fault detection circuitry to detect the problem and take action.

The PLL/IGBT Gate Driver, as the name implies, generates properly timed signals at sufficient power to directly drive the gates of the IGBTs of the modulator. Correct timing also requires that the signals sent to the IGBTs include some deadtime to ensure that two IGBTs in series are never turned on at the same time, thus avoiding shoot-through failures.

2.3 IGBT Modulator

The IGBT modulator consists of an ac/dc converter, a capacitor bank, and an IGBT H-bridge (Fig. 4). Each modulator will be powered by uninterruptible power to prevent a common mode failure due to the loss of ac input voltage. The ac/dc converter will charge up and maintain a constant voltage on the capacitor bank. Charge is drawn into and out of the capacitor bank by the H-bridge. The value of the dc output voltage of the power supply is dictated by system level requirements in that the dc voltage represents the rate of change of the current in the raster magnet inductance (V = L*dI/dt).

The dc voltage values are different for the x-axis magnets and y-axis magnets because the required peak deflections (i.e. peak B-field) differ. Final beam expansion and sizing is actually controlled by two quadrupole magnets located downstream of the raster magnets in the HEBT beamline as shown in Fig. 2. The dc capacitor bank exchanges reactive power with the magnet on a 1000 Hz timescale (twice per cycle). The IGBT H-Bridge circuit drives the raster magnets with a voltage square wave, resulting in a triangular current waveform. The timing of the IGBT gate circuit is controlled by the PLL/IGBT Gate Driver already mentioned.

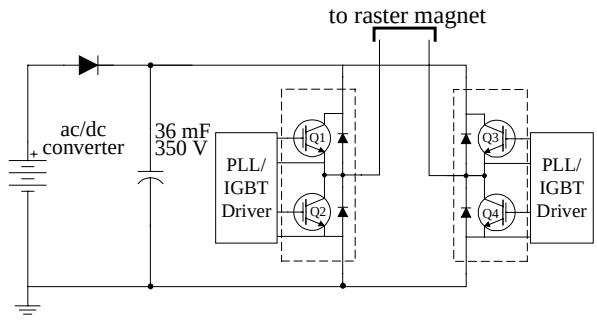

Figure 4: IGBT Modulator

The choice of IGBTs as the switches for the H-bridge was made on the basis of the operating frequency of 500 Hz and the low losses that these devices exhibit, in contrast to the choice of MOSFET switches in the system described in [2]. Freewheeling diodes are included across each switch to return the stored energy in the inductive load to the capacitor bank each half cycle, which is whenever the voltage applied to the load changes polarity. Because of this exchange of stored energy or reactive power between the capacitors and the magnet, the applied dc real power to maintain charge on the 36 mF capacitor bank is only 4% of the peak reactive power in the load, making this a very efficient system.

2.4 Fault Detection Circuit

The beam can not be allowed to stop sweeping across the target. The Fault Detection Circuit is the watchdog circuitry consisting of magnetic field and current sensors and the associated processing circuits that will check to be sure no serious failure modes exist in the Raster System. If a failure is detected, the Fault Detection Circuit removes the beam enable from the Linac, thus shutting down the beam until repairs can be made.

There are two B-dot pickup coils wound in each magnet that will have a voltage induced in them when there is a change in the magnetic field (dB/dt). Since the field is a triangular waveform, this induced voltage is essentially a square wave that can be used to detect a fault in either the magnet or the magnet drive. There are also two Rogowski current loops per magnet that will be used to measure the derivative of the triangular current. Each of these four sensors removes the beam enable signal from one of the four divisions of the Fault Detection Circuitry if it detects a fault. The beam is shut off if two or more of the four beam enable signals are missing.

2.5 Raster Magnet

The raster magnets are ferrite, 30-cm long with an 8-cm square aperture. A magnet cross-section is shown in Fig. 5. A prototype magnet has been built and tested which uses Ceramic Magnetics CMD5005 Hi-mu, low loss ferrite rather than the air core of [2]. This is a nickel-zinc material with a permeability of 4500 * μ_0 H/m at 1500 Gauss. The inductance with two 20-turn coils is 1.1 mH which produces peak fields of 640 Gauss at 100 A. From a radiation hardness standpoint, there is experience with ferrite cores as kicker magnets at Brookhaven National Laboratory that show that the ferrite material will outlast the coils.

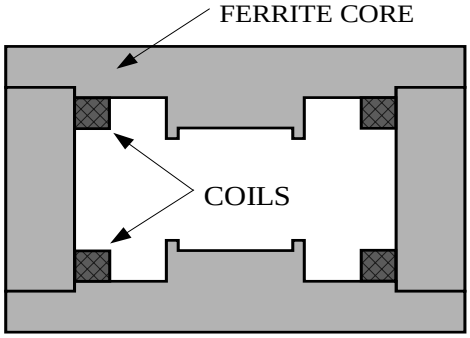

Figure 5: Raster magnet cross section

3 TEST RESULTS

A raster modulator and magnet have been successfully tested at LANL. A photo of the modulator and the resulting triangular current is shown in Fig. 6. The modulator is designed to operate at voltages up to 300 V and 1000 Hz. For this magnet with an inductance of approximately 1.1 mH, when the voltage is set to 243 V, peak operating current is +/- 100 A (59 A rms).

Figure 6: Modulator and test waveform
(+/-100 A, 500 Hz)

The output power capability of the power supply is based on the predicted losses in the load, which is the sum of the losses in the IGBT H-bridge, the cable, and losses in the magnet which include the magnet cable resistance and the magnet eddy current losses. At 243 V and 100 A peak current, the output power is essentially reactive and equal to 14,030 VARs. The measured input power (real) is only 925 Watts. With approximately 1000 joules stored in the 36 mF capacitor bank, the magnet field drops to the 1/e point in about 2 seconds if the dc charging circuit is turned off. Fig. 7 shows the raster waveforms as measured on an oscilloscope.

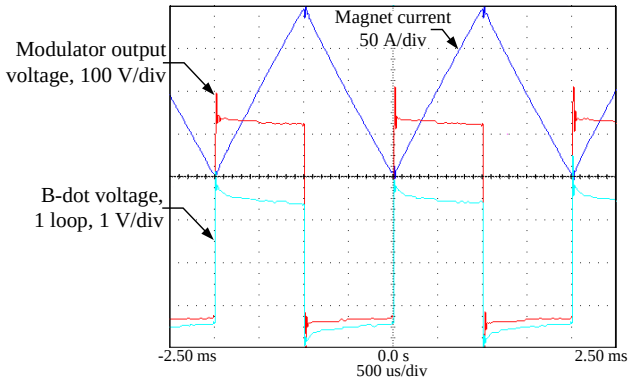

Figure 7: Measured waveforms of modulator

The spikes visible in the modulator voltage are caused by the stray inductances being switched by the IGBTs in the modulator. The peaking that is seen on the B-dot waveform, on the otherhand, has two distinguishable features:

- An overall L/R droop due to the resistance of the circuit, and
- A short overshoot of about 10% at the beginning, with a time constant of about 100 microsec. This is due to eddy currents in the coil that essentially shield part of the volume of the ferrite magnet. The voltage overshoot is thereby caused because the initial inductance is only 90% of its dc value.

4 CONCLUSIONS

A raster magnet system that is capable of safely and reliably expanding a proton beam onto the APT target has been developed and tested. Test data taken on a prototype indicate that the required ac power is about 4% of the peak reactive power in the raster magnet. The full-scale design is robust due to the application of redundancy as well as the use of independent fault detection circuitry that monitors the operation of the raster system. Based on the positive results of the prototype test, a complete system of eight magnets, modulators and fault detect circuits is currently being fabricated for full system evaluation and testing.

5 REFERENCES

[1] C.R. Rose and R.E. Shafer, "A 200-A, 500-Hz, Triangular Current Wave Modulator and Magnet Used for Particle Beam Rastering," Proc. 1997 Particle Accel. Conf., #7P089 (Vancouver, 5/97).

[2] C. Yan, et al., "Target Raster System at CEBAF," Nucl. Inst. and Meth., Vol. A365, pp 46-48 (1995).

LOW TO HIGH ENERGY BEAMSTOPS FOR APT

D. Doll, T. Van Hagan, K. Redler, J. Tooker, A. Baxter, M. Fikani - General Atomics, San Diego CA
D. Schneider, F. Spinos - Los Alamos National Laboratory, Los Alamos, NM
W. Funk – Westinghouse Savannah River Site, Aiken, SC

Abstract

Beamstops are required for commissioning and operating linear accelerators. The family of beamstops currently being developed for the DOE-sponsored Accelerator Production of Tritium (APT) program is addressed. The operational range encompasses proton energies of 6.7 MeV at the end of the radio-frequency quadrupole RFQ to 1.7 GeV at the target/blanket, and both pulsed and cw operating modes. An additional beamstop needed on a companion test facility to validate ion injector performance has been built and operated. This was the first of the series of cw beamstops; the second is under construction and will be operational by the end of 1998. Particle stopping distance and duty factor drive the size and heat transfer capacity of these beamstops; the need for low neutron production and activation potential drives the material selection. At energies above 6.7 MeV, the preferred beamstop material is graphite with aluminum the choice for structures and helium the choice for coolant. Boronated water is the preferred shielding below about 35 MeV, but is less suitable at higher energies because of the creation of Be-7. The evolution of the low-energy demonstration accelerator (LEDA) beamstops to 11 MeV and descriptions of APT beamstops are presented with performance ramifications and the status of the hardware and testing.

1 BACKGROUND

A linear accelerator operating cw at 0.100 A has been proposed for producing tritium to replace the nation's stock-pile as it continually dwindles due to natural decay. The APT program addresses this need and is being implemented by Burns and Roe, General Atomics (GA), and Los Alamos National Laboratory (LANL) in a facility to be located at the Savannah River Site (SRS). In support of this program, an Engineering Design and Development (ED&D) program is on-going simultaneously at LANL. The baseline APT facility will produce tritium at a rate of 3.0 kg/year. A two-phase approach now under consideration would accommodate an intermediate stage whereby a 1.5 kg/year production rate could be achieved and be upgradable with minimal schedule impact. The linac uses a rf driven ion injector that feeds into the RFQ at 75 kV. The RFQ accelerates the beam to 6.7 MeV; this is followed in ascending energy levels by a CCDTL (96 MeV), CCL (211 MeV), and high energy cryo-cooled (HE) linac (1700 MeV). In the two-phase program, the first-phase facility would have the proton beam turned 90^0 at 1032 MeV and directed to the target/blanket switch-yard instead of going to 1700 MeV, turning 180^0, and returning to the same switch-yard.

Beamstops are being designed and built to accommodate each stage of the linac assembly as well as on-line tune-up operation. This began with the ED&D [1] program which requires three beamtops, two of which have been built and operated; a third is being designed. This paper gives an overview of all these beamstops outlining the key requirements, basic approach to the designs, and a summary of the work completed.

2 REQUIREMENTS AND KEY CRITERIA

The obvious prime requirement for any beamstop is to stop the accelerated particles. Not so obvious is the need to do so in a manner that addresses both the linac operation and the need to minimize the effects of nuclear interactions produced. Above a few MeV, protons will activate a target as well as produce neutrons that escape the target and activate the surrounding materials. Since proton energies up to 1700 MeV will be produced, the APT beamstops will see the full range of nuclear reactions well into the spallation regime. The object is to select the solid target material that produces the fewest neutrons. A comparison of three candidates is shown in Fig. 1. Carbon is the clear winner throughout all energies. In the same way, the vacuum vessel and structures are aluminum because of its low production of long half-life isotopes; helium is the coolant because it is transparent to the neutrons.

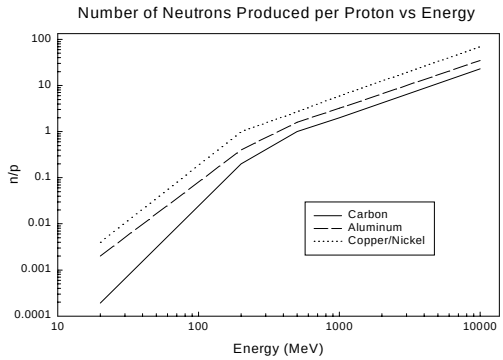

Fig. 1 Comparison of beam absorber materials

Spallation reactions with carbon produce a wide range of daughter isotopes but only Be-7 (0.48 MeV gamma, 53 day half-life) seriously affects shut-down access for

maintenance or replacement. The cross section for this reaction is shown in Fig. 2. The low and intermediate energy beamstops will not accumulate much Be-7 at 0.1 % duty unless long operating times (>>6 months) are used in linac commissioning. The 1700 MeV beamstop will build up 5.4 Curies (gamma-producing) over the projected 1000 initial hours of operation at 2% power. Man-access for repair or replacement will be affected.

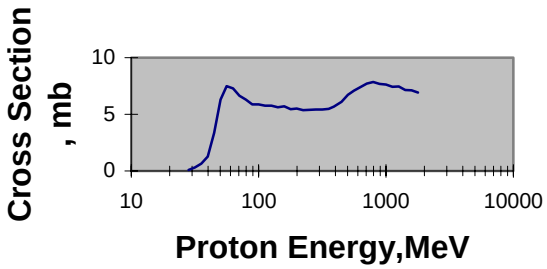

Fig. 2 Cross section for $^{12}C(p,n)^{7}Be$ reaction rises sharply above 32 MeV.

As the proton beam enters the graphite, it will penetrate as far as the initial energy will carry it. This stopping distance and the concomitant power deposition are the remaining key factors in the beamstop design. At energies up to 20 MeV, the heat deposition is essentially on the surface (2.75 mm); above this energy, the power is deposited into an ever increasing volume and depth until at 1700 MeV, 4.6 m of 1.8 g/cm^3 graphite is required to stop the beam. Fig. 3 shows the radial and axial power distributions for a 1 σ, 2.66 cm beam at 1700 MeV. This is used to design the array of cooling passages in the graphite target.

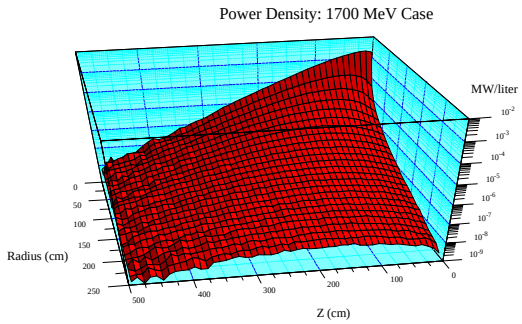

Fig. 3 Power density in graphite from a 1 σ = 2.66 cm 1700 MeV proton beam

Beamstop shielding requirements vary widely over the linac, driven by the effects of increasing proton energy. The neutron spectrum produced comes from three sources: 1) cascade neutrons that are produced from proton energies >20 MeV and can be as energetic as the incoming proton, 2) evaporation neutrons whose energies are <5 MeV, and 3) thermal neutrons arising from degradation of the cascade and evaporation neutrons. While the evaporation neutrons have an isotropic angular distribution, the cascade neutrons are forward scattered and become more so as the proton energy increases. Yields (n/p) range from $2x10^{-4}$ at 20 MeV to 2 at 1700 MeV with mostly evaporation neutrons at low energy and about half-and-half at high energy. One meter of water or concrete (4π) is adequate for neutron shielding for proton energies up to 20 MeV; it is also adequate at higher proton energy transverse to and upstream of the beam. Above 150 MeV, 6-8 m of concrete are required on the down-stream end to capture the high energy spallation neutrons. The latter may be made thinner by substituting an inner layer (20–30 cm) of steel. Unfortunately, this layer would become quite activated making it a solution of last resort.

3 COMMISSIONING BEAMSTOPS

The preliminary linac commissioning plan [2] calls for five beamstops. The first three will be used for commissioning and stored in shielded alcoves off the main tunnel after the linac has been built and tested to that point, i.e. 6.7 – 20, 211, and 470 MeV. The last two beamstops located at the end of the linac (1700 MeV. 0.1 %) and adjacent to the target/blanket (1700 MeV, 2%) are permanently integrated into the linac facility. The graphite targets of the three commissioning beamstops are cooled by thermal radiation to the respective vacuum vessels, thus eliminating the need for a window. Although larger, the 0.1% HE beamstop at the end of the linac is cooled similarly. The 2% 1700 MeV beamstop requires direct cooling of the graphite with helium and a window also cooled with helium.

The low energy beamstop will be used to commission the RFQ and as many CCDTL modules as practicable limited primarily by the increased forward scattered cascade neutrons (Fig. 4). The graphite beam target is located in the center of the shield tank and radiates the heat to the cylindrical housing which is in turn cooled by natural convection of the shield water. Air convection on the outside of the tank cools the shield water, resulting in completely passive thermal management.

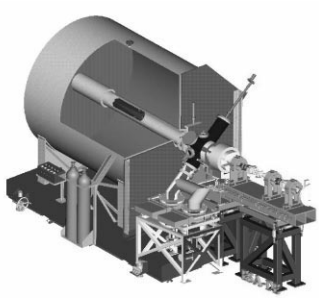

Fig. 4 Low energy beamstop to be used for commissioning at several energies starting at the RFQ

The preferred coolant is helium since it does not activate, has good heat transfer properties, and can heat-exchange to conventional cooling systems. The arrangement for the 470 and 1700 MeV (0.1%) beamstops will be designed similar to the low energy beamstop except elongated to accommodate the increased proton range and the vessel is cooled with helium. In all beamstops above 200 MeV, the shield will be concrete about 1 to 2 m thick radially to capture evaporation neutrons and 6 to 8 m thick downstream to stop the cascade neutrons.

The high energy beamstop is the final tune-up target before the beam is switched into the target/blanket. It is designed to absorb 2% of the 1700 MeV beam, or 3.5 MW. The graphite is arranged as vertical hexagonal blocks with coolant holes running transverse to the beam and spaced to keep the temperature as uniform as practicable. Helium is circulated through the blocks starting at the bottom (up-flow) with a large plenum that also acts as a support and terminating at the top where orifices are used to balance the flow through the differently heated zones. The heat is exchanged at a remote location with water to a conventional facility cooling system. The window separating the vacuum from the pressurized helium is aluminum, used to minimize the long-term activation products. It is cooled with helium through holes running transverse to the beam. The concrete shielding is similar to the intermediate energy beamstops except that special provisions are made to replace the window remotely should that become necessary.

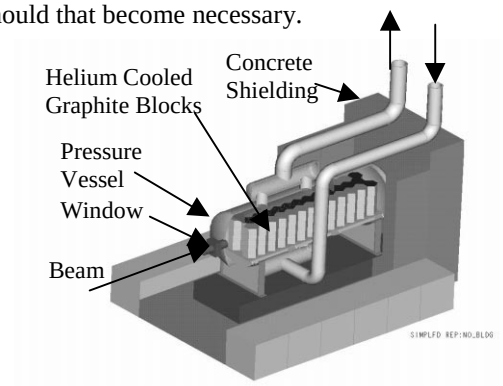

Fig. 5 High energy beamstop – 1700 MeV

4 ED&D BEAMSTOPS

Two beamstops [3] have been built in support of the ED&D program at LANL. Both use the same basic design approach to stopping the proton beam and dissipating the thermal energy, which is to use concentric thin-wall ogive (pointed arch) shapes with high velocity water flowing in the gap between them. The first one was built of copper and operated successfully in the Chalk River Injector Test Stand (CRITS) facility (Fig. 6 upper left) which reached 0.085 A at 1.2 MeV, the highest power cw beam yet achieved. The second was fabricated from electroformed nickel, chosen over copper because of the lower n/p at 6.7 MeV. This ogive is integrated into a cartridge that fits into a central chamber in an aluminum tank filled with boric acid saturated water which acts as a neutron and decay gamma shield (Fig. 6, lower right).

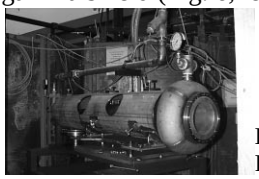

LEDA Beamstop
Boronated Water Filled Shield Tank
Coolant In/Out

CRITS Beamstop

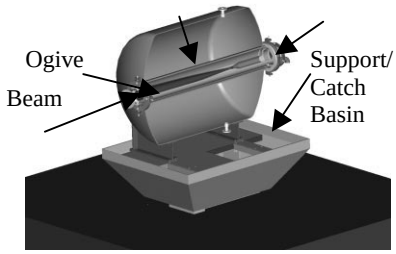

Fig. 6 Beamstops built and operated for ED&D

5 CONCLUSIONS

The development and commissioning plans for the APT linac have created unique requirements for the beamstops. These have been met with an array of designs that have taken advantage of graphite as the absorber, aluminum for structures, and helium for coolant. These materials minimize the production of neutrons and activation products which reduces the effects on worker safety and the need for remote handling. These designs give the greatest flexibility to the facility design and commissioning activities.

6 ACKNOWLEDGEMENTS

*This work was sponsored by the Department of Energy under Contract No. DE-AC04-96AL8907. The authors wish to thank GA beamstop team members Raj Acharya, Paul Wegner, Chuck Charman, Terry Figueroa, Hank Brodnick, Ralph Senior, and Craig Bystedt. We gratefully acknowledge the support of LANL staff members Joe Sherman, Herb Newman, Denise Pelowitz, Ross Meyer, Jr and Dave Hodgkins.

7 REFERENCES

[1] H. V. Smith, et al, ”Status Update on the Low-energy Demonstration Accelerator”, LINAC98 POSTER TU4014.

[2] L. Warren Funk, et al “Development of a Commissioning Plan for the APT Linac”,LINAC98 Poster TU4012

[3] T. H. Van Hagan, et al, “Design of an Ogive-Shaped Beamstop”, LINAC98 Poster TU4091.

LOW-STORED-ENERGY 100-kV REGULATOR FOR ION SOURCES AT LANSCE *

E. G. Jacobson, R. L. Haffner, W. B. Ingalls, B. J. Meyer, J. E. Stelzer
Los Alamos National Laboratory, Los Alamos, New Mexico 87545 USA

Abstract

At Los Alamos Neutron Science Center (LANSCE), as elsewhere, it is desirable to minimize the available stored electrical energy for the H^- ion sources to minimize accelerating column damage caused by uncontrolled energy release during arc-downs. The stored energy includes, in addition to the charge in the power supply output capacitance, the charge on the electronics racks. The racks are supported and insulated from ground by PVC pipe and have a capacitance to ground of approximately 900 pf. In 1988 LANSCE personnel designed a high-voltage current source using a low-stored-energy power supply and planar triode with the goal of eliminating uncontrolled release of charge stored in the power supply. Construction and testing were performed intermittently as resources permitted until 1993. When work on the Short-Pulse Spallation Source (SPSS) [1] started on the LANSCE Ion Source Test Stand (ISTS), it was recognized that a higher current power supply would be needed and work resumed on the regulator circuitry. A 120-kV power supply having low output capacitance and a planar triode have been used to supply 40 mA, 120-Hz, 12% duty-factor current for the ISTS beam. The triode's cathode current is controlled by circuitry operating both at power-supply voltage level and at ground level via a fiber optic link. Voltage droop is approximately 600 V during the 1 ms beam pulse. We present the status of the regulator and its special challenges.

1 BACKGROUND

Requirements for a low-stored-energy power source supplying 50 mA at 100 kV at 12% duty were defined a decade ago. A 120-kV, 25 mA power supply was specified and acquired. The power supply's output capacitance was to be charged during the 7.3 s periods that beam was not being extracted from the source, and its output voltage was to decrease during the 1 ms periods when H^- ions were being extracted. The tube would be controlled, if possible, such that plate voltage, relative to ground, would decrease 1 V for each 1 mA of increase in load during a beam pulse. One goal was to have the electronic circuitry, including the fiber optic components, have a frequency response of 1 MHz in order to minimize droop at the beginning of a pulse. Circuitry was also designed to turn the tube off quickly in case of an arc to ground at the output. Several operational amplifier configurations were tried, and by the spring of 1993, the electronics response was flat out to approximately 300 kHz, the components destined for oil immersion had run in air with an output of 7.5 kV for an input voltage of 10 kV, and preparations were made to test the regulator with a pulsed load.

When the supply and regulator were tested in preparation for use on the ISTS at LANSCE, the only detectable component failure resulting from the 4 years of storage was physical damage to one optical fiber conductor. The fiber optic transmitters were relocated from the ground level electronic chassis to the top of the oil tank to prevent recurrence. Approximately 5 m of optical fiber were replaced by copper. No performance degradation was detected when duplicating pre-1993 measurements in the fall of 1997.

The regulator and power supply were placed in service on the ISTS late in 1997 and they operated satisfactorily with a pulsed beam current (H^- plus electrons) up to 40 mA with droop of 600 V (15 V per mA). At current above 40 mA, droop was no longer linear due to operation of the current-limiting feature of the circuitry associated with the field-effect transistors (FETs). At some total beam current level above 60 mA, probably over 100 mA, operation of the power supply became erratic, and then the power supply failed.

All components of the regulator have been subjected to the transients associated with ion source arc-downs on the test stand and there have been no failures. The tube has an amplification factor of 1300 and with 120 kV across it, it is cut off with a grid-to-cathode voltage of –110 V, more than a factor of 3 below the rated drain-to-source voltage of the FETs. The high gain of the tube permits the FET circuitry to limit plate current during normal operation, including arcing to ground (through the source or otherwise) of the output.

2 SIMPLIFIED REGULATOR DESCRIPTION

A 0 to 10 V reference is supplied to the control circuitry located at ground and compared with the feedback voltage developed by the compensated divider Fig.1. The magnitude of the signal provided to the fiber optic transmitter is varied as necessary to make the magnitude of the feedback voltage equal to the reference. Tube cathode current is controlled by varying current in the

* Work supported by the U. S. Department of Energy

FET. For plate-to-cathode voltage of greater than 3 kV and plate current of less than 150 mA, grid-to-cathode voltage is negative and grid current is zero. Within those constraints, plate current is equal to FET current.

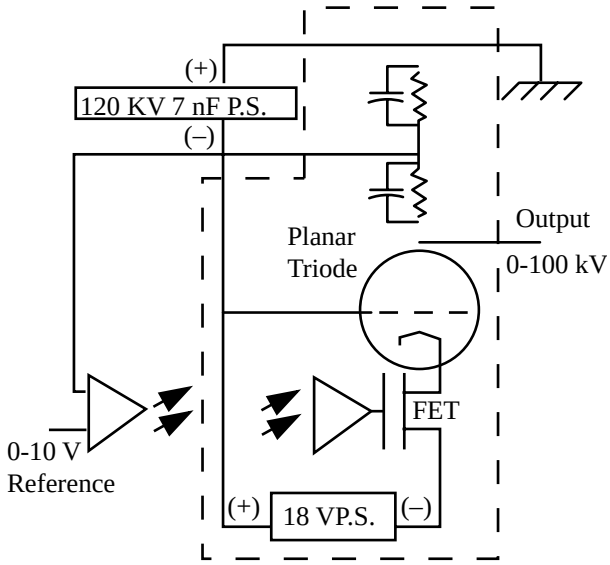

Figure 1: Simplified circuit diagram. Components represented by symbols inside the dotted line are in an oil-filled tank. The double arrows represent fiber optic transmission and detection.

3 COMPONENTS AT GROUND LEVEL

Reference to the summing junction of the regulator amplifier is provided by a 10.000 V, +/- 2.5 mV precision reference chip and a 10-turn potentiometer. The regulator amplifier is followed by three stages of amplification of gain seven each. The operational amplifiers used for these stages have a gain-bandwidth product of no less than 45 MHz. They are followed by a buffer amp of gain 0.9 which drives the fiber optic transmitter. The transmitter is mounted on the top of the oil tank.

4 COMPONENTS IN THE OIL TANK

Devices located in the tank filled with electrical insulating oil are mounted on a plate that is supported by rods connected to the removable tank top. All components are accessible when the tank top is lifted. A 120:24 V isolation transformer rated 120 kVDC and the compensated voltage divider are mounted on the plate. Also attached to the plate is a phenolic support structure on which is mounted:

- A printed circuit card holding the fiber optic receiver and three stages of amplification, FETs which provide on-off switching and cathode current control, and 18- and 23-V voltage regulators
- A 24:6 V filament transformer
- A planar triode and heat sink
- Light-emitting diodes that indicate circuit components' status outside the tank via light fibers

5 FIBER OPTIC LINKS

The printed circuit board in the oil tank has two fiber optic inputs from ground level. The analog control signal originates in the regulator module. A digital on-off signal comes from a transmitter that receives its input from an arc-down recovery card module that has several permissive inputs. The FET depicted in Figure 1 represents both the FET associated with the analog signal and the FET associated with the arc-down recovery card. Figure 2, though still simplified, is an expansion of the FET circuitry.

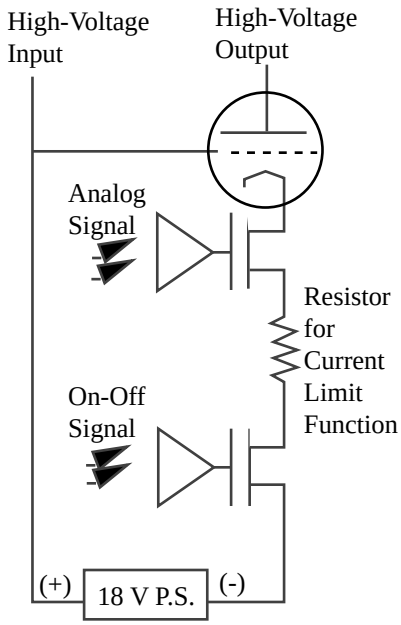

Figure 2: Simplified circuit diagram. Analog amplifier represents a detector diode and three stages of amplification. On-off amplifier represents a detector diode and a comparator.

The output of a comparator on the card in oil ensures that the FET associated with the permissive signal from the arc-down recovery card is either fully enabled or disabled. When enabled (effectively a short circuit), control of current in the FETs, and consequently the planar triode, is provided by the FET whose gate signal is a function of the output of the ground-level regulator circuitry.

6 CONTROL RESPONSE

The open-loop gain, from the reference input of the regulator to the gate of the controlling FET, is approximately 1600. Time to peak following an input step small enough not to cause any amplifier saturation,

2.5 mV through 1 kΩ into the summing junction, is approximately 850 ns. Time to reach steady-state is approximately 2.25 μs. Because of the limitations of the compensated divider, measurement of closed-loop response has been difficult due to the magnitude of the noise on the divider signal. Use of a commercial divider having a half-power frequency response of 5.7 MHz has been used to observe what we think is a truer representation of voltage applied to the ion source on the ISTS. The regulator has supplied 40 mA, 1 ms pulses at 120 Hz with a droop from 80 kV of 600 V.

7 COMPENSATED DIVIDER

The divider which generates the voltage feedback signal consists of three 300 pF vacuum capacitors and one 1 μF polystyrene capacitor in series that are in parallel with seventy-eight 1.283 MΩ resistors and one 10,001 Ω resistor in series. The 1.283 MΩ resistors are wound spirally around a phenolic tube that encloses the 300 pF capacitors. The first resonance of the vacuum capacitors, measured individually, in air, occurs at 33 MHz. The first resonance for the polystyrene unit occurs between 0.5 and 0.6 MHz.

The change in effective capacitance when the assembly is submerged in oil is not known. However, total capacitance of the three vacuum capacitors before submersion in 1990 was 116 pF. After the resistor, capacitors, and phenolic tube had been submerged in oil for 4 years, measured total capacitance was 256 pF. Measured individually, the increases were 70 to 80 pF per resistor-capacitor section. The effects on regulator performance of the variation from ideal have not been determined.

8 FUTURE WORK AND CONCERNS

The initial requirement of supplying a 50-mA pulsed load has changed to 100 mA and may be increased to 200 mA or more. A nonstandard power supply capable of 200 mA at 12% duty has been ordered. It is possible to add power supplies in parallel.

The manufacturer's experience with the planar triode indicates that, as operated in this application, it is capable of peak current of 350 mA without exceeding the anode dissipation capability of the tube or the tube's emission capability. Due to consequences of consolidations within the vacuum tube industry, tube procurement lead time has been long.

Considerable time was spent before 1992 in the effort to build a good high-frequency voltage divider. The original goal for frequency response had been 1 MHz for the electronics and 10 MHz for the divider. Although operation using the divider has been satisfactory, the signal it provides is noisy and needs to be improved. A chip capacitor whose first resonance is at 1.1 MHz is a possible replacement for the polystyrene capacitor if the chip's relatively inferior stability would not be a problem. Although short, 4 cm, the connection between the plate, made on the heat sink bolted to the triode, and the top of the divider is inductive, and the effect of varying the length has been investigated only briefly.

9 CONCLUSIONS

Regulation of -80 kV using a planar triode and a low-stored-energy power supply whose output droops from –120 kV during the time charge is being extracted from an ion source on the ISTS has been demonstrated. The capacity of the high-voltage supply has been exceeded with no apparent damage to the regulator components.

With an adequate power supply and modifications to the FET current limit circuitry, which floats at high voltage, it is anticipated that up to 350 mA at 12% duty could be supplied by the regulator using the present planar triode.

Future work will include investigation of the response time of on-off FET circuitry, reduction of compensated divider noise, determination of the cause(s) of the higher-than-designed-for droop, and testing with the new power supply.

ACKNOWLEDGMENT

Andrew A. Browman was the initial designer of the regulator, provided solutions to circuit limitations as they became apparent as portions were constructed and tested, and has continued to provide valuable suggestions when requested.

REFERENCE

[1] R. R. Stevens et al., "Beam Simulations for the H^- Upgrade at LANSCE," Proceedings of LINAC98, Chicago, August 23-28, 1998. XXX-XXX (1998).

TESTING OF VACUUM PUMPS FOR APT/LEDA RFQ*

K. Kishiyama, S. Shen, D. Behne
Lawrence Livermore National Laboratory, Livermore, CA and
N. G. Wilson, AMPARO, Inc., Los Alamos, NM and
D. Schrage, R. Valdiviez, Los Alamos National Laboratory, Los Alamos, NM

Abstract

Two vacuum systems were designed and built for the RFQ (Radio Frequency Quadrupole) cavity in the APT/LEDA (Low Energy Demonstration Accelerator) linac. The gas load from the proton beam required very high hydrogen pump speed and capacity. The gas load from the high power RF windows also required very high hydrogen pump speed for the RF window vacuum system. Cryopumps were chosen for the RFQ vacuum system and ST185 sintered non-evaporable getter (NEG) cartridges were chosen for the RF window vacuum system. Hydrogen pump speed and capacity measurements were carried out for a commercial cryopump and a NEG pump. This paper will discuss the test procedures and the results of the measurements.

1 INTRODUCTION

Cryopumps and NEGs are known for their high hydrogen pumping speed and capacity and are used widely in accelerators applications. Cryopumps were selected for the RFQ cavity due to the very high hydrogen gas load from the proton beam loss. A cost analysis showed that for the same cost, cryopumps could provide twice the pumping speed compared with turbomolecular pumps. NEGs were selected for the RF windows because in addition to the high hydrogen pumping speed, they are relatively small in size and lightweight. Size and weight were important requirements in the RF window vacuum system since space in the waveguide area was very limited.

The Ebara ICP200 cryopump was selected for the RFQ vacuum system because of its reasonable cost, very large hydrogen capacity and its flexible interface for remote operation. The SAES CapaciTorr B1300 NEG cartridge pump utilizing the sintered ST185 blades was selected for the RF window vacuum system. The manufacturer claims that the sintered ST185 blades has increased pump speed and capacity at room temperature over other types of NEGs.

Since LEDA is a demonstration facility for APT, beam availability must be high to prove that APT production goals can be met. Therefore, it was important to verify the performance of the cryopumps and NEGs to ensure they would support the operational requirements for LEDA.

2 TEST SETUP

The pump speed and capacity for the cryopump and the NEG pump were measured using test domes built to American Vacuum Society Standard 4.1 [1]. The pumps were tested using only hydrogen, since it is the primary gas load in APT. A schematic of the test setup is shown in Figure 1.

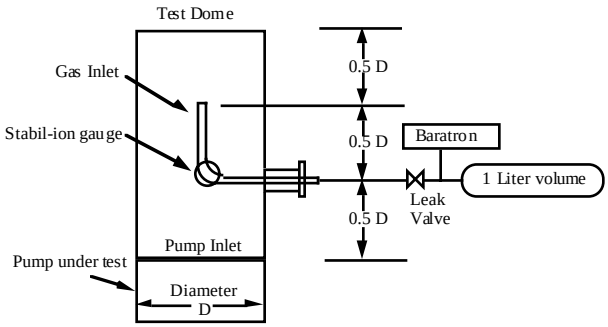

Figure 1. Test setup for pump speed measurement.

The pressure in the test dome was measured using Granville-Phillips 370 Stabil-ion gauges. These gauges were supplied with individual calibration data on memory modules that were downloaded into their controller. Granville-Phillip claims the measurement uncertainty is 3%. The gauges were calibrated at the factory for Nitrogen. All measurements were taken using the factory calibration and then corrected for hydrogen.

Gas flow into the test dome was established by charging a known volume to a set pressure, then measuring the change in pressure with respect to time. The gas flow into the test system was controlled by a Varian variable leak valve. The pressure in the known volume was measured using an MKS Baratron. The Baratron is a capacitance manometer with an accuracy of 0.5%.

The measurement of pump speed was similar to the flowmeter method as outlined in AVS Standard 4.1. However, this method varies from AVS Standard 4.1 in that the flow rate drops off as the pressure in the known volume drops. The LabView data acquisition system

*Work performed under the auspices of the U.S. Department of Energy by Lawrence Livermore National Laboratory under Contract W-7405-Eng-48

measures the pressure change in the known volume via the Baratron and the vacuum pressure via the Stabil-ion gauge at prescribed time intervals. For a given short time interval, we assume that the flow rate is constant. The pump speed can then be calculated using the equation $S = Q/(P - P_0)$ where the throughput Q is the change in pressure in the known volume during the sample time interval and P is the Stabil-ion gauge pressure in the test dome. P_0 is the base pressure in the test dome before the test gas is introduced.

For the pump speed measurements, a certified 1 liter volume was used as the known volume. By substituting the 1 liter volume with a larger volume and changing the Baratron to a higher range we used the same LabView system to measure pump capacity. LabView then calculated the total Torr-Liters of gas sorbed versus pump speed.

3 RESULTS AND DISCUSSION

Pump speed and capacity were measured for both the cryopump and the NEG. LabView recorded a timestamp, pressure in the test dome, and pressure of the test gas in the 1 liter volume.

3.1 Cryopump Data

The cryopump reached a base pressure of 1.78×10^{-10} Torr in the test dome. The pump speed was measured at over 2700 liters/sec. The pump speed test was repeated 5 times after the pump was conditioned as stated in the AVS Standard 4.1. (Pump Conditioning = pump speed x 0.03 Torr-liters. Using the manufacturer's specification of 2200 liters per second [2], the pump was conditioned after 66 Torr-liters.) See Figure 2 for a typical plot of cryopump pump speed versus sorption. The measurement shows that the manufacturer's specification is very conservative.

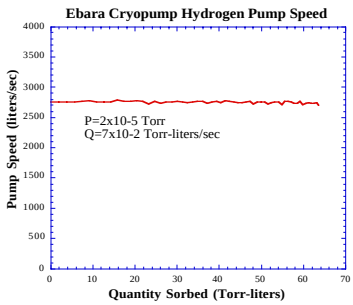

Figure 2. Measured Cryopump Pump Speed Versus Sorption.

The hydrogen capacity of the cryopump was measured to be over 30 standard liters at an operating pressure of 1×10^{-4} (H_2) Torr and a throughput of 2×10^{-1} Torr-liters/sec. This flow rate is over two orders of magnitude higher than the predicted gas load in APT/LEDA. Figure 3 shows the sorption plot at the high flow rate. At this very high flow rate the test took 33 hours.

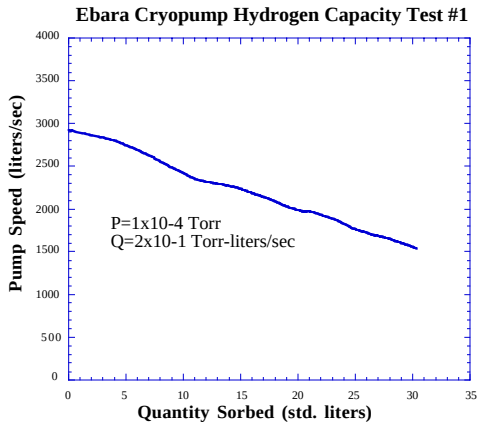

Figure 3. Measured Cryopump Capacity at High Flow.

The cryopump was then regenerated and after regeneration the cryopump reached a base pressure of 1.90×10^{-10} Torr. The hydrogen capacity of the cryopump was re-measured and found to be 32 standard liters at an operating pressure of 1.0×10^{-5} (H_2) Torr and a throughput of 2.0×10^{-2} Torr-liters/sec. This flow rate was still at least an order of magnitude higher than the predicted gas load in APT/LEDA. Figure 4 show the sorption plot at the lower flow rate. At this flow rate the test took 12.8 days and the results agreed very well with the previous test at the high flow rate.

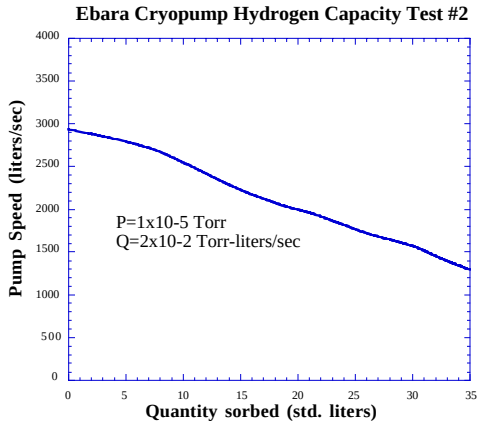

Figure 4. Measured Capacity at the Lower Flow Rate.

3.2 NEG Data

The ST185 NEG, like all NEG pumps, does not pump inert gases, therefore a small turbo pump was added to the system. The turbo was a Varian V70LP and has a specified hydrogen pump speed of 45 liters/sec. The hydrogen pump speed was measured in the test dome before the NEG cartridge was inserted and found to be 51 liters/sec.

The NEG cartridge pump was mounted in the optional 6" diameter body rather than the standard 4" body. According to SAES, this would increase pump speed from about 700 liters/sec to 1200 liters/sec [3].

It was observed during installation of the cartridge pump in its heater assembly that the thermocouple used by the NEG regeneration controller to control the heater was mounted very near the heater element and free standing. There was concern that the actual temperature of the NEG pump would not be what the thermocouple was reading since the ST185 blades are mounted radially outward and the view factor of the blade to the heater is small. It was felt that a thermodynamic analysis was not in the scope of this study, but it would have been interesting to mount thermocouples directly on NEG blades and measure the temperature gradient. Pump speeds could probably be further optimized by knowing this temperature gradient.

After the initial activation recommended by SAES of 500 C for 45 minutes, several pump speed measurements were made, followed by a regeneration. It was found that by increasing the regeneration to an indicated 550 C for 90 minutes produced higher pumping speeds. This agrees with tests performed by others [4]. Subtracting the pump speed of the turbo, the average speed of the NEG was 1380 liters/sec. Figure 5 shows a typical sorption plot for the NEG.

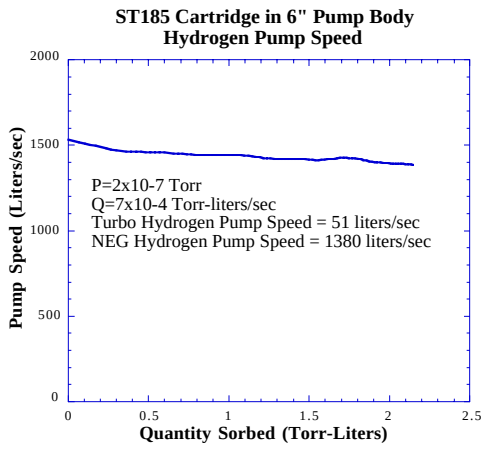

Figure 5. Measured Speed of ST185 Cartridge Pump.

A test of the hydrogen capacity of the NEG pump was performed after a regeneration. The objective of this test was to show that the NEG pump was capable of sorbing one standard liter of hydrogen at the rated pump speed. One standard liter was an arbitrary value that represents several months of normal RF window operation. As the data shows in Figure 6, the pump speed was 1150 liters/sec after 700 Torr-liters.

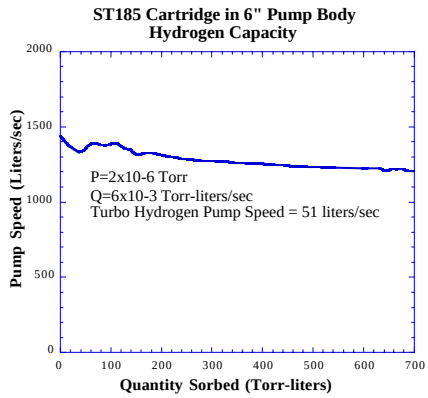

Figure 6. Measured Capacity of ST185 Cartridge Pump.

4 SUMMARY

We have measured the pump speed and capacity of the cryopump and NEG that are proposed for use in the RFQ vacuum system for APT/LEDA. The results verify the manufacturer's specifications and gives us confidence that these commercial pumps will provide the necessary vacuum performance for the operation of LEDA.

ACKNOWLEDGMENTS

Reference herein to any specific commercial product, process, or service by trade name, trademark, manufacturer, or otherwise, does not necessarily constitute or imply its endorsement, recommendation, or favoring by the United States Government or the University of California.

The authors wish to thank Jim Bowman, Tony DeCosta and Mark Harper, Wolfgang Stoeffl and Marshall Mugge for their technical assitance.

REFERENCES

[1] M. H. Halblanian, "Recommended Procedure For Measuring Pumping Speeds," J. Vac. Sci. Technol. A 5(4) July/Aug 1987

[2] Ebara ICP200 product data

[3] SAES CapaciTorr B1300 product data

[4] Y. Li et al., "Design and Pumping Characteristics of a Compact Titanium-Vanadium Non-Evaporable Getter (NEG) Pump", accepted, to be published, J. Vac. Sci. Technol 1998

MEDICAL APPLICATIONS OF C-BAND ACCELERATOR TECHNOLOGIES

E. Tanabe, AET Associates, Inc., 20370 Town Center Lane, Suite 252, Cupertino, CA 95014, USA
Y. Fineberg, Stanford University, PO Box 8205, Stanford, CA 94309, USA
H. Matsumoto, T. Shintake, High Energy Accelerator Research Organization (KEK), 1-1 Oho, Tsukuba, Ibaraki, 305 JAPAN

Abstract

Electron linacs have been widely used in medical applications. Most of these linacs use S-Band (about 3 GHz) microwave technologies. Recently, however, several new ideas in radiation therapy have been proposed that require new, higher power, higher gradient accelerators. In this paper, we propose the application of C-Band (5 to 7 GHz) technology for radiation therapy. Also, we describe the possible design of a new standing wave accelerator structure and R&D of C-Band technology in KEK.

1 INTRODUCTION

Cancer is the major cause of death in most developed countries, where approximately one in every four persons will develop a cancer at sometime in his or her lifetime. Modern society has recognized the immense value of linear accelerator technology as a powerful tool in medical technology. Today more than 5500 electron linacs are used for medical purposes, mainly for the treatment of cancer, in the world.

2 MEDICAL ACCELERATORS

Linacs play such an important role in radiation therapy because of its treatment efficacy and cost efficiency. One of the difficulties in treating cancer is targeting the treatment at the cancerous cells only, without putting the rest of the body at possible or certain risk, as does often surgery and chemotherapy.

Radiation therapy is a preferable alternative to chemotherapy and surgery, although it is often used in conjunction with both. Nearly half of all cancer patients in developed countries will receive radiation therapy, as definitive therapy, for palliation, or as an adjunct to surgery, and more than 50% will be cured by radiation therapy [1]. Linear accelerators direct the x-ray dosage at the target volume, the cancerous tumor cells, and control their reproduction capabilities. Radiation therapy offers these benefits:

1. It localizes the treatment to the tumor
2. No cuts or abrasions are made on the body
3. The process is moderately tranquil, not traumatic for patients
4. Patients usually do not suffer side effects from radiation therapy
5. Most patients do not need expensive hospital care
6. Smaller medical staff is involved in treatment

However, the x-rays are “equal opportunity destroyers,” killing healthy tissue while traveling to, and through, the target volume. The goal of new radiation therapeutic technology, therefore, is eradication of the tumor with minimal radiation damage to the surrounding healthy tissue while maintaining a high quality of life for the patient.

3 CURRENT RESEARCH IN RADIATION THERAPY

Tomotherapy [2] and stereotactic [3] radiotherapy are new radiation treatments that offer advanced solutions to this enduring problem. Currently, simulator and CT (computer tomography) imaging technology allowing radiation physicians the ability to precisely locate the tumor position before treatment. Modern medical accelerators utilize the most updated computer technology, which has allowed radiation to be delivered to the tumor as a function of time, space and dose rate. The time dependent dose delivery is called "physiological gating," wherein the beam is delivered only over certain time intervals in order to account respiration and heart motion. For space dependence, the multileaf collimator "MLC," which utilized a number of beam absorbing leaves to produce an irregular beam shape in order to "conform" the treatment beam to the prescribed 3-D treatment volume. However, these advanced techniques are still not based on real time tumor monitoring and treatment concurrently. Tomotherapy and stereotactic radiotherapy will allow physicians to locate the tumor position *during* treatment as well, and are able to make modifications to the beam based on real-time analysis, thus making the treatments more proficient and yielding a higher cure rate for its patients. Advances in the ratio of computational power to computer cost are now making

this form of therapy economically practical. Between 1970 and 1980, significant advancements in CT and MRI technology made radiation oncology a precise and predictable modality. As a result, the cure rate by radiation therapy has increased dramatically

Figure 1 shows the tomotherapy concept. Tomotherapy combines the precision of a helical CT scan with the potency of dynamic radiation therapy. Using an intensity-modulated fan beam, rotational radiotherapy delivery is achieved by moving multiple collimator vanes in and out of the beam path with speed and precision. By rotating the beam source around the patient, the beam is able to enter the patient from many different angles and to deliver more doses of lesser potency, thereby exposing the healthy tissue to a significantly lower dosage of radiation.

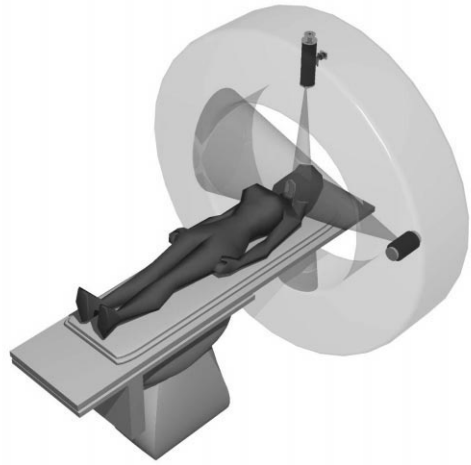

Figure 1: Tomotherapy concept

Thus, tomotherapy accurately controls the location and intensity of the radiation entering the patient with the joint advanced technology of the MLC system and helical CT imaging technology, and delivers highly conformal dose distributions. When using such a capable dynamic modulator, however, one must pay special attention to possible inaccuracies such as leaf transmission, leakage and alignment.

Stereotactic radiotherapy is often prescribed for brain tumors, using extreme precision and a finely focused radiation dosage to the target volume. By directing finely collimated beams of radiation from thousands of angles, the x-rays converge at one small spot, the tumor, while the healthy non-targeted tissue receives very little radiation.

This technique currently requires the use of a head ring, CT scan often in conjunction with magnetic resonance imaging or angiography, and 3-dimensional simulation and computerized dosimetry as well as treatment using a linear accelerator. Figure 2 shows a new concept of stereotactic radiotherapy, which utilizes two rotary joints that are placed on the side of the gantry and the top of ceiling. These provide all the necessary electrical powers and coolings to the accelerator and the X-ray source, which are free to rotate around all angles of the target volume.

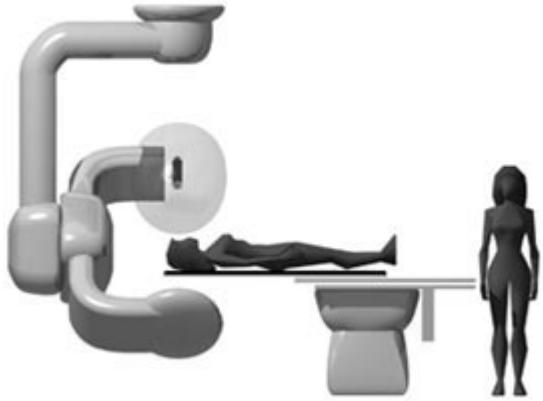

Figure 2: Stereotactic therapy concept

4 MEDICAL ACCELERATORS IN THE FUTURE

Even today's most sophisticated linear accelerator systems for radiation therapy still have many shortcomings. Both tomotherapy and stereotactic treatments require more advanced accelerators that can produce much more x-ray radiation and at a more stable rate, in time and space. They need:

1. A dose rate of 1 Gy/sec or higher
2. X-ray treatment beam position accuracy of 0.1 mm
3. Compact size of the linear accelerator
4. 100% temporal and spatial control of the x-ray beam.

In today's treatment, however, there is not 100% temporal and spatial control; tumor position monitoring is not done in real-time. Simulation is done in another room during the treatment, and what results is bombardment without knowing the exact target. A second issue is the undesirable shift of organs during the radiation treatment, where organs may potentially move 2 cm and thus interfere with the line of radiation.

Advanced equipment such as CT can be used merely for sending and storing information through the network in a sequential manner. What we need is interactive equipment that can produce real time imaging and can feed back immediately (to the degree of a millisecond) to the linear accelerator and deliver the dose at once, thereby eliminating bombardment without knowing the exact target location. This image-directed therapy modifies the radiation source so that the intended target is in the beam line instead of modifying patient position to align with the radiation source. Taking into account natural organ shifts, it is also necessary to deliver the dose in a very short time,

requiring a much higher dose rate and a more powerful linear accelerator.

5 C-BAND ACCELERATOR RESEARCH AND DEVELOPMENT

Hence, we propose high-power C-band accelerators to fit the requirements of the accelerators of future radiation therapy. The following summarizes the general description of these C-band accelerators:

1. Compact
2. High gradient
3. High current
4. Stable
5. Mechanically tolerant
6. More efficient

There are many advantages to using higher frequencies for compact accelerators, i.e. higher shunt impedance per unit length, smaller diameter, shorter filling time, and a higher breakdown threshold. Most electrical parameters can be scaled with frequencies but not for mechanical and thermal parameters. As a result, the shunt impedance can not be increased with the rate of $f^{1/2}$ as we wish. The filling time τ will decrease with a frequency of $f^{-3/2}$, which is the advantage for short pulse operation. The voltage breakdown threshold increases roughly by the square root of the frequency [4].

Meanwhile, there are currently several shortcomings in using a much higher frequency, such as a tighter mechanical tolerance, higher power density, and higher power transmission loss. These are true not only for the accelerator itself, but also for RF power sources such as klystrons and magnetrons. Because of tighter tolerance and higher power density, these microwave sources are difficult to make operating reliable at higher peak power.

The High Energy Accelerator Research Organization (KEK) in Japan has developed C-Band components and accelerators that bring solutions to the above-mentioned problems. Among their advanced solutions include:

1. C-Band klystron
2. Pulsed modulator for C-Band klystron
3. C-Band accelerating structure

KEK's C-Band 50MW klystron uses $\pi/2$ mode traveling wave structure in the output circuit in order to enhance the power-conversion efficiency and to reduce the electric field gradient in the output circuit. Operating at about 5700 MHz, the beam voltage reaches about 360 kV. Various tests have demonstrated that the KEK design is powerful and reliable for the multi-cell output structure.

The pulse modulator uses an inverter-type power supply, which eliminated the massive charging-transformer and also the de'Q-ing circuit from the traditional design. KEK's compact modulator design produces test output voltage of 23.4 kV, and a pulse width of 3.9 microseconds. Having followed the concept of the "Smart Modulator," this one tries to satisfy demands that it be reliable, simple, cheap, efficient, and easy to operate.

The C-Band accelerating structure is under development. Table 1 summarizes the design parameters of a proposed compact high power accelerator for medical applications, which utilizes the hybrid standing wave structure (patent pending).

This structure will be able to deliver a much higher dose rate (1Gy/sec) than currently used in the S-band accelerator, provided the successful operation of the new X-ray target concept.

Table 1: Specifications for C-Band accelerating structure

ACCELERATOR LENGTH (cm)	23
STRUCTURE	Hybrid Standing Wave
NUMBER OF ACC. CAVITIES	9
FREQUENCY (MHz)	5712
ENERGY (MeV)	10
BEAM CURRENT (mA)	600
BEAM PULSE WIDTH (μsec)	4
REPITION RATE (PPS)	240
RF PEAK POWER (MW)	11
SHUNT IMPEDANCE (MΩ/m)	140
LOAD LINE (MeV)	15-8 i

6 CONCLUSION

Electron accelerators have been key contributors to the success of radiation therapy. The medical community is always looking for new linac technologies that are more effective and can save more lives. C-Band frequency technology could be the best choice for future applications in radiation therapy.

REFERENCES

[1] C.J. Karzmak, et al., "Medical Electron Accelerators," McGraw Hill, Inc. (1993).

[2] T.R. Mackie, et al. "Tomotherapy: A new concept for the delivery of dynamic conformal radiotherapy," *Med. Phys.* **20**, 1709-1719 (1993).

[3] W. Lutz, et al. "A system for sterotactic radiosurgery with a linear accelerator," *Int. J. Radiation Oncology Biol.* **14**, 373-381 (1988).

[4] E. Tanabe, et al. "Voltage breakdown at X-Band and C-Band Frequencies," Linear Accelerator Conference Proceedings, 458-460 (1986).

AN UPDATED ASSESSMENT OF A MEDICAL CYCLOTRON AS AN INJECTOR FOR AN ENERGY UPGRADE

J. A. Clarke, D. M. Dykes, C. W. Horrabin, P A McIntosh, H. L. Owen, M. W. Poole, S. L. Smith and V. P. Suller CLRC Daresbury Laboratory, Warrington WA4 4AD, United Kingdom

A. Kacperek and B. Marsland, Douglas Cyclotron Unit, Clatterbridge Centre for Oncology, Wirral L63 4JY, United Kingdom

Abstract

The 60 MeV cyclotron at Clatterbridge operates as the UK centre for proton therapy, concentrating on treatment of eye tumours; the accelerator is a Scanditronix model MC60PF fixed energy isochronous cyclotron with a high current ion source. Although possible energy upgrades have been previously considered interest has now been reawakened by the activities of the Italian TERA Foundation, which has proposed a compact high frequency booster linac as a potential solution to achieve the 200 MeV needed for a broader therapy programme. The paper reports progress on studies to assess if the Douglas cyclotron is suitable for a test of such a prototype booster linac. The results demonstrate that a cyclotron beam pulse of about 25 microseconds can be achieved by application of amplitude and phase modulation to its RF system. The most recent measurements of output emittance and energy spread of the accelerator are presented and compared with the normal CW values. Compatibility with the acceptance of the proposed linac is discussed.

1 INTRODUCTION

An overview of the use of accelerators for medical applications has been given by Amaldi [1]; this includes the important technique of hadron therapy using a variety of particles. Of these the potential for proton therapy in the treatment of a broad range of cancers is now widely accepted and has already been identified by an EU Working Party as deserving of priority support [2]. It is already used effectively for eye melanomas in the range 60-70 MeV but for deep seated tumours requires energies of at least 200 MeV. Few hospitals have such higher energy facilities and most patients have had to be treated at nuclear physics laboratories, a less than satisfactory situation. What is needed is a compact, economical solution for provision of these 200 MeV proton beams.

One route proposed by the Italian TERA Collaboration [3] is the production of a novel 3 GHz protontherapy linac, using an injector followed by two side-coupled linac structures with energies respectively of 70 MeV and 200 MeV; this challenge has been taken up by the Frascati team in its TOP project [4].

An attractive option is to exploit the same economical technology to boost the energy of existing therapy facilities, especially those in medical centres. Many are intermediate energy cyclotrons and it is necessary to assess whether their extracted proton beams can be successfully matched into the small physical aperture and restricted longitudinal phase space of a high frequency linac structure. In particular the Italian design has an acceptance of about 10π mm-mrad and 0.1 % rms energy spread [5]. Beam intensities for treatment need only be 10-20 nA average current and the linac is assumed to have a typical duty cycle of about 0.1 %, leading to an instantaneous cyclotron current of a few 10ís of μA. Especially in a hospital environment it is crucial to minimise beam losses in the transfer between the two accelerators so that it will be important to develop pulsed operation of the cyclotron matching that of the linac (~10μs) as closely as possible.

The initial studies of the suitability of extracted beam characteristics of one such cyclotron, at the Clatterbridge Oncology Centre in the UK, were recently reported at the EPACí98 conference in Stockholm [6]; updated studies are reported in this paper. It may be possible for this accelerator to be used as a test bed for the proposed concept, perhaps in collaboration with the Italian project [7]. A suggestion to boost the energy of the Clatterbridge accelerator with a linac, albeit of somewhat lower frequency, had previously been made in an earlier study by AEA Industrial Technology [8].

2 THE CLATTERBRIDGE CYCLOTRON

The Douglas Cyclotron Unit at Clatterbridge has operated a cyclotron for proton therapy since 1988. However for several years before that tests were carried out on the efficacy of neutron therapy, necessitating an accelerator with exceptionally intense proton currents of at least 50-100 μA to produce the required neutron fluxes from its beryllium target. A large switching magnet steered the protons into a neutron area and this separate beam line still exists, providing a useful facility for test purposes.

The commercially supplied isochronous cyclotron is a Scanditronix model MC60PF, whose principal parameters are summarised in Table 1.

Table 1. Principal Cyclotron Parameters

Energy	(MeV)	62
Current	(μA)	50+
Emittance/1σ	(π mm-mrad)	2-3
Energy Spread	(%, FWHH)	0.25
Radiofrequency	(MHz)	25.7
Harmonic Number		1
Dee Voltage	(kV)	40
Bunch Length	(deg)	13

These are notional parameters, as specified by the manufacturer, and in some cases are probably conservative. The current rating reflects the earlier utilisation as a neutron source and in recent years the accelerator has rarely exceeded 50 nA in CW mode. Emittances were measured at the factory and the energy spread and phase length are assumed to be equal to that of another Scanditronix model (MC35). The energy has been estimated from transmission through aluminium foil absorbers and for this type of cyclotron is fixed.

The intense ion source is a cold cathode (PIG) discharge type. Extraction is by utilising a radial integer resonance, together with an electrostatic deflector and focusing magnetic channel. This makes it difficult to predict the exact properties of the output beam.

3 MODIFIED PULSE DURATION

The obvious and most straightforward method of modulating the beam in a cyclotron would be to pulse the source of ions whilst they are at low energy. Unfortunately the ion source of the Clatterbridge accelerator, as with the majority of medical cyclotrons, is positioned at the centre of the dees and is very inaccessible. Furthermore, no modifications to the cyclotron could be considered which might reduce its availability in its primary function as a source for therapy. For these reasons an alternative approach to achieving a pulsed output beam was selected, that is to modulate the RF accelerating voltage.

If the RF accelerating voltage is not optimum, the first few orbits of ions which have been emitted from the ion source are perturbed, resulting in them colliding with collimators which are critically placed near the centre of the dees. Running the cyclotron with reduced RF amplitude and pulsing the RF up to the correct level when the beam pulse is required will produce a pulsed output beam. In practice this technique must be constrained by the need to keep the RF within certain limits so that the auto-tuning loops remain functional.

An alternative technique is possible in cyclotrons of the type used at Clatterbridge where there are two pairs of dees used. Adjusting the relative phase of the drive to the separate RF amplifiers feeding the dee pairs can alter the RF accelerating voltage effectively seen by the ions. This has the advantage of not disturbing the tuning loops. A highly simplified block diagram of the RF system is given in fig 1, showing how the amplitude and phase modulating signals are applied. The Clatterbridge system was modified to allow the two types of modulation and a series of tests were made in which short rectangular pulses of both amplitude and phase shift were applied at a repetition rate of 50 Hz and synchronised to the electricity main.

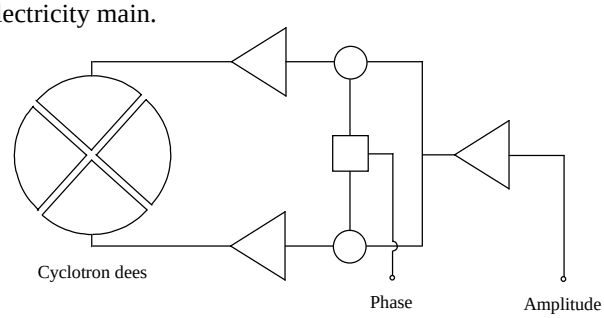

Figure 1: Block diagram of the modified RF system

The results showed that both modulations were fully effective in producing a pulsed output beam, which was detected from a faraday cup signal. The amplitude modulation was limited to the rise time of the RF system and gave a beam pulse of about 100 μs half width. Shorter pulses of about 25 μs were obtained by driving the RF rapidly through the optimum level, but this of course gave rise to 2 beam pulses, on the upward and downgoing edges of the drive pulse. The phase modulation system gave slightly shorter beam pulses of about 20 μs, as shown in fig 2, but a measurement of the basic system response to step phase changes has not yet been made so that it is not clear what the ultimate shortest pulse would be. At present it is likely that the best technique for generating a single short beam pulse is to apply shifted, overlapping, phase and amplitude modulations.

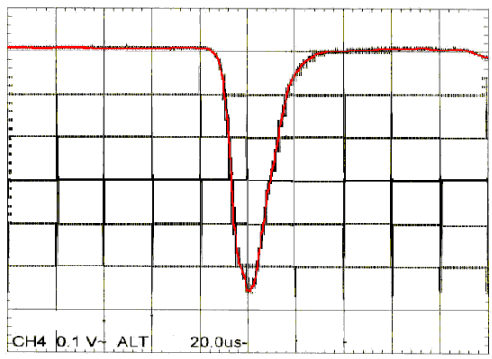

Figure 2. Successful RF pulsing of the cyclotron beam

4 EXTRACTED PROTON BEAM TESTS

The extracted beam properties have been assessed in an experimental programme making use of the beam line

previously devoted to feeding the neutron target. This line has quadrupole triplets before and after a 55^0 dipole magnet and the latter allows a large dispersion to be set if required. The available diagnostics in the experimental beam line has been quite limited; a fluorescent screen at the downstream end supplements spinning wire profile monitors at two fixed locations. Viewing the screen image with a CCD camera the beam sizes were estimated by fitting to Gaussian profiles using framegrabber and image analysis software written with LabVIEW [9].

Systematic scans of single quadrupoles with the beamline set to give both high and low dispersion at the screen [6] gave a range of data that was then fitted to a linear model of the beamline written using Microsoft EXCEL [10]; quadrupole field gradients were calibrated using a Hall plate. Although the predicted beam sizes are only weakly dependent upon the model energy spread an upper bound of 0.1% rms can be given for this cyclotron parameter; Twiss functions and emittances have also been estimated, the latter being consistent with those given in Table 1. An example is shown in Figure 3 where the horizontal beam size is compared with model energy spreads of 0.1%, 0.05% and 0.01%.

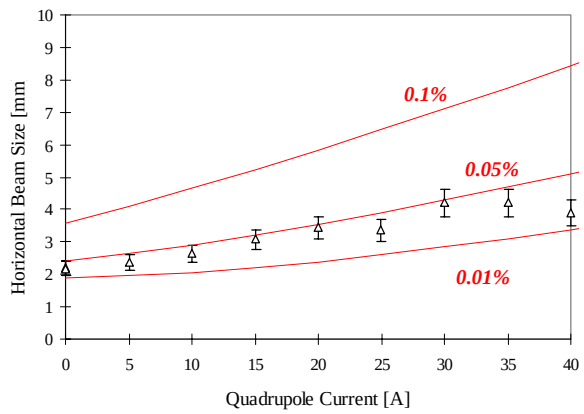

Figure 3. Typical fit of cyclotron parameters

5 CONCLUSIONS

The first phase of assessment of the properties of the extracted proton beam from the 62 MeV Clatterbridge cyclotron has been successfully completed. Emittances in both planes have been confirmed to be at or even below the expected values of about 2-3 mm-mrad and the energy spread appears to be exceptionally good, with an upper value (rms) of 0.1 % and probably considerably lower. Pulsed beam operation has been commissioned by modification to the RF drive circuitry and a pulse width of 20 μs at 50 Hz demonstrated; since the modulation is effectively onto the low energy beam acceptance in the accelerator it is not expected that the high energy beam properties will be adversely affected, but this has yet to be confirmed experimentally. Nevertheless it is clear that the cyclotron could be a suitable injector into a high frequency proton linac booster. The possibility of testing this with a real accelerating structure will now be pursued, perhaps in an international collaboration.

6 ACKNOWLEDGEMENTS

We wish to thank E. Wilson (CERN) and U. Amaldi (CERN and TERA Foundation) for helpful encouragement and advice. L.-O. Arlasjo (Scanditronix Medical AB) provided important technical advice on the cyclotron.

7 REFERENCES

[1] U. Amaldi, “Accelerators for Medical Applications”, Proceedings of the 5th European Particle Accelerator Conference, June 1996, Sitges, p 244.

[2] “European Strategy for Cancer Research”, Commission of European Communities DG XII - Medical Division (1991): XII/F-6/AV/nv/91001P

[3] “The RITA Network and the Design of Compact Proton Accelerators”, Eds: U. Amaldi, M. Grandolfo and L. Picardi, INFN, Frascati, 1996

[4] L. Picardi et al, “The TOP-ISS Linear Accelerator: A High Frequency Proton Linac for Therapy”, Proceedings of the 5th European Particle Accelerator Conference, June 1996, Sitges, p 2638

[5] M. Weiss, Private Communication

[6] J.A.Clarke et al. “An Assessement of a Medical Cyclotron as an Injector for an Energy Upgrade”, Proceedings of the 6th European Particle Accelerator Conference, June 1998, Stockholm.

[7] U. Amaldi, Private Communication

[8] M.P.S. Nightingale et al, Proceedings of the Linear Accelerator Conference, Ottawa, 1992, p 398

[9] National Instruments, 6504 Bridge Point Parkway, Austin, TX 78730-5039, USA.

[10] Microsoft Corporation, Redmond, Washington 98052-6399, USA.

LIBO — A 3 GHZ PROTON LINAC BOOSTER OF 200 MeV FOR CANCER TREATMENT

U. Amaldi, B. Szeless, M. Vretenar, E. Wilson
CERN, CH 1211 Geneva 23, Switzerland
K. Crandall
Consult Crandall, Edgewood, New Mexico 87015, USA
J. Stovall
Rutherford Appleton Laboratory, Chilton, Didcot, UK
M. Weiss
TERA, Foundation for Oncological Hadrontherapy, Via Puccini 11, 28100 Novara, Italy

Abstract

Several hospitals and laboratories possess proton cyclotrons with output energies of 60 to 70 MeV. A high frequency (3 GHz) booster linac (LIBO) is proposed to upgrade the cyclotron beam to an energy of 200 MeV, sufficient to treat deep seated tumours. LIBO is a side-coupled linac which can produce beams with a variable output energy. This paper presents the feasibility study of such an accelerator, together with the milestones planned for 1998-1999, including the machining of a part of LIBO and testing it with full RF power on a test stand at CERN.

1 INTRODUCTION

The design of a novel high-frequency proton linear accelerator of 200 MeV for medical purposes was proposed by the TERA Foundation in 1996 [1]. Such an accelerator has been further studied at ENEA, Frascati, Italy, and the low energy part of it is now under construction [2]. Reference [1] briefly describes a study of a booster linac, LIBO, intended to upgrade a cyclotron beam energy from about 60 MeV (already available in several hospitals and research institutions) to 200 MeV in order to treat deep seated tumours. In an earlier proposal [3] a similar but lower frequency upgrade was considered for the 62 MeV cyclotron of the Clatterbridge Centre for Oncology, UK. LIBO studies are also based on the Clatterbridge cyclotron, but the operating frequency has been pushed into the S-band in order to reduce the accelerator size and increase its breakdown limit.

LIBO is a side-coupled linac (SCL) operating at 2998 MHz. It is composed of 36 tanks, separated by permanent magnetic quadrupoles (PMQs). Four tanks are grouped into a module, an RF unit, fed by its own RF chain.

The average output beam required from LIBO is of the order of 10nA, and it must be possible to vary its energy from about 130 to 200 MeV. This constrains both the number of tanks in a module and their length.

The 3 GHz klystrons used to power the tanks operate in the pulsed mode with pulse lengths of up to 5 μs, but it is the average power a klystron can deliver that limits the LIBO duty cycle. The energy spread in the LIBO beam should be narrow enough to limit the distal fall off of the dose given to the patients to ≤ 2 mm. A beam pulse repetition rate of 400 Hz has been chosen to suit an active beam scanning method (e.g. pixel scanning). Preliminary tests have been performed to pulse the Clatterbridge cyclotron beam [4] to study its use as a LIBO injector

2 BEAM OPTICS

Beam optics studies have been made in order to find a suitable layout of LIBO. A high average axial accelerating gradient E_0 (15.3 MV/m) has been selected to limit the accelerator length and care has been taken to avoid synchro-betatron parametric resonances. The cyclotron beam will be matched transversely to LIBO by focusing elements placed between the two accelerators and the aperture radius of 4 mm will make the transverse acceptance A_t such as to contain the cyclotron beam emittance ($A_t \cong 12\ \pi$ mm mrad).

Longitudinally the situation is different. Only part of the low frequency cyclotron beam falls into the short LIBO buckets and many particles remain outside. This effect has been analysed by simulating the cyclotron beam, which appears continuous in phase when referred to the LIBO frequency of 2998 MHz, and dividing it into many thin phase slices which span 360 degrees. Each slice is followed through the linac with a beam dynamics program, and LIBO is optimised in a preliminary way, assuming no misalignments. It is then found that about 50% of the continuous beam can be transmitted and about 25% of the transmitted beam is fully accelerated. Thus the accelerated beam is about 12.5% of the input beam. Most of the rest of the beam leaves with energies below 70 MeV.

Misalignments of PMQs and linac tanks, and other errors, such as quadrupole gradient errors, can reduce the intensity of the accelerated beam. One can estimate the effect of quadrupole misalignments on the transmission by making a Monte Carlo optics calculation.

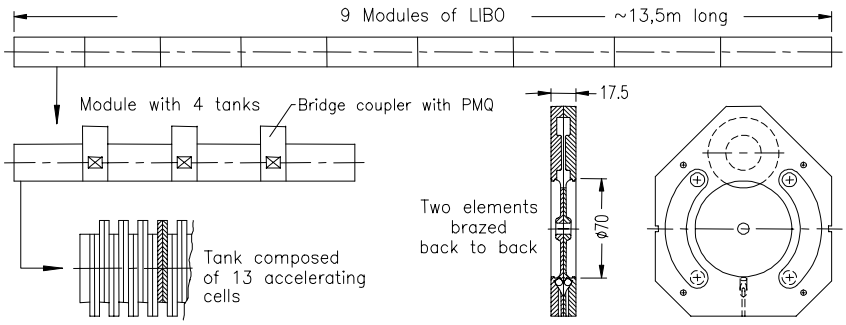

Figure 1: Schematic layout of LIBO

Four types of error have been analysed: quadrupole displacement errors of ±0.1 mm; tank displacement errors of ±0.1 mm; quadrupole rotation errors of ±1°; and quadrupole strength errors of ±1%. The only error that produces any significant reduction in the transmission is quadrupole displacement. For a displacement error tolerance of 0.1 mm there is a 90% probability that the transmission will be greater than 10%, and about a 50% probability that the transmission will be greater than 11%. With a 10% transmission and a beam duty cycle of 0.0018 (400 Hz and 4.5 μs) the LIBO trapping efficiency will be 1.8×10^{-4} and hence, in order to have an average output current of 10 nA, the peak intensity in the cyclotron beam pulse should be about 55 μA.

3 LIBO STRUCTURE

A schematic layout of LIBO is shown in Figure 1. Nine modules, each comprising four tanks, are mechanically coupled together to form the 13.5 m long accelerator. A tank has 13 accelerating cells, which are formed from 24 basic elements and from 2 half end cells. Each basic element consists of half of an accelerating cell and half of a coupling cell. The tanks of a module are resonantly coupled together via three bridge couplers. The central coupler is connected to the RF feeder line and the remaining two to a vacuum system. An RF pick-up is installed at either end of each tank and PMQs, placed between the tanks, form a FODO focusing lattice. The soft copper linac will be precisely aligned by fixing it on a rigid support with pre-adjusted keys.

The shape of the cells has been studied using the program SUPERFISH. Investigations have included, among other things, the effect of the accelerating cell diameter D and of the web thickness w (wall between two accelerating cells) on the effective shunt impedance ZT^2 and peak surface field E_{peak}. The shunt impedance includes the effect of slots for 3% coupling. The upper curve in Figure 2 shows that at the high energy end of LIBO (β=0.56), the chosen diameter D of 70 mm is optimum with respect to ZT^2. The lower curve shows that at the low energy end (β=0.35) there is little to be gained in ZT^2 by reducing D and that E_{peak} would increase rapidly. With D=70 mm, E_{peak} is limited to a conservative value of 1.6 times the Kilpatrick limit E_k.

Figure 3 shows that a thin web thickness w is preferable, as one might expect from the short cell lengths of LIBO. A 4 mm web has been chosen for a good mechanical rigidity of the pieces during machining and it has been decided to braze two basic elements back to back before the final machining of the accelerating cells. However, the really delicate issue is whether cooling channels are required in the web or whether circumferential cooling alone is sufficient. Cooling channels would necessitate a relatively thick web, which spoils the electrical characteristics and complicates the mechanical design, adding an extra risk and cost.

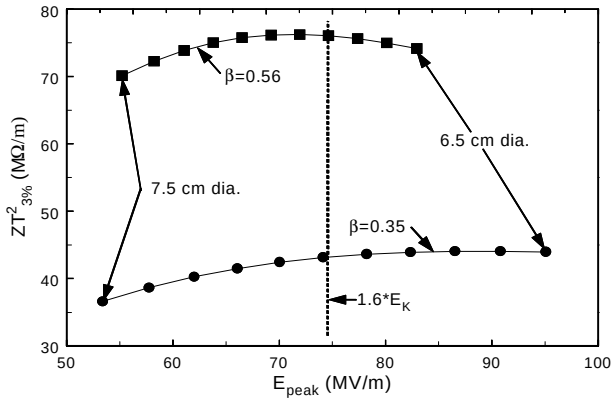

Figure 2: The points show the shunt impedances and the peak surface fields for 11 different cell diameters D, at the input (β=0.35) and output (β=0.56) energy. The web thickness w is 4 mm.

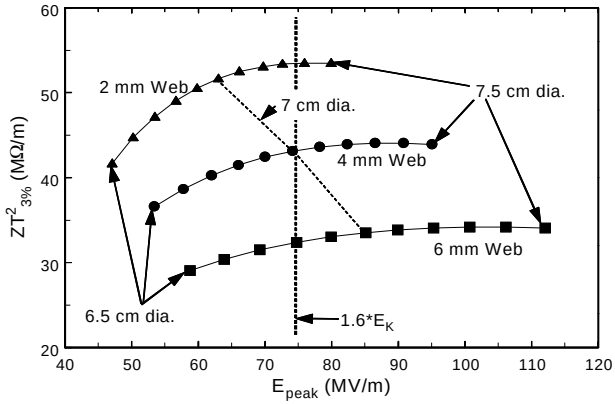

Figure 3: The points show the shunt impedances and the peak surface fields for 11 different cell diameters D and for 3 web thicknesses w, at the input energy (β=0.35).

The cooling problem has been studied assuming an RF duty factor of 0.2%, for which 150 W are dissipated in each accelerating cell of tank 1. Very little power is dissipated in the coupling cells because LIBO operates in the $\pi/2$ mode. The study has proceeded as follows:

- A table of surface coordinates of an accelerating cell and of the power density distribution on its walls is generated by SUPERFISH.
- The table is read by a finite element engineering code ANSYS, together with the specifications of the cell material. In our model this material extends to a radius of 40 mm, where a thermal boundary is defined. Simple cooling is simulated by fixing the sink temperature, T_{sink}, at this radius, where one may reasonably expect the temperature to be uniform. ANSYS computes the temperature distribution, the thermal stresses and the mechanical deformations of the cell. In our case, there was a temperature gradient between the nose (centre of the cell) and T_{sink} of about 7° C.
- A special code has been written to compute the frequency of distorted cells. The code reads the coordinates of the deformed cell surface from ANSYS, compares them with the original ones and computes the frequency detuning Δf by using Slater's perturbation theorem. The detuning is found to be about –250 kHz if T_{sink} is held at its ambient value.
- By lowering T_{sink}, the original cavity can be mechanically deformed in the opposite sense. Using ANSIS and the special code, it was found that changing T_{sink} by –5° C brings the cell back on tune; see Figure 4.

The conclusion is that circumferential cooling will be adequate for LIBO and that by controlling T_{sink} with the frequency feedback loop, it will be possible to keep the accelerator on tune.

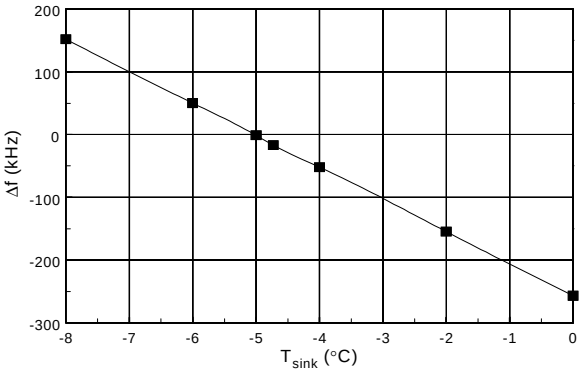

Figure 4: Detuning Δf as function of the lowering of the sink temperature T_{sink}.

The effects of coupling slots between cells have been studied with the 3-D program MAFIA. The PSPICE program, dealing with coupled circuits, has been used to assess the importance of various errors in the presence of incompletely closed stop bands. Cold RF measurements on a few cells of an aluminium model at CERN completed the studies of LIBO.

4 FEASIBILITY TEST

The SCL type of structure is usually used with lower frequencies or with higher β values than those foreseen for LIBO. It is therefore important to carry out a feasibility test prior to the construction of a complete medical booster linac. In a collaboration with High Vacuum Process (HVP), Parma, Italy, the following milestones have been set:

- Construction of a model of the first LIBO tank in copper (at HVP) in order to master the delicate parts of the production (machining, tuning, assembling, brazing, cooling etc). It should be completed in the second half of 1998.
- Construction of the complete first LIBO module (at HVP) to be tested with full RF power at CERN; the module will be pumped, water cooled and powered by a spare 3 GHz chain of LIL, and it will also contain pick-ups for RF feedback. The tests at CERN are planned for the end of 1999.

5 ACKNOWLEDGMENTS

Our CERN collegues, L. Bassi, P. Bourquin, A. Millich and R. Zennaro participated in several studies presented in this paper; A. Catinaccio, in particular, dealt with the deformations of the structure and the resulting detuning. J. Lipp of RAL assisted in this analysis. K. Hübner, D. Simon and the PS division of CERN supported this project in many ways and rendered, together with S. Ferrari (HVP), the fixing of our milestones possible. To all of them go our deepest thanks.

The financial support of the Price Foundation is gratefully acknowledged.

6 REFERENCES

[1] U. Amaldi, M. Grandolfo and L. Picardi, editors, "The RITA Network and the Design of Compact Proton Accelerators", INFN, Frascati 1996, ISBN 88-86409-08-7.

[2] L. Picardi, C. Ronsivalle and A. Vignati,"Progetto del TOP Linac", RT/INN/97/17, ENEA, Frascati 1997.

[3] M. P. S. Nightingale, A. J. T. Holmes and N. Griffiths, "Booster Linear Accelerator for Proton Therapy", Proceedings of the Linear Accelerator Conference, Ottawa, Canada, August 24-28, 1992, 398-401.

[4] J. A. Clarke, D. M. Dykes, C. W. Horrabin, H. L. Owen, M. W. Poole, S. L. Smith and V. P. Suller, "Assessing the Suitability of a Medical Cyclotron as an Injector for an Energy Upgrade", Proceedings of the EPAC – 98, Stockholm, Sweden, 1998.

MEDICAL ISOTOPE PRODUCTION WITH THE ACCELERATOR PRODUCTION OF TRITIUM (APT) FACILITY

M. R. Buckner, Westinghouse Savannah River Co., Aiken, SC 29802
M. Cappiello, Eric Pitcher, Los Alamos National Laboratory, Los Alamos, N.M. 87544
H. O'Brien, O'Brien & Associates, 107 LaSenda Road, Los Alamos, N.M. 87544

1 INTRODUCTION

In order to meet US tritium needs to maintain the nuclear weapons deterrent, the Department of Energy (DOE) is pursuing a dual track program to provide a new tritium source. A record of decision is planned for late in 1998 to select either the Accelerator Production of Tritium (APT) or the Commercial Light Water Reactor (CLWR) as the technology for new tritium production in the next century. To support this decision, an APT Project was undertaken to develop an accelerator design capable of producing 3 kg of tritium per year by 2007 (START I requirements). The Los Alamos National Laboratory (LANL) was selected to lead this effort with Burns and Roe Enterprises, Inc. (BREI) / General Atomics (GA) as the prime contractor for design, construction, and commissioning of the facility. If chosen in the downselect, the facility will be built at the Savannah River Site (SRS) and operated by the SRS Maintainance and Operations (M&O) contractor, the Westinghouse Savannah River Company (WSRC), with long-term technology support from LANL. These three organizations (LANL, BREI/GA, and WSRC) are working together under the direction of the APT National Project Office which reports directly to the DOE Office of Accelerator Production which has program authority and responsibility for the APT Project.

2 DESCRIPTION OF APT

The APT, which is shown schematically in Figure 1, is made up of four major subsystems which are described briefly below[1].

2.1 Accelerator System

The Accelerator System consists of the following subsystems:

- Proton injector to develop and maintain a continuous 100-mA current.
- Radio Frequency Quadrupole (RFQ) to focus and accelerate the proton beam to 7 MeV (kinetic energy)
- Coupled-cavity Linac (CCL) to accelerate the proton beam to 211 MeV.
- Superconducting Linac (SCL) to accelerate the proton beam to its final energy of 1700MeV. The design is modular so that the portion of the accelerator up to 1030 MeV can be completed to produce 1.5 kg/yr of tritium and then a decision can be made as late as 2002 to add the last section if the START I production level is still required.

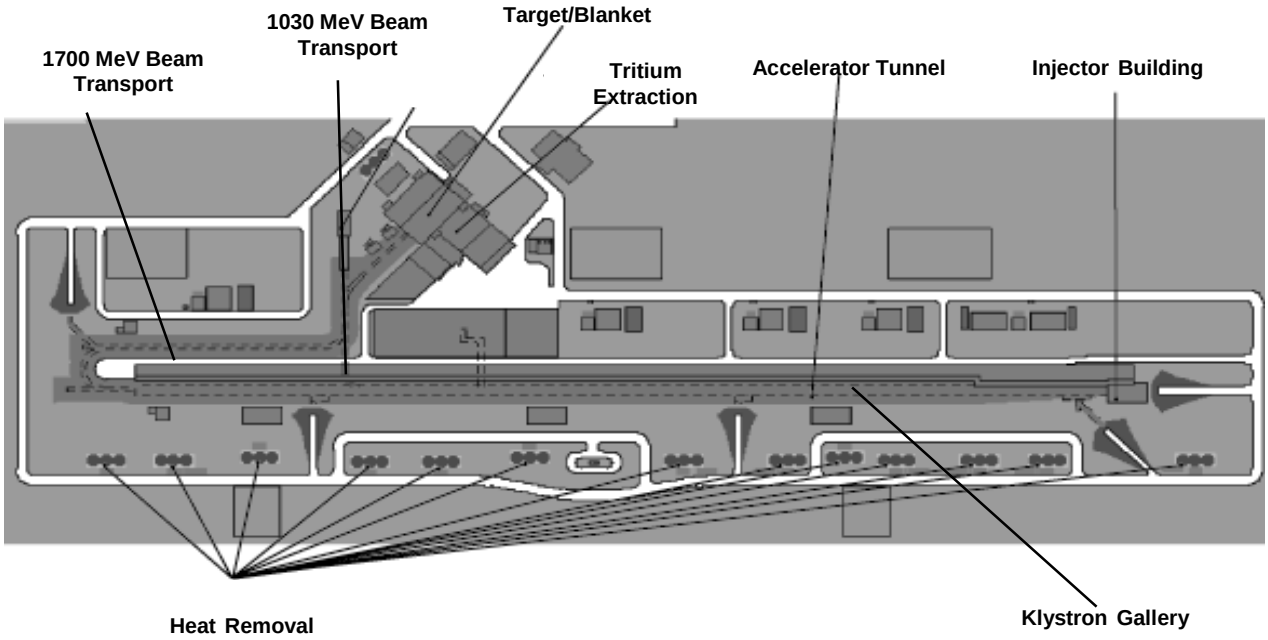

Fig. 1 APT Plant Layout

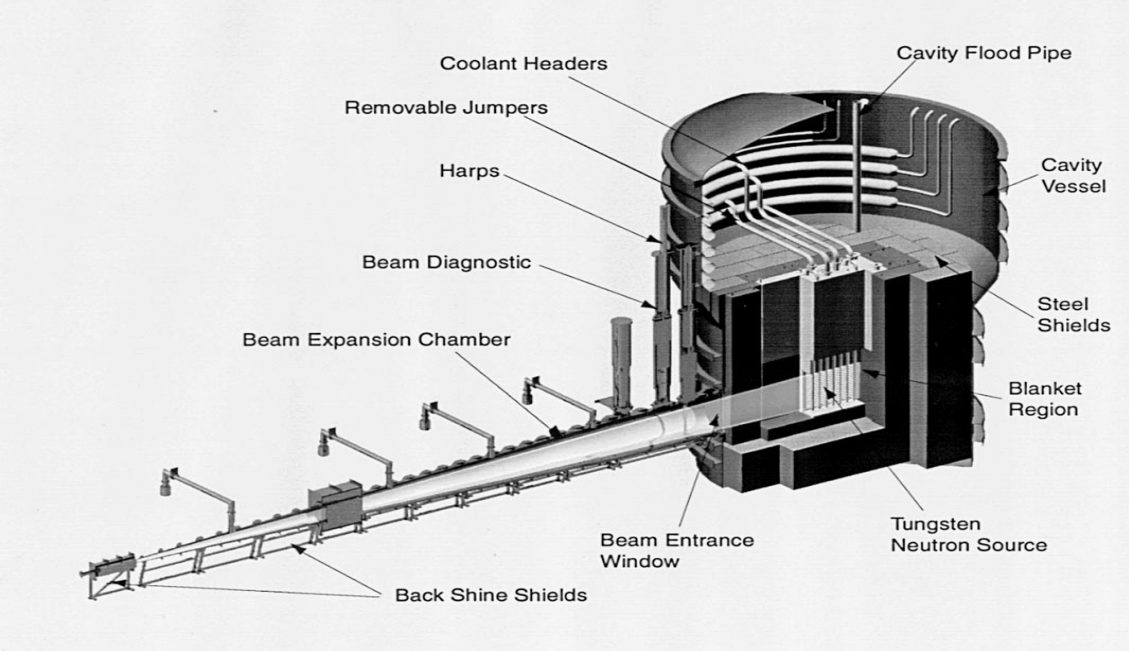

Fig. 2 APT Target/Blanket

2.2 Target/Blanket (T/B) System

The Accelerator System provides a proton beam that is expanded and directed to a T/B assembly shown in Figure 2. The T/B assembly consists of a tungsten clad target in which neutrons are produced by spallation surrounded by a blanket in which additional neutrons are produced in lead. The neutrons are thermalized by collisions in the lead and in light-water and are subsequently captured in He-3 to produce tritium.

2.3 Tritium Separation Facility (TSF)

The TSF operates by extracting tritium from a tritium, hydrogen, and He-3 mixture returned from the T/B System in a recirculating He-3 loop. The He-3, hydrogen and tritium mixture also contains impurities such as water, methane, ammonia and small quantities of radioactive materials. Hydrogen isotopes are separated from the He-3 and sent to an Isotope Separation System where the tritium is separated from hydrogen. The He-3 is purified and recycled to the T/B assembly.

2.4 Balance of Plant (BOP) Systems

The BOP Systems support the integrated operation of the accelerator, T/B, and TSF, and provide the facility buildings that house them. The BOP System designs are driven by the required electric power input, the generated waste heat to be removed throughout each facility and the need to handle radioactive materials remotely.

3 MEDICAL ISOTOPE PRODUCTION WITH APT

The APT T/B will produce a high energy, high flux proton and neutron irradiation environment that is unique in the field of isotope production[2]. In addition to converting He-3 to tritium, it can be used to create isotopes for medical applications. Although the primary mission of the APT is to create tritium for the nuclear weapons deterrent, an ancillary isotope production mission is possible without significantly impacting tritium production. Because of the unique irradiation environment, and the large volume of space available, the APT has the potential to provide a significant source of research, diagnostic, and therapeutic isotopes to the medical community.

The capability for the irradiation of medical isotope targets is feasible within the scope of the T/B material surveillance program. The centerpiece of this program is a “rabbit” system that allows the insertion and removal of material surveillance coupons directly into several (up to seven) locations within the T/B assembly. Double wall tubes with a continuous flow of water provide a cooled environment for small (approximately 1.4 cm diameter by 6.3 cm long) target capsules. These capsules are moved in and out of the irradiation positions using hydraulic pressure. The design of the tungsten neutron source in the APT T/B allows for a large volume of potential irradiation positions directly in the high proton and neutron flux regions.

A small hot cell located nearby in an adjoining room is used to remove the capsules from the ”rabbit” tubes and load them into shipping casks for transfer to a processing facility. Location of a private processing facility at the site boundary is a possibility. As an option to shipping casks, it is also possible to use pneumatic transfer tubes from the hot cell to the processing facility to speed the transfer.

Radioisotopes production in the APT target/blanket was analyzed to determine production rates and radiopurity of several isotopes that are of interest to the medical community. These include Cu-67, Ge-68, Sr-82, In-111, Re-186, Sm-153, Pd-103, P-32, Sc-47, and Ga-67. The isotopes were produced by nuclear spallation of natural (non-enriched) target materials by high-energy protons and neutrons. Significant production rates, high radiopurity and specific activity were achieved for most of the isotopes. In addition, the calculations showed that for 11 liters of target volume placed directly in the proton beam the decrease in tritium production was less than 2%.

4 THE POTENTIAL IMPACT OF APT ON MEDICAL ISOTOPE NEEDS

Leaders of the biomedical science community met recently in Dallas[3] to discuss the importance of developing an adequate supply of radionuclides to support clinical practice, research, education and training, and new treatments. The group acknowledged that the present supply of radionuclides is insufficient to meet current and projected future needs.

As an example, the recent development of specific delivery agents such as monoclonal antibodies that can target specific tumor cells and carry radiotherapeutic materials to those cells has led to a major advance in radiotherapy. Other healthcare areas with great potential include bone pain palliation, brachytherapy applications in inoperable tumors, nuclear cardiology and positron emission tomography (PET) procedures. For these to become available in routine practice there must be a supply of reasonably priced, high purity radionuclides

The proposed APT facility has the potential to supply the much-needed radionuclides. Although the charter for APT does not include radionuclide production, the facility has the potential to make a significant contribution with little impact on tritium production. The biomedical community leaders learned of preliminary calculations of production yields, specific activities and radionuclidic purities for the nuclides listed above. This wide variety is possible from APT because, unlike reactor facilities, both energetic protons and neutrons are available in quantity.

Working as a team, the group developed the following statement in support of including radionuclide production in the APT charter:

“The APT facility will provide a unique resource for the production of substantial quantities of high specific activity radionuclides resulting in enormous scientific, research and education opportunities. These radionuclides will be especially useful in advancing healthcare for diagnosis and in the rapidly growing area of radionuclide therapy. We therefore support an expansion of the APT project charter to include designing into a biomedical radionuclide production capability. This initiative should not draw from existing radioactive materials research or production programs, as it is fundamental to the overall DOE mission, extending rather than replacing existing efforts, with downstream benefits which are vast for the nation.”

There was general agreement within the group that any new opportunity for radionuclide production and development gained by construction of the APT facility should be jointly pursued by the National Institutes of Health (NIH), DOE, and the Department of Defense (DOD), with NIH being the lead agency.

5 CONCLUSIONS

The APT will produce a high energy, high flux proton and neutron irradiation environment that is unique. Medical isotope production in APT has the potential to provide downstream benefits which have been judged by the biomedical community to be “vast for the nation”. Although the primary mission of the APT is tritium production, significant medical isotope production is possible with little impact on tritium production.

REFERENCES

1. “Accelerator Production of Tritium Conceptual Design Report”, LA-UR-96-4847 (March, 1997).
2. Cappiello, M., E. Pitcher, H. O’Brien, “APT Design Overview and Isotope Production Capability”, LA-UR-98-1793, (May, 1998).
3. “Proceedings of the Medical Isotope Work-shop”, Medical University of South Carolina, Charleston, S.C. (June, 1998).

OPERATION OF HIGH-POWER 8.6 AND 17.1 GHz COAXIAL GYROKLYSTRONS*

W. Lawson, B. Hogan, M. Castle, V. L. Granatstein, M. Reiser, X. Xu
Institute for Plasma Research, University of Maryland, College Park, MD 20742

Abstract

At the University of Maryland, we have designed, constructed, and tested a number of gyroklystron tubes operating from X-Band to Ka-Band over the past several years [1]. The purpose of this effort is to examine the suitability of gyro-amplifiers as drivers for advanced accelerator applications such as the Next Linear Collider. We are currently conducting a series of experiments with coaxial tubes which are designed to produce peak powers in excess of 100 MW in X- and Ku-Band, increasing the state-of-the-art by a factor of 3-5. Preliminary results have indicated peak powers in excess of 75 MW at 8.6 GHz in a three cavity first-harmonic gyroklystron tube with a gain near 30 dB and an efficiency near 32%. In this paper we will detail the experimental results of this tube and discuss designs and preliminary cold test results of a 3-cavity second-harmonic device, which is expected to give comparable results at 17.14 GHz.

1 INTRODUCTION

At the University of Maryland, we have been investigating the suitability of high power gyro-amplifiers as drivers for linear colliders for over a decade. [1] To this end, we have designed, constructed, and tested a variety of gyroklystron and gyrotwystron tubes operating from X-Band to Ka-Band. With a 440 kV, 160-260 A beam, we were able to produce about 30 MW of peak power in 1 μs pulses near 9.87 and 19.7 GHz with first- and second-harmonic gyroklystron tubes, respectively. The peak efficiencies were near 30% and the large-signal gains were 25-35 dB. Circular electric modes were used in all cavities and the average beam velocity ratio was always near one. Efficiency was limited by instabilities in the beam tunnel preceding the input cavity and beam power was limited by the electron gun.

The focus in the past few years has been to upgrade the system to achieve peak powers approaching 100 MW in X- and Ku-Band. The increase in power results from a larger beam current, which is achieved by maintaining the same current density, but enlarging the average beam radius. Subsequently, the tube cross-sectional dimensions are increased and an inner conductor is required to maintain cutoff to the operating mode in the drift regions. To date, we have hot-tested a 2-cavity and a 3-cavity first harmonic tube and we are about to test a 3-cavity second harmonic tube.

In this paper we first discuss the experimental test facility. Then we discuss the computer simulations before describing the experimental results from our X-Band tubes. Finally, we mention our Ku-Band progress before closing with our near and long term goals.

2 EXPERIMENTAL TEST FACILITY

The voltage pulse is generated with a line-type modulator which is capable of producing 2 μs flat-top pulses at up to 2 Hz with voltages and currents up to 500 kV and 800 A, respectively. A capacitive voltage divider and a current transformer are used to measure the time evolution of the voltage and current. Our single-anode MIG is

Table I. The system parameters.

Beam parameters	
Beam Voltage (kV)	470
Beam Current (A)	505
Average Velocity Ratio	1.05
Axial velocity spread (%)	4.4
Magnetic field parameters	
Input cavity field (kG)	5.69
Buncher cavity field (kG)	5.38
Output cavity field (kG)	4.99
Input and buncher cavity parameters	
Inner radius (cm)	1.10
Outer radius (cm)	3.33
Length (cm)	2.29
Quality factor	70 ± 15
Output cavity parameters	
Inner radius (cm)	1.01
Outer radius (cm)	3.59
Length (cm)	1.70
Quality factor	135 ± 10
Drift tube parameters	
Inner radius (cm)	1.83
Outer radius (cm)	3.33
Length (between I-B) (cm)	5.18
Length (between B-O) (cm)	5.82
Amplifier Results	
Drive Frequency (GHz)	8.60
Output power (MW)	75
Pulse length (μs)	1.7
Gain (dB)	29.7
Efficiency (%)	31.5

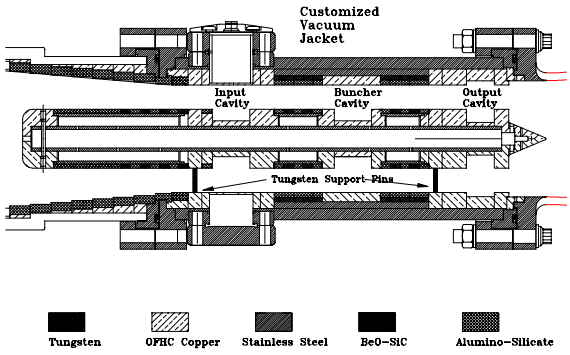

Figure 1. The three-cavity microwave circuit.

capable of producing a 500 kV, 720 A beam with an average orbital-to-axial velocity ratio of $\alpha = 1.5$ and an axial velocity spread of $\Delta v_z/v_z < 10\%$. The beam parameters are given in Table I for the operating point where maximum amplification occurs. The voltage and current are measured quantities; all other values come from the EGUN simulations and are based on the MIG geometry and the magnetic field profile. The actual theoretical fields at the centers of the three cavities are given in Table I. The axial field is detuned by -3.5% in the input cavity, -8.8% in the buncher cavity and -15.4% in the output cavity.

The 3-cavity microwave circuit is shown in Fig. 1 and the key dimensions are given in Table I. The inner conductor is supported by two thin tungsten pins and forces the drift tubes to be cutoff to the TE_{01} mode at 8.6 GHz. The inner conductor only extends a few centimeters into the downtaper and is rapidly terminated after the output cavity. Lossy ceramics are placed in the drift regions to suppress spurious modes. The rings on the inner conductor generally alternate between carbon-impregnated alumino-silicate (CIAS) and 80% BeO-20% SiC. Two layers of lossy ceramics are placed along the outer conductor in the drift regions. The outer layer is BeO-SiC and the inner layer is CIAS. The 2-cavity circuit omits the buncher cavity and has a longer drift region.

The input cavity is defined by a decrease in the inner conductor radius. The cavity loss is roughly evenly divided between the coupling aperture and a CIAS ring on the inner conductor which is placed adjacent to the cavity. The power to the input cavity is supplied by a 150 kW coaxial magnetron. The buncher cavity has identical dimensions for the metal components. However, the Q is determined entirely by CIAS ceramics.

The output cavity is defined by radial changes on both walls and the lip radii are equal to the drift tube radii. The quality factor is dominated by the diffractive Q which is adjusted by changing the length of the coupling lip.

3 THEORETICAL AND EXPERIMENTAL RESULTS

3.1 First-Harmonic Results

A partially self-consistent large-signal code is used to design the circuit and magnetic field configuration and to estimate the performance of the tube at the actual operating point. A small-signal start-oscillation code is used to determine the stability properties of the cavities and set limits on the cavity quality factors. The solid line in Fig. 2 shows the expected performance of the tube as a function of velocity spread for α=1.5. The simulation predicts a zero-spread efficiency of 43%, and an efficiency of 34% for 10% spread. For the 6% spread predicted for a 500 A beam, the simulated interaction efficiency is about 40%. All microwave cavities are expected to be stable at the design operating point for the quality factors indicated in Table I. The theoretical efficiency for the 2-cavity tube is slightly less, but the predicted gain is significantly lower. Consequently, the 2-cavity tube was gain-limited and produced less than 1 MW of output power.

The optimal parameters and experimental results have been listed in Table I. The values are all taken from anechoic chamber measurements. The time dependence of

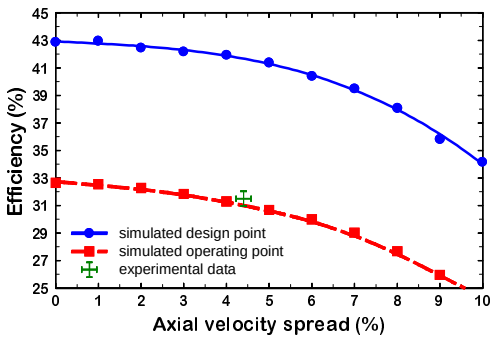

Figure 2. Efficiency versus velocity spread.

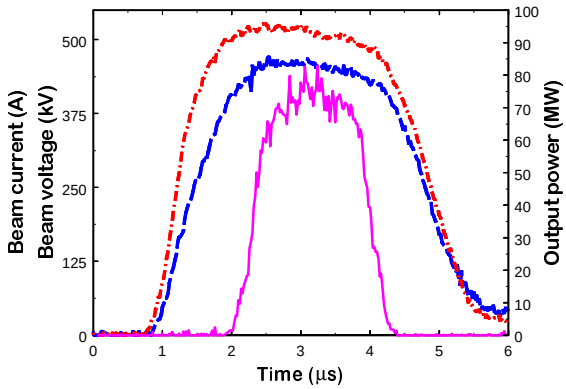

Figure 3. Time dependence of the output pulse.

the beam voltage (dashed line), beam current (dot-dashed line), and the amplified signal (solid line) are shown in Fig. 3. There is a slight droop on the flat top due to mismatches in the modulator. The peak values indicated in Table I represent the average value of the signal in the flat top region. The peak power is about 75 MW, which represents an efficiency of nearly 32%. The corresponding gain is almost 30 dB and the pulse width is 1.7 μs (FWHM). Attempts to increase the peak power further by raising the beam's velocity ratio result in a sharp cut in the output signal near the maximum value which is usually indicative of an instability (though none were detected by the microwave diagnostics).

An EGUN simulation using the parameters of the operating point indicate that the beam's velocity ratio at the entrance to the circuit is near one. There is a reasonably large uncertainty in this ratio due to the neglect of the self-axial magnetic field in EGUN and the uncertainty in the applied field at the cathode. In a previous experiment at the University of Maryland, for example, the measured average velocity ratio was consistently higher than the simulated ratio by about 15%. [2] Simulations of the amplifier performance at the operating point are given by the dashed line in Fig. 2. The simulated cathode magnetic field is adjusted slightly to produce the best match between the theoretical efficiency and the measured efficiency, which is indicated by the cross. The required field is about 20 G lower than the calculated ideal field and well within the uncertainties of the experimental data.

3.2 Second Harmonic Tube

The second harmonic tube is realized by keeping the first harmonic tube's input cavity but replacing the buncher and output cavities with ones that resonate at twice the drive frequency in the TE_{021} mode. Such cavities

Table II. The second harmonic design.

Beam voltage (kV)	500
Beam current (A)	770
Velocity ratio	1.51
Input cavity Q	50
Buncher cavity Q	389
Output cavity Q	320
Gain (dB)	49
Efficiency (%)	41
Output power (MW)	158

are normally difficult to realize, because the cavity's end walls generate other radial modes due to the beam tunnel opening. For cavity isolation, the fields must not leak substantially into the drift regions, yet the operating frequency is well above the cutoff of the TE_{01} mode. In circular waveguide systems, the usual way to avoid this problem is to introduce smoothly-varying wall radii, but the added length of these transitions is usually unacceptable. Fortunately, in coaxial tubes, making the radial wall transitions that define the TE_{021} cavity approximately

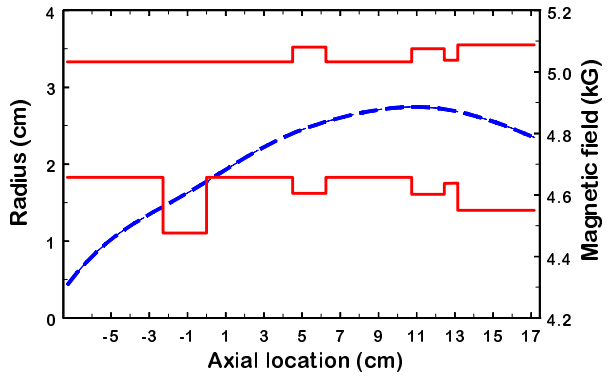

Figure 4. The shape of the second harmonic tube and the simulated optimal magnetic field profile (dashed line).

equal on the inner and outer walls naturally leads to a mode with very little conversion to the TE_{01} modes and subsequent leakage fields.

The principal design parameters for our three cavity second harmonic tube are given in Table II along with the simulated performance estimates. The cavity profile is shown in Fig. 4. The overall length is very similar to the first harmonic tube. At this point, the tube components have been constructed, the cavities have been adjusted to achieve the required frequencies and quality factors, and the tube is installed in our test facility. Hot testing should commence in the next few days.

4 SUMMARY

In summary, we have developed an X-band coaxial gyroklystron which has increased the state-of-the-art in peak power for gyroklystrons by nearly a factor of 3. In the near future we will test our 2nd harmonic tube, with the goal of obtaining about 100-150 MW of peak power at 17.136 GHz. We will investigate the limitations on velocity ratio in greater detail and attempt to increase the nominal velocity ratio to the original design value. In the long term we expect to build and power a 17.136 GHz accelerator structure with an accelerating gradient near 200 MV/m.

5 ACKNOWLEDGEMENTS

The authors would like to thank N. Ballew, P. Chin, J. Cheng, P. E. Latham, G. Nusinovich, and G. P. Saraph for their contributions to this work.

6 REFERENCES

[1] V. L. Granatstein and W. Lawson, "Gyro-Amplifiers as Candidate RF Drivers for TeV Linear Colliders," IEEE Trans. on Plasma Science, Vol. 24, pp. 648-665 (1996).

[2] J. P. Calame and W. Lawson, *IEEE Trans. Electron Devices*, vol. 38, p. 1538 (1991).

EXPERIENCE AT FERMILAB WITH HIGH QUANTUM EFFICIENCY PHOTO-CATHODES FOR RF ELECTRON GUNS

A. Fry,* E. Hahn, W. Hartung,† M. Kuchnir
Fermi National Accelerator Laboratory,‡ P. O. Box 500, Batavia, Illinois 60510 USA
P. Michelato, D. Sertore
INFN Milano—Laboratorio LASA, Via fratelli Cervi 201, 20090 Segrate (Milano), Italy

"Somebody leave the light on."
T. Amos

1 INTRODUCTION

As part of the A0 Photo-injector collaboration at Fermilab [1, 2] and the TeSLA collaboration [3], a high brightness, low emittance electron source has been developed. In the process, a system was constructed for coating molybdenum cathodes with a layer of cæsium telluride (Cs_2Te), a photo-emissive material of high quantum efficiency (QE). The use of Cs_2Te was first investigated at CERN [4] and LANL [5]. The development of the systems for the TeSLA Test Facility Linac and the Fermilab Photo-injector was done in Milano [6]. The system at Fermilab incorporates manipulator arms to transfer a cathode from the preparation chamber into a 1.3 GHz photo-electron RF gun while it remains in an ultra-high vacuum (UHV) environment, in order to avoid the deleterious effects of residual gases on the QE. A first prototype electron gun has been operated with a photo-cathode for several months [1]. This paper describes preliminary results obtained with the first 2 photo-cathodes and the first gun.

Some of the desired parameters for the TeSLA Test Facility beam are given in Table 1. The desired characteristics for the photo-cathodes include (i) high QE, (ii) high current density ($>$500 A/cm^2), (iii) long lifetime, and (iv) low field emission. The choice of Cs_2Te is a compromise between long lifetime, rugged metal cathodes with low QE (typically between 10^{-6} and 10^{-4}) and semiconductor cathodes with high QE ($>$10%), which generally have a short lifetime because of their sensitivity to contamination.

2 PREPARATION CHAMBER

To minimise the poisoning by residual gases, the cathodes must be coated under UHV conditions and remain in UHV throughout their useful lives. Thus, all components of the cathode preparation chamber (Figure 1) are compatible with UHV. The chamber is baked at 150 to 200°C after exposure to ambient air. The vacuum is maintained by 2 ion-getter pumps and a titanium sublimation pump. Ionisation gauges and a residual gas analyser (RGA) are used to monitor the pressure. The chamber can accommodate up to 5 cathodes, which could in principle all be used in turn without the need to bleed up the chamber. A cathode is moved from the coating chamber to the RF gun via one mechanical actuator and 2 magnetically-coupled actuators. The electrical contact between the cathode and the wall of the gun is made with a toroidal Be/Cu spring.

Table 1. Selected TeSLA Test Facility beam parameters.

Charge per bunch	8 nC
Bunch spacing	1 μs
Bunches per RF pulse	800
Repetition rate	10 Hz
Bunch σ_z in gun	4.3 mm

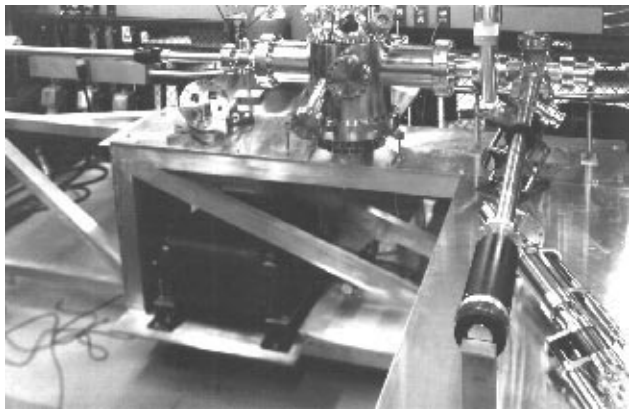

Figure 1. Cathode preparation chamber.

3 COATING OF THE CATHODES

Prior to coating, the sources are degassed by flowing a small amount of current through them. In the mean time, the molybdenum cathode is heated with a halogen lamp to encourage the evaporation of surface contaminants: the temperature is ramped up to 350°C and held at 350°C for 30 to 60 minutes. The cathode is then allowed to cool to 120°C and held at that temperature for the duration of the coating. A quartz crystal thickness monitor is inserted momentarily to calibrate the evaporation rates for the Cs and Te sources. Ultra-violet (UV) light from a mercury lamp (λ = 254 nm) is focussed onto the cathode and the photo-current is monitored during the deposition, as shown in Figure 2. Te is deposited for 10 minutes at a rate of 1 nm/minute, and then Cs is deposited at the same rate for 60 to 120 minutes. The pressure typically increases to between 1 and $4 \cdot 10^{-9}$ torr during evaporation of Cs or Te. The colour of the photo-emissive film was orange for the first cathode (Cs deposited for 63 minutes) and blue for the

*Department of Physics, University of Rochester. Present address: Positive Light, Inc, Los Gatos, California.
†Corresponding author.
‡Operated by the Universities Research Association under contract with the U. S. Department of Energy.

second cathode (Cs deposited for 110 minutes).

4 QE MEASUREMENTS

The UV beam from the mercury lamp is used to measure the QE while the cathode is in the preparation chamber. The QE is defined as

$$\mathrm{QE} = \frac{\text{Number of Emitted Photo-electrons}}{\text{Number of Incident UV photons}} .$$

The UV power is measured with a photo-diode. A bias of 200 V is applied between cathode and its surroundings to capture the photo-electrons. The photo-current is measured with a picoammeter; the background current (obtained by blocking the UV light) is subtracted. The DC QE is deduced from the ratio of the photo-current to the UV power. The UV spot size is typically about 5 mm during the DC measurements.

While the cathode is in the RF gun, the UV pulses from the laser (λ = 263 nm, 1 to 10 ps pulse length) are used to measure the QE. The UV energy per pulse is measured with a photo-diode. The photo-electron bunch produced by a laser pulse is accelerated by the gun. The charge per bunch is measured with an integrating charge transformer at the exit of gun. The pulsed QE is deduced from the ratio of the charge per bunch to the UV energy per pulse. As can be seen in Figure 3, there is a decrease in the measured pulsed QE at high charge per bunch. This might be due to space charge or an actual dependence of the photo-electron yield on UV intensity.

The QE measurements on the 2 cathodes are summarised in Figure 4. The initial QE of both cathodes exceeds 10%, but the QE after removal from the RF gun is less than 1%. The maximum charge extracted from the cathode was 30 nC for a single bunch and 15 nC per bunch for trains of 9 bunches.

5 GAS EXPOSURE

Exposure to residual gases, O_2, CO_2, and H_2O in particular, causes the QE to decrease with time. The base pressure in the preparation chamber was of order $5 \cdot 10^{-10}$ torr or lower; RGA measurements indicated that the dominant gas was H_2, with other species typically down by at least a factor of 4. The pressure in the gun without RF was about $2 \cdot 10^{-9}$ torr when the first cathode was inserted; it had fallen to $\leq 5 \cdot 10^{-10}$ torr by the time the second cathode was removed. The pressure with RF on was significantly worse; it got as high as $5 \cdot 10^{-8}$ torr initially, but did improve with time. Actuator motion inside the vacuum system also produced some short-term increase in pressure.

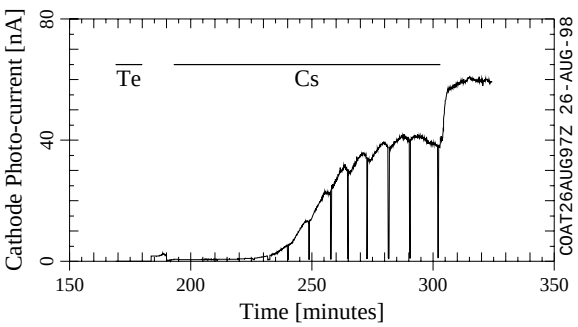

Figure 2. Photo-current as a function of time during the coating of the second photo-cathode. The times during which Te and Cs were being evaporated are indicated by the bars along the top. The downward spikes correspond to the UV light being blocked momentarily to check the background current.

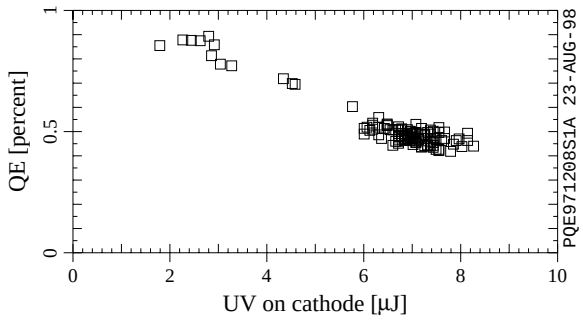

Figure 3. Dependence of the QE on the energy per laser pulse.

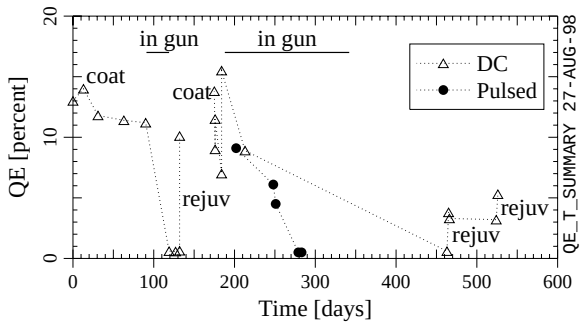

Figure 4. Time dependence in the QE.

6 REJUVENATION

The decrease in QE due to gas exposure can be partially reversed with a combination of heat and UV light [5, 7]. UV light from the mercury lamp is focussed onto the cathode with a spot diameter of about 10 mm; the UV power is between 6 and 40 μW. The cathode is heated to 230°C. The combination of heat and light causes improvement of the QE. The exact process is not yet clear; it may be desorption of residual gas from the surface or diffusion from the surface further into the photo-emissive layer.

Figure 5 shows the increase in photo-current during the rejuvenation of the first cathode. From time t = 30 minutes to t = 90 minutes, the cathode temperature was ramped up to 230°C; the temperature was held at 230°C until t = 190 minutes, at which time the temperature was ramped back to room temperature. As can be seen in Figure 5, the photo-current increases the most rapidly as the temperature is ramped up; it still increases by almost a factor of 2 as the temperature is ramped down (the latter increase was

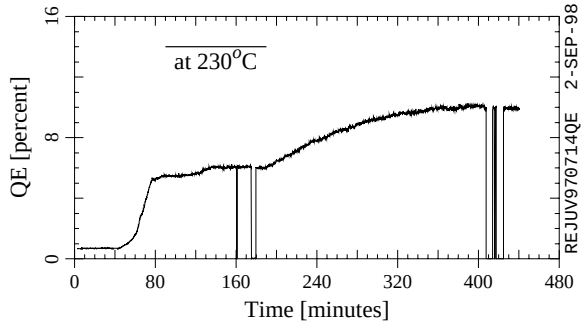

Figure 5. QE as a function of time during the rejuvenation of the first cathode. As before, the downward spikes correspond to the UV light being blocked momentarily.

not observed during the rejuvenation of the second cathode, however). The pressure was highest (between 1 and $2 \cdot 10^{-9}$ torr) while the temperature was ramped up.

As indicated in Figure 4, the QE of the first cathode increased from 0.65% to 10% during rejuvenation. The QE of the second cathode increased from 0.6% to 5% in 2 iterations.

7 MUTABILITY

After coating the second cathode, we observed an increase in the QE with time in the presence of UV light at room temperature, presumably due to the same mechanism as the rejuvenation at elevated temperatures. The QE increased from 7% to 15.5% in about 150 minutes. Much less mutability in the QE was seen after rejuvenation: the QE remained between 2.9 and 3.3% over 130 minutes. The time dependence in the QE is compared in Figure 6.

8 QE SCANS

Maps of the QE as a function of position on the cathode were obtained by focussing the UV light from the lamp to a small spot (about 1.25 mm diameter) and scanning the spot over the photo-emissive surface. A mirror on a kinematic mount (allowing us to translate and rotate the mirror reproducibly) was used to divert the UV spot onto a piece of graph paper in order to determine the location of the spot.

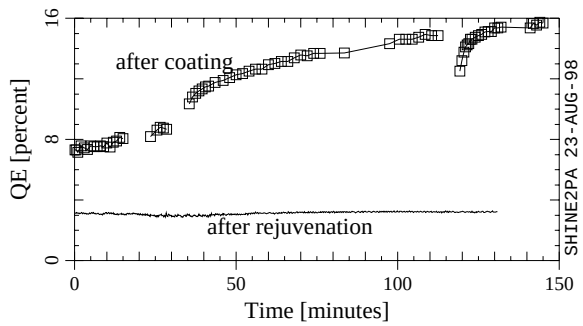

Figure 6. Comparison of the QE versus time before insertion into the gun and after rejuvenation for the second photo-cathode (UV power = 10 μW, spot size = 5 to 10 mm).

Visible light was used to determine the location of the cathode in the coordinate system of the graph paper. A QE map taken after the coating of the second cathode is shown in Figure 7. As can be seen, the QE is not uniform over the entire photo-emissive layer (15 mm diameter).

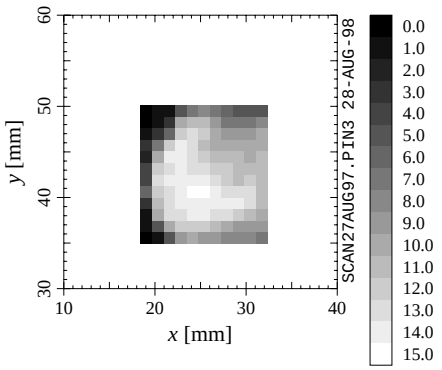

Figure 7. Map of the QE as a function of position on the surface of the second cathode the day after coating. Each pixel represents one QE measurement; the legend on the right indicates the QE values in percent.

9 CONCLUSION

We have coated and used two Cs_2Te photo-cathodes in the first prototype RF gun of the Fermilab photo-injector. We have extracted 30 nC from a single bunch and 15 nC per bunch from trains of 9 bunches. Under operating conditions, the QE falls from $\geq$8% to $<$1% over one or more months. Our QE measurements with DC and pulsed light are reasonably consistent, although we see a reduction in the pulsed QE at high UV intensity. Rejuvenation allows us to restore the QE to $\geq$5%, although we have not yet used a rejuvenated cathode in the gun. It would be desirable to improve the spatial uniformity and lifetime of the cathodes.

ACKNOWLEDGEMENTS

We thank our colleagues, especially E. R. Colby, M. J. Fitch, and C. Gesmundo for their help with this work, which would not have been possible without the support of H. T. Edwards and C. Pagani.

REFERENCES

[1] J.-P. Carneiro *et al.*, "Beam Transport, Acceleration and Compression Studies in the Fermilab High-Brightness Photoinjector," these proceedings.

[2] E. Colby, "A High Charge, High Duty Factor RF Photoinjector for the Next Generation Linear Collider," these proceedings.

[3] D. Trines, "Status of the TeSLA Design," these proceedings.

[4] E. Chevallay *et al.*, *Nucl. Instrum. Methods Phys. Res.* **A340**, p. 146–156 (1994).

[5] S. H. Kong *et al.*, *Nucl. Instrum. Methods Phys. Res.* **A358**, p. 276–279 (1995).

[6] P. Michelato *et al.*, in *Proceedings of the Fifth European Particle Accelerator Conference*, IOP Publishing, Bristol, 1996, p. 1510–1512.

[7] A. di Bona *et al.*, *J. Appl. Phys.* **80**, p. 3024–3030 (1996).

A HIGH CHARGE PHOTOINJECTOR FOR THE PULSED RADIOLYSIS FACILITY - ELYSE*

J.C. Bourdon, T. Garvey, J. Le Duff,
Laboratoire de l'Accélérateur Linéaire, Université de Paris-Sud, IN2P3 - CNRS, Orsay, France.

M. Gaillard,
Laboratoire de Photophysique Moléculaire, Université de Paris-Sud, CNRS, Orsay, France.

Abstract

The Physical Chemistry Department of the CNRS at the Université de Paris-Sud and the Laboratoire de l'Accélérateur Linéaire (LAL) will collaborate on a dedicated radiolysis user facility named ELYSE. The irradiation of users' samples will be performed using electron beams of energies varying from 4 to 9 MeV, produced from a laser triggered RF gun. The accelerator group at LAL, benefitting from the experience gained with their experimental RF gun (CANDELA), are responsible for the design and construction of the accelerator. The nominal beam requirements for ELYSE are 1 nC pulses of 5 ps width (FWHM). However there is a strong scientific interest in obtaining bunch charges of 10 nC for the same pulse width. The need to extract such high charges necessitates the use of Cs_2Te photocathodes with their high quantum efficiency. An essential user requirement is to keep the charge of the integrated dark current during the RF pulse width (3 microseconds) below 1% of the charge of the main beam. We will present the status of our studies aimed at construction of an RF gun and its associated transport optics capable of achieving these challenging goals.

1 INTRODUCTION

The ELYSE project is aimed at providing the French physical chemistry community with a facility for the study of fast chemical reaction dynamics. The increasing interest in such facilities has resulted in their study and construction elsewhere [1,2]. Irradiation of chemical samples will be possible with both electron beams (radiolysis) and laser beams (photolysis). A "probe" laser, synchronised with the excitation source, will then be used to examine the induced reactions. The Laboratoire de l'Accélérateur Linéaire has the responsibilty for the design and construction of the electron accelerator for the radiolysis experiments. Our design will benefit from the experience we have gained with our experimental RF gun project, CANDELA [3]. In this paper we will present the requirements of the accelerator and illustrate the status of our studies towards its design.

2 SPECIFICATION

The desired beam parameters for ELYSE are shown in table 1 below.

Table 1: Specification of the ELSYE Accelerator

Energy	4 - 9 MeV
Bunch charge	> 1 nC
Bunch duration	< 5 ps (FWHM)
Energy spread (RMS)	2.5%
Normalised RMS emittance	60 mm-mrad
Repetition rate	> 10 Hz
Beam diameter on target	2 - 20 mm

In addition to the above requirements there is a strong interest in pushing the bunch charge to 10 nC for the same bunch length and in having machine operation at frequencies up to 100 Hz. As the project requires a probe laser synchronised with the electron beam it seems natural to consider a laser triggered RF gun as the electron source. Following our previous experience with S-band structures we have opted for a 3 GHz RF gun. Good experimental conditions require the level of dark current charge incident on user samples to be less than 1% of the charge from the main electron pulse. As the RF pulse width will be typically 3 μs long it is clear that the dark current arriving in the experimental area must not exceed several μA and this condition is certainly one of the principal challenges of the machine.

3 THE ACCELERATOR

3.1 The Electron Gun

We aim to benefit as much as possible from existing RF gun experience and therefore we base our choice of gun on the one developed for the CLIC Test Facility (CTF) at CERN [3]. This 1-1/2 cell structure provides a beam of 4.5 MeV for a nominal electric field of 100 MV/m. As it is known that the dark current is a strongly increasing function of the cathode field (E_C) we aim to slightly modify the CERN geometry so as to permit operation at reduced fields. Calculations with the SUPERFISH code show that the introduction of a chamfer around the cathode plane can reduce E_C with respect to the maximum axial field by 17% [4]. With this modification we can envisage running the cathode at fields of typically 65 - 75 MV/m (79 - 91 MV/m peak axial field). In order to allow clean transmission of the beam for these reduced fields we open the iris diameter of the structure from 20 mm to 30 mm. PARMELA simulations indicate that such a gun should produce a

beam of 3.6 MeV for E_C = 65 MV/m (4.2 MeV for E_C = 75 MV/m).

The additional energy needed to reach 9 MeV will be provided by a "booster" cavity which will be identical to the one employed on the CTF. This is a four-cell standing wave structure operated in π mode. As the 10 nC bunch leaving the gun will be strongly affected by space charge forces a solenoidal focusing coil, placed at the gun output will be used to focus the beam through the booster. Table 2 shows a summary of the beam parameters as calculated by PARMELA at the exit of the booster. A schematic drawing of the RF gun and the booster is shown in figure1.

Table 2 Beam parameters as calculated by PARMELA.

	9 MeV/1nC	9 MeV/10 nC	4 MeV/1 nC	4 MeV/10 nC
RMS Bunch length (ps)	1.1	2.4	1.2	2.8
RMS energy spread (%)	0.8	2.6	1.7	6.0
RMS Norm Emittance (mm-mrad)	14	67	15	70

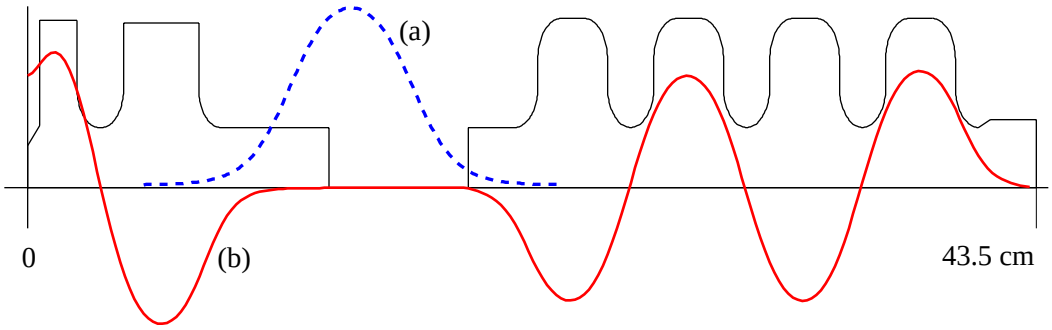

Fig. 1 Schematic of RF gun and booster showing (a) solenoidal magnetic field and (b) RF accelerating field.

The desire to have 10 nC bunch charges implies the use of Cs_2Te cathodes. Such cathodes have demonstrated quantum efficiencies in excess of 1% with life-times of several hundred hours [4]. We propose to use a 10 mm diameter cathode irradiated at near normal incidence by a 266 nm wavelength laser beam. A commercially available Titanium-Sapphire laser (800 nm) produces the UV light after frequency tripling. The UV pulses are typically of 1 ps RMS width and have an energy of 70 μJ.

3.2 The Transport Line

The beam from the booster can be delivered to any of three different experimental stations with the aid of two 30° bend dipole magnets (Fig.2). It is hoped that the dispersive nature of the dipoles will serve to reduce the level of dark current arriving at the targets of those users for whom this effect is particularly troublesome. Collimating slits between the two dipoles can be used to select a narrow energy band around the nominal beam energy. Until now we have checked the transport through the magnet elements with the TRANSPORT and TRACE-3D codes. Input to the codes was provided by outputs from PARMELA runs calculated from the cathode up to the exit of the booster cavity. PARMELA gives the distribution of the particles on the 2-D phase-space projections; x-x', y-y', and δφ-δE/E, where these symbols have their usual meaning. However, as TRACE-3D has no notion of particle distribution we make the following approximation; the elliptical phase-spaces used to start the TRACE-3D runs are chosen such that the values of the beam parameters are equal to the RMS values calculated by PARMELA (for which the 2-D projections are not necessarily enclosed by an elliptical contour).

As the arc, composed of the two dipoles, has a non-zero momentum compaction we have the possibility of bunch compression due to energy-dependent path length effects. Initially we run TRANSPORT to find settings for quadrupoles Q4 and Q5 which yield $R_{51} = R_{52} = 0$, where R_{51} and R_{52} are the φ-x and φ-x' elements of the transport matrix (calculated from the entrance of the first dipole to the exit of the second). We then run TRACE-3D to add the effects of linear space-charge forces and finally optimise the settings of Q4 and Q5 to obtain a minimum in the bunch length at the exit of dipole 2. In the absence of space charge forces the final phase width of the beam, $\Delta\phi_f$, is given by,

$$\Delta\phi_f = R_{56}\delta p/p + \Delta\phi_i$$

where $\Delta\phi_i$ is the initial length and R_{56} is the φ-δp/p element of the transport matrix. We have seen signs of such bunch compression from the TRACE-3D runs and experimental observations of this effect have been obtained recently using a two-dipole arc similar to the one which we propose [1].

Calculations indicate that compression is possible for all energies and charges of interest when the beam is transported to experimental area 3. In contrast we note that, for the case in which the space-charge is strongest (4 MeV, 10 nC), the bunch delivered to experimental area 1 is longer than the bunch which exits the booster. The PARMELA simulations indicate that the 4 MeV-10 nC beam exiting the booster has transverse phase space ellipses which are strongly distorted by non-linear space

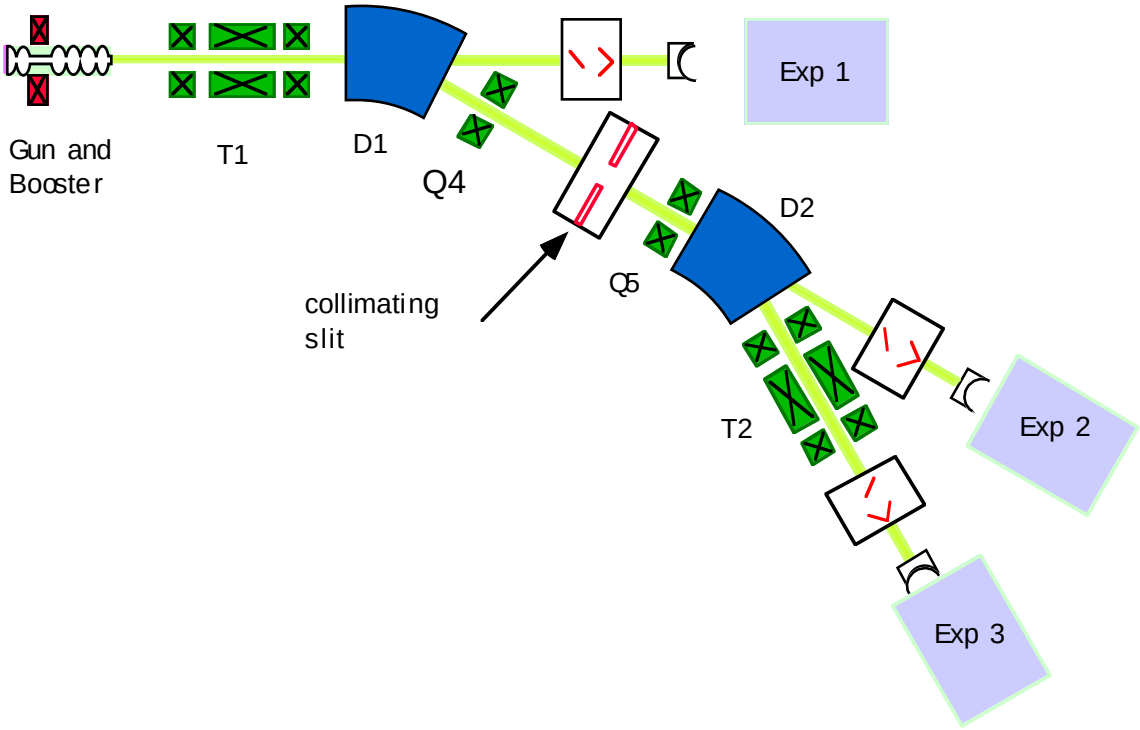

Fig.2 Schematic of the ELYSE accelerator showing the gun, booster, triplet magnets (T1, T2), dipoles (D1, D2), quadrupoles (Q4, Q5) and experimental areas (Exp 1, Exp 2, Exp 3).

charge effects. However, the input phase spaces for TRACE-3D simulations are ellipses with Twiss parameters which correspond to the RMS emittance, size and divergence of the PARMELA outputs. Therefore, the results of the TRACE-3D runs should be regarded with some caution. Now that we have some idea of the necessary quadrupole strengths required to confine the beam we intend to perform PARMELA simulations throughout the entire accelerator to verify the results of the TRACE-3D calculations.

ACKNOWLEDGEMENTS

We are indebted to R. Bossart and J.C. Godot of CERN for all the information they have provided us with concerning the CTF gun and booster cavity. The various simulation runs described above were performed by H. Monard and Y. Thiery with the aid of B. Mouton. The modifications to the CTF gun were suggested by J. Rodier. We thank P. Dufresne for the preparation of figure 2.

* Funding for ELYSE is provided by the CNRS, the MENRT, the Universite de Paris-Sud, the Conseil Regional Ile-de-France and the Conseil General de l'Essonne.

REFERENCES

[1] M. Uesaka et al., "Precise Measurement of a Subpicosecond Electron Single Bunch by the Femtosecond Streak Camera", Nucl. Inst. and Meth. A, **A 406**, 371-379 (1998).

[2] C. Creutz et al., "Report of the Workshop on the Proposed Pulsed radiolysis Facility at Brookhaven national laboratory", BNL Formal report BNL-52229 (1989).

[3] C. Travier et al., "Experimental Characterization of CANDELA photo-injector", Nucl. Inst. and Meth. A, **A 393**, 451-454 (1997).

[4] R. Bossart et al., "Modular Electron Gun Consisting of Two RF Sections and an Intermediate Focusing Solenoid", Nucl. Inst. and Meth. A, **A 340**, 157-163 (1994).

[5] E. Chevallay, et al., "Photocathodes Tested in the DC Gun of the CERN Photoemission Laboratory", Nucl. Inst. and Meth. A, **A 340**, 146 (1994).

FIRST PERFORMANCE OF THE RFD LINAC STRUCTURE*

D.A. Swenson, K.R. Crandall, F.W. Guy, J.W. Lenz, W.J. Starling
Linac Systems, 2167 N. Highway 77, Waxahachie, TX 75165

Abstract

Our "Proof-of-Principle" prototype of the RFD linac structure is fully assembled, tuned, and under vacuum, awaiting the delivery of the rf power system, which is now 15 months late and scheduled for delivery at the end of this conference (September 1998). Hence, we have no linac beam or full power performance to report. Nevertheless, we have some ion source beam, prototype assembly, and low-power linac performance to report.

1 THE RFD LINAC PROTOTYPE

A "Proof-of-Principle" prototype of the new RFD linac structure has been installed in the Linac System's laboratory in Waxahachie, TX. The purpose of this prototype is to demonstrate the validity of this new format of rf electric focusing and the practicality of using this new linac structure for a variety of scientific, medical, and industrial applications. The prototype is fully assembled, tuned, and under vacuum, awaiting the delivery of the rf power system, scheduled for delivery in the near future.

This prototype, comprising a 25-keV duoplasmatron ion source, a short two-element einzel lens LEBT, a 0.65-m-long, 0.8-MeV RFQ linac section, and a 0.35-m-long, 2.5-MeV RFD linac section, is shown in Fig. 1. The left-most section of the prototype, as shown in the figure, contains the ion source and LEBT, the middle section contains the RFQ linac, and the right-most section contains the RFD linac. The linac structures were designed to operate at 600 MHz; they both are currently tuned to 596.48 MHz.. The entire length of the prototype is 1.5 meters; the total length of the two linac structures is 1 meter.

The ion source, on loan from Los Alamos, is a scaled down version of the LAMPF ion source, designed and built for the PIGMI program in the late 1970s. It still produces more than 15 mA of proton current, which is more than adequate for this application. The ion source/LEBT vacuum enclosure is pumped by a single 400 l/s turbo pump and operates, under normal hydrogen gas flow, at a vacuum pressure of about $2x10^{-4}$ Torr.

The LEBT incorporates a small amount of electrostatic steering, a two-element einzel lens, and a small amount of beam diagnostics near the entrance to the RFQ linac. An excitation of 24.5 kV on each einzel lens element produces a small, well-centered beam spot at the entrance to the RFQ linac, without the use of any beam steering. A four-quadrant beam collection plate followed by a beam current transformer completes the Ion Source/LEBT portion of the system.

*Supported by National Inst. of Mental Health (NIMH).

The RFQ linac structure was fabricated as four separate pieces of OFE copper; two major pieces (the top and bottom vanes) and two minor pieces (the side vanes). The vane tips were contoured with a special, fixed-radius cutter, with a very small (3.5 mm) throat radius. The intent was to bolt the four pieces together for low power testing and to furnace braze them together for operation. However, for expedience, we chose to eliminate the final furnace brazing step.

For want of a proper machining fixture, the precision of the four RFQ pieces was not as high as expected. In spite of its short length, the RFQ tuning process was quite difficult. In the end, we found considerable help from the dipole-mode tuning rods developed by Los Alamos. Figure 2 shows the resulting mode spectrum and the field distribution at three places in each of the four quadrants. The quadrant fields appear to have an rms deviation of about 2.2%.

The RFQ vacuum enclosure is pumped by a single 400 l/s turbo pump. It typically operates at a vacuum pressure of $1x10^{-6}$ Torr. The RFQ assembly incorporates an ultra-thin (6.35 mm) beam line vacuum valve to provide vacuum isolation between the ion source/LEBT region and the RFQ region for maintenance purposes.

Fig. 1. 2.5-MeV RFD Linac Prototype.

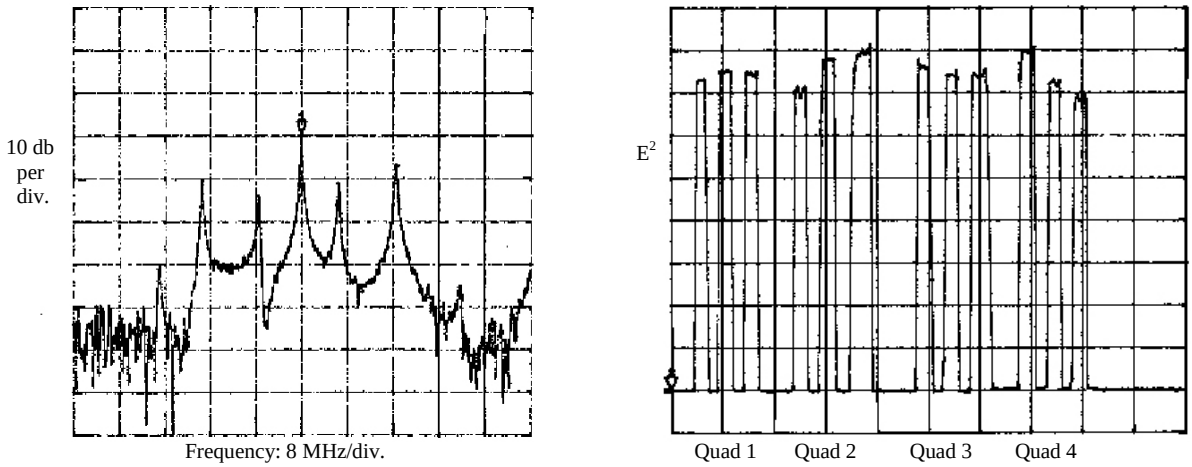

Fig. 2. Mode Spectra and Field Distribution in the RFQ Linac Structure.

The RFD linac structure is essentially a simple water-cooled cylindrical tank, loaded with RFD drift tubes. The RFD drift tube body and stem design comprises two half-body electrodes, with a total of four fingers to create the rf quadrupole field along the axis, supported on two water-cooled support blades that emanate from a single stem that mounts in a single hole through the linac tank wall. Both the drift tube and the hole are precision machined and no provision for additional alignment is planned.

The stem/blade assembly is a 4-layer stainless steel sandwich requiring two hydrogen-furnace braze cycles for completion. A portion of this assembly was machined to a circular cross section and precision ground to a cylindrical surface for installation into a reamed hole in the tank wall. The stem and hole is keyed to control the angular orientation of the drift tube. Fig. 3 shows two views of the RFD drift stem prior to adding the two half drift tube bodies. Several views of an RFD half drift tube body are shown in Fig. 4.

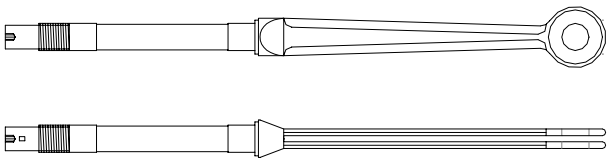

Fig. 3. RFD Drift Tube Stem.

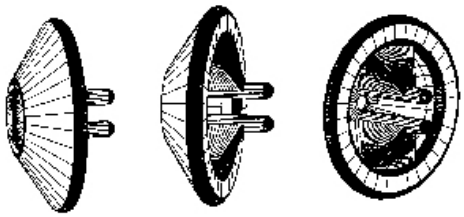

Fig. 4. Several Views of an RFD Half Drift Tube Body.

Soon after receiving the RFD drift tubes, we installed them in the RFD tank and checked the resonant frequency. It turns out to be about 595 MHz. As the RFQ frequency is about the same, we accepted 596.48 MHz for the Proof-of-Principle (POP) prototype.

We developed a way to measure the RFD lens excitation. By pulling a small "copper sponge" (diameter ~ 2.4 mm) along the axis of the linac, stopping inside each RFD drift tube, we shorted each RFD lens in succession, resulting in a frequency perturbation to the structure in proportion to the electrical stored energy in each lens. Initially, we employed the usual phase shift technique used for bead pull measurements. However, as the perturbation was larger than the Q-width of the structure, it was better to simply measure and record the resulting resonant frequency. The results are presented on the upper half of Fig 5. Next, we proceeded to measure the drift tube body gap, which has a direct effect on the expected lens excitation. The results are presented on the lower half of Fig. 5. Note the correlation! After inspection and adjustment of the RFD Drift Tube geometry, the uniformity of excitation was very good.

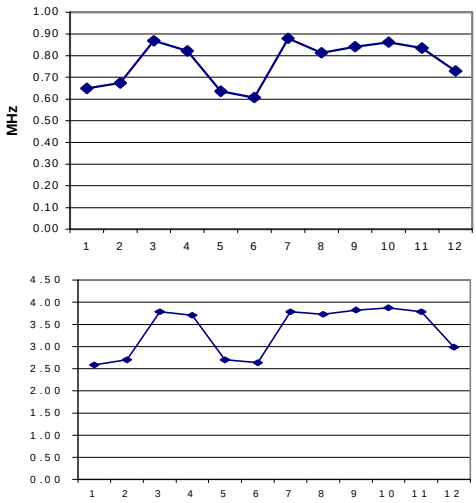

Fig. 5. RFD Lens excitation (upper) and Physical Misalignment (lower).

A resonant coupler, designed to couple the excitation of the two linac structures by locking their fields in phase and amplitude, is being employed. The resonant coupler extracts precisely the right amount of rf power from the RFD structure to excite the RFQ structure. It has the form of a quarter-wave stub in a cylindrical can as shown in Fig. 6. Slots near the base of the quarter-wave stub provide coupling to the fields of both the RFQ and RFD structures.

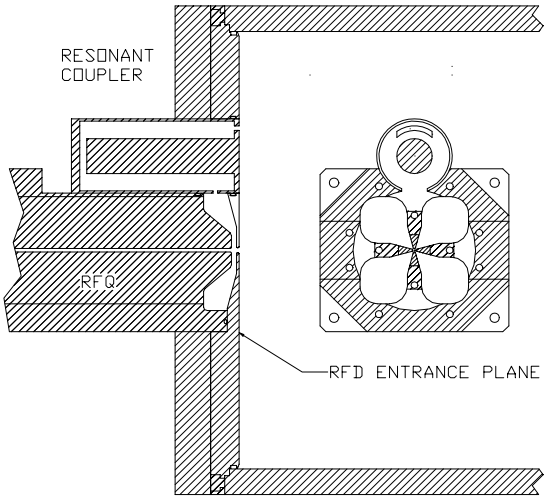

Fig. 6. The Geometry of the Resonant Coupler.

The two linac structures together with the resonant coupler form a chain of three coupled resonators that, when properly tuned, can be excited in three different modes corresponding to 0, $\pi/2$ and π phase shift between adjacent resonators. These three modes can be seen in the mode spectra of our coupled linacs shown in Fig. 7.

Our system is tuned to use the $\pi/2$ mode, which is well known for its ability to lock the phase and amplitude of the fields in adjacent cavities with great accuracy.

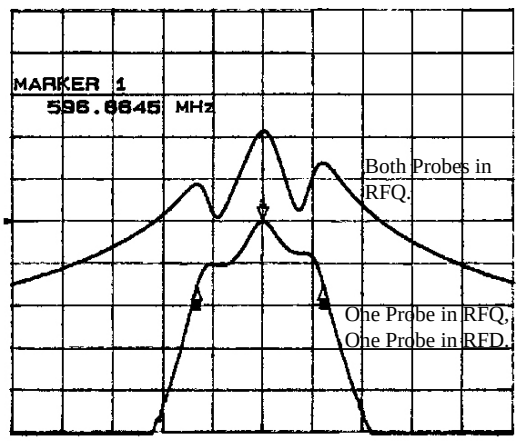

Fig. 7. Mode Spectra of the Coupled Linacs.

The rf power system is based on a multiplicity of high power YU-141 planar triodes. It is designed to produce a peak power of 240 kW at a pulse duty factor of 0.5%. It will consist of a chain of two intermediate power amplifiers (IPAs) and one final power amplifier (FPA). The IPAs will be rack mounted, while the FPA will be mounted directly above the RFD linac section, as shown in Fig. 1. The IPAs will use a total of 3 of the planar triodes. The FPA will utilize an all new single cavity configuration of 12 planar triodes in parallel.

This rf power system is nearing completion at JP Accelerator Works, Inc. It features easy tube replacement (individual cathode assemblies), a broadband cathode circuit (no tuning required), a light weight cavity assembly, built-in phase and amplitude control, a PC based control system with fiber-optically isolated control modules and professional controls software. The system is scheduled for delivery next month (September 1998).

We hope to demonstrate successful performance of this new linac structure in the very near future. The status of this effort will be reported promptly on our web pages at: **www.linac.com**

REFERENCES

1. D.A. Swenson, "RF-Focused Drift-Tube Linac Structure", 1994 Intern. Linac Conf., Tsukuba, Japan, 1994.
2. D.A. Swenson, "A New Linac Structure for the BNCT Application", Proc. First Intern. Workshop on Accelerator-Based Neutron Sources for BNCT, Jackson Hole, WY, 1994.
3. D.A. Swenson, Crandall, Guy, Lenz, Ringwall, & Walling, "Development of the RFD Linac Structure", Proc. of the 1995 Particle Accelerator Conference, Dallas, TX, 1995.
4. D.A. Swenson, F.W. Guy, K.R. Crandall, "Merits of the RFD Linac Structure for Proton and Light-Ion Acceleration Systems", Proc. of EPAC'96 Conference, Sitges, Spain, 1996.
5. D.A. Swenson, K.R. Crandall, F.W. Guy, J.M. Potter, T.A. Topolski, "Prototype of the RFD Linac Structure", 1996 Linac Conf., CERN, Geneva, Switzerland, 1996.
6. D.A. Swenson, "12-MeV Proton Linac for PET Isotope Production", Institute of Clinical PET Conf., Orlando, FL, 1996.
7. D.A. Swenson, "CW RFD Linacs for the BNCT Application", Fourteenth Intern. Conference on the Applications of Accelerators in Research and Industry, Denton, TX, 1997.
8. D.A. Swenson, Crandall, Guy, Lenz, Potter, "Status of the RFD Prototype", 1997 Particle Accelerator

THE PERFORMANCE OF THE 1.3 GHz SUPERCONDUCTING RF CAVITIES IN THE FIRST MODULE OF THE TESLA TEST FACILITY LINAC

Wolf-Dietrich Möller for the Tesla collaboration
Deutsches Elektronen Synchrotron DESY, 22603 Hamburg, Germany

Abstract

The design goal of the 1.3 GHz 9-cell superconducting RF cavities for the Tesla Test Facility (TTF) is a gradient Eacc ≥ 15 MV/m at a quality factor of Qo ≥ $3 \cdot 10^9$. The cavities are operated in pulsed mode: 0.8 ms constant gradient with 10 Hz repetition rate.

After the vertical acceptance test and prior to the assembly in the linac the cavities are tested in a horizontal cryostat fully equipped with helium vessel, high power input coupler, higher order modes coupler and tuning system. After installing module 1 the first 120 MeV beam has been delivered successfully.

We report about the measured results in vertical and horizontal tests, the processing of the superconducting cavity system in the first module and the performance of the cavity system before, during and after operating the linac.

1 INTRODUCTION

In order to prove the technical basis of TESLA[1] the TTF (Tesla Test Facility)[2] was established at DESY within the frame of an international collaboration. In May 1994 the infrastructure was ready to prepare and test superconducting cavities. Twenty-seven 9-cell cavities, manufactured by four different European companies have been processed and measured so far.

9 cavities from the first production are operating in the TTF linac and 8 more cavities are now being installed. In end of 1997 26 more cavities were ordered which are now under fabrication or final processing. Two of them have been measured already.

2 CAVITY TREATMENT

The standard cavity preparation before the vertical test consists of the following steps: 80 µm removal from the inner surface by buffered chemical polishing (BCP), a 2 h heat treatment (HT) at 800 ˚C, a 4 h HT at 1400 ˚C with titanium getter and additional 100 µm removal by BCP. The cavity is then rinsed with high pressure (100 bar) deionized ultra pure water. After welding the He-tank and prior to the horizontal test a 20 µm BCP and a high pressure water rinse takes place.

3 VERTICAL TEST RESULTS

The average gradient of the 27 cavities tested so far is 19.5 MV/m. The average gradient of the last 13 cavities measured is even 24.6 MV/m, 3 of them showed gradients Eacc > 28 MV/m (see Fig. 1). The main limitation now is field emission. It is remarkable, that all 4 manufacturers delivered cavities with gradients higher or close to 25 MV/m.

However at the time of selecting the capture cavity and the 8 cavities for module 1, only 4 cavities were available with gradients > 15 MV/m. 5 cavities were limited by quench below 15 MV/m in the vertical test (see table 1). The reasons for this limitation were found as foreign inclusions in the material and improper cleaning of weld area before welding[3,4]. In the future this type of defects will be excluded by eddy current scan of all niobium sheets and by the current fabrication method.

Table 1: Cavity performance during vertical and horizontal tests and after installation into the linac. The numbers are the gradients in MV/m. The 1. linac test was done before and the 2. test after 3 month of linac operation. At the vertical test the dissipated power is set to 100W in order to compare the cw measurement in the vertical test with the pulsed measurement (duty cycle 1%).

cavity	vertical test Pdiss <100W	horiz. test Pcryo <1W	linac 1. test Pcryo <1W	linac 2. test Pcryo <1W	linac 2. test Pcryo <3W
D3	25.3	21.0	15.5	19.1	19.5
S8	12.5	16.0	11.9	11.9	12.5
S10	14.2	13.4	13.2	14.7	15.9
D1	21.3	19.0	21.0	23.1	23.5
D2	17.7	23.5	23.6	24.5	25.6
S11	13.5	17.3	12.9	11.8	13.4
D4	13.3	13.5	11.5	12.4	13.5
S7	12.6	-	11.3	12.2	13.2
C19	19.6	19.0	12.7	-	-
sum	150	155*	134	142†	151†
average	16.7	17.2*	14.8	15.8†	16.8†

*: S7 test result taken from the vertical test
†: C19 test result taken from the 1. test of linac

4 HORIZONTAL TESTS

13 cavities for module 1, injectors and first for the module 2, equipped with all auxiliary components (helium-vessel, high-power-coupler, HOM-couplers, tuning mechanism and magnetic shielding) were tested in a horizontal cryostat. Because of the low Q_{ext} of the high power input coupler only measurements in the pulsed mode were

possible (500 μs rise time and 800 μs constant gradient at a repetition rate of 10 Hz)

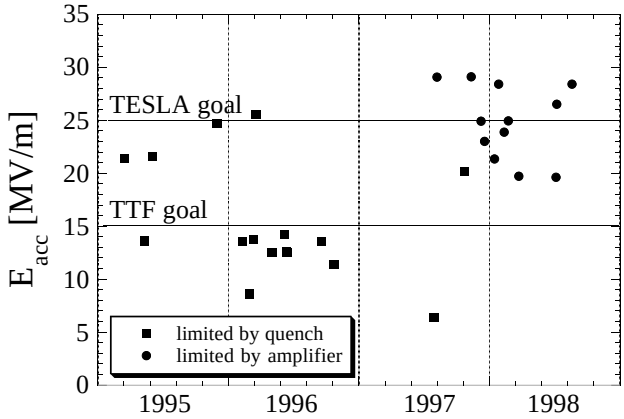

Fig. 1: Result of vertical cavity tests. The gradients below 15 MV/m before mid '97 are due to fabrication errors.

These 13 cavities reached an average gradient of 19.7 MV/m in the horizontal test compared to an average gradient of 20.3 MV/m in cw mode in the vertical test stand. In the horizontal tests, field emission has been observed higher intensities. The reason is probably particle contamination due to the more complicated assembly and the processing of the main power coupler. The higher field emission loading is responsible for the slight degradationin performance.

The performance of the cavities selected for module 1 are listed in table 1. Three cavities (D2, S8, S11) showed a higher field in the horizontal test under pulsed conditions than in the vertical cw test. This is most likely caused by the slow thermal development of the quench as compared to the rf pulse length. The other cavities sufferedfrom higher field emission or stayed constant.

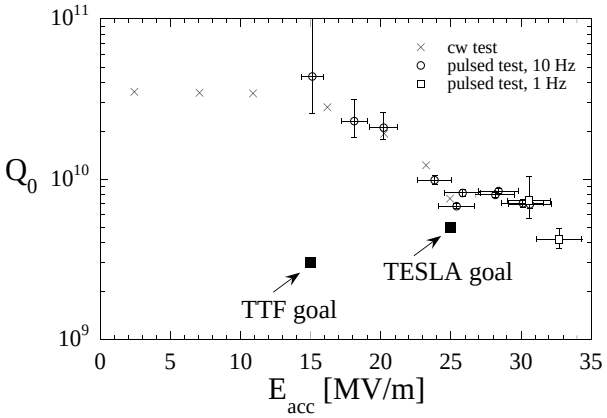

Fig. 2: The best horizontal test so far. The Q values during the pulse tests are calculated from the cryogenic losses. The cw measurement from the vertical test is given for comparison.

The best cavity tested so far in the horizontal test cryostat reached33 MV/m with a quality factor $Q = 4 \cdot 10^9$ (Fig. 2). At 34 MV/m a quench occurred. In the vertical test, this cavity reached25 MV/m, limited by available power.

Cavities showing strong field emission can be further improved by applying HPP[5]. For this purpose, short pulses of high instantaneous power (≤500 μs, up to 1 MW) are applied to destroy field emitters. The power coupler has to be carefully processed up to 1 MW, which may take several days. Due to a tight time-schedule HPP was not always applied during the horizontal test.

5 PROCESSING OF THE MODULE 1

5.1 High power input coupler

The two types (Fermilab and DESY design) of high power couplers[6] consist each of two RF vacuum windows. The coaxial window near the cavity at 70 K and the room temperature window in front of the wave-guide (Fermilab) or as a part of the wave-guide to coax transition (DESY) outside the cryostat. The coupler vacuum of all eight couplers on the module is connected and pumped by a common ion getter pump.

All 8 cavities in module 1 are driven by one 5 MW klystron. A linear RF distribution system is branching off identical amount of power for each cavity by directional couplers.

5.2 Processing couplers and cavities

The TESLA design parameters call for a transfer of 206 kW peak RF power per cavity to the beam with a pulse length of 1.3 ms and a repetition rate of 5 Hz. In addition it is also foreseen to apply HPP to the cavities in situ which requires1 MW at a maximum pulse length of 500 μs and at a repetition rate ≤ 1 Hz. Therefor the couplers have to be conditioned to this limits.

The coupler processing procedureat TTF starts with the cavity and coupler at room temperature. Therefor gases released by RF stimulated desorption can be pumped away. In the beginning of the conditioning the cavity is off resonance. The first power rise (dependent from the vacuum pressure and e^- and light in the vacuum) is done with a pulse length of 20 μs, then the pulse length is doubled for the next power rise and so forth. At the full pulse length the power is sweeped for some hours. After this the cavity and coupler are cooled down and the same processing procedureis carried out again. The last part of processing is done with the cavities on resonance.

5.1. Processing results on module 1

Due to limited time the processing of couplers in module 1 was restricted to 200 kW and 600 μs. The processing of the coupler on the module at room temperature was done at two couplers at a time in order to distinguish the vacuum reactions in the common coupler vacuum. It was always observed, that initially it is possible to rise the power very quickly without being

limited by outgassing, electron signals or light. After a sudden burst of outgassing on the coupler side of the cold window at a typical power level of 50 - 100 kW many hours are needed to once again reach the earlier achieved power level. Once the maximum power of 200 kW is reached for the shortest pulse length the power rises for longer pulses are straight forward. After about 48 to 72 h only one multipacting level at 125 kW is visible at the charged particle detectors. But the signals are smaller by a factor of 10 compared to the first processing hours. A second multipacting level at 65 kW is processed away.

When the module was cooled down to the operating temperature of 1.8 K the same processing procedure took place. All multipacting levels were processed after 30 h. The temperatures of the Fermilab cold window increased due to dynamic losses by about 5 K. Due to a fabrication failure during brazing metallization of the cold DESY windows occurred. This causes a much stronger temperature rise of about 100 K which does not effect the coupler behavior but creates higher losses at the 70 K shield circuit of the module.

When the cavities are on resonance the field distribution in the coupler differs from the off resonance full reflection condition. An additional processing is necessary. After only a few (1-5) more hours the couplers were fully operational without limiting the cavities. No interlock events were observed up to the TTF operating power of 125 kW during the first 30 days of operation time. After a few days power off time no new processing was needed to operate the module again.

6 OPERATION OF THE CAVITIES IN THE LINAC

After installation in the linac the cavities were measured again individually under pulsed conditions. Here the capture cavity C19 showed a reduced performance due to field emission loading (Tab. 1). The 8 cavities mounted in the module 1 reached almost the same results as in the vertical tests. One cavity D2 showed a slightly higher, one cavity D3 a slightly lower gradient, caused by field emission.

Operating all cavities with one klystron and a uniform power distribution the module performance is limited by the worst cavity. Therefor the quench of cavity S7 limits the maximum gradient of the module 1 to 12 MV/m at the full pulse length of 800 µs flat top and 10 Hz repetition rate. For shorter RF pulses of 300 µs rise time and 100 µs flat top at 2 Hz repetition rate acceleration gradients of 16.7 MV/m were obtained.

7 CAVITIES FOR MODULE 2

In Fig. 3 the vertical test results of the 8 cavities forseen for the module 2 are shown. The module 2 will be installed in the linac by end of September '98. The expected average gradient for this module is ≥20 MV/m.

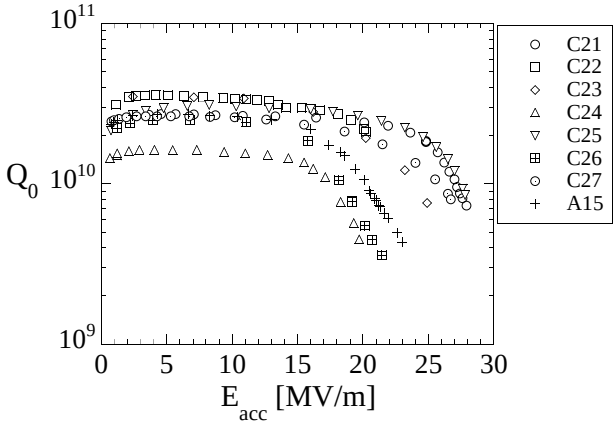

Fig. 3: Vertical test results of the 8 cavities selected for module 2.

8 CONCLUSIONS

Gradients well above 20 MV/m have been demonstratedwith 9-cell TTF cavities. Excluding only the cavities with a well identified fabrication error, the average gradient of 13 cavities is 24.6 MV/m.

The highest gradient in the horizontal cryostat with a fully equippedcavity was 33 MV/m.

The main limitation is field emission, indicating the high standardof niobium quality and fabrication methods. Further progress in gradient can be expectedby improving cleanliness during final treatment and assembly.

The first beam of 8 mA has been successfully accelerated. The average gradient of the first 8 cavity module is limited by one of the above mentioned cavity. Further improvement of the gradient is possible by optimizing the RF distribution.

A slight reduction in gradient from horizontal test to module operation was observedand is causedby high field emission loading. It shows that improvements in clean assembly and coupler handling is still necessary.

REFERENCES

[1] Conceptual Design of a 500 GeV e^+e^- Linear Collider with integrated x-ray Laser Facility, Ed. R. Brinkmann, G. Materlik, J. Rossbach, A. Wagner, DESY 1997-048, ECFA 1997-182.

[2] D.A. Edwards: `TESLA TEST FACILITY LINAC - Design Report', TESLA 95-01, 1995.

[3] W. Singer et. al.: Diagnoses of defectsin high purity niobium, Eighth Workshop on RF Superconductivity, Albano Terme (Padova), Italy, 1997.

[4] A. Brinkmann et. al.: Performance degradation in several TESLA 9-cell cavities due to weld imperfections, Eighth Workshop on RF Superconductivity, Albano Terme (Padova), Italy, 1997.

[5] J. Graber, Ph.D. thesis, Cornell University, 1993

[6] M. Champion, Seventh Workshop on RF Superconductivity, Gif Sur Yuette, France 1995.

SIMULATION OF BEAM DYNAMICS INCLUDING SPACE CHARGE IN PROTON LINAC WITH ERRORS*

D.V.Gorelov** and P.N.Ostroumov
Institute for Nuclear Research of the Russian Academy of Sciences, Moscow, 117312 Russia

Abstract

The LANA computer code (Linear Accelerators Numerical Analysis) has been modified in order to study the effect of random errors on beam dynamics in proton or heavy ion linacs. The standard well known set of different errors of the accelerating and focusing channel including geometry misalignments in all directions, magnetic and electric field imperfections and accelerating field instabilities are simulated. Partial as well as cooperative effects of the errors are analyzed. The LANA code includes space charge forces in the beam, using certain approximations. A comparison of the errors effect on the beam parameters with and without space charge in the 30 mA proton linac is presented. As was found the error effect on beam dynamics is a main contribution on halo formation as well as on beam losses.

1 INTRODUCTION

The present research has been done as part of the conceptual design of the 400 MeV proton linac for JHF at KEK, Tsukuba [1]. The linac includes an RFQ, MEBT, DTL and CCL. The errors study has been performed for the MEBT-DTL-CCL part of the whole linac – from 3 MeV up to 400 MeV. The CCL operates at the third harmonic of the fundamental frequency of 324 MHz, and a transition from the DTL to CCL occurs at 70 MeV. The structure of the linac has been designed for beam intensity of 30 mA.

This research has been done using LANA code [2], that has been developed in INR, Moscow since 1991. This code has been extensively used during the commissioning and operation of the Moscow Meson Factory linac [3]. LANA was also used during the commissioning of the Fermilab linac upgrade in 1993 [4]. Presently this code is being used at TRIUMF for the ISAC project [5] and at CERN for SPL design [6].

* Research was done in frames of the collaboration between INR, Moscow and KEK, Tsukuba and as part of the agreement between these institutions.

** At present time author has temporary position at NSCL, MSU

2 MODEL

The errors which influence the beam dynamics in linacs can be divided into three groups [7]. Beam related errors, e.g. displacements of the beam with respect to the accelerator axis, mismatched beam in phase space, energy shift and spread, etc, compose the first group. Only errors of the displacements of the beam were considered in this study, taking into account the periodical steering of the beam position.

The second group of errors include time-independent (slow) errors - misalignments, e.g. tanks and drift tubes length and positioning, quads gradients, length and positioning, accelerating field flatness and setting of the amplitude and phase during the tune-up procedures, etc. A full set of this kind of errors is considered in this work.

The third group of errors consists of time-dependent (fast) errors – instabilities, e.g. amplitude and phase from the rf source, mechanical vibrational errors, field distortion due to transient beam loading, etc. This group of errors is responsible for the jitter in the beam. Only the accelerating field amplitude and phase instabilities were considered during this study as the major errors of this kind.

A simplified space charge model of the beam is used in LANA. This is a model based on the analytic relations between the charge density and the space charge electric fields for a distribution with 3-D ellipsoidal symmetry in real space [8]. Therefore this model can be applied to bunched beams only.

When doing error studies LANA provides the following values at the end of every accelerating cell in the cavity or every intertank element, e.g. drifts or quads: the transverse coordinates and derivatives of the beam center; the longitudinal average phase and energy of the bunched beam; the maximal radial extent of the beam; vertical and horizontal maximal and rms sizes of the beam; phase and energy maximal and rms spreads; the normalized rms emittances and the normalized emittances containing 99% particles in all 3 dimensions; and a number of other quantities of interest. A well known set of different errors in the linac were simulated during this study. Table 1 shows the tolerance limits for all simulated errors which are the maxima of the allowed deviations of the corresponding variables, uniformly distributed around its design value. The rms value of errors is 3 times less than the values listed in the table 1.

Table 1: Maximal tolerances limits

Error Type	Tolerance Limit
1. Transverse beam displacement	500 μm
2. tilt	1 mrad
3. CCL section length	100 μm
4. alignment	100 μm
5. Drift tube length	100 μm
6. alignment	100 μm
7. Quadrupole gradient	1.5 %
8. Length	100 μm
9. Alignment	100 μm
10. Displacement	50 μm
11. Tilt	0.5 mrad
12. Rotation	10 mrad
13. Field difference between CCL sections in amplitude	1 %
14. in phase	1 °
15. Non-flatness of the accelerated field in the cavity	3 %
Average accelerating field amplitude over DTL or CCL tank:	
16. tune-up	3 %
17. instability	1 %
Phase difference between neighbor cavities:	
18. tune-up	3 °
19. instability	1 °

The errors of the first group (1. and 2.) were applied at the entrance of each section where the steering of the beam is provided after the centering the actual position of the beam.

3 COMPARISON OF THE PARTIAL CONTRIBUTION OF DIFFERENT SETS OF ERRORS

Five different sets of errors were considered in this study:

1. All errors listed in Table 1.
2. All errors, except the 17th and 19th – the instability errors.
3. RF system errors only, i.e. from 13th to 19th.
4. RF system errors except instabilities errors.
5. Geometry misalignments, quad errors and beam mismatches, i.e. from 1st to 12th.

All these simulations were performed both with and without space charge effects taken into account.

Figs. 1, 2 and 3 presents the results of the 1st set of error simulations, listed above. It could be seen in Fig. 1 that the space charge effects have a smaller impact on the maximal beam radius growth compared to the error effect. The error effect for the beam without space charge gives approximately a factor of 4 in the maximal beam radius growth, but the space charge effect gives approximately a factor of 3 for the beam without errors and a factor of 2 – with errors for the simulated number of particles ~1200.

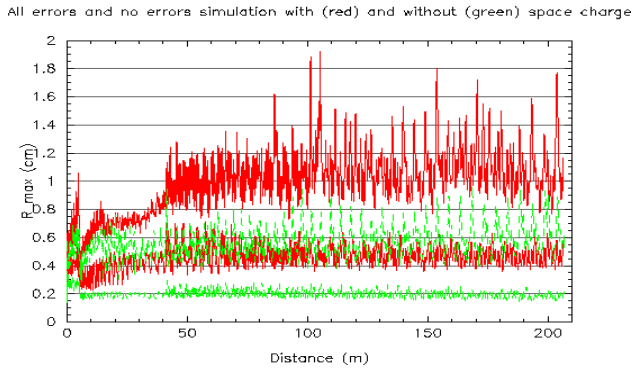

Figure 1. Evolution of the maximal beam radius along the linac with errors (upper lines) and without errors (i.e. design linac) with space charge (solid lines) and without space charge (dashed lines).

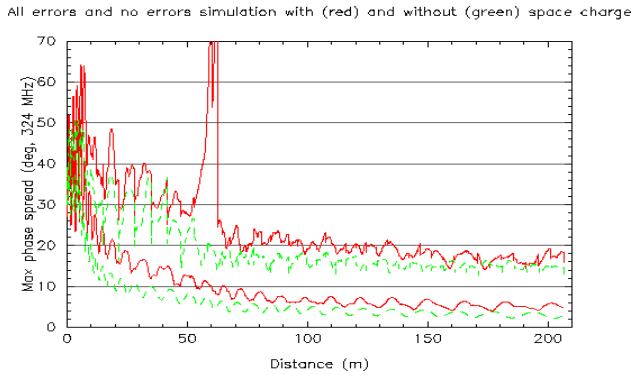

Figure 2. Evolution of the maximal phase spread along the linac with errors (upper lines) and without errors (i.e. design linac) with space charge (solid lines) and without space charge (dashed lines).

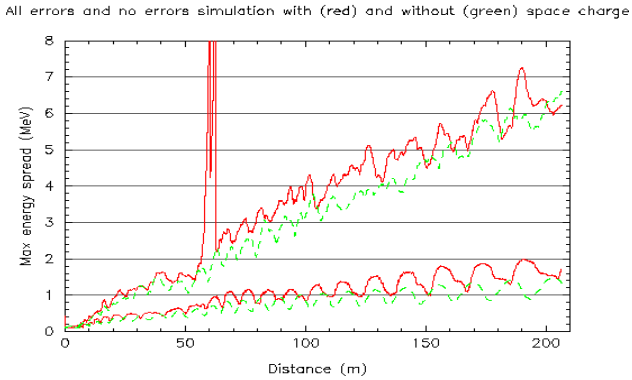

Figure 3. Evolution of the maximal energy spread along the linac with errors (upper lines) and without errors (i.e. design linac) with space charge (solid lines) and without space charge (dashed lines).

The interesting result is that the relative effect of the errors is smaller in the case of a charged beam (~3 times growth of the maximal beam radius) compared to the case of a non-charged beam (~4 times growth of the same parameter).

The halo formation process could not be studied in detail because of the limited number of particles used for the statistical simulations. But in some cases of charged beam simulation where the field instabilities were included a few particles were lost. These losses indicate intensive halo formation induced by instabilities of the accelerating field.

4 PROBABILITY ANALYSIS

The probability distributions of the maximal beam radius and the longitudinal effective emittance, containing 99% of particles, are presented in Figures 4 and 5 respectively. These figures show the probabilities for simulations without space charge for 400 and 100 random errors samples. Also the probability distributions of the simulations with space charge for 100 errors samples are shown on the same figure in a different scale.

The detailed consideration of the probability distributions, which could not be discussed here because of the limited space, show that the statistics of 400 errors samples is good enough for the transverse beam parameter study and reasonable for the longitudinal ones. The 100 errors samples analysis shows good qualitative results, but insufficiently reliable quantitative ones.

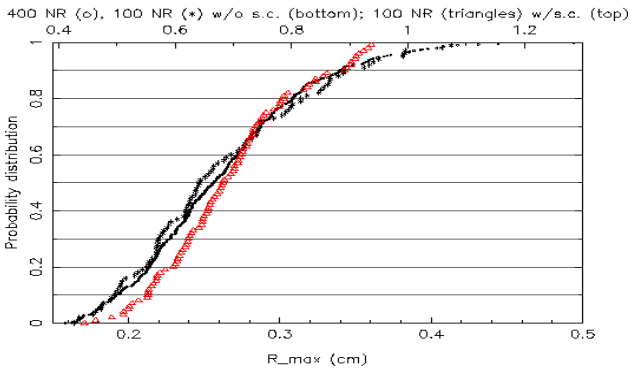

Figure 4. Probability distribution of the maximum beam radius from 400 NR (dots), 100 NR (asterisks) without space charge; and from 100 NR (triangles, upper scale) with space charge.

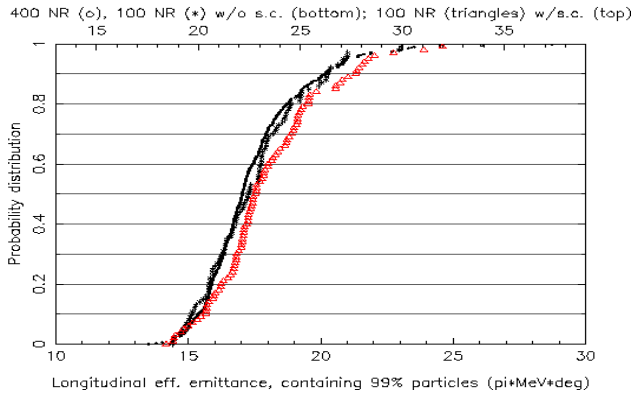

Figure 5. Same as in Figure 4, but for the longitudinal effective emittance, containing 99% of particles.

5 CONCLUSIONS

The time-consumptive calculations that were done for the statistical analysis of the errors influence on the charged beam dynamics provide interesting results and emphasizes the problem of halo formation which is not the subject of the present article. Though in the conclusion of this study we would like to state that the halo formation takes place in the regions of the non-adiabatic changes of the linac main parameters and is induced by the instabilities of the accelerating field.

The probability distributions study confirms that the number of samples for such a study could be chosen to be about 200-300 for the transverse beam dynamics and about 400-500 for the longitudinal ones.

These studies show that the given values of the tolerance limits (table 1) could be recommended in order to meet the requirements of low losses in the linac.

While the most sensitive error for the transverse emittance growth is quad rotations, the one for the longitudinal dynamics is the accelerating field instability.

The relative increase of the maximum beam radius is smaller in the case of the charged beam simulation compared to the relative growth of this quantity in the non-charged beam simulation. Nevertheless the cooperative effect of space charge and the errors could lead to halo formation if no special care is provided to control this process.

6 REFERENCES

[1] Y.V.Bylinsky, et al., “Conceptual Design of the JHF Linac,” Edited by P.N.Ostroumov, Internal Report, KEK, Tsukuba (1997).

[2] D.V.Gorelov and P.N.Ostroumov, “Application of LANA Code for Design of Ion Linac,” EPAC’96 Conf. Proc., Barcelona, (1996).

[3] S.K.Esin, et al., “Commitioning/Operation of the Moscow Meson Factory Linac,” LINAC’94 Conf. Proc., V.1, 31 (1994).

[4] M.Popovic, et al., “Measurements of the Longitudinal Beam Parameters in the Fermilab Linac,” LINAC’94 Conf. Proc., V.2, 896 (1994).

[5] R.E.Laxdal, D.V.Gorelov, “Optimization and Design Specifications for Tank1 of the ISAC Drift Tube Linac,” TRIUMF TRI-DN-ISAC-97-4 (1997).

[6] R.Garoby, et al., “Feasibility Study of a 2 GeV Superconducting H- Linac as Injector for the CERN PS,”, these proceedings.

[7] D.Raparia, et al., “Error and Tolerance Studies for the SSC Linac,” PAC’93 Conf. Proc., 3585-3587 (1993).

[8] R.W.Garnett and T.P.Wangler, “Space Charge Calculation for Bunched Beams With 3-D Ellipsoidal Symmetry,” PAC’91 Proc., 330-332 (1991).

BASIS FOR LOW BEAM LOSS IN THE HIGH-CURRENT APT LINAC

T. P. Wangler, E. R. Gray, F. L. Krawczyk, S. S. Kurennoy, G. P. Lawrence, and R. D. Ryne
Los Alamos National Laboratory, Los Alamos, NM 87545 USA
K. R. Crandall, TECHSOURCE, Santa Fe, NM 87594-1057

Abstract
The APT linac has been designed for very low beam loss. This important aspect of the design is supported by three main bases: 1) an understanding of the performance of the 800-MeV LANSCE proton linac at Los Alamos using measurements and simulations, 2) a theoretical understanding of the dominant halo-forming mechanism in the APT accelerator from physics models and multiparticle simulations, and 3) a conservative design approach for APT aimed at maximizing beam quality at low energies and providing large apertures at high energies to reduce beam loss to a very low value.

1 BEAM LOSS AND ACTIVATION

The APT accelerator [1] is a cw medium-energy proton linac with a design beam current of 100 mA, a number of particles per bunch equal to 1.8×10^9, and a final energy of 1030 MeV or higher, depending on the desired tritium production rate. It has been designed to operate with extremely low beam losses to avoid radioactivation of the machine components. It is important to achieve hands-on maintenance capability along the machine in order to meet overall plant availability requirements, although remote maintenance techniques could be employed at a few high-beam-loss locations without major impact.

The maintenance criterion limits post-shutdown activation levels to a few mrem/hr at the beamline. The corresponding beam loss rate that can be tolerated, as a function of beam energy, has been estimated in Ref. [2]. Expressed in beam power, the loss above 100 MeV is limited to a few tenths watt per meter, a value that is consistent with experience at the LANSCE linac, which operates with hands-on maintenance. LANSCE is the highest power operating proton linac in the world. It is a pulsed machine with multiple beam operation that includes a 6%-duty-factor 1-mA average current 800-MeV output beam. For LANSCE the average fractional H^+ loss rate above 100 MeV is about 10^{-6}/m. Excluding two hot spots at focusing transitions lowers this value to about a few times 10^{-7}/m. The number of particles per bunch in APT is only about 3.4 times greater than for LANSCE, and the beam focusing strength in the APT design is greater so that the beam-physics regimes of the two linacs are nearly the same. The APT peak beam current of 100 mA is by no means a record for proton linear accelerators; the Brookhaven and Fermilab injector linacs have operated with H^+ beams at peak proton currents near 300 mA. Nevertheless, the challenge for the APT linac is to deliver an average current 100 times higher than LANSCE in the same energy range, while achieving a beam-loss rate that is no larger in absolute terms. This scales for APT to an acceptable average fractional loss rate of about 10^{-8}/meter, or a total of about 10^{-5} fractional beam loss above 100 MeV. The design objective for APT is a factor of 10 smaller than these numbers.

2 APT BEAM-LOSS THREAT

Our evaluation of the beam-loss threat in APT and its impact on the linac design are based on a combination of operational experience, and theory plus simulation. The approach we have used has several aspects and components:

- Use of measurements of beam performance and activation levels in the LANSCE linac combined with computer simulations to determine the causes of beam loss in that accelerator.
- Choice of the APT linac design architecture and parameters to avoid the halo-generating and loss-mechanisms seen in LANSCE.
- Use of analytic modeling and computer simulation to understand the remaining physical mechanisms responsible for generating halo, and the amplitudes of particles projected into the halo.
- Confirmation of the predicted beam performance (at low energies) by measurements on the Low Energy Demonstration Accelerator (LEDA) now being built at Los Alamos. In the present schedule, initial data should be available in late FY99.

3 BEAM LOSS AT LANSCE

LANSCE routinely achieves hands-on maintenance at all locations in the accelerator and beam transport. Typical H^+ loss rates after the major focusing transitions in the linac are very low; the integrated fractional loss along the high-energy linac is normally less than 5×10^{-4} and never more than 10^{-3}. Simulations of the LANSCE linac [3] have shown several causes of beam loss. The main cause is the incomplete bunching action of the 2-cavity 201.25-MHz bunching system in the low-energy beam transport. This system, which pre-dates the development of the RFQ, produces a beam with an extended tail in longitudinal phase space, leading to poor longitudinal capture. A significant beam loss occurs downstream from the frequency jump at 100 MeV, where the 201.25-MHz drift-tube linac (DTL) transitions to the 805-MHz coupled-cavity linac (CCL); here both the transverse and the longitudinal acceptance decrease substantially, and the beam is also poorly matched longitudinally. Near 200 MeV, there is a sudden reduction in the transverse focusing strength, which leads to additional losses downstream.

Several other effects are believed to contribute to beam loss in LANSCE. First, the dual beam (H^+ and H^- accelerated together) operation of the accelerator limits the effectiveness of beam steering and other corrections.

In practice, beam steering is restricted to the low-energy beam transport and the transition region between the DTL and CCL, where the two beams are separated. Second, LANSCE is a pulsed linac, and as much as 40% of the beam loss occurs during the beam-turn-on transients. This loss can be caused by several factors, including beam-neutralization variations in the low-energy transport, and the beam-induced transient in accelerating-cavity fields, uncorrected by feedforward signals. Finally, the aperture radii in the LANSCE focusing elements and accelerating structures are relatively small, 1.6 to 1.9 cm in the high-energy linac, and the transverse focusing is relatively weak, because of the large spacing of quadrupole magnets. These two factors taken together result in a small "aperture ratio" (the ratio of physical aperture radius to rms beam radius), which varies from about 4 to 7 in the high-energy linac.

4 LANSCE LINAC AND APT DESIGN

How are the beam-loss mechanisms identified in LANSCE addressed in the APT linac design? First, the dominant loss mechanism in LANSCE, longitudinal tails caused by incomplete bunching, is almost completely eliminated in APT by the use of the RFQ, the modern replacement for the LANSCE injection and bunching architecture. Second, only one charge species, H^+, is accelerated in the APT linac, allowing uncompromised beam steering and matching. Third, APT is a cw linac with no pulse structure during normal operation, so there are minimal losses due to beam-turn-on transients; these should be managed to a greater degree than in LANSCE by the rf control loops planned for this system with feedback and feedforward. Fourth, APT is designed with much larger apertures than in LANSCE and with stronger transverse focusing. In the APT high-energy linac, the aperture radius is 8 cm. Combined with the stronger focusing in APT, the resulting aperture ratio ranges from 13 at 100 MeV to about 50 at 1030 MeV, compared with those given above for LANSCE. The very much larger aperture ratios in APT mean that beam halo is much more easily contained within the aperture. The large aperture ratios at high energies, where the activation threat is greatest, are a major benefit of using superconducting cavities for the high energy linac. Finally, improved longitudinal phase-space margin for APT is provided by conservative choice of the accelerating gradient in the superconducting linac. A 10% field increase above the design value is possible in most of the linac, which produces a 27% increase in bucket phase width and a 14% reduction in longitudinal beam size.

Improved matching is also addressed in the APT linac design. Beam-current-independent matching is obtained by maintaining the same transverse and longitudinal focusing strength across accelerating structure transitions, and focusing-strength changes are made adiabatically wherever possible. Operational setting errors that would lead to mismatch are reduced by providing adjustable focusing and appropriate beam diagnostics.

5 BEAM HALO IN APT

Given that the LANSCE beam-loss mechanisms have been addressed in the APT design, what remains as the main potential cause of APT beam loss? The beam spends only a short time transiting the linac (a few microseconds) and effects common in circular machines, such as intrabeam scattering from single Coulomb collisions have insufficient time to develop. Far more important are collective space-charge forces due to the beam as a whole. Numerical-simulation studies predict that the most important potential cause of beam loss is that associated with space-charge-induced halo caused by beam-optics mismatches [4]. These mismatches produce density oscillations of the beam core that can resonantly drive particles to larger radial amplitudes. Theoretical and numerical studies of halo formation show particle amplitudes resulting from single mismatches that extend well beyond the Debye tail of a matched beam, but not growing without limit.

Particle-core models of mismatched beams such as those in Refs.[5-14] have been constructed to provide quantitative estimates of the characteristics of halo-particle amplitudes caused by a single mismatch. In these models, the space-charge field from the oscillating beam core in a uniform linear-focusing channel is obtained from an oscillating density distribution. The amplitude of the core oscillation is directly related to the magnitude of the rms mismatch of the beam. The behavior of halo particles is studied by representing them with test particles that oscillate through the core and interact with it. A parametric resonance occurs [6] when the particle oscillation frequency is half the core frequency. The amplitude growth for the resonant particles is self limiting, because outside the core the space-charge force falls off and the net restoring force increases nonlinearly with radius, producing a dependence of frequency on the particle amplitude such that the particles drop out of resonance as their amplitudes grow. A simple scaling formula has been derived [11] from the transverse halo models that shows how the maximum amplitude for an rms mismatched beam decreases with increased focusing strength. Halo formation from the particle-core model has also been studied in 3D bunches with self consistent stationary distributions [14] with bunch parameters close to the APT case. Results for the transverse halo are similar to those from 2D models; the relative extent of the longitudinal halo has been found to be smaller than that of the transverse halo. The halo models have provided a basic understanding of the underlying physics of the most important beam-loss mechanism expected in the APT linac.

6 NUMERICAL-SIMULATION STUDIES

Numerical simulation studies are an important tool for the analysis of the beam behavior in APT. Simulations using several codes have been carried out to support the basic design of the linac. The forces acting on the particles in

the simulations include the external focusing fields and the direct space-charge fields; nonlinear force terms are included. Two-dimensional cylindrical-beam simulations with a single beam mismatch, initiating a breathing-mode core oscillation, were carried out for comparison with the particle-core halo models; these have shown remarkably good agreement in terms of maximum radial amplitude as a function of mismatch[11, 13].

End-to-end (from injector to linac output) simulation studies of the LANSCE accelerator have also been carried out for comparison with beam measurements [3] and loss estimates. The simulations agreed with measured rms quantities to within 10% to 15%. The major loss locations in the high-energy linac were correctly indicated by the simulations, but the loss magnitudes were overpredicted by about an order of magnitude. This discrepancy was not unexpected because of the sensitivity of the beam losses to the details of the particle distribution in the beam tails formed during the LANSCE bunching process, and the lack of longitudinal phase-space measurements, which are very difficult to make.

Both 2D(r-z) and 3D particle-in-cell space-charge routines have been compared and are in excellent agreement for APT, which suggests that 3D effects that account for x-y differences are not important. Nevertheless, precise calculation of the details of the particle distribution at the edges of the beam may be beyond our capabilities. Even assuming that the simulation code contains all the correct beam physics, and if sufficient numbers of particles could be run to eliminate artificial statistical fluctuations, as a practical matter the exact configuration of the machine errors can not be precisely known, nor can the initial phase-space distribution of the particles in the beam be precisely known. Because of these uncertainties, the numerical simulation studies can only make probabilistic predictions and at best have statistically validity. Given the expected statistical distributions of the errors, many computer runs are needed to predict statistical distributions of the beam parameters.

Supercomputers using massively-parallel processing are now being applied to these simulations. Some preliminary simulations looking at beam halo using up to 10^7 particles per run have already been done, and have shown the potential of applying increased computing power to the halo problem. Unlike the LANSCE simulations, the APT simulations for a linac with realistic errors produce zero beam loss above 100 MeV when using 10^7 particles per calculation. If the total fractional loss above 100 MeV was equal to 10^{-5} (an acceptable loss level), these simulations would yield an integrated loss of about 100 particles along the high energy APT linac. The absence of particle loss above 100 MeV is an encouraging result, and is positive evidence for a successful design.

At present, no direct measurements of beam-halo amplitude distributions are available for comparison with the codes, although such measurements will be carried out on LEDA. Such measurements are not trivial, and to be definitive must be carried out with careful characterization of the input beam in all six phase-space dimensions, and using precision beam diagnostics capable of taking measurements over a large intensity range.

7 BEAM-LOSS CONTROL

We believe that the practical approach to achieving very-low beam loss in the APT linac is to produce a strongly-focused well-matched high-quality beam in the low-energy normal-conducting linac, including an RFQ, and inject this beam into the large-aperture high-energy superconducting linac. Throughout the linac, rf phase and amplitude (feedback) control loops must keep the beam well centered within the longitudinal bucket, and beam steering must be provided to keep the beam well centered in the aperture. The beam halo observed in simulations with realistic errors does not extend radially beyond 5σ for a well-matched beam, or beyond about $10\,\sigma$ for a beam with mismatches; the maximum particle amplitudes are well within the apertures of the high-energy linac.

8 ACKNOWLEDGMENTS

The authors acknowledge support from the U.S. Department of Energy, and wish to thank Robert Gluckstern for useful discussions.

9 REFERENCES

[1] G.P. Lawrence, “High Power Proton Linac for APT; Status of Design and Development”, these proceedings.
[2] A.P. Fedotov and B. Murin, Proc. of the 1976 Linear Accelerator Conf., Chalk River, Canada, p.377.
[3] R.W. Garnett, R. S. Mills, and T. P. Wangler, Proc. 1990 Linac Conf., Sept. 9-14, 1990, Albuquerque, NM, Los Alamos Report LA-12004-C, pp. 347-350.
[4] A. Cucchetti, M. Reiser, and T. P. Wangler, Proc. 1991 Part. Accel. Conf., IEEE Cat. No. 91CH3038-7 (1991) 251.
[5] J. S. O’Connell, T. P. Wangler, R. S. Mills, and K. R. Crandall, Proc. 1993 Part. Accel. Conf., Washington, DC(1993) 3657.
[6] R. L. Gluckstern, Phys. Rev. Lett. 73 (1994) 1247.
[7] R.L. Gluckstern, W.H. Cheng, and H. Ye, Phys. Rev. Lett. 75, 2835 (1995).
[8] R.L. Gluckstern, W.H. Cheng, S.S. Kurennoy, and H. Ye, Phys. Rev.E 54, 6788 (1996).
[9] T.P. Wangler, R.W. Garnett, E.R. Gray, R.D. Ryne, and T.S. Wang, Dynamics of Beam Halo in Mismatched Beams, Proc. of the XVIII Int. Linear Accel. Conf., 26-30 August, 1996, Geneva, Switzerland, CERN 96-07, 372.
[10] J. Barnard and S. Lund, 1997 Particle Accelerator Conf., Vancouver, British Columbia, Canada, to be published.
[11] T.P. Wangler, K. R. Crandall, R. Ryne, and T. S. Wang, Particle-Core Model for Transverse Dynamics of Beam Halo, submitted to Phys. Rev. Special Topics-Accelerators and Beams.
[12] T.P. Wangler, E.R. Gray, S. Nath, K.R. Crandall, and K. Hasegawa, 1997 Particle Accelerator Conference, Vancouver, BC, Canada, to be published.
[13] R. L. Gluckstern, and S. S. Kurennoy, 1997 Particle Accelerator Conference, Vancouver, BC, Canada, to be published.
[14] R. L. Gluckstern, A. V. Fedotov, S. S. Kurennoy, and R. D. Ryne, Phys. Rev. E., to be published (Oct. 1998).

DESIGN SIMULATION FOR SPOT SIZE STABILIZATION IN ITS/DARHT*

Thomas J. T. Kwan, David C. Moir, Barbara G. DeVolder, Charles M. Snell, and Michael Kang
Los Alamos National Laboratory

Abstract

In high resolution flash x-ray imaging technology the electric field developed between the electron beam and the converter target is large enough to draw ions from the target surface. The ions provide fractional neutralization and cause the electron beam to focus radially inward, and the focal point subsequently moves upstream due to the expansion of the ion column. A self-bias target concept is proposed and verified via computer simulation that the electron charge deposited on the target can generate an electric potential, which can effectively limit the ion motion and thereby stabilize the growth of the spot size. A target chamber using the self bias target concept was designed and tested in the Integrated Test Stand (ITS). We have obtained good agreement between computer simulation and experiment.

1 INTRODUCTION

The stable propagation of a relativistic electron beam in vacuum requires balance between the electric and magnetic forces. For a charge unneutralized relativistic electron beam, the difference between its Coulomb repulsive force (radially outward) and its self magnetic force (radially inward) scales as $1/\gamma^2$, where γ is the relativistic factor. The Coulomb force always dominates slightly so the beam will diverge as it propagates in vacuum. However, if there is fractional charge and/or current neutralization of the electron beam, the dynamics of propagation can be quite different. For example, if the fractional charge neutralization is η, the net force acting on the beam scales (η - $1/\gamma^2$). For a highly relativistic electron beam, a small fractional charge neutralization can cause the magnetic force to dominate, resulting in radial pinching and the subsequent divergence of the beam after the pinch point. In x-ray radiography, the electron beam generates x-rays via the bremsstrahlung process in a converter target. For high resolution radiography, the energy density of the electron beam is sufficiently intense that an electric field can develop near the converter target such that ions can be extracted from its surface. Typical ions species are from contaminants such as hydrocarbons, water vapor, oxygen, etc. Among the various species, hydrogen is the most mobile and most prone to cause radial focusing of the electron beam. In our study, we assume hydrogen ions in all of our calculations. Once the ions are created, they are drawn toward the potential well near the axis of the electron beam form by its space charge. Such an ion column provides fractional neutralization of the electron beam locally and thus causes the beam to focus radially inward. Furthermore, as the ion column expands in the upstream direction, the location of the pinch point also moves in the same direction. The divergence of the beam immediately after the focal point causes the beam spot on the target to grow. The temporally increasing radiographic spot size is detrimental to high-resolution radiography. This dynamical phenomenon of the electron beam has been predicted in computer simulations[1] and confirmed by experiments at the Integrated Test Stand (ITS)[2] at Los Alamos National Laboratory

2 CONCEPT OF SELF BIAS TARGETS

In this paper, we present a novel idea of establishing an electrical potential between the target and ground that would overcome the space charge potential of the electron beam to confine the ions near the converter target. When an electron beam is incident on a target, a certain fraction of the charge will be deposited in the target in addition to the forward transmitted and the backward reflected components. The partition among the three components depends on beam energy, target material (atomic weight and mass density) and thickness (path length). In addition, there are low energy knock-on electrons coming off the surfaces. Through the variation of target thickness, one can achieve a charged state of the target ranging from positive to negative depending on the balance between the charge carried away by knock-ons and the charge deposited by the electron beam. If the target is charged negatively, an electric field will develop to attract the ions toward the converter. This can be an effective method to control the ion column, leading to the stabilization of the beam spot size. We have performed Monte Carlo electron transport calculations of the ITS electron beam and the DARHT electron beam in targets of different materials and thicknesses. The beam parameters for the ITS beam are 5.5 MeV, 3.8 kA, and 60 ns pulse length. The beam parameters for the DARHT beam are 20 MeV, 4.0 kA, and 60 ns pulse length. The target material used in the experiments was either copper or tantalum. To estimate the charge buildup and the resulting electric field in its vacinity, we will take the 1.5-mm-thick copper target as an example. From our Monte Carlo calculation, the fractional charge deposited on the target is 0.241. During the 10 ns rise of the ITS electron beam pulse, the electron energy is lower and fractional charge deposition will therefore be higher. From a rough estimate of the charge buildup on the target, we find that after approximately 3.5 ns into the rise of the electron beam pulse, an electric potential of 400 kV would be developed. At that time, excess charge needs to be drained from the target to avoid electrical breakdown between the target and the surrounding grounded conductors.

2 TARGET ASSEMBLY DESIGN

One of the major concerns of the target chamber design is field breakdown resulting from the bias potential across the collimator and the target assembly. The final design of the target chamber assembly is shown in Fig. 1. The critical surfaces are shaped in such a geometry to minimize electrical field stress. The design is aimed at a bias potential of 360 kV. The minimum distance between the target and the collimator was 2.0 cm. The diameter of the collimating aperture was chosen to be 2.0 cm. The finite element code FLUX2D was used to obtain the electric field profile in the target chamber. The maximum field strengths were found to be –175 kV/cm at the target holder position and 240 kV/cm at the tip of the collimator. In addition, the code calculated the capacitance of the target chamber to be 29.2 pF. Note that the resistance of the radial liquid resistor between the Rexolite can be varied easily by changing the salt concentration.

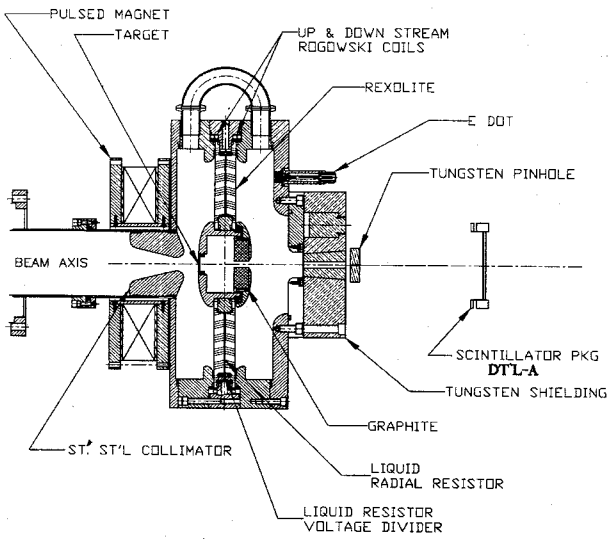

Figure 1 Experimental layout of the target chamber

3 PHYSICS DESIGN SIMULATION

The design of the target chamber was numerically simulated by using the large-scale, time-dependent, two-dimensional fully electromagnetic and relativistic particle-in-cell code MERLIN. An electron beam with the ITS parameters was injected at the left boundary and was focused on the target with a spot size of 1 mm in radius. The electron beam current was chosen to be 3.0 kA, corresponding to the experiment in which an emittance selector was inserted upstream in the beam pipe resulting in reduced current but higher beam quality. The transmitted and reflected electrons have the proper momentum and angular distributions determined by prior Monte Carlo calculations. The hydrogen ions are emitted from the target foil according to the space-charge-limited emission model. The liquid radial resistor was modeled in our simulation by a vacuum diode with its impedance determined by a properly chosen anode-cathode (AK) gap. In Fig. 2, we show the real space diagram of the target chamber assembly from our simulation. At this time, the beam current has achieved its full value of 3.0 kA. The bias potential has reached a steady state value of 360 kV after the rise time of the electron beam. We note that in Fig. 1, the axial length of the hydrogen ion column is clearly limited by the self bias potential. The ions execute vortex motion in the potential well, which limits its axial excursion. In the case where the ion column is not significantly larger than the betatron wavelength of the electron beam, the spot size on the target will not increase. The quarter betatron wavelength of the electron beam is estimated to be 3.3 cm for the parameters in our simulation. As a result, the spot size is expected to be stable. In Fig. 3, we show from our computer simulation the root-mean-square(rms) radius of the electron beam on the target plane. After the transient state due to the rise of the beam current (i.e., the development of the bias potential), the rms radius achieves a steady state value of about 0.5 mm. Note that the root-mean-square value is weighed by the beam current.

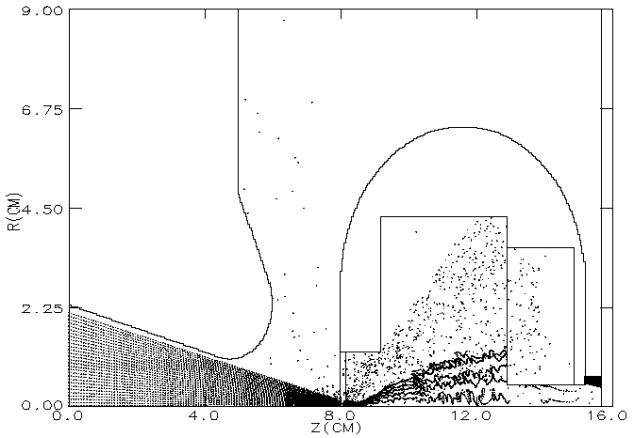

Figure 2 Physics simulation of the target chamber

4 EXPERIMENTAL COMPARISON

Experiments to validate the concept of a self bias target and the design of the target chamber were carried out at the ITS. Emittance selectors were used in the beam pipe to increase the quality of the electron beam and reduce the beam halo phenomenon. The experiment reported here had a beam current of 3.0 kA and a voltage of 5.6 MV. The radiographic spot size was monitored as a function of time. Its measured radius versus time is shown in Fig. 4. It is clear that after some transient behavior consistent with the development of bias potential, the spot size is stabilized. Besides the difference in a scaling factor due to normalization, the comparison with the simulation result in Fig. 3 is found to be quite favorable.

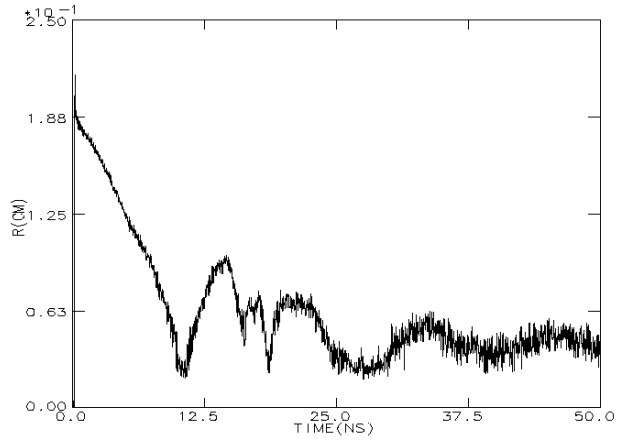

Figure 3 The rms radius of the electron beam at the target plane from the simulation

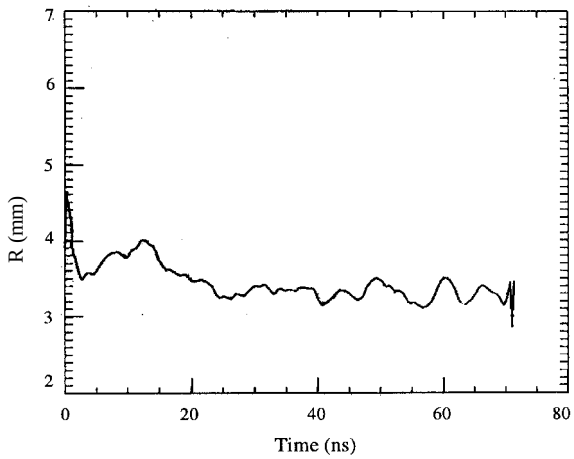

Figure 4 The radius of the radiographic spot obtained from the experiment

5 CONCLUSIONS

We found good agreement between experiment and simulation of the target chamber. The self bias potential between the target and the collimator is shown to be able to maintain the radiographic spot size in high dose radiography.

ACKNOWLEDGMENTS

The authors wish to thank B. DeVolder, T. Hughes, D. Prono, L. Thode, and D. Wolkerstorfer for many valuable discussions.

REFERENCES

1. Thomas J. T. Kwan, John C. Goldstein, and Barbara G. DeVolder, Los Alamos National Laboratory Research Note XPA-RN(U)97-021, June 1997.
2. David C. Moir, private communication.

*Work supported by USDOE

MODELING BEAMS WITH ELEMENTS IN PHASE SPACE*

E. M. Nelson
Los Alamos National Laboratory, Los Alamos, New Mexico 87545 USA

Abstract

Conventional particle codes represent beams as a collection of macroparticles. An alternative is to represent the beam as a collection of current carrying elements in phase space. While such a representation has limitations, it may be less noisy than a macroparticle model, and it may provide insights about the transport of space charge dominated beams which would otherwise be difficult to gain from macroparticle simulations.

The phase space element model of a beam is described, and progress toward an implementation and difficulties with this implementation are discussed. A simulation of an axisymmetric beam using 1d elements in phase space is demonstrated.

1 INTRODUCTION

Conventional particle codes represent beams as collections of macroparticles. This representation is adequate for many applications, but there are situations where relatively subtle details of the beam distribution are studied, and discretization noise in the macroparticle representation of the beam may obscure these details. Simulations of beam halo and emittance growth in space charge dominated beam transport are two examples. Algorithms which model a subset of the beam distribution have been successful. These include the δf algorithm[1, 2] and an algorithm[3] which employs a form of domain decomposition in phase space. Another approach is to model the Vlasov-Maxwell equation on a grid[4, 5]. Efforts using massively parallel computing paradigms with $\sim 10^8$ macroparticles are also providing significant advances in beam simulation[5].

This work discusses another model. In this model the beam is represented by a collection of elements in phase space instead of point-like macroparticles. Current is distributed over elements instead of being localized in macroparticles. This phase space element model of the beam represents a smooth phase space distribution better than a macroparticle model. Thus, this model might provide for beam transport calculations with less discretization noise. The motivation of this work is to develop improved models of emittance growth in DARHT[6].

2 PHASE SPACE ELEMENT MODEL

An element in phase space is a d dimensional simple shape embedded in a $2n$ dimensional phase space. The shapes are simplexes such as line segments, triangles or tetrahedra. Quadrilateral and hexahedral shapes may also be viable, as are shapes of four or more dimensions. Test particles at the element's vertices (and perhaps edges and faces) define the element's shape and location in phase space. Local coordinates are assigned to each point of phase space inside the element. There is a simple map from the element's local coordinates to global phase space coordinates.

Each element carries a number (or charge or current) density which is expressed in the element's local coordinate system. A number is obtained by integration of this density over the element's domain. In the jargon of differential geometry, the number density is a pseudo-d-form. This density is different from traditional densities where one integrates the density over a volume of configuration space to obtain a number.

The test particles evolve (e.g., over time) according to their equations of motion. The elements move with the test particles because each element's shape and location is defined by its test particles. The number density expressed in local coordinates on each element does not change. It is simply carried with the element. Collision-like effects are not being treated. The validity of this model depends on the interpolation of the evolved test particles being close to the evolution of an interpolated initial particle. Such tests can be performed to assess the accuracy of the model, and perhaps to adaptively refine the phase space elements which represent the beam.

3 AN IMPLEMENTATION

A code is being developed to model the transport of an intense steady-state axisymmetric beam in the presence of axisymmetric static fields. The phase space is $(x, y, ct, \gamma\beta_x, \gamma\beta_y, \gamma)$. The relativistic equations of motion for the particles are integrated in z. No paraxial approximation is used. Coordinates (x, y) are used instead of radius r to avoid potential difficulties pushing particles near the axis. Points (x, y) with the same radius r are equivalent. One can imagine revolving the phase space elements and particles about the axis in order to visualize the beam's particle distribution. Coordinate ct is computed for each particle, but this coordinate does not influence the particle motion.

The phase space elements are one dimensional line segments connecting two test particles. A local coordinate u, with $0 \leq u \leq 1$, labels points on each element. One test particle is $u = 0$ and the other is $u = 1$. The map from local coordinate u to global phase space coordinates is linear interpolation of the two test particles' phase space coordinates. Note that radius r is not linearly interpolated. It is computed from the interpolated values of x and y. This scheme better represents the beam's particles near the axis.

* Work supported by W-7405-ENG-36.

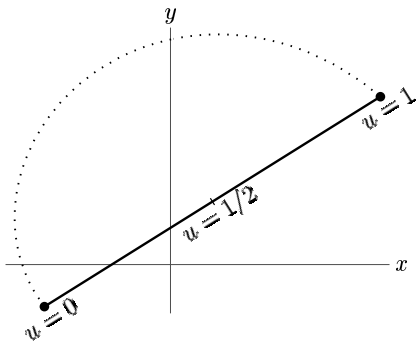

Figure 1: A one dimensional element (solid line) near the axis. Two test particles (filled circles) define the location and shape of the element. Local coordinate u identifies points on the element. The dotted line shows the effective element location if interpolation were performed in radius r instead of (x, y).

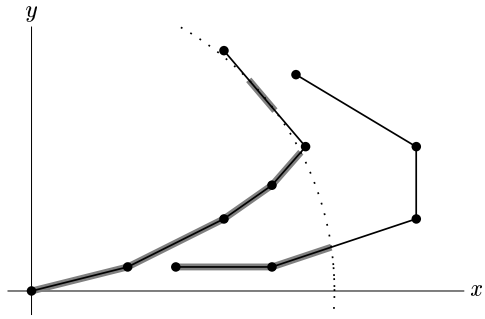

Figure 2: A collection of one dimensional phase space elements. For the self field calculation at the radius of the dotted circle, the current density is integrated over the region outlined in gray.

Fig. 1 illustrates a one dimensional element and the distinction among interpolation schemes.

An element's current density $\mathcal{J} = dI/du$ is a linear function of u. That is, the pseudo-one-form current density is $\mathcal{J} = (j_1 u + j_0)du$ with constants j_1 and j_0. This form for the current density $\mathcal{J}$ enables good representation of a uniform current density (traditional sense) beam.

The fields acting on the particles are external focusing fields, accelerating fields, and self-fields (including a flux conserving diamagnetic field). The self-fields are computed using Gauss' and Ampere's laws assuming the beam is uniform with respect to z. For example, Ampere's law gives

$$H_\theta(r) = \frac{I(r)}{2\pi r} = \frac{1}{2\pi r} \sum_i \int_{\mathcal{U}_i(r)} \mathcal{J}_i \qquad (1)$$

where $I(r)$ is the current enclosed by a circle of radius r, and i is a phase space element index. For the ith element, the domain of integration $\mathcal{U}_i(r)$ is the portion of the element inside of radius r,

$$\mathcal{U}_i(r) = \{u : 0 \le u \le 1, r_i(u) < r\}. \qquad (2)$$

The radius at u in the ith element is $r_i(u)$. An example is shown in Fig. 2. Notice that an element may have two intersections with the circle of radius r. The implementation splits elements into subelements during each self field calculation so that each subelement has at most one intersection with a circle.

Algorithms have been developed for higher dimensional phase space elements. Elements are first split into subelements so that intersections with circles are simple. A circle splits a triangle subelement into a triangular piece and a quadrilateral piece. The possibility that the triangle element encloses the axis has also been considered. A tetrahedral subelement splits into a tetrahedral piece and a prism piece, or into two prism pieces.

The motivation for using Gauss' and Ampere's law is to employ the simplest algorithm at this stage of the investigation. The integration in Gauss' and Ampere's law does not scale well with increasing number of phase space elements and test particles. However, the integration requires calculation of the intersection of elements with only one circle at a time. A better implementation will use a grid for the computation of self-fields, but such an implementation will have to deal with intersections of an element with two circles instead of just one. This adds complexity to the code.

Accelerating fields are treated crudely at this time. A fixed $\Delta\gamma$ is added to each test particle as it passes through a gap. The magnetic field on-axis is computed from a rational function approximation. Off-axis fields are computed using a four term Taylor's expansion. The equations of motion for the test particles are integrated using a fourth order Runge-Kutta algorithm.

4 AN EXAMPLE

An example is shown in Figs. 3-5. Nominal DARHT-I parameters are employed except for the beam's initial emittance. The beam is not matched with the accelerator. The initial beam is a laminar (zero emittance), uniform current density beam. The particle energies are corrected for space charge depression and all particles have zero canonical angular momentum. The initial beam is composed of 100 elements equally spaced in radius on the positive x-axis.

The example illustrates two issues. First, the beam model is wrapping itself around the axis. This will ultimately ruin the effectiveness of the element's interpolation scheme. The wrapping has two sources. One is the tune shift due to the beam's self-fields. The other is the non-conservation of canonical angular momentum, p_θ, introduced mainly by the self-field calculation scheme.

The assumption of uniformity with respect to z in the self-field calculation leads to errors in p_θ. The error for particles near the axis are opposite in sign from the error for particles near the beam edge. Using an improved self-field calculation or particle pushing scheme will reduce this effect, but the tune shift must still be dealt with when the

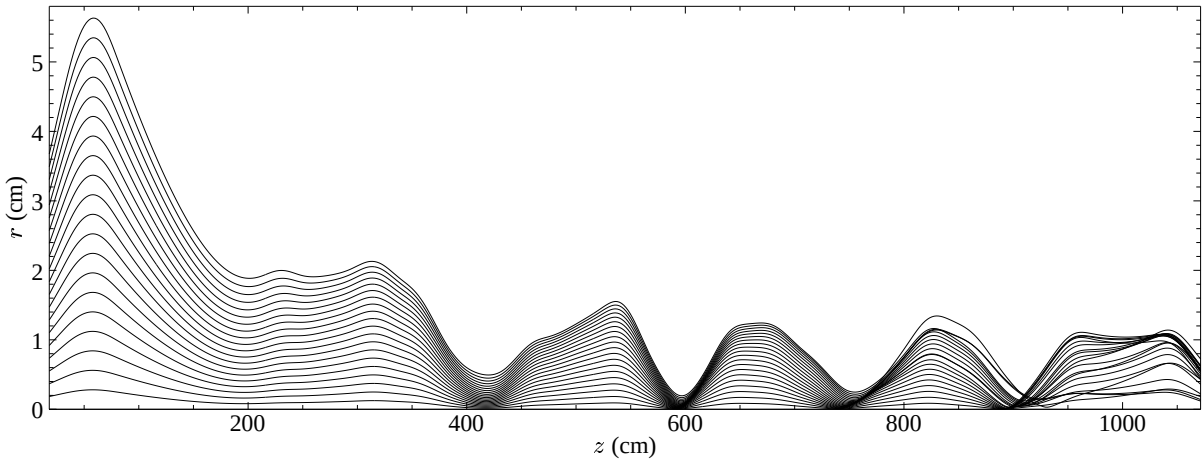

Figure 3: Trajectories of 20 particles (every 5th particle) of a mismatched laminar beam in the first 10 m of DARHT-I.

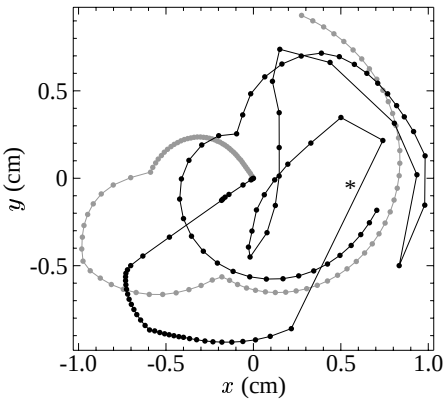

Figure 4: Configuration of the phase space elements of the beam at z=8.1 m (gray) and z=10 m (black). The gray curve clearly shows the beam model wrapping around the axis. The black curve shows that the model becomes very convoluted.

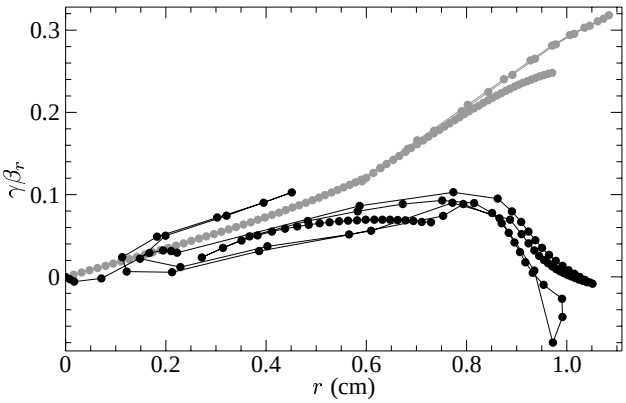

Figure 5: The beam model at z=8.1 m (gray) and z=10 m (black) projected onto the r-$\gamma\beta_r$ plane.

full accelerator is modeled.

One might modify the equations of motion to cancel the tune shift. Recall that the test particles in this axisymmetric simulation represent an equivalence class of particles at the same radius, so it is not absolutely necessary for their trajectories to coincide with real particles.

This leads to the second issue. The configuration of the beam at z=10 m (see Fig. 4) is quite convoluted. This casts doubt on the validity of the beam model. In fact, refinement of the model (i.e., more elements) shows that it is surprisingly good except near the large phase space element labeled *.

5 CONCLUSION

Some progress has been made in developing a phase space element model for a beam. More work is needed before this model's viability can be demonstrated concretely, but there are promising indications that the model will yield some improved beam simulations.

6 REFERENCES

[1] J. K. Coga and T. Tajima, "The δf Algorithm for Beam Dynamics," J. Comp. Phys. 116, 314-329 (1995).

[2] W. W. Lee, Q. Qian and R. C. Davidson, "Stability and Transport Properties of an Intense Ion Beam Propagating Through an Alternating Gradient Focusing Lattice," Phys. Lett. A 230, 347-352 (1997).

[3] T. Chen, J. Irwin and R. Siemann, "Simulation of the Beam Halo from the Beam-Beam Interaction," Phys. Rev. E. 49 (3), 2323-2328 (1994).

[4] A. Piquemal, "Renoir, a Numerical Simulation Code for the Study of Halo in Intense Charged Particle Beams," 1996 Computational Accelerator Physics, Williamsburg, VA, September 24-27, 1996, 137-142 (1997).

[5] R. Ryne and S. Habib, "Parallel Beam Dynamics Calculations on High Performance Computers," 1996 Computational Accelerator Physics, Williamsburg, VA, September 24-27, 1996, 377-388 (1997).

[6] M. J. Burns et al, "Status of the Dual-Axis Radiographic Hydrotest Facility," Proceedings of LINAC96, CERN, August 26-30, 1996, 875-877 (1996).

SURVEY TALK - NEW LASER AND OPTICAL RADIATION DIAGNOSTICS*

W. P. Leemans
Center for Beam Physics, Accelerator and Fusion Research Division
Ernest Orlando Lawrence Berkeley National Laboratory, Berkeley, CA 94720

Abstract

New techniques are reported for electron beam monitoring, that rely either on the analysis of the properties of wiggler radiation (from static magnetic fields as well as from laser "undulators", also referred to as Thomson scattering) or on the non-linear mixing of laser radiation with electron beam radiation. The different techniques reviewed are capable of providing information on femtosecond time scales and micron or even sub-micron spatial scales. The laser undulator is also proposed as a useful tool for non-destructive measurement of high power electron beams. An example is given of measuring electron beam energy and energy spread through spectral filtering of spontaneous wiggler radiation [1]. A novel technique based on fluctuational characteristics of radiation is described, for single shot, non-destructive measurement of the electron beam bunch length [2,3]. Thomson scattering based beam monitoring techniques are discussed which, through analysis of the radiated beam properties, allow non-destructive detailed measurement of transverse and longitudinal distributions of relativistic electron beams [4]. Two new techniques are discussed which rely on non-linear optical mixing of laser radiation with electron bunch emission: differential optical gating (DOG) [5] and electron bunch length measurement in a storage ring based on sum-frequency generation [6].

1 INTRODUCTION

Measurement of the transverse and longitudinal phase space properties of electron bunches produced in present and future high performance linacs [7-9], requires development of beam diagnostics with high spatial (micron or sub-micron) and temporal (femtosecond) resolution. Measurement of beam properties of high current, high power linacs [10] requires non-destructive diagnostics to be developed. Several diagnostics will be discussed, which rely on direct measurement of the properties of electron beam radiation, or on the interaction of that electron beam radiation with a laser beam. In each of the techniques discussed in this paper, the electron beam radiation is generated through interaction of the electron beam with static magnetic fields (e.g. wiggler radiation) or with electromagnetic radiation from a laser (Thomson scattering). Most of the techniques can be applied more generally to other types of radiation sources, except when the unique property of a one-to-one correlation between observation angle and wavelength of the emission is used, such as in radiation originating from the interaction with magnetic fields.

Wiggler radiation (from permanent magnets, electromagnetic undulators and lasers) has been used for diagnostic purposes [1-3, 11-13] in a wide range of beam energies, as the radiation contains the full signature of the electron beam. In Section 2, a technique for measuring energy and energy spread through spectral filtering of spontaneous emission of a wiggler will be discussed [1] as well as a technique for bunch length monitoring through fluctuational interferometry of the incoherent light [2,3]. In Section 3, experiments using radiation from laser Thomson scattering [4] (i.e. electromagnetic undulator) for beam characterization will be reviewed. In Section 4, non-linear optical mixing of laser radiation with radiation from electron beams for longitudinal bunch profile measurements [5,6,14] will be discussed.

2 WIGGLER RADIATION

2.1 Beam Energy Diagnostic

The wiggler emission cone contains information about the electron beam mean energy and energy spread [15,16]. A series of proof of principle experiments [1] have been carried out at the Accelerator Test Facility (ATF) at Brookhaven National Laboratory, demonstrating wiggler-based beam diagnosis in single shot mode, both for single micropulses and single macropulses. The experiments were performed using a high precision (0.08% peak amplitude rms) pulsed electromagnetic microwiggler from MIT, with a wiggler period of 8.8 mm. The high microwiggler field quality simplified the interpretation of the spectra defined by the convolution over many parameters: energy spread, divergence, spot size, matching, beam pointing and wiggler field errors. For a beam energy of 44-48 MeV, the wiggler emission was in the visible, where a wide range of optical diagnostics are available.

The wiggler emission profile was studied at the fundamental (532 nm). A narrow (1 nm) bandwidth interference filter was used to spectrally filter the radiation cones, and the full transverse far field pattern was recorded using a CCD camera. For a fixed wavelength, determined

* Work supported by the US Department of Energy under contract No. AC03-76SF00098.

by the filter, the cone radius depends on beam energy and wiggler field strength, and the cone width contains information of divergence and energy spread. Analytic expressions were derived, showing that for energy spreads realistic for the linac (0.5% FW) at 48 MeV, divergence dominates over both energy spread and natural linewidth at sufficiently large angles [1]. For small cones, both effects are important. The far-field profile provides an advantage over the spectrum in divergence sensitivity. A systematic set of experiments was carried out to study cone response to beam energy, energy spread, wiggler field strength, electron beam misalignment and filter central wavelength. An electron beam divergence of 0.25 mrad was extracted in a single shot measurement. Examples of spontaneous emission cones are shown in Figure 1. Note that with a wiggler length of 70 periods, sensitivity to as little as 0.5% change in central beam energy was demonstrated.

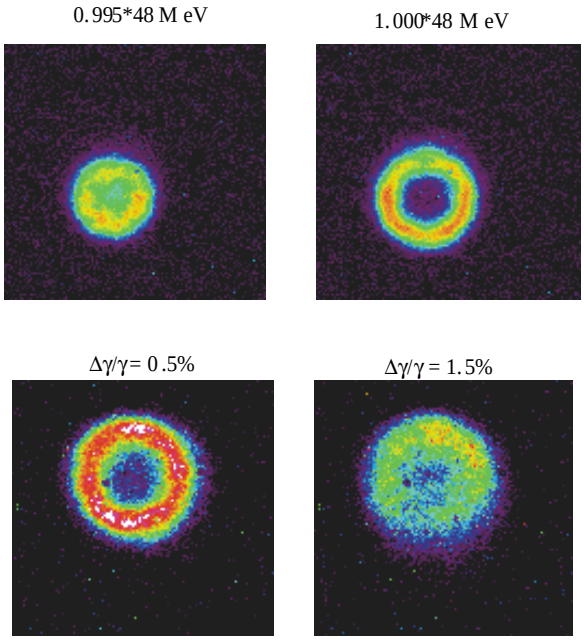

Figure 1. CCD images of a 1 nm portion of the far field wiggler spontaneous emission profile, showing sensitivity to beam energy (top pair – 48 MeV and 48*0.995) and energy spread (bottom pair – 0.5% and 1.5% FW). From Ref. 1.

2.1 Fluctuational Interferometry

In 1995, a fluctuational interferometry technique relying on the incoherent contribution to the radiation was proposed [2]. For a radiation pulse to be longitudinally incoherent, the spectral bandwidth $\Delta\omega$ must be much larger than the inverse of the pulse duration τ_p, i.e. $\Delta\omega\tau_p >> 1$. Using a bandpass filter, centered around ω_0 and with spectral width $\delta\omega$, temporal coherence can be imposed with an associated coherence time $\tau_{coh} \propto \delta\omega^{-1}$, effectively breaking the pulse up in N independent portions where $N = \tau_p / \tau_{coh}$. From shot-to-shot, the intensity will vary on the order of $1/\sqrt{N}$. Measurement of the variance of the intensity fluctuations will then give a measure for N and hence $\tau_p \approx N / \delta\omega$.

A proof of principle experiment was carried out at the ATF, in which the single shot spontaneous emission spectrum of the MIT microwiggler, was studied for a range of bunch lengths (1-7 ps) [1,3]. The microwiggler provided high brightness visible wavelength emissions for an electron beam energy of 44 MeV. A typical measured spectrum is shown in Figure 2a, revealing nearly 100% modulation and the presence of random spikes of a characteristic width, from which a bunch length of 2 ps was extracted. For comparison, a simulation for a similar bunch length including the measured instrumental resolution is shown in Figure 2b. The important features of the experimental data, the characteristic spike width and the level of modulation, are reproduced by the theory. Quantitative agreement has also been obtained between bunch length extracted from fluctuations and independent calibrations of beam bunch length [3].

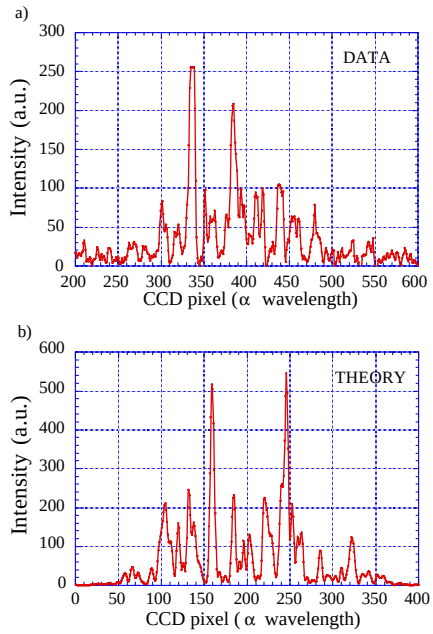

Figure 2. a) Single shot spontaneous emission spectrum from a microwiggler at 632 nm, showing nearly 100% modulation of the spectrum. Beam bunch length was extracted in a single shot measurement from the spectral fluctuations. b) A simulation for the same bunch length reproduces both the qualitative and quantitative features of the data.

3 LASER SCATTERING DIAGNOSTICS

A different approach to generating radiation from particle beams for beam monitoring is to use the interaction of the beam with high intensity laser fields. In effect, the laser acts as an electromagnetic undulator and the

properties of the emitted radiation can be accurately predicted using an equivalent undulator model [17]. The scattered radiation contains information on energy as well as on transverse and (for short laser pulses) longitudinal distributions of the electron beam.

At the Final Focus Test Beam (FFTB) at SLAC, transverse e-beam sizes as small as 70 nm were measured, by scanning a 50 GeV e-beam across the intensity fringes of an optical standing wave [7] produced by crossing two laser beams. The gamma ray yield depends on the number of photons with which the electron beam interacts and is therefore much larger at the peaks than at the valleys of the standing wave. Such resolution is beyond usual optical (e.g. optical transition radiation or synchrotron radiation) based methods.

A laser based beam diagnostic [4] which relies on analysis of the properties of the scattered radiation has been developed and used at the Beam Test Facility (BTF) [18] of the Center for Beam Physics at Lawrence Berkeley National Laboratory (LBNL). Some of the results of this experiment are discussed next.

3.1 Orthogonal Thomson Scattering Diagnostic

The experiment [4] was conducted at the BTF and used the 50 MeV (γ = 98) linear accelerator (linac) injector of the Advanced Light Source in conjunction with a high power (40 mJ in 100 fs) short pulse laser system operating at 800 nm wavelength. Electron bunches were transported using bend magnets and quadrupoles to an interaction chamber where they were focused and scattered against the laser beam. After the interaction chamber, a 60˚ bend magnet deflected the electron beam onto a beam dump, away from the forward scattered x-rays. A 75 cm radius of curvature mirror was used to focus the S-polarized amplified laser pulses to about a 30 μm diameter spot at the interaction point (IP) (measured by a charge coupled device (CCD) camera at an equivalent image plane outside the vacuum chamber).

To measure the spot size (and position) of the electron beam at the IP, an image of the electron beam was obtained by relaying optical transition radiation (OTR) [19] from a foil onto a 16 bit CCD camera or optical streak camera using a small f-number telescope. Electron beam spot sizes as small as 35 μm rms have been measured.

During the interaction of an electron beam and laser beam, scattered x-ray photons are produced with energy U_x, given by (for $\gamma >> 1$)

$$U_x = \frac{2\gamma^2 \hbar\omega_0}{1+\gamma^2\theta^2}(1-\cos\psi), \qquad (1)$$

where ω_0 is the frequency of the incident photons, ψ is the interaction angle between the electron and laser beam ($\psi=\pi/2$ in our experiments) , and θ is the angle at which the radiation is observed and assumed to satisfy $\theta << 1/\gamma$. In the experiment, x-rays with a maximum energy of 30 keV (0.4 Å) are generated.

To measure the transverse electron beam distribution for a given slice of the electron beam, we scanned the laser beam transversely across the electron beam in steps of 10 μm, by changing the tilt of the focusing mirror. and monitored the x-ray yield on the phosphor screen. It was found (Fig. 3) that the laser based technique and the results from OTR were in good agreement and give a half-width half maximum (HWHM) vertical size of 66 μm. However, the measurements for the beam edges differed and were both non-Gaussian. From the OTR data an HWHM horizontal size of 47 μm was obtained.

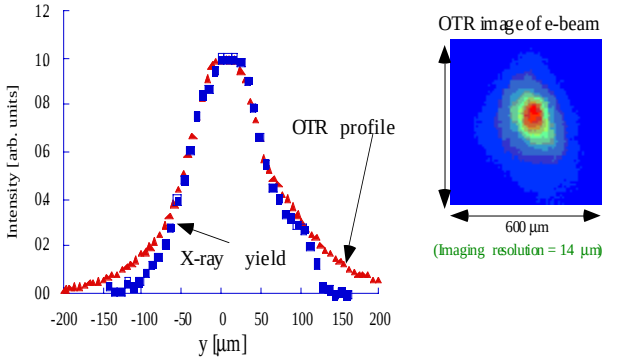

Figure 3: a) OTR image of the focused electron beam and b) triangle - vertical line-profile through the OTR image of the electron beam; square - x-ray yield vs. vertical laser beam position.

Measurement of the electron beam divergence for a fixed longitudinal location (i.e. fixed delay time between the laser and electron beam) of a time slice of the electron beam, with a duration equal to the convolution of the transit time of the laser pulse and the laser pulse duration, was done by monitoring the spatial x-ray beam profile on the phosphor screen using the CCD camera (see Fig.4). The scattered x-ray energy flux contains information of the angular distribution of the electron beam. By convoluting the single electron spectrum with a Gaussian distribution for the horizontal and vertical angles ($\sigma_{\theta x}$ and $\sigma_{\theta y}$ are the rms widths of the angular distribution of the electron beam in the horizontal and vertical direction respectively) and integrating over all energies and solid angle, the energy flux can be written as [4]:

$$\frac{dP}{d\theta_x d\theta_y} \propto \int_0^{2\pi} d\phi \int_0^1 d\kappa F(\kappa)\kappa\left[1-4\kappa(1-\kappa)\cos^2\phi\right]$$

$$\exp\left[-\frac{(\theta_x - \gamma^{-1}\sqrt{\frac{1}{\kappa}-1}\cos\phi)^2}{2\sigma_{\theta x}^2}\right]$$

$$\exp\left[-\frac{(\theta_y + \gamma^{-1}\sqrt{\frac{1}{\kappa}-1}\sin\phi)^2}{2\sigma_{\theta y}^2}\right] . \qquad (2)$$

Here dP is the radiated x-rays intensity in a solid angle $d\theta_x d\theta_y$, ϕ is the azimuthal angle, $F(\kappa)$ is an x-ray energy dependent function modeling the detector sensitivity and x-ray vacuum window transmission. Also, $\kappa = U/U_{max} = (1+\gamma^2\theta^2)^{-1}$ and $U_{max} = 2\gamma^2\hbar\omega$ and a single incident laser frequency is assumed.

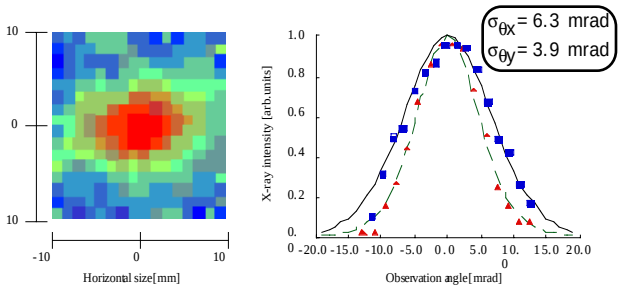

Figure 4. a) False color CCD image of the spatial profile of a 30 keV x-ray pulse on the phosphor screen, which is located 80 cm from the IP; b) square- horizontal line-profile and fitting curve (solid line), triangle -vertical line-profile and fitting curve (dashed line) from Fig. 4 (a). The scale has been converted into angular units.

By fitting the data (see Fig. 4) using Eq.(2), an electron beam divergence of $\sigma_{\theta x}$ ($\sigma_{\theta y}$) = 6.3 ± 0.2 (3.9 ± 0.2) mrad was found. F(κ) was adjusted to account for the spectral dependence of the x-ray window transmission. The difference between $\sigma_{\theta x}$ and $\sigma_{\theta y}$ is due to a combination of the electron beam being focused astigmatically at the IP, resulting in a tilted phase space ellipse (y, y′), and a laser spot size much smaller than the vertical electron beam size. As the laser beam crosses the focal volume of the electron beam, the complete horizontal (direction of propagation of the laser) phase space (x, x′) is sampled by the laser beam. However, only electrons occupying the region in the vertical phase space defined by the spatial overlap with the laser beam will contribute to the x-ray flux. As opposed to the transition radiation based detector, the laser beam therefore acts as an optical microprobe of a finite region of the transverse phase space. This value of the electron beam divergence is also consistent with an effective angular divergence of the electron beam of 3.5 - 4 mrad obtained from analyzing the x-ray spectra. Of course, the main difference is that measurement of the spatial profile is a single shot technique as opposed to measuring the x-ray spectra which requires accumulation of thousands of shots.

Finally, since the x-ray yield is sensitive to both the longitudinal bunch profile and the degree of transverse overlap between the laser and electron beam, time-correlated phase space properties of the electron beam can be studied. When an electron bunch, which exhibits a finite time-correlated energy spread (chirp), is focused at the IP with a magnetic lattice which has large chromatic aberrations, different temporal slices of the bunch will be focused at different longitudinal locations. The transverse overlap between e-beam and laser will therefore strongly depend on which time slice the laser interacts with. This in turn will lead to a time dependence of the x-ray yield varying faster than the actual longitudinal charge distribution. To illustrate this, the x-ray flux was measured as a function of the delay between laser and e-beam, for two different magnetic transport lattices. In both lattices, the magnet settings were optimized to obtain a minimum electron beam spot size in the horizontal and vertical plane (as well as zero dispersion at the IP), but chromatic aberrations were about 5 times larger in the second lattice. Result of a 60 ps long scan (time step of 1 ps) and time-resolved OTR from the streak camera for the lattice with low and high chromatic aberrations is shown in Fig. 5(a, b).

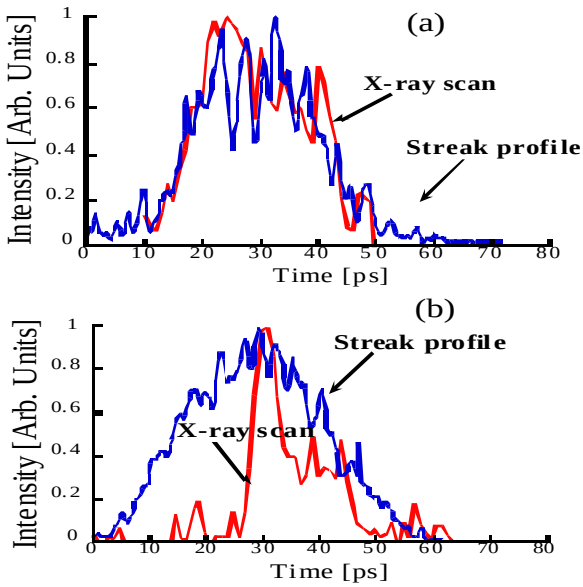

Figure 5: x-ray yield vs. delay time between laser and electron beam and profile of time resolved OTR image from a streak camera for a lattice with a) small and b) large chromatic aberrations.

Whereas the temporal scan for the lattice with low chromatic aberrations (Fig.5a) is in good agreement with the time-resolved OTR measured with a visible streak camera, the scans taken for the second configuration (Fig.5b) typically showed a 2-3 times larger amplitude 5 ps wide peak sitting on a 20 ps wide pedestal. This is to be compared to the time resolved OTR from the streak camera which typically showed a 25-30 ps wide electron beam without any sharp time structure. From lattice calculations, it is found that an energy change on the order of 0.25 % would increase the vertical spot size by a factor two at the IP, compared to best focus, resulting in a proportional reduction in vertical overlap between the laser and electron beam, and hence in x-ray yield. These measurements indicate the potential of the laser based Thomson diagnostic to measure time-correlated energy changes of less than a percent, with sub-picosecond time resolution.

It is important to note also that, due to the non-destructive nature of the Thomson scattering technique, it might prove to be a useful tool for the diagnosis of high current, high power electron beams, such as for the DAHRT project [10].

4 NON-LINEAR MIXING

Another new direction being pursued for developing beam diagnostics, is the non-linear mixing of laser radiation with radiation from electron beams [14]. Two recent

examples of the application of non-linear optics for bunch length monitoring are discussed next: one in which a tightly synchronized laser pulse is used to perform a cross-correlation measurement and one in which the laser pulse is loosely synchronized with respect to the electron beam.

4.1 Laser Correlation with Synchrotron Pulses

Experiments at the Advanced Light Source have recently shown [6] that a synchronized laser pulse can be used to measure femtosecond synchrotron pulses via frequency up-conversion. Visible synchrotron radiation from the ALS at 2 eV was sum-frequency mixed in a BBO crystal with 1.55 eV radiation from a short pulse (<100 fs) Ti:Al_2O_3 laser. By scanning the laser pulse in time with respect to the electron bunch, a 16.6 ps rms bunch length was measured, which is in good agreement with streak camera measurements. Furthermore, the technique was shown to detect sub-picosecond structure of the electron bunch, purposely imposed on the bunch by co-propagating an intense short laser pulse with the electron beam inside a wiggler. The laser beam, in the presence of a wiggler field, causes an energy modulation of a slice of the bunch via a FEL-like interaction. The energy modulation depth is determined by the wiggler and the laser pulse strength, and the duration of the slice is equal to the laser pulse length. By propagating the modulated electron beam through a dispersive section, this short slice can be separated from the main bunch, leaving a small density depression in the main bunch. The cross-correlation technique detected this few 100 fs long depression [6].

4.2 Differential Optical Gating

The second example relies on the use of a loosely-synchronized laser pulse as a gate in a non-linear medium for pulse length measurement in a technique which is called differential optical gating (DOG) [5]. DOG uses two non-linear media as gates and two detectors (A and B). The gate pulse and the electron beam radiation are optically split in two parts. The laser reaching gate B is delayed by a time δ with respect to the one reaching gate A. Under the assumption that the gate pulse is much shorter than the radiation pulse (and an instantaneous gate response), the signal seen by each detector can be written as [5]

$$\begin{aligned} A(t_1) &\propto E_G I_S(t_1) \\ B(t_1+\delta) &\propto E_G I_S(t_1+\delta) \end{aligned} \qquad (3)$$

where E_G is the energy of the laser gate pulse and $I_S(t)$ is the instantaneous intensity of the radiation. From this measurement, both the instantaneous intensity and its time derivative are then known, which allows bunch shape reconstruction. Through the loose synchronization, the laser pulse randomly "walks" across the bunch, much like interleaved sampling on digital oscilloscopes. In recent experiments at Stanford University, the technique has been applied to the pulse shape measurement of a picosecond free electron laser source, using both an instantaneous gate and a step function gate [5].

5 ACKNOWLEDGEMENTS

I would like to thank Palma Catravas for kindly contributing to the section on the fluctuational interferometry and wiggler radiation measurements, R. Schoenlein and M. Zolotorev for information on the non-linear mixing, C. Rella and T. Smith for the DOG information, as well as my collaborators on the laser based probing work. I also want to thank E. Esarey for many useful conversations.

6 REFERENCES

[1] P. Catravas, PhD thesis, MIT, 1998.
[2] M. S. Zolotorev and G. V. Stupakov, SLAC-PUB-7132 (1995); M. S. Zolotorev and G. V. Stupakov, Proc. 1997 Particle Accelerator Conference.
[3] P. Catravas et al., submitted to Phys. Rev. Lett.
[4] W.P. Leemans et al., Phys. Rev. Lett. **77**, p.4182 (1996); R.W. Schoenlein et al., Science **274**, pp.236-238 (1996); W.P. Leemans et al., IEEE Journal of Quant. Elect. **33**, pp. 1925-1934 (1997).
[5] C.W. Rella et al., submitted to Optics Comm.
[6] R.W. Schoenlein, M. Zolotorev et al., private communication.
[7] T. Shintake, Nucl. Inst. & Methods A**311**, pp. 453 (1992), Balakin, V. et al., Phys. Rev. Lett. **74**, p. 2479-82 (1995).
[8] P. Kung, H. Lihn and H. Wiedemann, Phys. Rev. Lett. **73**, 967 (1994).
[9] D. Umstadter et al., Phys. Rev. Lett. **76**, 2073 (1996); E. Esarey et al., Phys. Rev. Lett. **79**, 2682 (1997).
[10] H. Rutkowski et al., these proceedings.
[11] P. Heimann et al., Rev. Sci. Instrum., **66**(2) 1885-8 (1995).
[12] A. Lumpkin, Nucl. Instr. & Meth. A, **393**, 170-177 (1997).
[13] E. Tarazona and P. Elleaume, Rev. Sci. Instrum., 66(2), 1974-7 (1995).
[14] W.P. Leemans, Proc. Advanced Accelerator Concepts Workshop, AIP 398, Woodbury, NY (1997)
[15] K.-J. Kim, AIP Conf. Proc. **184**, Vol.1, 565-632 (1989).
[16] R. Barbini et al., Rivista del Nuovo Cimento, **13**(6), 1-65, (1990).
[17] K.-J. Kim, S. Chattopadhyay and C.V. Shank, Nucl. Instr. And Meth. A **341**, 351-354 (1994).
[18] W.P. Leemans et al., Proc. 1993 IEEE Part. Acc. Conf., 83, (IEEE, New York, 1993).
[19] L. Wartski et al., J. Appl. Phys. **46**, 3644 (1975); M.J. de Loos, S.B. van der Geer and W.P. Leemans, Proc. EPAC 94, 1679 (1994).

HIGH GRADIENT SUPERCONDUCTING RF STRUCTURES

H.Weise
Deutsches Elektronen-Synchrotron DESY, 22607 Hamburg, Germany

Abstract

Superconducting (s.c.) RF structures for the acceleration of electrons have been known for over 30 years (HEPL, Stanford). More than 10 years after their successful start a new generation (i.e. standing wave, π-mode cavities), made from niobium and operated at frequencies between 352 MHz and 3 GHz, was established at accelerators being operated for high energy physics (CERN, DESY, KEK) as well as nuclear physics (CEBAF, Darmstadt) experiments. Although the HEPL s.c. cavities were limited to a 10% duty cycle and the 2nd generation now allows continuous wave operation, the increase of the accelerating gradient was remarkably small with respect to the > 50 MV/m limit given by the physics of RF superconductivity.

Thirty years ago HEPL cavities reached about 2 MV/m; 15 years later DESY cavities achieved 4 MV/m. And the large 338-cavity CEBAF installation is based on a 5 MV/m gradient, the commissioning of the accelerator being less than 10 years ago. Since 1992 the TESLA (TeV Energy Superconducting Linear Accelerator) collaboration has studied the fundamental problems in cavity fabrication as well as operation. Last year an 8 mA electron beam was successfully accelerated in a 15 MV/m module containing 8 s.c. 9-cell cavities. Two more modules (20 to 25 MV/m) will be installed. From recent cavity tests a gradient of 25 MV/m can be taken as state of the art. Cavity production, preparation, and installation was remarkably improved, a prototype linac (TESLA Test Facility Linac) for a large linear collider shows good performance.

1 RF SUPERCONDUCTIVITY AND LINEAR ACCELERATORS

In 1961 Banford and Stafford [1] at Harwell proposed the feasibility of a superconducting proton linac, and have carried out experimental measurements on lead and niobium at 400 MHz using quarter-wavelength hairpin resonators. Similar measurements were started by Susini [2] and others at CERN and the University of Lausanne on lead and niobium surfaces at 300 MHz using a capacitively-loaded coaxial resonator. Here the interest was in building a s.c. separator. Also in 1961, a program was started at Stanford University to measure the properties of superconductors in a microwave cavity at 2856 MHz [3]. This program started the pioneering work for the application of superconducting RF structures for the acceleration of electrons.

The Stanford cavity was about 14 cm in diameter by 14 cm in length and was resonant at 2865 MHz in the TE011 mode. In this mode there is no current flux across the joints between the cavity side wall and the two end plates, so that the quality factor Q is independent of these joints. Several types of tin and lead surfaces were measured. Electroplated surfaces gave the highest Q's. A residual resistivity was always observed as T approached zero. Today we know from the theory of RF superconductivity that this is not due to improper cavity fabrication but can be explained by the BCS theory of superconductors. Nevertheless, material properties are limiting the achievable accelerating gradient. We characterize the state of the art material by the so-called RRR (residual resistivity ratio) which is a direct measure of the thermal conductivity.

At the 1963 International Conference on High Energy Accelerators in Dubna the Stanford group published a very preliminary design of a 20 GeV - 10% duty cycle superconducting accelerator. This at a time at which no real cavity has ever been built. The remarkable numbers were an assumed length of 3000 m corresponding to about 10 MV/m (active/total length ratio of 66%), and a power dissipated in the walls of the structure of 200 kW average, i.e. 100 W/m; the forward power was claimed to be 2 MW average, so that the total beam power of 1.8 MW average corresponded to almost 100 μA average electron beam current. Ref. [4] can be used to compare this design with the actual TESLA design [5] for a 500 GeV c.m. linear collider.

Based on the TE011 measurements the Stanford group designed and built the first two accelerating cavities, one TM010 and one 2 π/3 mode cavity. In 1965 an accelerating gradient of 3.7 MV/m was reached at an unloaded Q_o of $2.5 \cdot 10^8$ [6]. The cavity was electroplated with lead and operated close to 2856 MHz. Radiation exceeding 100 mR/h provoked the optimistic statement *The radiation provides indirect evidence of strong accelerating fields*. The explanation for the field emission limit was a possible local enhancement of the electric field by a factor 200 caused by sharp projections on typical surfaces [7]. Today we use enhancement factors of

100 to 1000 to explain the level of field emission using Fowler-Nordheim theory.

During the discussion of a LINAC 64 conference paper [8] the author felt that *the present state of knowledge of RF superconductivity was sufficiently discouraging to abandon further work on a superconducting proton linac.* Suelzle from Stanford wrote almost 10 years later *lower-than-expected accelerating gradients have necessitated the re-evalution of the energy objectives* [9]. The hope for getting roughly 14 MV/m in a 6-meter long, 1300MHz accelerating structure was not fulfilled. By the end of 1972 the 1300 MHz structures were limited to 3 MV/m. But the first superconducting electron linac was commissioned. It produced an 8 MeV, 250 μA beam with 12 keV · deg (FWHM) and a transverse emittance of less then 1 π mm mrad. Today the HEPL accelerator is used to drive different undulators and produce Free Electron Laser radiation in the infrared.

2 S.C. CAVITIES FOR STORAGE RINGS

The somewhat disappointing results from Stanford certainly have de-emphasized the search for high gradients. But in the late 70's the use of s.c. cavities in storage rings was considered. Here gradients of a few MV/m were sufficient. Important were instability thresholds - an adequate damping of higher order modes (HOMs) for multiturn operation was needed. Tests in existing storage rings led to promising results as reported [10-11]. Today we can find 352-MHz cavities in LEP as well as 500-MHz cavities in HERA. The first Workshop on RF Superconductivity, organized in 1980 by the Kernforschungszentrum Karlsruhe (KfK), summarized all activities aiming for the use of RF superconductivity for acceleration of ions as well as electrons.

While all first β=1 cavities were of cylindrical symmetry, i.e. a pill box with slightly smoothed out edges, one can find the first spherical resonators around 1980. According to [12] the Genoa / Italy 3-cell C-band structure was built in spherical geometry because of easier manufacturing. The result was amazing, the comparison of the maximum accelerating field shows the remarkable gradient of 8 MV/m. Somewhat later the spherical geometry was found to be the best in order to avoid multipacting. The high radiation levels in the HEPL tests were not only caused by simple field emission but by resonant electron emission, i.e. multipacting.

Within a short time the five laboratories being the driving forces towards high gradient β=1 structures, CERN, Cornell, DESY, KEK, and Wuppertal, concentrated on the spherical geometry. The E_{peak}/E_{acc} ratio was optimized to be about 2 for any geometry. Some cavities had a wall section being exactly perpendicular to the cavity axis (remains of the old pill box). Later the elliptical geometry was found to be best because of easier chemistry and water cleaning. The resonator frequencies and the number of cells varied from 352 MHz / 4-cell (CERN) to 3 GHz /5 & 20-cell (Cornell; Wuppertal - for the S-DALINAC / Darmstadt).

A significant frequency dependence of the maximum obtainable accelerating field could not be found. The choice of frequency was determined by the need to combine the cavity operation with other normal conducting structures or by the existence of klystrons. For most of the listed cavities the maximum number of cells was chosen from HOM calculations. The need to damp HOMs and to have sufficient coupling between the input coupler and the cavity led to slightly different designs.

3 HIGHER GRADIENTS, LOCALIZED DEFECTS, AND HIGHER RRR

For many years the design goal for superconducting structures was about 5 MV/m. This was based on experience with multicell cavities. Nevertheless, the goal of high gradients was never forgotten since the BCS theory predicted maximum gradients of almost 50 MV/m at 2 K. Considerable effort has been devoted to the understanding of surface defects. Larger defects could be localized and sometimes even eliminated by grinding. In 1979 the technique of temperature mapping was developed at CERN and it was demonstrated that well localized defects were one of the prime causes of quenching [13]. Over the years these temperature mapping devices have been improved, and more diagnostics like X-ray diodes and RRR measuring devices using eddy current induced by small coils have been introduced.

Cornell pointed out that the threshold for thermal instabilities could be increased if the thermal conductivity, i.e. the RRR of the cavity wall is improved. In a close collaboration with industry the RRR value for the used Nb material was raised from typically 40 (corresponding to a heat conductivity λ = 10 W/(m·K) at 4.2K) to values between 150 and 200. To increase the RRR even further yttrification at about 1250°C was used at Cornell. Later the use of 1400°C UHV baking in the presence of titanium vapor was established.

The combination of eliminating defects and using higher RRR has guaranteed a more reliable way towards accelerating fields of 5 to 10 MV/m in multicell cavities. As examples one can quote results from CEBAF prototype cavities which reached 6-8 MV/m, a single cell KEK 500 MHz cavity (RRR 80) with 7.6 MV/m, the first CERN LEP prototype cavity (4-cell, 352 MHz) with 7.5 MV/m, and last but not least one 20-cell 3GHz cavity for the S-DALINAC which reached 7.8 MV/m after the preparation at Wuppertal. Cornell was able to reach really high gradients in 1.5 GHz single cell cavities: 22.5 MV/m. Wuppertal followed with 23.1 MV/m for a 3 GHz single cell structure.

A few years later the standard material for s.c. cavities was RRR 280. The first multicell cavities reached again higher gradients but shortly after the installation of the first 20-cell cavity in the S-DALINAC the enthusiasm was damped by a new phenomenon. After keeping the cavity at temperatures just above nitrogen temperature (70 - 100K), which can happen in a linac installation, the quality factor dropped, the cryogenic losses were increased by a factor of 10. Darmstadt and DESY found the Q-degradation (sometimes also called Q-disease) at about the same week. Months later it was clearly identified as a clustering of hydrogen and therefore creation of normal conducting niobium hydride areas [14]. For increasing the RRR of the Nb material the oxygen was removed with the disadvantage that the hydrogen is not chemically bound anymore. A cooling of the acid during chemical polishing is necessary to avoid high hydrogen concentration in the niobium. Otherwise Niobium hydride areas start to grow. Baking at temperatures above 750°C can cure the problem.

4 THE STATUS BEFORE TESLA

At the LINAC 92 Conference R. Sundelin presented a good overview about the state of the art in s.c. cavity production [15]. Assembly in clean rooms was standard, the Cornell group had improved gradients using high peak power processing, and CERN used high pressure water rinsing to suppress field emission in the LEP cavities which are made from copper but sputter coated with Nb. The number of superconducting cavity operating hours in larger installations increased substantially.

Table 1:
S.c. cavities in operation as known at the time of the LINAC 92 Conference, i.e. before the start of the TESLA program. The CEBAF installation was ongoing at a rate of 16 cavities per month.

	Nbr.	of Cav.	MHz	m	MV/m
MACSE	5	5-Cell	1500	2.5	6.5
S-DALINAC	10	20-Cell	3000	10.0	5.9
HERA	16	4-Cell	500	19.2	3.6
HEPL				30.8	3.0
TRISTAN	32	5-Cell	508	47.2	6.6
CEBAF	106	5-Cell	1497	53.0	7.6
LEP	12	4-Cell	352	20.4	3.7

The achieved accelerating gradients of the different machines are listed above. The CEBAF installation was ongoing at a rate of 16 cavities per month.

5 CEBAF AND LEP INSTALLATION

The CEBAF recirculating superconducting electron linac at Jefferson Lab went in full operation and is now using 330 s.c. cavities operating at 2.0 K. The operation frequency is 1497 MHz. Four pairs of the 0.5-m-long cavities are contained in one cryomodule but each cavity is separately powered by one 5 kW klystron. According to [16] the distribution in the accelerating gradients has its maximum at about 7.5 MV/m with a spread of 5 MV/m FWHM. The principal limitation of the installed cavities is electron field emission and associated phenomena, such as X-ray production, charging and arcing at the cold ceramic RF window, and anomalous 2 K heat load. This affects about 80% of the cavities. Only 12% of the cavities are limited by quench. The average quench limit is at 13 MV/m.

The cavity operation in CEBAF has been quite stable and reliable. In 1997 the maximum energy delivered to the nuclear physics experiments was 4.4 GeV at a beam current of 115 μA. The RF could have supported 5.6 GeV with a five pass beam delivery. In-situ RF-helium processing of the cavities was tested and yielded an additional 41 MeV/pass. Jefferson Lab intends to upgrade the machine to the 6-8 GeV region by this method. Further steps towards higher electron beam energy are described elsewhere [17]. The Jefferson Lab Free-Electron Laser installation can operate above 10 MV/m.

In 1997 CERN operated 240 s.c. cavities in LEP. Out of the 240 cavities 16 were made from solid niobium and 224 were sputtered Nb/Cu cavities. The operation frequency is 352 MHz, the nominal operating field 6 MV/m. Eight cavities are grouped each and driven by one klystron. Two klystrons are connected to one HV power converter. According to [18] the overall performance of the s.c. RF system was good during the 1997 operation period. The average operational gradient of the 224 Nb/Cu cavities was 5.9 MV/m even though some cavities were limited at lower gradients. The four solid Nb modules were running at about 3.6 MV/m (nominal gradient 5 MV/m).

6 THE TESLA R&D EFFORT

Since 1991 the international TESLA collaboration [19] is following an approach to a 500 GeV linear collider using superconducting accelerating cavities. Altogether 35 institutes from nine countries are developing linac components as there are s.c. accelerating structures, couplers, cryostats, RF sources, beam diagnostics etc. The TESLA Collaboration tries in a joint effort to increase the usable accelerating gradient to more than 25 MV/m. A test facility, located at DESY with major components flowing in from members of the collaboration, is going to establish a well-developed collider design. The status of this design work is described elsewhere [5].

The TESLA Test Facility (TTF) includes cavity preparation and testing as well as the final test of cavities in a linac installation [20]. About 25 standard 9-cell 1.3 GHz structures operating in the pi-mode have been prepared and tested. Out of the first production series eight cavities were taken for the assembly of one TESLA cryogenic unit, the TTF module #1.

The goal for the accelerating gradient was set to 15 MV/m average (to be compared with the 1992 state of the art given in table 1) at an unloaded quality factor $Q_o=3\cdot10^9$. This goal was reached with module #1. Although some cavities are limited below 15 MV/m the maximum achieved electron energy was 125 MeV in short macropulses and 105 MeV in 800 µs long macropulses. The overall performance is limited by the weakest cavities since all eight cavities are driven by one common klystron and the RF forward power is equally split. Details about the operation can be found in [21].

7 THE FIRST TTF CAVITY PRODUCTION

About 25 cavities from 4 different manufacturers were tested in a vertical test cryostat. The average gradient was 19.2 MV/m at $Q_o > 3\cdot10^9$. 14 cavities showed $E_{acc} > 20$ MV/m, 3 cavities showed $E_{acc} > 28$ MV/m. The last 9 cavities delivered and tested had a clearly increased gradient of 24.3 MV/m at $Q_o > 3\cdot10^9$. Figure 1 shows the test results as a function of time. Maximum gradients are plotted as well as the usable gradient defined by the onset of increased cryogenic losses. Some of the very first cavities had maximum acceleration voltage being almost high enough for TESLA 500 but the strong field emission limited the usable gradient.

During 1996 the first group of cavities was tested. High pressure rinsing with ultraclean water reduced the field emission but most of the tested cavities were limited around 13 MV/m. The reason was found to be an insufficient cleaning after the preparation for electron beam welding of the equator. Since summer 1997 another 11 cavities were tested. The average maximum gradient is almost 25 MV/m. Field emission is still an issue and limits the usable gradient to roughly 22 MV/m. Nevertheless, all four manufacturers were able to produce cavities with gradients above or close to 25 MV/m. The gradient of the best TESLA 9-cell cavity is above 30 MV/m. Figure 2 shows the horizontal test result. This cavity is going to be used in the second cryogenic module.

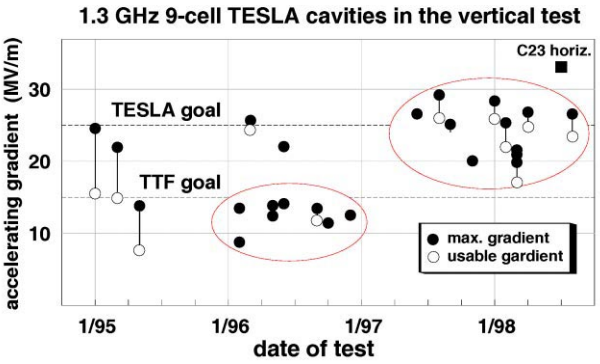

Fig. 1: Vertical test of 1.3 GHz 9-cell cavities.

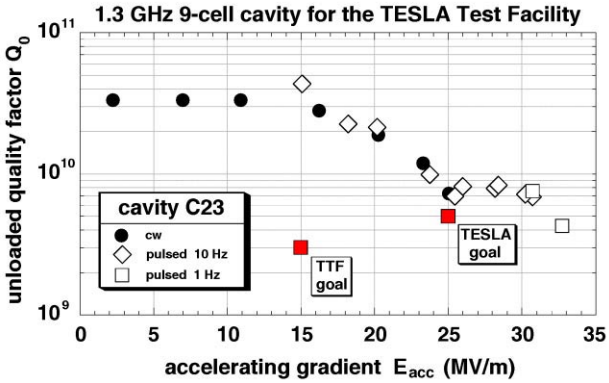

Fig. 2: The best TESLA 9-cell cavity measured in a horizontal test cryostat. For this test the cavity is equipped with the main RF input coupler and the HOM couplers.

8 OUTLOOK

The goal for the second TTF Linac module being just in the assembly phase is 20 MV/m. The third module is expected to reach 25 MV/m. All three modules will be used for a Free Electron Laser experiment in the UV [22]. Further modules will be built to finalize the design of accelerating units of the large TESLA machine [23]. Being installed in the TTF Linac they will finally drive a VUV free-electron laser. Therefore a new cavity production was started. A total number of 26 cavities is expected to be at DESY by end of 1998. The material for all cavities was scanned for inclusions of other metals. A special eddy current scanning apparatus was developed.

Single cell cavities have reached 40 MV/m accelerating field [24]. The members of the TESLA collaboration and also Jefferson Lab as well as KEK are still improving the gradients of resonators made from solid niobium. Electropolishing is studied again in order to smoothen the inner surface. High pressure water rinsing is the most successful method to decrease field emission. Nevertheless, the installation procedure of all RF couplers seems to be a main issue.

With the aim to decrease the cavity production costs two new fabrication methods are studied. Spinning of cavities is described elsewhere [25]. Hydroforming of multicell cavities is also under investigation. Both methods allowed the production of L-band single-cell cavities with accelerating gradients above 20 MV/m. A slightly decreasing Q vs. E_{acc} is not understood. Multicell-cavities are underway and will be measured next.

9 REFERENCES

[1] A. P. Banford and G. H. Stafford, Plasma Physics, J. Nucl. Energy, Part C, 3, 287 (1961).

[2] A. Susini, "Initial Experimental Results Concerning Superconductive Cavities at 300 MHz," CERN Internal Report 63-2, (Febr. 1963).

[3] P. B. Wilson, Nucl. Instr. And Methods, 20, 336 (1963).
[4] P.B. Wilson, H. A. Schwettman, W. M. Fairbank, "Status of Research at Stanford University on Superconducting Eletron Linacs", IV Int. Conf. on High Energy Acc., Dubna 1963, p. 694 (1963).
[5] D. Trines, "Status of the TESLA Design," this conference.
[6] H. A. Schwettman, P. B. Wilson, G. Y.Churilov, "Measurements at High Electric Field Strengths on Superconducting Accelerator Cavities", V Int. Conf. on High Energy Acc., Frascati 1935, p.690 (1965).
[7] H.A. Schwettman, J. P. Tourneaure, R. Waites,"Evidence for Surface-state-enhanced Field Emission in RF Superconducting Cavities", Journ. of Applied Physics, Vol.45, No.2 (1974).
[8] J. M. Dickson, "RF Superconductivity Measurements", LINAC 64 Conference, p. 540 (1964).
[9] L. R. Suelzle, "Progress on RF Electron Superconducting Accelerators", 1973 Part. Acc. Conf., San Francisco, p. 44 (1973).
[10] R. Sundelin, IEEE NS-32 (1985) 3570.
[11] H. Piel, IEEE NS-32 (1985) 3565 and LINAC 84 Conf., p. 260 (1984).
[12] C. Pagani, private communication.
[13] Ph. Bernard et al., XI Int. Conf. on High Energy Acc., Geneva 1980, p .878 (1980).
[14] W. Bonin and R. W. Roeth, "5th RF Supercond. Workshop, Hamburg 1991, DESY M-92-01.
[15] R. M. Sundelin, "Review of Progress in Superconducting High-Beta Structures", LINAC 92 Conf., p. 840 (1992).
[16] C.E. Reece, "Operating Experience with Superconducting Cavities at Jefferson Lab.," 8th RF Supercond.Worksh., Padova 1997, to be publ.
[17] J. R. Delayen, "Development of an Upgrade of the CEBAF Acceleration System", this conference.
[18] O. Brunner, "RF System Reliability and Performance in 1997", 8th LEP Performance Workshop, CERN Internal Reports, CERN-SL-98-006 DI.
[19] The TESLA (TeV Energy Superconducting Linear Accelerator) R&D effort is carried out by a number of institutions which includes: Armenia: Yerevan Physics Institute; China: IHEP, Academia Sinica, Beijing; Tsinghua-University, Beijing; Finland: Institute of Physics, Helsinki; France: CEA/DMS (DAPNIA, CE Saclay); IN2P3 (INP Orsay + LAL Orsay); Germany: RWTH Aachen; Max-Born-Institute, Berlin-Adlershof; TU Berlin; TU Darmstadt; TU Dresden; University of Frankfurt; GKSS, Geesthacht; DESY, Hamburg + Zeuthen; University of Hamburg; FZ Karlsruhe; University of Rostock; University of Wuppertal; Italy: INFN Frascati; INFN Legnaro; INFN Milano; INFN and University Roma II; Poland: Polish Academy of Science; University of Warsaw; Institute of Nuclear Physics, Cracow; Univ. of Mining & Metallurgy, Cracow; Pol. Atomic Energy Agency, Warsaw; Soltan Institute for Nuclear Studies; Otwock-Swierk; Russia: JINR, Dubna; IHEP Protvino; INP Novosibirsk; USA: ANL, Argonne IL; Cornell University, Ithaca NY; FNAL, Batavia IL, UCLA, Los Angeles CA.
[20] D. A. Edwards (ed.), TESLA Test Facility Linac - Design report, DESY-TESLA-95-01 (1995).
[21] W. D. Moeller, "The Performance of the 1.3 GHz Superconducting RF Cavities in the First Module of the TESLA Test Facility Linac", this conference.
[22] J. Rossbach, "The TESLA Free Electron Laser - Concept and Status", this conference.
[23] R. Brinkmann, G. Materlik, J. Rossbach, A. Wagner (eds.), "Conceptual Design of a 500 GeV e^+e^- Linear Collider with Integrated X-ray Laser Facility, DESY 1997-048 and ECFA 1997-182.
[24] M. Ono et al., "Achievement of 40 MV/m Accelerating Field in L-Band SCC at KEK", 8th RF Superconducting Workshop, Padova 1997, to be published.
[25] V. Palmieri, "Review of Fabrication of SC Cavity Structures", this conference.

CW RFQ FABRICATION AND ENGINEERING *

D. Schrage, L. Young, P. Roybal, A. Naranjo, D. Baca, W. Clark, F. Martinez,
H. Haagenstad, J. Mitchell, D. Montoya, A. Rendon, F. Krawczyk, T. Davis, D. Casillas,
A. Gonzales, G. Gonzales, S. Hidalgo, E. Kettering, G. Leeches, B. Ormond, R. Reinert,
O. Smith, & J. Tafoya
Los Alamos National Laboratory, Los Alamos, NM, 87545, USA

Abstract

The design and fabrication of a four-vane RFQ to deliver a 100 mA CW proton beam at 6.7 MeV is described. This linac is an Oxygen-Free Electrolytic (OFE) copper structure 8 m in length and was fabricated using hydrogen furnace brazing as the joining technology.

1 INTRODUCTION

The linear accelerator for the Accelerator Production of Tritium Project (APT) [1] will include a 6.7 MeV Radio Frequency Quadrupole (RFQ) linac. The first phase of this project, the Low Energy Demonstration Accelerator (LEDA) [2] consists of this RFQ plus a 20 MeV Cavity-Coupled Drift Tube Linac (CCDTL) [3]. The technical specifications for the APT/LEDA RFQ are given on Table 1.

Table 1: APT/LEDA RFQ Specifications

PARAMETER	VALUE
Frequency	350.00 MHz
Particle	H^+
Input Energy	75 keV
Input Current	105 mA
Input Emittance, trans./norm.	0.020 π-cm-mrad rms
Output Energy	6.7 MeV
Output Current	100 mA
Output Emittance, trans./norm. longitudinal	0.022 π-cm-mrad rms 0.174 deg-MeV
Transmission	95%
Duty Factor	100 %
Peak Surface Field	1.8 Kilpatrick
Average Structure Power	1.2 MW
Average Beam Power	0.7 MW
Average Total Power	1.9 MW
RF Feeds	12 Waveguide Irises
Average Heat Flux	11 W/cm^2
Maximum Local Heat Flux	65 W/cm^2
Resonant Segments	4 @ 2.0 m each
Brazed Sections	8 @ 1.0 m each
Slug Tuners	128 total
Length	8.0 m
Weight	5000 lb
Inlet Coolant Temperature	50°F
Operating Temperature	85°F

* Work supported by the US Department of Energy

These requirements presented significant challenges for the beam dynamics, cavity design, and thermal management. This was further exacerbated by the scarcity of similar devices which have been built and the limited operational experience. Indeed, none have been operated continuously for as long as one year. A comparison of CW RFQs is given in Table 2 on the following page. The CRNL1 RFQ, which has been moved to LANL and is now in operation as the CRITS (Chalk River Ion Source Test Stand), is the only device to have amassed significant operational time [4].

The original concept design for the APT RFQ was carried out in 1993 [5]. That concept incorporated a cavity that was segmented longitudinally as four resonantly-coupled cavities [6].

Because of the high output energy and current, there are some significant new features in the APT RFQ. Some of the issues and their resolution are:

- Long Electrical Length - This is possible through use of the segmented resonantly-coupled cavity [6]
- High Power - The use of a non-uniform vane-skirt width [7,8] reduces the peak and total cavity power.
- High Average Power Density - The average surface power of 11.4 W/cm^2 is a factor of four higher than CRNL1. Use of 24 longitudinal coolant passages in the cross section is required to dissipate the heat.

2 FABRICATION CONCEPT

The original fabrication concept [5] was based upon the electroformed joint which was developed by LANL, Northrop-Grumman, and GAR Electroformers for the BEAR RFQ [9] and later used for the CWDD [10] and SSC [11] RFQs. This method produces a monolithic cavity which has high structural efficiency and serves as an integral vacuum vessel. Electroforming is a room-temperature process and thus there is no concern regarding the maintenance of dimensional integrity. These advantages are largely offset by the high cost and long process duration.

Following completion of the conceptual-design study for the APT RFQ, LANL began an investigation of other manufacturing technologies in an attempt to reduce both cost and schedule. The primary focus was the joining technology. Welding, dip-brazing, plasma-spray, and hydrogen-furnace brazing were investigated. LANL has

extensive experience in hydrogen-furnace brazing of linear accelerators. The brazed joining concept was tested on a 525-MHz, 0.48-meter-long engineering model [12].

The brazed RFQ linac concept has the advantages of using OFE copper for its high thermal and electrical conductivity while facilitating the attachment of high-strength copper (C15715 GLIDCOP [13]) for high-stress areas such as flanges.

The 8-meter long APT RFQ cavity was fabricated as eight one-meter long "sections." A cross section of the cavity of the APT RFQ is shown on Fig. 1 with a schematic of the entire 8-meter structure shown on Fig. 2. The cavity is a major/minor vane arrangement. Each vane is fabricated as a vane tip brazed onto a base. This allows coolant passages to be machined in and located very near the vane tips. Plugs are brazed over the coolant passages. The brazed-on vane tips are the only water-to-vacuum braze joints in the structure. An alternative would have been to deep-hole-drill the passages and plug the ends by brazing.

The manufacturing plan allowed for each one-meter-long section to be mechanically aligned and for the RF-field distribution and resonant frequency to be measured prior to brazing. The alloy used to form the longitudinal joints, Cusil (AWS BAg-8), flows freely over copper surfaces and these joints could be assembled metal to metal. The alloy was supplied from wire placed into grooves. Thus it was not necessary to compensate for the thickness of the alloy in the mechanical alignment and RF measurements. After brazing, it was determined that the mechanical alignment had not changed more than 0.001 in and the resonant frequency had changed less than 75 KHz.

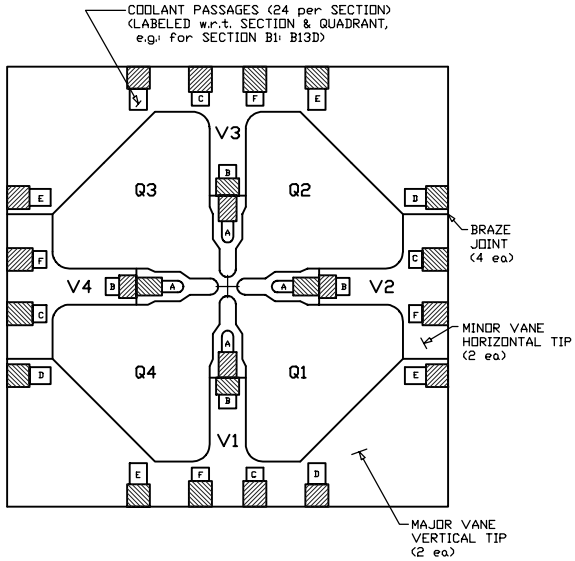

Figure 1: APT/LEDA RFQ Cross Section

Table 2: Comparison of CW RFQs

Parameter		**FMIT**	**CRNL**	**CRNL1 CRITS**	**CWDD**	**APT**
Particle		H_2+	H+	H+	D-	H+
Frequency	MHz	80	267	267	352	350
Injection Energy	MeV	0.075	0.050	0.050	0.200	0.075
Final Energy	MeV	2.000	0.600	1.270	2.000	6.700
Input Current	mA	105	90	86	92	110
Output Current	mA	100	75	75	80	100
Length	m	4.00	1.47	1.47	3.97	8.00
Wavelengths	λ	1.00	1.31	1.31	4.66	9.72
Intervane Voltage (Peak)	Kvolts	185.0	78.0	78.0	92.0	102.0
Peak Surf. Field	MV/m	27.2	25.0	28.8	33.7	33.6
Peak Surf. Field	Kilpatrick	1.00	1.50	1.75	1.80	1.80
Total Power	kW	600	133	254	304	1900
Beam Power	kW	193	50	105	144	700
Copper Power	kW	407	83	159	160*	1200
Avg. Cu Power/Length	kW/m	107	56	107	40	150
Avg. Cu Power/Area	W/cm^2	0.4	2.4	4.6	0.3*	11.4
Max Cu Power/Area	W/cm^2		8.7	16.7	2.7*	65.0
Operated		YES	YES	YES	NO	SOON
Reference		[14]	[15]	[4,16]	[10]	

* The CWDD RFQ was designed to operate at 35 K. The stated copper power includes the effect of enhanced surface electrical conductivity.

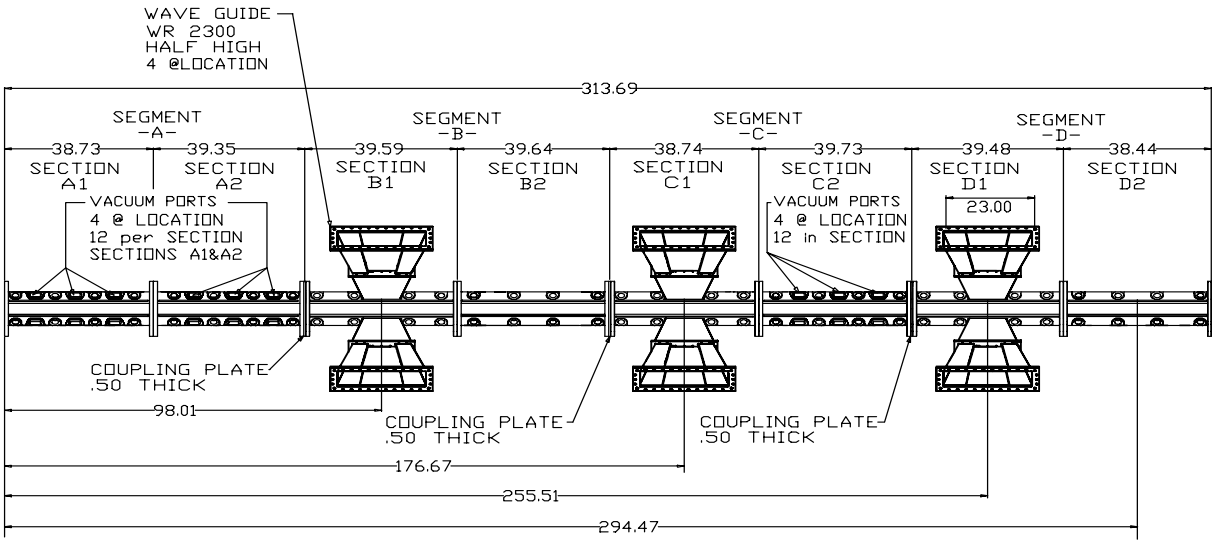

Figure 2: APT/LEDA RFQ Schematic

3 THERMAL MANAGEMENT

A total of 1.2 MW must be removed from the APT/LEDA RFQ cavity. With the average surface-power density being a factor of four higher than any earlier CW RFQ, thermal management was the major concern for the engineering analysis and design. The coolant passages were sized such that the bulk velocity did not exceed 15 ft/s to minimize flow erosion. The coolant passages were sized and located such that the heat gain per unit length in each passage was equal in the cross section. This was necessary in order to assure symmetric thermal distortion of the cavity.

A requirement that the longitudinal tilt of the local cavity frequency not exceed ±20 KHz in each one-meter long section established the number of cavity coolant passages (24 longitudinal passages in each section) and their locations. The "small" (350 MHz) cavity cross section did constrain the number, sizes, and locations of the coolant passages.

The RF field is ramped along the linac. The RF power in each of the four resonant segments is significantly different (A = 188, B = 318, C = 361, & D = 398 kW). In order to simplify manufacture, all segments have the same number and arrangement of coolant passages. The differences between the segment cooling requirements are addressed by having separate flow loops (including pumps and mixing valves) for each of the four resonant segments [17].

The resonance-control scheme provides coolant (360 GPM total) at a constant 50°F into the tip passages ("A" & "B" as identified on Fig. 1) while the temperatures of the coolant (1160 GPM total flow) fed to the cavity wall passages ("C," "D," "E," & "F") are modulated to maintain the cavity on resonance. The inlet coolant temperatures to the cavity walls of each segment are predicted to be 71, 65, 63, and 61°F respectively. Modulating only the cavity-wall-coolant temperature gives a positive derivative of the frequency with respect to the coolant temperature in the cavity-wall passages ($\partial f/\partial T = 1.7X10^4$ Hz/°F).

Each slug tuner (128), vacuum pumping port (36), RF iris/waveguide unit (12), coupling plate (3), and both end-walls are also supplied with coolant. There are 424 coolant passages.

The 50°F coolant temperature was selected in order to reduce the peak temperature of the cavity wall to about 100°F. (The highest temperatures, ~150°F, occur in the end undercut regions where the surface heat flux is 65 W/cm^2.) This serves to minimize longitudinal thermal expansion as well as cavity power which would have increased at higher surface temperatures. The 50°F inlet temperature requires the coolant water to be refrigerated rather than supplied from a cooling tower. A cooling tower would provide 105°F inlet water in the summer which would raise cavity-wall temperatures and power consumption significantly.

4 VACUUM SYSTEMS

The vacuum pumping system for the RFQ is designed to provide a cavity-vacuum level of better than $1X10^{-6}$ Torr. As much as 10 mA of the H^+ input beam will not be captured. This will form $1.0X10^{-3}$ Torr-l/s of H_2 in the first resonant segment. There is an additional $0.5X10^{-3}$ Torr-l/s of other species (H^+, H_2^+, H_3^+, & O_2) from the injector that must also be removed. There are 36 vacuum pumping ports, 12 each in Sections A1, A2, and C2. Each pumping port has local heat fluxes up to 40 W/cm^2 and therefore they must be actively cooled.

The vacuum-manifolding concept is based on that used for the SSC RFQ [11]. Five 8-in cryopumps are used. These are connected via manifolds to allow for operation during regeneration and to provide installed redundancy [18].

There are 12 RF windows [19] connected via ridged waveguide [20] to the quadrants of Segments B1, C1, and D1. Each window will transmit 250 kW thru a small (0.063 in wide by ~3.5 in long) iris. Because the vacuum conductance through these irises is very small (< 16 l/s) and the outgassing of the window and ridged waveguide assemblies is high (>$5X10^{-9}$ Torr-l/s), separate vacuum pumping units are required for each assembly. Direct-mounted non-evaporable getter (NEG) pumps will be used in these locations [21]. These have the advantages of being passive (no mechanical vibrations) and oil free. The selected units (SAES "CapaciTorr") have greater than 1000 l/s speed for H_2 and the predicted time between regenerations exceeds one year. There is no installed redundancy in the RF-window vacuum system.

5 STRUCTURAL SUPPORT

The cavity is a long, slender structure, sufficiently flexible that a statically-indeterminate support is required [22]. The cavity is suspended by five articulated links, one at the end of each resonant segment. This support meets the requirements that the gravitational deflection not exceed 0.0005 in and that the deflection due to predicted applied loads not exceed 0.005 in.

For assembly, the support structure was mounted in a vertical orientation on a pair of pyramidal towers (Fig. 3). The RFQ sections were stacked into the support structure. The entire assembly was then rotated to the horizontal and rolled into the linac tunnel. This concept was extrapolated from that used with the CWDD RFQ [10].

6 INSTALLATION STATUS

Fabrication of the cavity was completed in January of 1998, 28 months after commencement of the project. Preliminary RF tuning [23], vacuum testing, and assembly into the support structure was completed in the Spring of 1998. The unloaded Q of the cavity was measured at 8634, more than 80% of the value predicted by SUPERFISH. With the variable vane-skirt width, the Q calculated by SUPERFISH varies along the length of the RFQ so a length-weighted average value is quoted. Fig. 4 shows the complete 8-meter linac assembled for low power RF tuning.

The unit was installed in the linac tunnel in June of 1998. At the present time, the cavity vacuum system and cooling system are being installed. Fabrication of the ridged waveguide components [20] is underway at LANL and at AlliedSignal. Final testing of the RF-window vacuum systems is underway at LLNL [24]. High-power conditioning is scheduled to begin in the Fall of 1998.

7 SUMMARY

The detail design of the APT/LEDA RFQ cavity was scaled directly from the engineering-demonstration model [12]. The design, fabrication, and tuning tasks went smoothly were carried out at LANL and the original schedule was adhered to. The brazed-RFQ concept is robust and can be cost-effectively and predictably implemented at all duty factors up to CW and in the frequency range of about 200 to 800 MHz.

8 ACKNOWLEDGEMENTS

Other institutions participating in RFQ project include LLNL and TECH-SOURCE (vacuum system), AlliedSignal (resonance control cooling system), plus Northrop-Grumman (engineering support). Personnel from the Argonne National Laboratory (G. McMichael), the FERMILAB (M. May), General Atomics (C. Charman & L. Lommers), Northrop-Grumman (B. Abel & J. Rathke), TECH-SOURCE (P. Grande & N. Wilson), NOAO (E. Pearson), and LANL (T. Butler) served on the project's technical-review panels.

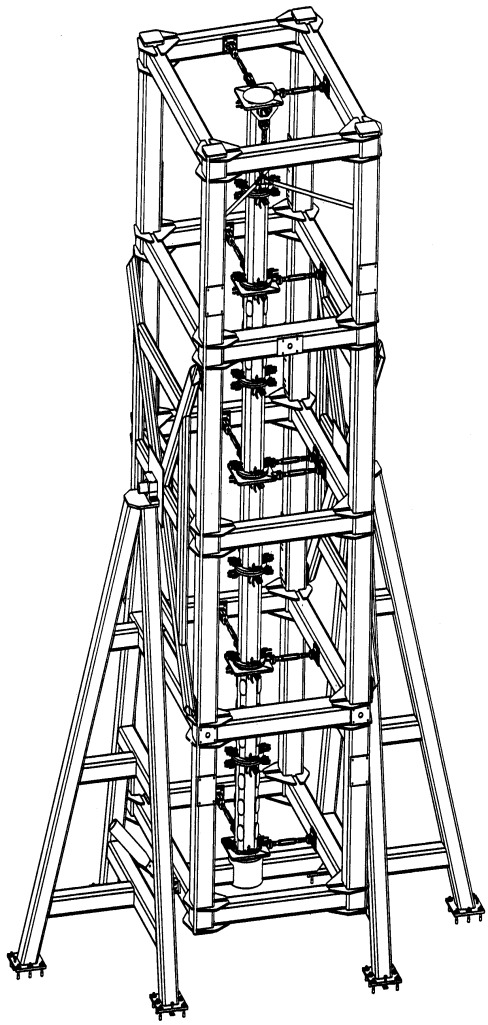

Figure 3: APT/LEDA RFQ in Support Structure

Figure 4: APT/LEDA RFQ Assembled for Pre-Installation RF Tuning

9 REFERENCES

[1] G. Lawrence, "High Power Proton Linac for APT; Status of Design and Development," these proceedings.

[2] H. V. Smith, "Status Update for the Low-Energy Demonstration Accelerator (LEDA)," these proceedings.

[3] R. Wood, et al, "Status of the Engineering Development of CCDTL for the Accelerator Production of Tritium," these proceedings.

[4] H. V. Smith, et al, "Comparison of Beam Simulations with Measurements for 1.25 MeV CW RFQ," these proceedings.

[5] D. Schrage, et al, "Conceptual Design of a 7-MeV RFQ Linac for the Accelerator Production of Tritium," LANL Report LA-UR-93-1790

[6] L. Young, "Segmented Resonantly-Coupled Radio-Frequency Quadrupole (RFQ)," Proceedings of the 1993 Particle Accelerator Conference," Washington, DC

[7] L. Young, "Simulations of the LEDA RFQ 6.7 MeV Accelerator," Proceedings of the 1997 Particle Accelerator Conference.

[8] D. Schrage, et al, "A 6.7 MeV CW RFQ Linac." Proceedings of the 1997 Particle Accelerator Conference.

[9] D. Schrage, et al, "A Flight-Qualified RFQ for the BEAR Project," Proceedings of LINAC88, Williamsburg, VA

[10] J. Rathke, et al, "Engineering Design of the Radio Frequency Quadrupole (RFQ) for the Continuous Wave Deuterium Demonstrator (CWDD)," Technical Symposium and Scientific Interchange on Neutral Particle Beam Technology, Monterey, CA, 1989

[11] D. Schrage, et al, Radio Frequency Quadrupole Linac for the Superconducting Super Collider," 12th Conference on the Application of Accelerators in Research & Industry, Denton, TX, 1992

[12] D. Schrage et al, "A New RFQ Fabrication Technique," Proceedings of LINAC94, Tsukuba, 1994

[13] GLIDCOP, OMG Americas, Triangle Park, NC

[14] W. Cornelius, "CW Operation of the FMIT RFQ Accelerator," Proceedings of the 1985 Particle Accelerator Conference, Vancouver, BC

[15] G. Arbique, et al, "CW Operation and Initial Beam Experiments with the RFQ1 Accelerator," Proceedings of the 1990 Linear Accelerator Conference, Albuquerque, NM

[16] G. Arbique, et al, "Beam Parameter Measurements on the CW RFQ1-1250 Accelerator," Proceedings of the 1992 Linear Accelerator Conference, Ottawa, ON

[17] R. Floersch, "Resonance Control Cooling System for the APT/LEDA RFQ," these proceedings.

[18] S. Shen, et al, "APT/LEDA RFQ Vacuum Pumping System, "Proceedings of the 1997 Particle Accelerator Conference," Vancouver, BC

[19] K. Cummings et al "Results and Lessons Learned from Conditioning 1 MW CW 350 MHz Coaxial Vacuum Windows," these proceedings

[20] R. Valdiviez et al, "The Mechanical Design & Fabrication of a Ridge-Loaded Waveguide for an RFQ," these proceedings

[21] S. Shen et al, "APT/LEDA RFQ RF Window Vacuum Pumping System - Conceptual Design Report," LLNL Report #APT/RFW-091797-001

[22] S. Ellis, "APT/LEDA RFQ and Support Frame Structural Analysis," LANL LA-UR #97-528

[23] L. Young, "Tuning of the LEDA RFQ 6.7 MeV Accelerator," these proceedings.

[24] K. Kishiyama et al, "Testing of Vacuum Pumps for the APT/LEDA RFQ," these proceedings

REAL-TIME TRANSVERSE EMITTANCE DIAGNOSTICS*

P. Piot, G.A. Krafft, R. Li, J. Song
Thomas Jefferson National Accelerator Facility, VA23606 Newport News, USA

Abstract

With the increasing interest in high-brightness beams and the recent advances in photoemission guns capable of producing such high-charge, low-emittance beams, measuring transverse emittance has become a primary concern, especially in driver accelerators for free-electrons lasers (FELs) where a degradation of this parameter could result in significant deterioration of the FEL gain. Hence frequent and fast measurement are needed, particularly when detailed parametric studies are required. Commonly used methods include optical transition radiation (OTR) based methods and trace space sampling methods. We will discuss these methods and provide motivation for our method of on-line emittance measurement in the Jefferson Lab FEL.

1 INTRODUCTION

The characterization and measurement of transverse phase space is a longstanding topic widely discussed in the literature [1]. In this paper we concentrate on methods that provide an on-line measurement of emittance and Twiss parameters. We quantify "on-line" as an update rate of the order of a second. Throughout this paper the JLab FEL driver-accelerator is taken as an example. In this paper we use the root mean square (rms) emittance. For the $x-x'$ trace space it is defined as:

$$\tilde{\varepsilon}_x = \kappa \left[\langle (x-x_0)^2\rangle\langle (x'-x'_0)^2\rangle - \langle (x-x_0)(x'-x'_0)\rangle^2\right]^{1/2} \quad (1)$$

where x and $x' = dp_x/dp_z = x/z$ are respectively the position and divergence coordinates. The $\langle . \rangle$ designates the average operator on the two-dimensional trace space distribution $\rho_2(x,x')$, the constants x_0 and x'_0 are the first order moments in position and divergence. κ is a scaling factor; henceforth we set its value to 1 to conform to the Sacherer [2] definition of rms emittance. Another commonly used definition of rms emittance was defined by Lapostolle [3] and now referred to as the effective rms emittance, defined by letting κ be 4. In this paper we will also use the normalized emittance defined as $\tilde{\varepsilon}^n_x = \beta\gamma\tilde{\varepsilon}_x$. The advantage of considering an rms-type emittance is that its definition is not as arbitrary as it is for the geometric emittance commonly used by experimentalists (which is defined as the trace space area of a contour encompassing a certain fraction of the beam particles). The rms emittance also allows comparison of beam quality from different facilities. Finally the concept of rms emittance is a figure of merit of the statistical properties of the beam since it is related to the beam entropy [4]. Along with the emittance, the trace space is also specified by the Twiss parmeters that are related to the moments: $\alpha_x = -\langle xx'\rangle/\tilde{\varepsilon}_x$, $\beta_x = \langle x^2\rangle/\tilde{\varepsilon}_x$, $\gamma_x = \langle x'^2\rangle/\tilde{\varepsilon}_x$. From Eqn.(1), the emittance measurement reduces to the measurement of the second order moments of the distribution.

We will use the JLab FEL photoinjector as a basis for numerical computations, it is worthwhile to recall in Tab. 1 the principal beam parameters at the two locations we wish to measure the transverse emittance. A more complete description of the injector is found in Ref. [5] and references therein. Our goal is to measure a normalized emittance ranging from 4 to 20 mm-mrad, with the nominal emittance being approximately 7 mm-mrad.

parameter	Location #1	Location #2
$\tilde{\varepsilon}^n_x$ (mm-mrad)	6.6	8.8
$\sigma_{x'}$ (mrad)	0.6	0.3
σ_x (mm)	2.3	1.9
$\tilde{\varepsilon}^n_y$ (mm-mrad)	6.0	6.2
$\sigma_{y'}$ (mrad)	0.5	0.2
σ_y (mm)	2.3	1.4

Table 1: Beam parameters predicted by PARMELA for the baseline design injector (Q=135 pC); the total energy is 10 MeV.

2 OTR-BASED TECHNIQUE

When a beam of charged particles has the electric permittivity of its environment changed, it emits transition radiation (TR). The use of this radiation for beam diagnostic purposes has become popular in recent years: in electron accelerators such radiation is generated by intercepting the beam with very thin metallic foils and observing the backward TR. For a single electron the TR angular distribution given by [6]:

$$\frac{d^2I}{d\omega d\Omega}(\theta,\gamma) = \frac{e^2\beta^3}{\pi^2 c} R \frac{\sin^2\theta}{(1-\beta^2\cos^2\theta)^2} \quad (2)$$

where $\beta^2 = 1 - 1/\gamma^2$ (γ being the usual Lorentz factor) and R is the reflection coefficient of the foil ($R \simeq 1$ for a metallic foil at optical wavelengths). The generated TR can be used to measure the rms beam spot size by computing the quantity:

$$\langle x^2\rangle = \frac{\int x^2 I(x,y)dxdy}{\int I(x,y)dxdy} \quad (3)$$

*Work supported by the US-DOE contract #DE-AC05-84ER40150, the Office of Naval Research, the Commonwealth of Virginia, and the Laser Processing Consortium.

where $I(x,y)$ is the two-dimensional density of the TR image on the foil. The beam divergence can be inferred from the observation of the TR angular distribution since it corresponds to the convolution of the TR intrinsic angular distribution with the beam angular density $P(x')$:

$$\frac{d^2I}{d\omega d\Omega}(\theta,\gamma) = \int \frac{d^2I(\theta-\alpha,\gamma)}{d\omega d\Omega} P(\alpha)d\alpha \qquad (4)$$

Hence if the upstream magnetic optics is properly tuned to achieve a waist at the location of the TR screen, the emittance can be estimated by computing the quantity:

$$\epsilon_x = \left[\langle x^2\rangle\langle x'^2\rangle\right]^{1/2} \qquad (5)$$

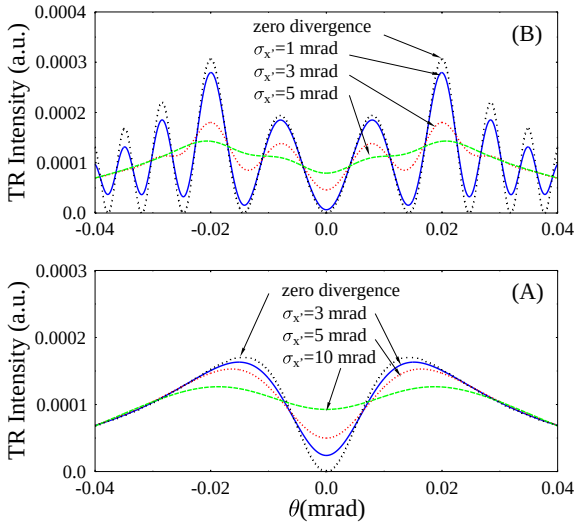

Figure 1: Dependence of the single foil TR angular distribution **(A)** and interferometric TR angular distribution **(B)** for different beam divergences. For case **(B)**, the wavelength of observation is λ =500 nm and the foil space is $L \simeq \lambda\gamma^2$.

Figure 1(A) shows the effect of beam divergence on the TR angular distribution for a beam of 38 MeV (at 10 MeV the effect is not very pronounced). The use of fitting to obtain the divergence (and subsequent emittance) measurement has been successfully implemented in several facilities [7, 8]: the experimental TR angular distribution is fitted with two parameters (energy and divergence). The minimum rms beam divergence that can be experimentally resolved is approximately $x' \simeq 0.15\gamma^{-1}$ [8]. Such a method was quickly replaced by a more precise method based on the Wartski [6] two-foil interferometer: instead of directly detecting the backward TR emitted from the foil, the interference pattern between the forward TR emitted as the beam crosses an upstream foil and the backward TR of a second foil is analyzed. The distance between the two foils must be larger than the far-field parameter $\Lambda = \lambda\gamma^2$ where λ is the wavelength at which the interference pattern is observed. In this case Eqn.(2) takes the form:

$$\frac{d^2I}{d\omega d\Omega} \propto \frac{\sin^2\theta}{(1-\beta^2\cos^2\theta)^2}\sin^2\left(\frac{\pi L}{\lambda}(1-\beta\cos\theta)\right) \qquad (6)$$

Simulations of the interference patterns for different beam divergences are presented in Fig. 1(B). In these numerical computations, we have simply convolved the Eqn.(6) with the beam angular distribution that is assumed to be gaussian, the beam energy being 38 MeV. The effect of increasing the divergence results in a blurring of the angular distribution. The previous remarks also pertains : for a 10 MeV beam we cannot resolve beam divergence comparable to the one expected in the JLab FEL injector (approximately 0.2 to 0.6 mrad). As in the single foil case, the experimentally obtained interference pattern is fitted using two parameters (divergence and energy) from which the divergence is computed, providing an emittance using Eqn.(5). The advantage of this method comes from the oscillations that occur at positions depending on energy, it generally gives more accurate fits compared to the single foil method. Also, because the distribution is dependent on the wavelength of observation and the distance between the two foils, it is possible, using these dependencies, to "tune" the interferometer in order to increase the accuracy of the measurement. TR-based methods are very attractive because of their simplicity, generally two CCD detectors and a beam splitter are needed. Unfortunately they have a number of drawbacks: Firstly, it is necessary to locate such devices at a beam envelope waist or to tune the upstream optics to achieve such waist. Secondly in the case of the two-foils scheme, the first foil used to emit forward OTR inevitably increases the beam divergence due to multiple scattering. This is especially important for low energy beams; typically this method is suitable only for a beam whose divergence $\sigma_{x'}$ and energy γ satisfy a relation of the type $\sigma_{x'} \gg f(Z,\Omega)/(mc^2\gamma)$ where f is a function of the foil atomic number Z and the mean number of collisions Ω, and can be estimated from results discussed in Ref.[9]. Also, both of these methods are difficult to apply to measure the emittance of a space-charge-dominated beam, e.g., as it is often the case for high-brightness injectors. Indeed, they can be used provided the beam sizes $\sigma_{x,y}$ at the horizontal waist satisfy the relation (the same equation obtains in the vertical plane replacing x subscript by y):

$$2K\sigma_x^2 / \left[\tilde{\varepsilon}_x^2\left(1+\frac{\sigma_y}{\sigma_x}\right)\right] \ll 1 \qquad (7)$$

where $K = 2I_p/((\beta\gamma)^3 I_A)$ is the normalized perveance (I_p and I_A are respectively the peak and Alfvèn current). Successful use of OTR interferometry has been reported by several groups, with an extensive study performed on the BOEING FEL facility [10]. A measurement of divergence of approximately 100 μrad for 650 MeV beam is planned on the APS undulator test line [11].

3 TRACE SPACE SAMPLING METHODS

Trace space sampling techniques are widely use to characterize the trace space density with high precision. The most popular example is the "slit and collector" method that has been used by several teams to characterize guns. Though it does not provide an on-line measurement, variants of this technique have been used to perform single shot measurements. In such methods a single slit is replaced by an interceptive mask where several apertures are bored. The different methods commonly in use differ in essentially two ways: in the shape of the sampling apertures but also in the type of "collector" device used to observe the beamlet profiles (fluorescent screens, optical transition radiation (OTR), wire scanner). The principle of the trace

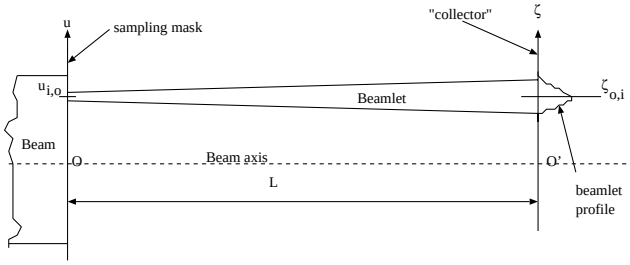

Figure 2: Basis of trace space sampling technique.

space sampling is sketched in Fig. 2, where we consider the one-dimensional case: the sampling aperture is assumed to have a zero-extension along the coordinate axis u. The generated beamlet strikes the collector device after propagating through a drift of length L. For the generated beamlet, the second order moments are $\langle u_{0,i}^2 \rangle$, $\langle ((\zeta - \zeta_{0,i})/L)^2 \rangle$ and $u_{0,i}\langle (\zeta - \zeta_{0,i})/L \rangle$. For a set of n beamlets, the second order moments are given by the relations:

$$\langle u^2 \rangle = \langle \sum_{i=1}^{n} u_{0,i}^2 \rangle, \langle u'^2 \rangle = \langle \sum_{i=1}^{n} \frac{(\zeta - \zeta_{0,i})^2}{L^2} \rangle \qquad (8)$$
$$\langle uu' \rangle = \langle \sum_{i=1}^{n} u_{0,i} \frac{(\zeta - \zeta_{0,i})^2}{L^2} \rangle$$

Using the set of Eqns.(8) and Eqn.(1), we can estimate the beam parameters of the incident beam.

In the case of on-line measurement, OTR screens or fluorescent screens are commonly used. The latter are generally preferred because they are very sensitive, but offer worse resolution, and care must be taken to use them in their linear response range. Also the persistence of such screens can be problematic for single-shot measurement. OTR screens, on the other hand, provide high resolution but the photon/electron conversion is very small (typically $1/\alpha$, α being the fine structure constant) and special attention must be directed toward maximizing the S/N ratio by reducing the background noise.

Another task common to all these method is the choice of mask material and thickness. If we restrict our discussion to uncooled systems, a high thermal conductivity material should be chosen to efficiently dissipate the beam deposited power. Also thermal bridges toward the exterior of the vacuum chamber should be used. Thermal analysis of the mask with the beam deposited power is necessary especially when OTR screens are used as collectors, since they require the highest possible average current to maximize the S/N ratio. Copper is a good choice because it offers a relatively good emissivity and therefore part of the deposited power is dissipated via black body type radiation. Other materials such as stainless steel are generally employed when the collector is a fluorescent screen. The deposited power may be reduced by choosing a proper beam temporal structure (micropulse frequency, and macropulse width and frequency) provided multi-bunch effects are not significant, a true assumption in the case of the JLab FEL where the bunches are separated by 8.03 m.

The thickness of the mask is a compromise between the S/N ratio on the collector and edge scattering of the electron on the aperture edge. Ideally, it is desirable to have a thickness that is of the order of the stopping thickness $\gamma mc^2/(dE/dx)$ where dE/dx is the energy loss per unit of pathlength in in the material. On the other hand, if the thickness is too large, particles can scatter on the aperture edges and thereby change their divergences [15]. The thickness can be determined by considering the rms scattering angle given by the Molière theory [12]:

$$\left[\langle \theta_{\text{scat}}^2 \rangle\right]^{1/2} = \frac{13.6}{\beta cp} z \sqrt{l/X_0}\,[1 + 0.038 \ln(l/X_0)] \qquad (9)$$

where p the momentum in MeV/c, z is the charge number, and l/X_0 is the mask thickness in units of radiation length X_0. Using the previous relation we can determine the thickness of the mask l so that the rms scattering angle is much larger than the angle subtended by the collector. In such cases, the scattered particles will contribute as a uniform background without biasing the beamlet pattern and one avoids erroneous values for the beam parameters. We have investigated the importance of edge scattering by using the PARMELA-generated phase space for the JLab FEL and numerically retracing each macroparticle through apertures. We found that in the case of the JLab FEL nominal emittance and divergence at the location where we perform the measurements, less than 5% of the particles were interacting with the edge even in the presence of a slight misalignment of the mask axis with respect to the beam axis of the order of 1 mrad. Therefore this latter effect is assumed to be insignificant, and no special care such as aperture tapering was considered for the case of the JLab FEL.

By a proper choice of aperture size, trace-space sampling allows the measurement of space-charge-dominated beams. The aperture size should be determined so that the space-charge contribution to the beamlets envelope equation is much smaller than the emittance contribution using

Eqn.(7). In such cases, the beam parameters can be inferred using Eqn.(8) since the beamlets are emittance dominated and their behaviour is governed by linear optics. If w_x and w_y are the characteristic sizes of the aperture, they should fulfill the relation:

$$\frac{K w_{x,y}^2}{6(\tilde{\varepsilon}_{x,y})^2 \left(1 + \frac{w_{y,x}}{w_{x,y}}\right)} \ll 1 \tag{10}$$

where the coefficients are as defined in Eqn.(7).
The separation between the apertures center d and the distance between the mask and the collector L depend on the beam size and beam divergence. By requiring the resolution to be the same in position and divergence a relation between the aperture spacing and distance can be derived:

$$\sigma_{x,y}/d \simeq L\frac{\sigma'_{x,y}}{r} \tag{11}$$

where r is the resolution of the detector. On the other hand, to ensure the beamlets do not overlap we must have:

$$4\sigma'_{x,y}L < d \tag{12}$$

Using the two latter equations we find for a given set of beam parameters all the geometric parameters of the mask.

The acquisition system requires a frame grabber to digitize the analog signal from the CCD detector. In the case of JLab FEL, we use a DATACUBE digitizer that operates under the EPICS environment. The digitized data are directly reduced on the same CPU as the one controlling the digitizer using the VxWorks language, and only results (values of beam parameters, trace-space plot) are broadcast on the network. These results can be accessed from any X-window stations using an EPICS-based screen [17].

3.1 The pepper pot method

In the pepper pot technique [13, 14], the mask consists of a matrix of generally circular apertures. The beamlets in the collector plane are given by:

$$I_{i,j}(x', y') \simeq \rho_4(x_i, x'; y_j, y')\delta S \tag{13}$$

where δS is the area of the apertures. The projection on the x-axis, i.e., summing on y_j and integrating on y' is:

$$P_i(x') \propto \rho_2(x_i, x')\delta S \tag{14}$$

From $P_i(x')$ we can compute the second order moments of the $x - x'$ trace space distribution $\rho_2(x, x')$ and deduce the beam parameters. In fact, the pepper pot method allows one to study coupling between the horizontal and vertical trace space; using Eqn.(13) the coupled second order moments $\langle xy\rangle$, $\langle x'y\rangle$, $\langle xy'\rangle$ and $\langle x'y'\rangle$ can be computed. Hence the rms hyper-transverse emittance can be estimated. Though this method can provide much information on the transverse trace space, it is difficult to get a decent signal by using an OTR screen as collector. In the JLab FEL case, the required aperture radius would be approximately 40 μm which implies that the average beamlet charge will be less than 6 pC, not a large enough number to produce enough OTR photons than can be detected with conventional CCD detectors.

3.2 The multislit method

In the case of the Jefferson Lab FEL, we have opted for this method which offers the same features of the pepper pot technique (without the possibility of measuring the hyper-emittance) with the advantage of providing much more signal. Its principal disadvantage is that the horizontal and vertical phase space measurements have to be performed separately and therefore the method requires two masks. Practically we have addressed this issue by mounting two sets of slits on the same mask, mounted on a two position air cylinder so that horizontal and vertical measurements can be performed one after the other. In the horizontal plane, the beamlets pattern generated by vertical slits centered at x_i is given by:

$$P_i(x') \propto w\rho_2(x_i, x') \tag{15}$$

where w is the slit width. When writing Eqn.(15) it is implicitly assumed that the slits are infinitely narrow. If such an approximation cannot be made; one should use formulae derived in Ref. [18]. For the JLab FEL we have carefully optimized the slits geometric parameters using PARMELA, taking as starting point numerical values computed from the previous discussion. For the baseline

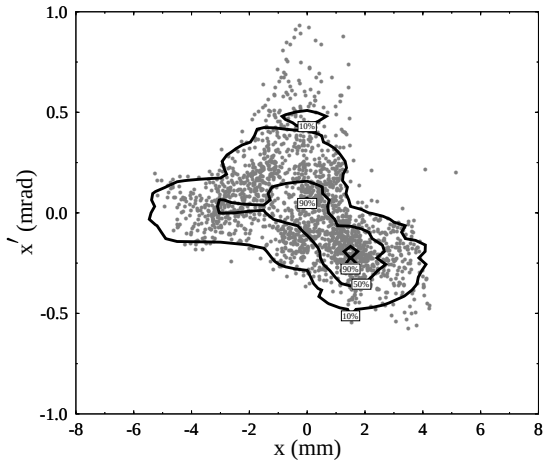

Figure 3: Simulation of emittance measurement with the multislit mask. The dots are macroparticles generated with PARMELA. The iso-contours are computed from the retrieved phase space after simulating the emittance measurement using the PARMELA distribution.

injector the optimized values for the multislit mask are: (1) a slit spacing of 1.5 mm, (2) a slit width of 0.75 μm, and (3) a mask thickness of 5 mm. In our case the distance between the mask and the OTR screen was set by mechanical constraints to 620 mm. With such parameters, a systematic error in the 10% range for the nominal emittance was found. In Tab. 2 we compare the PARMELA simulated emittance with the computed emittance simulating the emittance measurement, the initial and retrieved trace space are plotted in Fig. 3. Systematic errors are

numerically estimated using errors propagated with the anticipated distribution and include finite slit width effects. Other source of error such as remanent space-charge in the beamlets, space-charge field perturbation due to the slits have been considered and were found to be negligible. However, finite sampling error is a concern and should be reduced below 10% provided that 5 slits, at least, are illuminated by the incident beam. The first tests were performed

$\tilde{\varepsilon}^n_{\text{parmela}}$	$\tilde{\varepsilon}^n_{\text{retrieved}}$	$\Delta\tilde{\varepsilon}/\tilde{\varepsilon}$% **(a)**	$\Delta\tilde{\varepsilon}/\tilde{\varepsilon}$% **(b)**
8.094	8.077	0.2	9.9
3.947	4.014	1.7	19.9
24.282	23.016	5.2	2.7

Table 2: Simulation of emittance measurement for different emittance, after slit optimization. The quantity $\Delta\tilde{\varepsilon}/\tilde{\varepsilon}$ **(a)** is just a measure of the relative difference between the nominal and retrieved emittance while the quantity $\Delta\tilde{\varepsilon}/\tilde{\varepsilon}$ **(b)** represents the systematic error estimate.

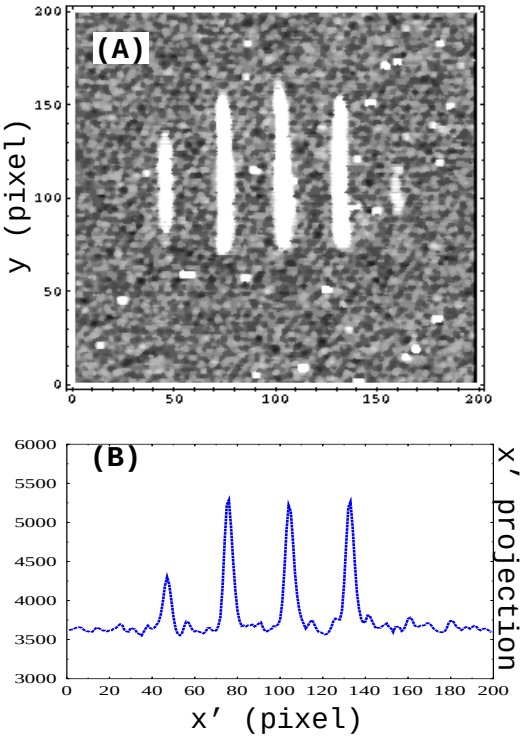

Figure 4: Typical beamlet pattern from a multislit mask. OTR image of the beamlets **(A)** and projection along the y-axis **(B)**.

in the JLab Injector Test Stand. Because of low energy, 350 keV, we were using, as collector, a fluorescent instead of an OTR screen. We compare the multislit method with the "slit and collector" apparatus [16, 17] and agreement at the 15% level was observed. Recent measurements performed in the JLab FEL operating at 60 pC (therefore with a lower beam emittance) are presented in Fig. 4. The emittance typically measured is approximately 6 mm-mrad which is somewhat larger than PARMELA prediction for this charge. Also because the beam divergence and size are different from those expected at 135 pC (the charge for which the mask has been optimized), the number of generated beamlets is only 4-5. This is a disadvantage of single shot phase space sampling method; they have to be designed for specific parameters and have a limited dynamic range. Multislit mask devices have been in use for several years in the UCLA group [19] to characterize a high brightness electron injector and in the CERN heavy ion injector to measure emittance of heavy ions beams [20].

The authors are indebted to the FEL commissioning team for support and operation of the machine.

4 REFERENCES

[1] C. Lejeune, et al., Advances in Electronics and Electron devices, Supp. **13A**, 159-259 (1980)

[2] F. Sacherer, IEEE Tran. Nuc. Sci. **NS 18** 1105-1107

[3] P. Lapostolle, CERN rep. CERN/**DI**-70-36 (1970)

[4] J.D. Lawson, et al., Part. Accel. **5**, 61 (1973)

[5] P. Piot, et al., proc of the Euro. Part. Acc. Conf.'98, (Stockholm, Sweden)

[6] L. Wartsky, PhD Thesis, Université Paris Sud (unpublished)

[7] X. K. Maruyama, et al., Nucl. Inst. Meth. **A272**, 237-240 (1987)

[8] R. Fiorito et al., AIP Conf. Proc. **319**, 21-37 (1994)

[9] P. Piot, et al., AIP Conf. Proc. **390**, 298-305 (1996)

[10] D. Rule, et al., Nucl. Inst. Meth. **A296**, 739-743 (1990)

[11] A. H. Lumpkin et al., Nucl. Inst. Meth. **A341**, 417-421 (1994)

[12] D. E. Groom et al., Eur. Phys. Journ. **C 3** Num. 1-4, 144 151 (1998)

[13] A. Vignati, et al., Nucl. Inst. Meth. **B66**, 503-507 (1992)

[14] Y. Yamazaki, et al., Nucl. Inst. Meth. **A322**, 139-145 (1992)

[15] E. D. Courant, Rev. Sci. Instr. **22** num 12, 1003-1005 (1951)

[16] P. Piot, et al., proc of the Part. Acc. Conf.'97 (Vancouver, Canada)

[17] J. Song, et al., Nucl. Inst. Meth. **A407**, 343-349 (1998)

[18] M. J. Rhee, et al., Rev. Sci. Instrum. **62(6)**, 1468-1470 (1991)

[19] S.C. Hartman, et al., proc of the Part. Acc. Conf.'93, 561-563 (1993); S.C. Hartman PhD Thesis, UCLA (unpublished)

[20] M. Crescenti, et al., Proc. of the Diag. Inst. Part. Acc, 66-68 (1995)

PERIODIC PERMANENT MAGNET DEVELOPMENT FOR LINEAR COLLIDER X-BAND KLYSTRONS*

D. Sprehn, G. Caryotakis, E. Jongewaard and R. M. Phillips
Stanford Linear Accelerator Center
Stanford University, Stanford, CA 94309

Abstract

The Stanford Linear Accelerator Center (SLAC) klystron group is currently designing, fabricating and testing 11.424 GHz klystrons with peak output powers from 50 to 75 MW at 1 to 2 μs rf pulsewidths as part of an effort to realize components necessary for the construction of the Next Linear Collider (NLC). In order to eliminate the projected operational-year energy bill for klystron solenoids, Periodic Permanent Magnet (PPM) focusing has been employed on our latest X-band klystron designs. A PPM beam tester has operated at the same repetition rate, voltage and average beam power required for a 75 MW NLC klystron. Prototype 50 and 75 MW PPM klystrons were built and tested during 1996 and 1997 which operate from 50 to 70 MW at efficiencies greater than 55 %. Construction and testing of 75 MW research klystrons will continue while the design and reliability is perfected. This paper will discuss the design of these PPM klystrons and the results of testing to date along with future plans for the development of a low-cost Design for Manufacture (DFM) 75 MW klystron and invitation for industry participation.

1 AN INTRODUCTION TO PPM

Periodic Permanent Magnet (PPM) focusing is utilized in Traveling-Wave Tube (TWT) devices for commercial and military applications. Instead of a solenoidal magnet with its associated overhead of power supply, cooling, and controls, permanent magnets are used to reduce operational cost and weight. In PPM focusing the axial field changes polarity with every magnet. If the magnetic period is small enough when compared to the beam plasma wavelength, λp/L, then sufficient beam stiffness can maintain the beam profile in the presence of large space charge forces due to the rf bunching.

Due to the high energy-products required for the magnets combined with geometrical constraints, it is usually not possible to thread as much flux through the cathode as it is with solenoidal focusing so particular attention must be paid to the gun design and beam transport issues.

The ratio of the axial field to the Brillouin field, Bz/Br, is shown in Table 1 along with other important parameters for three SLAC solenoidal-focused klystrons and three PPM designs. The Brillouin field is that value of magnetic focusing at which all forces operating on the beam are balanced and it is possible to transport the beam with a constant radius. All of the klystrons have output power levels from 50 to 75 MW except the 150 MW DESY klystron. The cathode-to-beam area convergence, A_c, is approximately 100 for all the X-Band klystrons because of the smaller drift tube dimensions. As can be seen the B_z/B_r ratios for the PPM klystrons are not all that different than those found for the solenoidal-focused klystrons. The loss in axial beam velocity, Δu_z, is higher for the PPM klystrons due to the full reversal of the field as seen by the beam.

Table 1: Comparison of SLAC Klystrons (see above text)

Tube	5045	Desy	XL-4	50XP	75XP	DFM
Beam Focusing	Sol.	Sol.	Sol.	PPM	PPM	PPM
frequency, GHz	2.86	3.00	11.42	11.42	11.42	11.42
Beam kV	350	525	440	464	490	490
uK	1.90	1.85	1.20	0.60	0.80	0.75
A_c	18	40	129	144	98	126
Cathode A/cm^2	6.34	5.04	8.75	7.39	7.71	7.23
B_z confined, T	0.12	0.20	0.45	0.20	0.17	0.23
Flux cath/beam	0.85	0.94	0.92	0.50	0.55	0.75
B_z/B_r, axis	1.90	2.82	2.54	1.15	1.20	1.51
B_z/B_r, drift tube	1.90	2.82	2.54	2.03	2.11	2.66
Δu_z	0.1%	0.1%	0.1%	1.6%	2.5%	4.8%

The drawback with PPM focusing is that the construction complexity of the tube may be increased so construction costs and failure rates could rise. The magnetic circuit is fixed and so there may be no easily accessible "knob" for the operator to turn in case adjustment is required. If the beam voltage is reduced enough, λp/L becomes small and the beam will impact the drift tube. This is known as the "stop-band" voltage. Since the high voltage beam pulse has a finite rise and fall time, then a portion of the beam pulse is below the stop-band and interception occurs. There are also areas of beam instability in PPM focused tubes and the possibility of coupling to modes which grow from an undulating beam.

* This work is supported by the Department of Energy under Contract DE-AC03-76SF00515

2 PPM DEVELOPMENT PROGRAM

PPM focusing had never been used successfully on very high-power klystrons and so there existed several unknowns with respect to the outcome of such an attempt. The large area beam convergence of 144:1, no axial field adjustability, possible interactions with an undulating beam, the presence of stop bands, and new materials and construction techniques presented several engineering challenges. It was decided to construct a beam-tester to test the gun optics followed by a 50 MW klystron, and lastly a 75 MW klystron. The 50 MW rf design was patterned closely after the successful solenoid X-band klystrons (XL series) at SLAC after allowances were made to drop the perveance to improve efficiency. The 75 MW klystron design requires a slightly higher perveance than the 50 MW design to keep the beam voltage below 500 kV to reduce modulator costs.

The beam-tester and 50 MW klystron were constructed with Samarium-Cobalt (SmCo) magnets and a gun coil. These magnets were die-pressed individually and a high level of quality control went into the manufacturing process. Inspection of the field on the axis agreed with simulation to within 1 %. To reduce cost, an experiment was performed on the 75 MW klystron by replacing the gun coil with permanent magnets and using Neodymium-Iron-Boron (NdFeB) magnets instead of SmCo. Replacing the gun coil forced large peak-to-peak variations in the field strength design on axis, and switching to bulk NdFeB resulted in a loss of control in material quality. These magnets were fabricated out of large blocks by slicing, core-drilling, and grinding to size. Magnetic, on-axis, field strengths of the individual magnets varied by as much as 20 % from simulation. The 75 MW design has more magnet periods in a plasma wavelength and a higher focusing field to Brillouin field ratio, both of which should allow for better focusing. Design parameters for both the klystrons are found in Table 2.

2.1 Beam-tester and 50 MW gun Design

In order to keep the cathode current density below an average value of 7.5 A/cm^2 for increased lifetime, a 2.25" diameter cathode was required which resulted in an area convergence ratio of 144:1. Since this value is higher than previous SLAC klystrons, a beam-tester was fabricated to prove gun and drift region optics for the PPM design. The design philosophy of the beam-tester was to eliminate all sources of trouble that could interfere with a study of the PPM beam formation and transmission. The issues of gun voltage breakdown, insufficient vacuum pumping, and collector power were addressed by using oversized components from previous klystron designs. This served to hasten the program and allowed for operation at higher voltages than the design required (in the interest of research into more powerful PPM designs). Furthermore, it was decided to control magnetic field in the gun with a standard bucking coil and the field in the region from the gun to the beam minimum with three compact coils closely wound around the drift tube. The gun and magnetic circuit were constructed so that operation with and without flux at the cathode was possible. The same general philosophy and beam focusing were used in the 50 MW klystron design.

Table 2: 11.424 GHz PPM klystron Specifications

rf power	50 MW	75 MW
Beam voltage	464 kV	490 kV
Beam current	190 A	257 A
rf pulsewidth	1.5μs @ 60Hz	1.5μs @ 60Hz
Cathode loading	7.4 A/cm^2	7.2 A/cm^2
A_c	144:1	98:1
RMS Gauss	1950	1680
Efficiency	55 %	55 %
Gain	55 dB	55 dB
Max gradients: Cavities	< 700 kV/cm	< 650 kV/cm
Anode	< 250 kV/cm	< 250 kV/cm
Focus electrode	< 220 kV/cm	< 210 kV/cm

The drift tube is constructed of alternating iron pole pieces and monel spacers that are brazed together in subassemblies and then welded together at specially split pole pieces. Each subassembly consists of eight permanent magnets where each magnet produces an axial field opposed in polarity to its immediate neighbor. EGUN[1] simulations were performed (Fig. 1) until the beam scalloping was less than 8 %. The testing began with the confined flow case because the beam is held in check by a larger magnetic field, and continued with the shielded flow case afterward.

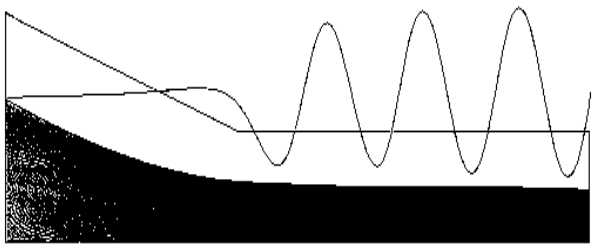

Figure 1: EGUN simulation of the beam as it enters the PPM stack as used for the beam-tester and 50 MW klystron.

When operated in the confined-flow condition the high-convergence gun design has 50 % of the beam flux threading the cathode (as measured at the axis). This is low for typical high-power klystrons. Ratios for other high-power klystron designs range from 80 to 95 %, which yield 1.7 to 3.2 times the Brillouin field condition. It is difficult to get large confinement ratios with PPM focusing because the pole pieces eventually saturate and

magnetic materials have finite strengths. There also exists a stability limit to the amount of field that may be applied because the axial velocity is reduced due to the large spin on the beam when the field is reversed from the direction of the field in the cathode. A value of 50 % yields 1.15 times the Brillouin field on the axis (Fig. 2) which increases to 2 times at the drift tube. This is an advantage because the further the beam strays from its radial position, the more focusing force it experiences. PPM focusing, as opposed to solenoidal focusing, increases as distance from the axis increases, which leads to a preference for focusing somewhat hollow beams. As such, hollow beams are a direct result of the gun design parameters in most high-power klystrons due to limitations in the possible emission current density of today's cathode materials for long-life.

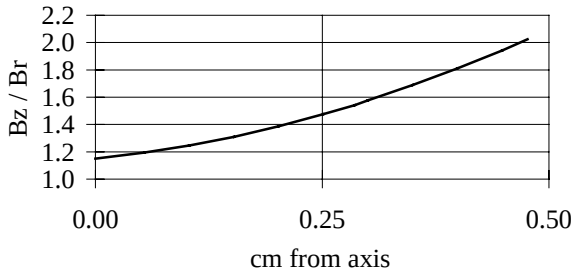

Figure 2: Variation of RMS magnetic field vs. radial distance from the axis for the PPM beam-tester and 50 MW PPM klystron.

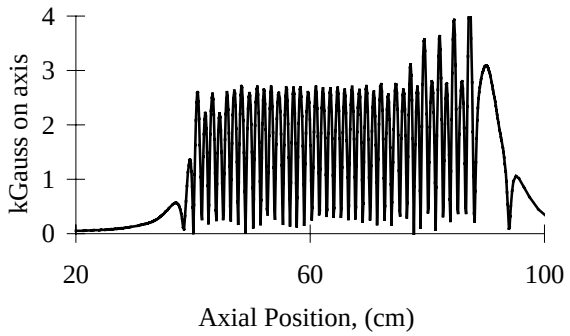

Figure 3: Axial field (Gauss) vs. axial distance (cm) for the 50 MW PPM klystron.

The 50 MW PPM klystron rf design was based on the highly successful XL-4 klystron development at SLAC. The PPM klystron, with its lower perveance, lossy materials, and higher operating voltage requires some modifications in the existing XL-4 rf circuit design. The rf circuit is adapted to the lower perveance beam by increasing the cavity spacings, altering tunings, and adding an extra cell in the traveling-wave output structure for a total of 5 cells. The number of cavities was kept constant and the bandwidth was reduced in order to maintain the required gain. This loss in gain between the two designs was primarily influenced by the lossy materials used in the PPM design. The PPM cavities have a lower Q_o than copper cavities and therefore suffer more rf heating. The lossy drift tube material may serve to dampen possible trapped oscillations and any coupling between the gun, cavities and collector. The magnetic field is very similar to the beam-tester until the last three cavities are reached where the field gradually tapers up to eventually peak (Fig. 3) in the output structure. Tapering serves to confine the beam as the space charge forces increase due to the growing rf current. The field in the output structure is unidirectional, unlike the rest of the klystron where it is periodic, and this forces the magnets to be larger.

2.2 Beam-tester and 50 MW Experimental Results

The beam-tester processing began with a 1 μs beam pulsewidth and proceeded up to 490 kV, 5 % above the design point, without incident. The beam microperveance was found to be 12 % higher than the design of 0.6 μK. The reason for this discrepancy is not fully known, although a full autopsy is scheduled to occur in October. To improve the reliability of beam transmission data, the pulse width was extended to 2.8 μs and the repetition rate increased to 120 Hz. At 490 kV, there was roughly 42 kW dissipated in the collector. The beam transmission at this point was found to be 99.9 %. This rather striking result is in direct contrast to experience with travelling-wave tubes (TWT) which traditionally are operated on a bench and iron shunts are placed along the magnet circuit to improve transmission. Such adjustments are not possible with this high-power device as most of the tube is covered in lead due to several kRads of radiation from the collector.

No instabilities or spurious oscillations arising from noise were detected at a 2.8 μs pulsewidth. No gas pressure rise other than that considered normal was seen and the collector vac-ion pump was running at about 10^{-8} Torr under full power and rep rate. With a design goal for the klystron of 1.5 μs and 465 kV, the operation of the beam-tester exceeded expectations and demonstrated the robustness of the design. The 490 kV level also happens to be that which is required for the 75 MW X-band klystron discussed later.

The three adjustment coils near the anode had negligible effect on the transmission data but one of the coils had a visible effect on the rising and falling edges of the collector current pulse. Most importantly of all, the shielded-gun operation and the confined-flow operation were essentially identical. Thus the formation and transport of the 144:1 area convergence beam into a shielded or an immersed PPM-focused drift tube for a high-power device has been proven feasible and robust.

Initial observations of the 50 MW klystron behavior revealed that the gun behaved identically to the beam-tester performance. An unusual gain curve

containing several jumps was believed to be due to multipactor in more than one location in the drift tube and/or cavities. The gain steps would decrease as beam voltage, drive frequency, or bucking coil setting was increased which means that the multipactor was not only a function of the rf drive but also of the rf current present on the beam and hence was located downstream of the input cavity. To eliminate these discontinuities, the tube was opened and the drift tube was coated with a titanium-nitride (TiN) layer roughly 100 Å thick to reduce the secondary emission coefficient of the surfaces subject to rf fields in the vacuum. After testing a second time, only one gain step remained.

Looking in the various coupling ports of the rf drive and rf output, and with a small antenna probe at the collector ceramic insulator, revealed no oscillations higher than 50 dB below the fundamental, which can easily be ignored. Small signal bandwidth was measured at 40 MHz, which closely agrees with the predicted value of 35 MHz. Measurements over a 70 dB range of rf drive power showed the small signal gain to be 65 dB at the design current, falling by 10 dB at the 50 MW power level.

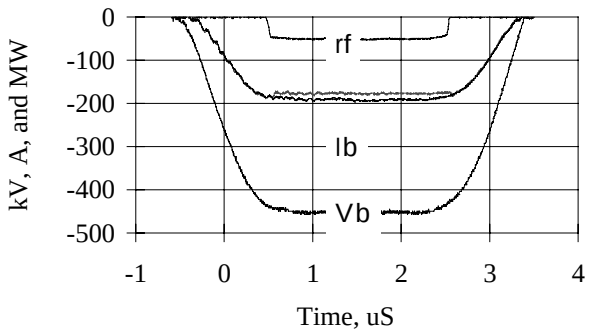

Figure 4: 50MW rf out, beam current (with and without rf present), and beam voltage vs. time for the 50 MW PPM klystron.

After removing the gun coils, replacing the first eight magnets, reducing the output magnet field, and applying prefabricated shunts along the whole magnet stack, the tube was tested in the shielded flow condition. The klystron reached 50 MW with essentially the same gain and efficiency with a 2 % increase in beam interception.

Despite the remaining step in the gain profile (believed to be in the input cavity due to an insensitivity to beam voltage) the PPM klystron reached the full operational specification (Fig. 4) of 50 MW at 2 μs. The efficiency at 50 MW was well over 55 %, and over 60 % at 60 MW, using calorimetric diagnostics. The intercepted beam power at 50 MW was about 1 % of the total beam power, but the beam current lost about 7 % while passing through the tube. This means that the energy of the electrons lost in the tube must be about 66 keV on average.

2.3 A 75 MW Experimental Design

In designing the 75 MW klystron, major changes made were enlarging the drift tube due to a higher beam current, a stainless steel drift tube, and the elimination of the gun focus coils. It was calculated that using a 5-cell travelling-wave output circuit would extract more than 75 MW. Opening the beam tunnel by 13 % to 0.425 inches reduced the efficiency of the beam-cavity interaction and thereby forced the inclusion of an extra gain cavity. This also allows more modes to propagate within the drift tube, including the second harmonic TM mode. The construction of the 75 MW PPM magnetic circuit differed in that the drift tube is a semi-continuous stainless steel structure interrupted by the cavities, with the iron pole pieces and non-magnetic spacers placed outside the vacuum envelope. This design change addresses three separate issues; avoiding the multipactor seen in the 50 MW klystron, taking a step toward the eventual low-cost design of a production klystron using a clamp-on magnetic circuit, and adding loss in the drift tube to increase the start-oscillation currents of the various parasitic modes which may arise.

The large drift tube opening resulted in a lower beam area convergence and lower current density in the beam, which in turn reduced the necessary magnet strength. On the other hand moving the pole pieces outside of the vacuum envelope increased the magnet strength required and the overall affect was a slightly higher energy-product required for the 75 MW design. Previously, SmCo magnets had been used that are highly resistant to radiation and temperature. The 75 MW design used NdFeB magnets which have higher energy-products, are easier to machine, are less brittle, but have a lower Curie temperature. However, at 500 keV photon levels, radiation effects do not seem to be an issue over the magnets projected lifetime. Furthermore, NdFeB magnets are less expensive in bulk quantities. Procurement of the NdFeB magnets presented many difficulties, as the vendor was unable to meet the required specifications. This material has been used in applications where the absolute value of the magnetic energy-product is not tightly held. This issue will be studied over the next few months and a decision will be made on the magnetic materials to be used in future designs.

Simulations of the klystron using CONDOR[2], a 2.5-D particle-in-cell code, show approximately 80 MW at the design beam power while maintaining low gradients in the output structure.

2.4 75 MW Experimental Results

Most of the completed magnets delivered to SLAC failed to meet the specification. Specifically the magnets at the beam convergence area near the gun, the gain cavity magnets, the penultimate cavity magnet, and the output magnets were all below specification. Due to time constraints it was decided to test the klystron and testing began with a 1 μs flattop beam pulse. Upon reaching 280

kV, an oscillation was noticed at the end of the beam pulse. The beam pulse was reduced to zero flattop, approximately 1 μs FWHM pulse, and the voltage was raised to 360 kV until the oscillation was again seen. A spectrum analyzer was used to carefully search for all frequencies between 11 GHz and 26.6 GHz and found only the fundamental, the second harmonic, and a signal at 20 GHz.

As the beam voltage was increased the oscillation could be damped by increases of the bucking coil, which tends to make the beam smaller, but the method has the limitation that too much of an increase and the beam impacts unpredictably on the vacuum envelope. Increasing the rf drive would also damp the oscillation but overdriving most klystrons will usually produce another set of instabilities. However, by combining the two methods it was possible to raise the voltage peak to 463 kV and attain 71 MW peak at a 200 ns pulsewidth. Despite the difficulties, gain was found to be between 55 and 60 dB and efficiency measured 60 % at the saturated rf output level of 70 MW.

The magnets have been removed from the klystron and are inserted on a full-scale model of the klystron circuit so that the field can be shunted on the bench to a desired profile. After simulation, theory, and measurement agree on the required field, the newly shunted stack will be installed on the klystron and testing will resume. It is expected that this will occur late in 1998.

2.5 A Low Cost Klystron

A low-cost design of a 75 MW klystron known as the Design For Manufacture klystron (DFM) has been under investigation for the past three years and seeks to minimize parts count, decrease complexity, reduce construction labor, and increase reliability of the klystron. A smaller gun and collector with reduced parts count, better output waveguide hardware such as mode converters and windows, and a simplified drift tube and magnet structure are the main areas of scrutiny. Industry participation will be solicited with several contracts awarded to build 50 MW klystrons. Close cooperation between industry and SLAC will be required for the successful construction and operation of several thousand 75 MW PPM klystrons. One key to the lower cost will be the development of a clamp-on magnet structure, which can be used repeatedly as klystrons reach the end of their useful lifetime. A clamp-on structure for evaluation purposes is currently under fabrication at SLAC and will be tested in the next few months.

Automated processing of the cathode activation, tube bake and rf processing must be implemented in order to keep up with the demand that will be an order of magnitude greater than any similar effort to date. It is currently planned that one or more factories on site will continuously build and repair klystrons while the accelerator is under construction and operation.

Eventually, the DFM klystron and the research prototypes along with industry efforts will merge in a single design using the best technologies from each.

3 CONCLUSIONS AND FUTURE WORK

The results of the 50 MW klystron testing exceeded the design goals in terms of output power, pulsewidth and efficiency, and provide a proof-of-principle for high-power PPM klystrons. The magnetic field difficulties with the 75 MW design can most likely be overcome by returning to a magnetic circuit similar to the 50 MW klystron. Further study is required to fully explore the failures and possible solutions concerning the 75 MW magnetic circuit. By early next year, a new design will be tested which relies on lessons learned from the previous 75 MW klystron. Furthermore, smaller gun and collector designs, elimination of some vacuum pumps, simpler output waveguide structures, and overall cost-reduction schemes will continue development.

Despite the requirement for further engineering work, this program has shown that a high-power PPM focused klystron is not only feasible, but has demonstrated to function in good agreement with simulation and engineering analysis. The elimination of the focusing solenoids for high-power accelerator sources is a major cost reduction in both the procurement and operational costs of such sources. It is likely that any future large-scale, linear electron accelerator constructed will be driven by PPM focused klystrons.

REFERENCES

[1] W. B. Herrmannsfeldt, "Electron trajectory program," SLAC 226, Stanford Linear Accelerator Center, Nov. 1979.

[2] B. Aimonetti, S. Brandon, K. Dyer, J. Moura, D. Nielsen Jr., "CONDOR user's guide," Livermore Computing Systems Document, Lawrence Livermore Nat'l Lab., April 1988.

REVIEW OF FABRICATION OF SC CAVITY STRUCTURES

V. Palmieri

Laboratori Nazionali di Legnaro, ISTITUTO NAZIONALE DI FISICA NUCLEARE, Legnaro (Padova), I-35020 ITALY

Abstract

The search for higher and higher accelerating fields with low rf losses, plus the need of know-how transfer from scientific laboratories to firms for industrial cavity production, have contributed to the establishment of fabrication technology standards. Over years of research both on high beta and on low beta superconducting resonators, various criteria improving resonator rf performances has been codified as guide-lines or canons in the fabrication process. However, the simple transfer of the standard cavity fabrication technology developed so far, is no longer sufficient for the new generation machines. Not only the progressive achievement of higher accelerating fields, but also the drastic reduction in resonator production time and costs (K$ per MV/m) is compulsorily for the feasibility of more and more powerful accelerators. This is the motivation under the research toward simpler and cheaper fabrication techniques as for instance seamless cavities. The paper reviews the status of those new forming techniques under development in several laboratories, as hydroforming, spinning, backextrusion or superconductor/normal metal coated cavities suitable for prototype fabrication and at least in principle, considerable for mass scale production.

1 INTRODUCTION

About ten years ago, the Argonne National Laboratories under the chairmanship of K. Shepard hosted the third Workshop on RF Superconductivity [1]. In this occasion everybody involved in the superconducting cavity field was proud to show his last and best result. At that time the LEP design value consisted in a gradient of 5MV/m at a Q-value of 3e+09 and the three industries involved in the Nb/Cu sputtered resonator production did not yet even start to acquire know-how. D. Proch in a talk on SC cavities in Storage Ring Beam Tests, was reporting values of the accelerating field values ranging from 1.9 MV/m to 6.5 MV/m [2]. The maximum accelerating field reported for the TRISTAN 500 MHz 5-cells was lower did not overcome the 10 MV/m [3], while G. Mueller reported even fields up to 24 MV/m but on a Nb single cell and at 3 GHz [4].

About 10 years later again under the ANL organization, the 98 LINAC conference will see the presentation of results such as the 30 MV/m in the high 1e+9 - low 1e+10 range in horizontal test for some TTF 1.3 GHz 9-cell resonators coming from the industrial production [5] or such as the 40 MV/m at a Q of 1e+10 obtained by K. Saito on a 1.3 GHz Niobium single cell [6]. The superconducting resonator fabrication technology has made great strides, improving the manufacture standards, and importing the know-how of the ultra-clean from the neighbouring field of semiconductors. In parallel to the traditional technology of Electron Beam (EB) welded cavities, already three laboratories are able to form seamless Niobium cavities of the TESLA shape [7-9]. Besides to whom is depositing Niobium onto Copper, who reinforces Niobium with Copper is also coming to the fore [10]. Last, the traditional separation between "low beta people" and "high beta people" is becoming weaker and weaker, since middle beta cavities are becoming a subject more and more investigated.

2 THE MOST SAFE APPROACH: THE BULK NIOBIUM TECHNOLOGY

It is not by accident that TTF is installing bulk Niobium 9-cell cavities. The TESLA goal is 25 MV/m at a Q-value of 5e+09 and the bulk Niobium technology is the only one capable to satisfy this requirement at industrial level in the shortest possible time. This does not mean no room for the Nb/Cu sputtering approach, but only that an eventual R&D for sputtered nine-cells has compulsorily much longer R&D times. On the other side it must be own that the traditional approach to EB weld half cells, both for material and for manufacture, has been convenient for the TJNAF 1.5 GHz 5-cell production, but it is is definitely too expensive for a possible mass production of 20,000 cavities, as in the TESLA Project.

The traditional fabrication approach for beta 1 resonators consists in forming the cavity cups by spinning or preferably by deep-drawing. The cup edge are trimmed by machining. The possible variation in wall thickness due to the mechanical tolerances of the drawing tool can influence the geometry so the resonant frequency (df/dl_{9cell} = 300 KHz/mm). Pad rubber forming has been proven to show the best reproducibility [11]. Facing the cups is the most crucial operation and it is performed on a rotating machine: any misalignment will certainly result in cracks along the EB weld. The thickness of the lip to weld is much smaller than the equator diameter, moreover the heated zone will thermically expand respect the cold one. This can seldom result into a trivial problem especially occurring when going to weld cups drawn from textured slabs: it is not said that the ending point of the weld will necessarily coincide with the point from where the EB started. However, nowadays the Niobium EB weld technology for SC cavities is well-established and has been transferred with full success from research laboratories to industrial partners. Prior to the welding, cups and beampipes are chemically treated by a Buffered Chemical Polishing (BCP) $HF/HNO_3/H_3PO_4$ 1/1/2 in

volume, followed by ultraclean water rinsing and handling in clean environment. The Niobium is oxidized by the nitric acid, then the oxydes if transformed in fluoride thanks to the high electronic affinity of fluorine. The Niobium fluoride is a salt highly soluble in water. The phosphoric acid mainly works as moderator.

After welding the cavity undergoes two main steps: titanified at 1400 C in UHV and chemically etched in a virgin 1/1/2 bath, then Rinsed with ultrapure water under High Pressure (HPR) usually at 100 bar.

Besides this elementary recipe some other fabrication steps have been found necessary in order to achieve voltages in the 20-30 MV/m regime and are clearly reported by Matheisen in his paper about the "Improvements on standard Fabrication methods" [11]. They can be listed in the following:

1) Since the Niobium ingot is Electron Beam melted in the UHV oven, already it is necessary to exercise a strict control that ultra clean conditions are respected. The use of a furnace seldom used for melting other elements is risky.

2) Rolling of sheets from ingot is not a less crucial step, since microparticles produced during rolling are pressed and embedded into the bulk.

3) The defect diagnostics of Niobium slabs by eddy current scanning provides a more accurate selection of sheets. It has been seen that by this method, the quench limitations can be sorted out in a very early step of the production.

4) The control of the BCP temperature kept lower than 15 C, in order to avoid hydrogen charging of Niobium.

5) The adoption of a wiggled beam with 50% penetration on the first welding turn, followed by a wiggled full penetration beam, since this sequence is less sensitive to fabrication tolerances.

6) The vacuum in the welding furnace must be lower than 5e-5 mbar, depending the Residual Resistivity Ratio (RRR) value on the chamber residual pressure.

Besides to this DESY experience seems to advice that quenches below 30 MV/m in multicell structures can be avoided by a strict application of cleanroom techniques followed by postpurification of Niobium.

Recently K. Saito has perturbed the common beliefs about the Niobium chemical treatment, sustaining the superiority of electropolishing over chemical polishing on high gradients [6]. The problem must be encountered in deeper detail, however the fact remains that he has reached 40 MV/m at 1e+10 on a 100 micron electropolished cavity. Electrochemical-mechanical buffing has been also proposed in the framework of a KEK-Mitsubishi collaboration in order to get the smoothest Niobium surfaces. The combination of mechanical polishing and electrochemical polishing is a well-known technique adopted for silicon wafer polishing.

Following the above mentioned basic fabrication rules, bulk Niobium and the related EB welding is a paying technology also for low beta cavities. Facco at LNL [12] has produced and recently installed 80 MHz Quarter Wave Resonators in the low beta section of ALPI. An average accelerating field of 7 MV/m at 7 Watt has been reached after HPR. In place of an electronic fast tuner a mechanical dissipator is inserted into the resonator shaft, in order to damp vibrations caused by the environment. An accelerating field of 5 MV/m at 7 Watt has been achieved in the bulk Niobium QWR prototype developed at NSC in New Delhi [13].

A masterpiece of EB welding is however the bulk Niobium RFQ for the PIAVE Injector of LNL [14], that in its complexity is up to now the most difficult bulk Niobium SC resonator ever built. Machining of the electrodes, Extrusion of the Cylinder on the back of the Electrodes, deep drawing of the stems, stiffening of the external tank by titanium liners, EB welding, and BCP are all operations that must be done within a few hundreds of tolerance.

Last we wish to mention in this paragraph the experiments conducted at Wuppertal with Nb_3Sn, since Nb_3Sn was prepared by vapour diffusion onto a bulk Niobium cavity [15]. The purpose consists in operating at 4.2 K instead than at 1.8 K, due to the higher critical temperature of the compound. At 4.2 the cavity arrived up to 30 MV/m of peak field; moreover at low field the Q-value was a factor 2 higher that the value of the Niobium substrate at 2 K. A similar slope of Q versus field is found also for NbN thermally diffused Niobium cavities [16]. The investigation carried on this material however is some order of magnitude lower than the efforts paied on bulk Niobium cavities. However the problems related to such multicompositional material are much more complex than those of Niobium.

3 ALL NIOBIUM DEEPER THAN A FEW LONDON PENETRATION DEPTHS IS UNNEEDED

The rf loss mechanism in a SC cavity is confined within the first 5,000 Å, approximately ten times the London penetration depth. That means that all the Niobium deeper is there only for providing mechanical rigidity. Moreover Niobium is neither a good thermal conductor. The first Copper-superconductor resonators were done by electroplating a Lead film. Lead has a critical magnetic field of only 500 G at 4.2, moreover its porosity and its density is dramatically sensitive to the action of moderators mixed into the plating solution. Without the right moderator indeed Lead would grow according to a dentritic structure. The main problem of surface instability has been solved [17]. Under the electrodeposition of Lead there is no black magic. All the black or yellowish spots people found after deposition were caused from residuals of the fluoborate plating solution coming from an imperfect rinsing of the surface, or from the dehydratation of Lead hydroxyde.

A very nice material to play with is the Japanese Niobium clad Copper slabs, since in RF it behaves as Niobium, while mechanically is workable as Copper. Both the Argonne National Laboratory Split Loops [18] and interdigital QWRs [19-20], and the JAERI cavities have only the external enclosure in Nb-Cu, being the loop or the shaft instead in bulk niobium. Split Loops are

cavities that by now have been tested for a very long time since two machines have been built in ANL and Stony Brook respectively. With interdigital also "there are no surprises", since they are operational from '93. Considerably high performances were achieved by JAERI niobium clad copper QWRs. Maximum accelerating fields are normally higher than 7 MV/m, even up to 13 MV/m, that for such a resonator geometry means an electric peak field of 60 MV/m and a magnetic peak field of about 1000 G.

The sputtering of high quality Niobium films onto OFHC Copper cavities has been invented at CERN by C. Benvenuti and it has been successfully applied to LEP cavities. After the successful transfer to the European Industry, This technology has been recognized as a valid and in some cases superior alternative to bulk Niobium resonators. Almost concluded the 352 MHz production CERN is dedicating not little effort in order to understand the mechanism preventing the achievement of theoretical performances. Smaller size cavities such as the 1.5 GHz monocells are very suitable for this purpose. The coating method is based on a Cylindrical magnetron configuration: in a noble gas atmosphere, generally argon, at a pressure of the order of 1e-03 mbar, a potential difference is established between the central cathode and the grounded cavity. The electrical current of the glow discharge is stabilized by a permanent magnet internal to the cathode. The sputtering temperature takes place at 150 C and the coating thickness is 1.5 microns obtained in 15 minutes of treatment. The films have a RRR of 11, the average grain size is around 1000 Å [21]. It is worthwhile to report that the Copper substrate plays a crucial role for the film growth. All Nb films sputtered onto spun substrates have lower losses and Q-slope than those on hydroformed substrates. The role of sputtering parameters on RF performances are investigated as well as the relevance of physical mechanisms acting on BCS and Residual Losses.

Nb sputtering onto Copper has been applied also to low beta cavities as QWRs at Legnaro National Laboratories The first cryostat with sputtered cavities was already installed in 1995 on the ALPI beamline [22]. The average field was of 4 MV/m. Subsequently last year these four cavities were substituted with other four sustaining an average field of 6 MV/m at 7 Watt. In parallel it has started the operation of resputtering with Niobium the old Lead electroplated QWR in the ALPI middle beta section. The average field achieved with the first four resonators is of 4 MV/m. The sputtering configuration chosen at LNL was that of a DC Biased Diode, because it is the simplest to operate. A DC cylindrical magnetron sputtering instead is the configuration designed and built at the Australian National University [23]. All the needed investigation of correlation of the deposition parameters with the superconducting properties of the films has been carried out; the subsequent phase of sputtering onto the real Copper cavity is under investigation.

Sputtering opens new roads to superconducting cavities as the one of NbTiN films onto Copper. Some investigation has been carried on at CERN and at Saclay, but as for Nb_3Sn the problems to solve are hugely more complex than those under Niobium, but up to now they have been faced with hugely less people and investments.

A totally new solution in the Nb/Cu framework has been recently proposed by the Orsay group [10]. Thin Niobium cavities are Copper reinforced outside by Copper Plasma spray. A series of 3 GHz cavities has been fabricated by deep drawing and EB welding using 40 RRR Niobium sheets of 0.5 mm thickness. The cavities were heat treated at 1200°C with a titanium getter before Cu plasma spray. The first two tested cavities have a Q in the range 10^9 at 1.8 K and are limited by quench at field values around 15 MV/m. Taking benefit from the thermal conductivity and porosity of the sprayed copper layer (resulting in an increase of the heat transfer surface in superfluid helium), the quench fields measured before and after Cu plasma spraying are the same. Tests with high purity Niobium and at 1.3 GHz are in programme.

4 SEAMLESS CAVITIES: A WAY TO REDUCE FABRICATION TIME AND SAVE MONEY

Even not mentioning that the equatorial weld is the main source of defects, whenever 20,000 cavities will be done it is compulsory to conceive a fabrication method able to output at least one ninecell per hour. A few laboratories are mainly involved in this search.

1) At LNL the author has succeeded in cold forming both Copper and Niobium multicells by spinning a simple circular blank onto a collapsible mandrel [7]. The strong advantage of this method lays in the total absence of intermediate annealings. Moreover the method does not regard of the possible ununiformity and texture of the starting material, since during spinning all the material is mixed up again. Spun cavities have been sent to CERN, DESY, TJNAF and to KEK for characterization. CERN has proved that spun copper monocells are superior to hydroformed ones, because of lower losses and lower Q-slope. Accelerating fields up to 25 MV/m have been measured at DESY on 1.3 GHz Niobium monocells, while 28 MV/m has been achieved on a 1.5 GHz Niobium monocell by P. Kneisel. Niobium fivecells have been already successfully spun and are waiting for characterization. Clad Nb/Cu slabs were also spun in the framework of a LNL-KEK collaboration. Low RRR Niobium has been adopted for first test, however up to now no positive result has been found yet, since the cavity annealing after forming seems to open crack in Niobium. According the author, however this is a problem easily solvable when spinning a thicker slabs instead than a rolled blank.

2) At DESY a 1.3 GHz Niobium monocell has been successfully hydroformed from a seamless tube jacketed into a steel matrix [8]. The steel was removed chemically and after a preliminary chemistry, the cavity reached already 14 MV/m in range 1e+10.

3) At Saclay, C. Antoine succeeded too in hydroforming a Niobium single cell. Two intermediate annealings were applied, but what is surprising is that the Niobium was

very poor in RRR, nevertheless the cavity reached 18 MV/m [9].
4) Seamless Copper cavities were produced by explosive forming in the framework of a KEK-Toshiba collaboration, that however in recent times is evaluating the possibility to combine explosive forming with hydroforming [24].
5) Copper Electroforming is instead under investigation at CERN [25] and at Protvino [26].

5 THE NEW ARRIVALS: THE MIDDLE BETA CAVITIES

It is probable that middle beta cavities will play the leading role in the next future. In this framework Los Alamos National Laboratories already fabricated 0.48 and 0.64 beta cavities standing over 1e+09 up to 40 MV/m of peak field [27].

The spoke resonators [28] proposed by Shepard and Delayen are also structures over which already a certain amount of work has been done. New structures as reentrant cavities [29] or shorter QWRs are also suitable for being considered. However besides to new structures also new materials should be investigated. For high intensity machines Copper for instance is not the best material, because of the possible activation. The sputtering onto Alluminum or onto Graphite with buffer layers would be worthy of investigation.

6 ACKNOWLEDGMENTS

This is review paper, hence it reports mainly the work of other people. Among all already quoted, the Author has reported material mainly got from C. Antoine, C. Benvenuti, G. Bisoffi, S. Calatroni, A. Facco, M. Fouaidy, T. Junquera, P. Kneisel, L. Lilje, A. Lombardi, M. Pekeler, A. Pisent, A. Porcellato, D. Proch, K. Saito, K. Shepard, W. Singer, S. Stark.

7 REFERENCES

[1] Proc. 3th Workshop on RF superconductivity, K.W. Shepard ed., ANL, Argonne (1987).
[2] D. Proch, ibid ref. 1, p. 29
[3] T. Furuya et al, ibid ref. 1 p. 95
[4] G. Mueller, ibid ref. 1 p. 331
[5] D. Proch, "Status of the TTF", Proceedings of the 8th Workshop on RF Supereconductivity, V. Palmieri, A. Lombardi eds., Abano, Italy (1997), on press.
[6] K. Saito, "Superiority of Electropolishing over Chemical Polishing on High Gradients", ibid ref. 5
[7] V. Palmieri, Seamless cavities: the most creative topic in RF Superconductivity", ibid ref 5
[8] W. Singer, private communication
[9] C. Antoine, private communication
[10] M. Fouaidy et al, "Copper Plasma sprayed Niobium Cavities", ibid ref 5.
[11] A. Matheisen, "Improvements on standard Fabrication methods", ibid ref. 5
[12] A. Facco, "Mechanical mode damping in superconducting low beta resonators", ibid ref 5
[13] P. Prakash et al, " QWcoaxial line cavity for New Delhi Linac Booster", ibid ref.5
[14] G. Bisoffi et al, " Status of the 80 MHz SC-RFQ development at LNL", ibid ref 5
[15] G. Mueller et al, " Proc. of the 7th Workshop on RF Superconductivity, B. Bonin ed, Gif sur Yvette, France (1995), p. 119.
[16] R. Parodi et al, " RF superconductivity in Genoa", ibid ref. 5
[17] S. Gustaffson, V. Palmieri, A.M. Porcellato, V.L. Ruzinov, S.Yu. Stark, F. Stivanello, S. Zandolin, ibid ref 15.
[18] K.W. Shepard, C.H. Sheibelhut, R. Benroya., L.M. Bollinger, IEEE Trans. Nucl. Sci. NS-24, 1147 (1977).
[19] K.W. Shepard, IEEE Trans. Nucl. Sci., 3574 (1985).
[20] K.W. Shepard, P.K. Markowich, G.P. Zinkann, Proc. 1989 IEEE Particle Accelerator Conf., March 20-23, 1989, Chicago Illinois, IEEE Cat. no.89CH2669-0 (1989) p.976.
[21] C. Benvenuti et al, " Niobium sputter-coated Copper Resonators", ibid ref. 5.
[22] S. Stark et al, "Niobium sputter-coated QWRs", ibid ref. 5.
[23] N. Lobanov et al, " NB Sputter coating on QWR in ANU", ibid ref. 5
[24] T. Ota, S. Sukenobu, Y. Tanabe, K. Takaishi, M. Yamada, S. Kawatsu, H. Inoue, S. Noguchi, M. Ono, K. Saito, T. Shishido, Y. Yamazaki, "Activities on Superconducting cavities at TOSHIBA", ibid ref. 5
[25] S. Parussatti, NT-CERN/94-10, CERN 1994
[26] A. Ageev et al Proceedings of the 6th Workshop on RF Superconductivity,October 1993, CEBAF, Newport News, R. Sundelin ed., p.802.
[27] B. Rusnak et al, " High intensity Proton Linac Activities at Los Alamos", ibid ref. 5.
[28] K. Shepard et al, "Accelerator development for a Radiactive beam facility based on ATLAS", ibid ref. 5
[29] M. Comunian et al, " A 100 MeV SC Proton Linac: beam Dynamic issues", this conference.

THE U.S. DOE GRAND CHALLENGE IN COMPUTATIONAL ACCELERATOR PHYSICS *

R. Ryne[1], S. Habib[1], J. Qiang[1], K. Ko[2], Z. Li[2], B. McCandless[2], W. Mi[2], C. Ng[2],
M. Saparov[2], V. Srinivas[2], Y. Sun[2], X. Zhan[2] V. Decyk[3], G. Golub[4]
[1]Los Alamos National Laboratory, Los Alamos, NM 87545
[2]Stanford Linear Accelerator Center, Stanford, CA 74702
[3]University of California, Los Angeles, CA 94550
[4]Stanford University, Stanford, CA 74702

Abstract

Particle accelerators are playing an increasingly important role in basic and applied science, and are enabling new accelerator-driven technologies. But the design of next-generation accelerators, such as linear colliders and high intensity linacs, will require a major advance in numerical modeling capability due to extremely stringent beam control and beam loss requirements, and the presence of highly complex three-dimensional accelerator components. To address this situation, the U.S. Department of Energy has approved a "Grand Challenge" in Computational Accelerator Physics, whose primary goal is to develop a parallel modeling capability that will enable high performance, large scale simulations for the design, optimization, and numerical validation of next-generation accelerators. In this paper we report on the status of the Grand Challenge.

1 INTRODUCTION

Several accelerator projects are planned or under consideration that will have major impacts in basic and applied scientific research. Examples include the Next Linear Collider (NLC),the Large Hadron Collider (LHC), the Spallation Neutron Source (SNS), and fourth-generation light sources. All of these projects will require high-resolution modeling far beyond that which has ever been performed by the accelerator community. Similar modeling will be needed for proposed accelerator-driven technologies, including Accelerator Production of Tritium (APT), Accelerator Transmutation of Waste (ATW), and Accelerator Driven Energy Production (ADEP).

For example, future high average power linear accelerators, such as the APT, will have to operate with extremely low beam loss (~ 0.1 nA/m) to prevent unacceptably high levels of radioactivity. To ensure that this requirement will be met, simulations with on the order of 100 million particles are needed. An equally challenging modeling problem exists in the NLC for which the linac design is dominated by the issue of beam emittance growth due to long-range transverse wakefields. To suppress this effect, a complex 3D accelerating structure, the Damped Detuned Structure (DDS), has been developed to control the wakefields and it is necessary to verify the effectiveness of the design by numerical simulation. This entails modeling a complete accelerator section that consists of 206 complex three-dimensional cavities requiring hundreds of GBytes of memory. It is evident that these simulations are beyond the desktop computer's capabilities, and can only be performed on the most advanced high performance computing (HPC) platforms using software and algorithms targeted to parallel and distributed environments.

In 1997 the U.S. Department of Energy initiated a Grand Challenge in Computational Accelerator Physics to support a collaborative effort involving LANL, SLAC, UCLA, and Stanford, together with two HPC centers, the National Energy Research Scientific Computing Center (NERSC) and the Advanced Computing Laboratory (ACL). The primary goal of this project is to develop a new generation of accelerator modeling tools for HPC platforms, and to apply them to large complex problems of importance in future accelerators, including those mentioned above. In this paper we will report the progress-to-date in two main thrust areas: electromagnetics and beam dynamics.

2 ELECTROMAGNETIC MODELING

The development of new electromagnetic tools for the Grand Challenge project originated from advanced accelerator structure research for the NLC. The main thrust of the effort is aimed towards large-scale simulations of realistic 3-D structures. Such a capability can be applied to system-scale analysis such as finding the wakefields in the entire DDS as described in Fig. 1, or to individual component design such as one cell in the DDS Fig. 2, by modeling with an accuracy approaching fabrication tolerance level. The new set of tools incorporates the following features to enable the high-resolution modeling required: (i) the use of unstructured grids to capture realistic geometries, (ii) the development of refinement algorithms to improve accuracy and optimize computing resources, and (iii) the implementation on parallel platforms to take advantage of the latest in HPC resources for large-scale simulations.

Presently, there are two types of solvers being developed for the tool set. The first type is formulated in the frequency domain using linear and quadratic finite elements on an ir-

* Work supported by the U.S. Department of Energy, Division of Mathematical, Information, and Computational Sciences, Division of High Energy Physics, and Office of Defense Programs.

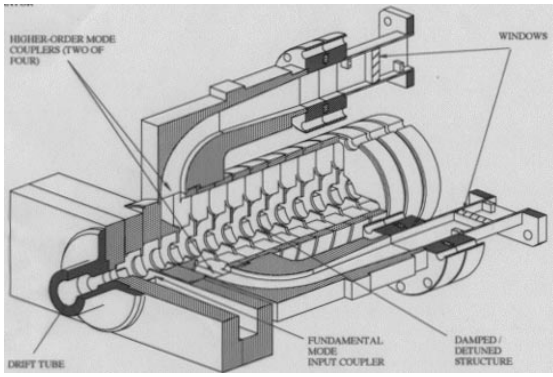

Figure 1: One end of the DDS 206-cell section including the input coupler and HOM load termination.

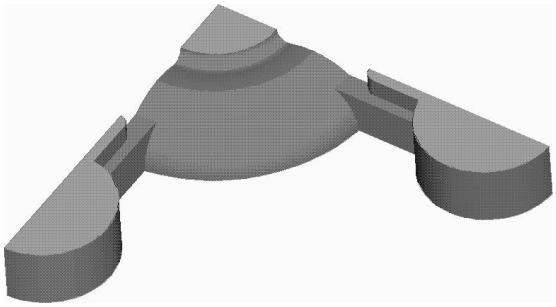

Figure 2: One-eighth of the DDS cell geometry from a solid model.

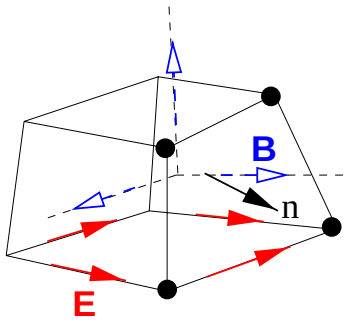

Figure 3: A non-orthogonal cell for the generalized Yee algorithm used in $\tau 3$.

regular grid, and includes eigenmode solvers in two and three dimensions, named $\Omega 2$ and $\Omega 3$ respectively. The parallel versions, $\Omega 2$P and $\Omega 3$P, use MPI and currently run on the SGI/Cray T3E at NERSC. In the case of $\Omega 3P$, the calculation proceeds in three steps: First, there is the mesh distribution step with a module called DistMesh that uses the parallel library ParMETIS for partitioning unstructured graphs. This is followed by the matrix assembly step which consists of the finite element formulation that provides the mass and stiffness matrices for the generalized eigenvalue problem. The final step is a solution step, with Lanczos or Jacobi-Davidson algorithms, that utilizes the parallel iterative library AZTEC to solve the sparse linear systems.

The other type of solver is a three-dimensional time-domain code, called $\tau 3$, that uses a generalized Yee algorithm on an unstructured grid [1][2], Fig. 3. A leapfrog time advancement scheme with filtering is implemented as well as a broadband termination at the waveguide ports. Therefore it is able to handle pulse transmission for S-parameter evaluations of RF components over a wide frequency range in a single run. Dipole excitation is also possible to calculate external Q's of waveguide-loaded cavities. A parallel version, $\tau 3$P, currently runs on a shared memory machine, like the 4-node Intel Xeon server, using threads while the distributed memory version for the T3E is presently under development. The inclusion of a transiting rigid beam to compute wakefields is planned.

2.1 *Examples*

We present here some recent results from $\Omega 3$P and $\tau 3$. First, we report the modeling of a single DDS cell using $\Omega 3$P on the T3E. Fig. 4 shows the cell geometry partition-

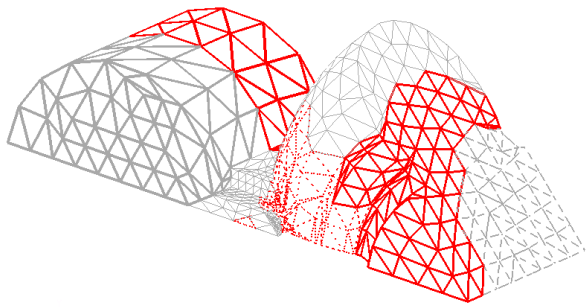

Figure 4: Domain decomposition of the DDS cell.

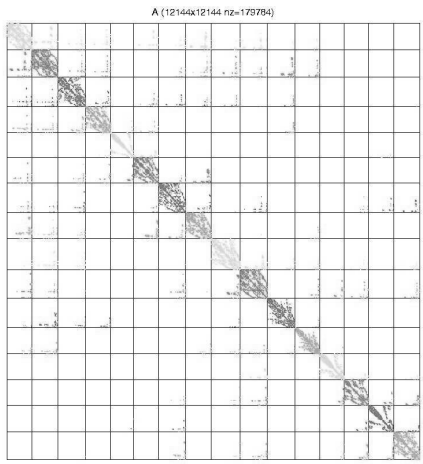

Figure 5: Mass matrix distribution over 16 processors.

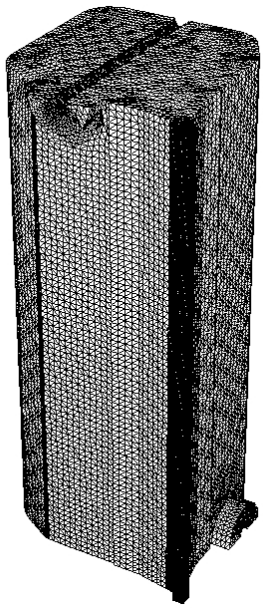

Figure 6: RFQ cavity for the SNS.

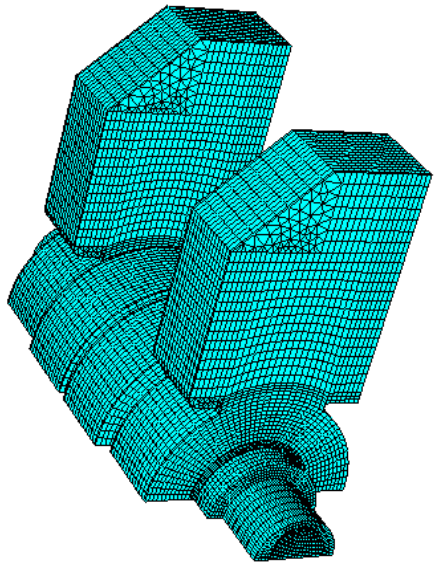

Figure 8: Input power coupler for the NLC linac modeled by $\tau 3$.

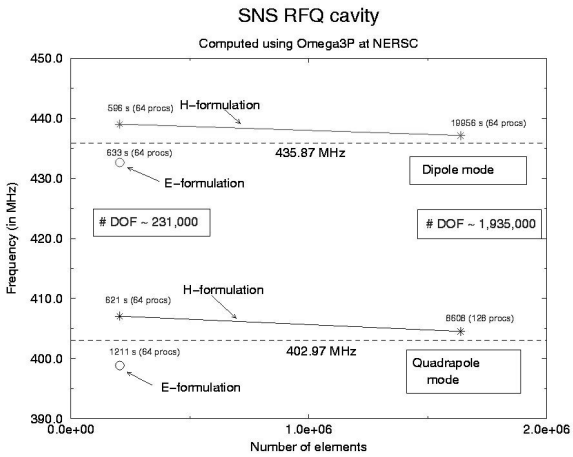

Figure 7: Calculated frequencies and measured data for two modes of the SNS RFQ cavity.

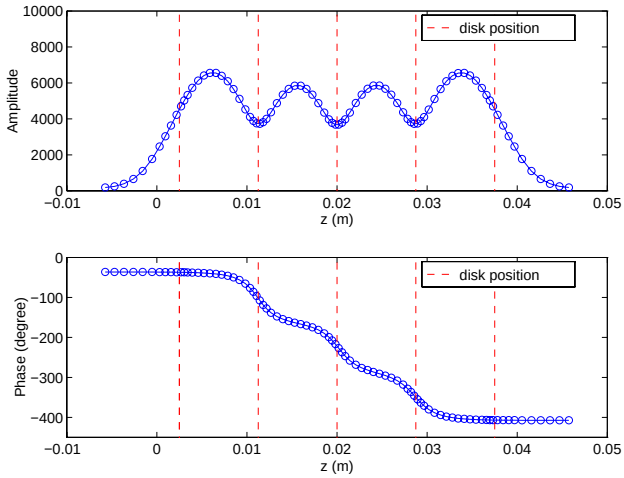

Figure 9: Field amplitude and phase of accelerating field at matched condition.

ing into 8 pieces using DistMesh/ParMETIS. Fig. 5 is the mass matrix distribution over 16 processors. Together they demonstrate the importance of domain decomposition to achieve load balancing. Currently, $\Omega 3$P is the tool we use to determine the new dimensions for improved versions of the DDS design. Another $\Omega 3$P result comes from the Spallation Neutron Source project for which we modeled the RFQ cavity as shown in Fig. 6. This cavity is difficult to simulate accurately due to the disparate lengthscales between the focusing vanes, the stabilizing rods, and the cavity proper. Fig. 7 shows the convergence of the calculated frequencies to measured data for the two modes of interest when the resolution is increased to require several million degrees of freedom in the simulation.

The $\tau 3$ capability is demonstrated by the matching and tuning of the input power coupler for the NLC accelerator section. Fig. 8 shows the mesh used in modeling a pair of couplers separated by two regular cells. $\tau 3$ finds the match by either single frequency or pulse excitation. The reflection is determined to be 0.005 at 11.424 GHz. The match is confirmed by the accelerating field amplitude and phase along the beam axis. Fig. 9 indicates the field that is due to a travelling wave with the correct phase advance of 120 degrees per cell from coupler to coupler. The advantage of $\tau 3$ over other commercial packages will be the ability to model much larger problems when the parallel version, $\tau 3$P, is completed.

3 BEAM DYNAMICS SIMULATIONS

Many systems involving intense charged-particle beams can be described by the Vlasov/Poisson equations. There are two main approaches to solving these equations: particle simulation techniques and direct methods.

In the particle simulation approach, the beam distribution function is represented by a number of macroparticles, typically 10's to 100's of millions in a large scale simulation. Often the single particle equations of motion are derived from a Hamiltonian which includes both externally applied fields and a mean field due to the beam's space charge: $H = H_{ext} + H_{sc}$. Such a form is ideally suited to the application of symplectic split-operator methods [3]. These methods provide a powerful framework capable of dealing with the complicated Hamiltonians often encountered in accelerator physics, where the Hamiltonian is usually approximated by a high-order polynomial in the phase space variables. Besides being able to treat Hamiltonians with many terms, the split-operator approach is easily generalized to high-order accuracy in time. A well-known fourth-order algorithm is due to Forest and Ruth [4], and an arbitrary-order scheme was derived by Yoshida [5]. There are also implicit symplectic methods that do not require the Hamiltonian to be split into a sum of exactly solvable pieces [3]. Finally, time-dependent systems are easily treated by "extending the phase space" [4].

Unlike some split-operator treatments that separate the Hamiltonian into terms involving only position and only momentum, our particle simulations separate the Hamiltonian into terms involving the external fields and terms involving the self fields. The external fields are treated using well-established techniques from magnetic optics. One advantage of this approach is that it enables one to take large time steps, since the dynamics due to external fields is usually dominated by a linear map which is easily obtained analytically or numerically. To treat the self fields, we use a 3D Particle-In-Cell (PIC) approach with area weighting. Open boundary conditions are treated using the convolution method of Hockney [6]. We are currently using and evaluating several methods of implementing our parallel particle simulation codes: High Performance Fortran (HPF), C++ with message passing via the POOMA framework [7], and Fortran 90 with message passing [8]. In our HPF codes, charge deposition and field interpolation are parallelized using the method of Ferrell and Bertschinger [9]. In our codes that use explicit message passing, a "particle manager" is used to make the data needed by processors local to the processors prior to charge deposition and field interpolation.

Stochastic corrections to Vlasov/Poisson evolution occur due to particle collisions and noise in external fields. To treat these effects we have modified our PIC codes to include Langevin forces and damping, which corresponds to solving the Fokker-Planck equation for the distribution function. An example is shown in the next section.

3.1 Examples

Fig. 10 shows the horizontal and vertical rms emittances from a 2D Langevin simulation of a beam in a potential that can produce chaotic dynamics. In the absence of damping and diffusion, the motion is governed by the Hamiltonian,

$$H = \frac{1}{2}(p_x^2 + p_y^2) + \alpha x^4 + \beta y^4 + \frac{1}{2}x^2y^2 + q\Psi, \quad (1)$$

where α and β are constants, and where Ψ is scalar potential associated with the beam space charge. Damping and diffusion were turned on at $t = 0$ in the simulation, and the beam approached thermal equilibrium quickly, as is evident from the emittance curves which reach their final values after about 20 units of time. As further evidence that that beam has reached equilibrium, we turned off the damping and diffusion at $t = 100$ and observed little or no change in the emittances.

Though early work in beam halo physics emphasized 1D and 2D models of the transverse beam halo, recent activity has turned to 3D models including longitudinal beam halo. We have developed a parallel PIC code called HALO3D specifically for studying beam halo formation in 3D bunches. Such a code is extremely useful for testing analytical models of halo formation, such as particle-core models. A unique feature of the code is that it has a capability to model a new 3D beam equilibrium distribution, developed by R. Gluckstern and A. Fedotov of the University of Maryland [10]. It also has the ability to include nonlinear rf focusing fields, a feature incorporated in collaboration with J. Barnard and S. Lund of Lawrence Livermore National Laboratory. Based on their CTP ("core test particle") code, Barnard and Lund had predicted that the period-2 parametric resonance widely known to be a major source of beam halo could be detuned by the presence of nonlinear rf fields. This was supported by HALO3D simulations, as shown in Figs. 11 and 12. These figures show a stroboscopic plot in longitudinal phase space of test particles moving in the field of a mismatched beam. The resonance is evident in Fig. 11, which has a linear model of the rf fields. In contrast, the resonance is absent in Fig. 12, which has a nonlinear model of the rf fields.

In addition to HALO3D, we are also developing a new 3D beam dynamics code called IMPACT (Integrated-Map and Particle Accelerator Tracking code). This code has an accurate and efficient treatment of RF accelerating gaps, obtained by numerical integration of the gap transfer map rather than integration of single particle trajectories. The code is especially useful for modeling superconducting proton linacs, where there are only a few types of accelerating cavities. An example input geometry that was used to test the code is shown in Fig. 13. The figure shows the quadrupole gradient in a FODO cell along with the electric field on-axis due to accelerating cavities between the quadrupoles. Finally, we have developed a parallel version of a code called LINAC, developed by K. Crandall, which is the primary code used by the APT project for halo simulations. In addition to parallelizing LINAC, we also added

a 3D space charge capability, as described in the preceding section.

4 ACKNOWLEDGMENTS

This research used resources of the National Energy Research Scientific Computing Center, which is supported by the Office of Energy Research of the U.S. Department of Energy under Contract No. DE-AC03-76SF00098. This research also used resources of the Advanced Computing Laboratory, located at Los Alamos National Laboratory, which is supported by the U.S. Department of Energy.

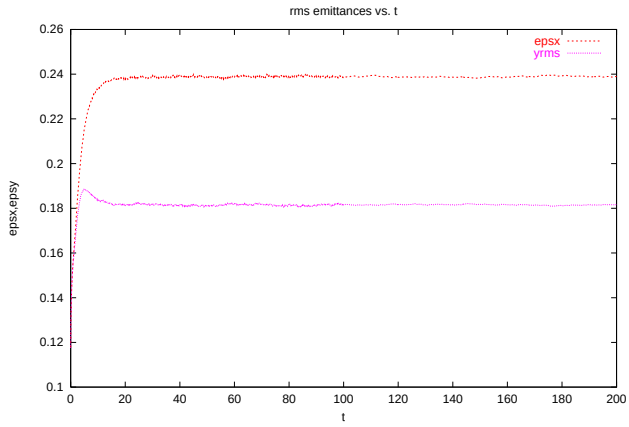

Figure 10: Emittance curves from a 2D Langevin simulation of a beam driven to thermal equilibrium.

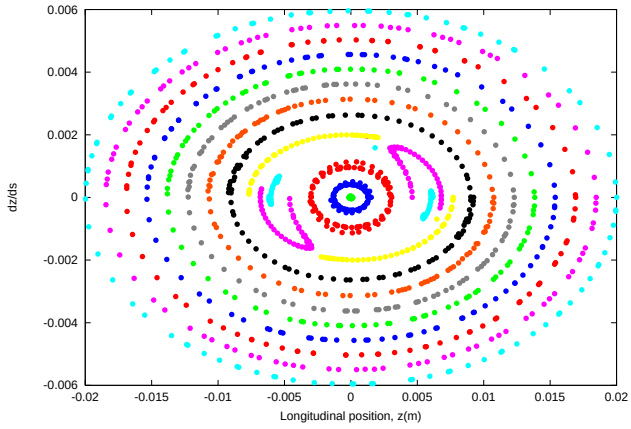

Figure 11: z-pz phase space plot from a HALO3D simulation *without* rf nonlinearity.

5 REFERENCES

[1] Proceedings of the 1998 International Computational Accelerator Physics Conference, in preparation.

[2] C. Ng et al.,, "Modeling Linear Collider RF Components in the Time Domain with Unstructured Grids," this conference.

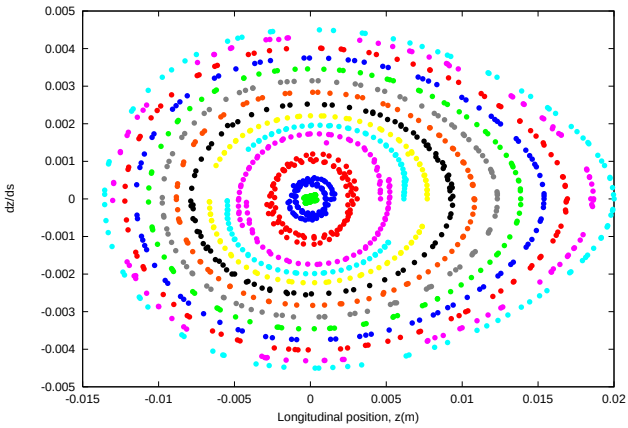

Figure 12: z-pz phase space plot from a HALO3D simulation *with* rf nonlinearity.

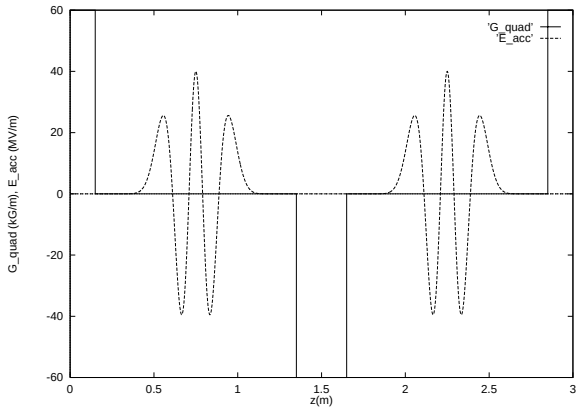

Figure 13: Example cell geometry for IMPACT simulation.

[3] E. Forest *et al.*, "Application of the Yoshida-Ruth Techniques to Implicit Integration and Multi-Map Explicit Integration," Phys. Lett. A 158, 99-101 (1991).

[4] E. Forest and R. Ruth, "Fourth-Order Symplectic Integration," Physica D 43, 105-117 (1990).

[5] H. Yoshida, Phys. Lett. A 150, 262 (1990).

[6] R. W. Hockney and J. W. Eastwood, *Computer Simulation Using Particles*, (Adam Hilger, NY, 1988).

[7] J. C. Cummings and W. F. Humphrey, "Parallel Particle Simulation Using the POOMA Framework," Proc. 8th SIAM Conf. on Parallel Processing for Scientific Computing" (1997)

[8] V. Decyk, "Skeleton PIC Codes for Parallel Computers," Comp. Phys. Comm. 87, 87-99 (1995).

[9] R. Ferrell and E. Bertschinger, "Particle-Mesh Methods on the Connection Machine," Int. J. Mod. Phys. C 5, 933-949 (1994).

[10] R. Gluckstern and A. Fedotov, "Halo Formation in 3-D Bunches," Phys. Rev. E, 58 (4), 4977-4990 (1998).

HIGH-INTENSITY LINAC STUDIES IN FRANCE

J-M Lagniel

CEA-Saclay, DSM-DAPNIA-SEA, 91191 Gif-sur-Yvette Cedex, France

Abstract

Teams from different French research agencies are working on high-intensity high-duty factor proton, H^- and deuteron linear accelerators for several applications (waste transmutation, spallation neutron sources, tritium production, materials irradiation facilities...). The conceptual design of the TRISPAL project achieved by the CEA for tritium production is presented. A separate R&D program undertaken by a CEA-CNRS (IN2P3) collaboration is also discussed. This program includes both the construction of a high intensity (100 mA), cw (continuous wave), 10 MeV, prototype linac (IPHI) and the fabrication and test of $\beta < 1$ superconducting cavities.

1 OVERVIEW OF THE HIGH-INTENSITY LINAC ACTIVITIES IN FRANCE

Proton and deuteron accelerators with average beam power greater than 1 MW are being studied all over the world for numerous applications (see [1-2] for reviews), mainly because they are increasingly considered as ideal sources of neutrons (high flux, broad energy spectra, cw or pulsed mode, safety associated with fast shut-down...).

In France, the CEA (Commissariat à l'Energie Atomique) started the study of the TRISPAL project for tritium production in 1992. In this project, a high-intensity cw proton beam is used to produce a high neutron flux through spallation process in a heavy metal target. These neutrons are then used to transmute ^{6}Li into tritium. The TRISPAL conceptual design is now complete [3]. The 24 MW beam power linac (40 mA, 600 MeV, cw, protons) designed by a team from CEA-Bruyères-le-Châtel, CEA-Saclay and Thomson-CSF-Airsys is described in section 2.

The CEA-Saclay team is also involved for the last several years in the IFMIF project (International Fusion Material Irradiation Facility). The aim of this IEA (International Energy Agency) activity is the design of a high-flux neutron source with an energy spectrum peaked near 14 MeV for research and development of materials for the next generation of fusion reactors. The IFMIF team has the distinction to have a broad community of scientists from different fields (accelerator, Li-target, test facility, users, design integration) and from different countries e.g. the European Union (EU), Japan and the United States of America, along with the Russian Federation as an associate member. The EU contribution in the accelerator field is done by a Frankfurt University - CEA-Saclay collaboration thanks to a support of the European Commission. The confrontation of ideas with scientists from different labs is very fruitful and the work with our European, Japanese, American and Russian colleagues has been and is still highly appreciated. The IFMIF design is based on two 125 mA, 35-40 MeV, cw deuteron linacs. A full description of the work done during the IFMIF Conceptual Design Activity (CDA, 1995 and 1996) can be found in ref. [4]. The project is now in the Conceptual Design Evaluation (CDE) phase. The CEA-Saclay team is working on the ion source, high-power 175 MHz RF systems (in collaboration with Thomson-Tubes-Electronics) and beam loss.

The CEA is also involved in the 5 MW European Spallation Source (ESS) project [5]. CEA-Saclay will participate in the R&D program for the linac (1.33 GeV, 107 mA H^- peak current, 6% duty cycle). R&D studies are being contemplated in the development of H^- ion source, the beam diagnostics and the design of the accelerating structures including the evaluation of a superconducting cavity option for the high energy part of the linac.

Two French research agencies, CEA and CNRS-IN2P3 (Centre National de la Recherche Scientifique - Institut National de Physique Nucléaire et de Physique des Particules), have started an evaluation program for the accelerator driven transmutation of waste (ADTW) technology. In such a system, spallation neutrons are used to transmute long lived nuclei with high radio-toxicity into short lived or stable nuclei. The accelerator is coupled to a sub-critical target where minor actinides and/or fission products for transmutation are located [6-7]. A beam power of 20 - 40 MW or more is needed. For this, 20 - 60 mA cw proton beam will be accelerated by a linac up to an energy range 600 - 1200 MeV. The choice of beam intensity and energy must result from a complex optimization process of the whole system and the design must take into account the severe constraints on the accelerator availability and beam losses [7-8].

A significant R&D program has been undertaken by the CEA-CNRS (IN2P3) collaboration in order to optimize the design of such a high-power proton linac which could be also used for the next generation of radioactive ion beam facilities and for muon colliders. The program includes the construction of a high intensity (up to 100 mA), cw, 10 MeV prototype (IPHI, section 3) and the fabrication and test of $\beta < 1$ superconducting RF (SRF) cavities (section 4).

2 THE TRISPAL PROJECT

TRISPAL is the CEA project for tritium production using spallation neutrons. The accelerator parameters have been optimized to produce the requested quantity of tritium per year. Optimization process has taken into account the fluctuation in the cost of electricity during the year (electricity in France is ten times more expensive during the winter). The process has lead to the choice of a beam power of 24 MW delivered by a 600 MeV 40 mA cw proton linac [3].

The main directive to the TRISPAL design team was to be as conservative as possible for the choice of the technology and parameters. This accelerator based tritium production system compete directly with the process based on a conventional nuclear reactor. Thus, the linac must be built as part of an industrial facility. The major considerations that went into the design of the accelerator are :

- limit beam losses to an extremely low level ($\sim\Delta I/I < 10^{-9}$) in order to allow hands-on maintenance.
- achieve a high reliability/availability (greater than 90%) and minimize the number of abrupt beam interruptions to limit the stress in the target. It has been calculated that the TRISPAL target (including the window) can accept up to 10000 abrupt beam stops (longer than 100 ms) per year. This approximately corresponds to a mean value of one stop per hour which seems to be realistic.
- Minimize the total cost of the machine (construction and operation) without compromising the two previous items.

Figure 1 shows the layout of the TRISPAL linac. The 24 MW proton beam is produced using 4 types of RF cavities, all operating at the same frequency (352 MHz). This minimizes bunch compression which is always a source of mismatch and halo formation. The front end is composed of an 95 kV ECR source, a low energy beam transport line with two solenoids and a 5 MeV RFQ. The main parameters of the RFQ are listed in Table 1. The maximum electric field is limited to 1.5 Kilpatrick to reduce the sparking rate. The price for this choice is a relatively low transmission.

Table 1, TRISPAL RFQ main parameters

Length	8 m (578 cells)
Vane voltage	88.5 kV (1.5 Kp)
R_0 (mean aperture)	4.38 mm (min a = 2.8 mm)
ρ (vane radius)	3.72 mm ($\rho/R_0 = 0.85$)
Input trans. Emit.	0.25 π mm mrad (rms norm)
Output trans. Emit.	0.23 π mm mrad (rms norm)
Output long. Emit.	0.12 MeV deg (rms norm)
Transmission	93% (for 50 mA input current)

The high output energy of the RFQ is achieved in a 8 m long structure thanks to the segmented coupled RFQ concept developed at LANL [9]. This capability of pushing up the RFQ energy is very useful because as $\beta = v/c$ increases, the first cells of the DTL become long enough (~ 8 cm) to accommodate electromagnetic quadrupoles. The front end cavities can then operate at a relatively high RF frequency allowing the construction of a high energy machine without a frequency jump (352 MHz for the TRISPAL basic design), or only with a jump of a factor of two if 704 MHz SRF cavities are used in the high energy part. This is an important point to facilitate the beam matching in the accelerator, to avoid halo formation, and unacceptable beam losses.

The medium energy part of the TRISPAL linac is made up of an RFQ to DTL matching section, a 29 MeV DTL and SDTL cavities up to 85 MeV. The beam matching between the RFQ and the DTL is done in a ~ 80 cm section using four quadrupoles and two 352 MHz bunchers. The phase advances per unit length are kept constant from the last cells of the RFQ to the first cells of the DTL and the beam envelope modulations are minimized as much as possible in order to obtain an intensity independent matching and to minimize emittance growth. The transmission through the 29 MeV DTL is 100% ; a full beam dynamics study including errors on both the beam and accelerator parameters has been completed to determine tolerances [10]. The DTL has two tanks, each fed by an 1.3 MW RF system similar to those used in LEP or ESRF accelerators. A SDTL (Segmented DTL), mechanically simpler to build than a standard DTL, is chosen for acceleration from 29 to 85 MeV. The SDTL is composed of short DTL cavities (5-7 cells) with simple drift tubes, the transverse focusing being provided by the quadrupoles located outside the cavities.

LEP-type CCL copper cavities (see figure 2) take the beam to the final energy (600 MeV). The beam dynamics beyond the DTL has been studied using a simplified linear model ; more accurate simulations using multiparticle codes (including error analysis) may lead to an adjustment of the transition energies. In the present TRISPAL design, each SDTL and CCL cavity is fed by couplers capable of maximum power of 125 kW (a conservative value). The RF power is supplied by 49 1.3 MW RF systems. A quadrupole doublet focusing lattice is chosen. The SDTL uses seven β families in a total of 40 cavities with beam apertures ranging from Φ 50 to 30 mm and effective shunt impedance ranging from 44 to 34 MΩ/m (80% SUPERFISH). The CCL uses twelve β families in a total of 344 cavities with beam apertures ranging from Φ 30 to 60 mm and effective shunt impedance of ~30 MΩ/m. An option using superconducting RF cavities is also presented in addition to this basic conservative design.

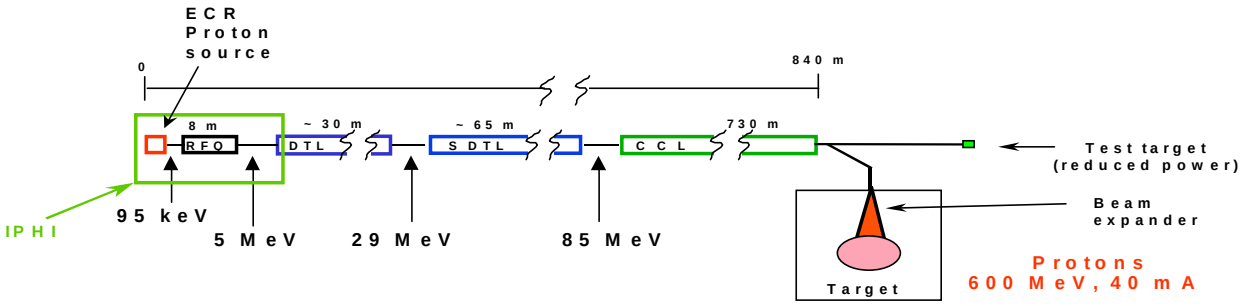

Figure 1 : TRISPAL layout

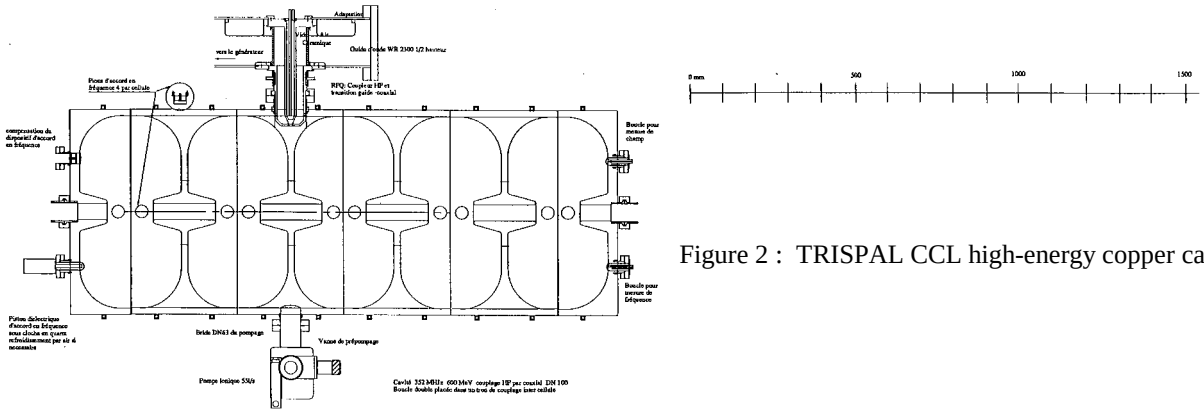

Figure 2 : TRISPAL CCL high-energy copper cavity

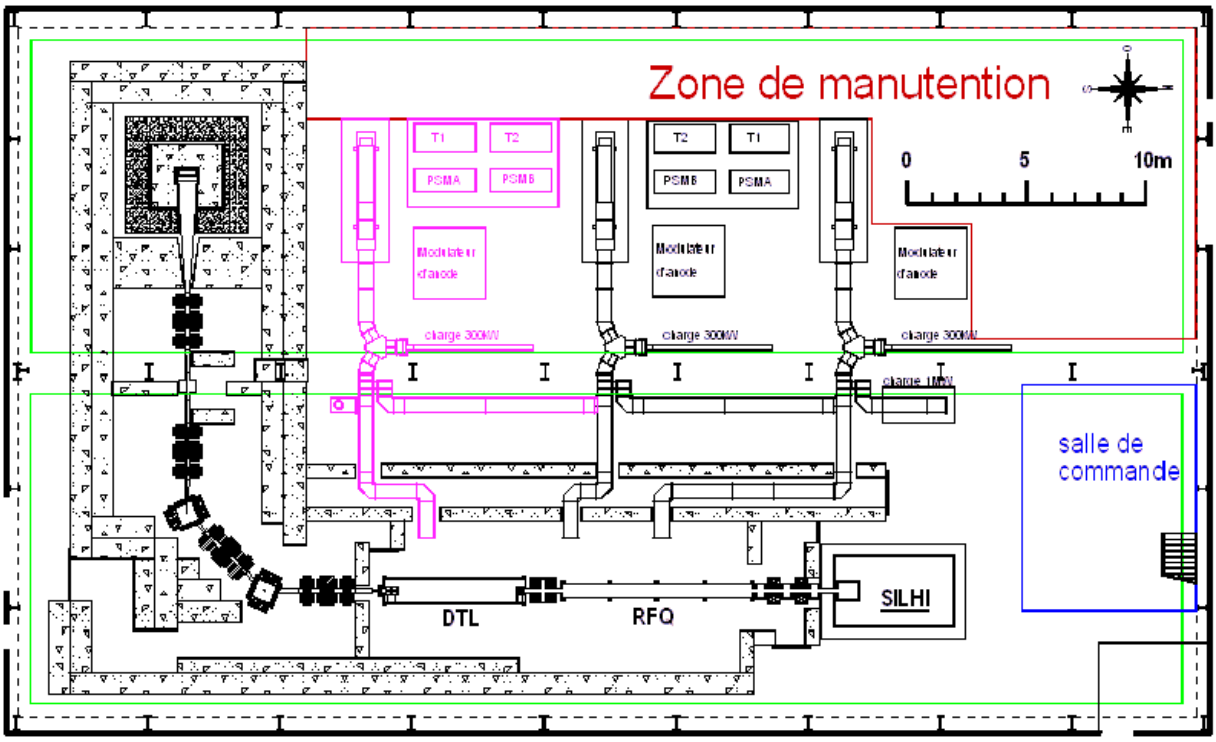

Figure 3 : General layout of the IPHI project

3 IPHI

IPHI (Injecteur de Protons Haute Intensité) is the name of the CEA-CNRS R&D program undertaken in 1997 for the front end of a typical high-power linac. The objective is to gain experience in this difficult part of the accelerator in order to optimize the whole machine in terms of performances, cost, reliability and availability. To summarize, the IPHI objectives are :

- validation of the beam dynamics codes in the low-energy sections where space-charge effects are dominant,
- knowledge of the beam distribution at an energy where halo considerations are crucial,
- demonstration of the merit of technological choices and adequacy of design codes,
- acquisition of data on reliability and availability, reality check on the cost of the components and ability of the manufacturers to build them.

The project goal is to build a 10 MeV "Injector for Protons with High Intensity" (up to 100 mA) and duty cycle up to 100%. The first stage is a High-Intensity Light-Ion Source, SILHI, designed to produce high-intensity proton or deuteron beams at 95 kV. This 2.45 GHz ECR source is now at a high performance level [11]. Table 2 shows the current performance data (consistent values except when specified) for two values of extraction diameter.

Table 2, status of the SILHI source

	Objective	Achieved	
Extraction Diameter (mm)	10	8	10
Proton current (mA)	100	91	98
Duty cycle (%)	100	100	100
Extraction voltage (kV)	95	95	92
Total current (mA)	~110	108	122.5
Proton fraction (%)	> 90	84	80
Plasma density (mA/cm^2)	140	215	156
RF power (W)	1200	1100	1200
Hydrogen mass flow (sccm)	< 10	2	3
Beam current noise (%)	± 1	± 2	NA
Norm. rms emittance (π.mm.mrad)	0.20	0.17 @ 80 mA	0.21 @ 97 mA

A first uninterrupted operation was done at the end of 1997 to measure the availability of the source. It was operated continuously for 100 hours (~5 days) at 100 mA cw. An availability of 96% was obtained with 1 h 45 mn for the Mean Time Between Failures and 4 mn 44 s for the Mean Time To Repair. Most of the beam interruptions occurred during the first day. When this conditioning period is not taken into account in the statistics, the source availability reach 99% (MTBF = 5 h 33 mn). EMC improvements made after this test and incorporation of an automatic restart controlled by computer is expected to improve these already high performance statistics.

No damage to the new HV extraction electrodes was observed after more than 300 hrs of cw operation at 100 mA. The stability and reproducibility of the beam are excellent. A non-interceptive emittance measurement system based on measurement of beam profiles with a CCD camera has been successfully tested recently [12].

The key parameters of the 5 MeV RFQ are now almost fixed. Table 3 shows that our objective to achieve a very high beam transmissions with a relatively low maximum electric field is at hand. The optimization of the beam dynamics has been done using a large set of codes developed at Saclay, LANL (PARMTEQM) and MRTI (LIDOS) [13]. An in-depth analysis of the different models used in these codes is underway [14].

Table 3 : IPHI RFQ main parameters

Length	8 m
Vane voltage	87.34 to 122.82 kV (1.7 Kp)
R_0 (mean aperture)	3.69 to 5.27 mm
ρ/R_0	0.85
A	3.56 to 4.41 mm
M	1.0 to 1.735
Input trans. Emit.	0.25 π mm mrad (rms norm)
Output trans. Emit.	0.25 π mm mrad (rms norm)
Output long. Emit.	0.18 MeV deg (rms norm)
Transmission (100 mA input current)	99.4% for 1.8 Kp 99.3% for 1.7 Kp 97.3% for 1.6 Kp

The thermo-mechanical analysis of the cavity and the study of the RFQ vacuum system has been successfully completed. Several prototypes will be built before the end of this year to validate the fabrication process. Financial commitment for the high-power RF system will be made in 1999 (klystrons, windows and circulators).

To optimize the geometry of the DTL, a full 3D magnetic analysis of the low energy quadrupoles (around 5 MeV) has been done. The field non-linearities have been calculated taking into account the effect of surrounding quadrupoles. The construction of a short tank (4 cells) for high-power tests will start at the end of this year. A affirmative decision for the construction of a 10 MeV tank is expected in 1999. Total investment for the IPHI prototype is ~8 M ECU (equipment only) and the CEA - CNRS-IN2P3 team consist of around 45 men-year/year. The key dates are :

Source / LEBT :
Test the matching conditions to the RFQ 1999

RFQ :
Tests of the 2 RF systems 01-06/2001
Tuning of the RFQ cavity 06-12/2001
Low beam current tests 01-06/2002
Nominal beam 06/2002

Diagnostic Line :
Beam measurements at nominal power 09-12/2002

DTL :

Short tank hot RF tests 04-08/2000

Start a 10 MeV tank 01/2001 (not yet funded)

4 SRF CAVITY STUDIES

A strong R&D effort on $\beta < 1$ SRF cavities is justified by the fact that this technology brings important advantages, the most obvious one being economy. In fact, the high RF to beam power efficiency (almost 100%) significantly reduces the operation cost. In addition, the investment cost can also be slightly reduced through length reduction. Standard copper RF cavities typically provide ~1.5 MeV/m with a shunt impedance ~35 MΩ/m. A 1 GeV linac is then ~ 670 m long and ~43 MW of RF power is lost in the copper (~ 70 MW from the plug).

An important know-how for the SRF cavity has been obtained by the CEA - CNRS-IN2P3 collaboration (CEA-Saclay, IPN-Orsay and LAL) and by the French industry (CERCA...) thanks to several studies and constructions done for the TESLA-TTF electron linac. This expertise is obviously very useful in the high-power proton linac field for which $\beta < 1$ SRF cavities must be developed. The first studies done in 1996 by a LANL - CEA-Saclay team demonstrated that beam losses as high as 10^{16} protons/cm^2/s do not affect the superconducting properties of niobium cavities [15-16]. In 1997, four 700 MHz single-cell cavities (β = 0.48 and 0.64) were successfully built and tested at LANL with participation of CEA-Saclay [17-18-19]. Several single cell 704 MHz β = 0.6 Nb cavities have been made by CERCA for CEA-Saclay ; low power RF tests will start very soon. Studies are also underway for the development of high-power RF couplers. "CRYHOLAB", the horizontal cryostat being built by CEA and CNRS, will be available in 1999 to test multicell cavities.

In the near future, a full study for the best choice of the RF frequency (352 vs 704 MHz) in terms of cost, beam dynamics and reliability-availability will be done. A new R&D programme called "ASH" (Accélérateur Supraconducteur pour Hybrides) [20] has also been proposed for high-power RF tests. The aim is to design a cryomodule fully equipped with high field cavities, high-power couplers and cryogenic connections, to measure the real cryogenic losses of the system. The ultimate objective of this proposal (1999-2002) is to transfer technology to the industry.

Together with the SRF cavity technology development, beam dynamics studies including errors on both beam and accelerator parameters need to be done. This would answer several basic questions such as - Are the long focusing periods due to the use of room temperature quadrupoles lead to acceptable beam losses ? - Must we limit the accelerating field to avoid emittance growth due to a strong transverse-longitudinal coupling ? - Must we use superconducting quadrupoles to shorten the focusing periods ? - What is the best choice for the beam aperture ? - Is 100 MeV the right energy to start SRF cavities ? An answer to the last question is definitely needed before starting the R&D on $\beta \sim 0.5$ SRF cavities. Analysis and improvement of the codes to achieve high precision for these beam dynamics calculations are an important part of the current effort [21-22]. For this, as well as for the development of the SRF cavity technology, a strong and productive collaboration is in place with several laboratories around the world, particularly with LANL (USA) and INFN (Italy).

REFERENCES

[1] S.O. Schriber, "Survey of proposed high intensity accelerators and their applications", EPAC94 proc. p.213

[2] M. Promé, "Major projects for the use of high power linacs", LINAC96 proc. p.9

[3] Rapport de faisabilité TRISPAL, CEA-DAM, 1998

[4] IFMIF Conceptual Design Activity final report, Edited by M. Martone, ENEA Frascati Report

[5] The European Spallation Source study, Volume III, The ESS technical study, ESS-96-53-M, November 1996

[6] See the proc. of the "Second International Conference on Accelerator-Driven Transmutation Technologies and Applications", June 1996, Kalmar, Sweden

[7] J-M. Lagniel, "A review of linac and beam transport systems for transmutation", EPAC98 proc.

[8] J-M. Lagniel, "Halos and chaos in space-charge dominated beams", EPAC96 proc. p.163

[9] L.M. Young, "Segmented resonantly coupled RFQ", PAC93 proc. p.3136

[10] D. Uriot, Internal memos, March and August 1998

[11] R. Gobin et al., "New performances of the cw high-intensity light-ion source SILHI", EPC98 proc.

[12] R. Ferdinand, "Non-interceptive emittance measurement of a high intensity beam at low energy", this conf.

[13] B. Bondarev et al., "CW RFQ designing using the LIDOS.RFQ Codes", this conference

[14] R. Duperrier et al., "Field description in an RFQ and its effect on beam dynamics', this conference

[15] B. Rusnak et al., "In-situ proton irradiation and measurement of superconducting RF cavities under cryogenic conditions", PAC97 proc.

[16] H. Safa et al., "A superconducting niobium RF cavity irradiated with a proton beam", Submitted to NIM

[17] B. Rusnak et al., "High intensity proton linac activities at Los Alamos", Proc. of the 8th workshop on RF superconductivity, Padova, Italy, October 1997

[18] H. Safa, "Optimum operating temperature of superconducting cavities", this conference

[19] H. Safa, "Multiple coupling and beam loading of an RF cavity", this conference

[20] H. Safa., "Le projet ASH", Internal memo, July 1998

[21] P. Lapostolle et al., "The SCHERM space charge routine, limitations and solutions", this conference

[22] N. Pichoff et al., "Simulation results with an alternate 3D space charge routine, PICNIC", this conf.

COMMISSIONING OF THE KEKB LINAC

Y. Ogawa, Linac Commissioning Group*
High Energy Accelerator Research Organization (KEK), Tsukuba, Ibaraki 305-0801 JAPAN

Abstract

The injector linac for the KEKB ring has been commissioned step by step since last autumn, while continuing the construction of the remaining parts as well as ordinary operation for beam injection into the Photon Factory. The commissioning has so far given quite satisfactory results: (1) A single-bunched beam with a charge of about 1.5 nC for direct injection into the ring was accelerated to the end of the linac (about 8 GeV). (2) A single-bunched beam with a charge of 6 nC for positron production was accelerated to a positron production target (3.3 GeV). Positron beams with a charge of about 0.5 nC have been successfully accelerated to the end of the linac (3.5 GeV) and transported to the beam line of the ring with a proper energy spread. (3) Various kinds of beam instrumentation have been employed and utilized for precise beam tuning and diagnosis.

1 INTRODUCTION

The construction of the KEKB linac [1] was completed on schedule at the beginning of May, 1998. The commissioning, which had been carried out step by step since October, 1997, has entered a full-commissioning phase at this moment so that two design beams for the KEKB ring could be realized: full acceleration of an electron beam (about 8.0 GeV) as well as the production of a large quantity of positrons and their acceleration (3.5 GeV).

The layout of the linac is shown in Fig. 1, comprising two parts: a newly constructed part (sectors A, B, C and J arc) and an upgraded part (sectors 1-5 and a beam switchyard). A beam starting from an electron gun passes two subharmonic bunchers (SHB1: 114.24 MHz and SHB2: 571.2 MHz) and an S-band bunching section (2856 MHz) to accomplish a single-bunched beam with a bunch width of about 10 ps (FWHM). After acceleration to the end of sector B (1.5 GeV), it enters into the J arc section, in which achromatic and isochronous conditions are fulfilled. It is then re-accelerated either to the end of the linac (8.0 GeV) or to the positron production target (3.3 GeV), depending on the operation mode. The 8-GeV electron beam is directly transported into the ring, while the produced positron beam is accelerated to the end of the linac (3.5 GeV) and passes into the ring injection line after an energy-compression system (ECS) located at the beam switchyard. In the case of positrons, the primary electrons also pass through a bunch-compression system (BCS) just before the target to decrease the bunch width so that a positron bunch-lengthening effect in the solenoids after the target can be partially compensated, realizing an appropriate bunch width for a positron energy spread.

Two operation modes (8-GeV, 1.2-nC electrons and 3.5-GeV, 0.64-nC positrons) have thus been almost established, realizing the designed beam characteristics.

For efficient commissioning, we have organized for the first time a linac-commissioning group comprising both members of the linac and the KEKB ring. We believe that it has made a great success in that linac beam parameters required for ring injection are being intensively pursued while sharing common commissioning experiences.

2 OUTLINE OF THE COMMISSIONING

Fig. 2 shows the results of commissioning concerning the beam positions and intensity in two operation modes of the KEKB linac: an 8-GeV electron beam and a 3.5-GeV positron beam. In the following sections, the beam-tuning process is discussed along with the beam flow of the linac.

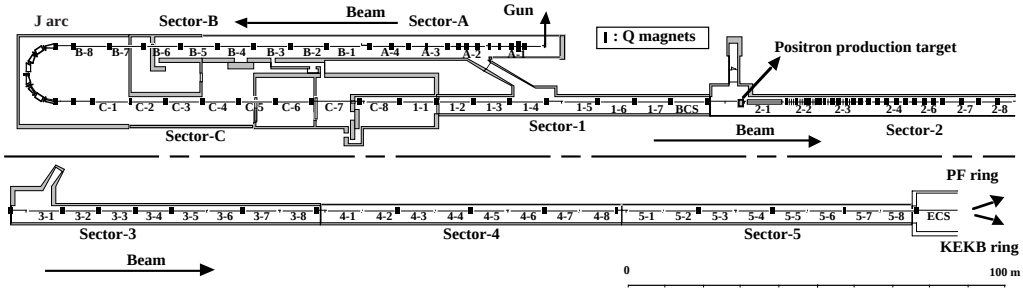

Figure 1: Layout of the KEKB linac. Sectors A, B, C and J-arc are newly constructed.

* N. Akasaka, A. Enomoto, J. Flanagan, H. Fukuma, Y. Funakoshi, K. Furukawa, T. Ieiri, N. Iida, T. Kamitani, T. Kawamoto, M. Kikuchi, H. Koiso, T. T. Nakamura, Y. Ogawa, S. Ohsawa, K. Oide, K. Satoh, M. Suetake, T. Suwada

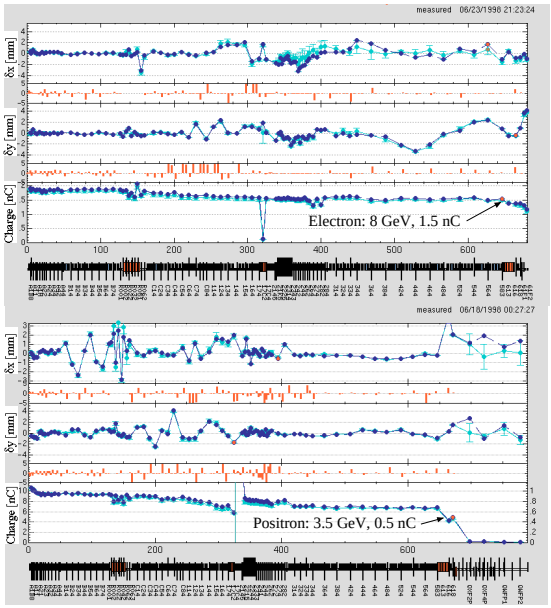

Figure 2: Two design beams have been achieved at the end of the linac: 8-GeV, 1.5-nC electron and 3.5 GeV, 0.5-nC positron beams.

2.1 Electron Gun and Its Orbit Measurement

The electron gun emits a beam with an energy of 200 keV and a pulse width of 2-3 ns (FW). The beam is immediately injected into the bunching section to form a single bunch in the S-band structure. Since the beam is still non-relativistic in this region, a solenoid-type focusing system is employed against strong space-charge forces among particles. It sometimes happens, however, that if a beam having even a slight inclination to the solenoid field axis is injected into this region, the central orbit may rotate in the magnetic field, causing an emittance growth. In order to prevent this kind of beam degradation, we not only checked the transverse components of the magnetic field, but also improved the alignment of the electron gun. As a result, the beam-orbit rotation is considerably minimized and the beam profile along the region becomes quite improved.

2.2 Tuning of Bunching Section

Tuning of the bunching section [2] has been carried out mainly by observing a bunch monitor with a streak camera (see Section 3.2) located at the end of the section. With proper powers fed into two SHB cavities, an S-band prebuncher and a buncher, as well as by precise tuning of the corresponding rf-phases, we succeeded to establish a single-bunched beam without any satellites. The bunch widths obtained in the 1.5-nC beam and the 10-nC primary beam for positron production are about 10 ps.

The energy spectrum is also measured at an energy-analyzing station at an energy of about 70 MeV, giving an energy spread of about 9% (FW).

2.3 Acceleration in Sectors A and B

In sectors A and B, the energy must reach the J-arc design energy of 1.5 GeV, which is realized by using 10 accelerator units with a margin of one unit. The last two units are used as a knob for adjusting the energy in a cross-phase configuration so as to compensate for any energy spread due to the slope of the sine function. In a high-current acceleration mode, the acceleration phase for the rest of units is set at an off-crest angle of about 15 degrees in order to minimize the energy spread, satisfying the J-arc energy acceptance of 2.8% (FW=4σ).

Beam transmission from the end of the bunching section to that of sector B is quite good, accomplishing almost 100% without any significant loss. It has been anticipated, however, that some problems related to wake-field effects might emerge for an intense primary electron beam with a charge of 10 nC. In fact, we sometimes observed some peculiar phenomena concerning beam profiles in high-current beam acceleration, while in beam acceleration with a small charge of 1.5 nC we found no such problems. Details concerning these items are discussed in Section 4.

2.4 Tuning of the J-arc Section

The J-arc section is designed to be achromatic and isochronous [3]. The achromaticity condition is fulfilled in the following manner:

- Measure the dispersion at all beam-position monitors (BPM: see Section 3.1) along the J-arc by changing the energy using the energy knob.
- Calculate the strengths of the quadrupole magnets so as to simulate the observed dispersion and obtain ratios to the set values.
- Set the strengths of the quadrupole magnets at the values calculated from the inverse ratios to the set values.
- Measure again the dispersion and iterate the process.

For the isochronicity condition, the same procedure is taken, except for the first step, which is replaced by:

- Measure the time delay with a streak camera system (see Section 3.2) at the end of the J-arc by changing the energy using the energy knob.

In achromaticity corrections, second-order effects are also cured by adjusting the strengths of the sextupole magnets.

The central energy in the J-arc is maintained at 1.5 GeV by introducing an energy feedback loop utilizing the energy knob. As mentioned in the previous section, we sometimes observed interesting phenomena related to a degradation of the beam quality, which made the beam transmission in the J-arc quite low. The cures obtained by using local bumps and adjusting the acceleration phases at sectors A and B were successfully tried, and are described in Section 4.

2.5 Acceleration in Sectors C and 1

In the midst of sectors C and 1, the newly constructed part and the upgraded part were joined together during the last week of March, 1998. In order to successfully make the prompt connection without causing any disturbances to the ordinary operation for the Photon Factory, we had prepared a temporary pre-injector comprising an electron gun and a bunching section at the first section of sector 1. Although two independent accelerators have been successfully connected without any obstacles, the short period for a connection has not allowed a satisfying alignment of the accelerator components. In fact, the beam losses in this region, which are suspected to be due to a misalignment, have so far not been avoided. A re-alignment of the linac is planned for this summer.

The largest amount of charge obtained for positron production was about 6 nC at the target, not reaching the design value of 10 nC. We expect a considerable improvement after a re-alignment.

2.6 Tuning of Primary Electrons at a e^+ Target

Primary electrons for positron production pass through BCS just before the target so as to partially compensate the bunch lengthening of positrons occurring in the following solenoids. The acceleration phases at sectors C and 1 are set at an off-crest angle of about 30 degrees, making the phase-space orientation for BCS. Although BCS worked quite well, fine-tuning will be carried out in the autumn.

Since the positron yield strongly depends upon the beam profile at the target, the beam waist was surveyed by changing the optics before the target. The minimum radius of the beam size was estimated to be around 1 mm, obtaining a maximum positron production.

2.7 Acceleration in Sectors 1-5

Acceleration in this region has proceeded without any problems for electron and positron beams. The beam characteristics have been measured for both beams at the end of sector 5, giving the quite satisfying results reported in Section 5.

2.8 ECS for e^+ beam

The energy acceptance required for the positron injection line to the KEKB ring is 0.5% (FW). In order to achieve this value, the positron beam is passed through ECS at the end of linac. An energy-compression ratio of about 0.5 was obtained: an energy spread of 1.7% (FW) became 0.8% (FW) after ECS. According to an analysis of the data (Fig. 3), it turns out that almost 90% of the positrons fall in the energy acceptance of the injection line. The remaining slight difference relative to the design value will be expected to be eliminated by fine tuning of the acceleration phases as well as that of BCS.

After passing through ECS, a positron beam with a charge of about 0.4 nC was successfully transported to the temporary beam dump in the midst of the injection line. Although the beam-loss monitors installed along the injection line showed an allowed level of radiation in this time of operation (5 pps), it turns out that for the full-injection mode (50 pps), the radiation level must be reduced by almost one half. This reduction will also be expected to be achieved with a proper tuning of the linac and the beam-transport line.

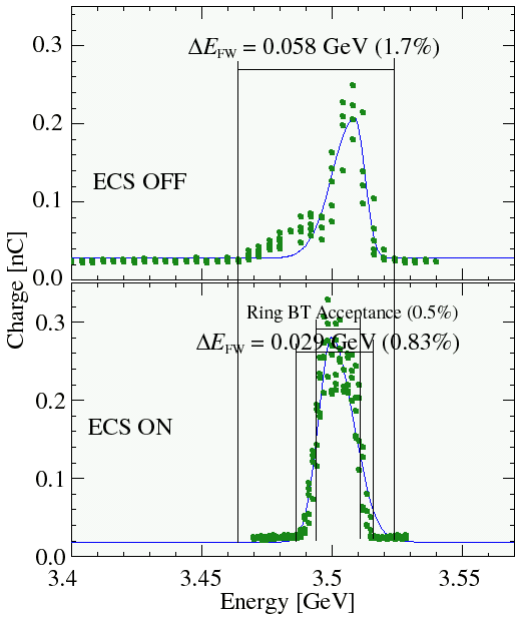

Figure 3: Energy spread of positron beams compressed into a half width by the ECS located at the end of linac, reaching almost the energy acceptance of the ring injection line.

3 BEAM INSTRUMENTATION

3.1 BPM Calibration

BPMs [4] installed in all quadrupole magnets have been quite efficient tools for beam diagnosis in the commissioning. We have performed several kinds of BPM calibrations using a beam: measurements of the position resolutions and offsets as well as estimations of the calibration factors by employing a recalibration method [5]. The obtained results are summarized in Table 1.

3.2 Bunch Monitor with a Streak-Camera System

Another important progress in beam diagnosis was the introduction of new streak-camera systems [6] for observing a bunch structure. Three systems (at the end of sector A and the J-arc, and just after the positron target) have been installed, while another one is being prepared at the end of the linac. One of the main features in the new

system is an integration of hardware and software; all of the necessary steps to observe streak-signals are integrated, and the handling becomes quite simplified. Detailed descriptions can be found in the reference.

3.3 Test of Wire Scanner

As non-destructive beam-profile monitors, wire scanners have been tested concerning several aspects: a detection scheme and its configuration as well as a radiation-shield method. The results indicate that with a suitable configuration of the detector, wire scanners give a sufficient signal-to-noise ratio against a strong radiation environment. We are planning to install three sets (each comprising three or four wire scanners positioned at proper distances) at the end of sector B, J-arc and the linac, respectively, so that the twiss parameters can be calculated in nearly real-time using signals from three or four wire scanners at the same time. Details are to be presented elsewhere [7].

3.4 Wall Current Monitor: Charge Calibration

Although the quantity of charge is one of the key parameters, the calibration is not a simple task, especially in the case of a very short pulse, like a single-bunch beam (10 ps) in the S-band linac. We employed two methods: a relative calibration utilizing a signal from the beam-induced field observed at the end of accelerator section as well as an absolute one using a Faraday cup installed in the straight branch line at the entrance of the J-arc. Details will be presented elsewhere.

4 FINE TUNING OF INTENSE BEAM

4.1 Acceleration-Phase Tuning

The acceleration phase for an intense beam has been set at an off-crest angle of about 15 degrees in sectors A and B for achieving an energy acceptance of the J-arc (Section 2.3). On the other hand, it has been about 30 degrees off-crest in sectors C and 1 for BCS (Section 2.6). The maximum beam transmission in these regions, however, was obtained by even a finer adjustment of the acceleration phases in sectors A and B, so that they were slightly shifted in the inverse direction relative to each other. In this way, the beam profiles in the J-arc were greatly improved, suggesting the existence of transverse wake-field effects, which are clearly shown in the next section. A detailed analysis will be carried out during the next commissioning period.

4.2 Orbit Tuning

Local bumps have been introduced somewhere in sectors A and B, depending upon the beam state to improve the beam transmission in the J-arc and sector C. In calculations of a bump, dipole transverse wake-field effects are taken into account so that the bump can be closed. The bump, however, sometimes failed to close the orbit, possibly because quadrupole wake-field effects emerged when the beam profile-deformation was large. Incorporating quadrupole wake-field effects in bump calculations might be necessary during the next opportunity.

4.3 Method of Downhill Simplex

Since the beam intensity at a certain point of the linac depends upon many parameters upstream, it may happen that searching the optimum combination of parameters would be practically difficult. We tried the method of downhill simplex [8] for obtaining the maximum positron yield by changing the strength of a few upstream steering coils together with some acceleration phases. The results suggest that this kind of method could be useful in some cases. A more elaborate application of the method will be introduced in the future.

5 BEAM CHARACTERISTICS

The beam characteristics obtained during the commissioning are listed in Table I, compared with the designed target values. As far as the beam intensity at the end of linac is concerned, the target values have been nearly realized for electron and positron beams, though a slight increase of positrons may be required. The single-bunch purity is practically 100%, while the bunch length is not in agreement with the design value, which does not seem to be a serious problem. The emittance growth observed in sectors A and B for an intense beam might be reduced by the effective use of local bumps or the method of downhill simplex. The energy margin for ring injection is rather poor at this time of commissioning, but can be considerably improved during the next commissioning period. The energy spread of both beams falls at almost the energy acceptance of the injection line.

6 CONCLUSIONS

The first commissioning of the KEKB linac was successfully completed, reaching two major goals: 8-GeV acceleration of electron beams and 3.5-GeV acceleration of positron beams with sufficient quantity and quality. High-quality hardware completion of the machine was also verified and confirmed through commissioning, satisfying the beam characteristics required for the KEKB ring.

7 ACKNOWLEDGEMENTS

The authors would like to thank to all of the staff members of linac for the high-quality completion of the construction. They also greatly appreciate various forms of support by the project leaders, Profs. K. Nakahara and S. Kurokawa.

Table I: Evaluation/Score of the KEKB Linac Commissioning

Beam Type	Electron Beam : 1.2 nC					Primary Electron Beam : 10 nC @ Target Positron Beam : 0.64 nC				
	Target Value		Achieved Value		Score	Target Value		Achieved Value		Score
Beam @ Gun										
Charge[*1]	1.5	nC	2	nC	A	13	nC	~ 14	nC	A
Pulse Width (FW)	2.0	ns	1.8	ns	A	2.0	ns	2.8	ns	B
Beam @ A1										
Charge[*1]	1.4	nC	1.9	nC	A	> 10	nC	11	nC	A
Satellite Bunch	< 2	%	0	%	A	< 2	%	~ 0	%	A
Bunch Width (FWHM)	5	ps	10	ps	B	16	ps	11	ps	A
Beam @ B8										
Charge[*1]	1.2	nC	~ 1.8	nC	A	> 10	nC	~ 9.5	nC	A
Transmission (A1-B8)	100	%	~ 95	%	A	100	%	~ 86	%	A
Energy	1.5	GeV	1.5 (Max 1.8)	GeV	A	1.5	GeV	1.5 (Max 1.8)	GeV	A
Energy Spread (±2σ)	±1.4	%	±0.58	%	A	±1.4	%	±0.75	%	A
Energy Stability (p-p)	< 0.2	%				< 0.2	%	fast 0.1	%	A
After Feedback								drift< 0.2	%/h	A
Beam @ C1										
Charge[*1]	1.2	nC	~ 1.8	nC	A	> 10	nC	~ 9.0	nC	A
Transmission (J-Arc)	100	%	~ 100	%	A	100	%	~ 95	%	A
Bunch Width (FWHM)						16	ps	18	ps	C
Beam @ e^+ Target										
Charge[*1]						> 10	nC	~ 6.0	nC	C
Transmission (C1-17)						100	%	~ 67	%	C
Transmission (A1-17)						100	%	~ 57	%	C
Energy						3.5	GeV	3.3	GeV	B
Beam @ 21_45										
Charge[*1]						(e^+) >2	nC	~ 1.5	nC	A
e+ Conversion (/GeV)								~ 7.6	%/GeV	
Beam @ 23_43										
Charge[*1]	(e^-)		1.6	nC		(e^+) > 0.6	nC	~ 0.8	nC	A
Transmission (21-23)						30	%	~ 53	%	A
Beam @ 58										
Charge[*1]	1.2	nC	1.5	nC	A	(e^+) > 0.6	nC	~ 0.7	nC	A
Transmission (23-58)	(e^-) 100	%	94	%	A	100	%	~ 88	%	A
Transmission (A1-58)	(e^-) 100	%	79	%	B					
Transmission (21-58)								~ 47	%	A
e+ Conversion (/GeV)						~ 1.8	%/GeV	~ 3.5	%/GeV	A
Energy	(e^-) 8.0+0.8	GeV	8.0+0GeV		A	3.5	GeV	3.5	GeV	A
Energy Spread (FW)								±0.8	%	
Beam @ ECS										
Charge[*1]						(e^+) > 0.6	nC	~ 0.5	nC	B
Transmission (ECS)						80	%	~ 70	%	A
Energy						3.5	GeV	3.5	GeV	A
Energy Spread (FW)						±0.25	%	±0.4	%	B
Norm. Emittance (B_{mag})										
Injector x(×10^{-6})	60	m	71 (1.2)	m	A	60	m	89 (1.0)	m	A
y(×10^{-6})	60	m	66 (1.2)	m	A	60	m	120 (1.1)	m	B
B8 x(×10^{-6})	< 1600	m	230 (1.6)	m	A	< 1600	m	770 (1.3)	m	A
y(×10^{-6})	< 750	m	500 (1.8)	m	A	< 750	m	760 (1.5)	m	B
C1 x(×10^{-6})								800 (1.6)	m	
y(×10^{-6})								820 (1.2)	m	
23 x(×10^{-6})						(e^+)		5600 (6.5)	m	
y(×10^{-6})						(e^+)		6600 (16)	m	
57 x(×10^{-6})	1100	m				(e^+) 1600	m	2000 (1.3)	m	B
y(×10^{-6})	1100	m				(e^+) 1600	m	2300 (1.6)	m	B
Orbit										
Deviation(rms) Δx	< 0.1	mm	< 0.1	mm	A	< 0.1	mm	0.3	mm	B
Δy	< 0.1	mm	< 0.1	mm		< 0.1	mm	0.3	mm	B
Variation Δx	< 0.1	mm	< 0.1	mm	A	< 0.1	mm	±0.2	mm	B
Δy	< 0.1	mm	< 0.1	mm		< 0.1	mm	±0.2	mm	B
BPM										
Resolution	< 0.1	mm				< 0.1	mm	~ 0.1	mm	A
Offset[*2]	< 0.1	mm				< 0.1	mm	0.1~0.2	mm	A
Repetition Rate	50	pps	5	pps		50	pps	5	pps	

[*1]Under calibration, [*2]Calibrated

8 REFERENCES

[1] A. Enomoto et al., "Commissioning of the KEKB 8-GeV e^- / 3.5-GeV e^+ Injector Linac", Proceedings of EPAC98, Stockholm, June 22-26, 1998.

[2] S. Ohsawa et al., "", Proceedings of APAC98, KEK, March 23-27, 1998, in press.

[3] T. Kamitani et al., "Optics", Proceedings of APAC98, KEK, March 23-27, 1998, in press.

[4] T. Suwada et al., "BPM", Proceedings of APAC98, KEK, March 23-27, 1998, in press.

[5] K. Sato et al., "Recalibration of Position Monitors with Beams", Proceedings of PAC95, Dallas, USA, May 1-5, 1995.

[6] Y. Ogawa et al., "New Streak-Camera System for the KEKB Linac", Proceedings of APAC98, KEK, March 23-27, 1998, in press.

[7] Y. Funakoshi et al., in preparation.

[8] J. Flanagan et al., "Downhill Simplex Method", presented in KEKB mini-workshop, KEK, July 21-23, 1998.

A REVIEW OF ACCELERATOR CONCEPTS FOR THE ADVANCED HYDROTEST FACILITY

Alan J. Toepfer
Science Applications International Corporation, Albuquerque, NM, USA

Abstract

The Advanced Hydrotest Facility (AHF) is a facility under consideration by the Department of Energy (DOE) for conducting explosively-driven hydrodynamic experiments. The major diagnostic tool at AHF will be a radiography accelerator having radiation output capable of penetrating very dense dynamic objects on multiple viewing axes with multiple pulses on each axis, each pulse having a time resolution capable of freezing object motion (≈ 50-ns) and achieving a spatial resolution ≈ 1 mm at the object. Three accelerator technologies are being considered for AHF by the DOE national laboratories at Los Alamos (LANL), Livermore (LLNL), and Sandia (SNL). Two of these are electron accelerators that will produce intense x-ray pulses from a converter target yielding a dose ≈ 1,000 - 2,000 Rads @ 1 meter. LLNL has proposed a 20 - 40 MeV, 3 - 6 kA linear induction accelerator (LIA) driven by FET-switched modulators driving metglas loaded cavities. SNL has proposed a 12-MeV, 40-kA Inductive Voltage Adder (IVA) accelerator based on HERMES III pulsed power technology. The third option is a 25 - 50-GeV proton accelerator capable of ≈ 10^{13} protons/pulse proposed by LANL. This paper will review the current status of the three accelerator concepts for AHF.

1. INTRODUCTION

X-radiography is a well-known diagnostic for nondestructive test measurements, both of static and dynamic systems. Pulsed x-radiography is commonly used for the study of a number of physical problems involving the hydrodynamics of materials, for example, the stability of accelerated material interfaces and the response of targets to ballistic penetration. Intense, single-pulse x-ray sources have been used for the past 30 years to study hydrodynamic phenomena at the extreme energy densities produced in the hydrodynamic stage of a nuclear detonation (before criticality). Traditionally this data, obtained in non-nuclear tests, has supplemented that available from underground nuclear tests.

With the advent of the Comprehensive Test Ban Treaty (CTBT), assurance of the safety and reliability of the U.S. nuclear stockpile in the absence of underground testing requires the development of high resolution pulsed radiography systems capable of obtaining multi-axis, multi-pulse data in a single dynamic test. The ultimate goal of this Advanced Hydrotest Facility (AHF) is to produce a high-resolution radiographic movie of a dynamic test object. Achievement of this goal requires the development of a number of new technologies including accelerators, converters, beam steering/optics, and detectors which make up the AHF system, as well as the computational tools needed to interpret and visualize the data. This paper reviews accelerator technologies proposed for AHF which are currently under development by the DOE laboratories at LLNL, LANL, and SNL.

2. TECHNOLOGY APPROACHES

There are presently two conceptual approaches to AHF radiography, the traditional x-ray source produced by the interaction of a beam of (12 - 40 MeV) electrons with a high Z "converter" target, and a newer approach using a pulsed beam of (25 - 50-GeV) protons to directly irradiate the test object, which are then imaged by an innovative magnetic lens system. Both approaches must be capable of penetrating the high density test object and achieving the required spatial and temporal resolutions to resolve phenomena of interest. The resulting radiographic source requirements for each approach are given in Table 1.

Table 1: AHF Radiographic Source Requirements

Parameter	X-ray	Proton
Pulse length (ns)	≤ 50	≤ 50
Resolution at object (mm)	0.5 - 1.0	0.5 - 1.0
Equivalent flux - kRads @ 1m - protons/sec	 1 - 2 -	 - 10^{17}
Number of pulses	5 - 10	5 - 10
Number of views (axes)	4 - 12	4 - 12
Pulse separation (μs)	0.2 -15	0.2 - 15
Temporal coverage (μs)	1.5 - 75	1.5 - 75

2.1 X-Radiography Approaches

The U.S. hydrodynamic x-radiography program has traditionally used electron linacs such as the 20-MeV Phermex rf-linac at LANL, and the 18-MeV FXR single-pulse, linear induction accelerator (LIA) at LLNL. For AHF, LLNL has proposed a 20 - 40 MeV, 3 - 6 kA, high repetition rate, solid-state modulator driven LIA, with injector and cavity designs closely related to an advanced LIA being developed for the Dual Axis Radiography Hydrotest Facility (DARHT) now being built at LANL. [1]

* Work supported by Sandia National Laboratories under Subcontract No. AV-0973

An alternate x-ray source based on high current, inductive voltage adder (IVA) technology developed for weapon effects simulation has been proposed by SNL. Pulsed power-based x-ray sources were first developed and have been used extensively by the British Atomic Weapons Establishment (AWE) for hydrotest radiography. These machines have typically been < 10-MeV in energy, but the Sandia-developed IVA technology has extended the capabilities of these accelerators to 20 MeV in the HERMES III accelerator. The IVA AHF proposal is an extension of a pulsed power radiography concept developed as one of the options for DARHT. [2]. For AHF, SNL has proposed a 12-MeV, 60-kA, 50-ns pulse length IVA.

2.2 Proton Radiography

Proton radiography may be capable of measuring both mass density and the atomic number of materials in the radiographed object. For AHF, LANL has proposed a 25 - 50 GeV proton synchrotron fed by an 800-MeV linac injector similar to LANSCE. The required beam flux is 5 x 10^{12} protons/pulse. A unique magnetic lens system is used to discriminate between Coulomb multiple scattering and nuclear (strong interaction) scattering effects to extract target information.

3. ACCELERATOR TECHNOLOGIES

In the following paragraphs we discuss the LLNL, SNL, and LANL - proposed accelerators for AHF in more detail, covering the unique features of each, the technology status, and the issues to be resolved.

3.1 Linear Induction Accelerator (LIA)

The demonstrated utility of LIAs for pulsed radiography accompanied by advances in solid-state modulator technology have led LLNL to develop the AHF system concept shown in Fig. 1. A 20 - 40 MeV, 3 - 6 kA accelerator produces a MHz train of pulses ranging from 200 ns to 2 μs in length. Fast kickers are used to direct the individual pulses to various beam lines and converters arranged about the object to be radiographed.

The Advanced Radiography Machine (ARM) induction accelerator cells are driven by FET-switched modulators. Prototype ARM modulators have been built and tested at LLNL. The 2-MHz, three-stage ARM-II modulator has 4,032 FETs in a series-parallel array and produces a flat-topped 45-kV open circuit voltage pulse with a maximum source current of 4.8 kA. The 10-MHz ARM III modulator, currently under development, will take advantage of the FET's active amplification region to produce arbitrary waveform shapes with a 20-kV open circuit voltage and 7.2-kA output. In both ARM II and III, a separate reset circuit is connected in parallel with the induction cell load.

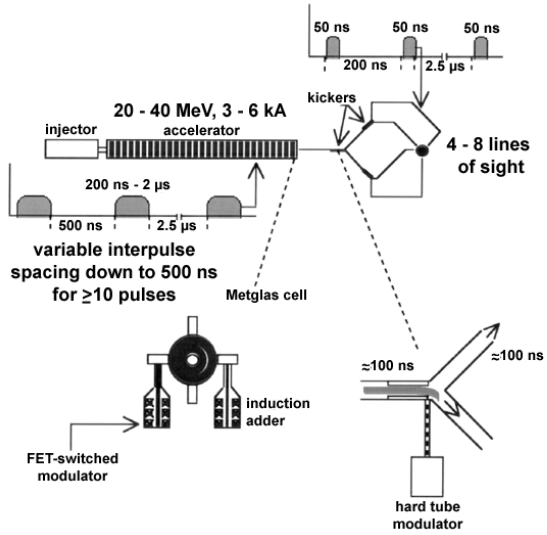

Fig. 1. Schematic of LIA AHF concept.

The LIA fast kicker system concept is shown in Fig. 2. It consists of four stripline electrodes and a fast pulser for driving the electrodes and deflecting the beam. A dc bias dipole wound over the kicker is used to steer the beam in the absence of a pulse to one of two or four desired output positions which are separated by several cm. The pulser drives the stripline electrodes to overcome the bias field and switch the beam to an output position. A drift space following the kicker amplifies the spatial separation, but not the angular separation. A DC septum magnet is used two steer the output beams apart and provide room for additional focusing magnets if necessary. A prototype kicker with two outputs has been installed on the ETA-II beamline at LLNL and preliminary tests give measured deflections consistent with theory.

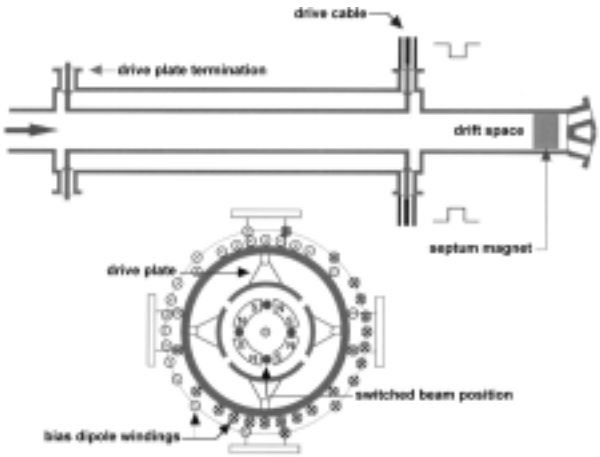

Fig. 2. LIA fast kicker system schematic.

Heating of the x-ray converter target by the incident electron beam will cause desorbtion of gas from the target, resulting in plasma formation and ion production which can defocus the incident beam and adversely impact the spot size. In addition shock waves induced in the target by the beam loading can alter the target for

succeeding pulses. LLNL is currently investigating several approaches towards alleviating these effects. In one, a retarding potential will be introduced at the target to reduce the accelerating fields produced by the beam and inhibit ion acceleration. An experiment using a modified ATA induction cell will test this concept. For multi-pulse systems, dynamic target concepts have been proposed, both linear (hypervelocity projectile or shaped charge jet) and rotating (flywheel). None of these concepts have been tested to date.

Two of the major technology issues raised regarding the LIA approach to AHF, namely the reliability of the solid-state electronics in the high voltage environment, and the feasibility of the kicker to maintain beam quality for suitable spot size have been addressed by LLNL in experiments and testing. Proof-of-principle tests have been encouraging. The remaining major issue to be addressed for the LIA accelerator concept is that of maintaining beam spot size at the target and developing a multi-pulse converter concept. The first of these will be addressed on DARHT. The second is the subject of ongoing research at LLNL, LANL, and SNL as part of the overall AHF program.

3. 2 Inductive Voltage Adder (IVA)

The SNL AHF concept is based on multiple modules incorporating the IVA pulse forming network shown in Fig. 3. The ≈ 1-μs, 3-MV output from a Marx generator is transformed through three successive pulse sharpening stages to a 1.5-MV, 60-ns pulse driving the cavities. Charging of eight metglas loaded cavities connected in series is synchronized with laser triggered gas switches to give a 12-MV voltage on the coaxial magnetically insulated transmission line (MITL). Electrons which are field emitted from the surface of the center charged conductor are trapped by the self-magnetic field of the current in the line. An ≈ 50-ns FWHM, 60-kA electron beam is produced at the cathode.

The engineering of IVA accelerators is well in hand, however the physics of the high current x-ray converter diode is complex. Electrons incident on the target are born at the cathode tip. Ions produced by beam interaction with the anode and ionization of neutral gas in the A-K gap stream counter to the electron flow. The diode geometry is designed to inhibit the flow of electrons born with large canonical angular momentum to the anode, and a 60-tesla, axial magnetic field is imposed on the cathode to inhibit the growth of ion hose instabilities in A-K region.

SNL has carried out proof-of-principle experiments at 9.2-MeV, 30-kA on the SABRE accelerator [3], achieving the anticipated 1.5-mm, FWHM x-ray spot. More recently, they have begun scaling experiments on HERMES III at 12 MeV, 150 kA; however, diode contamination on HERMES III caused premature shorting of the A-K gap. From this data summarized in Fig. 4, they have made substantial advances in understanding and modeling the physics of high current "immersed" diodes.

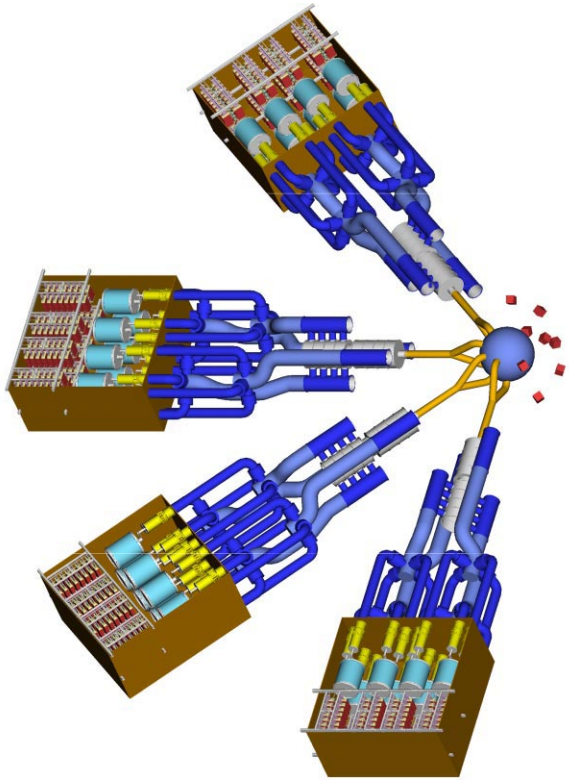

Fig. 3. IVA AHF concept.

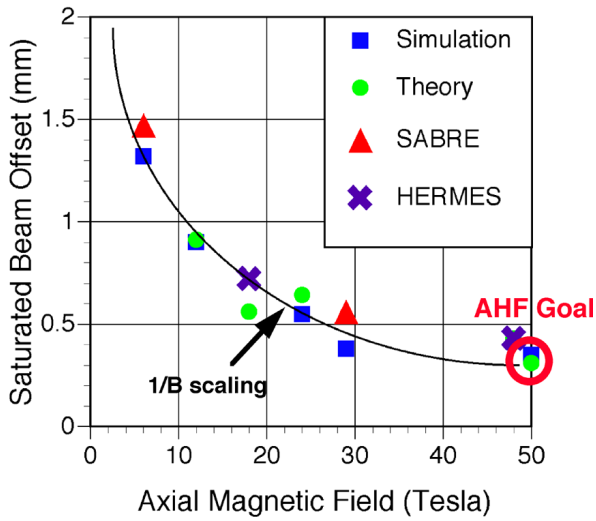

Fig. 4. IVA X-ray spot measurements and calculations.

The major issues confronting the IVA concept are the achievement of AHF parameters in the diode, the feasibility of multi-pulsing a single diode, and the feasibility of charging multiple transmission lines for a multi-axis system. To address the first issue, further experiments are planned on HERMES III. The second issue will be addressed by the construction of a Radiographic Integrated Test Stand (RITS). RITS can be configured to produce either a single 12-MeV pulse or two

6-MeV pulses along the same MITL with complete timing flexibility. The feasibility of splitting and combining pulses in multiple MITLs has been demonstrated in a number of pulsed power machines. Extension of this capability to an AHF accelerator should be straightforward, but is yet to be demonstrated.

3.3 Proton Radiography (PRAD)

The LANL concept for PRAD (Fig. 5) includes an 800-MeV H^- linac injector, a 20-GeV proton synchrotron low energy booster (LEB), and a 50-GeV high energy booster/ accumulator (main ring), and is based both on LAMPF technology and designs developed for the superconducting super collider (SSC). A fast kicker modulator extracts the beam from the LEB into the main ring, and a combination of ferrite kickers and electrostatic septum beam splitters transfers the beam bunches from the main ring into ultimately twelve separate beam lines at the test facility. The total number of 50-GeV protons stored in the main ring is $\approx 3 \times 10^{12}$. An earlier embodiment of this concept which assumed injection directly from the 800-MeV linac into a 50-GeV synchrotron was published in Ref. [4].

The rf technology assumed in the LANL PRAD concept is 45 MHz at injection (800 MeV), and is raised to 53.3 MHz at the entrance to the delivery system. Based on experience at Fermilab, the proton bunches should be less than 5 ns wide at extraction time, and if properly synchronized, the bunch pattern will be repeated once each 150 ns for as long as beam is delivered to the delivery system. At 800 MeV, a minimum 95% emittance of 4.7 π-mm-mrad is required.

From the requirements in Table I, he kicker modulator must be capable of pulsing up to 120 times on demand over a 1.5 - 75-μs interval. The ferrite kickers would be triode driven and operated with capacitors to make them resonant. Electrostatic septum splitters would be used to divide the beam transversely among two beam lines per stage.

The number of beam lines at the target is currently envisioned to be 8 - 12. Each beamline would transport up to 10 pulses to the target. In order to arrange that the beams all arrive at the target simultaneously, the lines must be equal in length. These long beam lines appear to be the dominant cost driver for the PRAD.

Interaction of the protons with the target occurs via three dominant processes:

- Multiple coulomb (elastic) scattering (MCS) from protons in the target nuclei. The MCS cross section increases with atomic number (A).
- Beam attenuation due to (inelastic) nuclear interactions with protons and neutrons in the target nuclei. The nuclear cross section decreases with increasing A.
- Energy loss due to collisions with target electrons. The cross section for this interaction increases very slowly with increasing A.

PRAD proposes to take advantage of the differing dependence of the elastic and inelastic cross sections on A to measure spatial and time resolved mass density and material composition of the target. To accomplish this, LANL has developed a two stage magnetic lens geometry (inset, Fig. 5) which differentiates between coulomb and nuclear scattered beam particles. [5] Since MCS scattered particles are deflected in the process, it is necessary to refocus them at the image plane following aperture 1. These particles are measured with the inelastic flux at the first detector. The MCS scattered protons are then stripped from the transmitted beam by aperture 2, so that the second detector measures only the beam component attenuated by nuclear scattering. Analysis of these two transmitted beam components should provide data on target mass distribution and A.

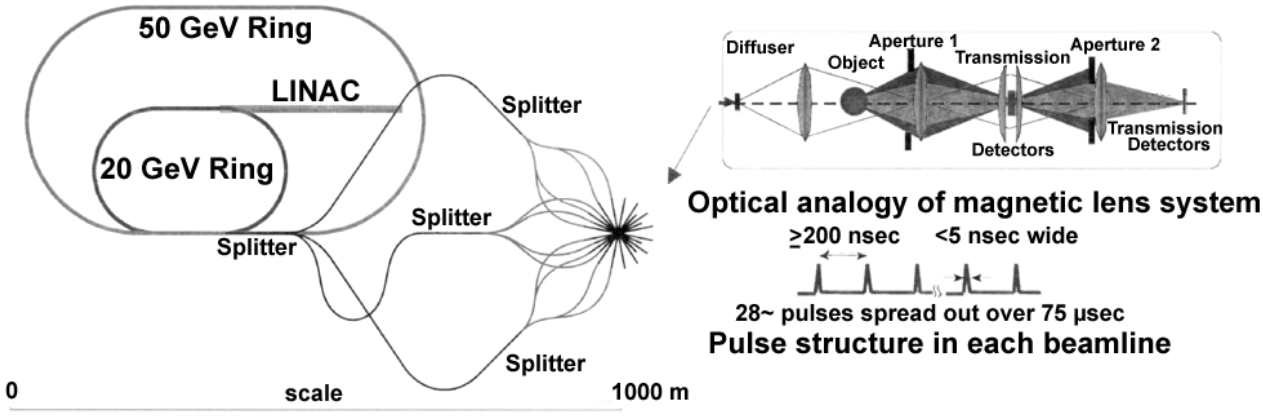

Fig. 5 Proton Radiography Concept

PRAD proof-of-concept experiments have been successfully carried out by LANL at 800-MeV on LANSCE and at 7 - 10 GeV on AGS at Brookhaven National Laboratory (BNL). Experiments at LANSCE (Fig. 6) have probed both static and dynamic targets, whereas only static target experiments have been carried out at AGS. A new beam line is currently under construction at AGS for 25-GeV, high intensity tests.

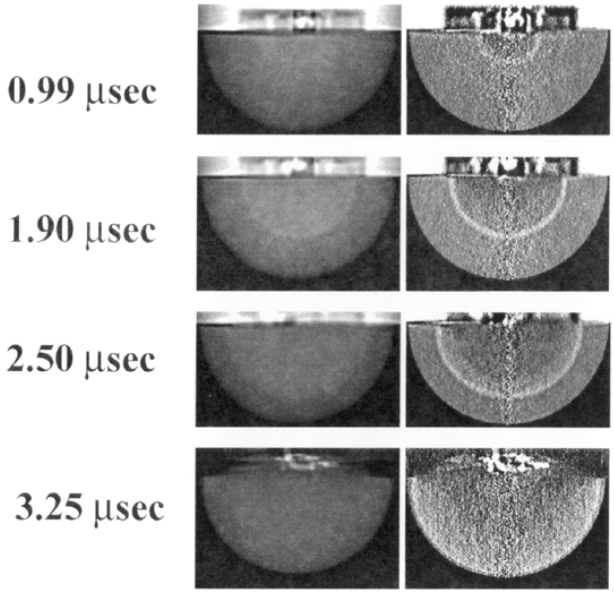

Fig. 6 Dynamic proton radiographs from LANSCE.

PRAD has the potential to significantly improve the utility of hydrodynamic radiography. The main technical issues associated with the accelerator and beam lines are the demonstration of the kicker modulator, resonant ferrite kicker, and electrostatic beam splitters required to extract and transport the beam bunches to the target. Proof-of-concept experiments must also be carried out at 30 - 50 GeV to demonstrate there are no "unknown unknowns" in the beam-target interaction that could give rise to inadequate resolution, loss of material discrimination capability, or unacceptable background.

The capability to discern material identity needs to be demonstrated. Experiments to date have shown excellent mass density resolution, but do not differentiate materials in the radiographed objects. This capability is a key feature of PRAD.

4. OUTLOOK

Achieving the AHF objective of a high-resolution radiographic movie of a dynamic test object extends the state of pulsed radiographic art well beyond present capabilities. The three approaches to developing a multi-pulse, multi-axis source each have their pluses and minuses. The LIA concept is an extension of existing systems to incorporate modern power electronics, and the IVA technology is an unproven, but potentially lower cost alternative. The major challenge facing these x-ray approaches is the development of multi-pulse converters having the radiation output and spot size necessary to do the job. PRAD is a potentially revolutionary approach which holds great promise for the long term, assuming no "unknown unknowns" are discovered, but may be too costly a system.

The DOE National Laboratories at Los Alamos, Livermore, and Sandia have embarked on a multi-year research and development effort to establish the capability of each approach and are making significant progress. The rate of progress is limited primarily by the availability of funds and facilities. DARHT, when it comes fully on line at the end of 2002, will help to address some of the multi-pulse issues in a real test environment that can only be approximated today.

5. ACKNOWLEDGMENTS

The author would like to thank George Caporaso of Lawrence Livermore National Laboratory, John McClelland of Los Alamos National Laboratory, and John Maenchen of Sandia National Laboratories for their cooperation in preparing this review paper.

6. REFERENCES

[1] G. J. Caporaso, "Linear Induction Accelerator Approach for Advanced Radiography," Proceedings of 1997 Particle Accelerator Conference, Vancouver. B.C., Canada, May 12-16, 1997, 3C005 (1997).

[2] D. L. Smith, *et. al.*, "Proposed Inductive Voltage Adder Based Accelerator Concepts for the Second Axis of DARHT," Proceedings of 11th IEEE International Pulsed Power Conference, Baltimore, MD, Vol. II, 1647 (1997).

[3] J. Maenchen, "Inductive Voltage Adder Driven Flash Radiography," Bull. Am. Phys. Soc. **43** (2), 1198 (April 1998).

[4] F. Neri, H.A. Theissen, and P.L. Walstrom, "Synchrotrons and Beamlines for Proton Radiography," Proceedings of 1997 Particle Accelerator Conference, Vancouver. B.C., Canada, May 12-16, 1997, 9B005 (1997).

[5] C.T. Mottershead and J.D. Zumbro, "Magnetic Optics for Proton Radiography," Proceedings of 1997 Particle Accelerator Conference, Vancouver. B.C., Canada, May 12-16, 1997, 4V006 (1997).

REVIEW OF BEAM DIAGNOSTICS IN ION LINACS

P.N. Ostroumov
Institute for Nuclear Research of Russian Academy of Sciences, Moscow 117312, Russia

Abstract

High quality beam diagnostics have been found to be useful for rapid commissioning and good operation of ion linacs, especially for linacs containing many separate rf cavities. Our group, at the INR, has been working on the development and practical use of several beam diagnostic tools. As such, we have been engaged in beam measurements on operating ion linacs in close collaborations with several laboratories: CERN, DESY, Fermilab, GSI, KEK, SSC and TRIUMF. Experience with commissioning these new beam diagnostic devices, their use for beam measurements, and studies of the machine performance will be discussed. In particular, a description of the new tools for time-of-flight (TOF) and bunch shape measurements, and the results of beam studies using them will be reported.

The purpose of the paper is not to review all types of beam diagnostic devices to be used in ion linacs, but to familiarize the reader with several modern techniques for the measurement of ion beam parameters.

1 BUNCH SHAPE MONITORS

A device, allowing the measurement of the bunch shape (or phase spectrum) of the proton beam with high precision has been developed and built for the first time at INR [1]. The principle of operation (see fig. 1) is based on the analysis of secondary electrons produced by a primary beam hitting a 0.1 mm diameter tungsten wire (position 1 in fig. 1), to which a potential of -10 kV is applied. In a BSM the longitudinal distribution of charge of the analyzed beam is coherently transformed into a spatial distribution of low energy secondary electrons through transverse rf modulation. The temporal distribution of the secondary electrons follows the distribution of the beam being measured with a time delay <5 ps. The historical view of the BSM development is elsewhere [2].

A number of modified BSMs has been built recently with additional functional abilities. The Bunch Length and Velocity Detector (BLVD) provides a measurement of the average beam velocity as well as the bunch shape [3,4]. The traditional BSM can be modernized to measure longitudinal and transverse distributions of beam bunches including two component H^+ and H^- beams [5]. A further modification of the monitor is a 3D-BSM - a detector, which allows the measurement of the charge density distribution in a 3-dimensional space [6]. A fairly high level of mechanical design has been demonstrated during the development of BSM for the installation on the inter-tank space between the Alvarez tanks of the DESY 50 MeV Linac. The detector, called IT-BSM, fits onto the existing 2 ports on the cylindrical surface of the inter-tank space [7].

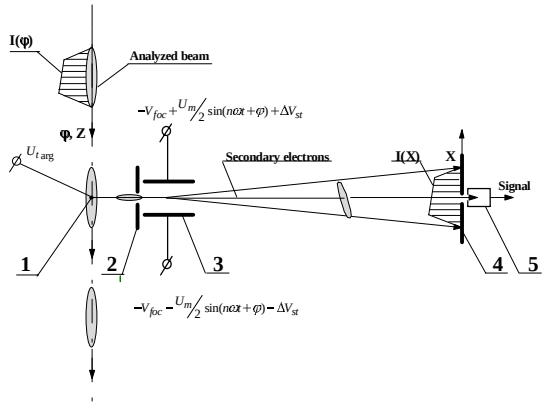

Figure 1: Principle of operation of the BSM. 1 – target, 2 – input collimator, 3 – rf deflector and electrostatic lens, 4 – output collimator, 5 – secondary electron multiplier (SEM).

BSMs have found applications in a number of accelerators [1-10]. Four BLVDs have been developed, designed and built at the INR for the meson factory linac (INR), CERN heavy ion linac [4], DESY H^- linac [7] and KEK H^- RFQ [9]. The 3D-BSM operates routinely in CERN proton linac [6]. IT-BSMs are installed at the DESY 50 MeV H^- linac. Similar IT-BSMs are being manufactured for the CERN proton linac.

1.1 Bunch Length and Velocity Detector

TOF methods have been used to measure the average velocity of beams with an rf bunch structure. Either two monitors installed a known distance apart [11] or a single movable one [12] can be used for this purpose. A BSM can be used as a movable detector [3]. When moving the BSM in a longitudinal direction one can observe a change in the bunch phase shape location by a value $\Delta\varphi_0=2\pi d/\beta\lambda$, where β is the relative velocity of the beam, λ is the wavelength of the deflector rf field and d is the distance of the monitor displacement. By measuring $\Delta\varphi_0$ and d one can find the beam velocity. For a high β it is expedient to use a higher harmonic for the deflecting field. The BLVD for the DESY Linac operates at the fourth harmonic f=810.24 MHz. For 50 MeV protons the value of the detector translation, $\beta\lambda/2$, is 60 mm. Fig. 2 shows the curves obtained during the

energy measurement output of the 50 MeV DESY linac. The phase positions of the centers of the bunches measured before and after the detector translation are practically the same and the energy found experimentally $W_{exp}=50.04$ MeV is practically equal to $W_{design}=50.00$ MeV.

The BLVDs provide energy measurements with an accuracy of about 0.15%.

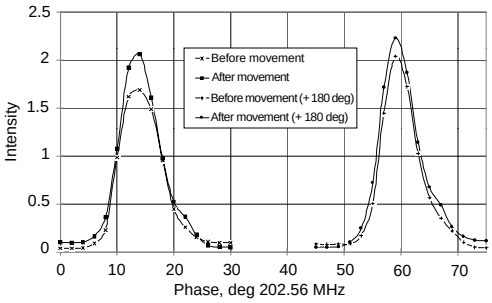

Figure 2: Bunch shapes during energy measurement.

1.2 Detectors to measure a three dimensional density distribution

In order to measure the 3-dimensional density distribution of a bunch, the following modifications of the BSM have been done: the target (pos. 1 in fig.1) is moved across the beam horizontally; the secondary electron beam is collimated by slit which is moved vertically and finally the electron beam is analyzed as in a standard BSM. Owing to the high strength of the electric field near the target, the electrons move practically horizontally and their vertical co-ordinates at the plane of the horizontal slit correspond to a short vertical section of the target wire determined by the position of the slit. Spatial distribution of the electrons after the passage through the rf deflector and drift space is measured with the 30 channel electron collector.

1.3 Phase resolution and sensitivity of BSM

The main parameter of the BSM is its phase resolution which depends upon a number of factors [1,2]. A resolution of 1° for frequencies up to 400 MHz can be achieved. The sensitivity of the BSM becomes important during the measurement of a low intensity beam or a longitudinal halo of a relatively high intensity beam. Normally electron multipliers are used in BSMs to detect secondary electrons. Typical values of the maximum gain of the multipliers for different types of the devices are ~10^5-10^8 and can be adjusted over three to four orders of magnitude by varying the HV. The multipliers can detect individual electrons so, as a matter of principle, by increasing the duration of the measurements it is possible to measure longitudinal parameters of extremely low intensity beams. Practically, the sensitivity is limited in any specific case. The minimum peak beam current we have made measurements by BSM was about 1 μA.

1.4 H^- beam measurements with a BSM

BSMs now operate with proton, H^- and lead ion beams. There are specific features of the BSM operation for each of these three types of ions. Particularly, for all type of ions there is a small fraction of high energy electrons (delta-electrons) but the number of such electrons compared to secondary ones is negligible and there is no real influence on operation of the bunch shape monitors. As for negative hydrogen ion beams, the electrons detached from the ions in a target can perturb the results of the measurements. An experimental study of the influence of detached electrons has been carried out during the commissioning of the DESY BSMs and KEK BLVD. In fig. 3 the bunch shape of the 30 MeV H^- beam is shown. The right bump in the figure is caused by the influence of the detached electrons. The secondary electrons can be separated from the detached electrons using a simple spectrometer located on the path of electrons to the electron beam detector [10].

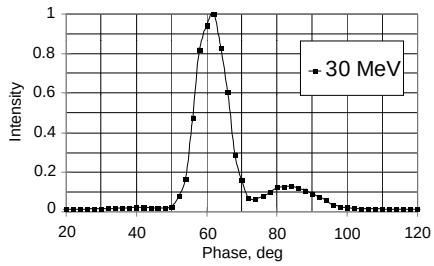

Figure 3: Bunch shape of 30 MeV H^- beam.

Further studies of the H^- beam have been made on the KEK 3 MeV RFQ with the help of a BLVD. In order to avoid the contribution of the detached electrons a 1 μm aluminum foil has been installed upstream of the BLVD wire target. The passage of the H^- beam through the foil produces a proton beam without any change of the longitudinal charge distribution. In order to measure the bunch shape in a wide dynamic range the measurements have been done with different gains of the SEM tube using the calibration curve. The longitudinal density distributions for H^- and proton beams are similar except for the halo region. Fig. 4 shows the particle fraction with respect to the phase extension for H^- and proton bunches. The proton beam contains much less particles in the halo, but still has a long tail. The

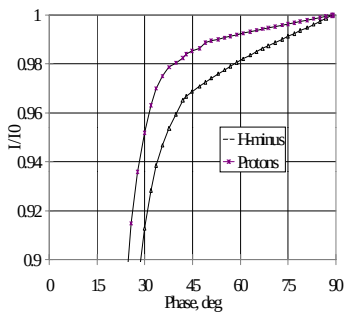

Figure 4: Particle fraction as a function of phase half-width for H– and proton

background for the proton beam is connected with a systematic error due to the electron beam interaction with the edge of collimator (pos. 2 in fig. 1) [9].

2 TRANSVERSE PARTICLE DENSITY MEASUREMENT

The use of high intensity beams for the irradiation of targets near the melting temperature requires control of the transverse beam density. The measurement of the profiles is not enough. As was mentioned the 3D-BSM could measure the density in three-dimensional space and the particle distribution on the transverse cross-section can be obtained by the integration along the longitudinal coordinate. However, the 3D-BSM has relatively small transverse aperture ~10x10 mm^2. For the measurement of the transverse particle density distribution a detector has been developed [13]. The electrons are produced due to the interaction of primary beam with the thin wire which is under negative potential. The electrons move on orbit in uniform magnetic field applied perpendicularly to the beam pipe axis. The secondary electrons are focused by electrostatic lenses in the vertical plane and by the magnetic field in the horizontal plane. The electron density distribution in the horizontal direction is transformed without distortion to the collector which is the multi-channel plate and located outside of beam pipe. The density distribution in the vertical direction is obtained with the help of wire movement along the vertical coordinate. The detector is installed in the 750 keV injection line of the MMF linac and an example of a beam density distribution is shown in fig. 5.

Another type of the particle transverse density measuring device is a residual gas monitor which is used on many accelerators. In Atomic Energy Institute, Moscow, this type of monitor has been modernized by adding an electrostatic analyzer which gives the possibility to observe on-line the density distribution of the particles [14]. The ions created in the residual gas are accelerated by the applied electric field and are collected by the multi-channel plate. The electrons at the exit of the multi-channel plate produce an image on the phosphor. After extraction from the beam pipe the trajectory of the residual ions is governed by the 45° electrostatic bend. Therefore the image on the phosphor directly corresponds to the density distribution of the primary beam. The use of ions, not electrons, allows one to deal with the signals with very low noise. The image from the phosphor is viewed by a CCD camera and is digitized. The residual ion beam current is directly proportional to the stopping power $d\varepsilon/dx$. The minimum collector current density which can be measured with good signal/noise ratio is ~10^{-16} A/mm^2. For example, for a 600 MeV proton beam with cross-section ~25 mm^2 the minimum peak current which can be observed by a residual gas detector at vacuum pressure of 10^{-6} torr is ~0.7 μA.

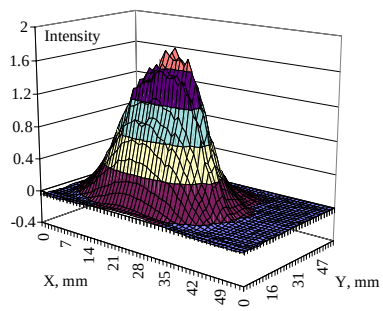

Figure 5: Transverse density distribution on 750 keV injection line of the MMF linac.

This type of monitor can be applied for all type of ions in wide energy range from several keV/n to hundreds of MeV/n. The range of beam current being studied is from nanoamps to hundreds of milliamps. The spatial resolution, whether one uses electrons or the ions, is limited, as space charge perturbs the trajectory of the collecting particles. This can be greatly improved upon applying high extraction voltages and a focusing magnetic field in the same direction.

3 WIRE-SCANNERS, HARPS

The wire scanners and harps are applied in all type of linacs. The use of wire-scanners is preferable for many reasons, but the harps are best for quick measurements in one beam shot. The spatial resolution of wire-scanners can reach a micrometer and with fast electronics, bunches can be observed individually. Their great sensitivity followed by the multi-gain amplifier allows the study of halos [15].

Carbon or SiC wires with a diameter > 0.002" are mostly used for high intensity beam diagnostics up to 1 mA average current for a 800 MeV beam. The wire scanners and harps must satisfy the following main specifications: 1) Multiple scattering of the primary must be small; 2) High vacuum; 3) Must not be destroyed by thermal expansion; 4) Must not melt; 5) Must be strong enough to withstand shock waves due to sudden vacuum failures; 6) Cooling is by radiation – the emissivity should be high; 7) The thermionic emission must be a small fraction of the secondary emission current. There are additional features in the design of scanners and harps for heavy ion [16].

4 TIME-OF-FLIGHT MEASUREMENTS

In a multi-cavity rf linac the measurements of relative as well as absolute energy is required. For this purpose TOF measurements are widely used [11]. The beam energy is calculated through the beam velocity. The TOF device includes a phase monitor and signal processing circuit. As a phase monitor coupling loop, capacitative pickup [16], wall current monitor [17], directional coupler [18] and rf resonators [19-21] have been used. The latter provides most sensitive measurements, a phase monitor capable to measure 1nA beam current has been reported [20,21].

In rf linacs the TOF is calculated through the measurements of phase difference. For relative

measurements it is enough to observe the phase difference between the induced signals. However to obtain the absolute beam energy the calibration is required. For calibration purposes two detectors must be excited by an external rf in phase. The relative velocity of bunched beam is calculated as $\beta = \frac{L}{\lambda}\frac{1}{n+\Delta\varphi/2\pi}$, where L is the distance between the monitors, $\Delta\varphi$ is the phase difference of the induced signals with wavelength λ, n is determined as a integer of $L/\beta_0\lambda$. The latter means that the beam velocity β_0 must be known roughly. The rough value of the absolute velocity β_0 can be found, for example, using one more phase probe [16] located closer to the other in order to have $n=0$. If a chopper exists in the linac one can produce single bunch mode for the measurement goals [17].

The precision of the velocity measurements is found as $\frac{\delta\beta}{\beta} = \frac{\delta L}{L} + \frac{\delta(\Delta\varphi)}{2\pi n + \Delta\varphi}$. By the selection of long enough distance the first term can be made negligibly small. An accuracy of phase measurement depends on processing circuit. Careful design of phase detectors can provide a precision of ~1° at a frequency of ~1 GHz. TOF measurements can be applied for beams with kinetic energy close to the rest energy of the particle. Relative energy measurements can be performed with resolution as low as $6\cdot10^{-5}$ [21], for absolute measurements the precision is $\sim10^{-3}$.

5 EMITTANCE MEASUREMENT

Conventional slit-collector measurements give detailed information about the emittance which may be neither elliptical nor symmetrical. They may be extended up to perhaps 200 MeV before multiple scattering in the slit ruins the profile resolution. Several methods have been reported in which the emittance is assumed to be elliptical (see references in [16]). For low energy beams <10 MeV/n the conventional method of the emittance measurement has been modified by using a phosphor screen instead of the particle collector. The beam image after the slit or pepper-pot is directly digitized by a CCD camera connected to a personal computer. This technique produces emittance during single shot and is successfully used for proton [22] or heavy ion beams [23,24].

New opportunities are being discovered for H^- beam diagnostics because of the simplicity of H^- beam neutralization by the laser beam [25]. H^0 transverse emittances are measured downstream of an H^- beam bending. To measure the longitudinal emittance the detached electron beam is analyzed.

5.1 Emittance measurement of 50 MeV H^- Beam

As an example, we describe a technique to measure the emittance in all 3 planes at the output of the DESY 50 MeV H^- linac. At the output of the linac the ellipse in the longitudinal phase space is assumed as a canonical shape. Then the longitudinal emittance is determined as a multiplication of the momentum spread and phase width. The longitudinal phase distribution has been measured with the help of a BLVD located close to the exit of the last tank. The momentum spread is measured by magnet spectrometer which operates on-line owing to a target converting H^- to protons. Owing to a narrow target (28 μm wire) and unit transformation of the transverse emittance from the target to the "momentum" harp location, the effect of the transverse emittance on the momentum measurement resolution is negligible. The horizontal profile determined by the harp well corresponds to the beam momentum distribution with a conversion ratio $\Delta p/p$ = 0.0526·x, where $\Delta p/p$ is in [%] and x is in [mm]. The spatial resolution of the "momentum" harp has been improved by sweeping the beam center at the harp position by the setting of several values of the bending magnetic field. Energy spread and phase spectrum measured at the signal level of 98% result in an emittance value of 2104 π·keV·deg, which is 5.05 times larger than the rms value.

For fast measurement of the transverse emittance on there is a procedure of the emittance restoration based on three profiles measured by the harps [26]. To improve the spatial resolution of the harps we have measured the beam profiles by sweeping the beam position on the harps. To produce a beam center deviation the steering magnets located upstream of the harps have been calibrated. The rms value of the density distribution has been calculated from 20-30 measurements on each harp. Emittance calculation has been done by using the least squares method. Table 1 shows rms emittance in all 3 planes.

5.2 Emittance measurement of 50 MeV Proton Beam

The proton Linac at CERN serves as an injector to the booster and operates with a peak current up to 170 mA in routine operation. For the emittance measurement during one shot in all 3 planes special equipment has been developed [27]. The transverse emittances are measured by the help of two kicker magnets for the sweeping of the beam position on the slit. Downstream of the slit a quadrupole doublet allows the adjustment of the resolution on the collector. Longitudinal measurement equipment contains two 54.3° bending magnets to provide the spectrometer function, rf cavity located downstream of the first spectrometer and slit. The rf cavity tuned to the linac frequency works as a rotating lens in the longitudinal phase space transforming the phase dispersion into an energy dispersion which is analyzed by the second spectrometer magnet. After the installation of the 3D-BSM 90 cm behind the last Alvarez tank, the measurements of both transverse and longitudinal rms emittances became available. The measurement of the transverse rms

emittance with the help of the 3D-BSM is performed by several (more than 3) settings of the quadrupole gradients and taking measurements for the calculation of rms radius. In table 2 the rms emittance data for a 170 mA proton beam is listed. The measurements performed by direct measurement of the emittance area in the phase space and by the help of 3D-BSM are consistent. The longitudinal rms emittance is determined as a multiplication of rms phase width by the rms energy spread from the spectrometer measurement.

Table 1: 50 MeV Beam Emittance

Lab	DESY	CERN,
H, normalized, π·mm·mrad	2.1	4.5
V, normalized, π·mm·mrad	1.8	4.1
L, π·deg·keV	417	780

6 ACKNOWLEDGEMENTS

The author gratefully acknowledges for the help during the commissioning of the detectors and work for this paper his colleagues from INR, IAE, MEPhI, CERN, DESY, KEK, TRIUMF and GSI.

7 REFERENCES

[1] A.V. Feschenko and P.N. Ostroumov. Bunch Shape Monitor and Its Application for an Ion Linac Tuning. Proc. of the 1986 Linac Conf., Stanford, June 2-6, pp. 323.

[2] A.V. Feschenko. Bunch Shape Monitors Using Low Energy Secondary Electron Emission. AIP Conf. Proc. 281, Proc. of the BIW, Berkeley, 1992, p.185.

[3] P.N. Ostroumov. Average Velocity Measurement of Accelerated Beam by Means of an Upgraded Bunch Length Detector. INR Preprint-812/93, May 1993.

[4] Yu.V. Bylinsky et al. Bunch Length and Velocity Detector and Its Application in the CERN Heavy Ion Linac. Proc. of the EPAC-94, London, 1994, p. 1702.

[5] A.V. Feschenko et al. A Detector to Measure Longitudinal and Transverse Distribution of a Two Component Ion Beam. Proceedings of the EPAC 92, Berlin, 1992, p.1073.

[6] A.V. Feschenko et al. A Three Dimensional Bunch Shape Monitor for the CERN Proton LINAC, Proc. of the 1996 Linac Conf., Geneva, 1996, p. 193.

[7] V.V. Feschenko at al. Bunch Shape Monitors For The DESY H^- Linac, Proceedings of PAC97, Vancouver, Canada, 1997. To be published.

[8] E.S. McCrory et al. Use of an INR-Style Bunch Length Detector in the Fermilab Linac. Proc. of the Linac-92, Ottawa, 1992, p. 662.

[9] A.V. Feschenko et al. Bunch Length and Velocity Measurement of the JHP-RFQ Beam with INR BLVD. This Proceedings.

[10] J.M. Hurd et al. Bunch Shape Monitor for SSCL Linac. Proc. of the 1993 PAC, Washington, 1993, p. 2426.

[11] Linear Ion Accelerators. Ed. by B.P. Murin, V.2, Atomizdat, 1978 (in Russian).

[12] A.V. Feschenko et al. Precise Energy Measurement of the Continuous Proton Beam. Proc. of the 1989 IEEE Particle Acc. Conf., Chicago, 1989, p. 1409.

[13] A.M. Tron and Vasilev. Secondary Electron Monitor of Beam's Two-Dimwnsional Transverse Current Density Distribution. EPAC-92, p.1124.

[14] V.G. Mikhailov et al. Muli-parameter Ionization Detectors for Measurement of Accelerated Particle Beams. PTE, 1995, No 6., p. 39.

[15] O.R. Sander et al. Recent Improvement in Beam Diagnostic Instrumentation. IEEE Trans., Vol. NS-26, No. 3, June 1979, p. 3417.

[16] P. Strehl. Ion Beam Diagnsotics. In "Handbook of Ion Sources", CRC Press, 1995, p. 385.

[17] M.B. Popovic et al. Time-of-Flight Measurements of Absolute Beam Energy in the Fermilab Linac", Proc. of the 1993 PAC, p.1689.

[18] J.D. Gilpatrick et al. Noninterceptive Beam Energy Measurements in Line D of the Los Alamos Meson Physics Facility. ibid, p. 485.

[19] A.V. Feschenko and P.N. Ostroumov. Velocity Measurement by Means of Mechanical Movement of a Detector. AIP Conf. Proc. 333. Proc. of the 1994 BIW, Vancouver, p. 478.

[20] J.M. Bogaty and B.E. Clifft. A Low-Cost Non-Intercepting Beam Current and Phase Monitor for Heavy Ions. Proc. of the 1995 PAC, p. 2625.

[21] P.N. Ostroumov et al. A very Sensitive Non-Intercepting Beam Average Velocity Monitoring System for the TRIUMF 300-keV Injection Line. AIP Conf. Proc. 390. Proceedings of the BIW, Argon, Illinois, p. 557.

[22] T. Shirai et al. One Year Operation of the 7 MeV Proton Linac. Proc. Of the 1993 PAC. p. 1697.

[23] M. Bourgeois et al. High Charge State Ion Beam Production from Laser Ion Source. Proc. of the 1996 Linac Conf., Geneva, 1996, p. 378.

[24] M. Domke et al. A Single Shot Emittance Measuring System for Intense Heavy Ion Beams. Proc. of 3rd European Workshop on Beam Diagnsotics and Instr. for Part. Accel. (DIPAC97). Frascati, Italy, 1997.

[25] W.B. Cottingame et al. Proc. of PAC85, IEEE Trans. Nucl. Scin. NS-32 (5) (1985), p. 1871.

[26] L. Criegee. Emittance measurement for Linac III. PLIN - Note 88-04, 1988.

[27] P. Tetu. New Linac Three Phase Planes Pulsed Emittance Measuremnt. Proc. of the 1979 Linac Conf., p.309.

HALO FORMATION IN INTENSE LINACS

Chiping Chen
Plasma Science and Fusion Center
Massachusetts Institute of Technology
Cambridge, Massachusetts 02139, USA

Abstract

Halo formation is an important issue in the development of high-power accelerators. In this paper, we discuss from the point of view of beam transport the mechanisms of halo formation in root-mean-square (rms) matched, high-brightness, space-charge-dominated beams in periodic focusing transport systems. In particular, it is shown theoretically that an important mechanism of halo formation in rms matched beams is due to chaotic particle motion induced by charge-density fluctuations about the ideal uniform density profile transverse to the direction of beam propagation. Experimental evidence is presented in support of the theoretical predication of halo formation in rms matched beams. Finally, to gain a better understanding of the equilibrium and stability properties of periodic focused intense charged particles, a rigid-rotor Vlasov equilibrium is discussed, and the effect of beam rotation on the phase space structure is studied.

1 INTRODUCTION

The problem of halo formation in intense charged-particle beams has been the subject of recent vigorous theoretical, computational and experimental investigations [1]-[19]. It is of fundamental importance in the development of next generation high-power accelerators for basic scientific research in high-energy and nuclear physics as well as for a wide variety of applications ranging from heavy ion fusion, accelerator production of tritium, accelerator transmutation of nuclear waste, spallation neutron sources, high-power microwave sources, to high-power free-electron lasers. In such high-power accelerators, beam halos must be controlled in order to keep beam losses at minimum.

It is well-known that a space-charge-dominated beam can develop a sizable halo if there is a root-mean-square (rms) mismatch between the beam and the focusing field [2]-[4],[6],[9]-[11]. The mechanism for halo formation in rms mismatched beams has been well described in the particle-core model [3, 6]. When there is a sizable mismatch, the halo can contain a substantial fraction (up to 15%) of the entire beam.

Recently, it has been shown theoretically [5, 8, 14, 15] that in periodic focusing transport systems, charge density fluctuations in rms-matched space-charged-dominated beams can also cause halo formation. An important mechanism of halo formation in rms matched beams has been identified with chaotic particle motion and nonlinear resonances occurring in the vicinity of the boundary of phase space occupied by the particles in the beam core. Invariant (Kolmogorov-Arnold-Moser) surfaces [20] play an important role in confining halo particles transverse to the direction of beam propagation. Because halos in rms matched beams are relatively tenuous compared with those in rms mismatched beams, experimental observations of halos in rms matched beams require detectors with a wide dynamic range. A recent observation of a halo in an rms matched potassium K^+ ion beam at the 2-MV Heavy Ion Beam Injector Experiment at Lawrence Berkeley National Laboratory (LBNL) [13] provides the first experimental evidence in support of the theoretical prediction [5, 8, 14, 15] of halo formation in rms-matched beams in periodic focusing transport systems.

For beam propagation through a *periodic* focusing transport system with the periodicity length S and the vacuum phase advance σ_0, a *space-charge-dominated* beam satisfies the condition [15]

$$\frac{SK}{4\sigma_0\varepsilon} > 1, \tag{1}$$

whereas an *emittance-dominated* beam satisfies the condition

$$\frac{SK}{4\sigma_0\varepsilon} \ll 1. \tag{2}$$

In Eqs. (1) and (2), $K = 2q^2N_b/\gamma_b^3\beta_b^2mc^2$ is the normalized beam perveance, ε is the unnormalized rms emittance of the beam, q and m are the particle charge and rest mass, respectively, N_b is the number of particles per unit length, $\beta_b c$ and γ_b are the characteristic velocity and relativistic mass factor of the particles, respectively, and c is the speed of light *in vacuo*. For an electron beam,

$$\frac{SK}{4\sigma_0\varepsilon} = 2.9\times10^{-5}\frac{1}{\sigma_0}\left(\frac{S}{\varepsilon_n}\right)\frac{I_b}{\gamma_b^2\beta_b^2}, \tag{3}$$

where I_b is the electron beam current in amperes, $\varepsilon_n = \gamma_b\beta_b\varepsilon$ is the normalized rms emittance in meter-radians, and S is in meters. For an ion beam,

$$\frac{SK}{4\sigma_0\varepsilon} = 1.6\times10^{-8}\frac{1}{\sigma_0 A}\left(\frac{q}{e}\right)\left(\frac{S}{\varepsilon_n}\right)\frac{I_b}{\gamma_b^2\beta_b^2}, \tag{4}$$

where A and q/e are the atomic mass and magnitude of the charge state of the ion, respectively, I_b is the ion beam

current in amperes, $\varepsilon_n = \gamma_b\beta_b\varepsilon$ is the normalized rms emittance in meter-radians, and S is in meters.

In this paper, we review recent theoretical, computational and experimental investigations of halo formation in high-brightness, space-charge-dominated beams that are rms matched but not fully matched (in terms of phase-space distributions) in periodic focusing transport systems. In particular, it is shown theoretically that the mechanism of halo formation in rms matched beams is due to chaotic particle motion induced by charge-density fluctuations about the ideal uniform density profile transverse to the direction of beam propagation. Experimental evidence is presented in support of the theoretical predication of halo formation in rms matched beams. Finally, to gain a better understanding of the equilibrium and stability properties of periodic focused intense charged particles, a rigid-rotor Vlasov equilibrium is discussed, and the effect of beam rotation on the phase space structure is studied.

2 MECHANISM OF HALO FORMATION IN RMS MATCHED BEAMS

It has been shown theoretically [5, 8, 14, 15] that in periodic focusing transport systems, charge density fluctuations in rms-matched space-charged-dominated beams can also cause halo formation. The mechanism of halo formation in rms matched beams has been identified with chaotic particle motion [20] and nonlinear resonances occurring in the vicinity of the boundary of phase space occupied by the particles in the beam core.

To illustrate the mechanism of halo formation in rms matched beams, we consider test-particle motion in the field configuration consisting of the self-electric and self-magnetic fields of a thin, continuous, intense charge-particle beam and the periodic solenoidal focusing field

$$\mathbf{B}_0(\mathbf{x}) = B_z(s)\mathbf{e}_z - \frac{1}{2}B_z'(s)(x\mathbf{e}_x + y\mathbf{e}_y). \qquad (5)$$

Here, $\mathbf{e}_x$ and $\mathbf{e}_y$ are unit Cartesian vectors perpendicular to the beam propagation direction, $s = z$ is the axial coordinate, $x\mathbf{e}_x + y\mathbf{e}_y$ is the transverse displacement from the beam axis at $(x, y) = (0, 0)$, the superscript 'prime' denotes d/ds with $B_z'(s) = dB_z(s)/ds$, and the axial component of magnetic field satisfies

$$B_z(s + S) = B_z(s), \qquad (6)$$

where S is the axial period of the focusing field.

The self-electric and self-magnetic fields [21] are readily determined from the steady-state Maxwell equations, assuming the following transverse density profile (Fig. 1)

$$n_b(r, s) = \begin{cases} \hat{n}_b + \delta\hat{n}_b[1 - 2r^2/r_b^2], & r < r_b(s), \\ 0, & r > r_b(s), \end{cases} \qquad (7)$$

where $r_b(s) = r_b(s + S)$ is the outermost radius for the rms-matched beam core, $\hat{n}_b(s) = N_b/\pi r_b^2(s)$ (with N_b being the number of particles per unit axial length), and $\delta\hat{n}_b(s) = \delta N_b/\pi r_b^2(s)$ is a measure of beam density fluctuations. The outermost beam radius $r_b(s)$ can be determined from the rms envelope equation. Note that the Kapchinskij-Vladimirskij (KV) beam equilibrium [22] corresponds to $\delta\hat{n}_b = 0$.

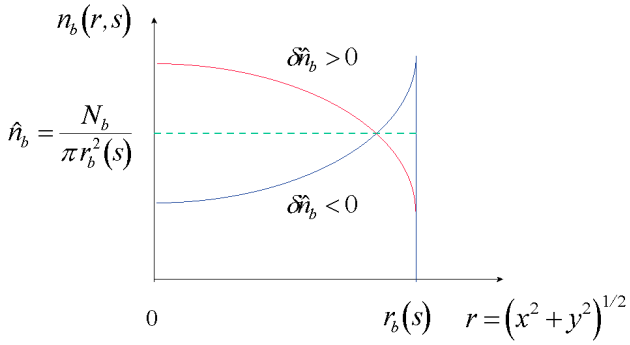

Figure 1: Transverse density profile described by Eq. (7).

It can be shown that in the Larmor frame of reference [23], the transverse equations of motion for a test particle in the combined periodic solenoidal and self fields are expressed as [15]

$$\frac{d^2x}{ds^2} + \kappa_z(s)x + \frac{q}{\gamma_b^3\beta_b^2mc^2}\frac{\partial}{\partial x}\phi^s(x, y, s) = 0, \qquad (8)$$

$$\frac{d^2y}{ds^2} + \kappa_z(s)y + \frac{q}{\gamma_b^3\beta_b^2mc^2}\frac{\partial}{\partial y}\phi^s(x, y, s) = 0, \qquad (9)$$

where $\kappa_z(s) = [qB_z(s)/2\gamma_b\beta_bmc^2]^2$, and the self-field potential ϕ^s is defined by

$$\phi^s = \begin{cases} -q(N_b + \delta N_b)r^2/r_b^2 + q\delta N_b r^4/2r_b^4, & r < r_b(s), \\ -q(N_b + \delta N_b/2) - 2qN_b\ln[r/r_b], & r > r_b(s). \end{cases} \qquad (10)$$

Figure 2 shows a Poincare surface-of-section plot in the phase space (x, x') for 2000 test-particle trajectories moving through 20 periods of a step-function lattice with filling factor η for a beam with a hollow density profile. The test particles are loaded initially on a circle defined by

$$W(x, y = 0, x', y' = 0, s = 0) = 1, \qquad (11)$$

where W is defined in [15]. The Poincare surface-of-section plot is generated by plotting the positions and momenta of the test particles as they pass through the lattice points $s/S = 0, 1, 2, \cdots, 20$. In Fig. 2, x and x' are scaled by the multiplication factors $r_b^{-1}(0)$ and $r_b(0)x'/4\varepsilon_m$, respectively, where $\varepsilon_m = (1 + 2\delta\hat{n}_b/3\hat{n}_b - \delta\hat{n}_b^2/3\hat{n}_b^2)^{-1}\varepsilon$. There is a pair of stable and unstable fixed points at the edge of the beam, i.e., at $x/r_b = \pm 1$ in the phase space. The unstable fixed point is located inside the beam,

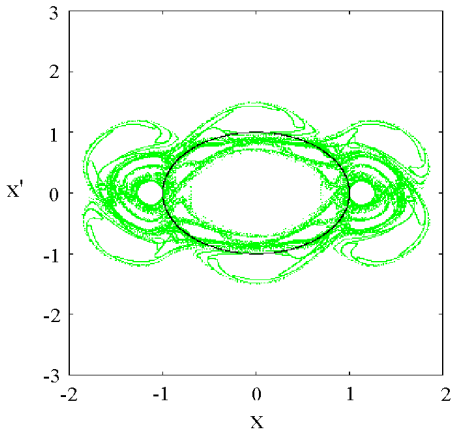

Figure 2: Poincare surface-of-section plot in the phase space (x, x') for 2000 test particles moving through 20 lattice periods. Here, the choice of system parameters corresponds to $\eta = 0.2$, $\sigma_0 = 88.8°$, $SK/4\sigma_0\varepsilon = 6.45$, and $\delta\hat{n}_b/\hat{n}_b = -0.95$.

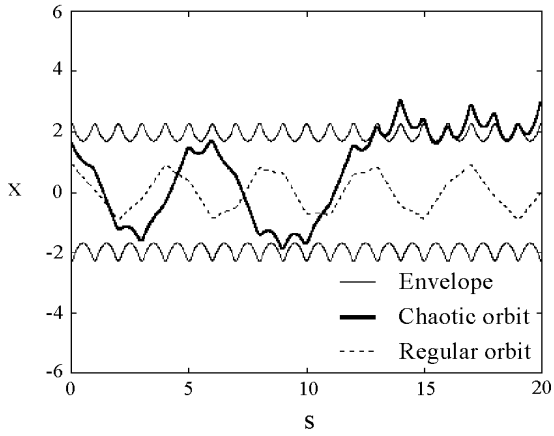

Figure 3: Shown as the dashed and bolded solid curves are, respectively, regular and chaotic trajectories for the same choice of system parameters shown in Fig. 2. Also shown as the two solid curves are the outermost periodic boundaries of the rms-matched beam core. The chaotic trajectory intersects the beam core envelope approximately at the thirteenth period of the focusing channel.

whereas the stable fixed point and associated island are located outside of the beam. Because of the symmetry in the underlying equations of motion (8) and (9), there is another pair of stable and unstable fixed points at $(x, x') \cong (-1, 0)$. These fixed points, which correspond to periodic solutions of the equations of motion (8) and (9), are induced by excessive space-charge at the edge of the hollow beam. Associated with the two unstable fixed points is a thin chaotic layer (separatrix) which occupies both the region with $W < 1$ and the region with $W > 1$ in the phase space. Particles in this thin chaotic layer can cross the beam envelope, forming a halo around a dense core of beam determined by $W \leq 1$ in the phase space. Although the chaotic layer has a sizable excursion along the x'-axis, it extends to $x/r_b \cong 1.8$ along the x-axis. Therefore, the halo size in this case is about 1.8 times the beam core radius. Because the chaotic layer is thin, the particle density in the halo region is expected to be very tenuous compared with that in the core region.

Shown in Fig. 3 as the dashed and bolded solid curves are, respectively, examples of regular and chaotic trajectories for the same choice of system parameters shown in Fig. 2. In Fig. 3, s is scaled by the multiplication factor S^{-1}, and both x and r_b are scaled by the multiplication factor $(4g\varepsilon S)^{-1}$, where $g = (1 - \delta\hat{n}_b/\hat{n}_b)^{-1}$. The regular trajectory is initialized well inside the beam envelope with $x' = 0$, whereas the chaotic trajectory is initialized near the unstable fixed point with $x' = 0$. Also shown in Fig. 3 as the two solid curves are the outermost periodic boundaries $\pm r_b(s)$ of the rms-matched beam core. The chaotic trajectory intersects the beam core envelope approximately at the thirteenth period of the focusing channel.

3 COMPARISON BETWEEN THEORY AND EXPERIMENT

Experimental evidence of halo formation has been observed in a space-charge-dominated potassium (K^+) ion beam in the 2-MV Heavy Ion Beam Injector Experiment at the Lawrence Berkeley National Laboratory (LBNL) [13]. In this experiment, a potassium ion beam was extracted from a 1-MV diode. The beam was then accelerated and transversely focused by four electrostatic quadrupoles (which correspond to two periods in a periodic focusing transport system). The four electrostatic quadrupoles add a total of 1 MeV to the ions at the end of the injector. Table 1 gives the basic system parameters measured at the end of the injector. The measured density profile at the end of the injector shows a density depression on the beam axis, and a halo extending 1.47 times the core envelope. The halo was tenuous, containing about 2% of the ions in the beam. A detailed description of the experimental setup and measurements can be found in [13].

A comparison between theory and experiment has been made. In the theoretical analysis, the electrostatic quadrupoles are treated as an alternating-gradient focusing system but the effect of acceleration is ignored. The elliptical cross section of the beam is incorporated. The transverse beam density profile is assumed to be

$$n_b(x, y, s) = \begin{cases} \hat{n}_b + \delta\hat{n}_b(1 - 2T), & T < 1, \\ 0, & T > 1, \end{cases} \tag{12}$$

where $T(x, y, s) = x^2/a^2(s) + y^2/b^2(s)$, and $a(s) = b(s + S)$ and $b(s) = b(s + S)$ are the outermost core envelopes in the x- and y-directions, respectively. For an rms matched

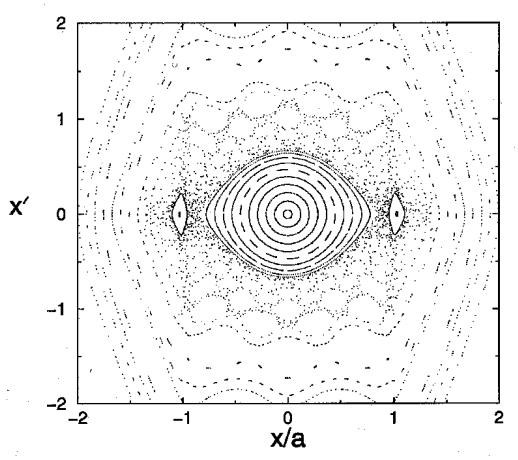

Figure 4: Poincaré surface-of-section plot in (x, x') phase space for 41 test particles in a nonuniform density beam. Here, the choice of system parameters corresponds to $\sigma_0 = 70°$, $\eta = 0.5$, $SK/4\varepsilon_x = 16$, $\varepsilon_x = \varepsilon_y$, and $\delta\hat{n}_b/\hat{n}_b = -0.2$.

beam, $a(s)$ and $b(s)$ are determined from the rms envelope equations.

Figure 4 shows the overall phase space structure for test-particle motion in a Poincaré surface-of-section plot for the nonuniform density beam. The choice of system parameters used to generate Fig. 4 is listed in Table 2, corresponding to the basic system parameters listed in Table 1. Shown in Fig. 4 are the trajectories

Table 1. Basic Parameters of the LBNL Experiment

Ion Type	Potassium
Beam Current	0.79 A
Ion Kinetic Energy	2.0 MeV
4 × Normalized Emittance	0.6 mm-mrad
Electrostatic Quad Period	0.8 m
Vacuum Phase Advance	70°

Table 2. Parameters in the Simulation

Vacuum Phase Advance σ_0	70°
Lattice Filling Factor η	0.5
$SK/4\sigma_0\varepsilon_x$ $(\varepsilon_x = \varepsilon_y)$	13.1
$\delta\hat{n}_b/\hat{n}_b$	-0.2

of 41 particles as they pass through the lattice points at $s = 0,\ S,\ 2S, \cdots, 400S$. The initial conditions for these particles are: $x(0)/a(0) = 0.1n$, $y(0) = 0$, and $x'(0) = y'(0) = 0$, where $n = 0, \pm 1, \cdots, \pm 20$. Note that for $y(0) = 0 = y'(0)$, the motion in (x, x') phase space is decoupled completely from that in (y, y') phase space. In Fig. 4, the vertical axis is scaled by the dimensionless quantity $(S/4g\varepsilon_x)^{1/2}$. There are two stable period-one orbits near the edge of the beam at $(x, x') \cong (\pm a, 0)$. These stable period-one orbits are accompanied by two *unstable* period-one orbits located approximately at $(x, x') \cong (\pm 0.9a, 0)$. It is the chaotic separatrix associated with the unstable period-one orbits that is responsible for particle escape from the beam interior to form a halo.

For beam propagation through several lattice periods, the Kolmogorov-Arnold-Moser (KAM) surface [20] at $(x, 0) = (\pm 1.42a, 0)$ is expected to determine the halo size. Therefore, the halo size in the x-direction is estimated to be $x_{\text{halo}} = 1.42a$, which is in good agreement with the measured halo size $x_{\text{halo}} = 1.47a$ [13]. Detailed numerical studies of the beam dynamics with a properly chosen initial distribution function show that a relatively small fraction (4%) of the particles in the beam become halo particles after five lattice periods, and the experimental measurements indicate that about 2% of the particles become halo particles in one lattice period.

4 RIGID-ROTOR VLASOV EQUILIBRIUM

The results presented in Secs. 2 and 3 show that charge-density fluctuations about the ideal uniform density profile induce chaotic particle motion and halo formation in rms matched space-charge-dominated beams in periodic focusing transport systems. Therefore, it is important to gain a better understanding of the equilibrium and stability properties of periodically focused beams. In this regard, we discuss a rigid-rotor Vlasov equilibrium [24, 25] discovered recently for intense beam propagation through a periodic solenoidal magnetic field.

The rigid-rotor Vlasov equilibrium distribution function can be expressed as [24, 25]

$$f_b^0(R, P_R, P_\Theta)$$

$$= \frac{N_b}{\pi^2 \varepsilon_T}\delta\left[P_R^2 + \frac{P_\Theta^2}{R^2} + R^2 + 2\omega_b P_\Theta - (1-\omega_b^2)\varepsilon_T\right]. \tag{13}$$

In Eq. (13), $\omega_b = \text{const.}$ $(-1 < \omega_b < 1)$ is a parameter measuring beam rotation relative to the Larmor frame. The normalized canonical phase-space variables $(R, \Theta, P_R, P_\Theta)$ are related to the Larmor-frame phase-space variables $(r, \theta, P_r, P_\theta)$ by

$$R = \frac{\sqrt{\varepsilon_T}}{r_b(s)}r, \quad \Theta = \theta, \tag{14}$$

$$P_R = \frac{1}{\sqrt{\varepsilon_T}}\left[r_b(s)\frac{d}{ds}r - r\frac{d}{ds}r_b(s)\right], \quad P_\Theta = P_\theta. \tag{15}$$

It can be shown that $n_b(r, s) = \int dx'dy' f_b^0$ is indeed identical to the step-function density profile defined in Eq. (7) with $\delta\hat{n}_b = 0$. It can also be shown that the well-known KV equilibrium corresponds to the special case with $\omega_b = 0$. Finally, a recent analysis [26] shows that beam rotation with $\omega_b \neq 0$ reduces the degree of chaotic behavior in phase space.

5 CONCLUSIONS

We have discussed several important mechanisms of halo formation in high-brightness, space-charge-dominated beams from the point of view of beam transport. In particular, it has been shown theoretically that the mechanism of halo formation in root-mean-square (rms) matched beams is due to chaotic particle motion induced by charge-density fluctuations about the ideal uniform density profile transverse to the direction of beam propagation. Experimental evidence is presented in support of the theoretical predication of halo formation in rms matched beams. Finally, to gain a better understanding of the equilibrium and stability properties of periodic focused intense charged particles, a rigid-rotor Vlasov equilibrium is discussed, and the effect of beam rotation on the phase space structure is studied.

6 ACKNOWLEDGMENTS

The author wishes to thank R. C. Davidson, Y. Fink, R. A. Jameson, R. Pakter, Q. Qian, and S. S. Yu for their contributions. This work was supported by the Department of Energy, High-Energy Physics Division under Grant No. DE-FG02-95ER40919, Air Force Office of Scientific Research under Grant No. F49620-97-1-0325, and Princeton Plasma Physics Laboratory under Subcontract No. S-03834-K.

7 REFERENCES

[1] *Space Charge Dominated Beams and Applications of High Brightness Beams*, edited by S. Y. Lee, AIP Conf. Proc. **377** (AIP, New York, 1996).

[2] I. Haber, D. Kehne, M. Reiser, and H. Rudd, Phys. Rev. **A44**, 5194 (1991).

[3] J. S. O'Connell, T. P. Wangler, R. S. Mills, and K. R. Crandall, Proc. 1993 Part. Accel. Conf. (IEEE Service Center, Piscataway, New Jersey, 1993), Vol. 5, p. 3657.

[4] C. Chen and R. C. Davidson, Phys. Rev. Lett. **72**, 2195 (1994); Phys. Rev. **E49**, 5679 (1994).

[5] Q. Qian, R. C. Davidson, and C. Chen, Phys. Plasmas **1**, 3104 (1994).

[6] R. L. Gluckstern, Phys. Rev. Lett. **73**, 1247 (1994).

[7] L. M. Lagniel, Nucl. Instrum. Methods Phys. Res. **A345**, 1576 (1995).

[8] Q. Qian, R. C. Davidson, and C. Chen, Phys. Plasmas **2**, 2674 (1995).

[9] C. Chen and R. A. Jameson, Phys. Rev. **E52**, 3074 (1995).

[10] S. Y. Lee and A. Riabko, Phys. Rev. **E51**, 1609 (1995).

[11] I. Haber, *et al.*, in Ref. 1, p. 105.

[12] F. L. Krawczyk, *et al.*, Proc. 1995 Part. Accel. Conf. (IEEE, Piscataway, New Jersey, 1995), p. 2306.

[13] S. Yu, S. Eylon, E. Henestroza, and D. Grote, in Ref. 1, p. 134.

[14] C. Chen, Y. Fink, R. C. Davidson, and Q. Qian, "Halo Formation in RMS Matched Intense Ion Beams," Proc. of the Eleventh Int. Conf. on High Power Particle Beams (Prague, Czech Republic, June 10-14, 1996), p. 1018.

[15] Y. Fink, C. Chen, and W. P. Marable, Phys. Rev. **E55**, 7557 (1997).

[16] M. Pabst, K. Bongardt, and A. P. Letchford, in Ref. 1, p. 343.

[17] R. W. Garnett, et al., in Ref. 1, p 60.

[18] R. Pakter and C. Chen, "Emittance Growth and Particle Diffusion Induced by Discrete Particle Effects in Intense Beams," Proc. 1997 Part. Accel. Conf. (1997), p. 1938.

[19] H. Okamoto and M. Ikegami, Phys. Rev. **E55**, 4694 (1997).

[20] A. J. Lichtenberg and M. A. Lieberman, *Regular and Chaotic Dynamics*, 2nd ed. (Springer-Verlag, New York, 1992).

[21] R. C. Davidson, *Physics of Nonneutral Plasmas* (Addison-Wesley, Reading, MA, 1990).

[22] I. M. Kapchinskij and V. V. Vladimirskij, in *Proceedings of the International Conference on High Energy Accelerators* (CERN, Geneva, 1959), p. 274.

[23] M. Reiser, *Theory and Design of Charged-Particle Beams* (Wiley & Sons, New York, 1994).

[24] C. Chen, R. Pakter, and R. C. Davidson, Phys. Rev. Lett. **79**, 225 (1997).

[25] R. C. Davidson and C. Chen, Part. Accel. **59**, 175 (1998).

[26] C. Chen, R. Pakter, and R. C. Davidson, "Phase Space Structure for Intense Charged-Particle Beams in Periodic Focusing Transport Systems," submitted for publication (1998).

RF PULSE COMPRESSION FOR LINEAR COLLIDERS

H. Mizuno
KEK, High Energy Accelerator Research Organization
Oho, Tsukuba-shi, Ibaraki-ken 305, JAPAN

Abstract

In the high gradient electron linacs at X or S band, a conventional klystropn driver cannnot supply short pulses that a linear collider operation requires. Therefore, some RF pulse compression system that can compress the RF pulse length and at the same time heighten the peak RF power become necessary. Such an RF pulse compression system has been already utelized successfully in the S-band electron linacs of several laboratories. In the studies of the X-band linear accelerators, such RF pulse compression systems, SLED (SLAC Linac Energy Doubler) [1] or its direct successors SLED2 [2] and VPM (VLEPP Pulse Multiplier) [3][4] were studied and developed as the RF pulse compression system for the future machines. These system are all based on the same principle that the RF pulse energy is once stored in some storage circuit (a resonance cavity or a delay line) and thereafter emitted within short time to create the shorter RF pulse. Instead of these schemes, BPC (Binary Pulse Conpression) [5] and DLDS (Delay Line Distribution System) [6] use the delay lines as the tool to make the RF pulse shorter (BPC), or to adapt the longer RF pulse into the shorter linac driving pulse (in case of DLDS). A DLDS was recently introduced as an RF pulse compression equivalent system based on the different operation principle from an ordinary pulse compression system. DLDS is expected as the RF pulse compression equivalent system for the future RF system of X-band linear colliders.

1 INTRODUCTION

As the typical example of the modern X-band linear collider, general parameters of JLC (Japan Linear Collider) are summarized in the Table 1 [7].

To achieve an accelerating gradient of ~70MeV/m or greater in an accelerating strcture with shunt impedencec of ~80Mohm/m, the RF power fed per unit length of the linear collider should be around 100MW/m or higher. Duration of the RF pulse should be 250nsec, which is the sum of the filling time of and to time length of the multi-bunch train that consist of 90 bunches each separated by 1.4 nsec.

In the JLC design, to provide a peak power up to 130MW/mto the accelerating structure, klystrons are distributed every 4-5m to feed 3-accelerating units with the RF power totaling 390MW. Clearly, such a high peak power is out of reach for a single klystron, even with the most advanced modern klystrion technologies. In addition, the required RF pulse duration of 250ns is too short to drive klystrons efficiently. Present high voltage modulators with a step-up pulse transformer can never drive a klystron with the rise time much shorter than 100ns.[7][8] Thus the klystron modulator systems will suffer from poor efficiency if it were to drive klystrons with output pulses of 250ns.

Table 1. General parameters for the next generation linear colliders

RF frequency(GHz)	11.4
Accelerating gradient(MeV/m)	
Unloaded/Loaded	76/57
Active linac length(km)	9.2
Total linac length(km)	10
Peak power /meter(MW/m)	100
Structures/power unit	6
Structure length per power unit(m)	7.8
Total number of power unit	1180
Total number of klystrons	4720
Total number of modulators	2360
Repetition rate(pps)	150
RF pulse length at str.(nsec)	250
Peak beam current(mA)	0.79
Total average RF power at Str.(MW)	34.5

Consequently, the RF power system of the X-band linear collider must supply the RF power that is shorter in pulse length and at the same time higher in peak power, than the present technology could achieve. This requirement imposes a notable change in the RF power system of the X-band linear colliders. As shown above, the energy consumption of the future collider is considered to reach to several hundred megawatts, it is quite important to supply these RF power with high conversion efficiency. Thus the major change was introduced to the X-band RF power system. It is, the introduction of the RF pulse compression stage to compress the klystron RF output pulse shorter about factor 4. This difference are due to the fact that the X-band RF power system has to deliver about factor 4 shorter RF pulse than S-band system. The most important difference between the S and X-band Rf power echnogy is that an RF pulse which dirves an X-band linac is about 4-times shorter than that of S-band case. Therefore, 4-times longer RF pulse that is created by the present klystron modulator technology limit must somehow adapted to this 4-times shorter linac driving pulse length. On this point, there is the absolute necessity of the RF pulse compression measure.[7][8]

2 RF PULSE COMPRESSION SYSTEMS

The RF pulse compression system is generally considered as the measure that can make an RF pulse shorter and higher while preserving its total RF pulse energy as much as possible. As an linac RF power sources, this condition is can be re-considered as follows. If an RF pulse that is several times longer than the linac driving pulse can drive a linac utilizing all its RF energy i.e. its longer pulse, this system has the same effct as the ordinary type pulse compression system driving a linac. Thus, the present Rf pulse compression methods can be divided into two categories. Firstly, the conventional RF pulse compression schemes such as SLED, SLED2 and VPM etc. [9] These methods are based on the same operational principle that the RF pulse are once stored in some energy storage system such as a resonnant cavity or cavity equivalent system, and later extracted as the shorter and higher RF pulse. In other words, the RF pulse is re-shaped into the shorter

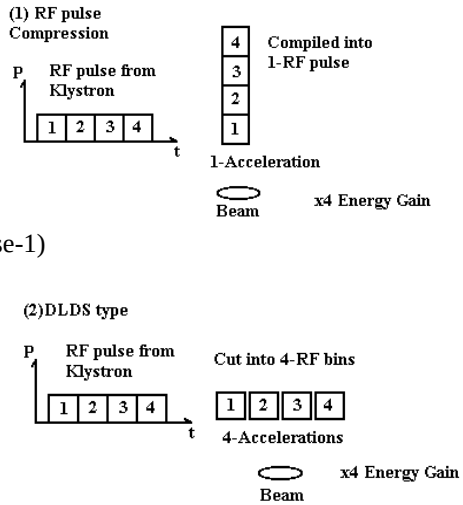

case-1)

case-2)

Fig. 1. Two types of RF shortening scheme

but higher RF pulse. On the other hand DLDS and its application are based on the fact that the RF pulse are applied on the beam in the different linac position to achieve the multiple acceleration by each RF bis that are cut from the longer original RF pulse. The main important feature of this DLDS like methods are that the RF pulse is divided into several shorter RF pulses (bins) and each pulse accelerates the same beam in the different position of the linac to adjust the time delay. Fig. 1 illustrates these operation principles in case of factor 4 compression ratio for each case. The ordinary RF pulse compression is illustarted in case-1) in this Figure. Longer RF pulse from the klystron is re-shaped into the shorter and higher RF pulse using the energy store system mostly resonnant cavities. On the other hand, as illustrated in case 2), RF pulse is divided into 4 RF bins in time domain and each shorter RF bin accelerates the same beam independently instead being piled up to the higher pulse like SLED type pulse compression system. In this DLDS system the longer RF pulse from the klystron are only divided into shorter pulses and steered into the different parts of the linac to meet the identical beam. These two systems can be considered as essentially the same, because both utilizes the longer Rf pulse to drive the linac that has 4-times shorter driving pulse. And the beam also gain the energy that is 4-times more than expected from the klystron output peakpower. Thus, this second type can be also called as the RF pulse compression system of the factor 4 compression ratio.

3 SLED SLED2 & VPM (SLED-FAMILY)

The operational principle of this SLED group is illustrated in Fig. 1.[1] All of this family has the same operational principle as the original SLED operation. As shown in the figure, RF energy is once stored in the resonnant cavities and later extracted through 3-dB hybrid which steers the RF pulse into the output port direction within short period.

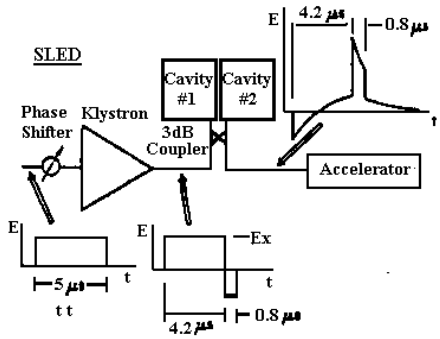

Fig. 2. Principle of operation of SLED

This kind of system necessarily has the two main causes of the energy loss in their operation process, firstly the reflection of the incoming RF pulse while the build up period especially at the early part of this stage and this reflection can never be avoided as long as the RF output pulse from the klystron are flat shape.[9] This device and the necessity of the time to build up RF energy in these storage cavity or cavities, mainly determines it's energy efficiency. The energy losses in this system are consist of following two categories, (1) The wall loss on the inner surface of the energy storage cavity, (2) the RF reflection while the storage period. and the RF energy left after extraction of the energy from the storage devices. The main part of loss in this stage, is the reflection of the input RF pulse while the build up period of the SLED operation. Thus the energy efficiency of this system is about 80% even neglecting the possible wall loss.

As illustrated above, this original SLED can only re-shape the RF pulse into the exponentially decaying pulse

waveform. However, several methods that can shape the RF pulse into a flat pulse are proposed. One is SLED2 that uses a pair of delay lines instead of the resonant cavities. Others uses the chain of the RF cavities for energy strage. One more possibility is to control the phase, amplitude or both to make a flat pulse. Detail of these sre omitted but the essential character of the system remains almost the same.[3][4]

4 BINARY PULSE COMPRESSION (BPC)

One more RF pulse compression system based on the different operational principle from these energy storage type pulse compression of the SLED family is the BPC (Binary Pulse Compression). This pulse compression system was proposed by D.Farkas and the first high power test was successfully achieved in SLAC.[10]

The operational principle of this BPC system is graphically illustrated in Fig. 3 in case of the compression factor of 4. This system is driven by two independently phased klystrons and their output pulses are divided into 4-short pulses respectively. The phase of each part of the RF pulse are coded as shown in Fig. 3. Through the 3-dB hybrid and delay lines, RF pulse trains from each klystron are combined and at the same time sterred to the two output port of the hybrid.

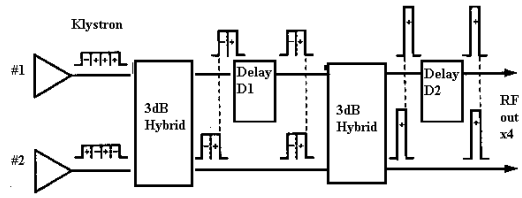

Fig. 3. Principle of ooperation of BPC

One port of the hybrid is connected to the delay lines which gives the necessary delay time to the first half of the RF pulse to meet with the following half of the RF pulse just in time at the input of the next 3dB hybrid. Through next hybrid, first and the second part of RF pulse are combined to give the twice peak power with one half of the original pulse duration. And as illustrated in the figure, this RF pulse again guided to the next stage as the figure illustrates. Repeating this process as shown in Fig. 3, 2^n pulse compression could be achieved. If the wall loss of the delay lines are neglected, it is quite easy to find that an n-stage of the BPC system can give the factor 2^n times higher pulse with 2n-th of a original pulse duration. It is also easy to recognize that in this BPC system the intrinsic energy efficiency could reach to 100% in case of the loss-less delay lines.

Due to this rather cumbersome configuration of the system, this BPC has been considered as of secondary importance even it can achieve better energy efficiency of close to or more than 90% in case of compression factor 4.[5]

5 DELAY LINE DISTRIBUTION SYSTEM (DLDS): A NEW RF POWER DISTRIBUTION METHOD EQUIVALENT TO A PULSE COMPRESSION SYSTEMS

Recently, the new RF power distribution system named DLDS(Delay Line Distribution System) which works as the replacement of an ordinary RF pulse compression system and has the better energy efficiency was proposed by the authors [6][7]. This system is based on the new operational principle different from the existing any other RF pulse compression systems. Like BPC, in this new DLDS, the short pulse trains that are divided into from the long klystron output pulse are led to the different parts of the linac respectively. The most specific point of this new system is that the divided RF pulses are never compiled again like SLED family or BPC. In this new system, the flight pass of the beam itself works as the delay line in the BPC, thus the half of the delay time necessary for the divided short RF pulse trains is given by the beam flight itself. In this new system, the length of the delay lines and consequently their losses can be decreased by about factor 2 compared to that of BPC. The operation principle of this new system DLDS is described in some detail below.

5.1 Basic factor 2 DLDS

In this new scheme, as shown in Fig. 4, the RF power from two klystrons that are independently phase controlled are combined together through the 3-dB coupler. One output port of the 3dB hybrid is connected to the upstream of the linac about one half of the linac operating time apart from the klystron location through the low-loss waveguide, and another port is connected to the structure located close to the klystron position. The first half of the RF pulse which is equal to the sum of the filling time and the bunch train is sent to the upstream of the linac through the delay line shown in the figure. The second part of the RF pulse is fed to the structure close to the klystron without delay. Delay line gives the delay time of Tdelay=L/Vg and the beam flight time between two structures is Tbeam=L/c. If these time delay satisfies next relation neglecting the delay time in the other RF transport system such as 3dB hybrid etc.,

$$T_{delay} + T_{beam} = L/V_g + L/c = t_a$$

where t_a is the pulse length of the linac operation, just the sum of the structure filling time and the duration of the bunch train. It is easily recognized that the timing of the bunch train and the RF pulse is adjusted to accelerate the beam and the beam is accelerated just as the ordinary linac pulses. Thus, The factor 2 DLDS (Delay Line Distribution System) which works equivalently as the factor 2 RF compression system can be constructed. The timing relation of this delay line scheme is illustrated in the “train diagram” shown in Fig. 5 in case of the RF

pulse from the klystrons are divide into two consecutive RF bins.

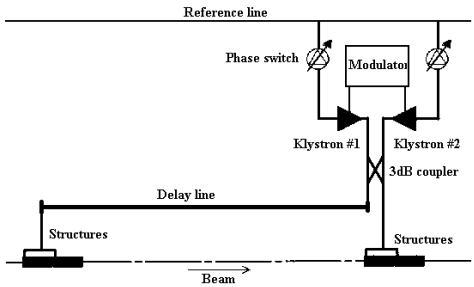

Fig. 4. A schematic diagram of the simplest factor-2 delay line distribution system

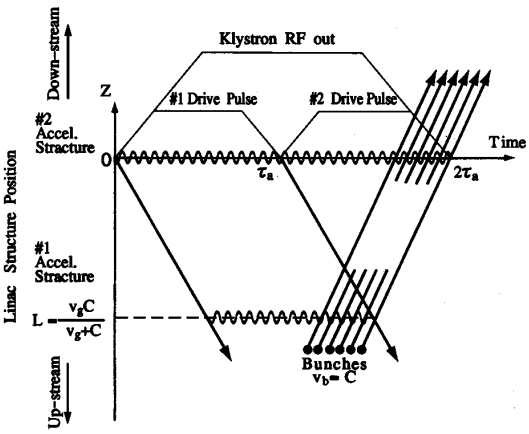

Fig. 5. A train diagram of factor 2 DLDS

In general , this scheme can be extended to the factor 2^n combined pulse height as follows. Each of the 2-klystrons in the factor-2 scheme mentioned in the previous section, can be replaced by the pair of 2-klystrons combined through a 3-dB hybrid coupler, thus this new system also works as factor-2 system, and remaining 2-output ports of the 2-hybrid couplers can be connected to the one more 3-dB hybrid coupler which serves as the additional factor 2 DLDS same as Fig. 4.

This process can lead to the construction of the factor-2^2 DLDS system. It may be easy to understand this procedure illustrated in the Fig. 6. Apparently, the train diagram of this factor factor-2^2 DLDS is easily understood as the extension from the factor 2DLDS case.

It should be noted that in this scheme the time domain compression equivalent factor i.e. klystron pulse length can be chosen from 1 to 2^n times longer than the linac operational RF pulse length. This system is generally noted as factor 2^n/m Delay Line Distribution System(2^n/m DLDS), 2^n represents the number of independent RF sources, and m represents the time domain compression equivalent factor. In this case, the (2^n - m) ports left unconnected to any structure.

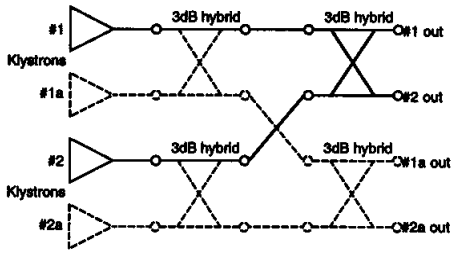

Fig. 6. A factor-4 DLDS built from factor-2 DLDS blocks.

Recently, an interesting application of this DLDS operation principle was proposed for a driving beam system for TBA (Two Beam Accelerator)[12]. Each RF bins in DLDS is replaced by the bunched beams that carries the RF power, and these bunch trains are transported to the counter direction to the accelerated beam like the RF bins in DLDS. The ssame operation principle as DLDS can be applied to the driving beam of TWA. Thus, even in TBA, an RF pulse compression equivalent system can be constructed and this scheme can replace the intense drive beam to the less intense but longer drive beam. It is expected that this new configuration could relax the technological problems on the drive beam compared to an ordinary co-direct drive beam cionfiguration.[12]

5.2 Design of a 4/3 DLDS for the JLC X-band main linacs

As an example of DLDS at X-band linear collider, 4/3 DLDS was designed as the RF pulse compression equivalent system for JLC. Fig. 7 schematically illustrates the 4/3 DLDS. Note that the 4-set of the klystrons and 3 groups of accelerating atructures that are seperated to adjust the time delay. The train diagram and the operational principle of this 4/3 DLDS are the essentially the same as factor 2DLDS, therefore further detailed explanation is unnecessary.

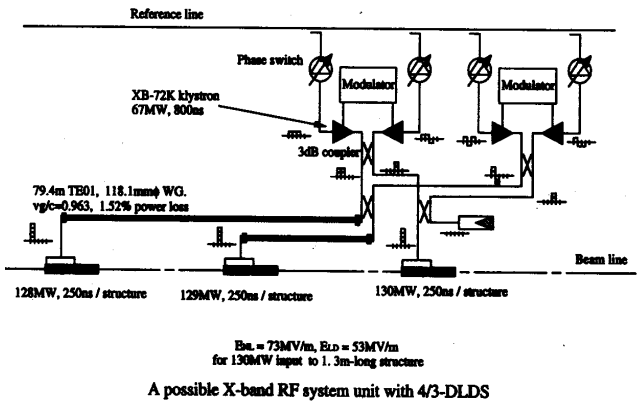

Fig. 7. 4/3 DLDS for JLC

6 MULTI-MODE DLDS

Recently, SLAC group proposed a clever configuration of DLDS which could save the delay line length by the use of multi-mode loading of the lines. This Multi-mode DLDS scheme works as follows. instead of the several delay lines, one delay line is set to have several mode extractor that are inserted on the one delay line to give the delay time as required by the DLDS operation.[11] Each mode extractor is designed as to extract only a specific mode and at the same time to transport the other modes completely. The one end of the delay line where RF sources are located, the mode launcher is attached. Primary RF pulse from the klystron is divided into the short RF bins and each RF bin is converted into the different mode through the mode launcher and lead into the delay line. Thus, each RF bin is extracted, in other words, distributed to the necessary location just as an ordinary DLDS. This new version of DLDS is currently considered as the best candidate for the next linear collider that is under study by joint effort of SLAC/KEK.

This multi-mode DLDS requires several new RF device such as a mode launcher, Intensive R&D plan is now going on at SLAC and KEK aiming the design of 4/4 multi-mode DLDS for their next linear collider.

7 CONCLUSION

The most important advantage of this new DLDS pulse compression equivalent system is firstly the high energy efficiency, as considered in the previous section its intrinsic efficiency could reach 100%. To compare this system efficiency with that of the ordinary SLED2 pulse compression system, , the efficiency of the DLDS is better than that of the SLED2 by about 20%. In comparison between an original DLDS and a muti-mode DLDS, if 4/4 DLDS is intended, a multi-mode DLDS is expected to be less cost due to the saving of delay length by its multi-mode loading of the delay lines. Considering the present status of R&D on the RF pulse compression schemes for an application to X-band linear colliders, following points can be pointed as a brief summary on this subject.

1) At X-band, DLDS especially muti-mode type is considered as the top ranked candidate as an RF pulse compression scheme for linear colliders.
2) DLDS has several advatage to other conventional RF pulse compression systems, howeveer DLDS can be applied only to a long linac such as a linear colilider.
3) traditional RF pulse compression schemes, such as SLED family, will remain as the useful measure for most of electorn linacs especially at S-band.
4) For the realization of the application of DLDS to linear colliders at X-band, technological R&D's such as high power tests, developments of several RF parts and beam operation oriented studies are still needed.
5) The operation principle of DLDS can alsobe applied to TBA drive beam system.

REFERENCES

[1] Z.D.Farkas et al. "SLED: A method of doubling SLAC's Energy"; Proc. 9th Int. Conf. High Energy Accelerators, SLAC. Stanford. 1974. P576.

[2] P.B.Wilson ;"RF Pulse Compression for Future Colliders" ; "AIP Conference Proceedings 337 (Pulsed RF Sources for Linear Colliders)", Montauk, NY 1994. P-293

[3] V.E.Balakin. I.V.Syrachev;"Status of VLEPP RF Power Multiplier" ; Proc. of EPAC92. March 1992 Berlin, Germany.; P1173.

[4] I.V.Syrachev; "The progress of X-band "Open" Cavity RF Pulse Compression Systems" ; Proc. of EPAC94. P375.

[5] Z.D.Farkas et al.; "Binary Peak Power Multiplier and its Application to Linear Collider design"; IEEE Trans. MTT-34(1986), P1036.

[6] H.Mizuno and Y.Otake;"A new RF power distribution system for X-band linac equivalent to an RF Pulse compression scheme of Factor 2n";Proceedings of the 17th International Linac Conference, Tsukuba, Japan, August 21-16 1994: P-463.

[7] "JLC-1"; KEK report 92-16, December 1992 A/H/M.

[8] "Zeroth-order Design Report for the Next Linear Collider"; SLAC Report 474. May, 1966.

[9] C.D.Nantista; "Radio frequency pulse compression for linear accelerators" Thesis, University of California 1994.

[10] T.L.Lavine, Z.D,Farkas et al.; "High Power RF Binary Pulse Compression Experiments at SLAC"; Proc. of the IEEE Particle Accelerator Conference May 1991. San Francisco. California. USA. P652.

[11] S.Tantawi et.al.; This Conference.

[12] J.P.Delahaye for the CLIC Study Team; "CLIC, a 0.5 to 5Tev e-p Compact Linear Collider"; CERN/PS 98-009(LP).CLIC-Note-360.

THE DESIGN OF AN ACCELERATOR FOR ADVANCED PULSE RADIOLYSIS EXPERIMENTS*

C. D. Jonah and R. A. Crowell
Argonne National Laboratory, Argonne, Illinois 60439 USA

Abstract

New accelerator techniques have made it possible to make shorter and shorter electron pulses. If appropriate detection techniques are available, these pulses make it possible to measure many important sub-picosecond chemical processes. We are proposing an accelerator system that can be used to measure important sub-picosecond chemical processes, such as solvation, vibrational relaxation, excited state relaxations and molecular fragmentation.

1 INTRODUCTION

It has long been known that radiation can induce highly complex reaction chemistry. At Argonne National Laboratory, one of the first pulse radiolysis experiments was done.[1] In pulse radiolysis a short pulse of ionizing radiation is used to create radicals and ions and the evolution of this chemistry is then observed.

In the more than 35 years since the first pulse radiolysis experiments, the time resolution of pulse radiolysis has increased from microseconds to under 5 ps.[2] With the advances in accelerator technology, it is now possible to push the time resolution to below a picosecond.

Pulse radiolysis and flash photolysis experiments are complementary. Pulse radiolysis excels in creating ions and in mimicking the chemistry that can occur in real-world systems such as waste storage tanks and biological systems after the impingement of ionizing radiation. In such systems, the concentration of reactants is very high and so the chemistry can occur at times less than a few picoseconds.

The important chemistry that needs study has prompted the Argonne Chemistry Division to propose a new pulse radiolysis facility. We envision a facility that will be used by the entire radiation chemical community to probe important chemical processes. In this paper we shall discuss

- The Chemical and Physical Processes that can occur.
- The design criteria for the facility.
- Some of the specific experiments that we plan to do

2 PHYSICAL AND CHEMICAL PROCESSES

Figure 1 displays a simplified picture of the chemical and physical processes that can occur after radiolysis. If there are high concentrations of reactants, they can easily compete with relaxation fragmentation and solvation.

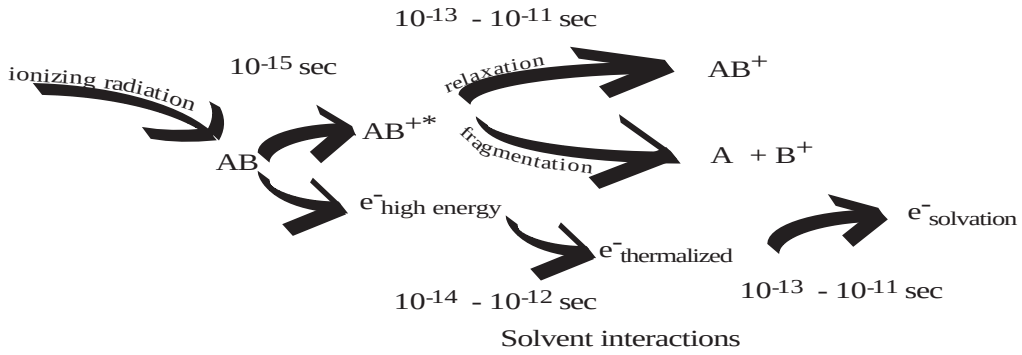

Figure 1: Schematic of the physical and processes occurring after radiolysis.

As one can see from looking at the figure, there are many processes that will occur at times where time resolution better than the 5-30 ps that are presently available in radiolysis experiments.

* Work performed under the auspices of the Office of Basic Energy Sciences, Division of Chemical Science, US-DOE under contract number W-31-109-ENG-38.

3 THE DESIGN CRITERIA FOR THE FACILITY

Recently there have been several reports of sub-picosecond pulses from linear accelerators.[3] However the goal of our project is to develop a sub-picosecond pulse radiolysis facility. This means that 1) there must be a sufficiently large concentration of species created and 2) there must be a detection technique that can make use of the short pulse and that will be of sufficient generality to

make meaningful measurements for a large variety of chemical systems. In addition, we had the desire to make a facility that would be usable for more general experiments and would not be limited to sub-picosecond experiments.

The initial design criterion was to create a system that could be used for optical absorption measurements. Optical absorption is applicable to a large variety of chemical systems. While single shot kinetics would be ideal, such measurements at short time scales are very difficult. Streak cameras are unsuited to such measurements. A typical experimental layout is shown in Figure 2.

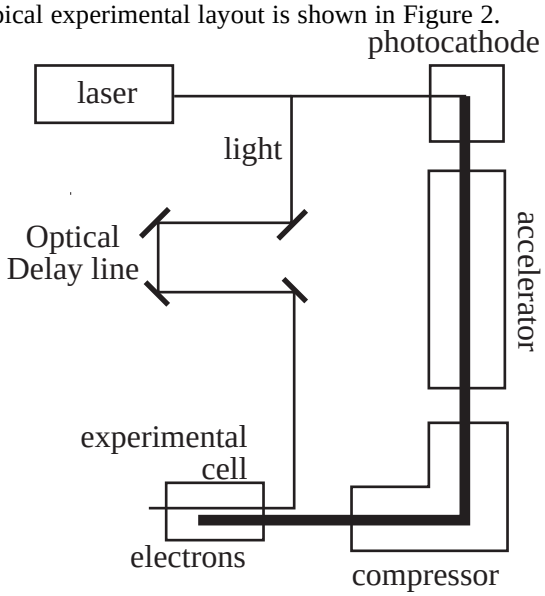

Figure 2: Pump probe measurement technique.

This figure shows a simple pump-probe detection technique. The time that the light strikes the cell can be altered by changing the length of the optical delay line. Thus time resolution depends only on the width of the electron pulse, the light pulse and the synchronism between them. Time resolution can then be reduced to a distance. For 1 ps, a distance of 0.3 mm is needed, easily measured and controlled. A similar technique could be used for fluorescence detection using upconversion or for 4-wave mixing techniques such as CARS (Coherent Antistokes Raman Scattering). These techniques make use of the availability of a synchronized laser.

3.1 General Requirements

To make use of the resolution available from the width of the accelerator pulse, it is necessary to

- Have the pulse width of the probe laser pulse to be less than the width of the electron pulse.
- Have the electron pulse and the accelerator pulse be synchronized as they pass through the sample cell
- Keep synchronization between the linac pulse and the laser pulse

The width of the laser will be narrower than the electron pulse. In fact, one of the problems will be stretching the laser pulse to a width that is appropriate for injecting electrons into the accelerator. Modern lasers will have a pulse width of a few hundred femtoseconds, too short for injecting electrons into an accelerator.

The synchronization between the light and the electrons can be assured by keeping the length of the cell sufficiently short. If we assume a refractive index of 1.5 for the sample, then the difference in transit times for the electrons and the light will be less than 0.5 ps if the sample length is less than 0.3 mm long. There is no difficulty in creating a cell of that depth; the primary difficulty is that such a short cell will limit the amount of optical absorption.

The most difficult problem will be the synchronization between the light and the electrons. While the electrons and the light should be synchronized when the electrons are formed, they may not be synchronized at the exit of the accelerator. Because the compressor works by changing the transit time through the magnets as a function of electron energy, anything that changes the energy of the electron pulse will change the time at which the electrons strike the cell relative to the light pulse. These can include different amounts of energy in the accelerating waveguides and the synchronization of the laser pulse relative to the RF of the accelerator. For example calculations suggest that a shift of 1 ps in the timing between the RF and the laser can yield a shift of 0.5 ps in the transit time.

Table 1 shows the proposed pulse widths. The larger pulses will be very useful for experiments when second order reactions are studied or when weakly absorbing species are formed.

Table 1 – Pulse characteristics.

Pulse Width	Charge
0.6 ps	2 nC
1.0 ps	5 nC
3 ps	10 nC
8 ps	50 nC
45 ps	90 nC
30 ps	25 nC (present linac)

3.2 Detection Options

A large variety of optical detection techniques are available that will make use of the synchronized probe light source. Figure 2 shows the experimental layout for optical absorption. The diagram suggests that the laser that ejects the electron will be used as the detection light source. This is clearly an over simplification because techniques such as optical parametric oscillators can produce a wide variety of wavelengths that can be used as probe sources. With the high powers available, continuum generation can be used, which will provide a white light source that can be used as a probe light source.

Present picosecond experiments have used Cerenkov light as the probe light. Experiments using this probe source have been limited in signal-to-noise because of the shot-noise limit. With a laser available as a probe light source, the signal-to-noise should be much larger.

Fluorescence can be detected either using a streak camera or fluorescence upconversion. With fluorescence upconversion, one can impinge the fluorescence signal and the probe light on a crystal. The probe light source can act as an optical gate that will sample the fluorescence when the probe light is there.

With the availability of intense, synchronized probe laser pulses, all the sophisticated techniques available in laser spectroscopy may be used when appropriate. One well-known technique is CARS spectroscopy where the vibrational state of a molecule can be measured using visible spectroscopy.

4 SCIENTIFIC GOALS FOR A SUB-PICOSECOND PULSE RADIOLYSIS FACILITY

As stated in the introduction, pulse radiolysis and flash photolysis are complementary techniques. While the time resolution of flash photolysis has always been greater than pulse radiolysis, there are experiments that are best done using pulse radiolytic techniques. These include:

Studies of the primary processes in radiation chemistry can only be studied using these techniques. The kinetics of the geminate recombination reactions of the electron in water has been studied using lasers. It has been shown that the rates of these reactions depend on the photon energy producing the hydrated electron.[4] This means that the spatial distribution of the electron depends on the photon energy. Thus there will be no straight-forward correlation between the laser experiments and the radiation experiments. These recombination reactions depend on the distance distribution that is created in the ionization event and the distribution depends on the source of ionization.

Laser studies have been very effective in studying the solvation of excited states (dipole solvation). However until radiation chemical techniques were used to study solvation, ionic solvation was not measured. The unexpected differences between ion solvation and dipole (excited state) solvation were only discovered with pulse radiolytic techniques.

Ionization by lasers depends on the optical cross sections while ionization by ionizing particles depends on the number of electrons present. These differences will allow one to probe a wide variety of chemical processes.

4.1 Nonhomogeneous processes

Radiation deposits energy nonhomogeneously, which leads to many of the important characteristics of radiation-induced chemistry. These high local concentrations of radicals and ions will recombine very quickly. The competition between the fast recombination and reaction with other species in the system will determine the efficacy of the radiation-induced reactions. With the new radiolysis facility, we will probe these reactions on faster time scales.

4.2 Chemistry before Relaxation

Radiation will produce radicals, ions and highly excited states in fluids. In traditional chemical experiments, the concentration of additives is low so that the reactions with the additives will occur much more slowly than the relaxation of the excited states and highly excited vibrational states of the solvent. However, when the concentration of reactants is high, one will have reaction competing with the relaxation process. Without an explicit understanding of the relaxation processes, it then is not possible to predict the final chemistry.

We have tried to summarize a few of the experiments that will require the very fast time resolution of a new facility. In such a short space and in this forum further details are not appropriate.

5 SUMMARY

In this short discussion we have tried to summarize our design goals for a subpicosecond pulse radiolysis facility. We have tried to show that such a facility is more than a short pulse – detection techniques must be taken into account when designing the facility because the goal is to make chemically significant measurements. We have tried to highlight a few fields of study for the future.

Details on the machine design have been ignored in the present discussion. Information about the design process can be found in the paper by Hans Bluem and coworkers in this conference. Details about the laser design can be found in the paper by Robert Crowell and his coworkers.

6 ACKNOWLEDGMENTS

We gratefully acknowledge the scientific discussions of the Radiation and Photochemistry Group, Alexander D. Trifunac, David M. Bartels, Ilya A. Shkrob and David W. Werst and discussions of the Electron Transfer and Energy Conversion Group, John R. Miller and Dani Meisel. Nothing could have been done without the simulations of Hans Bluem, Alan Todd and their collaborators at Northrop Grumman.

7 REFERENCES

[1] M. S. Matheson and L. M. Dorfman, Detection of short-lived transients in radiation chemistry. *J. Chem. Phys.* **32**, 1870-1 (1960).

[2] M. C. Sauer, Jr., Charles D. Jonah and C. A. Naleway "Study of Reactions of Geminate Ions in Irradiated Scintillator, Hydrocarbon Solutions Using Recombination Fluorescence and Stochastic Simulations" *J. Phys Chem.* **95**, 730-740 (1991).

[3] Kozawa, T.; Kobayashi, T.; Ueda, T.; Uesaka, M. **"**Generation of high-current (1 kA) subpicosecond electron single pulse"**.** *Nucl. Instrum. Methods Phys. Res., Sect. A* **399** 180-184 (1997).

[4] Crowell, Robert A.; Bartels, David M. **"**Multiphoton Ionization of Liquid Water with 3.0-5.0 eV Photons"**.** *J. Phys. Chem.* **100**, 17940-17949 (1996).

NEW TECHNIQUES FOR EMITTANCE TUNING IN THE SLC*

P. Raimondi, R.W. Assmann†, T. Barklow, J.R. Bogart, F.J. Decker,
C. Field, H. Hendrickson, D.J. McCormick, M. Minty, N. Phinney,
M.C. Ross, J.L. Turner, T. Usher, M.D. Woodley, F. Zimmermann
SLAC, Stanford, CA 94309, USA

Abstract

In the 1997-98 run, the luminosity of the SLAC Linear Collider (SLC) increased by about a factor of four compared to previous runs. A significant contribution to this improvement came from revised emittance tuning techniques throughout the accelerator. A new strategy was used to cancel wakefields and dispersion in the LINAC. Careful monitoring and control of the ARCs optic reduced the emittance growth due to coupling, wakefields and synchrotron radiation. New Final Focus optics and upgraded diagnostics improved the emittance measurement resolution and otpimization. These and other new procedures resulted in an average 25residual emittance growth in both planes from the damping rings to the interaction point.

1 LUMINOSITY OVERVIEW

During the 1997-98 run, a total of 350,000 Z^0s were recorded with an average electron beam polarization of 74%. This was nearly double the total sample of events from all previous SLD runs and reflected a substantial increase in luminosity of about a factor of four. The peak luminosity delivered was 300 Z^0s per hour or 3 10^{30} $cm^{-2}s^{-1}$ with a record of more than 5300 Z^0 events recorded in 24 hours. The luminosity steadily increased throughout the run bringing the SLC to within a factor of two of design [1]. The improvement was due almost entirely to changes in tuning procedures and reconfiguration of existing hardware with no major upgrade projects.

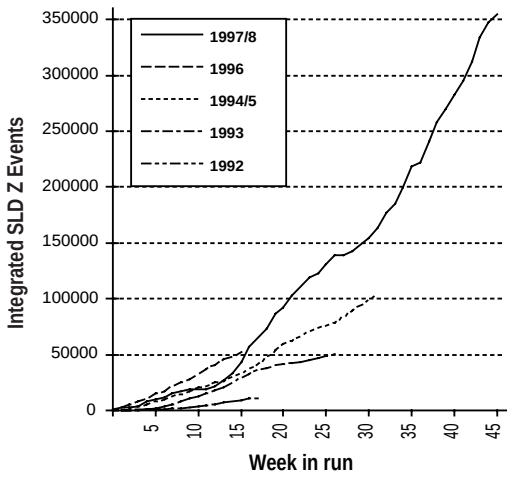

Figure 1: History of integrated SLD Z^0 events from 1992 through 1998, showing the steep increase in 1997-98.

* Work supported by the Department of Energy, contract DE-AC03-76SF00515

† present address: CERN, SL division, Geneva, Switzerland

The luminosity of a linear collider L is given by

$$L = \frac{N^+ N^- f}{4\pi\sigma_x\sigma_y} H_d, \quad (1)$$

where $N^\pm$ are the number of electrons and positrons at the interaction point (IP), f is the repetition frequency, $\sigma_{x,y}$ are the average horizontal (x) and vertical (y) beam sizes, and H_d is the disruption enhancement factor which depends on the beam intensities and on the transverse and longitudinal beam sizes. At the SLC, the repetition frequency is 120 Hz and the beam intensity is limited by wakefield effects and instabilities to about $4\ 10^{10}$ particles per bunch. The only route to significantly higher luminosity is by reducing the effective beam size. Using the definition of emittance as the product of the beam size and angular divergence ($\theta_{x,y}$), $\epsilon_{x,y} = \sigma_{x,y}\theta_{x,y}$, one may reexpress the luminosity as

$$L \propto \frac{\theta_x}{\epsilon_x}\frac{\theta_y}{\epsilon_y} H_d. \quad (2)$$

For higher luminosity, the basic strategy was to decrease the emittance and increase the angular divergence. Any reduction in beam size strengthens the disruption, or mutual focusing of the beams, and further increases the luminosity.

2 EMITTANCE TRANSPORT

A variety of new techniques were used to minimize the emittance growth from the damping rings to the final focus. In the ring-to-linac transfer lines where the bunch length is compressed, the horizontal beam size is large and fills the available aperture, causing emittance dilution and beam loss. Ballistic beam-based alignment minimized dispersion generated in the strong matching quadrupoles. A new optics with a larger momentum compaction factor better matched the beam size to the apertures and reduced losses [2]. Shielding sleeves were also added to reduce wakefields generated by the bellows in the beamline.

In the linac, a new implementation of two-beam dispersion free steering [3] constrained the electron and positron beams to follow the same trajectory, minimizing dispersion and wakefields. Once established, the trajectories were stable over several months, with only occasional resteering required. A stronger focusing lattice [4] improved the damping of incoming oscillations while ensuring compatibility with PEP-II (the SLAC B-factory) operation. This also allowed a reduction in the beam energy spread introduced for BNS damping which helped minimize chromatic emittance growth. Known sources of jitter from vibrations in the mechanical systems near 10 Hz and in the water cooling systems near 59 Hz were reduced by stiffened supports, upgraded water pumps [5], and special high-speed feedbacks.

Another important improvement was the development of a fast, accurate procedure for phasing the rf accelerating voltages. All of the 30 linac subboosters, each of which drives 8 klystrons, could be phased in about 2 minutes to an accuracy of 1-2 degrees. This provided a stable, well understood energy profile throughout the run [6].

In the collider arcs, emittance growth is inevitable due to the emission of synchrotron radiation in the bending dipoles. In addition, the non-planar geometry of these beamlines can cause transverse coupling. In this run, the optical properties of the arcs were more precisely optimized and maintained. First the beam trajectory was carefully centered through the magnets to reduce wakefields. Then the emittance growth was constantly monitored and minimized using refinements of the techniques first developed in 1990 [7]. The realization that the final focus dispersion matching quadrupoles strongly coupled the beam led to the development of new methods for matching dispersion in the arcs themselves.

Most importantly, the strategy for global optimization of the linac emittances was changed significantly. Since 1991, the SLC has used closed betatron oscillations early in the linac to cancel wakefield tails caused by residual structure misalignments [8]. Studies showed that where the energy spread is large, dispersion dominates the emittance growth. Oscillations used to cancel dispersion may generate additional wakefield tails. At low energy, the optics is also extremely sensitive to small errors in the energy profile. Tuning further downstream in the linac where the energy spread is small, produced more stable, reproducible results.

In previous runs, emittances were optimized using wire scanners located near the end of the linac at about the 90% point. Measurements in 1997 indicated that significant emittance growth can occur in the last 200 meters, as predicted by simulations [9]. The solution was to use wire scanners early in the final focus for the global optimization. To provide high precision measurements during luminosity running, several upgrades were required. Thin carbon wires were installed to allow measurements while the SLD detector was logging data. New optics improved the phase space coverage and high resolution (≈ 2 μm) beam position monitor electronics allowed precision correction for pulse-to-pulse orbit fluctuations. The revised optimization strategy produced not only a smaller emittance, but also much less variability without anomalous sources of emittance growth. Most significantly, for the first time, the emittance transport was qualitatively and quantitatively understood and controlled.

3 FINAL FOCUS IMPROVEMENTS

The key to improving the performance of the SLC final focus (FF) was the understanding that for non-Gaussian beam distributions, the beam sizes, $\sigma_{x,y}$, in Eq. 1 must be calculated from the integral over the beam overlap distributions and not from the root mean square (RMS) distribution. The upper curve in Fig. 2 shows the RMS beam size as a function of angular divergence for the 1996 FF optics. Because the RMS is dominated by tails containing only a small fraction of the beam, it increases after an optimum divergence value. The second curve shows the effective beam size when the integrals are properly evaluated and predicts higher luminosity for increased angular divergence. The third curve demonstrates the gains from a different FF optics used for this run where the final demagnification was moved closer to the interaction point (IP). With these optics, the divergence, beam size, and predicted disruption enhancement (assuming a 1 mm bunch length) were changed from $\theta_x = 350$ μrad, $\sigma_x = 2.0$ μm, $H_d = 1.3$ to $\theta_x = 470$ μrad, $\sigma_x = 1.5$ μm, $H_d = 2.0$. This was still less than the optimal values of $\theta_x = 530$ μrad, $\sigma_x = 1.3$ μm, and $H_d = 2.2$.

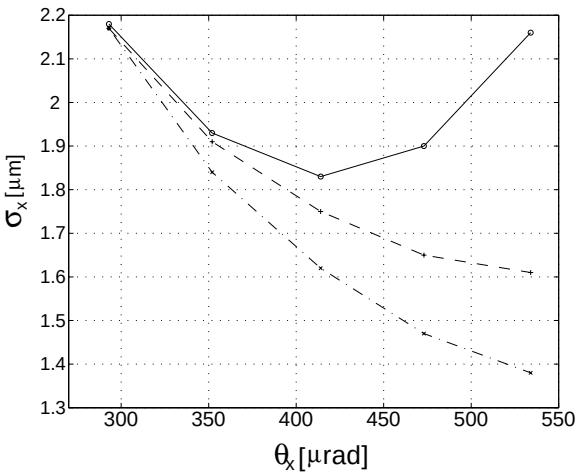

Figure 2: Horizontal beam size σ_y at the SLC IP as a function of angular divergence θ_y. Curves (solid), RMS, and (dashed), with proper integration, are for the 1996 optics. The dot-dashed is for 1997 optics.

At the SLC, the maximum achievable angular divergence is limited primarily by backgrounds in the SLD detector. In preparation for the 1997 run, changes were made to the FF collimation and to the masking near the IP. Collimators from the FF were moved to the arcs and rotated by 45° to allow for 'round' collimation. In addition, for most collimators ($\approx$60 jaws in total), a new technique ensured that they were properly centered on the beam to minimize wakefield kicks. Later, offline studies using upgraded tracking codes revealed that part of the detector backgrounds were generated by higher order chromatic terms ($\sim \delta^2$), specifically T_{266} and T_{226} in transport notation. Based on these results, permanent magnet sextupoles were installed just after the end of the linac and additional sextupoles were energized in the FF to cancel these contributions.

In addition to the new optics mentioned above, several other upgrades to the FF were implemented during the run to reduce the emittance growth due to synchrotron radiation and to cancel residual higher order aberrations. The additional FF sextupoles not only reduced backgrounds, but also reduced the contribution to the vertical beam size from two third-order aberrations, U_{3246} and U_{3244}, generated by the interleaved sextupoles. At the end of 1997, the average bend radius in the FF was increased by using offset quadrupoles and steering dipoles. This reduced synchrotron radiation emittance growth in both planes. In

February, permanent magnet octupoles were installed to further cancel the U_{3246} and U_{3244} vertical aberrations. The observed decrease in the vertical beam size was about 15%. Finally, in May the strength of the final quadrupole nearest the IP was increased to further raise the horizontal angular divergence. The horizontal and vertical beam sizes achieved were $\sigma_x = 1.5$ μm and $\sigma_y = 0.65$ μm, which together yield a beam area which is a factor of 3 smaller than the SLC design value.

4 LUMINOSITY OPTIMIZATION

To achieve and maintain the minimum beam size at the SLC IP, 5 final corrections are routinely optimized for each beam. These include centering of the x and y beam waist positions, zeroing of the dispersion η_x and η_y, and minimization of an $x-y$ coupling term. Since the first SLC collisions, an automated procedure has been used to scan the beam size as a function of each parameter and set the optimal value. The beam size was measured with a beam-beam deflection scan but this technique lacked the resolution required to measure micron-size, disrupted beams. It was estimated [10] that poor optimization caused a $20-30\%$ reduction in luminosity during the 1996 run. For 1997, a novel 'dithering' feedback was implemented which optimizes a direct measure of the luminosity (i.e. the beamstrahlung signal) as a function of small changes in each parameter [11]. By averaging over thousands of beam pulses, it was possible to improve the resolution by a factor of 10.

The feedback was configured to cycle through each of the 10 parameters automatically, typically every hour or two. In contrast, the old, slower, more invasive procedure was typically implemented only a few times per day. Because of the improved resolution, it was possible to align the FF sextupoles and new octupoles much more accurately and to develop new methods for cancelling all of the second order chromatic and geometric aberrations. An added benefit of the feedback optimization was that it was highly reproducible and no longer required operator intervention. Lastly, with the improved optimization and increased stability in the upstream systems, high luminosity was more quickly reestablished after any interruption.

5 DISRUPTION

In the 1997-98 SLC run, a significant luminosity enhancement from disruption was demonstrated for the first time. As the beams collide, each beam is focused by the field of the other beam, causing the transverse size to shrink. If the resultant focal length is shorter than the bunch length, the average beam size seen by the other beam decreases, which increases the luminosity. The magnitude of the disruption, or pinch effect, depends on the transverse beam size, the bunch length and the beam intensities. For this run, along with the significant reduction in beam size, the bunch length was carefully monitored and set to the optimum value [12]. In addition, the beam currents were maintained at record levels partly due to bunch precompression in the damping ring [13]. Fig. 3 shows the ratio of luminosity as recorded by SLD to that calculated from the measured beam parameters assuming rigid (i.e. undisrupted) beams. The data are in agreement with the theoretically calculated disruption enhancement. At the highest luminosity, the enhancement was more than 100%.

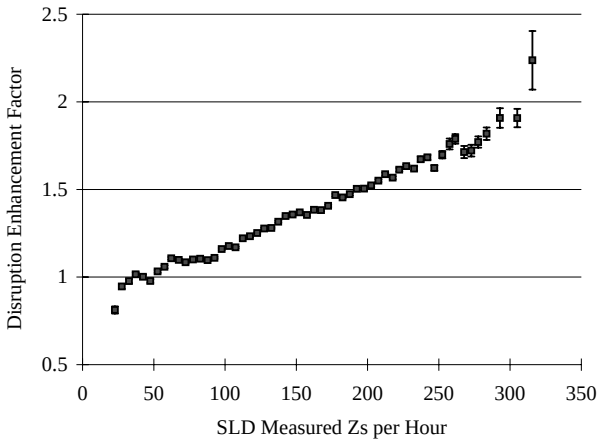

Figure 3: Ratio of luminosity measured by SLD to that calculated for rigid beams without disruption.

6 SUMMARY

The remarkable increase in luminosity after nearly a decade of operation demonstrates that the SLC remains on a steep learning curve and has far from exhausted its potential for further improvements and for a deeper understanding of linear colliders. The success of the 1997-98 SLD run was due to the hard work and dedication of many groups and individuals. In particular, we acknowledge the outstanding efforts of the operations crews and the engineering and maintenance staff as well as the physicists from SLD and the Accelerator Research departments.

7 REFERENCES

[1] SLC Design Report, R. Erickson (ed.), SLAC-PUB (1994).
[2] S. Kuroda, SLAC-CN-418 (1997).
[3] R. Assmann *et al*, this conference.
[4] Y. Nosochkov, unpublished (1997).
[5] R.E. Stege, J.L. Turner, Beam Instrumentation Wkshp (1998).
[6] J. Bogart *et al*, EPAC98.
[7] T. Barklow *et al*, AIP Conf. Proc **255**, (1992).
[8] J.T. Seeman *et al*, HEACC (1992).
[9] R. Assmann *et al*, SLAC-PUB-7577 (1997).
[10] P. Emma *et al*, IEEE PAC (1997).
[11] L. Hendrickson *et al*, ICALEPCS Conf. (1997).
[12] F. Zimmermann *et al*, EPAC98, and SLAC-PUB-7898.
[13] M. Minty *et al*, IEEE PAC (1997).

TOWARDS THE ZERO BEAM DIAGNOSTICS

A. Rovelli
INFN Laboratori Nazionali del Sud, via S. Sofia 44/a, 95123 Catania, Italy

1 INTRODUCTION

Low intensity beam diagnostics is a challenge that has involved the accelerator community in the last years. The interest in this activity is due to the fact that a number of applications are based on the use of low intensity beams. The produced effort is mainly oriented to improve the performances of the conventional beam diagnostics in order to work properly also when the beam intensity goes down to $10^8 \div 10^6$ pps. A very important incentive for this activity came few years ago with the development of a new type of beam facility for the production of radioactive ion beams (RIB) [1]. The new challenge was very hard because the required sensitivity for the beam diagnostics was in the range $10^{10} \div 10^5$ pps, or even lower. The necessity to measure the beam characteristics all over such a wide range and the variety of ions and energies involved forced the development of a complete set of beam instrumentation able to satisfy all the requirements.

2 THE PROBLEM EVALUATION

A facility for the production of radioactive ion beams is the best reference to evaluate all the problems related to the low intensity beam diagnostics; the typical variety of ions, energies and intensities involved, offers the meaningful scenery inside which the new apparatus have to be developed [2]. The first items to be considered are the expected intensity and energy range. From an overview all around the projects it is possible to individuate two ranges:

- beam intensity: $10^5 \div 10^{11}$ pps
- beam energy: $10^4 \div 10^7$ eV

Once fixed the operative ranges, it is necessary to fix also few general requirements related to the specific use of these devices. In addition to the typical parameters to characterize an ion beam in the longitudinal and in the transverse plane, a new request, typical for a RIB facility, is the unambiguous isotope identification. To perform all these measurements these devices have to guarantee:

- the highest sensitivity to the lower current;
- the highest sensitivity to the lower energy;
- the highest reliability;
- the highest strength;
- the highest simplicity to use and to maintain it.

Furthermore, all these requirements have to be added to the typical ones for standard beam diagnostics.

3 THE GUIDELINES

Two main guidelines are followed approaching the low intensity beam diagnostics problem. The first one, based on the performances improvement of conventional techniques, consists of a deep investigation about the typical sensitivity limitations of the beam diagnostics. The second one is based on the evaluation of using particle detection techniques very reliable for sensitivity and precision in nuclear as well as high energy physics research. It is evident that a realistic solution is represented by two different sets of devices with an overlapped operative range to perform relative calibrations for absolute measurements.

3.1 Conventional techniques

Conventional beam diagnostics is a very wide set of instrumentation: secondary electrons emission (wire, grids, etc.), light emission (screen, fiber, etc.), gas ionization (residual, chamber, etc.) and charge induction (pick-up, transformer, etc.) are the most diffused techniques. The typical advantages are the simplicity in their structure, use and maintenance. This is a very important consideration that has to be always taken in account also developing low intensity beam diagnostics. The reason of this simplicity is that they were developed mainly looking the operative procedures performed by the people (the console operators), which are not necessarily expert of particles detection techniques, that have to accelerate and transport the beam from the source to the experimental point. The low signal-to-noise ratio of a lot of these devices is the main limitation to their use for low intensity beam diagnostic. With the exception of the ionization chambers, extensively used also as particles detector, all the others techniques have to be subjected to a deep revision in order to increase the general performances toward the lower limits. This revision has to be performed following two directions: the research for new materials (as sensor) and the electronics improvement. The new materials have to guarantee:

- higher conversion efficiency;
- higher collection efficiency;
- lower background noise;
- higher radiation hardness;

The electronics improvement has to guarantee:

- lower electronic noise (connectors, contacts, cables, components, etc.);

- lower electromagnetic noise (grounding, shielding, etc.);
- higher signal first amplification;
- improving the read-out electronics;
- higher radiation hardness;

The goal is to reach the minimum sensitivity of $10^7 \div 10^5$ pps. In this way it will be possible to overlap the typical highest limit of the nuclear detectors and to perform absolute calibrations with respect reference devices.

3.2 Particles detection techniques

The typical instrumentation and techniques used in nuclear as well as high energy physics research can be used for low intensity beam diagnostics if they are modified looking the peculiarity of this application. Semiconductors, gas chambers and scintillators based detectors offer, together with other ones, a wide choice in terms of performances and versatility.

The advantages are the sensitivity, the precision and the absolute measurements that can be performed after a suited calibration. The main limitation is the setup complexity from the point of view of its structure and use. Beam diagnostic measurements require a fast read-out of the information, on-line if possible, and at the same time well understandable by the operators. In this sense the main effort has to be devoted to:

- reduce the setup complexity;
- reduce the measuring time;
- increase the general hardness;
- increase the automated procedures;

3.3 The ideal solution

All the arguments up to now mentioned allow the identification of the ideal solution. A list of the recommendations for such a device is the following:

- measure different beam characteristics;
- cover a wide intensity range;
- cover a wide energy range;
- allow self calibration;
- minimize the interferences with the beam;
- minimize maintenance operations and price;
- maximize reliability and versatility;
- allow different measurement modes:
  - charge/current collection;
  - continuous/pulsed acquisition;
  - integration time settable;

Very important is the integration of this instrumentation in the main control system of the facility. This feature means that the operator in the console must operate the beam management with no regard to the beam intensity. Furthermore, the choice of the right device has to be done considering that the setup structure has to be strong enough to resist to quick intensity changes. If necessary, a suited interlock system has to be provided in order to protect the device in case of mistakes or faults.

4 SEMICONDUCTORS

The semiconductors probably are one of the most popular materials category used to develop nuclear detectors. Their versatility allows the realization of different configurations very useful also for beam diagnostics. In the end of this chapter it will be reported also some applications based on a particular material, the diamond. It is an insulator but it can be considered, from the applications point of view, the most important alternative to the use of semiconductors.

4.1 Silicon based detectors

To state the reason for the wide use of the silicon as particles detector the best and the easiest way is to list its main characteristics:

- the mean energy to produce a pair is 3.62 eV;
- well suited for different configurations;
- good timing performances;
- medium price.

Unfortunately its radiation hardness is very low. This aspect limits its use for beam diagnostics; in particular, it can be used only in single particle counting mode and, in any case, great care has to be devoted to protect it.

Silicon based detectors can find useful applications for very low intensity beam diagnostics. Silicon micro-strips, for example, can be used as beam profile and position monitor. The sensitivity and the spatial resolution (higher than 100 μm over a 10×10 cm^2 area) are very good, but the electronics and the price are very expansive. Much more suited is the application for isotope identification [3]. A thin Au target is used and a silicon telescope is positioned at a suited angle in order to match a suited scattering counting rate. The ΔE-E information allows the isotope identification. The operative energy range depends by the silicon and dead layers thickness.

4.2 Germanium based detectors

This very sophisticated kind of detector is mainly used for high resolution gamma ray spectroscopy. Its main characteristics are.

- the mean energy for a pair production is 2.96 eV;
- operating at 77 °K;
- very low radiation hardness;
- very complex experimental setup;
- very high price.

It is obvious that such a detector has several limits for beam diagnostics application but, for a specific use, can be very useful. For example, it is a powerful tool for very rare radioisotope identification [4]. The main advantage of this setup is that implanting the radio-isotope at very low energy it is possible its identification just after its production, allowing an efficient tune of the transport line avoiding any beam contamination.

4.3 Diamond based detectors

The operating principle of this isolating material is the same of the semiconductors one. Its main features are:

- the mean energy to produce a pair is ~ 13 eV;
- the collection length is 50 ÷ 100 μm;
- very good radiation and power hardness;
- very good timing performances;
- versatility for different configurations;
- high price.

Nevertheless the higher energy to produce a pair, an important advantage with respect the semiconductors is the high energy gap that strongly reduces the noise. The strength of this material allows its use with high intensity as well as low intensity beams. The very short collection length, depending by the nature and density traps, determines very high performances in terms of spatial and time resolution. Can be used in pulses counting mode, for very low beam intensities, as well in current mode looking the continuous component of the signal produced by high intensity beams. An interesting application is the use of diamond film with 100 μm pitch micro-strips [5]; this setup allows the beam profile and position measurement. The increasing interest on such a material is due to the advanced techniques nowadays available for the production of synthetic diamonds at realistic prices. The CVD (Chemical Vapor Deposition) technique allows the production of very thin diamond films of some centimeter size; the possibility to realize wide homogeneous layers with controlled impurity characteristics, justifies the big effort that is devoted to test new devices for beam diagnostics.

5 GAS BASED DETECTORS

Many detectors are based on the ionization produced by a charged particle crossing a gas volume. The gas can be used to fill a chamber with thin entrance and exit windows, or can be the residual gas itself contained along the beam pipes used to transport the beam.

The most famous gas detector is the gas chamber; it founds many applications also for beam diagnostics. Its versatility in terms of dimensions and shapes allows to develope a variety of setups well suited for beam diagnostics applications. The signal is produced by the energy loss into the gas and its amplitude depends by the gas pressure and by the collecting electric field. The mean energy to produce a pair is about 30 eV, depending by the gas. Very important features are:

- very good radiation hardness;
- energy loss and charge multiplication effect;
- very good sensitivity;
- versatility for different configurations;
- medium price.

The most interesting configurations for beam diagnostics purposes are the wire chambers and the micro-strips chambers [6]. Their main are the sensitivity and the spatial resolution. Particular interest is devoted to the micro-strips chambers because the lithographic procedure to realize the strips on a suited substrate (typically glass) allows to obtain 100 ÷ 200 μm (the pitch) of spatial resolution. Also the chamber size can be reduced as well as the setup complexity.

Two very interesting devices were developed at the LNS to measure the beam profile [7] and for particles identification [8]. Both are based on the use of a 5×5 cm^2 glass plate with 200 μm pitch of Au strip. To measure the beam profile the strips are parallel with respect the beam direction, while for particles identification are perpendicular. The whole structure, very simple and light, can be inserted or removed, through a suited actuator.

5.1 Residual gas detectors

The ionization produced by the beam interaction with the residual gas contained along the beam pipes can be used to measure several beam properties without any interference with the beam itself. Generally and especially with low intensity beams, the ionization events are very rare then it is necessary some signal amplification. The typical setup foresees a charge collecting field and an electron amplifier, generally a micro-channel-plate (MCP), to collect the charges. This setup has no problems for the radiation damage, on condition that it is prevented from the direct beam interaction. The MCP choice depends by the application; several model with different characteristics and performances are available. Here is reported a brief description of two different techniques.

The MCP with electric readout is a detector where the signal coming from the collecting electrode is directly acquired and analyzed. This system, in different configurations, is very useful for both transversal and longitudinal beam profiles. To measure the transverse beam profile, as well as the position, the collecting electrode is coupled with a silicon micro-strips plate; the spatial resolution is very good (0.3 ÷ 1 mm). A similar setup [9], but coupled with a 50 Ω anode is used to measure the longitudinal beam profile with a very good time resolution (100 ÷ 200 ps).

The MCP with light readout is similar to the previous one; the only difference is that the electrons coming out from the amplification stage are sent onto a scintillating screen. The light produced by the electrons hitting the scintillator can be acquired through a common CCD camera [10] or directly through silicon strips. The signal is acquired by a frame-grabber PC board. A simple program allows displaying the on-line acquired images together with the beam profile and position information; is better to use a camera with gain and shutter control to match the setup sensitivity.

6 SEM BASED DETECTORS

Secondary electrons emission based devices probably are the most diffused ones for beam diagnostics. The ions hitting the outer layer of several materials produce an

electron emission that is proportional to the released energy. Because only the electrons contained in the first microns can exit from the material, the emission is a typical surface effect and it is proportional to the surface exposed to the beam. Moving wires, grids and thin foils are commonly used to measure several beam properties. The limitation of their use for low intensity beam diagnostics is mainly due to the bad signal-to-noise ratio. To improve their performances it is possible to devote particular care to the material selection and to the electronic noise reduction; in any case it is very difficult to increase their sensitivity more than 10^7 pps. To do that, it is necessary to develop most sophisticated apparatus based on such an amplification (MCP, channeltron, etc.) of the detected signal [11].

7 SCINTILLATORS BASED DETECTORS

As the previous category, also the scintillating materials are very well known and used for beam diagnostics applications. The main advantage with respect the SEM based devices is that the wide choice of materials and light detectors allows to develop several apparatus well suited also for low intensity beams. Very briefly, the main items for the scintillating materials are:

- fluorescent light due to the particles energy loss;
- mean energy to produce a photon is $10 \div 100$ eV;
- good radiation hardness for the inorganic ones;
- poor radiation hardness for the plastic ones;
- versatility for different configurations;
- medium price.

The first important question concerns the material choice. It is not so easy to have a global view on the scintillating materials because of their very big number, continuously in progress with the fast improvement of the technology to produce them. A significant contribute comes out also from other sectors of the scientific research where scintillating materials are employed for completely different applications. A simple way for a choice is to select them in terms of:

- the mean energy to produce a photon;
- the decaying time constant;
- the photon wave length;
- the refraction index of the material;
- the efficiency of photon collection;
- the radiation hardness.

Many other properties have to be taken in account: for examples, the mechanical features as well as the hygroscope one. In literature [12] are reported the most important features of the common organic and inorganic scintillators; also some amorphous materials like glasses, usually doped with rare earths elements (Tb, Gd, Ce, etc.), represent an alternative choice for radiation hardness and light emission efficiency. However, a scintillator based detector also consists of a suited photo-sensor and, sometime, a suited light-guide. Once fixed the scintillating material to be used, it is necessary to match its characteristics with the proper light-guide and photo-sensor. Also for the light detector there is a wide choice of devices. Rather than a long list of the available devices (photomultipliers tubes, photodiodes, avalanche photodiodes, hybrid photodiodes, etc.) it is better to do a brief overview of the most significant applications for low intensity beam diagnostics. Profile, total current and time measurements can be easily done using scintillating optical fibers and screens.

7.1 Beam profile and position monitor

The simplest setup is based on the use of a scintillating screen that intercepts the beam; the emitted light is collected through a quartz window by a CCD camera. The main limitation is the bad light collection efficiency that limits the use with low intensity beams. To improve its performances it is possible to use more efficient scintillating screens (Cr doped alumina, rare earths plastic sheets, etc.) or collecting with the same camera the light emitted at different solid angles.

A more sensitive setup was developed for very low intensity ($10^4 \div 10^6$ pps) and energy (higher than 10^4 eV) [13]. It is based on the use of the CsI(Tl). A small brick of this material is positioned behind a moving slit and it is coupled with a compact photo-tube by means of a PMMA prism. The photo-tube is completely shielded by the slit itself with respect to the beam. The use of faster scintillators (CsI, BaF_2, etc.) increases the upper limit of the count rate allowing absolute calibrations with normal intensities.

The scintillating fibers offer an interesting alternative. The advantage with respects the previous systems is that the efficiency in the light transmission is strongly improved. Plastics as well as glass fibers can be successful used depending by the application. A very simple setup was developed to measure the beam profile and position [14]. It is based on the same idea of the moving wires monitor. Sensitivity and spatial resolution depend by the fiber choice. Using glass fibers the radiation hardness is higher but the mechanical strength is lower. The light collection is performed through a compact photo-tube able to work also inside the beam pipe. A special I/V converter [15] was developed to get the continuous signal component as well as the impulsive one coming from the tube. This configuration allows to do measurements over the widest intensity range. The only limitations are the damage produced by the power released by the beam and the outer dead layer of the fiber (only the core is scintillating); this last problem limits its functionality at the lower energies.

7.2 Time structure and total current monitor

For this applications the best choice is the use of very fast organic scintillators. The high counting rate obtainable allows, if coupled with a suited photo-sensor, to get high time resolution and absolute current measurements over a wide intensities range.

To measure the phase of pulsed beams a useful setup is based on the use of a fast plastic scintillator [16]. The PILOT-U sensor is coupled with a photo-tube through a long optical fiber; the whole setup is mounted on a radial probe to measure the beam time characteristics inside the cyclotron. The operating range is $10^4 \div 10^6$ pps. The same setup can be also coupled with a silicon detector to perform ΔE-E measurements but at lower rates (10^3 pps).

Total current measurements can be performed using very fast scintillators after a suited calibration [17]. The short decay time of the polymeric plastic scintillators allows very high acquisition rates; they can be easily shaped in different geometry and are very cheap. The main drawback is their poor radiation hardness if used at low energies and high intensities.

8 SUMMARY AND PROSPECTS

It is not so easy to report a complete overview of the activities that are coming out developing low intensity beam diagnostics. The wide choice of materials, detectors and techniques involved produces an increasing quantity of experimental apparatus very different in terms of performances and operating ranges. In any case, this is an encouraging situation meaning that the interest is very high as well as the number of the possible applications.

At the end of this very general overview it is possible to draw some conclusions regarding the state of art and the prospects of this activity. To satisfy all the requirements for the low intensity beam diagnostics the investigation on the use of particles detecting techniques has produced the most promising results. Gas chambers as well as scintillators based detectors represent the preferred solutions for their versatility, reliability and cost. For the next future, also the diamond based detectors will represent a good alternative.

REFERENCES

[1] NuPECC Report, December 1997.

[2] J. D. Garret, *Nucl. Phys.* A 616 (1997) 3.
S. Kubono et al., *Nucl. Phys.* A 616 (1997) 11.
A. C. C. Villari, *Nucl. Phys.* A 616 (1997) 21.
D. Habs et al, *Nucl. Phys.* A 616 (1997) 29.
D. J. Morrissey, *Nucl. Phys.* A 616 (1997) 45.
I. Tanihata, *Nucl. Phys.* A 616 (1997) 56.
G. Ciavola et al, *Nucl. Phys.* A 616 (1997) 69.

[3] R. Pardo et al, presented at the RIB workshop, May 1997, Vancouver (Canada).

[4] B. Launé et al, presented at the RIB workshop, May 1997, Vancouver (Canada).

[5] H. Fenker et al., presented at *the IEEE Nucl. Sc. Symp.*, November 1995, S. Francisco (CA, USA).

[6] A.Oed, *NIM* A 263 (1988) 351.

[7] P. Finocchiaro et al., submitted to *NIM* A.

[8] S. Aiello et al., *NIM* A 400 (1997) 469

[9] J. P. Vignet et al, *AIP* 390 (1996) 223.

[10] A. Rovelli et al, *AIP* 390 (1996) 398.

[11] D. Shapira et al, presented at the RIB workshop, May 1997, Vancouver (Canada).

[12] G. F. Knoll, Radiation Detection and Measurement, 2nd edition.

[13] P. Finocchiaro et al., *IEEE Trans. on Nucl. Sc.*, in print.

[14] P. Finocchiaro et al., *NIM* A 385 (1997) 31.

[15] A. Amato et al., LNS Report 09-10-97.

[16] B. Launé et al, presented at the RIB workshop, May 1997, Vancouver (Canada).

[17] L. Rezzonico et al., presented at the RIB workshop, May 1997, Vancouver (Canada).

NONLINEAR SPACE CHARGE EFFECTS AND EMITTANCE GROWTH IN LINAC*

Yinbao Chen and Zhibin Huang
China Institute of Atomic Energy, P.O. Box 275(17), Beijing 102413

Abstract

The nonlinear space charge effect of bunched beam in linac is one of the important reasons that induce the emittance growth. The general formulas for calculating the potential of space charge with nonuniform distribution in surrounding structure are presented. For a bunched beam with different distribution in waveguide of linac, the expresses of the nonlinear field energy of a cylinder model of space charge are derived, and the numerical results of the nonlinear field energy for different density distributions are given. The emittance growth caused by these nonuniformities are discussed.

1 INTRODUCTION

In high-current beam for Free Electron Laser (FEL) and linear accelerator for high energy physics, induction linac for heave ion fusion, microwave devices and other applications, the space charge force is no longer small compared with the externally applied focusing forces. And the space charge effect is assumed to be one of the fundamental factors governing the beam dynamics.

Since the theoretical study and numerical simulation show that the nonuniform particle distributions have more electrostatic field energy per unit length than that of the equivalent uniform beam with the same current I, rms radius, and rms emittance. Therefore, it is suggested that this additional field energy is converted into particle kinetic energy and caused emittance growth as the distribution tends to become more homogeneous. This concept has been already accepted by many studies. Historically, the relationship between rms emittance and space charge field energy term for a continuous beam in a continuous focusing channel was firstly derived by Lapostolle [1]. The rms envelope equation with space charge was obtained by Sacherer [2]. An equation for emittance growth in space-charge-dominated beam having nonuniform density was derived by Struckmeier, Klabunde, and Reiser [3]. For a round continuous beam with an arbitrary distribution in a linear focusing channel, a differential equation for emittance change was derived by Wangler [4]. And, a generalized differential equation for a bunched beam was derived by Hofmann and Struckmeier [5]. Also, there are many further study results on the subject (see for examples Ref. [6] and [7]).

We should point it out that the above results concerning the calculation of the space charge field energy are based on the assumption of a continuous beam in a tube or a bunched beam in free space though involved with different density distributions. There is an obvious difference between these results and the reality of the electron (or ion) bunched beam in a linear accelerator or some microwave devices.

With regard to a bunched beam in surrounding structures, the space charge effects of nonuniform density distributions in waveguide of linac have been studied in our early work [8]. In this paper, first we review the main point of Ref. [8] to give the general formulas for potential induced by a cylinder of space charge with nonuniform density distribution in a surrounding cylinder (Section 2); in Section 3, for a bunched beam with nonuniform distributions in waveguide of linac, we present the expresses of the nonlinear field energy of a cylinder model of space charge; in Section 4, we show the numerical results of the nonlinear field energy for different density distributions; and finally, in Section 5, we discuss the emittance growth for a bunched beam in linac.

2 GENERAL FORMULAS FOR POTENTIAL OF NONUNIFORM CHARGE DISTRIBUTION

For the convenience of understanding and application, here we review the main point of Ref.[8] in which the general formulas for calculating the potential of space charge with nonuniform distributions in waveguide have been obtained.

A cylinder model of space charge is used to present a space charge bunch in linac as shown in Fig.1.

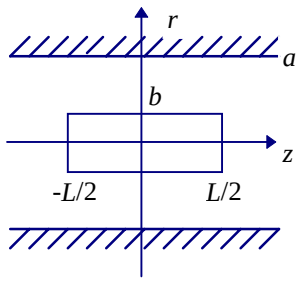

Figure 1. Cylinder model of space charge.

Letting a as the accelerator waveguide radius, b and $\pm L/2$ as the boundaries of the cylinder model in r and z directions,

* Supported by National Natural Science of China.

respectively. The potential induced by the space charge bunch with uniform distribution ρ in a cylindrical coordinate system can be written as follows [9]:

$$\varphi_0 = \rho\, f_0(r,z;b,L/2), \tag{1}$$

where f_0 is the potential induced by a unit space charge density.

According to the general formulas in Ref.[8], for the space charge bunch model with nonuniform charge density distribution $\rho(r,z)=\rho(r)\rho(z)$, we have the induced potential as follows:

$$\varphi = \int_0^{\frac{L}{2}}\int_0^b \rho(\xi,\zeta)\frac{\partial^2 f_0(r,z;\xi,\zeta)}{\partial\xi\partial\zeta}d\xi d\zeta\,. \tag{2}$$

Therefore, so long as the potential φ_0 (in the form of Eq.(1)) induced by a space charge bunch model with uniform distribution is known, the potential φ induced by the space charge with the same model but nonuniform distribution can be obtained from Eq.(2).

The potentials of a cylinder of space charge with uniform density distribution inside a conducting cylinder have been obtained : [9]

$$\varphi_{1,2} = \frac{2\rho ab}{\varepsilon_0}\sum_{l=1}^{\infty}\frac{J_1(k_l b)J_0(k_l r)}{(k_l a)^3 J_1^2(k_l a)}sh\frac{k_l L}{2}e^{-k_l|z|},\ \left(|z|>\frac{L}{2}\right), \tag{3}$$

$$\varphi_3 = \frac{2\rho ab}{\varepsilon_0}\sum_{l=1}^{\infty}\frac{J_1(k_l b)J_0(k_l r)}{(k_l a)^3 J_1^2(k_l a)}\left[1-ch(k_l z)e^{-\frac{k_l L}{2}}\right],\ \left(|z|<\frac{L}{2}\right), \tag{4}$$

where $J_i(k_l x)$ is the Bessel function of the ith order, and k_l is chosen so that $J_0(k_l a)=0$. Substituting Eqs. (3) and (4) into Eq. (2), we can rewrite the general formulas for calculating the potential induced by the same cylinder of space charge with nonuniform distribution as follows:

$$\varphi_{1,2} = \frac{2}{\varepsilon_0 a}\int_0^{\frac{L}{2}}\int_0^b \rho(\xi,\zeta)\sum_{l=1}^{\infty}\frac{\xi J_0(k_l\xi)J_0(k_l r)}{(k_l a)J_1^2(k_l a)}ch(k_l\zeta)e^{-k_l|z|}d\xi d\zeta,\ \left(|z|>\frac{L}{2}\right), \tag{5}$$

$$\varphi_3 = \frac{2}{\varepsilon_0 a}\int_0^{|z|}\int_0^b \rho(\xi,\zeta)\sum_{l=1}^{\infty}\frac{\xi J_0(k_l\xi)J_0(k_l r)}{(k_l a)J_1^2(k_l a)}ch(k_l\zeta)e^{-k_l|z|}d\xi d\zeta + \\ + \frac{2}{\varepsilon_0 a}\int_{|z|}^{\frac{L}{2}}\int_0^b \rho(\xi,\zeta)\sum_{l=1}^{\infty}\frac{\xi J_0(k_l\xi)J_0(k_l r)}{(k_l a)J_1^2(k_l a)}ch(k_l z)e^{-k_l\zeta}d\xi d\zeta,\ \left(|z|<\frac{L}{2}\right). \tag{6}$$

Suppose that the density is given by

$$\rho(r,z) = N_{t,l}\rho_{t,l}\,, \tag{7}$$

where the normalization constants $N_{t,l}$ are chosen to satisfy $2\pi\int_0^b\int_{-\frac{L}{2}}^{\frac{L}{2}}\rho(r,z)rdrdz = Nq$, where N is the total number of particles, the subscription t presents the distribution in transverse direction and l represents that in longitudinal direction. Therefore, t and l can be u (for uniform), w (for waterbag), p (for parabolic) and g (for Gaussian). We list all possible combinations of the four distributions in Table 1, where

$$\rho_{u,u}(r,z)=\frac{Nq}{\pi b^2 L}, \qquad \rho_{w,u}(r,z)=\frac{2Nq}{\pi b^2 L}\left(1-\frac{r^2}{b^2}\right),$$

$$\rho_{p,u}(r,z)=\frac{3Nq}{\pi b^2 L}\left(1-\frac{r^2}{b^2}\right)^2, \qquad \rho_{g,u}(r,z)=\frac{Nq}{2\pi\alpha^2 L}e^{-\frac{r^2}{2\alpha^2}},$$

$$\rho_{u,w}(r,z)=\frac{3Nq}{2\pi b^2 L}\left[1-\frac{z^2}{(L/2)^2}\right], \qquad \rho_{w,w}(r,z)=\frac{3Nq}{\pi b^2 L}\left(1-\frac{r^2}{b^2}\right)\left[1-\frac{z^2}{(L/2)^2}\right],$$

$$\rho_{p,w}(r,z)=\frac{9Nq}{2\pi b^2 L}\left(1-\frac{r^2}{b^2}\right)^2\left[1-\frac{z^2}{(L/2)^2}\right], \qquad \rho_{g,w}(r,z)=\frac{3Nq}{4\pi\alpha^2 L}e^{-\frac{r^2}{2\alpha^2}}\left[1-\frac{z^2}{(L/2)^2}\right],$$

$$\rho_{u,p}(r,z)=\frac{15Nq}{8\pi b^2 L}\left[1-\frac{z^2}{(L/2)^2}\right]^2, \qquad \rho_{w,p}(r,z)=\frac{15Nq}{4\pi b^2 L}\left(1-\frac{r^2}{b^2}\right)\left[1-\frac{z^2}{(L/2)^2}\right]^2,$$

$$\rho_{p,p}(r,z)=\frac{45Nq}{8\pi b^2 L}\left(1-\frac{r^2}{b^2}\right)^2\left[1-\frac{z^2}{(L/2)^2}\right]^2, \qquad \rho_{g,p}(r,z)=\frac{15Nq}{16\pi\alpha^2 L}e^{-\frac{r^2}{2\alpha^2}}\left[1-\frac{z^2}{(L/2)^2}\right]^2,$$

$$\rho_{u,g}(r,z)=\frac{Nq}{\pi b^2 LD}e^{-\frac{z^2}{2\beta^2}}, \qquad \rho_{w,g}(r,z)=\frac{2Nq}{\pi b^2 LD}\left(1-\frac{r^2}{b^2}\right)e^{-\frac{z^2}{2\beta^2}},$$

$$\rho_{p,g}(r,z)=\frac{3Nq}{\pi b^2 LD}\left(1-\frac{r^2}{b^2}\right)^2 e^{-\frac{z^2}{2\beta^2}}, \qquad \rho_{g,g}(r,z)=\frac{Nq}{2\pi\alpha^2 LD}e^{-\frac{r^2}{2\alpha^2}}e^{-\frac{z^2}{2\beta^2}}, \tag{8}$$

and

$$\alpha^2=\langle r^2\rangle,\ \beta^2=\langle z^2\rangle,\ D=\frac{1}{2}\int_{-1}^{1}e^{-\frac{L^2}{8\beta^2}t^2}dt\,. \tag{9}$$

Table 1. Density Distributions

Distribution in transverse direction	Distribution in longitudinal direction			
	uniform	waterbag	parabolic	Gaussian
uniform	$\rho_{u,u}$	$\rho_{u,w}$	$\rho_{u,p}$	$\rho_{u,g}$
waterbag	$\rho_{w,u}$	$\rho_{w,w}$	$\rho_{w,p}$	$\rho_{w,g}$
parabolic	$\rho_{p,u}$	$\rho_{p,w}$	$\rho_{p,p}$	$\rho_{p,g}$
Gaussian	$\rho_{g,u}$	$\rho_{g,w}$	$\rho_{g,p}$	$\rho_{g,g}$

Substituting the density distributions of Eq. (8) into Eqs. (3) to (6), we can get the potentials induced by the cylinder of space charge with different density distributions. (For details of the derivation see Refs. [10] to [12]).

3 NONLINEAR FIELD ENERGY OF A CYLINDER OF SPACE CHARGE IN LINAC

The nonlinear field energy of the cylinder model of space charge in a waveguide of linac can be found by integrating φdq over the entire volume occupied by the space charge: [9]

$$W = 2\pi\int_{r=0}^{r=b}\int_{z=-\frac{L}{2}}^{z=\frac{L}{2}}\rho\varphi rdrdz\,. \tag{10}$$

Substituting the different density distributions of Eq.(8) and the potentials φ induced by these space charge in the regime ($|z|<L/2$) from Eq.(6) into Eq.(10), we get the self-field energy of the cylinder of space charge in waveguide as the following.

For a bunched beam with longitudinal uniform distribution and different distributions in transverse direction, we get:

$$W_{u,u}=\frac{2N^2q^2a^2}{\pi\varepsilon_0 Lb^2}\sum_{l=1}^{\infty}\frac{J_1^2(k_lb)}{(k_la)^4J_1^2(k_la)}A_{kv}\ , \tag{11}$$

$$W_{w,u}=\frac{32N^2q^2a^4}{\pi\varepsilon_0 Lb^4}\sum_{l=1}^{\infty}\frac{J_2^2(k_lb)}{(k_la)^6J_1^2(k_la)}A_{kv}\ , \tag{12}$$

$$W_{p,u}=\frac{1152N^2q^2a^6}{\pi\varepsilon_0 Lb^6}\sum_{l=1}^{\infty}\frac{J_3^2(k_lb)}{(k_la)^8J_1^2(k_la)}A_{kv}\ , \tag{13}$$

$$W_{g,u}=\frac{N^2q^2}{2\pi\varepsilon_0 L}\sum_{l=1}^{\infty}\frac{e^{-k_l^2\alpha^2}}{(k_la)^2J_1^2(k_la)}A_{kv}\ , \tag{14}$$

where

$$A_{kv}=1-\frac{2}{k_lL}sh\frac{k_lL}{2}e^{-\frac{k_lL}{2}}\ . \tag{15}$$

For a bunched beam with longitudinal waterbag distribution and different distributions in transverse direction, we get:

$$W_{u,w}=\frac{18N^2q^2a^2}{\pi\varepsilon_0 Lb^2}\sum_{l=1}^{\infty}\frac{J_1^2(k_lb)}{(k_la)^4J_1^2(k_la)}A_{wb}\ , \tag{16}$$

$$W_{w,w}=\frac{288N^2q^2a^4}{\pi\varepsilon_0 Lb^4}\sum_{l=1}^{\infty}\frac{J_2^2(k_lb)}{(k_la)^6J_1^2(k_la)}A_{wb}\ , \tag{17}$$

$$W_{p,w}=\frac{10368N^2q^2a^6}{\pi\varepsilon_0 Lb^6}\sum_{l=1}^{\infty}\frac{J_3^2(k_lb)}{(k_la)^8J_1^2(k_la)}A_{wb}\ , \tag{18}$$

$$W_{g,w}=\frac{9N^2q^2}{2\pi\varepsilon_0 L}\sum_{l=1}^{\infty}\frac{e^{-k_l^2\alpha^2}}{(k_la)^2J_1^2(k_la)}A_{wb}\ , \tag{19}$$

where

$$A_{wb}=\frac{2}{15}-\frac{1}{3(k_lL/2)^2}+\frac{1}{(k_lL/2)^3}\left[1+\frac{1}{(k_lL/2)}\right]-$$
$$-\frac{1}{(k_lL/2)^3}\left[1+\frac{1}{(k_lL/2)}\right]^2e^{-\frac{k_lL}{2}}sh\frac{k_lL}{2}\ . \tag{20}$$

For a bunched beam with longitudinal parabolic distribution and different distributions in transverse direction, we get:

$$W_{u,p}=\frac{20N^2q^2a^2}{7\pi\varepsilon_0 Lb^2}\sum_{l=1}^{\infty}\frac{J_1^2(k_lb)}{(k_la)^4J_1^2(k_la)}A_{pa}\ , \tag{21}$$

$$W_{w,p}=\frac{320N^2q^2a^4}{7\pi\varepsilon_0 Lb^4}\sum_{l=1}^{\infty}\frac{J_2^2(k_lb)}{(k_la)^6J_1^2(k_la)}A_{pa}\ , \tag{22}$$

$$W_{p,p}=\frac{11520N^2q^2a^6}{7\pi\varepsilon_0 Lb^6}\sum_{l=1}^{\infty}\frac{J_3^2(k_lb)}{(k_la)^8J_1^2(k_la)}A_{pa}\ , \tag{23}$$

$$W_{g,p}=\frac{5N^2q^2}{7\pi\varepsilon_0 L}\sum_{l=1}^{\infty}\frac{e^{-k_l^2\alpha^2}}{(k_la)^2J_1^2(k_la)}A_{pa}\ , \tag{24}$$

where

$$A_{pa}=1-\frac{3}{(k_lL/2)^2}+\frac{63}{2(k_lL/2)^4}+\frac{945}{2(k_lL/2)^6}+\frac{2835}{2(k_lL/2)^7}+\frac{2835}{2(k_lL/2)^8}$$
$$-\frac{315}{2(k_lL/2)^5}\left[1+\frac{3}{(k_lL/2)}+\frac{3}{(k_lL/2)^2}\right]^2e^{-\frac{k_lL}{2}}sh\frac{k_lL}{2}\ . \tag{25}$$

For a bunched beam with longitudinal Gaussian distribution and different distributions in transverse direction, we get:

$$W_{u,g}=\frac{2N^2q^2a^2}{\pi\varepsilon_0 Lb^2}\sum_{l=1}^{\infty}\frac{J_1^2(k_lb)}{(k_la)^4J_1^2(k_la)}A_{ga}\ , \tag{26}$$

$$W_{w,g}=\frac{32N^2q^2a^4}{\pi\varepsilon_0 Lb^4}\sum_{l=1}^{\infty}\frac{J_2^2(k_lb)}{(k_la)^6J_1^2(k_la)}A_{ga}\ , \tag{27}$$

$$W_{p,g}=\frac{1152N^2q^2a^6}{\pi\varepsilon_0 Lb^6}\sum_{l=1}^{\infty}\frac{J_3^2(k_lb)}{(k_la)^8J_1^2(k_la)}A_{ga}\ , \tag{28}$$

$$W_{g,g}=\frac{N^2q^2}{2\pi\varepsilon_0 L}\sum_{l=1}^{\infty}\frac{e^{-k_l^2\alpha^2}}{(k_la)^2J_1^2(k_la)}A_{ga}\ , \tag{29}$$

where

$$A_{ga}=\frac{k_lL}{8D^2}\int_{-1}^{1}\left[\left(1-|t|\right)\int_{-1}^{1}e^{-\frac{L^2}{8\beta^2}\left(\frac{1-|t|}{2}v+\frac{1+|t|}{2}\right)^2-\frac{k_lL}{2}\left(\frac{1-|t|}{2}v+\frac{1+|t|}{2}\right)}dv\right]\times$$
$$\times e^{-\frac{L^2}{8\beta^2}t^2}ch\frac{k_lL}{2}tdt+\frac{k_lL}{8D^2}\int_{-1}^{1}e^{-\frac{L^2}{8\beta^2}t^2-\frac{k_lL}{2}|t|}\times$$
$$\times\left[|t|\int_{-1}^{1}e^{-\frac{L^2}{8\beta^2}\left(\frac{|t|}{2}v+\frac{|t|}{2}\right)^2}ch\frac{k_lL}{2}\left(\frac{|t|}{2}v+\frac{|t|}{2}\right)dv\right]dt\ . \tag{30}$$

4 NUMERICAL RESULTS OF NONLINEAR FILED ENERGY

As an example, take a cylinder model of space charge with total charge $Nq=6\times10^{-9}$ Coulomb in a surrounding cylinder with radius $a=0.015$m. The calculations of nonlinear field energy W versus b/a of the bunch and wall radius and b/L of the bunch radius and length are carried out. The related plots for different transverse distributions combining different longitudinal distributions are shown in Figures 2 and 3. As can be seen, first, the all nonuniform particle distributions have more nonlinear field energy than that of the equivalent uniform beam. Second, the nonlinear field energies increase as b/L increases and decrease as b/a increases for all distributions. Thirdly, from Fig.2, it can be seen that the smaller the b/a, the bigger the nonlinear field energy W. Therefore, it can be predicted, the nonlinear field energy tends its maximum in free space for a space charge bunch with any distribution.

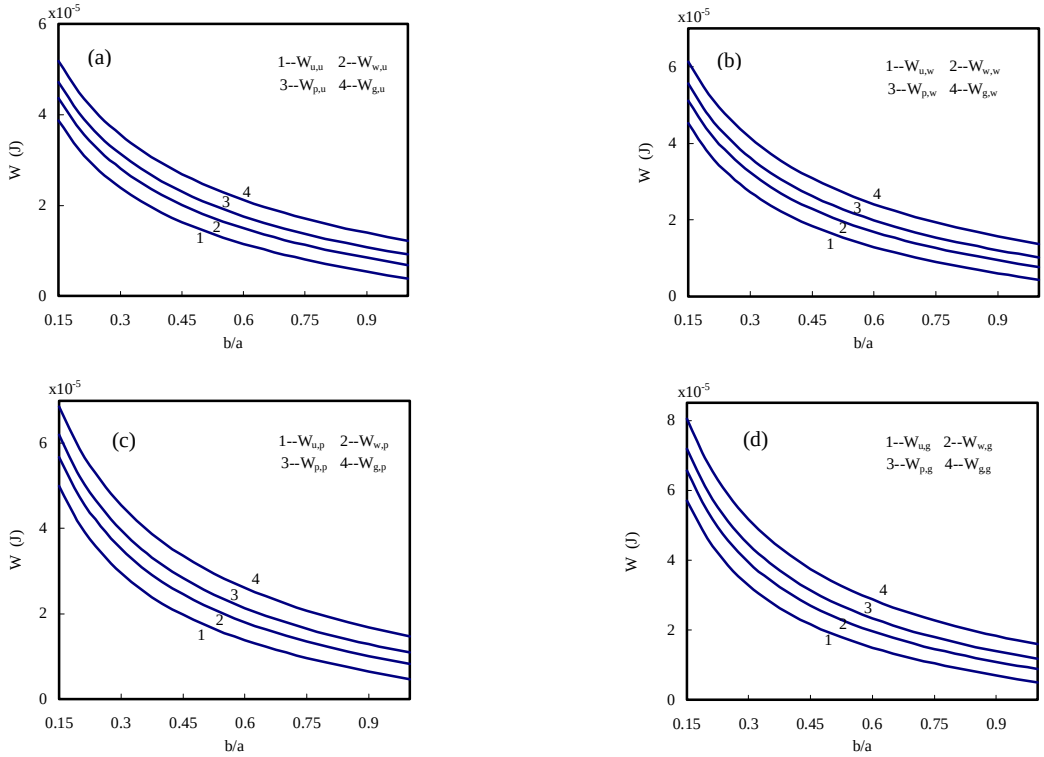

Figure 2. Field energy W versus b/a of the bunch and wall radius for different transverse distributions and (a) longitudinal uniform distribution; (b) longitudinal waterbag distribution; (c) longitudinal parabolic distribution; (d) longitudinal Gaussian distribution.

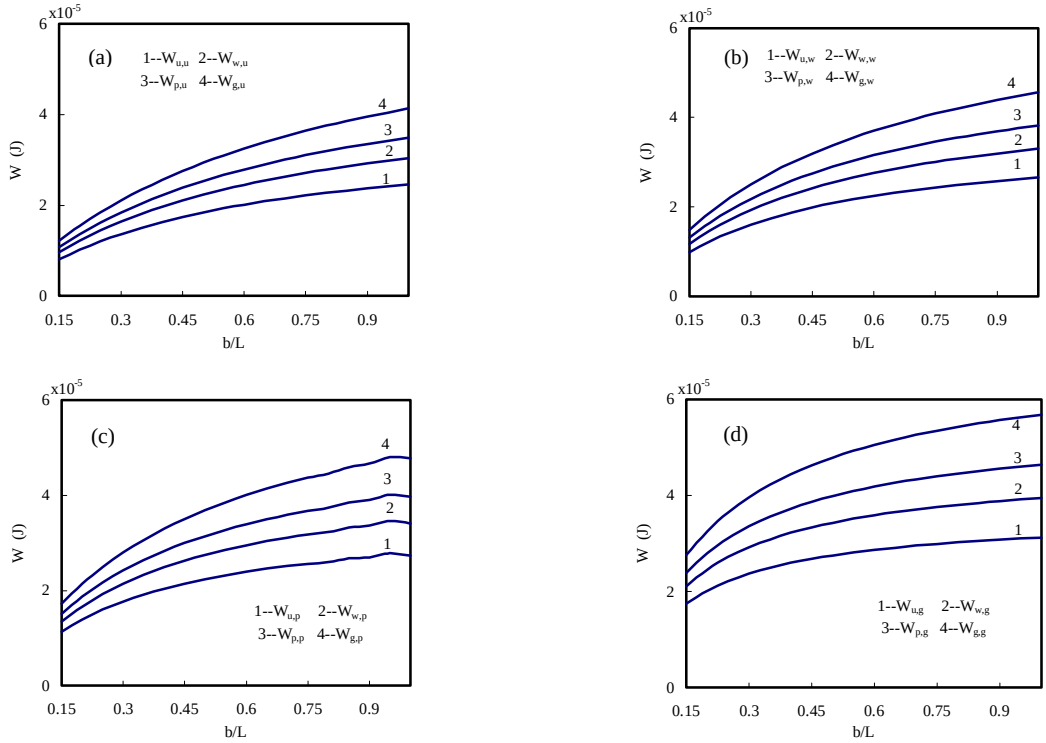

Figure 3. Field energy W versus b/L of the bunch radius and length for different transverse distributions and (a) longitudinal uniform distribution; (b) longitudinal waterbag distribution; (c) longitudinal parabolic distribution; (d) longitudinal Gaussian distribution.

5 EMITTANCE GROWTH FOR A BUNCHED BEAM IN LINAC

The generalized three-dimensional equation for the emittance and field energy of high-current beams in periodic focusing structure was derived by Hofmann and Struckmeier [5], and can be written for three degrees of freedom *x*, *y* and *z (*with linear focusing in each plane) as:

$$\frac{1}{x^2}\frac{d}{ds}\varepsilon_x^2+\frac{1}{y^2}\frac{d}{ds}\varepsilon_y^2+\frac{1}{z^2}\frac{d}{ds}\varepsilon_z^2=-\frac{32}{m\gamma^3v^2N}\frac{d}{ds}(W-W_u), \qquad (31)$$

where $s=v\cdot t$, ε_x , ε_y and ε_z present rms emittance in *x*, *y* and *z* directions, respectively, W and W_u are the space charge field energies of the real beam and equivalent uniform beam. The equation allows one to estimate the total emittance growth if the change of nonlinear field energy can be predicted.

In linear accelerator, the real beams have to be considered in some channels. And hence, the nonlinear field energy of the beam should be calculated in a surrounding structure. It can be seen clearly, from the Fig.2 and Fig.3, the nonlinear field energies are not only dependent of the ratio b/L of the bunch radius and length, but also dependent of the ratio b/a of the bunch and wall radius. It is also true for the free energy. Letting the quantity U_n:

$$U_n=(W-W_u)/W_u \ . \qquad (32)$$

U_n is a measure of the nonuniformity of the charge density and represents the field energy which can be converted into particle kinetic energy as the distribution tends to become more homogeneous. And hence it leads the emittance growth. As some examples, taking $W_u=W_{u,u}$, and W equals to $W_{w,w}$, $W_{p,w}$, $W_{g,w}$, $W_{w,p}$, $W_{p,p}$, and $W_{g,p}$ respectively, we obtain U_n versus b/a for these distributions as shown in Fig.4.

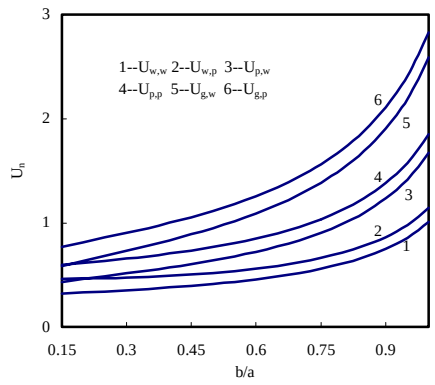

Figure 4. Free energy U_n versus b/a for some distributions.

Obviously, the emittance growth caused by the free energy U_n will be also dependent of the ratio of the bunch and wall radius, and may tend its minimum in free space. Therefore, it may be not enough to form a true estimation of the emittance growth if the change of nonlinear field energy is predicted with the value in free space in stead of that in a channel of linac.

REFERENCES

[1] M. Lapostolle, Possible emittance increase through filamentantion due to space charge in continuous beams, IEEE Trans. Nucl. Sci. NS-18, 1101 (1971).

[2] F. Sacherer, RMS envelope equations with space charge, IEEE Trans. Nucl. Sci. NS-18, 1105 (1971).

[3] J. Struckmeier, J. Klabunde and M. Reiser, On the stability and emittance growth of different particle phase space distributions in a long magnetic quadrupole channel, Part. Acc. 15, 47 (1984).

[4] T. P. Wangler, K. R. Crandall, R. S. Mills, and M. Reiser, Relationship between field and rms emittance in intense particle beams, IEEE Trans. Nucl. Sci. NS-32, 2196(1985).

[5] I. Hofmann and J. Struckmeier, Generalized three-dimensional equations for the emittance and field energy of high-current beams in periodic focusing structures, Part. Acc. 21, 69 (1987).

[6] T. P. Wangler, P. Lapostolle and A. Lombardi, Space-charge-induced emittance growth in an elliptical beam with a parabolic density distribution, Conference record of the IEEE 1993 particle Accelerator Conference, 93CH3279-7, p.3606.

[7] M. Reiser, Theory and Design of Charged Particle Beams, John Wiley & Sons, Inc., New York, 1994.

[8] Chen Yinbao, Xie Xi, Space charge effects of nonuniform density distribution in waveguide, Chinese Journal of Nuclear Physics, 1979, 1:107-128

[9] J.Hechtel, The effect of potential beam energy on the performance of linear beam devices", IEEE Trans. on electron devices, 1970, 15:999-1009

[10] Chen Yinbao, Nonlinear space charge effects of bunched beam in linac, China Nuclear Science & Technology Report, CNIC-00592, IAE-0100, 1992.

[11] Chen Yinbao, Fu Sinian, Huang Zhibin at el., Space charge effects of bunched beam with nonuniform distributions in both longitudinal and transverse directions, Chin. J. Nucl. Phys. 1995, 17(1):80.

[12] Chen Yinbao, Fu Sinian, Huang Zhibin at el., Space charge effects of bunched beam with Gaussian distribution in linac, Chin. J. Nucl. Phys. 1995, 17(2):174.

A HIGH CHARGE, HIGH DUTY FACTOR RF PHOTOINJECTOR FOR THE NEXT GENERATION LINEAR COLLIDER

E. Colby
Stanford Linear Accelerator Center, MS07, Stanford, CA, 94309 USA

Abstract

Testing of the prototype TESLA Test Facility (TTF) RF photoinjector has been completed, and fabrication of the high duty factor TTF injector is underway. Experimental results from the prototype tests conducted at Argonne National Laboratory will be presented. Engineering design work for the high power TTF gun will be discussed together with initial operating experience with a Cesium telluride photocathode in short (50 microbunch) pulse trains, and long RF pulses (1000 millisecond), conducted at Fermilab[1]. An outline of future advanced accelerator R&D activities at Fermilab will also be presented.

1 INTRODUCTION

The TeV Superconducting Linear Accelerator (TESLA) is unique among the world's linear electron accelerator proposals as the only scheme using superconducting radiofrequency (scrf) cavities for acceleration. The TESLA Test Facility (TTF) is being constructed at the Deutsches Elektronen-Synchrotron (DESY) to address engineering and economic questions about the viability of constructing superconducting electron accelerators at energies reaching to 0.5 TeV and beyond. Table 1, reproduced from the design report [1], outlines the parameters of both TESLA-500, a 0.5 TeV collider proposed as the first step towards a 5 TeV machine, and the parameters for the TTF.

Fermilab's participation in the planning and construction of the TTF has been extensive, including key contributions to the cryogen handling systems, cryomodule design, rf input power couplers, and the rf photocathode electron source for the second phase of the TTF testing program.

Initially, a conventional thermionic source was used to supply low bunch charge (37 pC) bunches to the TTF linac at a 216 MHz micropulse repetition rate to provide the correct beam loading current (8 mA) for rf and transport studies. The thermionic injector will be replaced by an rf photocathode gun capable of delivering the TESLA-500 bunch charge (8 nC) at the required repetition rate (1 MHz). Higher order mode power deposited by the bunch wakefields will be studied with the nearly 1 kA beams produced.

[1]Operated by the Universities Research Association for the U. S. Department of Energy. Work also supported in part by grants DE-FG03-ER40796 and W-31-109-ENG-38.

Table 1: TESLA-500 and TTF Parameters

Parameter	TESLA 500	TTF
Linac Energy	250 GeV	500 MeV
RF Frequency	1300 MHz	1300 MHz
Gradient	25 MeV/m	15 MeV/m
No. Cryomodules	~2500	4
Bunch population	5×10^9	5×10^9
Energy Spread[1]	0.15 %	0.1%
Energy Spread[2]	0.1 %	0.2%
Bunch Length[3]	1 mm	1 mm
Beam Current	8 mA	8 mA
Macropulse length	0.8 ms	0.8 ms
Injection Energy	20 MeV	20 MeV
Emittances[4]	20 x 1 μm	20 x 20 μm
Beam Size[5]	260 x 60 μm	3.5 mm
Beam Size	50 x 12 μm	0.5 mm
Micropulse spacing	1 μs	1 μs
Macropulse spacing	100 ms	100 ms

[1]RMS, single bunch
[2]RMS, bunch-to-bunch
[3]RMS, one-sigma
[4]RMS, one-sigma, normalized
[5]RMS, one-sigma

Once the wakefield and transport studies have been completed, plans call for replacement of the high charge gun with a low-charge low-emittance photocathode gun for the FEL experiments. A Self-Amplified Spontaneous Emission Free Electron Laser (SASE-FEL) will be installed, initially operating in the 100-25 nm range. Ultimately, plans call for a doubling of the linac energy, and modification of the undulator to produce radiation in the 20-6nm range [2]. Operation of the high-charge gun, with suitably altered laser parameters, may provide an effective interim alternative [3] for the first phase of the SASE-FEL studies while the new gun is being constructed.

2 INJECTOR DESIGN

Two rf photocathode guns have been built, and a third is currently in fabrication: a low duty cycle($<10^{-3}$) gun for single bunch testing, and two high duty factor guns incorporating differing methods of water channel fabrication.

The design has been described in detail elsewhere [4,5], with only a brief summary provided here. Electrons are produced from a cesium telluride photocathode (plain copper in the low duty cycle prototype) which is on the

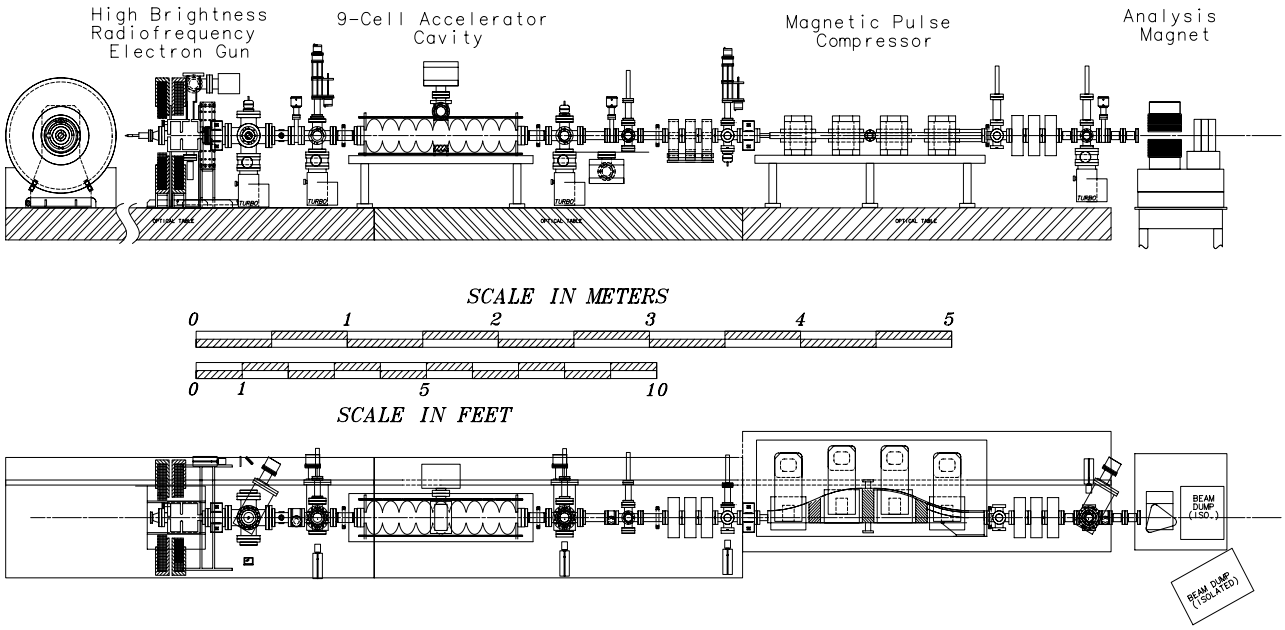

Figure 1: Layout of photoinjector components

rear conducting wall of a 25% elongated half cell. A system of four external solenoids (two focussing and two bucking) provide adjustment of both the strength and longitudinal profile of the magnetic field used to simultaneously focus and space charge correlation compensate ("emittance compensate" [7]) the electron bunch, permitting correlation compensation to be attained over a wide range of accelerating gradients. The bunch is accelerated in the low gradient (18 MeV/m) gun structure of 1.625 cells. The 3.9 MeV electron bunch exits the gun and drifts approximately half a plasma wavelength to the entrance of a superconducting 9-cell booster linac (normal conducting for the prototype).

In the booster it receives moderate acceleration (15 MeV/m) to approximately 18 MeV, and a modest phase-energy correlation. To preserve the transverse emittances, the initial bunch length is 2.2 mm, which is compressed to 1 mm in a dipole chicane (temporal dispersion: $(\phi|dp/p)=2.50$ rad) using the phase-energy correlation developed in the booster linac, which is run off-crest by some 15-20°.

An entrance quadrupole doublet and exit triplet permit beta function matching to the pulse compressor. At the TTF, several quadrupole doublets and triplets relay the beam from the exit of the pulse compressor to the first cryomodule. At Fermilab's A0 Photoinjector installation, quadrupole triplets will provide an interaction region for a variety of advanced accelerator experiments.

Experimental testing of the injector has been taking place in three separate phases:

- With single electron bunches and the low duty factor gun to establish the basic design;
- With short bunch trains (<50 microbunches) and the cesium telluride photocathode to study cathode lifetime effects [6], and with long rf pulses (1 ms), but low duty factor to test for rf breakdown problems;
- With the high duty cycle gun operated with long rf pulses (1 ms) and acceleration provided by a superconducting cavity to study long pulse train operation of the injector.

3 PROTOTYPE TEST PHASE

The prototype injector was installed in two steps at the Argonne Wakefield Accelerator Facility at Argonne National Laboratory. The gun was assembled with a short test beamline, to permit direct diagnosis of the beam produced by the gun, then the test beamline was removed and the booster linac and pulse compressor installed to permit testing of the completed injector.

Shown in figure 2 below is a slit mask emittance measurement of the horizontal emittance as a function of the gun solenoid field strength, made at 16.5 MeV. The emittance compensation minimum is clearly visible.

The energy spectrum of the uncompressed 8 nC bunch is shown in figure 3 below.

Measurement of the bunch length was done with a Hamamatsu streak camera (C1587 streak tube, 1 ps quoted resolution) examining the Cerenkov radiation from an aerojel target. Measured pulse lengths generally showed poor pulse compression, which from subsequent simulations of wakefield effects [8] is believed to have arisen from interactions with the irises in the gun and booster linac. Electron bunches as short as 12 ps FWHM were observed, corresponding to a peak current of more than 850 amperes. Table 2 below outlines the desired, predicted and measured parameters for the injector.

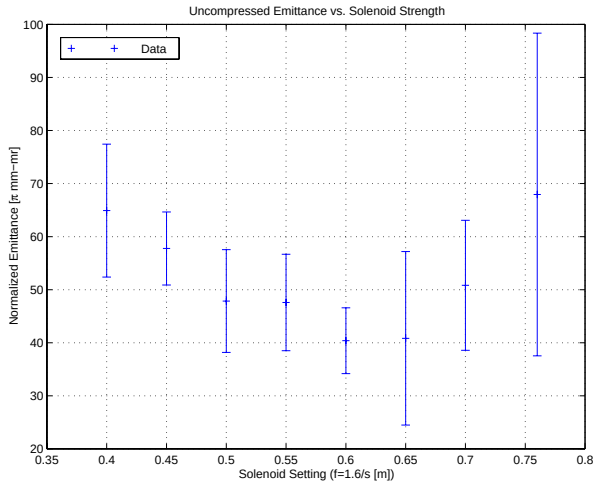

Figure 2: Horizontal emittance measurement versus gun solenoid strength. Error bars are sample variances from ten trials per point.

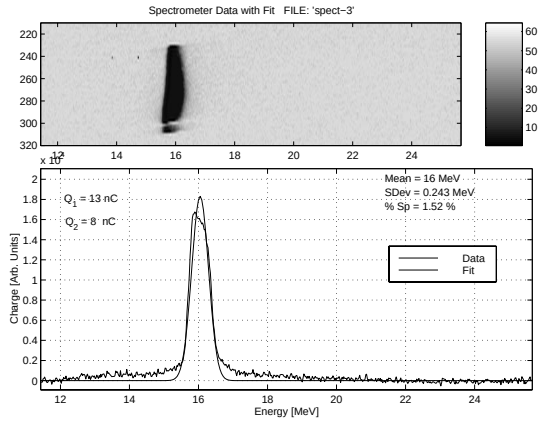

Figure 3: Energy spectrum of uncompressed 16 MeV beam at exit of injector.

Although design values for the injector meet or exceed the requirements for the TTF installation, the conditions under which the injector was tested were different from the idealization in the design. Simulation of the injector using a modified version of PARMELA and the measured values for the rf structure field balances and the measured spatio-temporal distribution of the laser pulse, but excluding wakefield effects shows reasonable correspondence to the measurements, as listed in table 2 below.

As before, quantities are RMS, one-sigma, and the emittances are normalized. It is worth noting that the dominant contributions to the emittance over the design values arise primarily from strong transverse filamentation and Gaussian temporal profile of the laser pulse, and from the unbalanced field strengths in the half and full cell of the gun. Incomplete pulse compression is seen in simulations [8] to be most likely from wakefield effects in the rf structures, which can be compensated effectively by further advancing the phase of the linac.

Table 2: Desired (D), predicted (P), and measured (M) Injector II parameters. 'NM'=not measured.

Parameter	D	P	M	Unit
Charge	8	8	8	nC
Energy	>10	18.3	17 ± 0.2	MeV
Energy Spread	<500	234	260 ± 200	keV
H. Emittance	20	37	40 ± 7	μm
V. Emittance	20	37	N.M.	μm
Bunch Length	1.0	1.6	1.4 ± 0.3	mm
Current, Peak	960	600	<850	A

4 HIGH DUTY CYCLE INJECTOR

With experimental evidence accumulating that the basic injector design was sound, work began to design a gun capable of sustaining the 1% duty factor (50 kW average power deposited in approximately a cubic foot) photocathode gun.

Detailed thermo-mechanical simulations were carried out [9] using Swanson's Ansys analysis system to establish that surface temperature rise due to rf pulse heating, peak surface stress levels, average temperature and average stress levels did not exceed the yield strength of OFE copper.

Given the long rf pulse length (Δt=1 ms) the expected thermal diffusion depth in copper is approximately:

$$\delta = \sqrt{4\alpha\Delta t} \approx 0.67 mm$$

where α is the linear coefficient of thermal expansion for copper. This implies that the deposited power does not reach the water channels during the rf pulse. Hence, the problem breaks into two parts: the pulsed-heating problem, which influences only the material choice and peak power, and the average power problem, which controls the water channel placement.

Peak surface temperature rise determines the peak surface stress and the vacuum outgassing, and is approximately:

$$\Delta T = 2\frac{dP}{dA}\frac{1}{\rho C}\sqrt{\frac{\Delta t}{\pi\alpha_{\varepsilon}}} \approx 29\,^{o}C$$

where dP/dA is the power flux (30 MW/m^2), ρ and c_ε the density and specific heat of copper, respectively.

Figure 4 below shows the predicted thermal cycling at depths of 0.0mm to 4.0mm in 0.5 mm steps, showing the peak surface temperature rise is $\approx 28^{o}$C, as predicted.

Simulation of the volumetric stress induced by the surface temperature rise shows that the peak stress of 79.7 MPa occurs on the iris, where the power density is a maximum. This value is comparable to the yield strength for pure copper, 76 Mpa, but as the surface is constrained by the underlying bulk material, it is not expected that surface spalling will occur at an appreciable rate.

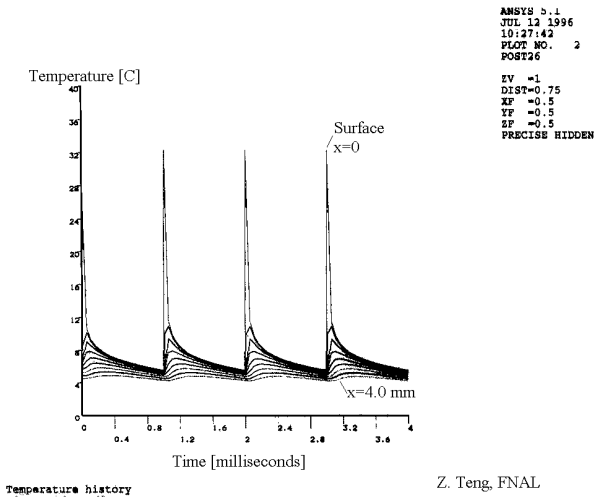

Figure 4: RF Pulse heating in the gun as a function of time.

Computation of the outer wall deflection was also carried out to determine the net cavity detuning that would take place during the RF pulse. The radial displacement before (lower trace) and after (upper trace) the 1 ms rf pulse are shown in figure 5 below. The initial net deflection corresponds to the "steady state" thermal distribution of the gun. The vertical scale is units of 10 microns, the horizontal is units of cm. An outward deflection (by ≈100 microns) of the outer wall close to the iris separating the half and full cell indicates the iris reaches a temperature slightly above the body at steady state.

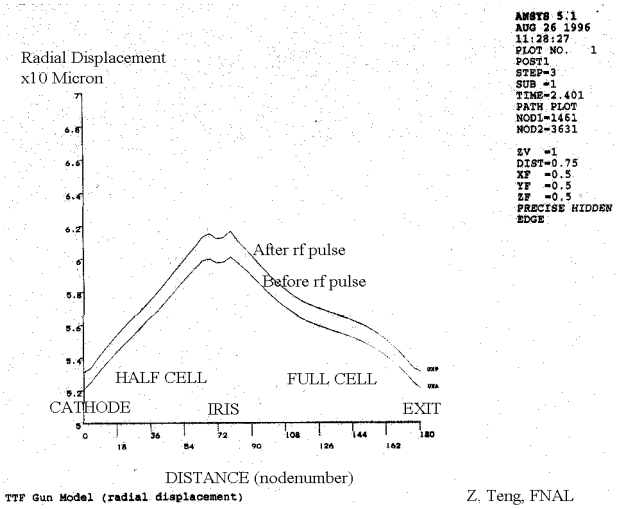

Figure 5: Outer wall radius change before and after rf pulse.

Owing to the high heat load in the thin iris separating the half and full cells of the gun, a cooling channel was machined into the iris to extract the heat. The low duty cycle gun and first high duty cycle gun had the iris cooling channel machined as an open channel (machined in from the full cell side) that was sealed shut by an electron beam welded annular cover. The iris face was machined after the electron beam weld some 0.080" to remove the weld fillet and produce a smooth surface for the high rf fields. This technique succeeded in the low duty cycle gun, but failed in two subsequent trials, fracturing open along and across the weld joint, and succeeded on the third trial with the high duty cycle gun. The reason for the failures is believed to be higher than acceptable impurity content in the copper, a problem worsened by annealing, which concentrates the impurities at the grain boundaries, giving sites of material weakness from which cracks can propagate. XDS analysis of the copper showed elevated levels of oxygen (but below the ASTM-F68-82 specification) and chlorine.

Consequently, another copper billet was purchased from Hitachi, and a fourth gun body produced, but with the iris cooling channel machined in from the gun exterior (not through the face of the full cell), and the channels brazed shut with copper water barriers.

5 HIGH DUTY CYCLE TESTS

Upon completion of the single bunch test at Argonne, the low duty factor injector was disassembled, transported to Fermilab's A-Zero experimental hall, and reassembled with a short diagnostic beamline. After brief rf testing to establish that the gun would successfully hold off much longer rf pulses (50 μs), the gun was dismounted and modified to accept the cesium telluride photocathode. RF conditioning, cathode lifetime and low energy beam experiments took place over the ensuing 6 months while the high duty cycle gun was being fabricated.

As the low and high duty cycle guns were in many respects equivalent for pulsed heating purposes (but not in average power dissipation) extensive rf conditioning of the low duty cycle gun was undertaken to discover limitations of the design. The low duty cycle gun conditioned unexpectedly well, holding off full klystron power (3.4 MW) for more than a millisecond with only occasional breakdown. Conditioning was halted by damage to the rf window incurred during the study. Vacuum was observed to rise from a base value in the 10^{-10} Torr range to the mid-10^{-8} Torr range during the long rf pulses, indicating that substantial rf conditioning will be necessary to obtain good vacuum at the full 1% duty cycle.

Photocathode lifetime was also investigated with the low duty cycle gun, and is described in detail elsewhere in these proceedings [4]. Once vacuum conditions had stabilized in the gun and beamline, we obtained 1.0% or better quantum efficiency from a cesium telluride cathode for more than four months, beginning from an initial QE value in excess of 10%.

Dark current was observed to be substantial (≈4 mA) from the low duty factor gun, and when imaged with the gun solenoid to a screen was seen to be composed of a ring with four or five bright spots on the periphery, implicating either (1) the cathode rf choke-joint spring,

(2) a sharp but recessed ridge in the cathode hole, (3) multipactoring brought on in the cathode-gun gap, perhaps exacerbated by the choke spring's silver plating, or (4) plasma formation, fed with gas by a nearby suspected virtual leak. The geometric features giving rise to (2) and (4) have been eliminated in the high duty cycle gun, and a plain beryllium copper spring has been used to reduce or eliminate the cause of (3).

Beam studies with short (10 microbunch) and longer (50 microbunch) pulse trains were undertaken, with the results being reported elsewhere in these proceedings[9]. Limitations of laser pulse energy limited the bunch charges to a nanocoulomb or less for long pulse trains, but short pulse trains of high charge bunches were also produced.

The first of the two high duty cycle guns was completed at the end of April, and has been successfully conditioned to accept full power, 1 ms rf pulses, with results reported in these proceedings [10]. The second high duty cycle gun should be completed by mid-September.

6 OPEN QUESTIONS

A number of physics issues remain to be resolved. The effect of variation of the solenoid "position" by adjusting the two gun focussing solenoid strengths has not been experimentally observed, and remains an interesting exploration of one facet of the space charge correlation compensation process. Pulse compression (to 1 mm and below) remains to be thoroughly investigated, both in itself, and for its potentially serious effects on the transverse phase space. Finally, finding the source and cure for the large dark current observed from the low duty cycle gun will be important.

7 FUTURE RESEARCH AT A-ZERO

A somewhat modified version of the photoinjector commissioned at DESY will be commissioned at Fermilab for use in an advanced accelerator R&D program. R&D projects which have real resources currently committed are:

- Electro-optically detected wakefield bunch profile measurement (Ph.D. research of M. Fitch, University of Rochester);
- Plasma wakefield acceleration experiments in the under-dense regime (J. Rosenzweig, UCLA, and P. Colestock, FNAL);
- High-efficiency photocathode material preparation and lifetime testing in RF cavity environment (Led by C. Pagani, Istituto Nazionale Di Fisica Nucleare, Milano)
- Fabrication and testing of superconducting rf cavities (H. Edwards, FNAL).

In addition, many more applications of the A0 facilities have been discussed:

- Polarized photocathode source development for RF injectors;
- Testing of next generation photoinjector structures;
- Bunched beam stochastic cooling;
- Impedance probing of stochastic cooling pickup/kicker antennae;
- Beam-beam tune shift neutralization in the Tevatron.

8 ACKNOWLEDGEMENTS

I gratefully acknowledge the support of the Fermilab Beams Division, under whose direction this work has been accomplished. Thanks also to the staff of the Argonne Wakefield Accelerator for their help in conducting the prototype experiments.

9 REFERENCES

[1] D. A. Edwards, Ed., "TESLA Test Facility Linac-Design Report", TESLA 95-01, (1995).
[2] "A VUV Free Electron Laser at the TESLA Test Facility at DESY", TESLA-FEL 95-03, (1995).
[3] J. Rosenzweig, et al, "Charge and Wavelength Scaling of RF Photoinjectors: a Design Tool", in Proc. Of the IEEE Part. Accel. Conf., Dallas, TX, p.957-60, (1995).
[4] W. H. Hartung, et al, "Experience at Fermilab with High Quantum Efficiency Photo-Cathodes for RF Electron Guns", in these proceedings, (1998).
[5] E. R. Colby, Ph.D. Dissertation, UCLA, September (1997).
[6] E. R. Colby, et al, Fermilab TM-1900, (1994).
[7] B. E. Carlsten, *NIM* **A285**, 313, (1989).
[8] P. Colestock, et al, Fermilab internal document (1997).
[9] Z. Teng, Fermilab internal document, (1996).
[10] J.-P. Carneiro, et al., "Beam Transport, Acceleration and Compression Studies in the Fermilab High-Brightness Photoinjector," in these Proceedings, (1998).

STATUS OF THE ISAC ACCELERATOR FOR RADIOACTIVE BEAMS

R. Laxdal, R. Baartman, P. Bricault, G. Dutto, R. Poirier, P. Schmor
TRIUMF, Vancouver, Canada

Abstract

The ISAC radioactive beam facility under construction at TRIUMF includes a 500 MeV proton beam ($I \leq 100\ \mu$A) impinging on a thick target, an on-line source, a mass-separator, an accelerator complex, and experimental areas. The accelerator chain includes a 35 MHz RF Quadrupole (RFQ) to accelerate beams of $A/q \leq 30$ from 2 keV/u to 150 keV/u and a post-stripper, 105 MHz variable energy drift tube linac (DTL) to accelerate ions of $3 \leq A/q \leq 6$ to a final energy from 0.15 to 1.5 MeV/u. The present status of the accelerator complex will be summarized. In particular, first rf and beam tests with the RFQ and the fabrication status of the DTL will be reported.

1 INTRODUCTION

A radioactive ion beam facility with on-line source and linear post-accelerator is being built at TRIUMF[1]. [1] In brief, the facility includes a proton beam (I$\leq$100 μA) from the TRIUMF cyclotron impinging on a thick target, an on-line source to ionize the radioactive products, a mass-separator for mass selection, an accelerator complex and experimental areas. Beams of $E \leq 60$ keV and $A \leq 238$ will be delivered to the low energy experimental area. The accelerator chain includes a 35 MHz RFQ to accelerate beams of $A/q \leq 30$ from 2 keV/u to 150 keV/u and a post stripper, 105 MHz variable energy drift tube linac (DTL) to accelerate ions of $3 \leq A/q \leq 6$ to a final energy between 0.15 MeV/u to 1.5 MeV/u. The accelerators have several noteworthy features. Both linacs are required to operate cw to preserve beam intensity. The RFQ, a four vane split-ring structure, has no bunching section; instead the beam is pre-bunched at 11.7 MHz with a single-gap, pseudo sawtooth buncher. The variable energy DTL is based on a unique separated function approach with five independent interdigital H-mode (IH) structures providing the acceleration and quadrupole triplets and three-gap bunching cavities between tanks providing transverse and longitudinal focussing respectively. A layout of the ISAC accelerator chain is shown in Fig. 1.

During 1998 TRIUMF management shifted the priority in ISAC to the target hall and mass-separator areas. Consequently progress on the accelerator has slowed somewhat. Nonetheless the building is complete and occupancy of the accelerator floor began in July 1997. In less than a year a source and injection line have been commissioned and initial rf and beam tests with the RFQ in an intermediate configuration have been successfully completed. In addition the first DTL buncher has been delivered in preparation for rf tests and the first DTL IH tank is ready for copper plating.

[1] http://www.triumf.ca/isac/lothar/isac.html

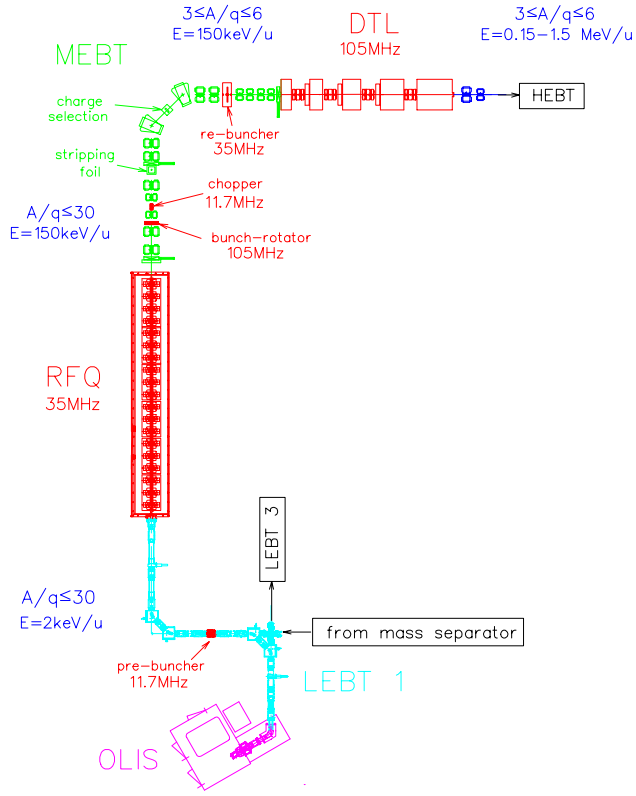

Figure 1: The ISAC linear accelerator.

2 LEBT

The low energy beam transport (LEBT) consists of electrostatic elements; quadrupoles, steering plates and spherical bends, that transport the exotic beams from the mass-separator and stable beams from an off-line ion source (OLIS) located on the accelerator floor[2]. An electrostatic switchyard allows selection of either the stable or unstable beam for acceleration while the other beam can be sent to the low energy experimental area.

The beam to be accelerated is pre-bunched at 11.7 MHz, the third sub-harmonic of the RFQ frequency, in a single gap, multi-harmonic pseudo-sawtooth pre-buncher. The pre-buncher frequency was selected at the request of experimenters to give a longer bunch spacing (86 ns), a useful feature for certain TOF and coincidence rejection techniques.

The pre-buncher is positioned ∼5 m upstream of the RFQ. The last four quadrupoles upstream of the RFQ match the beam to the RFQ acceptance.

Installation of the off-line ion source (OLIS) began in July 97 with first beam extracted in November 97. Commissioning of the LEBT from OLIS to the RFQ followed soon after. The saw-tooth prebuncher was installed and commissioned with three harmonics in February 98. The fourth harmonic will be added following an upgrade to the wide band amplifier. During commissioning the bunched beam structure was measured with a cone type fast Faraday cup. Tuning proved relatively straight forward, the phase of each harmonic was determined with the beam and the amplitudes were set to pre-determined values followed by empirical optimization.

3 RFQ

The 8 m long, 1m×1m ISAC RFQ tank (Fig. 2) houses 19 split ring structures each feeding 40 cm lengths of modulated electrode. Both rings and electrodes are water cooled to dissipate the expected 100 kW of rf power[3]. The design peak voltage between electrodes is 74 kV, with a bore radius of r_0=7.4 mm.

The buncher and shaper sections of the RFQ have been completely eliminated from the design in favour of a four-harmonic sawtooth pre-buncher[4]. This not only has the benefit of shortening the structure but also reduces the output longitudinal emittance. These gains are made at the expense of a slightly lower beam capture. We expect 81% of the beam will be accelerated in the 11.7 MHz buckets while ∼3.5% will be accelerated in the two 35 MHz side-buckets with ∼15% of the beam unaccelerated and lost in the MEBT.

The initial seven ring segment of the RFQ (2.8 m) has been installed for an interim rf and beam test[5]. A copper wall is located just downstream of the seven ring section to isolate the rf fields. The beam is accelerated to 55 keV/u and

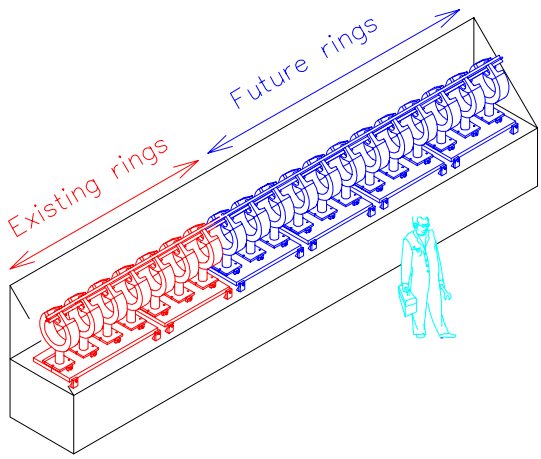

Figure 2: The ISAC 35 MHz RFQ.

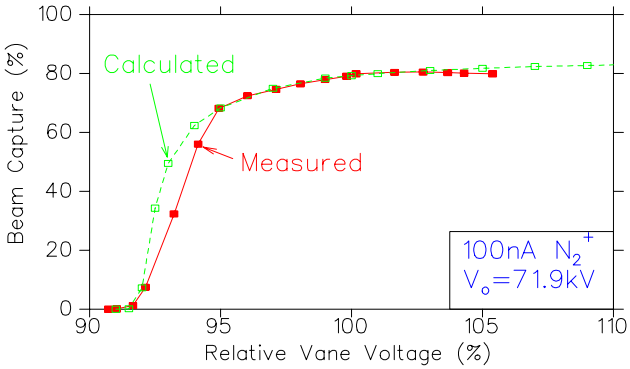

Figure 3: Beam test results from the RFQ. Shown is the capture efficiency of a N_2^+ beam as a function of relative vane voltage (solid line). The calculated capture efficiency is plotted (dashed line) for comparison.

then eight electrostatic quadrupoles, located inside the RFQ tank, transport the beam to a diagnostic station located at the exit of the RFQ. Signal level measurements of the rf have determined a frequency of 35.7 MHz, a shunt impedance of 292 kΩ·m and $Q = 8700$. Power level tests have confirmed stable operation in cw mode at peak voltage[3]. First beam was accelerated June 6/98. Since then both N^+ ($A = 14$) and N_2^+ ($A = 28$) have been accelerated testing performance at both low and high power with excellent results. In particular, in the case of N_2^+, 80% of the beam was accelerated with three harmonics on the pre-buncher in perfect agreement with PARMTEQ predictions (Fig.3). The beam quality also is as expected. The tests will continue through October 98. The remainder of the rings will then be installed with the commissioning of the full RFQ in the fall of 1999.

4 MEBT

The beam is stripped in the medium energy beam transport (MEBT) with a thin carbon foil (3 μgm/cm^2) to boost the charge state before acceleration in the DTL. The beam from the RFQ is focussed in three dimensions onto the stripping foil with quadrupoles and a 105 MHz double gap bunch rotator to minimize emittance growth due to multiple scattering and energy straggling. A chopper eliminates the small quantity of beam (∼3%) accelerated in the two 35 MHz buckets neighbouring the main pulse. After charge selection the beam is matched into the DTL with quadrupoles and a 35 MHz re-buncher.

All quadrupoles have been received. A two-gap spiral re-buncher is presently in development. A model has been completed to study the mechanical rigidity. The MEBT will be installed in the summer of 1999 in time to commission the full energy RFQ.

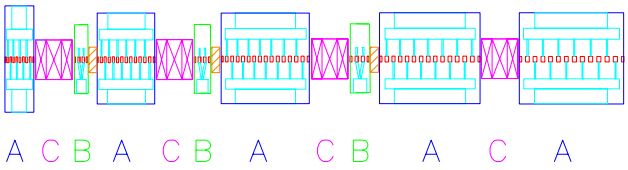

Figure 4: Schematic drawing of the ISAC variable energy separated function DTL. Five IH tanks (A) provide acceleration at 0° synchronous phase, three triple gap spiral resonators (B) provide longitudinal focus ($\phi_s \sim -60°$) and quadrupole triplets (C) provide transverse focus.

5 DRIFT TUBE LINAC

A schematic drawing of the DTL is shown in Fig. 4. The separated function design [6] offers the flexibility and beam quality of a super-conducting linac but at a reduced cost and complexity. To achieve a reduced final energy the higher energy IH tanks are turned off and the voltage and phase in the last operating tank are varied. The three-gap split ring cavities are adjusted to maintain longitudinal bunching. In this way the whole energy range can be covered with 100% transmission and no longitudinal emittance growth.

Fabrication of the first IH tank and the first split-ring buncher are proceeding in advance of the bulk of the DTL in order to get experience with the fabrication techniques. The stems and ridges of the first tank have been received. They are both fabricated from solid copper. The completed tank is being copper plated prior to final assembly. Power tests are scheduled for the fall.

The first DTL buncher[7], a split-ring three gap structure operating at 105 MHz, has been designed and fabricated at INR-RAS Troitsk and has been delivered to TRIUMF for power level tests. The fabrication of the remainder of the cavities will proceed after the acceptance tests are complete. The quadrupole triplets have been specified and are presently in design. Commissioning of the DTL is expected in the middle of 2000.

6 BEAM QUALITY

The beam from the source is expected to have a transverse emittance no larger than $\epsilon_{x,y} = 50\pi\mu$m corresponding at 2 keV/u to a normalized emittance of $\epsilon_n = \beta\gamma\epsilon = 0.1\pi\mu$m. The expected transverse and longitudinal emittances at various locations in the accelerator chain are shown in Table 6. The values quoted enclose 98% of the particles. Note the effect of multiple scattering and energy straggling in the stripping foil and the small emittance growth in the MEBT rebuncher. The transverse acceptance of the RFQ and DTL are large enough that no emittance increase is expected during acceleration. The technique of pre-bunching the beam entering the RFQ and eliminating the bunching and shaping section in the RFQ gives a very compact beam in longitudinal phase space. The longitudinal acceptance of the DTL and flexibility of the design are such that not more than 10% emittance growth is expected over the whole energy range.

Table 1: Simulation results showing the beam emittance at various locations in the ISAC accelerator chain. The values quoted enclose 98% of the particles.

Position	Transverse		Longitudinal	
	$\epsilon_{x,y}$	$\beta\epsilon_{x,y}$	ϵ_z	ϵ_z
	($\pi\mu$m)	($\pi\mu$m)	(π% ns)	(πkeV/u ns)
LEBT	50	0.1	DC	DC
After RFQ	5	0.1	0.33	0.5
After Foil	10	0.2	0.45	0.67
Before DTL	11	0.22	0.50	0.74
After DTL	$11\cdot(\frac{0.018}{\beta_{fin}})$	0.22	$0.5\cdot(\frac{0.15}{E_{fin}})$	0.74

7 FUTURE PLANS - ISAC2

TRIUMF is currently preparing a new five year plan requesting additional funding from the Canadian Government for the period beginning in April 2000. A major element of this plan includes an upgrade of the ISAC facility, ISAC2, to permit acceleration of radio-active ion beams up to energies of at least 6.5 MeV/u for masses up to 150[8]. In brief the proposed acceleration scheme would use the existing RFQ with the addition of an ECR charge state booster to achieve the required charge to mass ratio ($q/A \geq 1/30$) for masses up to 150. A new room temperature drift tube linac would accelerate the beam from the RFQ to 400 keV/u where the beam could be more efficiently stripped to give a charge to mass ratio greater than 1/7 for the full mass range. This beam would then be accelerated by a linac consisting of many short superconducting cavities. The design is compatible with staging scenarios that achieve beams up to ~5 MeV/u and A up to 60 as early as 2003 albeit with reduced ion intensity compared to the completed facility.

8 REFERENCES

[1] P. Schmor, *et al*, "The High Intensity Radioactive Beam Facility at TRIUMF", Proceedings of the 1998 European Part. Acc. Conf., Stockholm, to be published.

[2] R. Baartman, J. Welz, "60 keV Beam Transport Line and Switchyard for ISAC", Proceedings of the 1997 Part. Acc. Conf., Vancouver, 1997.

[3] R. Poirier, *et al*, "RF Tests on the Initial 2.8m of the 8m Long ISAC RFQ at TRIUMF", these proceedings.

[4] S. Koscielniak, *et al*, "Beam Dynamics Studies on the ISAC RFQ at TRIUMF", Proceedings of the 1997 Part. Acc. Conf., Vancouver, 1997.

[5] R.E. Laxdal, *et al*, "First Beam Test with the ISAC RFQ", these proceedings.

[6] R.E. Laxdal, *et al*, "A Separated Function Drift Tube Linac for the ISAC Project at TRIUMF", Proceedings of the 1997 Part. Acc. Conf., Vancouver, 1997.

[7] Y. Bylinsky, *et al*, "A Triple Gap Resonator Design for the Separated Function DTL at TRIUMF", Proceedings of the 1997 Part. Acc. Conf., Vancouver, 1997.

[8] R. Baartman, *et al*, "Long Range Plan Proposal for an Extension to ISAC", these proceedings.

THE SCHERM SPACE CHARGE ROUTINE - LIMITATIONS AND SOLUTIONS

P. Lapostolle*, J.M. Lagniel, S. Nath**, N. Pichoff, E. Tanke***, S. Valero
CEA/DSM/DAPNIA/SEA,
* Consultant, SEA/CEA, Saclay,
** On sabbatical from LANL, Los Alamos, NM, USA,
*** PS Division CERN, CH-1211, Geneva 23, Switzerland.

Abstract

The SCHERM space charge routine reported in the 1996 linac conference is based on a representation of the charge density distribution in a bunch with an Hermite series expansion. Approximate values of the field components are deduced from the properties of the Hermite functions. First applications of the method for the 180 mA CERN proton linac showed promising results, however the method has shown its limitations when it was tested in a periodic accelerating channel (6 MeV to 100 MeV) with highly tune-depressed beams. Problems underlying the approach are discussed, and solutions are proposed.

1 INTRODUCTION

A new type of approach for the space charge computation, without the need of a strict symmetry has been reported in [1]. It is based on the 3-dimensional representation of the charge density distribution with a Hermite-series expansion. Approximated values of the field components were deduced in order to be good in the bunch core where most of the particles lie. The method had been successfully applied at the 180 mA CERN proton linac beam. Results compared very well with those computed with SCHEFF for this beam. Emboldened by the initial success, we applied this approach to a periodic channel with highly tune-depressed beam. This exercise has revealed underlying limitation of the method. These limits are found to be purely mathematical in origin and lie with the limitations of Hermite-series expansion of the charge density distribution and the field components. Solutions for circumventing these difficulties are proposed in this article.

2 PROBLEMS WITH SERIES REPRESENTATION

The difficulties with series representation had been reported at the end of the eighteenth century. Dirichlet had shown (~1870) that the Fourier-series expansion of some class of functions does not always converge uniformly (e.g. Gibbs phenomena). Moreover, when they converge uniformly, they oscillate around the function in a random manner. Using the studies of Cesaro on the divergent series, Fejer (~1890) presented solutions to such problems. Here, one represents, for simplification, the process in one dimension, which can be extended in 3 dimensions. Among the two representations of the m-order Hermite series expansion $S_m(x)$ of the function f(x), only the expression proposed in [1,3], converges to zero, when x goes to infinity, and as such can be used for the charge density distribution representation as:

$$S_m(x) = \sum_{n=0}^{m} A_n \cdot H_n(x) \cdot \exp\left(-\frac{x^2}{2}\right). \qquad (1)$$

For functions f without Gaussian appearance (meaning continuous functions decreasing to zero at the infinity more rapidly that any power of 1/|x|), S_m usually does not converge uniformly to f when m increases. However S_m always minimises the quadratic means square I_m :

$$I_m = \int_{-\infty}^{+\infty} \left(f(x) - S_m(x)\right)^2 \cdot dx\,. \qquad (2)$$

Due to eq. (2), the Hermite series in eq. (1) oscillates around the function f(x) (Weisstrass Minimax theorem). If S_m converges uniformly to f, these oscillations disappear when m increases to infinity. As the value of m is always limited, S_m can have a random behaviour with unexpected effects when the function f(x) changes during the computation. Moreover, if S_m does not converge uniformly to f, these oscillations are amplified with increasing m. This problem can be circumvented with the Cesaro-Fejer transformation. Here, one replaces the Hermite series $S_m(x)$ by the Cesaro-Fejer series $\sigma_m(x)$:

$$\sigma_m(x) = \frac{1}{m+1} \sum_{n=0}^{m} S_n(x)\,. \qquad (3)$$

According to the Theorem of Cesaro, if the limit f(x) exists, the Cesaro-Fejer series in eq. (3), converges uniformly to f(x), when m increases. The unexpected oscillations are attenuated. An example can be seen in figure 1.

As presented in ref.[1], the local charge density expressed in terms of Hermite-series polynomial is given by:

$$\rho(x,y,z) = \exp\left(-\frac{u+v+w}{2}\right)\cdot \sum_i\sum_j\sum_k A_{ijk}\cdot H_i(u)\cdot H_j(v)\cdot H_k(w) \quad (4)$$

with :

$$A_{ijk} = \frac{q}{(2\pi)^{3/}\, i!\,j!\,k!\,abc}\cdot\sum_{n=1}^{N} H_i(u_n)\cdot H_j(v_n)\cdot H_k(w_n) \quad (5)$$

where u=x/a, v=y/b, w=z/c, a, b and c are the rms size of the bunch in the x, y and z directions respectively and N is the number of particles.

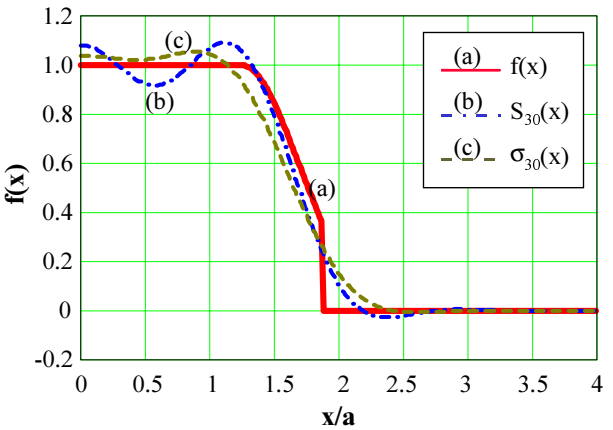

Figure 1: A function f(x) (in a) is represented by a 30-order Hermite series (in b). The oscillations practically disappears using a Cesaro-Fejer transformation (c).

The Cesaro-Fejer transformation of the one dimensional function in eq. (1) leads to :

$$\sigma_m(x) = \sum_{n=0}^{m} A_n\cdot\left(1-\frac{n}{m+1}\right)\cdot H_n(u)\cdot\exp\left(-\frac{u^2}{2}\right), \quad (6)$$

this can be extended to 3 dimensions.

From eq. (6), we see that Cesaro-Fejer transformation is an Hermite-expansion with attenuated high order coefficients. This plays the role of a low-pass filter in the Hermite base suppressing oscillations, but having a slope smaller than that of the Hermite-series.

The effect of the Cesaro-Fejer transformation can be seen in fig 2, where are presented the transverse emittance growth in a periodic accelerating channel with highly tune depressed beam (APT linac from 6.7 MeV up to 100 MeV). The computations are made for identical conditions with and without the Cesaro-Fejer transformation. It should be noted that the improvements in the field computation, explained below, have not yet been introduced. The difference in emittance growth, is due to the unexpected oscillations resulting from the Hermite series expansion of the charge density distribution. This oscillation of the charge density representation seems to introduce a diffusion like effect (or more precisely a stochastic coupling effect between directions) adding to the transverse emittance growth.

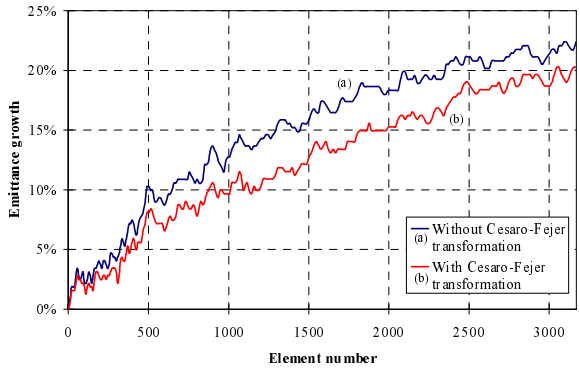

Figure 2 : Transverse emittance growth in a periodic accelerating channel (6.7 MeV to 100 MeV) with a highly tune-depressed beam. The results are obtained from the simple Hermite series expansion (a), and from the Cesaro-Fejer transformation (b).

3 SELECTION OF THE NUMBER OF TERMS IN THE HERMITE SERIES EXPANSION

It has been shown in [1], that the charge density distribution can be considered to be a Gaussian:

$$\rho_0(x,y,z) = A_{000}\exp\left(-\frac{u^2+v^2+w^2}{2}\right), \quad (7)$$

corrected by various terms (coefficients A_{ijk} in eq. (4)), each of them of total charge zero. In practice most of these coefficients can be neglected. It is essential to define a criterion, allowing the selection of the most significant terms. The Hermite polynomials $H_i(u)$ are obtained from the recurrence relation :

$$H_{i+1}(u) = u\cdot H_i(u) - i\cdot H_{i-1}(u). \quad (8)$$

Even and odd Hermite functions are represented in fig.3:

$$\mathcal{H}_i(u) = H_i(u)\cdot e^{-\frac{u^2}{2}}. \quad (9)$$

With even functions, the extremum is obtained when u=0. Near this point, from the Hermite recurrence relation, one obtains :

$$\left|H_{2l}(u)\right| \le (2l-1)\cdot(2l-3)\ldots 1. \quad (10)$$

For odd Hermite functions, the extremum lies between $0.5 < u < 0.75$, and one can write :

$$\left|H_{2l-1}(u)\right| \le (2l-2)\cdot(2l-4)\ldots 0.75. \quad (11)$$

Introducing the following numbers:

$$g(0) = 1$$
$$g(1) = 0.75 \quad (12)$$
$$g(n+2) = (n+1)\cdot g(n),$$

one obtains from eq. (10) and eq. (11) :

$$\left|A_{ijk}\cdot H_i(u)\cdot H_j(v)\cdot H_k(w)\right| \le \left|A_{ijk}\right|\cdot g(i)\cdot g(j)\cdot g(k). \quad (13)$$

Comparing the magnitude of the right term in eq. (13), relative to the Gaussian in eq. (7) allows us to select the more significant terms. They are chosen such that:

$$\left|A_{ijk}\right|\cdot g(i)\cdot g(j)\cdot g(k) \ge \delta\cdot A_{000}\,, \quad (14)$$

with δ = 0.1, 0.01, ..., depending on the accuracy desired. An estimation of the relative importance of the terms neglected can be obtained from eq. (14). The field contributions from only relatively more significant terms are considered.

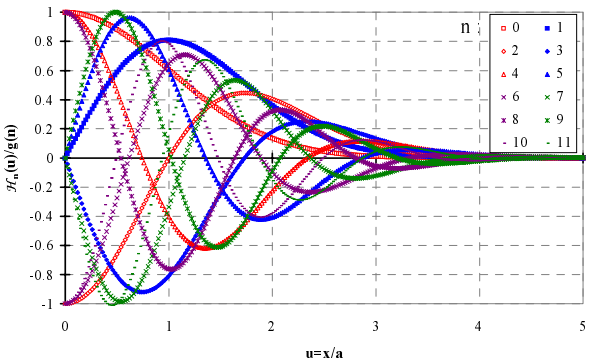

Figure 3 : The functions $H_n(u)/g(n)$ for n=0 to 11. They decrease rapidly to zero and might be considered null when u>5 (corresponding to 5 standard-deviation). The definition of g(n) is given in the text.

4 COMPUTATION OF THE FIELD COMPONENTS

Computation of the field components due to the dominant term A_{000} in eq. (7) is based on one quadrature calculation as explained in [2,3]. The field components due the other terms A_{ijk} are exactly calculated from the Poisson equation, instead of the approximated approach given in [1].

The corresponding potential from each term is given by the Poisson law :

$$\Delta U_{ijk}(u,v,w) = \frac{-A_{ijk}}{\varepsilon_0}\cdot \mathcal{H}_i(u)\cdot \mathcal{H}_j(v)\cdot \mathcal{H}_k(w) \quad (15)$$

Fourier transforms applied to eq. (15) leads to analytical expressions of the field components with a 3 dimensional (3D) integral in a 3D complex plane. Extensive effort was devoted to reduce the computation time of the field components.

The calculus of residues allows to reduce the 3D quadrature to a 2D one. This 2D quadrature is solved using numerical methods, which required several steps. Moreover, most of the values involved in these quadratures are independant of the particle co-ordinates and can be pre-calculated only once at the beginning of a simulation.

The analytical formulation of the method is quite extensive and beyond the scope of this paper.

5 CONCLUSION

Solutions to overcome the limits of the method presented in [1] are formulated. In particular:

- Cesaro-Fejer transformation would avoid the unexpected effects arising from the oscillations in the Hermite-series expansion, reducing the observed emittance growth.

- Criterion has been set (eq. (14)) to select the most significant terms of the series expansion. Computation have shown that only some tens of terms are sufficient for a suitable fit of the charge density distribution.

- Precision of field calculation has been improved and efforts have been done to reduce the computation time. Transformations applied to Poisson equation are being studied. Possibilities to reduce the 2D quadrature to a 1D one are also being looked out.

All the components of the above formualtion must be fully implemented in the space-charge code SCHERM before a fair beam-dynamics comparison could be done with DYNAC [4] and PARMILA [5] codes.

6 REFERENCES

[1] P. Lapostolle et al., Proceedings of LINAC96, CERN, August 1-5, 1996, Vol. 1, 375-377 (1996).

[2] R.W. Garnett and T. P. Wangler, IEEE PAC91 Conf., San Francisco, 330-332 (1991)

[3] P. Lapostolle et al., «A modified space-charge routine for high intensity bunched beams», *Nucl. Instr. and Meth. In Phys. Reach.*, **A379**, 21-40 (1996).

[4] P. Lapostolle, E. Tanke and S. Valero, «A new method in beam dynamics computation», *Part. Acc.*, **Vol. 44**, 215-255 (1994).

[5] G.P. Boiscourt, «Linear Accelerator and Beam Optics Codes», Proc. of AIP Conf., 177 (1988).

OPERATION OF THE APS RF GUN*

J.W. Lewellen, S. Biedron, A. Lumpkin, S.V. Milton, A. Nassiri, S. Pasky, G. Travish, M. White
Argonne National Laboratory, Argonne, Illinois 60439 USA

Abstract

The Advanced Photon Source (APS) has a thermionic-cathode rf gun system capable of providing beam to the APS linac. The gun system consists of a 1.6-cell thermionic-cathode rf gun, a fast kicker for beam current control, and an alpha magnet for bunch compression and injection into the APS linac line. This system is intended for use both as an injector for positron creation, and as a first beam source for the Low-Energy Undulator Test Line (LEUTL) project [1]. The first measured performance characteristics of the gun are presented.

1 INTRODUCTION

The APS injection system currently uses a 100-kV DC thermionic-cathode gun as its main electron beam source, followed by five 3-meter sections of S-band linac structures, as a means for providing beam to a positron conversion target. The principal measures of electron beam quality have been beam current at the positron target and positron generation efficiency. The transverse beam quality provided by the DC gun, however, is insufficient for many planned experiments utilizing the APS linac system.

The APS linac now includes a thermionic-cathode rf gun system. An alpha magnet bunch compressor is used to inject beam into the linac line between the first and second 3-meter linac sections. Although the rf gun system cannot provide as much current as the original DC gun system, the beam brightness is higher, and it is suitable as a source for some of the experiments slated to use the APS linac line. Because of the gun's placement in the APS electron linac line, beam energy at the positron target is limited to approximately 175 MeV instead of the nominal 220 MeV the full line can provide.

We have begun to characterize the performance of the thermionic-cathode gun in light of its potential as a hot spare for the DC gun. The performance measurements completed to date are presented, along with additional measurements relating to the suitability of this gun for other experiments using the APS linac line.

2 OVERVIEW OF THE RF GUN SYSTEM

The rf gun system includes the gun itself, the transport line from the gun to the entrance of the linac section, a fast crossed-field kicker used to limit injected charge, and various diagnostics. A schematic of the system is shown in Figure 1.

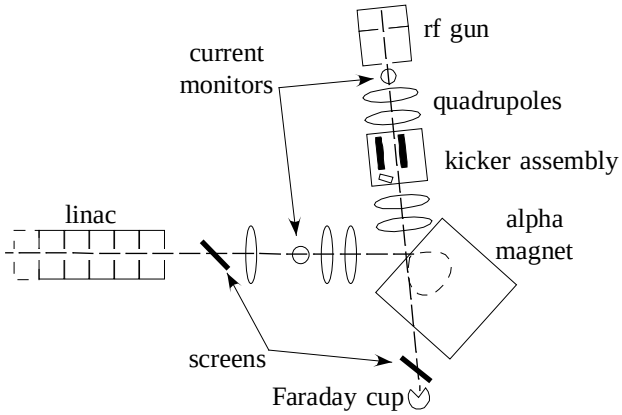

Figure 1. Schematic layout of the rf gun beam transport optics and diagnostics. Steering correctors are not shown.

2.1 Rf Gun Properties

The rf gun itself is a 1.6-cell π-mode structure. Up to 7 MW of rf power can be supplied to the full cell via an end-coupled waveguide, with a side-coupled cavity providing power transfer from the full cell to the cathode cell. The cathode used is a tungsten dispenser cathode with a diameter of 6 mm. The gun can produce peak beam energies of up to 4.5 MeV (kinetic) and peak macropulse currents of up to 1.3 A. Expected beam emittances and peak currents vary considerably with beam energy and current, but are expected to be as low as 5 π mm mrad (normalized rms) and as high as 150 A, respectively. More details of calculated gun performance may be found in [2].

2.2 Diagnostics

Several diagnostics are located along the rf gun beamline. A current transformer is located immediately after the exit of the gun and provides measures of beam current and total charge emitted. A combination Faraday cup and viewscreen is located on the far side of the alpha magnet from the gun, so kicker system tuning can be performed with the alpha magnet off.

Other diagnostics, such as fluorescent and transition radiation screens, beam position monitors (BPMs), spectrometers, and bunch length monitor cavities, are

* Work supported by US Department of Energy, Office of Basic Energy Sciences, under Contract No. W-31-109-ENG-38

present at various locations along the linac line for further characterization of the rf gun beam properties.

2.3 Gun-to-Linac Transport Line

The beam from the rf gun is injected into the second 3-meter linac structure via an alpha magnet. This alpha magnet also serves as a bunch compressor. An asymmetric transport lattice of four quadrupoles before the alpha magnet and three following the alpha magnet is used. The calculated beam size for a typical set of gun parameters is shown in Figure 2, from the exit of the rf gun to the entrance of the linac. The simulation code **elegant** [3] was used for all transport simulations external to the rf gun.

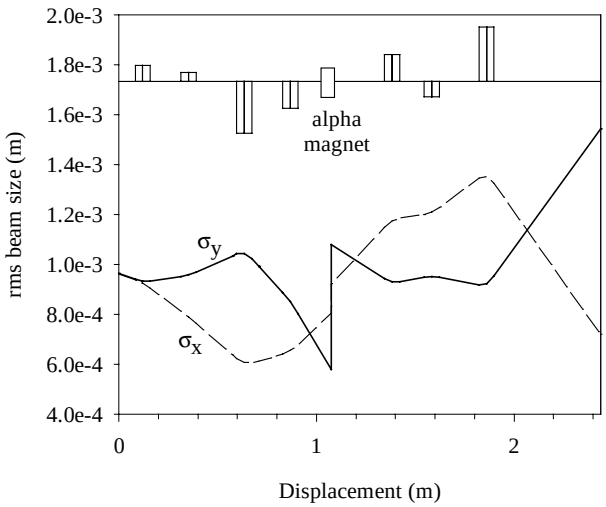

Figure 2. calculated beam spot size for a typical set of rf gun operating conditions. The discontinuity of the beam size at the alpha magnet is due to the use of transport matrix modeling formalism through the magnet.

2.4 Kicker System

The rf gun system includes an electric/magnetic crossed-field kicker system to limit the total current injected into the linac line. [4] A permanent magnet is used to deflect the beam from the gun into a beam dump; when the kicker fires, a delay line is used to provide a bucking E-field for 40 ns.

Proper kicker operation was verified by operating the rf gun and kicker with the alpha magnet off, and observing the current transmitted to the combination fluorescent screen and Faraday cup located straight-through the alpha magnet. A plot of the full current macropulse from the rf gun, and transmitted beam current detected on the Faraday cup, is shown in Figure 3. The noise on the current monitor signal trace is due to the kicker firing. Simulations indicate that a maximum of 75% of the total beam current can be transmitted to the Faraday cup if the beamline is optimized for such transport. For Figure 3, the beamline was optimized for injection into the linac so the transmitted current is slightly lower.

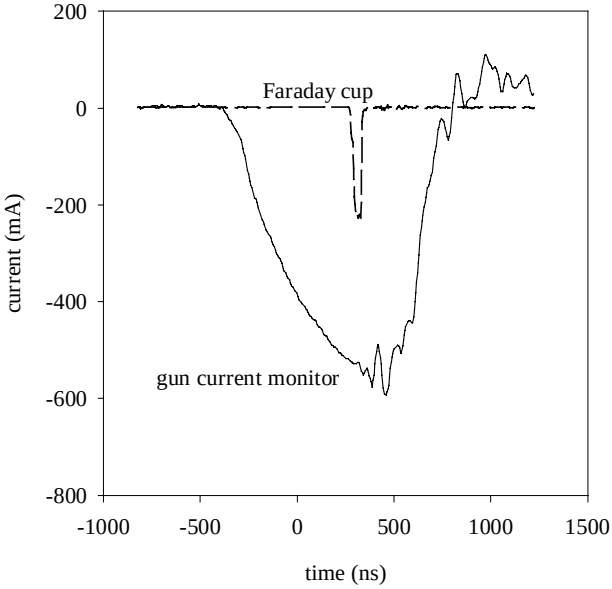

Figure 3. Gun current monitor and Faraday cup signals.

3 SYSTEM PERFORMANCE

3.1 Transport Efficiency and Energy Gain to the Positron Target

Electron beam transport efficiency measurements were made using the current monitors located in the rf gun beamline and the BPM sum signals from the APS linac diagnostics. Approximately 70% of the total charge emitted from the gun can be injected into the linac. The majority of the loss occurs over the length of the gun-to-linac transport line in the low-energy tail of the beam, which would be lost in any event during linac capture. Losses along the linac line are measured using the linac BPM sum signals. From after injection into the linac, about 85% of the beam can be transported to the positron target at high rf gun currents (~600 mA), and essentially all of the beam can be transported to the positron target at low rf gun currents (~200 mA).

An energy spectrometer immediately upstream of the positron target was used to measure the electron beam energy and energy spread at the end of the electron linac. The peak beam energy was found to be approximately 175 MeV. The beam energy was measured as a function of the phase between the linac sections and the rf gun, for a constant alpha magnet current (see Figure 4). The minimum rms energy spread found was 0.5% and was achieved by varying the linac-to-gun rf phasing and minimizing the spot size on the spectrometer screen.

Positron conversion efficiency was also measured at rf gun beam currents of 200 mA and 600 mA. In both cases, measured conversion efficiency was on the order

of 0.3% - 0.5%, depending more upon final focusing and positron linac setup than beam current. These efficiencies are in the expected range, given the target design and beam energy.

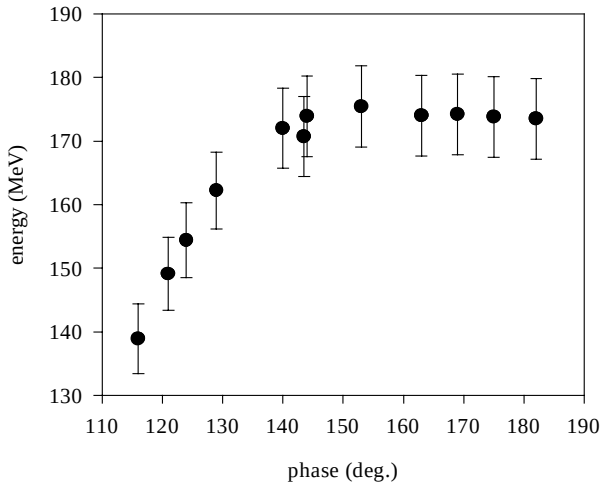

Figure 4. Peak electron beam energy vs. phase between the rf gun and linac. The error bars represent uncertainty in centroid location and spectrometer calibration.

3.2 Bunch Length Measurements

The APS linac includes a fifth-harmonic (of the linac frequency) rf cavity intended for real-time bunch length diagnostic measurements. The cavity is located upstream of the positron target and downstream of the energy spectrometer magnet [5].

No direct calibration of the cavity signal to actual bunch length has been made using the rf gun. We can vary the cavity output signal considerably simply by varying the linac-to-gun phase relationship while maintaining constant delivered current. Thus, the cavity appears to be functional and, once the cavity signal can be calibrated to beam current and correlated with streak-camera measurements, should provide real-time bunch length measurements.

Using a fast diode and scope, we can observe the buildup of rf power in the fifth-harmonic cavity. The signal builds up over a period of approximately 40 ns, then begins to decay. This is consistent with the duration of the electron beam passed by the kicker system.

A plot of observed signal strength vs. alpha magnet current is shown in Figure 5. For this measurement, the beam current from the gun was stabilized at 200 mA, with an input rf power of 3.5 MW. The relative rf phase between the gun and linac was varied to obtain the minimum energy spread on the spectrometer magnet, which should correspond to the minimum bunch length. In Figure 5, the fifth-harmonic cavity signal strengths have been normalized to the square of the beam current at the positron target.

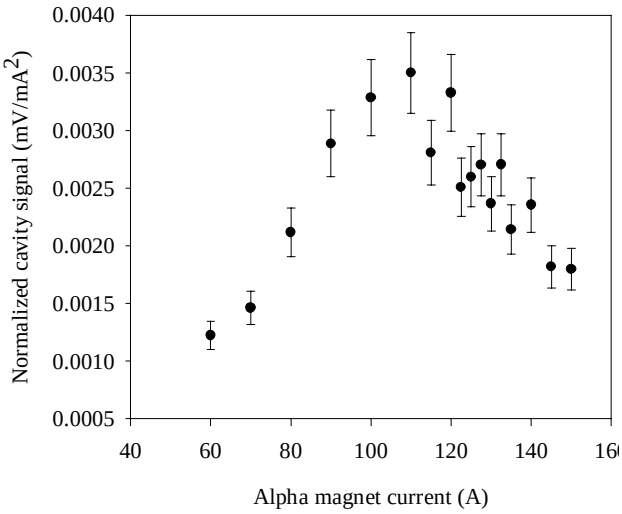

Figure 5. Fifth-harmonic cavity signal as a function of alpha magnet current, normalized to electron beam current. The signal strength is inversely proportional to the bunch length divided by the beam current squared.

We have also measured bunch lengths on the order of 3 – 6 ps using a streak camera and are in the process of calibrating the fifth-harmonic cavity with the streak camera measurements.

4 CONCLUSIONS

The commissioning process for the thermionic-cathode rf gun is proceeding well. Reasonable beam transport along the APS linac line has been achieved. Positron conversion efficiency has been measured and indicates that the rf gun could be used to fill the APS storage ring if required, albeit at a reduced rate. Bunch length measurements are in progress, and a fifth-harmonic cavity is being correlated to streak camera measurements for use as a real-time bunch length monitor. Beam emittance measurements are also planned.

5 REFERENCES

[1] S.V. Milton et al., "Status of the Advanced Photon Source low-energy undulator test line," *NIM A* **407** (1998) 210-214.

[2] M. Borland, private communication

[3] M. Borland, "User's Manual for **elegant**," APS online document, Program Version 12.4, December 1993

[4] Y. Kang et al., "Beam Chopper for the Low-Energy Undulator Test Line (LEUTL) in the APS," *Proc. 1997 Part. Acc. Conf.*, Vancouver, BC (to be published)

[5] A. Nassiri and A. Grelick, "A Fifth Harmonic RF Bunch Monitor for the ANL-APS Electron Linac," *Proc. 1993 Part. Acc. Conf.*, Washington, DC, 2412 (1993)

TPS ANALYSIS OF HEAVY-ELEMENT IONS FROM LASER-PRODUCED PLASMA*

L. Láska, B.Králiková, J. Krása, K.Mašek, M. Pfeifer, J.Skála, K. Rohlena
Institute of Physics, Acad. Sci. Czech Rep., Prague

E. Woryna, P.Parys, J. Wolowski
Institute of Plasma Physics and Laser Microfusion, Warsaw

W. Mróz
Institute of Optoelectronics, MUT, Warsaw

Abstract

The Thomson parabola spectrograph (TPS) is an excellent device to give a general overview of the charge states and the velocity (energy) distribution of all the types of ions produced by a single laser shot focused onto a target. Using the TPS and other diagnostics based on the time-of-flight method - ion collectors (IC) and a cylindrical electrostatic ion energy analyzer (IEA) – the laser produced plasma of different heavy elements was analyzed in a far expansion zone. As target material Ta, W, Pt, Au, Pb and Bi were chosen. The photodissociation iodine laser system PERUN was used for this purpose and results are compared with experiments obtained with the CO_2 laser ion source.

1 INTRODUCTION

The results of experiments on laser ion sources (LIS) performed up to now proved the feasibility of laser-production of highly-charged ions of heavy elements [1-4]. Current densities of multiply charged ions are about two orders of magnitude higher than those from the ECR ion source. This fact has lead to the construction of a LIS which may become a source for LHC. Nevertheless, the LIS still faces major technological problems as for applications of that kind.

TPS measurements [5,6] made it possible to analyze very effectively ions emitted from the target of different elements and also of ions in extracted ion beam [7]. A more detailed analysis of expanded ions was performed using a time-of-flight method.

In the presented contribution results obtained up to date with the photodissociation iodine laser at Prague are summarized and compared with those obtained with the CO_2 laser ion sources [1,3]. In addition, both the mentioned lasers are discussed with respect to their use for a considered LIS.

*This work was partially supported by a grant A1010819 from the Grant Agency of the ASCR

2 EXPERIMENT

The photodissociation iodine laser PERUN at Prague is operating at $\lambda = 1.315$ μm, with the energy up to 40 J and with the pulse-length of 300-500 ps. Focusing the laser beam with either lens optics or with a parabolic mirror to a spot size of about 100 μm means attainable power density on the target up to about 1×10^{15} W/cm^2 (reduced intensity $I\lambda^2 = 1.7\times10^{15}$ Wμm^2/cm^2).

The operation principle of the TPS is based on the passage of ions through parallel magnetic and electric fields, $\boldsymbol{B}$ and $\boldsymbol{E}$. From the solution of equations of motion for a charged particle we obtain the coordinates x and y of the point in the recording plane of a plane detector (a MCP in our case), onto which an ion of given parameters impacts. After eliminating the kinetic energy of ions E_i we obtain an equation, which describes the Thomson parabolas [5,6]. Points of intersection of parabolas with a straight line passing through the origin of coordinates, Oxy, correspond to ions of a fixed velocity v_i. To overcome difficulties with the identification of highly charged ions, to make the evaluation of parabolas easier and to help further data processing, the computer program THOMSON was developed [6,8].

Two types of ion collectors (IC) - a flat one and a ring (coaxial) one, which allows to measure the ion current close to the TPS or IEA axis - were used for a registration of the time-resolved ion current signal, from which the ion current densities can be derived. The humps on a collector signal usually indicate several ion groups which may be ascribed to different mechanisms of their production [2]. We also used a cylindrical electrostatic ion energy analyzer (IEA) for a separation of ions with different ratio of mass to charge state M_i/z to determine the relative abundance of ions produced. Experimental arrangement as well as the ion diagnostic tools are described, in a more detail, elsewhere [9,10].

The results obtained with the iodine laser used are summarized in the Table 1 (with exception of Ta for not fully optimized conditions). Paths of flight of ions ranged from 84 cm to 187 cm. The average total current densities

j_{th} and j_f are the peak values of the fast and thermal ion signals, recalculated to the distance of 100 cm according to a L^{-3} law, the widths (FWHM) of corresponding signals Δt_{th} and Δt_f are usually about 2 μs and 0.7 μs, respectively, or lower. Results for Ta and Pb ions produced by CO_2 laser [1,3] are included in this Table, too, for a comparison (Δt_{th} is about 5 μs in this case).

From the values of j_f, j_{th}, Δt_f and Δt_{th} the number (fluency) of considered ions can be estimated, if the relative abundance of ions in the group is known. Such estimations give for iodine laser produced Ta^{40+}ions the value of about $1x10^8$ ions/cm^2, for Ta^{20+} values about 6 times higher.

3 DISCUSSION

Table 1 shows that the short-wavelength and short-pulse iodine laser achieves much higher charge-states than the CO_2 laser and that the group of fast ions is missing in the second case. The ions are generated by an intense collisional ionization in the hot core of plasma, formed by a short intense laser pulse. Owing to a long wavelength of a CO_2 laser the critical density is low (about 65 times in comparison to that for iodine laser) and the ionization is slow. In the case of iodine laser the estimated electron temperature of plasma exceeded 1.5 keV, while in the case of CO_2 laser it is only about 400 eV [11].

The higher power density, the higher plasma temperature is and the higher charge states are produced [9,12]. Losses of the charge suffered by ions emitted from a laser plasma were studied recently for Ag, Cu, Ta and Pb using the iodine laser. Two ion collectors (a ring one and a flat one) were used to measure simultaneously ion current in the same direction and at two distances from the target (from 84 cm to 187 cm). It was confirmed that the decrease in the total charge carried by ions obeys nearly a L^{-2} law, as it is generally accepted, independently of the amount of transferred charge [13]. It means that recombination of ions does not proceeds at these distances and high charge states are really "frozen". Different situation is valid for the CO_2 laser. According to calculations of Roudskoy [11] the critical distance L_{cr} from the irradiated target, where the sharp rise of the recombination losses changes to a slow descend, may reach a few meters. The TPS, when installed at CERN, gave evidence for ion recombination not only in freely expanding plasma, but pictures of recombined ions were registered also after an extraction of Ta ion beam from the plasma [7].

4 CONCLUSIONS

From the experiments performed up to now it is possible to conclude:

a) Lasers with a shorter wave-length and shorter pulse-lengths can produce ions with higher charge-states much more easily than CO_2 laser.
b) Ions of heavy elements with charge states up to about 50+, and current densities above 10 mA/cm^2 at the distance of 1 m may be achieved with iodine laser at power densities of $1x10^{15}$ W/cm^2.
c) The occurrence of the highest charge states in the far expansion zone is ascribed to the presence of a fast ion group (fast electrons) [2].
d) Practical reasons (high energy at 1Hz repetition rate with 10^6 shots now achievable for an acceptable amount of money) dictated the use of the CO_2 laser as the first choice for a driver at CERN, considered as an alternative ion source for LHC [14]. Iodine, but more probably Nd lasers are predestined for a LIS of the next generation (smaller size, more progressive solution - one level of stripping might become superfluous, at least).
e) TPS seems to be a very good device for checking the LIS operation.

Table 1: Main parameters of laser produced ions of heavy elements.

	iodine laser						CO_2 laser	
	Ta	W	Pt	Au	Pb	Bi	Ta	Pb
z_{max}	55	49	50	51	51	51	25	35
$\langle z_f \rangle$	42	45	40	38	40	40		
$\langle z_{th} \rangle$	35						20	30
$E_{i,max}$, MeV	8.8	4.9	8.5	4.8	5.1	5.1	0.5	0.5
$\langle E_{i,f} \rangle$, MeV	3.4	2.4	3.1	3.1	3.3	2.7		
$\langle E_{i,f} \rangle / A$, keV/u	18.7	13.1	15.9	15.7	15.9	12.9		
$\langle E_{i,th} \rangle$, keV	700						58	100
$\langle E_{i,th} \rangle / A$, keV/u	3.9						0.32	0.48
j_f , mA/cm^2	17.4	8.6	11.5	11.0	6.6	8.6		
j_{th} , mA/cm^2	35.3	12.1	10.1	21.9	11.1	13.0	8.5	40.5

5 REFERENCES

[1] V. Yu. Baranov et al., Laser and Particle Beams 14 (1996) 347.
[2] K. Rohlena et al., Proc. LINAC'96, Geneva, Vol. 1, p. 169.
[3] H. Haseroth et al., Rev. Sci. Instrum. 69 (1998) 1051.
[4] L. Láska et al., Rev. Sci. Instrum. 69 (1998) 1072.
[5] E. Woryna et al., Laser and Particle Beams 14 (1996) 293.
[6] W. Mróz et al., Proc. 23th ECLIM, Madrid, 1996, p.71.
[7] H. Haseroth et al., to be published.
[8] M. Pfeifer et al., Proc. Int. Symp. PLASMA´97, Jarnoltowek (Poland), 1997, Vol.1., p.425.
[9] L. Láska et al,. Czech. J. Phys. 46 (1996) 1099.
[10] E. Woryna et al., Apl. Phys. Lett. 69 (1996) 1547.
[11] I.V. Roudskoy, Laser and Particle Beams, 14 (1996) 369.
[12] S.V. Homenko et al., Proc. 23th ECLIM, Madrid, 1996, p.239.
[13] J. Krása et al., 12 th Int. Conf. BEAMS'98, Haifa.
[14] H. Kugler, private communication.

NON-INTERCEPTIVE EMITTANCE MEASUREMENT OF A HIGH INTENSITY BEAM AT LOW ENERGY

R. Ferdinand, P.-Y. Beauvais, D. Bogard, R. Gobin, B. Pottin, CEA/Saclay,
DSM/DAPNIA/SEA, Bat 706, 91191 GIF-sur-Yvette FRANCE

Abstract

A CW Electron Cyclotron Resonance source has been constructed at CEA-Saclay and is now under test. The aim is to reach a 100-mA proton current at 95 keV with an rms normalized emittance smaller than 0.2 π.mm.mrad and a very high reliability. In order to match this beam into the Radio Frequency Quadrupole linac (RFQ), its characteristics have to be monitored on-line. An emittance measurement unit (EMU) located close to the RFQ entrance is a very powerful diagnostic tool. We developed a non-interceptive EMU based on the video analysis of the residual gas illumination. Methods and results are presented and discussed.

1 INTRODUCTION

This work is a part of a wide range of activities presently being undertaken at the CEA in the field of high power proton or deuteron linear accelerators. We are studying the CW IPHI demonstration project [1]. This accelerator will consist of a high intensity light ion source (SILHI) [2], an RFQ [3] and a DTL up to 10 or 11 MeV. The main application of this kind of accelerators is the production of high flux neutrons by spallation reactions, for use in the IFMIF and nuclear waste treatment projects.

The SILHI requirements are: 100 mA proton or 140 mA deuteron in more than 90% of the total extracted beam, at 95 keV and with a rms normalized emittance of 0.2 π.mm.mrad. The ECR ion source operates at 2.45 GHz with an approximately 875 G axial magnetic field. The first proton beam was produced in July 1996.

In order to match the beam into the RFQ accurately, a precise knowledge of its characteristics measured close to the cavity entrance is required. Presently, beam position and size along the low energy test line are obtained from the CCD video cameras. The emittance is measured by means of a classical "hole-slit" type Emittance Measurement Unit (EMU). This kind of EMU is esteemed for its precision but presents several disadvantages (slow mechanism, interceptive system, r-r' emittance…). Moreover, the power density allowed by the sampler, (limited to 1 kW/cm^2), prohibits us from tuning the beam around the cross-over. So it was felt necessary to develop a fast and non interceptive EMU. We decided to study a CCD video camera based system and calibrate this EMU with the classical one.

Here, we present the method and the first results obtained.

2 METHOD

For the beam monitoring, four CCD video cameras - (MICAM VHR 2000 Model) - are in operation on the Low Energy Beam Transport (LEBT) line. Two cameras are located between the extraction system and the first solenoid and another set of two 1.5 meter behind this solenoid. In both the locations, H and V planes can be observed. The MICAM camera is equipped with a 752×582 pixel matrix, its sensitivity is 0.25 lux for a 1.2 F/D ratio. The beam area observed is about 120×90 mm. Remote controls, data acquisition and analysis are performed by using LABVIEW™.

The CCD cameras give directly a signal proportional to the light emitted by the residual gas integrated over the observed plane. It means that we can acquire only transverse (x-x') emittance. The light is considered proportional to the current density and to the residual gas pressure. The logical way to obtain the beam emittance is to employ the well-known 3 gradients method. We want to obtain the emittance value ε and the Twiss parameters of the beam (α, β, γ). Due to the relation $\alpha^2 = \beta\gamma - 1$, we have in fact only 3 unknown parameters. The beam radius x is related to β, and the beam angle x' is related to γ. The principle consists in measuring the beam profile for at least three different solenoid currents. We then adjust the unknown parameters and transport the beam from upstream of the solenoid to the measurement position. The difference between the measured values and the calculated ones is the number we minimize. The beam transport has to be done with space charge. From the experience of previous measurements we take a beam neutralization of 97% [4]. Space charge and solenoid focusing (transfer from one plane to the other) imply that we cannot use a matrix formalism. The beam transport is calculated with the well known envelope equation :

$$\begin{cases} \tilde{x}'' + k^2(z)\cdot\tilde{x} - \dfrac{K}{2\cdot(\tilde{x}+\tilde{y})} - \dfrac{\tilde{\varepsilon}_x^{\,2}}{\tilde{x}^3} = 0 \\ \tilde{y}'' + k^2(z)\cdot\tilde{y} - \dfrac{K}{2\cdot(\tilde{x}+\tilde{y})} - \dfrac{\tilde{\varepsilon}_y^{\,2}}{\tilde{y}^3} = 0 \end{cases}$$

where $\tilde{x}$ and $\tilde{y}$ are the rms transverse dimensions, $K = \dfrac{qI}{2\pi\varepsilon_0 m(\gamma\beta c)^3}$ is the defocusing factor due to space charge forces, $k^2(z) = \dfrac{q^2B^2}{4\gamma^2m^2\beta^2c^2}$ is the confinement term due to the magnetic field and

$\tilde{\varepsilon} = \sqrt{\langle r^2 \rangle \langle r'^2 \rangle - \langle r \cdot r' \rangle^2}$ is the rms emittances to be calculated

At present time, we use only the camera that looks at the horizontal plane behind the solenoid. With the assumption of a cylindrical beam, the space charge forces can still be calculated. We do not expect a big difference in that case.

It is more reliable to optimize the values with about 10 measurements. Moreover, we improve the S/N ratio by averaging about 20 video columns.

The measurement code has been developed using Labview 4.0. It automatically acquires the beam and line parameters (energy, current, solenoid currents...), proposes some solenoid current values and acquires the data. It then launches the optimization code developed in C^{++}, and displays the result.

3 RESULTS

3.1 Qualitative approach.

By changing the solenoid current we can obtain a convergent beam, a divergent beam or a cross over in front of the video diagnostics. We call the “cross-over curve” as the curve of the beam size as a function of the focusing:

A complete analysis as a function of the position of the measured points on this “cross-over curve” has been done. We considered the localization of the acquisition points on this curve as shown in Figure 1 :

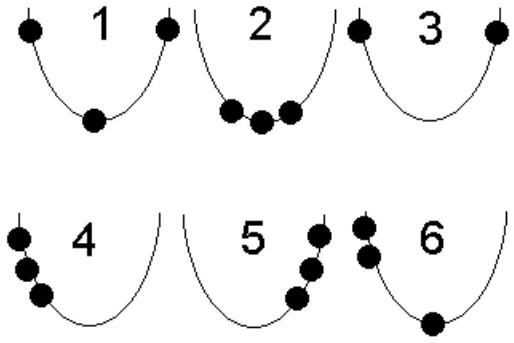

Figure 1 : Different locations of acquisition points on the "cross-over curve".

Cases 4 trough 6 generate the worst solutions: the minimization algorithm converges rarely and the results are never reproducible. Case 3 produces uncertain results. Case 1 with points equally spaced, represents the best compromise for fitting a curve that describes the dots. It produces the most reliable results and is also the "closest" to the reference EMU ones.

Preliminary exploration of the system shows that it is better to limit the beam size at the acquisition point to 2 to 3 times the cross over size. This is probably due to some optics limitation in the acquisition system.

This emittance measurement is fast. It takes about 1 minute to acquire and obtain the twiss parameters. Under the conditions defined earlier, it is a reproducible measurement, which is one of our main criteria.

3.2 Quantitative comparisons.

In order to validate this EMU, a complete comparison has to be made with a reference system. We have developed several years ago a precise "hole-slit" measurement unit. The smallest step size of the sampler is 0.6 µm, but we normally never work below 0.2 mm. Under such conditions, the acquisition takes about 10 min to be completed. A typical example is given in Figure 2.

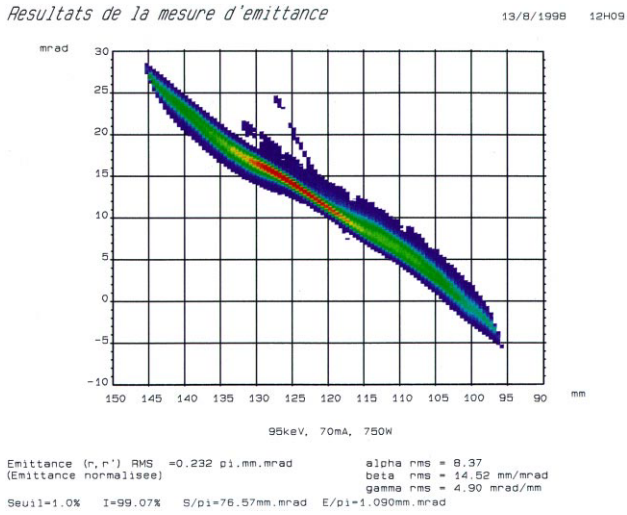

Figure 2 : Typical measurement with the reference EMU.

Typical values obtained with this reference unit are in the range of $0.23\,\pi$.mm.mrad (rms, r-r’). It depends mostly on the extracted current, pressure and the potential on the intermediate electrode. With the assumption of a cylindrical beam and a cylindrical velocity distribution inside the beam, the r-r’ value equals to $\sqrt{2}$ times the x-x’ emittance value. This gives us an rms x-x’ emittance of $0.16\,\pi$.mm.mrad. Under the same conditions, we measured the emittance with the video EMU. The result is around $0.3\,\pi$.mm.mrad, with a standard deviation of 0.0028.

We are able to produce an emittance increase of about 20% by changing the source parameters. In that case, both EMU measurements show an increase of 20%.

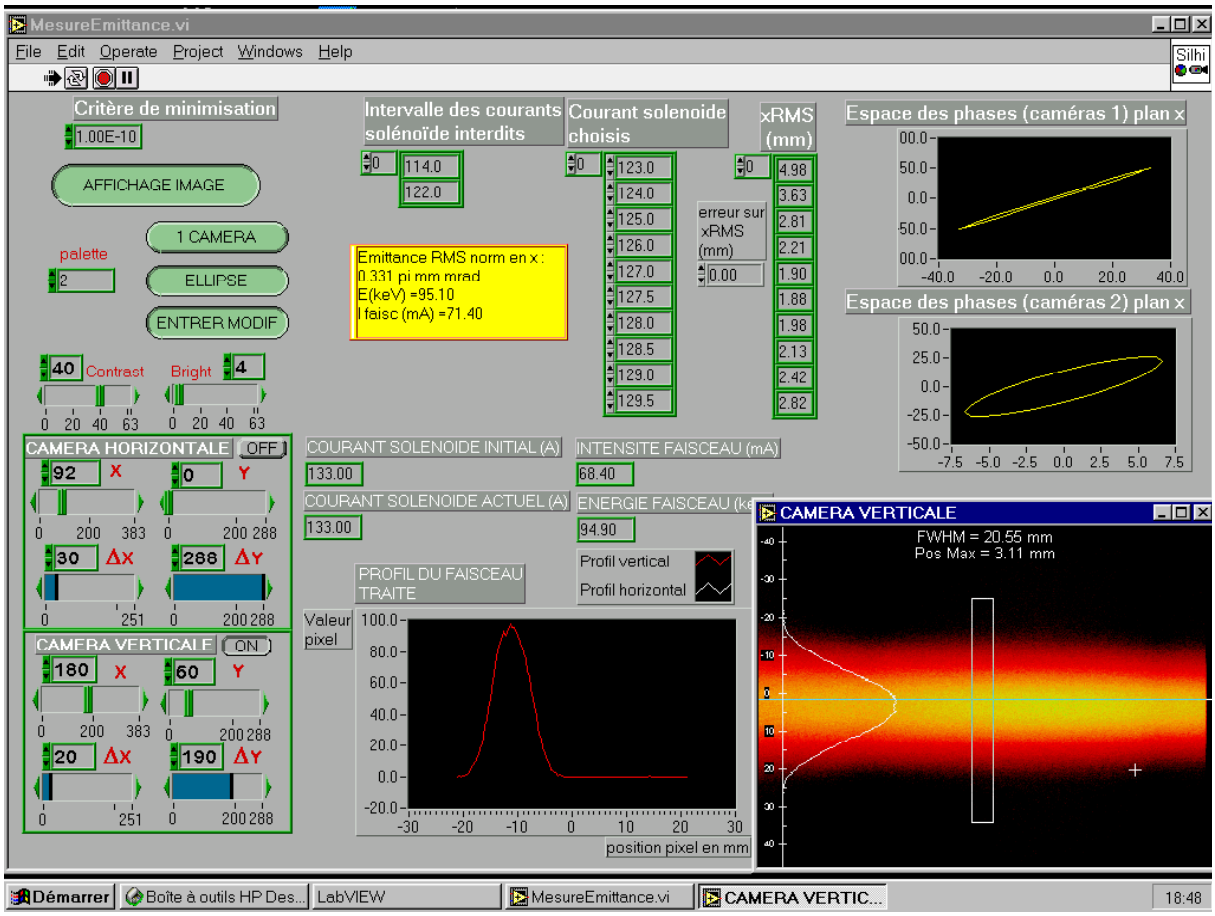

Figure 3: Front image of the video EMU.

3.3 Interpretation.

To explain this discrepancy between the two measurements, we have to carefully consider the nature of the information given by the video EMU. The light emitted originates from the background gas de-excitation. The profile measured on the video camera suffers from an enlargement due to the diffusion of the excited particles before they emit. In that case the profile increase should have a fixed error, independent of the beam size but will depend on the background pressure. Based on this assumption, we have subtracted 0.4 mm from all the measured rms beam size. It then produces a nice reproducible value of about 0.18 π.mm.mrad for the video rms emittance measurement.

Other acquisition errors are certainly present. For example, we can list the possible errors due to the optics and possible non-linearity of the CCD with light intensity.

4 CONCLUSION

So far, the EMU provided reproducible measurements with the use of some hypotheses. The measurements are fast and easy to perform. Extensive set of measurements will be needed to validate the method. A complete analysis of the collected light has also to be performed, in order to confirm the systematic observed rms error. Studies are underway for different source/LEBT tunings conditions (pressure, current…).

5 ACKNOWLEDGMENTS

The authors would like to thank the other team members for their contribution to this work and especially Nicolas Pichoff for discussions on some of the results. We would also like to thank S. Nath from LANL for is fruitful help during the writing of this document.

6 REFERENCES

[1] J-M. Lagniel, “High-Intensity Linac Studies in France”, these proceedings.

[2] R. Gobin et al, “New performances of the CW High-Intensity Light Ion Source (SILHI)”, EPAC 98, Stockholm.

[3] B. Bondarev et al, “Using of LIDOS.RFQ Codes for CW RFQ designing”, these proceedings.

[4] R. Ferdinand, J. Sherman, R. R. Stevens Jr., and T. Zaugg, “Space-charge neutralization measurement of a 75-kev, 130-mA hydrogen-ion beam”, PAC 97, Vancouver Canada.

PERFORMANCE OF AN S-BAND KLYSTRON AT AN OUTPUT POWER OF 200MW

S. Choroba, J. Hameister, S. Jarylkapov*
DESY, 22603 Hamburg, Germany, * on leave from INR, 117312 Moscow, Russia

Abstract

In order to provide RF power to the accelerating sections of a future S-Band linear collider, klystrons producing 150MW of output power at a frequency of 2.998GHz are required. Two S-Band klystrons with a nominal output power of 150MW at a pulse duration of 3μs and a repetition rate of 50Hz were developed in a collaboration between SLAC, Philips, TH Darmstadt and DESY [1]. They were built and successfully tested at SLAC in 1994 and 1995 and then shipped to DESY to feed the accelerating sections of the S-Band test facility linac. In order to explore their power potential one of the klystrons was operated at an even higher output power of more than 200MW at the test facility. HV pulses up to 610kV at a current of 780A were applied to the klystron cathode. This paper reports the results of the measurements of the various parameters of the klystron at this power level (e.g. output power, efficiency, perveance). It describes the performance and the limitations of the klystron in this power range.

1 INTRODUCTION

A possible future S-Band linear collider would require more than 5000 klystrons, capable of an output power of 150MW at a pulse duration of 2.8μs and repetition rate of 50Hz. Until 1992 klystrons meeting these demands were not available. The well known SLAC 5045 klystron achieved 65MW at a pulse duration of 3.5μs [2]. A klystron with an output power of 150MW at 1μs pulse width was developed at SLAC in 1985 [3]. In 1992 a collaboration between SLAC, TH Darmstadt, Philips and DESY was settled to develop a klystron meeting the demands of an S-Band linear collider. Two klystrons were built and successfully tested at SLAC. The results are reported in [1]. Table 1 shows the design and the parameters of the two klystrons, which were measured during the tests at SLAC.

Later C. Bearzatto and G. Faillon of Thomson in France reported, that they had developed and tested an S-Band high power klystron with an output power of 150MW at a pulse width of 1μs [4].

Both klystrons, built at SLAC, are now in operation at the S-Band test facility at DESY. The second tube was used to investigate whether an even higher peak output power than 150MW is possible. The output waveguides of the klystron were connected to RF water loads. The klystron cathode voltage was carefully raised from 550kV to a higher voltage. In the following we describe the klystron operation at the higher power level. The results of the measurements are presented.

Table 1: Parameters of the klystrons for the S-Band test facility (design and measured during tests at SLAC)

	Design	Tube#1	Tube#2
Power Out	150 MW	153 MW	150 MW
Pulse Duration	3 μs	3 μs	3 μs
Repetition Rate	60Hz	60Hz	60Hz
Beam Voltage	535 kV	527 kV	508 kV
Beam Current	700 A	680 A	652 A
Microperveance	1.79	1.78	1.80
Efficiency	40 %	43 %	45 %
Gain	> 50 dB	56 dB	57 dB

2 THE KLYSTRON

Figure 1 shows klystron #1. The total height is 2.6m, the diameter of the anode housing is 40cm and the weight is about 300kg. The cathode has a diameter of 13.3cm and a cathode loading of 6.12A/cm^2. The beam area convergence is 40:1. The maximum electric fields on the focus electrode and anode are 180kV/cm and 210kV/cm, respectively. Seven cavities including the input and output cavities are in the 3.2cm wide drift tube.

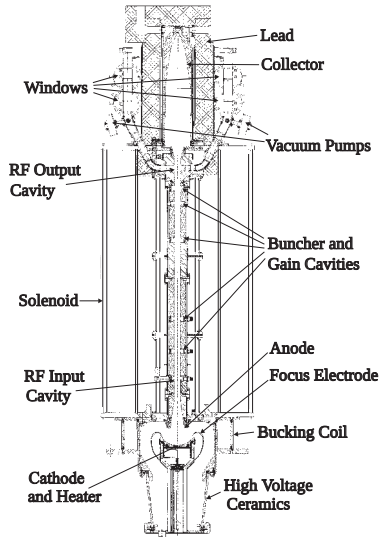

Figure 1: Layout of klystron #1

The klystron has two output waveguides, which are splitted and recombined again, so that there are two RF windows in each output waveguide. The waveguide assembly on each side is the well proven design of the SLAC 5045 klystron.

The klystron requires a solenoid with a magnetic field of 1800G and a power consumption of 14kW. A bucking coil is needed to achieve zero magnetic field on the cathode surface.

Although the two tested tubes are very similar in general, there are three major differences between tube #1 and #2. Already at the design state it was decided to use different output cavities for the two tubes. Tube #1 has one single cavity, whereas tube #2 has two coupled cavities at the output. The expectation was, that the second tube would have a slightly better efficiency than the first tube. During the tests of tube #1 an oscillation at 8.1GHz was observed depending on the beam voltage and solenoid field settings. Therefore it was decided to fabricate tube #2 with a stainless steel drift tube between the cavities 3 and 4, and 4 and 5 instead of using only copper for the drift tube as for klystron #1. This added additional losses to the disturbing oscillation. No oscillations were observed during testing of tube #2. The cathode of tube #2 was changed to a scandate cathode for tube #2, whereas tube #1 uses an osmium coated M-type cathode. More details can be found in [1].

3 OPERATION OF KLYSTRON #2

Since klystron #2 did not show disturbing oscillations up to an output power of 150MW and in addition has a slightly better efficiency than klyston #1, it was chosen to investigate the power potential of this type of klystron. Whereas klystron #1 has to provide RF power to the accelerating sections of the test facility, two sets of high power water loads, made by Nihon Koshuha, Yokohama, Japan, were installed at the two output waveguides of klystron #2. Each of the loads consists of a splitting T which devides the output power of each output waveguides. At the end of each waveguides the power is absorbed by water flowing behind a thin ceramic window. The VSWR of the loads is less than 1.10 at 2.998GHz.

Two 75dB hole coupler were installed at each output waveguide to measure the forward and reflected output power. A 2.998GHz band pass filter (30MHz bandwidth) was used to eliminate other frequency components in the measurements. In addition the output power could be determined by calorimetric measurements by measuring the water flow rate through the loads and by taking the loads water in and outlet temperatures. By taking into account these numbers, the repetition rate and the output pulse shape it was possible to calculate the klystrons peak output power. Since we were also able to measure the temperatures and flow rates in the klystron coolant circuits, e.g. the collector and body cooling circuit, we were also able to determine the power absorbed in the klystron itself. The difference between the power absorbed in the klystron at operation with and without RF power generation gives the klystron output power, too.

The high voltage pulse duration could be changed by adding or removing capacitors of the line type modulators pulse forming network. A detailed description of the modulator can be found in [5].

4 MEASUREMENTS

The measurements were performed at a high voltage flat top pulse duration of 1μs and a repetition rate of 12.5Hz, because both, klystron and modulator, were operated beyond their peak power specification during the tests. The cathode voltage was slowly raised from 550kV up to the maximum possible voltage of 610KV at a current of 780A. At a voltage level of 600kV it was necessary to increase the magnetic field in the solenoid by about 6%. Otherwise the RF output power would break down at the end of the 1μs long RF pulse. Later it turned out, that by adjusting the independent coils of the solenoid, operation at a beam voltage up to 610kV could be achieved even with a lower setting of the solenoid currents. Figure 2 shows the waveforms at a voltage of 610kV and total output power of 213MW.

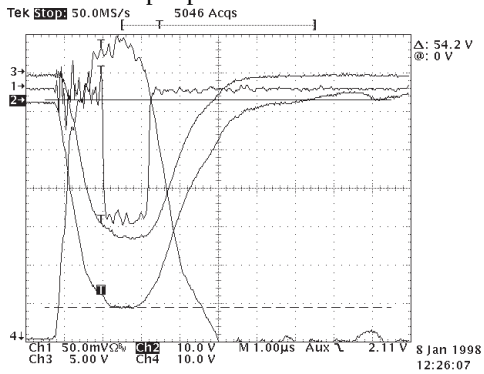

Ch1 RF output power out of waveguide 2 107MW
Ch2 Klystron cathode voltage 610kV
Ch3 Klystron collector current 781A
Ch4 Klystron gun current 778A
Time 1 s/div

Figure 2: Waveforms at a voltage of 610kV

The measurement of the perveance of klystron #2 gives numbers lower than in the SLAC measurements. Although klystron #1 is operated at a different modulator with different devices for voltage and current measurement as klystron #2, we measure also a lower perveance than in the SLAC tests. The reason for the difference is not clear up to now. Figure 3 shows perveance and efficieny as a function of the beam voltage. The klystron efficiency increases with increasing beam voltage and reaches 47%. Figure 4 shows the output power as function of the beam voltage. At a voltage of 610kV a power of 213MW in a 1μs long pulse can be extracted from the klystron. Figure 5 shows the dependence of the output power from the drive power for different beam voltages. Four data points are included, which were taken at four different beam voltages but at fixed drive power.

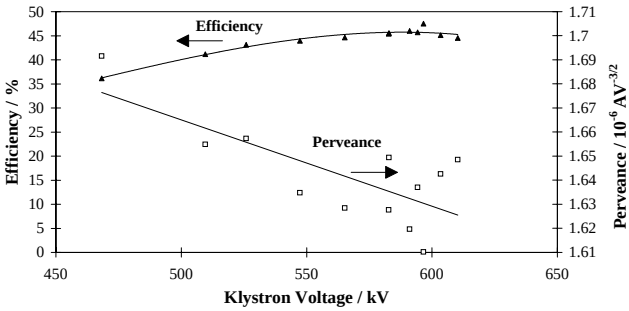

Figure 3: Efficiency and perveance as function of beam voltage

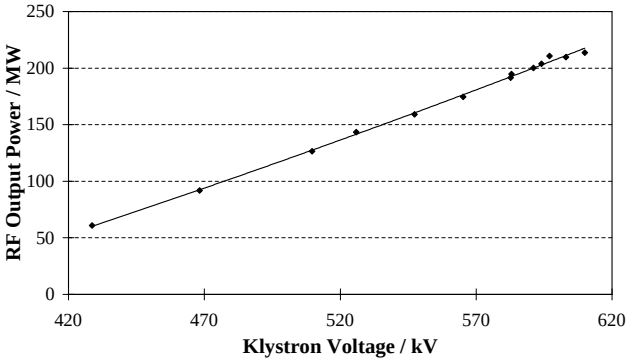

Figure 4: Output power versus beam voltage

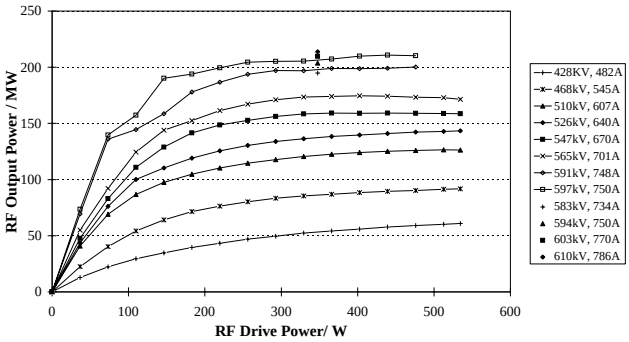

Figure 5: RF output power versus RF drive power for different klystron voltages and currents at an RF pulse duration of 1μs

At a drive power of 300W the output power is saturated. The saturated gain at this point is 58dB for an output power of more than 200MW. For beam voltages above 550kV the curves start to show a strange behavior on the rising part of the curve, where bumps appear. This can be seen more easily in figure 6, which shows the gain at a beam voltage of 583kV. The gain, which usually decreases with increasing drive power, shows a bump at 95W of forward drive power. Since the reflected drive power increases almost linearly as function of the forward drive power and shows no distinct bump, the drive power absorbed by the klystron should show a similar behavior. The vacuum pressure in the tube was not conspicuous in any way. A variation of the solenoid filed affected the bumps. The bumps could be shifted to other points or could be made more or less distinct. It is even possible to find curves which show two or three of these bumps on the gain curve. The reason for this behavior is not clear up to now. It might be, that it indicates multipacting in the tube.

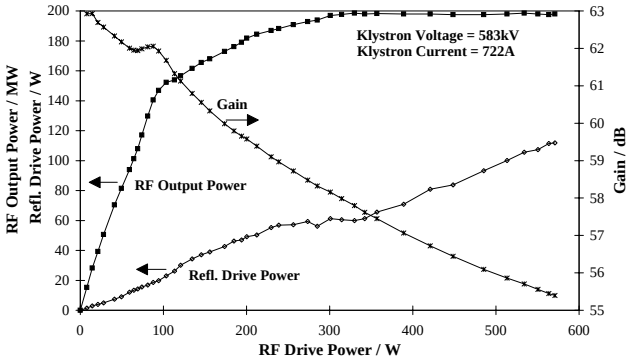

Figure 6: RF output power, gain and reflected drive power at 583kV and 722A

5 CONCLUSION

It is possible to operate an S-Band klystron at a pulse duration of 1μs at more than 200MW of output power. Even longer RF pulses at this power level might be achievable. Since we wanted to use the klystron to provide RF power for the test facility, we refrained from trying to reach more than 200MW at longer pulse duration. Both, the klystron and the modulator, were operated beyond their original specification. The e-beam needs careful focussing when the beam voltage is in the 600kV range. The reason for the bumps on the gain curves is not clear. Since these can be affected by varying the magnetic field, this might indicate multipacting in the tube.

6 REFERENCES

[1] D. Sprehn, G. Caryotakis, R.M. Phillips, "150-MW S-Band Klystron Program at the Stanford Linear Accelerator Center", Proceedings of the RF96, Kanagawa, Japan, April 8-12, 1996, P 91-99

[2] T.G. Lee, J.V. Lebacqs, G.T. Konrad, "A Fifty Megawatt Klystron for the Stanford Linear Collider", SLAC-Pub-3214, September 1983

[3] T.G. Lee, G.T. Konrad, Y. Okazaki, M. Watanabe, H.Yonezawa, "The Design and Performance of a 150MW Klystron at S-Band", SLAC-Pub-3619, April 1985

[4] C. Bearzatto, G. Faillon, "Short Presentation of High Peak Power TH 2153 Klystrons", Proceedings of the RF96, Kanagawa, Japan, April 8-12, 1996, P 116-122

[5] S. Choroba, M. Bieler, J. Hameister, Y. Chi, "A 375MW Modulator for a 150MW Klystron at the S-Band Linear Collider Test Facility at DESY", Proceedings of the XVIII International Linear Accelerator Conference, Linac 96, Geneva, Switzerland, 26 -30 August, 1996, P 785-787

DEVELOPMENT OF THE X-BAND KLYSTRON MODULATOR AT KEK

M. Akemoto, S. Anami, H. Mizuno and S. Tokumoto
High Energy Accelerator Research Organization (KEK)
Oho 1-1, Tsukuba-shi, Ibaraki-ken, 305-0801 Japan

T. Majima and Y. Kobayashi
Ishikawajima-Harima Heavy Industries Co., Ltd.
Toyosu 3-1-15, Koto-ku, Tokyo, 135-8732 Japan

Abstract

A line type modulator with a Blumlein pulse-forming network (PFN) to drive a 75 MW pulsed klystron for the main linac of an X-band Linear Collider is under development at KEK. This Blumlein modulator yields a reasonably fast rise time and hence, an improved efficiency. A high power test of the modulator showed that an output pulse with a rise time(10%-90%) of less than 350ns can be generated for the klystron. This paper describes the design, specifications and results of the performance tests of the Blumlein modulators.

1 INTRODUCTION

The klystron pulse modulator for an X-band Linear Collider requires to produce a 454kV, 367A, 1.5μs flat-top pulse to drive a 75MW klystron[1]. The present configuration of the 0.5TeV linear collider requires more than 3200 modulators. The large number of klystrons and modulators dictate the need for a reliable and efficient system.

The power efficiency of the modulator are extremely important. The effective output power of the modulator is the power of the flat-top portion of the high voltage output pulse and hence, the pulse with a fast rise time and fall time is required. The main contributor to the pulse waveform is a pulse transformer(PT) as well as a pulse-forming network(PFN). For these designs, the transformer turns ratio plays a very important role. Using a Blumlein method allows a lower transformer turns ratio, which yields a reasonably fast rise time and hence, an improved efficiency. The efficiency target for the modulator system (wall plug to usable pulse flat-top) is 75%.

The R&D's of the Blumlein type modulator, which is based upon conventional technology and components that exist at present, are being performed at KEK.[2] Two kinds of modulators have been developed. First modulator, which is called Modulator #1 after this, has been built to study the practical application of Blumlein type modulator. The second modulator, which is called Modulator #2 after this, has been built to study a compact and high performance Blumlein modulator.

2 KLYSTRON

The X-band klystron development program at KEK had been originally designed for 80 MW peak power at 400ns pulse length. The rf parameters of the main linac were recently changed after reconsidering the rf system. The main parameters of the klystron developing at present are given in Table 1.[3]

Table 1. Specifications of X-band klystron

Operating frequency	11.424 GHz
RF pulse length	1.5μs
Peak output power	75MW
Repetition rate	120pps
RF efficiency	45%
Beam voltage	454kV
Beam current	367A
Perveance	1.2μ
Gain	53-56dB

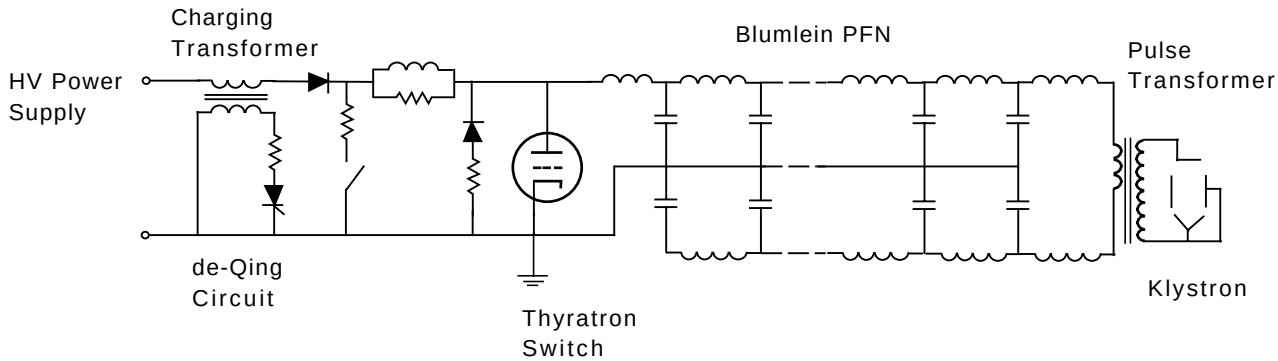

Figure 1. Circuit of the Blumlein type modulator.

3 BLUMLEIN CIRCUIT

The basic circuit of the Blumlein type modulator is shown in Figure 1. It consists of a conventional PT, a Blumlein PFN, a single-thyratron switch tube and a resonant charging circuit with a de-Qing circuit.

4 MODULATOR #1

4.1 Hardware

The modulator components shown in Figure 1 are all housed in air. The main parameters of the modulator #1 are given in Table 2. Maxwell mini double-ended capacitors were used as a PFN capacitor. The internal inductance of the PFN capacitor itself should be lower for faster discharge and it limits the shortness of the rise time. The internal inductance of this capacitor is approximately 20nH. Each section capacitor consists of two these capacitors which are placed in series to get 100kV. These capacitors have a standard value of 7nF and a rated voltage of 50kV. The thyratron EEV CX1937A with a rated voltage of 80kV was used as a switch tube which discharges the Blumlein PFN.

Table 2. Main parameters of the modulator #1

	unit	Design	Upgrade
Output pulse			
Secondary voltage(Max.)	kV	560	560
Secondary current(Max.)	A	503	503
Pulse width	μs	0.8	2.4
Flat-top	ns	400	1500
Repetition rates	pps	50	50
Pulse transformer			
Step-up ratio		1:8	1:8
Blumlein PFN			
PFN impedance/line	Ω	8.7	17.4
No. of sections		13	20
Inductance/section	μH	0.265	1.06
Capacitance/section	nF	3.5	3.5
Total capacitance	nF	91	280
Charging voltage(Max.)	kV	70	70

4.2 Output pulse waveform and circuit analysis

The solid line in Figure 2 shows an example of the klystron voltage waveform. An output pulse with a peak voltage of 470kV, a rise time(10%-90%) of 350ns, a flat-top width(flatness ±1%) of 400ns and a fall time(10%-90%) of 350ns was successfully generated. The rise time is a sufficiently short because the rise time of the requirement is less than 400ns.

We have analyzed the modulator circuit by a simulation method. The broken curve in this figure shows result simulated by a computer code Micro-Cap IV. The simulation gives a good fit to the measured data. From this analysis, it was found that total distributed capacitance in the pulse transformer, the tank and the klystron is about 180pF. This large value mainly limits the rise time of output pulse. The calculated values of distributed capacitances for the klystron and the PT are about 80pF and 40pF, respectively.

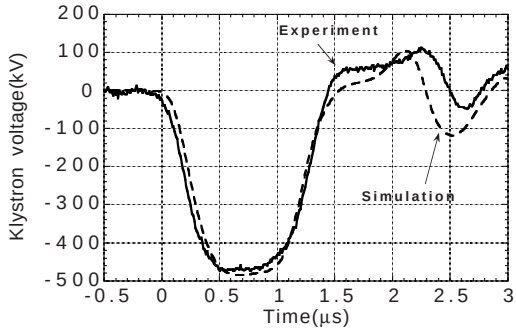

Figure 2. Output pulse waveform at the klystron.

4.3 Upgrade

We upgrade the modulator #1 to produce a pulse with a flat-top of 1.5μs. To increase the pulse width, the number of the PFN section is increased up to 20. Each line is made in two parallel lines to increase the value of the section inductance in order to improve the PFN characteristic. The charging transformer and the PT are also remade. The parameters of the upgrade modulator are given in Table 2. We simulated the output pulse waveform by using circuit parameters obtained by the circuit analysis above subsection. Figure 3 shows the result for a charging voltage of 70kV. The simulation shows that an output pulse with a rise time(10%-90%) of 350ns and a flat-top width of more than 1.5μs can be achieved.

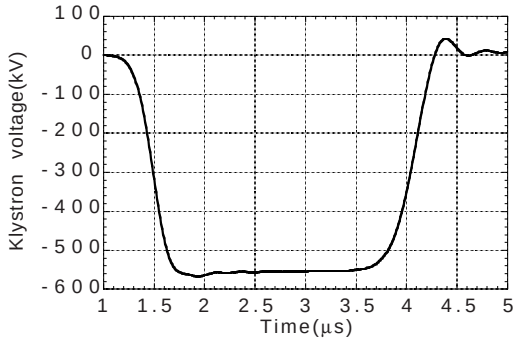

Figure 3. Output pulse waveform simulated by a computer code Micro-Cap IV.

5 MODULATOR #2

5.1 Hardware

The modulator components shown in Figure 1 are all housed in a cylindrical stainless oil tank which also mounts the klystron. This allows to make all circuits

significantly compact, and also to make circuit wiring short. The slow rise time caused by stray inductance of wiring is therefore improved and it makes modulator efficiency better. Figure 4 is a photograph of the modulator #2. The size of the oil tank is 1.8m in diameter and 1.6m in height. The thyratron EEV CX2199 with a rated voltage of 100kV was used as a switch tube. For the Blumlein PFN, a compact double-ended capacitor with a capacitance of 1.9nF, a rated voltage of 80kV, a voltage reversal of 65%, an internal inductance of 40nH and a design life of $2x10^8$ shots was developed by Maxwell Energy Products, Inc.. The size of the capacitor is 4''wide x 6''deep x 10.25''high. The main parameters of the modulator are given in Table 3.

Table 3. Design parameters of the modulator #2

Output pulse	
Secondary voltage(Max.)	560kV
Secondary current(Max.)	503A
Pulse width	700ns
Flat-top	400ns
Repetition rates	50pps
Pulse transformer	
Step-up ratio	1:7
Blumlein PFN	
PFN impedance/line	11.5Ω
No. of sections	16
Inductance/section	252nH
Capacitance/section	1.9nF
Charging voltage(Max.)	80kV

Figure 4. Photograph of the modulator #2.

5.2 High-voltage test

A preliminary test has been performed to confirm the performance of the modulator. The secondary side of the PT was connected to a 1120Ω ceramic resistor. The modulator was operated up to a charging voltage of 80kV without any faults. Figure 5 shows the output waveforms obtained for a charging voltage of 40kV. An output pulse with a peak voltage of 280kV, a rise time(10%-90%) of 210ns, a flat-top width(flatness ±4.5%) of 400ns and a fall time(10%-90%) of 280ns was successfully generated.

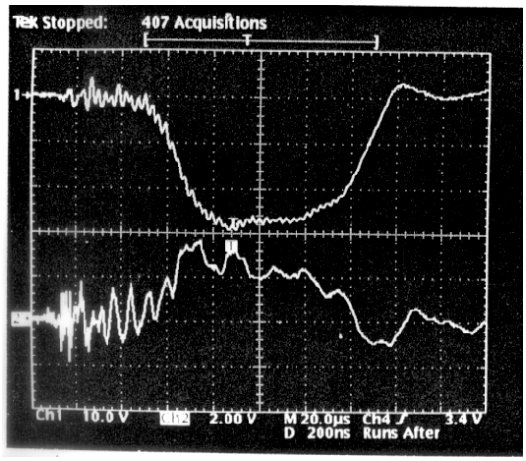

Figure 5. Output pulse waveform at the resistor load.
Upper trace: Output voltage(100kV/div)
Lower trace: Output current(200A/div)
Horizontal: 200ns/div

6 FUTURE PLANS

The upgrade work of the modulator #1 is now in progress and will be completed on October, 1998. We plan to test the modulator #2 connecting to a XB72K klystron to confirm its performance in this winter. In order to reduce both production costs and spaces of the modulators, we make a design study of the modulator operating two or four klystrons.

REFERENCES

[1] JLC Design Study Group, "JLC Design Study," KEK Report 97-1, 1997.

[2] H. Mizuno, T. Majima, S. Sakamoto and Y. Kobayashi, "A Blumlein type Modulator for a 100MW-class X-band klystron," Proc. of the Eupopean Particle Accelerator Conference, 1994.

[3] Y.H. Chin et al., "The 120 MW X-band Klystron Development at KEK," Proc. of the Eupopean Particle Accelerator Conference, 1998.

PROGRESS OF APT SUPERCONDUCTING LINAC ENGINEERING DEVELOPMENT*

K. C. D. Chan, B. M. Campbell, R. C. Gentzlinger, P. Balleyguier**, J. A. Waynert, F. Krawczyk, W. B. Haynes, J. P. Kelley, B. Rusnak, and H. Safa**
Los Alamos National Laboratory, Los Alamos, NM 87545 USA

Abstract

We have initiated a program to develop superconducting (SC) RF technology for high-power proton linacs. These linacs are useful in accelerator-driven transmutation applications and the Accelerator Production of Tritium (APT) Project. We are developing 5-cell niobium cavities with elliptical-cell shapes at 700 MHz. These cavities, unlike most elliptical cavities for electron accelerators, are designed to accelerate protons at $\beta<1$. Coaxial power couplers are being developed to transmit high (250 kW) CW RF power to the cavities. The couplers will be tested both at ambient temperature and at 2-K temperature, and power-handling and thermal properties measured. The cavities and power couplers will be integrated into a prototype cryomodule, which will be tested and characterized with RF under cryogenic conditions as required for a high-power proton linac.

1 INTRODUCTION

We have a program to develop SCRF technology for proton linacs in Los Alamos. Although this program has been initiated to support the APT SCRF linac [1], the technology development will be useful for all SC proton linacs with high CW power and current. The merit of using SCRF linacs for high-power applications, like accelerator-driven transmutation technology, has been described in Ref. 2. In this paper, we describe the issues encountered in the development of cavities, power couplers, and cryomodules. Design features of these components are given in Ref. 3 and will be repeated here only to the extents of explaining the issues.

2 CAVITY SHAPES

Figure 1 shows the cell-shape used for the APT 5-cell cavities, usually known as the elliptical cell shape which has been widely adopted in SCRF cavities that accelerate relativistic electrons. For proton linacs, the lengths of the cells are reduced to maintain synchronism with the slower proton beams (β=0.64 and 0.82). The shorter cell lengths lead to cell walls that have smaller slopes that could easily collapse under vacuum pressure and prone to multipacting. We have designed the APT cavities with a 10-degree slope for the cell wall. This is the optimum slope to minimize peak electric and magnetic peak fields and to maximize mechanical stability. With a slight increase in wall thickness (from 3 to 4 mm), we can eliminate the need of costly stiffeners that are otherwise needed to withstand the vacuum load. We have tested single-cell cavities [4]. Results (Fig. 2) show the APT cavity field can be achieved with more than a factor of two margin, and with no limitations due to multipacting, even in the case of β=0.48.

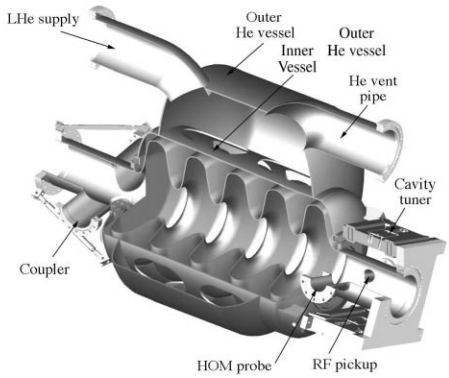

Figure 1: Illustration of β=0.64 cavity design.

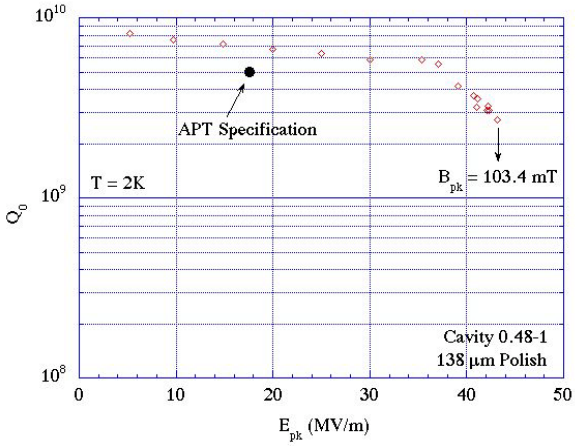

Figure 2: Typical test results of a β=0.48 cavity

3 POWER COUPLER ENGINEERING DESIGN

Figure 3 shows an illustration of the APT power coupler. Because of the high beam power, each coupler needs to deliver 210 kW of CW power to the beam. This

*Work supported by US Department of Energy
**On sabbatical leave from CEA Saclay, 91191 Gif-sur-Yvette, France

power level was achieved only recently by a waveguide-type coupler; and it has not been achieved by coaxial-type couplers [5]. Additionally, since the APT-linac is required to produce tritium with high availability over 40 years, it is important that APT coupler operate reliably at high power.

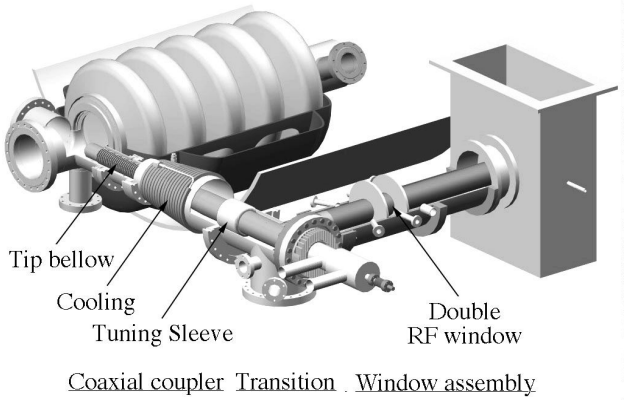

Figure 3: Illustration of the APT power coupler.

Based on experience from other laboratories, we have chosen a coupler design [3] with features that enhance reliability. Usually, RF windows are the primary source of coupler failure. In our design, we use warm RF windows with two ceramic pieces for redundancy, no direct line of sight to the beam, and window diagnostics to detect signs of the onset of failures. These windows, fabricated as complete assemblies by the klystron industry, have been designed, and will be tested to 1 MW.

The APT coupler consists of three sections: the RF-window assembly, the transition, and the coaxial coupler. To minimize reflected power during operation, extensive 3D electromagnetic modeling has been done to attain a good match between sections. The modeling procedure started with the design of separate components and benchmarking the simulations by building and measuring some of these components. Finally, a fully integrated study was performed. As a result, a coupler has been designed that has an excellent power transmission at and around the 700-MHz operation frequency. We have also minimized the electromagnetic interactions between the RF-window assembly with the transition and coaxial-coupler sections. The transmission of the coaxial-coupler section is maximized by adjusting the length of a quarter-wave stub and the shape of a tuning sleeve. The RF window as a complete assembly has also been simulated extensively with respect to thermal performance to minimize thermal stress.

There are two features in the coupler that can potentially reduce the reliability of the coupler: bellows and copper plating. First, two bellows will be used in a coupler, one to allow the joining between the RF-windows and the transition sections, and one (close to the tip of the inner conductor) for changing the length of the inner conductor and consequently the coupling to the cavities. These bellows could become work-hardened and yield after repeated elongation, compression and thermal cycling. Bellows made of BeCu are ideal for our application, but their availability is expected to be limited because of the toxicity of machining Be. We are studying options including copper alloys, electroformed copper bellows, and copper-plated or sputtered stainless-steel bellows. Second, copper plating will be used on the inside surface of the stainless-steel outer conductor. Stainless steel is chosen as structural material for the outer conductor because of its low thermal conductivity. Unfortunately, it also has high RF resistivity and RF heat loss. Copper has low electrical resistivity and RF heating. Copper-plated stainless steel will offer both low RF loss and low heat transfer at 2-K temperature. To maintain reliable performance, it is important that plating have a low outgassing rate and good adhesiveness to stainless steel. The plating process must produce these performance and thickness uniformity consistently. There are three ways to achieve copper plating: plating with UBEC (Ultra Bright Electroplated Copper), plating with OFE (oxygen-free electrolytic) copper, and plating with vacuum sputtering. We plan to perform outgassing and adhesive tests on plating samples produced using these three methods. We will also construct couplers with these plating methods and tests them at high RF power.

4 COUPLING COEFFICIENTS OF POWER COUPLER

For the amount of power needed to accelerate the beam, we need to obtain an external-Q (Q_L) of 2.5×10^5. This Q_L will be provided by two couplers, each having a Q_L of 5×10^5. We have investigated different coupler geometries to provide this Q_L. Results [6] show that we need to expand the beamtubes for the β=0.64 cavities from 6.5 cm to 8 cm. Lower coupling can further be achieved by slightly expanding the tip of the coupler center conductor. We have also extended the standard beam-loading theory for beam loading with multiple couplers [7]. Reflected powers resulting in failure scenarios and when the two couplers are not exactly identical were calculated.

5 OPERATING TEMPERATURE

The cavity operating temperature has been set at 2.15 K [8]. This temperature was chosen for two reasons. First, we evaluated the total cryoplant cost, including the capital cost and operating cost, as a function of the operating temperature. The total cost has a minimum around 2.4 K caused by a tradeoff between higher cryogenic efficiency at higher temperature and lower surface resistance at lower temperature. The minimum is broad, with the total cost increased by 3% by operating at 2.15 K. Second, we decided to operate in the temperature regime of superfluid for better helium heat-transfer properties and better margins against quench. An operating temperature of 2.15-K is the highest temperature for which that we presently feel confident to control the LHe temperature so

that LHe remains superfluid. It may be lowered in the future.

6 HEAT LOADS AND POWER COUPLER COOLING

We are designing our components and cryomodules to maximize cryogenic efficiency and to minimize the required cryogenic power. Table 1 shows a summary of the baseline heat loads for a $\beta = 0.82$ cryomodule. Such a cryomodule will have 4 cavities and 8 power couplers. For this case, heat is removed by LHe boiloff and at an intermediate temperature of 45 K.

Table 1: Typical heat loads of a β=0.82 cryomodule

	2.15-K (W)	45-K (W)
Cavities	96.4	0
Power Couplers	40.0	176
HOM	6.8	0
Others	8.0	90.9

The major heat loads are from the RF losses in the cavities. The Qo used to calculate this load is $5x10^9$. The second major heat load is the power coupler. The power couplers are the primary thermal connections between room temperature and the 2.15-K temperature. They are also major heat sources because the RF losses in the couplers. Typically, the RF losses are 230 and 50 W, respectively, for inner and outer conductor. It is important to prevent these losses from reaching the 2.15-K temperature. We have developed a thermal model to explore a wide range of cooling schemes and operating conditions. This model includes heat-transfer mechanisms like conduction, radiation, RF heating, and cooling by forced convection. We considered cooling of the outer conductor with single- and two-temperature thermal intercepts and with a counter-flow heat exchanger. Results [9] showed that the power-coupler heat loads could be reduced to 16W at 2.15 K using counter-flow heat exchangers. Results from the model also showed that the inner conductor could be cooled using room-temperature gaseous helium.

7 CRYOMODULE ASSEMBLY

For high-performance of SC cavities and power couplers, it is important to maintain clean assembly of the cryomodule. For our power coupler design [10], with the absence of a cold RF window to seal off the cavity, we are required to assemble the power couplers with the cavities in a cleanroom (Class-100) environment. Figure 4 shows the assembly that will be assembled in the cleanroom. After cleanroom operation, we will rotate the assembly through the axis by 90-degrees to facilitate the installation of superinsulations, magnetic shields, LHe tubings, and instrumentation. After that, we will install all the LHe and vacuum connections and the two endcaps and test for vacuum.

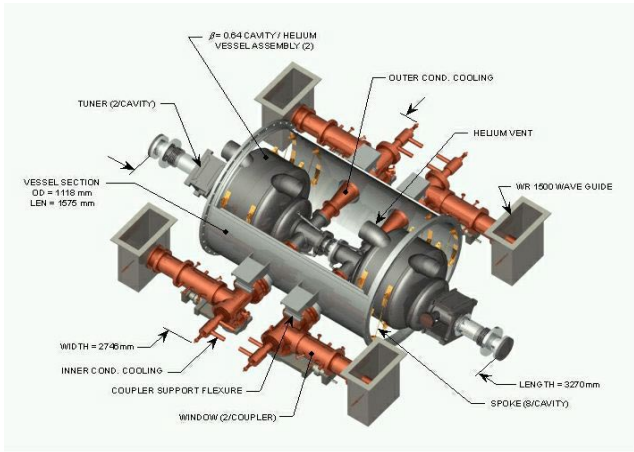

Figure 4: Part of cryomodule assembled in a Class-100 cleanroom

8 SUMMARY

We are developing SC RF cavities, couplers, and cryomodules to accelerate high-intensity proton beams. Issues identified during this development have been described in this paper.

9 REFERENCES

[1] G.P.Lawrence, High-Power Proton Linac for APT; Status of Design and Development, presented in this conference.

[2] K.C.D.Chan, et al., Development of RF Linac for High-Current Applications, presented at the 5th Euro. Conf. On Accel. In Applied Res. and Techn., Einhoven, The Netherlands, Aug. 26-30, 1997.

[3] K.C.D.Chan, Engineering Development of Super-conducting RF Linac for High-Power Applications, presented at the 6th European Particle Accelerator Conference, Stockholm, Sweden, June 22-26, 1998.

[4] W.B.Haynes et al., Medium-Beta Superconducting Cavity Tests at Los Alamos National Lab for High-Current Proton Linac, presented to the 8th Workshop on RF Superconductivity, Oct. 6-11, 1997, Padova, Italy.

[5] Waveguide-type coupler achieved 210 kW at Cornell in June 1998. The highest CW power transferred to beam by coaxial-type coupler is 168 kW at KEK, Japan.

[6] P. Balleyguier, External Q Studies for APT Superconducting Cavity Coupler, presented in this conference.

[7] H. Safa, Multiple Coupling and Beam Loading of An RF Cavity, ibid.

[8] H. Safa, Optimum Operating Temperature of Superconducting Cavities, ibid.

[9] J.A. Waynert, et al., A Thermal Analysis And Optimization Of The Apt 210 kW Power Coupler, ibid.

[10] B. M. Campbell, Engineering Design of the APT Cryomodule, ibid.

DEVELOPMENT OF A FAST TRAVELING-WAVE BEAM CHOPPER FOR THE SNS PROJECT*

S.S. Kurennoy and J.F. Power
Los Alamos National Laboratory, Los Alamos, NM 87545, USA

Abstract

High current and stringent restrictions on beam losses, below 1 nA/m, in the designed linac for the Spallation Neutron Source (SNS) require clean and fast – with the rise time from 2% to 98% less than 2.5 ns – beam chopping in its front end, at the beam energy 2.5 MeV. The development of new traveling-wave deflecting current structures based on meander lines is discussed. Three-dimensional time-domain computer simulations with MAFIA are used to study transient effects in the chopper and to optimize current structure design. Two options for the fast pulsed voltage generator – based on FETs and vacuum tubes – are considered, and their advantages and shortcomings for the SNS chopper are discussed.

1 MEBT CHOPPER SYSTEM

The SNS is a next-generation pulsed spallation neutron source designed to deliver 1 MW of beam power on the target at 60 Hz in its initial stage [1,2]. It will consist of a 1-GeV linear H^- accelerator and an accumulator ring. The SNS storage ring accumulates the linac beam during a few hundred turns (a macropulse, about 1 ms) using H^--injection through a carbon foil. The beam injected into the ring is stacked into a single long bunch, and the linac macropulse must be chopped at near the ring revolution frequency 1.188 MHz to provide a gap required for the kicker rise time during a single-turn ring extraction. The final clean beam chopping in the linac is to be done in the Medium Energy Beam Transport (MEBT) line.

The MEBT transports 28 mA of peak beam current from a 2.5-MeV 402.5-MHz RFQ to a drift-tube linac. A 0.5-m space is allocated for the chopper that deflects the beam into a beam stop during the 35% beam-off time. The chopper parameters are summarized in Table 1.

Table 1: MEBT Chopper Specifications

Parameter	Value	Comment
Beam energy	2.5 MeV	β=0.073
Length	≤0.5 m	Shorter is better
Gap	1 cm	adjustable
Pulser voltage	±900 V	Currently achievable with FETs
Deflection angle	18 mrad	
Chopping period	841 ns	
Duty factor	35 %	65 % beam on
Rise / fall time	< 2.5 ns	2–98 % (final goal)

To mitigate the effects of a partial chopping or small errors in the timing system, an identical "anti-chopper" is placed in the MEBT line at an optically symmetric point from the chopper to return uncollimated beam to the axis. Two preliminary chopping stages (at the ion source and in the LEBT line, at 100 keV, see [2]) are introduced to reduce the beam power deposited at the MEBT beam stop.

At any given moment of beam passing through, there are about ten bunches along the chopper length. Even having an ideal pulse generator, the only way to avoid partially chopped bunches is to apply a traveling-wave current structure. The deflecting electric-field pulse fills the chopper with the phase velocity along the beam path matching the beam velocity and propagates together with the beam. The bunches following the pulse front are fully deflected while those ahead of the front are not disturbed. Providing the field-pulse front (and its end) shorter than the bunch-to-bunch spacing (2.5 ns, or about 5 cm) is the most challenging requirement to the chopper system. As an initial goal, the rise/fall time below 5 ns is acceptable; it will lead to one partially chopped bunch at the front and the end of each chopper pulse.

2 CHOPPER CURRENT STRUCTURE

A traveling-wave chopper for $H^{\pm}$ beams at 750 keV [3] has been working successfully for many years at LAMPF. It provides the rise time of about 7 ns, mostly due to the pulse modulator. Its coax-plate current structure itself is capable of providing a pulse front about 2-3 ns with an overshoot on the 10% level ringing for a few ns. The 1-m long structure consists of two parallel plates, each interfaced with many small strip segments connected with coaxial cables on the reverse side of each plate to form a continuous circuit along the structure. The voltages on the upper and lower plates are synchronized and have opposite signs so that the resulting vertical electric field deflects the beam. The structure rise and fall time limitations are caused by stray capacitance between the segments and by multiple coax-to-segment transitions.

A new current structure based on a meander line with separators (Fig.1) has been proposed in [4]. A strip line forming the meander can be either straight or notched (as the one shown in Fig. 1). The line parameters are adjusted to provide the line characteristic impedance 50 Ω. The meander bends are chamfered to avoid pulse reflections.

* Work supported by the US Department of Energy.

The separators (or guard barriers) rising from and electrically connected to the ground plane are used to reduce the coupling between the adjacent sections of the meander line, see in Fig.2. The new design has no multiple coax-to-plate transitions and is easier for manufacturing.

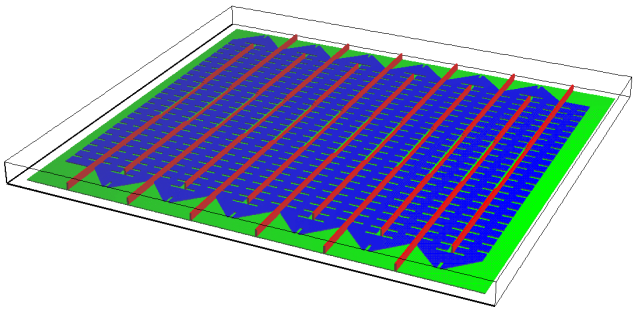

Figure 1: 1/4-length model of meander current structure: notched meander strip line (blue) above the ground plate (green) with separators (red), cf. Fig.2. Only the lower plate is shown.

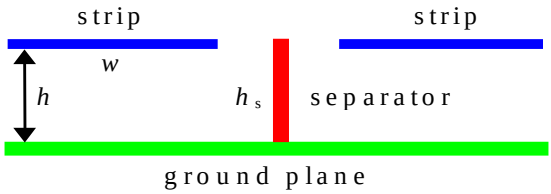

Figure 2: A partial vertical cut in the beam path plane of the meander current structure: the separator is inserted between two adjacent pieces of the transmission line.

3-D time-domain simulations with the electromagnetic simulator MAFIA [5] have been used to study transient effects in the current structure. It was shown [4] that even without separators, the meander structure has a rise time 2–2.5 ns; with separators it can be reduced down to 1–1.25 ns, depending on the separator height. The structure fall time was found to be about the same as the rise time. High separators, however, reduce the effective field on the beam path by 10–20% depending on their height h_s.

Our previous work [4] dealt mostly with straight-strip meander structures. Using a notched strip line in the meander instead of a straight one has some advantages. First, the notches provide an additional inductive load that slows down the wave along the strip. It increases the field efficiency due to a larger ratio of the strip width w to the strip-to-strip gap width g: the notched-strip width w is 8 mm compared to 5 mm for a straight line. The meander width transverse to the beam is about 11 cm, h=1 mm and g=2 mm in both cases. In addition, the notches also reduce the magnetic coupling between adjacent strips since the wave magnetic field is concentrated closer to the strip center. As a result, our recent efforts have been directed toward optimizing the notched-strip design.

For earlier simulations [4] we needed to load a TEM wave into the structure. The latest version of MAFIA [5] allows simply to feed the strip with a voltage having any time profile. We have used voltages shaped as either step-functions (often smoothed by a squared *sin* to filter out very high frequencies) or as finite-length pulses. As the voltage pulse propagates along the structure, the electric field on the beam path is recorded. As an example, Fig.3 shows the deflecting field created by a voltage pulse with 1-ns sin^2 front, flat top at 1 kV for 3 ns, and 1-ns sin^2 end, in the full-length 50-cm model of the type shown in Fig.1. Such a pulse would kick out exactly two linac bunches. As the pulse propagates, its shape is slightly distorted by developing an overshoot, but its front and end remain well within 2-ns range, see also Fig.4.

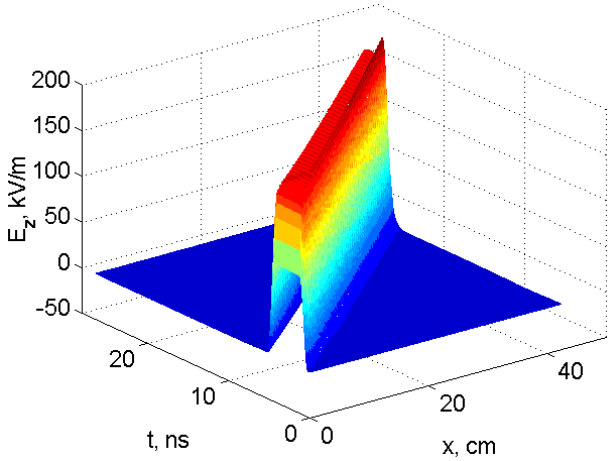

Figure 3: Deflecting field on the beam path versus time and position in the notched-strip meander structure for a 1-3-1-ns 1-kV driving pulse.

Cross-sections of the surface plot in Fig.3 for a given position x along the structure show time dependence of the field at this location, cf. Fig.4. Straight-strip meanders produce slightly larger pulse distortions, see in [6].

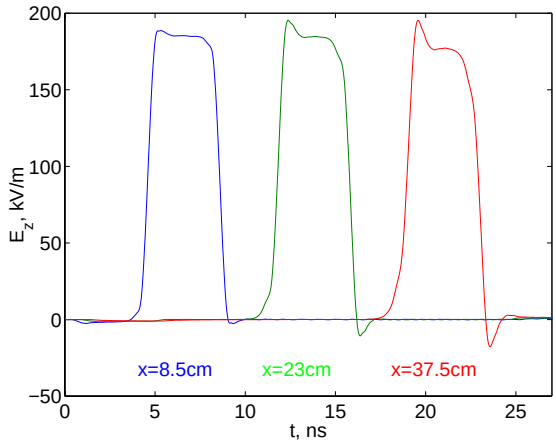

Figure 4: Deflecting field versus time in 3 different points on the beam path in the notched-strip meander structure.

Cross-sections of Fig.3 taken at given time t produce snapshots of the deflecting field as shown in Fig.5. Small wiggles on the pulse tops are due to differences of the field in points above the middle of the strip and above the separators. In fact, these field variations will even help to spread the deflected beam slightly on the beam stop.

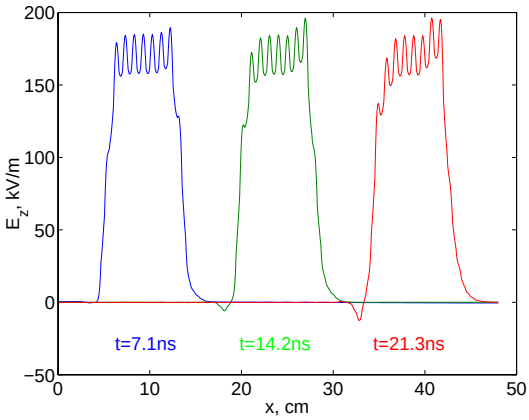

Figure 5: Snapshots of the deflecting field on the beam path in the notched-strip meander structure (cf. Fig.3).

As a result of our design optimization, the notched-meander structure looks as shown in Fig.1. Extra notches on the bends have been added to eliminate reflections. To increase the effective field on the beam path without increasing the rise time, the profiled separators have been introduced: they are low (flash with the strip line) near the beam and higher near the edges, see Figs.1-2.

3 CHOPPER PULSE GENERATOR

There are two technologies applicable to generating the required chopping voltage. These are the planar triode vacuum tubes and power FET devices.

Planar triodes, such as the Eimac 8940, could be used as switches to generate the required pulses. A number of difficulties would be challenging to overcome. The duty factor rating of these small triodes is a factor of ten lower than needed, so multiple tubes must be connected in parallel. Increasing the number of tubes increases the stray capacitance and the current rise time. These tubes are designed for operation at several kilovolts, which results in high grid currents at low voltage operation (such as 2 kV). Excessive grid power dissipation is a concern [7]. Generating the grid-drive will be as difficult as producing the output pulse. On the positive side, sub-nanosecond rise time has been demonstrated with these tubes at low duty factors [7,8] and a previous LANSCE chopper using six tubes produced 3-ns rise times and 4.5-ns fall times at 500 volts with similar duty factors [9].

Power FETs, such as the DEI 102N02, are capable of switching high currents at the <1-kV level at high repetition rates. A FET-switched pulser should be able to meet all of the specifications fairly easily, except for the rise time. The available FETs from current manufacturers are inherently limited to rise times on the order of 3-4 ns, with 5 ns being a demonstrated number [10]. We feel that the power FET devices are the best choice for the switching technology for the chopper application.

Starting next year we will build and test a proof-of-principle chopper pulser using FET devices that are currently available. This will be a low-average-power system whose purpose is to verify what level of performance can be expected using existing technology. We will build both a positive-output and negative-output polarity pulsers that are capable of generating 900-V pulses across 50-Ω loads. Each pulser consists of two high-voltage FETs, their gate-drive circuits, optical trigger links, an impedance-matched chassis assembly, power supplies and instrumentation. Output rise times and fall times are expected to be on the order of 5 ns.

In parallel with the proof-of-principle chopper pulser work we will attempt to develop FET devices which are faster than presently available. This entails fabricating new FETs whose bulk-silicon and doping characteristics will be specifically optimized for fast switching. Directed Energy Inc. (DEI) feels [10] that they can produce a significantly faster device, but the development cost will be significant. We will contract out this work to a suitable company with experience in the production of similar devices. If this effort is successful, we will incorporate these new FETs into our proof-of-principle pulser design.

4 CONCLUSIONS

A new current structure based on a meander line has been developed. The 3-D time-domain modeling shows that the structure is capable to provide the rise and fall times on the order of 1 ns. Further simulations will include more engineering details like supports, as well as beam dynamics and PIC-simulations. Manufacturing of the prototypes and their measurements are also planned.

The voltage generator development remains the most important and challenging issue. We will proceed with the proof-of-principle pulser design using currently available technology, while continuing to work with manufacturers on development of faster powerful FETs.

Useful discussions with Andy Jason and Frank Krawczyk are gratefully acknowledged.

5 REFERENCES

[1] B.R. Appleton et al., Proceed. of EPAC (Barcelona, 1996), p.575. – IOP Publishing, Bristol (1996).
[2] NSNS Collaboration, “NSNS Conceptual Design Report.”– NSNS/CDR-2/V1, Oak Ridge, TN (1997).
[3] J.S. Lundsford and R.A. Hardekopf, IEEE Trans. NS, **NS-30**, 2830 (1983).
[4] S.S. Kurennoy, A.J. Jason, F.L. Krawczyk, and J.F. Power, in Proceed. PAC97 (Vancouver, BC, 1997).
[5] *MAFIA release 4.00.* – CST, Darmstadt, 1997.
[6] S.S. Kurennoy, “Beam Chopper System for SNS”, Report LA-CP-98-156, Los Alamos (1998).
[7] Paul Larson, Private communication, CPI Eimac, July 1996.
[8] Howard Rinehart, Private communication, IROC Inc. August 1996.
[9] J.F. Power, “H^- Chopper Modifications”, AT-3 Tech Note 132, Los Alamos (1986).
[10] George Krausse, Private communications, DEI Inc. August 1996 - August 1998.

CHARACTERIZATION OF A VARIABLE ENERGY DEUTERON RFQ SYSTEM FOR NEUTRON PRODUCTION

R.W. Hamm[1], C.B. Franklyn[2], J. Guzek[3], B.R. Kala[3], U.A.S. Tapper[3], J. I. W. Watterson[3]

[1]AccSys Technology, Inc., 1177A Quarry Lane, Pleasanton, CA 94566 USA
[2]Atomic Energy Corporation of South Africa, PO Box 582, Pretoria 001, South Africa
[3]Schonland Research Centre, University of Witwatersrand, Private Bag 3, Wits 2050, Johannesburg, South Africa

Abstract

A variable energy radio-frequency quadrupole (RFQ) linac system, the LANSAR™ Model DL-5, has been developed at AccSys Technology, Inc. as a fast neutron source. The energy variation is accomplished by coupling two RFQ cavities with an adjustable rf power phase shift between them to provide two modes of operation, beam acceleration or beam transport. The beam dynamics code PARMTEQ was used to model this system and calculate the output beam parameters as a function of phase shift between the two RFQs. Output beam measurements were performed using a Rutherford back-scattering (RBS) technique and beam scanner developed for this system. The results are compared to the calculations.

1 INTRODUCTION

A compact variable energy RFQ linac, the LANSAR™ Model DL-5, has been developed by AccSys Technology, Inc. for the production of fast neutrons for resonance neutron radiography. The system was designed to accelerate deuterium ions to two discrete energies for injection into a high pressure windowless deuterium gas target that employs a rotating shutter. Precise deuteron beam energies are required for the neutron radiographic imaging technique being employed. The beam size at the gas target must also be small as this determines the spatial resolution of the imaging system.

This system produces a deuteron beam in the selected energy range of 3.60–4.90 MeV by directly coupling two RFQ cavities with an rf power phase shift between them to provide two modes of operation, beam acceleration or beam transport. Depending on the relative rf phase shift between RFQ1 and RFQ2, RFQ2 can either add or subtract energy from the 3.94 MeV deuteron beam from RFQ1. However, the large bore and strong transverse focusing permits most of the particles to be transmitted through RFQ2, regardless of phase.

2 SYSTEM DESCRIPTION

The Model DL-5 linac system consists of a deuterium ion injector and two close-coupled RFQ resonators. Each RFQ is powered by an rf amplifier supplying up to 300 kW of peak rf power via a semi-rigid coaxial cable. The high energy beam transport system (HEBT), consists of a beamline, a toroid for monitoring the pulsed output beam current, two orthogonal steering magnets and a quadrupole triplet for beam focusing. The performance specifications of the LANSAR™ Model DL-5 system are presented below in Table 1.

Table 1. Model DL-5 Performance Specifications

Operating frequency	425	MHz
Injector output energy	25	keV
RFQ1 output energy	3.94	MeV
RFQ2 output energy via transport mode via acceleration mode	 3.90 4.86	 MeV MeV
Injector output current (pulsed)	12	mA
RFQ2 output current (pulsed)	6-8	mA
Maximum average current	0.1	mA
Linac total length	4.4	m
Maximum beam pulse width	90	μs
Repetition rate (variable)	20-200	Hz
RF power (RFQ1/RFQ 2)	280/160	kW
Maximum rf duty factor	1.5	%
Nominal beam transmission (RFQ1/RFQ2)	84/95	%
Nominal HEBT beam transmission	> 95	%

3 VARIABLE BEAM ENERGY

The beam dynamics code PARMTEQ was used to model the linac design. As shown in figure 1, the calculated beam dynamics indicates a strong periodic variation of the accelerator output energy as a function of the relative phase shift between the two RFQ structures.

The Rutherford back-scattering (RBS) technique was used to measure the output deuteron energy as a function of the relative rf phase shift between RFQ1 and RFQ2. A water-cooled, thick tantalum target was mounted at 45° to the beam direction. The scattered particles were counted with a silicon surface barrier detector which was calibrated using an ^{241}Am α-source and positioned at 90º to the beam direction.

Significant pile-up and detector dead-time were initially observed in the RBS measurements due to the linac's low duty cycle (1.5%), high peak current (6–8 mA), and low repetition rate (100–200 Hz). Significant beam de-focussing and collimation had to be employed in order to avoid the pile-up effects, resulting in an average acquisition time of ~15 min per RBS spectrum.

The measurements were performed with the linac operating at two duty cycles: 0.32% (repetition rate of 80 Hz, beam pulse width of 40 μs) and 0.6% (repetition rate of 125 Hz, beam pulse width of 40 μs). The results of the RBS measurements are presented in figure 2. These measurements correlate very well with the calculations presented in figure 1 and display the calculated periodicity. The variations of the beam energy for the two selected duty cycles are within the measurement errors.

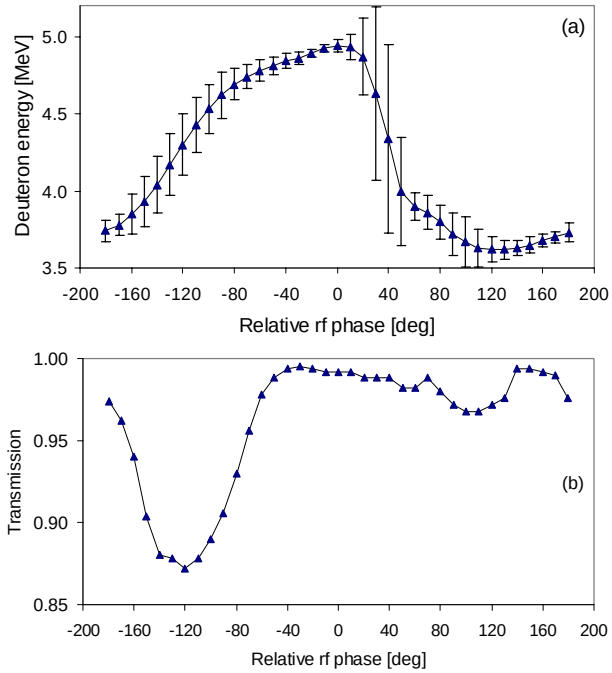

Figure 1. Calculated beam energy (a) and transmission (b) as a function of relative phase shift.

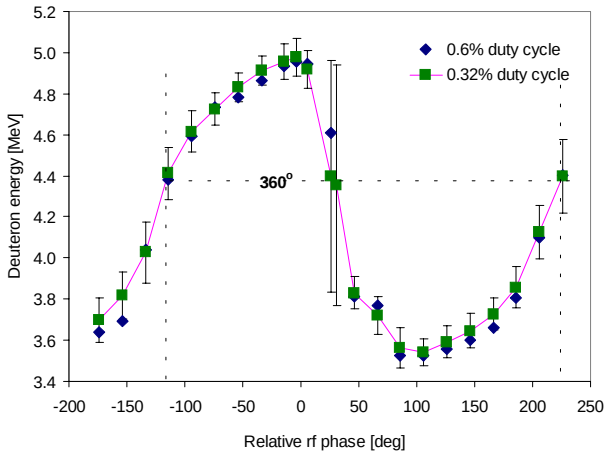

Figure 2. RBS measured beam energy as a function of relative rf phase shift at two beam duty factors.

The output deuteron energy is stable in the 4.7-4.9 MeV energy region over the relative phase range from 0° to -60° about the design synchronous phase of –28°. It is also stable over the 3.5 – 3.7 MeV energy range for relative input phases from 80° to 180°. The mean value of the output energy varies from 3.62 MeV to 4.93 MeV over the full 360° phase range. The exact amplitude and phase settings for operation in the dual energy mode depend on the operating duty factor, since the operating frequency and hence the phase relationship change slightly with the duty factor. However, for the two duty factors used for the RBS measurements, these changes were within the experimental measurement error.

The deuteron beam energy was also measured with RFQ2 switched-off, i.e. in the condition where the ions are only accelerated in RFQ1 but subsequently drift through RFQ2. The measured beam energy was 3.90±0.05 MeV.

4 BEAM CURRENT PROFILES

A standard National Electrostatic Corporation beam profile monitor (Model BPM-45) was used to measure the output deuteron beam profile. In this BPM, a single wire formed into a 45° helix is rotated about the axis of the helix at a frequency of about 16 Hz. It sweeps across the beam in two independent directions in every cycle. The secondary electron current released from the wire as it intercepts the beam is a measure of the beam intensity.

The normal use of this BPM is not effective with the linac operating at a beam repetition rate of 100 Hz and beam pulse width of 100 μs. Primarily due to the frequency mismatch, the BPM's wire misses most of the beam pulses. In order to use the BPM more effectively the trigger signal generated by the BPM during every revolution (traditionally used as a trigger signal for the oscilloscope) was used to trigger the accelerator. By varying the delay of the trigger signal, the deuteron beam pulses were probed at different spatial positions, and the intensity of the beam was measured on a digital oscilloscope. Knowing the trajectory of the wire, its dimensions and rotation frequency, the trigger delay time was scaled into the linear extent of the beam.

The toroid, steering magnets and quadrupole magnets were removed from the HEBT to provide access to the beamline for the BPM. The beam spot dimensions were measured at several positions downstream from the exit aperture of RFQ2 at different settings of the relative rf phase, i.e. energy. A gaussian function was fit to all measured beam profiles and the FWHM was calculated. An example of the beam profiles obtained at 284 mm from the RFQ2 aperture, for the relative rf phases of -80° (E_d~4.65 MeV), 0° (E_d~4.90 MeV) and 160° (E_d~3.70 MeV), is presented in figure 3.

The results of measurements of the deuteron beam profiles as a function of the relative rf phase shift are presented in figure 4 for a distance of 284 mm and 404 mm from RFQ2 exit. The beam diverges in both planes as it travels down the beamline because the focusing elements have been removed. There are two regions of relative rf phase (deuteron energies) where the beam

dispersion is small and varies little with small changes in the relative rf phase.

These regions are separated by a region of high beam dispersion, which corresponds to a transition region between high and low deuteron energy, as seen in figure 4. The large beam dispersion in this region is caused by the large deuteron energy spread within the bunch, which results in spatial de-focusing.

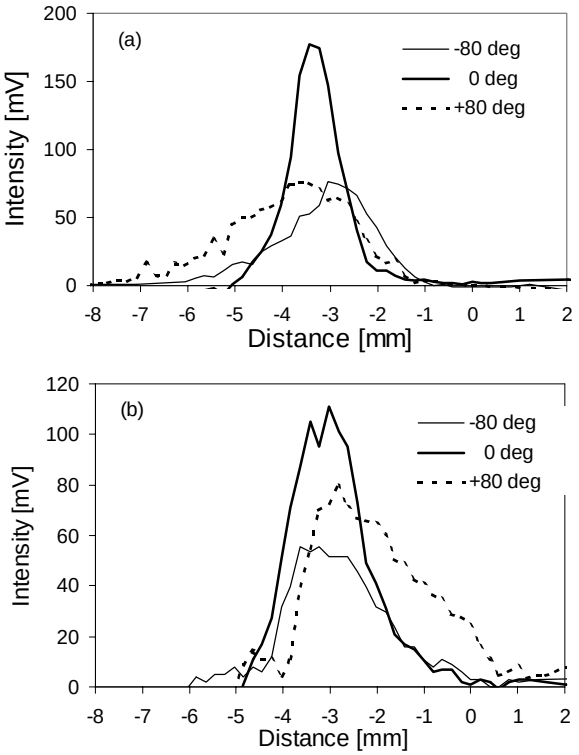

Figure 3. Measured x (top) and y (bottom) beam profiles at a distance of 284 mm from RFQ2 exit. The *x*-axis is the distance from the center of BPM's helix axis.

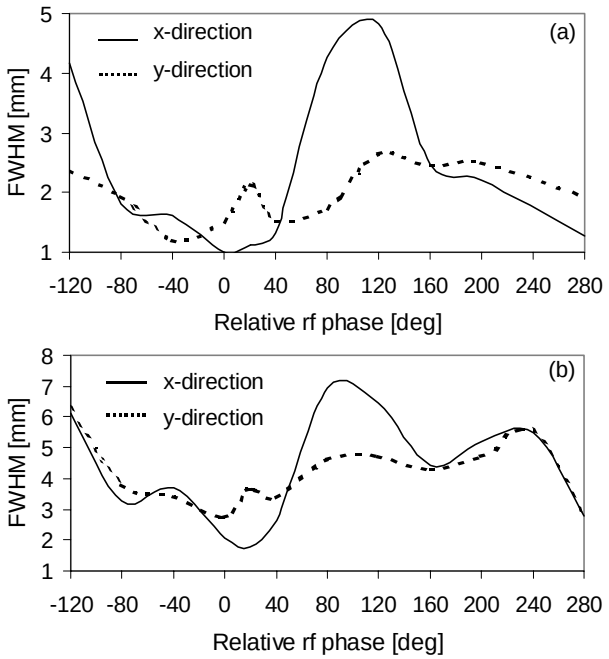

Figure 4. Measured beam dimensions at 284 mm (top) and 404 mm (bottom) distance from RFQ2 exit.

The calculated output beam size is shown in figure 5. There is good agreement between the measurements and the calculations. The smallest beam size is both predicted and observed in the high energy range, and is half the minimum value in the low energy range. The calculations indicate that at the maximum beam energy, the beam diameter is <1 mm at the exit of RFQ2.

The measurements indicate that the operation of the linac is very stable in the "acceleration" mode, where the beam has a well-defined energy with the smallest spatial dispersion. When operating with the relative rf phase outside these conditions, RFQ2 has both accelerating and decelerating modes as the beam passes through it. This results in significant beam energy spread and a larger beam spot size on the target.

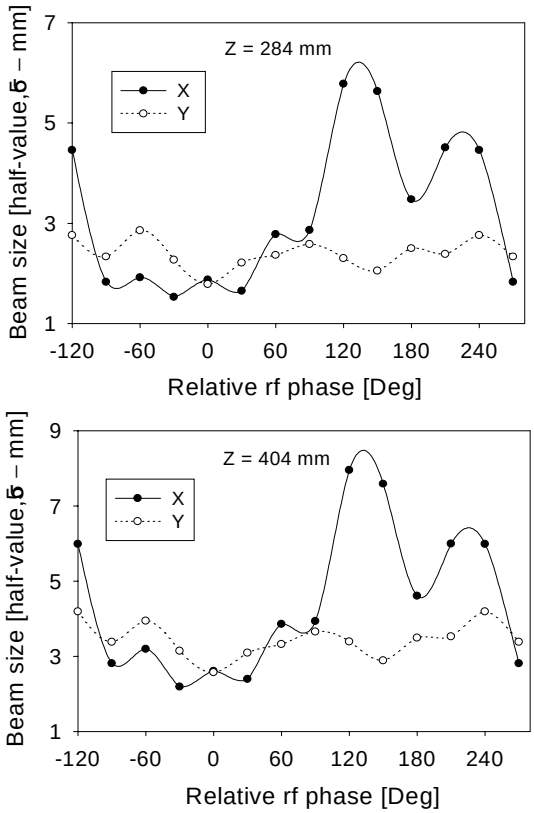

Figure 5. Calculated output beam dimensions at 284 mm (top) and 404 mm (bottom) from RFQ2 exit.

5 CONCLUSION

Output beam measurements on the LANSAR™ Model DL-5 variable energy RFQ linac have been performed and compared to PARMTEQ calculations. The experimental measurements are in good agreement with the beam dynamics calculations and prove that the system performance does indeed satisfy the stringent requirements imposed upon it as a dual energy neutron source. The system was installed in the spring of 1997 in a radiographic test facility in South Africa and has been in routine use for more than one year.

STATUS OF THE INFN HIGH CURRENT SC PROTON LINAC FOR NUCLEAR WASTE TRANSMUTATION

C. Pagani, D. Barni, G. Bellomo, R. Parodi[†], P. Pierini,
INFN Milano LASA, Via Fratelli Cervi, 201, I-20090 Segrate (MI), Italy
[†]INFN Genova, Via Dodecanneso 33, Genova, I-16146, Italy

Abstract

INFN, jointly with ENEA, is working at the design study for an accelerator driven waste transmutation subcritical system, TRASCO. In particular, our group is studying the high energy section, above 100 MeV, of the high power (> 30 MW) proton linac driver at 352 MHz, following the guidelines we presented at the Linac'96 Conference. The funded activities include the overall conceptual design of the three section SC linac and the development and tests of prototypes for the cavities and cryomodules. An overview of the status and perspectives of these activities will be given in this paper.

1 THE TRASCO PROJECT

The TRASCO Project is a two year funded (10 M$) program in which INFN, jointly with ENEA and various Italian industries, will work on the design study of an accelerator driven waste transmutation subcritical system. TRASCO is an Italian acronym for Transmutation (TRAsmutazione) of Waste (SCOrie).

This program is in line with the growing European consensus, promoted by Carlo Rubbia through the idea of the Energy Amplifier, on a long term reconsideration of the civil use of nuclear power, based on a final solution of the waste accumulation problem. While similar programs are underway in the US and in Japan, in Europe the various national efforts are coordinating through the signature of Memoranda of Understanding, like the one recently signed by INFN, CEA and IN2P3 for a common effort in the accelerator technology development. Another MOU signed with the CERN group led by E. Chiaveri will give us the opportunity to make use of the wide experience gained so far in the production and commissioning of the LEP2 cavities. In particular, the cavity prototypes planned for TRASCO will be treated and tested at the CERN premises.

The aim of our specific effort in this preliminary, and short-termed, program is to set the feasibility of a high beam power proton linac based, whenever possible, on the "cheap" CERN technology developed for the LEP2 superconducting cavities. This is an extremely attractive option, since it allows the possibility to make use of large and expensive facilities, existing at CERN and at various European companies, for the studies on prototypes.

The low energy section of the machine, up to 6 MeV, is under study by others INFN groups (at LNL and LNS), in the framework of the collaboration with CEA and IN2P3. While a working prototype of the source is in operation at Saclay, the design and development of the CW, 6 MeV, RFQ, similar to the one developed for APT at LANL, is considered one of the major technological tasks.

The medium energy part, up to 100 MeV, is in study by INFN/LNL, and will take advantage of a contract signed with a qualified industry.

2 THE LINAC DESIGN

The reference linac design for the high energy section of the TRASCO linac has been set in Refs. [1] and [2]. The 100 to 1600 MeV linac is split three sections, with synchronous cavity β of 0.5, 0.65 and 0.85. Transverse focusing is provided by a periodic doublet lattice, with cell length of 8, 11.2 and 15.3 m, respectively.

2.1 Beam dynamics simulations

An intensive beam dynamics activity has started, in order to verify the performances of the linac design with multiparticle codes. An "ad hoc" simulation code has been developed for the beam dynamics in the elliptical shaped cavities, employing a fast 3D Poisson solver, based on multigrid algorithms, for the treatment of the nonlinear space charge fields. The results of this simulations are presented in a separate contribution to these Proceedings[3]. In Figure 1 we show the rms, 90% and 100% emittances along the linac for the nominal current of 25 mA, and a typical simulation of 100.000 particles. The cells at the transitions have been used for transverse and longitudinal matching across the three sections. The rms emittance growth is limited to below 10% and the total emittance increases by a factor smaller than 2.

The ratio between the beam aperture and the transverse rms beam size is well above 25 all along the linac. This, together with the small number of betatron wavelengths in the linac (few tens), gives us a great confidence that, with such a design, the halo formation in the SC linac would not be a serious problem.

The simulations were performed for a nominal current of 25 mA, the goal being that of a driver for a prototype transmutation plant. An increase of the linac current up to 100 mA has not been studied yet in full details.

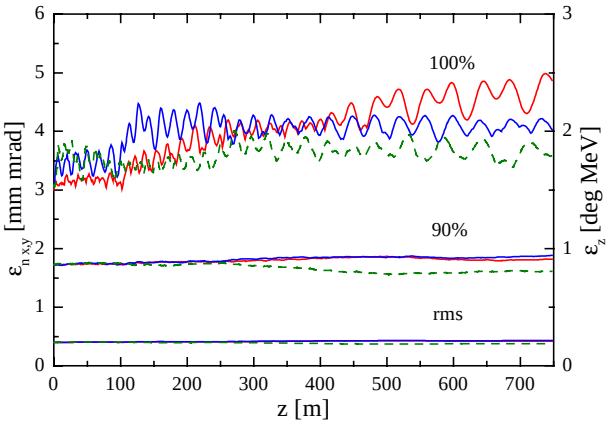

Figure 1: The rms, 90% and total (100%) emittances along the linac The solid curves are the transverse emittances, (left axis) and the dashed curve is the longitudinal emittance (right axis). The simulation has been performed with 100.000 particles.

However, to allow for this current increase it seems that either a shorter focussing period should be provided in the first linac section, or the normal conducting DTL to SC transition should be raised to higher energies.

2.2 Reliability of the proposed design

Having assessed that the basic design does not show serious limitations in achieving the objectives for a transmutation plant, we are now planning the inclusion of spare linac focussing cells in order to achieve full reliability in the case of klystron or cavity/coupler faults.

In spite of the demonstrated high reliability of the existing large scale superconducting RF accelerators (LEP, CEBAF, HERA and TRISTAN), a driver for a nuclear waste transmutation plant needs to satisfy the stringent requirements imposed by its specific use. In particular, a beam stop due to any failure of one of its components causes an interruption of the spallation neutron flux sustaining the subcritical system. If this interruption exceeds a fraction of an hour (the exact time depending on the details of the core design), the fuel bar poisoning rises: i.e. a new start up procedure needs to be performed and the waste cleaning process is partially lost.

For this reasons we are considering a linac design which includes two spare cryomodules for the low and intermediate energy sections. These two sections are the most critical, since they need to provide the correct transition energy to the following sections. A 10% spare contingency of three additional cryomodules is planned for the (less critical) high energy section. The lengthening due to the amount of contingency hardware is around 80 m, for a new total length of 800 m.

In the case of failure, a spare component will take the place of the faulty, and the beam will be back on the target in the time required by the reactor design. Some of the components, like the klystrons, could be repaired or replaced during the regular linac operation, while others, like the cavities or the RF couplers, will have to wait for the planned reactor maintenance shutdown.

The best use of these spare components when they are not needed (whether they are kept on or off at all times) needs to be analyzed on the basis of both capital and operational costs.

3 R&D ACTIVITIES ON THE SUPERCONDUCTING CAVITIES

The design of the three accelerating structures has been presented in detail at EPAC'98[4]. The geometry of a five cell cavity with an elliptical shape both at the iris and at the equator has been optimized in each linac section. The following design goals for the cavity operating conditions were chosen:

1. a peak surface electric field below 16 MV/m
2. a peak surface magnetic field below 40 mT
3. a good cell to cell coupling factor of 1.7%.

The cavities have been analyzed both with respect to the electromagnetic performances and with respect to the mechanical loads on the structures. Structural stiffening is required only for the lowest beta structure (β=0.5), and either a standard stiffening structure will be employed or a structural stiffening via copper spraying with a plasma jet (as proposed for the Tesla cavities[5]) will be performed.

Table 1 summarizes the main electromagnetic parameters of the TRASCO cavities, while Table 2 lists the geometrical parameters of the three structures. For an explanation of the symbols refer to the geometry sketched in Fig. 2.

The cavities will operate with an accelerating field of 4.6, 5.7 and 6.7 MV/m, respectively. A synchronous phase of 30 degrees has been chosen to provide the necessary longitudinal focusing.

Table 1: Main e.m. characteristics of the three structures.

β_c	E_p/E_{acc}	B_p/E_{acc} [mT/MVm^{-1}]	Cell to cell coupling [%]
0.5	3.4	8.1	1.8
0.65	2.7	6.5	1.7
0.85	2.3	4.6	1.7

Table 2: Geometrical parameters (in mm) for the internal cell geometry, at the working cryogenic temperature.

β_c	**0.5**	**0.65**	**0.85**
A	47.1	71.6	131.3
B	80.1	121.8	196.9
a	33.4	44.8	35.4
b	60.1	89.6	56.7
d	26.8	32.8	26.8
L	101.1	132.6	175.7
D	392.2	392.7	385.2
R_{iris}	99.4	109.3	114.3

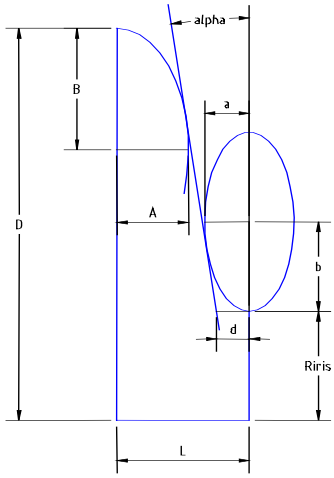

Figure 2: Reference geometry for the cavity shape.

3.1 Cavity prototypes

An agreement with CERN has been established in order to fabricate and test a full β=0.85 five cell cavity and a single cell test structure, on the basis of our design. The cavities will be ready for tests at CERN at the end of 98.

The Italian company Zanon will build a second β=0.85 cavity, a single cell Nb β=0.5 cavity and a complete copper model of the five cell structure. These additional cavities will be tested at CERN.

3.2 High order modes and multipactoring

An analysis of the high order modes distribution in the structure has been performed with the OSCAR2d code[6], showing modes with a very low R over Q. The choice of a beam tube diameter equal to the cavity inner irises helped in easing the behavior of the high order mode, since the field can freely propagate for any frequency above the tube cut-off. No trapped tube modes, like the ones measured on the LEP cavities, are possible.

Possible electron loading effects (multipactoring) were investigated, but the low magnetic fields and the elliptic shape of the equator resulted in a very safe cavity operation. In particular, the elliptical equator gives a stronger longitudinal component of the electric field along the surface, which pushes the electrons towards the equator, where the resonant condition for one point multipactoring is broken.

3.3 Preliminary design of the cryomodules

Based on the expertise gained in the design of the second and third generation of Tesla Test Facility cryostats we have started the design of the cryomodules for the superconducting linac. The design is still at a preliminary state, but various solutions have been chosen because of their success in the Tesla Test Facility design[7]. The cryostat will have a single thermal shield, made by self-sustained aluminum sheet or by a thin copper sheet kept by a stainless steel frame, and will be cooled by a finger welded pipe, to reduce production cost and assembling time. The cryomodule will be extremely modular, each module holding a single cavity in a titanium and stainless steel frame. The other guideline for the cryomodule design is a cost-effective solution, keeping in mind that extremely low thermal losses are not necessary when operating at 4.2 K. The vacuum vessel is open, similar to that one used in the LEP2, with a thin stainless steel sheet closing it, to guarantee easy access during the assembling and to reduce the assembling costs.

4 CONCLUSIONS

We have summarized here the status of the R&D activities for the TRASCO superconducting linac, aimed as a driver for nuclear waste transmutation and energetic applications. For sake of completeness we report in Table 3 an updated parameter list of the linac sections, where we explicitly indicated the necessary contingency for operational reliability.

Table 3: Summary of the SC TRASCO linac parameters.

	SI	**SII**	**SIII**
Section β_c	0.5	0.65	0.85
Section length [m]	96	146	475
Injection Energy [MeV]	100	190	428
Cell period [m]	8.0	11.2	15.3
# focussing cells/section	12+2	13+2	31+3
Max. ΔE/cavity [MeV]	4.0	6.5	10.0
E_{acc} [MV/m]	4.6	5.7	6.7
# cavities/section	24	39	124
# cavities/cryomodule	2	3	4
# cryomodule/klystron	1	1	1
Beam power/cryom. [kW]	200	500	1000
The additional focusing cells indicated after the plus sign are the needed contingency required for the linac reliability			

REFERENCES

[1] C. Pagani, G. Bellomo, P. Pierini in Proceedings of the XVIII Int. Linear Acc. Conf. Editors C. Hill and M. Vretenar, CERN 96-07 (1996), p. 107.

[2] C. Pagani, G. Bellomo, P. Pierini, G. Travish, D. Barni, A. Bosotti, R. Parodi, in Proceedings of the 1997 Part. Acc. Conf., Vancouver, Canada.

[3] G. Bellomo, P. Pierini, these Proceedings, paper number MO4046, and G. Bellomo, P. Pierini, in Proceedings of the 1998 European Part. Acc. Conference, Stockholm, Sweden..

[4] D. Barni, A. Bosotti, C. Pagani, P. Pierini, S. Visonà, in Proceedings of the 1998 European Part. Acc. Conference, Stockholm, Sweden.

[5] S. Bousson et al., in Proceedings of the 1998 European Part. Acc. Conference, Stockholm, Sweden.

[6] P. Fernandes, R. Parodi, IEE Trans. Magn. 24 (1998), p. 154

[7] D. Barni, C. Pagani, P. Pierini, report TESLA 98-16, DESY, June 1998 and references therein.

DESIGN AND CONSTRUCTION OF THE BPL-RFQ

Deng-Ming Kong , Zi-Hua Luo, Ji-Min Qiao, Shu-Hong Wang and Wen-Wu Xu
Institute of High Energy Physics, Chinese Academy of Sciences
P. O. Box 918 , Beijing 100039, China

Abstract

BPL-RFQ is a four-rod type linac structure, currently under construction, that will be operated at a radio frequency of 201.25 MHz. According to the design, it can accelerate protons from 40 keV to 750 keV with a pulse beam current of 60 mA. BPL-RFQ is planned as the Beijing Proton Linac's injector instead of the present bulky Cockroft-Walton accelerator. This paper describes the general layout, dynamics design features, four-rod structure, field distribution measurements, and recent status of the BPL-RFQ.

1 INTRODUCTION

In August 1993, it was considered to construct an RFQ system as BPL's injector. Since then the design of beam dynamics, the design and the manufacture of a cold model had been done. The cold model of four-rod structure had been measured and tested. The mechanical design of RFQ structure, the construction of rf power supply, the reconstruction of the ion source have been done also. The formal electrode modules and the cavity is being assembled and tested. The control subsystem, emittance measurement devices, and solenoids have been tested also.

2 GENERAL LAYOUT AND DESIGN FEATURE

The construction of BPL-RFQ is based on the consideration for replacement of the present Cockroft-Walton accelerator, which has been used for BPL's injector near two decades. In order to meet the need as BPL's injector, some performance requirements for the BPL-RFQ had been proposed as follows: frequency of 201.25 MHz, output energy of 750 keV, pulse beam current of 60 mA, maximum repetition rate of 12.5 Hz, output transverse normalized emittance of less than 3 π-mm-mrad and the output energy spread of ±25keV.

BPL-RFQ system is composed of three sections:[1,2] including of RFQ section, IS-RFQ match section, and RFQ-DTL match section as shown in Fig.1.

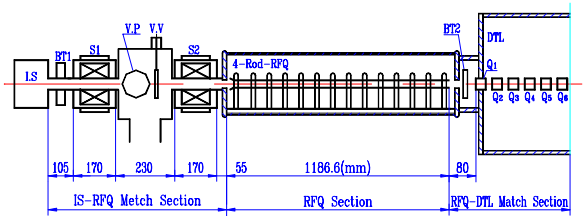

Fig.1: Scheme of the BPL-RFQ system

The RFQ is chosen to be a four-rod structure, because it has the advantages of easy manufacture and tuning, and the other features on feasibility of circular rods as electrodes giving very good mechanical as well as very good beam dynamic properties. Also four-rod RFQ has been successfully tested and used[3-5].

The RFQ beam dynamics design consists of four segments: the radial matcher, the shaper, the buncher and the acceleration. The first four cells is the radial matching segment , where the protons are gradually matched to the time dependent transverse focusing system. The next 51 cells is the shaper segment where the bunching process is initiated with a slow decrease of the stable phase from -90°to -77.2°and with a slow increase of the modulation parameter of m from 1 to 1.150. In the next 52 cells, the stable phase is reduced to -30°, the parameter of m is increased to 1.824, the protons are brought to 417 keV and fully bunched. The final 8 cells is the acceleration segment, the stable phase and parameter of m are kept constants of -30°and 1.824 respectively, the protons are accelerated to 750 keV by the end of RFQ. BPL-RFQ has a total of 115 cells and is 118.7 cm long. The main parameters of BPL-RFQ are listed in Table 1.

Table 1: Main Parameters of the BPL-RFQ

Particle	proton
Input energy	40keV
Output energy	750keV
Input pulse beam current	>100mA
Output pulse beam current	>60mA
Pulse length	180 micro-sec.
Input r.m.s. emittance:	
(x,x′)	<0.34 π-mm-mrad
(y,y′)	<0.32 π -mm-mrad
Output r.m.s. emittance:	
(x,x′)	<0.56 π -mm-mrad
(y,y′)	<0.54 π -mm-mrad
Frequency	201.25 MHz
Repetition rate	1-12.5 Hz
Maximum surface field (Es.max)	24.9MV/m
Inter-electrode voltage (V)	130.2kV
Characteristic radius	0.708 cm
Aperture radius (a)	1.962 - 0.492 cm
The length of electrode	~120 cm
Number of modules	13
Number of stems	14
Total number of cells (N_T)	115
Modulation parameter (m)	1-1.824
Trans. focu. parameter (B)	0.8-6.136
Stable phase	-90°— -30°

In the front of RFQ , there is an IS-RFQ matching section which consists of two solenoids and a beam transformer. Two solenoids are used for focusing and matching the beam into RFQ. Behind the RFQ there is an RFQ-DTL matching section which is composed of first six quadrupoles of DTL. In order to reduce the beam longitudinal mismatch, our RFQ is located very close to the DTL entrance. The distance between RFQ's electrode and first quadrupole of DTL is 8 cm only. The computer simulation for the 100 mA of beam motion from the exit of RFQ to the end of DTL had been done by PARMILA code. The simulation indicates that more than 98 mA of beam can be accelerated to the end of DTL.

The BPL-RFQ has some design features as follows:

- High transmission efficiency of 97% and 92% for the input beam current of 0 mA and 100 mA respectively.
- Low input energy of 40 keV even for an input beam current of 100 mA.
- The initinal focusing parameter of B_i and the radial matching cell number of N_{rm} have been chosen 0.8 and 4 respectively.
- The length of BPL-RFQ is short (~ 120 cm) . And the inter-electrode voltage is high (~130 kV).

3 FOUR-ROD STRUCTURE AND THE FIELD DISTRIBUTION MEASUREMENT

3.1 Four-Rod Structure

We chose a simplified structure (see Photo 1). The RFQ is brazed on a massive rail and can be aligned and tuned outside the cavity on a bench and then screwed into the cavity. The cylindrical electrodes with cones and cylinders of variable diameter have been used for our four-rod-RFQ.

Two pairs of the electrode rods form RFQ fields, each pair being held by seven stems. There are fourteen stems in total. The stems are equally spaced. Each electrode pair is supported by a common leg. The module geometry dimensions of our RFQ had been calculated by MAFIA.

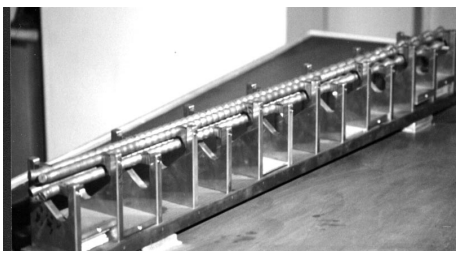

Photo 1: Electrodes and stems and substrate of the BPL-RFQ's model on the bench

3.2 Field Distribution Measurement

A cold model with full scale had been constructed for the field measurement and adjustment. Two kinds of electrodes, which are un-modulated and modulated, had been made and respectively assembled into the model. The field distribution had been measured by using bead pull perturbation method. When a bead is pulled into the cavity, the resonant frequency of the cavity will be shifted by a Δ f which satisfies the formula

$$\frac{\Delta f}{f} = -\left[\frac{\varepsilon}{\mu}\int_{v_b} E^2 dv - \int_{v_b} H^2 dv\right] / (2\int_{v_c} H^2 dv) \qquad (1)$$

where v_b and v_c are volumes of the bead and cavity respectively .

If the measurement is done at near beam axis where H apprixiates zero, so

$$(\Delta f / f) \propto \int_{v_b} E^2 dv \qquad (2)$$

The $\Delta f / f$ can be got by measuring the $\Delta\phi$ which satisfies $\Delta\phi = tg^{-1}\left[\frac{2\Delta f}{f} Q_L\right]$. We expect to look for a method to calculate the theoretical design values of $\int_{v_b} E^2 dv$ for the RFQ. For a RFQ, the electrical field components can be expressed by formula [6]

$$\left.\begin{aligned} E_z &= \frac{kAV}{2} I_0(kr)\sin kz.\sin(\omega t+\varphi) \\ E_r &= -\left[\frac{GV}{a^2} r\cos 2\theta + \frac{kAV}{2} I_1(kr)\cos kz\right].\sin(\omega t+\varphi) \\ E_\theta &= \frac{GV}{a^2} r\sin 2\theta.\sin(\omega t+\varphi) \end{aligned}\right\} \qquad (3)$$

where V–inter-electrode voltage, I_0 and I_1–modified Bessel functions

$$\left.\begin{aligned} k &= 2\pi / \beta\lambda \\ A &= (m^2-1)/\left[m^2 I_0(ka) + I_0(mka)\right] \\ G &= 1 - A I_0(ka) \end{aligned}\right\} \qquad (4)$$

According to the (3), the electrical field amplitude of E_m is given by

$$E_m^2 = E_{zm}^2 + E_{\theta m}^2 + E_{rm}^2 = L_{(r,\theta,Z,G,k,A)} V^2 \qquad (5)$$

where

$$L_{(r,\theta,z,G,k,A)} = \left[\frac{G}{a^2} r\cos 2\theta + \frac{kA}{2} I_1(kr)\cos kz\right]^2 + \\ + \left(\frac{G}{a^2} r\sin 2\theta\right)^2 + \left[\frac{1}{2} kA I_0(kr)\sin kz\right]^2 \qquad (6)$$

The L depends on the r,z,θ and the RFQ parameters of G,k,A. We are interested in field amplitude, so let's put (6) into the (2) and consider that V is constant for our RFQ, then

$$\frac{\Delta f}{f} \propto \int_{v_b} L_{(r,\theta,z,G,k,A)} dv \qquad (7)$$

Define $$\eta = \int_{v_b} L_{(r,\theta,z,G,k,A)} dv \qquad (8)$$

which indicates the field distribution at the position appointed and usually it is not constant. η is called the field distribution factor by us.

In the BPL-RFQ, the cell length is short and the variations of field near beam axis are very sharp. Therefore when we calculate the integration of the formula (8), the variation of field in the range of bead size can not be neglected. We do the measurement at the $\theta = \pm 45°$ and $\theta = \pm 135°$, because the calculations of η

are easy there.

For each cell of RFQ, there are maximum and minimum η at the positions of Z where coskz=1, sinkz=0 and coskz=0, sinkz=1 respectively. So

$$\eta_{\min} \approx 4\pi . r_b^3 \left[\frac{G^2}{a^4} \left(\frac{1}{3} r_a^2 + \frac{2}{15} r_b^2 \right) + k^4 A^2 \left(\frac{r_a^2}{48} + \frac{r_b^2}{40} \right) \right] \quad (9)$$

$$\eta_{\max} \approx 4\pi . r_b^3 \left[\frac{1}{12} k^2 A^2 + \left(\frac{G^2}{a^4} + \frac{1}{8} k^4 A^2 \right) \left(\frac{1}{3} r_a^2 + \frac{2}{15} r_b^2 \right) + \frac{k^6 A^2 r_a^2}{48} \left(r_a^2 + \frac{r_b^2}{5} \right) \right] \quad (10)$$

where r_b is the bead radius and r_a is the radial distance from bead center to the beam axis. The average of η, $\eta_{Av} = (\eta_{\min} + \eta_{\max}) / 2$, can be calculated also for each cell of RFQ. We like to use a relative normalized $\eta_{N,AV}$, because the calculated and measured field distribution are relative. The $\eta_{N,AV}$ can be as theoretical design values of field distribution, and it is shown in the Fig.3 for the BPL-RFQ.

In order to obtain a good result and to get a stronger signal for avoiding the noise perturbation and to reduce the image effect, it is important to choose an appropriate bead position, size, and material. We do measurement at the position off beam axis and use a dielectrical bead with a radius of 2mm . The measurement results are shown in the Fig.2 and Fig.3.

In the case of un-modulated electrodes, the results were: the field distribution unblance is less than ±1.5% azimuthally and the field flatness is less than ±4.0% longitudinally. In the case of modulated electrodes, the results were not so good as in the case of un-modulated one, but the measurement values correspondingly agree with theoretical values.

Fig.4 shows the measured field distribution of three modes in the case of un-modulated electrodes and without cavity shell. The nearest mode spacing is about 30 MHz.

4 OTHERS

4.1 RF Power Supply

There was a 50 KW rf power supply, which was initially used for a buncher supply of the BPL. We decided to upgrade it to satisfy the need of rf power for our RFQ by adding a new final power amplifier, which uses a TH-116 triode. Therefore the upgraded rf power supply system can provide the power output of more than 300 KW.

4.2 Ion Source

A dualplasma type ion source has been chosen for our RFQ system. A beam current of 140 mA has been reached under 40 kV.

4.3 Emittance Device

The emittance device is of "a slit and multi - wires" type. It is temporarily located behind of second solenoid for measuring the emittance at the entrance of RFQ.

4.4 Solenoids

Two pulsed solenoids had been made. The coil of the solenoid consists of 12 "cakes" with different inner diameters to obtain the wanted magnetic field shape. Two solenoids had been tested under the maximum magnetic field of 7.5 KGass. The measured effective magnetic length is 12.9 cm.

4.5 Status

The mechanical engineering for the BPL-RFQ is almost completed. It is being installed and commissioned.

5 ACKNOWLEDGMENT

Authors thank Prof. Dr. A. Schempp for the helpful discussion during the design and construction, and thank all staff of Proton Linac Division of IHEP for their work on the BPL-RFQ.

6 REFERENCES

[1] Luo Zi-hua, Wang Shu-Hong, Summary of Beam Dynamics Design for BPL-RFQ, Internal Report IHEP-BPL-Note-01, March 20,1994.
[2] S.H.Wang et al., Proc .of 1994 Linac Conf. (1994), P.830.
[3] A.Schempp et.al., N.I.M B10/11(1985)P.831.
[4] A.Schempp, CAS CERN 92-03 Vol. II P.522.
[5] A.Schempp, EPAC88 , World Sci. (1989) P.464
[6] K.R. Crandall et al., BNL 51143 (1980) P.205

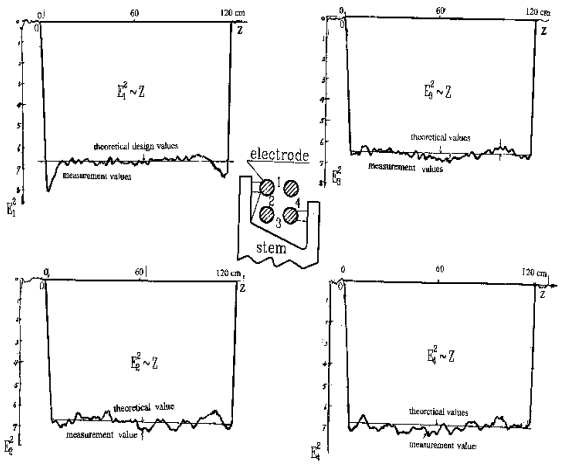

Fig.2: E^2 Vs Z at four quadrants(with unmodulated electrodes and 9mm of bead center to beam axis)

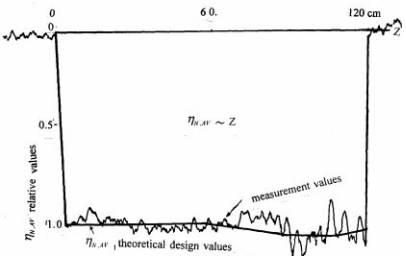

Fig.3: $\eta_{N,AV}$ Vs Z at a quadrant (with modulated electrodes and 5mm of bead center to beam axis)

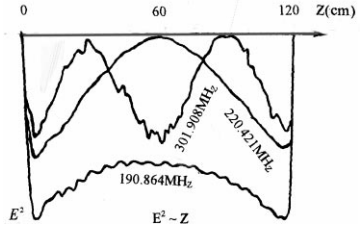

Fig.4: E^2 Vs Z for three modes

TESTING OF NEW 2 MeV RFQ AND PERSPECTIVE OF 433 MHz LINAC FOR APPLIED PURPOSES

Yu.A.Svistunov, Yu.V. Afanasiev, Yu.N.Gavrish, A.K.Liverovsky,
V.G.Mudrolubov, A.P.Strokach, M.F.Vorogushin

Scientific Research Efremov Institute of Electrophysical Apparatus

Abstract

A new 2 MeV 433 MHz RFQ has been built and tested with proton beam up to 15 mA. It has been fabricated from AMG-6 aluminium alloy and installed instead of previous 1.8 MeV RFQ. The results of frequency adjustment and field alignment are presented. There are significant improvements in field distribution and beam emittance of output injector in comparison with 1.8 MeV accelerator data. Simultaneously the working out of alternate phase focusing (APF) structure with input energy 2 MeV and output one 11 MeV was continued. Theoretical and experimental researches connected with different applications of 2 MeV linac or 11 MeV tandem RFQ and APF linacs are carrying out at NPK LUTS of the Efremov Institute last years. Methods and devices of elemental analysis and contraband detection system for 2 MeV linac and use of 11 MeV tandem for PET-system or as part of a big linac are discussed briefly.

1 INTRODUCTION

Since 1990 Linear Accelerators and Cyclotrons Division of the Efremov Institute (NPK LUTS) makes researches to create compact rf linear ion accelerators which may use as part of different complexes for applied purposes. Different output devices are worked out too. Choice of the working frequency is 433 MHz. There are five directions of researches:

- elemental express-analysis of materials or environment;
- contraband detection system (in particular detection of explosives and fission's);
- PET-system with ion rf linac;
- transported safe atomic station with undercritical nuclear reactor controlled by ion rf linac;
- rf linac as injector for medical proton synchrotron.

If one mean to use accelerated protons for all over these cases required range of final energies is from 2 up to 100 MeV.

2 ELEMENTAL ANALYSIS AND CONTRABAND DETECTION SYSTEM

Each of system consists of ion injector, 433 MHz RFQ, 433 MHz RF system, injector feed system, fast measuring and processing complex. Description of injector, RFQ and RF system was given in paper [1].

Neutron activation's analysis is used for express-analysis of environment. Maximal effect may be achieved by application of bicyclical registration method. Neutrons are produced by $Li_3^7(p,n)Be_4^7$ reaction and they are used as source of activating radiation. Pulsed sequence of radiation repeats sequence of accelerator's pulses. Tested sample, block of target change, neutron radiation monitor and semiconductor detector of induced g-ray are placed inside of interaction's chamber. There are two regimes of elemental analysis. Registration of short-lived isotopes (half live time 10^{-4} ...10^{-3} s) is produced between current pulses of accelerator. For determination long-lived isotopes is used standard neutron activation method. Detector is defended by protective gear from directed action of ionized radiation. Detector is blocked when neutron radioactive activation and thermolysation take place. Data process and spectral analysis are produced between blocking pulses. Sensitivity of different elements is 10^{-4} ...10^{-9} g/g. This method may be used for element analysis of isotopes that have atomic masses from 9 to 209.

Scheme of contraband detection complex is shown on fig.1. Explosive's detection is based on g-ray registration which is induced by non-elastic scattered fast neutrons and registration of induced activation on nuclei of specific elements (N,O,C) as result of thermal neutron capture. Fission's are registered by measuring of temporal neutron spectra. Specific change of neutron radiation's parameters permit to determine fission in observed object.

2 MeV RFQ is need for these purposes. In period 1993...1997 two RFQ had been fabricated and tested on laboratory stand at NPK LUTS. First of RFQ was fabricated from alloy D16. It had output energy 1.8 MeV. Results of it's tests were given in paper [1]. Second one was fabricated from aluminium alloy AMG-6, it's output calculated energy is 2 MeV. It was supposed to electroplate cavity's inner surfaces by copper but this plan was not fulfilled because financial and organizational prob-

lems. Testing of AMG-6 alloy RFQ showed correctness it's fabrication and tuning. Eigenfrequencies and field distributions of their oscillations in cavity were according to calculations ISFEL3D code [2]. Measuring of electrical field z-component along longitudinal axis showed accordance amplitude's meanings to theoretical meanings of effectiveness q. Field symmetrization of resonator's quadrants was better then 2%. Irregularity of field distribution along z-axis was less then ±2%. Convergence geometric and electromagnetic axes were less then 30 mkm along z. Dependencies of full current and energetical spectra on voltage vane were according to dynamics calculations although maximal beam energy was less then 2 MeV because bad quality of AMG surface and therefore additional electron load [3].

A new original 2 MeV RFQ is worked out now. Resonator is dismountable parallelepiped which has four rigid walls and two bottoms. Four copper vanes are placed inside parallelepiped together with plattings which are welded to vanes. Reliable mechanical contacts join the platting. Cavity's hermetization will be proved after receiving of geometric and electrodynamical parameters.

3 PET-SYSTEM

PET-system need accelerated protons of 11...16 MeV energy to produce four types of isotopes C^{11},N^{13},F^{18},O^{15}. It is evidently that first stage of accelerator is 2 MeV RFQ. But acceleration from 2 up to 11 or 16 MeV will be realized by accelerating structure with drift-tubes and crossed transversal holders (CTH) which was described in [2]. Distribution H-field of working type oscillation look like H-field in four-chamber's RFQ. CTH-structure have high shunt-impedance in energetical diapason from 2 up to 15 MeV. It is possible to use the same scheme of RF feeding for CTH-cavity as for RFQ. Using alternate phase focusing in CTH-structure permit to manage without magnetic lenses inside drift-tubes. Other advantages of this type resonators were described in [2]. If they are used as second stage accelerator and have the same working frequency as RFQ therefore here is not big problems to match RFQ then CTH-structure. 433 and 866 MHz CTH-cavities were successfully tested at NPK LUTS laboratory stands.

Required for PET's target and chemistry modules may be designed and fabricated by Efremov Institute and Main Science Research Radiological Institute at St. Petersburg in cooperation.

4 SAFE ATOMIC ENERGETICAL INSTALLATION

At the last time proposals to use accelerator as driver of under-critical reactor are discussed by many scientists. As rule there are considered schemes with big accelerators [4]. Their output beam power may be several megawatts or several tens of megawatts. Such power are need for driving of reactors with thermal power in few gigawatts. In these works cyclotrons are proposed to use as drivers. Output energy of these accelerators is supposed from 0.4 to 1 GeV. Aspiration for big accelerator drivers is explained by wish to obtain sufficient energetical gain (relation thermal power of reactor to beam power) 30 and higher. But for transported atomic installations main factor is safety. Their power may be several hundreds of megawatts. For example thermal power of transported station with ship reactor KH-3 is 300 MW. Therefore it may appear profitable that such energetical installations will be controlled by compact rf linac with about 300-500 kW beam power.

Comparison of electron, proton and deuteron beams as producers of neutrons under different targets was made in paper [5]. For produce the same quantity of neutrons power of the electron beam must be much more (approximately on order) then power of ion beams. On other hand efficiency of deuteron beam as neutron producer for energies more then 50 MeV just a little higher then proton beam one. Fabrication and exploitation of deuteron linac will be more expensive then proton linac. Therefore, best choice is proton rf linac as driver. Here is considered scheme of proton linac as energetical amplifier for reactor which works on high-enriched uranium 235. Following factors determine main parameters of accelerator. With energy's growth number of neutrons which are produced by only accelerated particle on target of total absorption are increased and compromise choice of final energy against average beam current is determined by allowable accelerator clearance and accelerating structure's acceptance which permits to pass required current without loss. For transported atomic station with thermal power 300 MW maximal proton energy 80-100 MeV will be good practice. Total density of neutron flow which proves normal working of reactor must be about 10^{14} neutron/sec×cm^2. Average linac current 3-5 mA is according to this flow density.

Accelerator-driver must be compact enough to work with reactor inside the compartment of limited sizes. 80 MeV proton linac with working frequency 433 MHz satisfies this condition. RFQ is used as first stage of accelerator which is accelerating particles up to 2 MeV and permit to capture about 100% ions into acceleration. For acceleration from 2 up to 10 MeV may use CTH-structure and alternate phase focusing. Modification of CTH-structure which has focusing magnetic lenses inside some of drift-tubes is used for acceleration from 10 up to 50...80 MeV. Pulsed mode must be used instead of CW-mode because scattered power inside cavity's walls will be too big to prove reliable thermal regime for CW-mode. If duty circle is 0.1 wall scattered power density will be 2 W/cm^2 and required cooling one may proves. It is expediently to build up RF system

multisectioned accelerator as separate amplificating lines. Dividing of RF power is made on low level. As output amplifier of line may be used klystron or endotron type devices to prove parameters

output pulse power	350-400 kW
average power	40 kW
pulse length	60 mks

Scheme of key blocks of accelerator-driver where is supposed dividing of the beam into seven ones before injection to reactor is given on fig.2.

REFERENCES

[1] Yu.A.Svistunov et al. // Advances at NPK LUTS 433 MHz Ion Linac. Proceedings of the XVIII International Linear Accelerator Conference, August 1996, Geneva, v.2, p.869.

[2] S.A.Minaev, Yu.A.Svistunov, S.A.Silaev. // Modelling and Testing of APF Cavity RF Field. Proceedings of International Workshop BDO-95, July 1995, Saint-Petersburg, p.130.

[3] Yu.V.Afanasiev et al. // Tuning and Testing of New 2 MeV RFQ of Aluminium Alloy. Abstracts of International Workshop BDO-98, June-July 1998, Saint-Petersburg, p.8 (to be published in Proceedings).

[4] H.Dariel, Yu.V.Petrov. // Feasibility Study of an Subcritical Fission Reason Driver by the Low Power Accelerator. Preprint 1989, Gutchina, 1994.

[5] Yu.N. Gavrish et al. // Choice of Accelerator's Type for Driving of Under-Critical Reactor. Proceedings of 15 Workshop on Charged Particle Accelerators, Protvino 1966, v.2, p.338 (in Russian).

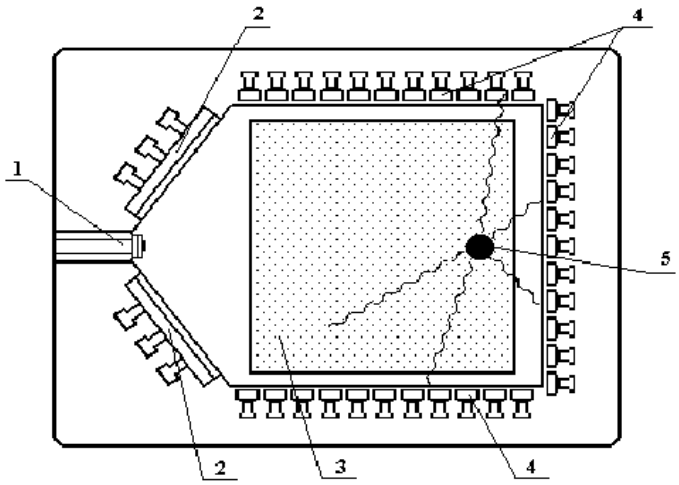

Figure 1: General view of contraband detection system. 1-target; 2-fission detection system; 3-investigated object; 4-explosive detection system; 5-location of fission or explosive.

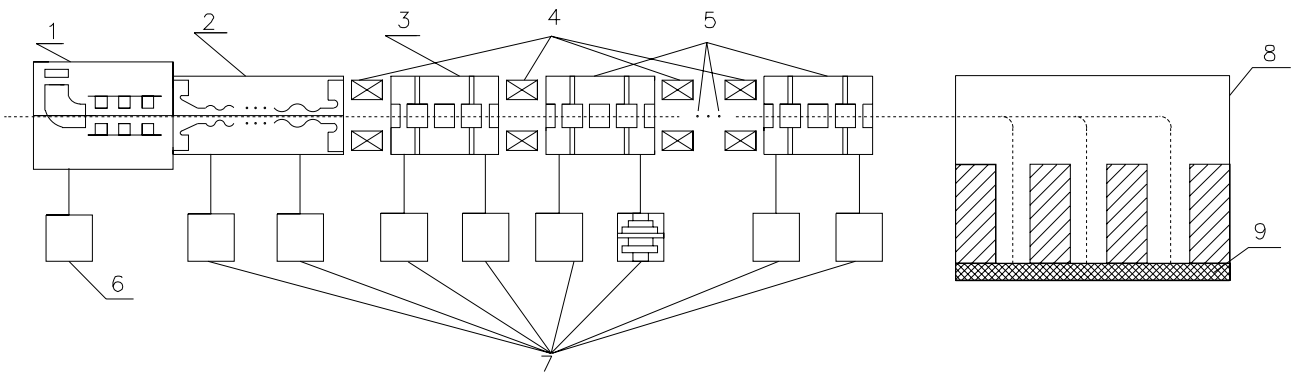

Figure 2: Key blocks of accelerator-driver.
1 - injection system; 2 - RFQ; 3 - cavity of APF; 4 - magnetic lenses; 5 - 10 cavities with drift-tubes; 6 - injector's feeding system; 7 - RF system; 8 - output pulsed magnetic system; 9 - targets.

HIGH POWER CONDITIONING OF THE 202 MHZ IH TANK 2 AT THE CERN LINAC3

J. Broere, H. Kugler, M. Vretenar
PS Division, CERN, CH 1211 Geneva 23, Switzerland
U. Ratzinger
GSI, Planckstrasse 1, D-64291 Darmstadt, Germany
B. Krietenstein
Technical University, Schlossgartenstrasse 8, D-64289 Darmstadt, Germany

Abstract

High accelerating gradients are very interesting for future machines, and, in particular, for high-current heavy-ion linac projects like the "Inertial Fusion Driver". In order to explore the maximum field achievable in an Interdigital-H type structure (IH), an experiment has been carried out at CERN with the Lead Ion Linac (Linac3). After the 1997 run, the RF amplifiers were rearranged in order to allow the feeding of the IH Tank number 2 (1.54 m long, 28 gaps, frequency of 202.56 MHz) with up to 2 MW pulsed RF power. After two weeks of conditioning at pulse lengths varying between 200 μs and 1 ms with a constant pulse repetition rate of 0.8 Hz, the maximum effective accelerating gradient achieved was 10.7 MV/m. This corresponds to a local field maximum of 75 MV/m, and to fields in excess of 50 MV/m (3.5 times the Kilpatrick limit) on large portions of the drift tube surfaces. This paper reports the conditioning procedure used, the measurements of field emission current at different voltages and pulse lengths, the determination of the surface field enhancement factor as well as the calculation of the electric field distribution for the gap with the highest surface fields.

1 SET-UP

For the normal Pb^{27+} operation of Linac3 [1], the IH Tank 2 requires 320 kW of RF power, which corresponds to a voltage gain of 9.09 MV. Its amplifier can deliver 800 kW, and during a test in 1996 the cavity was easily conditioned up to this power [2].

In order to increase the output power, a special amplifier arrangement has been prepared at the end of the 1997 Linac3 run. The tube TH170R, used in the final stages for Tanks 2 and 3, can deliver power levels up to 2.5 MW at a low duty cycle if enough power from the driver stage is available. By inserting the final amplifier stage of Tank 3 temporarily into the Tank 2 chain, between the driver and the final stage, more than 2 MW output RF power became available. The maximum pulse length in this configuration was 1 ms. This corresponds to a duty cycle of 0.08% at the Linac3 repetition rate of 0.8 Hz.

2 CONDITIONING

A two week period was made available for the high power tests, before the CERN winter shutdown. Part of this already short time was used for cabling the new amplifier arrangement, for improving the radiation safety of the installation (high X-ray levels were reached during the tests), and finally for some repairs to the amplifier electronics. The effective time available for conditioning amounted to 230 hours (i.e. slightly less than 10 days).

First of all, the power was gently increased with a pulse length of 200 μs. Breakdowns with associated strong degassing started from about 700 kW. The pumping rate of the vacuum system finally determined the acceptable number of breakdowns and therefore the speed of the conditioning process. Under normal conditions, the vacuum in Tank 2 is the best of the Linac3 complex, $4 \cdot 10^{-9}$ mbar. During the conditioning, it was noticed that the cavity was not able to recover from a series of breakdowns when the pressure entered in the 10^{-6} range, thus the power was reduced in order to stay within the 10^{-8} and 10^{-7} mbar region. The conditioning was done manually, but a computer was used to register the vacuum level at regular intervals, to log the breakdowns, and to calculate automatically cavity voltage, power levels and tube gains.

Figure 1 shows the integrated number of breakdowns (pulses where the cavity could not reach the programmed voltage) and the corresponding pressure during one night (15 hours at 780 kW) of the pre-conditioning phase.

After four days of pre-conditioning up to about 800 kW, the degassing from the surfaces decreased drastically, and the power could be pushed up more rapidly. Finally, a power of 1.21 MW was reached with only occasional breakdowns, however with dark current emission absorbing about 6% of the input RF power. At this point, instead of trying to push the field higher, the pulse length was increased to 500 μs. After 48 hours of reconditioning starting from 1 MW, the maximum stable level reached was as high as 1.3 MW. Beyond this input power level heavy sparking started with high degassing. Next, the pulse length was further increased to 1 ms and the conditioning restarted at 800 kW and reaching

1.2 MW after 3 days. Increasing the field beyond this level led again to heavy sparking with an almost immediate degradation of the vacuum.

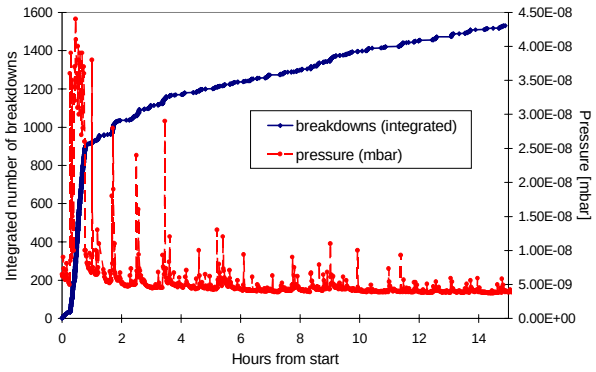

Figure 1: Integrated number of breakdowns and pressure during 15 hours pre-conditioning at 780 kW.

Figure 2 shows the power delivered to the tank as a function of time from the start of the tests. Table 1 gives the maximum gap voltage achieved, in units of the nominal voltage for Pb^{27+}, and the corresponding surface electric field at two positions, on the drift tube face and on the edges (see next Section).

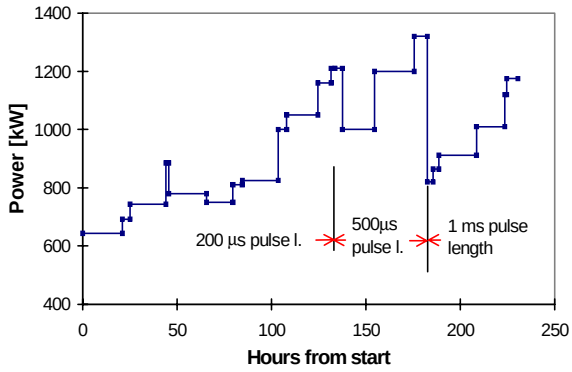

Figure 2: Conditioning history (RF power vs. time).

Table 1: Voltage and peak surface field achieved.

Pulse length	Voltage	*E*-field on tube	Max. *E* on tube	Eff. tank acc. field
[µs]	units of Pb^{27+} voltage	[MV/m]	[MV/m]	[MV/m]
200	1.71	51	70	10.1
500	1.82	54	75	10.7
1000	1.67	49	69	9.8

The radiation level (X-rays) during the tests was permanently monitored. The dose rates measured at 1.35 MW and 500 µs were about 5 mSv/h at 80 cm from the cavity axis and 2543 mSv/h at the tank surface [3].

3 SURFACE FIELD DISTRIBUTION

Figure 4 shows gap voltage and on-axis field distributions in Tank 2, derived from a bead-pull measurement scaled to the maximum voltage achieved during the tests (1.82 times the nominal). The electric field distribution in gap number 9, where the voltage is maximum, has been calculated with the code MAFIA to find the value of the surface field reached in the cavity during the tests. Figure 5 shows the calculated electric field in the plane of the stems and the value of the electric field at four representative points on the drift tube surface.

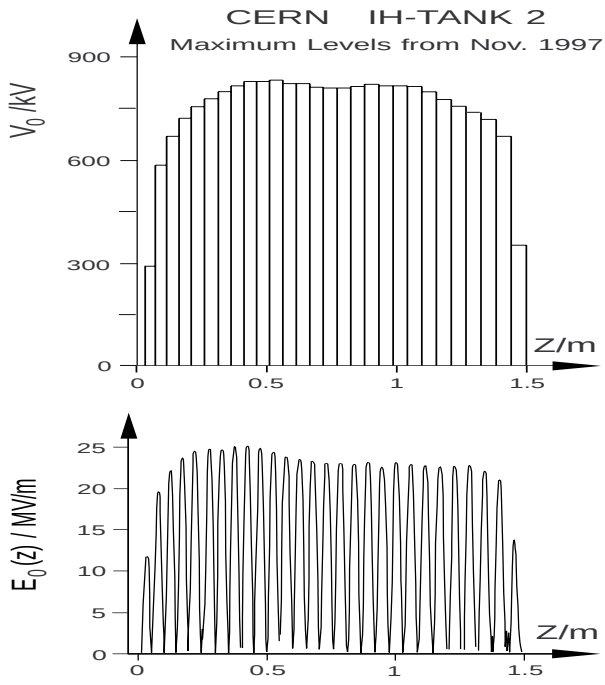

Figure 4: Voltage and electric field distribution (Tank 2).

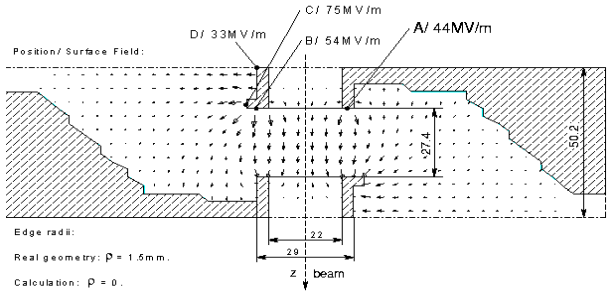

Figure 5: MAFIA calculation of field distribution in gap number 9 for 830 kV gap voltage.

In the MAFIA simulation the drift tube edges are not rounded, in contrast to the real geometry, and this leads to an underestimation of the field at point A (tube edge). At the other points, the values should be realistic, since they are calculated far enough from the square edges, as compared to the mesh step of 0.6 mm. Thus the field at point B can be taken as representative of the field on the

drift tube face, while point C represents a maximum field reached only on an area of about 0.5 cm^2 per drift tube.

In conclusion, fields of about 54 MV/m were reached on the drift tube face (~ 6 cm^2 per tube) in more than 20 gaps. This corresponds to 3.5 times the Kilpatrick level at 202 MHz (14.8 MV/m).

4 FIELD EMISSION MEASUREMENTS

The high electric field reached during the tests led to high levels of field-emitted current (dark current). The dark current level was measured at regular intervals by monitoring the cavity voltage for different RF input levels.

Without dark current, the power is proportional to the voltage squared, the coefficient being the inverse of the shunt impedance. When at high voltages dark current appears, the electrons are accelerated over the cavity gaps and extract an additional power $P=I\times U$ from the generator, I being the overall electron current and U the average gap voltage. The electron transit time factor is unity for the gap size and frequency of this case. When plotting P vs. U^2, the deviation from a straight line at high power gives the power driving the dark current; the dark current value is obtained by dividing this power by the average gap voltage. Figure 7 shows the measured dark current as a function of cavity voltage in units of the nominal Pb^{27+} voltage, at the end of the conditioning process for the three different pulse lengths. In all cases, appreciable dark current emission starts at 1.4 to 1.5 times the nominal voltage, and then rapidly grows with voltage. The highest dark current measured absorbed 9% of the input RF power.

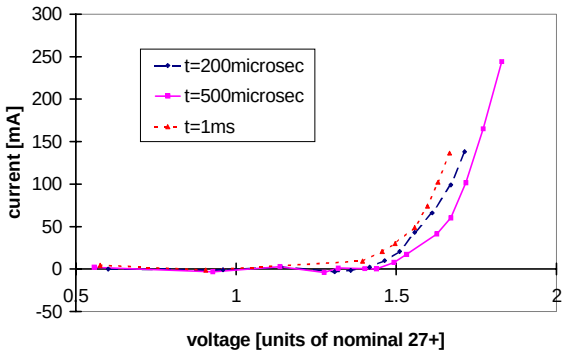

Figure 7: Overall field emission current vs. field level (units of nominal) for three pulse lengths.

The three measurements can be re-drawn in the usual "Fowler-Nordheim" form $\ln(I/E_s^{2.5})$ vs. $1/E_s$ (Figure 8), where field emission is represented by a straight line with a slope equal to the inverse of the surface field enhancement factor beta.

From the curves, it can be seen that β did not change appreciably during the conditioning process, being always between 100 and 114, values that indicate clean electrode surfaces. For comparison, β measured with the same technique on the CERN RFQ2 at different times ranged between 67 - very clean - and 920 – heavily polluted [4]. As expected, the conditioning process changed the intercept of the straight line, which is proportional to the overall emission, i.e. to the number of emitting spots on the surface. Between the first two measurements (200 μs and 500 μs pulse length) there is a reduction in the emitted current. When the pulse length was further increased to 1 ms, however, the emission went up again.

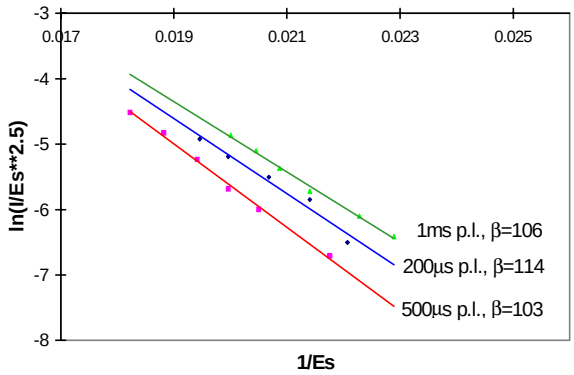

Figure 8: Fowler-Nordheim plot for the cases of Fig 7.

5 CONCLUSIONS

IH cavities of this type, with small diameter drift tubes, can stand fields of 50 MV/m (3.5 Kilpatrick) on large fractions of the drift tube surfaces, for low duty cycles and at pulse lengths up to 1 ms. Local maxima can be as high as 75 MV/m. These field levels were achieved after only a few days of conditioning with a cavity which has been in routine linac operation since 1994. Field emission was observed at surface field levels above 45 MV/m. Higher "clean" levels may be reached by applying an extended RF conditioning concept.

6 ACKNOWLEDGEMENTS

The authors are grateful to W. Pirkl who suggested the amplifier arrangement and to J.M. Hanon, R. Hajdas and R. Simitsch for their help during the tests.

7 REFERENCES

[1] H.D. Haseroth, "Pb Injector at CERN", Proc. of the 1996 Linac Conf., Geneva, CERN 96-07, p. 283.

[2] R.Scrivens, "High Power Measurements and Segmented Phase Probe Improvements on Linac3", PS/HP/Note 97-08 (MD).

[3] J.-M.Hanon, "Rapport de Surveillance Radiation", RSR/PS/98-02/jmh.

[4] M.Vretenar, "Field Emission Measurements on RFQ2 and Re-calibration of the Vane Voltage", PS/RF/Note 97-11 (MD).

DESIGN OF THE KOMAC H^+/H^- RFQ LINAC

J. M. Han, Y. S. Cho, B.J. Yoon and B. H. Choi
Korea Atomic Energy Research Institute, P.O.Box 105, Yusong, Taejon, Korea
Y. S. Bae and I. S. Ko
Dept. of Physics, Pohang Univ, of Science and Technology, Pohang, Korea
B. S. Han
Samsung Heavy Industries Co., Ltd., P.O.Box 43, Taejon, Korea

Abstract

A 350MHZ, cw Radio-Frequency Quadrupole (RFQ) will be built to produce 20mA of proton beam at 3MeV for the KOrea Multipurpose Accelerator Complex (KOMAC) projects 1GeV linac. The beam dynamics and the engineering design of the RFQ linac are described. The length of the RFQ is 324cm long and the longitudinal stability is mitigated by the coupled-cavity concept. In order to minimize the power deposited on the cavity walls, the longitudinal variation of the width of the vane base is given. The peak temperature on the cavity wall is 50C, the displacement is about 18 μm.

1 INTRODUCTION

The Radio Frequency Quadrupole (RFQ) linac proposed for the Korea Multipurpose Accelerator Complex (KOMAC)[1-3]. Project is a cw linac which will produce a 20 mA beam of H^+/H^- with energy of 3 MeV. This paper addresses the physics and engineering design plus the present status of the KOMAC RFQ. The RFQ concept is shown on Figure 1 with the parameter values given on Table 1.

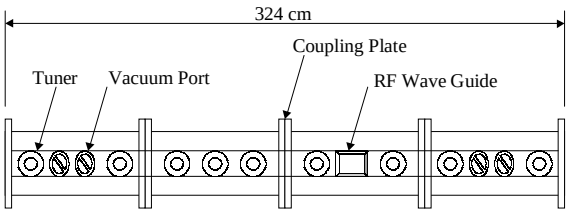

Figure 1. Preliminary drawing of a 3MeV 350MHz RFQ linac for the KOMAC.

The main focuses of this physics and engineering design in the KOMAC RFQ are as follows:

- To obtain the focusing required to match the H^+/H^- beam to the RFQ..
- To maintain a constant capacitance per unit length along the axis of the RFQ.
- To minimize the power dissipated on the cavity walls and the end region of the vanes.
- To stabilize the longitudinal mode in the structure.

The physics design study is presented in section 2. The physics design codes used for RFQ include space- and image–charge effects and have been proved against existing linacs [4-6]. The engineering design of the RFQ is described in Section 3. The thermal analysis is studied by ANSYS code. The section 4 describes the fabrication status of the KOMAC RFQ.

Table 1. RFQ linac parameters for the KOMAC

PARAMETER	VALUE
Operating frequency	350 MHz
Particles	H^+ / H^-
Input / Output Current	23 / 20 mA
Input / Output Energy	0.05 / 3.0 MeV
Input / Output Emittance, Transverse/norm.	0.02 /0.023 π-cm-mrad rms
Output Emittance, Longitudinal	0.246 MeV-deg
Transmission	95.4 %
RFQ Structure Type	4-vanes
Duty Factor	100 %
Peak Surface Field	1.8 Kilpatrick
Structure Power	350.0 kW
Beam Power	67.9 kW
Total Power	417.9 kw
Length	324.0 cm

2 PHYSICS DESIGN

The KOMAC system requires 20 mA of H^+/H^- beams from the 350 MHz RFQ. The proper energy needs for injection into the coupled cavity drift tube linac(CCDTL). The maximum vane voltage is given by the peak electric field that could cause sparking. In this design, the peak electric field was limited to 1.8 times the Kilpatrick criterion [7].

Figure 2 shows the various parameters defining the KOMAC RFQ design versus position. These parameters

were obtained by CURLI, RFQUICK, PARI, and PARMTEQM [4]. The curves labeled “V”, “Phase”, ”B”, “A”, “r”, “ a”, “m”, “E_z” and ”W” show the voltage difference adjacent vane-tips, synchronous phase, focusing strength, accelerating efficiency, average radius, aperture radius, modulation factor, average axial electric field and beam energy along the RFQ, respectively.

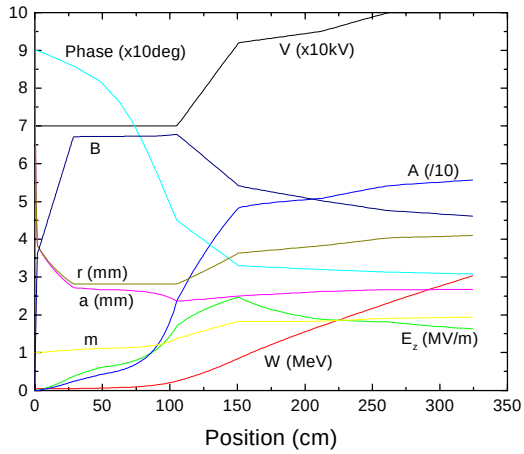

Figure 2. Various parameters defining the RFQ design versus position.

To obtain the focusing required to match the beam from LEBT to the RFQ requires a weaker focusing and a larger aperture at the entrance of the RFQ. However, the transmission rate of the beam decreases with the inverse of the aperture at the entrance of the RFQ. In order to design a radial matching section with a weak focusing and large aperture, we used CURLI and RFQUICK. The aperture in the KOMAC RFQ is smoothly reduced as it moves from the entrance to z=26.8 cm where the focusing strength is peak , as shown in Figure 2. In general, the end of the gentle buncher is a point where significant beam loss occurs. By the proper combination of V, a and B, the beam loss at the end of the gentle buncher was reduced. At about 104cm, the vane gap voltage, V, and aperture, a, start increasing and the focusing strength, B, starts decreasing. The increase in the vane gap voltage increases the accelerating gradient in the high-energy portion. The increase in the vane gap voltage also decreases the design length of the RFQ

Another important factor in the RFQ design is to maintain a constant capacitance per unit length along the axis of the RFQ. In order to maintain a constant capacitance, the average radius from the vane tip to the axis of the RFQ is changed, as shown in Figure 2. A change in the average radius would result in a change in the capacitance and in the local resonant frequency of the waveguide by a severe tilt in the fields. To maintain a constant capacitance per unit length, we fix the ratio of the vane tip transverse radius of curvature, ρ, to the average radius, r. For the KOMAC RFQ, the value of ρ/r is kept constant at 0.792. The resonant frequency is kept constant by varying the cavity cross-section by adjusting the width of the vane base while r changes. Because the power dissipated in the cavity walls will not be longitudinally uniform, this also minimizes the structure power.

We used PARMTEQM to match the beam into the CCDTL. Figure 3 shows the result of the PARMTEQM simulation. The percentage transmission is 95.4%.

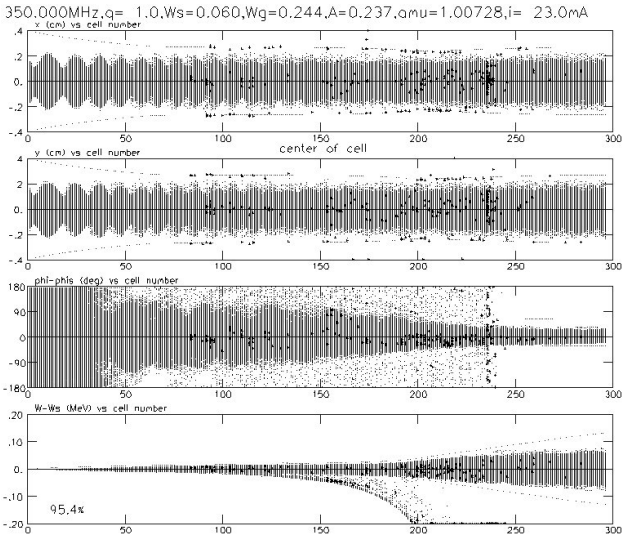

Figure 3. PARMTEQM simulation of the RFQ using 5000 particles. From top to bottom are: x, y, phase, and energy coordinates versus cell number. Bold black points indicate lost particles in the RFQ.

3 ENGINEERING DESIGN

The length of the KOMAC RFQ is 3.24 m long and consists of two resonantly coupled 1.62m sections. The length is determined by the final energy which is 3.0 MeV. The resonant coupling provides the longitudinal field stabilization and a stop band in the dipole mode, which is improved the transverse stability by eliminating dipole modes. In order to tune the resonant frequency of the end regions of the RFQ, we have used the three-dim. MAFIA code [8]. There is the rectangular undercut of the vanes. However, the exact shape of the undercut will be determined empirically by the cold model which is being fabricated into the aluminum alloy. The cavity cross-section is four triangular shape with the axial variation in the width of the vane base as shown in Figure 4. The vane-cavity will be joined longitudinally by a brazing. Thus the RFQ is the completed monolithic structure and the vanes are permanently aligned. This structure serves to mitigate the cost and to simplify the mechanical support system.

A serious problem in the design of the KOMAC RFQ with cw operation result from the rf thermal loads on the

cavity walls. The average structure power by rf thermal loads is 0.35 MW and the peak surface heat flux on the cavity wall is 0.13 MW/m^2 at the high energy end. In order to remove these heat, we consider 24 longitudinal coolant passages in each of the sections, as shown in Figure 4. Figure 4 also shows a temperature distribution of the cavity at the high energy end. The material is oxygen-free copper. The thermal loads was given by the SUPERFISH [9] analysis. The heat transfer coefficients is between 11kW/m^2-C to 15 kW/m^2-C. Because of the flow erosion of the coolant passages, we consider the maximum allowable bulk velocity of the coolant as 4.5 m/sec. From the thermal-structural analysis of ANSYS, the peak temperature on the cavity wall is 50C, the displacement is about 18 μm and the intensity stress .is 30 MPa.

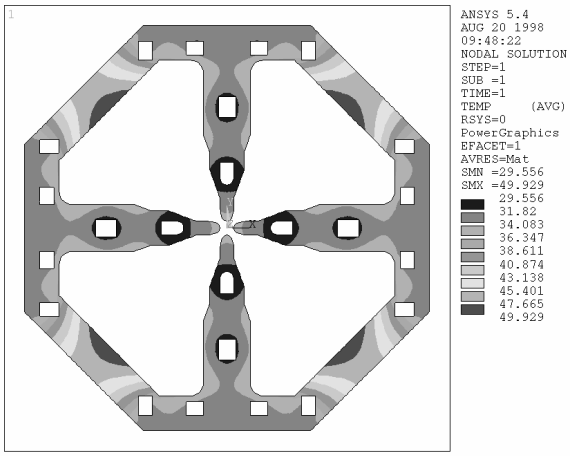

Figure 4. Temperature distribution of the cavity at the high energy end of the KOMAC RFQ.

4 PRESENT STATUS

A prototype of the RFQ is being machined at the Samsung Heavy Industies Co., Ltd and the Dae-Wung Engineering Co.. We are going to test a brazing of one section at next month.

5 ACKNOWLEDGMENT

We are grateful to Dr. Kazuo Hasegawa at JAERI and Dr. Lloyd M. Young at LANL. This work has been supported by the Korea Ministry of Science and Technology (MOST) and by the Korea Electric Power Co. (KEPCO).

6 REFERENCES

[1] C. K. Park et al., "The Komac Project: Accelerator and Transmutation Project in Korea", Proceeding of APAC98, Tsukuba, March 23-27 (1998).

[2] Y. S. Cho et al., "Conceptual Design Study of KOMAC DTL ", Proceeding of APAC98, Tsukuba, March 23-27 (1998) .

[3] T. Y. Eom et al., "A Study on the Development Plan and Preliminary Design of Proton Accelerator for Nuclear Application", KAERI/RR-1769/96.

[4] K. R. Crandall et al., "RFQ Design Codes", LA-UR-96-1836, (Revised February, 1997)

[5] L. M. Young, "Simulations of the LEDA RFQ 6.7-MeV Accelerator'", LA-UR 97-2582, July, 1997.

[6] K. Hasegawa et al., "Development of a High Intensity RFQ at JAERI", J. Nuc. Sci. and Tech., 34, 622 (1997).

[7] W. D. Kilpatric, "Criterion for Vacuum Sparking Designed to Include Both rf and dc", Rev. Sci. Instr. 28, 824 (1957).

[8] R. Klatt et al., "MAFIA-A Three-Dim. Electromagnetic CAD System for Magnets, RF Structures, and Transient Wake-field Calculations", SLAC-303, 276 (1986).

[9] J. H. Billen and L. M. Young, 'POISSON SUPERFISH", LA-UR-96-1834 (Revised December, 1997)

DESIGN AND STATUS OF THE RFQ FOR REX-ISOLDE*

T. Sieber, D. Habs, O. Kester, A. Kolbe, LMU München, Am Coulombwall 1, Garching, Germany
A. Schempp, J.W.Goethe Universität, Robert Mayer-Str. 2-4, Frankfurt/Main, Germany

Abstract

The first module of the REX-ISOLDE-Linac is a 4-Rod-λ/2-RFQ-structure, which is - together with the REX- IH-DTL - built up and tested at Munich.

In this Paper, the electrode design and the mechanical characteristics of the REX-RFQ are presented. Furthermore, the results and the principle of our low-level rf-measurements are discussed, and PARMTEQ-calculations for several measured voltage distributions are shown.

1 INTRODUCTION

At CERN a new concept for the efficient post-acceleration of radioactive ions will be realized with REX-ISOLDE [1]. REX-ISOLDE is a compact experiment, at which neutron-rich isotopes from the online mass separator ISOLDE are firstly accumulated, cooled and bunched in a Penning-Trap, afterwards charge breeded in an Electron-Beam Ion-Source (EBIS) and finally accelerated by a Linac to energies between 0.3 MeV/u and 2.2 MeV/u [2].

The Linac consists of a 4-Rod-RFQ and an Interdigital-H Drift-Tube-accelerator, followed by three seven-gap resonators for energy variation from 1.1 MeV/u to 2.2 MeV/u. The RFQ will accelerate the radioactive ions (design-ion: $^{36}Na^{8+}$) with an A/q of 3 - 4.5 from 5 keV/u to 300 keV/u. The according electrode-voltage is 28 to 42 kV, which will require an rf-power of about 30 to 40 kW. It has a total length of 3 m (18 stems) and operates at a resonant frequency of 101.28 MHz (duty-cycle: 10%).

Table 1: Parameters of the REX-RFQ, theoretical values are marked with '*'.

frequency	101.2 [MHz]
Input energy	5 [keV/u]
Final energy*	300 [keV/u]
duty-cycle	10 %
q/A	1/3 - 1/4.5
Electrode voltage	28 – 42 kV
rel. field deviation	≈ 1%
Transmission*	98%
max. input emittance	200 πmmmrad
phase	-90° to –13°
Energy spread*	±1%
Rp (pert.cap.)	171 [kΩm]
Quality-factor Q_0	3894
accelerator cells	233
electrode length	2925 [mm]
tank length	3000 [mm]
tank diameter	320 [mm]
stem height	189 [mm]
number of stems	18

* Work supported by the BMBF under contract 06 LM 868 I / TP : 4

2 ELECTRODE DESIGN

The calculations for the electrode-design of the REX-RFQ were made with a modified version of the multi- particle code PARMTEQ. For the input, an in both phase planes convergent beam (α=0.66) with emittances of 200 π mmmrad and a distribution with a randomly filled transverse phase-space, uniform phase and no energy spread was assumed. Because of the very low beam-currents at REX-ISOLDE (10000 particles per 100μs-EBIS-pulse), a zero-current electrode design could be generated, which was optimized to a high transmission (98%) and - due to the small longitudinal acceptance of the following IH-0°-synchronous phase structure - small energy spread (±1%).

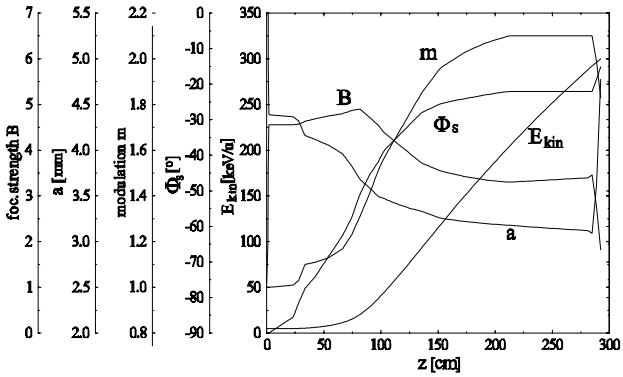

Figure 1: Electrode parameters calculated with the code PARMTEQ.

Figure 1 shows the electrode-parameters charted as a function of the accelerator-length. The strongly reduced focusing strength in the last three cells (which is the result of the increasing aperture: $B \propto 1/a^2$), corresponds to the matching-out section of the RFQ. By decreasing the phase in this section from -22° to -13° the energy spread could be kept constant. The simultaneous reduction of the modulation has simply mechanical reasons. Because of the increased aperture, a continuous modulation would have reached to close to the cooling channel inside the mini-vane profile (see below) of the electrodes.

The matching out section produces a decreased divergence of the output-beam, which reduces the required field strength of the following magnetic quadrupole lenses and avoids particle losses during the beam transport from the RFQ to the IH-structure. Fig. 2 shows the calculated output-emittances with (below) and without (above) matching-out section.

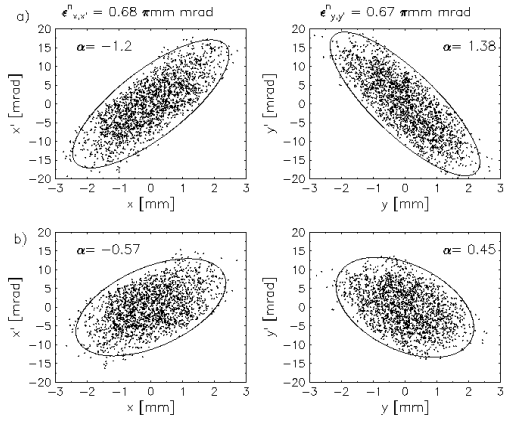

Figure 2: Output-emittances for $\varepsilon_{n,in}$=0.65 π mm mrad.

PARMTEQ calculations with the output emittance of the REX-ISOLDE mass-separator used as input emittance of the RFQ showed, that - due to the large acceptance of the given electrode design - the (in x-direction divergent) beam from the separator is matched and accelerated with the same excellent transmission and energy-spread as the design beam. Figure 3 shows the resulting RFQ-in- and output emittances. The separator output emittances have been calculated to third order with the COSY infinity code for an EBIS emittance of 14 πmmmrad [3].

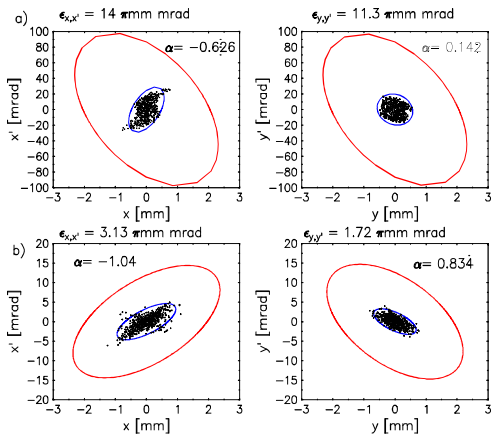

Figure 3: In and output emittances for the design beam (large ellipses) and the separator beam (small ellipses with α and ε specified).

3 MECHANICAL CHARACTERISTICS OF THE RESONATOR

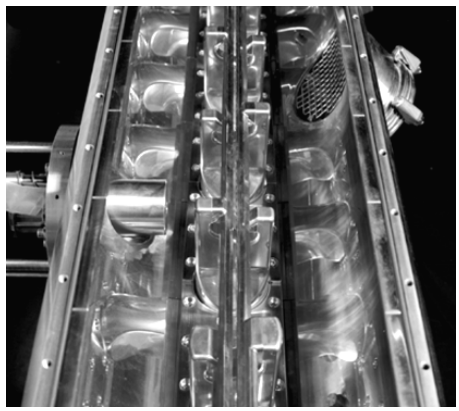

Figure 4: The inside of the RFQ tank (view from the low-energy end).

The resonator of the REX-RFQ is similar to the GSI High Charge-State-Injector- and to the Heidelberg High-Current-Injector-RFQ. Figure 4 shows a photo of the structure. The stems have a total height of 180 mm, the stem-foot (with circular cross-section) has a height of 40 mm, what defines the maximum thickness of the plates for frequency and Flatness tuning. For the quadrupole electrodes so called 'mini-vanes' with a cooling water channel inside (see Fig.6) were used. The mini-vanes allow a very good cooling of the electrodes, what avoids misalignment caused by heating.

The Flatness tuning is done with single plates, which are mounted between neighbouring stems. The plates are contacted to the stems by silver plated springs lying in a groove at the edge of the plates. The advantage of this principle is, that the deformation of the contact springs during operation of the resonator is reversible. Fig. 5 shows a tuning plate and the way it is contacted to the stems.

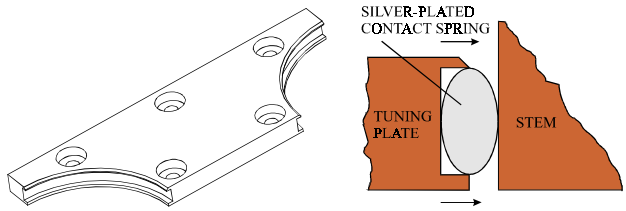

Figure 5: Tuning plate and contacting.

The channels for the water supply of the electrodes are drilled inside of the six waterleading stems. This design, which was developed for the Heidelberg High-Current-Injector-RFQ, avoids the (former used) little tubes on the outside, which turned out to be sensitive to corrosion and mechanical resonances. Figure 6 shows a Pro/E-Plot of a waterleading stem and a cross section of a stem with mounted electrodes. The electrode alignment is (because of the O-Ring between electrode-holder and stem) only

possible in the range ±1/10mm horizontally and ±5/10mm vertically.

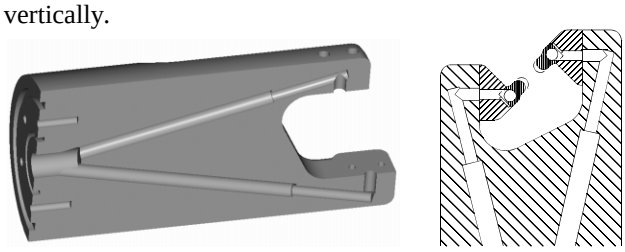

Figure 6: Waterleading-stem used in the REX-RFQ (see also Fig. 4 in the foreground).

4 MEASUREMENT OF THE RF-PARAMETERS

The measurement of the frequency and the quality factor resulted (with a distribution of tuning plates as seen in Fig. 7) in f=101.2 MHZ and Q=3894.

The theoretical description of the RFQ-resonator as a resonant circuit tells us, that the pertubation capacity, which is used for the measurement of the Rp-value must be small in comparison to the rod-capacity (≈190 pF). In this case $Rp=2Q\Delta f/\pi f^2\Delta C$, with ΔC being the pertubation capacity. Only if *all* values in this formula are kept constant, the electrode voltage is (because of the definition of the Rp-value: $U^2=Rp/N$) proportional to the square root of the frequency difference caused by the additional capacity.

To find out the upper limit of usable capacitors, and to investigate wether there is a convergence to the real voltage distribution when steadily smaller capacities are used, we measured the Flatness with three different pertubation capacitors.

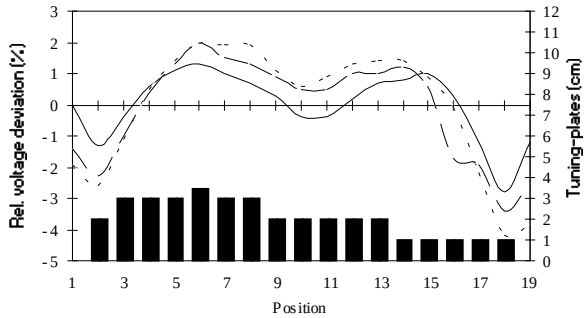

Figure 7: Voltage distribution of the REX-RFQ measured with 1.2pF (solid line), 2.2pF (dashed line) and 3.3pF (dotted line). The bars indicate the thickness of the Tuning-plates.

Figure 7 shows the expected steady increase of the 'Unflatness' at smaller capacitors. With an average Δf of the 1.2 pF measurement, the Rp-value of the REX-RFQ amounts to 171 kΩm.

In this context it is important to mention, that a Flatness and Rp-value measurement with the often used crocodile-clip-capacitor arrangements does not fit exactly to the theory. Because of the arrangement's own capacity (switch etc.), not the real Flatness is measured but the relative difference between f. ex. a 0.5 pF and a 1.2 pF measurement (analogue to Fig. 7). For the determination of the Rp-value this method provides strictly speaking no constant f in the above mentioned formula. The most accurate way of measurement is to contact the smallest available capacitor (≤ 1pF) directly to the electrodes and to determine its capacity as exact as possible (f. ex. with a capacity measurement-bridge).

The measured voltage distributions were used to calculate the influence of the Unflatness on the particle dynamics in the RFQ. Table 2. shows the results of the PARMTEQ-calculations. Note (from Fig. 7), that the maximum field deviation refers only to the end cells! On the average, the field deviation (except for the the untuned measurement) is around ±1%.

Table 2: Transmission and energy-spread for the untuned voltage distribution and for the tuned distri-bution measured with three different capacitors.

	max. field deviation	ΔE (90%)	Trans-mission	x,y-output-emittances ε_n
(untuned)	±20%	5.3%	97.9%	0.648; 0.659
3.3 pF	±2.8%	2.5%	97.3%	0.648; 0.659
2.2 pF	±3.4%	2.52%	97.15%	0.647; 0.658
1.2 pF	±4.2%	2.54%	96.95%	0.651; 0.656

5 PRESENT STATUS

Currently the REX-RFQ is on its test stand at the Munich accelerator lab ready for vacuum testing and final alignment of the electrodes. Two of the three piston tuners have been mounted (see Fig. 4), and provide (from a middle position) a frequency shift of ± 200 kHz. The vacuum test will take place after mounting of a cooled ground plate, which is the last missing component of the resonator. The electrode alignment was measured after mounting in the range of 1/10 mm, With the final alignment after the vacuum test, we want to reach an accuracy of 5/100 mm.

REFERENCES

[1] D. Habs et al., "The REX-ISOLDE Project", Proc. ECAART-5, NIM B 139 (1998).

[2] O. Kester et al., "The REX-ISOLDE LINAC", Proc. of EPAC '98, June 1998.

[3] R. Rao et al., "Beam Optics Design of the REX-ISOLDE q/m-Separator", Proc. of EPAC '98, June 1998.

RECENT DEVELOPMENTS OF THE FOLDED-COAXIAL RFQ FOR THE RIKEN HEAVY ION LINAC

O. Kamigaito, A. Goto, Y. Miyazawa, T. Chiba, M. Hemmi,
M. Kase, S. Kohara, E. Ikezawa, T. Nakagawa, M. Kidera, and Y. Yano
The Institute of Physical and Chemical Research (RIKEN),
Wako-shi, Saitama, 351-0198 Japan

Abstract

The beam intensity available with the RIKEN heavy-ion linac (RILAC) has remarkably increased since the installation of a new injector in 1996, which consists of an 18-GHz ECR ion source and a variable-frequency RFQ based on a folded-coaxial resonator. Since August 1997, the maximum extraction voltage of the ECR ion source has been raised from 10 kV to 20 kV in order to upgrade the intensity further. The RFQ vanes were re-designed and replaced at the same time. Now the intensity has increased by about one or two orders of magnitude compared with those formerly available with the Cockcroft-Walton injector. The maximum power of the beam extracted from the RILAC and that from the ring cyclotron have reached 560 W and 2 kW, respectively. Another important result we have obtained is that the transmission efficiency through the RILAC is much improved by use of a prebuncher placed before the RFQ. Operational experiences of the RFQ as well as recent developments are described in this paper.

1 INTRODUCTION

As already reported[1], the new injector consisting of an 18-GHz ECR ion source (ECRIS) and a variable-frequency RFQ based on a folded-coaxial resonator has been working in the RIKEN heavy ion linac (RILAC) since August 1996. Figure 1 shows the RFQ along with the six tanks of the RILAC. Acceleration tests of the RILAC and the ring cyclotron (RRC) have been carried out continually using the beams from the new injector since the installation.

The beam intensity has remarkably increased owing to the high performance of the 18-GHz ECRIS[2]. In December 1996, we achieved the beam current of 1 pμA from the RRC for the first time using $^{36}Ar^{5+}$ beam supplied with the new injector.

One of the advantages of the new injector is that highly charged ions are readily generated with the ECRIS. The charge stripper between the RILAC and the RRC has become unnecessary for low-energy beams of medium-heavy ions such as Argon, so that the stability of the beam has been improved.

However, the extraction voltage of the ECRIS was quite low for the highly charged ions, because the maximum voltage was initially chosen to be 10 kV. The voltage was, for example, only 3 kV in the beam test mentioned above. This low voltage caused bad effects both on the intensity and the emittance of the extracted beams.

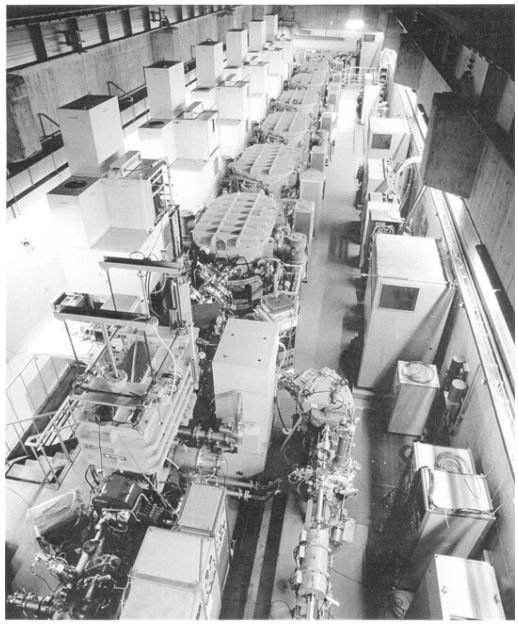

Figure 1: The RILAC and the RFQ seen from the upstream.

2 RECENT DEVELOPMENTS

2.1 New Vanes

Since August 1997, the maximum extraction voltage of the ECRIS has been raised to 20 kV in order to upgrade the beam intensity further. The RFQ vanes were re-designed and have been replaced.

The length of the initial sections of the vanes has increased, because the velocity of the input beam to the RFQ has become higher by about 40%. In order to keep the vane length less than the inner length of the resonator, we have raised the intervane voltage by about 5% and reduced the total number of the cells from 78 to 72. The mean aperture (r_0) have been slightly increased to reduce the capacitance between the vanes. All the parameters have been optimized by using the PARMTEQ code.

The vane parameters are listed in Table 1. Although the length has increased by 8%, the change of the frequency-

Table 1: Main Parameters of the RFQ

	~ 07.1997	08.1997 ~
Frequency (MHz)	17.7 - 39.2	17.4 - 39.0
Mass-to-charge ratio (m/q)	6 - 26	6 - 26
Input energy (keV/q)	10	20
Output energy (keV/q)	450	450
Input emittance(mm•mrad)	145 π	145 π
Vane length (cm)	142	153
Intervane voltage (kV)	33.6	36.8
Mean aperture (r_0:mm)	7.70	8.08
Min. aperture (a_{min}:mm)	4.17	4.67
Max. modulation (m)	2.70	2.41
Beam margin	1.7	1.6
Focusing strength (B)	6.8	6.8
Max. defocusing strength	-0.30	-0.30
Final synchronous phase	-25°	-30°

range could be made very small. The vanes were three-dimensionally machined within the accuracy of ±50 μm and aligned within the same accuracy.

2.2 Transmission Efficiency

At the same time of the replacement of the vanes, an additional Faraday cup was installed just after the RFQ, as shown in Fig. 2, for the measurement of the transmission efficiency through the RFQ alone. The efficiency is defined by the ratio of the measured beam currents with the two Faraday cups (FC-R1 and FC-R2) shown in Fig. 2.

The maximum efficiency ever achieved is 92 %, being good enough compared with the calculated value of 94 %. The typical efficiency is about 80 to 90%, which depends on the input beam emittance varying with respect to the ion species and the extraction voltage.

One of the problems annoying us is that the efficiency up to the entrance of the RILAC is not so good as expected. Although the best efficiency is 80%, only 50 to 70% of the beam entering the first Faraday cup (FC-R1) is usually transported to the entrance of the RILAC. This means that some portion of the beam is lost in the matching section between the RFQ and the RILAC.

The RFQ can accept a beam having an emittance larger

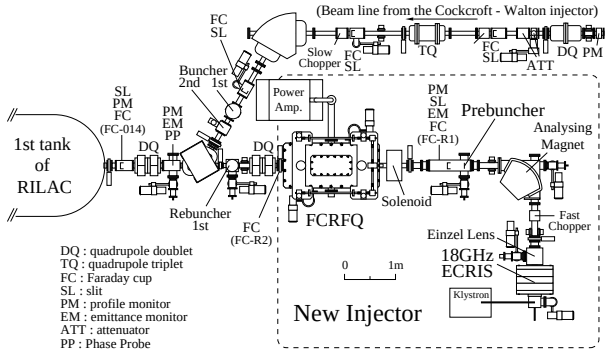

Figure 2: Schematic drawing of the new injector.

than the designed value of 145π mm•mrad, because the beam margin is large as shown in Table 1. However, the beam size exceeds the aperture diameter of the rebuncher when the input beam emittance is larger than the designed value or the beam ellipse does not match the designed ellipse. The aperture diameter of the rebuncher has been therefore enlarged from 40 mm to 50 mm, which does not help us so much. Additional devices such as quadrupole magnets is needed in the LEBT section to achieve more effective beam-transport.

2.3 A Prebuncher for the RFQ

As shown in Fig. 2, a prebuncher has been used in the LEBT section since the new injector was installed in the RILAC beam line. Its electrode consists of two mesh plates made of copper with a gap distance of 5 mm. A transformer is employed in the feeder line so that the termination register of 200 Ω matches the standard impedance of 50 Ω. The rf-power is supplied with a wide-band amplifier which transmits the maximum power of 1 kW in the frequency range from 5.5 MHz to 40 MHz.

This system was originally introduced to generate "single-bunch" beams by applying sub-harmonic (1/3 - 1/5 of the fundamental frequency) rf-voltage to the mesh electrode while a fast-chopper placed in the LEBT section sweeps the main part of the extracted beam from the ion source, based on the same method already established in the injection line of the AVF cyclotron[3]. It has been found that this method also works well in the RILAC.

On the other hand it has been reported elsewhere that the longitudinal emittance can be reduced by using the prebuncher with the fundamental frequency. We examined this effect by measuring the transmission efficiency through the RILAC, using Argon and Xenon beams from the new injector. In the test, the effect of the second and third harmonic components was also studied by adding these components to the fundamental rf-voltage.

A result measured with Ar^{5+} beam at the frequency of 18.8 MHz is shown in Table 2. As shown there, the transmission efficiency through the RILAC was much improved when the prebuncher was used, while that through the RFQ did not change so much. This result qualitatively agrees with the PARMTEQ simulation,

Table 2: Effect of the prebuncher on the transmission.

prebun.	FC-R1	FC-R2	FC-014*	FC-A02**
No Use	23.0μA (100%)	20.1μA (87%)	15.9μA (69%)	8.0μA (35%)
1f	23.0μA (100%)	20.1μA (87%)	16.9μA (73%)	12.1μA (53%)
1f - 3f	23.0μA (100%)	21.0μA (91%)	16.9μA (73%)	13.0μA (57%)

*The Faraday cup placed at the entrance of the RILAC (shown in Fig. 2).
**The Faraday cup placed at the exit of the analyzing magnet after the RILAC.

which shows little effect on the transmission efficiency through the RFQ but great reductions of longitudinal emittance of the accelerated beam.

It was hard to observe the effect of the higher harmonic components because the gap distance of the mesh electrode was too wide and the impedance-matching of the transformer in the high frequency region was not so good. Systematic study of the higher components as well as measurements of the longitudinal emittance are under preparation.

3 PRESENT STATUS AND OUTLOOK

The beam intensity from the ECRIS has increased by a few times since the extraction voltage was raised. The maximum current ever extracted from the RRC is 2 pμA for Argon and 200 pnA for Xenon. Comparing these values with the beam current formerly available with the Cockcroft-Walton injector, the intensity of Argon beams has increased by one order of magnitude. For Xenon beams, the intensity has become larger by two orders. The ions accelerated so far are summarized in Fig. 3.

Figure 4 shows the maximum transmission efficiency ever achieved up to the exit of the RILAC. It has become 1.5 times larger than that using the Cockcroft-Walton injector. Typical transmission efficiency from the ECRIS to the exit of the RRC is 10 to 20 %. The maximum beam power ever provided with the RRC is 2 kW (2 pμA of Argon at 24 MeV/u) and that with the RILAC is 560 W (13 pμA of Oxygen at 2.5 MeV/u). Considering the high beam power, the transmission should be further improved.

We are planning to construct an improved prebuncher system for the RFQ, which can generate "saw-tooth" wave-form. The design is under progress.

4 ACKNOWLEDGEMENTS

The authors are grateful to Dr. N. Tokuda at KEK for the usage of the program for vane-cutting. They are also grateful to the operating staffs for their efforts and cooperation.

5 REFERENCES

[1] O. Kamigaito et al., "Acceleration test of the folded-coaxial RFQ linac for the RILAC," Proceedings of PAC97, Vancouver, BC, Canada, May 12-16, 1997.

[2] T. Nakagawa et al., "Development of RIKEN 18-GHz ECRIS," Proceedings of EPAC96, Sitges (Barcelona), Spain, June 10-14, 1996, 1478-1480 (1996).

[3] N. Inabe et al., "Development of a New Type of Single-Bunch Selector," RIKEN Accel. Prog. Rep. 29 (1996), p. 214.

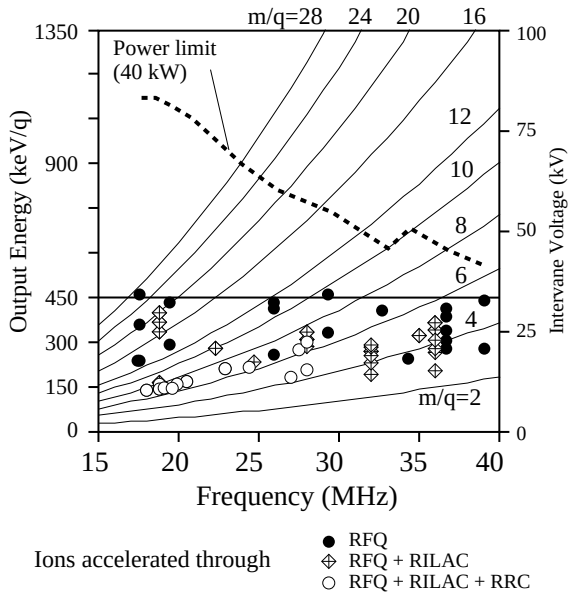

Figure 3: Performance of the RFQ linac. The abscissa and the ordinate represent the resonant frequency and the output energy, respectively. The intervane voltage, which is proportional to the output energy, is also indicated. The ions accelerated until July 1998 are indicated by the closed circles, diamonds, and open circles. The solid curves represent the acceleration condition of ions, each of which is indicated by the m/q-value. The dashed curve shows the maximum attainable voltage with the present power amplifier (40 kW).

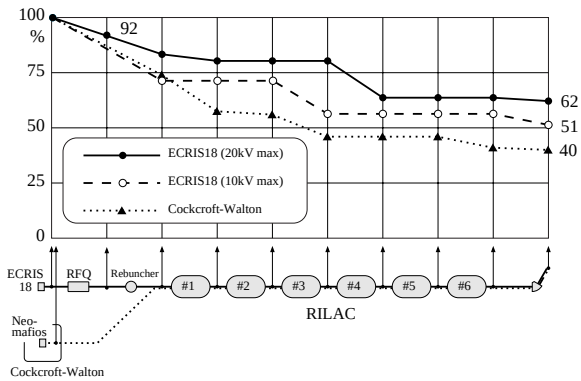

Figure 4: The best transmission efficiency ever achieved through the RILAC.

FIRST BEAM TEST WITH THE ISAC RFQ

R. Laxdal, R. Baartman, P. Bricault, G. Dutto, K. Fong, K. Jayamanna, M. MacDonald,
G. Mackenzie, R. Poirier, W. Rawnsley, L. Root, P. Schmor, B. Uzat, J. Welz
TRIUMF, Vancouver, Canada

Abstract

The ISAC RFQ is a 35 MHz, split-ring, four vane structure designed to accelerate ions of $A/q \leq 30$ from 2 keV/u to 150 keV/u in cw mode. When completed the RFQ will comprise 19 split rings and modulated electrodes in quadrature for a total length of about 8 m. The first 7-ring portion of the RFQ is being tested with beam in an interim configuration. A copper wall internal to the RFQ tank isolates the rf power to the electrode region. Electrostatic quadrupoles are installed in the remainder of the tank to transport the beam to a downstream diagnostic station. An injector composed of an ion source and an electrostatic LEBT and matching section delivers stable light ions to the RFQ. The beam is pre-bunched with an 11.7 MHz pseudo saw-tooth waveform across a single gap. The diagnostic station consists of Faraday cups, a fast Faraday cup, an emittance rig, and an analyzing magnet. The complete test set-up will be described and the results of commissioning the injector and testing the RFQ will be presented.

1 INTRODUCTION

A radioactive ion beam facility with on-line source and linear post-accelerator is being built at TRIUMF[1]. The accelerator chain includes a 35 MHz RFQ, operating cw, to accelerate beams of $A/q \leq 30$ from 2 keV/u to 150 keV/u.

The ISAC RFQ (Fig. 1) is a split ring 4-rod structure[2]. A total of 19 split rings, each feeding a 40 cm length of modulated electrodes, are housed in a square 1m×1m tank with a total length of almost 8 m. The gross specifications include a bore radius of $r_0 = 7.4$ mm, and a maximum inter-vane voltage of 74 kV corresponding to a power of 85 kW. Rings and electrodes are water cooled. A unique feature of the design is the constant synchronous phase of -25°[3]. The buncher and shaper sections of the RFQ have been eliminated in favour of a four-harmonic sawtooth prebuncher located ∼5 m upstream of the RFQ in the low energy beam transport (LEBT). This shortens the RFQ but in addition, injecting a pre-bunched beam yields a smaller longitudinal emittance at the expense of a slightly lower beam capture. The pre-buncher operates at a fundamental frequency of 11.7 MHz, the third sub-harmonic of the RFQ. This introduces an 86 nsec bunch spacing that is useful for some physics experiments. We expect 81% of the beam to be accelerated in the 11.7 MHz bunches, ∼4% accelerated in the two neighbouring 35 MHz buckets, with 15% of the beam unaccelerated.

It was decided to proceed with a two-stage installation. We have installed the first seven rings of the RFQ for an interim beam test subsequent to installation of the remaining twelve rings. The test allows us to perform rf measurements, establish alignment procedures, commission the injection line, determine matching conditions and establish capture efficiencies all well in advance of the RFQ completion in 1999.

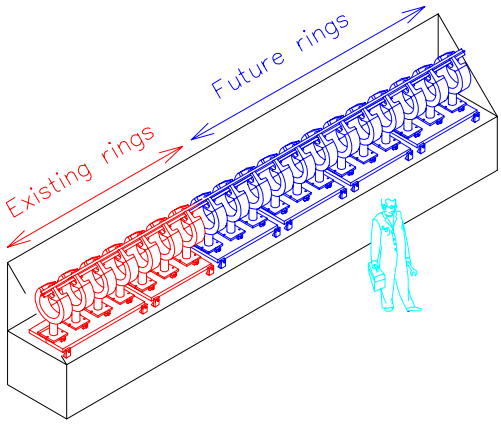

Figure 1: The ISAC 19 ring 35 MHz RFQ.

2 THE TEST SET-UP

A schematic of the test set-up is shown in Fig. 2. A copper wall installed downstream of the seven ring section provides rf containment. Beams produced in the ISAC off-line ion source (OLIS) are transported through a ∼15 m long LEBT section to arrive at the RFQ. The beam is accelerated

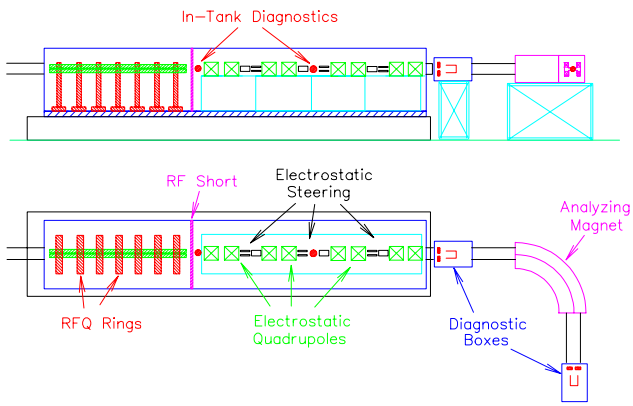

Figure 2: A schematic view of the RFQ and test station.

to 53 keV/u, then a series of eight electrostatic quadrupoles transports the beam to a diagnostic station just downstream of the RFQ tank.

2.1 OLIS and LEBT

A schematic of the ion source (OLIS) and injection line (LEBT) are shown in Fig. 3. Wire-scanners and Faraday cups are positioned throughout the line. In addition a transverse emittance rig is located after the OLIS analyzing magnet. A fast Faraday cup is located just upstream of the RFQ and was used to commission and tune the pre-buncher.

A 2.45 GHz micro-wave source with a magnetic cusp plasma confinement is installed. The LEBT consists of electrostatic elements; quadrupoles, steerers and spherical bends[4]. The source efficiently produces positive ions of gaseous species from Hydrogen to Argon. The ions for the initial RFQ tests are $^{14}N^{+}$ and $^{28}N_2^{+}$ with transverse emittances measured to be $20\pi\mu$m and $10\pi\mu$m respectively.

2.2 Pre-buncher Commissioning

The pre-buncher consists of two circular electrodes spaced 8 mm apart forming a single gap with a beam aperture of 7 mm radius. The fundamental frequency of 11.7 MHz and the first three harmonics are individually phase and amplitude controlled and combined at signal level. The signal is amplified by an 800 W broad-band amplifier that drives the two plates in push-pull mode with a peak voltage of about 200 V (400 V between plates). Optimization of amplitude and phase of each harmonic results in an almost saw-tooth modulation on the beam velocity. The variation in the gap-crossing efficiency for each harmonic means that the driving voltage is far from a sawtooth, being dominated by the higher, less efficient harmonics. In fact the present amplifier band width rolls off after 35 MHz and so initial testing was done with only three harmonics.

The time structure of the bunched beam as measured on a 50Ω co-axial fast Faraday cup[5] for one, two and three harmonic bunching are shown in Fig. 4. The buncher was tuned by setting the phase of each harmonic individually, then adjusting the voltage to previously calculated values followed by empirical optimization. The tuning was straightforward and the performance matches the predictions of simulation studies.

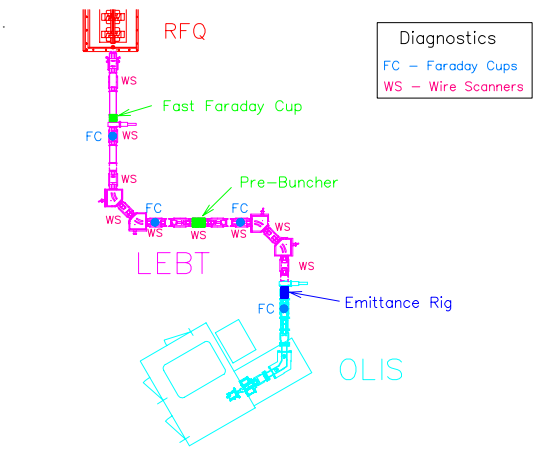

Figure 3: The layout of the off-line ion source (OLIS) and low energy beam transport (LEBT) upstream of the RFQ. The commissioning diagnostics are indicated.

2.3 In-Tank Beam Transport

The beam from the RFQ is brought to a double waist after the first four quadrupoles and again at the exit of the RFQ. The quadrupoles are each 30 cm long with a 2.5 cm half aperture and require maximum voltages of just under 10 kV for $A = 30$. For mechanical reasons the RFQ vanes are orientated at 45° to the horizontal. As a consequence the first four electrostatic quadrupoles are also at 45°. The transverse reference frame is rotated to the normal after the first double waist where the beam is round.

2.4 Diagnostic Station

The diagnostic station is designed around a $\rho = 1.5$ m analyzing magnet with a dispersion of 3 cm/%. [1] The magnet is placed symmetrically between horizontally defining object and image slits 1.5 m upstream and downstream of the magnet respectively. A Faraday cup upstream of the object slit measures the final beam intensity and when compared with the last Faraday cup in LEBT gives the relative beam capture. Unaccelerated beam is lost in the electrostatic quadrupoles. A Faraday cup just downstream of the image slit records the transmitted beam and the energy and energy spread are derived from the magnetic field. A slit and harp transverse emittance rig and fast Faraday cup have recently been placed upstream of the magnet.

3 RFQ BEAM TESTS

The initial set of rf and beam tests have been successfully completed. The RFQ was operated in cw mode for all beam tests. The operation of the RFQ at peak voltage (74 kV) is

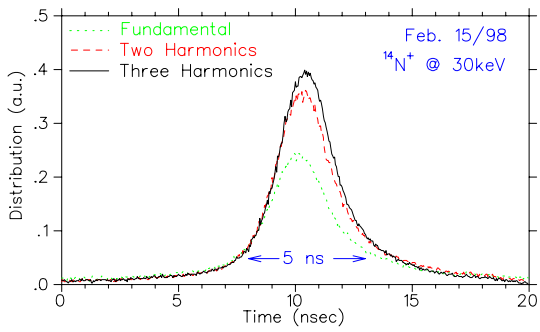

Figure 4: Beam bunches measured on the fast Faraday cup in LEBT for one, two or three harmonic bunching.

[1] The magnet was generously donated by the Nuclear Physics Institute in Rez, Czech Republic.

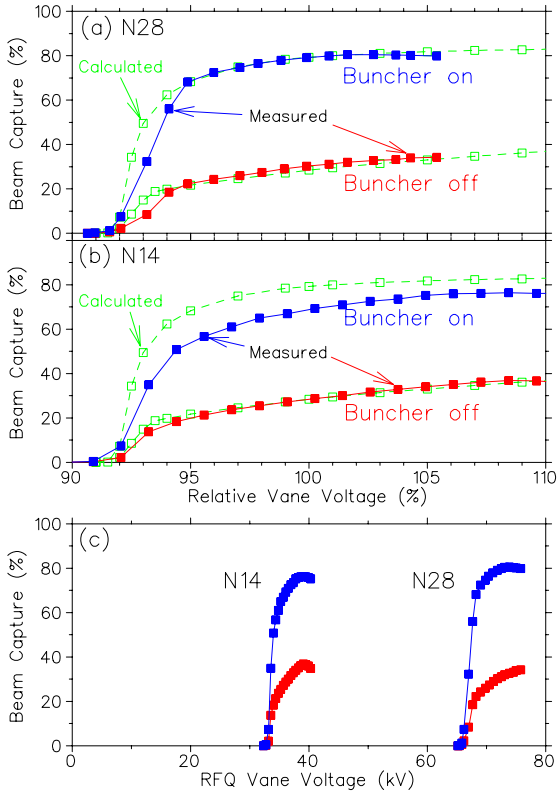

Figure 5: RFQ beam test results showing capture efficiency as a function of relative vane voltage for (a) N_2^+ and (b) N^+. The nominal vane voltage in each case was 71.9kV and 36 kV respectively. The beam capture for both bunched and unbunched initial beams are recorded (solid line) and are compared with PARMTEQ calculations (dashed lines). In (c) the results are plotted with respect to absolute vane voltage.

stable[2]. Beams of both N^+ and N_2^+ have been accelerated to test the RFQ at both low and high power operation.

Beam capture as a function of RFQ vane voltage measurements have been completed for each ion and for both unbunched and bunched input beams. The results are given in Fig. 5 (solid lines) along with predicted efficiencies based on PARMTEQ calculations (dashed lines). The N_2^+ capture efficiency at the nominal voltage is 80% in the bunched case (three harmonics) and 30% for the unbunched case in agreement with predictions. (The capture is lower than the 85% quoted earlier since we are presently operating with only three harmonics on the pre-buncher.) The capture for one harmonic and two harmonic pre-bunching are 63% and 74% respectively. The results for N^+ are somewhat lower in the bunched case (70%) due, we think, to the larger transverse emittance reducing the bunching efficiency. In theory the LEBT and RFQ have an acceptance of eight times the measured emittance of N^+ so this result may be significant. However it may also be the result of a poor LEBT tune generating a non-achromatic condition in the electrostatic bend. It warrents further investigation.

The energy of the beam as measured with the analyzing

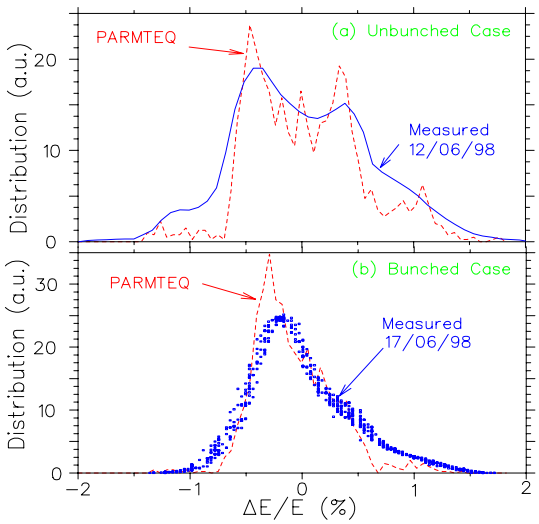

Figure 6: Results of energy spread measurements of accelerated N^+ beams for both (a) unbunched and (b) bunched cases. PARMTEQ simulation results are plotted for comparison.

magnet is 55 keV/u. The beam energy is higher than originally quoted since the RFQ test frequency is 2% higher than the design frequency. (The actual frequency is expected to drop with the addition of the remaining 12 rings.) The energy spread for the bunched and unbunched cases were measured at $\pm 0.4\%$ and $\pm 0.7\%$ respectively and compare well with PARMTEQ predictions (Fig. 6).

The results demonstrate a strong confirmation of both the beam dynamics design and the engineering concept and realization. We are presently installing diagnostics for a further set of tests [6] including measurements of longitudinal and transverse emittance and acceptance. These measurements will proceed through October 98 before we commence with the installation of the rest of the rings. Commissioning of the RFQ in the final configuration is expected in Fall 99.

4 REFERENCES

[1] P. Schmor, *et al*, "The High Intensity Radioactive Beam Facility at TRIUMF", Proceedings of the 1998 European Part. Acc. Conf., Stockholm, to be published.

[2] R. Poirier, *et al*, "RF Tests on the Initial 2.8m of the 8m Long ISAC RFQ at TRIUMF", these proceedings.

[3] S. Koscielniak, *et al*, "Beam Dynamics Studies on the ISAC RFQ at TRIUMF", Proceedings of the 1997 Part. Acc. Conf., Vancouver, 1997.

[4] R. Baartman, J. Welz, "60 keV Beam Transport Line and Switchyard for ISAC", Proc. of the 1997 Particle Acc. Conference, Vancouver, 1997.

[5] J. Bogaty, *et al*, "A Very Wide Band-Width Faraday Cup...", Proceedings of the 1990 Linear Accelerator Conference, 1990.

[6] R. Laxdal, "Testing the RFQ at 53 keV/u", TRIUMF-ISAC Design Note, July 1997.

OPERATION OF THE VE-RFQ INJECTOR FOR THE ISL-CYCLOTRON*

O. Engels, F. Höllering, A. Schempp Institut für Angewante Physik,
Johann Wolfgang Goethe-Universität, Frankfurt am Main, Germany
A. Denker, H. Homeyer, W. Pelzer, Hahn-Meitner-Institut, Berlin, Germany
J. Häuser, NTG, Neue Technologien, Gelnhausen-Hailer, Germany

Abstract

The VE-RFQ-injector for the cyclotron at HMI in Berlin is now in operation. The ECR-source together with the RFQ's [1,2] supply heavy ion beams with 90 - 360 keV/u for q/A > 0.15, matched to the isochronous cyclotron. Properties of the new injector and results of rf-measurements, high power tests and beam measurements are presented.

1 INTRODUCTION

The Ionen Strahl Labor (ISL), the former VICKSI-facility, at the Hahn-Meitner-Institut in Berlin has installed a second injector for the separated sector cyclotron. A combination of an ECR-ion source with a two stage 4-Rod-VE-RFQ (VE = variable energy) [3] replaces the former Tandem-injector to meet the demands of solid state physics [4,5] as shown in figure 1.

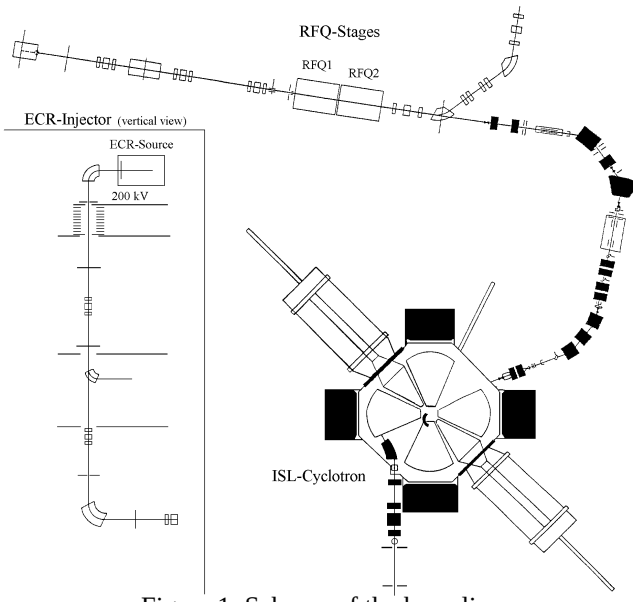

Figure 1: Scheme of the beamline

The VE-RFQ works at a high duty factor (cw-mode) and covers a frequency-range from 85 MHz to 120 MHz. It is designed to accelerate ions with an q/A from 1/8 to 1/2 with input energies from 15 to 30 keV/u to output energies between 90 and 360 keV/u. The final energies out of the cyclotron cover the range between 1.5 and 6 MeV/u [5]. Table 1 gives the parameters of the new injector and figure 2 shows a view of the RFQ.

To achieve this energy variation the RFQ is split into two stages. The second stage is designed to operate either as an accelerator or as an radial focusing transport channel [7,8,9] in an operational mode which has not been tested before with a bunched beam.

Figure 2: View into the two stage RFQ

After the assembly and first high power test at NTG in Gelnhausen the RFQ has been transported to ISL in December 1997 and has been installed at the cyclotron during the first half of 1998.

Length (split into two stages)	[m]	3
diameter	[m]	0.5
number of stems per stage		10
minimum aperture	[mm]	2
min/max Ein	[keV/u]	15.16/29.72
min/max Eout	[keV/u]	178.35/355.09
charge-to-mass-ration		1/8 - 1/2
frequency	[MHz]	85 - 120
duty factor		100% (cw)
max power consumption p. stage	[kW]	20

Table 1: ISL-VE-RFQ parameters

2 GAMMA-SPETROSCOPY

A first set of high power rf-tests was done to check the functionality after transport.

To ensure that the RFQ reaches the necessary electrode voltage and to calibrate the RFQ-probes several high power tests at different frequencies have been made. At a power-consumption of 10 kW the gamma-emission from the cavity has been measured and the results have been extrapolated for a power consumption of 20 kW.

Figure 3 shows the extrapolated electrode voltage and the necessary electrode voltage for minimum q/A proportion of the first RFQ stage.

The bend in the design voltage curve results from the limited preacceleration of 200 kV, so that the necessary injection energy into the RFQ could not be reached for all q/A proportions. The measurements show, that the design voltage can be reached for all frequencies.

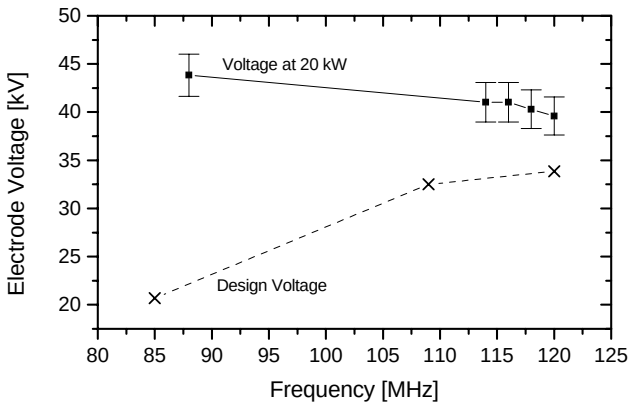

Figure 3: Electrode voltage as a function of RFQ frequency

3 BEAM MEASUREMENTS

The second set of tests were experiments with a beam from the ISL DC-injector. Figure 4 and 5 show the results of O^{4+}- and He^{+}-beams at a frequency of 120 MHz. The second RFQ has been operated in accelerating mode and in transport mode.

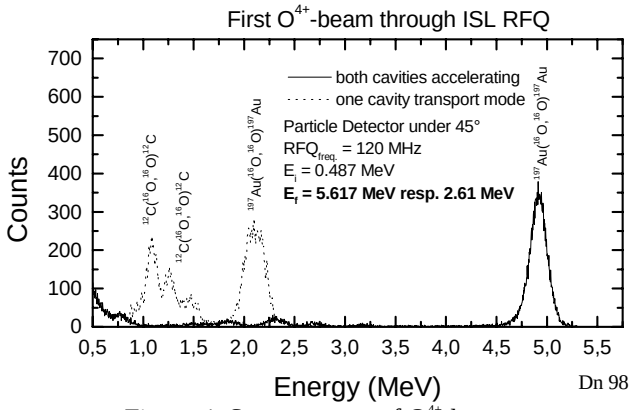

Figure 4: Spectroscopy of O^{4+}-beam

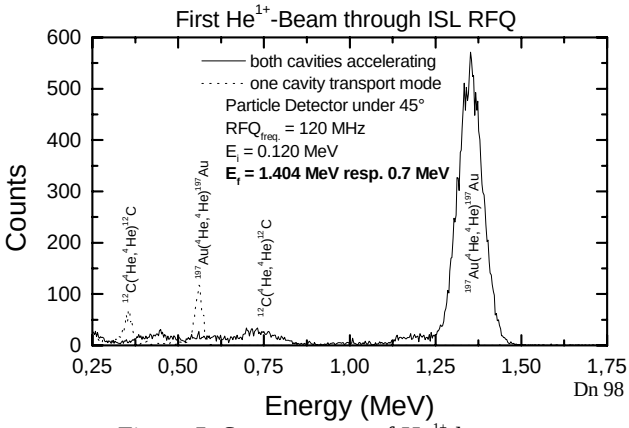

Figure 5: Spectroscopy of He^{1+}-beam

The results of the spectroscopy show that the RFQ works well and provides the calculated energies. It also shows, that the concept of using the second RFQ as a transport channel works, though more efforts on a better coordination between the two stages to improve the transmission in transport mode have to be done.

4 CONCLUSIONS

The series of high power and beam tests showed a good performance of the RFQ. The accelerator provides the correct energies and can be operated in the transport mode. More tests for an optimization of the transport mode have to be done.

At ISL the work is now focused on integrating the RFQ-system in existing controlsystem and on optimizing the rf-systems. In the beginning of September a first injection into the cyclotron is planned.

REFERENCES

[1] I.M. Kapchinskiy and V. Teplyakov, Prib. Tekh. Eksp 119, No. 2 (1970) 17

[2] K.R. Crandall, R.H. Stokes, T.P. Wangler, Linac 79, BNL 51134 (1979) 205

[3] A. Schempp, NIM B40/41 (1989) 937

[4] H. Hohmeyer, K. Ziegler, NIM B64 (1992) 937-942

[5] H. Hohmeyer, W. Pelzer, „Vorschlag zur Realisierung eines Ionenstrahllabors am HMI (ISL-Berlin)“, HMI-Berlin, (1992)

[6] O. Engels et al., NIM B113 (1996), p. 16-20

[7] A. Schempp, O. Engels, F. Marhauser, H. Hohmeyer, W. Pelzer., IEEE PAC 1995, Dallas, TX, p. 914

[8] H. Dehnen, H. Deitinghoff, W. Barth, A. Schempp, „Transport of Ions in a RFQ Accelerator“, EPAC 1992,Ed. Frontiers (1992), p. 967-969

[9] F. Marhauser, diploma thesis, IAP, Frankfurt am Main (1996)

DESIGN OF A HIGH CURRENT RFQ INJECTOR WITH HIGH DUTY FACTOR *

H. Vormann [1], A. Schempp [1], U. Bessler [1], A. Letchford [2], C. W. Planner [2],
[1] Institut für Angewandte Physik, Johann Wolfgang Goethe-Universität,
Frankfurt am Main, Germany
[2] Rutherford Appleton Laboratory, Chilton Didcot, Oxfordshire, Great Britain

Abstract

An RFQ injector with a duty factor up to 10 % is planned for the spallation source ISIS at Rutherford Appleton Laboratory (RAL). The accelerator will be a Four-Rod RFQ with directly cooled electrodes, operating at 202 MHz.

The RFQ will provide a H^--beam current up to 50 mA with an output energy of 665 keV (input energy 50 keV). The beam dynamics, rf and mechanical designs are presented.

1 INTRODUCTION

The ISIS neutron source at the Rutherford Appleton Laboratory presently consists of a H^--Penning source (extraction voltage 35 kV), a Cockroft-Walton injector (output energy 665 keV), an Alvarez Drift Tube Linac (output energy 70 MeV), the ISIS synchrotron (final energy 800 MeV) and a heavy metal target (average beam current 0.2 mA, average beam power 160 kW) [1].

The Cockroft-Walton is now going to be replaced by a new RFQ accelerator [2, 3] with the same figures of energy. The resonance frequency of the RFQ will be the same as the one of the Alvarez linac, 202.56 MHz. The beam current will be 50 mA with high transmission, allowing a later upgrade to 100 mA with 85 % transmission.

ISIS has reached a maximum beam current of more than 55 mA with a stable operation at 2.5 % duty cycle in early 1997. The new RFQ is planned for 10 % duty cycle. These values are not far away from the proposed values for the next generation of neutron source, the European Spallation Source ESS, where 6.5 % and 5 MW beam power (1.34 GeV) are planned. So the ISIS upgrade is a test bench for the future ESS injector. The present plans for the ESS project provide 107 mA, achieved with two RFQs (54 mA each) at 175 MHz.

2 HIGH DUTY CYCLE RFQ

The HLI-RFQ at GSI Darmstadt is an operating RFQ with high duty cycle: It operates at 15 kW/m average power (duty cycle 25 %) [4]. Its resonance frequency is 108.5 MHz, lower than the frequency of the RAL RFQ (202.56 MHz). Lower frequencies go along with larger resonator structures and a distribution of the power to a larger surface. Such a higher thermal stress has been applied to a short test model (202.56 MHz) with 20 kW/0.3 m in c.w. operation. This model worked well and showed that an RFQ resonator with completely cooled electrodes works well even at 60 kW/m [5].

3 RF CALCULATIONS

MAFIA Calculations and experiments have been made to investigate the magnetic field distribution around the stems and for optimizing the input coupling loop. The magnetic field in a groove, milled into the surface of the copper stem, is very weak, compared to the field strength around the stem (<1%).

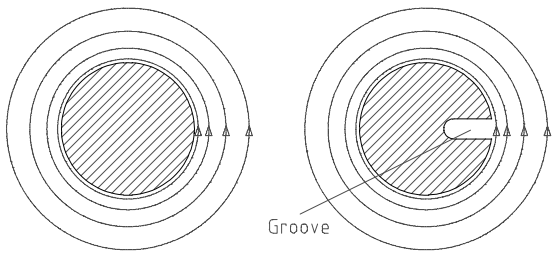

Figure 1: Magnetic field around stems.

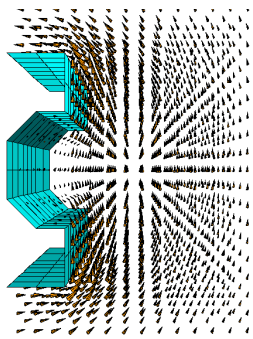

Figure 2: Magnetic field (arrows) on a grooved stem's surface.

To decrease the sensitivity of the loop, caused by the inhomogeneous magnetic field, the effect of a groove, milled into the stem has been tested. With this groove the loop can "dive" into the stem, thus giving a stronger coupling, as shown in figurs 1 and 2.

Another subject within the RF calculations was the influence of the electrode cooling pipes on the field distribution and the resonator properties.

It has been shown that multipole components of the electrodes with cooling pipes differ less than 0.1 % from the values of regular rods (circle shaped), and remain in the same range of difference from the hyperbolical (ideal) quadrupole geometrie, as shown in figure 3. The flatness (percentage rate of the intervane voltage) is shown in figure 4.

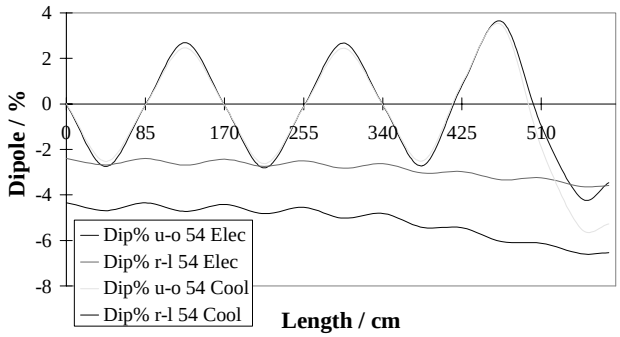

Figure 3: Influence of the cooling pipes on the field components.

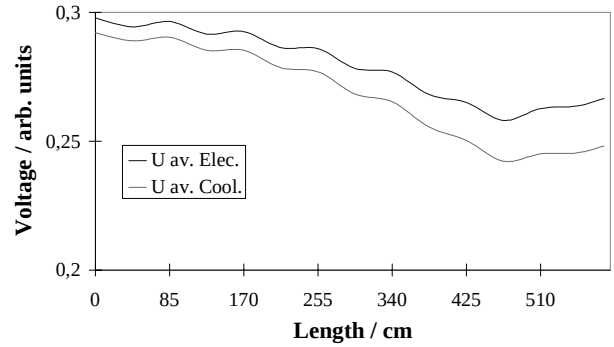

Figure 4: Influence of the cooling pipes on the field distribution along the beam axis.

The calculated values of Q-value and shunt-impedance differ less than 1 %, what is a negligible variation of change.

The geometry of the electrodes with the cooling pipes has an influence on the electric field distribution and the resonator properties. MAFIA calculations and measurements have been made to investigate that effect, particularly the ratio of aperture to rod radius is important for the capacitance of the electrodes, what has a big influence on the resonance frequency and the flatness and field distribution along the beam axis.

4 PARTICLE DYNAMICS

For the particle dynamics design, the methods for compact RFQs are used [6]. With adiabatic variation of parameters and 80 kV electrode voltage a high acceptance at large aperture is reached. The beam dynamics parameters are shown in table 1. Figure 5 shows results for simulations using the ideal two term potential.

Letchford [7] has developed a code which solves the field equations with respect to higher multipole components. The result was, that the design chosen for ideal shaped electrodes must be only slightly modified when it is used with rod electrodes, to match the properties of a hyperbolical shaped quadrupole.

Another special feature is used for this RFQ: The last cell consists of half an RFQ-cell and half a cell with a symmetrical output matcher to achieve a good output emittance matching [8].

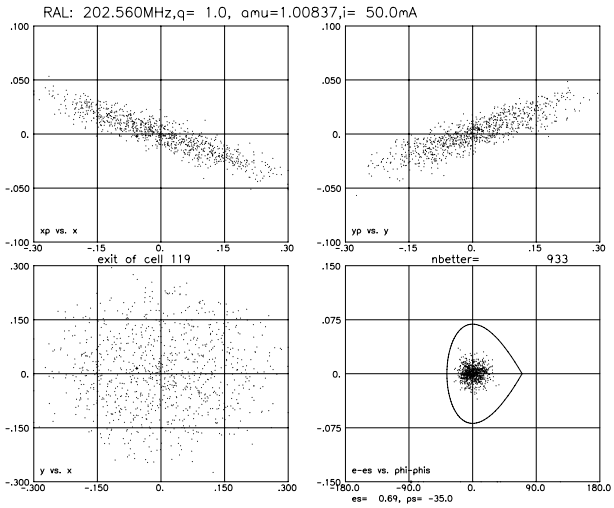

Figure 5: Particle Output Distribution.

5 MECHANICAL DESIGN

Results of MAFIA calculations have shown that 34 % of the power is lost on the electrodes, 44 % on the stems and 22 % on the ground plate. To get the temperature distribution on a stem, ANSYS calculations have been made. These calculations showed that a cooling of the end cells with only one coaxial cooling channel or with water flow split into two channels (figure 6) is not sufficient: So a "one way cooling channel" has been chosen, as shown in figure 7. The channel is milled into the stem and covered by a brazed plate, avoiding any direct water-to-vacuum seals [9, 10].

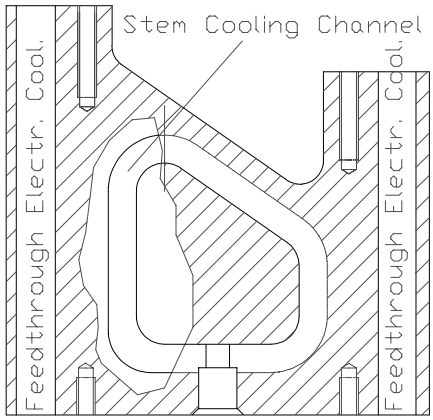

Figure 6: Cooling of the endstem with split water flow.

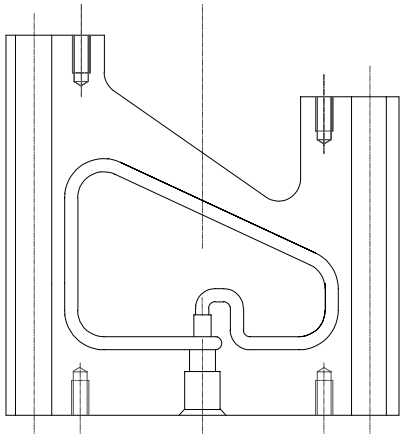
Figure 7: One way cooling channel of the endstems.

At present the tank is ready for copper plating. The parts of the RFQ insert should be ready in September, so that electrode alignment and cavity tuning can be done in Fall 1998.

ACKNOWLEDGEMENTS

We would like to thank the colleagues from RAL for collaboration and our group members for help and support.

Table 1: RFQ specifications and beam parameters of the RFQ.

Total Length	1190 mm
Diameter	250 mm
Frequency	202.56 MHz
Q-Value	3000
Shunt Impedance	65 kΩ
E in	35 keV
E out	665 keV
ε^{in}_{norm}	1.00 π mm mrad
ε^{out}_{norm} (50 mA)	1.05 π mm mrad
ε^{out}_{norm} (100 mA)	1.15 π mm mrad
ε_{rms}	0.07 °MeV

REFERENCES

[1] C. W. Planner et al, "High Stability Operation of the ISIS Pulsed Spallation Neutron Source at 200 mA", EPAC96, Sitges, Spain (1996), p. 584,

[2] I. M. Kapchinskij, V. A. Tepljakov, "Linear Ion Accelerator with Spatially Homogeneous Strong Focusing", Prib. i Techn. Exper., No. 2, 1970, p. 17,

[3] K. R. Crandall, R. H. Stokes, T. P. Wangler, "RF-Quadrupole Beam Dynamics Design Studies", BNL-51143, 1980, p. 250,

[4] J. Klabunde, E. Malwitz, J. Friedrich, A. Schempp, "Upgrade of the HLI-RFQ Accelerator", Linac94, KEK (1994), p. 704,

[5] A. Schempp, H. Vormann,"Design of a High Current H^--RFQ injector", PAC97, Vancouver,

[6] A. Schempp,"Design of compact RFQs", Linac96, CERN (1996), p. 53,

[7] A. Letchford, "A Comparison of 4-Rod and 4-Vane RFQ Fields", EPAC98,

[8] Ken Crandall, "Ending RFQ Vane Tips with quadrupole symmetry", Linac94, KEK (1994), p.227,

[9] G. R. Murdoch, H. Vormann, "Thermal Design of an RFQ Cell for the Radio Frequeny Quadrupole under Construction for ISIS", EPAC98,

[10] H. Vormann, A. Schempp, U. Bessler, C. W. Planner, A. Letchford, "A New High Duty Factor RFQ Injector for ISIS", EPAC98.

PROPOSAL TO USE PIVAIR AS A 30 GHZ HIGH-POWER GENERATOR

J. Gardelle, T. Lefevre, J. L. Rullier
CEA/Centre d'Etudes Scientifiques et Techniques d'Aquitaine, B.P.2, 33114 LeBarp, France
J. T. Donohue
Centre d'Etudes Nucléaires de Bordeaux-Gradignan,. B.P.120, 33175 Gradignan, France

Abstract

The Two-Beam Accelerator (TBA) is under active study both at Lawrence Berkeley National Laboratory (LBNL) and at CERN. In the TBA, an extremely intense low-energy electron beam is bunched at the desired operating frequency and, upon passing through resonant cavities, it generates radio-frequency (RF) power for accelerating the main beam. Among the different approaches to the production of a suitable drive-beam, the use of a free-electron laser has been proposed. Recently at CEA-CESTA, encouraging results in this direction have been obtained. To extend this work, we propose the use of the induction accelerator "PIVAIR" at CESTA (7.2 MeV, 3 kA) as a test stand for high power RF structure experiments at 30 GHz. Our research program for PIVAIR includes:

1 Production of a drive beam current profile designed to compensate beam loading,

2 High power tests of a CLIC Transfer Structure,

3 Tests of the 30 GHz RK-CLIC components.

1 INTRODUCTION

As a power source candidate for linear colliders, the highly developed klystron technology provides reliable and economic RF power at frequencies of order 3-12 GHz, but its extension to higher frequencies represents a difficult task. As alternatives to klystron technology, the TBA, suggested by A. Sessler at Lawrence Berkeley National Laboratory (LBNL) [1], is under active study both at LBNL [2] and at CERN, where the project bears the name Compact LInear Collider (CLIC) [3]. For multi-TeV TBA designs, both groups are considering operating frequencies around 30 GHz. Among the many technological difficulties in the TBA approach, the production of a suitable drive beam (DB) constitutes a major challenge. The research program outlined in the present document is devoted to a scheme of generating such a beam, based on the bunching that naturally occurs in a Free-Electron Laser (FEL) powered by an induction accelerator capable of producing kiloampere currents of electrons with energies in the several MeV range.

In a series of experiments performed at CEA/CESTA with the LELIA induction linac, the capacity of a FEL, powered by an induction accelerator, to generate an intense bunched beam has been demonstrated [4]. The next step, which is being pursued actively at CESTA, is the extraction of the bunched beam and its propagation into a resonant cavity [5]. The aim is to demonstrate the ability of this scheme to generate the required amounts of RF power by the passage of the bunched beam through the extraction cavity [6]. Although this program is proceeding as planned, a major difficulty must be surmounted, namely the tendency of a tightly bunched beam to debunch under the influence of longitudinal space charge forces. In the case of LELIA, the usual relativistic factor $\gamma = 5.3$, whereas at the nominal energy of the PIVAIR accelerator, $\gamma = 15.1$, and the correspondingly increased debunching distance is roughly an order of magnitude greater.

We propose here a continuation of the TBA R&D in a 4-year experimental program. This proposition is in fact a testbed for high frequency and high power RF acceleration. Many tests of interest are planned, thanks to the powerful PIVAIR accelerator [7], which is a unique tool capable of producing a bunched beam with specifications very close to the final DB for both TBA designs: CLIC and RK-TBA.

2 EXPERIMENTAL PROGRAM

The PIVAIR accelerator delivers a 3 kA, 7.2 MeV low emittance electron beam which will be transported to a high gain FEL amplifier operating at 30 GHz. A similar experiment was performed in the past at Lawrence Livermore National Laboratory at a beam energy of 6 MeV [8]. In the wiggler magnet, the beam undergoes the FEL process and becomes bunched at the resonant frequency. The interaction is stopped at a length where the bunching is maximum. The bunched beam is then ready to be used for various tests.

To compensate for transient beam loading effects in the accelerating cells, the front end of the current must be ramped with a profile adapted to produce the desired power extraction from the transfer cavity (TC). This shaping of the front end of the beam is necessary for the FEL to remain a viable candidate for DB production.

The PIVAIR energy is high enough to ensure bunched beam propagation through one or more TC. High power operation of the TC would permit us to test its operating limits. The breakdown threshold, dark current capture threshold, and maximum gradient are measurements of prime importance.

The RK-CLIC scheme is an extension to 30 GHz of the work in progress at LBNL for the RK-TBA project at 11.4 GHz. Idler and open cavities are its basic components. The coupling is stronger than in the other scheme and a re-acceleration of the electron beam is necessary by means of an induction cell. Tests of beam transport, high output power production, compact induction modules are proposed.

3 THE PIVAIR INDUCTION LINAC

A photograph of PIVAIR is displayed in Fig. 1. The high voltage pulse generator of the injector was developed by Pulse Science Incorporated (PSI) for the Dual Axis Radiographic Hydro-Test Facility (DARHT) and the diode was designed by Los Alamos National Laboratory (LANL). It is a single shot device whose repetition rate is once every 5 minutes. A 3 kA, 3.6 MeV electron beam is extracted from a velvet cathode with excellent reproducibility. Upon exiting the injector, the electron beam is accelerated to 7.2 MeV by 16 induction cells, which are fed by external high voltage generators producing 250kV, 75 ns pulses with 1% voltage spread. Each generator drives two induction cells. The beam energy spread is less than 1% over 60 ns and the normalized edge emittance is 1000 π-mm-mrad. PIVAIR has an excellent reliability when operating at 7.2 MeV.

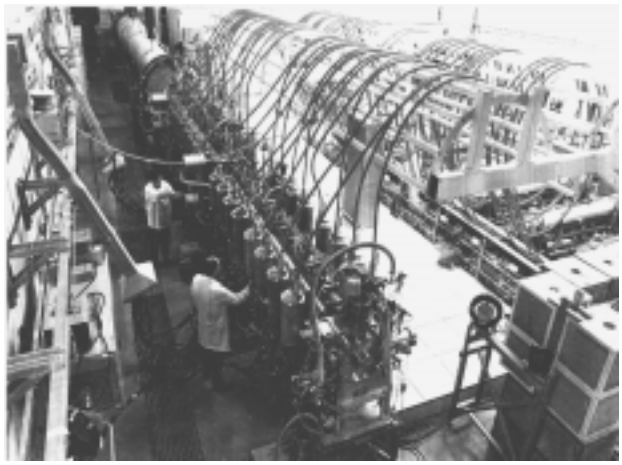

Figure 1: Photograph of the PIVAIR facility.

4 THE FEL AMPLIFIER AT 30 GHZ

In the proposed experiment the wiggler is a pulsed bifilar helix. The external EM wave is produced by a 30 GHz microwave source such as a magnetron or traveling-wave tube. Since the FEL efficiency varies slowly with the wiggler period, the length required to reach saturation does too. We choose a wiggler period short enough for the total length of the wiggler to be reasonable (a few meters).

FEL numerical simulations are performed using the code SOLITUDE. We present here the results obtained for a 7 m long wiggler with 6 adiabatic entrance periods, at 7.2 MeV. For these calculations, the beam current and beam radius have been chosen to be 1 kA and 1cm, respectively, while the waveguide diameter was 60 mm. Power levels close to 1 GW are expected at resonance for B_w = 1900 G. In Fig. 2, we have plotted the power as a function of the interaction length showing that saturation occurs at period 27 (5.40 m). The bunching is maximum just before this point with a maximum bunching parameter (average over the electrons phase in the longitudinal phase space) of 0.5. Consequently, the wiggler length should be around 5 meters to obtain the maximum bunching.

The beam is adiabatically extracted to remove the transverse momentum imparted by the wiggler field. Simulation with PARMELA indicates that the beam remains bunched at a significant level for a distance greater than 3 m permitting all the DB tests.

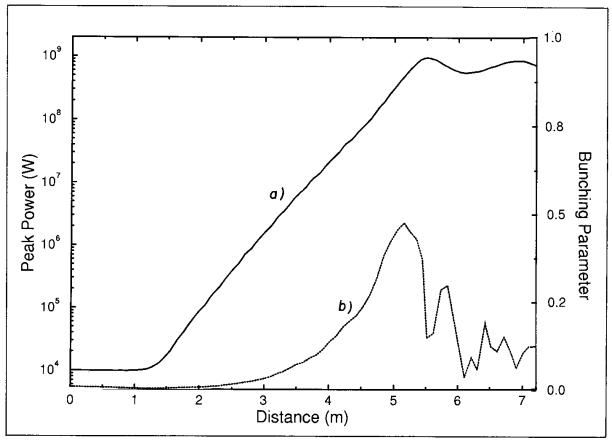

Figure 2: FEL simulations with the code SOLITUDE for the best resonant magnetic field (1900 G): a) power vs. z and b) bunching parameter vs. z.

5 PRODUCTION OF THE BEAM CURRENT PROFILE

Ramping of the current profile is a necessary requirement in any system that seeks to produce usable RF power to drive multi-bunch, high-gradient accelerating structures. Without any profiling, the transient response of the accelerating structure will cause an intolerable energy spread in the accelerated pulse train. By including an initial ramp to the drive beam, the transient filling of the accelerating structure will be accomplished before the main beam arrives, and constant transfer of energy will occur over the entire pulse train.

We propose the use of a pulsed quadrupole and a beam scraper to induce a ramped current profile. The quadrupole field is produced by a stripline device [9]. Initially, the beam is defocused in one plane by the quadrupole at the aperture position, and only a part of the total current is allowed to pass. As the quadrupole field decreases, the beam is more and more focused, until at zero field all the current is transported through the aperture. The quadrupole is pulsed and decays over a duration corresponding to the desired current ramp.

6 HIGH POWER OF A CTS

The multi-kiloamp PIVAIR beam current opens up interesting possibilities for testing future CTS. These would allow us to test both the extremely high field effects and long pulse periods that are required for multi-TeV colliders. At present, three CTS parameters sets have been studied in detail with MAFIA (See Table 1).

The electron beam requirements for full-field tests are easily calculated using the expression for structure output power.

$$P = \frac{(r/Q)q_d^2\omega}{2d}$$

where q_d is the beam charge passing through the structure during the drain time

$$d = (s/c)(1/\beta_g - 1)$$

The charge is supposed to be concentrated in infinitely short bunches spaced by $g=c/f$=1cm (f=30 GHz). The necessary beam charge per drain time is obtained from the above expression as:

$$q_d = \sqrt{\frac{2dP}{(r/Q)\omega}}$$

Furthermore, the charge per bunch (for a train of delta-function drive bunches) is obtained as $q_b = 2q_d/fd$. The Fourier analysis of a beam with these infinitely short bunches spaced in time by $1/f$ yields a peak current component at f of $I=2fq_b$. Note that the CTSs are tuned to the frequency component at f = 30 GHz. Assuming a RF current bunching factor of 0.6 at 30 GHz, the required PIVAIR beam DC current amplitude becomes $2fq_b/0.6$. Numerical values for the three drive beam cases are summed up in the table.

	1 TeV Single DB	1 TeV Multi DB	3 TeV Multi DB
CTS output power: P (MW)	550	309	600
CTS length: s (m)	0.92	1.028	1.028
Drain time: d (ns)	5	5.14	5.14
Relative group velocity: β_g	0.38	0.4	0.4
Beam charge / d: q_d (nC)	2325	673	798
r/Q of CTS (circuit Ω)	5.2	51.4	51.4
CTS peak deceleration (MV)	1.18	2.5	3.87
FEL mean current (A) (for delta-function)	465	123	155
Peak 30 GHz FEL current (A)	930	247	310
FEL mean current: (A) (for I_{rf} = 0.6 at 30 GHz)	1550	411	517

Table 1: CTS parameters for different DB possibilities.

7 RK-CLIC STUDIES

The existing effort at LBNL seeks to realize the RK-TBA concept by construction and successful operation of a full-scale, prototype device [10]. This will be a 11.42 GHz version and will test all the key components and design elements of a complete system. PIVAIR operated as a test stand will provide a valuable resource in the effort to examine beam dynamics and to test designs of beamline components for a high frequency RK-TBA.

A key point in the beam dynamics of an RK-TBA is the stability of the bunching against space charge forces and longitudinal impedances. The RF cavities are designed to be 'inductively detuned' to provide a net re-bunching force on the beam as it travels through the structure, and to maintain stable synchrotron (longitudinal) oscillation. The cavities themselves are designed to act upon the beam to maintain stable bunches.

The induction cells may take on a very compact design, increasing the efficiency of the re-acceleration units. However, decreasing the beampipe diameter tends to increase the transverse impedance and peak surface electric field in the induction modules. Innovation is required in the cell geometry, induction core material, and high gradient insulation. These may all be tested at PIVAIR.

The RF cavities are the centerpiece in any RK-TBA system. Their microwave properties are crucial to the generation of useful power by the drive beam. The idler, standing-wave (SW) and travelling-wave (TW) output cavities all have unique interactions with the beam that need to be measured and analyzed experimentally. Important tests that need to be performed include: generation of high output power , high-voltage holdoff, low Q, longitudinal impedance characterization.

8 CONCLUSION

The PIVAIR accelerator is a useful research tool, capable of providing an intense high-quality electron beam of energy 7.2 MeV. This machine may be used in a variety of scientific and technological projects, among which figures prominently the generation of high-power, high-frequency microwaves. A major application of these consists in powering the next generation of linear colliders which will operate at high frequencies, such as 30 GHz. In the present project, we propose to use PIVAIR in conjunction with a FEL to produce an intense bunched beam, and to test structures designed to extract power at 30 GHz from such a beam.

Some of the technical aspects of our proposal have been contributed by members of different groups. We express to them our thanks, and acknowledge the helpful remarks offered by members of the CLIC collaboration and the RKTBA group.

9 REFERENCES

[1] A. M. Sessler, The Laser Accel. of Part., AIP Conf. Proc. n° 91 (American Institute of Physics, New York, 1982), p. 151.
[2] G. Westenskow, et. al., Proc. of the Part. Accel. Conf., IEEE eds., Dallas, 737 (1995).
[3] W. Schnell, CERN/SL 92-51 and CLIC Note n°184; K. Hubner, CERN/PS 92-43, CLIC Note n°176; S. Van der Meer, CERN/PS 89-50, CLIC Note n°97.
[4] J. Gardelle, J. Labrouche, and J. L. Rullier, Phys. Rev. Lett. 76, 4532 (1996); J. Gardelle, et. al., Phys. Plasmas 3, 4197 (1996); J. Gardelle, et. al., Phys. Rev. Lett. 79, 3905 (1997).
[5] J. Gardelle, et. al., Proc. of the European Part. Accel. Conf., Stockholm, Sweden, (1998).
[6] S. M. Lidia, et. al., These Proceedings.
[7] P. Anthouard, et al, Proc. of the Part. Accel. Conf., Vancouver, Canada, (1997).
[8] W. E. Nexsen, et. al., Nucl. Instrum. Methods Phys. Res. A 296, 54 (1990).
[9] K-Y Ng, Part. Accel. 23, 93 (1988).
[10] T. Houck, et. al., IEEE Trans. Plasma Sci. 24, 938 (1996).

FIRST ORDER DESIGN STUDY OF AN ACCELERATOR BEAMLINE FOR THE PEARL FEL

M. C. Lampel, G. H. Gillespie Associates, Inc., J. M. J. Madey, U. of Hawai'i, R. J. Burke, Arcata Systems

Abstract

The Pan-Oceanic Environmental and Atmospheric Research Laboratory (PEARL) consortium has proposed the deployment of a ship-based FEL facility in order to carry out advanced atmospheric and environmental research for a variety of applications. The FEL is intended to have an optical output from approximately 20 microns down to 1/3 micron, with up to 1 kW average power. The accelerator will operate over a wide range of beam currents and energies to meet these goals. Clearly, the proposed shipboard FEL must meet many design constraints in compactness and efficiency. The accelerator beamline, upstream of the FEL resonator, includes a 4.5 MeV rf gun, pulse length compression chicane, and four (4) 1.26 meter long traveling wave (TW) accelerator sections. First order focusing along the beamline is provided by quadrupole magnets. First order beam dynamics for this beamline are studied using TRACE 3-D with a self-consistent TW accelerator model incorporated into it. Parametric studies of current and beamloading effects on accelerator efficiency and beam transport are performed. Beamline layouts, taking into account the physical dimensions and operating parameters of the equipment will be studied to determine the baseline beamline design for further, higher order simulations, on the way towards an optimized design.

1 THE PEARL FEL

The PEARL consortium has proposed use of a powerful lidar system [1-3] for application to the problems of remote sensing and pollution monitoring. Air quality is affected by emissions of NOx, CO, CO_2, SO_2, hydrocarbons, CFCs, Ozone, and aerosols, etc. In addition there is an interest in detecting illegal drug manufacturing, chemical and biological warfare agents, and clandestine nuclear tests. Concentrations of the emissions of interest range from ppb to ppm, with a need for temporal and spatial resolution. Remote detection lidar processes available include Rayleigh scattering, Mie scattering, Raman scattering, absorption, and DIAL (differential absorption of two laser lines).

The FEL at the core of this lidar system is intended to have an optical output from approximately 20 microns down to 1/3 micron, with up to 1 kW average power. Macropulses of 3-5 microseconds, average currents of hundreds of milliamperes, and electron beam energies ranging from 20 MeV to 120 MeV are being considered as operating parameters of the accelerator/driver. In addition, high peak power requirements translate to a high micropulse current, 500-1000 Amps over 2-4 picoseconds. To begin translation of earlier system studies into specification of an accelerator beamline, several first order designs are being compared to gain insight into the problem. The remainder of this paper discusses four beamlines looked at using TRACE 3D. This version of TRACE 3D has been modified to incorporate traveling wave accelerator structures, both constant gradient and constant impedance [4].

2 THE BEAMLINES

The baseline accelerator design is taken from the 1 kW FEL concept of Cover, et. al. [5]. A 1.5 cell rf gun produces a 4.5 MeV electron beam [6]. This beam is

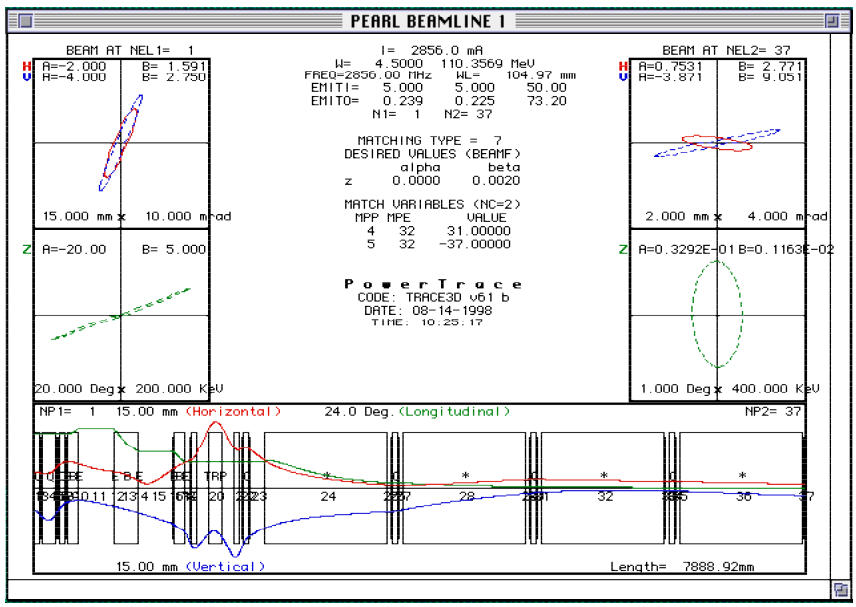

Figure 1: The Baseline PEARL Magnetic Chicane Buncher and Four Accelerator Structures

bunched in a variable magnetic chicane consisting of two 5" diameter dipole magnets placed about a large central magnet. The central magnet was designed to provide a path length equal to the combined path lengths of the two outside dipoles for any angle of entry. Bend angles up to 40 degrees can be accommodated, giving great flexibility in pulse compression. The beam is matched into the first of four 1.26 meter accelerator sections, which are derived from the SLAC 3 m structure. Three of them incorporate higher order mode outcouplers to extend BBU thresholds and limit emittance growth. Quadrupole magnets are placed in between the structures to provide focusing. Figure 1 illustrates this baseline, with a beam of 1 nC every eighth rf bucket accelerated to 110 MeV. Initial conditions for the TRACE 3D simulations are given in Table 1.

Table 2 summarizes the parameters for the different beamlines. Two beamlines use chicanes and two use six accelerator structures. This preliminary study indicates that, with the option to select phase lag for each accelerator structure individually, a chicane buncher is useful, but causes some emittance growth. However, a shorter, <20 psec pulse is probably needed out of the rf gun if the chicane is to be eliminated. Power requirements for the four beamlines are: 112, 104, 79, and 77 MW respectively.

Each beamline transports and accelerates the initial beam (see Table 1) to a final energy of 110 MeV. Parameters have been chosen to obtain this final energy and an upright longitudinal phase space ellipse at the end of the beamline. Table 3 summarizes final emittances and pulse lengths.

3 CONCLUSIONS

The four beamlines examined indicate that shorter and/or lower power alternatives can meet the operating parameters needed for PEARL. A chicane buncher provides greater flexibility at the expense of emittance growth. Future analysis will extend these preliminary results through higher order modeling.

Table 1: Initial Beam Parameters

Beam Kinetic Energy	4.5 MeV
Macropulse Beam Current	357 mA
Micropulse Charge	1 nC
Initial Pulse Length	20 (no ch.) 30 psec (w/ch.)
Correlated Energy Spread	125 - 210 keV
Longitudinal Emittance (z)	50 π deg-keV (eq. unif.)
Transverse Emittance (x,y)	5 π mm-mrad (eq. unif.)

Table 3: Final Beam Parameters

z-emittance (π deg-keV)	73	51	86	51
pulse length (psec)	0.6	1.0	1.0	1.0
x-emittance (π mm-mrad)	0.24	0.23	0.24	0.23
y-emittance (π mm-mrad)	0.23	0.23	0.23	0.23

ACKNOWLEDGEMENTS

The authors would like to thank Drs. C. K. Patel, S. Sharma, C. Helsley, D. Tratt, and R. Collins for

Table 2: Beamline Parameters; chicane is specified by initial bend angle (deg.), accelerator structures by initial gradient (MV) and phase lag (deg.).

Beamline #	Chicane	Acc1	Acc2	Acc3	Acc4	Acc5	Acc6
1	26˚	26.5/-15.6˚	29/-30˚	31/-37˚	31/-37˚	----------	----------
2	----------	15.8/-11.8˚	30/-30˚	32/-20˚	32/-20˚	----------	----------
3	28˚	18/-16˚	12.6/-12˚	12.6/-12˚	24.5/-20˚	24.5/-20˚	24.5/-20˚
4	----------	13.5/-10˚	17.3/-19.2˚	21.7/-25˚	21.7/-25˚	21.7/-25˚	21.7/-25˚

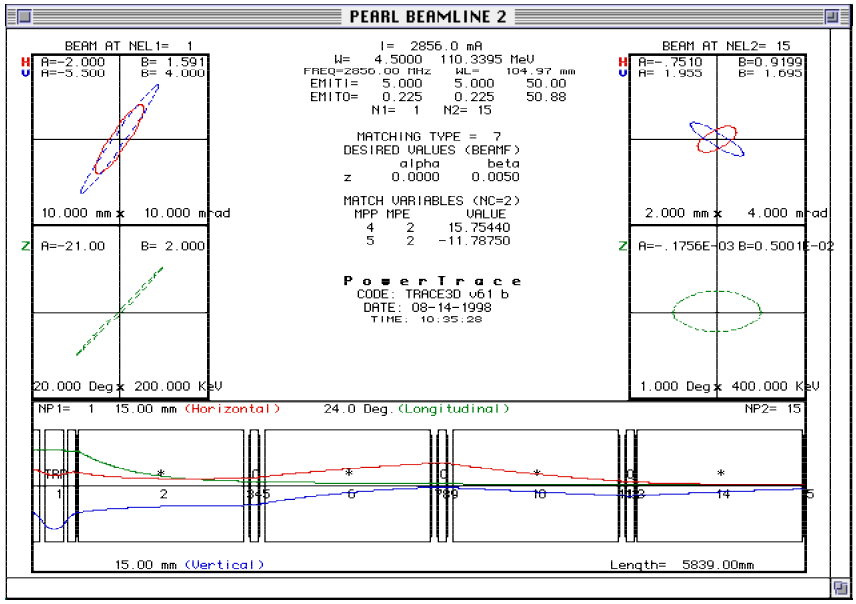

Figure 2: Pulse Compression with Four Accelerator Sections

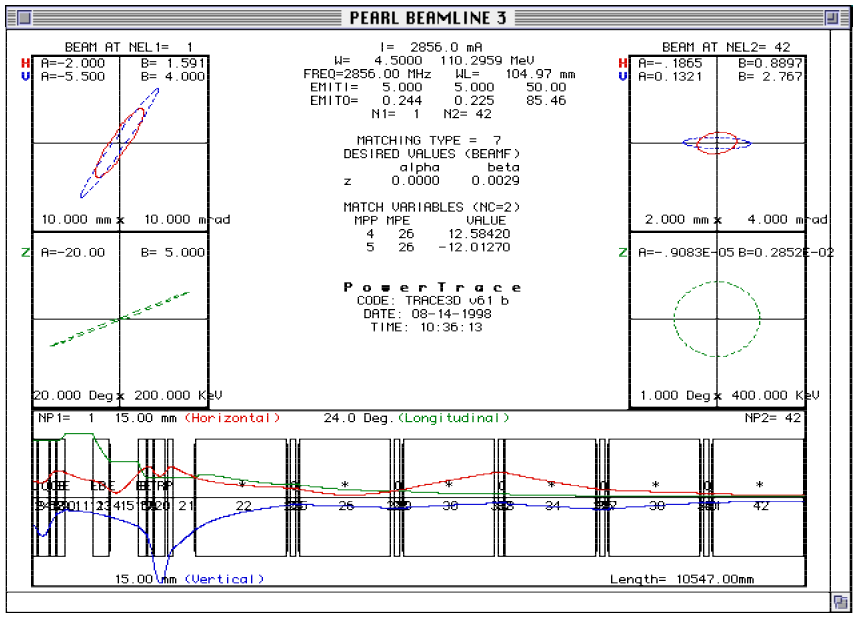

Figure 3: Pulse Compression with Magnetic Chicane Buncher and Six Accelerator Sections

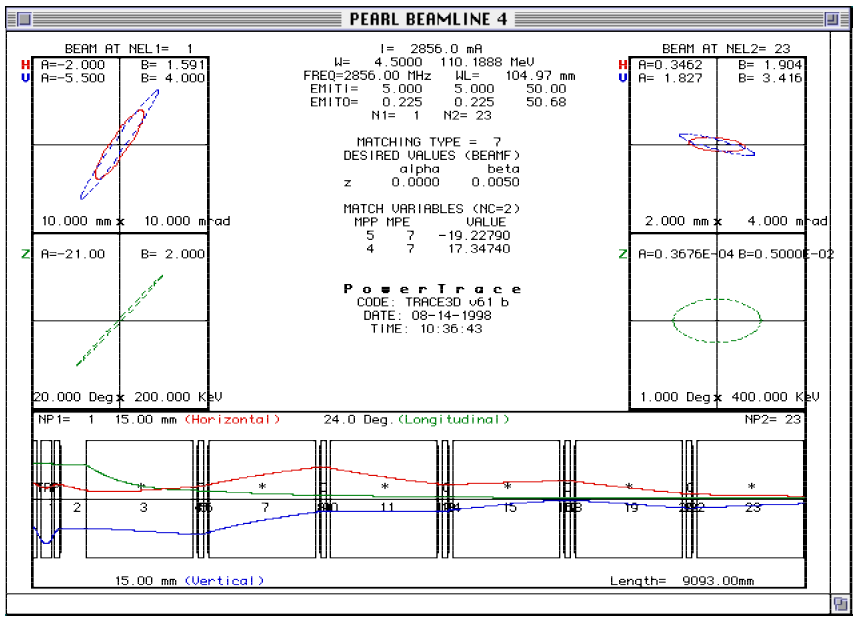

Figure 4: Pulse Compression with Six Accelerator Sections

information on the applications of this technology. Calculations were performed with the PowerTrace™ [7] implementation of TRACE 3D. This work was supported in part by G. H. Gillespie Associates, Inc., Arcata Systems, and the U. of Hawaii.

REFERENCES

[1] J. Madey, R. Burke, C. Helsley, S. Sharma, C. K. Patel, D. Tratt, M. Kennedy,"The PEARL Initiative: Applications of FEL Technology in Support of Atmospheric Research and Remote Sensing", 1998 Int.'l FEL Conf. to be published in NIM A.

[2] C. K. Patel, S. Sharma, C. Helsey, R. Burke, D. Tratt, and R. Collins, "Laser Development from Carbon Dioxide to Free Electron and Their Applications to Remote Sensing and Pollution Monitoring", 19'th Int'l. Laser Radar Conference, Annapolis, MD, July 6, 1998.

[3] S. Sharma, C. Helsley, R. Burke, D. Tratt, and R. Collins, C. K. Patel, "Ship-based Free Electron Laser (FEL) LIDAR for Oceanic and Atmospheric Research", PACON INTERNATIONAL 1997.

[4] M. Lampel, "A Self-Consistent Beam Loaded Traveling Wave Accelerator Model for Use in TRACE 3D", Particle Accelerator Conf., Vancouver, BC, 1997.

[5] R. Cover, G. Bennett, R. Burke, M. Curtin, M. Lampel, G. Rakowsky, J. Quant. Elect. **27**, pp2598-2604, Dec. 1991.

[6] M. Curtin, M. Lampel, J. Hall, R. Burke, R. Cover, "Initial Results from the Rocketdyne Photocathode RF Injector", 16th Int.'l FEL Conf., Stanford, 21-26 Aug. 94.

[7] PowerTrace™ is available from AccelSoft Inc.

FIRST LASING OF THE JAERI FEL DRIVEN BY THE SUPERCONDUCTING RF LINAC

E.J. Minehara, M. Sugimoto, M. Sawamura, R. Nagai, N. Kikuzawa,
T. Yamanouchi and N. Nishimori
Japan Atomic Energy Research Institute, Tokai, Naka, Ibaraki, 319-1195 Japan

Abstract

First and strong laser oscillation has been obtained in the wavelength ranging from 24 to 28μm using the JAERI (Japan Atomic Energy Research Institute, Tokai) 500MHz superconducting rf linac based FEL driver and far infrared FEL device. Electron beam energy and resolution are around 16MeV and 0.6%, respectively, the beam current between 2 and 4mA, and pulse width between 0.1ms and 0.9ms, respectively. A near-concentric optical resonator with a 52 period of 33mm length hybrid planer undulator (K=0.7) is 14.4m long, and uses Gold-coated Copper mirrors of 120mm diameter. The optical axes and distance of the mirrors are precisely adjusted by remotely controlled actuators in order to coincide with the electron beam and micro pulse repetition rate, respectively, before the oscillation. The power has been measured and scattered from 10^7 to 10^8 times higher than that of the spontaneous emission. During the first successful operation, the highest FEL power was measured to be about a hundred watts in average. The FWHM of the FEL spectrum is around the Fourier-transform limited value, and less than 0.09 μm, which corresponds to $\Delta\lambda/\lambda$=0.37%. The detuning curve of the cavity is asymmetrically-peaked over about 3 μm in the longer side, and spanned over about 15μm.

1 INTRODUCTION

A prototype for a quasi-cw or very long-pulse, and high-average power free electron laser(FEL) driven by the 15 MeV superconducting rf linac has been developed, and constructed at Tokai, JAERI (Japan Atomic Energy Research Institute) since 1989 [1-4]. Both high performances of cryogenic stand-by loss<3.5W at 4.5K and accelerating fields' Eacc < 8.3MV/m and Q < 2 x10^{+9} in the JAERI superconducting rf linac modules have been successfully realized as a so-called zero-boil-off and world-first transportable capabilities without any serious vibrational problem in the JAERI FEL accelerator vault.

Since modification and related maintenance of the cryogenic refrigerator system for the driver were completed in the middle of October 1995, the system has run with no trouble, and the driver has been continuously run very successfully up to now. The optical resonator system and related electron beam transport system were modified to realize larger acceptance than the old for both of the undulator radiation and energetic electron beam. An alignment and distance measurement system was newly developed, and successfully applied to actual preparatory measurement for lasing in the JAERI FEL. A far-infrared light transport line and detector room was built to realize a low-loss and low-noise measurement near the accelerator vault in April, 1996.

In order to realize the quasi-cw and very long-pulse operation, we have improved the electron gun grid-pulsar and high voltage power supply, and rf amplitude and phase control systems for the JAERI superconducting rf linac. The improvements in the electron gun and the related with the rf system are still under way.

A beam test and commissioning of the JAERI superconducting rf linac as an FEL driver was successfully performed to get an electron beam ranging from 10 to 23 MeV with a nearly full transmission and a full current, and relatively short macro pulse of 0.01ms. Strong and stable oscillation in the wavelength of around 24 μm have been observed by using the Ge(Cu) detectors with a home-made fast current amplifier system, commercially-available MCT detectors and thermopiles. As shown in Fig. 1, a sudden increase of the light signal were observed after a few tens of microseconds later from the onset of beam current pulse.

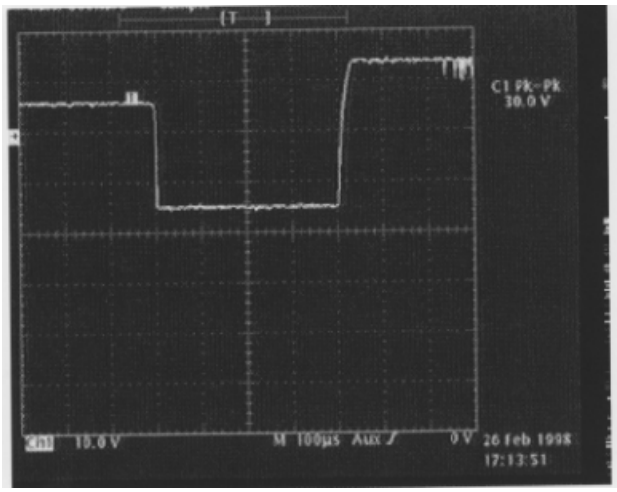

Figure 1: Stable oscillation in the wavelength of around 24 μm. The pulse duration is continued over 0.4ms, the beam current ranging from 2 to 4mA, and the maximum laser power about a hundred watts in average.

2 EXPERIMENT

Fig. 1 shows the first and stable laser oscillation with the JAERI superconducting rf linac based FEL. The average current for a macro pulse is measured to be around 4mA. The lower trace of the figure is a far-infrared light signal waveform of a Ge-Cu detector. The total cavity loss and the FEL gain are scattered between 1.1 and 1.9%, and estimated to be from 10% to 30%, respectively, which were obtained from decay and rising times of the output pulse.

Fig. 2 shows the e-beam current signal of the lower part and FEL light output signal of the upper over a half millisecond. As shown in Fig. 3, the FEL spectrum was measured with a grating spectrometer and a commercially-available pyroelectric line-sensor of 64 channels located at the focal plane during the operation.

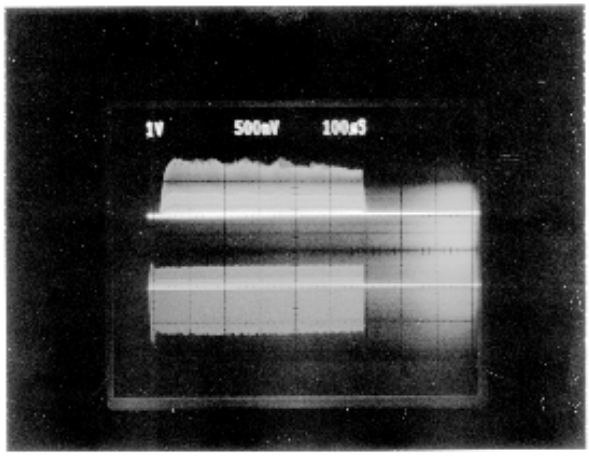

Figure 2: Electron-beam current signal of the lower part and FEL light output signal of the upper over a half millisecond.

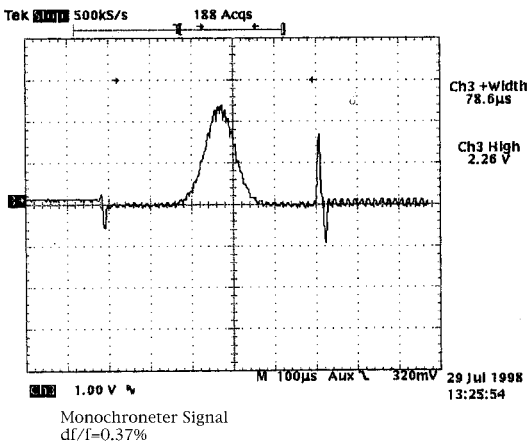

Figure 3: The FEL spectrum was measured with a grating spectrometer and a commercially-available pyroelectric line-sensor of 64 channels fixed at the spectrometer focal plane during the operation. The FWHM of the FEL spectrum is less than 0.09 µm, which corresponds to $\Delta\lambda/\lambda$=0.37%.

The FWHM of the FEL spectrum is less than 0.09 µm, which corresponds to $\Delta\lambda/\lambda$=0.37%. The tuning range of the cavity is spanned over about 15µm.

The detuning curve was measured reliably to be asymmetric, long-tailed in the shorter cavity-length side, and short-tailed or quickly-disappeared in the longer.

An FEL beam spot was observed using a pyro-camera fixed in the optical measurement room neighboring the FEL accelerator vault.

Divergence of the beam is estimated to be the same order of a diffraction limit value in the figure 4.

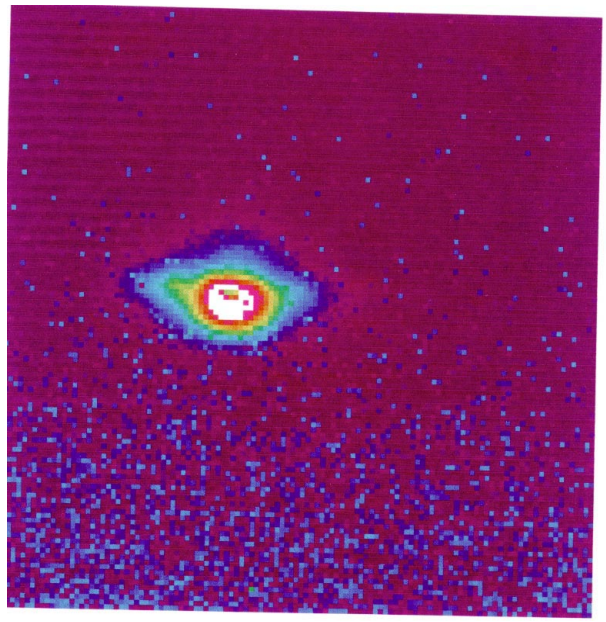

Figure 4: FEL beam spot observed using a pyro-camera fixed in the optical measurement room neighboring the FEL accelerator vault.

Stable laser oscillation has been obtained at a wavelength of 24µm using the JAERI superconducting rf linac based FEL driver. During the first successful operation, the highest FEL power was measured to be about a hundred watts in average. The JAERI superconducting rf linac operational parameters are summarized in the following; 1) Electron Beam Energy of 15.8 MeV from 0.1 to 0.9ms, 4) Beam current ranging from 2mA to 4mA, 5) Energy resolution around 0.6%, and 6)Repetition Rate 10.4125MHz.

A near-concentric optical resonator with a 52 period of 33mm length hybrid planer undulator (K=0.7) is 14.4m long and uses Gold-coated Copper mirrors of 120mm diameter. The optical axes and distance of the mirrors is adjusted by remotely controlled actuators in order to coincide with the electron beam and micro pulse repetition rate, respectively, before the oscillation. The power has been measured and scattered from 10^7 to 10^8 times higher than that of the spontaneous emission.

3 REFERENCES

[1] E.J. Minehara et al., Nucl. Instrum. Method. A 331 (1993) 276.

[2] M. Sawamura et. al., Nucl. Instrum. Method. A318 (1992) 127.

[3] R. Nagai et al., Nucl. Instrum. Method. A 358 (1995) 403.

[4] E.J. Minehara, et al., Proceedings of Particle Accelerator Conference, 1995, Dallas, 159-161 (1995).

RECENT PERFORMANCE OF THE JAERI SUPERCONDUCTING LINAC FOR FEL

M. Sawamura, R. Nagai, N. Kikuzawa, N. Nishimori, E.J. Minehara
Japan Atomic Energy Research Institute (JAERI), Tokai, Ibaraki 319-1195 Japan

Abstract

Far-infrared FEL oscillation using the superconducting linac has succeeded in JAERI. The linac consists of a 250kV electron gun, a subharmonic normal-conducting buncher (SHB) of 83.3MHz, two single-cell and two 5-cell superconducting cavities of 499.8MHz. The gun was typically operated around 200 kV to reduce space charge effects.

The combination of the SHB and two single-cell cavities enabled high current beam of more than ten amperes by utilizing a thermionic cathode and a grid pulsing. Calculations utilizing the modified PARMELA code showed that the electron bunch of 3 ns from the electron gun was finally compressed to be 20-35 ps after the two single-cell cavities. FWHM bunch length and 80% emittance were measured to be 22ps and 35 pi mm mrad.

1 INTRODUCTION

Many kinds of free-electron laser (FEL) facilities exist in the world. Some are striving to develop a short wavelength FEL while others are trying to find applications in various fields, such as medical and scientific research. The purpose of the Japan Atomic Energy Research Institute (JAERI) FEL project is to develop a high-average-power, high-efficiency FEL for research and industrial use[1,2]. The stable FEL oscillation was achieved in March 1998. Figure 1 shows the schematic layout of JAERI superconducting linac. This paper describes the detail design of JAERI FEL linac and the measurement of bunch length and emittance.

2 CONCEPTUAL DESIGN OF THE JAERI FEL LINAC

The average power of an FEL is determined by multiplying the peak power by the repetition rate and pulse length. Thus, to create a high-average-power FEL, it is necessary to increase the peak power, the repetition rate, and the pulse length. The peak power is proportional to the peak current of the electron beam. The peak current of the linac is normally a few hundred amperes maximum for an RF linac. Though an RF gun and photocathode are used to obtain the high-current beam, it is difficult to

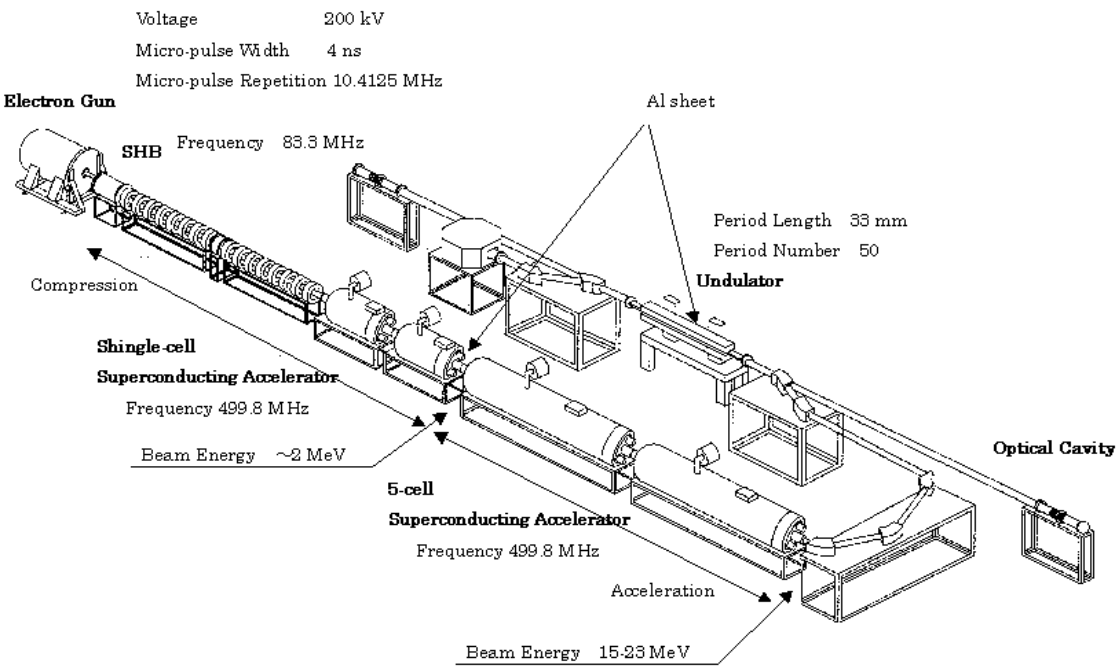

Figure 1: Schematic Layout of the JAERI Superconducting Linac

operate them with a high-repetition rate and a long pulse length. From this standpoint, a linac with a high repetition rate and a long-pulse or continuous-wave (CW) mode operation is suitable for a high-average-power FEL. Therefore, superconducting accelerators are superior.

The electron beam power is converted to laser power with an efficiency of only a few percent or less. When the electron beam is dumped, most electron beam power is wasted. Therefore the efficiency of an FEL is usually very low. Reusing the electron beam and reducing the RF loss increase the efficiency. Superconducting cavities have a very small RF power wall loss, which makes them superior to normal conducting cavities for a high-efficiency FEL linac.

Thus, we conclude that superconducting accelerators used as the main accelerating components are best to realize a high-power, high-efficiency FEL.

3 DESIGN DETAILS OF COMPRESSING SECTION OF THE JAERI FEL LINAC

For the electron gun, the thermionic cathode is the most acceptable choice presently available. However, it is difficult to obtain a high-current electron beam that has a current of more than a few hundred milliampere and also has good emittance. Therefore, a beam compressing system is necessary to produce a high-peak-current beam.

A frequency of 500 MHz was selected for the main accelerating components. A period of 500 MHz is 2 ns and at least half of that is unavailable for compressing the beam. Therefore, to compress the beam bunch of more than 1 nanosecond, a subharmonic buncher (SHB) is required. When the bunch length from the electron gun is 3-4 ns, the subharmonic frequency must be less than a quarter of the main frequency, 500 MHz. Though an SHB using lower subharmonics can compress a beam bunch to a shorter length than one using higher subharmonics, it requires a higher buncher voltage, which results in a larger RF loss in the SHB. Considering long-pulse or CW mode operation, low-power loss is desirable. We chose a subharmonic number of 6 for the SHB.

When the charge density increases by shortening the bunch length or when the beam current is originally high, beam compression with only the SHB does not work well because of the space charge effects. A means of resolving this problem is to install an additional element that works not only as a buncher but also as an accelerator that decreases the space charge force. Since we are considering a high-average-power, high-efficiency FEL, the accelerating section of the linac must be superconducting. If a multicell superconducting module is adopted for this element, it causes not only less effective acceleration but also an increase in the energy spread. When the phase in the first cell of a multicell is adjusted to enhance both compression and acceleration, the remaining cells are out of the phase of maximum accelerating. That causes an expansion of the energy spread because the accelerating field of the maximum accelerating phase has the smallest energy spread. Therefore, the multicell superconducting accelerator is unsuitable, whereas the single-cell element is suitable. Thus, two single-cell superconducting modules are installed after the SHB section to accelerate the beam to almost the speed of light.

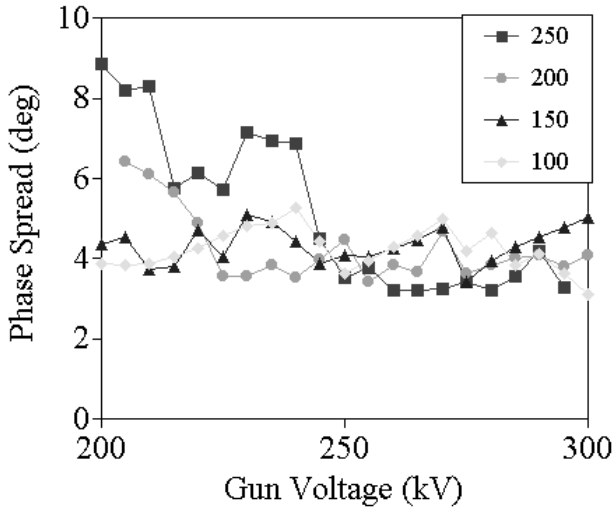

Figure 2: Calculated phase spread with different gun voltage and with different beam current.

The voltage of the electron gun influences the phase spread. Figure 2 shows the phase spread of the compressed bunch with the SHB and two single-cell cavities calculated with PARMELA. The initial phase spread was 3 ns. The 80 % phase spread was calculated by optimizing the phases of SHB and two single-cell cavities and the amplitude of SHB.

The figure shows that this compression system works well. For high beam current such as 200 mA and 250 mA, increasing the gun voltage has an advantage of making the beam spread small. For low beam current such as 100 mA and 150 mA, the phase spread does not change so much according to the gun voltage. Therefore, 200 kV gun voltage is sufficient for the beam current less than 150 mA.

4 MEASUREMENT OF THE BEAM BUNCH LENGTH AND EMITTANCE

The bunch length was measured at the middle of the undulator. The bunch length is estimated to be several tens picoseconds. The beam bunch length was measured with a steak camera made by Hamamatsu Photonics Co. An aluminum plate profile monitor was installed within the undulator duct. When the electron beam collided with an aluminum plate, optical transition radiation (OTR) was emitted. The bunch length was measured by detecting the OTR by the streak camera. Figure 3 shows the result of

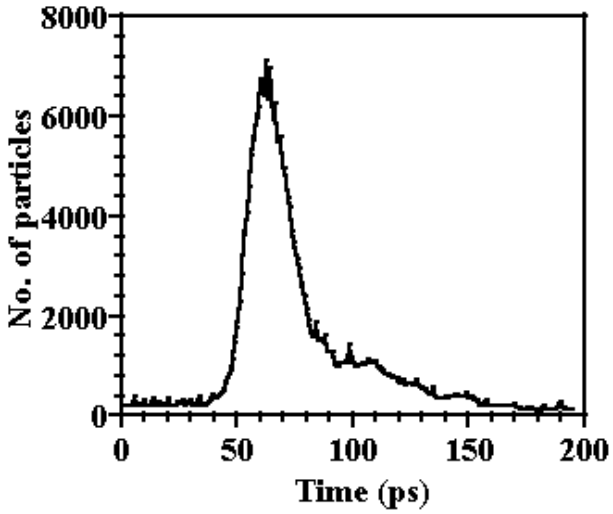

Figure3: Measured bunch length

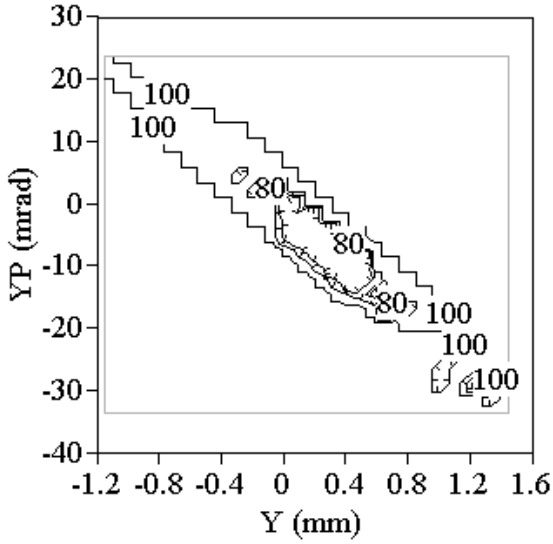

Figure 4: Reconstructed phase space contour of 100 % and 80 % emittance.

the bunch length measurement. It indicates a bunch length of 22 ps, which corresponds to 4.0 degrees.

The beam eminence was measured by measuring the beam distribution on the profile monitor with different quadrupole fields. Then the emittance was reconstructed with tomography method[3]. Figure 4 shows the result of the reconstruction. This indicates that 80 % normalized emittance is 35 pi mm mrad and that 100 % emittance is about 5.6 times larger than 80 %. This was achieved before the succession of the FEL oscillation and under adjustment of the accelerator parameters.

5 REFERENCES

[1] Y.Kawarasaki et al.: *Nucl. Instr. Methods in Phys. Res.*, **A285**, 338 (1989)

[2] M.Takao et al.: *Nucl. Instr. Methods in Phys. Res.*, **A331**, 218 (1993)

[3] C.B.McKee et al.: *Nucl. Instr. Methods in Phys. Res.*, **A358**, 264 (1995)

ELECTRON BEAM CHARGE STATE AMPLIFIER (EBQA)-- A CONCEPTUAL EVALUATION*

J. C. Dooling and J. A. Nolen
Argonne National Laboratory, Argonne, Illinois 60439 USA

Abstract

A concept is presented for stripping low-energy, radioactive ions from 1+ to higher charge states. Referred to as an Electron Beam Charge State Amplifier (EBQA), this device accepts a continuous beam of singly-charged, radioactive ions and passes them through a high-density electron beam confined by a solenoidal magnetic field. Singly-charged ions may be extracted from standard Isotope-Separator-Online (ISOL) sources. An EBQA is potentially useful for increasing the charge state of ions prior to injection into post-acceleration stages at ISOL radioactive beam facilities. The stripping efficiency from q=1+ to 2+ (η_{12}) is evaluated as a function of electron beam radius at constant current with solenoid field, injected ion energy, and ion beam emittance used as parameters. Assuming a 5 keV, 1 A electron beam, η_{12} = 0.33 for 0.1 keV, ^{132}Xe ions passing through an 8 Tesla solenoid, 1 m in length. Multi-pass configurations to achieve 3+ or 4+ charge states are also conceivable. The calculated efficiencies depend inversely on the initial ion beam emittances. The use of a helium-buffer-gas, ion-guide stage to improve the brightness of the 1+ beams [1] may enhance the performance of an EBQA.

1 INTRODUCTION--MOTIVATION FOR THE EBQA

The production and acceleration of radioactive nuclides far from stability is an area of significant interest in nuclear physics [2,3]. Generating these nuclides in specific charge states selectively and efficiently are important goals in the development of a cost-effective Radioactive Ion Beam (RIB) facility. To increase efficiency and reduce cost, it is desirable to strip singly-ionized species to higher charge states while still at low energy in the post-accelerator. RIBs typically employ low charge state ions (usually 1+) at the front end of the post-accelerator; these ions are often generated within Isotope Separation On-Line systems (ISOLs) [4]. For A>30-60 amu, higher charge states are desired to simplify the post accelerator. For example, ISAC [5] presently under construction at TRIUMF, requires a source capable of generating heavy ions with charge to mass ratios (q/A) greater than 1/30. Elevated charge states are available at low energy from Electron Cyclotron Resonance Ion Sources (ECRIS) [6] and Electron Beam Ion Sources (EBIS) [7]. The ISOL-MAFIOS [8] system combines properties of both ECRIS and EBIS by electrostatically "catching" singly-charged ions injected into the minimum B-field ECR region; stripped ions then effuse continuously. However, ECR sources tend to generate beams of relatively large emittance and produce a broad range of charge states. The EBIS is typically a pulsed machine which generates higher charge states by first trapping ions in an electrostatic well then "cooking" them in an electron beam for a period of time. A large EBIS is planned for the REX ISOLDE facility at CERN [9]. If the 1+ ions are first accelerated by a low q/A structure, such as an RFQ, they can be stripped afterwards to higher charge states. A post accelerator based on this concept is being developed at Argonne [2,10,11]. The EBQA concept discussed here is an alternative method of increasing the charge state of a DC beam at ion source energy.

The primary components of an EBQA are presented in Figure 1. Though in principle it should be possible for the EBQA to generate ions of arbitrarily high charge state by recirculating the beams, the present analysis focuses on advancing q from 1+ to 2+.

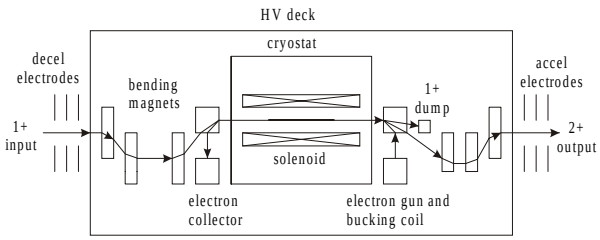

Figure 1: The EBQA in single-pass mode.

2 EBQA ANALYSIS

Simulating the detailed ion and electron orbits within the solenoid requires a full 4-D emittance distribution (e.g., f(x,x',y,y')). Angular momentum effects arise from xy' and x'y phase-space pairs. A Kapchinsky-Vladimirsky (K-V) distribution is chosen for the injected beam [12]. The solenoid is modeled as an ideal cylindrical coil. All ion trajectories are assumed to be near the axis; therefore, analytical expressions for B_z and B_r can be obtained.

2.1 Matching

To optimize stripping efficiency and minimize envelope oscillations, the ions and electrons must be

* Supported by U.S. DOE, Contract W-31-109-ENG-38

properly matched into the solenoid. Assuming the ion starts from a shielded source (**B**=0), the matched beam radius is just twice the Larmor radius, $r_m=2\rho_o$,

$$r_m = \left[\frac{2\varepsilon_n m_o c}{qB_{zo}}\right]^{1/2} \quad (1)$$

where the normalized emittance is $\varepsilon_n = \beta\gamma\varepsilon_o$. Note that the matched radius is not a function of injected energy.

2.2 Electron Injection

Magnetic field at the cathode plays an important role in determining the matched e-beam radius. Because of the relatively low electron energy and high field intensity, electron rigidity is low. The cathode immersion field can be used to control the beam size within the solenoid to maximize stripping efficiency or brightness. High field and low rigidity mean that both electron gun emittance and gun alignment errors must be small.

The EBQA requires a large perveance from the electron gun; thus, space charge neutralization must occur over a short distance. The doubling distance of a 5 keV, 1 A electron beam extracted through a 1 cm^2 aperture is approximately 4 cm. The necessary neutralization of the e-beam space charge is facilitated by dc extraction. Employing a background hydrogen gas at a pressure of 10^{-6} Torr, the neutralization time, $\tau_n=(n_b<\sigma_{01}v>)^{-1}$, is on the order of 1 ms for 5 keV electrons [13].

2.3 Stripping Efficiency--Analytical Results

Stripping efficiency in the EBQA depends upon solenoidal field intensity, beam energies, emittances, ion charge state, and stripping cross sections. Cross sections are estimated using empirical formula [14,15] or from data [16] where available. Multi-step ionization is ignored as are cross sections for excited states. Assuming uniform density profiles for both ions and electrons, stripping efficiency can be estimated. The stripping efficiency for singly-charged ions, fully immersed in the e-beam can be expressed as,

$$\eta_s(t_i) = 1 - \exp\left[-\frac{L_s\sigma_{12}I_e\beta_e}{e\pi r_e^2\beta_i c\beta_{e\|}}\right] \quad (2)$$

To determine actual efficiency, overlap of the electron and ion beams must be included (this does not take into account orbital effects). For a matched ion beam radius, r_m the efficiency is given as,

$$\eta_{12} = \eta_s(t_i)\frac{r_e^2}{r_m^2} \qquad r_e < r_m \quad (3a)$$

$$\eta_{12} = \eta_s(t_i) \qquad r_e > r_m \quad (3b)$$

The effect of nonlocalized charge on stripping efficiency is discussed in the following section with simulation results. In the limit where stripping efficiency is relatively weak (<10 percent) and $r_e \le r_m$, the efficiency can be approximated by Equation 4. In this case, the efficiency is roughly independent of r.

$$\eta_{12} \approx \frac{L_s\sigma_{12}I_e\beta_e}{e\pi r_m^2\beta_i c\beta_{e\|}} \quad (4)$$

Continued stripping of the 2+ beam to higher charge states must also be considered. If interest is in q=2+ only, ions stripped to higher charge states would be considered lost. The time it takes to maximize the q=2+ state may be expressed as,

$$t_{max} = \frac{\ln(\sigma_{12}/\sigma_{23})}{n_e\beta_e c(\sigma_{12}-\sigma_{23})} \quad (5)$$

Using ^{132}Xe as an example, $\sigma_{12}=1.5\times10^{-21}$ m^2 and $\sigma_{23}=0.84\times10^{-21}$ m^2 at 5 keV, t_{max}= 215 μs (r_e = 0.7 mm). Inserting t_{max} into the 2+ rate equation, the maximum efficiency for the production of Q=2+ is 47.9 percent; at this time the density of q=3+ is 21.4 percent. In the single-pass mode, this represents the maximum theoretical efficiency; however, in a multipass system, one could do better if trying to attain q>2+.

2.4 Stripping Efficiency and Orbit Effects

Stripping efficiency is found to be maximized when electron and ion beam diameters are the same; however orbital effects complicate the picture. Figure 2a shows an x-y projection of two ion orbits entering the solenoid.

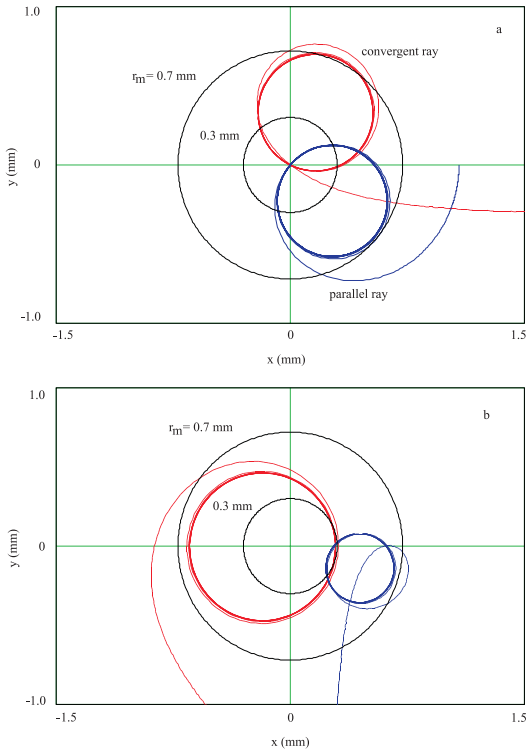

Figure 2: a) End-on view of matched orbits within the solenoid (x-y plane) starting with zero angular momentum, and b) with finite angular momentum.

The electron beam is contained within a circle of radius r_e. The ion trajectories are matched into the solenoid with a radius r_m=0.71 mm. Both trajectories enter the solenoid with zero angular momentum; however, they are separated in phase space to indicate maximum displacement and divergence. In Figure 2b, trajectories are shown which include angular momentum satisfying the K-V distribution. Stripping can only take place while ions are within the region occupied by the electron beam; i.e. $r<r_e$. Because of the complex orbits that result from the inclusion of angular momentum, it is necessary to use a numerical model to determine the stripping efficiency within an EBQA.

3 NUMERICAL MODEL

A random number generator is used to produce a set of Cartesian input phase space coordinates satisfying the K-V distribution. A predictor-corrector algorithm is employed to step each trajectory through the solenoid; this method has been benchmarked against a Runge-Kutta algorithm to insure accuracy. Depending upon initial positions in phase-space, some ions never encounter the e-beam and therefore cannot be stripped. For those ions that do enter the e-beam, a finite stripping probability is assigned. Total efficiency is determined by summing the probability for all trajectories and then dividing by the total number of particles. The trajectories possessing a nonzero stripping probability are used to calculate the emittance of the stripped, doubly-charged beam. Stripping efficiencies, determined in simulations of 2000 particles per electron beam radius are presented in Figure 3 for ion beam emittances of ε_n=0.005, 0.010, and 0.020 π-mm-mrad (ε=39, 77.5, and 155 π-mm-mrad at 1 keV, A=132 amu). The results in Figure 3 are obtained for constant e-beam current and energy (1 A, 5 keV) assuming a stripping cross section of 1.5×10^{-21}m^2. In the case of 0.1 keV injection into an 8 T field, the maximum efficiency is 38.6 percent with a charge state distribution of 33.4 percent in 2+, 4.9 percent in 3+, and 0.3 percent in 4+ and above. The stripping efficiency is seen to be inversely proportional to injected ion beam emittance.

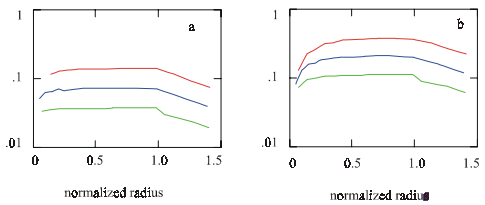

Figure 3: Stripping Efficiency versus electron beam radius at 0.005, 0.010, and 0.020 π mm mrad a) 1.0 keV, 8 T and b) 0.1 keV, 8 T.

A comparison of numerical and analytical stripping efficiency is presented in Figure 4. In this case, the injected ion beam energy and emittance are 1.0 keV and ε_n=0.005 π-mm-mr and the solenoid field strength is 8 T. Efficiency is plotted against electron beam radius assuming constant current. Near the matched radius, good agreement exists between both efficiency models; however, away from matched radius, the numerical result is larger. The deviation of the numerical result from Eq. 3 is indicative of orbital effects within the solenoid. Similar behavior is observed for the other injection cases.

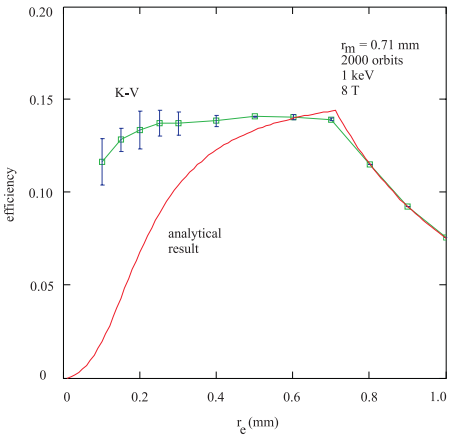

Figure 4: Comparison of numerical and analytical stripping efficiency models with electron beam radius.

4 ACKNOWLEDGEMENTS

The authors would like to thank Drs. P. Schmor, P. Van Duppen, and M. Reiser for their valuable comments.

5 REFERENCES

[1] M. D. Lunney, et al., Ref. 34 in U. Koster, et al., Rev. Sci. Instrum., 69(3), 1316(1993).
[2] J. A. Nolen, Proc. 1996 LINAC Conference, CERN
[3] D. K. Olsen, Proc. 1995 Particle Accelerator Conf., Dallas, TX, p. 312.
[4] H. L. Ravn and B. W. Allardyce, in Treatise on Heavy Ion Science, ed. by D. A. Bromley, Plenum, New York, 1989, Vol. 8, p 363.
[5] P. G. Bricault, Rev. Sci. Instrum., 67(3), 1277(1996).
[6] Y. Jongen and C. M. Lyneis, in The Physics and Technology of Ion Sources, ed. by D. A. Bromley, Plenum, New York, 1989, Vol. 8, p 207.
[7] E. D. Donets, in The Physics and Technology of Ion Sources, ed. by I. G. Brown, Wiley, New York, 1989, p. 245.
[8] R. Geller, et al., Rev. Sci. Instrum., 67(3), 1281(1996).
[9] REX-ISOLDE, CERN Rep. ISC 94-25, Geneva, Nov., 1994.
[10] K. W. Shepard and W. C. Sellyey, Proc. 1996 Linac Conf., CERN.
[11] P. Decrock, et al., Rev. Sci. Instrum., 68(6), 2322(1997).
[12] M. Reiser, Theory and Design of Charged Particle Beams, Wiley, New York, 1994, p. 62.
[13] M. Reiser, ibid., p. 274.
[14] W. Lotz, Z. Phys., 216, 341(1968), and Z. Phys., 220, 466(1969).
[15] T. A. Carlson, et al., Atomic Data, 2, 63(1970).
[16] A. Müller, et al., J. Phys. B, 13, 1877(1980).

LONG RANGE PLAN PROPOSAL FOR AN EXTENSION TO ISAC

R. Baartman, R. Laxdal, L. Root, TRIUMF, Vancouver, Canada

Abstract

A radioactive ion beam facility, ISAC, is presently under construction at TRIUMF. The post-accelerator comprises a 35 MHz RFQ to accelerate ions of $A/q \leq 30$ from 2 keV/u to 150 keV/u and a post-stripper room temperature 105 MHz DTL to accelerate ions of $3 \leq A/q \leq 6$ to a final energy fully variable up to 1.5 MeV/u. Both linacs are required to operate in cw mode. For the next five year plan, it is intended to increase the final energy above the Coulomb barrier (roughly 6.5 MeV/u) and broaden the mass range up to roughly $A = 150$. The ISAC-2 proposal will utilize the existing RFQ. Masses higher than 30 will require ECR ion sources and/or charge boosters. The optimum design consists of an IH linac to reach a 400 keV/u stripping energy, and superconducting modules to reach the final energy. The superconducting option is preferred because the short modules allow significantly higher energy – up to 13 MeV/u – for light ions. In this paper we compare the various ISAC2 options and present first order linac designs and staging scenarios.

1 INTRODUCTION

The ISAC facility currently under construction at TRIUMF[1] (ISAC1) will have the capability of accelerating singly-charged radioactive ion masses up to 30 atomic mass units ($A = 30$) to an energy of 1.5 MeV per amu (MeV/u). As a next step, experimenters would like to go to the Coulomb barrier (roughly 6.5 MeV/u) with masses up to roughly 150.

One option considered[2] was to take the singly-charged ions up to 12 keV/u with a low frequency RFQ (11.67 MHz), use a gas stripper to reach $A/q = 60$, then with a combination of RFQ and IH linac accelerate to 0.55 MeV/u, strip to $A/q = 6$ and finally accelerate to 6.5 MeV/u using more IH linacs. Although this is an intensity-efficient option, it is expensive, requiring 60 m of linac.

Ions of mass A can be accelerated in ISAC1 if their charge is greater than $A/30$. The first step in an upgrade is therefore to upgrade to a higher charge state. ECR ion sources can easily reach the required $A/q = 30$. Such sources which can withstand the radiation fields due to the 500 MeV, 10-100 μA primary beam are already under development at TRIUMF. Another possibility is a device which boosts the charge state of the 60 keV beam from the ion source. Such charge state boosters are under intensive development at GANIL/Grenoble[3]. For example, from singly-charged initial ions they have achieved Kr^{9+} with an efficiency of 9% and Zn^{7+} with an efficiency of 2%.

An attractive option is to develop a charge state booster which would give $A/q \leq 6$. This would obviate the need for any stripping and the ISAC1 stripper could be discarded. Subsequent linacs could then be optimally short and inexpensive. However, there is no guarantee that such high charge states ($q = +25$ for $A = 150$) can be obtained. Moreover, experiments indicate that the higher the charge state, the longer the 'cooking' time needed in the charge booster: up to 100 ms for very high charge states. This obviously would make it difficult to use isotopes far from stability in ISAC2.

Although ISAC1 would allow acceleration of all masses to 1.5 MeV/u, intensities for masses beyond ~70 would be too low to be useful. The reason is that the stripper in ISAC1 is at an energy of 0.15 MeV/u and $A/q \leq 6$ required for the Drift Tube Linac (DTL) cannot be achieved for masses beyond about 70. This rules out a simple extension to the ISAC1 DTL to take the ions from 1.5 to 6.5 MeV/u, unless the ISAC1 MEBT and DTL are upgraded to higher A/q. The drawback of this approach is that approximately an order of magnitude in intensity would be lost because a second stripper would be needed after ISAC1 to lower the A/q else the 1.5 MeV/u to 6.5 MeV/u linac would be too expensive.

A better approach would be to optimize the total design to use only one stripper to reach 6.5 MeV/u while keeping the total linac length to a minimum. In that case, the optimum stripping energy is 0.4 MeV/u with a maximum $A/q = 7$ for $A = 150$. A higher stripping energy makes the pre-stripper linac (where A/q is 30) too long. A lower stripper energy does not strip to a high enough charge state, making the post-stripper linac too long.

2 ISAC2 DESIGN

2.1 Acceleration from 0.15 MeV/u to 0.4 MeV/u

A cost effective configuration to reach 400 keV/u is to continue the acceleration straight north of the RFQ MEBT1 line (Fig. 1). This would require an addition to the present building to widen it northward. The energy gain of 0.25 MeV/u requires a total rf voltage of ($0.25 \times 30 =$) 7.5 MV. A DTL very similar to the ISAC1 DTL IH linac[4] would be about 5 m long assuming an average gradient of 1.5 MV/m and could be placed downstream of the first MEBT bender after a short matching section.

After the new DTL, the beam would go through a beam

transport system (MEBT2) consisting of a short matching section, stripping foil, a 90° bend for charge selection and a matching section to the post-stripper linac.

2.2 Acceleration from 0.4 Mev/u to 6.5 MeV/u

To reach 6.5 MeV/u from 0.4 MeV/u with $A/q = 7$ requires a total voltage gain of 42.7 MV. A room temperature linac should be composed of long, many-gap modules (like the ISAC1 IH DTL), else the rf power supply and running costs become prohibitively large. Such a structure running cw would have a gradient of 2.2 MV/m and including the required focusing quadrupoles between tanks would therefore be at least 28 m in length. Higher electrical gradients are possible in principle, but in cw operation rf power dissipation in the drift tubes becomes a limiting factor. These problems disappear if we instead use superconducting cavities. In that case, an accelerating gradient of 3 MV/m is conservative (5 MV/m has been achieved).

Superconducting technology is technically more difficult than the room temperature IH structure but would offer a shorter more flexible accelerating structure. Typically superconducting booster linacs are composed of two- to four-gap cavities. Two gaps give a larger velocity acceptance at the expense of a reduced voltage gain per cavity when compared to three- and four-gap cavities. Two-gap cavities have been made in both a spiral and QWR (quarter wave resonator) configuration. Three-gap cavities have been made in a split-ring structure. The four-gap cavities are constructed in a QWR geometry. The QWR shape has been found to be inherently more stable than the ring structures[5]. Acceleration efficiencies (= energy gain/($q \times$ peak voltage)) are more than 80% for the velocity range $0.81 \leq \beta/\beta_0 \leq 1.60$ for two-gap cavities and $0.85 \leq \beta/\beta_0 \leq 1.34$ for three-gap cavities.

2.3 Cavity Dimensions

A zeroth order linac concept is presented here as an example. Obviously a full optimization considering cavity type, stability, cost, etc, is required to achieve a first order design. This example consists of three different cavity geometries. The three models have design velocities of 3.5%, 7% and 11% respectively with the lowest velocity cavity being a two-gap resonator and the other two models being three-gap resonators. The two-gap cavity is chosen in the low velocity section because of its broader velocity acceptance but also because the device is inherently more phase stable and the longitudinal emittance in this region is relatively large. Cavity details are presented in Table 1, Table 2 and Table 3. In Table 1 ($A/q = 7$) and Table 2 ($A/q = 3$) the efficiency of acceleration can be determined from the ratio of the velocity to the cavity design velocity. The regions have been chosen to yield at least ∼80% acceleration efficiency for acceleration of the higher masses ($A/q = 7$). In Table 2 the particle velocity is estimated for the case where $A/q = 3$ assuming a flat velocity acceptance for the cavities. This shows that energies of 15 MeV/u can still be accelerated with reasonable efficiency.

Table 1: Energy range, velocity range and maximum voltage gain required for the three cavity types for $A/q = 7$.

Cavity	Cells	E (MeV/u)	β (%)	ΔV (MV)
1	2	0.4 – 1.5	2.9 – 5.6	7.7
2	3	1.5 – 3.5	5.6 – 8.6	14
3	3	3.5 – 6.5	8.6 – 11.7	21

Table 2: Energy range, velocity range and voltage gain for $A/q = 3$ assuming a flat effective energy gain for the three cavity types.

Cavity	Cells	E (MeV/u)	β (%)	ΔV (MV)
1	2	0.4 – 3.0	2.9 – 8.0	7.7
2	3	3.0 – 7.7	8.0 – 12.8	14
3	3	7.7 – 14.7	12.8 – 17.6	21

In Table 3 the cell structure for each cavity type is given assuming rf frequencies of 105, 140 and 175 MHz (resp. 3, 4 and 5 times the RFQ frequency). The rf frequency can be increased down the line as the relative longitudinal emittance is reduced. (The frequencies are conservative compared to the room temperature equivalent due to the higher Q and possible resultant reduction in longitudinal acceptance.) The length of the two-gap cavity is $L_2 = \beta\lambda$ and of the three-gap cavity is $L_3 = 3\beta\lambda/2$. A conservative gradient of 3 MV/m is assumed to calculate the effective voltage gain per cavity.

Table 3: Specifications for the three cavity types. The effective voltage assumes an accelerating gradient of 3 MV/m.

Cavity	Cells	β_0 (%)	f (MHz)	L (cm)	V_{eff} (MV)
1	2	3.5	105	10	0.3
2	3	7.0	140	22.5	0.68
3	3	11.	175	28.2	0.85

The proposed structure was used to estimate expected final energies. Assuming a conservative gradient of 3 MV/m, ISAC2 could reach 13 MeV/u for the lightest ions decreasing monotonically to 10 MeV/u at $A \sim 60$ and to 6.5 MeV/u at $A = 150$.

3 STAGING

The flexibility of short superconducting modules has other advantages as well. Since they are short and have wide

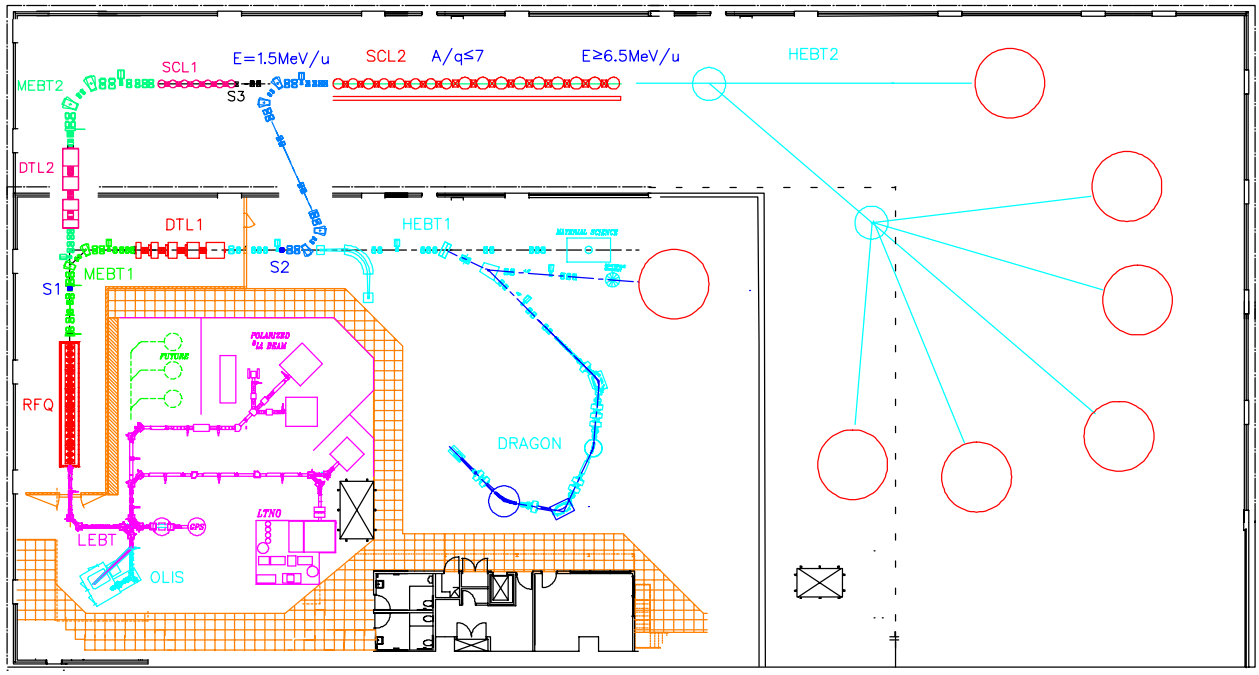

Figure 1: ISAC2 layout, including link from ISAC1, as would be needed for a 2-stripper stage

velocity acceptance, they can be built and tested even before the building addition for ISAC2 (see Fig. 1) is completed. Modules can be installed downstream of DTL1 as they become available and before the building needs to be expanded. At reduced, but usable intensity, masses up to 60 and energy up to 7 MeV/u could be available with an outlay of as little as 1/3 the cost of the complete ISAC2. This is stage 1 in Fig. 2.

Intensity for masses higher than 60 are low in stage 1 because the ISAC1 DTL requires $A/q \leq 6$ and the stripping energy is 0.15 MeV/u. However, by pushing the DTL voltage, raising the top fields of the MEBT dipoles and the DTL quads by a factor of 7/6, $A/q \leq 7$ becomes possible. This allows acceleration by ISAC1 up to mass 110 before intensity drops off. Accordingly, the ISAC1 design has been upgraded from $A/q = 6$ to 7. This is stage 2 in Fig. 2. In this stage, the building would have the expanded size shown in Fig. 1, the superconducting modules would be installed in their final location in preparation for ISAC2, and a transfer line would be used to bring the beam from DTL1 to SCL2.

Finally, DTL2 and MEBT2 would be installed to allow stripping at 400 keV/u to reach $A = 150$. This is stage 3 in Fig. 2.

4 REFERENCES

[1] P. Schmor et al., "The High Intensity Radioactive Beam Facility at TRIUMF", Proceedings of the 1998 European Part. Acc. Conf., Stockholm, to be published.

[2] P. Ostroumov, "ISAC-II: A Proposal for the ISAC Facility Expansion", TRIUMF internal note (Sept. 1997).

[3] C. Tamburella et al., "Production of Multicharged Radioactive Ion Beams: ...", Rev. Sci. Instrum. **68** (6), 2319-2321 (1997).

[4] R.E. Laxdal et al., "A Separated Function Drift Tube Linac for the ISAC Project at TRIUMF", Proc. Part. Acc. Conf. (Vancouver, 1997).

[5] J.W. Noe et al., "A Retro-fit/Upgrade of the Stony Brook Linac", Nucl. Instrum. Meth. **A287**, 240-246 (1990).

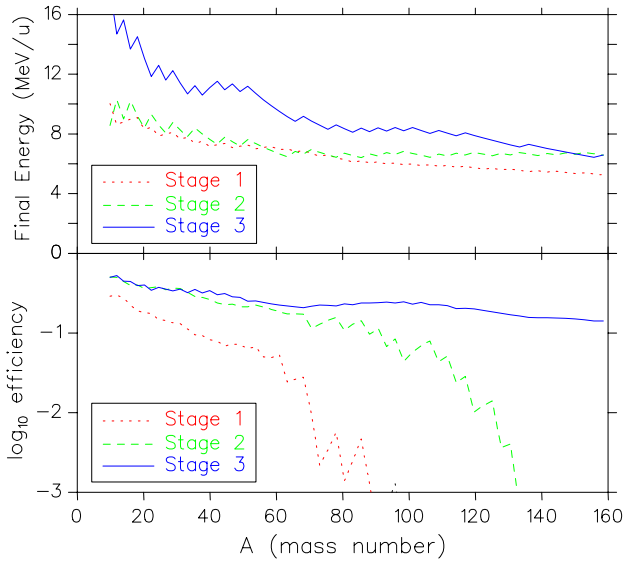

Figure 2: Relative intensities and energies for the 3 stages

STATUS OF THE REX-ISOLDE LINAC*

O. Kester, D. Habs, R. Rao, K. Rudolph, T. Sieber, H. Bongers, A. Kolbe, P. Thirolf
LMU München, Garching, Germany
R. von Hahn, H. Podlech, R. Repnow, D. Schwalm, MPI für Kernphysik, Heidelberg, Germany
A. Schempp, K.-U. Kühnel, C. Welsch, J.W. Goethe-Universität, Frankfurt, Germany
U. Ratzinger, GSI, Darmstadt, Germany
and the REX-ISOLDE collaboration

Abstract

The Radioactive beam Experiment (REX-ISOLDE) [1] a pilot experiment testing a new concept of post acceleration of radioactive ions at ISOLDE/CERN is under progress. Radioactive singly charged ions delivered by the on-line mass separator ISOLDE are accumulated in a Penning trap, then charge bred to A/q < 4.5 in an electron beam ion source (EBIS) and finally accelerated in a LINAC from 5 keV/u to a final energy between 0.8 and 2.2 MeV/u. The resonant structures of the LINAC consist of a Radio Frequency Quadrupole (RFQ) accelerator, a 3-gap split ring buncher, an interdigital H-type structure and three 7-gap spiral resonators, which allow to vary the final energy. New beam line calculations of the mass separator and the matching section between the RFQ and the IH-structure have been done. A test beam line including a duoplasmatron ion source, an electrostatic quadrupole lens system and a prototype of a diagnostic box is assembled. The vacuum tank of the IH-structure is in production as well as the buncher. The RFQ is assembled and ready for first vacuum tests. The first 7-gap resonator is almost completed and first tests are sheduled. The present paper describes the status of the separator and the REX-ISOLDE LINAC.

1 INTRODUCTION

REX-ISOLDE is a first generation Radioactive Ion Beam (RIB) project to explore the structure of neutron rich Na, K, Ca and Mg isotopes and the possibilities of an effective post acceleration of exotic ions due to charge breeding with dedicated state of the art machines. The frame parameters of the LINAC are an operation frequency of 101.28 MHz which is the half frequency of the CERN proton LINAC II, the timing of the extraction and a repetition rate of up to 50 Hz require a maximum duty cycle of 10%. To be flexible in the kind of experiment and for different ion species the exit energy has to be variable between 0.8 and 2.2 MeV/u. [2]. The radioactive ions are injected into the LINAC with an A/q-ratio between 3 and 4.5. The used structures is a 4-rod RFQ similar to the first RFQ of the Heidelberg high current injector [3] using mini-vanes as electrodes.

* Work supported by the BMBF under contract 06 LM 868 I / TP:4 and 06 HD 802 I

In addition an IH-structure is used as a booster structure which is a small version of the tank1 of the lead LINAC-IH-structure at CERN [4]. For matching the phase spread of the ion beam out of the RFQ to the longitudinal phase acceptance of the IH-structure a 3-gap split ring resonator is used. The energy variation is done by three 7-gap spiral resonators similar to the structures used at the Heidelberg high current injector [5]. The complete experiment is shown in Fig.1 including the beam optics and the target region.

2 HARDWARE STATUS

All resonance structures of the LINAC are now in production or already delivered. Hence an overview of the hardware status can be given. The installation of the LINAC at ISOLDE takes place in the next shut down period. The Penning trap is fully assembled and first tests of the injection system have been done [6]. The beam line trap-EBIS has been calculated and is now under construction. The cryostat of the EBIS was damaged after a He-quench test and is now in repair. The vacuum system of the EBIS as well as the collector and the gun are completed and shipped to CERN.

2.1 The q/A separator

The ion beam leaving the EBIS contains impurities from residual gas inside the EBIS. Therefore a q/A-separator is required with a resolving power of about 150. In order to be independent in the resolving power from the energy spread of the ions due to the potential depression of the electron beam of the EBIS an achromatic system was chosen, where the resolving power is dependent on the EBIS emittance [7]. The amount of radioactive isotopes from ISOLDE can be down to 100 times lower than the number of residual gas ions. Thus the overlap of the mass peaks at the mass separation slit must not be higher than 0.01%. Therefore the EBIS emittance has to be lower than 10 π mm mrad (2σ) to get a resolving power of 150. The hardware of the separator is in production, the vacuum system is delivered. The electrostatic quadrupole quadruplet (EQQ1) is completed and built into the test beam line.

The deflector tank is in production as well as the deflector. The construction of the electrostatic lenses is

completed. The deflecting magnet with a maximum field of 0.2 T is ordered.

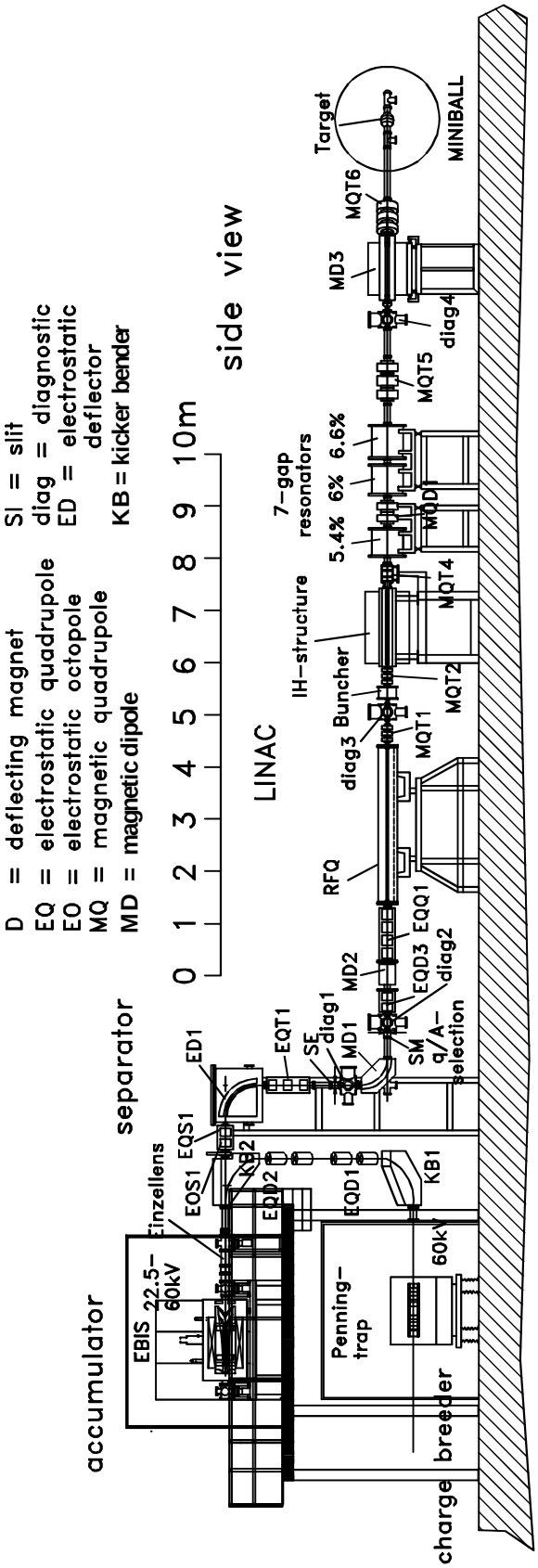

Figure 1: Layout of REX-ISOLDE.

This magnet has the possibility to shape the exit pole face for higher order corrections by iron fingers mounted at the mirror plates.

2.2 The four-rod RFQ

The REX-ISOLDE-RFQ has been assembled and a first frequency tuning has been done. In these measurements the flatness of the rod voltage, the quality factor and the shunt impedance have been determined. The resonator is ready for the first vacuum test. For the power test the water cooled ground plates have to be mounted and the final alignment has to be done. More details about the RFQ are presented in [8] on this conference.

2.3 The buncher

The vacuum tank for the Split Ring Buncher has been manufactured and leak checked. Next step is copper plating at GSI. An 1:1 model of the resonator has been built and tuned to the proper frequency. The final drift tube assembly has been manufactured. Fig.2 shows a view of the present tank with the split rings.

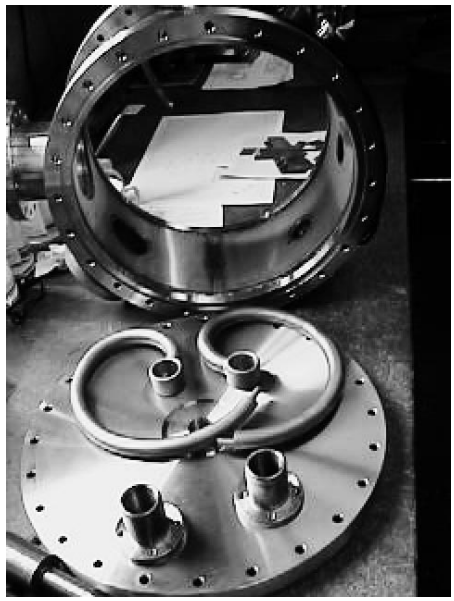

Figure 2: Vacuum tank of the buncher and the split ring structure.

2.4 The IH-Structure

The booster part of the LINAC is a short IH-structure with a maximum resonator voltage of 5.04 MV. Identical to the twin brother structure tank1 of the CERN lead LINAC the REX-ISOLDE-IH-structure consists of a center frame which carries the drift tubes and two half shells which are double walled for water cooling reasons. In fig.3 one can see the two walls of both half shells and the center frame with the support of the drift tubes. The photo was taken before the frequency tuning via the half shell length has been done. The big holes in the half shells are for the pumping flange, the incoupling loop and the inner-tank triplet lens. The triplet lens mounted in the IH-

vacuum tank is now completed and will be delivered from DANFYSIK within the next three weeks. After the final production of the tank all parts will be copper plated until the end of the year. The drift tubes will now be brazed to the supports and both will than be copper plated.

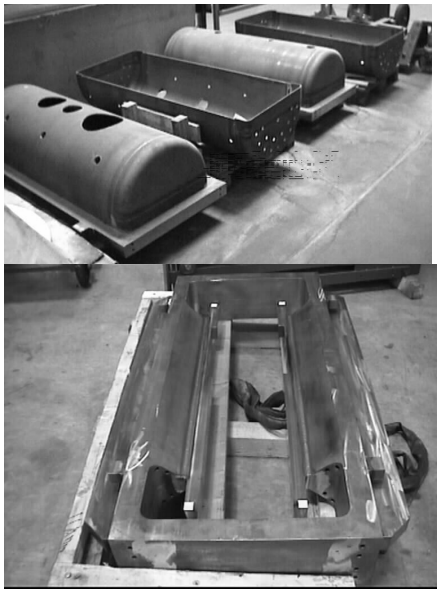

Figure 3: Half shells and center frame of the IH-structure before the final assembly at the company NTG.

2.5 The 7-gap resonators

The high energy section of the REX-ISOLDE LINAC consists of three 7-gap resonators each with a single resonance structure. It consists of a copper half shell to which three copper arms are attached on each side. Each arm consists of two hollow profiles, surrounding the drift tubes and carrying the cooling water. Copper segments on both sides allow to tune the resonator to the required frequency. The optimization of all model resonators is finished. The resonators will achieve the design voltage of 1.75 MV at 90 kW incoupled rf-power.

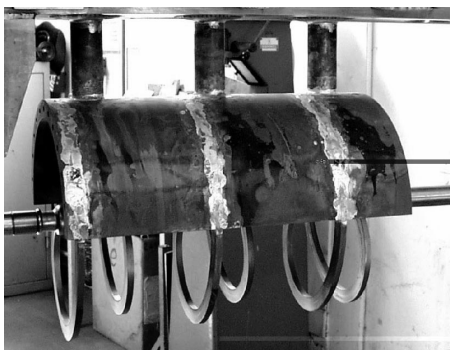

Figure 4: Resonance structure of the 5.4% power resonator directly after brazing of the arms into the half shell.

All components of the power resonators (tank, half shells, arms and drift tubes) are in production (fig.4) or already finished. The first half shell (5.4% resonator) is brazed and will be assembled into the tank after cleaning and polishing of the surface. After the tuning to the right frequency the resonator will be ready for vacuum, power and beam tests. The production of the resonators are well within the time schedule, expecting the first accelerated beam in 1999.

3 TEST BEAM LINE

In order to test the RFQ as the first acceleration stage, an injection system as well as an ion source are required. Therefore a duoplasmatron ion source has been borrowed from the university of Frankfurt. For the present geometry the calculated current of 1^+ He-ions is about 38 μA assuming 20 kV extraction voltage. This current will be reduced by collimators and slits down to 1 μA in order to reduce the emittance to the EBIS emittance. For beam diagnostic the prototype of a diagnostic box for REX-ISOLDE developed at KU Leuven will be used. In order to get the right beam slope in both transverse directions for the injection into the RFQ the electrostatic quadrupole quadruplet of the mass separator will be used. In the first stage the beam leaving the RFQ will be examined. Later the matching section will be included and the buncher will be tested with the He-beam as well.

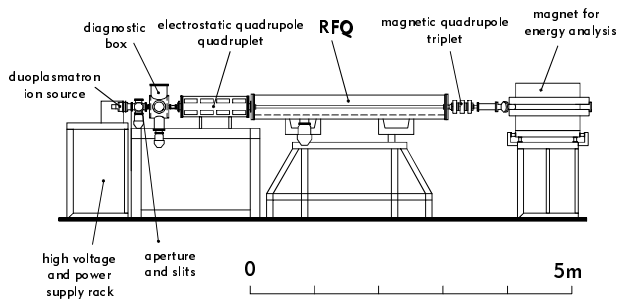

Figure 5: Lay-out of REX-ISOLDE test beam line for beam analysis of the RFQ beam

REFERENCES

[1] D. Habs et al., CERN-ISC94-25

[2] O. Kester et al., "The REX-ISOLDE Project", proc. CAARI'96, Denton, USA, AIP 392

[3] M. Madert et al., "The RFQ-Accelerator for the Heidelberg High Current Injector", *Nucl. Instrum. and Meth.* **B 139**,437-440 (1998).

[4] N. Angert et al., "The IH LINAC of the CERN Lead Injector", LINAC94, Tsukuba, Japan, 1994.

[5] R. von Hahn et al., *Nucl. Instrum. and Meth.* **A 328**, 270-274 (1993).

[6] F. Ames et al., „REX TRAP an ion buncher for REX-ISOLDE", proc. ENAM98, Michigan USA, June 98.

[7] R. Rao et al., "The q/m-Separator for REX-ISOLDE", proc. EPAC98, Stockholm, June 1998.

[8] T. Sieber et al., „Design and Status of the RFQ for REX-ISOLDE", this conference, TH4006.

RTA GUN PERFORMANCE

G. A. Westenskow, T. L. Houck
Lawrence Livermore National Laboratory, Livermore, CA 94550 USA
D. E. Anderson, S. Eylon, E. Henestroza, S.M. Lidia, D. L. Vanecek, S. S. Yu
Lawrence Berkeley National Laboratory, Berkeley, CA 94720 USA

Abstract

The technical challenge for making two-beam accelerators into realizable power sources for high-energy colliders lie in the creation of the drive beam and in its propagation over long distances through multiple extraction sections. This year we have constructed a 1.2-kA, 1-MeV, electron induction injector for the RTA accelerator. The electron source will be a 8.9 cm diameter, thermionic, flat-surface cathode with a maximum shroud field stress of approximately 165 kV/cm. The injector's pulse length should be over 120-ns flat top (1% energy variation) with a normalized edge emittance of less than 300 π-mm-mr. Details of the design and performance of the injector, beam line, and diagnostics will be presented.

1 INTRODUCTION

Induction accelerators are a unique source for high-current, high-brightness, electron beams. A collaboration between the Lawrence Livermore National Laboratory (LLNL) and Lawrence Berkeley National Laboratory (LBNL) has been studying rf power sources based on the Relativistic Klystron Two-Beam Accelerator (RK-TBA) concept for several years [1, 2]. Demanding beam parameters are required of the electron source, an induction injector, to achieve the transport goals. A test facility, called the RTA, has been established at LBNL [3] to verify the analysis used in the design study. The primary effort of the facility is the construction of a prototype RK-TBA subunit that will permit the study of technical issues, system efficiencies, and costing. In this paper, we will discuss the development of the RTA electron source and it's pulsed power system, which has recently been constructed and is now undergoing testing. Figure 1 is a photograph of the gun undergoing initial tests. Beam tests will be performed this fall.

2 RTA GUN

A major part of our effort during the past year has been towards the design of a low emittance electron source for RTA accelerator. We expect to produce an electron source with a much lower emittance than typical induction guns. The electron source will be a 8.9-cm-diameter, thermionic, flat-surface M-type cathode with a maximum shroud field stress of approximately 165 kV/cm. An emission density of 20 A/cm^2 is required from the cathode to produce a 1.2 kA beam.

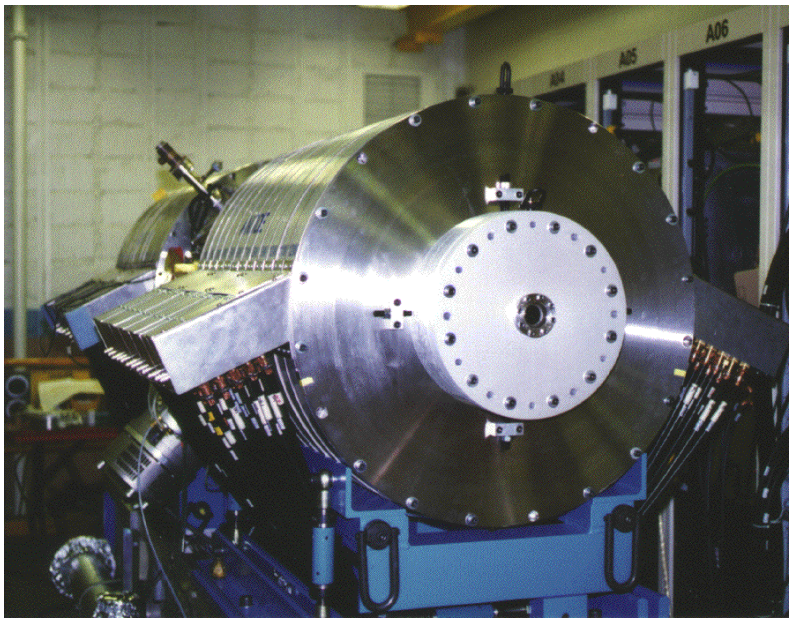

Figure 1. RTA Gun during pulsed power test.

The RTA gun has 72 induction cores, each driven at 14 kV. The voltage from the cores are summed across the A-K gap to produce 1 MV. The cells are segmented radially to reduce the individual aspect ($\Delta r/\Delta z$) ratio of the cores. The lower aspect ratio reduces the variation in core impedance during the voltage pulse simplifying the pulse forming network (PFN) design.

We have done high-voltage tests on the gun. In operation a 500 kV potential is developed across each of the two 30-cm-ID PYREX insulators producing a 5.1 kV/cm average gradient along the insulator. The maximum fields at the triple points, the intersection of insulator, vacuum, and metal, is less than 3.5 kV/cm. Maximum surface field in the cathode stalk of the gun is about 85 kV/cm. The maximum field is about 116 kV/cm on the anode stalk.

Initial beam focusing in the gun is accomplished by large-bore air-core solenoids installed on the central pumping spool. The first solenoid is operated to null the magnetic field from the other solenoids at the cathode front surface. With a flat cathode a high dB/dz is needed to prevent the beam from hitting the anode surfaces. The magnetic field at a distance of 20 cm from the cathode is about 650 gauss. There are seven smaller solenoids located within the anode stalk to provide additional focusing to transport the beam to the end of the gun.

2.1 Pulsed Power System for the RTA Gun

The pulsed power system for the gun consists of a 20-kV High-Voltage Power Supply, 6-kJ Energy Storage Bank, two Command Resonant Charging (CRC) Chassis, 24 Switched Pulse Forming Networks, and four Induction Core Reset Pulsers. Each PFN will drive a single 3-core induction cell of the gun.

Segmenting the core in the induction cell and driving the individual core segments avoids a high-voltage step-up transformer. This reduces the developmental effort needed to achieve a "good" flattop pulse (minimal energy variation) with fast risetime and improves the efficiency of the overall pulsed power system. Our system of low-voltage PFNs driving multiple core induction cells is similar to the system envisioned for the full scale RK-TBA design. For the gun core material we choose 20-μm-thick 2605SC METGLAS. In the RTA main extraction section we will use a lower loss 2714AS METGLAS for the induction cores.

Design of the switched PFNs follows easily from published METGLAS core loss data [4]. For the RTA induction cells, a flux swing of 2.6 T in 400 ns (FWHM) results in a magnetization rate of 6.5 T/μs. At this rate, a loss density of 1800 J/m^3 translates into 30 J lost in a cell with $16.7x10^3$ cm^3 of 2605SC METGLAS. For a cell input voltage of 14 kV applied for 400 ns, these losses require that 5900 A be supplied to the three radial cores. An additional 3600 A is required to supply beam current (1200 A x 3 cores/cell), resulting is a total current of 9 kA. The required drive impedance for a cell is then 1.5 Ω, which is provided by the PFN module.

An area of concern was the variation of the energy loss for different METGLAS cores. Experience [5] with the 72 cores in the gun leads us to believe that for a large RK-TBA, matching cell cores should permit acceptable energy loss variation.

2.1 Gun Voltage Waveform

Achieving the fast risetime necessary to minimize the volt-seconds required for the injector cores presented a challenge. Budget constraints coupled with the large availability of EEV CX1538 thyratrons from the ATA program at LLNL made these tubes an attractive option. However, their poor time rate of current change (4 kA/μs rating) made them questionable for this application, which requires about 40 kA/μs. A variety of techniques were tried to decrease the risetime. In a 1.5 Ω system, stray circuit inductances must be maintained at or below 100 nH to achieve a 10-90% risetime of 150 ns. This was accomplished by placing the thyratron between two current sheets connecting the PFN output to the output cables. The ionization time of the thyratron was substantially reduced by applying a 1-2 A pre-pulse to the keep-alive grid 300-400 ns prior to the arrival of the main control-grid pulse. Faster risetimes were achieved with Triton F-130 ceramic thyratrons. An upgrade of the current thyratrons in the gun pulsed power system should allow us to achieve the design 100-ns risetime.

At the 1-MV, 1.2-kA operating conditions we hope to produce a ±1% gun voltage flat waveform for 120 ns. We will need to adjust the number of turns in appropriate sections of individual PFNs to achieve this goal. Insertion of ferrite material in the center of the inductors coils will allow additional small corrections to the waveform.

2.3 Diagnostics for the RTA Gun

A variety of diagnostics [6] will be used to determine the performance of the gun, both permanently installed monitors for general operations and temporary diagnostics specific to the injector commissioning and troubleshooting. Planned diagnostics include an isolated cathode with resistive divider for direct measurement of current emission, resistive-wall and magnetic probe current monitors for measuring beam current and centroid position, capacitive probes for measuring A-K gap voltage, an energy spectrometer, and a pepper-pot emittance diagnostic.

The majority of the diagnostics will be installed after the gun. The first 1.4 m of beam line after the gun will

include two beam position and current monitors to allow the offset and angle of the beam at the exit of the injector to be measured. A pop-in probe will be incorporated in a pumping port to allow the beam profile to be viewed.

The current density profile will be measured using Cherenkov and/or optical transition radiation from intercepting foils. A primary concern with using foils is possible damage from beam energy deposition. Average heating of the foil can be controlled by adjusting the repetition rate of the injector. The difficulty is the single shot heating where material can be melted and ejected before the heat is conducted away. As an example, to avoid damage for a thin quartz foil, the beam diameter must be larger than 2 cm for a 1-kA, 300-ns, relativistic electron beam. The significant levels of energy deposited in the foil could affect the dielectric constant or generate a surface plasma that could be confused as a variation in beam parameters.

Three different methods may be used to determine the A-K voltage and beam energy. The first method involves measuring the applied voltage to the induction cores at the connection of the power feeds to the induction cells. Capacitive dV/dt pickup probes [6] are used for a more direct measurement of the A-K gap voltage and also to provide greater bandwidth with respect to the resistive dividers. We also hope to employ a conventional energy spectrometer comprised of an on-axis collimator, dipole magnet, scintillator, and viewing port to directly measure the beam energy.

2.4 Emittance measurement for the gun

We plan to use a pepperpot emittance diagnostic to help characterize the beam. Measuring the beam emittance is expected to be very difficult as the beam is highly space charged dominated. Our aperture plate will consist of a rectangular pattern of 121 (11x11) 250-μm apertures with 7 mm spacing on a 500-μm thick tungsten plate. The emittance term that is responsible for spot size growth of the beamlets after the aperture plate is approximately an order of magnitude larger than the space charge term.

Another serious problem concerns the effect of the conductive aperture plate on the beam. It has been demonstrated [7] that, while the local distribution in phase space can be determined, the global x–x' curve is dominated by the non-linear focusing of the aperture plate. EGUN simulations performed for our beam parameters indicate that the beam emittance determined from the pepperpot data will be as much as six times the actual emittance in the absence of the aperture plate. This effect can be accounted for in the analysis. However, the accuracy in the final emittance value will suffer.

3 ACCELERATOR SECTION DESIGN

Design of the full-scale RK-TBA system has an accelerator section after the gun that raises the beam energy from 1 MeV to 2.5 MeV before starting to bunch the beam at 11.4 GHz. In the full-scale RK-TBA system we expect to use a pulse power system similar to that demonstrated in the gun system for this section. The accelerator cells will be segmented to reduce the required drive. However, to reduce RTA's cost we are planning on using a 120-kV MARX spark-gap pulsed power system to drive 16 unsegmented accelerator cells in this section of RTA. The design is not acceptable for the full-scale machine because of the high gap erosion rates. The spark-gap system can provide a faster risetime than the thyratron system which will reduce the required cross sectional area of the induction cores. The volt-second rating of the accelerator cores (operated at 120 kV) will limit the flat top of the beam pulse in the RTA. Installation of additional cells (future upgrade), and operating all the cells at a lower voltage, will increase the useful duration of the current pulse. We also plan to test a High-Gradient Insulator [8] in the first of these accelerator cells. If successful we would like to construct the 16 cells for RTA accelerator section using High-Gradient Insulators.

4 ACKNOWLEDGEMENTS

The work was performed under the auspices of the U.S. Department of Energy by LLNL under contract W-7405-ENG-48, and by LBNL under contract AC03-76SF00098. We thank Andy Sessler and Swapan Chattopadhyay for their support and guidance and thank Wayne Greenway, William Strelo, Bob Benjegerdes and Bob Candelario for their excellent technical support

.

5 REFERENCES

[1] Sessler, A.M. and Yu, S.S., "Relativistic Klystron Two-Beam Accelerator," *Phys. Rev. Lett.* **54**, 889 (1987).

[2] Westenskow, G.A., and Houck, T.L., "Relativistic Klystron Two-Beam Accelerator," *IEEE Trans. on Plasma Sci.*, **22**, 750 (1994).

[3] Houck, T.L., and Westenskow, G.A., "Prototype Microwave Source for a Relativistic Klystron Two-Beam Accelerator" *IEEE Trans. on Plasma Sci.*, **24**, 938 (1996).

[4] Smith, C.H., and Barberi, L., "Dynamic Magnetization of Metallic Glasses," in Proc. of the 5th. IEEE Int'l Pulsed Power Conf., 1985.

[5] Westenskow, G.A., et al., "Relativistic Klystron Two-Beam Accelerator Studies at the RTA Test Facility", Proc. of the 1997 Particle Accelerator Conference, Vancouver, Canada, 1997.

[6] Houck, T.L., et al., "Diagnostics for a 1.2-kA, 1-MV Electron Induction Injector," Proc. of the 8th Beam Instrumentation Workshop, SLAC, 1998.

[7] Hughes, T.P., Carlson, R.L., and Moir, D.C., *J. Appl. Phys.* **68**, 2562–2571 (1990).

[8] Houck, T.L., et al., "Stacked Insulator Induction Accelerator Gaps", Proc. of the 1997 Particle Accelerator Conference, Vancouver, Canada, 1997.

ACHROMAT WITH LINEAR SPACE CHARGE FOR BUNCHED BEAMS

D. Raparia, J.G. Alessi, Y. Y. Lee and W. T. Weng
Brookhaven National Laboratory
Upton, NY 11973, USA

Abstract

The standard definition for an achromat is a transport line having zero values for the spatial dispersion (R16) and the angular dispersion (R26). For a bunched beam with linear space charge this definition of achromaticity does not hold. The linear space charge in the presence of a bend provides coupling between (a) bunch spatial width and bunch length (R15) and (b) bunch angular spread and bunch length (R25). Therefore, achromaticity should be redefined as a line having zero values of the spatial dispersion (R16), the angular dispersion (R26), and matrix elements R15 & R25. These additional conditions (R15=R25=0) can be achieved, for example, with two small RF cavities at appropriate locations in the achromat, to cancel space charge effects. An example of the application of this technique to the Spallation Neutron Source (SNS) high energy beam transport line will be presented.

1 INTRODUCTION

A transport line is said to be achromatic if spatial & angular widths of the beam are independent of its momentum spread. In other words, the spatial dispersion (R16) and the angular dispersion (R26) have zero values. The spatial & angular widths are also independent of the bunch length in absence of linear space charge. The beam ellipse is upright in the x-z plane. A property of an achromatic bend is that the total phase advance should be $n\pi (n = 1, 2 \cdots)$ if all dipoles in achromat bend the beam in the same direction, or $2n\pi$ if some of the dipoles in achromat bend the beam in the opposite direction. In the presence of linear space charge the transport line no longer remains achromatic for two reasons. (1) The total phase advance is no longer $n\pi$ or $2n\pi$ due to tune depression. The total phase advance can be changed back to $n\pi$ or $2n\pi$ by readjusting quadrupoles in achromat. (2) When beam passes through the bend it is no longer upright in x-z plane because space charge provides coupling between (a) bunch spatial width and bunch length (R15) and (b) bunch angular width and bunch length (R25). The beam ellipse can be made upright in x-z plane by introducing two rf cavities in the achromat.

2 ACHROMAT WITH LINEAR SPACE CHARGE FOR BUNCHED BEAM

2.1 Linear Space Charge for Bunched Beams

Following the formulism of TRACE3D [1], the electric field components due to a uniformly charged ellipsoid are given by [2]

$$E_x = \frac{1}{4\pi\epsilon_0}\frac{3I\lambda}{c\gamma^2}\frac{(1-f)}{r_x(r_x+r_y)r_z}x,$$

$$E_y = \frac{1}{4\pi\epsilon_0}\frac{3I\lambda}{c\gamma^2}\frac{(1-f)}{r_y(r_x+r_y)r_z}y,$$

$$E_z = \frac{1}{4\pi\epsilon_0}\frac{3I\lambda}{c}\frac{f}{r_x r_y r_z}z,$$

where r_x, r_y and r_z are the semi-axes of a ellipsoid, I is the average electrical current over one RF period, λ is the free-space wavelength of the RF, c is the velocity of light, and ϵ_0 is the permittivity of the free space. The form factor f is a function of $p \equiv \frac{\gamma r_z}{\sqrt{r_x r_y}}$ given by

$$f(p) = \begin{cases} \frac{1}{1-p^2} - \frac{p}{(1-p)^{3/2}}\cos^{-1}p & \text{if } p < 1 \\ \frac{p\cosh^{-1}p}{(p^2-1)^{3/2}} - \frac{1}{(p^2-1)} & \text{if } p > 1 \\ \frac{1}{3} & \text{if } p = 1 \end{cases}$$

where $\cosh^{-1}p = \ln\left(p + \sqrt{p^2-1}\right)$.

The space charge is applied in the kick approximation as a change in the normalized momentum components as the beam traverses Δs, and is given by

$$\Delta(\beta\gamma)_u = \frac{qE_u\Delta s}{m_0c^2\beta}$$

where u represents x, y, or z. This kick formulation is correct as long as the ellipsoid is upright in local x-y, y-z, and z-x planes. When beam traverses the bend the ellipsoid is tilted in the local x-z plane. To calculate the space charge kick first one has to transform to the coordinate system in which the ellipsoid is upright. The ellipsoid is transformed back to the local coordinate system after applying the space charge kick. The transfer matrix for the space-charge kick is

$$R_S = \begin{pmatrix} 1 & 0 & 0 & 0 & 0 & 0 \\ \frac{qE_x\Delta s}{m_0c^2\beta} & 1 & 0 & 0 & 0 & \\ 0 & 0 & 1 & 0 & 0 & 0 \\ 0 & 0 & \frac{qE_y\Delta s}{m_0c^2\beta} & 1 & 0 & 0 \\ 0 & 0 & 0 & 0 & 1 & 0 \\ 0 & 0 & 0 & 0 & \frac{qE_z\Delta s}{m_0c^2\beta} & 1 \end{pmatrix}.$$

2.2 *Coupling Between Bunch Length and Bunch Spatial & Angular Widths*

This coupling is induced by linear space charge, which can be shown as follows. The transfer matrix of a bending magnet for bend angle α and length L is

$$R[xx]_B = \begin{pmatrix} \cos(k_x L) & \frac{1}{k_x}\sin(k_x L) \\ -k_x \sin(k_x L) & \cos(k_x L) \end{pmatrix}$$

$$R[xz]_B = \begin{pmatrix} 0 & \frac{h(1-\cos(k_x L))}{k_x^2} \\ 0 & \frac{h\sin(k_x L)}{k_x} \end{pmatrix}$$

$$R[yy]_B = \begin{pmatrix} \cos(k_y L) & \frac{1}{k_y}\sin(k_y L) \\ -k_y \sin(k_y L) & \cos(k_y L) \end{pmatrix}$$

$$R[zx]_B = \begin{pmatrix} \frac{-h\sin(k_x L)}{k_x} & \frac{-h(1-\cos(k_x L))}{k_x^2} \\ 0 & 0 \end{pmatrix}$$

$$R[zz]_B = \begin{pmatrix} 1 & \frac{-1}{\rho^2 k_x^3}(k_x L\beta^2 - \sin(k_x L)) \\ & +\frac{L}{\gamma^2}(1 - \frac{1}{\rho^2 k_x^2}) \\ 0 & 1 \end{pmatrix}$$

$$R[xy]_B = R[yx]_B = R[yz]_B = R[zy]_B = \begin{pmatrix} 0 & 0 \\ 0 & 0 \end{pmatrix}$$

where

$$h = \frac{1}{|\rho|}\frac{\alpha}{|\alpha|}$$

$$k_x = \sqrt{(1-n)h^2}$$

$$k_y = \sqrt{nh^2}$$

$$L = |\rho|\,\alpha$$

$$\rho = \frac{m_0 c\beta\gamma}{qB_y}$$

$$n = -\left(\frac{\rho}{B_y}\frac{\partial B_y}{\partial x}\right)_{x=0,y=0}$$

When space-charge is included in the calculation for the bending magnet in the kick approximation, the two matrices R_S and R_B are multiplied, and the resultant matrix R_{SB} will have $R_{SB}15$ and $R_{SB}25$ non-zero and given by

$$R_{SB}15 = R_B16 * R_S65 = \frac{h(1-\cos(k_x L))}{k_x^2} \times \frac{qE_z L}{m_0 c^2 \beta}$$

$$R_{SB}25 = R_B26 * R_S65 = \frac{h\sin(k_x)L}{k_x} \times \frac{qE_z L}{m_0 c^2 \beta}.$$

Even after applying the usual conditions for an achromat, R16=R26=0, the system is not achromatic. To completely remove coupling between x-x' and z-z' planes, not only the determinant of sub-matrix R[xz] has to be zero, but all of its elements have to be zero. If any element of this sub-matrix is non-zero, it means that beam is not upright in the x-z plane. The coupling provided by the space charge will effectively produce dispersion (R16), angular dispersion (R26) and non-zero matrix elements R15 & R25. The beam ellipse can be made upright in x-z plane by introducing two rf cavities in the achromat.

3 EXAMPLE

As shown, all four elements of the R[xz] sub-matrix should have zero values for a transport line to be achromatic. We will use as an example proposed Spallation Neutron Source (SNS) high energy transport line [3]. This transport line is about 180 meters long and has an achromat which is six cells long, with a total phase advance of 360 degrees. The layout of HEBT is shown in Figure 1, and the corresponding amplitude and dispersion functions are shown in Figure 2.

The transfer matrix of the achromat in the HEBT for the zero current (using TRACE3D) is

$$R_{acro} = \begin{pmatrix} 1 & 0 & 0 & 0 & 0 & 0 \\ 0 & 1 & 0 & 0 & 0 & 0 \\ 0 & 0 & 1 & -1.305 & 0 & 0 \\ 0 & 0 & 0.01778 & 0.98846 & 0 & 0 \\ 0 & 0 & 0 & 0 & 1 & 14.15989 \\ 0 & 0 & 0 & 0 & 0 & 1 \end{pmatrix}$$

with the following units

$$\begin{pmatrix} 1 & m & 1 & m & 1 & m \\ m^{-1} & 1 & m^{-1} & 1 & m^{-1} & 1 \\ 1 & m & 1 & m & 1 & m \\ m^{-1} & 1 & m^{-1} & 1 & m^{-1} & 1 \\ 1 & m & 1 & m & 1 & m \\ m^{-1} & 1 & m^{-1} & 1 & m^{-1} & 1 \end{pmatrix}$$

The R[xz] sub-matrix of the achromat plus the following two cells, for zero current, is

$$R[xz]_{acro+2c} = \begin{pmatrix} 0 & 0 \\ 0 & 0 \end{pmatrix}$$

The R[xz] sub-matrix for the achromat, with 28 mA current, is

$$R[xz]_{acro} = \begin{pmatrix} 0.133349 & -0.18495 \\ 0.00469 & 0.8130 \end{pmatrix}$$

Now one can apply the conditions R16 = R26 = 0, by adjusting two families of quadrupoles in the achromat, and the resultant R[xz] sub-matrix of the achromat is

$$R[xz]_{acro} = \begin{pmatrix} 0.14278 & 0 \\ 0.00339 & 0 \end{pmatrix}$$

The R[xz] sub-matrix of the achromat plus the following two cells, for the 28 mA, is then

$$R[xz]_{acro+2c} = \begin{pmatrix} -0.00608 & -0.68454 \\ -0.01605 & 0.01919 \end{pmatrix}$$

This shows the condition R16 = R26 = 0, will not yield a achromatic system if one includes space charge. Figure 3 shows the space charge induced dispersion at end of the SNS achromat as function of half bunch length at beginning of the HEBT.

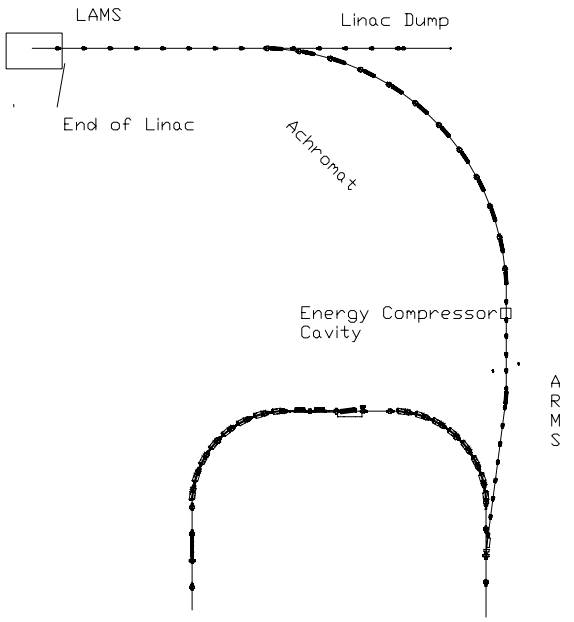

Figure 1: Layout of the SNS HEBT line.

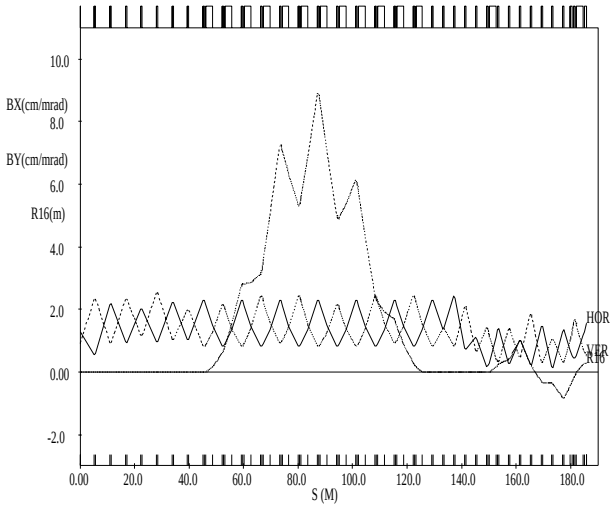

Figure 2: TRANSPORT output for the amplitude (β) functions and dispersion function (η) along the SNS HEBT.

Next, one can apply the conditions R16 = R26 = R15 = R25 = 0 (instead of R16 = R26 = 0) by adjusting the two families of quadrupoles in the achromat, and adding two small 1 meter RF cavities in the 2nd and 5th cells of the achromat set at appropriate voltages. One can then get the following R[xz] sub-matrix, similar to the zero current case.

$$R[xz]_{acro} = \begin{pmatrix} 0 & 0 \\ 0 & 0 \end{pmatrix}$$

For this case, however, the R[xz] sub-matrix for the achromat plus the following two cells, for 28 mA, is

$$R[xz]_{acro+2c} = \begin{pmatrix} 0 & 0 \\ 0 & 0 \end{pmatrix}$$

Therefore, for bunched beams achromaticity should be redefined as a line having zero values of matrix elements R15, R25, R16 and R26. The additional condition can be achieved with two small rf cavities.

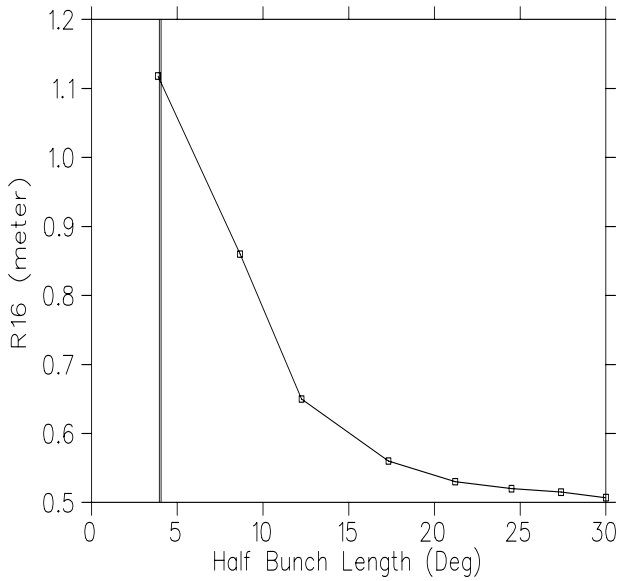

Figure 3: Space-charge induced dispersion (R16) at the end of the SNS achromat as a function of bunch length at the beginning of HEBT. Vertical line shows the design bunch length.

4 REFERENCES

[1] K. R. Crandall and D. P. Rusthoi, Los Alamos Report LA-UR-97-886.

[2] P. M. Lapostolle, CERN report AR/Int. SG/65-15, Geneva, Switzerland, July 1965.

[3] D. Raparia, J. Alessi, Y.Y. Lee, W. T. Weng, to be published in Proceedings of 1997 Particle Accelerator Conference, Vancouver, B.C. Canada, May 12-16, 1997.

A POSSIBLE PARTICLE-CORE APPROACH TO MISMATCHED BEAMS IN A PERIODIC FOCUSING CHANNEL

M. Ikegami and M. Mizumoto
Proton Accelerator Laboratory, Japan Atomic Energy Research Institute
Tokai-mura, Naka-gun, Ibaraki-ken, 319-1195 JAPAN

Abstract

A method is derived for applying the particle-core analysis to mismatched beams in a periodic focusing channel. By carefully choosing the parameters to yield a favorable core frequency, Poincaré surface of section plots are obtained. The plots for a periodic solenoid channel exhibit a striking resemblance with the continuous focusing case, while those for an FODO channel exhibit strong chaosity which is not seen in the corresponding continuous situation. Some typical numerical results and a way to find adequate parameters are presented.

1 INTRODUCTION

In recent years, halo formation in intense ion beams has been extensively studied in both theoretical and numerical ways. In these studies, the so-called *particle-core model* [1] has been frequently used. In this model, we usually consider a beam propagating in a continuous focusing channel and assume that its core has the Kapchinskij-Vladimirskij (KV) distribution. In the macro-particle simulation studies of the continuously focused beams, features such as the separatrix and fixed point locations are found to be in good agreement with those obtained with the particle-core model [2].

The halo properties in periodically focused cases have also been studied self-consistently, and a close resemblance to the continuous focusing cases is found for a periodic solenoid channel unless instabilities due to structure-driven resonances occur [3]. Though the role of the particle-core resonance in periodic focusing situations can be directly investigated by applying the particle-core model, it has never been done in mismatched cases mainly due to the difficulty in finding the fundamental frequency of the system. In the particle-core model, Poincarémapping technique is an essential tool to examine the stability properties of test particles, but we need to know the fundamental frequency of the system to use this technique. It is generally difficult to know the fundamental frequency in periodic focusing cases because there are two sources of periodicity, namely; the external focusing field periodicity and that due to initial beam-size mismatch. As the envelope is known to be stable with a reasonable choice of parameters, we try to obtain the fundamental core frequency restricting our interest to the cases where core oscillation is stable.

2 PERIODIC SOLENOID CHANNEL

Assuming the axial symmetry of the focusing channel, the time evolution of the beam envelope is governed by the envelope equation,

$$\frac{d^2 R_b}{ds^2} + \kappa(s) R_b - \frac{K}{R_b} - \frac{\varepsilon^2}{R_b^3} = 0, \qquad (1)$$

where R_b is the beam radius, $\kappa(s)$ is the periodic function representing the external focusing field strength, K is the generalized perveance, ε is the rms emittance of the beam, and independent variable s is the distance measured along the beam line. Then, in terms of dimensionless variables, Eq. (1) becomes

$$\frac{d^2 R}{d\tau^2} + \vartheta(\tau) R - \frac{\Gamma}{R} - \frac{1}{R^3} = 0, \qquad (2)$$

where $\tau = s/S$ is taken as the independ variable with S being the focusing period. The function $\vartheta(\tau)$ is related to the zero-current phase advance σ_0, and Γ is related to the tune depression η, namely, the ratio of the space-charge depressed phase advance to the zero-current phase advance. The matched solution R_0 of Eq. (2) can be obtained with the help of an optimization code. For later reference, we here introduce a mismatch factor defined as

$$M = \left[R(0) - R_0(0)\right] / R_0(0). \qquad (3)$$

It should be noted that $R_0(0)$ corresponds to the maximum of the matched beam radius since the origin of the coordinate τ is located at the center of a focusing solenoid. With use of the smooth-approximation, Eq. (2) can be written as

$$\frac{d^2 R_s}{d\tau^2} + {\sigma_0}^2 R_s - \frac{\Gamma}{R_s} - \frac{1}{R_s^3} = 0, \qquad (4)$$

where R_s is the scaled beam radius in the approximation. In weakly mismatched cases, the phase advance of the breathing mode oscillation of the envelope can be approximated by

$$\sigma_m = \sqrt{2\left(1+\eta^2\right) + \frac{1}{2}\left(1+9\eta^2\right) M^2}\,\sigma_0, \qquad (5)$$

where we use a combination of a simple perturbation method and an averaging method.

We here assume that the oscillation of the core can be approximated by a simple composition of two oscillation modes, namely; one is excited by the initial beam-size mismatch (*mismatch mode*) and the other is excited by the periodic nature of a focusing structure (*structure mode*). Based on the smooth-approximation analysis above, the phase advance of the mismatch mode is expected to be σ_m. On the other hand, the fundamental period of the structure mode is apparently synchronized with the focusing structure. Thus, it is obvious that if $\sigma_m/2\pi$ is a rational number *n/m*, the mismatched envelope is exactly periodic in τ with the period of *m* times a focusing period. In such cases, we can easily obtain a Poincaré surface of section plot by plotting test particle location every *m* focusing periods. That is our strategy to apply the particle-core method to mismatched beams in a periodic channel.

Finally, we write down the equation of motion for a test particle. Assuming that the core has a KV distribution and test particles have no augular momentum, the equation of motion in terms of the dimensionless variables is given by

$$\frac{d^2x}{d\tau^2} + \vartheta(\tau)x - \frac{\Gamma}{R^2}x = 0 \quad (|x| \le R), \tag{6a}$$

and

$$\frac{d^2x}{d\tau^2} + \vartheta(\tau)x - \frac{\Gamma}{x} = 0 \qquad (|x| > R). \tag{6b}$$

Figure 1 shows an example in which we consider a periodic solenoid channel having σ_0=45° and a 50% filling factor, and the beam parameters are set to be η=0.5 and M=0.3. These parameters are determined to yield σ_m=360/5=72° by Eq. (5) with the help of an optimization code. As shown in Fig. 1, the fundamental period of the core oscillation coincide with five focusing periods with a very good accuracy. We can also see in Fig. 1 that the core oscillation is almost dominated by the mismatch mode, and the contribution from the structure mode is fairly small. Plotting the single particle position every five focusing periods, we successfully obtain a Poincaré surface of section shown in Fig. 2, which exhibits a striking resemblance with continuous focusing cases.

3 FODO CHANNEL

The same method is also applicable to the beams in channels without an axial symmetry such as FODO channels. Assuming that the zero-current phase advance and emittance are the same in the horizontal and vertical directions, the envelope equations are given in terms of dimensionless variables as

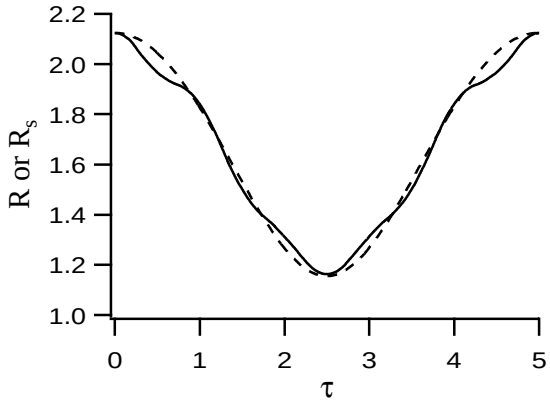

Figure 1: Time-evolution of the beam envelope in a periodic solenoid channel. Solid line: periodic solenoid channel. Broken line: smooth-approximation.

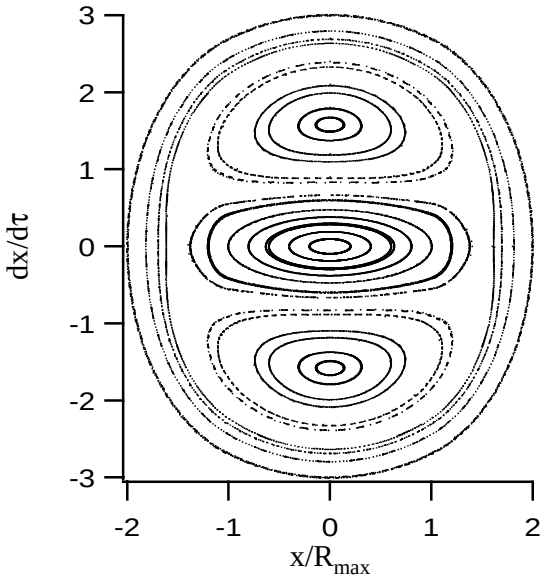

Figure 2: Poincaré surface of section plot for a periodic solenoid channel. The same parameters with Fig. 1 are employed.

$$\frac{d^2X}{d\tau^2} + \vartheta(\tau)X - \frac{2\Gamma}{X+Y} - \frac{1}{X^3} = 0, \tag{7a}$$

and

$$\frac{d^2Y}{d\tau^2} - \vartheta(\tau)Y - \frac{2\Gamma}{X+Y} - \frac{1}{Y^3} = 0, \tag{7b}$$

where X and Y are, respectively, the scaled beam half-width for the horizontal and vertical directions.

Note here that not only the breathing but also quadrupole mode oscillation can be excited in an FODO channel. For the quadrupole mode oscillation, the frequency of the mismatch mode is given by

$$\sigma_m = \sqrt{1+3\eta^2+5\eta^2 M^2}\,\sigma_0 . \qquad (8)$$

The equations of motion for a test particle initially located on the horizontal plane can be written [4] as

$$\frac{d^2x}{d\tau^2} + \vartheta(\tau)x - \frac{2\Gamma}{X(X+Y)}x = 0 , \qquad (|x| \le X) \text{ (9a)}$$

and

$$\frac{d^2x}{d\tau^2} + \vartheta(\tau)x - \frac{2\Gamma}{x^2 + |x|\sqrt{x^2+Y^2-X^2}}x = 0 . \ (|x| > X) \text{ (9b)}$$

First, we will consider the case where the breathing mode oscillation of the core is excited. Figure 3 shows an example in which we consider an FODO channel having σ_0=45° and a 50% filling factor, and the beam parameters are set to be η=0.5, and M=0.3. We can see in Fig. 3 that the modulation of the core oscillation due to the periodic nature of the focusing field is much larger than in periodic solenoid cases. A Poincaré surface of section plot is obtained as shown in Fig. 4.

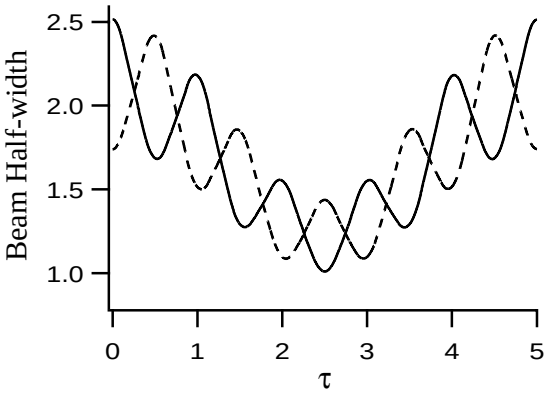

Figure 3: Time-evolution of the beam envelope in an FODO channel (breathing oscillation case). Solid line: horizonral half-width. Broken line: vertical half-width.

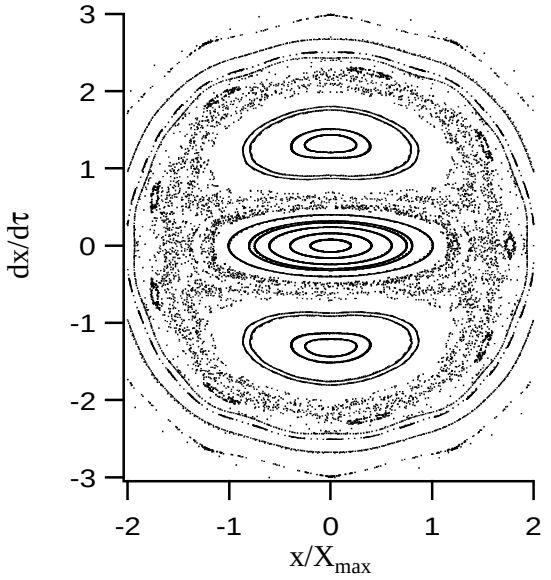

Figure 4: Poincaré surface of section plot for an FODO channel (breathing oscillation case). The same parameters with Fig. 3 are employed.

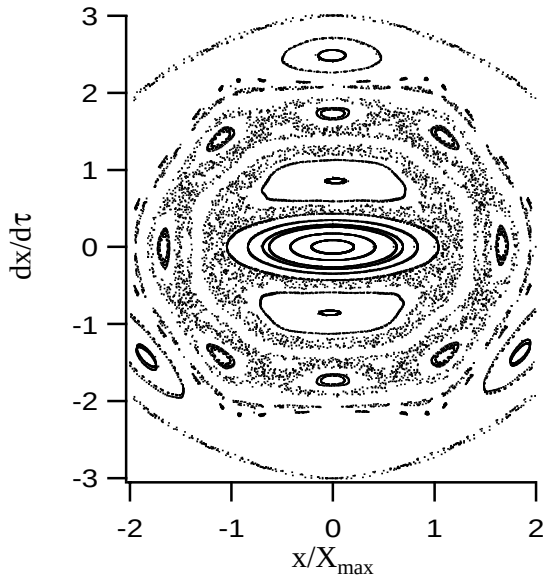

Figure 5: Poincaré surface of section plot for an FODO channel (quadrupole oscillation case).

Second, we consider the case where the quadrupole mode oscillation is excited. Figure 5 shows the Poincaré plot for a core executing the quadrupole mode oscillation. An FODO channel having σ_0=52° and a 50% filling factor is considered, and the beam parameters are set to be η=0.5, and M=0.3. These parameters are determined again to yield σ_m=72°.

Both pictures show strong chaosity which is not observed in solenoid cases. It suggests that the strong modulation of the core oscillation due to an alternating-gradient focusing field affects test particle stability, and causes an increase of the halo intensity.

4 ACKNOWLEDGEMENTS

We thank Dr. R. A. Jameson and Dr. S. Machida for helpful discussions on several points in this paper.

5 REFERENCES

[1] For exmaple, A. Riabko *et. al.*, Phys. Rev. E **51**, 3529 (1995).

[2] R. A. Jameson, LA-UR-93-1209, 1993; H. Okamoto and M. Ikegami, Phys. Rev. E **55**, 4694 (1997).

[3] M. Ikegami and H. Okamoto, Jpn. J. Appl. Phys. **36**, 7028 (1997).

[4] J. M. Lagniel, Nucl. Inst. Meth. A **345**, 405 (1994).

HALO FORMATION BY MISMATCH FOR HIGH INTENSITY BUNCHED BEAMS

K. Bongardt, M. Pabst, FZJ, Jülich, Germany
A. Letchford, RAL, Didcot, U.K.

Abstract

In high intensity proton linacs even small particle loss causes activation of the accelerator components [1]. Minimizing the losses is therefore a major task of the beam dynamical design. Losses are strongly correlated to the formation of a halo around the beam core. Monte Carlo simulations are presented for bunched beam transfer lines with varying tune depressions and equipartitioning ratios showing halo formation by mismatch due to parametric resonance excitation. For large tune depressions and/or quite unequal transverse and longitudinal temperatures substantial halo formation even for a matched beam occurs due to temperature exchange and/or exciting a higher order mode instability. An envelope instability can be excited in addition. A conservative criteria is presented for identifying parameters for reduced halo formation due to mismatch.

1 INTRODUCTION

In recent years substantial progress has been achieved by identifying the parametric resonance conditions as a major source of halo production in DC and bunched beams [2]. For realistic particle distributions with nonlinear space charge forces particles inside the core have a tune spread. Parametric resonances can occur between single particle tunes and the frequency of the oscillating mismatched beam core.

In this presentation the one dimensional parametric resonance model is generalized to bunched beams. Due to one longitudinal and the two transverse bunch dimensions, 3 eigenmodes exist for the mismatched envelopes.

The three eigenmodes of bunched beams are described in section 2. Correlation between enhanced halo production due to mismatch and parametric resonances are verified by Monte Carlo simulation in section 3. In section 4, halo production even for a matched beam due to the excitation of an envelope or higher order mode instability or as a result of temperature exchange is demonstrated. A conservative criteria is presented for identifying parameters for reduced transverse and longitudinal halo formation due to mismatch.

2 THE THREE ENVELOPE MODES OF MISMATCHED BUNCHED BEAMS

For the analytical approximation of the eigenfrequencies (modes) of the mismatched envelopes it is assumed that the beam is of ellipsoidal shape with uniform charge density giving linear space charge forces. In the rest frame of the bunch, the bunch radii are denoted by a_x, a_y and a_z. The bunch length b in the laboratory system is given by $b = a_z/\gamma$, where γ is the relativistic mass factor. The external forces for are assumed to be linear and periodic in the longitudinal direction s with period length L. The envelope equations are given by

$$a_x'' + k_{xo}^2 a_x - \frac{IK_x}{a_y b} - \frac{\epsilon_t^2}{a_x^3} = 0,$$

$$a_y'' + k_{yo}^2 a_y - \frac{IK_y}{a_x b} - \frac{\epsilon_t^2}{a_y^3} = 0,$$

$$b'' + k_{zo}^2 b - \frac{IK_z}{a_x a_y} - \frac{\epsilon_z^2}{b^3} = 0.$$

Here k_{xo}, k_{yo} and k_{zo} are the external periodic force constants. K_x, K_y and K_z are proportional to the elliptical formfactors and depend on the bunch dimensions too. I is the bunch current and ϵ_t and ϵ_z are the transverse and longitudinal emittances. This system of nonlinear coupled differential equations exhibits oscillating stable or unstable solutions. 'Matched' solutions have the same periodicity as the external focusing system. The oscillation of small mismatched solutions can be characterized by three eigenfrequencies, a pure transverse **quadrupolar mode**

$$\sigma_{env,Q} = 2\sigma_t$$

and a **high** and **low mode** which couple the transverse and longitudinal directions

$$\sigma_{env,H}^2 = A + B,\ \sigma_{env,L}^2 = A - B$$

with

$$A = \sigma_{to}^2 + \sigma_t^2 + \frac{1}{2}\sigma_{lo}^2 + \frac{3}{2}\sigma_l^2$$

and

$$B = \sqrt{\left(\sigma_{to}^2 + \sigma_t^2 - \frac{1}{2}\sigma_{lo}^2 - \frac{3}{2}\sigma_l^2\right)^2 + \left(\sigma_{to}^2 - \sigma_t^2\right)\left(\sigma_{lo}^2 - \sigma_l^2\right)}.$$

The mismatch mode tunes are expressed by the full and zero current transverse and longitudinal tunes σ_t, σ_{to}, σ_l and σ_{lo}.

The high mode represents a 'breathing' of the ellipsoidal bunch [3]. For the low mode, the bunch breathes in the transverse direction, but the oscillation in the longitudinal direction is of opposite phase.

In Fig. 1, the optical elements and the three matched beam radii are shown for a bunched beam transportline corresponding to the first period at 70 MeV of the coupled cavity (CCL) of the proposed European Spallation Source (ESS). By varying the beam current, the transverse and longitudinal emittance and the quadrupole gradient, a range

of full and zero current tunes can be obtained. The radii shown in Fig. 1 correspond to the 214 mA ESS bunch current and 60^o transverse full current tune.

3 HALO FORMATION BY PARAMETRIC RESONANCE EXCITATION

It is important to do multiparticle calculations of the bunched beam transfer line and compare the results with the model as due to phase space filling the multiparticle simulations have nonlinear space charge forces included. However the rms quantities are mainly determined by the linear part of the space charge forces. Monte Carlo simulations are done with 20 000 particles which interact fully in 3d. A 6d waterbag distribution is used as input.

Due to the nonlinear space charge forces, particles have tunes which are distributed between the full current and zero current tune. Due to oscillation of the mismatched radii single particles can experience parametric resonances. The condition for exciting a parametric resonance either radially or longitudinally is given by

$$\frac{\sigma^p_{t,l}}{\sigma_{env}} = \frac{m}{n} = \frac{1}{2}, \frac{1}{3}, \ldots$$

with

$$\sigma_t \leq \sigma^p_t \leq \sigma_{to},$$
$$\sigma_l \leq \sigma^p_l \leq \sigma_{lo}$$

where σ_{env} is one of the three envelope tunes of the mismatched radii and $\sigma^p_{t,l}$ the single particle tune.

The low order resonances are the most dangerous ones. For the radial direction the 1/2 parametric resonance is always excited by the quadrupolar mode. The high or low mode can excite a parametric resonance either in the transverse or longitudinal direction. The frequency of the high mode should be limited below 180^o in order to avoid an envelope instability.

Figs 2 and 3 are the results of Monte Carlo simulations of the bunched beam transfer line in Fig. 1. Shown is the 99.9% total to rms emittance ratio in x-direction. The transverse and longitudinal rms emittances stay constant for a 20% initial mismatch. In Fig. 2 the matched case is compared to a 20% quadrupolar mode excitation. An increase of the 99.9% emittance is visible due to exciting the 1/2 parametric resonance. Fig. 3 compares the matched case with a 20% radially and 30% longitudinally excited high mode with a numerically determined mode frequency of 168^o. No halo formation due to mismatch is visible here as no single particles have a transverse tune of 84^o. The full current transverse design tune is 60^o.

4 STABILITY CRITERIA FOR HALO FORMATION DUE TO MISMATCH

Halo production due to mismatch gets complicated if the rms emittances are changing. Reasons for emittance

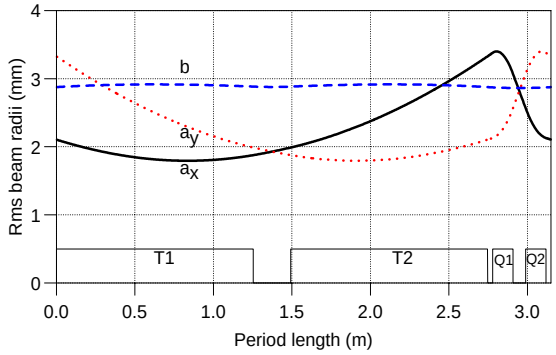

Figure 1: The matched beam radii along one period. T1, T2 bunching cavities, Q1, Q2 quadrupoles

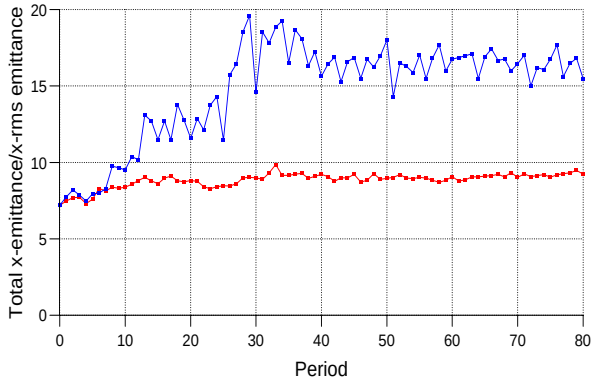

Figure 2: 99.9% total to rms emittance ratio for a matched (bottom) and a quadrupolar mode excited case (top)

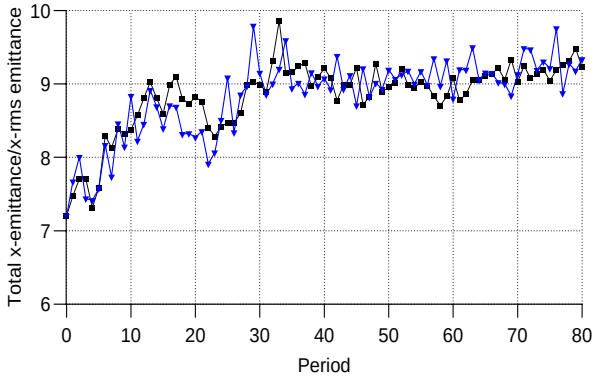

Figure 3: 99.9% total to rms emittance ratio for a matched (squared) and a high mode excited case (triangles)

change can be an envelope instability, temperature exchange or particle redistribution under high space charge forces. Substantial halo production even for a matched beam will occur in these cases.

4.1 High Mode Envelope Instability

The coupled set of bunched beam envelope equations with linear space charge forces can have unstable solutions due to the periodic external focusing. This is expected to hap-

pen if one of the envelope tunes is close to or above 180^o. Fig 4 shows a Monte Carlo simulation for an unstable bunched beam transfer line, which has a high mode frequency of almost 180^o. Clearly visible is a dramatic increase of the transverse total emittance.The transverse rms emittances grow by a factor of 4.

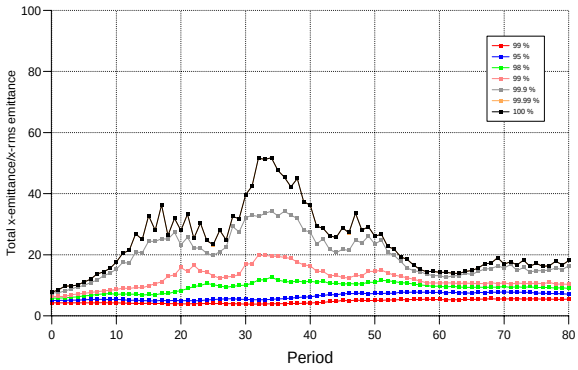

Figure 4: Excitation of the high mode envelope instability.

4.2 *Temperature exchange*

In Fig. 5 the transverse and longitudinal rms emittances are shown for an initially matched beam, where the transverse temperature is chosen to be a factor 2.3 higher than the longitudinal one. Visible is an exchange of emittance at the beginning, followed by damped oscillation afterwards. The ratio of total to rms emittance stays constant in all three planes. This is consistent with a temperature exchange [4,5].

4.3 *Higher Order Mode Instability*

Results of Monte Carlo simulations for an initially matched, equipartitioned beam with transverse and longitudinal tune depressions below 0.4 are shown in Fig. 6. Visible is the excitation of a higher order mode instability [6,7]. The total emittance growth is earlier and much more pronounced than the rms emittance growth which is not shown.

4.4 *Stability Criteria for Halo Formation due to Mismatch*

Based on Monte Carlo simulations for designs of bunched beam transferlines, a conservative stability criteria for halo fromation due to mismatch can be given. If the high mode envelope instability is avoided then a linac design insensitive to mismatch is given if the tune depressions are above 0.8 and the transverse to longitudinal temperature ratios between 1/3 and 2. The asymmetric temperature boundary reflects the situation of a bunched beam. Two hot transverse temperatures feeding one cold longitudinal are more dangerous than vice versa.

It should be pointed out that 'islands of stability' for a matched beam can exist outside this boundary [8] but they may suffer from substantial halo production due to mismatch. For a larger initial mismatch, pronounced halo formation has been observed in DC beams [9] and for equipartitioned, self-consistent bunched beams [10].

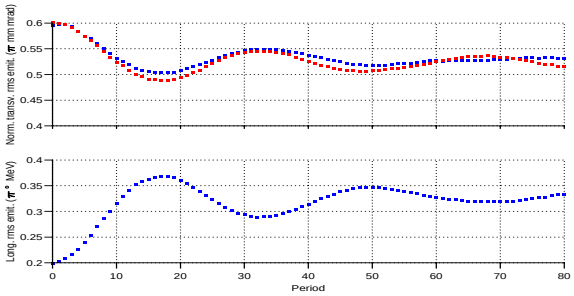

Figure 5: Rms emittances showing temperature exchange from the transverse (top) to the longitudinal (bottom) plane

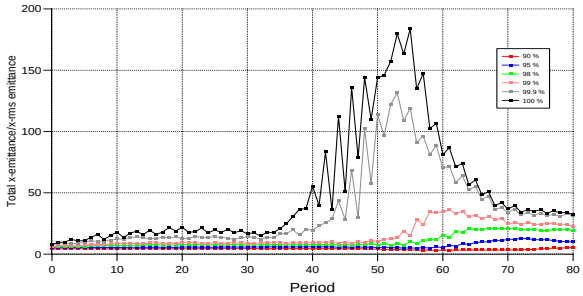

Figure 6: Excitation of a higher order mode instability

5 REFERENCES

[1] K. Bongardt et al., "High Intensity Injector Linacs for Spallation Sources", these proceedings

[2] M. Pabst et al, "Progress on Intense Proton Beam Dynamics and Halo Formation", Proc. EPAC '98, Stockholm, Sweden

[3] J. J. Barnard and S. M. Lund, "Theory of Longitudinal Beam Halo in RF Linacs", Proc. of the PAC 1997, Vancouver

[4] M. Reiser, "Theory and Design of Charged Particle Beams", John Wiley, New York, p. 575, 1994

[5] S. M. Lund et al., "Temperature Anisotropy Instabilities in Space Charge Dominated Beams", these proceedings

[6] R. L. Gluckstern et al., Phys. Rev. E, vol. 54, 1996, p. 6788

[7] C. Chen et al., "Halo Formation in Intense Linacs", these proceedings

[8] T. P. Wangler et al, "New High Power Linacs and Beam Physics", Proc. PAC '97, Vancouver

[9] C. Chen and R. A. Jameson, Phys. Rev. E, 1995, p. 3074

[10] A. V. Fedotov et al., "Halo Formation in Spheroidal Bunches with Self-Consistent Stationary Distributions", Proc. EPAC '98, Stockholm, Sweden.

SELF-CONSISTENT 3D SIMULATIONS OF LONGITUDINAL HALO IN RF-LINACS*

John J. Barnard[1], Steven M. Lund[1], and Robert D. Ryne[2]
1. Lawrence Livermore National Laboratory, L-645, Livermore, CA 94550
2. Los Alamos National Laboratory, H817, Los Alamos, NM 87545

Abstract

In order to prevent activation of the beam pipe walls and components of a high power ion accelerator, beam loss must be minimized. Here we present self-consistent, 3D particle-in-cell simulations of longitudinally mismatched beams, including the effects of rf non-linearities, using parameters based on the Accelerator Production of Tritium linac design. In particular, we explore the evolution of the longitudinal halo distribution, i.e. the distribution of particles in longitudinal phase space with oscillation amplitudes significantly larger than amplitudes of particles in the main body or "core" of the beam. When a particle reaches a sufficiently large amplitude longitudinally, it can be lost from the rf bucket, and consequently loses synchronism with the rf wave. Such particles will lose energy and so be poorly matched to the transverse focusing field and consequently can be lost transversely. We compare the present simulations, in which all particles contribute self-consistently to the self-field, to predictions of a core/test particle model, in which the core distribution has uniformly distributed charge and does not evolve self-consistently. Effects of self-consistent, non-linear space-charge forces, non-linear rf focusing on envelope mismatch induced beam halo are explored through comparisons of both models.

1 INTRODUCTION

Requirements on accelerator activation in high power proton linacs, have led to stringent limits on particle loss from the beam. Transverse mismatches have been shown to lead to large transverse particle oscillation amplitudes, leading to large apertures (up to a factor of 20 rms in conservative designs) to avoid intercepting the transverse beam halo (cf. refs.[1]-[4]). In the longitudinal case, the width of the stable rf bucket replaces the physical aperture as the dimension which determines when a particle can be lost from the beam. Since the half-width of the bucket can be as small as 2.3 longitudinal beam radii, a careful understanding of longitudinal halo is also warranted. Recently, the development of halos in the longitudinal direction has been explored using core test-particle models (cf. ref. [5],[6]), and using 3D PIC simulations, (ref. [7], and [8]) using rf fields which varied linearly with distance from the bunch center. In this paper we focus on the effects of the non-linear rf-focusing field, and compare numerical results of a 3D PIC code, known as Langevin3d, to the core-test particle code (CTP) reported on in references [5] and [6].

* Work performed under the auspices of the U.S. D.O.E. at LLNL under contract W-7405-ENG-48 and at LANL under support of the Division of Mathematics, Information, and Computational Sciences, the Division of High Energy Physics, and Office of Defense Programs.

2 PARAMETERS USED FOR EXAMPLES

For concreteness, we will refer to a design of the Accelerator Production of Tritium (cf. ref. [9]) for numerical examples (see table). The undepressed synchrotron wavenumber, k_{s0} represents the zero-current oscillation wavenumber of a particle at infinitesimal amplitude about the synchronous phase, k_s/k_{s0} is the tune depression due to space charge. Also, $k_{\beta 0}$ is the zero current transverse betatron frequency, and $k_\beta/k_{\beta 0}$ is the transverse tune depression. The quantities $r_{\perp 0}$ and r_{z0} are $\sqrt{5}$ times the rms radius in the transverse and longitudinal directions, respectively in the lab frame. The quantity α represents the ratio of transverse to longitudinal radius in the comoving frame, and is the quantity of physical relevance when evaluating the fields (cf.ref[5]). Note that although the beam is nearly spherical in the lab frame at the 500 MeV point, in the comoving frame $\alpha = 0.68$ and at other energies it is even more elongated. $\Delta z_{max} \cong \beta_s c(-\phi_s)/2\pi\nu$ and $\Delta z_{min} \cong \beta_s c(2\phi_s)/2\pi\nu$ are the approximate rf-bucket half-widths longitudinally, where ϕ_s is the synchronous phase, $\beta_s c$ is the velocity of the synchronous particle, and ν is the rf frequency.

Energy (GeV)	0.1	0.5	1.0	1.8
k_{s0} (rad/m)	0.285	0.107	0.055	0.030
k_s/k_{s0}	0.31	0.31	0.23	0.20
$k_{\beta 0}$(rad/m)	0.474	0.160	0.151	0.147
$k_\beta/k_{\beta 0}$	0.35	0.32	0.48	0.65
r_{z0} (mm)	6.53	4.61	4.90	4.62
$r_{\perp 0}/r_{z0}$	0.53	1.04	0.62	0.46
$\alpha \equiv r_{\perp 0}/\gamma_s r_{z0}$	0.48	0.68	0.30	0.16
$\Delta z_{max}/r_{z0}$	2.34	5.87	6.37	7.26
$\lvert\Delta z_{min}/r_{z0}\rvert$	4.68	11.7	12.7	14.5

Table APT parameters in superconducting coupled cavity linac, at four representative points along the linac.

3 CORE-TEST PARTICLE CODE, CTP

In the code CTP (refs. [5,6]), test particles are allowed to evolve from both external and space charge fields, in all three spatial directions (although the fields themselves are cylindrically symmetric). The external longitudinal field is a sinusoidally varying rf electric focusing field with the intrinsic non-linearity of a sine wave, and the external transverse field is assumed to be uniform focusing, representing the effects of the quadrupoles, in an average sense. The

space charge field is that of a uniformly charged spheroid, calculated for arbitrary α (prolate, oblate or spherical). The spheroid is set to oscillate in linearized normal modes of the coupled transverse and longitudinal envelope equations, at the linearized mode frequencies, each with assumed sinusoidal time dependence. Arbitrary amplitudes and phases of the two envelope modes are allowed. Particles are typically loaded with radial coordinate $r = 0$, and distributed in longitude either over a bunch length or a bucket length, although more complicated loads are also possible. Stroboscobic plots of particle energy and phase relative to the synchronous particle are made at the same phase of each envelope period. CTP is well suited for studying particle resonances and the overall structure of the phase space.

4 3D PIC CODE, LANGEVIN3D

The code Langevin3d (see ref. [10,7] for details) is a Particle-In-Cell (PIC) code that allows 3D space charge field calculations as well as 3D particle orbits. The boundaries are placed at infinity by using the method of ref. [11], which is a good approximation in accelerators with large beam pipe radii. One option in the code uses a modified symplectic integrator, to allow inclusion of artificial damping and diffusion. Use of this feature drives beams to a Boltzmann distribution, to allow thermal equilibrium initial conditions. The parallel processing architecture of Langevin3d permits the use of large particle numbers, which minimizes statistical fluctuations and maximizes accuracy. Typical results displayed here were run with 0.5 million particles, but runs with several million particles are not extraordinary. Phase space plots of a randomly chosen fraction of all the particles can be viewed at a fixed time or test particles can be viewed stroboscopically. Plots with a "density cut" can be viewed which display particles up to a specified maximum density. This feature allows viewing the low density halo regions without saturating the higher density core.

5 COMPARISON OF RESULTS

Figure 1, shows a comparison between the longitudinal phase space ($d\Delta z/ds$ vs. Δz generated by Langevin3d (top two plots) and CTP (lower plot). Here Δz is the longitudinal particle position relative to the synchronous particle, and s is distance along the accelerator. In the top plot, a density cut was made allowing the details of the halo to be observed. The relative intensity of the halo is better characterized by the middle plot, in which the density of particles displayed is proportional to the actual distribution. In the lower plot the solid line represents the position of the equilibrium bunch, with dotted lines indicating the extent of the excursions from the beam mismatch. It is apparent that the main two-lobe structure (due to the resonance between the particle oscillation frequency and half the envelope frequency) in phase space is clearly visible in the results of both codes. The extent of the halo in both Δz and $d\Delta z/ds$ is also quite similar for both CTP and Langevin3d. Higher order resonances appearing within the beam in the CTP plots do not appear to be as significant in the self-consistent simulations.

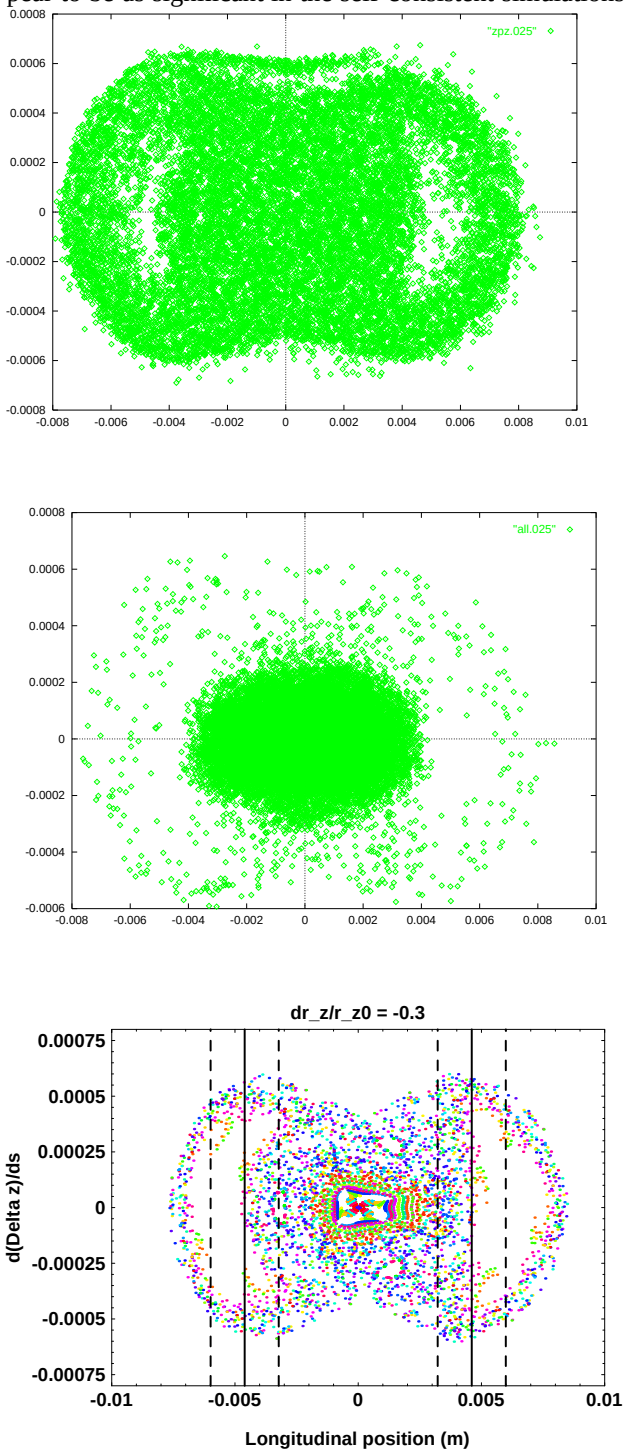

Figure 1 Comparison of Langevin3d (top, middle) and CTP results (bottom) of $d\Delta z/ds$ versus $\Delta z(\mathrm{m})$ for a 30% mismatched beam at the 500 MeV point in the APT linac. Top: Density cut; Middle: Full distribution; Bottom: Stroboscopic test particle plot.

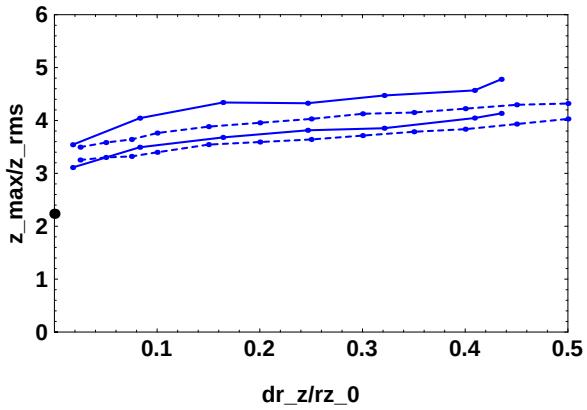

Figure 2 Comparison of the maximum longitudinal excursion in CTP and Langevin3d simulations as a function of mismatch parameter $\delta r_{z0}/r_{z0}$ using parameters from the 500 MeV point. Dashed lines indicate CTP results; solid are from Langevin3d. The upper curve of each pair is the absolute value of the negativemost excursion in Δz, the lower is the maximum of the positive particle excursion.

Figure 2 indicates that CTP tracks the Langevin results well as a function of envelope mismatch amplitude, although the maximum excursion is somewhat less than that found in Langevin3d. Note that the particles all remain within the stable bucket, and so no particles were lost at these amplitudes.

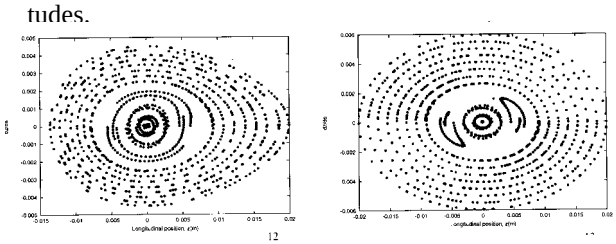

Figure 3 Langevin3d stroboscopic test particle plots for an average current per bunch of 5 mA (rather than 200 mA) but otherwise parameters for the 100 MeV APT normal conducting linac tabulated in ref.[5], loaded over the width of the bucket, with $d\Delta z/ds = 0$. Left: with non-linear rf-focusing; Right: with linear focusing.

6 NON-LINEAR RF HALO SUPPRESSION

In ref. [6] it was shown that for fixed focusing strengths and emittances, at very low or high currents the resonance disappears. Because the rf focusing field varies sinusoidally, the particle oscillation frequencies do not tend to an asymptotic frequency as they would in a strictly linear external focusing field. Rather, a maximum oscillation frequency is reached at some radius generally outside the bunch, and the frequency decreases for larger amplitudes. If that maximum frequency lies below half the longitudinal envelope frequency no resonance is possible. Parametrically it was found that at very low and high currents (when focusing and emittance is held fixed) the maximum frequency is below half the envelope frequency and simulations with CTP found an absence of resonance. Simulations using Langevin3d verified that for a low current case the resonance indeed vanished. Figure 3 illustrates this effect, by showing the phase space with linear focusing in which the resonance persists and sinusoidal rf focusing which suppresses the resonance.

7 CONCLUSIONS

We have performed 3D PIC simulations of beams with longitudinal mismatches, and have found general agreement between PIC simulations and the Core/Test Particle model, particular with respect to the size of the resonant region. The suppression of the envelope-particle resonance by the sinusoidal rf field under certain conditions predicted using CTP has been confirmed using Langevin3d. Using both codes, no particle loss through the rf bucket has been observed for mismatch amplitudes below 0.5.

8 ACKNOWLEDGMENTS

The authors wish to thank Bob Gluckstern, Ingo Hofmann, Alexei Fedotov, and Tom Wangler for valuable discussions on beam halo. This research used resources of the National Energy Research Scientific Computing Center, which is supported by the Office of Energy Research of the U.S. D.O.E. under contract DE-AC-03-76SF00098.

9 REFERENCES

[1] J.S. O'Connell, T.P. Wangler, K.R. Krandall, Proc. 1993 Part. Accel. Conf., Washington DC, p. 3657.
[2] R.A. Jameson, 1993 Part. Accel. Conf., Washington DC, p. 3926.
[3] R.L. Gluckstern, Phys. Rev. Letters, **73**, 1247, (1994).
[4] R.D. Ryne, T.P. Wangler, Proc. Accel. Driven Transmutation Tech. Conf., Las Vegas, NV, July 1994.
[5] J.J. Barnard and S.M. Lund, "Theory of Longitudinal Beam Halo in RF Linacs: I. Core/Test-Particle Formulation," Proc. of the 1997 Particle Accelerator Conf.
[6] S.M. Lund and J.J. Barnard "Theory of Longitudinal Beam Halo in RF Linacs: II. Envelope/Particle Resonances," Proceedings of the 1997 Particle Accelerator Conference.
[7] R.L. Gluckstern, A.V. Fedotov, S.S. Kurenoy and R. D. Ryne, "Halo Formation in three-dimensional bunches," Phys. Rev. E., in press, (October 1998).
[8] M. Pabst, K. Bongardt "Progress on Intense Proton Beam Dynamics and Halo Formation" Proceedings of the European Particle Accelerator Conference, held Stockholm, Sweden, 1998.
[9] T. Wangler, private communication (1997). [10] R. Ryne et al, "The DOE Grand Challenge in Computational Accelerator Physics," 1998 International Linear Acc. Conf. (these proceedings).
[11] R.W Hockney and J.W. Eastwood, "Computer Simulation Using Particles," [Adam Hilger, Bristol], 1988.

ANALYTIC MODEL OF ION EMISSION FROM THE FOCUS OF AN INTENSE RELATIVISTIC ELECTRON BEAM ON A TARGET

George J. Caporaso and Yu-Jiuan Chen
Lawrence Livermore National Laboratory, Livermore, California 94550 USA

Abstract

Advanced radiographic systems for stockpile stewardship require very small x-ray sources to achieve the required resolution. Focusing multi-kiloampere beams to diameters on the order of 1 mm onto a Bremsstrahlung target leads to the generation of axial electric fields on the order of several MV/cm which act to extract ions out of the surface plasma and accelerate them upstream into the beam. These backstreaming ions act as a distributed electrostatic lens which can perturb the focus of the electron beam in a time varying manner during the pulse. An analytic model of the ion extraction is presented for a particular target geometry along with scaling laws for the perturbation of the focal spot.

1 INTRODUCTION

High resolution x-ray radiography requires the production of a small (≈1 mm diameter) spot on the surface of a Bremsstrahlung converter target by a relativistic electron beam of at least several kiloamperes [1]. A mechanism that might possibly disrupt the focal spot was proposed by D. Welch [2]. Bombardment of the target by a high power electron beam would lead to the rapid formation of a surface plasma. A large axial electric field would appear at the surface due to the charge redistribution on the target arising from cancellation of the beam's *radial* electric field. This axial field would expel the ions into the beam. These *backstreaming* ions would acquire energies on the order of the space charge depressed potential of the beam and would propagate upstream at very high speeds where they would act as an electrostatic focusing lens. The focusing due to these moving ions would cause the electron beam to pinch upstream of the target and then rapidly diverge. The result would be a spot size that would rapidly increase in time at the converter target.

An analytic model is presented for a "beer can" geometry in which a close fitting conducting tube surrounds the beam right up to the target. A beam envelope equation is used to derive scaling laws for the effect of the backstreaming ions on the focal spot size at the target.

2 TARGET GEOMETRY AND MODEL

We will model the "beer can" geometry shown in Figure 1. In this target arrangement, a conducting tube with the same radius as the electron beam is connected to the target. The presence of the tube limits the space charge depression of the beam which will in turn reduce the emitted ion current.

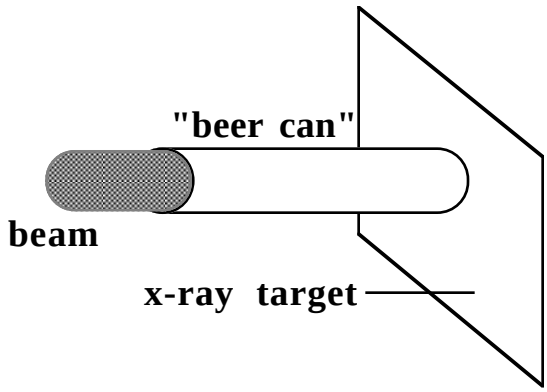

Fig. 1. "Beer can" geometry proposed to reduce the space charge depressed potential of the beam which would reduce the backstreaming ion current.

We will assume that the target surface is sufficiently rich in ions that flow will be space charge limited. The steady state emission is determined by Poisson's equation for the electrostatic potential (in c.g.s. units)

$$\nabla^2\Phi = -4\pi\rho \tag{1}$$

where ρ is the sum of the beam's charge density and the density of the emitted ions. Since the target (and the tube) are assumed to be grounded, we may use the conservation of energy to obtain the ion velocity as

$$v_i = \sqrt{-2e\Phi / M} \tag{2}$$

where M is the ion mass and e is the ion charge. The ion charge density is given by

$$\rho_i = J(r) / v_i \tag{3}$$

where J(r) is the ion current density.

Equation [1] is two dimensional (r and z). A great simplification is made possible by choosing the beam profile to be of the form

$$\rho_b = -\rho_o J_o(\alpha r) \tag{4}$$

where J_0 is the zeroth order Bessel function and $\alpha = x_{01} / a$. Here a is the radius of the beer can, x_{01} is the first root of J_0 and $-\rho_0$ is the on-axis charge density of the beam.

Let us seek solutions which have the following form:

$$\Phi(r,z) = -\psi(z) J_o(\alpha r) \tag{5}$$

and

$$J(r) = \Lambda_o J_o^{3/2}(\alpha r) \tag{6}$$

where $\psi(z)$ and Λ_o are to be determined.

Substitution of Equations [2] through [6] into Equation [1] yields

$$\psi - \frac{d^2\psi}{d\zeta^2} = -\frac{4\pi\rho_o}{\alpha^2} + \frac{4\pi\Lambda_o}{\alpha^2}\sqrt{\frac{M}{2e}}\frac{1}{\sqrt{\psi}} \tag{7}$$

where we have defined a dimensionless axial coordinate $\zeta=\alpha z$. If we multiply Equation [7] by $d\psi/d\zeta$ we can obtain a first integral

$$\left(\frac{d\psi}{d\zeta}\right)^2 = \psi^2 - \frac{8\pi\rho_o}{\alpha^2}\psi + \frac{16\pi\Lambda_o}{\alpha^2}\sqrt{\frac{M}{2e}}\sqrt{\psi} \tag{8}$$

where we have used the condition for space charge limited emission to eliminate the constant of integration (i.e., $d\psi/d\zeta=0$ at the emitting surface $\zeta=0$ where $\psi=0$).

To proceed further we define a dimensionless variable Ω and a dimensionless constant μ as

$$\Omega \equiv \sqrt{\alpha^2\psi / 8\pi\rho_o} \tag{9}$$

and

$$\mu \equiv \frac{16\pi\Lambda_o}{\alpha^2}\sqrt{\frac{M}{2e}}\left(\frac{\alpha^2}{8\pi\rho_o}\right)^{3/2}. \tag{10}$$

With these definitions we may solve Equation [8] as (we choose the positive root since we expect ψ to increase with ζ)

$$\int_0^{\Omega}\frac{\sqrt{\Omega'}}{\sqrt{\Omega'^3 - \Omega' + \mu}}d\Omega' = \frac{\zeta}{2}. \tag{11}$$

We expect that as $\zeta \to \infty$, Ω will approach a finite asymptotic value corresponding to the space charge depressed potential of the beam. Thus μ must have a value such that the integral in Equation [11] $\to \infty$ as $\Omega \to \overline{\Omega}$ the asymptotic value. We note that the radical in the denominator of Equation [11] must be real for a physical solution to exist. Let us find its minimum. Defining the radicand as χ we have

$$\chi \equiv \Omega^3 - \Omega + \mu \tag{12}$$

and

$$d\chi / d\Omega = 3\Omega^2 - 1 = 0 \tag{13}$$

so that

$$\Omega_o = \pm\sqrt{1/3}. \tag{14}$$

From the derivative of Equation [13] we see that the positive root of Equation [14] will correspond to a minimum of the radicand

$$\chi_{\min} = -2/3\sqrt{3} + \mu. \tag{15}$$

Note that if this minimum value is greater than zero then the integral will be finite regardless of the upper limit of integration in Equation [11] and thus will not be a solution. Therefore μ must have a value such that $\chi_{\min} = 0$. That is, we must have

$$\mu = 2/3\sqrt{3} \quad \text{and} \quad \overline{\Omega} = \Omega_o = 1/\sqrt{3}. \tag{16}$$

Using this result we can solve Equation [11]. The solution is shown in Figure 2. Note that the potential changes rapidly over a distance of order the beam radius.

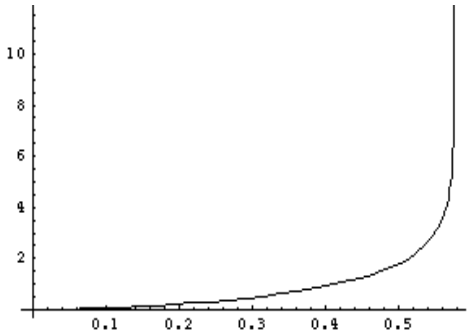

Fig. 2. Solution of Equation [11]. ζ is plotted vs. Ω.

With the solutions given by equation [16] we can immediately determine the asymptotic potential as

$$\psi \to \psi_{\max} = 8\pi\rho_o / 3\alpha^2 \tag{17}$$

and the ion current constant as

$$\Lambda_o = \frac{2}{3\sqrt{3}}\frac{\alpha^2}{16\pi}\sqrt{\frac{2e}{M}}\left(\frac{8\pi\rho_o}{3\alpha^2}\right)^{3/2} \propto \frac{\psi_{\max}^{3/2}}{a^2}. \tag{18}$$

Note that the final result for the ion current resembles the classical Child-Langmuir law for a diode with a potential given by the beam potential and an "A-K gap" given by the beam radius.

By integrating over the beam profile we find that

$$\psi_{\max} = \frac{4}{3}\frac{I}{x_{01}J_1(x_{01})c} \cong 32.04 I_{kA} \text{ (kV)} \tag{19}$$

and that the asymptotic neutralization fraction of the beam by the ions is

$$\rho_{ion}(r, z\to\infty) / \left|\rho_{beam}(r)\right| = 1/9\sqrt{3} = 0.064. \tag{20}$$

The potential gives rise to an asymptotic ion speed given through Equation [2] as

$$v_{\max} = 2.48x10^8\sqrt{I_{kA}Z/A} \text{ (cm/sec)} \tag{21}$$

where Z and A are the charge state and atomic number of the ions respectively.

3 FOCUSING EFFECTS OF BACKSTREAMING IONS

Examination of Equation [21] reveals that substantial motion of backstreaming ions is possible during a single electron beam pulse. For example for a 4 kA beam protons will propagate approximately 50 cm upstream after 60 ns, singly charged carbon ions would travel 14 cm in the same time and singly charged tantalum ions (a typical target material) would move only about 3.5 cm.

These propagation distances are comparable to the focal length of the final focusing lens in radiography systems and so would be expected to exert a substantial focusing force on the electron beam.

An estimate of the effects of these ions can be obtained by using an envelope equation for the beam. By computing the radial electric field produced by the ions and averaging the product of this field with radius over the beam profile it is possible to derive a simple equation for the rms (root mean square) radius of the beam [3]. Assuming a uniform distribution for the beam profile and using the Lapostolle emittance (E) we can then obtain an equation for the edge radius R of the beam (without space charge) as

$$R'' = \frac{E^2}{R^3} - \frac{2 f_n I}{\gamma\beta^2 I_o R} \qquad (22)$$

where f_n is the neutralization fraction (given in the "beer can" model by Equation [20]), $I_o = mc^3/e \approx 17$ kA and E is the Lapostolle emittance.

As the ions propagate upstream we expect the type of behavior shown in Figure 3a to occur. Equation [22] can be solved for different "slices" of the beam corresponding to different distances from the head of the beam. Each slice will experience an ion column of different length and so will have a different history of R vs. z. If the head of the beam is arranged to hit the target at a waist then ion backstreaming will initially lead to a smaller spot on target as the additional electrostatic focusing in close proximity to the target pinches the beam. However, as the ions move further upstream this pinching will occur progressively farther upstream leading to a divergent beam at the target. The behavior of the focal spot at the target as a function of time is shown in Figure 3b. The time at which the spot radius equals R_S, the spot size at the head of the beam is the *disruption time* τ_d.

By numerically solving a dimensionless, scaled version of Equation [22] the length of uniform ion column required to disrupt the focal spot is found to be

$$z_o \approx R_s \sqrt{\pi\gamma\beta^2 I_o / f_n I} \qquad (23)$$

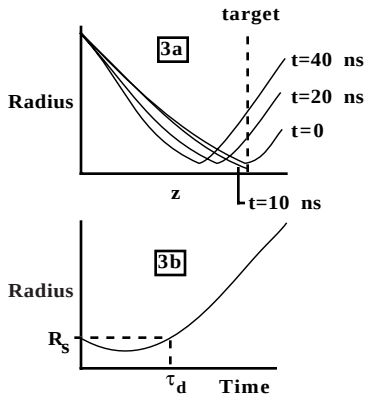

Fig. 3. (a) Trajectories of different beam "slices". (b) Radius as a function of time at the target plane.

and the disruption time follows from Equations [21] and [23] as

$$\tau_d = z_o / v_i \approx 29.5 R_s \sqrt{\gamma\beta^2 A / f_n Z} / I_{kA} \text{ (ns)}. \qquad (24)$$

For example if R_S=0.05 cm, I=2kA and γ=12.7 we find that z_o=3.64 cm and τ_d=10.4 ns for proton emission.

4 CONCLUSIONS

We have provided an exact analytic solution to the problem of the space charge limited flow of ions off the surface of a target surrounded by a tight fitting cylindrical tube of the same diameter as the electron beam. The effects of these ions have been treated with an envelope equation and the scaling laws for the disruption of the focal spot have been derived.

5 ACKNOWLEDGMENTS

This work was performed under the auspices of the U.S. Department of Energy by LLNL under contract W-7405-ENG-48.

6 REFERENCES

[1] G. J. Caporaso, "Linear Induction Accelerator Approach to Advanced Radiography", Proceeding of 1997 Particle Accelerator Conference, Vancouver, Canada, May 1997.

[2] Dale Welch, Target Workshop, Albuquerque, NM. Feb. 6, 1997.

[3] G. J. Caporaso and A. G. Cole, "High Current Beam Transport" in Frontiers of Accelerator Technology, World Scientific, 594-615 (1966).

TRAPPING BACKSTREAMING IONS FROM AN X-RAY CONVERTER USING AN INDUCTIVE CELL

J. McCarrick, Y.-J. Chen, T. L. Houck, B. R. Poole
Lawrence Livermore National Laboratory, Livermore, California 94550 USA

Abstract

High current electron beams have been used as x-ray drivers for x-ray radiography. Typically, several thousand amperes of electron beam current at 20 MeV is focused to a millimeter spot size on a x-ray converter. Within a single pulse, the heating of the target by the electron beam will lead to rapid desorption of surface contaminants. The space charge potential of the electron beam will pull ions out of this plasma layer upstream into the beam. These backstreaming ions can act as a focusing lens which cause the beam to be overfocused at a waist upstream. The final beam spot size on the target would then be larger than intended, and the x-ray radiography resolution is reduced. We have designed a self-biased ion trap for the Experimental Test Accelerator (ETA-II) beam by using an Advanced Test Accelerator (ATA) inductive cell to prevent the backstreaming ions from moving upstream and forming a long ion focusing channel. We have studied the effects of this type of ion trap on the final focusing of the electron beam with the ETA-II beam parameters. Simulation results will be presented.

1 INTRODUCTION AND MOTIVATION

The use of electron beams in high-resolution x-ray radiography requires that a high-current beam be focused on a millimeter-sized spot for the duration of the beam pulse. The energy deposited in a small volume of target material is enough to generate a plasma of heavy target material, along with any lighter species that contaminated the target surface, such as hydrogen or carbon. Once these light ions are present, they are rapidly accelerated upstream in the strong axial electric field produced by the beam at the metallic surface of the target, in a process called "backstreaming." The presence of this excess positive charge in the beam upsets the balance of electric repulsive forces and magnetic pinching forces which determine the radius of the beam. The radial electric force is reduced, causing the magnetic forces to pinch the beam to a premature focus and then expand well past the desired spot size at the target. This reduces the achievable resolution of the radiographic image and is an undesirable effect.

Only a small quantity of positive charge is required to have an impact on the target spot size. We can compare the extraction of ions from the target plasma to the operation of an ion diode under the conditions of space-charge limited (SCL) flow. The accelerating potential is that of the beam with respect to the grounded metallic target, which has the well-known form

$$\phi_o = 30I\left(1 + 2\ln\frac{r_w}{r_b}\right) \tag{1}$$

where r_w is the beampipe radius, r_b is the beam radius, and I is the beam current. For the ETA-II accelerator with a millimeter spot radius, 3 cm beampipe radius, and 2 kA of beam current, this potential is 468 kV. Assuming that the extracted ion current satisfies the Child Law for SCL conditions, and neglecting the small initial thermal energy of the ions compared to the beam potential, the neutralization fraction f of ion space charge to beam space charge is given by

$$f = \frac{r_b^2\left(1 + 2\ln\frac{r_w}{r_b}\right)}{9d_{eff}} \tag{2}$$

where d_{eff} is the effective diode gap. Consideration of Poisson's equation in the vicinity of the target shows the potential has the approximate form [1]

$$\phi(r=0,z) \approx \phi_o\left(1 - e^{-z/d}\right) \tag{3}$$

where the scale length d is approximately the beam diameter. Choosing $d_{eff} \sim 3d$ as the total acceleration gap in the ion-diode model gives a neutralization factor of 2.5%, corresponding to a number density of $\sim 10^{17}$ m^{-3}. Thus, a 25 cm channel of hydrogen ions requires a mere 2.5×10^{11} atoms, easily supplied by surface contaminants. At ETA-II parameters the asymptotic velocity for protons is $\sim 9.5 \times 10^6$ m/s, so that this channel can form in about 25 ns, about the mid-point of a pulse.

The effect of such an ion channel on the beam radius can be estimated by a simplified form of the envelope equation:

$$\frac{d^2R}{dz^2} = \frac{\varepsilon^2}{R^3} + \frac{k}{R}\left(\frac{1}{\gamma^2} - f\right) \quad (4)$$

where R=R(z) is the radius of the beam, ε is the un-normalized beam emittance, γ is the usual relativistic factor, f is the neutralization fraction, and the constant k is γ^2 times the generalized perveance of the beam. A comparison of beam envelope with and without the ion channel is shown in figure 1. This behavior is also seen in self-consistent PIC simulations which capture other effects such as emittance growth [2], and has been seen experimentally based on recent data from the ETA-II accelerator [3].

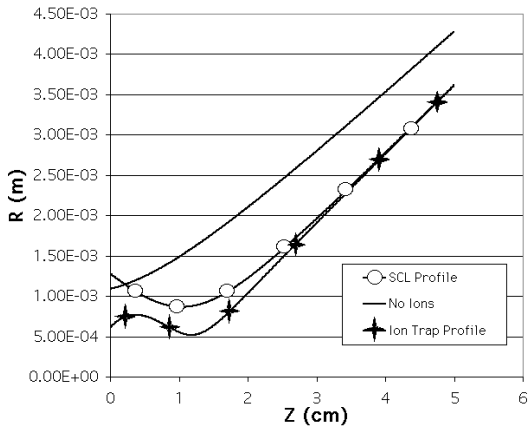

Figure 1. Beam envelope in the presence of no ions, ions with a SCL profile, and ions with the inductive trap profile.

2 APPLICATION OF AN INDUCTIVE ION TRAP

To preserve the minimum spot size of the beam throughout the pulse, it is desirable to either prevent ion emission altogether, or at least confine the ions to a sufficiently small channel such that the net effect on the beam is small. It is not feasible to bias the target with an external DC voltage due to the magnitude of the beam potential; however, it is possible to use the beam current as a "self-biasing" source. One method involves using an induction cell where the accelerating gap (or "decelerating gap", in this case) is formed between the target material and an annular electrode placed slightly upstream in the beampipe. Such a cell has been designed for ETA-II, based on an induction cell used in the Advanced Test Accelerator (ATA) [4]. A schematic of the cell is shown in figure 2.

During a beam pulse, the large inductance of the core will prevent the return current of the beam from traveling the preferred DC path A+B, forcing it instead through the shunt resistor in path A+C and causing the voltage $I_{beam}R$ to appear across the gap. This potential drop serves a dual purpose. Firstly, for a sufficiently high value of R, the sum of the cell potential and the beam potential will form a well, trapping ions in a channel of length the order of the gap size. Secondly, as charge builds up in the channel, the net electric field at the surface of the target will decrease and lower the rate of subsequent ion emission.

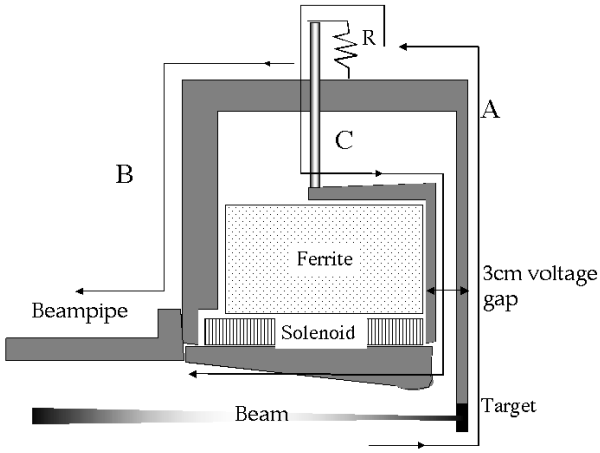

Figure 2. Schematic of Inductive-Cell Ion Trap.

There are difficulties associated with such a design. The potential provided by the cell must be of the same order as the beam potential, and the gap size must be kept as small as possible to minimize ion channel length. Such gradients could cause the electric fields in the gap to exceed the breakdown voltage. In addition, expansion of the plasma of target material could cause conducting plasma to fill the gap, causing a short. The present design has a gap size of 3 cm and a maximum desired voltage of 450 kV, producing electric fields of magnitude 150 kV/cm. By placing high-gradient insulator in the portions of the gap away from the beam, these parameters should be achievable [5].

3 NUMERICAL RESULTS

During the flattop of the current pulse, the inductive voltage across the gap should remain approximately constant, allowing it be modeled as a simple DC voltage. PIC simulations have been run on space-charge limited proton emission from the target in a 2 kA, 1mm spot radius ETA-II beam, with the ion trap operating at 400 kV. Note this value is less than the "bare" beam potential because of the ameliorating effect of the ion space charge which builds up in front of the target.

The simulation is run for 20 ns, allowing enough time for the ions to complete a full round-trip in the potential well. To reduce computation time, the electron beam particles are fixed in time, so that the effect of the ions on the beam is not simulated. The geometry along with the distribution of ions at 5ns and 20ns is shown in figure 3; note almost all of the ions have collected within the gap region, with only a small stream managing to escape the trap. Figure 4 shows the axial positions of all 50,000 particles in the simulation at 20ns; 94% of the particles are trapped within about 2.5 cm of the target.

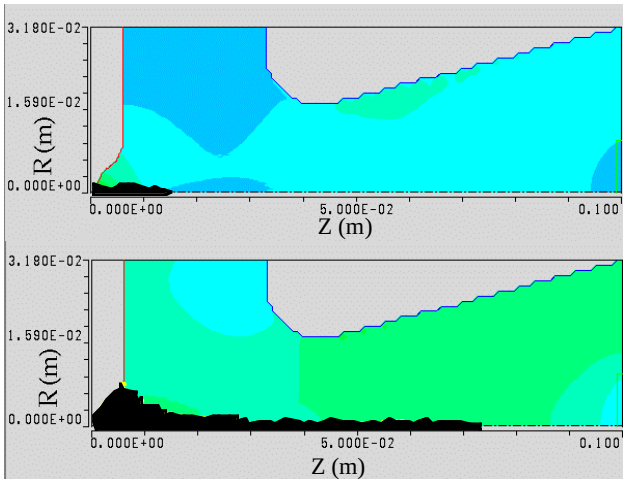

Figure 3. Inductive trap simulation geometry, showing ion distribution at 5ns (top) and 20ns (bottom) after onset of emission.

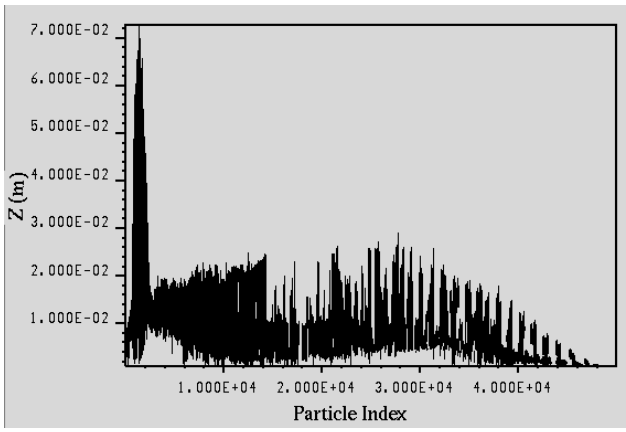

Figure 4. Axial coordinate of each particle at 20ns, showing 2.5cm trapping length.

However, figure 5 shows that ion charge density in the gap is much higher than the unconfined SCL value. The electron beam charge density is about 2 C/m^3, meaning that the neutralization "fraction" is in fact much greater than unity. Using a smooth approximation to this profile in an envelope-equation calculation yields the third curve in figure 1, showing confined oscillations of the beam envelope below the nominal profile. While these results suggest that such a tailored profile of high-density ions could prevent the growth of the beam spot, the varying divergence angle of the beam as it enters the target is not desirable for radiographic purposes. In addition, such constant-emittance envelope calculations are questionable in the presence of beam oscillations, and complete self-consistent PIC simulations including the electron beam are required.

4 CONCLUSIONS

The presence of backstreaming ions from target material in high-current electron accelerators causes undesirable growth in beam size, reducing the achievable resolution of radiographic images. We have examined the use of an inductive ion trap to confine the length of the backstreaming ion channel. PIC simulations show that an ion trap based on an ATA induction cell will confine 94% of emitted protons in the ETA-II accelerator. However, the resulting density of ions in the confinement region is much higher than the unconfined value. Preliminary envelope calculations show that this density profile confines the beam envelope to oscillations below the nominal beam radius. However, further PIC simulations which include the electron beam self-consistently must be performed to confirm this behavior. In addition, the radiographic quality of such an oscillating beam may not be acceptable.

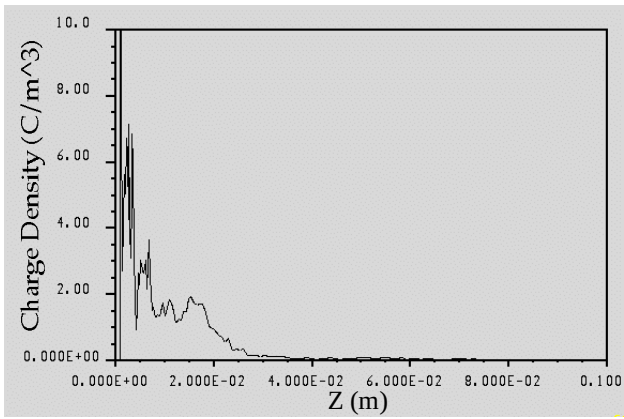

Figure 5. Ion charge density along beam axis. Beam density is 2.12 C/m^3

5 ACKNOWLEDGEMENTS

This work was performed under the auspices of the U.S. Department of Energy by the Lawrence Livermore National Laboratory under contract No. W-7405-Eng-48

6 REFERENCES

[1] Y.-J. Chen, et. al., "Controlling Backstreaming Ions from X-ray Converter Targets with Time Varying Final Focusing Solenoidal Lens and Beam Energy Variation," this conference.

[2] P. Rambo, et. al., "EM-PIC Simulations of e-Beam Interaction with Field Emitted Ions from Bremsstrahlung Target," this conference.

[3] S. Sampayan, et. al., "Experimental Investigation of Beam Optics Issues at the Bremsstrahlung Converters for Radiographic Applications," this conference.

[4] S. Humphries. "Principles of Charged Particle Acceleration." Wiley Interscience, New York, NY 1986 p. 289

[5] S. Sampayan, et. al., "High Performance Insulator Structures for Accelerator Applications," Proceedings 1997 Particle Accelerator Conference, (IEEE), New York, NY (1997)

ANALYSIS OF THE FREQUENCY DEPENDENCE OF THE LONGITUDINAL COUPLING IMPEDANCE OF A SMALL HOLE IN A COAXIAL LINER *

Alexei V. Fedotov, Robert L. Gluckstern
Physics Dept., University of Maryland, College Park, MD 20742

Abstract

We recently developed a general analysis for an azimuthally asymmetric rectangular slot in the inner conductor of a coaxial liner, which allowed us to investigate the coupling impedance numerically. In the present paper we obtain analytic expressions for a small hole of arbitrary shape. Specifically, we go beyond the quasi-static (Bethe) approximation to explore and understand the structure of the impedance in the frequency region near the cutoffs of the inner beam pipe and outer coaxial structure. Finally, we extend our analytic analysis to a hole in a wall of finite thickness.

1 INTRODUCTION

In an earlier work, Gluckstern and Neri [1] analyzed the impedance of a small azimuthally symmetric pill-box in a beam pipe at frequencies of the same order as the cutoffs of the TM_{0n} modes in the pipe. They found that the admittance could be written as the sum of a term depending primarily on the pill-box width and thickness, and a term depending primarily on the pipe radius. In fact, the broad resonance used frequently by others to describe the behavior near cutoffs, was shown to be due to a change of sign of the imaginary part of the admittance.

We recently constructed a variational form for the impedance of a rectangular hole in the wall of a coaxial liner [2]. Our analysis allowed us to study numerically the frequency dependence of the coupling impedance of a transverse rectangular slot, small square hole [2] and a longitudinal rectangular slot, including the resonances due to the slot length [3]. However, it is possible to obtain an approximate analytic expressions, analogous to that obtained in [1], for a small hole of arbitrary shape which would allow us to understand the structure of the impedance in the frequency region near the cutoff of the beam pipe. In the case of a narrow pill-box the dominant contribution comes from the magnetic portion of the problem; therefore, in [1], only the magnetic part was considered. In the present paper we extend the analysis to the azimuthally asymmetric problem of a hole in the wall of a coaxial liner. We also consider both the electric and magnetic portions of the problem. Finally we extend our analysis to a hole in a wall of finite thickness.

* Work supported by the U.S. Department of Energy

2 THE LONGITUDINAL COUPLING IMPEDANCE

The source fields in the frequency domain generated by the driving current

$$J_z(x,y,z;k) = I_0\delta(x)\delta(y)e^{-jkz} \tag{1}$$

are the following:

$$E_r^{(s)}(r,z;k) = Z_0 H_\theta^{(s)}(r,z;k) = \frac{Z_0 I_0}{2\pi r}e^{-jkz}, \tag{2}$$

$$E_z^{(s)}(r,z;k) = 0, \tag{3}$$

where $Z_0 = 120\pi\ [\Omega]$, $k = \omega/c$. The definition of the frequency dependent longitudinal coupling impedance of any obstacle can be taken to be

$$Z_\parallel = \frac{-1}{I_0}\int_{-\infty}^{\infty} dz e^{jkz} E_z(0,\theta,z;k), \tag{4}$$

where $E_z(r,\theta,z;k)$ is the axial electric field in the frequency domain, with frequency dependence $\exp(j\omega t)$, where $\omega = kc$. This expression can be rewritten as

$$\frac{Z_\parallel(k)}{Z_0} = -\frac{1}{2\pi a Z_0 I_0}\int dS E_z(a,\theta,z;k)e^{jkz}, \tag{5}$$

where the surface integral is only over the hole, since E_z vanishes on the liner wall. Since the driving current on axis is proportional to $\exp(-jkz)$, the problem is simplified by obtaining results for an even driving current $\cos kz$ and an odd driving current $-j\sin kz$ separately [2]. We use the superscript (e) for the even problem and the superscript (o) for the odd problem. The field matching is performed at the radius of the inner conductor (liner) in the opening. We call the region inside the inner conductor $r \le a$ the "pipe region" and the region outside the inner conductor $a \le r \le b$ the "coaxial region".

3 THIN WALL ANALYSIS

3.1 Odd Part

We now assume that the hole dimensions are small compared to the wavelength, and we can use the quasi-static solutions for the field components in the vicinity of the hole. For the odd part of the impedance we obtain

$$\frac{Z_\parallel^{(o)}}{Z_0} = -\frac{jk}{8\pi^2 a^2}\chi\Big[1 + \frac{\chi}{8\pi^2}W\Big], \tag{6}$$

with W being defined as

$$W = \sum_n \Big(\int dq[q^2 P_n(q) - \frac{n^2 k^2}{\kappa^2 a^2} Q_n(q)] \Big), \qquad (7)$$

where κ, defined by $\kappa^2 = k^2 - q^2$, is the radial propagation constant, χ is the electric polarizability of a hole, and symbol n stands for the azimuthal index of the modes. Functions P_n and Q_n contain Bessel functions and their derivatives and can be found in [2]. For a small hole, the term proportional to χW will be small compared to 1 and we can write an expression for the admittance as

$$Z_0 Y_{\parallel}^{(o)} = \frac{j8\pi^2 a^2}{k\chi} - \frac{ja^2}{k} W. \qquad (8)$$

3.2 Even Part

Similarly to the odd part we obtain

$$\frac{Z^{(e)}}{Z_0} = \frac{jk}{8\pi^2 a^2} \psi_\theta \Big[1 - \frac{\psi_\theta}{8\pi^2} V \Big], \qquad (9)$$

where ψ_θ is the transverse magnetic susceptibility of a hole, and V is defined as

$$V = \sum_n \Big(\int dq[k^2 P_n(q) - \frac{n^2 q^2}{\kappa^2 a^2} Q_n(q)] \Big). \qquad (10)$$

As before, for $\psi_\theta V \ll 1$ we can write

$$Z_0 Y_{\parallel}^{(e)} = -\frac{j8\pi^2 a^2}{k\psi_\theta} - \frac{ja^2}{k} V. \qquad (11)$$

We can also combine Eqs. (6) and (9) to obtain the expression for the total impedance

$$\frac{Z_{\parallel}}{Z_0} = \frac{jka}{8\pi^2 a^3} \Big(\psi - \chi - \frac{1}{8\pi^2} (\psi^2 V + \chi^2 W) \Big). \qquad (12)$$

The structure obtained in Eq. (12) is similar to the one presented in [4], but we now have additional contribution from the modes in the coaxial region.

3.3 Discussion

We now examine our results in Eqs. (8) and (11). One sees that each admittance separates into a part which includes the geometry of the hole (parameters ψ and χ), and the term involving the pipe and the coaxial region. In the present case the real part includes dependence on parameters b and a (where b is the radius of the outer pipe), and is present even below all possible cutoffs because of the existence of the TEM mode in the coaxial region. Additional energy is lost when other outgoing propagating modes are generated in the "coaxial" and the "pipe" region. In fact, experience with [1] suggests that these expressions are valid in the region of the mode cutoffs where ka and $k(b-a)$ are of the order of 1. This speculation is confirmed by the numerical studies [5].

3.4 Numerical Implementation

It is clear from Eq. (12) that the departure from the usual small hole (Bethe) approximation is contained in the quantities W and V defined in Eqs. (7) and (10). The real parts of W, V contribute to the imaginary part of the impedance. From numerical studies [5] we find that for low frequencies $V_r, W_r \sim k^2$, and that below all possible cutoffs imaginary part of $V, W = \pi/[ln(b/a)]$, with additional energy being lost when other outgoing propagating modes are generated.

To compare the frequency behavior of the admittance of a small hole with the one presented for a pill-box [1], we perform numerical calculations for the square hole with the following parameters $b/a = 1.3125$, $w/a = 0.25$. Results are shown in Figs. 1 and 2 for the imaginary and real part of the admittance, respectively. Figure 2 clearly shows the steps which occur as ka passes the cutoffs corresponding to the TM amd TE modes. For the odd part one sees the cutoffs corresponding to the $\mathrm{TE}_{11}^{(coax.)}$, $\mathrm{TE}_{21}^{(coax.)}$, $\mathrm{TE}_{11}^{(pipe)}$, $\mathrm{TE}_{31}^{(coax.)}$ modes, while for the even part one sees the cutoff corresponding to the $\mathrm{TM}_{01}^{(pipe)}$ mode. This leads to the conclusion that, for a small hole, the odd (electric) part primarily couples to the TE modes, while the even (magnetic) part primarily couples to the TM modes near the cutoffs. This behavior can be also shown analytically (see for example [6]). We also confirmed numerically that this behavior holds for slots with $l/a < 1$ and $kl < 1$, in agreement with [6]. If one goes to very high frequency ($kl \sim \pi$), the imaginary part of the admittance in Fig. 1 eventually crosses the zero axis and changes sign. This behavior corresponds to a resonance due to the hole length. Note that the resonances occur at different frequencies for the odd and even parts.

4 THICK WALL ANALYSIS

When the field is incident on a hole in a wall of finite thickness the usual approach is to split it into two components: one with an asymmetric potential and one with a symmetric potential about the midpoint of the wall [7]. The parameters ψ and χ come from both the symmetric and antisymmetric problems. We then define the magnetic susceptibility and electric polarizability seen within the liner as

$$\psi_{in} = \psi^s + \psi^a, \;\; \chi_{in} = \chi^s + \chi^a, \qquad (13)$$

while the susceptibility and polarizability outside the liner are defined by

$$\psi_{out} = \psi^s - \psi^a, \;\; \chi_{out} = \chi^s - \chi^a. \qquad (14)$$

4.1 Even Part

For the even part of the impedance we obtain [5]:

$$\frac{Z^{(e)}}{Z_0} = \frac{jk}{8\pi^2 a^2} \psi_{in} \Big[1 - \frac{\psi_{in}}{8\pi^2} \tilde{V} \Big], \qquad (15)$$

where

$$\tilde{V} = \sum_n \int dq \Big[k^2 \Big(\frac{J_n'(\kappa a)}{\kappa a J_n(\kappa a)} - \frac{\psi_{out}^2}{\psi_{in}^2} \frac{F_n'(\kappa a)}{\kappa a F_n(\kappa a)} \Big)$$

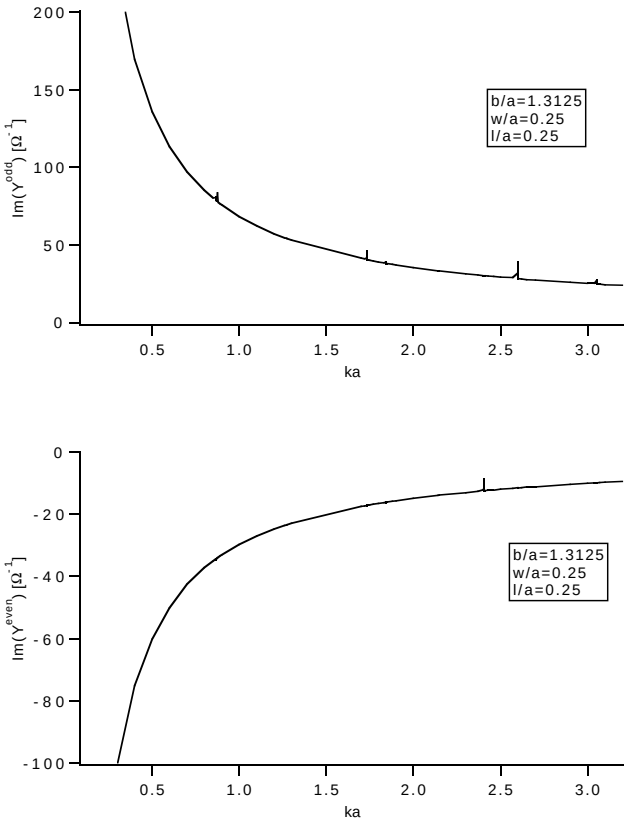

Figure 1: Imaginary part of the admittance near the cutoff frequencies.

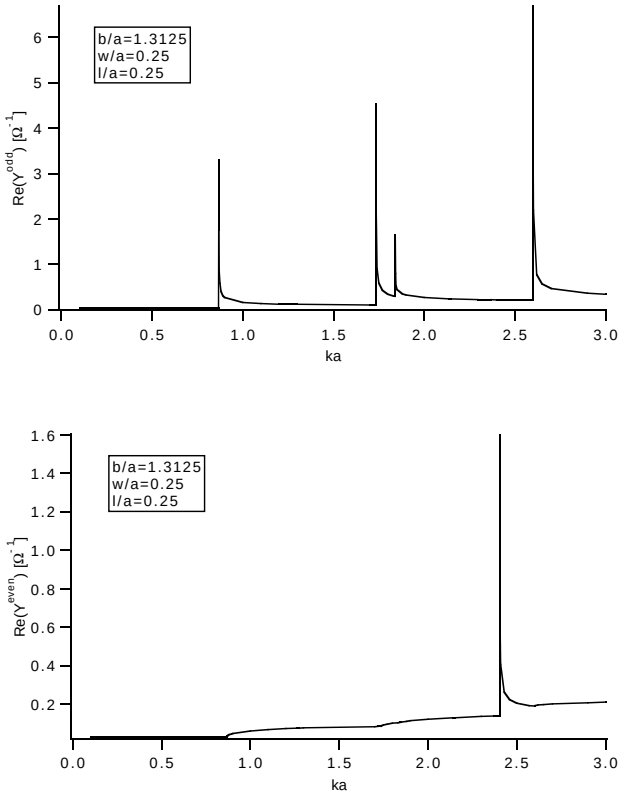

Figure 2: Real part of the admittance near the cutoff frequencies.

$$- \quad \frac{q^2 n^2}{\kappa^2 a^2}\Big(\frac{J_n(\kappa a)}{\kappa a J_n'(\kappa a)} - \frac{\psi_{out}^2}{\psi_{in}^2}\frac{G_n(\kappa a)}{\kappa a G_n'(\kappa a)}\Big)\Big]. \quad (16)$$

4.2 Odd Part

For the odd part of the impedance we obtain [5]:

$$\frac{Z^{(o)}}{Z_0} = -\frac{jk}{8\pi^2 a^2}\chi_{in}\Big[1 + \frac{\chi_{in}}{8\pi^2}\tilde{W}\Big], \quad (17)$$

where

$$\tilde{W} = \sum_n \int dq \Big[q^2\Big(\frac{J_n'(\kappa a)}{\kappa a J_n(\kappa a)} - \frac{\chi_{out}^2}{\chi_{in}^2}\frac{F_n'(\kappa a)}{\kappa a F_n(\kappa a)}\Big) - \frac{k^2 n^2}{\kappa^2 a^2}\Big(\frac{J_n(\kappa a)}{\kappa a J_n'(\kappa a)} - \frac{\chi_{out}^2}{\chi_{in}^2}\frac{G_n(\kappa a)}{\kappa a G_n'(\kappa a)}\Big)\Big]. \quad (18)$$

Expressions for $\tilde{V}$ and $\tilde{W}$ include the parameters ψ and χ; and, therefore, for the case of a wall of finite thickness, the admittance does *not* separate into a part which includes only the geometry of a hole and a term which includes the geometry of a pipe. But this separation *is* still valid for a thin wall ($\chi_{out} = \chi_{in}$, $\psi_{out} = \psi_{in}$) and for a very thick wall ($\chi_{out} = \psi_{out} = 0$).

5 SUMMARY

We obtained analytic expressions for the impedance of a small hole which includes effects of energy propagation along the inner beam pipe and/or outer coaxial pipe. This allow us to understand the structure of the impedance in the frequency region near the cutoffs of the inner beam pipe and outer coaxial structure. We then extended our analytic treatment to a wall of finite thickness and discussed the resulting expressions, and concluded that the admittance could no longer be separated into a part depending only on the pipe geometry and a part depending primarily on the hole geometry.

6 REFERENCES

[1] R.L. Gluckstern and F. Neri, in Proceedings of the 1989 Particle Accelerator Conference (IEEE, Chicago, IL, 1989), p. 1271.

[2] A.V. Fedotov and R.L. Gluckstern, Phys. Rev. E, 56, N. 3, 3583 (1997).

[3] A.V. Fedotov and R.L. Gluckstern, Phys. Rev. E, 56, N. 6, 7217 (1997).

[4] S.S. Kurennoy, R.L. Gluckstern and G.V. Stupakov, Phys. Rev. E, 52, N. 4, 4354 (1995).

[5] A.V. Fedotov and R.L. Gluckstern, Phys. Rev. ST Accel. Beams 1, 024401 (1998).

[6] G.V. Stupakov, in Proceedings of the 1995 Particle Accelerator Conference (IEEE, Dallas, TX, 1995), p. 3306.

[7] R.L. Gluckstern and J.A. Diamond, IEEE Trans. on Mic. Theory and Techn., 39, N. 2, 274 (1991).

BEAM DYNAMICS SIMULATIONS OF THE LANSCE LINAC

Frank Merrill and Lawrence Rybarcyk
LANSCE Division, Los Alamos National Laboratory, Los Alamos, New Mexico 87545 USA

Abstract

Detailed beam dynamics calculations of the LANSCE Linac have been performed using multi-particle simulation codes. The LANSCE accelerator produces both H^+ and H^- beams and is comprised of Cockcroft-Walton injectors, a 100 MeV drift-tube linac and an 800 MeV side-coupled linac. Several improvements to the simulations of H^+ and H^- beams have recently been made. These include the use of more accurate input distributions and a better estimate of beam neutralization in the low-energy beam transport. Better estimates of the accelerating fields in the drift-tube linac have also been determined through measurements and modeling. With these improvements better agreement has been achieved between the predictions and measurements of RMS beam parameters and beam losses for both beams. The details of the simulations along with predictions are presented in comparison with measurements for both H^+ and H^- beams.

1 INTRODUCTION

The LANSCE accelerator begins with two Cockcroft-Walton injectors that accelerate H^+ and H^- beam to 750 keV. Each beam is transported in a separate low-energy beam transport (LEBT) to a common LEBT that transports both beams to the drift-tube linac (DTL). The DTL operates at 201.25 MHz and accelerates the beams from 0.75 to 100 MeV. The transition region (TR) consists of two beam lines, one for H^+ and the second for H^-, and transports both beams from the DTL to the Side-Coupled Linac (SCL). The SCL operates at 805 MHz and accelerates the beams to 800 MeV.

Each LEBT contains quadrupole magnets set to transport and transversely match each beam into the DTL. A single-cell 201.25 MHz buncher in each upstream LEBT, referred to as the pre-buncher, and an identical buncher in the common LEBT, referred to as the main buncher, are used to prepare the longitudinal phase-space of the beams for DTL injection.

The DTL consists of four tanks, referred to as modules 1 through 4. Each DTL tank is driven by a separate rf power source. Quadrupole magnets inside the DTL drift-tubes are used to establish a singlet FODO lattice.

The two beam lines in the TR each contain four quadrupole magnets for transporting and transversely matching the beams into the SCL. The SCL is made of 44 modules, each fed by a separate rf power source. The SCL modules 5 through 12 accelerate beam from 100 to 211 MeV and consist of four bridge-coupled tanks each with 32-36 cells. Modules 13 through 48 accelerate from 211 to 800 MeV and consist of two bridge-coupled SCL tanks with 49-61 cells. Quadrupole doublets between tanks provide the focusing lattice required for transport of the beams through the SCL.

During typical LANSCE operation an average current of 1 mA of H^+ is delivered to one experimental area while an average current of 76 μA of H^- is transported to the Proton Storage Ring (PSR) for compression and subsequent delivery to a neutron spallation target. The 1 mA of H^+ beam is presently achieved by accelerating a peak current of 16.5 mA at a pulse rate of 100 Hz and a pulse length of 625 μs. The 76 μA of H^- is delivered at 20 Hz and 575 μs length with a 9.5 mA peak current. The H^- beam must also be "chopped" for injection into the PSR with a chopping duty factor of ~70%.

2 SIMULATION TECHNIQUE

A modified version of PARMILA was used to model the beam transport through the LEBT, DTL and TR. The beam transport through the SCL was modeled using a modified version of CCLDYN, a PARMILA-like code used to model beam dynamics through coupled-cavity linacs. These simulation codes were used in previous studies[1] of the LANSCE linac and were modified to incorporate more of the details of the beam transports and accelerator.

Both the H^+ and H^- simulations were performed using 1×10^5 macro-particles to represent 6.2×10^8 H^+ ions or 3.7×10^8 H^- ions at DTL injection. The two-dimensional mesh used by PARMILA and CCLDYN to calculated space-charge forces consisted of 800 mesh points, 20 radial points and 40 longitudinal points.

2.1 Input Distributions

The transverse phase-space input distributions were derived from measurements made at TDEM1, a slit-and-collector emittance station upstream of the DTL. To discriminate between signal and noise on the collector wires only those data bins above 2% of the peak were included in the generation of the input distribution. The measured distributions were then normalized and used as a discrete probability distribution for the Monte-Carlo creation of the horizontal and vertical input distributions.

The longitudinal phase-space input distributions were estimated with PARMILA by transporting mono-energetic, unbunched H^+ and H^- beams through their

respective pre-bunchers and the common main buncher to the slit of TDEM1.

The transverse and longitudinal phase-space distributions were combined without correlations to produce the final input distributions. The resulting H^+ and H^- input distributions at the entrance to the DTL are shown in Fig. 1 and 2, respectively.

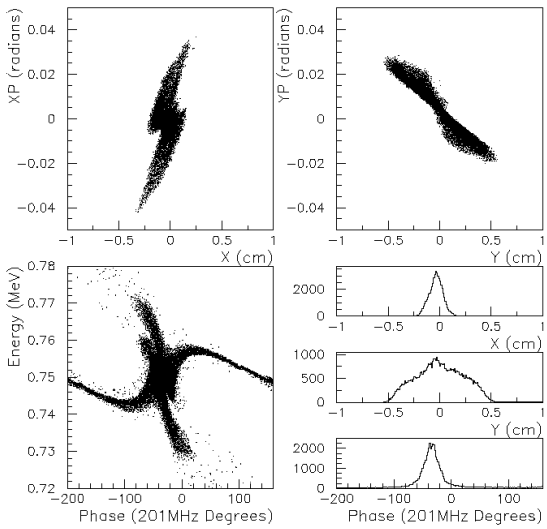

Figure 1: The simulated transverse and longitudinal H^+ beam distributions at injection to the DTL.

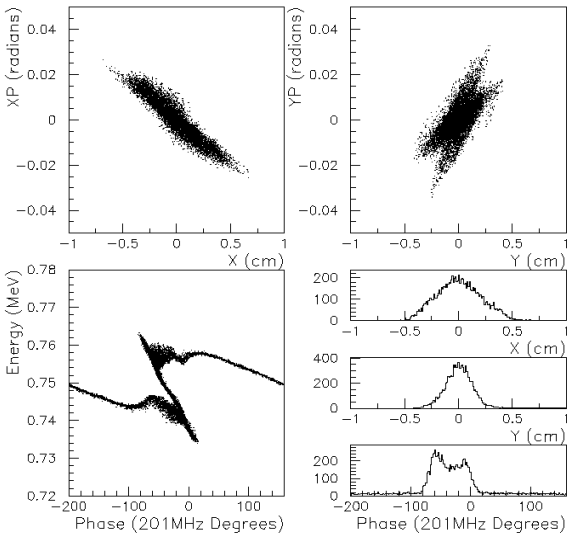

Figure 2: The simulated transverse and longitudinal H^- beam distributions at injection to the DTL.

2.2 Space-Charge Neutralization

The effects of space-charge neutralization in the common LEBT were estimated for both H^+ and H^- beams from measurements made with TDEM1. For each beam the horizontal and vertical phase-space distributions at the slit position were measured along with the beam profiles at the collector position. The measured phase-space distributions were used as input in a PARMILA calculation to predict the beam profiles after a drift to the collector location. An iterative search routine was used to determine the effective charge of the beam that resulted in the best agreement between the measured and predicted profiles. An effective peak of 85% of the measured H^+ peak current and 75% of the measured H^- peak current were found to best reproduce the measured data.

The measured H^+ and H^- currents were used in the DTL and SCL since the large magnetic and electric fields in these structures would quickly remove electrons or ions from the beam column. No neutralization effects were included in the simulations of the TR.

2.3 LEBT, DTL, TR and SCL Parameters

The field strengths of the quadrupoles in the LEBT, DTL, TR and SCL were determined from field-map data and present operating set points.

The phase and amplitude of the rf fields in the buncher and DTL cavities were determined through a combination of measurements and simulations. For these estimates a version of the PARMILA code was modified to include an option for simulating "phase scans". This phase scan procedure uses an absorber-collector diagnostic to measure the transmitted beam current above an energy threshold versus the cavity rf phase. The phase centroid and width of the resultant distribution are related to the phase and amplitude of the rf fields in the cavity. For the bunchers, phase and amplitude settings were adjusted until measured phase scan results matched simulations that were based upon desired operating set points. For the DTL, phase scan simulations were performed for a range of amplitude and phase values that produced the desired output energy. Phase scan measurements were then performed with the DTL tanks at their production settings. Simulation results were interpolated to these measured phase scan parameters to extract an operating amplitude relative to the design amplitude for each tank. Simulations were then performed with these amplitudes and compared with measurements to obtain the operating phase set points of each of the DTL tanks.

The design phase and amplitude set points of the rf fields in each SCL module were used in the simulations.

3 SIMULATION RESULTS

The simulations were performed with beam started in the 750 keV LEBT and transported through the DTL and TR to the exit of the SCL at 800 MeV. Particle distributions were saved at various locations along the accelerator for analysis and comparison to measurements.

3.1 DTL Capture

The DTL capture ratio is the percent of the injected beam that is properly accelerated to 100 MeV through the exit of the DTL. This ratio is primarily determined by the longitudinal distribution at injection into the DTL and the settings of the DTL parameters. The two-buncher system

used at LANSCE results in a complicated longitudinal phase-space distribution at injection to the DTL. The simulated longitudinal H^+ and H^- distributions at injection are shown in Fig. 1 and 2, respectively.

Simulations have shown that the structure of these distributions is primarily determined by the rf field strengths in the bunchers and the level of space-charge neutralization in the LEBTs. With the estimates of these parameters, described in section 2, the simulations accurately predict the capture for both H^+ and H^- beams. The H^+ capture was measured to be 82±1% while simulations predict 80%. For the H^- beam a capture ratio of 81±1% was measured while the simulations predict a ratio of 80%.

3.2 Beam Emittance

The measured transverse phase-space distributions at TDEM1 were used as input distributions for both H^+ and H^- beam simulations. The next two emittance stations that were used for comparison with the simulations are located in the TR. Station one (TREM1) is located at the exit of the DTL and station two (TREM2) at the entrance to the SCL. The simulated and measured normalized RMS emittances at these locations are summarized in Table 1.

Table 1: Comparison of simulated and measured normalized RMS emittances for H^+ and H^- beams in horizontal (H) and vertical (V) planes.

Emittance Station		H^+ RMS Emittance (π cm-mrad)		H^- RMS Emittance (π cm-mrad)	
		Sim.	**Meas.**	**Sim.**	**Meas.**
TDEM1	H	$.93\times10^{-2}$	$.93\times10^{-2}$	1.9×10^{-2}	1.9×10^{-2}
	V	$.92\times10^{-2}$	$.92\times10^{-2}$	2.5×10^{-2}	2.5×10^{-2}
TREM1	H	5.2×10^{-2}	3.1×10^{-2}	3.2×10^{-2}	2.8×10^{-2}
	V	2.7×10^{-2}	2.8×10^{-2}	5.1×10^{-2}	3.4×10^{-2}
TREM2	H	5.2×10^{-2}	3.7×10^{-2}	3.2×10^{-2}	2.9×10^{-2}
	V	2.7×10^{-2}	2.0×10^{-2}	5.0×10^{-2}	2.6×10^{-2}

Although the simulated and measured RMS emittances agree, the higher order moments of the beam distributions in phase-space are different. The 95% emittance, which is the emittance value that includes 95% of the beam, includes information about these higher order moments. The predicted 95% emittance of the H^+ beam in the TR is 2 times larger than the measured 95% emittance and the H^- 95% emittance in the TR is 1.5 times larger than the measured value.

3.3 TR and SCL Losses

The simulations also predict the expected level of losses and the distribution of these losses along the SCL. Measurements of total losses have been made with current monitors that measure average current with an accuracy of ~1 μA. The loss distribution along the linac has also been measured with loss monitors located along the SCL. A comparison between simulation and typical measured losses is shown in Table 2. The simulated and measured distribution of these losses is plotted in Fig. 3. Relatively good agreement has been achieved between simulation and measured losses, although the measured trend of increasing H^- losses along the linac has not yet been understood.

Table 2: Comparison of simulated and measured losses for H^+ and H^- beams.

Between Modules	H^+ Losses		H^- Losses	
	Sim.	**Meas.**	**Sim.**	**Meas.**
3-12	0.04%	0.1%	0.15%	< 1%
12-48	0.28%	< 0.1%	0.24%	< 1%

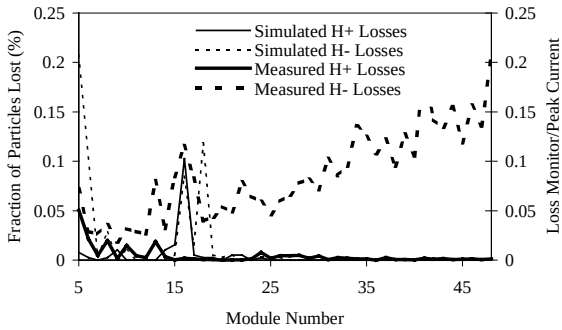

Figure 3: Fraction of particles lost versus module number from simulations (plotted against left axis) and measured losses scaled by peak current (plotted against right axis).

4 CONCLUSIONS

The recent improvements made to the beam dynamics simulations of the LANSCE linac have resulted in better agreement between simulation results and measurements. The most important of these were the use of input distributions derived from measurements, better estimates of space-charge neutralization effects in the LEBTs and the use of accurate estimates of the phase and amplitude of the DTL rf fields.

Because of the improved agreement between simulations and measurements this new model has been used to investigate upgrade scenarios with more confidence. The model is also presently being used to investigate possible sources of the smaller than predicted 95% emittance for both beams in the TR and possible effects that create the observed H^- losses along the SCL.

5 ACKNOWLEDGEMENTS

This work was supported by the U.S. Department of Energy.

6 REFERENCES

[1] R.W. Garnett et al. "Simulation Studies of the LAMPF Proton Linac", Proceedings of the Particle Accelerator Conference, Dallas Texas, May 1-5, 1995.

THE NONLINEAR TRANSERVERSE RF FIELD EFFECTS ON THE BEAM DYNAMICS*

Sun Xiang and Lin Yuzheng
Department of Engineering Physics, Tsinghua University, Beijing 100084, PRChina

Abstract

The nonlinear transverse RF field effects on the low energy and emittance dominated electron beams are investigated theoretically including the bunching and accelerating. Without any external magnetic focusing devices and in pursuit of high shunt impedance, the nonlinear transverse RF field effects should not be neglected. The evolution of the beam phase space distribution in asymmetric cavity is studied by taking into account the nonlinear transverse RF fields. As a result of the nonlinear transverse RF field effects, the emittance growth occurs mainly in the first cavity of bunchers and is associated with the relative position of the particles deviating from the axis, the nonlinearity of the RF fields and the synchronous state of the beam. A few formulas for energy, phase and emittance growth are derived.

1 INTRODUCTION

Low energy electron linacs used for industry, medicine and research need the higher quality beam. The nonlinearity of RF fields, magnetic focusing fields and space charge will cause the phase space tearing and emittance growth. And this distortion of the phase space can not be corrected.

The RF fields in S-band low energy electron linacs are considered as linearity and this approximation are good enough due to a smaller ratio of beam size to beam aperture. In order to get higher breakdown threshold and shunt impedance, higher microwave frequencies should be used (e.g. X-band linacs). Then the nonlinearity of RF fields becomes serious. With the increasing of RF frequencies, $r/(\beta_p\lambda)$ (r: the particle radial position; λ: the RF field wavelength; β_p: the relative phase velocity) increases and a decreases correspondingly (a: the iris radius). The cavities are optimized for higher shunt impedance by decreasing a and r/a is larger. In the meantime the magnetic focusing lens is not used to keep linac size small and r/a can not decrease. The condition of paraxial beam is no long satisfied in our case.

In NLC design, the beam sizes are microns and the iris radius is 4 mm, so the cubic term is down by about $(10^{-3})^2$ from the linearity[1]. But in our case, the beam radius is about 1 mm and the iris radius is no larger than 2 mm.

The nonlinear effects of magnetic focusing fields and space charge have been studied[2][3]. An approximate theory of electron beam dynamics in laser-driver RF guns has been developed[4] and the emittance growth due to the effects of nonlinear RF fields in laser-driver RF guns has been studied by simulations[5].

In low energy and low current SW linacs, the electron beams are emittance dominated. The beams are bunched in the first a few cavities and accelerated along the tube. Contrary to the laser-driver RF guns, the initial phase region of captured particles is very large (e.g. 120^0) and usually in the decelerating region. In the following discussion, the influence of initial phase should be considered. The initial emittance is set to zero and the space charge forces are turned off. There is no magnetic focusing lens and the beam is not paraxial.

2 RF FIELDS IN SW LINACS

In order to represent the fields near the axis of a multi-cell π-mode structure, the RF fields are approximated by a power expansion truncated after r^3, yielding

$$E_z = \sum_{n=1}^{\infty} a_n Sin\left(\frac{nkz}{\beta_p}\right) + \frac{k^2 r^2}{4}\sum_{n=2}^{\infty} a_n Sin\left(\frac{nkz}{\beta_p}\right) \quad (1.1)$$

$$E_r = -\frac{kr}{2\beta_p}\sum_{n=1}^{\infty} n a_n Cos\left(\frac{nkz}{\beta_p}\right) - \frac{k^3 r^3}{16\beta_p^3}\sum_{n=2}^{\infty} n\left(n^2-1\right) a_n Cos\left(\frac{nkz}{\beta_p}\right) \quad (1.2)$$

$$H_\theta = \frac{jkr}{2\mu_0 c\beta_p}\sum_{n=1}^{\infty} a_n Sin\left(\frac{nkz}{\beta_p}\right) + \frac{jk^3 r^3}{16\mu_0 c\beta_p^3}\sum_{n=2}^{\infty}\left(n^2-1\right) a_n Sin\left(\frac{nkz}{\beta_p}\right) \quad (1.3)$$

where, $a_i = \frac{2}{D}\int_0^D E_z(r=0) Sin\left(\frac{kz}{\beta_p}\right) dz$; $D = \frac{\beta_p \lambda}{2}$ is the cell length; $i = 1,2,3,\cdots$.

It is because the coefficient of the first harmonic nonlinear term is zero that the π-mode structure is used. If we use symmetric cavities, the coefficient of the second harmonic nonlinear term is zero.

So called symmetric cavity is the one that has a symmetry plane perpendicular to the axis and asymmetric cavity is the one which has not such plane.

3 ANALYSIS OF LONGITUDINAL BEAM DYNAMICS

The low energy linacs consist of a first cavity, bunchers and relativistic cavities. In analysis, the first cavity is the phase oscillation section and bunchers and relativistic cavities are the quasi-synchronous section (shown in Fig. 1). For convenient, we neglect the nonlinear of longitudinal electric fields.

*Work supported by the National Science Foundation of China

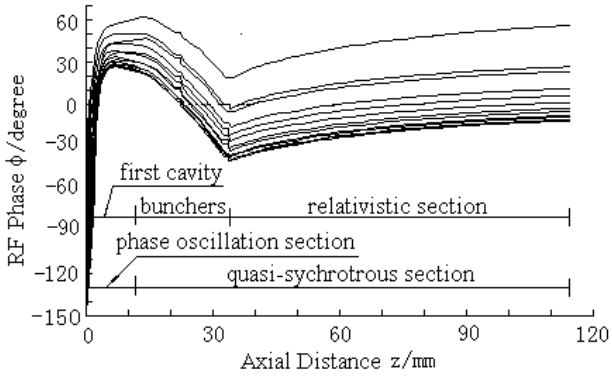

Fig. 1 Schematic of linac distributions

Because the particles are in the decelerating region when they are injected, we assume D_0 is the length of decelerating region (shown in Fig. 2) and $\overline{\beta}_{e0}$ is the average velocity over D_0. ϕ_0 is the initial phase of particles and γ_0 is the initial relativistic factor. γ_i and ϕ_i are the relativistic factor and the phase at the exit of *ith* cavity separately. D_i is the cell length of *ith* cavity. $\overline{\beta}_{ei}$ is the average velocity in the *ith* cavity except $\overline{\beta}_{e1}$ which is the average velocity over $(D_1\text{-}D_0)$ in the first cavity.

We assume $\frac{k}{\overline{\beta}_{e0}} D_0 + \phi_0 = 0 \Rightarrow D_0 = -\frac{\overline{\beta}_{e0}}{k}\phi_0$.

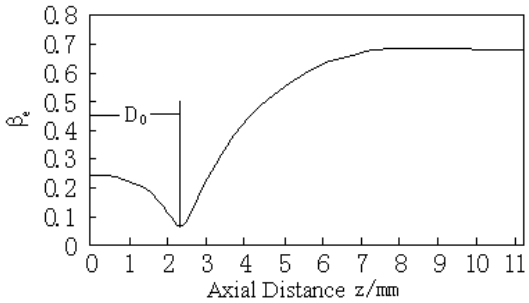

Fig. 2 Schematics of β_e in the first cavity

The average relative velocity is assumed to be constant over its integral region below. At the exit of the first cavity, the relativistic factor particles is

$$\gamma_1 = \gamma_0 + \int_0^{D_0} \frac{e}{m_0 c^2} E_z(z) Sin(\omega t + \phi_0) dt + \int_{D_0}^{D_1} \frac{e}{m_0 c^2} E_z(z) Sin(\omega t + \phi_0) dt$$

$$= \gamma_0 + \frac{e}{m_0 c^2}\frac{\overline{\beta}_{e0}}{k}\left[\sum_{n=1}^{\infty} a_n \frac{Sin\left(\frac{n\overline{\beta}_{e0}}{\beta_{p1}}\phi_0\right) - \frac{n\overline{\beta}_{e0}}{\beta_{p1}} Sin(\phi_0)}{1-\left(\frac{n\overline{\beta}_{e0}}{\beta_{p1}}\right)^2}\right]$$

$$+ \frac{e}{m_0 c^2}\frac{\overline{\beta}_{e1}}{k}\sum_{n=1}^{\infty} a_n \left[\frac{-Cos\left(\frac{\overline{\beta}_{e0}}{\overline{\beta}_{e1}}\phi_0\right) Sin\left(\frac{n\overline{\beta}_{e0}}{\beta_{p1}}\phi_0\right)}{1-\left(\frac{n\overline{\beta}_{e1}}{\beta_{p1}}\right)^2}\right.$$

$$\left. + \frac{n\overline{\beta}_{e1}}{\beta_{p1}} \frac{(-1)^n Sin\left(\frac{\beta_{p1}}{\overline{\beta}_{e1}}\pi\right) + Sin\left(\frac{\overline{\beta}_{e0}}{\overline{\beta}_{e1}}\phi_0\right) Cos\left(\frac{n\overline{\beta}_{e0}}{\beta_{p1}}\phi_0\right)}{1-\left(\frac{n\overline{\beta}_{e1}}{\beta_{p1}}\right)^2}\right] \quad (2)$$

Corresponding, the phase at the exit of the first cavity

$$\phi_1 = k\int_0^{D_1}\frac{dz}{\beta_{e1}} + \phi_0 = k\int_0^{D_0}\frac{dz}{\overline{\beta}_{e0}} + k\int_{D_0}^{D_1}\frac{dz}{\overline{\beta}_{e1}} + \phi_0 = \frac{k}{\overline{\beta}_{e1}}(D_1 - D_0) \quad (3)$$

In the quasi-synchronous section,

$$\gamma_i = \gamma_{i-1} + \int_0^{D_i}\frac{e}{m_0 c^2} E_z(z) Sin(\omega t + \phi_{i-1}) dt$$

$$= \gamma_{i-1} - \frac{e}{m_0 c^2}\frac{\overline{\beta}_{ei}}{k}\frac{\overline{\beta}_{ei}}{\beta_{pi}}\sum_{n=1}^{\infty} n \frac{Sin\left(\frac{\pi}{\left(\overline{\beta}_{ei}/\beta_{pi}\right)} + \phi_{i-1}\right) + Sin\phi_{i-1}}{1-\left(\frac{n\overline{\beta}_{ei}}{\beta_{pi}}\right)^2} \quad (4)$$

$$\phi_i = k\int_0^{D_i}\frac{dz}{\beta_{ei}} + \phi_{i-1} = \frac{k}{\overline{\beta}_{ei}}(D_i - D_{i-1}) + \phi_{i-1} \quad (5)$$

4 ANALYSIS OF TRANSVERSE BEAM DYNAMICS

In the following, the radius r and the average relative velocity are assumed to be constant over their integral region. After the first cavity,

$$\Delta P_{r1}\big|_{non} = \int_0^{D_0}\frac{F_r\big|_{non}}{m_0 c\overline{\beta}_{e0} c} dz + \int_{D_0}^{D_1}\frac{F_r\big|_{non}}{m_0 c\overline{\beta}_{e1} c} dz$$

$$= \frac{\pi^2 D_1 e}{2m_0 c^2}\left(\frac{r}{\beta_{p1}\lambda}\right)^3\left(\frac{1}{\beta_{p1}} - M_0^2\right)\sum_{n=2}^{\infty}\frac{n(n^2-1)a_n}{1-(nM_0)^2}\left[Cos(nM_0\phi_0) - Cos(\phi_0)\right]$$

$$- \frac{\pi^2 D_1 e}{2m_0 c^2}\left(\frac{r}{\beta_{p1}\lambda}\right)^3\sum_{n=2}^{\infty}\frac{(n^2-1)a_n}{1-(nM_1)^2}\left\{M_1\left(\frac{n^2}{\beta_{p1}} - 1\right)Sin\left(\frac{M_0}{M_1}\phi_0\right)Sin(nM_0\phi_0)\right.$$

$$\left. + n\left(\frac{1}{\beta_{p1}} - M_1^2\right)\left[-(-1)^n Cos\left(\frac{\pi}{M_1}\right) + Cos\left(\frac{M_0}{M_1}\phi_0\right)Cos(nM_0\phi_0)\right]\right\} \quad (6)$$

where $M_0 = \overline{\beta}_{e0}/\beta_{p1}$, $M_1 = \overline{\beta}_{e1}/\beta_{p1}$. $\Delta P_{r1}\big|_{non}$ is the transverse momentum changing due to the nonlinear components of RF fields through the first cavity.

From eq.(6), the nonlinear transverse effects come from three facts.

(1) $(r/\beta_{p1}\lambda)^3$ expresses the relative radial position of particles.

(2) a_n indicates the nonlinear components of RF fields. They are determined by the shapes of the cavities. $a_{2n}=0$ in the symmetric cavities. But the RF fields in the asymmetric cavity lift slowly along the axis and the decelerating force exerted on the particles in the asymmetric cavity is smaller than the force exerted on the particles with the same initial phase in the symmetric cavity over the decelerating region. The synchronous state of particles in the asymmetric cavity is better than in the asymmetric cavity over the decelerating region.

(3) M_0, M_1 and ϕ_0 show the synchronous state between particles and RF fields. We can change the synchronous state by changing injecting voltage and RF field amplitude in the first cavity.

After one cavity in quasi-synchronous section,

$$\Delta P_r\big|_{non} = \int_0^D \frac{F_r\big|_{non}}{m_0 c\beta_e c}dz = -D\frac{2e}{m_0c^2\pi}\frac{\pi^3}{2}\left[\frac{1}{\beta_p}-\left(\frac{\beta_e}{\beta_p}\right)^2\right]\left(\frac{r}{\beta_p\lambda}\right)^3 \bullet$$

$$\bullet\left\{\frac{2\cdot 3a_2}{1-\left(\frac{2\beta_e}{\beta_p}\right)^2}Sin\left[\frac{\pi}{2\left(\frac{\beta_e}{\beta_p}\right)}+\phi\right]Sin\left[\frac{\pi}{2\left(\frac{\beta_e}{\beta_p}\right)}\right]\right.$$

$$\left.+\frac{3\cdot 8a_3}{1-\left(\frac{3\beta_e}{\beta_p}\right)^2}Cos\left[\frac{\pi}{2\left(\frac{\beta_e}{\beta_p}\right)}+\phi\right]Cos\left[\frac{\pi}{2\left(\frac{\beta_e}{\beta_p}\right)}\right]+...\right\} \quad (7)$$

where $(\beta_e/\beta_p) \to 1$, $\beta_p \to 1$, $\phi \to 1$,. So $\Delta P_r|_{non} \to 1$ in quasi-synchronous section.

From eq.(6) and (7), the nonlinear transverse effects occur in the first cavity and the nonlinear transverse effects in the bunchers are more serious than in relative section.

5 EMITTANCE GROWTH

The rms normalized transverse emittance is

$$\varepsilon_{xn} = 4\pi\sqrt{\langle P_{xn}^2\rangle\langle x^2\rangle - \langle P_{xn}x\rangle^2}$$

where <> denotes an average over *N* particles at *z*.

For convenient, $p_{xn0}=0$ is assumed at the entrance of one cavity, or $\varepsilon_{xn0}=0$.

After one cavity which length is $\beta_p\lambda/2$, we have

$$P_r = \Delta P_r = L(\phi_0)\left(\frac{r}{\beta_p\lambda}\right) + N(\phi_0)\left(\frac{r}{\beta_p\lambda}\right)^3 \quad (8)$$

from eq.(6) and (7), where $L(\phi_0)$, $N(\phi_0)$ is the function of ϕ_0 alone. Then,

$$P_x = \Delta P_x = L(\phi_0)\left(\frac{1}{\beta_p\lambda}\right)x + N(\phi_0)\left(\frac{r}{\beta_p\lambda}\right)^2\left(\frac{1}{\beta_p\lambda}\right)x. \quad (9)$$

$$\Delta\varepsilon_{xn} = \varepsilon_{xn} - \varepsilon_{xn0} = 4\pi\left(\frac{1}{\beta_p\lambda}\right)^3|N(\phi_0)|\sqrt{\langle r^4x^2\rangle\langle x^2\rangle - \langle r^2x^2\rangle^2} \quad (10)$$

If the distribution of electrons is uniform distribution at the plane which is perpendicular to the axis,

$$\Delta\varepsilon_{xn} = 4\pi\left(\frac{R}{\beta_p\lambda}\right)^3|N(\phi_0)|\times 0.06R \quad (11)$$

where *R* is the envelope radius of the beam.

From eq.(11), $\Delta\varepsilon_{xn}$ and ΔP_r are the same form. So the analysis and conclusion about ΔP_r can apply to $\Delta\varepsilon_{xn}$ too.

6 CONCLUSION

A simple theory to investigate the nonlinear transverse RF field effects on the emittance dominated beam in low energy SW electron linacs has been performed. The nonlinear transverse effect of RF fields on the beam is associate with the relative radial position of particles, the nonlinear components of RF fields and the synchronous state between particles and RF fields. The nonlinear transverse effects of RF fields on the beam and the emittance growth mainly occurs in the first cavity, especially over the decelerating phase region. These effects weaken quickly and vanish in the quasi-synchronous and synchronous section. In the symmetric π mode cavities, the nonlinear components of RF fields are least. But the nonlinear effects on the beam in an asymmetric first cavity can be less than on the beam with the same initial phase in a symmetric one. It is because the radial RF fields lift slowly in an asymmetric first cavity than in a symmetric one that the synchronous state of particles over the decelerating region in an asymmetric first cavity is better than in a symmetric one, even though the nonlinear components of RF fields in asymmetric cavity are larger.

A few formulas for longitudinal and transverse dynamics have been derived including bunching, accelerating and higher space harmonics. They should be useful in design the low energy SW linacs operating in higher frequencies. The comparison of this theory with the simulation is reported in ref.[6] and they are agreement on the whole.

ACKNOWLEDGMENT

The authors thank M. Reser, K. McDonald, Y. Batygin, R. Gluckstern, C. Bohn and R. Jameson for useful discussions.

REFERENCES

[1] John Irwin, private communication.

[2] P. Loschialpo, et al., Effects of Space Charge and Lens Aberrations in the focusing of an Electron Beam by a Solenoid Lens, Jounal Applied Physics, Vol. 57, No. 1(1985)

[3] M. Reiser, Theory and Design of Charge Particle Beams(1994)

[4] Kwang-Je Kim, RF and Space-charge Effects in Laser-driven RF Electron Guns, Nuclear Instruments and Methods in Physics Research, A275 (1989)

[5] Kirk T. McDonald, Design of the Laser-driver RF Electron Gun for the BNL Accelerator Test Facility, IEEE Transactions on Electron Devices, Vol. 35, No. 11(1988)

[6] Sun Xiang and Lin Yuzheng, Simulations of the Nonlinear Transverse RF Field Effects on the Beam Dynamics in Low Energy X-band SW Linacs, These proceedings.

A MULTI-PLATFORM GRAPHIC USER INTERFACE FOR THE PARTICLE OPTICS CODE MARYLIE

George H. Gillespie, Barrey W. Hill, Michael C. Lampel, Hendy Martono, John M. Moore, Kyle J. Ryan
G. H. Gillespie Associates, Inc., P.O. Box 2961, Del Mar, CA 92014, U.S.A
and
Alex J. Dragt
Department of Physics, University of Maryland, College Park, MD 20742, U.S.A.

Abstract

An advanced graphic user interface (GUI) is being developed for use with the particle optics code MARYLIE. MARYLIE is based on a Lie algebra formulation of charged particle trajectory calculations and is particularly useful for particle tracking and the analysis of linear and nonlinear lattice properties. The GUI for MARYLIE uses the Multi-Platform Shell for Particle Accelerator Related Codes, a software framework developed specifically to support accelerator modeling and simulation. Transport element icons are selected from a palette and assembled into beamlines by graphical construction. Optical cells and lattices composed of element groups may be defined as sublines, and any element or subline can be replicated using an alias element. The icon-based beamlines generate entries for the #beam, #menu and #lines components of the MARYLIE Master Input File (MIF). Frequent computations, such as creating maps or generating particle distributions, are encapsulated into interactive GUI commands which create corresponding entries in the #menu, #lines and #labor components of the MIF. An icon-based description of procedural processes is being developed to support the more complex MARYLIE analysis tasks that utilize the #lumps and #loops components. Progress on the development of this GUI for MARYLIE is described and illustrations from the Windows95/NT GUI implementation are presented.

1 INTRODUCTION

The Multi-Platform Shell for Particle Accelerator Related Codes (S.P.A.R.C. MP) software technology provides a framework for implementing cross platform graphical interfaces. The software architecture was designed to run on different operating systems including 32-bit Windows, UNIX/X-Windows and the Mac OS. The approach to developing the cross platform code is to implement platform specific interface libraries, each of which encapsulates an individual operating system. These interface libraries provide a common application programming interface (API) between the S.P.A.R.C. MP source code (C++) and each target operating system. The API libraries, which are a collection of basic functions utilizing OS native routines, provide a means of interacting with the different platform specific operating systems to maintain the native "look and feel" of the graphic interfaces associated with each platform, while providing a single programming interface to all supported platforms. This approach yields a single version of the S.P.A.R.C. MP source code for all platforms. Platform specific executable applications are created by linking the compiled S.P.A.R.C. MP code with the appropriate API for that platform.

S.P.A.R.C. MP was developed to interface with a variety of accelerator modeling and simulation programs. The software uses a modular approach that allows new programs to be added to the framework, without affecting the functionality of existing programs. This paper summarizes progress on the interfacing of the MARYLIE [1] code with S.P.A.R.C. MP.

2 GRAPHIC USER INTERFACE (GUI)

The graphic interface for MARYLIE is patterned after that developed for the Particle Beam Optics Laboratory (PBO Lab™). The PBO Lab [2,3] has four major components: (1) a graphic user interface shell, (2) a graphic beamline construction kit, (3) a set of physics and technology tutorials, and (4) modules for various charged particle optics computation engines. Each component is described elsewhere [2,3,4,5]. A MARYLIE Module is being developed to provide significant new optics modeling and simulation capabilities.

A principle requirement for the GUI is to assist users in the set up and running of MARYLIE without requiring any knowledge of the format, syntax, or similar requirements of the input. Beamlines are graphically constructed on the computer screen using drag and drop icons. Default parameters are incorporated for all required inputs so that both the topology of the beamline and a complete set of input data are defined automatically during the graphical construction. Setting up a specific problem then involves editing the values of parameters. The S.P.A.R.C. MP graphic user interface shell and the beamline construction kit [3] provide this capability for the MARYLIE GUI. Figures 1 and 2 illustrate selected windows for the GUI running under Windows 95.

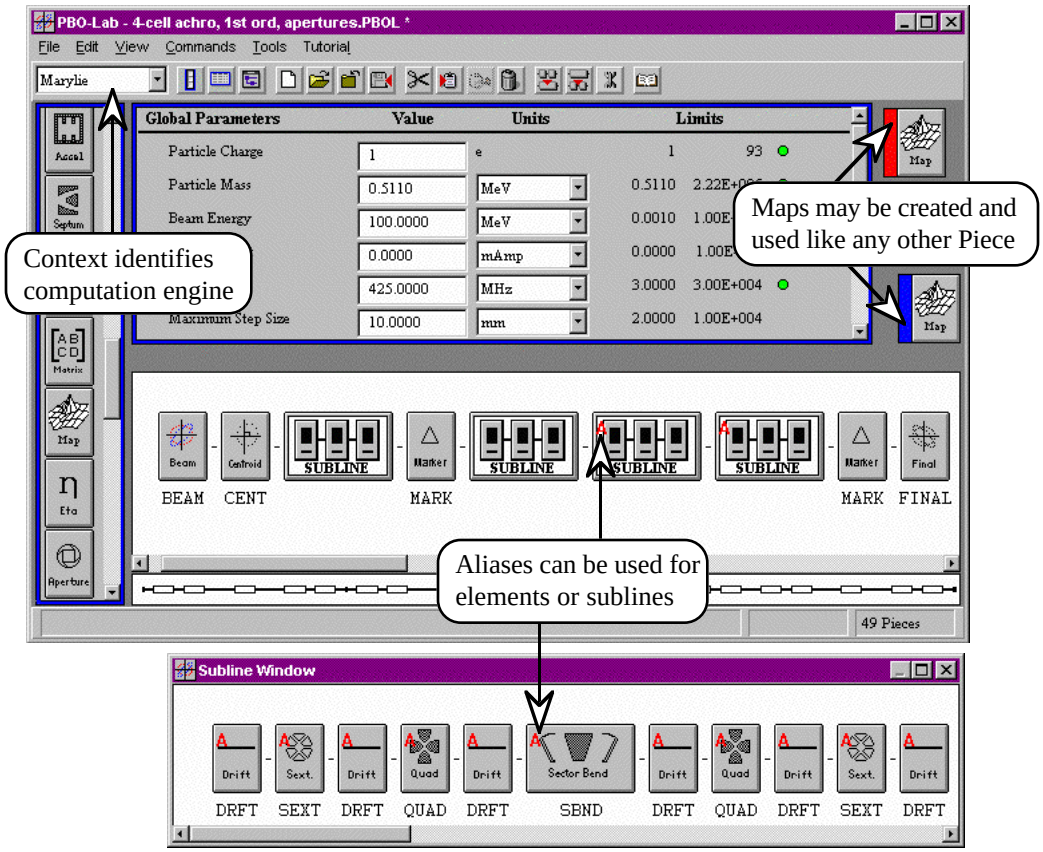

Figure 1. Example Document Window and Subline Window of the graphic user interface for MARYLIE.

Several new GUI features have been added in order to support the extensive capabilities of MARYLIE. Figure 1 illustrates the second-order achromat described in [5] in a new version of the Document Window [2,3] developed for MARYLIE. Figure 1 also illustrates two new elements of the GUI developed for MARYLIE: Alias Pieces and Map Pieces.

The Map Piece is an important new element of the GUI for MARYLIE. Its full functionality is still being defined, but currently the Map Piece can be used to enter a user specified map, to create a map from a given selection of Pieces or Sublines, and to save a map for later use.

The Alias Piece is one of the components of an innovative object model [6] that has been developed to describe beamlines. S.P.A.R.C. MP beamlines can be modeled using hierarchical (Sublines), flat (individual Pieces), or mixed representations that contain both Sublines and individual Pieces. This object model provides the basis for the functionality of the beamline construction kit. An alias in this object model is a Piece or Subline which is represented by a persistent link to another Piece or Subline, and is also capable of storing deviations from the original parameters without duplication of redundant data. The Alias Piece thus provides an element that can be used to efficiently replicate any other Piece, including Sublines: the only persistent data is a pointer to the original Piece or Subline. However, Alias Pieces can also contain deviations (e.g. to represent errors) from the original data. Figure 1 illustrates an example of Alias Subline use, where the second Subline (describing the 2nd cell of the achromatic) has been used to define an Alias which is then replicated to define the 3rd and 4th cells. Alias Sublines contain Aliases to individual Pieces or Sublines.

Figure 2 illustrates an Alias Window for a magnetic bend, together with the Piece Window [3] for the original bend element. In the example illustrated, a deviation of 0.1% of the magnetic field has been entered. Figure 2 also shows some of the new features that have been added to the Piece Windows for all elements to support MARYLIE. The new features for magnetic elements include tab panels for additional data that describe fringe fields, magnet geometry parameters and beamline location (position and orientation) information.

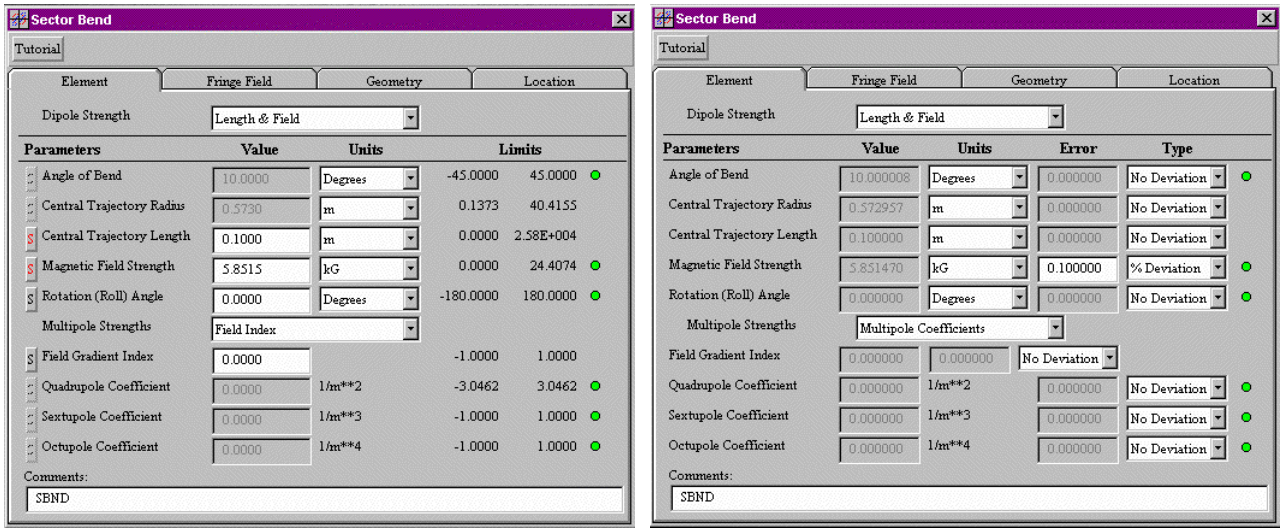

Figure 2. Example of Piece Window (left) and Alias Window (right) for editing parameters of a magnetic bend element.

3 MARYLIE MASTER INPUT FILE

MARYLIE is executed with a Master Input File (MIF) which contains six components referred to as #beam, #menu, #lines #lumps, #loops and #labor [1]. The requirements for the GUI to provide for all of these components are still under development, but the central features can be summarized. The graphic interface writes to each component all of the necessary data to accomplish a given task. The Global Parameters generate entries in the #beam component, and individual Pieces generate entries in the #menu component. Commands and other data also create entries in the #menu component, since this component defines all data used in subsequent components. Commands determine most of the structure of the #labor component. Sublines generate entries in the #lines component. Aliases (with no deviations) are utilized in the data for the #lines component, and the complete beamline also creates an entry in the #lines component. Map Pieces create entries in the #menu component, but may be used in a number of different ways, for example to create an entry in the #lumps component.

4 SUMMARY

A graphic user interface is being developed for MARYLIE that promises improved productivity for researchers working on the design and analysis of accelerators and beamlines. Substantial progress has been made in developing a MARYLIE Module for integration with S.P.A.R.C. MP.

ACKNOWLEDGMENT

This work has been supported by the U. S. Department of Energy under SBIR grant number DE-FG03-95ER81975.

REFERENCES

[1] A. J. Dragt, D. R. Douglas, F. Neri, C. T. Mottershead, R. D Ryne, E. Forest, L. M Healy, P. Schutt and J. van Zeijts, "MARYLIE 3.0 User's Manual, A Program for Charged Particle Beam Transport Based on Lie Algebraic Methods," July draft, 460 pages (1998).

[2] G. H. Gillespie, B. W. Hill, N. A. Brown, H. Martono and D. C. Carey, "The Particle Beam Optics Interactive Computer Laboratory," AIP Conference Proceedings 391, 264-269 (1996).

[3] G. H. Gillespie, B. W. Hill, H. Martono, J. M. Moore, N. A. Brown, and M. C. Lampel, "The Particle Beam Optics Interactive Computer Laboratory for Personal Computers and Workstations," to be published in the proceedings of the 1997 Particle Accelerator Conference, 3 pages (1997).

[4] N. A. Brown, G. H. Gillespie, B. W. Hill, M. C. Lampel, H. Martono and J. M. Moore, "The Particle Beam Optics Laboratory (PBO LAB™): A New Education and Training Aid," to be published in the proceedings of Sixth European Particle Accelerator Conference, 3 pages (1998).

[5] G. H. Gillespie, B. W. Hill, H. Martono, J. M. Moore, M. C. Lampel, and N. A. Brown, "Using the Particle Beam Optics Laboratory (PBO LAB™) for Beamline Design and Simulation," to be published in the proceedings of the 15th International Conference on Cyclotrons and Their Applications, 4 pages (1998).

[6] B. W. Hill, H. Martono and J. S. Gillespie, "An Object Model for Beamline Descriptions," AIP Conference Proceedings 391, 361-365 (1996).

X-BAND KLYSTRON OUTPUT CAVITY SIMULATION

H. Tsutsui
The Graduate University for Advanced Studies, 1-1 Oho, Tsukuba, Ibaraki, 305-0801 Japan

S. Matsumoto, S. Michizono, Y. H. Chin and S. Fukuda
High Energy Accelerator Research Organization (KEK),1-1 Oho, Tsukuba, Ibaraki, 305-0801 Japan

Abstract

Two-dimensional modeling of klystron output cavity coupler is presented. The coupler is considered to be the mode converter between TE10 mode of the rectangular waveguide and TM0*0 mode of the cavity cell. The components of the scattering matrix are calculated using MAFIA eigenmode solver. For the simulation by MAGIC2D 2.5 dimensional particle-in-cell code, finite-conducting material is set in the coupler region to match S11. Output powers, which are calculated from the Poynting vector, are compared with the measured values of KEK XB72K#9 and SLAC XL-4 klystrons.

1 INTRODUCTION

Development of X-band (11.424GHz) klystrons capable of 120MW(XB72K series) is undergoing at KEK [1-3]. To reduce the maximum electric field in the output cavity, traveling wave type structures are used. Output structures of XB72K#8 and #9 were designed at BINP using one dimensional simulation code DISKLY [4]. Due to the limitation of one-dimensional design, not enough powers were extracted with these output structures. MAGIC2D [5], a 2.5 dimensional particle-in-cell code, was introduced in KEK in 1997 for the design of the next klystron XB72K#10 with a 4-cell traveling wave type output cavity. Since the coupler of the output cavity is not axisymmetrical, the structure cannot be simulated directly by 2 dimensional codes. To make it possible, the notion of scattering matrix is introduced, and is calculated using the eigenvalue solver of MAFIA [6] codes. Output powers calculated by MAGIC2D are compared with the measured values of KEK XB72K#9 and SLAC XL-4 [7] klystrons. In section 2, calculation of scattering matrix is shown. In section 3, output cavity simulation by MAGIC2D is presented. Design of XB72K#10 klystron output structure is briefly discussed in section 4.

2 SCATTERING MATRIX

Though there are many modes around operating frequency with the multi cell output structure, the field pattern around the output cell of these modes are similar to TM0*0 mode. The phasor of the electric field in the region can be approximated as the following,

$$E_{CAV} = a_{1in} H_0^{(1)}(kr) + a_{1out} H_0^{(2)}(kr), \quad (1)$$

where H is the Hankel function, $k=\omega/c$ is the wave number. Time dependence of the electric field is assumed to be $\exp(-i\omega t)$. The electric field in the waveguide can be described as,

$$E_{WG} = a_{2in} \exp(-ik_g y) + a_{2out} \exp(ik_g y), \quad k_g = \sqrt{(\omega/c)^2 - (\pi/a)^2}, \quad (2)$$

where a is the width of the rectangular waveguide, y is the distance from the center of the coupler. If the output coupler is considered as the mode converter between TM0*0 of the cavity cell and TE10 mode of the rectangular wave guide, the scattering matrix can be defined as follows,

$$a_{1out} = S_{11} a_{1in} + S_{12} a_{2in}, \quad a_{2out} = S_{21} a_{1in} + S_{22} a_{2in.} \quad (3)$$

The variables $\xi_1$and ξ_2 are defined as the ratio between the amplitudes of the incoming and outgoing waves,

$$\xi_1 = a_{1out} / a_{1in}, \ \xi_2 = a_{2out} / a_{2in}. \quad (4)$$

Using (4), (3) becomes

$$(S_{11} - \xi_1)(S_{22} - \xi_2) = S_{12} S_{21} \quad (5)$$

If the values of three (ξ_1,ξ_2) pairs are known, S_{11}, S_{22} and $S_{12}S_{21}$ can be calculated.

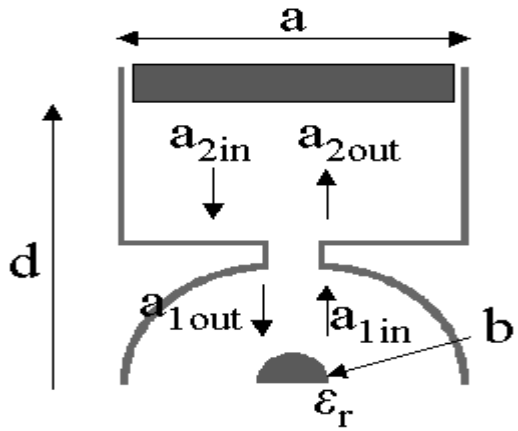

Figure 1: Configuration for MAFIA calculation.

MAFIA eigenmode solver is used to calculate three (ξ_1,ξ_2) pairs. As shown in figure 1, the waveguide is short at distance d, and the dielectric material is set at the center of the cavity cell. Since the electric field on the plane y=d is zero, ξ_2 is,

$$\xi_2 = -\exp(-2ik_g d). \quad (6)$$

By putting dielectric material at the center of the coupler cell, the parameter ξ_1 can be varied as,

$$\xi_1 = \frac{kJ_0(k'b)H_1^{(1)}(kb) - k'J_1(k'b)H_0^{(1)}(kb)}{k'J_1(k'b)H_0^{(2)}(kb) - kJ_0(k'b)H_1^{(2)}(kb)}, \quad (7)$$
$$k' = \sqrt{\varepsilon_r}\,\omega / c,$$

where b is the radius of the dielectric material, ε_r is the relative dielectric constant, J is Bessel function.

From the energy conservation, the following equations

$$|S_{11}| = |S_{22}|, S_{11}S_{22} - S_{12}S_{21} = S_{22}/S_{11}^*, \quad (8)$$

are obtained. These are used to check the calculation of scattering matrix.

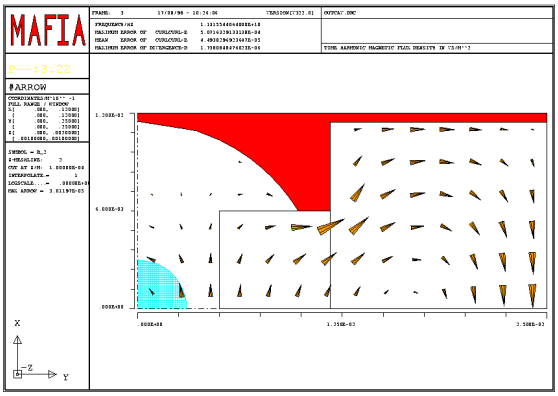

Figure 2: An example of MAFIA calculation.

Figure 2 shows the example of eigenmode solver calculation using MAFIA. The structure is from KEK XB72K#9. Three relative dielectric constants ε_r=1,3,5 are used to obtain three different ξ_1. The distance d is changed to find the frequency dependence of the scattering matrix. Reflection coefficient S_{11} for XB72K#9 output cavity coupler is shown in figure 3.

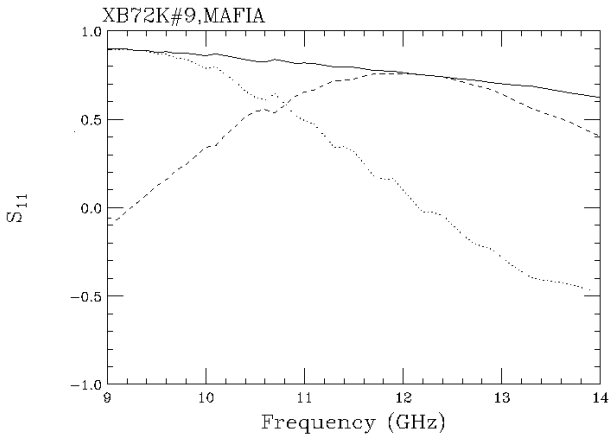

Figure 3: Reflection coefficient S_{11} as a function of frequency. Dotted and broken lines are real and imaginary parts, respectively.

3 MAGIC2D SIMULATION

Since the reflection coefficient r at the rectangular waveguide looked from the center of the cell is usually designed to be zero, the reflection coefficient at the coupler looked from the center of the cell can be assumed to be S_{11}. If the reflection coefficient r is not negligible, S_{11} should be replaced by the parameter S, which is defined by,

$$S = S_{11} + S_{12}(r + r^2 S_{22} + r^3 S_{22}^2 + \cdots)S_{21} = S_{11} + rS_{12}S_{21}/(1 - rS_{22}). \quad (9)$$

In order to realize the reflection coefficient S_{11} in the MAGIC2D simulation, a finite conducting material is set in the coupler region as shown in figure 4.

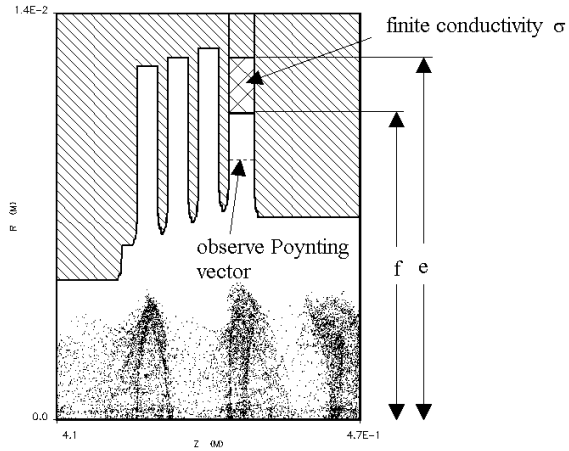

Figure 4: An example of MAGIC2D simulation. A finite conducting material is set in the coupler region to match S_{11}. Output power is calculated by time average of the area integral of Poynting vector. This structure is KEK XB72K#9 output cavity.

With this configuration, S_{11} is,

$$S_{11} = \frac{k\alpha H_1^{(1)}(kf) - k''\beta H_0^{(1)}(kf)}{k''\beta H_0^{(2)}(kf) - k\alpha H_1^{(2)}(kf)},$$
$$\alpha \equiv H_0^{(1)}(k''e)H_0^{(2)}(k''f) - H_0^{(2)}(k''e)H_0^{(1)}(k''f),$$
$$\beta \equiv H_0^{(1)}(k''e)H_1^{(2)}(k''f) - H_0^{(2)}(k''e)H_1^{(1)}(k''f),$$
$$k'' = \sqrt{(\omega/c)^2 + i\mu_0\sigma\omega}, \quad (10)$$

where e is the outer radius, f is the inner radius, σ is the electric conductivity, of the material. The reflection coefficient S_{11} in (10) is fitted to the value calculated from (5) at operating frequency 11.424GHz by changing three parameters (σ, e, f) with the aid of Mathematica [8]. Since number of unknown parameters (σ, e, f) are three, and number of known parameters (Real(S_{11}), Imag(S_{11})) are two, one parameter is free. In many cases, the outer radius e is fixed to one of the outer radii of the upstream cells in order that Courant stability criterion,

$$\sum_i \frac{\beta c \Delta t}{\Delta x_i} < 1, \quad (11)$$

is satisfied in the MAGIC simulation. In this equation, βc is the velocity of the particle, Δt is the time step, Δx_i is the grid size of i-th coordinate. For XB72K#9, the parameter e is fixed to the outer radius of the second cell, as can be seen in figure 4. The conductivity σ should be small so that the skin depth

$$\delta = \sqrt{2/\mu\sigma\omega} \qquad (12)$$

is larger than the grid size. Since the conductivity is chosen to be 2.5/Ωm in case of XB72K#9, skin depth is 3mm, which is larger than the grid size of 0.2mm. Figure 5 shows the frequency dependence of S_{11}, which is calculated from (10).

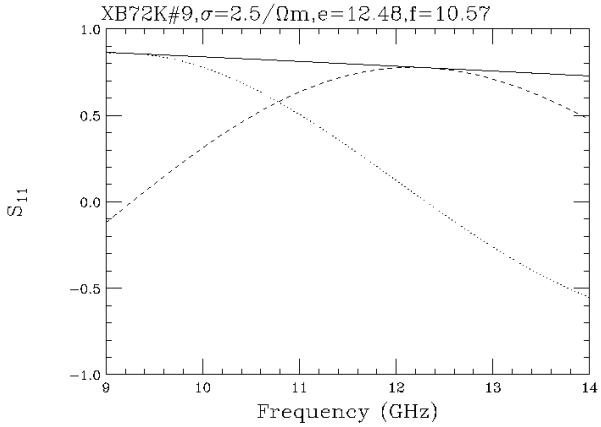

Figure 5: Frequency dependence of the S_{11} calculated from (10). Parameters of the conductor are obtained by fitting S_{11} at the operating frequency of 11.424GHz.

Output cavity simulations are done with imported bunches and space-charge waves, which are created by buncher section simulation [3]. Output power is calculated from time average of Poynting vector just below the finite conductor, as shown in figure 4. Saturated output powers of XB72K#9,10 and SLAC XL-4 are shown in figure 6. For SLAC XL-4, simulation results and measured values are consistent within a few percent. For XB72K#9, simulation results are about 10 percent lower than measurements. We think that accuracy of the measured cathode voltage is not good due to the capacitance in gun region. We have a plan to test XB72K#9 again with longer pulse.

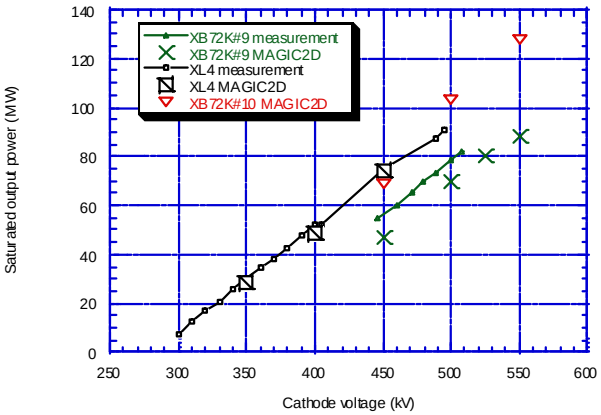

Figure 6: Saturated output power as a function of cathode voltage for XB72K#9,10 and SLAC XL-4.

4 DESIGN OF XB72K#10 OUTPUT STRUCTURE

How to reduce the maximum electric field in 120MW output structure design is the problem. By choosing 2π/3-like mode instead of π/2, we can make the width of the cells wider than that of SLAC XL-4. Since the electric field was high at the disk between third and fourth cell, we increased the width of the disk. After hundreds of simulations, we decided the approximate structure, which has the maximum electric field less than that of SLAC XL-4. The structure was slightly changed in order to separate the resonant frequencies of transverse deflecting modes from the operating frequency. Figure 7 shows one example of the MAGIC2D simulations of XB72K#10 output structure. Saturated output powers by MAGIC2D simulation are plotted in figure 6. XB72K#10 is being manufactured at TOSHIBA. We will test it in November this year.

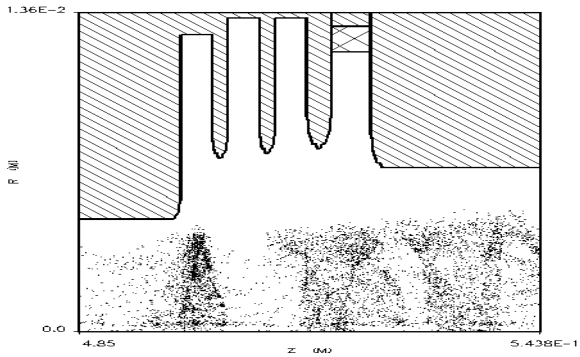

Figure 7: An example of MAGIC2D simulation of XB72K#10 output structure.

5 REFERENCES

[1] Y.H. Chin et al., "Modeling and Design of Klystron", in these proceedings.

[2] S. Michizono et al., "Electron Gun Simulation Using MAGIC", in these proceedings.

[3] S. Matsumoto et al., "Simulation Study of the Bunching Section of X-band Klystrons", in these proceedings.

[4] V.E. Teryaev, "DISKLY Code for Calculation and Optimization of Klystrons"
S. Kazakov, "One method of output structure simulation", RF'93, 161-166, (1993)

[5] http://www.mrcwdc.com/magic/homepage.htm

[6] http://www.cst.de

[7] G. Caryotakis, "Development of X-Band Klystron Technology at SLAC", SLAC-PUB-7548, (1997)

[8] http://www.wri.com

DESIGNING DOUBLE-GAP LINEAR ACCELERATORS FOR A WIDE MASS RANGE

W. P. Lysenko, E. A. Wadlinger, B. Rusnak, F. Krawczyk
Los Alamos National Laboratory, Los Alamos, NM 87545 USA

K. Saadatmand, Z. Wan
Semicond. Equip. Operations, Eaton Corp., Beverly, MA 01915 USA

Abstract

For applications like ion implantation, rf linacs using double-gap structures with external resonators can be used because they are practical at low frequencies. However, since the two gaps associated with a given resonator cannot be individually phased, it is not obvious how to build a linac that can efficiently accelerate particles having different mass/charge ratios. This paper describes the beam dynamics of double-gap rf linacs and shows how to maximize the range of mass/charge ratios. Our theory also tells us how to rescale a linac tune (i.e., reset the voltages and phases) so that a new particle, having a different mass or charge, will behave similarly to the original particle.

1 INTRODUCTION

Eaton Corporation builds high-energy ion implanters for semiconductor device fabrication. These machines are rf linear accelerators that accelerate ions to energies up to several MeV. Recently, Eaton has been working with Los Alamos to study ways to improve their machines to meet the future needs of Eaton's customers[1]. The main requirements for a near-future ion implanter linac are

- Various ion species. From $^{11}B^{+}$ to $^{75}As^{+}$.
- Variable energies. Up to several MeV.
- High current. Several mA.
- Short length. Not more than about 2 m long.

Additional requirements are low power consumption and low energy spread. This project consists of analyzing the present Eaton linac, studying new approaches for improved performance, and determining the best design based on present double-gap technology. The main part of this paper describes a new theory and design procedure, which we developed to determine the maximum performance of double-gap structures.

2 BACKGROUND

2.1 Study of Present Eaton Machine

The Eaton linac uses 13.56 MHz rf cells to accelerate and provide longitudinal focusing. Each cell consists of a drift tube, fed by an external helical resonator, in a grounded cavity. This provides two rf gaps per cell and is a practical way to get a compact and efficient structure at low frequencies. Electrostatic quadrupole lenses, in an alternating-gradient arrangement, provide transverse focusing. In general, accelerator performance can be limited by weak focusing, poor matching, or poor bunching. We found that the present machine has adequate focusing for accelerating $^{11}B^{+}$ at 3 mA but transmits only about a third of the particles injected. The losses are caused mainly by emittance growth in the rf gaps. This is a nonlinear effect caused by different particles seeing different rf phases as they cross the rf gaps. Improved bunching and matching could double the output current. To further increase the current or to get good performance for heavier ions, we need to improve the transverse focusing.

2.2 Study of New Approaches

New structures and focusing A single-gap rf structure (resonant cavity) has the advantage that we can phase each gap independently. We investigated the feasibility of resonant cavities at low frequencies (40 MHz). While it is possible to get a cavity of reasonable size at this frequency, we found the efficiency to be low. We studied variable-frequency radio frequency quadrupole (RFQ) structures. The high cost of variable-frequency rf power is a problem. The high transmission of most RFQ linacs is the result of adiabatic bunching. However, this is not practical for an ion implanter because of the length constraint. A segmented RFQ or an RFQ with a separate buncher may turn out to be feasible. We studied modifications to the drift tube noses in a gap structure to introduce quadrupole fields that would contribute to transverse focusing. We also studied alternating phase focusing (APF). As in previous investigations, we found that the acceptance of such machines is low.

Improved bunching A well-designed linac with a conventional (single frequency) buncher can accelerate about 75% of the particles injected. While multiple-frequency bunchers are probably not worthwhile, two separated cavities are desirable even for a single-frequency approach, because of the range of particle velocities associated with different particle masses.

Scaling studies We determined optimum quadrupole strengths and period lengths required for an alternating gradient focusing system, taking into account the defocusing

effect of the rf gaps. We also verified that we can reduce the length of the linac by raising the frequency while maintaining the electrostatic and rf voltages. This is beneficial when the quadrupoles and the rf gaps are voltage (not field) limited.

3 IMPROVED DOUBLE-GAP DESIGNS

We developed a new theory (see [2] for earlier version) and design procedure for linacs having double-gap resonators and electrostatic quadrupoles. Our goal is to determine the maximum performance using technology proven at Eaton. The basic idea is that we design the linac for a certain design-reference particle. Then we scale the design-reference tune (voltages and phases) to new particles.

3.1 Theory for Double-Gap Structures

The new theory is useful for the situation in which we are voltage rather than field limited. In existing machines, power limitations limit maximum gap voltage.

In each double-gap resonator, the two gaps are separated by a distance of

$$L = \frac{\beta_o \lambda}{2\pi}(\phi_{o2} - \phi_{o1} + \pi), \tag{1}$$

where β_o is the velocity of the design-reference particle and ϕ_{o1} and ϕ_{o2} are the synchronous phases at the two gaps. As we will see, we need the flexibility to allow the two synchronous phases to be different, even for the design-reference particle.

Once the machine is designed and built, we can no longer change any of the L values, but we are free to retune the machine, i.e., to change gap voltages and phases and to inject different particles.

To see how a new particle of different mass, charge, or velocity will behave,[1] let us define some ratios, which are various quantities relative to their values for the design-reference-particle design. The focusing ratio refers to the focusing strength of the rf gaps.

$$\begin{aligned}
k_{m/q} &= \frac{m/q}{m_o/q_o} && \text{(mass/charge ratio)} \\
k_q &= \frac{q}{q_o} && \text{(charge ratio)} \\
k_\beta &= \frac{\beta}{\beta_o} = \frac{\Delta\beta}{\Delta\beta_o} && \text{(velocity ratio)} \\
k_W &= \frac{W}{W_o} = \frac{m\beta^2}{m_o\beta_o^2} && \text{(energy ratio)} \\
k_f &= \frac{1/f_e}{1/f_{eo}} && \text{(focusing ratio)} \\
k_v &= \frac{VT}{(VT)_o} && \text{(voltage ratio)}
\end{aligned} \tag{2}$$

[1] We are including the situation in which the "new" particle is the same as the design-reference particle but run at a new velocity (energy).

We assume all ratios are the same at every cell in the linac. (A constant velocity ratio β/β_o implies the velocity ratio equals the velocity-gain-per-cell ratio $\Delta\beta/\Delta\beta_o$.)

We assume all the ratios of Eq. 2, except for k_v, as given and determine the new rf voltage and phase required to achieve them. The change in energy in crossing the two gaps is given by

$$\Delta W = qeVT(\cos\phi_1 + \cos\phi_2), \tag{3}$$

where ϕ_1 and ϕ_2 are the synchronous phases on the two gaps, V is the gap voltage, and T is the transit-time factor. We assume that V and T are the same for both gaps. By evaluating Eq. 3 for both the design-reference and the new particles, and using $\Delta W = mc^2\beta\Delta\beta$, we get the following expression for the voltage ratio:

$$k_v = k_{m/q}k_\beta^2\frac{\cos\phi_{o1} + \cos\phi_{o2}}{\cos\phi_1 + \cos\phi_2}. \quad \text{(acceleration condition)} \tag{4}$$

Once we set the phase at the first gap, the phase at the second is determined by the gap separation and the velocity.

$$\phi_2 = \phi_1 - \pi + \frac{1}{k_\beta}(\phi_{o2} - \phi_{o1} + \pi). \tag{5}$$

The effective longitudinal focusing strength (reciprocal of focal length) of the two gaps is given by

$$\frac{1}{f_e} = -\frac{2\pi qeVT}{\beta^3\lambda mc^2}(\sin\phi_1 + \sin\phi_2), \tag{6}$$

where we have added the two strengths and neglected the fact that the two gaps are separated. The focusing strength in the transverse direction is one-half of the value given by Eq. 6 and of the opposite sign. Thus the focusing ratio is the same for both transverse and longitudinal focusing.

If we compute the focusing strengths for the design-reference particle and for the other particle, take their ratio, and rearrange, we get the following expression:

$$k_f = \frac{k_v}{k_{m/q}k_\beta^3}\,\frac{\sin\phi_1 + \sin\phi_2}{\sin\phi_{o1} + \sin\phi_{o2}}. \quad \text{(focusing condition)} \tag{7}$$

If we eliminate $k_v/k_{m/q}$ in Eqs. 4 and 7, we get the following expression for how to set the phase of the first gap for the new-particle tune.

$$\tan\phi_1 = \frac{(1-c_o)k_f k_\beta S + s_o C}{(1-c_o)C - s_o k_f k_\beta S}, \tag{8}$$

where

$$\begin{aligned}
c_o &= \cos\left(\frac{\phi_{o2} - \phi_{o1} + \pi}{k_\beta}\right), \\
s_o &= \sin\left(\frac{\phi_{o2} - \phi_{o1} + \pi}{k_\beta}\right), \\
C &= \cos\phi_{o1} + \cos\phi_{o2}, \\
S &= \sin\phi_{o1} + \sin\phi_{o2}.
\end{aligned} \tag{9}$$

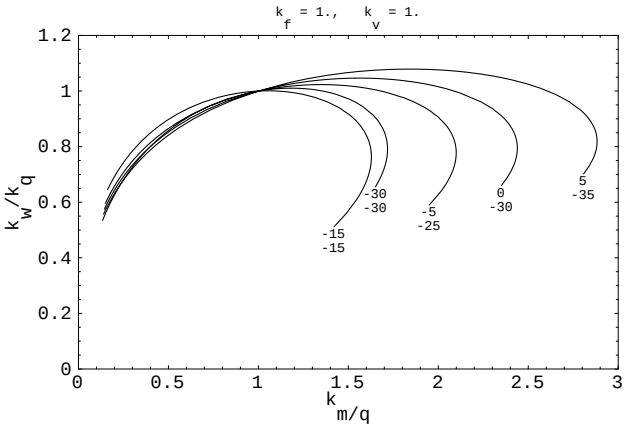

Figure 1: This shows how the energy changes when we retune a linac to a new particle. The quantity k_W is the energy ratio, k_q is the charge ratio, and $k_{m/q}$ is the charge/mass ratio. For a fixed charge, therefore, the curves show the energy as a function of mass. All ratios are relative to the design-reference particle, which is the particle for which the synchronous phases at the two gaps are ϕ_{o1} and ϕ_{o2}. The curves are labeled by the values of these phases.

Knowing ϕ_1, we determine the new voltage from Eq. 4.

Now let us determine over what range of mass/charge values a given design will work. Because we want the new particle to behave similarly to the design-reference particle, we set the focusing ratio to k_f=1. Assume our accelerator was designed to work at the maximum rf gap voltage. As a result, we want to fix the voltage ratio at k_v=1, as we cannot go any higher in voltage for the new particle. Now if we eliminate ϕ_1 in Eqs. 7 and 8 (we can do this numerically), we get a relation between the velocity ratio and the mass/charge ratio, with ϕ_{o1} and ϕ_{o2} as parameters. Figure 1 shows the result, which we express in terms of the energy instead of velocity.

There are five curves in the figure. Each curve is labeled by the values of the synchronous phases at the two gaps for the design-reference particle, ϕ_{o1} and ϕ_{o2}. Notice the large mass range over which an accelerator with phases of (5°,-35°) can operate. The cases (-5°,-25°) and (0°,-30°) have the same rf focusing strength as (5°,-35°) but work over a more restricted range of mass values. What is happening here is that making the synchronous phase on the first gap positive reduces the distance between the two gaps, which is beneficial for heavier (slower) particles. Figure 1 shows that we can accelerate particles over a mass/charge range of about three to one to about the same energy as the design-reference particle. Quite low masses can also be accelerated, but only to somewhat lower energies.

Now consider the electrostatic quadrupoles and space charge. The quadrupoles can be set to provide the same focusing strength for the new particle by setting the voltage according to

$$qV_q/W = \text{const.}, \qquad (10)$$

where V_q is the voltage on the quadrupole electrodes.

For a focusing ratio k_f of unity, and with the quadrupoles set according to Eq. 10, the beam bunch size will be the same as for the design-reference particle if the emittance of the new particle is the same. In this case, the space-charge effects will be the same for the new particle. If we change the beam size by changing the emittance or focusing strength, we can maintain space-charge effects the same as before by adjusting the beam current.

3.2 New Design Procedure

We start with the TRACE 3-D code with user-defined elements for electrostatic quadrupoles and the double-gap rf cells. These elements operate in two modes. In the design mode, the code sets the rf gaps automatically to get the specified synchronous phases. Also, the quadrupole lengths and the gap voltages are automatically set to achieve the specified phase advance per focusing period in all three directions. We do this for each focusing period, getting the maximum focusing possible without exceeding the voltage limits of the gaps and taking care to avoid cell-to-cell discontinuities. In the retune mode, an existing design is retuned to a new particle according to our theory. Once we have a TRACE 3-D design, we use the PARMELA particle-tracking code to determine the fraction of the beam transmitted by the machine. We finish our design by using an optimizing version of PARMELA to fine tune the quadrupole and buncher settings. We find that our new designs have substantially improved performance while still using proven technology.

4 DISCUSSION

The new approaches need further study. However, we found that the present approach of using double-gap resonators and electrostatic quadrupoles can provide ion implanters of substantially improved performance over a wide range of mass/charge values. The design procedure we developed ensures we get the good bunching, matching, and the maximum transverse focusing. Improvements in the rf resonators could further improve performance. The rf gap voltage limitation makes it impossible to obtain significantly higher energies within the length constraint.

5 REFERENCES

[1] Z. Wan, K. Saadatmand, F. Sinclair, W. Lysenko, B. Rusnak, L. Young, "Linac Simulation for high energy ion implantation," 11th International Conference on Ion Implantation Technology, 16–21 June 1996, Austin, TX, USA, p. 371–4.

[2] E.A. Wadlinger, W.P. Lysenko, B. Rusnak, and K. Saadatmand, "Beam Dynamics of a Double-Gap Acceleration Cell for Ion Implantation with Multiple Atomic Species," AIP Conference Proceedings 392, Applications of Accelerators in Research and Industry, edited by J.L. Duggan and I.L. Morgan, AIP Press, New York, 1997, p. 941–4.

PHYSICS DESIGN OF THE DARHT 2ND AXIS ACCELERATOR CELL*

T.L. Houck Y-J Chen, and C. Shang
Lawrence Livermore National Laboratory, Livermore, California 94550 USA
L.L. Reginato and S.S. Yu
Lawrence Berkeley National Laboratory, Berkeley, California 94720 USA

Abstract

The next generation of radiographic machines based on induction accelerators require very high brightness electron beams to realize the desired x-ray spot size and intensity. This high brightness must be maintained throughout the beam transport, from source to x-ray converter target. The accelerator for the second-axis of the Dual Axis Radiographic Hydrodynamic Test (DARHT) facility is being designed to accelerate a 4-kA, 2-μs pulse of electrons to 20 MeV. After acceleration, the 2-μs pulse will be chopped into a train of four 50-ns pulses with variable temporal spacing by rapidly deflecting the beam between a beam stop and the final transport section. The short beam pulses will be focused onto an x-ray converter target generating four radiographic pulses within the 2-μs window. Beam instability due to interaction with the accelerator cells can very adversely effect the beam brightness and radiographic pulse quality. This paper describes the various issues considered in the design of the accelerator cell with emphasis on transverse impedance and minimizing beam instabilities.

1 INTRODUCTION

A DARHT Second Axis Technology Options Study (TOS) was initiated in September 1996 to determine if advances in technology since the design of the first axis induction accelerator warranted a new design for the second axis. The "Long Pulse" option, an induction accelerator that would produce a 2-μs, 4-kA electron beam pulse that could be divided into several shorter pulses, was eventually selected to be the basis for a new design [1]. A preliminary accelerator cell design for the "Long Pulse" option had been presented to the TOS Committee. This preliminary design evolved into the "initial" design described below as detailed engineering design work and beam transport studies were accomplished.

The principle issues necessitating changes to the preliminary cell design involved the material for the vacuum interface insulator and the transport solenoidal magnet field strengths. The dielectric constant for the current insulator is about three times larger than that for the original insulator. The cross sectional area also changed to accommodate fabrication. These changes altered the rf characteristics of the cell and the mode damping scheme for was revised. A more important issue involved the solenoid fields required to transport the beam from the injector into the accelerator. The growth in the beam's transverse centroid motion (instability) is strongly influenced by the transverse impedance of the cell and the transport solenoids' magnetic field strength. See equation (2). Very low solenoidal fields at the front of the accelerator placed a severe constraint on the maximum impedance.

Nearly half of the transverse motion growth occurred in the first 10% of the accelerator with the preliminary design. Thus, it was decided to increase the cell inner radius to reduce the transverse impedance and alter the gap/insulator design to shift the impedance spectrum for the first eight cells. The new gap/insulator design proved to be more compact longitudinally and offered some mechanical advantages over the initial cell design. This design is now the "current" design described below for the first eight larger bore cells and the main accelerator.

2 INITIAL DESIGN

This design evolved directly from the TOS "Long Pulse" design. Improvements were made in vacuum surface field stresses, transverse impedance, fabrication ease, and vacuum integrity. Figure 1 is a schematic of this initial accelerator cell design.

2 .1 General Design Criteria

The cross sectional area of the induction cores was set by the required voltage, V, pulse duration, $\Delta\tau$, and core material: $V \cdot \Delta\tau = \Delta B \cdot A \cdot pf$, where (1)
ΔB is the magnetic flux swing, A is the cross sectional area, and pf is the packing fraction of the core material.

The desired maximum growth in the traverse instability and number of cells was used to estimate the maximum transverse impedance. A minimum inner radius consistent with this impedance was then chosen. The following equations are pertinent [2]:

$$\Gamma = \frac{c}{2}\frac{Z_\perp}{l}\frac{I}{I_o}\int_0^L \frac{dz}{B_z}, \text{ and} \quad (2)$$

$$Z_\perp = 120\frac{W}{r_p^2}\eta \ (\Omega/\text{m}), \text{ where} \quad (3)$$

Γ is the number of e-folds of growth, $Z_\perp$ is transverse impedance, l is the cell longitudinal length, I is beam current, I_o is 17 kA, L is length of the accelerator, B_z is solenoid field strength, r_p is beam pipe radius, W is cell gap width, and η is a form factor of order unity. Note that

*The work was performed under the auspices of the U.S. Department of Energy by LLNL under contract W-7405-ENG-48, and by LBNL under contract AC03-76SF00098.

W is approximately the total energy gain of the accelerator divided by number of induction cells and maximum vacuum surface electric field stress. Constraints on the length of the accelerator limited flexibility in determining the outer radius of the induction core.

Determining the optimum B_z involves simulating the beam transport from source to x-ray converter and requires information on expected current and energy variation, location/alignment of components, and cell impedance. This process requires several iterations as the accelerator design matures. The preliminary design assumed the transport fields would be similar to those planned to be used for the first axis accelerator and a conservative value, 12.7 cm, was chosen for r_p.

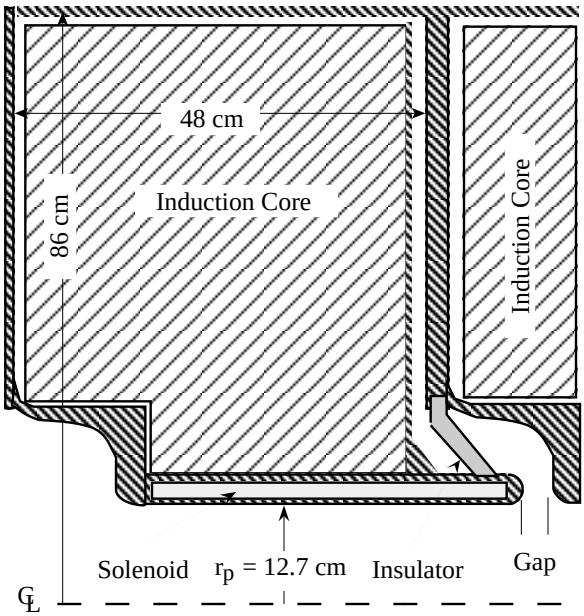

Figure 1. Schematic of the initial accelerator design.

2 .2 Insulator and Field Stress Issues

The insulator has to provide a mechanical interface between the beam line vacuum and the cell insulating oil while withstanding the applied voltage pulse of, in this instance, about 200 kV. It is highly desirable for the insulator to be hidden from line-of-sight view of the beam. See reference [3] for an alternative approach. The simplest design would have been to locate the insulator at the outer radius of the induction cores. Unfortunately, insulating materials, e.g. plastics, that could be fabricated with the required large inner radius, presented an unacceptable gas load due to the large surface area.

A shielded gap design, illustrated in Fig. 2, was used as it permitted the insulator to be placed at a smaller radius (less surface area) while preventing direct line-of-sight with the beam. Rexolite was initially chosen as the insulator material based on performance in operating, short pulse (~100 ns), induction accelerators. However, during long pulse, high-voltage testing performed at LBNL, a Rexolite insulator did not fully recover after experiencing an electrical arc. The insulator was changed to Mycalex to remove any concerns related to insulator performance for long pulses.

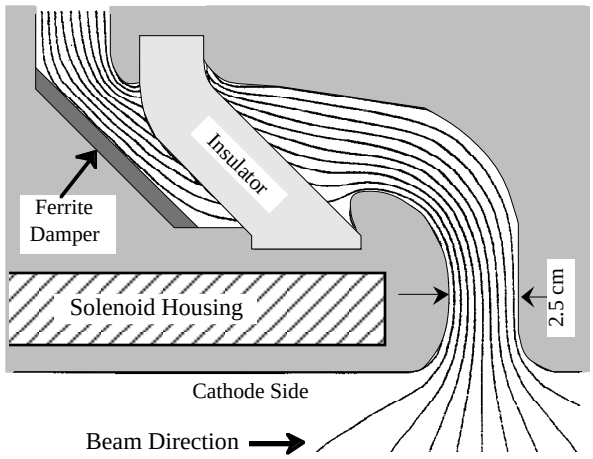

Figure 2. Illustration of the insulator and gap in the initial design. Equipotential lines are shown for the vacuum and oil regions. Each line represents ~20 kV potential change.

Design goals were for vacuum surface electric fields (negative polarity) to be ≤ 100 kV/cm and insulator surface fields ≤ 40 kV/cm. The primary limitation on positive polarity surfaces was to maintain ≤ 100 kV/cm during pulsed power reversals. As the maximum reversed voltage expected is less than 30% of the forward, this was not a difficult requirement. Care was taken to minimize electric fields at triple points (vacuum, metal, and insulator interfaces). Equipotential lines generated by Poisson are shown in Fig. 2 for the vacuum and oil regions of the cell. Maximum fields for the negative polarity (cathode) side of the gap occurred towards the top of the gap nose and were about 100 kV/cm. The maximum field across the insulator occurred towards the top and was about 40 kV/cm. Maximum stress on the positive polarity surfaces was about 130 kV/cm along the curve surfaces approaching the top of the insulator.

2 .3 Transverse Impedance

The transverse impedance of the induction cell was calculated using the AMOS Code [4]. Cell damping was simulated with ferrite, modeled after the TDK PE11B used in the DARHT first axis induction cells, located in the oil region after the insulator as shown in Fig. 2 and on a small section of the outer radius of the core material (not shown). The simulations results are shown in Fig. 3.

3 CURRENT DESIGN

The large radius and low B_z transport fields needed to match the beam from the injector into the accelerator argued for increasing the accelerator bore in the first eight-cell block. Increasing the cell inner radius to 17.8 cm was expected to reduce the impedance by half. See eq. 3.

Desire to reduce the length of the accelerator, while also including more longitudinal space for beam diagnostics,

encouraged compactness in the gap/insulator design. The current cell design, shown in Fig. 4, has been adopted for both the larger bore cells and the main accelerator. The notch in the beam pipe wall downstream of the gap is a recess for diagnostics. This design with diagnostic recess has about the same cross section as the initial design.

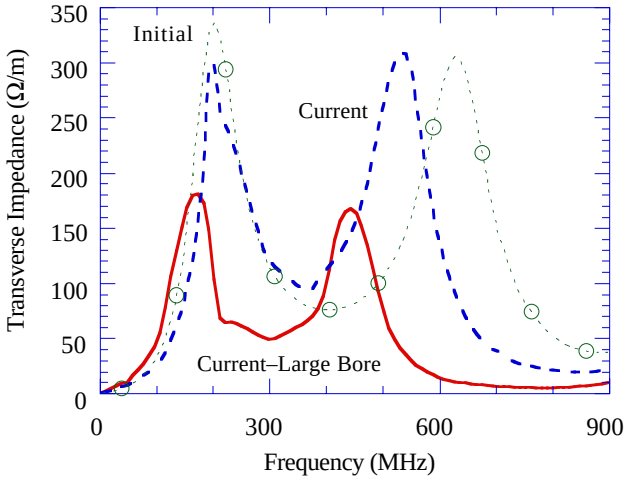

Figure 3. Calculated transverse impedances, $Z_{\perp}$, for the initial and current designs. $Z_{\perp}$ for the first eight larger bore cells using the current design is also shown.

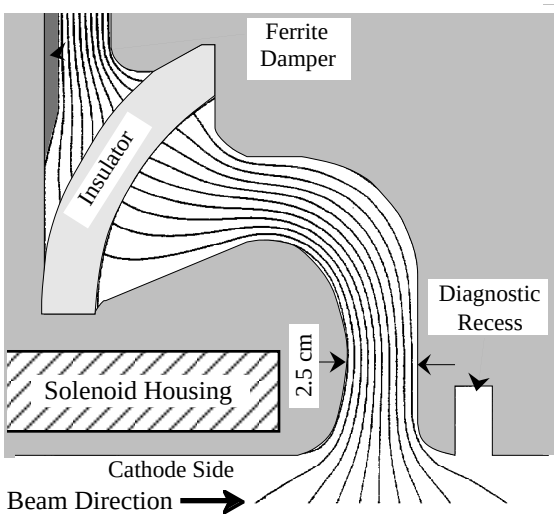

Figure 4. Illustration of the insulator and gap for the current design. Equipotential lines are shown for the vacuum and oil regions. Each line represents ~20 kV potential change.

3 .1 Field Stresses

The first step in arriving at the current design was a series of electrical field stress calculations using Poisson. The current cell design, with equipotential lines plotted, is shown in Fig. 4. The angle of the insulator with respect to the equipotentials was the most significant departure from the initial design with respect to electrical field stress management. Tests with relatively short pulses have determined that the maximum field stress across an insulator can be increased significantly if the electric field makes an angle of 30-45° with respect to the insulator surface [5]. The initial cell design took advantage of this phenomena. It is believed that the field stress in the current design is sufficiently low, < 35 kV/cm for the main accelerator and < 30 kV/cm for the large bore cells, that insulator breakdown will not occur. All conducting surfaces have field stress levels below 100 kV/cm.

3 .2 Transverse Impedance

The transverse impedance of the current induction cell design was also calculated using the AMOS Code and modeling the ferrite damping material as TDK PE11B. The simulations results are shown in Fig. 3. Modest lowering of the impedance can be seen at 200 MHz. The impedance for the larger, 17.8 cm, radius cell is lowered by about half, as expected, and shifted in frequency.

4 SUMMARY

The basic induction cell design for the DARHT second axis accelerator has remained essentially unchanged from the preliminary "Long Pulse" option design. However, the gap/insulator configuration evolved as the engineering design of the accelerator matured, comprehensive beam dynamics simulations were completed, and developmental testing performed. Two gap/insulator configurations have been proposed, a conservative design with respect to the electric field stress on the insulator and a longitudinally compact design. For both configurations, the first eight cells have a larger bore, inner radius of 17.8 cm, than the main accelerator cells, inner radius of 12.7 cm. The compact design is preferred, but the final selection will be made after high-voltage testing of both designs.

5 ACKNOWLEDGMENTS

A very large number of people associated with the DARHT program contributed towards the cell design. In particular, we thank D. Birx, R. Briggs, G. Caporaso, D. Prono, C. Peters, D. Vanecek, and G. Westenskow.

6 REFERENCES

[1] H. Rutkowski, "An Induction Linac for the Second Phase of DARHT," this conference MO2001

[2] Y-J Chen, "Study of the Transverse Beam Motion in the DARHT Phase II Accelerator," this conference TU4033

[3] S. Sampayan, et al., "High-Performance Insulator Structures for Accelerator Applications," Proceedings 1997 Particle Accelerator Conference, (IEEE), New York, N.Y. (1997).

[4] J. Deford, et al., "The AMOS Wakefield Code," *Workshop on Accelerator Computer Codes*, Los Alamos, NM, January 1990.

[5] I. Smith, Proc. First Int. Symp. Discharges and Elec. Insul. in Vac., MIT, Cambridge MA, 1964, p. 261.

THE PERFECT BOUNDARY APPROXIMATION TECHNIQUE FACING THE BIG CHALLENGE OF HIGH PRECISION FIELD COMPUTATION*

B. Krietenstein[1], R. Schuhmann[1], P. Thoma[2], T. Weiland[1]
[1]Darmstadt University of Technology, TEMF, Schloßgartenstr. 8, D-64289 Darmstadt, Germany
[2]CST GmbH, Lauteschlägerstr. 38, D-64289 Darmstadt, Germany

Abstract

Computational tools for the design of accelerating structures are in use since decades. While highly accurate methods exist for quasi two dimensional cavities, fully three dimensional modeling with high precision is still a 'big challenge'.

The most widely used computer code in this area is MAFIA, basing on the Finite Integration Theory (FIT, [1,2]). While being well known for its robustness and reliability, MAFIA nevertheless suffers somewhat from a deficiency in being able to model very complicated 3D-cavities including curved boundaries with high precision.

In this paper we present two recently developed algorithms, facing this challenge within FIT: the usage of generalized non-orthogonal computational grids (NO-FIT), and the so-called Perfect Boundary Approximation (PBA) technique. Both methods represent consistent extensions of FIT, preserving all important properties as second order accuracy and stability of the transient solver. Especially the PBA technique reveals to be a highly efficient method, as it combines easy-to-use Cartesian grids with a perfect approximation of boundaries.

We compare MAFIA with the PBA technique for typical accelerator components, and it turns out, that the PBA technique is more than one order of magnitude faster than the conventional method if many non Cartesian metallic boundaries appear inside the modeled structure.

1 INTRODUCTION

The most common disadvantage of the Finite Integration Technique in three dimensions is the usage of Yee-type [3] cartesian meshes (cf. Fig. 1a), being quite inflexible, if complex, non-orthogonal structures have to be discretized. Even with the concept of triangular fillings (cf. Fig. 1b), not only the local electric and magnetic field, but sometimes also global quantities like resonance frequencies and Q-values suffer from the modeling errors along curved boundaries.

In the field of the FDTD-method, which is equivalent to FIT for transient calculations, several approaches have been published in the last years, trying to overcome this problem. Most of these algorithms, however, either suffer from stability problems, or do not show the same high efficiency properties as FDTD referred to both memory and CPU-time requirements. In this paper we present two algorithms, which can handle curved boundaries and are not only provably stable, but also highly accurate and efficient. Included in the matrix-formalism of the FIT, these algorithms are not only applicable to RF-problems, but also to the calculation of static fields, time-harmonic fields, the interaction with charged particles, and other related problems.

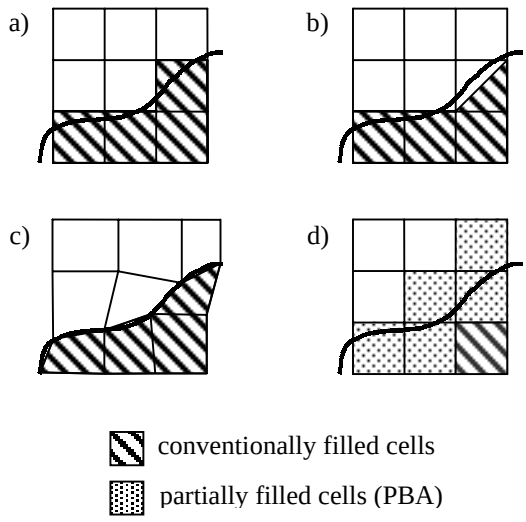

Figure 1: Grid approximations of rounded boundaries: Standard (a), triangular (b), non-orthogonal (c), PBA

2 ALGORITHMS

2.1 FIT on Non-Orthogonal Grids

The most general approach to handle curved boundaries is to allow generalized non-orthogonal grids (Fig. 1c). The basic idea to extend the FDTD-method on such grids has already been formulated in 1983 [4], including a local interpolation scheme for field components. Fulfilling the symmetry-condition in this interpolation process, we get an explicit time-stepping method with proven stability properties [5].

* Work of B. Krietenstein supported in part by DESY, Hamburg.

The non-orthogonal algorithm has been implemented in MAFIA (experimental status), and successfully applied to several transient RF-calculations, as well as to 2D and 3D eigenvalue computations. As the method reduces to standard FIT for orthogonal meshes, interfacing orthogonal with non-orthogonal grids is trivial. The numerical cost is increased by the interpolation scheme by a factor between 2 and 3 for 2D- or 3D-problems, respectively.

2.2 Perfect Boundary Approximation Technique

The application of the non-orthogonal algorithm is sometimes limited by the increase of the numerical cost, and, last but not least, by the requirement to supply a body-fitted, structured, non-orthogonal grid.

As an even more efficient approach we implemented the Perfect Boundary Approximation (PBA) Technique. In this method, the (orthogonal) computational grid does not have to be conformal to the rounded boundaries (Fig. 1d). Instead, also sub-cellular information is taken into account, leading to an algorithm with second order accuracy for arbitrary shaped boundaries. Except for a somewhat more complicated preprocessing, there is only slightly additional numerical cost during the iteration (the factor being near to one). Moreover, the grid generation becomes very easy, as there is no need for a highly resolved mesh near by non-orthogonal shapes. In most cases, even equidistant meshes produce highly accurate results. However, adaptive mesh generation has been implemented to achieve the highest possible accuracy for a given number of mesh cells, including user defined accuracy requirements.

The application of the PBA-technique to several problems from microwave- and accelerator-components is presented in the next chapter.

3 NUMERICAL EXAMPLES

3.1 Twisted Waveguide

In the first example, the reflection parameter S11 at the input port of a twisted waveguide has been calculated. Fig. 2 shows the discrete model using a non-orthogonal mesh, and in Fig. 3 the broadband results for three grid resolutions are shown. All three curves are very close

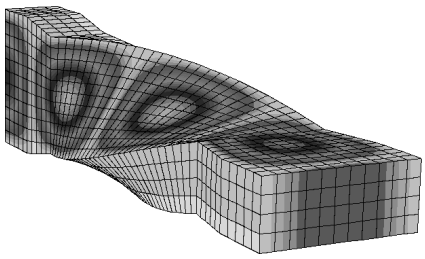

Fig. 2: Twisted Waveguide: non-orthogonal grid-model and electric field (steady state).

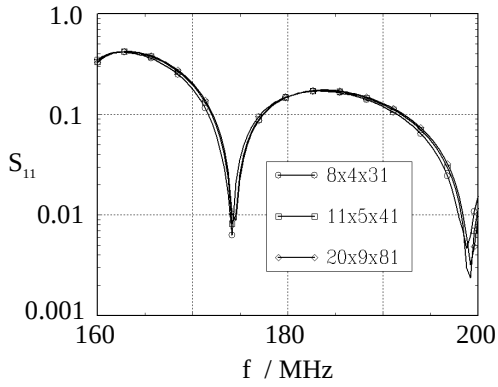

Fig. 3: Twisted Waveguide: reflection coefficient S_{11} for different grid resolutions

together. The result is already well converged for the coarsest grid.

3.2 TESLA Input Coupler

This example (cf. Fig. 4) shows a planned new input coupler for the TESLA superconducting cavities[1]. A rectangular coupler in-between two cavity cells is connected to an elliptical waveguide. A ceramic window is located

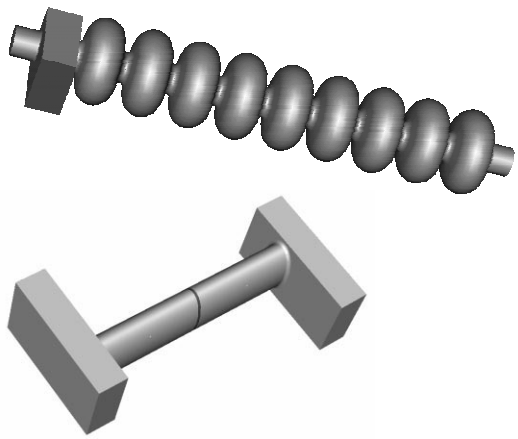

Fig. 4: TESLA 9-cell cavity with planned input coupler structure.

in the middle of the elliptical guide, followed by a second rectangular waveguide.

Fig. 5 shows the geometry of the transition of the rectangular guide to the elliptical one. The connection be-

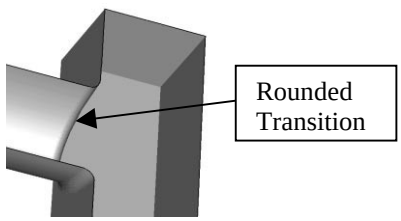

Fig. 5: Transition rectangular to elliptical waveguide.

[1] Design by M. Dohlus and A. Jöstingmeier (DESY)

tween the two waveguides was rounded with a rounding radius of 1cm.

Some more geometric details, the dielectric window and two matching rods (radius 2mm) inside the elliptic waveguide, are shown in Fig. 6.

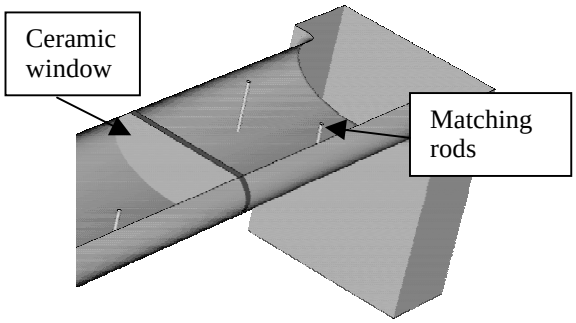

Fig. 6: Details inside the elliptical waveguide.

After a transient field simulation including an on-line DFT transformation we obtain the entire spectrum for the S-parameters, as shown in Fig. 7:

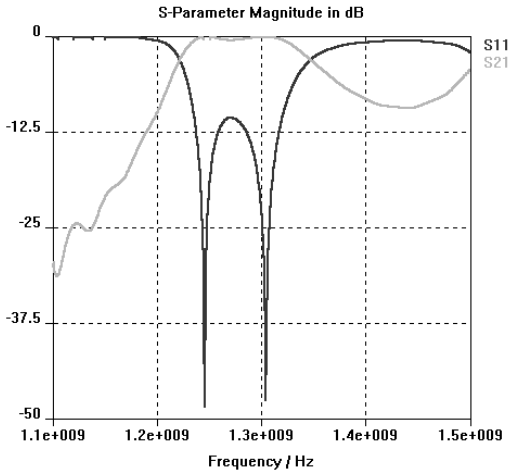

Fig. 7: S-Parameter of the Waveguide Transition.

The design shows a very good reflection property at the design frequency of 1.3 Ghz, although it was not yet optimized and was meant to serve here only as a demonstration example for the new PBA-algorithm.

3.3 Coax to Waveguide Coupler

The last example is the (mismatched) coax to waveguide coupler structure shown in Fig. 8. It has been simulated with both the new PBA-technique and standard MAFIA.

The results for the transmission coefficient demonstrate the high accuracy of the PBA-method: even the calculation with the coarsest grid resolution (10 mesh steps per wavelength) yields a S_{12}-curve close to the final result, whereas the standard method needs more than 60 steps/λ to achieve a comparable accuracy. The numerical cost of the simulation thus can be reduced by about two orders of magnitudes, which is a typical result for structures containing many non Cartesian geometrical details.

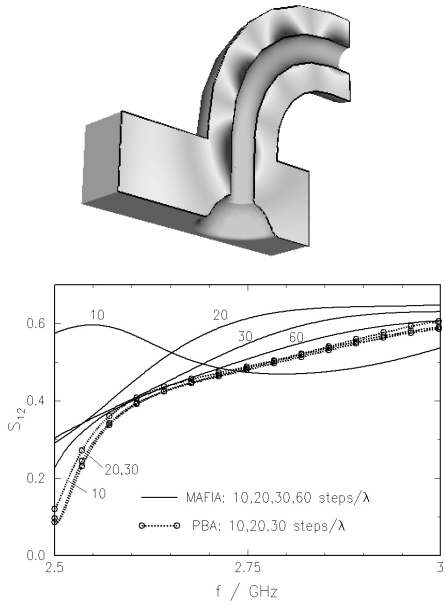

Fig. 8: Coax to waveguide coupler (with electric field in steady state), transmission coefficient for different grid resolutions (MAFIA and PBA results).

4 CONCLUSION

The Finite Integration Theory, combined with either non-orthogonal computational grids or with the newly developed Perfect Boundary Approximation Technique, is able to model structures with very fine geometric details with high accuracy. The application especially of the PBA-technique to typical accelerator devices demonstrates the high efficiency of the method compared to conventional FD- or FE-approaches.

5 REFERENCES

[1] T.Weiland, “A Discretization Method for the Solution of Maxwell’s Equations for Six-Component Fields,” Electronics and Communication 31, p.116 (1977).

[2] T.Weiland, “Time Domain Electromagnetic Field Computation with Finite Difference Methods,” Int. Journal of Numerical Modelling 9, 295-319 (1996).

[3] K.S.Yee, “Numerical Solution of Initial Boundary Value Problems in Isotropic Media,” IEEE Trans. on Antennas and Propagation AP-14, 302-307 (1966).

[4] R.Holland, “Finite-Difference Solution of Maxwell’s Equations in Generalized Nonorthogonal Coordinates,” IEEE Trans. on Nucl. Sciences NS-30,6, 4589-4591 (1983).

[5] R.Schuhmann, T.Weiland, “Stability of the FDTD Algorithm on Nonorthogonal Grids Related to the Spatial Interpolation Scheme,” Proc. of the 11th Conf. on the Computation of Electromagnetic Fields (COMPUMAG), 211-212 (1997).

CHALLENGES OF OPERATING A PHOTOCATHODE RF GUN INJECTOR*

X.J. Wang. M. Babzien, I. Ben-Zvi, R. Malone, J. Sheehan, J. Skaritka, T. Srinivasan-Rao,
M. Woodle, V. Yakimenko and L.H. Yu
Brookhaven National Laboratory, Upton, New York 11973 USA

Abstract

The major challenges in operating a photocathode RF gun based injector are its stability and reliability. This report discuss two important subjects which affect the performance of photocathode RF gun, high efficiency photocathode and experimental technique characterizing the RF gun injector. A Mg cathode was manufactured and routinely operated at 100 MV/m field with quantum efficiency on the order of 10^{-3}. By measuring the photoelectron charge as function of RF gun phase, we can monitor the RF gun driving laser pulse length variation, and measuring the laser arrive time variation on the cathode with Pico-second accuracy.

1 INTRODUCTION

The superior performance of photocathode RF gun based injectors have been experimentally demonstrated in many laboratories [1-3], all proposed fourth generation light source, such as X-ray and UV free electron lasers are based on the photocathode RF gun injector [4-6]. The performance of those future light sources will be determined by the photocathode RF gun injector. One of most challenging area in photocathode RF gun research is to improve the stability and reliability of its operation.

Brookhaven Accelerator Test Facility (ATF) is a facility dedicated to the beam physics and advanced accelerator physics research. It is one of few user facilities based on photocathode RF gun injector. It has a unique opportunity to address those challenges, demonstrate the feasibility of photocathode RF gun based user facility. The reliability and stability of the photoinjector are determined by the RF gun and its driving laser. The procedure developed in manufacture and operating RF gun reach in such stage that, it is mainly determined by the photocathode. The stability and reliability of the laser system for photocathode RF gun is the area much improvement is needed. Develop high efficiency, reliable photocathode, and laser diagnostic techniques, specially the longitudinal profile measurement, are critical to improve the stability and reliability of the photoinjector. We will first present experimental results of Mg cathode measurements at the ATF. Then we discuss a simple technique to study the laser longitudinal profile and laser intensity front variations on the cathode.

* Work supported by U.S. DOE

2 MAGNESIUM PHOTOCATHODE

As we pointed out earlier, photocathode is one of the critical links to improve the RF gun operation for both metal and semiconductor materials. The life time and quantum efficiency (QE) stability of the cathode is the major concern for a user facility. We choose metal cathode at the ATF mainly due to its robustness. Magnesium (Mg) has demonstrated relative high QE under modest vacuum condition [7,8]; the challenge is to find reliable way to attach Mg cathode to the Copper. Many techniques were tested, such as press fitting and sputtering, to attach the Mg cathode to the Copper. The Mg cathode made of press fitting suspect to the temperature variation due to vacuum bake out, while sputtered Mg can be damaged by RF break down. We were able to work with NCT Inc of Connecticut to develop a frictional welding technique to attach the Mg to the Copper with reliable vacuum seal. The Mg cathode was prepared according to the procedure we have developed [9], the cathode surface was polished using three different sizes diamond polishing compound, as polish progressing, the diamond in the polishing compounds were reduced from 9 μm, to 6 μm, then to 1 μm. The polished surface was rinsed with Hexane before immersed in the Hexane bath for 20 minutes ultra-sound cleaning. After the cathode surface was blowed dry with dry nitrogen, it was placed inside a UHV vacuum chamber for 200 °C bake out. It was installed on the RF gun under dry nitrogen (Fig.1).

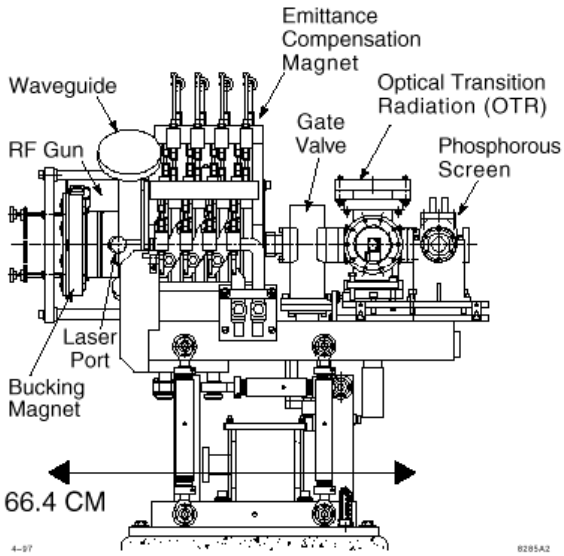

Figure 1: Layout of the ATF photoinjector.

Fig.1 shows the ATF photocathode RF gun injector. The RF gun was mounted directly on the emittance compensation solenoid magnet. There is a Electron beam diagnostic station, which is a multi-function device can be used as a beam profile monitor (BPM) and Faraday cup for photoelectron charge measurement. Fig. 2 is the measurement of photoelectron charge as function of the laser polarization and QE improvement after laser cleaning. The laser energy density used for the cleaning is about 7 mJ/cm^2. One of the most important improvement with frictional welding Mg cathode is its stability comparing to the sputtered Mg cathode [8], which decays by an order of magnitude after couple days operation. The QE measured is on the order of 10^{-3} for a peak field of 100 MV/m after laser cleaning.

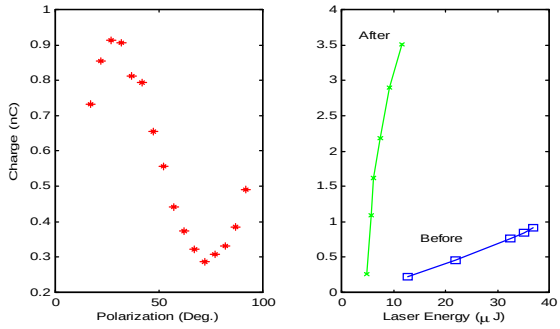

Figure 2: Photoelectron charge as function laser polarization (left) and laser cleaning (right).

3 LONGITUDINAL LASER PROFILE STUDIES

The photoinjector driving laser stability is determined by its energy fluctuation, point stability, timing jitter, transverse and longitudinal longitudinal profiles distribution. Develop experimental technique to characterize those laser properties are critical to improve laser performance. We have developed a technique to study laser longitudinal profile variation and timing jitter by measuring the photoelectron charge as function of the RF gun phase.

The photoelectron current density can be described by the following formula,

$$j = AI(t)(h\nu - \varphi + \alpha\sqrt{\beta E(t)})^2$$

Where I (t) is the time dependent laser intensity, hν is the photon energy, φ is the cathode work function, E(t) is RF field, and β is the field enhancement factor. Using frequency quadrupled Nd:Yag laser (266 nm), the first two terms in above equation is much smaller than the last term for Copper and Mg, so the photo-emission is dominated by the so called Schottky effect. The total photoelectron charge as function of the RF gun phase is,

$$Q(\phi) = \int_{-\infty}^{\infty} d\tau AI(\tau)(h\nu - \varphi + \alpha\sqrt{\beta E(\phi - \tau)})^2$$

The above equation shows that, the charge $Q(\phi)$ is the convolution of the laser intensity distribution $I(\tau)$ and RF field $E(\phi)$. So in principle, we could deduce the laser longitudinal distribution by measuring the photoelectron charge through deconvolution.

Measuring the photoelectron charge as function of the RF gun phase is one of the simplest, but most import measurement in photocathode RF gun operation. Fig.3 is the experimental measurement for both Copper and Mg cathodes. We could obtain following information from Fig.3,

- **Absolution RF gun phase:** both photoelectron beam transverse emittance and bunch length are the function of the RF gun phase [10], accurate measure of the absolute RF gun is essential any stable photoinjector operation. For Schottky effect dominated photoemission, the peak of $Q(\phi)$ corresponding to the RF field crest (90 deg).
- **Timing Jitter:** taking advantage of $Q(\phi)$ dependency on the RF gun phase, we can measure the timing jitter between the RF system and RF gun driving laser. Notice the asymmetry in Fig.3, the falling edge of the $Q(\phi)$ curve is much more sensitive to the laser timing jitter. For a maximum charge of 1.5 nC, the sensitivity of the measurement can be 35 pC/deg. For a S-band RF gun, one degree RF phase is almost equal to 1 ps, this easily allows us to measure femto-seconds timing jitter between the laser and RF system if laser energy fluctuation can be simultaneously take into consideration. To deduce the laser system timing jitter, the timing jitter dependency on the RF gun phase must be taken into consideration [11].

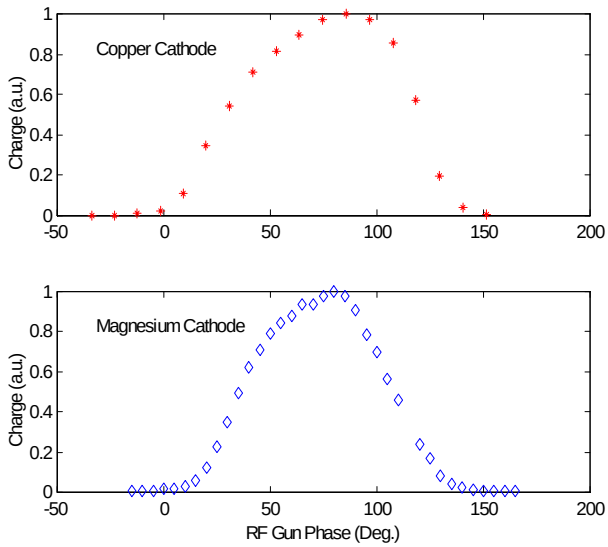

Figure 3: Photoelectron charge as function of RF gun phase for different cathode materials.

The $Q(\phi)$ curve was extensively used at the ATF for photocathode RF gun injector stability studies. We have measured the effect of the frequency doubling crystal on the longitudinal profile distribution of the RF gun driving

laser system (Fig.4). As we increase the laser energy to saturate the frequency doubling crystal, the laser profile change significantly, this is indicated by the variation of the rising edge of the $Q(\phi)$ curve, and broadening the range of the $Q(\phi)$ curve. From convolution theorem [12], the variance of the convolution equal to the sum of the individual function's, so laser pulse length increase will lead to the broadening of the $Q(\phi)$ curve.

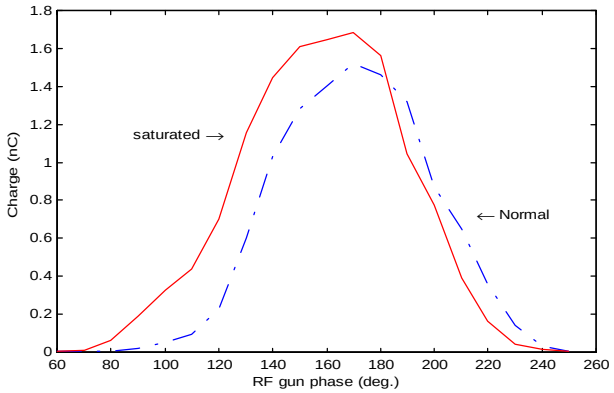

Figure 4: Photoelectron charge as function of RF gun phase for two different longitudinal laser profiles.

Fig. 5 shows variation of the $Q(\phi)$ curve FWHM from normal laser operation condition (80 deg) due to the laser pulse lengthening. We first confirmed this finding by measuring the electron beam bunch length, the laser pulse length inferred is 20 to 25 ps (FWHM). A streak camera with 2 ps resolution was employed to study the laser pulse length, and the laser pulse length obtained is 10 to 14 ps. tremendous efforts was devoted to investigate the inconsistency of those results. Since a grating was used to correct the laser intensity front tilt caused by the oblique laser incidence. We suspected that might cause the effective laser lengthening. We developed a technique of measuring the laser intensity front tilt on the cathode using $Q(\phi)$ curve. A $Q(\phi)$ curve was first obtained for normal laser spot on the cathode (2 mm diameter). Then a laser aperture was used to reduce the spot to 0.3 mm, the second $Q(\phi)$ curve for the smaller laser spot was compared with the first one. It was found that the RF gun phases corresponding to the maximum charge are different. This led us to believe that the laser arrives time varying with the position on the cathode. Further more, $Q(\phi)$ curves were measured as we move the small laser spot on the cathode. Comparing the RF phases for different positions we concluded that, the laser arrive time on the cathode vary as much as 10 ps with position.

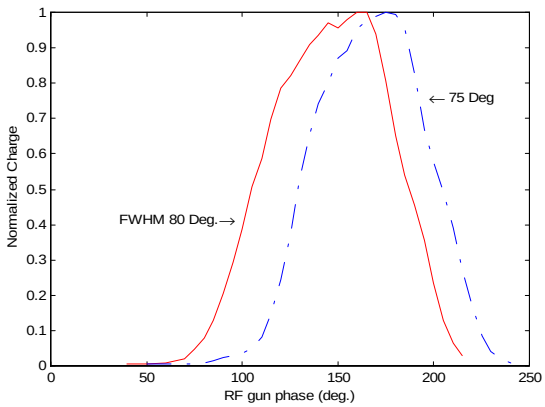

Figure 5: Q curve Width variation due to laser intensity front tilt leads to effective laser lengthening.

4 ACKNOWLEDGEMENT

We would like to acknowledge the technical support from B. Cahill, R. Harrington, M. Montemago and J. Schill.

5 REFERENCES

[1] P.G. O'Shea *et al*, Nucl. Instr.and Mth. A331(1993) 62-68.
[2] X.J. Wang *et al*, Nucl. Instr. And Meth A375 (1996) 82-86.
[3] D.T. Palmer *et al*, to be published in the Proceeding of PAC 97, Vancouver, Canada May12-16, 1997.
[4] The Brookhaven National Laboratory DUV Free Electron Laser CDR, BNL-49713, Jan. 1994.
[5] LCLS Design Study Report, SLAC-R-521, April 1998.
[6] A VUV Free Electron Laser at the TESLA Test Facility at DESY, DESY TESLA-FEL 95-03, 1995.
[7] X.J. Wang et al, Nucl. Instr. And Meth A356 (1995) 159-166.
[8] X.J. Wang et al, to be published in Nucl. Instr. And Meth A, BNL – 65002 (1997).
[9] T. Srinivasan-Rao *et al*, Study on the Sensitivity of Quantum Efficiency of Copper Photocathodes on Sample Preparation, BNL-62626 (1996).
[10] X.J. Wang *et al*, Phys. Rev.E.54 R3121 (1996).
[11] P.G. O'Shea, Nucl. Instr. And Meth A 358 (1995) 36-39.
[12] Deconvolution of Images and Spectra, edited by P.A. Jansson, Academic Press.

SUPPRESSION OF THE 1MHZ BEAM CURRENT MODULATION IN THE LEDA PROTON SOURCE

Pascal Balleyguier, CEA, Bruyeres-le-Chatel, France
Joseph Sherman, Thomas Zaugg, LANL, Los Alamos, USA

Abstract

Earlier operation of a microwave proton source exhibited an approximate 1-MHz modulation in the beam current. This oscillation could cause instabilities at higher energy in the linac, as the low-level RF control for linac operation rolls off at 200 kHz. Tests on a dummy load showed the modulation was created by the magnetron itself. Since the magnetron exhibits better behavior at higher levels, an RF power attenuator was inserted to force the magnetron to run at a higher power. This attenuator is made of two antennas plunged a quarter of guided wavelength apart in the waveguide and connected to dummy loads by a coaxial line. Magnetron operation at the higher power level gives a beam current spectrum free of the 1-MHz modulation, showing the coherent beam noise is not generated by plasma chamber phenomena.

1 MAGNETRON CHARACTERIZATION

Recent operations of the LEDA proton source [1-2] showed that the beam current was modulated in amplitude at a frequency of approximately 1 MHz. Earlier works already mention this kind of problem [3]. In the future downstream accelerator, any beam current variation would result in a varying beam-loading and could cause serious RF field instabilities. A challenge was to find out how to get rid of this modulation.

Previous measurements showed that the modulation was present in the 2.45 GHz RF power injected in the source plasma. In order to tell if the beam modulation was caused by a plasma resonance or by the RF generator itself, we connected the magnetron to a dummy load and measured the RF spectrum via a directional coupler (fig. 1). At 680 W (typical RF level for this application), its output still exhibited a strong 1 MHz modulation. Varying the RF power resulted in different spectra, and we established that the spectrum was completely free of modulation at higher powers, (see for example, the spectrum for 975 W in figure 2). The plot on figure 3 shows that the modulation strongly depends on the magnetron output power. The sideband effect is probably caused by a resonance in the tube.

Unfortunately, the useful power range for our ion source operation (500 to 800 W) is in the middle of this resonance. The good behavior of the magnetron above 800 W suggests to run it at a higher power range in order to get rid of the modulation. The magnetron can provide 750 to 1200 W of power and one third of this power can be dissipated in a power coupler.

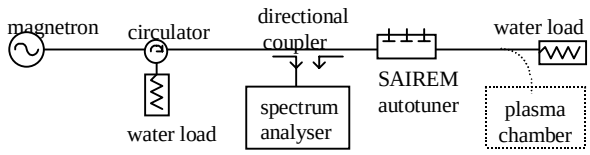

Figure 1: Measurement of the magnetron RF spectrum.

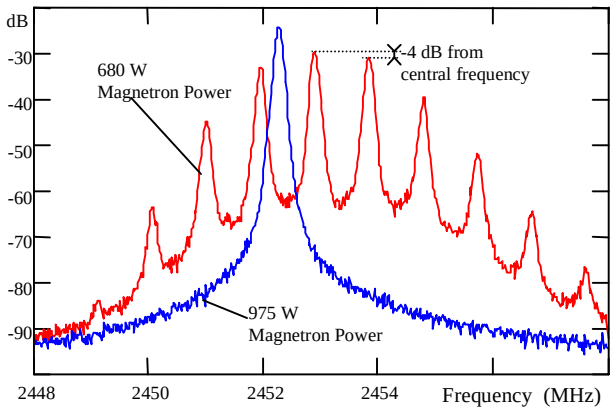

Figure 2: Magnetron power spectra at 680 and 975 W

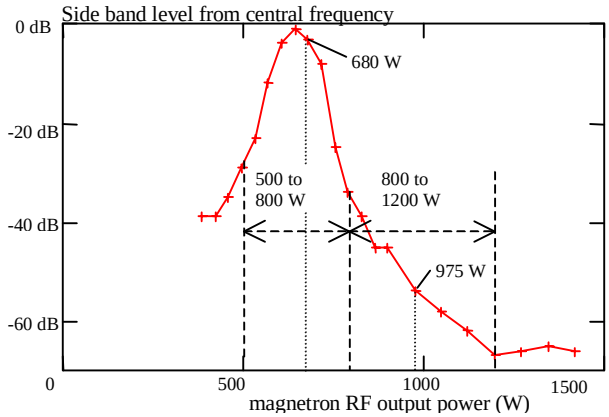

Figure 3: Sideband level vs. RF power

2 POWER EXTRACTOR

The device we need is an RF attenuator that transmits 66.7% of the input power. Such an attenuator (-1.78 dB, dissipating up to 400 W on a WR284 waveguide at 2.45 GHz), is not a standard product and would have a high price and a long delay if ordered from a manufacturer. Therefore, we decided to build it within the laboratory. It is easy to extract some RF power from a waveguide by inserting an electric antenna in the high electric field region and connecting the antenna to a coaxial load. The antenna length can be adjusted to attain a given coupling value, but this generates a local mismatch and results in

a reflected wave in the guide. If the power extractor consists of two identical antennas a quarter of guided wavelength apart, the two reflected waves are out of phase and approximately cancel each other. Moreover, as each of the antennas has to extract only 1/6 of the input RF power, they can be smaller in size, and this also reduces the mismatch effects of the device.

2.1 Single antenna pick-up theory

Consider a $\lambda_g/4$ long piece of lossless waveguide. The transfer coefficient between the input and output planes is the complex number *i*. Introducing an antenna in the middle of this device can lower the transfer coefficient modulus, and also alter the phase by $\Delta\varphi$. The original $\pi/2$ phase can be restored (fig. 4) by shifting the reference planes by :

$$\Delta l = -\frac{\Delta\varphi}{2\pi}\lambda_g . \quad (1)$$

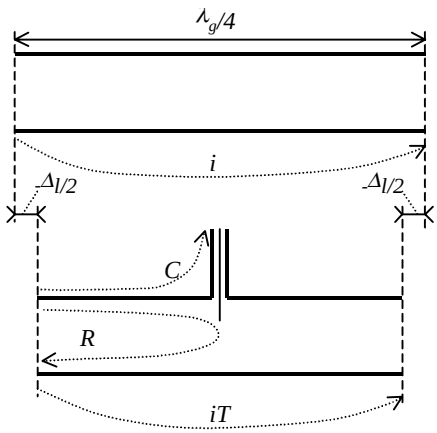

Figure 4: Single antenna pick-up. The reference planes have been displaced in order to keep the forward transfer coefficient a purely imaginary number.

The transfer coefficient of this "single antenna pick-up" is *iT, T* being a positive real number. In the coaxial line, the reference plane is chosen so the coupling coefficient *C* is also a positive real number. The antenna causes a reflected wave in the waveguide with an a priori arbitrary phase. Let *R* be the complex reflection coefficient seen from the input reference plane. Energy conservation implies:

$$|R|^2 + C^2 + T^2 = 1 . \quad (2)$$

As seen in the following section, *R* must also be a real number. That physically means that the reflection coefficient phase on the antenna is null if seen from a reference plane $\lambda_g/8$ upstream from the antenna (Δl is neglected here). In other words, the reflection phase is $\pm\pi/2$ if the reference plane is on the antenna itself.

2.2 Dual antenna pick-up theory

The dual antenna pick-up is obtained by cascading two devices identical to the single antenna pick-up described above (fig.5). We will assume that the inter antenna distance ($\lambda_g/4+\Delta l$) is large enough that the field patterns perturbation caused by one antenna is not seen by the other one. If the perturbation was non-negligible, the antennas could be separated by an additional integer number of $\lambda_g/2$.

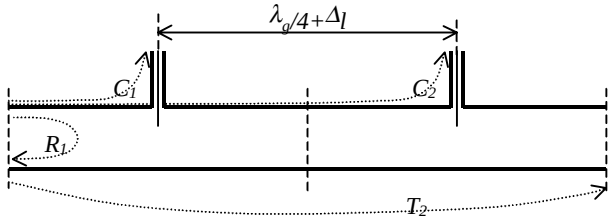

Figure 5: Dual antenna pick-up

Let T_2 be the global transfer coefficient. The incoming wave is multiplied by *iT* by the first antenna and *iT* again by the second antenna, giving $-T^2$ as the first term in T_2. The reflection on the second antenna creates a wave that is partially reflected again by the first antenna. At this point (medium reference plane), the transfer coefficient is $iT.R^2$. Going through the second antenna, this secondary waves reaches the output plane with a transfer coefficient multiplied again by *iT*, resulting in $iT.R^2.iT=-T^2R^2$. Considering now the wave doing one more round trip between the two antennas results in $iT.R^4.iT=-T^2R^4$. And so on... The summation of all these waves gives the actual transmitted wave:

$$T_2 = -T^2 + \sum_{k=1}^{\infty} -T^2R^{2k} = -\frac{T^2}{1-R^2} . \quad (3)$$

The same kind of argument gives the global reflection coefficient R_1, and the two coupling factors C_1 and C_2:

$$R_1 = R + \sum_{k=1}^{\infty} -T^2R^{2k-1} = R\left(1-\frac{T^2}{1-R^2}\right), \quad (4)$$

$$C_1 = C + \sum_{k=1}^{\infty} -iTCR^{2k-1} = C\left(1+i\frac{RT}{1-R^2}\right), \quad (5)$$

$$C_2 = iTC\sum_{k=1}^{\infty} -iTCR^{2k} = i\frac{TC}{1-R^2} . \quad (6)$$

Conservation of energy implies:

$$|R_1^2| + |C_1^2| + |C_2^2| + |T_2^2| = 1 \quad (7)$$

With equations (2) to (6), (7) can easily be proven if *R* is a pure real number. It is more difficult to prove the reciprocal proposition, but one can easily be convinced (by some numerical tests) that equation (7) can only be true if *R* is real, as mentioned in previous section.

Equation (4) shows that, as expected, the global reflection coefficient has been reduced by the second antenna, though it has not been completely cancelled because the second antenna receives a signal that has been already attenuated by the first one. For the same

reason, the two coupled output coefficients $|C_1|$ and $|C_2|$ are roughly equal to *C*.

The goal is to reach a specific transfer value $|T_2|$. From equation (3), one can see that T^2 must be chosen slightly greater than $|T_2|$, as R^2 is expected to be much smaller than unity. To be more precise, the link between *R* and *T* is needed, or equivalently because of equation (1), the link between *R* and *C*. While this link cannot easily be predicted, it can be measured experimentally.

2.3 Realization

A single antenna has been installed in the waveguide. A 9 mm hole has been drilled in the upper wall guide, and a connector socket (N type) fixed on the external side in a way that the socket pin would make an electrical antenna within the guide. As this antenna proved to be too short, a screw was placed in the socket pin (fig. 6) to increase the coupling coefficient *C*.

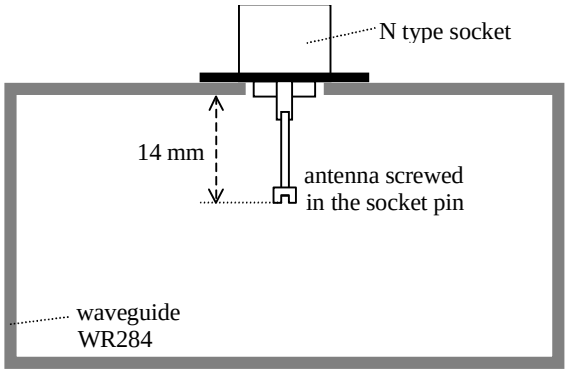

Figure 6: Mechanical design of the pick-up antenna. The two antennas are 51 mm apart.

After testing different antenna lengths, we established that the link between R and C was approximately:

$$C = 0.85 \cdot R + 0.18 . \qquad (8)$$

The goal value for C was computed numerically from equations (2)(3)(8) and from T_2^2=0.667: C=0.414. With a 14 mm antenna, we measured C≈0.399, and considered it was close enough to the goal. The phase shift introduced by a single antenna on the transmission coefficient was measured by comparing the waveguide phase transmission successively with and without the antenna: Δφ=11°. From eq.(1), the waveguide width and the operating frequency (a=72 mm, f=2.45 GHz), we computed the correct distance between the antennas:

$$\lambda_g/4+\Delta l=233/4-7\approx 51 \text{ mm}.$$

After installing the second antenna at this distance, we measured the dual antenna device characteristics:

$|R_1|$=0.028 (-30.8 dB), $|C_1|$=0.435 (-7.22 dB),
$|C_2|$=0.350 (-9.11 dB), $|T_2|$=0.822 (-1.70 dB).

The power transmission coefficient ($|T_2^2|$=0.675) is close to the design value (0.667), and the reflection coefficient is even better than predicted (SWR =1.06): the objective of power extraction without important mismatching has been reached. When operating the magnetron up to 1200 W, the loads have to dissipate up to 227 and 147 W, respectively. The loads installed can hold up to 250 W RF power, and a fan has been installed to cool them.

3 CONCLUSION

We tested the source performance with the same RF power delivered to the plasma chamber with and without the power extractor installed. With power extractor, the magnetron delivers 1010 W and the plasma chamber sees 682 W. The current source spectrum is now free of any 1 MHz modulation and cannot be distinguished from the background noise (fig. 7).

We proved that the 1 MHz modulation on the source current was entirely due to the magnetron, and was not generated by any phenomenon in the plasma chamber, and we found a simple and efficient way to get rid of this modulation.

The source current noise spectrum is now low enough to accurately identify the influence of various ion source parameters on the current spectrum.

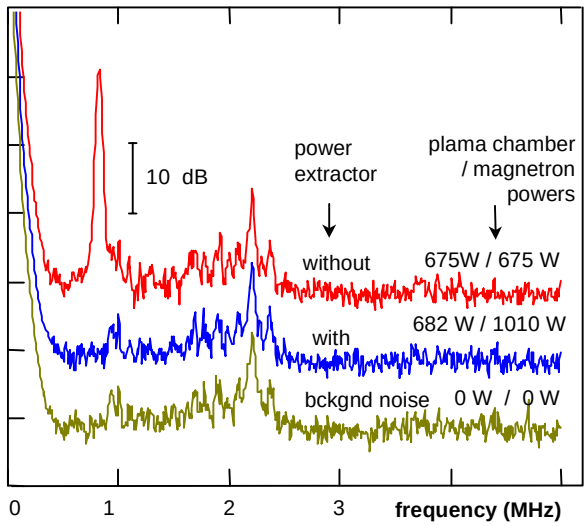

Figure 7: Current spectra comparison at constant RF power in the plasma chamber.
(For clarity, the "without" and "with" curves have been shifted up by 20 and 10 dB respectively).

REFERENCES

[1] J.Sherman et al., "Status report on a DC 130 mA 75 keV proton injector", Rev. of Sci. Instr., Vol 69, p 1003, (1998).

[2] J. Sherman et al., "A DC Proton Injector for Use in High-Current CW Linacs", submitted to European Particle Accelerator Conference, Stockholm, 22-26 June 1998.

[3] I. Soloshenko, "Physics of Ion Beam Plasma and Problems of Intensive Ion Beam Transportation", Rev. Sci. Instrum., Vol 67-4, p. 1646(1996).

PHOTO-CATHODES FOR THE CERN CLIC TEST FACILITY

E. Chevallay, J. Durand, S. Hutchins, G. Suberlucq, H. Trautner
CERN 1211 Geneva 23 Switzerland

Abstract

Since 1993 the CLIC Test Facility (CTF) has used laser-illuminated Tellurium Alkali photo-cathodes as intense electron sources (up to 50 nC in 10 ps), for the Drive Beam of a two-beam accelerator. These cathodes have been produced and tested in our photo-emission laboratory and transported under vacuum to the CTF. They are placed in a 3 GHz RF gun with a 100 MV/m electric field. This RF gun produces a train of 48 pulses, each of 13.4 nC charge and 10 ps length. The CTF Probe Beam has used air-transportable cesium iodide + germanium photo-cathodes in another RF gun, which produces a single pulse of the same duration but with only 1 nC charge. The optical damage threshold in the laser is the main limitation of energy available on the photo-cathode. From an operational point of view, the photo-cathode lifetime is defined to be the time during which the cathode is able to produce the nominal charge with the nominal laser energy. After having recalled the main characteristics of the photo-cathodes tested, this note describes in more detail the performance obtained in operation. The possibility of photo-cathode production at the RF gun in a simplified evaporation chamber will also be discussed.

1 INTRODUCTION

The CLIC Test Facility (CTF) produces and tests two different electron beams: one, with a high charge (up to 640 nC in 48 pulses), called the "Drive Beam" (DB) is used to produce 30 GHz radio frequency power. The other, called the "Probe Beam" (PB), with a lower charge of 1 nC in a single pulse, is used to sample the 30 GHz accelerating fields. A summary of results from CTF-II is reported in [1]. The electron source for each beam is a 3 GHz RF gun equipped with a laser-driven photo-cathode. The photo-cathode requirements are closely related to the electron beams and the laser characteristics.

2 PHOTOCATHODE REQUIREMENTS

2.1 Electron beam specifications

The electron beam specifications are summarized in Table 1. The repetition rate was reduced from 10 to 5 Hz to improve the vacuum in the DB RF gun and consequently to improve the photo-cathode lifetime.

Table 1 : Electron beams specifications.

		DB	PB
Charge per bunch	nC	13.4	1 - 2
Number of bunches	-	48	1
Pulse width FWHM	ps	10	10
Δt between pulses	ps	330	-
Charge stability	% rms	1	5
Jitter laser / RF	ps	$\pm$ 1	$\pm$ 1
Jitter DB / PB	ps	$\pm$ 1	$\pm$ 1
Delay PB / DB	ns	-	14
Cathode electric field	MV/m	100	70
Repetition rate	Hz	5	5

2.2 The CTF-II laser system

The laser (Fig. 1 and Ref. 2) is a "Master Oscillator-Power Amplifier" (MOPA) system in which 2 pulses are selected from a 250 MHz Nd:YLF mode-locked oscillator. The pulses are 8 ps and they have an energy of 0.5 nJ per pulse. They are amplified in a Regenerative Amplifier (RA), followed by power amplifiers to 7 mJ per pulse. The power density is 10 GW/cm^2 at the final power amplifier. This is close to the damage threshold since the beam is limited to 4.5 mm diameter due to the size of the components. The wavelength is converted from 1047 nm to 262 nm (the 4th harmonic). The 2 UV pulses are then progressively "split" with appropriate delays in a "Pulse Train Generator" (PTG) to produce the DB train of 48 pulses with 333 ps separation. The separation is exactly one 3 GHz RF period so that each light-pulse will illuminate the photo-cathode at the same RF phase and the resulting electrons will then be equally accelerated. The timing for the laser and the 3 GHz RF generator are synchronized.

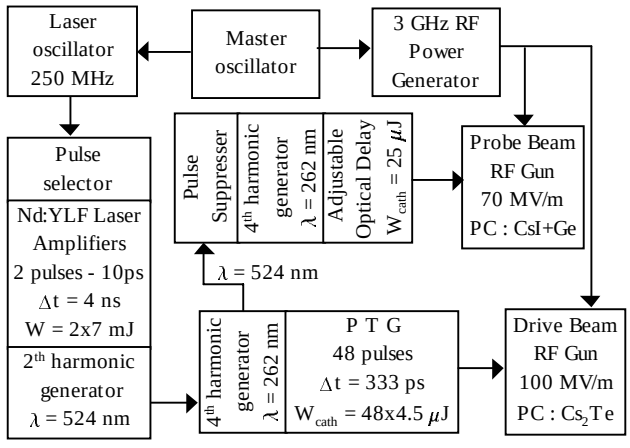

Figure 1: Laser layout for the Probe and Drive Beam

The residual green light from the initial 4th harmonic generator is used to produce a pulse for the PB. This initially passes through a Pockels cell that rotates the polarization of the second green pulse by 90°, this is then rejected by a polarizing plate. The remaining pulse is converted to UV.

The two light beams are imaged to their respective cathodes, for the DB the distance is 32 m with a magnification of 2x. The PB is delayed to arrive at the accelerating section in the linac when the 30 GHz power has been generated, making its path length equal to 36 m.

Finally, 48 pulses of 4.5 μJ at 262 nm arrive at the DB photo-cathode, and a single pulse of 25 μJ with the same wavelength on the PB photo-cathode.

2.3 Photo-cathode requirements

The photo-cathodes are characterized by their quantum efficiency (QE, the ratio of emitted electrons to incident photons) at a given wavelength and by their lifetime under operating conditions. Taking into account the available laser energy, QE must be greater than 1.5 % at 262 nm for the DB, and greater than 0.02 % for the PB at the same wavelength. The lifetime required is at least one week for an electric field in the DB RF gun of 100 MV/m. When a new cathode is installed in the PB RF gun to be operated at a field of 70 MV/m, it is necessary to bake-out the gun due to air contamination. For this reason, the lifetime must be at least one month for continuity of operation. The charges produced must be linearly related to the laser energy up to 640 nC (48 pulses of 13.4 nC) for the DB and 2 nC for the PB. In both cases, the time response must be less than a few ps.

3 PHOTO-CATHODES TESTED IN THE RF GUN

The photo-cathodes are produced and tested in a separate photo-emission laboratory. Only cathodes with properties near-nominal are installed in the CTF guns. Metallic cathodes were also tested [3], a magnesium cathode could be a candidate for the PB, but its QE is low and it has a high dark current. In the context of an informal collaboration with the Stanford Linear Accelerator Center, non-activated GaAs cathodes were tested in the DB gun with electric fields up to 87 MV/m. An activation process for GaAs is under development. The results are reported in [4,5].

Between December 1990 and October 1993 CsI photo-cathodes were used because they can be transported in air [6]. Unfortunately, their photo-emission threshold is high (6.3 eV) involving the use of the fifth harmonic of a Nd:YLF laser (λ=209 nm). This wavelength was found to be impractical, so the possibility of using photo-cathodes at the fourth harmonic (λ=262 nm) were investigated, and a system for transferring the cathodes under vacuum was developed. At this wavelength alkali photo-cathodes are able to produce high charges, and many were tried in the photo-emission lab [3]. Two kinds which matched our laser equipment and the CTF specifications were selected. The first type, for the PB, is a cesium iodide cathode with a coating of germanium. This cathode can be transported in air at the expense of a moderate QE at 262 nm. For the DB, cesium telluride was chosen because of its high QE at 262 nm and long lifetime, but it must be transported under vacuum. The complete results for these two cathode types are reported in [7,8]

3.1 CsI+Ge photo-cathodes

A thin 2 nm coating of germanium over a CsI cathode decreases the QE at 213 nm by a factor of 10, but improves it at 262 nm from $7x10^{-5}$ to 0.13 % [3]. This coating does not change the air exposure property of the CsI. To improve adhesion, a 200 nm layer of aluminum is deposited on the copper cathode plug before the 350 nm CsI layer, which is then coated with 2 nm of Ge. These photo-cathodes are stored in a desiccator. Finally they are installed, in air, in the RF gun which is then baked to 150°C to improve the vacuum. These cathodes require a delicate conditioning process using high electric fields and laser pulses to remove the oxidized surface without destroying the thin germanium layer. After 10 to 15 hours of processing, the QE reaches up to 0.2 % with an electric field of 70 MV/m. The lifetime is quite long: the time constant τ (the time to drop down to QE_{max}/e) is more than one year. In the PB gun, the same cathode has been used since October 1996.

3.2 Alkali telluride photo-cathodes

Four kinds of alkali telluride photo-cathodes were produced and tested on different substrates: Cs_2Te, K_2Te, Rb_2Te and RbCsTe. Only the first one is routinely used in the DB RF gun. All require UV light (λ < 270 nm) for operation.

Cs_2Te : about 10 nm of Te is deposited at room temperature on various substrates (Cu, Mo, Mg). The Cs is evaporated with the substrate at 110 °C until the photo-emission reaches a maximum. Typically 15 nm of Cs gives a QE of 7 %. These cathodes are very robust compared to the alkali antimonide cathodes. The working pressure is about 10^{-9} mbar. The main contamination comes from oxygen [9]. A satisfactory behavior was observed in the RF gun up to 127 MV/m. At this field level, the initial QE is close to 10 %. The QE drops during the first 50 hours with a $\tau \approx 40$ hours, followed by a slower decrease with a $\tau \approx 350$ hours. The time response is less than 2ps; the measurement is limited by the resolution of the streak camera. An electric field dependence of the QE was observed this is probably a Schottky effect [10], and seems to be independent of the Cs_2Te photo-cathode aging rate.

K_2Te : This was found to be a robust photo cathode, but with a QE between 1 to 3 % at 262 nm.

Rb_2Te and RbCsTe : About the same properties as Cs_2Te

cathodes. These cathodes seem very promising for QE rejuvenation after exposure to air. Nevertheless their performance in the RF gun must be demonstrated.

The photo-cathode substrate : Various kinds of substrates have been used : molybdenum, magnesium, and copper, the best results were obtained with Mo and Mg. Due to its higher dark current Mg was eliminated. In terms of charge availability, (QE > 2 % during a few weeks), the substrate is not so important. The second slope of the lifetime curve seems to be almost independent of the substrate.

Between November 1993 and July 1998, 50 alkali photo-cathodes were produced. Twenty eight were used in the RF gun : 26 Cs_2Te, 1 K_2Te and 1 Rb_2Te. Table 2 summarizes the statistics (mean and standard deviation values) for the produced and used alkali photo-cathodes. The cathodes were measured in the DC gun at electric fields between 6 and 9 MV/m. R is the layer thickness ratio of alkali over tellurium. T is the total time of the photo-cathode in the RF gun, and $\tau_{QE>2\%}$ is the time during which the QE is greater than 2 %. About 30 % of the time mentioned in Table 2 was with RF power and laser. The vacuum pressure was about 10^{-9} mbar.

Table 2: Alkali photo-cathodes : Production and use.

Cathode type		Cs_2Te			All	
Substrate type		Cu	Mo	Other		
Production	Numb.	31	6	8	52	-
	QE_{MOY}	4.7	8.8	7.8	5.8	%
	QE_{STDV}	1.9	3.8	2.5	3	%
	R_{MOY}	1.2	1. 5	2.6	1.6	-
	R_{STDEV}	0.5	0.2	2.5	1.3	-
Used in the CTF 70 < E < 125 MV/m	Numb.	15	6	5	28	-
	T_{TOTAL}	362	160	142	693	days
	T_{MOY}	24	27	28	25	days
	T_{STDEV}	23	23	24	22	days
	$\tau_{QE>2\%}$	20	17	14	19	days
	τ_{STDEV}	23	17	14	17	days

4 PHOTO-CATHODE PREPARATION

Three kinds of photo-cathode preparation can be identified depending on the QE and lifetime specifications. When high charge (> 10 nC per pulse), high QE and long lifetime are required (as for CTF DB), the cathode should be prepared by real time monitoring of the QE, then transported and installed in the RF gun in an ultra-high vacuum environment. For up to 1 nC per pulse, CsI+Ge photo-cathodes which can be transported in air give good performances, and lifetimes of a few months. For 1 to 10 nC per pulse it may be possible to produce photo-cathodes using more simple methods. One method would be to prepare the photo-cathode for a high QE, transport in air, then rejuvenate it in the RF gun, or in a vacuum chamber attached to the RF gun. We have tried two different rejuvenation processes: heating, and ion-bombardment etching. A Rb_2Te cathode was exposed to air during 7 minutes and its QE dropped to 10^{-5}. After heating to 200°C in vacuum, the QE improves to 0.5 %. We did not observe any further QE change during 1 week. Another RbCsTe cathode was exposed to air for 2 minutes, its QE dropped down to 0.1 %. After ion bombardment cleaning, its QE improved to 0.7 %.

The second possibility to obtain a medium charge i.e. a medium QE, is to prepare the photo-cathodes in a simplified preparation chamber linked to the RF gun. By monitoring only the layer thickness, the production of photo-cathodes with a QE between 1 and 3 % is possible. Such a cathode, with an initial QE of 2.5 %, has been used in the DB for 78 days with a QE > 2 %.

5 CONCLUSIONS

Cs_2Te and CsI+Ge cathodes fulfil the drive and probe beam CTF-II specifications. The Rb_2Te cathode, using a rejuvenation process, may be a good alternative to Cs_2Te. It is possible to produce Cs_2Te cathodes in an easier and cheaper way by monitoring only the layer thickness, this is however obtained at the expense of a lower mean QE.

A new vacuum chamber will be attached to the PB RF gun to enable laser alignment of the PB. This chamber will be equipped for a simplified cathode production and rejuvenation.

6 REFERENCES

[1] H.H. Braun, and 13 co-authors, “Demonstration of Two Beam Acceleration in CTF II”, this conference.

[2] S. Hutchins, “The CTF-II Laser System”, CERN CTF Note 98-18.

[3] E. Chevallay, J. Durand, S. Hutchins, G. Suberlucq, M. Wurgel, “Photo-cathodes tested in the dc gun of the CERN photo-emission laboratory”, NIM A 340 (1994), p. 146.

[4] K. Aulenbacher and 9 co-authors, “RF Guns and the Production of Polarized Electrons”, CERN-CLIC Note 298, SLAC-NLC-Note 20, March 1996.

[5] G. Suberlucq, and 8 co-authors, “Gallium Arsenide Photo-cathodes used in high electric fields”, CERN CTF Note 98-13.

[6] G. Suberlucq, “Photocathodes en iodure de césium utilisées à fort courant”, CLIC Note 162, May 1992.

[7] G. Suberlucq, “Développement et production de photo-cathodes pour le CLIC Test Facility”, CERN CLIC Note 299, 15-5-1996.

[8] G. Suberlucq, “Development and production of photo cathodes for the CLIC Test Facility”, Free Electron Lasers 1996, p. II-131, 1997 Elsevier Science B.V.

[9] A. Di Bona, F. Sabary, S. Valeri, P. Michelato, D. Sertore, G. Suberlucq, “Auger and X-ray Photo-emission Spectroscopy Study on Cs2Te Photo-cathodes”, J. Appl. Phys, 80 (5) 1 September 1996.

[10] R. Bossart, H. Braun, M. Dehler, J.C. Godot, “A 3 GHz Photo-electron Gun for High Beam Intensity”, CLIC Note 297, CERN 1995.

OPERATION OF THE UPGRADED H⁻-INJECTION SYSTEM OF THE LINAC III AT DESY

C.-M. Kleffner, N. Holtkamp, M. Nagl, H. Poggensee, J. Peters
Deutsches Elektronensynchrotron DESY, D-22603 Hamburg, Germany
A. Schempp, IAP, University of Frankfurt, Germany

Abstract

During the winter shutdown 1997/98, the injection system of the H⁻-Linac III was upgraded. At present two different kinds of H⁻-sources are operated at DESY. The new cesium-free rf ion source is planned to operate parallel to the magnetron ion source.

In addition a new MEBT (Medium Energy Beam Transport line) between two distinct RFQ accelerators and the Alvarez accelerator of Linac III was installed to match the beam of each ion source to the Alvarez acceptance. This scheme makes it possible to operate either H⁻-source with the Alvarez linac with a miniumum of effort to switch from one to the other. The design of the transport line also facilitates the development and tests of newly proposed ion sources, for example deuterium and polarized proton sources.

After assembly of the RFQs and ion sources as well as the new components for the MEBT, a relatively easy commissioning could be demonstrated, although the ions have to be transported on a long distance from the RFQ to the Alvarez linac. First results of measurements will be presented.

1 INTRODUCTION

Linac III at DESY started operating as an H⁻-injector for the DESY III synchrotron in 1989 [1] and is part of the injector chain for the HERA collider. The negative charged ions are produced by a surface-plasma magnetron source at 18 keV and are accelerated with an RFQ to an energy of 750 keV. A conventional Alvarez linac is used to obtain the injection energy of 50 MeV into DESY III.

Further developments at the DESY cesium-free rf-volume source led to an operable and reliable design [2]. To integrate this volume source into the proton linac for standard operation it was desirable to find a technical solution to switch back to the magnetron source at any time. This improves the reliability of the proton injector chain to HERA. It was therefore decided to reconstruct the pre-accelerator of the linac to allow both ion sources to operate for the linac simultaneously.

The upgraded injection system in front of the Alvarez linac consists of the existing devices as well as of a new beamline with an additional RFQ and a rebuncher cavity. The assembly of the new MEBT beamline and the two ion sources also necessitated an extension of the accelerator tunnel. The shutdown period of the DESY accelerators

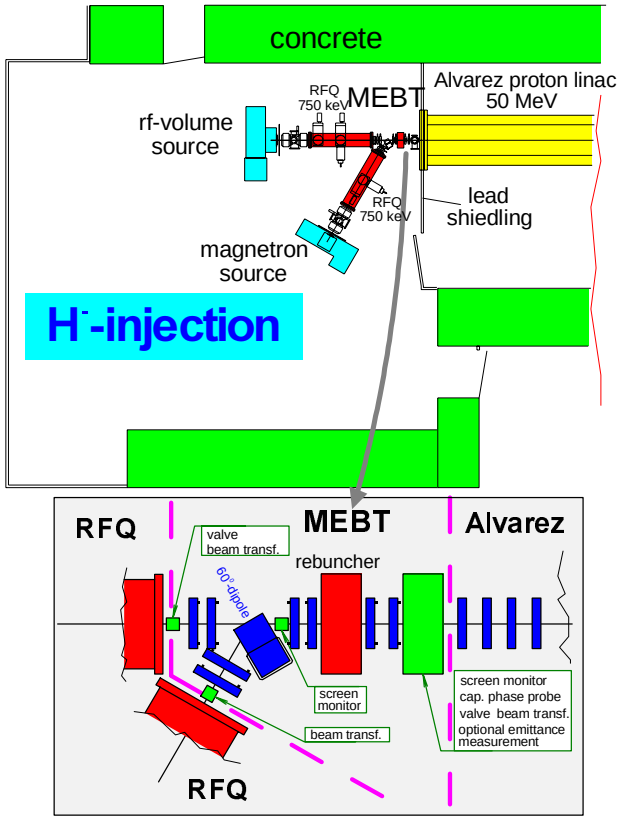

Figure 1: Floor plan of the injection system and a detailed view on the MEBT.

in winter 1997/98 was used for dismantlement of the pre-accelerator, the reconstruction of parts of the tunnel and related facilities and the assembly of the new components.

The low beam energy of 750 keV, small beam losses and a new arrangement of lead- and concrete-shielding permits access to the injection system during linac operating time.

2 CHARACTERISTICS OF THE MEBT

Beam transport of ions under space charge conditions at low energies reduces the variety of possible transport line designs. The goal was to control the longitudinal bunch shape with only one rebuncher cavity between the RFQs and the Alvarez linac. Therefore it was essential to keep the overall length of the transport line below 1 m. The mechanical components had to be composed in a very compact manner. Details of the MEBT have been given previously

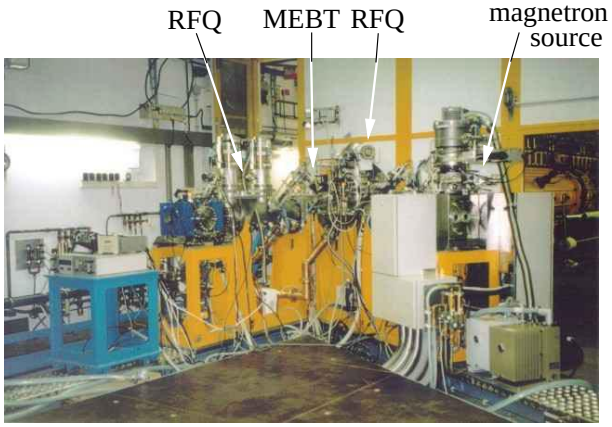

Figure 2: View of the rebuilt injection system in the Linac III tunnel.

[3], briefly the design is as follows:

The new rf-volume source is installed on the axis of the Alvarez linac, whereas the beam coming out from the magnetron source is bent by a 60°-dipole to this axis. Fig. 1 shows a survey of the injection system.

The main components including ion sources, RFQs and the MEBT are mounted independently on frames made of aluminium. These frames are put onto a rail system and are thus retracktable along the beam axis. It is therefore easy to install additional beam diagnostic elements for further investigation of beam properties at any place in one of the paths. Fig. 2 and Fig. 3 show the arrangement of the injection system and details of the MEBT transport line.

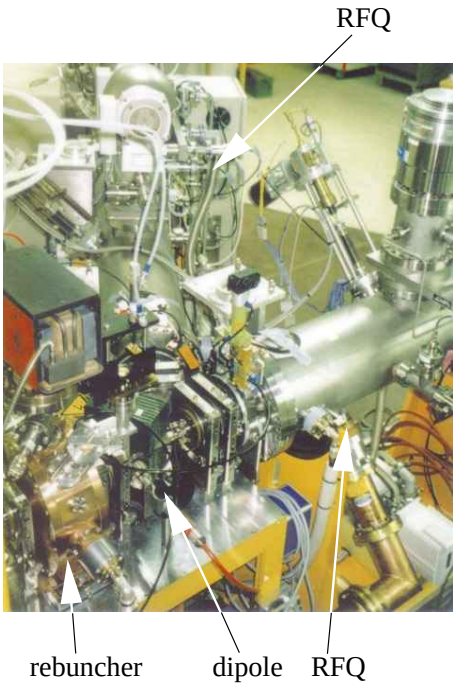

Figure 3: Side view of the MEBT beam transport line.

Table 1: Basic parameters of the new cavities for the injection system.

	RFQ	rebuncher
f_0	202 MHz	202 MHz
U_{rod} / U_{eff}	80 kV	58 kV
P	80 kW	4 kW
L	120 cm	12 cm

The 4-rod RFQ and the rebuncher cavity were delivered by the University of Frankfurt [3]. A parameter list is given in Table 1. The rf-amplifier for the rebuncher was designed and constructed at DESY. The design is based on the rf-preamplifier of the existing rf-amplifiers for Linac III.

3 FIRST OPERATION WITH THE MEBT

After the assembly and adjustment of the new injection system first acceleration tests with the magnetron source were performed. The rf-volume source is already assembled in position but not in operation yet. It is expected, that first beam tests with the new source can be performed in autumn.

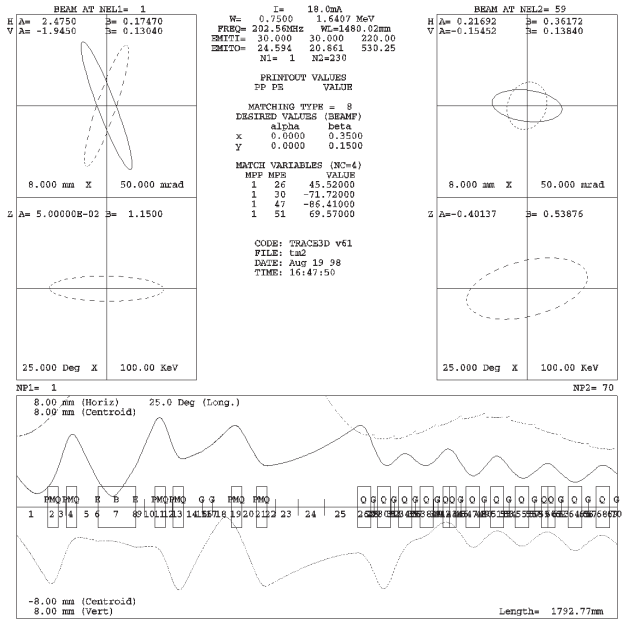

Figure 4: Matched beam envelopes (5σ) calculated by TRACE3D.

Once the beam delivered by the magnetron coasted through the MEBT line, only little empirical tuning of the MEBT quadrupole focusing strength was necessary. The numerical simulations (s. Fig. 4) led to a solution with good transmission through MEBT and the Alvarez linac. Only one quadrupole was displaced by 0.7 mm for beam steering reasons. Whereas the transmission of the solenoid focusing channel in front of the RFQ is found to be limited under space-charge conditions to 50 % [4], the transmission from the RFQ up to the end of the high energy transport line after the Alvarez linac under typical conditions

reaches 75 %. At the injection point to DESY III currents of 10 to 15 mA are obtained, depending on the current of the magnetron source of typically 30 to 65 mA.

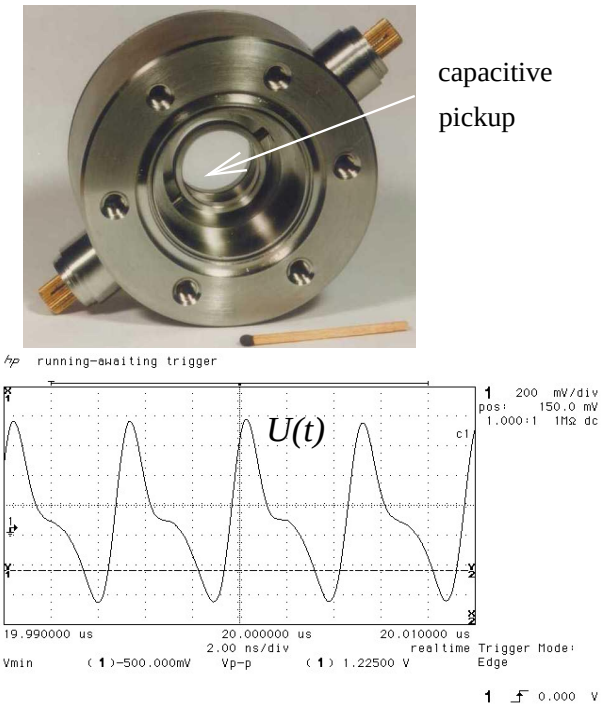

Figure 5: Signal of a bunched beam with $\Delta\varphi\,(2\sigma) = \pm 30°$ measured with the capacitive probe above.

The cavity phase and amplitude settings of the RFQ and rebuncher with respect to the Alvarez tanks was to be found more laborious. The phase settings of the cavities is based mainly on the measurements of energy and momentum spread after the Alvarez linac. A capacitive phase probe built at DESY (see Fig. 5) between rebuncher and the Alvarez was used to estimate the longitudinal bunchlength at the end of the MEBT.

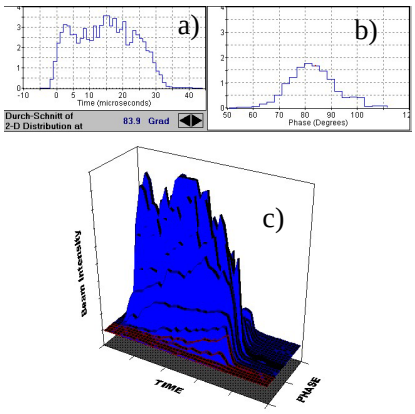

Figure 6: Current density along the bunch train **(a)**, phase spread **(b)** and a 3D-view **(c)** of the buch train measured with the bunch shape monitor at the Alvarez Tank 1.

The bunch shape monitor [5] in the Alvarez Tank 1 was used for fine tuning of the relative phase setting between the rebuncher cavity and the Tank 1 as well for the amplitude settings of these cavities. Fig. 6 shows a offline estimated 3D-view of the bunch train.

The phase tuning was to be found slightly depending on the beam current delivered by the ion source. Fig. 7 shows a typical devolution of momentum spread and energy during tuning of the cavity settings.

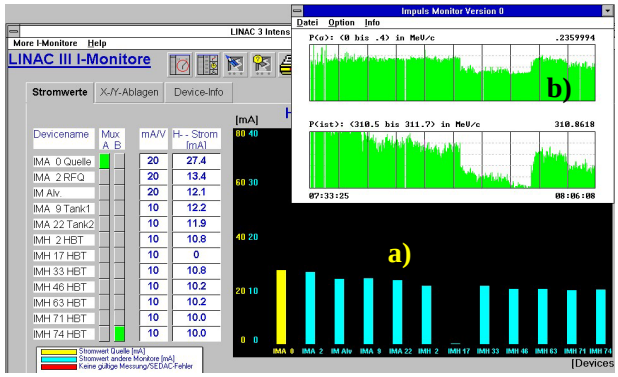

Figure 7: Transmission along the linac **(a)** and a history of evaluated beam properties **(b)** shown on a PC console station.

4 ACKNOWLEGMENT

The authors wish to thank all contributing colleagues and the collaborating institutes for their technical support and helpful discussions.

5 REFERENCES

[1] LINAC III collaboration, Rev. Sci. Instruments **62** (4), April 1991.

[2] J. Peters, Review of Negative Hydrogen Ion Sources High Brightness/High Current, this conference.

[3] C.-M. Kleffner, G. Jacobs, N. Holtkamp, M. Nagl, I. Peperkorn, J. Peters, Deutsches Elektronen Synchrotron DESY, Germany, A. Schempp, IAP, Universität Frankfurt, Germany, and V. Paramonov, INR Moscow, Russia, Upgrade of the H^--Injection System at the DESY Proton Linac III, Proc. of the 1997 PAC, Vancouver, Canada, 12-16 May 1997.

[4] A. Sauer, diploma thesis, IAP Frankfurt, 1998.

[5] A.V. Feschenko, A.V. Liiou, A.N. Mirzojan, A.A. Menshov, P.N. Ostroumov, N. Holtkamp, C.-M. Kleffner, M. Nagl, I. Peperkorn, Bunch Shape Monitors for the DESY H^--Linac, Proc. of the 1997 PAC, Vancouver, Canada, 12-16 May 1997.

BEAM TRANSPORT, ACCELERATION AND COMPRESSION STUDIES IN THE FERMILAB HIGH-BRIGHTNESS PHOTOINJECTOR

J.-P. Carneiro, R. A. Carrigan, M. S. Champion, A. Cianchi, E. R. Colby, P. L. Colestock,
H. T. Edwards, J. D. Fuerst, W. H. Hartung, K. P. Koepke, M. Kuchnir, L. K. Spentzouris
Fermi National Accelerator Laboratory, Batavia, Illinois 60510 USA
M. J. Fitch, A. R. Fry, A. C. Melissinos, B. D. Taylor
Univ. of Rochester, Rochester, New York
P. Michelato, D. Sertore, C. Pagani
INFN-Milano-LASA, Milano, Italy
J. B. Rosenzweig
University of California at Los Angeles, Los Angeles, Ca.

Abstract

A photoinjector is being constructed in order to produce a pulse train of up to 800 electron bunches, each with 8 nC of charge and a 3.5 ps rms bunch length. The spacing between bunches within a train is 1 μs and the train repetition rate is 1–10 Hz. The desired transverse emittance is $<20\pi$ mm $\cdot$ mrad. An rf photo-gun delivers a bunched 4–5 MeV beam which will be accelerated to 14–18 MeV by a 9-cell superconducting cavity and compressed magnetically. Measurements have been done on the beam delivered by a first prototype rf gun; installation of a new rf gun, the 9-cell cavity, and the bunch compressor is in progress.

1 INTRODUCTION

A high-brightness electron source is being constructed at Fermilab as part of an ongoing collaboration with the TeSLA Test Facility (TTF) [1], and to provide an R&D facility for advanced accelerator research at Fermilab. The facility consists of a high quantum efficiency photocathode in a 1.3 GHz normal conducting rf gun, a 9-cell superconducting cavity for acceleration, and a magnetic bunch compressor (chicane). Thus far, an initial test with an rf gun has been completed. In particular, the important operational issues of dark current production and beam transport through the rf gun were studied. In this paper, we outline the results of the gun and beam studies thus far. When completed, the facility will be used to study beam transport through the cavity and the physics of compression with the high brightness beam. In the longer term, the facility will be used to explore a number of new acceleration schemes and to provide an R & D tool for a variety of new concepts relevant to high-energy, high-intensity machines, as will be described herein.

2 DESCRIPTION OF FACILITY

The beam line consists of a normal conducting rf gun, a superconducting acceleration cavity, a magnetic chicane, a low-β section, a spectrometer, and diagnostics. In addition, there is a separate chamber for coating photo-cathodes and transferring them to the rf gun. The upstream portion of the beam line is shown in Fig. 1.

2.1 RF Gun

The rf gun consists of a 1.625-cell 1.3 GHz π mode copper cavity side-coupled to a waveguide in the full cell [2, 3]. The first prototype gun was intended for a low duty cycle ($\sim 10^{-4}$). However, it was operated with a peak surface field on the cathode of E_c = 39 MV/m with a pulse length of up to 400 μs at a 1 Hz repetition rate; a 1 ms pulse was reached with E_c = 36 MV/m at 0.1 Hz. The gun was used to produce beam at Argonne [2, 3] and Fermilab (see § 3).

A second generation gun has been designed for a high duty cycle (1%). The design parameters were (i) a beam energy of 3.9–5.5 MeV, which corresponds to E_c = 35–50 MV/m and a peak power dissipation of 2.2–4.5 MW; (ii) an rf pulse duration of 800 μs; (iii) a repetition rate of 10 Hz. The high average power (up to 36 kW) is removed by cooling channels machined into the walls of the cavity, with $\sim$4 L/s of water flow. The first of the new guns has been fabricated and is presently being conditioned. To date, it has been operated with E_c = 40 MV/m (2.7 MW peak power) with a 800 μs pulse length at 1 Hz. Dark current measurements have also been done (see § 3.2).

2.2 Nine-cell Cavity

The superconducting accelerating cavity is a 9-cell structure made from sheet Nb [1]. Sub-systems include a high-power coaxial input coupler (Q_{ext} = 10^6 to $9 \cdot 10^6$), a cold tuner (range $\approx \pm$ 400 kHz), and 2 coaxial higher-order mode couplers. The current cavity, named S12, is a prototype fabricated by industry for TTF. It was etched, rinsed, heat treated, and tested with rf at DESY. The cavity is one of a batch with a low quench field (13 MeV/m in CW), attributed to contamination in the electron beam welds at the equator. The horizontal cryostat was designed at Orsay [4] for the TTF capture cavity and built by industry. After shipment to Fermilab, the cavity and cryostat were assembled, cooled to 1.8 K, and tested (without beam). With 800 μs useful pulse length and 1 Hz repetition rate, the cryogenic load was tolerable at a gradient of $\geq$12 MeV/m. Further rf tests are needed to verify the field level calibration and measure the cryogenic losses versus field level.

2.3 Laser System

The ultra-violet (UV) laser for photo-electron production is a phase-stabilized mode-locked Nd:YLF oscillator (λ = 1054 nm) and a chain of Nd:glass amplifiers, using chirped pulse amplification [5]. Seed pulses from the oscillator are stretched and chirped in an optical fiber, then selected by a fast Pockels cell (PC). A second fast PC is

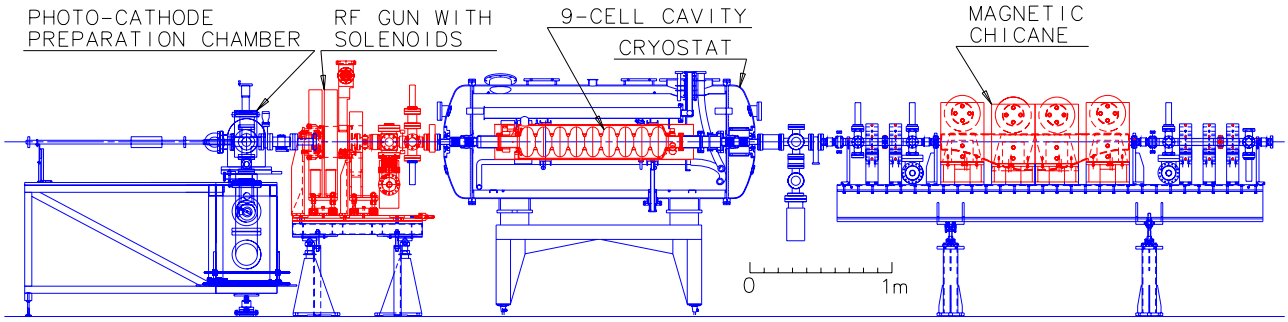

Figure 1. A0 beam line layout from the cathode preparation chamber through the chicane.

used to trap and eject the pulses into a multi-pass amplifier (see Fig. 2). After a 2-pass amplifier and spatial filtering, a grating compressor achieves a short, selectable pulse length (1–20 ps). Two stages of second harmonic generation are used to reach the UV wavelength (263 nm). The system is designed to produce 5 μJ per pulse of UV, in the following temporal pattern: pulse repetition rate of 1 MHz, pulses grouped into trains of 800, with 1 Hz repetition rate for the trains. The amplitude across the train is shaped via a third (slow) PC prior to amplification, to compensate for the time-dependent gain of the amplifiers, in order to produce a pulse train with a flat envelope.

2.4 *Photo-cathode*

The primary photo-cathode figure of merit is the quantum efficiency (QE), the ratio of the number of emitted electrons to the number of incident photons. The cathode is a Cs_2Te film on a Mo substrate. Cs_2Te can have a QE of up to 10–15%; for comparison, the QE of a metal cathode is typically 10^{-4}–10^{-6}. However, the QE of Cs_2Te is degraded by residual gases, so a Cs_2Te cathode must remain in ultra-high vacuum (UHV) for its entire useful life. A UHV system for coating cathodes and transferring them into the rf gun is hence required. So far, 2 cathodes have been coated and used with the first gun. For both, the QE was $>$10% immediately after coating, about 0.6% after being used in the gun, and $\geq$5% after rejuvenation [6].

2.5 *Diagnostics*

The beam diagnostics include integrating current transformers (ICT), Faraday cups, beam position monitors (BPM), screens, emittance slits, and a magnetic spectrometer. The BPM's employ a heterodyne scheme to avoid rf noise and enhance signal strength. The screens are YAG, Cr-doped alumina, and Al, the latter being used for optical transition radiation (OTR) measurements with an intensified camera. The emittance slits consist of a rotatable array of 10 μm slits approximately 20 mm high and 6 mm thick.

3 BEAM OPERATION

A first round of experiments was done at Argonne with the low duty cycle gun, a Cu cathode, and a Cu 9-cell cavity [2, 3]. A second round of experiments was done at Fermilab with the same gun (after retrofit for a Cs_2Te cathode), without a 9-cell cavity, as will be described in this section. The next step will be further experiments with the new high

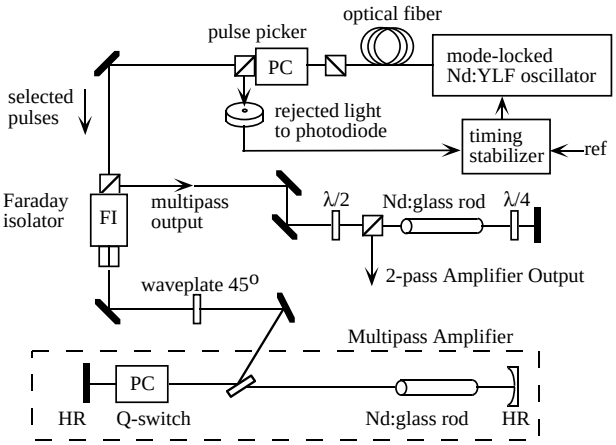

Figure 2. Block diagram of the laser system through the 2-pass amplifier.

duty cycle gun, 9-cell superconducting cavity, and chicane.

3.1 *Photo-Current Measurements*

Photo-electrons have been produced in pulse trains up to 50 μs long, as shown in Fig. 3. At present, the limit on train length is set by the laser. The maximum charge per bunch extracted from the cathode and accelerated by the gun was 30 nC, 15 nC, and $\sim$1 nC for trains of 1, 9 and 50 bunches, respectively.

The maximum beam energy measured with the spectrometer was 4.7 MeV, with a corresponding RMS energy spread of 5 to $8 \cdot 10^{-3}$. The normalized horizontal and vertical emittances were 9π and 7π mm $\cdot$ mrad, respectively, as measured via a quadrupole scan (with 10 bunches, 1.2 nC/bunch, 4.5 MeV).

A scan of rf phase shows the expected peak of transmitted current around the operating phase (Fig. 4). Direct measurements of jitter show the laser-rf jitter to be less than 10 ps, which is the limiting resolution of the measurement.

A preliminary round of measurements was done with the BPM's, ICT's, Faraday cups, and the OTR screen. Various problems were identified, e.g. amplitude modulation in the low-level rf system and inadequate alignment of the gun and focussing solenoids to the beam line.

3.2 *Dark Current Measurements*

A large amount of dark current was generated in the first rf gun after retrofit. Since field emission is strongly dependent on the rf field strength, one would expect that the dark

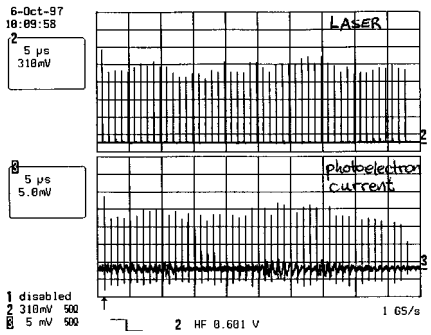

Figure 3. UV light incident on the cathode (top) and beam current (bottom) as a function of time (5 μs/division). Vertical scales are uncalibrated.

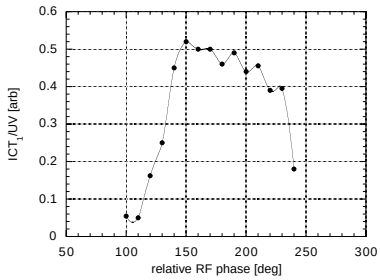

Figure 4. Normalized beam current versus rf phase.

current is generated at nearly full field, and thus emerges at full energy, but with a large energy spread. This was confirmed in spectrometric measurements. With the focussing solenoids set to image the emission on a screen downstream of the gun, it was inferred that the dark current was emitted primarily near the edge of the cathode, where a toroidal spring provides the rf contact between the cathode and the Cu wall of the gun.

In the second generation gun, the measured dark current is smaller by a factor of 20 at E_c = 38 MV/m. We attribute this to careful cleaning procedures and to the use of a slightly different geometry and a new type of spring; however, the measurements on the second gun were made 0.2 m further downstream, which may account for some of the difference. Further tests on the new gun are underway.

4 PLANNED EXPERIMENTS

In addition to those described below, experiments are planned on the measurement of the longitudinal charge distribution of short bunches and on channelling acceleration.

4.1 Chicane Operation

In order to qualify the facility for future high-brightness applications, it is necessary to further compress the bunch length using a magnetic compressor, or chicane. While this procedure is routine, there are issues that need to be studied, including the effect of strong space charge forces on the transport through the chicane [7].

4.2 Plasma Accelerator Experiments

A key test of the plasma wake field accelerator (PWFA) [8] is planned among the first applications of this facility. Since the beam is of such high brightness, it provides an excellent driver of plasma waves in the PWFA, and should be the most definitive test of the achievable gradient to date. A plasma of $1–3 \cdot 10^{13}$ cm^{-3} is created in a target chamber located in a low-β section of the beamline, shown in Fig. 5. Expectations are that gradients of 1 GeV/m should be achievable in this plasma.

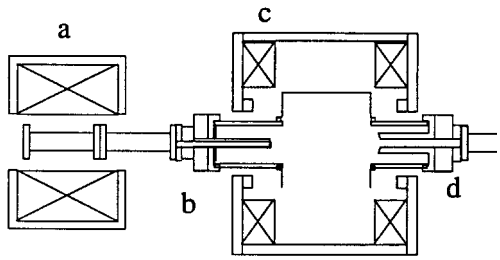

Figure 5. Plasma target chamber for PWFA, consisting of (a) matching solenoid, (b) cathode assembly, (c) plasma vessel with confinement solenoid, and (d) anode assembly. The plasma is generated between the 2 coaxial electrodes.

5 CONCLUSIONS

A flexible, high-brightness photoinjector is under construction; it will provide an intense source of electrons for a variety of experiments. Initial experiments with a prototype rf gun have shown the expected beam properties, albeit accompanied by relatively large dark current. A second-generation gun has shown a promising reduction in dark current. Further work is now in progress to commission a chicane, and to optimize performance. Experiments on such concepts as the plasma wake field accelerator will commence in the near future.

ACKNOWLEDGEMENTS

We thank our colleagues at Fermilab and in the TeSLA collaboration, especially S. Buhler, J. Crandall, R. H. Flora, T. Garvey, J. Gastebois, E. H. Hahn, M. Julliard, T. Junquera, T. W. Koeth, J. R. Le Duff, A. Matheisen, W.-D. Möller, W. Muranyi, F. A. Nezrick, J. R. Noonan, M. J. Pekeler, P. S. Prieto, D. Reschke, J. K. Santucci, S. N. Simrock, J. J. Urban, M. M. White, and D. A. Wolff, for their participation in and many contributions to this project.

REFERENCES

[1] D. A. Edwards, Ed., "TeSLA Test Facility Linac—Design Report," TeSLA 95-01, DESY (1995).
[2] E. Colby, "A High Charge, High Duty Factor RF Photoinjector for the Next Generation Linear Collider," these proceedings.
[3] Eric R. Colby, Ph. D. Thesis, UCLA (1997).
[4] S. Buhler et al., in *Proc. of the 7th Workshop on RF Superconductivity*, CEA/Saclay 96 080/1, p. 689–693 (1996).
[5] Alan R. Fry, Ph. D. Thesis, University of Rochester (1996).
[6] A. Fry et al., "Experience at Fermilab with High Quantum Efficiency Photo-Cathodes for RF Electron Guns," these proceedings.
[7] Bruce E. Carlsten, *Phys. Rev. E* **54**, p. 838–845 (1996).
[8] J. Rosenzweig et al., "Proposal for Staged Plasma Wake-Field Accelerator Experiment at Fermilab," P890 Proposal, Fermilab (1997).

ION SOURCES FOR THE NEW HIGH CURRENT INJECTOR AT GSI

P. Spädtke, H. Emig, K.D. Leible, C. Mühle, H. Reich, B.H. Wolf*
GSI Darmstadt

The new high current injector at GSI will replace the existing prestripper accelerator of Wideröe type by a RFQ and an IH structure [1]. This new accelerator will increase the possible particle currents by 2 orders of magnitude. For the design ion Uranium, the particle current will be increased from presently 20 pμA (U^{10+}) to 4 pmA (U^{4+}). As ion sources for such high currents, a multi cusp ion source (for gases) or a vacuum arc ion source (for metals) are foreseen. The existing Penning ion source, which is well experienced for all elements of the periodic table, will be used in the future as well and has to be improved in current performance for this new operating regime. For these ion sources two 320 kV high voltage terminals are presently used.

1 HIGH CURRENT TERMINAL

The high current terminal will be equipped either with a MEVVA (Metal Vapor Vacuum Arc)[1] ion source (for metals) or with a MUCIS (Multi cusp ion source)[2] ion source (for gases). Because of the high current required from this terminal, we have to replace the existing 320 kV/20 mA high voltage power supply by a new power supply 130 kV/150 mA.

The ion sources are already in use with the existing Wideröe accelerator, however not with the full ion current available from these sources. We had several beam times, mainly for accelerator experiments, with the MUCIS ion source (Ne^{+}, Ar^{2+}, H_3^+, D_3^+) and the MEVVA ion source (Ni^{3+}, Mg^{+}, Mg^{2+}). Total ion currents extracted from the sources were in the order of 100 mA for all ions mentioned above. The preparations and tests of the MUCIS and MEVVA ion sources are performed at a special test bench. Beside the ion source power supplies, the test bench consists of a 8m long beam transport line with two quadrupole triplets, a dipole analyzing magnet and a number of ion beam diagnostic elements. Typical ion beam currents, charge state distributions (CSD) and signal to noise ratios (S/N) measured at the test bench are listed in table 1. The listed values of total current (I_{tot}) depend on the extraction voltage (U_{ex}) applied, and are measured values for ion source settings with minimized beam noise. The S/N ratios listed in the tables are defined by the averaged ion current S and the intensity fluctuations N during a typical beam pulse [repetition rate: 1/s, duration: 1ms]. The listed CSD are for standard ion source settings. For both ion sources it is possible to shift the CSD to lower or higher mean charge state, adjustment parameters are: additional gases, magnetic fields, discharge power.

Table 1: Ion currents from the MUCIS (gases) and from the MEVVA (metals) measured at the test bench.

spec.	I_{tot} /mA	CSD ion : fraction	S/N	U_{ex} /kV
H	≈60	H^+:0.4,H_2^+:0.1,H_3^+:0.5	≤50	10
D	≈60	D^+:0.4,D_2^+:0.1,D_3^+:0.5	≤50	10
Ne	≈50	Ne^+:0.9,Ne^{2+}:0.1	≤50	10
Ar	≈80	Ar^+:0.6,Ar^{2+}:0.3	≤50	25
N_2	≈80	N^+:0.8,N^{2+}:0.2	≤50	25
Mg	≈160	Mg^+:0.5,Mg^{2+}:0.5	≤20	25
Cu	≈100	Cu^+:0.2,Cu^{2+}:0.5	≤10	25
Au	≈80	Au^{2+}:0.4,Au^{3+}:0.5	≈10	25
U	≈80	U^{3+}:0.3,U^{4+}:0.4	≈10	25

During accelerator experiments, we experienced some problems in the transport of the ion beam,whenever the beam was not stable enough along the pulse.Especially we encountered that problem with the MEVVA ion source, whereas the beam transport to the RF structure seemed to be less critical with quiet beams as extracted from the MUCIS. Because the same extraction system was used at both sources, we conclude that the problem is not an emittance problem, but a question of space charge compensation of the beam, which is much more effectiv for quiet beams. Therefore, to reduce the noise of the MEVVA source to the level achieved for the MUCIS is our main development goal.

The higher noise level of the ion beam extracted from the MEVVA ion source compared to the noise level of the ion beam extracted from the MUCIS is strongly connected to the very different plasma generation process. Whereas the homogenious plasma of the MUCIS has its origin in a quiet gas discharge, the plasma of the MEVVA has its origin in a number of non-stationary cathode spots[3, 4]. Moreover the charge state distribution (CSD) of the ions produced in a specific spot scatter during the life time (several μs) of the spot[5]. A number of modifications have been applied to quiet the MEVVA plasma and to influence the CSD[6]. Although the ion beam noise is a principle problem caused by the MEVVA plasma generation process its significance is for some metals (e.g. Al, Cu, U) more pronounced than for others (e.g. Mg, Cr).

* as guest from Australia

It was possible to produce high intensity Mg^+ and Mg^{2+} ion beams with high stability and low noise comparable to the quality of MUCIS ion beams, whereas Al^+ and Al^{2+} ion beams were very noisy with the same MEVVA setup. Mg and Al have similiar values of ionization energies, electric properties, chemical properties and similiar melting points (Mg: 648°C, Al: 660°C). The vapor pressure of these two metals are very different at the melting point (Mg: ≈ 2 mbar Al: $\approx 10^{-8}$ mbar). The boiling point is 1090 °C for Mg, and 2467 °C for Al.

There are indications from our experiments that for metals used as cathodes in the MEVVA ion source, a lower vapor pressure at the melting point results in more noisy ion beams. In comparison to the pure metals, metaloxides have usually a higher melting point but their vapor pressure curves do not differ too much from the pure metal ones. Experiments have been performed with these pure metal cathodes of Mg, Al and Cu and additional gas flows of O_2 and Ar into the MEVVA. A sufficient gas flow was chosen to allow the cathodes surfaces to be covered by Ar or to be oxidized by oxygen in the time between two MEVVA shots (repetition rate 1/s, pulse width 1 ms).

A preliminary evaluation of the experimental data showed a general decrease in ion beam noise and a shift in the CSD to lower charge states. The latter is well known and results from charge exchange processes in the residual gas (O_2, Ar), additionally, the increased residual gas pressure enhances the space charge compensation in the beam line. It could be shown that in the case of Mg the metal surface could be modifiedby oxygen. The ion beam produced from the oxidized Mg cathode surfaceremained low noisy for about 100 MEVVA shots after switching off theoxygen gas flow, whereas the ion beam noise with Ar auxiliary gasincreased instantly after the disconnection of the Ar gas flow.This measurement showed that a less noisy ion beam could be produced by the use of the higher vapor pressure metal compound MgO compared to pure metal Mg.Presently experiments with U and UO_2 are under preparation.The melting points of U and UO_2 differ drastically(U: 1130 °C,UO_2: $\approx$ 2500 °C), their vapor pressure as functionof temperature behaves similiar. The electrical conductivity of UO_2 should be high enough to make it usable as a cathode in a MEVVA ion source. Measurements of the ion beam noise and ion beam CSD will be performed in the near future.

2 PENNING ION SOURCE TERMINAL

To provide with the PIG source the same beam quality for the new acclerator as for the still existing Wideröe accelerator two general problems have to be solved. First the beam line has to be adapted to the new injection energy of 2.2 keV/u instead of 11.6 keV/u. Second, to make use of the capability of the new injector to accept ions with a m/q-value (m: ion mass, q: ion charge state) of up to 65 instead of 24, one has to improve the already shown capability of the source to produce lower charge states [7].

In the existing beam line there is a multi gap structure for the electrostatic acceleration. Experiments at an energy as low as 2.2 keV/u with the multi gap structure had shown that the focusing strength is too small to transport the beam through the accelerating tube with sufficient efficiency. Therefore a moveable single gap was designed, installed and first tests have been made (see figure 1). The gap width can be varied from 50 mm up to 250 mm without breaking the vacuum. In addition a screening electrode has been installed shortly behind the ground electrode to preserve the space charge compensation of the beam on ground potential.

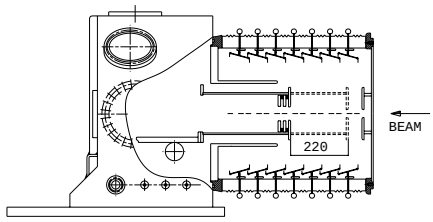

Figure 1: Sketch of the single gap structure. The most right electrode represents the high voltage potential. The moveable electrode is on ground potential. The inner diameter of the electrodes is 50 mm.

The high volatage stability of the movable single gap was tested to be very reliable. Without beam 100 % of the present available acceleration voltage (320 kV) could be applied without any breakdown. The tests with beam at the moveable single gap were carried out with Ar and Bi to have of sample of a light gas and of a heavy monoisotopic solid. For Ar^{2+} the current and emittances were measured for different gap widths. The Faraday cup (FC) and the emittance measurment device were installed about 1 m behind the single gap. The current measured in the FC behind the gap has shown a maximum value in dependence of the gap width (min. 0.9 mA max. 2.2 mA). However, it can be assumed, that this strong variation is just an optical effect (acceptance of the FC), because of the fact that losses in the order of 1 mA would create remarkable sparking in the accelerating tube. The dependence of the emittance from the gap width exhibited a not simple behaviour, created by the superposition of aberations, space charge effects and limitation by apertures. Therefore a final analysis cannot be done before a complete computer simulation is finished, which is in preparation. Furtheron Argon charge states Ar^+, Ar^{2+} and Ar^{3+} at the future injection energy (2.2 keV/u) of the new injector were compared. This showed the technical limits of the system for light ions. For Ar^{2+} the shortest possible gap width was the optimum. For Ar^{3+} the focusing was too small because of the large distance. The beam could not been focused any more. The problems for small m/q-values became obvious. Especially the splitting of extraction voltage U_{ex} and acceleration voltage U_{acc} gets difficult. On one hand one would like to increase the extraction voltage (to extract higher cur-

rents), on the other hand there is not enough voltage for the focusing any more. Further experiments were carried out with $Bi^{6+...9+}$ at optimized gap width (0.55 mA, 0.50 mA, 0.50 mA, 0.20 mA) and with Bi^{8+} with different gap widths (min. 0.25 mA, max. 0.50 mA) at the energy of 2.2 keV/u.

Almost all measured emittances of the above described experiments were within the acceptance of 140 $\pi\, mm\, mrad$ of the new RFQ-structure. Therefore, from the emittance point of view the RFQ should be accept the beam without losses. The use of the screening electrode increased the current in the FC by 5 to 10%. So we can state there is at least a partial space charge compensation. An optimization of the electrode diameters will be carried out in the beginning of the next year.

The maximum m/q-value of 65 for the new injector allows the use of lower charged ions (e.g. Bi^{4+} instead of Bi^{9+}). Therefore several experiments were carried out at the test bench. To apply high enough extraction voltages for the lower charge states the magnetic field had to be increased. The idea of changing the potential of the anti-cathode [8] (by connecting to the anode, by leaving it floating or by connecting via a resistor to cathode) to shift the CSD to lower charge states did not yield good results. With the anti-cathode on anode potential and with floating anti-cathode no ingnition at all was possible. A resistor of about 1 kΩ allowed to shift the maximum of the CSD to Bi^{4+}, but decreased the over all performance of the source. Under normal source conditions it was possible to produce a higher current of Bi^{4+}, but the maximum particle currents were observed for $Bi^{5+...7+}$ depending on the sputter gas used. Currents of about 120 pμA were measured for these ions with the standard extraction system about 1.5 m behind the source. For Au^{6+} 2 mA were measured, which corresponds to ealier measurements [9], in which 4 mA were measured with a by a factor of 2.6 enlarged extraction are. For optimized generation of charge states 5 to 7 of these ions a slightly increased source pressure was necessary. Under these conditions the source discharge was more quiet. Even at a repetition frequency as low as 1/s ignition was no problem with slightly increased heating.

To improve extractable ion currents from the source the increasing of the extraction voltage is one possibility. Because of the insulation distances in our vacuum chamber we are limited to 25 kV. Experiments with additional insulators yielded only small improvements [10]. Therefore we decided to develop an accel-decel extraction system. This gives the possibility to increase the extraction field strength without the necessity of increasing the high voltage at the source. In addition it will help to overcome the above described problem with light ions because it makes high extraction field strength at low beam energy possible. First experiments with a very simple accel-decel design were performed and showed good agreement with raytracing KOBRA3-INP [11] simulations. With +8 kV source potential and -6 kV at the accel electrode, similiar currents could be extracted as with 14 kV extraction voltage with the normal extraction system ($\approx$ 2.5 mA Ar^{2+}). Further development is focused on the cooling and the mechanical stability of the accel-decel extraction system.

3 REFERENCES

[1] U. Ratzinger, The New GSI Prestripper Linac for High Current Heavy Ion Beams, Proc. of the 1996 Linac Conf., Geneva, p. 288

[2] R. Keller, Multicharged ion production with MUCIS *in GSI Sci. Rep. 1987*, 1988.

[3] I.G. Brown, Vacuum Arc Ion Sources, Rev. Sci. Instrum., vol. 65, pp. 3061 - 3081, 1994

[4] B. Jttner, Formation Time and Heating Mechanism of Arc Cathode Craters in Vacuum, J. Phys. D: Appl. Phys., 14(1981), 1265 - 1275

[5] A. Anders et.al., Time Depend. of Vac. Arc Parameters, IEEE Trans. Plasma Sci., vol. PS-21, pp. 305 - 311, 1993

[6] E. Oks et.al., Ion CSDs in High Current Vacuum Arc Plasmas in a Magnetic Field, IEEE Trans. Plasma Sci., vol. 24, Nr.3, 1996, pp. 1174- 1183

[7] B. Gavin, PIG Ion Sources, *in The Phys. & Techn. of Ion Sources*, ed. by I. Brown, Wiley and Sons, 1989

[8] G. Korschinek et.al., A Study of Different Ion Sources for Use in the ^{205}Pb Experiment, Nucl. Instr. and Meth. in Phys. Research A271, (1988) pp. 328– 331.

[9] M. Mller et.al., Unilac Injector Improvement, *in GSI Sci. Rep. 1981*, 1982

[10] C. Mhle et.al., Development of the PIG source for higher current, Proc. of the 7. Int. Conf. on Ion Sources, Taormina, p. 1057, 1998.

[11] INP, Junkernstr. 99, 65205 Wiesbaden, Germany

ENHANCED H⁻ ION SOURCE TESTING CAPABILITIES AT LANSCE*

W. B. Ingalls, M. W. Hardy, B. A, Prichard, O. R. Sander, J. E. Stelzer, R. R. Stevens
Los Alamos National Laboratory
K. N. Leung, M. D. Williams
Lawrence Berkeley National Laboratory

Abstract

As part of the on-going beam-current upgrade in the Proton Storage Ring (PSR) at the Los Alamos Neutron Science Center (LANSCE), the current available from the H⁻ injector will be increased from the present 16 to 18 mA to as much as 40 mA. A collaboration between the Ion Beam Technology Group at Lawrence Berkeley National Laboratory (LBNL) and the Ion Sources and Injectors Section of LANSCE-2 at Los Alamos National Laboratory (LANL) has been formed to develop and evaluate a new ion source. A new Ion Source Test Stand (ISTS) has been constructed at LANSCE to evaluate candidate ion sources . The ISTS has been constructed to duplicate as closely as possible the beam transport and ancillary systems presently in use in the LANSCE H⁻ injector, while incorporating additional beam diagnostics for source testing. The construction and commissioning of the ISTS will be described, preliminary results for the proof-of principle ion source developed by the Berkeley group will be presented, and future plans for the extension of the test stand will be presented.

1 INTRODUCTION

The surface-conversion H⁻ ion source used to supply production beam at LANSCE has been in use since 1984. References [1] and [2] describe the development of this ion source. A new collaboration between LBNL and LANL has been formed to develop an ion source [3] capable of providing 40 mA of H⁻ beam to the LANSCE linac. A new test stand has been constructed at LANL to provide a place to evaluate the new ion source before it is moved to the equipment dome of the LANSCE H⁻ Ion Injector. The test stand has been constructed to duplicate as closely as possible the low energy column and beam transport system presently installed in the equipment dome of the H⁻ Injector.

2 H⁻ ION INJECTOR BEAM TRANSPORT

The 750 keV beam produced by the H⁻ Injector is obtained from a surface-conversion H⁻ ion source on an 80 keV transport system located inside the equipment dome of a 670 kV Cockcroft-Walton. As shown in the schematic representation in Figure 1, the transport system inside the dome consists of an 80 kV accelerating column and a two-solenoid transport. A beam deflector between the two solenoids permits changing the length and repetition rate of the beam pulse delivered to ground while the ion source remains operating at a 10 to 12% duty factor (835 to 1000 μsec pulse length at 120 Hz rep rate). Beam diagnostic devices in the dome consist of four current monitoring toroids placed along the 80 keV transport and slit and collector emittance gear capable of measuring emittance in the horizontal and vertical planes. The emittance station is located mid-way between the two transport solenoids.

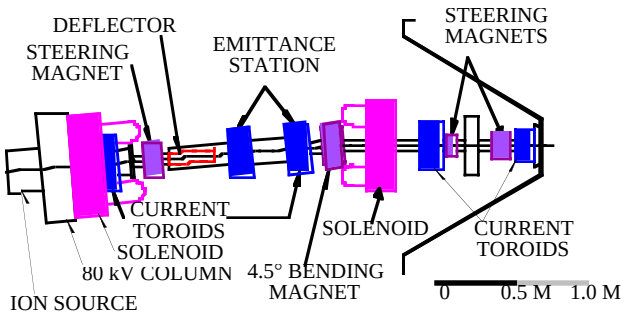

Figure 1. Schematic depiction of the major components of the 80 keV beam transport inside the LANSCE H⁻ Ion Injector.

3 ION SOURCE TEST STAND CONSTRUCTION

Constructing ISTS to duplicate the configuration of the existing H⁻ Ion Injector is highly desirable. Not only can the test stand provide an emergency supply of critical components for the injector while LANSCE is in production, but also unforeseen surprises, when a new ion source is finally moved to the injector, can be minimized by the experience gained in operating the source on a nearly identical beam transport. A test stand that closely duplicates the conditions of the H⁻ Injector dome also provides a place for off-line testing of ancillary equipment [4] that might be considered for use in the dome.

The ISTS is located in the same room that had housed an old H⁻ test stand. That stand [5] was completely removed except for its 50 KVA isolation transformer and isolated electronics racks, which were relocated in the room to provide space for the new, larger ISTS. The

* Work supported by the U. S. Department of Energy.

existing 2000 l/s turbo pump and attendant backing pumps were returned to service on the new test stand.

To begin experiments with beam early in the development of the new ion source, the construction of the initial ISTS transport was terminated at a Faraday cup installed just after the mid-transport emittance station. The remainder of the transport, including a bending magnet and second transport solenoid, will be installed later. An additional diagnostic station will also be added to measure the emittance at a distance from the transport equivalent to the entrance of the 670 kV column in the H^- Injector. The ISTS as presently constructed contains sufficient diagnostic gear to allow comparison of ISTS beam experimental results with those routinely performed during LANSCE beam production cycles in the H^- Ion Injector dome. Figure 2 shows the ISTS in its present configuration.

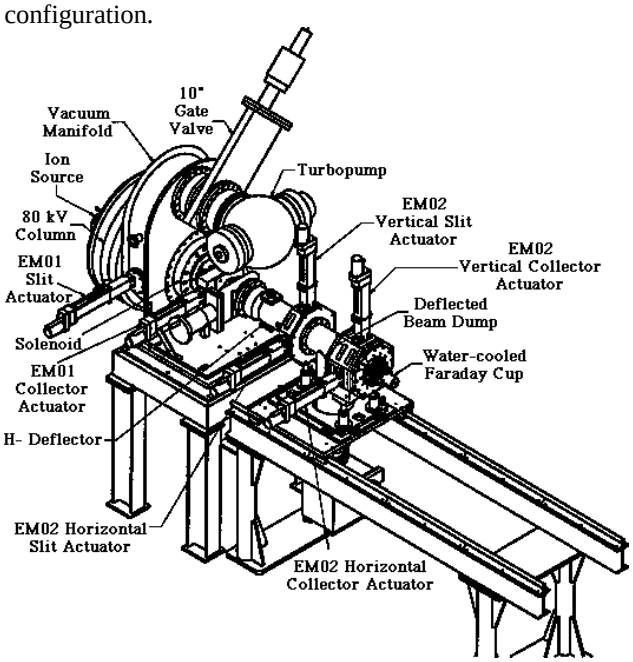

Figure 2. Isometric drawing of the beam line components assembled for the first phase of construction of the ISTS.

4 BEAM DIAGNOSTICS

4.1 Emittance Measurements

Slit and collector emittance gear identical to the gear in the H^- Injector dome was installed on the ISTS in the same relative location along the beam transport. On ISTS this gear is referred to by the acronyms EM02H for horizontal and EM02V for vertical plane. The test stand has an additional diagnostic station, not found in the H^- dome, which is used to measure the horizontal-plane beam emittance directly after the 80 kV accelerating column. This gear is referred to as the EM01H gear. There is no space available to install vertical plane actuators. A water-cooled carbon slit capable of withstanding the full duty factor of the anticipated beam (almost 400 watts) is mounted in the side of the main vacuum manifold directly after the 80 kV column. The corresponding collector is mounted just downstream of the x-y steering magnet, which follows the first focusing solenoid. Use of this diagnostic thus requires turning off the solenoid and steering magnets.

It was long thought that the 80 kV accelerating column was causing emittance growth in the dome transport, but use of this new diagnostic on the ISTS has demonstrated that the measured beam at the exit of the accelerating column is almost exactly that of the geometrical admittance of the ion source. The capability to measure emittance directly after the 80 kV accelerating column provides us with data which can be compared to ray-tracing simulations of the column dynamics. Another contribution [6] to these proceedings discusses some of these results.

4.2 Steering Magnets and Current Toroids

In the H^- Injector dome there are three sets of steering magnets located along the 80 keV transport and four current monitoring toroids. The ISTS has, at present, only one set of steering magnets, located immediately downstream of the first focusing solenoid. The primary use of the steering magnet is to sweep electron contamination out of the ion beam during emittance measurements at EM02. This same technique is used in the H^- Injector during emittance measurements.

In the H^- Injector the first two current toroids are located directly downstream of the first focusing solenoid and directly after the collectors of the emittance gear located at the mid-point of the transport. On ISTS we have exactly duplicated the second current toroid, but the inclusion of the EM01H emittance diagnostics on ISTS precluded the inclusion of a beam current toroid immediately downstream of the first solenoid. A toroid was mounted inside the vacuum manifold on ISTS and provided useful beam current information during the initial commissioning of the test stand. It did not survive the transition to a source with higher apparent electron content and has subsequently been removed.

5 COMMISSIONING

Following the cessation of LANSCE accelerator operations in mid-August of 1997, injector personnel concentrated on getting the new ISTS assembled and operational. One of the LANSCE production ion sources was mounted on the test stand for initial commissioning experiments. First beam was transported to the end of the transport on September 25, 1997 and operation of the beam current monitors and the EM02 gear was verified.

Beam current was measured at the exit of the 80 kV column and directly after the EM02 emittance gear by current toroids (1.6 m apart) with apertures of approximately 7.5 cm. The 80 keV beam is dumped into a Faraday cup with an entrance aperture of 4.4 cm. located 15 cm. after the second toroid. An additional indication of

beam current is provided by monitoring the total current drain on the 80 kV beam energy supply. Representative data of such measurements are presented in Table 1.

Table 1. Beam current measurements along the ISTS 80 kV transport. The steering magnet has been adjusted to remove the electron contamination for the data shown in the last two columns.

80 kV supply drain current, mA	80 kV column toroid, mA	Toroid after EM02 station, mA	Faraday Cup Beam Dump, mA
20	20	7.9	7
30	28	6	6
50	45	16	
40	33	16	15.6
40	32	15.2	14.8

Several hundred emittance measurements have been made to commission the operation of the ISTS emittance diagnostics and compare the results with those routinely obtained over the years in the H^- Injector dome. Agreement between H^- Injector dome data and ISTS data has generally been acceptable; emittance on ISTS is generally 5 to 10% larger than historical measurements in the dome. A sample of better agreement is presented in Table 2.

Table 2. Comparison of mid-transport emittance measurements for the ISTS and the H^- Injector dome.

Parameter	ISTS	H^- Injector
Date/Plane	5-Dec-97/H	2-May-92/H
Run Number	265	3003
E(Tot) Measured	7.305	7.627
E(Tot) Normalized	0.095	
E(RMS) Measured	1.218	1.116
E(RMS) Normalized	0.016	
Alpha	0.263	0.083
Beta	0.361	0.445

The calculated mismatch factor [7] is 0.16

Once satisfied that measurements of emittance and beam current on the test stand were in agreement with similar measurements made in the H^- Injector dome, we proceeded to test the proof-of principle (POP) ion source [3,8] that has been developed at LBNL. Further discussion of the development of this source is given elsewhere [3] at this conference.

6 INITIAL POP ION SOURCE TESTS

The Ion Beam Technology Group at LBNL developed a proof-of-principle ion source capable of producing the desired beam current of 40 mA in the Fall of 1997 [8]. The configuration of this early POP ion source evolved into the "Axial" source delivered to Los Alamos and mounted on ISTS earlier this calendar year. At LBNL at least 40 mA of 250 eV H^- current has been observed in a biased Faraday cup located directly after beam exits the ion source. In early experiments with this source we have obtained good agreement with this result in that we have observed up to 33 mA of 75 keV H^- beam through the current toroid and Faraday cup at the end of our present transport. Because the Axial source is a POP device, it does not lend itself to extensive experimentation with, for example, changes in alignment. Future measurements of its characteristics have been deferred.

7 FUTURE CONSTRUCTION

Assembly of components to complete the ISTS is underway. We will next mount a bending magnet and second solenoid to complete the duplication of the devices in the H^- Injector dome. The beam line will end with a third emittance station for studies of emittance growth and beam dynamics. Additional beam diagnostics such as current toroids will be placed along the added beam line.

8 SUMMARY

We have assembled and commissioned a test stand for H^- ion sources which closely duplicates the existing low-energy transport located in the LANSCE H^- Ion Injector equipment dome. The new test stand allows off-line measurement of ion source performance with direct comparison of results to the existing injector. The new test stand not only provides a locale to study the performance of next-generation H^- ion sources for LANSCE, but also serves as ready source of spares of critical components of our existing injector. It offers the opportunity for evaluation of H^- ion sources for others who might wish to use this new capability.

9 REFERENCES

[1] R. l. York, R. R. Stevens, Jr., R. A. DeHaven, J. R. McConnell, E. P. Chamberlin and R. Kandarian, Nucl. Instr. and Meth. B **10/11**, 891-895 (1985)

[2] K. W. Ehlers and K. N. Leung, Rev. Sci. Instrum. **51**(6), 721-727 (1980)

[3] M. Williams, et al., "Ion Source Development for LANSCE Upgrade", TU4054 of these proceedings.

[4] E. G. Jacobson, et al., "Low Stored Energy 100 kV Regulator for Ion Sources at LANSCE", TU4094 of these proceedings.

[5] R. l. York and R. R. Stevens, Jr, IEEE Trans. Nuc. Sci., **NS-30**(4) 2705-2707 (1983).

[6] R. R. Stevens, et al., "Beam Simulations for the H^- Upgrade at LANSCE", TU4053 of these proceedings.

[7] J. Guyard and M. Weiss, "Use of Beam Emittance Measurements in Matching Problems," Proc. 1976 Linear Accel. Conf., Atomic Energy of Canada, AECL-5677 (1976) p.254.

[8] A. B. Wengrow, et al., Rev. Sci. Instrum., **69**(2) 989-991 (1998).

DEVELOPMENT AND TEST RESULTS OF THE LOW-ENERGY DEMONSTRATION ACCELERATOR (LEDA) PROTON INJECTOR ON A 1.25 MeV cw RADIO FREQUENCY QUADRUPOLE*

J. Sherman, G. Bolme, L. Hansborough, T. Hardek, D. Hodgkins, D. Kerstiens, E. Meyer, J. D. Schneider, H. V. Smith, Jr., M. Stettler, R. Stevens, Jr., M. Thuot, T. Zaugg (LANL, Los Alamos, NM), A. Arvin, A. S. Bolt, M. Richards (SRS, Aiken, SC), P. Balleyguier (CEA-Bruyeres le Chatel, France), J. Kamperschroer (GA, San Diego, CA)

Abstract

The low-energy demonstration accelerator (LEDA) 75-keV proton injector is being developed for tests of high-current (100-mA) cw linacs. The injector comprises a microwave proton source and a space-charge neutralized magnetic low-energy beam-transport system (LEBT). The LEDA injector has been configured to provide flexible 50-keV beam matching into a cw 1.25-MeV radio-frequency quadrupole (RFQ) brought from Chalk River Laboratories (CRL). The LEBT has two solenoid focus magnets separated by 117 cm. Between the solenoids are two steering magnets and diagnostic stations for measuring the beam current, profile, and position. The ion-source extraction system was modified to a 50-keV triode to test the injector/RFQ system. Beam-matching tests showed that injector-RFQ transmission is 90% for 50-mA RFQ current. At the RFQ design current of 75 mA the beam transmission decreased to 80 - 85%. Optimized injector tuning led to 100-mA beam accelerated through the RFQ.

1 INTRODUCTION

In 1993, a 1.25-MeV cw RFQ designed for 75-mA beam current operation[1] was brought to Los Alamos from CRL for continuation of proton beam testing[2]. The final operation at CRL led to 55-mA current accelerated by the RFQ[3] using a direct-injection single-solenoid focus LEBT with no beam-steering capability[4]. Problems encountered using this LEBT for RFQ matching were discussed, but no further injector technology development was possible at CRL.

A more advanced proton injector is under development at Los Alamos for the LEDA project. This effort culminated in demonstration of a 75-keV, 130-mA proton injector[5] appropriate for the 6.7-MeV LEDA RFQ. After completion of the 75-keV injector demonstrations, the LEDA injector was modified to operate at 50-keV proton beam energy to make integration tests with the 1.25-MeV cw RFQ. This injector includes two solenoid focusing magnets, and two pairs of steering magnets for increased beam steering and matching flexibility to a RFQ. Modification of the ion extraction system from 75 to 50 keV led to a 50-keV injector whose operating parameters are shown in Table 1.

*Work supported by the US Department of Energy.

Table 1. 50-keV LEDA proton injector operation.

Parameter	Design	Measured
Beam current (mA)	100	150, max.
Proton fraction (%)	90	95, max.
Beam energy (keV)	50	50
2.45 GHz power (W)	600-800	1000-1500
Axial magnetic field (G)	875	875-960
Beam duty factor (%)	100	100
Emission radius (mm)	3.4	3.4
Extraction gap (mm)	8.1	8.1
Inj. $E_{rms,n}$ (πmm-mrad)	0.20	0.15
RFQ output current (mA)	75	100, max
RFQ acceptance (πmm-mrad)	0.5	

2 50-KEV INJECTOR DEVELOPMENT

The first 50-keV LEDA injector beam tests were completed on the prototype injector shown in a line drawing in Fig. 3 of ref.[5]. A microwave proton source[6] is used to generate a dense plasma with proton fractions in the 90 - 95% range[5,7]. Fifty-keV ion beam extraction was first attempted with the tetrode (four-element) extractor (Fig. 2 of ref.[5]) where the full acceleration voltage is held across a single gap between the first (plasma) and second (extraction) electrodes. The third electrode (electron trap) is held at -1500 V while the fourth electrode is at ground potential to terminate the electric fields from electrode 3. The beam-current requirement is transmission of 100-mA current through the LEBT solenoids. Only 50% beam transmission was observed with the tetrode, and the poor transmission was traced to higher beam divergence at 50 keV. The increased divergence arises from an increase of beam perveance, P_b, of the I_b=90-mA, V_b=50000-V injector P_{50keV}= $42.9X10^6(I_b(A)/V_b^{3/2})$=0.34 μP compared to the 130-mA, 75-keV injector where P_{75keV}=0.27 μP. A series of PBGUNS beam simulations comparing a triode (three-electrode accel-decel system) with the tetrode extractor is shown in Fig. 1, where the calculated maximum angle is plotted vs. P_b at fixed 50-keV beam energy. Four calculations for both extractors were done using a 9.2 mm

extraction gap with a r_{em} = 3.4 mm emission aperture radius. They are connected by solid lines. The letter "D" appended to a point indicates the extracted beam is divergent and the letter "C" indicates a convergent beam. The reduced triode divergence arises from an approximate 1-cm reduction of unneutralized space-charge beam transport achieved by the more compact triode extractor. The beam transmission through the LEBT solenoids on the prototype injector increases to > 90% when the triode

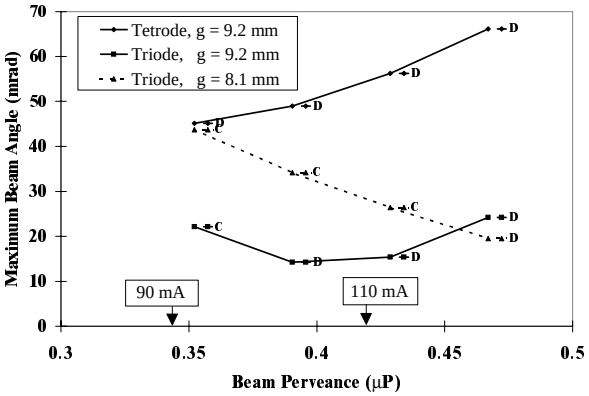

Figure 1. Maximum angle predictions from the PBGUNS code for the 50-keV ion extraction systems.

produced 90-mA beam with an extraction gap g=9.2 mm. The first focus solenoid is located 79 cm from the ion extractor, thus a beam with 45 mrad divergence (the 50-keV tetrode extractor, cf Fig. 1) at extraction position will grow to 3.5 cm radius - too large for good transmission through the 10 cm (diameter) aperture LEBT solenoids.

Baseline injector beam phase-space data using the triode extractor were accumulated on the prototype injector for use in follow-on LEBT/RFQ matching calculations[8]. These data were accumulated in dc mode, and were measured a distance of 213 cm from the ion extractor. The rms normalized emittance, $E_{rms,n}$ is 0.15 (πmm-mrad), and nearly constant over the P_b range. The data were projected back to the ion source by use of the TRACE code[9] using four times rms laboratory emittance ($4E_{rms}$). The Courant-Snyder α,β parameters extracted at the ion source are plotted vs proton beam perveance in Figs. 2 (A) and (B) respectively. The TRACE calculations used an effective transport current of $0.02I_b$ (1.8 mA) based on proton beam neutralization measurements[10]. Fig. 2(A) shows that this procedure leads to a convergent beam (α>0), which agrees with the 90 mA (0.34 μP) PBGUNS triode calculation shown in Fig. 1. The average β from Fig. 2 is 0.023 (cm/mrad) thus yielding $X_{max} = (\beta 4E_{rms})^{1/2}$ = 3.7 mm, which agrees adequately well with r_{em} = 3.4-mm.

The triode ion source was installed on a 2.54-m long version of the LEDA injector LEBT attached to the 1.25-MeV RFQ. This injector is shown in Fig. 3, and has all the ion-optical transport features of the final 2.8-m proton injector[11]. During injector operation with the g = 9.2 mm triode, it became evident that injector currents greater

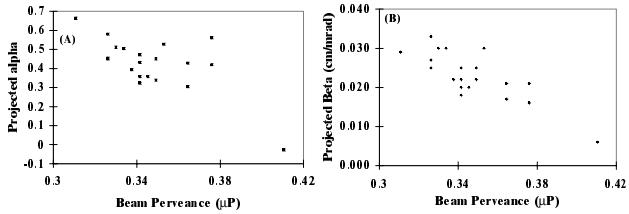

Figure 2. (A) Shows the baseline α and (B) the baseline β parameters projected to the 50-keV triode extractor installed on the prototype injector. Calculations based on these measurements are used in the 1.25 MeV cw RFQ calculations.

than 90 - 100 mA could not be efficiently transported through the LEBT, and the 75-mA RFQ design current could not be reached. As currents increased above 90 mA in DC1 the beam-profile widths in video diagnostics 1 (VD1) became unacceptably large. This has two effects: the LEBT beam transmission decreases, and the non-interceptive DC2 current monitor becomes increasingly

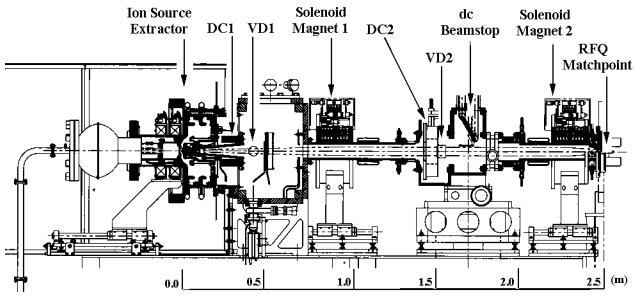

Figure 3. First version of the LEDA injector used for the 1.25 MeV cw RFQ tests.

susceptible to secondary electrons and beam plasma as the 50-keV beam approaches the vacuum wall. For these reasons, g was decreased from 9.2 to 8.1 mm. This step led to increased LEBT transmission (defined as DC2/DC1) for beam currents in the 110 - 115 mA range

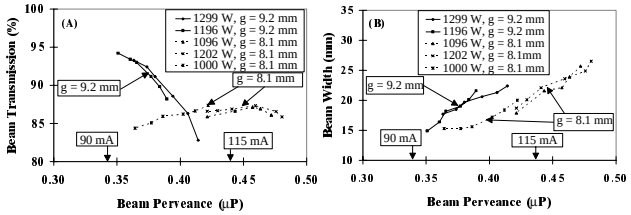

Figure 4. (A) Shows the increased beam transmission from DC1 (ion source) to DC2 (mid-LEBT), when the ion source extraction gap is decreased from 9.2 to 8.1 mm. (B) Shows the measured full-width, half maximum beam widths at VD1 for two data sets at g=8.1 and 9.2 mm extraction gaps. The lines are drawn to guide the eye.

(Fig 4(A)). The reduced extraction gap also decreased the beam size at VD1 for 110 - 115 mA beam currents (Fig. 4(B)). Plotting the beam transmissions and widths vs P_b suggests these parameters follow unique curves defined

by the extraction gap and P_b. The highest DC1 current recorded in Fig. 4 at 50 keV is 125 mA, giving P_b=0.477 μP. The improved injector optics with g=8.1 mm is also indicated in Fig. 1; the dashed curve shows that PBGUNS predicts a converging beam up to P_b=0.45 μP. The RFQ results reported below used g=8.1 mm.

3 TEST OF A 1.25 MeV cw RFQ

The basic 1.25-MeV RFQ design parameters are listed in ref. [1]. The primary diagnostic in the present measurement was to record the current transmitted through the RFQ with a third dc beam current monitor (DC3) located at the RFQ exit. See ref. [8] for a line drawing of the injector, RFQ, and CW beam dump installation. Other details on the operation of this RFQ at Los Alamos are given in ref. [12].

The RFQ transmission (%) is defined as 100(DC3/DC2). The present DC2 location tends to overestimate the RFQ input proton current which would indicate a lower-than-actual RFQ transmission. Secondary electron production and beam-plasma effects in the LEBT may also affect the accuracy of the DC2 measurement. Electrons flowing in the beam direction would produce a DC2 response lower than actual beam current, and would indicate a greater than actual RFQ transmission. An uncertainty of 5 mA in the DC2 current monitoring may be expected while the injector is operating at 75-mA RFQ design currents.

A check on the DC3 current monitor was made by doing calorimetry on the RFQ beam stop. At RFQ design current and energy there is 94-kW power in the RFQ beam. The agreement between the power measured by calorimetry and the power calculated from DC3 current assuming acceleration to full beam energy is good, varying from -6 to +2% depending on the RFQ exit quad excitation.

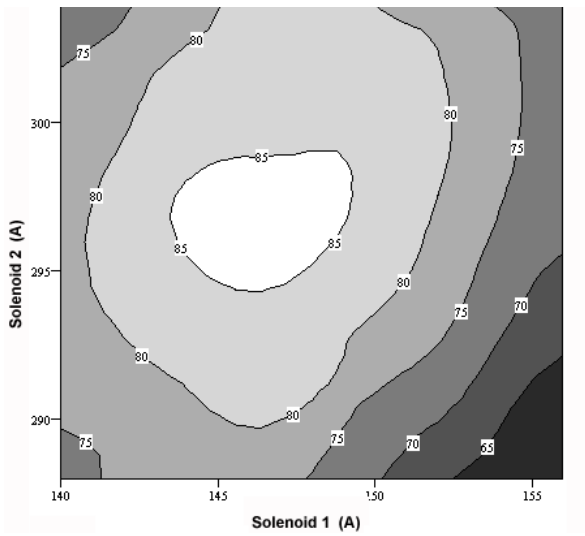

Figure 5. Contour plot of beam transmission through the 1.25 MeV RFQ as a function of the LEBT solenoid one and two currents. The RFQ is operating at 75-mA design output current for the 85% contour.

A systematic search of LEBT solenoids one and two led to the data shown in the contour plot of Fig. 5. The contour lines represent equal transmission in the solenoid tuning space. At the 75-mA RFQ design current, measured RFQ transmissions are 85%. On one occasion, while attempting to establish the maximum RFQ current, 100 mA was observed briefly in DC3. This high-current operation was limited by the injector's ability to deliver proton current to the RFQ matchpoint, and the limits of the RFQ rf power system [12]. DC1 current was 150 mA during the 100-mA RFQ current measurement. At 150-mA DC1 current, the beam is very large in the LEBT, and almost certainly the DC2 current monitor is adversely affected by secondary electron and beam plasma effects.

REFERENCES

[1] B. G. Chidley, F. P. Adams, G. E. McMichael, T. Tran Ngoc, and T. S. Bhatia, "New Vanes for RFQ1", 1990 Linear Accelerator Conference Proc., LA-12004-C, 42.

[2] J. D. Schneider, et. al., "Installation of a CW Radiofrequency Quadrupole Accelerator at Los Alamos National Laboratory, Proc. of the 1994 Linear Accelerator Conf., (Aug., 1994, Tsukuba, Japan), 149.

[3] G. M. Arbique, et. al., "Beam Parameter Measurements on the CW RFQ1-1250 Accelerator", Proc. of the 1992 Linear Accelerator Conf., (Aug., 1992, Ottawa, Ontario, Canada), 55.

[4] G. M. Arbique, et. al., "High-Current Direct Injection to a cw RFQ Using an ECR Proton Source", Proc. of the 1992 Linear Accelerator Conference., (Aug., 1992, Ottawa, Ontario, Canada), 52.

[5] Joseph Sherman, et. al., Rev. Sci. Instrum. 69(2), 1003(1998).

[6] Terence Taylor and Jozef F. Mouris, Nucl. Instrum. Methods, Phys. Res. A 336, 1 (1993).

[7] Jim Kamperschroer, "Doppler-shift Proton Fraction Measurement on a CW Proton Injector", these Conference Proceedings.

[8] H. Vernon Smith, et. al., "Comparison of Beam Simulations with Measurements for a 1.25 MeV, CW RFQ", these Conference Proceedings.

[9] K. R. Crandall and D. P Rusthoi, Los Alamos National Lab Report LA-UR-90-4146 (1990).

[10] Robin Ferdinand, et. al., "Space-Charge Neutralization Measurement of a 75-keV, 130-mA Hydrogen-Ion Beam", to be published, Proc. of the 1997 Particle Accelerator Conf., (May, 1997, Vancouver, B.C., Canada).

[11] L. D. Hansborough, et. al., "Mechanical Engineering of a 75-keV Proton Injector for the Low-Energy Demonstration Accelerator", to be published, Proc. of the 1997 Particle Accelerator Conf., (May, 1997, Vancouver, B.C., Canada).

[12] G. O. Bolme, et. al., "Proton Beam Studies with a 1.25 MeV, cw Radio Frequency Quadrupole Linac", these Conference Proceedings.

OPERATION OF A MICROWAVE PROTON SOURCE IN PULSED MODE*

T. Zaugg, C. Rose, J. D. Schneider, J. Sherman, R. Stevens, Jr.
Los Alamos National Laboratory, Los Alamos, NM 87545

Abstract

Initial beam operation of the cw radio-frequency-quadrupole (RFQ) built for the Low Energy Demonstration Accelerator (LEDA) project requires the injection into the RFQ of a 75-keV, pulsed, H^+ beam with a rise and fall time less than 10 microseconds and a pulse width from 0.1 to 1 millisecond at a repetition rate up to 10 Hz. The ion source for the accelerator is a microwave proton source driven by a 2.45-GHz magnetron. Pulsed beam for the RFQ is accomplished by modulation of the magnetron tube current. The magnetron provides microwave pulses to the ion source, and a medium-bandwidth, extraction power supply produces the H^+ ion beam using a four-electrode extractor. A similar ion source with a three-element extractor operating at 50 kV has also been tested with this magnetron modulator. We report the results of modulating the ion-source microwave power and extracting a pulsed proton beam using both a triode and a tetrode extractor.

1 INTRODUCTION

The LEDA accelerator [1] is being constructed to test and verify critical accelerating components that will be part of the Accelerator Production of Tritium (APT) plant facility. A line drawing of the LEDA ion source and extraction region is shown in Figure 1. The 75-keV injector [2] for the LEDA accelerator consists of a microwave source, a tetrode extractor and a low-energy-beam-transport (LEBT) [3] that includes two solenoid magnets. A magnetron provides 500 to 700 watts of microwave power to the ion-source plasma chamber. Two solenoid magnets in the injector produce an axial magnetic field of approximately 875 gauss to create an electron-cyclotron-resonance condition in the plasma chamber. The four elements of the tetrode extractor are the ion-source aperture electrode at 75-kV, the extraction electrode at ground, the electron suppressor electrode at -1.5-kV and a second ground electrode used to quickly establish beam neutralization.

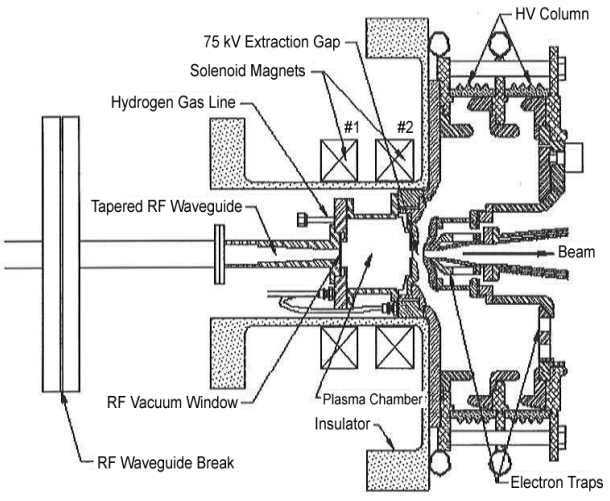

Figure 1. LEDA microwave proton source.

The current from the extraction power supply is sampled by a Pearson transformer (I_{ps}). Low-frequency components of the beam current are measured using two parametric current transformers (PCT) [4], one at the exit of the ion source (PCT1) and the second between the two solenoid magnets of the LEBT (PCT2). An ac current transformer at the exit of the ion source measures the high-frequency beam-current components. A beam stop, known as the plunging beam stop, can be inserted into the beamline between the solenoid magnets of the LEBT and also provides a means of measuring beam current (I_{pbs}).

Although dc (100% duty factor) operation is the normal operating mode, initial beam testing will be done in pulsed-mode conditions. This pulsed-mode, low-duty-factor operation is necessary to minimize equipment damage during beam impingement. The ion-source pulsing described herein is our preferred means of accomplishing this mode of operation.

2 MODULATOR DESIGN

A sketch of the magnetron modulator [5] is shown in Figure 2. A dc set point value for the desired magnetron

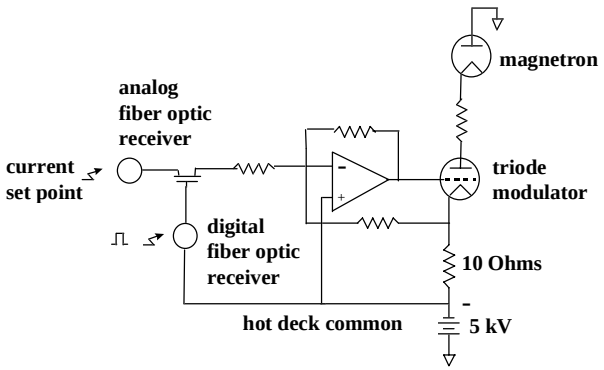

Figure 2. Magnetron current-modulator diagram.

* Work supported by the US DOE, Defense Programs.

current is compared to the voltage developed across the modulator tube's cathode resistor. The modulator acts as a current source that sets the magnetron current to zero when the digital pulse is not present and controls the magnetron current to a value determined by the set point when the digital pulse is present. The modulator tube and the feedback components are raised to the hot-deck voltage set by the -5 kV power supply. Filament supplies for the magnetron and modulator also must be isolated at this voltage level.

Our magnetron is sensitive to cathode-to-anode voltage and generates full output power variation for a few hundred volts change in voltage. Our current-controlled modulator design takes advantage of the more linear power response characteristics of the magnetron as the tube current is varied. Figure 3 shows the typical linearity of magnetron output power versus magnetron current when the magnetron is controlled by the current modulator.

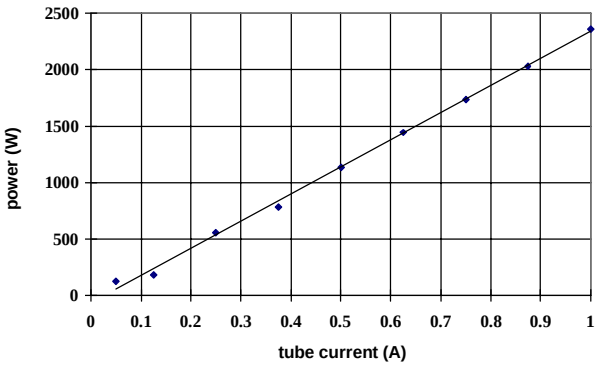

Figure 3. Microwave power versus tube current.

The output power is measured using a waveguide-directional-coupler and a calibrated diode with an error less than 0.5-db over the range of 500 W to 2500W.

3 PULSED OPERATION OF THE LEDA INJECTOR

Figure 4 shows the leading edge of the extracted beam current from the LEDA injector when the magnetron is producing a 750-W pulse. The limited bandwidths (4 kHz for PCT1 and 20 kHz for PCT2) of the two parametric current transformer devices are evident in the delayed and relatively slow risetimes seen for these two signals. Displayed difference in measured current for PCT1 and PCT2 is typical for this injector and reflects the beam-transport characteristics of the LEBT. The ac beamline transformer has a bandwidth greater than 10 MHz and droop of approximately 0.4%/μsec for a square wave of current. The plunging-beam- stop current measurement nearly equals the PCT2 measurement. (PCT2 and I_{pbs} are located close together on the beamline.)

A set of oscilloscope traces of these same five signals on the trailing edge of a 1 ms pulse is shown in Figure 5.

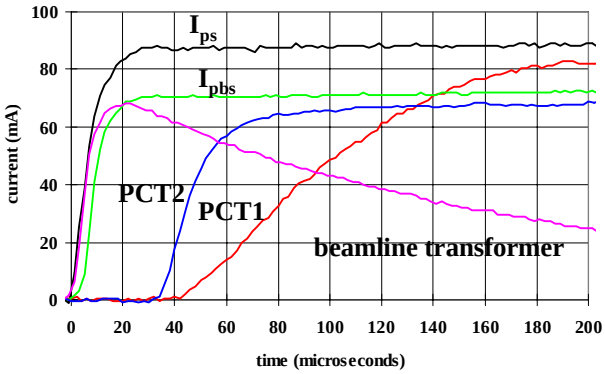

Figure 4. Leading edge of the extracted current from the LEDA injector.

The beam current response time meets the specification required for RFQ commissioning.

Longer pulse lengths show a slight rise in current as the pulse length increases. A 10 ms pulse shows a 10% increase in the current from beginning to end of the pulse. This effect is believed to be due to temperature effects in the plasma chamber that cause the source characteristics to change The flattop response of the beam current is acceptable with the modulator loop controlled around the magnetron tube current, but an improved flattop response is likely if the loop is closed around the extracted beam current

The effect of magnetron power on the extracted beam current can be seen in Figure 6. Measured values are

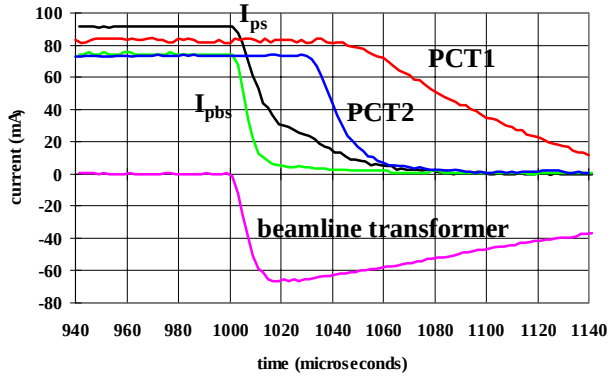

Figure 5. Trailing edge of the extracted current from the LEDA injector.

averaged over 50 samples near the end of 1 ms pulses. The solid lines are second-order polynomial fits to the data points used only to focus the eye on the trend in the data. The extractor power-supply current (I_{ps}) and PCT1 current continue to rise with increasing input power but the PCT2 and I_{pbs} currents reach a maximum value and then fall off as beam transport is affected by the beam

divergence from the source. (Standard CCD cameras are used to observe the transverse beam profile.) The measurements shown in Figure 6 were made without any

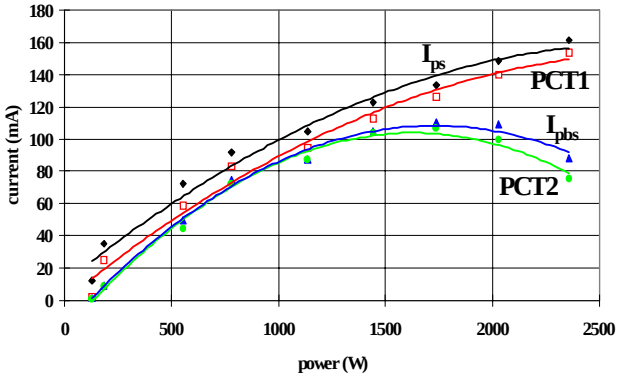

Figure 6. Beam current versus microwave power for the 75-kV tetrode extractor.

other change in the ion-source settings; the ion-source was adjusted for best operation at a microwave power of 750-W. It should be noted that a single setting is not ideal for this broad range of power.

4 PULSED OPERATION OF THE TRIODE INJECTOR

The current- modulator was also tested on a 50 kV triode injector. The LEDA microwave injector was converted from a tetrode extractor to a triode extractor. (The three elements of the triode extractor are the ion-source aperture electrode at 50-kV, an accel-decel electrode at -2.0-kV and an electrode at ground.) This injector was used to deliver a dc beam to a cw, 1.25-MeV RFQ and was conveniently available for pulsed operation into the plunging beam stop.

The time-response of the extracted beam for this injector is dramatically different from that seen for the tetrode extractor. Figure 7 is a plot of I_{ps}, PCT1, PCT2 and I_{pbs} currents with a 100 ms pulse. The extractor power supply initially supplies almost twice the current that is transported through the LEBT. Beamline current rises rapidly to about 10% of the final value and then slowly rises to its final value with a time constant of approximately 10 ms. No serious attempt has been made to discover why the extraction and transport response of the triode injector is so different from the tetrode injector. It is known that the electron suppressor voltage is not significantly affected and that electron production at the extractor electrode is not contributing to the problem.

5 SUMMARY

A linear, current-controlled magnetron modulator has been used to produce pulsed proton beams from a microwave ion source. The extracted beam from the tetrode injector produces acceptable pulsed beam for the

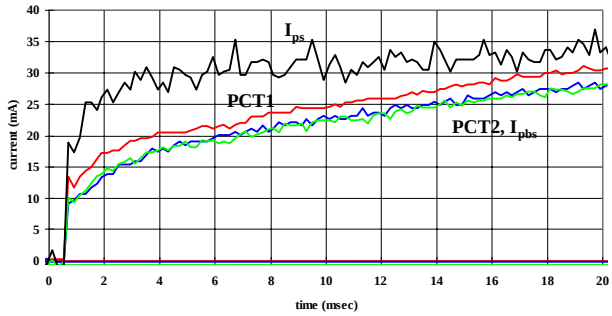

Figure 7. Leading edge of the beam current extracted from the 50-kV triode injector.

LEDA RFQ. Use of this modulator on a triode extractor is less satisfactory since extraction and transport effects cause a slowly rising beam-current pulse. Similar pulsed-beam effects from a microwave source have been observed at the Saclay laboratory [6].

REFERENCES

[1] J. D. Schneider and K. C. D. Chan, "Progress Update on the Low-Energy Demonstration Accelerator (LEDA)" Proc. of the 1997 Particle Accelerator Conf. (May, 1997, Vancouver, Canada)

[2] J. Sherman, et. al., "Status Report on a dc 130-mA, 75-keV Proton Injector", Rev. Sci. Instrum., 69 (2) , 1003 (1998).

[3] H. Vernon Smith, et. al., "Simulations of the LEDA LEBT H^+ Beam", Proc. of the 1997 Particle Accelerator Conf. (May, 1997, Vancouver, Canada)

[4] K. Unser, "A Toroidal DC Beam Current Transformer with High Resolution", IEEE Trans. Nucl. NS-28 (1981) 2344-2346

[5] C. Rose and D. Warren, "Performance and Test Results of a Regulated Magnetron Pulser", 23rd International Power Modulator Symposium, Rancho Mirage, CA, June 1998

[6] R. Gobin, et. al., "New performances of the CW High-Intensity Light Ion Source (SILHI)", to be published in the Proceedings of the 1998 European Particle Accelerator Conference, (Stockholm, Sweden)

THE FRANKFURT H$^-$ SOURCE FOR THE EUROPEAN SPALLATION SOURCE*

K. Volk, A. Maaser, H. Klein
Institut für Angewandte Physik, Universität Frankfurt, 60054 Frankfurt, Germany

Abstract

The **E**uropean **S**pallation **S**ource (ESS) requires two ion sources, each delivering a pulsed 70 mA H$^-$ beam with a pulse length of 1.2 ms and a repetition rate of 50 Hz. At the University of Frankfurt, an H$^-$ volume source based on the HIEFS (**Hi**gh **Ef**ficiency **S**ource) has been developed and tested. The source consists of a cesium seeded multicusp plasma generator, in which negative ions are produced via volume and surface processes. Due to improvements of the cesium injection method, the beam current density has been enhanced up to 153 mA/cm^2. Thus, an H$^-$ beam current of 120 mA has been extracted using an aperture radius of 5 mm.

This paper reports about these recent developments of the Frankfurt H$^-$ source. After a description of the experimental setup, measurements of the beam current density, the electron to H$^-$ ratio and the lifetime will be presented followed by a beam emittance estimation.

1 INTRODUCTION

For the ESS, two H$^-$ sources, each delivering a 70 mA H$^-$ beam in 1.2 ms pulses at a repetition rate of 50 Hz (duty cycle = 6 %) are foreseen [1,2]. The normalized rms beam emittance in front of the first RFQ should be 0.1π mm mrad or smaller. These requirements have to be fulfilled with great constancy and reliability. The source must operate over an acceptable period of time.

Within the ESS study, the Institut für Angewandte Physik of the Frankfurt University is concerned with the development of the accelerator part and especially with the development of H$^-$ ion source prototype. As promising candidate for this task, the so-called HIEFS was chosen. It was developed in Frankfurt [3] and belongs to the volume type family. In case of positive ion production (H^+, H_2^+, D^+, He^+, N^+, Ar^+, and Bi^+) this source has proven its capability to produce high current ion beams of a single mass to charge ratio at very low beam emittances (200 mA H^+ [4], 80 mA D^+ [5], 70 mA Bi^+ [6]).

2 EXPERIMENTAL SETUP

A schematic cross-sectional view of the experimental setup is shown in Figure 1. The plasma chamber of the ion source is made of a water-cooled copper cylinder. It is surrounded by 10 CoSm magnets in cusp field arrangement. Near the chamber axis, four tungsten filaments (1.8 mm diameter) are mounted. The front end of the chamber is enclosed by the plasma electrode. It is electrically connected with the anode. An electromagnet is installed in the flange of the plasma electrode. Its transverse magnetic field (B_f) acts as an electron filter.

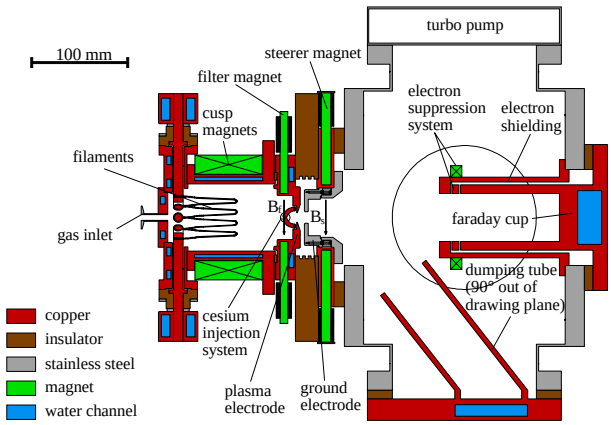

Figure 1: Schematic drawing of the experimental setup.

The arc power is provided by an array of capacitors (C_{tot} = 0.53 F) and gated by a high current switch. The used pulse generator allows arc powers up to 50 kW during 0.15 to 1.2 ms pulses and variable repetition rates from 1 to 400 Hz. Furthermore, for beam currents beyond the current limit of our extraction power supply (65 kV/300 mA), its charge also has to be accumulated in a capacitor (C = 3.5 μF). A wiring diagram of the ion source is presented in Figure 2.

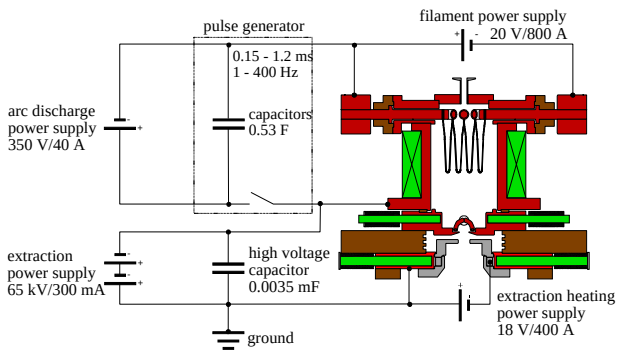

Figure 2: Wiring diagram of the H$^-$ ion source.

An external oven is mounted on the flange of the plasma electrode for introducing cesium. By means of two small pipes, the cesium vapor is deposited close to the outlet aperture. The whole system is temperature controlled.

* Work supported by BMBF under contract number 06OF841I and FZJ GmbH.

In order to extract the H^- ions, a single hole diode extraction system with an aspect ratio of 0.8 is used. A heater is integrated in the ground electrode to run the extractor at temperatures around 250 °C. That way, a cesium deposition on the ground electrode is avoided which would lead to high voltage breakdowns in the extraction gap otherwise.

As the extraction of H^- ions is always accompanied by the extraction of electrons, a device for electron beam removal is necessary. Our concept is to dump the electron beam behind the extractor at full beam energy in a water-cooled cup. Due to the extension of the filter magnet field into the gap of the extractor, the electron beam is deflected out of the beam axis. As the deflection angle of the electron beam depends on the filter field strength and the extraction energy, an additional so-called "steerer magnet" is necessary (B_s) to contrive the electron beam in the dumping tube.

The ion beam diagnostic consists of a water-cooled Faraday cup, encapsulated in a grounded screen. It is equipped with an electrostatic and magnetic electron shielding.

3 EXPERIMENTAL RESULTS

There are two dominant processes for H^- generation in this ion source: volume and surface production. Both processes can be intensified by supplying cesium to the plasma chamber [7]. In operation with cesium, the H^- emission current is up to 4.5 times higher and the e/H^- ratio is about 7 times lower compared to an operation without cesium.

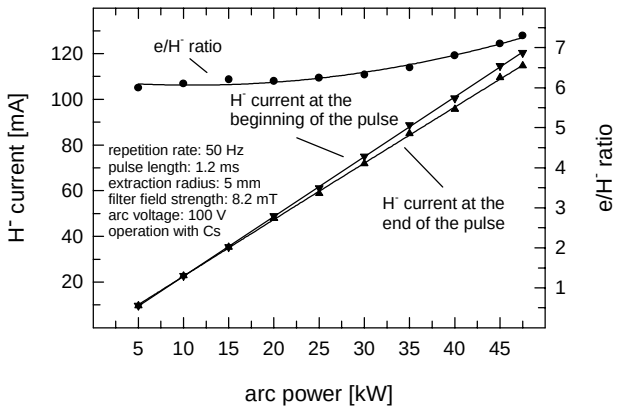

Figure 3: H^- current and e/H^- ratio vs the arc power.

Figure 3 illustrates the H^- current as function of the arc power for a cesiated source operation. The graph is split for higher arc powers: the upper graph shows the H^- current at the beginning of the pulse, the lower graph indicates the H^- current at the end of the pulse. This splitting, or current decrease during the pulse, is due to the "burn in" of the arc discharge. Especially for higher arc powers, it takes more time until the discharge achieves its balance. For an arc power of 47.5 kW, the ion source produces 120 mA H^- at the beginning of the pulse and 115 mA H^- at the end of the pulse. The former value corresponds to an emission current density of 153 mA/cm^2. In this mode of operation, the required extraction voltage for a matched beam is 33 kV (E_{gap} = 5.3 kV/mm). It is remarkable that the H^- current increases linearly as function of the arc power. Hence, a further enhancement of the H^- current is expected for arc powers beyond 50 kW. For short times 140 mA have already been achieved.

Figure 3 also shows the e/H^- ratio as function of the arc power. The plot displays a small growth rate. For full arc power the e/H^- ratio is about 7. This value corresponds to an electron current of 850 mA, equivalent to a mean electron beam power of 1.7 kW. Almost 100 % of the electron beam is captured in the dumping tube where the deposited energy of the electron beam is removed easily.

Figure 4 presents the evolution of the H^- current during a 1.2 ms pulse. After a rise time of 75 µs the curve reaches its maximum, shows a reduction of 4 %, and falls down within 35 µs.

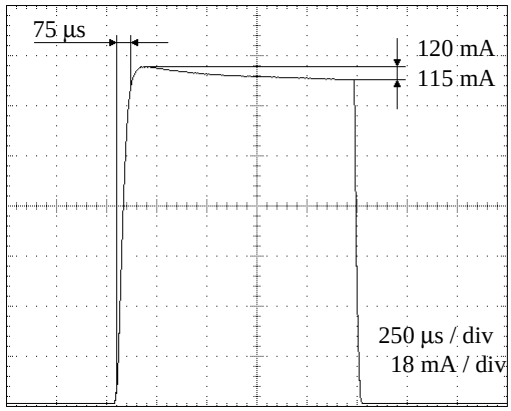

Figure 4: Oscillogram of the H^- beam.

For an arc power of 47.5 kW and a matched beam the noise level is less than 1.5 % (peak to peak). To attain such a low level, both the H^- and the electron beam must not hit any electrodes.

An ion source operation without cesium leads to a considerably faster current decrease during the pulse. Also, the beam noise level is dramatically higher.

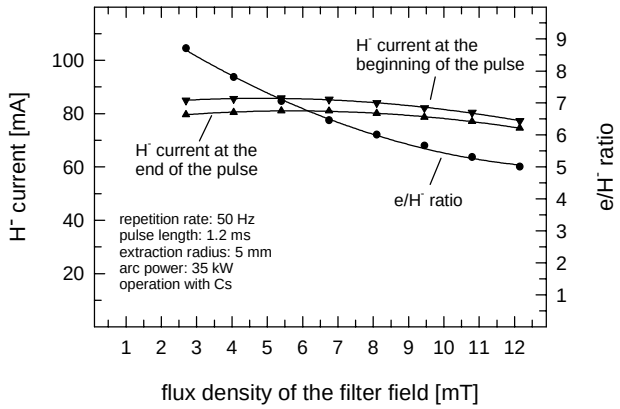

Figure 5: H^- current and e/H^- ratio vs filter field strength.

In a further experiment, the influence of the filter field strength on the H^- current and the e/H^- ratio was investigated. The measurements were made at an arc power of 35 kW. As illustrated in Figure 5, rising the filter field strength reduces the e/H^- ratio while having little influence on the H^- current. Consequently, the ion source is operated with a filter field strength of 8.2 mT.

In the course of the experiments, the dependence of the H^- current and the e/H^- ratio on the plasma electrode temperature was investigated. As depicted in Figure 6, an increase of the temperature yields higher H^- currents. For about 200 °C, the H^- current is about 1.3 times larger compared to its value at room temperature. Over the same temperature range, the e/H^- ratio drops by a factor of 2.

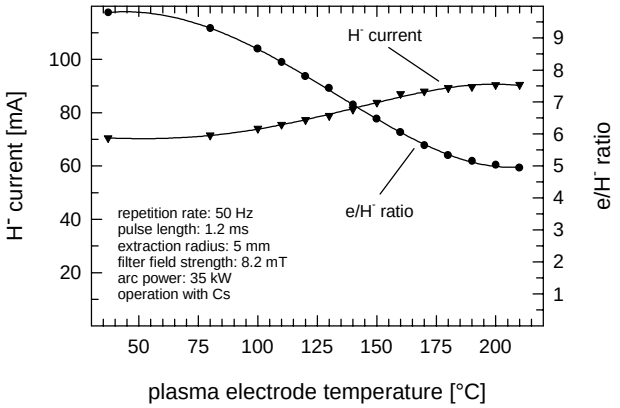

Figure 6: H^- current and e/H^- ratio vs plasma electrode temperature.

Besides a high H^- current, an appropriate ion source lifetime is another important requirement. For a given operational gas, the lifetime is limited by the wear of the filament which is approximately antiproportional to the duty cycle and the arc power. In order to obtain a long ion source lifetime, one should employ several filaments with large cross sections. This of course requires a filament power supply of the proper size. In other words, many thick filaments - which unfortunately have to be operated with a large power supply - are favorable for a long lifetime of the ion source. With the configuration described in this paper, the ion source was operated for 190 h at an arc power of 40 kW. After this time, the experiment was interrupted to check the condition of the filaments. Their diameter was reduced from 1.8 mm at the beginning to 1.5 mm. Since the filament can be used down to a thickness of about 0.9 mm, the ion source lifetime would be about 15 to 20 days.

As cesium is injected on demand only, in the normal mode of operation the injection system is off. That means, there is also a wear of the cesium layer which has to be rebuilt every 10 to 18 h. To achieve a controlled cesium deposition, a specific temperature profile of the plasma generator has to be kept. To account for this fact, the arc power has to be reduced for about 15 min. At the moment, a cesium injection system is developed, which will allow the cesium injection at high arc powers.

So far, the beam emittance has been not measured with our slit-grid emittance measurement device. Nevertheless, the H^- beam was recorded with a video camera to get a rough emittance estimation. After an optical analysis, the beam radius and the divergence angle of the 120 mA - 33 keV H^- beam could be estimated to 3 mm respectively 10 mrad. Hence, a phase space area emittance of 30π mm mrad is covered. For a KV distributed beam, the rms emittance is 7.5π mm mrad, the corresponding normalized rms emittance is 0.063π mm mrad.

4 CONCLUSIONS

In the present article, the status of the Frankfurt high duty cycle H^- ion source is described. The investigations have shown that the ion source is capable of producing a 120 mA H^- beam at an arc power of 47.5 kW (50 Hz, 1.2 ms, duty cycle = 6 %). This corresponds to an emission current density of 153 mA/cm^2. The required extraction voltage for a matched beam is 33 kV. A rough estimation indicates an excellent beam emittance of $\varepsilon_{rms,\ norm} \sim 0.06\pi$ mm mrad only. The achieved current is much lager as required for ESS, but further work has to be done to improve the lifetime of the source. A long-standing milestone is to have an ion source which satisfies simultaneously all the ion source requirements for ESS, a goal that is now within sight.

5 ACKNOWLEDGMENTS

The authors would like to thank Dr. Ka-Ngo Leung (LBNL) for the good cooperation and many fruitful discussions. We are also thank the members of the electronic lab and the mechanical workshop for their technical support as well as the ion source group members for their assistance with this work.

6 REFERENCES

[1] H. Klein, "Spallation Neutron Sources," Proceedings of LINAC94, Tsukuba, August 21-26, 1994.

[2] ESS Council, "The European Spallation Source Study, Vol. III Technical Study," ESS 96-53-M, November, 1996.

[3] K. Volk et al., "A Compact High Brilliance Ion Source for RFQ Injection," Proceedings of EPAC94, London, June 27 - July 1, 1994.

[4] R. Hollinger et al., to be published.

[5] A. Maaser et al., "Development of a D^+ source for International Fusion Materials Irradiation Facility," *Rev. Sci. Instrum.* **67** (3), 1054 (1996).

[6] M. Weber et al., "Development of a Bi^+ source for heavy ion fusion," *Rev. Sci. Instrum.* **69** (2), 1066 (1998).

[7] Ka-Ngo Leung, "Radio frequency driven multicusp sources," *Rev. Sci. Instrum.* **69** (2), 998 (1998).

IMPLEMENTATION OF IMPROVED INTERACTIVE IMAGE ANALYSIS AT THE ADVANCED PHOTON SOURCE (APS) LINAC

N. Arnold, W. Berg, S. Biedron, A. Lumpkin, S. Milton, M. White, B. Yang
Argonne National Laboratory, Argonne, Illinois 60439 USA

Abstract

An image-analysis system, based on commercially available data visualization software (IDL [1]), allows convenient interaction with image data while still providing calculated beam parameters at a rate of up to 2 Hz. Image data are transferred from the IOC to the workstation via EPICS [2] channel access. A custom EPICS record was created in order to overcome the channel access limit of 16k bytes per array. The user can conveniently calibrate optical transition radiation (OTR) and fluorescent screens, capture background images, acquire and average a series of images, and specify several other filtering and viewing options. The images can be saved in either IDL format or APS-standard format (SDDS [3]), allowing for rapid postprocessing of image data by numerous other software tools.

1 INTRODUCTION

The Advanced Photon Source [4] linear accelerator system [5] consists of a 200-MeV, 2856-MHz S-band electron linac and a 2-radiation-length-thick tungsten target followed by a 450-MeV positron linac. The linac is designed to accelerate 30-ns-long pulses containing 50 nC of electrons to an energy of 200 MeV at 48 pulses per second. The 480-W beam is focused onto a tungsten target that serves as a positron converter. Positrons [and electrons] are re-accelerated from the target to 450 MeV.

The linac was recently outfitted with a thermionic rf gun [6]. A BNL-Gun IV photocathode rf gun [7] and glass drive laser will be added in the next few months, thus allowing the linac to become a free-electron laser (FEL) driver [8]. The ability to extract accurate, on-line measurements of important beam parameters from image data has become ever more important in view of the recent upgrades, thus the imaging system has been significantly improved over the past few months. Beam emittance, profiles, spot size, and spot shape are all valuable in tuning and debugging the linac and understanding its behavior.

The APS linac's original image analysis systems were based on high-performance pipelined image processing hardware (Datacube MV20/MV200 [9]) residing in a VME crate and controlled with EPICS software. The pipeline architecture of the Datacube modules allows for pixel manipulation while the image is being digitized and routed to image memory. Additional on-board hardware provides arithmetic operations and statistical analysis. These capabilities can be used to implement many image-processing algorithms, which can function at the full 30-Hz frame rate of the incoming video.

This advanced capability has a price. In addition to a sizable investment in hardware, extensive knowledge and training are required to properly configure, program, and test the pipelined hardware. All processing must be done in the VME environment, which requires a system reboot when new features or changes are implemented. The learning curve is substantial, thus many desirable features are never actually implemented.

Since the original image analysis system was implemented five years ago, significant increases in workstation and network performance have made it feasible to accomplish limited image analysis with a workstation-based tool. The advantages are:

- Able to use high-level software, such as IDL
- Easy to modify, enhance, and debug
- User-friendly access to file systems for saving, restoring, and manipulating data
- GUI interface
- Video-capture hardware knowledge is unnecessary

The disadvantage is that speed is compromised.

Table 1 lists benchmarks of some typical image analysis operations. These statistics demonstrate that if system requirements demand frame-by-frame processing, the only solution is an image processing system designed for that task. If, however, it is sufficient to perform the analysis at a 1-Hz rate, other options can be considered.

Table 1. Benchmarks of Some Typical Image Analysis Operations

	MVME 167	**Sun Ultra 2**	**Pentium 90MHz**	**MV200 512×480**
Proc. / **Function**	68040 - 25MHz	IDL	IDL	Image Processor
Backgr. Subtr.	146 ms	14 ms	55 ms	No O/head
Sum X	263 ms	24 ms	90 ms	2.3 ms
Sum Y	166 ms	10 ms	25 ms	2.3 ms

A workstation-based image analysis program that maximizes the capabilities of our hardware was developed and is currently in use at the APS linac. It was written in IDL (Interactive Data Language), a powerful

* Work supported by the U.S. Department of Energy, Office of Basic Energy Sciences, under Contract No. W-31-109-ENG-38.

4GL application development software package for data analysis and visualization.

2 SYSTEM OVERVIEW

The existing MaxVideo MV20 image processor is used to digitize the video image in the VME chassis. Through a new EPICS record type, an "image record," the raw image data is made available to workstation-based clients via EPICS channel access. Since there is a 16-kbyte limit for each waveform in channel access, the image record presents the data as N scanlines of M pixels, where N is the vertical resolution of the camera and M is its horizontal resolution. For a typical camera of 480×512 pixels, the entire image can be fetched by retrieving 480 arrays of 512 bytes. This retrieval takes approximately 0.4 seconds on a typical 10-Mbit Ethernet network. A "smart" client will minimize retrieval time by only fetching the scanlines within a region of interest (ROI).

All other functionality is provided in an IDL application named "imageCatcher." Standard EPICS provides a library such that channel access functions can be called directly from within the IDL code. The entire raw image can be fetched with the single IDL statement:

stat = caGet(pvNames, image, max=512, type=1)

where "pvNames" is a string array of the process variable (pv) names representing each scanline, and "image" is an IDL variable for a 2-dimensional array. The user-friendly "imageCatcher" main control screen is shown in Figure 1.

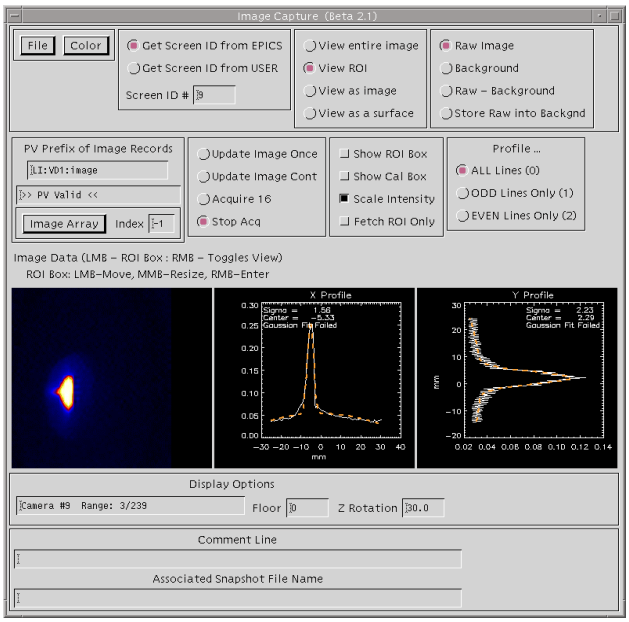

Figure 1: The "imageCatcher" main control screen. The user can easily select from several acquisition, calibration, and display options for any of the linac OTR, YAG, or Chromox screens.

The advanced IDL instruction set can easily be used to perform analysis functions on the IDL image data. Some features currently implemented in "imageCatcher" are:

- Background definition and subtraction
- Image display with pseudocolor surface view
- Surface intensity characterization with adjustable rotation and tilt
- Calculation and plotting of X and Y profiles
- Interactive screen calibration for conversion from pixels to mm
- Gaussian fit of profiles, with evaluation of fit quality
- Calculates position of peak intensity and sigma
- Performs online average of 16 consecutive images
- Saves image data in IDL or SDDS format for further analysis

The images can be saved in either IDL format or SDDS format, allowing for postprocessing of image data by other software. Figure 2 is an example of an "sddscontour" plot showing intensity versus position.

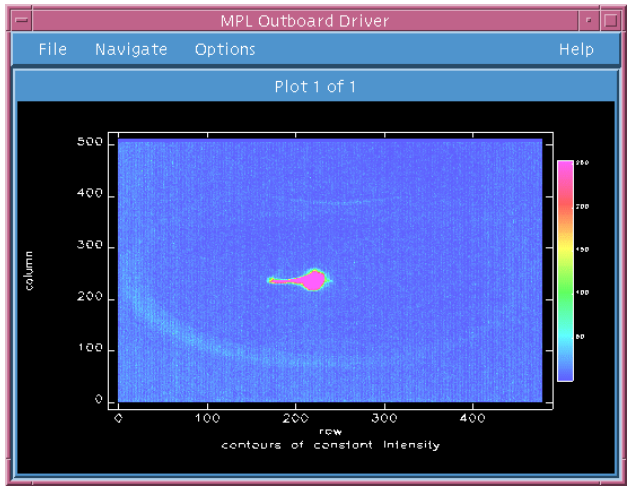

Figure 2: Contour plot of a thermionic rf gun beam spot on a Chromox screen obtained with "imageCatcher."

3 APPLICATIONS

The APS linac is equipped with 10 Chromox fluorescent screens, 2 OTR screens, and 2 YAG crystals. These screens can be viewed with any of the standard CCD or CID cameras. Bunch length data can be obtained from the OTR screens by means of a streak camera. The Chromox screens and fiducials are at 45 degrees to the beam. The calibration procedure redefines the fiducial area to compensate for any angular dependence as well as for optical alignment errors. Many of the cameras allow the user to zoom, focus, and change the iris setting; therefore, the ability to rapidly establish a calibration before capturing the image is critical. "imageCatcher" allows rapid screen calibrations to be performed and to be associated with each measurement. The screen calibration utility is shown in Fig. 3. Beam emittance, profile, spot size, and spot shape are all extremely valuable in tuning the accelerator, debugging problems, carrying out accelerator studies, and generally understanding machine behavior.

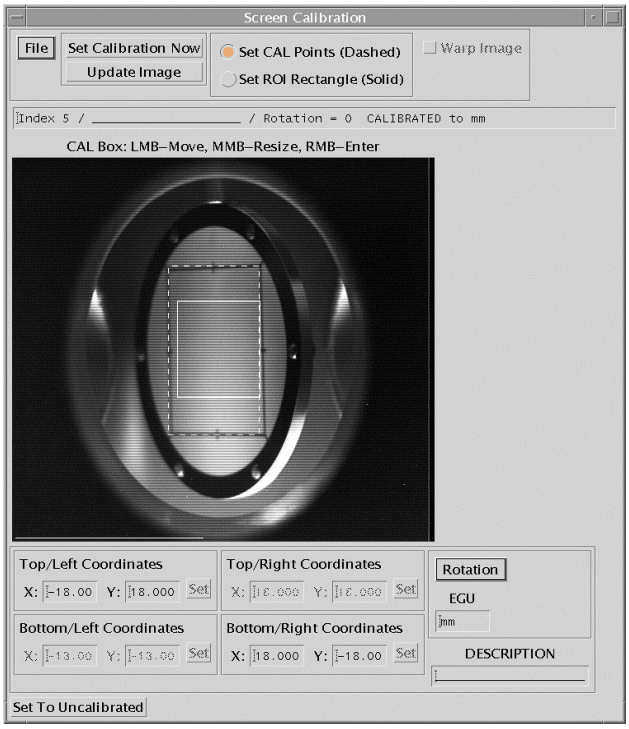

Figure 3: "imageCatcher" calibration mode is shown. The solid box is the ROI and the dashed box is the calibration box. After drawing the calibration box, known coordinates of the four corners are entered at the bottom of the screen.

Transverse profiles at each screen can be compared to beam images on the same screen or on other screens from current and previous runs.

"imageCatcher" has been used to collect data for quadrupole-scan based emittance measurements and for the characterization of Chromox (Chromium doped Al_2O_3) screens. Figure 4 shows transverse beam size data from a quadrupole-scan emittance measurement using the DC thermionic gun. Image information was saved and later processed with SDDS tools.

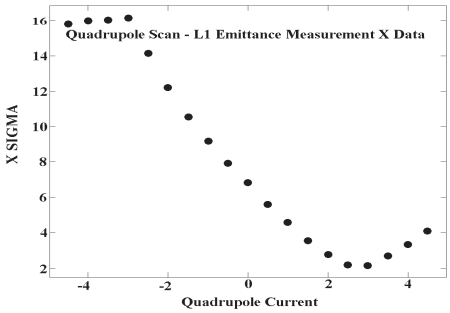

Figure 4: "imageCatcher" data; transverse beam size vs. quadrupole current, used to determine the emittance.

4 FUTURE PLANS

Future plans include upgrading the network to 100MBit, adding capability to correct the image for distortion due to the optics, and integrating "real time analysis" into the IOC so simple analysis can be done fast and more advanced analysis can be done on the workstation.

5 REFERENCES

[1] IDL, product of Research Systems, Inc., Boulder, CO www.rsinc.com.

[2] W. P. McDowell, et al., "Status and Design of the Advanced Photon Source Control System," Proc. of the 1993 Particle Accelerator Conference, Washington, DC, May 17-20, 1993, pp. 1960-1962 (1993).

[3] SDDS Reference: M. Borland, "Applications Toolkit for Accelerator Control and Analysis," Proceedings of the 1997 Particle Accelerator Conference, Vancouver, BC, Canada, to be published.

[4] 7-GeV Advanced Photon Source Conceptual Design Report, ANL-87-15, April 1987.

[5] M. White, N. Arnold, W. Berg, A. Cours, R. Fuja, A. E. Grelick, K. Ko, Y. L. Qian, T. Russell, N. Sereno, and W. Wesolowski, "Construction, Commissioning and Operational Experience of the Advanced Photon Source (APS) Linear Accelerator," Proceedings of the XVIII International Linear Accelerator Conference, Geneva, Switzerland, 26-30 August, 1996, pp. 315-319 (1996).

[6] M. Borland, "An Improved Thermionic Microwave Gun and Emittance Preserving Transport Line," Proc. of the 1993 Particle Accelerator Conf., Washington, DC, May 17-20, 1993, pp. 3015-3017 (1993).

[7] F. Sakai, X. Wang, et al., "Development of High Duty Operation Rf Photoinjector," BNL Report BNL-65003, December 1997.

[8] S. V. Milton, J. Galayda, E. Gluskin, "The Advanced Photon Source Low-Energy Undulator Test Line," Proc. of the 1997 Particle Accelerator Conference, Vancouver, BC, Canada, to be published.

[9] MaxVideo Image Processing Products, Datacube, Inc., Danvers, MA, www.datacube.com.

BUNCH LENGTH AND VELOCITY MEASUREMENT OF THE JHP-RFQ BEAM WITH INR BLVD

P. N. Ostroumov, A.V. Feschenko, V.A. Gaidach, S.A. Krioukov, A. A. Menshov
Institute for Nuclear Research, Moscow, 117312 Russia
A. Ueno
Accelerator Laboratory, High Energy Accelerator Research Organization, KEK
1-1 Oho, Tsukuba-shi, Ibaraki-ken, 305-0801 Japan

Abstract

The bunch length and velocity of a beam accelerated with the 432-MHz, 3-MeV JHP-RFQ (Japanese Hadron Project - Radio Frequency Quadrupole) linac were measured by using a Bunch Length and Velocity Detector (BLVD) developed by INR. The measured velocity (0.08002±0.00016)c showed a good agreement with the design value. The longitudinal profiles of the bunch have been measured for various setting of the RFQ. The bunch shapes of H^- beam as well as proton beam (produced by the stripping of H^- ions) have been studied. Although the BLVD has been designed for measurement of beam core (~99% of particles) the accurate study of a beam halo has been done. An almost uniformly distributed background was observed. The amount of the integrated background signal was about 1% of the beam intensity. A possible source of the background is analyzed.

1 INTRODUCTION

Well understanding of the beam characteristics output of the JHP RFQ operating at high duty cycle [1] is major step in the design of front end of the linac for future Hadron Facility [2]. For the study of longitudinal beam parameters as well as for the beam energy measurement the BLVD has been used. The design of the BLVD was based on the long-term experience of the INR group [3]. The BLVD is an extension of the Bunch Shape Monitor (BSM) to measure absolute velocity of a bunched beam [4].

2 GENERAL DESIGN OF THE DETECTOR

The technical specifications for the BLVD are shown in Table 1. The target is a tungsten wire with a diameter of 100 μm. A proton or H^- beam with energy of 3 MeV has 57.3 mg/cm^2 or 28 μm range in tungsten, therefore total beam energy will be dissipated in the target. The heating of the wire, located on the beam axis per beam pulse can be roughly estimated using the formula $\Delta T = \frac{4WI\tau}{(\pi R)^2 \rho C_p d}$, where *W[eV]* is the beam energy, *I[A]* is the beam current, *τ[s]* is the pulse duration, *R[m]* is the beam radius, *ρ[kg/m^3]* is the target density, C_p *[J/(kg·K)]* is the specific heat of the target material, *d[m]* is the target wire diameter. Assuming a beam radius to be equal to 2·rms value and using beam parameters for the most powerful beam one can get $\Delta T \approx 4700$ °K. The maximum temperature for the tungsten is restricted by thermal emission of electrons ~1500 °K. The simplest way to avoid target overheating is the use of a slit collimator upstream of the target. The 0.2 mm slit located 130 mm upstream of the target decreases the beam density at the target by a factor of 6 allowing to make safe measurements for whole beam pulse with maximum current of 40 mA and 50 Hz repetition rate, if necessary.

Table 1: BLVD specifications

1	Type of particles	H^- or H^+
2	Energy of particles	3 MeV
3	Minimum pulse current	0.1 mA
4	Maximum pulse current	40 mA
5	Pulse length	600 μs
6	Repetition rate	50 Hz
7	Accelerating frequency	432 MHz
8	Geometrical size along the beam	360 mm
9	Phase resolution at 432 MHz	2°
10	Range of phase measurements	180°
11	Accuracy of velocity measurement	0.2 %
12	Beam line aperture	32 mm

The simplified general assembly drawing of the BLVD is shown in Fig. 1. The beam to be analysed is moved perpendicularly to the plane of drawing. The BLVD consists of the following main elements: body of the detector (1), target actuator (2) with the target unit (9), rf deflector combined with electrostatic lens (3), registration unit (4), permanent magnet with adjustable field (5) to steer the electrons vertically, glider (6) with the actuator (7) to shift the longitudinal position of the detector. The extra port (8) is assigned for vacuum pump. The horizontal 0.2 mm slit is not seen in the drawing and

located 130 mm upstream of the wire. The vertical position of the slit is adjusted by a stepping motor. There is a permanent magnet located upstream of the slit. We can select one of the two positions (one is on the beam axis and the other is far from the beam axis) of the magnet remotely. By locating the magnet on the beam axis, we can bend the small amount of particles, which are not accelerated in the RFQ, far from the target. The longitudinal glider has been designed using the Linear Motion Guide Actuator manufactured by THK, the position reproducibility is ~3 μm. In order to minimise a space along the beam pipe the stepping motor of the longitudinal glider is located off-axis, parallel to the beam pipe. The glider can move the detector over the distance of $\sim\beta\lambda/2\approx 56$ mm.

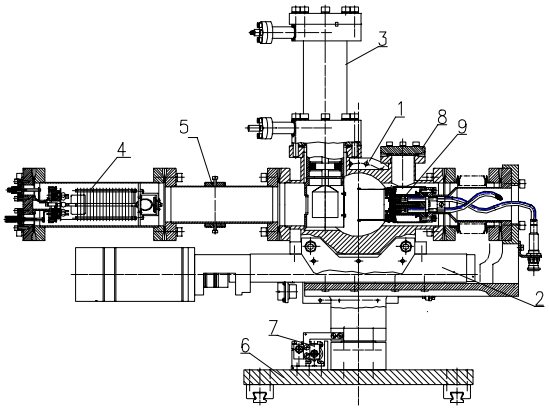

Figure1: General assembly drawing of the BLVD.

3 DATA ACQUISITION AND CONTROL SYSTEM

In order to detect secondary electrons produced on the target, a secondary electron multiplier (SEM) tube of the type of Hamamatsu R596 is used. The amplification gain of the electron multiplier can be varied within 5 orders of magnitude by changing supplied high voltage. The signal from the SEM tube is amplified by the fixed gain (0.5 V/μA) amplifier located directly on the registration unit output flange. The amplifier has an internal pulse generator to test the signal propagation. The response time of the whole signal chain is less than 1 μsec.

The control system is based on IBM PC and one CAMAC crate. Special electronic modules are housed in an additional NIM crate. There are two modes of the measurements. In the 'fast' mode the phase of the deflecting field is varied with the beam pulse and the bunch shape is measured within a beam pulse. It means that the different points of the longitudinal intensity distribution are taken along the beam pulse. In the 'slow' mode the phase is varied between the beam pulses and different points of the bunch shape are obtained for different beam pulses. In this case digitizing of the signals with 1 μsec intervals for each phase position enables to find behavior of the longitudinal distribution during the beam pulse. Obviously this procedure requires the stability from pulse-to-pulse which is perfectly provided by the accelerator.

The software for control and data acquisition system for the detector has been developed using new 32-bit version of the MOON Lab technology running under Microsoft Windows95, developed at the INR [5]. While processing the detector control and acquiring data, the software can post-process and present the data.

4 RESULTS

After the commissioning of the BLVD and optimum setting of its parameters the 3-MeV beam accelerated by the 432 MHz RFQ has been studied. The RFQ beam parameters are rather different from those in Table 1, mainly due to the performance of the ion source under development. The typical peak beam current, the maximum repetition rate and the maximum pulse length were 13 mA, 25 Hz and 300 μs respectively. In order to avoid the sputtering problem of the collimator slit, the measurements were performed with the pulse length shorter than 130 μs. Under these conditions, the wire also survives with any repetition rate less than 25 Hz. (Therefore, the collimator slit was used in order to study the relationship between the bunch shape and the vertical position.)

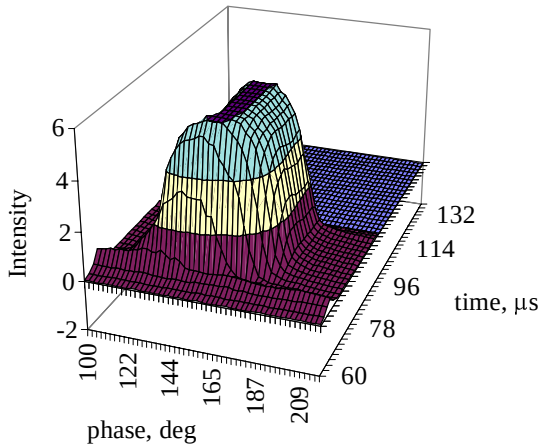

Figure 2: Bunch shape evolution along beam pulse.

In Fig. 2 the bunch shape evolution along the beam pulse is shown. Duration of the beam pulse injected to the RFQ was longer than the rf pulse length. The rf filed in the RFQ has been well stabilized on the top of beam pulse but there was some rf field parameters distortion in the transient. Therefore the bunch center at the beginning of the pulse is shifted in phase and due to the low level of the accelerating field in the beginning of pulse there is a fraction of unaccelerated particles. As for the top of the rf pulse from theory it is very unlikely to have unaccelerated particles after the long 3-MeV RFQ. However it was found that about (1÷2)% of integrated signal arises from the almost uniformly distributed in phase background. The insertion of the 1000 Gs bending

magnet upstream of the BLVD do not indicate any reduction of the background. It was supposed that the possible source of the background is the contribution of the detached electrons from H^-. In order to avoid the contribution of the detached electrons 1 μm aluminum foil has been installed upstream of the target. The passage of the H^- beam through the foil produces a proton beam without any change of the longitudinal charge distribution. In order to measure bunch shape in wide dynamic range the measurements have been done with different gains of the SEM tube using the calibration curve. The measured particle fractions as a function of phase half-width for H^- and proton beams are shown in Fig. 3. The bunch shape of the proton beam in logarithmic scale is shown in Fig. 4. These measurements show that the background noise for proton beam is smaller than that for H^- beam (see Fig. 3), however the longitudinal tail containing ~1% of particles still remains.

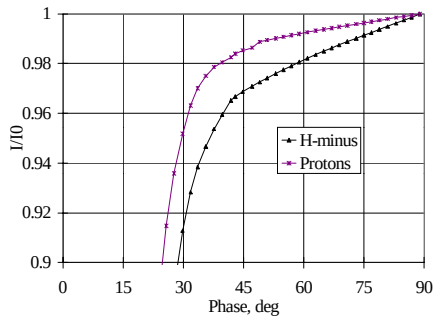

Figure 3: Particle fraction as a function of phase half-width for H^- and proton beams.

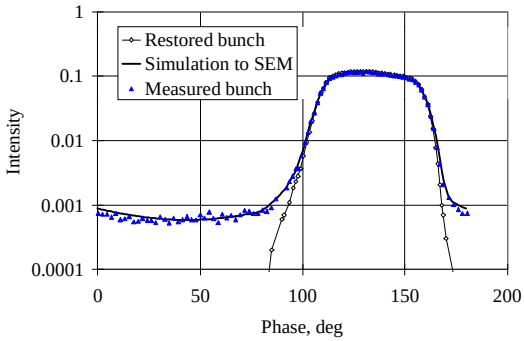

Figure 4: Bunch shape of proton beam in logarithmic scale.

Both of the H^- and proton beams have a similar longitudinal density distributions except of the halo region. The proton beam contains much less particles in the halo, but still has long tail. In order to understand the source of such signal, the secondary electron beam motion has been analyzed. A possible reason of the background formation is an interaction of the electrons with the edge of the collimator installed at the entrance of the deflector. This interaction results in increasing of energy dispersion as well as scattering of the small part of secondary electrons. In addition the beam optics can produce some aberrations. All these effects result in a diffusion of the electron beam on the detector. The secondary electron distribution $f(V_{st})$ as a function of the steering voltage V_{st} applied to the deflector plates has been measured without any rf field in the deflector. For ideally focused electron beam this function must be very narrow distribution without any background. However, in practice the very low level of background signal has been observed for whole range of steering voltage. It confirms the existence of scattered secondary electrons. The function $f(V_{st})$ has been used in order to exclude the systematic error in the measurements. Fig. 4 shows the "restored" bunch shape after excluding systematic error and the simulated bunch shape which is produced numerically using the "restored" bunch and the function $f(V_{st})$. For the restored bunch shape the bunch width on the base (see Fig. 4) is ±50° which corresponds to $3.27 \cdot \Delta\varphi_{rms}$. Where $\Delta\varphi_{rms}$ is the rms bunch width.

An ability of the target displacement across the beam provides possibility to obtain transverse parameters of the beam by processing the results of the standard measurements taken at different position of the target. The transverse profiles have been measured for different rf power levels in the RFQ. There is no change of the beam transverse position with rf power variation which means that the RFQ is well aligned and there is no transverse coherent oscillation.

The total error of energy measurement is ±12 keV (rms error is 0.13%) (including calibration of BLVD glider, statistical error due to multi bunch measurements, finding of the bunch center using longitudinal density distribution). The output energy of the RFQ is (3.02 ± 0.012) MeV which is equal to the design value.

5 CONCLUSION

A detector for the measurement of the bunch shape and average velocity for 3-MeV JHP RFQ has been developed and built. The detector has been successfully commissioned and is being used for the studies of the RFQ beam parameters.

6 REFERENCES

[1] A.Ueno et al. Beam Test at the Pre-Injector and the 3-MeV H^- RFQ with a New Field Stabilizer PISL. Proc. of LINAC96, Geneva, 1996, p. 293.

[2] Y.Yamazaki et al. JHF Accelerator Design Study Report, KEK Report 97-16.

[3] S.K. Esin et al. INR Activity in Development And Production of Bunch Shape Monitors, Proc. of the 1995 PAC and Int. Conf. on High-Energy Accelerators, Dallas, 1-5 May, 1995, V.4, p. 2408.

[4] P.N. Ostroumov. Average Velocity Measurement of Accelerated Beam by Means of an Upgraded Bunch Length Detector. INR Preprint - 812/93.

[5] S.A. Kryukov, On-Line and Off-Line Multi-Dimensional Data Presentation, Proc. CHEP'97, Berlin, p. 109.

ROLL BAR X-RAY SPOT SIZE MEASUREMENT TECHNIQUE*

R. A. Richardson, T. L. Houck
Lawrence Livermore National Laboratory, Livermore, California 94550 USA

Abstract

A time dependent x-ray spot size measurement is critical to understanding beam target physics such as target plasma generated beam instabilities. The so-called roll bar measurement uses a heavy metal material which is optically thick to X-rays, to form a 1D shadow of the x-ray origination spot. This spot is where an energetic electron beam interacts with a high Z target to produce the x-rays. The material (the "roll bar") has a slight radius to avoid alignment problems. If a beam profile is assumed (or measured by other means), the equivalent x-ray spot size can be calculated from the x-ray shadow cast by the roll bar. Typically a radiographic film is exposed over the duration of the beam pulse, and the shadow is analyzed for a time integrated measurement. This paper explores various techniques to convert the x-rays to visible photons which can be imaged using a gated camera or streak camera for time evolved x-ray spot size. Data will be presented from the measurements on the ETA II induction linac.

1 INTRODUCTION

This diagnostic is used to measure the spot size of an x-ray source. A bar that is optically thick to x-rays is used shadow the source, acting as a knife edge. This produces a shadow that is effectively the integral of the x-ray profile. We assume that the profile here is Gaussian in shape. The profiles are fitted to a erfc function, which is the integral of a Gaussian. The Gaussian assumption is verified using other diagnostics such an x-ray pinhole camera and OTR (optical transition radiation) of the focused electron beam striking the surface of an x-ray target.

The shadowed x-rays are then converted to visible photons for imaging using commercial cameras. The image is corrected for flat field using an image taken without the rollbar present. The image is averaged in the dimension orthogonal to the rollbar edge to increase photon statistics.

The full-width half maximum (FWHM) of the Gaussian (from the fitted erfc function), corrected for magnification, is reported as the spot size. The magnification of the rollbar is simply the distance from the rollbar to the x-ray image converter (scintillator) divided by the distance from the x-ray source to the rollbar (Fig. 1).

* Work performed under the auspices of the U.S. Dept. of Energy by the Lawrence Livermore National Laboratory under contract No. W-7405-ENG-48.

Limitations of this diagnostic are the blurring effects due to the finite thickness of the image converter. This can be reduced by increasing the magnification, but at a cost of reduced x-ray flux. The photon conversion efficiency is low, so that detection is marginal for short gate widths and large magnification.

2 EXPERIMENTAL SETUP

This diagnostic is used to measure the x-ray spot on the ETA II linear electron accelerator. The machine parameters are 5.5 MeV energy, 2 kA current, 50 ns pulse width. X-rays are created when the beam is focused on a (typically) 0.040" Tantalum target. The diagnostic setup (Fig. 1) consists of a heavymet (mostly Tungsten) rollbar, which is a 8x8x3 cm block with a 1 meter radius machined on one face. This bar is located a distance 108 cm from the target (x-ray source). Between the target and the rollbar is a 0.060" aluminum vacuum window. At a distance of 427 cm there is a 90x90x19 mm BC-400 scintillator. The magnification is therefore 3.95. We use a 0.010" tantalum sheet in front of the scintillator to convert the x-rays to electrons which are detectable by the scintillator. Black cloth between the tantalum and scintillator absorbs reflections.

The scintillator is imaged using a gated camera. We have used a Cohu SIT camera (10 ns gate) and a Princeton Instruments CCD camera (5 ns gate). Both cameras use a microchannel plate to intensify and gate the image.

Typically a short lead bar is placed directly in front of the scintillator-Tantalum stack orthogonal to the direction of the rollbar edge, partially blocking the x-rays. This is done to provide an edge that is representative of the blurring introduced by the scintillator and camera. The optical resolution is typically much less than the scintillator blur.

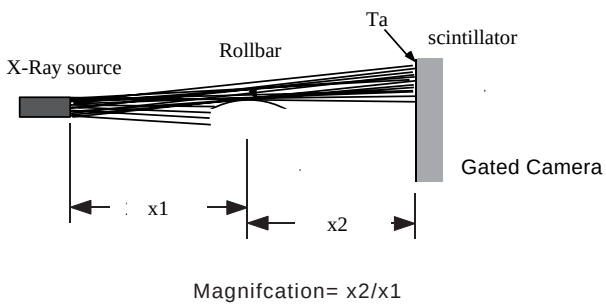

Figure 1: Sketch of rollbar diagnostic.

3 DATA

An example rollbar image is shown in Fig. 2. This is the raw scintillator image, uncorrected for flat field. The scintillator is imaged with the Princeton Instruments camera (ICCD-576). The 5 ns gate of the camera is timed to the middle of the accelerator pulse. The dark frame around the scintillator is clearly visible. The rollbar in this case is vertical, and an averaged lineout in the horizontal direction is analyzed to get the spot size of the x-ray source. The sharper horizontal shadow in the lower half of the image is due to a 0.25 inch thick lead bar placed immediately in front of the scintillator. Lineouts in the vertical direction are analyzed to approximate the blurring due to x-ray and electron scattering in the scintillator and tantalum backing, as well as optical blurring.

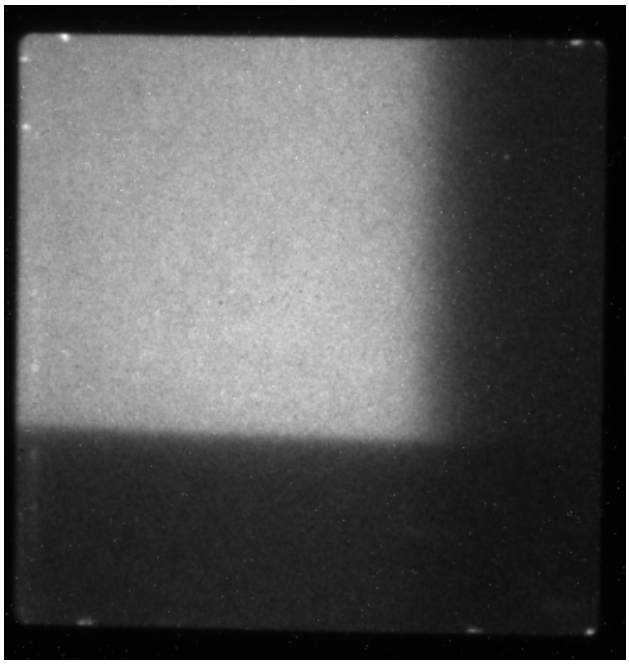

Figure 2: Scintillator image showing rollbar and edge blur x-ray shadows.

A horizontal lineout and erfc fit are shown in Fig. 3. This is the raw data, uncorrected for any blur. A lineout of the image in the vertical direction, which shows the shadow from the lead bar is shown in Fig. 4. An erfc fit is done on the data to quantify the blur produced. As expected, the fit is not perfect, but gives a representation of the spot size error, in this case around 1 mm.

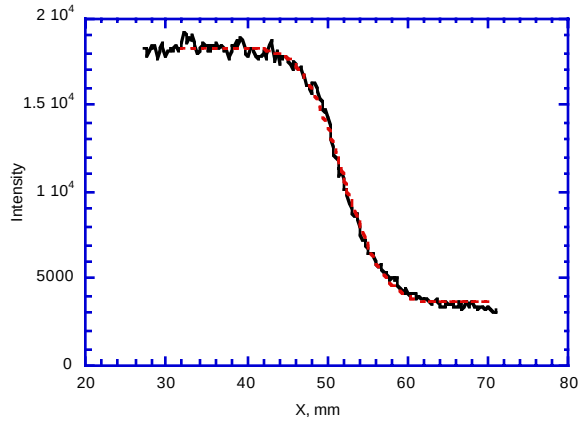

Figure 3: Rollbar data with erfc fit. Magnification=4, Gaussian FWHM = 2.4 mm.

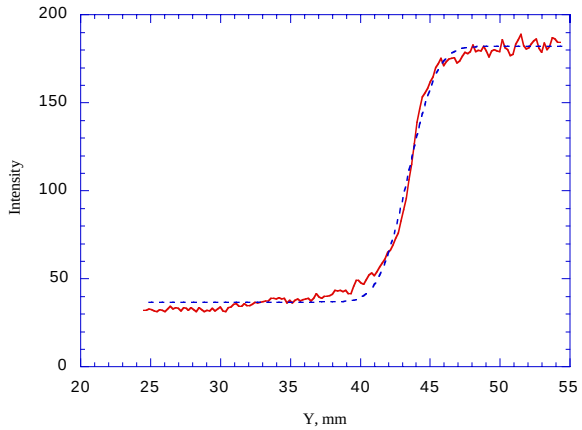

Figure 4: Scintillator blur with erfc fit. The equivalent spot size is 0.97 mm.

The scintillator blur can be corrected for by deconvolution of the data with the blur[1]. This is done using Fourier transforms of the data. First the data is smoothed and differentiated. The Fourier transform of the data is taken and normalized to give the modulation transfer function (MTF). The spot size can be obtained by finding the frequency (f_0) at which the MTF = 0.5. The equivalent Gaussian spot size is then FWHM = $0.447/f_0$. The resulting transforms are shown in Fig. 5. The spot size of 2.5 mm when corrected for scintillator blur drops to 1.9 mm. This method of spot size determination is more effected by noise. Note there is a slight difference in the uncorrected spot size when determined by FFT or erf fit to the raw data (2.5 versus 2.4 mm).

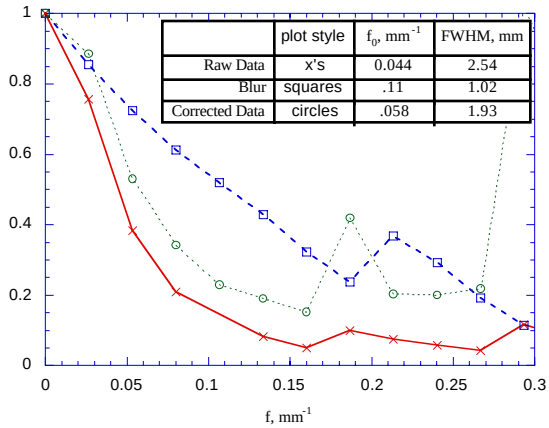

Figure 5: Fourier transforms of image lineouts, with corrected data.

4 RESULTS

The rollbar diagnostic is useful for final tuning of the accelerator. The image data is recorded real time electronically. The lineouts and fit can be done in a manner of minutes, and a tuning curve can be generated rapidly, Fig. 6.

The rollbar diagnostic can also be used to determine the time history of the x-ray spot, Fig. 7. For this data, each point represents a different shot, so some shot-to-shot stability must be assumed.

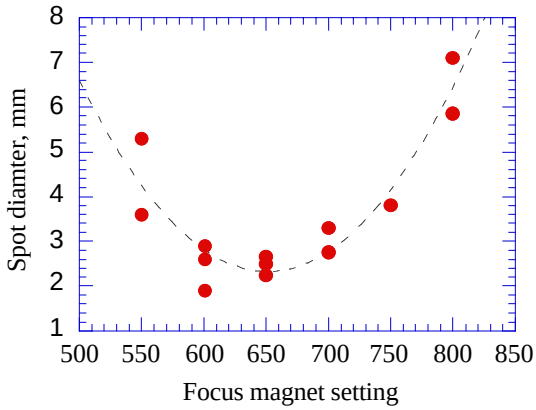

Figure 6: X-ray spot size tuning curve.

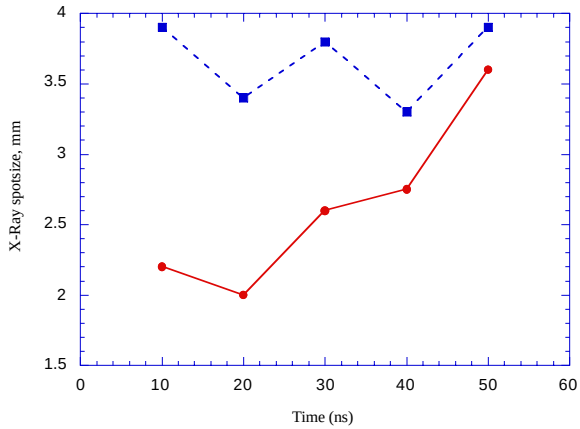

Figure 7: X-ray spot size versus time for two different magnet settings (solid and dashed curves).

5 ACKNOWLEDGMENTS

The authors wish to thank the ETA II experimental staff for their support.

6 REFERENCES

[1] N. Back., internal LLNL memo

DEVELOPMENT OF NANOMETER RESOLUTION C-BAND RADIO FREQUENCY BEAM POSITION MONITORS IN THE FINAL FOCUS TEST BEAM*

T. Slaton and G. Mazaheri
Stanford Linear Accelerator Center, Stanford University, Stanford, California 94309 USA

T. Shintake
KEK: National Laboratory for High Energy Physics, 1-1 Oho, Tsukuba-shi, Ibaraki 305 Japan

Abstract

Using a 47 GeV electron beam, the Final Focus Test Beam (FFTB) produces vertical spot sizes around 70 nm [1]. These small beam sizes introduce an excellent opportunity to develop and test high resolution Radio Frequency Beam Position Monitors (RF-BPMs). These BPMs are designed to measure pulse to pulse beam motion (jitter) at a theoretical resolution of approximately 1 nm [2]. The beam induces a TM_{110} mode with an amplitude linearly proportional to its charge and displacement from the BPM's (cylindrical cavity) axis. The C-band (5712 MHz) TM_{110} signal is processed and converted into beam position for use by the Stanford Linear Collider (SLC) control system. Presented are the experimental procedures, acquisition, and analysis of data demonstrating resolution of jitter near 25 nm. With the design of future e^+e^- linear colliders requiring spot sizes close to 3 nm [3], understanding and developing RF-BPMs will be essential in resolving and controlling jitter.

1 INTRODUCTION

Because of the small vertical spot sizes in the FFTB and a horizontal to vertical aspect ratio of almost 17 to 1, the RF-BPMs were designed to measure only vertical beam motion. At the end of the SLAC linac or entrance to the FFTB, vertical jitter is typically 30% of σy [4]. Assuming contribution to jitter from the FFTB is negligible, a design βy^* of 100 μm at the Final Focal Point (FFP) and measured $\gamma\varepsilon y$ of 1.5 μm at the entrance to the FFTB would produce vertical beam jitter on the order of 20 nm. Interest in tracking and recording this jitter led to the development of these BPMs.

Although the FFTB is equipped with 34 strip-line BPMs, each with a jitter resolution of about 2 μm at a beam intensity of 6e9 [5], a direct measurement of the jitter at the FFP is very difficult. BPMs near the FFP (in the final transformer) are $n\pi/2$ out of phase measuring only angular divergence jitter. Farther away, BPMs can be found which are in phase, but are limited by their resolution and the accuracy of the transport optics model used to project the jitter to the FFP. Another concern of using BPMs which are not in the vicinity of the FFP is structural vibrations in the final transformer that could contribute to vertical jitter and would not be detected.

To make a direct measurement of the beam's motion at the FFP a single RF-BPM was installed 6.35 cm downstream of the KEK Beam Size Monitor (BSM). Because of the RF-BPM's compactness, placement close to the FFP is possible (see table 1).

Table 1. RF-BPM parameters.

PARAMETERS OF A RF-BPM	
Frequency	5712 MHz
BPM length	50 mm
cavity length	5 mm
BPM diameter	96 mm
cavity diameter	60.07 mm
beam pipe diameter	20 mm
loaded Q factor	130
signal into 50 ohms	25 μV/nC/nm

Figure 1 shows a set of three RF-BPMs which were installed at the entrance to the final transformer, an image focal point (IMFP). The final transformer has a demagnification of 7, so the jitter will be on the order of

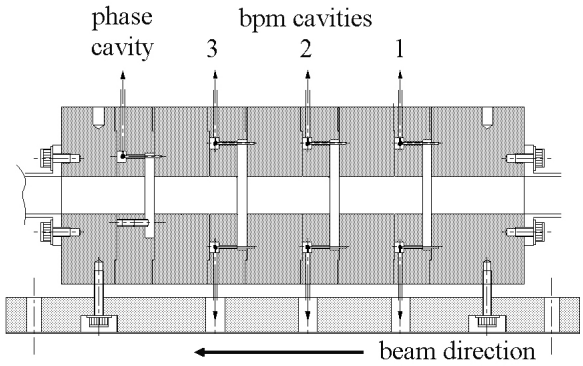

Figure 1. Mechanical drawing of the triplet RF-BPM set used for measuring the BPMs' resolutions.

* Work supported by the Department of Energy, contract DE-AC03-76SF00515.

140 nm at these BPMs. This set of BPMs is used for the resolution measurement, as well as for characterizing the beam's jitter parameters before entering the final transformer.

2 EXPERIMENT CONFIGURATION

The RF-BPMs are a typical pill box cavity design producing a signal containing four components

$$Vrf = A1qy + jA2qy' + jA3qy^{O} + Vnoise, \quad (1)$$

where q is the beam charge, y is the beam's offset with respect to the center of the cavity, y' is the beam's angle with respect to the cavity ($y'=dy/dz$), y^0 is an offset which comes from the TM_{010} signal (common mode), and j denotes the imaginary terms.

The signals from the RF-BPM are sent through a 180° hybrid that significantly reduces the second and third term in equation 1. The difference signal from the hybrid is passed into a RF receiver circuit. The RF receiver circuit is set up as a heterodyne synchronous detector that extracts the amplitude and polarity of the BPM signal. The beam induced waveform is filtered at 5712 MHz and mixed down to 500 MHz. The 500 MHz signal is then filtered, amplified, and mixed down to 50 MHz. This signal is again filtered and amplified and passed to a dual track and hold (NiTNH) module, a 16 bit digitizer with a ±2 volt limit and a 300 MHz bandwidth. The digital signal is converted into beam position and read by the SLC Control Program (SCP).

The measured dynamic range of the receiver is 51 dBm with measured noise of -82 dBm or 1 nm for a beam charge of 1 nC. The gain factor for the system is measured by moving the BPMs with respect to the beam (see section 3 below for this process).

3 DATA ACQUISITION

Before being used for data acquisition, the RF-BPMs were phased to the electron beam and a signal to position calibration constant was measured. Phasing was accomplished by using a fourth cavity which is located at the end of the triplet stack (see figure 1). Since the BPMs were phased to the beam, drifting due to timing signals were eliminated. The calibration constant was measured by moving the BPMs with respect to the beam. Calibrated linear variable differential transformers (LVDTs) measured the change in the BPM's position while the change in the BPM's signal is recorded. Within the dynamic range of the receiver, position verses signal is linear and the slope is the gain or calibration constant. This calibration constant is stored in the SCP's database for use with the BPM acquisition software. The maximum beam rate of the FFTB is 30 Hz. The signals from RF-BPMs are acquired simultaneously with the signals from standard BPMs up to the acquisition rate of 30 Hz. This allows for the comparison of the beam positions measured by the RF-BPMs to that measured by the standard BPMs.

4 DATA ANALYSIS

The top plot in figure 2 displays beam trajectories for approximately 300 machine pulses at an acquisition rate of 30 Hz. The beam's waist at the IMFP is close to the middle RF-BPM of the triplet set. With only drift spaces between the BPMs, the calculation of the slope and offset for each beam trajectory at the center BPM does not require knowledge of beam line optics. The bottom plot in figure 2 shows angles verses positions with a one sigma ellipse. This is a measurement of the jitter emittance which is equal to 1.533 μm. The equation for the emittance is

$$\varepsilon_{\text{jitter}} = \sqrt{\langle y \cdot y \rangle \langle y' \cdot y' \rangle - \langle y \cdot y' \rangle^2}, \quad (2)$$

where y is the measured position at the center BPM, y' is the measured angle using all three BPMs ($y'=dy/dz$), and <…> means an average over a series of measurements with a fixed time limit. The jitter emittance is close to one tenth of the beam emittance, which is expected for the observed beam jitter to beam size fraction of 30% in the SLC. This is an important measurement because it shows that the RF-BPMs agree with standard BPMs.

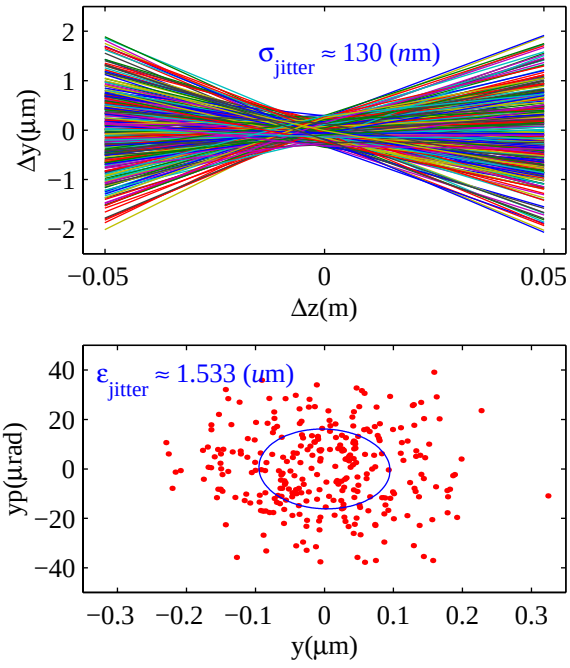

Figure 2. The top plot displays the measured beam trajectories. The bottom plot shows the calculated jitter emittance.

The resolutions of the RF-BPMs were measured using the triplet stack. With the BPMs in the triplet set being equally spaced and the beam's trajectory through them a straight line, the position from the middle BPM should equal the average of the positions from the outer BPMs. Assuming each BPM has the same resolution and uncorrelated noise, the resolution of the BPMs can be calculated from the standard deviation of the difference (residual) between the center position and the averaged positions for many beam trajectories. The equation is

$$\sigma_{bpm} = \sqrt{\frac{2}{3}}\sigma_{residual} \quad (3)$$

The first plot in figure 3 displays the distribution of the residuals with a sigma of 31 nm from a gaussian fit. This gives a BPM resolution of 25 nm for a 1 nC beam charge. The second and third plots show the time and frequency domain of the residual, respectively. It appears to be mostly white noise. The peak around 1 Hz is of some concern because it is a signature of beam motion in the SLC. The signal from the beam angle has not been completely eliminated. The fourth plot shows the integral of the residual in the frequency domain. Although the 1 Hz peak is of concern, its contribution to the overall residual is a small percentage.

If the RF-BPMs had a correlated noise source, for example a mechanical vibration or electronic noise, the resolution of the measured jitter would be understated for the rest of the beam line. To confirm the RF-BPM resolution measured by the triplet set, standard BPMs, one before and after the triplet set, were incorporated into fitting beam trajectories. All five BPMs were simultaneously fitted to the beam line model in an iterative least squares method until the resolution of each BPM converged [6]. Displayed in table 2 are the results for the triplet set and the two strip-line BPMs. The Yrslt column gives the resolutions of the RF-BPMs (The RF-BPM names are CB02 5032, 5034, and 5036).

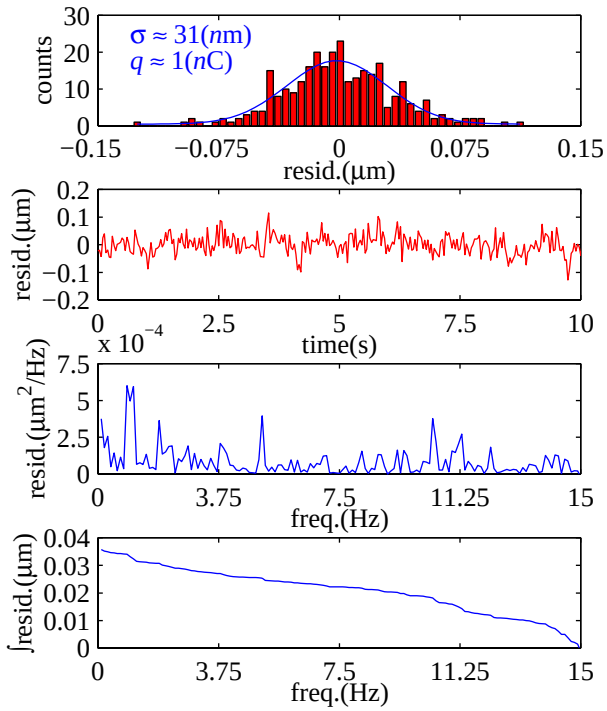

Figure 3. The histogram, time and frequency structure, and integrated amplitude of the residual from top to bottom, respectively.

Table 2. RF-BPMs resolutions.

BPMS RESOLUTIONS(μm)				
BPMS	Yest	Yrslt	Yrsdl	Yrms
CB01 5020	0.400	0.400	0.025	207.8
CB02 5032	0.045	0.045	0.040	1.8
CB02 5034	0.023	0.023	0.014	1.3
CB02 5036	0.054	0.054	0.051	1.6
CB01 5030	2.640	2.640	2.640	31.4

5 DISCUSSION AND CONCLUSION

Although the resolution of approximately 25 nm was measured for the RF-BPMs from the triplet set, the measured resolution of the RF-BPM at the FFP was around 80 nm. This is attributed to the beam's large angular divergence (460 μrad) and is not completely understood. Even though the FFP BPM was not able to measure beam motion below 80 nm, it was very efficient in minimizing beam aberrations before using the KEK BSM.

ACKNOWLEDGEMENT

The authors of this paper would like to thank Dr. David Burke for the opportunity and the beam time to develop these C-Band RF-BPMs, D. Walz for mechanical support, S. Smith, B. Traller, and K. Bouldin for electronic support, N. Spencer for control system support, and P. Raimondi for his analytical advice.

REFERENCES

[1] D. L. Burke, *et. al.*, SLAC-PUB-6609, Proceedings of EPAC 1994:23-27; V.A. Alexandrof, *et. al*, KEK-PREPRINT-9I, IEEE PAC 1995:2742-2746
[2] S.C. Hartman, *et. al.*, SLAC-PUB-95-6908, IEEE PAC 1995:2655-2657
[3] R.H. Siemann, SLAC-PUB-6244, IEEE PAC 1993:532-536
[4] T.O. Raubenheimer, SLAC-PUB-7308, Proceedings of Linac 1996:270-274
[5] H. Hayano *et. al.*, SLAC-PUB-5691, Nucl. Inst. Methods A320:47-52
[6] P. Emma, T. Lohse SLAC-CN-364

A HIGH PEAK POWER S-BAND SWITCHING SYSTEM FOR THE ADVANCED PHOTON SOURCE (APS) LINEAR ACCELERATOR (LINAC)*

A. E. Grelick, N. Arnold, S. Berg, R. Fuja, Y. W. Kang,
R. L. Kustom, A. Nassiri, J. Noonan, M. White
Argonne National Laboratory, Argonne, Illinois 60439 USA

Abstract

An S-band linear accelerator is the source of particles and front end of the Advanced Photon Source [1] injector. Additionally, it will be used to support a low-energy undulator test line (LEUTL) and to drive a free-electron laser (FEL). To provide maximum linac availability for all uses, an additional modulator-klystron subsystem has been built, and a waveguide-switching and distribution subsystem is now under construction. The combined subsystems provide a hot spare for any of the five S-band transmitters that power the linac and have been given the additional function of powering an rf gun test stand whenever they are not otherwise needed. Design considerations for the waveguide-switching subsystem, topology selection, timing, control, and system protection provisions are described.

1 DESIGN CONSIDERATIONS

The APS linac [2] uses five 35-MW peak power output, pulsed klystrons, numbered in order from L1 to L5. L1 drives the first 2856-MHz accelerating structure, located just downstream of the electron gun, and L3 drives the sixth 2856-MHz accelerating structure located immediately downstream of the positron conversion target. The L2, L4, and L5 klystrons each drive a SLED cavity assembly [3] that in turn drives four 2856-MHz accelerating structures. A sixth klystron-modulator system has been installed in the linac gallery. Design work is in progress on a waveguide distribution and switching system that will allow the sixth subsystem to serve as a hot spare for any of the others.

The most critical design issues for this system are waveguide switch reliability at 35 MW of peak power and reducing losses to an acceptable operational level.

1.1 Losses and Topology

The loss issue was addressed first because of its critical effect on system topology. A loss budget was established based on maintaining operational characteristics that should allow filling of the storage ring under almost all conditions without adding unnecessary complexity and cost. A basic requirement is to be able to provide good-quality beam at the 400-MeV positron accumulator ring (PAR)/booster-synchrotron injection energy in the event of failure of any one of the klystron-modulator systems. The loss-budget allocations are: 15% power loss at L4 and L5, 25% power loss at L1 and L2, and 25% to 40% power loss at L3. The higher loss at L3 was included specifically to allow consideration of a parallel extra-low-loss path feeding L1 and L2.

There is very little unused space in the linac gallery, restricting long waveguide runs to heights sufficient to clear most other equipment. A height of 15 feet, 4 inches, was chosen in order to allow the run to be placed in front of the klystrons while allowing adequate clearance for smooth replacement of a faulty klystron. The reference design uses WR284 waveguide, which drops down to a waveguide switch located approximately at penetration height near each klystron. This results in a total length of more than 250 feet between L6 and L1 and a predicted loss of just over half the incident power. A modified topology, using an additional waveguide switch located at the height of the main waveguide run, but above each intermediate klystron, reduces the total length to 200 feet. The predicted loss in the modified topology is reduced to 41% of the incident power. With the modified topology, the predicted loss is further reduced to 28% by changing the waveguide size to WR340. This exceeds the 25% loss-budget at L1. Losses at all other klystrons, including L4 which is critical for determining positron injection energy, are within budget. Parallel, more direct waveguide runs, especially using circular waveguide can produce lower losses at L1. However, it is hard to justify the considerable extra expense, since the loss at L4 would not be improved. To verify this reasoning, tests were made of linac operation at reduced L1 power. Reductions much greater than 28% were made without unacceptable performance degradation.

Numerous configurations were evaluated over the course of this effort. When compared to alternatives, the modified daisy-chain design in WR340 either had lower losses at all klystrons or had lower cost with equal or better loss at L4. Losses at L1, L2, and L3 have been determined to be acceptable with this design, although some higher cost designs produced lower losses at one or more of these klystrons. On the basis of the above design analysis process and supporting test results, the modified daisy-chain topology, using two waveguide switches per klystron in WR340 oxygen-free high-conductivity copper waveguide, was selected for the switching system.

* Work supported by the U. S. Department of Energy, Office of Basic Energy Sciences under Contract No. W-31-109-ENG-38.

The original design concept directed power from L6 to a full-power dummy load when L6 was not needed as a hot spare for one of the other linac transmitters. This load is still included in the current design and will be used to verify operational readiness of a transmitter that has been repaired. The addition of two more waveguide switches allows for extra flexibility in the system. Various thermionic rf guns and photocathode rf guns in the linac and in the rf gun test stand can be powered whenever the hot spare function is unused.

1.2 High-Power Reliability

Waveguide switch reliability has been the subject of an ongoing investigation. Thomson CSF indicated that they preferred not to supply 35-MW klystrons for use with SF6 pressurized waveguide because breakdown and conditioning are significant issues above 30 MW [4]. Tests conducted by ANL personnel at SLAC confirmed that breakdown occurred above that level in pressurized WR284. It was also determined that the switches can be severely damaged if breakdown occurs [5].

Two approaches have been considered to increase the power level at which breakdown occurs. The use of a circulator-dehydrator to keep the SF6 both moisture-free and moving has been successfully used at the Duke University Free-Electron Laser Laboratory for trouble-free operation at 34-MW peak power [6]. The decision to build much of the distribution waveguide in WR340 suggests a second approach for which no previous experience is known. Scaling suggests that the breakdown vulnerability threshold at 30 MW in WR284 would occur above 40 MW in WR340.

A test was performed at ANL, in which a WR340 switch was successfully operated at 35 MW using WR284 windows and pressurized tapered transitions.

Additional tests will be conducted at SLAC in the near future to quantify the difference in performance between the two waveguide sizes. In the upcoming tests, all pressurized components, including windows, will be implemented in the waveguide size under test. WR340 windows will be included in the WR340 test set-up. In-house construction of WR340 windows is now underway.

We are proceeding with a design that incorporates both of the above approaches, as shown in Figure 1. WR340 had already been selected for the major portion of the switching and distribution system. Using WR340 for essentially all of it has significant standardization advantages while incurring some additional space problems that have now been solved. Use of a circulator-dehydrator is the practical approach for a relatively large, spread out system in any event.

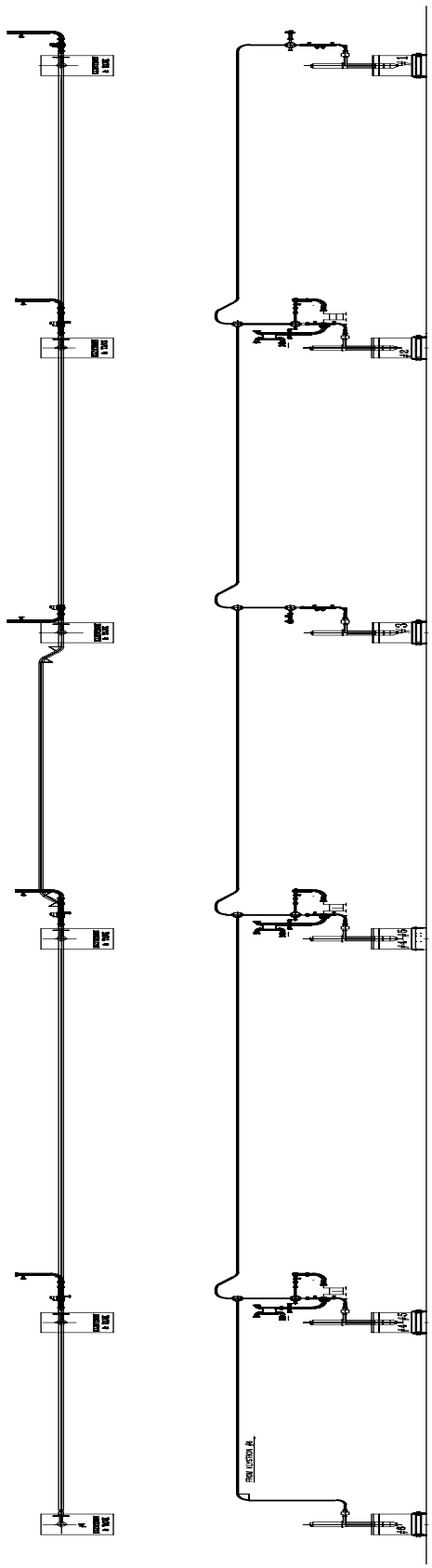

Figure 1: Mechanical layout of the klystron-switching system, by means of which the sixth klystron can be selected in place of any of the five others.

2 TIMING

Each modulator-klystron subsystem receives two modulator triggers, an rf drive gate and a SLED PSK trigger. Each trigger has unique timing requirements that are a function of trigger distribution delays, internal delays, and beam transmission time.

Therefore, a separate timing selection software window will be provided for each linac sector when driven by each allowable modulator-klystron subsystem. The switching control subsystem will provide confirmation of operational mode to EPICS [7], in order to ensure that the correct screens for the confirmed mode are active.

The linac uses two separate trigger repetition rates. The rf repetition rate is a uniform 60 Hz, or sub-multiples thereof, chosen to minimize load-regulation requirements on the modulators. The nominal rf rate is 30 Hz. The beam repetition rate and bunch pattern are completely flexible, up to a maximum of 60 Hz.

Ordinarily, each klystron is triggered synchronously at the rf repetition rate. If a klystron (L1 or L6; possibly L3 in the future) is driving an rf gun that provides beam to the linac, that klystron will be triggered at the beam rate. L6 can also drive the rf gun test stand with asynchronous, stand-alone timing.

3 CONTROL AND PROTECTION

Switching is performed under local control. The system is interlocked so that both the klystron drive and the modulator PFN voltage must be removed from all klystrons that are in the switching path. Klystron drive can be only reapplied following confirmation of successful switch transfer.

Interlocks and auxiliary reflected power protection are automatically switched in tandem with waveguide switching. SLED de-tuning needle position, water flow to the high-power rf components, and vacuum are among the categories included in the switched interlocks.

4 CURRENT STATUS

Our first priority has been the design and construction of items that support linac operation with a photocathode rf gun. Construction of a flexible rf gun test facility that can be operated without interruption, while the linac is injecting into the storage ring, is next on the priority list. Waveguide switches have been ordered. Detailed design is in progress for the main waveguide run and the L1/gun area switching. Our goal is to achieve both of these operating modes very early in 1999, and all activities are progressing well.

Switching between L1 and L6 will follow during the first half of 1999 when the initial part of the control and protection subsystem (or its prototype) can be completed and installed.

Implementation of redundancy-switching of the original five klystrons awaits detailed design and fabrication of the intermediate waveguide drops. Verification of the design and reliability of the control and protection subsystem is also a prerequisite.

5 ACKNOWLEDGMENTS

The authors gratefully acknowledge T. Jonasson for mechanical construction of the ANL test setup; D. Jefferson for instrumentation and calibration; D. Meyer and G. Trento for operation and support of the tests; H. Deleon for water support; J. Hoyt, V. Svirtun, and D. Wyncott for vacuum component setup and troubleshooting; S. Hanuska for producing the system design drawings, and C. Eyberger for editorial assistance.

6 REFERENCES

[1] 7-GeV Advanced Photon Source Conceptual Design Report, ANL-87-15, April 1987.

[2] M. White, N. Arnold, W. Berg, A. Cours, R. Fuja, A. E. Grelick, K. Ko, Y. L. Qian, T. Russell, N. Sereno, and W. Wesolowski, “Construction, Commissioning and Operational Experience of the Advanced Photon Source (APS) Linear Accelerator,” Proceedings of the XVIII International Linear Accelerator Conference, Geneva, Switzerland, 26-30 August, 1996, pp. 315-319, (1996).

[3] Z. D. Farkas et al., “SLED: A Method of Doubling SLAC’s Energy,” SLAC-PUB-1453, June 1974.

[4] J. P. Ichac, private communication.

[5] A. Nassiri, A. E. Grelick, R. L. Kustom, M. White, “High Peak-Power Test of S-Band Waveguide Switches,” Proceedings of the 1997 Particle Accelerator Conference, Vancouver, BC, Canada, to be published.

[6] P. G. O’Shea et al., “Accelerator Archaeology-The Resurrection of the Stanford Mark-III Electron Linac at Duke,” Proceedings of the 1995 Particle Accelerator Conference, May 1-5, 1995, Dallas, TX, pp. 1090-1092 (1996).

[7] W. P. McDowell et al., “Status and Design of the Advanced Photon Source Control System,” Proceedings of the 1993 Particle Accelerator Conference, Washington, DC, May 1993, pp. 1960-1962 (1993).

OVERVIEW OF THE APT RF POWER DISTRIBUTION SYSTEM*

M. McCarthy, T. Overett, G. Spalek, J. Tooker
General Atomics, 2237 Trinity Dr., Los Alamos, NM 87544
M. Lynch, D. Rees
Los Alamos National Laboratory (LANL), Los Alamos, NM 87544

Abstract

The Accelerator Production of Tritium (APT) [1] project requires a linac of nearly a kilometer in length. Accelerating potential for the 100-mA CW proton beam is provided by 350 and 700 MHz klystrons. The radio frequency (RF) power distribution for the planned 244 1MW klystrons has a wide range of design requirements and constraints. Efficient transport, control of phase, control of fault events, thermal dissipation and coupling considerations will be discussed. A description of the currently proposed configurations will be presented.

1 PLANT OVERVIEW

The primary purpose of the RF Power Distribution System is to safely and efficiently couple up to 244 MW of RF power to the APT linac in a reliable manner and to respond to fault conditions with minimum impact on beam operations. The APT linac will deliver a 1700 MeV 100mA CW proton beam to a tungsten based target that generates neutrons used in the production of tritium. 3.0 KG of tritium can be produced yearly at this power level. An alternative modular design has been conceived to allow the accelerator to be built in two stages. Stage 1 would produce 1.5 kilograms of tritium yearly, using 160 klystrons rather than 244. Stage 2 could be added while the accelerator is in operation if additional tritium is required. The design issues of this paper are applicable to either schedule, however, where absolute numbers are given, the number in parenthesis is for a 1.5 kilogram system.

APT will be located at the U.S. Government's Savannah River Site (SRS) near Aiken, South Carolina. The entire accelerating portion of the linac is about 1032 (735) meters in length. One MW klystrons provide the RF power that generates the accelerating potential in the cavities along the linac. The klystrons are located in a gallery that runs parallel to the linac tunnel.

The APT linac has three distinct sections with unique power coupling characteristics for the RF power. Power coupling to the linac under full beam (100 mA) conditions is designed to be optimum, i.e., no reflected power. Under off-normal (no beam) conditions, the coupling is inversely proportional to the Q of the cavity. Q is defined as the ratio of energy stored to energy dissipated per RF cycle. The three linac sections with distinct Q's are 1) the Radio Frequency Quadrapole (RFQ), 2) the low energy normal conducting (NC) section and 3) the medium and high-energy superconducting (SC) sections. The amount of reflected power from each section determines the size of the RF load necessary to absorb this power. Under start-up conditions, a three-stage process to bring the beam up to full current (100 mA) requires full RF fields in the cavities continuously.

1.1 RFQ

The RFQ follows the proton injector and its function is to bunch the proton beam while accelerating it to 6.7 MeV. Three 350 MHz klystrons drive the RFQ. It has an unloaded (no beam) match of approximately 2:1 which means about 1/3 of the incident power is reflected when no beam is present. Only two klystrons of the three are required to drive the RFQ. This redundancy allows three klystrons to operate at 67% of maximum power or two at 100%.

1.2 NC Section

Fifty-one 700 MHz klystrons drive the normal conducting section. The NC linac accelerates the beam from 6.7 to 211 MeV. The NC section is composed of one CCDTL (Coupled Cavity Drift Tube Linac) driven by a single klystron and ten 'supermodules' (either CCDTL's or CCL's (Coupled Cavity Linac)) each driven by multiple (up to seven) klystrons. The 'supermodule' technique provides redundancy by allowing beam operation even with a failure of one klystron per module. The phase of the RF power delivered to the cavities in any supermodule must be equal. The Low Level RF (LLRF) system [2] measures the phase at selected linac ports and controls the klystron phase to ensure phase alignment. The unloaded match for this section is approximately 4:1 resulting in reflected power of about 60% when no beam is present.

1.3 SC Section

One hundred fifty four (or seventy) 700 MHz klystrons drive cryomodules containing super conducting (SC) cavities. These boost the beam energy from 211 to 1700 (1030) MeV. The unloaded match is approximately 4000:1. Essentially all of the incident power is reflected when no beam is present. Each cryomodule has two, three, or four SC cavities with a pair of RF ports per cavity. The RF phase of each pair must be identical. As the phase relationship between pairs changes along the length of the linac with increasing beam velocity, the proportion of the reflected power going to RF loads changes. This complicates the placing and sizing of the loads.

*Work supported by DOE contract: DE-AC04-96AL89607.

2 RF SECTIONS

2.1 Klystron Gallery

The physical spacing of the klystrons in the gallery lines up closely with their respective coupling ports on the linac in the tunnel. Klystron garages house the klystron tubes and shield the gallery from klystron generated X-rays. The garage mechanically supports the five electric power and five water-cooling connections to the klystrons. Breaking these connections is all that is required to remove and replace a defective klystron. The water connections are at the front of the garage, the electrical connections at the rear. A trough in the concrete floor near the front of the garage contains supply and return water pipes that provide cooling water for the klystrons. This keeps the pipes short and unobtrusive.

A mezzanine running above the garages supports the control racks for the klystrons, linac magnet supplies, diagnostics and the 'transmitter' unit of the high voltage power supply (HVPS). This close proximity reduces cable length with a corresponding reduction in stored energy and enhances maintenance and troubleshooting. An HVAC duct hung under the mezzanine will connect with short spur ducts to each garage to provide cooling for the klystron solenoid coils and the garage in general. The HVPS for the klystrons sit in groups of four just across a maintenance access way and outdoors, behind the gallery building. A 95 kVDC cable from each HVPS runs through conduits in the concrete floor and up to the transmitter on the mezzanine.

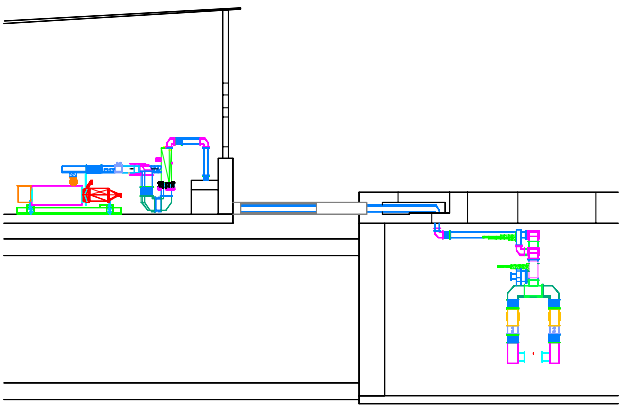

Figure1: Waveguide run between gallery and tunnel.

2.2 Waveguide System

Aluminum WR-1500 waveguide (15"x7.5") transports the 1 MW RF power from each klystron in the gallery to the linac couplers in the tunnel. A typical WG run from klystron includes the following:
1) Harmonic filter; absorbs higher order harmonics from the klystron to prevent harmful feedback. 2) Circulator; directs RF energy to the linac and routes RF energy reflected from the linac to a water load to protect the klystron. 3) Directional Couplers; detects the level of forward and reverse RF power in the waveguides, used for fault detection and phase balancing. 4) Loads: absorb incident RF power without significant reflection. 5) Magic-tees and hybrid splitters: divides RF power into two legs. 6) WG switches (remotely controlled); selects a different waveguide path. 6) Bellows; compensates for thermal expansion. 7) Linac Couplers: Air to vacuum transition between the waveguide and linac incorporates an alumina window [4]. Several waveguide components have been developed and tested [5] on the Low Energy Demonstration Accelerator (LEDA) at LANL with direct applicability for APT.

The waveguide run between the circulator and the gallery wall contains a loop which serves two functions: 1) Provide a clear walkway on the tunnel side of the gallery and 2) Provide a mechanism for equalizing the lengths of the waveguides on a supermodule by shimming. For reliability and efficiency the waveguide (WG) runs are as short, straight, and simple as feasible.

Between the klystron and the first power splitter in the tunnel, each aluminum waveguide carries 1MW with an expected loss of 250 W per foot. Waveguide temperatures of 80-100 C have been measured at English Electric Valve Ltd., in a test garage with little ventilation. In the gallery, where personnel are present, exposed waveguide should not exceed 60 C. A physical shield will envelop the guide and water-cooling is being considered. In the concrete conduit between the tunnel and gallery, the temperature may not exceed 65 C to prevent long term damage from excessive drying. An air cooling scheme forces HVAC tunnel air under and over the waveguide to keep the guide well within limits. In the tunnel, the RF power is typically divided into four equal legs before mating with the couplers. This reduces the power to the individual vacuum windows and couplers to no more than 250 KW under normal conditions. The tunnel HVAC system will be expected to handle the heat deposited such that the ambient temperature doesn't rise above 37 C. Circulating air is expected to uniformly cool individual waveguide legs such that they don't differ in temperature by more than 5 C. This last requirement ensures that differential temperatures don't contribute to significant differences in waveguide length from thermal expansion and hence RF phase differences between coupler pairs.

2.3 Phase Control

Magic-tees are four port waveguide splitters that have the characteristic of equally dividing incoming RF power between two output legs. These devices will be used to divide the RF power in the tunnel. The RF phase at each coupler pair should be equal within $\pm$ 0.5 degree. To minimize phase discrepancy, the legs to the couplers will be as short as feasible and the length of each leg uniform within $\pm$ 0.015" (standard EIA tolerance).

3 OFF-NORMAL CONDITIONS

The linac is designed such that if any klystron in a NC supermodule goes off-line, the remaining klystrons can be boosted in power to compensate. The SC linac also compensates for an RF system failure by adjustment of the RF phase and amplitude. This function is performed by the LLRF system.

The three most likely RF system faults are klystron or HVPS failure, waveguide arcs and window failure.

3.1 Klystron or HVPS failure

The klystron or HVPS is taken off line. The beam is shut off for approximately six seconds while a waveguide switch is thrown which presents the proper impedance to the cavity. If the failed klystron drives a supermodule, then the power on remaining klystrons on the supermodule is raised. If the failure is in a cryomodule, the offending cryomodule's cavity is de-tuned (no beam interaction) and the power on the remaining downstream klystrons is raised and rephased.

3.2 Waveguide arcs

An arc in the waveguide is effectively a short that will cause 100% reflection in that particular leg. This usually occurs near a window or discontinuity. The fiber optic arc detector system (part of the Low-Level RF system) shuts down the klystron and beam momentarily (<150 ms) then brings them back on. If the arc persists, the associated klystron is shut down and the waveguide switch thrown. During the arc, the klystron power is reflected into the local magic-tee load.

3.3 Window failure

Impending window failure can usually be detected by a temperature excursion at the thermal sensors. RF power to the window is shut down. If the window can be isolated and power can still be sent to other couplers driven by the same klystron, then only a coupler pair (rather than a klystron) will be taken out of service. In the event of an actual vacuum window leak, the RF and beam will be shut down. If the window is in the NC section, a vacuum gate valve may be incorporated to separate the window from the linac, and operations would resume. If the window is in the SC section, a double window is employed. The volume between the windows is evacuated, the RF is removed from the defective window, and the associated cavity is detuned (no RF from the beam will couple to the window). Beam operation can then begin with that cryomodule cavity off line.

4 SAFETY

Safety is a main driving force in the APT design. All systems must pass a rigorous safety review. A concerted effort is being made to incorporate safety by design rather than add on. Physical access, for both safety and maintenance, thermal surfaces, electrical procedures, RF and radiation, noise and ambient temperature are all factors in the overall plant safety design.

For radiation shielding purposes, the gallery is broken into three sections along its length. At the low energy (injector) section of the linac, up to 211 MeV, the distance between the gallery and the tunnel is 7' of soil. Between 211 and 471 MeV, the gallery is 12' from the tunnel. And above 471 MeV to the end of the accelerator at 1700 (1030) MeV, the separation is 17' of soil. The waveguide run is imbedded in the four-foot thick tunnel ceiling resulting in a tenfold reduction of neutron streaming. Borel lined shield blocks form an igloo around the aperture where the waveguide enters the gallery from the tunnel. This attenuates neutrons streaming through the waveguide into the gallery [6] to a level below requirements. An air block between gallery and tunnel prevents potentially activated tunnel air from permeating the gallery. The waveguides and klystrons are shielded physically and electrically. Dual redundant RF and radiation detection systems are planned.

ACKNOWLEDGEMENTS

Many thanks to Karen Cummings, William Roybal, Amy Regan and Dale Schrage, of LANL for generous sharing of their time and experience on the LEDA accelerator from which much of the RF design of APT is based. And to Harry Yip for klystron support in the gallery layout and Mark Pippenger for his many practical suggestions.

REFERENCES

[1] George Lawrence, "High-Power Proton Linac for APT; Status of Design and Development", Proceedings of LINAC98, Chicago, August 24-28, 1998.

[2] A. Rohlev et al., " Characterization of High Power CW klystrons and Application to the APT LLRF Control System", Proceedings of LINAC98, Chicago, August 24-28, 1998.

[3] R. Street, et al., " Advanced Buck Converter Power Supply "ABCPS" for APT", Proceedings of LINAC98, Chicago, August 24-28, 1998.

[4] K. Cummings, "Results and Lessons Learned from Conditioning 1-MW CW 350 MHz Coaxial Vacuum Windows," Proceedings of LINAC98, Chicago, August 24-28, 1998.

[5] W. Roybal et al., " LEDA RF Distribution Design and Component Test Results," Proceedings of LINAC98, Chicago, August 24-28, 1998.

[6] E.C. Snow, E. Pitcher, " Port to Klystron Gallery Streaming Calculations", Bectel Nevada Interoffice Memorandum No.2612-ES-98-0179, June 8, 1998.

A CONCEPTUAL DESIGN OF RF SYSTEM IN THE NSP SUPERCONDUCTING LINAC AT JAERI

E. Chishiro, Y. Honda*, N. Ouchi, Y. Touchi**, K. Hasegawa, J. Kusano and M.Mizumoto
Proton Accelerator Laboratory, Japan Atomic Energy Research Institute
*Mitsubishi Heavy Industries, Ltd., **Sumitomo Heavy Industries, Ltd.
Tokai-mura, Naka-gun, Ibaraki-ken, 319-1195 Japan

Abstract

We have performed a conceptual design work of an RF system for a superconducting (SC) linac proposed for Neutron Science Project (NSP) at JAERI. An accelerating structure of the SC linac is divided into 8 different β-sections. The linac has 284-cavities and the length of 690-m. The 8 sections system suppresses the beam emittance growth and reduces the linac length. In the steady state, beam loading for three operation modes is calculated. For a pulse operation with a peak beam current of 30mA (chopping factor of 0.6), the peak RF power of 138kW is required at the high-β cavity. The power of 41kW is required for CW operation at a beam current of 5.33mA. Tuning errors on coupling and cavity resonant frequency are evaluated. In the conceptual design in which an RF power of klystron is distributed to 4-cavities, supply power is estimated. The supply power of about 20 MW is required for both operation modes.

1 INTRODUCTION

The NSP accelerator will consist of RFQ, DTL, Separated-type DTL and SC linac [1]. The SC linac accelerates hydrogen ions from 0.1 to 1.5GeV. It should be operated both in pulse and CW for demands in the applications. This requirement is the essential feature for the RF system. Table 1 shows a preliminary specification for the SC linac. Beam dynamics study has been carried out to determine the SC linac structure. RF system design work is performed under those parameters.

2 SC LINAC STRUCTURE DESIGN

The relative particle velocity (β) gradually increases from 0.43 to 0.92 along the SC linac. Therefore, accelerating cavities are divided into several sections with different β values to match to the particle velocity. The β-section is determined in the view of the bunch phase slip. The SC linac divided by many β-sections has the advantage of accelerating efficiency and less emittance growth because of the less phase slip. For the capital and maintenance cost, number of sections should not be increased so much.

Table 1: Preliminary specification of the SC linac

Energy	0.1 to 1.5GeV
Final beam power	8 MW
Accelerating particle	H^- , H^+
Frequency	600 MHz
Synchronous phase	-30 degree
Beam operation	1st stage pulse
	2nd stage pulse/CW
Peak current	16 mA at 1st stage
	30 mA at 2nd pulse mode
	5.33 mA at CW mode
Repetition rate	50 Hz
Macro pulse width	2 to 5.9 ms, CW
Intermediate pulse width	400 ns (interval 270 ns)

Prior to the β-section decision, basic parameters were prepared [2]. The number of cells per cavity is 5. The peak surface electrical field (Epeak) is limited to be 16 MV/m. The cavity surface resistance is estimated to be 15 nΩ. The number of cavities excited by an amplifier is set to be 4. It is indicated that the 4 cavities are fed with the same RF power.

The number of β-sections is decided by considering the RMS emittance growth and the linac length [3]. As the result of the study, the length and the emittance growth can be saturated over 8 β-sections. In the conceptual design, we chose the linac structure with 8 β-sections. The diagram is shown in Fig. 1 and its RF parameters are listed in Table 2. The linac has 284-cavities and the 690-m length.

3 STEADY-STATE BEAM LOADING

We calculated the required peak RF power in the steady state for each operation modes. The required power (P_f) is given by [4]

$$P_f = \frac{(1+\beta_c)^2 V_{acc}^2}{4\beta_c R} \times \left\{ (1-\tan\psi_b/\tan\phi)^2 + (\tan\psi_c - \tan\psi_b)^2 \right\}, \quad (1)$$

where β_c is the coupling factor to the cavity, ϕ is the synchronous phase and R is the cavity shunt impedance defined by $R=V_{acc}^2/$(cavity wall loss). Beam-loading detune angle (ψ_b) and cavity detuning angle (ψ_c) are defined by following equations, respectively.

$$\tan\psi_b = -\frac{R \cdot I_b}{(1+\beta_c)V_{acc}}\sin\phi \ , \quad (2)$$

$$\tan\psi_c = \frac{\omega_c - \omega_{rf}}{\omega_c}\frac{2Q_0}{1+\beta_c} \ , \quad (3)$$

where I_b is beam current, ω_c is cavity resonant frequency, ω_{rf} is driven frequency and Q_0 is unloaded Q value. To minimize the P_f , those angles have to be set to $\psi_b = \psi_c = -\phi$. Therefore, the optimum β_c and ω_c are obtained by

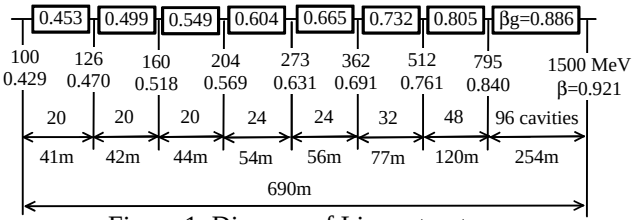

Figure 1: Diagram of Linac structure

Table 2: Design parameters of SC linac

Section No.	1	2	3	4	5	6	7	8
β	0.43 -0.47	0.47 -0.52	0.52 -0.66	0.57- 0.63	0.63 -0.69	0.69- 0.76	0.76 -0.84	0.84 -0.92
Vacc (MV/cav.)*	1.34- 1.60	1.78- 2.11	2.35- 2.74	3.03- 3.56	3.96- 4.51	4.95- 5.69	6.26- 7.13	7.85- 8.82
TTF	0.53 -0.65	0.55-0.67	0.58- 0.69	0.60- 0.71	0.62- 0.72	0.63-0.73	0.64-0.73	0.66 -0.74
Q_0	8.31E9	9.16E9	1.01E10	1.11E10	1.22E10	1.32E10	1.44E10	1.57E10
R/Q (Ω/cav.)	38.5- 58.5	58.8- 86.4	86.6- 122	121- 170	172- 227	223- 295	289- 377	370- 470

* Cavity accelerating voltage = Average electric field x Cavity length x TTF (Transit Time Factor)

$$\beta_{copt} = 1 + \frac{RI_b \cos\phi}{V_{acc}}, \qquad (4)$$

$$\omega_{copt} = \omega_{rf}\left\{1 - \frac{I_b}{2V_{acc}}(R/Q_0)\sin\phi\right\}. \qquad (5)$$

Under the optimum condition, the required power is given by $P_{fopt}=(1+\beta_c)^2 V_{acc}{}^2/(\beta_c R)$.

In the SC cavity, the required RF power is almost the same as beam loading under the optimum condition. The required power is shown in Fig. 2. The power is gradually increasing with the cavity number and the power at the high-β end is 6.6 times as large as that at the low-β end. For the pulse operation, the maximum power of 138 kW/cav. is needed at the high β-section. On the other hand, the power of 41 kW/cav. is required for the CW operation. There is difference of 3.4 times in the power between CW and pulse operations. The RF system including tuner, coupler, amplifier and so on have to manage this difference.

Tuning errors on β_c and ω_c cause the increase of the required RF power. Those tuning errors are evaluated for the SC linac. Figure 3 shows the dependence of the power enhancement on the coupling error (normalized by the optimum power P_{fopt} and the coupling factor β_{copt}). For the coupling error of +/-30 %, the power to keep the V_{acc} in the cavity increases 1.7% at over coupling and 3.2 % at under coupling. The coupling error does not seriously affect the power enhancement.

The cavity tuning error is evaluated for the cavity detuning angle (ψ_c). Figure 4 shows the dependence of the power on the ψ_c. The power is minimized at ψ_c =30 degree (=ψ_b). Over the 30 degree, the power is rapidly increased. For the shift of +/-30 degree from the optimum detuning angle, the power increases 8 % at –30 degree shift and 33 % at +30 degree. Using the parameters seen in Table 2 and the described equations, resonant frequency error of the cavity #1 at the 2nd stage CW mode is calculated. The tuning error of +/-30 degree corresponds to the resonant frequency error of -24 Hz and +47 Hz, respectively. The precise tuning is needed for the cavity pre-detuning.

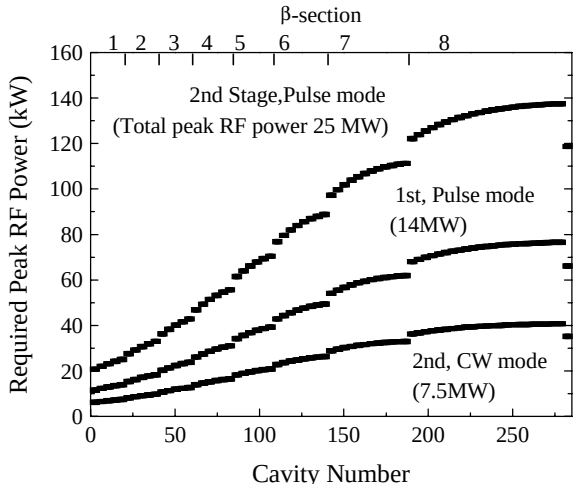

Fig. 2: Peak RF Power Requirement for the SC Linac

4 RF SYSTEM OF SC LINAC

4.1 Klystron

The design study of the RF system has been performed on the basis on klystrons, which are well suited to accelerator use. In the SC linac RF system, the klystron has to operate in the high power pulse mode and low power CW mode. In addition, the klystron also has to cover wide power range because of varying the required power along the SC linac. We have selected the klystron with modulating anode. Klystrons with property of UHF-band (508 MHz), high power (1MW) and CW operation have been already operated in TRISTAN and SPring-8. The maximum power satisfies our request (138kWx 4cavites + α).

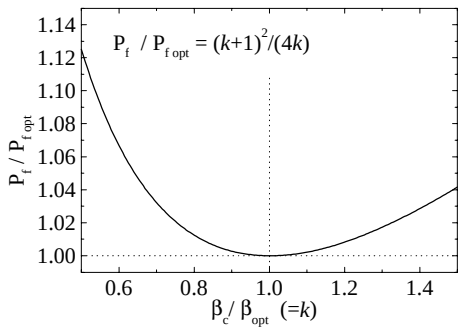

Fig 3: Required Power Enhancement for Coupling Error

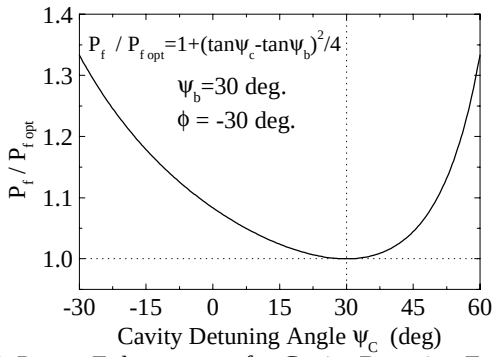

Fig 4: Power Enhancement for Cavity Detuning Error

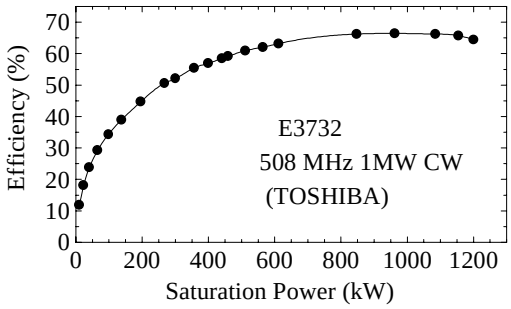

Fig.5: Efficiency Characteristic of the Klystron

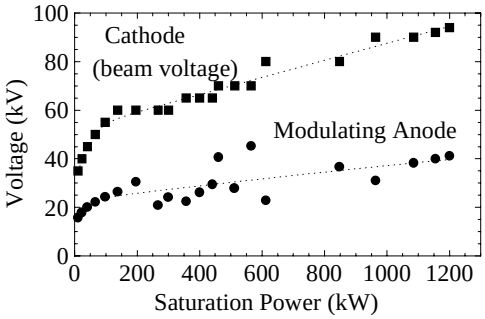

Fig.6: Cathode and Anode Voltage for Saturation Power

Klystron is manufactured such that its maximum efficiency becomes at the full saturation power. When the klystron operates below the saturation, the efficiency falls if the klystron beam power is not reduced. To keep higher efficiency in the low power range, the beam voltage is reduced. We have measured the efficiency characteristics using a 508 MHz klystron (E3732, TOSHIBA). Figure 5 shows dependence of the efficiency on the saturation power. Figure 6 shows the cathode and anode voltage where the power is saturated, respectively. The efficiency below 50% is measured at the power of 250 kW or less.

4.2 System efficiency and supply power

The RF system efficiency and supply power are estimated on the basis of the characteristic seen in Fig 5[5]. The result is given in Table 3. Since the klystron drives the 4-cavities, klystrons of 71 unit are needed in the RF system. High power tubes (44 units) with 1MW output and low power tubes (27units) with 400 kW are arranged in the linac to cope with the varying RF power requirement along the linac. To control the cavity field, some amount of RF margins are necessary. In this design, the margin of 15% is assumed. Considering power loss of 5 % in the transmission line, the klystrons are operated at 80% for the saturation power. Therefore operation efficiency becomes 0.8 times of saturation efficiency.

In the 2nd stage pulse operation, maximum output power of 690 kW (138 kW x 4 cavities x 1/0.8) is required at high β-end klystron. Since the efficiency at the saturation power is 64 % (see in Fig. 5), operating efficiency is estimated to be 51 % (64 % x 0.8). The supply power to the klystron is calculated to be 1082 kW (138kW x 4 cavities / 0.51 %).

The estimation is carried out for the klystrons of 71 units at each operation mode. At CW operation, averaged klystron efficiency is 33% due to operate the klystrons at low power. Averaged supply power is calculated to take into account the duty including time to rise field in the cavity. The averaged supply power to the RF system needs of about 20 MW for both of CW and pulse mode at the 2nd stage.

4.3 IOT system

Another choice of the SC linac RF system is a scheme that one-cavity is driven by one-IOT (Inductive Output Tube). This system is regarded as a suitable system for an RF control. In addition, the IOT is compact and is kept with high efficiency at low output power. In a rough estimation, the supply power at CW operation is reduced to 14 MW. However, high power IOT (more then 120kW) does not exist at present. In the case that the IOT is applied as all amplifiers, 568 tubes including pre-amplifiers are needed. Using many tubes may cause decrease of accelerator reliability. At present, we have done the preparation to evaluate the performance of a CW-35 kW IOT.

5 CONCLUSION

The SC linac with 8 β-sections is determined in the view of the bunch phase slip with respect to the RF phase in the cavity. This linac is an effective option for its shorter length and lower emittance growth. In steady state, the beam loadings under the optimum conditions were calculated. The maximum RF power requirements of 138kW at pulse operation and 41kW at CW operation are estimated. As a result of consideration on the tuning error, the precise tuning is needed for the cavity pre-detuning. In the conceptual design there the output power of a klystron is distributed to 4-cavities, the averaged supply power is estimated. The powers of about 20 MW are needed for both operation modes at 2nd stage.

Table 3: Efficiency and Supply Power in the RF System

Operation Mode	1st	2nd stage	
	Pulse	Pulse	CW
Beam pulse width (ms)	2	5.9	cw
Peak RF power (MW)	14	25	7.5
Klystron efficiency (%)	41	48	33
Peak supply power (MW)	34	53	23
Averaged duty *	0.18	0.38	1
Averaged supply power (MW)	5.8	20	23

* Including time to rise field in cavity

REFERENCES

[1] M. Mizumoto et al., "High Intensity Proton Accelerator for Neutron Science Project at JAERI", Proc. of EPAC98, Stockholm, June 22-26, (1998).

[2] N. Ouchi et al., "Proton Accelerator Activities in JAERI", Proc. of the 8th Workshop on RF Superconductivity, Italy (1997).

[3] Y. Honda et al., "A Conceptual Design Study of Superconducting Proton Linear Accelerator for Neutron Science Project", Proc. of 1st APAC, KEK, March 23-27, (1998).

[4] T. P. Wangler, "Principles of RF Linear Accelerators", John Wiley & Sons Inc., (1998).

[5] E. Chishiro et al., "An RF Power System for NSP High Intensity Proton Accelerator at JAERI", Proc. of 1st APAC, KEK, March 23-27, (1998).

A NEW RF SYSTEM FOR THE DEBUNCHER AT THE KEK 40-MEV PROTON LINAC

Z. Igarashi, E. Takasaki, T. Takenaka and K. Nanmo
High Energy Accelerator Research Organization, KEK
1-1 Oho Tsukuba-shi Ibaraki-ken, 305-0801, Japan

Abstract

The rf system for the debuncher at the KEK 40-MeV proton linac was renewed to an all solid-state one during the long shut down last summer. Since the amplifier of this system, containing one hundred and eight power transistors on its' final stage, can deliver a stable 20kW at 201MHz, the momentum spread of the linac beam can be decreased to less than 1%. This new rf system for the debuncher and its operational results are described.

1 INTRODUCTION

Although the debuncher cavity was replaced by the reentrant type with a single gap when the linac was upgraded from 20MeV to 40MeV in 1980 [1], the vacuum tube amplifier had been used since the linac construction as the rf source for the debuncher. This vacuum-tube amplifier had caused problems due to the short-lived vacuum-tube; furthermore production of the vacuum-tube for the final stage of the amplifier was discontinued. It was thus decided to replace it by a new amplifier which is the same as those of the predrivers of the rf systems for the DTLs [2] and the prebuncher [3].

2 NEW RF SYSTEM

The new rf system consists of nine transistor amplifier modules, rf power divider/combiners, dc power supplies and a control system. Figs. 1 and 2 show this system and a block diagram [4].

The transistor amplifier module, which was originally developed for cw operation of a TV transmitter, was refined for pulse operation, and can deliver more than 2kW.

Figure 1: New rf system.

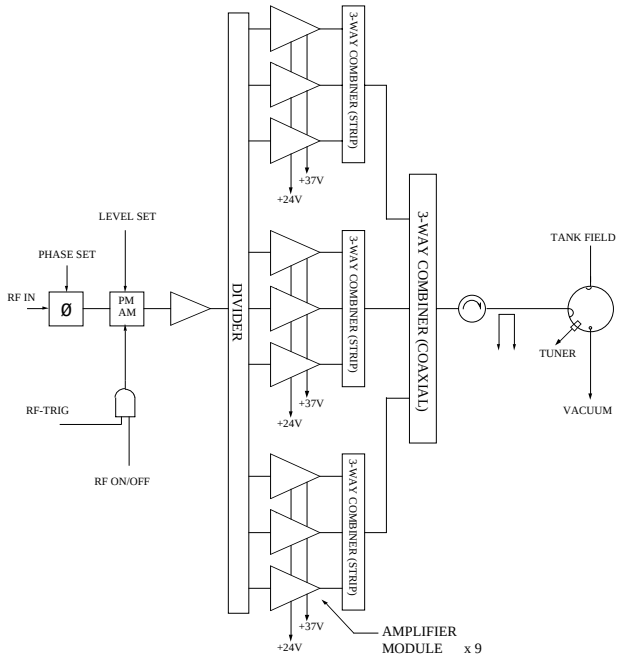

Figure 2: Block diagram of the new rf system.

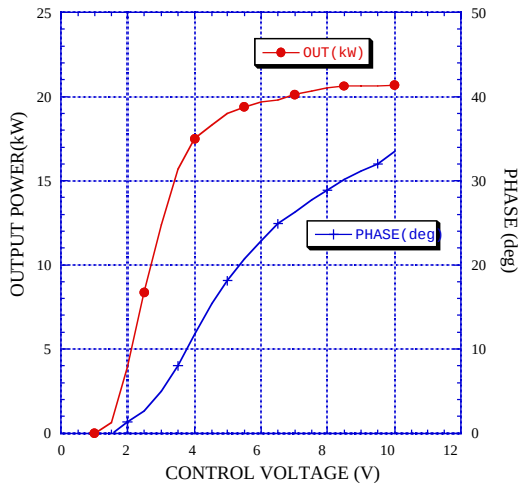

Figure 3: Output characteristics of the new rf system.

The rf power transistor used in the final stage of the module is the 2SC3286-M, which adops the so-called Gemini package, in which two transistor chips are mounted for push-pull operation, and generates about 200W.

The outputs of the nine modules are first summed up by three stripline 3-way combiners, and then by a coaxial 3-way combiner.

The output power and phase of the system are shown in Fig. 3. Control of this new rf source is achieved using a programmable logic controller [5]. The screen for control and status display of the system is shown in Fig. 4.

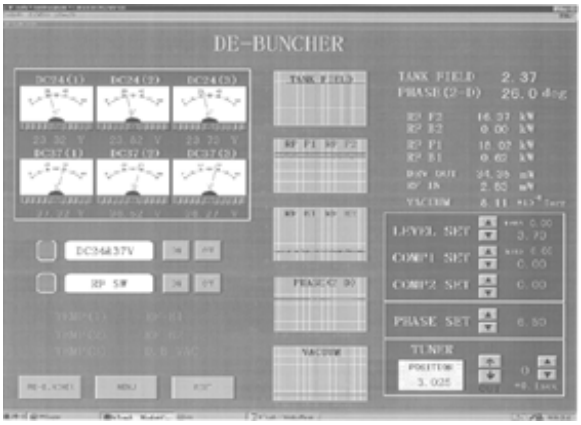

Figure 4: The screen for control and status display.

3 OPERATIONAL RESULTS

The field waveform of the debuncher and the beam-energy variations by the debuncher phase are shown in Figs. 5 and 6.

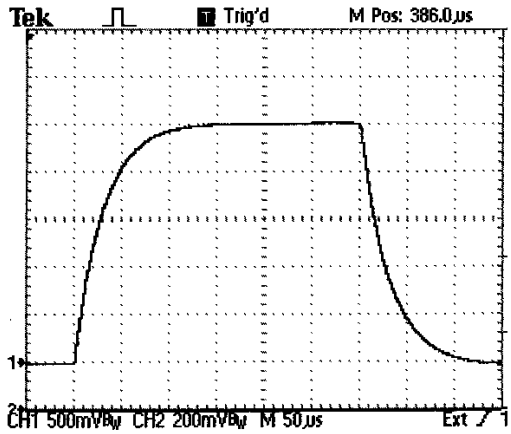

Figure 5: Waveform of the tank field.

The energy variations shown in Fig. 6, which were measured by the velocity monitor [6], are in good agreement with the calculated values. The upper part of the momentum-analyzer output in Fig. 7 is for the debuncher being off, and the lower one is for the input power being 19kW.

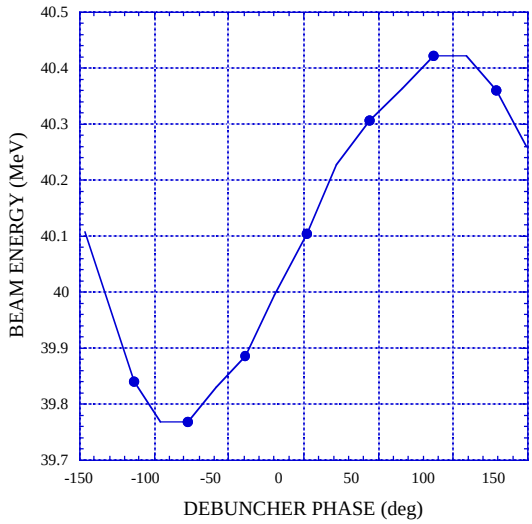

Figure 6: Beam energy versus debuncher phase.

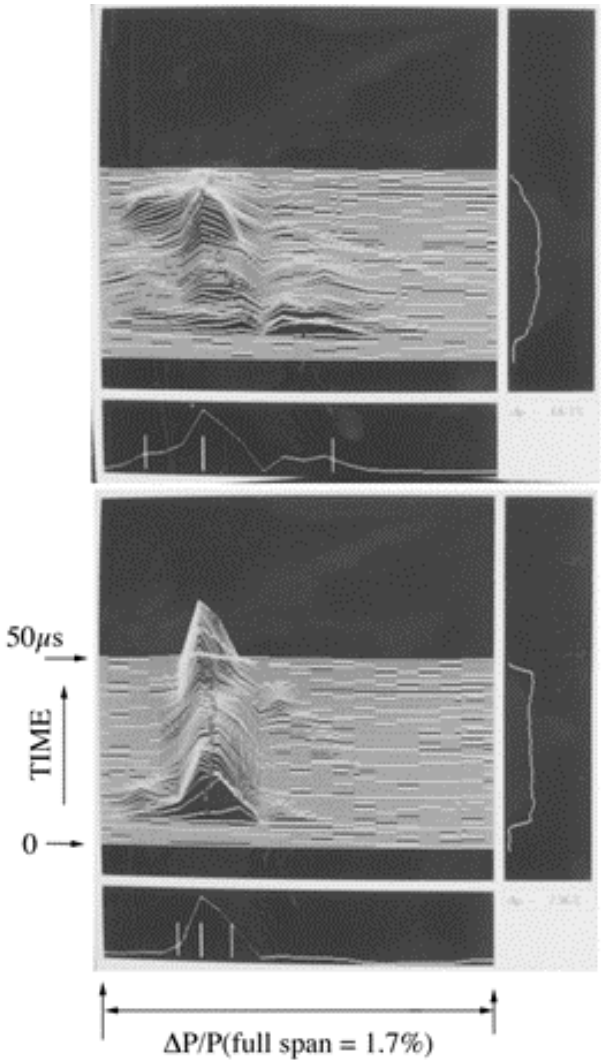

Figure 7: Momentum-analyzer outputs.
Upper : debuncher off
Lower : Pin=19kW

The momentum spread of the linac beam(ΔP/P) versus the debuncher field and the bunch length of the 500MeV booster synchrotron before extraction versus ΔP/P varied by the debuncher are given in Figs. 8 and 9. These results show that the debuncher is effetive to decrease ΔP/P of the linac and the booster synchrotron.

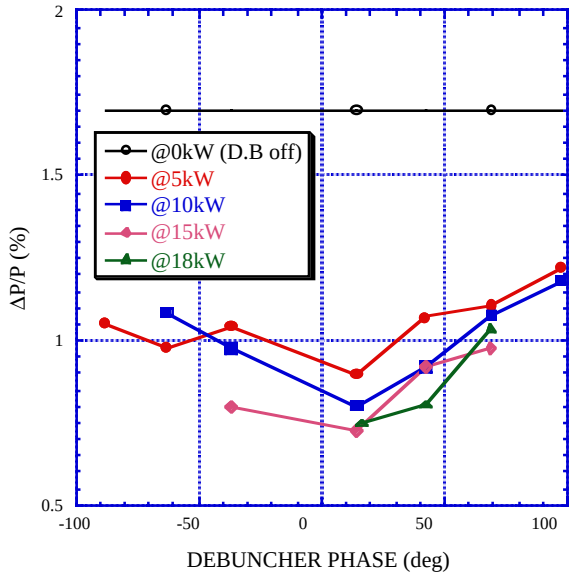

Figure 8: ΔP/P versus debuncher field.

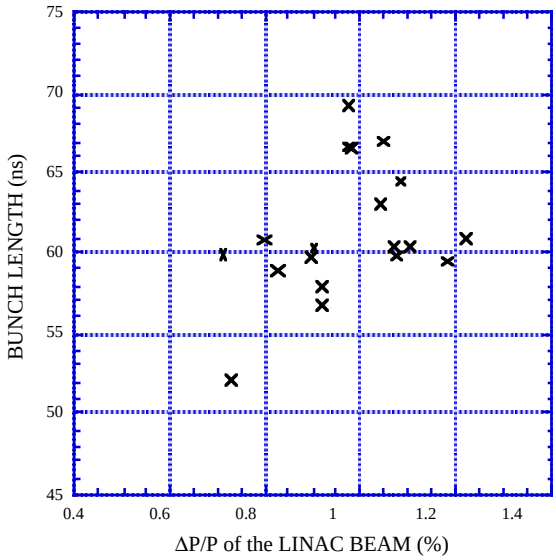

Figure 9: Booster bunch length versus linac ΔP/P.

4 CONCLUSION

The momentum spread of the linac beam has been decreased from 1.4% to 0.7% by the renewing of the rf system for the debuncher. Throughout the operations for about one year, it was proved that the new system is very stable and reliable without any problems; furthermore, the debuncher is much more useful for the tuning the linac and the booster synchrotron, consequentry all of the 12-GeV proton synchrotron, than before.

REFERENCE

[1] T.Kato et.al., “Debuncher for the 40MeV Proton Linac”, Proceedings of the 11th Linac Meeting in Japan, 111-113 (1986).

[2] Z.Igarashi et al., “10kW All Solid State RF Power Amplifier ”, Proceedings of the 13th Linac Meeting in Japan, 34-36 (1988).

[3] Z.Igarashi et al., “Renewal of the RF Source for the Prebuncher at KEK Proton Linac”, Proceedings of the 21st Linac Meeting in Japan, 195-197 (1996).

[4] Z.Igarashi et al., “Renewal of the RF Source for the Prebuncher at KEK Proton Linac”, Proceedings of the 22nd Linac Meeting in Japan, 131-133(1997).

[5] E.Kadokura et.al., “Improvement of PS Linac Control System”, Proceedings of the 20th Linac Meeting in Japan, 215-217 (1995).

[6] Z.Igarashi et.al., “Velocity Monitor for the KEK 40MeV Proton Linac”, Proceedings of LINAC92, Ottawa, August 23-28, 1992, 112-114 (1992).

THE C-BAND 50MW KLYSTRON USING TRAVELING-WAVE OUTPUT STRUCTURE

Y. Ohkubo, H. Yonezawa, TOSHIBA Co., 1385, Shimoishigami, Ohtawara, Tochigi, 324, Japan
T. Shintake, H. Matsumoto and N. Akasaka, High Energy Accelerator Research Organization (KEK), 1-1 Oho, Tsukuba, Ibaraki, 305, Japan

Abstract

The second tube of the C-band 50 MW klystron (model TOSHIBA E3746 series) has been developed in the course of the C-band rf-system R&D [1]. It uses the half-π mode traveling-wave structure in the output circuit in order to enhance the power-conversion efficiency and reduce the electric field gradient in the output circuit.

The three-cell traveling-wave structure was analyzed by the coupled-resonator model, and parameterized in a 3-by-3 impedance matrix form. The electrical performance at a hot condition was evaluated by a particle-in-cell simulation code: FCI, which predicted a power efficiency of 44%. The agreement of the simulation of FCI-code and test result was within 1%.

1 INTRODUCTION

In the future accelerators such as e+e- linear colliders, the system has to be highly reliable and efficient. The R&D of C-band accelerator system has been carried out at KEK since 1996.

Among the R&D work, two 50 MW C-band klystrons (TOSHIBA E3746 series) have been developed. The first tube using a conventional single gap in the output circuit was tested in August 1997, and generated a 50 MW peak power in 1 μs pulse duration at 20 pps pulse repetition rate, and also in a long pulse mode it generated 46 MW in 2.5 μs at 50 pps [2,3].

In the second tube, the output circuit was replaced to a traveling-wave structure to achieve over 50 MW peak power in 2.5 μs pulse width. The drift tube diameter at the output structure was enlarged to reduce the beam loss. The second tube was tested in April 1998, and generated a stable output power of 54 MW with 2.5 μs pulse duration, and 44% power efficiency at 50 pps repetition rate. The performance of the developed klystron agreed well with the predictions by the FCI-code.

2 DESIGN

The target performance of the E3746 klystron is shown in Table 1. The target value of peak power was chosen by scaling from the existing S-band klystrons to the C-band frequency.

The cross-sectional view of the E3746 klystron is shown in Fig.1. The left half in Fig.1 shows the first tube and the right half shows the second tube.

The output circuits consists of two output waveguides and two output windows, and they are recombined to one output port at the external circuits after the ceramic windows.

Table1:Main target parameters

Parameter		Unit
Output Power	50	MW
Operating Frequency	5712	MHz
Beam Voltage	350	kV
Beam Perveance	1.53	$\mu A/V^{3/2}$
RF Pulse Width	2.5	μs
Pulse Repetition Rate	50	pps
Drive Power	< 500	W
Power Efficiency	45	%
Gain	> 50	dB

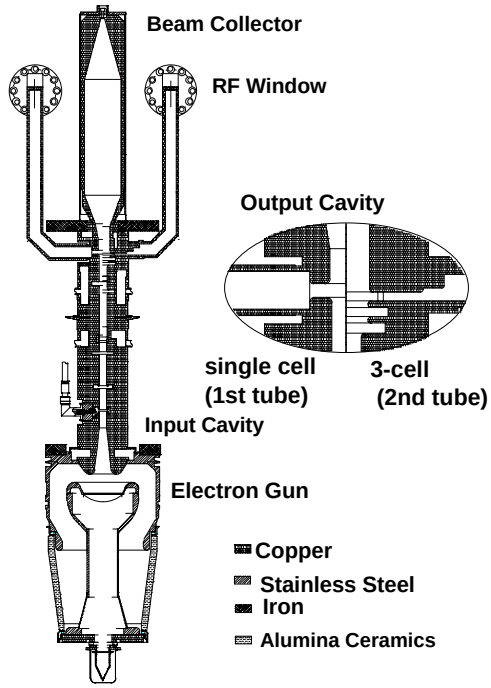

Figure 1: Cross sectional view of E3746 Klystron.

At the high power test of the first tube, the electron gun operated stably without diode-oscillation or high-voltage breakdown, and also rf windows showed nice high power performance. A stable 50 MW output power was generated in 1 μs pulse width. However the measured power efficiency was slightly lower than the target value.

The second tube uses a half-π mode traveling-wave output structure, which has advantages described below.

(1) Electric field gradient in the output cavity is reduced.

(2) The drift tube-diameter at downstream side of the output cavity can be enlarged without deteriorating the power efficiency, thus a high-voltage breakdown associated with the beam loss can be eliminated.

(3) Since the traveling-wave smoothly decelerates the electron beam in synchronous with the beam velocity, the power conversion efficiency is enhanced.

The multi-cell coupled cavity type output structure has been recently used for high power pulse klystrons, such as X-band klystrons at SLAC [4], where successful results were obtained. However there are still some problems in design described below.

(a) Optimum design procedure of the multi-cell cavity is not fully established.

(b) Countermeasure to prevent the parasitic oscillation phenomena is not fully established.

Thus, we decided to develop advanced design procedure for a traveling-wave structure. To do this, we laid the following basic guidelines.

(1) An equivalent circuit model is used for analyzing the multi-cell output cavity.

(2) To prevent the parasitic oscillation, the three-cell structure was chosen, which is the minimum number of cells to realize a traveling-wave.

(3) The half-π mode was chosen, since the impedance matrix becomes a simple form, also it makes frequency tuning simple.

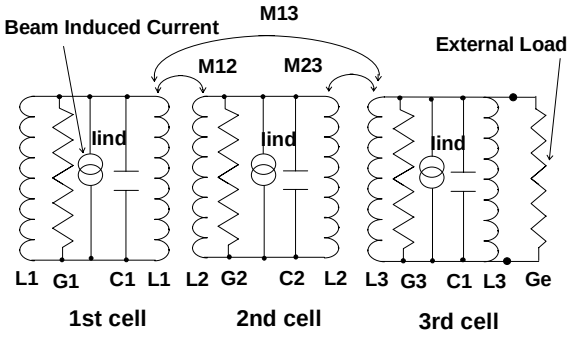

Figure 2: The equivalent circuit model.

The equivalent circuit for the three-cell structure is shown in Fig.2. Three resonator circuits are coupled each other through the mutual inductances M12, M23, M13. The current source in each circuit represents induced current by the beam. The conductance at the 3rd cell shows the output waveguide and external load. This equivalent circuit is identical to the coupled resonator model which has been widely used to analyze various kinds of accelerator structures. A special situation in klystron analysis is that the next neighbor coupling M13 plays an important role. Klystron output structure requires so large coupling coefficients between neighbor cells that the next neighbor coupling becomes non negligible.

The design procedure is,

(1) The beam rf current and beam energy at cavity center location of each cell are estimated by the beam simulation (FCI-code), mounting a single cell output cavity.

(2) The shunt impedance R/Q and the beam coupling coefficient of each cell are estimated from numerical simulation code, such as SUPER FISH, etc.

(3) Assume the same amount of the deceleration voltage in each cell. Compute the cell-voltage from the beam coupling coefficient.

(4) The mutual inductances M12, M23, M13, the external-Q and the cell resonance frequencies at half-π mode are computed by the impedance matrix using the estimated induced currents and the cell voltages.

(5) The physical dimensions of each cell are determined by numerical simulations. We repeat process (4) to (5) using the estimated R/Q and the beam coupling coefficient by the code.

(6) We run the FCI-code using the circuit parameters obtained above, and check the output power with the target value.

(7) The 3rd cell is connected to the output waveguides, thus we use 3D-simulation code HFSS, by which we decide the optimum iris size and cavity diameter.

At the actual design, almost all the cavity parameters were determined by the method described above in one process. We did not use FCI-code for a try-and-error parameter search.

The simulation result of the second tube is shown in Table 2. FCI said that the output power of 49 MW and the power efficiency as high as 44% can be obtained at the beam voltage of 350 kV.

Table 2: Design parameters (Values in parenthesis show the design parameter of the first tube.)

Parameter		Unit
Output Power	49	MW
Operating Frequency	5712	MHz
Beam Voltage	350	kV
Beam Current	317	A
Drive Power	300	W
Power Efficiency	44	%
Electric Field Gradient in Output Cavity	29.2 (45)	kV/mm
Drift Diameter of Collector Side	14 (9.5)	mm

In the second tube, the drift tube-diameter at the output structure was enlarged by 1.4 times than the first tube, and the electric field gradient in the output structure was reduced to 0.7 times lower than the first tube. Thus the second tube has more safety margin against rf-breakdown and beam-loss damage around the output structure.

3 TEST RESULT

The second tube was tested at KEK in April 1998. In this test, the output power was measured by the absolute calorimetric method. In this method, the output power is measured from the water temperature rise at the rf dummy load. In order to calibrate the temperature rise, an electrical heater was loaded in the water cooling system after the rf dummy load. The heat dissipation can be simply determined by the product of the terminal voltage and the current. This method is independent from the

error in the flow rate of water measurement, thus it is very reliable.

Table 3 shows the experimental result, and Fig.3 shows the rf output power and the beam voltage waveforms. This klystron achieved 54 MW output power at the beam voltage of 369 kV, 2.5 μs pulse width and 50 pps repetition rate. The output waveform was always steady and stable for wide range of operating conditions. We tested the effect of reducing the focusing field, where no oscillation nor beam loss was observed.

Fig.4 shows the saturated output power as a function of the beam voltage and Fig.5 shows the input-output characteristic at the beam voltage of 362 kV. No unstable phenomena was observed in the input-output characteristic.

The test result of saturated output characteristics agreed well with the FCI simulation result. The difference between the measured output power and the simulation was within 1%.

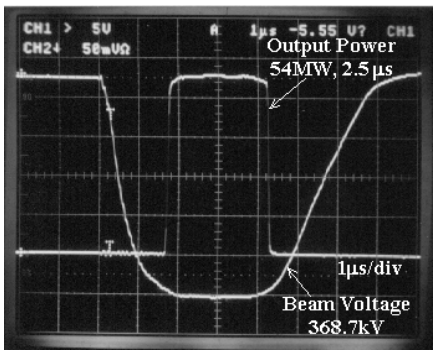

Figure 3: Output power and Beam voltage waveform.

Table 3: Test result

Parameter	1st tube	2nd tube	Unit
Operating Frequency	5712	5712	MHz
Beam Voltage	360.4	368.7	kV
Beam Current	326.4	333.0	A
Output Power	50.1	53.9	MW
RF Pulse Width	1.0	2.5	μs
Pulse Repetition Rate	20	50	pps
Drive Power	259	323	W
Power Efficiency	42.6	43.9	%
Power Gain	52.9	52.2	dB
Beam Perveance	1.51	1.49	$\mu A/V^{3/2}$
Solenoid Coil Power	6.38	4.55	kW

4 CONCLUSION

The second C-band klystron which uses the three-cell traveling-wave output structure successfully generated a stable 54 MW output power at 369 kV beam voltage, 2.5 μs pulse width, 50 pps repetition rate.

The test result showed a good agreement with the FCI-code simulation. It demonstrated that the design procedure established here is powerful and reliable for the design of multi-cell output structure.

As the next step, in order to improve the system efficiency, we will start development of a periodic permanent magnet (PPM) focused klystron from 1998, which eliminates the focussing magnet power.

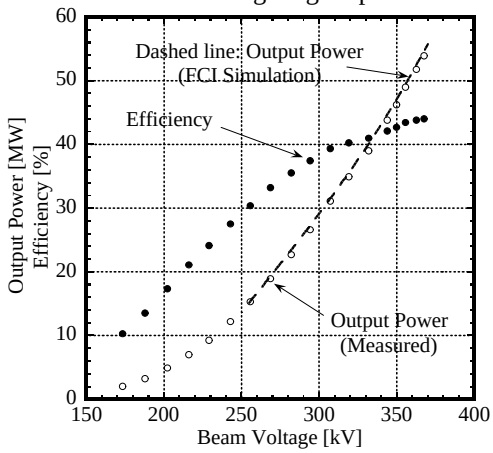

Figure 4: Saturated output characteristics.
(2 μs pulse width and 50 pps repetition rate)

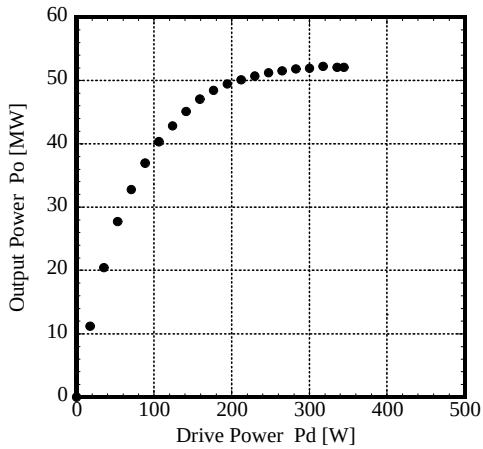

Figure 5: Input-output characteristics.
(2 μs pulse width and 50 pps repetition rate)

ACKNOWLEDGEMENT

We thank to Mr. Kazuharu Nishitani and Mr. Kensuke Watanabe for their effort on preparing the experimental set up.

REFERENCE

[1] T.Shintake, et. al., "C-band Main Linac System for e+e- Linear Colliders", EPAC96, Barcelona Spain, 1996.

[2] T.Shintake, et. al., "Development of C-band 50 MW Pulse Klystorn for e+e- Linear Collider", PAC97, Vancouver, BC, Canada, 1997.

[3] H.Matsumoto, et. Al., "Operation of the C-band 50 MW Klystron with Smart Modulator" , '1st Asian Particle Accelerator Conference, Tsukuba, Japan, 1998.

[4] G.Caryotakis, “The X-band Klystron Program”, RF96, Kanagawa, Japan, 1996.

[5] T.Shintake, "Resent Status of FCI: PIC Simulation of Coupled-Cavity Structure", Proc. of Linac96.

[6] Please refer the detail to http://C-band.kek.jp.

EFFICIENCY AND GAIN ENHANCEMENT OF RF-PULSE COMPRESSOR FOR C-BAND RF SYSTEM

M.Yoshida,
International Center for Elementary Particle Physics, University of Tokyo, Tokyo 113, Japan
T. Shintake,
High Energy Accelerator Research Organization (KEK), 1-1 Oho, Tsukuba, Ibaraki, 305, Japan

Abstract

In order to make use of the additional energy in the front part of the modulator output pulse, the phase modulation system was proposed for the efficiency enhancement in various RF system. The phase modulation system compensates the undesirable phase rotaion associated with the rising power of the klystron to store the additional energy in the RF-Pulse Compressor. This idea leads the enhancement of the RF-Pulse Compressor in both respect of the power efficiency and gain which are keys of the e^+e^-linear collier.

To demonstrate the efficiency and gain enhancement of the RF-Pulse Compressor, we confirmed the complete phase compensation of the klystron and observed the gain enhancement of 125% using the cold model of the RF-Pulse Compressor in the C-band RF system.

1 INTRODUCTION

In the oridinary RF system with the RF-Pulse Compressor in the electon linear accelerator, only the flat top of the modulator pulse is used. The conventional modulator using the line-type PFN(pulse forming network circuit) with the thyratron switch usually generates a pulse with the considerable settling time(Fig. 1), and it is technically difficult to reduce this time. The front part of the pulse contains a large amount of energy. However this useful energy cannot be used due to the undesirable phase rotation associated with the rising voltage of the modulator output pulse.

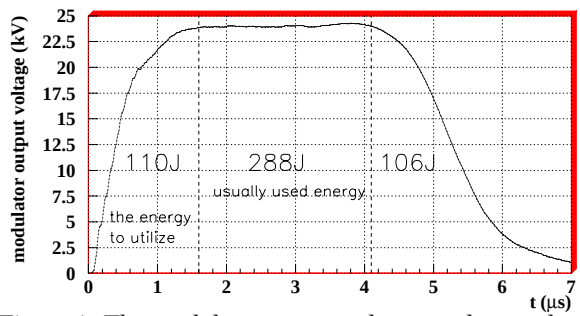

Figure 1: The modulator output voltage on dummy load

If we can utilize the energy in the front part of the modulator output pulse, the gain enhancement factor of $1.38(=(110+280)/280)$ will be roughly estimated in the ideal case. Considering the klystron efficiency, this factor becomes to $1.32(=(40+126)/126)$. If we assume 30% of the energy loss in the RF-Pulse Compressor, the gain enhancement factor of $1.22(=(40\times 0.7+126)/126)$ is finally expected.

To do this, we employ the phase modulation system to compensate the phase rotation in the klystron. Then the integrated energy of the front part can be stored in the pulse compression cavity, which contributes to increase the power gain of the compressed output pulse.

Furthermore this phase modulation system with the adaptive feedback may be used as a multipurpose apparatus as follows.

- A compensation of the ringing response of the RF-Pulse Compressor associated with the coupled-resonator circuit.
- A beam-to-rf phase adjustment.
- An energy gain adjustment.
- A frequency locking by rotating the phase: $\Delta f = \frac{1}{2\pi}\frac{d\phi}{dt}$ where Δf is the frequency shift and ϕ is the phase.

2 PHASE MODULATION SYSTEM

The schematic diagram of the phase modulation system for the C-band RF system [1, 2] is shown in Fig. 2.

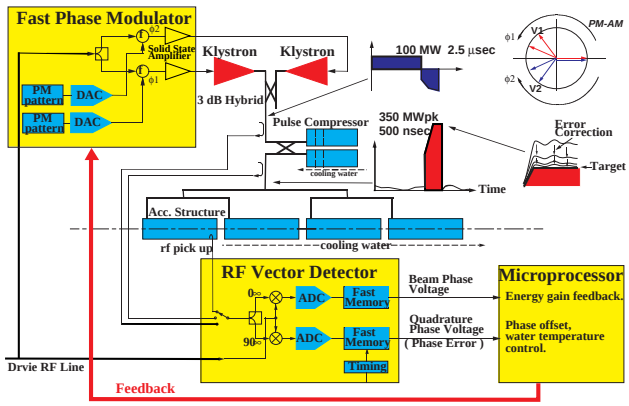

Figure 2: The schematic diagram of the phase modulation system.

It consists of the fast phase modulator, the vector rf voltage detector, the solid-state driver amplifier and the feedback control computer.

In this system, the vector-rf-voltage detector monitor the power flow at the several points; klystron output, pulse compressor output and the output coupler of the acceler-

ating structure. The software computes errors from the target value and stores the phase modulation pattern to the memory in the fast phase modulator. This feedback loop is repeatedly applied on the successive pulses to maintain a constant energy gain. The feedback is automatically controlled corresponding to the various situation: some system failures, temparature change and timing drift etc.

In the two klystrons system as shown in Fig. 2, the Phase-to-Amplitude conversion is performed to flip the input voltage of the RF-Pulse Compressor. The single klystron configuration is also possible, but it is more difficult than the two klystron system because the klystron is usually operated in the saturated region for the high effiency and the stability, and furtheremode the nonlinearity must be compensated.

3 SIMULATION

To find the optimized parameters of the RF-Pulse Compressor, the computer simulation was performed using the measured data of the C-band modulator [3] pulse and the klystron characteristics. The C-band RF-Pulse Compressor was designed for the multi-bunch operation in the future e^+e^- linear collider. The concept is: (1) the multi-cell coupled cavity is used to delay the energy output, (2) the input pulse is controlled to obtain a flat-pulse output.

In the simulation, we used a 3-cell non-uniform coupled cavity pulse compressor whose characteristics had been measured in 1997 using the cold model [4].

Fig. 3 shows the simulated output from the RF-Pulse Compressor. The dashed line shows the normalized input voltage, the light solid line shows the gain for the square input pulse, and the dark solid line shows the gain for the extended input pulse with the phase compensation. The phase compensation started at the period of 50% peak power.

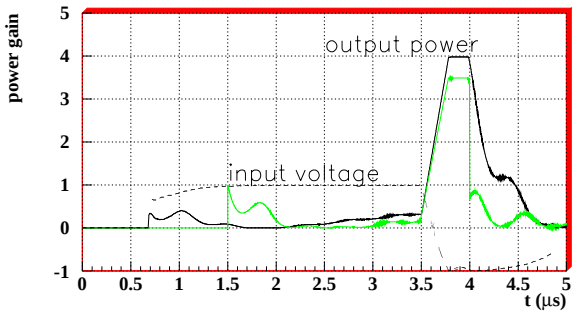

Figure 3: The simulated RF-Pulse Compressor output. Vertical axis is the normalized power gain.

The rf energy from 0.7 to $1.5\mu sec$ in Fig. 3 was stored additionally in the RF-Pulse Compressor. Futhermore we found that the lower side band through the smooth input contributes to reduce the reflection power so that the power gain reached to 4.0.

As described in Section. 1, the gain enhancement factor of 1.32 and the the maximum gain of 4.6 is expected in the ideal case. The optimization will enhance the gain.

4 EXPERIMENTAL TESTS

To demonstrate the efficiency and gain enhancement of the RF-Pulse Compressor, we performed the experimental test with the single klystron configuration using the cold model of the C-band RF-Pulse Compressor, the 50MW klystron(Toshiba, E3746) and the pulse modulator(Nihon Koshuha, KLY-M-104). The phase modulation system mainly consists of double balanced mixer(Stellex, M14A), CAMAC 100MHz 8bit Flush-ADC, VME 250MHz Programable Pattern Generator, VME 12bit DAC, VME board computer(force CPU 5V), and the feedback software which was written in Perl with SWIG, Perl/Tk, Perl/MesaGL and C++. Fig. 4 shows an experimental setup.

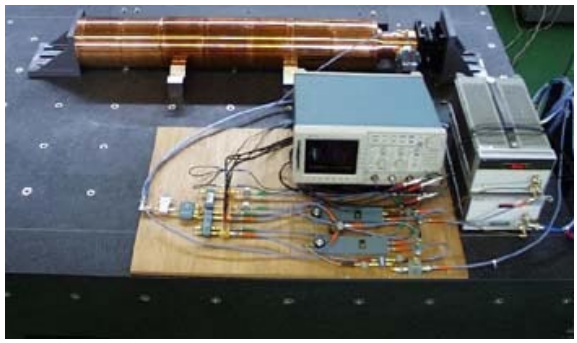

Figure 4: An experimental setup.

4.1 Phase Compensation of Klystron

At the first step, the undesirable phase rotation in the klystron associated with the rising cathode voltage was compensated by the feedback loop. The procedure of the phase compensation is as follows.

- Timing Adustment: It is important to adjust the timing of the fast phase modulator and the vector-rf-detector because it seriously affects the accuracy of the adaptive feedback. To correct the timing, we used a step pulse modulation and detecteted the timing of the rising edge.
- Calibration: The vector modulator invariably has the in-phase and quadrature (called I-Q) errros and the amplitude error. The I-Q errors affect only the settling time of the feedback, but the amplitude error causes the error in controlling the klystron output voltage. A few times of measurement was enough to determine the vector errors by setting the manual phase shifter at various phase points.
- Feedback: The vector rf voltage detector monitors the I-Q components and the amplitude of the klystron output. In the software, the I-Q sampled data is used to compute the phase correction data. Considering the characteristics and errors of the system, the software generates the I-Q modulation pattern from the phase correction data. The AM modulation pattern for the RF-Pulse Compressor must be also considered in this time. Then the I-Q pattern is stored to the memory of

DACs. When the next pulse is triggered, DACs generates the I-Q modulation waveforms.
This feedback loop is repeatedly applied on the successive pulses to maintain a constant energy gain.
In this experiment, the quadrature component of the klystron output was reduced to the noise level after 4 times feedback processes.

The Fig. 5 shows the the I-Q components of the vector demodulator versus time for the klystron output, and their X-Y(I-Q) display is shown in Fig. 6. We can interpret the I-Q display by $A(t)e^{j\phi(t)}$ where $A(t)$ and $\phi(t)$ is the amplitude and phase of the klystron output respectively, so we find that the phase rotates to the positive direction associating with the rising amplitude.

The Fig. 7 and 8 show the temporal display and I-Q display of the klystron output with the phase compensation.

It was found that the phase rotation of both the rising and falling part was completely compensated.

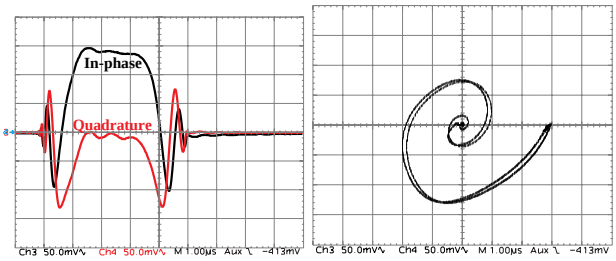

Figure 5: I-Q demodulator pulse without the phase compensation

Figure 6: I-Q display without the phase compensation

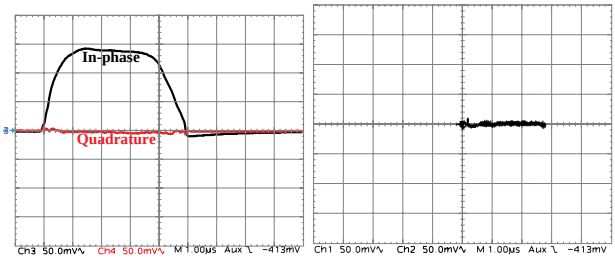

Figure 7: I-Q demodulator pulse with the phase compensation

Figure 8: I-Q display with the phase compensation

4.2 *Gain Enhancement of RF-Pulse Compressor*

Using the monitor signal from a Bethe-hole coupler at the klystron output, the pulse compression was demonstrated with the phase compensation of the klystron. The RF-Pulse Compressor in this measurement was the cold model of the C-Band RF-Pulse Compressor with a 3-cell non-uniform coupled cavity and we used the single klystron configuration. As the pulsed klystron modulator had been already tuned up to generate the $2\mu s$ flat pulse, the expected gain with the phase compensation was 3.5.

For the AM modulation to control the RF-Pulse Compressor output, we must consider the non-linear characteristic of klystron, not only for phase but also for amplitude.

Fig. 9 shows the power gain of the RF-Pulse Compressor output. The light line shows the gain for the square input pulse, and the dark line shows the gain for the extended input pulse with the phase compensation. We observed the gain enhancement factor of 1.25 and obtained the power gain of 3.5. It should be noted that the $2.5\mu s$ flat pulse was required for this power gain without the phase compensation.

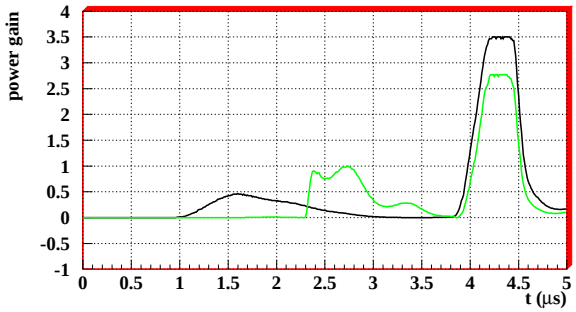

Figure 9: The power gain of the RF-Pulse Compressor.

5 DISCUSSION

We successfully demonstrated the phase modulation system. We confirmed that this phase modulation system provides a important gain enhancement with no hardware modification in high-power components.

For the further R&D, it is neccessary to optimize the parameters of the C-band RF-Pulse Compressor for a higher gain and to develop the phase modulation module for common uses. Especially, the solid-state RF amplifier is an important R&D task to drive each klystron at 500W level. It must be compact, minimum phase walk and low cost. A pulsed-class-A amplifier will be suitable for this purpose.

6 ACKNOWLEDGMENTS

We thank to Prof. Hiroshi Matsumoto, and Mr. Kensuke Watanabe for their supports.

7 REFERENCES

[1] T.Shintake et al., "C-band RF-system Development for e^+e^- Linear Collider", APAC98, KEK, March 23-27, 1998.
[2] http://c-band.kek.jp
[3] H.Baba et al., "Pulsed Modulator for C-band Klystron", APAC98, KEK, March 23-27, 1998.
[4] T.Shintake et al., "Development of C-band RF Pulse Compression System for e^+e^- Linear Colloder", PAC97, Vancouver, May 12-16, 1997.

RESULTS AND LESSONS LEARNED FROM CONDITIONING 1 MW CW 350 MHZ COAXIAL VACUUM WINDOWS*

K. Cummings, R. Cordova, D. Rees, W. Roybal, Los Alamos National Laboratory, Los Alamos, NM 87545 and
S. Risbud, University of California, Davis, CA 95616 and
D. Wilcox, EEV, Ltd. Chelmsford, England

Abstract

The reliability of the radio frequency (RF) windows on the Low Energy Demonstration Accelerator (LEDA) is critical to the success of the Accelerator Production of Tritium Program (APT). On the APT accelerator there will be over 1000 windows, each passing on the order of 250 kW of CW RF power. This power level is well above power levels historically used in RF windows. Based on the high-power RF test results of the RF window prototypes from vendors, the coaxial windows made by EEV Ltd. of Chelmsford, England, were selected for LEDA. This paper describes the high-power RF testing of the 16 EEV coaxial windows. The RF window diagnostic equipment, data acquisition system and test stand are described. The results of the high power RF testing of the windows are presented. The successes and failures in the conditioning, manufacturing and testing techniques of the windows are presented. The conditioning timeline, power profile and the conditioning waveform are also discussed.

1 INRODUCTION

To select a reliable RF window for the radio frequency quadrapole (RFQ), prototype windows were tested from three different vendors. Based on the prototype test results EEV, Ltd. of Chelmsford, England was selected as the vendor for the 350 MHz RF windows. This paper describes the high power acceptance testing of the windows ordered for the RFQ. Under normal operating conditions these windows are required to transmit up to 250 kW of continuous wave (CW) RF power. Prior to acceptance from the vendor each window was conditioned to 1 MW of CW RF power and run at 1 MW for four hours to obtain steady state results. The power was generated by a EEV klystron capable of producing 1.2 MW CW RF power at 350 MHz.

2 EXPERIMENTAL SETUP

2.1 Window Geometry

The cross section of the EEV window is shown in Fig. 1. The window is a coaxial AL300 alumina ceramic. The air and vacuum side flanges are half height WR2300 and T-bars are used on the air and vacuum sides of the window to transition to the coaxial line. The waveguide transition on the vacuum side is copper plated stainless steel waveguide, and on the air side it is aluminum.

2.2 Test Stand

The experimental test stand is capable of testing four windows at a time. The four windows are in two pairs in a back to back configuration. The test stand is capable of passing 1 MW CW RF power through the windows. The windows are both air and water cooled. The water cooling is circulated through the vacuum side T-Bar. The air cooling goes through the air side T-bar,down the inner conductor, exits the inner conductor through a series of

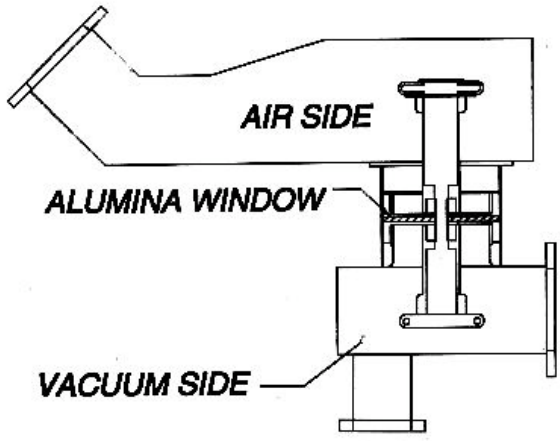

Figure 1: Sketch of the EEV Window

Figure 2: RF Window Pair on the Test Stand

*Work supported by U.S. Department of Energy.

holes and is directed over the ceramic. Then the air exits the outer conductor through a series of holes. A RF window pair in a back to back configuration is shown in Figure 2.

2.3 Diagnostic Equipment

The RF window test stand includes many diagnostics. The vacuum pressure is measured at three places in each window pair. It is interlocked to the RF power. The pressure setting for the RF interlock is adjusted during the conditioning routine. Each RF window has two fiber optic arc detectors, one on the air side and one on the vacuum side. The arc detectors are also interlocked with the RF power and will shut down the RF drive for 1.6 seconds upon detection of an arc. The water and air inlet and exit temperatures are monitored and interlocked with the RF power. In addition, the temperature of the outer coaxial surface in the region of the alumina ceramic is also monitored and recorded. An infrared camera was used to obtain the temperature distribution across the ceramic.

2.4 Data Acquisition System

The data acquisition system is used to record data from the RF window test stand and the klystron. The coaxial RTD and vacuum and arc detector data is read by a LabView program and archived. The air and water temperatures are recorded by the klystron transmitter PLC. The RGA data are read from a second LabView program. A master processor has access to all the data and allows for a common display.

3 EXPERIMENTAL RESULTS

3.1 Processing Results

The ceramic on the prototype windows was coated with copper black to prevent multipacting. During the high temperature bakeout, the coating was discolored and redistributed over the ceramic and metal surfaces. These surfaces were grit blasted to remove the coating. The prototype windows conditioned to 1 MW in 26 hours and no excessive heating or arcing were observed. The first two windows after the prototypes were not grit blasted. Excessive heating and arcing were seen as shown in Figure 3, and one of these windows failed at 500 kW. From then on, all the windows were grit blasted.

All the grit blasted windows achieved the expected power level of 1 MW and conditioned in a timely manner. Windows that were originally grit blasted at EEV had to be grit blasted again at LANL. The difference in the grit blasting is assumed to be due to differences in nozzle size and geometry. At LANL a small nozzle with a 90° bend was used allowing easy access to the corners and back sides. EEV has now adapted the same nozzle as at LANL. The windows were grit blasted with 220 alumina grit at 55 psi.

3.2 RF Conditioning Results

A low vacuum pressure is essential during RF conditioning. At higher pressures, more arcing and heating occurred. The vacuum interlocks were set at 1 x 10^{-5} Torr for power levels less than 100 kW, 5 x 10^{-6} Torr for power levels between 100 kW and 500 kW, and 2 x 10^{-6} Torr for power levels above 500 kW.

During conditioning it is important to monitor the rate of temperature increase as a function of RF power. By conditioning 4 windows at a time, nonlinear temperature increases are easier to detect. An example of the nonlinear temperature increase is illustrated by the windows that were not grit blasted as shown in Figure 3. If a large temperature increase is detected, the power level is immediately reduced until the temperatures are more typical.

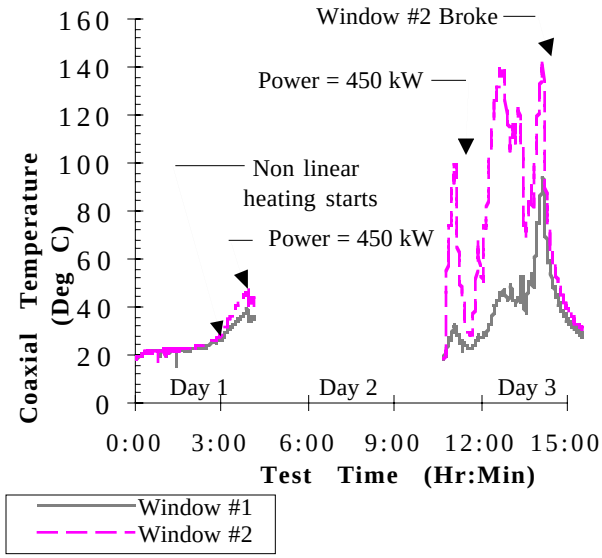

Figure 3: Window Temperature vs. Test Time of Two Windows that were not Grit Blasted.

3.2 High Power Test Results

The time to condition the windows to 1 MW is shown in Figure 4. The average conditioning time is approximately 19 hours and the average outer coaxial temperature near the ceramic at 1 MW is approximately 75 degrees C.

Different RF waveforms used in conditioning included CW, pulsed, and amplitude modulation. In CW conditioning the power could only be increased in discrete steps. The power is increased in decibels, thus, the steps are quite large at high RF power levels. At times, large gas loads were seen due to the large power increase. Pulsed conditioning helps decrease the average power and the heating in the window; however, it does not eliminate or reverse the nonlinear heating which leads to the failure of the window. Amplitude modulation was used as a conditioning method to pass a power region of high outgassing. CW conditioning is easily compared to amplitude modulation in Figure 5. In this particular case, CW conditioning was used during the first four hours and amplitude modulation was used the remainder of the test time. The increased speed of conditioning the windows with amplitude modulation is easily observed.

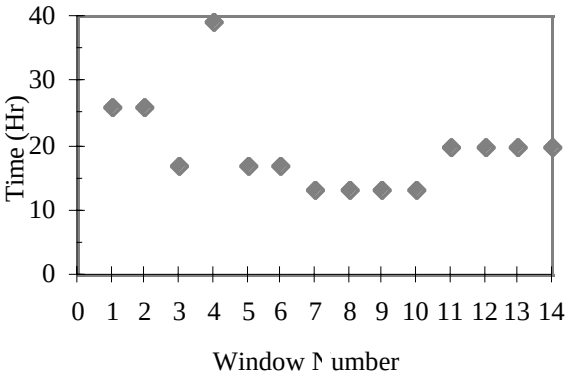

Figure 4: Comparision of Conditioning Times to 1 MW.

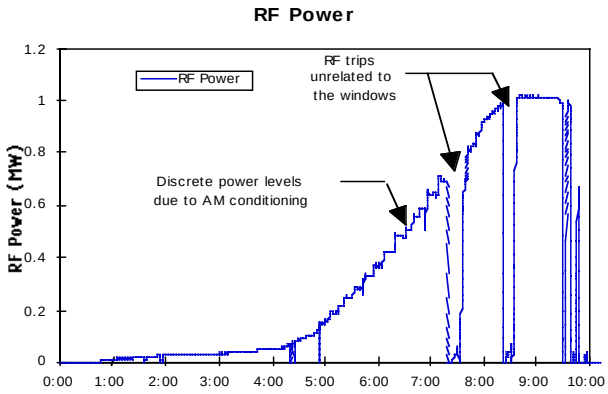

Figure 5: RF Power vs. Test Time with CW Conditioning until 4 hrs. and Amplitude Modulation after 4 hrs.

4 DISCUSSION

Grit blasting is believed to reduce cause of the nonlinear temperature increase by cleaning the surface and changing the surface topography[1]. Changes in the surface topography dull the potential field enhancement sites which reduces multipacting. Surface characterization work showed the grit blasted samples to have a higher carbon content on the surface than non-grit blasted samples[2].

In amplitude modulation a continuous range of power levels are conditioned. As previously discussed, in CW conditioning discrete power levels are conditioned, and when returning to a previously conditioned power level, multipacting may still be seen. With amplitude modulation there are no discrete power levels and multipacting does not reoccur at specific power levels.

During conditioning, two separate phenomena, multipacting and ion bombardment, are thought to be occurring[1]. The signs of multipacting are rapid fluctuations in the vacuum pressure and nonlinear temperature increases with power[3,4]. Multipacting tends to occur at specific power levels for a given window geometry. The second phenomenon is believed to be due to ion bombardment. As electrons are freed from the surface, they are colliding with molecules in the vacuum chamber which produces ions. The ions collide with the surfaces on the vacuum chamber, which causes heating and additional electrons to be freed due to the high kinetic energy of the ions at the time of the collision. As more electrons are freed, more ions are made. Ions may also form when molecules are exposed to small electric fields at less than very good vacuum conditions and the electric fields pull the molecule apart. These ions are then accelerated by the Lorenz forces into a surface where they cause heating and liberate more gas that further drives the process. The ion bombardment can be observed by a slow steady increase in the vacuum pressure. Following the slow steady pressure increase, nonlinear heating can be observed.

5 CONCLUSIONS

Sixteen windows passed 1 MW of power and stabilized to steady state conditions. Grit blasting was found to be a critical processing step to avoid excessive heating and arcing at higher power levels. Amplitude modulation is the recommended method of RF conditioning because it conditions a continuous range of power levels while minimizing the gas load.

6 ACKNOWLEDGEMENTS

The authors would like to thank the people from LANL that helped with the experimental set up, especially Michael Borrego, Jeff Espinoza, Don Clark, J.D. Smith, Stephen Ruggles, Phil Torrez, Manuelita Rodriguez and Michael Collins.

REFERENCES

[1] K. Cummings, "Theoretical Predictions and Experimental Assesments of the Performance of Alumina RF Windows," Ph.D. Dissertation, University of California-Davis, June 1998.

[2] T. Taylor, "Surface Analysis of RF Window Materials", MST-6, Internal LANL Memo, 3/30/98

[3] A.H. Pickering, "Multipactor Discharges on Coaxial Waveguide Windows," Internal Report, EEV Ltd., Chelmsford, England, 1997.

[4] D.H. Priest, R.C. Talcott, "On Heating of Output Windows of Microwave Tubes by Electron Bombardment," IRE Trans. on Elect. Dev., Vol. ED8, July, pp. 243-251, 1961.

SOLID STATE POWER AMPLIFIER AS 805 MHZ MASTER SOURCE FOR THE LANSCE COUPLED-CAVITY LINAC*

J. T. M. Lyles, J. L. Davis
Los Alamos National Laboratory, Los Alamos, New Mexico 87545 USA

Abstract

From 100 to 800 MeV, the Los Alamos Neutron Science Center (LANSCE) proton linac receives RF power from forty-four 1.25 MW klystrons at 805 Megahertz (MHz). A single master RF source provides a continuous high level phase reference signal which drives the klystrons along the 731 meter-long linac through a coaxial transmission line. A single point failure of this system can deenergize the entire coupled-cavity linac (CCL) RF plant. The authors replaced a physically large air-cooled tetrode amplifier with a compact water-cooled unit based on modular amplifier pallets developed at LANSCE. Each 600 Watt pallet utilizes eight push-pull bipolar power transistor pairs operated in class AB. Four of these can easily provide the 2000 watt reference carrier from the stable master RF source. A radial splitter and combiner parallels the modules. This amplifier has proven to be completely reliable after two years of operation without failure. A second unit was constructed and installed for redundancy, and the old tetrode system was removed in 1998. The compact packaging for cooling, DC power, impedance matching, RF interconnection, and power combining met the electrical and mechanical requirements. CRT display of individual collector currents and RF levels is made possible with built-in samplers and a VXI data acquisition unit.

1 INTRODUCTION

The LANSCE linac is an 800 MeV proton machine capable of accelerating high average current, up to 1 mA of H^+. In addition, a 70 uA H^- beam is accelerated for the proton storage ring; the accumulated charge is extracted and directed to a spallation target for neutron production.

The CCL accelerates the two proton beams from 100 to 800 MeV. It is supplied with pulsed radio frequency power at 805 MHz from forty-four klystrons capable of producing up to 1.25 MW. These are driven by the RF reference source, which is located near the 100 MeV end of the structure. The RF source used a Burle Industries 8501 Cermolox® tetrode. The source generates 2000 watts of continuous RF. It is distributed to each klystron via directional coupler taps along a single temperature-stabilized drive line, located adjacent to the linac structure. This series-feed technique is simple and reliable, as long as the coaxial drive line is not compromised. In over twenty-five years of operation, this has not been a problem. For redundancy, the RF source itself is duplicated in a main/backup switched configuration. In 1993, the 8501 tetrode became obsolete. With an immediate purchase of enough tubes to supply operations for five years, we began searching for an alternative amplifier.

2 NEW POWER AMPLIFIER

2.1 Existing Transmitters

We considered developing a new cavity amplifier around another available UHF television transmitting tetrode. This idea was eliminated when we observed that fewer transmitters were being designed around medium power tetrodes, as all solid-state (transistorized) amplifiers were coming to market. LANSCE is situated at an elevation of 2120 meters above sea level, so the air density is reduced by 22% from sea level. We prefer water cooling where it is practical to remove the heat load from RF equipment. It is cooled in plant cooling towers, so that the water is continuously recycled though the RF system. There were no commercial water-cooled solid-state TV transmitters in this power range when this work began.

2.2 Solid-State Amplifier Concept

We developed a water-cooled amplifier module, using bipolar power transistors developed for cellular telephone stations. This began in 1992, and by 1993 the basic RF amplifier board was operating as designed. A multiple amplifier module was designed with four printed circuit boards mounted on two sides of an aluminum block with water passages drilled through the central core for heat removal.

2.3 RF Amplifier Module

The transistors used are Motorola part number MRF899, which are actually two bipolar transistors on a single flange. They contain gold-metallized NPN silicon transistors rated for 230 Watts of dissipation and are characterized for 150 Watts of output at 900 MHz. These transistors are factory-tested with a 5:1 load voltage standing wave ratio (VSWR) at all phases, while operating at 150 Watts at 26 Volts DC. We only operate with 22 Volts for an additional safety factor. The two devices are operated in class AB push-pull and are in common-emitter (CE) configuration, advantageous for high gain at UHF frequencies. Push-pull operation with

* Work supported by the US Department of Energy

the MRF899 minimizes the emitter-to-emitter inductance to the bonds between the devices on the flange, instead of the higher emitter to ground inductance of separate CE transistors [1]. Only the DC current flows to ground in the MRF899.

Push-pull operation of the device uses coaxial line baluns on the input and output sides. Matching to raise the transistor impedance to the coaxial line impedance is accomplished with microstrip over the PTFE/glass (ε_r'= 2.55) board and discrete chip capacitors to ground. Each push-pull amplifier is combined with an adjacent one on the same printed circuit board using Wireline® 3 dB quadrature hybrids, made by Sage Laboratories, Inc. Thick film resistors mounted on the pallet terminate the forth port of these hybrids. In figure 1, the "U"-shaped baluns are seen, along with the straight sections of Wireline® used for power dividing and combining. Two MRF899 devices are on each printed circuit board, which is mounted in a machined recess in the aluminum block. There are four boards and eight push-pull transistors per pallet. A total of 32 of these bipolar transistors are used in this amplifier on four pallets.

2.4 Cooling

The water cooling passages are drilled with three long passages along the length of the block, and short intersecting passages drilled at right angles to make the crossovers. Pipe plugs are used to block the drill holes after the passages are joined. Water enters the fitting at the bottom (see figure 1) and circulates along a serpentine path shown by the dotted line. In worst-case testing, we operated one push-pull transistor with 130 Watts of RF, and the semiconductor junction temperature was 135 degrees Celsius. Good engineering practice suggests limiting this to no more than 150 degrees [2]. In actual operation, each device operates at 80 Watts, with a generous safety margin which should ensure transistor lifetimes above 50,000 hours.

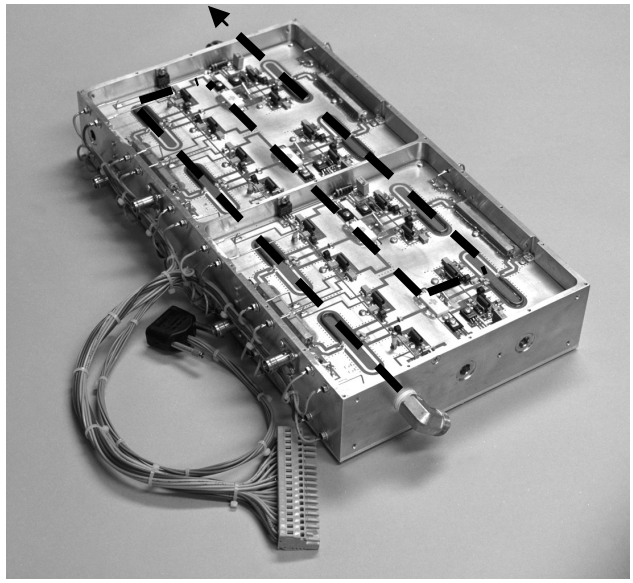

Figure 1. Basic pallet, one of four used in amplifier

2.5 Combined Amplifier

After the basic module and pallet concept was developed and tested, we completed the design of the splitting/combining networks, the overall packaging, cooling, monitoring, and control circuitry. Four of the pallets are arranged in a compact 48.3 cm-wide enclosure, with cooling paths in series. Sixteen amplifier boards are available, but only fourteen are combined

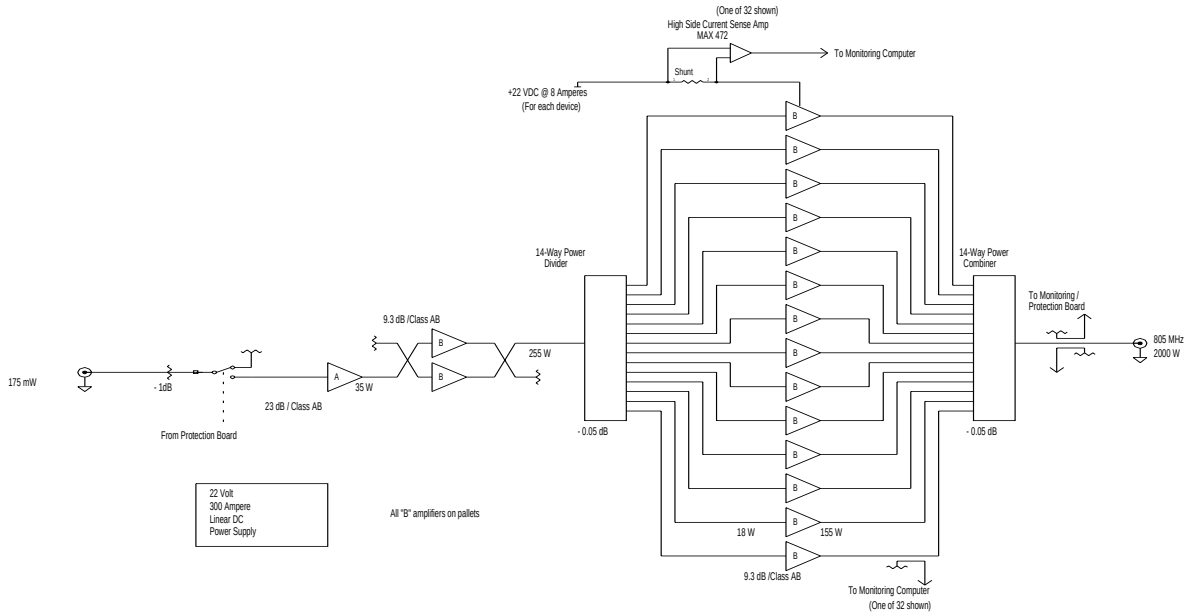

Figure 2. Block diagram of solid-state power amplifier

for the final stage, each supplying 155 Watts. Two are used as an intermediate stage, to drive the 14-way splitter with 255 Watts of power. These two boards (one half pallet) are driven and combined with 3 dB quadrature hybrids with isolation loads. In the block diagram the driver stage (marked "A") uses a commercial 35 Watt amplifier, also operated in class AB.

A 14-way radial "Tee" divider and combiner was supplied by Werlatone, Inc. Radial combiners have a good active match at each port, as long as each port is being driven by an equal source. The effects of complete failure of one amplifier in the 14-way device would theoretically create only a 1.15:1 VSWR at the remaining ports. RF power transistors typically do not fail in a shorted mode, at least not for very long. The worst case failure mode would most likely be if several transistor failures (open collector to emitter) or open terminations on the Wireline® hybrids reflected a short into the center of the output combiner. Our transmission line lengths transform an open circuit on any board to an open at the center of the combiner. This has worked well, as evident when we operated at full power for many days while one collector tab was disconnected on a board. No long term damage was sustained by the amplifier.

The amplifier load is a very long transmission line terminated in a fifty Ohm dummy load. There is no isolator needed since a fast-acting reflectometer/detector commands the protective logic to remove drive and power from the amplifier if the output reflected power becomes excessive.

2.6 Control System

For control, protection and monitoring, two separate schemes are used. An internal logic board handles the RF-on command, and monitors pallet temperatures, water flow, power supply voltage, and output reflected power. It protects the amplifier by switching off the 22 Volt DC power, and muting the RF drive.

A second system scans the DC bus voltage, the water temperature rise across the amplifier, the individual input and ouput RF levels from each amplifier board, and the collector currents from each transistor. This monitoring system uses a VXI-based data acquisition system from Hewlett-Packard, using a workstation/controller. A CRT screen provides all the amplifier parameters, along with a printer for hardcopy. We examine and track individual transistor and board performance; no major variations have been noted in over a year of operation of two amplifiers. Thirty-two surface mounted high-side current-sensing integrated circuits were incorporated to measure the collector currents from a shunt resistor on each connection to the DC bus bar. They provide ground-referenced zero to five volt analog levels to the multiplexer, without the common-mode DC bus voltage.

2.7 Power Supply

The RF reference must have low sideband noise as it could be amplified by the klystrons and be within the modulation bandwidth of the RF controls. We designed the amplifier for low phase noise and low modulation sidebands with respect to carrier. Massive linear power supplies were obtained from Kikusui Electronics, instead of lighter switchmode or SCR-type supplies, to eliminate the possibility of power supply noise sidebands. 250 Amperes DC is the normal operating current for 2000 Watts.

3 RESULTS AND CONCLUSION

The new amplifiers can provide as much as 2800 Watts of CW power at 805 MHz, with 40 dB of power gain. The DC-to-RF efficiency is 36%. The first amplifier was installed in 1996 and has operated continuously without failure. A second amplifier was installed in 1997, along with an RF switchover system and controls. Each amplifier in a single equipment rack (see figure 3) is much more compact than the four racks containing each original tetrode system.

ACKNOWLEDGEMENTS

The authors wish to thank Irene DeBaca, Mark Doub, Andrew Espinoza, Diane Johnson and Roger Johnson of LANSCE for their skillful work and dedication.

REFERENCES

[1] N. Dye, H. Granberg, *"Radio Frequency Transistors – Principles and Practical Applications"*, Butterworth-Heinemann, 1993, p. 92.
[2] Dye and Granberg, p. 73.

Figure 3. Two amplifiers (center of racks) and monitoring computer on right. DC power supplies are at lower left.

LEDA LLRF CONTROL SYSTEM CHARACTERIZATION*

A.H. Regan
Los Alamos National Laboratory, Los Alamos, NM 87545
P. Balleyguier
Commissariat a l'Energie Atomique, Bruyeres-le-Chatel, France
C.D. Ziomek
ZTEC, Inc., Albuquerque, NM 87109

Abstract

The Low Energy Demonstration Accelerator (LEDA) for the Accelerator for the Production of Tritium (APT) project will be built at Los Alamos National Laboratory. The low-level RF (LLRF) control system portion of this accelerator must perform many functions, of which the primary one is controlling the RF fields in the accelerating cavities. Plans have been made to provide for on-line characterization of the LLRF control system and the complete RF system through use of stimulus and response buffers, and a digital signal processor built into the field control system electronics. The purpose of this circuitry is to characterize the behavior of the entire RF system (klystron, waveguides, high power splitters, accelerator cavity, etc.). This characterization feature can be used to measure the performance of the closed loop system with respect to the open loop system, to provide an automated way to set loop parameters, to determine the cavity Q-curve, and to detect any abnormal behavior in the RF chain. The types of measurements include frequency and time-domain responses to given perturbations, amplitude modulations, etc. This paper will discuss types of algorithms that can be implemented and present a description and block diagram of the electronics to be used.

1 BACKGROUND MOTIVATION

Initially LEDA will be operated "manually" as we bring systems on-line individually. However, in planning for the APT plant, it is realized that we will be operating an accelerator with upwards of fifty control systems. Automatic calibration and test sequences will enable the operators to quickly diagnose a system and anticipate possible failures. In addition, performing a dynamic frequency response measurement of the RF chain around its normal working point, will provide for characterization of individual control systems throughout their "lifetime."

Here the RF chain refers to part of the LLRF control system hardware, the preamplifier, the klystron, waveguide, high power splitters, couplers, cavity, pickup loop, downconverter, and return signal cable. This measurement will be a special mode of operation, incompatible with the normal control algorithm. The aim is to measure how a known perturbation at a given frequency is transmitted along the RF chain.

Uses of such measurements include:

- Optimizing performances of the control system, by predicting ultimate loop gain possibilities
- Checking performance of closed loop operation with respect to open loop
- Setting the correct loop phase shift
- Detecting any abnormal behavior in the RF chain

2 DISCUSSION

One of the primary functions of the low-level RF control system is to maintain the field levels inside the accelerating cavities. The basic VXIbus module architecture for the LEDA LLRF control system has been described previously[1] as well as some preliminary low-level RF modeling for the APT[2]. By implementing a LLRF control system that provides easy software/hardware interaction, other functions can be implemented besides simple real-time setup by the accelerator operators. Software can also be used to perform RF system analysis.

A fundamental component of the LLRF control system is the Field Control Module (FCM). This module is a feedback/feedforward controller used to regulate the RF field parameters of the accelerator cavity. The FCM performs cavity field feedback and beam feedforward control algorithms in both digital and analog circuitry. The digital processing on the FCM is centered around a Texas Instruments TMS320C50 fixed point digital signal processor (DSP). The DSP processor provides powerful control algorithms and flexible operational scenarios. The digital processing provides precision detection and flexible control signals to bandwidths around 10 kHz. In order to extend the bandwidth beyond this, analog circuitry is used to process the field and beam signals in parallel with the DSP. The analog circuitry is more susceptible to errors and noise, and is less flexible, but provides control signal bandwidths to around 1 MHz. A block diagram of the FCM is depicted in figure 1.

The flexibility of the digital processing on the FCM is demonstrated by its ability to function in significantly different operating modes. The operating modes encompass many different operational scenarios including continuous operation, pulsed operation, amplitude modulation, phase modulation, frequency modulation, amplitude and phase control, amplitude-only control, open-loop operation, and closed-loop operation. Also, setpoints, gains, bandwidths, and algorithms can be adjusted by the operator through the VXIbus interface. In

addition to the control circuitry, the FCM includes circuitry that performs self-calibration and system characterization. The calibration and characterization functions are accomplished with either frequency modulation or arbitrary waveform modulation.

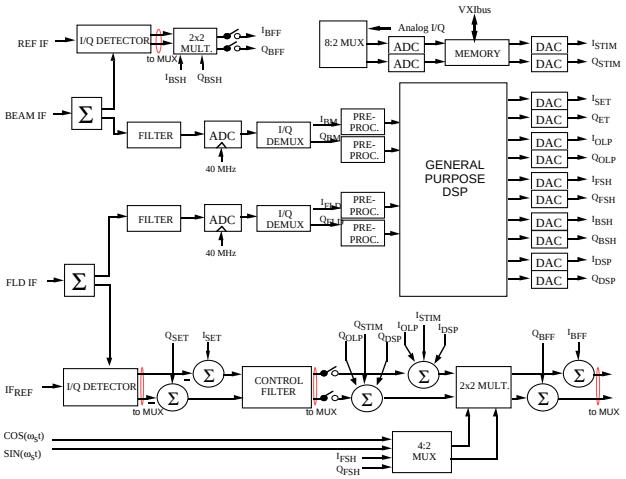

Figure 1. Block Diagram of Field Control Module

The frequency modulation functionality can be used for self-calibration of the in-phase/quadrature (I/Q) detectors on the FCM and other modules in the system. The FCM can be placed into an operating mode where it generates a control output that applies a frequency shift to the master oscillator frequency. The original purpose of this shift is to provide a means of resonance tracking to rapidly heat the accelerating structure after a RF fault.[3] It has the additional feature though, of providing us with a means of inputting a test frequency for measurement of the offsets, quadrature errors, and gain imbalances in the I/Q detectors. This frequency modulation functionality will also allow us to modulate the klystron drive with a swept FM signal, something SLAC has found quite useful for processing cavities.

The arbitrary waveform modulation functionality can be used to characterize the RF system response and configure the RF system control parameters. The arbitrary waveform functionality is provided by stimulus and response waveform buffers on the FCM. The stimulus waveform buffer allows loop excitation with arbitrary modulation signals stored in memory and converted to analog signals in DACs operating at 10 MHz. The response waveform buffer captures the response of the RF system to the stimulus. Various points along the signal path in the FCM can be multiplexed and their data stored for later analysis. The cavity field feedback signal can be examined to characterize and configure the total RF system. In effect, this can be thought of as a baseband arbitrary waveform generator, with the ability to perform baseband network analysis.

The first step to system characterization is to set the DSP outputs to a constant value such that the normal field level is measured in the cavity (without beam). A generated perturbation (test signal) is then added to the normal output values to generate the perturbed input signal (I_{STIM} and Q_{STIM}). We will operate the klystrons some percentage below saturation, in order to allow operating room for the disturbance input. The modulation we place on the drive will be simply some small noise on top of a baseband level. One type of test signal consists of a succession of pre-calculated samples at a certain frequency rate and during a certain period of time. While this test signal is being injected into the system, the cavity field perturbed inputs to the DSP are measured and stored for future analysis. Therefore, the only real-time process would be to read a pre-calculated complex signal, add it to a constant value, output this signal at a certain frequency rate, acquire the perturbed signal at the same frequency rate, subtract the constant value, and store it in memory. All other analysis could be done after this sequence, in a non-real time mode by the supervisory system software, EPICS.

Some of the input test signals will be time domain versions of single frequency tones at known system-problem frequencies. Other possible input test signals include chirp pulse-compression waveforms. This methodology will also allow us to modulate the RF drive with a swept frequency signal for frequency-domain analysis of the RF system. In another test scenario, a small amount of white noise can be injected. Such a technique has been used with success on the ELSA linac at Bruyeres le Chatel.[4] The test signal was actually a special kind of noise: constant in amplitude and random in phase in the frequency domain. We anticipate bandwidth-limiting the noise for better measurements, and more realistic inputs.

Off-line processes include generating the desired input test signals and performing data analysis. One nice feature about EPICS is its ability to incorporate MATLAB functions. MATLAB, a control system design and analysis software package, has a very useful function known as TFE. The Transfer Function Estimate simply requires a set of system inputs and outputs, for which it returns the system's transfer function. The complex frequency response can then be plotted in the complex plane with frequency as a parameter, or as a Bode diagram. Once transfer functions are calculated, they can be compared to models for determining desirable operating parameters

3 HARDWARE SPECIFICS

A photograph of the Field Control VXIbus Module is shown in figure 2. The analog electronics are along the bottom of the module, while the digital hardware is located in the upper two thirds. The analog circuitry consists of two intermediate frequency I/Q detectors, baseband analog PID control circuitry, analog switches and multipliers for adjustments, and the analog control

output drivers. The digital circuitry consists of quadrature-sampling ADCs, decimating digital filters, the DSP, the control output DACs, the DSP memory resources, and the VXIbus interface. In addition, The FCM contains the stimulus waveform memory banks and DACs and response waveform memory banks and ADCs.

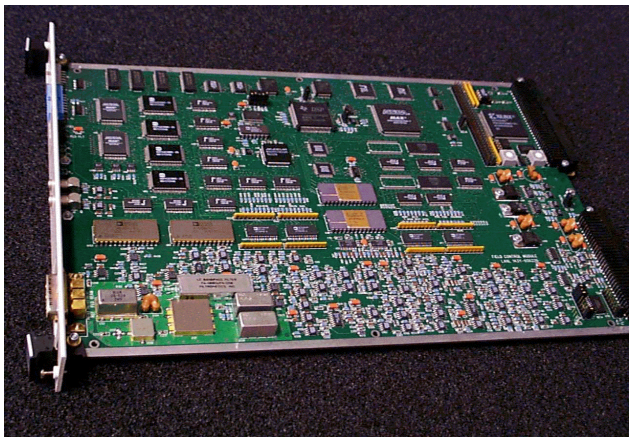

Figure 2. Field Control VXIbus Module

The EPICS interface to the stimulus/response functionality is accomplished with two sets of read/write registers that have been designated as the Stimulus I (or Q) Memory Register and the Response I (or Q) Memory Register. These registers provide access to the First-In, Last-Out (FILO) memory buffers for the stimulus DACs and response ADCs. Each FILO memory is 256 kwords in length, providing a time duration of approximately 26 ms at the 10 MHz DAC and ADC rate. In order to measure the response of the system, the FILO memory buffers are placed in their record mode, thus capturing response waveforms from the control system. There are two possibilities for the time-duration of the stimulus/response signals. The continuous duration causes the stimulus waveforms to be generated repeatedly and the response waveforms to be captured repeatedly. The single duration causes the stimulus DACs and response ADCs to generate and capture data only once until the waveform buffers are full. After the response waveform buffers are full, the FILO memory buffers stop and the VXIbus host processor is notified.

4 CONCLUSION

The FCM is one of five fundamental modules in the APT LEDA LLRF control system. It not only performs analog and digital field control, but has some features built in to allow us to perform on-line RF system characterization. This will be useful in determining various operational parameters, as well as provide a means for conditioning cavities. We expect to integrate the first LLRF control system with the rest of LEDA later this year. Once commissioning commences, one of the first LLRF tests we will perform is RF system characterization.

REFERENCES

[1] Regan, A.H., et al, APT LLRF Control System Functionality and Architecture," Proceedings of Linear Accelerator Conference 1996, Geneva, Switzerland, August, 1996, pp. 225-227.

[2] Regan, A.H., Ziomek, C.D., "APT LLRF Control System Model Results," Proceedings of PAC '97, Vancouver, Canada, May 1997.

[3] Rees, D.E., et al, "Design and Test Results Of The Low Energy Demonstration Accelerator (LEDA) RF Systems, " Proceedings of EPAC '98, Stockholm, Sweden, June, 1998.

[4] Balleyguier, P. "Pulsed Network Analysis with Random Signal for RF Feedback Optimization," IEEE Trans. Nucl. Sci., Vol. 43, No. 4, August 1996, pp. 2337-2342.

LEDA RF DISTRIBUTION SYSTEM DESIGN AND COMPONENT TEST RESULTS*

William T. Roybal, Daniel E. Rees, Heather L. Borchert
Los Alamos National Laboratory
Michael McCarthy, General Atomics, Loren Toole, Savannah River Site

Abstract

The 350 MHz and 700 MHz RF distribution systems for the Low Energy Demonstration Accelerator (LEDA) have been designed and are currently being installed at Los Alamos National Laboratory. Since 350 MHz is a familiar frequency used at other accelerator facilities, most of the major high-power components were available. The 700 MHz, 1.0 MW, CW RF delivery system designed for LEDA is a new development. Therefore, high-power circulators, waterloads, phase shifters, switches, and harmonic filters had to be designed and built for this application. The final Accelerator Production of Tritium (APT) RF distribution systems design will be based on much of the same technology as the LEDA systems and will have many of the RF components tested for LEDA incorporated into the design. Low power and high-power tests performed on various components of these LEDA systems and their results are presented here.

1 WAVEGUIDE SYSTEMS

The first accelerating section of LEDA is the radio frequency quadrupole (RFQ). Three 350 MHz 1.3 MW CW klystrons can deliver RF power to the RFQ.[1] Each of the waveguide runs from the klystron contain several important components that will be described in the next section

The RFQ is followed by the Coupled Cavity Drift Tube Linac (CCDTL). This section of the accelerator is driven by a single 700 1.0 MW CW klystron.[2] Many of the components used in the 350 MHz system are also used in the 700 MHz systems. The 700 MHz RF systems will comprise most of the RF systems used on the APT accelerator. [3]

WR2300 full-hcight waveguide is used for delivering up to 1.2 MW of CW RF power at 350 MHz to the RFQ. In order to minimize the RF power passed through the vacuum windows to the RFQ the power is divided into equal parts. Hybrid couplers (3 dB) are used to split the power. After the power division, the waveguide size transitions to half-height and the power from one klystron is delivered to the RFQ through four waveguide feeds. Since the RFQ serves as the power combiner, the effective electrical length of the waveguide runs must be controlled. High-power phase shifters are introduced to the waveguide runs to set the phase at the proper value and to make adjustments when needed. A typical waveguide configuration from the klystron to the RFQ is shown in Figure 1.

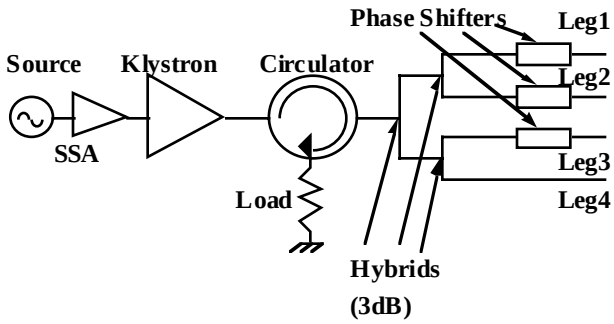

Figure 1: Schematic of LEDA RFQ RF power delivery system.

2 RF COMPONENTS

2.1 Circulators

Both the 350 and 700 MHz RF delivery systems use a high-power circulator to protect the klystron from excessive reflected power. The circulators used on LEDA are manufactured by Advanced Ferrite Technology (AFT). The circulators have a measured insertion loss of less than 0.05 dB at the center frequency. The isolation for the three ports of each circulator is greater than 30 dB.

2.2 Phase Shifters

Phase shifters supplied by Mega Industries are used to correct any phase differences introduced to the waveguide runs that lead to the accelerator. The phase shifters adjust the phase in the waveguide up to 45 °. The phase shifters move three posts in and out of a section of waveguide (0.0 to 2.5") to introduce the required phase shift. They are adjusted manually with a knob or electronically with a motor. A photograph of a 350 MHz WR2300 phase shifter is shown in Figure 2.

The WR2300 half-height phase shifters were tested on the test stand for 4 hours at 200 kW CW. The 45 ° of phase shift was demonstrated at this power level. A WR2300 full height phase shifter was tested on the up to 1.0 MW CW over the 45° range at 350 MHz for several hours. The external temperature near the base of one of

* Work supported by the US Department of Energy.

the posts (with the posts fully inserted into the waveguide) reached a constant temperature of 154 °F at this power level. The posts were extracted with the power held constant and the temperature at that location reduced to 135 °F.

Figure 2: Photograph of 350 MHz WR2300 half-height Phase Shifter.

2.3 Waveguide Switches

A three port waveguide switch, also manufactured by Mega Industries, is used to isolate a klystron from the accelerating structure. The APT accelerator has installed redundancy on each copper structure and the waveguide switch is used to isolate a failed RF station from the cavity. A phase shifter and a shorting plate on the third port of the waveguide switch is used to present a short at the proper phase to the accelerating cavity iris to allow operation with one system removed.

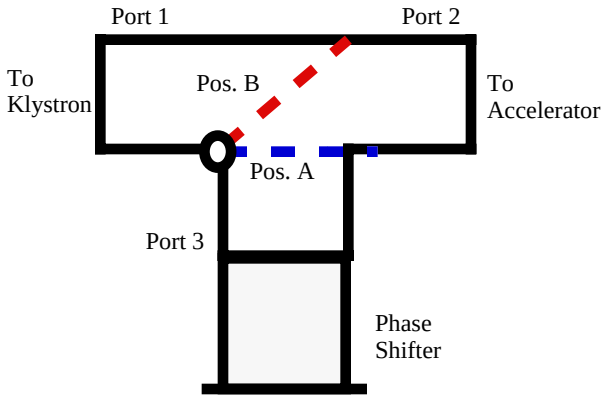

Figure 3: Schematic of a Waveguide Switch in its typical configuration.

As shown in Figure 3, with the waveguide switch in position A the power is directed to the accelerating structure. In position B a short circuit at the correct phase is presented to the coupling iris of the accelerator and any power from the klystron is reflected back to the circulator load.

2.4 Harmonic Filters

Harmonic filters are used between each klystron and circulator to de-Q any potential resonant circuits at the harmonic frequencies. The harmonic filter occupies a 46" section of waveguide. It has 6 antennas protruding into the narrow wall of the waveguide which are terminated in 200 W, 50 Ohm, air cooled loads. A photograph of a 350 MHz harmonic filter is shown in Figure 4.

Figure 4: Photograph of LEDA 350 MHz Harmonic Filter.

Since the fundamental frequency is carried in the TE_{10} mode with the electric fields orthogonal to the broad wall, the antennas are inserted through the narrow wall of the waveguide to couple out harmonic power in the TE_{11} and TM_{11} modes. [4] If the antenna is too thick, it can couple a significant amount of power at the fundamental frequency. An optimal length and thickness for the antennas were chosen.

The diameter of all antennas is 0.0787" (2 mm). The length of antennas for the harmonic filter for the 350 MHz system is 3.88" (9.85 cm) and 1.75" (4.44 cm) for the 700 MHz. The measured insertion loss for the harmonic filters are 0.04 dB and 0.01 dB for the 350 and 700 MHz filters, respectively. The measured antenna coupling value for either fundamental frequency is -60 to -70 dB. For the first through the third harmonic, the coupling value varied between -20 to -30 dB. Currently, several harmonic filters at 350 MHz are installed and have been in use for hundreds of hours without a failure. As much as 20 Watts of harmonic power have been measured on some antennas during operation of the klystrons at full power.

2.5 RF Loads

RF loads are used on the all high-power RF systems. Except for the test stand, 200 kW loads are placed on the return leg of the 3 dB hybrids and circulators. For testing

RF components, the test stands use RF loads that are capable of taking the full power out of the klystron.

The 350 MHz full power loads were developed by Titan Beta. They are used on the test stand for testing components up to 1.2 MW CW. To reduce the length of these water loads, they operate using a 70% water and 30% propylene glycol mixture. At this mixture, the VSWR for the loads according to factory low power testing is 1.05:1, however the best achieved under high power conditions is 1.07:1.

Similar loads are used for the test stand at 700 MHz. Premier Microwave (now Atlantic Microwave) provided the 1.0 MW CW RF water loads. Deionized water is used in these loads. The body of the load is stainless steel. The VSWR for these loads is also 1.05:1. This load has been operated at 1.1 MW for 24 hours of continuous operation for a klystron test.

Altronics Research supplies a coaxial mounted 50 Ohm film resistor rated at 200 kW. Five resistors of this type are used on each RF transmitter. It is based on a shell-and-tube design and is cooled with deionized water.

The resistor's transient rating is about 22 joules. It can accept 6 times the average rated power for 100 microseconds. Coolant flow results in a rated pressure drop of 50 psi at 20 gpm. All resistors are continuously monitored for flow and temperature. The flow rate is monitored using a Rosemount flowmeter coupled to a Oripac orifice plate. Omega RTD probes are used for all temperature measurements in the cooling systems. An Allen-Bradley system is used to monitor these sensors and software interlocks will recognize the effect of transients and the associated time constant of the piping system and instrumentation.

The robustness of this design has been an ongoing concern in relation to offnormal conditions expected during acceleration operation. At outlet temperatures above 90 °C, localized boiling has been observed to occur in the cooling channel, reducing the film's heat transfer coefficient and potentially creating conditions for failure. However, the rate of failure has yet to be determined. Preliminary acceptance tests of 21 resistors have accumulated nearly 100 hours of test stand time at rated power. Of the 21 loads, 18 passed the 4 hour full power test, 2 required rebuilding and passed the 4 hour test on the second attempt, and 1 was rebuilt twice before finally passing the 4 hour acceptance test.

2.6 Flexible Waveguide

Sections of flexible waveguide are located in every leg of every waveguide run to accommodate thermal expansion between fixed points. Ultraflexible pieces are used to connect critical components such as the klystron and RF windows [5] to the rest of the system.

Ultraflexible WR2300 half-height guide with a 90° E-plane bend incorporated into it is used as the last sections of waveguide that connects the RF windows to the RFQ. These sections allow for the expansion of the RFQ due to heating. The manufacturer of these flexible sections is Mega Industries. These sections have been tested and installed on the waveguide runs. The results of the mechanical testing is given in Table 1. The measured results for the compression and expansion displacement and the horizontal offset were not compliant with the original requirement. The results of all the mechanical tests were reevaluated and later determined to be sufficient.

	Measured	Expected
Çompression with 12.5 lbs force	0.109"	0.125" min.
Expansion with 12.5 lbs force	0.045"	0.125" min.
Vertical Tilt force to get 1° tilt	18 ft-lbs	25 ft-lbs max.
Horizontal Tilt force to get 1° tilt	14 ft-lbs	25 ft-lbs max.
Vertical Offset force to achieve 0.0625" offset	+7 lbs & -5 lbs	15.7 lbs max.
Horizontal Offset force to achieve 0.0625" offset	+18 lbs & -21.5 lbs	15.7 lbs max.
Clockwise Twist with 20 ft-lbs of torque	0.165"	0.10" min.
CounterClockwise Twist with 20 ft-lbs of torque	0.165"	0.10" min.

Table 1: Mechanical test results of the 90° E-bend flexible half-height WR2300 waveguide.

High-power electrical tests were performed on one WR2300 half-height flexible 90° E-bend. It was tested for 4 hours at 900 kW CW without failure.

REFERENCES

[1] D. Rees et al., "Operation and Test Results of 350-MHz LEDA RF System," Proceedings of LINAC98, Chicago, August 24-28, 1998.

[2] D. Rees et al., "Accelerator Production of Tritium 700-MHz and 350-MHz Klystron Test Results," Proceedings of LINAC98, Chicago, August 24-28, 1998.

[3] K. Cummings et al., "Results and Lessons Learned from Conditioning 1-MW CW 350 MHz Coaxial Vacuum Windows," Proceedings of LINAC98, Chicago, August 24-28, 1998.

[4] H. Frischholz, "The LEP RF Power Generation and Distribution System", LANL Colloquium, 1997

[5] M. McCarthy et al., "Overview of the APT RF Power Distribution System," Proceedings of LINAC98, Chicago, August 24-28, 1998.

A THERMAL ANALYSIS AND OPTIMIZATION OF THE APT 210 kW POWER COUPLER*

J.A. Waynert, F.C. Prenger
Los Alamos National Laboratory, Los Alamos, New Mexico 87545 USA

Abstract

This paper presents the thermal analysis and heat load optimization of the continuous power 210 kW, 700 MHz RF power coupler (PC) for the Accelerator Production of Tritium (APT). The PC is a co-axial design with RF power transmitted in the annular region between two concentric cylinders. Thermally, the PC represents a link from room temperature to the superconducting niobium cavities operating at 2 K. The analysis includes all the major heat transfer mechanisms: conduction, RF joule heating in normal and superconducting materials, infra-red radiation, and, forced and natural convection cooling of the inner and outer conductors. A performance comparison is given for one and two single point thermal intercepts, versus a counter-flow heat exchanger on the outer conductor. The benefits of reducing the operating temperature of the center conductor are discussed. The variation in thermal performance of the inner and outer conductors for several operating modes is also presented.

1 INTRODUCTION

The APT utilizes a linear accelerator to produce energetic protons, which strike a metal target of tungsten and lead, producing neutrons through spallation. The neutrons are captured in ^{3}He, producing tritium. The low energy portion of the accelerator uses conventional normal-conducting components, after which, the protons enter the superconducting accelerator section. The superconducting portion of the APT has cryomodules containing superconducting RF accelerating cavities separated by resistive focusing quadrupole magnets. The RF cavities are cooled by saturated superfluid helium at 2.15 K. Although there are two and possibly three variations of cryomodule, depending on the location of the module within the linac relative to the proton energy, this paper will focus on only the β=0.82 cryomodule.

Within a cryomodule, the PCs represent the second largest thermal load on the 2 K system, only the cavities generate a larger heat load. There are several objectives of the PC thermal analysis:

- Develop a model which accounts for the major heat loads and can be used to explore a wide range of geometries, material properties, and operating conditions;
- Ensure viable thermal operation of the PC; and
- Optimize total system refrigeration input power.

This paper will discuss each of the objectives in detail. Section 2 provides a description of the PC and the thermal model that has been developed. Section 3 presents the results for the inner and outer conductors and considers the implications of various cooling schemes on the cryomodule system total refrigeration input power. Section 4 gives a summary and discussion of the work.

2 DESCRIPTION OF THERMAL MODEL

Figure 1 shows a cut-away view of the PC as modeled, with a simple illustration of a counterflow heat exchanger for cooling of the outer conductor. The total length of the PC is about 1006 mm. Not shown are the two RF windows which couple the microwave power from the wave guide to the PC, mating at a 90^o angle to the coupler at the 300 K end.

The outer conductor is 152.4 mm ID at the 300 K end and tapers to 100 mm ID at the 2.15 K end where it attaches to the beam tube. The co-axial inner conductor has a similar taper, going from 66.7 mm OD to 43.5 mm OD at the beam tube end. The outer conductor is 2.4 mm thick stainless steel plated with a 15 μm copper film on the inside. About 120 mm from the beam tube end, the outer conductor mates with a niobium nipple with RRR=40 and a wall thickness of 3.2 mm. The inner conductor is solid copper with RRR=50 and wall thickness of 1.5 mm. There is a concentric stainless steel tube within the copper tube (see Fig. 1) which provides coolant for the inner conductor. Helium gas enters the ID of the stainless tube from the left of Fig. 1, passes to the right end of the PC, and returns through a 3.2 mm radial gap between the stainless and copper tubes.

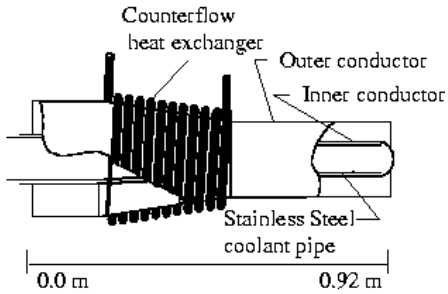

Figure 1: Schematic of the PC with a simple illustration of a counterflow heat exchanger on the outer conductor.

* Work supported through U.S. Department of Energy

The thermal model is axisymmetric, one-dimensional, and uses a finite difference approximation. There are over 200 nodes. Temperature dependent properties are used for the thermal conductivity, RF resistivity (RRR = 2, for 750 MHz), and specific heat and enthalpy of the helium gas coolant. Infra-red radiation heating is calculated assuming gray body, diffuse scattering through a CAD based program called RadCAD [1]. SINDA [2] is used for the thermal analyzer.

The heat transfer mechanisms considered for the inner conductor are:

- Conduction through copper (RRR=50)
- Radiation (gray body, diffuse, emissivity=0.3);
- RF heating (distributed or constant current); and
- Internal forced convection (supercritical helium in annular region).

The outer conductor heat transfer mechanisms considered are:

- Conduction through stainless steel (304L) and copper plating (thermal conductivity ratio=50);
- Radiation (gray body, diffuse, emissivity=0.3);
- RF heating (distributed or constant current); and
- Cooling - through localized single point thermal intercepts or distributed through forced convection counterflow cooling.

The emissivity value for copper has been chosen as 0.3. Typical values range from about 0.05 to 0.9 depending on the condition of the surface. We believe our selection of 0.3 represents a conservative choice for copper. How the emissivity will change over the 40 year life of the accelerator is unknown. The emissivity for niobium was also chosen as 0.3.

The inner and outer conductors are joined by a 1.27 mm thick copper plate at the furthest most position to the left of Fig. 1. This plate is the electrical shorting plate of the RF quarter-wave stub.

3 RESULTS

The analysis naturally divides into separate consideration of the inner and outer conductors. The temperature distribution on the inner conductor is only marginally coupled, via radiation, to the temperature distribution on the outer conductor, and hence, may be considered independent of the cooling scheme for the outer conductor.

3.1 Inner Conductor Results

The temperature distribution on the inner conductor was calculated for 210 kW traveling and standing wave (TW, and SW respectively) conditions, and for the special test condition of 500 kW TW. Figure 2 shows the RF-induced power distributions on the inner conductor for the 210 kW, 750 MHz TW and SW as calculated from MAFIA [3]. In Fig. 2, 0.0 represents the leftmost end of the PC shown in Fig. 1, and the beam tube interface is roughly at 0.92 m. Although the RF analysis shows an azimuthal power variation in addition to the axial dependence, the maximum circumferencial value of power dissipation at each axial position was chosen as a conservative and simplifying assumption. The data points show the power values as used at the individual nodal coordinates.

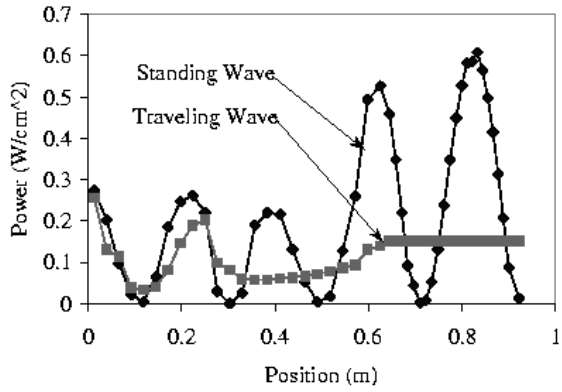

Figure 2. RF-induced heating distribution on the inner conductor for both the 210 kW standing wave and traveling wave.

Figures 3 and 4 show the resulting temperature distributions on the inner conductor and the coolant fluid, assumed to be 3 g/s, 300 K helium at 3 atmospheres at the inlet, in all cases. The temperature distributions from using a constant current with the same total power dissipation in the inner conductor are also shown.

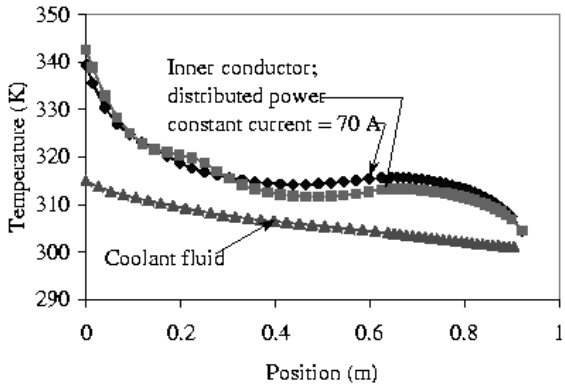

Figure 3. Temperature distribution in inner conductor (upper two curves) and cooling fluid (lower curve) for 210 kW TW. (235 W dissipated on inner conductor).

As seen in Fig. 3, the difference in temperature distribution between distributed power and constant current, is less than 5 K. The difference in the fluid temperatures for constant current vs distributed power is even less, so only one is shown in Fig. 3. The same small difference in temperature between distributed power and constant current is seen in the 210 kW SW results, Fig.4.

The results for the 500 kW TW are not plotted due to space limitations in this article. The highest temperature in the inner conductor is 365 K (at the leftmost end of Fig. 1) and the coolant fluid outlet temperature is 330 K. The results of the analysis of the inner conductor

demonstrate that, for the operating conditions considered, the inner conductor is adequately cooled.

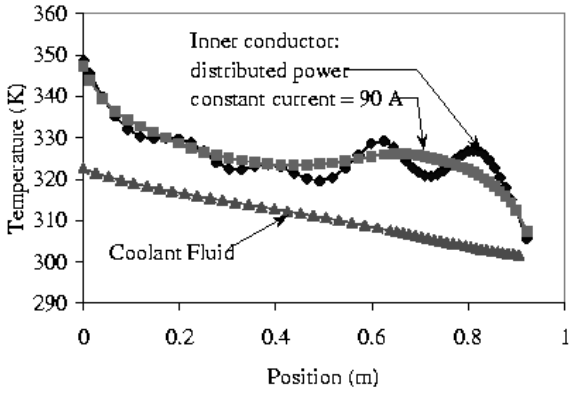

Figure 4. Temperature distribution in the inner conductor (upper two curves) and cooling fluid (lower curve) for 210 kW SW. (310 kW dissipated on inner conductor).

3.2 Outer Conductor Results

The outer conductor analysis focuses on the total room temperature refrigeration input power as a function of two different cooling approaches:

- The distributed cooling of the counterflow vs
- The localized cooling of single point intercepts.

Regardless of which cooling approach is chosen, the heat load to 2.15 K is largely determined in the niobium nipple. This may be understood by reference to the solution of the one-dimensional heat diffusion equation with constant thermal conductivity, k, and uniformly generated heat load, Q_{gen}. Equation 1 shows the solution for a Nb nipple of length, L and heat conduction cross-sectional area, A. The hot end is assumed to be at T_h, while the cold end is at T_c = 2.15 K. If the Nb is kept below its superconducting transition temperature of 9.2 K, the heat load generated in the Nb is mainly due to IR radiation = Q_{gen}. Q_c is the heat load at 2.15 K.

$$Q_c = \frac{kA}{L}(T_h - T_c) + \frac{Q_{gen}}{2} \qquad (1)$$

There is an optimum length, L, since Q_{gen} will vary linearly with L, but, generally, L is chosen for mechanical or manufacturing reasons. To minimize Q_c, A should be made as small as practical, and k should also be small, i.e. RRR should be low. Q_{gen} can be reduced by lowering the emissivity of the materials (this has been discussed in an earlier section), or the inner conductor temperature can be reduced (this will be discussed later). In a typical situation, with geometry, emissivities and inner conductor temperature fixed, T_h, and hence, Q_c, are determined by the temperature developed by the cooling configuration at the stainless steel, Nb interface. Table 1 presents the heat loads at 2 K and at the various intercept temperatures, plus the resulting room temperature refrigeration input power. For example, the third configuration, with two single point intercepts, one at 7.8 K at the stainless steel niobium interface, and the other at 56 K at the location for minimum refrigeration input power, has respective heat loads of 7 W and 23 W, and a total 310 K refrigeration input power of 3550 W. Refrigeration input power is based on real refrigerator efficiencies of 0.13 and 0.18 (0.25 and 0.27) for 2.1 K (4.6 K) liquefaction and refrigeration loads respectively. When the lowest temperature intercept is above 9.2 K, a copper strap was used to connect the stainless steel/Nb boundary to the 2.15K helium vessel, which increases the 2 K heat loads.

Table 1. Calculated heat loads at 2 K, intercept 1 at T1, and intercept 2 at T2 for point intercepts, with T2 at optimal location. Calculated 2 K load for counterflow heat exchanger for coolant inlet temperatures of 2.6 K or 4.6 K. Wtot = total refrigeration input power.

Thermal intercept configuration	**Q at 2K (W)**	**Q at T1 (W:K)**	**Q at T2 (W:K)**	**W total (W)**
1 single point	1.8	15:4.6	-	5525
1 single point	4.3	53:15	-	7570
2 single points	2.4	7:7.8	23:56	3550
2 single points	4.1	6.2:15	24:56	4400
Counterflow 2.6 K, 0.07 g/s	1.9	-	-	3070
Counterflow 4.6 K, 0.07 g/s	2.0	-	-	3371

Lowering the inner conductor temperature can reduce the 2 K radiation load, Q_{gen}, but the work required to remove the inner conductor heat load at the reduced temperature increases. Using the double point intercept at 7.8 K and 56 K as an example, the total refrigeration input power can be reduced by as much as 26% by lowering the inner conductor coolant temperature to 200 K.

4 SUMMARY

A thermal model has been built which accounts for the major heat loads in the 210 kW PC. Inner conductor results indicate adequate cooling under TW and SW conditions. There is a 14% reduction in refrigeration input power by using 2.6 K counterflow cooling on the outer conductor over the best double point cooling approach. Further trade-off studies on the outer conductor cooling scheme are required. Lowering the inner conductor temperature adds complexity to the system, but offers a 26% reduction in PC refrigeration input power.

5 REFERENCES

[1] CAD based thermal radiation analyzer, Cullimore and Ring Technologies, Inc, Littleton, CO, crtech@netcom.com.

[2] Systems Improved Numerical Differencing Analyser, Cullimore and Ring Technologies, Inc, Littleton, CO, crtech@netcom.com.

[3] Electromagnetic Simulator, CST, D-64289 Darmstadt, Germany, info@sct.de

DEEP X-RAY LITHOGRAPHY FABRICATION OF mmWAVE CAVITIES AT THE ADVANCED PHOTON SOURCE*

J.J. Song, Y.W. Kang, R.L. Kustom, A. Nassiri
Argonne National Laboratory, Argonne, IL 60439, USA
G. Caryotakis, E.N. Jongewaard, SLAC, Klystron Dept., Stanford, CA, USA
V. White, U. of Wisconsin at Madison, Center for X-ray Lithography, Madison, WI 53706, USA

Abstract

Millimeter-wave (mmWave) accelerating cavity structures have been manufactured using the deep x-ray lithography (DXRL) technique. These cavity structures have potential applications as parts of linear accelerators, microwave undulators, and mm-wave amplifiers. The microfabrication process includes manufacturing of precision x-ray masks, exposure of positive resist by x-rays through the mask, resist development, and electroforming of the final microstructure. Prototypes of a 32-cell, 108-GHz constant-impedance cavity and a 66-cell, 94-GHz constant-gradient cavity were fabricated at APS. Using an HP8510C 26-GHz vector network analyzer, rf measurements are being prepared with a frequency up- and down-converter before and after a test cavity structure. Preliminary design parameters for a 91-GHz multi-module klystron along with an overview of the DXRL technology are also discussed.

1 INTRODUCTION

A potential advantage of mmWave accelerators for particle physics is a higher accelerating gradient. It is known from experience with S- or X-band accelerating structures that gradients are limited by dark current capture, which is the acceleration of field-emitted electrons to relativistic energies, and by rf breakdown. The maximum gradient from these phenomena scales approximately inversely with wavelength; scaling accelerating structures to significantly higher frequencies could provide a higher field gradient as proposed by P.B. Wilson [1].

The new micromachining technology, known as LIGA, consists of deep-etched x-ray lithography (DXRL), electroplating, and micromolding. The microfabrication processes have been developed by W. Ehrfeld and co-workers to the degree that submillimeter actuators, motors, and gears can be built with great accuracy and a high aspect ratio. Electric field levels as high as 50 MV/m and magnetic field levels of 1 T have been achieved with these components [2]. Specifically, this technology could offer significant advantages over conventional manufacturing methods in such areas as precision fabrication and mass production.

The concept of applying these techniques to develop rf cavities for mm-wave linacs [3], undulators [4], free-electron lasers [5], and mm-wave amplifiers originated at Argonne National Laboratory. A meter-long structure with similar accuracy that also provides channels for vacuum pumping, adequate cooling, and focusing elements is feasible. Major challenges of the DXRL techniques are: fabrication of the wafers into three-dimensional rf structures, alignment and overlay accuracy of the structures, adhesion of the poly-methylmethacrylate (PMMA) on the copper substrate, and selection of a developer to obtain high resolution.

2 FABRICATION

The simplified version of the DXRL process is shown in Fig. 1. It consists of making an x-ray mask, preparing a sample and x-ray exposure, developing, and electroplating the structure. The process is related to the fabrication of semiconductor integrated circuits and requires similar tooling, in addition to a high-energy light source and electroplating equipment. In DXRL, no dissolution of unexposed positive thick resist is allowed during development, and good adhesion of the high-aspect ratio resist structure to the copper substrate is essential. In addition, the microstructures must have high mechanical stability and low internal stresses to prevent stress corrosion during exposure and development. Also, the resist material must be compatible with the electroplating process.

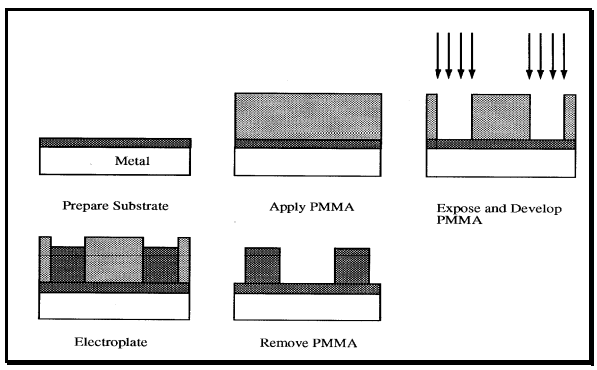

Figure 1: Simplified DXRL process.

DXRL with high-energy synchrotron radiation allows resists up to 1 mm thick to be fabricated with submicron accuracy. A high-accuracy DXRL mask was made by means of an intermediate mask--that is in two steps. The first step was the photolithography. A plating base of Ti/Au 75/300 Å was used for the e-beam writer and then a

*This work was supported by the U.S. Department of Energy, Office of Basic Energy Sciences, under Contract No W-31-109-ENG-38.

3-μm-thick layer of Au was plated on the intermediate mask. The second step used soft x-ray lithography at the Center for X-ray Lithography in Stoughton, Wisconsin (1-GeV Aladdin). For the DXRL mask, a 45-μm-thick layer of Au was plated over a 300-μm-thick Si wafer where the x-ray was exposed and the resist removed. To observe the high depth-to-width aspect ratio in the final product, micron-range structures were patterned on the DXRL mask. To avoid alignment problems and x-ray diffraction, these two steps were done on the same sample substrate without a physical gap.

PMMA up to 1 mm thick was used as a positive resist. The copper substrate was diamond-finished to have a flatness of 1 μm over 4 inches. Then either an oxide film was grown to one micron thick or an equally thick Ti coating was deposited in order to promote better adhesion to the copper substrate. Through these processes, the flatness of the copper surface is maintained, but is still rough enough to give good adhesion to the PMMA sheet, which has a roughness of less than 0.1 μm [6].

When the PMMA film was cast onto the copper substrate, it was annealed at various temperatures from 110 to 170° C for one to three hours [7]. The APS 2-BM-A beamline was used to expose the sample. The transmitted x-ray intensity was calculated based on the APS bending magnet parameters and is plotted in Fig. 2. The ratio of the top dose to the bottom dose for the 1-mm-thick PMMA is about 1.1. During the exposure, the sample was enclosed in a He-purged housing with a Kapton window, and the sample holder baseplate was water cooled. The first platinum (Pt) mirror with a grazing angle of 0.15° was used to cut off all the high-energy x-rays above 40 keV as shown in Fig. 2. More information on the APS 2-BM beamline for the DXRL can be found in Ref. 8.

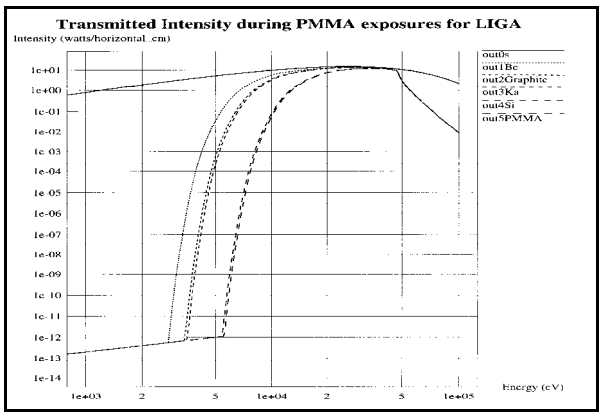

Figure 2: Transmitted x-ray intensity during PMMA exposures for DXRL at APS, energy vs. intensity.

Two different developers were used in the developing process. The first developer, so-called GG, was a mixture of 60% vol 2-(2-butoxy-ethoxy) ethanol, 20% tetrahydro-1, 4-oxazine, 5% 2-aminoethanol-1, and 15% deionized water. The allowed dose range was from 3 to about 10 kJ/cm^3. Below that threshold the crosslinked resist could not be dissolved, and above that range damage to the resist can occur from production of gases in the PMMA. The second developer was methyl-iso-butyl ketone (MIBK) diluted with 2-propanol. After developing the microstructure, copper can be electroplated to the positive resist and the surface can be diamond-finished.

3 MM-WAVE STRUCTURES

Due to DXRL's ability to maintain precise tolerances, it is ideally suited for the manufacture of rf components operating at frequencies above 30 GHz. The first two structures fabricated were a 32-cell, 108-GHz constant-impedance cavity and a 66-cell, 94-GHz constant-gradient cavity. A 32-cell, 108-GHz constant-impedance cavity is a planar accelerating structure with parameters as shown in Table 1. The change from a typical cylindrical symmetrical disk-like structure to a planar accelerating structure results in a loss in shunt impedance and Q value of less than 5%. An accelerating gradient of 50 MV/m is chosen for a practical 50-MeV microlinac application, but it is not limited to 50 MV/m when the rf system is operational in the pulse mode with less repetition rate.

Table 1: The Design rf Parameters of a 32-Cell, 108-GHz Constant-Impedance Cavity

Frequency	f	108 GHz
Shunt impedance	R	312 MΩ/m
Quality factor	Q	2160
Operating mode	TW	2π/3
Group velocity	v_g	0.043c
Attenuation factor	α	13.5 m^{-1}
Accelerating gradient	E	50 MV/m
Peak power	P	750 kW

For a constant-impedance planar structure, the double-periodic structures with confluence in the p-mode design were considered. The 2π/3-mode operation in these structures can give high shunt impedance, group velocity, and low sensitivity on dimensional errors. More detailed descriptions, such as rf simulation using the MAFIA computer code and the thermal analysis related to this structure, can be found in Ref. 9.

Constant-gradient accelerating structures are used in many present-day accelerators because of their higher energy gain and better frequency characteristics, such as higher shunt impedance, more uniform power dissipation, and lower sensitive to frequency deviations, when compared to the constant-impedance structure. Tapering the cells along the structure while keeping the gap and cell depth constant is difficult. Since the structure needs to be manufactured on a planar wafer, adjusting the cell width and length while maintaining a constant depth within the structure is necessary. Figure 3 shows the constant-gradient structure with cuts in the irises; its rf parameters can be found in Ref. 10.

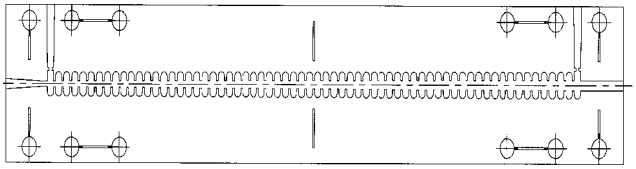

Figure 3: The 66-cell, 94-GHz constant-gradient cavity: side-coupling for mm-wave transmission and circled hole for the alignment.

4 KLYSTRON DESIGN

The mm-wave amplifier is designed to meet a pulsed klystron operating at a high voltage, high current, by combing multi-cells and multi-modules as shown Figure 4 [11]. Beam optics become easier and permanent periodic magnet (PPM) focusing is possible. A higher efficiency also results, because of the low beam perveance. A number of klystrons can then be fabricated on a single substrate, using a deep-etch lithography technique. They can be water-cooled individually and operated in parallel. Several such modules can be stacked to form a klystron "brick," requiring a relatively low voltage for the peak and average power produced. The brick can be provided with a single output, or with individual, spatially combined radiators. The klystron consists of a 4×10×l.5-inch module producing 500 kW peak, 500 W average at 91 GHz, operating at 120 kV, 10 A in total. Its main parameters are summarized in Table 2.

Table 2: Detailed Klystron Design Parameters

Frequency	9l GHz
Voltage	120 kV
Current	2.5 A
Perveance	0.06×10^{-6}
Output power	125 kW
Pulse length	1 μs
Drift tube diameter	0.8 mm
Beam diameter	0.5 mm
Cavity gap length	0.4 mm
Brillouin field	2.7 kG
Cathode current density	15 A/cm^2
Magnetic period	6 mm
Duty cycle	0.1%
Beam area convergence	85:1

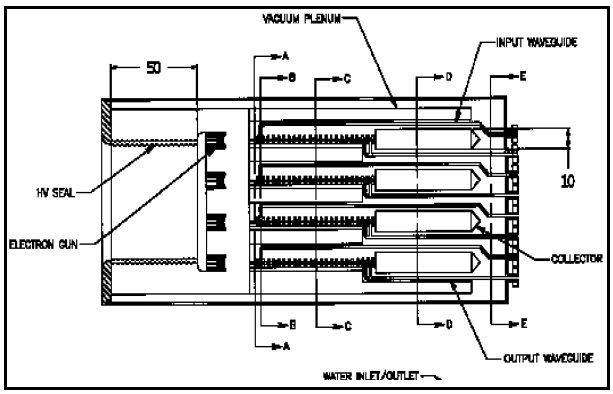

Figure 4: Four-klystron module layout.

The cathode loading and beam convergence parameters are quite conservative, except for the low perveance and PPM focusing. The beam voltage is very high for the power produced by a single klystron due to the low perveance required for PPM focusing (and for good efficiency). However, it is the PPM-focusing feature that makes the module design and tube paralleling possible.

5 SUMMARY AND FURTHER WORK

The final electroplated structure for the prototype of the 108-GHz constant-impedance cavity is shown in Fig. 5. The size of the cavity cell appears to be a few microns off from the design, but the size is controllable by adjusting the x-ray mask to meet the specification. The roughness and flatness of the sidewall of the cavity cell were measured to be 0.05 μm and 2 μm, respectively.

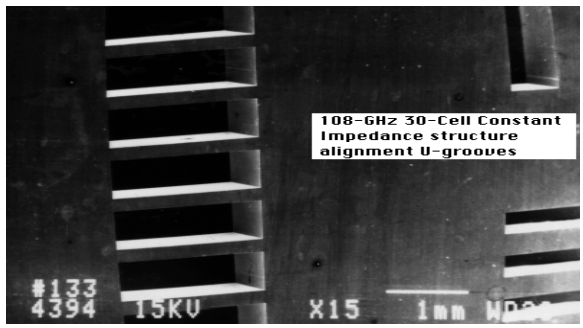

Figure 5: Scanning electron microscopy picture of the 108-GHz constant-impedance cavity structure.

Two mirror-imaged fabricated structures were aligned and measured on a network analyzer. The initial measurement of the quality factor is about 800, which is only 40% of the calculated value. The main contribution to the low value of Q is the MIBK chemical processing used to make the sample above. When the GG chemical was applied to develop the sample, the contrast between the exposed area and unexposed area was at least one order of magnitude higher than MIBK. The metallurgical study of the copper-electroplated sample shows that the level of oxygen in the sample appears to be too high. The electroplating process must be improved so that the structure can sustain against the vacuum and high-power rf.

REFERENCES

[1] P.B. Wilson, SLAC-PUB-7263, Oct. 1996.
[2] W. Ehrfeld and D. Muechmeyer, Nucl. Instr. and Methods in Physics Res., A203, 523 (1991).
[3] Y.W. Kang et al., Proc. of the 1993 Particle Accelerator Conference, 549 (1993).
[4] J.J. Song et al., SPIE-Micromachining and Microfabrication'96, Austin Texas, V2888 (1996).
[5] A. Nassiri et al., IEEE, International Electron Device Conference, Washington DC, 169 (1993).
[6] F. DeCarlo et al., submitted to 42nd International Conf. on Electron, Ion, and Photon Beam Tech '98, Chicago (1988).
[7] H. Guckel et al., MEMS'91, Nara, Japan, January, 1991.
[8] B. Lai et al., SPIE-Micromachining and Microfabrication'96, Austin Texas, V2888 (1996).
[9] P. Matthews, and A. Khounsary, private communication.
[10] J.J. Song et al., presented to HARMST'97, to be published in Microsystem Technologies.
[11] G. Caryotakis et al., SPIE-Conf. of International Society of Optical Engineering'97, San Diego, CA.

DEVELOPMENT OF NIOBIUM SPOKE CAVITIES FOR A SUPERCONDUCTING LIGHT-ION LINAC

K. W. Shepard and M. Kedzie
Argonne National Laboratory, Argonne, Illinois 60439 USA

J. R. Delayen and C. Piller
Jefferson Lab, Newport News, Virginia 23606 USA

A. M. Porcellato
INFN, Legnaro ITALY

Abstract

This paper reports the development of 350 MHz niobium superconducting cavities for the velocity range $0.2 < v/c < 0.6$. Such cavities could be used to form a linac of exceptional flexibility, capable of efficiently accelerating beams of either protons, deuterons, or any of a wide range of light ions, at intensities sufficient for a production beam for a radioactive beam facility. Results of numerical modeling for several resonator geometries are presented. The design and construction status of prototype niobium cavities is discussed.

1 INTRODUCTION

For more than a decade, various concepts for an ISOL-type (isotope separator on-line) radioactive ion beam facility have been developed and discussed within the nuclear physics community [1,2]. The Argonne Physics Division several years ago put forward a concept requiring a linac for protons and light ions as a driver for spallation sources [3]. As initially proposed, the driver linac would be a fixed velocity profile, 220 MV, normally-conducting linac which could provide various beams of protons or light ions at a output energy of 100 MeV per nucleon with a total beam power of 100 kW. The different beams would be used in a variety of different production mechanisms.

To be cost-effective, however, a normal-conducting linac would have several limitations. To maximize shunt impedance, the velocity profile would need to be fixed. Consequently, for the lighter ions, particularly protons, the linac would have to be operated at substantially less than its maximum gradient. Also, operation would be pulsed, at 120 Hz, with a duty factor of at most a few percent. This mode of operation would aggravate heating problems in the spallation source and might also make voltage stability of the radioactive ion source problematic.

These limitations could be overcome by making the driver linac superconducting [4]. In this case, shunt impedance would not be a strong consideration, and the linac could be formed of short independently-phased cavities. The resulting broadly variable velocity profile would enhance performance, for example roughly doubling the maximum proton energy.

A superconducting linac would provide for cw operation, which would be advantageous in several respects beyond that of reducing target heating transients. Requirements for the injecting ion sources would be simplified. The reduction of space charge effects could provide for increased beam currents, opening, for example, the possibility of driving several targets simultaneously.

However, to date little development work has been done on superconducting cavities with the characteristics required for such a machine, most particularly in the upper part of the required velocity range . Before such a machine can be designed in detail, suitable cavities need to be fully developed and characterized.

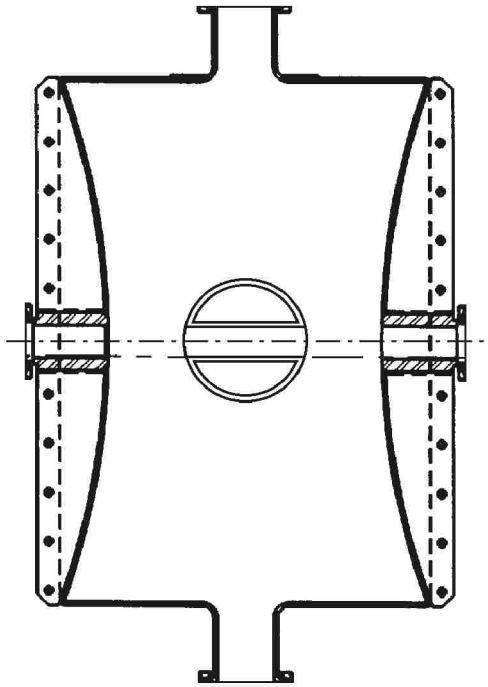

Figure 1: Section for a 44 cm diameter, 350 MHz spoke cavity

Medium-beta cavities are currently being developed for protons of 200 MeV and higher energies, in the form of foreshortened versions of the multi-cell elliptical cavities long used for electron acceleration [5]. The present application, however, is aimed at energies below 200 MeV, and the cavities required would be excessively foreshortened, with several adverse consequences. To obtain a reasonable accelerating voltage, particularly in single or double cell structures, cavities of adequate length would require large diameters, approaching a meter. Construction, handling, and cryostat design would all be rendered more difficult. Also, the mechanical stability of such large, highly foreshortened cavities would be marginal.

For the present application, a more promising geometry is the spoke resonator, which has been successfully prototyped in the form of an 855 MHz, single-cell superconducting niobium cavity [6, 7]. For the linac contemplated here, a substantially lower frequency is desirable. As will be shown below, a frequency choice in the range 300-400 MHz can provide for increased voltage, larger beam aperture, and enable higher operating temperatures. This frequency range differs nearly a factor of three from the single spoke cavity tested to date. Further prototyping is required to establish reliable estimates of the performance of the needed structures.

We have evaluated several possible configurations. In what follows, we discuss parameter choices for several prototype cavities, describe the resulting designs, and report the status of construction and tests.

2 PROTOTYPE CAVITY DESIGN AND CONSTRUCTION

The spoke resonator, in either single or double cell configuration, has a broad enough velocity acceptance

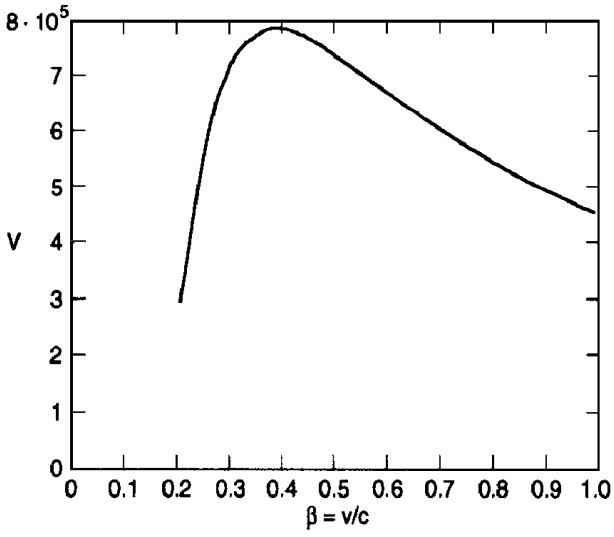

Figure 2: Velocity acceptance characteristic for the two-gap, $\beta = 0.4$ spoke cavity. The voltage gain is given in volts for an rf energy content of 1 joule, corresponding to an accelerating field of 3.4 MV/m in the 22.9 cm long structure.

Table I: Calculated and measured parameters for the $\beta = 0.4$ prototype niobium spoke cavity

Parameter	Calculated	Measured
Frequency	351.89 MHz	348.56 MHz
Active Length	-	22.9 cm
Q (niobium)	5491	5223
U_0*	80.4 mJ	85.3
Peak Electric Field*	4.0 MV/m	-
Peak Magnetic field*	107 Gauss	-
Optimum β (v/c)	0.40	0.39

* At an accelerating field of 1 MV/m

that for the linac contemplated here only two different types of structure are required to cover efficiently the velocity range $0.2 < \beta = v/c < 0.7$ [4]. We need consider only the velocity range above 0.2c, since many resonator types have been successfully developed for the velocity range below 0.2c [8].

The prototype design, shown in Figure 1, was chosen to minimize the number of sheet-metal forming dies required. To further minimize time and cost, we form spoke cavities for two different velocities by changing only the cavity length and spoke diameter.

The cavity housing is formed from 1/8 inch sheet, and the central spoke of 1/16 inch sheet niobium. The 17 inch diameter bulkheads at either end are dished inwards by 1.2 inches to reduce cavity deformation under external pressure. However, numerical finite element analysis indicated that to obtain adequate mechanical stability, a series of support ribs should be welded to the bulkhead exterior, as shown in Fig. 1.

The 2.5 cm diameter beam aperture could be increased with little effect on either energy gain or peak surface electric field. The two coupling ports provide access for vacuum and rf coupling, and also for chemical processing.

2.1 Prototype Cavity for $\beta \geq 0.4$

The first of the two prototype cavities is sized for an optimum particle velocity $\beta = 0.4$ and is shown in Figure 1. The active length of the structure, *i.e.* the interior distance between beam ports, is 22.9 cm. The diameter of the central spoke is 10 cm.

The electromagnetic properties of the prototype cavities have been calculated by numerical modeling using MAFIA. In Table 1 the calculated values are compared with values measured for the recently completed prototype $\beta = 0.4$ niobium cavity.

Figure 2 shows the voltage gain as a function of particle velocity through the two-gap cavity, for an rf field level corresponding to an energy content of one joule. The broad velocity acceptance of the structure makes it particularly suitable for the present application.

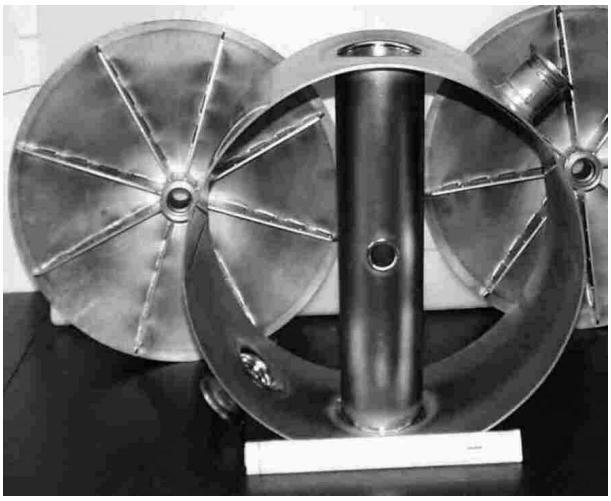

Figure 3: Elements of the prototype niobium cavity just before closure welds attached end sections to the spoke mid-section. A twelve-inch scale is shown.

2.2 Prototype Cavity for $\beta \geq 0.29$

Also under construction is a prototype cavity sized for an optimum particle velocity β = .29. The cavity differs from that shown in Fig. 1 in that the active length is shortened to 18 cm, and the diameter of the central spoke is reduced to 6.25 cm. For use in a linac, the cavity diameter would need to be reduced slightly to bring the frequency to 350 MHz to match the β = .4 cavity. But for purposes of evaluating resonator performance, the slightly lower frequency that results from using the same tooling as for the higher velocity cavity is of no consequence. Table II details the main parameters of the cavity. As in the section above, the electromagnetic properties shown are the results of numerical modeling (MAFIA).

3 RESULTS AND CONCLUSIONS

Designs for spoke cavities operating at 350 MHz have been developed which have low rf losses and low peak surface fields. Room temperature measurements have been made on the recently completed β = .4 cavity, and are compared in Table I with the design values. The measured Q agrees well with the calculated value, confirming that the rf losses for these structures are quite low. With niobium surfaces of good, currently attainable quality, i.e. residual resistivity of 10 nΩ or less, economic operation of the 350 MHz structures at 4.2 K should be feasible. Also, preliminary indication that the mechanical stability of the β = .4 structure is very good.

Plans for further work include finishing the β = .29 prototype, which is nearly complete, and performing low temperature tests of both prototypes. The major remaining question for these cavity designs is the nature of multipacting and other electron loading properties, which can be resolved only by cold tests.

Table II: Parameters for the β = 0.29 Prototype Niobium Spoke Cavity

Parameter	Design Value
Frequency	338.05 MHz
Active Length	18.0 cm
Q (niobium)	5384
U_0*	51.4 mJ
Peak Electric Field*	4.24 MV/m
Peak Magnetic field*	90.4 Gauss
Optimum β (v/c)	0.29

* At an accelerating field of 1 MV/m

4 ACKNOWLEDGEMENTS

The authors wish to acknowledge the help received from several people. Renzo Parodi of INFN, Genoa performed an initial MAFIA evaluation of possible multipacting behavior. John Brawley of JLAB provided many techniques for critical electron beam welds. Don Henley of Argonne's TD Division performed numerical analysis of the mechanical properties of the cavities.

This work was supported by the U. S. Department of Energy, Nuclear Physics Division, under contract number W-31-109-ENG-38.

5 REFERENCES

[1] "Proceedings of the Accelerated Radioactive Beams Workshop", September 5-7. 1985, Parksville, Canada, eds. L. Buchmann and J. M. D'Auria, TRIUMF report TR-85-1.

[2] J. A. Nolen, in the "Proceedings of the 1996 Linear Accelerator Conference", August 26-30, 1996, Geneva, Switzerland, 32 (1997).

[3] "Concept for an Advanced Exotic Beam Facility"', a working paper, Physics Division, Argonne National Laboratory, February, 1995.

[4] K. W. Shepard, et al., in Proc. of the 8th Workshop on RF Superconductivity, October 6-10, 1997, Padua, Italy (to be published in Particle Accelerators).

[5] K. C. D. Chan, et al., in the proceedings of this conference.

[6] J. R. Delayen, W. L. Kennedy, and C. T. Roche, in Proc. 1992 Linear Acc. Conf., August 24-28, 1992, Ottawa, Canada, AECL-10728, 695 (1992).

[7] J. R. Delayen, et al., in Proc. 1993 Particle Acc. Conference, May 17-20, 1993, Washington D. C. , IEEE93CH3279-7, 1715 (1993).

[8] K. W. Shepard, Nuclear Instruments and Methods **A382**, 125 (1996).

A TAPERED DAMPED ACCELERATING STRUCTURE FOR CLIC

M. Dehler, I. Wilson, W. Wuensch
CERN, Geneva, Switzerland

Abstract

A new 30 GHz multibunch accelerating structure incorporating both damping and detuning has been designed for the Compact LInear Collider (CLIC). Each cell of the 150-cell structure is damped by its own set of four radial waveguides resulting in a *Q* of 16 for the lowest dipole mode. A simple linear taper of the beam-pipe dimension provides a detuning frequency spread of 2 GHz (5.4%). Predictions of the transverse wakefield levels in this structure have been made using both uncoupled, and two-band coupled equivalent circuit models with non-perfect loads. The short-range wakefield has been calculated to be about 1000 V/(pC.mm.m) decreasing to less than 1% at the second bunch (0.67 ns) and with a long time level below 0.1%.

1 INTRODUCTION

The CLIC study of a 0.5 to 5 TeV $e^{\pm}$ linear collider [1] proposes the use of 30 GHz normal-conducting structures operating at high accelerating fields (100 to 200 MV/m) to reduce the length and, in consequence, the cost of the main linacs. In order to reach the required luminosities (10^{34}-10^{35} cm^{-2} sec^{-1}) it is necessary to accelerate and collide multiple bunches per RF pulse. The present CLIC parameter list has 150 bunches each with 4.10^{9} particles spaced at 0.67 ns.

The luminosity that can be achieved depends strongly on the vertical emittance at the interaction point. The main source of emittance dilution in CLIC comes from the strong transverse wakefields produced by the accelerating structures. Beam dynamics simulations show that transverse wakefield levels of about 1000 V/(pC.mm.m) decreasing to less than 1% at the second bunch and continuing to decrease thereafter, are required to limit the vertical emittance blow-up along the linac to reasonable values [2]. These wakefield levels cannot be obtained by detuning only, because of a limited bandwidth and recoherence effects [3] nor by a combination of detuning and light damping as proposed for NLC [4]. The required levels were obtained using a structure with four T-cross-sectioned damping waveguides per cell terminated by perfect loads [5]. This structure was considered too difficult to fabricate. It became evident that the problematic stem of the T-shape waveguide could be eliminated if the beneficial detuning effects of a quasi-constant gradient structure were included in the analysis. This has finally resulted in a multi-bunch structure design suitable for CLIC.

2 THE TAPERED DAMPED STRUCTURE

The new structure geometry is shown in Fig. 1. It incorporates both damping and detuning, but does not rely on a high degree of optimization of either. Each cell of the 150-cell structure is damped by its own set of four radial waveguides. The damping waveguides have a rectangular cross-section (4.5 mm x 1.39 mm) with a cut-off frequency above the 30 GHz fundamental but below all higher-order modes. Higher-order mode energy propagates out via the waveguides to small individual RF loads. A taper of the iris dimension from 3.5 mm to 4.5 mm provides a detuning frequency spread of 2 GHz (5.4%) for the lowest dipole mode which helps to decrease the roll-off time. The detuning also plays an important role in reducing the levels of all higher longitudinal and transverse modes.

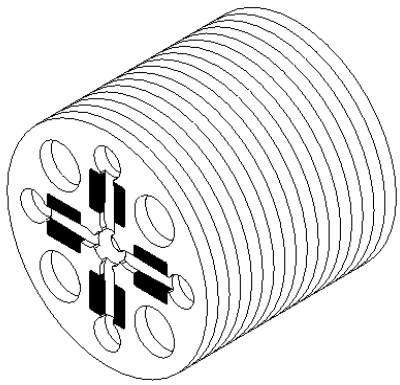

Figure 1: 30 GHz Tapered Damped Structure.

The transverse wakefield of the standard CLIC structure without damping or detuning is dominated by the lowest transverse passband with the higher bands contributing at the 5-10% level. The damping waveguides produce a $Q < 20$ for the lowest dipole band and a $Q \approx 100$ for the next transverse band. The synchronous mode of the lowest band propagates with a velocity of 3% of the speed of light and is attenuated by 5×10^{-3} per cell. The energy does not propagate very far along the structure so the behaviour of this mode can be estimated very well using an uncoupled model.

2.1 Uncoupled-cell analysis

A good estimate of the transverse wake behaviour can be obtained from a simple RLC lumped-element single-cell circuit analysis of the lower band. The values of *L* and *C* were chosen to make the circuit resonant at the

synchronous frequency of the equivalent undamped constant impedance (CI) structure with $2a$ = 4mm. From [5] it is known that a Q of 16 is obtained for this mode for the chosen waveguide dimensions. Below cut-off the Q is assumed to be 4000 (the Q of an undamped cell). These effects were simulated in the circuit by an abrupt change of R at cut-off. The Fourier transform of the frequency response of this circuit gives the wakefield time response (Fig. 2). It can be seen that the wakefield does not always decrease exponentially-the long range wakefield is affected by the waveguide cut-off.

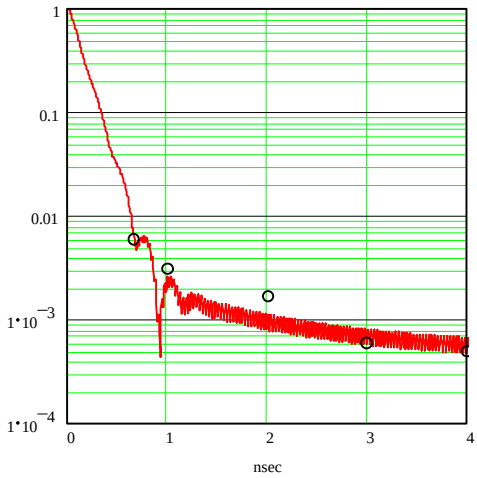

Figure 2: Normalised wakefield using only damping for single-band uncoupled model with perfect loads.
(o MAFIA analysis).

Results from a complete MAFIA time-domain multi-cell analysis of the T-waveguide damped CI structure with perfect loads [5] are given in Fig. 2 for comparison. The stem part of the T-waveguide takes out the contribution to the wake of the upper band. The simple model predicts the basic behaviour very well.

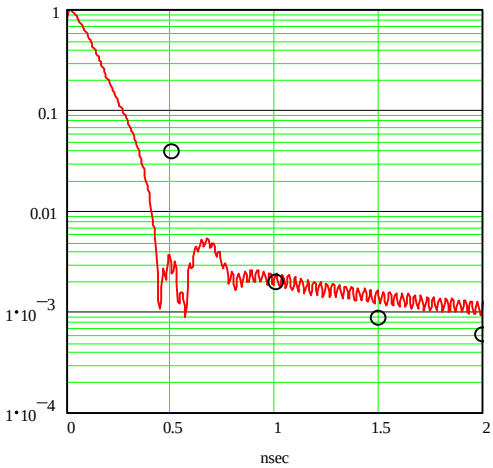

Figure 3: Normalised wakefield with damping and detuning for single-band uncoupled model with perfect loads. (o Two-band coupled-cell results)

The effects of detuning were included by adding the responses of 150 different circuits covering the detuning range ($2a$ = 3.5 mm to 4.5 mm). The wakefield for these damped-detuned uncoupled cells is given in Fig. 3 together with results obtained from a complete two-band coupled-cell analysis (see Section 2.2). To improve the overall model, the upper band of the first pass band which contributes at the 5-10% level to the undiluted wake was treated in the same way as the lower band. The waveguides damp this primarily TE-like mode to a $Q \approx 100$ which alone results in a wakefield level at the second bunch which would be too high. The level is however further reduced by the detuning. As done previously, the responses of 150 different circuits covering the detuning range ($2a$ = 3.5 mm to 4.5 mm) were added to produce the wakefield shown in Fig. 4.

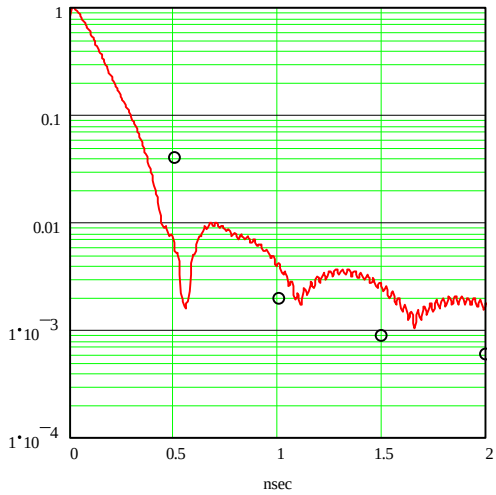

Figure 4: The normalised wakefield with damping and detuning for the double-band uncoupled model with perfect loads. (o Two-band coupled-cell results)

2.2 Coupled-cell double-band analysis

A complete double-band coupled-cell analysis of this new structure has been made using a more complete equivalent circuit model [6]. The damping waveguide, which couples only to the TM part of the circuit, is modeled by a resistor in parallel with the TM inductance. The waveguide load is incorporated into the circuit directly in the form of a table of scattering parameters calculated by MAFIA. The determination of the damped circuit parameters follows the procedures of Bane and Gluckstern [7] for the detuning, and Kroll and Yu [8] for the damping. Circuit voltages are determined as a function of frequency and phase advance by the spectral function method [9]. Calculation of the transverse wakefield from the results of this circuit analysis is not straightforward. For high-Q structures the beam sees a real transverse impedance only at discrete frequencies which are synchronous with the velocity of

light. For low-*Q* structures the resonances spread out such that there is interaction with the beam over a continuous range of phases and frequencies. In this case, the usual Brillouin diagram has to be replaced by a two-dimensional broad-band impedance function depending on frequency and phase advance.

For this particular analysis, the detuning distribution used was not quite linear - it had slight rounding at the ends to improve the long time response, and a conservative value $Q = 200$ was used for the upper-band damping (MAFIA results gave 80 to 130). The load consists of two SiC slabs which sit in the side walls of the waveguide (see Fig. 1) giving a good absorption behaviour close to cut-off. The reflection coefficient data obtained from a MAFIA analysis of this load assuming a dielectric constant of 30 and a loss tangent of 0.5 for all frequencies is given in Fig. 5. The calculated transverse wakefield is given in Fig. 6. The levels obtained are below those determined by beam dynamics simulations for beam stability and good emittance preservation in the CLIC main linac.

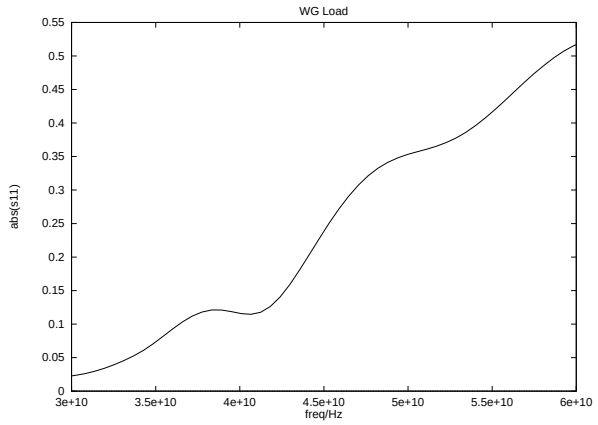

Figure 5: Reflection coefficient versus frequency.

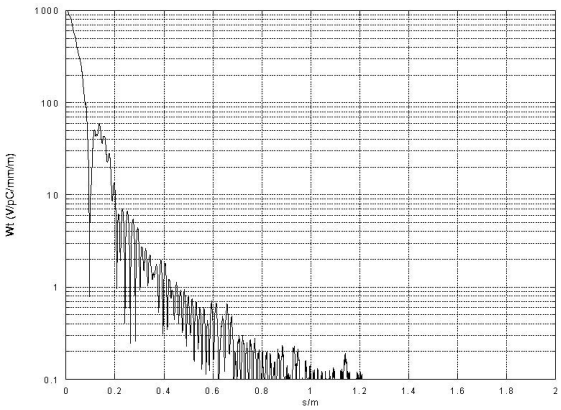

Figure 6: The wakefield obtained for the double-band coupled model plus RF load.

3 CONCLUSIONS

A 30 GHz tapered damped accelerating structure has been designed for CLIC which gives very low transverse wakefields. The wakefield behaviour has been analysed by simple single-cell equivalent circuits assuming perfect loads, and by a very complete two-band coupled-cell analysis with a real load. The single-cell analysis provides a quick and simple way to calculate the wakefield envelope with sufficient accuracy to establish, and study the influence of changing basic design parameters such as the damped *Q*, detuning range, waveguide cut-off frequency and number of cells. The full analysis is however essential for a detailed design. Cold model tests are presently underway to confirm the calculated values, and prototype structures are foreseen. In particular, it is planned to build an X-band scale model for tests in the ASSET facility at SLAC.

4 REFERENCES

[1] J-P. Delahaye and 30 co-authors., “CLIC, a 0.5 to 5 TeV Compact Linear Collider”, Proceedings of EPAC98, Stockholm, June 22-26, (1998).

[2] G. Guignard, J. Hagel, “MBTR Simulations for Different Multibunch Structure Models”, CLIC Note 348, November 1997.

[3] I. Wilson, W. Wuensch, “Multibunch Studies for CLIC", Proceedings of PAC93, Washington, May 17-20, 1993, 641-643 (1993).

[4] M. Dehler, I. Wilson, W. Wuensch, “CLIC Waveguide Damped Accelerating Structure Studies", Proceedings of LINAC96, CERN, August 1-5, 1996, 734-736 (1996).

[5] M. Dehler, I. Wilson, W. Wuensch, R.M. Jones, N.M. Kroll, R.H. Miller, “Design of a 30 GHz Damped Detuned Accelerating Structure", Proceedings of PAC97, Vancouver, May, 1997.

[6] M. Dehler, “Modelling a 30 GHz Waveguide Loaded Detuned Structure for CLIC”, CLIC Note 358, April 1998.

[7] K. Bane, R. Gluckstern, “The Transverse Wakefield of a Detuned X-band Accelerator Structure”, Particle Accelerators, Vol.42, 213 (1993).

[8] N.M. Kroll, D. Yu, “Computer Determination of the External Q and Resonant Frequency of Waveguide Loaded Cavities”, SLAC-PUB-5171 (1990).

[9] R.M. Jones, K. Ko, N.M. Kroll, R.H. Miller, “A Spectral Function Method Applied to the Calculation of the Wake Function of the NLCTA”, Proceedings of LINAC96, CERN, August 1-5, 1996, 650-652 (1996).

Π/2 INTERLEAVED CAVITY DEVELOPMENTS FOR THE MUON COLLIDER COOLING EXPERIMENT

A. Moretti, FNAL, Batavia, IL USA
J.N. Corlett, D. Li, W.C. Turner, LBNL, Berkeley, CA, USA
H. G. Kirk, R.B. Palmer, Y. Zhao, BNL, Upton, NY USA

Abstract

In this paper we discuss the development of a π/2 interleaved standing wave linac for the proposed muon cooling experiment. The nominal beam momentum is 186 MeV/c (beta=0.87). Each muon cooling channel section contains a 1.3m rf accelerating linac separated by 0.64m of liquid hydrogen absorbers immersed in a alternating superconducting solenoidal magnetic transport line. Instead of conventional open cavity beam apertures, the 805 MHz linacs have thin Be windows covering the iris apertures. The accelerating cavities closely resemble pillbox cavities and have little or no field enhancement due to iris aperture corners. Further, since the peak field is on the axis, the shunt impedance is about a factor 2 larger than conventional designs. It is also proposed to cool the cavity to liquid nitrogen temperature to reduce the losses and increase the shunt impedance. Our π/2 interleaved cavity design is essentially two chains of side coupled π/2 cavities interleaved to form a continuous chain of accelerating cells on the beam axis. Each accelerating cell has a phase advance of π/2 and, therefore, a favorable transit time factor. This paper will discuss the design of the cavity, MAFIA calculations, low-power rf model cavity measurements, low-temperature effects with Be windows, design of high-power rf test models and a proposed high-power rf test facility.

1 INTRODUCTION

Studies of muon colliders have been going on for about five years and more recently a international collaboration has been formed to study the feasibility of muon colliders for high energy physics research. The collaboration is focused at BNL, Fermilab, and LBL [1,2]. For a practical high-luminosity collider, large numbers of muons must be produced and transported through the collider complex. Because of the short lifetime of the muon, this must be accomplished very quickly to minimize loss of muons and to preserve the machine luminosity. The muons are generated from the decay of pions produced in proton-nucleus interaction in a high-Z target and collected in a solenoidal decay channel. This produces muons with a large initial phase volume which must be reduced (cooled) quickly by several orders of magnitude. The technique of ionization cooling has been adopted to reduce the phase-space volume of the muons. In this technique, muons lose both transverse and longitudinal momentum while passing through low-Z material and the longitudinal momentum is then restored by acceleration in rf cavities. This process is repeated numerous times to reduce the phase-space volume sufficiently for acceptance by the acceleration system of the collider complex.

After studying a number of cavity designs, the interleaved π/2 side coupled cavity, Fig. 1, with thin (125 μm) beryllium windows over the cavity apertures was selected [3,4,5]. This design resembles a pillbox cavity and achieves a high shunt impedance over the required large beam aperture (16 cm). The peak accelerating electric field and maximum surface field are identical. This gives a maximum possible accelerating field limited only by electrical breakdown. In addition, the π/2 interleaved pillbox design gives a transit time factor of 0.90. This design has the highest group velocity (being in the center of the passband) and is more tolerant of dimensional errors, beam and mechanical perturbations. The pillbox design is made possible because of the low scattering rate of muons in matter, especially low-Z beryllium. Further, the cavity is to be cooled to liquid nitrogen temperature to increase the shunt impedance by about a factor two and reduce the large peak power requirements of the muon cooling channel. This feature requires the design of bi-metallic transitions between the copper cavity walls and Be window foils to compensate for differences in the material thermal expansions and keep the window flat during cool-down and operation. Also, the high group velocity of the π/2 mode will make it more tolerant of thermal distortions during cool-down and operation.

2 RF CAVITY DETAILS

The cooling channel rf cavity details are shown in Fig. 1. It is a 805 MHz interleaved side-coupled π/2 cavity. (The same frequency as the Fermilab Upgrade Linac commissioned in 1993.) The interleaved design was chosen over the more conventional side-coupled cavity design because of its larger shunt impedance (ZTT=38MOhm/m and Q=19,600 from MAFIA calculations). The conventional design, because of the required large beam aperture of 16 cm, had a ZTT about a factor two smaller. The operating principle can be understood with reference to Figs. 1 and 2.

The upper part of figure 1 shows cells labeled C coupled together to form a side-coupled cavity while the cells labeled D form another independent side-coupled cavity. Structures C and D have been designed with the computer program MAFIA to resonate in the π/2 mode and are excited with high fields in the on-axis accelerating cells

*Supported by the US DOE under contract numbers DE-AC03-76-SF00098, DE-AC02-76-CH00016 and DE-AC02-76-CH03000.

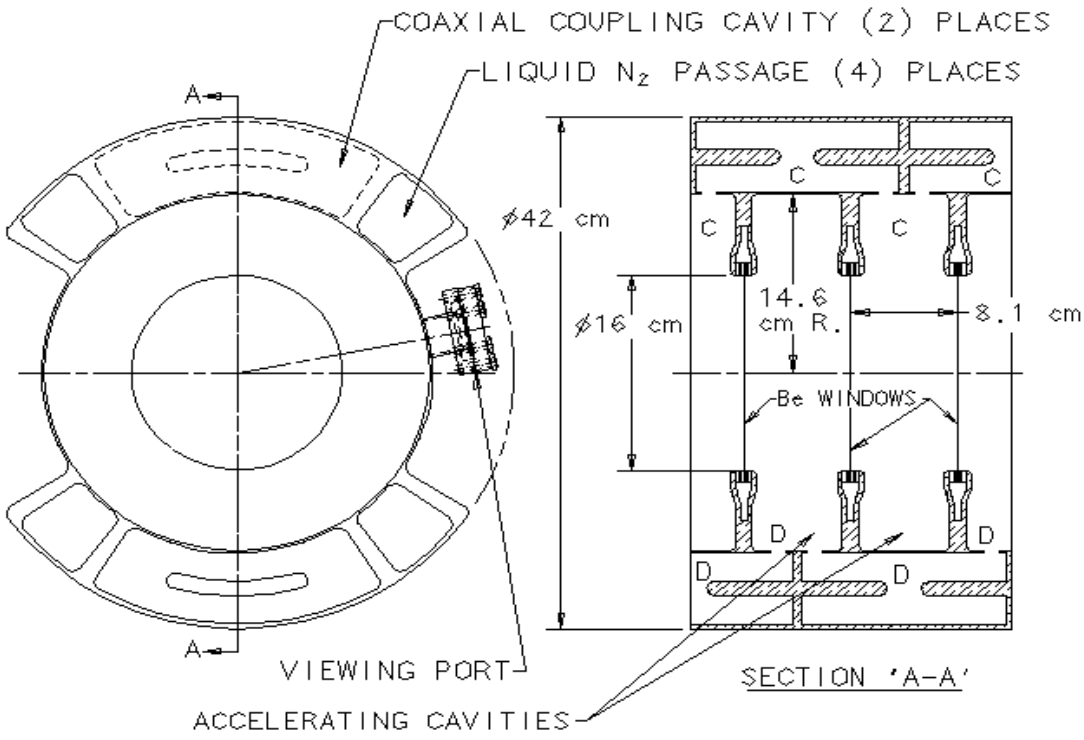

Figure 1: $\pi/2$ Interleaved Cavity Cross Section

and near zero fields in the off-axis coupling cells. The on-axis cells of the C structure and the D structure each have a phase advance of π per cell, but together have the transit time factor of 0.90 of a $\pi/2$ mode cell rather than 0.637 of a conventional side-coupled structure. Fig. 2 shows the method of excitation. Two independent waveguides are slot coupled to adjacent accelerating cells and are driven $\pi/2$ apart in phase through a 90 degree waveguide hybrid.

Figure 1 gives some details of the bi-metallic transition between the outside cavity iris walls and the central 125 μm Be foil. Because of the large difference in thermal expansion between copper and beryllium from room temperature to liquid nitrogen temperature, a buffer material must be used to bridge this difference. Large distortions will otherwise occur resulting in detuning of the cavity and distortions in the required fields. Molybdenum has been chosen as the buffer material. Its Young's modulus is about the same as Be and three times that of copper at room temperature. Its thermal expansion coefficient is about 30% less than Be. With proper design (ANSYS calculations are under way) this should result in slight tension on the Be foil and keep it flat at liquid nitrogen temperatures. Keeping the foil flat will preserve the cavity tune and field flatness. This is illustrated by the rings of different material surrounding the Be window foils in Fig. 1.

3 EXPERIMENTAL STATUS

The design of a low-power three cell test cavity has been completed at LBL using MAFIA. Copper for the cavity has been ordered by the University of Mississippi where the final machining will be done. Testing of this cavity to liquid nitrogen temperature will take place at LBL in the next few months. Studies of the electrical properties of Be at liquid nitrogen temperature are underway at BNL and Mississippi. A high-power three cell cavity is currently being designed at LBL. This cavity will also be machined at Mississippi and then tested at low power at LBL. A high-power 805 MHz test facility is now being planned at Fermilab. It will use a high-power Litton klystron and a Fermilab built modulator to produce up to 15 MW of rf power for 50 μs at 15 Hz. Testing will take place to determine the upper power limit of the klystron. The cavity will be put in a pair of 5.5T superconducting solenoids to simulate the alternating solenoid environment of the cooling channel. The solenoids are being designed and built at LBL and will be shipped to Fermilab as part of the test facility.

4 REFERENCES

[1] R. Palmer, A. Tollestrup and A. Sessler, Proc. Of 1996 DPF, DPB Summer Study "New Directions for High Energy Physics", Snowmass, Co (1996).

[2] Status of Muon Collider Research and Development and Future Plans, Fermilab-PUB-98/179.

[3] E.A. Knapp, B. C. Knapp, and J. M. Potter, Rev. Sci. Instr. 39, 979 (1968).

[4] V. A. Vagine, IEEE tr NS, Vol.NS 24, p1084, No. 3, June, 1977.

[5] A. Moretti, J. N. Corlett, D. Li, W. C. Turner, H.G. Kirk, R. B. Palmer and Z. Zhao, to be published in EPAC, June, 1998.

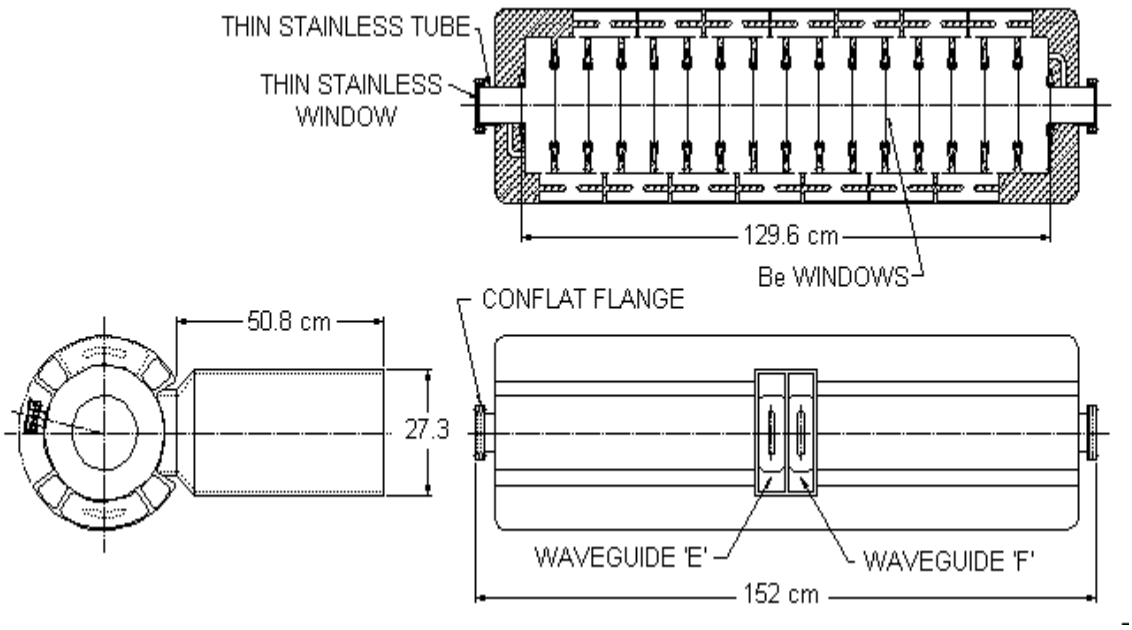

Figure 2: Cooling Channel rf Cavity

SCALE ROOM TEMPERATURE MODEL OF THE SUPERCONDUCTING RFQ1 FOR THE PIAVE LINAC

V. Andreev, G. Bisoffi, M. Comunian, A. Lombardi, A. Pisent, A.M. Porcellato
INFN-LNL, Padova, Italy
T. Shirai
Nuclear Science Research Facility, Kyoto University, Kyoto, Japan

Abstract

The new injector PIAVE (Positive Ion Accelerator for Very low Energy) will use two bulk niobium (Nb) superconducting RFQs (SRFQ1 and SRFQ2), which will be operated at 80 MHz. The electrode length of SRFQ1 is about twice as long as the being built SRFQ2 thus requiring an EBW vacuum chamber larger than the previously available one. A principal decision was hence taken to split the electrodes and the tank into two parts. A half-scale room temperature model was built at LNL in order to test RF characteristics of the structure and to determine its exact dimensions. Results of the model measurements and M.A.F.I.A. code simulations are presented.

1 INTRODUCTION

PIAVE injector is now under construction at LNL for the superconducting (SC) linac ALPI. The beam, generated by an ECR source, will be bunched by a three harmonic buncher and accelerated by two SC RFQs, followed by eight SC QWRs, for an equivalent voltage of 8 MV (U^{+28} beam) [1]. The cavity design of both SRFQ1 and SRFQ2 is based on the 4-rod structure with 90°-apart-stem arrangement [2]. The components of the cavities will be manufactured from 3 mm thick niobium (Nb) sheet and will be assembled by electron beam welding (EBW). SRFQ2 is being already manufactured in LNL [3]. A design of SRFQ1 was done based on the M.A.F.I.A. code simulation for the case of unmodulated electrodes [4]. Since SRFQ1 electrodes are about twice as long as those of SRFQ2, it is impossible to weld them in the EBW vacuum chamber used for SRFQ2. We decided to split the vanes and the tank into two parts. Finally the two tanks will be welded by EBW into a single cavity. The cutting point of the unmodulated electrodes should be at the center between the stems (the point of zero longitudinal current) in order to minimize the field disturbance of the gaps. However, for modulated electrodes, the point should be slightly shifted to the position of electric field minimum closest to the position of zero longitudinal current. Since the welding of the electrode tips is technically impossible, a 1 mm gap between electrode parts is foreseen. RF contact between them will be provided by welding only proper Nb strips to avoid mode disturbance.

A half scale aluminum model of SRFQ1 with modulated electrodes was constructed having the goal:

1) to determine the tank diameter for the required resonant frequency;

2) to optimize the stem position in order to obtain proper field distribution;

3) to test the effect of the vane cutting and the strip connecting the gap;

4) to determine alignment error tolerance.

2 ALUMINUM MODEL DESIGN

The model (Fig.1) allowed easy access to the central part of the structure and hence proper alignment of the electrodes.

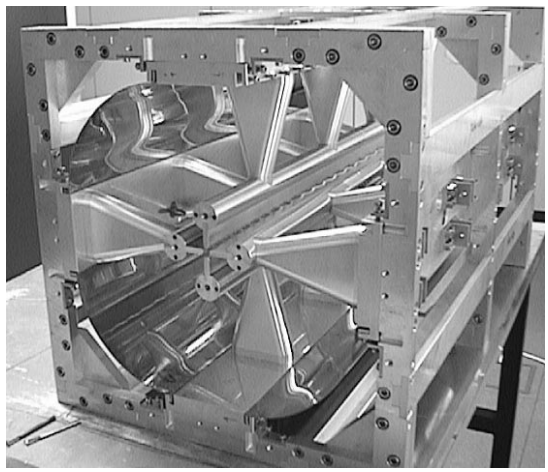

Figure 1: View of the half scale model of SRFQ1 (end flanges and one of the shells are not installed)

It is first assembled in 4 parts by means of longitudinal and transverse aluminum bars. The assembling procedure of the structure was the following.

At first each 1/4 structure was assembled independently: four stems, supporting the split (with 0.5 mm gap) electrode were installed onto the longitudinal bar and fixed. Then four such parts were assembled with respect to an external frame and aligned. After that four copper cavity shells were slided into proper slits with good RF contact. Finally two end flanges closed the structure. The first alignment procedure was the longitudinal positioning of the electrodes. Transverse positioning of the electrodes was obtained with respect to reference planes manufactured on each electrode.

Positioning of the electrodes was provided with an accuracy of $\pm$ 25 μm.

3 RESULTS OF MEASUREMENTS

3.1 Resonant frequency, Q-factor and mode separation

A comparison between M.A.F.I.A. simulations, performed using unmodulated electrode because of mesh number constraints, and measurements (modulated electrodes) is shown in Table 1.

Table 1 : RF parameters of the model

	M.A.F.I.A. simulations	Measurements
Frequency of quadrupole mode [MHz]	158.038	158.546
Q-factor	7400	3700
Frequencies of dipole modes [MHz]	181.169	178.197 179.440
Capacitance [pF/m]	141	_

As it can be seen from Table 1 simulated value of the quadrupole mode frequency for unmodulated electrodes is slightly lower than measured one with modulated electrodes, but it should be higher since the modulation results in lowering resonant frequency. It means that the simulation underestimated the frequency value mainly because of the unavoidable roughness of the mesh size in the simulation, especially around the vane tips. The modulation of the electrodes can result also in tilt of the longitudinal inter-electrode voltage distribution due to a change of inter-electrode capacitance, since modulation factor changes from 1.2 to 2.8. Instead of direct simulation of the version with modulated electrodes we calculate the capacitance variation along the regular channel of the structure for several cells by means of M.A.F.I.A. static solver. The input geometry used for calculation included one cell with vane tip and cilindrical part of the electrode. Figure 2 shows results of the calculations.

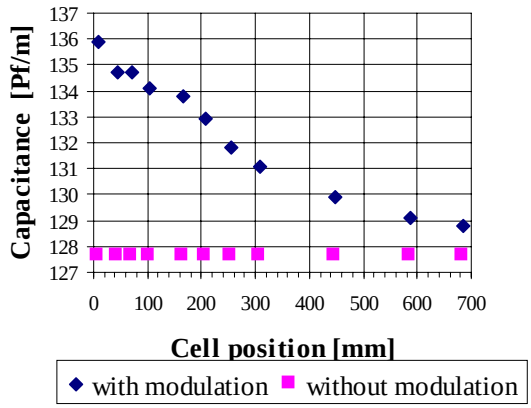

Figure 2. Inter-electrode capacitance variation

The effect of frequency shift due to the modulation was estimated to be 2.7 MHz ($\delta f = (f*\delta C)/(2*C_t)$, where C_t - total capacitance of the RFQ, and δC is change of it.

Measured frequencies of the dipole modes are split owing both to electrode modulation and to not ideal alignment. The frequency separation between the qudrupole mode and dipole ones is about 20 MHz. For 80 MHz Nb SRFQ1 it will be 10MHz, but it is enough to prevent the mode mixing. Measured Q value is also lower than simulated one due to not ideal RF joints.

3.2 Field distribution measurements

Measurements of the fields were carried out by means of standard bead-pull technique. We used for transverse field measurements a plexiglas bead (6 mm in diameter) and for longitudinal ones an aluminium cylindrical rod (1 mm in diameter and 3 mm in length). The inter-electrode voltage distribution (transverse E) along the structure was measured for each pair of neighbouring electrodes. To reduce effects of the modulation, the bead was pulled between electrode cylindrical parts at a distance of 30 mm from the beam axis. The results of field measurements were obtained after averaging 8 runs for each position. Standard deviation was 0.5%.

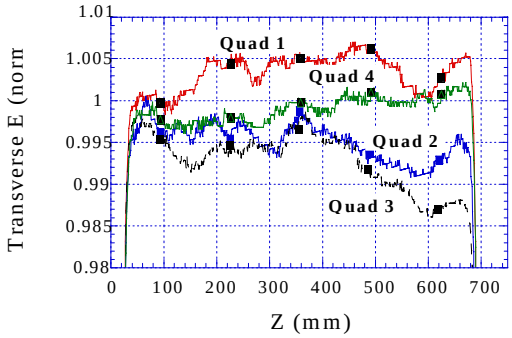

Figure 3: Close view of normalized transverse electric field distribution for 4 quadrants

As can be seen from figure 3 electric field unbalance among four qudrants is within ± 1%. Upper curves correspond to quadrants in which the distance between electrodes at the exit of the structure. is slightly smaller (~0.02 mm) than in the other two. The tilt of electric field distribution less 1% and no correction of the stems position is hence required. Electric field distribution at the beam axis is shown in figure 4.

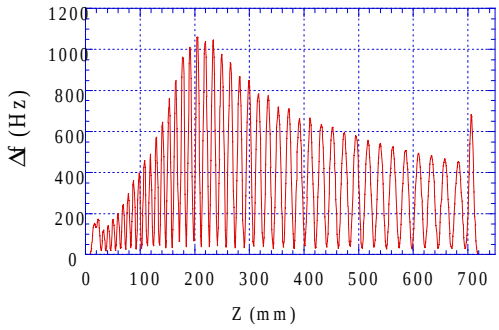

Figure 4: $\Delta f (\propto E_z^2)$ distribution at beam axis

The increase of E_z^2 in the initial part (0-200 mm) of the structure is due to the change of the modulation factor

(m) from 1.2 to 2.8 The behaviour of the rest of the curve is explained by the constant value of m. More detailed distribution (E_z^2) in the 8 mm long gaps between the end flanges and the electrodes are shown in figure 5 (a, b). Like all 4-rod structures a voltage difference exists in the gap between end flanges and ends of the electrodes. The effect of the exit gap voltage is used here in order to create an additional accelerating cell [5]. The different shapes of the electric field distribution in the input and output gaps are due to the termination of the electrodes (SRFQ1 adopts a half cell termination at the end) and the positioning of the stems.

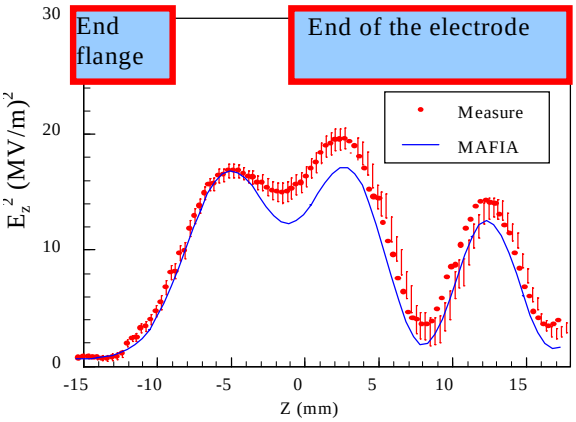

Figure 5 a): E_z^2 distribution at the entrance of the RFQ

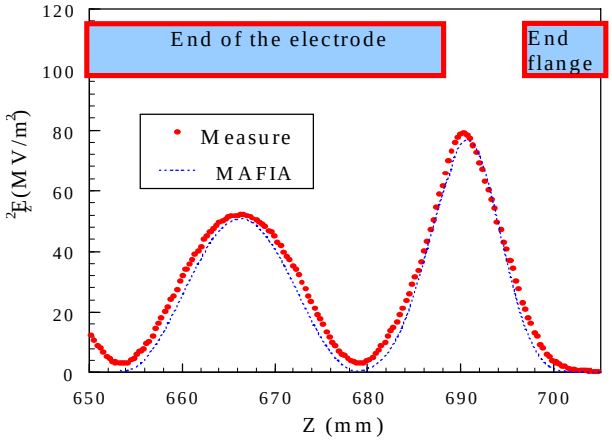

Figure 5 b) E_z^2 distribution at the exit of the RFQ

Field measurement were carried out along the beam axis near the electrode spliting points to observe effect of the split electrodes when RF strips were installed. M.A.F.I.A. static solver simulation predicted very small (~0.2%) field drop. No effect was consistently observed on the 0.5 mm gap with measurement accuracy. In order to estimate sensitivity to alignment errors the upper electrode was moved downwards by 0.1 mm. The resonant frequency of quadrupole mode was decreased by 257 kHz as a consequence. The measured transverse electric field distribution for the 4 quadrants is shown in figure 6.

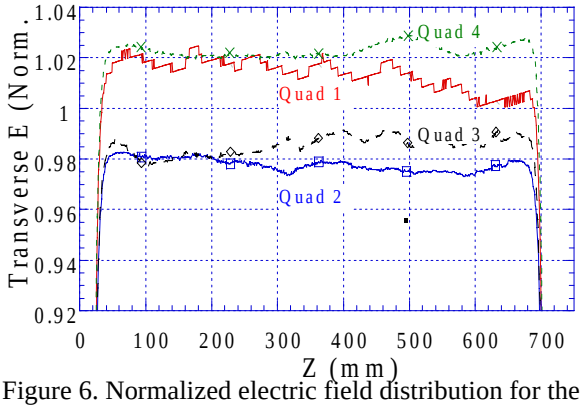

Figure 6. Normalized electric field distribution for the 4 quadrants after 0.1 mm misalignment of one of them

As it is shown by figure 6, transverse electric field in the upper quadrants (1 and 4) were increased and in lower ones (2 and 3) reduced. Total unbalance between the quadrants of the RFQ does not exceed ± 2% (i.e . ± 1% in the full-scale 80 MHz Nb structure).

4 CONCLUSION

Cold model measurements allowed to answer all the questions and to get results which will be a guideline in the construction of the full scale Nb SRFQ1.

Tank diameter for required resonant frequency was determined. Tolerance for the electrode misalignment should not exceed ± 0.1 mm in the 80 MHz SRFQ1.

A 1 mm gap between split electrodes parts will not affect the field distribution appreciably.

M.A.F.I.A. static solver simulations and experimental results obtained for E_z^2 distribution on the beam axis are in very good agreement.

5 REFERENCES

[1] A. Lombardi et al."The new Positive Ion Injector Piave at LNL" Proc. Of the 1997 Particle Acceleration Conference, Vancouver, B.C. , Canada 12-16 May 1997 (to be published).

[2] V.A. Andreev, G. Parisi "90°-apart-stem RFQ Structure for Wide Range of Frequencies", Proc. of the 1993 Particle Acceleraton Conference Proc., Washington ,DC., May 1993, p.3124.

[3] G. Bisoffi et al., " Status of the 80 MHz superconducting RFQ development at LNL", Proc. Of the Eight Workshop on RF Superconductivity, Abano Terme, 6-10 October 1997 (to be published).

[4] T. Shirai, G.Bisoffi, V.Andreev, " Design of the superconducting RFQ1 cavity for the PIAVE linac" Proc. Of the Eight Workshop on RF Superconductivity, Abano Terme, 6-10 October 1997 (to be published).

[5] A.Pisent, M.Comunian "Complete Simulation of the Heavy Ion Linac PIAVE" Proc. Of the 1997 Particle Accelerating Conference, Vancouver, B.C. , Canada 12-16 May 1997 (to be published).

EQUIVALENT LUMPED CIRCUIT STUDY FOR THE FIELD STABILIZATION OF A LONG FOUR-VANES RFQ

A. Pisent, R. Celentano* and R. Zennaro#
INFN-Laboratori Nazionali di Legnaro, Padova (Italy)

Abstract

The possibility to design an RFQ long respect to the RF wavelength is very important for the feasibility of linacs with different applications, from the high power CW linacs for neutron production to the low power high frequency linacs proposed for hadrotherapy. In particular INFN has been funded for the study of the critical parts of a waste transmutation linac. In this framework the field stabilization of a 352 MHz RFQ has been studied, using the LANL resonant coupling technique; an equivalent lumped circuit approach has been used, and compared with MAFIA simulations. Based on the results of these studies an aluminum model (1:1 scale, 0.04 mm tolerances) has been built and we are now ready for the test of the tuning procedure.

1 CIRCUIT MODEL

A four vanes RFQ resonator is based on a transfer line quadrupolar mode, with dispersion relation:

$$\omega^2 = \omega_o^{\ 2} + k^2 c^2 \qquad (1)$$

where ω_0 is the cut-off frequency, k is the wave number and c is the asymptotic phase velocity. In an RFQ the boundary conditions are such that the eigen modes are given by $k\ell = \pi n$, with ℓ cavity length and n (integer) mode number. The same dispersion relation (1) is valid for the circuit in Fig. 1, governed by the equation:

$$\frac{d^2V}{dz^2} = -Z_L Y_0 V \qquad (2)$$

with V intervane voltage, $Z_L dz = i\omega L_1\, dz$ coupling impedance, L_1 coupling inductance per unit length, and

$$Y_0 dz = \left(\frac{1}{i\omega L} + i\omega C\right)dz = \frac{1}{i\omega L}\left(1 - \frac{\omega^2}{\omega_0^2}\right)dz$$

with L inductance length, C capacitance per unit length. The solution of (2) can be written as:

$$V = V_0 e^{ikz} \qquad k^2 = -\frac{L_1}{L}\left(1 - \frac{\omega^2}{\omega_0^2}\right)$$

All these parameters have for a RFQ a straightforward meaning; $\omega_0 = 1/\sqrt{LC}$ is the frequency of operation, C is mainly the capacitance per unit length of the quadrupolar vane tips, (of the order of 120pF/m), that can be evaluated with the help of SUPERFISH. Moreover $L_1 / L = \omega_0^2 / c^2$, so as to have the asymptotic phase velocity equal to c. This model can be discretized, keeping the same meaning of the parameters involved, as long as we are only interested in the first modes and the upper cut-off in frequency can be neglected. The resulting dispersion relation is:

$$\left(\frac{\omega_n}{\omega_0}\right)^2 = 1 + \frac{L}{L_1 dz^2} 2(1 - \cos\alpha n)$$

with dz (finite) discretization step and $\alpha = \pi\, dz/\ell$. In the limit of dz→0 this relation reduces to (1), but if one is only interested in the first two modes (n=0,1), one can take $dz = \ell/2$, and the two frequencies correspond to the α=0 and α=π modes by imposing $L_1 / L = 32/\lambda^2$, with $\lambda = 2\pi c/\omega_0$; we shall use this result in the following.

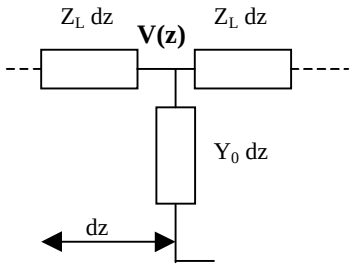

Figure 1: Equivalent circuit for the longitudinal dependence of the quadrupole modes a four vanes RFQ.

In a four vanes RFQ the operating frequency is ω_0, and therefore the field cannot be stabilized as foreseen by the resonant coupling theory, since ω_0 is never between an upper and lower symmetrical frequency[1]. As a consequence some drop of the voltage along the RFQ can be expected in presence of mechanical errors for a long RFQ, since the distance of the operating frequency respect to the first mode frequency is function of λ/ℓ.

A possible way to stabilize the RFQ is suggested by our circuit; we introduce a capacitance every two cells. In other words we cut the transmission line into segments of

* from University of Naples, Italy
# from University of Ferrara, Italy

length 2dz, for each segment we consider only the n=0 and 1 modes, and we couple the segments with an impedance $Z_{Ca} = 1/i\omega C_a$. The result is a biperiodic system governed by the equations

$$\begin{cases} (1 - x - \beta\gamma x + \gamma)u_n + \beta\gamma x u_{n-1} - \gamma u_{n+1} = 0 \\ (1 - x - \beta\gamma x + \gamma)u_m - \gamma u_{m-1} + \beta u_m = 0 \end{cases}$$

with m=2j+1, n=2j, j integer,

$$\omega_c \equiv \frac{1}{\sqrt{L_1 2dz C_a}}, \quad \beta \equiv \frac{\omega_c^2}{\omega_0^2}, \quad \gamma \equiv \frac{2C_a}{Cdz}, \quad x \equiv \frac{\omega_0^2}{\omega^2}.$$

It is interesting to observe that the unknown x appears in the non-diagonal terms and this is therefore a so-called extended eigen value problem. Nevertheless, since we have a lossless chain, one can look for a solution of the form: $u_n = e^{i\alpha} u_{n-2}$. This condition leaves two independent voltages, for example u_n and u_{n+1}, and therefore the recursive relations determine a couple of linear equations that have solution different from zero if:

$$x = \frac{[\beta\gamma^2(1-\cos\alpha)+1+\beta\gamma+\gamma] \pm \sqrt{[\beta\gamma^2(1-\cos\alpha)+1+\beta\gamma+\gamma]^2 - (1+2\beta\gamma)(1+2\gamma)}}{(1+2\beta\gamma)} \quad (3)$$

This is the new dispersion relation. The two bands, corresponding to the two sign determination of the square root, have even dependence on α, and the fundamental frequency $x=1$, corresponding to $\alpha=0$, is not any more the lowest. Moreover we have the coalescence of the two bands at $\alpha=0$ when the square root vanishes, i.e. for $\beta=1$. Therefore the stabilization of the fundamental mode is realized when $\omega_0=\omega_C$, condition that resembles the coalescence condition for the coupled pillbox biperiodic chains.

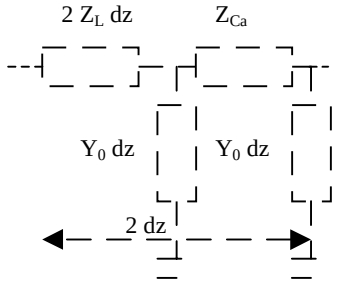

Figure 2: Biperiodic equivalent circuit.

In Fig. 3 we show the numerical solution a chain of 10 resonators (γ=.024, β=1). In the upper part we plot the normalized frequency of the modes, together with the dispersion relation (3) for an infinite chain of resonators; the agreement is good, meaning that in this case the termination conditions do not play an important role. The fundamental mode and the two neighbor modes are plotted in the lower part of Fig 3. These two modes have the same long range dependence, but the oscillation between next cells is in opposite phase. As a consequence, for a small (1%) perturbation in the eigen-frequency of the first resonator, the long range drop of the field is compensated, but the short range oscillation (first mode for each wave-guide segment) is enhanced. In this sense the stabilization is not complete.

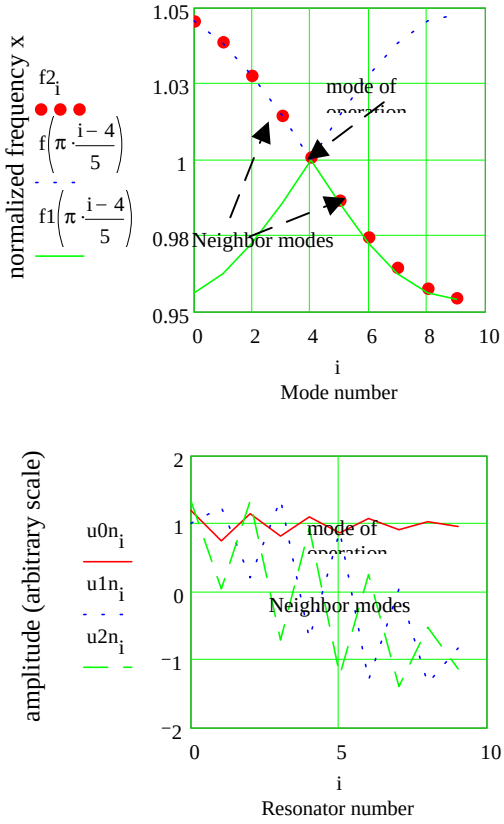

Figure 3: Numerical solution of the equivalent circuit (γ =.024, β =1, 1% perturbation in the frequency of the first resonator) and dispersion relation for an infinite chain of resonators.

2 SCALING FOR A SEGMENTED RFQ

The lumped circuit model of the previous section has been developed so to dimension a 352 MHz RFQ (about 6 m long) using the LANL technique for field stabilization[2]. We just remind that the RFQ is split in segments (of length 2 dz) coupled throw a coupling cell with the geometry shown in the MAFIA plot of fig. 4.

The impedance of this coupling-cell has in general an inductive (L_A) and a capacitive component (C_A), determined by the cross talk of the magnetic fields of the neighbor RFQ throw the opening, and by the capacitance of the facing electrode terminations respectively. Nevertheless for practical range of parameters the capacitive term is the dominating one:

$$Z_a = \frac{1}{i\omega C_A}\left(1 - \omega^2 L_A C_A\right) \approx \frac{1}{i\omega C_A}\left(1 - \omega_0^2 L_A C_A\right) = \frac{1}{i\omega C_a}$$

With these assumptions we can get very practical scaling relations. From the resonant coupling condition β=1 we calculate the desired coupling capacitance:

$$C_a = \frac{C}{dz}\frac{\lambda^2}{64} \quad (4)$$

that determines the gap between electrode terminations. Moreover the coupling strength is:

$$\gamma = \frac{1}{64}\frac{\lambda^2}{dz^2} \qquad (5)$$

The relative strength of the geometrical errors that can be corrected (for example the relative error of the local frequency) scales like γ; therefore short RFQ segments give a better correction but a higher coupling capacitance and a shorter gap. A short gap can be a problem because of the construction tolerances even if in the lumped circuit model we saw that the tolerances in β are rather loose, and for example for the case in Fig. 3 β=1.2 still gives significant field stabilization.

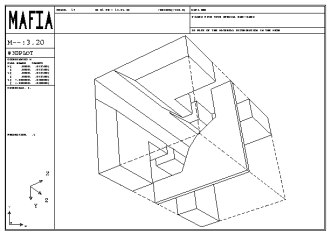

Figure 4: MAFIA simulation geometry in the coupling cell.

3 SIMULATIONS WITH MAFIA

One quarter of the structure has been simulated with MAFIA. Moreover, to reduce the number of mesh points we employed a simplified geometry, six times shorter, that resonates at 5.9 times higher frequency, but preserving the 352 MHz electrode geometry as much as possible (Fig. 4). In this way the "ratio limit", that is substantially the ratio between the smallest mesh size required (in the gap) and the total structure length, is kept reasonable, and the CPU time required for simulations is affordable.

In Fig. 5 and Fig 6 we show some typical. In Fig 5 the frequencies of the fundamental and of the two neighbor modes are plotted as a function of the gap length. The fundamental mode frequency is of course untouched by the change of capacitance. The equidistance of the spurious modes is reached for a gap of 3.3 mm. With the rough approximation of a planar condenser we get C_a=0.27 pF.

From equation (4), taking into account that for our simplified transverse C=80 pF/m, the capacitance for the coalescence of modes is C_a=0.32 pF. If we consider that the magnetic effects in the coupling cell and the edge electric field due to the finite dimensions of the electrode cross section have been neglected, the 16% agreement achieved is fair.

To test the compensation we have compared the longitudinal behavior of the voltage between the segmented and the uncoupled RFQ in thee presence of a perturbing piston tuner (fig 6).

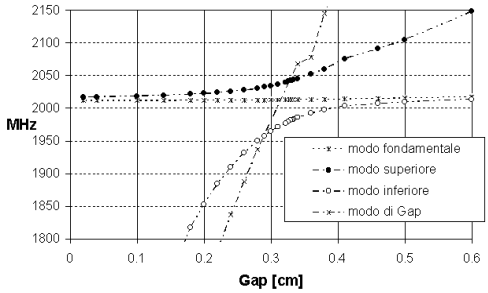

Figure 5: Frequencies of the most relevant modes as a function of gap length.

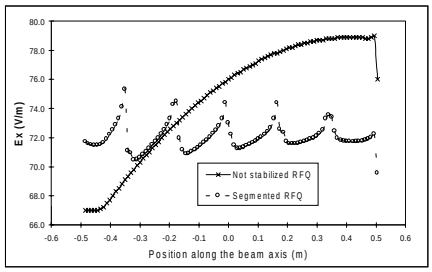

Figure 6: Effect of a perturbation on the RFQ with and without coupling cells. .

4 CONCLUSIONS

We have introduced an equivalent circuit to model an RFQ stabilized with the LANL technique. We think that this rough model catches the essence of the problem, giving the coalescence condition and the pass band amplitude (related to the error correction capability) as a function of few RFQ parameters, namely the operating frequency, the length, the quadrupole capacitance per unit length and the capacitance of the coupling cell. The comparison with MAFIA confirms our scaling laws; however we are not able to test the entire tuning procedure (including the influence of dipole modes) with MAFIA. For these reasons we have built an aluminum model, 3 m long, 352 MHz. The RF measurements are in progress.

5 ACKNOWLEDGMENTS

We thank Prof, V.G. Vaccaro, Prof. L. Verolino and Prof. P. Dalpiaz for the precious supervision of the two undergraduate theses that are the starting point of this paper. The discussions with M.Vretenar (CERN) and A. Lombardi have clarified many points.

REFERENCES

[1] G. Dome, Linear Accelerators, P.M. Lapostolle and A.L. Septier editors p. 665-673 (1970)

[2] M.J. Browman and L. M.Young, Proceedings of 1990 Linac Conference, p 70.

THE POSSIBILITY OF MULTIPACTOR DISCHARGE IN COUPLING CELLS OF COUPLED CELLS ACCELERATING STRUCTURES

V.V. Paramonov, S.G. Tarasov
Institute for Nuclear Research, 117312, Moscow, Russia

Abstract

The Multipactor Discharge (MD) takes place at low values of electric rf field. Operating values of the field in accelerating cells are usually match more higher than the upper threshold of the discharge and this phenomenon take place during structure conditioning. In operating regime, during rf pulse, weak electric field, linearly decreasing from the point of the rf drive to the end of the cavity, exists in coupling cells to provide rf power flux along the cavity. Depending on cavity operating regime and coupling cells parameters, the value of this field can be in limits of the discharge. In this paper parameters of coupling cells for Side Coupled (SCS), On-axis Coupled (OCS) and Annular Coupled (ACS) structures are considered and estimations for electric field are given. Results of numerical simulations of the discharge in coupling cells are presented.

1 INTRODUCTION

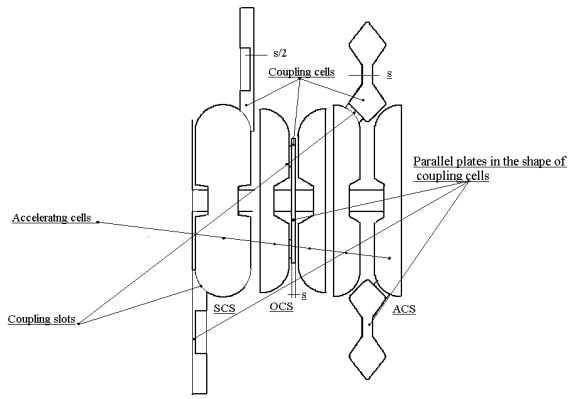

Figure 1: A sketch of SCS, OCS and ACS structures

The effect of the MD in accelerating cells of Coupled Cells (CCL) structures is straightforward, because parameters of accelerating cells directly define parameters of the cavity and the discharge is equivalent to additional parasitic conductivity. In operating regime coupling cells in first order do not excite, the MD in coupling cells may be simulated as additional rf losses, leading to reduction of quality factor for coupling cell and has not such evident sequences on operating parameters. To decrease dimensions of coupling cells, one need provide capacitive load by providing 'noses' in the region of strong electric field of the coupling mode. As the result, coupling cells have parallel plates, like capacitor (Fig.1). Such shape is favourable for MD excitation.

The MD in coupling cells of CCL structures was not described in papers directly, just indications that OCS was rejected for application in TRISPAL project due to MD possibility [1] or private communications [2]. The purpose of this paper is to discuss the possibility of most popular first order two-surface MD in coupling cells, to compare different types of coupling cells and specify operating parameters of the structure, which can provide conditions for MD in coupling cells.

2 STEADY-STATE CONDITIONS

2.1 The energy stored in coupling cells

If the steady-state operating regime of the CCL structure is specified, one can easy find the energy W_a of electric field stored in accelerating cell:

$$W_a = \frac{c\beta_p Q_a (E_0 T)^2}{4\pi f_0^2 Z_e}, \qquad (1)$$

where Q_a is quality factor for accelerating cells, Z_e - effective shunt impedance, f_0 - operating frequency, β_p - relative velocity of particles, c - velocity of light, E_0 - average electric field along axis, T -transit time factor. To find stored energy in coupling cells, one can use conclusions both lumped circuit [3] and electrodynamical [4] approaches, which coincide for coupling cells. The energy stored in coupling cells W_c is

$$W_c = W_a \alpha^2 (n - N)^2, \qquad (2)$$

where α is attenuation constant per period, n - number of the coupling cell from the point of rf input, N - number of the structure periods from the point of rf input to the end of the cavity. If the beam loading is not strong $I_b Z_e cos^2\varphi_s \leq E_0 T$, attenuation constant α may be estimated as:

$$\alpha \approx (1 + \frac{I_b Z_e cos\varphi_s}{E_0 T}) \frac{2}{k_c Q_a} \qquad (3)$$

where k_c is the coupling coefficient of the CCL structure, φ_s - synhronous phase. For strong beam loading attenuation should be founded as the result of solution for the power balance equation [4]. Combining (1-3), one can define W_c for any operating regime given. For proton linacs at typical values f_0=805 MHz, β_p=0.5, Q_a=20000, k_c=5%, Z_e=35 MOhm/m, supposing I_b=0 and N=40 (total tank has 80 accelerating cells and rf input is in the middle of the tank) dependencies of W_c on the accelerating gradient $E_0 T$ and n are plotted in Fig.2. As one see, W_c may varies in wide range, depending on $E_0 T$ and N values.

2.2 Estimations for MD threshold

In typical shape of coupling cells there are parallel plates (Fig.1) with electric field of coupling mode between them. Because the gap length s between plates is small, we can suppose uniform electric field between plates, considering this region as a capacitor. Simple estimations for the MD range may be obtained by using the model of single electron sheet ([5],[6] and relates references). The resonant condition for electric field strength E_r in coupling cells for two electrode MD is:

$$E_r = \frac{4\pi^2 f_0^2 sG}{(e/m)}, \tag{4}$$

$$G = [(\frac{k_v+1}{k_v-1})(2n_p-1)\pi cos\phi_e + 2sin\phi_e]^{-1}, \tag{5}$$

where e/m is the ratio of electron charge and mass, n_p - order of MD (number of rf halfperiods needed for electron to pass distance s, k_v is assumed constant ratio of electron emission to impact velocities and ϕ_e is secondary emission electron starting phase. Below we consider mostly first order $n_p = 1$ MD. For phase stable MD the phase of electron impact with second plate ϕ_i should be $\phi_i \approx \phi_e + n_p\pi$ with the condition of stability $-1 \geq d\phi_i/ \geq 1$ [6]. The minimum value of E_r depends on $G(k_v, \phi_e)$ and G_{min}= 0.27 (k_v=0), G_{min}=0.23 (k_v=0.1), G_{min}=0.21 (k_v=0.25). The assumption $k_v = const$ has no physical basement, but due to week dependence, results obtained are in good agreement with experiments [7] and direct numerical MD simulation [6] and assumption k_v=0 is a good approximation.
From (4) one can see, that rf resonant rf voltage for MD excitation $V_r = E_r s$ does not depend on frequency f_0 if scaling is applied for dimensions of coupling cell.
Another important value for MD exitation is the energy of impact electrons W_i (supposing nonrelativistic electrons):

$$W_i = 8\pi^2 m(\frac{f_0 sGcos\phi_e}{1-k_v})^2 \tag{6}$$

For high order (n_p=2,3,4..) MD estimations for resonant rf voltage V_{rn_p} and impact energy W_{in_p} may be obtained using G-factor, if equivalent values for n_p=1 discharge are known ($V_{rn_p} \approx V_{r1}/n_p$, $W_{in_p} \approx W_{i1}/n_p^2$).

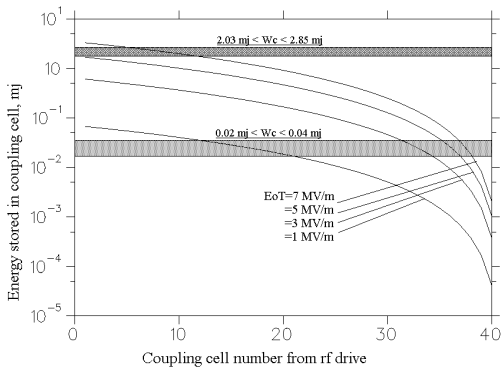

Figure 2: The energy stored in coupling cells, mj

2.3 Coupling cells parameters

To compare parameters of different cells, three types of structures - SCS, ACS and OCS (Fig.1) were calculated at the same frequency 805 MHz for $0.45 \leq \beta_p \leq 0.8$. By using powerful 3D code Mafia, one can calculate field distribution for coupling mode and define simply, what value of electric field E_c or rf voltage V_c between plates in coupling cell corresponds to stored energy W_c. To describe the this parameters for coupling cell, the best way is to introduce "equivalent capacitance" C_e:

$$C_e = \frac{2W_c}{V_c^2} \tag{7}$$

If this C_e value is known at the given frequency, for another value it can be estimated from scaling relation $C_e \sim f^{-1}$. For SCS geometry is the same as for [8], ACS geometry was scaled from [9]. For OCS structure the length of coupling cells was 0.1 from the length of accelerating one. Last OCS example for β_p=1, f_0=2797 MHz is from reference [10]. For OCS structure V_c is calculated at radius of beam aperture. If dimensions of coupling are specified, one can estimate $f_0 s$ value, which is of main importance for calculation of V_r (4) and estimate energy stored in coupling cell $W_{c1} = C_e V_r^2/2$ and impact energy W_{i1} (6) which correspond to condition of n_p=1 stable ($0 \leq \phi_e \leq 33^o$ [6]) discharge. Results are summarised in Table 1, W_c and W_i are estimated for n_p=1 MD.

Table 1: Parameters of coupling cells

CCL	β_p	$f_0 s$	C_e	W_{c1}	W_{i1}
			pF	mj	keV
SCS	0.45	705	4.42	0.02÷0.03	1.1÷2.3
	0.50	834	3.87	0.03÷0.05	1.6÷3.2
	0.70	1545	2.34	0.24÷0.34	5.5÷11
ACS	0.52	1503	21.9	2.03÷2.85	5.2÷10
	0.78	2177	33.7	13.7÷19.3	11÷22
OCS	0.50	563	14.0	0.02÷0.04	0.7÷1.5
	0.70	837	12.4	0.11÷0.16	1.6÷3.2
	1.0	1200	3.39	0.12÷0.18	3.3÷6.6

3 DISCUSSION

3.1 Conditions of discharge

To have stable discharge, one need fulfil three conditions:
a) - space stability;
b) - phase stability;
c) - impact electron energy should be in range where secondary emission coefficient $\sigma_e \geq$1.0. For copper this range is from $\approx$ 200 eV to $\approx$ 2 keV, depending on surface quality. As one see from Table 1, conditions b) and c) are valid for

low β_p SCS and OCS structures. Not so big energy 0.02 mj $\leq W_{c1} \leq$ 0.04 mj should be stored in coupling cells to provide conditions for n_p=1 discharge. This range is shadowed at Fig.2 and one can see these values realistic for proton linacs. In accelerating cavity several coupling cells may be in range of possible discharge. For ACS structure impact electron energy is too big even for low β_p (due to big $f_0 s$ value) to provide conditions for n_p=1 discharge. Only high order MD n_p=2,3,4 are possible in ACS structure at low β_p.

3.2 Numerical simulations

Special code was written for direct tracking of electrons in calculated fields of coupling cells. Main purpose of this tracking was to check space stability of discharge. Results of simulations confirm good analytical estimations for n_p=1,2 MD at low β_p for all structures. For SCS and ACS structures at low β_p electric field is practically constant both in longitudinal and in transverse directions in the space between noses. It means, that MD (if exists) takes practically all space between noses, but MD range in respect of W_c is limited. With increasing of β_p distance s rises, becomes comparable with transversal dimensions of noses. For ACS and SCS structures the approximation of plane capacitor becomes not acceptable. Direct numerical simulation shows no stable electron trajectories in the space $\approx 1.5s$ from outer side of the nose. It is sequence of nonuniform electric field in this region. It is especially important for ACS structure because nose is open both from top and bottom sides. For $\beta_p \geq$0.7 results show no stable trajectories for ACS coupling cells and reduced region (near centre of nose) of space stability n_p=1 MD in SCS coupling cells. Condition of the space stability for high order MD with respect field homogeneity are more rigid than for n_p=1 MD.

For OCS coupling cell is narrow cylindrical cavity. Electric field varies as Bessel J_0 function along radius. Nonuniform fields are only near beam aperture and coupling slots. Results of simulation show, that if MD exists at W_{c1} given, it takes a part of coupling cell and for $W_{c11} \geq W_{c1}$ it may displays to another part of the cell with lower electric field. All time there are regions with space stability of discharge. If for β_p =1 the impact energy W_i for n_p=1 MD is too big, conditions for high order MD may be fulfilled.

3.3 Effect of MD in coupling cells

It is known [6], [11], that the discharge current is limited by space charge effect and for maximum value of current density for n_p=1 MD is:

$$j_{1\ max} \simeq \frac{\epsilon_0 m f_0^3 s}{e}. \qquad (8)$$

For typical values f_0=805 MHz, s=1 cm, $j_{1\ max}$=2500A/m^2. For high order discharge n_p=2,3,4.. $j_{n_p\ max}$ value is 3(n_p+3) times less. Suppose n_p=1 discharge exists in one SCS coupling cell (nose radius is r_n=3.0437 cm [8]). The total MD current I_{MD} is estimated as $I_{MD} = \pi r_n^2 j_{1\ max} \sim 7$ A. With impact energy $W_{i1} \approx 1$ keV it leads to additional rf power dissipation $P_{rf} = I_{MD} W_{i1}/e \sim 7$ kW (upper estimation). It is not so big value to see drastic disappearance of rf power from rf generator with total power in several MW. But quality factor Q_l for this cells decreases to value $Q_l = 2\pi f_0 W_{c1}/P_{rf} \sim 20$. Such low Q cell do not keep amplitude and phase stability for operating $\pi/2$ mode so good as high Q one.

4 SUMMARY

Results of analytic estimations and numerical simulations show that first order multipactor discharge of is possible in SCS and OCS coupling cells for low $\beta_p \approx 0.4$. In ACS only high order discharge is possible. for low $\beta_p \approx 0.4$. With β_p increasing the gap between cell noses increases too, leading to nonuniform field between noses, reducing possible space for stable MD in SCS and eliminating it in ACS structure.

The best way to decrease MD possibility is trancformation of parallel plates into conical surface.

For coupling cells of OCS structure at β_p=1 condition for higher modes of discharge may be fulfilled.

5 ACKNOWLEDGMENTS

The authors thank Prof. L.V. Kravchuk, Prof. Y. Yamazaki, Dr. G.V. Romanov for valuable discussions and help for this investigation.

6 REFERENCES

[1] M. Prome, Major Projects for Use High Power Linacs. Proc. of the 1996 Linac Conf., v.1 p9, (1996)

[2] Y. Yamazaki, private communication.

[3] E.A. Knapp, Standing wave high energy accelerating structures, Rev. of Sci. Instr. v. 39, p. 979, (1968)

[4] V.G. Andreev, V.V. Paramonov. The distortions of the accelerating field... . Proc. 1995 Part. Accel. Conf., p. 1702, (1995)

[5] A.J. Hatch, H.B.Williams., Multi-pacting modes of high frequency breakdown, Phy. Rev., v. 112, n.3, p. 681, 1958

[6] I.N. Slivkov, Process at high voltage in vacuum, Energiatomizdat, Moscow, 1986 (in Russian).

[7] D. Proch, D. Einfeld, R. Onken, Measurement of multi pacting currents... . Proc. 1995 PAC Conf., p. 1776-1778, (1995)

[8] FNAL Linac Upgrade, Conseptual design report, FNAL, Nov. (1989)

[9] T. Kageyama et al., A high-power model og the ACS cavity. Proc. 1990 Linac Conf., LA-12004-C, p.150, (1990)

[10] B.V. Zverev, N.P. Sobenin, Parameters of accelerating cavities, Energoatomizdat, Moscow, (1993) (in Russian)

[11] D. Callebout, Secondary electron resonance discharge. Phys. v. 29, n. 7, p. 784, 1963

PROGRESS ON A 27 MHZ HEAVY ION RFQ*

A.A.Kolomiets, V.A.Andreev, D.A.Kashinsky, S.A.Minaev, V.I.Pershin,
R.M.Vengrov, V.L.Zviagintsev, S.G.Yaramishev *ITEP, Moscow*
G.Parisi, *IAP-Frankfurt*

Abstract

A 27 MHz heavy ion RFQ is now under construction at ITEP. It based on new ring-connected resonant structure. This structure is low frequency version of previously described "four – ladder" structure. The RFQ has been designed for acceleration of heavy ions with charge to mass ratio of 1/60 (U^{4+}) to energy 100 keV/u. At present the manufacture of the structure is completed, RFQ is assembled and installed into a vacuum tank. The RF measurements confirm the expected parameters calculated by MAFIA and SOPRANO codes – resonant frequency, very reliable mode separation and perfect electrical field distribution.

The carried out numerical simulations and experimental results show that given RFQ type is considerably promising candidate for use as initial part of high current heavy ion linac for HIF.

1 INTRODUCTION

The RFQ for acceleration of intense pulse beam of ions with charge to mass ratio 1/60 up to energy 100 keV/u is under construction in ITEP during last years. The main goal of this work is a maintenance of experimental base for reaserches of interaction of the heavy ion beam with dense plasma. At the time the accelerator was considered as a prototype of an initial part of the linac driver for heavy ion fusion. This work allow to test experimentally the results of investigations and developments for heavy ion high-power accelerator made during last years in ITEP. The main requirements produced to driver are effective acceleration of an intense beam with minimum particles losses and emittance growth. The design of the RFQ is completely based on new ITEP approach to the construction of initial part of high intensity heavy ion linac. A version of "90^0 - apart stem structure" named "ring - connected structure" has been chosen for the RFQ. The structure is the best choice to reach perfect field distributions in low frequency RFQ. Beam dynamics has been designed to minimize emittance growth for intense pulsed beam current.

The important factor influenced the design of the RFQ was very limited financial resources. It means, that from economy purposes some deterioration of radiotechnical, mechanical and operational parameters were allowed. At present the accelerator has been assembled and RF tuning is being carried out.

2 RFQ DESIGN

The described RFQ is the version of "90^0 - apart stem" structure proposed in ITEP for initial part of intense heavy ion linac. The detailed description of the structure and data of both computer simulations and results of RF measurements at the cold models are given in the earlier published works [1,2].

The basic advantages of described structure in comparison with known are:

- rather small transversal dimension;
- high RF parameters;
- reliable mode separation that provides proper field distribution;
- simplicity of mechanical design and low cost of manufacturing;
- low sensitivity to mechanical tolerances.

The mechanical construction of the RFQ is presented in Figure 1, where the RFQ is shown at assembling place before its installation into vacuum tank. The resonant structure consists of octangular shape "rings" produced together with stems. Rings are connected by longitudinal bars. Rings, bars and basements of the electrodes are manufactured of copperplated aluminum alloy. OFHC copper is used for tips of the electrodes. The stem pairs at adjacent rings are perpendicular to each other and to the beam direction. The stems in horizontal and vertical planes are connected by cylindrical electrode basements. The assembled structure represents a rigid 3-D construction allowed to reach required accuracy of electrode positioning. The thickness of the copper layer is not less

Figure 1: RFQ view at assembling place

* The work is supported by GSI, Germany

than 60 microns. The accuracy of machining of the structure parts was not worse than 20 microns.

The basic parameters of the RFQ construction are given in Table 1.

Table 1: Basic RFQ geometry.

Maximum outer ring size, mm	880
Maximum inner ring size, mm	780
Ring thickness, mm	50
Distance between adjacent rings, mm	580
Ring number	22
Cross-section of bars, mm x mm	50x25
Height of stems, mm	280
Height of electrode tips, mm	26
Thickness of electrodes, mm	10
RFQ length, m	12

As mentioned above the mechanical design of the RFQ was largely defined by the limited financial opportunities. In particular the cooling required for high average currents operation has been not provided. Not all of the structure elements connections design have been optimized for highest Q - factor. The expected Q factor is approximately 2 times lower then calculated one. However, it is enough to provide RFQ operation with acceptable RF losses. The improvement of RF contacts does not represent a basic problem, but would result in increasing the total cost of the RFQ.

3 BEAM DYNAMICS

Beam dynamics in the RFQ has been calculated using developed in ITEP procedure for high current linac design. The main goal of the procedure is to achieve maximum value of accelerated beam current with at least 95% transmission and minimum emittance growth.

The modulation parameter along part of initial bunch formation in early RFQ designs was chosen to keep geometrical length of separatrix approximately constant. If particle distribution in separatrix is uniform this method allow to keep constant space charge forces along RFQ. It should minimize beam emittance growth [3]. However, using of monochromatic beam for injection to RFQ leads to considerable variations of space charge density along formation part. The result is noticeable emittance growth for high intense beam at this part. It is also troublesome to propose in advance optimal synchronous phase and modulation along RFQ.

The described RFQ has been designed using some modification of the above mentioned approach. Cell geometry is calculated taking into account real particle distribution in phase space, obtaining from beam dynamics simulations in preceding cells. The simulation takes into account as space charge forces as real external field distribution.

In the procedure the geometry of cell is chosen to fulfill some requirements and limitations for RFQ parameters:

- space charge forces do not exceed some prescribed value;
- longitudinal stability has to be obtained not less than for 95% of particles;
- phase advance doesn't change more than on ±10 % of its chosen value;
- maximum strength of electric field on electrodes surface doesn't differ more than on 1% of its chosen value.

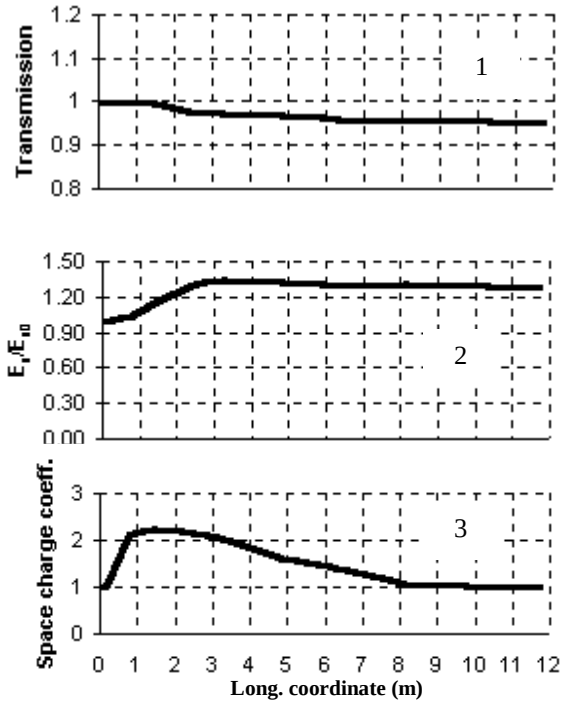

Figure 2: Calculated beam transmission (curve 1), relative transverse emittance growth (2) and Coulomb parameters (3) *h* relatively to its initial value along RFQ

These requirements has to minimize emittance growth due to space charge effects and mismatching of the beam in channel with changing phase advance.

The RFQ generating procedure controls space charge effects using Coulomb parameter *h*, introduced in [3]:

$$h = \frac{\lambda}{\mu_0 \beta \gamma^2 I_0} \frac{I}{V_p},$$

where I - peak current of the beam, V_p - normalized transversal emittance, λ - wave length, β - relative velocity of particles, γ - relativistic factor, μ_0 - phase advance, I_o - characteristic current, equal $3.13 \cdot 10^7$ *A/Z*, *A/Z* - mass to charge ratio. Peak current and emittance are calculated by simulations in preceding cells.

As a rule, the monochromatic beam is injected to RFQ. It means that at bunching of the beam in initial part of structure peak current can change in width enough range with formal maintenance of separatrix length. In this case *h* in bunch formation part is always higher than

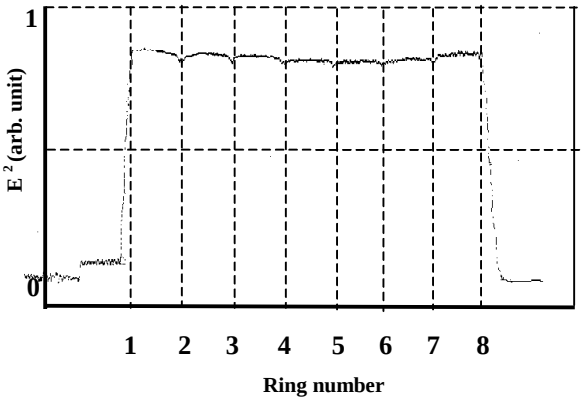

Figure 3: Measured field distribution along 8 ring assembly

in injected beam. The procedure of RFQ generating should to keep *h* lower than some prescribed upper limit.

Some results of RFQ design using described procedure are presented on Fig. 2. The simulations were carried out using written in ITEP code DYNAMION for beam current 12 mA and initial emittance 0.3 mm*mrad. Curve 3 shows Coulomb parameter along RFQ. At pre-bunching part (0 -1 m) Coulomb parameter smoothly increases to its prescribed value h_{max}. At formation part (1 - 3 m) *h* is kept under h_{max}. At gentle buncher *h* decreases because phase advance is dominated factor at this part. At main accelerating part the geometrical length of separatrix is constant and *h* is practically equal to its value in injected beam.

Curve 2 on Figure 2 shows relative growth of normalized rms emittance along RFQ. It can be seen from picture that rms emittance increases on ≈25% and main growth happens in the part of RFQ corresponding to the maximum value of Coulomb parameter. It has to be noticed that high enougth value of h_{max} = 0.34 was chosen only due to necessity of accelerating of particles up to 100 keV/u on the length limited by existing vacuum tank. Curve 1 shows that some particle losses are appeared at beam current 12 mA in spite of the fact that ratio acceptance to emittance is approximately factor 2.5. The explanation is that at given h_{max} the process of halo formation plays significant role [4].

4 FIRST RF MEASURMENTS

Measurements of the fields were carried out by means of standard bead-pull technique. Inter-electrode voltage distribution along the structure was measured for each pair of neighboring electrodes. On Figure 3 the distribution of the normalized inter-electrode voltage along structure for one pair adjacent electrodes is shown. The measurements have been carried out for the part of RFQ - 8 rings assembly. The measured non-uniformity of the field along the section is 1.5 %. It is mainly due to the measurements have been carried outside of the tank and end regions of the structure were tuned for lower frequency. The field distributions for other pairs of the electrodes have the same character. The average fields for different pairs electrodes differ within the limits of 3 %, that can be explained by the fact that the a preliminary alignment had more pure accuracy then it is foreseen for final one. Since this first measurements were made on a part of the structure, for whole structure it is possible to expect the aspiring of the frequency to design value 27.14 MHz and increasing of Q-factor. However even the given results of measurements completely confirm advantages of this variant RFQ for low working frequencies.

Table 2: Calculated and measured RF parameters

	Calculated	Measured
Frequency of quadrupole mode, MHz	27.14	27.66
Q-factor	13000	5650
Frequency of dipole mode, MHz	37.2	36
Shunt-impedance, MOhm ∗ m	1.1	0.48

5 CONCLUSION

The 27 MHz heavy ion RFQ has been designed in ITEP using new resonant structure and original procedure of RFQ generating. The computer simulations as well as RF measurements show that new resonant structure allow:

- to improve the linearity of focusing field due to significant shift of the dipole mode of oscillations;
- to have uniform field distribution along axis;
- to minimize the emittance growth due to improvement of field distribution and minimization of space charge effects;
- to decrease essentially the total cost of the RFQ due to using compact and simple construction.

Final adjustment of structure nowadays is close to completion. The first beam experiments are scheduled for the end of the 1998. In case of experimental confirmation of calculated parameters of the RFQ it will be possible to assert, that RFQ of the given type is a good option for an initial part of HIF driver.

6 REFERENCES

[1] V.A. Andreev, G.Parisi "90°-apart-stem RFQ Structure for Wide Range of Frequencies", Proc. of the 1993 Particle Acc. Conf., Washington DC.

[2] V.A. Andreev, A.A. Kolomiets, V.I. Pershin, V.N. Sydorenko, R.M. Vengrov, S.G. Yaramyshev, O.V. Ershov, G. Parisi, " Development of the ITEP 27 MHz Heavy Ion RFQ", Proc. of the 1997 Particle Acc. Conf., Vancouver, 1997

[3] I.M. Kapchinsky, Theory of Linear Resonant Accelerators, Moscow, Energoizdat,1982

[4] A. Kolomiets, S.Yaramishev, "Comparative Study of Accelerating Structures Proposed for High Power Linac", PAC-97, Vancouver, 12-16 May 1997, Bulletin of the American Phys. Soc., May 1997, Vol. 42, N 3, p.1387

CALCULATIONS OF EXTERNAL COUPLING TO A SINGLE CELL RF CAVITY*

Derun Li, Robert Rimmer, Shakti Kosta, LBNL, One Cyclotron Road, Berkeley, CA 94720, USA

Abstract

A method is proposed to calculate the intrinsic and external Q values of a cavity coupled to a waveguide using MAFIA code in time domain. Typical methods used for the Q calculation in time domain are also reviewed. The method works efficiently for high Q cavities with coupling strengths close to critical coupling case. Applications of the method to a single cell RF cavity coupled to a waveguide are presented. The comparisons between simulation and experimental results are given for a set of different coupling iris apertures.

1 INTRODUCTION

Calculations of external coupling to a resonant RF structure is important in many accelerator applications. There have been a few methods available for specific systems. The methods range from analytical approximations based on the equivalent circuit theory or analytical field solutions to numerical simulations. With the development of powerful computer codes such as MAFIA, SUPERFISH etc., numerical methods are favored for their versatility. Among the numerical methods, two types of the simulation techniques are often used: frequency domain and time domain. In the frequency domain, The Kroll-Yu method [1] has been used widely and proven to be efficient in the external Q calculations for systems having low Q values and strong coupling. The Kroll-Yu method uses the resonance frequencies computed from the MAFIA for different lengths of the waveguides and fits the induced phase variations with a theoretical formula. Both the loaded resonant frequency and the external Q are then obtained from the fitting. When the coupling becomes weak and Q gets higher, to fit the phase variation curve requires very high accuracy of the resonant frequency. This is difficult for many simulation codes. An improved version of this method is Kroll-Lin method, but we do not have enough data and experience to comment about it. We developed a method using the MAFIA time domain simulation results. Unlike the conventional decay method in the time domain, which calculates the natural decay time constant, we calculate the Q_0, $Q_{\rm ext}$ using an energy method [2]. The method involves the use of waveguide boundary condition which is available in the MAFIA time domain module. Application of this method to a single cell RF cavity coupled to a rectangular waveguide, shown in Figure 1 will be presented. Comparisons between simulations and experimental measurement will be given for a set of different coupling iris apertures.

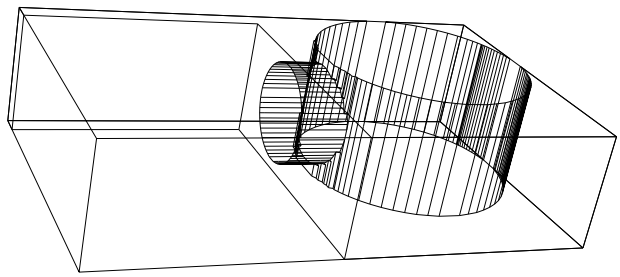

Figure 1: A 3D MAFIA model of a single cell pill-box cavity coupled to a rectangular waveguide through an open iris. The design resonant frequency for the cavity is 1.5 GHz.

2 THE METHOD

We define a cavity (or a chain of coupled cavities) coupled to an external RF component such as a waveguide or a coaxial line, through an open iris or a probe as a cavity-coupler system. The system, in a narrow band around its natural resonant frequency, can be very well presented by an equivalent RCL circuit coupled to a transmission line through a transformer. Due to the presence of the coupling between the cavity and the coupler, the electro-magnetic fields become quite complicated in the iris region. Numerical simulation codes are often used to model this region. The resonant frequency of the system will depend on how the coupler is terminated as well. In analogy to the definition of the unloaded quality factor Q_0, an external quality factor $Q_{\rm ext}$ is defined in such a way that makes the coupling and the resonant frequency of the system unique by terminating the coupler with a matched load. It is difficult to numerically simulate a matched load in the frequency domain. We instead take the advantage of the built-in waveguide boundary condition in the MAFIA time domain, calculate the instantaneous stored energy and power loss over one RF period based on the time domain simulation results. We assume the following relations hold at any instant,

$$Q_0 = \omega_0 \frac{U(t)}{P_w(t)}, \quad Q_{\rm ext} = \omega_0 \frac{U(t)}{P_{\rm out}(t)} \tag{1}$$

where ω_0 is the natural angular resonant frequency; $U(t)$ and $P_w(t)$ are respectively the stored energy and power loss on the cavity averaged over one RF period at time t; $P_{\rm out}(t)$ is the RF power flowing out from the waveguide port over one RF cycle at time t. Two time domain runs are needed to determine both the resonant frequency and the $Q_{\rm ext}$ of the system: one for the resonant frequency and the other

* This Research Work is supported by the Director, Office of Energy Research, Office of High Energy and Nuclear Physics, High Energy Physics Division, of the U.S. Department of Energy, under Contract No. DE-AC03-76SF00098

for the $Q_{\rm L}$ which is given by,

$$\frac{1}{Q_{\rm L}} = \frac{1}{Q_0} + \frac{1}{Q_{\rm ext}}. \qquad (2)$$

As the MAFIA time domain module can handle lossy dielectric materials, system involving coupling with ceramic windows and lossy materials can also be simulated correctly.

2.1 Resonant Frequency of the System

We first drive the cavity-coupler system with a broad band dipole pulse with its center frequency approximately around the natural resonant frequency of the system. A Gaussin pulse built-in in MAFIA is often used with its bandwidth wide enough to cover the natural resonant frequency, but not to excite high order modes. The location and the polarization direction of the dipole should be at the place where the mode of interest has a strong electric field component in the same direction. Waveguide boundary condition at the waveguide port must be used. The bandwidth of the waveguide should be wide enough so that there are no reflected fields coming back from the port. The induced time varying electro-magnetic fields in the cavity are also monitored at a place where the mode of interest has a strong component, but not too close to the driving point. The electro-magnetic field whose frequency is equal to the natural resonant frequency of the system will be coherently excited, and be built up. If the driving source is removed, the field decays with its natural time constant. For high Q cavities, the decay time, therefore the CPU time is so long that makes it in-efficient to calculate Q in this way. Nevertheless this field does provide enough information to determine the resonant frequency. Having carefully chosen the driving bandwidth, the only field left after the driving source will be the field with the natural resonant frequency. A Fast Fourier Transform (FFT) of the field then can be used to find the frequency. However better accuracy of the frequency can be determined by measuring the oscillation period of the time varying field signal using the last 5 to 10 RF cycles. Based on our experiences, typically less than 30 RF cycles are long enough to get a good measurement. Figure 2 shows an example of the time varying electric field signal excited by a pulse. The field is calculated by the MAFIA time domain module, T3.

2.2 The Energy Method

The same procedure used to measure the resonant frequency is repeated except the dipole excitation will be at a single frequency equal to the resonant frequency obtained from the 1st time domain simulation. In addition to monitoring the time varying electro-magnetic fields at the same location, 3D electro-magnetic fields in the system are recorded as well at time $t_0 \pm \Delta t$. The t_0 is chosen at a time when the relative energy contribution from the excitation source to the total stored energy in the cavity is negligible. In order to calculate the average stored energy and the

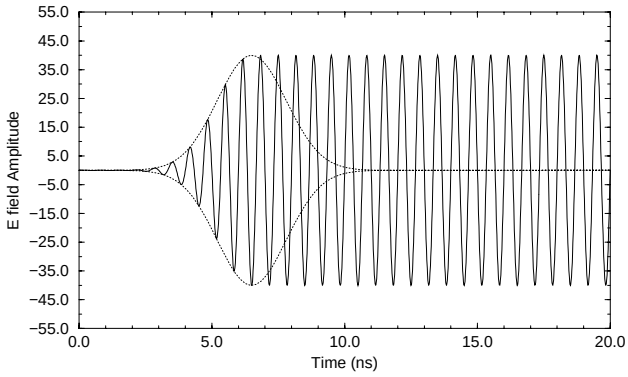

Figure 2: An electric field component is plotted as a function of time (solid line). The envelop of the driving pulse is plotted at the same time with dotted line. Only the last 5 to 10 RF cycles are used to calculate the resonant frequency of the system.

power loss at t_0, we take,

$$\Delta t = \frac{1}{4 f_{\rm drv}}, \qquad (3)$$

with $f_{\rm drv} = \omega_0/2\pi$ as the driving frequency and ω_0 as the angular resonant frequency. With this driving source, the electro-magnetic fields will be building up coherently with time, e.g.,

$$\Phi(t) = \Phi_\infty \left(1 - e^{\frac{t}{\tau}}\right) \sin(\omega_0 t + \theta_0), \qquad (4)$$

where $\Phi(t)$ may denote any field component of $\vec{E}(\vec{r},t)$ or $\vec{B}(\vec{r},t)$, and Φ_∞ is the field amplitude at steady state. $\tau = \frac{2Q_{\rm L}}{\omega_0}$ is the time constant of the system. θ_0 is an initial phase. For a high $Q_{\rm L}$ system it is impractical to run MAFIA in time domain to obtain either an accurate value for the decay time or until the steady-state field amplitude Φ_∞ is reached. We find that it is convenient to record the 3D fields at t_0 and $t_0 \pm + \Delta t$ during the time while the fields build-up and use the fields to re-construct a quasi-time harmonic field (mode). Taking the advantage of many built-in features in the MAFIA post-processor (P code), the quasi-time harmonic field can be used readily for the calculation of Q_0 and $Q_{\rm ext}$.

As indicated in Equation (4), the field build-up is approximately linear when $\frac{t}{\tau} << 1$. Figure 3 shows an electric field component as a function of time calculated by MAFIA during the field build-up. A linear build-up pattern of the field is exhibited. The same cavity-coupler system shown in Figure 1 is used for the simulation. The system is driven at its resonant frequency, obtained from the first time domain simulation discussed in Section 2.1.

As we pointed out earlier, the excitation dipole will inevitably contribute its energy to the total stored energy in the cavity, but its relative contribution decreases with time. Therefore it is preferable to record the fields at several times until we are sure that approximately the same Q values are obtained. Usually about 30 RF cycles are needed. To calculate $U(t), P_w(t)$ and $P_{\rm out}(t)$, the MAFIA P code

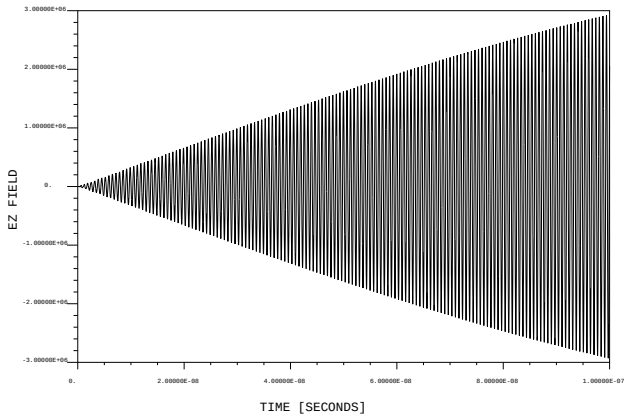

Figure 3: An electric field component is built up linearly as a function of time for a high Q cavity-coupler system driven at its resonant frequency.

is needed. In fact, the P code treats the electro-magnetic fields at time t_0 and $t_0 \pm \Delta t$ as time harmonic fields. Both the energy and power loss calculations from the P code have phase dependent terms. However, the phase dependent terms are cancelled out automatically by the careful choice of Δt in Equation (3). The stored energy at t_0 is then given by,

$$U_\Phi(t_0) \approx \frac{\alpha}{2} \oint_V \left\{ \Phi^2(t_0) + \Phi^2(t_0 \pm \Delta t) \right\} dv \qquad (5)$$

with

$$\alpha = \begin{cases} \epsilon_0 & \text{electric energy, } \Phi = \vec{E} \\ \frac{1}{\mu_0} & \text{magnetic energy, } \Phi = \vec{B} \end{cases}$$

Similarly the power loss is calculated by,

$$P_w \approx \frac{R_s}{2} \oint_S \left\{ H(t_0)^2 + H(t_0 \pm \Delta t)^2 \right\} ds \qquad (6)$$

The unloaded Q_0 is then computed by,

$$Q_0 \approx \omega_0 \frac{U_E(t_0) + U_B(t_0)}{P_w(t_0)}. \qquad (7)$$

2.3 Poynting Vector Calculations

To calculate $Q_{\rm ext}$, $P_{\rm out}$ has to be calculated using the Poynting vector $\vec{S} = \vec{E} \times \vec{H}$, which is constructed by the MAFIA P code using the recorded fields at t_0 and $t_0 \pm \Delta t$,

$$P_{\rm out}(t_0) \approx \frac{1}{2} \int_s \{ S_\perp(t_0) + S_\perp(t_0 \pm \Delta t) \} ds \qquad (8)$$

$S_\perp$ is the transverse component of the Poynting vector in the waveguide. The integral in Equation (8) may be conducted at any cross section s in the waveguide away from the iris. It is also worthy to point out that $E_\perp$ and $H_\perp$ are in phase in the waveguide, therefore the phase dependent terms are cancelled out in Equation (8) for the same reason stated earlier.

Considering the simple geometry of the rectangular waveguide, $P_{\rm out}(t_0)$ may be computed by an analytical formula combining with an energy density $W_{\rm wg}$ obtained from MAFIA by,

$$\begin{aligned} P_{\rm out}(t_0) &= c\sqrt{1 - \left(\frac{f_c}{f_{\rm drv}}\right)^2}\, W_{\rm wg}(t_0) \\ W_{\rm wg}(t_0) &= \frac{1}{d} \left[U_E(t_0) + U_B(t_0) \right]_d , \end{aligned} \qquad (9)$$

where $v_g = c\sqrt{1 - \left(\frac{f_c}{f_{\rm drv}}\right)^2}$ is the group velocity; f_c is cut-off frequency determined by the geometry of the waveguide; $W_{\rm wg}(t_0)$ is stored energy per unit length in the propagation direction with d as the length used for the stored energy calculation. The same $P_{\rm out}$ values are achieved from either Equation (8) or Equation (9). $Q_{\rm ext}$ is then directly calculated from Equation (1).

3 NUMERICAL RESULTS

Numerical simulations of the system have been performed for a set of different iris apertures, and compared with experimental measurements on a simple cold-test model. The results are shown in Figure 4.

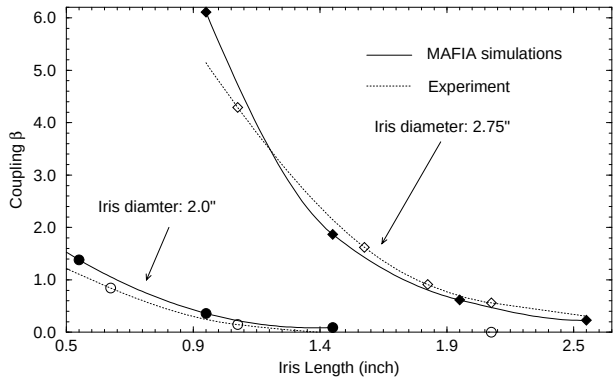

Figure 4: Coupling coefficient $\beta = \frac{Q_0}{Q_{\rm ext}}$ is plotted as a function of iris length for two different iris diameters.

4 CONCLUSION

The time domain method works efficiently for the cavity-coupler system with high Qs and weak coupling. Good agreements are achieved between the MAFIA simulations and the experimental measurements. The method can be easily applied to other systems as well.

5 REFERENCES

[1] N. Kroll, D. Yu *Computer Determination of the External Q and Resonant Frequency of Waveguide Loaded Cavities*, SLAC-PUB-5171

[2] D. Smith, et al. *Recent Progress on Photonic Band Gap Accelerator Cavities*, p518, AIP Conference Proceedings 398 (1996)

MECHANICAL DESIGN, CONSTRUCTION AND ALIGNMENT OF THE ISAC RFQ ACCELERATOR AT TRIUMF

G. Stanford, P. Bricault, G. Dutto, R. Laxdal, D. Pearce, R.L. Poirier, R. Roper
TRIUMF, Vancouver, BC, Canada
R. Obidowski, W. Teskey
University of Calgary Geomatics Engineering, Calgary, AB, Canada

Abstract

The ISAC RFQ is an 8 meter long, 4-rod split-ring structure operating at 35 MHz in cw mode. The rods are vane-shaped and supported by 19 rings spaced 40 cm apart. The stringent, $\pm$ 0.08 mm, quadrature positioning tolerance of the four rod electrodes over the 8 m length was met by adopting a design philosophy based on manufacturing 19 identical rings and mounting them on precision ground plates which are accurately aligned in the vacuum tank prior to ring installation. The vacuum tank is also unique in that it is square in cross-section and split diagonally to obtain full unobstructed side access to the RFQ modules. A seven ring section of the RFQ has been successfully tested with beam at full power.

1 INTRODUCTION

The accelerating system of the ISAC radioactive ion beams facility consists of an RFQ and a post - stripper DTL. Ion beams with A/q $\leq$ 30, from the on line mass separator will be accelerated from 2 keV/u to 150 keV/u through the RFQ and then to an energy up to 1.5 MeV/u through the DTL structure. The reference design[1] for the RFQ is a four rod split ring structure operating cw at 35 MHz. The RFQ accelerator section is 8 meters long and is designed in 40 cm long modules with a peak potential between the electrodes of 74 kV. Full power tests on a single module[2] and on a three module assembly[3] enabled us to complete the basic electrical and mechanical design for the RFQ accelerator. The alignment philosophy was based on manufacturing 19 identical rings and mounting them on precision ground platens which are accurately aligned in the vacuum tank prior to ring installation. The theodolite intersection method was used to align two platen bases in the tank to allow 7 of the 19 rings to be installed in the first section of the vacuum tank. The alignment of the ring assemblies on the platens was accomplished by the same method. Because of the manufacturing procedures and alignment philosophy adopted, when the electrodes were installed on their mounting surfaces they were aligned by definition, assuming that the fabrication tolerances were met.

2 VACUUM TANK

The vacuum tank for the RFQ accelerator is square in cross section (approx. 1 m x 1 m) and 8 m long. It is welded in mild steel and made in two pieces, a base and a lid, with a diagonal split line (Fig. 1) sealed with an 'O' ring. The intent is to provide a very rigid base and heavy back wall on which to mount the turbo pumps, diagnostics, gauges and rf coupling loop; leaving the lid a lighter structure easily removable for access. The diagonal split line provides exceptional accessibility. Cooling water manifolds run along the front floor of the tank fed by penetrations in the tank floor. The inside of the tank is completely cyanide bath copper plated. This was accomplished by using each half of the tank as its own bath vessel – tipped 45°. All the mounting pads on the floor are machined in one pass to ensure they are co-planar. The tank base is mounted on a 9 m x 1.5 m x 0.5 m concrete pad with 22 imbedded studs to match the 7 mounting flanges on the tank base. In order to avoid distortion, the tank is set down on epoxy grout which is allowed to set before the nuts are torqued. After final adjustment no movement of the tank base was observed when the lid was bolted down or when the tank was evacuated. Each half of the tank has forty-two 500 W heaters uniformly installed, covered with a glass fiber blanket, for bake out. A tank temperature of 60°C is reached in less than 2 hours creating a longitu-

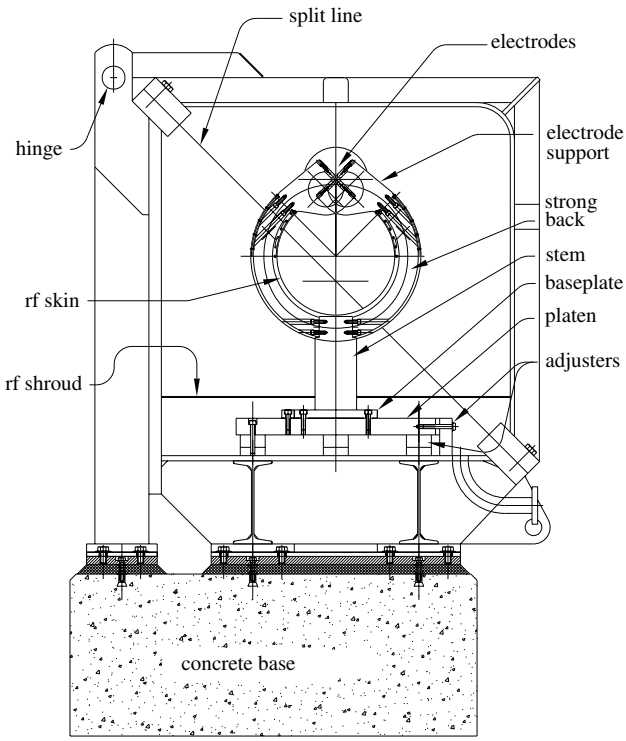

Figure 1: End view of RFQ tank assembly.

dinal growth of $\sim$ 2.0 mm. The elasticity of the mounting system copes with this and growth returns to zero at operating temperature.

3 ACCELERATOR COMPONENTS

3.1 Design Considerations

Each ring is identical and consists of a base, a stem, a split strong back, two electrode supports and an rf skin (Fig. 1). To achieve thermal stability all rf surfaces are water cooled (except for the outer rf skin). This is done by using two separate water circuits. Circuit 1 supplies cooling water from the inlet manifold to a tube array soldered on the inside of the inner rf skin; from there the water enters a circuit drilled into the electrode support (Fig. 2) and then returns to the outer manifold. Circuit 2 transports water from the inlet manifold to the electrode supports through the electrodes to the adjacent ring. Hence, with a 3-ring platen, number 2-ring supplies water to the 4 electrodes, and number 1 and 3 rings receive and return the water. The rf skin encloses the strong back but is attached only where it meets the electrode supports, thus allowing for thermal growth of the skin without loading the structure and causing electrode misalignment. Prototype tests indicate a very small movement during voltage ramp-up but this returns to zero at steady state. Tests on the seven rings showed no movement at all.

As mentioned the philosophy of mechanical positioning, or alignment of the rings, in order to control the accuracy of the electrodes around a true datum line in space (i.e., beam centerline), is to make each ring identical such that when sitting in a jig on its baseplate the electrode mounting pads are within 25 μm, of true position. In the tank there are 6 platens – the first supports 4 rings, and the remaining five 3 rings each. Each platen consists of a special steel 63.5 mm thick with an offset longitudinal rail bolted and doweled in place. The platen and rail are accurately ground in one set up, thus providing accurate datums for mounting and locating the ring bases (the flatness tolerances, i.e., < 12 μm). The platens have 5 adjustable mounting points - 3 vertical and 2 lateral. Each platen is adjusted in the tank using special targets for each platen and aligned by the theodolite intersection procedure which is covered in a later section. Once the platens are aligned they are locked in position and are ready for installation of the rings.

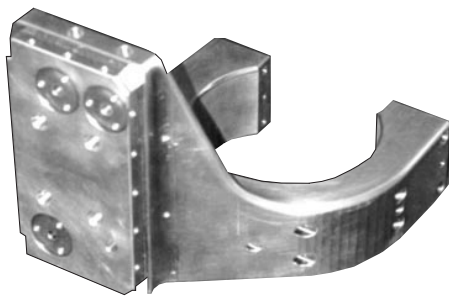

Figure 2: Electrode support showing holes drilled for water cooling circuits.

3.2 Fabrication Considerations

In order to achieve the manufacture of identical rings a philosophy of fabrication and assembly had to be decided upon. The key to this is that the mounting surface on which the vane shaped electrodes are mounted are machined as the last major operation. In order to achieve this with such an awkward shape it was decided to use Electrical Discharge Machining (EDM) and employ a master fixture that would engage datum features on the ring base (the same features that would eventually engage the datums on the platen) and accurately hold the ring in the EDM machine for final machining, thus ensuring that all rings are machined in an identical set up. This master fixture also had provision for addition of inspection tooling to check the result. The same fixture was also used to manufacture special targets previously mentioned which are used to align the platens. Finally, each ring is inspected by an independent organization using a coordinate measuring system. This method of ring manufacture means that individual components can be held to reasonable tolerances with enough machine allowance on the electrode platform to accommodate the accumulated assembly tolerances. Prior to EDM machining at final assembly, all components are doweled together and cleaned.

The electrode support is also of some complexity due to the cooling circuits drilled within the shape of this component (see Fig. 2). This is a fully NC machined component produced to a better than 0.80 μm surface finish in chromium copper (tellurium copper was chosen due to a higher machinability and conductivity rating but pieces of this size are unavailable).

The only other components that require special mention are the electrodes and the rf skin. The electrodes are $\sim$ 13 mm x 38 mm x 120 cm long (except the first two sets which are 80 cm long) and made from tellurium copper for improved machinability and good conductivity. The rods are rough machined, gun drilled for water cooling channels and straightened by the supplier. The cooling holes are plugged at either end with silver soldered plugs. They are then finally machined and profile cut on an NC machine to an overall tolerance of $\sim$ 25 μm. Both the electrode and electrode support quality and accuracy met or exceeded our expectations.

The rf skin is made from 2.2 mm thick C110 copper and the u-shaped ring was created by spinning over a mandrel in two pieces that were later brazed together. Mounting frames and flanges are soldered and finished machined and the cooling array is then soldered in position.

3.3 *Assembly*

Rings were assembled in a semi-clean room environment. The base, stem and strong back and electrode supports were bolted together and aligned in a fixture. These components were then drilled and reamed to allow repeatability during the cleaning and subsequent disassembly in order to fit the rf skin. Once the ring was completely assembled it was shipped to the EDM shop in a special protective container. Handling was a major issue due to the awkward shape, high centre of gravity, and fragility of the rings, hence several handling devices were employed to avoid accidents.

After final EDM machining and inspection the rings were cleaned and installed onto the previously aligned platens and the accuracy of their placement in situ was measured, the results of which are discussed in the next section.

4 ALIGNMENT OF PLATENS AND RINGS

Alignment of the first 2 platens was done as a two step process involving a direct on beam axis sighting with an alignment telescope to position the platens, and confirmation of the position using a three dimensional theodolite intersection technique. Four alignment monuments with targets on the beam axis for direct position and off the beam axis to eliminate rotation about the beam axis were manufactured in the ring assembly jig using EDM. These monuments which simulated the rings were placed on the upstream and downstream ends of both platens. The platens were then adjusted so that the monument targets were on beam axis defined by a line of sight telescope with a resolving power of 3.4 arc sec (0.08 mm) and offset micrometer resolution of 0.001".

The three dimensional theodolite technique involves locating two theodolites within a known grid then measuring the angles to monument targets to compute their coordinates. Two 1 sec electronic theodolites (KERN E2) and their in-house software, SIMS (SLAC industrial measurements system), were used to process the data. Simulations using a grid of five fixed points and two independent measurements of the targets with both theodolites indicated measurement accuracy of 0.04 mm in the vertical off axis and on beam axis directions and 0.075 mm in the horizontal off axis direction. Physical constraints that required the theodolites and the grid to be only along one side of the RFQ meant that the horizontal off axis measurement are less accurate because they are along the theodolite sight line.

The grid was established by measuring angles to 17 points with both theodolites and the distance between two of the points which was defined by an invar scale with a tolerance of ± 0.013 mm. All measurements were done twice to improve the accuracy. Five points in the concrete base beneath the RFQ were used to establish the fixed points for the grid. The alignment of the platens was then confirmed by theodolite intersection of the alignment monuments to be on a straight line within 0.010 ± 0.025 mm vertically and within 0.080 ± 0.100 mm horizontally. Following this measurement the seven rings were installed on the platens and a datum face on one side of each ring was measured with the theodolites. The relative aligment of the rings shown in Fig. 3 shows that the rings were aligned to a straight line within 0.060 ± 0.045 mm horizontally and 0.040 ± 0.010 mm vertically which is well within the strident alignment requirement of ± 0.080 mm. The remaining 12 rings will be aligned by extending the grid to the adjacent platen to be aligned and then aligning the platen to the line defined by the previously aligned platens. This process will be repeated as the grid is extended to the next platen to be aligned. Each platen will be aligned to the new straight line.

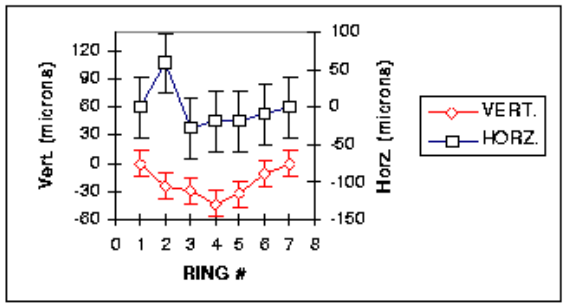

Figure 3: Relative alignment of RFQ rings.

5 CONCLUSION

The outstanding results obtained with beam at full power[4] is a positive indication that the mechanical design, construction and alignment philosophy adopted was a success.

6 ACKNOWLEDGEMENT

A special thanks to Bhalwinder Warich, Peter Harmer and Tim Emmens for the assembly and installation of the RFQ components, and the beam line/alignment group for their help in the alignment of the tank, platens and rings. TRIUMF would also like to thank the alignment group at SLAC for the loan of the two theodilites and their in-house software.

7 REFERENCES

[1] P.G. Bricault and H.R. Schneider, "Simulation of the TRIUMF Split Ring 4-Rod RFQ with MAFIA", Proc. 1995 Particle Accelerator Conf. and Int. Conf. on High-Energy Accelerators, 1125 (1995).

[2] R.L. Poirier, P.J. Bricault, K. Jensen and A.K. Mitra, "The RFQ Prototype for the Radioactive Ion Beams Facility at TRIUMF", Proc. XVIII LINAC Conference, CERN, 405 (1996).

[3] R.L. Poirier, P. Bricault, G. Dutto, K. Fong, K. Jensen, R. Laxdal, A.K. Mitra, and G. Stanford, "Construction Criteria and Prototyping for the ISAC RFQ Accelerator at TRIUMF", Proc. 1997 Particle Accelerator Conference.

[4] R. Laxdal, "First Beam Tests with the ISAC RFQ", this conference.

ENGINEERING DESIGN OF THE APT CRYOMODULES*

B.M. Campbell, M.J. Fagan, J.P. Kelley, A.D. Puckett, R. Valicenti, J.A. Waynert
Los Alamos National Laboratory, Los Alamos, New Mexico 87545 USA

Abstract

The high energy section of the Accelerator Production of Tritium (APT) linac uses Superconducting Radio Frequency (SRF) cavities to accelerate a 100 mA proton beam from 211 MeV to 1700 MeV. Since these SRF cavities can accept protons over a wide velocity range, only 2 different β designs are required. However, 3 different length cryostats, or cryomodules, are required primarily to accommodate the changing magnet focussing lattice. The comparatively short development time span for these cryomodules has inclined us to adopt many design features from proven operating cryomodules. What sets the APT cryomodules apart is the comparatively high RF power; making design to minimize refrigerator work a high priority.

1 INTRODUCTION

A cryomodule containing 2 β=0.64 cavities (β=particle-velocity/speed-of-light) is under design at Los Alamos as part of the Engineering Development and Demostration (ED&D) program. The other types of cryomodules will be designed by General Atomics, one type for 3 β=0.64 cavities and another type for 4 β=0.82 cavities. A modular approach has been adopted that will reduce the total engineering and design effort required to produce these cryomodules.

2 THE β=0.64 ED&D CRYOMODULE

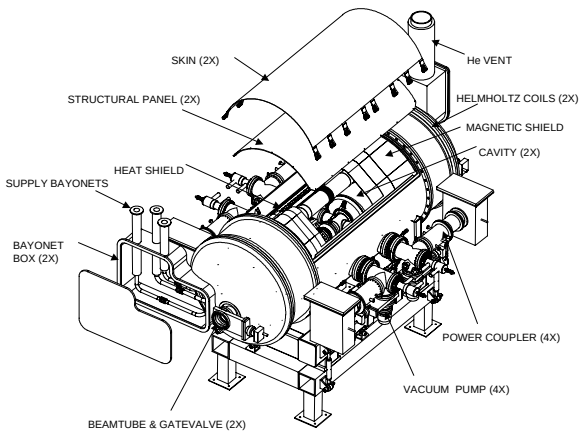

Figure 1: The β=0.64, 2 cavity, ED&D Cryomodule.

The β=0.64 ED&D cryomodule is pictured in Figure 1. The length is 4.9 m, width is 2.7 m, diameter is 1 m, and it weighs 3100 kg .

The extension sections, domed ends, and bayonet boxes are identical modules for all 3 types of cryomodules. Only the length of the RF Section, pictured in Figure 2, varies for the other types of cryomodules.

2.1 Vacuum Tank

The 120° [angle] top opening in the vacuum tank can be seen in Figure 1 with the structural panel and vacuum skin popped up. This design was adopted from the CERN-LEP cryomodule. A similarly large lower opening provides excellent access for assembly and laminar air flow in the clean room.

The center section of the vacuum tank is designed to be easily cleaned before going into the clean room. The side walls are formed from 310 stainless steel plate with a ground finish. No tapped or blind holes are used.

2.2 Heat Shield

The heat shield installed in the complete RF Section is pictured in Figure 2. The heat shield is assembled from top and bottom parts and two end parts. The parts are made from aluminum sheet with a tube trace attached by welding. Slots in the sheet relieve stresses during cool down as in the Tesla Test Facility (TTF) cryomodule.

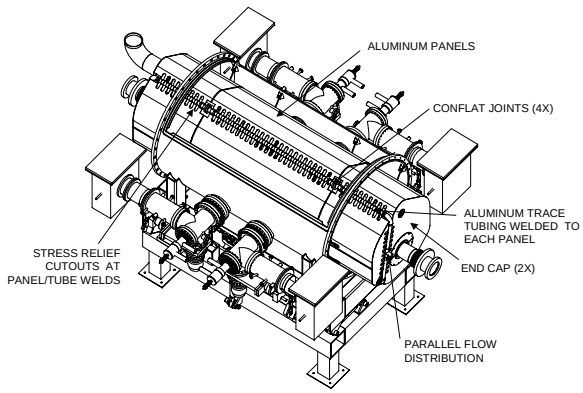

Figure 2: Complete RF Section with heat shield installed.

* Work supported by US Department of Energy

2.3 Magnetic Shield

The magnetic shielding is designed to attenuate the earth's magnetic field reaching the cavity to about 10 mGauss. Two passive shields will be used to attenuate the radial fields and Helmholtz coils used for the axial fields.

2.4 Helium Venting for Fault Conditions

With a loss of vacuum, the liquid helium in the helium vessels will boil and rapidly evolve helium vapor that is vented to prevent over pressurizing the helium vessels and cavities. Four separate vent systems are required to handle the various fault conditions. The worst case is a breach in the beam tube outside the cryomodule that allows air to rush into the 2-K cavity. The air condenses on the cavity wall and deposits a heat flux of 3.8 W/cm^2 into the helium bath. The helium vessels vent through the 15-cm duct to pressure relief devices that discharge the helium directly into the tunnel.

2.5 Vacuum System

Separate vacuum systems provide the insulating vacuum and the power coupler and cavity vacuum. Turbo molecular pumps were selected over ion pumps because design advances have improved reliability and there is less risk of contamination from back streaming.

2.6 Cryomodule Heat Loads

Table 1: β = 0.82 Component Heat Loads

	β = 0.82 Cryomodule	
	2-K (W)	45-K (W)
Cavity (each)	24.1	0
Power Coupler (each)	5	22
HOMs (per cavity)	1.7	0
End Beam Tubes (2)	1.84	24
Radiation - MLI	2.2	19.4
Other	4	47.5

Table2: β = 0.64 Component Heat Loads

	β = 0.64 Cryomodule	
	2-K (W)	45-K (W)
Cavity (each)	15.4	0
Power Coupler (each)	3.5	15
HOMs (per cavity)	1.2	0
End Beam Tubes (2)	1.64	24
Radiation - MLI	0.92	9.1
Other	3	47.5

Tables 1 & 2 summarize the various heat loads, both static and dynamic, that the cryomodule components place on the refrigeration.

2.7 Cryomodule Assembly

The couplers and cavities are assembled and hermetically sealed in a class 100 clean room. The center section of the vacuum vessel goes into the clean room for assembly because the power coupler windows are located outside the vacuum vessel. This approach follows the procedure at CERN. The thermal intercept, cryogenic plumbing, and remaining components are installed outside the clean room with the cryomodule rotated 90°.

3 CAVITIES

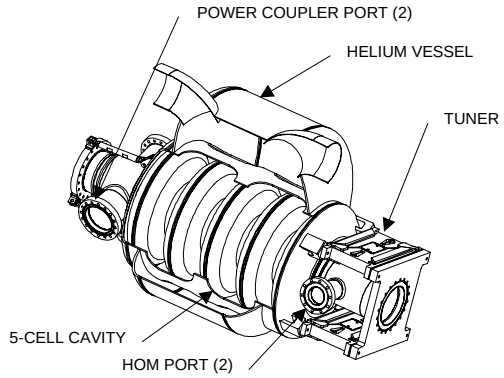

Figure 3: A β=0.64 Cavity and Helium Vessel

3.1 Cavity Design

A cavity and helium vessel, with ¼ of the wall cut away, is pictured in Figure 3. Table 1 gives a summary of the cavity design. The cavities are made from RRR 250 niobium that is formed and e-beam welded following well established cavity fabrication methods. The thickness of the niobium sheet is 3-mm for the β=0.82 cavity and 4-mm for the β=0.64 cavity.

Table 1: Cavity Design Summary

	β=0.64	**β=0.82**
Aperture Radius	65 mm	80 mm
Cavity Radius	194 mm	200 mm
Wall slope	10°	10°
Number of cells	5	5
Length	685 mm	878 mm
Frequency	700 MHz	700 MHz
Peak surface field	15 to 17 MV/m	14 to 17 MV/m
Accelerating gradient	4.7 to 5.0 MV/m	Constant 5.5 MV/m
RF losses @ $Q_0 = 5 \times 10^9$	15.4 W	24.1 W

After fabrication the cavities are chemically etched and high pressure water rinsed using state-of-the art procedures.

3.2 Helium Vessel Design

The helium vessels are made from grade 2 titanium that nearly matches the expansion rate of niobium and avoids possible residual magnetic fields inside the shielding. In the cryomodule the helium vessels are connected by an upper 15-cm vapor return duct and a lower 2-cm liquid transfer line. The liquid helium level at 2.15-K is 7-cm above the cavity. Sufficient ullage is provided in the helium vessel to allow the helium to expand in the event sub-atmospheric pumping is interrupted causing the helium to warm to 4.5-K. The purpose is to keep the return duct free of liquid to reduce recovery time after pumping resumes.

3.3 Cavity Frequency Tuner

Each cavity can be tuned to its 700 MHz resonant frequency by a magnetostrictive linear actuator that either compresses or lengthens the 5 cells. The actuator acts through a flexure device that provides parallel action and 4:1 leverage. The tuning range is ±324 KHz and the resolution is 10 Hz. The actuator travel of 2-cm is obtained by alternately clamping each end of the magnetostrictive rod. The tuner can also be used to de-tune the cavity 20 KHz to take it off line so that proton bunches do not excite cavity fields.

3.4 Cavity Microphonics

Cavity vibration and its effect on the RF frequency will be measured on the prototype 5-cell β=0.64 cavity that is currently being fabricated. The cavity will be installed in its inner perforated shell, shown in Figure 3, but without the outer helium vessel. This permits access to the cavity for installing accelerometers and also for adding cavity supports if needed. The RF control system has been extensively modeled [1] and this measured data will be used with the model to assess microphonic instability.

The next phase will be testing the cavity in the ED&D cryomodule at 2-K. A wire position monitor will be used to measure helium vessel vibration.

4 POWER COUPLERS

Each cavity is powered by 2 coaxial couplers [2], each rated at 210 kW for the β=0.82 and 140 kW for the β=0.64 cavities. A power coupler is pictured in Figure 4. Dual RF windows are warm and located outside the vacuum tank.

The losses from the high RF power transmitted by the couplers can result in large heat loads on the refrigeration plant. The power coupler cooling must be carefully designed to minimize these loads.

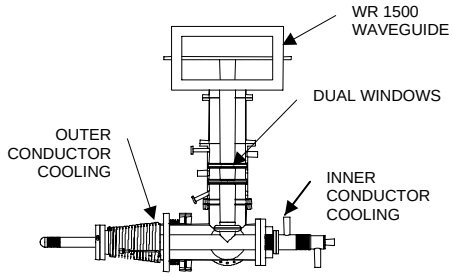

Figure 4: Coaxial Power Coupler

The power coupler cooling naturally divides into two separate considerations: maintaining thermal stability of the inner conductor under various operating scenarios, such as traveling and standing wave RF; and, outer conductor cooling to reduce the heat conducted to the low temperature superconducting cavities. Analysis has shown that the inner conductor is adequately cooled with 3 g/s of helium gas at 3 atm and 300 K. The maximum temperature rise of the inner conductor is limited to 50 K under 210 kW standing wave condition.

Two basic approaches have been considered for cooling the outer conductor: one or two localized thermal intercepts, and distributed cooling from counterflow heat exchange [3]. Independent of the cooling approach, the 2 K heat load is about 2 W, if the niobium is maintained in the superconducting state. The total room temperature refrigeration input power will depend on the details of the cooling approach, but a trade-off study considering additional factors such as manufacturability, reliability, and controllability will ultimately determine which cooling approach is used.

5 STATUS

We are currently in the final design phase and planning a design review for November. Testing is scheduled to begin in April of year 2000.

6 REFERENCES

[1] A. Regan, “APT LLRF Control System Model Results”, 1997 Particle Accelerator Conference, Vancouver, May 1997.

[2] B. Rusnak, et al., “Power Coupler Design for the APT Linear Accelerator”, Proc. Eighth Workshop on RF Superconductivity, Abano Terme (Padova), Italy, October 1997.

[3] J.A. Waynert et al., “A Thermal Analysis and Optimization of the APT 210 kW Power Coupler,” Proceedings of LINAC98, Chicago, Aug 24-28, 1998, to be published.

ANALYSIS OF PERFORMANCE LIMITATIONS FOR SUPERCONDUCTING CAVITIES *

J. R. Delayen, L. R. Doolittle, and C. E. Reece
Thomas Jefferson National Accelerator Facility, Newport News, Virginia 23606 USA

Abstract

The performance of superconducting cavities in accelerators can be limited by several factors, such as: field emission, quenches, arcing, rf power; and the maximum gradient at which a cavity can operate will be determined by the lowest of these limitations for that particular cavity. The CEBAF accelerator operates with over 300 cavities and, for each of them, we have determined the maximum operating gradient and its limiting factor. We have developed a model that allows us to determine the distribution of gradients that could be achieved for each of these limitations independently of the others. The result of this analysis can guide an R&D program to achieve the best overall performance improvement. The same model can be used to relate the performance of single-cell and multi-cell cavities.

1 MODEL AND ANALYSIS

We assume n independent random variables X_i, each with probability density $f_i(x)$ and probability distribution $F_i(x) = \int_{-\infty}^{x} f_i(t)dt$.

We define a new random variable X as $X = \min(X_i)$. Its probability density $f(x)$ and distribution $F(x)$ are related to those of the X_i by:

$$1 - F(x) = \prod_i [1 - F_i(x)]$$

$$f(x) = (1 - F(x)) \sum_i \frac{f_i(x)}{1 - F_i(x)}$$

While $f(x)$ and $F(x)$ are directly observable, the above relations are not sufficient to determine the $f_i(x)$ and $F_i(x)$. This can be done, however, if for each realization of X we can identify for which variable X_i we had $x = x_i$.

In the application to superconducting cavities this means that for each cavity, not only do we know the maximum gradient at which it will operate but also which limitation prevents it from operating at a higher field. This is shown in figure 1. For each variable X_i, we can then define the function $g_i(x)$ as:

$$g_i(x)dx = \text{Prob}\{x < X_i \leq x + dx,\ X_j > x \text{ for } j \neq i\}$$

$$= f_i(x)dx \prod_{j \neq i} [1 - F_j(x)]$$

* Work supported by the U.S. DOE Contract # DE-AC05-84ER40150

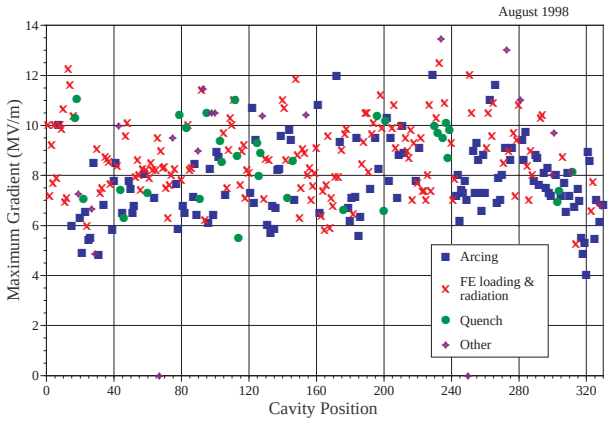

Figure 1: Maximum useful gradient and type of limitation for CEBAF cavities.

$$g_i(x) = \frac{f_i(x)}{1 - F_i(x)} \prod_j [1 - F_j(x)] \qquad (1)$$

The functions $g_i(x)$ are directly observable and the corresponding histograms are shown in figure 2 for our application. Note that the functions $g_i(x)$ are not true probability densities but represent how often a particular variable will be the minimum for a particular value x. Their primitives, G_i which are shown in figure 3, are the cumulative rate of occurrence for each limitation. The functions $g_i(x)$ also satisfy

$$\sum_i g_i(x) = f(x)$$

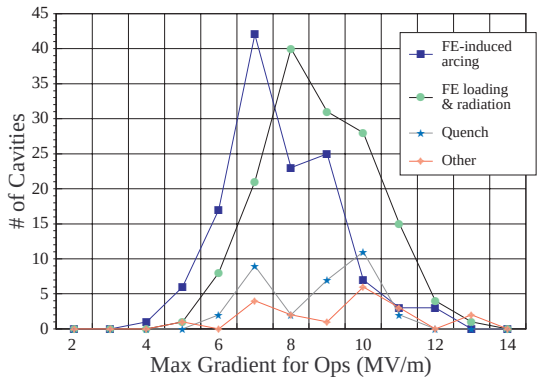

Figure 2: Histograms of the cavity gradients for the different limitations.

Equation (1) can be rewritten as:

$$\frac{f_i(x)}{1 - F_i(x)} = \frac{g_i(x)}{1 - F(x)}$$

Since $f_i(x)$ is the derivative of $F_i(x)$ the above equation can be simply integrated to yield:

$$F_i(x) = 1 - \exp\left(-\int_{-\infty}^{x} \frac{g_i(t)dt}{1-F(t)}\right) \qquad (2)$$

$$f_i(x) = \frac{g_i(x)}{1-F(x)} \exp\left(-\int_{-\infty}^{x} \frac{g_i(t)dt}{1-F(t)}\right)$$

For a finite number of cavities, the measured probability densities $f_i(x)$ are constructed from delta functions. For n cavities, each with a limit of type l_k at energy E_k,

$$g_i(x) = \frac{1}{n}\sum_k \delta(x - E_k)\delta_{i,l_k},$$

where l_k ranges over the same set of integers as i (arcs, radiation, etc.). The distribution F and the individual G_i are easily computed by integration of g_i. As shown in figure 3, they are summations of step-functions.

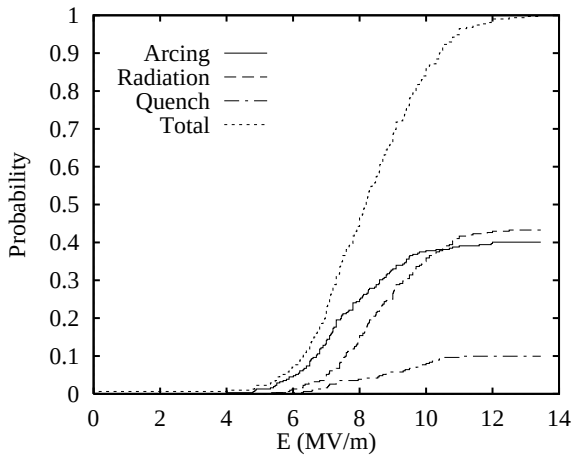

Figure 3: Measured distributions F and G_i vs. energy.

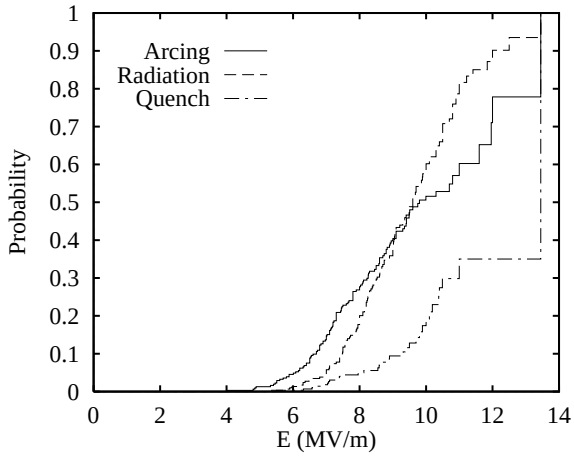

Figure 4: Calculated distributions F_i vs. energy.

Equation (2) also integrates sums of delta functions into sums of step-functions. The resulting derived probabilities F_i are shown in figure 4, and the corresponding density functions f_i are again sums of delta functions. To be shown in a useful form one could sort them into bins; instead, we assumed they have an approximate log-normal form, and chose coefficients for that distribution based on the calculated F_i.

The smoothed probability densities $f_i(E)$ for the 3 main limitations are shown in figure 5, along with the overall density $f(E)$. The same analysis was performed in 1995 on data collected at that time, and is shown in figure 6.

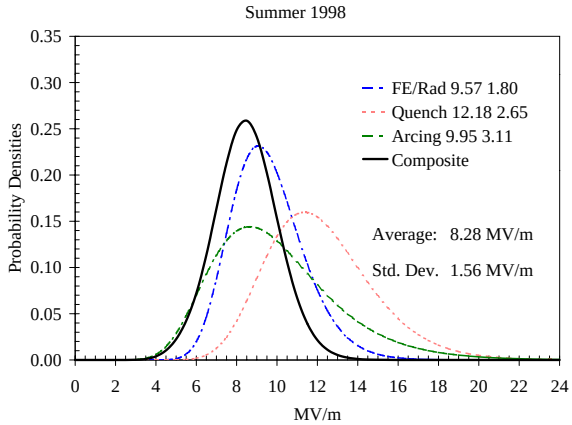

Figure 5: Probability densities for 1998 limitations.

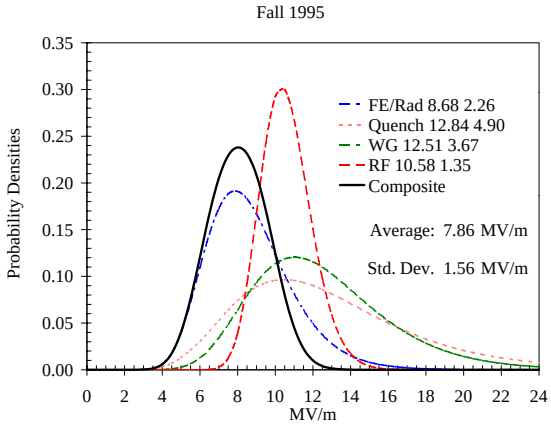

Figure 6: Probability densities for 1995 limitations.

2 DISCUSSION

Two of the important limitations which were present in 1995 have been eliminated. At that time, the beam current required of the machine was modest, so to reduce power consumption, the output power of the klystrons was limited to 2 kW. This imposed a limit on the gradient that some cavities, whose external Q was not optimal, could achieve. In 1998, with the klystrons operating at 5 kW output power, rf is not a limitation anymore.

Another limitation which was present in 1995 (labelled WG in the figure) was due to pressure fluctuations in the

waveguide section between the cold and warm windows leading to an rf trip. Since then a program to improve *in situ* the performance of the cavities has been implemented. This program includes a cryocycle of the cryomodules to about 40 K to outgas the waveguide section, followed by rf conditioning of the same section. As a result, waveguide pressure fluctuations and their associated rf trips have been eliminated as an important performance limitation [1].

The main limitation, as can be seen from figure 6, was field emission in the cavities. This was the main target of the *in situ* processing of the cavities and, although not yet completed, has resulted in raising the field-emission-limited performance by 1 MV/m. When this improvement program is completed in February 1999 it is expected to have raised the operational energy of CEBAF from 5 to 6 GeV.

As indicated in figure 5 a new limitation has appeared which was not included in the 1995 data. It is due to occasional arcing or flashover on the cold window, which is located close to the beam line, and is probably caused by slow charging from field-emitted electrons. This limitation is different from the others in that it is operational in nature, and not as hard a limitation as the others. Although arcing is infrequent (which is why is was not identified in the 1995 commissioning data), with more that 300 cavities in operation it can have a significant impact on accelerator up-time. We have set a limit of less than one arc-related trip every eight hours for each of the cavities which display this behavior, and some of these cavities have had their operating gradient reduced as a result.

A new configuration for the cold window, which places it further from the beam line and shields it from field-emitted electrons, has been developed and tested, and has led to a virtual elimination of arcing in laboratory tests. While this modification cannot be done on cryomodules while they are installed in the accelerator, it is being implemented on new cryomodules which are under construction for the FEL, and will be incorporated in the CEBAF cryomodules when the opportunity presents itself.

3 PERFORMANCE OF MULTI-CELL CAVITIES

The same model can be used to predict or compare the performance of cavities composed of different numbers of cells under the same set of assumptions: each individual cell's performance is independent of other's and governed by the same variables, and the performance of a multi-cell cavity is limited by its weaker cell.

If f_1, resp. F_1 are the probability density, resp. distribution for the operating gradient of single-cell cavities and f_n and F_n the same functions for n-cell cavities, then:

$$F_n(E) = 1 - [1 - F_1(E)]^n$$

$$f_n(E) = n f_1(E) [1 - F_1(E)]^{n-1}$$

In particular, if $\langle E_1 \rangle = \int_0^\infty E f_1(E) dE$ and $\langle E_n \rangle = \int_0^\infty E f_n(E) dE$, under reasonable assumptions on $F_1(E)$ one can estimate the reduction in performance $\langle E_n \rangle / \langle E_1 \rangle$ from 1 to n cells. It is found that $\langle E_n \rangle / \langle E_1 \rangle$ is relatively insensitive to the actual shape of $f_1(E)$ but depends strongly, as should be expected, on its normalized standard deviation $\sigma / \langle E_1 \rangle$.

An example is shown in figure 7 where we assumed a log-normal distribution for $f_1(E)$. Figure 8 shows the decrease in average gradient as a function of the number of cells for normalized standard distributions between 0.1 and 0.4. This shows that the expected gradient in multi-cell cavities has a negative power-law dependence on the number of cells. This is similar to the apparent negative power-law dependence on the cavity surface area [2].

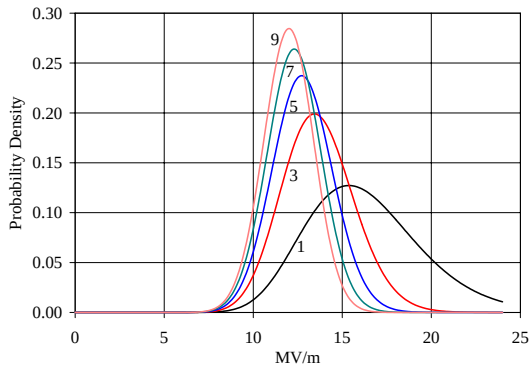

Figure 7: Probability densities for the gradient of single and multi-cell cavities.

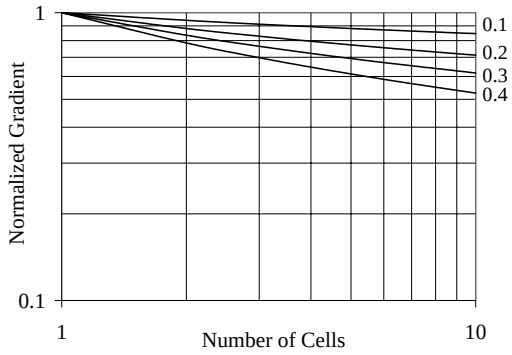

Figure 8: Normalized gradient of multi-cell cavities as a function of the number of cells. The parameter is the normalized standard deviation for gradient of a single-cell cavity.

4 REFERENCES

[1] C. E. Reece *et al.*, "Improvement of the Operational Experience of SRF Cavities via in situ Helium Processing and Waveguide Vacuum Processing," Proc. PAC 97.

[2] H. Padamsee, "Superconducting RF," in AIP Conference Proceedings 249, pp 1402-1482, American Institute of Physics, New York, 1992.

RESONANCE CONTROL COOLING SYSTEM FOR THE APT/LEDA RFQ*

R. Floersch, G. Domer
AlliedSignal Federal Manufacturing & Technologies**, Kansas City, Missouri 64141 USA

Abstract

The Radio Frequency Quadrupole (RFQ) [1] resonance control cooling system (RCCS) for the Low Energy Demonstration Accelerator (LEDA) [2] in support of the Accelerator Production of Tritium (APT) [3] is described. Constant flow regulating valves to distribute the required flow to the 424 channels and to permit use of centrifugal pumps is discussed. Control system schema are described to regulate resonance frequency during steady state operation.

1 CONTROL OF RESONANCE FREQUENCY

Resonance frequency in the RFQ is manipulated by changing the gap between opposing vane tips in each of the four Segments. The quadrupole vanes are cooled with constant temperature 50 degree Fahrenheit water to hold their geometry constant. The RFQ cavity wall and all of the systems interfacing through the cavity wall are cooled with temperature controlled water. By manipulating the cavity wall water temperature, the vane tip gap will either increase or decrease based on whether the cavity wall diameter grows or shrinks, thus manipulating the rf resonant frequency.

2 COOLING SYSTEM

The resonance control cooling system is comprised of two subsystems, one open loop and one closed loop.

2.1 Open Loop Subsystem

The open loop subsystem supplies constant temperature coolant to the vane and coupling plate channel passages. The open loop subsystem dissipates approximately 350 kilowatts of heat. To dissipate that heat, 360 gallons per minute of constant temperature 50 °F water is supplied to 84 individual channels. The 84 channels are subdivided into 4 channel types that are common to each of the four 2-meter RFQ Segments. Four sets of supply and return pipes connected directly to the chilled water system distribute approximately 90 gallons per minute of the coolant to/from each of the four Segments.

Parallel piped constant flow regulating valves are used to assure the correct total flow is supplied to each of the channel types within each Segment. Each constant flow-regulating valve supplies a manifold which distributes the coolant among the individual channels.

2.2 Closed Loop Subsystem

The closed loop system supplies temperature controlled water to five different channel types in the cavity wall to dissipate approximately 910 kilowatts of heat. To dissipate that heat, a total of 1160 gallons per minute is supplied to 340 individual channels.

The closed loop subsystem is comprised of four pump loops which circulate coolant through the cavity wall channels of the four RFQ Segments. Connecting the four pump loops is an outer piping loop whose purpose is to control the water temperature being supplied to the four pump loops.

Due to the different amounts of heat dissipated in each RFQ Segment, the inlet water temperature to the cavity wall channels of each Segment must be adjustable and no two will be the same. Figure 1 illustrates a single pump loop. The inlet temperature to the cavity wall channels of each Segment is established by fixing the ratio of the mass flow of the RFQ heated returning coolant that is diverted to mix with the entering mass flow from the outer loop. Setting the stem position of each pumping loop's diverting valve controls that mass flow ratio. The final stem position will be a function of desired inlet temperature and the heat dissipated by the loop and, once established, is not changed during steady state operation.

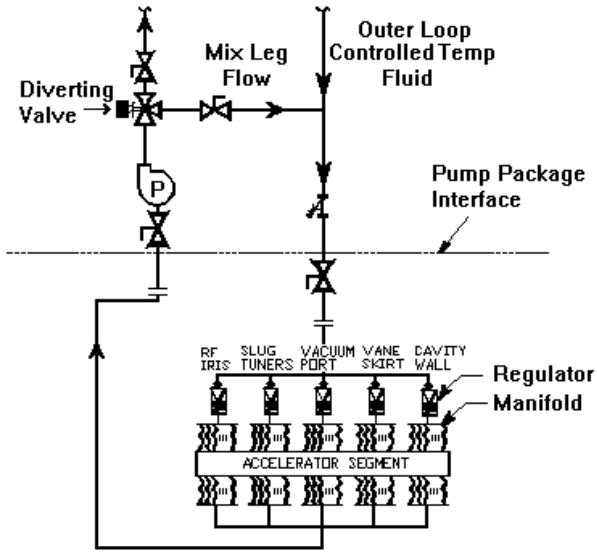

Figure 1: One of four Pump Loops

* Work supported by the US Department of Energy.
** Operated for the United States Department of Energy under Contract No. DE-ACO4-76-DP00613.

To force the cavity to the desired resonant frequency, the rf frequency controller manipulates an outer loop control valve to allow more or less constant temperature chilled water to enter the outer loop and mix with the water from the Segments which is not diverted down the mix leg. The amount of mass flow entering either lowers or raises the outer loop temperature. When the outer loop temperature changes incrementally, the inlet temperatures of all four of the RFQ Segments will increase or decrease by the same incremental amount as long as the rf power is at steady state.

2.3 Constant Flow Regulating Valves

Parallel piped constant flow regulating valves are employed to assure the correct proportion of the total pump flow is supplied to each of the closed loop channel types within each Segment. Each constant flow regulating valve supplies a manifold that distributes the coolant among the individual channels within a channel type.

Flow through the regulating valve is described by the following equation.

$$Q = Cv*SQRT(dP)$$

The flow coefficient (Cv) of the constant flow regulating valves, changes as the differential pressure (dP) across the valve changes. Figure 2 depicts the internals of the AutoFlow regulating valve manufactured by Flow Design Inc. [4].

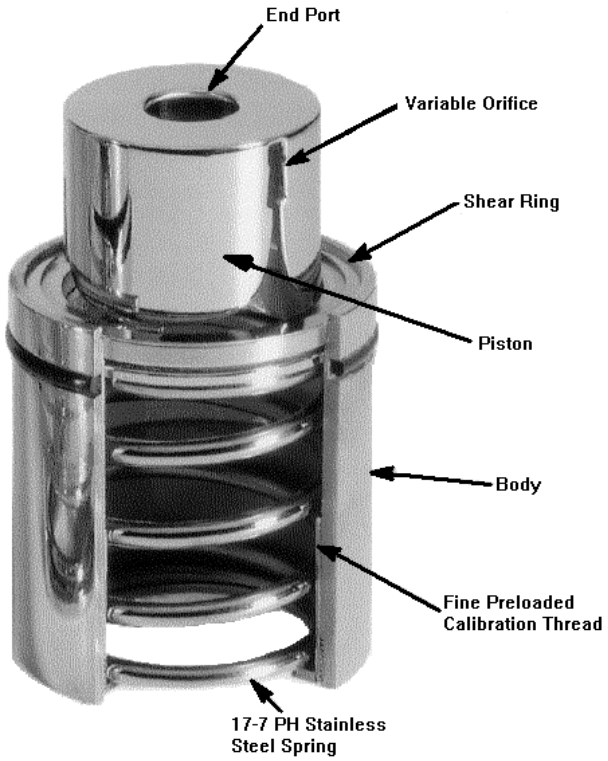

Figure 2: Internals of Constant Flow Regulating Valve

As the pressure drop increases, the piston depresses, reducing the exposed orifice area, thus reducing the Cv. The opposite is true when the pressure drop decreases. The valve's Cv increases/decreases in proportion to the square root of the differential pressure. The net effect is that the flow (Q) through the valve will remain at the designed flow rate (within +/- 5%) as long as the spring is not fully compressed or extended. Spring ranges can be purchased for two pressure drop ranges, 2-30 psi and 5-60 psi.

These flow-regulating valves are used to regulate the flow to each different channel type within a one meter RFQ Section. Since all flow paths utilize a regulating valve, the total volumetric flow of the pump is clamped to the sum of the designed regulating valve flows as long as the pressure drop variance among the channels doesn't exceed the valves spring range. Figure 3 shows the effect that the constant flow-regulating valves have on each loop's loss curve. The discontinuity in the loop loss curve begins when all valves are in the regulating range and ends when the first valve saturates. That discontinuity establishes a window that permits use of centrifugal pumps. A centrifugal pump whose head gain curve intersects the discontinuity of the loop loss curve will provide the desired volumetric flow.

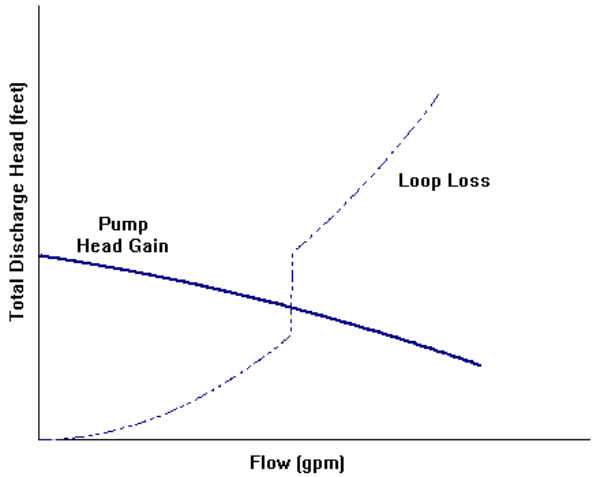

Figure 3: Loop Loss Curve with Regulating Valves

The height of the discontinuity window is dependent on the spring range of the regulating valves and the pressure drops of each of the channel types.

3 RESONANCE FREQUENCY CONTROL

The RFQ RCCS provides continuous and discrete control of the cooling system. Operator interface screens are provided to change setup parameters for continuous control and to initiate discrete controls. Status screens are also provided to display information about the RFQ cooling system.

The RCCS is implemented using Experimental Physics and Control System (EPICS) based hardware and software and is integrated with other networked LEDA EPICS systems. Figure 4 shows the network connections of the RCCS system. The other LEDA systems act in a supervisory role by providing information to the RCCS via EPICS Channel Access to the RCCS Input/Output Controller (IOC) database to initiate actions. Status information from the RCCS is accessible via Channel Access.

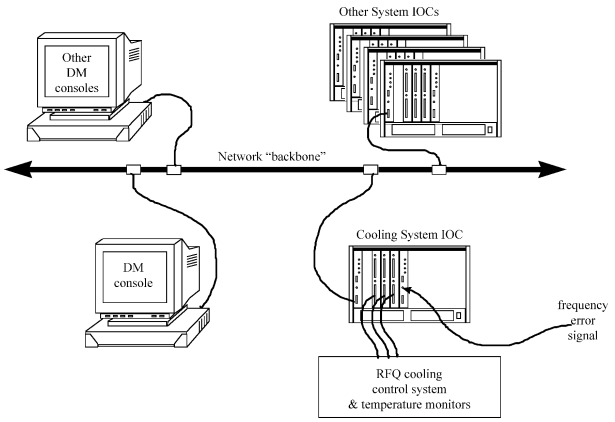

Figure 4: Network Configuration

The RCCS software is constructed using EPICS State Notational Language (SNL) to track the condition of the system and to allow certain control actions to take place. Additional C programs are used to perform the control algorithms and file operations. Figure 5 shows the state diagram that represents the overall conditions of the RCCS. Resonant Frequency Control (RFC) is obtained by going through one of two defined sequences of operations, Startup or Conditioning.

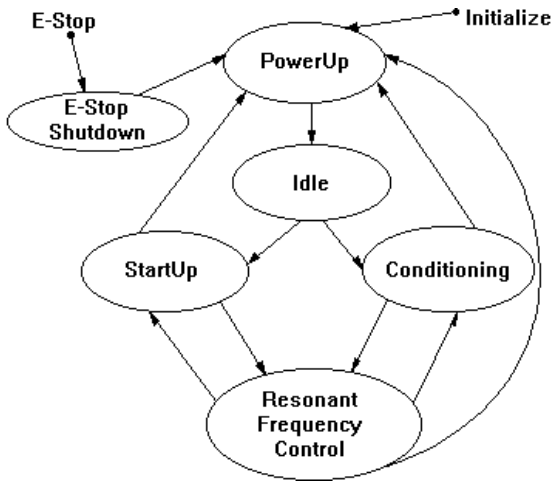

Figure 5: System Level State Diagram

RFC regulates the resonant frequency of the RFQ using a single loop Proportional Integral Derivative (PID) control algorithm that adjusts the setting of the outer loop control valve based on the frequency error provided by the Low Level RF (LLRF) control system. The valve adjustments will alter the temperature of the water flowing in the outer loop, thereby changing the frequency of the RFQ. RFC is the normal operating state of the RCCS.

RFC begins when a valid frequency error from the LLRF system is detected, ending startup or conditioning. The PID algorithm regulates the resonant frequency of the RFQ to +/- 8KHz, which corresponds to a change in water temperature supplied to the inner pumping loops of +/- 0.5°F.

The frequency error, received via an analog signal from the LLRF system, ranges from 0 to 10V DC, where +0.5V represents -50KHz error and +9.5V represents +50KHz error. Any error reading outside the +0.5V to +9.5V range is considered an invalid signal.

If the frequency error signal is lost, RFC is halted and temperature control is started to regulate the Outer Loop Common Supply at the current temperature, until the supervisory system dictates a change to another state or the frequency error returns. The setpoint for temperature control will be the average of sampled temperatures before the error signal was lost. When the frequency error signal returns, temperature control is halted and RFC is restarted.

RFC can only be halted and directed to make a transition to the proper state by the supervisory system or an emergency stop condition.

4 INSTALLATION STATUS

Installation of the RCCS Pump Package and under floor piping was completed in January 1998. Installation of the remainder of the distribution piping is scheduled for completion along with the control system hardware and software in September 1998.

5 ACKNOWLEDGEMENTS

An immense amount of technical insight and installation assistance was provided by Dale Schrage, Lloyd Young, Dave Gurd, Amy Regan, and Frank Spinos, LANL.

6 REFERENCES

[1] D. Schrage, et al, "CW RFQ Fabrication and Engineering", these proceedings.
[2] H. V. Smith, "Status Update for the Low-Energy Demonstration Accelerator (LEDA)", these proceedings.
[3] G. Lawrence, "High Power Proton Linac for APT; Status of Design and Development", these proceedings.
[4] AutoFlow Valves manufactured by Flow Design Inc., 8908 Governors Row, Dallas Texas 75247.

FIRST TESTS OF A TRAVELING-WAVE CHOPPER FOR THE ATLAS POSITIVE ION LINAC

R.C. Pardo, J.M. Bogaty, B.E. Clifft
Argonne National Laboratory, Argonne, IL 60439
USA

Abstract

A ten segment traveling-wave chopper has been constructed and successfully tested at 5% of the design 12 MHz repetition rate. The chopper must remove unbunched tails from a partially bunched heavy-ion beam in order to avoid undue emittance growth in the linac and the production of undesirable satellite beam bunches. When poorly bunched beams traverse a chopper, the traditional sine wave chopper produces unacceptable transverse emittance growth and unnecessary beam loss. Emittance growth and unnecessary beam losses are expected to be much reduced in the traveling wave chopper. These first tests have confirmed the validity of these claims, clearly showing much reduced transverse emittance growth as compared to the original sine wave chopper and excellent selectivity for the desired beam. Details of these tests will be presented and compared to calculations. Operation of the new chopper at the full 12 MHz rate is the next goal. Development of a driver power supply capable of full CW operation will also be described.

1 INTRODUCTION

Excellent beam quality is an important feature of heavy-ion beams provided to the research program by the ATLAS superconducting linear accelerator. The measure of beam quality includes relatively low emittance, small spot sizes with little or no halo, small energy spread, and when requested excellent bunch time width (<200 ps FWHM) on target. In order to make use of these properties, a rather larger bunch period of 82.4 ns is provided meaning that only every sixth or eighth RF bucket is filled with beam.

To achieve these beam quality goals, a two stage bunching systems converts the DC beam from the ion source into a beam with a 12.125 MHz bunch structure. The system is able to adequately bunch approximately 70% of the DC beam into acceptable pulses, but the remainder of the DC beam must be removed in order to provide the correct bunch structure and beam quality. This unbunched beam 'tail' is removed with a vertically deflecting electric beam chopper.

The beam chopper which has been used up to now at ATLAS is a resonant 'sine wave' chopper. Bunches are phased so as to arrive at the center of the chopper plates as the sine wave passes through the zero voltage point. The chopper therefore operates at half the frequency of the bunch structure deflecting the unwanted tails both 'up' and 'down'. Since the good beam also sees some voltage due to the finite transit time of the beam bunch through the plate region, portions of the beam pulse are deflected slightly both up and down causing an emittance growth of the transmitted beam. A similar energy gain effect also takes place due to the entrance and exit fringing fields of the chopper. Thus such a device has a significant detrimental effect on beam emittance. The magnitude of the effect depends on the time width of the beam bunch at the chopper. If the chopper can be located in a location with a narrow bunch width these effects can be minimized and acceptable performance is possible. The geometry of a new bunching system in the ion source region of the ATLAS Positive Ion Injector(PII) does not allow the chopper to be located at a location where the beam time width is narrow and the resulting emittance growth from a sine wave chopper will be unacceptable.

Therefore a new non-resonant traveling-wave transmission-line chopping system (TWC) is being developed which can largely eliminate the emittance growth effects described above. The conceptual design and modeled performance has been previously reported [1]. This paper describes the final design and first low duty factor tests of the chopper.

2 CHOPPER DESIGN

The TWC consists of ten shielded plate pair segments arranged transversely to the beam, like rungs on a ladder. The top plates of each section are a portion of one continuous impedance-matched transmission line as are the lower plates. Such a system can propagate a well-formed voltage pulse down the line with a group velocity matched to the velocity of the bunched beam traveling between the plates. The deflector plates have a center-to-center spacing of 4.5 cm which corresponds to a 17.6 ns ion transit time between plates. The deflector plates are isolated from each other by field clamp electrodes which also can be biased with a DC voltage to fine tune any slight beam deflection from incomplete voltage shutoff on the deflector plates. Stripline electrodes are supported by plexiglass plastic strips which provide critical spacing to maintain the proper RF impedance. Three sections of the chopper plate assembly are shown schematically in Figure 1 in relation to the beam direction.

The deflector's characteristic impedance is 125Ω which results from the stripline electrode gap of 3.8 cm and width of 1.5 cm. Each of the stripline electrodes is attached to a pair of 125Ω coaxial connectors. Coaxial cable delay lines are connected in series with the stripline

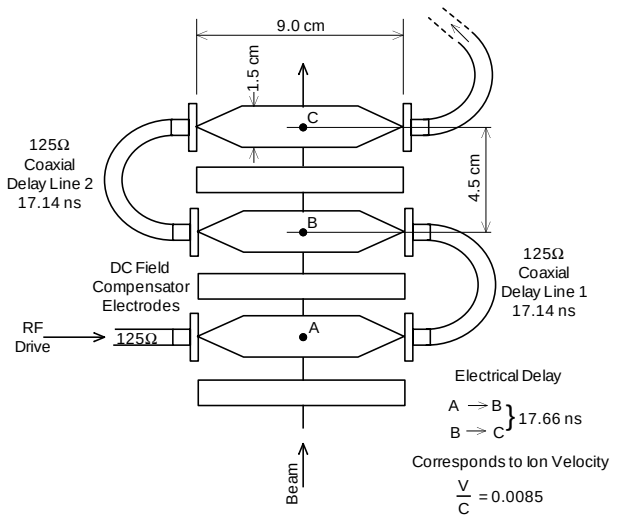

Figure 1: Schematic of TWC deflector plate assembly and its incorporation into the overall transmission line.

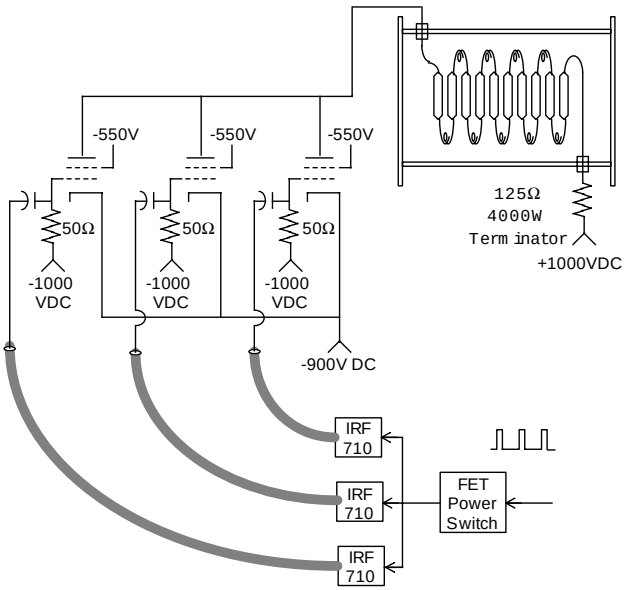

Figure 2: Schematic of the TWC and tetrode final stage with FET grid drivers.

deflectors. The delay lines are used to match the chopper pulse propagation time to the beam velocity. Transition from stripline geometry to coaxial geometry is facilitated by tapering the stripline electrode ends. The tapered ends are paired with a special ground plane electrode assembly (not shown in figure 1) that maintains the 125Ω impedance. The chopper electrodes and water-cooled delay lines are contained in a 0.56 m long by 0.44 m inner diameter cylindrical vacuum chamber.

Each of the nine 3.35m-long delay lines are made from 122.5Ω semirigid coaxial cable[3]. The coax center conductor diameter is approximately 0.0325 cm. The small cross section results in significant ohmic heating which requires direct cooling. A water cooled stainless steel form is used to support the nine delay lines and provide cooling. The delay lines are coiled on the water cooled form and indium soldered for good thermal contact. About 120 watts will be disipated along the delay line during normal chopper operation. The last stripline deflector is terminated in a 125Ω, 4000 watt air-cooled resistor array.

In the quiescent mode, the plates have a vertically deflecting voltage of up to 1000 volts, effectively blocking the transmission of any beam through the device by deflecting all particles vertically onto a set of slits 2 meters downstream. When a bunched beam pulse arrives at the start of the deflecting plates, a zero voltage pulse of 17 ns width or greater is propagated down the chopper, providing a transmission window with no deflecting voltage as seen by the desired beam pulse. At a repetition rate of 12.125 MHz this generates up to 1648 watts of heat into the termination resisitor.

Three Eimac [4] 4CW2000A tetrode vacuum tubes are used in parallel as an electronic switch. The plates of the tubes connect to the chopper transmission-line assembly as shown in figure 2. When the vacuum tubes are cut off, chopper electrode voltage is maintained at the cutoff value of up to 1000V. Pulsing the tubes into conduction causes 8.0 amperes of plate current to flow for about 20 ns. The pulse of current reduces the deflector electrode voltage to zero just as an ion bunch enters the deflector array. The zero volt window propagates through the transmission line array in phase with the desired beam pulse terminating in the 125Ω resistor load. This occurs at a 12.125 MHz CW rate.

Particles in the timing tails will see some deflection. This is minimized by producing as fast a fall and rise time as possible in the voltage pulse. The effect is weighted by the fraction of transmitted particles in the tail regions. Even this effect is lessened compared to the sine wave chopper since the deflection is always in the same direction for the traveling wave chopper, whereas the leading and trailing beam tails are deflected in opposite directions in a sine wave chopper.

3 FIRST TEST RESULTS

The prototype chopper system was mounted in a vacuum chamber on the PII injection beamline. A photo of the prototype assembly is shown in Figure 3. The delay line for this test was made from RG-63 coaxial cable with the outer insulator removed to improve it vacuum properties. Even so the vacuum obtained was barely adequate for these tests and even at 5% duty cycle, noticeable outgassing of the cable occurred.

A beam of 538 keV $^{16}O^{5+}$ with a velocity of 0.0085c was provided by the ATLAS ECR ion source and bunched by a 4-harmonic buncher operating at 12.125 MHz. For this beam, a voltage of 500 V was adequate for complete beam cutoff using only the upper delay line. The lower delay line was used as a DC ground plane. A DC offset voltage of -150 volts was applied to the lower ground

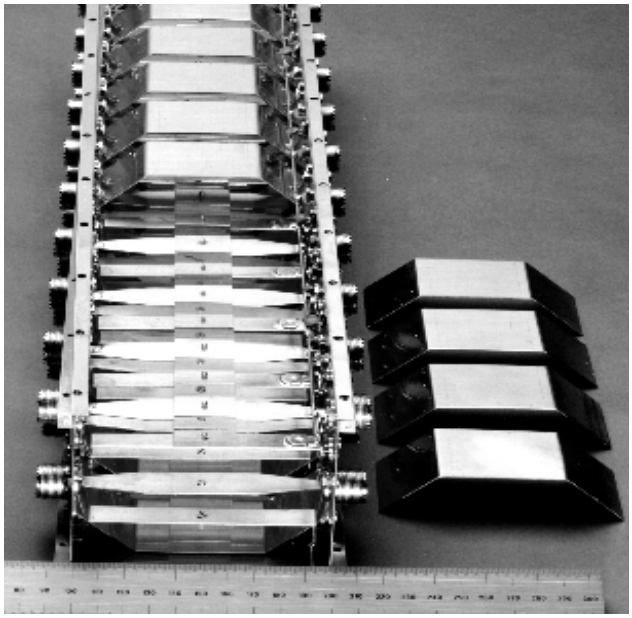

Figure 3: Photo of travelling wave chopper transmission line deflection plate assembly with clamp electrodes in place. A portion of the ground plane electrodes are shown to the side.

plane electrodes to minimize beam steering arising from the inability to completely achieve 0 volts on the transmission-line electrodes. For these tests, a power supply with the required power and rise time was not available and a smaller supply was used, limiting the tests to a 5% duty cycle.

At 500 volts applied deflection, excellent pulse definition was achieved. The achieved voltage pulse waveform is shown in Figure 4. No beam leakage between pulses was observed. 100% cutoff was achieved. These results are in agreement with the calculated voltage and indicated the system was working as expected.

The transverse beam emittance was also measured using the quadrupole method [2]. The original, and still used, sine wave chopper was also immediately upstream of the new chopper and so it was possible to measure the transverse beam emittance with both devices and obtain a direct comparison. Emittance measurements were obtained using both choppers for beam bunch widths of 3 ns and 18 ns FWHM as the beam traversed the chopper plates. Table 1 shows the results of those measurements. The emittance degradation in the chopping plane caused by the sine wave chopper is dramatically demonstrated, especially for the poorly bunched beam. In contrast the TWC shows no emittance growth for narrow pulses and less than a 25% increase in emittance for an 18 ns wide beam. Completion of a full power version of the TWC is expected by the end of the year.

This work was supported by the U.S. Department of Energy, Nuclear Physics Division, under contract W-31-109-ENG-38.

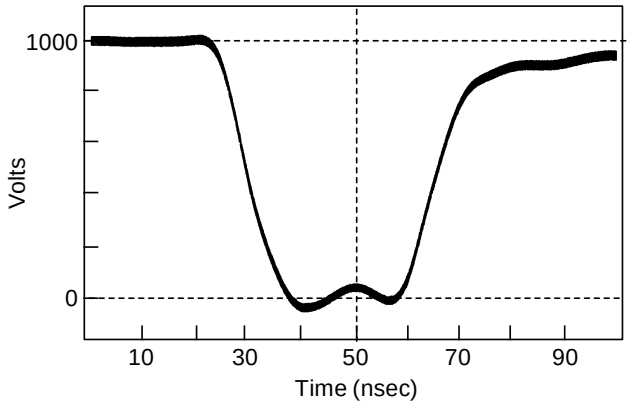

Figure 4: Actual pulse shape waveform achieved in prototype tests of the TWC. Total voltage fall time is approximately 15 ns.

Table 1: Measured growth of the beam emittance of) 538 keV $^{16}O^{5+}$ beam due to the effects of a sine wave and traveling-wave chopper (TWC).

Bunch Width (ns)	Chopper Type	ε^{x}_{n} (πmm•mr)	ε^{y}_{n} (π mm•mr)
3.0	none	0.09	0.09
3.0	sine		0.13
18	sine		0.17
3	TWC		0.10
18	TWC		0.12

REFERENCES

[1] R. C. Pardo, et al., 'A Study of Beam Chopping Options for the ATLAS Positive-Ion Linac', Proc. Of LINAC96, CERN, August 1-5, 1996, 65-67(1996).

[2] Y. Qian, et al., 'Beam Parameter Measurements for the APS Linac System', Proc. 1994 Int. Linac Conf., Japan, Aug. 21-26, 1995, 899-901(1994).

[3] Micro-Coax Inc., Pottstown, PA 19464

[4] Eimac, Varian Associates, San Carlos, CA

SIMULATION AND MEASUREMENT OF THE ELECTROSTATIC BEAM KICKER IN THE LOW-ENERGY UNDULATOR TEST LINE*

G.J. Waldschmidt, Y.W. Kang
Argonne National Laboratory, Argonne, Illinois 60439 USA

Abstract

An electrostatic kicker has been constructed for use in the Low-Energy Undulator Test Line (LEUTL) at the Advanced Photon Source (APS). The function of the kicker is to limit the amount of beam current to be accelerated by the APS linac. Two electrodes within the kicker create an electric field that adjusts the trajectory of the beam. This paper will explore the static fields that are set up between the offset electrode plates and determine the reaction of the beam to this field. The kicker was numerically simulated using the electromagnetic solver package MAFIA [1].

1 INTRODUCTION

The kicker is positioned just downstream of a 2.856-GHz high-brightness thermionic-cathode rf gun. The rf gun produces peak beam energies of up to 4.5 MeV and peak macropulse current of up to 1.3 A at a repetition rate of 10 Hz. This greatly surpasses the operational limit of the thermionic gun currently in use by the APS. The APS linac then accelerates this beam to energies of approximately 650 MeV before being transported to the LEUTL beamlines. However, this output exceeds the radiation safety restrictions on the linac vault [2,3].

The kicker was designed to dump much of the beam before it reaches the linac and to retain only a fraction of the total beam produced by the rf gun. To achieve this, the kicker is physically surrounded by a constant magnetic field. The field envelopes the kicker, thus deflecting the beam into a dump positioned just past the kicker. The kicker is pulsed by a 150-ns generator, which raises the potential of the electrode plates to 25 kV. When this potential exists, it is sufficient to nullify the effects of the magnetic field, thereby enabling the bunch to pass the kicker and continue along the LEUTL beamline.

Since the bunch length is on the order of picoseconds while the electrodes are pulsed for nanoseconds, the field is considered static. The uniformity of this field, as well as effects due to fringing are discussed in this paper.

2 DESCRIPTION

As shown in Figure 1, the kicker consists of dielectric standoffs, two electrodes, and a feedthrough. The stainless steel electrodes are 10 cm long and separated by 1 cm. They are electropolished with rounded edges in order to improve their reliability under high voltage. An electron beam passing through the kicker can be deflected by nearly 4 mm due to the constant magnetic field. In order to prevent beam scraping, the electrodes are offset from the beamline axis by roughly 2 mm in the direction of the magnetic force. This asymmetry creates a potential perturbation in the electric field that may result in irregularities in the electric field pattern between the electrodes.

The dielectric standoffs serve a dual purpose. They function as a mechanical support for the electrodes and as an alignment device to ensure that the electrodes are positioned within 0.1 mm of specifications. The 35-kV vacuum rated, angled feedthrough supplies the 25-kV potential from the constant current supply through coaxial cables [2].

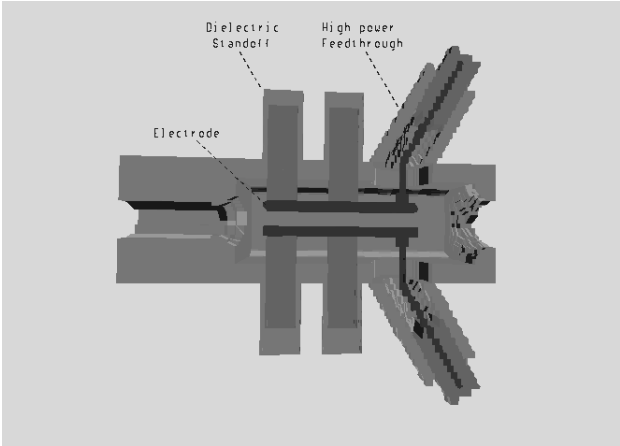

Figure 1: MAFIA rendition of kicker

3 NUMERICAL SIMULATION

Simulations were done with MAFIA 4.01 ECAD software. Two questions were primarily investigated during the simulations. The first question concerns the possible effects of shifting the electrodes off-axis. The second question arises from the actual design criteria, that is, how does the beam behave as is traverses the enclosure. In order to evaluate these issues, the structure was first modeled as accurately as possible within the capabilities of MAFIA. The simulated structure faithfully modeled the important electrical and physical properties

* work supported by U.S. Department of Energy under Contract No. W-31-109-ENG-38

of the kicker. The offset electrodes consisted of rounded edges as did the corners of the interior chamber walls to prevent radiating sources from potentially corrupting the computational domain. The angle of the feedthrough was also considered in order to allow for any slight variation in the field that this produced. The simulation model can be seen in Figure 1.

3.1 Static Solver

The uniformity of the electric field between the electrode plates is of great importance to the reliability and predictability of the kicker. A 25-kV potential was created across the plates be means of the MAFIA static solver module. Using the cgxyz solver, the field strength throughout the volume of the kicker was evaluated. Although the electrodes were offset 20% from the axis, the uniformity of the field strength was verified. An arrowplot showing the constant E-field as well as a visual representation of the fringing fields can be seen in Figure 2. Note that the electrodes are variously colored in order to allow different potentials to exist on each surface.

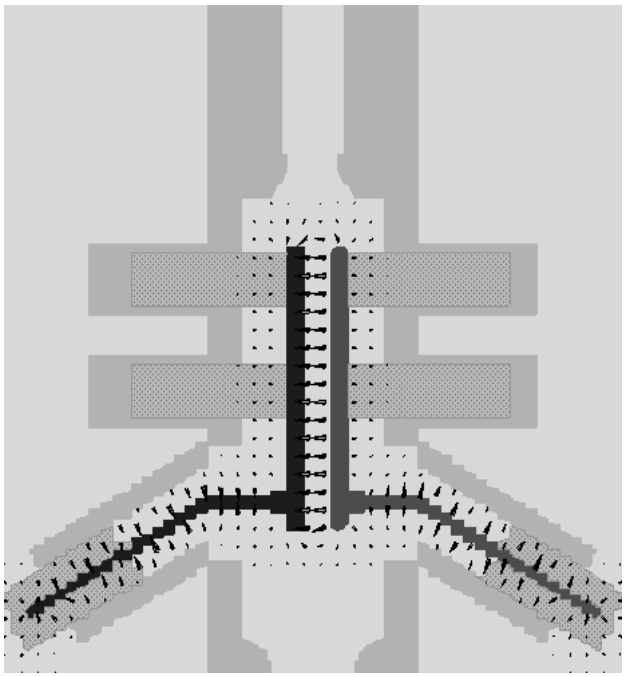

Figure 2: Electric field distribution

Of primary concern is the uniformity of the field along the beam axis, since this is the potential imposed on an intruding beam. Ideally, there exists no field outside the electrodes, while a strong transverse field serving to deflect the beam upward would exist between the plates. The actual field strength along the beam axis is plotted in Figure 3. Since the gap between the electrodes in 1 cm, the maximum electric field between the plates is 2.5 MV/m. In the plot, the electrodes begin at approximately 3.9 cm and extend to 13.9 cm. The virtually constant field strength may be viewed along the entire surface of the electrodes in Figure 4.

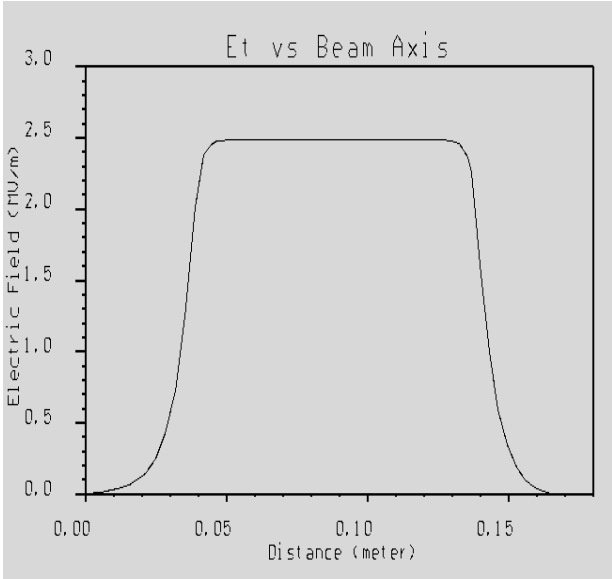

Figure 3: Transverse electric field vs. distance

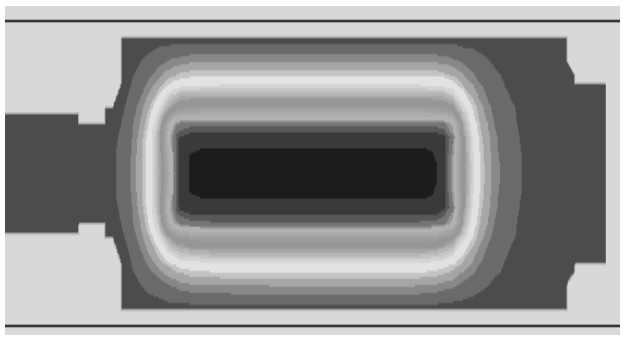

Figure 4: Contour plot of electric field

3.2 Particle-in-Cell Solver

The module TS3 was executed in order to evaluate the overall impact of the kicker with an actual electron bunch passing through the static field. The gaussian beam used in the simulation had a bunch length of 20 ps with an energy of 3.5 MeV and a charge of 350 pC. Given these parameters, a beam deflection of 3.57 mm was calculated analytically. Numerical simulations that account for the effects of fringing fields found the deflection to be approximately 10% greater as the beam traveled the entire length of the kicker chamber.

A plot of the beam can be seen in Figure 5. In this plot, the path of the beam is traced to show the aggregate deflection resulting from the electrodes.

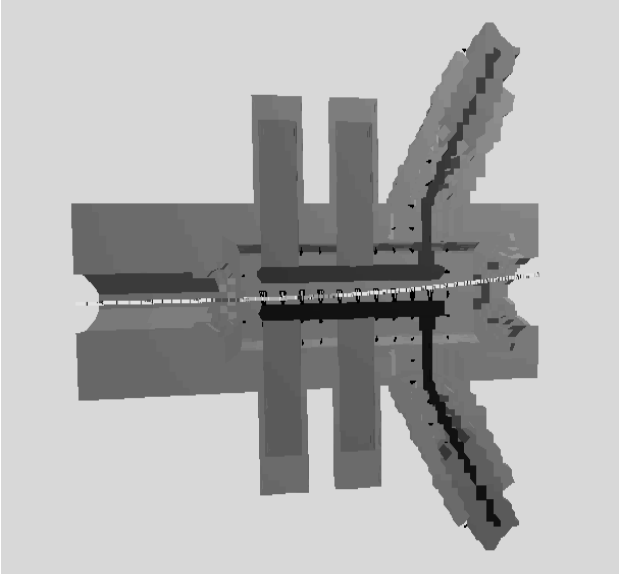

Figure 5: Beam trajectory

4 MEASUREMENT

Preliminary measurement on the relative field distribution in the kicker was made using the HP8753C vector network analyzer. Initially a two-port through calibration was made with a thin plastic line positioned between the electrodes. A small metallic disk, 0.125 inches long with a 0.125 inch diameter, was attached to the line and pulled along the beam axis between the electrode plates. The presence of the disk modified the capacitance of the electrodes. Since the capacitance due to the disk is dependent upon the magnitude of the electric field, the field strength was derived from the power transfer through the plates. This transfer characteristic was then recorded by the network analyzer. The limited distortion of the electric field due to the disk was ignored.

Assuming that the structure is much smaller than a wavelength of the excitation signal, approximate field distributions can be derived. As expected, lower signal frequencies gave noisy results since the coupling was small, whereas higher frequencies gave a distorted field distribution due to transmission line effects. It was found that for 10 cm long electrodes, a few MHz to tens of MHz gave results considered dependable. Figure 6 shows the measured field strength along the beam axis for a 10 MHz signal. The relative electric field distribution can be approximated from this data as:

$$U = \sqrt{|S_{21}|^2 - 1}$$

The above rf technique was used to approximate the static electric field strength. However, there exist reports on the measurement of these fields using a truly static approach [4,5]. At this time, techniques for such measurements are not as well developed as those for magnetic fields.

5 DISCUSSION

The numerical simulation demonstrates the effectiveness of the kicker as a beam chopper. In spite of the offset electrodes, the uniformity of the field was analyzed and found to be satisfactory. The numerical simulation as well as the attempted measurement of the electric field strengths provided results close to those calculated. However, the method used for static field measurements will need to be refined in order to provide more dependable results.

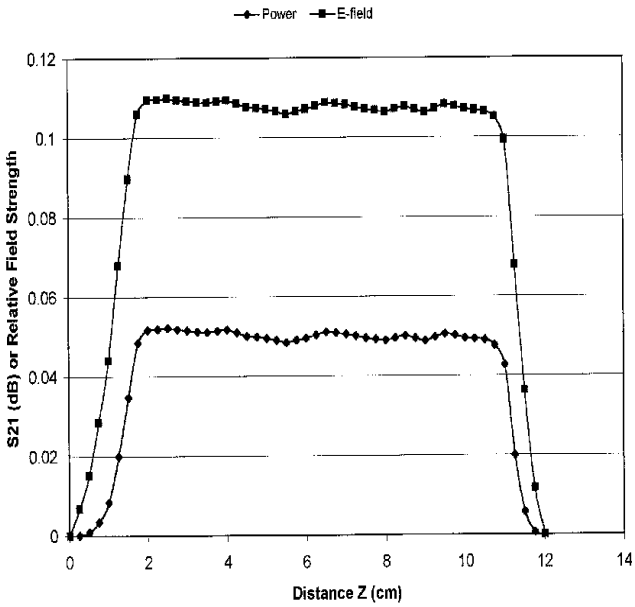

Figure 6: Measured electric field uniformity

6 ACKNOWLEDGEMENT

The authors would like to thank X. Jiang and W. Yoder for their assistance in the setup and measurement of the kicker.

7 REFERENCES

[1] MAFIA ECAD v. 4.01, Gesellschaft fur Computer Simulationstechnik mbH.

[2] Y.W. Kang et al., "Beam Chopper for the Low-Energy Undulator Test Line (LEUTL) in the APS, Proceedings of PAC97, to be published.

[3] S.V. Milton et al., "The Advanced Photon Source Low-Energy Undulator Test Line," Proceedings of PA97, to be published.

[4] W. Lou et al., "Measurement of Electrical Field Uniformity in a Electrostatic Separator," Proceedings of PAC95, Houston, TX, 2138.

[5] A.B. Temnykh et al., "Improved Measurement of Electric Field Uniformity in Horizontal Electrostatic Separator," Proceedings of PAC97, to be published.

IMPROVED TEMPERATURE REGULATION OF APS LINAC RF COMPONENTS*

R. Dortwegt, S. Pasky, M. White
Argonne National Laboratory, Argonne, Illinois, USA 60439

Abstract

The temperature of the APS S-Band linac's high-power rf components is regulated by water from individual closed-loop deionized (DI) water systems. The rf components are all made of oxygen-free high-conductivity copper and respond quickly to temperature changes. The SLED cavities are especially temperature-sensitive and cause beam energy instabilities when the temperature is not well regulated. Temperature regulation better than ± 0.1 °F is required to achieve good energy stability. Improvements in the closed-loop water systems have enabled us to achieve a regulation of ± 0.05 °F over long periods. Regulation philosophy and equipment are discussed and numerical results are presented.

1 INTRODUCTION

The Advanced Photon Source [1] linear accelerator system [2] consists of a 200-MeV, 2856-MHz S-band electron linac and a 2-radiation-length-thick tungsten target followed by a 450-MeV positron linac. The linac is designed to accelerate 30-ns-long pulses containing 50 nC of electrons to an energy of 200 MeV at 48 pulses per second. The linac rf system includes accelerating structures and SLED cavities that require temperature stability of ± 0.1° F or better. Stability is achieved using closed-loop water systems that provide constant temperature water to the SLEDs, accelerating structures, waveguide, loads, and to the rf reference and drive line.

The optimum temperature of each linac closed loop (LCL) system is found by a standard procedure. Water temperature is varied, and the setpoint is the value that maximizes beam energy. Results from one LCL system are shown in Figure 1. Each LCL has a unique setpoint in the range of 105-116 °F. Absolute knowledge of the temperature is not essential since the setpoint is chosen by direct measurement, but long-term stability is important.

2 GENERAL SYSTEM DESCRIPTION

All linac high-power rf components are temperature conditioned within ± 0.05 °F with DI water from the LCL pumping systems. One LCL is depicted in Figure 2 along with the klystron gallery secondary (DI process water) system (KGSS) that supplies coolant to the heat exchanger (HX) in the closed loop. The APS primary (DI process water) system (APS-PS), from which heat is ultimately rejected, is also shown in the figure. There are five LCLs, all with identical hardware components. Three of the LCLs provide total flows of 80 gpm and the other two provide 25 and 40 gpm.

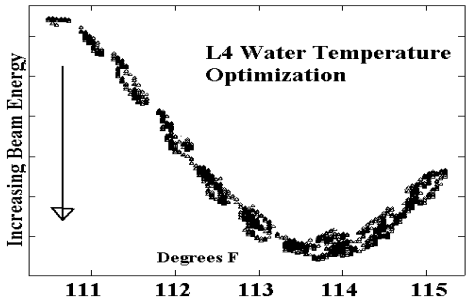

Figure 1: The optimal temperature for L4 is ≈113.7 °F.

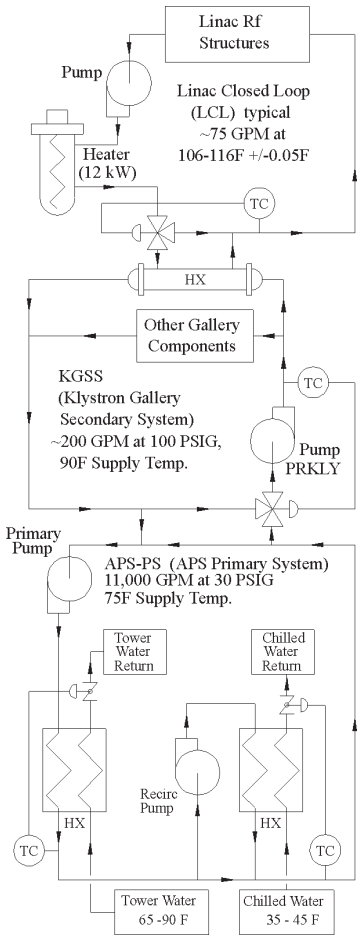

Figure 2: Overview of the linac water system.

* Work supported by the U.S. Department of Energy, Office of Basic Energy Sciences, under Contract No. W-31-109-ENG-38.

LCL components include an end-suction centrifugal pump, a 12-kW electric heater, a shell-and-tube heat exchanger, and a 3-way mixing valve to regulate the temperature. The heater serves two functions. It provides energy input to the system on cold startup so the setpoint value is reached in a reasonable time. It also matches steady-state energy input with heat rejection capacity, as the temperature control valve and heat exchanger capacities are more than adequate to remove heat from rf power input and frictional flow losses.

All LCLs are cooled by water circulated by the KGSS pump. KGSS water temperature is controlled at 90 °F by a 3-way mixing valve. Water from the primary system at 75 °F is admitted to the recirculating KGSS.

Whenever possible, cooling of the APS-PS water is done using cooling-tower water. When the cooling tower water is too warm, an additional exchanger cools the primary water using chilled water.

2.1 Brief History of the Linac Water System

The original linac water system provided long-term temperature stability no better than ± 0.5 °F compared to the required ± 0.1°F at steady state. Human intervention was required following significant power transients or equipment upsets. Inadequate performance was primarily due to: 1) poor resolution of the temperature-sensing elements (temperature control instruments only detected changes of the same order as the required steady-state tolerance); 2) installation of thermal sensors in thermowells resulting in very slow response times; 3) variation of KGSS coolant temperature by ≥ ± 1.0 °F.

By the end of 1995 control was improved to ± 0.2 to 0.3 °F. The most notable changes were the installation of direct-immersion RTDs (resistance temperature detectors), and series installation of heater and HX units. Performance periodically became unstable due to a significant derivative term in the control algorithm.

2.2 KGSS and APS-PS Temperature Stability

Efforts to stabilize the temperature of the coolant side of the LCL heat exchangers were initiated in early 1996. A 30-gallon holding tank was installed on the coolant inlet side of the exchanger to average out the fluctuations. A similar tank was installed on the linac side of the heat exchanger to increase capacitance. These modifications reduced temperature fluctuations in the LCL to ± 0.15 °F. Linac mixing valve actuators were also upgraded to the current Worcester models at that time.

In October of 1996, attempts were made to tune the proportional-integral-derivative (PID) loop of the KGSS with partial success. It was possible to tune the system using PI control (P=400, I=1000 s). KGSS stability was ± 0.1 °F, but the system was unable to handle transient heat loads, and equipment trips resulted. Studies indicated that it took ≈60 seconds for output control signal changes to actually be noticed by the sensor due to the long distance between the KGSS RTD and the mixing valve, and because the KGSS RTD was installed in a thermowell.

In order to improve the KGSS's response, its RTD was replaced by a direct-immersion RTD and was relocated immediately downstream of the pump. This permitted improved tuning of the secondary loop with PI control. The control algorithm, executed by the Johnson Metasys system, included a “tune override” feature that imposed “stronger” PID control parameters if the temperature deviated from the setpoint by a preset amount. This feature was removed, and traditional PI tuning was implemented.

These modifications resulted in KGSS stability on the order of ± 0.1 to 0.2 °F and LCL stability of ± 0.1 °F.

2.3 Upgrades to the LCL Control Systems

In early 1997, it became clear that valve tuning was a critical element in system control and that tuning the 3-way mixing valves in the LCLs (controlled by Johnson Controls LCP controllers) was not routine. The Johnson LCP has no specific “tune override” feature, but its response to temperature disturbances did not seem “classical.” As a test, a Watlow 965FDO controller was substituted for one of the Johnson LCP controllers for a short time, during which it was observed that valve tuning in the classic closed loop manner was possible [3]. Based on these results, it was decided to search for a high-resolution, stand-alone temperature controller that could be tuned to the required tolerance.

Valve tuning experience up to this time made it clear that, while a feedback control system functions to correct an error, such a correction can occur only after the error is detected. It was necessary to be able to discern changes in temperature significantly smaller than the acceptable tolerance. The Johnson Controls LCP was able to discern changes only as small as 0.06 °F. Thus, 60% of the available tolerance had already been expended before control action was initiated.

The Honeywell Progeny, whose A/D converter can resolve changes less than 0.01 °F when scaled across the 40 °F range of the applicable transmitter, was chosen as the stand-alone controller. Using this controller, it was demonstrated that steady-state temperature could be controlled to within ± 0.05 °F.

During this time, attempts were made to reduce coolant flow through the LCL heat exchangers so that the control valves would pass 65-75% of the load-side flow through the exchanger. It was felt that more precise temperature regulation would be possible if a larger flow of water were heated or cooled. As the coolant flow was reduced below 2 or 3 gpm, the exchanger demanded 100% of the load flow yet process temperature continued to climb. At such a reduced flow, the coolant flow transitioned from turbulent to laminar resulting in a loss of overall heat transfer coefficient. The surface area of the heat exchanger was reduced by 50% by rotating one end cap

of the 4-pass shell-and-tube unit by 90° so that coolant would pass through only half of the tubes.

Coolant flowrate in each LCL is now regulated at a fixed, heat-load-dependant value of 7-10 gpm by Griswold flow control cartridges. The coolant flowrate for a given station is determined by varying the flowrate until the 3-way control valve on the linac (load) side is ≈65-75% open at 100% load. The output of the electric heaters is set at a constant value to fix the heat load.

In the most recent upgrade, the Johnson Controls LCPs, the original Barber-Coleman control units, and the Honeywell Progeny were replaced by Allen-Bradley PLC-5/20 processors with 1771-N4BS analog I/O modules. Temperature changes on the order of 0.003 °F can be discerned. Previously, the system noise levels were on the order of 0.015 °F above the applicable system resolution.

Other benefits of the Allen-Bradley processors include the ability to tune valves with response characteristics that permit LCL startup from a cold condition to a steady operating temperature without supervision. This was never possible in the past. It has also been found that most rf power transients are handled well within the ± 0.05 °F tolerance range, as shown in Figure 3.

Use of Allen-Bradley PLCs permits communication between the LCL water stations and the APS control room. The LCLs can now be operated remotely in "real time" via the EPICS [4] control system.

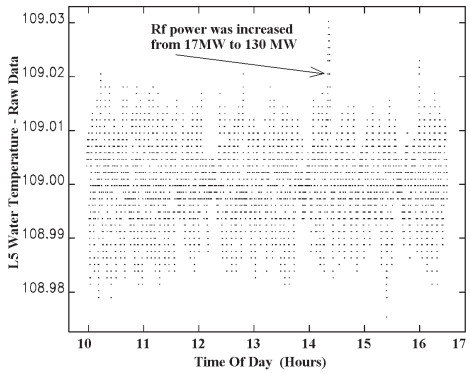

Figure 3: Temperature stability of one LCL over seven hours in April of 1998. The temperature only changed by 0.03 °F in response to an 80-MW increase in the SLED forward power.

2.4 Linac Temperature Control Systems

The LCL temperature control systems now consist of:

1) 3-way Durco ball-type control valves that divert water through or around the heat exchanger as required for stable temperature regulation.
2) Worcester series 75 electric control valve actuators with AF-17 positioners with a resolution of 0.5%.
3) Electric heaters providing fixed heat input rates; rates between 0% and 100% are chosen at setup.
4) 3-wire, direct immersion, 4-s time constant, Minco S603PD8 RTDs.
5) Analog temperature transmitters scaled in the range 85-125 °F (Minco TT676PD1QG).
6) Allen-Bradley PLC-5/20s with P/N 1771-NB4S high-resolution analog I/O cards for PID temperature control (the D feature is not used).

Use of a 3-way diverter valve in the load stream rather than a throttling valve in the coolant stream is especially important. An order of magnitude faster temperature response is obtained with the diverter valve since the final temperature is a result of mixing, and flow ratio changes are immediate upon valve movement. Throttling of the coolant flow results in relatively slower response, since the entire mass of the load stream and the mass of the heat exchanger surfaces must change temperature.

3 CONCLUSIONS

Temperature regulation of high-power rf components to within ± 0.05 °F has been achieved at the APS linac. The system responds quickly to changes in rf power load and maintains long-term temperature stability. The water system and the techniques to optimize the temperature are described more completely in [5]. System studies continue including an effort to find a source for a digital temperature transmitter with suitable resolution to address possible drift issues.

4 ACKNOWLEDGMENTS

The authors would like to acknowledge R. Damm for leading efforts to improve system performance; E. Swetin for installing holding tanks, downsizing heat exchangers, and assisting with KGSS tuning; C. Putnam and H. DeLeon for implementing the PLCs; N. Arnold and M. Kramer for implementing network communication; R. Kneebone and W. Matz for implementing changes prior to 1996; and C. Eyberger for editorial assistance.

5 REFERENCES

[1] 7-GeV Advanced Photon Source Conceptual Design Report, ANL-87-15, April 1987.

[2] M. White, N. Arnold, W. Berg, A. Cours, R. Fuja, A. E. Grelick, K. Ko, Y. L. Qian, T. Russell, N. Sereno, and W. Wesolowski, "Construction, Commissioning and Operational Experience of the Advanced Photon Source (APS) Linear Accelerator," Proc. of the XVIII Intl. Linear Accelerator Conf., pp. 315-319 (1996).

[3] P. W. Murrill, "Fundamentals of Process Control Theory," 2nd Ed., Instrument Society of America, pp. 126-129 (1991).

[4] W. P. McDowell, et al., "Status and Design of the Advanced Photon Source Control System," Proc. of the 1993 Particle Accelerator Conference, Washington, DC, May 1993, pp. 1960-1962 (1993).

[5] R. Dortwegt, S. Pasky, and M. White, "Temperature Regulation of the APS Linac High-Power Rf Components," APS-LS Note, to be published.

EXPERIMENTAL RESULTS OF THE ACTIVE DEFLECTION OF A BEAM FROM A KICKER SYSTEM*

Y. J. (Judy) Chen, G. Caporaso, J. Weir
Lawrence Livermore National Laboratory, Livermore, CA 94550 USA

Abstract

A high current kicker has been designed and tested on the ETA-II beam line. A bias dipole which surrounds the kicker acts to deflect the beam in the DC mode. High voltage pulsers (10kV) with fast rise times (10ns.) are connected to the internal strip lines of the kicker. They are used to manipulate beams dynamically.

Camera photos which show the switching of the beam from one position to another will be presented. Beam bug measurements of beam-induced as well as active steering will be shown. These will be compared with theoretical predictions.

1 INTRODUCTION

Recently there has been considerable interest in providing advanced flash x-ray radiography capability for stockpile stewardship[1][2]. A multi-axis capability is required in order to produce a tomographic reconstruction of an imploding assembly. It would be economical to produce many lines of sight using a single high current electron accelerator if a kicker could be used to axially section a long beam pulse into pieces which could be directed to different beam lines.

The kicker for this application must be able to handle continuous kilo-ampere beams with great precision and high speed. Switching times of order 10 ns are required in order to make maximum use of the available beam charge. In addition, beam induced fields arise in the kicker and cause additional deflections which must be compensated for by modifying the external pulser voltage waveform.

In order to improve field quality the kicker was fitted with curved strip line electrodes approximating a cylindrical boundary as shown in Fig. 1. The resulting structure strongly resembles a strip line beam position monitor that is in wide use in the high energy accelerator community [4]. These kickers are to be used to handle continuous relativistic electron beams of at least several kilo-amperes so that wake fields in the kicker are significant even for a single passage of the beam. The wake fields for structures of this type are strong enough to significantly steer the beam. The input condition on the beam centroid is amplified as a function of beam current [2] for both a passive and kicked mode of operation. The shaped electrodes improves field quality but residual higher order moments still exist. The strongest field after the dipole moment is the sextupole moment. The nonlinearity of a sextupole field can shape the beam into a triangle and introduce a small amount of emittance growth [5].

* This work was performed under the auspices of the U.S. Department of Energy by the Lawrence Livermore National Laboratory under Contract No. W-7405-Eng-48.

Figure 1: Photo of kicker cross-section which shows kicker plates

2 DESCRIPTION OF EXPERIMENT

The kicker experiment, which comprises high voltage pulsers and the kicker itself with a bias dipole magnet wound around the outside, sits in the transport section of a linear induction accelerator (Fig. 2). A complete system would also include a septum magnet downstream of the kicker. It is the only active component in that section. Experiments to test the system have been and are still being conducted on the Experimental Test Accelerator - II (ETA-II) at the Lawrence Livermore National Laboratory. Two existing pulsers can provide $\pm$10kV into a 50Ω load with a 10-90% risetime of 10 nsecs. The pulser is shown in Fig. 3.

Two different beam line configurations were used. The original layout proved to be inadequate for the set of beam-induced steering experiments. Two resistive wall monitors (known locally as beam bugs) upstream of the kicker were needed to measure input displacement and angle [6]. In fig. 4a, these were labeled BBT08 and BBT09. However, a large focusing magnet, C4A, resided between the two and was necessary to transport the beam to the output of the kicker. It was quickly realized that incorporation of the C4A in the analysis meant the assumption that the magnet was perfectly aligned. A new beam line was designed such that two beam bugs can be placed upstream of the kicker without a magnet between them, as shown in fig. 4b. The spacing between the input bugs must be comparable to the length of the kicker to minimize measurement error in angle.

The first set of results shows that the predicted amplification due to beam-induced steering in a passive kicker matches well with experimental data. These cases were all taken at I_b=1700A where amplification is 1.47 in initial offset and 1.08 and initial angle is 1.15. There is a small background magnetic field that points in both the x and y direc-

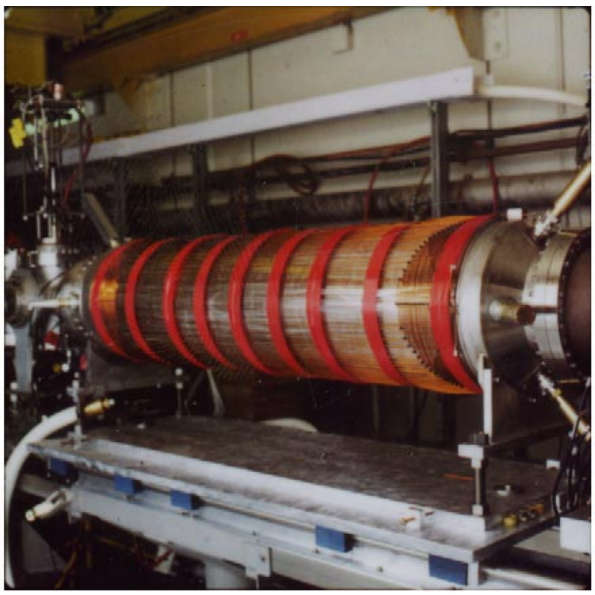

Figure 2: Photo of kicker on ETA-II beam line. White cables (unconnected in this picture) connect pulsers to kicker. Red tape holds bias dipole magnet windings to outer shell of kicker.

Figure 3: Kicker pulser.

tion that is folded into the data analysis. The magnetic field pointed in the $-y$ and $-x$ directions (defined by propagation of the beam in the $+z$ direction) with magnitudes of .3-.6G and .1-.3G respectively. This added an error in beam steering in the $-y$ and $+x$ direction. Fig. 5 shows time-averaged location of the beam at BBT10 for both theoretical projection and actual data for various current values. The error bars on the theory values stems from an assumption that beam bugs have a ± 1.4mm error [6]. For large offsets the error is closer to $\pm .7$mm. This implies that at BBT10, the error should be $\pm(1.4\text{mm} \times 2.41\text{m}/1.33\text{m} + .7\text{mm}) = \pm 3.2$mm. The error bars on the beam bug data include an

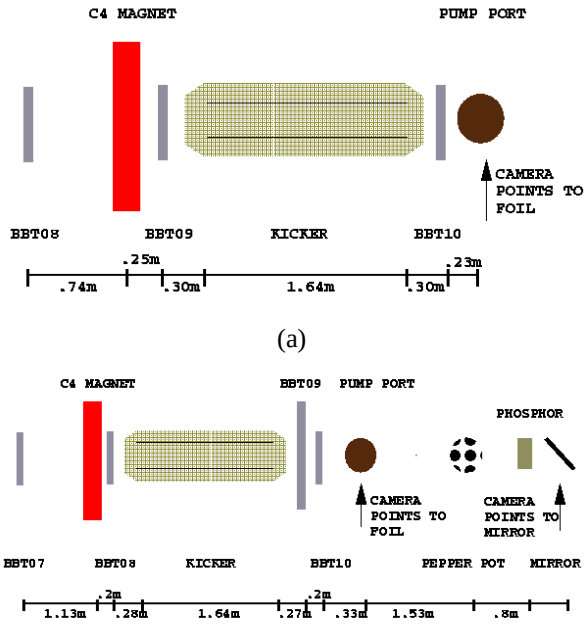

Figure 4: a) Old beam line layout. b) New beam line layout.

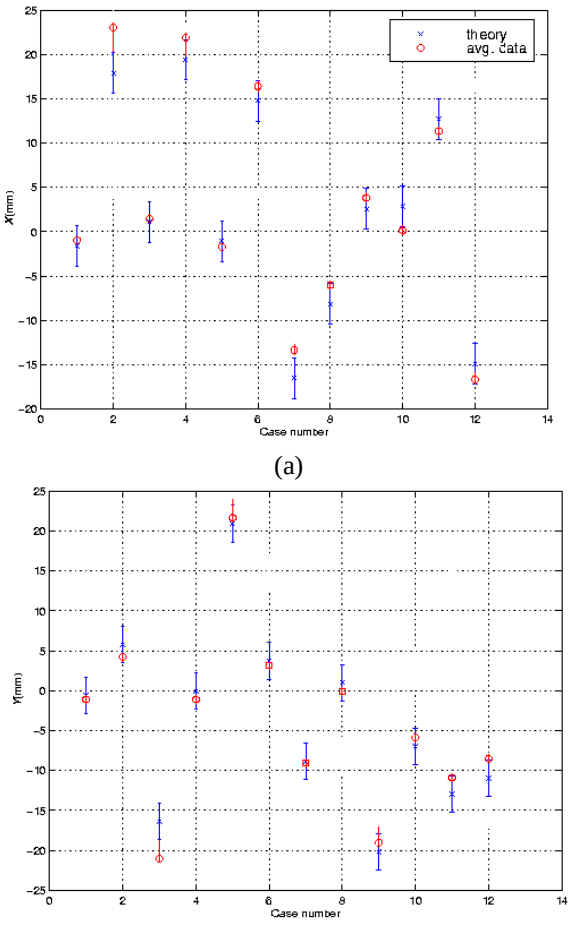

Figure 5: a) Time-averaged x displacement at output of kicker (at BBT10) and b) y displacement show amplification is a function of beam current.

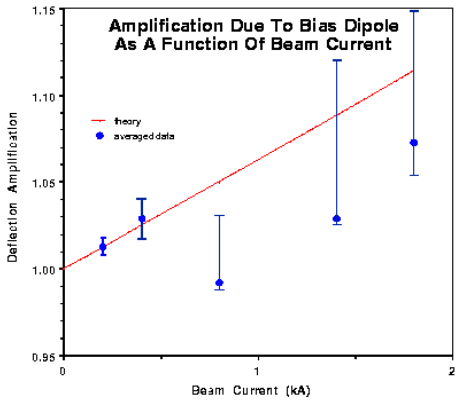

Figure 6: x displacement at BBT09 (old beam line) due to dipole magnet

additional contribution due to the inherent nonlinearity of beam bugs for off-axis measurements. The data are time-averaged over a 40nsec. window.

Case 1 was the zero case where the beam entered the kicker on-axis with little to no angle. Cases 2 to 5 were different combinations of initial offsets in x and y, again with no angle. In cases 6 to 9, the beam is steered into the kicker close to axis but with a large angle. Cases 10-12 is another set similar to cases 2 to 5. These sets of data were taken on three different days.

Fig.6 shows the amplification of bias dipole magnet steering as a function of I_b. This data was collected on the old beam line configuration. Centroid location was derived from finding the geometric center of TV camera images of the beam. The kick due to the magnet is normalized to the predicted steering given no beam-induced effect (setting $I_b = 0$). Here we are trying to trace an amplification factor that at the maximum is only 8% as shown in the last data point in figure 6. Although the error bars are large, the general trend fits well with theory.

A series of tests were conducted using the pulsers to kick the beam. Fig. 7 shows a TV image of a 200nsec. time slice of an electron beam at I_b=1000A hitting a quartz foil (see Fig. 4a). The electron beam on impact produced Cherenkov radiation that a camera can detect. The total beam pulse length is only 70nsec. so the camera captured the electron beam as it was kicked from one position to the other. It shows a beam kicked with V_p=9kV and at an estimated energy of 6.3MeV. The total displacement at the camera foil is 4cm. Fig. 8 shows that if the beam is large entering the kicker it can pick up a sextupole moment created by the applied voltage and consequently have a triangular shape at the output [5].

3 CONCLUSION

The kicker as a viable technology in the advancement of multi-axis multi-pulse radiography has been experimentally demonstrated. The physics characterization of the kicker itself is almost complete.

Beam deflection experiments has shown that the kicker can switch the beam in 21ns (10-90%). The experimental

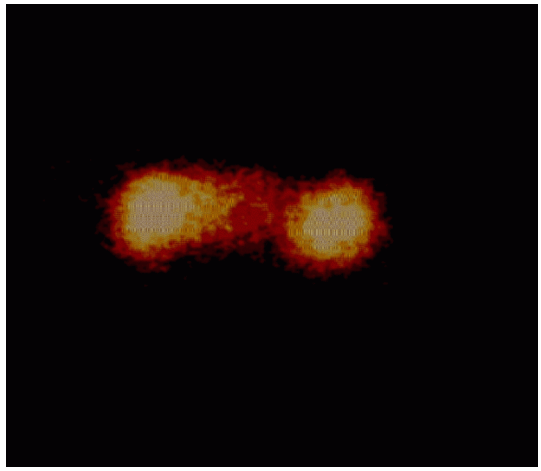

Figure 7: TV camera downstream of kicker which captured the beam as it deflected from one side to the other.

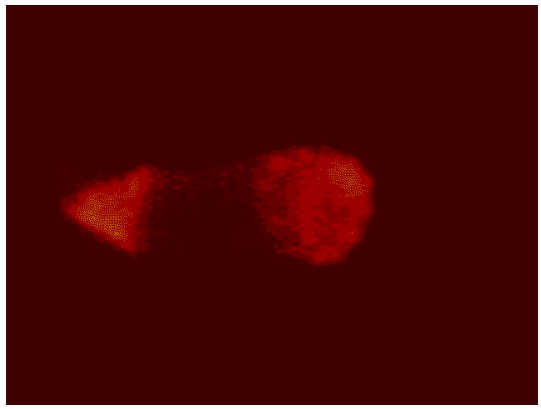

Figure 8: TV camera downstream of kicker which captured a triangularly shaped beam shaped by the sextupole moment inherent in the fields due to the stripline voltages.

characterization of beam-induced effects in the kicker fits well with theory. The predicted sextupole shaping of the beam was also seen.

4 ACKNOWLEDGMENTS

We gratefully acknowledge the assistance of the entire ETA-II and Bechtel-Nevada staff. We acknowledge the contribution of both B. Poole and S. Nelson [7] for their EM numerical and experimental analysis of the kicker.

5 REFERENCES

[1] Caporaso, G. J., Frontiers of Accelerator Technology, World Scientific, (1996).
[2] Caporaso, G. J. et al., "Transmission line analysis of beam deflection in a BPM stripline kicker," *Proceedings of the Particle Accelerator Conference*, (1997), to be published.
[3] Coffield, F. et al., Nucl. Instr. and Methods in Phys. Research, **A293**, 296, (1990).
[4] Ng, K.-Y., Particle Accelerators, **23**, 93, (1988).
[5] Poole, B. et al., "Analysis and modeling of a stripline beam kicker and septum," *this conference*.
[6] Chen, Y. J. and T. Fessenden, "Improvements on the accuracy of beam bugs,"*this conference*.
[7] Nelson, S. D., "Electromagnetic cold-test characterization of the quad-driven stripline kicker,"*this conference*.

CHARACTERIZATION OF HIGH POWER CW KLYSTRONS AND ITS APPLICATION TO LOW LEVEL RF CONTROL*

A.S. Rohlev, D.E. Rees
Los Alamos National Laboratory, Los Alamos, NM 87545

Abstract

The power gain, phase delay, and line harmonic spectrum of a 1.3 MW, 350 MHz, CW klystron amplifier have been measured as a function of input power. These measurements of the klystron were taken at several constant perveance and constant impedance operating points. The results are used to enhance the performance of the low level RF control system.

1 INTRODUCTION

Accelerator control systems attempt to maintain a constant cavity field by monitoring the field and modulating the driving RF amplifiers to cancel out any perturbations. The extent to which this can be done depends on the characteristics of the cavity, the strength of the amplifiers, and the quality of the control system. An accurate characterization of the cavity and the amplifiers can be used to improve the performance of the control system. The purpose of this paper is to show results from measurements made on a 350 MHz 1.2 MW klystron amplifier. The measurement technique, while not unique, is relatively simple and can be used on a variety of CW amplifiers.

The 350 MHz klystron tested will be used to drive the RFQ on the Low Energy Demonstration Accelerator (LEDA) for the APT project. The RF architecture of LEDA places several constraints on the low level control system which were quantified by these tests. The LEDA RFQ will be driven by three klystrons operating at 2/3 power or, if one fails, two klystrons operating at full power. In either case the DC bias parameters of the klystrons will be set to allow for an amplitude control margin of about 10%. One control system will be used to drive these klystrons so having the proper phase relationship between the klystrons is critical. Since the klystrons will be operating near saturation it was necessary to get accurate gain curves for a variety of DC bias conditions. Also line harmonic frequencies on the output RF were measured since regulating these could decrease the control margin. Finally, the phase length of the klystron was measured as a function of the DC bias and the input power.

*Work supported by Department of Energy.

2 EXPERIMENTAL SETUP

Figure 1 Shows a block diagram of the experimental setup.

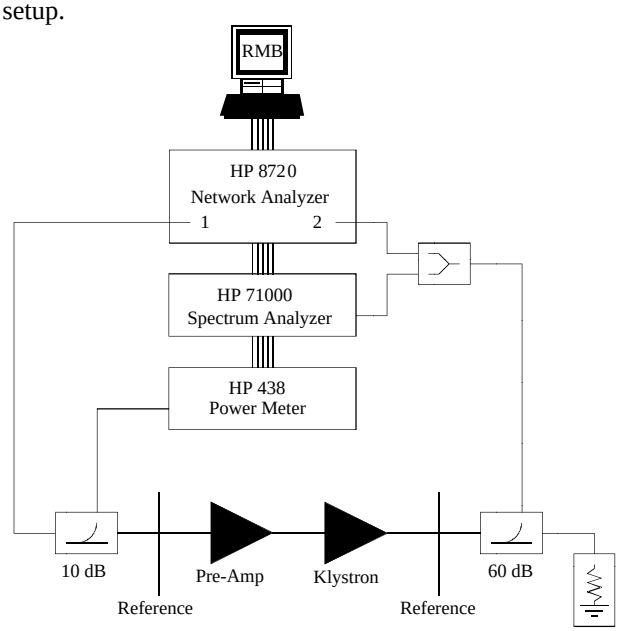

Figure1. Experimental Setup

A HP 8720 network analyzer operating in CW mode at 350 MHz was used to drive the klystron and measure its output power and phase length. A HP 71000 series spectrum analyzer was used to measure line harmonic sidebands (N*60 Hz) on the output RF. Lastly, a HP 438 power meter was used to measure and adjust the RF output power of the network analyzer. The three instruments were controlled, and data was collected, via HPIB by a PC running Rocky Mountain Basic. All measurements were made as a function of input power once the DC bias of the klystron had been established. The line losses from port 1 of the network analyzer to Reference Plane 1 as well as from Reference Plane 2 to port 2 were carefully measured and recorded. The measurements proceeded as follows. First the computer instructed the network analyzer to go to a prescribed output power. The power meter measured the true output power using a well defined 10 dB directional coupler. The true power was relayed back to the computer which used a converging algorithm to adjust the output of the network analyzer until the prescribed RF power was present at Reference Plane 1. The network analyzer then measured the magnitude and angle of S_{21} after which, at the operators request, the input power was incremented and another test point was taken.

From the magnitude of S_{21} the gain between Reference Plane 1 and 2 could be calculated since the line losses were known. Also, since the input power at Plane 1 was known, the output power at Plane 2 could be derived. The angle of S_{21} was the phase length between Planes 1 and 2 plus a fixed angle due to the lines. At several points along a curve the spectrum analyzer was poled to get the output RF spectrum. The spectrum analyzer would measure the main klystron peak as well as any other peaks within 750 Hz of the center. The sidebands occurred exclusively at line harmonic frequencies, and their power relative to the main peak was recorded.

Once the DC bias for the klystron was fixed the input power was initially set at a low level generating less than 50 kW output from the klystrons. The input power was then raised in 1 dB increments, 0.2 dB increments, and finally 0.1 dB increments as the klystron neared saturation. Table 1 shows the different DC bias conditions for which the klystron was tested. The beam current was set to maintain a constant tube perveance in points 1-4 and a constant tube impedance in points 4-7.

Test Point	Beam Current (A)	Cathode Voltage (kV)	Saturated Pout (kW)	Number of Data Points
1	9.85	60.0	279	51
2	15.3	80.0	725	40
3	17.6	88.0	963	42
4	19.4	93.9	1161	50
5	18.3	88.4	1008	30
6	16.4	80.4	806	42
7	12.4	60.2	365	46

Table 1.

3 RESULTS

The test results are summarized in Figures 2, 3, and 4 which respectively show the power, efficiency, and phase characteristics for the klystron.

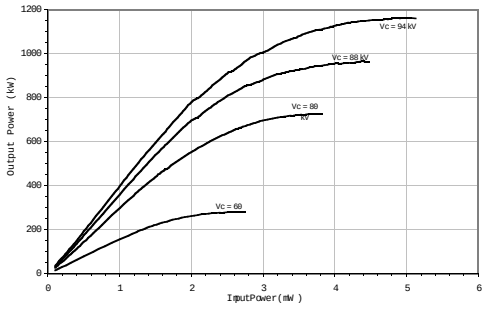

Figure 2. Output power characteristics.

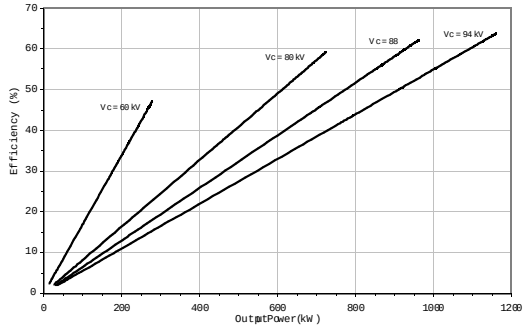

Figure 3. Power efficiency characteristics.

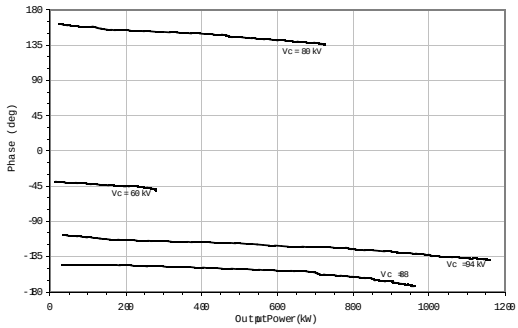

Figure 4. Output phase characteristics.

The figures show the results for bias points 1 through 4. The efficiency is calculated as the ratio of the output RF power to the input DC power. Table 2 show the line harmonic data at several output power levels for bias point 4. There was no appreciable power in the line harmonics above 120 Hz, and only at 1000 kW output was there power in the 60 Hz harmonic.

Pout (kW)	60 Hz Power (dBc)	120 Hz Power (dBc)
117	< -70	-52.8
504	< -70	-53.2
1000	-55.7	-46.9
1159	< -70	-48.3

Table 2. Line harmonic data.

4 CONCLUSION

Several observations about the architecture and performance requirements of the control system can be made from the above data. Measurements of the line harmonic power show that it will introduce about 0.5% error in the cavity voltage and will not seriously reduce the control margin of the system. With respect to the klystron phase data, it is obvious that some sort of individual phase control is necessary for each klystron.

The phase length of the klystron can change by many tens of degrees with cathode voltage and by ten degrees or more for a set DC bias condition. For LEDA three klystrons will drive a single cavity and be controlled by a single system. The cavity phase is the superposition of the three klystron phases and will be maintained at a constant value by the control system. However, without individual control of each klystrons phase, large inefficiencies in transmitted power can occur which will degrade the control margin of the system.

RF SYSTEM DEVELOPMENTS FOR CW AND/OR LONG PULSE LINACS *

Michael Lynch
Los Alamos National Laboratory, Los Alamos, New Mexico 87545 USA

Abstract

High Power Proton Linacs are under development or proposed for development at Los Alamos and elsewhere. By current standards these linacs all require very large amounts of RF power. The Accelerator for Production of Tritium (APT) is a CW accelerator with an output current and energy of 100 mA and 1700 MeV, respectively. The Spallation Neutron Source (SNS), in its ultimate configuration, is a pulsed accelerator with an average output power of 4 MW of beam. Other accelerators such as those that address transmutation and upgrades to LANSCE have similar requirements. For these high average power applications, the RF systems represent approximately half of the total cost of the linac and are thus key elements in the design and configuration of the accelerator. Los Alamos is fortunate to be actively working on both APT and SNS. For these programs we are pursuing a number of component developments which are aimed at one or more of the key issues for large RF systems: technical performance, capital cost, reliability, and operating efficiency. This paper briefly describes some of the linac applications and then provides updates on the key RF developments being pursued.

1 APPLICATIONS OF HIGH POWER PROTON LINACS

APT is by far the highest average power accelerator ever proposed. A table showing pertinent parameters for APT is shown below. 244 klystrons are required for the currently planned 1700 MeV version [1]. A reduced power variation is under consideration due to changing tritium requirements, but even that design is higher in average power than any proposed accelerator. The reduced power version has a final energy of 1300 MeV and requires 160 CW klystrons. In both versions of the linac, a klystron is required about every 4.5 m, so the average power per unit length is very high.

Table 1: Pertinent Parameters of APT Linac

Proton Energy	1700 MeV
Beam Current	100 mA
Beam Power	170 MW
AC Power (for RF)	386 MW
Peak Coupler Power	210 kW
Klystrons (1 MW)	243
Linac Length	1104 m

* Work supported by the US Department of Energy

The RFQ for APT operates at 350 MHz and requires 3 klystrons [2]. The remainder of the accelerator operates at 700 MHz, so the majority of the klystrons are at 700 MHz. Each RF system for APT is generally laid out as shown in Fig. 1. [3]. Each klystron is split 4 ways to drive 4 ports on the accelerator. This splitting arrangement was deemed necessary to ensure reliable operation of the window/coupler assemblies. It was felt that reliable operation could be achieved with up to 250 kW of CW forward power through each window. This allows for situations with high-reflected power in which the RF fields in the window might double.

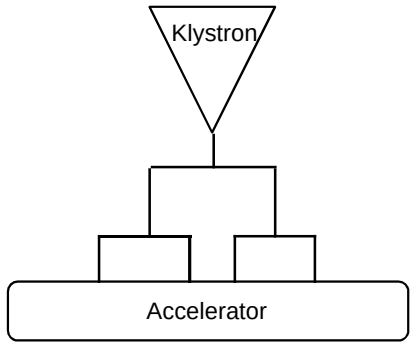

Figure 1: Typical RF System Layout for APT

The Spallation Neutron Source (SNS), in its ultimate configuration, will have an average output current and energy of 4 mA and 1000 MeV, respectively, providing 4 MW of average beam power. In its initial configuration the beam power is 1 MW. A table of the parameters for the 1 MW version is given below. It requires 59 klystrons with most at 805 MHz and 2.5 MW peak power. The remaining 3 are 1.25 MW peak at 402.5 MHz. At the full 4 MW of beam power, the number of klystrons required is 83.

Table 2: Pertinent Parameters of SNS Linac

Proton Energy	1000 MeV
Beam Current	27.7 mA, peak 1.04 mA, average
Beam Power	1.04 MW, average
Pulse Width	1.0 ms
Repetition Rate	60 Hz
Klystrons 805 MHz, 2.5 MW peak 402.5 MHz, 1.25 MW peak	 56 3
Linac Length	486 m

Other accelerators that address transmutation and upgrades to LANSCE have similar requirements. For transmutation, one version uses multiple CW

accelerators, each with a current of 40-mA and output energy of 1 GeV. A table of pertinent parameters for an ATW linac is given below. A significant portion of this linac could be superconducting (from 21 MeV to 1 GeV), but it would still require 56 CW klystrons of 1 MW output power. To achieve complete burn of the nuclear waste, a total of 20 of these machines would be needed. They would be built over about a 25-year period and each would need to operate for 40 years.

Table 3: Pertinent Parameters of ATW Linac

Proton Energy	1000 MeV
Beam Current	40 mA
Beam Power	40 MW
AC Power (for RF)	95 MW
Peak Coupler Power	200 kW
Klystrons (1 MW)	56
Linac Length	355 m

For all of these high average power applications, the RF systems are very key elements of the overall accelerator because they represent approximately half of the total cost of the linac.

2 DEVELOPMENT THRUST AREAS

2.1 System Design Developments

Development is taking place both in system design and in component design to address one or more of the key items: capital cost, operating cost, availability, or technical performance. In terms of system design, APT is planning a supermodule scheme for the normal conducting linac portion (up to 211 MeV). Supermodules allow quick return-to-service in the event of a failure of a component in the RF system. A diagram of a supermodule is given in Fig. 2.

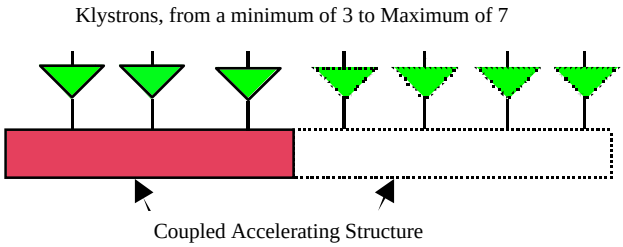

Figure 2: A Block Diagram of a supermodule showing the size variation. Each supermodule has one more klystron than is needed for full-current operation.

In analyzing the availability of the RF system with a large number of generators, we found that the failure and repairs would lead to excessive down time and insufficient production by the machine. The use of supermodules greatly improves the availability of the normal conducting portion of the accelerator. The supermodule is simply a long coupled structure, which requires multiple RF generators to achieve sufficient power. In configuring the RF system an 'extra' RF station is added such that any one RF system can fail, and in a very short time (5 to 10 minutes), the failed unit can be taken off line and operation resumes with the remaining stations. The supermodules vary in size from 3 klystrons (2 required) to 7 klystrons (6 required).

For the superconducting portion of the linac the availability is achieved by installing more modules than are needed to achieve the rated production. If a module fails, it is detuned so the beam will not drive the cavity, and the adjacent modules are adjusted in amplitude and phase to 'make up' the difference. Approximately 5% more cavities are installed than are needed. This adds complication for the control system, but the controls are being developed to handle these complications. An additional feature of the superconducting module is that one klystron drives more than one resonant structure (either 2 or 3) as shown in Fig.3.

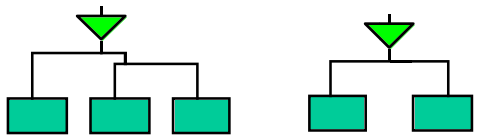

Figure 3: Block diagram of RF system for the superconducting cavities. Each klystron drives either 2 or 3 cavities. The medium and high ß refer to the two types of superconducting structures used in APT. [1]

The overall linac is thus a combination of normal conducting 'supermodules' and a large number of superconducting modules as shown in Table 4.

Table 4: Breakdown of RF Systems for the APT Linac

Accelerator System	Klystrons	Super-modules	Cavities/Klystron
RFQ (350 MHz)	3	1	
CCDTL	22	6	
CCL	29	5	
SC, ß=0.64	36		2 for 6 klystrons, 3 for 30 klystrons
SC, ß=0.82	154		2

2.2 Operating Efficiency

In a simple analysis of the overall efficiency of the accelerator, approximately 44% of the input AC power is converted to beam power. To reach this efficiency, many parts of the RF system are being pushed to their limits. The HVPS must deliver the DC power with 95% efficiency. The RF transport, which includes the circulator, splitters, the RF window, and any phase and amplitude variations in the various drives, must deliver to the cavity at least 94% of the power from the klystron. The beam loading percentage is addressed with the conversion to superconducting cavities for the majority of the accelerator. In the superconducting cavities, the beam loading is 100%. Only in the normal conducting section of the linac (up to 211 MeV) is RF power dissipated in the cavity walls.

Since there is a potential savings of $1M in operating cost for each percentage point improvement in operating efficiency, developments are taking place with the RF generators to develop higher efficiency generators, and generators which have less loss of efficiency when operating below their 'saturated' or 'maximum' output level.

2.3 Low Level RF Controls (LLRF)

We are working to develop LLRF controls for APT which only require 10% excess drive capability in the generator to deal with system disturbances (beam noise, power supply ripple, etc.) In addition we are incorporating DSP technology into the design for advanced capabilities and enhanced flexibility. [4] For SNS, since it is a pulsed application, we will require 20% or more excess drive capability. For both CW and pulsed systems, the LLRF must control fields in the cavities, provide the resonance control signals, provide the RF reference along the entire linac, provide the proper timing signals for the RF system, and provide the proper protection signals. There are, in addition, particular requirements related to the CW or pulsed application.

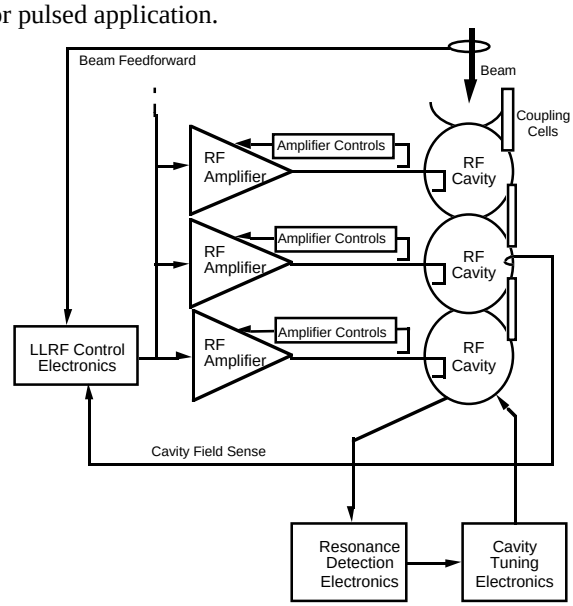

Figure 4: LLRF control diagram for a supermodule. The long coupled accelerator structure is driven by multiple klystrons and controlled with one feedback system. To equalize the klystrons, each one has a control loop.

The Low Level RF (LLRF) controls must be designed differently for the normal conducting and superconducting portions of the accelerator. Figures 4 and 5 show the block diagram for the LLRF controls for these two portions. In the normal conducting portion, the supermodule has multiple drives for one resonant cavity. The implication for the LLRF for this portion is that the separate RF systems must be properly phased and the drives must be 'equalized'. In the superconducting system, one RF drive provides power to multiple cavities (2 or 3). The cavities must be maintained properly relative to each other.

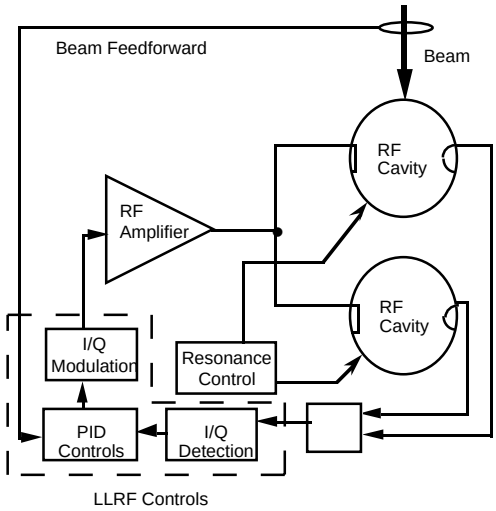

Figure 5: LLRF control diagram for a superconducting module. Each klystron drives more than one cavity.

2.4 Component Design Developments

First and foremost for APT is the 700 MHz RF generator. We are currently pursuing 2 main avenues with an additional pursuit occurring externally. One main avenue is the development of a conventional 'superpower' klystron at 700 MHz [5], which is derived from the CERN 352 MHz CW klystron. The other is a new type of tube, referred to as an HOM-IOT, which promises again the same output characteristics as the conventional klystron, but very high operating efficiency. The external pursuit is an advanced klystron, which is striving for equivalent output characteristics as the conventional klystron, but at higher efficiency.

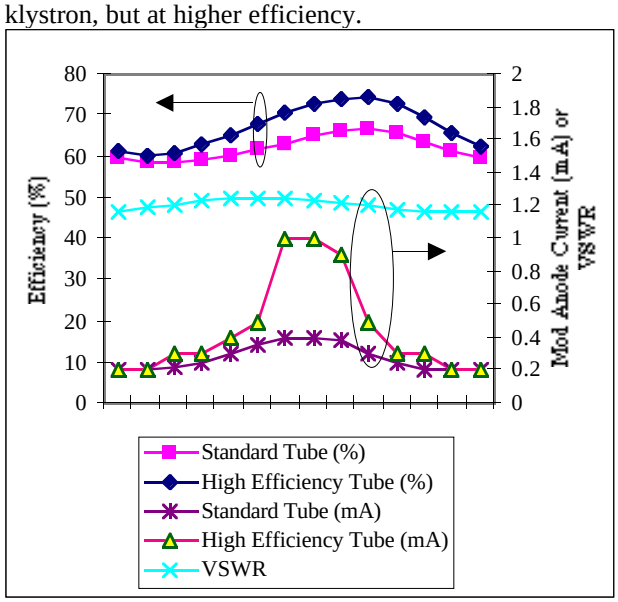

Figure 6: Test results of the standard and 'advanced' 700 MHz klystron from EEV. The advanced tube shows higher overall efficiency, but also shows more sensitivity to the 1.2:1 VSWR test.

The conventional 700 MHz klystron is being developed at CPI and at EEV. The tube has a modulating anode to optimize the efficiency. The tube is expected to operate at

65% efficiency when saturated and should average about 58% in actual operation (due to the need to operate below saturation to enable the feedback control system to work correctly). The advanced klystron is an internally funded venture by EEV. If it is successful, the saturated efficiency will be 70% or greater.

Test results of the standard and high efficiency klystron are shown in Fig. 6. The high efficiency klystron had very good results, although less efficiency than expected. In addition the high mod anode currents indicate that the tube has potential stability problems. Nevertheless, the results are encouraging and further development is taking place.

In both types of klystron, the tube must 'sacrifice' some of its efficiency to allow margin for control [6]. This sacrifice can be recovered with a depressed collector. This was considered but has not been pursued. A new type of tube proposed by CPI has an inherently good efficiency and could eliminate most of the operating penalty. The tube is referred to as a High-Order Mode Inductive-Output Tube (HOM-IOT) and is a density modulated device in which the amount of beam in the tube is determined by the input RF level. The expected efficiency of the HOM-IOT and a conventional klystron, as a function of output power, is shown in Fig. 7. As can be seen, even at half the rated output power, the efficiency is 60% or better compared to less than 50% for the klystron. A diagram of the tube is shown in Fig. 8.

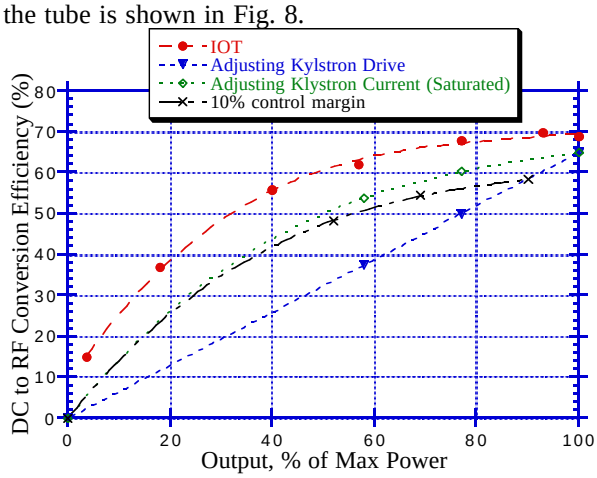

Figure 7: Comparison of the operating efficiency characteristics of the HOM-IOT and a standard klystron.

Other components being developed for APT include High Voltage Power Supplies (HVPS), high power circulators at 700 MHz, and RF windows. The HVPS is the single biggest cost item in the RF system, and there is room for improvement in the operating efficiency and reliability. There are several options being considered for the APT HVPS, from a conventional SCR-controlled supply to various versions based on IGBT technology. [7,8]

The RF windows represent the biggest impact to system reliability. The full APT has approximately 1000 windows, and their reliability is a key issue for APT. In addition there is a complication arising from the mixture

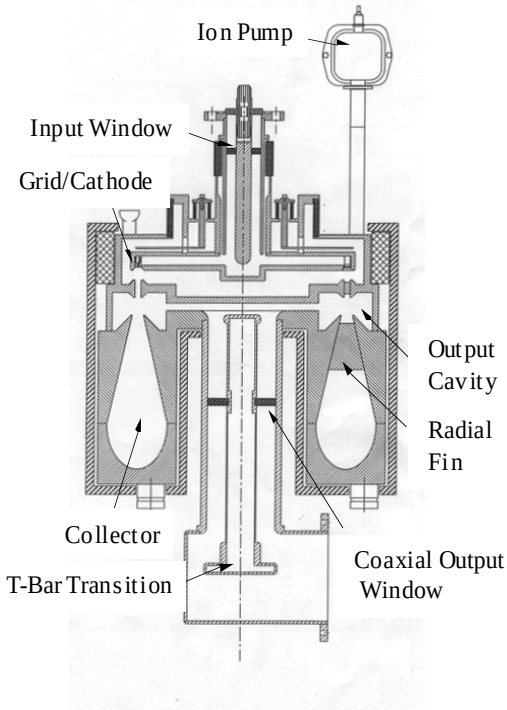

Figure 8: Outline drawing of the HOM-IOT. The tube is rotationally symmetric about the centerline, with the exception of the ion pump and output starting at the t-bar transition.

of normal conducting and superconducting cavities. The normal conducting windows are all based on klystron window technology. [9] For the superconducting cavities, the window design starts with standard klystron window design, but then must accommodate the tough problems of connecting to the power coupler for the superconducting cavity. A sketch of the basic window layout for superconducting cavities is shown in Fig. 9.

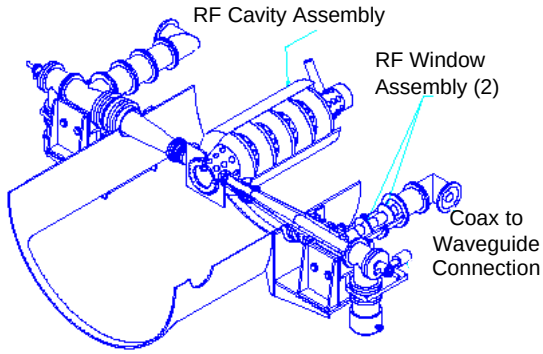

Figure 9: Layout drawing of the RF/vacuum window for a superconducting cavity. Dual windows are used for reliability considerations.

For SNS, a new klystron is being developed to provide 2.5 MW peak at 805 MHz and 7% duty factor with a pulse width of more than 1 ms. [10] Two development contracts have been placed for one klystron, one with CPI

and one with Litton. In addition, options for the High Voltage modulator are being pursued which take advantage of developments in IGBT technology.

In all, IGBT technology is being considered in three different topologies. [7,8] Two different topologies are being pursued for APT. One is an extrapolation of a commercial unit designed for Voice of America installations (Fig. 10). The other is a new design, which has associated risks, but looks to be able to provide cost savings. In both cases, the IGBT technology promises to offer considerable technological advantages over a standard SCR-type of HV power supply. They should eliminate the need for a crowbar, offer significant cost savings, and provide graceful degradation and easy repair. In the case of the commercial unit, the supply utilizes 96 modules wired in series to produce the high voltage. Each module contains a full-wave, 3-phase rectifying bridge, which produces 1.1 kV DC across a small filter capacitor. The module circuitry and controls allows the power supply to continue to operate with approximately 5% failed modules without degradation in performance. The failed modules can then be repaired during a scheduled shutdown.

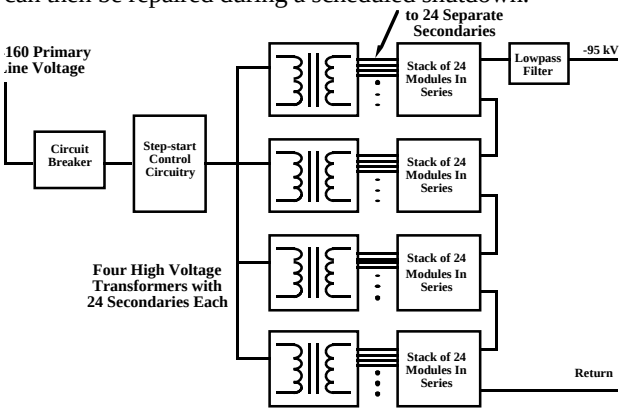

Figure 10: 95 kV advanced HVPS based on IGBT technology features graceful degradation and low stored energy (and thus does not require a crowbar).

The IGBT system being pursued for SNS combines the functions of the HVPS and the HV modulator needed for pulsing of the klystron into a single small unit. The crowbar is eliminated, and significant cost savings are expected.

3 PROJECTED TIMELINE

For the larger version of APT (1700 MeV), the need for the start of Tritium production is 2007. If the smaller version (1030 MeV) is opted for, the need date for start of production moves to 2011 because the existing Tritium can decay further before additional amounts are needed to replenish the decaying amounts. Assuming the smaller version of APT, tube production must begin around 2001 and be complete by 2009. SNS is currently expecting to be completed by 2005. Initial installation of the RF hardware must occur in 2000 and be completed by 2004. Finally, a reasonable assumption at this point is that the first ATW accelerator begins installation in 2007 and is completed by 2012.

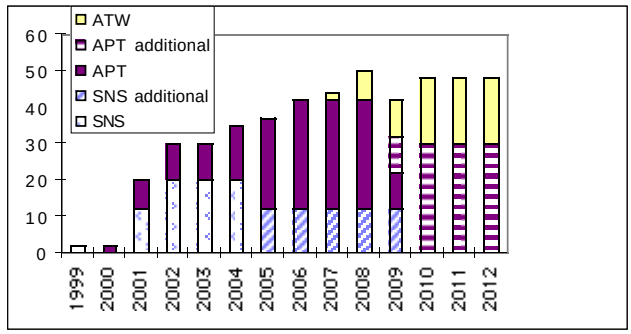

Figure 11: The tube requirements for the APT, SNS, and ATW for the next several years add up to a significant number of high power tubes.

Figure 11 shows all of the needs for these three programs compiled together based on the above dates and assumes that 20% of the initial 'need' for klystrons is produced for 5 years after completion in order to provide spares and replacements for infant failures. As can be seen by the table, the production total reaches a maximum of approximately 50 tubes for one year, and after about 2005 the production maintains a level of 40 or more tubes for over 7 years. There is a similar need for all of the associated RF hardware such as HV power supplies, waveguide, capacitors, circulators, etc.

4 REFERENCES

[1] G.P. Lawrence, "High-Power Proton Linac For APT: Status of Design and Development", This conference.

[2] D. Rees et al, "Design, Operation, and Test Results of 350 MHz LEDA RF Systems", This conference.

[3] W.T. Roybal et al, "LEDA RF Distribution System Design and Component Test Results", This Conference.

[4] A.H. Regan et al, "LEDA LLRF Control System Characterization", This Conference.

[5] D. Rees et al, "Accelerator Production of Tritium 700 MHz and 350 MHz Klystron Test Results", This Conference.

[6] A.S. Rohlev, "Characterization of High Power CW Klystrons and its Application to Low Level RF Control", This Conference.

[7] J.T. Bradley, III, et al, "Design, Construction, and Operational Results of the IGBT Controlled Solid State Modulator (SSM) High Voltage Power Supply used in the High Power RF Systems of the Low Energy Demonstration Accelerator (LEDA) Portion of the APT Project", This Conference.

[8] R.W. Street et al, "Advanced Buck Converter Power Supply 'ABCS' for APT", This Conference.

[9] K. Cummings et al, "Results and Lessons Learned from Conditioning 1 MW CW 350 MHz Coaxial Vacuum Windows", This Conference.

[10] P.J. Tallerico et al, "The RF Power System for the SNS Linac", This Conference.

LINAC R&D IN KOREA*

Won Namkung
Pohang Accelerator Laboratory, POSTECH, Pohang 790-784, Korea

Abstract

A 2-GeV linear accelerator is constructed as an injector to the Pohang Light Source (PLS), the first large-scale accelerator complex in Korea. It is a national synchrotron radiation users' facility for basic and applied science research. The PLS storage ring is a third generation machine with a low-emittance, and it has been serving users since September 1995. With the success of this construction project, there are strong demands on accelerator facilities for various applications, such as a neutron facility for transmutation and energy production called the KOMAC-project, a nuclear data center, a mini-cyclotron for radioisotope production. Most of linac R&D programs are subsystems in the low-energy end/or special components to improve the performance of the existing subsystems of the PLS linac. We present the current accelerator status, R&D activities related to linear accelerators at PAL, and the proposed accelerator programs in Korea.

1 INTRODUCTION

In the early 1960's, there were three particle accelerators in Korea: a 1.5-MeV cyclotron at the Seoul National University (SNU) and two Cockcroft-Walton type accelerators both at the Korea Atomic Energy Research Institute (KAERI) and at the Yonsei University. The cyclotron at SNU was used for accelerator physics studies. While the KAERI machine was used for neutron production via the D-T fusion reaction by 240-keV beams, the 300-keV machine at Yonsei produced proton and Lithium beams for various physics experiments. In the late 1970's, SNU constructed a 1.5-MV Tandem Van de Graaff for materials research.

Recently, there are many imported facilities and equipment related to the particle accelerator technology mainly for medical and industrial applications. In 1980's, the Korea Cancer Center Hospital (KCCH) imported a 50-MeV cyclotron and a 22-MeV microtron for medical treatment. A survey of research and medical accelerators in Korea is listed in Table 1.

The PLS is, therefore, the first large-scale accelerator complex in Korea. It is a national synchrotron radiation users' facility for basic and applied science research consisting of a 2-GeV linear accelerator as a full-energy injector and a low-emittance storage ring.

In 1988, the Pohang University of Science and Technology (POSTECH) initiated the PLS project with financial support from the Pohang Iron and Steel Company (POSCO), and the government joined in the project in 1989. The accelerator construction was officially completed at the end of 1994, and it was open to users in September of 1995 with two beamlines initially. There are now eight beamlines. A commercial company, LG-Semiconductor, built its own beamline for lithography, and the Kwangju Korea Institute of Science and Technology (KJIST) built its own beamline with support from the Kumho Business Group.

With the success of the PLS project, there are strong demands on accelerator facilities for various applications: the KOMAC-project for nuclear transmutation and energy production, a neutron facility for nuclear data production and evaluation, a FEL driver, industrial accelerators, and a 13-MeV cyclotron for medical radioisotope production, and others. We describe briefly recent activities for these accelerators along with R&D activities in the following sections.

Table 1: Survey of accelerators in Korea.

Research Accelerators			
Ion	0.4–3.0 MV Van de Graaff	8 Research institutes	Basic R&D
Electron	1.0 MeV Electro-Static	SHI	Environment R&D
	2.0 MeV ES	ADD	NDT
	8.0 MeV Microtron	KAERI	FEL
	0.1 GeV	PAL	Nuclear Data
	2.0 GeV	PAL	Light Source

Medical Accelerators			
Linac	5 ~ 20 MeV	~60 Hospitals	Therapy
Microtron	22 MeV	KCCH	RI production
Cyclotron	50 MeV 18/13 MeV 16/13 MeV	KCCH SNU Samsung	Therapy, PET PET PET

* This work is supported both by the Ministry of Science and Technology, Korea and the Pohang Iron & Steel Company.

2 POHANG ACCELERATOR LABORATORY

2.1 PLS Status

The 2-GeV injector linac consists of a 100-MeV preinjector and 10 SLAC-type regular modules, with 4 accelerating sections fed by each klystron [2]. Recently, we installed another module with 2 accelerating sections to improve the machine availability. Each module also has a SLAC-type Pulse Compressor with an average energy gain factor of 1.5. Since we use 80-MW-class high-power klystrons, each regular module is able to provide beam energy of 200 MeV with microwave power of 50 MW. The beam injection to the storage ring takes usually 2-5 minutes with 10-Hz and 1.5-ns pulses.

The PLS Storage Ring has a TBA-lattice structure with 12 super-periods with circumference of 280 m. There are two straight sections allocated for the RF-cavities and the injection system. Aluminum vacuum chambers are machined by an outside vendor and welded in-house. The RF system uses 4 RF klystrons of 60-kW to support a beam current of 400 mA at 2.0 GeV and 250 mA at 2.5 GeV. We demonstrated beam energy ramping to 2.5 GeV from 2.0 GeV, and we will provide 2.5 GeV beams from the second half of 1998.

Table 2 shows hours of the total machine operation and user service mode. We operated the linac for 5,480 hours and the storage ring for 4,840 hours in 1997. The user service time is 3,600 hours with the machine availability of 91.4% in 1997 and 92.4% in the first half of 1998. The machine fault statistics are shown in Table 3 for both the injector linac and the storage ring. The most frequent failure was the modulators in the linac and the injection system in the storage ring. We have experienced various beam instabilities, especially the coupled-bunch instability in high-current operations. Therefore, we are developing the longitudinal feedback system in collaboration with SLAC.

Table 2: Statistics for total machine operation and user service mode.

Machine operation (hours)				
	'95[1)]	'96	'97	'98[2)]
Linac	1,870	4,810	5,480	2,848
SR	1,820	4,680	4,840	2,657
User service				
Plan	1,275	3,236	3,960	2,400
Actual	1,142	3,034	3,618	2,222
Availability	89.6 %	93.8 %	91.4 %	92.6%

[1)] 2nd half year, [2)] 1st half year.

2.2. PAL Test-linac and Nuclear Data Center

Another electron linac, called PAL Test-linac with a beam energy of 100 MeV, was recently constructed in the PLS linac tunnel for R&D activities, such as experiments for development of special electron guns, a free electron laser (FEL), neutron generation, and a slow positron source.

The PAL Test-linac consists of a thermionic RF-gun, an alpha magnet, four quadrupole magnets, two SLAC-type accelerating sections, a quadrupole triplet, and a beam analyzing magnet [3]. With a temporary klystron-modulator, it produces 75 MeV, 30 mA beams at 3 μs and 10 Hz. The machine parameters and achieved values are shown in Table 4.

As applications of the PAL Test-linac, we proposed a pulsed neutron facility for nuclear data production and evaluation. In order to support the nuclear-power development program and the nuclear R&D applications in Korea, KAERI decided to establish the Nuclear Data Center to produce and evaluate nuclear data. Among various kinds of neutron sources (reactors, accelerators, and radio-isotopic neutron emitters), an accelerator-based neutron source is the most efficient one for high-resolution measurements of microscopic neutron cross sections. It produces short bursts of neutrons with a broad continuous energy spectrum by nuclear reactions of energetic photons or charged particles. Especially, an electron linac is a useful tool for the neutron time-of-flight (TOF) measurement as an intense pulsed source. The Test-linac will be jointly utilized for the Nuclear Data Center.

Table 3: Machine fault statistics in 1996-1997.

Storage Ring		Linac	
RF system	65	Modulator	127
MPS system	48	Control system	35
Control system	28	MPS system	30
LCW system	19	Timing system	25
Vacuum system	18	Vacuum system	8
Interlock system	13	Power failure	8
Timing system	12	Microwave system	3
Power failure	6		
Injection system	5	E-gun	1
Total	**214**	Total	**231**

Table 4: Machine parameters of Test-linac.

Beam Energy	100 MeV (75 MeV*)
Beam Current	100 mA (30 mA*)
Pulse Width	6 μs (3 μs*)
Energy Spread	< 1 % (3 %*)
Repetition Rate	60 Hz max. (10 Hz*)
Norm. Emittance	< 30 πmm-mrad

* Achieved values

For the pulsed neutron facility, the machine is to be upgraded with following parameters; The beam energy is at least 100 MeV with beam currents of 0.3 –5.0 A. The

pulse width is in the range of 10-1000 ns, and the repetition rate is 30–300 Hz. The target system uses water-cooled Tantalum. The average neutron yield is approximately 10^{13} n/sec. There will be three time-of-flight beamlines of 10 – 100 meters.

2.3 Linac R&D activities at PAL

There are several R&D programs at PAL to improve the existing machine and to explore possibilities for the future facility expansion and other applications. These are described in the followings.

2.3.1 RF-gun: A one-cell S-band RF-gun is fabricated in-house with a dispenser cathode and installed to the Test-linac. It is capable to produce beams of 1.0 MeV and average 600 mA with 2.0 MW RF-power [4]. It shows the beam energy range of 0.4-1.0 MeV with the peak energy of 0.9 MeV. Therefore, one needs an alpha magnet before injection into the main accelerating section.

2.3.2 Triode RF gun: The triode RF gun is a conventional triode gun with its pulser replaced by a S-band RF power source. A preliminary experiment to investigate the feasibility of this scheme shows that electrons could be bunched at 2.856 GHz, although the extracted bunch current would be relatively low. Presently, a coaxial cavity is being prepared in order to increase the bunch current.

2.3.3 Polarized electron source (PES): The PLS 2-GeV electron linac at PAL is the only facility applicable for nuclear and high-energy experiments in Korea. However, it is very difficult to have meaningful experiments due to the lower duty-factor for nuclear experiments. One of ways to utilize the existing 2-GeV electron beams to nuclear experiments is to use a polarized electron source for studying spin dependencies in the nuclear systems.

The polarized electron source consists of a polarized electron gun with a GaAs-type photo-cathode, a laser system operated at the wavelength near the GaAs band gap, and a polarimeter. In the first stage, we designed and constructed a test stand, which consists of a photo-cathode gun, a light source, a cylindrical condenser and a Mott chamber to develop the polarized electron source.

We used a bulk GaAs as a photo-cathode and supplied a few kV high-voltage. The energy of the emitted laser light is sufficient to photo-excite electrons to just above the photo-threshold for GaAs. Thus, a diode laser with photon energy of 1.56 eV and a maximum power of 20 mW will be used for the light source. The polarized electrons are bent to 90-degrees by a cylindrical condenser and measured the polarization by the Mott polarimeter.

2.3.4 Klystron-Modulator: A new modulator is designed to improve the current PLS 200-MW modulator. It employs an inverter type switching power supply to charge high energy density PFN capacitors, a command charging method to improve the system reliability, and a computerized automatic control system with a microprocessor. This modulator is compact, highly efficient, and reliable with easy remote-control capability. On the other hand, in the electron-positron linear collider program, the modulator efficiency is one of the most important issues in the operating cost. A prototype modulator, called the smart-modulator, is developed in collaboration with the C-band group at KEK. The initial test result shows that the efficiency of the 111-MW modulator system is 47.9% in compare with the design value of 59.3%.

2.3.5 Resonant ring: An S-band traveling-wave resonant ring is constructed for high-power RF tests on microwave components, such as ceramic windows and waveguide valves. This system is capable of delivering traveling microwaves of 4 μsec and 30 Hz with more than 200 MW power level, even though the peak power from the E3712 klystron is limited by 80 MW.

2.3.6 Waveguide valve: There needs a proper waveguide valve for the 80-MW RF system. It is very useful one for easy replacement and quick maintenance of klystrons. We adopted a new concept without limitations on power transmission. The new S-band waveguide valve consists of a U-shaped waveguide section with a pushrod assembly, a vacuum chamber with two H-corner sections and a scaling plate with two viton o-rings. We achieved a power transmission of more than 65 MW at a pulse with of 3.5 μsec and a pulse repetition rate of 30 Hz. It also shows an excellent reliability of the vacuum seal.

2.3.7 Portable cooling-water system; A stand-alone cooling-water system with the precision temperature control for the use of RF tests of microwave components, such as a resonant ring, a energy-doubler, and RF loads. The system consists of a centrifugal circulating pump, electric heater, air-cooled heat exchanger, direct digital temperature controller, and auxiliary components. The capacity of the maximum thermal dissipation is 3 kW with the temperature control range of $24 - 45 \pm 0.2^{o}$C.

3 KOREA ATOMIC ENERGY RESEARCH INSTITUTE: KOMAC-PROJECT

There has been a great demand on electricity along with a rapid economic growth in Korea. The national policy for constructing more nuclear power plants requires spent fuel treatment. As an optional concept, the Korea Atomic Energy Research Institute (KAERI) proposed an accelerator-based transmutation and energy production project called the KOMAC; the Korea Multi-purpose Accelerator Complex [5]. It adopts a 1 GeV and 20 mA CW proton linac for the driver of a 1000 MWth test reactor with electrical power of 300-400 MW. It is

capable to handle spent fuels from 2 units of 1 GW Light Water Reactors (LWR). There are two beam extraction areas, at 100 MeV for fast neutron generation and 260 MeV for medical application. The basic parameters of the KOMAC system are listed in Table 5.

In the first R&D phase of 1997-2001, it is to develop a low-energy end of 20 MeV consisted of an ion-source, RFQ, and CCDTL(I). It requires both positive and negative ion sources for beam extractions at 100 and 260 MeV. The RFQ operates at 350 MHz CW for 3 MeV and 20 mA. The minimum aperture of the vanes is 4.6 mm, and the total length is 2.4 m. The operating frequency of CCDTL is 700 MHz, and the length for 20 MeV is 30 m. The participating institutes in this R&D program are KAIST, PAL, and SNU: KAIST for ion sources, PAL for RFQ, and PAL and SNU for RF sources.

The main linac is suggested to use super-conducting structures for large apertures and reducing operating costs. Since the super-conducting linac technology is now being developed in many places, for example, at TESLA and JAERI, it is desirable for the KOMAC team to participate in collaboration research among interested groups.

Table 5: KOMAC basic parameters

Parameter	Specification
Beam energy	1.0 GeV
Beam current / power	20 mA / 20 MW
Particle	H+ (18 mA) / H- (2 mA)
Operational mode	CW (final), Pulsed (initial)
Accelerator Type	Ion Source / RFQ / CCDTL / Super-conducting Linac
RF system	31 Klystrons (700 MHz)
Beam extractions	100 MeV / 250 MeV
Electricity	68.5 MW
Cooling water capacity	60.0 MW (excluding reactor)
Overall Length	705.4 m

3.1 Ion Sources

A duoplasmatron H^+ ion source has been built at KAERI. It has a peak current of 30 mA with a normalized 90% emittance of 0.5 mm-mrad. While the Korea Advanced Institute of Science and technology (KAIST) is developing an H^- ion source, KAERI is responsible for an injector delivering both H^+ and H^-.

3.2 Radio frequency Quadrupoles (RFQ)

PAL is developing a 350 MHz RFQ which accelerates 50 keV H^+/H^- up to 3 MeV. The total length is to be 3 m with a minimum aperture of 2.4-mm radius. Full beam current will require 68 kW. Because of RF loss on wall surface, we still need total power of 400 kW.

3.3 Phase Matching Section

A phase matching section is required after RFQ for H^- since the frequency of CCDTL becomes 700 MHz. This section will be used as an alignment steer (two beams can be aligned independently). A system of quadrupoles and bunchers for transverse matching is also required in this matching section.

3.4 Coupled-cavity drift-tube linac (CCDTL)

KAERI is developing a CCDTL with the features of conventional DTL and CCL. The CCDTL accelerates both positive and negative ions from 3 to 100 MeV. It is easy to fabricate and install it on the structure without breaking vacuum. The total length is 29.8 m with total RF power of 1.5 MW. As an option, a 5-MeV RFQ is also considered. In the first phase, the first part of CCDTL is to be fabricated to deliver 20-MeV beams. In the second phase, 94.2-m CCDTL is to accelerate beams to 100 MeV.

3.5 Beam Extraction

A partial extraction of H^- beams is planned at both 100 and 260 MeV. A magnetic-stripping study shows that the threshold field for stripping an electron at 100 MeV is 1 T and one for 260 MeV is 0.8 T. Since one expects the emittance degradation in this system, there need more studies on a special magnet with a very sharp peak-field and a laser extraction method.

3.6 Super-conducting linac

A SNU team studies on this subject due mainly to save RF power and to have a large aperture size to reduce beam loss. However, there need more detailed studies on the capital investment cost and availability for the related technologies. In the preliminary investigation, there are three cryomodules: 100-140 MeV, 140-260 MeV, and higher than 260 MeV. The cryostats contain four 4-to 6-cells of 700 MHz niobium cavities. The transverse focus requires doublet quadrupoles in the outside of cryostats.

4 SEOUL NATIONAL UNIVERSITY AND SAMSUNG HEAVY INDUSTRY

4.1 Seoul National University (SNU)

SNU constructed a 1.5 MeV cyclotron in Physics Department in the early 1960's and a 1.5 MV Tandem Van de Graaff in Nuclear Engineering Department in the late 1970's. These are constructed as a graduate program. The 1.5 MV Tandem is being used for Rutherford back scattering (RBS), Photon induced x-ray emission (PIXE) analysis, and various nuclear cross-section measurements.

The Users Support Center at SNU purchased a Tandetron AMS from the High Voltage Engineering Europa. The nominal terminal voltage is 2.5 MV with the maximum of 3.0 MV.

4.2 Samsung Heavy Industry (SHI)

During the last few years, many industrial processes using the electron beam irradiation have been developed. In order to meet the industrial needs for irradiation technology, Samsung Heavy Industry established the accelerator development center and employed an ELV-type industrial electron accelerator developed by the Institute of Nuclear Physics (INP) in Novosibirsk, Russia in the mid-1970s. The ELV accelerator is characterized by the high voltage generation with a cascade coreless transformer.

The main parameters for ELV-type accelerators are as follows; Electron energy is 0.4 - 2.0 MeV, and beam power is no less than 20 kW within the whole energy range. SHI began to commercially manufacture ELV-type accelerators in collaboration with INP for various industrial applications, such as waste-water treatment, flue-gas purification, cross-linking of polyethylene, hardening of coatings and paints, graft polymerization, vulcanization of rubbers, deinsectization of grain, and fabrication of fiber glass plastics.

5 SUMMARY

We believe that we have established technological basis for accelerator related sciences, especially, through experience of the PLS construction. This accelerator community is to contribute the country for advancing basic and applied science research.

6 REFERENCES

[1] I. S. Ko, “Status of Pohang Light Source,” Proceedings. of EPAC’98 (Stockholm, Sweden, June 22-26, 1998).

[2] M. H. Cho, K. R. Kim, J. S. Oh, S. H. Park, I. S. Ko, and W. Namkung, “Status of PLS 2-GeV Electron Linac Performance,” these proceedings.

[3] H. S. Kang, J. Y. Choi, Y. J. Park, S. H. Kim, G. N. Kim, M. H. Cho, and I. S. Ko, “Beam Acceleration Results of Test Linac,” Proceedings of APAC’98 (Tsukuba, Japan, March 23-27, 1998).

[4] H. S. Kang, G. N. Kim, M. H. Cho, I. S. Ko, and K. H. Chung, “High Power Test of Thermionic RF-gun at the Pohang Accelerator Laboratory,” IEEE Trans. NS-44, 1639 (1997).

[5] B. H. Choi, C. K. Park, T. Y. Eom, H. E. Ahn, Y. S. Cho, J. M. Han, J. H. Lee, W. S. Park, S. S. Kang, W. S. Song, Y. K. Kim, C. K. Hwang, J. H. Chang,, S. Y. Suh, M. H. Yang, and J. K. Chung, “The KOMAC Project,” these proceedings.

REVIEW OF NEGATIVE HYDROGEN ION SOURCES HIGH BRIGHTNESS/HIGH CURRENT

J. Peters
Deutsches Elektronen-Synchrotron, DESY, Notkestraße 85, 22607 Hamburg, Germany

Abstract

Due to the development of reliable H^- ion sources, charge-exchange injection into circular accelerators has become routine. This paper reviews recent developments in negative hydrogen ion sources. The underlying physics, operating parameters and beam characteristics of selected sources will be described and compared.

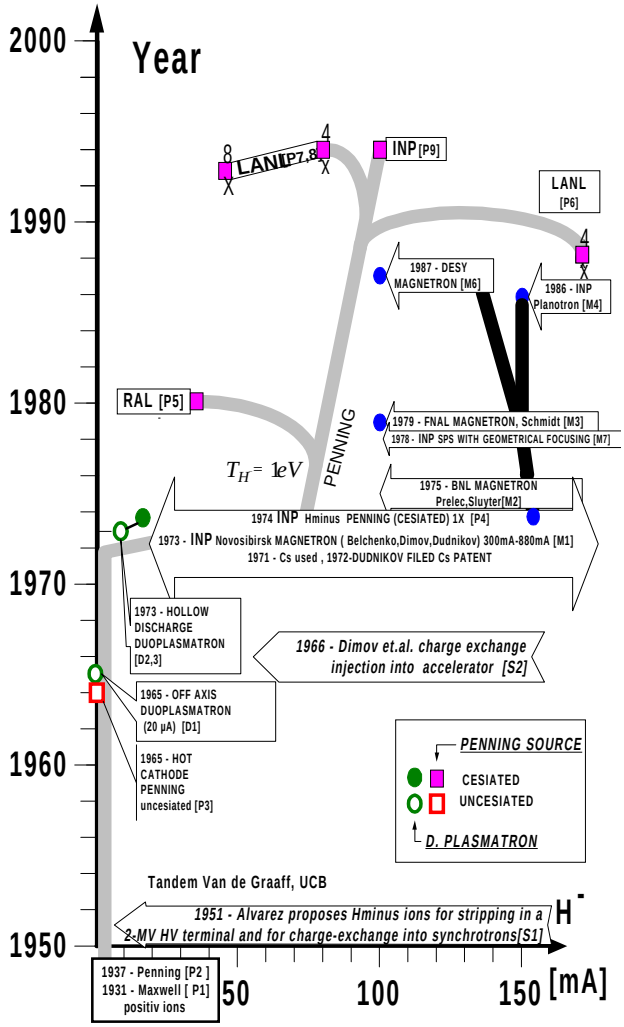

Figure 1: History of duoplasmatron and surface source development.

1 INTRODUCTION

This paper will deal primarily with H^- sources used as injectors for high energy accelerators. Usual (high) H^- currents are 10 to 100 mA dependent on the duty factor. It has taken two decades to reach these currents since Alvarez proposed H^- ions for stripping in a high voltage terminal and for charge-exchange injection into synchrotrons (Fig.1 S1) [1].

Duoplasmatrons (D1,2,3) with their low currents are excluded as well as multi aperture sources which have high currents but low brightness .

1.1 Definition of Brightness and Emittance

Several definitions of brightness are in use. The following relation is adopted here :

$$B = \frac{I}{\varepsilon^N_{x,90\%} \quad \varepsilon^N_{y,90\%}} \quad ,$$

where $\varepsilon^N_{x,90\%}$ is the energy normalized emittance in the (x ,x') plane for the contour containing 90% of the brightest beam and

$$\varepsilon^N = \varepsilon \beta \gamma \quad ,$$

with : $ß = v_{BEAM}/c$ and $\gamma = 1/(1-\beta^2)^{1/2}$.

In the ideal case the contour is an ellipse and ε is the product of the semimajor and semiminor axes times π. Emittances quoted in conventions other than 90% area values can be converted using the following equations :

$\varepsilon_{90\%} = 4.6\ \varepsilon_{rms}$ and $\varepsilon_{90\%} = 1.125\ \varepsilon_{4rms}$ assuming a Gaussian distribution.

1.2 Emittance Scanners and Emittance Errors

Emittance values found in the literature may differ very much even for the same source type and current. For this paper the labs were asked for emittances and the related current, type of emittance scanner, distance from scanner to extractor and other relevant source data. Most labs now use slit-multiwire scanners [DESY, BNL, RAL] or electrostatic sweep scanners (Allison) [LANL, LBL]. These devices are able to measure rms and area emittances. The pepperpot is also still in use. It measures only area emittances. In recently published emittance collections [2] area definitions have been used.

2 SURFACE SOURCES (SPS)

After the discovery of cesiation of surfaces at INP in 1971, the attainable H^- currents increased dramatically. The magnetron was invented (see Fig.1 M1)[3] and the penning source developed to its present standard (P4) [4] in Novosibirsk at INP .

2.1 Magnetron

Magnetron technology was transferred from INP to BNL (M2) [5] and from there to FNAL (M3) [6]. There was a mutual exchange between these two labs. In 1987 magnetron plans were brought from FNAL to DESY.

Figure 2 shows the structure of a magnetron in front and side views. It consists of a central cylindrical cathode surrounded by an anode. The discharge voltage, U_D , is typically ≈150 V and the current 40 A. A magnetic field (≈0.17 T) is parallel to the cathode axis. Hydrogen gas is introduced from the top by a pulsed gas valve.

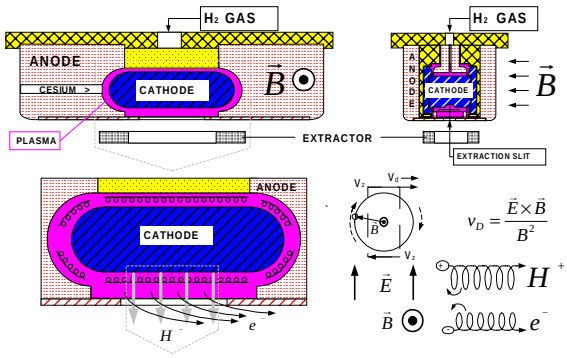

Figure 2: Magnetron source and E×B drift.

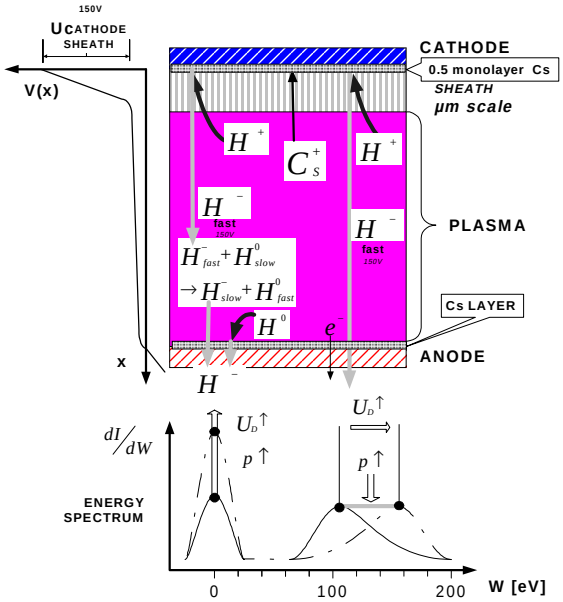

Figure 3: Production of H^- at cathode and anode of the source and their energy spectrum.

Cesium is obtained by heating metallic cesium or a mixture of cesium chromate and titanium. The mixture is available as pellets or powder.

H^- ions are extracted at 18 kV (FNAL, DESY) or 35 kV (BNL) together with electrons. Modern magnetrons have geometric focussing, developed at INP in 1978, with a groove in the cathode and slit extraction followed by a bending magnet [7]. Another possibility is to dimple the cathode and to use a hole as aperture toward the extractor electrode [8].

The electric field between anode and cathode leads to an E×B drift around the cathode, which is shown on a magnified scale Fig.2 (lower part). Positive and negative ions move in the same direction. There is no movement parallel to E as particles gain as much energy as they lose. But parallel to E×B there is a resulting difference v_d (see Fig.2). Charges are not separated due to this effect. A dense plasma is produced.

If one looks with a bigger magnification at the space between anode and cathode (Fig. 3) one notices a transition zone, the so-called sheath, between the plasma and the cathode. Here the potential drops to cathode level. There is only a small potential difference across the plasma. H^+ ions generated in the plasma are accelerated through the sheath. They produce H^- ions at the cathode surface, which is covered in the ideal case with approximately half a mono layer of Cs in order to minimize the surface work function. These H^- particles are then accelerated to U_D passing through the sheath. Some move through the plasma and are extracted. They form a maximum in the energy spectrum (Fig.3 lower part). Others hit slow H^0 particles and exchange speed and charge; this is resonant charge exchange. In this way slow H^- ions are produced. Slow H^- can also be produced by H^0 hitting the cesiated anode surface.

Due to these mechanisms a low and a high energy peak appear in the energy spectrum. To increase the fraction of low temperature ions one can increase the source pressure and discharge voltage U_D, as indicated in the plot. In addition, the position of the high energy peak can be changed by varying U_D and the amplitude lowered by increasing the pressure.

2.2 Semiplanotron

The semiplanotron (see Fig. 4) is an optimized magnetron, with geometric focussing and without a discharge at the back of the cathode. These modifications make it more efficient. Operational experience is, however, limited. Source lifetime may be limited by the accumulation of sputtered particles from the cathode as a result of their drift path being blocked. This might result in a short circuit, consistent with DESY experience.

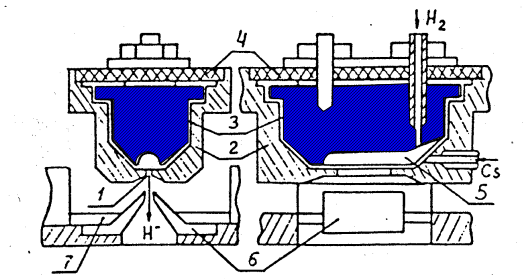

Figure 4: The semiplanotron source. 1. emission slit, 2. anode, 3. cathode, 4. insulator, 5. groove, 6. extractor, 7. steel inserts.

2.3 Penning

In order to avoid the high energy peak of the magnetron spectrum the cathode surface should not face the ion extraction aperture. This is how the penning source is constructed (see Fig. 5).

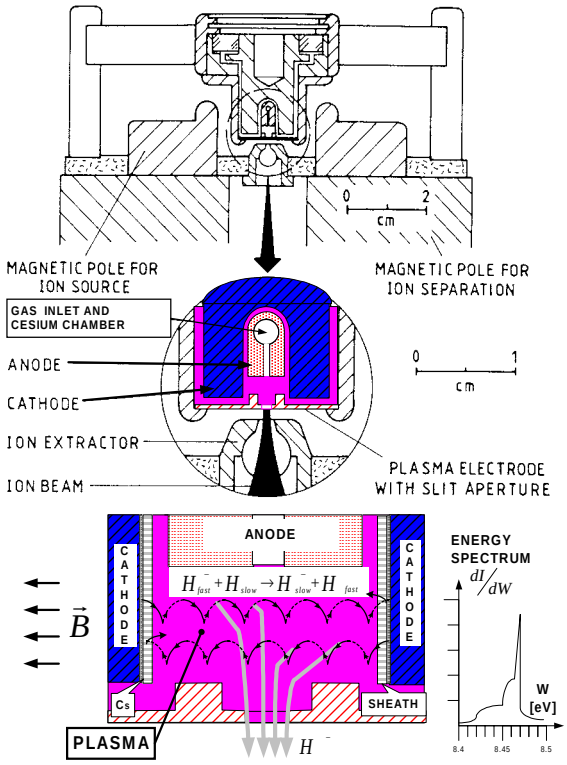

Figure 5: Penning source schematic and its energy spectrum.

A strong magnetic field parallel to the electric field of the sheath guides electrons and ions on cyclotron spirals from cathode to cathode. Fast H^- ions are generated at the cathodes as in the magnetron. They are slowed down due to the charge exchange reaction as they migrate to the plasma aperture. There is only one low energy peak and the H^- temperature has been measured to be less than 1eV [9].

2.4 Multicusp Surface-plasma (converter) Source

Fig. 6 shows a multicusp surface-plasma source. A discharge is produced with filaments. The plasma is confined by a multicusp field. A converter biased at ≈300 V is located in the middle of the source. Secondary emission of negative ions takes place. The H^- ions are produced by H^+, H_2^+ and H_3^+ bombarding the converter. Cesium is injected into the source to increase the H^- yield. Self extraction of H^- takes place with focussing provided by the curvature of the converter. A magnetic filter is used to repel electrons.

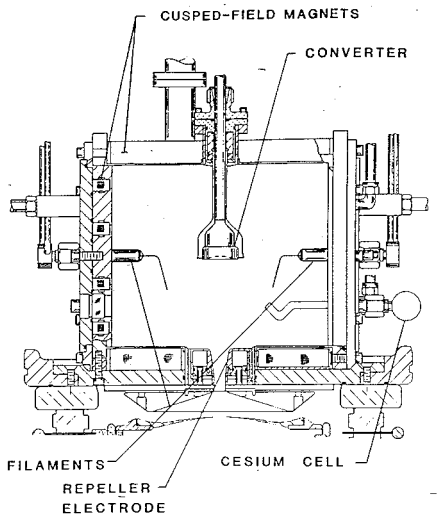

Figure 6: LANL surface production multicusp.

3 VOLUME SOURCES

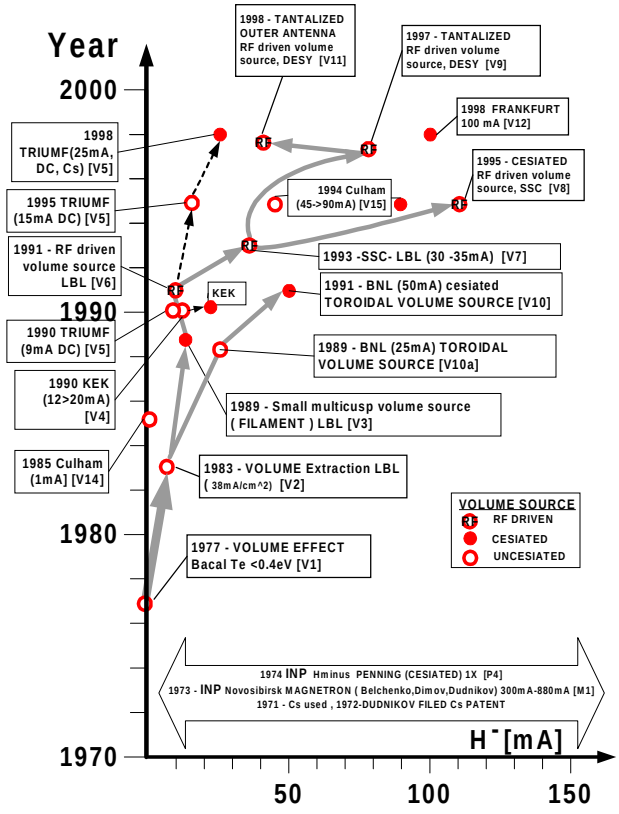

Figure 7: History of volume source development.

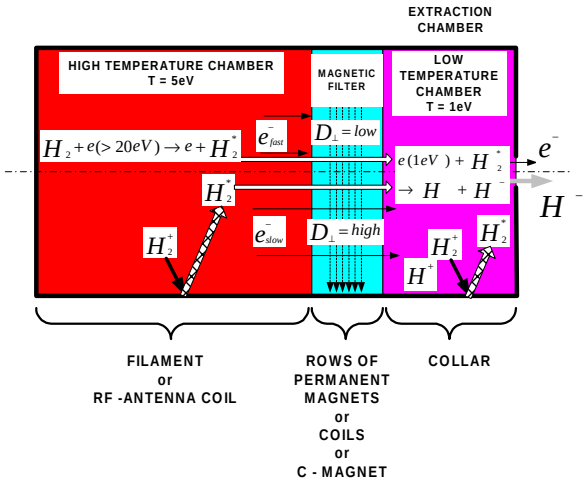

Figure 8: Tandem source for volume production.

In 1977 M. Bacal [10] discovered volume production for H^- generation. This started the development of a new type of sources (Fig. 7). The volume source consists of two chambers, which are connected by a magnetic filter (Fig. 8). In the high temperature chamber energetic electrons hit H_2, which become vibrationally excited. Excited molecule are also produced at the chamber walls out of H_2^+ and H^+. Electrons from the high temperature chamber move by diffusion through a perpendicular magnetic field into a second chamber. Whereas high energy electrons are effectively blocked, slow electrons collect in the second chamber. In this low energy chamber, low temperature 1eV electrons attach to the H_2^* producing H^- ions.

Multi-cusp magnets are used to confine the plasma.

3.1 Filament Volume Source

The first volume sources were uncesiated and had filaments. Currents of up to 20 mA DC [11] were reached with small sources and 45 mA [12] (Fig. 6 V15) with larger ones. Cesiated currents of 25 mA DC [13] and 90-100 mA at 6% duty factor [12,14] V12 have been achieved. The lifetime of these sources is limited by that of the filament.

3.2 RF Volume Source

The filament was first replaced by an rf antenna coil in 1991 [15]. Fig. 9 shows the DESY RF volume source; it is similar to the sources of LBL and SSC. The antenna heats the high temperature chamber and the filter is constructed with two rows of permanent magnets. The low temperature chamber is located inside a collar.

The antennas are coated to reduce plasma modulation by the rf voltage and sputtering. With uncesiated rf volume sources 35 mA were reached. At DESY the collar was biased and tantalum coated, and currents of 80 mA were achieved uncesiated.

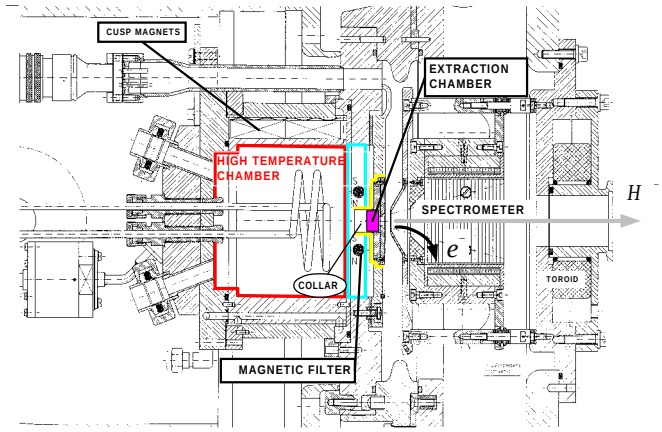

Figure 9: RF driven volume source.

The antennas used by LBL, SSC and DESY were all coated by the same manufacturer. An analysis of the coating found a high percentage of K and Na (Table 1). Different contents of potassium might have contributed to reported differences in source performance.

Table 1: Results of Analyses of the Antenna Coating

ELEMENT	PERCENTAGE
Si	46.9 %
Ti	29.6 %
K	15.2 %
Al	5.7 %
Na	2.6 %

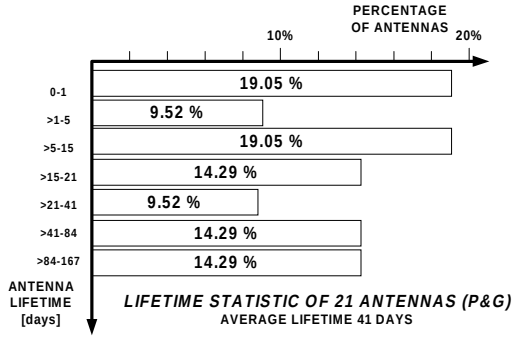

Figure 10: Lifetime statistic of the coated antennae.

DESY has the longest experience in running this type of volume source with the P&G antenna. The performance of the antennae is first limited by spots in the coating. If it survives this period then cracks due to sputtering of the coating material become the lifetime limitation. The average lifetime of only 41 days is higher than that of a filament. However ≈50% of all antennae fail during the first 15 days. This unpredictability is a serious problem for reliability.

In addition it was found that sputtered glass from the coating insulates the chamber walls. After such an event it is necessary to do a careful time consuming cleaning of the whole source. Based on this experience a new rf coupling was developed, which couples through a ceramic of Al_2O_3. This type of ceramic has a sputter rate seven times lower than that of glass and three times lower than Ti.

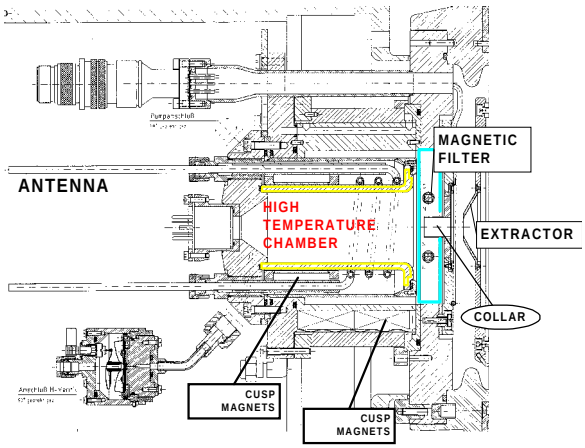

Figure 11: The DESY volume source with an rf coil shielded by Al_2O_3 ceramic.

A source of this type, Fig. 11, was run for 2800 h at 40 mA with a duty factor of 0.05 % and a pulse length of 100 µsec. No degradation in performance was observed.

4 SUMMARY

Table 2: Collection of Source Data

tested uninterrupted run [h]	SOURCE TYP	DUTY FACTOR [%]	$\varepsilon_{n,90\%}$ [π mm mrad]	REF.	BRIGHTNESS [mA/m² mrad²]	C_s CONS [mg/day]	CURRENT I/mA
7224 4320	MAGNETRON 16 years a.	0.05 0.48	.98 1.2	[16] [17]	6.4 4.9	2.8	60 (->120 75
	PLANOTRON	0.25	0.14	[19]	500	24	100
960	PENNIN 15 years. exp	2.5 2.5	0.3 ->0.1	[18] [19]	670	24	35 (->170 80
500	VOLUM FILAMEN 9 years a.	100	0.75	[20]	3.6	NO	20
	FILAMEN	100 6	0.52(0.6 ≈0.23	[21] [22]		5 29	20 100
72-984	RF Antenna Plasm	0.1	0.5	[23]	12	NO but K	30 (->80
	RF Antenna Plasm	0.1	0.5	[24]	28	Cs	91 (->120
2800	RF out of	0.05	0.75	[25]	7.2	NO	40

For high energy accelerators it is important to have a reliable source. Magnetrons have been used for the longest time in accelerators and have tested runs of 7000 h. They have, however a poor brightness. Penning sources provide the highest brightness but run for only about 900 h.

The best tested volume source is a DC 6 - 20 mA source, which runs (limited by the filament) for 500 h.

A new rf volume source with an rf coil shielded by ceramic exhibited no degradation in performance after a run of 2800 h.

According to recent results [11, 14] the future prospects of filament volume sources as high duty factor accelerator sources are very good.

Since the antenna problem was solved [27] rf sources are expected to replace magnetrons. They have a higher brightness, higher reliability and are easier to maintain.

5 ACKNOWLEDGEMENTS

The author is grateful for the contribution of the following colleagues at DESY :

N.Holtkamp, I.Hansen, H.Sahling and R.Subke. I wish to thank the technical groups at DESY for their support, and M. Lomperski of DESY for helpful suggestions to the wording of the report. The support of the source groups of BINP, BNL, FNAL, LANL, LBL, RAL and TRIUMF is gratefully acknowledged.

6 REFERENCES

[1] L.W. Alvarez, Rev. Sci. Instrum. 22,705(1951)

[2] J. R. Alonso, Rev. Sci. Instrum., Vol. 67, No.3, March 1996

[3] Yu.I. Belchenko, G.I. Dimov, V.G. Dudnikov, NUCLEAR FUSION 14 (1974)

[4] V.G. Dudnikov, Proc. IV All-Union Conf. on Charged Particle Accelerators, Moscow, 1974,Nauka 1975, Vol 1, p. 323

[5] K.A. Prelec, Th. Sluyters, M. Grossman, IEEE Trans. Nuc. Sci. NS-24(1977) 1521

[6] C.W. Schmidt, C.D. Curtis, IEEE Trans. Nuc. Sci. NS-26 (1979) 4120 }

[7] C.W. Schmidt, Proceedings of LINAC90, Albuquerque, New Mexico, September 10-14, 1990, 259-263 (1990).

[8] J.G. Alessi et al., BNL – 42426, ICIS 1989, Lawrence Berkeley Lab, July 10-14, 1989

[9] J.D.Sherman et al., Rev. Sci. Instrum. 62 (10), October 1991

[10] M. Bacal et al., Phys. Rev. Lett. 42 1538, J. Phys. (Paris) 38, 1399 (1977)

[11] T. Kuo et al.,Rev. Sci. Instrum. 67 (3), March 1996 and private communication

[12] A.J.T. Holmes et al, Rev. Sci. Instrum. 65 (4) April 1994

[13] private communication with T. Kuo , TRIUMF

[14] private communication with K. Volk and A. Maser

[15] K.N. Leung, G.J. DeVries, W.F. DiVergilio and R.W. Hamm, Rev.Sci.Instrum.62(1),100(1991)

[16-27] private communication with DESY, BNL, RAL, BINP, TRIUMF, TRIUMF, FRANKFURT UNIVERSITY, LBL, LBL, DESY, LANL, DESY

EMERGING INDUSTRIAL APPLICATIONS OF LINACS

A. M. M. Todd
Northrop Grumman Advanced Energy Systems
9 Jeffrey Lane, Princeton Junction, New Jersey 08550, USA

Abstract

Three emerging linac market areas are discussed: contraband detection using tandem ion accelerators; x-ray sterilization of food using high-power electron linacs; and large volume material surface processing with radiation from superconducting RF accelerator-driven free electron lasers. The opportunities are described and simple economic models are applied to assess the viability of linac technology market penetration. The high cost of ownership is considered a potential problem for accelerator systems in the inelastic contraband detection market. However, the food sterilization and material processing markets appear to have sufficient headroom to permit successful accelerator technology penetration. Of these three areas, food sterilization is likely to be the application that could first experience significant growth early next century.

1 INTRODUCTION

Medical applications, particularly clinical x-ray systems, continue to dominate the industrial market for linear accelerators. However, several developments suggest that significant new markets may soon emerge.

Among these markets is food irradiation which for some time has been pushed within the technical community but has never developed sufficient market pull to secure a commercial foothold. Irradiation should benefit from the recent Food and Drug Administration (FDA) approval of x-rays for the cold pasteurization of red meat, poultry and pork.

Another growth area, driven by Federal Aviation Administration (FAA) and Department of Defense (DoD) funding, is contraband detection. In addition to airport hand baggage, inspection of large cargo volumes and containers at airports, seaports, road and rail border crossings and military bases is a growing market. The current market surge is dominated by advanced x-ray devices and chemical detection "sniffers", but larger linac systems may have a niche in container inspection. Increasing terrorist activity is once again focusing a spotlight on higher performance explosive detection systems (EDS).

Further off in time, ultraviolet (UV) and infrared (IR) micromachining and surface material processing with high-power, linac-driven, Free-Electron Lasers (FEL) has the potential to evolve into a major and varied market. Many applications, principally in polymer and metal processing, are already established and their commercialization is limited only by the economics of available light sources.

The following three sections focus on Contraband Detection Systems (CDS) utilizing tandem ion accelerator-generated gamma-rays for resonance imaging, cold pasteurization of red meat using high-power electron accelerator-generated x-rays, and high-volume surface material processing with UV and IR radiation from a superconducting-RF FEL. The applications, their performance requirements and their economic potential to achieve market penetration are assessed.

We stress the platitudes that successful technology insertion requires market pull and not simply technology push, and that a technology cannot simply be thrown over the wall to thrive without nurturing. Economic considerations are almost always critical, but market infrastructure, operational simplicity, robustness, reliability, availability, maintainability, inspectability (RAMI or the "ilities") and after sale support are all vital.

2 CONTRABAND DETECTION

A principal motivation for contraband detection systems is the increasing number of successful terrorist incidents. Most recently, the Nairobi and Dar es Salaam US Embassy attacks and the despicable incident in Omagh have again heightened awareness of terrorist activities. While we are all aware of the PanAm 103 and TWA 800 incidents, one of which was definitely caused by a bomb, it is not so widely known that there are hundreds of annual attacks at US bases abroad, though few are as severe as the recent al Khobar Towers incident.

Hence, there is a significant opportunity for contraband and explosive detection systems of various kinds: at seaports and airports to inspect hand baggage, cargo and to otherwise detect smuggling; for force protection of bases and embassies; and at border crossings to inspect trains and trucks.

The market characteristics are somewhat fickle with significant peak-to-peak funding oscillations and sales opportunities that often seem to parallel occasional tragedies. The market also remains largely inelastic due to the high cost of ownership (COO) of effective detection systems coupled with the low probability of incidents actually occurring in the first place or being prevented by the system.

InVision Technologies is the market leader with the $1M CTX 5000 x-ray device that is deployed at airports worldwide and is the only presently FAA certified EDS for hand baggage. Lockheed Martin has recently introduced the cheaper L-3 system, while Vivid Technologies and

others market simpler units. Thermedics is a leading supplier of competing chemical "sniffer" systems.

The FAA certification requirement for baggage inspection systems is a throughput of 450 bags per hour. False Alarm Rate (FAR) and detection rates are not public, but simple intuition suggests that values of FAR ≤ 10% and detection probabilities ≥ 90% are probably required to prevent significant transit delay. An interesting economic point is that the cost to install CTX 5000 systems in the 75 busiest airports is estimated at around $2.2B [1]. This figure is greater than the entire 1995 airline industry profit and explains the COO market penetration difficulty of EDS, given the very few US airline bomb incidents to date.

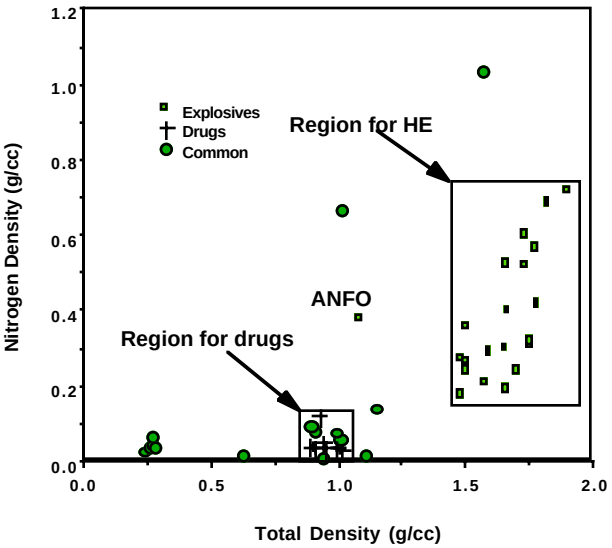

Figure 1: Nitrogen-based High Explosive (HE) identification using the gamma resonance CDS technique [2].

Gamma resonance imaging holds great promise as an EDS technology. Here 1.76 MeV protons impinging on a ^{13}C target produce γ-rays that are arranged to pass through an inspection target. A high-current tandem accelerator is selected for wall-plug efficiency reasons. At a particular detection angle, the γ-rays are resonant with ^{14}N. Hence, measuring the resonant γ-rays determines the sample nitrogen density, while the non-resonant γ-rays yield the total sample density. Figure 1 illustrates that these two simultaneous measurements provide excellent discrimination and the potential for high detection probabilities with corresponding low FAR for nitrogen-based explosives. Tomographic inversion leads to small voxel identification of suspicious material that in principle permits the identification of sheet explosives. Gamma resonance CDS is a relatively immature technology, which is projected to meet FAA throughput and performance targets, but at a higher cost than the competing systems.

In analyzing EDS systems, we have assumed a 15% cost of capital, a 5% of capital cost per annum maintenance expense, $150K annual operating cost comprised of $100K for operating personnel and $50K for other costs and services over a 7 year system lifetime with straight line depreciation. This results in a net present COO of ~$2.0M for a $1M x-ray system and ~$4.0M for a gamma resonance CDS. An interesting figure of merit is that 450 bags/hour, 18 hours a day, 350 days a year for 7 years result in a cost of 5¢/bag per $1M COO. Even if gamma resonance technology matures and can outperform multiple units of other systems as is projected, the high COO will remain a problem in this market unless the driving forces change significantly.

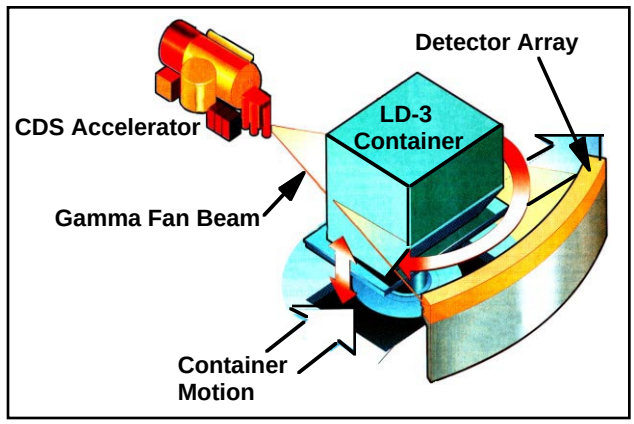

Figure 2: LD-3 airline cargo container CDS interrogation concept [2].

Force protection and airline cargo examination, as indicated in figure 2, have been projected as possible niche markets for the higher potential performance of gamma resonance CDS. Heimann Systems already markets static and transportable x-ray systems, based on conventional electron linac technology, that are used to inspect trucks and other cargo. However, despite strong DoD and Congressional interest, until the recent Embassy bombings, US action on force protection was proceeding conventionally and somewhat slowly, and the need for airline cargo inspection was again being questioned. US Customs interest for train and road border crossings, airframes and sea containers continues to lag DoD, State Department and FAA interest.

Thus, we are forced to conclude that the present outlook for market insertion of accelerator-based gamma-resonance CDS is mixed. However, the rapid swings in attention and funding within this market place suggest that the situation could again quickly reverse in the future.

3 COLD PASTEURIZATION

The motivation for cold food pasteurization is strong and receiving increasing recognition. The US Department of Agriculture (USDA) estimates that $30B in annual hospitalization costs and lost earnings result from contaminated food. The Council for Agricultural Science and Technology (CAST) estimates greater than 33 million annual US cases of food contamination illness and more

than 9000 deaths. Recently, the National Academy of Science, asked by Congress to review the situation, estimated 81 million annual cases of food contamination illness, higher than CAST, and expressed the need for a more centralized and modern Government food safety administration.

In addition to illness, radiation treatment reduces spoilage and adds shelf life of up to a month. This results in additional home market value added and opens new overseas markets because of the economic opportunity for seaborne transportation of US produce.

The FDA has recently approved x-ray cold pasteurization in addition to γ-ray and electron sterilization of red meat, poultry & pork. USDA radiation dose and packaging guidelines are imminent with a 30 to 60 days public review period to follow. We have chosen here to focus on x-rays because they permit significantly more uniform irradiation of thicker product. Within the permitted dose range, direct electron irradiation, while possible at tens rather than hundreds of kilowatts, is limited to boneless product such as ground beef patties.

An important paradigm changes is the recent emergence of a significant fraction of consumers (> 20%) who are willing to pay a premium for safe meat and the impending availability of economic, high-power electron accelerators. This yields the opportunity for near term market insertion shortly after the year 2000 because of the existence of value added headroom through market acceptance of a premium product. This leads to the price elasticity that was missing in the previous EDS market and opens the door for the introduction of a new accelerator product.

We have long been promised that the medical and food sterilization markets have been ready to explode. However, although imported spices have been irradiated for years, only 1B lbs of food is presently irradiated annually worldwide. Of interest is Food Technology Services in Florida, which already produces the premium brand "Nations Pride" poultry with cobalt source irradiation. However, radioactive sources cannot be turned off like accelerator-based sources, have a high environmental disposal cost and issues associated with high throughput.

Similarly, in the more accessible, lower throughput, higher value added medical sterilization market, Impela devices, Titan Scan systems, and most recently the Ion Beam Applications Rhodotron, have been competing for a limited number of orders. The continual drive towards the "greening" of processing technologies suggests that present chemical sterilization will continue to be displaced.

In evaluating the market economics, we assume a service provision business structure for the plant and present year money throughout. A 0.5 MW electron accelerator can generate 40 kW of x-rays that deliver a 1.8 kilogray exposure to 200 metric tons of red meat per 8 hour accelerator shift. At 50 mils/ kW-hour and greater than 50% wall plug efficiency, this leads to a $200K annual cost of electricity and other services. Splitting the mark up that consumers have indicated a willingness to pay for a safe premium product, yields ~ 5¢/lb added cost for irradiation to the service provider, plus a further 10-15¢ for the meat processor and retailer for around 5% of the final product cost. We baseline a $7.5M plant capital cost for the high-power accelerator, conveyor system, shielding and support systems, a 15% cost of capital, 2.5% of capital cost per annum maintenance expense, $100K annual personnel operating cost for a 7 year system lifetime with straight line depreciation.

As shown in figure 3, this leads to a 2.5¢/lb earned value break-even point. Earned value is defined to be the net present value of the free cash flow over the lifetime of the plant. In the vicinity of the nominal 5¢/lb charge, which is removed from the break-even point, there is relative insensitivity to interest rate, plant capital cost and electrical efficiency, which influences the choice of drive accelerator. It is this insensitivity that suggests there is a high probability of successful technology insertion at price levels the market will tolerate. However this also implies that early on in the development of the market, competition for the large available sales volume, which will expand beyond premium brands, will drive the acceptable processing cost for the customer much closer to break-even. Here, sensitivity to efficiency and plant capital cost will become critical discriminators in obtaining adequate margin and the successful accelerator technology will have to be both very affordable and highly efficient.

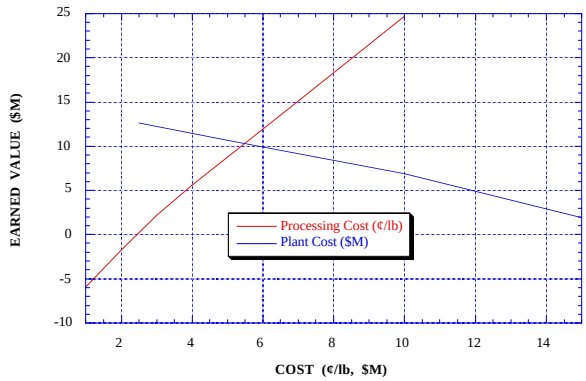

Figure 3: Earned value as a function of plant cost ($M) and unit processing cost (¢/lb).

4 FEL MATERIAL PROCESSING

The third area we consider is large volume material processing with an IR or UV FEL. A superconducting-RF accelerator driver has been assumed because of the high wall-plug efficiency at the very high power level projected. The envisaged system is based on the Jefferson Lab IR FEL that recently set the FEL power record of 311W [3], and is pushing on towards kW power levels to provide market evaluation quantities from some of the processes described below.

The motivation in this case is that future US prosperity is strongly linked to on-shore manufacturing strength. Radiation processing offers the opportunity to widen product value and choice by surface modification, can reduce resource intensity by optimal use of prior investment, may provide near real-time response to consumer demands and leads to reduced environmental impact over competing chemical processing by minimizing waste and improving efficiency.

Many of the metal and polymer applications are proven and patented [4], and the issues for deployment are the available power level and the economics at the desired wavelength. Excitation is vibrational in the IR and electronic in the UV. For instance, many of the processes have already been demonstrated with conventional lasers or lamps, but the cost of these radiation sources is too high and their power levels are too low for practical application. In particular, UV excimer lasers have opened the way to surface modification via transform chemistry, morphology or topography changes dependent on fluence, irradiance and wavelength.

On the other hand, the vacuum lasing medium of the FEL still promises to yield very efficient, high-power lasing, while the wide tunability leads to versatility with respect to processing applications and permits matching to narrow-band absorption. The ultra-short and intense pulse structure gives rise to optimum surface coupling, very high peak powers, as well as the highest heating and cooling rates available for surface modification. In addition, the short pulses minimize collateral damage due to bulk heating and the dry chemistry enables increasingly economic "green" processing.

Polymers are a huge, highly cost sensitive business. 1994 US synthetic fiber production was 9.5 B lbs, while the 1993 World artificial fiber production was 40 B lbs. 1994 US resin production was 5.7 B lbs for food packaging within flexible packaging sales of 14.7 B lbs, but this is dwarfed by the huge food packaging potential in the Third World.

Commercially important polymer applications include improved adhesion for forming multi-component film products or composite structures, more effective fibers for use in filters, and improved feel and appearance of synthetic fiber fabrics. Other applications would yield more easily recyclable food packaging, more durable and attractive carpeting, stronger and more versatile composite materials, and antimicrobial surfaces for shipment or storage of food without the need for refrigeration. As with food sterilization, the latter application has great potential impact in the Third World.

Figure 4 shows an electron micrograph of a polyester fabric surface microroughened with exposure to ultraviolet light from a conventional laser that illustrates the effects of surface texturing. This processing leads to improved look, feel and dye uptake that translates into value added that can be successfully charged to the consumer.

The present hierarchy of polymer processing can be expressed in energy density order as follows. Enhanced adhesion of amorphized PET with UV radiation occurs at 25 mJ/cm^2. Surface roughening of PET leading to enhanced feel, look, mechanical interlock, dye uptake or enhanced filtration via rapid thermal processing with UV and IR radiation occurs at 0.5 J/cm^2. Finally, photochemical anti-microbial surface activation of nylon with 193 nm radiation requires 2.5 J/cm^2. An equivalent suite of high-power metal applications, and micromachining at 2-10 kW, exist but are not described here. In all cases, the true need for FEL-specific properties, as opposed to a tailored, cheaper and smaller conventional laser, must be fully considered.

Figure 4: Excimer-treated polyester fiber showing surface roughening for improved look and feel [5].

We again assume a service provider business structure and present year money. In this case, the FEL power level is 100 kW and 80% annual availability is postulated. A $175K charge is applied for other services plus the annual cost of electricity at 50 mils/ kW-hour and a 20% overall wall plug efficiency. A 3.5 mils/kJ radiation cost, $20M plant capital cost, 15% cost of capital, 2.5% of capital cost per annum maintenance expense, $400K annual personnel operating cost, 10 year system lifetime and 7 year straight line depreciation are also nominally assumed.

This leads to a 2.2 mils/kJ earned value break-even point where plant capital cost is a key parameter in this case. Economics competition considerations similar to sterilization will likely move the system parameter choice from 3.5 mils/kJ towards break-even, thereby determining the accelerator choice and other factors. For this reason we believe that a superconducting-RF-driven linac is the FEL driver of choice. Again, there is clear market opportunity and head room, if accelerator plant cost targets can be met.

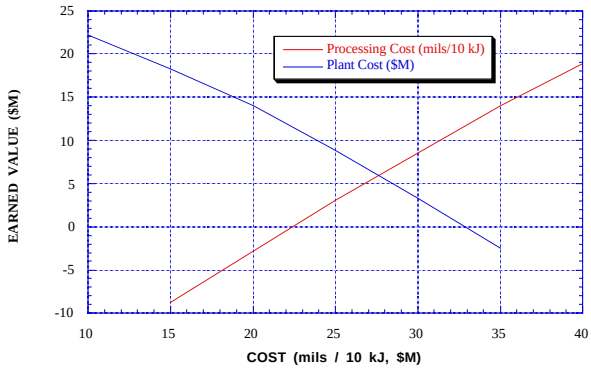

Figure 5: Earned value as a function of plant cost ($M) and unit processing cost (mils/10 kJ).

5 SUMMARY

New linear accelerator product opportunities seem to be immanent. In developing these new products, market and economic forces must always be recognized and observed. Contraband Detection has great potential, but sales are highly politicized and thus the market future is unclear. Sterilization has true and significant market potential and is finally almost here. FEL Material Processing is a potentially huge opportunity worldwide, but is still a few years off

ACKNOWLEDGMENTS

The author gratefully acknowledges utilizing information provided on contraband and explosive detection systems by Joseph Sredniawski of Northrop Grumman [2], on food sterilization by Locke Bogart [6] of Pepco, and on polymer processing by Michael J. Kelley of Dupont [4, 5].

REFERENCES

[1] USA Today, August 8, 1996.

[2] J. Sredniawski, “Detecting Concealed Explosives with Gamma Rays”, The Industrial Physicist, 24 (March 1997).

[3] S. Benson et al., “First Lasing of the Jefferson Lab. IR Demo FEL”, to appear in Proceedings of the 20th International FEL Conference, Williamsburg, VA, August 16-21, 1998.

[4] M. J. Kelley, “An FEL for the Polymer Processing Industries”, *SPIE* **2988,** 240-244 (1997).

[5] Reproduced courtesy of M. J. Kelly from the Jefferson Lab Laser Processing Consortium at “http://www.jlab.org/fel/lpc/index.html/”.

[6] E. L. Bogart, *priv. comm.*

THE CHALLENGE OF INERTIAL FUSION DRIVEN BY HEAVY ION ACCELERATORS

I. Hofmann*
GSI Darmstadt, 64291 Darmstadt, Germany

Abstract

Accelerators have a chance to participate in the enormously growing energy market of the 21st century if inertial confinement fusion can be shown to be competitive with fossil and fission alternatives. While it is expected that ignition and gain of fusion pellets will be demonstrated by the National Ignition Facility after 2005, the development of a suitable driver with high efficiency and rep-rate capability remains the next challenging issue. We review the status of the European HIDIF study group which has set itself the goal of demonstrating the feasibility of the RF linac based heavy ion driver. Related experimental investigations (beam halo) are briefly discussed.

1 INTRODUCTION

Thermonuclear fusion promises a long-term supply of energy under all presently discussed scenarios of population development and environmental constraints (CO_2). It can be assumed that the expected expansion of the energy market in non-OECD countries within the next fifty years will dramatically increase the need for new, affordable energy sources other than fossil. It is estimated that the non-OECD energy market doubles every 25 years; on the other hand stabilization of the CO_2-level at 550 ppm (parts per million, with presently 350 ppm and a pre-industrial value of 270 ppm) would require 15 TW of additional carbon-free primary energy by the year 2050 [1]. Note that the present total energy consumption is 13 TW. This perspective describes the tremendous potential of fusion energy.

Although enormous progress has been achieved in both approaches to fusion energy, magnetic confinement (MFE) and inertial fusion energy (IFE), the gap between scientific understanding and attractive commercial realization is still big. One of the crucial questions is the complexity of a thermonuclear energy plant, which seems to exceed significantly that of fission reactors. The presently most advanced study exists for the tokamak based ITER (International Thermonuclear Experimental Reactor), which is designed for 1 GW fusion power and has a volume exceeding that of the Westinghouse AP-600 light water reactor by two orders of magnitude. We expect that inertial fusion reactors are significantly more compact and offer a number of conceptual advantages, for the following reasons :

- decoupling of driver and reactor chamber, which reduces the complexity of the overall system and allows to use several chambers for one driver; this could also shorten substantially the development path of a commercial system.
- liquid blanket protection, which offers the potential for lifetime reactor chambers, instead of solid walls (as in MFE) that would be exposed to serious radiation damage requiring frequent replacement [2].
- while the standard fuel is an equimolar D-T mix, it is not excluded for IFE to consider (at a more advanced stage) fuels with significantly less or no T inventory, for instance D-^{3}He; in MFE the only option is D-T due to excessive bremsstrahlung losses at the higher temperatures required for all other reactions.

The next milestone in inertial fusion is the expected low-gain target ignition with the laser driven "National Ignition Facility" at Livermore (NIF) and "Megajoule" in Bordeaux, France. These facilities are designed to demonstrate (beyond the year 2006) for the first time propagating fusion burn in D-T fuel on a single-shot basis, which would clearly set inertial fusion to the forefront of fusion development.

In parallel to this the development of a suitable driver with a rep-rate capability of the order of 10 Hz is the next most important requirement for advancing inertial fusion energy. For heavy ion accelerators the necessary rep-rates are common standard, but the required intensities and phase space densities have yet to be demonstrated. Heavy ion accelerators can satisfy the efficiency requirement of 20-30% which follows from the relationship $\eta G \geq 7-10$ needed for a reasonably small re-circulating energy. Here G is the target gain and η the driver efficiency. An η of 20% is consistent with a low-risk gain $G \approx 40$ and achievable with the RF driver. This perspective of heavy ion drivers applies equally to the RF linac/storage ring concept as to the induction linear accelerator, a concept pursued by the US community [3].

Other presently discussed options are high rep-rate diode pumped glass lasers developed at Livermore and expected to get from the presently 1 J per unit to the 100 J level

* this paper summarizes the work of the HIDIF study group with the following members: S. Atzeni[1], R. Bär[2], M. Basko[3], R. Bock[2], K. Bongardt[4], J. D'Avanzo[2], H. Deitinghoff[5], C. Deutsch[6], H. Eickhoff[2], A. Faltens[7], G. Franchetti[2,8], R.W. Hasse[2], H. Klein[5], J. Meyer-ter-Vehn[9], D. Möhl[10], U. von Möllendorff[11], R.W. Müller[2], U. Oeftiger[2], G. Parisi[5], M. Perlado[12], W. Pirkl[10], G. Plass[10], C. Prior[13], R. Ramis[14], U. Ratzinger[2], G. Rees[13], G. Rumolo[2,15], A. Schempp[5], H. Schönauer[10], P. Spiller[2], P. Strehl[2], [1]*ENEA Frascati,* [2]*GSI Darmstadt,* [3]*ITEP Moscow,* [4]*FZ Jülich,* [5]*Frankfurt,* [6]*Orsay,* [7]*Lawrence Berkeley Laboratory,* [8]*Bologna,* [9]*MPQ Garching,* [10]*CERN,* [11]*FZK Karlsruhe,* [12]*DENIM Madrid,* [13]*Rutherford and Appleton Laboratories,* [14]*Madrid,* [15]*Napoli*

at 10 Hz in 2-3 years [4]. Electron beam pumped KrF laser concepts have been proposed at NRL/USA [5] and in Japan [6], which are expected to deliver up to 200 J at a few Hz. For the long–term future of GSI a 100 T-m synchrotron is presently explored, which would deliver up to 10^{13} U^{4+} ions and 40-50 kJ total energy in a single bunch. The SIS heavy ion synchrotron at GSI can in principle operate at 1 Hz, but public grid load restrictions limit the present rep-rate to 0.5 Hz. Using an Ar^{10+} beam at 300 MeV/u and the highest presently achieved intensities (5×10^{10} particles) it is able to produce bunches with 100 J energy at this rate. The next step will be in 1999 the possibility of accelerating highest currents of U^{28+} after completion of the new IH-structure high-current injector for UNILAC. With the expected 10^{11} U ions in the SIS the bunch energy can be raised to close to 1 kJ.

2 THE HIDIF-STUDY

The scope of the HIDIF study has been to demonstrate the feasibility of an RF linac and storage ring based scheme for high repetition rate ignition consistent with an indirectly driven low-gain target. It has been carried out within the framework of a European Study Group in the years 1994-98. Collaborators in the field of the accelerator have been individuals from GSI, CERN, Rutherford, Frankfurt University (IAP) and FZ Juelich. The most challenging issue is the requirement of small beam loss and minimum dilution in all of the six-dimensional phase space in order to match the requirements of short pulse lengths (6 ns) and small focal spots (1.7 mm radius) at the target. The study succeeded to show that the designed driver satisfies the requirements of producing the necessary beam power. The concept of indirectly driven targets has been chosen since it appears difficult with heavy ion beams to achieve a 1% symmetry of implosion as required by direct drive (see Fig. 1 and Ref. [7]).

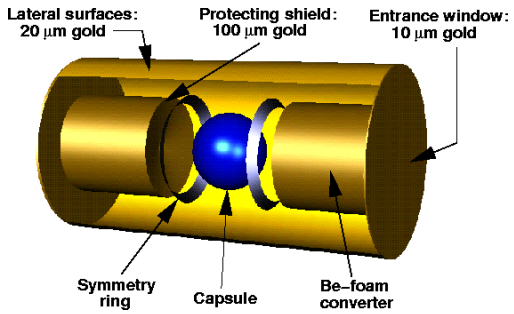

Figure 1: Indirectly driven reference target proposed for HIDIF. The heavy ion beams are converted into x-rays by two Be converters. The fusion capsule implosion is driven by the symmetrized radiation (courtesy of R. Ramis).

The HIDIF driver has a number of characteristic features, which are summarized in the following:

- charge state 1+ to reduce space charge effects,
- 3 ion species (for telescoping, see below) accelerated in the same linac but stored in different rings,
- 16 ion sources of each species,
- four funneling stages for RFQ's and DTL's and one main high-current DTL linac up to 10 GeV and a total pulse current of 400 mA,
- simultaneous two-plane multi-turn injection into storage rings to minimize injection losses,
- multi-turn injection into RF barrier buckets and, after filling of all rings, adiabatic prebunching,
- final bunch compression (fast) in induction bunchers with multiple beam lines to obtain the required 6 ns pulse length,
- conventional focusing using super-conducting quadrupoles in matrix array.

The funneled linac tree is shown schematically in Fig. 2 (see also Ref. [8]) assuming ion sources for Bi^{1+} with a current of 25 mA (for a prototype ion soutce see section 3).

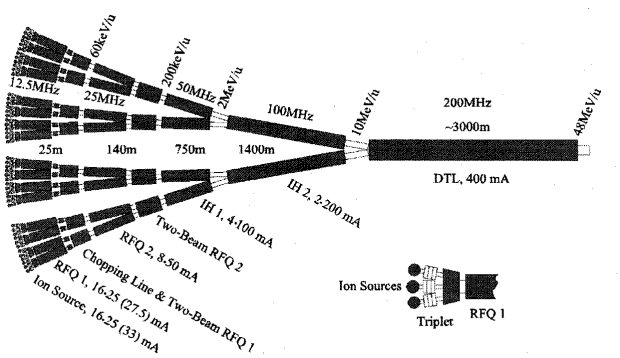

Figure 2: Scheme of a linac funnel tree for HIDIF (courtesy of A. Schempp).

The envisaged linac peak current of 400 mA and the gaps between different barrier buckets as well as the switching of the linac beam to different storage rings and to different ion species lead to a total pulse duration of 1.5 ms, which is also the duration of the RF power cycle (see Fig. 3).

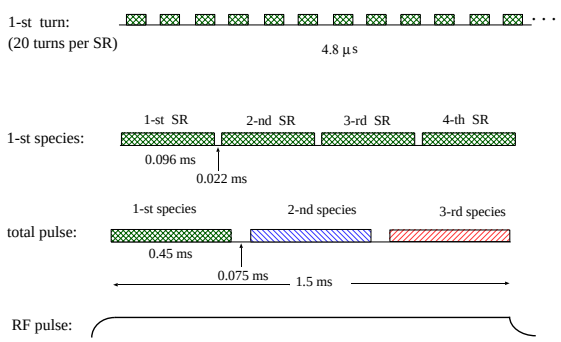

Figure 3: Linac pulse structure.

As a result the average linac current in this period is 192 mA. The scenario assumes 12 bunches per storage ring, which is equivalent to a stored energy of 250 kJ per ring.

The full scenario is shown in Fig. 4 for the reference case with 3 MJ requiring a total of 12 storage rings. Single-charged ions of three atomic species are accelerated in the same linear accelerator to identical momenta and stored and bunched in a set of 4 storage rings per species. The bunches are synchronized by delaying them in sets of delay lines (one set per storage ring) so that they coincide per species in time at the entry into the induction bunchers. Each bunch will at this stage travel on a separate trajectory, each induction buncher carrying 36 beam lines in parallel. In the final transport towards the target, bunches of each of the three species are merged together in a common beam line. This "telescoping" goes back to an idea originally discussed by Burke [11]. Bunches of different ion species (here masses varied by 10%) but identical momenta can be superimposed in the longitudinal phase space in the final beam lines, which saves beam lines and final optics by the number of species (here three). The number of beam lines converging on the reaction vessel is now 48, which is reduced by a factor of three with respect to a single ion species (non-telescoping) scenario.

It is generally desirable to have the average linac current as high as possible as this determines the driver efficiency and helps to minimize beam loss in the storage rings due to ion-ion charge exchange. The linac efficiency is estimated to 30%, the total driver efficiency to close to 20% for the maximum rep-rate of 50 Hz.

2.1 Computer Modeling

The issue of space charge makes it necessary to model key issues by means of computer simulation. The following sub-sections of the driver have been studied with 2d or 3d codes:

- drift tube linac above 10 MeV/u (3d),
- debunching and capture in barrier buckets of rings,
- two-plane multi-turn stacking (2d with preliminary 3d), showing that the beam losses can be kept at the level of 1-2% [12]
- prebunching and final bunch compression,
- final focusing system to target.

The drift tube linac simulation shows that the required output results for current, emittance and momentum spread ($\epsilon_N = 1.2$mm mrad and $\Delta p/p \leq 0.1\%$) can be satisfied [13]. A full linac simulation starting from injection into the first RFQ throughout the main linac remains a goal for future work. This includes the issue of beam loss throughout the linac and storage rings and the resulting activation, which must be considered carefully.

Driver parameters (for Bi^+ and similar mass ions) for this standard target are summarized in Table 1. The scheme is modular in the sense that doubling of the energy requires doubling of the number of storage rings and bunches. For future work it is planned to study in more detail the option of a DTL based on H-mode cavities, which promises significantly higher linac current than the above considered 400 mA [14]. Such structures have been successfully taken into operation for the CERN Pb-Linac and the GSI U^{4+} high-current injector [15], which operates at 36 MHz and assumes a space charge limited current of I(emA)$= 0.25A/q$. It accelerates U^{4+} at 16 mA current from a MEVVA ion source which has recently shown to exceed the required current on the test bench [16]. The main advantage of this structure for fusion applications is the high acceleration efficiency at relatively low values of β. The possibility is discussed of using multiple beam cavities for an IH-RFQ as well as an IH-DTL at relatively low frequencies (10 rsp. 20 MHz). The design is eased by the fact that quadrupoles are not used internal to the RF tanks (see Fig. 5). This concept requires a special funneling technique, which is possibly easier than the funneling of separate accelerator lines as in the usual approach. The maximum gradient that can be expected is about 7 MV/m using cavities in an H_{211} mode, which is another attractive feature of this scheme.

ion energy (GeV)	10
total driver energy (MJ)	3
linac current (mA)	400
storage rings	12
number of stored bunches	144
stored bunch length (ns)	250
ion species (telescoping)	3
final pulse length (ns) (base line of main pulse)	6

Table 1: Parameters of HIDIF driver for two-converter reference target.

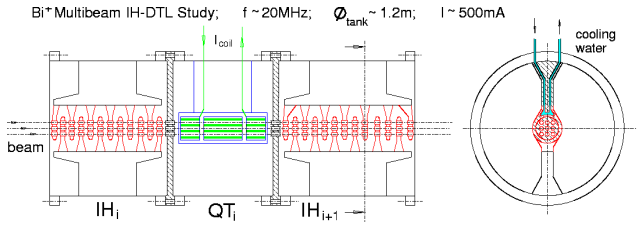

Figure 5: Schematic view of multiaperture IH mode DTL for heavy ion fusion (courtesy of U. Ratzinger).

3 EXPERIMENTS

A prototype Bi ion source at Frankfurt (IAP) has recently been shown to deliver 21 mA [9] (Fig. 6). The source has a seven hole extraction system with a maximum extraction voltage of 27 kV. The fraction of Bi^{1+} in the ex-

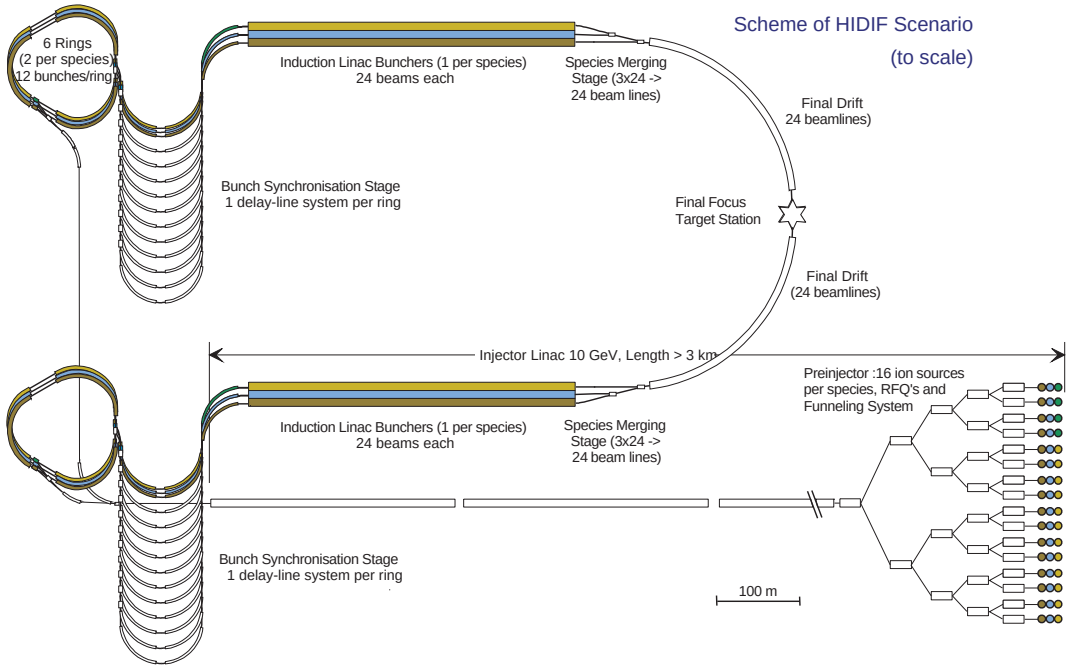

Figure 4: HIDIF layout for reference energy of 3 MJ.

tracted current was measured as 93%. The RFQ funneling concept is studied in another experiment at Frankfurt in a scaled version using two He^{+} beams from 2 identical ion sources [10].

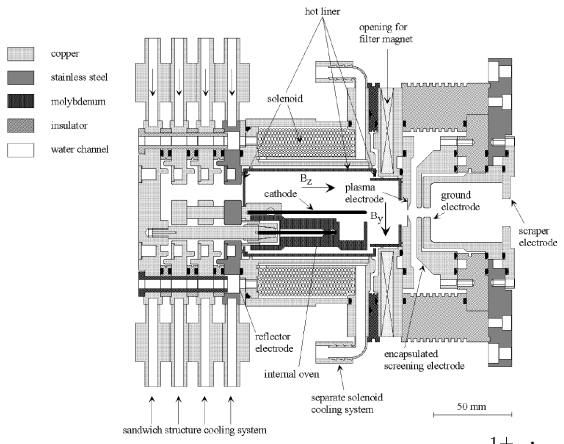

Figure 6: Schematic drawing of prototype of Bi^{1+} ion source and extraction (courtesy of M. Weber).

Beam loss plays an important role for high average beam power. The total activation of 10 GeV Bi ions is reduced by approximately two orders of magnitude compared with that of 1 GeV protons due to the substantially shorter Coulomb range of the heavy ion [17]. For a fusion driver at 10 Hz and 50 MW beam power the average linac current is ≈5 mA, and a loss of 10^{-3} seems acceptable. This is less stringent than the requirements of future high-current proton linacs discussed for various applications. A critical area appears to be the injection into the storage rings (operated at 2-5 MW beam power), where the presently studied two-plane injection with 1-2% loss would require a further reduction of the losses by an order of magnitude.

This leads to the conclusion that the study of halos in linacs and rings requires more attention than previously assumed. One of the first steps is experimental verification of the standard picture of halo formation driven by mismatch (envelope) modes [18, 19]. Such experiments are difficult to carry out in any existing linac. Since it is commonly accepted that the strength of space charge is less important, we are lead to the conclusion that such basic studies can be carried out in a synchrotron or storage ring as well. We have made some preliminary computer simulation studies of the effect of mismatch for a beam injected into the synchrotron SIS. Using a Ne^{10+} beam at the injection energy of 11 MeV/u and a current of 2.5 mA we have found that a mismatch of 1.5 leads to more than doubling of the rms emittance after 20 turns (corresponding to 200 cells). The phase advance per period is $\sigma_{0,h} = 130^{o}$ in horizontal and $\sigma_{0,v} = 99^{o}$ in vertical direction. The tune depression is only as small as 0.98. The initial distribution in the simulation is assumed as waterbag (see Fig. 7).

Comparing different values of mismatch and of current we have found that higher beam current primarily accelerates the emittance growth, whereas the mismatch is responsible for the size of the emittance growth as is shown in Fig. 8. It should be noted that the effect is unexpectedly large and presumably related to a resonance phenomenon with the FODO lattice, since a corresponding calculation for constant focusing gave only 1/4-th of the emittance growth.

As a next step we plan to realize this in an experiment at the SIS by extracting the beam after a variable number of turns and transport it to a plastic scintillator to observe its transverse density distribution with a gated CCD camera.

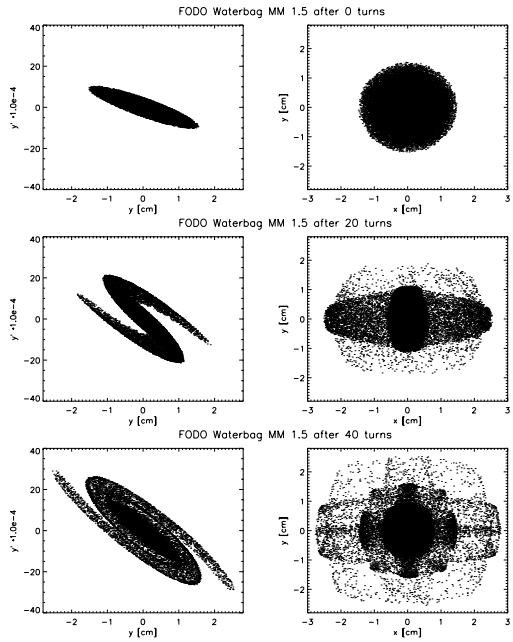

Figure 7: 2d-simulation (particle-in-cell) of halo development for a coasting beam in a FODO synchrotron lattice with weak space charge and 50% mismatch (shown are y-y' and x-y projections after 0,20,40 turns).

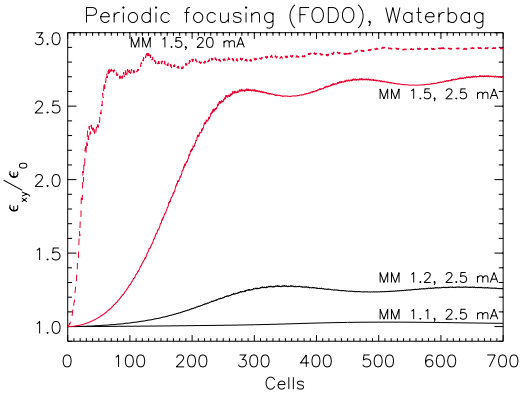

Figure 8: RMS emittance growth of simulated mismatched coasting beam in a FODO synchrotron lattice.

An important ingredient to the halo formation is the frequency of the mismatch oscillations, which is shifted by space charge. In this context it is also worth mentioning that we have recently measured in the SIS the frequency shift of these mismatch oscillations, both the "breathing" and the "quadrupolar" mode. The beam was excited by a quadrupolar exciter in the frequency band considered and the response signal on a quadrupolar pickup was evaluated [20].

4 CONCLUSIONS

The HIDIF accelerator study has for the first time considered detailed computer simulation studies of key areas in the RF linac/storage ring approach to inertial fusion. Future work will have to concentrate on the low-energy part of the linac (in particular funneling) and include new developments like the H-mode structure. Developments on the side of the target play an important role, in particular if novel concepts like the "fast igniter" [21] are better understood and their relevance for energy producing targets is consolidated. The expected reduction in Megajoules could result in significant reduction of the complexity of the driver. Accelerator experiments on key issues, including beam halo, are needed to verify the increasingly demanding computer simulation.

ACKNOWLEDGMENTS

The author wishes to acknowledge the help of O. Boine-Frankenheim in performing the beam halo simulations.

5 REFERENCES

[1] L.J. Perkins, Proc. Int. Symposium on Heavy Ion Inertial Fusion, Heidelberg, Sept. 22-27, 1997, to be published in Nucl. Instr. Meth. **A**

[2] R.W. Moir et al., *Fusion Technology* **25**, 5 (1994)

[3] R.O. Bangerter, Fus. Eng. Des. **32-33**, p. 27 (1996)

[4] S.A. Payne, Proc. of the IAEA Technical Committee Meeting on Drivers and Ignition Facilities for Inertial Fusion, Osaka University, Japan, March 10-14, 1997

[5] J.D. Sethian et al., ibid.

[6] I. Okuda et al., ibid.

[7] R. Ramis, Proc. Int. Symposium on Heavy Ion Inertial Fusion, Heidelberg, Sept. 22-27, 1997, to be published in Nucl. Instr. Meth. **A**

[8] A. Schempp, Proc. Int. Symposium on Heavy Ion Inertial Fusion, ibid.

[9] M. Weber et al., Proc. Int. Symposium on Heavy Ion Inertial Fusion, Heidelberg, ibid.

[10] A. Firjahn-Andersch et al., these Proceedings

[11] R. Burke, Argonne National Laboratory unpublished note (1978)

[12] C.R. Prior and G.H. Rees, Proc. Int. Symposium on Heavy Ion Inertial Fusion, Heidelberg, Sept. 22-27, 1997, to be published in Nucl. Instr. Meth. **A**

[13] G. Parisi et al., these Proceedings

[14] U. Ratzinger and R. Tiede, Proc. Int. Symposium on Heavy Ion Inertial Fusion, Heidelberg, Sept. 22-27, 1997, to be published in Nucl. Instr. Meth. **A**

[15] W. Barth et al. these Proceedings

[16] P. Spädtke et al., these Proceedings

[17] K.-H. Schmidt, private communication (1998)

[18] J.S. O'Connell, T.P. Wangler, R.S. Mills and K.R. Crandall, Proc. 1993 Part. Accel.Conf., Washington DC, 3651 (1993)

[19] R.L. Gluckstern, *Phys. Rev. Lett.*, **73**, 1247 (1994)

[20] R. Bär et al., Proc. Int. Symposium on Heavy Ion Inertial Fusion, Heidelberg, Sept. 22-27, 1997, to be published in Nucl. Instr. Meth. **A**

[21] M. Tabak et al., Phys. Plasmas **1**, 1626 (1994)

TOWARD A FOURTH-GENERATION X-RAY SOURCE *

David E. Moncton
Argonne National Laboratory, Argonne, IL 60439 U.S.A.

Abstract

The field of synchrotron radiation research has grown rapidly over the last 25 years due to both the push of the accelerator and magnet technology that produces the x-ray beams and the pull of the extraordinary scientific research that is possible with them. Three successive generations of synchrotron radiation facilities have resulted in beam brilliances 11 to 12 orders of magnitude greater than the standard laboratory x-ray tube. However, greater advances can be easily imagined given the fact that x-ray beams from present-day facilities do not exhibit the coherence or time structure so familiar with the optical laser. Theoretical work over the last ten years or so has pointed to the possibility of generating hard x-ray beams with laser-like characteristics. The concept is based on self-amplified spontaneous emission (SASE) in free-electron lasers. A major facility of this type based upon a superconducting linac could produce a cost-effective facility that spans wavelengths from the ultraviolet to the hard x-ray regime, simultaneously servicing large numbers experimenters from a wide range of disciplines. As with each past generation of synchrotron facilities, immense new scientific opportunities would result from fourth-generation sources.

1 INTRODUCTION

The rapid growth in the field of synchrotron radiation research over the last 25 years has been the most exciting period in the history of x-rays since the period immediately after they were discovered by Röntgen over 100 years ago. The brilliance of x-ray beams versus time since their discovery in 1895 (Fig. 1) shows that the technology was unchanged for more than six decades. Remarkably, however, x-rays had unprecedented scientific impact. X-rays garnered the first Nobel Prize and some 20 more, all based on x-rays provided by only minor improvements of tubes that Röntgen used for his first experiments. From the first generation of parasitic synchrotron facilities that appeared in the 1970s through the second-generation facilities that were designed explicitly to produce synchrotron radiation, to the third generation that use an optimized magnet lattice and insertion devices, synchrotron x-ray research has enjoyed gains in beam brilliance that are 11 to 12 orders of magnitude greater than the standard laboratory x-ray tube. Given that this rate of improvement exceeds Moore's Law for semiconductors by approximately a factor of two, it is reasonable to ask, What could be a better source of x-rays than the insertion device (ID) upon which the Advanced Photon Source (APS) and other third-generation sources are based?

* Work supported by the U.S. Department of Energy under contract W-31-109-Eng-38.

2 SOURCE CHARACTERISTICS

An ID x-ray beam from a third-generation x-ray synchrotron radiation facility, while highly directional and monochromatic, does not have the full coherence of an optical laser. The transverse coherence length of radiation from an ID at the APS is ~10 μm, which is useful to condensed-matter physicists and others in understanding the dynamics of solids. However, the coherence length is small compared to the size of the source itself (170 mm), which means the source is only very weakly coherent. Making up for that shortfall represents an enormous opportunity. If the technology can be developed to make a source fully coherent, it would be orders of magnitude better than those existing today.

Another major opportunity to exceed the limits of existing x-ray sources lies with the time structure of the beam. Current machines produce bunch lengths in the 100-psec regime. This structure enables science well beyond the reach of steady-state x-ray tubes, and many experiments exploit this time dependence.

However, 100 psecs is longer than the time associated with many interesting physical phenomena. In the optical

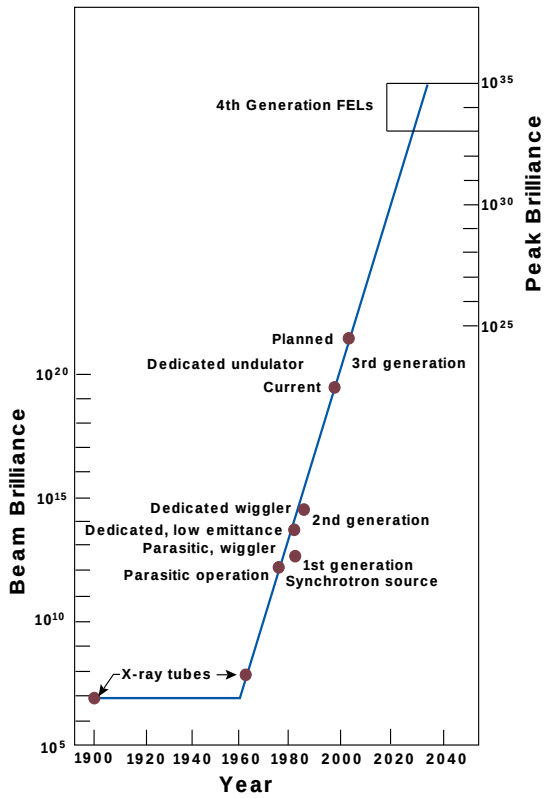

Fig. 1: History of (8-keV) x-ray sources, beam brilliance vs. time.

regime, femtosecond lasers have existed for quite some time and have made the first forays into this time domain. The ability to bring x-ray time scales down into the sub-picosecond regime is very compelling, since many of the most interesting physical phenomena cannot be studied with long-wavelength optical radiation.

3 TECHNOLOGICAL CHALLENGES

It now appears that substantial improvements in source characteristics can be achieved with the development of x-ray free-electron lasers (FELs). The technologies to produce FEL-based radiation for ultraviolet and shorter wavelengths have been under consideration for some time using different accelerator-FEL configurations. At this time, neither the optical cavity approach[1] nor the seeded amplifier concept[2] appears to be workable in the hard x-ray range, although future developments could change this situation. Recently, the concept[3,4,5,6] of self-amplified spontaneous emission (SASE) has captured the imagination of the synchrotron radiation community. The SASE concept eliminates the need for optical cavities or input seed radiation. The very stringent electron beam qualities required for SASE operation in the hard x-ray region can be met with the recently developed laser driven radio-frequency (rf) photocathode gun[7] and in the beam compression and linear acceleration technology in connection with the high-energy linear collider program.[8] Recent measurements by the University of California, Los Angeles group at Los Alamos National Laboratory[9] have shown the first convincing evidence of SASE gain at 16-μm wavelengths.

The Stanford Synchrotron Radiation Laboratory has developed a SASE-based concept[10] called the Linac Coherent Light Source, which would use the Stanford linac and theoretically produce a gain of 8 or 9 orders of magnitude over third-generation undulator beams in the hard x-ray range. This would be an excellent R&D project to supply the necessary experience for a new fourth-generation user facility. And it would be reasonably cost-effective since the linac already exists. However, it would not be sufficient to meet the needs of the synchrotron community at large, because the facility would only support a few experimental stations, at most. This limitation is due to the pulse rates associated with conventional linear accelerators.

A newer alternative, the superconducting linac, is in principle capable of supplying the pulse rate needed to support a farm of x-ray undulators, as shown in Fig. 2. This approach is based upon the anticipated maturity of the superconducting rf technology for the high-energy linear collider program. A group at the Deutsches Elektronen-Synchrotron[11] is pursuing the concept of a superconducting linac that can support the very high pulse rates necessary to feed a large number of SASE undulators for x-rays. Such a facility would also be able to produce ultraviolet beams either at lower energy points on the linac or by using spent electron beams after they have produced the SASE x-rays. Research and development is expected to go forward internationally over the next few years, yielding a decision on whether to proceed with such a facility in conjunction with a new high-energy physics linear collider.

At Argonne National Laboratory, we are installing a low-energy (750 MeV) undulator test line (LEUTL) (Fig. 3) on the APS linac.[12] The LEUTL is located in a 50-m-long extension of the linac tunnel that is configured to enable study of SASE in the 100-nm-wavelength range.

4 SCIENTIFIC RESEARCH

A fourth-generation light source will support a wide range of disciplines and a large number of individual experiments. It is therefore difficult to be specific about the scientific opportunities in a short article. To provide summary information, Figs. 4 and 5 attempt to simply characterize the advances from one generation of light source to the next in terms of our ability to extract spatial and temporal information from material systems, which is the essence of virtually all x-ray research. Focusing on spatial information to begin with in Fig. 4, we can see the

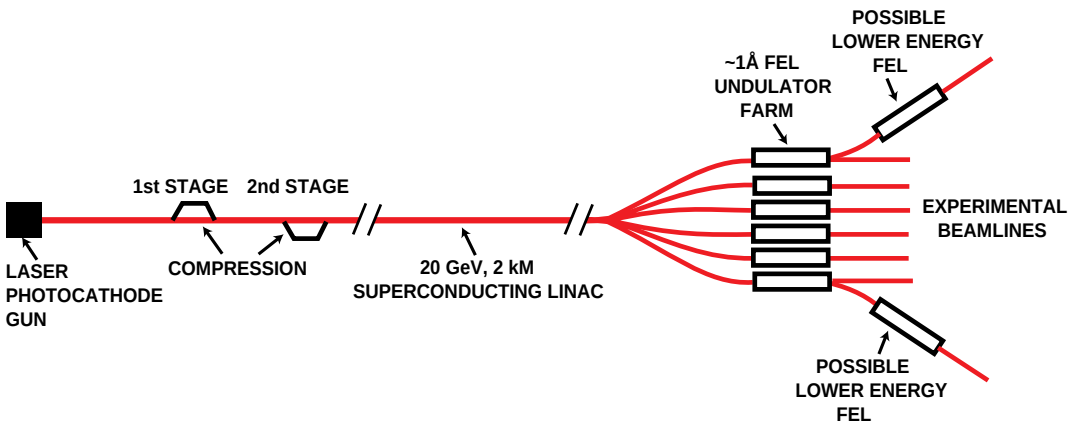

Fig. 2: Diagram of a possible fourth-generation synchrotron facility using self-amplified spontaneous emission free-electron lasers.

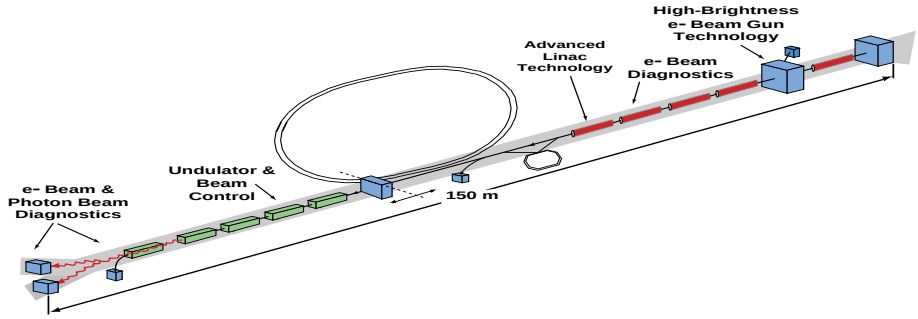

Fig. 3: Drawing of the low-energy undulator test line at Argonne National Laboratory.

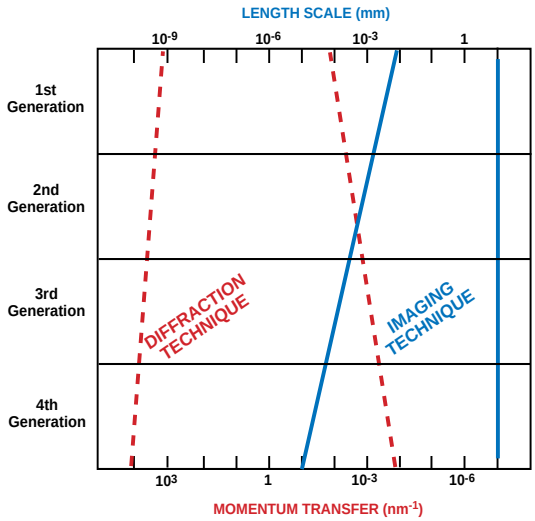

Fig. 4: Research opportunities with synchrotron radiation: spatial structure.

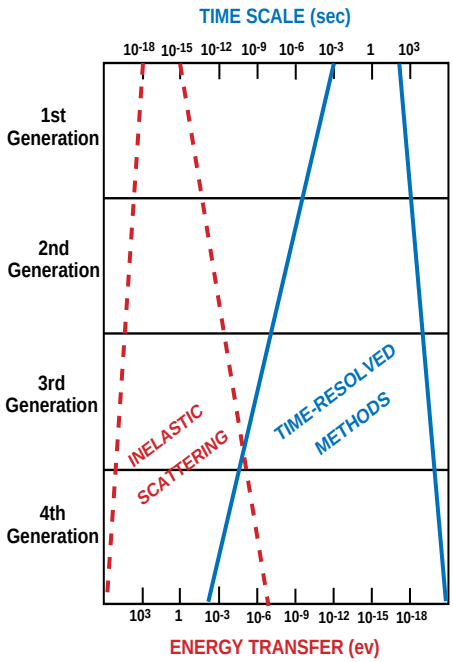

Fig. 5: Research opportunities with synchrotron radiation: temporal structure.

general evolution of imaging methods in direct space or diffraction methods in momentum or reciprocal space. Generally, information on the structure of materials is extracted over a length scale from 1 mm to atomic dimensions. As the brilliance of x-ray beams has improved, higher fluxes, coupled with much higher degrees of collimation, have expanded the boundaries of various diffraction and imaging techniques.

This progress is very tangible now at the APS, where imaging and diffraction methods overlap to cover the entire range of spatial length scales, from the atomic up to the macroscopic, particularly in the 1-μm regime. That is the very important length scale on which information is stored in the human gene, as well as in integrated circuits. For example, protein crystallography is arguably the most challenging area of x-ray diffraction today. Two years ago, the first protein crystal structure solved with the APS was a complex, 100,000-atom molecule.[13] Data sets for proteins of this complexity can now be obtained at the APS in less than an hour, and in some cases less than 15 minutes. With the APS operating 5000 hrs/yr, the possibility of achieving within a decade a storehouse of comprehensive data on all proteins that are important to life seems realistic.

As one looks at the region of Fig. 4 that pertains to fourth-generation sources, there is growing overlap between imaging and diffraction methods. In practice, this overlap actually represents the emergence of integrated imaging and diffraction approaches, which are only possible with highly coherent sources. As an example of what may be possible with the enormous increase in coherence from x-ray FELs, consider how we now obtain information on the structure of complex molecules. The major prerequisite to an x-ray diffraction experiment of the type mentioned above is a crystal in which some 10^{18} copies of the molecule are arranged in a nearly perfect crystalline array. The need for this form of the sample is a consequence, in principle, of the relative weakness of the source of x-rays and the associated scattering cross-section. Furthermore, it is a tremendous burden to the researcher interested in the structure to be required to have such a sample of the molecule of interest. It is now the

most significant limitation in the rate of protein structure determination. One of the most compelling aspects of the x-ray FEL source is the possibility to eliminate the need for this form of the sample and to be able to extract molecular structure, using new x-ray holographic methods,[14] from a single molecule or a relatively small number of identical molecules in solution. One cannot underestimate the impact of this evolution on biology and chemistry. It is beyond the scope of this paper to discuss this method further, but this will be the subject of upcoming fourth-generation scientific workshops in the next few years.

The other complementary aspect of x-rays is the ability to extract information on the dynamic structure of materials. Figure 5 shows how information is extracted using direct time-resolved x-ray studies and the reciprocal method known as inelastic x-ray scattering. On early storage-ring sources, these two techniques were separated by many orders of magnitude and their ability to extract information in the very important intermediate regime (millivolts or picoseconds) was essentially non-existent. With better beam sources, this gap has narrowed. On third-generation sources, phonon dispersion curves[15] are studied in order to conduct inelastic experiments that have millivolt energy resolution. Time-resolved experiments are moving into the sub-nanosecond region. Investigations of complex materials, such as proteins, are benefiting from third-generation sources, which allow imaging a high-quality diffraction pattern in the time of a single intense pulse—about 100 psecs.

We now proceed to the area of the Fig. 5 that relates to the fourth-generation sources. Here it is anticipated that the improvements in source characteristics made possible by x-ray FELs will finally lead to the closure of the "dynamics gap" shown in the figure. While this appears to be only a quantitative improvement in the range of the two principal methods, it is actually much more than that because it allows access to the energy range in which most phenomena of interest in chemistry, biology, and the physics of technologically-relevant materials occur. It is not yet clear specifically how experimental methods will evolve to permit the anticipated extensions of resolution. Like x-ray holographic methods discussed briefly above, which are a blend of imaging and diffraction methods, we expect that new approaches will be devised to take advantage of the extraordinary time-structure and peak brilliance of the source. The objective will be to provide movie-like representations of molecular motion at the sub-picosecond level. It is critically important that these new methods provide information in direct space where motion is more naturally related to function, as in catalytic reactions or biological processes. In traditional crystalline solid-state systems where crystal momentum is a good quantum number, inelastic methods are very powerful. But in complex aperiodic systems, real-space methods for elucidating dynamics will be much more readily interpreted. If this challenge can be met, fourth-generation sources will have immense impact.

5 CONCLUSION

One can easily imagine that extraordinary science would result from the use of x-ray sources based on FELs. The higher coherence and greater spatial resolution afforded by FELs, together with a two- or three-order-of-magnitude improvement in time resolution to the 100-fsec range would prove invaluable for determining molecular structures and watching atomic and molecular processes. Furthermore, beyond the examples mentioned above, the high intensities in these short pulses would provide intriguing opportunities for non-linear physics, and perhaps offer powerful new opportunities for applications in microscopy.

6 REFERENCES

[1] M. E. Couprie, *Nucl. Instrum. Methods A* **393**, 13 (1997)

[2] *UV Free-Electron Laser: Preliminary Design Report*, I. Ben-Zvi, ed., BNL-48565 (February 1993).

[3] Y. S. Derbenev, A. M. Kondratenko, and E. L. Saldin, *Nucl. Instrum. Methods A* **193**, 415 (1982).

[4] R. Bonifacio, C. Pellegrini, and L. M. Narducci, *Opt. Commun.* **50**, 6 (1985).

[5] K.-J. Kim, *Phys. Rev. Lett.* **57**, 1871 (1986).

[6] J.-M. Wang and L.-H. Yu, *Nucl. Instrum. Methods A* **250**, 396 (1986).

[7] R. L. Sheffield, in *Physics of Particle Accelerators*, M. Month and M. Dienes, eds., AIP Conf. Proc. **184**, 1500 (1989).

[8] G. Loew, *International Linear Collider Technical Review Committee Report*, SLAC-R-95-471 (1995).

[9] M. Hogan et al., *Phys. Rev. Lett.* **80**, 289 (1998).

[10] *Linac Coherent Light Source (LCLS) Design Study Report*, SLAC-R-521 (April 1998).

[11] *Conceptual Design.of a 500 GeV e^+e^- Linear Collider with Integrated X-ray Laser Facility, Vol. II*, DESY 1997-048 (1997).

[12] S. V. Milton et. al, *Nucl. Instrum. Methods A* **407**, 210 (1998).

[13] C. D. Lima, K. L. D'Amico, I. Naday, G. Rosenbaum, E. M. Westbrook, and W. A. Hendrickson, *Structure* **5** (6), 763, (1997).

[14] B. Adams, D. V. Novikov, T. Hiort, G. Materlik, and E. Kossel, *Phys. Rev. B* **57** (13), 7526, (1998).

[15] M. Schwoerer-Böhning, A. T. Macrander, and D. A. Arms, *Phys. Rev. Lett.* **80** (25), 5572, (1998).